ANIV
Associazione Nazionale
per l'Ingegneria del Vento

UNIVERSITÀ DEGLI STUDI
DI GENOVA

GENOVA
UNIVERSITY
PRESS

Wind Engineering in Italy

Proceedings of the XIII Conference
of the Italian Association for Wind Engineering

In-Vento 2014

Genova 22-25 giugno 2014

Edited by Luigi Carassale and Maria Pia Repetto

Associazione Nazionale
per l'Ingegneria del Vento

UNIVERSITÀ DEGLI STUDI
DI GENOVA

Conference Organization

Local Organizing Commitee
Lorenzo Banfi
Massimiliano Burlando
Luigi Carassale (Co-chair)
Patrizia De Gaetano
Andrea Freda
Marco Lepidi
Michela Marrè-Brunenghi
Mirko Maurici
Marina Pizzo
Maria Pia Repetto (Co-chair)
Alessio Ricci
Marco Tizzi
Federica Tubino

Scientific Commitee
Giuliano Augusti (Italy)
Gianni Bartoli (Italy)
Bert Blocken (The Netherlands)
Claudio Borri (Italy)
Guido Buresti (Italy)
Luca Caracoglia (USA)
Piero D'Asdia (Italy)
Vincent Denoël (Belgium)
Giorgio Diana (Italy)
Yaojun Ge (China)
Massimiliano Gioffrè (Italy)
Vittorio Gusella (Italy)
Ruediger Hoeffer (Germany)
Ahsan Kareem (USA)
Gino Materazzi (Italy)
Masaru Matsumoto (Japan)
Daniele Rocchi (Italy)
Vincenzo Sepe (Italy)
Gianni Solari (Italy)
Paolo Spinelli (Italy)
Ted Stathopoulos (Canada)
Mark Sterling (UK)
Yukio Tamura (Japan)
Alberto Zasso (Italy)

Organizing Secretariat
Asap S.r.l.
Via B. Bosco, 57/9 A
16121 Genova
Italy

Sponsors
Erg Renew
BMT Fluid Mechanics
Leosphere

Exhibitors
Gerb
Redaelli
Danetech
Luchsinger

With the support of
Università degli Studi di Genova
Ordine degli Ingegneri di Genova
Autorità Portuale di Genova

Conference Venue
Polytechnical School (Architecture) of the University of Genova
Stradone S.Agostino, 37
16123 Genova
Italy

The logo of In-Vento 2014 has been conceived and drawn by Michela Marrè Brunenghi; it represents a sail billowing in the wind fastened to the Lighthouse of Genova.

The photo on the cover of this volume has been shot by Paolo Picasso (Terminal San Giorgio - Gavio SpA).

Programme at a glance

Sunday, June 22nd, 2014

6:00 PM	-	8:00 PM	Registration
6:30 PM	-	9:00 PM	Welcome cocktail

Monday, June 23rd, 2014

8:00 AM	-	5:00 PM	Registration
8:30 AM	-	9:00 AM	Opening addresses
9:00 AM	-	10:00 AM	**Keynote lecture** by Horia Hangan
10:00 AM	-	10:30 AM	Coffee break
10:30 AM	-	12:00 PM	**Technical session - Wind-Induced Vibrations 1**
12:00 PM	-	1:00 PM	**Special session** - Ph.D. theses in wind engineering
1:00 PM	-	2:00 PM	Lunch
2:00 PM	-	3:30 PM	**Technical session - Aerodynamics 1**
3:30 PM	-	4:00 PM	Coffee break
4:00 PM	-	5:30 PM	**Technical session - Bridges**
5:30 PM	-	6:45 PM	**Technical session - Urban wind flows**
6:45 PM	-	7:15 PM	ANIV General Assembly

Tuesday, June 24th, 2014

8:00 AM	-	5:00 PM	Registration
8:30 AM	-	9:30 AM	**Keynote lecture** by Tracy Kijewski-Correa
9:30 AM	-	10:00 AM	Coffee break
10:00 AM	-	11:30 AM	**Special session** - Random vibration of dynamic systems driven by non-Gaussian actions
11:30 AM	-	1:00 PM	**Technical session - Wind energy**
1:00 PM	-	2:00 PM	Lunch
2:00 PM	-	3:30 PM	**Technical session - Aeroelasticity**
3:30 PM	-	4:00 PM	Coffee break
4:00 PM	-	5:15 PM	**Technical session - Wind flows and natural ventilation**
5:15 PM	-	6:30 PM	**Technical session - Buildings and roofs**
6:30 PM	-	8:00 PM	Guided tour to historical city center
8:00 PM	-	10:00 PM	Social Dinner

Wednesday, June 25th, 2014

8:00 AM	-	12:00 PM	Registration
8:30 AM	-	9:30 AM	**Keynote lecture** by Fernando Porté-Agel
9:30 AM	-	10:30 AM	**Panel session** on Wind flows in the atmospheric boundary layer: physical modeling, numerical simulation, in-site measurements
10:30 AM	-	11:00 AM	Coffee break
11:00 AM	-	1:00 PM	**Technical session - Wind field modeling**
1:00 PM	-	2:00 PM	Lunch
2:00 PM	-	3:15 PM	**Technical session - Aerodynamics 2**
3:15 PM	-	3:45 PM	Coffee break
3:45 PM	-	5:15 PM	**Technical session - High-rise buildings & towers**
5:15 PM	-	6:15 PM	**Technical session - Wind-induced vibrations 2**
6:15 PM	-	6:30 PM	Closing ceremony

XIII Conference of the Italian Association for Wind Engineering
in·vento·2014
JUNE 22-25 · Genova · ITALY
www.invento2014.org

ANIV
ASSOCIAZIONE NAZIONALE PER L'INGEGNERIA DEL VENTO

Italian section IAWE
INTERNATIONAL ASSOCIATION FOR WIND ENGINEERING

UNIVERSITÀ DEGLI STUDI DI GENOVA · DICCA
DIPARTIMENTO DI INGEGNERIA CIVILE, CHIMICA E DELL'AMBIENTE

Technical programme

Monday, June 23rd, 2014

10:30 AM – 12:00 PM. Technical session - Wind-Induced Vibrations 1

Chair: Federica Tubino, Luca Facchini

Optimization of Passive Tuned Mass Damper Systems to reduce Tower Vibrations of Wind Turbines
Meinhardt, C., Dalmer, F., Bottoni, F.

Performance prediction and validation of a tuned liquid column damper with internal baffles
Cammelli, S., Li, Y.F., Hsu, L.

Prediction of the buffeting response of ice-accreted stay cables
Demartino, C., Ricciardelli, F.

Aerodynamic stability of dry stay cables using different quasi-steady models
Demartino, C., Ricciardelli, F.

Efficient Monte-Carlo method for the wind-induced "fragility analysis" of tall buildings
Cui, W., Caracoglia, L.

Compactly supported wavelet-Galerkin analysis method for the wind-induced stochastic dynamic response of a tall building
Le, T-H., Caracoglia, L.

12:00 PM – 1:00 PM. Special session – Ph.D. Thesis in wind engineering

Chair: Gianni Bartoli, Alberto Zasso

A new aerodynamic phenomenon and its effects on the design of ultra-high cylindrical towers
F. Lupi

Probabilistic Tools for the Qualitative Analysis of Wind Actions on Structures
M. Marrè-Brunenghi

Aeroelastic Effects on Tall Buildings: Performance-Based Comfort Analysis
C. Pozzuoli

2:00 PM – 3:30 PM. Technical session - Aerodynamics 1

Chair: Giorgio Diana, Valerio Iungo

Aerostatic loading on the deck of cable-stayed bridge during erection stage under skew wind
Li, M., Li, S., Zeng, J., Liao, H.

Base-drag reduction of an axisymmetric bluff body through boundary-layer and near-wake modifications
Mariotti, A., Buresti, G., Salvetti, M.V.

Aerodynamic forces on a NACA 0015 airfoil in dry and iced states
Mattiello, E.

Pressure field around a rectangular 5:1 cylinder in smooth flow
Mannini, C., Allori, D., Pigolotti, L., Marra, A.M., Bartoli, G.

Numerical and experimental investigations of wind flow around ground mounted solar panels
Jubayer, C.M., Hangan, H.M., Siddiqui, K.

Sand transverse dune aerodynamics: a computational study
Bruno, L., Fransos, D., Merlo, A., Preziosi, L.

4:00 PM – 5:30 PM. Technical session - Bridges

Chair: Francesco Ricciardelli, Francesco Petrini

Investigation of vortex-induced vibrations of the Ewijk Bridge during different stages of refurbishment
Argentini, T., Rocchi, D., Zasso, A.

Implementation of the non-flutter design principle
Andersen, M.S., Sahin, E., Laustsen, B.

Flutter of suspension bridges under nonuniform wind profiles
Arena, A., Lacarbonara, W., Marzocca, P.

Lifetime cost analysis against flutter riskiness for long-span bridges
Seo, D.W., Caracoglia, L.

Wind Resistance Performance of Long-Span Steel Truss Bridges Across Gorges in Mountainous Area
Wang, K., Liao, H., Liu, J.

Early damage detection in wind-excited suspension bridges
Comanducci, G., Ubertini, F., Materazzi, A.L.

5:30 PM – 6:45 PM. Technical session - Urban wind flows

Chair: Massimiliano Burlando, Hrovje Kozmar

Wind comfort on building balconies: CFD simulation, validation and application for a high-rise tower
Montazeri, H., Blocken, B., Janssen, W.D., van Hoof, T.

A comparison of wind comfort criteria for a complex case study
Blocken, B., Janssen, W.D., van Hoof, T.

Risk analysis of pedestrian and vehicle safety in windy environments
Baker, C.J.

Research on the wind damage of urban roadside trees based on local wind field numerical simulation
Ai, X.Q., Li, J.

Wind spectral analysis in Northern Tyrrhenian ports
Tizzi, M., Repetto, M.P.

10:00 AM – 11:30 AM. Special session - Random vibration of dynamic systems driven by non-Gaussian actions

Chair: Richard Field, Mircea Grigoriu

Calculation of third order joint acceptance function for line-like structures
Blaise, N., Canor, T., Denoël, V.

Probabilistic Models for Wind Loads and Response Analysis
Zhao, H., Grigoriu, M.

Characterization of wind-induced pressure on solar updraft tower
Facchini, L., Lupi, F., Borri, C.

Wavelet-Galerkin solution for nonlinear dynamic systems
Le, T-H., Caracoglia, L.

Analysis of linear systems driven by non-Gaussian noise
Field, R.V., Grigoriu, M.

Efficient estimation of the high-order response statistics of a wind-excited oscillator with nonlinear velocity feedback
Denoël, V., Carassale, L

11:30 AM – 1:00 PM. Technical session - Wind energy

Chair: Claudio Borri, Yongbo Peng

Experimental investigation on small size wind turbines renovated
Burlando, M., Pagnini, L.C., Repetto, M.P., Rosasco, M.

Aerodynamics of 5 MW Wind Turbine Using Boundary Element Method
Al-Esbe, I., Abdel-Maksoud, M.

Wake characteristics of an offshore wind turbine in the vicinity of a coastal mountain
Kozmar, H., Allori, D., Marino, E., Bartoli, G., Borri, C.

Wind farm operation on complex terrains: numerical and experimental analysis
Castellani, F., Burlando, M., Astolfi, D., Terzi, L.

Experimental characterization of wind turbine wakes: wind LIDAR measurements and wind tunnel tests
Iungo, G.V., Viola, F., Porté-Agel, F.

Piezoelectric energy harvesting under air flow excitation
Petrini, F., Gkoumas, K., Bontempi, F.

2:00 PM – 3:30 PM. Technical session - Aeroelasticity

Chair: Luca Caracoglia, Daniele Rocchi

Aeroelastic instabilities of rectangular cylinders with various side ratios
Mannini, C., Marra, A.M., Massai, T., Bartoli, G.

Predictions of VIV-mathematical models for a rectangular 4:1 cylinder
Marra, A.M., Mannini, C., Bartoli, G.

Wind tunnel tests on "Arco estetico Expo 2015"
Belloli, M., Robustelli, F., Rosa, L.

Sectional load characteristics of a dry inclined helically filleted cable
Christiansen, H., Jakobsen, J.B., Macdonald, J.H.G., Larose, G.L., Bosch, H.

Qualitative analysis of the motion-excited forces acting on a square prism
Carassale, L, Freda, A., Banfi, L.

Bridge decks flutter derivatives identification via RANS turbulence models
de Miranda, S., Patruno, L., Ubertini, F., Vairo, G.

4:00 PM – 5:15 PM. Technical session - Wind flows and natural ventilation

Chair: Luca Bruno, Piero D'Asdia

Evaluation of the thermal comfort by natural ventilation in hot climates
Castillo, J.A., Huelsz, G., van Hoof, T., Blocken, B.

Numerical evaluation of evaporative cooling by mist spraying systems: validation and application
Montazeri, H., Blocken, B., Hensen, J.L.M.

Natural ventilation for the "Limestor" in Dalkingen (Germany): analysis and measurements
Lanza Volpe, A.

A generalised model of the lodging of cereal crops
Baker, C.J., Sterling, M., Berry, P.

CFD simulation of cross-ventilation for a one-sided wind catcher system
Azizian, R., Montazeri, F., Montazeri, H.

Tuesday, June 24th, 2014 (continued)

5:15 AM – 6:15 PM. Technical session - Buildings and roofs

Chair: Bert Blocken, Chris Baker

An efficient method for wind-induced vibration responses of long-span roofs
Luo, N., Liao, H., Li, M.

Wind Loading on a cube and portal framed buildings subject to transient winds
Jesson, M., Sterling, M., Letchford, C., Haines, M.

The debate on the strengthening of San Gaudenzio's dome in Novara (1931-1945): a contribution to the history of wind engineering
Calderini, C., Pagnini, L.C.

Design of hyperbolic paraboloid roofs with circular and elliptical plan shape
Rizzo, F., D'Asdia, P., Speziale, F.

Wednesday, June 25th, 2014

9:30 AM – 10:30 AM. Panel session - Wind flows in the atmospheric boundary layer: physical modeling, numerical simulation, in-site measurements

Chair: Horia Hangan, Giovanni Solari

Panelists:

Christopher Baker, University of Birmingham, UK.
Bert Blocken, Eindhoven University of Technology, The Netherlands.
Andrea Buzzi, Isaac CNR Bologna, Italy.
Stefano Cammelli, BMT Fluid Mechanics, UK.
Paolo Schito, Politecnico di Milano, Italy.

11:00 AM – 1:00 PM. Technical session - Wind field modeling

Chair: Fernando Porté-Agel, Luisa Carlotta Pagnini

The European project "Wind, Ports, and Sea"
Burlando, M., Repetto, M.P., Solari, G., De Gaetano, P., Pizzo, M., Tizzi, M., Iafolla, L., Carmisciano, C., Iafolla, V.

Wind characteristics on a suspension bridge at the inlet of a fjord
Cheynet, E., Jakobsen, J.B., Snæbjörnsson, J.Þ.

The Orographic influence in European wind load standards
Lieb, R-D., Paul, J.

Tornado-like vortex simulations in Model WindEEE Dome
Refan, M., Hangan, H.M.

Spatial estimation of future typhoon genesis considering climate change
Kim, G.Y., Lee, S., Ham, H.J.

Development of probabilistic wind load model for South Africa
Botha, J., Retief, J.V., Holicky, M., Barnardo-Viljcen, C.

Velocity profile of the gusty Bora wind
Lepri, P., Kozmar, H., Večenaj, Ž., Grisogono, B.

Physical modeling of spatial fluctuating wind fields and its applications
Li, J., Peng, Y.B., Yan, Q.

2:00 PM – 3:15 PM. Technical session - Aerodynamics 2

Chair: Kenny Kwok, Guido Buresti

Experiments on static and moving scale trains in crosswinds
Dorigatti, F., Quinn, A.D., Sterling, M., Baker, C.J.

Cross wind and rollover risk on lightweight railway vehicles
Cheli, F., Giappino, S., Rocchi, D., Tomasini, G.

Experimental Techniques for Super and Mega Yacht Aerodynamics Assessment
Fossati, F., Muggiasca, S., Robustelli, F.

Numerical and experimental optimization of a time-trial cycling helmet
Belloli, M., Giappino, S., Schito, P., Tenni, M.

Wind Loading on Multi-Layer Open Frame Structures: A Comparison of International Code Provisions
Nelson, J.K.

3:45 PM – 5:15 PM. Technical session - High-rise buildings and towers

Chair: Tracy Kijewski-Correa, Stefano Cammelli

The effects of wind-induced building motion on occupant wellbeing and work performance
Lamb, S., Kwok, K.C.K., Walton, D.

Building occupants' comfort assessment in the PBWE framework
Petrini, F., Olmati, P., Bontempi, F.

Design of Industrial Chimneys for Gust and Vortex Resonance: Practice and Perspectives
Lupi, F., Borri, C., Niemann, H-J., Hoeffer, R.

Risk-consistent cladding pressures on the Isozaki tower in Milan
Pozzuoli, C., Mola, F., Segato, C.

A robust optimization framework for wind-excited cable stayed masts
Venanzi, I., Materazzi, A.L., Ierimonti, L.

Modelling of wind action on high-rise buildings – Warsaw Trade Tower case study
Cwik, M.

5:15 PM – 6:15 PM. Technical session - Wind-induced vibrations 2

Chair: Vincent Denoël, Ilaria Venanzi

Targeted-Energy-Transfer devices for stay-cable vibration mitigation
Izzi, M., Caracoglia, L., Noè, S.

Galloping of slender tower buildings based on a shear-shear torsional equivalent beam model
Piccardo, G., Tubino, F., Luongo, A.

Coupled dynamic simulations of offshore wind turbines: influence of wave modeling on the fatigue load assessment
Marino, E., Lugni, C., Stabile, G., Borri, C., Manuel, L.

Structural dynamics modelling of floating wind turbines: a preliminary study on the role of large rotation
Giusti, A., Marino, E., Borri, C.

Design of hyperbolic paraboloid roofs with circular and elliptical plan shape

Fabio Rizzo[1], Piero D'Asdia[1] and Federica Speziale[1]

[1]Department of Engineering and Geology, University of Chieti-Pescara, Italy
Corresponding author: Federica Speziale, federica.speziale@libero.it

Abstract

On the basis of a research aimed at the parameterization of the structural responses and aerodynamic behavior of hyperbolic paraboloid cables nets with four different footprints, respectively, square, rectangular, circular and elliptical, this paper focuses on the circular and elliptical shape showing two interesting case studies. The first case study is about the design of a tensile structure with circular shape proposed as alternative roof for the multipurpose building called "Entertainment Centre" which is part of a larger environmental redevelopment project of a portion of land in the town of Massafra (TA) in order to show that this type of roof is highly competitive compared to traditional structures; the second one presents the design of a tensile structure with elliptical shape proposed to reorganize a part of the town of Agnone (IS). The structural analysis were performed by applying wind action evaluated by using the mean experimental pressure coefficients acquired in the wind tunnel. They show the optimum behavior of the hyperbolic paraboloid shape both for wind angle at 0°, parallel to the stabilizing cables, and 90°, parallel to the load bearing cables (that represents the worst load condition).

1 Introduction

In architecture, lightweight structures offer the possibility to create flexible and dynamic spaces. Flexibility in the design, interpreted as the availability of the building to easily change its intended use, it is often manifested in the need to create space without intermediate supports, imagining large containers whose only role is to capture the dynamism of activities. Therefore, the desire to meet these needs leads to design large span roofs. Among large covers, a valid alternative is offered by tensile structures that are very lightweight structures that can assume different configurations to create interesting architectural effects. In fact, they offer numerous structural and architectural possibilities. These structures have become increasingly common in the architectural environment. They are used to roof stadiums, station platforms, arenas, exposition halls, recreational facilities, festival tents, bandstands and other buildings (Majiowiecki, 2004).

Tensile structures represent one of the most interesting and current building systems, whose potential has not yet been fully investigated and developed by the designers. It is therefore still a field open to experimentation and research. Being characterized by lightweight and flexibility, they are optimal in seismic areas but highly susceptible to the snow and the wind action. This makes their design very complex and this is mainly due to 2 basic problems: the lack of parameters for the structural pre-sizing and the lack of data such as pressure coefficients for calculation of wind action on unconventional shapes, which this type of structure requires. Consulting the Italian regulations, which include the "Technical Construction Standards, Ministerial Decree 14-01-2008 - 3.3 Action of the wind", and the "CNR (National Research Council), 2008. CNR-DT 207/2008 Guidelines on Actions and Effects of Wind on Structures", do not include the hyperbolic paraboloid shape and therefore do not provide any guideline for those who want to design a tensile structure with this shape. There are no guidelines also in the main international technical Standards such as the European "CEN (Comité Européen de Normalisation) 2005. EN 1991-1-4: Eurocode 1: Actions on structures - Part 1-4: General actions – Wind actions", the american"ASCE (American Society of Civil Engineers) 2005. Minimum Design Loads for buildings and other Structures, ASCE 7-05" or "Australian/New Zealand Standard 2002. Structural design actions; Part 2: Wind actions. AS/NZS 1170.2:2002, which only contain

guidelines for portico hyperbolic paraboloid structures, open at the side and of a small size. For these reasons, the only way to study wind-structure interaction is to perform experimental tests in the wind tunnel.

Thus, considering the development obtained by the research aimed at studying the structural and aerodynamic behavior of hyperbolic paraboloid cables net with square, rectangular, circular and elliptical plane shape, shown in previous papers (Rizzo et al., 2011, 2012), this work wants to show 2 case studies: one concerning the circular shape and one concerning the elliptical ones. This in order to demonstrate the real possibility to design hyperbolic paraboloids with circular and elliptical footprint using pressure coefficients acquired in the wind tunnel on a rigid model for this shape.

2   Case studies

2.1   *Hyperbolic paraboloid roof with circular shape (Case Study 1 - CS1)*

Case Study 1 –CS1- shows the design of a tensile structure with circular shape and hyperbolic paraboloid cables net roof (Fig. 1) proposed as alternative roof for the multipurpose building called "Entertainment Centre" which is part of a larger environmental redevelopment project of a portion of land in the town of Massafra (TA) (Carbotti, 2013).

The aim of this case study is to present an interesting comparison between the approved structure to be realized with glued laminated timber roof and concrete beams and the cables net tensile structure here proposed, in order to show the high performance that this second type of structures can offer in terms of weight and cost reduction.

Figure 1. "Entertainment Centre" tensile structure.

In Table 1, geometric characteristics of the hyperbolic paraboloid cables net with circular shape are reported; α indicates the ratio between cables span (L), H (= $f_1 + f_2$, sum of cables sags) indicates the height of the roof, H_b is the distance between ground level and roof level, while subscripts 1 and 2 indicate, respectively, bearing cables and stabilizing one (Rizzo et al., 2011).

Table 1. Geometric characteristics of the hyperbolic paraboloid cables net with circular shape.

$\alpha=L_1/L_2$	L_1 [m]	L_2 [m]	f_1 [m]	f_2 [m]	H [m]	H_b [m]
1	80.00	80.00	2.67	5.33	1/10 L_{max}	1/6 L_{max}

The adopted tensile structure system is composed of a hyperbolic paraboloid cables net, a border arch, an anchoring system consisting of inverted V columns placed in pairs and an intermediate arch that circle the structure in order to avoid columns instability.

Table 2 is a summary of weights, sections and materials used in the project; A indicates the cables area and ε the cables deformation while subscripts 1 and 2 indicate, respectively, bearing cables and stabilizing ones.

Table 2. Summary of the elements used in the project.

Load-bearing cables	$A_1 = 31.49$ cm^2	$\varepsilon_1 = 0.003540$
Stabilizing cables	$A_2 = 3.83$ cm^2	$\varepsilon_2 = 0.005132$

Columns	Cross-section: tubular 1000x50 mm	Material: steel S420
Border arch	Cross-section: tubular 1200x50 mm	Material: steel S420
Intermediate rings	Cross-section: tubular 500x20 mm	Material: steel S420

2.2 *Hyperbolic paraboloid roof with elliptical shape (Case Study 2 - CS2)*

Case Study 2 -CS2- regards the design of a tensile structure with elliptical shape and hyperbolic paraboloid cables net roof proposed to reorganize a part of the town of Agnone (IS) (Latino, 2013). In this area, covering about 20.000 m^2, there are sports facilities that are underused and poorly connected to each other. This project is configured as a structure that is on one hand container and on the other hand connector. In Figure 2 some significant images of the project are reported. In particular, Figure 1a shows the plan of the sports center while Figure 2b an internal three dimensional view of the complex.
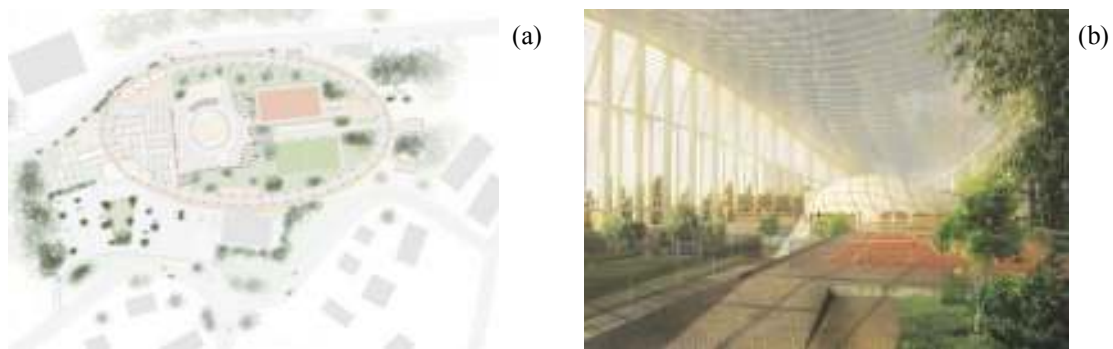
Figure 2. Tensile structure used to cover a Sports center (a) plan (b) internal three dimensional view.

In Table 3, geometric characteristics of the hyperbolic paraboloid cables net with elliptical shape are reported (Rizzo et al., 2012).

Table 3. Geometric characteristics of the hyperbolic paraboloid cables net with elliptical shape.

$\alpha=L_1/L_2$	L_1 [m]	L_2 [m]	f_1 [m]	f_2 [m]	H [m]	H_b [m]
2	160.00	80.00	8.88	24.91	1/4 L_{max}	1/12 L_{max}

The adopted tensile structure system is composed of a hyperbolic paraboloid cables net, a border arch, an external perimeter colonnade that is used as anchoring system and of two intermediate arches that circle the structure in order to avoid the problem of columns instability. Table 4 is a summary of the weights, sections and materials used in the project.

Table 4. Summary of the elements used in the project.

Load-bearing cables	$A_1 = 80.37$ cm^2	$\varepsilon_1 = 0.011281$	$T_1 = 2023.59$ KN
Stabilizing cables	$A_2 = 43.58$ cm^2	$\varepsilon_2 = 0.004265$	$T_2 = 332.77$ KN
Columns	Truss cross-section composed of 4 tubular 300x10 mm		Material: steel S460
Border arch	Truss cross-section composed of 4 tubular 200x10 mm		Material: steel S460
Intermediate rings	Truss cross-section composed of 4 tubular 200x10 mm		Material: steel S460
Roof structural weight	1.09 kN/m^2: - Roof covering: 0.04 kN/m^2 (membrane) - Structure: 1.03 kN/m^2 (self-weight of cables net + connections) - Installations: 0.02 kN/m^2 (not installed on roof)		

3   Non Linear Static Analysis

Using a finite element model (Fig. 3), non-linear static analysis were performed considering the extreme load conditions that are the maximum snow action and the maximum wind depression (Simiu & Scanlan, 1996) using the research program *TENSO*, a non-linear static and dynamic analysis software of three-dimensional structures composed of cable and beam elements.
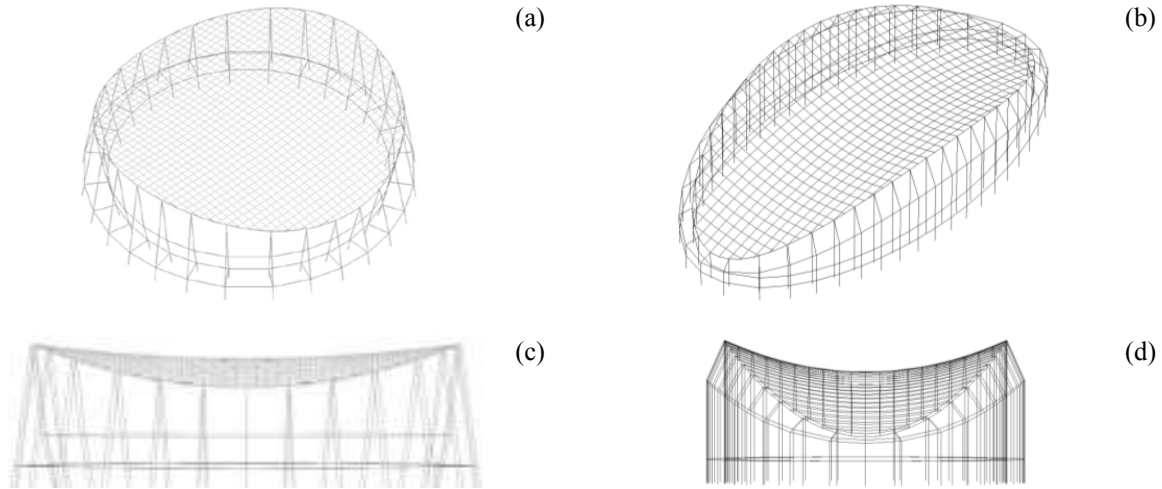

Figure 3. FEM model (a) CS1 3D view (b) CS2 3D view (c) CS1 elevation (d) CS2 elevation.

Wind action was evaluated using the mean experimental pressure coefficients for circular and elliptical shapes tested in the wind tunnel (Rizzo et al., 2011, 2012) for two wind angles, 0° that is parallel to the stabilizing cables and 90° that is parallel to the bearing one. The data obtained by experimental tests were pressure coefficient time-histories from which mean values have been evaluated using a probabilistic theory according to the Gumbel method (Cook & Mayne, 1978, 1979, 1980). Analysis were performed by applying, on the cables net nodes, forces calculated multiplying the mean pressure coefficients for the kinetic pressure $q=(\frac{1}{2}\rho V^2)$ and for the considered area of influence of each net node.

Non-linear static analysis were carried out considering the following load combinations:

- COMB1a (foundamental): $G_K*1.3+G_P*1.5+Pret*1+N*1.5*0.5+V(0°)*1.5*0.6$
- COMB1b (foundamental): $G_K*1.3+G_P*1.5+Pret*1+N*1.5*0.5+V(90°)*1.5*0.6$
- COMB2 (end construction): G_K+G_P
- COMB3 (snow action): $G_K*1.3+G_P*1.5+Pret*1+N*1.5$
- COMB4a (wind action 0°): $G_K*1.3+G_P*1.5+Pret*1+V(0°)*1.5$
- COMB4b (wind action 90°): $G_K*1.3+G_P*1.5+Pret*1+V(90°)*1.5$

Maps of the mean pressure coefficients acquired in the wind tunnel for circular and elliptical shape are shown in Figure 4. (Rizzo, 2014)
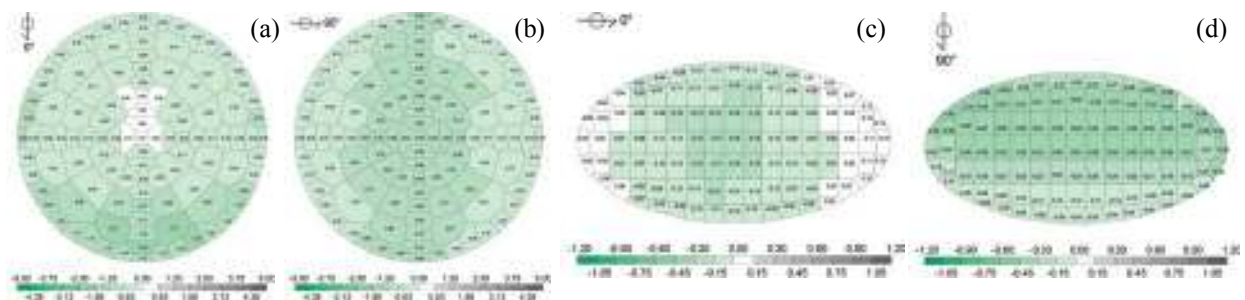
Figure 4. Mean Pressure coefficient (a) (b) Circular shape CS1, 0°,90° (c) (d) Elliptical shape, CS2, 0°,90°.

Table 5 summarizes the main results for each considered load combination; it also shows the maximum and minimum values of deformations (ε), displacements (d) and traction force (T) moved by cables to the border structures; subscripts 1 and 2 indicate, respectively, bearing cables and stabilizing ones.

Table 5. Output data - CS1, CS2.

CS1										
Load combination	ε_1		ε_2		T_1 (kN)		T_2 (kN)		d (m)	
	max	min	max	min	max	min	max	min	max	min
Fund. 0°	0.0057	0.0020	0.0031	0.0020	75467	26104	22108	14115	0.06	-0.01
Fund. 90°	0.0055	0.0021	0.0032	0.0021	73426	27816	23041	15052	-0.15	0.06
End Constr.	0.0057	0.0020	0.0031	0.0020	76158	26249	22260	14211	0.09	-0.01
Snow	0.0048	0.0023	0.0034	0.0023	63147	30541	24130	16529	-0.32	0.01
Wind 0°	0.0067	0.0018	0.0028	0.0017	88969	22784	20644	12320	0.29	-0.01
Wind 90°	0.0063	0.0019	0.0031	0.0019	83907	25541	22104	13815	0.20	-0.01
CS2										
Load combination	ε_1		ε_2		T_1 (kN)		T_2 (kN)		d (m)	
	max	min	max	min	max	min	max	min	max	min
Fund. 0°	0.0085	0.0046	0.0051	0.0031	61140	34510	59950	41550	-0.40	0.10
Fund. 90°	0.0085	0.0033	0.0081	0.0033	107856	43464	61090	32590	-0.27	0.16
End Constr.	0.0082	0.0042	0.0058	0.0032	59260	31720	76670	41950	-0.20	0.19
Snow	0.0087	0.0049	0.0046	0.0030	62750	35560	59950	39700	-0.74	0.06
Wind 0°	0.0083	0.0041	0.0059	0.0032	59700	29930	42670	78520	0.18	-0.10
Wind 90°	0.0081	0.0041	0.0064	0.0032	58830	28410	85190	42990	0.26	-0.05

As regards to CS1, non-linear static analysis were carried out for the two different types of roofs, the glued laminated timber roof with concrete beams which is under construction and the hyperbolic paraboloid cables net roof proposed as alternative roof. The result is the identification of the structural weights of both construction in order to make a comparison in terms of weight and behavior of the building under the action of loads.

Modal static analysis were performed by applying, on the FEM model, nodal masses of about 10 kg. The first six modal shapes are shown in Figure 5 while in Table 6 the Modal Analysis Output, for the first ten modes of vibration of the cables net, is summarized.

Table 6. Cables net frequencies and periods

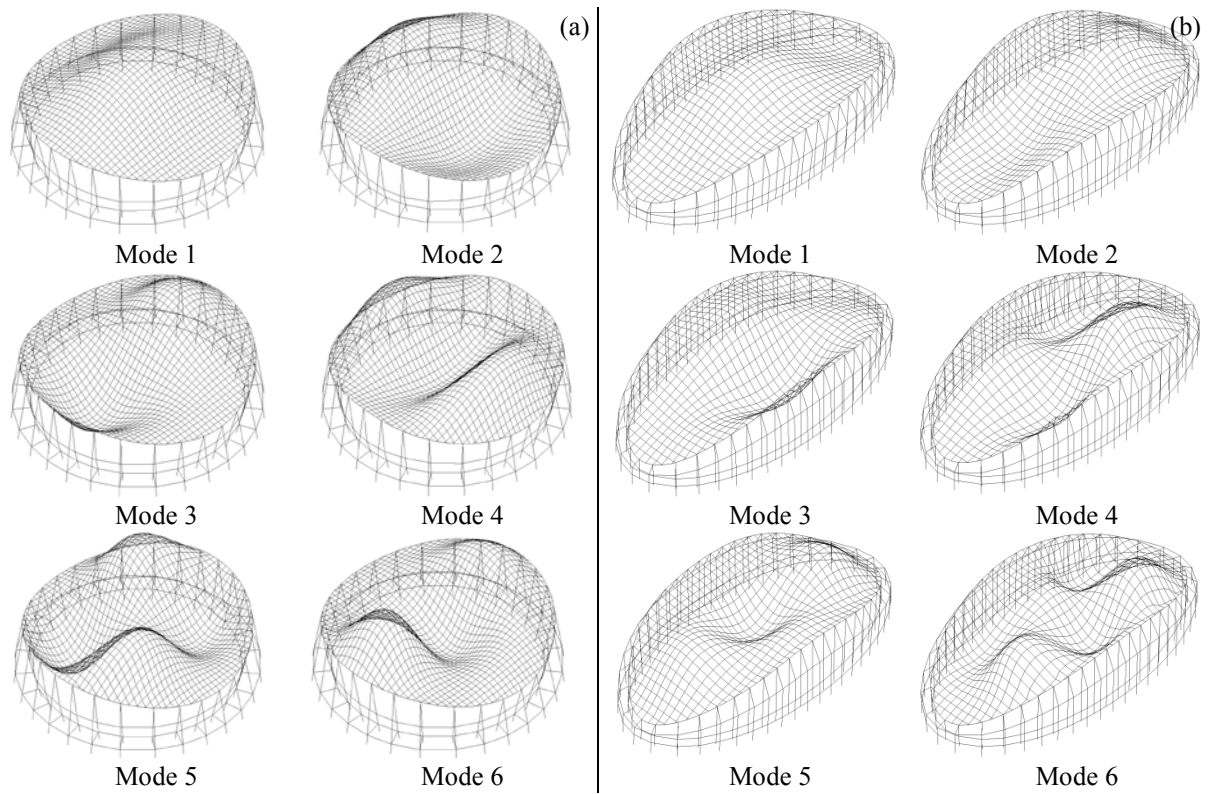|	CS1		CS2	
Modes	Frequencies (Hz)	Periods (s)	Frequencies (Hz)	Periods (s)
1	0.19	5.26	0.34	2.97
2	0.21	4.79	0.35	2.88
3	0.23	4.28	0.37	2.72
4	0.27	3.74	0.38	2.65
5	0.26	3.79	0.44	2.26
6	0.22	3.17	0.47	2.13
7	0.31	3.18	0.48	2.07
8	0.32	3.12	0.49	2.02
9	0.36	2.82	0.51	1.95
10	0.37	2.70	0.52	1.93

Figure 5. Modal shapes (a) CS1 (b) CS2.

Figures 6-10 show the structural response to the main load combinations. The maximum displacement of 32 cm for CS1 and 64 cm for CS2, downward, occurs in the snow combination. As can be seen from the graph, the net nodes displacements are never less than 40 cm for CS1 and 80 cm for CS2, which corresponds to 1/200 of the span (as set in NTC 2008 – Table 4.1.X); no cable exceeds the maximum strength value preset in the hypotheses (f_y=1.70E+06 KN/m^2), remaining at average values, and no cable is slack.
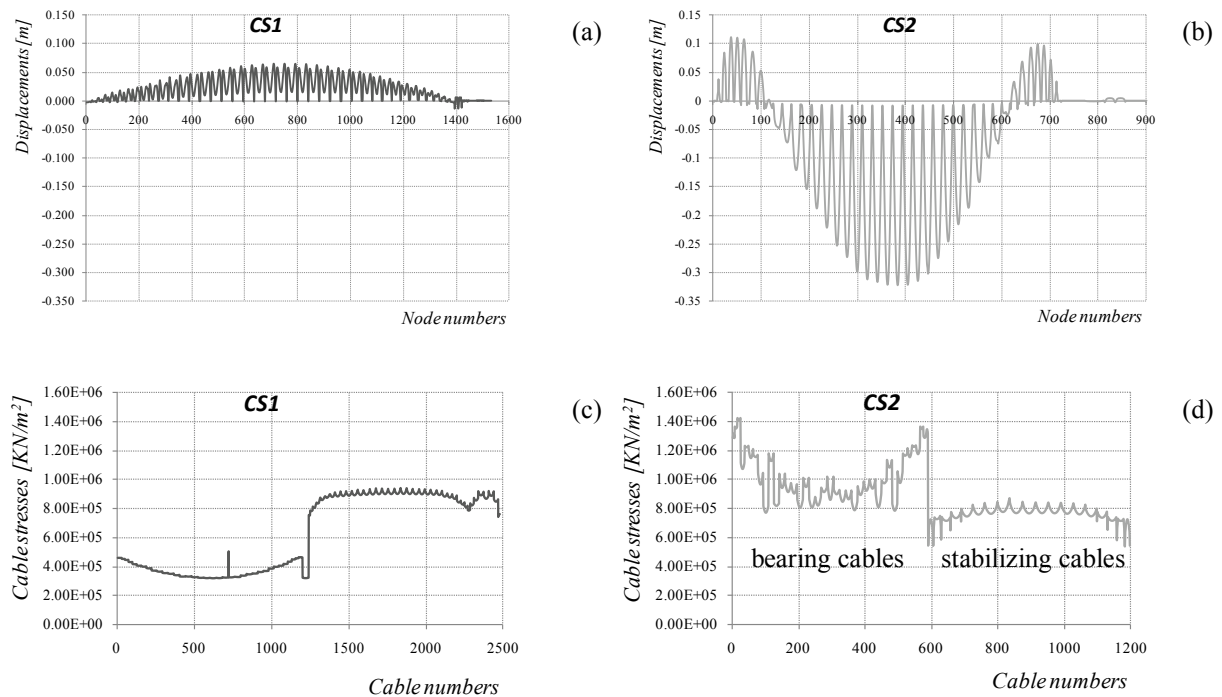
Figure 6. Fundamental combination, wind 0° (a) displacements CS1 (b) displacements CS2 (c) cables stresses CS1 (d) cables stresses CS2.
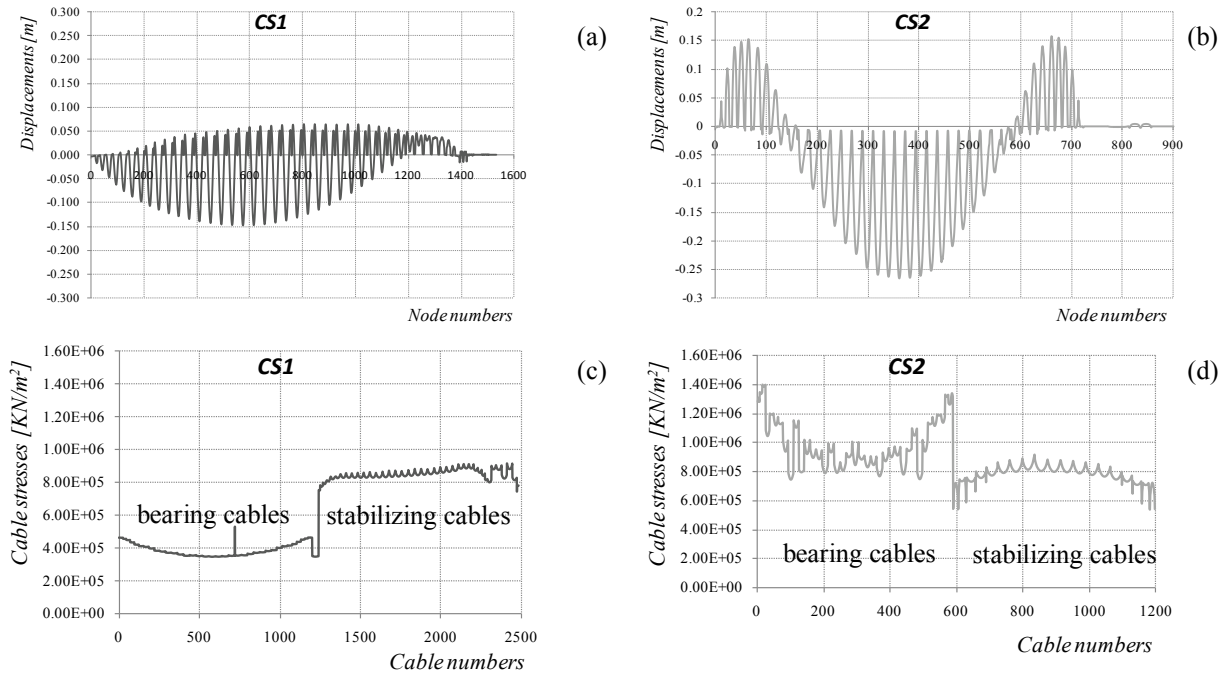
Figure 7. Fundamental combination, wind 90° (a) displacements CS1 (b) displacements CS2 (c) cables stresses CS1 (d) cables stresses CS2.
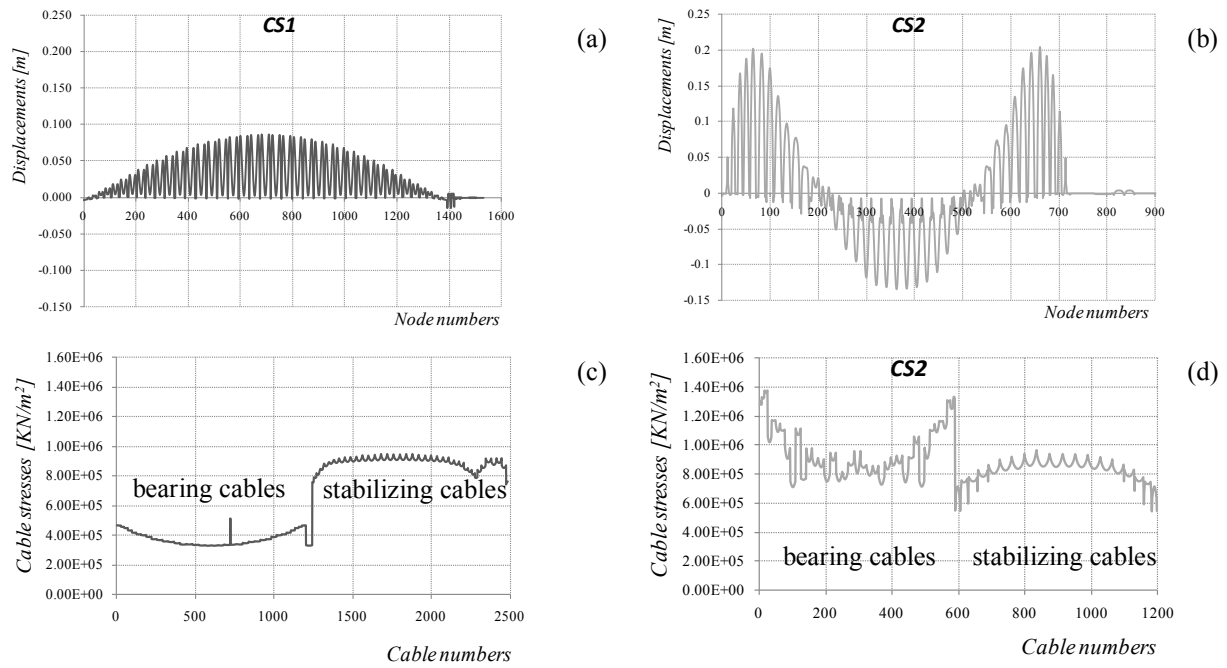
Figure 8. End Construction load combination (a) displacements CS1 (b) displacements CS2 (c) cables stresses CS1 (d) cables stresses CS2.
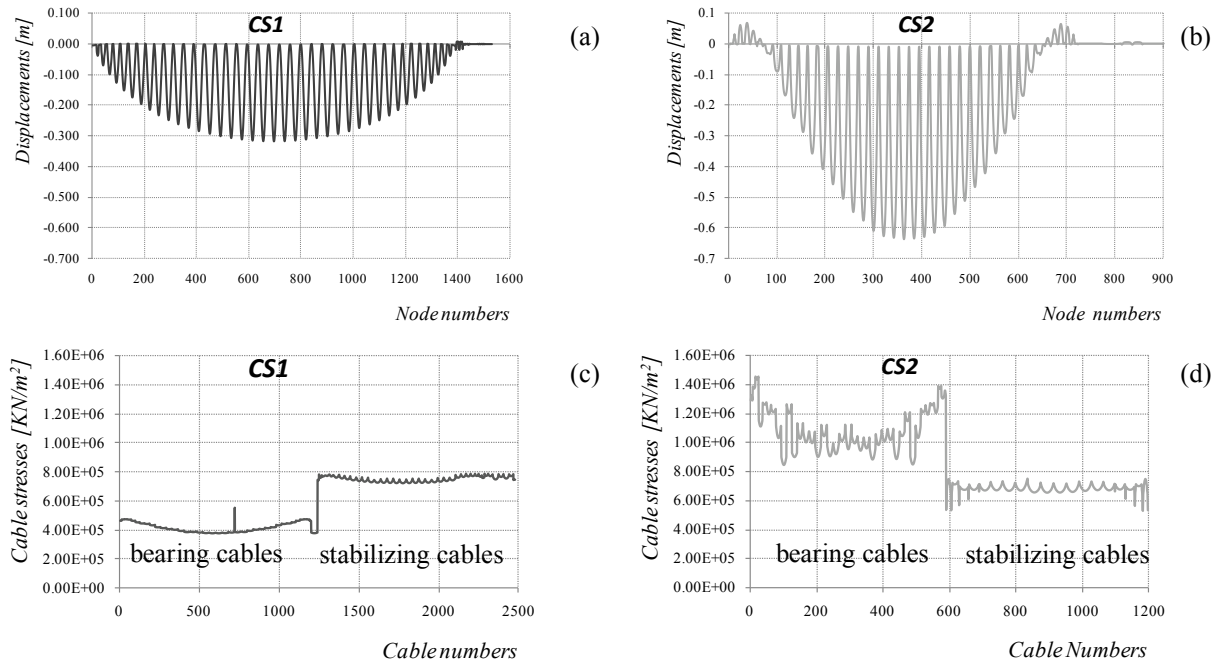
Figure 9. Snow load combination (a) displacements CS1 (b) displacements CS2 (c) cables stresses CS1 (d) cables stresses CS2.
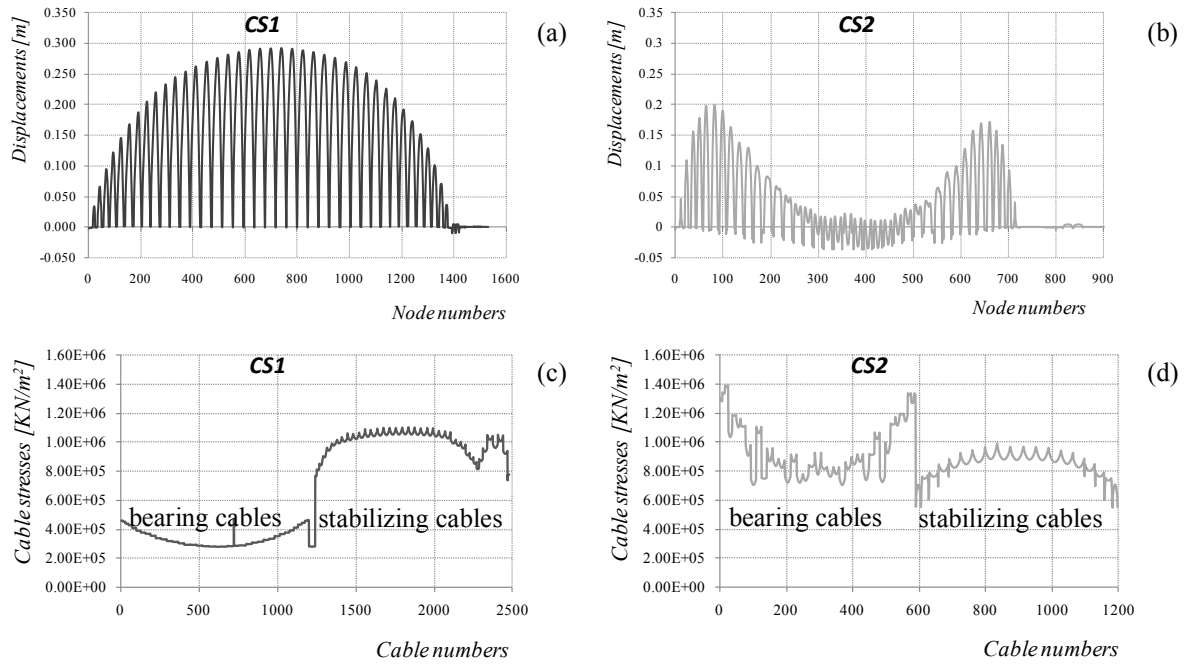
Figure 10. Wind 0° load combination (a) displacements CS1 (b) displacements CS2 (c) cables stresses CS1 (d) cables stresses CS2.
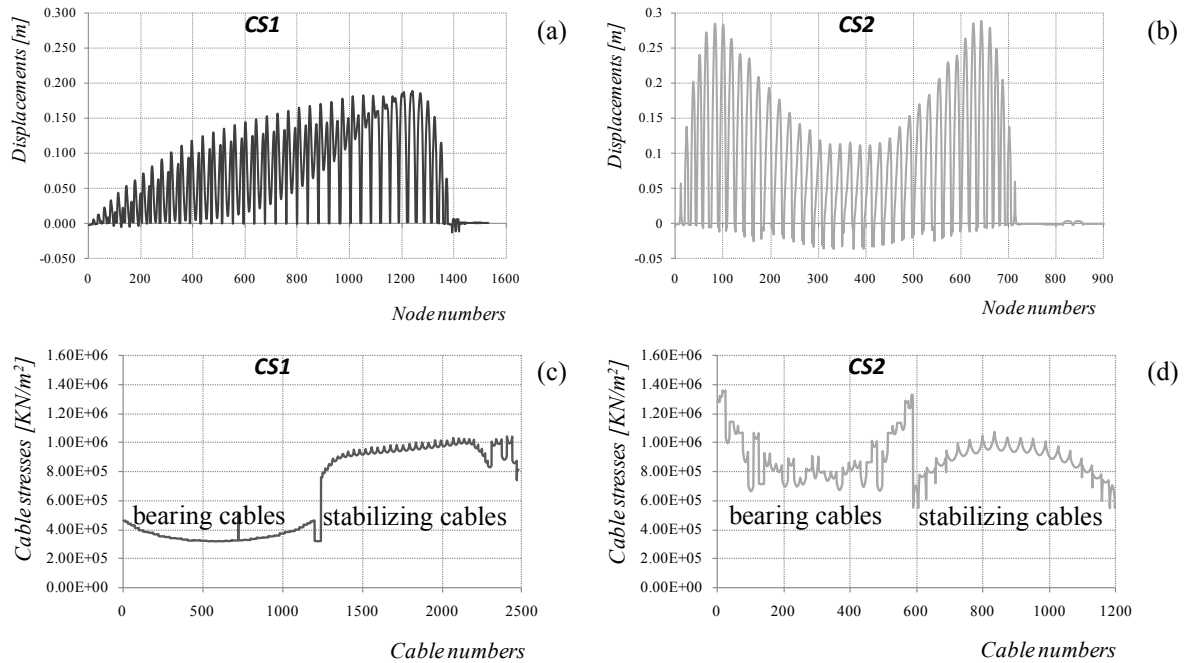
Figure 11. Wind 90° load combination (a) displacements CS1 (b) displacements CS2 (c) cables stresses CS1 (d) cables stresses CS2.

4 Conclusions

These project are extremely important because they apply experimental data for wind loads to real design to highlight the possibility to cover large spans without intermediate supports and through structures with a dead load much lower than traditional structures such as steel or concrete plates or plywood roofs. In fact, CS2 proposes a hyperbolic paraboloid roof with elliptical shape with a maximum span of 160 m, with a cables net weighing only 103 kg/m^2 and supported structures of small dimensions. Moreover, as regards to CS1, comparing the data of Table 7 the cables net roof (Fig. 12b) has a structural weight of 123 kg/m^2 compared to the 342 kg/m^2 of the glued laminated timber roof and concrete beams (Fig.12a) which is under construction resulting in a substantial saving of 53% in terms of weight.

Figure 12. CS1 (a) Glued laminated timber roof -approved project- (b) HP Cables net roof -alternative proposal-.

Table 7. Summary of the weights of the compared structures for CS1.

Glued laminated timber roof (approved project)		Cables net roof (alternative proposal)	
Glued laminated timber beams self-weight	46.00 kg/m^2	Cables net self-weight	14.61 kg/m^2
Concrete beams self-weight	186.00 kg/m^2	Border arch self-weight	71.26 kg/m^2
Roof covering self-weight	110.00 kg/m^2	Roof covering self-weight	37.40 kg/m^2
Total weight	**342.00** kg/m^2	**Total weight**	**123.27** kg/m^2

It is understandable how important is the advantage of using cables net roof in terms of both architectural and structural lightness. Although tensile structure are lightweight structures sensitive to environmental actions, they perfectly meet the safety requirements laid down by Italian national code for construction under seismic, wind and snow action. Regards to seismic action, the reduced weight of the proposed structure results into better static performance generating a direct reduction of the seismic forces that are known to be proportional to the weight of the building; regards to the wind action, high performance in windy conditions, both at 0°, parallel to the stabilizing cables, and 90°, parallel to the load bearing cables, are found; so, the values of the aerodynamic coefficients acquired in the wind tunnel on a rigid model that simulates the undeformed configuration, are also valid for cables net deformed by the wind action. This means that the hyperbolic paraboloid shape has a very good behavior under the wind action. Finally, regards to the snow action, deformations do not exceed the limit of $1/200L_{max}$ (40 cm for CS1 – 80 cm for CS2) provided by NTC 2008 – Table 4.1.X for covers in general. This allows to cover large spans without intermediate supports, with the minimum amount of material and savings in terms of total cost of the building.

References

Carbotti, M. (2013). Progetto di una copertura alternativa per l'Entertainment Centre nel comune di Massafra: tensostruttura in rete di funi. Degree thesis.

Cook, N.J., Mayne, J.R. (1978). On design procedures for wind loading. Building Research Estabilishment, Garston.

Cook, N.J., Mayne, J.R. (1979). A novel working approach to the assessment of wind loads for equivalent static design, Journal of Wind Engineering and Industrial Aerodynamics, Vol. 4, pp. 149-164.

Cook, N.J., Mayne, J.R. (1980). A refined working approach to the assessment of wind loads for equivalent static design, *Journal of Wind Engineering and Industrial Aerodynamics*, **6**, 125-137.

Gumbel E.J., Statistic of extremes, Columbia University, Press: Lieblein J. (1974). Efficient methods of extreme value methodology, Report 74-602, National Bureau of Standards: Washington

Latino, M. (2013). Progettazione di una tensostruttura per la connessione delle attività sportive e infrastrutture del centro polisportivo del comune di Agnone. Degree thesis.

Majiowiecki M. (2004). Tensostrutture: Progetto e Verifica. Edizioni Crea, Milano.

Rizzo, F., D'Asdia, P., Lazzari, M., Procino, L. (2011). Wind action evaluation on tension roofs of hyperbolic paraboloid shape, *Engineering Structures*, **33**(2), 445-461.

Rizzo F., D'Asdia P., Ricciardelli F., Bartoli G. (2012). Characterization of pressure coefficients on hyperbolic paraboloid roofs, *Journal of Wind Engineering & Industrial Aerodynamics*, **102**(C), 61-71.

Rizzo, F. (2012). Wind tunnel tests on hyperbolic paraboloid roofs with elliptical plane shapes. *Engineering Structures,* **45**, 536-558.

Rizzo, F. (2014). Aerodynamics of tensile structures. Silvana Editoriale, Milano.

Simiu, E., and Scanlan, R.H. (1996). *Wind effects on structures*. Third edn. John Wiley & Sons, Ltd.

Research on the wind damage of urban roadside trees based on local wind field numerical simulation

X. Q. Ai[1] and J. Li[12]

[1] Shanghai Institute of Disaster Prevention and Relief, Tongji University，China
[2] State Key Laboratory for Disaster Reduction in Civil Engineering, Tongji University，Chin

Corresponding author: X. Q. Ai, aixiaoqiu@tongji.edu.cn

Abstract

Every year China's coastal city's landscaping will be affected and damaged seriously by typhoons. In this paper the modelling for urban roadside trees was conducted. CFD was adopted for wind field numerical simulation and the effect of buildings on the near surface wind field was studied. Combining with numerical wind field analysis, the wind damage of roadside trees was investigated. The result shows that because of the change of local wind environment, the wind damage would be differential. The method presented can be used to evaluate the loss assessment of the urban roadside trees as well as other wind vulnerable structures.

1   Introduction

The typhoon will damage a city more than buildings and structures. Every year China's coastal city's landscaping will be affected and damaged seriously by typhoon. Known from typhoon disaster documents, the wind damage of urban roadside trees on a city mainly including: 1) The urban green space landscape would be serious damaged; 2) Safety problems, such as hurting passengers, crushing cars and houses, destroying power supply and telecom lines; 3) Blocking traffic. At the present, there is less study on the analysis and evaluation for urban roadside trees under wind disaster. On the other hand, the wind field distribution near the surface would change with the layout of urban buildings and form local wind environment, which may be important for wind disaster. According to the above, in this paper the modelling for urban roadside trees is conducted. CFD software was adopted for wind field numerical simulation and the effect of buildings on the near surface wind field is studied. Combining with numerical wind field analysis, the wind disaster losses of roadside trees is investigated.

2   The modelling of urban street trees

2.1 Simplified analysis model

Tree type is an important factor affecting the wind resistance ability of roadside trees. Different tree species differ greatly in wind resistance. It has been shown that there are four tree fundamental characteristics for the wind resistance capability: 1) Physical and mechanical properties include the flexural strength and the dry gas density; 2) Crown characters include the crown, the diameter at breast height, the tree height and the crown type; 3).Branches features include the crown density; 4) Root characters include deep root or shallow root.

According to the shape, the tree crown can be assumed as a body revolving with the trunk. The tree can be also regarded as a cantilever beam structure and the wind action is concentrated on the crown.

The wind load of the tree is shown in Figure 1, there H is the total height，Hs is the trunk height, L is the crown height , B is the tree crown, D is the trunk diameter and q is the wind pressure.
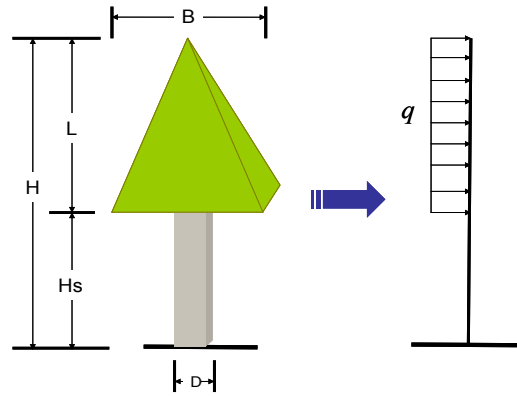
Figure 1. The wind load of a tree

2.2 Wind resistance analysis

Define the coefficient of air infiltration is C_t and air pressure can be transferred to wind force

$$F = \left(1 - C_t\right) \cdot w_0 \cdot A \tag{1}$$

There A is the crown cross-sectional area

$$A = \frac{1}{2} \cdot B \cdot L \tag{2}$$

If the wind force centre is the point of application by wind force on a tree, the height of wind force centre H_0 can be defined as

$$H_0 = H_s + \frac{1}{3}L \tag{3}$$

The wind pressure acting on the tree crown will cause wind moment through the wind force centre. Obviously the wind moment is the biggest at the root, and reduced with the increase of the height from the ground. The maximum wind moment M_{max} is

$$M_{max} = F \cdot H_0 \tag{4}$$

But it is noting that the actual broken usually appears in the tree height of 1/5 ~ 1/3.

Therefore, the wind resistance strength condition for tree break can be defined as

$$\sigma_s = \frac{M_{max}}{W_s} < \sigma \tag{5}$$

There W_s is the cross section flexure coefficient. That means the actual stress of any part of the trunk should be less than the ultimate strength of the trunk; otherwise the tree would be snapped. If the wind is bigger, and when the actual stress is less than the ultimate strength of trunk, the tree might happen flattened. In this paper the tree flattened is not considered temporarily.

According to the wind disaster survey, the wind damage of urban roadside trees can be classified to five Classes by different stress condition, which is figured as Table 1. There   is the maximum stress of the trunk section, f is the bending strength of certain tree species.

Table 1. Wind Damage Classification

	Damage Class	Damage Phenomenon	Strength Condition
I	Undamaged	Twig and leaf loss < 1/2	
II	Slight damaged	Twig and leaf loss > 1/2	
III	Medium damaged	Trunk lean angle< 30	
IV	Severe damaged	Trunk lean angle >30	
V	Full damaged	Trunk break	

3   The numerical simulation of wind field

In the paper, PHOENICS is used to simulate the flow field of a buildings compact district. The area of the group buildings is 188m*279m*98m and P1 to P3 are the object points as shown in Figure 2(a). The area for calculation is 800m*1000m*400m.The calculating mesh is local refined in the core subdomain as shown in Figure 2(b)
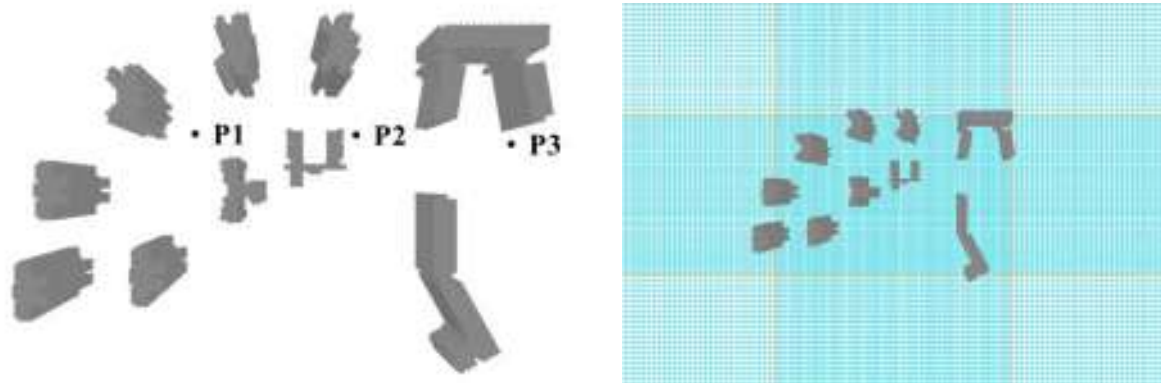
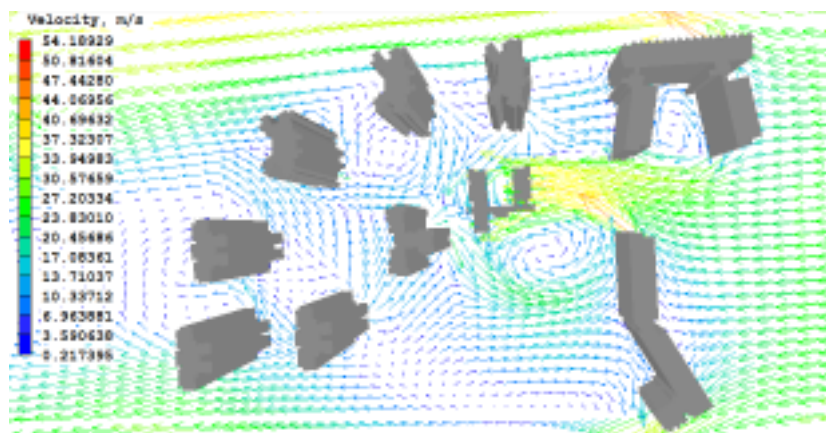Figure 2. Wind Mode (a) Group of Buildings (b) Calculating Mesh
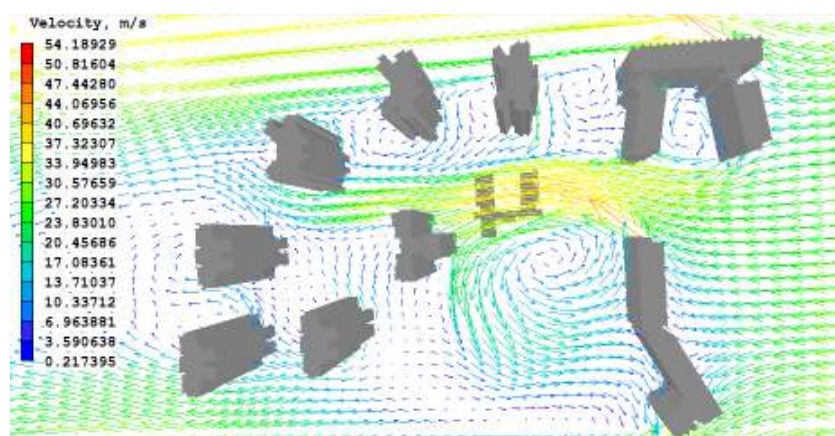

Figure 3. Wind Speed Section (2m height)

Figure 4. Wind Speed Section (20m height)

The k-εMode is accepted as a turbulent mode. The wind direction is south and the exponential wind profile is adopted with the wind speed at 10m as 30m/s, the terrain roughness parameter as 0.25.

The simulation results are showed as Figure 3 and Figure 4, which are the wind speed section at 2m and 20m height respectively. As is shown, because of the funnelling between the high buildings, the local wind field is significantly different.

4 The wind damage analysis

For the maidenhair tree as an example, assuming the total height as 6 m, the tree crown as 5m, the crown height as 4m ,the trunk diameter as 15cm and the coefficient of air infiltration as 0.5, the bending strength is adopted as77.8 MPa. The wind speed of different object points is used to calculate the maximum stress of the trunk section and the damage class. The Result is presented in Table 2.

Table 2. Wind damage of tree

Inflow Direction	Object Points	1	2	3
South	Wind Speed (m/s)	11.6	39.1	28.9
	Maximum Stress(MPa)	4.2	47.2	25.8
	Damage Class	I	III	II

5 Conclusions

The result shows that because of the change of local wind environment and the street trees distribution, the wind damage would be differential. The method presented can be used to evaluate the loss assessment of the urban roadside trees as well as other wind vulnerable structures. The further investigation considering the root characters would be continued.

Acknowledgement

References

Sellier D., Brunet Y. and Fourcaud T.(2008). A numerical model of tree aerodynamic response to a turbulent airflow. *Forestry* 81, 279-297

Gardiner B., Peltola H. and Kellomaki S.(2000). Comparison of two models for predicting the critical wind speeds required to damage coniferous trees. *Ecological Modelling* 129, 1-23

Cheng J.Q., Yang J.J. and Liu P.(1992). *Chinese wood records*. China Forestry Press.

Natural ventilation for the "Limestor" in Dalkingen (Germany): analysis and measurements

A. Lanza Volpe[1]

[1]Department of Architecture, University of Palermo, Italy
Corresponding author: A. Lanza Volpe, annalavolpe@virgilio.it

Abstract

The paper presents the results of fluid dynamic simulations of the glass structure that protects the remains of the Roman gate "Limestor", at Dalkingen (Germany). Specifically, thanks to the collaboration with the I.F.I. Institute (*Institut für Industrieaerodynamik*), Aachen, the climatic conditions inside the glass cover have been verified. Inspections and measurements have allowed us to validate the obtained results with real data. The study has been carried out in the context of a PhD thesis on glass covers used to protect archaeological sites.

1   Introduction

At Dalkingen, Germany, a fully glazed covering structure designed by Isin Architekten (Aalen, Germany) protects the remains of a Roman gate in the course of the famous Roman Limes (Fig. 1a, b); it is an almost cube-shaped glass structure with edges measuring about 20 m in length. The cube slants upwards towards the south, from a height of 8 m to 15 m, at an angle of 23° to the horizontal, which allows a 12 m high replica of the arch of the gate to be fitted on top of the remains. For management of the microclimate, a natural ventilation system was adopted. The openings are at the bottom, along the entire perimeter of the enclosure, and at the top, along the upper edge of the southern façade. The inclination of this protective shelter enhances the resulting chimney effect, as the hot air is dissipated at the highest point (Graf, 2010). Temperature and wind speed sensors are used to set the openings, preventing overheating inside the fully glazed enclosure. Measurements and calculations were carried out in order to verify the functioning of the ventilation system. Simplified calculations (Lanza Volpe, 2012) were carried out already during the design stage of the ventilation system (Lieb, 2009). Measurements and calculations were now carried out by us to verify the functioning of this ventilation system.

Figure 1a, b. External views of the glass cover, Limestor, Dalkingen (Germany).

2   Verification of natural ventilation

Natural ventilation is an effective way of removing accumulated heated air from rooms (specially with glass surfaces) and supplying colder from outside. The design of a correct ventilation system is of great importance; in fact, the air flow effect increases the exchange of indoor air, safety in the event of fire, the comfort of visitors and, in the case of archaeological site location, the preservation of the enclosed remains.

In the *InVento 2012 Conference* (Lanza Volpe, 2012) we have discussed the simplified methods used for dimensioning such ventilation systems. The methodology for the design of ventilation openings in glass roofs was borrowed from Rolf-Dieter Lieb, *Freie Durchströmung großer Glashallen* (Lieb, 2010), presented by Lieb in the above mentioned conference in the paper titled: *An easy approach to calculate natural ventilation and get an adapted design* (Lieb, 2012). This simplified method allows us to calculate geometric and physical parameters: given the dimensions and position of its openings, it is possible to calculate the flow rate and temperature difference between internal and external air; given the temperature difference, it is possible to obtain the flow rate and its dimension. In order to evaluate heat and mass transfer more accurately, CFD simulations were conducted to obtain an efficient representation of air flows and observe the trends over time as inside the covered area as well.

The CFD simulation of a building is a mathematical representation of its physical behavior. However, a simulation cannot precisely replicate a real construction, because all the simulations are based on a number of key assumptions and simplifications that affect the accuracy of results. In addition, the scant understanding of methodological limitations may lead to over- or underestimation of input data, or it may lead to unprecise results. Consequently, the interpretation of results requires particular attention, as they are only a partial representation of a building-environment system (Bottiglioni and Mingozzi, 2008). The I.F.I Institute's collaboration enabled us to carry out inspections and measurements on site for validation of simulation results. Each model needs to be validated with methods of comparison, since a software simulation is unable to accurately represent reality in all its aspects and in any situation. The simulations were validated by analytical and empirical methods. The analytical method is a comparison between simulation results and simplified calculation method results; on the other hand, empirical validation plus additional calibration allowed us to confirm the ability of models to give a valid image of reality, through comparison of calculation output, interview and values measured on site. For this purpose, the archaeological site "Limestor" at Dalkingen, in Germany, was visited.

3   The visit

The visit at the site was on July 28, 2013, at about 12:30 h. An interview with the guide of the archaeological site has allowed us to obtain the users' experiences and considerations on the adequacy of the climate inside the covered area. The tourist guide awaited visitors outside because of the high temperature inside the glazed cover near the entrance on hot summer days; the situation in winter is different, when the rise of temperatures is ideal and people enter inside with pleasure. On sunny days the perceived temperature is greater than the effective; this is due to the lack of shading and to an effect of reflection on the plastic replica of the ancient gate (Fig. 2a) as showed our measurements. In addition, the entrance is on the south side and this further increases perceived temperatures, while they are lower north of the gate and in the shadows of artifacts and replica.

The cover had been mainly designed for protection from cold, so the architects have given greater importance to the fact that snow and frost in cold weather should be absolutely avoided. This in fact works: as stated in the interview, snow does not accumulate along the perimeter of the glass enclosure during the winter, thanks to the grids for the air inlet at the bottom and higher temperature inside. These ventilation grids are covered with perforated plate (Fig. 2c), in order to prevent animals to enter. However, they increase the warm up effect on hot summer days, as they limit the open diameter for the entering air as well.

The measurements, made within a short-time interval, were conducted with calibrated measurement equipment of I.F.I. Institut für Industrieaerodynamik, including an IR temperature meter for measurements of the surface temperatures without contact (*Voltcraft IR-2200-50D USB Infrared Thermometer Optics*), a hot wire anemometer for measuring flow speeds and air temperatures (*Airflow's TA5 Thermal Anemometer*), a lux meter for measuring luminance (*Testo 545*) and a laser distance measurer to control the built dimensions versus the plan dimensions (*Leica*) .

Voltcraft IR-2200-50D USB Infrared Thermometer Optics is a measuring device for non-contact temperature measurement. It determines the temperature based on the emitted infrared energy and the emissivity of an object. This type of measurement is very useful to measure objects that are difficult to reach. The device allowed us to measure the average surface temperature of sample remains.

Airflow's TA5 Thermal Anemometer is a portable air velocity and temperature measurement calibrated to an internationally recognised standard. Measurements were carried out in simple spot checks, automatically temperature compensated. The air velocity has been checked over large areas. A number of spaced readings has been taken. The average of these readings gave the average velocity.

Testo 545 light intensity measuring instrument was used for testing average light intensity on exposed and shaded surfaces. The mean value has been calculated at the touch of a button from measured lux values. *Leica* laser distance measurer allowed us to verify some distances and sizes. Quantitative data, corresponding to theoretical expectations, were recorded and used. Data to be quantify (temperatures, velocity, etc.) fluctuate periodically, so the precision in the measurements was not considered important for the purpose of validation (semi-quantitative method). The following table shows the most important data collected on site with this equipment:

Table 1. Measurements on site.

Outside
Air temperature: about 32° C
Blue sky with hardly no clouds
Full insolation from Southern Direction, approx. > 120.000 lux (beyond range of luminance meter)

Inside
Air temperature: about 34° C
At the openings, at the bottom (inlet), the air velocity is about 0.3 m/s, at the door it is about 1.0 m/s
Air temperature at inlets equals outside air temperature
Floor temperature: about 38° C
Archaeological ruins temperature: about 38° C.
Temperature of the reconstructed gate: about 42° C (with possible influence of reflected radiation)
Roof temperature: about 44-45° C (this is expected to be equal to the air exhaust temperature, as those surfaces laid in the shadow)
Temperature of the steel structure: about 47° C
Shadow luminance: approximately 8000 lux
Luminance in the shade south of the replica varied from 18000 to 20000 lux

The glazed cube is made of a steel structure with light grey coating of the members and a single pane laminated security glass made from clear glass without e.g. a sun protection or low-E coating. There is no sun shade installed inside or outside the cube. Thus solar irradiation can enter without more resistance than the transparent glass (the expected total energy transmission is g = 0.85, daylight transmission being in the same order), which is shown as the luminance meter has a range of 100.000 lux and the irradiation was still slightly over this value for direct incidence behind the glass.

 The perceived temperature was uncomfortable under these conditions when entering the cube. As it was not outside, neither in the rear of the cube, we wondered, why it was obviously so much worse at the entrance, even though the protected entrance allowed for some additional shading (see fig. 2b). The answer was found with the lux meter and is given in table 1 as well. While luminance in the

shadow through diffuse sun light was only about 8000 lux we measured more than double of this in the shadow in the entrance area, both values being measured in a horizontal plane. When we tilted the luminance meter to the outside and to the inside, we could detect, that the additional portion of luminance was caused by the diffuse reflection of direct sun light from the material of the replica, which is essentially a printed plastic tissue in light beige colours, as seen in fig. 2a.

Figure 2. Internal views: the plastic replica of the ancient Roman gate (a). Openings at the top of the southern façade (b) and at the bottom of the entire perimeter (c).

4 Simulation model

In order to calculate the natural air flow through the cube a Computational Fluid Dynamics (CFD) software was used. As most of the flow is non-isothermal and dominated by free convection in a larger volume (i.e. the cube) a Large Eddy Simulation (LES) model was chosen, that showed all the necessary thermal parameters, such as e.g. a full calculation of effects of thermal buoyancy instead of the use of the Boussinesq approximation.

The simulation model is made up of three main categories of component (ASHRAE, 2005):

1. geometry, parameters and properties for its physical description;
2. input variables, such as the outdoor air temperature and solar radiation on surfaces;
3. output data that describes the system response when it is subject to variable inputs.

The calculation was performed with the CFD program fds (Fire Dynamics Simulator) in version 5.5.3. The inside and outside volume of and around the Glass Cube was discretized on the basis of 5 cm Hexaedral cells in a structured mesh. As such a mesh does not allow for directly inclined surfaces, all inclined surfaces were described in two ways:

- The first model is normal to the base plane (i.e. terrain plane) and inclined surfaces were modelled as stepping obstacles with a correction in order not to produce additional turbulence as those geometry steps

- The second model uses the rectangular shape of the Cube and therefore all of its surfaces are plane obstacles with the sole exception of the terrain plane and natural convection is correctly simulated by inclining the vector of Gravity.

Both models are not completely detailed, as the remains were not exactly known before the visit and obviously should not have too much of an influence, they were left away. The same was decided for the steel frame of the cube, as its members had a height unknown before the visit and only in the range

of 2-3 cell dimensions, so that their flow effects could not have been reproduced sufficiently with the coarse grid possible for the research due to limited computational time resources.

From the physical point of view, if we consider the energy balance for a glass covering structure, the flows involved are:

- heat flow through the envelope due to the temperature difference between outdoor and indoor air;
- flow due to solar radiation (short wavelength irradiation);
- long wavelength irradiation from outside;
- air flow due to ventilation;
- heat given off by the materials inside the covering structure (high wavelength irradiation from inside);
- heat inside the covering structure generated by people, motors, artificial light, etc.

The physical conditions of these flows and the conditions in the simulation models are described below.

- Heat flow through the envelope due to the temperature difference between outdoor and indoor air.

The regime of simulations is periodic. The simulations start from a situation of equilibrium in which the outside temperature is the same as inside. Therefore, in the numerical model the indoor temperature calculated depends on solar radiation and it is not a function of the temperature difference between outside and inside. This difference in temperature is not an important parameter for energy performance because the solar radiation energy flux is certainly predominant. With lower external air temperatures, the internal absolute air temperature will be lower and thus probably more acceptable (Lieb, 2010).

- Flow due to solar radiation (short wavelength irradiation)

In the case of glazed buildings the solar energy contribution is the most significant portion of the total load (Lieb, 2010). This highlights the importance of solar radiation modeling, as it affects the accuracy of global performance.

Short wavelength solar radiation on external surfaces is partly reflected and partly transmitted inside the volume. The radiative wave passing through the glass is partly absorbed, causing a rise in temperature, while the remaining portion continues along its path. This increase in temperature brings about a swifter conduction process and more convective motions. Finally, the surface temperature itself affects the amount of long wavelength radiative emissions. The component of the transmitted incident beam will strike some of the inside surfaces with an imperceptible time lag. Then it acts like the radiation striking the external surfaces: in the case of opaque surfaces there is absorption and reflection, while in the case of transparent surfaces there is absorption, reflection and transmission.

In the simulated models the maximum incoming solar radiation under clear-sky conditions and its component passing through the glass were examined, taking into account the solar factor. Accurate modeling of solar radiation would require calculation methods for the prediction of surface position relative to the solar beam; in addition, the thermo-physical properties involved include coefficients of absorption, reflection and emission of the elements, which depend on angle of incidence, wavelength of the incident light, time of day, month and year (Binotto, 2009).

- Long wavelength irradiation from outside.

The exchange of energy, by long-wave radiation, between external surfaces and the sky, or between the surrounding buildings and the ground, can result in a substantial lowering of surface temperatures, especially under clear sky conditions and at night. This energy flow modeling requires the estimation of many factors including: the effective air temperature as a function of cloud covering structure type, temperature of surrounding buildings, soil temperature as a function of its conditions (humidity, composition, surface coverage), surface heating caused by incident short wavelength radiation and by factors based on the coupling between the above-mentioned elements (Binotto, 2009).

In the calculations the maximum solar radiation under a clear sky and a constant external floor surface temperature are considered to safety advantage.

- Air flow due to ventilation.

Ventilation due to temperature difference is considered in the numerical calculation while the presence of external wind is not modeled, to safety advantage. This is due to the fact that the wind cannot be called a reliable source of ventilation in all but a very few sites around the world during the hottest days of a year (Lieb, 2012).

- Heat given off by the materials inside the covering structure (long wavelength irradiation from inside).

Inter-surface, long wavelength radiation is a function of temperature, emissivity, the extent to which the surfaces are in visual contact (represented by a view factor) and of the nature of the surface reflection (diffuse, specular or mixed). The flow-path will tend to establish surface temperature equilibrium by cooling hot surfaces and heating cold ones (Binotto, 2009).

Archaeological remains are different in shape and materials, with different heat absorption and reflection properties and therefore with different energy interchange between surfaces.

A flat stone surface is considered inside the protective covering structure in the simulated cases, with a thickness of 20 cm, conductivity of $\lambda = 1.83$ W/m^2 K, emissivity $\varepsilon = 0.67$, specific heat c = 0.712 kJ/(kg K) and density d = 2200 kg/m^3. The increase in internal temperature, which brings about the so-called greenhouse effect, is dependent on the wavelength of the radiation.

In the simulated model the transmission of heat does not vary with wavelength variation and the glass emissivity is supposed to be constant over the whole spectral range, equal to 0.837. In addition, over time, the solar flux determines an increase in internal temperature, especially with regard to the glazed, closed configurations. This is also associated with the increase in absolute humidity, which is the amount of water vapor in the air usually expressed in grams per cubic meter. So we might expect the following causal chain: as the temperature rises, evaporation increases; the water absorbs more heat, further warming the air and causing more evaporation (greenhouse effect), with a similar mechanism to the one occurring in our atmosphere. In the numerical model this combination of heat and humidity was not considered.

- Heat inside the covering structure generated by people, motors, artificial light, etc.

The thermal load for people, motors, artificial light, etc. was not evaluated in the simulation model.

5   Results of simulations

Using simulations we observed that external air-flows enter through the openings at the bottom and through the door as designed, all results are given for the first model in the following, as the differences to model two were sufficiently small. The inclination of the protective cover structure enhances the resulting chimney effect, as the hot air is dissipated at the highest point and thus no heat accumulation can develop below the roof. Substantial agreement was found between real and theoretical results as well.

Considering the effective surface opening area (approximately 12 m^2) and using the simplified methods of calculation, we apprehend that, at 2 m in height (head height and maximum height of the remains), the indoor temperature may exceed the external by approximately 0.33 degrees. This value is close to the one obtained by simulations at about the same height (Fig. 3a - d). The results of numerical simulation have qualitatively matched with simplified methods results and with on site measurements. Otherwise, unexpected results would indicated problems with the procedure or materials, or suggested that the theories on the topic of testing were incorrect. The effect of the entrance on the south side and the reflection of the plastic replica that increase the perceived temperatures were not considered in the design phase, nor could be found without special treatment in the CFD.
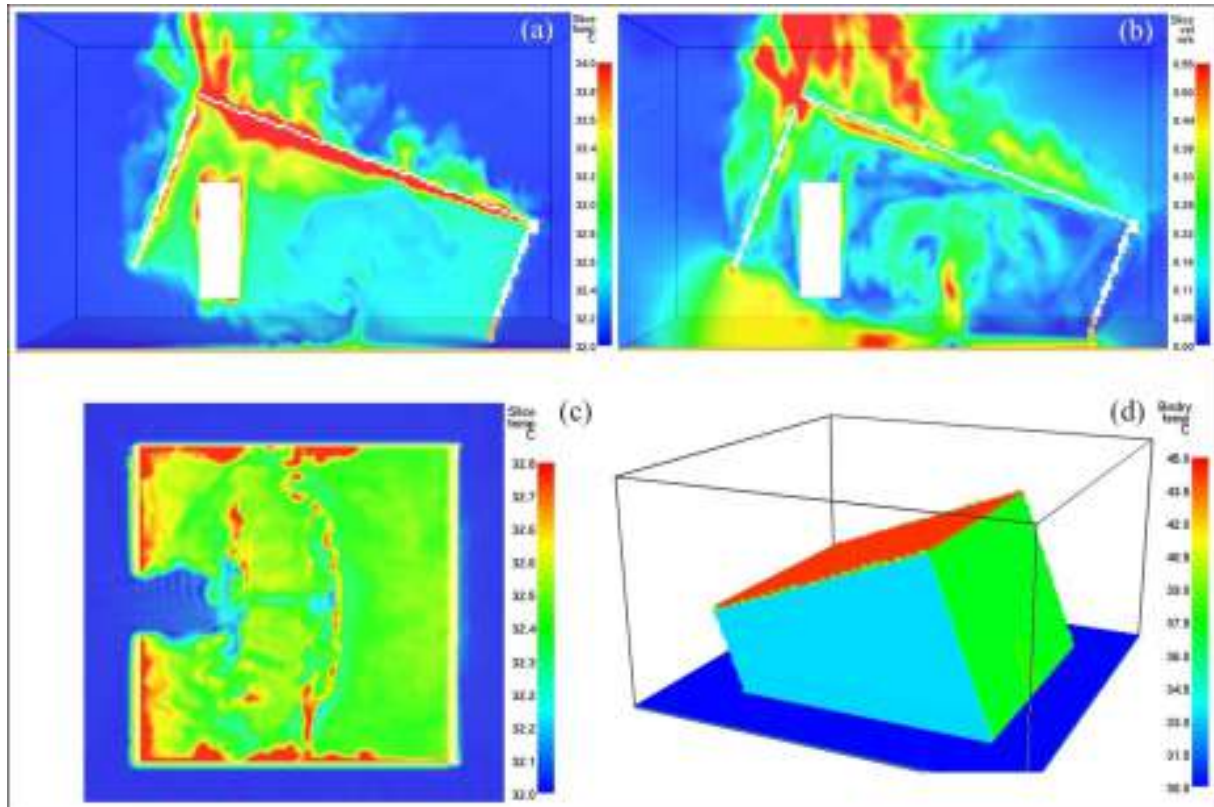
Figure 3. Vertical section for temperature (a); vertical section for velocity, (b). horizontal section, height of 2 m from the ground, for temperature (c). Surfaces temperatures (d).

6   Conclusions

The study assessed the efficacy of natural ventilation. The average values of air temperature and velocity, luminance and surface temperature were ascertained on site. The evaluation of the profiles shows qualitative and general quantitative agreement between the simulations, the simplified method and the measurements. The defined model represents the existing building, thus allowing a more accurate prediction of its behaviour under certain circumstances.

References

ASHRAE (2005). Energy estimating and modeling methods, *ASHRAE Handbook 2005 - Fundamentals (SI)*, 32.

Binotto, M., Prof. Zecchin, R. (rel.), (2009-10). *Software di simulazione energetica degli edifici e loro validazione*, Tesi di Laurea - Università degli Studi di Padova.

Bottiglioni, S. Mingozzi, A. (2008). *Programmi di calcolo delle prestazioni energetiche degli edifici*, Progetto BREA, Bologna.

Graf, J. (2010). A glass palace for the Limes Gate at Dalkingen, *Engineered transparency. International Conference at Glasstec, Sept. 29 -30, Düsseldorf*.

Lanza Volpe, A. (2012). Application of natural ventilation to archaeological sites with glass covers. *XII Convegno Nazionale di Ingegneria del Vento, Oct. 7-10, Venezia* (going to press).

Lieb, R. D. (2009). *Limestor Dalkingen. Entwärmung der Glaseinhausung,* Aachen (not published publically).

Lieb, R. D. (2010). *Freie Durchströmung großer Glashallen*, Universität Stuttgart - IGE Institut für GebäudeEnergetik, N. 20, Stuttgart.

Lieb, R. D. (2012). An easy approach to calculate natural ventilation and get an adapted design, *XII Convegno Nazionale di Ingegneria del Vento, Oct. 7-10, Venezia* (going to press).

Risk analysis of pedestrian and vehicle safety in windy environments

Chris Baker

Department of Civil Engineering, University of Birmingham, United Kingdom
c.j.baker@bham.ac.uk

Abstract

Recent events in the UK have highlighted the need for a consistent set of criteria that can be used to assess the effect of new buildings on the safety of vehicles and pedestrians around the base of the building. This paper presents a risk analysis for assessing the risk of such incidents. The paper first discusses the nature of current methodologies, and argues that methods that are based on the probability distribution of wind velocities alone are not wholly adequate. The new methodology takes the wind velocity probability distribution functions that can be obtained from wind tunnel measurements and convolutes these with the cumulative distribution functions for human and vehicle instability in high winds to give a risk of an accident occurring. It is argued that such a risk based methodology allows for greater consistency in the application of any pedestrian / vehicle movement restrictions or alleviation methods.

1 Introduction

In the design of tall buildings it is normal practice to carry out a wind comfort study to assess the pedestrian wind environment around the base of the building, usually through a wind tunnel test or through CFD calculations. The data obtained from such a study is used in conjunction with local wind data to find the probability that, at different points around the building, specific wind speeds will be exceeded. These wind speed probabilities are then compared with a range of different criteria that indicate whether that particular point around the building will be suitable for different activities – e.g. sitting, walking etc. In some situations where high winds are expected, the possibility of "distress" is also considered – i.e. the probability of wind speeds exceeding levels that are regarded as dangerous for pedestrians. The wind speed criteria themselves can take on a variety of different forms and can be based on mean wind speeds, gust wind speeds, or some combination of mean and gust – see table 1 for a collation of criteria. In 2011 in Leeds in Northern England, a large lorry blew over close to the base of a recently erected tall building during windy conditions, killing one pedestrian and injuring another (figure 1) (Daily Telegraph 2011). Since this building was completed in 2007, there have been numerous reports of pedestrians finding the wind conditions in the vicinity of the building uncomfortable at best and dangerous at worst, with a number of incidents of pedestrians being blown off their feet. This has led to a renewed interest in the distress criteria that are currently being used in the UK, and in the development of criteria for the stability of vehicles around new developments. In this paper we consider these effects further and develop a consistent risk based analysis that enables the risk of pedestrian injury and vehicle accidents to be considered in a way that is consistent with other risks. In section 2 we consider the requirements for building design and operation to ensure pedestrian and vehicle safety. In sections 3 and 4 we consider the wind speed safety limits for pedestrians and vehicles, and the risk analysis framework is described in section 5. An example of the use of the framework is presented in section 6 and suggestions made for further work. Two appendices are given – the first of which derives the form of the Weibull probability distribution as it applies to gust speeds, and the second gives the application of the current methodology to the determination of vehicle instability caused by train slipstream effects.

Figure 1. Bridgewater Place in Leeds UK and the accident of March 2011

Table 1 Wind speeds for pedestrian distress.

Author	Mean wind speed m/s	Gust wind speed m/s	Notes
Melbourne (1978)		23	Mean plus 3.5sd's
Penwarden	15 to 20		
Hunt (1976)		15 (control of walking)	Mean plus 3sd's
		20 (danger)	
Lawson (2001)	14.1 to 17.3		
Soligo (1998)	11.9 to 15	22.2 to 27.8	Mean plus 3.5sd's Compilation
Bottema (1992)	10	15 (elderly people)	Mean plus 2sd's
		20 (young people)	
White (1992)		20	Compilation
LDCC (in Lawson, 2001)		15	
Peters (1999)		12.5 to 20	Train gust
BRB (1971)		11 (passengers)	Train gust
		17 (trackside workers)	
CEN (2009)		15.5 (passengers)	Train gust
		22.0 (trackside workers)	

2   Design and operation requirements and wind speed criteria

In the terms of this paper, when a building is being designed, the information that is required is an indication of the risk that pedestrians or vehicles will be blown over, that can be compared with a range of other risks and assessed for their acceptability. If these risks are not acceptable, then either building modifications will be required to bring the risk values to acceptable levels, or some operational criteria will need to be developed to exclude pedestrians or vehicles from specific areas, again such that the risk of an incident falls to acceptable levels. Such a consideration of risk requires both a consideration of the wind conditions around the building and of the behaviour of pedestrians or vehicles in high winds. Now, in so far as there is an agreed current practice, this is not the procedure

that is generally carried out, with pedestrian distress and vehicle restriction criteria being based on wind speed magnitudes and probabilities of exceedence only – i.e. the effect of the wind on pedestrians and vehicles themselves is not usually considered. The author would contend that, although such methodologies might be simple and pragmatic, they do not address the fundamental issue of the risk of an incident occurring. This paper will seek to address this point in what follows.

3   Pedestrian stability in high winds

In terms of response to wind gusts, there is a very great deal of person to person variation, as might be expected. This variation was assessed in Jordan et al (2008), through the use of wind tunnel experiments where groups of students of both sexes were subjected to sudden gusts and there displacement measured. Note that these gusts are not necessarily representative of wind conditions around the base of buildings. Typical results are shown in figure 2 for pedestrians facing the oncoming wind. These show the cumulative probability distribution of subject instability for different categories of subject. From a range of data such as this, for different pedestrian stances relative to the wind, we can express the c.d.f. of a particular group of individuals becoming unstable in a particular gust velocity u_i in a simple linear form

$$\mu = 0 \; for \; u_i < a$$
$$\mu = \frac{u-a}{b} \; for \; a < u_i < a + b \tag{1}$$
$$\mu = 1 \; for \; a + b < u_i$$

where a and b take on values that one would expect to be a function of size / weight / gender proportion etc.
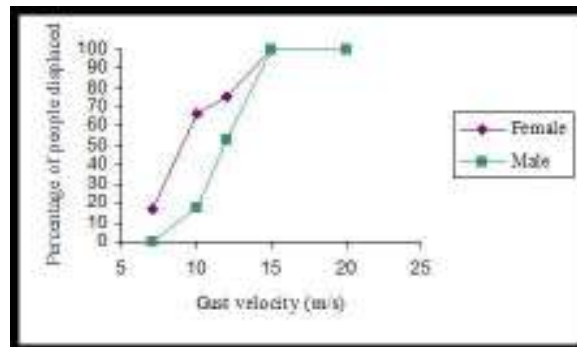
Figure 2. CDF of displaced sample in sudden wind gust (facing oncoming wind) (Jordan et al 2008)

4   Road vehicle stability in high winds

The vehicles that are of particular concern in this paper are large vans and lorries, of the type studied in Sterling et al (2010). Before considering how vehicle instability in high winds should be calculated, two observations need to be made. Firstly, whilst a number of investigations have carried out studies of vehicles in high winds, using models of the vehicle dynamic system of varying levels of complexity, all of these are too complex for routine use in the situation studied here, where the level of uncertainty concerning the nature of the wind field, acceptable risk etc., implies a simple, easily applied method is required. Secondly observations suggest that the type of accident of overwhelming concern is when such vehicles overturn about their leeward wheels. This in fact offers a possible way forward for a simplification. If we assume that this is the only instability mechanism of importance, a simple calculation can be carried out that only requires information on the rolling moment coefficient about

the leeward wheel track – in a very similar way to that reported for trains in Baker (2013). That paper shows that, in the low yaw angle (ψ) range, these coefficients collapse onto a simple form if plotted in the following way

$$\frac{C_{RL}(\psi)}{C_{RL}(40)} = \left(\frac{\sin(\psi)}{\sin(40)}\right)^{n} \qquad\qquad \frac{C_{RL}(\psi)}{C_{RL}(40)} = R \tag{2}$$

for the low and high yaw angle ranges respectively. Here ψ is the yaw angle and $C_{RL}(\psi)$ is the lee rail rolling moment coefficient at that yaw angle. n is a parameter that depends upon train type, but for many trains is close to 1.5, and R is a constant. Now a study of the available data for the lee rail rolling moment for lorry overturning, shows that these forms also apply in this case. The available data is summarised in figure 3 and it can be seen that values of $n = 0.9$ and $R = 1.3$ give a conservative envelope to nearly all the data for a range of vehicle types. Through a consideration of the wind vectors and a simple dynamic model of the train overturning problem, Baker (2013) than arrives at a definition of a parameter that he refers to as the characteristic velocity c, defined by

$$c^2 = \frac{\alpha M g p\,(\sin(40))^{n}}{0.5\rho C_{RL}(40)Ah} \tag{3}$$

Here M is the vehicle mass, p the wheel base semi-width, ρ the density of air, A the reference area, h the reference height. α is a parameter that allows for a specified degree of wheel unloading (usually 0.9) and also takes into account suspension, road curvature and cant and aerodynamic force correlation effects. This leads to the following expressions for a generic cross wind characteristic that relates the gust wind speed at which an incident will occur u_i, to the train speed v and the wind direction relative to the track β. At low yaw angles

$$\left(\left(\frac{v}{c}\right)^2 + \left(\frac{u_i}{c}\right)^2 + 2\left(\frac{u_i}{c}\right)\left(\frac{v}{c}\right)\cos(\beta)\right) = \left(\left(\frac{u_i}{c}\right)\sin(\beta)\right)^{2n/(n-2)} \tag{4}$$

and at high yaw angles

$$\left(\left(\frac{v}{c}\right)^2 + \left(\frac{u_i}{c}\right)^2 + 2\left(\frac{u_i}{c}\right)\left(\frac{v}{c}\right)\cos(\beta)\right) = ((\sin(40))^{-n})/R \tag{5}$$

Note that c thus effectively acts as a normalisation velocity. A numerical solution for these equations shows that they have a minimum value for a value of β somewhat less than 90^0 (figure 4) when the wind is normal to the road This value is of most significance to the overturning issue as the probability of these incident wind speeds being exceeded decreases very rapidly away from these minima. For $n=0.9$ and $R=1.3$ the variation of minimum normalised accident wind speed with normalised vehicle speed is shown in figure 5, and can be seen to be of a relatively simple form. This curve is given to a good approximation by the polynomial fit.

$$\left(\frac{u_i}{c}\right) = 1.0691 - 0.3623\left(\frac{v}{c}\right) - 0.0251\left(\frac{v}{c}\right)^2 + 0.0201\left(\frac{v}{c}\right)^3 \tag{6}$$

This curve thus gives the generic cross wind characteristic and the curve for a particular type of vehicle can be calculated through a knowledge of the characteristic velocity c. Having thus obtained a relatively simple formula for the accident wind speed for a range of vehicles, the question then arises as to what is the cumulative probability distribution for this wind speed, for a range of vehicle types /

weights etc. This can be found for a particular location by assuming a typical set of vehicle parameters and speeds, and the uncertainties around these parameters, and then, through a large number of probabilistic realisations, calculating values of c and u_i, to give a cumulative probability distribution of u_i. This is illustrated in figure 6 below using the parameters given in table 2. Such curves can be approximated by linear formulae that are identical to those given in equation (1) above.
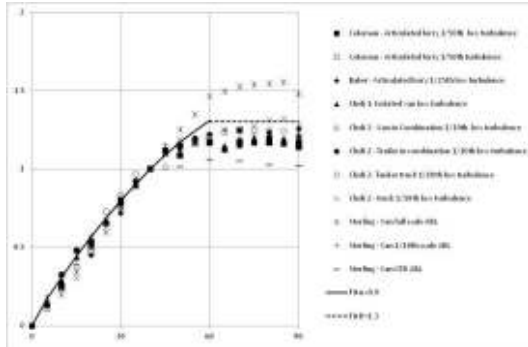
Figure 3. Compilation of rolling moment coefficient data
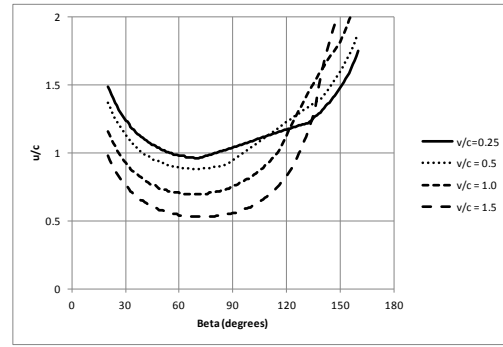
Figure 4. Critical wind speed as a function of vehicle speed and wind direction
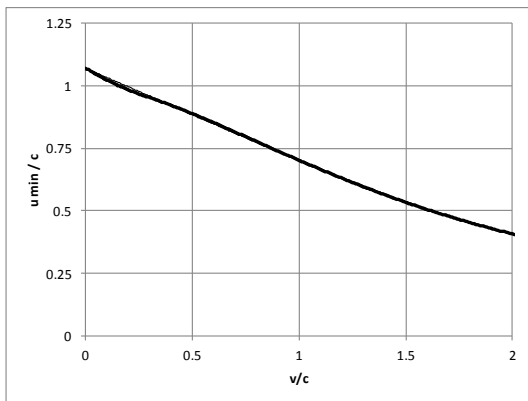
Figure 5. Minimum critical wind speed as a function of vehicle speed
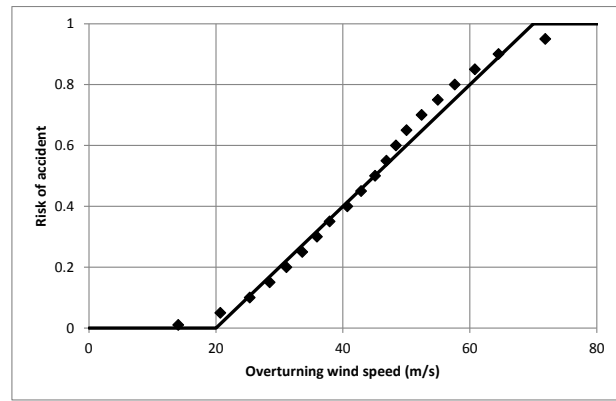
Figure 6. Cumulative probability distribution accident wind speeds for lorries

Table 2. Parameters used in calculation of lorry accident wind speeds

	v (m/s)	α	M (kg)	P (m)	C_{RL}	A (m^2)	h(m)
Mean	15	0.8	10000	1	0.5	20	4
Standard deviation	5	0.1	4000	0.2	0.1	3	1

5   Risk analysis

From wind tunnel tests and available meteorological data, it is possible to find, for a particular site, the probability distribution function (p.d.f.) for the exceedence of a specified wind gust at the site. In what follows it will be assumed that this can be given by a Weibull distribution. In Appendix 1 it is shown that if the p.d.f. of the mean velocity is given by a Weibull distribution, and the instantaneous wind speed is distributed normally about the mean, then the instantaneous wind speed will also be given by a Weibull distribution, with different parameters to those for the mean p.d.f.. We thus assume that the gust wind speed p.d.f. is given by

$$f = \frac{k}{\lambda^{k'}} u_i^{k'-1} e^{-\left(\frac{u_i}{\lambda}\right)^{k'}} \tag{7}$$

where k' and λ are the appropriate Weibull parameters. Appendix 1 shows that k' varies from that for a mean speed p.d.f, decreasing as turbulence intensity increases, but λ stays the same as for the mean speed p.d.f.. Now the risk of a person or a vehicle blowing over is thus given by a convolution of equations (1) and (7). This can be expressed in a dimensionless form as follows.

$$\Omega = \int_0^\infty f\mu du_i = \int_{\frac{a}{\lambda}}^{\frac{a}{\lambda}\left(1+\frac{b}{a}\right)} k'\left(\frac{u_i}{\lambda}\right)^{k'-1} e^{-\left(\frac{u_i}{\lambda}\right)^{k'}} \frac{(u_i/\lambda)-(a/\lambda)}{(b/a)(a/\lambda)} d\left(\frac{u_i}{\lambda}\right) + \int_{\frac{a}{\lambda}\left(1+\frac{b}{a}\right)}^\infty k'\left(\frac{u_i}{\lambda}\right)^{k'-1} e^{-\left(\frac{u_i}{\lambda}\right)^{k'}} d\left(\frac{u_i}{\lambda}\right)$$

$$\tag{8}$$

In this case this formula has to be evaluated numerically, with the risk being a function of a/λ, b/a and k'. The risk level can be calculated using the Weibull parameters obtained from the wind tunnel study and meteorological data, and can also be used to evaluate the effect on risk of changes to these parameters caused by geometric modifications to the structure. This expression can also be used "in reverse" for a specific set of Weibull parameters – to calculate a wind speed level for a specified value of risk.

Finally, Appendix 2 sets out a similar analysis for calculating the risk of a passenger becoming unstable in the slipstreams of trains. It can be seen that in this case it is possible to obtain an explicit expression for the risk, because the underlying probability distribution is normal rather than Weibull and is thus integrable. This is not taken further in this paper, but may be useful in future studies.

6   Example of the Methodology

We can use the above formulation of risk to calculate the risk that a pedestrian or vehicle accident might occur for a particular situation. Figures 7 and 8 show the variation of risk with a/λ for a range of values of *b/a* and *k*. It can be seen that the risk is mostly dependent on the value of a/λ, which positions the cumulative distribution curve for pedestrian or vehicle instability in relation to the Weibull distribution for wind gust probabilities. As the values of this ratio increase, any incidents will take place in the lower probability regions of the Weibull tail. The risk also decreases as *b/a* increases – i.e. the broader the cdf of the incident probability and as k increases which implies lower values of turbulence intensity – see Appendix 1. Now let us calculate some actual numerical risk values. For pedestrian stability we assume that for a mixed age and gender population *a* = 12.5 and *b*=12.5. The numerical values have been chosen to be broadly consistent with those of table 1, although it has to be acknowledged that these values are very uncertain. In physical terms, these values suggest that some in this population would become unstable in a gust of 12.5m/s, and all would be unstable in a gust of 25m/s. Whilst there must be some doubt concerning the appropriateness of these numerical values for typical wind gusts (the available data varies widely and is not always for conditions similar to that found in the natural wind) they will serve in what follows to illustrate the proposed methodology. Similarly for the population of vehicle considered in figure 5, we take *a* = 20m/s and *b* = 50m/s. The lower figure has been shown to be around the level that high sided vehicle accidents begin to occur (Reynolds and Baker 1990). The risk of an accident occurring if a pedestrian or vehicle is at a particular location is then given by equation (8), with or without wind restrictions. Some factor then needs to be applied to allow for the presence or otherwise of a person or vehicle at that point, at that time. For the calculation of pedestrian risk we conservatively assume that this factor is 1.0. For vehicles, considering a particular stretch of road of length *L*, with vehicles with an average speed *v*, and a number of vehicle per hour of *N*, then the reduction factor beomes *LN/3600v*. Table 3 shows the results of these calculations, for a turbulence intensity of 30%, a mean wind speed Weibull *k* factor 2.0 (resulting in *k'*=1.65 – appendix 1) and different values of the parameter λ. It can be seen that the risk

is a very strong function of the latter i.e. the strength of the wind at a particular site. The risks of a lorry accident are, as would be expected, much less than the risk of a pedestrian accident. The question then arises as to how the risk might be affected by a restriction in either pedestrian or vehicle movement. Figure 9 shows the calculated risk variation for the lorry situation with different wind speed limits imposed. The most notable point is the rapid rise in risk when the initial rise velocity of the c.d.f. (20m/s) is exceeded – indicating that most of the risk comes from wind speeds of around this value, when the wind p.d.f is relatively high. This implies that the only sensible wind speed restriction is at this level. Finally it is possible to calculate risk contours as a function of wind parameters, specifically the Weibull parameter λ and the turbulence intensity I – figure 10. This gives areas of different risk levels in this plane, and can be used as a guide fro assessing the outcome of wind tunnel tests – for each measurement point the results should lie in a region of acceptable risk.
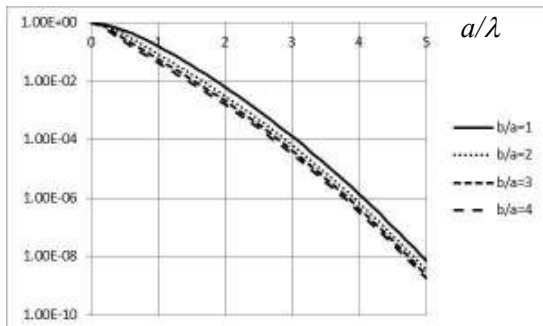
Figure 7, Variation of risk with a/λ and b/a (k'=1.7)   Figure 8. Variation of risk with a/λ and k' (b/a=2.0)
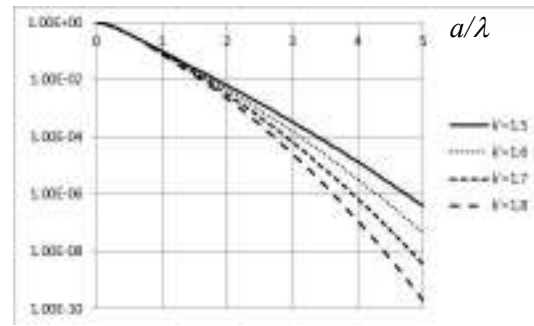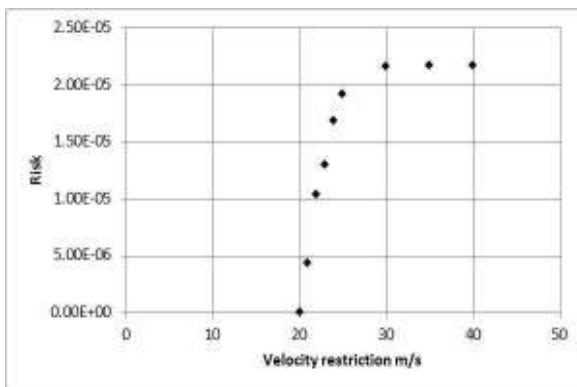
Figure 9. Effect of vehicle restrictions on lorry   Figure 10. Lorry accident risk as a function of Weibull
accident risk (λ=6m/s, k'=1.7) λ and turbulence intensity I

Table 3 Typical values of calculated risk

λ m/s	Pedestrian accident risk	Vehicle accident risk
4.0	1.25×10^{-4}	1.07×10^{-8}
5.0	1.32×10^{-3}	1.24×10^{-6}
6.0	5.79×10^{-3}	2.17×10^{-5}
7.0	1.54×10^{-2}	1.42×10^{-4}

It can be seen from the above that the above methodology can, in principle, act as a tool in providing a consistent way for assessing the risk of an accident to a pedestrian or a vehicle around a high rise building. However before this can be done, the nature of the cumulative probability distributions for both pedestrian and high sided vehicle instability needs to be much better designed. In addition it would be useful to determine such distributions for other vulnerable classes of vehicle – specifically cycles and motor cycles.

References

Baker C J (1987), Measures to control vehicle movement at exposed sites during windy periods, *Journal of Wind Engineering and Industrial Aerodynamics* 25, 2, 151-161.

Baker C J (2013) A framework for the consideration of cross wind effects on trains, *Journal of Wind Engineering and Industrial Aerodynamics* 123, 130–142

Baker C J, Reynolds 3. 1991. Wind induced accidents of road vehicles, *Accident Analysis and Prevention 24*, 6, 559-575

Bottema M, Leene J A, Wisse J A, (1992). Towards forecasting of wind comfort. *Journal of Wind Engineering and Industrial Aerodynamics* 44, 1-3 2365–2376

BRB (1971). High Speed Tests at Cheddington, 1970. Design project no.80068, British Railways Board, Chief Mechanical and Electrical Engineer's Department

CEN (2009) Railway applications — Aerodynamics — Part 4: Requirements and test procedures for aerodynamics on open track, CEN EN 14067-4:2005+A1

Cheli F, Corradi R, Sabbioni E,Tomasini G (2011) Wind tunnel tests on heavy road vehicles: Cross wind induced loads—*Part 1, Journal of Wind Engineering and Industrial Aerodynamics* 99, 1000–1010

Cheli F, Ripamonti F, Sabbioni E, Tomasini G (2011) Wind tunnel tests on heavy road vehicles: Cros Fs wind induced loads—*Part 2, Journal of Wind Engineering and Industrial* Aerodynamics 99 1011–1024

Coleman S A, Baker C J. (1994). An experimental study of the aerodynamic behaviour of high sided lorries in cross winds, *Journal of Wind Engineering and Industrial Aerodynamics* 53, 3, 401-431

Daily Telegraph (2011) http://www.telegraph.co.uk/motoring/news/8374281/Police-investigate-Dalek-after-man-killed-by-overturned-lorry.html

Hunt J C R, Poulton E C, Mumford J C (1976) The effects of wind on people; new criteria based on wind tunnel experiments. *Building and Environment* 11:15–28.

Jordan S C, Johnson T, Sterling M, Baker C J, (2008) Evaluating and modelling the response of an individual to a sudden change in wind speed, *Building and Environment* 43, 1521-1534

Lawson T V (2001) *Building Aerodynamics*, Imperial College Press

Melbourne W H (1978) Criteria for environmental wind conditions. *Journal of Industrial* Aerodynamics 3, 241–9.

Peters J W H (1999). Air movements and human postural stability. Arbo Management Groep, Ergonomics 2109-E (AM) Project Organisation High Speed Line South Infrastructure (HSL South Infra), Utrecht, Netherlands,

Soligo M J, Irwin P A, Williams C J, Schuyler G D (1998) A comprehensive assessment of pedestrian comfort including thermal effects, *Journal of Wind Engineering and Industrial Aerodynamics* 77/78,753–66.

Sterling M , Quinn A, Hargreaves D, Cheli F, Sabbioni F, Tomasini G, Delaunay D, Baker C J , and Morvan H , (2010) A comparison of different methods to evaluate the wind induced forces on a high sided lorry, *Journal of Wind Engineering & Industrial Aerodynamics* 98, 10–20

White B R (1992) Analysis and wind tunnel simulation of pedestrian level winds in San Francisco, *Journal of Wind Engineering and Industrial Aerodynamics* 41-44, 2353-2364

Appendix 1 Gust probability distributions

The probability density function (pdf) for mean hourly wind speeds m_u is given by the Weibull distribution

$$f_{mu} = \frac{k}{\lambda^k} m_u^{k-1} e^{-\left(\frac{m_u}{\lambda}\right)^k} \tag{A1.1}$$

where λ and k are the well documented Weibull parameters. The cumulative density function (cdf) for a specific gust speed u with an overall mean m_u and standard deviation s_u is given by the normal distribution

$$\mu_u = 0.5 \, erfc\left(\frac{1}{\sqrt{2}}\left(\frac{u - m_u}{s_u}\right)\right) \tag{A1.2}$$

Through a process of convolution the overall probability that the gust speed will be greater than the incident (accident) wind speed $u_{i,}$ is given by

$$\mu_i = \int_0^\infty f_{mu} \, \mu_{u_i} dm_u \tag{A1.3}$$

This can be written in a dimensionless form as

$$\mu_i = \int_0^\infty k \left(\frac{m_u}{\lambda}\right)^{k-1} e^{-\left(\frac{m_u}{\lambda}\right)^k} 0.5 \, erfc\left(\frac{1}{\sqrt{2}}\left(\frac{\left(\frac{u_i}{\lambda}\right) - \left(\frac{m_u}{\lambda}\right)}{I\left(\frac{m_u}{\lambda}\right)}\right)\right) d\left(\frac{m_u}{\lambda}\right) \tag{A1.4}$$

where I is the turbulence intensity s_u/m_u. This expression needs to be evaluated numerically and a typical example is given in figure A1.1. This is plotted in the form of $\log(-\log(\mu_i))$ against $\log\left(\frac{u_i}{\lambda}\right)$, and can be seen to be a very good ft to a straight line. This implies that this characteristic follows the form of the v.d.f. of a Weibull distribution and can be empirically expressed as

$$\mu_i = e^{-\left(\frac{u_i}{\lambda}\right)^{k'}} \tag{A1.5}$$

Here k' is the modified Weibull parameter and is given by the empirical curve fit

$$k' = (1 + 0.5088I - 1.0747I^2)k - (0.3404I + 0.1395I^2)k^2 \tag{A1.6}$$

The values of k' are plotted against k and I in figure A1.2. It can thus be seen that the gust values follow a Weibull distribution, provided that modified values of the k parameter are used, and from the above equations one can specify the incident probability μ_i in a reasonably straightforward manner. Note that k' decreases as turbulence intensity decreases, which results in the expected spreading of the p.d.f at high and low wind speeds.
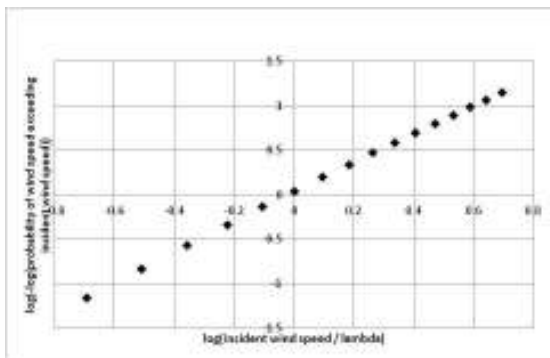
Figure A1.1 Fit of overall cumulative probability distribution to Weibull format (k=2.0, I=0.3)
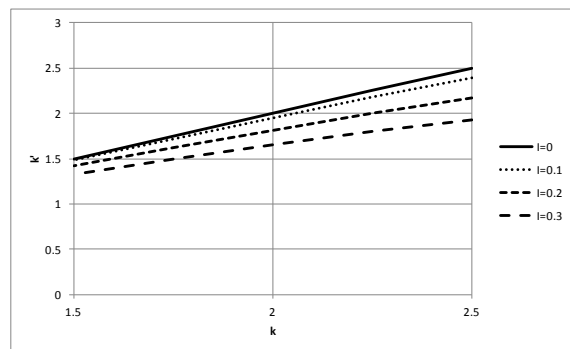
Figure A1.2 Variation of modified Weibull parameter k' with k and I

Appendix 2 Application of the methodology to train slipstreams

For the case of waiting passengers or trackside workers becoming unstable due to the air velocities in train slipstreams or wakes the current CEN procedures (CEN 2009) requires that data from at least 20 train passes be analysed. A one second moving average is applied to all the data and the peak value found for each train pass. This forms an ensemble of at least twenty gust values. The TSI velocity is then calculated as the mean plus two standard deviations of this ensemble, and is compared with the specified limit values. However this information can also be used to specify the pdf of the one second velocity in a train slipstream exceeding a certain value s. If it is assumed that this is normal, one can write

$$f_i = \frac{1}{s_s\sqrt{2\pi}} e^{-\frac{1}{2}\left(\frac{s-m_s}{s_s}\right)^2} \tag{A2.1}$$

where m_s is the mean value of the TSI velocity and s_s is the standard deviation. These values can be obtained from full scale or model scale tests for specific points relating to either trackside workers or passengers on platforms.

As in section 3, we can express the c.d.f. of a particular group of individuals becoming unstable in a particular slipstream gust velocity as

$$\mu_r = 0 \; for \; s < a$$

$$\mu_r = \frac{s-a}{b} \; for \; a < s < a + b \tag{A2.2}$$

$$\mu_r = 1 \; for \; a + b < s$$

We then need to obtain the combined probability that human instability will occur in a specified slipstream velocity through the convolution

$$\mu_{i,r} = \int_0^\infty f_i \mu_r ds \tag{A2.2}$$

which gives

$$\mu_{i,r} = 0.5(1 - \text{erf}(\beta)) + \frac{1}{\beta-\alpha}\left(\frac{1}{\sqrt{\pi}}\left(e^{-\alpha^2} - e^{-\beta^2}\right) + \frac{\alpha}{2}(\text{erf}(\alpha) - \text{erf}(\beta))\right) \tag{A2.3}$$

$$\alpha = \frac{a-m_s}{\sqrt{2}s_s} \qquad \beta = \frac{a+b-m_s}{\sqrt{2}s_s} \tag{A2.4}$$

The overall risk is then given as

$$\Omega = \left(0.5(1 - \text{erf}(\beta)) + \frac{1}{\beta-\alpha}\left(\frac{1}{\sqrt{\pi}}\left(e^{-\alpha^2} - e^{-\beta^2}\right) + \frac{\alpha}{2}(\text{erf}(\alpha) - \text{erf}(\beta))\right)\right) \tag{A2.5}$$

A series of specific reference routes can then be defined (different ratios of male to female, with and without platforms). In vehicle certification the risk off an incident on such reference routes can be determined. For route risk calculations, the risks should be calculated for every platform etc and the total risks summed and then multiplied by the number of train passes in a year to get the annual risk of an incident.

Early damage detection in wind-excited suspension bridges

Gabriele Comanducci[1], Filippo Ubertini[1], and A. Luigi Materazzi[1]

[1]Department of Civil and Environmental Engineering, University of Perugia, Italy
Corresponding author: Gabriele Comanducci, comanducci@strutture.unipg.it

Abstract

Continuous structural health assessment based on data recorded by monitoring sensors permanently installed in structures is an important challenge of the modern civil engineering. Among the various methodological approaches for structural health monitoring, methods of multivariate statistical analysis are currently receiving a deep attention because of their ability to early detect, in a fully automatic way, possible anomalies in the structural behaviour using either static or dynamic structural output response data.

With this paper, the authors propose the use of a mathematical technique based on principal component analysis and novelty detection for early damage detection in wind-excited long-span bridges. The effectiveness of the proposed technique is investigated by application to pseudo-experimental vibration response data, obtained by means of a continuum model of damaged suspension bridge under wind loading and accounting for aeroelastic effects and measurement noise.

1   Introduction

The problem of damage identification via vibration-based non-destructive testing techniques has been investigated for several years. This task can be pursued by Structural Health Monitoring (SHM) systems that link the experimental observation of the in-service response of a structure to its structural integrity. Permanent monitoring systems have been installed on many strategic structures worldwide, with several applications in bridges; sensitive features commonly considered in damage detection strategies are obtained either from their static (Alvandi and Cremona, 2006) or dynamic (Deraemaeker et al., 2008) responses.These quantities are typically affected by changes in environmental and operational conditions (Sohn, 2007), such as temperature, humidity, wind speed and traffic, that may hide the effects induced by damage. From this reason, the need for appropriate strategies able to eliminate such effects arises.

Multivariate statistical techniques based on Principal Component Analysis (PCA) (Yan et al., 2005) and novelty detection are currently being established as very powerful tools to eliminate the effects of changes in environmental/operational conditions and to detect the damage. In such techniques, data obtained from structural response in operational conditions are acquired and used to build a reference model. Deviations from such a reference model are identified on a statistical basis and associated with a possible damage (Magalhaes et al., 2012).

Within the context of SHM, wind sensitive slender structures, such as long-span bridges, pose the additional challenge of exhibiting significant apparent variations of their modal parameters with incoming wind speed as a consequence of aeroelastic effects. The removal of such aeroelastic effects from monitoring data have been rarely investigated in the literature. For this reason, following previous research on the topic (Ubertini, 2013, 2014), in the present paper the authors propose the application of a technique for wind effects removal and early damage detection in wind-excited long-span bridges.

The paper is organized as follows. Section 2 presents the theoretical background; Section 3 briefly introduces the analytical model and discusses the results of some parametric analysis; Section 4 model investigates damage detection applied to pseudo-experimental data generated from the same analytical

and Section 5 concludes the paper.

2   Theoretical background

In the practice of the health assessment one of the first basic step consists of the choice of proper quantities suitable for damage identification purposes. Many of these quantities, often already available in the literature, are generally related to the dynamic properties of the structure. In the present paper, natural frequencies are chosen as features enabling condition assessment of long-span bridges because they are easily identifiable even with a limited number of sensors.

A commonly adopted multivariate statistical analysis technique is then employed to depurate frequency estimates from the effects of changes in the incoming wind speed and for damage detection. This part of the paper is therefore devoted to briefly presenting the theoretical background on the two main tools of the procedure: PCA and novelty detection.

2.1   Principal Component Analysis

PCA is a multivariate statistical method *explaining the variance-covariance structure of a set of variables through a few linear combinations of these variables*. The field of application of such method is rather wide and, in the specific case of structural dynamics, PCA has been often applied in reduced-order modeling and modal analysis. In more recent years, such technique has revealed to be particularly effective for damage detection purposes: indeed it is capable to efficiently remove environmental and operational factors from damage-sensitive features, and, if compared to other methods, presents the main advantage of working without the knowledge of the environmental parameters which are taken into account as embedded variables.

In the context of the investigated problem, PCA tries to reduce the variability of natural frequency estimates by removing linear correlations among the data, entailing, in this way, the compression of the same data without loss of essential information. The effectiveness of the procedure is bonded to the respect of the hypothesis that most of the variability of the natural frequencies is explained by environmental factors which produce linear or weakly non-linear effects on these.

Let us denote with $\mathbf{Y} \in \mathrm{R}^{n \times N}$ the observation matrix containing N samples of the frequency estimates of n vibration modes of the structure. These data are remapped into the vectorial space generated by the so-called Principal Components (PCs) that constitute an orthogonal basis. The remapped matrix, $\mathbf{X} \in \mathrm{R}^{n \times N}$, called the score matrix, is written as

$$\mathbf{X} = \mathbf{TY} \tag{1}$$

where $\mathbf{T} \in \mathrm{R}^{n \times n}$ is the loading matrix, obtained by performing the Singular Value Decomposition (SVD) of the covariance matrix of the original data as follows:

$$\mathbf{YY^T} = \mathbf{U\Sigma^2 U^T} \tag{2}$$

and setting

$$\mathbf{T} = \mathbf{U^T} \tag{3}$$

Each column of the loading matrix contains the coefficients of a singular PC, while Σ^2 is a diagonal matrix containing the singular values of the covariance matrix, which represent the variance contribution of each PC.

Dealing with experimental data, a limited number, l, of PCs usually suffice to reconstruct the major part of the variance allowing to reduce the loading matrix to the rectangular matrix $\hat{\mathbf{T}} \in \mathrm{R}^{n \times l}$ obtained by taking into account only the first l columns of the matrix $\mathbf{T}$. The retained information in this step is described by the residual error matrix $\mathbf{E}$ which can be estimated by first remapping the data into the original space using $\hat{\mathbf{T}}^{\mathrm{T}}$, and then computing $\mathbf{E}$ as

$$\mathbf{E} = \mathbf{Y} - \hat{\mathbf{Y}} = \mathbf{Y} - \hat{\mathbf{T}}^T \mathbf{X} = \mathbf{Y} - \hat{\mathbf{T}}^T \mathbf{T} \mathbf{Y} \tag{4}$$

By performing the SVD of the covariance matrix on data collected within a training period t_0 of sufficient length, during which the structure can be assumed in a reference healthy state, the residual error matrix $\mathbf{E}$ is expected to be relatively insensitive to variations in environmental factors and should be capable of highlighting anomalies that were not observed during the training period: for example those induced by the occurrence of a damage. Literature results suggest that t_0 should be long enough, so that a nearly complete record of environmental and operational conditions is considered during the training period. On the other hand, in the present paper the authors are interested to check the effectiveness of the methodology also in the case of shorter training periods, for instance lasting just a few months, which is of interest for new bridges.

2.2   Novelty Index Analysis for damage detection

Once the quantity insensitive to environmental factors, that is the residual error, has been defined using Eq. (4), a novelty detection algorithm is implemented to automatically detect anomalies in the data: each observation that deviates so much from other observations is called an *outlier* and it is designated to be generated by a different mechanism, for example the occurrence of a damage.

In the present paper, novelty detection is pursued by computing the following novelty index:

$$T^2 = r \cdot \left(\overline{\mathbf{E}} - \overline{\overline{\mathbf{E}}} \right)^T \cdot \mathbf{S}^{-1} \cdot \left(\overline{\mathbf{E}} - \overline{\overline{\mathbf{E}}} \right) \tag{5}$$

and constructing a proper control chart. In Eq. (5), r is an integer parameter, $\overline{\mathbf{E}}$ is the mean of the residuals in the subgroup of the new r observations, while $\overline{\overline{\mathbf{E}}}$ and $\mathbf{S}$ are the mean of the residuals and the covariance matrix of the original data, respectively, computed in the training period t_0. An outlier, that is a value of T^2 greater than an Upper Control Limit (UCL), is likely considered to be an indication of the damage. In the paper, the UCL is statistically computed as the value corresponding to a cumulative frequency of 95% in the training period. According to the adopted damage detection procedure, the novelty index is updated after a group of r new observations, is acquired and the probability of having a false alarm is equal to 5%.

3   Damage versus aeroelastic effects in long-span bridges

In the case of long-span bridges, one of the environmental factors producing the most significant effects on structural dynamic properties is represented by the speed of the incoming wind flow. The reason is that self-excited aeroelastic loads acting on the deck are directly related to wind speed and determine apparent modifications of modal parameters. In the specific case of natural frequencies, it is worth to underline that the effects produced by wind are greater, or at least comparable, than those in duced by damage. Such circumstance makes the identification of damage through a simple and direct observation of the natural frequencies unfeasible. Therefore, the present section is devoted to quanti-

Figure 1. Continuum model of suspension bridge with damaged main cable (a), lift and pitching moment per unit length acting on the deck (b).
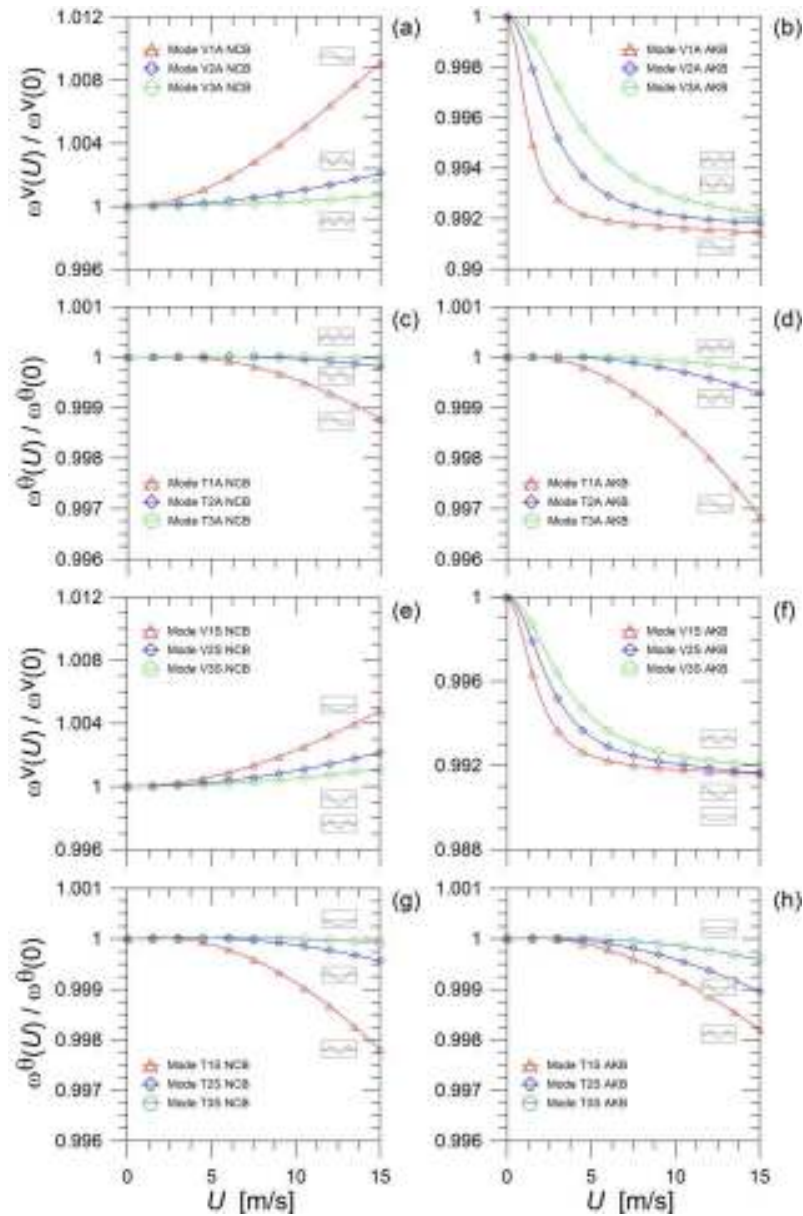
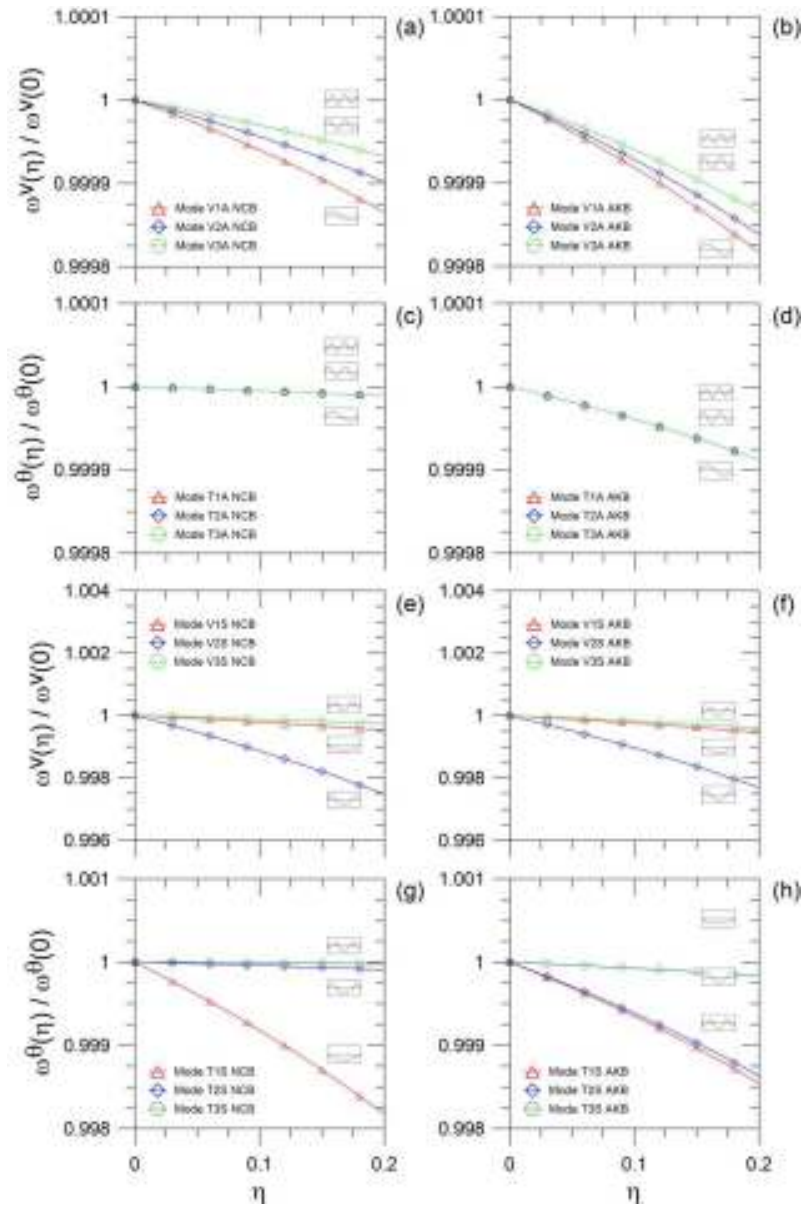Figure 2. Aerodynamic effects on symmetric and antisymmetric, vertical and torsional, modal frequencies for the New Carquinez Bridge (left side) and the Akashi Kaykio Bridge (right side).

fying and comparing variations in modal frequencies caused by damage with those produced by changes in the incoming wind speed.

3.1 Analytical model

The model adopted in the following analysis is a continuum model of a single-span, damaged suspension bridge whose coupled vertical-torsional motion is produced by the excitation of a turbulent wind which blows in the cross-deck direction and has a mean speed, U (Figure 1).

The bridge is composed by two shallow main cable, a stiffening girder and a uniform distribution of vertical hangers. The main cables, placed at a distance $2b$, are hinged at fixed anchors placed at the same vertical elevation and are modeled as mono-dimensional linearly elastic continua with negligible flexural and shear rigidities. The deck is modeled as a uniform, linear elastic beam with Euler-Bernoulli flexural behaviour and classic De Saint Venant torsional behaviour. The hangers are uniformly distributed, massless and inextensible. Modal damping ratios of 0.5% are assumed for all modes retained in the model. The damage scenario in the bridge is represented by a diffused cross-

Figure 3. Damage effects on symmetric and antisymmetric, vertical and torsional, modal frequencies for the New Carquinez Bridge (left side) and the Akashi Kaykio Bridge (right side), for varying the damage intensity factor η.

section reduction of one main cable near the tower saddle, which is region mostly prone to fretting fatigue. The considered damage is fully described by three non-dimensional parameters: damage intensity factor, $\eta \in [0; 1]$, extension factor, δ, and position factor, γ, respectively.

The wind loading on the bridge induces aerodynamic and aeroelastic loads on the deck which are represented by the lift, L_{tot}, and the piching moment. M_{tot} per unit length. The classic hypothesis of superposition principle allows to write such loads as sums of buffeting and self-excited components. The former are digitally generated under the assumption of modelling the turbulent wind field as a multivariate Gaussian stochastic process (Carassale and Solari, 2002), while the latter are modelled through the widely adopted formulation based on indicial functions (Chobsilprakob et al., 2011).

After straightforward computations, the equations of motion of the aeroelastic system can be written in the classical first order form as follows

$$\dot{\mathbf{x}} = \mathbf{A}\mathbf{x} + \mathbf{B}\mathbf{\Lambda} \qquad (6)$$

where $\mathbf{x}$ is the state vector, $\mathbf{A}$ is the aeroelastic system matrix, containing inertial, damping and stiffness terms, including aerodynamic contributions to these quantities, $\mathbf{\Lambda}$ is the buffeting wind
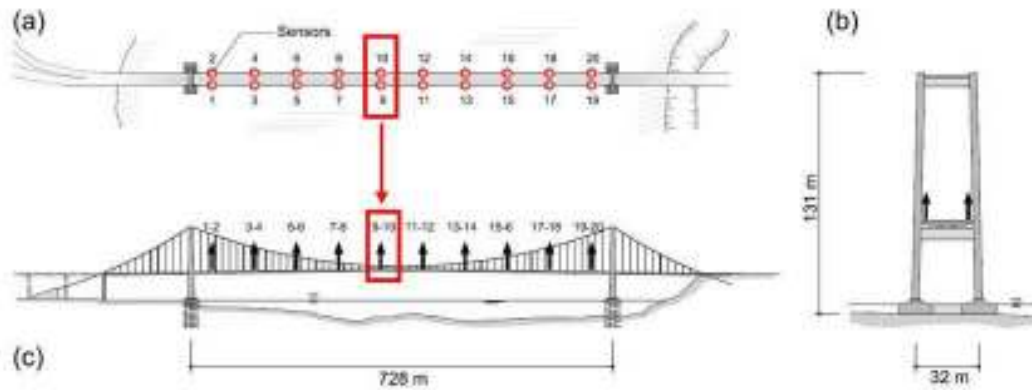
Figure 4. Case study bridge with ideal sensors' layout: plan (a), cross section (b) and elevation (c).

loading vector and **B** is the collocation matrix.

It is noteworthy that the aeroelasic system matrix **A** , and consequently the modal properties of the system, depend upon both damage characteristics and wind speed. All the details concerning the formulation of the analytical model can be found in Ubertini (2013, 2014).

3.2 Wind effects

Variations of eigenfrequencies with wind speed are investigated by solving the eigenvalue problem of the aeroelastic system, Eq.(6), assuming different values of wind speed (varied from 0 to 15 m/s). Moreover, with the purpose of enhancing the role played by the aerodynamic properties of the deck, the tests are carried out for two different bridges with different deck types. The first one is the New Carquinez Bridge (NCB) characterized by a streamlined cross section, flexible under an aerodynamic point of view. The second one is the Akashi Kaikyo Bridge (AKB) which has a truss-type stiffened cross-section and can be considered as rigid under wind action.

In Figure 2 some of the obtained results are shown. The charts concern the apparent variations of the natural frequencies of the first three symmetric and antisymmetric, vertical and torsional modes expressed in terms of ratios between apparent frequencies, obtained for $U > 0$, and structural ones (obtained for U=0). Because of their different aerodynamic properties, substantially different trends can be observed for the two different deck types, especially in the case of the vertical modes. Moreover, it is worth noting that the frequency ratios of vertical modes of the Akashi Kaikyo Bridge are seen undergo greater variations at lower values of the wind speed, while they tend to stabilise above a certain threshold, around 5 m/s. On the contrary, the behaviour of the frequency ratios of the New Carquinez Bridge is more uniform both for torsional and vertical modes.

The hereafter, the following notation will be adopted to state the modes: V stands for vertical, T for torsional, A and S stand for antysimmetric and symmetric, respectively, while the number denotes the order of the mode.

3.3 Damage effects

In order to evaluate damage effects on natural frequencies and successively have a direct comparison with those induced by wind action, an analysis similar to that presented in Section 3.2 is carried out.

As demonstrated in previous works (see for instance Ubertini, 2014), natural frequencies are almost not influenced by damage position, while they are affected in quantitatively similar ways by damage intensity and extension. For this reason, the following parametric analysis is conducted for fixed values of δ and γ , equal to 0.05 (which means the 5% of the cable length) and 0.025, respectively, while only the damage intensity, η, is varied from 0 to 0.2, corresponding to a cross section reduction in one main cable ranging from 0 to a remarkable 20%.

Figure 3 shows the results of the parametric analysis in terms of ratio between damaged and unda-

maged frequencies both for the New Carquinez Bridge and for the Akashi Kaykyo Bridge. As it can be observed from these results, damage-induced frequency variations are comparatively more significant in symmetric modes than in antisymmetric ones for both bridges. The most sensitive modes are the second symmetric vertical and the first symmetric torsional ones, exhibiting frequency variations with an average rate of about 0.015%, for every 1% reduction in cable cross-section, η. Changes in frequencies of other modes are so small that they essentially lose any practical interest.

The comparison between wind and damage effects highlights that wind effects on frequencies, even if decreasing in the higher order modes, are always more significant than those induced by damage. This may suggest that the identified modal parameters, in general, cannot be directly used for damage detection purposes because the effects of environmental factors (wind speed) are superimposed to damage effects.

4   Damage detection

Application of the damage detection technique reviewed in Section 2 to pseudo-experimental dynamic response data is presented in this section. To this purpose, 365 consecutive days of aeroelastic dynamic response of the analytical model briefly introduced in the previous section is simulated under turbulent wind action.

Considering the hypothesis of linear or weakly non-linear dependence of natural frequencies upon environmental factors in the application of PCA, the analytical model is specialized with the geometric, mechanical and aerodynamic properties of the New Carquinez Bridge which better fits with this condition, as shown in the previous parametric analysis.

Vertical accelerations of the bridge are generated in 20 points along the main span. These points, whose spatial layout is shown in Figure 4, ideally represent the locations of the sensors of a monitoring system installed on the bridge. The position of the sensors, located on both the sides of 10 equidistant cross-sections of the girder, allows to identify both vertical and torsional modes.

The generation of the wind-excited response of the bridge is carried out with a time step of 0.05 sec. Consecutive one-hour-long time histories of structural response are generated by using one-hour mean wind speed data obtained from a real wind time history downloaded from National Data Buoy Center for an open sea site at 10 m elevation. The overall 10-minutes mean wind speed historical data collected in 2005 and 2006 for station no. 46026, LLNR 357, are selected in this work, hourly down-sampled and converted to the site and elevation of the NCB by using the classic logarithmic law for the wind profile (roughness length of 0.001 m and boundary layer height of 300 m).

Data generated from the analytical model are corrupted by adding a white noise with a standard deviation of 6e-5 m/s^2 which could be considered as a quite high noise level. Figure 5 depicts the difference between a typical acceleration signal before and after being corrupted by noise. The selected signal represents the acceleration at mid-span for a typical wind event.

4.1   Frequency tracking and removal of wind effects

Modal properties of the bridge are identified from simulated responses by means of a fully automated data-driven Stochastic Subspace Identification procedure applied to time windows of one-hour length. The first three symmetric and antisymmetric vertical and torsional identified frequencies ($n = 12$) are considered in the observation matrix, $\mathbf{Y}$, introduced in Section 2.

The $\mathbf{Y}$ matrix is built through an automated frequency tracking procedure, based (i) on a double similarity check on both frequency values and mode shapes (MAC value) which allows to avoid multiple modes selection and (ii) on the probabilistic procedure of the *Expectation Maximization algorithm* which permits to replace the missing identified modes. These last are probably due to low signal to noise ratios leading to inability to identify higher order modes.

Because estimated modal frequencies are closely correlated with wind speed, they are also correlated with each other. This is the reasone why the time histories of identified modal frequencies, obtained by applying the automated tracking technique, highlight wind-induced fluctuations, with superimposed random errors associated with the inherent approximations in output only modal identification.

The first step towards damage detection consists in a preliminary analysis aimed at evaluating the
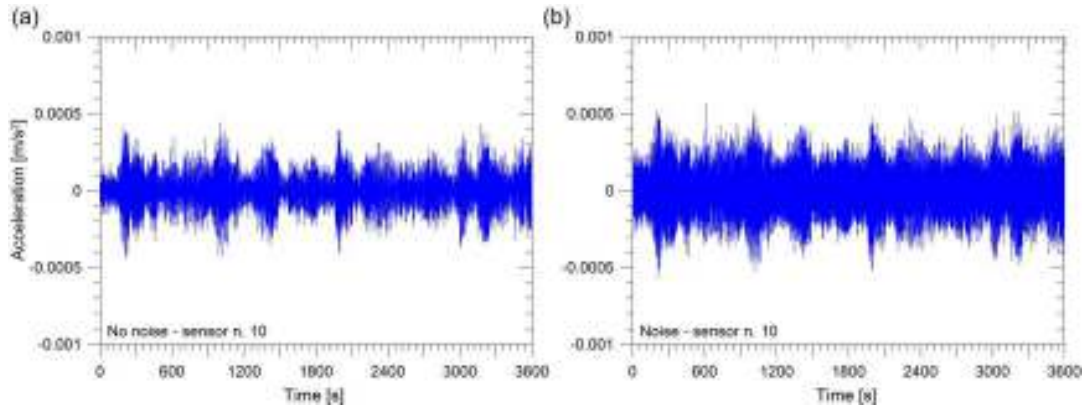
Figure 5. One hour of acceleration registration acquired by sensor n. 10, before (a) and after (b) noise addition.

importance of each PC in terms of variance of the data. A proper choice of the number of retained PCs should allow to accurately remove wind effects from identified eigenfrequencies, by reducing the dimension of the problem without loss of effectiveness in damage detection. Such analysis whose results are not reported here for sake of brevity, suggests to retain 6 PCs. The cleaned data are those contained in matrix $\hat{\mathbf{Y}}$, Eq. (4), and the PC coefficients are computed considering a training period t_0 of 240 days. In the present application, the need for eliminating a relatively large number of PCs can be justified by the circumstance that the PCs have comparable weights in terms of variance, because of the presence of one single variable (the wind speed) affecting the data. Figure 6 shows raw and cleaned data for the first vertical antisymmetric mode when retaining 6 PCs, in the case of original and noised data, respectively. The difference between the two frequency time histories is not very marked because of the effectiveness of modal identification procedure. However it is noted that a quite larger number of missing modes was observed in the case of data corrupted by noise.

4.2   Damage detection and outlier analysis

Damage effects are simulated by imposing, at a given date (t_d, day n° 300), a shift in identified frequencies that is computed through the analytic model for varying damage parameters (Section 3). The artificially imposed damage, although relatively severe (γ =0.025, δ=0.05, η=0.10), is not visible even in the detailed view of the frequency time histories of the most damage-sensitive modes. Thus, damage identification through a simple visual inspection of frequency time histories is unfeasible.
The effectiveness of the damage detection procedure described in Section 2 is tested by considering three damage scenarios. They are all characterized by the same damage position, close to one support (γ =0.025) and extension δ=0.05, while they are characterized by different damage inten sities: (i) η=0.025 (small damage), (ii) η=0.05 (moderate damage) and (iii) η=0.10 (severe damage).
   Such damage scenarios produce relative changes, Δf_{max}, of the most damage-sensitive frequency (the one of the second symmetric vertical mode) equal to: (i) 0.02%, (ii) 0.05% and (iii) 0.11%. The
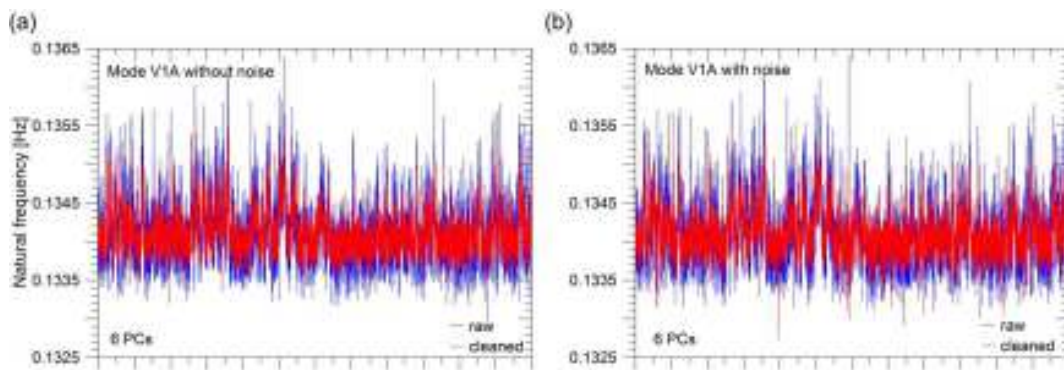
Figure 6. Time history of identified frequency of the 1st antisymmetric vertical mode before and after application of the PCA: results obtained with the original (a) and noised (b) data.
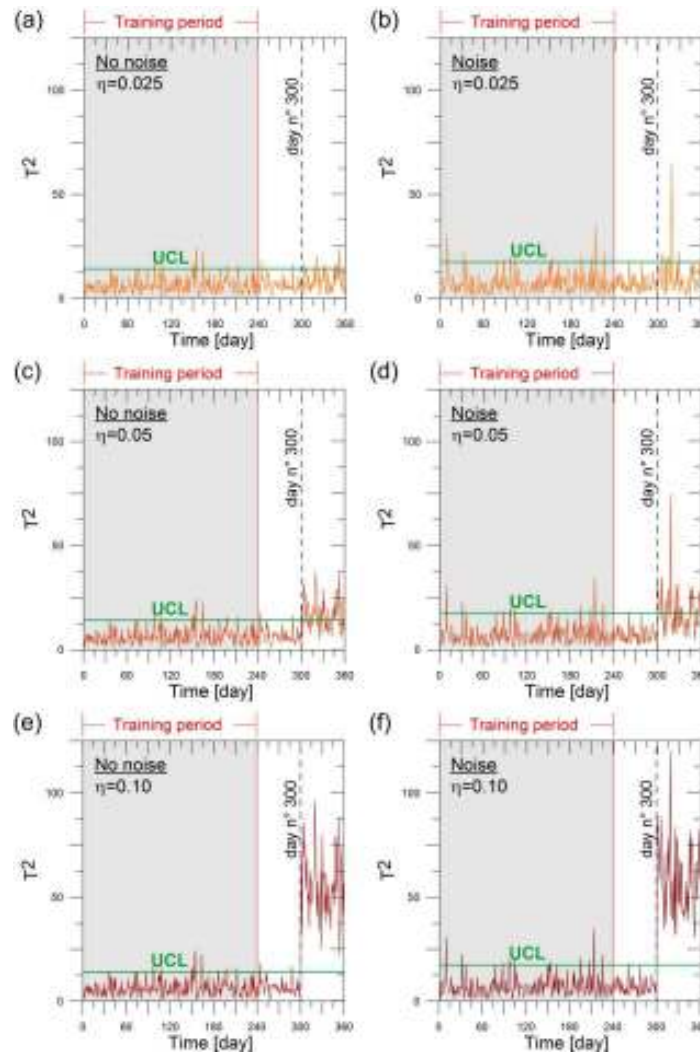
Figure 7. Control charts of three different damage intensity scenarios for original (a,c,e) and noised (b,d,f) data.
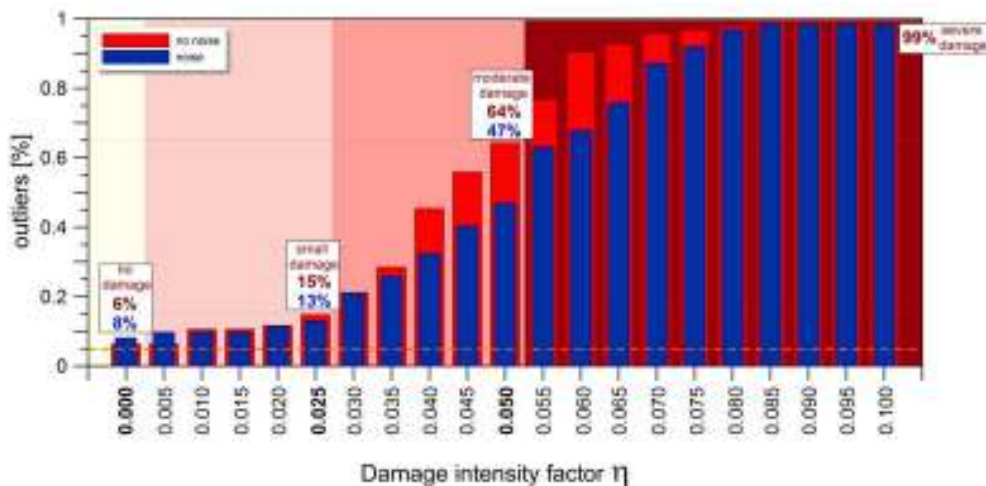
Figure 8. Outlier analysis on original and noised data for varying the damage intensity factor η .

control charts obtained in these three scenarios are depicted in Fig. 7 retaining 6 PCs, assuming t_0=240 and t_d=300 and choosing $r = 24$, Eq. (5).

The presented results show that, at first glance, there is not much noise effect and that theprocedure is effective regardless the level of noise. However, the difference is apparent in term of percentage of outliers in the damaged period, as shown in Figure 8. In such figure, the results of a

systematic outlier analysis are presented for varying damage intensity factor, η, and computing the corresponding percentage of outlier in the damaged period (from t=300 to t=360). From the obtained results it is clear that the presence of noise determines an increase of outliers in the undamaged case and a loss of accuracy of the procedure in the region of small and moderate damage, while the procedure can be considered equally effective for severe damage.

5   Conclusions

The paper has investigated the use of natural frequency tracking and multivariate statistical analysis for vibration-based damage detection in long-span bridges under wind loading with particular reference to short monitoring periods. Taking suspension bridges as meaningful examples, an elastodynamic parametric bridge model with damage in one main cable and subjected to turbulent wind loading has been adopted for comparing damage-induced variations of natural frequencies with apparent variations of frequencies associated with changes in incoming wind speed and produced by aeroelastic effects. This first analysis has been carried out by considering two sample suspension bridges with different deck sections, in order to highlight the role played by the aerodynamic properties of the bridge.

The analytic model has been also used for generating bridge response data under turbulent wind loading. Natural frequency estimates have been extracted from such pseudo-experimental data and have been used for damage detection through a technique based on principal component analysis and novelty detection. The results demonstrated that, with a proper tuning of some salient parameters, such mutivariate statistical analysis procedure is able to remove aeroelastic effects from frequency estimates and enables detection of small damages consisting of little reductions of the cross-section of one main cable also in the case of data corrupted by a significant level of measurement noise.

References

Alvandi, A., Cremona, C., (2006). Assessment of vibration-based damage identification techniques, *J. Sound Vib*, **292** (1-2), 179-202.

Deraemaeker, A., E., R., De Roeck, G., Kullaa, J., (2008). Vibration based structural health monitoring using output-only measurements under changing environment, *Mech. Syst. Signal Pr*. **22** (1), 34-56.

Sohn, H., (2007). Effects of environmental and operational variability on structural health monitoring, *Phil. Trans. R. Soc. As.*, **365** (1851), 539-560.

Yan, A., Kerschen, G., De Boe, P., Golinval, J., (2005). Structural damage diagnosis under varying environmental conditions part i: a linear analysis, *Mech. Syst. Signal Pr.*, **19** (4), 847-864.

Magalhaes, F., Cunha, A., Caetano, E., (2012). Vibration based structural health monitoring of an arch bridge: From automated oma to damage detection, *Mech. Syst. Signal Pr.* **28**, 212-228.

Ubertini, F., (2013). On damage detection by continuous dynamic monitoring in wind-excited suspension bridges, *Meccanica* **48** (5), 1031-1051.

Ubertini, F., (2014). Effects of cables damage on vertical and torsional eigenproperties of suspension bridges, *J. Sound Vibr.* **333** (11), 2404-2421.

Carassale, L., Solari, G., (2002). Wind modes for structural dynamics: a continuous approach, *Probabilistic Eng. Mech.*, **17** (2), 157-166

Chobsilprakob, P., Suthasupradit, S., Kim, K., (2011). Aeroelastic analysis of long span bridges via indicial functions considering geometric and material nonlinearity, *Int. J. Steel Struct.*, **11** (2), 215-226.

Aerodynamic forces on a NACA 0015 airfoil in dry and iced states

Emanuele Mattiello

Hydro- and Aerodynamics, FORCE Technology, Denmark
emmi@force.dk

Abstract

Denmark is designing a novel aeroacoustic-aerodynamic National Wind Tunnel (NWT) facility specifically dedicated to testing of wind turbine blades. FORCE Technology is involved in the design of this new wind tunnel, which will not be equipped for icing test. In this perspective the author conducted a test campaign on a NACA 0015 airfoil section model, to measure aerodynamic forces in dry and iced conditions. The tests were performed in the DTU/FORCE Technology's Climatic Wind Tunnel (CWT), which was demonstrated suitable for ice testing of airfoil profiles. The results obtained from the tests were compared with literature, both in term of ice accretions and aerodynamic coefficients. The work conducted so far is planned to be extended to further develop the simulation of in-cloud icing as well as tune a CFD code for aerodynamics prediction of iced airfoil.

1   Introduction

1.1   Research framework

The Danish Ministry of Science, Innovation and Higher Education decided in May 2012 to establish a new wind tunnel at Risø Campus - Technical University of Denmark (DTU), as a part of the national research infrastructure for the development of next generation's wind turbines, in the frame of the ambitious target to set the entire Danish energy supply as fully-renewable by 2050 (Bak et al., 2011).

The wind tunnel is being designed by specialists from DTU, FORCE Technology and two Swedish consultancy companies, Fluid Thinking and CreoDynamics. According to the specifications, the tunnel will be capable of reaching wind speeds up to 105m/s inside the 2.2x3.3m^2 test section. The latter will be equipped with 'Kevlar' walls and surrounded by an anechoic room – similarly to that of Virginia Tech Wind Tunnel (Remillieux et al., 2008) - to satisfy both aerodynamic and aeroacoustic requirements, making the facility unique worldwide. Another requirement of the Danish national research infrastructure is to include a facility to perform climatic wind tunnel tests. FORCE Technology is actively collaborating to reach this target, upgrading one of its in-house facilities, the DTU/FORCE collaborative Climatic Wind Tunnel (CWT), to test airfoils and wind turbine components in a velocity range up to 32m/s, in critical climatic conditions, i.e. with ice accretion. The CWT has a test section of 2x2m^2 and its cooling unit is capable of controlling and keeping a long-term average temperature down to -10°C, depending on the wind speed (Georgakis et al., 2009). A rotatable spray bar system is located in the settling chamber after the honeycomb, and allows the simulation of in-cloud icing conditions, (Demartino, 2014).

The work presented here was initiated to confirm the potential of the CWT facility, originally designed specifically for experiments with structural cables, for testing of wind turbine blade sections and components. Static tests were conducted on a NACA 0015 airfoil in the CWT, in dry and iced states. Drag, lift and pitching moment were measured via force gauges for different wind angles of attack from horizontal to approximately stall. Results from the tests were compared to literature.

1.2   Icing on airfoils

Non- conventional sites, e.g. cold climates, are becoming more and more exploited for the installation of wind turbines, due to lack of more favourable sites and the increasing demand for the use of

renewable resources, (Hudecz et al., 2013). In Denmark as in other Nordic countries including Greenland, the right atmospheric conditions for the ice to accrete on rotor blades of wind turbine can be found for significantly long periods over the year. During the rotation of the blades, more and more ice is collected around the stagnation point of the airfoil, with increasing thickness towards the outer part of the blade, due to the increased velocity, see Figure 1.1, (Seifert and Richert, 1997). Drag and pitching moment increase and the lift diminishes, affecting significantly the power production of the wind turbine. The accreted ice can cause long term vibration and fatigue problems as well. Icing on wind turbine blades has been studied by many, both experimentally and numerically, e.g. (Seifert and Richert, 1997, Jasinsky et al., 1998 and Makkonen et al., 2001). More generally, the effects of ice on wing aerodynamics have been extensively reviewed by Lynch and Khodadoust (2001).

Nevertheless, icing wind tunnel tests of blades remain a challenge. In particular in-cloud icing tests that simulate the in-cloud atmospheric icing in a controlled environment, require special facilities that produce a cloud, a mix of air and water with the proper liquid water content - LWC≈0.2g/m^3 - and median volume diameter - MVD≈10-50μm - (Demartino, 2014), and at the same time are capable of controlling the temperature of air in the tunnel, making the right conditions for in-could icing to happen. In-cloud icing is classified in rime, glaze and mixed ice, see e.g. (Cattin, 2012).

Rime ice is formed when super cooled liquid water droplets from clouds or fog are transported by the wind and hit a surface, freezing immediately. If the droplets are rather small, soft rime is formed, if the droplets are bigger, hard rime is formed. Soft rime typically forms at temperatures below -8°C while hard rime typically forms between -2°C and -8°C. Hard rime is an opaque/white ice formation which adheres firmly on surfaces. The density of hard rime ice ranges typically between 600 and 900kg/m^3, (ISO 12494). Soft rime is a fragile, snow-like formation consisting mainly of thin ice needles or flakes of ice. The growth of soft rime starts usually at a small point and grows triangularly into the windward direction. The density of soft rime is usually between 200 and 600 kg/m^3, (ISO 12494). Glaze is caused by freezing rain, freezing drizzle or wet in-cloud icing and forms a smooth, transparent and homogenous ice layer with a strong adhesion on the structure. It usually occurs at temperatures between 0 and -6°C. Glaze is the type of ice having the highest density of around 900 kg/m^3. Wet in-cloud icing occurs when the surface temperature is near 0°C. The water droplets which hit the surface do not freeze completely. A layer of liquid water forms which, due to wind and gravity, may flow around the object and freeze also on the leeward side. The liquid accretion is accompanied by the formation of icicles, whose growth is driven by a balance between gravity and wind drag. Mixed ice is the mixture of glaze and rime ice.

Besides the flow and cloud conditions, thermodynamics is the other aspect ruling the accretion process. Considering a steady-state heat balance of the icing surface, its temperature depends on several processes such as dynamic heating, freezing of droplets, ice sublimation and heat exchange between droplets and surface, (Mazin et al. 2001). The accretion type and shape are therefore significantly affected by the thermal properties of the structure/surface where the ice accretes.
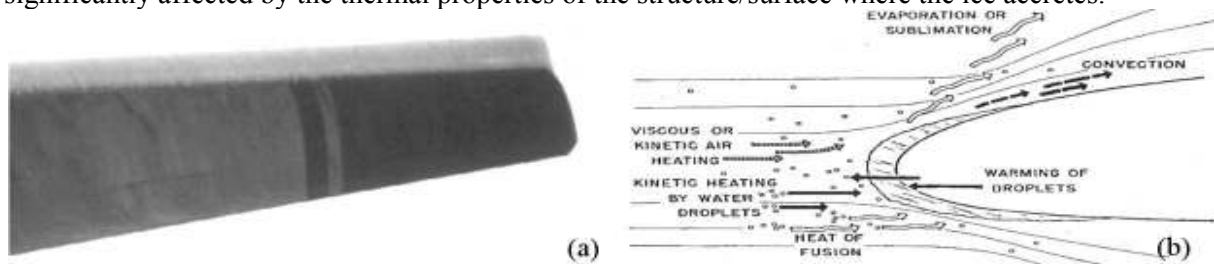
Figure 1.1. Iced wind turbine blade (Seifert and Richert, 1997) (a), and illustration of the thermodynamic processes at the icing surface (Mazin et al., 2001) (b).

When considering cold climatic simulations, that maintain air temperature below freezing and include clouds of supercooled droplets, it is extremely important to control the flow uniformity, air temperature and its stability, liquid phase characteristics (LWC and MVD), cloud uniformity as well as surface temperature distribution and local heat transfer coefficient during the accretion process, in order to have a better understanding of the phenomena. For the present test campaign, flow and cloud variables as well as the aerodynamic coefficients were monitored during the accretion process while the liquid phase characteristics were estimated on average ex post.

2   Experimental work

The closed-circuit CWT at FORCE Technology has originally been designed for testing of structural cables, (Georgakis et al., 2009). Extensive research work on cable aerodynamics has been done so far, in the frame of a joint research project between DTU and FORCE Technology, founded by Femern A/S, (Georgakis et al., 2013). Plain cables have been studied by Matteoni and Georgakis (2012) with focus on surface roughness and cross-sectional distortion, Figure 2.1a. Twin cables have been studied statically and dynamically by Acampora and Georgakis (2013) and Mattiello el al. (2013), respectively, Figure 2.1b. Today's cable surface modifications have been investigated and innovative surface modifications to prevent rain-wind induced vibrations (RWIV) have been proposed by Kleissl and Georgakis (2012), Figure 2.1c. The research was conducted in both dry and simulated rain conditions.

Figure 2.1. Wind tunnel test on a plain cable (Matteoni and Georgakis, 2012) (a), a filleted twin-cable (Mattiello et al., 2013) (b) and a new cable surface modification (Kleissl and Georgakis, 2012) (c).

The CWT is equipped with a 15 nozzles spray bar for testing of models in simulated in-cloud icing conditions, see Figure 2.5a. Section models of plain bridge cable hangers and stays were tested with ice accretion by Demartino (2014), Figure 2.2a and Figure 2.2b, respectively. Similarly, Koss et al. (2013) tested iced filleted and pattern-indented cables. Preliminary icing tests on a NACA 64-618 airfoil were performed by Hudecz et al. (2013), see Figure 2.2c.

Figure 2.2. In-cloud ice accretion on a bridge hanger (a), and on a stay cable (b) (Demartino, 2014) and on a wind turbine blade (Hudecz et al., 2013) (c).

To support the research on airfoils being established at the National Wind Tunnel (NWT) and continue with the development of the CWT including the in-cloud icing system, a new experimental work on an airfoil was initiated in the CWT. Static tests were conducted on a symmetric airfoil section model, NACA 0015, both in dry and iced states. Dry static tests were conducted for varying wind angle of attack until approximately the beginning of the stall region and served as reference case. The iced state was investigated simulating two in-cloud icing conditions – generating rime and glaze accretions - for three different model pitch angles. The effect of the ice presence on the airfoil aerodynamics was measured for several wind angles of attack. Parallel to this, a numerical study is ongoing considering both dry and iced states. For the latter, the 'Dispersed Multiphase model' is employed, see (FORCE, 2014). The present paper describes the results obtained to date.

The hand made section model of a NACA 0015 tested by Gaunaa (2002), was restored to fit the CWT. It is a symmetric airfoil with a chord length of c=0.38m and a span-wise length of l=1.98m. The central section of the model is cladded by 'Plexiglas' due to the presence of pressure tap rings, Figure 2.3b, while the rest of the model is made of high density foam 'Divinycell H' supported by an aluminium core. For the present test campaign the model was coated with a self-adhesive black plastic foil 'd-c-fix', Figure 2.3c, to better homogenize the surface of the model and improve the visual contrast of the ice accreting on the surface, during icing tests. The model was connected to a 3-component static gauge in either end. The newly designed static rig, Figure 2.3a, supported the load gauges which were positioned outside the test section to maximize the model aspect ratio and

minimize the air flux from the test section to the instruments. The rig is also capable of controlling the pitch angle of the model with 1° precision.
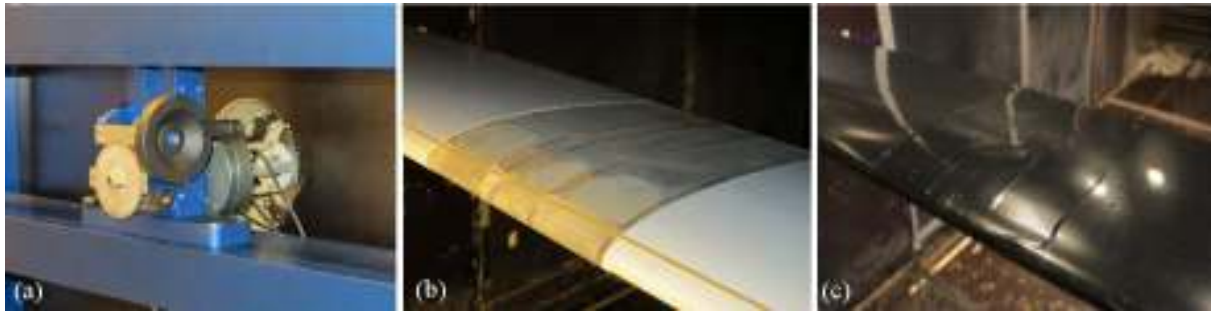
Figure 2.3. Static rig (a) and uncoated (b) and coated (c) NACA0015 section model mounted in the CWT.

The model was positioned horizontally at test section mid-height. The gauges measure X- and Y-forces and Z-moment about the centre of rotation of the section model, defined at 1/4 of the chord length downstream of the leading edge, Figure 2.4. The reference pressure was measured with a Pitot tube placed 2.3m upstream the model and 0.4m below the test section ceiling. A second reference Pitot tube was placed 2.3m upstream of the model and 0.55m from the test-section floor. A third Pitot tube was used for preliminary measurements in the wake. It was positioned at a distance 3/4 of the chord length downstream of the trailing edge and moved vertically. The entire set-up and measuring chain was verified by testing a 40mm by 40mm square cylinder as reference.
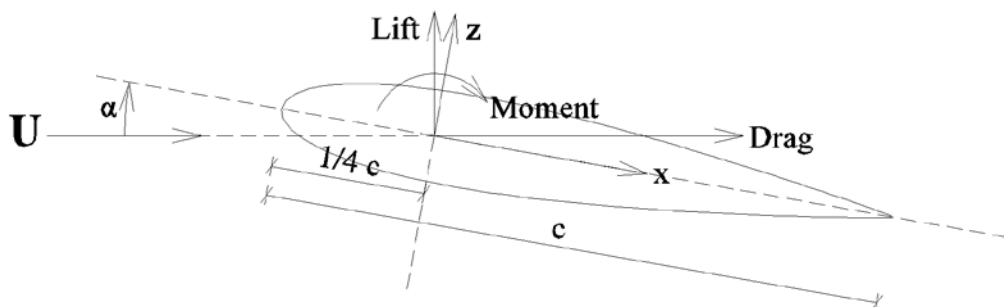
Figure 2.4. Reference coordinate system and definition of angle of attack α.

The spray bar currently installed in the CWT was designed by Demartino (2014) based on previous experiments in the CWT. Few components, e.g. air caps, fluid caps, gaskets and connection fittings are cleaned and substitute regularly to keep optimal the spray, see Figure 2.5a-b. Air compressors and water pump have been optimized and now capable of feeding the nozzles with nearly constant pressures over time, up to one hour and more, see Figure 3.2a. Profile measurements were conducted at the inlet and at the model location, in the empty wind tunnel except for the icing spray bar placed horizontally, see Figure 2.5a. At the inlet of the test section the longitudinal turbulence intensity was found to be I_u=0.67% in the free stream and 0.96% in the wake of the spray bar. At the model location the turbulence intensity was I_u=0.70% and 0.81% in the free stream and in the wake of the spray bar, respectively. Overall, the smooth flow condition was respected being I_u<1%. The longitudinal component of the velocity was found to be uniformly distributed across the test section.
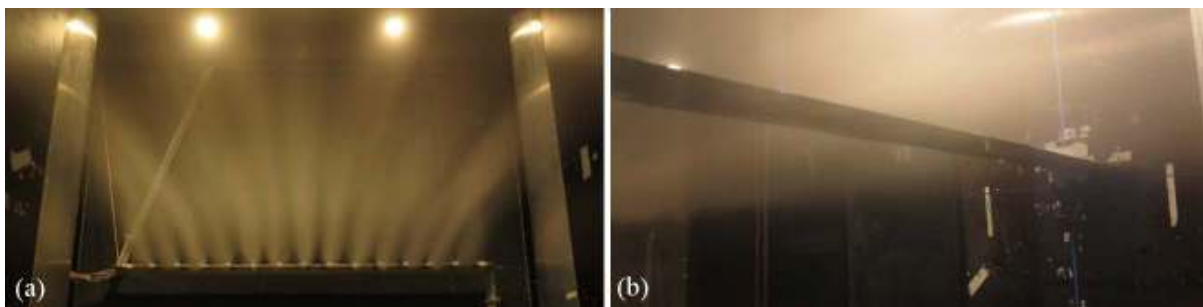
Figure 2.5. Uniformity of the cloud exiting the spray bar (a) and impacting the model (b).

3   Results and discussion

3.1   Dry state

Results of tests in dry conditions are presented in Figure 3.1 in terms of aerodynamic force coefficients defined as $C_i=F_i/(qcl)$, where F_i is the measured force in the i-direction, q is the dynamic pressure, c the chord length and l the section model length. Moment coefficients are also included and defined similarly, except for the factor c^2 instead of c, at the denominator. Blockage correction was applied according to ESDU 76028. The largest blockage area ratio, at 15° wind angle of attack, was estimated to be 5.5%. At 0° wind angle of attack the blockage area ratio was 2.9%. Lift and drag forces and pitching moment were measured for three wind velocities corresponding to Reynolds number (Re, based on c) of about $2.5 \cdot 10^5$ ($\triangleright$), $3.8 \cdot 10^5$ ($\bigcirc$) and $5.5 \cdot 10^5$ ($\Diamond$). No significant Re dependency was observed in the range ±10° of wind angles of attack. The test results (black curves) were compared to literature (colored curves) both experimental data (Gaunaa, 2002 – solid line and Sheldahl and Klimas, 1981 – dash-dotted line) and numerical data (Airfoil Tools, 2013 – dotted line and preliminary CFD data (FORCE, 2014) – dashed line). The lift coefficient was found in good agreement with literature in the full range of the investigated wind angles of attack. Stall was observed for wind angles of attack larger than |10°| with a lift coefficient around ±1.0. The drag coefficient from force balance measurements was observed to be larger ($C_d \approx 0.016$) than reported in literature ($C_d \approx 0.01$-0.014). The deviation is possibly explained by differences in model surface roughness, boundary conditions and/or measuring technique among the compared set-ups. The drag coefficient at 0° was estimated to be $C_d \approx 0.014$ from preliminary wake measurements. The measured moment coefficient resembled the overall trend of literature data, but the scatter between the different curves is significantly large from 10° and above. From the test results it seemed that the model was not completely symmetric being $C_l \neq 0$ at 0° angle of attack and the slightly asymmetry of C_d and C_m curves.
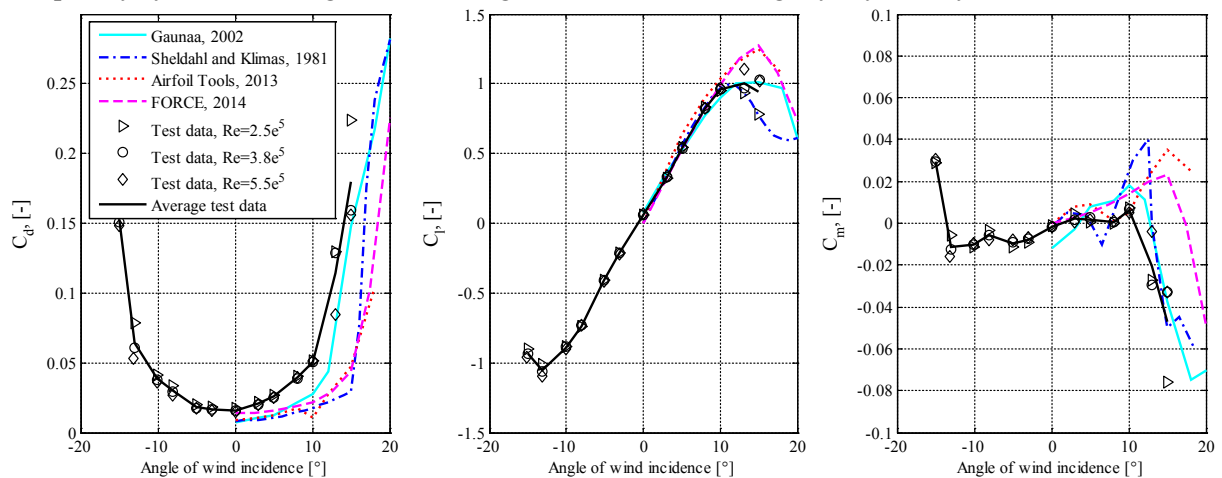
Figure 3.1. Aerodynamic coefficients of NACA 0015 in dry state.

3.2   Iced state

The iced state was investigated by reproducing in the CWT favourable climatic conditions for the formations of two types of ice: rime ice and glaze ice. The boundary and climatic conditions applied during the accretion phase are shown in Table 3.1 for all six accretion tests. All the reported values in Table 3.1 are values averaged over one hour of ice accretion. The temperature inside the test section was oscillating harmonically around the mean value with a period and amplitude of approximately 600s and 1.2°C, see Figure 3.2a. The air pressure was very stable around the mean value over time, while the water pressure assumed a 'saw-tooth' pattern due to the activation of the pump at intervals of about 350s, see Figure 3.2a. The dynamic pressure at the test section was also found to decrease over time – about 10% after one hour of in-cloud exposure, see Figure 3.2a. This was due to the circulation of the droplets inside the tunnel and the consequent accumulation of ice on several components of the tunnel such as guide vanes, fan supports, etc. Improvement of the heating of those components is ongoing, to further limit the dynamic pressure loss during ice accretion simulations.

Table 3.1. Boundary and climatic conditions during icing tests.

Accretion test ID	Model pitch angle	Wind speed	Temperature	Air pressure	Water pressure	LWC*	MVD**	Mass accreted	Max accretion
	[°]	[m/s]	[°C]	[Pa]	[Pa]	[g/m³]	[µm]	[g/m]	[mm]
R0	0	9.8	-5.3	3.9	3.7	0.23	10	245	24
R5	+5	9.4	-5.4	4.1	3.7	0.22	9	188	22
R10	+10	9.2	-5.4	4.1	3.7	0.22	9	167	25
G0	0	9.4	-0.9	4.1	3.7	0.22	9	238	13
G5	+5	9.7	-1.7	3.6	3.7	0.23	12	363	10
G10	+10	9.7	-1.8	3.6	3.7	0.23	12	310	13

*   based on measurements of the spray in the CWT, after Demartino (2014)
**   estimated from spray nozzle supplier 'Spraying System Co.'

From the analysis of the boundary and climatic conditions during the accretion tests, mean water pressure values were very consistent while the mean air pressure was varying a little between the tests, leading to homogeneous values of MVD. LWC was also very consistent given the small variation in wind speed. The difference in wind speed for the rime ice tests, R#, linked linearly to the difference in accreted mass of ice. The higher temperature of test G0 compared to G5 and G10, is reflected in a lower accreted mass of ice. A distinct feature found on the accretion for all six tested cases was the reduced ice thickness in the central section of the model, accompanied by a more compact and dense ice formation, see Figure 3.2b-c. It is conjectured that this is a direct consequence of the thermodynamic process, namely the heat exchange between droplets and surface, (Mazin et al., 2001). In fact there is a material discontinuity at the model mid-section, see Section 2 and Figure 2.3b. The Plexiglas of the central segment of the model has a thermal conductivity $\lambda \approx 0.17$, while the value for foam is typically $\lambda \approx 0.035$. Therefore, even if the distribution of surface temperature of the model was not monitored during the accretion phase, it was no doubt higher in the mid section, affecting considerably the ice accretion.
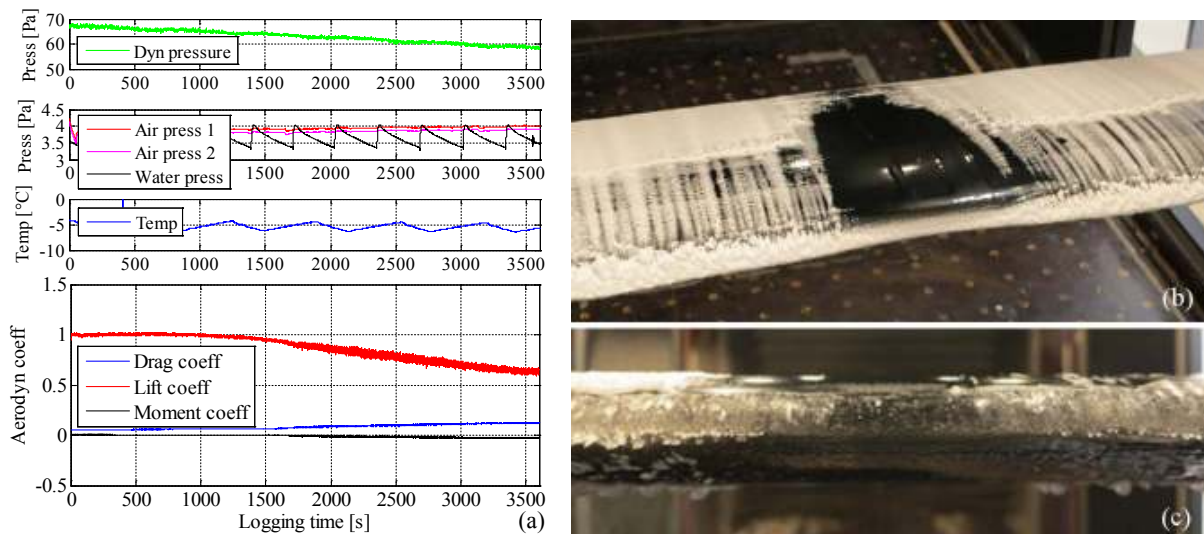
Figure 3.2. Variation of boundary and climatic conditions and aerodynamic coefficients during the accretion phase of test R10 (a), and different ice accretion at the model mid-section due to uneven thermal properties, for test R0 (b) and test G0 (c).

The particular arrangement of the test set-up, see Section 2, allowed a reliable and continuous monitoring of the aerodynamic forces and moment of the airfoil as the ice accretion was progressing. None of the earlier icing tests in the CWT achieved this. An example of variation of aerodynamic coefficients is plotted in Figure 3.2a, for test R10. The frequency content of the measured aerodynamic forces and moment during accretion and their variation over time during the accretion phase was post-processed by means of wavelet analysis, see (Ansell and Bragg, 2013). The main features of the wavelet transform were found substantially independent of the pitch angle of the model during accretion, and similar for rime and glaze accretions. A representative wavelet power spectrum is

presented for accretion test R10. It showed a decrease over time of the third lowest eigen-frequency from 39Hz to 36Hz. This is believed to be linked to the increasing mass of accreted ice. The first two eigen-frequencies, 18.5Hz and 28Hz, appeared stable during the ice accretion. Noticeable is also the increased spectrum values for frequencies around and below the first eigen-frequency after approximately half an hour of in-cloud exposure. This is reflected by the increased rms response of the lift coefficient, see Figure 3.2a, indicating the possible activation of a dynamic mechanism. In this perspective, no further analysis has been conducted to date.
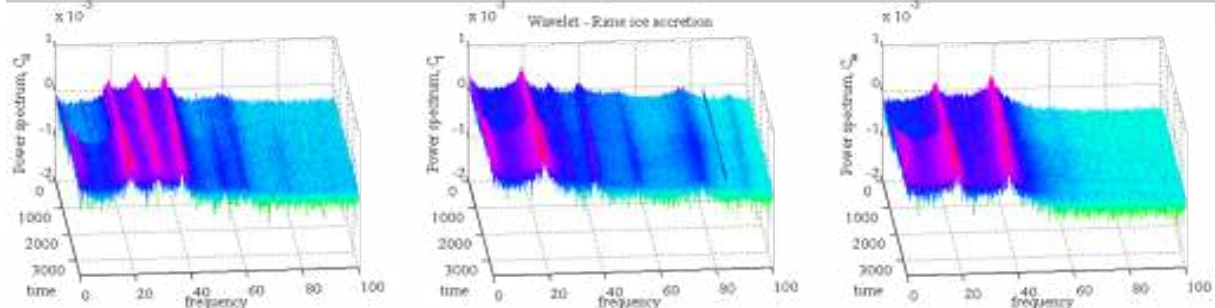
Figure 3.3. Wavelet power spectrum of aerodynamic coefficients during accretion test R10.

3.2.1   Rime ice accretion

The main characteristics of the rime ice accretion observed after the in-cloud icing simulations R0, R5 and R10, are documented in Figure 3.4 by means of pictures and sketches of the ice cross section determined by cutting the ice at the end of each test. The accretion in all three tests presented a distinct horizontal core wall indicating the stagnation line. The line was present throughout the entire span of the model and its position obviously depended of the angle of the approaching wind compared to the airfoil. Above and below the stagnation line, an area covered with hard rime in a feather like pattern was found. The distance from the feathers front to the root in the upper side and lower side of the airfoil was found dependent of the model pitch angle during accretion, see contour trace in Figure 3.4. Downstream the feathers root a flow out area with flow out accumulation was present, while towards the tail, the wing was covered with soft rime.
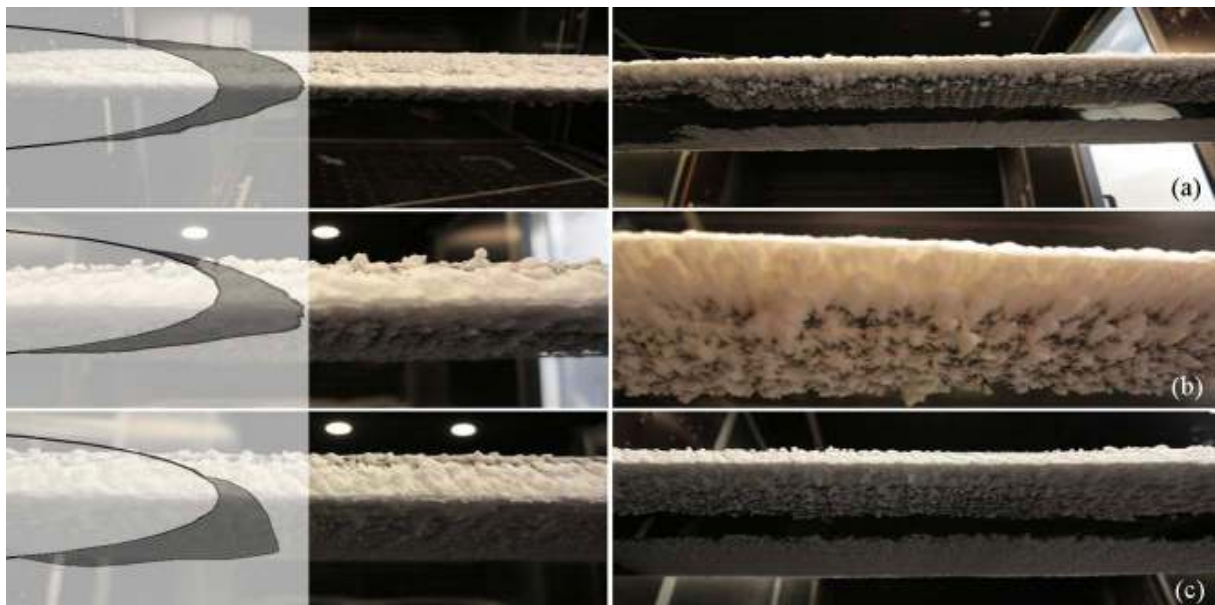
Figure 3.4. Rime ice accretion, R0 (a), R5 (b) and R10 (c).

3.2.2   Glaze ice accretion

Similarly to the rime ice tests, the main characteristics of the glaze ice accretion observed in tests G0, G5 and G10, are documented in Figure 3.5 by means of pictures and sketches of the ice cross section. The accretion in all three tests presented a distinct horizontal core wall indicating the stagnation line. The line was present throughout the entire span of the model and its position was a function of the

wind pitch angle during accretion. Directly above the stagnation line a glazed area was found with sharp spikes pointing against the wind and glazed smaller feathers, compared to the rime ice tests. After the glazed area, runback water traces were found. At the tail of the wing, a layer of soft rime was accumulating. Below the stagnation line the glazed area was less wide then above and icicles were forming at approximately regular spacing. The orientation of the icicles was a function of aerodynamic and gravity forces. Further downstream, traces of soft rime built up in the wake of the icicles.
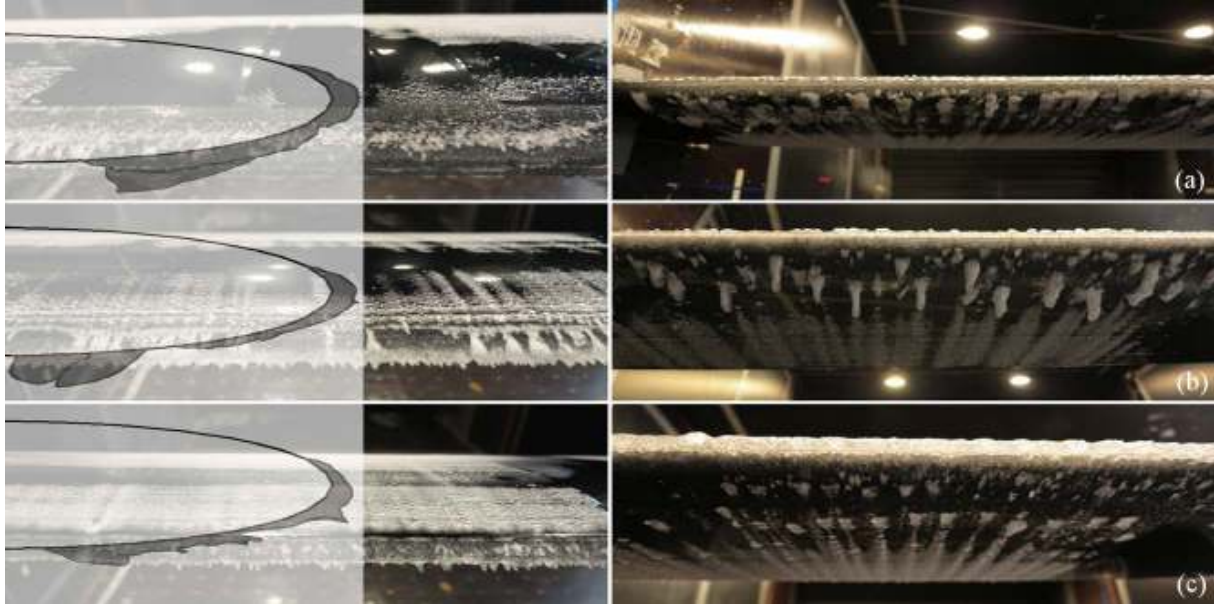
Figure 3.5. Glaze ice accretion, G0 (a), G5 (b) and G10 (c).

3.2.3   Aerodynamics of iced NACA 0015

The aerodynamics of the rime ice accreted airfoil was studied measuring the aerodynamic coefficients at $0°$, $\pm 3°$, $\pm 5°$, $\pm 8°$, $\pm 10°$, $\pm 13°$, $\pm 15°$ wind angle of attack after one hour ice accretion at $0°$, $+5°$ and $+10°$, tests R0, R5 and R10, see Table 3.1. The aerodynamic coefficients were defined based on the original chord length c, similarly to the dray case. Blockage correction was applied in a similar manner, (ESDU 76028). Coefficients were measured at two different Re number, showing an overall independency of the aerodynamics to the wind speed. Results are plotted against the reference data, i.e. airfoil in dry state without ice, see Figure 3.6.
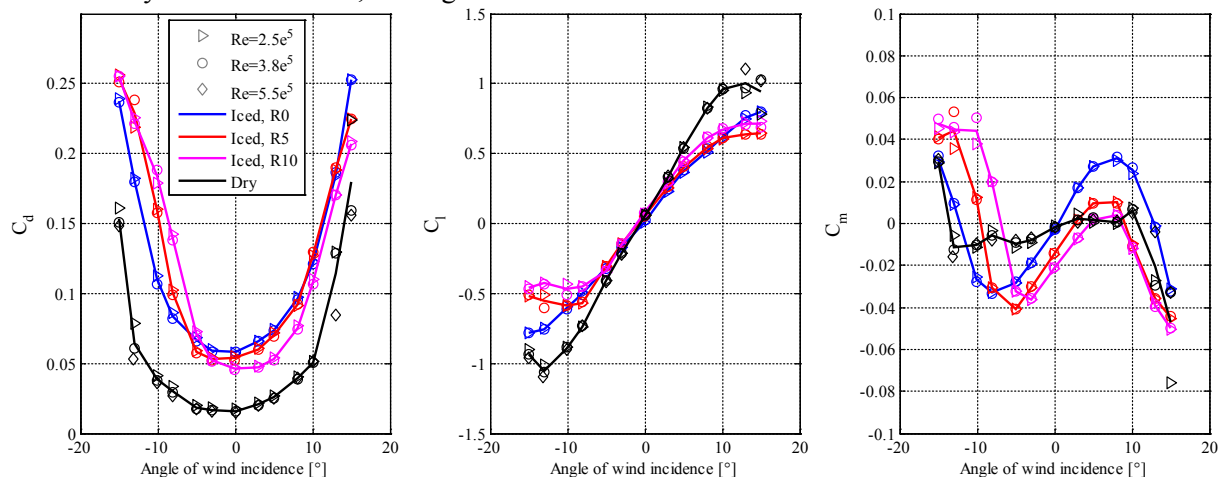
Figure 3.6. Aerodynamic coefficients of NACA 0015 with rime ice accretion.

The drag coefficients were significantly increased, $\approx 200\%$, $C_d \approx 0.05$, for the iced airfoil compared to the dry case, in agreement with Lynch and Khodadoust (2001). The increase in drag was reducing from test R0 to R10 in a linear fashion. For positive wind angles of attack the results showed higher drag for R0 compared to R5 and R10 respectively, while the trend was reversed for negative angles of attack. A degradation of the lift coefficient for the iced airfoil was found. It became significant, 20-

50%, above ±8° pitch angle in agreement with Lynch and Khodadoust (2001). Furthermore, the lift curve became more and more asymmetric from test R0 to R10, and stall occurred 4-6° earlier compared to the dry state. Lift at 0° remained in the range $C_l \approx 0$-0.05 for all tested conditions. Similarly to the lift, the moment coefficient curves became more and more asymmetric from R0 to R10. The moment coefficient at 0° was found to decrease from 0 to -0.02 from test R0 to R10. Overall, due to the presence of ice, i.e. growth of the chord length, the moment coefficient was increasing dramatically, see (Seifert and Richert, 1997).

The aerodynamics of the glaze ice accreted airfoil was studied with the same approach followed for the rime ice case. Three accretion cases were considered, G0, G5 and G10, see Table 3.1. Coefficients were found to be Re independent. Results are plotted against the reference data, i.e. airfoil in dry state without ice, see Figure 3.7.
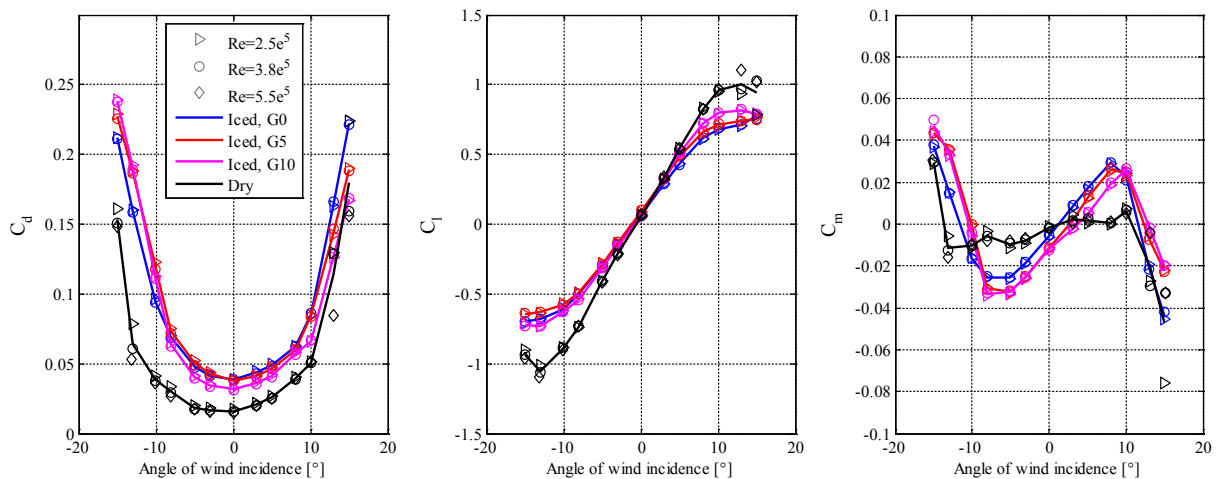
Figure 3.7. Aerodynamic coefficients of NACA 0015 with glaze ice accretion.

The drag coefficients were significantly increased, ≈100-150%, $C_d \approx 0.04$, for the iced airfoil compared to the dry case, in agreement with Lynch and Khodadoust (2001). The increase in drag was found lower for test G10 compared to test G0 and G5. Generally, the drag of the iced airfoil was higher for negative wind angles compared to positive angles. The difference in drag values between G0, G5 and G10 was less pronounced compared to the tests with rime ice, R0, R5 and R10. A consistent degradation in the lift coefficient of about 30% was found for the iced airfoil throughout the entire wind angle of attack range, (Lynch and Khodadoust, 2001). Lift at 0° remained at $C_l \approx 0.06$ for all tested conditions. Lift of the airfoil with glaze ice was found less dependent to the pitch angle of the accretion, compared to the rime ice case. The moment coefficient at 0° was found to decrease from nearly 0 to -0.01 from test G0 to G10. Also in this case the moment coefficient was increasing noticeably, see (Seifert and Richert, 1997). The difference between G5 and G10 was less evident though, compared to the rime case, R5 and R10.

4   Conclusion

The aerodynamics of a NACA 0015 airfoil was wind tunnel studied in dry and iced states. In-cloud icing conditions were successfully recreated in a climatic wind tunnel. Climatic conditions and aerodynamic coefficients were monitored during the accretion process. The degradation of the performance of the airfoil during accretion will be further analyzed. The aerodynamics of the ice accreted airfoil was measured for different ice types and accretion angles. The results compared well with literature. Further work is ongoing to tune a CFD code for prediction of iced airfoil performance.

References

Acampora, A., and Georgakis, C. T. (2013). Aerodynamic coefficients of plain and helically filleted twin circular cylinders for varying wind angles of attack. *6th European and African Conference of Wind Engineering, Cambridge, UK.*

Airfoil Tools. (2013). Tools to search, compare and plot airfoils.
   url: *http://airfoiltools.com/airfoil/details?airfoil=naca0015-il*

Ansell, P. J., and Bragg, M. B. (2013). Characterization of ice-induced low-frequency flowfield oscillations and their effect on airfoil performance. *31st AIAA Applied Aerodynamics Conference, San Diego, California, USA.*

Bak, C., Sørensen, J. N., Rasmussen, F., Madsen, H. A., Sørensen, N. N., Gaunaa, M., Mikkelsen, R., Mann, J., Hansen, M., Koss, H. H., and Georgakis, C. T. (2011). Large national wind tunnel facility at DTU, Denmark: Suggested specifications. *Risø-I-3188(EN), Technical University of Denmark, Roskilde, DK.*

Cattin, R. (2012). Icing of wind turbines. Vindforsk projects, a survey of the development and research needs. *Elforsk report 12:13, Stockholm, SE.*

Demartino, C. (2014). Aerodynamics and aeroelastic behaviour of ice accreted bridge cables. *Ph.D. thesis. Department of structures for engineering and architecture, University of Naples Federico II, Naples, IT.*

ESDU 76028. (1995). Lift-interference and blockage corrections for two-dimensional subsonic flow in ventilated and closed wind tunnels.

FORCE Technology. (2014). 114-20840. CFD prediction of aerodynamic forces on NACA 0015 airfoil. Preliminary internal report. *Kgs. Lyngby, DK.*

Gaunaa, M. (2002). Unsteady Aerodynamic Forces on NACA 0015 Airfoil in Harmonic Translatory Motion. *Ph.D. Thesis, Technical University of Denmark, Kgs. Lyngby, DK.*

Georgakis, C. T., Koss, H. H., and Ricciardelli, F. (2009). Design specifications for a novel climatic wind tunnel for testing of structural cables. *8th International Symposium on Cable Dynamics, Paris, FR.*

Georgakis, C. T., Jakobsen, J. B., Koss, H. H., Larsen, S. V., Macdonald, J. H. G., Riccardelli, F., and Svensson, E. (2013). Understanding and controlling wind-induced vibrations of bridge cables: Results from the Femern Crossing research project. *6th European and African Conference of Wind Engineering, Cambridge, UK.*

Hudecz, A., Koss, H. H., and Hansen, M. O., (2013). Ice accretion on wind turbine blades. *15th International Workshop on Atmospheric Icing of Structures. St. John's, Newfoundland and Labrador, CA.*

ISO 12494. (2001). Atmospheric icing of structures.

Jasinski, W. J., Noe, S. C., Selig, M. S. and Bragg, M. B. (1998). Wind turbine performance under icing conditions. *Journal of Solar Energy Engineering* **120**, 60-65.

Kleissl, K., and Georgakis, C. T. (2012). Comparison of several innovative bridge cable surface modifications. *7th International Colloquium on Bluff Body Aerodynamics and Applications, Shanghai, CN.*

Koss, H. H., Henningsen, J. F., and Olsen, I. (2013). Influence of icing on bridge cable aerodynamic. 1*5th International Workshop on Atmospheric Icing of Structures. St. John's, Newfoundland and Labrador, CA.*

Lynch, F., and Khodadoust, A. (2001). Effects of ice accretions on aircraft aerodynamics. *Progress in Aerospace Science* **37**, 669-767.

Makkonen, L, Laasko, T., Marjaniemi, M., and Finstad, K. J. Modelling and prevention of ice accretion of wind turbines. *Wind Energy* **25(1)**, 3-21.

Matteoni, G., and Georgakis, C. T. (2012). Effects of bridge cable surface roughness and cross-sectional distortion on aerodynamic force coefficients. *Journal of Wind Engineering and Industrial Aerodynamics* **104-106**, 176-187.

Mattiello, E., Eriksen, M. B., and Georgakis, C. T. (2013). Determination of aerodynamic damping and force coefficients of filleted twin cables in dry conditions through passive-dynamic wind tunnel tests. *6th European and African Conference of Wind Engineering, Cambridge, UK.*

Mazin, I P., Korolev, A. V., Heymsfiel, A., Isaac, G. A. and Cober, S. G. (2001). Thermodynamics of icing cylinder for measurements of liquid water content in supercooled clouds. *Journal of Atmospheric and Ocean Technology* **18**(4), 543-558.

Remillieux, M. C., Crede, E. D., Camargo, H. E., Burdisso, R. A., Devenport, W. J., Rasnick, M., Van Seeters, P., and Chou, A. (2008). Calibration and demonstration of the New Virginia Tech anechoic wind tunnel. *14th AIAA/CEAS Aeroacoustic Conference, Vancouver, British Columbia, CA.*

Seifert, H., Richert, F. (1997). Aerodynamics of iced airfoils and their influence on loads and power production. *European Wind Energy Conference '97, Dublin Castle, IE.*

Sheldahl, R. E. and Klimas, P. C. (1981). Aerodynamic characteristics of seven symmetrical airfoil sections through 180-degree angle of attack for use in aerodynamic analysis of vertical axis wind turbines. *SAND80-2114, Sandia National Laboratories, New Mexico, USA.*

Physical modeling of spatial fluctuating wind fields and its applications

J. Li[1], Y.B. Peng[1] and Q. Yan[1]

[1]State Key Laboratory of Disaster Reduction in Civil Engineering,
Tongji University, Shanghai 200092, P.R. China
Corresponding author: J. Li, lijie@tongji.edu.cn

Abstract

A stochastic model of fluctuating wind fields represented by Fourier spectrum functions is proposed in physical scenario of atmospheric turbulence, which includes three components related to amplitude spectrum, phase spectrum and phase delay spectrum, respectively. According to the law exposed in the energy spectrum of fluctuating wind speeds, an exponential amplitude model in form of bilinear functions in log-log coordinates defined as stochastic Fourier wave-number spectrum is first estabilished. A univariate phase model defined as stochastic Fourier phase spectrum is then developed which relies upon just a random argument associated with the concept of starting-time of phase evolution. A phase delay spectrum model towards the representation of spatial coherence of stochastic wind fields is proposed. For validatied purpose, the measurement data of wind field at a certain site East China is used. A TV tower with height of 388 m subject to spatial fluctuating wind field is explored, which indicates the proposed stochastic model exhibiting the potential application for the accurate analysis and reliability evaluation of random wind-induced responses of engineering structures.

1   Introduction

The modeling of fluctuating wind speeds is a challenge in the investigation of wind engineering, which underlies the computation and analysis of wind-induced structural responses. The fluctuating wind flow could be viewed as a non-stationary component of atmospheric turbulence in essence. It is a traditional thought in wind engineering that the energy distribution of fluctuating wind speeds is represented by density function of a certain power spectrum. A number of models, in the context of this thought, has been proposed and investigated for decades (Von Karman,1948; Davenport, 1961; Kaimal et al, 1972), which gains the benefits from the engineering applications. Due to the complexity of the turbulence, however, the probabilistic information inherent with the fluctuating wind speeds is extremely difficult to be secured just using the density function of power spectrum. For the wind-excited structure, moreover, only the second-order statistics of its responses can be afforded through the scheme of power spectrum, which results in the impossibility of accurate assessment of structural reliability.

Using the stochastic Fourier functions, however, the model of dynamic excitations can be obtained (Zhang et al, 2008). This model includes the physical essence of excitations, and the complete probabilistic information as well. Besides, the stochastic Fourier functional scheme is readily to be integrated with the probability density evolution method (PDEM) (Li and Chen, 2008; 2009), allowing for an accurate reliability assessment of highly-dimensional nonlinear systems subjected to complex random excitations. It was demonstrated to be an efficient method for the reliability analysis of wind-excited structural systems (Zhang et al, 2008). Having this knowledge, the present paper is dedicated to establishing a stochastic model for spatial fluctuating wind speeds. This model is derived from the physical perspective of atmospheric turbulence by implementing the representation of succinct parameters of the model towards securing the probabilistic behaviors of spatial fluctuating wind speeds in a more rational manner.

2   Modeling of Amplitude Spectrum Component (Modeling I)

It was shown from theoretical analysis and measured data on the energy spectrum of turbulence that the mathematical structure of the energy-containing sub-domain at energy-containing scale conforms with the rule of "-1" power law while that of the inertial sub-domain at energy-balance scale conforms with the rule of "-5/3" power law (Hinze, 1975). An exponential amplitude model in form of bilinear functions in log-log coordinates is defined as stochastic Fourier wave-number spectrum:

$$|F(k)| = \begin{cases} \sqrt{\alpha_1} \dfrac{u_*}{(\kappa z k_c)^{1/3}} k^{-1/2} & (k_l < k \le k_c) \\[3mm] \sqrt{\alpha_1} \dfrac{u_*}{(\kappa z)^{1/3}} k^{-5/6} & (k \ge k_c) \end{cases} \tag{1}$$

where α_1 denotes the Kolmogorov constant of one-dimensional energy spectrum; k_c denotes the cut-off wave number; k_l denotes a lower-boundary of wave number; u_* denotes the shear wave speed; κ denotes the von Karman's constant; z denotes the height of spatial point of interest. These parameters eventually connect to the ground roughness length z_0 and 10-min mean wind speed U_{10}, which are referred to as the elementary random variables of this component model.

Towards obtaining the measured data of strong winds, we built up an observation platform at a certain site of East China in 2006. Four supersonic anemometers were mounted on the main tower at 10m, 20m, 28m and 43m along the height of the anemometer tower, respectively, as shown in Figure 1.
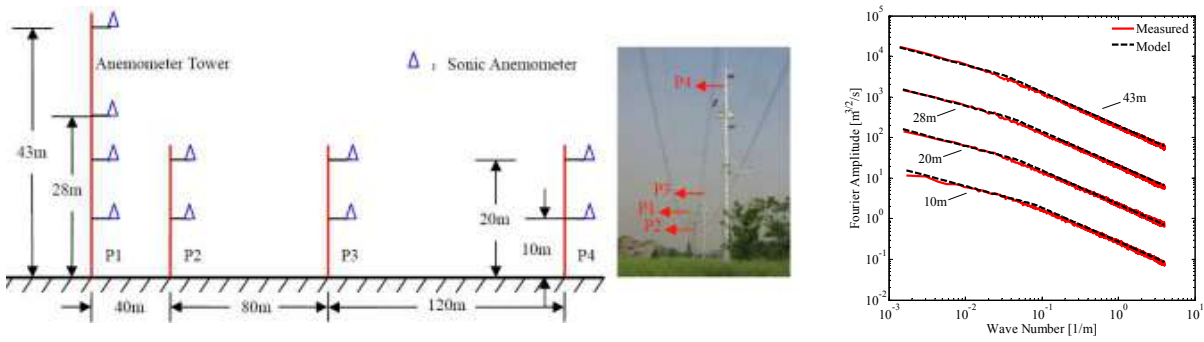
Figure 1. Schematic diagram of four supersonic anemometers mounted on the anemometer tower. Figure 2. Mean of model and measured Fourier amplitude spectrum at height 10m; 20m; 28m and 43 m.

A collection of sample wind speeds from measured data at different heights of the anemometer tower can be obtained. The mean of model and measured Fourier amplitude spectrum at height 10m, 20m, 28m and 43 m are shown in Figures 2. For the clear exposure, the curves labeled 20m, 28m and 43m all move up parallelly along vertical axis of which the amplitude is enlarged 10, 100 and 1000 times, respectively. It is seen, nevertheless, that the mean of model and measured Fourier amplitude spectrum is numerically very close.

3   Modeling of Phase Spectrum Component (Modeling II)

It is noted that a time-history sample of wind speed can be viewed as the integration of a series of harmonic waves propagating from the time where all the inertial phases are zeros to the time T_e. the simulated phase spectrum of real time history can thus be readily built up as the following univariate function:

$$\varphi(n, T_e) = v(n)k(n)T_e \tag{2}$$

where T_e denoes the starting-time of phase evolution, which is the only random variable in this component model. Figure 3 shows the simulated and measured principal phase spectrum of wind speed at the height 28m. It is thus concluded that the simulating objective is achieved.
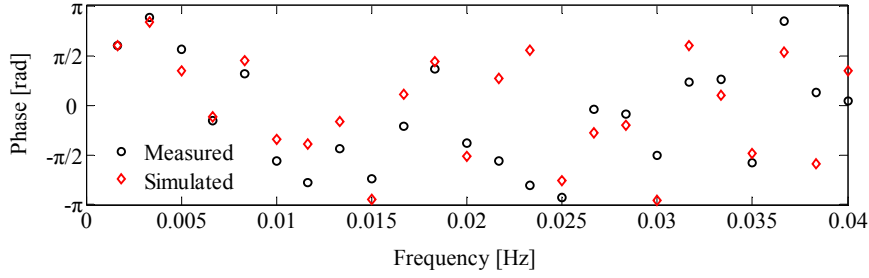
Figure 3. comparison of simulated and measured principal phase spectrum of wind speed at height 28m.

4   Modeling of Phase Delay Spectrum Component (Modeling III)

The investigations reveal that the primary factors affecting the phase delay spectrum include: (i) the natural frequency n that is in positive relationship to the phase delay; (ii) the spatial distance r_y and r_z between two points that are also in positive relationship to the phase delay; (iii) the mean wind speed $\overline{U}$ that is in negative relationship to the phase delay; (iv) the shear rate $d\overline{U}/dz$ that is in positive relationship to the phase delay.

$$\Delta\phi_y(n) = \frac{\beta_y r_y \left(n\dfrac{d\overline{U}}{dz}\right)^{0.5}}{\overline{U}} \qquad \Delta\phi_z(n) = \frac{\beta_z r_z \left(n\dfrac{d\overline{U}}{dz}\right)^{0.5}}{\overline{U}} \tag{3}$$

where β_y and β_z denote the magnification coefficient of phase delay spectrum along horizontal direction and vertical direction, respectively, whereby the phase delay spectrum with different amplitudes can be obtained.

Using the mentioned three component models, the simulated time histories of fluctuating wind speed in wind field are shown in Figure 4. It is seen that the simulated time histories numerically very close to the measured time histories.
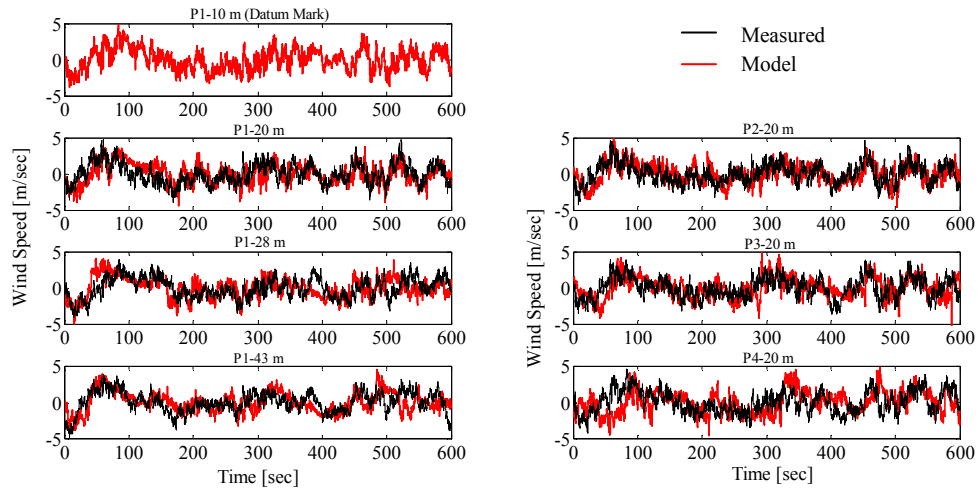
Figure 4. Simulated and measured fluctuating wind speed at typical spatial points of wind fields.

5   Stochastic Dynamic Response and Reliability of Wind-Excited TV Tower

A TV tower with height of 388 m subject to spatial fluctuating wind field is explored. 37 spatial points along the height of tower, 150 groups wind speed time series simulated for its stochastic dynamic response analysis and reliability assessment employing the PDEM. The probability density function (PDF) and cumulative density function (CDF) of extreme Mises stress at bottom of compressed column of the tower are shown in Figure 5. The standard distribution function EVD-I with the same

mean and standard deviation with the result of PDEM are also included in this figure. It is seen that the real PDF of structural response emloying the PDEM does not meet with the EVD-I, and their CDFs indicate an ignorable error on the EVD-I in cases of low reliability with threshold 80MPa and high reliability with threshold 150MPa.

(a)   (b)
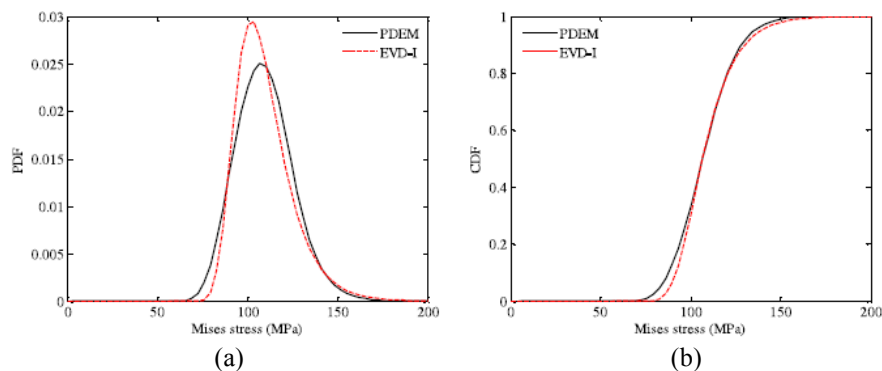
Figure 5. Probability density function and cumulative density function of extreme Mises stress at bottom of compressed column of the TV tower: (a) PDF of Mises stress; (b) CDF of Mises stress.

6 Concluding Remarks

This paper provides a physical scheme for stochastic modeling of spatial fluctuating wind fields represented by Fourier spectrum functions. Some concluding remarks are included as follows:

- Exponential amplitude model defined as the stochastic Fourier wave-number spectrum exhibits succinct formulation and well-understood physical accounts.
- Univariate phase spectrum in function of the starting-time of phase evolution provides a new perspective towards the efficiently modeling of random processes and random fields.
- Phase delay spectrum model is proved to be of rationality and of applicability using the measured data at spatial points of wind fields.
- The scheme of simulation of spatial fluctuating wind fields is proved to be of applicability for dynamic analysis and reliability assessment of randomly wind-excited structures.

References

Davenport, A. G. (1961). The spectrum of horizontal gustiness near the ground in high winds. *Quarterly Journal of the Royal Meteorological Society* **87**, 194-211.

Hinze, J. Q. (1975). *Turbulence*. McGraw-Hill.

Kaimal, J. C., Wyngaard, J. C., Izumi, Y., and Cote, O. R.. (1972). Spectral characteristics of surface-layer turbulence. *Quarterly Joural of the Royal Meteorological Society* **98**, 563-589.

Katul, G., and Chu, C. R. (1998). A theoretical and experimental investigation of energy-content scales in the dynamic sublayer of boundary-layer flows. *Boundary-Layer Meteorology* **86**, 279-312.

Li, J., and Chen, J.B. (2008). The principle of preservation of probability and the generalized density evolution equation. *Structural Safety* **30**, 65-77.

Li, J., and Chen, J.B. (2009). *Stochastic Dynamics of Structures*. John Wiley & Sons.

Von Karman, T. (1948). Progress in the statistical theory of turbulence. *Proceedings of the National Academy of Science of the United States of America*, **34**, 530-539.

Zhang, L. L., Li, J., and Peng, Y. B. (2008). Dynamic response and reliability analysis of tall buildings subject to wind loading. *Journal of Wind Engineering and Industrial Aerodynamics*, **96**, 25-40.

Analysis of linear systems driven by non-Gaussian noise

R. V. Field, Jr.[1] and M. Grigoriu[2]

[1]Sandia National Laboratories[*], Albuquerque, New Mexico, USA
[2]Cornell University, Ithaca, New York, USA
Corresponding author: R. V. Field, Jr., rvfield@sandia.gov

Abstract

A method is developed for approximating the properties of the state of a linear dynamic system driven by a broad class of non-Gaussian noise, namely, by polynomials of filtered Gaussian processes. The method involves four steps. First, the mean and correlation functions of the state of the system are calculated from those of the input noise. Second, higher order moments of the state are calculated based on Itô's formula for continuous semimartingales. It is shown that equations governing these moments are closed, so that moment of any order of the state can be calculated exactly. Third, a conceptually simple technique, which resembles the Galerkin method for solving differential equations, is proposed for constructing approximations for the marginal distribution of the state from its moments. Fourth, translation models are calibrated to representations of the marginal distributions of the state as well as its second moment properties. The resulting models can then be utilized to estimate properties of the state, such as the mean rate at which the state exits a safe set. The proposed method is applied to assess the turbulence-induced random vibration of a flexible plate motivated by problems in wind engineering.

1 Introduction

Classical linear random vibration theory provides equations for calculating the first two moments of the state $\mathbf{X}(t)$ of a linear system subjected to input or driving noise characterized by its first two moments. The theory provides no information beyond the second moment properties of $\mathbf{X}(t)$ unless the noise is Gaussian, in which case the state $\mathbf{X}(t)$ is a Gaussian process. There are no efficient methods for calculating properties of $\mathbf{X}(t)$, and functionals of this process, for the general case of non-Gaussian driving noise. This study develops a practical and efficient method for constructing approximate representations for the state $\mathbf{X}(t)$ of a linear dynamic system driven by a class of non-Gaussian noise that can be used to calculate properties or functionals of $\mathbf{X}(t)$. Developments are based on linear random vibration (Soong and Grigoriu, 1993, Chapter 5), Itô's formula for continuous semimartingales (Grigoriu, 2002, Section 4.6), an elementary solution for the problem of moments (Shohat and Tamarkin, 1943), and translation models $\mathbf{X}_{\mathrm{T}}(t)$ for $\mathbf{X}(t)$ (Grigoriu, 1995, Section 3.1.1). Herein, we consider the driving noise to be from the class of non-Gaussian processes defined by polynomials of filtered Gaussian processes (Grigoriu, 1986; Grigoriu and Ariaratnam, 1988).

In Grigoriu and Ariaratnam (1988), the objective was to calculate the mean upcrossing rate of level x for scalar process $X(t)$ driven by a polynomial of a Gaussian process. Hermite approximations were developed for the joint density of $(X, \mathrm{d}X/\mathrm{d}t)$, and the approximations were used to find the mean upcrossing rate of level x. In the current study, the objective is to estimate the probability law of $\mathbf{X}(t)$, and the development is not limited to scalar-valued processes. It is assumed herein that $\mathbf{X}(t)$ can be approximated by a translation process, so that the marginal distribution of $\mathbf{X}(t)$ and its correlation function are needed. The construction of the marginal distribution is as in Grigoriu and Ariaratnam (1988), generalized for the case of vector-valued processes. The construction of the correlation function for the input involves novel aspects of linear random vibration. Translation models are very flexible and have been

used in a wide variety of modeling applications, including wind pressure fluctuations on bluff bodies (Gioffrè et al., 2000), the description of irregular masonry walls (Spence et al., 2008), and damage in glass plates (Gioffrè and Gusella, 2002).

For demonstration purposes, the vibration response of a flexible plate subjected to turbulent flow is presented. The random pressure fluctuations applied to the plate surface are proportional to the square of the velocity field, which is assumed to be Gaussian. Hence the applied pressure field is non-Gaussian. Muscolino and co-workers worked on a related problem assuming a SDOF oscillator (Benfratello et al., 1996; Gullo et al., 1998).

2   Correlation function and moments

Let $\mathbf{X}(t)$ be an $\mathbb{R}^d$-valued stochastic process defined by the following linear differential equation

$$\dot{\mathbf{X}}(t) = \mathbf{a}(t)\,\mathbf{X}(t) + \mathbf{b}(t)\,\mathbf{Z}(t),\ t \geq 0, \tag{1}$$

where $\mathbf{a}(t)$ and $\mathbf{b}(t)$ are $d \times d$ and $d \times d'$ matrices with real-valued, time-dependent entries, $\mathbf{Z}(t)$ denotes an $\mathbb{R}^{d'}$-valued input process, and $\mathbf{X}(0)$ is the initial state specified by its mean vector $\boldsymbol{\mu}_0 = \mathrm{E}[\mathbf{X}(0)]$ and covariance matrix, $\boldsymbol{\gamma}_0 = \mathrm{E}[(\mathbf{X}(0) - \boldsymbol{\mu}_0)\,(\mathbf{X}(0) - \boldsymbol{\mu}_0)']$. Vector $\dot{\mathbf{X}}(t)$ has coordinates $\dot{X}_k(t) = \mathrm{d}X_k(t)/\mathrm{d}t$, $k = 1, \ldots, d$. It is assumed that input $\mathbf{Z}(t)$ is a weakly stationary process with mean $\boldsymbol{\mu}_{\mathbf{Z}} = \mathrm{E}[\mathbf{Z}(t)]$ and covariance function $\mathbf{c}_{\mathbf{Z}}(\tau) = \mathrm{E}[(\mathbf{Z}(t+\tau) - \boldsymbol{\mu}_{\mathbf{Z}})\,(\mathbf{Z}(t+\tau) - \boldsymbol{\mu}_{\mathbf{Z}})']$.

It can be shown (Soong and Grigoriu, 1993, Section 5.2.1) that the time evolution of $\boldsymbol{\mu}(t) = \mathrm{E}[\mathbf{X}(t)]$ and $\mathbf{c}(t, s) = \mathrm{Cov}[\mathbf{X}(t), \mathbf{X}(s)]$, the mean and covariance of state $\mathbf{X}(t)$ described by Eq. (1), are given by

$$\dot{\boldsymbol{\mu}}(t) = \mathbf{a}(t)\,\boldsymbol{\mu}(t) + \mathbf{b}(t)\,\boldsymbol{\mu}_{\mathbf{Z}},\ t \geq 0, \tag{2}$$

and

$$\frac{\partial}{\partial t}\mathbf{c}(t, s) = \mathbf{a}(t)\,\mathbf{c}(t, s) + \mathbf{d}(t, s),\ t > s, \tag{3}$$

where

$$\mathbf{d}(t, s) = \mathbf{b}(t)\int_0^s \mathbf{c}_{\mathbf{Z}}(t, u)\,\mathbf{b}(u)'\,\boldsymbol{\theta}(s, u)'\,\mathrm{d}u, \tag{4}$$

and $\boldsymbol{\theta}(t, s)$ is a system property satisfying the differential equation $\frac{\partial}{\partial t}\boldsymbol{\theta}(t, s) = \mathbf{a}(t)\,\boldsymbol{\theta}(t, s)$, $t \geq s$, with $\boldsymbol{\theta}(s, s)$ equal to the identity matrix $\forall s \geq 0$.

Next let $\mathbf{Y}(t)$ be an $\mathbb{R}^n$-valued Gaussian process defined by

$$\mathrm{d}\mathbf{Y}(t) = \boldsymbol{\alpha}(t)\,\mathbf{Y}(t)\,\mathrm{d}t + \boldsymbol{\beta}(t)\,\mathrm{d}\mathbf{B}(t),\ t \geq 0, \tag{5}$$

where $\boldsymbol{\alpha}(t)$ and $\boldsymbol{\beta}(t)$ are $n \times n$ and $n \times n'$ matrices, respectively, with real-valued, time-dependent entries, $\mathbf{B}(t)$ is an $\mathbb{R}^{n'}$-valued Brownian motion with independent coordinates, and $\mathbf{Y}(0) \sim N(\boldsymbol{\mu}_{\mathbf{Y},0}, \boldsymbol{\gamma}_{\mathbf{Y},0})$ is a Gaussian random vector independent of $\mathbf{B}(t)$ that defines the (random) value for $\mathbf{Y}$ at time $t = 0$. We refer to $\mathbf{Y}(t)$ as a filtered Gaussian process since it is the output of a linear filter to Gaussian white noise. It is assumed that process $\mathbf{Z}(t)$ that serves as the driving noise in Eq. (1) is expressed as a polynomial function of $\mathbf{Y}(t)$, the solution to Eq. (5).

The coordinates $\{Z_k(t)\}$ of $\mathbf{Z}(t)$ are polynomials of $\mathbf{Y}(t)$ that have the form

$$Z_k(t) = \sum_{m_1, \ldots, m_n \geq 0} \lambda_{k; m_1, \ldots, m_n} \prod_{r=1}^n Y_r(t)^{m_r},\ k = 1, \ldots, d', \tag{6}$$

where $\lambda_{k; m_1, \ldots, m_n}$ are real-valued coefficients and $m_r \geq 0$ are integer powers. Indeed, the class of input processes defined by Eq. (6) are very general and can represent a broad range of non-Gaussian probability

laws. The mean and correlation functions of $\mathbf{Z}(t)$ have the expressions

$$\mathrm{E}[Z_k(t)] = \sum_{m_1,\ldots,m_n \geq 0} \lambda_{k;m_1,\ldots,m_n} \,\mathrm{E}\!\left[\prod_{r=1}^{n} Y_r(t)^{m_r}\right] \quad \text{and}$$

$$\mathrm{E}[Z_k(s)\,Z_l(t)] = \sum_{m_1,\ldots,m_n \geq 0} \lambda_{k;m_1,\ldots,m_n} \sum_{m'_1,\ldots,m'_n \geq 0} \lambda_{l;m'_1,\ldots,m'_n} \,\mathrm{E}\!\left[\prod_{r=1}^{n} Y_r(s)^{m_r} \prod_{q=1}^{n} Y_q(t)^{m'_q}\right]. \quad (7)$$

The expectations in the second formula of Eq. (7) can be calculated from the observation that, for $t > s$,

$$Y_q(t) = \sum_{i=1}^{n} \theta_{qi}(t,s)\, Y_i(s) + G_q = V_q(t,s) + G_q, \quad (8)$$

where $(G_1,\ldots,G_n)$ is a Gaussian vector independent of $\mathbf{Y}(s)$ with mean $\mathbf{0}$ and covariance matrix $\int_s^t \boldsymbol{\theta}(t,u)\,\boldsymbol{\beta}(u)\,\boldsymbol{\beta}(u)'\,\boldsymbol{\theta}(t,u)'\,\mathrm{d}u$. Accordingly, the expectations in the second formula of Eq. (7) have the form

$$\mathrm{E}\!\left[\prod_{r=1}^{n} Y_r(s)^{m_r} \prod_{q=1}^{n} Y_q(t)^{m'_q}\right] = \mathrm{E}\!\left[\prod_{r=1}^{n} Y_r(s)^{m_r} \prod_{q=1}^{n} \left(V_q(t,s) + G_q\right)^{m'_q}\right]$$

$$= \sum_{p_1=0}^{m'_1} \cdots \sum_{p_n=0}^{m'_n} \frac{m'_1!}{p_1!\,(m'_1 - p_1)!} \cdots \frac{m'_n!}{p_n!\,(m'_n - p_n)!} \times$$

$$\mathrm{E}\!\left[\prod_{r=1}^{n} Y_r(s)^{m_r} \prod_{i=1}^{n} V_i(t,s)^{p_i}\right] \mathrm{E}\!\left[\prod_{i=1}^{n} G_i^{m'_i - p_i}\right]. \quad (9)$$

The expectations in the expression of $\mathrm{E}\!\left[\prod_{r=1}^{n} Y_r(s)^{m_r} \prod_{q=1}^{n} Y_q(t)^{m'_q}\right]$ represent higher order moments of Gaussian variables, that is, the coordinates of $\mathbf{Y}(s)$ and of the coordinates of $(G_1,\ldots,G_n)$. Properties of Gaussian variables can be used to calculate these expectations; see, for example, Papoulis (1991, Section 5.4).

3   Approximate model for the state

The method in Section 2 delivers the marginal moments of any order of the state $\mathbf{X}(t)$ of a linear system driven by a polynomial of a filtered Gaussian process, as well as the correlation function of this process. In this section, we use this information to construct a translation model $\mathbf{X}_{\mathrm{T}}(t)$ for $\mathbf{X}(t)$. The construction involves two steps. First, approximations are developed for the marginal distributions of $\mathbf{X}(t)$ based on higher order moments of this process. Second, $\mathbf{X}_{\mathrm{T}}(t)$ is selected to match the marginal distributions of $\mathbf{X}(t)$ and approximate, or match whenever possible, the correlation function of this process.

3.1   Marginal distributions

The construction of approximations for the marginal distributions of $\mathbf{X}(t)$ from their moments constitutes the solution of an inverse problem, referred to as the problem of moments (Shohat and Tamarkin, 1943). Our objective is to develop a conceptually simple and efficient method for solving the problem of moments for the marginal distributions of $\mathbf{X}(t)$. The posed problem has a solution since the prescribed moments correspond to distributions. However, it does not have a unique solution since the available information on the probability law of $\mathbf{X}(t)$ is incomplete. We construct approximations for the marginal distributions of $\mathbf{X}(t)$ that are optimal in some sense. For clarity, we limit the following discussion to stationary, scalar-valued processes $\mathbf{X}(t) = X(t)$; the extension to the case of non-stationary $\mathbf{R}^d$-valued processes is direct and will be used in Section 4.

Suppose $X(t)$ is a real-valued stationary process with unknown marginal distribution $F(x)$ and known first $n \geq 1$ marginal moments $\mu(r) = \mathrm{E}[X(t)^r]$, $r = 1,\ldots,n$. As previously stated, our ob-

jective is to construct an approximation $\tilde{F}(x)$ for $F(x)$ based on the available information, that is, the moments $\mu(r)$, $r = 1, \ldots, n$, of $X(t)$. Various approximations can be constructed for $F(x)$; we shall consider approximations $\tilde{F}(x)$ and $\tilde{f}(x)$ for the marginal distribution and density functions, $F(x)$ and $f(x)$, of $X(t)$ that resemble the Galerkin method (Grigoriu and Lind, 1980). It is assume that $\tilde{f}(x)$ is a member of the linear space spanned by a finite collection of densities $\{f_k(x)\}$, $k = 1, \ldots, b$, that is,

$$\tilde{f}(x) = \sum_{k=1}^{b} p_k \, f_k(x), \tag{10}$$

where the constants $\{p_k\}$ are such that $p_k \geq 0$, $k = 1, \ldots, b$, and $\sum_{k=1}^{b} p_k = 1$, so that $\tilde{f}(x)$ is a density for any parameters $\{p_k\}$ satisfying the above constraints. The corresponding approximate distribution function has the expression

$$\tilde{F}(x) = \sum_{k=1}^{b} p_k \, F_k(x) \tag{11}$$

with $F_k(x) = \int_{u \leq x} f_k(u) \, \mathrm{d}u$, $k = 1, \ldots, b$. The densities $\{f_k(x)\}$ may or may not be completely specified; for example, some densities may depend on a collection of unknown parameters. However, we will consider the case in which the densities $\{f_k(x)\}$ are fully specified, so that the probabilities $\{p_k\}$ are the only uncertain parameters of $\tilde{f}(x)$ and $\tilde{F}(x)$.

The optimal values for $\{p_k\}$ defined by Eqs. (10) and (11) minimize the discrepancy

$$e(p_1, \ldots, p_b) = \sum_{r=1}^{m} v(r) \left(\mu(r) - \sum_{k=1}^{b} p_k \, \mu_k(r) \right)^2 \tag{12}$$

between the exact moments $\mu(r) = \mathrm{E}[X(t)^r]$ of $X(t)$ and their approximations

$$\tilde{\mu}(r) = \int x^r \, \tilde{f}(x) \, \mathrm{d}x = \int x^r \sum_{k=1}^{b} p_k \, f_k(x) \, \mathrm{d}x = \sum_{k=1}^{b} p_k \int x^r \, f_k(x) \, \mathrm{d}x = \sum_{k=1}^{b} p_k \, \mu_k(r), \tag{13}$$

under the constraints $p_k \geq 0$, $k = 1, \ldots, b$, and $\sum_{k=1}^{b} p_k = 1$. Further, $m \geq 1$ is an integer denoting the largest moment considered in the analysis and $v(r) \geq 0$ denotes a weighting function, for example, $v(r) = 1/\mu(r)^2$. As in the Galerkin method, the accuracy of $\tilde{f}(x)$ is essentially controlled by the properties of the densities $\{f_k(x)\}$.

Heuristic arguments and/or prior information may be used to select the basis $\{f_k(x)\}$ for $\tilde{f}(x)$. For example, we may require that the skewness and kurtosis coefficients of $\{f_k(x)\}$ bracket the corresponding coefficients of $f(x)$ and that the first two moments of $\tilde{f}(x)$ coincide with those of $f(x)$ for all value of $\{p_k\}$. In addition, knowledge regarding the behavior of dynamic systems may provide information on the properties of $f(x)$, for example, the state of linear systems under driving noise with a symmetric density is known to have an even density.

3.2 Translation model

Let $\mathbf{X}(t)$ be a stationary $\mathbb{R}^d$-valued stochastic process specified partially by its second moment properties and marginal distributions $F_i(x)$, or approximations $\tilde{F}_i(x)$, $i = 1, \ldots, d$, of these distributions. Methods for calculating these properties of $\mathbf{X}(t)$ have been discussed above. In this section, we develop translation models for $\mathbf{X}(t)$, denoted by $\mathbf{X}_{\mathrm{T}}(t)$, which can be used to approximate properties of $\mathbf{X}(t)$. For example, let $\mathbf{X}(t)$ denote the state of a dynamic system, and suppose that whenever the state resides within a "safe set" $\mathcal{S}$, the system performance is known to be satisfactory. A typical property of interest for this scenario is the mean rate at which $\mathbf{X}(t)$ exits out of $\mathcal{S}$, since this property can be used to estimate system reliability (Soong and Grigoriu, 1993, Chapter 7).

Translation models are defined by nonlinear transformations of Gaussian random functions (Grigoriu,

1995, Section 3.1.1). By careful selection of the properties of the Gaussian function and the functional form of the transformation, it is possible to calibrate the translation model to match a wide variety of prescribed marginal CDFs and second moment properties. However, translation models matching exactly specified marginal distributions and second moment properties may not exist. If there exists no translation model matching these properties, we construct an $\mathbb{R}^d$-valued translation model $\mathbf{X}_{\mathrm{T}}(t)$ that matches exactly the marginal distributions $\{F_i(x)\}$ of $\mathbf{X}(t)$, or their approximate representations $\{\tilde{F}_i(x)\}$, and characterizes approximately the covariance functions of $\mathbf{X}(t)$.

Let

$$X_{\mathrm{T},i}(t) = F_i^{-1} \circ \Phi\big(G_i(t)\big), \quad i = 1, \ldots, d, \tag{14}$$

denote the coordinates of $\mathbf{X}_{\mathrm{T}}(t)$, where $\mathbf{G}(t) = (G_1(t), \ldots, G_d(t))$ is an $\mathbb{R}^d$-valued stationary Gaussian process with $\mathrm{E}[G_i(t)] = 0$, $\mathrm{E}[G_i(t)^2] = 1$, and $\mathrm{E}[G_i(t+\tau)\,G_j(t)] = \rho_{ij}(\tau)$. The marginal distributions of $\mathbf{X}_{\mathrm{T}}(t)$ in Eq. (14) coincide with those of $\mathbf{X}(t)$. The covariance function of $\mathbf{X}_{\mathrm{T}}(t)$ depends on the mapping in Eq. (14) and the covariance function of $\mathbf{G}(t)$. If there are no correlation functions $\{\rho_{ij}(\tau)\}$ such that the scaled covariance functions

$$\xi_{\mathrm{T},ij}(\tau) = \frac{\mathrm{E}\{(X_{\mathrm{T},i}(t+\tau) - \mathrm{E}[X_{\mathrm{T},i}(t+\tau)])\,(X_{\mathrm{T},j}(t) - \mathrm{E}[X_{\mathrm{T},j}(t)])\}}{\mathrm{Std}[X_{\mathrm{T},i}(t+\tau)]\,\mathrm{Std}[X_{\mathrm{T},j}(t+\tau)]} \tag{15}$$

of $\mathbf{X}_{\mathrm{T}}(t)$ match the corresponding scaled covariance functions $\{\xi_{ij}(\tau)\}$ of $\mathbf{X}(t)$, we select $\{\rho_{ij}(\tau)\}$ such the discrepancy between $\{\xi_{T,ij}(\tau)\}$ and $\{\xi_{ij}(\tau)\}$ is minimized in some sense.

4   Engineering application: turbulent flow over a flat plate

In this section, we apply the proposed method to study the flow-induced random vibration of a flexible plate. Consider Fig. 1, which illustrates a thin flexible plate that is simply supported along all four edges. Fluid flows from left to right at constant speed v_0 over the surface of the plate, resulting in a turbulent boundary layer. Random pressure fluctuations within this layer, denoted by Z, provide a time-varying excitation to the top surface of the plate; the resulting (random) displacement response at the neutral axis of the plate is denoted by W. This class of problems has seen much attention; see, for example, Blake (1986), Corcos (1963), Strawderman and Brand (1969), and Tack and Lambert (1962). Most of these studies assume the applied pressure field is Gaussian. Herein we study non-Gaussian excitations. The velocity field is assumed to be composed of a collection of processes that each satisfy a Langevin equation. The surface pressure driving the plate response is then assumed to be the dynamic pressure, which is proportional to the square of the velocity field. Properties of the plate response, such as the mean rate at which W crosses a prescribed level, are then calculated and can be used to estimate time-dependent reliability of the plate structure (Soong and Grigoriu, 1993, Chapter 7). These estimates are not possible by classical linear vibration theory unless the applied pressure field is assumed Gaussian.

4.1   The fluctuating pressure field

Recall Fig. 1 and consider flow moving at constant speed v_0 in the $+u_1$-direction over the surface of a thin plate with length l, width h, and thickness $\epsilon \ll l, h$. Pressure fluctuations in the boundary layer, modeled by a space-time random field, induce structural vibration. As per Lin and Cai (1995, Section 2.3.2), we assume the flow moves uniaxially over the plate, and the only component of the velocity field driving the plate response is that component which acts normal to the plate surface. Let $V(t)$ denote fluid particle velocity in turbulent flow; its motion can be modeled by the Langevin equation:

$$\mathrm{d}V(t) = -\alpha\,V(t)\,\mathrm{d}t + \beta\,\mathrm{d}B(t), \tag{16}$$

where $\alpha > 0$ is the "inverse integral time scale" (Pope, 2000, Section 12.3.1), and $\beta > 0$ denotes the scale of the driving noise.

   To model fluid velocity over the entire plate, we construct a velocity field composed of a collection
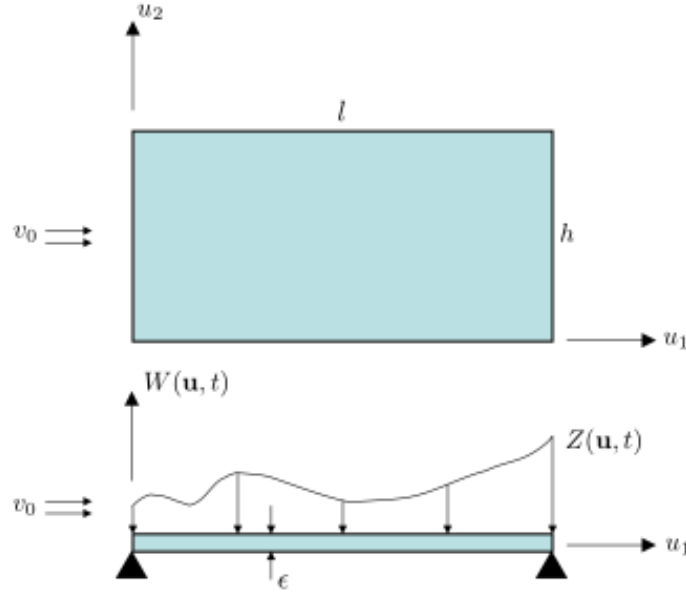
Figure 1. Flexible plate subject to flow-induced vibration.

$\{V_k(t)\}$ of iid copies of $V(t)$ defined by Eq. (16) with associated parameters $\{\alpha_k, \beta_k\}$. Let

$$Y(\mathbf{u}, t) = \sum_{k \geq 1} \sqrt{b_k}\, \phi_k(\mathbf{u})\, V_k(t), \tag{17}$$

denote the velocity of the fluid at location $\mathbf{u} = (u_1, u_2)' \in [0, l] \times [0, h]$ on the surface of the plate, where $\{b_k > 0\}$ and $\{\phi_k(\mathbf{u})\}$ are deterministic constants and basis functions, respectively. The second-moment properties of Y, assuming each $V_k(0) = 0$ almost surely, are

$$\mathrm{E}[Y(\mathbf{u}, t)] = 0$$

$$\mathrm{Cov}(Y(\mathbf{u}, t), Y(\mathbf{v}, s)) = \sum_{k \geq 1} b_k\, \phi_k(\mathbf{u})\, \phi_k(\mathbf{v})\, \mathrm{Cov}(V_k(t), V_k(s))$$

$$= \sum_{k \geq 1} b_k\, \phi_k(\mathbf{u})\, \phi_k(\mathbf{v})\, \frac{\beta_k^2}{2\alpha_k} \left(1 - e^{-2\alpha_k \min(t, s)}\right) e^{-\alpha_k |t - s|} \tag{18}$$

demonstrating that the covariance function of Y is time/space separable. Further, it is clear by Eq. (18) that the spatial covariance of Y is controlled by $\{b_k > 0\}$ and $\{\phi_k(\mathbf{u})\}$ defined by Eq. (17). The corresponding dynamic pressure applied to the top surface of the plate is given by

$$Z(\mathbf{u}, t) = \kappa_0\, \frac{\rho_0}{2}\, Y(\mathbf{u}, t)^2, \tag{19}$$

where ρ_0 denotes the density of air, and κ_0 is an empirical parameter that depends on the speed and temperature of the flow (Laganelli et al., 1983).

4.2   The structural model

Let κ, γ, and ρ denote the elastic modulus, Poisson's ratio, and mass density of the plate material, respectively. The equation of motion of an undamped thin flat plate with thickness ϵ driven by applied pressure field Z, based on the theory by Kirchhoff (Leissa, 1993), is

$$\delta\, \nabla^4 W(\mathbf{u}, t) + \rho\, \epsilon\, \frac{\partial^2}{\partial t^2} W(\mathbf{u}, t) = -Z(\mathbf{u}, t), \quad \mathbf{u} = (u_1, u_2) \in [0, l] \times [0, h], \ t \geq 0, \tag{20}$$

where W denotes the vertical displacement of the neutral plane of the plate, $\delta = \kappa\,\epsilon^3/(12(1-\gamma^2))$ is a parameter defining the effective plate flexural rigidity, and $\nabla^4(\,\cdot\,) = \frac{\partial^4}{\partial u_1{}^4}(\,\cdot\,) + 2\,\frac{\partial^2}{\partial u_1{}^2}\frac{\partial^2}{\partial u_2{}^2}(\,\cdot\,) + \frac{\partial^4}{\partial u_2{}^4}(\,\cdot\,)$ is the biharmonic operator. We assume the plate is simply supported along each edge and initially at rest.

Denote by $\psi_{mn}(\mathbf{u})$ and ω_{mn}, $m, n \geq 1$, the undamped natural modes and frequencies of free vibration of the structure, *i.e.*, the solution to

$$\rho\,\epsilon\,\omega_{mn}^2\,\psi_{mn}(\mathbf{u}) = \delta\,\nabla^4\psi_{mn}(\mathbf{u}), \quad \mathbf{u} \in [0, l] \times [0, h]. \tag{21}$$

For a simply supported plate with length l and width h, we have (Leissa, 1993)

$$\omega_{mn} = \sqrt{\frac{\delta}{\rho\,\epsilon}}\left[\left(\frac{m\pi}{l}\right)^2 + \left(\frac{n\pi}{h}\right)^2\right] \text{ and } \psi_{mn}(\mathbf{u}) = \frac{2}{\sqrt{\rho\,\epsilon\,h\,l}}\,\sin\left(\frac{m\pi u_1}{l}\right)\,\sin\left(\frac{n\pi u_2}{h}\right), \tag{22}$$

where the mode shapes form an orthonormal basis with respect to the mass of the plate, *i.e.*,

$$\int_0^l \int_0^h \rho\,\epsilon\,\psi_{mn}(\mathbf{u})\,\psi_{qr}(\mathbf{u})\,\mathrm{d}u_2\,\mathrm{d}u_1 = \begin{cases} 1 & m = q \text{ and } n = r \\ 0 & \text{else} \end{cases} \tag{23}$$

The displacement of the plate can be expressed as

$$W(\mathbf{u}, t) = \sum_{mn \geq 1} \psi_{mn}(\mathbf{u})\,Q_{mn}(t), \tag{24}$$

where $\{Q_{mn}(t)\}$ form a set of generalized modal coordinates. Applying a constant damping factor $0 < \zeta < 1$ to each mode, each $Q_{mn}(t)$ is the solution to the following ordinary differential equation

$$\ddot{Q}_{mn}(t) + 2\,\zeta\,\omega_{mn}\,\dot{Q}_{mn}(t) + \omega_{mn}^2\,Q_{mn}(t) = A_{mn}(t), \ t \geq 0, \tag{25}$$

where $Q_{mn}(0) = \dot{Q}_{mn}(0) = 0$ are the initial conditions, and

$$\begin{aligned} A_{mn}(t) &= \int_0^l \int_0^h Z(\mathbf{u}, t)\,\psi_{mn}(\mathbf{u})\,\mathrm{d}u_2\,\mathrm{d}u_1 = \int_0^l \int_0^h \kappa_0\,\frac{\rho_0}{2}\,Y(\mathbf{u}, t)^2\,\psi_{mn}(\mathbf{u})\,\mathrm{d}u_2\,\mathrm{d}u_1 \\ &= \sum_{k,l \geq 1} \kappa_0\,\frac{\rho_0}{2}\,\sqrt{b_k\,b_l}\,V_k(t)\,V_l(t) \int_0^l \int_0^h \phi_k(\mathbf{u})\,\phi_l(\mathbf{u})\,\psi_{mn}(\mathbf{u})\,\mathrm{d}u_2\,\mathrm{d}u_1 \\ &= \sum_{k,l \geq 1} \lambda_{kl}\,V_k(t)\,V_l(t), \end{aligned} \tag{26}$$

where the third line follows from Eq. (17), and parameters $\{\lambda_{kl}\}$ are introduced to simplify notation.

4.3   Moments and correlation function of state vector

For numerical illustration, we truncate Eq. (26) at two terms and assume the plate displacement can be approximated by its first structural mode. Therefore

$$W(\mathbf{u}, t) \approx \psi_{11}(\mathbf{u})\,Q(t), \tag{27}$$

where $Q(t) = Q_{11}(t)$ satisfies

$$\ddot{Q}(t) + 2\,\zeta\,\omega\,\dot{Q}(t) + \omega^2 Q(t) = \sum_{k,l=1}^2 \lambda_{kl}\,V_k(t)\,V_l(t), \tag{28}$$

$\omega = \omega_{11}$ is the first resonant frequency of the plate given by Eq. (22), and $\{V_k(t)\}$ are iid copies of $V(t)$ defined by Eq. (16) with associated parameters $\{\alpha_k, \beta_k\}$, driven by Brownian motions $\{B_k(t)\}$. We limit the discussion that follows to the case of a single structural mode and two fluid particles for clarity;

additional structural modes and fluid particles can be added to the formulation if necessary.

Let $\mu(t; p, q, r, w) = \mathrm{E}[X_1^p(t) X_2^q(t) V_1^r(t) V_2^w(t)]$ define the moments of the state vector. It can be shown that (Grigoriu and Field, 2014)

$$
\begin{aligned}
\dot{\mu}(t; p, q, r, w) = {}& p\,\mu(t; p-1, q+1, r, w) + q\Big[-\omega^2\,\mu(t; p+1, q-1, r, w) - 2\,\zeta\,\omega\,\mu(t; p, q, r, w) + \\
& \lambda_{11}\,\mu(t; p, q-1, r+2, w) + (\lambda_{12} + \lambda_{21})\mu(t; p, q-1, r+1, w+1) + \\
& \lambda_{22}\,\mu(t; p, q-1, r, w+2)\Big] - r\,\alpha_1\,\mu(t; p, q, r, w) - w\,\alpha_2\,\mu(t; p, q, r, w) + \\
& \beta_1^2\,\frac{r(r-1)}{2}\,\mu(t; p, q, r-2, w) + \beta_2^2\,\frac{w(w-1)}{2}\,\mu(t; p, q, r, w-2)
\end{aligned}
\tag{29}
$$

is a family of differential equations describing the time evolution of the moments of the state. For calculations, we solve this system of equations for $m = 1$ and increasing r, w, then solve the system for $m = 2$ and increasing r, w. Further, it can be shown that the covariance function of the state is, for $t > s$,

$$
\mathbf{c}(t, s) = \boldsymbol{\theta}(t - s)\,\mathbf{c}(s, s) +
$$

$$
\sum_{k,l=1}^{2} \lambda_{kl} \int_s^t \boldsymbol{\theta}(t - u) \begin{bmatrix} 0 & 0 \\ \mathrm{E}[V_k(u)\,V_l(u)\,X_1(s)] & \mathrm{E}[V_k(u)\,V_l(u)\,X_2(s)] \end{bmatrix} \mathrm{d}u
\tag{30}
$$

where (Soong and Grigoriu, 1993, p. 177)

$$
\boldsymbol{\theta}(t) = e^{-\zeta\,\omega\,t} \begin{bmatrix} \cos(\omega_d\,t) + \dfrac{\zeta\,\omega}{\omega_d}\sin(\omega_d\,t) & \dfrac{1}{\omega_d}\sin(\omega_d\,t) \\[2ex] \dfrac{-\omega^2}{\omega_d}\sin(\omega_d\,t) & \cos(\omega_d\,t) - \dfrac{\zeta\,\omega}{\omega_d}\sin(\omega_d\,t) \end{bmatrix}
\tag{31}
$$

4.4 Translation model

In this section, we apply the techniques from Section 3 to approximate process $Q(t)$ defined by Eq. (28) by a translation model, denoted by $Q_{\mathrm{T}}(t)$. The corresponding approximation for the plate displacement response is then given by Eq. (27), *i.e.*, $W_{\mathrm{T}}(\mathbf{u}, t) = \psi_{11}(\mathbf{u})\,Q_{\mathrm{T}}(t)$.

Following the discussion from Section 3.1, let

$$
\tilde{f}(x; t) = \sum_{k=1}^{b} p_k(t) f_k(x; q_k, \eta_k)
\tag{32}
$$

denote an approximation for the marginal PDF of $Q(t)$, where each trial density f_k is the PDF of a gamma random variable with parameters (q_k, η_k), $k = 1, \ldots, b$. We note that $\tilde{f}(x; t)$ is time-varying and is a generalization to Eq. (10), and $\tilde{F}(u; t) = \int_0^\infty \tilde{f}(y; t)\,\mathrm{d}y$ is the corresponding marginal CDF.

Figure 2(a) illustrates the optimal solution $\{p_k(t)\}$ to Eq. (32) based on the moment calculations from Section 4.3. The solution minimizes the discrepancy defined by Eq. (12) at each time t, assuming weight function $v(t; r) = 1/\mu(t; r)^2$ and $b = 10$; the time-evolution of the discrepancy is illustrated by Fig. 2(b). We note that, in general, the solution improves with increasing t.

$W_{\mathrm{T}}(\mathbf{u}, t)$, the translation model for the plate displacement response $W(\mathbf{u}, t)$, is completely defined by the second-moment properties and marginal CDF of Q_{T}, as well as $\psi_{11}(\mathbf{u})$, the first mode shape of the plate defined by Eq. (22). We now can use this model for W to approximate various output properties of interest. For example,

$$
\nu_{\mathrm{T}}(x; \mathbf{u}) = \frac{\sigma}{2\pi} \exp\left[-\frac{1}{2}\left(\Phi^{-1} \circ \tilde{F}_{\mathrm{s}}\left(\frac{x}{\psi_{11}(\mathbf{u})}\right)\right)\right]
\tag{33}
$$

is the mean x-upcrossing rate of process $W_{\mathrm{T}}(\mathbf{u}, t)$, where $\tilde{F}_{\mathrm{s}}(x) = \lim_{t\to\infty} \tilde{F}(x; t)$ denotes the stationary version of the marginal CDF of Q_{T}, and parameter $\sigma > 0$ denotes the standard deviation of the process defined as the mean square time derivative of $\Phi^{-1} \circ \tilde{F}(Q_{\mathrm{T}}(t))$. Quantity $\nu_{\mathrm{T}}(x; \mathbf{u})$ defined by Eq. (33) is illustrated by Fig. 3 for $0 \le u_1 \le l$ and $u_2 = h/2$ as a function of level x. This quantity can be used,
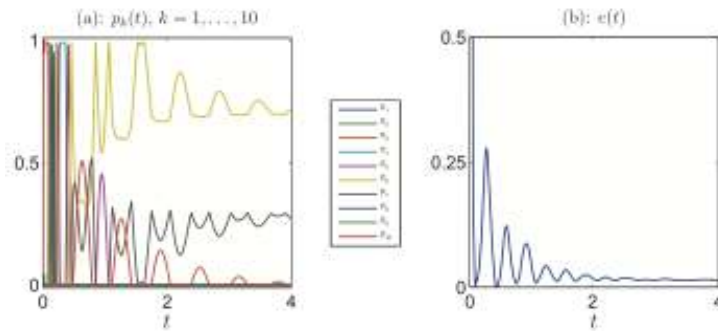
Figure 2. Optimal solution for translation model of process $Q(t)$: (a) probabilities $p_k(t)$, $k = 1, \ldots, 10$, and (b) discrepancy $e(t)$ defined by Eq. (12).
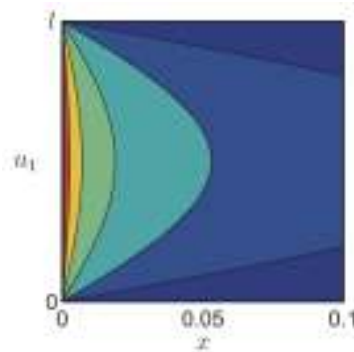
Figure 3. Mean x-upcrossing rate, ν_{T}, of plate displacement as a function of level x and spatial coordinate u_1.

for example, to make estimates of the probability that W will exceed level x within a prescribed time interval (Soong and Grigoriu, 1993, Chapter 7).

5 Conclusions

A method has been developed for approximating the properties of the state of a linear dynamic systems driven by a broad class of non-Gaussian noise, namely, by polynomials of filtered Gaussian processes. The method involved four steps. First, the mean and correlation functions of the state $\mathbf{X}(t)$ of the linear system were calculated from those of the input. Second, equations were developed for higher order moments of $\mathbf{X}(t)$ based on Itô's formula for continuous semimartingales. It was shown that these equations are closed, so that moment of any order of $\mathbf{X}(t)$ can be calculated exactly. Third, a conceptually simple method was proposed for constructing approximations for the marginal distributions of $\mathbf{X}(t)$ from its moments. The method resembles the Galerkin method for solving differential equations. Fourth, translation models were calibrated to representations of the marginal distributions of $\mathbf{X}(t)$ and the second moment properties of this process. The resulting models were then utilized to estimate properties of $\mathbf{X}(t)$, such as the mean rate at which the state exits a safe set. The implementation of the proposed method was demonstrated by numerous examples, including the turbulence-induced random vibration of a flexible plate.

References

Benfratello, S., Falsone, G., and Muscolino, G. (1996). Influence of the quadratic term in the alongwind stochastic response of SDOF structures. *Engineering Structures* **18**.9, pp. 685–695.

Blake, W. K. (1986). *Mechanics of Flow-Induced Sound and Vibration. Volume I: General Concepts and Elementary Sources*. Academic Press.

Corcos, G. M. (1963). Resolution of pressure in turbulence. *The Journal of the Acoustical Society of America* **35**.2, pp. 192–199.

Gioffrè, M. and Gusella, V. (2002). Damage accumulation in glass plates. *Journal of Eng* **128**.7, pp. 801–805.

Gioffrè, M., Gusella, V., and Grigoriu, M. (2000). Simulation of non-Gaussian field applied to wind pressure fluctuations. *Probabilistic Engineering Mechanics* **15**.4, pp. 339–345.

Grigoriu, M. (1986). Response of linear systems to quadratic Gaussian excitations. *Journal of Engineering Mechanics* **112**.6, pp. 532–535.

— (1995). *Applied Non-Gaussian Processes*. Englewood Cliffs, NJ: P T R Prentice-Hall.

— (2002). *Stochastic Calculus: Applications in Science and Engineering*. Boston, MA: Birkhäuser.

Grigoriu, M. and Ariaratnam, S. T. (1988). Response of linear systems to polynomials of Gaussian processes. *Journal of Applied Mechanics* **55**, pp. 905–910.

Grigoriu, M. and Field Jr., R. V. (2014). A method for analysis of linear dynamic systems driven by stationary non-Gaussian noise with applications to turbulence-induced random vibration. *Applied Mathematical Modelling* **38**.1, pp. 336–354.

Grigoriu, M. and Lind, N. C. (1980). Optimal estimation of convolution integrals. *Journal of the Engineering Mechanics Division* **106**.EM6, pp. 1349–1364.

Gullo, I., Muscolino, G., and Vasta, M. (1998). Non-Gaussian probability density function of SDOF linear structures under wind actions. *Journal of Wind Engineering and Industrial Aerodynamics* **74–76**, pp. 1123–1134.

Laganelli, A. L., Martellucci, A., and Shaw, L. L. (1983). Wall Pressure Fluctuations in Attached Boundary-layer Flow. *AIAA Journal* **21**.4, pp. 495–502.

Leissa, A. (1993). *Vibration of Plates*. Acoustical Society of America.

Lin, Y. K. and Cai, G. Q. (1995). *Probabilistic Structural Dynamics*. New York, NY: McGraw-Hill.

Papoulis, A. (1991). *Probability, Random Variables, and Stochastic Processes*. 3rd ed. New York, NY: McGraw-Hill, Inc.

Pope, S. B. (2000). *Turbulent Flows*. Cambridge, UK: Cambridge University Press.

Shohat, J. A. and Tamarkin, J. D. (1943). *The Problem of Moments*. Vol. 1. The American Mathematical Society.

Soong, T. T. and Grigoriu, M. (1993). *Random Vibration of Mechanical and Structural Systems*. Englewood Cliffs, NJ: P T R Prentice-Hall.

Spence, S. M. J., Gioffrè, M., and Grigoriu, M. (2008). Probabilistic models and simulation of irregular masonry walls. *Journal of Engineering Mechanics* **134**.9, pp. 750–762.

Strawderman, W. A. and Brand, R. S. (1969). Turbulent-Flow-Excited Vibration of a Simply Supported, Rectangular Flat Plate. *The Journal of the Acoustical Society of America* **45**.1, pp. 177–192.

Tack, D. H. and Lambert, R. F. (1962). Response of bars and plates to boundary layer turbulence. *Journal of the Aerospace Sciences* **29**, pp. 311–322.

The effects of wind-induced building motion on occupant wellbeing and work performance

S. Lamb[1], K.C.S. Kwok[1] and D. Walton[2]

[1]Institute for Infrastructure Engineering, University of Western Sydney, Australia
[2]Health Promotion Agency, Wellington, New Zealand
Corresponding author: S. Lamb, 17097433@student.uws.edu.au

Abstract

This paper presents findings from two studies showing that individual susceptibility to motion sickness moderates the effect of building motion on symptoms of motion sickness. While highly susceptible individuals indicate a preference to avoid working in tall buildings, they are no less likely to work in tall buildings than the least susceptible individuals. During building motion, participants report low-dose motion sickness (tiredness, low motivation and distraction) at levels 2-3 times the baseline rate. High levels of motion sickness reduce work performance by up to 0.90 standard deviations below baseline. Affected individuals attempt to manage their own discomfort, and indicate a preference to work a different location during motion, take 30-40% longer breaks, and attempt to self-medicate.

1   Introduction

Tall buildings vibrate at low frequencies and accelerations in response to strong winds at or near their resonant frequency. This vibration can be perceptible to building occupants and in some cases can cause motion sickness (Hansen, Reed & Vanmarke, 1973; Goto, 1983; Burton, 2006). Most research has focused on the threshold of motion perception (e.g. Tamura et al., 2006), favouring artificial motion simulator studies over realistic field studies, largely due to the difficulty of accessing tall buildings. Motion simulator studies have found no significant motion-induced reduction in cognitive or work performance (Burton, 2006; Denoon et al., 2000; Jeary, 1988). While offering a high degree of experimental control, motion simulators cannot adequately mimic the complexity of a real office environment. Only field studies can assess the real influence of tall building motion on occupants.

While building motion researchers have considered the classic symptoms of motion sickness, nausea and dizziness, fewer researchers have examined early onset motion sickness, known as sopite syndrome (Graybiel & Knepton, 1976). Sopite syndrome is characterised by tiredness, distraction, low motivation and low mood. Given the low acceleration nature of building motion, sopite syndrome may be more likely to affect occupants than classic motion sickness (Walton et al., 2011).

Two studies examine the occupant response to motion, both in Wellington, New Zealand, known for its consistently high wind climate. Study 1 surveyed central city workers about their experiences of wind-induced tall building motion. Study 2 uses a longitudinal method to assess changes in wellbeing and work performance of occupants of wind-sensitive buildings.

2   Method

In Study 1, the investigators distributed 4000 surveys in the Wellington Central Business District (CBD). 1014 completed surveys were returned (response rate: 25.4%). The survey measured reported effects of motion, individual susceptibility to motion sickness (Motion Sickness Susceptibility Questionnaire; Golding, 2006), complaint, and work environment preferences.

Study 2 uses a longitudinal design to examine changes in occupants comfort and work performance in a sample of 47 Wellington CBD office workers working on high floors in tall buildings over 8 months. A quasi-experimental longitudinal design compares the responses of tall building occupants to a sample of 53 office workers near the ground floor. Occupant responses to motion were collected using short 5-minute online surveys. Participants completed 2,261 surveys across a range of wind conditions from calm days to high winds. The survey measured a range of potential symptoms of motion sickness, work performance (objective and subjective measures), wellbeing, and reported building motion.

3   Results

In Study 1, 42% of respondents ($N = 229$) reported that they had felt wind-induced building motion, observed across 29 different tall buildings. Individuals highly susceptible to motion sickness reported a strong preference to work on the lowest floors of tall buildings rather than the highest floors. However, the most susceptible individuals worked on the same mean floor as the least susceptible individuals. Highly susceptible individuals reported the avoidance of common nauseogenic environments, which indicates that these individuals are constrained in their ability to avoid working in tall buildings. Highly susceptible individuals were subsequently more likely to experience motion sickness (reported by a fifth of occupants). Building motion induced symptoms of sopite syndrome, mainly difficulty concentrating, were reported in almost half of occupants, shown in Figure 1. Despite respondents judging building motion as unpleasant and causing occupant discomfort, occupants almost never formally complained, contradicting the belief that formal complaint is a reliable indicator of building performance. However, just under half of occupants complained informally to friends, family and colleagues. Some participants indicated constraints on the ability to complain, reporting that complaint might jeopardise their employment. Formal complaints indicate poor building performance, but the absence of formal complaint is not evidence of acceptable building performance.
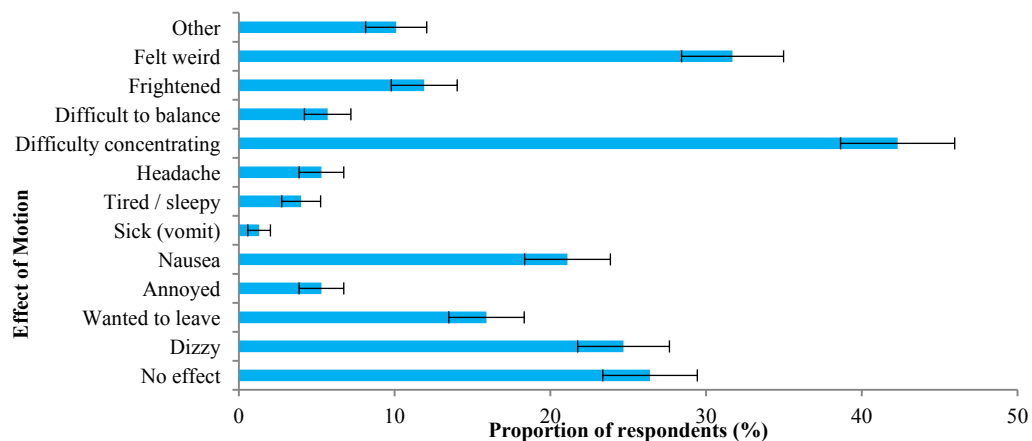
Figure 1. Building occupants reported effects of building motion (error bars indicate 95% confidence intervals)

In Study 2, building occupants were significantly more likely to report both high-dose (nausea and dizziness) and low-dose symptoms of motion sickness (tiredness, distraction and feeling 'off', low mood and motivation) during building motion (including barely perceptible or "possible" and "definite" motion) than during baseline (no motion).
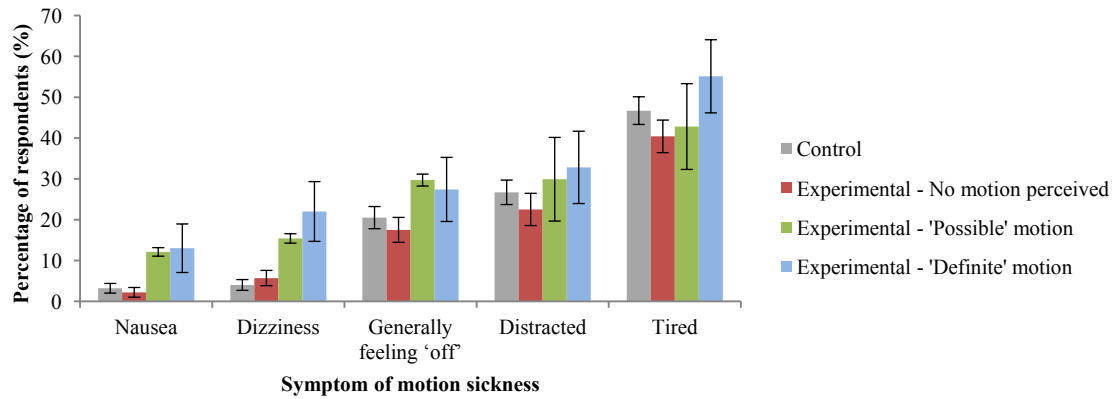
Figure 2. The frequency of reported symptoms of motion sickness across reported perception of motion in the experimental condition compared with the control condition (Error bars represent 95% confidence intervals)

Clusters of both low- and high-dose symptoms were 2-3 times more likely to occur during building motion than at baseline on the Combine Motion Sickness Scale (CMSS). Self-reported work performance decreased significantly during reported building motion. Reported symptoms of motion sickness accounted for more variation in work performance than the occurrence of building motion. Building occupants affected by 'moderate' to 'high' levels of motion sickness report performance impairments of .76 to .90 standard deviations below their normal performance. Objective measures of task performance support these trends. Up to 30% of building occupants attempted to manage their discomfort by taking analgesic medication. The most susceptible individuals to motion sickness took 31% longer breaks to reduce their exposure to motion, and those suffering motion sickness took 40% longer breaks.
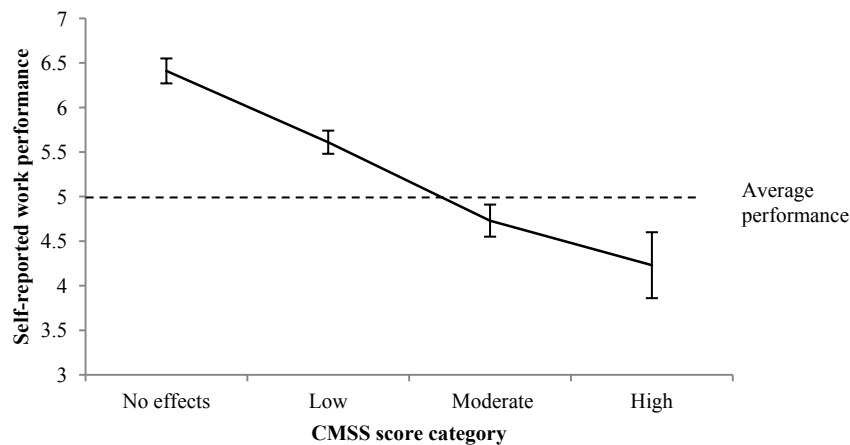
Figure 3. The effect of CMSS scores on self-reported work performance compared to average in the experimental condition, higher scores indicating above average performance (Error bars represent standard error).

4   Discussion

Motion sickness is clearly the most significant effect of building motion. Study 1 shows that individual susceptibility to motion sickness moderates the effect of building motion on symptoms of motion sickness, and Study 2 shows that symptoms of motion sickness mediate the effect of building motion on work performance. Building occupants have limited freedom to avoid working in tall buildings, therefore most sensitive individuals are forced to endure motion-induced discomfort.

Study 2 shows that the effects of building motion are emergent, as motion sickness develops after a duration of exposure to motion, which mostly manifests as symptoms of sopite syndrome, including

tiredness, low motivation, distraction from work activities, and low mood. During building motion, participants report these symptoms at 2-3 times the baseline rate, which significantly reduces work performance by nearly one standard deviation. That performance reductions are limited to those experiencing motion sickness, suggests that direct or immediate effects of motion, such as vibration interference with tasks, has a minimal effect at low accelerations. Affected individuals attempt to manage their own discomfort, and indicate a preference to work a different location during motion, take 30-40% longer breaks, and attempt to self-medicate using analgesic medication, which is unlikely to effectively treat motion sickness.

Long duration exposure to low accelerations, around or possibly below the threshold of perception, may cause a greater discomfort than previously thought. To improve serviceability criteria, future research could determine the motion dose that produces the effects observed in this series of studies, in terms of both low- (e,g. tiredness and distraction) and high-dose motion sickness (i.e. nausea). The motion sickness dose is likely a complex interaction of the duration, strength and frequency of motion, moderated by individual susceptibility to motion sickness.

Building occupants rarely make formal complaints about building motion. Rather than complain, occupants adapt to environmental stressors, continue their work activities, but at reduced levels of performance and comfort. Office design criteria should minimise the environmental stress of building motion on work performance and wellbeing, rather than evaluate building performance based on misleading indicators such as occupant complaint. Robust design standards for building motion will reduce the likelihood that future buildings undergo unacceptable accelerations adversely affect building occupants.

5   References

Burton, M. (2006). *Effects of Low Frequency Wind-Induced Building Motion on Occupant Comfort*. PhD Thesis, Hong Kong University of Science and Technology.

Denoon, R.O., Roberts, R.D., Letchford, C.W., and Kwok, K.C.S. (2000). *Field experiments to investigate occupant perception and tolerance of wind-induced building motion*. Research Report No. R803. Department of Civil Engineering, University of Sydney, Australia.

Golding, J. F. (2006). Predicting individual differences in motion sickness susceptibility by questionnaire. *Personality and Individual Differences, 41*, 237-248.

Goto, T. (1983). Studies of wind-induced motion of tall buildings based on occupants' reactions. *Journal of Wind Engineering and Industrial Aerodynamics, 13*, 241-252.

Graybiel, A., & Knepton, J. (1976). Sopite syndrome: A sometimes sole manifestation of motion sickness. *Aviation, Space, and Environmental Medicine, 47*, 873-882.

Hansen, R.J., Reed, J.W. and Vanmarcke, E.H. (1973). Human response to wind-induced motion of buildings. *Journal of the Structural Division ASCE,* **99(ST7)**, 1589-1605.

Jeary, A.P., Morris, R.G., & Tomlinson, R.W. (1988). Perception of vibration - tests in a tall building. *Journal of Wind Engineering and Industrial Aerodynamics, 29*, 361–370.

Tamura, Y., Kawana, S., Nakamura, O., Kanda, J., & Nakada, S. (2006). *Evaluation perception of wind-induced vibration in buildings*. Proceedings of Institution of Civil Engineers, Structures and Buildings 159 (SB5).

Walton, D., Lamb, S. & Kwok, K. (2011). *A review of two theories of motion sickness and their implications for tall building motion sway. Wind and Structures, 14*, 499-515.

Aerodynamic stability of dry stay cables using different quasi-steady models

Cristoforo Demartino[1] and Francesco Ricciardelli[2]

[1]Dept. of Structures in Engineering and Architecture, University of Naples Federico II, via Claudio 21, 80125 Naples, Italy

[2]Dept. of Informatics, Infrastructures and Sustainable Energy, University of Reggio Calabria, via Graziella, 89122 Reggio Calabria, Italy

Corresponding author: Cristoforo Demartino, cristoforo.demartino@unina.it

Abstract

Galloping vibrations due to critical Reynolds number effects, have recently been identified as a potential problem for dry stay cables. These are mainly connected to complex inclined-flow aerodynamics and to superficial imperfections characterizing real stay cables. The analysis of the forces causing them is usually made using a quasi-steady approach. Several models have been developed with the aim of predicting cable aerodynamic instabilities, each of which considering different aspects of the dynamic and aerodynamic behaviour. In this paper, different models are used to investigate the stability of dry stay cables using aerodynamic data deriving from wind tunnel tests. A comparison of the results has highlighted that the use of multi-DoF models is not justified, as 1-DoF models are sufficient to predict aerodynamic instability.

1   Introduction

Despite the amount of research carried out in recent years, large amplitude vibrations of stay cables is still of concern. Two types of dry cable excitation have been observed in inclined flow. Cables can either undergo a divergent motion with increasing wind speed (dry galloping) or a limited-amplitude motion in a narrow wind speed range (high reduced wind speed vortex induced vibration). Large galloping vibrations of dry stay cables have been observed through long-term monitoring of cable stayed bridges. The aerodynamic action on stay cables is made complicate by the three-dimensional nature of the wind flow and by Reynolds number effects, leading to a steep drop in the drag coefficient and strong variations of the lift coefficient. As a matter of fact, it has been demonstrated that for circular cylinders drag crisis is significantly more likely to occur in inclined flow than in cross flow (Matsumoto *et al.*, 2010). Moreover, Matteoni and Georgakis (2012) highlighted that bridge cables are commonly characterized by local surface roughness perturbations and cross-sectional shape distortion, which alter the flow around the cylinders and promote or inhibit aerodynamic regimes.

With the aim of investigating galloping instability of inclined cylinders, several quasi-steady models have been developed, each of which considering different aspects of the dynamic and aerodynamic behaviour. The first galloping criterion for cylinders in inclined flow is that of Carassale *et al.* (2004), who presented a 2-DoF model for the case of coupled and uncoupled across- and along-wind vibration. In this model, the aerodynamic coefficients depend on the angle of attack and on the wind-cable angle. Macdonald and Larose (2006) derived a general theoretical expression for the quasi-steady aerodynamic damping of stay cables, accounting for the dependence of the aerodynamic coefficients on the angle of attack, on the wind-cable angle and on the Reynolds number. Macdonald & Larose (2008a,b) improved the model of Carassale *et al.* (2004) by including the dependency of the aerodynamic coefficients on the Reynolds number. Finally, Gjelstrup and Georgakis (2011) derived a quasi-steady 3-DoF model, accounting for the dependency of the aerodynamic coefficients on the angle of attack, on the wind-cable angle and on the Reynolds number; the model also accounts for possible inertial coupling.

In the following the results of the application of the above models to wind tunnel data obtained by the authors on a full scale section model of a bridge stay cable, will be shown.

2   Reference wind tunnel data

Wind tunnel tests were performed in the DTU/Force Technology collaborative Climatic Wind Tunnel (CWT) in Lyngby, Denmark. The technical specifications of the facility are reported by Georgakis *et al.* (2009). The model was made of a plain black HDPE tube, provided by bridge cable suppliers, with a nominal diameter of 0.16 m, stiffened with a spacer-separated inner aluminium tube (Demartino, 2014). The length of the model was 1.42 m. Aerodynamic forces were measured at both ends using two 6-DOFs force transducers (AMTI MC3A-500), installed between the model and the supports. The definition of the angles of rotation of the cable is shown in Figure 1, where Θ is the inclination and β is the yaw. The inclination is the angle between the cable axis and the horizontal plane. The yaw is the angle between U and the projection of the cable axis on the horizontal plane. The aerodynamics of a circular cylinder in inclined flow is usually described as a function of the wind-cable angle:

$$\Phi = \arccos(\cos\Theta\cos\beta) \tag{1}$$

In this context U is decomposed into two components: one perpendicular to the cylinder axis, named *normal flow*, U_N, and one parallel to the cylinder axis, named *axial flow*, U_A. Force measurements were performed for $\Theta = 30°$, for yaw angles in the range of 0° to 180° at intervals of 10° and for wind speeds in the range of 8 to 29 m/s ($Re = 0.98\times10^5$ to 3.52×10^5), with steps of approximately 2 m/s. The dynamics of this system is described with respect to the in-plane direction and to the out-of-plane direction perpendicular to the former (Figure 1). As a matter of fact, due to the cable sag the frequencies in these two DoFs are different (Irvine, 1981), as also demonstrated by field observations on real stay cables (Acampora and Georgakis, 2011).
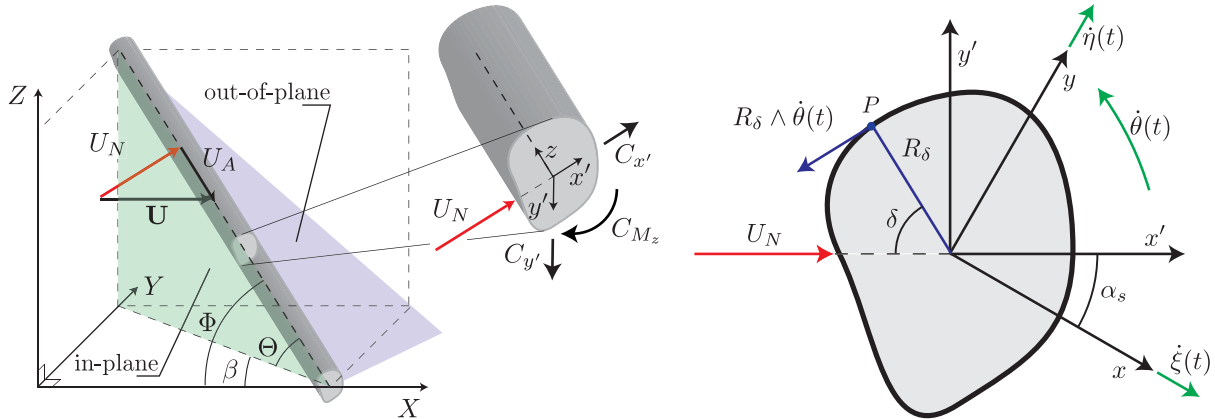
Figure 1. Stay cable orientation, flow and DoFs definitions.

The mean aerodynamic force coefficients were evaluated with respect to the mean wind tunnel speed, U, and to the diameter of the cable of 0.16 m. The variation of the projected area due to the variation of β was not considered. No blockage correction was performed. C_x is the force coefficient associated with the force component parallel to U_N. C_y is the across-wind force coefficient in the direction perpendicular to C_x. C_M is the moment coefficient about z (Figure 1).

In Figure 2 the variation of C_x, C_y and C_M and of their derivatives with respect to Φ and Re is shown. To obtain values of comparable magnitude, the Re derivatives were multiplied by Re; this is also in agreement with fact that they are indeed multiplied by Re in the galloping equations. The derivatives were evaluated in terms of Newton's difference quotient. The values obtained well agree with the results from the literature (Larose *et al.*, 2005; Matteoni and Georgakis, 2012). An increase of C_x was observed in the range of $\Phi = 30°$ to 90°, and a reduction in the range of $\Phi = 90°$ to 150°.

This variation is mainly due to a geometric effect, as the projected area of the model increases in the range of $\Phi = 30°$ to $90°$ and decreases in the range of $\Phi = 90°$ to $150°$. C_x is roughly symmetric with respect to $\Phi = 90°$, and its dependency on Re is more pronounced for Φ around $90°$. The slight asymmetry is generated by the small superficial imperfections of the cable model. At $\Phi = 90°$, C_x decreases approximately from 1.1 to 0.5 with increasing Re, while for $\Phi = 30°$ and $\Phi = 180°$ it decreases approximately from 0.4 to 0.2. This reduction is the effect of critical Reynolds conditions, where a single laminar bubble forms on one side of the cable creating a steady asymmetric pressure distribution. Accordingly, the derivative of C_x with respect to Re has a minimum for Φ around $90°$, and is approximately 0 for Φ approaching $30°$ and $150°$. At $\Phi = 80°$, C_x reaches the value of 0.5 for $Re = 2.95 \times 10^5$ and remains constant when the Reynolds number is further increased; as a result the derivative with respect to Re goes to zero. The derivative of C_x with respect of Φ decreases in the entire range investigated of $\Phi = 30°$ to $150°$.
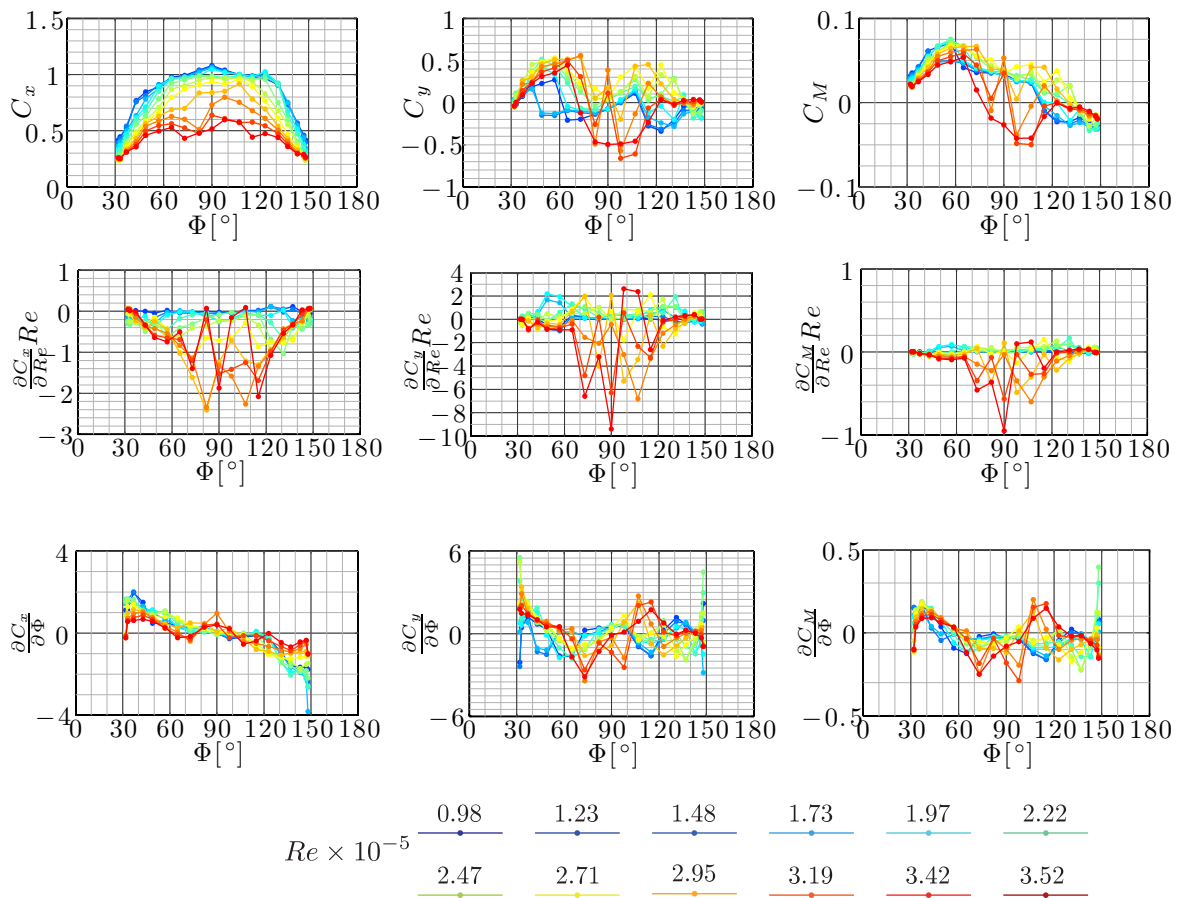
Figure 2. Variation with Φ of C_x, C_y and C_M and of their derivatives, for different values of Re.

The reduction of C_x is accompanied by large (either positive or negative) values of C_y, otherwise small when Φ is close to $30°$ and $150°$. As the yaw moves away from the two limiting cases, an increase in the values of C_y and of their dependency on Re was observed, together with pronounced sign reversals. In a perfectly symmetric setup, the sign of C_y can be either positive or negative, depending on the side where the separation bubble forms; this is very sensitive to small perturbations (Schewe, 1986) and can therefore change in time. In an actual setup, perfect symmetry is never achieved, therefore when the model was rotated of $90°$ about its axis the variations of C_y in the critical regime changes completely, and proves dependent on the surface imperfections of the model (Matteoni and Georgakis, 2012). The derivative of C_y with respect to Re reaches a minimum value (as low as -10) for Φ approaching $90°$ and is approximately 0 for Φ close to $30°$ and $150°$. In particular, for $\Phi = 90°$ and $Re = 3.42 \times 10^5$ the lowest value of the derivative of C_y with respect to Re was found. This derivative is strongly influenced by the superficial imperfections of the cable model. The

derivative of C_y with respect to Φ ranges between ± 3, and has maxima for $\Phi = 30°$ and $150°$. C_M was found to be in the narrow range of -0.05 to $+0.075$ and globally follows the same trend as C_y, confirming that moment is the effect of a variable transverse force with a fixed arm. Also the derivative of C_M with respect to Re follows a similar trend as that of C_y. The derivative of C_M with respect to Φ is similar to that of C_y, with lower values, in the range ± 0.25, with the exception of peaks at $\Phi = 150°$ and $Re = 1.97 \times 10^5$ and 2.22×10^5.

3   Application of galloping stability criteria

In the following the parameters used in the application of the galloping models are given. The diameter $D = 160$ mm is the same as that of the wind tunnel model, and typical of medium- to long-span bridge stay cables. The mass and mass moment of inertia per unit length are taken as typical value for bridge cables of this size: 100 kg/m and 0.32 kg·m^2/m. The value of the first out-of-plane natural frequency of $\omega_y = 2\pi$ chosen for the calculations is comparable with typical values applying to long bridge cables; in a first stage an unrealistic perfect tuning of the in-plane frequency, $\omega_x = \omega_y$, is assumed; in a second stage the effects of detuning are investigated. The detuning is expressed in terms of the detuning parameter $k_{i,j} = \omega_i/\omega_j$, with $i,j = x, y, \theta$ and ω_i being the circular natural frequency in the DoF i. The torsional natural frequency is much larger than the remaining frequencies, thus making $k_{\theta,y} \gg 1$ and $k_{\theta,x} \gg 1$. $R_\delta = 80$ mm and $\delta = 90°$ are typical values used to describe the torsional aerodynamics of circular sections (Gjelstrup and Georgakis, 2011). R_δ and δ are the cylindrical coordinates of the reference point P (Figure 1) representing the velocity field on the cross section boundary. Some of the parameters were then varied with respect to the reference value, in order to understand their influence. When the 2-DoFs and 3-DoFs models were applied, the assumption was made that the damping ratio is the same in all DoFs, $\xi_x = \xi_y = \xi_\theta$.

1-DoF stability of inclined stay-cables was investigated using the model of Macdonald and Larose (2006) for different values of the structural angle α_s, considering and neglecting the dependency of the aerodynamic coefficients on Re and on the wind-cable angle Φ. The structural angle α_s (Figure 1) is the angle between x', i.e. the direction of U_N, and x, i.e. the direction of vibration. Coupled and uncoupled 2-DoFs in-plane and out-of-plane stability was investigated using the model of Macdonald and Larose (2008a,b). Finally, the coupled and uncoupled 3-DoFs stability was analysed using the model of Gjelstrup and Georgakis (2011).

3.1   1 DoF stability

In Figure 3 the regions of potential instability for different values of α_s evaluated using the model of Macdonald and Larose (2006), are shown in the $Re - \Phi$ plane. The contour lines are the instability thresholds. In Figure 3a the regions of potential instability considering the Re- and Φ-dependency of the aerodynamic coefficients, are shown, while, in Figures 3b and 3c the same regions obtained neglecting the Re- or Φ-dependency are shown, respectively. In Figure 3a, two major regions of instability are observed. The first region is approximately in the range of $\Phi = 70°$ to $120°$ for $Re > 2.5 \times 10^5$. The extension of the instability region is larger for $\alpha_s = 0°$, $150°$ and $120°$, reduces for $\alpha_s = 30°$ and $60°$ and completely disappears for $\alpha_s = 90°$. This region of instability exists only considering the Re-dependency of the aerodynamic coefficients, and is mainly related to the large values of the derivative of C_x and C_y with respect to Re (Figure 2). A second, narrow region of instability is found, located approximately in the range of $Re = 1.5 \times 10^5$ to 3×10^5 and in the range of $\Phi = 30°$ to $35°$, which exists only considering the Φ-dependency. Globally, the results appear in agreement with those of Macdonald and Larose (2006), which used aerodynamic data of a cylinder with an inclination of $60°$ in the range of $\Phi = 60°$ to $90°$.
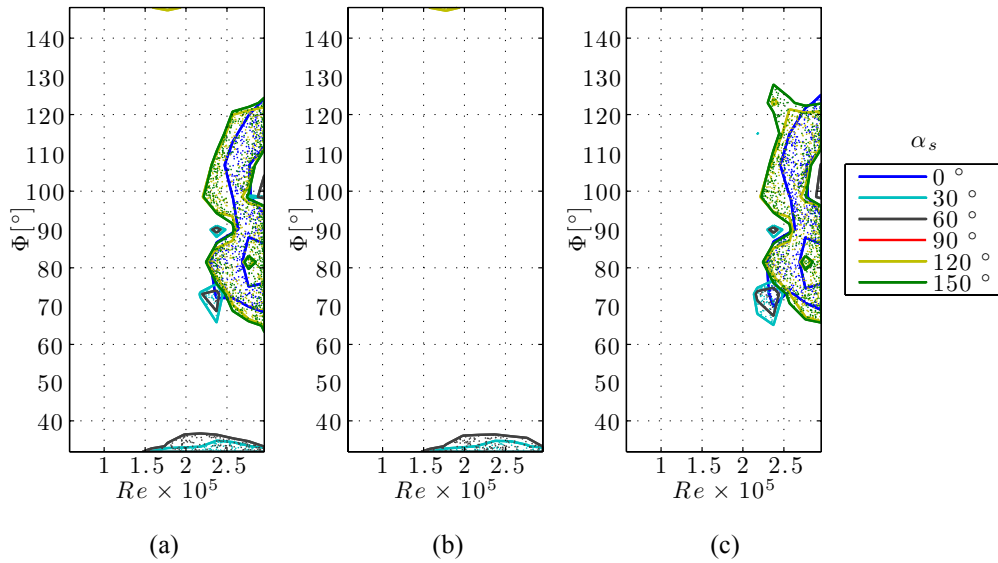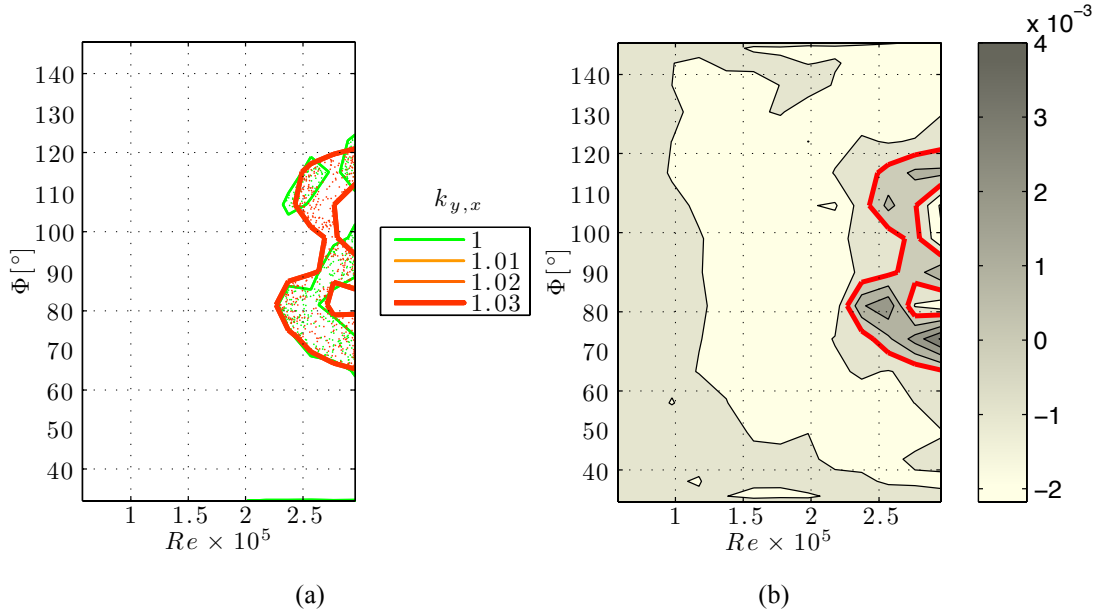
Figure 3. Regions of potential instability for different values of α_s, using the model of Macdonald and Larose (2006), considering (a) and neglecting the dependency of the aerodynamic coefficients on Re (b) or on Φ (c).

The minimum structural damping required to avoid instability for any α_s, is shown in Figure 4 in the $Re - \Phi$ plane. In Figure 4a the results considering the Re- and Φ-dependency of the aerodynamic coefficients, are shown, while, in Figures 4b and 4c the results obtained neglecting the Re- or Φ-dependency are shown, respectively. The regions reported in Figure 4 are the envelope of the maxima of ξ_x obtained with varying α_s. Considering all the dependencies, the maximum value of the minimum structural damping required to stabilize the cable is $\xi_x = 1.2\%$, much larger than the value of $\xi_x = 0.24\%$ found when the Re-dependency is neglected. This difference is the effect of neglecting the drag crisis-type instability. On the other hand, neglecting the Φ-dependency of the aerodynamic coefficients makes instability in the second region disappear, and brings only small changes in the extension of the first region.
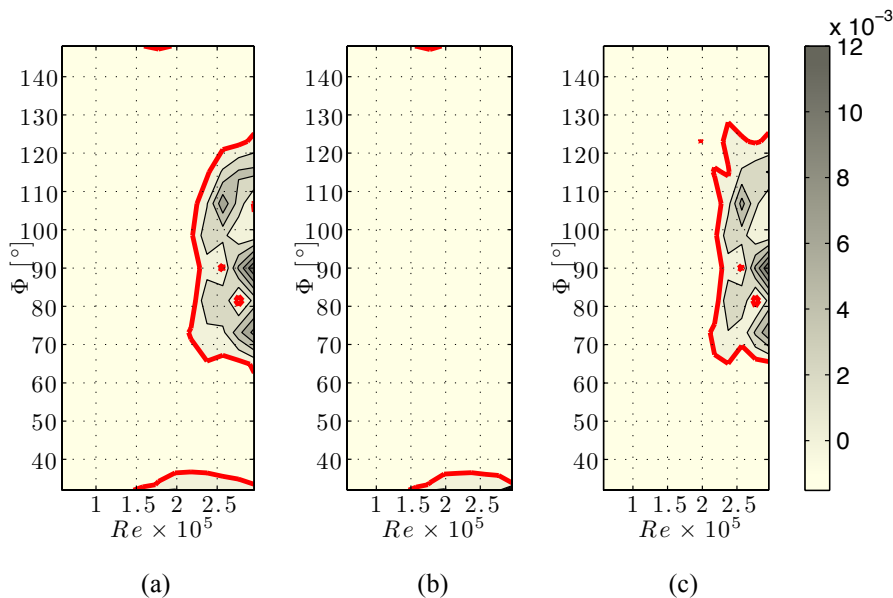
Figure 4. Minimum required structural damping needed to avoid instability for any α_s, using the model of Macdonald and Larose (2006) considering (a) and neglecting the dependency of the aerodynamic coefficients on Re (b) or on Φ (c). The red contour lines are the instability thresholds.

Torsional vibrations are not an issue for bridge cables and the results obtained are of no interest for practical application to bridge cables. Therefore, the values predicted by applying the model of Gjelstrup and Georgakis (2001) considering only the torsional aerodynamic damping are reported only for the sake of completeness, in summary form in Table 1.

3.2   2 DoF stability

In Figure 5a the comparison of the potential instability regions found applying the 1-DoF model of Macdonald and Larose (2006) for $\alpha_s = 0°$ and applying the tuned 2-DoF model of Macdonald and Larose (2008a), is shown. For stay cables, the perfectly tuning is not realistic, as the vertical sag makes the in-plane and the out-of-plane natural frequencies differ (Irvine, 1981). The case of perfectly tuning is considered here with the only purpose of comparison. Globally, the regions of instability found using the 1-Dof and the tuned 2-DoFs models are similar in extension.

In Figure 5b, the minimum required structural damping evaluated using the tuned 2-DoF model of Macdonald and Larose (2008a), is shown. The maximum value found of $\xi_x = \xi_y = 0.25\%$ is quite lower than that found for the 1-DoF instability of $\xi_x = 1.2\%$ (Figure 4a). The prediction of the model of Macdonald and Larose (2008a) considers both DoFs simultaneously and does not depend on the value of α_s (because the stiffness matrix and the mass matrix do not vary with α_s, i.e. they are spherical tensors), as in the case of the 1-DoF model of Macdonald and Larose (2006). Therefore, it can be concluded that for tuned DoFs the use of the maximum required damping from 1-DoF models is conservative. Nevertheless, as already pointed out, this is an unrealistic circumstance for stay cables.

(a)   (b)
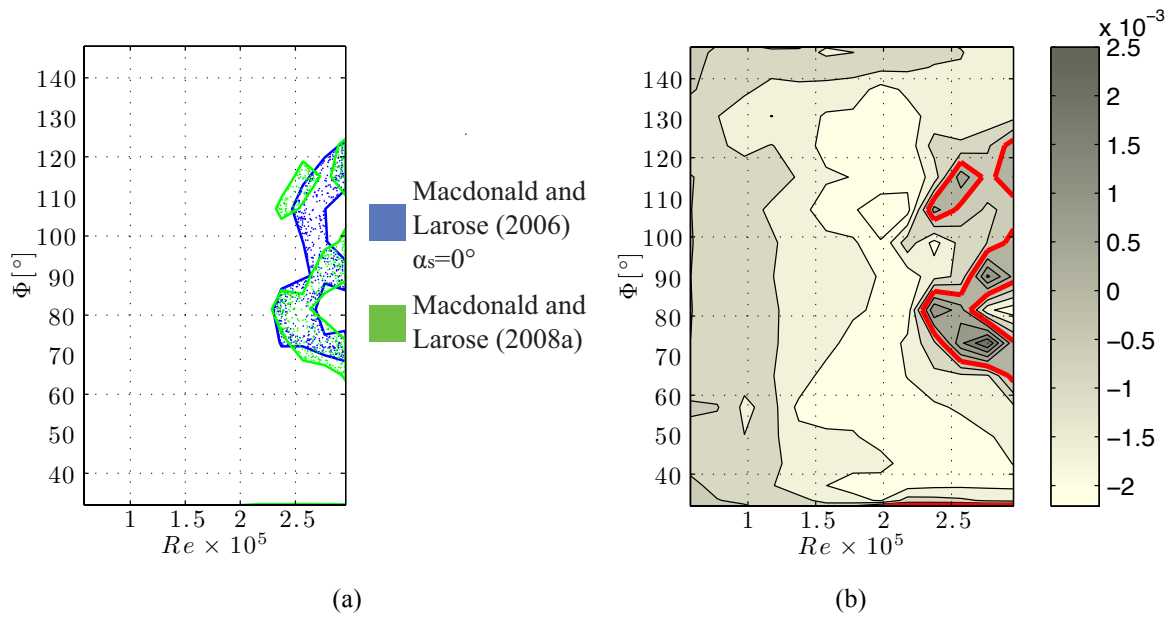
Figure 5. Comparison of the potential instability regions applying the 1-DoF and the tuned 2-DoF models (a). Minimum required structural damping $\xi_x = \xi_y$ needed to avoid instability using the tuned 2-DoF model of Macdonald and Larose (2008a) (b). The red contour lines are the instability thresholds.

In Figure 6a the effects of detuning ($k_{y,x}$) on the extension of the regions of potential instability evaluated using the model of Macdonald and Larose (2008b), are shown. To express the detuning between the in-plane and out-of-plane directions (Figure 1), the structural angle is written as:

$$\alpha_s = \arccos\left(\frac{\tan\Theta}{\tan\Phi}\right) \qquad (2)$$

Small values of $k_{y,x}$ are sufficient to make the system behave as it were uncoupled in the x and y directions, the transition between the coupled and the uncoupled behaviour being rather abrupt. As a matter of fact, for values of $k_{y,x}$ in excess of 1.01 the predicted potential instability regions are already independent of $k_{y,x}$, and overlap to those predicted using the 1-DoF models evaluated in the in-plane

and out-of-plane directions. In Figure 6b the minimum required structural damping $\xi_x = \xi_y$ for $k_{y,x} = 1.03$ and α_s as in Eq. 2 (detuning between the in-plane and out-of-plane directions) is shown. In this case, the minimum required structural damping tends to the maximum value between the predictions of the 1-DoF model of Macdonald and Larose (2006) in the in-plane and out-of-plane directions (α_s as in Eq. 2 and α_s as in Eq. 2 $+90°$) (Table 1).

(a)   (b)

Figure 6. Regions of potential instability for different values of $k_{y,x}$, using the 2-DoF model of Macdonald and Larose (2008b) for α_s as in Eq. 2 (a). Minimum required structural damping $\xi_x = \xi_y$ needed to avoid instability using the 2-DoF model of Macdonald and Larose (2008b) for $k_{y,x} = 1.03$ and α_s as in Eq. 2 (b).

3.3 3 DoF stability

3-DoF stability was evaluated using the model of Gjelstrup and Georgakis (2011). As explained above, the analysis of the 3-DoF model with three coincident frequencies (perfectly tuned system) is lacking of practical interests, since it is not representative of any real situation. Also in this case, small deviations from 1 of $k_{\theta,x}$ and $k_{\theta,y}$ make the potential instability regions tend to the superposition of those pertaining to the 1-DoF and to the tuned 2-DoF systems, taken separately. In conclusion, it appears that when one DoF is detuned with respect to the remaining two, the potential instability regions are the superposition of those pertaining to the 1-DoF and to the tuned 2-DoF systems taken separately. Similarly, if all the three DoFs are detuned, the potential instability regions are the superposition of the three 1-DoF systems taken separately.

4   Discussion

The minimum required structural damping ratios are summarised in Table 1, with different models predicting different values. In particular, the model of Macdonald and Larose (2006) for any α_s predicts a very large value of the minimum required structural damping of 1.2%. Differently, considering only the dependency of the aerodynamic coefficients on Φ, the minimum required structural damping ratio drops to 0.24%.

Table 1. Minimum required structural damping ratio [%] found using the different models. Stable indicates that no structural damping is required for stability. ([*]Adapted torsional model from the damping matrix derived by Gjelstrup and Georgakis (2011)).

Model	DoFs	α_s	Tuned	Dependency		
				Re - Φ	Re	Φ
Macdonald and Larose (2006)	x	any	n/a	1.20	1.20	0.24
Macdonald and Larose (2006)	x	0°	n/a	0.25	0.27	stable
Macdonald and Larose (2006)	x	90°	n/a	stable	stable	stable
Macdonald and Larose (2006)	x	Eq. 2	n/a	0.13	0.10	stable
Macdonald and Larose (2006)	x	Eq. 2 + 90°	n/a	0.44	0.39	stable
Adapted torsional model[*]	θ	n/a	n/a	0.14	0.14	0.12
Macdonald and Larose (2008a)	x and y	Eq. 2 or any	✔	0.25	0.23	0.01
Macdonald and Larose (2008b)	x and y	Eq. 2	$k_{y,x} = 1.03$	0.42	0.37	stable

In order to better understand the difference in the prediction between the 1-DoF for any α_s and the 2-DoF tuned models, some observations are in order. For $\alpha_s = 0°$, the 2-DoF damping matrix is (Macdonald and Larose, 2008a):

$$C_a(\alpha_s = 0°) = \frac{\rho DU}{2} \begin{bmatrix} \left(2C_x + \frac{\partial C_x}{\partial \text{Re}}\text{Re}\right)\sin\Phi + \frac{\partial C_x}{\partial \Phi}\cos\Phi & \left(-C_y + \frac{\partial C_x}{\partial \alpha}\right)\frac{1}{\sin\Phi} \\ \left(2C_y + \frac{\partial C_y}{\partial \text{Re}}\text{Re}\right)\sin\Phi + \frac{\partial C_y}{\partial \Phi}\cos\Phi & \left(C_x + \frac{\partial C_y}{\partial \alpha}\right)\frac{1}{\sin\Phi} \end{bmatrix} \tag{3}$$

The diagonal terms correspond to the aerodynamic damping appearing in the 1-DoF model of Macdonald and Larose (2006) for $\alpha_s = 0°$ and 90°. The aerodynamic damping for other values of α_s can be calculated by applying a rotation to the 2-DoF damping matrix:

$$C_a(\alpha_s) = R(\alpha_s)C_a(\alpha_s = 0°)R^T(\alpha_s) \tag{4}$$

where $R(\alpha_s)$ is the rotation matrix. The 1-DoF model of Macdonald and Larose (2006) considers only the first diagonal term in eq. (3), which varies with varying α_s. The large value of the minimum required structural damping of 1.2% is primarily associated with the large values of the derivative of C_y with respect to Re (Figure 2), appearing in the first diagonal term as an effect of rotation. When applied to the tuned 2-DoF system, the model of Macdonald and Larose (2008a) predicts much smaller values of the required damping than those predicted with the model of Macdonald and Larose (2006) for any α_s. Smaller values of the required damping can be explained through decomposition of the damping matrix in symmetric and skew-symmetric parts:

$$C_a(\alpha_s) = C_a^{sym}(\alpha_s) + C_a^{skew} \tag{5}$$

When the symmetric part is diagonalized, the minimum and maximum damping values for any α_s, appear on the diagonal, being the matrix eigenvalues. The skew-symmetric part of the damping matrix is responsible for the energy transfer between the two eigen-directions; energy migrates from the least dissipative direction to the most dissipative one, in which it is eventually dissipated; this produces elliptical trajectories. The additional energy dissipated in this mechanism, not accounted for by 1-DoF models justifies the lower required damping. The vibration eigen-directions are governed by the damping values as long as the system is tuned, i.e. until the stiffness is the same in all directions (spherical stiffness matrix).

When the 2-DoF model is applied to a detuned system with $k_{y,x} = 1.03$ (detuning between the in-plane and out-of-plane directions), the minimum required structural damping is equal to the maximum between the values predicted by the 1-DoF model of Macdonald and Larose (2006) in the in-plane and out-of-plane directions (α_s as in Eq. 2 and $\alpha_s + 90°$). In this case, the system tends to vibrate in the eigen-direction to which the lowest damping is associated, becoming unstable when this is negative.

When the same model is applied to a detuned system for any α_s, the minimum required structural damping tends to the maximum value predicted by the 1-DoF model of Macdonald and Larose (2006) for any α_s. This confirms the findings of Macdonald and Larose (2008b).

(a)   (b)

(c)   (d)
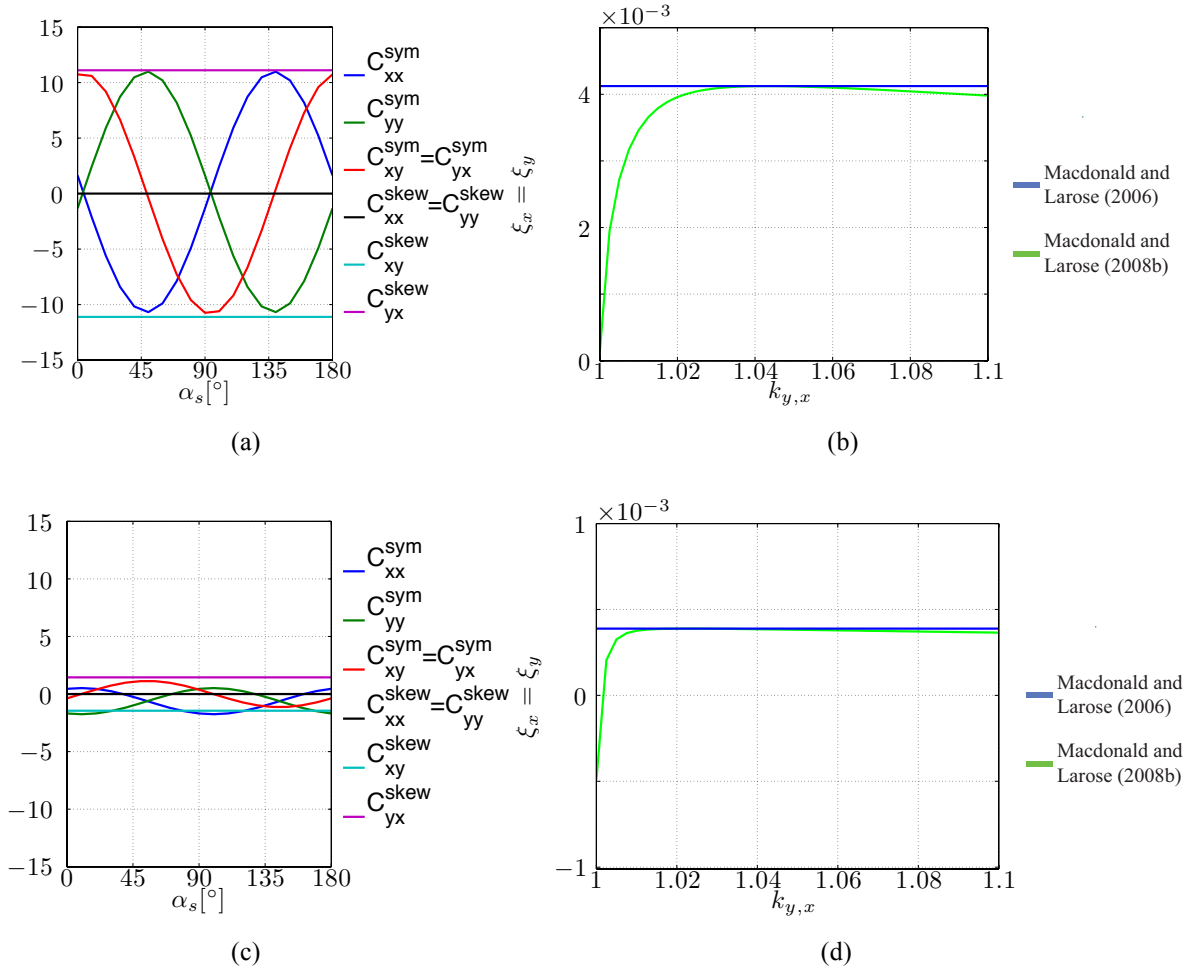
Figure 7. Symmetric and skew-symmetric terms of the aerodynamic damping matrix of the 2-DoF model of Macdonald and Larose (2008a) with varying α_s (a, c). Comparison of the minimum required structural damping predicted using the 1-DoF (Macdonald and Larose, 2006) and 2-DoFs (Macdonald and Larose, 2008b) models for different values of k_{yx} (b, d). $\Phi = 73°$ and $Re = 3.52\times10^5$ (a, b) and $\Phi = 98°$ and $Re = 3.42\times10^5$ (c, d).

To understand the beneficial effect of the skew-symmetric part of the aerodynamic damping matrix in tuned systems, two different conditions characterized by different values of C_a^{skew} are analysed in Figure 7. In Figures 7a and 7c, the symmetric and skew-symmetric parts of the aerodynamic damping matrix of the 2-DoF model of Macdonald and Larose (2008a) are shown as a function of the structural angle, α_s. In Figures 7b and 7d, the minimum required structural damping $\xi_x = \xi_y$ using the model of Macdonald and Larose (2008b) is shown with a green line, while the maximum between the prediction of the model of Macdonald and Larose (2006) in the in-plane and out-of-plane directions is shown with a blue line, for different values of $k_{y,x}$. In Figure 7a, the skew-symmetric terms of the damping matrix, $C_{yx}^{skew} = -C_{xy}^{skew}$, take larger values with respect to Figure 7c. Accordingly, the beneficial effect of detuning is more pronounced in the first case than in the second case. In Figure 7b the minimum required structural damping $\xi_x = \xi_y$ is approximately 0 for $k_{y,x} = 1$ and increases up to 4×10^{-3} for $k_{y,x} = 1.03$, and tends to the value pertaining to the 1-DoF solution. In Figure 7d, the minimum required structural damping $\xi_x = \xi_y$ is approximately -0.05×10^{-3} for $k_{y,x} = 1$ and increases up to 0.4×10^{-3} for $k_{y,x} = 1.01$, and also in this case tends to the value pertaining to the 1-DoF solution.

5   Conclusions

Application of a 1-DoF stability model for the in-plane and out-of-plane vibration of a dry stay cable predicts two regions of potential instability. Application of the 2-DoFs stability model to a tuned system predicts less extended regions of instability and lower values of the required structural damping, indicating that tuning can have a beneficial effect. However, a detuning as low 3% is sufficient to make the 1-DoF and the 2-DoFs predictions coincident. For inclined stay cables perfectly tuning is an unrealistic assumption, due to sag effects. Concluding, it is observed that the use of multi-DoFs models would be justified only in the case of perfectly tuned frequencies, and is unconservative in other cases. It was also shown that neglecting some of the derivatives of the aerodynamic coefficients heavily modifies the galloping predictions. Finally, an explanation of the beneficial effect of the tuning of the M-DoF galloping models has been given.

References

Acampora, A., and Georgakis, C.T. 2011. Recent monitoring of the Øresund Bridge: Observations of rain-wind induced cable vibrations. In: 13th Int. Conf. Wind Eng., Amsterdam.

Carassale, L., Freda, A., and Piccardo, G. 2004. Quasi-static model for aerodynamic instability of yawed circular cylinder. Proc. 5th Int. Coll. on Bluff Body Aerodyn. and App., Ottawa, 401–404.

Demartino, C. 2014. Aerodynamics and aeroelastic behaviour of ice accreted bridge cables. PhD Thesis. Dipartimento di Strutture per l'Ingegneria e l'Architettura, Università di Napoli Federico II.

Georgakis, C.T., Koss, H.H., and Ricciardelli, F. 2009. Design specifications for a novel climatic wind tunnel for the testing of structural cables. Proc. 8th Int. Symp. on Cable Dyn., Paris, 333–340.

Gjelstrup, H., and Georgakis, C.T. 2011. A quasi-steady 3 degree-of-freedom model for the determination of the onset of bluff body galloping instability. J. Fluids and Structures, **27**(7), 1021–1034.

Irvine, H.M. 1981. Cable structures. The Massachusetts Institute of Technology Press, Cambridge.

Larose, G.L., Zasso, A., and Giappino, S. 2005. Experiments on a yawed stay cable in turbulent flow in the critical Reynolds number range. 6th Int. Symp. Cable Dynamics, Charleston, 279-286.

Macdonald, J.H.G., and Larose, G.L. 2006. A unified approach to aerodynamic damping and drag/lift instabilities, and its application to dry inclined cable galloping. J. of Fluids and Structures, **22**(2), 229–252.

Macdonald, J.H.G., and Larose, G.L. 2008a. Two-degree-of-freedom inclined cable galloping part 1: general formulation and solution for perfectly tuned system. J. Wind Eng. Ind. Aerodyn., **96**(3), 291–307.

Macdonald, J.H.G., and Larose, G.L. 2008b. Two-degree-of-freedom inclined cable galloping part 2: analysis and prevention for arbitrary frequency ratio. J. Wind Eng. Ind. Aerodyn., **96**(3), 308–326.

Matsumoto, M., Yagi, T., Hatsuda, H., Shima, T., Tanaka, M. and Naito, H. 2010. Dry galloping characteristics and its mechanism of inclined/yawed cables. J. Wind Eng. Ind. Aero., **98**(6), 317-327.

Matteoni, G. and Georgakis, C.T. 2012. Effects of bridge cable surface roughness and cross-sectional distortion on aerodynamic force coefficients. J. Wind Eng. Ind. Aero., **104**, 176-187.

Schewe, G. 1986. Sensitivity of transition phenomena to small perturbations in flow round a circular cylinder. Journal of fluid mechanics, 172, 33-46.

Velocity profile of the gusty Bora wind

Petra Lepri[1], Hrvoje Kozmar[2], Željko Večenaj[3] and Branko Grisogono[3]

[1]Meteorological and Hydrological Service, Grič 3, 10000 Zagreb, Croatia,

[2]Faculty of Mechanical Engineering and Naval Architecture, University of Zagreb,
Ivana Lučića 5, 10000 Zagreb, Croatia,

[3]Department of Geophysics, Faculty of Science, University of Zagreb,
Horvatovac 95, 10000 Zagreb, Croatia

Corresponding author: Hrvoje Kozmar, hrvoje.kozmar@fsb.hr

Abstract

Vertical velocity profile of the gusty Bora wind blowing on the eastern Adriatic coast is analysed based on the meteorological-tower measurements carried out during summer. Those high-frequency field measurements are taken at three heights up to 40 m. The observed experimental data in this near-ground layer are generally in good agreement with the power-law and the logarithmic-law approximations. However, the most fascinating finding is an increase in the power-law exponent, friction velocity and aerodynamic surface length with decreasing Bora wind velocity that indicates an urban-like velocity profile for smaller wind velocities and a rural-like velocity profile for larger wind velocities.

1   Introduction

Effects of the classical atmospheric boundary layer flow on engineering infrastructure, traffic and human activities are more or less known, but there are some very unique local winds whose characteristics still need to be fully resolved. One example is the gusty Bora wind that blows along the eastern Adriatic coast, and many other dynamically similar places, such as Japan, Russia, Kurdistan, Iceland, Austria, Rocky Mountains in the Northern America, etc. (e.g. Grisogono and Belušić, 2009), significantly influencing local wind energy yield, fatigue of wind energy structures, agriculture and optimal functioning of transportation network (e.g. Kozmar et al., 2012a, 2012b).

Bora is a very strong, usually dry and gusty wind that blows from the northeast across the coastal mountain ranges on the eastern coast of the Adriatic Sea, from Trieste to Dubrovnik and further south (e.g. Belušić and Klaić, 2006). It is spatially and temporally very variable and generally occurs more frequently in winter when it can last up to several days (e.g. Jurčec and Visković, 1994). Bora's mean velocity, 10 to 20 m s^{-1}, is not as substantial as its gusts that can reach velocities up to three or even five times the average value (e.g., Belušić and Klaić, 2006). Bora can be cyclonic, anticyclonic or frontal, depending on the triggering baric system. Cyclonic or 'dark' Bora usually brings clouds with a high possibility for precipitation, while anticyclonic or 'clear' Bora is usually accompanied with clear weather (e.g. Jurčec and Visković, 1994). Frequency of Bora occurrence in the eastern Adriatic decreases from northwest to southeast, and its strength weakens seaward from the shore in a way that it is rarely stormy in the western Adriatic (e.g. Enger and Grisogono, 1998; Grisogono and Belušić, 2009).

2   Methodology

The measurements data discussed in this study were conducted at the meteorological tower on Pometeno brdo in the lee side of the central Dinaric Alps close to the city of Split. Eastern, northern and vertical velocity components and ultrasonic temperature were measured at the sampling frequency

of 5 Hz at 10, 20 and 40 m heights. An isolated summer Bora event, which lasted from 24 to 27 July 2010 (Magjarević et al., 2011) is analysed. The Bora velocity profiles are compared against the power- and the logarithmic-law. The power-law is commonly used in wind power assessment where wind at a certain level has to be estimated from wind measurements at another level. Originally, it was suggested by Hellman (1916) as:

$$\frac{\overline{u}_z}{\overline{u}_{\text{ref}}} = \left(\frac{z-d}{z_{\text{ref}}-d} \right)^{\alpha},$$ (1)

with $\overline{u}_z$ as time averaged mean wind velocity in x-direction at the height z, $\overline{u}_{ref}$ as time averaged mean wind velocity in x-direction at the reference height z_{ref}, d as displacement height and α as the power-law coefficient dependent on atmospheric stability, local terrain roughness and the time averaging interval.

The logarithmic-law:

$$\frac{\overline{u}_z}{u_*} = \frac{1}{\kappa} \ln \frac{z-d}{z_0},$$ (2)

where u_* represents shear velocity, κ von Kármán constant with the value of 0.41 and z_0 aerodynamic surface roughness length, can be considered valid within the inertial sublayer (Thuillier and Lappe, 1964). Considering that a potential applicability of the power- and logarithmic-law for Bora wind profiles in the mean wind direction is tested, the appropriate coordinate system is considered to be the one with the x-axis aligned along the mean wind direction. Time averaged wind speed is calculated using moving average with averaging scale of 17 min which represents a suitable turbulence averaging scale for that type of Bora (Magjarević et al., 2011). In order to test the applicability of the power-law, the time averaged mean wind speeds in x-direction at three levels are normalized using the time averaged mean wind speed in x-direction at 40 m height. Therefore, the power-law exponent α is obtained by data fitting where the displacement height equals zero. For the logarithmic-law testing, u_* and z_0 were calculated in two different ways, i.e. (a) by data adjustment to the logarithmic-law, and (b) by directly applying the logarithmic-law to a layer between 10 and 40 m (both with $d = 0$ m).

3 Results and discussion

In this section applicability of the empirical power-law and the logarithmic-law on the Bora wind velocity profiles, as well as velocity profile characteristics during different wind velocity periods are discussed.

Generally, the results show that both the logarithmic-law and the power-law fit the Bora wind velocity profiles very well, as reported in Fig. 1. For this particular Bora episode, the logarithmic-law and the power-law fit the measured data better when performing the analysis by using the median rather than using the arithmetic mean wind velocity due to a drifting of z_0 values during the recording time.

A decrease in α, u_* and z_0 values with increasing Bora wind velocity can be noticed in Fig. 2 indicating a rural-like velocity profile for larger wind velocities and an urban-like velocity profile for smaller wind velocities. As the time averaged Bora mean wind velocity reaches its local maxima, the corresponding α, u_* and z_0 reach their local minima, and vice versa. In general, the mean value of α for rural terrain is 0.19 and 0.35 for urban terrain, as reported in ESDU 72026 (1972). Moreover, it needs to be mentioned that the reported trends apply to measurements at this specific site only. In addition, more work still needs to be done to fully investigate the applicability of α, u_* and z_0 at other locations, different thermal stability conditions and seasons as well as for the different height ranges of measurement points.
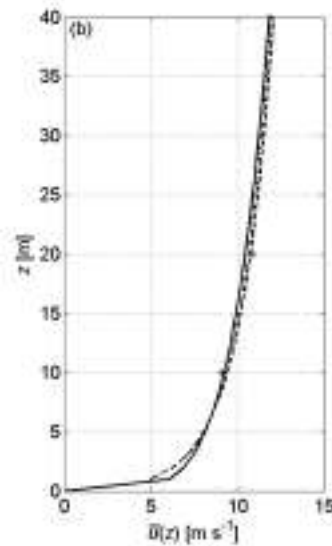
Fig. 1: Vertical velocity profile of the Bora wind; comparison of result measured at the meteorological tower with the empirical logarithmic- and power-law comparison based on calculation using the median value. Legend: star – measured median value, black solid line – power-law, black dotted line – logarithmic-law, black dashed line – logarithmic-law applied to a layer between 10 and 40 m.
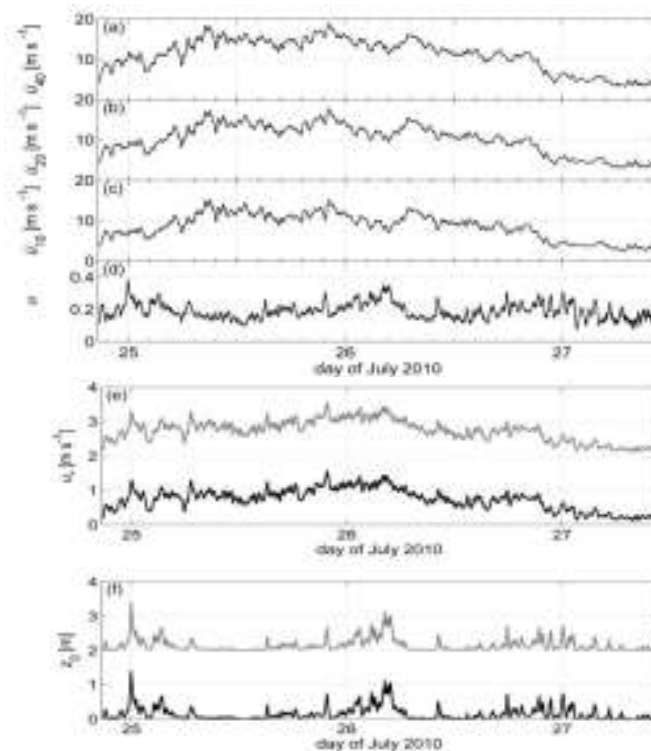
Fig. 2: Mean wind velocity at (a) 40 m, (b) 20 m and (c) 10 m height; (d) power-law exponent α; (e) friction velocity u_* calculated using two approaches: the black curve is obtained by applying the logarithmic-law to a layer between 10 and 40 m and the grey curve is calculated using the logarithmic-law adjustment. The grey curve is artificially shifted upwards for 2 m s^{-1} in order to create a better visual presentation; (f) aerodynamic surface roughness length z_0 calculated using two approaches: the black curve is obtained by applying the logarithmic-law to a layer between 10 and 40 m and the grey curve is obtained using the logarithmic-law. The grey curve is artificially shifted upwards for 2 m in order to create a better visual presentation.

4   Concluding remarks

A summertime vertical velocity profile for the gusty Bora wind was studied. The power-law and the logarithmic-law performance is tested based on 3-level high-frequency velocity measurements carried out on the meteorological tower Pometeno brdo, Croatia. For the first time it is recognized that the observed profiles of the average wind velocity along the dominant Bora wind direction agree well with the power-law and logarithmic-law approximations. An interesting property is an increase in α, u_* and z_0 with decreasing Bora mean wind velocity and vice versa, indicating rural-like velocity profile for larger wind velocities and an urban-like velocity profile for smaller velocities. The logarithmic-law is applied to determine u_* and z_0 by using two different approaches. While both approaches give the same value for u_*, z_0 shows mild discrepancies. The trends mentioned above apply to measurements at the specific site and future work is required to investigate Bora turbulence characteristics at other locations, during potentially different thermal stratifications, seasons and for different elevations of measurement points.

Acknowledgments

References

Belušić, D., and Klaić, Z. B. (2006). Mesoscale dynamics, structure and predictability of a severe Adriatic Bora case. *Meteorol Z* **15**, 157-168.

Enger, L., and Grisogono, B. (1998). The response of bora-type flow to sea surface temperature. *Quart J Roy Meteorol Soc* **124**, 1227-1244.

ESDU Data Item No. 72026 (1972). Characteristics of wind speed in the lower layers of the atmosphere near the ground: strong winds (neutral atmosphere), Eng Sci Data Unit, London, UK.

Grisogono, B., and Belušić, D. (2009). A review of recent advances in understanding the meso- and micro-scale properties of the severe Bora wind. *Tellus* **61A**, 1-16.

Hellman, G. (1916). Über die Bewegung der Luft in den untersten Schichten der Atmosphäre. *Meteorol Z* **34**, 273-285.

Jurčec, V. and Visković, S. (1994). Mesoscale characteristics of southern Adriatic Bora storms. *Geofizika* **11**, 33-46.

Kozmar, H., Butler, K., and Kareem, A. (2012a), "Transient cross-wind aerodynamic loads on a generic vehicle due to bora gusts", *J Wind Eng Ind Aerod* **111**, 73-84.

Kozmar, H., Procino, L., Borsani, A. and Bartoli, G. (2012b). Sheltering efficiency of wind barriers on bridges. *J Wind Eng Ind Aerod* **107-108**, 274-284.

Magjarević, V., Večenaj, Ž., Horvath, K. and Grisogono, B. (2011). Turbulence averaging interval for summer Bora flows at the middle of the NE Adriatic coast. *Poster, 31st International Conference on Alpine Meteorology, May 23 – 27 2011, Aviemore, Scotland*.

Thuillier R. H., and Lappe U. O. (1964). Wind and temperature profile characteristics from observations on a 1400 ft tower. *J Appl Meteorol* **3**, 299–306.

A comparison of wind comfort criteria for a complex case study

B. Blocken[1,2], W.D. Janssen[1] and T. van Hooff[1]

[1]Department of the Built Environment, Eindhoven University of Technology, the Netherlands
[2]Department of Civil Engineering, Leuven University, Belgium
Corresponding author: B. Blocken, b.j.e.blocken@tue.nl

Abstract

A wide range of criteria exist for wind comfort assessment around buildings. This paper compares and evaluates the results by four different criteria as part of a complete wind comfort assessment study. The case study area is the campus of Eindhoven University of Technology. The 3D steady Reynolds-averaged Navier-Stokes (RANS) equations and the realizable k-ε model are used to provide part of the aerodynamic information. The CFD simulations are performed on a high-resolution grid based on grid-sensitivity analysis. Validation is conducted with on-site measurements. Part of the wind comfort assessment procedure is performed with the Dutch wind nuisance standard NEN 8100. The criteria compared in this study are the four complete criteria by Isyumov and Davenport (1975), Lawson (1978), Melbourne (1978) and NEN 8100 (2006a). It is shown that the different criteria can lead to very different conclusions about the wind comfort.

1   Introduction

A wide range of different wind comfort criteria exist. Most of these criteria consist of a threshold wind speed and a maximum allowed exceedance probability of this threshold. Many criteria also distinguish between various activities, such as sitting, strolling, walking fast, etc. In that case, either different values for threshold wind speed, or different maximum exceedance probabilities, or both, are imposed for these different activities. In the past, several comparisons of wind comfort criteria have been performed, the most extensive one being that by Bottema (2000). While this study provided a very valuable and systematic way of comparing different criteria, it also has some limitations. The wind amplification factor was assumed to be wind-direction independent, and the practical consequences of differences between criteria were rather difficult to interpret, visualise and communicate. In this respect, analysis of differences between criteria by means of illustrative case studies would be beneficial. The goal of this paper is therefore to provide an illustrative case study based on CFD as a framework for the comparison of different wind comfort criteria and to compare and evaluate the results by the different criteria as part of a complete wind comfort assessment study. This comparison study is different from previous comparison studies, because of several reasons: (1) it is based on a complex case study; (2) it is performed based on whole-flow field data obtained by CFD; (3) it includes the recently established criteria in the Dutch wind nuisance standard; (4) it is based on a detailed categorization of the four different comfort criteria based on the original articles and on the level of activities in these criteria.

2   Four complete wind comfort criteria

Four different wind comfort criteria are compared in this study, i.e. those by (1) Isyumov and Davenport (1975), (2) Lawson (1978), (3) Melbourne (1978) and (4) the Dutch wind nuisance standard NEN 8100 (2006a). While more criteria exist, these four criteria were selected in this study because they are considered as "complete" criteria, as they address a wide range of activities, including "sitting/standing long", "sitting short" and "strolling". The criteria all consist of a threshold

value of the wind speed U_{THR} and a maximum allowed exceedance probability P_{max} of this threshold value. For comparison purposes, we have clustered these criteria according to the activities for which they define a "moderate/tolerable" situation, and we have provided this information in an overview table that will be provided in the full paper (due to space limitations). The categorization distinguishes between four main categories of activities in terms of wind comfort: (A) Sitting long; (B) Sitting short; (C) Strolling; (D) Walking fast. Two additional categories are "Danger" and "Unacceptable – Poor wind climate", where the latter is considered for a situation that is unacceptable for all activities but not yet dangerous. Therefore this category is situated between category "D" and "Danger". The categorization was based on the categorization and description of different pedestrian activities by Koss (2006). However, the clustering operation which resulted in the overview table was not straightforward and unambiguous, for several reasons, which are reported in Janssen et al. (2013).

3   CFD simulations

Figure 1 shows the campus of Eindhoven University of Technology. The computational domain was selected based on best practice guidelines (Franke et al. 2007, Tominaga et al. 2008). Special care was given to the development of a high-quality and high-resolution grid that consists of only hexahedral and prismatic cells and that does not contain any tetrahedral or pyramidal cells, using the grid generation technique presented by van Hooff and Blocken (2010) (Fig. 1b and d). The grid resulted from a grid-sensitivity analysis (see Blocken et al. 2012) and consisted of about 7.5 million cells. At the inlet of the domain, neutral atmospheric boundary layer profiles of mean wind speed, turbulent kinetic energy and turbulence dissipation rate are imposed. At the walls, the standard wall functions by Launder and Spalding (1974) with the sand-grain roughness modification by Cebeci and Bradshaw (1977) were used with appropriate roughness parameters according to the relationship between z_0 and the parameters k_S and C_S by Blocken et al. (2007). For Fluent 6.3, this relationship is $k_S = 9.793z_0/C_S$. The CFD simulations are performed using the commercial CFD code Fluent 6.3.26 (2006) and the 3D steady RANS equations. Closure is provided by the realizable k-ε turbulence model (Shih et al. 1995). Pressure velocity-coupling is taken care of by the SIMPLE algorithm. Pressure interpolation is second order. Second-order discretization schemes are used for both the convection terms and viscous terms of the governing equations. Convergence is obtained when the scaled residuals showed no further reduction with increasing number of iterations and at that time the residuals reached the following minimum values; x-, y- and z-momentum: 10^{-8}, k and ε: 10^{-7} and continuity: 10^{-6}. The CFD simulations were successfully validated based on field measurements at the campus terrain. The validation study will be reported in the full paper.

4   Wind comfort assessment

The assessment of wind comfort is performed with the procedure of the Dutch wind nuisance standard NEN8100 (2006a, 2006b) in which each of the four comfort criteria are used. The results are shown in Figure 2. The following main observations are made:

- Overall, the application of the different criteria shows large differences in the results on wind comfort and wind danger. This confirms the importance of standardization of studies of wind comfort and wind danger, especially concerning the comfort and danger criteria.
- Concerning the most problematic areas, only the criterion by Melbourne (1978) identifies some areas of wind danger, while neither NEN 8100 nor Isyumov and Davenport (1975) indicate areas of poor wind climate or wind danger.
- Concerning the best areas in terms of wind comfort, NEN 8100 provides the most positive outcome, in clear contrast to Lawson (1978), where the largest part is labelled as only suitable for "walking fast". The criterion by Melbourne (1978) on the other hand shows that a large part of the campus area is suitable for strolling, but on the other hand another large part is not labelled ("unclassified"), meaning that according to Melbourne (1978), it is not suitable for strolling.
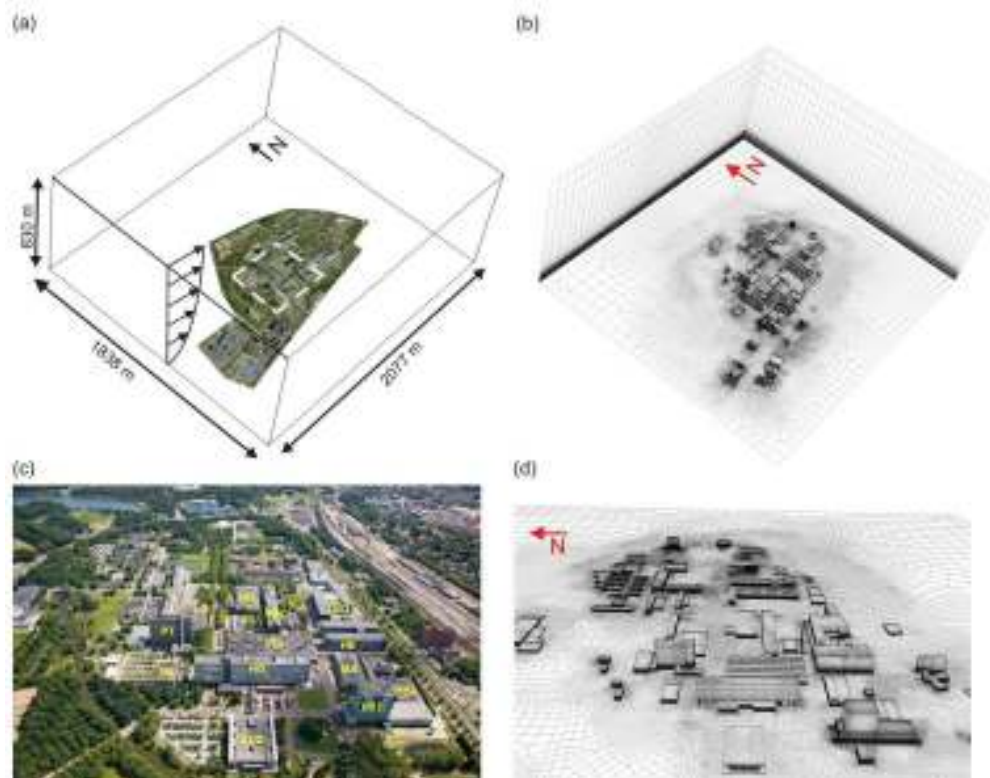
Figure 1. (a) Computational domain with aerial photo of the explicitly modelled buildings; the area of interest is indicated by the dashed rectangle. (b) Corresponding computational grid on the building surfaces, ground surface and two side faces of the domain. (c) Photo of the TU/e campus terrain, taken from west, with indication of abbreviated building names. (d) Corresponding high-resolution computational grid (7.554.091 cells).
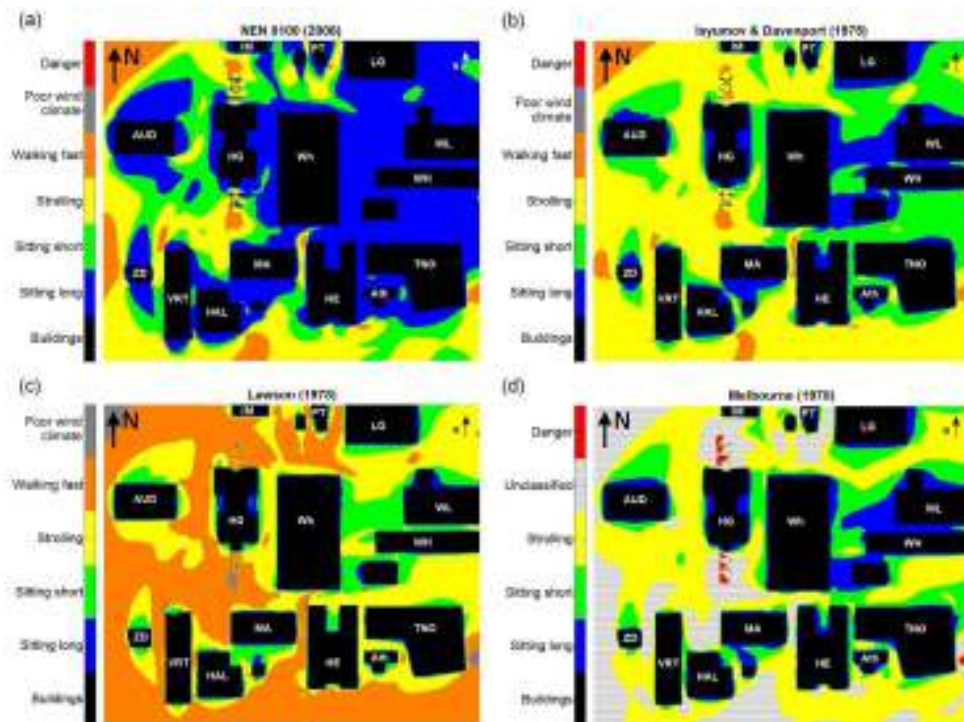
Figure 2. Assessment results for pedestrian wind comfort (moderate/tolerable wind climate for different pedestrian activities) and wind danger according to four different criteria: (a) NEN8100 (2006a); (b) Isyumov & Davenport (1975); (c) Lawson (1978); (d) Melbourne (1978).

5   Conclusions

This study showed that the different criteria can lead to very different conclusions about the wind comfort situation in the complex urban area under study. The criteria by Lawson (1978) and by Melbourne (1978) were shown to be most restrictive, while the criteria by Isyumov and Davenport (1975) showed the best agreement with those of NEN 8100. The latter criterion is considered to be the most lenient of the four complete criteria considered in this comparative study. The resulting wind comfort predictions sometimes shift two classes; from a wind climate that is tolerable for "sitting long" according to NEN 8100 to a wind climate that is only tolerable for "strolling" according to Lawson (1978) and Melbourne (1978). Note that even the criteria by NEN 8100 (2006a) and Isyumov and Davenport (1975), which correspond best to each other, locally can yield differences up to two activity classes. This stresses the importance of standardization of the wind comfort assessment procedure, especially concerning the comfort criterion.

References

Blocken B, Stathopoulos T, Carmeliet J. (2007). CFD simulation of the atmospheric boundary layer: wall function problems. *Atmos Environ* 41: 238-52.

Blocken B, Janssen WD, van Hooff T. (2012). CFD simulation for pedestrian wind comfort and wind safety in urban areas: General decision framework and case study for the Eindhoven University campus. *Environ Modell Softw* 30: 15-34.

Bottema M. (2000). A method for optimisation of wind discomfort criteria. *Build Environ* 35(1): 1-18.

Cebeci T, Bradshaw P. (1977). *Momentum transfer in boundary layers*, Hemisphere Publishing Corporation, New York.

Fluent Inc. (2006). *Fluent 6.3 User's Guide*. Fluent Inc., Lebanon.

Franke J, Hellsten A, Schlünzen H, Carissimo B. (2007). *Best practice guideline for the CFD simulation of flows in the urban environment*. COST Action 732: Quality Assurance and Improvement of Microscale Meteorological Models.

Isyumov N, Davenport AG. (1975). The ground level wind environment in built-up areas. In: *Proc. 4th Int. Conf. Wind Effects on Buildings and Structures*. Heathrow, UK, 403-422.

Janssen WD, Blocken B, van Hooff T. (2013). Pedestrian wind comfort around buildings: comparison of wind comfort criteria based on whole-flow field data for a complex case study. *Build Environ* 59: 547-562.

Koss HH. (2006). On differences and similarities of applied wind comfort criteria. *J Wind Eng Ind Aerodyn* 94: 781-797.

Launder BE, Spalding DB. (1974). The numerical computation of turbulent flows. *Comput. Method. Appl. M.* 3: 269-289.

Lawson TV. (1978). The wind content of the built environment. *J Ind Aerodyn* 3: 93-105.

Melbourne WH. (1978). Criteria for environmental wind conditions. *J Ind Aerodyn* 3: 241-249.

NEN (2006a). *Wind comfort and wind danger in the built environment*, NEN 8100 (in Dutch) Dutch Standard.

NEN (2006b). *Application of mean hourly wind speed statistics for the Netherlands*, NPR 6097:2006 (in Dutch). Dutch Practice Guideline.

Shih TH, Liou WW, Shabbir A, Zhu J. (1995). A new k-ε eddy-viscosity model for high Reynolds number turbulent flows – model development and validation. *Comput Fluids* 24 (3): 227-238.

Tominaga, Y., Mochida, A., Yoshie, R., Kataoka, H., Nozu, T., Yoshikawa, M., Shirasawa, T. (2008). AIJ guidelines for practical applications of CFD to pedestrian wind environment around buildings. *J Wind Eng Ind Aerodyn* 96(10-11): 1749-1761.

van Hooff T, Blocken B. (2010). Coupled urban wind flow and indoor natural ventilation modelling on a high-resolution grid: A case study for the Amsterdam ArenA stadium. *Environ Modell Softw* 25(1): 51-65.

Wind comfort on building balconies: CFD simulation, validation and application for a high-rise tower

H. Montazeri[1], B. Blocken[1,2], W.D. Janssen[1] and T. van Hooff [1]

[1]Building Physics and Services, Eindhoven University of Technology, The Netherlands
[2]Building Physics Section, Department of Civil Engineering, Leuven University, Belgium
Corresponding author: H. Montazeri, h.montazeri@tue.nl

Abstract

High-rise buildings can cause high wind speed near ground level and on building balconies necessitating remedial action. In order to reduce wind discomfort on balconies, different measures can be taken. This paper presents the evaluation of a new second-skin facade concept to improve wind comfort at building balconies. The concept consists of a staggered semi-open second-skin facade in front of the balconies, which partly shields them from the wind. CFD simulations are performed for the building with and without second-skin facade concept. Validation is conducted using wind-tunnel measurements of surface pressure distribution on a building model with balconies. Next, the CFD results are combined with wind speed statistics and a comfort criterion to judge wind comfort on the balconies, according to the Dutch wind nuisance standard. The analysis shows that this concept is effective in providing a zone with pressure equalisation at the balconies. The related reduction in pressure gradients across the width of the facade strongly decreases the local wind speed. At many positions along the balconies this yields a wind comfort improvement of one or even two classes in the Dutch wind nuisance standard compared to the situation without implementation of this concept.

1   Introduction

Wind comfort and wind safety for pedestrians are important requirements in urban areas (Blocken et al., 2012). Although many studies of pedestrian-level wind speed conditions have been performed in the past, they almost exclusively focused on wind speed near ground-level. To the best of our knowledge, only one CFD study has yet been published with focus on wind conditions on building balconies (Murakami, 1990). Attention for wind conditions and wind comfort at building balconies on high-rise buildings is important, because they can be exposed to strong winds and comfort and safety of the pedestrians at the balconies needs to be ensured. In order to reduce wind discomfort on balconies, different measures can be taken, such as closing the balcony or adding partition walls, as in the study by Murakami (1990). Recently a new facade concept was developed by ELD Partnership, which provides another way of shielding the balcony area from strong winds. It consists of a staggered semi-open second-skin facade that partly shields the balconies from the wind (Fig. 1a). The concept is intended to provide a semi-outdoor environment at the balconies, which also includes significant improvement of wind comfort on the building balconies. The concept is implemented in the Park Tower ("Parktoren"), which is a new 78 m high-rise building in the urban area of Antwerp, Flanders, Belgium (Fig. 1b). In this paper, the performance of this concept for this tower is evaluated by CFD simulations based on the 3D steady RANS equations and application of the Dutch wind nuisance standard NEN8100, and by comparing the results for the situation with and without application of this new facade concept. The CFD simulations are subjected to a detailed validation study based on a sub-configuration validation methodology.
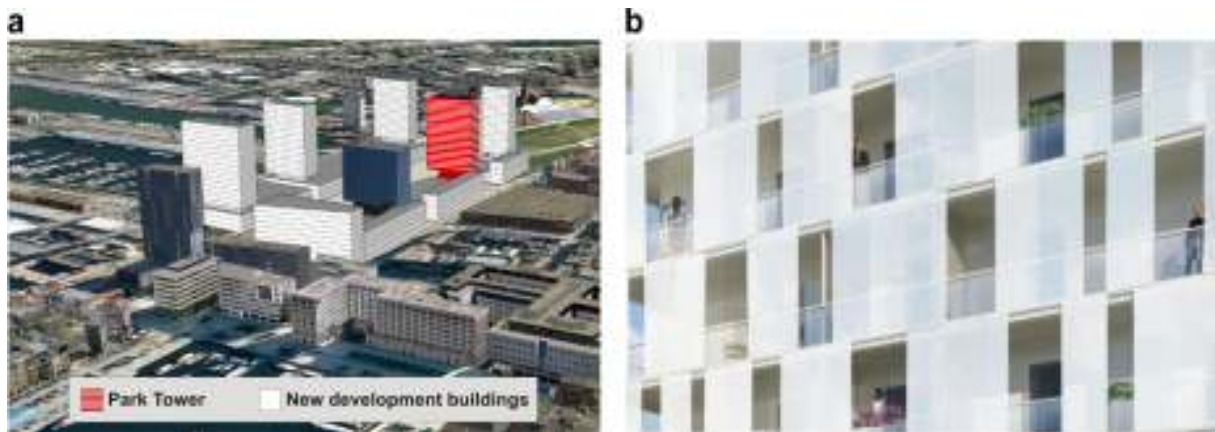
Figure 1. (a) View of Park Tower (red), other new buildings under development (white) and already existing urban surroundings; (b) Building facade with second-skin staggered facade concept.

2   Description of building and urban area

The new high-rise building Park Tower ("Parktoren") is located in Park Spoor Noord in the northern part of the city of Antwerp, Flanders, Belgium. The tower is north-south oriented and surrounded by other high-rise and low-rise buildings (Fig. 1b). It has dimensions L × W × H = 21.87 × 50.88 × 78.18 m³ (Fig. 2a). The depth of the balconies on the north, east, south and west side of the tower is 1.32 m, 1.3 m, 1.59 m and 1.56 m, respectively (Fig 2b). The facade concept is a second-skin concept, where a second outer skin is placed in front of the first and inner skin. The inner skin acts as traditional facade and the outer skin as a wind shield for the balconies between both skins. The second skin consists of a staggered semi-open glass facade, as indicated in Fig. 1a. It has a permanent solid glass balustrade of 1.2 m high, while above this 1.2 m, solid glass facade panels are applied in a staggered configuration. The width of the openings in the second-skin façade ranges from 0.69 to 2.45 m. Note that no partition walls are present in the balcony area, and that this area is completely open for wind flow all along the circumference of the facade. For the comparison study, a reference high-rise building with only the 1.2 m high and non-porous balustrade will be considered. Fig. 1b shows a perspective view of some of the surrounding buildings. The buildings in "white" are all part of the new developments in this area.
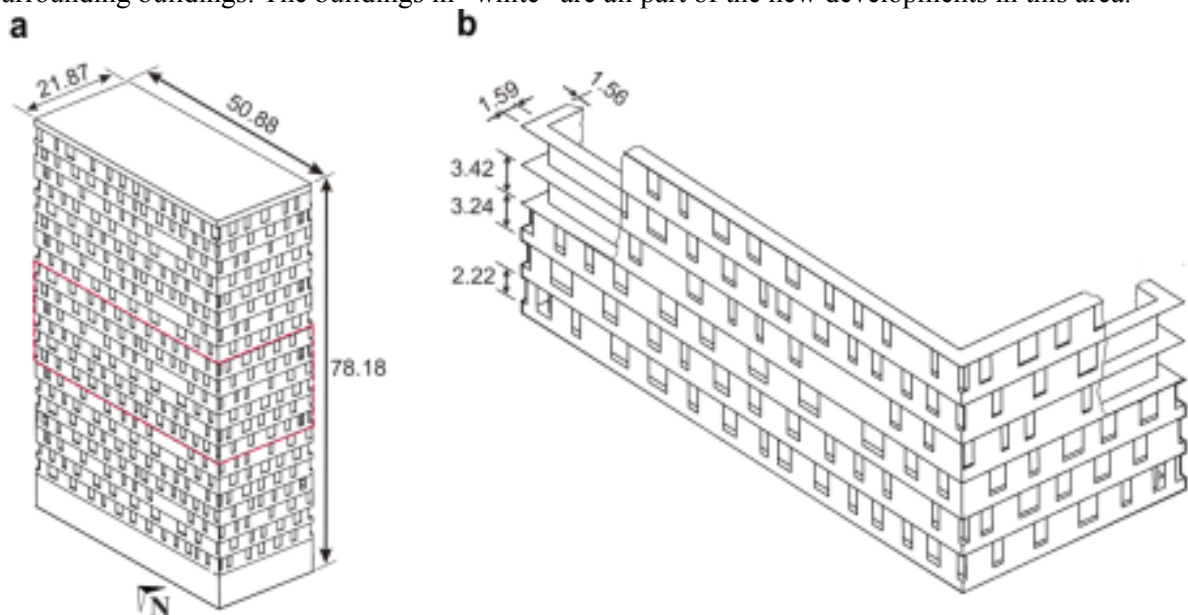
Figure 2. (a,b) Geometry of Park Tower and of part of second-skin facade. Dimensions in metre.

3   CFD validation

CFD simulations based on the 3D steady RANS equations in combination with a turbulence model require validation. As mentioned before, the present study employs "sub-configuration validation". Because the validation study has been published as a separate paper (Montazeri and Blocken, 2013), only the headlines are briefly repeated here.

3.1   Wind-tunnel measurements

Atmospheric boundary layer wind tunnel measurements of wind-induced surface pressure on the facade of a reduced-scale model (1:30) of a medium-rise building were conducted by Chand et al. (1998). The incident vertical profile of mean wind speed (i.e. at the location of the test model) can be described by a logarithmic law with aerodynamic roughness length $z_0 = 0.008$ m and friction velocity $u^* = 0.72$ m/s. Longitudinal turbulence intensity ranged from 13% near ground level to about 3% at gradient height. The building had dimensions $w_m \times d_m \times h_m = 0.25 \times 0.60 \times 0.50$ m^3 (reduced scale, see Fig. 3a) corresponding to full-scale dimensions $W_m \times D_m \times H_m = 7.5 \times 18 \times 15$ m^3, resulting in a blockage ratio of about 6.6%. To evaluate the effect of building balconies on mean pressure, the measurements were carried out for an isolated building with and without balconies. Three balconies each with length 0.15 m, width 0.05 m and height 0.03 m were positioned at each floor (Fig. 3a). Surface pressures were measured along three vertical lines on the windward and leeward facade. Each line was in the middle of the balconies and 45 pressure taps were implemented along these lines. Pressure coefficients were related to the incident wind speed at building height (7.1 m/s).

3.2   Comparison of CFD results and wind tunnel measurements

The wind tunnel experiments are reproduced by solving the 3D steady RANS CFD simulations combined with the realizable k-ε model (Shih et al., 1995) and following the best practice guidelines by Franke et al. (2007) and Tominaga et al. (2008). Fig. 3b compares the numerically simulated and measured pressure coefficients at the windward facades of the buildings with balconies for the wind direction = 0°. The pressure coefficients are computed as $C_p = (P-P_0)/(0.5\rho U_{ref}^2)$ where P is the pressure at the surface, P_0 the reference static pressure, $\rho = 1.225$ kg/m³ the air density and U_{ref} is the reference wind speed at building height ($U_{ref} = 7.1$ m/s at z = 0.5 m). It shows that for the windward facades, the trends are well predicted by the CFD simulations. For the building without balconies, the deviations between the experimental and CFD results is about 10%, while for the building with balconies, it can locally increase up to 20%.
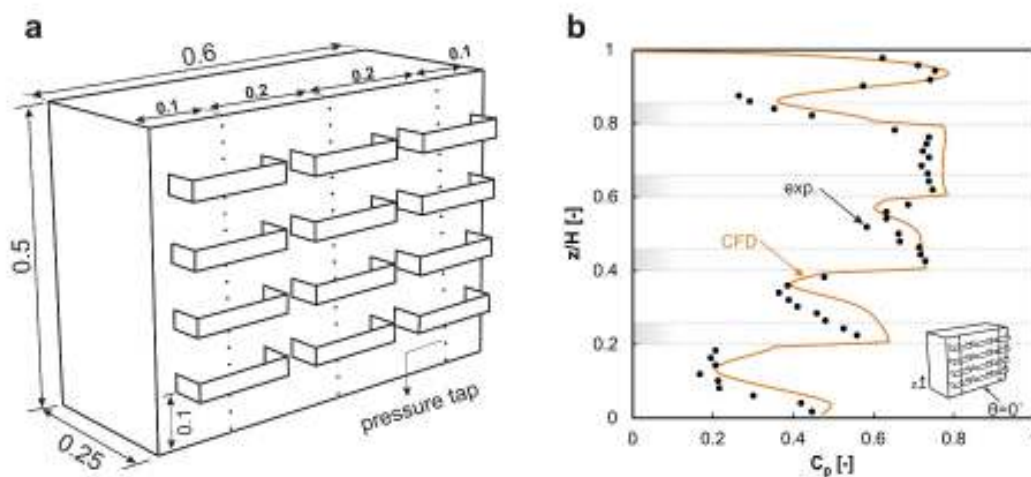
Figure 3. (a) Wind tunnel model of building with balconies and three vertical lines for pressure measurements (reduced-scale dimensions in m); (b) Comparison of wind tunnel and CFD results: pressure coefficient (C_p) along vertical line near building edge.

4   CFD simulations for the case study: computational settings and parameters

4.1   *Computational geometry and domain*

The Park Tower and its urban surroundings are placed in a computational domain with dimensions $W_d \times D_d \times H_d = 2076 \times 1963 \times 400$ m^3. This actual computational domain consists of a subdomain containing the explicitly modelled buildings (i.e. those included in the computational domain with their actual main dimensions) and an additional downstream subdomain, as shown in Fig 4b. The explicitly modelled buildings are the tower itself and the surrounding buildings in a rectangle of 1037 by 632 m² around the tower. The tower is modelled in detail, including second-skin facade with the details of the staggered facade elements as shown in Fig. 2, while the surrounding buildings are included only with their main shape. Special attention is given to the generation of a high-quality and high-resolution grid. The grid is constructed using the surface-grid extrusion technique presented by van Hooff and Blocken (2010), which allows a large degree of control over the quality of the grid and its individual cells. It consists of only hexahedral and prismatic cells and does not contain any tetrahedral or pyramid cells. The grid resolution at the building balconies is based on the one used in the validation study, with at least 10 (hexahedral) cells across the depth of the balconies. A typical cell size at the balconies is 0.1 m. The resulting grid has a total of 16,292,495 hexahedral and prismatic cells. The computational grid is shown in Figs. 4b and 5. For comparison purposes, a similar computational domain and grid are made for the Park Tower without second-skin facade. This grid consists of 15,536,529 hexahedral and prismatic cells (Fig. 5b).
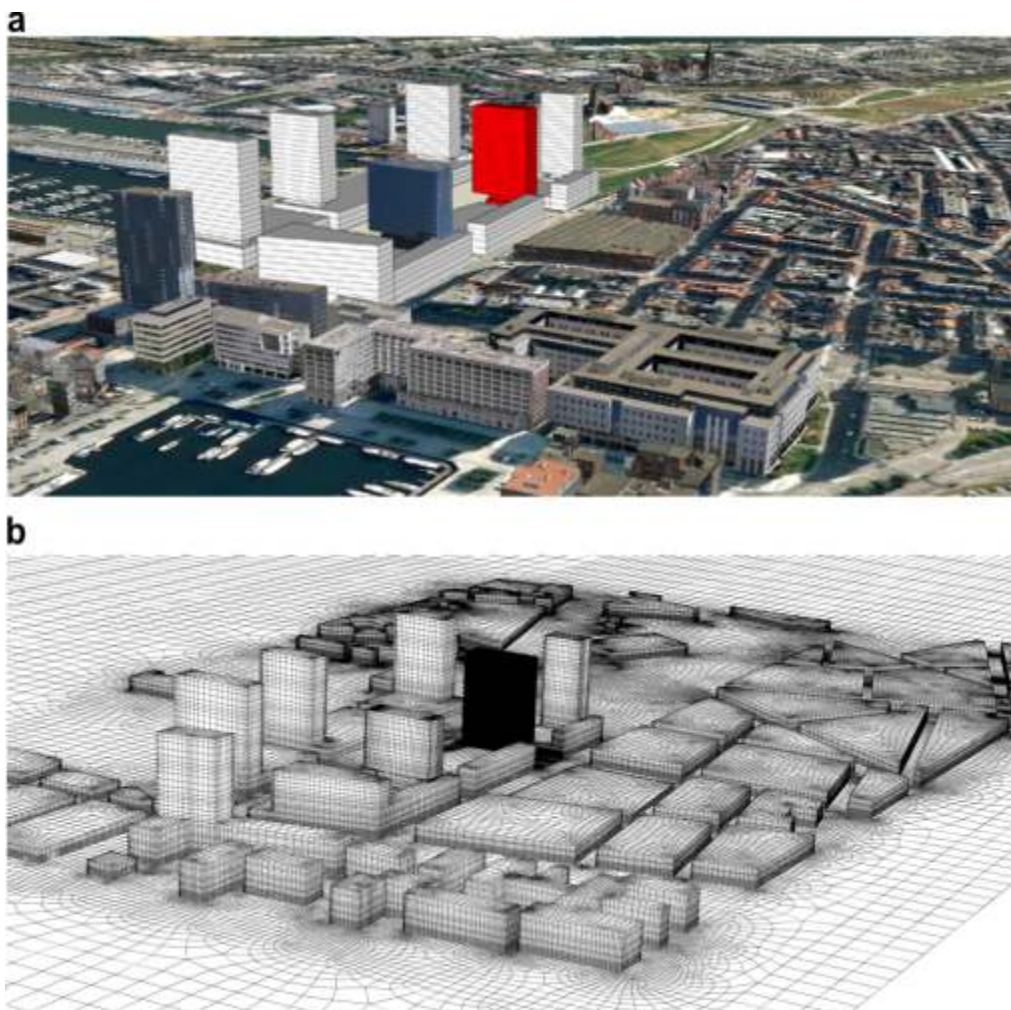
Figure 4. (a) Aerial view of the Park Tower (red) and surrounding buildings. (b) Corresponding high-resolution computational grid (16,292,495 cells).
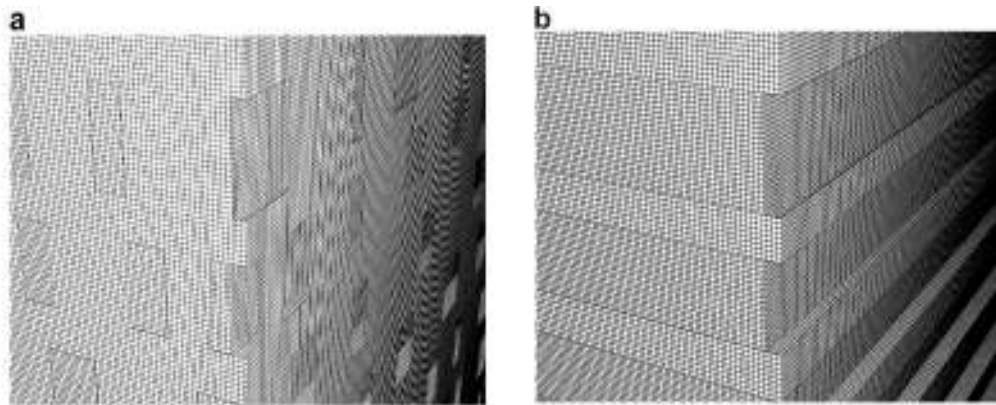
Figure 5. Detail of computational grid near the southwest corner of the 15th floor for the case (a) with second-skin facade concept (16,292,495 cells) and (b) without this concept (15,536,529 cells).

4.2   Boundary conditions

At the inlet of the domain, neutral atmospheric boundary layer inflow profiles of mean wind speed, turbulent kinetic energy and turbulence dissipation rate are imposed. These profiles are based on the aerodynamic roughness length z_0 of the upstream terrain that is not included in the computational domain. At the outlet, zero static pressure is specified. At the sides and the top of the domain, symmetry boundary conditions are imposed. At the ground surface, the standard wall functions by Launder and Spalding (1974) with the sand-grain roughness modification by Cebeci and Bradshaw (1977) are used in which the equivalent sand-grain roughness height k_S and roughness constant C_S are determined based on their relationship with z_0 according to Blocken et al. (2007). At the building surfaces, also standard wall functions are used, with the assumption of smooth walls ($k_S = 0$ m).

4.3   Solver settings

The CFD simulations are performed using the commercial CFD code Fluent 6.3.26. The 3D steady RANS equations are solved with the realizable k-ε turbulence model (Shih et al. 1995). The choice for this turbulence model is based on the recommendations by Franke et al. (2007) and on earlier successful validation studies for pedestrian-level wind conditions with this turbulence model (Blocken et al., 2012). Pressure velocity-coupling is taken care of by the SIMPLE algorithm. Pressure interpolation is second order. Second-order discretisation schemes are used for both the convection terms and viscous terms of the governing equations. The simulations performed for the 12 wind directions θ = 0-330° in 30° intervals.

5   CFD simulations for the case study: computational settings and parameters

Fig. 6 provides contours of the amplification factor in a horizontal plane at the 15th floor, at 1.7 m above the balcony floors for the two cases: with and without implementing the second-skin facade concept. The amplification factor is defined as the ratio between the local mean wind speed and the "undisturbed" mean wind speed at the same height, i.e. the wind speed that would occur without the buildings present. The amplification factor is therefore a direct indication of the influence of the buildings on the local wind-flow pattern. The wind direction is 210°, which is the prevailing wind direction in Antwerp. By comparing the results with and without the second-skin concept, the following observations are made: (1) At the west (windward) facade, the second-skin concept provides a more uniform and also lower value of the amplification factor. (2) At the south (windward) facade, the amplification factor does not become more uniform, but overall it is reduced. (3) At the north and east (leeward) facades, the concept increases the amplification factor. (4) Overall, the second-skin facade seems to provide a more uniform amplification factor over the entire balcony area, i.e. the whole circumference of the building. An exception to this are the north-west and south-east corner, where pressure short-circuiting between windward and leeward facade parts very locally yields a local

amplification factor of about 1. It should be noted that no partition walls are present in the balcony area, and that this area is completely open for wind flow all along the circumference of the facade.
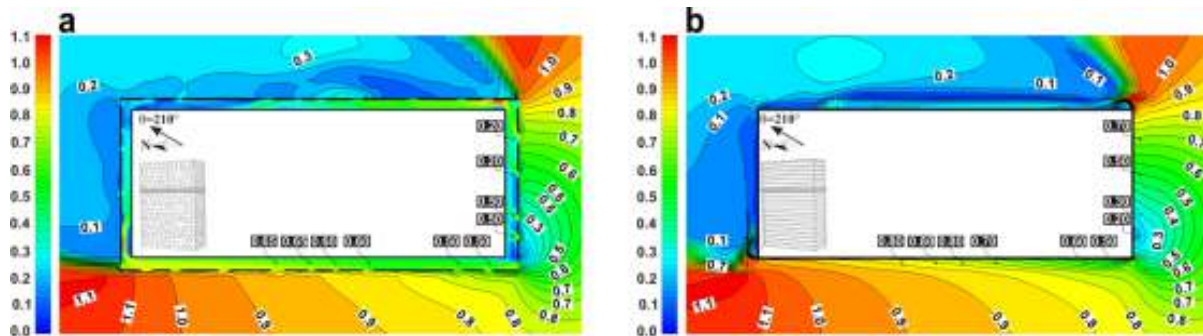
Figure 6. Top view of contours of amplification factor in a horizontal plane at a height of 1.7 m above balcony level for wind direction 210° at 15th floor of the tower (a) with second-skin facade concept and (b) without this concept.

6   Assessment of wind comfort

Wind comfort assessment in this case study is performed with the Dutch standard for wind comfort and wind safety (NEN, 2006a; NEN, 2006b). It contains an improved and verified transformation model for the terrain-related contribution that can provide the wind statistics at every location in the Netherlands, however without including the local building aerodynamic effects. In the standard, the comfort criterion has a threshold of the mean wind speed U_{THR} = 5 m/s for all types of activities. Depending on the type of activity and the maximum allowed discomfort probability, the code defines fives grades of wind comfort A–E (see Table 1). Although the standard does not specify requirements for balconies, one could assume that class A or B are required, which implies P < 5% and a good or moderate comfort for sitting.

Table 1. Criteria for wind nuisance according to NEN 8100 (2006)

P(U_{THR} > 5 m/s) (in % hours per year)	Grade	Activity		
		Traversing	Strolling	Sitting
< 2.5	A	Good	Good	Good
2.5 – 5.0	B	Good	Good	Moderate
5.0 – 10	C	Good	Moderate	Poor
10 – 20	D	Moderate	Poor	Poor
> 20	E	Poor	Poor	Poor

For the present study, the wind statistics of Eindhoven are used, given its proximity to Antwerp and the absence of statistical meteorological data for Antwerp. The wind statistics for the 12 wind directions for Eindhoven are provided by the Dutch Practice Guideline NPR 6097. The total discomfort probability is the sum of the probabilities for the 12 wind directions. Fig. 7 shows these discomfort probabilities for the 15th floor. By comparing the results with and without the second-skin concept, the following observations are made: (1) At the west (windward) facade, the second-skin concept substantially reduces the exceedance probabilities. The size of the reductions is very location dependent, but at many positions it exceeds a factor 2. (2) At the south (windward) facade, also significant reductions are observed. These reductions are most pronounced for higher floors (not shown in this figure). (3) At the north and east (leeward) facades, the second-skin concept increases the exceedance probability. This is also most pronounced for higher floors.
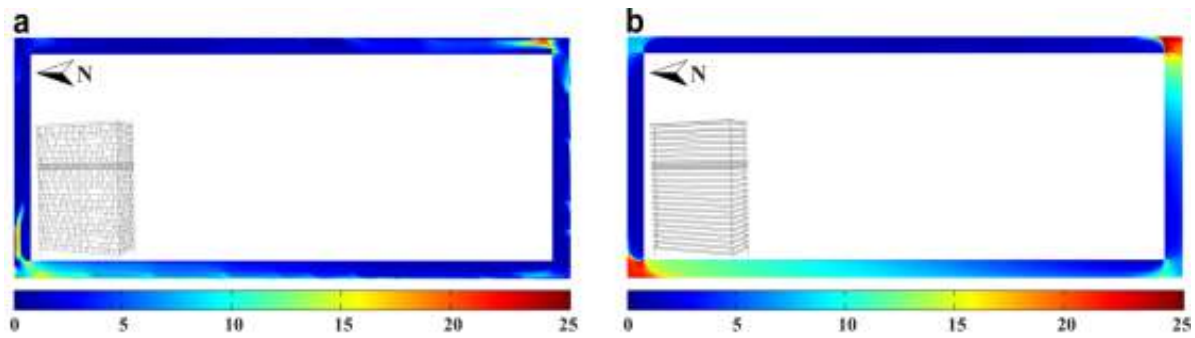
Figure 7. Top view of contours of exceedance probability for wind nuisance in a horizontal plane at a height of 1.7 m above balcony level of the 15th floor of the tower (a) with second-skin facade concept and (b) without this concept.

Fig. 8 labels the balconies according to the five quality classes in Table 1 of the Standard. For sitting, class A is good and class B is moderate, while classes C-E are considered to represent a poor wind comfort for this activity. The figure shows that the second-skin facade concept substantially improves the wind comfort on the balconies on the west and south facade. At most positions, the wind comfort improves with one class, and at some positions even with two classes. On the other hand, the concept causes some decrease in wind comfort on the balconies at the leeward facade. This is for example clear at the east facade at the 15th floor, where the wind comfort at a large part of the balconies shifts from class A to class B.
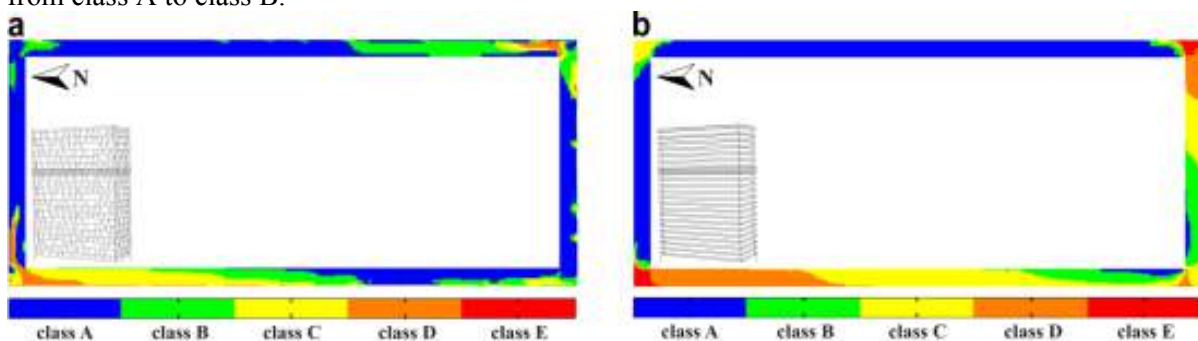
Figure 8. Top view of contours of wind comfort quality classes according to NEN8100 in a horizontal plane at a height of 1.7 m above balcony level of the 15th floor of the tower (a) with second-skin facade concept and (b) without this concept.

7   Discussion

Steady RANS is not suitable for separated regions, but for wind comfort the high-speed regions are most of interest, and only high wind speeds contribute to the exceedance probability of dis-comfort threshold of wind speed (i.e. 5 m/s in the Dutch Standard). Moreover, because of the complexity of the geometry grid-sensitivity analysis was not possible to be performed in this study. However, the computational grid has been made based on guidelines and on previous and similar studies including gird-convergence analysis as recommended by Blocken et al. (2012). In spite of the mentioned limitations, this paper has provided a detailed evaluation of a new facade concept in improving wind comfort on the balconies of a high-rise building.

8   Conclusion

This paper has presented the evaluation of a new facade concept that is intended to significantly reduce the wind speed and therefore improve wind comfort on the balconies of high-rise buildings. The concept consists of a staggered semi-open second-skin facade in front of the balconies, which partly shields them from the wind. The concept is implemented in the Park Tower ("Parktoren"),

which is a new 78 m high-rise building in the urban area of Antwerp, Flanders, Belgium. In this paper, the performance of this concept for this tower has been evaluated by CFD simulations based on the 3D steady RANS equations and application of the Dutch wind nuisance standard NEN8100, and by comparing the results for the situation with and without application of this new facade concept. The CFD simulations have been subjected to a detailed validation study based on the sub-configuration validation methodology. The analysis has shown that the second-skin facade concept is effective in providing a zone with pressure equalisation at the balconies. The related reduction in pressure gradients across the width of the facade strongly decreases the local wind speed. At many positions along the balconies this yields a wind comfort improvement of one or even two classes in the Dutch wind nuisance standard compared to the situation without implementation of this concept. This improvement is more pronounced for floors near the top of the tower. Further detailed information on the can be found in the paper by Montazeri et al. (2013).

References

Blocken, B., Stathopoulos, T., and Carmeliet, J. (2007). CFD simulation of the atmospheric boundary layer: wall function problems. *Atmospheric Environment* **41,** 238-252.

Blocken, B., Janssen, W.D., and van Hooff, T. (2012). CFD simulation for pedestrian wind comfort and wind safety in urban areas: General decision framework and case study for the Eindhoven University campus. *Environmental Modelling & Software* **30,** 15-34.

Cebeci, T., and Bradshaw, P. (1977). Momentum Transfer in Boundary Layers, Hemisphere Publishing Corporation, New York.

Chand, I., Bhargava, P.K., and Krishak, N.L.V. (1998). Effect of balconies on ventilation inducing aeromotive force on low-rise buildings, *Building and Environment* **33,** 385-396.

Franke, A.H. J., Schlünzen, H., Carissimo, B. (2007). Best practice guideline for the CFD simulation of flows in the urban environment.

Launder, B.E., and Spalding, D.B. (1974). The numerical computation of turbulent flows. *Computer Methods in Applied Mechanics and Engineering* **3**, 269-289.

Montazeri, H., and Blocken, B. (2013). CFD simulation of wind-induced pressure coefficients on buildings with and without balconies: validation and sensitivity analysis. *Building and Environment* **60**, 137-149.

Montazeri, H., Blocken, B., Janssen. W.D., van Hooff, T. (2013). CFD evaluation of new second-skin facade concept for wind comfort on building balconies: Case-study for the Park Tower in Antwerp. *Building and Environment* **68**, 179-192.

Murakami, S. (1990). Computational wind engineering. *Journal of Wind Engineering and Industrial Aerodynamics* **36**, 517-538.

NEN, Wind comfort and wind danger in the built environment, NEN8100 Dutch Standard, (2006).

Shih, T.H., Liou, W.W., Shabbir, A., Yang, Z., and Zhu, J. (1995). A new k-ε eddy viscosity model for high Reynolds num-ber turbulent flows, *Computers & Fluids* **24,** 227-238.

Tominaga, Y., Mochida, A., Yoshie, R., Kataoka, H., Nozu, T., Yoshikawa, M., and Shirasawa, T. (2008). AIJ guidelines for practical applications of CFD to pedestrian wind environment around buildings. *Journal of Wind Engineering and Industrial Aerodynamics* **96**, 1749-1761.

van Hooff, T., Blocken, B. (2010). Coupled urban wind flow and indoor natural ventilation modelling on a high-resolution grid: a case study for the Amsterdam ArenA stadium. *Environmental Modelling & Software* **25**, 51-65.

Performance prediction and validation of a tuned liquid column damper with internal baffles

Stefano Cammelli[1], Yin Fai Li[2] and Leejay Hsu[2]

[1]BMT Fluid Mechanics, Teddington, UK
[2] BMT Fluid Mechanics, Kuala Lumpur, Malaysia
Corresponding author: Stefano Cammelli, *scammelli@bmtfm.com*

Abstract

During the early design stages of a relatively slender 42-storey high-end residential building located in the Middle East, a series of high-frequency force balance (HFFB) wind tunnel tests highlighted that the highest occupied floors could experience wind-induced motion which – depending on the inherent damping of the finished structure – had the potential to exceed standard industry occupant comfort criteria. In order to mitigate these excessive vibrations, a Tuned Liquid Column Damper (TLCD) was proposed for this building. The performance prediction and validation of the behaviour of such device involved: an initial campaign of full scale measurements to validate frequencies and inherent damping of the structure near completion; a series of shake table tests employing a 1:20 scale physical model; and a final full scale extrapolation study using Computational Fluid Dynamics (CFD).

1 Introduction

The location of the site of the proposed development considered within this technical paper was approximately 1 km from the Mediterranean coastline, with the immediate surrounding area consisting of densely populated low to mid-rise urban sprawl. The 50-yr return period mean-hourly basic wind speed for the region was ~25 m/s (10 m reference height in $z_0 = 0.03$ m) and the characteristic product of the local wind climate was ~4.

The height of the building was ~180 m, with a ~22 m × ~44 m rectangular floor plan. The lateral stability of the tower was provided by a central reinforced concrete core. The numerically predicted structural frequencies of the three fundamental modes of vibration of the building were: 0.19 Hz, 0.26 Hz and 0.53 Hz, with the first two describing pure sway of the structure along the principal axes of the central core (exponent of these mode shapes were ~1.5) and the third one being torsional.

The damper study, which this paper is focused on, was part of a wider range of wind engineering consultancy services which included: wind climate study, pedestrian and terrace / balcony level wind microclimate study, overall wind loading study and cladding pressure study.

2 On-site full scale measurements

When the construction of the super-structure of the tower approached its completion – and before commencement of the installation of the cladding, a campaign of on-site full scale measurements was conducted to detect some of the key structural parameters of the building; in order to achieve this, the 34th level of the tower was instrumented with a number of low-range high-resolution accelerometers with the aim of acquiring a large number of ambient data records. Before commencement of post-processing, the different time-histories of recorded wind-induced accelerations have been digitally low-pass filtered at a frequency of 1 Hz to remove high-frequency noise content which – due to the nature of the site – have inevitably been picked up during the measurements.

The different time-histories have then been analysed making use of the so-called random decrement (RD) technique (Tamura et al., 2000 and Li et al., 1998 & 2003), which enabled the random and chaotic part embedded in the actual measured signals associated with the excitation from the atmospheric turbulence to be fully removed, revealing the far more regular 'signature' left by the structure itself.

Subsequently, modal identification techniques (Tamura, 2005) were applied to the RD signatures in order to identify the frequencies and damping of the tower during construction. The first two modes of vibration of the structure (for the specific construction stage the tower was at during monitoring) have been found well aligned with the two principal axes of the structural core of the building and their frequencies in very good agreement with the prediction of the finite element model. The level of inherent structural damping associated with these two modes of vibration of the structure was found to be in the region of ~1.0% of critical. It should be noted that during the period of monitoring the strength of the wind storms that passed through the region was lower than what expected for a typical 1-yr return period event.

3   Concept design of the TLCD

A detailed review of the HFFB wind tunnel tests results, performed during the early design stages of the design, revealed that the motion along the weak direction of the building was the key contributor to the peak combined wind-induced acceleration. It was also estimated that, in order to achieve the desired level of occupant comfort at the highest occupied levels of the building – for both the more frequent (1-yr return period) and the less frequent (10-yr return period) wind events, a total damping of ~2.0% of critical in the first mode of vibration of the structure was required.

Amongst the different types of auxiliary damping devices which could be installed on a tall building, tuned liquid dampers (TLDs) are the most cost-effective.

The preliminary design of the damper was conducted following the guidance provided in Vickery (2006). It was estimated that the damping system employed would require a total effective mass of ~80,000 kg, equating to ~0.5% of the modal mass of the first mode of vibration of the tower, and a natural frequency of ~99.5% of the first mode frequency of the building. These estimates were made assuming an efficiency of the damping device of ~75%. Deviation from zero main damping was also duly taken into consideration during concept design.

Due to the relatively slender nature of the building here examined (the slenderness ratio of the building in its weak axis was ~1:9), the more compact tuned liquid column damper (TLCD) solution was adopted from the very start of the concept design study. The TLCD damper comprises an auxiliary vibrating system consisting of a column of liquid moving in a tube-like container. The restoring force is provided by gravity, whilst the energy dissipation is achieved at the baffles installed within the horizontal duct.

The above estimates and considerations led to the selection of a pair of identical TLCDs in the form of a "U-tube" water tank to be installed just below the roof level of the building.

The internal dimensions (i.e. exclusive of the thickness of the RC wall) of one of the two identical TLCDs are reported in Table 1 below:

Table 1. Internal dimensions of one of the two identical TLCDs.

Dimensions (mm)	
Length of the U-tube, L_o	7600
Internal width of each riser, W	1650
Internal breadth of the TLCD, B	4925
Internal height of the horizontal duct, H	1100
Internal free board in each riser, R	900

The overall arrangement of one of the TLCD is illustrated in Figure 1 below:
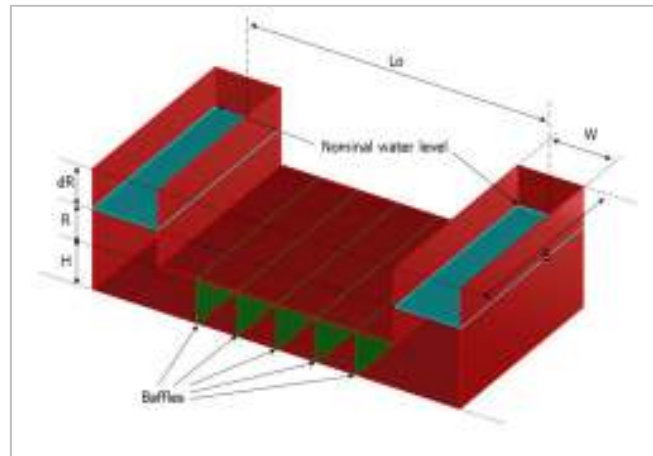
Figure 1. Internal arrangement of one of the two identical TLCDs.

It was estimated that the internal headroom for sloshing 'dR' during a typical 10-yr return period wind event was ~1000mm. It should be noted that the number and location of the required internal baffles was – at this stage of the design – only indicative.

4   Detail design of the TLCD – Physical model testing

The concept design of the damper was tested in the 6 degree-of-freedom (6DOF) shake table facility of the Department of Civil Engineering of the University of Bristol. The aim of the model testing was not only to verify the key resulting parameters of the concept design but also to derive the optimal geometry and internal arrangement of the baffles within the TLCD.

4.1   Experimental setup

A 1:20 model of the damper was constructed in Plexiglas. The construction of the damper allowed up to five interchangeable porous screens to be inserted within its horizontal duct. The working fluid in the model was water. The model damper was mounted on the shake table via a piezoelectric load cell (see Figure 2). The motion of the shake table was programmed according to the solution of the equation of motion of the first mode of the actual building at various levels of structural damping computed based on wind tunnel measurements. The motion of the shake table was then measured simultaneously with the load cell signal using non-contact displacement transducers.
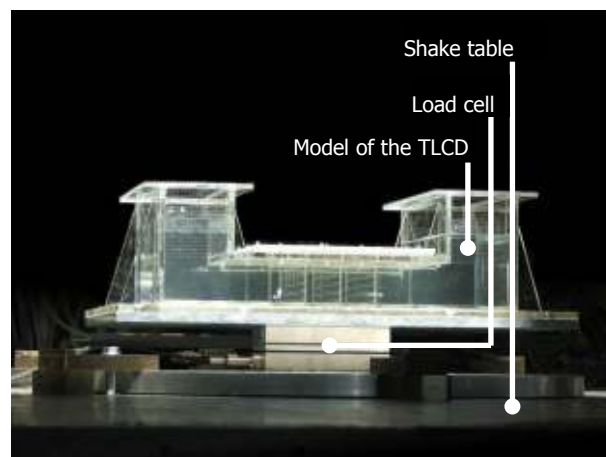
Figure 2. Experimental setup of the 1:20 TLCD model.

A video of the model scale experiment is presented in Figure 3.

Figure 3. Video of the physical model scale shake table testing (press ▶ on the still image to run).

4.2   Results and discussions

The energy dissipated within the model can be derived from the simultaneous measurements of the base force reaction and motion of the damper as follows:

$$W = \int F dx = \int F \dot{x} dt \tag{1}$$

where $F, x, \dot{x}$ denotes the measured force, displacement, and time derivative of the displacement (i.e., velocity). The equivalent damping ratio of the TLCD, i.e. the damping ratio of a non-viscous device that would dissipate the same amount of energy per cycle of vibration as a perfectly viscous device at the same amplitude, can be defined as follows:

$$\int F \dot{x} dt = \int -c_{eq} \dot{x}^2 dt = \int -2\zeta_{eq} m \omega_n \dot{x}^2 dt$$

$$\zeta_{eq} = \frac{\int F \dot{x} dt}{\int -2m\omega_n \dot{x}^2 dt} = \frac{1}{-2m\omega_n} \frac{\int F \dot{x} dt}{\int \dot{x}^2 dt} = -\frac{1}{2m\omega_n} \frac{\sigma_{F\dot{x}}^2}{\sigma_{\dot{x}}^2} \tag{2}$$

where $\zeta_{eq}, m, \omega_n, \sigma_{F\dot{x}}^2, \sigma_{\dot{x}}^2$ are the damping ratio expressed as fraction of critical, mass (in kg), and natural circular frequency (in rad/s) of the system, covariance between measured force and velocity (in N·m/s) and variance of velocity (m²/s²). It should be noted that the measured ratio of the two covariances is not dimensionless and had therefore to be converted to full scale in order for the equation above to apply. A dimensional analysis revealed that the scaling of the $\frac{\sigma_{F\dot{x}}^2}{\sigma_{\dot{x}}^2}$ term would follow the geometric scale of the model raised to the power of 2.5, i.e.:

$$\zeta_{eq} = -\frac{NR_L^{2.5}}{2m\omega_n} \frac{\sigma_{F\dot{x}}^2}{\sigma_{\dot{x}}^2} \tag{3}$$

where R_L and N are the geometric scale and the number of TLCDs installed in the building. Eq. (3) therefore represents a direct relationship between the equivalent damping ratio of the full scale damper system and the model scale $\frac{\sigma_{F\dot{x}}^2}{\sigma_{\dot{x}}^2}$ term, which was measured as a function of standard deviation of excitation displacement.

In the case of a TLCD installed on a building with fixed structural frequencies and inherent damping, the standard deviation of excitation amplitude during a wind event is controlled by total system damping, which is in turn contributed significantly by the added damping of the TLCD itself.

Figure 4 plots the equivalent added damping ratio versus total system damping. It is clear from this graph that for all configurations of porous baffles tested, the equivalent damping generally increased with excitation magnitude, or decreased total damping. Configurations with a larger number of porous baffles generally showed higher energy dissipation at low amplitude, as more energy was dissipated when water moved across the screen. While, on the other hand, configurations with many baffles had the potential to prohibit the build-up of vibration amplitude of the water, hence hindering the damping performance.

The actual damping performance, taking into account the inherent damping of the structure, is denoted in Figure 4 by the intersection points between different baffle configurations and different levels of inherent damping. From this plot it is clear that both the '3 baffles' and the '5 baffles' configurations gave rise to an equivalent damping ratio of ~1.2% of critical which – together with a ~1.0% of inherent structural damping – corresponded to ~2.0% of critical of total system damping.
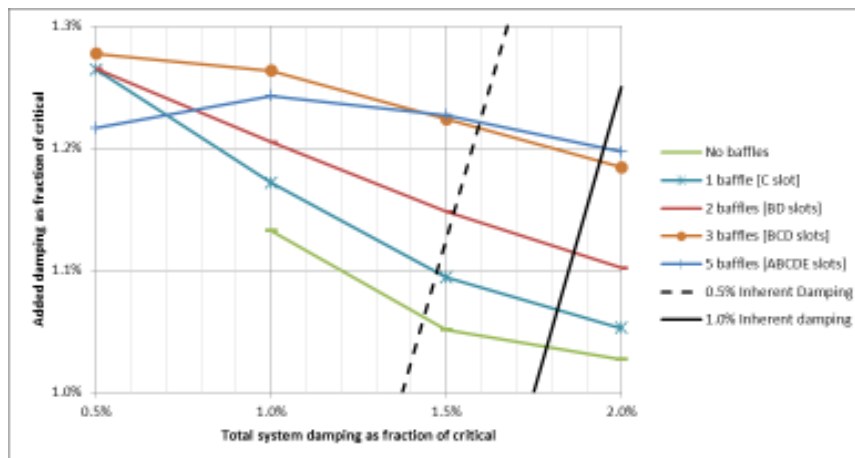
Figure 4. TLCD performance curves (75% porous baffles).

The geometrical arrangement of the best performing baffle arrangement (75% porous) is presented in Figure 5.
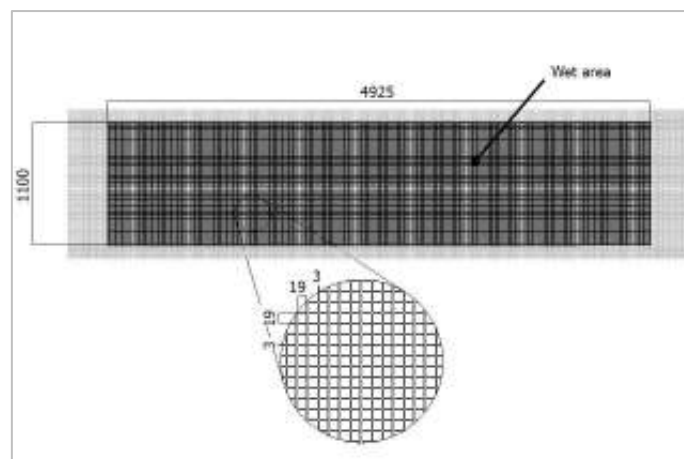
Figure 5. Arrangement of a 75% porous baffle (dimensions in millimetres).

4.3   Comparison with the solution of 2DOF equation of motion

In order to further inspect and understand the measured results in terms of total system damping performance, the time domain solution of equation of motion based on Clough and Penzien (1993) for the first mode has been extended to a 2 degree-of-freedom (2DOF) system to incorporate the addition of the TLCD. In order to solve the equation of motion in the time domain the knowledge of the internal damping of the TLCD is required.

   The internal damping of the damper system with optimal baffle configuration was evaluated via a series of free decay model testing. The free decay of base shear force was measured after the damper was subjected to a step excitation. The internal damping was calculated by applying the logarithmic decay to the measured time histories. It was found that the damping generally reduces with amplitude and, for the operating conditions here examined (10-yr return period wind event), the damping is of the order of ~3.7% – 3.9% of critical. A sample of a free decay time history is shown in Figure 5 with damping estimates for different section of the time history.
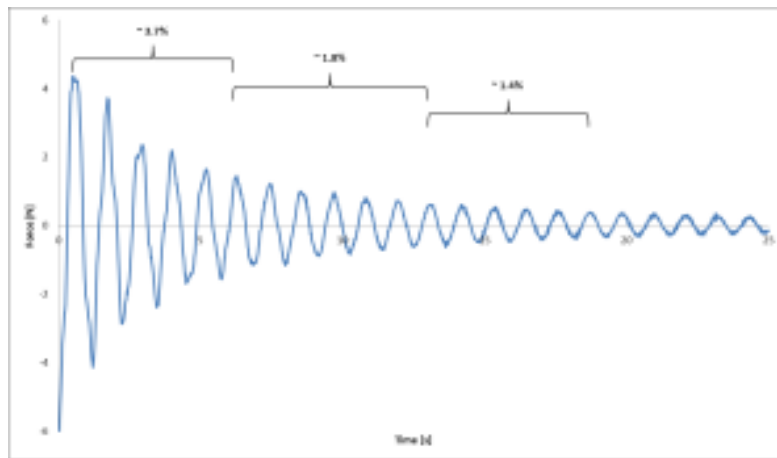
Figure 5. Example of free decay force time history of the physical model of the TLCD.

   The 2DOF equation of motion was solved for the measured wind excitation, damping ratio and frequency of the TLCD for each time step and the response with and without the TLCD is presented in Figure 6. The peak acceleration response of the primary mass, i.e. the building itself, has reduced from ~21.5 milli-g to ~15.5 milli-g, which is equivalent to an increase in total system damping from ~1.0% of critical to ~1.9% of critical.
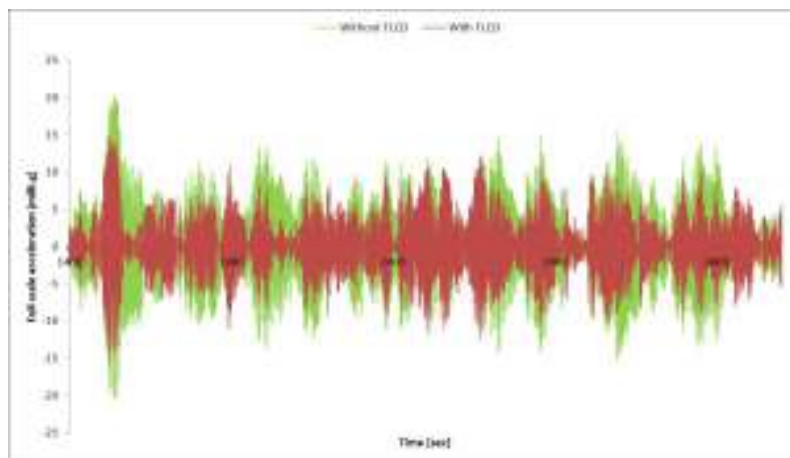
Figure 6. Solutions of the equation of motion in the time domain, with and without TLCD.

5   Detail design of the TLCD – CFD study

The 1:20 scale physical model testing inevitably left the authors of this technical papers with some uncertainties over the potential for scale effects to affect the performance of the full scale TLCDs. In order to try to quantify these, a number of CFD studies have been undertaken.

5.1   Analysis software

The multi-purpose CFD software OpenFOAM® (*www.openfoam.com*) was used for the study. OpenFOAM® is an open source CFD package which has gained a large user base in commercial and academic applications which features a wide variety of validated solvers in the area of oscillatory and sloshing flow.

5.2   Geometry and grid

The numerical work was focused on a single TLCD, the internal volume of which was discretised with a 3D structured mesh. Areas of particular interest were modelled with a higher level of geometrical detail, such as the regions around each baffle.

Figure 7 shows the complete structured mesh of a single TLCD. The green regions are open to atmospheric pressure. The blue regions represent areas of high mesh density near the baffles: properly capturing the flow behaviour in these regions was a high priority.
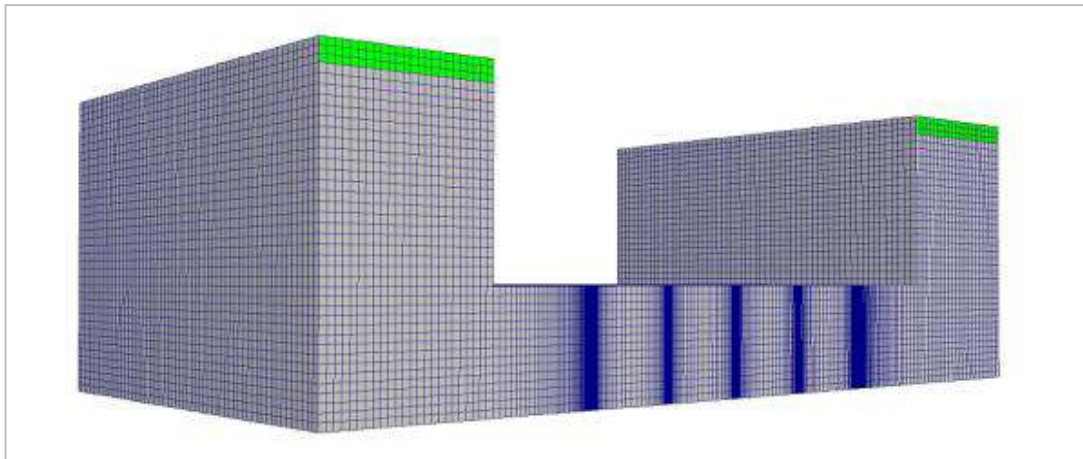
Figure 7. Perspective view of the spatial mesh.

5.3   Porous regions

The baffles were modelled as anisotropic porous regions using the Darcy-Forchheimer approach. This model is composed of two parts: a viscous loss term known as the Darcy permeability (first term on the right hand side of Eq. (4)) as well as an inertial loss term known as the Forchheimer term (second term on the right hand side of Eq. (4)):

$$S_i = -\left(\sum_{j=1}^{3} D_{ij}\mu U_j + \sum_{j=1}^{3} F_{ij}\rho\bar{U}U_j\right) \tag{4}$$

Where S_i is the volumetric source term added to the momentum equations of the baffle zones, D_{ij} and F_{ij} are the prescribed porous media tensors, μ is fluid dynamic viscosity, ρ is fluid density, U_j is the jth component of the velocity vector, and $\bar{U}$ is the velocity magnitude.

5.4   Boundary conditions

Rough walls with a no-slip condition (u, v, w = 0) were assumed for all internal surfaces. A turbulent viscous wall function and mean roughness height of 0.025mm (uniform sand grain roughness) were used to simulate the surface roughness of the smooth-finish concrete walls in the full scale simulations of the TLCD. The lateral pressure release openings were modeled as constant atmospheric pressure openings in the CFD grid.

5.5   Turbulence model

The standard k-ε turbulence model was employed in the CFD simulations when assessing the internal flow of the water tank in order to capture recirculation and eddy phenomena (such as the recirculation near the inside corners as illustrated in Figure 8). This turbulence model is one of the most widely used turbulence models for its combination of computational speed and accuracy.
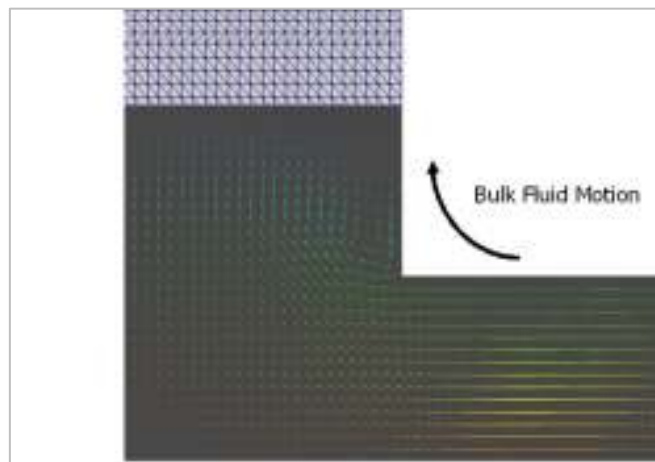
Figure 8. Recirculation near the internal corner of the TLCD.

5.6   Solver

OpenFOAM®'s interDyMFoam solver was used for the study. This solver is compatible with 2-phase, isothermal, incompressible, immiscible flows. InterDyMFoam uses a finite volume approach to represent the Navier-Stokes equations, in which each cell in the computational mesh is assigned a single value for each fluid property (i.e. velocity and pressure) that represents the average of these properties over the whole volume of the cell.

5.7   Methodology

A 1:20 scale numerical model was initially set-up with the aim of generating results which could have been directly compared with the ones obtained from the physical model testing campaign. A number of mesh independence studies was conducted to determine an optimal computational mesh, as well as to locate potential areas which would benefit from mesh refinement (e.g. regions in which vortices and recirculation were expected, see Figure 9). Once the 1:20 numerical model was finalised, the results were compared to experimental shake table results before performing full scale computational analysis.
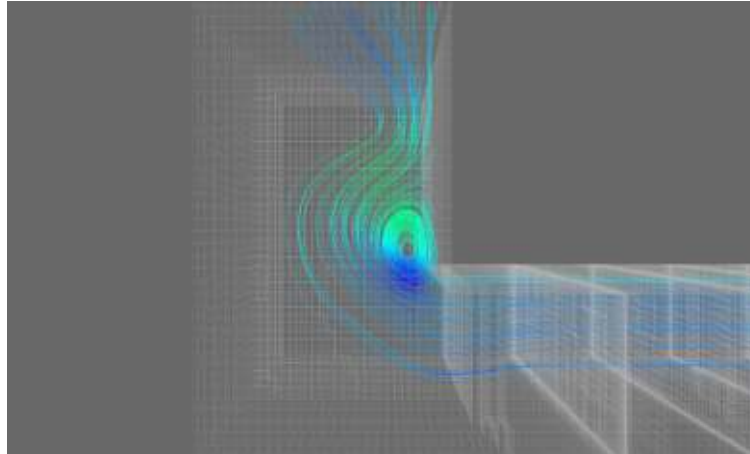
Figure 9. Streamlines under free decay motion.

The free-decay logarithmic decrement approach was used to quantify the performance of each simulated TLCD. This method included the excitation of the CFD model with a sinusoidal input wave until the system reached a periodic steady state. The forced movement of the TLCD was then stopped, and the decay of the overall net force was measured over time. The net force measured included the contribution from dynamic pressure acting on the walls and baffles of the TLCD in the direction of the first mode of vibration of the tower.

Comparison of damping performance ('3 baffles' configuration), as simulated in CFD and experimentally gathered in the shake table experiments ($\sim$4.2 – 4.5% and $\sim$3.7 – 3.9% respectively), was satisfactory given the complex nature of unsteady multi-phase flow (see Figure 10).
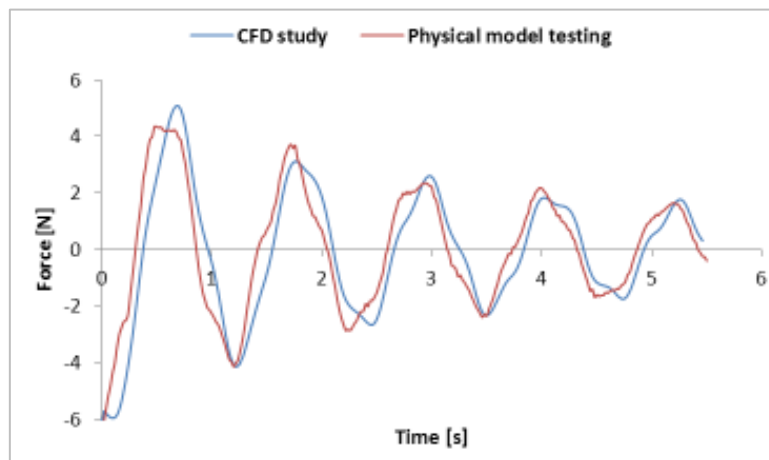
Figure 10. Example of free decay force time history of the model TLCD, CFD vs. physical testing.

Numerically computed studies on a full scale TLCD showed that the damping of the device itself during operating conditions (10-yr return period wind event) decreased by $\sim$10%. This was believed to be due to the different physics controlling the energy dissipation at the two scales: at model scale, in fact, the contribution coming from viscous forces is expecting to be larger than at full scale where, on the other hand, damping at full scale will be more dominated by inertial forces and recirculation within the TLCD.

6   Conclusions

A pair of identical TLCDs has been designed to mitigate the excessive wind-induced motion of a 42-storey residential tower located in the Middle East.

Their concept design, based on an initial desktop study approach, has been subsequently validated via a series of scale model tests performed on a shake table which in turn allowed an optimal configuration of internal porous screens to be obtained. The internal dissipation of each TLCD, in the form of equivalent viscous damping ratio, was extracted from the shake table experiments using energy dissipation considerations as well as directly solving the 2DOF equation of motion: these two analyses led to very consistent results.

Finally, the performance of the full scale TLCDs has been evaluated using CFD in an attempt to gain insights on the differences between model scale study and full scale implementation.

7   Acknowledgments

References

Clough, R.W. and Penzien, J. (1993). *Dynamic of Structures*. 2nd Ed. McGraw Hill.

Li, Q.S., Fang, J.Q, Jeary, A.P., Wong, C.K. (1998). Full Scale Measurements of wind effects on Tall buildings. *Journal of Wind Engineering and Industrial Aerodynamics* Vol 74-76, pp 741-750.

Li, Q.S., Yang, Ke., Wong, C.K., Jeary, A.P. (2003). The effect of amplitude-dependent damping on wind induced vibrations of a super tall building. *Journal of Wind Engineering and Industrial Aerodynamics* Vol 91, pp 1175-1198.

Tamura Y. (2005). Damping in buildings and estimation techniques. *Proceedings of APCWE-VI*, Seoul, Korea.

Tamura, Y., Suda, K., Sasaki, A. (2000). Damping in Buildings for Wind Resistant Design. *International Symposium on Wind and Structures for the 21st Century*, 26-28 Jan, Cheju, Korea.

Vickery, B.J. (2006). On the Preliminary Design of Passive Tuned Mass Dampers to Reduce Wind Induced Accelerations. *Australasian Wind Engineering Society Workshop*, Queenstown, New Zealand, February.

Wind Loading on Cubic and Portal Framed Buildings Subject to Transient Winds

Michael Jesson[1], Mark Sterling[2], Chris Letchford[3] and Matthew Haines[4]

[1]Research Fellow, School of Civil Engineering, University of Birmingham, Birmingham, UK,
[2]Beale Professor of Civil Engineering, School of Civil Engineering, University of Birmingham, Birmingham, UK
[3]Professor, School of Civil and Environmental Engineering, Rensselaer Polytechnic Institute, New York, USA
[4]PhD Student, School of Civil Engineering, University of Birmingham, Birmingham, UK
Corresponding author: Michael Jesson, m.a.jesson@bham.ac.uk

Abstract

In many parts of the world, the study of transient winds such as thunderstorm downbursts has increased in recent years. This paper describes a series of experiments performed in the University of Birmingham Transient Wind Simulator to measure the wind loading on structures subject to such wind loading. The simulator uses a 1m diameter, vertical, impinging jet to mimic a full-scale downburst at 1:1600 scale, using a flap mechanism to achieve the required high flow accelerations. Comparison with full-scale is made, which shows that the simulator is successfully capturing the main features of a full-scale downburst. Pressure coefficients on a cubic and portal framed building are presented. Extremes of negative pressure on the roof are found to occur when the approaching wind corresponds to a 45° yaw angle. It is postulated that such an arrangement leads to the formation of intense vortices on the leading corners of the roof. It is noted that negative pressures on the roof are greater for the portal framed building than the cube.

1 Introduction

Transient winds resulting from convection in thunderstorm cells, such as tornadoes and thunderstorm downbursts, have been shown to be the cause of design wind speeds in many parts of the world (Chay and Letchford 2002). This realisation has led to increased interest in quantifying the impact of transient winds, and in particular thunderstorm downbursts. Downbursts, have been simulated in a number of ways, from very small-scale density driven flows (Lundgren et al. 1992) to pulsed impinging jets (Mason 2003; Mason et al. 2009; McConville et al. 2009; Haines et al. 2013).

In order to examine the wind loading of structures in downburst winds, a number of researchers have measured pressure distributions over model buildings in simulated downbursts. Measurements on cubic buildings exposed to a steady, translating, impinging jet were made by Chay and Letchford (2002) and Sengupta et al. (2008). Butler et al. (2010) examined the pressures on prismatic buildings of varying heights in a downburst simulator while portal framed buildings have been investigated by Zhang et al. (2013) using steady-state, impinging jet flow, with two roof angles.

From their comparison of experimental data with pressure coefficients obtained in atmospheric boundary layer (ABL) and uniform flow, Chay and Letchford (2002) discovered that downburst windward wall pressure coefficients are more uniform, and of a larger magnitude. Additionally, flow separation over the roof is delayed in the downburst case, and flow reattachment is very much slower than the ABL in some cases. Roof suction (uplift) reaches its maximum behind the windward eaves, while leeward face suctions due to downbursts are *ca.* 5 times the magnitude of those seen in ABL flow.

This paper will build on the aforementioned work and examine the interaction of transient winds (at model scale, 1:1600) with two building shapes: a typical portal framed structure and a cube.

2   Experimental facility

The experimental facility used for the current work is outlined in detail in McConville et al. (2009). A circular, impinging jet of diameter D = 1m is used, with a set of flaps initially blocking the flow from a circular contraction. The fans and flaps are computer controlled, with the flaps released once the fans have achieved full speed, creating a rapid acceleration of the flow The velocity of the jet (V_j) immediately below the contraction attains a mean value of 13.7 ms^{-1}, with a corresponding turbulence intensity (standard deviation / mean) of 13%.

Comparison with the full-scale event at Andrews Air Force Base (AAFB; see (Fujita 1985)) gives approximate length, velocity and time scales of 1:1600, 1:2.6 and 1:600 respectively (see Figure 1). The velocity data were obtained using Cobra probes manufactured by Turbulent Flow Instrumentation (TFI). The maximum velocity was seen to occur at a height of $z/D = 0.2$ and radial position $x/D = 1.5$, where z is the perpendicular distance above the ground and x is the radial distance from the centre of the impingement. Two model buildings were used for this research, each 3-D printed with built-in pressure tappings, see Table 1 for the relevant dimensions. The pressure was measured at a rate of 500Hz using a bespoke, 64-channel digital pressure measurement system (DPMS), designed and manufactured by Solutions for Research Ltd. For both the velocity and the pressure measurements, a 10-run ensemble mean was calculated in order to compensate for run-to-run variation, similar to the variation seen between full-scale events.
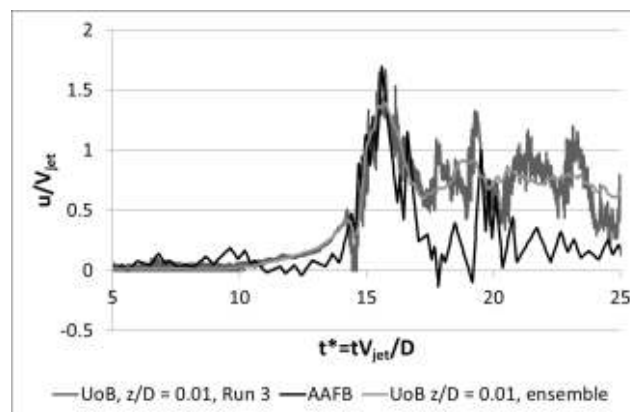
Figure 1 Non-dimensionalised radial velocity time-series for the UoB simulations and the AAFB full-scale event

Table 1 Model building dimensions

Model	Height (mm)	Width (mm)	Length (mm)
Portal	42 (eaves) 53 (peak)	130	240
Cube	60	60	60

3   Results

Analysis of the experimental data is ongoing and more detail will be presented at the conference. Pressure coefficients, C_p, as defined by (Eq. 1) have been calculated, where p_i is the pressure corresponding to tapping point i, p_{atm} is the atmospheric pressure (measured away from the influence of the impinging jet) and U_m is the maximum radial velocity found when the flow field was mapped. U_m occurred at $x/D = 1.5$ (the same location was used for the model), at height of $z/D = 0.2$.

$$C_{pi} = \frac{p_i - p_{atm}}{\frac{1}{2}\rho U_m^2} \tag{1}$$

Preliminary results are shown in Figure 2 and expressed in terms of the maximum magnitude of C_p at each point over the building surface. This gives an indication of the maximum cladding load seen over the building – wind loading (in terms of drag coefficients) will be given in the presentation. With yaw angle 0° (i.e. the dominant, radial wind direction perpendicular to one face of the cube), the maximum value of C_p on the windward face of the cube is *ca.* 0.7 and occurs at the midpoint of face, with a reduction closer to the ground before a small increase at the base of the cube. Along the roof centreline, the maximum suction occurs approximately in the centre of the roof ($C_p \approx$ -0.66) and values at the windward and leeward edges are of a similar magnitude. The maximum suction over the entire roof occurs away from the centreline, with $C_p \approx$ -0.75 in the windward, left-hand corner. The asymmetry may be due to slight misalignment of the model, or asymmetry of the outflow. At a yaw angle of 45°, an increase in the magnitude of the roof negative pressure occurs over the windward corner and eaves, with maximum suctions of $C_p \approx$ -1.1 occuring under the delta vortices, at the eaves but away from the corner. It is postulated that this is due to the formation of high intensity vortices at the leading edge. Figure 2(b) shows higher suction on the right-hand side of the leading edge, but again this is thought to be caused by either a slight misalignment of the model, or asymmetry of the outflow.

In the case of the portal framed building, corresponding to a yaw angle of 0°, a maximum C_p of ca. 0.56 occurs in the centre of the windward face of the portal building (Figure 2(c)). The maximum roof negative pressures, *ca.* -0.81 and -0.90, occur at the two windward corners. It should be noted that the animated distribution (available for viewing on the project website, *www.birmingham.ac.uk/transient-winds*) indicate that the asymmetry seen for the 0° case in Figure 2(c) is exaggerated. C_p reduces towards the ridgeline of the roof and over the leeward roof face, with $C_p \approx$ -0.34 at the leeward edge. The majority of the leeward face has $C_p \approx$ -0.1, with C_p increasing to as high as 0.2 towards the side edges. Suction is seen along the side faces, with C_p remaining approximately constant at $C_p \approx$ -0.4. The right-hand face has greater suction, again possibly due to asymmetry of the outflow. With a 45° yaw angle, a maximum suction of $C_p \approx$ -1.6 is seen at the leading corner (Figure 2(d)). Suction remains high (*ca.*-0.8) along the leading edges of the roof and, unlike the 0° yaw case, a region of increased suction (*ca.*-0.6) is seen along the back of the ridge line in the windward half of the roof. The left and right windward walls have a positive pressure at the leading edge (*ca.* 0.6 and *ca.* 0.5 respectively), with suction at the trailing edge of $C_p \approx$ -0.1 for both. The leeward walls show the same pattern of increasing suction, though with suction the full length (-0.3 to -0.4 on the left wall, -0.2 to -0.3 on the right wall).

4   Acknowledgements
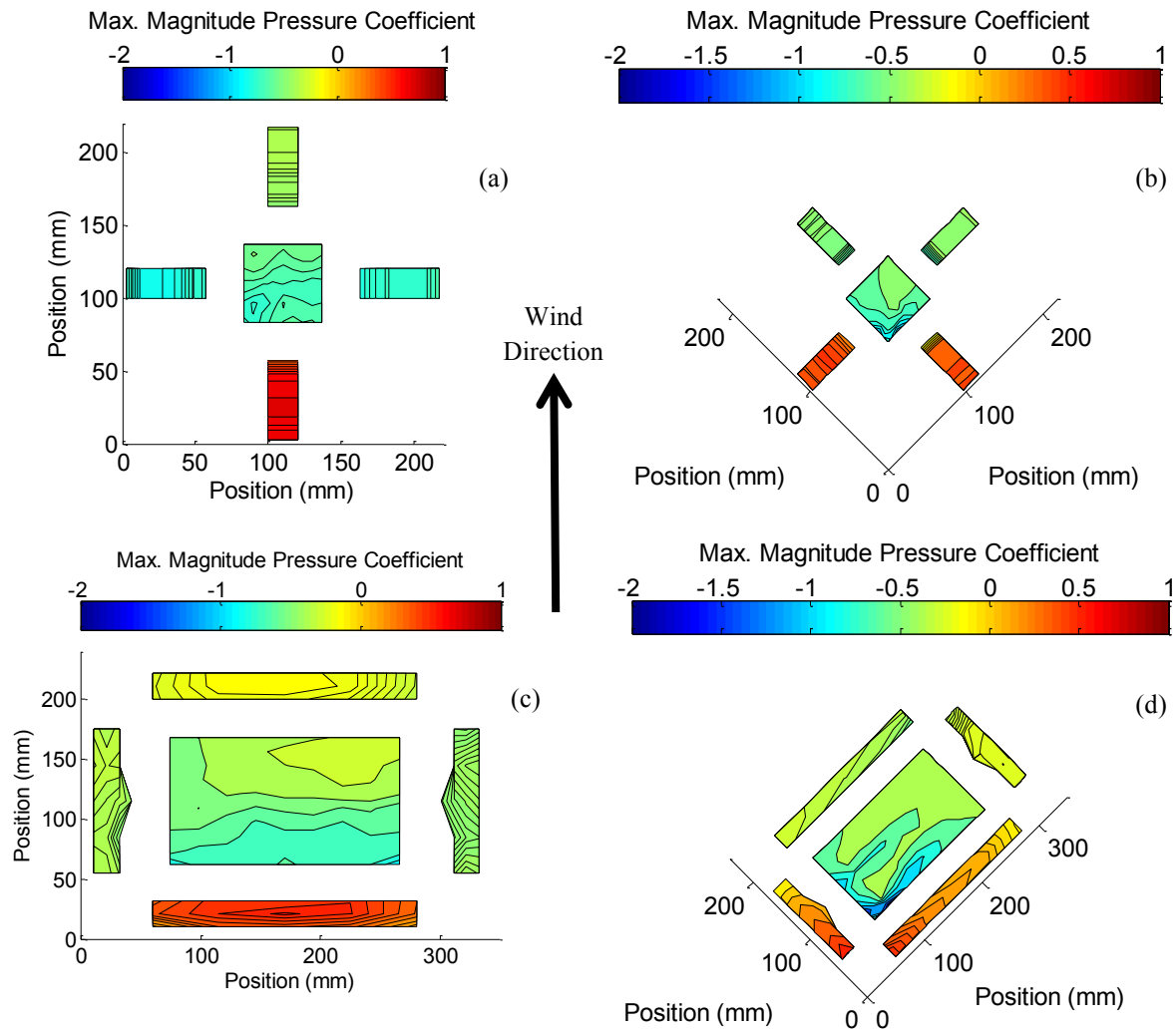
Figure 2. Maximum magnitude pressure coefficients on the cube at 0° yaw (a), cube at 45° yaw (b), portal building at 0° yaw (c) and portal building at 45° yaw (d). Wind direction is from the bottom of the page.

Selected References

Chay, M. T. & Letchford, C. W. 2002. Pressure distributions on a cube in a simulated thunderstorm downburst - Part A: stationary downburst observations. *Journal of Wind Engineering and Industrial Aerodynamics,* 90 (7), 711-732.

Fujita, T. T. 1985. *Downburst: Microburst and Macroburst,* Chicago, Illinois, University of Chicago Press.

Haines, M., Sterling, M. & Quinn, A. 2013. Interference effects around two model high rise buildings in a simulated non-synoptic event. *European-African Conference on Wind Engineering.* Cambridge, UK.

Mcconville, A. C., Sterling, M. & Baker, C. J. 2009. The physical simulation of thunderstorm downbursts using an impinging jet. *Wind and Structures,* 12 (2), 133-149.

An efficient method for wind-induced vibration responses

of long-span roofs

Nan Luo[1,2], Haili Liao[1,2] and Mingshui Li[1,2]

[1]Research Centre for Wind Engineering, Southwest Jiaotong University, Chengdu, China
[2]Key Laboratory for Wind Engineering of Sichuan Province, Chengdu, China
Corresponding author: Nan Luo, nanluo@swjtu.edu.cn

Abstract

The CQC method can carry out an exact calculation of wind-induced vibration responses, but its efficiency is difficult to meet the computing needs of long-span roofs. In this paper, an efficient method is proposed for wind-induced vibration of long-span roofs including both background response and resonant response, meanwhile the modal coupling effects of background and resonant component are considered. The difference with the CQC method is that the modal coupling effects between the background and resonant component are ignored as their contribution to total response is minimal. As the total response is divided into the background and resonant component, and each component is calculated independently, the computational efficiency is improved.

1 Introduction

Wind-induced vibration responses of long-span roofs are one of main concerns for both structure and wind engineers. The CQC method can perform an exact calculation for wind-induced vibration responses of those structures, but its efficiency is difficult to meet the computing needs of long-span roofs. Load-Response-Correlation method(LRC) use the correlation coefficient between the loads and the response to calculate wind-induced vibration response. In this method, only the background response is considered, so it has some limitations in dealing with the resonant response of long-span roofs. Another simplified method is dividing the pulse response in the frequency domain into two parts to calculate the background and resonance. Holmes[1]gives the combination of the mean wind loads, background wind loads and the resonant wind loads, but the method assumes that a good separation between each part of the vibration modes, ie, without considering the mode coupling effect. However, Coupling effects in solving the strong coupling structure of wind-induced response should be considered. Xie and Ni [2] used the LRC method of combination the wind vibration force which contains the background, resonance and its coupling item. The precision meets the requirements, but the CQC method was used to calculate the response, computational efficiency is equivalent to the CQC method. Denoël [3] and Gu [4] proposed a new method considering the mode coupling, but the formula is still complex.

Based on the above methods, an efficient method was proposed to calculate the wind-induced vibration response which includes the contribution of background response, resonant response and modal coupling. With considering the mode coupling, this method has high accuracy. The high efficiency is realized by dividing wind-induced vibration response into the background and resonant component. This paper briefly introduces this method and presents its application to a large-roof structure.

2 Theoretical analysis

The structural dynamic displacement can be expressed as,

$$\{y(t)\} = \Phi\{q(t)\} = \sum_{i=}^{n} \phi_i q_i(t) = \sum_{i=}^{m} \phi_i q_i(t) + \sum_{i=m+}^{n} \phi_i q_i(t) = \{y(t)\}_{b,n} + \{y(t)\}_{r,m} \tag{1}$$

where, n is the mode number concerned, Φ is the modal matrix, $q(t)$ is the modal coordinate, ϕ_i is the vibration mode vector of i, $q_{i,b}(t)$ is the displacement response vector containing only the quasi-static contribution to the i-order background, $q_{i,r}(t)$ is the displacement response vector contains only the contribution to the i-order response, $\{y(t)\}_{b,n}$ is the response vector containing all modal quasi-static contribution to the background. $\{y(t)\}_{r,m}$ is the main m contribution modes (which may be the displacement of the higher modes). How to choose the main contribution modes can be found in the literature [5].

2.1 The background response

The background response under wind loads can be calculated by quasi-static method which is expressed as follows,

$$\{y(t)\}_{b,n} = [I]\{F(t)\} \tag{2}$$

where, $[I]$ is the influence coefficient matrix, $\{F(t)\}$ is the external wind loads vector, so the contribution of the background response is,

$$\left[\sigma_b \right] = [I]\left[\sigma_F \right][I]^T \tag{3}$$

2.2 The resonant response

The structural displacement response variance can be obtained by using modal decomposition method,

$$\sigma_y = \sum_{j=}^{n}\sum_{k=}^{n} \phi_j \phi_k^T \int \lambda_{jk} S_{F_j F_k} \, d\omega = \int \sum_{j=}^{n} \sum_{k=}^{n} \phi_j \phi_k^T \lambda_{jk} S_{F_j F_k} \, d\omega$$
$$\lambda_{jk} = H_j^*(i\omega) H_k(i\omega) \tag{4}$$

where, ϕ_j is the j modal column vector, ϕ_k^T is the transpose of the k modal column vector, $S_{FjFk}(\omega)$ is the modal force spectrum, $H_k(i\omega)$ is the frequency response function of the k modal, $H_j^*(i\omega)$ is the complex conjugate of $H_j(i\omega)$, λ_{jk} is the transfer function of the modal frequency response.

The modal frequency response transfer function is a complex function, in this paper, it will be divided into real and imaginary parts. And as the modal force spectrum matrix is a Hermite matrix, the structural displacement response variance can be simplified into，

$$\sigma_y = \int \sum_{j=}^{n} \sum_{k=}^{n} \phi_j \phi_k^T \operatorname{Re}[\lambda_{jk}] \operatorname{Re}[S_{F_j F_k}] \, d\omega - \int \sum_{j=}^{n} \sum_{k=}^{n} \phi_j \phi_k^T \operatorname{Im}[\lambda_{jk}] \operatorname{Im}[S_{F_j F_k}] \, d\omega \tag{5}$$

where, $\operatorname{Re}[\lambda_{jk}]$ is the real part of λ_{jk}, $\operatorname{Im}[\lambda_{jk}]$ is the imaginary part of λ_{jk}, $\operatorname{Re}[S_{F_j F_k}]$ is the real part of $S_{FjFk}(\omega)$, $\operatorname{Im}[S_{F_j F_k}]$ is the imaginary part of $S_{FjFk}(\omega)$.

As shown in Figure 1, the distribution of $\operatorname{Re}[\lambda_{jk}]$ in the frequency domain, its value near the natural vibration frequency has a narrow peak value, the other is smaller. The maximum and minimum values appear near the natural vibration frequency.
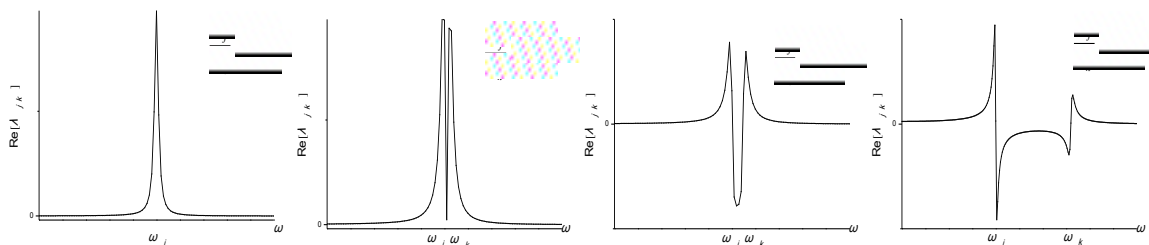
Figure 1. Real part of modal frequency response function of modal coupling part

In the narrow peak area, $S_{FjFk}(\omega)$ can be considered as an approximate white noise excitation (as in Den09, SEM-32(6)2009), i.e. $S_{FjFk}(\omega)$ is a constant. By applying integral to each resonance interval, the real part of the resonant response is,

$$\left[\sigma_{rRm}\right]=\sum_{j=}^{m}\sum_{k=}^{m}\phi_{j}^{T}\phi_{k}\left(\alpha_{k}\beta_{k}\left\lceil S_{F_{j}F_{k}}\right\rceil_{j}+\alpha_{j}\beta_{j}\left\lceil S_{F_{j}F_{k}}\right\rceil_{k}\right) \tag{6}$$

As shown in Figure 2, the distribution of $\mathrm{Im}\left[\lambda_{jk}\right]$ in the frequency domain, its value near the natural vibration frequency has a narrow peak value, the other is smaller, and the maximum value appears at the natural vibration frequency position.
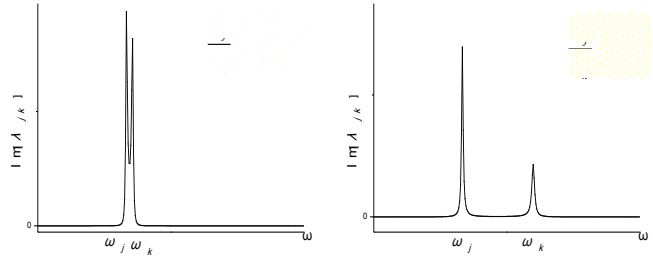
Figure 2. Imaginary part of modal frequency response function of modal coupling part

Then, the imaginary part of the resonant response can be expressed as,

$$\left[\sigma_{rIm}\right]=\sum_{j=}^{n}\sum_{k=}^{n}\phi_{j}^{T}\phi_{k}\left(\alpha_{k}\beta_{j}\left\lceil S_{F_{j}F_{k}}\right\rceil_{j}+\alpha_{k}\beta_{j}\left\lceil S_{F_{j}F_{k}}\right\rceil_{k}\right) \tag{7}$$

2.3 The total response

Based on the above analysis, the total response which contains the background response, resonant response and the modal coupling can be expressed as,

$$\left[\sigma_{y}\right]=\left\lfloor\sigma_{b}\right\rfloor+\left\lfloor\sigma_{rRm}\right\rfloor+\left\lfloor\sigma_{rIm}\right\rfloor \tag{8}$$

3 Working example

3.1 Wind tunnel test and preliminary analysis

A swimming pool shaped like a gull wing is a novel, unique shell structure. The long span is 167.5m, the short span is 141.7m. The test was carried out in the Southwest Jiaotong University Wind Engineering Research Center XNJD-1 industrial wind tunnel, shown in Figure 3.

The finite element model of the swimming pool is shown in Figure 4, and the six typical nodes were marked out. The vertical displacement response power spectral density function diagram of the central node (Node 2) calculated by CQC method is shown in Figure 5. And the main resonant modes were marked out. As can be seen, for such long-span roof, background and resonant components all can not be ignored, and the resonant effect caused by structural modes is not unique, not just the low order modes.
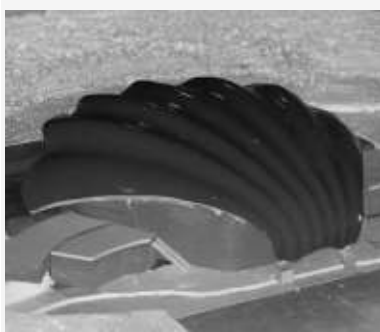
Figure 3. Model in wind tunnel   Figure 4. Finite element model   Figure 5. Displacement response power spectrum of the central node
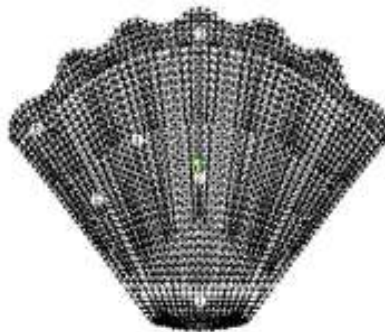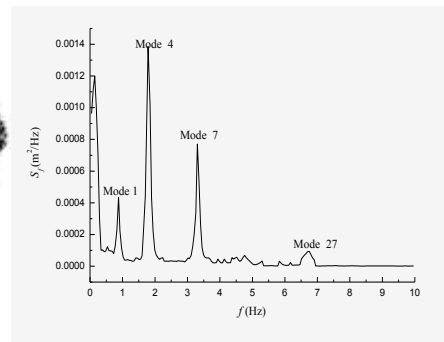
3.2   Wind-induced vibration response analysis

The response was obtained by this efficient method, the traditional three-component method, and the CQC method. The root variance for wind-induced response of typical nodes was shown in Table 1. As can be seen, the calculation error of traditional three-component method is large without considering the coupling effect. For some nodes, it can be conservative, such as node 4, the error is 9.44%, for some nodes, it can be unsafe, such as node 3, the error is -8.35%. The calculation results of this efficient method agree well with the CQC method, the maximum error is only -2.14%. The error comes mainly from the modal coupling effects between the background and resonant components.

Table 1. Root variance for fluctuating wind-induced response of typical node

node number	CQC method /mm	traditional three-component method		this efficient method	
		response/mm	error/%	response/mm	error/%
1	12.21	12.67	3.77	12.11	-0.82
2	30.22	32.15	6.39	30.36	0.46
3	21.31	19.53	-8.35	21.49	0.84
4	8.79	9.62	9.44	8.66	-1.48
5	5.79	6.02	3.97	5.83	0.69
6	31.38	29.71	-5.32	30.71	-2.14

4   Conclusions

In this paper, an efficient method for wind-induced vibration response of long-span roofs which considering the background response, resonant response and mode coupling was proposed. The main conclusions are,

(1) The traditional three-component method, which does not consider the modal coupling effect, should not be used to solve strong coupling structure.

(2) The wind-induced response calculated by this present method agrees well with the CQC method.

(3) The computational efficiency of proposed method is much higher than one of CQC method by considering background and resonant components separately.

5   Acknowledgements

References

Holmes, J.(2002). Effective static load distributions in wind engineering. *Journal of Wind Engineering and Industrial Aerodynamics*, 90(2), 91-109.

Xie, Z.N., Fang, X.D., and Ni, Z. H.(2008). Equivalent static wind loads on tall building-the extended load-response-correlation (ELRC) approach. *Journal of Vibration Engineering,* 21(004),398-403.

Denoël, V.(2009). Estimation of modal correlation coefficients from background and resonant responses. *Structural Engineering and Mechanics: an International Journal,* 32(6),725-740.

Gu, M. and Zhou, X.Y.(2009). An approximation method for resonant response with coupling modes of structures under wind action. *Journal of Wind Engineering and Industrial Aerodynamics*, 97(11-12),573-580.

Nakayama, M., Sasaki, Y., Masuda, K. et al.(1998). An efficient method for selection of vibration modes contributory to wind response on dome-like roofs. *Journal of Wind Engineering and Industrial Aerodynamics,* 73,31-43.

Base-drag reduction of an axisymmetric bluff body through boundary-layer and near-wake modifications

A. Mariotti[1], G. Buresti[1] and M. V. Salvetti[1]

[1]DICI, Aerospace Engineering Division, University of Pisa, Italy
Corresponding author: A. Mariotti, alessandro.mariotti@for.unipi.it

Abstract

In the present work, the main findings of an experimental and numerical research activity aimed at characterizing and reducing the base drag of bluff bodies are presented. We consider the flow around an axisymmetric body, which can be viewed as a simplified model of a road vehicle. The results of experiments, LES and DNS simulations show that the base suctions − and thus the base drag − decrease in direct proportion to the increase of the length of the mean recirculation region behind the body which, in turn, can be obtained by increasing the boundary layer thickness before separation. Although the different set-ups and Reynolds numbers in the experiments and numerical simulations imply significant differences in the near wake dynamics, in all cases the length of the mean recirculation region present behind the body seems to be connected with the location of the incipient instability of the detaching shear layers. It is shown that the location of this instability can be moved downstream, and thus base drag can be reduced, by increasing the thickness of the separating boundary layer. The results of the present analysis may be useful to devise further strategies for pressure drag reduction.

1 Introduction

A large contribution to the aerodynamic drag of a bluff body is given by the low pressures acting on its base, which is the surface lying within the separated wake. In many engineering applications, such as the design of low-consumption road vehicles, decreasing the base drag would then have a significant importance. However, the present understanding of the geometrical and flow features influencing the base pressure of bluff bodies cannot yet be considered completely satisfactory, and considerable research work is still needed. In particular, a preliminary critical issue is characterizing the relationship between the base pressure and the parameters defining a particular flow configuration.

Some indications exist in the literature that the characteristics of the boundary layer developing over the lateral surface of a bluff body and separating at its base contour may influence the base pressure. This effect is particularly significant for bodies whose base is a sharp-edged flat surface perpendicular to the free stream. In the two-dimensional case, the base drag was found to be reduced by increasing the boundary-layer thickness (see, e.g., Rowe et al., 2001). As for axisymmetric bodies, although some experimental data on the connection between separating boundary layer and base drag are available in the literature (see, e.g., Porteiro et al., 1983), to our knowledge the first experimental systematic investigation on this topic is documented in Mariotti and Buresti (2013), in which the increase of the boundary layer thickness was confirmed to produce a reduction of the base suctions. It was also suggested that this effect may be connected with an increase of the length of the mean recirculation region present behind the body, and with the downstream movement of the incipient instability of the detaching shear layers.

In the present work, the results of the above mentioned experimental campaign are compared with those of numerical simulations that were carried out to widen the analysed flow conditions and to try to attain a deeper understanding of the parameters and flow features that are responsible for the observed connection between boundary layer characteristics, base pressure and near-wake flow field. In particular, the results of Variational MultiScale (VMS) Large-Eddy Simulations (LES), carried out on the same nominal geometry and at the same Reynolds number of the experiments in Mariotti and Buresti (2013), are first described. These simulations present two significant differences compared to the experiments in Mariotti and Buresti (2013): (i) the model support is not considered; (ii) the free-stream turbulence

is not accounted for, i.e. laminar free-stream conditions are used. These differences were maintained to ascertain whether general conclusions may be drawn in spite of them. Direct numerical simulations were also carried out at Reynolds numbers roughly two orders of magnitude lower than in the experiments and in the VMS-LES simulations, in order to investigate on the sensitivity of the observed trends to the Reynolds number. The analysis of the results of the experiments and simulations permits to identify the main parameters influencing the base drag and their relationship with the thickness of the detaching boundary layer. Furthermore, by exploiting the detailed information on the near wake dynamics provided by the numerical simulations, the base pressure variations could be connected with the changes in the formation and evolution of the vorticity structures that are present in the near wake.

2   Problem definition and methodology

The experimental tests of Mariotti and Buresti (2013) were carried out in the closed-return, subsonic wind tunnel of the University of Pisa, which is characterized by a circular open test section $1.1m$ in diameter and $1.42m$ in length. The model, whose diameter to length ratio is $d/l = 0.175$, has a forebody with with a 3:1 elliptical contour and a cylindrical main body with a sharp-edged base perpendicular to the axis. The model was supported above a flat plate by means of a faired strut (see Fig. 1a). The chosen support implies that the flow is not symmetrical in the vertical plane, while it remains symmetrical in the horizontal plane; nonetheless, it was preferred to a rear sting support, which directly interferes with the near-wake flow development and effectively changes the free body base to an axisymmetric backward-facing step. The pressures acting over the lateral and base surfaces of the body were obtained through a total of 121 pressure taps distributed over the surface of the model, 65 of which were positioned over the base, while the boundary layer profiles and the wake velocity field were measured through hot-wire anemometry (see Mariotti and Buresti, 2013 for further details on the experimental apparatus and on the measurement techniques). The tests were carried out at $Re = u_\infty d/\nu = 9.6 \times 10^4$, where u_∞ is the free-stream velocity. Due to the wind tunnel turbulence level, in these operating conditions the boundary layer over the lateral surface of the model becomes turbulent before separating at the sharp-edged base contour. Strips of emery cloth were wrapped in various positions around the body circumference in order to move transition upstream, and, thus, to increase the thickness of the boundary layer. In particular, the boundary layer transition was either kept natural or fixed at $x_t/l = -0.70$ and at $x_t/l = -0.875$ (see Fig. 1a).
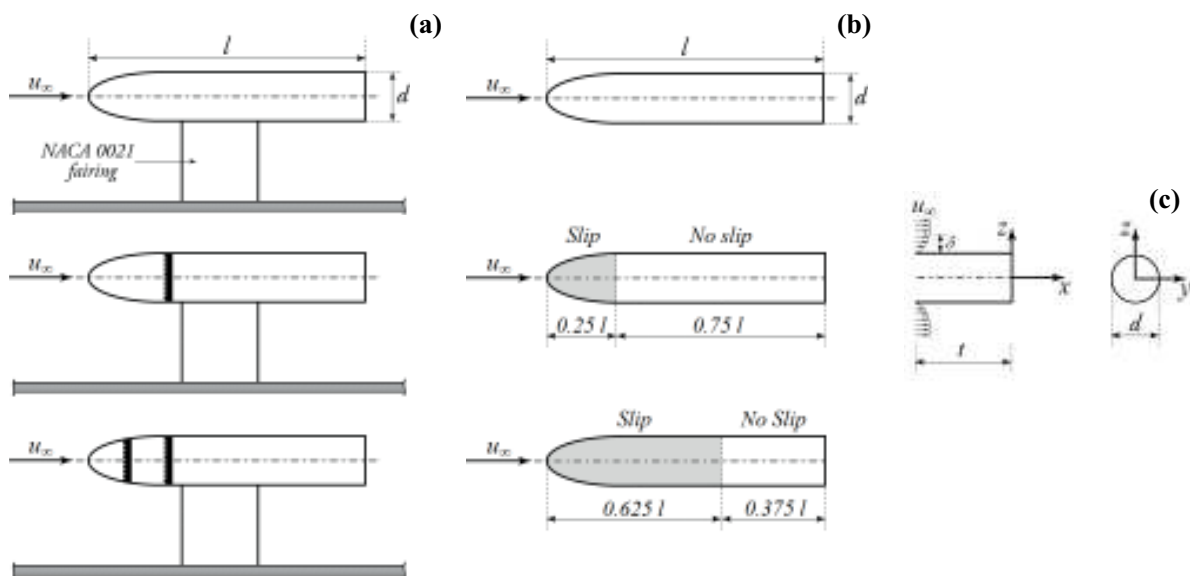
Figure 1. Geometries and boundary layer control: experiments (a), VMS-LES (b) and DNS (c).

The VMS-LES simulations were carried out on the same body and at the same Reynolds number of the experiments. As already pointed out, the differences are that simulations were carried out for laminar freestream conditions, while a freestream turbulence intensity of 0.9% was present in the experiments, and that the faired strut supporting the model in the experiments was not present in the simulations (see Fig. 1b). The method to change the boundary layer thickness is also different: in the numerical simulations a reduction of the boundary layer thickness was obtained by using a free-slip boundary condition over different initial portions of the body surface. In particular, three simulations are presented here, which correspond to no-slip over the entire body, over the last 75% and over the last 37.5% of the body lateral surface (see Fig. 1b). The VMS-LES simulations were carried out by using AERO, an in-house developed numerical code based on a linearized implicit time advancing and on a mixed finite-volume/finite-element method, applicable to unstructured grids for space discretization. The accuracy of the numerical method is second order both in space and time and the Smagorinsky model was used as subgrid scale model. The VMS-LES approach adopted in the present work was successfully validated for the simulation of bluff-body flows in the past (see, e.g., Ouvrard et al., 2010 and Wornom et al., 2011). The computational domain is cylindrical, with a diameter of $15d$ and a length of $50d$ ($30d$ being the distance from the body base to the outflow); it was discretized through an unstructured grid having approximately 2.4×10^6 nodes. The grid is particularly refined near the body surface and in the near wake (the wall y^+ is lower than 1). Characteristic-based boundary conditions were used at the inflow, outflow and lateral surfaces of the computational domain. The boundary conditions on the body lateral surface were chosen, as previously explained, in order to vary the boundary-layer thickness on the lateral surface; in all cases, no-slip was imposed on the base.

The DNS simulations were carried out only for a final portion of length $t = 2d$ of the previously described axisymmetric body (see Fig. 1c). The computational domain is cylindrical, with a diameter of $10d$ and a length of $30d$ ($28d$ being the distance from the body base to the outflow); it was discretized through a hexahedral structured grid having approximately 3.5×10^6 nodes. An axisymmetric self-similar boundary-layer velocity profile was assumed at the inlet of the computational domain, with four different values of the thickness δ/d, viz. $\delta/d = 0$, $\delta/d = 0.1$, $\delta/d = 0.2$, and $\delta/d = 0.3$. The Reynolds number of the simulations was $Re = u_\infty d/\nu = 1500$; no-slip was imposed on the body while free slip was used on the domain lateral boundary, together with pressure outflow conditions. The simulations were carried out by using the open-source code OpenFOAM and the accuracy of the numerical method was second order both in space and time. The DNS set-up was validated through comparison against results available in the literature for the same type of bodies at low Reynolds numbers. A thorough description of the DNS code validation, together with further numerical details on both the VMS-LES and DNS simulations, are reported in Mariotti (2014)).

3   Discussion of the results

The mean values of the boundary layer thickness, δ/d, at $x/d = -0.1$ obtained in the experiments of Mariotti and Buresti (2013) and in the two types of numerical simulations are reported in Table 1, where the corresponding mean values of the displacement thickness δ^*/d, of the momentum thickness θ/d and of the shape factor H are also given. As the considered position lies within a region where a negative pressure gradient along the surface is present, with a consequent accelerating velocity at the edge of the boundary layer, the values of δ/d were obtained by identifying the distance normal to the surface at which the mean velocity was equal to the 99% of the maximum one in the considered section. Within numerical uncertainty, this position coincided with the one corresponding to 99% of the integral of the vorticity in the normal direction. As can be seen, the whole set of cases comprises a wide range of boundary layer thicknesses; furthermore, the values of the shape factor witness that in the experiments all boundary layers were turbulent at separation, whereas they were laminar or in incipient transition for the VMS-LES and DNS simulations.

In all the considered operating conditions, the boundary layer remains completely attached over the lateral surface of the model up to the separation at the sharp-edged base contour. The flow separation at the base leads to the development of a free shear layer and to a flow recirculation behind the base, with the creation of a trailing stagnation point. Therefore, the streamlines bounding the recirculation zone have a

	Case	δ/d	δ^*/d	θ/d	H
	Smooth model	0.107	0.0121	0.0086	1.41
Experiments	One strip of emery cloth	0.143	0.0171	0.0121	1.41
	Two strips of emery cloth	0.171	0.0194	0.0144	1.35
	No-slip over 37.5% of the body	0.0306	0.0078	0.0036	2.15
VMS-LES	No-slip over 75% of the body	0.0411	0.0107	0.0050	2.14
	No-slip over the entire body	0.0663	0.0146	0.0072	2.03
	$\delta_{in}/d = 0$	0.131	0.0433	0.0184	2.35
DNS	$\delta_{in}/d = 0.1$	0.171	0.0539	0.0232	2.32
	$\delta_{in}/d = 0.2$	0.234	0.0739	0.0321	2.30
	$\delta_{in}/d = 0.3$	0.318	0.1024	0.0441	2.32

Table 1. Boundary layer characteristics evaluated at $x/d = -0.1$

curvature that is first convex and then concave, and this leads first to an increase and then to a decrease of the velocity. As already observed in Mariotti and Buresti (2013), the amount of velocity increase outside the separating boundary layer and along the first part of the free shear layer bounding the recirculation region is directly linked to the value of the pressure on the body base. The effect of increasing the boundary layer thickness on the shape and dimension of the recirculation region may be appreciated from Fig. 2a and Fig. 2b, which show, respectively for the VMS-LES and the DNS simulations, the mean flow streamlines bounding the recirculation region − i.e. averaged in time and in the azimuthal direction − together with the wake edges evaluated as the positions corresponding to 99% of the integral of the vorticity in the cross-flow direction. As already found in the experiments, increasing the boundary layer thickness leads to an increase of the recirculation length l_r/d, which may be determined from the position along the wake axis were the velocity value is equal to zero. As a consequence, the curvature of the streamlines bounding the first part of the recirculation region decreases, causing an analogous reduction of the velocity. As can be seen from the mean pressure distributions reported, for the two types of simulation, in Fig. 3a and Fig. 3b, the result is an increase of the mean base pressure and, thus, a reduction of the base drag.
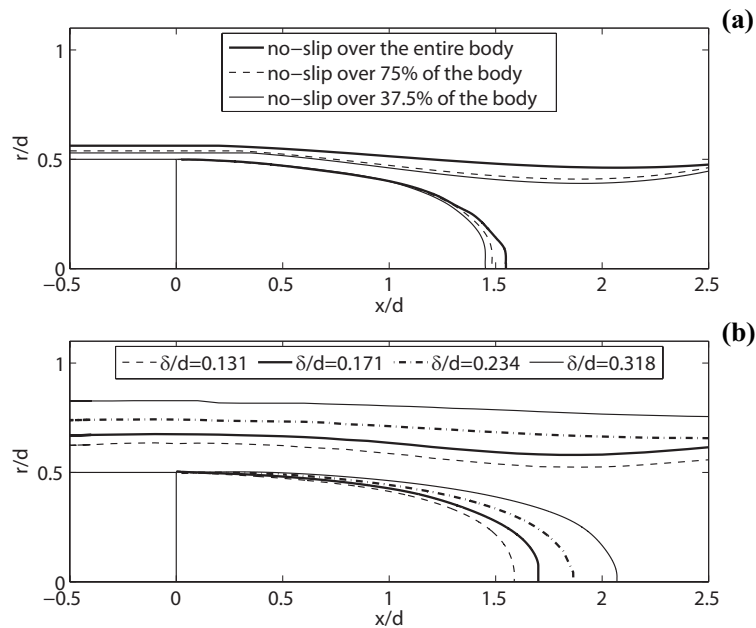
Figure 2. Mean flow streamlines bounding the recirculation zone and wake edges: VMS-LES (a) and DNS (b).
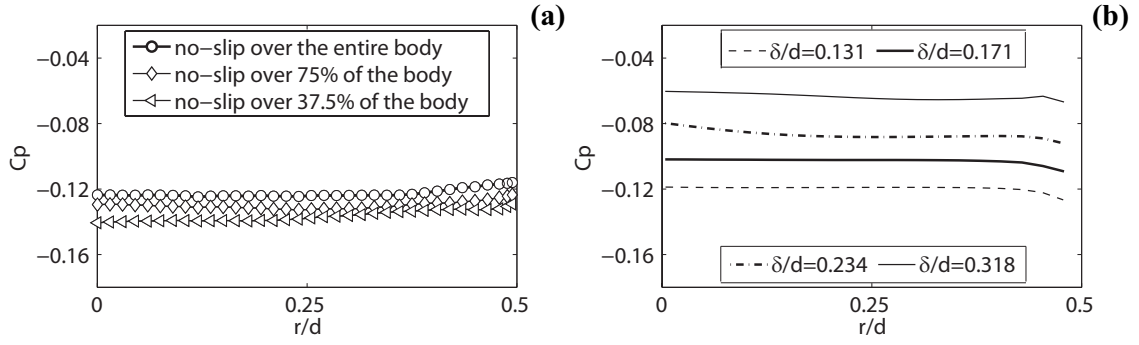
Figure 3. Variation of the averaged Cp over the base: VMS-LES (a) and DNS (b).

The experimental pressure measurements described in Mariotti and Buresti (2013) were obtained only for $r \leq 0.4$. Therefore, in order to directly compare the effects of the boundary layer thickness on the base drag obtained in the experiments and in the two types of numerical simulations, the numerical mean pressure coefficients were averaged over this limited portion of the base, and the corresponding values are denoted as $Cp_{base}^{r \leq 0.4}$. The complete set of values obtained for this parameter is reported as a function of the boundary layer thickness in Fig. 4a. From this figure one may immediately observe that for all the considered cases $Cp_{base}^{r \leq 0.4}$ increases almost linearly with increasing δ/d. However, significant quantitative differences are found between the experiments and the present numerical methods; in particular, it is immediately apparent that comparable values of the boundary layer thickness may give rise to quite different base pressures. This result may be readily explained by considering the different conditions corresponding to the various cases, and by analyzing the variations of the recirculation length as a function of the boundary layer thickness, which are shown in Fig. 4b. Actually, the values of l_r/d could not be accurately measured in the experiments of Mariotti and Buresti (2013), but they could be inferred from the positions corresponding to maximum fluctuations in the axis, as described in Mariotti (2014). Figure 4b shows that the trends of l_r/d as a function of δ/d are similar to those of $Cp_{base}^{r \leq 0.4}$, and that similar differences between the experimental and numerical results are found. For instance, the lower experimental base pressures − and thus higher drags − in Fig. 4a correspond to lower values of l_r/d in Fig. 4b.

The similarity of the trends in Figs. 4a and 4b immediately suggests the existence of a direct connection between the mean base pressure and the recirculation length, and this is indeed what derives from Fig. 5, where $Cp_{base}^{r \leq 0.4}$ is reported as a function of l_r/d. As is apparent, all the experimental and numerical data of the base pressure are seen to follow a common and almost linear relationship with the recirculation length. This result strongly indicates that the parameter directly controlling the base pres-
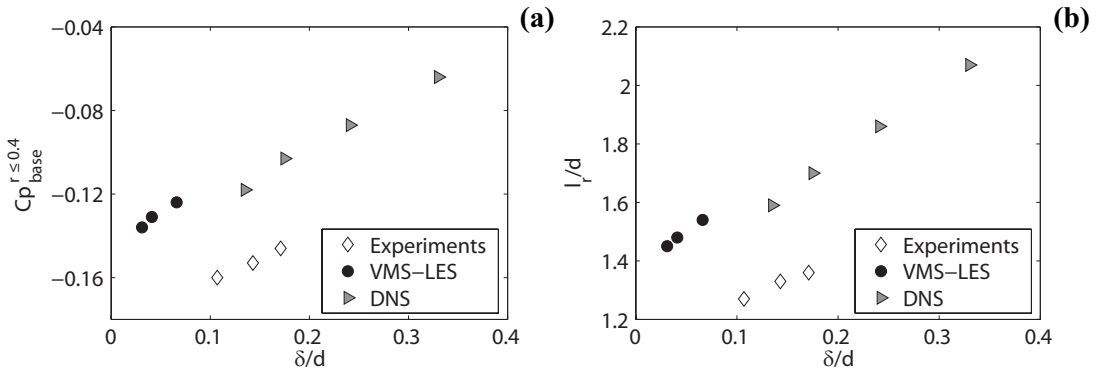
Figure 4. Comparison between the experimental, the VMS-LES and the DNS results: $Cp_{base}^{r \leq 0.4}$ vs. δ/d (a) and l_r/d vs. δ/d (b)
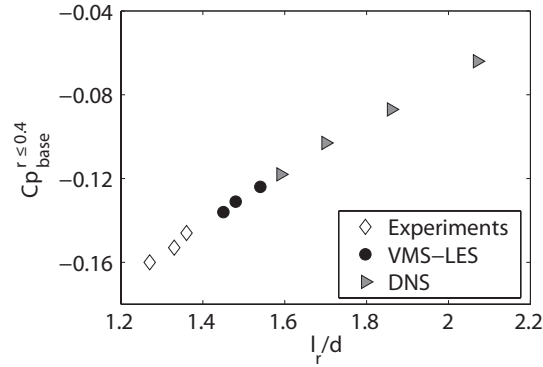
Figure 5. Comparison between the experimental, the VMS-LES and the DNS results: $Cp_{base}^{r\leq0.4}$ vs. l_r/d.

sure, and thus drag, is the recirculation length, independently of the status of the boundary layer before separation, of the turbulence level of the oncoming flow and of the Reynolds number. In particular, the base suctions and drag decrease with increasing l_r/d.

The above finding suggests the need of carrying out a deeper investigation on the physical mechanisms that influence the length of the recirculation region, and a significant clue in this direction is provided by the analysis of the fluctuating flow field. Indeed, the mean flow features in the near wake are the result of the instantaneous flow dynamics. In all cases, the near wake is found to be characterized by the formation and evolution of hairpin vortices, as schematically depicted in Figs. 6a and 6b, in agreement with the results obtained on similar bodies and on spheres at low Reynolds numbers (see, e.g., Meliga et al., 2009 and Sevilla and Martinez-Bazan, 2004). In this general framework, differences are again observed between the results of the experiments and of the numerical simulations. In the latter, these vortical structures form and evolve on planes rotating with time but, due to the higher Reynolds number, their formation is more upstream and their evolution more rapid in the VMS-LES simulations than in DNS ones. This can be qualitatively seen, for instance, in Figs. 7a and 7b, where the isosurfaces of the vortex-indicator λ_2 (see, e.g., Jeong and Hussain, 1995) are shown for the VMS-LES with no-slip condition over the whole body and for the DNS simulation. In the experiments of Mariotti and Buresti (2013), the hairpin vortices had been found to form only on a preferential fixed plane due to the presence of the fairing.

In view of the complexity of the wake dynamics and the differences between the various cases, it might seem surprising that the present analysis suggests that the value of the mean recirculation length
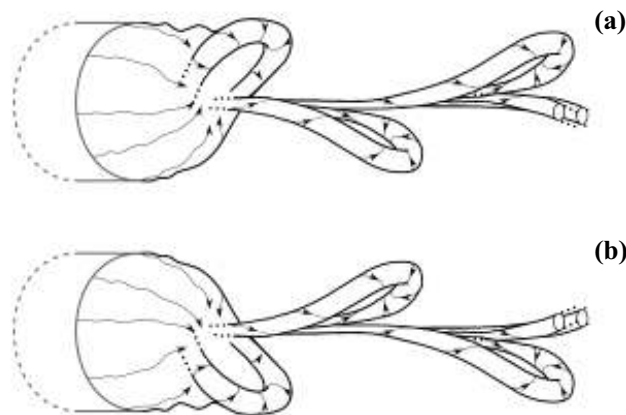
Figure 6. Sketch of the hairpin vortices downstream of the axisymmetric body: time $t = t^*$ (a) and time $t = t^* + \frac{1}{2}T$ (b), where T is the hairpin vortex shedding period.
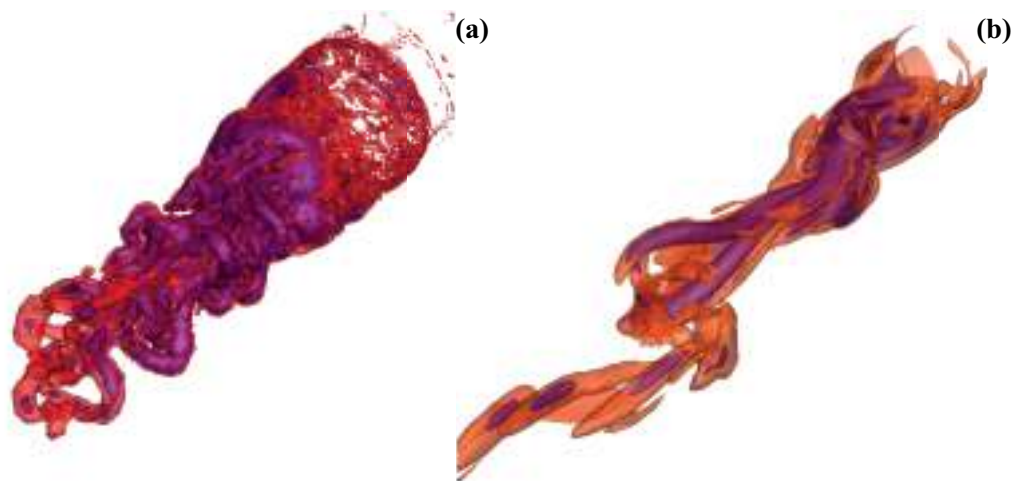
Figure 7. Isosurfaces of the vortex-indicator λ_2: VMS-LES (a) and DNS (b).

is a fundamental parameter associated with the base drag. Nonetheless, it is possible to explain the connection between the mean and fluctuating flow fields by considering the different locations where the instability of the shear layers bounding the near-wake occurs. As already suggested in Mariotti and Buresti (2013), this location may be identified by analysing the trends of the standard deviation of the velocity fluctuations along the edge of the near-wake, which are shown, for all the different experimental and numerical cases, in Figs. 8a, 8b, and 8c. As may be seen, the fluctuations start increasing at a certain distance from the base which, in all cases, increases with increasing boundary layer thickness; furthermore, the increase occurs progressively more downstream going from the experimental results to those of the VMS-LES and of the DNS simulations. It is then plausible to deduce that this growth of the velocity fluctuations may be associated with the onset of the instability in the separated shear layer bounding the near wake which, in turn, is directly connected with the formation of the vorticity structures and with the length of the mean recirculation region.
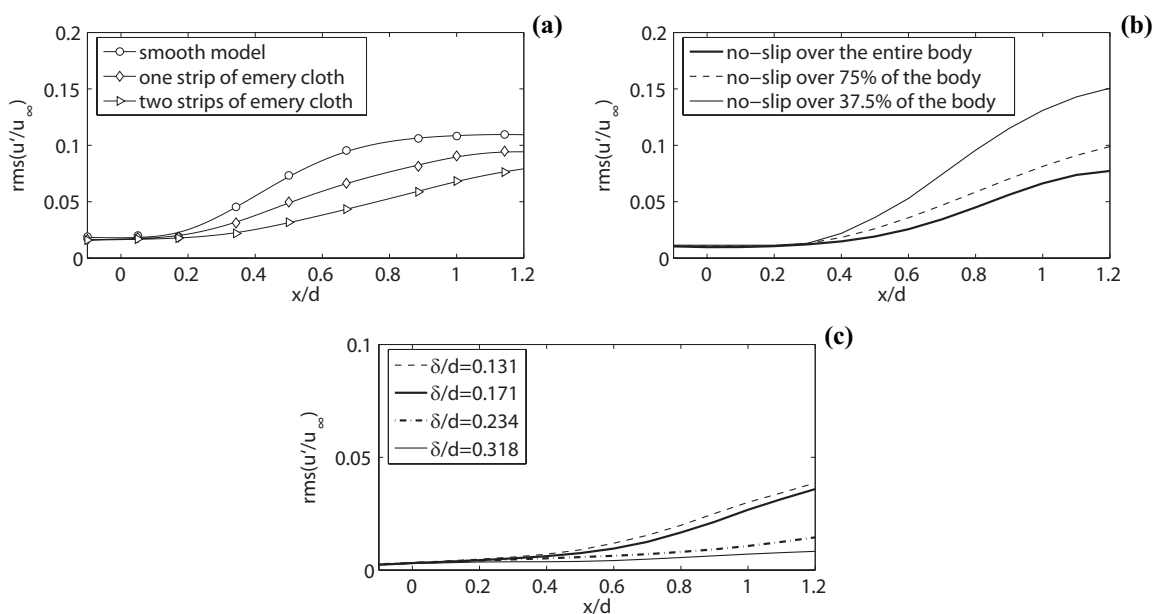
Figure 8. Intensity of the velocity fluctuations along the edge of the near wake: experiments (a), VMS-LES (b) and DNS (c).

4   Conclusions

In the present work the effect of varying the boundary layer thickness on the lateral surface of an axisymmetric blunt-based body was analysed through VMS-LES and DNS simulations, and the results were compared with available experimental data. The experiments and the VMS-LES simulations were carried out at the same Reynolds number but the free stream and boundary layer turbulence levels were different. On the other hand, the DNS simulations were carried out at a significantly lower value of the Reynolds number.

The results showed that in all cases the base drag of the body decreased when the thickness of the separating boundary layer increased; the trend of this variation was the same for all the considered cases but significant quantitative differences were present, in strict connection with the different flow conditions as regards turbulence level and Reynolds number. However, considering the effect of the variation of the boundary layer thickness on the length of the mean recirculation region present in the near wake, it could be shown that, independently of the status of the boundary layer before separation, of the turbulence level of the oncoming flow and of the Reynolds number, a single linear relationship exists between the base pressure and the mean recirculation length, which is then found to be the key parameter connected with the value of the base drag. In particular, the base suctions and drag decrease with increasing l_r/d, and this highlights the importance of identifying the flow parameters and features that mainly influence the mean recirculation length. In the present work we focussed on the effect of the thickness of the separating boundary layer, but it was also possible to highlight the role of the location of the onset of the instability in the shear layer bounding the near wake. Therefore, it may be concluded that any geometrical or flow parameter influencing the start of this instability may be expected to also affect the length of the recirculation region and thus the base drag of a blunt-based bluff body.

References

Jeong, J. and Hussain, F. (1995). On the identification of a vortex. *J. Fluid Mech.* **285**, pp. 69–94.

Mariotti, A. (2014). Experimental and numerical investigations for the characterization and control of separated flows. *PhD. Thesis, Scuola di Dottorato in Ingegneria "Leonardo da Vinci", University of Pisa.*

Mariotti, A. and Buresti, G. (2013). Experimental investigation on the influence of boundary layer thickness on the base pressure and near-wake flow features of an axisymmetric blunt-based body. *Exp. Fluids* **54 (11): 1612**.

Meliga, P., Chomaz, J. M., and Sipp, D. (2009). Unsteadiness in the wake of disks and spheres: Instability, receptivity and control using direct and adjoint global stability analyses. *J. Fluid Struct.* **25**, pp. 601–616.

Ouvrard, H., Koobus, B., Dervieux, A., and Salvetti, M.V. (2010). Classical and variational multiscale LES of the flow around a circular cylinder on unstructured grids. *Comput. Fluids* **39**, pp. 1083–1094.

Porteiro, J. L. F., Przirembel, C. E. G., and Page, R. H. (1983). Modification of subsonic wakes using boundary layer and base mass transfer. *AIAA J.* **21**, pp. 665–670.

Rowe, A., Fry, A. L. A., and Motallebi, F. (2001). Influence of boundary-layer thickness on base pressure and vortex shedding frequency. *AIAA J.* **39**, pp. 754–756.

Sevilla, A. and Martinez-Bazan, C. (2004). Vortex shedding in high Reynolds number axisymmetric bluff-body wakes: Local linear instability and global bleed control. *Phys. Fluids* **16**, pp. 3460–3469.

Wornom, S., Ouvrard, H., Salvetti, M.V., Koobus, B., and Dervieux, A. (2011). Variational multiscale large-eddy simulations of the flow past a circular cylinder: Reynolds number effects. *Comput. Fluids* **47**, pp. 47–50.

Aerostatic loading on the deck of cable-stayed bridge during erection stage under skew wind

Mingshui Li[1,2], Shaopeng Li[1], Jiadong Zeng[1] and Haili Liao[1,2]

[1]Research Centre for Wind Engineering, Southwest Jiaotong University, Chengdu, China
[2]Key Laboratory for Wind Engineering of Sichuan Province, Chengdu, China
Corresponding author: M. Li, lms_rcwe@swjtu.edu.cn

Abstract

It is assumed that aerostatic load coefficients along a bridge deck follow the strip assumption in conventional buffeting theory. The validity of this assumption is suspended for a cable-stayed bridge under construction stages due to the effect of significant aerodynamic interference from the pylon. This situation may be aggravated because of the presence of skew wind. Based on the full bridge aero-stiff model, aerostatic loads on each deck segment are measured in smooth oncoming flow with various yaw angles. The results show that the pylon's shelter effect may not be ignored and can amplify the aerostatic forces on the leeward deck, and consequently results in the so-called "cosine rule" to be invalid for the buffeting estimation of cable-stayed bridge during erection under skew wind.

1   Introduction

Cable-stayed bridges under construction are usually susceptible to wind actions. Auxiliary pier or wind cable is taken to prevent them from exceeding buffeting responses induced by occasional storms. The wind normal to the bridge axis is assumed to be the worst case in estimating buffeting response and the design of these auxiliary structures. However, larger buffeting response under skew wind rather than normal wind observed during an aeroelastic model test of a cable-stayed bridge in erection stage (Zan, 1987) seems to infer the limitation of assumption mentioned above.

Tanaka and Davenport (1982) proposed so called "cosine role", skew wind decomposition method, to predict the buffeting response of the structure under skew wind in frequency domain. By introducing effective mean wind speed, deck width, and ellipse coherence model of turbulent flow, Xie and Tanaka (1991) developed an extended approach to estimate buffeting response of long span bridge in completed stage under skew wind. Scanlan (1993) took the similar method but introduced six aerodynamic coefficients. Zhu (2002) proposed a modified buffeting analysis method by introducing a concept of oblique strip along the mean wind direction. In his research, the wind coordinate system was selected as the coordinate for analysis, which required complicated wind tunnel tests to obtain the aerodynamic coefficients, aerodynamic admittance and flutter derivatives along the oblique strip. All analytical methods assumed that aerostatic load coefficients along a bridge deck keep constants and the strip assumption can be applied to calculate the total buffeting forces along span. However, the aerostatic force distribution along the span under skew wind is not confirmed yet, which may have important effect on the evaluation accuracy of wind induced response. Therefore, it is essential to obtain aerostatic wind force distribution on the girder varying with skew wind, including possible aerodynamic interference of the pylon.

In this paper, the full aero-stiff model of a cable-stayed bridge during double cantilever erection stage was adopted to obtain aerostatic loading on deck segments. To investigate effects of skew wind and pylon on aerostatic loads, the yaw angle is varied from -90° to 90°. The error margin of the "cosine rule" is estimated by comparing testing results with static loads derived from conventional section model testing technique. Furthermore CFD simulation is conducted to study the flow field of

the bridge to verify pylon's shelter effect and account for the invalidation of the traditional "cosine role" partly.

2   Experimental Technique

The full aero-stiff models of the cable-stayed bridge in erection stage was designed and manufactured using the conventional aerelastic model technology, i.e. the structural stiffness was provided by a metal spine assembly; the external shape was provided by cladding elements. In contrast to an aeroelastic model, a full aero-stiff model has sufficient high stiffness and keeps stationary under action of wind. This technology makes it possible to measure aerostatic forces on each segment by a force balance attached to the spine structure.

The metal spine assembly of the main girder was designed as a rectangular steel beam with high stiffness. The external shapes of the girder were made of fibre glass and ABS materials. To avoid interaction between two adjacent sections, a 3mm gap between sections was reserved, see Fig.1.

Two sets of balance systems were employed to measure two sections simultaneously. The balances were fixed on the metal spine (Fig.1), and then the drag force, axis force and lift force on each section would be measured in body coordinate. As shown in Fig.2, these two balance measurement systems can be moved from section 1# to section 5# with the wind yaw angle varying from -90° to 90°. 0° yaw angle was defined as the wind direction normal to the bridge deck axis, and the yaw angle 90° was defined as the measured sections located at upstream, the contrast was the yaw angle -90°.

Figure 1. Full bridge aero-stiff model of a cable-stayed bridge (left) and force balance inside deck segment (Right)
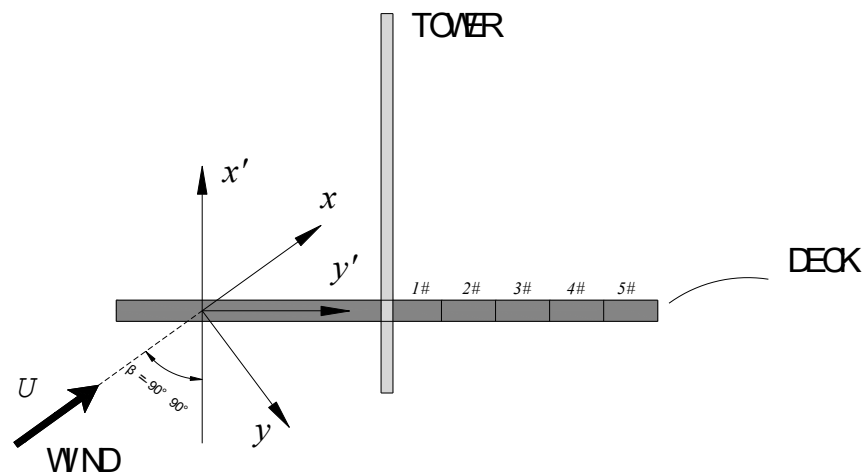
Figure 2. Deck segments and definition of coordinate systems

The tests were carried out in an industrial wind tunnel (type: XNJD-1) of Southwest Jiaotong University, which is a closed circuit wind tunnel with two tandem closed test sections. The first test section, 3.6m(width)×3.0m(height)×8.0m(length), was used. Its wind speed is adjustable from 0.5m/s to 22.0m/s. The aerostatic loading on deck segments was investigated under smooth oncoming flow, turbulent intensity~0.5%.

3   Results and Discussion

Fig.3 shows lift coefficients of each segments corresponding to the wind normal to the bridge axis. A load amplification area about 1/3 cantilever length from the tower is found due to the tower shelter effect, and this tendency become more obvious as the attack angle increased. Lower loading on segment 5 is expected due to possible 3-D flow influence at the tip of the deck. When the oncoming flow is not normal to the bridge axis, the influence of the tower is more significant to loading on sections in the leeward side, as shown in Fig. 4. The maximal sectional lift forces appear while the yaw angle varying from -10° to -20°. It is naturally to concluded that the "cosine rule" is just approximately applicable to the sections located in upwind side, whereas, it may underestimate the wind load and risk the bridge into danger for the leeward sections, especially as the yaw angle varying from 0° to -30°, see Fig.5. The possible explanation is that the tower shelter effect changes the flow field, and generates complex vortex in the leeward side, which may induce larger surface pressure at some area behind the tower even for comparatively small yaw angles. In order to demonstrate the complex wind field caused by the tower shelter, CFD simulation was carried out to visualize the flow filed of the model. As shown in Fig.6, the flow around the tower and the vortex in tail flow could be observed, which may partly account for these complicate experiment phenomena.

In the end, the experimental result was employed to calculate the aerostatic response and the error margin of the "cosine rule" was estimated approximately.
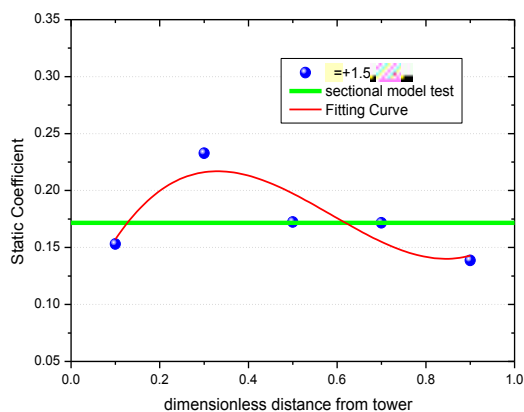
Figure 3. Influence of attack angle and tower on spanwise lift distribution
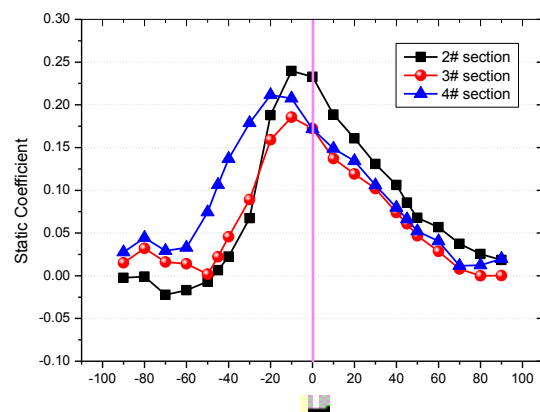
Figure 4. Influence of yaw angle and tower on sectional lift distribution (α=+1.5°)

4   Conclusions

The full bridge aero-stiff model was taken to investigate the sectional aerostatic force distribution on the deck of cable-stayed bridge in cantilever erection stage under skew wind. In comparison with the discrepancies of the sectional forces on upwind sections and leeward sections, it can be deduced that tower's shield effect plays an essential role in reshaping the deck surface pressure, which may result in invalidity of "cosine role" for estimation of aerostatic loading on sections in the leeward side. The finding is also verified partly by the flow filed of CFD simulation.
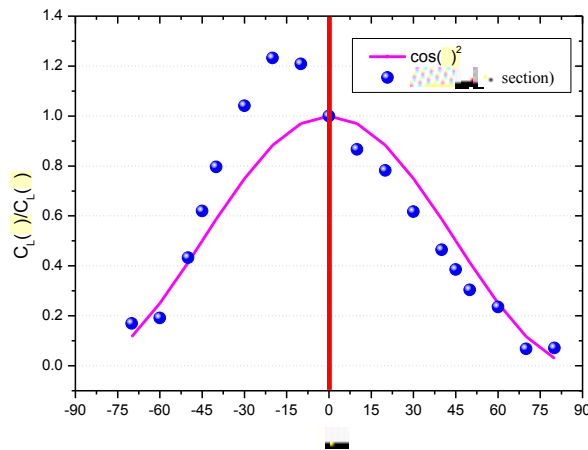
Figure 5. Error margin of the "cosine rule"
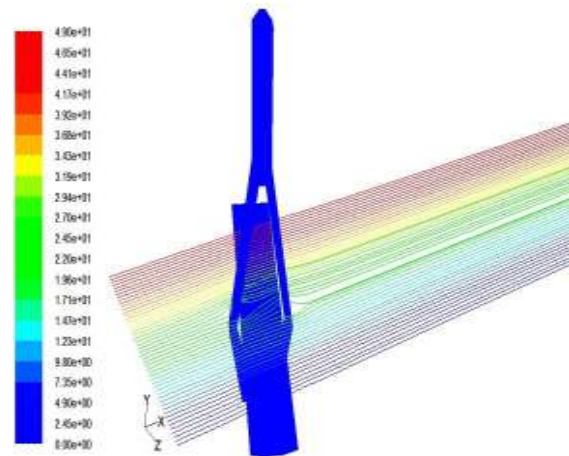
Figure 6. The flow field by CFD Simulation

5   Acknowledgements

References

Zan, S. J. (1987). The effects of mass, wind angle and erection technique in the aeroelastic behaviour of a cable-stayed bridge model. *NAE-AN-46*, NRCC.

Tanaka, H. and Davenport, A.G. (1982). Response of taut strip models to turbulent wind, *Journal of the Engineering Mechanics Division*, ASCE, 108(1), 33-49.

Xie, J. and Tanaka, H. (1991). Buffeting analysis of long span bridges to turbulent wind with yaw angles, *Journal of Wind Engineering and Industrial Aerodynamics*. 37(1), 65-77

Scanlan, R. H. (1993). Bridge buffeting by skew winds in erection stages. *Journal of Engineering Mechanics*, ASCE, 119(2), 51-269.

Zhu, L.D. (2002). Buffeting response of long span cable supported bridges under skew winds: field measurement and analysis, PhD Thesis, The Hong Kong Polytechnic University, China.

Development of probabilistic wind load model for South Africa

J. Botha[1], J.V. Retief[1], M. Holický[2] and C. Barnardo-Viljoen[1]

[1]Department of Civil Engineering, Stellenbosch University, South Africa
[2]Czech Technical University, Prague, Czech Republic

Corresponding author: J. Botha, jacquesb@sun.ac.za

Abstract

There exists an acute need to improve the probabilistic wind load models used in calibration of national load standards in order to achieve specified target levels of reliability. The representation of wind load probabilities and the combination of time variant and invariant uncertainties are discussed. A procedure is presented for determining partial factors and for deriving distribution properties for the purposes of reliability calibration based on a set of extreme value models and climatic strong wind characterization. Representative models of the South African annual extreme wind pressure are developed and used to compare two methods for calculation of design wind loads. It is shown that the standard partial factor method taking into account both time variant and invariant components results in significantly greater design pressures than pressures calculated using a design quantile approach considering the time variant component only.

1   Introduction

Wind is an intrinsically variable natural phenomenon. This variability is a critical aspect of wind actions as structural loads that can only be treated probabilistically. The probability models used to describe the various factors in the wind load process form the basis for calibration of design procedures to achieve sufficient levels of reliability over a range of design situations.

Much work has been done on the proper probabilistic representation of strong wind loading mechanisms. In spite of this, there is still an acute need to improve probability models for strong winds in order to address specific needs. One such need is to improve the representation of the strong wind climate and probability models for a specific region, making use of the latest series of observations. A recent study of the South African strong wind climatology (Kruger et al., 2011) provides an opportunity to improve the South African probabilistic wind load models.

The wind load design process may broadly be divided into the description of the free-field wind at the location of the structure and the conversion of the free-field wind into wind pressure loading on the structure. The free-field wind is predominantly modeled by time variant probability models representing the stochastic nature of strong wind conditions. Probability modeling of the wind pressure loading process is predominantly a time invariant representation of uncertainties of predicting wind pressure conversion and distribution across the structure. This paper discusses the combination of uncertainties of the time variant and time invariant components, probability models of the time variant component for the South African wind climate and the contribution of the time invariant components to the total uncertainty of design wind loads.

2   General Wind Load Probability Representation

The general formulation of design wind load is given in Equation 1. The variables are defined in Table 1, along with indicative statistical parameters which have been adopted from JCSS (JCSS, 2001-2002). The parameters are given for normalized distributions – the relative mean value of a given variable is the ratio of the mean to characteristic value of that variable – which are typically used for probabilistic investigations. It should be noted that the given parameters are significantly dependent on particular conditions

and may be changed to better represent specific structural and environmental situations. However, for the purpose of this investigation the indicative parameters are sufficient. The wind load formulation is a function of wind pressures, given in Equation 2, which is dependent on air density (ρ) and wind speed (V).

$$Q = Q_{Ref}\, c_r\, c_a\, c_g\, c_d \tag{1}$$

$$Q_{ref} = 0.5\, \rho\, V^2 \tag{2}$$

Table 1. Indicative distribution parameters and time dependence of wind load variables.

Symbol	Variable	Time Dep.	Dist. Type	Relative Mean	CoV
Q_{Ref}	Annual extreme pressure	Yes	Gumbel	0.8	0.25
c_r	Terrain roughness	No	Normal	0.8	0.15
c_a	Pressure coefficient	No	Normal	1.0	0.20
c_g	Gust factor	No	Normal	1.0	0.15
c_d	Dynamic effects	No	Normal	1.0	0.15

For the purposes of structural reliability the distribution of the extreme maximal wind speed and pressure values is of import. The extreme value distribution of type I, commonly called the Gumbel distribution, is typically used in the description of annual extreme wind speed values. This distribution is described in Equation 3, and the shape coefficient (a) and mode (B) distribution parameters which are related to the mean (μ) and standard deviation (σ) are given in Equations 4 and 5 respectively. The quantile (X_T) for a given return period (T) may be determined using Equation 6 (Holický, 2009)

$$F(x) = exp\left(-exp\left(\frac{B - x}{a}\right)\right) \tag{3}$$

$$a = \sigma\sqrt{6}/\pi \tag{4}$$

$$B = \mu - 0.577a \tag{5}$$

$$X_T = B - a\,ln\left[-ln\left(1 - \frac{1}{T}\right)\right] \tag{6}$$

Assuming a Gumbel distribution for the design wind load, including all time variant and invariant components, expressions may be formulated for the design value (Q_d) and characteristic value (Q_k) of the design wind load in terms of the mean value (μ_q), the target level of reliability (β_T), the coefficient of variation of the design wind load (w_Q), the sensitivity factor for action effects (α_E), the time-sensitivity factor (α_T), and the ratio (N) of the reference period to the design life (Holický, 2009). The sensitivity factor for action effects is taken as $\alpha_E = -0.7$ for Eurocode and the South African load standard (Retief and Dunaiski, 2009). The time-sensitivity factor is given by the ratio of the coefficient of variation of the time dependent component to the coefficient of variation of the total design wind load. Assuming the time dependence of components as given in Table 1 holds, the time sensitivity factor may be calculated using Equation 7. The coefficient of variation of the design wind load is determined using Central Limit Theorem, as shown in Equation 8 (Montgomery and Runger, 2007).

$$\alpha_T = \frac{w_{Q,Ref}}{w_Q} \tag{7}$$

$$w_Q = \sqrt{\sum w_i^2} \tag{8}$$

For a characteristic value defined as the wind speed with an exceedance probability of 0.02 per annum, the ratio of the characteristic value to mean value is given in Equation 9. The ratio of the design value for a specified design working life to mean value is given in Equation 10. The partial load factor (γ_Q) may

then be calculated using Equation 11 (Retief et al., 2013). This method for calculation of partial factors effectively incorporates the uncertainties of both time dependent and independent wind load components.

$$\frac{Q_k}{\mu_Q} = 1 - w_Q(0.45 + 0.78ln(-ln(0,98))) \tag{9}$$

$$\frac{Q_d}{\mu_Q} = 1 - w_Q(0.45 - 0.78\alpha_T ln(N) + 0.78ln(-ln(\Phi^{-1}(-\alpha_E\beta)))) \tag{10}$$

$$\gamma_Q = Q_d/Q_k \tag{11}$$

By using the indicative parameters given in Table 1 and parametrically varying the annual extreme pressure coefficient of variation, partial load factors for a gi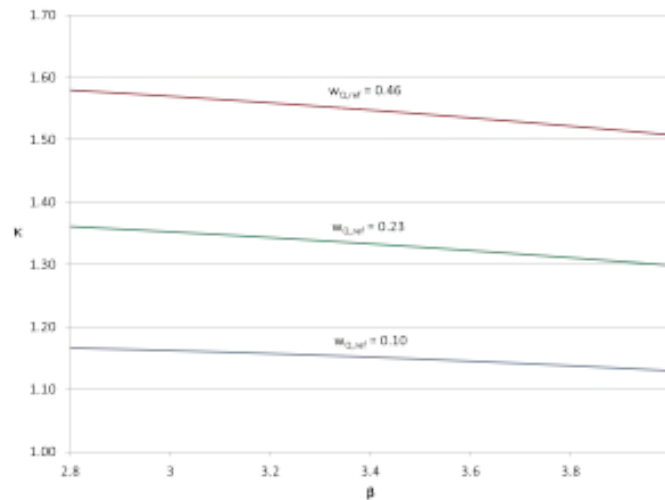ven target reliability value may be found using this method. The variation of the partial load factors with the reliability index for selected values of the annual extreme pressure coefficient of variation is shown in Figure 1, and Table 2 gives partial factor values for the typical target reliability levels used in Eurocode and South African standards.
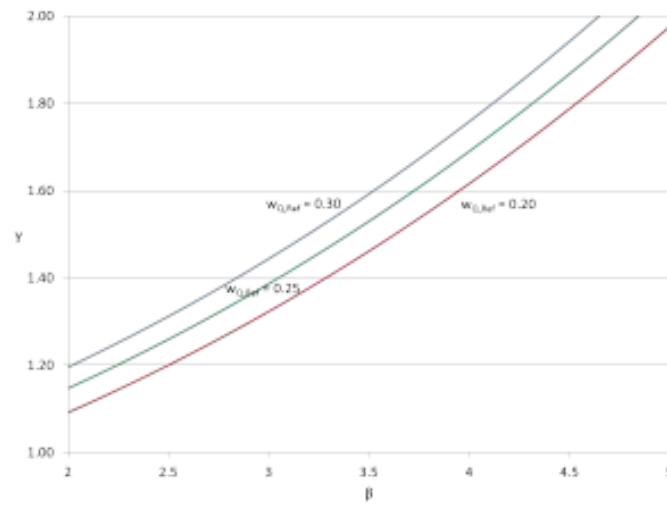
Figure 1. Variation of the partial load factor γ_Q with the reliability index β for selected values of the annual extreme pressure coefficient of variation $w_{Q,Ref}$ using indicative distribution parameters, $N = 50$.

Table 2. Partial load factor γ_Q values for typical target reliability levels β for selected values of the annual extreme pressure coefficient of variation $w_{Q,Ref}$ using indicative distribution parameters, $N = 50$.

$w_{Q,Ref}$	w_Q	α_T	γ_Q for $\beta_T = 3.0$	γ_Q for $\beta_T = 3.5$	γ_Q for $\beta_T = 3.8$
0.20	0.38	0.52	1.32	1.46	1.55
0.25	0.41	0.61	1.39	1.53	1.62
0.30	0.44	0.68	1.44	1.59	1.69

3   Strong Wind Statistical Parameters for South Africa

The South African strong-wind climate consists of multiple strong wind generating mechanisms with a complex geographical distribution. Chief among these are synoptic scale weather systems which dominate along the coast, and meso-scale events, mainly thunderstorms, which are more prevalent in the internal parts of the country (Kruger et al., 2011). These strong wind mechanisms need to be considered when developing probability models for wind speeds.

The current South African design wind maps are based on records from 14 weather stations with
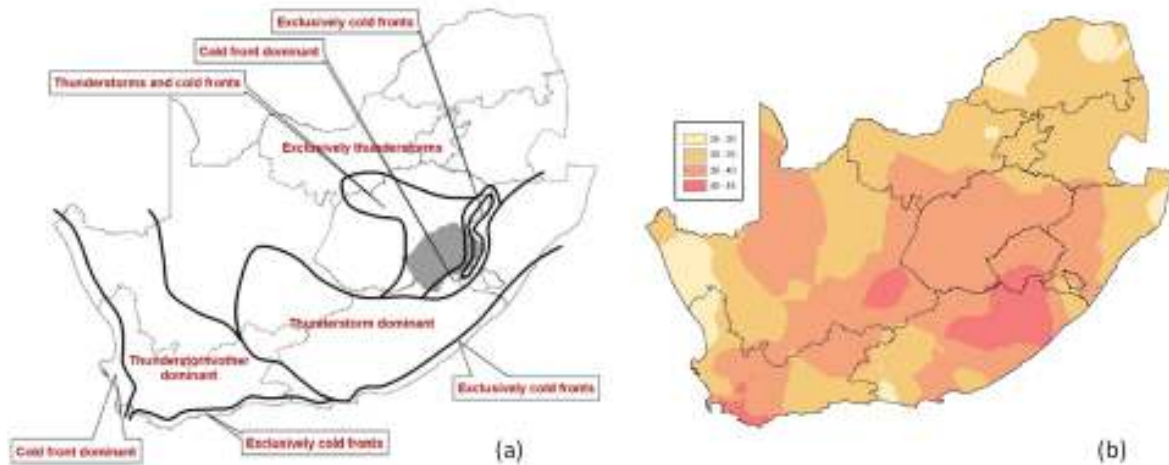
Figure 2. (a) Geographical distribution of strong wind gust mechanisms and (b) characteristic gust wind speed values (Kruger et al., 2011).

average record lengths of 26 years. A new design wind map is in development using wind speed records from a network of 172 new generation automatic weather stations (AWS) deployed since 1990 (Kruger et al., 2011). After a quality audit, 74 AWS record sets were selected and predictive wind speed models were established for each station. Various models were employed to account for short record lengths and mixed strong wind generating mechanisms, however it was found that the Gumbel distribution models were sufficient to represent the South African annual extreme wind speeds. Cluster analysis was used to identify zones with similar distribution parameter values and strong wind generating mechanisms, which enabled mapping of characteristic wind speeds and primary strong wind mechanisms across the country, as shown in Figure 2 (Kruger et al., 2013).

Wind maps are conventionally expressed in terms of characteristic wind speed values defined as the wind speed value with an exceedance probability of 0.02 per annum. This characteristic value corresponds to a return period of 50 years. The distribution models were therefore normalized with respect to the characteristic value ($V_{0.02}$) at each station, converting the distributions to standard form as used in probabilistic investigations and allowing comparison of distribution models across a large region. Furthermore, the models were disaggregated according to the primary strong wind mechanisms in order to determine the effects of the mechanisms on the models. The upper and lower limits of the distribution models were then selected to determine a range of extreme wind speed models over the region for each strong wind mechanism. This range is shown in Figure 3, and the distribution parameters of the selected models are given in Table 3.

Table 3. Range of distribution parameters of normalized South African extreme wind speed (V) probability models for thunderstorm and synoptic winds.

Mechanism	Model	a	B	w_V
Thunderstorm	Upper Bound	0.11	0.56	0.22
	Lower Bound	0.04	0.83	0.06
Synoptic	Upper Bound	0.09	0.61	0.18
	Lower Bound	0.03	0.86	0.05
Combined	Average	0.07	0.73	0.11

By evaluating the integrals of the distribution functions on the probability interval $[0.001, 0.02]$ to compute the areas bounded by the functions, it was found that there is an 84.4% overlap between the
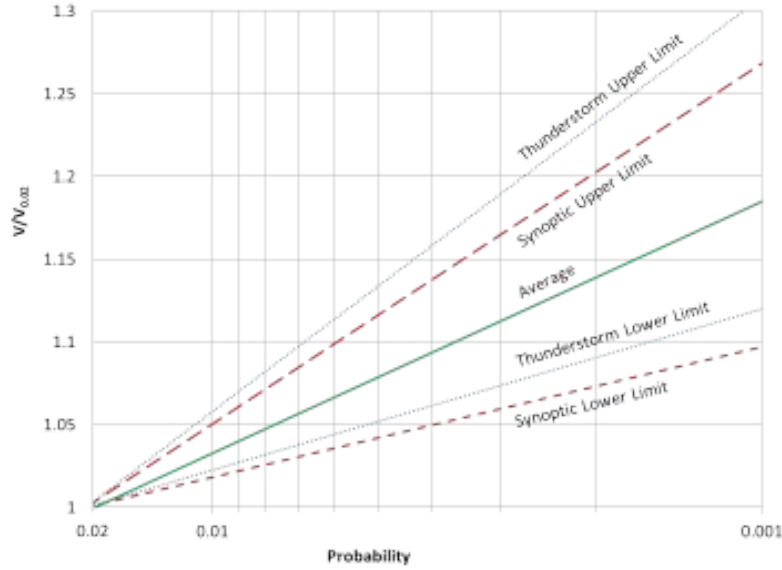
Figure 3. Upper and lower bounds of normalized South African extreme wind speed (V) probability models for thunderstorm and synoptic winds.

synoptic and thunderstorm envelopes. This indicates that the difference between the average wind speed models of the two wind generating mechanisms is insignificant when compared to the difference between the upper and lower bounds of each range. The conclusion that may be drawn from this is that influence of the different strong wind generating mechanisms on the ranges of distribution parameters of annual extreme wind speeds is negligible. These parameters may therefore be determined directly from predictive models for a range of strong wind conditions over a large region.

4   Comparison of Design Wind Load Calculation Methods

In order to investigate the influence of the time invariant components of the wind load formulation on the total uncertainty of the design wind load, a comparison was drawn between two methods prescribed in ISO 4354 (ISO, 2009) for the calculation of design wind loads. The first is the standard partial factor method whereby the annual extreme pressure is calculated using the characteristic 50 year wind speed ($V_{0.02}$). The design wind load is then determined by factorizing the annual extreme pressure with a partial factor and multiplying by the product of the means of the time invariant wind load components (C), as shown in Equation 12. As explained in Section 2, this method incorporates the uncertainty of both the time dependent and time independent components.

$$Q_{d,1} = \gamma_Q \, 0.5 \, \rho \, V_{0.02}^2 \, C \qquad (12)$$

In the second method, which shall be referred to as the design quantile approach, the contribution of the time invariant components to the total uncertainty of the design wind load is ignored. The design load is calculated as shown in Equation 13 by directly using the quantile wind speed (V_p), with a probability of exceedance (p) corresponding to the target level of reliability, to determine the extreme wind pressure. The quantile wind speed is determined using Equation 6. The formula for the calculation of the probability of exceedance is given by Equation 14.

$$Q_{d,2} = 0.5 \, \rho \, V_p^2 \, C \qquad (13)$$

$$p = 1 - \Phi(\alpha_E \beta) \qquad (14)$$

4.1 Methodology

The two methods described above were compared using the South African regional wind speed models discussed in Section 3. From within the envelopes of distribution parameters given in Figure 3 and Table 3 three representative wind speed models were selected. These models were selected by determining the maximum, average and minimum coefficients of variation within the dispersion envelopes and selecting the models corresponding to those values. The selected models were the upper bound thunderstorm model, the lower bound synoptic model and the average model.

In order to determine partial factors, annual extreme wind pressure models are required as opposed to annual extreme wind speed models. From Equation 2 it may be seen that a quadratic relationship exists between wind speed and pressure. The representative wind speed models were therefore transformed into representative wind pressure models by determining the mean ($\mu_{Q,Ref}$) and standard deviation ($\sigma_{Q,Ref}$) of the wind pressure models using Equations 15 and 16. A value of unity was assumed for air density. The mean (μ_{V^2}) and standard deviation (σ_{V^2}) of the squared wind speed were calculated using standard moment identities as given in Equations 17 and 18, which are dependant on the mean (μ_V), standard deviation (σ_V) and skewness (α_V) of the wind speed models (Holický, 2009). The distribution parameters of the representative wind speed models and transformed wind pressure models are given in Table 4.

$$\mu_{Q,Ref} = 0.5\rho\mu_{V^2} \tag{15}$$

$$\sigma_{Q,Ref} = 0.5\rho\sigma_{V^2} \tag{16}$$

$$\mu_{V^2} = \mu_V^2 + \sigma_V^2 \tag{17}$$

$$\sigma_{V^2} = 2\sigma_V\sqrt{\mu_V^2 + \mu_V\sigma_V\alpha_V} \tag{18}$$

$$\alpha_{V^2} = \frac{8\mu_V^3\sigma_V^3(\alpha_V + 3w_V)}{\sigma_{V^2}^3} \tag{19}$$

It was conservatively assumed that the transformed wind pressure models are described by Gumbel distributions even though the value of the skewness as calculated using Equation 19 may differ from the skewness value of a Gumbel distribution. However, this assumption is unimportant as these models were only used in the calculation of partial load factors, and the partial factor method described in Section 2 is only dependent on the coefficient of variation of the annual extreme wind pressure and not specific distribution parameters. The initial assumption of a Gumbel distribution for the design wind load should however be reconsidered, as it is not the wind annual extreme pressure which is typically described by a Gumbel distribution but rather the annual extreme wind speeds.

Table 4. Distribution parameters for representative South African annual extreme wind speed and wind pressure models.

Model	Speed			Pressure		
	a	B	w_v	a	B	$w_{Q,Ref}$
Maximum	0.11	0.56	0.22	0.08	0.16	0.46
Average	0.07	0.73	0.11	0.05	0.27	0.24
Minimum	0.03	0.86	0.05	0.03	0.37	0.10

Using the coefficients of variation of the representative wind pressure models the method for calculation of partial factors as given in Equations 9 to 11 was applied. The indicative statistical parameters of the time invariant components as given in Table 1 were used, and the indicative coefficient of variation of the annual extreme wind pressure was replaced with each of the representative South African coefficients of variation in turn. The time-sensitivity factor and the coefficient of variation of the design wind load were recalculated using Equations 7 and 8 respectively. The partial factor values for the three representative models are given in Table 5.

Finally, the characteristic ($V_{0.02}$) and design (V_p) wind speeds were calculated using the predictive

Table 5. Partial load factor γ_Q values for typical target reliability levels β for representative values of the South African annual extreme pressure coefficient of variation $w_{Q,Ref}$ using indicative distribution parameters of time invariant wind load components, $N = 50$.

$w_{Q,Ref}$	w_Q	α_T	γ_Q for $\beta_T = 3.0$	γ_Q for $\beta_T = 3.5$	γ_Q for $\beta_T = 3.8$
0.46	0.57	0.82	1.59	1.76	1.87
0.24	0.41	0.59	1.37	1.52	1.61
0.10	0.34	0.30	1.18	1.31	1.40

models for each of the 74 AWS stations across South Africa for a range of target levels of reliability. Partial load factors were also calculated for values within the same range using the three representative South African annual extreme pressure models. The design wind loads could then be calculated for both the standard partial factor method (Equation 12) and the design quantile approach (Equation 13) described at the beginning of this Section.

4.2   Comparison

The ratio of the design pressures (κ) as calculated using Equation 20 was determined for a range of target levels of reliability. As the time invariant components cancel out, κ is effectively the ratio of the annual extreme pressures. The variation of the average ratio across all stations with the target level of reliability is shown in Figure 4.

$$\kappa = \frac{Q_{d,1}}{Q_{d,2}} \tag{20}$$

Figure 4. Variation of partial factor with the reliability index for selected values of the annual pressure coefficient of variation.

It may be seen that the partial factor method results in design pressure values which are between 13% and 58% greater than those obtained using the design quantile approach, depending on which representative annual extreme pressure model is considered. It is expected that the partial factor method will result in greater values as it incorporates the uncertainties of both the time variant and time invariant components, whereas the design quantile approach solely uses the annual extreme wind speed model in its formulation and therefore the uncertainty of the time invariant components is ignored. However, the magnitude of the difference of the values obtained for these methods clearly illustrates that the time invariant components have a significant influence on the uncertainty of design wind loads. It is therefore not sufficient to use indicative models of these components, and a clear need exists to develop more

accurate models of the time dependant wind load components.

Furthermore, the choice of the representative model of the annual extreme pressure used to calculate partial factors has a considerable impact on the final design wind load values. This raises the question of which distribution parameters should be selected from within the range of calculated extreme wind speed models for a given region for the purposes of reliability calibration of wind load standards. Further research regarding the choice of distribution parameters is required.

5   Conclusion

From this investigation the following was concluded:

- For parametrically varied coefficients of variation of the annual extreme pressure over the interval $[0.20, 0.30]$, time-sensitivity factors range between $\alpha_T = 0.52$ and $\alpha_T = 0.68$.

- By further parametrically varying target levels of reliability over the interval $[3.0, 3.8]$ using the same range of coefficients of variation of the annual extreme pressure, partial load factors were found to vary between $\gamma_Q = 1.32$ and $\gamma_Q = 1.69$.

- The areas bounded by the distribution functions of representative South African extreme wind speed models for two primary wind generating mechanisms were found to overlap by 84.4%. Therefore, the influence of the different strong wind generating mechanisms on the ranges of distribution parameters of annual extreme wind speeds is negligible.

- Design wind loads calculated using the standard partial factor method taking into account both time variant and invariant components are between 13% and 58% greater than design loads calculated using a design quantile approach considering the time variant component only, depending on the coefficient of variation of the annual extreme pressure selected.

Further investigation regarding the influence of the skewness on extreme wind speed models and the choice of distribution parameters for the purposes of reliability calibration is required.

References

Holický, M. (2009). *Reliability Analysis for Structural Design*. First. SUN MeDIA. ISBN: 978-1-920338-10-7.

ISO (2009). *ISO 4354 - Wind actions on structures*.

JCSS (2001-2002). *Joint Committee on Structural Safety Probabilistic Model Code, Parts 1 to 4*.

Kruger, A.C., Retief, J.V., and Goliger, A.M. (2011). An updated description of the strong wind climate of South Africa. *13th International Conference on Wind Engineering*.

— (2013). Strong winds in South Africa: Mapping of updated statistics. *Journal of the South African Institute of Civil Engineering* **55**, pp. 46 –58.

Montgomery, C.D. and Runger, G.C. (2007). *Applied Statistics and Probability for Engineers*. Fourth. John Wiley & Sons. ISBN: 978-0-471-74589-1.

Retief, J.V. and Dunaiski, P.E. (2009). *Background to SANS 10160*. First. SUN MeDIA. ISBN: 978-1-920338-10-7.

Retief, J.V., Barnardo-Viljoen, C., and Holický, M. (2013). Probabilistic models for design of structures against wind loads. *Research and Application in Structural Engineering, Mechanics and Computation*.

Compactly supported wavelet-Galerkin analysis method for the wind-induced stochastic dynamic response of a tall building

Thai-Hoa Le[1,2] and Luca Caracoglia[1]

[1]Department of Civil and Environmental Engineering, Northeastern University, USA
[2]Department of Engineering Mechanics, Vietnam National University, Hanoi, Vietnam
Corresponding author: Thai-Hoa Le, ho.le@neu.edu

Abstract

This study explores the utilization of a novel Wavelet-Galerkin (WG) analysis approach, which combines a Galerkin approximation method with compactly discrete wavelets as a basis function for analyzing the wind-induced stochastic response of a linear or nonlinear tall building subjected to stationary or transient wind loads. A reduced-order model of the tall building is examined to study the stochastic dynamic response; both time-dependent turbulent-induced buffeting forces and motion-induced aerolastic forces are taken into consideration. The WG method with compactly supported Daubechies wavelets is used to decompose the coupled stochastic dynamic equations of the tall building into random algebraic equations; this decomposition allows obtaining the solution in an approximate yet accurate way. The CAARC tall building is utilized as a benchmark simulation example. Results of an investigation on the influence of the wavelet order and resolution of the WG solutions are also discussed.

1 Introduction

A tall building is sensitive due to wind excitation; it is often exposed to large wind-induced dynamic response. The study of the building's stochastic dynamics often requires to take into consideration nonlinear structural behaviour, nonlinear and nonstationary stochastic wind loading (e.g., Kareem and Wu, 2013). Nevertheless, assumptions such as the stationarity in wind loading and the linear structural behaviour are usually postulated for simplicity. Moreover, system coupling during the motion is often neglected. The wind-induced stochastic structural dynamics of tall buildings can be usually analysed in adequate form by a reduced-order model of the system, which retains some selected fundamental vibration modes of the building along with the main aerodynamic properties. The stochastic dynamic response of tall buildings via reduced-order models has been successfully investigated in the literature (e.g., Kareem, 1985; Piccardo and Solari, 2000; Caracoglia, 2013). The reduced-order model is usually composed of coupled differential equations because of the combination of the time-dependent buffeting forces with the motion-induced aeroelastic forces. Solution to the dynamic response is usually determined in the frequency domain using the Fourier transform (e.g., Kareem, 1985; Piccardo and Solari, 2000); the Fourier transformation can deal with the stochastic dynamics of the building by using empirical power spectral density functions of the wind turbulence as well as it enables transforming the coupled equations of motion into a simpler algebraic form. In contrast, the solution of the coupled motion equations in the time domain, for example needed in the case of nonlinear structural response, is not usually pursued since it may lead to complex and computationally demanding numerical solution procedures (e.g., Caracoglia, 2013). A simplified solution for the stochastic dynamics of the buildings has been, on occasion, proposed to decouple the equations of motion by omitting the motion-induced wind loads.

Recent investigations on wind loading and wind environment have also clarified that the random wind field processes in extreme, local and convective wind events can exhibit transient/nonstationary behaviour. The non-synoptic pattern of the turbulence is observed, for example, in thunderstorms, downbursts, tornadoes and hurricanes; this feature can result in temporal dependence of both amplitude and frequency of the loading processes (e.g., Xu and Chen, 2004). Furthermore, the

stochastic response of tall structures under the extreme wind events might become nonlinear (e.g., Kareem and Wu, 2013). Thus, common assumptions of a stationary wind loading, used to analyse the structural dynamics, can be inadequate in the case of extreme and locally convective winds with transient/nonstationary turbulence, and insufficient for observing any transient response. In addition, it has been noted that existing methods for studying the transient structural dynamics can lead to computationally-demanding numerical solutions in the case of wind-induced stochastic dynamics (e.g., Chen, 2008).

Wavelet-based computational tools have emerged in structural dynamics since 1998, when Daubechies first introduced the compactly supported wavelets, known as Daubechies wavelet family. The use of wavelets later expanded to various fields of science and engineering. The Daubechies wavelets possess the advantageous properties of compactness, orthogonality and ability to perform multi-resolution analysis. The latter property implies that wavelets can be used to represent "computational solutions" at any pre-selected level of resolution; this property makes them particularly attractive for developing approximating solutions to complex dynamic problems by Galerkin projection. The wavelet-Galerkin method (WG) is a powerful instrument for the purpose of approximations to engineering problem solutions. For example, Daubechies wavelets have been used as basis-functions in conjunction with the Galerkin projection to solve ordinary differential equations (Amartunga and Williams, 1997), for the identification of nonstationary model parameters in single-degree-of-freedom systems (Ghanem and Romen, 2001), for investigating simplified continuous mechanical systems (Gopalakrishnan and Mitra, 2010) and the seismic response of simplified systems (Basu and Gupta, 1998).

One of the potentially novel applications of the WG method is the solution of stochastic dynamic equations with a nonlinear structure and transient/nonstationary wind loads. Nevertheless, limitations and computational challenges of the WG method have been observed for ordinary differential equations. Issues include the treatment of the boundary conditions, the wavelet resolution, the finite or infinite duration of the dynamics in time, and a supplementary computational complexity. These issues have initially prevented the expansion of the WG method towards an application to a wide spectrum of stochastic dynamic problems (Latto et al., 1991; Gopalakrishnan and Mitra, 2010). Fortunately, the treatment of boundary conditions, the resolution and an improved numerical approach for computing the wavelet "connection coefficients" have been recently resolved (Romine and Peyton, 1997; Le and Caracoglia, 2014).

This study exploits these latest developments to advance the study of the WG method for the stochastic structural dynamics of realistic structural systems. This paper proposes a novel WG analysis method to compute the stochastic structural response of a reduced-order model of a tall building accounting for both transient/nonstationary wind loads and the coupling between turbulent-induced forces and motion-induced forces. The CAARC tall building (Melbourne, 1980) is utilized as a benchmark for demonstration of this method. Realizations of the evolutionary transient wind fields along the building height are artificially simulated from a stationary wind processes by amplitude-modulation function technique (Chen, 2008). Numerical investigations are employed to study issues such as the orders of the Daubechies wavelets and the resolution needed for the transient response analysis of the building.

2   Compactly Supported Wavelet-Galerkin Method

Compactly-supported wavelet functions have non-zero values exclusively within a finite domain (interval) and are identically zero outside this interval. The family of compactly supported Daubechies wavelets (DB) is very well suited due to the properties of orthogonality and compactness. The "father" scaling functions $\varphi(x)$ of a wavelet of order N, with support over the finite interval $[0, N-1]$, can "dilate" and "translate" in the domain of continuous signal at any resolution; these functions are (Daubechies, 1998):

$$\varphi(x) = \sum_{k=0}^{N-1} a_k 2^{j/2} \varphi(2^j x - k) \tag{1}$$

where a_k: scaling coefficients, satisfying $\sum_{k=0}^{N-1} a_k = 2$; k, j: translation and dilation parameters. The scaling functions satisfy the condition $\int_{-\infty}^{\infty} \varphi(x)dx = 1$; they also have compact support on the interval $[0,N$-1$]$; the index N designates the order of the wavelets. Figure 1 shows examples of the Daubechies "father" scaling functions for $DB1$, $DB6$, $DB8$ and $DB10$.
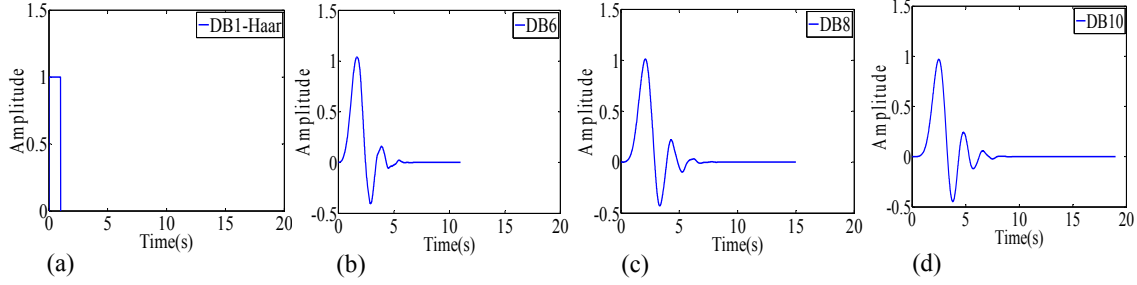
Figure 1. Some examples of Daubechies "father" scaling functions: (a) $DB1$, (b) $DB6$, (c) $DB8$, (4) $DB10$

The Galerkin projection approximates the exact solution *u(x)* to an equation *Bu=f*, by projecting it into a subspace using the basis-function $\varphi(x)$. The basis function is a piecewise function, containing multiple sub-functions; each sub-function is projected into a certain interval of the basis function's domain. In the WG method, the orthonormal and compactly supported Daubechies wavelets can be employed as basis-functions for the Galerkin projection of the approximate solution to a time-dependent dynamic problem. If the independent time variable is denoted by *t*, the motion in the WG transform can be expressed, at a preselected level of resolution *j* of the wavelet, as:

$$u(t) = \sum_{l=1}^{N_x} u_l \varphi_l(t) \tag{2}$$

In the previous equation u_l are approximation coefficients, derived from the inner product $u_l = \langle u(t), \varphi(t) \rangle = \int_{-\infty}^{\infty} u(t)\varphi(t)dt$. Similarly, the first and second derivatives $\dot{u}(t), \ddot{u}(t)$ can be approximated, in the Daubechies wavelet subspace $\varphi(t)$, as:

$$\dot{u}(t) = \sum_{l=1}^{N_x} u_l \dot{\varphi}_l(t), \qquad \ddot{u}(t) = \sum_{l=1}^{N_x} u_l \ddot{\varphi}_l(t) \tag{3}$$

The derivatives of the wavelets can be obtained in closed form in the support, i.e., in the interval $[0,N$-1$]$. The inner products between approximating solutions of the velocity and acceleration in Eq. (3) and each term of the expansion φ_k are required by the Galerkin expansion. Due to the orthogonality property of the Daubechies wavelets, these are:

$$\langle \varphi_k, \sum_{l=1}^{N_x} u_l \varphi_l \rangle = \sum_{l=1}^{N_x} u_l \, \delta_{lk}, \langle \varphi_k, \sum_{l=1}^{N_x} u_l \dot{\varphi}_l \rangle = \sum_{l=1}^{N_x} u_l \Omega_{l-k}^{0,1}, \langle \varphi_k, \sum_{l=1}^{N_x} u_l \ddot{\varphi}_l \rangle = \sum_{l=1}^{N_x} u_l \Omega_{l-k}^{0,2} \tag{4}$$

$$\delta_{lk} = \int_{-\infty}^{+\infty} \varphi_k(t)\varphi_l(t)dt, \; \Omega_{l-k}^{0,1} = \int_{-\infty}^{+\infty} \varphi_k(t)\dot{\varphi}_l(t)dt, \; \Omega_{l-k}^{0,2} = \int_{-\infty}^{+\infty} \varphi_k(t)\ddot{\varphi}_l(t)dt \tag{5}$$

In the previous equations the operator $\langle \; \rangle$ denotes the inner product operation; δ_{lk} is the Kronecker delta; $\Omega_{l-k}^{0,1}, \Omega_{l-k}^{0,2}$ are 2-term connection coefficients of the Daubechies wavelets; the integer *l-k* is the index of appearance that depends on the support or the order of the wavelet.

It is noteworthy that the connection coefficients exclusively depend on the scaling functions within their limit support and the wavelet resolution; in contrast, they not to depend on the analytical signal. The 2-term connection coefficients are usually needed for second-order dynamical systems. If higher-order derivation and cross terms exist in the equation of motion to represent nonlinearity and coupling, the 3-term connection coefficients or possibly higher multi-term coefficients may appear. Since the wavelets are compactly supported, the connection coefficients are also determined within a limited interval. For the adequate implementation of the WG method, a sparse matrix form has been used for the compactly supported connection coefficients. For instance, the Daubechies wavelet of order N (DBN) are compactly supported at (N-1) discrete points, $0 \leq l, k \leq (N-1)$, thus requiring a total of ($2N$-3) pairs of connection coefficients; furthermore, ($2N$-3) 2-term connection coefficients can be determined with the indices of (*l-k*) varying on the support of $[-N+2,-N+3,..,0,…,N-3,N-2]$.

Computation of the connection coefficients of the Daubechies wavelets and accurate treatment of the boundary conditions are essential for the implementation of the WG method. The 2-term

connection coefficients, exclusively applicable to approximations with unbounded time interval and only for the *DB*6 with wavelet resolution *j*=1, were computed by Latto et al.(1991). Romine and Peyton (1998) extended this methodology (Latto et al., 1991) to simulate the two ends of a bounded time interval and for resolutions other than *j*=1, providing an efficient generalized approach for the management of arbitrary boundary conditions and arbitrary wavelet resolution.

This study employs the approach proposed by Romine and Peyton (1998), which is briefly described below. It is based on the expansion of the original computational domain of the signal (N_n discrete points) by adding (N-1) points to the left of the domain (before initial time) and (N-1) points to the right of original computational domain (beyond final time). The new computational domain has ($N_x=N_n+2N$-1) wavelet expansion points. The WG method uses N_x independent scaling functions. The WG transform expands the time-varying signal at a pre-selected resolution (*j*); therefore an initial choice of wavelet resolution (*j*) is required for the computation of the connection coefficients. The resolution parameter of the Daubechies wavelets is known as 2^j at a scale *j*. The resolution must be determined so that the scaling function is centered, given the number of discretization points, i.e., the sampling time of the original signal. The wavelet resolution (*j*) can be approximately found from the number of samples of the signal per unit time ($\bar{N}_x$) with $\bar{N}_x = 2^j$ (Le and Caracoglia, 2014).

3   Stochastic Dynamic Response of a Tall Building: Background

The reduced-order motion equations of the tall building, after decomposition into generalized modal coordinates, which only retain information on the fundamental modes (the first lateral modes in the *x* and *y* directions - Figure 2), can be written as (Piccardo and Solari, 2000; Caracoglia, 2013):

$$M_r \ddot{r}(t) + C_r \dot{r}(t) + K_r r(t) = \bar{Q}_f + Q_{bf,r}(t) + Q_{acf,r}(t,r,\dot{r},\ddot{r}) \qquad (6)$$

where M_r, C_r, K_r are generalized mass, damping and stiffness of *r*-th mode; the variable $r = \{x,y\}$ is also used to designate the generalized coordinate of the fundamental modes: (*x*) "along-wind" lateral mode in the plane of the mean wind direction, (*y*) "cross-wind" transverse mode; $\bar{Q}_{f,r}, Q_{bf,r}(t)$, $Q_{acf,r}(t,r,\dot{r},\ddot{r})$ are, respectively, the generalized mean wind load, the generalized time-dependent buffeting and aeroelastic loads. System and loading quantities in the generalized coordinates, indicated in Eq. (6), can be found:

$$M_r = \int_0^h \Phi_r^2(z)m(z)dz, \ K_r = 4\pi^2 n_r^2 M_r, \ C_r = 4\pi\zeta_r n_r M_r \qquad (7)$$

$$\bar{Q}_{f,r} = \int_0^h \Phi_r(z)\bar{F}_r(z)dz, Q_{bf,r}(t) = \int_0^h \Phi_r(z)F_{b,r}(z,t)dz, Q_{acf,r}(t,r,\dot{r},\ddot{r}) = \int_0^h \Phi_r(z)F_{ac,r}(z,t,r,\dot{r},\ddot{r})dz \ (8)$$

where h: total height of the building; z: generic elevation along the height of the building, $\Phi_r(z)$: mode shape function; $m(z)$: distributed mass per unit height of the building; n_r, ζ_r: fundamental natural frequencies and damping ratios; $\bar{F}_r, F_{b,r}, F_{ac,r}$: respectively, distributed mean forces, buffeting forces and aeroelastic forces per unit height in the plane (direction) of the "*r*-th" mode. The global response (R) can be reconstructed from the generalized response (r) as:

$$R = \Phi_r r \qquad (9)$$
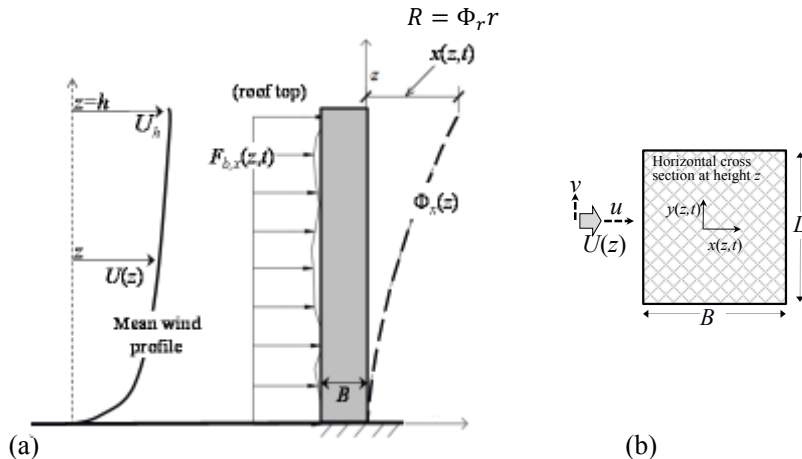
(a)   (b)
Figure 2. Coordinate system of a tall building and sectional forces: (a) lateral view; (b) cross-section

The mean wind direction is orthogonal to the face of dimension D in Figure 2. Distributed wind forces $\bar{F}_r(z), F_{b,r}(z,t), F_{ac,r}(z,t,r,\dot{r},\ddot{r})$ per unit height z corresponding to the two primary motion planes $r=x$, $r=y$, compatible with the definition of generalized coordinates in Figure 2, are (Caracoglia, 2013):

$$\bar{F}_x(z) = \left(\tfrac{1}{2}\right)\rho U(z)^2 DC_D, \ F_{b,x}(z,t) = \left(\tfrac{1}{2}\right)\rho U(z)D\left[2C_D u + \left(C_D^{'} - C_L\right)v\right]$$

$$F_{ac,x}(z,t,\dot{x},\dot{y},\theta) = \left(\tfrac{1}{2}\right)\rho U(z)D\left[-2C_D\dot{x} - \left(C_D^{'} - C_L\right)\dot{y}\right] + \left(\tfrac{1}{2}\right)\rho U(z)^2 D\left[C_D^{'}\theta\right] \tag{10}$$

$$\bar{F}_y(z) = \left(\tfrac{1}{2}\right)\rho U(z)^2 DC_L, \ F_{b,y}(z,t) = \left(\tfrac{1}{2}\right)\rho U(z)D\left[2C_L u + \left(C_L^{'} - C_D\right)v\right]$$

$$F_{ac,y}(z,t,\dot{x},\dot{y},\theta) = \left(\tfrac{1}{2}\right)\rho U(z)D\left[-2C_L\dot{x} - \left(C_L^{'} - C_D\right)\dot{y}\right] + \left(\tfrac{1}{2}\right)\rho U(z)^2 D\left[C_L^{'}\theta\right] \tag{11}$$

where $\rho, U(z), t$ respectively are air density, mean-wind velocity profile and time; B, D are the width and depth of the cross-section; $C_D, C_L, C_D^{'}, C_L^{'}$ are quasi-static force coefficients, normalized with respect to B, and their derivatives; $u(z,t), v(z,t)$ are fluctuating components of wind turbulence; $\theta, \dot{x}, \dot{y}$ are the building's torsional rotation, the derivatives of the along-wind lateral and the across-wind transverse displacements at each floor. The distributed wind forces in Eqs. (10-11) are coupled.

4   Stochastic Building Response of a Tall Building: Wavelet Domain

The coupled equations of motion in the generalized coordinates can be found in Eq. (6), while the generalized system parameters and generalized forces are Eqs. (7-8) and Eqs. (10-11). As a result, two global equations of motion in the modal structural coordinates, denoted by x and y, can be obtained from the relationship in Eq. (9) as

$$M_x\ddot{x}(t) + [C_x - Q_{xx}]\dot{x}(t) - Q_{yx}\dot{y} + K_x x(t) = Q_{b,x}(t) \tag{12}$$

$$M_y\ddot{y}(t) + [C_y - Q_{yy}]\dot{y}(t) - Q_{xy}\dot{x} + K_y y(t) = Q_{b,y}(t) \tag{13}$$

where M_x, M_y, C_x, C_y, K_x, and K_y are derived from Eq. (7); Q_{xx}, Q_{yx} are motion-induced forces associated with the x-coordinate; $Q_{b,x}(t)$ is the generalized buffeting load of the x-coordinate; $Q_{xx}, Q_{yx}, Q_{yy}, Q_{xy}$ are the aeroelastic forces and $Q_{b,y}(t)$ is the generalized buffeting load of the y-coordinate. These quantities are determined as follows (Le and Caracoglia, 2014):

$$Q_{xx} = -\int_0^h \phi_x [0.5\rho U(z)DC_D]dz, \ Q_{yx} = -\int_0^h \phi_x \left[0.5\rho U(z)D\left(C_D^{'} - C_L\right)\right]dz \tag{14}$$

$$Q_{xy} = -\int_0^h \phi_y [2(0.5)\rho U(z)DC_L]dz, \ Q_{yy} = \int_0^h \phi_y \left[0.5\rho U(z)D\left(C_L^{'} - C_D\right)\right] \tag{15}$$

$$Q_{b,x} = -\int_0^h \phi_x(0.5)\rho U(z)D\left[2C_D u + \left(C_D^{'} - C_L\right)v\right]dz, \ Q_{b,y} = \int_0^h \phi_y\left(\tfrac{1}{2}\right)\rho U(z)D\left[2C_L u + \left(C_L^{'} - C_D\right)v\right]dz \tag{16}$$

It is generally agreed that solution of the coupled stochastic dynamic equations in Eqs. (12-13) in the time domain by numerical integration or other discrete numerical methods is often extremely challenging and, on occasion, poorly accurate or even impossible. In contrast, the WG analysis method transforms the coupled motion equations in Eqs. (12-13) to the wavelet domain. The steps of the computational procedure are: (1) all time-dependent quantities are approximated by the Galerkin projection in Eqs. (2-3); (2) the Galerkin-based approximating quantities are found by inner product, using the orthogonality property of the wavelets, and are subsequently assembled into the "connection coefficient matrices" in Eqs. (4-5); (3) the resultant algebraic system of equations in matrix form is solved numerically; (4) lateral displacement, velocity and acceleration of coupled stochastic dynamics at each floor are estimated. The solution of the coupled stochastic motion equations can be rewritten in the wavelet domain as:

$$\left\{M_x \sum_{l=1}^{N_x} \Omega_{lk}^{0,2} + (C_x - Q_{xx})\sum_{l=1}^{N_x}\Omega_{lk}^{0,1} + \sum_{l=1}^{N_x}K_x\delta_{kl}\right\}x_l - \left\{Q_{yx}\sum_{l=1}^{N_x}\Omega_{lk}^{0,1}\right\}y_l = q_{bxl} \tag{17}$$

$$\left\{M_y \sum_{l=1}^{N_x} \Omega_{lk}^{0,2} + (C_y - Q_{yy})\sum_{l=1}^{N_x}\Omega_{lk}^{0,1} + \sum_{l=1}^{N_x}K_y\delta_{kl}\right\}y_l - \left\{Q_{xy}\sum_{l=1}^{N_x}\Omega_{lk}^{0,1}\right\}x_l = q_{byl} \tag{18}$$

where N_x is the computational domain; x_l, y_l are WG-based approximate displacement in the x, y generalized coordinates in Eq. (2); q_{bxl}, q_{byl} are WG-based approximate generalized buffeting forces in the x, y coordinates, similar to Eq. (2); $\Omega_{lk}^{0,1}, \Omega_{lk}^{0,2}$ are 2-term connection coefficients, obtained in Eqs.

(5). The time-varying coupled stochastic equations of motion are reduced to a system of two random matrix algebraic equations (after combining all indices):

$$[A_{11}]\{x_l\} + [A_{12}]\{y_l\} = \{B_1\} \tag{19}$$

$$[A_{21}]\{x_l\} + [A_{22}]\{y_l\} = \{B_2\} \tag{20}$$

in which the following terms are derived:

$$[A_{11}] = M_x[\Omega^{0,2}] + (C_x - Q_{xx})[\Omega^{0,1}] + K_x[I], [A_{12}] = -Q_{yx}[\Omega^{0,1}]$$

$$[A_{21}] = -Q_{xy}[\Omega^{0,1}], \ [A_{22}] = M_y[\Omega^{0,2}] + (C_y - Q_{yy})[\Omega^{0,1}] + K_x[I], \{B_1\} = \{q_{bxl}\}, \{B_2\} = \{q_{byl}\} \tag{21}$$

In Eq. (21) $[\Omega^{0,2}]$ and $[\Omega^{0,1}]$ denote the connection coefficient matrices; $[I]$ is the identity matrix.

Finally, the linear random algebraic equations (19-20) can be solved numerically to find the motion of the building. The WG-based approximate displacements $\{x_l\}$ and $\{y_l\}$ are random since the generalized wavelet-domain loading terms, B_1 and B_2, are random. The resultant random velocities and accelerations in the x and y coordinates can be estimated as

$$\{\dot{x}_l\} = [\Omega^{0,1}]\{x_l\}, \quad \{\dot{y}_l\} = [\Omega^{0,1}]\{y_l\} \tag{22}$$

$$\{\ddot{x}_l\} = [\Omega^{0,2}]\{x_l\}, \quad \{\ddot{y}_l\} = [\Omega^{0,2}]\{y_l\} \tag{23}$$

where $\{\dot{x}_l\}, \{\dot{y}_l\}, \{\ddot{x}_l\}, \{\ddot{y}_l\}$ are the WG-based approximate velocities and accelerations in the x and y coordinates, respectively.

5   Transient Wind Loading on a Tall Building: Simulation

Multivariate transient wind fields must be digitally simulated along the height of the building at a series of discrete nodes in order to synthetically generate time-histories of the wind load (see Figure 2a). The digital simulation of a transient/nonstationary process can be based on the theory of evolutionary power spectral density or EPSD (e.g., Priestley, 1965; Liang et al., 2007). This approach exploits the property that a multivariate nonstationary process can be expressed as a sum of partially-correlated stationary processes, modulated by a deterministic time function. The spectrum of the stationary processes and the deterministic time-dependent modulation function can be obtained by matching a prescribed evolutionary spectrum. Therefore, a multivariate set of time-histories of transient winds can be generated by identifying a suitable deterministic time-dependent function to modulate a synthetically-generated realization of a multivariate stationary fluctuating wind process. The realization of the stationary process can be synthetically generated using a spectral representation approach (e.g., Deodatis, 1996). A suitable model for transient/nonstationary wind fields for the tall buildings is:

$$U_j(z,t) = \bar{U}_j(z,t) + u'_j(z,t), \quad v_j^j(z,t), j=1,2,...,M \tag{24}$$

where M is the number of building nodes, need to discretize the integrals in Eqs. (14-16); z is a generic height variable; $\bar{U}(z,t)$ is the time-varying mean wind velocity; $u'(z,t)$, and $v'(z,t)$ are the random fluctuating components of the transient turbulence, which are found from the zero-mean stationary random process by means of a deterministic modulating function $A_j(\omega,z,t)$ as:

$$u'_j(z,t) = A_j(\omega,z,t)u_j(z,t), \quad v'_j(z,t) = A_j(\omega,z,t)v_j(z,t) \tag{25}$$

Suitable examples of modulating functions for transient wind simulations have been developed by Holmes and Oliver (2000), Chen (2008). The theory of evolutionary power spectra of nonstationary stochastic processes (Priestley, 1965) defines the elements of the evolutionary cross-spectral matrix as:

$$S_{jj}(\omega,z,t) = |A_j(\omega,z,t)|^2 S_{jj}^0(\omega,z), \ S_{jk}(\omega,z_1,z_2,t) = A_j(\omega,z_1,t)A_k^{T*}(\omega,z_2,t)S_{jk}^0(\omega,z_1,z_2) \tag{26}$$

In the previous equation T and "*" denote the transpose and complex conjugate operators, respectively; $S_{jj}^0(\omega,z), S_{jk}^0(\omega,z_1,z_2)$ are the stationary auto- and cross-power spectra of turbulence, noting that $S_{jk}^0(\omega,z_1,z_2) = Coh_{jk}(\omega,z_1,z_2)\sqrt{S_{jj}^0(\omega,z_1)S_{kk}^0(\omega,z_2)}$ with $Coh_{jk}(\omega,z_1,z_2) = \exp(-\frac{C\omega|z_1-z_2|}{\pi(\bar{U}(z_1)+\bar{U}(z_2))})$ being the coherence function of the spectra between nodes j and k. The Cholesky decomposition is

used to decompose the evolutionary cross spectral matrix $S(\omega, z, t)$, which is real and symmetric by construction, as follows:

$$S(\omega, z, t) = H(\omega, z, t)H^{T*}(\omega, z, t) \tag{27}$$

$$S(\omega, z, t) = |A(\omega, z, t)|^2 H(\omega, z)H^{T*}(\omega, z) \tag{28}$$

in which $H(\omega, t)$ denotes a lower triangular matrix and the superscript symbol "$T*$" indicates complex-conjugate transpose matrix operation.

A realization of the multivariate nonstationary processes $u'_j(z, t), j = 1, 2, \ldots, M$ can be numerically generated (e.g., Liang et al., 2007) as:

$$u'_j(z, t) = 2\sqrt{\Delta\omega} \sum_{m=1}^{M} \sum_{l=1}^{n} |A(\omega_l, z, t)||H_{jm}(\omega_l, z)|\cos[\omega_l t - \vartheta_{jm}(\omega_l, z, t) + \phi_{ml}] \tag{26}$$

In the previous equation $\Delta\omega$ is a circular frequency interval or "step" $\Delta\omega = \omega_{up}/n$; ω_{up} is the upper cut-off circular frequency; n is the number of circular frequencies used by the wave-superposition; ω_l is a generic circular frequency ($\omega_l = l\Delta\omega$); the matrix decomposition is $H_{jm}(\omega, z) = |H_{jm}(\omega, z)|e^{i\vartheta_{jm}(\omega, t)}$ with $\vartheta_{jm} = tan^{-1}(Im[H_{jm}(\omega, t)]/Re[H_{jm}(\omega, t)])$; ϕ_{ml} are independent random phase angles distributed uniformly in the interval $[0, 2\pi]$.

6 Numerical Example: CAARC Building

The building model is derived from the CAARC benchmark structure (Melbourne, 1980) of dimensions B=30.5m, D =45.7m and h = 183m. Uniform mass per unit height is used with $m(z)$=220,800 kg/m. The fundamental natural frequencies of the first along-wind lateral mode (x) and cross-wind transverse mode (y) are n_x=0.20Hz and n_y=0.22Hz. Torsional effects are neglected for mean wind direction parallel to x. The modal damping ratios are ζ_x=ζ_y=0.01. The mode shapes of the two fundamental modes are approximated as $\Phi_x(z) = \Phi_y(z) = (z/h)$. The Aerodynamic static coefficients and their first-order derivatives per unit height are assumed as constant, independent of the height (Caracoglia, 2013): $C_D = 1.2, C_L = -2.2, C'_D = -1.1, C'_L = -0.1$. The building is discretized into 41 floor nodes along the height at an equally-spaced distance of 4.575m. In this study, the mean wind profile of the transient/nonstationary wind model exclusively varies with the height variable (z); furthermore, the power-law model with the factor $\alpha = 0.25$ (Melbourne, 1980) and the exponential-law model are used to approximately describe the mean wind profile. It is noteworthy (e.g., Holmes and Oliver, 2000; Chen and Letchford, 2004) that the mean-wind velocity profile in a non-synoptic wind, like a thunderstorm or a downburst, is different from either power-law or exponential boundary layer models. Nevertheless, in this first application example of the WG method a more rigorous characterization of the wind profile with elevation was considered as unnecessary.

Evolutionary transient fluctuating wind velocities of the along-wind (u) and cross-wind (v) components in the x and y global structural coordinates have been synthetically simulated at the building nodes using the modulation function method (Chen and Letchford, 2004; Chen, 2008). Power auto-spectral density functions of the stationary wind turbulence employ the Harris's empirical spectrum (Melbourne, 1980) as: $nS_{kk}(\omega)/\sigma_k^2 = 0.6X/(2 + X^2)^{5/6}$, with $X = 1600n/\bar{U}(z)$ and n being a frequency (Hz), k=u and k=v, σ_k being the standard deviation of the stationary wind turbulence. The coherence function uses Davenport's empirical formula. The mean wind velocity ($\bar{U}(z)$) used in Harris's spectrum and Davenport's coherence are the mean wind velocity values evaluated at the vertical coordinate z. The reference mean wind velocity (U_h) is taken at the node 41. In this preliminary application example (Le and Caracoglia, 2014), simplified modulation functions are utilized: (*i*) cosine modulation function, $A(\omega, t) = ((1 - \cos(2\pi t/T_0)/2)^\eta$ with η a positive even integer and T_0 a reference duration, and (*ii*) exponential modulation function, $A(\omega, t) = \alpha_0 t^{\beta_0}e^{-\lambda t}$, $\alpha_0 > 0, \lambda, \beta_0 \geq 0$ (Chen, 2008).

7 Results and Discussion

Figure 3 shows a 200-second realization of a simulated time series of u along-wind transient fluctuations of wind velocity of the cosine modulation function and the exponential modulation

function, and the stationary fluctuating wind velocities at selected building nodes (nodes 41, 30) for top-floor mean wind velocity U_h=20m/s at z=h=183 m.
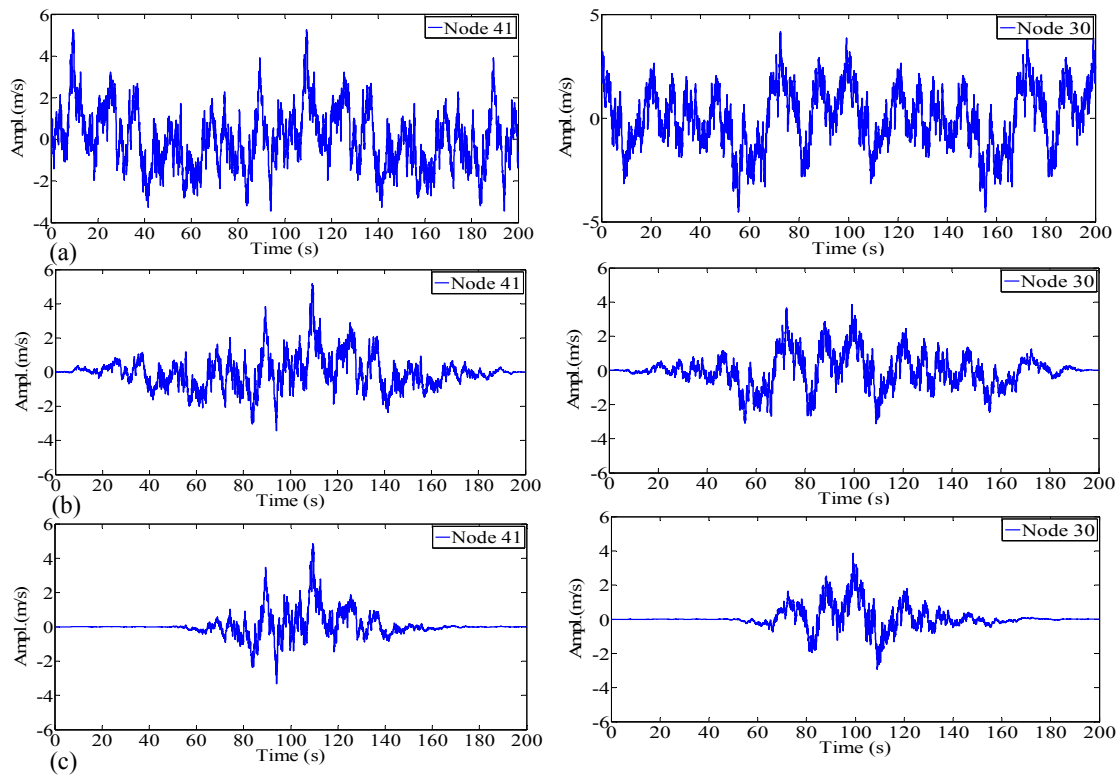
Figure 3. Simulated realization of u along-wind velocity transient fluctuations at nodes 30, 41 (roof-top) for a reference mean wind speed U_h=20m/s: (a) stationary wind, (b) transient wind with cosine modulation, (c) transient wind with exponential modulation
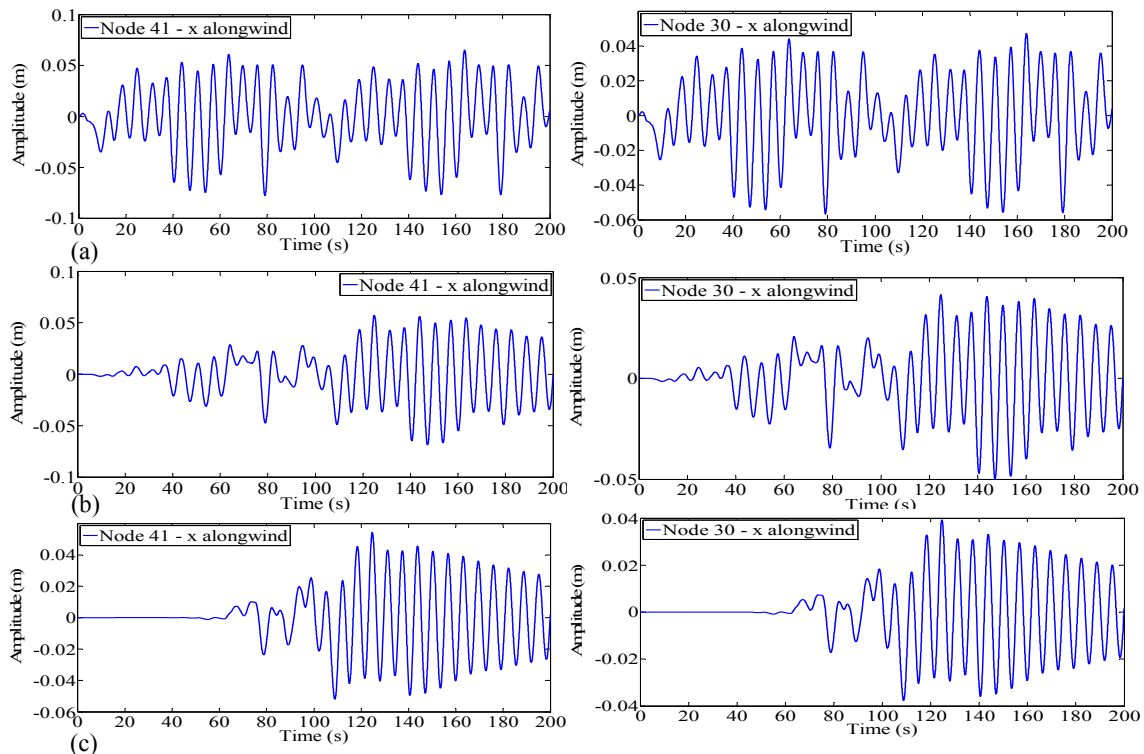
Figure 4. Along-wind dynamic displacements at nodes 30, 41 for a reference mean speed U_h=20m/s: (a) Stationary wind, (b) transient wind with cosine modulation, (c) transient wind with exponential modulation

200-second time series of the dynamic displacements in physical coordinates in the x or along-wind direction at nodes 41 and 30 are presented in Figure 4, from which it can be noticed that the response is dominated by the two fundamental lateral and transverse modes of the building. Maximum global displacements at all building nodes can be estimated from the time series of the global displacements at all nodes. The envelope of the maximum lateral displacements (drift) of the building along its height can also be determined.

(a)   (b)
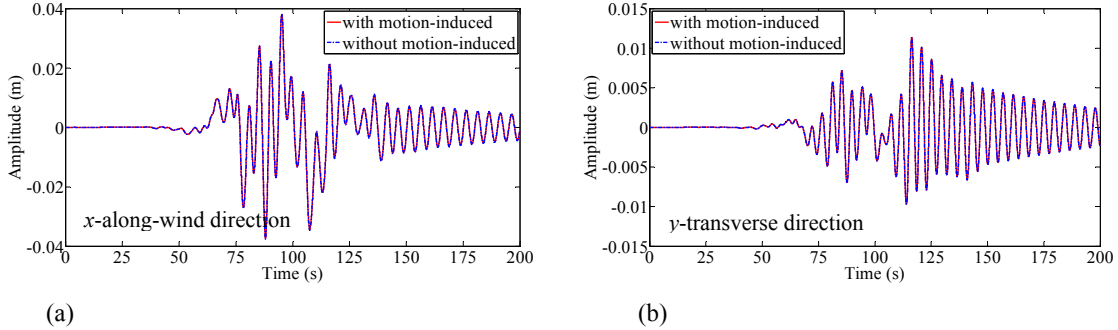
Figure. 5. Coupling effect of motion-induced forces on the transient displacement at roof-top node 41: (a) x along-wind direction, (b) y transverse direction

(a)   (b)
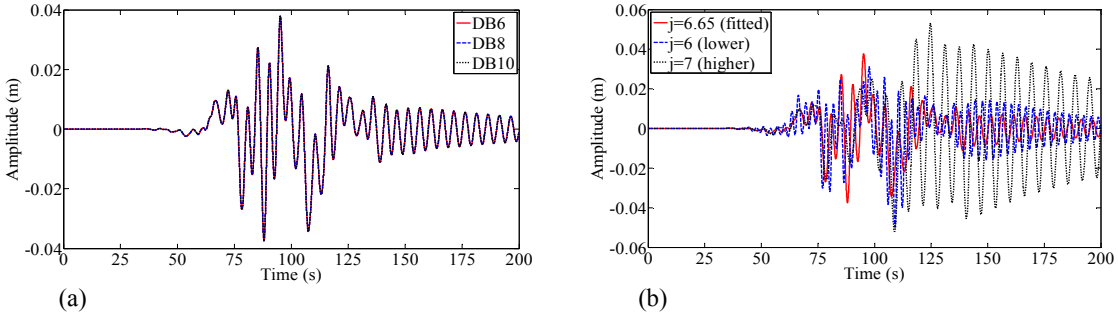
Figure 6. Influence of the wavelet order and wavelet resolution on the transient displacement at roof-top node 41: (a) Order of the Daubechies wavelet, (b) Wavelet resolution

Figure 5 illustrates the effects of the coupling on the transient dynamic displacements at the roof-top node 41 for U_h=20m/s. In this example computed at U_h=20m/s, there is little difference in the global response between the two cases with and without motion-induced forces. Figure 6 examines the influence of the selection of the Daubechies wavelet and wavelet resolution on the numerically-computed response of the building; the x-direction roof-top dynamic displacement is analyzed. The *DB6*, *DB8* and *DB10* Daubechies wavelets (refer to Figure 1 for the shapes of *DB6, DB8* and *DB10*) and three levels of wavelet resolutions have been investigated. In Figure 6b, the wavelet resolution j=6.65 is chosen to fit the sampling time of the input wind and turbulence signals. Two other values of j, either somewhat higher or lower than the "fitted" value, are utilized for comparison. No difference in the computed building response can be observed if the Daubechies wavelets *DB6, DB8* or *DB10* is utilized (Figure 6a), even though the computational time, required by higher-order Daubechies wavelets, is longer. It is also observed that the selection of wavelet resolution is crucial for the WG method, since an incorrect choice may significantly overestimate or underestimate the stochastic building response (Figure 6b).

8   Conclusion

The WG method has been explored to estimate the coupled transient dynamic response of the 183m CAARC tall building by reduced-order structural model and by synthetically-generated transient wind field realizations. Two modulation functions have been used for simulating the transient wind fields. The resultant transient response of the tall building has been examined by comparing the two cases with modulation function against the stationary wind load case; the transient dynamic "zero-mean" response of the tall building is larger than the stationary-wind dynamic response. Preliminary

investigation on the influence of the aerodynamic coupling effect, the order of selected Daubechies wavelet and the "fitted" wavelet resolution has also been carried out. The coupling effect and the wavelet order do not significantly influence the building response; in contrast, accurate estimation of the wavelet resolution is crucial. The study proves that the WG is a powerful analysis method for the solution of coupled, transient/nonstationary structural dynamic problems of tall building structures under wind loading.

Acknowledgements

This material is based upon work supported in part by the National Science Foundation (NSF) of the United States under CAREER Award, CMMI 0844977. Any opinions, findings and conclusions or recommendations are those of the authors and do not necessarily reflect the views of the NSF.

References

Amaratunga, K., and Williams, J. R. (1997). Wavelet-Galerkin Solution for Boundary Value Problems. *Archives on Computational Methods in Engineering*, **4**(3), 243-285.

Caracoglia, L. (2013). Effect of State-augmentation Numerical Scheme on the Stochastic Dynamics of a Tall Building under Wind Loading Uncertainty. *12th Americas Conference on Wind Engineering (12ACWE), Jun. 16-20, Seattle Washington, USA.*

Chen L, and Letchford C. W. (2004). Parametric study on the along-wind response of the CAARC building to downbursts in the time domain. *Journal of Wind Engineering and Industrial Aerodynamics*, **92** (9), 703-724.

Chen, X. (2008). Analysis of Along-wind Tall Building Response to Transient Nonstationary Winds. *Journal of Structural Engineering*, **134** (5), 2008, 782-791.

Daubechies, I. (1988). Orthogonal Bases of Compactly Supported Wavelets. *Communications on Pure and Applied Mathematics,* **XLI**, 909–996.

Deodatis, G. (1996). Simulation of Ergodic Multivariate Stochastic Processes. *Journal of Engineering Mechanics*, ASCE, **122**(8), 778-787.

Ghanem, R., and Romeo, F. (2001). A Wavelet-based Approach for Model and Parameter Identification of Nonlinear Systems. *International Journal of Nonlinear Mechanics*, **36**, 835-859.

Gopalakrishnan, S., and Mitra, M. (2010). *Wavelet Methods for Dynamical Problems*. CRC Press.

Holmes, J. D, and Oliver S. E. (2000). An empirical model of a downburst. *Engineering Structures*, **22**(9), 1167-1172.

Kareem, A (1985). Lateral-torsional Motion of Tall Buildings to Wind Loads. *Journal of Structural Engineering, ASCE*, **111** (11), 2479-2496.

Kareem, A., and Wu, T. (2013). Wind-induced Effects on Bluff Bodies in Turbulent Flows: Nonstationary, Non-Gaussian and Nonlinear Features. *Journal of Wind Engineering and Industrial Aerodynamics*, **122**(10), 21–37.

Latto, A., Resnikoff, H., and Tenenbaum, E. (1991). The Evaluation of Connection Coefficients of Compactly Supported Wavelets. *Proceedings of the French-USA Workshop on Wavelets and Turbulence*, Princeton, New York, Springer-Verlag.

Le, T. H., and Caracoglia, L. (2014). Coupled Wind-induced Stochastic Response of a Reduced-order Building Model using a Wavelet-Galerkin Method. *National Symposium on Vibration and Control of Structures under Actions of Wind*, February 24-25, Hanoi, Vietnam.

Liang, J., Chaudhuri, S., and Shinozuka, M. (2007). Simulation of Nonstationary Stochastic Processes by Spectral Representation, *Journal of Engineering Mechanics*, ASCE, **133**(6), 616-627.

Melbourne, W. H. (1980). Comparison of Measurements on the CAARC Standard Tall Building Model in Simulated Model Wind Flows, *Journal of Wind Engineering and Industrial Aerodynamics*, **6** (1-2), 73-88.

Piccardo, G., and Solari, G. (2000). 3D Wind-excited Response of Slender Structures: Closed-form Solution, *Journal of Structural Engineering*, *ASCE*, **126** (8), 936-943.

Priestley, M. B. (1965). Evolutionary Spectra and Non-Stationary Processes, *Journal of the Royal Statistical Society - Series B*, **27** (2), 204-237.

Romine, C. H., and Peyton, B. W. (1997). Computing Connection Coefficients of Compactly Supported Wavelets on Bounded Intervals. *Computer Science and Mathematics Division*, Report ORNL/TM-13413.

Xu, Y. L., and Chen, J. (2004). Characterizing Nonstationary Wind Speed Using Empirical Mode Decomposition. *Journal of Structural Engineering*, **130** (6), 912-920.

Wavelet-Galerkin solution for nonlinear stochastic dynamical systems

Thai-Hoa Le[1,2] and Luca Caracoglia[1]

[1]Department of Civil and Environmental Engineering, Northeastern University, USA
[2]Department of Engineering Mechanics, Vietnam National University, Hanoi, Vietnam
Corresponding author: Thai-Hoa Le, ho.le@neu.edu

Abstract

This paper explores at the first time the utilization of a wavelet-Galerkin method for solving nonlinear stochastic systems subjected to stationary and transient/nonstationary wind loads. Compactly supported Daubechies wavelets are used as orthonormal basis functions in conjunction with the Galerkin projection scheme to analyze the motion of some special cases of single-degree-of-freedom stochastic systems, which include stiffness nonlinearity (Duffing type) and damping nonlinearity (Van de Pol type), and to demonstrate the applicability of the wavelet-Galerkin method. Computation of the connection coefficients, study of boundary conditions, resolution analysis of the Daubechies wavelets, corresponding to analytical signals, are further extended for a comprehensive simulation of full-scale multi-degree-of-freedom systems and arbitrary parameters. Random white noise loading, stationary wind loading and transient/nonstationary wind loading are digitally simulated in the numerical computations.

1 Introduction

In recent decades, wavelets and wavelet transform (WT) have gradually emerged as a powerful tool for engineering and scientific computations in the mixed time-frequency domain. Wavelets are either piecewise functions or a family of functions, containing multiple sub-functions, in which each sub-function can dilate and translate from a basic function (or mother wavelet) within the signal domain (Daubechies, 1988). Wavelets are characterized as localized, rapidly-decaying, zero-mean oscillatory functions. The wavelet transform (WT) computes the convolution operation between a signal and a family of wavelets. The advantage of the WT over Fourier transform (FT) is that, instead of using a family of complex harmonic functions to decompose an aperiodic signal by FT, a family of wavelets is employed. Wavelets can represent not only symmetric, smooth or regular signals, but also asymmetric, sharp or irregular signals, which are typical of nonstationary and nonlinear phenomena, simultaneously on the time-frequency plane and in the multi-resolution analysis (MRA). The continuous wavelet transform (CWT) is applicable for signal analysis in the time-frequency domain using both orthogonal and non-orthogonal wavelets. In contrast, the discrete wavelet transform (DWT) is utilized for signal analysis and signal processing using only orthogonal wavelets. In the context of the MRA, the WT analyzes high-frequency components of the signal with a "fine" frequency resolution but "coarse" time resolution, while the WT examines low-frequency components with "fine" time resolution and "coarse" frequency resolution.

Wavelets have attracted the interest of the engineering community in computations since Daubechies (1988) derived the theory for compactly supported wavelets in orthonormal bases, known as the Daubechies wavelet family. Daubechies wavelets allow for a wide range of localization and dilation with the multi-resolution framework. Daubechies wavelets have the capability of representing the analysed signal at various levels of resolution, which make them also particularly attractive for developing approximations to exact solutions in a dynamic problem. The orthogonal-basis and multi-resolution features of the compactly-supported Daubechies wavelets have been integrated with a Galerkin expansion method to approximately solve various kinds of ordinary differential equations (Amaratunga et al., 1994; Amartunga and Williams, 1997) and dynamical differential equations (Ghanem and Romeo, 2000). This wavelet-Galerkin method (WG) is progressively emerging as an

approach to build approximate solutions to various engineering problems. In structural dynamics, the WG method has been employed in dynamics and vibrations of continuous single-degree-of-freedom, two-degree-of-freedom systems with linear and nonstationary parameters (Ghanem and Romeo, 2001), continuously simplified mechanical systems (Gopalakrishnan and Mitra, 2010), stochastic response of long-span bridges (Le and Caracoglia, 2014). Additionally, the WG method has been intensively employed in earthquake engineering to synthetically decompose seismic motions and to investigate the seismic response of simplified systems (e.g., Basu and Gupta, 1998). This partial review of the existing literature shows that this numerical method is progressively receiving more and more attention from the technical community, also in consideration of the progressive technological evolution of computational capabilities.

Some limitations and computational challenges of the WG method have been observed. These include an accurate treatment of boundary conditions, arbitrary time range, resolution analysis and computational complexity in comparison with finite-difference methods. Among the aforementioned limitations, the management of boundaries and the resolution analysis are the main problems. Many recent applications of the WG solution for ordinary differential equations have dealt with unit time (e.g., Amaratunga et al., 1994; Gopalakrishnan and Mitra, 2010); in these applications the resolution analysis of the wavelets can be neglected and the treatment of boundary conditions can be drastically simplified. These aspects have limited the evolution of the WG method to a wide range of problems, until recently. Fortunately, the problem of "adaptable" treatment of boundary conditions to better model the two ends of a finite-duration analytical signal along with an improved computation of the wavelet "connection coefficients" (Latto et al., 1991) has been solved recently (Romine and Peyton, 1997; Le and Caracoglia, 2014). Initial attempts to address the issue of treatment of boundary conditions were carried out by Latto et al., 1991, which did not provide correct computation at endpoints in bounded domain. Romine and Peyton (1997) developed a flexible treatment for the boundary conditions of the differential equations and improved the computation of the connection coefficients of the Daubechies wavelets. The WG method was modified to better model the two ends of a finite-duration analytical signal by extending the original WG method to any boundary conditions and by suitable "assemblage" of the connection coefficients in matrix form, which incorporates boundary conditions in the first and the last rows of this matrix (e.g., Le and Caracoglia, 2014). The open question on the resolution of the computed wavelets has been lately solved thanks to the fitting with the resolution of analytical signal (e.g., Le and Caracoglia, 2014).

In wind engineering, the continuous wavelet transform, using either real or complex Morlet mother wavelets, has been applied to the representation of turbulence and to the detection of correlation and coherence in the pressure or wind loads (e.g., Kareem and Kijewski, 2002). Nevertheless, no research studies exist on the application of the WG method for modelling of wind fields and simultaneous simulation and analysis of the stochastic response of civil structures. Recent investigations on wind loading and environment have also indicated that wind processes in extreme wind events can originate from non-synoptic winds such as thunderstorms, downbursts, tornadoes and hurricanes, in which either amplitude or frequency of the wind processes is transient in time (e.g., Xu and Chen, 2004). Nevertheless, the assessment of the structural loads and dynamic response has often been based on stationary wind assumptions because of the lack of computational resources and the inherent modelling challenges in the case of transient/nonstationary winds. Furthermore, stochastic response of structures during extreme wind events might no longer be linear but nonlinear (e.g., Kareem and Wu, 2013). Unfortunately, the numerical solution of nonlinear dynamic equations with transient/nonstationary loads can be extremely complex and problematical (Huang and Iwan, 2006); Therefore, the use of the WG method could be of great support to this task.

One of the potential applications of the Daubechies wavelets to study wind effects on structures is to solve stochastic dynamic equations of both single-degree-of-freedom and multi-degree-of-freedom systems with random wind loads, especially for nonlinear dynamical systems. This paper introduces the WG solution for nonlinear stochastic dynamical systems with emphasis on some special cases of stochastic loads and typical nonlinear single-degree-of-freedom systems. The paper also investigates recent shortcomings of the WG method in managing boundary conditions, estimating wavelet

resolution, which are required in order to extend the WG method for full-scale linear and nonlinear structures subjected to both the stationary and the transient/nonstationary wind loads.

2   Daubechies Wavelets

The wavelets $\psi_{a,b}(x)$ are defined as a family of functions generated from a mother wavelet by scaling (a) and translation (b) as follows:

$$\psi_{a,b}(x) = \frac{1}{\sqrt{|a|}}\psi\left(\frac{x-b}{a}\right) \tag{1}$$

Wavelets possess very useful properties, which make them particularly attractive to represent in compact and unique form nonstationary signals, such as a transient wind record (e.g., a thunderstorm). Localization and dilation with an adaptive multi-resolution are allowed with wavelets, which enable the signal to be "observed" simultaneously in time-frequency domains. Dyadic wavelets with $a = 2^{-j}; b = k2^{-j}$ are often exploited in a discrete sampling.

Daubechies wavelets are compactly supported functions, which have non-zero values within a finite domain (or duration) and a zero value elsewhere. A wavelet system is composed of a pair of functions, the father scaling function $\varphi(x)$ and the mother wavelet function $\psi(x)$; the former is defined recursively while the latter is found in terms of the scaling one (Daubechies, 1988):

$$\varphi(x) = \sum_{k=0}^{N-1} a_k \varphi(2x-k) = \sum_{k=0}^{N-1} a_k \varphi(2x) \tag{2}$$

$$\psi(x) = \sum_{k=-1}^{N-2} (-1)^k a_{k+1} \varphi(2x+k) \tag{3}$$

where a_k: scaling coefficients; N: order or "genus" of Daubechies wavelets; k: translation parameter of scaling function. Daubechies wavelets define a limit set of non-zero scaling coefficients, satisfying the condition $\sum_{k=0}^{N-1} a_k = 2$, having a limit support in the interval $[0, N-1]$. The following conditions are also necessary: $\int_{-\infty}^{\infty} \varphi(x)dx = 1$ and $\int_{-\infty}^{\infty} x^k \psi(x)dx = 0$ $(k = 0, \dots, N/2 - 1)$; these functions form an orthogonal basis because of the following properties: $\langle \varphi_k, \varphi_m \rangle = \int_{-\infty}^{\infty} \varphi_k(x)\varphi_m(x)dx = \delta_{km}$ (δ_{km}: Kronecker delta), $\langle \psi_k, \psi_m \rangle = \delta_{km}, \langle \varphi_k, \psi_m \rangle = 0$. The d-th-order derivative of the scaling function is denoted as $\varphi_k^d(x) = \partial^d \varphi_k(x)/\partial x^d$. Scaling coefficients can be determined by several methods, such as a cascade algorithm, by successive approximations and by Daubechies algorithm (Daubechies, 1988). The scaling function also holds for $\varphi(2x)$ and by induction for all $(2^j x)$; thus a general form can be written for all dilations and translations of $\varphi(x)$ as $\varphi(x) = 2^{j/2}\varphi(2^j x - k)$ where j is the resolution parameter of the wavelet. An example of dilated and translated $DB4$ wavelets and the concept of multi-resolution analysis of $DB4$ are illustrated in Figure 1. Figure 2 shows pairs of the father scaling function $\varphi(x)$ and the mother wavelet function $\psi(x)$ of $DB1$, $DB6$ and $DB20$ Daubechies wavelets.
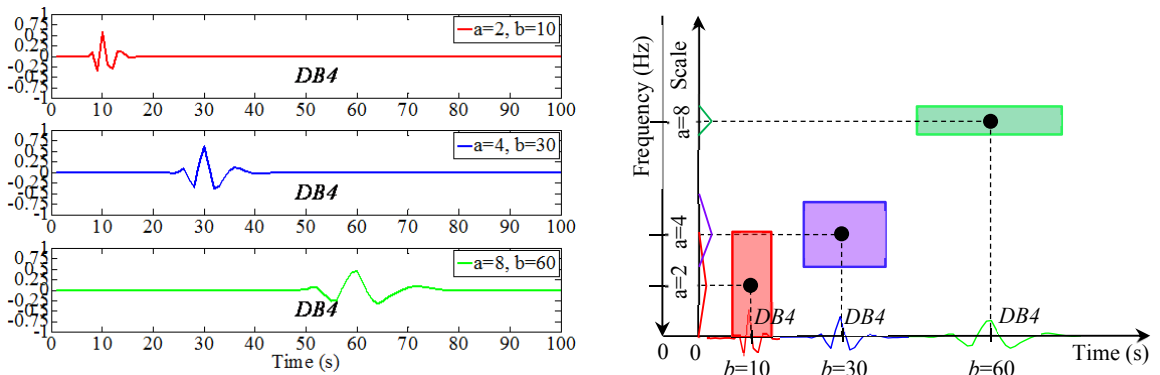
Figure 1. Wavelet analysis: (a) $DB4$ Daubechies wavelet $\psi_{a,b}(x)$ in dilation and translation, (b) concept of multi-resolution analysis

In discrete wavelet transform (DWT), the Daubechies wavelets facilitate the MRA of a signal $u(x)$, which can be exactly decomposed by a scaling function at a certain resolution j and a series of wavelet functions at lower resolutions $1 < a < j$ (i.e., higher frequencies) (Daubechies, 1998):

$$u(x) = \sum_{l=0}^{N_x} c_l \varphi_l(x) + \sum_{a=0}^{j} \sum_{l=0}^{N_x} c_{al} \psi_{al}(x) \tag{4}$$

in which c_l are approximation coefficients at certain j resolution, $c_{jl} = \langle u(x), \varphi_{jl}(x) \rangle$; c_{al} are the coefficients at lower resolutions $a < j$, with $c_{al} = \langle u(x), \varphi_{al}(x) \rangle$; l is a translation parameter; N_x is an integer index used to denote the size of the computational domain.
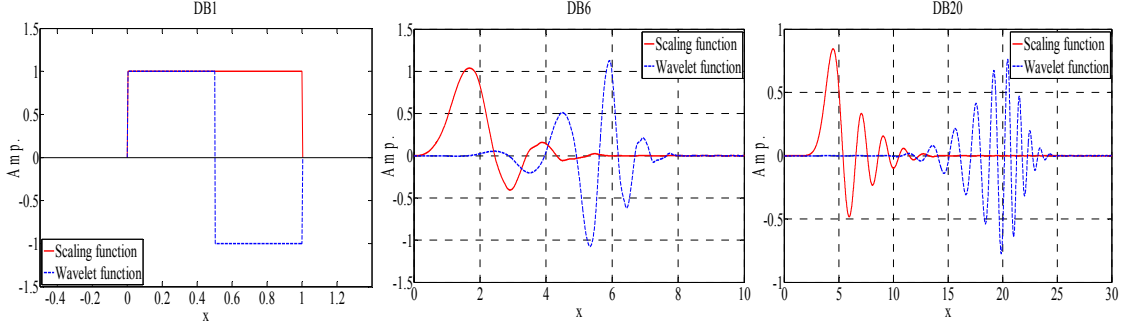
Figure 2. Pairs of scaling functions and wavelet functions of Daubechies wavelets (a) $DB1$, (b) $DB6$, (c) $DB20$

If the decomposition in Eq. (4) is truncated at the j-th level (i.e., a pre-selected resolution), the approximation of $u(x)$ is $u(x) \approx \sum_{l=0}^{N_x} c_{jl} \varphi_{jl}(x)$.

3   Wavelet-Galerkin Method

The Galerkin projection approximates an exact solution $u(x)$ to an equation $Bu=f$ by projecting it into a subspace using $\varphi(x)$ as a basis-function. The basis function is a "piecewise function", which contains several sub-functions, each of which is applied within a certain interval of the basis function's domain. In the WG method, the orthonormal and compactly supported Daubechies wavelets are used as basis-functions in the Galerkin projection to find the approximate solution. Also, the generic solution $u(t)$ to time-varying dynamic problem as a function of time t can be approximated by WG transform, at a selected resolution level j of the wavelet (Amaratunga et al., 1994):

$$u(t) = \sum_{l=1}^{N_x} u_l \varphi_l(t) \tag{5}$$

where u_l are approximation coefficients, derived through the inner product $u_l = \langle u(t), \varphi(t) \rangle = \int_{-\infty}^{\infty} u(t)\varphi(t)dt$. The first and second derivatives with respect to t, $\dot{u}(t), \ddot{u}(t)$ are found as:

$$\dot{u}(t) = \sum_{l=1}^{N_x} u_l \dot{\varphi}_l(t), \;\; \ddot{u}(t) = \sum_{l=1}^{N_x} u_l \ddot{\varphi}_l(t) \tag{6}$$

where $\dot{\varphi}_l(t) = (d\varphi_l(t)/dt), \ddot{\varphi}_l(t) = (d^2\varphi_l(t)/dt^2)$ are the derivatives of Daubechies wavelets in the "limit support", i.e., in the interval $[0, N-1]$, which can be obtained correctly, N_x: computational domain (consisting of the originally bounded domain of the analytical signal N_n and additional endpoints used to solve the issue of the boundary conditions).

Since the WG method decomposes a time-varying signal at a selected resolution (j), the initial choice of wavelet resolution (j) is important for computation of the connection coefficients. The resolution parameter of the Daubechies wavelets at the scale j is 2^j; the resolution is determined so that the scaling function is centered within the domain, given the number of discretization points of the original signal. The wavelet resolution j can be approximately found from $\overline{N}_n = 2^j$, with $\overline{N}_n$ being the number of samples of the signal per unit time, i.e., the sampling frequency of the loading and response.

4   Connection Coefficients of Daubechies Wavelets

For a correct use of the orthonormal basis of Daubechies wavelets, the inner products of the approximating solutions for the dynamic motion and its derivatives in Eq. (5) have been utilized:

$$\langle \varphi_k, \sum_{l=1}^{N_x} u_l \varphi_l \rangle = \sum_{l=1}^{N_x} u_l \int_{-\infty}^{+\infty} \varphi_l(t)\varphi_k(t)dt = \sum_{l=1}^{N_x} u_l \Omega_{l-k}^{0,0} \tag{7}$$

$$\langle \varphi_k, \sum_{l=1}^{N_x} u_l \dot{\varphi}_l \rangle = \sum_{l=1}^{N_x} u_l \int_{-\infty}^{+\infty} \dot{\varphi}_l(t)\varphi_k(t)dt = \sum_{l=1}^{N_x} u_l \Omega_{l-k}^{1,0} \tag{8}$$

$$\langle \varphi_k, \sum_{l=1}^{N_x} u_l \ddot{\varphi}_l \rangle = \sum_{l=1}^{N_x} u_l \int_{-\infty}^{+\infty} \ddot{\varphi}_l(t)\varphi_k(t)dt = \sum_{l=1}^{N_x} u_l \Omega_{l-k}^{2,0} \tag{9}$$

where $\Omega_{l-k}^{d_1 d_2} = \int_{-\infty}^{+\infty} \varphi_l^{d_1}(t)\varphi_k^{d_2}(t)dt$: 2-term connection coefficients of Daubechies wavelets; d_1, d_2: derivative orders of two generic wavelets with the special cases $\Omega_{l-k}^{0,0} = \int_{-\infty}^{+\infty} \varphi_l(t)\varphi_k(t)dt = \delta_{lk}$, $\Omega_{l-k}^{1,0}$, $\Omega_{l-k}^{2,0}$. The connection coefficients depend on the scaling functions themselves within their limit support, while they do not depend on the analytical signal and the wavelet resolution. If higher-order derivatives and nonlinear constitutive relationships are present in the dynamic model of a nonlinear system, multi-term connection coefficients can be used to represent the nonlinear terms (Romine and Peyton, 1998):

$$\Omega_{l_1 l_2 \ldots l_n}^{d_1, d_2, \ldots, d_n} = \int_{-\infty}^{+\infty} \varphi_{l_1}^{d_1}(t)\varphi_{l_2}^{d_2}(t) \ldots \varphi_{l_n}^{d_n}(t)dt = \int_{-\infty}^{+\infty} \prod_{i=1}^{n} \varphi_{l_i}^{d_i} dt \tag{10}$$

Only 2-term and 3-term coefficients $\Omega_{l-k}^{d1,d2}$, $\Omega_{l-k,k-m}^{d1,d2,d3}$ are needed for 2nd-order dynamical systems, in which $\Omega_{l-k,k-m}^{d_1 d_2 d_3} = \int_{-\infty}^{+\infty} \varphi_l^{d_1}(t)\varphi_k^{d_2}(t)\varphi_m^{d_3}dt$ are the 3-term connection coefficients.

The 2-term, 3-term connection coefficients are used for second-order linear and nonlinear dynamical systems. The 2-term connection coefficients can be estimated as described by Latto et al. (1991) for the unbounded domain, by noting that the d-th derivative of the scaling function is $\varphi_k^d = 2^d \sum_{k=0}^{N-1} a_k \varphi_k^d(2t - k)$, as:

$$\Omega_{l-k}^{d_1 d_2} = \int_{-\infty}^{\infty} \varphi_l^{d_1}(t)\varphi_k^{d_2}(t)dx = 2^{d_1+d_2-1} \sum_{p,q} a_p a_{q-2(l-k)+p} \int_{-\infty}^{\infty} \varphi^{d_1}(t)\varphi_q^{d_2}(t)dx \tag{11}$$

The Daubechies wavelets are compactly supported on $(N-1)$ discrete points, since the subscript indices l, k in Eqs. (7-8) vary as $0 \leq l \leq (N - 1)$ and $0 \leq k \leq (N - 1)$; a total of $(2N-3)$ pairs of connection coefficients are necessary. For example, the *DB6* Daubechies wavelet requires nine 2-term connection coefficients with indices ranging for $(l-k)$=-4,-3,..,3,4. Computation of the connection coefficients and adequate treatment of boundary conditions are essential to the implementation of the WG method. Latto et al. (1991) proposed a method for computing the 2-term connection coefficients with *DB6* Daubechies wavelet and resolution *j*=1 for unbounded domain. Romine and Peyton (1997) extended the methodology by Latto et al. (1991) to the case of a finite-interval signal (bounded domain) and to *j*>1, i.e., to a set of arbitrary boundary conditions. The approach by Romine and Peyton (1997) is used herein, in which the computational domain of the original signal (N_n discrete points) is expanded by adding $(N-1)$ points to the left of the original computational domain (before initial time) and $(N-1)$ points to the right of the original domain (beyond final time). The modified domain has ($N_x = N_n + 2N-1$) wavelet expansion points.

Table 1. Connection coefficients of Daubechies wavelets $\Omega_{l-k}^{d_1 d_2}(N,j)$

Dau.	l-k	-6	-5	-4	-3	-2	-1	0	+1	+2	+3	+4	+5	+6
DB4	$\Omega_{l-k}^{0,1}(4,6)$					5.333	-42.666	0	42.666	-5.333				
DB4	$\Omega_{l-k}^{1,2}(4,6)$					131070	262140	0	262140	131070				
DB6	$\Omega_{l-k}^{0,1}(6,6)$			-0.021	-0.935	9.293	-47.693	0	47.693	-9.293	0.935	0.021		
DB6	$\Omega_{l-k}^{0,2}(6,6)$			350	7490	-57420	222200	-345230	222200	-57420	7490	350		
DB8	$\Omega_{l-k}^{0,1}(8,6)$	0	0.011	0.142	-2.149	12.287	-50.752	0	50.752	-12.287	2.149	-0.142	-0.011	0
DB8	$\Omega_{l-k}^{0,2}(8,8)$	-5	-110	-690	9890	-45740	173150	-273020	173150	-45740	9890	-690	-110	5

Le and Caracoglia (2014) constructed an efficient matrix form for computing the connection coefficients; this matrix [*A*] becomes an (N_x-*N*+1) by (N_x-*N*+1) square matrix. The boundary conditions (for instance, the initial displacement and initial velocity of the *sdof* system) are treated and assembled in the first and last rows of [*A*]. Computation of the coefficient matrix [*A*] has been coded in MATLAB® for any Daubechies wavelet. Table 1 shows an example of 2-term connection

coefficients $\Omega_{l-k}^{d_1 d_2}$ (N,j) of $DB4$, $DB6$ and $DB8$ (order $N=4,6,8$) computed for selected wavelet resolutions ($j=6,8$). It is noted that the WG method relies on the initial choice of wavelet resolution (j).

5   Wavelet-Galerkin Solutions for Stochastic Dynamics

5.1   Single-degree-of-freedom Linear Stochastic System Subjected to White Noise Loading

The governing motion equation of an *sdof* system subjected to random white noise loading is:

$$m\ddot{u}(t) + c\dot{u}(t) + ku(t) = f(t) \tag{12}$$

where *m, c, k*: known mass, damping and stiffness coefficient; *f(t)* is a white noise force.

System responses *u(t), ü(t), u̇(t)* and white noise force *f(t)* can be approximated in the wavelet domain using the WG method presented in Sections 3 and 4. First, the time-varying responses and the random force are approximated using the Daubechies wavelet (the scaling function) in Eqs. (5-6). In a second step, the inner product operation described in Eqs. (7-9) is subsequently applied to both sides of the motion equation in the wavelet domain Eq. (in order to take an advantage of orthogonality of the Daubechies wavelet. Thus, Eq. (12) is converted to the wavelet domain as:

$$m\sum_{l=1}^{N_x} \Omega_{l-k}^{0,2} u_l + c\sum_{l=1}^{N_x} \Omega_{l-k}^{0,1} u_l + k\sum_{l=1}^{N_x} \delta_{kl} u_l = f_l \tag{13}$$

where $\Omega_{l-k}^{0,2}$, $\Omega_{l-k}^{0,1}$ denote the 2-term connection coefficients of Daubechies wavelet, f_l: scalar force vector, u_l: resultant scalar response vector. One could write the Eq. (13) in a matrix form with compact notation; we have:

$$[A]\{u_l\} = \{f_l\} \tag{14}$$

where [A] is the connection coefficient matrix. The time-varying second-order stochastic equation has been transformed into first-order algebraic equation, the solution of which is much simpler and computationally advantageous. Assemblage of the connection coefficient matrix, estimation of the resolution and treatment of the boundary conditions, which are key issues of the method, are presented hereafter. $DB6$ wavelet ($N=6$) is used for demonstrating the assemblage of the connection coefficient matrix [A]. The computational domain is [-N+1,N_n+N-1], with total discrete points $N_x=N_n+2N-1$. It uses N_x "moving" scaling functions at discretized points of the computational domain. Wavelet resolution (j) can be approximately estimated by fitting $2^j = \bar{N}_n$. The 2-term connection coefficients of $DB6$ wavelet $\Omega_{l-k}^{0,2}$, $\Omega_{l-k}^{0,1}$ have (2N-3)=9 coefficients, respectively, with the indices $l-m$=-4,-3,…,3,4 (see Table 1). The matrix [A] becomes a square matrix of dimension (N_n+2N-2) ×(N_n+2N-2), of which the first (9×9) block can be assembled as:

$[A]$
$$= \begin{bmatrix}
m\Omega_0^{0,2}+c\Omega_0^{0,1}+k & m\Omega_1^{0,2}+c\Omega_1^{0,1} & m\Omega_2^{0,2}+c\Omega_2^{0,1} & m\Omega_3^{0,2}+c\Omega_3^{0,1} & m\Omega_4^{0,2}+c\Omega_4^{0,1} & 0 & & 0 & 0 & \cdots \\
m\Omega_{-1}^{0,2}+c\Omega_{-1}^{0,1} & m\Omega_0^{0,2}+c\Omega_0^{0,1}+k & m\Omega_1^{0,2}+c\Omega_1^{0,1} & m\Omega_2^{0,2}+c\Omega_2^{0,1} & m\Omega_3^{0,2}+c\Omega_3^{0,1} & m\Omega_4^{0,2}+c\Omega_4^{0,1} & & 0 & 0 & \cdots \\
m\Omega_{-2}^{0,2}+c\Omega_{-2}^{0,1} & m\Omega_{-1}^{0,2}+c\Omega_{-1}^{0,1} & m\Omega_0^{0,2}+c\Omega_0^{0,1}+k & m\Omega_1^{0,2}+c\Omega_1^{0,1} & m\Omega_2^{0,2}+c\Omega_2^{0,1} & m\Omega_3^{0,2}+c\Omega_3^{0,1} & & m\Omega_4^{0,2}+c\Omega_4^{0,1} & 0 & \cdots \\
m\Omega_{-3}^{0,2}+c\Omega_{-3}^{0,1} & m\Omega_{-2}^{0,2}+c\Omega_{-2}^{0,1} & m\Omega_{-1}^{0,2}+c\Omega_{-1}^{0,1} & m\Omega_0^{0,2}+c\Omega_0^{0,1}+k & m\Omega_1^{0,2}+c\Omega_1^{0,1} & m\Omega_2^{0,2}+c\Omega_2^{0,1} & & m\Omega_3^{0,2}+c\Omega_3^{0,1} & m\Omega_4^{0,2}+c\Omega_4^{0,1} & \cdots \\
m\Omega_{-4}^{0,2}+c\Omega_{-4}^{0,1} & m\Omega_{-3}^{0,2}+c\Omega_{-3}^{0,1} & m\Omega_{-2}^{0,2}+c\Omega_{-2}^{0,1} & m\Omega_{-1}^{0,2}+c\Omega_{-1}^{0,1} & m\Omega_0^{0,2}+c\Omega_0^{0,1}+k & m\Omega_1^{0,2}+c\Omega_1^{0,1} & & m\Omega_2^{0,2}+c\Omega_2^{0,1} & m\Omega_3^{0,2}+c\Omega_3^{0,1} & \cdots \\
0 & m\Omega_{-4}^{0,2}+c\Omega_{-4}^{0,1} & m\Omega_{-3}^{0,2}+c\Omega_{-3}^{0,1} & m\Omega_{-2}^{0,2}+c\Omega_{-2}^{0,1} & m\Omega_{-1}^{0,2}+c\Omega_{-1}^{0,1} & m\Omega_0^{0,2}+c\Omega_0^{0,1}+k & & m\Omega_1^{0,2}+c\Omega_1^{0,1} & m\Omega_2^{0,2}+c\Omega_2^{0,1} & \cdots \\
0 & 0 & m\Omega_{-4}^{0,2}+c\Omega_{-4}^{0,1} & m\Omega_{-3}^{0,2}+c\Omega_{-3}^{0,1} & m\Omega_{-2}^{0,2}+c\Omega_{-2}^{0,1} & m\Omega_{-1}^{0,2}+c\Omega_{-1}^{0,1} & & m\Omega_0^{0,2}+c\Omega_0^{0,1}+k & m\Omega_1^{0,2}+c\Omega_1^{0,1} & \cdots \\
0 & 0 & 0 & m\Omega_{-4}^{0,2}+c\Omega_{-4}^{0,1} & m\Omega_{-3}^{0,2}+c\Omega_{-3}^{0,1} & m\Omega_{-2}^{0,2}+c\Omega_{-2}^{0,1} & & m\Omega_{-1}^{0,2}+c\Omega_{-1}^{0,1} & m\Omega_0^{0,2}+c\Omega_0^{0,1}+k & \cdots \\
\vdots & \vdots & & & & & & \vdots & \vdots & \ddots
\end{bmatrix}$$

$$\{u_l\} = \{u_{-N+1}, u_{-N+2}, \dots u_0, \dots, u_{N_n+N-1}\}^T; \{f_l\} = \{f_{-N+1}, f_{-N+2}, \dots f_0, \dots, f_{N_n+N-1}\}^T \tag{15}$$

Initial displacement and velocity are often used in the dynamical problems as $u(0) = u_0$, $\dot{u}(0) = \dot{u}_0$. Transforming the initial conditions into the wavelet domain via Eqs. (5-6) leads to $u(0) = \sum_{l=1}^{N_x} u_l \varphi_l (0))$, $\dot{u}(0) = \sum_{l=1}^{N_x} u_l \dot{\varphi}_l (0))$. Then, using the inner products in Eqs. (7-8) and noting that $\int_{-\infty}^{\infty} \varphi(t)dt = 1$, equivalent boundary conditions in the wavelet domain are obtained as:

$$\sum_{l=1}^{N_x} u_l \delta_{lk} = u_0, \sum_{l=1}^{N_x} u_l \Omega_{l-k}^{0,1} = \dot{u}_0 \tag{16}$$

If Eq. (16) is expanded at the initial time *t*=0 (backwards in time) in the computational domain [-N+1,N_n+N-1], it requires establishing the condition at *l-k*=0. Thus, initial conditions in Eq. (16) can be assembled in the first row and the last row of the connection coefficient matrix [A], in which a unit

value is placed at the index $l\text{-}k=0$ on the first row, while $\Omega_0^{0,1}$ must be placed in the column with the same index $l\text{-}k=0$ on the last row, as expressed in Eq. (17) for $DB6$. A similar approach can be applied to another arbitrary initial or boundary conditions.

$$[A] = \begin{bmatrix} 0 & 0 & 0 & & 0 & 1 & 0 & & 0 & 0 & 0 & 0 & 0 & \dots \\ \vdots & \vdots & \vdots & & \vdots & \vdots & \vdots & & \vdots & \vdots & \vdots & 0 & 0 & \vdots \\ \Omega_{-4}^{0,1} & \Omega_{-3}^{0,1} & \Omega_{-2}^{0,1} & \Omega_{-1}^{0,1} & \Omega_0^{0,1} & \Omega_1^{0,1} & \Omega_2^{0,1} & \Omega_3^{0,1} & \Omega_4^{0,1} & 0 & 0 & \dots \end{bmatrix}, \{f_l\} = \begin{Bmatrix} u_0 \\ \vdots \\ \dot{u}_0 \end{Bmatrix} \qquad (17)$$

Solving the stochastic equation Eq. (12) employs the aforementioned procedures. A realization of random white noise forces is digitally simulated by Monte Carlo method. Figure 3a shows an example of dynamic displacement and velocity of given system parameters, obtained by using the WG method, in comparison with the Newmark-Beta (NM) numerical integration method ($\alpha = 1/2$, $\beta = 1/4$). The initial conditions are assumed as $u(0) = 0$, $\dot{u}(0) = 0$.

(a)   (b)
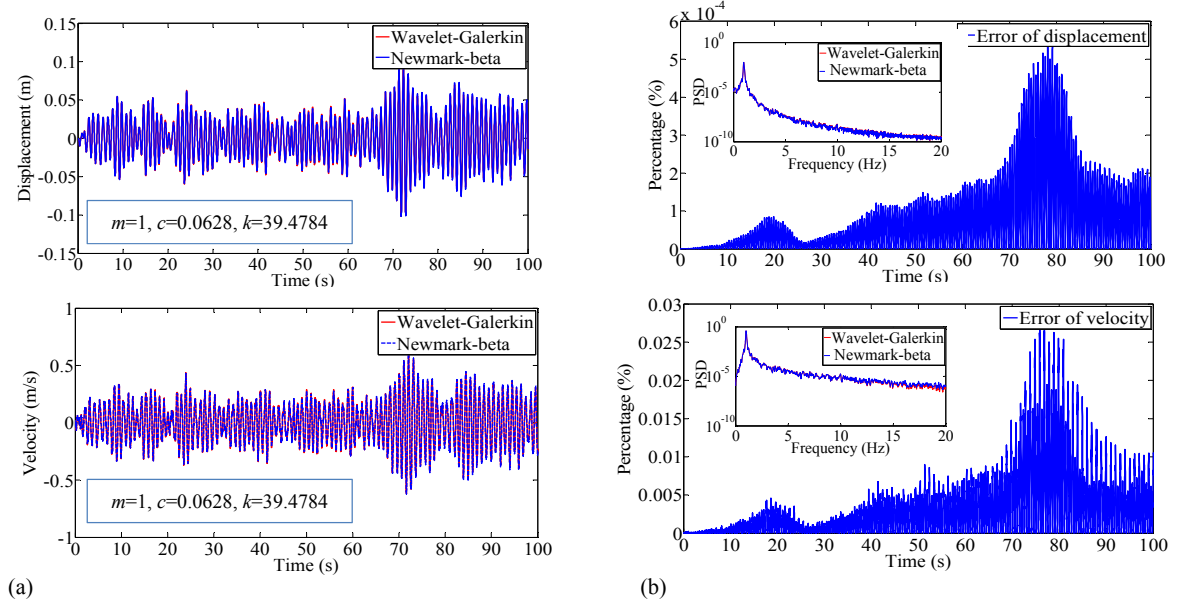
Figure 3. WG solution due to white noise loading: (a) Responses, (b) Error functions and PSD functions

The error function of the response obtained by the WG method and the NM method is defined as $E(\%) = (x_{NM} - x_{WG})^2 / x_{NM}^2$ (in which x stands for resulting responses). Error functions and PSD functions are portrayed in Figure 3b. Good agreement in the solutions estimated by the WG method and the "exact" NM method is observed.

5.2 Single-degree-of-freedom Stochastic System with Stiffness Nonlinearity Subjected to Stationary Wind Load

The dynamic equation of an *sdof* system with cubic-stiffness nonlinearity (Duffing type), subjected to a stationary fluctuating wind load, is:

$$m\ddot{u}(t) + c\dot{u}(t) + k(1 + \varepsilon u(t)^2)u(t) = \tfrac{1}{2}\rho \bar{U}^2 A_p C_D \frac{2w(t)}{\bar{U}} \qquad (18)$$

where m, c, k: known mass, damping and stiffness coefficient; ε: nonlinear stiffness parameter; $\rho, \bar{U}, A_p, C_D$: air density, mean wind velocity, projected area and drag coefficient, respectively; $w(t)$ is the along-wind fluctuating velocity component. Univariate stationary fluctuating wind time histories are simulated by using the spectral representation method. The power spectral density (PSD) function of the fluctuating wind velocity exploits Harris's empirical model. Initial conditions are assumed as $u(0) = 0$, $\dot{u}(0) = 0$. As in the previous sections, the equation of motion is transformed into the Daubechies wavelet domain by following the two steps of the proposed procedure, i.e., WG approximation and inner product operation. The following equation is obtained:

$$\left\{ m \sum_{l=1}^{N_x} \Omega_{l-k}^{0,2} u_l + c \sum_{l=1}^{N_x} \Omega_{l-k}^{0,1} u_l + k \sum_{l=1}^{N_x} \delta_{kl} u_l \right\} + \left\{ k\varepsilon \sum_{l=1}^{N_x} \delta_{kl} u_l^3 \right\} = \bar{w}_l \qquad (19)$$

where $\bar{w}_l = 0.5\rho U A_p C_D w_l$. Here the DB6 wavelet is used. It is noted that the nonlinear stiffness term $k\varepsilon u(t)^3$ in Eq. (18) has been approximated in the wavelet domain as $k\varepsilon \sum_{l=1}^{N_x} u_l{}^3 \Omega_{l-k}^{0,0} = k\varepsilon \sum_{l=1}^{N_x} \delta_{kl} u_l^3$. After replacing $[A]$ as in the previous section and $[B] = k\varepsilon[I]$ in Eq. (19) as the connection coefficient matrices, an algebraic equation of power three in the wavelet space is determined:

$$[A]\{u_l\} + [B]\{u_l^3\} = \{\bar{w}_l\} \tag{20}$$

The connection coefficient matrices $[A]$, $[B]$ and vector $\{\bar{w}_l\}$ are assembled after incorporating the effects of the boundary conditions and the wavelet resolution analysis in the same manner as the one presented in sub-Section 5.1.
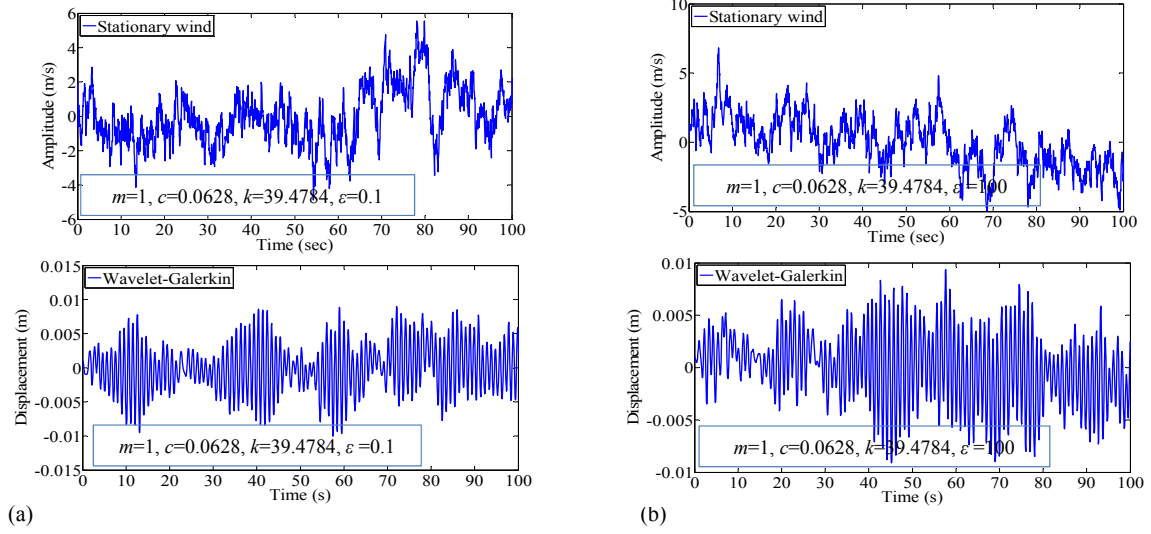
Figure 4. WG solution of an oscillator with nonlinear stiffness, subject to stationary wind: (a) case 1, (b) case 2

Wind parameters are $\rho = 0.0125 t/m^3$, $\bar{U} = 10 m/s$, $A_p = 2m$, $C_D = 1.2$. Figure 4 shows the dynamic response of a stochastic system with stiffness nonlinearity induced by stationary fluctuating wind load; two different cases of nonlinear-stiffness system parameter are analysed: $\varepsilon = 0.1$ (weak nonlinearity, case 1) and $\varepsilon = 100$ (strong nonlinearity, case 2).

5.3 Single-degree-of-freedom Stochastic System with Damping Nonlinearity Subjected to Stationary Wind Load

The motion of an *sdof* system with nonlinear damping (Van-der-Pol type), subjected to stationary wind load, is analyzed:

$$m\ddot{u}(t) + c(1 - \mu u(t)^2)\dot{u}(t) + ku(t) = \frac{1}{2}\rho \bar{U}^2 A_p C_D \frac{2w(t)}{\bar{U}} \tag{21}$$

where μ: nonlinear damping parameter; *w(t)*: along-wind stationary wind velocity. Other system parameters are taken, in this example, as: $\rho = 0.0125 t/m^3$, $\bar{U} = 10 m/s$, $A_p = 2m^2$, $C_D = 1.2$.

After applying the WG transformation, the stochastic nonlinear dynamic equation in Eq. (21) can be rewritten in the wavelet domain, in a scalar form at a generic index *l* and in matrix form, as:

$$\left\{ m\sum_{l=1}^{N_x}\Omega_{l-k}^{0,2} u_l + c\sum_{l=1}^{N_x}\Omega_{l-k}^{0,1} u_l + k\sum_{l=1}^{N_x}\delta_{kl}u_l \right\} + \left\{ c\mu\sum_{l=1}^{N_x}\Omega_{l-k}^{0,1} u_l^3 \right\} = \bar{w}_l$$

$$[A]\{u_l\} + [B]\{u_l^3\} = \{\bar{w}_l\} \tag{22}$$

where matrix $[B]$ contains the connection coefficient. It is noted that the nonlinear damping term in Eq. (22) is approximated in the wavelet domain as $u(t)^2\dot{u}(t) \to c\mu \sum_{l=1}^{N_x} u_l{}^3 \Omega_{l-k}^{0,1}$. Moreover, the nonlinear coefficient equation in Eq. (22) is similar to Eq. (19), whereas the matrix $[B]$ is different.

Figure 5 shows two examples of dynamic displacement solution (stochastic realizations) for a system with nonlinear damping due to stationary wind in the two cases: $\mu = 0.1$ (weak nonlinearity, case 1) and $\mu = 100$ (strong nonlinearity, case 2).
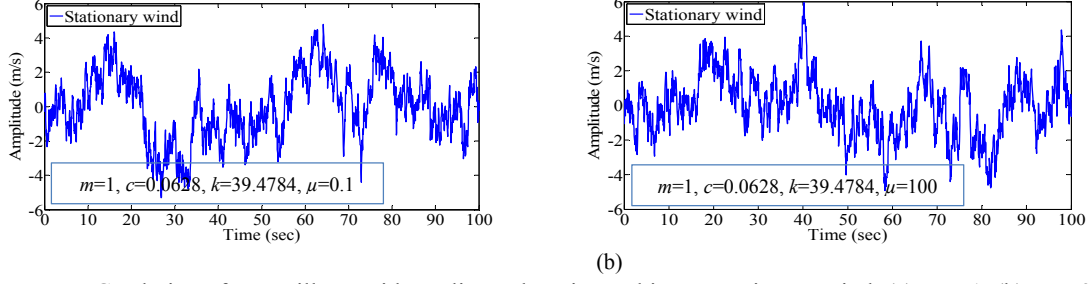
(a)   (b)

Figure 5. WG solution of an oscillator with nonlinear damping, subject to stationary wind: (a) case 1, (b) case 2

5.4 Single-degree-of-freedom Stochastic System with Stiffness Nonlinearity Subjected to Simulated Downburst Wind Loading

In this final section, the WG method is used to investigate the response of a nonlinear stochastic system subjected to a transient wind load in a thunderstorm downburst. The total along-wind wind speed $U(t)$ in the thunderstorm downburst consists of a time-varying mean wind velocity $\bar{U}(t)$ and an "evolutionary" or transient wind velocity fluctuation $w'(t)$. The equation of motion an *sdof* stochastic system with stiffness nonlinearity, subjected to downburst transient wind, is:

$$m\ddot{u}(t) + c\dot{u}(t) + k(1 + \varepsilon u(t)^2)u(t) = \frac{1}{2}\rho\bar{U}(0)^2 A_p C_D \frac{U(t)}{\bar{U}(0)} \qquad (23)$$

where U(t) is the total downburst transient wind velocity, expressed as $U(t) = \bar{U}(t) + w'(t)$ and with $\bar{U}(0)$ the mean wind velocity at initial time t=0; other wind load and system parameters are: $\rho = 0.0125 t/m^3$, $\bar{U}(0) = 37m/s$, $A_p = 2m^2$, $C_D = 1.2$, m=1, c=0.0628, k=39.4784. The time-varying mean wind velocity is determined from an empirical downburst model (Holmes and Oliver, 2000), while the transient wind velocity fluctuation is simulated from a realization of stationary wind turbulence by means of an amplitude modulating function.

As in sub-Section 5.2, the equation of motion can be obtained in the wavelet domain as:

$$[A]\{u_l\} + [B]\{u_l^3\} = \{\bar{w}_l'\} \qquad (24)$$

Generally, Eq. (24) is similar to Eq. (20), except for the force vector in the wavelet domain, which is based on the transient loading (and velocity) with slowly time-varying mean.
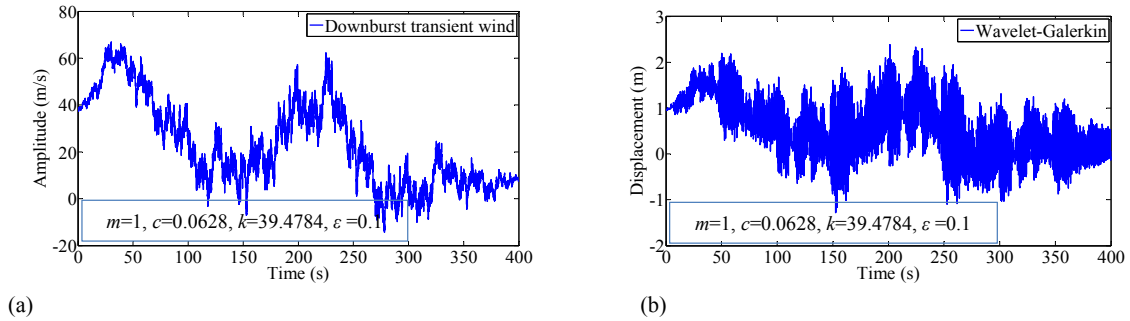
(a)   (b)

Figure 6. Stiffness-nonlinear WG solution due to downburst transient wind loading: (a) Downburst transient wind velocity realization, (b) Nonlinear transient response

Figure 6 shows the dynamic displacement of a stochastic system with nonlinear stiffness due to a downburst transient wind with nonlinear stiffness parameter $\varepsilon = 0.1$.

6   Conclusion

The WG method has been investigated to estimate the response of stochastic nonlinear dynamical systems. Representative examples of nonlinear dynamic *sdof* oscillators have been studied: stiffness nonlinearity (Duffing type) and damping nonlinearity (the Van-der-Pol type). The analyzed random

load cases include: white noise loads, stationary and transient/nonstationary wind loads. The paper has also examined and solved existing shortcomings of the WG method, necessary for the successful extension to full-scale nonlinear tall building structures subjected to transient/nonstationary wind loads.

Acknowledgements

References

Amaratunga, K., Williams, J., Qian, S., Weiss, J. (1994). Wavelet-Galerkin Solutions for One dimensional Partial Differential Equations. *Journal on Numerical Methods in Engineering*, **37**, 2703-2716

Amaratunga, K. and Williams, J. R. (1997). Wavelet-Galerkin Solution for Boundary Value Problems. *Archives on Computational Methods in Engineering.* **4**(3), 243-285.

Basu B., Gupta V.K. (1998). Seismic Response of SDOF Systems by Wavelet Modeling of Nonstationary Process. *Journal of Engineering Mechanics*, ASCE, **124** (1). 1998, 1142-1150.

Daubechies, I. (1988). Orthogonal Bases of Compactly Supported Wavelets. *Communications on Pure and Applied Mathematics,* **XLI**, 909–996.

Ghanem, R., and Romeo, F. (2000). A Wavelet-based Approach for the Identification of Linear Time-varying Dynamical Systems. *Journal of Sound and Vibration*,**234**(4), 555-574.

Ghanem, R., Romeo, F. (2001). A Wavelet-based Approach for Model and Parameter Identification of Nonlinear Systems. *International Journal of Nonlinear Mechanics*, **36**, 835-859.

Gopalakrishnan, S., and Mitra, M. (2010). W*avelet Methods for Dynamical Problems*, CRC Press.

Holmes, J.D. and Oliver, S.E. (2000). An Empirical Model of A Downburst. *Journal of Engineering Structures*, **22**, 1167-1172.

Huang, C. T., and Iwan, W. D. (2006). Equivalent Linearization of the nonstationary response analysis of nonlinear systems with random parameters. *Journal of Engineering Mechanics* ASCE, **132**, 465-474.

Kareem, A., and Kijewski, T. (2002). Time-frequency Analysis of Wind Effects on Structures. *Journal of Wind Engineering and Industrial Aerodynamics*, **90**, 1435-1452.

Kareem, A., Wu, T. (2013). Wind-induced Effects on Bluff Bodies in Turbulent Flows: Nonstationary, Non-Gaussian and Nonlinear Features. *Journal of Wind Engineering and Industrial Aerodynamics*, **122**(10), 21–37.

Latto, A., Resnikoff, H., Tenenbaum, E. (1991). The Evaluation of Connection Coefficients of Compactly Supported Wavelets. *Proceedings of the French-USA Workshop on Wavelets and Turbulence*, Princeton, New York, Springer-Verlag.

Le, T.H., Caracoglia, L. (2014). Wind-induced Stochastic Dynamic Response Analysis of a Bridge in the Wavelet Domain. *National Symposium on Vibration and Control of Structures under Actions of Wind* (V&C2014), February 24-25, Hanoi, Vietnam.

Romine, C. H., and Peyton, B. W. (1997). Computing Connection Coefficients of Compactly Supported Wavelets on Bounded Intervals. *Computer Science and Math. Div.*, **ORNL/TM**-13413.

Xu, Y.L., Chen, J. (2004). Characterizing Nonstationary Wind Speed using Empirical Mode Decomposition. *Journal of Structural Engineering*, **130** (6), 912-920.

Efficient Monte-Carlo method for the wind-induced "fragility analysis" of tall buildings

Wei Cui and Luca Caracoglia

Department of Civil Engineering and Environmental, Northeastern University, Boston, MA, 02115, USA

Corresponding author: Luca Caracoglia, lucac@coe.neu.edu

Abstract

This paper presents a computationally-efficient algorithm for predicting the wind-induced response of tall building, both in the along-wind and cross-wind directions. The numerical procedure, derived from standard frequency domain analysis, is employed to compute the power spectral density (PSD) of the loading and to derive the dynamic response. The CAARC prototype building is utilized to validate the proposed algorithm. This paper also describes the computation of structural fragility curves for the CAARC building, accounting for experimental measurement errors and using Monte-Carlo methods (MCM). A novel computationally-efficient procedure for fragility analysis is proposed, employing both an interpolation method (stochastic collocation) and the least-squares fitting method. The procedure is used for performance analysis, based on simulated response and serviceability limit states.

1 Introduction

Fragility analysis is a standardized methodology, utilized for performance-based structural design. In wind engineering, fragility curves or surfaces (e.g., Smith and Caracoglia, 2011, Pozzuoli et al., 2013) can be used to quantify the likelihood of structural damage on a building, conditional on the "intensity of the hazard" (i.e., mean wind velocity at a reference height, mean wind direction). A set of thresholds (displacement, acceleration, etc.) can be selected to represent different service limit states, which are either required by building standards or prescribed by designers. Eq. (1) presents the mathematical definition of fragility of a structure when the mean wind velocity, designating the hazard intensity, is V_z at the height h.

$$F_T = P[X > T | V_z = \bar{U}(h)] \tag{1}$$
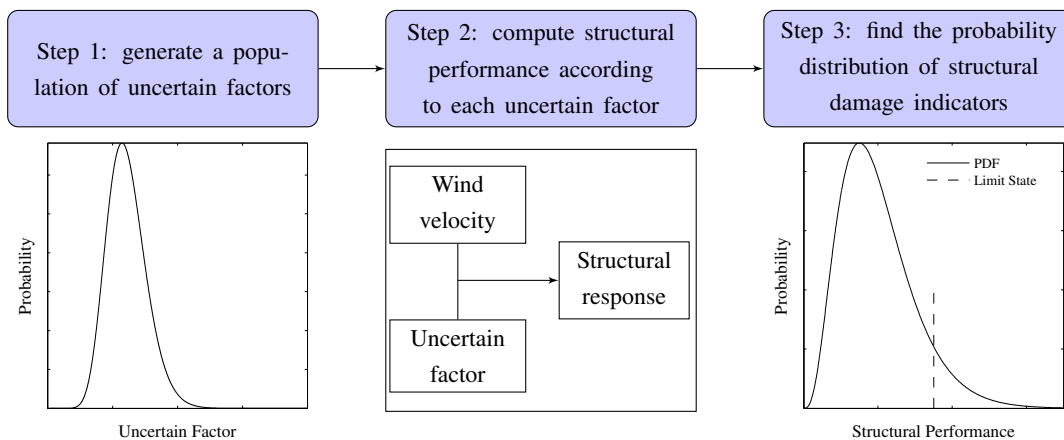
Figure 1. procedure of fragility analysis

In the analysis of the wind-induced response of tall buildings, there is considerable uncertainty as a result of the unpredictable modeling of the wind and the partially unknown loading parameters and

mechanical properties of the structure. Errors from the above uncertainties, especially those related to the estimation of the wind loads, will contaminate response simulations and bring uncertainties into the predicted results. The standard fragility analysis procedure (e.g., Smith and Caracoglia, 2011) can be usually summarized in three steps, shown in Figure 1. This standard approach has been used for decades in earthquake engineering, but the computing time demanded by this method can become significant in wind engineering. The reason is that, in order to obtain the probability of exceedance in Eq. (1), a large number of uncertain factors should be generated and the procedure for calculating the structural response should repeatedly be run several times for each factor. In this paper, an alternative and computationally efficient numerical method is presented to enable engineers and researchers to efficiently perform the fragility analysis of a high-rise building.

2   Background on Structural Dynamics and Wind-induced Response

The proposed methodology employs standard frequency domain random vibration analysis for the estimation of the wind-induced loading and the dynamic response on a high-rise building (Davenport, 1971). As the research described herein primarily focuses on serviceability limit states for high-rise buildings, the proposed procedure utilizes a linear elastic structural model and modal superposition. This study primarily concentrates on the magnitude of lateral displacements at roof-top rather than other quantities relevant to structural vibration (i.e., acceleration, velocity). Furthermore, as stated in reference (Piccardo and Solari, 2000), only few fundamental modes are usually necessary to fully describe the main features of the structural response. Consequently, only the first fundamental mode was considered in this investigation.

The simplified building is considered as a slender prismatic vertical cantilever with a rectangular floor-plan section, which is symmetrical to both (strong and weak) axes of bending. The mean wind direction coincides with direction "x" in Figure 2 and is perpendicular to one of the vertical faces of the structure. Due to the geometrical symmetry and loading planes, torsional effects are ignored in the proposed method. The turbulence-induced aerodynamic loading is derived from equivalent quasi-static theory (Davenport, 1971; Kareem, 1982). From this theory, the power spectral density (PSD) of the generalized buffeting force can be described in Eq. (2) for along-wind direction and Eq. (3) for cross-wind direction.
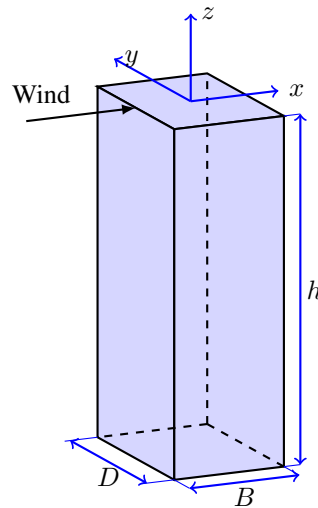
Figure 2. Schematic view of the CAARC building

$$S_{Q_x Q_x}(n) = \iint_h C_D^2 \rho^2 D^2 \Phi_x(z_1)\Phi_x(z_2)\bar{U}(z_1)\bar{U}(z_2)S_{uu}(n, z_1, z_2)\mathrm{d}z_1 \mathrm{d}z_2 \qquad (2)$$

$$S_{Q_{b,y}Q_{b,y}}(n) = \iint\limits_{h} \left[C_L^2 S_{vv}(n, z_1, z_2) + \frac{1}{4}\left(\frac{\partial C_L}{\partial \alpha} + C_D\right)^2 S_{uu}(n, z_1, z_2) \right]$$
$$\times \rho^2 D^2 \Phi_y(z_1)\Phi_y(z_2)\bar{U}(z_1)\bar{U}(z_2)\mathrm{d}z_1\mathrm{d}z_2 \tag{3}$$

where ρ is the air density, $\Phi_x(z)$, $\Phi_y(z)$ are model shape functions in along-wind direction and cross-wind direction, $\bar{U}(z)$ is the mean wind velocity at height z, and C_D is drag coefficient, C_L is the lift coefficient, and $\frac{\partial C_L}{\partial \alpha}$ is the derivative of C_L with respect with wind direction α.

From the frequency domain theory, the PSD of building's response can be directly calculated from the PSD of dynamic force, which is shown in Eq. (4). The two equations above, Eq. (2) and Eq. (3), require performing a double integration, which may become computationally demanding; this step is often recognized as the "bottle-neck" of any wind-induced dynamic analysis. Monte-Carlo integration algorithms (Seo and Caracoglia, 2012) and other numerical integration methods (Simpson's rule, Newton-Cotes formulas, etc.) can significantly improve the computational speed. Description are omitted but details can be found in (Seo and Caracoglia, 2012; Smith and Caracoglia, 2011). The PSD of the dynamic response can be directly estimated from the previous equations. As an example, the PSD of the along-wind response in the x direction between any two points (e.g., floors) at height z_1 and z_2 is:

$$S_{xx}(z_1, z_2, n) = \Phi_x(z_1)\Phi_x(z_2)\frac{S_{Q_xQ_x}}{16\pi^2 M_{g,x}^2 \left[\left(n_{0,x}^2 - n^2\right)^2 + [2nn_{0,x}\left(\zeta_{s,x} + \zeta_{a,x}\right)]^2\right]} \tag{4}$$

In the cross-wind direction, the quasi-steady aerodynamic force model is insufficient to describe the full loading and response. Vortex-induced vibration may occur when vortices are shed alternately in the wake of the building (e.g., Dyrbye and Hansen, 1997). Loading will reach its maximum effect when the frequency of vortex shedding approaches the fundamental frequency of building. Also, because of the effect of turbulence, the lift coefficient $C_L(z, t)$, which can be associated with vortex-shedding effects, can be considered as a stochastic Gaussian process with zero mean rather than a constant term as the C_D coefficient.

In the atmospheric boundary layer, it is a good approximation to assume that the turbulence follows a Gaussian Process (Dyrbye and Hansen, 1997). Thus, it is adequate to express the auto-spectrum of the lift coefficient fluctuation due to vortex shedding, $S_{C_L}(z, n)$, using Eq. (5) (Vickery and Clark, 1972).

$$\frac{nS_{C_L}(z, n)}{\tilde{C}_L^2(z)} = \frac{n}{\sqrt{\pi}B_w(z)n_s(z)}\exp\left[-\left(\frac{1 - \frac{n}{n_s(z)}}{B_w(z)}\right)^2\right] \tag{5}$$

where $\tilde{C}_L$ is the standard deviation of C_L; n_s is the frequency of the vortices, $n_s = S_t D/\bar{U}(h)$; S_t is the Strouhal number; B_w is the band width.

For vortex-shedding, in most cases, it is sufficiently accurate to assume that the force correlation only depends on the distance between two nodes considered, rather than each one of the coordinates. Thus an evaluation of double-fold integral can be reduced to single-fold integral. Based on the above assumption and Eq. (5), the generalized force caused by vortex-shedding can be expressed as:

$$S_{Q_{vr,y}Q_{vr,y}}(n) = \frac{2L_s}{\sqrt{\pi}n_{0,y}}\times$$
$$\int_0^h \left(\frac{1}{2}\rho\bar{U}^2(z)D\tilde{C}_L\Phi_y(z_1)\right)^2 \frac{n}{B_w(z)n_s(z)}\exp\left[-\left(\frac{1 - \frac{n}{n_s(z)}}{B_w(z)}\right)^2\right]\mathrm{d}z \tag{6}$$

in which L_s stands for correlation length.

Based on the assumption that the cross-wind buffeting forces and vortex-shedding loads are mutually independent (Piccardo and Solari, 1998), the PSD of the cross-wind dynamic response can be derived according to Eq. (7):

$$S_{yy}(z_1, z_2, n) = \Phi_y(z_1)\Phi_y(z_2) \frac{S_{Q_{b,y}Q_{b,y}} + S_{Q_{vr,y}Q_{vr,y}}}{M_{g,y}^2 \left[\left(1 - \frac{n^2}{n_{0,y}^2}\right)^2 + \left[2\frac{n}{n_{0,y}}\left(\zeta_{s,y} + \zeta_{a,y}\right)\right]^2 \right]} \tag{7}$$

At last, the evaluation of root mean square (RMS) dynamic response at each floor of the building can be found by converting the PSD of response to RMS values for one-sided spectral in Eq. (8):

$$\sigma_i(z) = \sqrt{\int_0^\infty S_{ii}(z, z, n)\mathrm{d}n} \tag{8}$$

in which i could be x or y.

3   Description of the Simulated Building Model and Simulation Results

The CAARC building had been proposed as a benchmark model for the comparison of the experimental techniques and results among various wind tunnels all over the world after a meeting of the Commonwealth Advisory Aeronautical Research Council (Melbourne, 1980). Figure 3 shows a schematic view of the CAARC building with an indication of the main dimensions (depth D, width B, height h).
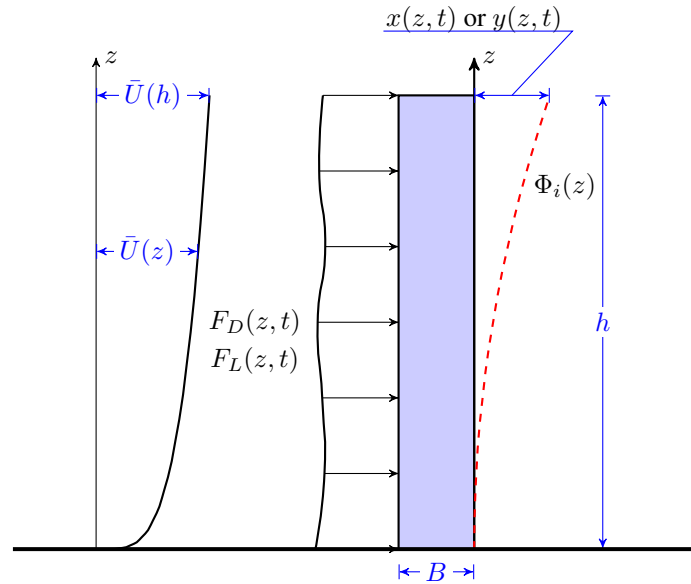
(a) Lateral view of tall building
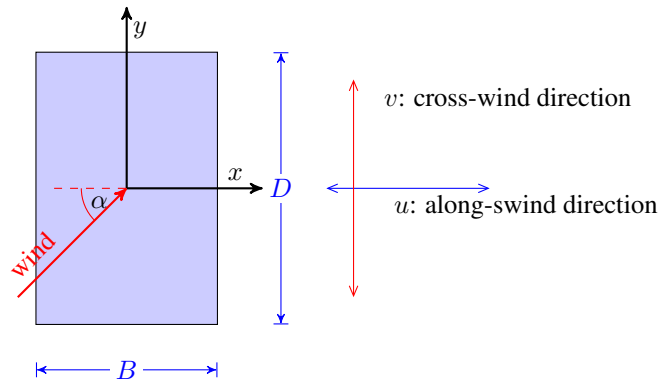
(b) Horizontal plane and wind load directions

Figure 3. Schematic of tall building and wind load directions. (α: relative wind direction)

Table 1(a) and Table 1(b) summarize the CAARC building full-scale model parameters and related wind field parameters that are employed in this paper.

Table 1. Model Parameters

(a) Structural parameters

Quantity	Value Assigned
B	30.5m
D	45.7m
h	183 m
$m(z)$	223224.4kg/m
$\zeta_{s,x}\ \zeta_{s,y}$	0.01
$n_{0,x}\ n_{0,y}$[Hz]	0.2
$\Phi_x(z)\ \Phi_y(z)$	$(z/h)^\gamma; \gamma = 1$
C_D	1.54
C_L	0
$\partial C_L/\partial\alpha$	-3.50
$\widetilde{C}_L$	0.287
S_t	0.116
L_s	$1.5 \times B$

(b) Wind field parameters

Quantity	Value Assigned
ρ	1.25 kg/m^3
Roughness z_0	0.5m
$\bar{U}(z)$ [m/s]	$\bar{U}(h)\left(\dfrac{z}{h}\right)^{0.28}$
$\bar{U}(h)$	0-50 m/s
u^*	$\bar{U}(h)/\left(2.5\ln\dfrac{h}{z_0}\right)$
I_u	$0.53/\left(\ln\dfrac{h}{z_0}\right)$
C_{zu}	12
C_{zv}	$0.667C_{zu}$

In Table 1(a), for simulating vortex shedding effects, the standard deviation of lift coefficient $\widetilde{C}_L$, the Strouhal number S_t and the correlation length L_s are derived according to the method described in (ESDU, 2004). The derivative of C_L with respect to the attack angle is calculated from (Richardson Jr, 1989). Normally, the decay coefficients of the co-coherence function are: $C_{zu} = 12$ (Dyrbye and Hansen, 1997) and $C_{zv} = 0.667C_{zu}$ (Simiu and Scanlan, 1986).

Although the turbulence spectrum, needed by Eq. (2) and Eq. (3) to calculate the generalized force PSD, was found in Melbourne (1980), the original turbulence PSD function was only suitable when $z = \frac{2}{3}h$; also data on the cross-wind direction were not reported. As a result, in this study the Kaimal's Model is employed (Kaimal et al., 1972) instead of the turbulence PSD function in Melbourne (1980). The turbulence PSD functions are described in the equations below:

$$\frac{nS_u(z;n)}{u_*^2} = \frac{105f}{(1+33f)^{\frac{5}{3}}} \tag{9}$$

$$\frac{nS_v(z;n)}{u_*^2} = \frac{17f}{(1+9.5f)^{\frac{5}{3}}} \tag{10}$$

where $f = nz/\bar{U}(z)$ is the Monin coordinate.

An example of simulated along-wind and cross-wind RMS response is depicted in Figure 4a and Figure 4b; In Figure 4(a)a the numerical solution of the RMS and mean response in the along-wind direction is compared to wind tunnel experiments results in Melbourne, 1980, as a function of the reduced velocity, $\bar{U}(h)/(n_0D)$. The along-wind building response is normalized with respect to the building width B. The curves in Figure 4 are plotted using a "spline interpolation" (C^2 continuity) to connect the simulation points. Similarly, in Figure 4b, the CF numerical results in the cross-wind direction are compared to the test results. Excellent correspondence can be found in all three curves, which is an evidence of verification of the reference numerical model built above.

In the above simulation, C_D and $\widetilde{C}_L$ are two important parameters, respectively converting air flow to quasi-static pressure loads and vortex-shedding loads respectively. According to the algorithm in Smith and Caracoglia (2011), when parameters uncertainty is included in the simulations, the fragility curve in Eq. (1) of the roof-top RMS response in the along-wind and cross-wind directions can be calculated by the Monte Carlo method, which is given by

(a) Along-wind response   (b) Cross-wind response
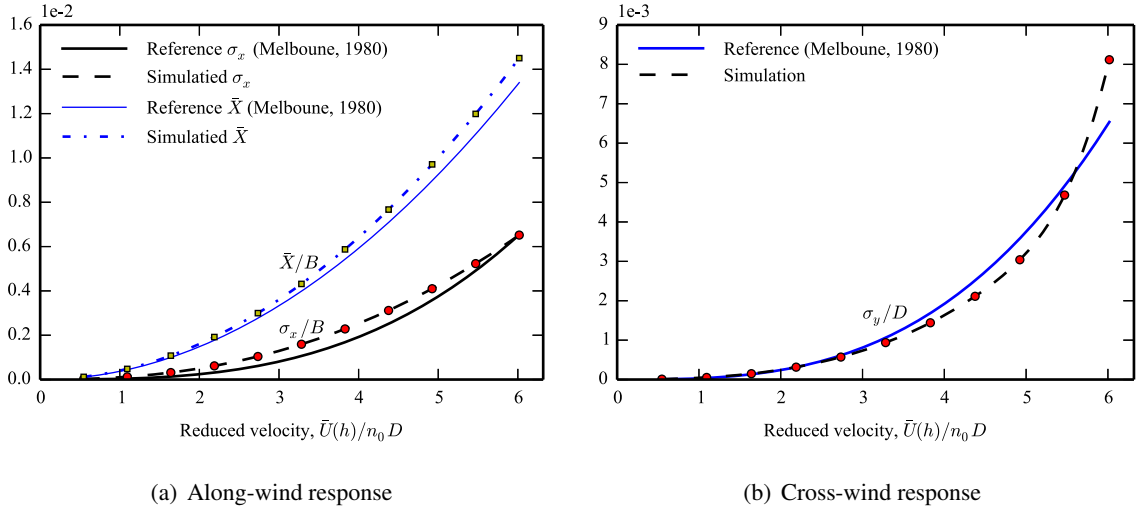
Figure 4. Comparision between simulated roof-top response of the CAARC building derived fromand aeroelastic model results (Melbourne, 1980); D building depth, B building width, n_0 first-mode frequency

$$F_{T_j}(V_z) \cong \frac{1}{N} \sum_{i=1}^{N} \delta(X_i) \tag{11}$$

where X_i is the i-th realization of the random variable corresponding to the different coefficients considered in the analysis; N is the total number of sets of the random variables; T_j is the threshold value for the j-th limit state. In this study, the T_1 threshold is designated for the roof-top lateral displacement in along-wind direction, and the T_2 threshold is used for the roof-top lateral displacement in the cross-wind direction. The function $\delta(X_i)$ is defined as:
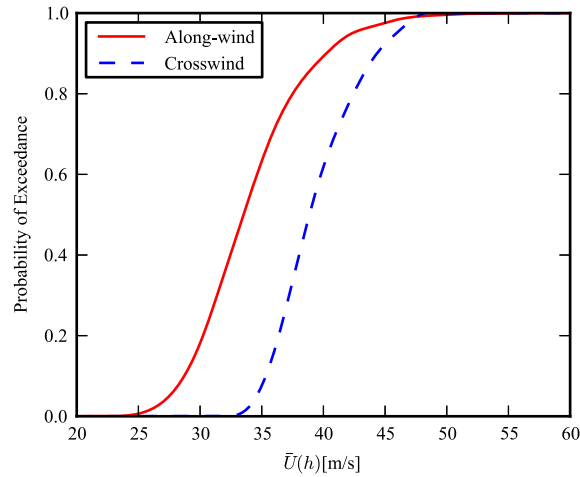
Figure 5. Example of fragility curves of along-wind and cross-wind RMS roof-top response

$$\delta(X_i) = \begin{cases} 1 \text{ if } Z(X_i) > T_j \\ 0 \text{ if } Z(X_i) \leq T_j \end{cases} \tag{12}$$

where $Z(X_i)$ is a generic function of the desired building response feature (e.g., top-floor lateral displacement) for the random the input variable X_i

If the threshold for the RMS lateral displacement on the along-wind direction is defined as $T_1 = 0.2\%B$, and $T_2 = 0.2\%D$ for the cross-wind direction, the two typical fragility curves are shown in Figure 5.

4   Novel Fragility Analysis Method
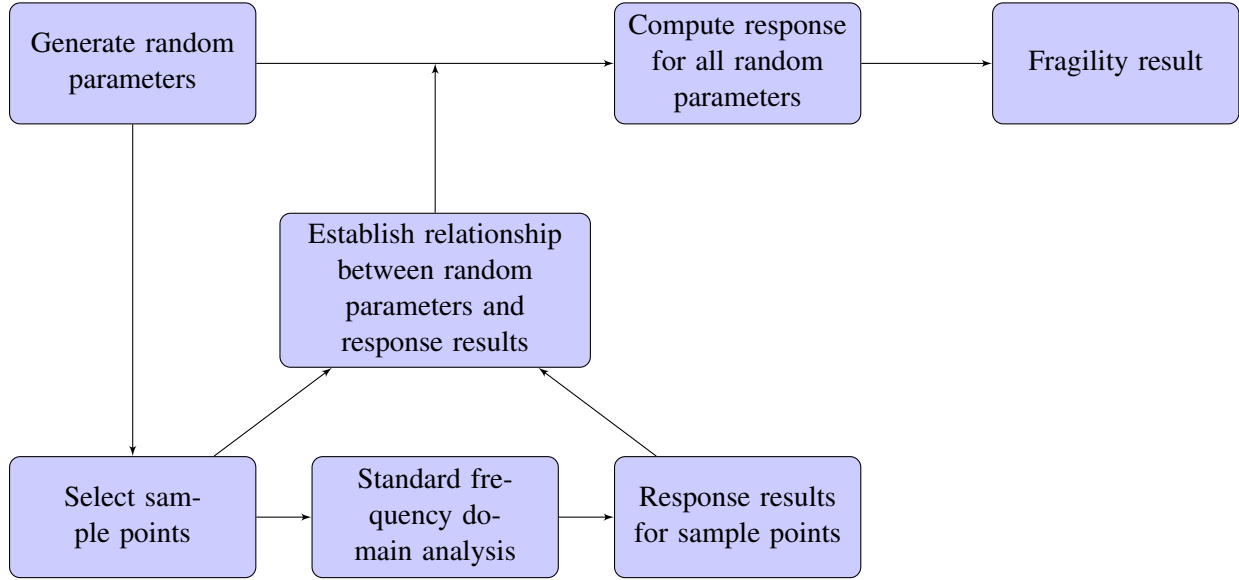
Figure 6. Flow chart of the computationally-efficient method for fragility analysis

The standard process shown above section is reliable and has been previously used (Smith and Caracoglia, 2011). Nevertheless, its greatest disadvantage is the large computation time. In order to to improve this limitation, functional relationship between input random parameters and the desired output response can be used. If so, the result (e.g., peak or RMS displacement) can be estimated directly from the random parameters (e.g., C_d) through this function. There are two practical methods to establish this relationship. The first method is the least-squares "curve fitting", while the second method is uses Lagrange interpolation (stochastic collocation) (Le Maître and Knio, 2010). The flow chart, describing the steps of the improved method, is shown in Figure 6.

For the least-squares method, a predefined function with initially unknown parameters (a, b, c and e) should be given. Inspired by Eq. (4) and Eq. (7), the function between RMS roof-top response σ_x, σ_y and random input C_d and $\frac{\partial C_L}{\partial \alpha}$ can be defined as in Eq. (13) and Eq. (14):

$$\sigma_x^2(C_d) = \frac{C_d^2}{a + bC_d + cC_d^2} \tag{13}$$

$$\sigma_y^2(C_d, \widetilde{C}_L) = \frac{\left(C_d + \frac{\partial C_L}{\partial \alpha}\right)^2 + e\widetilde{C}_L^2}{a + b\left(C_d + \frac{\partial C_L}{\partial \alpha}\right) + c\left(C_d + \frac{\partial C_L}{\partial \alpha}\right)^2} \tag{14}$$

The second method, proposed to determine the $\sigma_x(C_d)$, employs Lagrange interpolation method (Le Maître and Knio, 2010) as Eq. (15) and Eq. (16):

$$L(x) = \sum_{j=0}^{k} y_j l_j(x) \tag{15}$$

$$l_j(x) = \prod_{i=0,i\neq j}^{k} \frac{x - x_i}{x_j - x_i} \tag{16}$$

As an example, when $\bar{U}(h) = 55\text{m/s}$, the relationship between C_D and σ_x is depicted in Figure 7a. Figure 7b shows the relationship between $C_D, \widetilde{C}_L$ and σ_y. Since five sample points are only required to approximate Eq. (13), the computational time is 1000 times faster than the case with the standard procedure (Section 3) needing 5000 points (Smith and Caracoglia, 2011). In contrast, for the deflection in cross-wind direction, the fitting function with two independent variables in Eq. (14) necessitates a grid with 25 points to generate the surface in Figure 7b. As a result, the computation time for the fragility curve of the cross-wind response is as large as square of one for along-wind direction.

(a) Along-wind response   (b) Cross-wind response
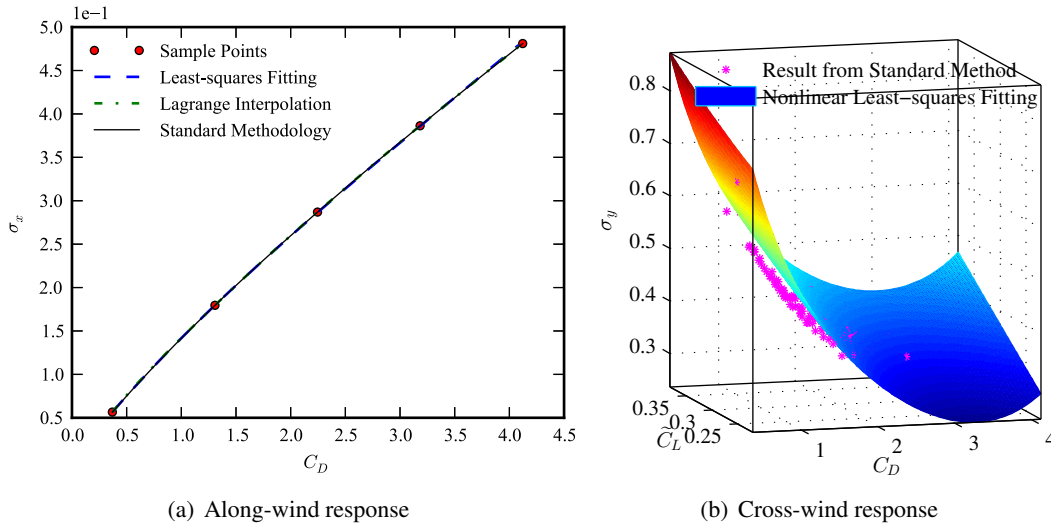
Figure 7. RMS response computed by various methods, $\bar{U}(h) = 55\text{m/s}$

The Figure 8 summarizes and compares the fragility curves obtained from the standard methodology and the computationally-efficient method, introduced in this section. For the along-wind direction, the result from standard method and the two "fast" methods (interpolation and fitting) are almost identical, while the results for the cross-wind direction show some minor differences because the fitting function in Eq. (14) for the cross-wind response has two variables (C_D and $\frac{\partial C_L}{\partial \alpha}$).
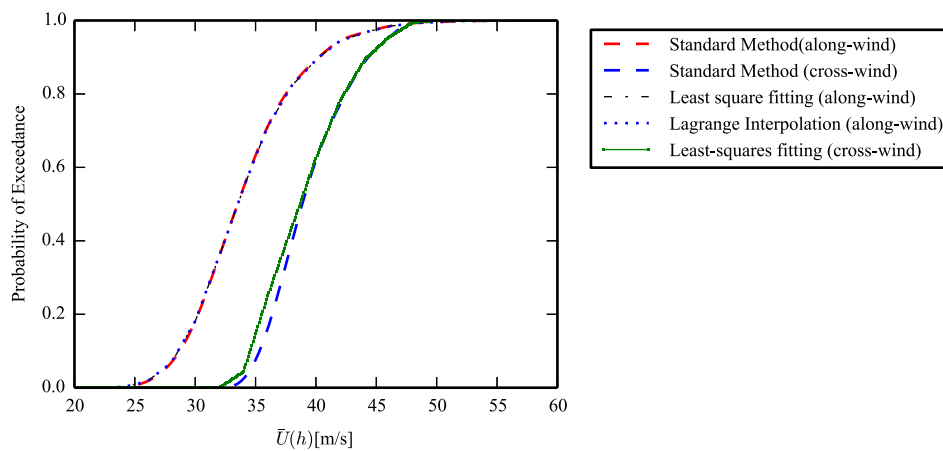
Figure 8. Example of fragility curves for both along-wind and cross-wind RMS roof-top response

5   Conclusion

This study firstly applied the standard frequency-domain analysis method in wind engineering to the estimation of high-rise building response from a given wind force. As the wind force on the structure is usually random in time and location due to wind turbulence, the random wind force will result in random building response. Therefore, the fragility analysis of the building at various mean wind speeds is necessary.

Nevertheless, it has been shown that the standard Monte-Carlo-based fragility analysis requires significant computing time because the frequency domain analysis is calculated for every realization of the wind force parameter. The two alternative procedures, proposed in this study, employs either the nonlinear least-squares method to determine a pre-defined response function or the Lagrange Interpolation method to establish the relationship between the force parameters and response results. Therefore, the large computing time, spent on the frequency-domain analysis, can be circumvented and avoided. The fragility analysis can be executed as accurately as with the standard procedure, by significantly improving the computational efficiency. The two alternative "fast" fragility analysis methods are therefore recommended for applications in the engineering research field.

6   Acknowledgments

References

Davenport, A. G. (1971). The response of six building shapes to turbulent wind. *Philos T Roy Soc A* **269**.1199, pp. 385–394.

Dyrbye, C. and Hansen, S. O. (1997). *Wind loads on structures*. 1st ed. New Jersey, USA: John Wiley & Sons.

ESDU (2004). *Standard 90036: Structures of non-circular cross section: dynamic response due to vortex shedding*. London, UK.

Kaimal, J., Wyngaard, J., Izumi, Y, and Coté, O. (1972). Spectral characteristics of surface-layer turbulence. *Q J Roy Meteor Soc* **98**.417, pp. 563–589.

Kareem, A. (1982). Acrosswind response of buildings. *J Struct Div* **108**.4, pp. 869–887.

Le Maître, O. P. and Knio, O. M. (2010). *Spectral methods for uncertainty quantification: with applications to computational fluid dynamics*. Heidelberg, Germany: Springer.

Melbourne, W. (1980). Comparison of measurements on the CAARC standard tall building model in simulated model wind flows. *J Wind Eng Ind Aerodyn* **6**.1, pp. 73–88.

Piccardo, G. and Solari, G. (1998). Closed form prediction of 3-D wind-excited response of slender structures. *J Wind Eng Ind Aerodyn* **74**, pp. 697–708.

— (2000). 3D wind-excited response of slender structures: Closed-form solution. *J Struct Eng-ASCE* **126**.8, pp. 936–943.

Pozzuoli, C., Bartoli, G., Peil, U., and Clobes, M. (2013). Serviceability wind risk assessment of tall buildings including aeroelastic effects. *J Wind Eng Ind Aerodyn* **123, Part B**, pp. 325 –338.

Richardson Jr, A. (1989). Guidelines for Vibration Contral of Tower Guy Cables. *National Association of Broadcasters Engineering Conference Proceedings*. Natick, Massachusetts: The MathWorks Inc., pp. 500–510.

Seo, D. W. and Caracoglia, L. (2012). Statistical buffeting response of flexible bridges influenced by errors in aeroelastic loading estimation. *J Wind Eng Ind Aerodyn* **104**, pp. 129–140.

Simiu, E. and Scanlan, R. H. (1986). *Wind effects on structures: fundamentals and applications to design.* 2nd ed. New Jersey, USA: John Wiley & Sons.

Smith, M. A. and Caracoglia, L. (2011). A Monte Carlo based method for the dynamic "fragility analysis" of tall buildings under turbulent wind loading. *Eng Struct* **33**.2, pp. 410–420.

Vickery, B. J. and Clark, A. W. (1972). Lift or across-wind response to tapered stacks. *J Struct Div* **98**.1, pp. 1–20.

Wind Resistance Performance of Long-Span Steel Truss Bridges Across Gorges in Mountainous Areas

Kai Wang, Haili Liao and Jun Liu

Research Centre for Wind Engineering, Southwest Jiaotong University, Chengdu 610031, China
Corresponding author: Kai Wang, wangk1010@126.com

Abstract

This paper has carried out a comprehensive description on two long-span steel truss suspension bridges in China's western area, which includes the selection of design wind parameters, results of section model tests and process of optimizing the aerodynamic shape. The methods and results of selecting design wind parameters of the bridges in the mountainous valley are firstly introduced in the paper. Then the process and results of section model tests of the two bridges are presented. Next a series of optimization tests are conducted aiming at the wind-induced vibration of the main beam and analysis of all the optimization tests have been made to select the best measure for vibration suppression of the wind-resistance characteristics. It not only meets the need of bridge wind-resistance design, but also provides a reference for future design.

1 Introduction

Comprehensive studies have been conducted on wind-resistance performance of long-span steel truss bridges in plains and coastal areas. However for long span bridges especially with steel truss girder across gorges in mountainous areas, the wind-resistance performance are still in question. Comparing with wind in plain and coastal areas, the wind in the gorges is stronger, more frequent and high turbulent with prominent non-stationary characteristics. The spatial distribution of its wind velocity field is complex and has significant three-dimensional characteristics. The prediction and measurements of wind-induced vibration response in the gorges are obviously different from other areas. The special case is that the long-span steel truss bridges are always built between two peaks with the gorge area below the bridge which makes the condition more complex. The wind field is different not only between the middle of the bridge and both sides of the slopes, but also between the location of the bridge and the surroundings of the bridge. Because of the mountain topography, airflow may be wavy so that non-stationary characteristics of natural wind will have a very negative impact on the bridge structure. Lacking of observation materials and due to regulation limitations, if the design wind speed is obtained based on conventional method which are later used to do wind-resistance test, it might lead to unsafe results. Two long-span steel truss bridges, Baling River Bridge and Dimu River Bridge, which are constructed across gorges, are discussed in this paper to show the particularity of wind field in the mountainous areas and the likely occurrence of the wind-induced vibrations of long-span steel truss bridges. Measures to suppress the flutter of steel truss bridges are also presented.

Baling River Bridge and Dimu River Bridge are two large steel truss suspension bridges. Both two bridges cross big gorges that are steep on both sides with abrupt topographical changes and uneven terrain, the depths of which are all several hundred meters. The two bridges both located in the karst topographical area. Weather conditions, typical mountainous gorge wind, are similar at the bridge sites. Baling River Bridge is a steel truss suspension bridge with its main span 1088 meters. The width of the main beam is 28m and the height is 10 m (Figure 1). Dimu River Bridge is also a steel truss suspension bridge with its main span 538 m. The width of main beam is 27 m, which is composed of a steel beam with a height of 4.5 m and orthotropic plate with a height of 0.8 m (Figure 2). With long span, low self-vibration frequency, sensitivity to the wind qualities of both the two bridges, the flutter

stability becomes the key problem that is also typical in wind resistance and stability of the bridges under complex wind conditions in China's western mountainous areas. The dynamic characteristics of the two bridges are listed in Table 1.
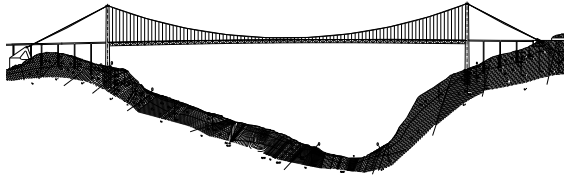
Figure 1 Arrangement of Baling River Bridge　　　　Figure 2 Arrangement of Dimu River Bridge
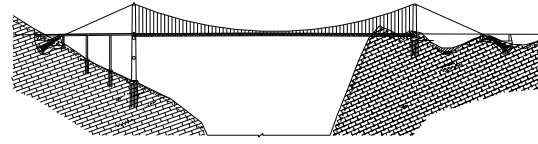
Table 1 Dynamic characteristics of the Two Bridges

Mode of vibration	Baling River Bridge	Dimu River Bridge
	Frequency /(hz)	Frequency /(hz)
The first symmetrical vertical bending	0.157	0.229
The first antisymmetry vertical bending	0.112	0.188
The first symmetric reverse	0.273	0.477
The first antisymmetry reverse	0.329	0.526

2　Wind Parameters at bridge site

Both bridges are located in the southwestern China, famous for its gorge topography. Both sides of the bridges are cliffs and steeps that are precipitous and complex. When natural wind flows though the gorge, it will be zoomed in or zoomed out, reversed or turned and then produces a number of vortices. All the above reasons make the wind field extremely complex. In order to determine the actual wind environment at the bridge site, taking Baling River Bridge as an example, the basic design wind of the bridge is determined as 24.9 m/s through in-situ measurement, numerous simulation (CFD) and topography tests at the bridge site.

According to Wind-resistant Design Specification for Highway Bridges, the maximum wind speed with recurrence period 100 years can be obtained using extreme value distribution Gumbel Type I and yearly extreme wind records of nearby metrological stations. The basic wind speed of Dimu River Bridge can be predicted as 26.92 m/s.

Since the bridge is located across a gorge, the determination of the design wind speed on the deck must take the gorge's complex terrain effects into consideration, by which the design wind speed will be modified. Assuming basic wind speed from gorge bridges virtual weather station is the inlet wind speed in the gorge, basic design wind speed of bridges built across gorges can be obtained from the following formula

$$u_{\mathrm{d}} = \left[\right] \tag{1}$$

In the formula, ud is basic design wind speed, u10 is basic wind speed from virtual weather station, H is the depth of the gorge, when a bridge is built across a gorge, H can be the height from the deck to the bottom of the gorge. B1 is the width of the gorge, it is usually the length of the bridge. B2 is the width of the bottom of the gorge, κ is gorge effect correction coefficient. From formula (1), design basic speed of Dimu River Bridge can be predicted as 34.80m/s.

Figure 3 Observation Tower at the Bridge Site   Figure 4 Calculation Area 3d View   Figure 5 Terrain Model in Wind Tunnel
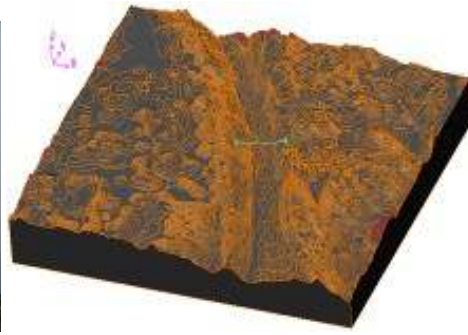
3   Section Model Test

3.1   Static Loading

Static load coefficient is a non-dimensional coefficient that represents the magnitude of the force under the mean wind for the various structure sections and reflects aerostatic reaction of the bridge due to the wind. Now with the development of theory and computer technology, many people often use CFD software calculate the three component force coefficient for main beam. But for steel truss beam, there are obvious error between the results from CFD software and from actual. For truss beam, wind tunnel test is still required. In figure 6 and figure 7, there are steel truss beam cross section of Baling River Bridge and Dimu River Bridge.
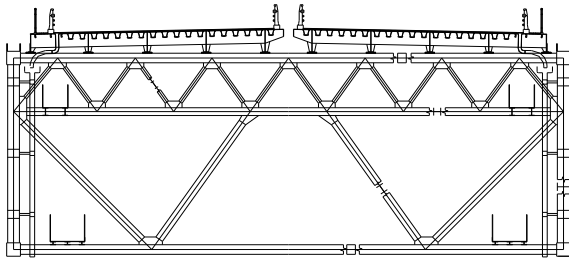
Figure 6 Main Beam Cross Section of Baling River Bridge   Figure 7 Main Beam Cross Section of Dimu River Bridge
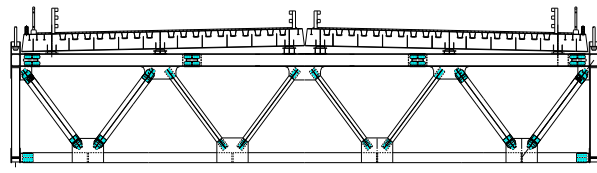
There are two ways to express the effect on the main girder of the static force components by the coordinate system of the three different, as the body axis coordinate system (coordinate system along the section centroid axis) and the wind axis coordinate system (coordinate system along the direction of the wind). The static three component coordinate system is shown in figure 6. The three static force coefficients under the wind axis coordinate system Press the type definition:

$$\text{Resistance Coefficient:} \quad C_D(\alpha) = F_D(\alpha) \Big/ \left(\frac{1}{2}\rho \upsilon^2 HL\right)$$

$$\text{Lift Coefficient:} \quad C_L(\alpha) = F_L(\alpha) \Big/ \left(\frac{1}{2}\rho \upsilon^2 BL\right)$$

$$\text{Torque Coefficient:} \quad C_M(\alpha) = M_Z(\alpha) \Big/ \left(\frac{1}{2}\rho \upsilon^2 B^2 L\right)$$

Type: α is the flow angle of attack; $\frac{1}{2}\rho \upsilon^2$ is the air pressure; H, B, L were the height, width, length; $F_D(\alpha)$, $F_L(\alpha)$, $M_Z(\alpha)$ were the resistance coefficient, lift coefficient, torque coefficient under the wind axis coordinate system. The resistance coefficient and lift coefficient could be got through change $F_D(\alpha)$ into $F_H(\alpha)$ and change $F_L(\alpha)$ into $F_V(\alpha)$, $M_Z(\alpha)$

and $C_M {'} \alpha$ are the same under the two axis coordinate system, but resistance coefficient and lift coefficient need to coordinate conversion relations as shown in figure 8.
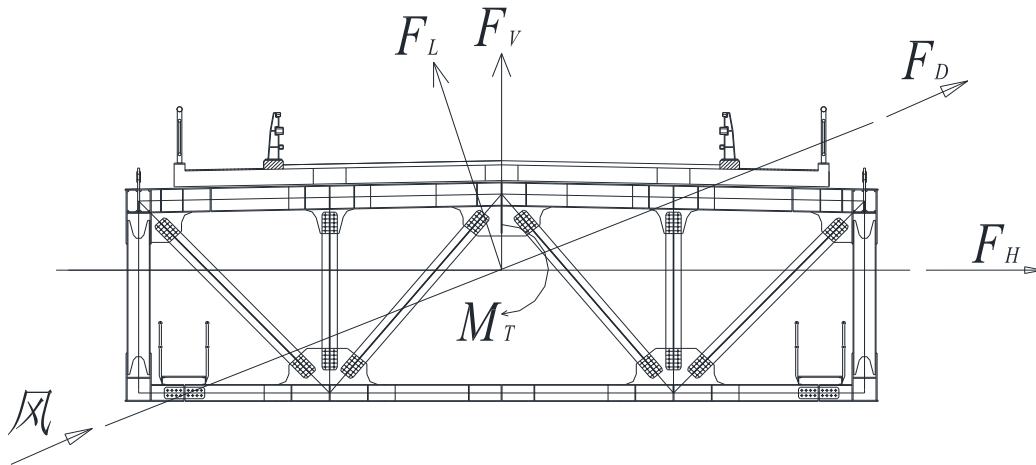
Figure 8 Schematic Plot of Body Axis Coordinate System and Wind Axis Coordinate System

For Baling River Bridge, the width of main beam is 28 m, the height is 10 m, the distance between each mode is 10.8 m. For the wind tunnel test of the main beam static section model, a geometrical scale of 1:47.5 with a 2.095 m in length is selected for section model. For Dimu River Bridge, its main span is 538 meters. The width of main beam is 27 meters, which is consisted of steel beam with the height of 4.5 meters and orthotropic plate with the height of 0.8 meter. A geometrical scale of 1:50 with a 2.095 m in length is selected for section model. Tests are carried out under uniform flow condition, the attack angle of the incoming flow is from -12° to 12°, the increment is 1°. Under the wind speed which is 15 m/s, the standard beams of Baling River Bridge and Dimu River Bridge in the completed state are tested. Testing results are shown in Figure 9 and Figure 10.
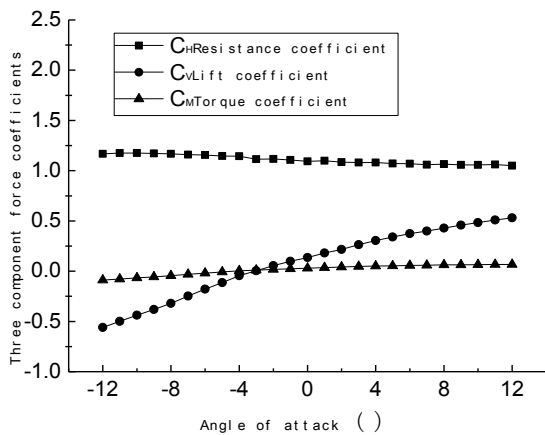
Figure 9 Curves of Three Component Force Coefficients of Baling River Bridge   Figure 10 Curves of Three Component Force Coefficients of Dimu River Bridge
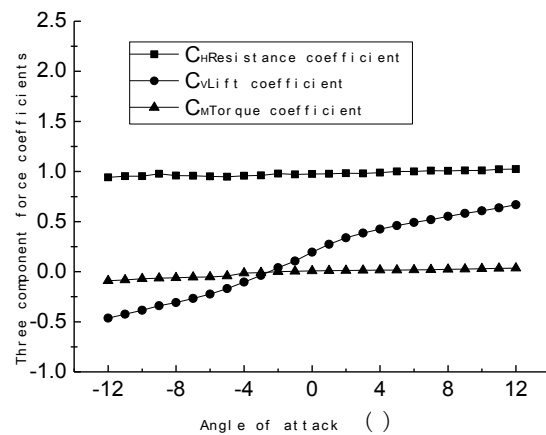
3.2   Dynamic Response

In order to simulate the elastic restraint between test section and other main beam section, the model of dynamic test is suspended by four string in the wind tunnel. Spring coefficient is determined by the similar conditions. Tests can be used to find flutter critical wind speed under different attack angle and verify vortex-induced vibration and galloping if applicable. The tests can also determine the wind speed, the amplitude of vibration and strouhal number of the main beam when vortex-induced vibration happens. Thus flutter and vortex-induced vibration performance of the main beam can be evaluated.

Tests are carried out under smooth oncoming flow, figure 11 and figure 12. The damping ratio is assumed to be 0.5% relative to the critical. Considering the adverse wind flow in the gorge, five attack

angles, 0°,+3°,-3°,+6° and -6°, were carried out. No vortex-induced vibration in vertical and torsional direction of the two bridges was observed. The flutter wind speed two bridges are listed in Table 2. It can be seen in the Table 2 that when the attack angle of the incoming flow is -3°, the flutter critical wind speed of Baling River Bridge is less than flutter checking wind speed. The amount of surplus with 0° attack angle is very small, so the main beam section need to do optimization test. When the attack angle of the incoming flow is 0°, -3° or -6°, the flutter critical wind speed of Dimu River Bridge are larger than flutter checking wind speed. But when the attack angle of the incoming flow is +3° or +6°, the flutter critical wind speed of Dimu River Bridge are less than flutter checking wind speed. Then they don't meet the requirements of bridge design. So main beam of both two bridges need to do aerodynamic optimization test.

Figure 11 Section Model of Baling River Bridge

Figure 12 Section Model of Dimu River Bridge

Table2 Flutter Critical Wind Speed of the Two Bridges

Baling River Bridge				Dimu River Bridge			
Attack angle	Flutter Critical Wind Speed /(m·s⁻¹)	Flutter checking Wind Speed /(m·s⁻¹)	Safety evaluation	Attack angle	Flutter Critical Wind Speed /(m·s⁻¹)	Flutter checking Wind Speed /(m·s⁻¹)	Safety evaluation
-6°	51.3		Safe	-6°	>64		Safe
-3°	38.8		Unsafe	-3°	>64		Safe
0°	43.7	41.3	Safe	0°	>64	57.6	Safe
+3°	71.2		Safe	+3°	53		Unsafe
+6°	48.6		Safe	+6°	50		Unsafe

4   Aerodynamic Optimization Test on Main Deck

Basis on the results of section model tests, when the attack angle of the incoming flow is -3°, the flutter critical wind speed of Baling River Bridge is less than flutter checking wind speed. The amount of surplus with 0° attack angle is very small, so the main beam section need to be tested optimization test. When the attack angle of the incoming flow is +3° or +6°, the flutter critical wind speed of Dimu River Bridge are less than flutter checking wind speed. In order to make the bridges meet the design requirements, and avoid bridges destructed by flutter, wind tunnel test is needed to do a serious of aerodynamic optimization test studies on main beam of the two bridges.

4.1   Baling River Bridge

For Baling River Bridge, this paper have tested two types of tests, single wing plate and double wing plate section model test. Flutter test has been tested after the groove of the deck is sealed, the results of it have been compared with the results come from tests that when unsealed groove and aerodynamic wing plate work together. Double wing plate are supported by upright columns, which is made of ABS plate, that beside the maintaining roadway. The section of it is ellipse with long axis of 23.3 mm and short axis of 2.5 mm. (Figure 12 and Figure 13). The results from the tests when unsealed groove and double aerodynamic wing plate have worked together are in Table 3.
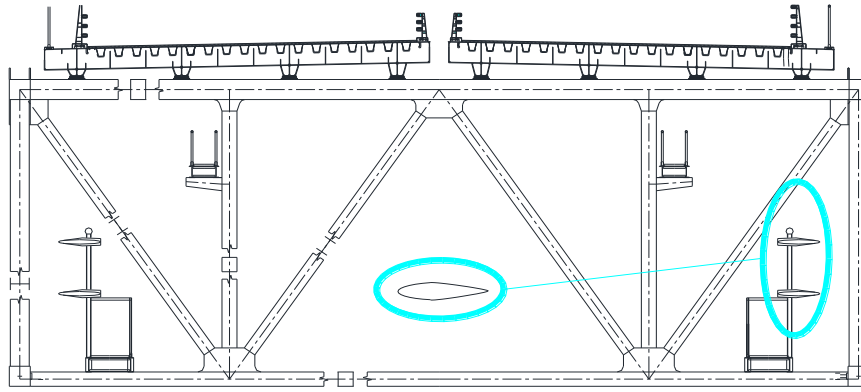
Figure 12 Truss Beam Section with Double Wing Plate
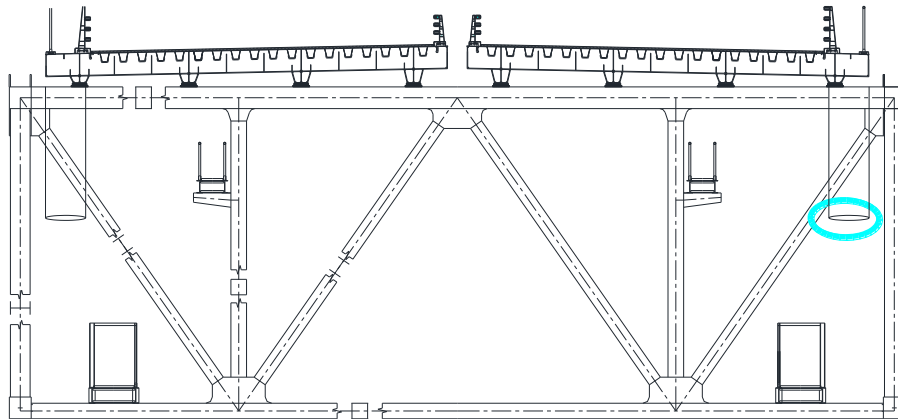
Figure 13 Truss Beam Section with Single Wing Plate

Table 3 Flutter Divergence Wind Speed
When Unsealed Groove and Double Aerodynamic Wing Plate Have Worked Together

Anti-vibration Measures	Attack angle (°)	Flutter Divergence Wind Speed /(m·s⁻¹)	Measures	Attack angle (°)	Flutter Divergence Wind Speed /(m·s⁻¹)
Double wing plate and the groove is 10mm	-3	>107.7	Double wing plate and the groove is sealed	-3	81.3
Double wing plate and the groove is 10mm	0	>107.7	Double wing plate and the groove is sealed	0	67.6
Double wing plate and the groove is 10mm	+3	56.3	Double wing plate and the groove is sealed	+3	49.9
the groove is 10mm	-3	>102.8	the groove is sealed	-3	75.9

| the groove is 10mm | 0 | 72.5 | the groove is sealed | 0 | 51.4 |
| the groove is 10mm | +3 | 53.9 | the groove is sealed | +3 | 45.5 |

Based on a serious of section model tests, different types of aerodynamic wing plate that are installed on the deck and have obviously different characteristics to affect flutter stability. Aerodynamic wing plate have obvious positive impact on flutter stability, but it can be significantly affected by wind attack angle and the number of plates. Single wing plate in proper position can increase flutter critical wind speed by 15%. If wind attack angle is 0°, double wing plate have a better function. The highest flutter critical wind speed can be increased by 48%. The location that the wind plate installed can affect flutter critical wind speed.

4.2 Dimu River Bridge

For selecting the best program, the worst effects wind attack angle, which is +6°, is been chosen to do aerodynamic optimization test. The optimization programs and results of the main beam are listed in table 4. The data in the table are converted to actual data that of actual bridge not of model.

Table 4 Aerodynamic Optimization Programs
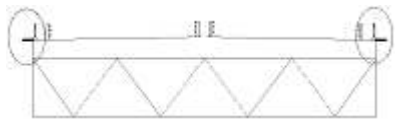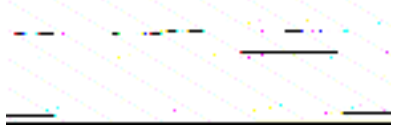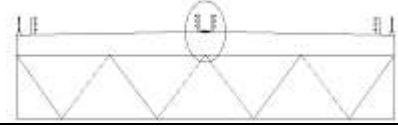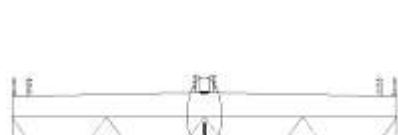
Anti-vibration Measures	Graphic	Program	Flutter Divergence Wind Speed /(m·s^{-1})
Install horizontal deflector		Program 1 the width of horizontal deflector is 1.5 m	52
Seal the groove of main beam		Program 2	52
Seal the groove of main beam and install central stabilized plate above the deck		Program 3 the height of central stabilized plate is 0.55 m Program 4 the height of central stabilized plate is 1.10 m	54 57
Seal the groove of main beam and install central stabilized plate below the deck		Program 5 the height of central stabilized plate is 1.0. m Program 6 the height of central stabilized plate is 1.50 m Program 7 the height of central stabilized plate is 1.75 m Program 8 the height of central stabilized plate is 2.00 m	53 55 63 63
Use grille seal the groove		Program 9 Ventilation rate of the grille is 50%	53
Use grille seal the groove and install central stabilized plate below the deck		Program 10 Ventilation rate of the grille is 25% and the height of central stabilized plate is 1.00 m Program 11 Ventilation rate of the grille is 50% and the height of central stabilized plate is 1.00 m Program 12 Ventilation rate of the grille is 50% and the height of central stabilized	55 56 58

plate is 1.00 m, which are installed at intervals.	
Program 13 Ventilation rate of the grille is 50% and the height of central stabilized plate is 1.00 m, which are installed at intervals, and the upper edge of stabilized plate close to surface of main truss beam)	64

As table 4 shows, based on a serious optimization section model tests. All programs have certain effects on increasing flutter critical wind speed, but the effects are different. The differences are as follows.

Installing horizontal deflector, or sealing the groove, or using grille to seal the groove, every method can only increase flutter critical wind speed by 2-3 m/s. They practically don't improve the aerodynamic performance of main beam. And the horizontal deflector has a bad effect on the appearance of the bridge.

Sealing the groove completely and installing central stabilized plate with the height of 0.55 m or 1 m above the deck, they can increase flutter critical wind speed, and the higher the central stabilized plate, the higher the flutter critical wind speed. But all flutter critical wind speed in these condition are less than flutter checking wind speed. And the central stabilized plate also has a bad effect on the appearance of the bridge.

Sealing the groove completely and installing central stabilized plate with the height of 1 m, 1.5m, 1.75 m or 2 m below the deck, they all can increase flutter critical wind speed. When the height of central stabilized plate is less than 1.75m, the flutter critical wind speed increases with the central stabilized plate's height. But when the height of central stabilized plate is more than 1.75m, the flutter critical wind speed doesn't increase any more. Therefore, if using the method that seal the groove completely and install central stabilized plate below the deck to increase flutter critical wind speed, the highest of central stabilized plate should be 1.75 m, and now the flutter critical wind speed is 63 m/s. But if the central stabilized plate is high, it will waste material and increase difficulties to installation.

Using grille seal the groove and installing central stabilized plate with the height of 1m above the deck at intervals. Through several programs, when the ventilation rate of the grille is 50%, the grille is discontinuously arranged and the upper edge of plate close to surface of main beam, the flutter critical wind speed is 64 m/s. This program save materials, such as grille and central stabilized plate, and reduce the wind load of main beam. And the height of central stabilized plate is reduced to 1 m. It is convenient for installation.

Based on the above analysis, this paper recommend that for Dimu River Bridge the following optimization measures are adopted, which is using grille with ventilation rate in 50% seal the groove of the beam and installing central stabilized plate at intervals, which is disconnected at the crossbeam, and its upper edge close to the surface of main beam (Figure 9 and Figure 10).
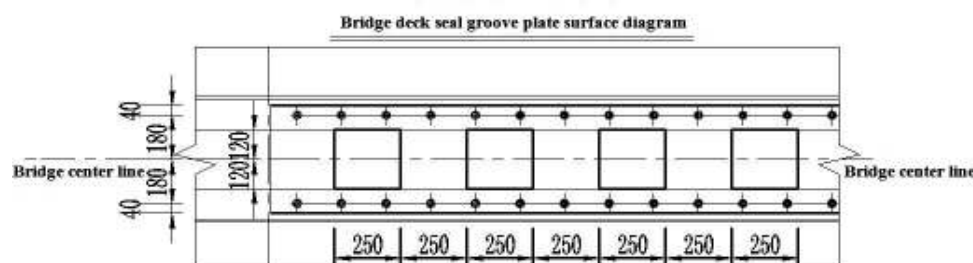
Figure 9 Use Grille Seal the Groove of Main Beam of Dimu River Bridge
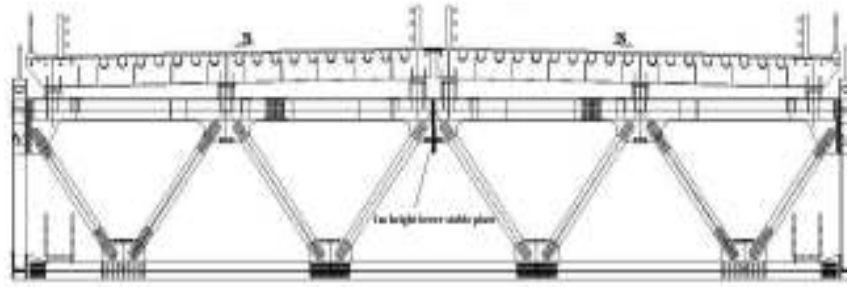
Figure 10 Center Stabilized Plate of Dimu River Bridge

5   Conclusions

Based on studies on the selection of wind parameters, section model test and anti-vibration measures of Baling River Bridge and Dimu River Bridge. This paper have got the following conclusions.

In the gorge of mountain area, the average wind speed can be obvious amplified, and in different gorge wind speed and the amplification are different. Every gorge has its own characteristic.

For different truss beam, even if the width of main beams are same, the aerodynamic characteristics are different. And this paper recommend the aerodynamic forces of truss girder should be obtained by wind tunnel tests

For long-span suspension bridges that are constructed in the mountain areas, flutter instability is a key factor in bridge design. The flutter instability of main beam is low when wind attack angle of incoming flow is positive, then the main beam usually needs aerodynamic shape optimization.

Installing aerodynamic wing plate or central stabilized plate can help to increase flutter critical wind speed. The location, continuity and height of aerodynamic wing plate and central stabilized plate have a great impact on flutter critical wind speed.

References

Wang Kai, et al. 2013. Determination method for basic design wind speed of mountainous valley bridge[J]. *Journal of Southwest Jiaotong University*, 48(1): 29-36.

Scanlan, R.H. 1978. The action of flexible bridges under wind, I: flutter theory. *Sound Vib*, 60(2),187-199.

Agar, T. J. A. 1989. Aerodynamic flutter analysis of suspension bridges by a modal technique. *Eng.Struct*, 11(2),75-82.

Beith J.G. 1998. A practical engineering method for the flutter analysis of long-span bridges. *Wind.Eng.Ind.Aerodyn*, 77-78,357-366.

Chen, Z. Q. Agar T. J. 1994. Finite element-based flutter analysis of cable-suspended bridges (discussion), *Struc.Eng,* ASCE, 120(3),1044-1046.

Tanaka H. Yamamura N. Tatsumi M. 1992. Coupled mode flutter analysis using flutter derivatives. *Wind Eng.Ind.Aerodyn*, 42(1-3),1279-1290.

Katsuchi ,H. Jones N. P. ,Scanlan R. H. 1999. Coupled flutter and buffeting analysis of the Akashi-Kaikyo Bridge. *Struct.Eng.*,ASCE, 125(1),60-70.

Miyata T.Yamada H. 1990. Coupled flutter estimate of a suspension bridge. *Wind. Eng.Ind. Aerodyn*, 33(1-2),341-348.

Dung N. N. Miyata T. Yamada H. Minh N. N. 1998. Flutter responses in long span bridges with wind induced displacement by the mode tracing method. *Wind. Eng.Ind. Aerodyn*. 77-78,367-379.

Ge Y. J. Tanaka H. 2000. Aerodynamic flutter analysis of cable-supported bridges by multi- mode and full-mode approaches. *Wind.Eng.Ind.Aerodyn*, 86(2-3), 123- 153.

Scanlan R. H. 2000. Motion-related body-force functions in two-dimensional low-speed flow. *Fluids Strcut*., 14(1),49-63.

Bucher C. G. Lin Y .K. 1988. Effect of span wise correlation of turbulence field on the motion stochastic stability of long-span bridges. *Fluids and Structures*, 2(5), 437-451.

Lin Y. K. Li Q. C. 1993. New stochastic theory for bridge stability in turbulent flow. *Eng. Mech*., 119(1),113-128.

Chen X.. Matsumoto M. Kareem A. 2000. Time domain flutter and buffeting response analysis of bridges. *Eng.Mech.*,ASCE, 126(1),7-16.

Scanlan R H Tomko J. 1971. Airfoil and bridge deck flutter derivatives. *Journal of Engineering Mechanics*. ASCE, 97(6):1717-1237

Xu Hongtao, Liao Haili, Li Mingshui. 2009. Wind tunnel test study of sectional model of baling river bridge[J]. *World Bridges*, 37(4): 83-89.

Scanlan R H, Tomko J J. 1971. Airfoil and Bridge Deck Flutter *Derivatives*.ASCE. 97(6):1717-1737

Xu Fuyou, Chen Airong, Zhang Zhe. 2008. Practical technique for determ ining critical flutterw ind speed of bridgemodel. *Journal of Vibration and Shock,* 27(12): 97-102.

Chen Zhengqing, OuYang Kejian, Niu Huawei. 2009. Aerodynamic mechanism of improvement of flutter stabil ity of truss-girder suspension bridge using central stabil izer. *China Journal of Highway and Transport*, 22(6):53-59.

Zhu L D, Wang M, Wang D L. 2007. Flutter and buffeting performances of third Nanjing bridge over Yangtze river under yaw wind via aeroelastic model test [J]. *Journal of Wind Engineering and Industrial Aerodynamics*, 95(9-11): 1579-1606.

Characterization of wind-induced pressures on solar updraft towers

Luca Facchini[1] , Francesca Lupi[1] , Claudio Borri[1]

[1]Department of Civil and Environmental Engineering, University of Florence, Italy
Corresponding author: L. Facchini, luca.facchini@unifi.it

Abstract

In some previous research works, the Authors addressed the problem of the characterisation of wind induced loads on solar updraft towers; such structures exhibit some peculiarities such as the existence of a bi-stable flow which induces, on certain zones of the structural surface, pressures characterised by bimodal probability densities. Past contributions were devoted to the definition of a nonlinear filter fed with a Gaussian white noise, whose output could resemble, from a statistical point of view, the pressure coefficients derived from measurements carried out in the WiSt and CRIACIV boundary layer wind tunnels. In the present work the procedure is applied to all the pressure measurements carried out on a ring of the tower, in order to characterize the stress distribution and determine a first estimate of the design loads on the tower section.

1 Introduction

Experimental tests carried out on a circular cylinder stiffened by a certain number of rings placed regularly along its height brought evidence of the presence of a bi-stable turbulent flow around the cylinder itself, which induced pressures endowed with a bi-modal probability density function.

In some previous research work, (Borri et al., 2012, Lupi et al., 2013), wind induced pressures in a particular tap were modelled as the output of a properly designed non-linear filter subject to a white noise. The filter was able to exhibit an output endowed with a bi-modal probability distribution; now, non-linear filters are designed to model the statistical characteristics of the pressures measured all around a ring of the tower model.

Therefore, a stochastic model can be set for the excitation and the structural response, thus leading to a better description of the distribution tails for the loads and for the structural response.

Hopefully, the process will help to gain insight for the definition of wind induced loads on a solar updraft tower.

2 Wind tunnel tests

A cross-checked wind tunnel investigation was performed at WiSt (Ruhr-University Bochum) and at CRIACIV (University of Florence) boundary layer wind tunnels.

The object of the investigation is a hollow circular cylinder of finite aspect ratio (h/d = 6.67, h = 1.0 m and d = 0.15 m) immersed in turbulent atmospheric boundary layer flow. The peculiarity of the model is the presence of a certain number of rings placed along the height of the cylinder and on top. From the structural point of view, spanwise rings are often used as stiffeners in the design of high and thin cylindrical shells. The wind tunnel investigation addressed in this paper is focussed on the aerodynamic effect created by the presence of rings along the height of the cylinder. The wind tunnel model is rigid and thus aeroelastic effects are not included.

Within the whole wind tunnel investigation at WiSt and CRIACIV, tests are done both on the circular cylinder without rings and with 10, 7 or 5 rings of different sizes (w/d = $4.67*10^{-2}$ and $2.33*10^{-2}$, being w the width of the ring). Different atmospheric boundary layers (including uniform flow), as well as different Re and roughness conditions of the cylinder surface are tested. The effect of

the efflux inside the chimney is also investigated. Wind pressures are measured at 17 levels along the height and in the circumferential direction at 18 positions, i.e. starting from the stagnation angle (0°) and proceeding at an angular spacing of 20°. Internal pressures are also measured along the height of the internal cylinder and along the circumference. For further details the reader is referred to Lupi et al. (2013). In particular, the effective Reynolds number is applied according to ESDU 80025 and a discussion on Reynolds effects and surface roughness is addressed in Lupi et al. (2013).

The presence of spanwise rings reveals a complex three-dimensional flow pattern around the circular cylinder and a bistable asymmetric load condition, due to the interaction of rings with the vortex structures in the tip region. A physical interpretation of the aerodynamic phenomenon - based on wind tunnel tests and further supported by numerical CFD simulations - is discussed in Lupi et al. (2013), together with the evaluation of its effects on the design of a ultra-high tower.

Among the results of the whole experimental campaign, this paper focuses on the wind pressures measured at CRIACIV wind tunnel around the circumference at the level z/h = 0.95. This level is in the highest compartment in between two rings, placed at z/h = 0.90 and on top at z/h = 1.0, respectively. The following configuration is selected for this study:

10 rings equally spaced along the height of the cylinder (at a distance of 10 cm in the wind tunnel scale), $w/d = 4.67*10^{-2}$);

rough cylinder: ribs of 0.25 mm in thickness, at an angular spacing of 20°;

turbulent atmospheric boundary layer ($I_{v,max} \approx 14\%$, see Lupi et al., 2013, for details)

no-efflux in the chimney;

$Re = 2.8*10^5$.

3   Correlations of Wind Pressures

The correlation coefficients around the circumference are governed by the mean flow pattern. Because of that, the circumferential correlations of the stagnation point with all the other points around the circumference resemble the mean pressure distribution. Stagnation and maximum suction have a strong negative correlation; stagnation and wake area have small negative correlations. It means that the fluctuations around the circumference appear to be organized by the mean flow and a considerable portion of them may be understood as a "breathing" of the mean flow. The cross-correlations of stagnation and of rear stagnation (i.e. 0° and 180°) are the only ones which are symmetric around the circumference. In general, the correlation coefficients depend on the reference position and on the direction of movement. The reference position can be classified in two groups: points before separation and points after separation. The direction of movement is either downstream or upstream.
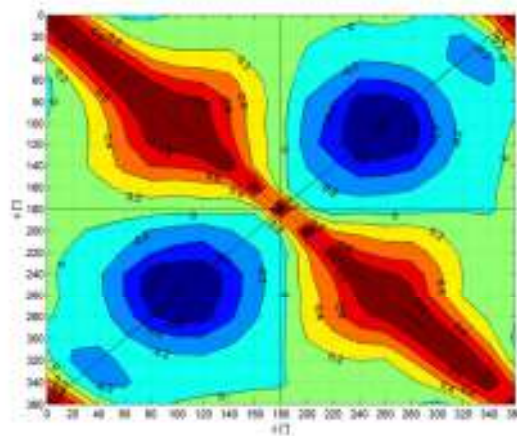
Figure 1. Correlation matrix of pressure coefficients at level z/h = 0.95 resulting from wind tunnel tests at CRIACIV

By definition, the correlation matrix is symmetric with respect to the main diagonal, whose values are equal to 1. Furthermore, due to the symmetry between the two sides of the cylinder, the matrix is also symmetric with respect to the secondary diagonal. However, this is not anymore true in presence of rings, because they create the aerodynamic effect of asymmetric flow past the circular cylinder (Lupi et al., 2013).

The cross-correlation matrix of the coefficients measured at z/h = 0.95 at CRIACIV wind tunnel is reported in Figure 1. The values of the cross-correlation coefficients are integrals over frequencies of the cross-spectra. Similarly, in the time domain, they express the zero-lag spatial correlation. Therefore, in the calculation of the structural response, the cross-correlation matrix is an input load parameter which accounts for the stochastic wind loading process without including the dynamic resonant contribution. For that, as well as to describe the time evolution of the bistable flow, correlation functions are required. Their structure is known by wind tunnel tests and it is used in this paper as target to develop a non-linear filtering of properly correlated white noises.

4   Theoretical background

A non-Gaussian stationary process can often be modelled as the output of a proper nonlinear filter to a stationary Gaussian white noise with intensity S_0 ; this result, originally due to Kramers (1940), was successively developed by Caughey (1964) and utilized by various Authors in several applications, see f.i. Alaoui Ismaili and Bernardt (1997), especially in the case of linear viscous damping. The scalar equation of the nonlinear filter may be expressed as

$$\ddot{x} + H(E)\dot{x} + g(x) = f(t) \tag{1}$$

Caughey (1964) expressed the probability distribution of the response as

$$p_{x,\dot{x}}(x,\dot{x}) = C \exp\left(-\frac{1}{\pi S_0}\int_0^E H(u)\,du\right); \quad E(x,\dot{x}) = \frac{\dot{x}^2}{2} + \Phi(x); \quad \Phi(x) = \int_0^x g(u)\,du \tag{2}$$
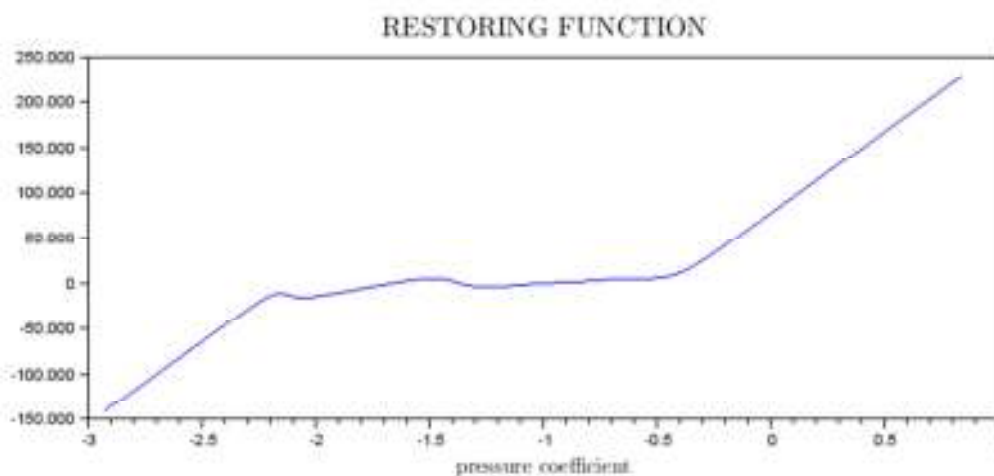
Figure 2: the nonlinear restoring function determined for the examined pressure coefficient.

In the case of linear viscous damping, Alaoui Ismaili and Bernardt (1997), utilized the function

$$H(E) = 2\nu\omega \quad \Rightarrow \quad p_{x,\dot{x}}(x,\dot{x}) = C \exp\left[-\frac{2\nu\omega}{\pi S_0}E(x,\dot{x})\right] \tag{3}$$

where C is a proper normalization constant for the probability distribution.

Parameter identification, based on the pressures measured in one of the taps which exhibited the most accentuated deviation from normality, led to the definition of a nonlinear system in the form

$$\ddot{c} + \frac{\pi S_0}{\sigma_{\ddot{c}}^2} \dot{c} + g(c) = f(t) \qquad (4)$$

where $c(t)$ is the examined pressure coefficient and $g(c)$ is a nonlinear restoring function. The behaviour of the restoring function $g(c)$ was best described by a sum of Gaussian bells; the result is shown in Figure 2.

The pdf and power spectral density of the forcing process $f(t)$ are shown in Figure 3, which clearly shows that the forcing process can well be modelled as a Gaussian white noise.
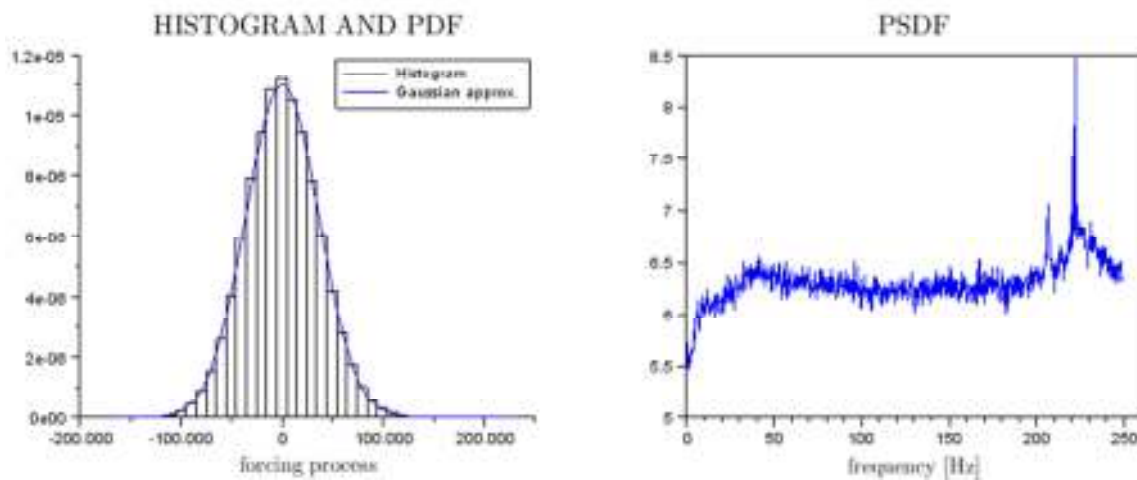
Figure 3: Probability distribution (left) and power spectral density (right) of the forcing process

Such kind of filters are currently being designed for all the taps around a ring on the model; therefore, a stochastic model for the loads and the structural response can be set, thus gaining insight in the definition of design loads for the solar updraft tower.

References

Alaoui Ismaili M., Bernardt P. (1997). Asymptotic analysis and linearization of the randomly perturbed two-wells Duffing oscillator, *Prob. Engng Mech.*, **12**, No. 3, pp. 171-178.

Borri C., Facchini L., Lupi F. (2012). Caratterizzazione del campo di pressione indotto dal vento sul modello di una torre solare, (in Italian) Proceedings of the XII Convegno Nazionale di Ingegneria del Vento In–Vento 2012 , Venice 7 – 10 October 2012

Caughey T.K. (1964). On the response of a class of nonlinear oscillators to stochastic excitation, *Proc. Coll. Int. du Centre Nat. de la Rechercher Scient.*, No. 148, Marseille, France, pp. 393-402.

Kramers H. A. (1940). Brownian motion in a field of force and the diffusion model of chemical reactions, *Physica*, **7**, pp. 284-304.

Lupi F., Borri C., Facchini L., Niemann H.-J., Peil U. (2013). A New Type of Bistable Flow around Circular Cylinders. Journal of Wind Engineering and Industrial Aerodynamics, **123** (B), December 2013, Pages 281–290.

Piezoelectric Energy Harvesting under Air Flow Excitation

Francesco Petrini, Konstantinos Gkoumas and Franco Bontempi

Department of Structural and Geotechnical Engineering, Sapienza University of Rome, Italy
Corresponding author: Francesco Petrini, francesco.petrini@uniroma1.it

Abstract

This study focuses on the numerical analysis of a high efficiency Energy Harvesting device, based on piezoelectric materials, for the sustainability of smart buildings, structures and infrastructures. Before that, a comprehensive literature review on the topic takes place. The device consists in an aerodynamic fin attached to a piezoelectric element that makes use of the air flow to harvest energy. The principal utilization of this device is for energy autonomous sensors, with applications in bridges, transportation networks and smart buildings. The results are corroborated by advanced analytical and numerical analyses (in ANSYS®) that demonstrate the energy harvesting capacity.

1   Introduction

There is a strong consensus in the engineering community and the society for the realisation of enhanced structures and infrastructures. In addition to safety and functionality requirements, collectively addressed by the so-called "Performance-Based Design" (SEAOC, 1995; Spekkink, 2005), one of the pillars of contemporary structural engineering, today the attention focuses on the most broad and profound notion of "sustainability" (Ehrenfeld, 2008). In this sense, the modern construction industry embraces the concept of smart structural systems that behave optimally with respect to the human needs, being at the same time coherently collocated in the environment (Srinivasan & McFarland, 2001) and inserted in a context of resilient cities (Rose, 2011). Smart structural systems combine their primary function with additional capabilities. For instance, a bridge can pair its primary function of carrying vehicular traffic with several secondary features, such as an embedded set of sensors that constantly monitor the structural condition, or devices able to provide power to the bridge itself and make it (partially) self-sufficient, more sustainable and environmentally friendly. This study investigates this latter type of smart features, with focus on structural and mechanical models for piezoelectric energy harvesting devices under airflow excitation.

Energy Harvesting (EH) can be defined as the process of collecting energy from the environment or from a surrounding system and converting it to useable electrical energy. The idea of harvesting freely available energy is not new, and dates back to the invention of windmills and watermills. Modern wind turbines can be considered the direct and straightforward evolution of ancient windmills. However, today EH is performed with a much broader set of devices and techniques, and has become a prominent research topic also in the field of civil engineering, with several promising applications to structural and infrastructural systems. For instance, current popular areas of application extend from powering small autonomous wireless sensors (thus eliminating the need for wires) up to large auxiliary systems (e.g., road lights, signs or information panels, in the case of transportation infrastructure), thus contributing towards the pursue of sustainable structures and infrastructures (Gkoumas, 2012).

From this point of view, EH in civil engineering is part of a global clean energy trend that encompasses several aspects and disciplines, and focuses on the use of renewable sources and the reduction of fossil fuel usage for a more sustainable development (Adams, 2006).

Several proposals and applications can be found in literature and practice, mostly using solar and wind energy. The latter is of particular interest for high-rise buildings and long span bridges, due to the superior characteristics of the wind field.

2   Energy harvesting for smart buildings, structures and transportation infrastructures

So far, EH for smart buildings, structures and infrastructures has been focusing mostly on the production of small amounts of energy for powering SHM (Structural Health Monitoring) systems, so the topics of EH and SHM are strictly related in the literature. Some more recent applications, still mostly at a conceptual level, aim at supplying power to auxiliary systems (e.g. road lights or information panels), thus, contributing to the development of sustainable and self-sufficient infrastructure systems. More recently, EH is implemented in devices for smart building automation.

Spencer & Cho (2011) reviewed the recent developments in SHM technologies, including an energy harvesting options for sustainable operation. The same paper reports on a number of recent full scale implementations of EH for SHM networks. Gkoumas (2012) provided a literature review and a framework for the optimal implementation of EH applications in transportation networks. A review of the EH applications on this topic can be found also in Park et al. (2008). The authors, after providing an overview of SHM, focus on the energy generation from mechanical vibrations as a powering option. In the same paper, the power requirements of existing and emerging sensing modalities are discussed, and future directions are given.

In the field of piezoelectric material modelling, several alternatives have been proposed in literature. Erturk and Inman, 2008, provide a critical review and identify the principal issues in the mechanism of piezoelectric coupling and the basic excitation relation. Numerical (Finite Element) modelling of piezoelectric material presents many challenges for what regards the coupling between the deformation and diffusion in the piezoelectric material. De Miranda et al. (2009) studied the coupled piezo-diffusion in elastic solids and provided indications and examples for the accurate modelling, overcoming simplistic assumptions of displacement and concentration of the material as independent variables in the model.

Focusing on the specific application proposed in this research (piezoelectric benders), recent developments seem promising in terms of EH capacity. In a recent study by Weinstein et al (2012), the EH potential is investigated, both analytically and experimentally, in heating, ventilation and air conditioning flows. The energy effectively harvested is augmented by means of an aerodynamic fin attached at the end of the piezoelectric cantilever and the vortex shedding downstream from a bluff body placed along the airflow in front of the fin/cantilever assembly.
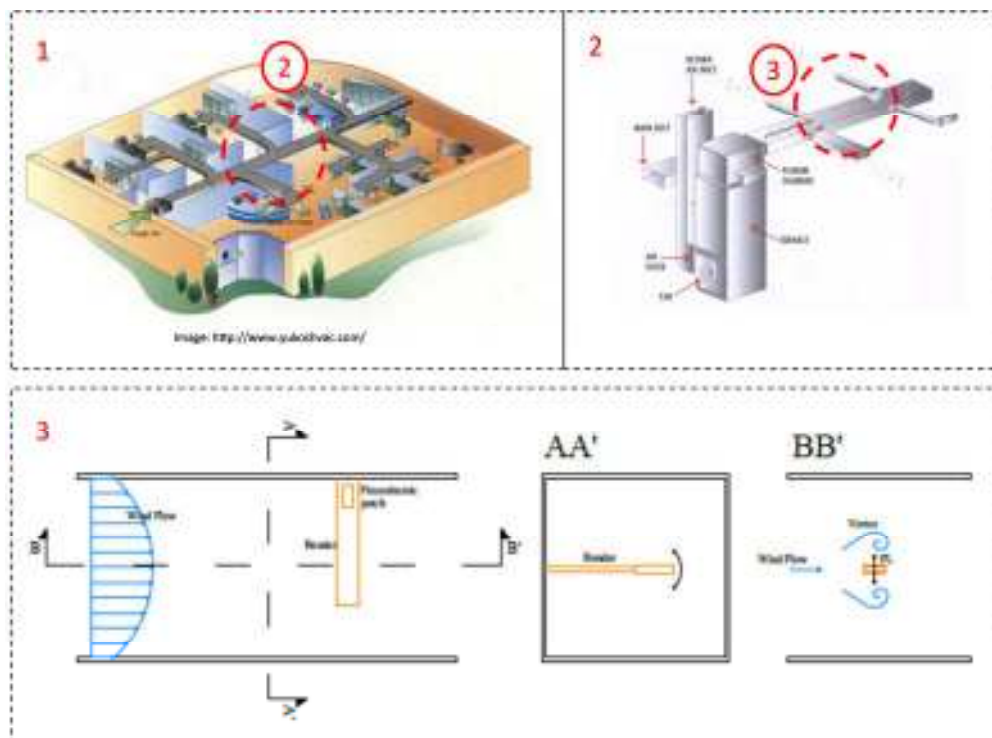
Figure 1. The device for EH (in orange in the figure) and its collocation inside a HVAC duct.

Figure 1 provides a schematic representation of a possible application of the EH device, object of this study. The EH device, could harvest the airflow powered inside Heating, Ventilation and Air Conditioning (HVAC) systems, using a piezoelectric component and an appropriate customizable aerodynamic appendix or fin that takes advantage of specific air flow effects (principally Vortex Shedding), and can be implemented for optimising the energy consumption inside buildings. The possibility to implement autonomous sensors inside a building that monitor relevant parameters (temperature, humidity, chemical agents concentration etc.), and transmit intermittently data to a central unit is a recent and rapidly grown business, helped by the standardisation of wireless (wi-fi) data transmission.

3   Numerical modelling

The proposed research focuses on the numerical modelling of different configurations of a piezoelectric bender and an attached fin (Figure 2).

The ANSYS® numerical code is used for the analyses (ANSYS, 2011). In the analysis, different air-flow intensities are considered.
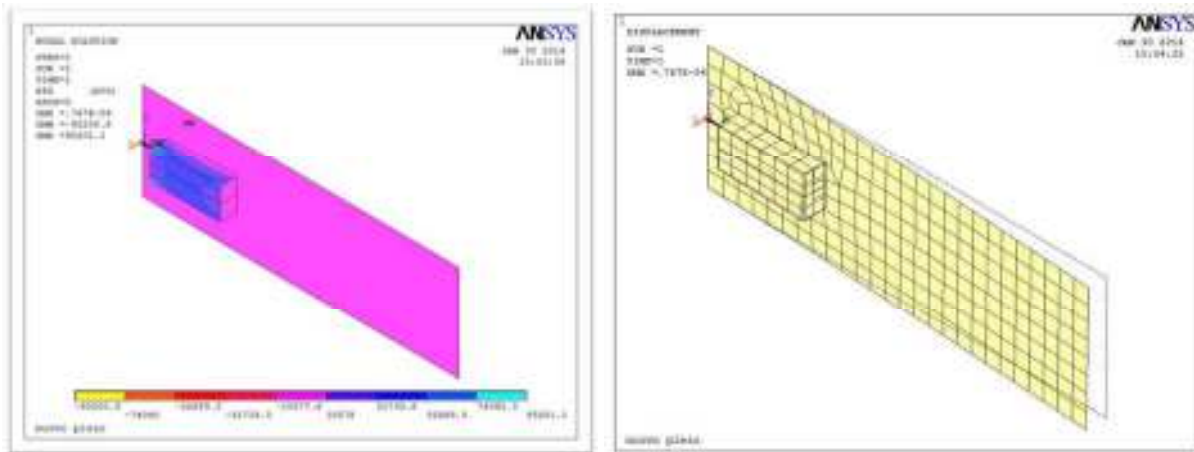
Figure 2. Numerical model of the piezoelectric bender and the fin (left); deformed shape of bender and the fin under air flow excitation.

A performance-based parametric analysis is conducted in order to assess the optimal values of some design and operating condition parameters, including length, width, thickness, constitutive material of the bender and velocity and turbulence intensity of the incoming airflow. The response parameters used for evaluating the performances include:
-   The bender max tip displacement;
-   The bender vibration frequency;
-   The rms of the voltage generated by the device.

Considerations are made for the harvested energy potential and possible applications in structures, infrastructures and smart buildings.

References

Abdelkefi, A., Nayfeh, A.H., Hajj, M.R., 2012. Design of piezoaeroelastic energy harvesters. Nonlinear Dynamics 68 (4), 519-530.

Adams, W.M. (2006). The Future of Sustainability: Re-thinking Environment and Development in the Twenty-first Century. Report of the IUCN Renowned Thinkers Meeting, 29-3.

ANSYS (2011). ANSYS FLUENT Theory Guide. Release 14.0. ANSYS, Inc.

De Miranda, S., Garikipati, K., Molari, L. and Ubertini, F. (2009). A simple solution strategy for coupled piezo-diffusion in elastic solids. Computational Mechanics, **44**, 191-203.

Doaré, O., Michelin, S., 2011. Piezoelectric coupling in energy-harvesting fluttering flexible plates: linear stability analysis and conversion efficiency. Journal of Fluids and Structures 27 (8), 1357-1375.

Ehrenfeld, J.R. (2008). *Sustainability by Design: A Subversive Strategy for Transforming Our Consumer Culture*. Yale University Press.

Erturk, A. and Inman, D.J. (2008). Issues in mathematical modeling of piezoelectric energy harvesters. Smart Materials and Structures, **17**, 14pp.

Gkoumas, K. (2012). Energy harvesting in bridges and transportation infrastructure networks: state of art, recent trends and future developments. *IABMAS 2012 - The 6th International Conference on Bridge Maintenance, Safety and Management, July 8-12, Stresa, Lake Maggiore, Italy*.

Kwon, S.-D., Lee, H., Lee, S., Wind energy harvesting from flutter. In: Proceedings of the 13th International Conference on Wind Engineering (ICWE-13), Amsterdam, NL, July 10-15, 2011, paper No. 071 (CD-ROM).

Park, G., Rosing, T., Todd, M.D., Farrar, C.R. and Hodgkiss, W. (2008). Energy Harvesting for Structural Health Monitoring Sensor Networks. ASCE Journal of Infrastructure Systems, **14**(1), 64-79.

Priya, S., Inman, D.J., 2009. Energy harvesting technologies. Springer Science, New York, NY, USA.

Rose, A. (2011). Resilience and sustainability in the face of disasters. Environmental Innovation and Societal Transitions, **1**, 96-100.

SEAOC. (1995). Vision 2000 - A Framework For Performance Based Design. Volumes I, II, III. Structural Engineers Association of California, Vision 2000 Committee.

Spekkink, D. (2005). Performance based design: bringing Vitruvius up to date, PeBBu Domain 3 Report, Rotterdam, 52 pp.

Spencer, B.F. Jr. and Cho., S. (2011). Wireless Smart Sensor Technology for Monitoring Civil Infrastructure: Technological Developments and Full-scale Applications. *The 2011 World Congress on Advances in Structural Engineering and Mechanics (ASEM'11+), September 18-22, Seoul, Korea*.

Srinivasan, A.V. and McFarland., D.M. (2001). *Smart Structures*. Cambridge University Press.

Tang, L., Païdoussis, M.P., Jiang, J., 2009. Cantilevered flexible plates in axial flow: Energy transfer and the concept of flutter-mill. Journal of Sound and Vibration 326 (1-2), 263-276

Weinstein, L.A., Cacan, M.R., So, P.M. and Wright, P.K. (2012). Vortex shedding induced energy harvesting from piezoelectric materials in heating, ventilation and air conditioning flows. Smart Materials and Structures, **21**(4), 10pp.

Building occupants' comfort assessment in the PBWE framework

Francesco Petrini, Pierluigi Olmati and FrancoBontempi

Department of Structural and Geotechnical Engineering, Sapienza University of Rome, Italy
Corresponding author: Francesco Petrini, francesco.petrini@uniroma1.it

Abstract

This research deals with the problem of the comfort assessment of high-rise building occupants under wind action. Also if the problem has been studied by the researchers and by the civil engineering industry during last thirty years, appropriate methods to handling the design of high-rise buildings in order to avoid wind-induced occupant discomfort has not been defined yet, mainly due to the high uncertainties involved in the determination of both the demand and the sensitivity of the building occupants to wind-induced vibrations. The main issues related with this problem are first summarized, then the growing, pioneering performance-based wind engineering (PBWE) approach is proposed as tool to handle the problem. The required analyses are presented and discussed on both the conceptual and operational point of view. A case-study is then presented in order to demonstrate the effectiveness of the proposed approach. In the PBWE view, the contribution of the work is focused on the procedural step identified as "damage analysis", something that, in authors' knowledge, has not been yet developed in the literature.

1 Introduction

Performance-Based Wind Engineering (PBWE) is a new branch of performance-based engineering gaining interest in the last years (Ciampoli et al. 2011, Spence and Gioffrè 2012, Pozzuoli et al. 2013). As defined in Ciampoli et al. (2011), the central objective is the assessment of the adequacy of the structure through the probabilistic description of a set of Decision Variables (DVs). Each decision variable is a measurable attribute that represents a specific structural performance, which can be defined in terms of the interest of the users or the society. The problem of risk assessment is addressed by means of the resolution of the integral shown in Eq. (1). Thus, the risk is disaggregated into different elements: site and structure-specific hazard analysis; structural characterization; interaction analysis; structural analysis; damage analysis; and loss analysis.

$$G(\text{DV}) = \iiiint G(\text{DV}|\text{DM}) \cdot f(\text{DM}|\text{EDP}) \cdot f(\text{EDP}|\text{IM,IP,SP}) \cdot f(\text{IP}|\text{IM,SP}) \cdot f(\text{IM}) \cdot f(\text{SP})$$
$$\cdot \, d\text{DM} \cdot d\text{EDP} \cdot d\text{IM} \cdot d\text{IP} \cdot d\text{SP} \tag{1}$$

In Eq. (1), $G(\bullet)$ is the complementary cumulative distribution function and $G(\bullet|\bullet)$ the conditional complementary cumulative distribution function; $f(\bullet)$ is the probability density function, and $f(\bullet|\bullet)$ the conditional probability density function; DM is a proper damage measure; EDP is an engineering demand parameter; the basic parameters characterizing the Aeolian hazard, the interaction phenomena and the structural systems and non-environmental actions are described respectively to IM, IP and SP. In Equation 1, IM and SP are assumed as uncorrelated and independent on IP, while IP is dependent on both IM and SP. The flowchart of the PBWE is shown in Figure 1.

Considering the last two risk assessment elements (damage and loss analysis), even though there is a great deal of literature on Performance-Based Design (PBD) in earthquake engineering, but also, for example, in hurricane engineering, these elements have not been investigated thoroughly in the PBWE for non-hurricane winds. Especially with regard to the comfort assessment of high-rise buildings under wind, additional research efforts are needed in order to complete the PBWE procedure.
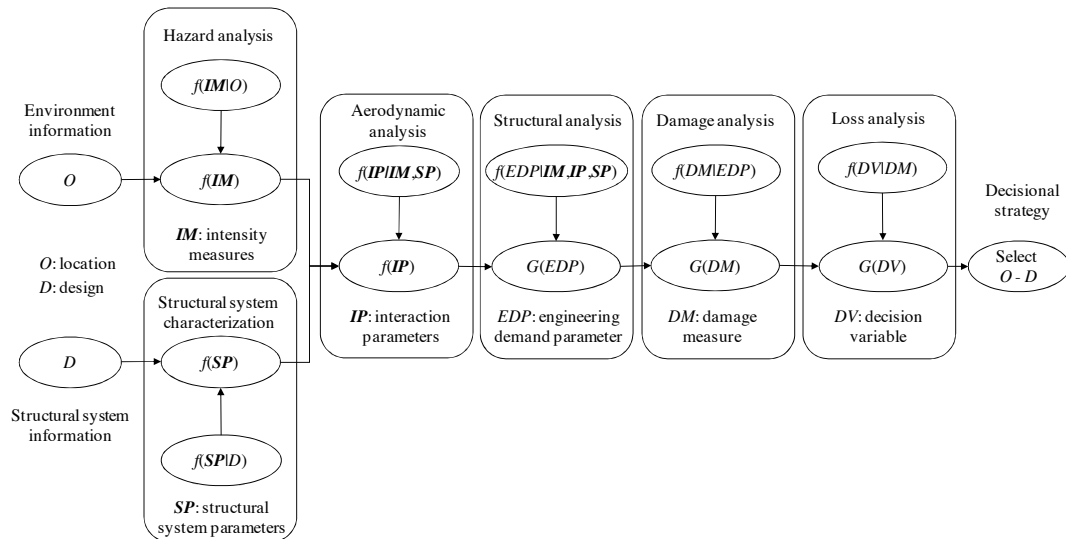
Figure 1. Flowchart of the PBWE procedure

In a first step, that in the PBWE framework can be identified as damage analysis, appropriate criteria need to be defined in order to characterize the uncertainty affecting the response thresholds assumed for the evaluation of the serviceability levels. This is particularly difficult in the evaluation of the building residents comfort (Bashor et al. 2005). In addition, in conducting the loss analysis, the monetary quantification of the loss of serviceability is required. In the authors' knowledge this aspect is, at the moment, poorly treated in literature on tall building serviceability under wind action.

2   Case study building

The damage analysis is carried out considering the results obtained by Ciampoli and Petrini (2012). The peak accelerations (the engineering demand parameter for the serviceability) are provided for a case-study tall building, and two structural configurations of the case-study tall building are considered: i) the original design and ii) the modified design by a Tuned Mass Damper (TMD).

The case-study building (Fig. 2) has a square plan, the side is 50 m long and the total height is 305 m; the number of floors is 74. The structural system is composed by both a central core (a 3D frame with 16 columns) and a 3D frame (composed by 28 columns) on the external perimeter. The two substructures are connected at three levels (at 100 m, 200 m and 300 m) by stiffening systems extended for 3 or 2 floors. The columns have a hollow square section, with dimensions and thickness varying with the height (between 1.20 m and 0.50 m, and 0.06 m and 0.025 m respectively). The beams are double-T steel beams and the beam-column joints are considered as being rigid in the structural model. The bracing system is composed by hollow square struts. Figure 2 shows both the finite element model and the three subsystems of the case-study tall building.

In Ciampoli and Petrini (2012) the model of the wind actions is calibrated on the basis of experimental results consisting in the time series of the global floor forces available by tests on a 1:500 scale rigid model. These tests have been carried out at the Boundary Layer Wind Tunnel of CRIACIV (Inter-University Research Centre on Buildings Aerodynamics and Wind Engineering) in Prato, Italy.

By the mentioned experimental test it was been assessed that the energy content of the global force spectra for various directions of the wind velocity increases due to the vortex shedding generated at the sharp edges of the building. By the analytical model of the lift force spectrum in across-wind direction this phenomenon is taken into account summing up an ad-hoc triangular function
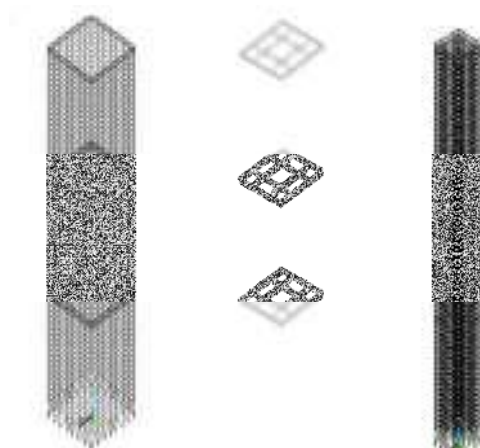
Figure 2: Finite element model of the structural system: the 3D frame on the external perimeter (left), the bracing system (central), the central core (right)

Figure 3 summarizes the response of the building to different wind intensities (represented by the 10-mins mean wind velocity at ten meters height V_{10}) in terms of the peak acceleration both in the original and modified design configuration. The study on the damage analysis about the serviceability takes place by the results of Figure 3.
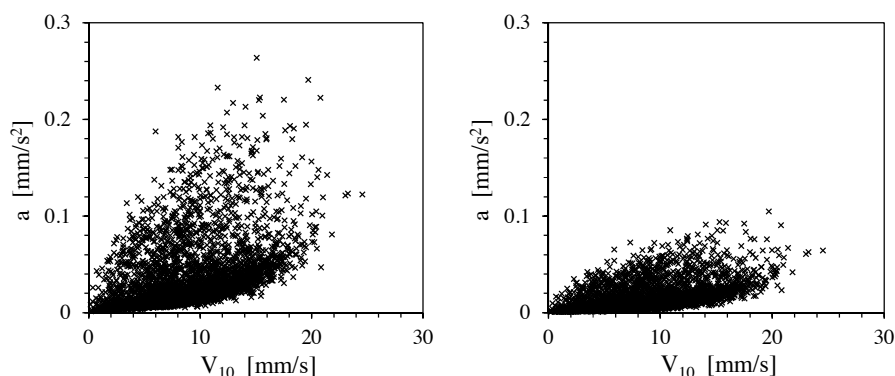
Figure 3. Samples of the peak acceleration (Monte Carlo simulation: 5000 runs) as a function of V10 provided by Petrini and Ciampoli (2012). Original design (left), modified design (right)

Three probability density functions are considered for fitting the peak acceleration samples shown in Figure 3: the linear piecewise (kernel probability density function in Matlab®), the log-normal, and the Wald probability density function. The probability of exceeding the defined serviceability limit states is computed by these three density functions and for the original and modified design of the case-study tall building. The damage analysis consists in the definition of the fragility in terms of damage measure, namely $G(DM \geq DM^*|EDP)$, being DM^* a threshold value for DM. In this case the fragility can be specialized as $G(N_P \geq n_p|a)$, where N_p is the number of people perceiving the motion (in percentage with respect to the total building users), and n_p is an acceptable number of people perceiving the motion (then identifying a limit state).

For computing the $G(N_P \geq n_p|a)$ the results of several experimental tests as taken from the literature are considered. Each of these results is given by a number of curves representing the motion perception threshold (in terms of floor acceleration a) as a function of the fundamental natural frequency of the building. Each curve is associated with a value of N_p, and it can be assumed as the determinist threshold of the acceleration for which N_p people perceive the motion. Here, in order to model the uncertainties affecting these threshold values, N_p is assumed as a stochastic variable having a lognormal distribution, the dispersion and the mean value of this distribution are evaluated, as a function of the acceleration a, on the basis of the above-mentioned experimental results. Then, for a fixed a value n_p, and a fixed value of a, the fragility function can be simply evaluated as the ratio

between the number of experimental results being greater than a (for that n_p) and the total number of experimental results available in literature for that n_p (see Fig. 4). The fragility curves are shown in Figure 5 referring to the 74th floor of the building, both for the original and the modified design configurations.
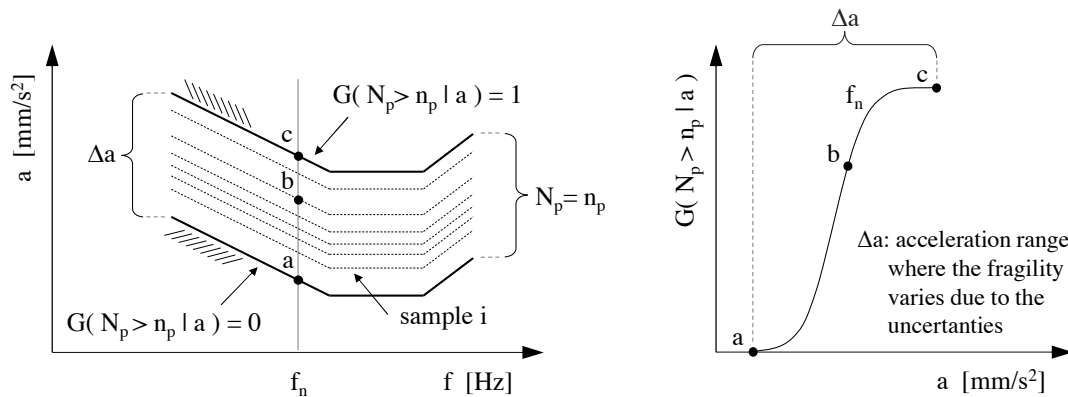
Figure 4. Extrapolation of the fragility fragility curves from experimental results available in literature. Threshold curves taken from the literature for a certain value of n_p (left), example of fragility curve (right).
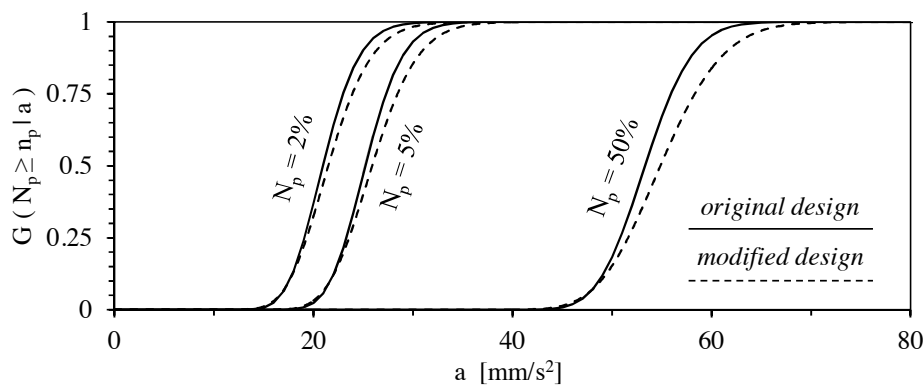
Figure 5. Fragility curves obtained from the analysis.

References

Ciampoli, M., Petrini, F. and Augusti, G. (2011). Performance-Based Wind Engineering: Towards a general procedure. *Structural Safety,* **33**(6), 367-378.

Ciampoli, M. and Petrini, F. (2012). Performance-Based Aeolian Risk assessment and reduction for tall buildings. *Probabilistic Engineering Mechanics,* **28**, 75–84.

Bashor, R., Kijewski-Correa, T., and Kareem A. (2005). On the wind-induced response of tall buildings: the effect of uncertainties in dynamic properties and human comfort thresholds. *Proceedings of Americas Conference on Wind Engineering*, Baton Rouge, LA, Vol. 31, 2005.

Pozzuoli, C., Bartoli, G., Peil, U., Clobes, M. (2013). Serviceability wind risk assessment of tall buildings including aeroelastic effects. *Journal of Wind Engineering and Industial Aerodynamic,* **123**, 325–338.

Spence, S.M.J., Gioffrè, M. (2012). Large scale reliability-based design optimization of wind excited tall buildings. *Probabilistic Engineering Mechanics,* **28**, 206-215.

Experimental characterization of wind turbine wakes: wind LiDAR measurements and wind tunnel tests

Giacomo Valerio Iungo, Francesco Viola and Fernando Porté-Agel

Wind Engineering and Renewable Energy Laboratory (WIRE),
École Polytechnique Fédérale de Lausanne (EPFL), Lausanne, Switzerland
Corresponding author: F. Porté-Agel, fernando.porte-agel@epfl.ch

Abstract

Wind energy is growing in popularity and becoming one of the most profitable renewable energy source. Consequently, optimized and improved wind turbines and wind farms are needed, which require a better characterization of their interaction with the atmospheric boundary layer (ABL) flow. Of particular interest it is also the mutual interaction of wind turbine wakes within wind farms, which is responsible for reduction in power harvesting and increase in fatigue loads for waked wind turbines (see e.g. Barthelmie et al., 2010). Moreover, downstream evolution and recovery of wind turbine wakes are strongly affected by atmospheric conditions, and in particular by the ABL thermal stability (Baker and Walker, 1984; Zhang et al., 2013; Iungo and Porté-Agel, 2014).

Wind turbine wake flows have been investigated via computational fluid dynamics (CFD) techniques, with different degrees of complexity and accuracy. Early CFD tools have adopted the Reynolds-averaged NavierStokes (RANS) approach, in which the mean flow is computed and the effects of the turbulence are parameterized using closure models (Sørensen et al., 2002; Gomez-Elvira et al., 2005). More recently, large eddy simulation (LES) frameworks have also been developed for wind energy applications (Jimenez et al., 2008; Calaf et al., 2010; Lu and Porté-Agel, 2010; Porté-Agel et al., 2011; Wu and Porté-Agel, 2011).

The above-mentioned numerical models need a significant amount of experimental data for their assessment and optimization. Experimental research in wind energy consists mainly in wind tunnel tests and field measurements. Wind tunnel investigations present the advantage of reproducing a broad range of well characterized wind conditions. However, the used downscaled models represent a strong limitation, especially for the near wake where geometrical details of the models might produce significant discrepancies with respect to real wind turbine wake flows. On the other hand, field measurements of the wake produced by real wind turbines still represent a challenge for the available measurement techniques, which is mainly due to the large measurement volumes connected with a wind turbine wake, and the varying wind conditions. In this paper, wind tunnel measurements of downscaled wind turbine models are presented together with wind velocity measurements of the wake produced from a 2-MW Enercon E-70 wind turbine, which were performed with the Doppler wind Light Detection and Ranging (LiDAR) measurement technique.

Velocity measurements of the wake produced by downscaled wind turbine models were performed in the boundary layer wind tunnel of the Wind Engineering and Renewable Energy Laboratory (WIRE) of the École Polytechnique Fédérale de Lausanne (EPFL), Switzerland. The used wind turbine model is a three-bladed GWS/EP-6030x3 anticlockwise, which was mounted on a vertical support in order to place the turbine outside the boundary layer. The uniform oncoming flow had a mean velocity, U_{hub}, of 5.8 m/s and a turbulence intensity of 7%. Measurements of the three velocity components were performed with a customized fast-response four-hole pressure probe. Wake measurements were also performed with hot-wire anemometers, both single-component or cross-wire probes.

The velocity field of the wind turbine wake obtained via wind tunnel measurements is presented in Figure 1. The axial velocity component is characterized by a significant velocity deficit at the wake location, which gradually recovers to the incoming wind velocity, U_{hub}, by moving downstream (Figure 1a). The wake recovery, which is strongly affected by the performance of the turbine and turbulence characteristics of the oncoming wind, is an essential feature for the estimation of the turbine separation distance within a wind farm. In Figure 1b significant peaks of the azimuthal velocity are detected for radial positions $r/d \approx 0.15$, which are connected to the rotational velocity induced by a vorticity structure mainly oriented along the streamwise direction, referred to as hub vortex. The azimuthal velocity induced by the hub vortex rapidly reduces by moving downstream, and the hub vortex can be considered as completely diffused for downstream distances larger than $4d$. Secondary peaks of the azimuthal velocity are also observed for radial positions $r/d \approx 0.5$, which are connected with the presence of the helicoidal tip vortices. The axial normal stress, which is plotted in Figure 1c, has an enhanced intensity in the near-wake,
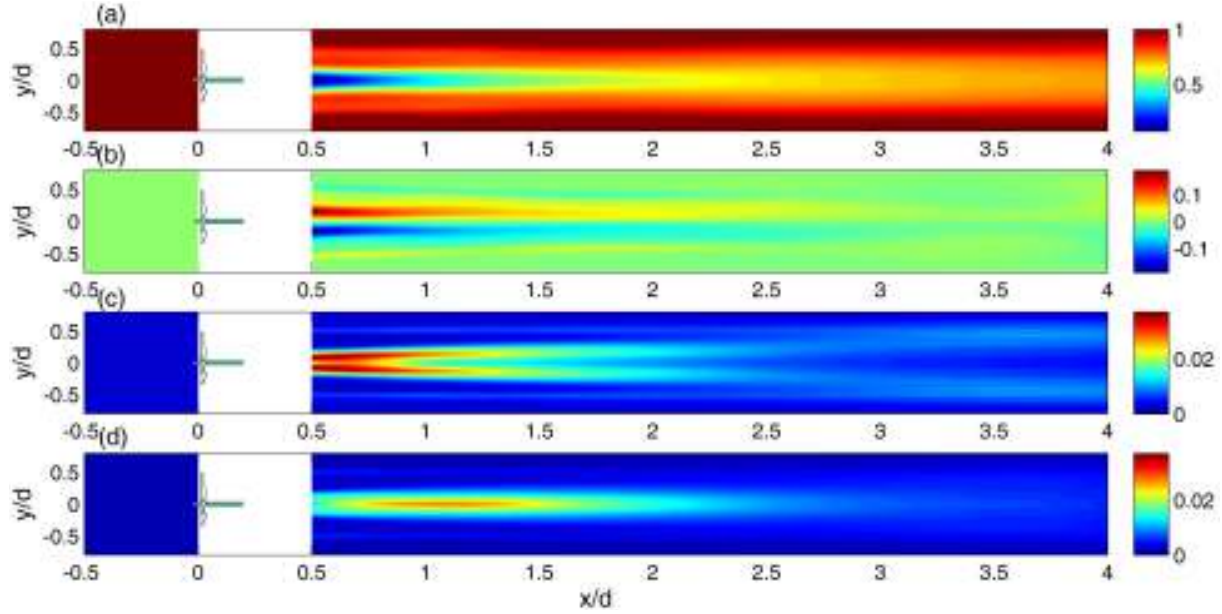
Figure 1. Wind tunnel velocity measurements of the wind turbine wake: (a) non-dimensional axial velocity, U/U_{hub}; (b) non-dimensional azimuthal velocity, V_θ/U_{hub}; (c) non-dimensional variance of the axial velocity, $\overline{(U-\overline{U})^2}/U_{hub}^2$; (d) non-dimensional variance of the azimuthal velocity, $\overline{(V_\theta-\overline{V_\theta})^2}/U_{hub}^2$.

which represents the mechanically produced turbulence due to the presence of the wake axial velocity deficit. This wake turbulent energy gradually dissipates by moving downstream, while the wake diffuses and increases its transversal width. Moreover, velocity fluctuations associated with the helicoidal tip vortices are also detected from the axial normal stress for the locations $r/d \approx 0.5$. Tip vortices diffuse by moving downstream, and for this particular experiment they start interacting with the wake core at a downstream distance of $x/d \approx 3$.

Differently, the normal stress connected with the azimuthal velocity component gradually increases by moving downstream up to $x/d \approx 1$, then it reduces further downstream. This feature indicates that the velocity fluctuations connected with the wake swirl induced by the hub vortex are not related to its turbulent diffusion. Moreover, spectral analysis of the velocity signals shows not only the presence of the spectral component connected to the helicoidal tip vortices, but also the presence of a low frequency contribution equal to about 0.34 times the hub rotational frequency. Summarizing, the analysis of the velocity field of the wind turbine wake indicates the presence of an instability of the hub vortex. Therefore, temporal and spatial linear stability analyses were performed on a base flow obtained from the time-averaged wind tunnel velocity measurements. This study shows that the low-frequency spectral component detected experimentally matches the most amplified frequency of the counter-winding single-helix mode downstream of the wind turbine, which is spatially reconstructed as shown in Figure 2 (see Iungo et al., 2013b for more details). Furthermore, simultaneous hot-wire measurements confirm the presence of a helicoidal unstable mode of the hub vortex with a streamwise wavenumber roughly equal to that predicted from the linear stability analysis. Further temporal and spatial stability analyses were also performed by taking into account the Reynolds stresses by means of turbulence eddy viscosity models, which are calibrated on the wind tunnel data. This new formulation for stability analysis allows a univocal detection of the hub-vortex instability as the most unstable mode with the largest growth rate, and the prediction of its connected instability frequency.

Besides wind tunnel tests, the wake flow produced by a 2 MW Enercon E-70 wind turbine was characterized under different atmospheric conditions via velocity measurements performed with three scanning Doppler wind LiDARs. One LiDAR was typically devoted to the characterization of the incoming wind, in particular mean wind velocity, shear and turbulence intensity at the height of the rotor disc. The other two LiDARs performed different types of scans in order to characterize the wake velocity field produced by the tested wind turbine.

Doppler wind LiDARs are laser-based instruments that allow the measurement of the wind velocity component in the laser beam direction, which is denoted as radial velocity or line-of-sight (LOS) velocity. This remote sensing technique consists in the emission of a laser beam into the atmosphere, which is back-scattered due to the presence of aerosol in the ABL. The radial wind velocity is then measured through the evaluation of the Doppler frequency shift on the back-scattered laser beam. Consequently, different LiDAR measurement techniques with different levels of complexity can be designed in order to perform 2-D and 3-D characterizations of the mean
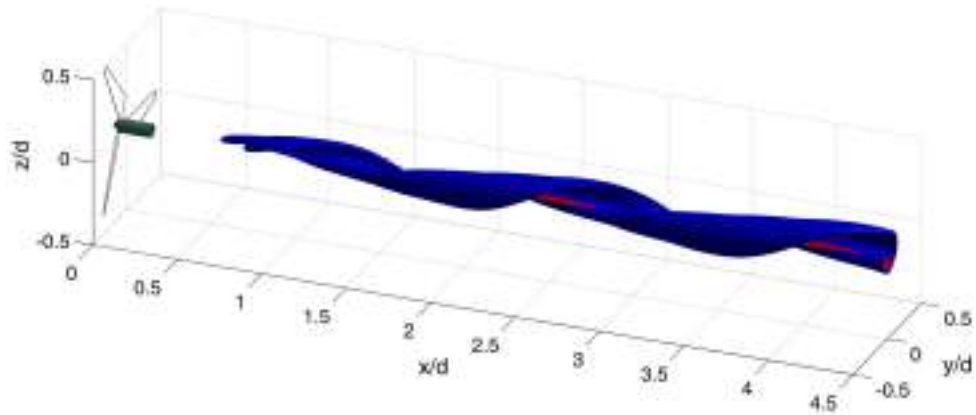
Figure 2. Spatial reconstruction of the counter-winding single-helix instability mode of the hub vortex present in a wind turbine wake. Iso-surface of the axial vorticity.

wake velocity field. However, larger measurement volumes and higher spatial resolution require longer sampling periods; thus, to investigate wake turbulence tests were also performed by staring the LiDAR laser beam over fixed directions and with the maximum sampling frequency. More details about LiDAR measurement procedures for the characterization of wind turbine wakes can be found in Iungo and Porté-Agel, 2013; Iungo et al., 2013a; Carbajo-Fuertes et al., 2014.

This study is mainly focused on a particular LiDAR measurement technique for the characterization of wind turbine wake flows, i.e. volumetric scans performed with two simultaneous LiDARs. For these tests two LiDARs were deployed at a downstream distance of $12d$. The measurements were carried out by varying both elevation and azimuthal angles of the LiDAR laser beams, in particular the azimuthal angle within a range of $20°$, centred with the wind turbine hub and with angular steps of $2°$, while the elevation angle was varied from $2°$ up to $16°$ with an angular step of $2°$. In order to reduce the sampling period required for each volumetric scan, measurements were performed simultaneously with two LiDARs, and each LiDAR measured over half measurement volume. A typical wake velocity field measured through a volumetric scan is reported in Figure 3, where transversal planes are reported for different downstream locations allowing the characterization of the wake morphology.

For the wake velocity fields obtained from each volumetric scan, the minimum wake velocity deficit was evaluated as a function of the downstream distance from the turbine, then fitted through a power law. This analysis shows that the ABL thermal stability has a significant effect on the wake evolution; in particular the wind turbine wake recovers faster under convective conditions, compared with the neutral ones. This enhanced wake recovery rate is
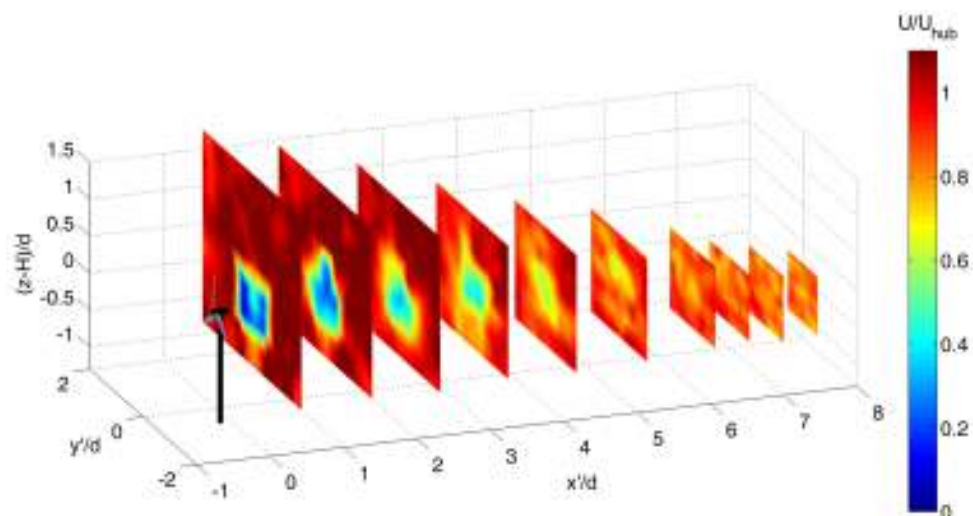
Figure 3. Velocity field obtained through a LiDAR volumetric scan. Transversal planes at different downstream locations ($x/d = 0.6; 1; 2; 3; 4; 5; 6; 7; 7.6; 8$).

likely related to increased turbulence levels within the ABL surface layer, which promote ABL flow entrainment into the wake. This noticeable effect of ABL stability on the downstream evolution of wind turbine wakes should be definitely considered for improved wake models, which are essential for numerical simulations of wind turbine wake flows, and for prediction of wind power harvesting. A good comprehension of the variability of wind turbine wakes under different ABL regimes is also crucial for the evaluation of the environmental impact of wind turbine wakes on the local micro-climate. Overall, the field wake measurements presented here provide a valuable dataset for the improvement and validation of numerical models (e.g., analytical models and large-eddy simulations) of wind turbine wakes.

References

Baker, R.W and Walker, S.N. (1984). Wake measurements behind a large horizontal axis wind turbine generator. *Solar Energy* **33**, pp. 5–12.

Barthelmie, R. J., Pryor, S. C., Frandsen, S. T., Hansen, K. S., Schepers, J. G., Rados, K., Schlez, W., Neubert, A., Jensen, L. E., and Neckelmann, S. (2010). Quantifying the impact of wind turbine wakes on power output at offshore wind farms. *J. Atmos. Ocean. Tech.* **27**.8, pp. 1302–1317.

Calaf, M., Meneveau, C., and Meyers, J. (2010). Large eddy simulation study of fully developed wind-turbine array boundary layers. *Physics of Fluids* **22**.1, p. 015110.

Carbajo-Fuertes, F., Iungo, G. V., and Porté-Agel, F. (2014). 3D turbulence measurements using three intersecting Doppler LiDARs: validation against sonic anemometers. Submitted to J. Atmos. Ocean. Tech.

Gomez-Elvira, R., Crespo, A., Migoya, E., Manuel, F., and Hernandez, J. (2005). Anisotropy of turbulence in wind turbine wakes. *J. Wind Eng. Industr. Aerodyn.* **93**.10, pp. 797–814.

Iungo, G. V. and Porté-Agel, F. (2013). Measurement procedures for characterization of wind turbine wakes with scanning Doppler wind LiDARs. *Adv. Sci. Res.* **10**, pp. 71–75.

— (2014). Volumetric LiDAR scanning of wind-turbine wakes under different atmospheric conditions. Submitted to J. Atmos. Ocean. Tech.

Iungo, G. V., Wu, Y-T., and Porté-Agel, F. (2013a). Field measurements of wind turbine wakes with LiDARs. *J. Atmos. Oceanic Technol.* **30**, pp. 274–287.

Iungo, G. V., Viola, F., Camarri, S., Porté-Agel, F., and Gallaire, F. (2013b). Linear stability analysis of wind turbine wakes performed on wind tunnel measurements. *J. Fluid Mech.* **737**, pp. 499–526.

Jimenez, A., Crespo, A., Migoya, E., and Garcia, J. (2008). Large-eddy simulation of spectral coherence in a wind turbine wake. *Environ. Res. Letters* **3**.1, p. 015004.

Lu, H. and Porté-Agel, F. (2010). A modulated gradient model for large-eddy simulation: application to a neutral atmospheric boundary layer. *Physics of Fluids* **22**.1, p. 015109.

Porté-Agel, F., Wu, Y-T., Lu, H., and Conzemius, R.J. (2011). Large-eddy simulation of atmospheric boundary layer flow through wind turbines and wind farms. *J. Wind Eng. Ind. Aerodyn.* **99**.4, pp. 154–168.

Sørensen, J. N., Michelsen, J. A., and Schreck, S. (2002). Navier-Stokes predictions of the NREL phase VI rotor in the NASA Ames 80 ft x 120 ft wind tunnel. *Wind Energy* **5**, pp. 151–169.

Wu, Y-T. and Porté-Agel, F. (2011). Large-eddy simulation of wind-turbine wakes: evaluation of turbine parametrisations. *Boundary-Layer Meteor.* **138**.3, pp. 345–366.

Zhang, W., Markfort, C. D., and Porté-Agel, F. (2013). Wind-turbine wakes in a convective boundary layer: a wind-tunnel study. *Bound. Layer Meteorol.* **146**, pp. 161–179.

Wind farm operation on complex terrains: numerical and experimental analysis

Francesco Castellani[1], Massimiliano Burlando[2], Davide Astolfi[1] and Ludovico Terzi[3]

[1]Department of Engineering, University of Perugia, Italy
[2]Department of Civil Engineering, University of Genoa, Italy
[3]Sorgenia Green s.r.l., Italy
Corresponding author: Francesco Castellani, francesco.castellani@unipg.it

Abstract

Wind farm operation in very complex terrains generally involves complicated and severe environment for the turbines. Strong speedups, extreme wind veer and high turbulence create a harsh framework for turbine safety and durability.

A detailed analysis of the wind field can be very useful in order to isolate the most dangerous conditions and prevent exceptional loads.

In the present work a very complex terrain wind farm site has been investigated through numerical calculations and experimental data analysis. The wind field induced by the complex orography has been calculated with two different numerical approaches: CFD (Computational Fluid Dynamics) and mass consistent modeling. Results have been compared and validated with experimental measurements from anemometer met-masts and from the wind farm SCADA (Supervisory Control And Data Acquisition) database. The analysis demonstrates that wind field models can give very useful information on rotor misalignment and on the overall park performance.

1 Introduction

Knowledge of wind field features can be fundamental to understand the complex behavior of a wind farm operating in very complex terrains. This is particularly important when severe climate conditions (such as icing and lighting) and difficult accessibility can also affect wind farm reliability; in such situations the effects of wind flow singularities induced by high slopes (Castellani and Franceschini, 2005) on the actual production can be difficult to discern. A deep analysis of the actual performance of a wind farm operating in complex terrain should consider the main drivers of the physics interactions between the main wind field (Makridis and Chick, 2013) and the wind farm such as the wakes evolution, the evolution of turbulence or the wind direction spatial variation driven by ridges and valley. The numerical study of such a complex flow is a challenge and not always meets the need of the wind farm operator to understand the overall park behaviour in a straight way. Due to the site characteristics the analysis was focused on the terrain effect on the undisturbed wind flow.

2 The wind farm under investigation

The wind farm under investigation is placed in Southern Italy on a very complex terrain area; on site 17 aerogenerators are installed, each producing a rated power of 2.3 MW at around 12 m/s with a rotor diameter of 93 m and a hub height of 80 m. The terrain is quite awkward, with very high slopes (up to 60%) close to the turbines; also the layout is complex and large, resulting in non trivial combination effects of complex wind flow and wake interactions. The main wind directions according to the reference met-mast (Fig. 1-b) are $30\,°$, $240\,°$, and $270\,°$; the overall topography of the site is characterized by three ridges with different orientation so that very strong variations in wind intensity and directions can be observed. The site is also characterised by significant icing and lighting effects. Prior the installation of the turbines site assessment was done using met-mast measurements; an anemometer is still operating as
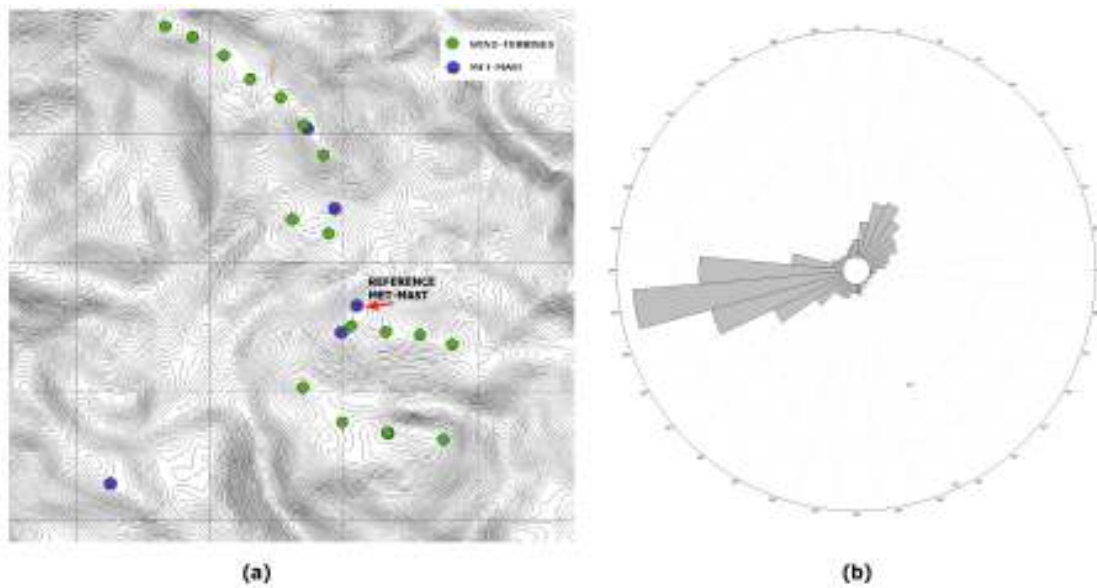
Figure 1. (a) - The wind farm layout (green circles), met-masts (blue circles) and topography (contour lines) - (b) The wind rose at hub height (b)

a reference measurement in the center of the layout collecting wind speed and directions at hub height level.

3   The numerical analysis

The numerical analysis was implemented using two different models: a CFD (Computational Fluid Dynamics) model and a mass-consistent model. For CFD simulation the Windsim (Moreno et al., 2003) numerical tools were used: this code is based on the numerical core PHOENICS, which solves the Reynolds Averaged Navier-Stokes (RANS) equations on a Cartesian grid; different solvers can be used but in the present work the General Collocated Velocity method (GCV) was preferred due to its capability to reach convergence even with uneven grid architectures. The simulations with the mass-consistent model have been performed by means of the numerical code WINDS (Burlando et al., 2005; Burlando et al., 2007), developed at the University of Genoa (Ratto et al., 1990). It reconstructs the three-dimensional wind field by means of a two-step procedure: firstly, a three-dimensional "first guess" wind field is obtained through the interpolation/extrapolation of measurements or BPL parametrisation. Then the interpolated field is adjusted by the minimum possible number of modifications in order to obtain the "final" three-dimensional wind field such that the mass is conserved locally everywhere within the entire domain. Both Windsim and WINDS simulations have been performed with the same geometric conditions in terms of topography (see the contour map in Figure 1a) and terrain roughness length (not constant within the domain). The volume of the three-dimensional computational domain, which is about 6.5 km X 4.1 km in longitude and latitude, respectively, and slightly more than 3 km in the vertical, has been discretized with a Cartesian grid for the horizontal directions with constant spacing of 23 m and with 30 unevenly-spaced conformal coordinates along the vertical axis. The volume is described by terrain-following surfaces, close to the topographic surface, and flat surfaces at the top of the computational domain. Table 1 reports some details concerning the extension and the discretization of the computational domain.

The inlet boundary condition is also the same for both models. It is assumed to be a logarithmic profile with the wind speed growing up to 10 m/s at the top of the boundary layer, which is assumed equal to 500 m, and constant above it. Only neutral atmospheric conditions have been simulated, which are typical of stronger wind situations and more interesting for wind energy purposes.

Table 1. The computational domain

Longitude (m)	Latitude (m)	Δx (m)	Δy (m)	Colums	Rows
530491.0-536977.0	4503227.0-4507344.0	23	23	282	179

4   Results

SCADA data mining techniques are extremely fruitful for assessing wind farm performances and to investigate how wind conditions variability and farm layout affect power production (Castellani et al., 2013). Six months of SCADA measurements on 10 minutes time basis have been post processed as follows in order to check goodness of the numerical analysis: only time steps during which every turbine of the wind farm was productive have been kept. On this filtered time series, nacelle positions and wind speeds from each turbine and from the meteorological mast have been recorded. Turbine number 10 has been chosen as the references turbine because it is placed in the center of the wind farm and the near the met-mast. Figure 2 shows that the ratio of turbine wind speeds to reference turbine speed can fairly be considered independent of speed at high values of the speed itself. Therefore, only the SCADA measurements concurrent to the wind speed ranging from 6 to 15 m/s at the reference met-mast have been used for the models validation. This range has been chosen because the atmosphere, within this wind speed interval, is expected to be to a fairly good approximation in neutral conditions, which is also the regime assumed for the simulations.
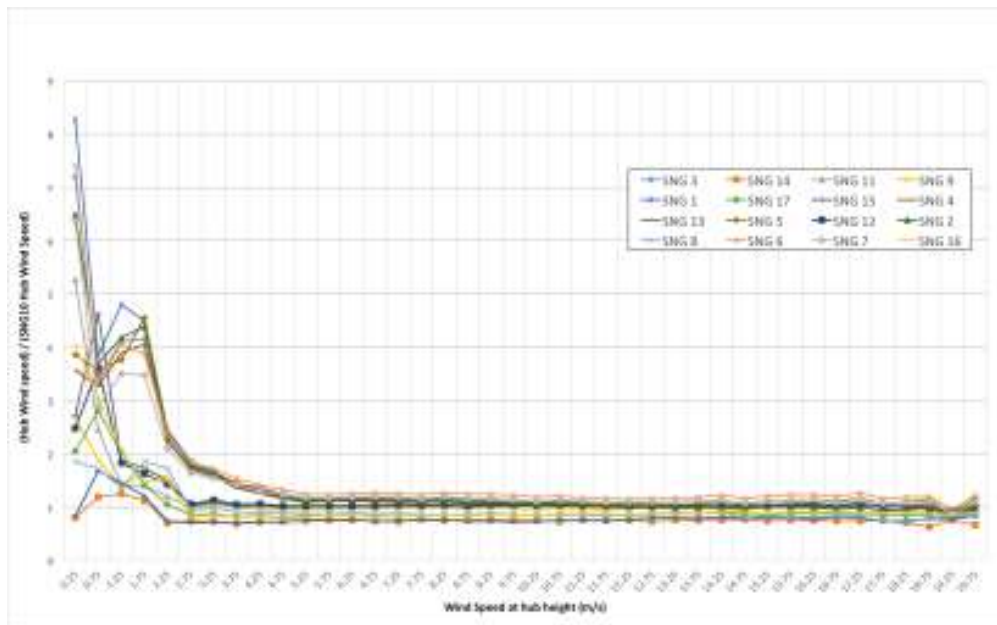
Figure 2. Variations of the wind speed ratio to the reference wind speed at hub height level.

Then, nacelle positions and wind speeds of each turbine have been stored in 12 direction sectors, centred with respect to the North, according to the measured direction of the reference met-mast. For each turbine, the speed-up ratios, η (defined as the ratio between the wind speed, simulated or measured, at the turbine with respect to the wind speed at the reference turbine) and the directional shifts $\Delta\phi$ (the difference in wind direction between reference turbine and every turbine along the farm) have been computed and averaged within each sector. The directional shift with respect to the reference turbine has been chosen as indicator of the goodness of the numerical results, since complexity of the terrain causes huge misalignment, affecting sensibly power production and rotor response to the variability of the wind direction, and makes too uncertain the prediction of single turbine nacelle position. Therefore computing the mean misalignment with respect to a reference becomes a useful indicator of the capability of turbine

to follow wind variability, and of how these effects distribute along the wind farm.

Three sectors have been chosen because mostly populated: $30°$, $240°$ and $270°$.

Eventually, for each of the three sectors, goodness of numerical simulations has been evaluated as mean percentage error between predicted and actual speed up ratios and as mean absolute error between predicted and actual directional shift with respect to the reference turbine, as in the following equations (1) and (2).

$$\epsilon_{\text{speed up}} = \frac{100}{16} \sum_i \left(1 - \frac{\eta_i^{\text{model}}}{\eta_i^{\text{actual}}} \right) \tag{1}$$

$$\epsilon_{\text{dir shift}} = \frac{1}{16} \sum_i \left| \left(\Delta\phi_i^{\text{actual}} - \Delta\phi_i^{\text{model}} \right) \right|, \tag{2}$$

where 16 is the number of wind turbines except for the reference one. Table 2 shows the errors for the two models considered. They turn out to be absolutely comparable as far as the simulation of the wind direction is concerned, whereas they both overpredict, on average, the speed-up at the turbines position. The site complexity stresses the closure of the wind field so that CFD could not give reliable results as the mass consistent model do; this demonstrates that in such complex situations mass-consistent model can give very useful and stable information despite its inability in reproducing recirculations.

Table 2. Estimated errors on the speedup ratio (%) and directional absolute shift ($°$) of the two numerical models: WindSim (WS) and Winds (WN)

Direction	WS speedup (%)	WS dir$^{(\circ)}$	WN speedup (%)	WN dir$^{(\circ)}$
30°	31.05	8.34	15.35	6.36
240°	13.27	4.61	6.37	4.19
270°	17.36	4.89	6.11	2.5

References

Burlando, M., Carassale, L., Borghesi, M.V., Tubino, F., Ratto, C.F., and Solari, G. (2005). Numerical simulation of turbulent wind fields at airports in complex terrain. *Proceedings of The Fourth European & African Conference on Wind Engineering, Praha, Czech Republic*, pp. 11–15.

Burlando, M., Carassale, L., Georgieva, E., Ratto, C.F., and Solari, G. (2007). A simple and efficient procedure for the numerical simulation of wind fields in complex terrain. *Boundary-layer meteorology* **125**.3, pp. 417–439.

Castellani, F. and Franceschini, G. (2005). A new technique to improve expected aep estimation in very complex terrain. *AIAA/ASME Wind energy symposium*.

Castellani, F., Garinei, A., Terzi, L., Astolfi, D., Moretti, M., and Lombardi, A. (2013). A new data mining approach for power performance verification of an on-shore wind farm. *DIAGNOSTYKA* **14**.4.

Makridis, A. and Chick, J. (2013). Validation of a CFD model of wind turbine wakes with terrain effects. *Journal of Wind Engineering and Industrial Aerodynamics* **123, Part A**.0, pp. 12 –29. ISSN: 0167-6105. DOI: *10.1016/j.jweia.2013.08.009*.

Moreno, P., Gravdahl, A.R., and Romero, M. (2003). Wind flow over complex terrain: application of linear and CFD models. *European Wind Energy Conference and Exhibition, Madrid*, pp. 16–19.

Ratto, C.F., Festa, R., Nicora, O., Mosiello, R., Ricci, A., Lalas, D.P., and Frumento, O.A. (1990). Wind field numerical simulations: a new user-friendly code. *1990 European Community Wind Energy Conference*, pp. 10–14.

A robust optimization framework for wind-excited cable stayed masts

Ilaria Venanzi[1], Annibale Luigi Materazzi[1] and Laura Ierimonti[1]

[1]Department of Civil and Environmental Engineering, University of Perugia, Italy
Corresponding author: Ilaria Venanzi, ilaria.venanzi@unipg.it

Abstract

Optimization methods are widely used in the design of structures in order to reduce costs and improve the structural performance. In engineering problems, where randomness of the parameters characterizing the system play an important role, stochastic optimization methods have gained an increasing importance.
This paper is concerned with the problem of optimizing the configuration of cable-stayed masts subjected to wind load, taking into account the uncertainties on the characteristics of the structure and on the wind excitation. A robust design framework is proposed, that limit the variability of the structural performance caused by parameters randomness and guarantees a prescribed safety level.

1   Introduction

All structural engineering problems are affected by uncertainties on the excitation and the parameters characterizing the system. The traditional design approach considers deterministic models and parameters and accounts for uncertainties in a simplified manner, for example through the introduction of appropriate safety factors. This can lead to non-economical solutions and cannot provide a quantitative estimation of the risk associated with the randomness of the parameters.

With the current trend of designing challenging and at the same time economical structures there is the need of using optimization methods. Among the procedures accounting for uncertainties, *robust optimization* methods look for designs which are relatively insensitive with respect to uncertain parameters changes and provide satisfactory performance of the system. Although many robustness indices are defined in the literature, in most cases the structural robustness is assessed by measures of the performance variability around the expected value, like variance or higher momentum indices (Beyer and Sendhoff, 2007). The robustness measures can be computed from the information obtained by simulation. Monte Carlo simulation is regarded as the most general simulation technique. Among the Monte Carlo-based methods, the Importance Sampling, the Latin Hypercube Sampling, the Line Sampling, and the Subset Simulation are available tools for efficient sampling.

This paper is concerned with the problem of optimizing the configuration of cable-stayed masts subjected to wind load, taking into account uncertainties on the characteristics of the structure and on the wind excitation. The need of optimizing the structural configuration of cable-stayed masts, accounting for uncertainties in the problem modeling, derives from their sensitivity to the change in modal and wind load parameters and also descends from the need of designing light structures with small environmental impact. The Authors recently started a research program on robust optimization of structural systems (Venanzi and Materazzi, 2013). The proposed optimization framework is based on the use of an enhanced Monte Carlo simulation method and the genetic algorithm. The large computational effort required by the Monte Carlo method is reduced by the use of the Latin Hypercube Sampling. The robust design procedure is capable of limiting the variability of the structural performance caused by parameters randomness and guarantees a prescribed safety level.

2   The robust optimization framework

Robust optimization (RO) is aimed at providing a solution that is relatively invariant with respect to uncertain parameters changes.

A general optimization task can be stated by the following mathematical problem:

$$
\begin{aligned}
&\text{find } \mathbf{y} \\
&\text{minimizing } F(\mathbf{y},\boldsymbol{\theta}) \\
&\text{subject to } g_i(\mathbf{y},\boldsymbol{\theta}) \leq 0 \quad i = 1,\dots I \\
&\qquad \mathbf{y}_{min} \leq \mathbf{y} \leq \mathbf{y}_{max}
\end{aligned}
\tag{1}
$$

where $\mathbf{y}$ is the vector of the design variables, $\boldsymbol{\theta}$ is the vector of the uncertain parameters, F is the objective function, g_i are the functions defining the set of inequality constraints, $\mathbf{y}_{min}$ and $\mathbf{y}_{max}$ are the lower and upper bounds of the design variables. In structural engineering problems, the constraints functions g_i can be limit state functions assuring the structural safety:

$$
g_i(\mathbf{y},\boldsymbol{\theta}) = x_i(\mathbf{y},\boldsymbol{\theta}) - LS_i
\tag{2}
$$

where x_i are the peak response functions and LS_i are the limit states.

The task of robust structural design optimization is to improve the design by minimizing the variability of the structural performance while meeting the requirements of optimum performance and constraint conditions. To achieve these goals, the robust design optimization problems is formulated as follows:

$$
\begin{aligned}
&\text{find } \mathbf{y} \\
&\text{minimizing } \left\{ p_{\mathrm{E}} \cdot \mathrm{E}\left[F(\mathbf{y},\boldsymbol{\theta}) \right] + p_\sigma \cdot \sigma\left[F(\mathbf{y},\boldsymbol{\theta}) \right] + P(\mathbf{y},\boldsymbol{\theta}) \right\} \\
&\text{subject to } G_i = \left\{ \mathrm{E}\left[g_i(\mathbf{y},\boldsymbol{\theta}) \right] + \beta_i \cdot \sigma\left[g_i(\mathbf{y},\boldsymbol{\theta}) \right] \right\} \leq 0 \quad i = 1,\dots I \\
&\qquad \mathbf{y}_{min} \leq \mathbf{y} \leq \mathbf{y}_{max}
\end{aligned}
\tag{3}
$$

where $\mathrm{E}\left[F(\mathbf{y},\boldsymbol{\theta}) \right]$ denotes the expected value of the objective function, $\sigma\left[F(\mathbf{y},\boldsymbol{\theta}) \right]$ is its standard deviation, p_{E} and p_σ are suitable weighting coefficients. P is a penalty function that is added when the constraints are violated. The constraint functions G_i are the values of the original constraint functions g_i that correspond to a prescribed probability of non exceedance and the quantity β_i is a prescribed feasibility index.

The first step of the procedure is the application of a Monte Carlo procedure for the simulation of a large number N of vectors $\boldsymbol{\theta}_j$ ($j = 1,\dots,N$) whose components follow a suitable probability distribution. In order to reduce the high computational effort inherent in the use of a crude Monte Carlo simulation technique, the Latin Hypercube Sampling (LHS) is adopted.

At each iteration of the optimization, the structural analysis is performed for the N realizations of the uncertain parameters and the probability distribution of the objective function and the constraint functions are computed. In order to assure a prescribed safety level (1-P_f) with P_f probability of failure, the values G_i are computed from the cumulative distribution functions (CDF) of the constraint functions g_i. If the inequality constraints in Eq. (3) are not satisfied, a large value is attributed to the penalty function, and the solution is automatically discarded.

In the multi-objective robust optimization problem formulated in Eq. (3), the mean value and the standard deviation of the objective function are competing between each other. Therefore, Pareto-optimal solutions are provided to show the precise trade-off information among the components of the objective function.

3   Description of the case study

3.1   Structural modelling

The problem of optimizing the structural configuration of a cable-stayed mast is considered. The height of the pole is H=33 m and the distance between the stays anchorages is d=6 m (Fig. 1). The main pole is built with a steel hollow circular cross-section, 12 mm thick, whose cross-section is constant along the height. The mast is supported by two orders of stays having diameter 2.7 cm. Without any restriction to the applicability of the procedure, a two-dimensional analysis is carried out.

In addition to the self weight and the dead load supported by the mast, the mass of the antennas, located at the top of the mast, is considered one of the uncertain parameters (see Sect. 3.3). The structural response is computed by time integration accounting for the geometric non-linearity.
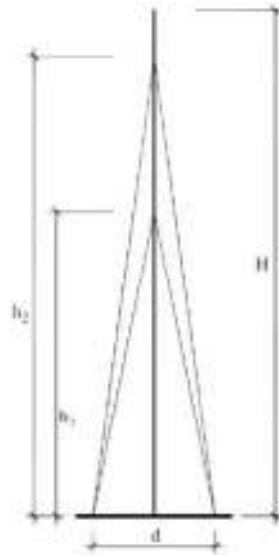
Figure 1. Geometry of the cable-stayed mast.

3.2   Wind load modelling

The reference wind speed V_r is considered one of the uncertain parameters (see Sect. 3.3). The mean wind velocity varies with the height following the logarithmic low. The simulation of the stochastic process representing the wind velocity is performed using a well known technique available in literature modeling the time-dependent unsteady component of the wind velocity as a null-mean Gaussian random process, whose probabilistic structure is completely defined by its power spectral density function. The drag coefficients C_d used to compute the wind loads are those obtained by wind tunnel tests on the same structure (Gioffrè et al., 2004). For the computation of the tributary area of each node a constant width of 0.5 m is adopted, that accounts for the size of the supported equipment.

3.3   Uncertain parameters sampling

The uncertain parameters are collected in vector $\mathbf{\theta} = \{V_r, m\}$, where V_r is the mean reference wind velocity and m is the mass corresponding to the weight of the antennas located at the top of the pole. Without loss of generality, the lognormal distribution is here adopted for all the uncertain parameters. In Table 1 are shown the mean values and the coefficients of variation of the uncertain parameters.

Table 1. Mean values and coefficients of variation of the uncertain parameters.

	Uncertain parameter	
	V_r	m
Mean value	25 m/s	100 kg
Coefficient of variation	0.01	0.3

The Monte Carlo sampling is based on the use of the Latin Hypercube Sampling (LHS) technique. To generate N samples from a random variable, its range is subdivided into N non overlapping intervals of equal probability. From each interval one value is randomly selected according to the probability density of the interval. A parametric analysis allowed setting the number N=500 of random samples.

3.4   Optimization problem

The optimization problem is expressed by Eq. (3). The design variable vector is $\mathbf{y} = \{\phi\}$, where ϕ is the pole's outer diameter. The function F in Eq. (3) is the weighted sum of the total weight of the structure W and the maximum absolute value of the top displacement of the pole δ_{max}:

$$F(\mathbf{y},\boldsymbol{\theta}) = c_W W(\mathbf{y},\boldsymbol{\theta}) + c_\delta \delta_{max}(\mathbf{y},\boldsymbol{\theta}) \tag{4}$$

The constraint functions are limit state functions, defined as follows:

$$g_1(\mathbf{y},\boldsymbol{\theta}) = \delta_{max}(\mathbf{y},\boldsymbol{\theta}) - \bar{\delta} \qquad\qquad g_2(\mathbf{y},\boldsymbol{\theta}) = \sigma_{max}(\mathbf{y},\boldsymbol{\theta}) - \bar{\sigma} \tag{5}$$

where $\bar{\delta}$ and $\bar{\sigma}$ are the allowable top displacement and internal stress, σ_{max} is the maximum absolute value of the internal stress.

The parameters of the Genetic algorithm are set on the basis of a preliminary sensitivity analysis.

Figure 2 shows the relative frequency diagrams of: a) the objective function F and b) the constraint function g_2 obtained in correspondence of the optimal value of the design variable. The dashed line in Figure 2b represents the value G_2 in Eq. (3).
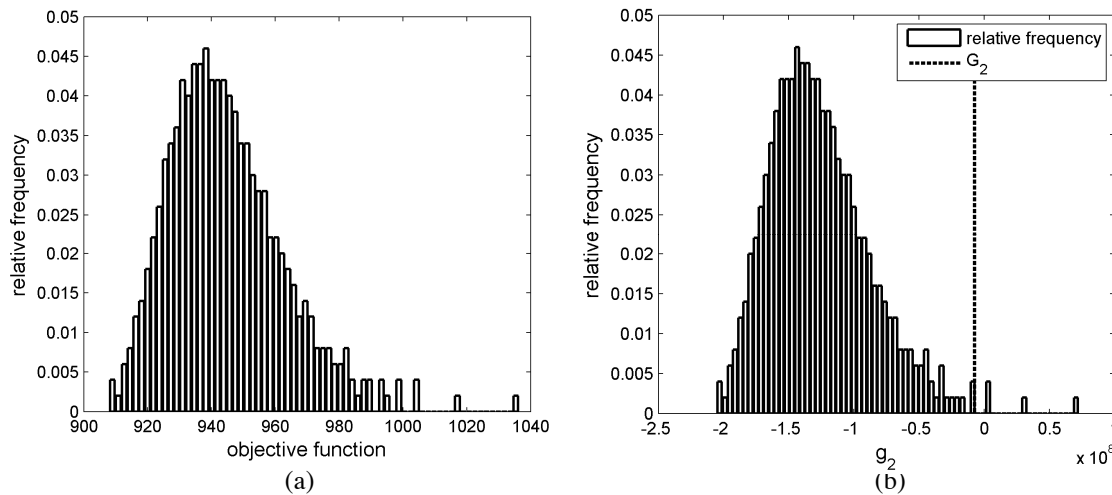
Figure 2. Relative frequency diagrams of: a) the objective function F and b) the constraint function g_2 obtained in correspondence of the optimal value of the design variable.

References

Beyer, H.G., Sendhoff, B. (2007). Robust optimization - A comprehensive survey. *Comput. Methods Appl. Mech. Engrg.*, 196:3190-3218.

Gioffrè, M., Gusella, V., Materazzi, A.L., Venanzi, I.(2004). Removable guyed mast for mobile phone networks: wind load modeling and structural response, *Journal of Wind Engineering and Industrial Aerodynamics*, 92: 463–475.

Schueller, G.I., Jensen, H.A. (2008). Computational methods in optimization considering uncertainties - An overview. *Computer Methods in Applied Mechanics and Engineering*, **198,** 2-13.

Venanzi, I., Materazzi, A.L. (2013). Robust optimization of a hybrid control system for wind-exposed tall buildings with uncertain mass distribution. *Smart Structures and Systems* **12**(6), 641-659.

Numerical and experimental investigations of wind flow around ground mounted solar panels

Chowdhury M. Jubayer[1], Horia M. Hangan[1] and Kamran Siddiqui[1]

[1]The Wind Engineering, Energy and Environment (WindEEE) Research Institute, Western University, London, Ontario, Canada

Corresponding author: Chowdhury M. Jubayer, cjubayer@uwo.ca

Abstract

We report on study conducted to investigate flow around a stand-alone ground-mounted solar panel using numerical and experimental approaches. Numerical simulations were performed using 3D unsteady Reynolds-Averaged Navier-Stokes (RANS) while Particle Image Velocimetry (PIV) technique was used to measure two-dimensional flow fields in a wind tunnel setup. A full scale model with Reynolds number of 2.1×10^6 based on the wind speed at the lower edge height of the panel and the chord length was employed in the numerical simulations whereas a 1:10 scale model with Reynolds number of 8.4×10^4 was used in the wind tunnel experiment. Four different approaching wind directions (0°, 45°, 135° and 180°) were considered in this study. Aerodynamic flow features around the solar panel were analyzed. Overall, results obtained by both numerical and experimental approaches were compared both qualitatively and quantitatively.

1 Introduction

Solar farms or photovoltaic power stations are gradually becoming a significant contributor to the electricity generation as the utility scale solar farms (capacity > 10MW) has experienced a growth of around 900% from 2009 to 2013 (Wiki-Solar.org). Solar farms consist of arrays of ground mounted solar panels in a vast open field. Despite the growing interest on solar farms, published literatures on the ground mounted solar panels are very few (Abiola-Ogedengbe, 2013; Bitsuamlak et al., 2010; Shademan and Hangan, 2010; Jubayer et al., 2012; Aly and Bitsuamlak, 2013) compared to the roof mounted solar panel study (Radu et al., 1986; Radu and Axinte, 1989; Wood et al., 2001; Kopp et al., 2002, 2012; Chung et al., 2008, 2011; Meroney and Neft, 2010; Kopp and Banks, 2013, Pratt and Kopp, 2013). Most of the studies on the ground mounted solar panel focused on the wind loading of the panel either using numerical (Bitsuamlak et al., 2010; Shademan and Hangan, 2010; Jubayer et al., 2012) or experimental (Abiola-Ogedengbe, 2013; Aly and Bitsuamlak, 2013) approach. Bitsuamlak et al. (2010) investigated the aerodynamic features of a stand-alone PV system and it was found that the pressure coefficients on the panel were underestimated by CFD when compared with full-scale experimental results. Also, when arranged in tandem, sheltering effect from the upwind panels reduced wind loads on the adjacent panels. Shademan and Hangan (2010) performed unsteady Reynolds-Averaged Navier-Stokes (URANS) simulations to measure wind loading on the ground mounted PV panels. For validation, a 2D flat plate simulation was performed and the mean pressure coefficients (C_p) values obtained at the upper windward surface of the plate for 0° wind direction were compared with Fage and Johansen (1927). A good match was found when Reynolds stress model (RSM) was used. Wind load on a ground mounted solar panel using Shear Stress Transport (SST) k-ω turbulence closure was estimated by Jubayer et al. (2012) for four different wind directions (0°, 45°, 135° and 180°). Mean pressure coefficients on the surfaces of the solar panel for all four wind directions were then validated with a surface pressure experiment performed in the Boundary Layer Wind Tunnel Laboratory (BLWTL) I at the University of Western Ontario. Kopp et al. (2012) studied wind loading on the ground mounted array to illustrate the effect of the building for the roof mounted solar panel arrays. In this study wind tunnel pressure measurements were performed in the BLWTL II at the

University of Western Ontario. The primary focus of this study was roof mounted arrays and it was found that there was a substantial difference in aerodynamics loading between ground mounted and roof mounted solar panel arrays due to the interaction of the flow with the building itself. Abiola-Ogedengbe (2013) performed pressure tests on the 1:10 scale model of a ground mounted solar panel in the BLWT I at the Western University, Canada for different inclination angles (25° and 40°) under four different wind directions (0°, 30°, 150° and 180°). 150° and 180° wind directions were found to be critical in terms of maximum lift. Particle Image Velocimetry (PIV) was also performed on the same solar panel system by Abiola-Ogedengbe (2013). However, measurements were taken only at the upstream of the solar panel for 0° wind direction .

The aforementioned literature reviews indicate that there is a clear lack of study that describes the wind flow structures as well as the underlying physics of the flow around a ground mounted solar panel. In this study, an effort has been made not only to investigate the wind flow around a ground mounted stand-alone solar panel by using unsteady Reynolds-Averaged Navier-Stokes (URANS) model as the Computational Fluid Dynamics (CFD) approach and Particle Image Velocimetry (PIV) as the experimental approach but also evaluates the performance of these two approaches by comparing results for a range of wind directions (0°, 45°, 135° and 180°).

2   Numerical Model

3D unsteady RANS simulation of wind flow over a full scale ground mounted stand-alone PV system is performed in this study. The overall dimension of the stand-alone system is 2.48 m (B) x 7.29 m (W) x 1.65 m (H) (Fig. 1) obtained from the specification provided by the manufacturer. The inclination of the panel with the horizontal is 25°. The computational domain and grid (Fig. 2) are created according to the COST guidelines (Franke et al, 2007). For four different wind directions, computational domains and grids are modified accordingly. Blockage ratio is around 2% and the total number of cells is 1.6 to 1.8 million for all four domains. At the domain inlet, velocity and turbulence intensity profiles are obtained from ESDU (ESDU 82026, 83045) for wind speed of 26 m/s at 10 m height and with aerodynamic roughness length of 0.03 m which represents open terrain. This resulted in the Reynolds number of $2.13x10^6$ based on the wind speed at the panel's lower edge height and chord length (B) of the panel. The turbulent kinetic energy profile, calculated from the ESDU velocity and turbulent intensity, is matched with Yang's profile (Yang et al, 2009) to get equilibrium atmospheric boundary layer (ABL). Equilibrium ABL, which is one of the pre-requisite for an accurate ABL simulation, means the stream-wise gradients of the flow parameters (e.g., velocity, turbulent kinetic energy (k), turbulence dissipation rate (ε) and specific turbulence dissipation rate (ω)) should be zero in an empty domain. The bottom of the domain is modeled as no-slip rough wall. Velocity and turbulence properties from the top of the inlet profile are imposed at the top of the domain. Panel and support structures surfaces are treated as no-slip smooth walls. At the outlet of the domain, zero gradient boundary condition is used. Simulation is performed using the SST k-ω turbulence model. Turbulence model constants are modified based on Menter (1994), Yang et al (2008) and Yang et al (2009) according to the nature of the flow. To check the horizontal homogeneity of the flow, simulations of wind flow inside an empty domain is performed. Figure 3 shows the inlet and incident velocity and turbulence intensity profiles obtained from the empty domain simulation which confirms equilibrium ABL is accomplished. In Figure 3, velocity and distance are normalized by the velocity at the top of the domain (U_R) and the height of the domain (y_R) respectively.
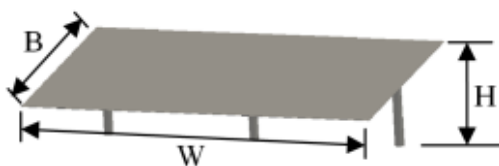
Figure 1. Schematic of the solar panel.
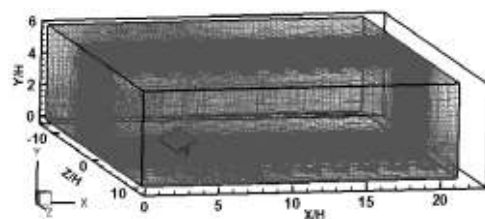
Figure 2. Computational grid.
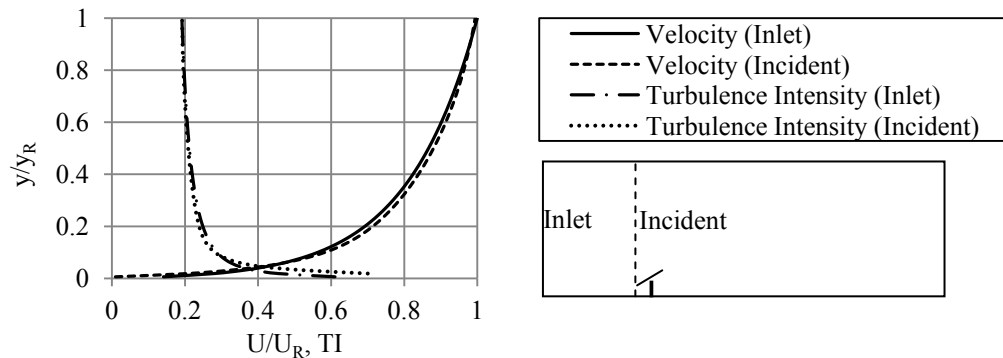
Figure 3. Inlet and incident velocity and turbulence intensity profiles.

Open source CFD toolbox OpenFOAM v2.1.0 (ESI Group) is used for the simulation. In this study pisoFoam, which is a transient solver for incompressible flows that uses PISO (Pressure -Implicit with Splitting of Operators) algorithm, is employed. Convergence criteria of 10^{-6} are employed for all variables. Linear interpolation scheme, Gauss limited linear divergence scheme and cellMD limited Gauss linear gradient scheme are used for discretizations. Time step size of 10^{-5} s is employed. Simulations are run for a total of 20 s of flow time and average of last 15 s is taken to analyze results. During the simulation the flow reaches steady state after around 5 s of flow time based on the panel surface pressures. Hence, averaging of last 15s of flow time should provide enough data to compute the results. Simulations are performed over the SHARCNET (Shared Hierarchical Academic Research Computing Network, www.sharcnet.ca) cluster using 128 processors. Each simulation takes approximately 300 hours of elapsed real time to converge on this cluster.

3   Experimental Method

The experiment was performed at the BLWTL I at the University of Western Ontario, Canada. The tunnel is an open circuit type and has the cross-section of 2.4 m (width) x 2.15 m (height) at the test section with an upstream fetch of 33 m. A 1:10 geometric scale model of the solar panel (Fig. 1) was chosen for this experiment. As for the incoming wind profiles, the target ABL profile was the ESDU profiles (ESDU 82026, 83045) for open terrain roughness (aerodynamic roughness length, $y_0 = 0.03$ m). However, boundary layer wind tunnels are designed to test models with geometric scale from 1:100 to 1:500 and to use this scale range for smaller structures such as solar panels has two major concerns; one, the test model will be too small, posing difficulty in measurements and two, the placement of the test model in the lowest part of the boundary layer which may not be the true representation of the ABL. Developing wind profiles at 1:10 scale in a wind tunnel, which is designed for 1:100 to 1:500 geometric scales, is challenging. To obtain the required wind profiles for 1:10 geometric scale, previously measured wind profiles in the BLWTL I for different roughness (Open (y_0 = 0.03 m), suburban ($y_0 = 0.3$ m) and urban ($y_0 = 1$ m)) were compared with ESDU ABL profiles (ESDU 82026, 83045) for an open terrain roughness ($y_0 = 0.03$ m). It was found that the urban profiles in the BLWTL I gave better match with the ESDU profiles for open terrain for 1:10 model scale (Fig. 4). Therefore, a boundary layer profile corresponding to $y_0 = 1$ m was used in this experiment. In this study, wind tunnel speed of 10.9 m/s, measured by a Pitot tube placed at the height of 1.47 m from the tunnel floor, was used. In Figure 4, the distances are normalized with the pitot tube height (y_{ref}) (1.47 m) and wind speeds are normalized with the tunnel wind speed (U_{ref}) (10.9 m/s). In this experiment the model scale Reynolds number was 8.44 x 10^4 based on the wind speed at the panel's lower edge height, chord length of the panel (B) and the air properties at 20°C.

The laser used in this experiment is from Litron Lasers (Model: Nano L 50-100 PIV) which is a water cooled Nd:YAG (Class 4) compact dual head laser, with output energy of 200 mJ at 532 nm wavelength for each laser. The repetition rate was set at 80 Hz (maximum repetition rate: 100 Hz) for each laser head to avoid damage to the laser and the power supply as the voltage measured in the wind tunnel lab was around 205V. The diameter of the laser beam was 4 mm. A mirror and a cylindrical lens were used to change the direction of the laser beam and to create a laser sheet from the beam

respectively. The camera used in this study was of 4 Megapixel with 2052 x 2048 pixel image resolutions and was based on CMOS image sensors (Flare 4M180MCL, IO Industries). The camera was connected to a digital video recorder (Core DVR Express, IO Industries) and was controlled by a DVR software package CoreView (IO Industries). Model 555 digital pulse delay generator (Berkeley Nucleonics Corporation) was used to generate timing signals for the laser and also to synchronize the camera exposures with individual laser pulses.
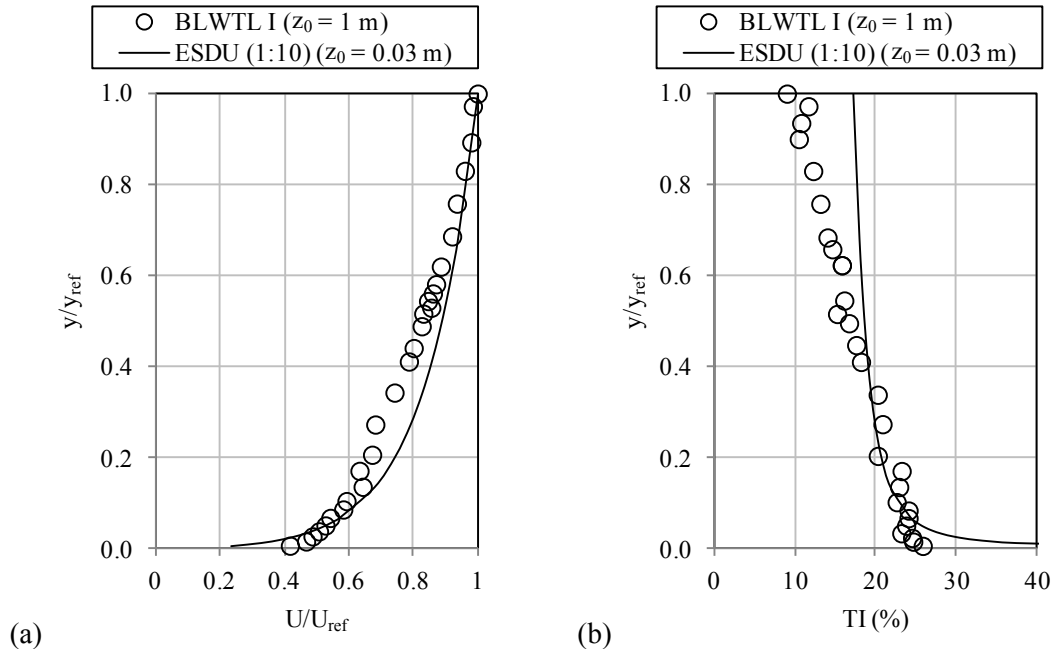
Figure 4. (a) Velocity and (b) Turbulence Intensity (TI) profiles for 1:10 geometric scale.

In this experiment measurements were taken at the plane between the two support legs of the panel (Plane 1) for 0° and 180° wind directions (Fig. 5a). For the 45° and 135° wind directions, measurements were taken at the centre plane of the panel parallel to the side walls of the wind tunnel (Plane 2) (Fig. 5b). For each planes, measurements were taken at 3 to 4 frames of size 18 cm x 18 cm each to capture the wind flow field around the solar panel. For the windward frames (coloured red, Fig. 6), the laser was shot from upstream of the solar panel, whereas for the leeward frames (coloured blue, Fig. 6), the laser was moved back and shot from a downstream location. For both scenarios, existing holes on the side walls of the wind tunnel were used as drilling new holes were not permitted by the BLWTL authority. Because of this, the distance between the downstream location of the laser and the solar panel was higher than the upstream location, resulting in the lowest intensity of the laser and posing challenges during analysis of the leeward frames. Two olive oil seeders were used to seed the wind tunnel. The seeders were place outside the tunnel with flexible plastic tube running into the tunnel carrying the olive oil smoke. Both tube outlets are placed upstream of the solar panel with one being closer than the other. However, the distances of the tube outlets were varied for one field of view to another to get uniform seeds in an image. Also, a small PVC pipe (around 300 mm in length) with several holes (similar to a flute) was attached to the each tube outlet to get a uniform distribution of the olive oil particles. Overall, as the wind tunnel was an open circuit type, it was very challenging to seed the wind tunnel especially when the wind speeds at the leeward frames were measured. During the experiment, images were captured at a rate of 56 fps for 1 minute for each frame which resulted in about 1680 image pairs.
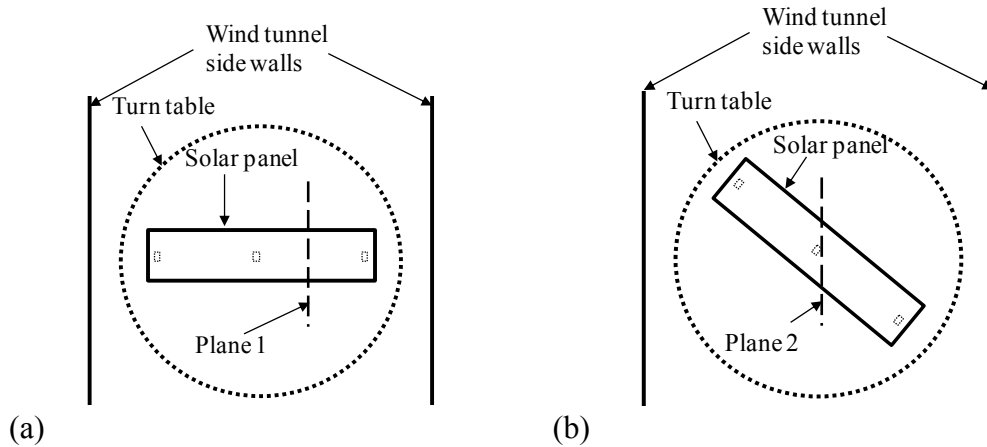
Figure 5. Schematics of the measurement planes in a plan-view (not to scale) for (a) 0° and 180° and (b) 45° and 135° wind directions.
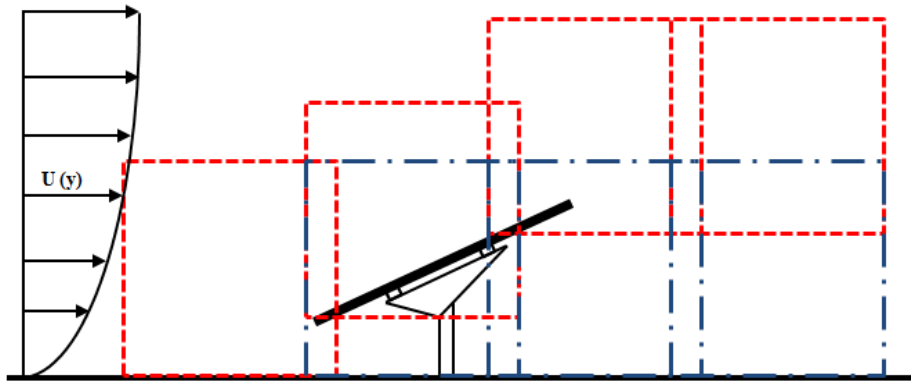
Figure 6. Location of measurement field of views on a plane (for 0° wind direction). Dashed line (red) represents when the laser was upstream and dash-dotted (blue) when the laser was downstream of the solar panel.

4   Results and Discussion

Aerodynamic features of wind flow around the ground mounted stand-alone solar panel subjected to four different wind directions (0°, 45°, 135° and 180°) obtained using both numerical (CFD-URANS) and experimental (PIV) techniques are presented here in this section. Normalized mean velocity magnitude contours along with the stream-lines using PIV and CFD are shown in Figure 7 and 8 respectively. In both Figures 7 and 8, distances are normalized with the lower edge height of the panel (Yr) (0.6 m full-scale) and the wind speeds are normalized by the stream-wise wind speed at the lower edge height in the undisturbed flow (Ur). Origin of the co-ordinates in these figures (Fig. 7 and 8) is at the lower edge of the panel. In Figure 7, mean velocity magnitude on both upstream and downstream sides of the solar panel for 0° and 180° wind directions are presented in the same figure; 0° in Figure 7a and 180° in Figure 7b. However, for 45° and 135° wind directions, results on the upstream and downstream sides of the solar panel are shown in separate figures (Figures 7c, d, e, f) for better visualization. Getting PIV images for 45° and 135° was challenging because of the significantly higher amount of reflections due to the angled orientation of the panel than 0° and 180° wind directions. As a consequence of these reflections, more data had to be discarded for 45° and 135° wind directions than 0° and 180° wind directions. For 0° wind direction (Fig. 7a), flow remains attach on the upper surface of the solar panel accelerating towards the trailing edge of the panel and separates at the leading edge towards the lower surface of the solar panel forming a separation bubble. Here, the centre of the separation bubble is closer to the trailing edge than the leading edge. On the other hand, for 180° wind direction (Fig. 7b), flow remains attached on the lower surface of the panel forming a jet like
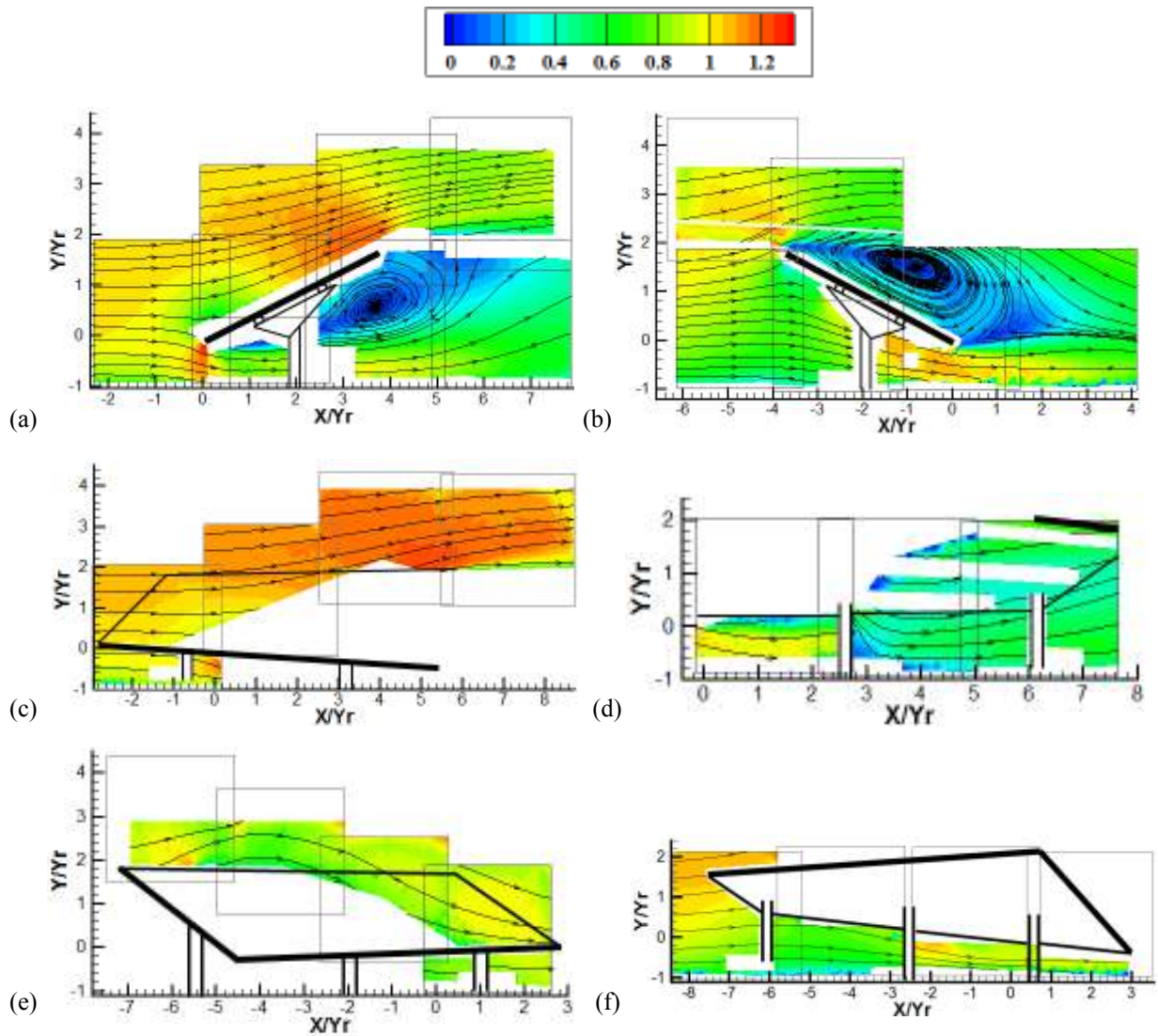
Figure 7. Normalized mean velocity magnitude contours along with stream-lines using PIV for (a) 0°, (b) 180°, (c) 45°- upstream (d) 45°- downstream (e) 135° - downstream and (f) 135° - upstream. Here, distances are normalized with the lower edge height of the panel (Yr) and velocities are normalized with the stream-wise velocity at the lower edge height of the panel in the undisturbed flow (Ur).
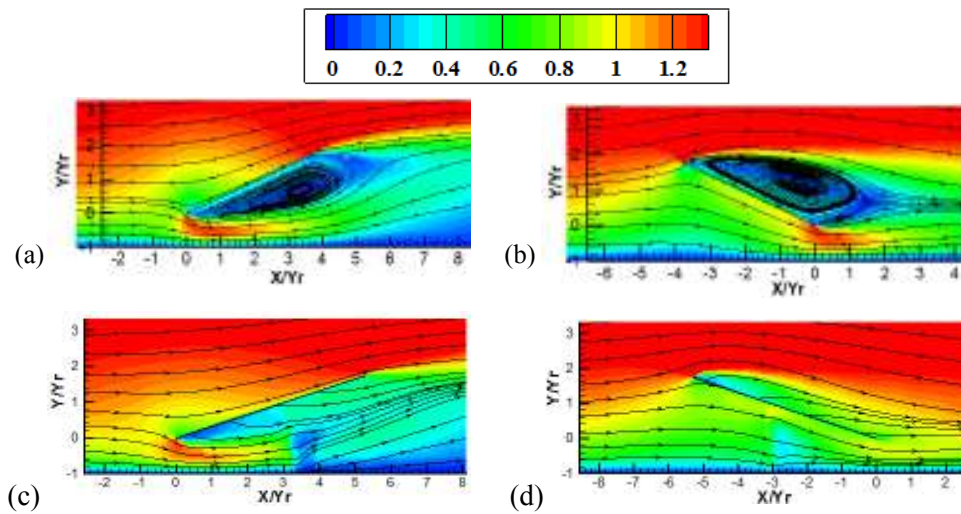
Figure 8. Normalized mean velocity magnitude contours along with stream-lines using URANS-CFD for (a) 0°, (b) 180°, (c) 45° and (d) 135°.
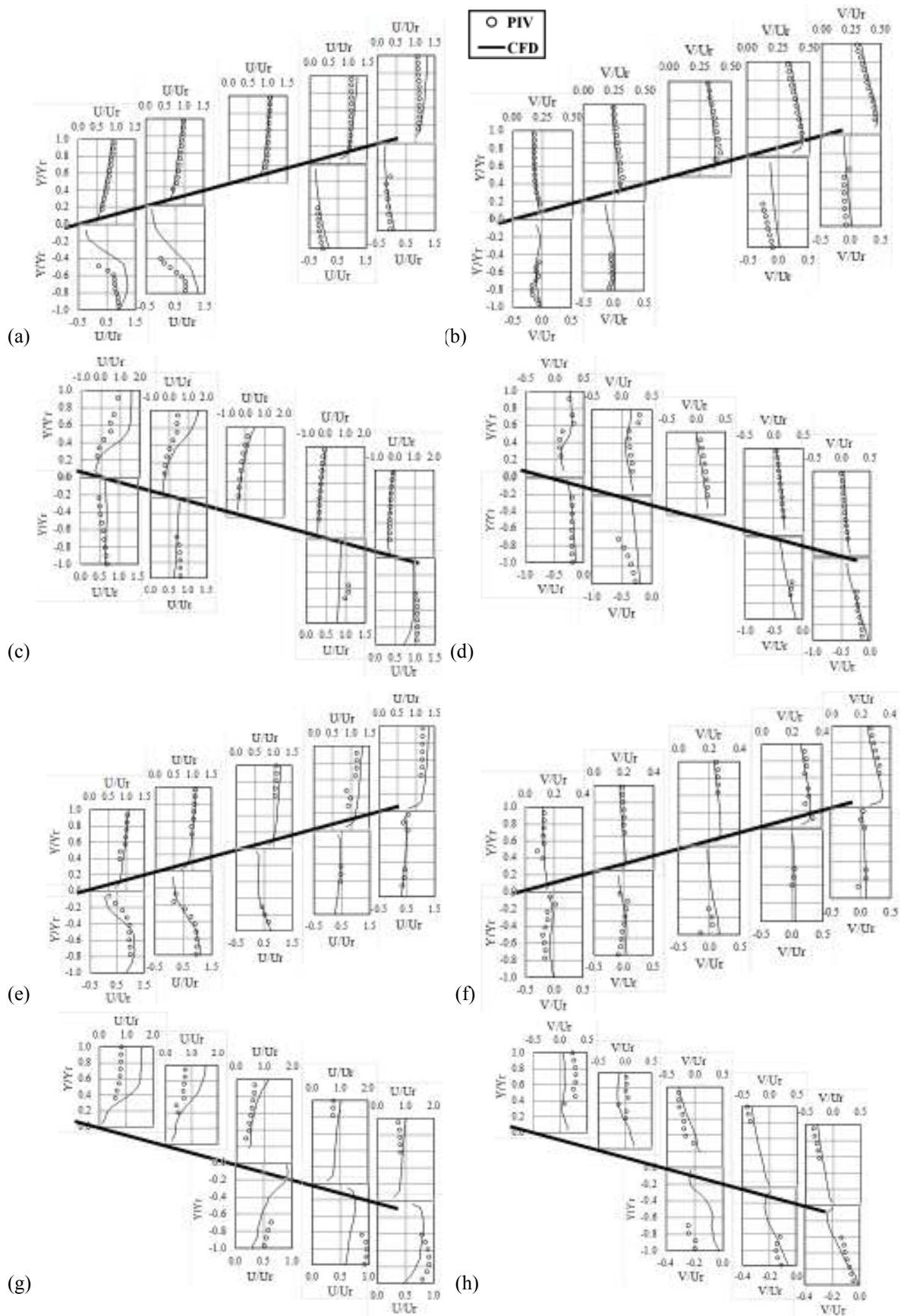
Figure 9. Mean stream-wise (U) and vertical (V) velocity profiles on the surfaces of the solar panel for wind directions (a) 0°-U, (b) 0°-V, (c) 180°-U, (d) 180°-V, (e) 45°-U, (f) 45°-V, (g) 135°-U and (h) 135°-V. The incoming wind is from left to right.

flow between the trailing edge and the tunnel floor, and separates at the leading edge creating a separation bubble on the upper surface of the solar panel. Contrary to the 0° wind direction, here the centre of the separation bubble is close to the centre of the solar panel. Similarly as 0° wind direction, attached flow is observed on the upper surface for 45° wind direction (Fig. 7c). Although the flow separates at the leading edge for 45° wind direction, a vortex like structure is not observed on the lower surface of the solar panel (Fig. 7d). For 135° wind direction, flow separates on the upper surface (Fig. 7e). On the lower surface (Fig. 7f), it is apparent that the flow remains attached on the lower surface though flow separation may occur locally at the lateral support beams underneath the panel but is not evident due to the lack of data on this surface. To compare the results between PIV and CFD qualitatively, normalized mean velocity magnitude contours obtained from the URANS are plotted in Figure 8. From the streamlines in Figure 7 and 8, it can be seen that the aerodynamic features between PIV and CFD match fairly well. CFD is able to capture the mean flow features around the solar panel as in PIV results. However, in terms of normalized mean velocity magnitudes, higher wind speed is observed above the upper edge of the solar panel in CFD than PIV. To compare wind speeds around the solar panel quantitatively, profiles of mean stream-wise (U) and vertical (V) components of wind velocity at five different locations (at B/8, B/4, B/2, 3B/4, 7B/8 from the leading edge, B is shown in Fig. 1) on both upper and lower surfaces of the panel for all four wind directions are plotted in Figure 9. Again, distances are normalized with Yr and the velocities are normalized with Ur. Profiles at B/2 from the leading edge on the lower surface for 0° and 180° wind directions are not plotted due to the lack of data at this location as the support structure was obstructing the field view. Similarly for 135° wind directions, profiles at B/8 and B/4 on the lower surfaces are not plotted because of the laser reflection from the panel surface and horizontal support beams underneath the panel. For 0° wind direction, U and V profiles match very well between PIV and CFD on the windward side of the panel (Fig 9 a, b). The differences between PIV and CFD are up-to 20% for U and 9% for V components. However, on the leeward side the match is not as good as the windward side, especially for U at B/8 and B/4 from the leading edge. This could be due the support beams at the back of the solar panel which resulted in bigger separation bubble in PIV than CFD. For 180° wind direction (Fig. 9 c, d), except for U profiles at B/8 and B/4 from the leading edge on top of the solar panel and V profiles at B/4 on the bottom of the solar, U and V profiles match within 11% between PIV and CFD. The U profiles at B/8 and B/4 from the leading edge on top of solar panel indicates a bigger separation bubble in PIV than CFD. This could be due the differences in Reynolds number in CFD ($2.1x10^6$) and PIV ($8.4x10^4$) (Song and Eaton, 2006). For 45° wind direction, mean U and V profiles between PIV and CFD are well in agreement at all locations plotted in Figure 9 (e, f). For 135° wind direction, poor agreement for U and V profiles are observed close to the leading edge on the both leeward and windward side of the solar panel. Structural support elements underneath the panel in the experimental model which is not present in the numerical model might have affected the flow at this wind direction. Also, for 135° wind direction, the higher amount of reflection of the laser from the angled orientation of the solar panel has resulted in fewer data and thus limits the comparison between CFD and PIV.

5   Conclusions

Wind flow-field around a stand-alone ground mounted solar panel system has been studied by using Computational Fluid Dynamics (CFD) and Particle Image Velocimetry (PIV) approaches for four different wind directions (0°, 45°, 135° and 180°). Overall the aerodynamic flow features around the solar panel is well captured in CFD compared to PIV. For 0° wind direction, the flow remained completely attached on the upper surface of the solar panel whereas for 180° wind direction, flow separated at the leading edge and formed a separation bubble which enveloped almost the entire upper surface of the panel. For both 45° and 135° wind directions, flow separated at the leading edge towards the leeward side of the panel but vortex like structures were not observed. Mean stream-wise (U) and vertical (V) velocity profiles on the windward surfaces of the solar panel for 0° and 180° wind directions obtained from PIV and CFD matched reasonably well (within 20%) except close to the support leg for 180° wind direction. However, on the leeward side of the solar panel for 0° and 180° wind directions, some discrepancy was observed closed to the leading edge which might be due the

different shapes of the separation bubble in PIV and CFD. Between, 45° and 135° wind directions, 45° case showed better agreement between PIV and CFD for U and V profiles than 135° case which might be due to the flow being affected by the structural support elements at the back of the solar panel for 135° wind direction case. Results presented in this study should be useful to numerical modelers to validate their models as well as to experimentalists to understand the important aerodynamic flow features for designing an experiment for solar panels.

References

Abiola-Ogedengbe, A. (2013). Experimental investigation of wind effect on solar panels. *University of Western Ontario - Electronic Thesis and Dissertation Repository*. Paper **1177**.

Aly, A. M., and Bitsuamlak, G. (2013). Wind induced pressures on solar panels mounted on residential homes. *Journal of Architectural Engineering*. DOI: 10.1061/(ASCE)AE.1943-5568.0000132

Bitsuamlak, G. T., Dagnew, A. K. and Erwin, J. (2010). Evaluation of wind loads on solar panel modules using CFD. *The Fifth International Symposium on Computational Wind Engineering, Chapel Hill, North Carolina, USA, May 23-27.*

Chung, K. M., Chang, K. C. and Chou, C. C. (2011). Wind loads on residential and large-scale solar collector models. *Journal of Wind Engineering and Industrial Aerodynamics* **99**, 59-64.

Chung, K., Chang, K., Liu, Y., 2008. Reduction of wind uplift of a solar collector model. *Journal of Wind Engineering and Industrial Aerodynamics* **96**, 1294-1306.

ESDU, 1982. *Strong winds in the atmospheric boundary layer. Part 1: Mean hourly wind speeds.* Engineering Science Data Unit Number 82026.

ESDU, 1983. *Strong winds in the atmospheric boundary layer. Part 2: Discreet gust speeds.* Engineering Science Data Unit Number 83045.

Fage, A. and Johansen, F. C. (1927). On the flow of air behind an inclined flat plate of infinite span. *Proceedings of the Royal Society of London. Series A, Containing Papers of a Mathematical and Physical Character 116, 170-197.*

Franke, J., Hellsten, A., Schlünzen, H. and Carissimo, B. (2007). *Best practice guideline for the CFD simulation of flows in the urban environment.* COST Action 732; Quality assurance and improvement of microscale meteorological models.

Jubayer, C., Abiola-Ogedengbe, A., Siddiqui, K., and Hangan, H. (2012). Numerical and experimental study of wind effects on photovoltaic (PV) panels. *3rd American Association for Wind Engineering Workshop, Massachusetts, USA.*

Kopp, G. A. and Banks, D. (2013). Use of wind tunnel test method for obtaining design wind loads on roof-mounted solar arrays. *Journal of Structural Engineering* **139**, doi: 10.1061/(ASCE)ST.1943-541X.0000654.

Kopp, G. A., Farquhar, S., and Morrison, M. J. (2012). Aerodynamic mechanisms for wind loads on tilted, roof-mounted, solar arrays. *Journal of Wind Engineering and Industrial Aerodynamics* **111**, 40-52.

Kopp, G. A., Surry, D. and Chen, K. (2002). Wind loads on a solar array. *Wind and Structures* **5**, 393-406.

Menter, F. R. (1994). Two-equation eddy-viscosity turbulence models for engineering applications. *American Institute of Aeronautics and Astronautics (AIAA) Journal* **32**, 1598-1605.

Meroney, R. N. and Neft, D. E. (2010). Wind effects on roof-mounted solar photovoltaic arrays: CFD and wind-tunnel evaluation. *The Fifth International Symposium on Computational Wind Engineering, Chapel Hill, North Carolina, USA*.

Pratt, R. N. and Kopp, G. A. (2013). Velocity measurements around low-profile, tilted, solar arrays mounted on large flat-roofs, for wall normal wind directions. *Journal of Wind Engineering and Industrial Aerodynamics* **123**, 226-238.

Radu, A. and Axinte, E. (1989). Wind forces on structures supporting solar collectors. *Journal of Wind Engineering and Industrial Aerodynamics* **32**, 93-100.

Radu, A., Axinte, E., and Theohari, C. (1986). Steady wind pressures on solar collectors on flat-roofed buildings. *Journal of Wind Engineering and Industrial Aerodynamics* **23**, 249-258.

Shademan, M. and Hangan, H. (2010). Wind loading on solar panels at different azimuthal and inclination angles. *The Fifth International Symposium on Computational Wind Engineering, Chapel Hill, North Carolina, USA.*

Song, S and Eaton, J.K. (2004). Reynolds number effects on a turbulent boundary layer with separation, reattachment, and recovery. *Experiments in Fluids* **36**, 246-258.

Wood, G. S., Denoon, R. O., and Kwok, K. C. S. (2001). Wind loads on industrial solar panel arrays and supporting roof structure. *Wind and Structures* **4**, 481-494.

Yang, W., Quan, Y., Jin, X., Tamura, Y. and Gu, M. (2008). Influences of equilibrium atmosphere boundary layer and turbulence parameter on wind loads of low-rise buildings. *Journal of Wind Engineering and Industrial Aerodynamics* **96**, 2080-2092.

Yang, Y., Gu, M., Chen, S. and Jin, X. (2009). New inflow boundary conditions for modelling the neutral equilibrium atmospheric boundary layer in computational wind engineering. *Journal of Wind Engineering and Industrial Aerodynamics* **97**, 88-95.

Lifetime cost analysis against flutter riskiness for long-span bridges

Dong-Woo Seo[1], Luca Caracoglia[2]

[1]Structural Engineering Research Division, Korea Institute of Construction Technology, Korea
[2]Department of Civil and Environmental Engineering, Northeastern University, USA
Corresponding author: Dong-Woo Seo, dwseo@kict.re.kr

Abstract

Flutter derivatives of bridge decks are fundamental for the assessment of bridge response to wind loading. Flutter derivatives are routinely extracted from wind tunnel section-model experiments. As suggested by the results of the "United States - Japan Benchmark Study on Flutter Derivatives", completed a few year ago, the analysis of experimental errors in the extraction of flutter derivatives from wind tunnel tests is of great relevance. In this study, wind tunnel experimental data of a truss-type deck girder are employed for the validation of a recently-developed computational framework for the lifetime cost analysis of long-span bridges, induced by damage produced by high winds. Replacement costs due to structural collapse, caused by incipient torsional flutter instability, are analyzed. The flutter probability is used, together with information on the probability of wind velocity at a given site, to predict the expected value of the replacement cost at the end of the bridge lifetime, using Monte-Carlo simulation for probability analysis and the Scanlan's frequency-domain approach for flutter examination.

1   Introduction

Flutter instability is one of major matters of concern in the design of long-span flexible bridges due to its potential for catastrophic structural failure. Aeroelastic stability can be predicted by analyzing the aeroelastic coefficients of bridge decks (flutter derivatives, FDs) (Scanlan and Tomko 1971). FDs of bridge decks are routinely measured in wind tunnel by section model experiments. However, as outlined in recent studies, aeroelastic coefficients are random due to experimental uncertainty. It is therefore useful to determine the flutter probability by performing a probabilistic analysis. Many existing long-span bridges are susceptible to single-mode torsional flutter (e.g., (Caracoglia et al. 2009)). This dynamic instability phenomenon coincides with a torsionally-driven unstable motion of the bridge deck; it is mainly associated with a vibration in the first torsional structural mode, being the most vulnerable to the unstable excitation.

An algorithm for the analysis of the bridge torsional-flutter probability (TFP), contaminated by errors in the flutter derivatives, was proposed by the authors (Seo and Caracoglia 2011). The proposed procedure models a selected group of FD curves, for moderate to highly bluff deck sections, as second-order polynomials as a function of the reduced velocity. The dynamic response at the onset of flutter was examined by single-mode analysis. The Monte-Carlo (MC) simulation algorithm was utilized to determine the TFP of the structure. In this study, the TFP is combined together with information on the probability of the annual maxima of the mean wind velocity at a given bridge site to predict the expected value of the replacement costs due to the chance of collapse.

2   Flutter analysis: torsional flutter and polynomial representation of FDs

The formulation is based on the aeroelastic torsional moment per unit length of the deck, simplified for torsionally-driven deck motion at flutter onset, as (Scanlan and Tomko 1971):

$$M_{ae} \cong \frac{1}{2} 0.5\rho U^2 B^2 \left[KA_2^* \frac{B\dot{\alpha}}{U} + K^2 A_3^* \alpha \right] \tag{1}$$

where B is the bridge deck width, U is the mean wind velocity, ρ is the air density, the α variable represent the pitching motion (heave motion is neglected) and $\dot{\alpha}$ its time derivative. Flutter derivatives A_j^* ($i = 2, 3$) are a function of the reduced frequency $K = \omega B/U$ where $\omega = 2\pi n$ is the circular frequency of vibration (rad/sec), which is proportional to the reciprocal of the reduced velocity $U_R = U/(nB) = 2\pi/K$ (with n frequency in Hz). Lateral force component (drag) was not considered.

Flutter can be determined after representing the simple harmonic motion at flutter in terms of a critical reduced frequency ratio $\chi = K/K_{t1}$ (e.g., (Dragomirescu et al. 2003; Jones and Scanlan 2001)). The problem can be reduced to the nontrivial solutions of a complex algebraic equation in the case of torsional flutter, dominated by fundamental torsional mode "t_1", with $i = \sqrt{-1}$ in Eq. (2) below, which neglects any source of coupling with other modes usually acceptable for moderately aerodynamically bluff decks.

$$E_{2,2}(K,\chi) = \left[-\chi^2 + 1 - q_{t1}\chi^2 A_3^*(K)G_{t1,t1} + i\left(2\zeta_{t1}\chi - q_{t1}\chi^2 A_2^*(K)G_{t1,t1} \right) \right] \tag{2}$$

The vanishing of the real and imaginary parts of $E_{2,2}$ in Eq. (2) (Jones and Scanlan 2001)leads to flutter. The torsional-flutter velocity can be determined by inspection of the roots satisfying the zero damping condition. Since flutter derivatives A_2^* and A_3^* are measured in wind tunnel as a function of the reduced speed, U_R, experimental data are usually available at discrete points on the U_R axis. A second order polynomial curve for A_2^* and A_3^*, as a function of U_R, was used in this study (Seo and Caracoglia 2011). This model is

$$A_3^*(U_R) = C_1 U_R^2 + C_2 U_R, \qquad A_2^*(U_R) = C_3 U_R^2 + C_4 U_R \tag{3}$$

where $C_1,\ldots,C_4$ are four parameters, which can be determined from regression of the experimental data points measured at various U_R.

3   Preliminary prototype application: Bridge model and flutter derivatives

The structural properties of the bridge model is the Golden Gate Bridge in San Francisco, California (USA), with main span $\ell = 1200$ m, deck width $B = 28$ m, torsional inertia $I_0 = 4.4\times106$ kg$\times$m^2/m of the moving deck and cables (Jain et al. 1996). This structure is characterized by a skew-symmetric fundamental torsional mode with frequency equal to 0.192 Hz. The modal damping is assumed as equal to 0.3% with respect to critical (Jain et al. 1996).

In Fig. 1 the A_2^* (a) and A_3^* (b) data sets, related to the truss-type deck girder, are shown as a function of U_R. Two sets are shown, respectively measured for a mean static attack angle of the wind α_0, with respect to horizontal reference position, equal to 0 degrees (Jain et al. 1996) and +5 degrees. The FD curves clearly show local irregularities as the reduced velocity increases above 6; dependence of the curves on the mean angle α_0 can be observed, especially for A_2^* in Fig. 1.
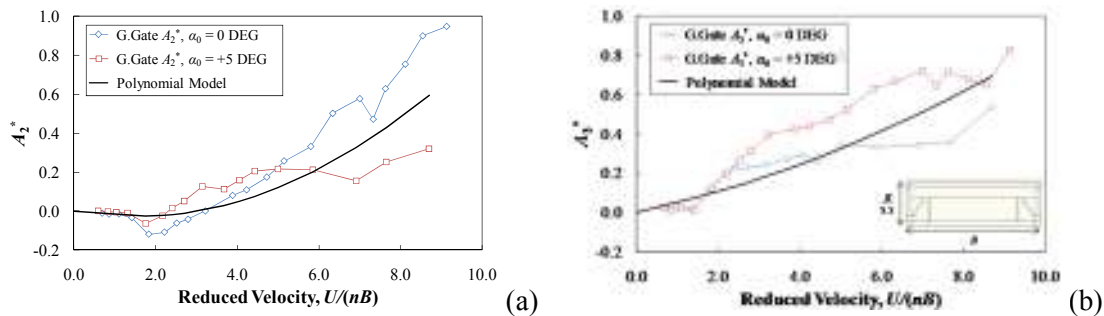
Figure 1. Flutter derivatives A_2^* (a) and A_3^* (b) of a truss-type bridge deck with aspect ratio $B/D = 3.5:1$. Experimental data are reproduced from (Jain et al. 1996)

Data from the two sets are used as the input for the polynomial model in Eq. (2), derived by least squares as indicated in (Seo and Caracoglia 2011). The average or "reference" values of the four

parameters of the polynomial models, $C_1^*,...,C_4^*$, can be directly evaluated from the data sets in Fig. 1. The reference polynomial model is also shown in the figure. The choice of the polynomial model for FD curves, which possesses physical foundation, approximately preserves good fidelity with the experimental data.

The randomness in the approximating polynomials of A_2^* and A_3^* curves is subsequently estimated under the hypothesis that the observed distinct pattern in the FD curves at $\alpha_0=0$ deg and $\alpha_0=+5$ deg can be linked to the effect of "measurement errors". Nevertheless, this assumption that the differences in the FDs measured at $\alpha_0=0$ deg and $\alpha_0=+5$ deg, can be related to randomness, does not exclude the fact that modifications in the local flow characteristics during section-model experiments may also be responsible for such variations. In any case, it was accepted for the purposes of this study since it enables evaluating torsional flutter velocity and the implementation of the computer model for cost analysis.

4   Expected lifetime cost based on torsional flutter probability

Over a time period (t, in years), which may be the design life of a new bridge or the remaining life of a retrofitted bridge, the expected replacement cost can be expressed as a function of t as follows (Wen and Kang 2001); in the equation below the expected value of lifetime replacement cost based on flutter probability, $C_{F,E}(t)$, normalized with respect to the initial construction cost C_0 at $t=0$ is

$$C_{F,E}(t) = E\left[C(t) - C_0 \right] / C_0 = E\left[\sum_{i=1}^{N(t)} e^{-\lambda t_i} P_f \right] \tag{4}$$

where $E[]$ denotes expected value; C_0 is the construction cost and $C(t)$ is the total cumulative cost; i is an integer positive index describing the occurrence of a severe wind event; $0 < t_i \leq t$ is the occurrence time of event "i", a random variable. Moreover, $N(t)$ is the total number of wind damaging events over time t; $e^{-\lambda t_i}$ is the "discounted factor" (Wen and Kang 2001) of the costs over time t with λ being a constant discount rate per year. In Eq. (4) P_f is the flutter probability. The number of occurrences for moderate wind storms $N(t)$ was modelled by a Poisson Process with mean occurrence rate 0.01 (as a first approximation).

The probability P_f was calculated by applying the MC methods. The random coefficients $C_1,...,C_4$ were assumed as either jointly Gaussian or jointly log-normal. The mean, standard deviation and correlation coefficients of $C_1,...,C_4$ were assessed from Fig. 1 and the wind tunnel data; the statistical moments were applied to the simulations utilizing normal and log-normal distributions for $C_1,...,C_4$.

The flutter probability was assessed by Monte Carlo methods as P_f=Prob($g\leq0$) with limit state function g(U_{cr}, U_{site})=U_{cr}-U_{site}, i.e., the difference between critical wind speed and mean wind speed at the bridge site (annual maxima). Standard algorithms for MC statistical analysis were considered employed (Bucher 2009) with appropriate sample of computer generated events (usually greater than 5×10^5). In order to analyze the effects of a partial correlation between C_1, C_2 and C_3, C_4 (Seo and Caracoglia 2011) a sensitivity analysis was also carried out by suitably varying the correlation coefficients among the variables (e.g., $0 \leq \rho_{C_3,C_4} < 1$ to study the mutual influence between C_3 and C_4).

Figure 2(a) summarizes, as an example, the analysis of the influence of ρ_{C_3,C_4} on the generalized safety index β (Bucher 2009), associated with torsional flutter. The histograms compare the numerical results obtained by MC methods for jointly Gaussian (N) and jointly log-normal (LN) parameters $C_1,...,C_4$.

Figure 2(b) depicts a detailed analysis of the influence of $\rho_{C_3^*,C_4^*}$ on the expected replacement cost at the end of the lifetime. For most cases in Fig. 2(b) the expected cost, based on flutter probability, appears to be more than 1.5 times the construction cost; the presented case is, however, a special limiting case. The safety indices suggest, in this example, moderately small dependence on the selected probability distribution of $C_1^*,...,C_4^*$.
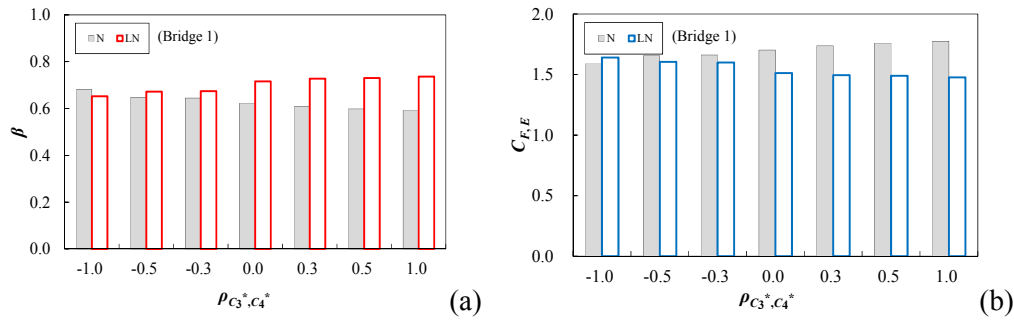
Figure 2. (a) Safety indices β and (b) expected relative cost $C_{F,E}$ after t=50 years for jointly normal (N) and jointly log-normal (LN) parameters $C_1^*,\ldots,C_4^*$, *, as a function of $\rho_{C_3^*,C_4^*}$.

5   Discussion and concluding remarks

A numerical procedure is presented for the solution of the torsional flutter problem under random perturbation of the aeroelastic input parameters, employed to simulate propagation of modeling and measurement error in the flutter derivatives. This procedure enabled the estimation of the torsional-flutter probability and of the replacement cost at the end of bridge lifetime. Limited influence of the correlation coefficient of the random flutter derivatives has been noted on the replacement cost for a truss-type bridge example, in a preliminary example. More cases will be discussed in the final presentation of this work.

In any case, it must be noted that the objective of the study was not to replace more sophisticated and accurate techniques but to propose a simple numerical method, useful for preliminary bridge analysis. The procedure could for example assist the engineer during early investigations, by utilizing the replacement cost variable as a simple scalar quantity for examining the feasibility of various design solutions.

6   Acknowledgements

7   References

Bucher, C. (2009). *Computational analysis of randomness in structural mechanics*, Taylor Francis Group, London, UK.

Caracoglia, L., Sarkar, P. P., Haan Jr, F. L., Sato, H., and Murakoshi, J. (2009). "Comparative and sensitivity study of flutter derivatives of selected bridge deck sections, Part 2: Implications on the aerodynamic stability of long-span bridges." *Engineering Structures*, 31(9), 2194-2202.

Dragomirescu, E., Miyata, T., Yamada, H., and Katsuchi, H. (2003). "Probabilistic approach of structural reliability applied to bridge components." *11th International Conference on Wind Engineering (11-ICWE)*, Texas Tech University, Lubbock, Texas, USA, 789-796.

Jain, A., Jones, N. P., and Scanlan, R. H. (1996). "Coupled aeroelastic and aerodynamic response analysis of long-span bridges." *Journal of Wind Engineering and Industrial Aerodynamics*, 60(1-3), 69-80.

Jones, N. P., and Scanlan, R. H. (2001). "Theory and full-bridge modeling of wind response of cable-supported bridges." *Journal of Bridge Engineering, ASCE*, 6(6), 365-375.

Scanlan, R. H., and Tomko, J. J. (1971). "Airfoil and bridge deck flutter derivatives." *Journal of Engineering Mechanics, ASCE*, 97(EM6), 1717-1737.

Seo, D.-W., and Caracoglia, L. (2011). "Estimation of torsional-flutter probability in flexible bridges considering randomness in flutter derivatives." *Engineering Structures*, 33(8), 2284-2296.

Wen, Y. K., and Kang, Y. J. (2001). "Minimum building life-cycle cost design criteria. I: Methodology." *Journal of Structural Engineering*, 127(3), 330-337.

Prediction of the buffeting response of ice-accreted stay cables

Cristoforo Demartino[1] and Francesco Ricciardelli[2]

[1]Dept. of Structural Engineering, University of Naples Federico II, via Claudio 21, 80125 Naples, Italy
[2]Dept. of Informatics, Infrastructures and Sustainable Energy, University of Reggio Calabria, Via Graziella, 89122 Reggio Calabria, Italy
Corresponding author: Cristoforo Demartino, cristoforo.demartino@unina.it

Abstract

Buffeting of iced stay cables is addressed in the paper. Numerical simulations of the 3-D cross-sectional response are carried out in the time domain. The quasi steady assumption is used for evaluating buffeting and self-excited forces. A specially derived numerical model accounts for the dependency of the aerodynamic coefficients on the angle of attack, on the wind-cable angle and on the Reynolds number. The final goal of the study is that of producing relationships between the mean wind velocity and direction and the statistics of the cable displacements, for use in fatigue calculations.

1 Introduction

Wind induced cable vibrations have been the topic of many studies carried out in the last decades. These mainly focus on the unstable behaviour deriving from a variety of causes, e.g. vortex shedding, galloping (in its many forms), shape modifications due to rain and ice. What has received less attention is the stable buffeting response. This becomes of interest when fatigue calculations have to be carried out.

For the particular case of stay cables, quasi-steady aerodynamics is governed by three parameters, the wind-cable angle Φ, the angle of attack α, and the Reynolds number Re, on which the aerodynamic coefficients depend. An analytical 3-D time domain model has recently been developed (Demartino (2014)) for description of the self-excited and buffeting forces arising on a vibrating cylinder inclined to the mean flow, accounting for the dependencies above. When implemented numerically, the model allows evaluation of the buffeting response of sectional a 3-D, 2-DoFs system representing a cable section.

In this paper the model above is shortly summarised and its relationship to other existing buffeting models is discussed. Then, for the particular case of an ice accreted cable the sensitivity of the response of the different terms appearing the excitation equation is investigated. Finally, the results of Monte Carlo simulations aimed at establishing a relationship between the mean wind velocity and direction and the statistics of the structural response of ice accreted cables, are presented. The latter must be considered as a first step towards fatigue assessments of stay cables.

The aerodynamic data of ice accreted stay cable used in the calculations derive from wind tunnel tests performed at the DTU/Force Technology collaborative Climatic Wind Tunnel (CWT) in Lyngby, Denmark. The experimental procedure and results are fully described in Demartino (2014).

2 Aerodynamic forces

A cylinder of arbitrary cross section (Figure 1) is considered, exposed to a turbulent flow. The total wind velocity $\mathbf{U}(t)$ is given by:

$$\mathbf{U}(t) = \mathbf{U} + \mathbf{U}'(t) = \begin{bmatrix} U & 0 & 0 \end{bmatrix}^T + \begin{bmatrix} u'(t) & v'(t) & w'(t) \end{bmatrix}^T \tag{1}$$

in the global reference system (X, Y, Z). The attitude of the cylinder to the flow is described by the *inclination*, Θ, i.e. the angle between the cylinder axis z and its projection on the horizontal plane, and the *yaw*, β, i.e. the angle between $U(t)$ and the projection of the cylinder axis on the horizontal plane. These two angles can be condensed in a single parameter, the *wind-cable angle*, Φ. In this context $\mathbf{U}(t)$ is usually decomposed into two components: one perpendicular to the cylinder axis named *normal flow*, $U_N(t)$, and one parallel named *axial flow*, $U_A(t)$ (Figure 1).
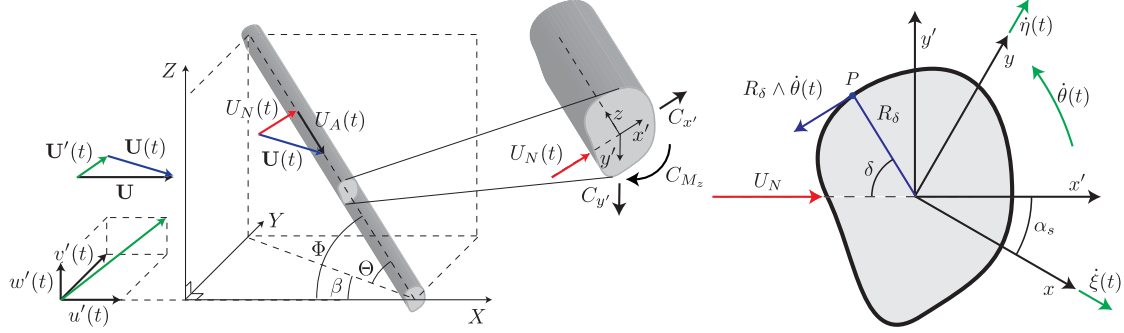
Figure 1. Stay cable orientation, wind velocity and DoFs orientation in the cross section plane.

The quasi-steady theory assumes that the wind sees the cylinder as a stationary object, and the aerodynamic forces can be evaluated using the mean aerodynamic force coefficients measured in static wind tunnel tests. The motion of the cylinder cross section is described in term of 2-DoFs defined at the shear centre, represented by the vector $q(t) = [\xi(t) \quad \eta(t)]^T$, ξ and η being two mutually orthogonal displacements of the section. The displacements ξ and η, are taken in the (x, y) reference system, that is rotated of $-\alpha_s$ with respect to the (x', y'). The angle α_s between $U_N(t)$ and x is termed the *structural angle*.

The instantaneous relative velocity, $U(t)$, is evaluated as the difference between $U_N(t)$ and the cylinder velocity vector, $\dot{\xi}(t)$ and $\dot{\eta}(t)$, in the (x', y') reference system. $U_R(t)$ and $U(t)$ define the relative angle of attack, $\alpha_R(t)$, and $U_R(t)$ and the cable axis define the relative wind cable angle of attack, $\Phi_R(t)$.

The vector $\mathbf{F}_a = \mathbf{F}_a(\dot{\mathbf{q}}(t), \mathbf{q}(t), \mathbf{U}(t))$ containing the aerodynamic forces is given as:

$$\mathbf{F}_a = \frac{1}{2}\rho D |\mathbf{U}_R|^2 \mathbf{R}_z \mathbf{C} \qquad (2)$$

where ρ is the fluid density, D is a characteristic dimension of the cross section, $\mathbf{U}_R = \mathbf{U}_R(\dot{\mathbf{q}}(t), \mathbf{q}(t), \mathbf{U}(t))$ is the squared norm of the instantaneous relative velocity vector, $\mathbf{R}_z = \mathbf{R}_z(\dot{\mathbf{q}}(t), \mathbf{q}(t), \mathbf{U}(t))$ is the rotation matrix between the aerodynamic force directions and the DoFs considered, and $\mathbf{C} = \mathbf{C}(\dot{\mathbf{q}}(t), \mathbf{q}(t), \mathbf{U}(t))$ is the vector containing the aerodynamic force coefficients.

The aerodynamic forces are expanded in Taylor series for $\dot{\mathbf{q}}(t)$ and $\mathbf{U}(t)$ at the equilibrium point $P = \{\dot{\mathbf{q}}(t) = \mathbf{0}, \mathbf{q}(t) = \mathbf{0}, \mathbf{U}(t) = \mathbf{U}\}$. To this aim, the aerodynamic force coefficients measured in the wind tunnel for different values of $Re = UD/\nu$, α and Φ must be expressed as a function of $\dot{\mathbf{q}}(t)$, $\mathbf{q}(t)$ and $\mathbf{U}(t)$; this is done applying the derivation chain rule. The result of the Taylor expansion is:

$$\mathbf{F}_a(\dot{\mathbf{q}}(t), \mathbf{q}(t), \mathbf{U}(t)) = \mathbf{F}_a(\mathbf{P}) - \mathbf{C}_a \dot{\mathbf{q}}(t) + \mathbf{B}_a \mathbf{U}'(t) \qquad (3)$$

The first term of the expansion represents the mean forces, the second term $\mathbf{C}_a = -J_{\dot{\mathbf{q}}(t)} \mathbf{F}_a\big|_{\mathbf{P}}$ is the Jacobian matrix of the aerodynamic forces, and represents the opposite of the aerodynamic damping matrix (Macdonald and Larose (2008)), the third term $\mathbf{B}_a = J_{\mathbf{U}(t)} \mathbf{F}_a\big|_{\mathbf{P}}$ is the Jacobian matrix of the aerodynamic forces, and represents the aerodynamic buffeting matrix.

Using Eq. (3), the linearized equation of motion is obtained:

$$\mathbf{M}_s \ddot{\mathbf{q}}(t) + (\mathbf{C}_s + \mathbf{C}_a)\dot{\mathbf{q}}(t) + \mathbf{K}_s \mathbf{q}(t) = \mathbf{F}_a(\mathbf{P}) + \mathbf{B}_a \mathbf{U}'(t) \qquad (4)$$

Eq. (4) can be written in the state space form and solved for a generic wind velocity time history adding an initial condition, $\mathbf{x}_0$.

The derived buffeting matrix is:

$$\mathbf{B}_a = \begin{bmatrix} \cos\alpha_R\left(C_x + \dfrac{\partial C_x}{\partial \mathrm{Re}}\mathrm{Re}\right) - \sin\alpha_R\left(C_y + \dfrac{\partial C_y}{\partial \mathrm{Re}}\mathrm{Re}\right) & \sin\alpha_R\left(C_x + \dfrac{\partial C_x}{\partial \mathrm{Re}}\mathrm{Re}\right) + \cos\alpha_R\left(C_y + \dfrac{\partial C_y}{\partial \mathrm{Re}}\mathrm{Re}\right) \\ -\left(\sin\alpha_R C_x + \cos\alpha_R C_y\right)R_1 + \cos\alpha_R R_3 - \sin\alpha_R R_4 & \left(\cos\alpha_R C_x - \sin\alpha_R C_y\right)R_1 + \sin\alpha_R R_3 + \cos\alpha_R R_4 \\ \left(-\sin\alpha_R C_x + \cos\alpha_R C_y\right)R_5 + \cos\alpha_R R_6 - \sin\alpha_R R_7 & \left(\cos\alpha_R C_x - \sin\alpha_R C_y\right)R_5 + \sin\alpha_R R_6 + \cos\alpha_R R_7 \end{bmatrix}^T \quad (5)$$

where:

$$R_1 = \frac{\sin\theta\left(1+\tan^2\beta\right)}{\left(\sin^2\theta+\tan^2\beta\right)} \quad R_2 = \frac{\cos\theta\sin\beta}{\sin\Phi} \quad R_3 = \left[-\frac{\partial C_x}{\partial\Phi}R_2 + \frac{\partial C_x}{\partial\alpha}R_1\right] \quad R_4 = \left[-\frac{\partial C_y}{\partial\Phi}R_2 + \frac{\partial C_y}{\partial\alpha}R_1\right]$$

$$R_5 = \frac{\sin\beta\cos\theta}{\cos^2\beta\left(\sin^2\theta+\tan^2\beta\right)} \quad R_6 = \left[\frac{\partial C_x}{\partial\Phi}\frac{\sin\theta}{\sin\Phi} + \frac{\partial C_x}{\partial\alpha}R_5\right] \quad R_7 = \left[\frac{\partial C_y}{\partial\Phi}\frac{\sin\theta}{\sin\Phi} + \frac{\partial C_y}{\partial\alpha}R_5\right] \quad (6)$$

The buffeting matrix in Eq. (5) evaluated for $\alpha_R = 0°$ and $\beta = 0°$, and neglecting the derivatives of the aerodynamic coefficients with respect to Re and Φ is the same used in buffeting analyses by Piccardo and Solari (2000).
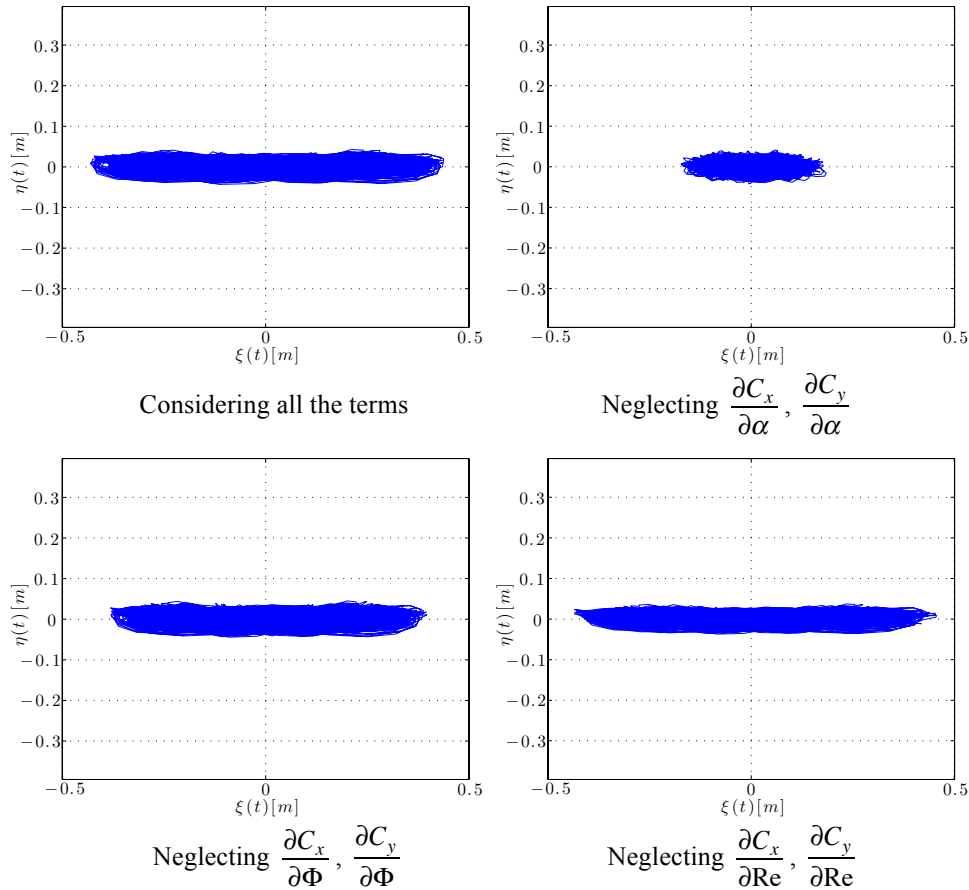
Figure 2. Motion of the ice-accreted stay cable subject to turbulent flow, in the plane $x - y$ considering all the derivatives of the aerodynamic coefficients and neglecting those respect Φ, α, and Re, respectively. ($\theta = 30°$, $\beta = 140°$, $f_x = 0.5Hz$, $f_y = 1Hz$, $\xi_x = \xi_y = 0.13\%$, $U = 28m/s$, $I_u = 13\%$).

3   Preliminary results and discussion

Numerical simulations of the cross-sectional response of an ice-accreted stay cable are carried out in the time domain. The turbulence intensity of the input wind time history is 13%. Different synthetic generation of wind data series are used in the analyses.

(a)   (b)
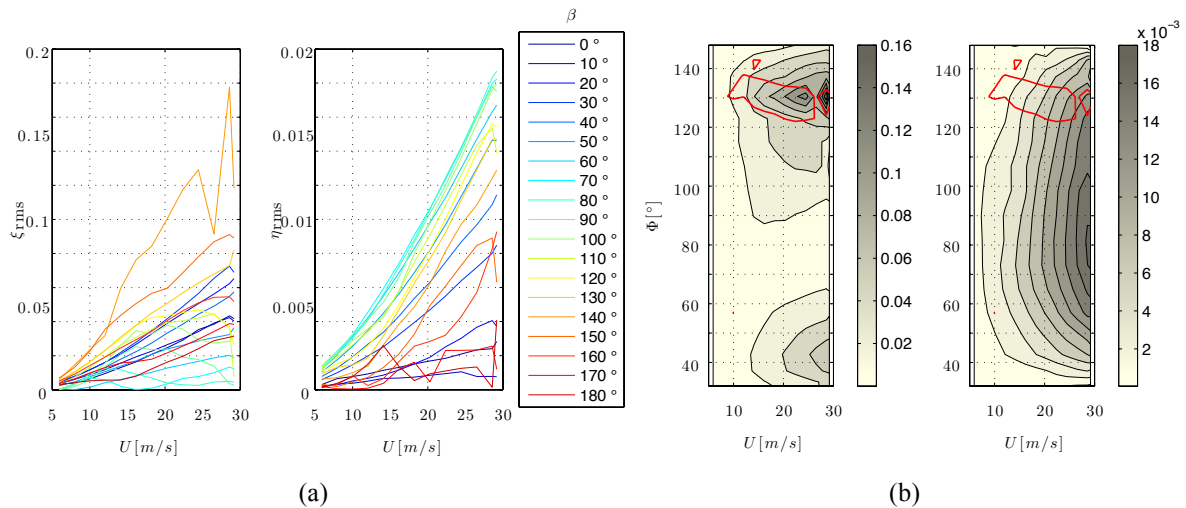
Figure 3. Diagrams (a) and contour plots (b) of the RMS of $\xi(t)$ and $\eta(t)$ $[m]$ for different values of U and β. The red line on the right figures (b) indicates the instability thresholds (Macdonald and Larose (2008)). ($\theta = 30°$, $f_x = 0.5Hz, f_y = 1Hz, \xi_x = \xi_y = 0.13\%, I_u = 13\%$).

Numerical analyses were performed with the aim of assessing the contribution of each derivative of the aerodynamic coefficients to the response. In the analysis a value of damping ratio of $\xi_x = \xi_y = 0.13\%$ was used; this value ensures the stability in the entire domain investigated. The other cases will be showed in the full-paper version. In Figure 2, the motion of the ice-accreted stay cable subject to turbulent flow in the in the $x - y$ plane is shown. It can be observed that neglecting the derivatives of the aerodynamic coefficients on α considerably underestimates the response.

In Figure 3 the RMS of $\xi(t)$ and $\eta(t)$ is shown for different values of U and of β. From Figure 3a, it is observed that the maximum ξ-response is found for $\beta = 130°$, which corresponds to the potentially instable behaviour (red line) shown in Figure 3b. Large value of ξ_{rms} are also obtained for approximately $\beta = 0°$ and $\beta = 180°$ and large values of η_{rms} are obtained for $\beta = 90°$.

References

C. Demartino (2014). *Aerodynamics and aeroelastic behaviour of ice-accreted bridge cables*. Ph.D. thesis. University of Naples, Federico II.

Druez, J., Louchez, S., & McComber, P. (1995). Ice shedding from cables. *Cold regions science and technology*, **23**(4), 377-388.

Macdonald, J.H.G., and Larose, G.L. 2008. Two-degree-of-freedom inclined cable galloping part 2: analysis and prevention for arbitrary frequency ratio. *J. Wind Eng. Ind. Aerodyn.*, **96**(3), 308–326.

Piccardo, G., & Solari, G. (2000). 3D wind-excited response of slender structures: Closed-form solution. *J. Struct. Eng. ASCE*, **126**(8), 936-943.

Scanlan, R. H. (1984). Role of indicial functions in buffeting analysis of bridges *J. Struct. Eng. ASCE*, **110**(7), 1433-1446.

Spatial Estimation of Future Typhoon Genesis considering Climate Change

Ga Young Kim[1], Sungsu Lee[2], Hee Jung Ham[3]

[1]Department of Civil System Engineering, Chungbuk National University, South Korea
[2]School of Civil Engineering, Chungbuk National University, South Korea
[3]Department of Architecture, Kangwon National University, South Korea
Corresponding author: Ga Young Kim, enthusiasm3535@gmail.com

Abstract

In this paper, we present spatial estimation of future typhoon genesis considering climate change scenario. For this analysis, we first calculated Genesis Potential Index(GPI) using RCP 8.5 monthly data of IPCC AR5 during 1982~2100, which corresponds to a high greenhouse gas emissions pathway compare to the scenario literature. By spatially comparing monthly averaged GPIs with typhoon genesis locations for 1982~2010, a probability distribution of the typhoon genesis is developed for the monthly averaged GPIs in Pacific basin. With developed PDF of the typhoon genesis, spatial distributions of probability on the typhoon genesis are estimated for the periods of 2011~2040, 2041~2070 and 2071~2100. Using this result, we can estimate potential region of the typhoon genesis in the future.

1 Introduction

Typhoons in North West Pacific have inflicted numerous properties and people in East Asia including Korea. About 26.1 typhoons have annually occurred in North West Pacific and 3.65 typhoons directly or indirectly affected Korea every year. According to archive of direct damages and losses in Korea, a typhoon 'RUSA (2002)' is ranked in 1st place with about 5.1 billion USD followed by a typhoon 'MAEMI (2003)' with 4.2 billion USD in direct loss. In order to mitigate the damages from wind event of typhoons, estimation of extreme wind speed is essential.

It is generally known that typhoon is influenced by several climatic factors such as sea surface temperature (SST), actively convective activity, vertical wind shear, Southern Oscillation Index (SOI) and Rossby wave of upper troposphere in Northern latitude 5° ~20°. In many studies, they were trying to find the cause of the typhoon activity from these climatic factors. In particular, SST is one of the main factors for typhoon genesis and, increase in SST can bring about increase in typhoon activity and intensity (Gray, 1968). Motivated by the work of Gray, Emanuel and Nolan(2004) developed GPI(Genesis Potential Index) with on the basis of the PI(Potential Intensity), relative humidity, absolute vorticity at various levels and wind shear. Following this, several researcher investigated climate change and oceanic environment as ENSO using GPI (Suzana J. Camargo, 2007). In addition, Murakami and Wang (2010) used the GPI to assess tropical cyclone genesis in global climate models.

In this paper, a genesis model is proposed using GPI (Emanuel (2004) on the basis of several climatological factors. With comparison of past genesis of typhoons in Pacific and GPI computed using RCP 8.5 data of 1982 ~ 2010, high correlation was found between them. In addition, we estimated future's typhoon genesis area using RCP 8.5 data of 1982~2100. Based on these correlations, we developed the statistical model of genesis using GPIs in the future.

2   Methodology

The study process can be summarized by the following six steps.

(a) Collect typhoon genesis data and RCP 8.5 monthly data during 1982 ~ 2100.
(b) Compute GPI by using the RCP 8.5 monthly data in the study area.
(c) Update the GPI by using the information of the typhoon genesis point during 1982 ~2010.
(d) Estimate the probability distribution of the GPI obtained at (c) step.
(e) Conduct the statistical analysis which is given by

   i.   Initialize the GPI ranges to be corresponded to density of 0.15, 0.1 and 0.05 according to the probability distribution
   ii.   Count the region corresponding to each GPI range for each month.

We divided the duration from 1982 to 2100 into four period, 1982~2010, 2011~2040, 2041~2070, and 2071~2100. Then, following three steps were conducted as the statistical analysis.

   iii.   Calculate the probability of each cells by employing below equation (x: number of cells)
$$\frac{x}{348} \times 0.15 (or\ 0.1\ or\ 0.05)\ \text{ in } 1982\text{~}2010$$
$$\frac{x}{360} \times 0.15 (or\ 0.1\ or\ 0.05)\ \text{ in } 2011\text{~}2040, 2041\text{~}2070 \text{ and } 2071\text{~}2100$$
   iv.   Calculate the number of typhoon genesis in each cell which was as same as the one used to obtain the GPI
   v.   Obtain the probability at each cell by multiplying the area resulted from the step iv with the number of the typhoon genesis.

(f) Estimate the result of step v to be potential region on the typhoon genesis.

3   Data

The typhoon data were obtained from Regional Specialized Meteorological Center (RSMC) best tracks of 1982 ~ 2010. A total number of 685 typhoons have generated through the study area of 0.625°N ~ 40.625°N and 111.5625°E ~ 171.5625°E which covers Korean peninsula in that duration (see Figure 1).
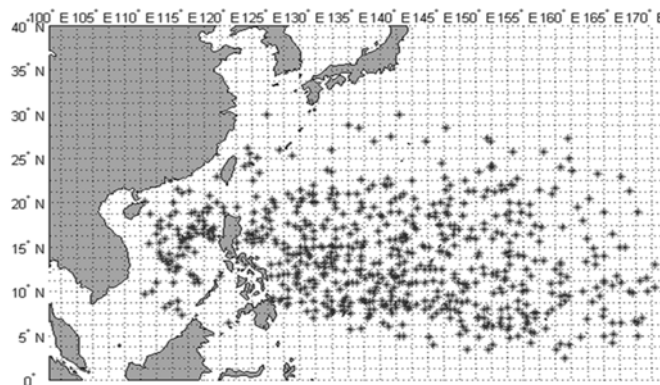
Figure 1. The black points show individual genesis event over the period from 1982 to 2010.

To calculate GPI, we used RCP (Representative Concentration Pathway) data of IPCC AR5. We also used RCP 8.5 (monthly data) scenario which corresponds to a high greenhouse gas emissions pathway compare to the scenario literature. The RCP scenario provides parameters to compute GPI suggested by Emanuel (2004) given by

$$GPI = \left|10^5 \eta_{850}\right|^{\frac{3}{2}} (1 + 0.1 V_{shear})^{-2} \left(\frac{PI}{70}\right)^3 \left(\frac{H_{700}}{50}\right)^3, \tag{1}$$

where η is the absolute vorticity at 850hPa in s[-1], H is the relative humidity at 700hPa in percent, PI is the potential intensity in ms^{-1}, and V_{shear} is the magnitude of the vertical wind shear between 850 and 200hPa in ms^{-1}. The technique used to compute potential intensity, PI, is a generalization of that described in Emanuel (1995) to take into account dissipative heating, in addition to SST, atmospheric temperature and mixing ratio at various pressure levels.

4   Distribution of GPI based on RCP 8.5 monthly data

We studied the GPI space distribution using RCP 8.5 monthly data during 1982~2100. The GPI was calculated at 1,089 points with intervals of 1.25°, and 1.875° at latitude and longitude, respectively, in the area of 0.625°N ~ 40.625°N and 111.5625°E ~ 171.5625°E.

To estimate the typhoon genesis points based on the GPI, the monthly GPI corresponding to each typhoon occurred during 1982 ~2010 has been calculated. And we estimated the probability distribution of GPI. As shown in figure 2, the ranges of GPI are 0~5, which are available to describe as the GEV(Generalized Extreme Value) distribution. The GEV distribution consists of σ=2.1633, μ=2.4865, and K=0.2217. The GPI ranges corresponding to 2σ about the mean μ is from 0.3232 to 4.6498．The number of typhoon included in this range is approximately 57.2% out of the total number of typhoon.
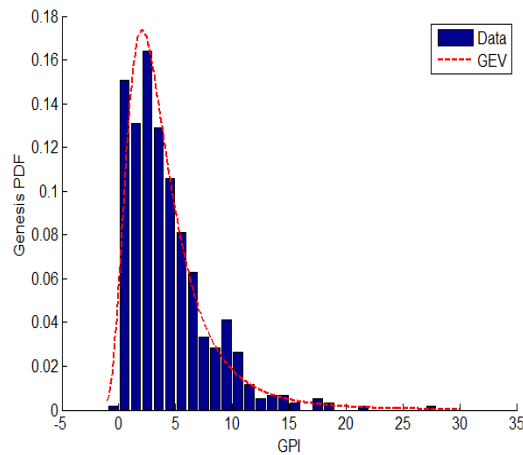
Figure 2. Distribution of GPI corresponding to the historical typhoon genesis points.

We calculated the GPI ranges when the probability density was greater than 0.15, 0.1 and 0.05 on the GPI distribution (see Figure 2). Each case is called as 0.15GPI, 0.1GPI and 0.05GPI, respectively. The corresponding GPI ranges are $1.1385 \leq 0.15GPI \leq 3.22511, 0.4314 \leq 0.1GPI \leq 4.63055$, and $0 \leq 0.05GPI \leq 6.918$. Using these results, we estimated flow of the GPI distribution with particular range during 1982~2100.

Figure 3 shows increase and decrease of GPI during 1982~2100. Each figure describes differences of time-averaged GPI between 2011~2040 and 1982~2010, 2041~2070 and 2011~2040, and 2100~2071 and 2070~2041. All panels in Figure 3 show that the GPIs are increasing around Northwest Pacific. Particularly, the GPIs in the area of 20~30° N are highly increased than other area.

Here, we analyzed spatial probability distribution based on 0.05/0.1/0.15GPI. Calculation procedure is the same as step e)-iii, iv and v mentioned in Section 2. Figure 4 shows normalized probability distribution corresponding to 0.15GPI during each period. Each max probability was 0.06767, 0.06833,

(a)   (b)   (c)
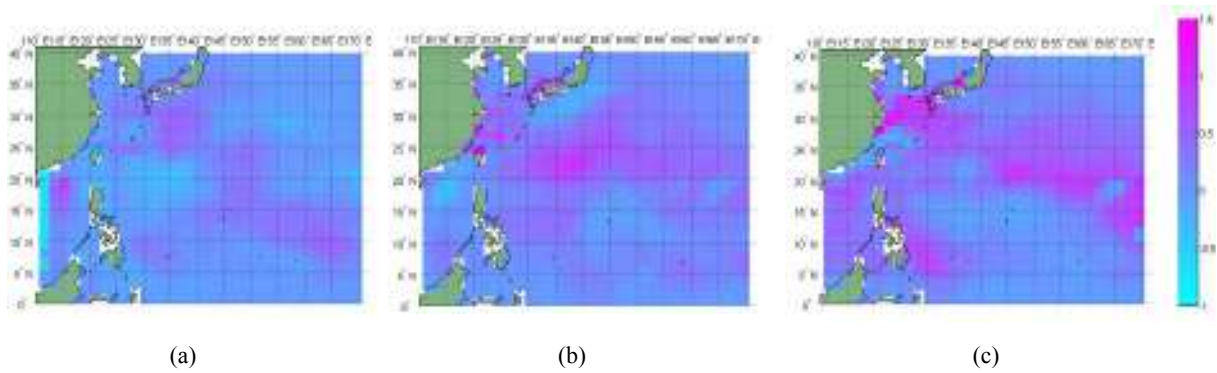
Figure 3. Differences of time-averaged GPI between (a) 2011~2040 and 1982~2010, (b) 2041~2070 and 2011~2040, and (c) 2100~2071 and 2070~2041. These figures show the increase and decrease of GPI during 1982~2100.

0.07 and 0.06875. Those values are closely calculated. Comparing the overall probability distributions, the areas with the high probability are heading southward s while the areas with the low probability are heading eastwards.

1982~2010   2011~2040

2041~2070   2071~2100
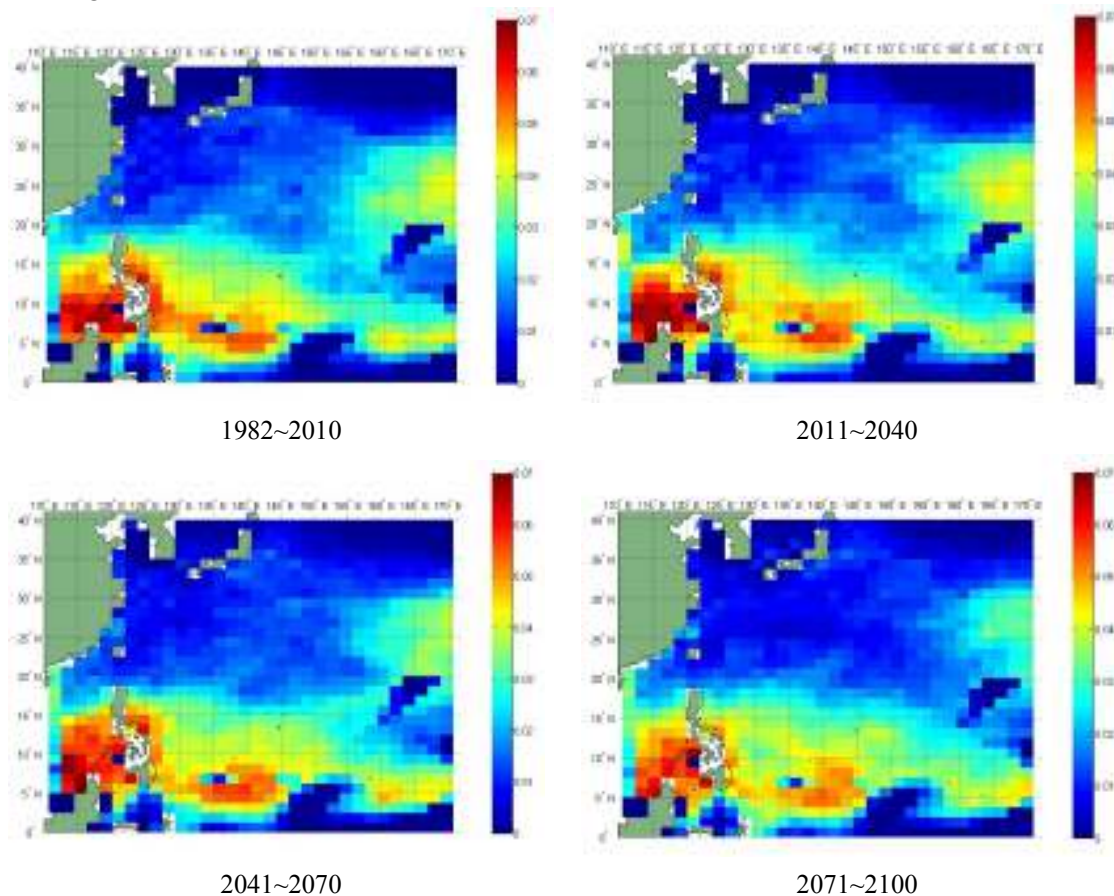
Figure 4. Probability distribution of 0.15GPI during four periods.

Lastly, we calculated the number of typhoon genesis in each cell which was as same as the one used to obtain the GPI. We obtained the density at each cell by multiplying the probability resulted from the step ii with the number of the typhoon genesis. As going to the far future, the areas with low probability are having even lower values while the areas with high probability are having even higher values.

1982~2010   2011~2040

2041~2070   2071~2100
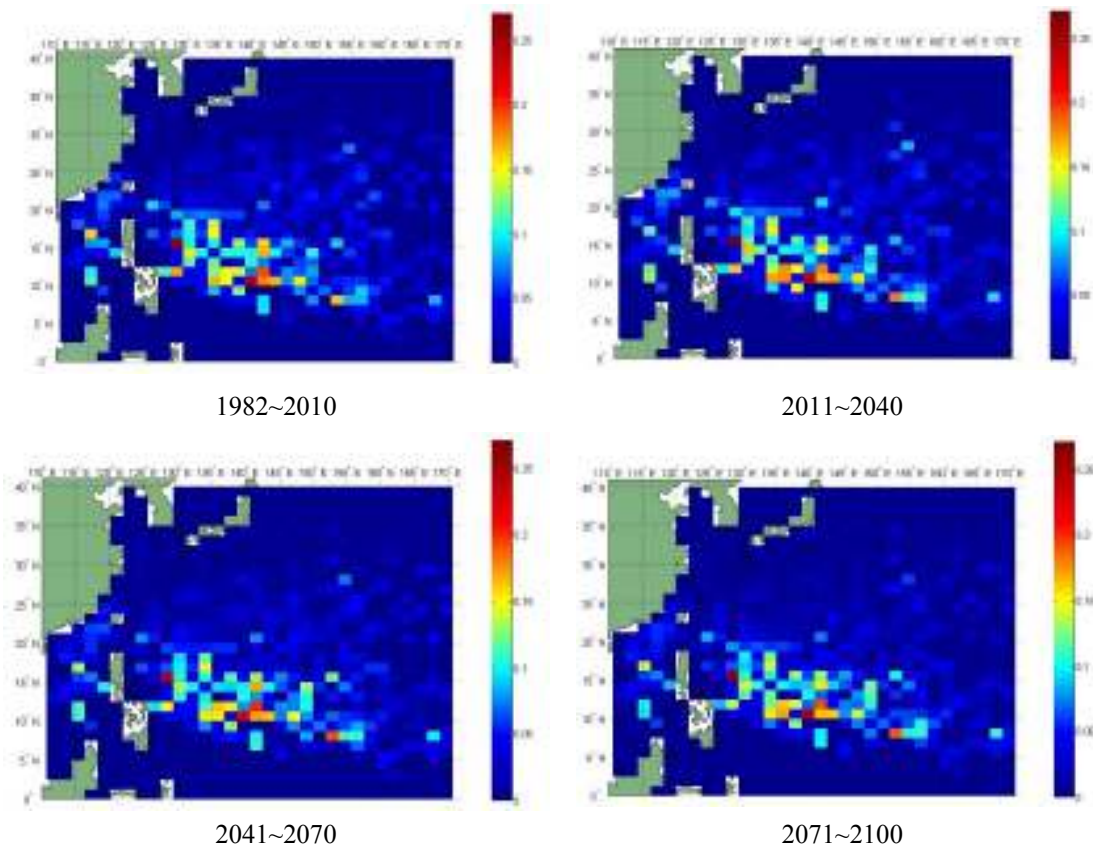
Figure 5 Spatial density of 0.15GPI during four period

5   Conclusion

In this paper, we analysed the spatial estimation of future typhoon genesis using climate change scenario. To this end, we firstly calculated Genesis Potential Index (GPI), which have developed by Emanuel(2004), using RCP 8.5 monthly data of IPCC AR5 during 1982~2100. This index included the Potential intensity (PI), relative humidity, absolute vorticity at 850hPa and wind shear at 850hPa and 200hPa. Also, the spatial distributions of GPI were analyzed by calculating the GPIs at 1,089point with intervals of 1.25°, and 1.875° at latitude and longitude, respectively, in the area of 0.625°N ~ 40.625°N and 111.5625°E ~ 171.5625°E.

To estimate the typhoon genesis point based on GPI, the monthly GPI corresponding to each typhoon occurred during 1982 ~2010 has been calculated. And we estimated the probability distribution of GPI. The ranges of GPI are 0~5, which can be plotted with the GEV(Generalized Extreme Value) distribution. And we define 0.05, 0.1 and 0.15GPI using the density of GEV distribution. The typhoon genesis probability distributions were obtained during 1982~2010, 2011~2040, 2041~2070 and 2071~2100 using 0.05/0.1/0.15GPIs. The distribution of all period showed that area with high value occurred in the lower latitude. The area with low value was going eastward around 15~30N °, the east area shown low value with the passage of time. And Philippines area had high probability than other area during all periods. Also, we estimated potential region on the typhoon genesis using typhoon genesis probability distribution and historical typhoon information. As probability distribution of four periods, the spatial density shows that east area shown low value with the passage of time. Using this result, we can estimate the potential region on the typhoon genesis in the future. As a results, it can be expected that we can take advantage of the genesis model development by estimating the points of the typhoon genesis resulted from this study.

Acknowledgement

References

Camargo, Suzana J.; Kerry A. Emanuel; Adam H. Sobel, (2007). Use of a Genesis Potential Index to Diagnose ENSO Effects on Tropical Cyclone Genesis. *J. Climate, 20, 4819–4834.*

Kerry A. Emanuel; David S. Nolan, (2004), Tropical cyclone activity and the global climate system, *26ᵗʰ conf. on Hurricanes and Tropical Meteorology, Miami, FL, Amer. Meteor. Soc., 10A.2-3*

IPCC, (2007). Climate Change 2007*, Report of the Intergovernmental Panel on Climate Change, UNEP*

Marja Bister; Kerry A. Emanuel, (2002). Low frequency variability of tropical cyclone potential intensity 1. Interannual to interdecadal variability, *Journal of geophysical research*, vol. 107, no. D24, 4801.

Murakami, H., and B. Wang, 2010: Future change of North Atlantic tropical cyclone tracks: Projection by a 20-km-mesh global atmospheric model. *J. Climate*, 23, 2699–2721

Modelling of wind action on high-rise buildings
– Warsaw Trade Tower case study

Michal Cwik[1]

[1]Faculty of Civil Engineering, Warsaw University of Technology, Poland
Corresponding author: Michal Cwik, michal.cwik@op.pl

Abstract

This paper presents a wind-modelling study of 208 m high Warsaw Trade Tower (WTT) building which is a subject of author's doctoral dissertation. The study includes full-scale measurements, wind-tunnel tests and computational fluid dynamics (CFD) simulations. The basis of the project was a proposed approach in which the assessment of structural health of high-rise buildings can be carried out by modelling and evaluating its response to wind action. In the first section, a general idea and an overview of the research project are described. Full-scale measurements, aimed at determining the displacement of the WTT building with simultaneous measurements of wind speed and direction, are presented in the second section. The third section provides a description of the wind-tunnel investigation. In fourth section CFD simulations are described. The aim of these parts of the research was to determine pressure distribution over the façade of the WTT building. A summary and conclusions of the research, as well as the future research are described in last section of the paper.

1 Introduction

The design working life of the high-rise buildings usually ranges between 50 to 100 years, sometimes even more. At that period a structure should remain safe, serviceable and durable without major repair being necessary. Obviously it is impossible to fulfil these requirements without appropriate maintenance. Apart of the standard maintenance activities, it is necessary to undertake periodic inspections of the structure. Such inspections should provide information on the condition of the building. Due to the possibility of fatigue, corrosion as well as the deterioration caused by other phenomena, comprehensive inspections require access to all components of a structure. For a number of reasons, such typical inspections are expensive, time-consuming and sometimes introduce significant technical challenges. Consequently, these problems may result in adjusting or even limiting the scope of inspections to suit the needs of specific buildings. This situation can be considered as inappropriate and requiring the development of relevant solutions.

Having regard that it is almost impossible to access and evaluate every part of a structure, Cwik et al. (2013) proposed solution, referring to high-rise buildings, which principle is not to examine the structure itself but rather to examine and analyse its response to a known loading. A comparison of the theoretical and measured responses would then constitute the indicator of a structural condition. Authors expect to obtain a fair degree of similarity in theoretical and physical displacements of high-rise buildings which are in a good structural condition, and clear differences for buildings with structural deficiencies. Proposed method is based on comparison of displacements of the top of the high-rise building caused by wind action. Such an approach requires evaluating wind pressure distribution over the building's façade, which would be used for determining theoretical displacement of the building's structure.

The primary aim of the project was to investigate a possibility of evaluating average wind pressure distribution over building's façade, corresponding to conditions observed during full-scale measurements of building's displacement. The aim refers to the proposed method of assessing of structural health of high-rise buildings with a use of wind-modelling. The scope of the project includes full-scale measurements, wind-tunnel tests and CFD simulations of the WTT building.

2   Full-scale measurements

The research project deals with wind-modelling study of 208 m high (184 m excluding the spire) WTT building (Fig. 1a). Constructed during 1997-1999 and mainly used for commercial purposes, it is currently the third tallest building in Poland. Building structure is composed of a covered exterior steel framed tube lateral system and an interior reinforced-concrete core. It is 52×27 m in plan. The shape of the building reminds semi-cylinder with flat western façade and with cuboids intersecting the curved rest of the façade. According to field measurements of the height of surrounding buildings and terrain elevation, the nearest surroundings are 18.4% built-up with buildings exceeding 3 m and 10.5% with buildings exceeding 15 m. The average height of the roughness elements is of 4 m. Field measurements showed also that analysed area has a constant elevation and is representative for other surrounding areas.

The aim of full-scale measurements was to evaluate physical response of the WTT building caused by measured wind action. The scope of this part of the research included displacement measurements of the building's roof and simultaneous measurements of wind speed and direction.

Measuring system was based on Real-Time Kinematic Global Navigation Satellite System (RTK-GNSS) devices manufactured by Leica Geosystems and a weather station manufactured by Vaisala. Two GNSS receivers (rover stations) together with the weather station were installed on the roof of the WTT building (Figs 1b, c, d). The third receiver (reference station) was located on the roof of Faculty of Civil Engineering of Warsaw University of Technology building (Fig. 1e). Sampling frequency of rover stations was of 20 Hz and 1 Hz. Weather station measurements were conducted with a frequency of 1 Hz. General operating scheme of the measuring system is shown in Figure 2.

The accuracy of the RTK-GNSS measurements was estimated with a use of: part per million values of GNSS receivers, Coordinate Quality indicators introduced by devices manufacturer and measurements of the top of the WTT building during negligible environmental actions, in particular minimal wind speed. Analysis showed that accuracy is of ±10 mm for horizontal coordinates and ±30 mm for vertical. These values refer to visibility of 6-8 satellites and 90% level of confidence.

(a)   (b)   (c)   (d)   (e)

Figure 1. Warsaw Trade Tower building (a) and full-scale measuring equipment:
RTK-GNSS rover stations (b, c), weather station (d) and RTK-GNSS reference station (e).
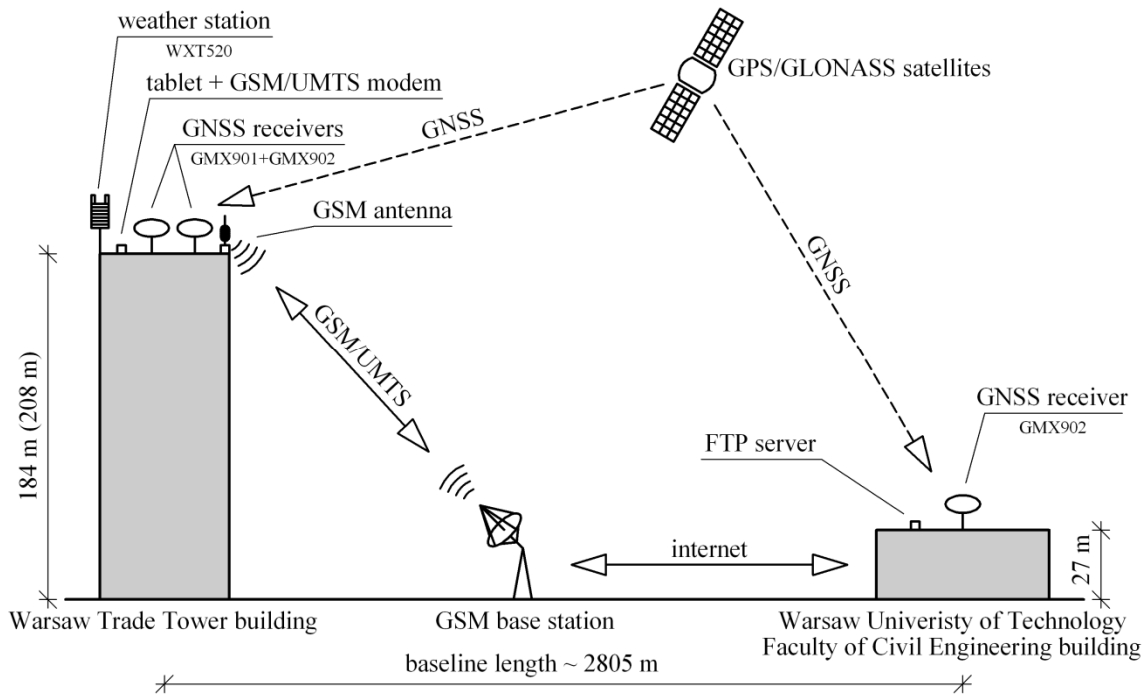
Figure 2. General operating scheme of the full-scale measuring system.

From a set of 6-month observations, 30-second measurement period from 11.03.2012 and time from 6:36:00 to 6:36:30 am was chosen for final analysis. Figure 3 presents time history of wind speed and direction measurements for selected period together with preceding and following 30-second periods. The measurements refer to the position of the weather station which was located in 1/3 distance between the lowest and the highest point of the upper edge of western façade, 2 m above interior edge of the parapet wall of the roof at height of 181.5 m above ground. During measurements, precipitation with intensity of 2.5 cm/h was observed. Temperature was of 1.9°C and humidity of 86%. The displacement of the top of the WTT building was estimated with a use of information derived from 15 satellites (GPS and GLONASS). The number of positions determined during selected period was of 516. Results of the RTK-GNSS measurements are shown in Figure 4. Due to the downtown character of the surrounding area and the early hours of the measurements, i.e. 38 minutes after sunrise, the possible displacement of the top of the building due to non-uniform thermal load of the façade was considered as negligible. Table 1 presents averaged results of full-scale measurements.
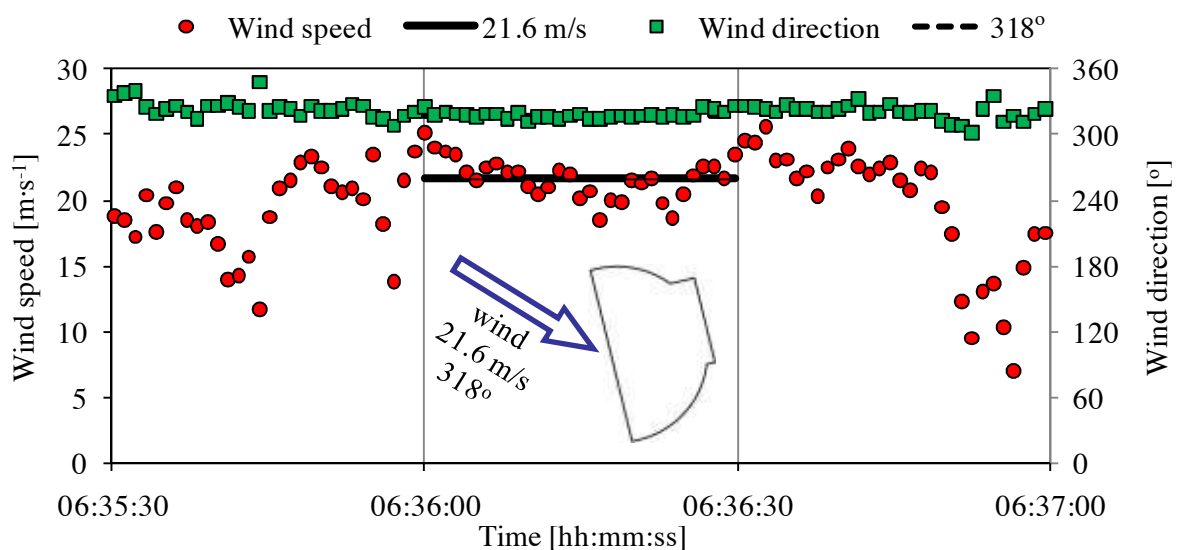
Figure 3. Time history of wind speed and direction for selected, preceding and following 30-second periods.
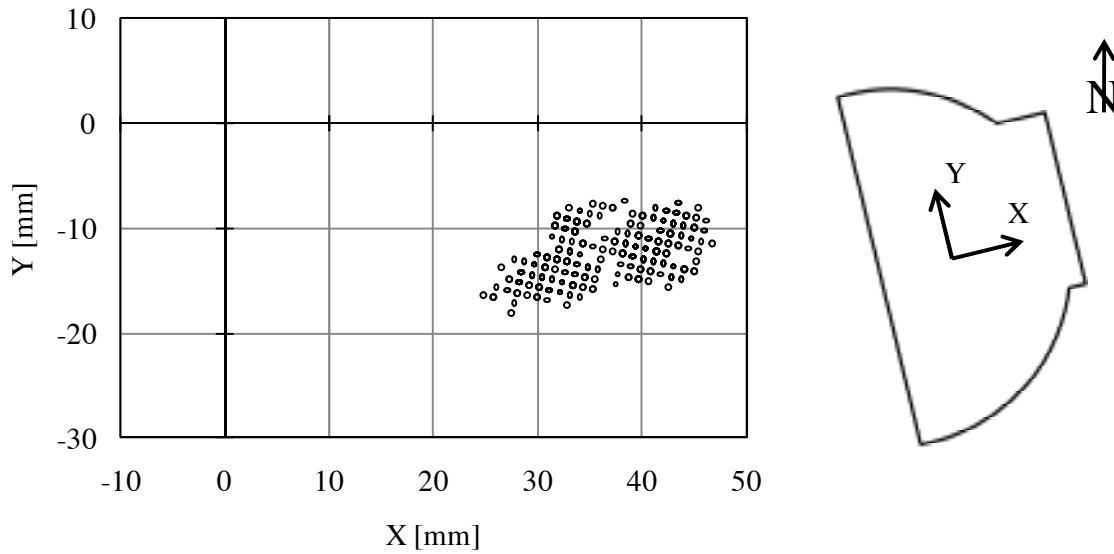
Figure 4. Horizontal position of the top of the WTT building for the selected 30-second period.

Table 1. Average 30-seconds values of WTT building displacement, wind speed and direction.

Wind		Displacement [mm]		
speed [m/s]	direction [°]	X	Y	Z
21.6	318	37	12	2

3   Wind-tunnel tests

The aim of wind-tunnel tests was to evaluate average pressure distribution over the façade of the WTT building under certain wind conditions. The scope of the study included determination of wind pressure values at 117 measuring points distributed over all façades of the model. Research has been conducted at a Boundary-Layer Wind-Tunnel (BLWT) located at the Council for Scientific and Industrial Research (CSIR) in Pretoria, South Africa (Fig. 5).

CSIR's BLWT was established in the early 1980s. Since then several improvements were introduced to the instrumentation and the data acquisition system. CSIR's BLWT is an open-circuit type with a boundary-layer development length of 14 m and a cross-section of 2 m by 1 m with a turntable of 1.8 m diameter. It is equipped with a single centrifugal fan powered by a thyristor-controlled 75 kW variable-speed motor which allows obtaining variable air speeds of up to 22 m/s. The inlet area consists of 50 mm tripping wall and four 250 mm high x 100 mm wide triangular spires.
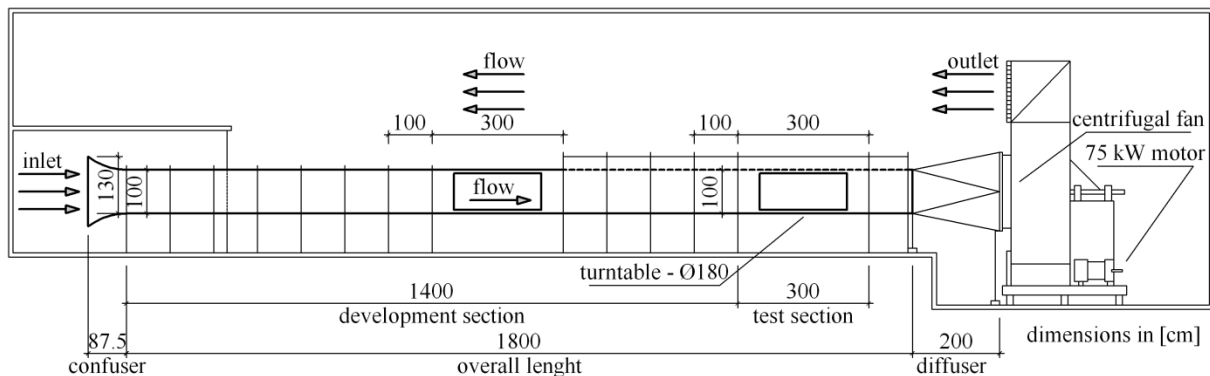
Figure 5. Schematic diagram of the CSIR's Boundary-Layer Wind-Tunnel.

The WTT building model (Fig. 6) and the model of its immediate surroundings (Fig. 7) were constructed at a geometric scale of 1:500. The surrounding model contained an area of the city within a circle with a radius of 450 m around the WTT building. Objects with height less than 3 m were not included in the modelling. The overall number of structures in the analysed area exceeded 250.
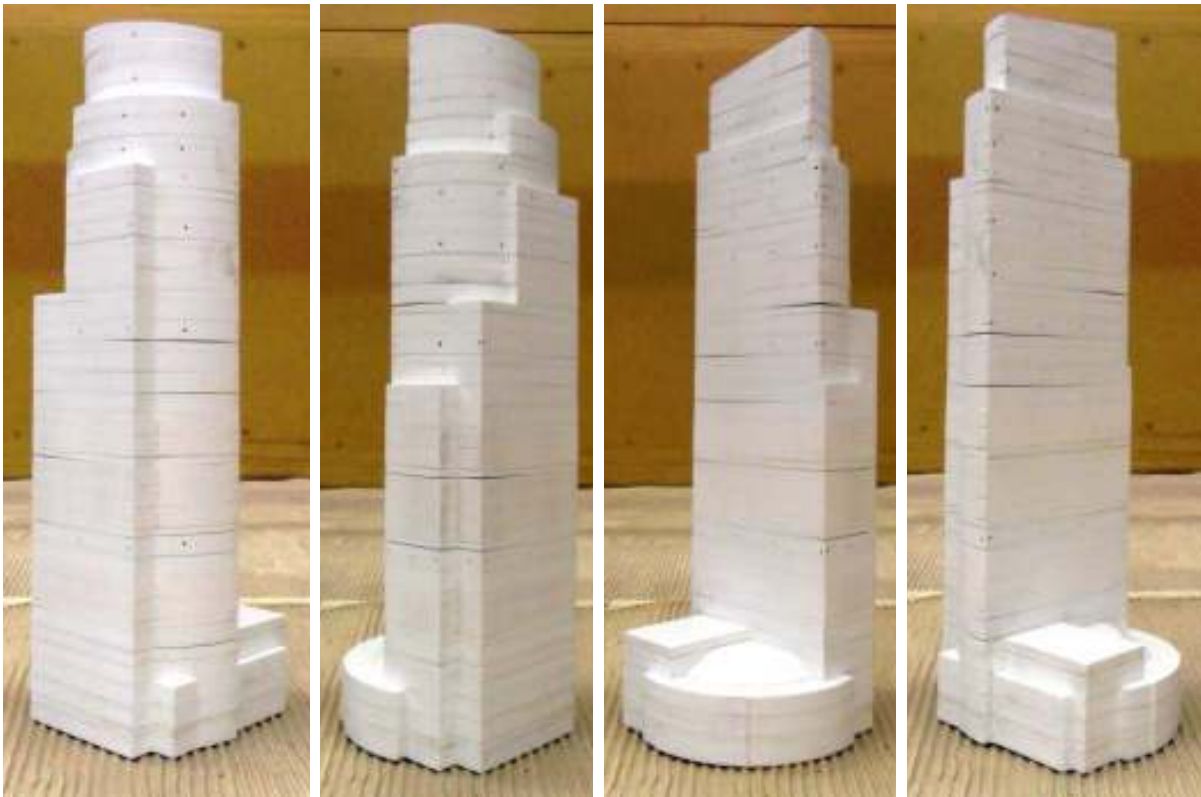
Figure 6. WTT building model used for wind-tunnel tests.

Figure 7. Surroundings model used for wind-tunnel tests.

Initially, measurements of the horizontal wind speed and turbulence intensity profiles were conducted. In accordance to field measurements, it was assumed that analysed area corresponds to terrain category between III and IV according to code EN 1991-1-4:2005 with emphasis on the category IV. A comparison between the wind speed and turbulence intensity profiles obtained in tunnel tests with those specified by the loading standard showed fair similarity. Subsequently, pressure measurements for a full range of wind azimuths have been carried out. Measurements included 25 wind directions. Synchronous Multi-Pressure Sensing System (SM-PSS) was used for pressure measurements. Finally, measurements of the wind speed at a location corresponding to the position of the weather station in full-scale were carried out. These measurements, which included 35 wind directions, were done in order to correlate the results obtained in wind-tunnel tests, CFD simulations and full-scale measurements.

Average values of the external pressure over building façade, shown in Figure 8, were calculated for undisturbed wind speed of 24.2 m/s at height of 181.5 m and direction of 320°. These conditions, according to correlation analysis carried out using measurements at the location of the weather station, correspond to conditions observed during full-scale measurements. All results are given in Pa.
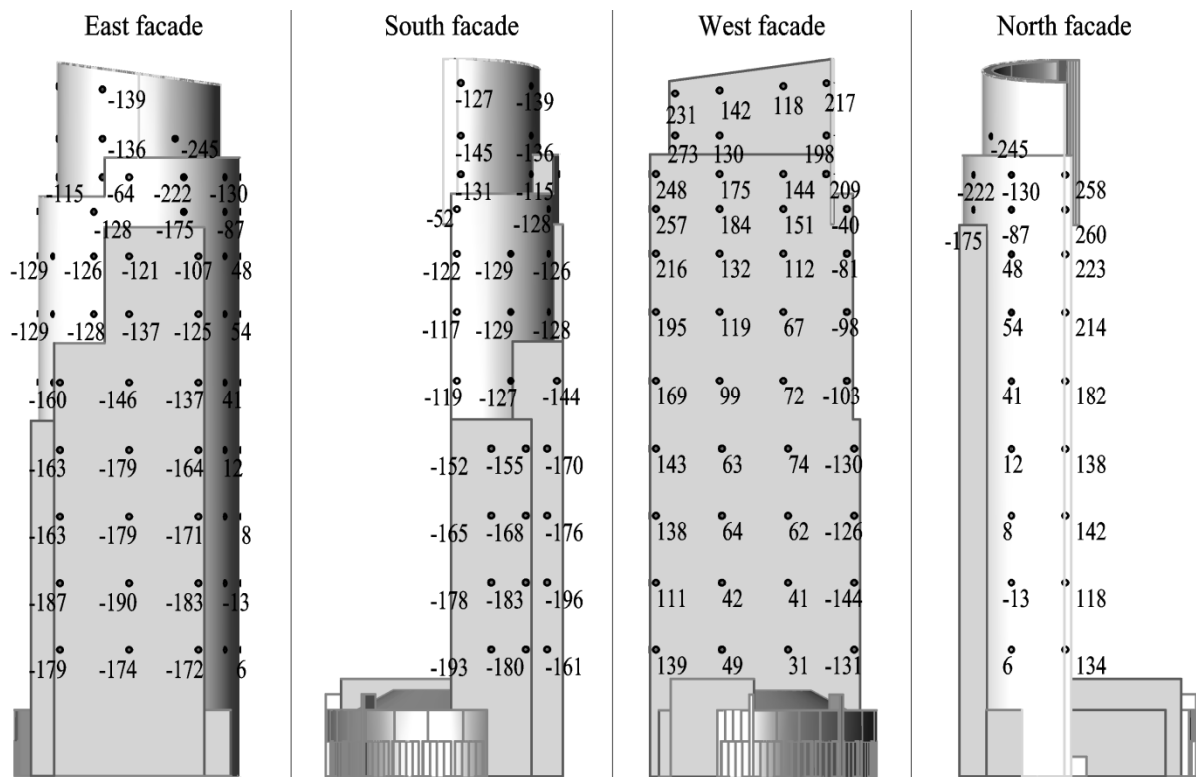
Figure 8. Average wind pressure over WTT facades.

4   CFD simulations

The aim of CFD simulations was to evaluate average pressure distribution over the entire façade of the WTT building under conditions corresponding to wind-tunnel tests. The scope of the study also included verification of simulations and validation of results.

Numerical model of the WTT building and surroundings (Fig. 9) was similar to physical model used in wind-tunnel tests. Computational domain (Fig. 10) was of 9 m long, 1 m high and 2 m wide. Dimensions of the cross-section of the domain correspond to wind-tunnel geometry. Length of the domain was determined having regard to the height of the WTT building. The distance between the inflow boundary and the WTT building was of ~8·H and the distance between WTT building and outflow boundary was of ~15·H, where H is the WTT building height. Considering relatively large size of the domain, it was decided to divide the domain into 62 parts. This allowed applying different

discretization parameters separately for each part of the domain. As a result, in areas with less impact on the simulation number of finite volumes was significantly reduced. Whereas thickened grid was used in areas with a major impact on results. Blockage effect ratio varied from 1.3% up to 2.4% depending on flow direction. For flow direction of 320°, which corresponds to conditions observed during full-scale measurements, blockage effect ratio was of 1.6%.

Figure 9. 3D digital WTT building and surroundings model – central section of the computational domain.
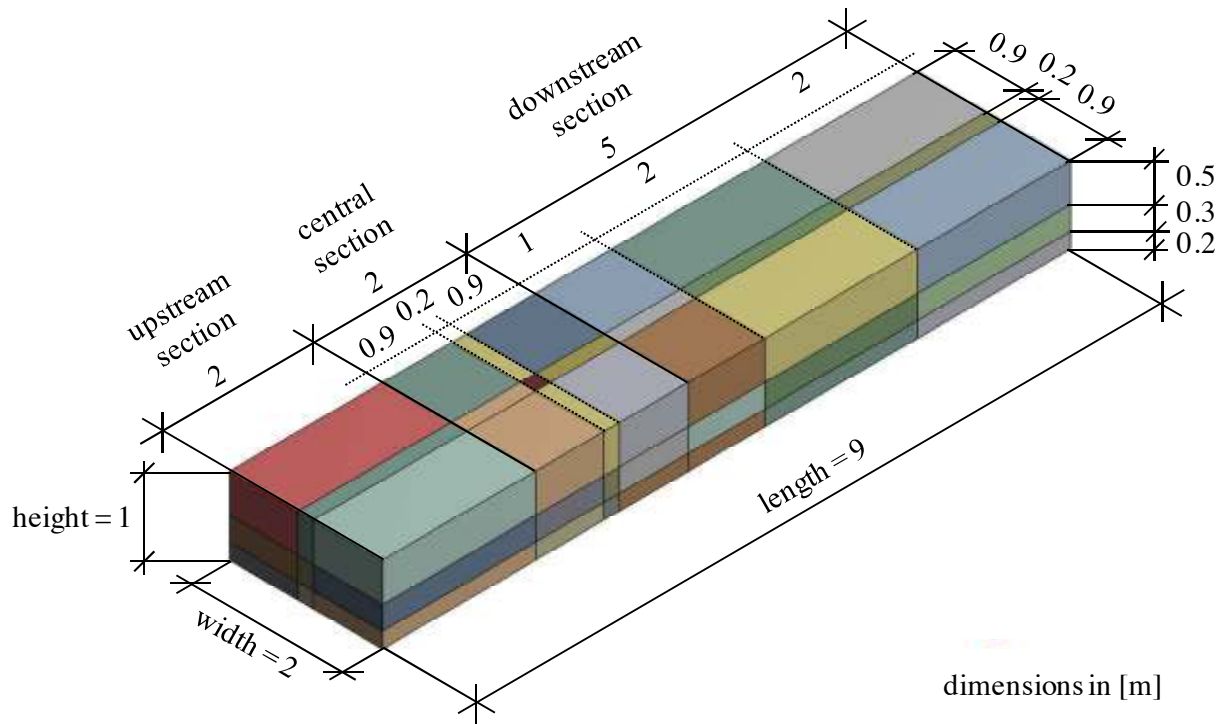
Figure 10. Computational domain.

The set of boundary conditions used in simulations are shown in Figure 11a. No-slip wall boundary condition was used to model top, sides and bottom of the domain. The same condition was used for surroundings and the WTT building models. The inlet area was prescribed by wind speed and turbulence intensity profiles obtained from wind-tunnel tests. The flow exit was modelled by outflow boundary condition. Calculations were performed using Ansys Fluent 13.0 software. Steady Reynolds Averaged Navier-Stokes (RANS) equations were solved using k-ε turbulence model with Renormalization Group Theory (RNG) modification.

In terms of verification, four cases of grids were considered: coarse (297,000 elements), medium (693,000), fine (1,411,000) and super-fine (4,016,000). Verification included comparative analysis of solution convergence, wind speed and direction at the location of weather station and wind pressure over WTT building façade. Figure 12 shows an example of the comparison of wind pressure over WTT façades at the model height of 0.238 m (119 m in full-scale) for four types of grids. Complete analysis showed that with an increase in grid density the solution is converging. Therefore, final calculations were performed with a use of super-fine grid (Figs 11a, b).

(a)   (b)
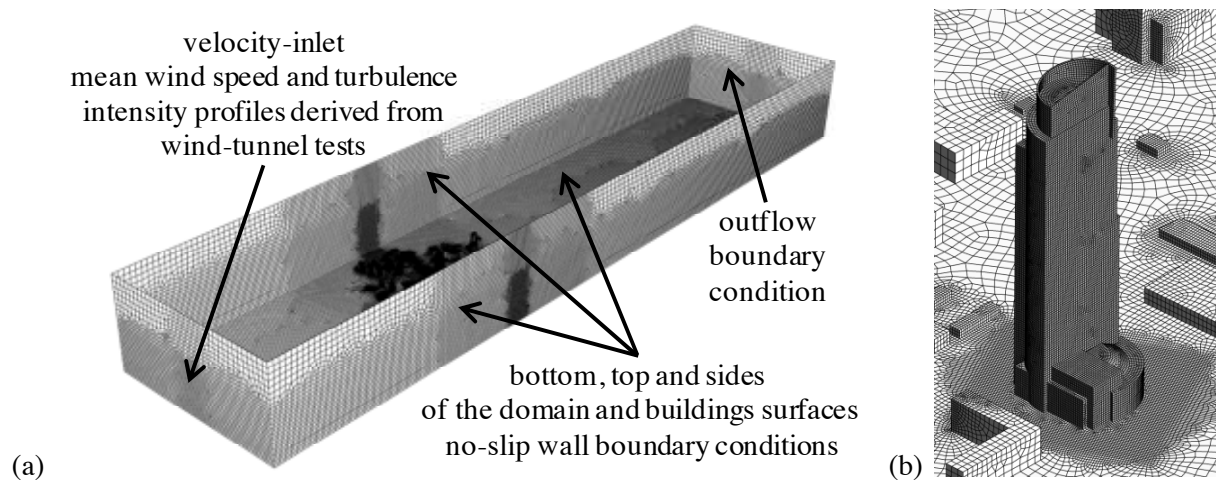
Figure 11. Computational super-fine grid at entire domain with boundary conditions indicated at each surface (a) and at WTT building surfaces and nearest surroundings (b).
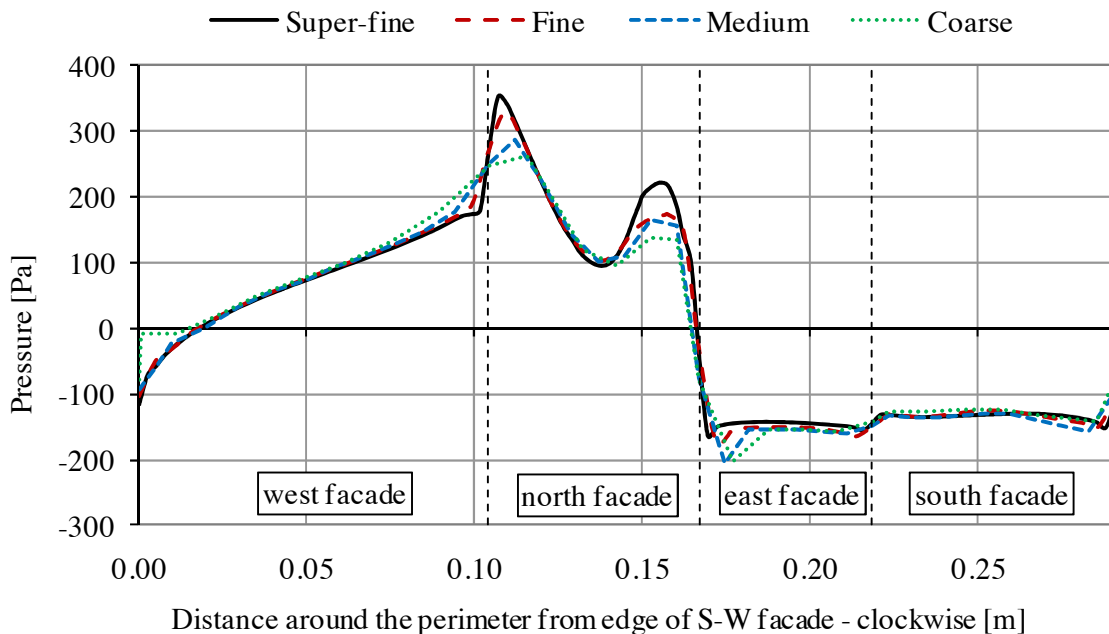
Figure 12. Comparison of wind pressure over WTT building façades at height of 0.238 m for four types of grids.

Firstly, measurements of the wind speed at the location of the weather station were carried out. As well as in the wind-tunnel tests, these were done in order to the correlation of the results obtained in full-scale measurements with the results from model tests and numerical calculations.

Next, simulations with conditions corresponding to those observed in full-scale measurements, were performed. Validation of the results obtained in CFD simulations with results from wind-tunnel tests included comparative analysis of wind speed profile, wind speed at the weather station localisation and average wind pressure over WTT building façade. Figure 13 shows an example of the comparison of average wind pressure over WTT building façades at the model height of 0.238 m (119 m in full-scale) from tunnel tests and numerical simulations. Comprehensive validation showed good agreement of the results obtained in CFD simulations with results derived from wind-tunnel tests.

Calculated average wind pressure distribution over building façade is shown in Figure 14. Wind speed and direction correspond to conditions observed during full-scale measurements.
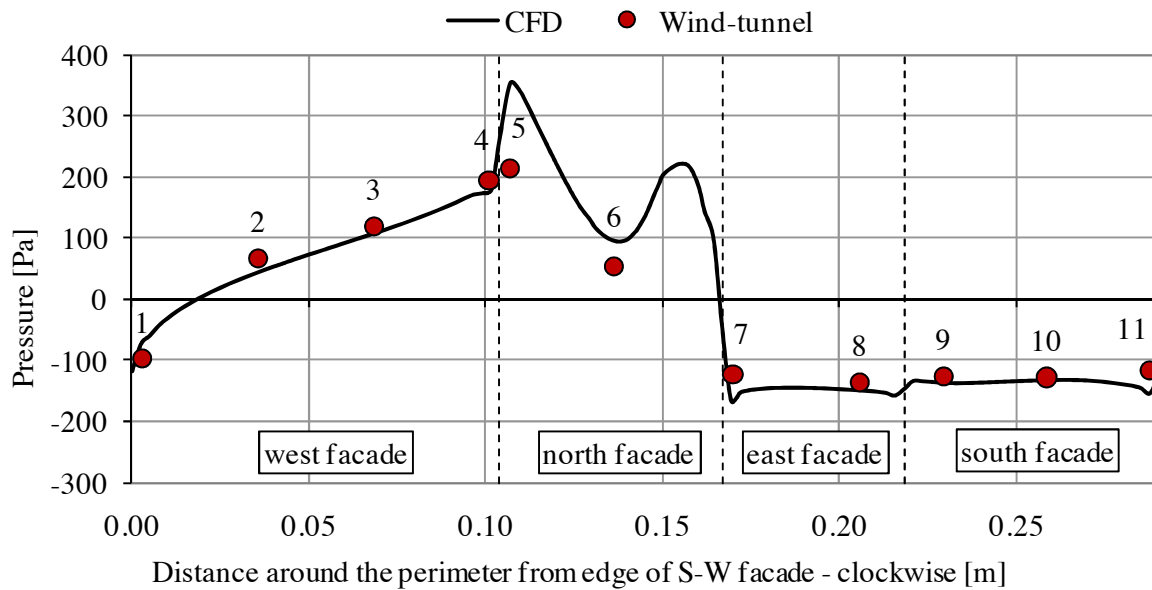
Figure 13. Comparison of average wind pressure over WTT building façades at height of 0.238 m derived from wind-tunnel tests and CFD simulations.
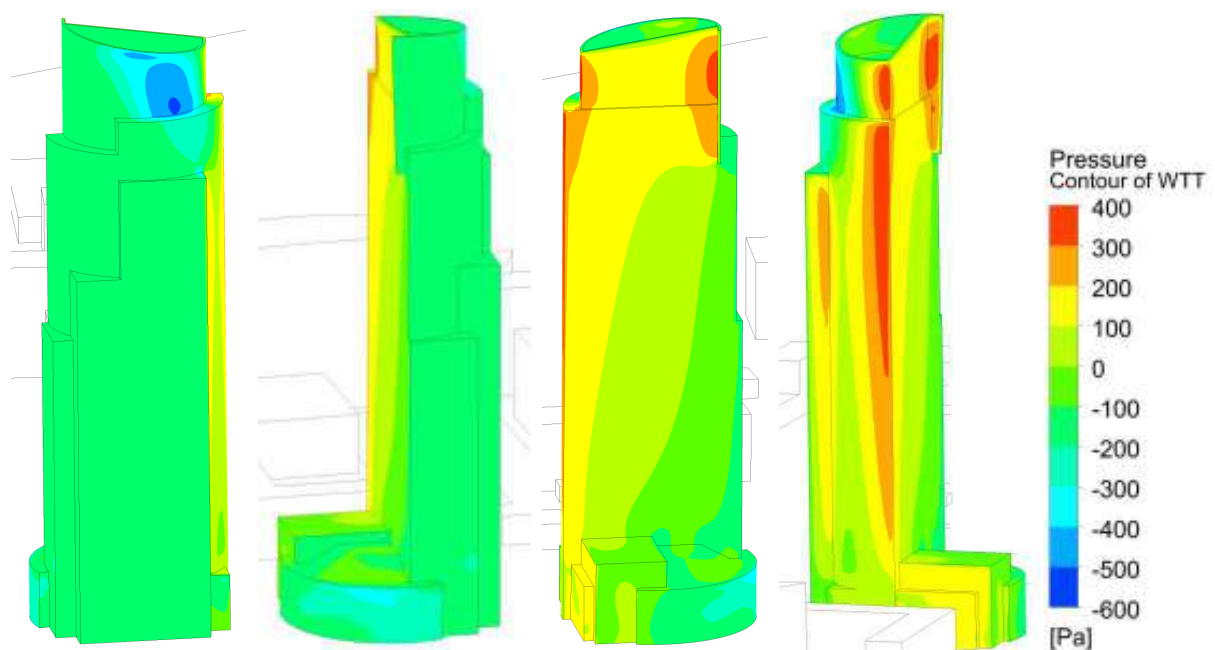
Figure 14. Contour maps of average wind pressure distribution over WTT building facades.

5   Conclusions and future research

Full-scale measurements of the high-rise WTT building with a use of RTK-GNSS technology and the weather station, are described. Observed displacement of the top of the WTT building, as well as wind speed and direction, are presented. Average wind pressures distribution over the façade of the WTT building, evaluated with the use of wind-tunnel technology and CFD simulations, are shown.

Obtained results proved the possibility of evaluating average wind pressure distribution over the building's façade, corresponding to conditions observed during full-scale measurements of building's displacement. Evaluated average wind pressure distribution and measured displacement of the top of building could be used for identifying potential structural deterioration of the WTT building.

The scope of future research includes finite element method (FEM) calculations. The aim is to evaluate theoretical displacement of the WTT building caused by wind loads derived from wind-tunnel tests and CFD simulations. The result would represent the theoretical response of the structure subjected to wind loads, which correspond to those observed in full-scale measurements. A comparison of the theoretical and measured responses would then constitute the indicator of structural condition. This part of the research is currently ongoing. Preliminary results show high degree of similarity in theoretical and physical displacements.

Nevertheless, as the accuracy of the RTK-GNSS measurements was of 25% of maximum building's roof displacement, further work is required to obtain more reliable results. This is planned to be achieved by improving the measuring system as well as continuing full-scale measurements in anticipation of higher wind speeds and consequently more significant displacements.

Moreover, future research includes analysis of the dynamic response of the building. It is considered that the comparison of theoretical (derived from FEM) and physical (measured in full-scale) dynamic characteristics of the building could also constitute the indicator of structural condition. This research would be an attempt to implement to high-rise buildings the method proposed by Chmielewski et al. (2009) who presented results of comparison of theoretical and measured response of the Stuttgart TV Tower. The assumption of the research conducted by Chmielewski et al. was that the changes in the first natural frequency may indicate potential damage of the tower. It is expected that similar approach could also be useful for structural health assessment process in reference to high-rise buildings.

6   Acknowledgement

References

Cwik, M., Gizejowski, M. A., and Goliger, A. M. (2013). Wind-tunnel investigations of pressure distribution over high-rise buildings. *In: Research and Applications in Structural Engineering, Mechanics & Computation: Proceedings of the Fifth International Conference on Structural Engineering, Mechanics & Computation (ed. A. Zingoni), Sep 2-4, Cape Town, RSA*, 235-236 [full text on CD, 645-650].

Chmielewski, T., Breuer, P., Gorski, P. and Konopka, E. (2009). Monitoring of tall slender structures by GPS measurements. *Wind and structures*, Vol. 12, No. 5, 401-412.

EN 1991-1-4:2005, Eurocode 1: Actions on structures - Part 1-4: General actions - Wind actions. CEN.

Numerical evaluation of evaporative cooling by mist spraying systems: validation and application

H. Montazeri[1], Bert Blocken[1,2] and J.L.M. Hensen[1]

[1]Building Physics and Services, Eindhoven University of Technology, The Netherlands
[2]Building Physics Section, Department of Civil Engineering, Leuven University, Belgium
Corresponding author: H. Montazeri, h.montazeri@tue.nl

Abstract

Mist spraying systems are increasingly used as efficient and environmentally-friendly systems to provide cooling and to enhance comfort in built environments. Computational Fluid Dynamics (CFD), among other methods, has been used in many occasions in the past to evaluate the performance of spray systems for different applications. To the best of our knowledge, a detailed evaluation of the Lagrangian-Eulerian (LE) approach for predicting evaporative cooling performance in an urban area has not yet been performed. This paper presents steady RANS CFD simulations of evaporative cooling provided by the use of mist spraying systems around and on balcony spaces of a medium-rise building. The evaluation is based on a grid-sensitivity analysis and on a two-part validation with wind-tunnel measurements. A parametric analysis is performed for different air flow conditions and spray characteristics to evaluate the performance of the spray system in mitigating the heat stress around the generic building. The thermal comfort is assessed with the Universal Thermal Climate Index (UTCI). The results show that evaporative cooling is an effective approach in providing cooling and improving thermal conditions in urban areas.

1 Introduction

Increased frequency and intensity of heat waves and heat stress are likely to cause increased illness and death as occurred in the hot summer of 2003. These problems are aggravated by the urban heat island effect (UHI). Therefore, different adaptation strategies such as evaporative cooling need to be evaluated and implemented to reduce heat stress of the outdoor and indoor environment. Mist spraying systems are increasingly used as efficient and environmentally-friendly systems to provide cooling and to enhance comfort in built environments (Montazeri et al., 2014). In a water mist spray, a cloud of very fine water droplets is produced using atomization nozzles. It enhances mixing and increases the contact surface area between the air stream and water droplets resulting in a higher rate of evaporation, which allows the ambient air to cool down.

Computational Fluid Dynamics (CFD), among other methods, has been used in the past to evaluate the performance of spray systems for different applications. In the vast majority of these studies the Lagrangian-Eulerian (LE) approach has been used in which the continuous phase (air in this study) is represented in an Eulerian reference frame while the discrete phase (water droplets in this study) is represented in a Lagrangian reference frame.

To the best of our knowledge, a detailed evaluation of the LE approach for predicting evaporative cooling in urban areas has not yet been performed. This paper presents steady RANS CFD simulations of evaporative cooling provided by the use of mist spraying systems with hollow-cone nozzles at the pedestrian level around and on balcony spaces of a medium-rise building. The evaluation is based on a grid-sensitivity analysis and a two-part validation with wind-tunnel measurements. A parametric analysis is performed for different air flow conditions and spray characteristics to evaluate the performance of the spray system in mitigating the heat stress around the generic building. The thermal assessment is performed with the Universal Thermal Climate Index (UTCI) (Błażejczyk et al, 2013).

2   Description of building

The isolated building has dimensions $W_m \times D_m \times H_m = 7.5 \times 18 \times 15$ m^3 (Fig. 1). Three balconies were positioned at each floor. Each balcony has length 4.5 m, width 1.5 m and height 0.9 m. A spray system including five hollow-cone nozzles is placed upstream of the building. The isolated building is considered to be north-south oriented and located in the city of Rotterdam, the Netherlands.
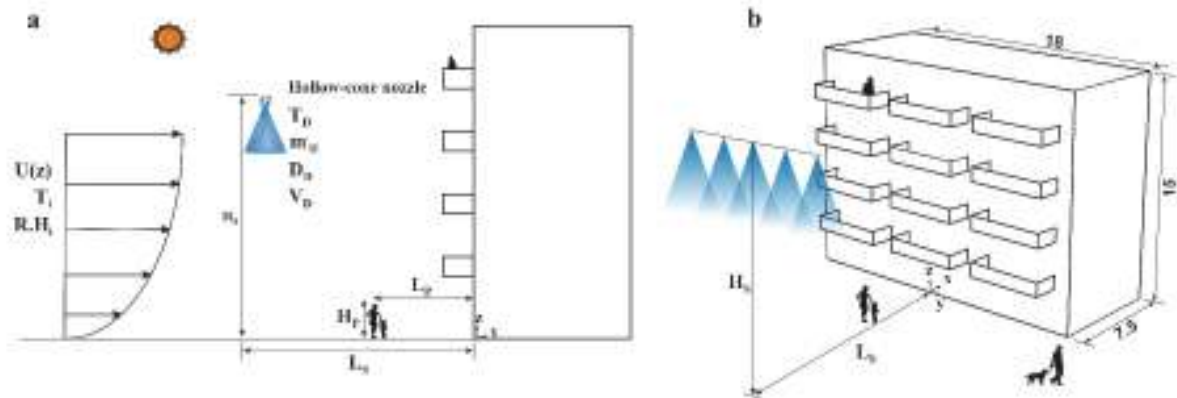
Figure 1. View of the generic building with a hollow-cone spray nozzle.

3   CFD validation study

In this paper, a two-part validation study is performed: (1) comparison of simulations and wind-tunnel measurements of pressure distribution across windward and leeward sides of a reduced-scale equivalent of the building model; (2) comparison of simulations and wind-tunnel measurements of dry-bulb temperature (DBT) and wet-bulb temperature (WBT).

3.1   Validation of surface pressure coefficients

Atmospheric boundary layer wind tunnel measurements of wind-induced surface pressure on the facade of a reduced-scale model (1:30) of the generic building were conducted by Chand et al (1998). The building had dimensions $w \times d \times h = 0.25 \times 0.60 \times 0.50$ m^3 (reduced-scale) resulting in a blockage ratio of about 6.6%. Mean surface pressures were measured along three vertical lines on the windward and leeward facade. Because of space limitations, the computational parameters and results are only briefly reported here. A detailed report can be found in Montazeri and Blocken (2013). The wind tunnel experiments are reproduced by solving the 3D steady RANS CFD simulations combined with the realizable k-ε model (Shih et al., 1995) and following the best practice guidelines by Franke et al. (2007) and Tominaga et al. (2008). The grid resolution resulted from a grid-sensitivity analysis, yielding a hybrid grid with 2,102,250 prismatic and hexahedral cells. The results show that steady RANS, in spite of its limitations, can accurately reproduce the mean wind pressure distribution across the windward facade of the building. The average deviations from the wind-tunnel measurements are 12% and 10% for the building with and without balconies, respectively.

3.2   Validation of DBT and WBT

In this paper, the experiments by Sureshkumar et al. (2008) are used for validation. In these experiments the evaporative cooling performance of a mist spray system with a hollow-cone nozzle configuration was investigated. The experiments were performed in an open-circuit wind-tunnel with a uniform air velocity profile. The test section of the wind tunnel was 1.9 m long with a cross section of 0.585×0.585 m^2 (Fig. 2a). The dry-bulb temperature (DBT) and wet-bulb temperature (WBT) variations of the air stream between the inlet plane of the test section, where the spray nozzle was installed, and its outlet plane were measured for different air flow conditions and spray characteristics. A computational model was made of the wind-tunnel test section resulting in a grid with 1,018,725

hexahedral cells. For the continuous phase flows, the 3D steady RANS equations for conservation of momentum, energy and mass were solved in combination with the realizable k-ε turbulence model by Shih et al. (1995). The discrete phase interacts with the continuous phase, and the discrete phase model sources are updated after each continuous phase iteration. The results show that CFD simulation of evaporation by using the Lagrangian-Eulerian approach can predict the evaporation process with an acceptable accuracy: the local deviations from the wind-tunnel measurement are within 10% for DBT and 5% for WBT (Figs. 2b-c).
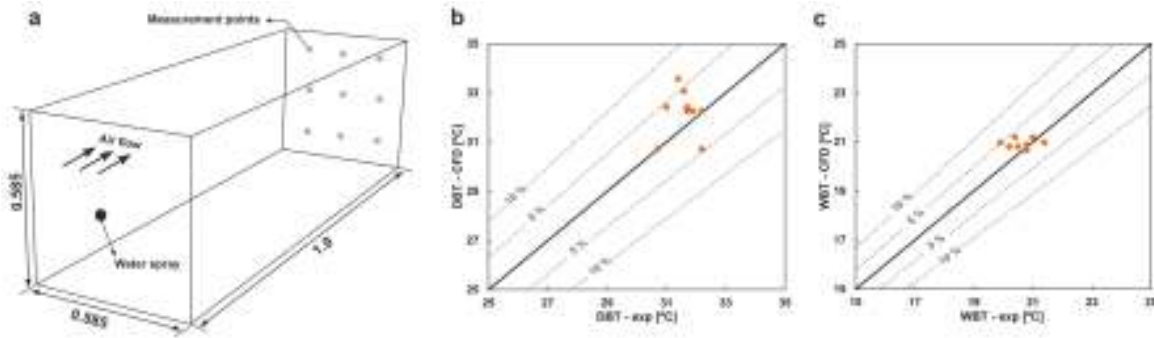
Figure 2. (a) Wind-tunnel along with measurement point positions at the outlet plane (dimensions in meter). Comparison of calculated (CFD) and measured (Sureshkumar et al 2008) (b) DBT and (c) WBT.

4   CFD simulations: computational model and parameters

A computational model was made of the building (full-scale), shown in Fig.1, according to the best practice guidelines by Franke et al. (2007) and Tominaga et al. (2008). The procedure was executed with the aid of Gambit 2.4.6, resulting in a hybrid grid with 3,755,370 prismatic and hexahedral cells.

4.1   Boundary conditions and solver settings

At the inlet of the domain, neutral atmospheric boundary layer inflow profiles of mean wind speed U (m/s), turbulent kinetic energy k (m^2/s^2) and turbulence dissipation rate ε (m^2/s^3) are imposed. The 3D steady RANS equations are solved in combination with the realizable k-ε turbulence model by Shih et al. (1995). As recommended by Blocken et al. (2007), the absence of unintended streamwise gradients in the vertical profiles of mean wind speed and the turbulence parameters is confirmed by performing simulations in an empty domain (i.e. without building present). The SIMPLE algorithm is used for pressure-velocity coupling, pressure interpolation is second order and second-order discretization schemes are used for both the convection terms and the viscous terms of the governing equations. The thermal boundary condition at the inlet is a constant temperature (35°C). A fixed vapour mass fraction is also calculated and imposed at the inlet based on the meteorological data (relative humidity 50%) of the 2003 European heat wave for the city of Rotterdam, where the generic building is assumed to be located. The Rosin-Rammler model (Rosin and Rammler, 1933) is used to determine the droplet size distribution. To analyse the performance of the spray system, a parametric analysis is performed for different spray characteristics. Because of space limitation, the results for one case are provided (see Table 1).

Table 1. Spray characteristics including water velocity (V_w), temperature (T_w) and flow rate ($\dot{m}_w$) as well as half-cone angle ($\alpha/2$).

V_w (m/s)	T_w (°C)	$\dot{m}_w$ (kg/s)	Position		$\alpha/2$ (deg)	Droplet diameters (Rosin-Rammler)				
			L_s	H_s		DRR (μm)	n	D_{min} (μm)	D_{max} (μm)	N
20	25	50	H_m	$2/3H_m$	30	369	3.67	74	518	20

5   CFD simulations: results

Fig. 3 shows the air velocity, temperature and relative humidity contours in the vertical centre plane. It can be seen that the air temperature decreases considerably close to the spray system. This reduction is extended downstream resulting in an air temperature decline area at the pedestrian level next to the building and on balcony spaces. Fig. 3c shows that the air velocity increases considerably close to the spray. This is because of the fact that the momentum lost by the droplets is obtained by the air. The CFD results in combination with the mean radiant temperature are used to assess the thermal comfort by using the UTCI.
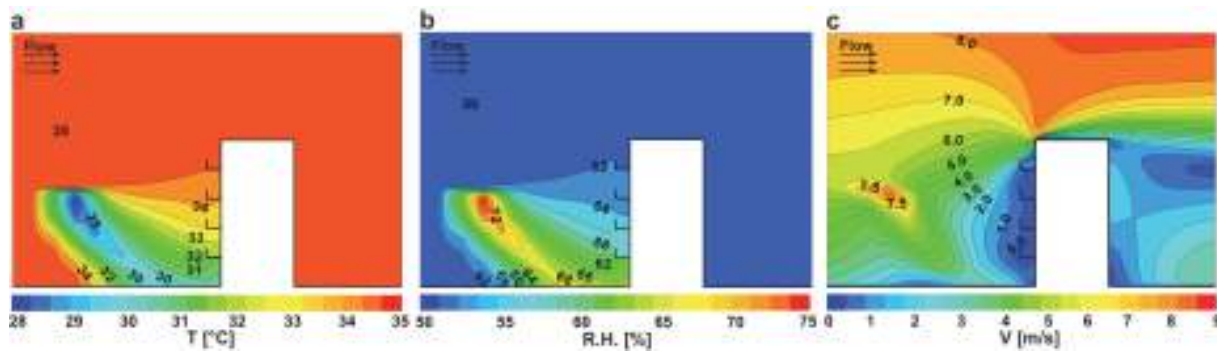
Figure 2. (a) Side view of contours of air (a) temperature, (b) relative humidity and (c) velocity in cross section.

References

Blocken, B., Stathopoulos, T., Carmeliet, J. (2007). CFD simulation of the atmospheric boundary layer: wall function problems. Atmospheric Environment **41**, 238-252.

Błażejczyk, K., Jendritzky, G., Bröde, P., Fiala, D., Havenith, G., Epstein, Y., Psikuta, A., Kampmann, B. (2013). An introduction to the Universal Thermal Climate Index (UTCI). *Geographia Polonica* **86**, 5-10.

Chand, I., Bhargava, P.K., and Krishak, N.L.V. (1998). Effect of balconies on ventilation inducing aeromotive force on low-rise buildings. *Building and Environment* **33,** 385-396.

Franke, A.H. J., Schlünzen, H., Carissimo, B. (2007). Best practice guideline for the CFD simulation of flows in the urban environment.

Montazeri, H., and Blocken, B. (2013). CFD simulation of wind-induced pressure coefficients on buildings with and without balconies: validation and sensitivity analysis. *Building and Environment* **60**, 137-149.

Montazeri H., Blocken B., Hensen J.L.M. (2014). Evaporative cooling by water spray systems: CFD simulation, experimental validation and sensitivity analysis. *Building and Environment*. http://dx.doi.org/10.1016/j.buildenv.2014.03.022.

Rosin, P., Rammler, E. (1933). The Laws Governing the Fineness of Powdered Coal. *Journal of the Institute of Fuel* **31**, 29–36.

Shih, T.H., Liou, W.W., Shabbir, A., Yang, Z., and Zhu, J. (1995). A new k-ε eddy viscosity model for high Reynolds num-ber turbulent flows. *Computers & Fluids* **24,** 227-238.

Sureshkumar, R., Kale, SR, Dhar, PL. (2008). Heat and mass transfer processes between a water spray and ambient air–I. Experimental data. *Applied Thermal Engineering* **28**, 349–360.

Tominaga, Y., Mochida, A., Yoshie, R., Kataoka, H., Nozu, T., Yoshikawa, M., and Shirasawa, T. (2008). AIJ guidelines for practical applications of CFD to pedestrian wind environment around buildings. *Journal of Wind Engineering and Industrial Aerodynamics* **96**, 1749-1761.

Bridge decks flutter derivatives identification via RANS turbulence models

Stefano de Miranda[1], Luca Patruno[1], Francesco Ubertini[1] and Giuseppe Vairo[2]

[1]DICAM, University of Bologna, Italy
[2]DICII, University of Rome "Tor Vergata", Italy
Corresponding author: Luca Patruno, luca.patruno@unibo.it

Abstract

Thanks to the rapidly growth of the available computer power and capability, Computational Fluid Dynamics (CFD) techniques are becoming an increasingly attractive tool for studying the aerodynamic behaviour of bridge decks. Although the computational cost of such simulations may be still remarkable, they allow to efficiently explore multiple scenarios and technical solutions in early design stages. In many published studies, several computational approaches have been applied with varying degree of success, often on a few specific and model-based geometries, and without a systematic comparison with experimental data, thereby preventing a general and effective assessment of the modeling strategy. As a matter of fact, the complex fluid patterns arising around bridge decks at Reynolds numbers typical for wind flows, may be oversimplified by the computational modeling technique, especially if RANS turbulence models are used. Accordingly, a deep investigation and validation of such a kind of methodology is needed. In this framework, this paper shows the results of preliminary numerical analyses based on a RANS formulation. Forced vibration tests are numerically simulated by considering different bridge-deck sections and flutter derivatives are estimated. Comparisons with available experimental and numerical data allow to assess strengths and limitations of the tested models. Finally, referring to different test structures, the influence of turbulence models on the assessment of critical wind conditions is highlighted.

1 Introduction

Wind tunnel tests still represent a fundamental step in the design of long span bridges. Nevertheless, a continuous progress in computational technologies and modeling approaches has allowed the development of numerical methods oriented to the simulation of fluid-structure interaction mechanisms and turbulent flows. In previous works (Larsen and Walther, 1998; Vairo, 2003; Sun et al., 2009; Brusiani et al., 2013), such techniques have been applied with varying degree of success, often on a few geometries and without systematic comparison with experimental data. The complex flow fields encountered around bridge decks at high Reynolds numbers (Re), may be drastically simplified by available computational techniques, so that a deep investigation and validation of these kind of methodology is needed before its practical application. In particular, for Re ranging from $1.0E5$ to $1.0E8$, in agreement with typical wind tunnel conditions and operational scenarios, the flow is extremely unstable, turbulent and generally characterized by a significant three-dimensionality of the medium- and small-scale turbulent structures.

Considering the particular case of aeroelastic loads, it should be noticed that the structure motion is often extremely slow if compared to the time scale of the eddies which can develop and shed from the deck section (namely, signature effects), and that the flow unsteadiness may be retained mainly provided by the structure motion itself. In this conditions, Scale Resolving turbulence models lead to long simulations while the RANS-based approaches might be usually acceptable, despite the unsteadiness of the flow. Nevertheless, the problem lies in the fact that the flow field around bluff bodies is deeply affected by the stability conditions of the shear layers which detach from the separation points. These flow structures, characterized by extremely high vorticity, damp out or amplify small disturbances, roll-up and eventually reattach depending on the local flow conditions. Such effects are accounted for only in an oversimplified way when RANS turbulence models are used, so that the model prediction can be inaccurate even in the simplest cases.

The authors conducted systematic simulations of the flow field around vibrating rectangular prisms

Table 1. Data of the structures used in critical flutter speed calculation.

	Str. 1	Str. 2	Str. 3	Str. 4
B $[m]$	30	40	50	60

ρ $[kg/m^3]$	Mass $[kg/m]$	Inertia $[kg \cdot m]$
1.225	5.0E4	1.0E7
Fq_h $[Hz]$	Fq_α $[Hz]$	$\xi_h = \xi_\alpha$ $[\%]$
0.2	0.4	1.0

of increasing aspect ratio reproducing the experiments performed by Matsumoto (1996), as well as on some typical bridge-deck sections, aiming at assessing the robustness of such simulations strategies in predicting the flutter derivatives and critical wind conditions inducing flutter onset.

2   Simulation strategy

A two-dimensional simulation approach is adopted coupled with a $k - \omega$ sst turbulence model. The coupling between the fluid and the mesh movement is obtained following the well known ALE formulation. In order to handle the body motion a rigid mesh zone is defined close to the immersed body so avoiding degradation of the mesh in critical zones. A deforming zone, meshed with triangular elements, is deformed, smoothed and remeshed during the calculation in order to allow the mesh movement. A fixed zone is then used to mesh the rest of the computational domain (considered as rectangular).

The adopted boundary conditions are velocity inlet and pressure outlet for the left and right side of the computational domain, respectively, while symmetry condition has been adopted for the upper and bottom sides of the domain.

Second order schemes are selected for all quantities and upwinding enabled for convected ones. Node based gradient approximation is chosen and a PISO scheme used for velocity-pressure coupling. Time advancement is first-order implicit.

The time step is chosen to be $1/500$ of the non-dimensional time unit, S, defined as $S = B/U$. Such choice is expected to lead to accurate description of the unsteady fluid behaviour and limits the Courant number, Co, to a maximum of 6 in extremely small areas close to the corners and well below 1 everywhere else.

In the following, numerical results will we shown both for $Re = 1.5E5$ and $Re = 37.5E5$. Such variation should not be interpreted only in analogy to a Re number variation in experiments. Instead, it should be considered as a drastic change in the whole simulation strategy because, form the numerical point of view, it implies a completely different treatment of the boundary layer representation. In fact, the mesh has been kept constant in the two cases so that, for $Re = 1.5E5$, the non-dimensional wall distance $y^+_{max} \simeq 5.0$ allows direct integration through the boundary layer while, for $Re = 37.5E5$, $y^+_{max} \simeq 125.0$ so that wall functions are used. Indeed, the two approaches are not directly comparable so that differences between the two simulation strategies should be interpreted as the results of both the variation in Re number and the wall treatment description.

3   Numerical results

In this section, some results obtained on rectangles with varying aspect ratio are presented together with a preliminary validation on a deck of technical interest. With the aim of assessing the usefulness of such procedures in technical applications, the critical flutter speed has been calculated for a set of test structures. The mechanical properties of such structures have been defined in order to explore various flutter conditions characterized by increasing critical reduced velocity, U_{red}. This has been obtained by considering as fixed the mass properties, the first (flexural and torsional) structural natural frequencies, and the structural damping ratios, and by varying the deck characteristic dimension B, as reported in Table 1.
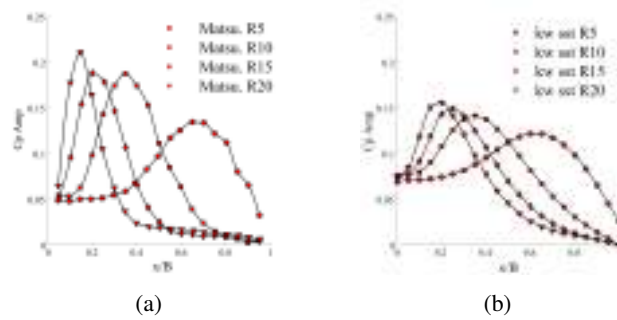
Figure 1. Amplitude of the motion-induced pressure coefficient with varying aspect ratio at $Re = 1.5E5$ along the upper side of the section: (a) experimental results from Matsumoto (1996) and $k - \omega$ sst at $U_{red} = 20$.
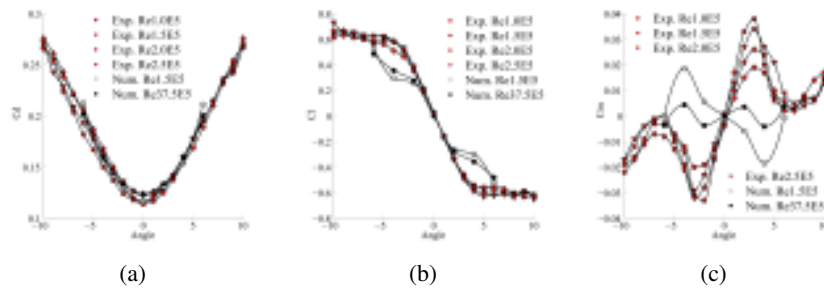
Figure 2. Variation of the dimensionless aerodynamic coefficients with the attack angle for R8. Experimental data are from (Starossek, 2013), numerical results refer to the $k - \omega$ sst model.

3.1   Rectangular prisms

As a preliminary validation of the approach, simple vibrating rectangular cylinders have been considered. In particular, Fig. 1 shows the comparison between the mean amplitude of the motion-induced pressure coefficient for $R5$, $R10$, $R15$ and $R20$ at $U_{red} \simeq 20$. The benchmarking experimental results have been taken from Matsumoto (1996).

It can be noticed that, in the experimental results, an increase in the aspect ratio corresponds to a migration toward the leading edge of the peak pressure and a decrease of the dispersion along the side. When numerical results are considered, the observed trends are confirmed but the peaks appear to be offset toward the trailing edge and not as sharp as in the experimental results. This effect systematically leads to an underestimation of the critical flutter speed on the test structures (tests not in here reported).

For a more detailed investigation, the rectangle $R8$ has been considered. The drag coefficient variation with the attack angle, reported in Fig. 2a, is in extremely good agreement with experimental results while the lift coefficient variation is in reasonable agreement for small attack angles but the stall condition is not captured correctly (Fig. 2b). The pitching moment appears to be not accurate and the two simulated Re number provide opposite sign for the coefficient variation (Fig. 2c). This is due to the fact that the considered aspect ratio has an almost symmetric aerodynamic centre so that its position can lead to positive or negative pitching moment when different Re numbers are considered. Also in this case the bluffness of the body is overestimated.

The critical flutter conditions evaluated by numerically extracting the flutter derivatives and referring to test structures with a $R8$-based section are reported in Table 2. The analyses confirm that the numerical simulations overestimate the bluffness of the body, probably due to an overestimation of the shear layers stability.

3.2   Chongqing

The procedure have been applied to the Chongqing bridge deck. The experimental data regarding such case are provided by Starossek (2013), with the indication of details relevant to the deck geometry.

Table 2. Comparison between critical flutter speed values for $R8$ in $[m/s]$.

	Str. 1		Str. 2		Str. 3		Str. 4	
	U	U_{red}	U	U_{red}	U	U_{red}	U	U_{red}
Exp. $Re2.0E5$	129	11.7	116	8.3	109	6.7	104	5.7
Num. $Re1.5E5$	80	6.9	83	5.7	87	5.2	87	4.9
Num. $Re37.5E5$	88	7.8	92	6.4	94	5.7	93	5.2

$4° \ Re = 1.5E5$ $6° \ Re = 37.5E5$
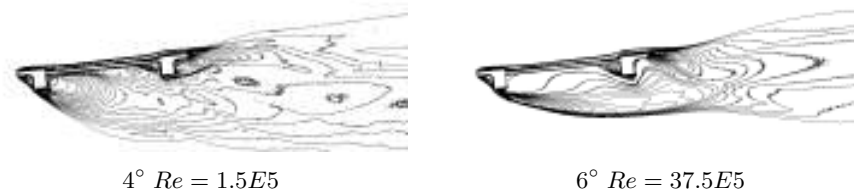
Figure 3. Time-averaged vorticity contours for the Chongqing deck section for different values of Re.

Synthetically, this is a deck with poor aerodynamic design, characterised by a C-shaped section which leads to strong flow separations as shown in Fig. 3.

The main trends of the flutter derivatives are captured by numerical simulations and the calculated critical flutter speed reported in Table 3 are in very good agreement with experimental data. It is noticed that, also in this case, results are mainly conservative with respect to safety structural conditions.

Further validation of the methodology is needed but, from these preliminary tests, it seems that the RANS-based methodology might be profitably applied to cases of technical interest even though it often underestimates the critical flutter speed. A deep validation on a variety of deck typologies is needed before its practical application to individuate further possible limits of applicability.

Table 3. Comparison between critical flutter speed values for Chongqing bridge in $[m/s]$.

	Str. 1		Str. 2		Str. 3		Str. 4	
	U	U_{red}	U	U_{red}	U	U_{red}	U	U_{red}
Exp. $Re2.0E5$	113	9.8	105	7.1	97	5.8	92	4.5
Num. $Re1.5E5$	109	9.4	100	6.2	95	5.2	90	4.4
Num. $Re37.5E5$	98	8.1	93	6.2	95	5.2	95	4.6

References

Brusiani, F., de Miranda, S., Patruno, L., Ubertini, F., and Vaona, P. (2013). On the evaluation of bridge deck flutter derivatives using RANS turbulence models. *J. Wind. Eng. Ind. Aerodyn.* **119**, pp. 39–47.

Larsen, A. and Walther, J.H. (1998). Discrete vortex simulation of flow around five generic bridge deck sections. *J. Wind Eng. Ind. Aerodyn.* **77-78**, pp. 591–602.

Matsumoto, M. (1996). Aerodynamic damping of prisms. *J. Wind Eng. Ind. Aerodyn.* **59**, pp. 159–175.

Starossek, U. (2013). *Online page of Technische Universitat Hamburg-Harburg.* URL: http://www.tuhh.de/sdb/starossek/.

Sun, D., Owen, J.S., and Wright, N.G. (2009). Application of the $k - \omega$ turbulence model for a wind-induced vibration study of 2D bluff bodies. *J. Wind. Eng. Ind. Aerodyn.* **97**, pp. 77–87.

Vairo, G. (2003). A numerical model for wind loads simulation on long-span bridges. *Simulation Modelling Practice and Theory 11*, pp. 315–351.

Tornado-like vortex simulations in Model WindEEE Dome

M. Refan[1] and H. Hangan[1]

[1]WindEEE Research Institute, Western University, London, Canada
Corresponding author: M. Refan, mrefan@uwo.ca

Abstract

The flow field of tornado vortices simulated in the 1/11 scaled model of the Wind Engineering, Energy and Environment (WindEEE) Dome is characterized. Flow visualizations, surface pressure tests and Particle Image Velocimetry measurements were performed to investigate the flow dynamics for a wide range of Swirl ratios (0.12≤S≤1.29) and at various heights above the surface. It is shown that this simulator is capable of generating a wide variety of tornado-like vortices ranging from a single-celled laminar vortex to a multi-celled turbulent vortex.

1   Introduction

The strongest tornado of the 2013 season struck Moore, OK in May 20th, resulted in 25 dead and hundreds injured. Peak velocities of 330 km/hr were reported by National Weather Service for this tornado. This was perhaps the worst tornado disaster since the Joplin, MO tornado in May, 2011. Since the return period of a disaster in tornado prone areas is well beyond what buildings are designed for, the main focus in these regions is on preserving human lives with safe rooms rather than designing tornado-resist residential dwellings. The recent study performed by the National Institute of Standards and Technology (NIST) on the impacts of the May 22, 2011 tornado that struck Joplin, MO has revealed the inefficiency of safe rooms in tornado-prone regions (Kuligowski et al., 2013). This 2-year technical investigation showed that safe areas (tornado shelters and safe rooms) did not adequately protect occupants. The conclusion of this study is strongly supported by another recent NIST report in which impacts of the May 20, 2013, tornado in the Newcastle-Moore area of Oklahoma are provided. These reports emphasize on the needs for more in-depth investigations of tornado flows and the damage associated with them.

Herein, the recently constructed wind facility at Western University, the Wind Engineering, Energy and Environment (WindEEE) Dome, is introduced. This work is mainly focused on tornado simulations in the 1/11 scaled model of the WindEEE Dome. The simulated tornado flow field is characterized qualitatively and quantitatively. The effect of Swirl ratio (S) on the core radius (r_c), maximum tangential velocity (V_{tan}) and axial profile of the radial velocity (V_r) is investigated. The Swirl ratio is defined as $S = r_0\Gamma_\infty/2Qh$ where, r_0 is the updraft radius, $\Gamma_\infty=2\pi r_c V_{tan,max}$ is the maximum circulation, Q is the flow rate, h is the inflow height and $V_{tan,max}$ is the maximum tangential velocity. All experimental studies are performed for eight Swirl ratios in the range of 0.12<S<1.29 and at a constant radial Reynolds number of 6.7×10^4. The radial Reynolds number is defined as $Re_r=Q/2\pi v$, where v is the kinematic viscosity of the fluid.

2   Wind Engineering, Energy and Environment (WindEEE) Dome

The WindEEE Dome is a three-dimensional wind facility capable of simulating various wind systems such as tornadoes, downbursts and gust fronts. The 1/11 scaled model of this facility, called Model WindEEE Dome (MWD), was designed and constructed in 2011 with a design concept very similar to the full-scale facility. MWD is a closed loop wind chamber consisting of two hexagonal chambers;

one at the top with 18 fans and one at the bottom with 100 fans (see Figure 1). Each fan can be controlled individually and the upper fans are reversible. Adjustable louvers, installed in front of all lower fans, produce the desired swirl. The lower chamber is connected to the upper chamber through a bell-mouth which is 0.4 m wide. The tornado can be translated at a maximum speed of 0.25 m/s using a single axis traverser system. Tornado-like vortices can be produced inside the dome using top fans as a source of suction and periphery louvers to generate swirl.

Figure 1. The Model WindEEE Dome.

3   Flow Visualization

Dry ice was used to obtain qualitative information on the tornado-like vortex at 8 different louver angles. Figure 2 displays evolution of the tornado-like vortex as the Swirl ratio increases. Overall, the flow pattern in MWD is in very good agreement with previously simulated vortices in Tornado Vortex Chambers (Ward, 1972; Church et al., 1979).

   At low Swirl ratio of S=0.12, the vortex core is laminar and its variation with height is negligible (Figure 2a). As the Swirl ratio increases, the core suddenly broadens aloft and a turbulent vortex breakdown bubble forms. Figure 2b demonstrates the vortex breakdown as it occurs in MWD for 0.35<S<0.57. By further increasing the Swirl ratio, the breakdown bubble moves downward until it touches the ground at around S=0.57 and the flow becomes fully turbulent. At this point, two intertwined helical vortices form and then a two-celled vortex appears (see Figure 2c and Figure 2d).

a)   b)   c)   d)
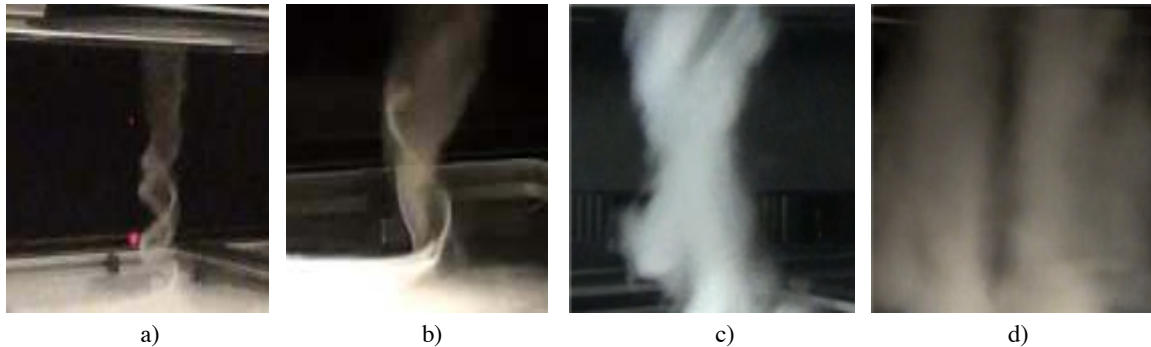
Figure 2. a) laminar core, S=0.12, b) vortex breakdown and touch down, S=0.35-0.57, c) two intertwined helical vortices, S=0.57-0.96 and d) two-celled vortex, S=0.96-1.29.

4   Surface Pressure Test

The surface static pressure distribution of tornado-like vortices and its variation with the Swirl ratio provides useful insights into the vortex dynamics. A pressure measurement system and a floor panel with several pressure taps were used to measure the surface static pressure deficit. Figure 3a shows the

center floor panel of the simulator with 413 static pressure taps distributed on concentric circles (with a maximum diameter of 56cm) around the simulator centerline.

Figure 3b displays the pressure deficit, ΔP^*, as a function of radial distance, r, from the center of the simulator, normalized by $1/2\rho V_{ax}^2$ (where V_{ax} is the average axial velocity at the updraft) and r_0, respectively. For small swirls, the radius at which the minimum surface pressure deficit occurs is not at the geometric center of the simulator. This is due to the wandering characteristics of the vortex and as a result, the vortex center shifts towards the center of the simulator as the flow becomes turbulent. Experimental results were compared with the surface pressure deficit suggested by the modified Rankine vortex model. A better match was achieved at radial locations away from the center. Also, the analytical model estimation improved as the Swirl ratio increased.

a)   b)
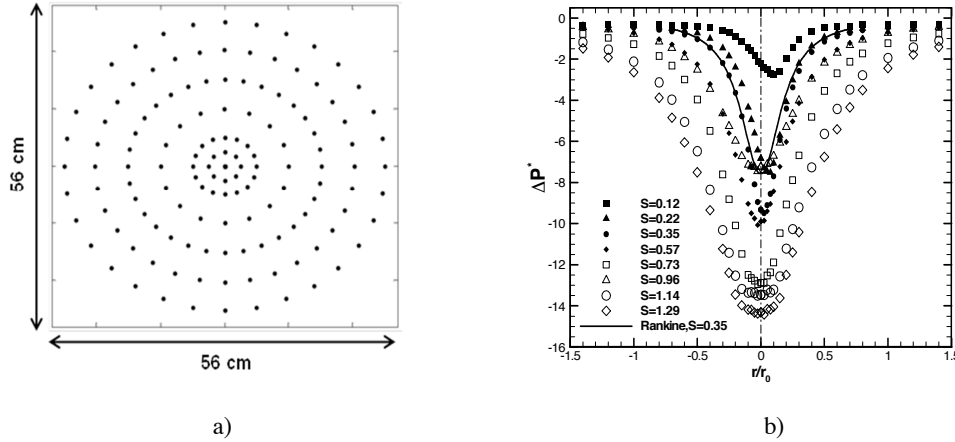
Figure 3. a) Surface pressure taps configuration and b) radial profile of the pressure deficit for various S.

5 Particle Image Velocimetry

The velocity field of simulated tornado-like vortices were investigated using Particle Image Velocimetry (PIV) method. A 120 mJ/pulse Nd:YAG laser generator with a wavelength of 532 nm was used as a source of illumination. A CCD camera with a spatial resolution of 2336×1752 pixels was employed to capture images. A light sheet with a uniform thickness of 2 mm was created inside the chamber using optics. The camera was connected to an image acquisition system that acquires 8-bit images. A pulse/delay generator was used to control the timing of the laser pulses and camera frames. An aerosol generator was utilized to seed the tornado chamber with Di-Ethyl-Hexyl-Sebacate particles with an average diameter of 1 μm. For each experimental run, 4000 images were acquired at a rate of 30 Hz resulting in 2000 vector maps. The horizontal velocity field was measured at the center of the simulator and at 8 different heights ranging from 3.5 to 15 cm. The vertical velocity field was only investigated at the updraft region to calculate the flow rate. The TSI software was used to extract vector maps and to perform post-processing of the data. The velocity measurement error in horizontal planes was estimated to be 2.2%. Since the spatial resolution of PIV measurements is 1-2 orders of magnitude larger than the Kolmogorov dissipation scale of the flow, no attempt was presently made to resolve the smallest scales of the tornado-like flow.

As an example, azimuthally and time averaged tangential velocity profiles at various heights for S=0.73 are shown in Figure 4a. The maximum tangential velocity and the corresponding radius at each height are used to normalize the velocity and the radius, respectively. Also, results are compared with the Rankine vortex model. For small Swirl ratios, S≤0.22, most of the experimental results and the analytical model match fairly well. At and after touch-down a clear variation in the experimental values with height is observed. In addition, the Rankine model shows agreement with only the upper level measurements for S>0.35. These observations can be explained by the increased surface friction as the flow becomes turbulent. The azimuthally and time averaged radial velocities are investigated as a function of height for various swirls and at four radial locations (one inside the core and the rest

outside of the core flow). Figure 4b shows a sample result for S=0.73. Radial velocities are normalized by V_{ax} and a negative value of radial velocity represents a converging inflow. It is observed that the radial velocity values close to the surface rise as the swirl increases. This is attributed to the intensified tangential velocities close to the ground. In addition, variation of the radial velocity with height is more noticeable for higher swirls which can be explained by the flow regime being fully turbulent for $S \geq 0.57$.

a)   b)
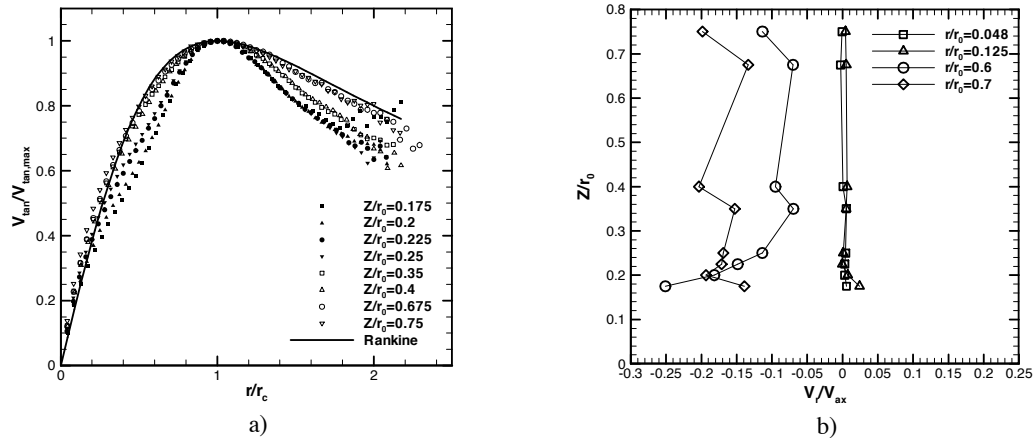
Figure 4. a) radial profiles of the normalized tangential velocity at various heights and b) vertical profile of the normalized radial velocity at four radial locations, S=0.73.

The vertical structure of the vortex core, the maximum tangential velocity variation with height and the three-dimensional structure of the vortex were also studied at different Swirl ratios and will be reported in the final paper.

6   Conclusions

The flow field characteristics of tornado-like vortices simulated in Model WindEEE Dome were studied experimentally. The vortex core development with increasing the swirl in the flow was captured using flow visualizations and well matched the ones reported in previous physical simulations. The surface pressure deficit was measured for the simulated vortex and compared with the modified Rankine vortex model. It was concluded that accuracy of this analytical model in estimating the surface pressure distribution is higher in the outer core regions of the vortex and increases with the Swirl ratio. The radial profiles of the normalized tangential velocities were in close agreement with that of the modified Rankine vortex model except for heights very close to the surface. In the next step, the simulated vortex flow characteristics will be compared with real tornado data in order to identify the geometric and kinematic scaling of the simulation.

7   References

Church, C. R., J. T. Snow, G. L. Baker, and E. M. Agee, 1979: Characteristics of tornado-like vortices as a function of swirl ratio: a laboratory investigation. *Journal of Atmospheric Sciences*, 36, 1175.

Kuligowski, E. D., F. T. Lombardo, L. T. Phan, M. L. Levitan, and D. P. Jorgensen, 2013: Draft Final Report, National Institute of Standards and Technology (NIST) Technical Investigation of the May 22, 2011, Tornado in Joplin, Missouri. NIST NCSTAR 3.

Ward, N. B., 1972: The exploration of certain features of tornado dynamics using a laboratory model. *Journal of Atmospheric Sciences*, 29, 1194.

The Orographic influence in European wind load standards

Dr.-Ing. Rolf-Dieter Lieb[1] and Dipl.-Ing. (FH) Jantje Paul[1]

[1]I.F.I. Institut für Industrieaerodynamik GmbH, Aachen, Germany
Corresponding author: Dr.-Ing. Rolf-Dieter Lieb, Lieb@ifi-aachen.de

Abstract

Embankments, escarpments, hills and ridges are typical orographic anomalies that standards across Europe consider in the calculation of wind loads through multiplication of a factor. The designation of this factor differs in several countries. Most common are "topography factor" and "orography factor" respectively their literal translations into the official national languages. In the Eurocode and its National Annexes these are used like synonyms and are referred to as "c_o".

Regular CEN-members mostly use Annex A.3 of the EN 1991-1-4 to calculate the orography factor. Some countries alter or extend the standard procedure, while others make up a procedure on their own. Few countries do not mention orographic influences in their standards at all.

The different ways to consider orographic influences among European wind load standards are described and compared. The scientific reasoning is examined as far as such documentation was available. Finally the different methods are compared in a sample calculation.

1   Current state of Standards used in Europe

This article focuses on the situation in countries which are regular members of the CEN, even though there might be some notes on neighbouring countries as well.

The following countries adopted the EN 1991-1-4 and published a National Annex until 5/2014:

Austria, Belarus, Belgium, Bulgaria, Croatia, Cyprus, Czech Republic, Denmark, Estonia, Finland, France, Germany, Greece, Hungary, Ireland, Iceland, Italy, Latvia, Lithuania, Luxembourg, Netherlands, Norway, Poland, Portugal, Rumania, Slovakia, Slovenia, Sweden and United Kingdom.

Bosnia and Herzegovina, Macedonia, Malta, Moldova, Montenegro, Serbia, Spain, Switzerland and Turkey have published the EN 1991-1-4 but not the corresponding National Annex yet. Spain, Switzerland and Turkey still have valid national standards that are not related to the Eurocode.

2   Calculation of orographic influences

The standard procedure described in Annex A.3 of the EN 1991-1-4 [1] is used in the following countries:

Belarus [3], Belgium [4], Bulgaria [5], Croatia [6], Cyprus [7], Czech Republic [8], Denmark [9], Estonia [10], Germany [13], Greece [14], Hungary [15], Iceland [16], Italy [18], Latvia [19], Lithuania [20], Luxembourg [21], Netherlands [22], Poland [24], Portugal [25], Rumania [26], Slovakia [27], Slovenia [28] and Sweden [29].

Finland [11], Ireland [17] and the United Kingdom [30] use the Annex A.3, but make some additions or changes to it. Austria [2], France [12], Norway [23] and Switzerland [33] consider the orographic influence in a different way. Turkey [34] gives a standard value for all topographic anomalies. Spain [32] does not consider topographic influences of any kind up to our knowledge.

3   Eurocode 1, EN 1991-1-4, Annex A.3

The annex A.3 from EN 1991-1-4 [1] is the most common approach to calculate orographic influences in the EU. The EN 1991-1-4 gives it as a recommended procedure.

The description in Annex A.3 seems to originate from the previous British standard BS 6399-2 [35]. According to [40] this method "has been in use since 1986". Even though in the British Standard the orography factor was still part of the altitude factor. The British and Irish National Annexes keep the altitude factor, but extract the orography factor into Annex A.3. Besides the slight corrections in the equations and the better structure, the calculations and diagrams stay the same. The same procedure as in Annex A.3 was also used in the 2005 version of DIN 1055-4 [31]. While DIN 1055-4:2005-03 and BS 6399-2:1997 give diagrams to determine the location factor s, Annex A.3 additionally provides three pages of formulae for its calculation.

Chapter 4.3.3, Topography, Paragraph (1) (of EN 1991-1-4 [1]) states that topographies like mountains, cliffs etc., which increase the wind speed by more than 5% have to be factored in. But paragraph (2) then declares that topographic effects may be ignored if the windward terrain slope is less than 3°. The windward terrain up to ten times the height of the topography has to be considered.

Annex A.3 explicitly reminds the reader that it is not supposed to be used for rippled or mountainous regions. For that reason in the UK a commentary [39] gives additional guidance to the use of EN 1991-1-4 and offers an alternative procedure for such areas. This might also be the reason why Switzerland, Austria and Norway do not adopt the method of Annex A.3 in their National Annexes.

After describing the areas in which the topography factor has to be calculated, (this is well illustrated in the British and Irish Annex Figure NA.2, also see section 7 below, Ireland and the United Kingdom) the basic formulae (A.1 to A.3) are given to calculate the topography factor.
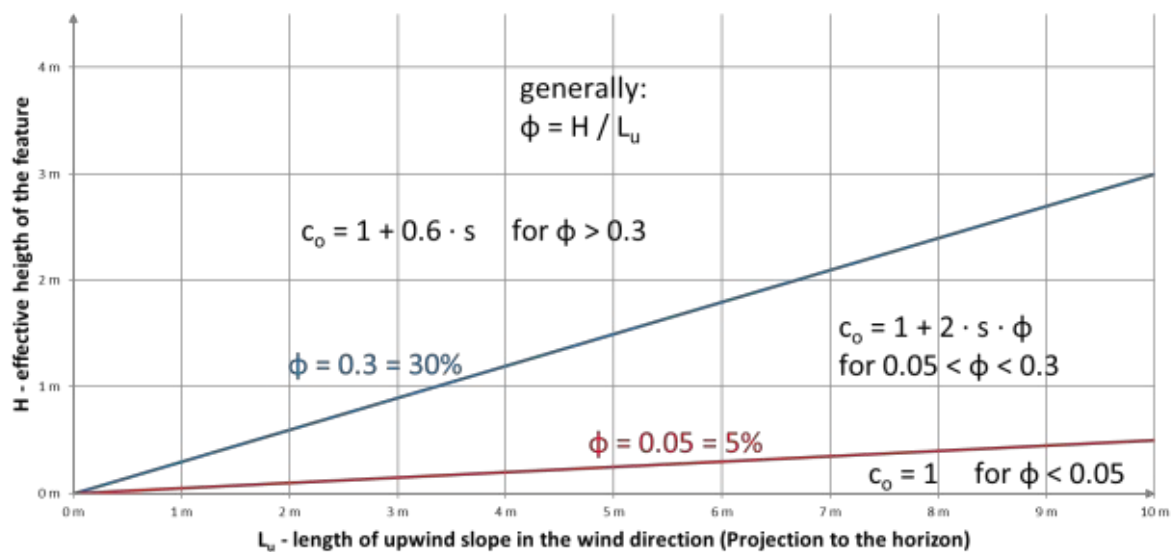
Figure 1. Orography factor c_o as a function of the windward slope Φ as known from the equations in the standard

with
Φ windward slope $\Phi = H / L_u$ (0.05 = 5% slope ≈ 2.8°; 0.3 = 30% slope ≈ 16.7°)
s   location factor (from Figure A.2 or A.3) (s can never have a negative value)
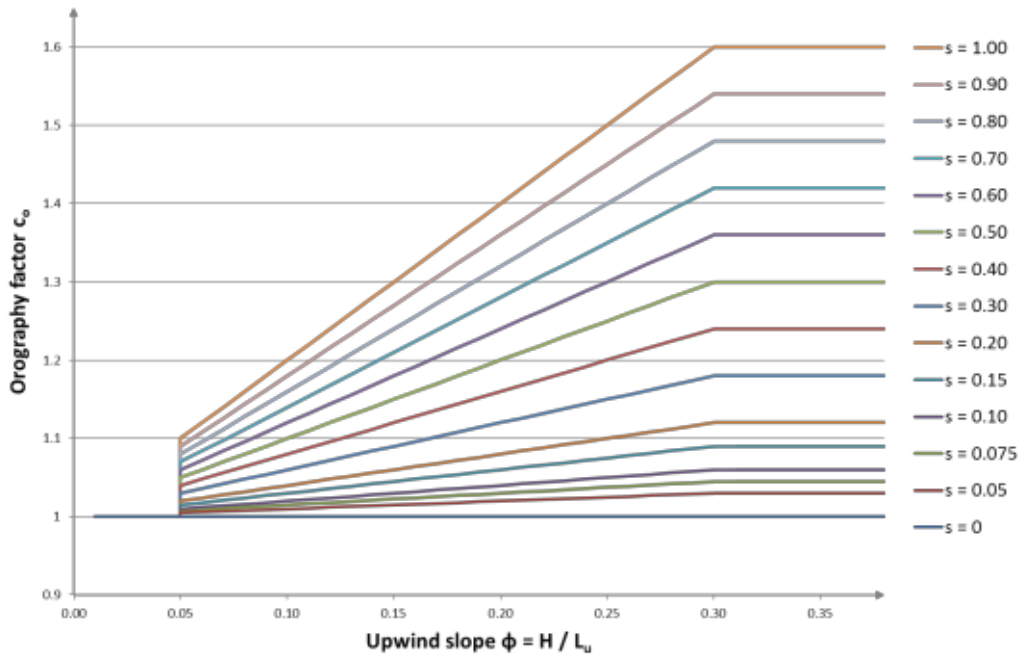
Figure 2. Orography factor c_o as a function of the upwind slope Φ

Figure A.2 shows a hill or ridge and Figure A.3 shows an escarpment. The diagramms should be used to determine the location faktor s. Obviously c_o can never be smaller than $c_{o,min} = 1.0$. The topographic influence in this description does never cause a reduction of windloads. In accordance with the approximation formulae given as equation A.4 to A.13 the maximum location factor s is unlikely to be significantly bigger than 1. Consequently the maximum orography factor is about $c_{o,max} \approx 1.6$.

When determining the location factor s the effective slope length L_e has to be calculated with the formulae in table A.2. This table shows that up to an upwind slope Φ of 0.3 the effective slope length L_e equals the length of the upwind slope L_u. For steeper slopes the effective length grows. The steeper the slope the longer the outreach of the topographic influence into the lee side. But steeper slopes also have shorter upwind slopes L_u.

$$L_e = L_u \qquad \qquad \text{for } 0.05 < \Phi < 0.3$$
$$L_e = H / 0.3 = L_u \cdot \Phi / 0.3 \qquad \qquad \text{for } \Phi > 0.3$$

In valleys c_o may be set to 1.0 when the accelarations due to channel effects can be eliminated. [1]
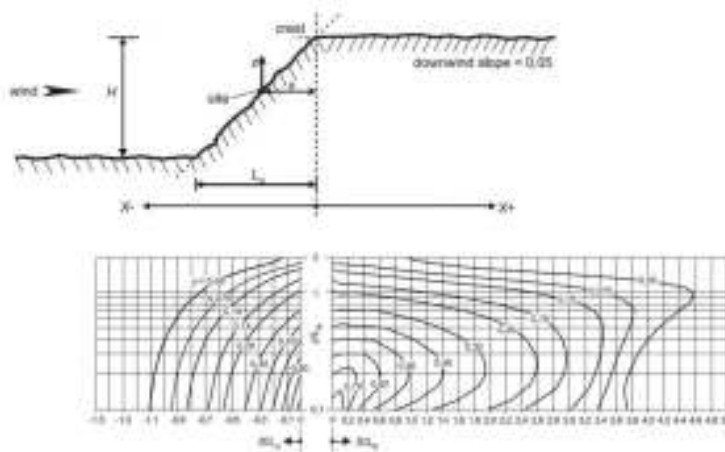
Figure 3. Figure A.2 out of the Eurocode EN 1991-1-4 [1]
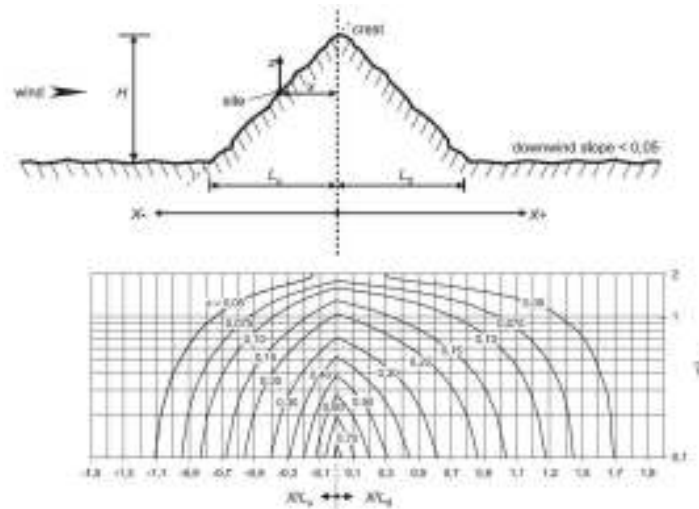
Figure 4. Figure A.3 out of the Eurocode EN 1991-1-4 [1]

4 Austria

Austria sets $c_o = 1$ for every situation. They explicitly state that Annex A.3 should not be used. According to Prof. Dr. Helmut Sockel, Convenor of the National Annex committee, the orographic influences in Austria are too complex to be considered with the approach used in Annex A.3. Annex A.3 assumes that approaching flows pass plain surfaces before hitting a topographic anomaly. This situation is rather rare in Austria. For that reason they considered the topographic influence within the basic wind velocities $v_{b,0}$ instead.

Basic wind velocities $v_{b,0}$ are given for nearly every small municipal. They also give an altitude above sea level (ASL) for each municipal. If the building sites' height ASL differs from the given height ASL for more than 250 m the higher values for $v_{b,0}$ from Table A.2 should be used.

The Austrian standard also gives the factor f_s which allows to reduce the air density ρ due to the height ASL. [2]

5 Finland

For buildings and structures smaller than 100 m in height, the procedure described in Annex A.3 of standard EN 1991-1-4 can be used to determine the orography factor c_o.

For high-rise structures (h > 100 m) the possibility of "thermal surface inversion" should be considered. The designer can either use meteorological data on local conditions or can consider it by defining an additional loading case. c_o is therefore multiplied with the factor c_{INV}.

$$\eta = z + H_s$$

$$c_{INV}(\eta) = 1 + \frac{H}{H_{ref}} \cdot 0.8 \qquad\qquad \text{for } \eta > H$$

$$c_{INV}(\eta) = 0.5 \qquad\qquad \text{for } \eta \leq H$$

H   is the height of the feature as defined in A.3 of standard EN 1991-1-4 and $H_{ref} = 400$ m,
H_s elevation of the site in comparison with the average terrain elevation
z   building height

The finish authorities considered long-term meteorological data from measurements in northern Finland to define this loading case. A stratified wind flow arises due to temperature inversion and causes a sudden change in the wind profile. [11]

6   France

The French National Annex offers two different procedures. The orographic influence **has to be** considered for slopes of more than 5%.

Procedure 1 gives formulae to calculate an average height A_m within a Radius of 1 km which is needed to calculate the relative building height ΔA_c.

$$c_o(z) = 1 + 0.004 \cdot \Delta A_c \cdot e^{-0.014 \, z10)} \qquad \text{for } z \geq 10 \text{ m}$$

$$c_o(z) = c_o(10) \qquad \text{for } z < 10 \text{ m}$$

This simplified procedure has been based on a statistical analysis of numerous real cases. The standard only allows this procedure for resulting values of $1.0 \leq c_o \leq 1.15$. A reduction of wind loads due to orography is not eligible. For values of $c_o > 1.15$ specific studies based on numerical models or wind tunnel experiments are advised.

Procedure 2 is a bit more detailed and the same as in ISO 4354:1997 [37]. It gives one formula which has several constants.

$$c_o(z) = 1 + S_{max}\left(1 - \frac{|X|}{k_{red} \cdot L}\right) \cdot e^{\frac{-\alpha z}{L}} \qquad \text{for } \Phi \geq 0.05$$

S_{max} is the relative "speed-up" factor at the crest near the surface, α is a decay coefficient for the decrease in "speed-up" with height. A simplified sketch that shows the "speed-up" is given in Figure 5. For these constants different values are given for different terrains. As for procedure one c_o may not be smaller than 1.0.

The standard does not detail the circumstances under which each procedure should be used. So the authors assume that you should calculate c_o with both procedures and choose the more critical value.
[12]

7   Ireland and the United Kingdom

Ireland and the UK basically use the standard procedure, but graphically display the limits where it has to be used. The orographic factor only has to be calculated for the shaded areas indicated in Figure NA.2. EN 1991-1-4 describes the same in Paragraph (3) of Annex A.3. Besides the confusing double information, the British and Irish Figure NA.2 is much easier accessible than the half page of text and formulae in Annex A.3.
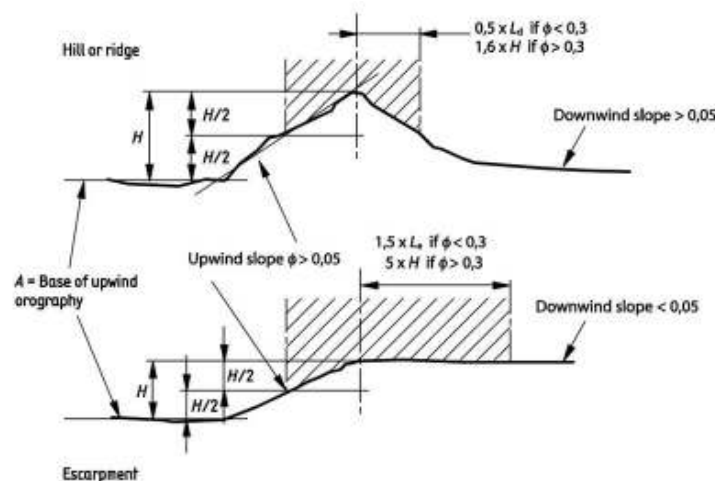
Figure 5. Figure NA.2 out of the Irish National Annex [17]

The BSI additionally published background information to their National Annex [39]. (Note: [39] is not to be regarded as a British Standard.) In this publication they describe an alternative procedure for undulating terrain in Figure 2 [39]. This procedure basically explains a way to define an adequate substitute hill, for sites that do not exactly match Figure NA.2 [17]. You print out a longitudinal cut of the terrain for 8 km in front of the site. By a geometrical construction the substitute is constructed and the values needed for the procedure described in Annex A.3 can be obtained from the sketch.

The standard procedure from Annex A.3 first appeared in a slightly different form in the British Standard BS 6399-2 [35]. The previously used CP3 [36] only allowed to choose the topography factor S_1 from Table 2. Table 2 described three categories of topography. Accordingly one chose a value of the three offered ones: 0.9; 1.0; 1.1. The value of 0.9 still leaves some engineers thinking they could reduce the topography factor below 1.0; but the EN 1991-1-4 does not allow any topography factor smaller than 1.0.

8 Norway

Among the researched countries Norway is probably the one that put the most attention to the influence of orography. Previously the recommended method, which is based on a paper of Lemelin, Surry and Davenport [42], which was used as a base for ISO 4354:1997 [37]. For the Eurocode this method was extended for a third dimension. For the third dimension a term that involves the length and width of a hill or escarpment was added. (B/L_0 may not be smaller than 0.5)

$$c_o(z) = 1 + S_{max} \left(\frac{\dfrac{B}{L_0}}{\dfrac{B}{L_0} + 0{,}4} \right) \cdot \left(1 - \frac{|X|}{k_{red} \cdot L} \right) \cdot e^{\frac{-\alpha z}{L}} \qquad \text{for } \Phi \geq 0.05$$

But Norway has plenty of topographic sites, which are more complex. For such cases Harstveit and Sandvik [41] compared several real life situations, scientific papers, damage reports and numerical studies. Usually it is considered that the topography leads to a "speed-up" in the mean wind velocity but does not affect the turbulence. They concluded that in the lee of mountains with slopes of about 30° the gust of wind increases by 10% over a length of 15 mountain heights. With slopes steeper than 40° the gust of wind increases by 20% over a length of 10 mountain heights. The mean wind speed on the other hand is not affected or decreased by 10%. Therefore the Norwegian standard increases the turbulence factor k_I by up to 75% for the lee side of such mountains, while leaving the topography factor at 1.0 or decreasing it to 0.9. So in the end the peak wind velocity pressure is significantly increased, while the mean wind velocity pressure is not affected or slightly decreased. [41] For more precise considerations a boundary layer wind tunnel study would be advised.
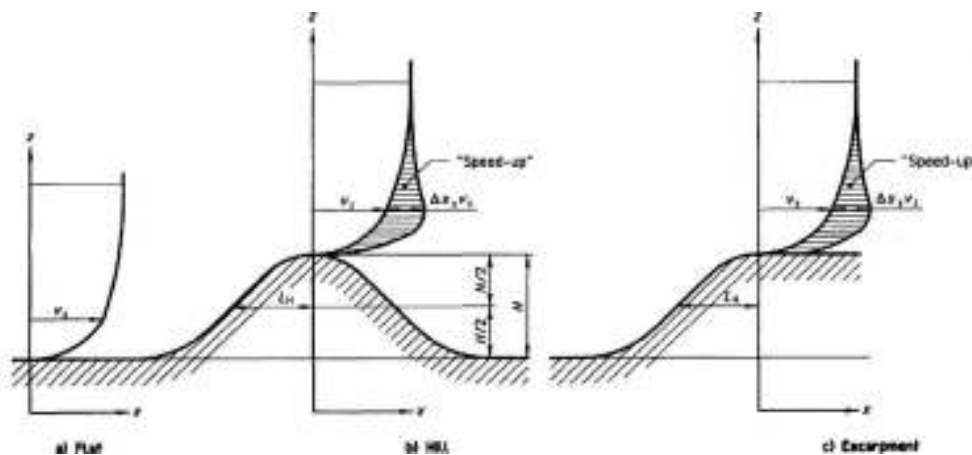
Figure 6. Figure C.2 out of ISO 4354:1997 [37]

9   Switzerland

The SiA 261 [33] states under 6.2.1.4 that for building sites with unusual wind conditions, for example on mountain tops or locations on a slope an increase of $q_{p,0}$ has to be considered. Besides that the standard does not give any further information on how to consider this situation.

The document D0188 [38] is a commentary on Chapter 6 of SIA 261 and 261/1. Under point 3.4 it explains that the typically used concepts to consider orographic influences, like those in Annex A.3 of EN1991-1-4, may not be used in a mountainous region like Switzerland. These concepts were designed for isolated hills or ridges. In Switzerland such topographic anomalies are usually not isolated. In other words Switzerland's topography is too complex to consider it with the simple, but common approaches. Even though no Swiss document explicitly requires or recommends it, a wind engineer should be consulted for building sites that might have unusual wind conditions.

10 Turkey

Turkey defines a peak velocity pressure for steep hills, which are not defined in detail. This peak velocity pressure is the same as the peak velocity pressure for buildings with a height of 21 to 100 m. In case of topographic influence this value would not even rise for buildings with a height of more than 100 m. Apparently it even would decrease the peak velocity pressure for buildings higher than 100 m from 1.3 kN/m² to 1.1 kN/m², but this is not commented on in the standard. [34]

11 Example calculation

In the following the orographic influence in a simple example is investigated, a 2-dimensional escarpment with the height H. The building was placed on the edge of the escarpment with a small distance of only x = 2 m being considered. The cubical building has a height of 10 m. Three slope angles Φ and two escarpment heights H are compared. Table 1 shows the dimension for the six sample cases.
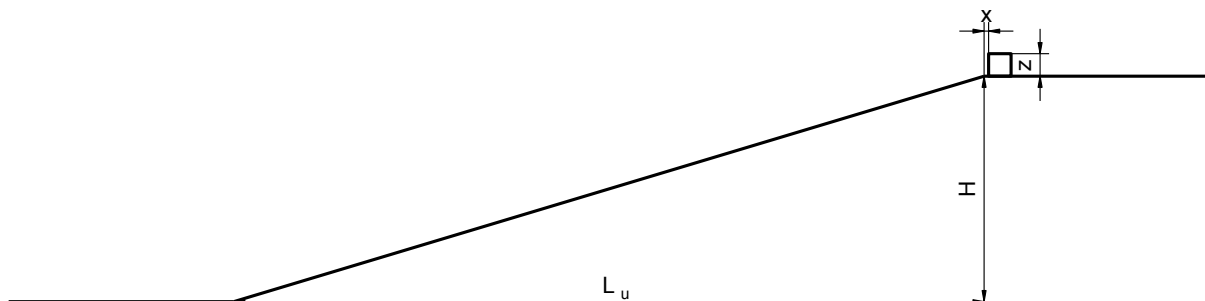
Figure 7. Example situation

Table 1. Example dimensions

H in m	L_u in m	Φ in %	Φ in °	x in m	z in m
10	200	5	2.9	2	10
10	100	10	5.7	2	10
10	33	30	16.7	2	10
50	1000	5	2.9	2	10
50	500	10	5.7	2	10
50	167	30	16.7	2	10

Figure 8 shows the orography factor c_o as it can be calculated according to Annex A.3, and the National Annexes of France (procedure I and II) and Norway. As mentioned, Austria considered the orography in the basic wind velocity and can consequently not be compared to other standards.

Finland's changes to Annex A.3 only affect high-rise structures with a height above 100 m. Spain does not consider orographic influences at all and Switzerland does not give a standardized method. Germany, Poland, Sweden, Ireland and the United Kingdom modify their wind profiles. Most of these countries prefer the power law over the logarithmic law. This causes slight differences in the peak wind velocity pressure. Since this effect was already researched in a previous paper [43], we chose to focus on the logarithmic profile. Just Poland and Sweden show an interesting anomaly. Poland and Sweden only consider the orographic influence in the mean wind velocity pressure, but not in the peak wind velocity pressure instead of vice versa.

Figure 9 shows the peak wind velocity pressure q_p in kN/m² calculated with the corresponding orography factor c_o from Figure 8 and the value for Turkey. The Turkish standard just gives one elevated value for situations with orographic influences. As can be seen the values given by Annex A.3 and France II are mostly governed by the slope angle. In Norway the height of the escarpment has a much more significant influence. (Since Norway does not consider 2-dimensional escarpments, the width of the escarpment was assumed with 1000 m.) Within the French standard procedure 2 seems to be the more conservative approach.
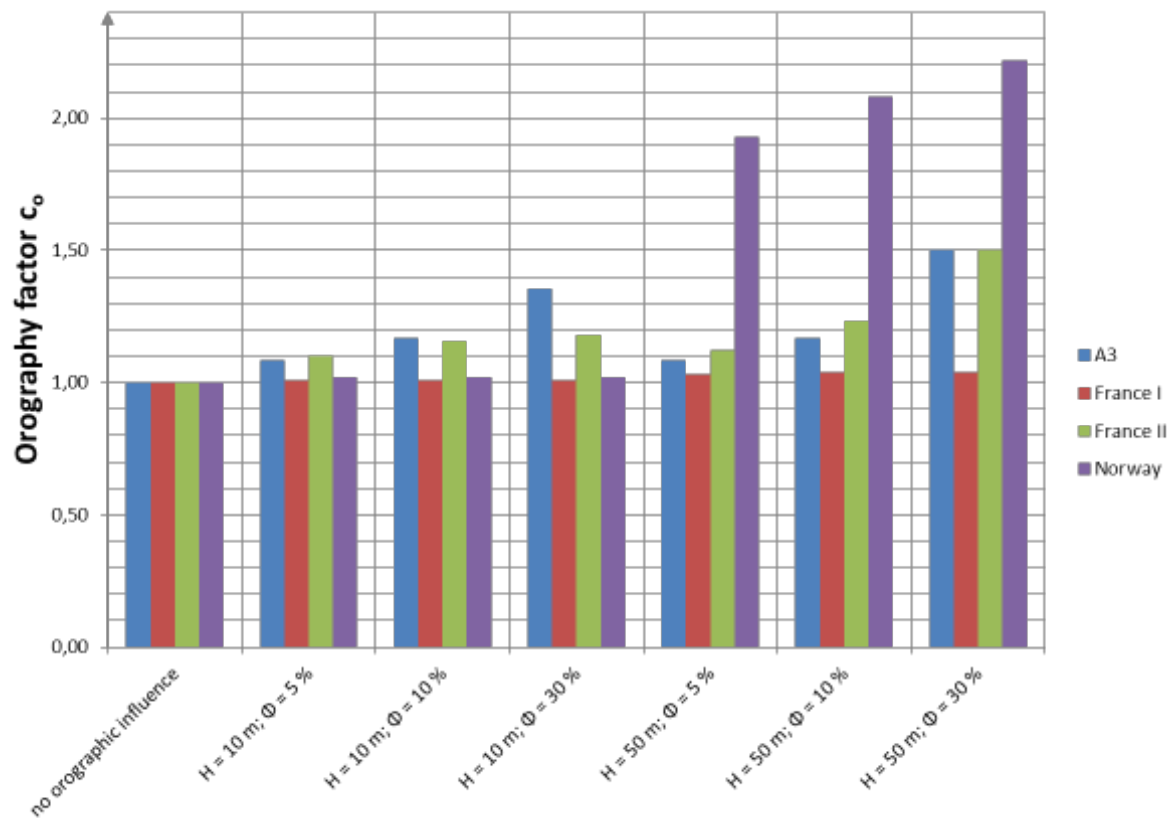
Figure 8. Orography factor c_o

12 Conclusion

Most countries follow the recommendations from Annex A.3 which is mainly focussed on the slope angle rather than the slope height. However this procedure describes the effect on attached wind flow in a plain, which suddenly hits an isolated topographic anomaly. Regular Hills, rugged or rippled terrain and mountains are not described by this procedure, even though a first mountain at the side of a larger plain or even lake might well be represented. The decision for application is therefore dependent on the assumption if upwind terrain will allow for the formation of a standard boundary layer or not (in the respective wind direction).

Mountainous countries like Austria, Norway and Switzerland have yet dismissed this procedure at all and chosen other ways to cope for such effects. In Austria and Switzerland the basic wind speeds and design wind pressures are adapted. France (in a second procedure) and Norway rather stick to the 2D-LSD-method as used in ISO 4354:1997 or even develop it further for three dimensions (Norway).

The topographic influence as used in EN 1991-1-4 does not cause any reduction of windloads however. On the save side is always assumed, that in harsh conditions high turbulence and wind speeds could well fill any valley or wind protected terrain as well. In fact it seems very difficult to define a situation of terrain were such effects could really be impossible.

One fact needs to be emphasized in any case: All discussion of standard procedures and their applications does only help, if civil engineers keep in mind to use it instead of just ignoring the topography factor c_0, as often seen in simple buildings or wind load calculations for e.g. photovoltaic installations. This is an interesting topic for professional education.
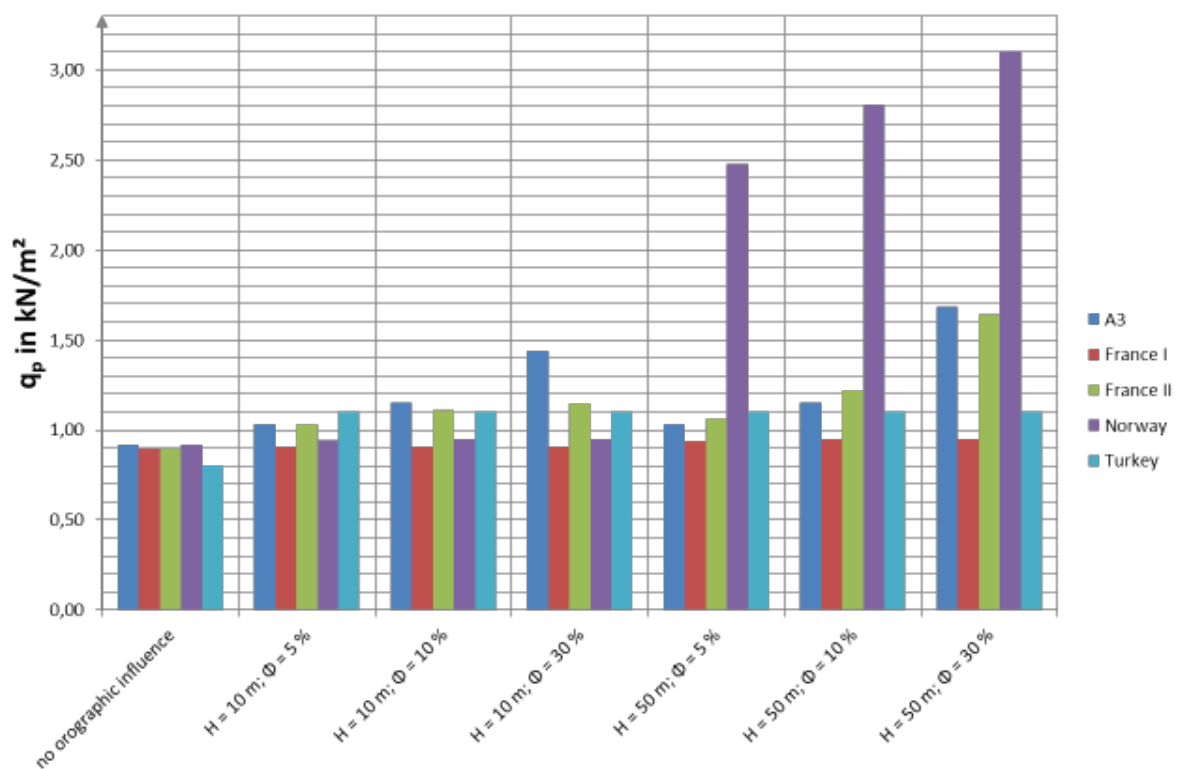
Figure 9. q_p in kN/m²

References

Eurocode and National Annexes ([2] to [30] index by country of publication)

[1]   EN 1991-1-4:2005: Eurocode1: Actions on structures – Part 1-4: General actions – Wind actions, CEN, 2005

[2]   ÖNorm B 1991-1-4:2013-05-01: Nationale Festlegungen zu ÖNORM EN 1991-1-4 und nationale Ergänzungen, Österreichisches Normeninstitut (ON), Wien, 2013

[3]   ТКП EN 1991-1-4-2009: National Annex to technical code TCP EN 1991-1-4-2009 Eurocode 1 ACTIONS ON STRUCTURES Part 1-4. General actions. Wind actions; Министерство архитектуры и строительства Республики Беларусь; Стройтехнорм; Minsk; 2010

[4]   NBN EN 1991-1-4-ANB:2010-12: Eurocode 1 : Actions sur les structures - Partie 1-4 : Actions générales - Actions du vent - Annexe nationale, Bureau de Normalisation, Bruxelles, 2010

[5]   BDS EN 1991-1-4/NA:2011-01: Eurocode 1 – Actions on Structures Part 1-4: General actions – Wind actions - National Annex to BDS EN 1991-1-4:2005, BIS, Sofia, 2011

[6]   HRN EN 1991-1-4:2012/NA:2012: Croatian National Annex to Eurocode 1 – Actions on Structures Part 1-4: General actions – Wind actions, Croatian Standards Institute - HZN, Zagreb, 2010

[7]   NA to CYS EN 1991-1-4:2005:2010-10: National Annex to CYS EN 1991-1-4:2005 Eurocode 1: Actions on Structures, Part 1-4: General actions – Wind actions, CYS, Nikosia, 2010

[8]   ČSN EN 1991-1-4/NA:2008-05: National Annex to Eurocode 1 – Actions on Structures Part 1-4: General actions – Wind actions, Česky normalizačni institute, Prag, 2008

[9]   DS/EN 1991-1-4 DK NA:2010-03: National Annex to Eurocode 1 – Actions on Structures Part 1-4: General actions – Wind actions, www.ds.dk, 2010

[10]   EVS EN 1991-1-4/A1:2010/NA:2010: Eurocode 1: Actions on structures, Part 1-4: General actions; Wind actions, Estonian National Annex; Estonian Center for Standardisation, Tallin, 2010

[11]   SFS-EN 1991-1-4/NA:2010: National Annex to Eurocode 1 – Actions on Structures Part 1-4: General actions – Wind actions, Finnische Normenwebseite, Helsinki, 2010

[12]   NF EN 1991-1-4/NA:2008-03: Annexe nationale à la NF EN 1991-1-4:2005 Actions générales — Actions du vent, AFNOR, La Plaine Saint-Denis Cedex, 2008

[13]   DIN EN 1991-1-4/NA:2010-12: Nationaler Anhang – National festgelegte Parameter – Eurocode 1: Einwirkungen auf Tragwerke – Teil 1-4: Allgemeine Einwirkungen – Windlasten, Deutsches Institut für Normung e. V., Beuth-Verlag, 2010

[14]   ΕΛΟΤ EN 1991-1-4:2005/NA: Greek National Annex to Eurocode 1 – Actions on Structures Part 1-4: General actions – Wind actions, Hellenic Standards, Peristeri, 2010

[15]   MSZ EN 1991-1-4:2007-12: NA nemzeti melléklet (előírás), Magyar Szabványügyi Testület, Budapest, 2007

[16]   ÍST EN 1991-1-4:2005/NA:2010-12: National Annex to Eurocode 1 – Actions on Structures Part 1-4: General actions – Wind actions, Staðfestur af Staðlaráði Íslands, Reykjavík, 2010

[17]   NA to I.S. EN 1991-1-4:2013: Irish National Annex to Eurocode 1 – Actions on Structures Part 1-4: General actions – Wind actions, NSAI, Dublin, 2013

[18]   UNI EN 1991-1-4/AN:2007-07: Appendice Nazionale UNI-EN 1991-1-4 "Azioni sulle costruzioni – Parte 1-4: Azioni in generale – Azioni del vento", Webseite UNIN, Rom, 2007

[19]   LVS EN 1991-1-4/NA:2011-09: 1.Eurokodekss. Iedarbes uz konstrukcijām. 1-4. Daļa: Vispārīgās iedarbes. Vēja iedarbes. Nacionālais pielikums, LVS Latvijas Standarts, Riga, 2011

[20]   LST EN 1991-1-4/NA: Eurokodas 1. Poveikiai konstrukcijoms. 1-4 dalis. Bendrieji poveikiai. VVejo poëikiai, Lietuvos Standartizacijos Departamentas, Vilnius, 2012

[21]   EN 1991-1-4:2005/AN-LU:2011: Actions sur les structures – Partie 1-4: Actions générales — Actions du vent, ILNAS, Luxemburg, 2011

[22]   NEN EN 1991-1-4 +A1+C2:2011/NB:2011: Nationale bijlage bij NEN-EN 1991-1-4 Eurocode 1: Belastingen op constructies – Deel 1-4: Algemene belastingen – Windbelasting, Nederlands Normalisatie-instituut, Delft, 2011

[23]   NS-EN 1991-1-4:2005+NA:2009: Eurokode 1: Laster på konstruksjoner, Del 1-4: Allmenne laster, Vindlaster, standard norge, Lysaker, 2009

[24]   PN-EN 1991-1-4:2008/NA:2010-09: Dotyczy PN-EN 1991-1-4:2008 Eurokod 1 Odd¬ziaływania na konstrukcje Część 1-4: Oddziaływania ogólne Oddziaływania wiatru, PKN, Warszawa, 2010

[25]   NP-EN 1991-1-4:2010: Eurocódigo 1 – Acções em estruturas, Parte 1-4: Acções gerais, Acções do vento;Instituto Português da Qualidade, Caparica, 2010

[26]   SR EN 1991-1-4/NB:2007-06: Eurocod 1: Acţiuni supra structurilor Partea 1-4: acţiuni generale – Acţiuni ale vântului – Anexa naţională, Asociaţia de standardizare din România, Bucureşti, 2007

[27]   STN EN 1991-1-4/NA:2008-07: National Annex to Eurocode 1 – Actions on Structures Part 1-4: General actions – Wind actions, Slovenský ústav technickej normalizácie, Bratislava, 2008

[28]   SIST EN 1991-1-4:2005/A101:2008-01: Evrokod 1: Vplivi na konstrukcije – 1-4. del: Splošni vplivi – Obtežbe vetra – Nacionalni dodatek, Slovenski institute za standardizacijo, Ljubiljana, 2008

[29]   SS-EN 1991-1-4:2005/Bilaga NA:2008-10: Eurokod 1: Laster på bärverk – Del 1-4: Allmänna laster – Vindlast, Swedish Standards Institute, Stockholm, 2008

[30]   NA to BS EN 1991-1-4:2008-09: UK National Annex to Eurocode 1 – Actions on Structures Part 1-4: General actions – Wind actions, BSi, London, 2008

Other standards ([31] to [37] index by country of publication)

[31]   DIN 1055-4:2005-03: Einwirkungen auf Tragwerke – Teil 4: Windlasten, Deutsches Institut für Normung e. V., Beuth-Verlag, Berlin, 2005

[32]   Documento Básico SE-AE: Seguridad Estructural Acciones en la edificación, AENOR, Madrid, 2003

[33]   SiA 261/1:2003: Bauwesen, Einwirkungen auf Tragwerke – Ergänzende Fest-legungen, Schweizerischer Ingenieur- und Architektenverein, Zürich, 2003

[34]   TS 498:1987 + T1:1997 dahil: YAPI ELEMANLARININ BOYUTLANDIRILMASINDA ALINACAK YÜKLERİN HESAP DEĞERLERİ, TÜRK STANDARDLARI ENSTİTÜSÜ, Ankara, 1997

[35]   BS 6399-2:1997, British Standard, Loading for buildings – Part 2: Code of Practice for wind loads, BSi, London, 2002

[36]   CP3: Chapter V: Part 2:1972, British Standard, Basic data for the design of buildings, Chapter V. Loading, Part 2. Wind loads, BSi, London, 1972

[37]   ISO 4354:1997(E), Wind actions on standards, International Organization of Standardization, Genève, 1997

Further publications

[38]   D0188, Wind, Kommentar zum Kapitel 6 der Normen SIA 261 und 261/1 (2003), Einwirkungen auf Tragwerke; Schweizerischer Ingenieur- und Architektenverein, Zürich, 2006

[39]   PD 6688-1-4:2009, Background information to the National Annex to BS EN 1991-1-4 and additional guidance, BSi, London, 2009

[40]   Cook, Nicholas J.; Wind loading a practical guide to BS 6399-2 Wind loads on buildings, Thomas Telford Publishing, London, 2005

[41]   Harstveit, Knut; Sandvik, Rune; Behandling av topografi I ny norsk standard for vindlaster, NS3491-4, Rapport Klima 11, Det Norske Meteorologiske Institutt, Oslo, 2001

[42]   Lemelin, D. R.; Surry, D.; Davenport, A. G.; Simple Approximations for Wind Speed-up over Hills, Journal of Wind Engineering and Industrial Aerodynamics, 28, pp. 117-127, 1988

[43]   Kray, T; Paul, J.; Lied, R.-D.; Harmonisierte Windlastansätze in Europa (Stand 2013), Windeinwirkung in urbaner Umgebung, Vortragsband der 13. Dreiländertagung D-A-CH 2013, Windtechnologische Gesellschaft e.V., pp. 97-107, Wien, 2013

CFD simulation of cross-ventilation for a one-sided wind catcher system

R. Azizian[1], F. Montazeri[2] and H. Montazeri[3]

[1]Department of Mechanical Engineering, Islamic Azad University, South Tehran Branch, Iran
[2]Department of Mechanical Engineering, Islamic Azad University, Science and Research Branch, Iran
[3]Building Physics and Services, Eindhoven University of Technology, the Netherlands
Corresponding author: F. Montazeri, Montazeri_f66@yahoo.com

Abstract

A wind-catcher, as a natural ventilation system, consists of a tower located at the roof of a building to capture wind from external air stream and induce it into the building. The system is employed in different heights, cross sections and number of openings. However, the aerodynamic characteristic of such a structure is important in providing sufficiently large pressure differences at the openings. Computational Fluid Dynamics (CFD) has been used in many occasions in the past to investigate the impact of these characteristics on natural ventilation performance of these systems. The vast majority of these studies, however, focused on four-sided wind-catcher in which there are four openings on the tower. In a four-sided wind catcher, the channel is divided into four parts leading to a considerable reduction in the captured air and efficiency of the system. Short-circuiting between the four openings also has a negative impact on the performance of such a system. This paper presents 3D steady Reynolds Average Navier-Stokes (RANS) CFD for predicting the captured air flow rate and mean wind pressure distributions on internal surfaces of a one-sided wind-catcher. The evaluation is based on a grid-sensitivity analysis and on validation using wind-tunnel measurements. The results show that one-sided wind catchers are effective in providing natural ventilation. The best performance of the system is achieved for a perpendicular wind direction to the opening. Moreover, steady RANS, in spite of its limitations, can accurately reproduce the mean air flow rate through the wind catcher channel. The deviation from the experiments is about 2.2 and 14.1% for 0° and 180°, respectively. In this case, the CFD simulations of surface pressures inside the channel is also in a good agreement with the experimental data. In addition, the important impact of the turbulence model is demonstrated.

1 Introduction

Wind catchers have been used in arid central regions of Iran to provide natural ventilation and passive cooling. For a multi-opening wind catcher, when wind is blowing over the tower and the building it severs, a wind pressure develops on various apertures. Air enters from the windward openings and leaves the openings with lower pressure coefficients (Bahadori, 1994). Wind-catchers come in different configurations, heights and number of openings. However, the aerodynamic characteristic of such a structure is important in providing sufficiently large pressure differences at the openings.

CFD already used in many occasions in the past to evaluate the performance of wind catchers with different configurations (e.g. Montazeri, 2011). However, the vast majority of these studies focused on the performance of four-sided wind catchers (e.g. Hughes and Ghani, 2008). To the best of our knowledge, a detailed evaluation of steady RANS CFD has not yet been performed for a one-sided wind-catcher. This paper presents 3D steady RANS CFD for predicting the captured air flow rate and mean wind pressure distributions on internal surfaces of a one-sided wind-catcher. The evaluation is based on a grid-sensitivity analysis and on validation with wind-tunnel measurements. In addition, the important impact of the turbulence model is investigated.

2   Wind-tunnel measurements

The experiments were conducted in an open working section wind-tunnel. The wind-tunnel was 3.6 m long and had a test section of 0.46×0.46 m^2. A 1:40 scale model of an ancient one-sided wind catcher was employed, resulting to a blockage ratio of 5%. The measurements were performed for approaching air angles of 0–180° in 15 increments. 20 Pitot and 5 static tubes were employed at the bottom of the wind-catcher channel to measure the air velocity at different positions. For the wind angles in which the wind-catcher acts as a suction device (75 – 180°), 10 Pitot and 5 static tubes were installed at the top of the wind-catcher. The induced air flow rate into the channel is determined based the measured velocities. In addition, 23 internal pressure taps were installed at different internal surfaces of its channel to measure static pressure at those points. Fig. 1 shows the constructed model with the attached pressure taps along with the Pitot and static tubes at the bottom of the channel. The room model, which had a single vertical window, was located underneath the model and out of the wind-tunnel test-section. Note that the area of the window was equal to the area of the opening of wind catcher.

A uniform wind profile was applied resulting in a Reynolds number Re = 1.8×10^5 based on the wind-catcher height (H = 0.145 m). A detailed report on the measurement procedure and experimental uncertainties can be found in Montazeri and Azizian (2008).
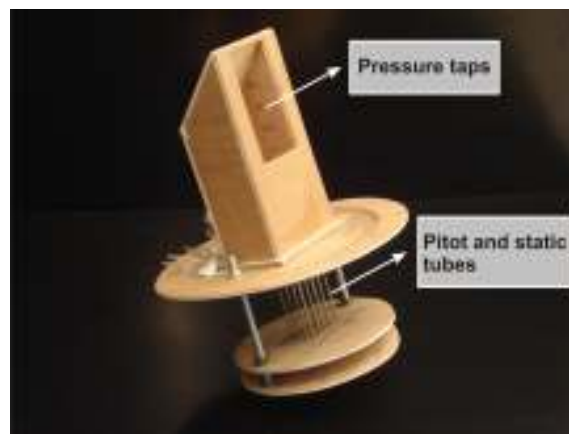
Fig. 1. One-sided wind-catcher model with the attached pressure taps, Pitot and static tubes.

3   CFD simulations: computational model and parameters

3.1 Computational geometry and grid

A computational model is made of the wind-catcher model including the room model in the wind-tunnel (Fig. 2). The size of the three-dimensional computational domain is based on the guidelines by Franke et al. (2007) and Tominaga et al. (2008). The upstream and downstream domain lengths are 5H and 10H, respectively. The computational grid was generated with the aid of the pre-processor Gambit 2.4.6, resulting in a hybrid grid with 7,265,421 prismatic and hexahedral cells. The grid is shown in Fig. 2. 25 and 26 cells are used along the width and depth of the wind-catcher opening, respectively. A maximum stretching ratio of 1.2 controls the cells located in the immediate surroundings of the wind-catcher model. y* values varies between 30 and 90. As standard wall functions (Launder and Spalding, 1974) are used in this study, these values ensure that the centre point of the wall-adjacent cell is placed in the logarithmic layer.

3.2 Boundary conditions and solver settings

The CFD simulations are performed using the commercial CFD code Fluent 6.3.26. The 3D steady RANS equations are solved in combination with the realizable k-ε turbulence model by Shih et al. (1995).
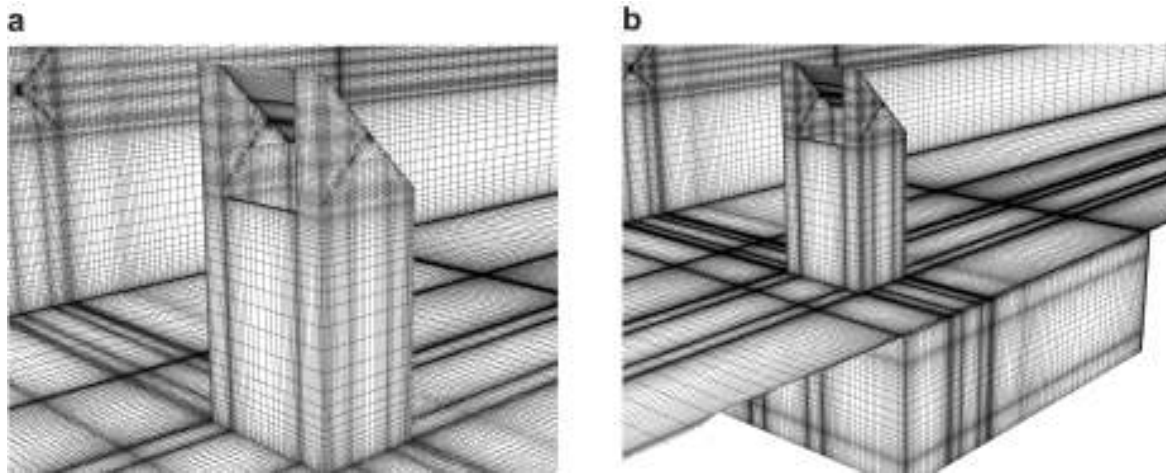
Fig. 2. Computational grid: (a) Detail of grid near wind-catcher. (b) Grid at bottom and side faces of the domain along with the room (7,265,421 cells).

The SIMPLE algorithm is used for pressure-velocity coupling, pressure interpolation is second order and second-order discretization schemes are used for both the convection terms and the viscous terms of the governing equations. At the inlet of the domain, a uniform mean wind speed profile is imposed. At the outlet, zero static pressure is specified. The simulations performed for the wind directions 0 and 180°. As recommended by Blocken et al. (2007), the absence of unintended stream-wise gradients in the vertical profiles of mean wind speed and the turbulence parameters is confirmed by performing simulations in an empty domain (i.e. without building present).

4   CFD simulations: results

The CFD results are compared with the wind-tunnel measurements by Montazeri and Azizian (2008). The pressure coefficients are computed as $C_P = (P - P_0)/(0.5\rho U_{ref}^2)$ where P is the pressure at the surface, P_0 the reference static pressure, $\rho = 1.225$ kg/m^3 the air density and U_{ref} is the reference wind speed. Fig. 3 compares the CFD results and the wind-tunnel results of C_P along the vertical measurement lines on two internal surfaces of the wind-catcher. The general agreement is good for the measurement points at the upper part of the lines. For the points in the middle of the channel, CFD tends to overestimate the C_p values. The maximum deviation can be observed in the vicinity of the flow separation. The main reason can be related to the well-known deficiencies of steady RANS CFD to reproduce separating and recirculating flow. For the point near the bottom of the channel a very good agreement can also be observed.
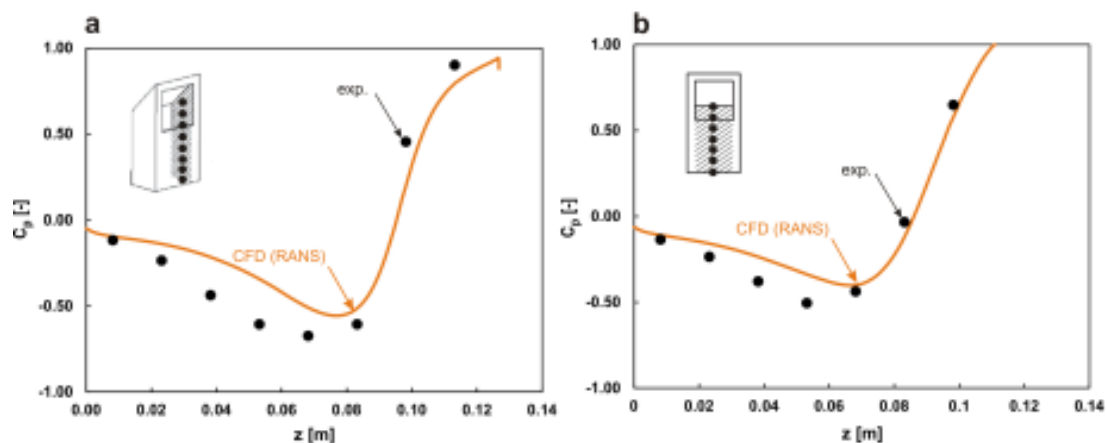
Fig. 3. Comparison of pressure coefficient (C_P) by CFD simulation results and wind-tunnel experiments along lines on (a) side plane and (b) centre plane of the wind-catcher channel.

Figure 4 compares the simulated and measured air flow rate for the two approaching wind angles 0° and 180°. It can be seen that the agreement for the air flow rate is quite good with the average deviations of 2.2% and 14.1%, respectively. This figure also shows that the performance of the one-sided wind-catcher is reduced by about 29% as the opening is located in the leeward side (i.e. θ = 180°). Note that in this case the wind-catcher system acts as a suction device as also pointed out by Montazeri and Azizian (2008). It shows that a one-sided wind catcher is capable of providing natural ventilation for different approaching wind angles.
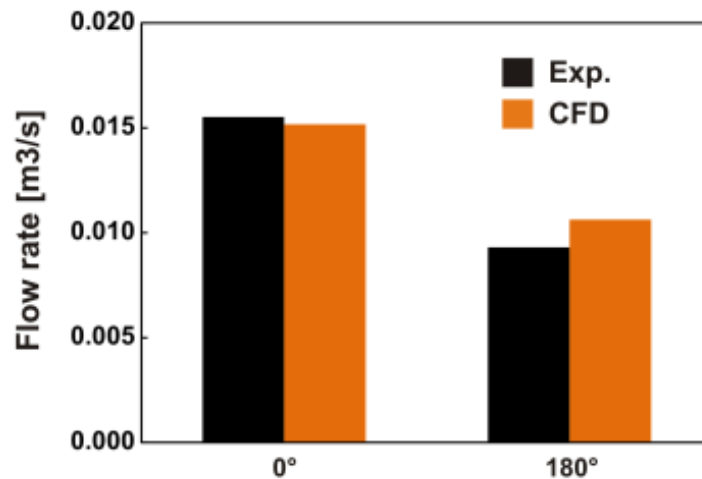
Fig. 4. Comparison of air flow rate (m^3/s) by CFD simulation results and wind-tunnel experiments for two wind angles 0° and 180°.

References

Bahadori, M.N. (1994). Viability of wind towers in achieving summer comfort in the hot arid regions of the Middle-East. *Renewable Energy* **5**, 879–892.

Blocken, B., Stathopoulos, T., and Carmeliet, J. (2007). CFD simulation of the atmospheric boundary layer: wall function problems. *Atmospheric Environment* **41**, 238-252.

Franke, A.H. J., Schlünzen, H., and Carissimo, B. (2007). Best practice guideline for the CFD simulation of flows in the urban environment.

Hughes B.R. and Ghani S.A.A. (2009). Investigation of a wind vent passive ventilation device against current fresh air supply recommendations, *Energy and Building* **40**, 9159-9151.

Launder, B.E., and Spalding, D.B. (1974). The numerical computation of turbulent flows. *Computer Methods in Applied Mechanics and Engineering* **3**, 269-289.

Montazeri, H., and Azizian R. (2008). Experimental study on natural ventilation performance of one-sided wind catcher, *Building and Environment* **43**, 2193–2202.

Montazeri, H., (2011). Experimental and numerical study on natural ventilation performance of various multi-opening wind catchers, *Building and Environment* **46**, 370–378.

Shih, T.H., Liou, W.W., Shabbir, A., Yang, Z., and Zhu, J. (1995). A new k-ε eddy viscosity model for high Reynolds num-ber turbulent flows, *Computers & Fluids* **24**, 227-238.

Tominaga, Y., Mochida, A., Yoshie, R., Kataoka, H., Nozu, T., Yoshikawa, M., and Shirasawa, T. (2008). AIJ guidelines for practical applications of CFD to pedestrian wind environment around buildings. *Journal of Wind Engineering and Industrial Aerodynamics* **96**, 1749-1761.

Evaluation of the thermal comfort by natural ventilation in hot climates

J. A. Castillo[1,2], G. Huelsz[1], T. van Hooff[2] and B. Blocken[2,3]

[1]Instituto de Energías Renovables, Universidad Nacional Autónoma de México, Priv. Xochicalco s/n
Col. Centro, Temixco Morelos, México
[2]Building Physics and Services, Eindhoven University of Technology, P.O. Box 513, 5600 MB
Eindhoven, The Netherlands
[3]Building Physics Section, Department of Civil Engineering, Leuven University, Kasteelpark Arenberg
40 bus 2447, 3001 Heverlee, Belgium
Corresponding author: J. A. Castillo, jacat@ier.unam.mx

Abstract

Natural ventilation is an alternative to create comfortable and healthy indoor conditions. This work presents the development of a method, named, the Heat Balance Index, HBI. This new index evaluates the occupant thermal comfort produced by natural ventilation in hot climates. It is based on the Heat Stress Index, HSI, model. The HBI gives the comfort velocity range, which is useful to calculate the well-ventilated percentage of a space. The numerical simulation of the cross ventilated building using Computational Fluid Dynamics was validated with experimental results. Numerical simulation of a cross ventilated building is used as an application example.

1   Introduction

Natural ventilation is an alternative to create comfort and healthy indoor conditions, reducing the energy consumption, for ventilation in general and in hot climates also for improving hygrothermal comfort. Typically, the energy cost of a naturally ventilated building is 40% less than that of an air-conditioned building (Energy Efficiency Best Practice Programme (EEBPP), 1993). For dry hot climates, it has been found that night ventilation is an effective method to promote thermal comfort conditions (Bleem et al., 1987), while for humid hot climates full day ventilation is the better strategy to promote thermal comfort conditions (Liping and Hien, 2007). Thus it is important to asses the indoor natural ventilation in hot climates in terms of the thermal comfort of the occupants.

The parameters used to evaluate the ventilation performance are the mean velocity at the space, V, and the average velocity coefficient at a slice of a given height, C_{Vh} (Prianto and Depecker, 2002). Bastide et al. (2006) have introduced the concept of well-ventilated percentage of a space, P, that is defined as the percentage of the volume with velocities within a velocity range, (U_{min}, U_{max}). They show that the results are very sensitive to the choice of U_{min} and U_{max}, but they do not give a methodology to select these values.

For the evaluation of thermal comfort, the most common method is the Predicted Mean Vote, PVM, with the Predicted Percentage Dissatisfied, PPD, (Fanger, 1970; ASHRAE, 2005), however, it has been proven that the $PVM - PPD$ method is inadequate in case of natural ventilation (De Dear et al., 1997). By contrast, the Heat Stress Index, HSI (Givoni, 1969), is a method used to evaluate thermal comfort for ventilated indoors in hot climates. It is defined as the ratio of the required evaporation to the maximum evaporative capacity of the air. The required evaporation is given by the total heat stress acting on the body (metabolism $\pm$ radiation $\pm$ convection).

This work presents the development of a method, the Heat Balance Index, HBI, to evaluate the indoor natural ventilation in hot climates in terms of the thermal comfort of the occupants. This index is developed using the assumptions and starting from the Heat Stress Index model and gives a method to define the comfort velocity range (U_{min}, U_{max}) useful to calculate the well-ventilated percentage of

a space, P. As example of application, a simulation, by Computational Fluid Dynamics (CFD), of a cross ventilated building (Kurabuchi et al., 2004) was evaluated with the climate conditions of Temixco, Morelos, which is a Mexican city with hot climate.

The fundamentals of the developed methodology are presented in Section 2. Section 3 describes the study case used to show the applicability of the proposed methodology. Conclusions are given in Section 4.

2   Methodology

The Heat Balance Index, HBI, is defined as the ratio between the heat balance of the body and the metabolic gain, which depends on the activity. The heat balance of the body is given by the algebraic sum of the metabolic gain and the heat transfer between the body and the surroundings given by the mechanisms of radiation, R (W/m^2), convection, C (W/m^2), and evaporation, E (W/m^2),

$$HBI = \frac{M \pm R \pm C - E}{M},\qquad(1)$$

where M (W/m^2) is the metabolic gain. The following empirical expressions for R, C and E (McIntyre, 1980; Wang et al., 2011) are used,

$$R = 4.4\,(T_s - T_r)\,,\qquad(2)$$

$$C = 4.6U^{3/5}\,(T_s - T_a)\,,\qquad(3)$$

$$E = 7.0U^{3/5}\,(P_s - P_a)\,,\qquad(4)$$

where $T_s = 35°C$ is the skin temperature, T_r $(°C)$ is the mean radiant temperature, U (m/s) is the air velocity, T_a $(°C)$ is the air temperature, $P_s = 56 \times 10^2 Pa$ the vapor saturation pressure at T_s and P_a $(10^2 Pa)$ is the partial pressure of water vapor at T_a. As the evaporation is only possible if $P_s > P_a$, if this condition is not fulfilled $E = 0$ in Eq. (4).

Table 1 shows the range of conditions covered by the empirical expressions (Eqs.2 -4). This range of conditions allows a proper application in hot climates, as the climate studied in this paper, which will be detailed in Section 3.

Table 1. The range of conditions covered by the HBI.

Lower limit		Upper limit
$65W/m^2$	$\leq M \leq$	$327W/m^2$
$21°C$	$\leq T_a \leq$	$49°C$
$0.25m/s$	$\leq U \leq$	$10.00m/s$
$3 \times 10^2 Pa$	$\leq P_a \leq$	$56 \times 10^2 Pa$

The HBI of 0 represents the neutral thermal condition, where the heat generated by the body (M) is exactly equal to the heat dissipated to the surroundings. For this work, the range $-0.2 \leq HBI \leq 0.2$ is considered the comfort range (Givoni, 1969; McIntyre, 1980). $HBI < -0.2$ indicates that the body has an overdissipation greater than the 20%, with respect of M, causing a cold uncomfort. On the other hand, $HBI > 0.2$ signifies that the body has a subdissipation greater than the 20%, thus the body feels a hot uncomfort.

In order to evaluate the range for thermal comfort of the magnitude of the air velocity produced by natural ventilation, U is solved from Eq. (1),

$$U = \left[\frac{M\,(1 - HBI) - R}{4.6\,(T_s - T_a) + 7.0\,(P_s - P_a)}\right]^{5/3}.\qquad(5)$$

As can be observed, U depends on HBI. Three magnitudes of U are distinguished: U_{max}, U_{neu} and U_{min}, for the HBI values of -0.2, 0.0 and 0.2, respectively. Thus $U_{min} \leq U \leq U_{max}$, represents the comfort air velocity range given an activity (M) and air temperature (T_a) and relative humidity (RH). When the value of U obtained from Eq. 5 is negative, this indicates that the air is unable to dissipate the heat generated by the body. The values of U_{max}, U_{neu} and U_{min} can be used to evaluate the comfort generated by the air velocity distribution into the building interior.

3   HBI example

3.1   CFD simulation

The cross ventilation in a scaled building (1/15), studied by Kurabuchi et al. (2004), of $0.3m \times 0.3m \times 0.15m$ ($l \times b \times h$) with two axial openings (Figure 1a) was simulated using the commercial CFD code FLUENT14.0 (ANSYS, 2011). The openings have dimensions $0.06m \times 0.03m$ ($w_w \times h_w$) and were installed at the middle of each wall, leeward and windward, respectively (Figure 1b). The CFD simulation reproduces the building geometry (small scale) and uses the reference velocity, $U_{ref} = 7m/s$, measured at h (Kurabuchi et al., 2004). The wind direction is parallel to the measurement plane. The building Reynolds number is $Re = U_{ref}h/\nu = 6.69 \times 10^4$ where ν is the dynamic viscosity of the air.
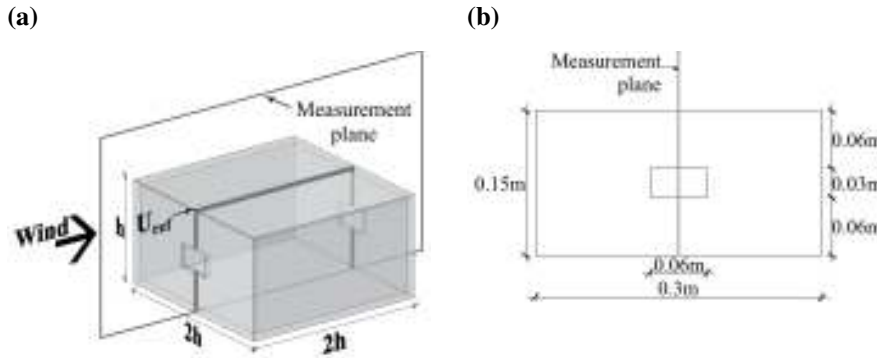
Figure 1. Scaled model of a building with two axial openings (Kurabuchi et al., 2004): (a) Right isometric view with measurement plane; (b) Front view with dimensions.

The 3D steady RANS equations were solved in combination with the shear-stress transport (SST) $k - \omega$ model (Ramponi and Blocken, 2012). The SIMPLEC algorithm was used for pressure-velocity coupling, pressure interpolation was second order and second-order discretization schemes were used for both the convection terms and the viscous terms of the governing equations. The convergence was assumed to be obtained when all the scaled residuals be less than 10^{-6}. The domain dimensions and the computational grid were based on the guidelines by Franke et al. (2007); Tominaga et al. (2008); Hooff and Blocken (2010); Ramponi and Blocken (2012), which dimensions were $W_d \times L_d \times H_d = 1.8 \times 3.0 \times 0.9m^3$ (Figure 2a). The computational base grid, formed by 1,448,712 hexahedral cells (Figure 2b), was created. The inlet boundary conditions were the wind velocity profile defined by the logarithmic law, $U(z) = (u^*_{ABL}/\kappa)ln((z+z_0)/z_0)$, with the atmospheric boundary layer (ABL) friction velocity, $u^*_{ABL} = 0.75m/s$, the von Karman constant, $\kappa = 0.42$, the roughness length, $z_0 = 0.0027m$, and the height coordinate, z. The turbulent kinetic energy (TKE) profile, $k(z) \cong \sigma^2_u(z)$, was obtained from the standard deviation of velocity in the x-direction, σ_u. The turbulence dissipation rate (TDR) and the specific dissipation rate (SDR) profiles were calculated, $\varepsilon(z) = u^{*3}_{ABL}/\kappa(z + z_0)$ and $\omega(z) = \varepsilon(z)/C_\mu k(z)$, respectively, with the empirical constant $C_\mu = 0.09$ (Tominaga et al., 2008). The standard wall functions with roughness modification (Cebeci and Bradshaw, 1977) were imposed on the ground surface. The values of the sand-grain roughness height, $k_S = 9.793z_0/C_S = 0.0039m$, and the roughness constant, C_S, were determined by using the relationship with the aerodynamic roughness length z_0 derived by Blocken et al. (2007). The standard wall functions were also used at the building surfaces, but with zero roughness height ($k_S = 0$). At the outlet plane, the zero static pressure was applied. Symmetry conditions were applied at the top and the lateral sides of the domain.

(a)   **(b)**
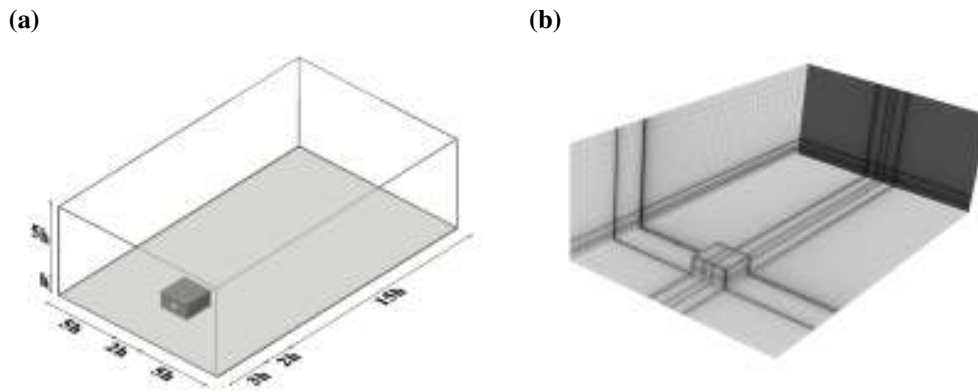
Figure 2. Computational domain with the building with two axial openings: (a) Perspective view with dimensions of the domain; (b) Perspective view of grid at bottom, side and back face (Base grid with 1,448,712 cells).

Figure 3 shows the velocity profile at inlet and at incident building position, which are an important quality criterion for the simulations (Blocken et al., 2007), in the empty domain. The test is to assess the extent of unintended streamwise gradients of the mean wind speed and the turbulence parameters, between the vertical profiles at inlet and at incident building position. In Figure 3, the inlet vertical profile (solid line) and the incident vertical profile (dashed line) are presented. Minor streamwise gradients are observed.

(a)   **(b)**
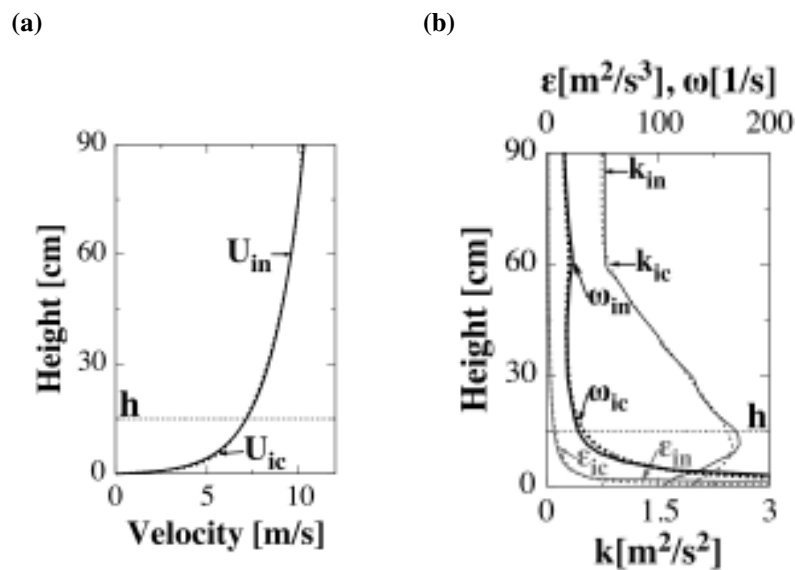
Figure 3. Vertical profiles of (left) the mean wind speed, U; (right) the turbulent kinetic energy (thin line), k, the turbulence dissipation rate (thick line), ε, and the specific dissipation rate (gray line), ω, at the inlet (solid line) and at the incident position (dashed line) in the empty domain. The subscripts "in" and "ic" refer to inlet and incident, respectively. The height of the model (h) is 0.15 m (SST $k-\omega$ model, Base grid with 1,448,712 cells).

Three grids with 728,724 cells (Coarse grid), 1,448,712 cells (Base grid) and 2,537,020 cells (Fine grid) were constructed (Figure 4). The grids were obtained by refining the Coarse grid twice by a factor of 2.

The vector field in the centerplane shows a close qualitative agreement between experimental and numerical results (Figures 5a and 5b). The simulation reproduces the main vortexes of the flow, such as the one formed by the floor and the windward wall, the one formed by the roof and the windward wall, and the biggest one in the rear of the building. The simulation tends to overestimate the structure size of the external vortexes round the scaled building. Besides, at interior of scaled building the simulation

(a)   **(b)**   **(c)**
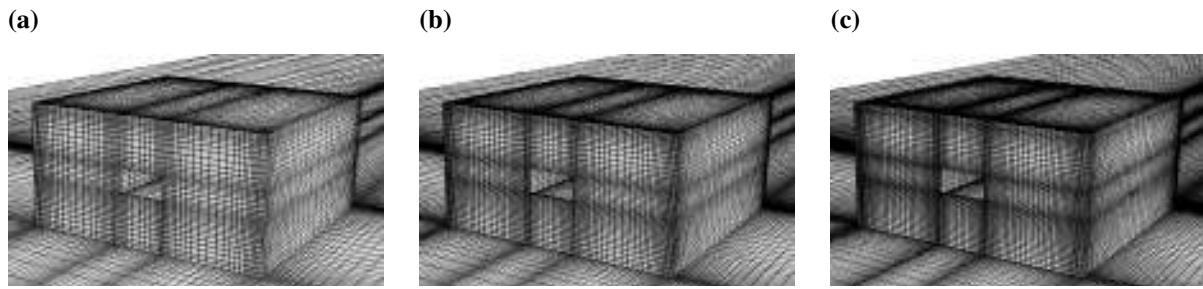
Figure 4. Isometric view of a building with two axial openings: (a) Coarse grid with 728,724 cells; (b) Base grid with 1,448,712 cells; (c) Fine grid with 2,537,020 cells.

reduces the wind speed magnitude and the size of the structures. In Figure 5c, the grid sensitivity is small along the center line, L_r. The difference of the wind speed ratio, u/U_{ref}, between the Coarse grid and Base grid at the building interior is around 7%, while between the Base grid and the Fine grid is lower than 2%. The percentage average difference between the experimental, PIV, and the numerical results, CFD, of the wind speed, $\Delta u = (PIV - CFD/U_{ref}) * 100$, along L_r is for the Base grid 6% at the interior building. Therefore, the Base grid is a suitable grid to use. Thus the validated numerical simulation of a building with two axial openings is used for the application example of the HBI.

(a)   **(b)**

(c)
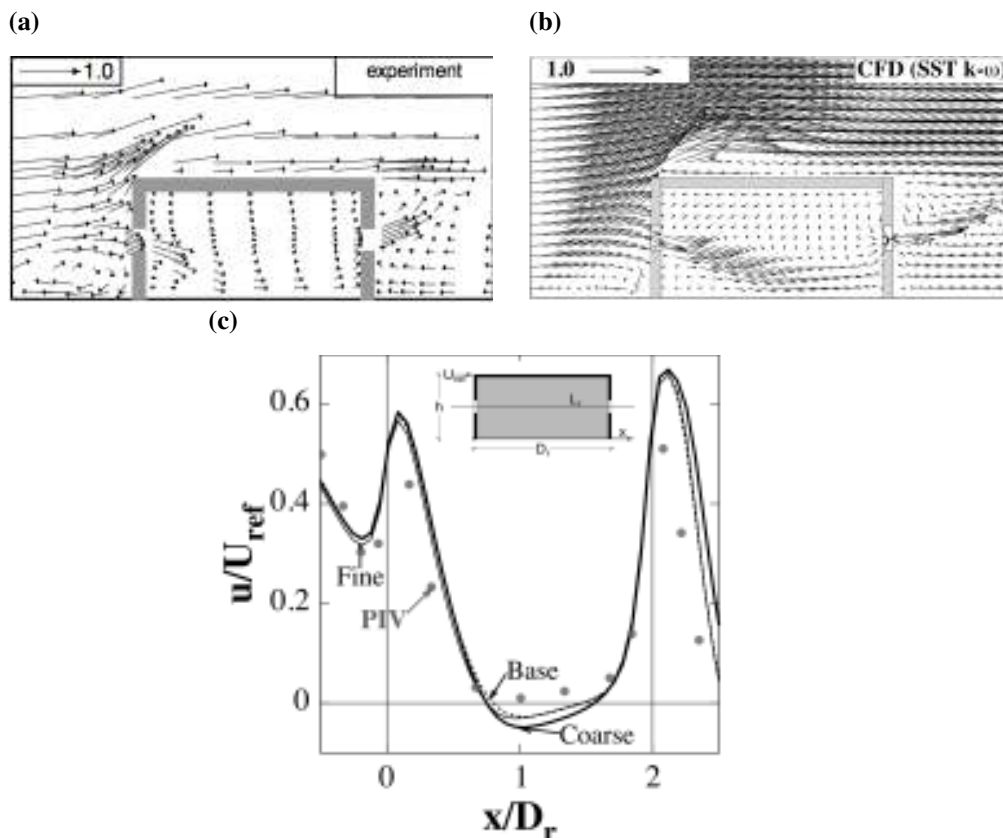
Figure 5. Comparison of mean wind vectors on the vertical centreplane and of wind speed ratio, u/U_{ref}, along the center line, L_r. (a) Experimental results from Kurabuchi et al. (2004), (b) simulation results using CFD SST $k - \omega$ turbulence model and (c) grid sensitivity analisys.

3.2   Application example

The HBI application example is performed with the climate conditions of the hot and humid season in the Temixco city located in Morelos, Mexico. The average conditions are $U_r = 1.04 m/s$ (the reference

air velocity at $H_r = 2.25m$ building height), $T_r = T_a = 33°C$ and $RH = 72\%$. The $U(z)$ from the real scale were modeled as inlet boundary condition, in the validated numerical model, by applying the dynamic similarity with $Re_r = (U_r H_r)/\nu = 1.49 \times 10^5$. For thermal comfort evaluation by natural ventilation, the interior volume simulated was discretized in 4000 cells. Then, the U values obtained from each cell were scaled to real scale by using Re_r. Figure 6 shows the comfort evaluation by natural ventilation of the building with cross ventilation (Figure 1), applying Eq. (5) and considering a Metabolic rate of $M = 93W/m^2$ (light activity). Therefore, the interior volume can be zoned as: discomfort by low ventilation, D_{lv}, comfort, C_m, and discomfort by high ventilation, D_{hv}, represented by 85.8%, 12.6% and 1.7%, respectively.

Volume	Cells	Percentage
D_{lv}	3430	85.8
C_m	504	12.6
D_{hv}	66	1.7
Total	4000	100.0
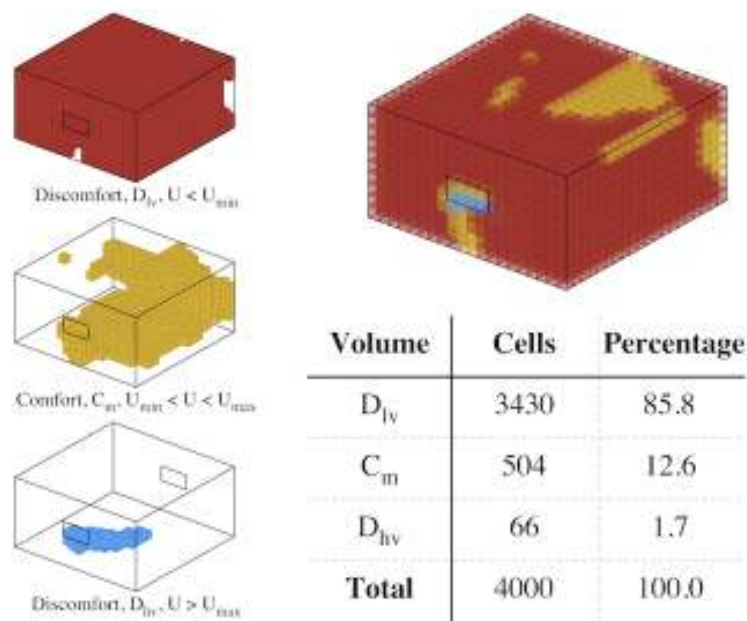
Figure 6. Evaluation of the comfort by natural ventilation of a building with cross ventilation. The interior volume is zoned as: discomfort by low ventilation, D_{lv}, comfort, C_m, and discomfort by high ventilation, D_{hv}. The range $U_{min} \leq U \leq U_{max}$ refers to the comfort air velocity range.

4   Conclusions

A methodology to evaluate the indoor comfort by natural ventilation in hot climates based on a heat balance index has been proposed. The methodology allows to evaluate CFD simulations as well as measurements taken from experiments (small or real scale). More research is needed to further verify the applicability of this methodology to select the best natural ventilation strategy.

Acknowledgements

References

ANSYS (2011). *ANSYS FLUENT user's guide*. ANSYS Inc, Pennsylvania.

ASHRAE (2005). *2005 ASHRAE Handbook fundamentals, Si Edition*. American Society of Heating, Refrigerating and Air Conditioning Engineers, Atlanta, GA.

Bastide, A., Lauret, P., Garde, F., and Boyer, H. (2006). Building energy efficiency and thermal comfort in tropical climates. Presentation of a numerical approach for predicting the percentage of well-ventilated living spaces in buildings using natural ventilation. *Energy and Buildings* **38**.9, pp. 1093–1103.

Bleem, J., Burns, P., and Winn, C. B. (1987). NIGHT VENTILATION STRATEGIES IN DRY CLIMATES. *Solar Engineering*. Vol. 2, pp. 959–966.

Blocken, B., Stathopoulos, T., and Carmeliet, J. (2007). CFD simulation of the atmospheric boundary layer: wall function problems. *Atmospheric Enviroment* **41**, pp. 238–252.

Cebeci, T. and Bradshaw, P. (1977). *Momentum transfer in boundary layers*. New York: Hemisphere Publishing Corp.

De Dear, R.J., Brager, G.S., and Cooper, D. (1997). *Developing an adaptive model of thermal comfort and preference, ASHRAE RP-884 Final report, ASHRAE Inc. and Macquarie Research Ltd., Sydney MRL*.

Energy Efficiency Best Practice Programme (EEBPP) (1993). *Energy Consumption Guide 19, Energy Efficiency in Offices, Energy Efficiency Office/HMSO, London*.

Fanger, P.O. (1970). *Thermal Comfort Analysis and Applications in Environmental Engineering*. New York: EngineersMcGraw-Hill.

Franke, J., Hellsten, A., Schlunzen, H., and Carissimo, B. (2007). Best practice guideline for the CFD simulation of flows in the urban environment. *COST office*.

Givoni, B. (1969). *Man, Climate and Architecture. Elsevier Architechtural Science Series*. Elsevier, Amsterdam - London - New York.

Hooff, T. van and Blocken, B. (2010). Coupled urban wind flow and indoor natural ventilation modelling on a high-resolution grid: a case study for the Amsterdam Arena stadium. *Environ Modell Softw* **25**, pp. 51–65.

Kurabuchi, Takashi, Ohba, Masaaki, Endo, Tomoyuki, Akamine, Yoshihiko, and Nakayama, Fumihiro (2004). Local Dynamic Similarity Model of Cross-Ventilation Part 1 - Theoretical Framework. *International Journal of Ventilation* **2**.4, pp. 371–382.

Liping, W. and Hien, W. N. (2007). The impacts of ventilation strategies and facade on indoor thermal environment for naturally ventilated residential buildings in Singapore. *Building and Environment* **42**.12, pp. 4006–4015.

McIntyre, D. A. (1980). *Indoor Climate*. Applied Science Publishers LTD, London, UK.

Prianto, E. and Depecker, P. (2002). Characteristic of airflow as the effect of balcony, opening design and internal division on indoor velocity: A case study of traditional dwelling in urban living quarter in tropical humid region. *Energy and Buildings* **34**.4, pp. 401–409.

Ramponi, R. and Blocken, B. (2012). CFD simulation of cross-ventilation for a generic isolated building: Impact of computational parameters. *Building and Environment* **53**, pp. 34–48.

Tominaga, Y., Mochida, A., Yoshie, R., Kataoka, H., Nozu, T., and Yoshikaw, M. (2008). AIJ guidelines for practical applications of CFD to pedestrian wind environment around buildings. *J Wind Eng Ind Aerodyn* **96**, pp. 1749–1761.

Wang, L., Liu, J., Liu, Y., Wang, Y., and Chen, J. (2011). Study on thermal environment of traditional architecture in tropic climate. *Advanced Materials Research*, pp. 6857–6861.

Probabilistic Models for Wind Loads and Response Analysis

H. Zhao[1] and M. Grigoriu[1]

[1]School of Civil and Environmental Engineering, Cornell University, USA
Corresponding author: H. Zhao, hz289@cornell.edu

Abstract

Probabilistic models are developed for structural responses of linear systems induced by wind loads corresponding to mean wind velocities that are orthogonal to a building surface. The focus is on the calculation of mean rates at which response processes exit safe sets. The analysis involves three steps. First, along-wind forces, across-wind forces, and torques are defined as superpositions of turbulence fluctuations and wake excitations, assumed to be independent filtered Gaussian processes. The models are calibrated to experimental observations. Second, structural responses are modeled by translation processes that match target second-moment properties and marginal moments. Linear random vibration theory is applied to find second-moment response properties. Itô's formula is used to develop moment equations for responses corresponding to the non-Gaussian components of the wind loads. Third, crossing theory for translation vector processes is applied to assess structural performance. Numerical results are presented for a simple oscillator and a single story with three degrees-of-freedom.

1 Introduction

Experimental and mathematical approaches are used to characterize structural responses to wind. Full-scale and wind tunnel tests provide invaluable information on both wind loads on structures and structural responses. Cost limits the use of this approach (Barlow et al., 1999). Mathematical approaches provide deterministic and probabilistic models for wind loads that can be used to calculate properties of structural responses. We propose a mathematical approach to model wind loads, calibrate these load models to experiments, and find response statistics for linear systems.

Our probabilistic model for wind loads is based on developments in Solari (1994). Wind tunnel records from Shimizu Corporation Laboratories (Kikuchi et al., 1997) are used to calibrate the model. The model relates wind loads with turbulence fluctuations. A linear term is added to capture effects of wake excitations in the rear region of the building. The proposed wind load model has three components that correspond to along-wind forces, across-wind forces, and torques. Along-wind forces are described by polynomials of along-wind Gaussian turbulence fluctuations. Across-wind forces and torques are linear combinations of loads associated with across-wind turbulence fluctuations and wake excitations. The turbulence fluctuation and wake excitation terms are modeled by filtered Gaussian processes.

A translation model of the type in Grigoriu and Field (2014) is used to characterize structural responses. The model is fitted to second-moment properties and marginal distributions of structural responses. The first two response moments are calculated by methods of linear random vibration theory (Grigoriu and Field, 2014; Soong and Grigoriu, 1993). Marginal distributions are calibrated to higher order marginal moments that are obtained by Itô's formula following an approach in (Grigoriu and Ariaratnam, 1988). Alternative methods can be used for this purpose, e.g., linear combinations of specified distributions with weights selected to minimize the discrepancy between moments of these models and target moments (Grigoriu and Ariaratnam, 1988) and C-type Gram-Charlier series expansion (Gullo et al., 1998).

Two examples are presented to illustrate the proposed methodology and assess its accuracy, a simple oscillator and a three degrees-of-freedom structure subjected to wind loads. The proposed method is applied to find mean rates at which responses of these structures exit safe sets. Results by the proposed method and Monte Carlo simulation are similar.

2   Wind-load model

We define probabilistic model for wind loads acting on buildings and calculate the second-moment property of the wind-load vector process.

2.1   Aerodynamic wind loads on rigid building

Consider an n-story building immersed in an ideal bi-dimensional wind field. Let $F_{xi}(t)$, $F_{yi}(t)$, and $M_{zi}(t)$ denote the along-wind force, the across-wind force, and the torque at floor i. Denote by ρ, B, $\varphi(t)$, $\bar{u}_i$, $\tilde{u}_i(t)$, and $\tilde{v}_i(t)$ the air density, building's width, instantaneous angle-of-attack of wind speed relative to building, mean wind velocity, along-wind turbulence, and across-wind turbulence fluctuations, respectively. Under the assumptions that the turbulence intensities are small and the wake excitations contribute insignificantly to along-wind forces, the dimensionless along-wind force $C_{xi}(t)$, across-wind force $C_{yi}(t)$, and torque $C_{zi}(t)$ have the expressions (Solari, 1994)

$$C_{xi}(t) = \frac{F_{xi}(t)}{\frac{1}{2}\rho \bar{u}_i^2 B} = c_{di,0} + \frac{2c_{di,0}}{\bar{u}_i}\tilde{u}_i(t) + \frac{c_{di,0}}{\bar{u}_i^2}\tilde{u}_i^2(t), \tag{1}$$

$$C_{yi}(t) = \frac{F_{yi}(t)}{\frac{1}{2}\rho \bar{u}_i^2 B} = \frac{c_{di,0} + c_{li,0}'}{\bar{u}_i}\tilde{v}_i(t) + \tilde{w}_{yi}(t), \text{ and} \tag{2}$$

$$C_{zi}(t) = \frac{M_{zi}(t)}{\frac{1}{2}\rho \bar{u}_i^2 B^2} = \frac{c_{mi,0}'}{\bar{u}_i}\tilde{v}_i(t) + \tilde{w}_{zi}(t), \tag{3}$$

where $c_{di,0} = c_{di}(\varphi(t))|_{\varphi(t)=0}$, $c_{li,0}' = dc_{li}(\varphi(t))/d\varphi(t)|_{\varphi(t)=0}$, $c_{mi,0}' = dc_{mi}(\varphi(t))/d\varphi(t)|_{\varphi(t)=0}$, $c_{di}(\varphi(t))$, $c_{li}(\varphi(t))$, and $c_{mi}(\varphi(t))$ denote the drag, lift, and torsional load coefficients at $\varphi(t)$, and $\tilde{w}_{yi}(t)$, $\tilde{w}_{zi}(t)$ are dimensionless, independent loads caused by wake excitations.

The turbulence fluctuation and wake excitation terms $\tilde{u}_i(t)$, $\tilde{v}_i(t)$, $\tilde{w}_{yi}(t)$, and $\tilde{w}_{zi}(t)$ in Eqs. (1)-(3) can be modeled by filtered Gaussian processes (Benfratello and Muscolino, 1999; Grigoriu and Field, 2014), e.g., $\tilde{u}_i(t)$, $\tilde{v}_i(t)$ are described by Ornstein-Uhlenbeck processes

$$d\tilde{\eta}_i(t) = -\alpha_{\tilde{\eta}i}\tilde{\eta}_i(t)dt + \sigma_{\tilde{\eta}i}^2\sqrt{2\alpha_{\tilde{\eta}i}}dB_{1i}(t) \tag{4}$$

and $\tilde{w}_{yi}(t)$, $\tilde{w}_{zi}(t)$ are modeled by the responses of a linear system driven by Gaussian processes

$$d\tilde{\mathbf{w}}_{\xi i}(t) = \mathbf{D}_{\xi i}\tilde{\mathbf{w}}_{\xi i}(t)dt + \mathbf{g}_{\xi i}dB_{2i}(t), \tag{5}$$

where $\tilde{\eta}_i = \tilde{u}_i, \tilde{v}_i$, $\tilde{w}_{\xi i} = \tilde{w}_{yi}, \tilde{w}_{zi}$, $\tilde{\mathbf{w}}_{\xi i}(t) = \begin{bmatrix} \tilde{w}_{\xi i}(t) & \dot{\tilde{w}}_{\xi i}(t) \end{bmatrix}^T$, $\mathbf{D}_{\xi i} = \begin{bmatrix} 0 & 1 \\ -\theta_{\xi i}^2 & -2\gamma_{\xi i}\theta_{\xi i} \end{bmatrix}$, $\mathbf{g}_{\xi i} = [0 \ \beta_{\xi i}]^T$, and $\{B_{1i}(t) \ B_{2i}(t)\}$ are independent standard Brownian motions. The parameters $\alpha_{\tilde{\eta}i}, \sigma_{\tilde{\eta}i}, \theta_{\xi i}, \gamma_{\xi i}, \beta_{\xi i}$ in the above equations need to be estimated.

2.2   Second-moment characterization

Let $\mathbf{C}_i(t) = [C_{xi}(t) \ C_{yi}(t) \ C_{zi}(t)]^T$ denote the dimensionless wind-load vector process at floor i. It is assumed that $\mathbf{C}(t) = [\mathbf{C}_1(t) \ \dots \ \mathbf{C}_n(t)]^T$ is a weakly-stationary $3n$-dimensional vector process. Let $\Gamma_{ij}^{ab}(\tau) = E[C_{ai}(t)C_{bj}(t+\tau)]$, denote the correlation function between two arbitrary components of $\mathbf{C}(t)$, where τ denotes the time lag, $a, b = x, y, z$ denote components of the wind load vector process, and $i, j = 1, \dots, n$ floor numbers. The cross spectral density of wind loads is $S_{ij}^{ab}(\nu) = \mathcal{F}\left[\Gamma_{ij}^{ab}(\tau)\right]$, where ν denotes the frequency and $\mathcal{F}$ is the Fourier Transform operator. These cross spectral densities

have the expressions

$$S_{ij}^{xx}(\nu) = \frac{6c_{di,0}c_{dj,0}S_{ij}^{\tilde{u}}(\nu)}{\bar{u}_i\bar{u}_j} + \frac{c_{di,0}c_{dj,0}S_{ij}^{\tilde{u}^2}(\nu)}{\bar{u}_i^2\bar{u}_j^2}, \tag{6}$$

$$S_{ij}^{yy}(\nu) = \frac{(c_{di,0} + c'_{li,0})(c_{dj,0} + c'_{lj,0})S_{ij}^{\tilde{v}}(\nu)}{\bar{u}_i\bar{u}_j} + S_{ij}^{\tilde{w}_y}(\nu), \tag{7}$$

$$S_{ij}^{zz}(\nu) = \frac{c'_{mi,0}c'_{mj,0}S_{ij}^{\tilde{v}}(\nu)}{\bar{u}_i\bar{u}_j} + S_{ij}^{\tilde{w}_z}(\nu), \tag{8}$$

$$S_{ij}^{xy}(\nu) = S_{ij}^{xz}(\nu) = 0, \text{ and} \tag{9}$$

$$S_{ij}^{yz}(\nu) = \frac{(c_{di,0} + c'_{li,0})c'_{mj,0}S_{ij}^{\tilde{v}}(\nu)}{\bar{u}_i\bar{u}_j}, \tag{10}$$

where $S_{ij}^{\tilde{\eta}}(\nu) = \mathcal{F}\{E\left[\tilde{\eta}_i(t)\tilde{\eta}_j(t+\tau)\right]\}$, $S_{ij}^{\tilde{u}^2}(\nu) = \mathcal{F}\left\{E\left[\tilde{u}_i^2(t)\tilde{u}_j^2(t+\tau)\right]\right\}$,
and $S_{ij}^{\tilde{w}_\xi}(\nu) = \mathcal{F}\{E\left[\tilde{w}_{\xi i}(t)\tilde{w}_{\xi j}(t+\tau)\right]\}$, in which $\tilde{\eta} = \tilde{u}, \tilde{v}$, $\tilde{w}_\xi = \tilde{w}_y, \tilde{w}_z$. The spectral densities associated with turbulence fluctuations and wake excitations $S_{ii}^{\tilde{\eta}}(\nu)$, $S_{ii}^{\tilde{u}^2}(\nu)$, $S_{ii}^{\tilde{w}_\xi}(\nu)$ in the above equations have the forms

$$S_{ii}^{\tilde{\eta}}(\nu) = \mathcal{F}\{E\left[\tilde{\eta}_i(t)\tilde{\eta}_i(t+\tau)\right]\} = \frac{2\alpha_{\tilde{\eta}i}\sigma_{\tilde{\eta}i}^2}{\left[\pi(\nu^2 + \alpha_{\tilde{\eta}i}^2)\right]}, \tag{11}$$

$$S_{ii}^{\tilde{u}^2}(\nu) = \mathcal{F}\left\{E\left[\tilde{u}_i^2(t)\tilde{u}_i^2(t+\tau)\right]\right\} = \frac{8\alpha_{\tilde{u}i}\sigma_{\tilde{u}i}^4}{\left[\pi(\nu^2 + 4\alpha_{\tilde{u}i}^2)\right]}, \text{ and} \tag{12}$$

$$S_{ii}^{\tilde{w}_\xi}(\nu) = \mathcal{F}\{E\left[\tilde{w}_{\xi i}(t)\tilde{w}_{\xi i}(t+\tau)\right]\} = \frac{\beta_{\xi i}^2}{\left[(\nu^2 - \theta_{\xi i}^2)^2 + 4\mu_{\xi i}^2\nu^2\theta_{\xi i}^2\right]}, \tag{13}$$

which result from Eqs. (4) and (5). The cross spectral densities $S_{ij}^{\tilde{\eta}}(\nu)$, $S_{ij}^{\tilde{u}^2}(\nu)$, $S_{ij}^{\tilde{w}_\xi}(\nu)$, $i \neq j$, are derived from, e.g., $S_{ij}^{\tilde{\eta}}(\nu) = \sqrt{S_{ii}^{\tilde{\eta}}(\nu)S_{jj}^{\tilde{\eta}}(\nu)}\Lambda_{ij}^{\tilde{\eta}}(\nu)$, where $\left\{\Lambda_{ij}^{\tilde{\eta}}(\nu)\right\}$ denote coherence functions for turbulence fluctuations (Simiu and Scanlan, 1985, p. 60).

3   Model calibration

Wind tunnel records from Shimizu Corporation Laboratories are used for wind-load model calibration. The records are for a 25-story building model with square cross-section has 500 wind pressure taps uniformly distributed on its sides. The length scale used for the model is 1:400. The mean wind velocity profile of the wind tunnel records corresponds to the urban terrain, and $Re = 1.4 \times 10^5$ at the top level of the building. Dimensionless pressure coefficients are recorded with 1000 Hz measurement frequency, and 32768 measurement points are obtained continuously. Further details can be found in (Kikuchi et al., 1997).

The parameters of the wind-load model defined in the previous section are fitted to experimental observations. Let $S(\nu; \Theta)$ be the functional form of the spectral density defined up to a vector Θ of parameters, e.g., $\Theta = [\alpha_{\tilde{u}i}\ \sigma_{\tilde{u}i}]$ for the spectral density of the along-wind force. The following algorithm is used for model calibration. First, spectral densities of the wind loads are estimated from observations. Denote by $\hat{S}(\nu)$ the corresponding estimate of spectral density. Second, spectral parameters Θ are selected to minimizes the error $\int[S(\nu; \Theta) - \hat{S}(\nu)]^2 d\nu$.

Figure 1 shows examples of model calibration at the 14th floor of a building. The solid lines are the estimates $\hat{S}(\nu)$ obtained from observations. The dash lines are the spectral densities $S(\nu; \Theta)$ fitted to $\hat{S}(\nu)$ by the above algorithm.
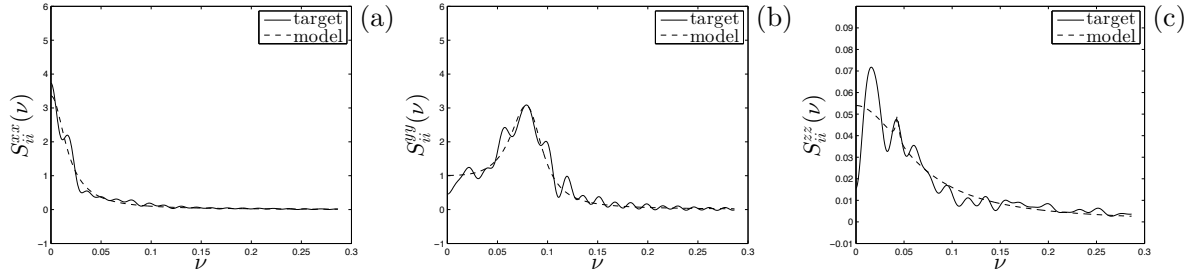
Figure 1. Examples of model calibrations for
(a) along-wind force, (b) across-wind force, and (c) torque at floor 14

4   Response analysis

Let $\mathbf{X}(t) = [\mathbf{X}_1(t) \ldots \mathbf{X}_i(t) \ldots \mathbf{X}_n(t)]^T$ denote the $3n$-dimensional response vector process for a linear systems. The components of the 3-dimensional vector $\mathbf{X}_i(t)$ are along-wind displacement $X_{1i}(t)$, across-wind displacement $X_{2i}(t)$ and torsional angle $X_{3i}(t)$. The process $\mathbf{X}(t)$ satisfies the equation

$$\mathbf{M}\ddot{\mathbf{X}}(t) + \mathbf{C}\dot{\mathbf{X}}(t) + \mathbf{K}\mathbf{X}(t) = \mathbf{F}(t) \tag{14}$$

where $\mathbf{M}$, $\mathbf{C}$, and $\mathbf{K}$ are the mass, damping and stiffness matrices of the system and $\mathbf{F}(t) = [\mathbf{F}_1(t) \ldots \mathbf{F}_i(t) \ldots \mathbf{F}_n(t)]^T$ is the wind-load vector process with components $\mathbf{F}_i(t) = [F_{xi}(t) \; F_{yi}(t) \; M_{zi}(t)]^T$, where $F_{xi}(t)$, $F_{yi}(t)$, and $M_{zi}(t)$ are given by Eqs. (1)-(3). Let $\mathbf{\Psi} = [\psi_1 \ldots \psi_k \ldots \psi_{3n}]$ be a $(3n, 3n)$-matrix whose columns are modal shapes. Denote $\mathbf{Y}(t)$ by the vector of modal responses, we have

$$\mathbf{X}(t) = \mathbf{\Psi}\mathbf{Y}(t) = \sum_{k=1}^{3n} \psi_k Y_k(t) \tag{15}$$

The components $\{Y_k(t)\}$ of $\mathbf{Y}(t)$ satisfy the equations

$$\ddot{Y}_k(t) + 2\zeta_k\omega_k\dot{Y}_k(t) + \omega_k^2 Y_k(t) = \frac{\tilde{F}_k(t)}{M_k}, \quad k = 1, \ldots, 3n, \tag{16}$$

where ζ_k, ω_k, and M_k are modal damping ratios, natural frequencies, and modal masses. The modal forcing functions have the form $\tilde{F}_k(t) = \left[\mathbf{\Psi}^T\mathbf{F}(t)\right]_k$. Without loss of generality, set $M_k = 1$.

The following subsections calculate the second-moment property of $\mathbf{X}(t)$ (Section 4.1), develop approximation for the marginal distribution of this process (Section 4.2), construct translation model for $\mathbf{X}(t)$ (Section 4.3), and find mean rate at which the response process $\mathbf{X}(t)$ exists safe sets (Section 4.4).

4.1   Second-moment property

Expectation $E[\mathbf{X}(t)]$ and cross spectral density $\mathbf{S_{XX}}(\nu)$ fully characterize the second-moment property of $\mathbf{X}(t)$.

$E[\mathbf{X}(t)]$ is defined by $E[\mathbf{X}(t)] = \sum_{k=1}^{3n} \psi_k E[Y_k(t)]$ which results from Eq. (15). Under the assumption that $Y_k(t)$ is stationary, taking the expectations on both sides of Eq. (16) and substituting the form of $E[Y_k(t)]$ in the above equation gives

$$E[\mathbf{X}(t)] = \sum_{k=1}^{3n} \psi_k \frac{E\left[\tilde{F}_k(t)\right]}{\omega_k^2} \tag{17}$$

The spectral density $\mathbf{S_{XX}}(\nu)$ has the expression

$$\mathbf{S_{XX}}(\nu) = \sum_{k=1}^{3n} \sum_{l=1}^{3n} \psi_k \psi_l^T S_{Y_k Y_l}(\nu) \tag{18}$$

where $\{S_{Y_k Y_l}(\nu)\}$ denote the cross spectral densities of arbitrary modal displacement pairs $\{Y_k(t), Y_l(t)\}$, $k, l = 1, \ldots, 3n$. For pair $\{k, l\}$, $Y_k(t), Y_l(t)$ are governed by (Soong and Grigoriu, 1993, p. 189)

$$\frac{d}{dt}\tilde{\mathbf{Y}}(t) = \mathbf{A}\tilde{\mathbf{Y}}(t) + \mathbf{g}\tilde{\mathbf{F}}(t) \tag{19}$$

where $\tilde{\mathbf{Y}}(t) = \begin{bmatrix} Y_k(t) & \dot{Y}_k(t) & Y_l(t) & \dot{Y}_l(t) \end{bmatrix}^T$, $\tilde{\mathbf{F}}(t) = \begin{bmatrix} \tilde{F}_k(t) & \tilde{F}_l(t) \end{bmatrix}^T$, $\mathbf{g} = \begin{bmatrix} 0 & 1 & 0 & 0 \\ 0 & 0 & 0 & 1 \end{bmatrix}^T$, and $\mathbf{A} = \begin{bmatrix} \mathbf{A}_k & \mathbf{0} \\ \mathbf{0} & \mathbf{A}_l \end{bmatrix}$, in which $\mathbf{A}_k = \begin{bmatrix} 0 & 1 \\ -\omega_k^2 & -2\zeta_k\omega_k \end{bmatrix}$ and $\mathbf{0}$ is a 2×2 null matrix.

The unknown cross spectral densities $\{S_{Y_k Y_l}(\nu)\}$ in Eq. (18) are calculated by the method in Soong and Grigoriu (1993, p. 195). Let $\mathbf{S}_{\tilde{\mathbf{Y}}\tilde{\mathbf{Y}}}(\nu) = \mathcal{F}\left\{E\left[\tilde{\mathbf{Y}}(t)\tilde{\mathbf{Y}}^T(t)\right]\right\}$ and $\mathbf{S}_{\tilde{\mathbf{F}}\tilde{\mathbf{F}}}(\nu) = \mathcal{F}\left\{E\left[\tilde{\mathbf{F}}(t)\tilde{\mathbf{F}}^T(t)\right]\right\}$ denote the cross spectral densities of $\tilde{\mathbf{Y}}(t)$ and $\tilde{\mathbf{F}}(t)$ in Eq. (19), respectively. $\mathbf{S}_{\tilde{\mathbf{Y}}\tilde{\mathbf{Y}}}(\nu)$ relates $\mathbf{S}_{\tilde{\mathbf{F}}\tilde{\mathbf{F}}}(\nu)$ through the equation

$$\mathbf{S}_{\tilde{\mathbf{Y}}\tilde{\mathbf{Y}}}(\nu) = \mathbf{H}^*(\nu)\mathbf{S}_{\tilde{\mathbf{F}}\tilde{\mathbf{F}}}(\nu)\mathbf{H}^T(\nu) \tag{20}$$

where the $*$ indicates complex conjugate and $\mathbf{H}(\nu)$ is a system matrix which has the form $\mathbf{H}(\nu) = (\sqrt{-1}\nu\mathbf{I} - \mathbf{A})^{-1}\mathbf{g}$, in which $\mathbf{I}$ is a 4×4 identity matrix. $S_{Y_k Y_l}(\nu)$ is the component $(1, 3)$ or $(3, 1)$ in $\mathbf{S}_{\tilde{\mathbf{Y}}\tilde{\mathbf{Y}}}(\nu)$.

4.2 Marginal moments and distribution

The kth modal displacement $Y_k(t)$ is governed by Eq. (16). Note that $\tilde{F}_k(t)$ has the expression $\tilde{F}_k(t) = \sum_{i=1}^n \psi_{k,3i-2}F_{xi}(t) + \sum_{i=1}^n \psi_{k,3i-1}F_{yi}(t) + \sum_{i=1}^n \psi_{k,3i}M_{zi}(t)$, where $\psi_{k,3i-2}$, $\psi_{k,3i-1}$ and $\psi_{k,3i}$ are the $(3i - 2)^{th}$, $(3i - 1)^{th}$ and $3i^{th}$ components in the kth mode ψ_k. Substituting the above expression in Eq. (16) gives

$$\ddot{Y}_k(t) + 2\zeta_k\omega_k\dot{Y}_k(t) + \omega_k^2 Y_k(t) = \sum_{i=1}^n \psi_{k,3i-2}F_{xi}(t) + \sum_{i=1}^n \psi_{k,3i-1}F_{yi}(t) + \sum_{i=1}^n \psi_{k,3i}M_{zi}(t) \tag{21}$$

Since the defining equation of $Y_k(t)$ is linear, we have $Y_k(t) = \sum_{i=1}^n \psi_{k,3i-2}Y_{k,xi}(t) + \sum_{i=1}^n \psi_{k,3i-1}Y_{k,yi}(t) + \sum_{i=1}^n \psi_{k,3i}Y_{k,zi}(t)$, where $Y_{k,xi}(t)$, $Y_{k,yi}(t)$ and $Y_{k,zi}(t)$ are the responses corresponding to wind loads $F_{xi}(t)$, $F_{yi}(t)$ and $M_{zi}(t)$, respectively.

Marginal moments of $Y_k(t)$ are calculated from the marginal moments of $Y_{k,xi}(t)$, $Y_{k,yi}(t)$ and $Y_{k,zi}(t)$. Since $F_{yi}(t)$ and $M_{zi}(t)$ are Gaussian processes so are the responses $Y_{k,yi}(t)$ and $Y_{k,zi}(t)$ so that moments of any order of these responses result from the second-moment properties of $F_{yi}(t)$ and $M_{zi}(t)$. The stationary moments $\mu_{k,xi}^y(p, q, r) = E\left[Y_{k,xi}(t)^p \dot{Y}_{k,xi}(t)^q \tilde{u}_i(t)^r\right]$ of $Y_{k,xi}(t)$ satisfy the following ordinary linear differential equation

$$0 = p\mu_{k,xi}^y(p-1, q+1, r) - q\omega_k^2\mu_{k,xi}^y(p+1, q-1, r) - (2q\zeta_k\omega_k + r\alpha_{\tilde{u}i})\mu_{k,xi}^y(p, q, r)$$
$$+ qc_{di,0}\mu_{k,xi}^y(p, q-1, r) + q\frac{2c_{di,0}}{\bar{u}_i}\mu_{k,xi}^y(p, q-1, r+1)$$
$$+ q\frac{c_{di,0}}{\bar{u}_i^2}\mu_{k,xi}^y(p, q-1, r+2) + r(r-1)\alpha_{\tilde{u}i}\sigma_{\tilde{u}i}^2\mu_{k,xi}^y(p, q, r-2) \tag{22}$$

by following arguments in (Grigoriu and Ariaratnam, 1988). The set of these moment equations is closed so that the response moments $\mu_{k,xi}(p, q, r)$ can be exactly calculated. Marginal moments of $\mathbf{X}(t)$ result

from moments of $\{Y_k(t)\}$ and the definition $\mathbf{X}(t) = \sum_{k=1}^{3n} \psi_k Y_k(t)$ of this vector.

Let $\mu_k^x(p, q, r)$ denote the marginal moments of $X_k(t)$, the kth component of $\mathbf{X}(t)$. The set of moments $\{\mu_k^x(p, 0, 0), p = 1, \ldots, 4\}$ is used to calibrate the model $\hat{F}_k(x) = \sum_{j=1}^{N} p_{kj} \hat{F}_{kj}(x)$ for the marginal distribution of $X_k(t)$, where $\left\{\hat{F}_{kj}(x)\right\}$ are the distributions with the mean $\mu_k^x(1, 0, 0)$ and variance $\mu_k^x(2, 0, 0) - \mu_k^x(1, 0, 0)^2$, $\{p_{kj} \geq 0\}$ are parameters selected to minimize the error $\sum_{p=1}^{4} [\mu_k^x(p, 0, 0) - \hat{\mu}_k^x(p, 0, 0)]^2$ under the constraint $\sum_{j=1}^{N} p_{kj} = 1$, in which $\{\hat{\mu}_k^x(p, 0, 0), p = 1, \ldots, 4\}$ are the marginal moments of $\hat{F}_k(x)$. We use the approximate marginal distribution $\hat{\mathbf{F}}(x) = \left[\hat{F}_1(x) \ldots \hat{F}_k(x) \ldots \hat{F}_{3n}(x)\right]$ to characterize the response process.

4.3   Response translation model

The response process $\mathbf{X}(t)$ is approximated by the translation model (Grigoriu and Field, 2014)

$$X_{T,k}(t) = \hat{F}_k^{-1}\big(\Phi[Z_k(t)]\big) \tag{23}$$

where $\{X_{T,k}(t)\}$ are the components of the translation vector process $\mathbf{X}_T(t)$ of $\mathbf{X}(t)$ with marginal distribution $\hat{F}_k(x)$, Φ denotes standard Gaussian cumulative density function and $\{Z_k(t)\}$ are the components of $\mathbf{Z}(t)$ which is a Gaussian vector process with zero mean, unit variance and spectral density $S_{\mathbf{ZZ}}(\nu)$ such that $\mathbf{X}_T(t)$ matches exactly or as close as possible the spectral density $S_{\mathbf{XX}}(\nu)$ of $\mathbf{X}(t)$. Eq. (23) indicates a nonlinear transformation from the standard Gaussian distribution to the marginal distribution $\hat{\mathbf{F}}(x)$. Generally, $S_{\mathbf{ZZ}}(\nu)$ is difficult to select and may not exist if it is required that the spectral densities of $\mathbf{X}_T(t)$ and $\mathbf{X}(t)$ coincide. Based on the observation that the discrepancy between the spectral densities of $\mathbf{X}_T(t)$ and $\mathbf{X}(t)$ is small, we use for $S_{\mathbf{ZZ}}(\nu)$ a normalized version of $S_{\mathbf{XX}}(\nu)$. The probability law of the translation process $\mathbf{X}_T(t)$ so defined is characterized completely.

4.4   Response crossing rates

Suppose the system in Eq. (14) is safe if its response approximated by $\mathbf{X}_T(t)$ does not leave the safe rectangular set $D_x = \times_{k=1}^{3n} [-\xi x_k, \xi x_k]$, where $x_k > 0$ are constants and $\xi > 0$ is scale factor controlling the size of the safe set. The image of the safe set D in the Gaussian space is $D_z = \times_{k=1}^{3n} [z_k^-, z_k^+]$, where $z_k^+ = \Phi^{-1}\left[\hat{F}_k(\xi x_k)\right]$ and $z_k^- = \Phi^{-1}\left[\hat{F}_k(-\xi x_k)\right]$. The mean rate at which the Gaussian vector process $\mathbf{Z}(t)$ exits D_x has the form

$$\lambda_{D_z} = \int_{\partial D_z} u(\mathbf{z}) f(\mathbf{z}) dS, \tag{24}$$

∂D_z denotes the boundaries of the safe set D_z, $f(\mathbf{z})$ is the probability density function of $\mathbf{Z}(t)$ conditional on $\mathbf{Z}(t) \in \partial D_z$, dS is the surface area measured on ∂D_z,

$$u(\mathbf{z}) = E\left[\dot{\mathbf{Z}}_n(t) + |\mathbf{Z}(t) = \mathbf{z}\right], \tag{25}$$

where $\dot{\mathbf{Z}}_n(t)+$ denotes the projection of $\dot{\mathbf{Z}}(t)$ on the exterior normal $\mathbf{n}(\mathbf{z})$ to ∂D_z (Soong and Grigoriu, 1993, p. 300).

Consider for illustration the special case in which the processes $\dot{\mathbf{Z}}(t)$ and $\mathbf{Z}(t)$ are independent so that $u(\mathbf{z})$ in Eq. (25) simplifies to $u = E\left[\dot{\mathbf{Z}}_n(t)+\right]$. For a planar boundary $\partial D_{z_k^+}$ at distance z_k^+ from the origin and exterior normal $\mathbf{n}_\mathbf{k}^+$ along the axis corresponding to $Z_k(t)$, the function $u(\mathbf{z})$ in Eq. (25) has the expression $u_k^+ = E\left[\dot{\mathbf{Z}}_{n_k^+}(t)+\right] = E\left\{\left[\sum_{j=1}^{3n} n_{k,j}^+ \dot{Z}_j(t)\right]+\right\}$, where $\dot{\mathbf{Z}}_{n_k^+}(t)$ denotes $\dot{\mathbf{Z}}_n(t)$ on the boundary $\partial D_{z_k^+}$ and $n_{k,j}^+$ is the jth component of $\mathbf{n}_\mathbf{k}^+$. Note that $\dot{\mathbf{Z}}_{n_k^+}(t) = \sum_{j=1}^{3n} n_{k,j}^+ \dot{Z}_j(t)$ is a Gaussian variable with zero mean and variance $\sum_{j=1}^{3n} \sum_{m=1}^{3n} n_{k,j}^+ n_{k,m}^+ \Gamma_{\dot{X}_j \dot{X}_m}$ for each $t \geq 0$, where $\Gamma_{\dot{X}_j \dot{X}_m} = \int_0^\infty \nu^2 S_{X_j X_m}(\nu) d\nu$ and $S_{X_j X_m}(\nu)$ is the cross spectral density of $X_j(t)$ and $X_m(t)$. Accordingly, we

have

$$u_k^+ = \left(\frac{1}{2\pi} \sum_{j=1}^{3n} \sum_{m=1}^{3n} n_{k,j}^+ n_{k,m}^+ \Gamma_{\dot{X}_j \dot{X}_m} \right)^{1/2} \tag{26}$$

The mean outcrossing rate $\lambda_{D_{z_k^+}}$ for this boundary has the form

$$\lambda_{D_{z_k^+}} = u_k^+ P(\mathbf{Z}_{\neq k}(t) \in \partial D_{z_k^+} | Z_k(t) = z_k^+) f(z_k^+) \tag{27}$$

where $\mathbf{Z}_{\neq k}(t)$ denotes $\mathbf{Z}(t)$ excluding $Z_k(t)$. The same procedure can be used to calculate $\lambda_{D_{z_k^-}}$ with threshold value z_k^-. The total mean outcrossing rate has the expression

$$\lambda_{D_z} = \sum_{k=1}^{3n} \left[\lambda_{D_{z_k^+}} + \lambda_{D_{z_k^-}} \right] \tag{28}$$

The determination of the mean outcrossing rates from Eq. 24 or even Eqs. 27-28 can be computationally intensive. We propose to estimate mean outcrossing rates for relatively small values of ξ from samples of $\mathbf{X}(t)$ and approximate these rates by $\lambda_{D_{z_k^+}} \simeq u_k^+ f(z_k^+)$ since $P(\mathbf{Z}_{\neq k}(t) \in \partial D_{z_k^+} | Z_k(t) = z_k^+) \simeq 1$ for relatively large rectangular safe.

5   Applications

Mean crossing and outcrossing rates are calculated for responses of two simple structural systems subjected to wind. Results are based on actual response statistics and translation models.

5.1   Single degree-of-freedom

Let $X(t)$ be the displacement of a simple oscillator with damping ratio ζ and natural frequency ω_0 subjected to the dimensionless along-wind force $C_x(t) = c_{d,0} + \frac{2c_{d,0}}{\bar{u}} \tilde{u}(t) + \frac{c_{d,0}}{\bar{u}^2} \tilde{u}^2(t)$. Then $X(t)$ is defined by

$$\ddot{X}(t) + 2\zeta\omega_0 \dot{X}(t) + \omega_0^2 X(t) = C_x(t) \tag{29}$$

The spectral density of the stationary response is

$$S_{XX}(\nu) = \frac{S_{C_x C_x}(\nu)}{(\nu^2 - \omega_0^2)^2 + (2\zeta\omega_0)^2}, \tag{30}$$

where the spectral density $S_{C_x C_x}(\nu)$ has the functional form of $S_{ij}^{xx}(\nu)$ in Eq. (6) with $i = j$.
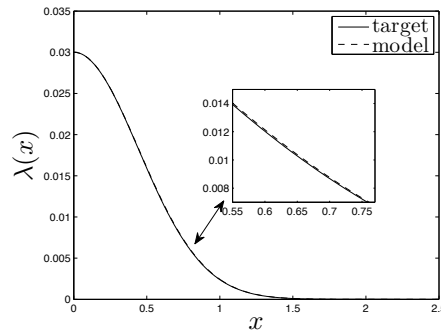
Figure 2. Mean crossing rates of the responses of single degree-of-freedom system

The first four marginal moments for $X(t)$ in Eq. (22) are used to calibrate a translation model $X_T(t)$

for $X(t)$. The mean crossing rate in Eq. (27) becomes

$$\lambda(x)^+ = \frac{\sigma_{\dot{Z}}}{\sigma_Z \sqrt{2\pi}} \phi(z) \tag{31}$$

where $\lambda(x)^+$ denotes the mean upcrossing rate of $X_T(t)$, $\sigma_{\dot{Z}}$ and σ_Z are the standard deviations of $\dot{Z}(t) = dZ(t)/dt$ and $Z(t)$, respectively, and ϕ is the standard Gaussian density. The same procedure is utilized for calculating the mean downcrossing rate $\lambda(x)^-$. The total mean crossing rate is expressed by $\lambda(x) = \lambda(x)^+ + \lambda(x)^-$.

The solid line in Figure 2 is an estimate of the mean crossing rate of $X(t)$ obtained from 1000 samples of this process. The dash line is the mean crossing rate of $X_T(t)$ given by Eq. (31).

5.2 Multi degrees-of-freedom

Consider an single-story structure with two translation and one rotation degrees-of-freedom. The structure is subjected to along-wind force $C_x(t)$, across-wind force $C_y(t)$ and torque $C_z(t)$. The components of the responses $\mathbf{X}(t)$ are along-wind displacement $X_1(t)$, across-wind displacement $X_2(t)$ and torsional angle $X_3(t)$. The equation of motion in the modal coordinates is Eq. (16) with $k = 1, 2, 3$.

Spectral density of $\mathbf{X}(t)$ is obtained by Eqs. (15) and (20). Figure 3 shows the spectral densities of modal displacements $Y_1(t)$, $Y_2(t)$ and $Y_3(t)$. The solid line is the spectral densities estimated from response samples, and the dash line is the spectral densities calculated from Eqs. (15) and (20).
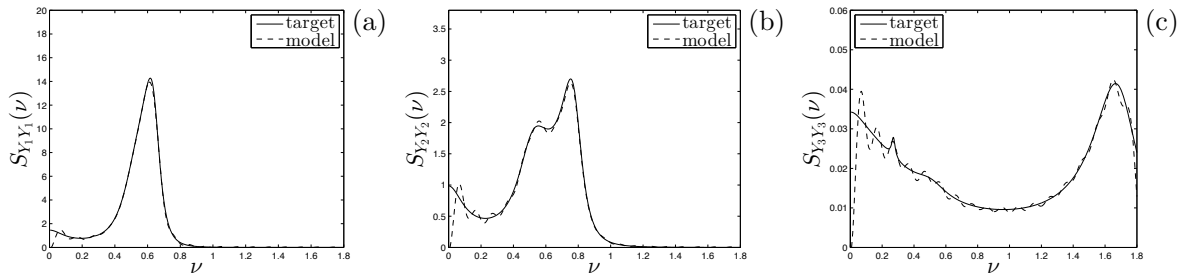
Figure 3. Spectral densities of (a) $Y_1(t)$, (b) $Y_2(t)$, and (c) $Y_3(t)$ at floor 14

The first four stationary moments of $X_1(t)$, $X_2(t)$ and $X_3(t)$ are used to construct approximations for the marginal distributions $\hat{F}_1(t)$, $\hat{F}_2(t)$, and $\hat{F}_3(t)$ of these processes.

Mean outcrossing rate of $\mathbf{X}(t)$ is estimated by both approaches described in Section 4.4. The solid lines in the left panel of Figure 4 is the mean outcrossing rate estimated from response samples, the dash line is the one calculated from Eqs. (27) and (28), and the dash dot line shows the proposed approximation of the mean outcrossing rate. The right panel is the mean outcrossing rates in the logarithmic coordinates.
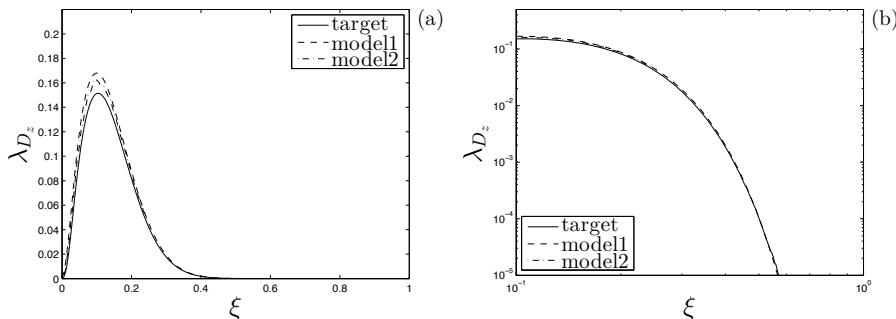
Figure 4. Mean crossing rates of 3-dimensional vector process $\mathbf{X}(t)$ in
(a) linear coordinates and (b) logarithmic coordinates

6   Conclusions

Existing wind velocity models and wind tunnel experiments have been used to construct probabilistic models for wind loads that capture their non-Gaussian features. A practical method has been developed for calculating response statistics of linear structural systems to the proposed wind-load models. The method is based on translation processes calibrated to marginal moments and spectral properties of linear structural responses. Numerical results have been obtained for two structural systems subjected to wind loads, a simple oscillator and a single story with three degrees-of-freedom.

Acknowledgment

References

Barlow, J. B., Rae, W.H., and Pope, A. (1999). *Low-Speed Wind Tunnel Testing*. Third. Canada: John Wiley & Sons.

Benfratello, S. and Muscolino, G. (1999). Filter Approach to the Stochastic Analysis of MDOF Wind-excited Structures. *Probabilistic Engineering Mechanics* **14**, pp. 311–321.

Grigoriu, M. and Ariaratnam, S. T. (1988). Response of Linear Systems to Polynomials of Gaussian Processes. *Journal of Applied Mechanics* **55**, pp. 905–910.

Grigoriu, M. and Field, R. V. (2014). A Method for Analysis of Linear Dynamic Systems Driven by Stationary Non-Gaussian Noise with Applications to Turbulence-induced Random Vibration. *Applied Mathematical Modelling* **38**, pp. 336–354.

Gullo, I., Muscolino, G., and Vasta, M. (1998). Non-Gaussian Probability Density Function of SDOF Linear Structures Under Wind Actions. *Journal of Wind Engineering* **74-76**, 11231134.

Kikuchi, H., Tamura, Y., Ueda, H., and Hibi, K. (1997). Dynamic wind pressures acting on a tall building model proper orthogonal decomposition. *Journal of Wind Engineering and Industrial Aerodynamics* **69-71**, pp. 631–646.

Simiu, E. and Scanlan, R. H. (1985). *Wind Effects on Structures*. 2nd. USA: John Wiley Sons, Inc.

Solari, G. (1994). Wind-excited Vibrations of Structures. Texts in statistical sciences. NY, USA: Springer Verlag, Wien. Chap. Gust-excited vibrations.

Soong, T. T. and Grigoriu, M. (1993). *Random Vibration of Mechanical and Structural Systems*. Englewood Cliffs, NJ, USA: Prentice Hall.

Optimization of Passive Tuned Mass Damper Systems to reduce Tower Vibrations of Wind Turbines

Christian Meinhardt[1], Frank Dalmer[1] and Fulvio Bottoni[2]

[1]GERB Vibration Control Systems, Berlin, Germany
[2]GERB Italia SRL,Milano, Italy
*Corresponding author: Christian Meinhardt,*christian.meinhardt@gerb.de

Abstract

To reduce fatigue loading, enhance the structural integrity for extreme wind events and to avoid effectivity losses due to resonance hold ups (Sommerfeld Effect), the increase of structural damping of the tower structure of wind turbines is a probate measure. This can be achieved with Tuned Mass Damper Systems (TMDs). Active Systems may reveal benefits with regards to their adaptive capabilities, but by optimizing the parameters of a passive TMD system a similar robustness can be achieved and the system will be effective for all types of dynamic loading the wind turbine tower structure is subjected to. To understand the requirements for such a robust setup, the types of dynamic loading and the effect on the TMD setup will be examined. For a practical application the design principles will be itemized and examples for a practical design and application will be introduced. For these examples experimental tests have been performed to verify the effectiveness of the implemented TMD and the results herein presented.

1 Introduction

Tower vibrations of Wind turbines can be caused by dynamic loads due to operation but also due to ambient wind excitation or transient operations of the wind turbine itself such as braking, pitching or yawing. Besides the dynamic loading during extraordinary wind events, which can affect the structural integrity immediately, tower vibrations induce fatigue problems especially when the support structure exhibits low structural damping ratios. For this case the structure is prone to resonance effects which lead to increased deflections and stress levels. Although aerodynamic damping increases the overall system damping ratio, for resonance phenomena the aerodynamic damping can decrease as described in [Kareem et al., Cerda Salzmann et. al.]. Also the aerodynamic damping is only effective in along wind direction and can only be encountered during operation. So increasing the system damping or more precise the structural damping by applying damping devices is an effective measure to reduce the vibration susceptibility of the support structure. Furthermore the increase of structural damping will reduce the effectivity loss of the wind turbine that occurs due to the Sommerfeld effect ([Brasil et al.]). Passive Damping devices such as Tuned Mass Dampers are one effective measure. They can be designed to be maintenance free devices and the parameters such as tuning frequency and internal damping ratio can be chosen to provide a robust setup to be effective for all types of dynamic loading.

2 Characteristics of the Dynamic Loading for Wind Turbine Towers

For an optimization as described in Chapter 1 it is crucial to understand the characteristics of the dynamic loading wind turbine support structures are subjected to. The dynamic loading can be classified into stochastic loading (such as wind gust loading or wave impacts at offshore structures), into harmonic excitations (during operation i.e. due to stall/ blade passage or rotor imbalances, vortex shedding at the tower structure and interferences) and into transient dynamic loading (emergency stops, nacelle yawing etc.). Figure 1 for example shows the occurring vibrations of a tower structure during

an emergency stop. It can be seen that the inert forces cause an almost static deflection and that the low damped tower structure responds to that with free vibrations that slowly decay.
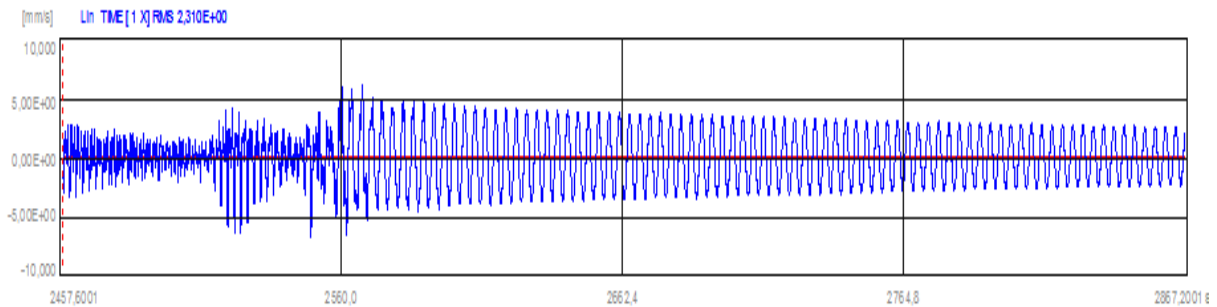
Figure 1. Occurring horizontal vibrations in wind direction after an emergency stop of a wind turbine

The optimum TMD parameters are usually specified according to the Den Hartog optimization. This approach has been done for harmonic loading. But the tower structure is also subjected to stochastic loading – mainly when the turbine is not operating, for example when strong winds occur and the facility is shut down. Figure 2 shows the frequency content of the measured vibrations at a wind turbine tower over a time period of 7000 seconds while the turbine was operating and stopped. It can be seen that the structure not only responds in its fundamental frequency but that an excitation in a close range can already cause significant vibrations. For this case, the TMD system requires a robust setup to be effective also for the close range excitation.
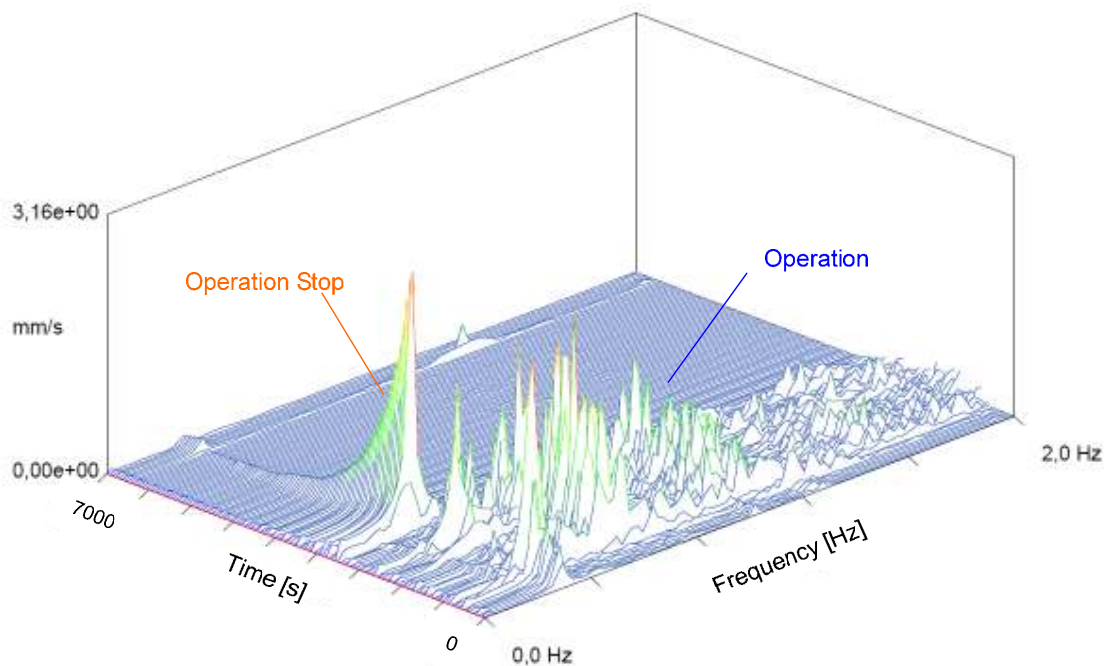
Figure 2. Waterfall diagram from a 7000 s in situ time record of the horizontal vibrations in wind direction

Figure 3 shows the results of a numerical analysis for which the stochastic wave loading for an offshore wind park has been simulated. It can be seen, that for the Fatigue Load State a reduction can be achieved with an optimized TMD system for which the max. allowable travel had to be considered due to space restrictions.
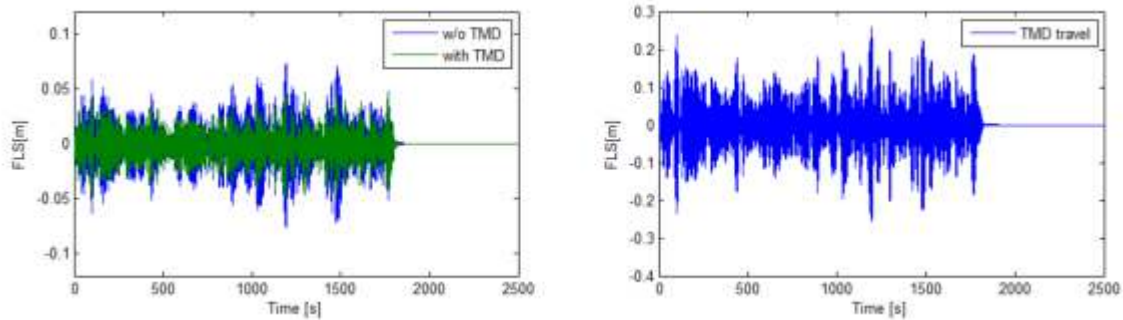
Figure 3. Calculated horizontal dynamic response of an offshore structure for a FLS wave loading time series

3   Passive Devices – Design Principles

One of the benefits for a passive TMD system is that these devices don't require any power supply or control units, so they can be designed to be maintenance free for the design life of the wind turbine. To avoid nonlinearities and to allow the passive TMD system to be effective for already small tower deflections, a frictionless pendulum type system is preferable. Furthermore the use of internal damping devices that provide a linear behaviour, so the resulting damping coefficient is direct proportional to the velocity and constant for either small or big deflections (see Figure 4) is beneficial for that purpose.
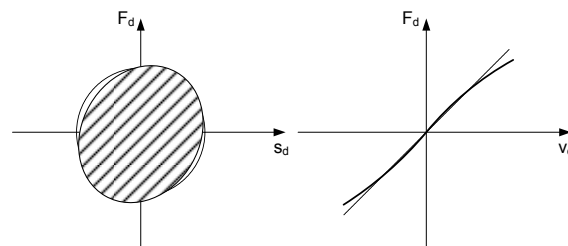
Figure 4. Force Deflection Diagram and Force Velocity Diagram of an ideal damper (dotted) and the applied damping devices (solid)

For the practical application, the systems need to be designed to ensure a feasible installation and adjustment that reflects the difficulties and site conditions.
Hereby the most governing parameter for the overall TMD design is the limitation of the resulting TMD deflections.

4   Optimization Approaches

Optimization approaches should consider 2 main issues – a) the determination of the optimum TMD parameters according to the characteristics of the dynamic loading and b) to achieve a certain robustness to cope with the change of modal parameters such as the fundamental tower frequencies and the system damping.

For harmonic loading, a proven optimization approach has been presented by Den Hartog way back in the past, but for stochastic loading, this approach is not valid. To derive an optimal specification for the TMCS, the characteristics of seismic loading has to be approximated. A legitimate approach is the assumption that stochastic gust loading excitation can be approximated with sufficient accuracy by a stationary white noise stochastic process. According to [Ayorinde et al.] for an analogous model (see Figure 5) the optimization can be found by minimizing the variance σ_x^2 of the structural displacements X.
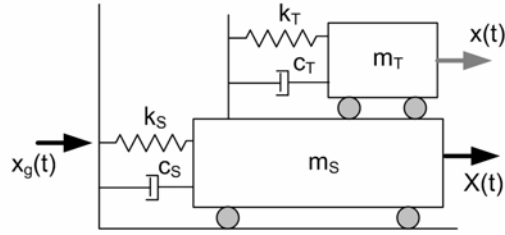
Figure 5. TMD model as 2DOF appendage

The displacement **X** is related to the constant white noise spectral density **S_0** (see (1)) in which **H(v)** is the complex response function of the displayed analogous model with the tuning frequency of the TMCS **f_T** and the natural frequency of the structure **f_S**.

$$\sigma_x^2 = \left[E(x^2(t))\right] = S_0 \int_{-\infty}^{\infty} \left| H(v) \right|^2 dv \tag{1}$$

The complex response function amounts to:

$$H(v) = \frac{\dfrac{m_T}{m_S} + \dfrac{(\frac{f_T}{f_S})^2 + 2i\zeta_T(\frac{v}{f_S})(\frac{f_T}{f_S})}{(\frac{f_T}{f_S})^2 - (\frac{v}{f_S}) + 2i\zeta_T(\frac{v}{f_S})(\frac{f_T}{f_S})}}{\dfrac{m_T}{m_S}(1 - (\frac{f_T}{f_S})^2 + 2i\zeta_T(\frac{v}{f_S})(\frac{f_T}{f_S}))} \cdot (\frac{v}{f_S})^2 \cdot (\frac{f_T}{f_S})^2 \tag{2}$$

To optimize the TMD parameters **f_T** and **ζ_T** a performance index J_0 has to be introduced that complies with the mentioned variance **σ_x^2** (3).

$$J_0 = S_0 \int_{-\infty}^{\infty} \left| H(v) \right|^2 dv \tag{3}$$

The minimization process of **J_0** can be expressed for slightly or better un-damped structures such as wind turbine towers in an analytical solution (see (4) and (5)).

$$\left(\frac{f_T}{f_M}\right)_{opt} = \frac{\sqrt{1 - \dfrac{m_T}{2 \cdot m_S}}}{1 + \dfrac{m_T}{m_S}} \tag{4}$$

$$\zeta_{opt} = \sqrt{\frac{\dfrac{m_T}{m_S}(1 - \dfrac{m_T}{4 \cdot m_S})}{4 \cdot (1 + \dfrac{m_T}{m_S}) \cdot (1 - \dfrac{m_T}{2 \cdot m_S})}} \tag{5}$$

Considering that aerodynamic damping may significantly increase the system-damping ratio, the influence of the overall damping ratio damping has to be considered as well as the nonlinear damping behaviour due to the wind-structure-interaction. So there are other approaches by solving the complex eigenvalue problem $\left| A - \lambda I \right|$ (see (6)) that derives from the free vibration equation for a system matrix

A which contains the stiffness and damping information of the main system (ω_0 & β), the mass ratio between the main structure and the TMD and the TMD parameters for the tuning - frequency and internal damping ratio.

$$
\left(\frac{\lambda}{\omega_0}\right)^4 + \left[2\left(\frac{f_T}{f_M}\right)\zeta_T\left(1+\frac{m_T}{m_S}\right) + 2\beta\right]\left(\frac{\lambda}{\omega_0}\right)^3 +
$$
$$
\left[1 + \frac{m_T}{m_S}\left(\frac{f_T}{f_M}\right)^2 + 4\left(\frac{f_T}{f_M}\right)\zeta_T\beta\right]\left(\frac{\lambda}{\omega_0}\right)^2 +
$$
$$
2\left(\frac{f_T}{f_M}\right)\left(\zeta_T + \beta\left(\frac{f_T}{f_M}\right)\right)\left(\frac{\lambda}{\omega_0}\right) + \left(\frac{f_T}{f_M}\right)^2 = 0
$$

(6)

The solution of the eigenvalue problem is in complex conjugate pairs with complex eigenvalues (see (7)). The optimum TMCS specification is determined, when the difference between the damping values ζ_{T1} and ζ_{T3} which result from the eigenvalues is minimal.

$$
\lambda_{r,r+1} = -\varpi_r\zeta_r \pm i\varpi_r\sqrt{1-\zeta_r^2}
$$

(7)

The iterative analysis can be done numerically [Sadek F. et al.] and leads to the optimum values, shown in Figure 6 and Figure 7. As a comparison, the resulting values for an optimization according to Den Hartog and for an approach using white noise excitation are displayed as well.
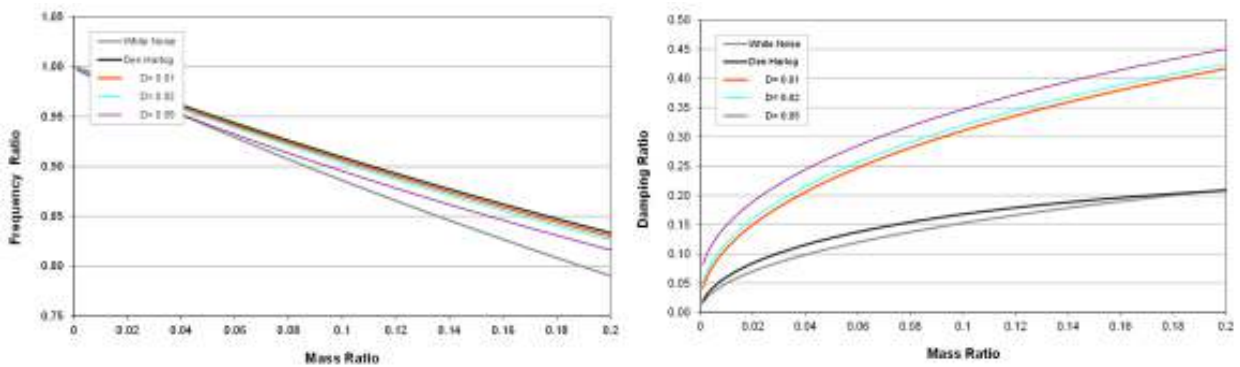
Figure 6.   Left: Optimum frequency ratio as a function of the mass ratio for different inherent damping ratios –
Right: Optimum internal damping ratio as a function of the mass ratio

In addition the theoretical approach has been verified with a numerical model of a wind turbine tower which was subjected to a wind pressure distribution loading. The time variance of the simulated gust loading resulted from time histories that were generated for a duration of 1250 s from a standard Davenport Gust Load spectrum (see Fig. 7).
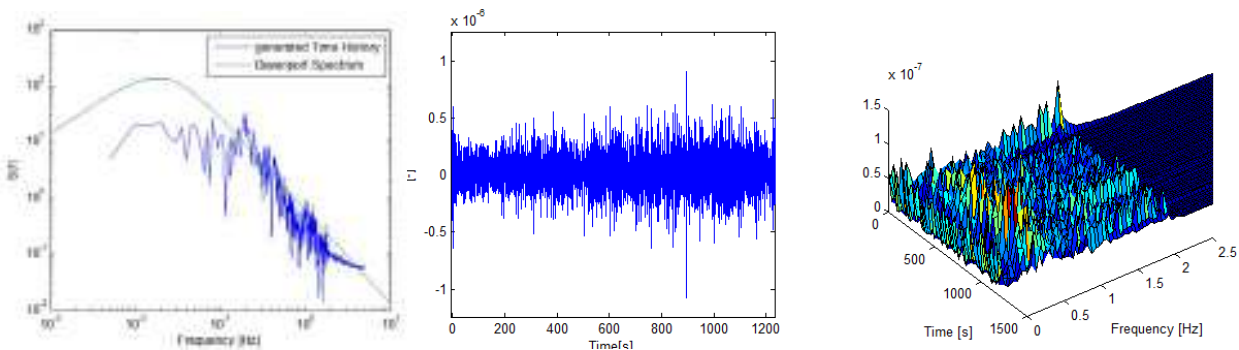
Figure 7: Generated Time Series for Gust loading (centre)- in comparison with the Davenport Spectrum (left)-
Waterfall Diagram of the generated time history (right)

Figure 8 (left) shows the dynamic response of the turbine tower structure due to the above described loading without an additional TMD and with TMD. A significant reduction can be identified – especially for the amplified passages. The reduction factor, which allows a direct comparison of TMD setups can be defined as factor between the RMS values of the complete time record were compared in relation to the values for the occurring displacements without TMD (see Figure 8-right). According to the numerical results and the simulated gust loading, an optimum reduction can be achieved for internal damping values above the optimum value according to Den Hartog. This differs from the previously introduced theoretical approaches.
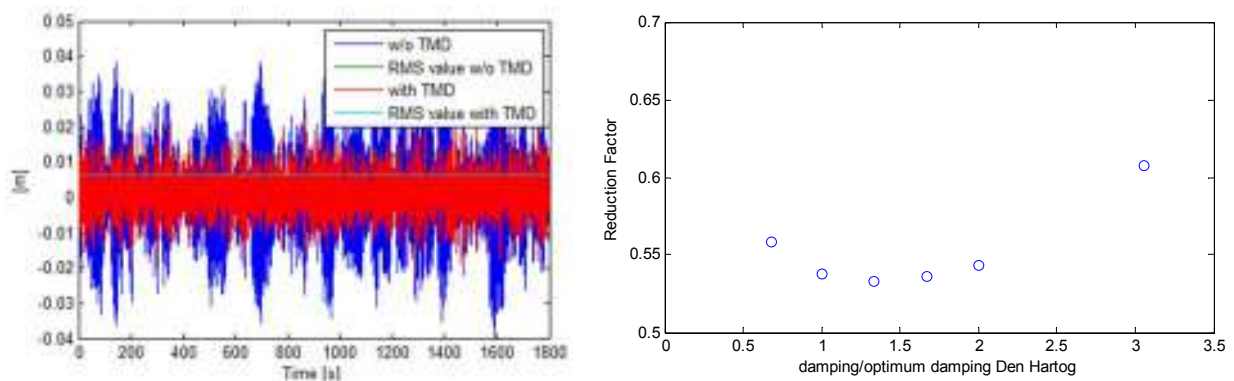
Figure 8: Left: Dynamic response of the tower structure due to the generated gust loading without TMD and with TMD – Right: Reduction factors for varying internal damping ratios

Long-term monitoring data of wind turbine towers (Hu W.H. et al.) show variations of the system damping, most likely by the portion of additional aerodynamic damping. Also it has been observed that the fundamental frequencies vary with the loading. So the optimization hast to consider robustness against frequency shifts and to ensure the max. effectiveness for varying system damping ratios. Neglecting that these effects mainly occur during operation and therefore a harmonic excitation as relevant loading, the numerical analysis has been used to assess the achievable reduction for higher system-damping-ratios and for frequency shifts or varying excitation frequencies. Figure 9 (left) shows the overall reduction that can be achieved for stochastic gust loading, depending on the inherent damping ratio. Figure 9 (right) shows the reduction of the max. displacements for an inherent damping of D=3% depending on the frequency ratio TMD tuning frequency in relation to the optimum tuning frequency. According to these results a robust setup of the TMD is given.
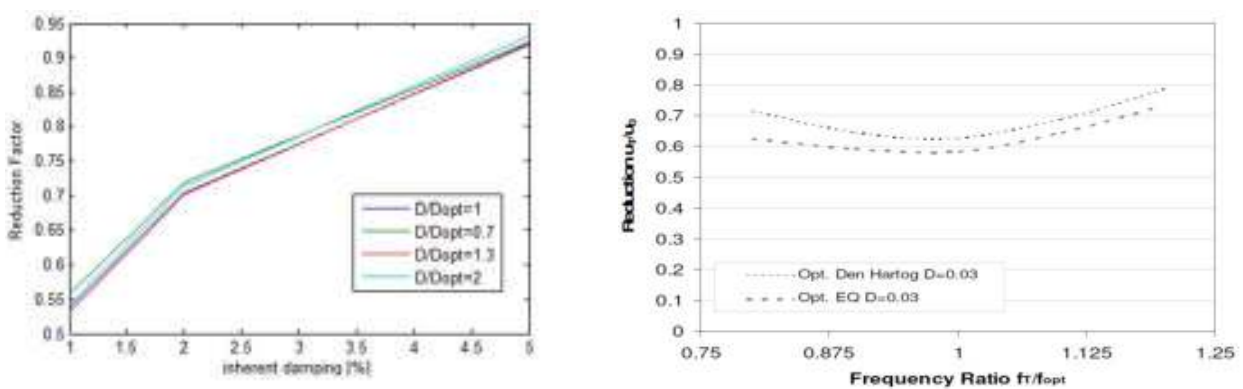
Figure 9: Generated Time Series for Gust loading (centre)- in comparison with the Davenport Spectrum (left)- Waterfall Diagram of the generated time history (right)

5   Design Examples- Practical Applications

The Figures 5 and 6 show practical applications of passive TMD systems. One example is from an offshore wind park for which the system has been installed within the transition piece with the purpose to protect the structure from wave induced vibrations. The other example is from two TMD systems implemented to reduce fatigue loading during operation in the first mode and to reduce the dynamic response of Mode 2 due to gust loading.

Figure 10. Passive Tuned Mass Damper applied at a transition piece to reduce wave induced vibrations

Figure 11. Tuned Mass Damper for Mode1 and Mode 2 of a wind turbine tower

6   In Situ verification

In line with commissioning works of the previously introduced applications, the effectiveness of the installed TMD systems resp. the increase of structural damping could be documented. Figure7 and 8 show some of the experimental results.
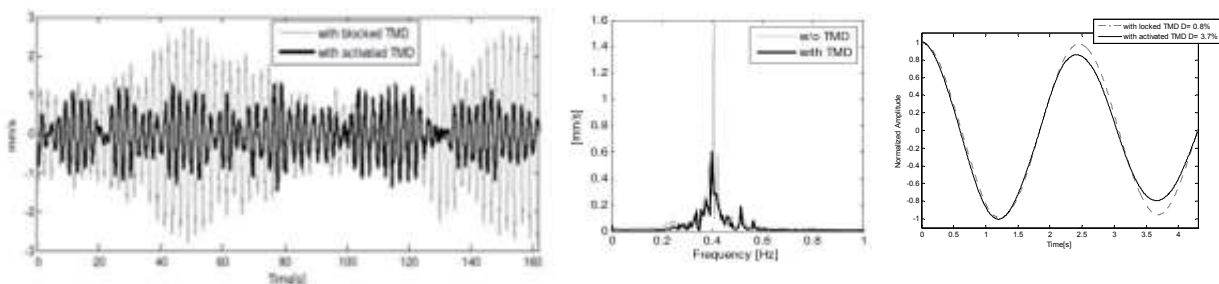
Figure 12.Measured time stories of the resulting vibrations at the offshore structure without and with TMD system (left), corresponding frequency spectra (centre), resulting Random Decrement Signature from the time domain damping assessment (right)
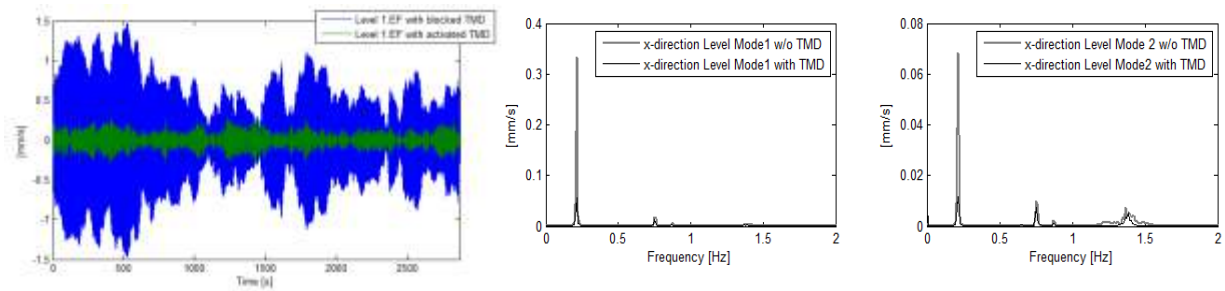
Figure 13.Measured time stories and corresponding Auto Power Spectra of the ambient vibrations at the wind turbine tower with and without TMD

7   Summary

It has been shown that passive Tuned Mass Damper (TMD) systems can be applied to reduce the occurring tower vibrations for several types of dynamic loading and are a maintenance-free and cost effective alternative. An optimization of the TMD parameters with regard to the loading characteristics, the required additional structural damping or space restrictions within the structure ensures and the use of damping devices with a linear behaviour ensure that the system provides effectiveness, either for extreme stochastic wind loads or for vortex shedding induced harmonic loading. Furthermore the dynamic response for resonance effects will be reduced and the production hold up due to the Sommerfeld Effect can be reduced.

References

Kareem A. and Gurley K. (1996). Damping in structures: its evaluation and treatment of uncertainty. *Journal of wind engineering and industrial aerodynamics* **59**: 131-157.

Brasil R.M.L.R.F., Feitosa L.C.S. and Balthszar J.M. (2006) A nonlinear and non-ideal wind generator supporting structure. *Applied Mechanics and Materials* **5-6**: 433-442.

Salzmann D.J.C. and Van der Tempel J. (2005). Aerodynamic damping in the design of support structures for offshore wind turbines. *Proceedings of the Copenhagen offshore wind conference, European offshore wind conference & exhibition, Copenhagen, Denmark.*

Ayorinde A.O. and Warburton G.B. (1980). Minimizing structural vibrations with absorbers. *Earthquake Engineering and Structural Dynamics* **8**: 219-236.

Hu W.H., Rohrmann R.G., Said S., Rücker W. (2013). Development of a vibration-based structural health monitoring system for wind turbines. *Proceedings of Structural Health Monitoring of Intelligent Infrastructure, Hong Kong*

Sadek F., Mohraz B. , Taylor A.W. and Chung R.M. (1997). A Method of estimating the parameters of Tuned Mass Dampers for seismic applications, *Earthquake Engineering and Structural Dynamics, Volume 26*: **617-635**.

Experiments on static and moving scale trains in crosswinds

F. Dorigatti[1], A.D. Quinn[2], M. Sterling[2] and C.J. Baker[2]

[1]RWDI, Dunstable, UK
[2]School of Civil Engineering, University of Birmingham, UK
Corresponding author: F. Dorigatti, francesco.dorigatti@rwdi.com

Abstract

This paper analyses the effects of the vehicle movement on the aerodynamic behaviour of trains in crosswinds. An assessment is carried out based on the comparison between static and moving model experiments on a scale-model. These experiments were undertaken in the University of Birmingham TRAIN (Transient Railway Aerodynamic INvestigation) rig facility and investigated the leading car of a 1:25 scale Class 390 Pendolino train subject to a 30° yaw angle crosswind. A bespoke stand-alone pressure measuring and data acquisition system was developed and installed on-board the scale-model, so that surface pressure measurements could be collected during both series of tests. Small discrepancies between static and moving model tests in the time-averaged pressure distribution are found only on the nose of the train. The time-averaged coefficients for side force, lift force and rolling moment are in good agreement. This provides evidence that supports the use of static tests for measuring the aerodynamic mean load coefficients. However, differences in the correlation of the pressure fluctuations along the train warn about unsteady aerodynamic effects of the vehicle movement.

1   Introduction

As a bluff body moving through a turbulent natural wind, a train travelling through the atmospheric boundary layer is surrounded by a complex flow field which leads to a series of steady and unsteady aerodynamic forces and moments. In the presence of strong winds these aerodynamic loads may become sufficiently high to cause serious accidents (Baker et al., 2009). Therefore, to reduce the risk of wind-induced accidents, the assessment of the train stability in crosswinds is prescribed by national and European railway standards (CEN, 2010). Although a variety of methods can be applied to carry out this assessment, most of the current standards require wind tunnel tests on static scale-models to measure the aerodynamic non-dimensional force and moment coefficients for trains. These experiments are common practice because they offer the best compromise between the demand of resources (e.g., facilities, equipment and time) and the accuracy of the results. Nevertheless, since a static test does not reproduce the vehicle movement, it inevitably provides an approximate representation of a train operating in reality. To evaluate the effects of this approximation a number of studies have compared crosswind static tests with moving model tests. However, the technical challenges inherent in latter led to carry out only a limited number of these studies and affected their accuracy, as echoed by the lack of agreement in the results (Baker, 1986; Humphreys, 1995; Cheli et al., 2011). In addition, the lack of detailed surface pressure data relating to moving model tests prevents the validation of the corresponding CFD simulations. This, hence, warrants further investigations.

To assess the aerodynamic effects of the train movement, this paper presents a further comparison between static and moving model tests carried out on a scale train in crosswinds. However, to address the challenges outlined by crosswind moving model tests in the past, the experiments of this research were undertaken in the TRAIN rig, a dedicated moving model test facility. In addition, a novel on-board stand-alone measuring and data acquisition system was employed to carry out surface pressure - rather than force – measurements during both static and moving model tests. In what follows, section 2 describes the test facility, the case study and methodology adopted for the tests; section 3 illustrates and discusses the results and section 4 draws the conclusions.

2   Experimental campaign

The TRAIN rig is a test facility built by British Rail Research in Derby (UK) at the end of 1980's and is currently operated by the University of Birmingham (*www.youtube.com/watch?v=8dqh936Bp-I*). As a moving model test facility, the rig consists of three straight parallel tracks 150 meters long and is equipped with a mechanical propulsion system that can catapult a 1:25 scale model up to 75 m/s. The mechanism that accelerates the scale-model employs a series of pre-tensioned elastic ropes driven by pulleys, while the brake dissipates the kinetic energy of the scale train through a piston deformable tube. Originally designed for investigating train aerodynamics in open-air and tunnels, the TRAIN rig has been upgraded as part of this project by implementing a new crosswind generator (CWG). Therefore, moving model experiments in the presence of crosswinds can currently be undertaken.

The case study considered in this work examined the leading car of a 1:25 scale Class 390 Pendolino train. Static and moving model tests were carried out investigating this scale-model on a flat ground (FG) scenario and subject to a side wind at 30° yaw angle (i.e. the angle between the relative wind and the direction of travel). The crosswind simulation was provided within a track portion 6.35 m long. The mean wind speed was ~12 m/s and the turbulence intensity was ~17 % (both taken as spanwise averages at 3 m FS equivalent height from the ground). The Reynolds numbers for the tests were within 1 to 2×10^5 (Dorigatti, 2013).

The on-board stand-alone measuring and data acquisition system that was employed for these tests was developed at the University of Birmingham Centre for Railway Research and Education (BCRRE). Entirely accommodated inside the scale-model, it consisted of 16 miniaturized differential pressure transducers in combination with a bespoke data logger. This data logger could monitor 16 channels with a 16-bit resolution sampling at rates up to 4 kHz. Given the limited number of channels that could be monitored simultaneously, series of successive runs were carried out during both static and moving model tests to measure the pressure on the train leading car on a total of 110 pressure taps.

Similar to a wind tunnel test, for the TRAIN rig static tests the train model was mounted statically inside the CWG and rotated with respect to the onset wind to simulate a 30° yaw angle. During each run time histories of the surface pressure were recorded for 60 s to enable stable time-averages to be computed. For the moving model tests the train was run on the track at approximately 20.8 m/s. Provided the crosswind mean velocity of 12 m/s, this train speed ensured that a 30° yaw angle was simulated also in these tests. However, given the span of the CWG along the track, it also implied that the scale train travelled through the simulated crosswind in ~0.3 s. To account for the run-to-run variability of the time histories recorded within such a short time interval, the methodology adopted for the moving model tests relied on carrying out sets of 15 runs monitoring the same pressure taps. For each tap, this enabled a stable ensemble average time series to be calculated based on 15 individual time histories. From this, the mean pressure was obtained as a time-average excluding the transitions at the entry and exit of the crosswind section (Dorigatti, 2013).

3   Results and discussion

The results presented in what follows are expressed in terms of non-dimensional coefficients relating to the mean (i.e. time-averaged) pressure on the train surface at the generic pressure tap i (C_{pi}) and to the resultant mean aerodynamic forces and moments (C_j and C_{Mj} , respectively):

$$C_{p_i} = \frac{P_i - P_0}{\frac{1}{2}\rho V_{rel}^2} \qquad C_j = \frac{F_j}{\frac{1}{2}\rho A_{ref} V_{rel}^2} \qquad C_{Mj} = \frac{M_j}{\frac{1}{2}\rho A_{ref} H_{ref} V_{rel}^2} \qquad (1)$$

where: P_i, is the mean pressure; P_0 is the reference pressure; F_j and M_j are the generic mean force and mean moment, respectively; ρ is the air density; A_{ref} is the reference nominal side area of the train (77 m^2 at FS); H_{ref} is the reference nominal train height (3.1 m at FS); V_{rel} is the mean wind velocity relative to the train. Note that for static tests V_{rel} was the onset mean wind velocity while, for moving

model tests, it was the vector combination between the train speed and the double-average (i.e., the spanwise and time-average (Dorigatti, 2013)) of the onset wind velocity. Four different load coefficients are examined: C_y and C_z for the side and lift force, respectively, and both C_{mx} and $C_{mx,lee}$ for the rolling moment (depending whether the moment is reduced to a central longitudinal axis at the ground or to the leeward rail, respectively). According to a right-handed co-ordinate system, C_y and C_z are defined positive for forces directed towards the leeward side of the train and upwards, respectively, while rolling moments tending to overturn the vehicle are negative.
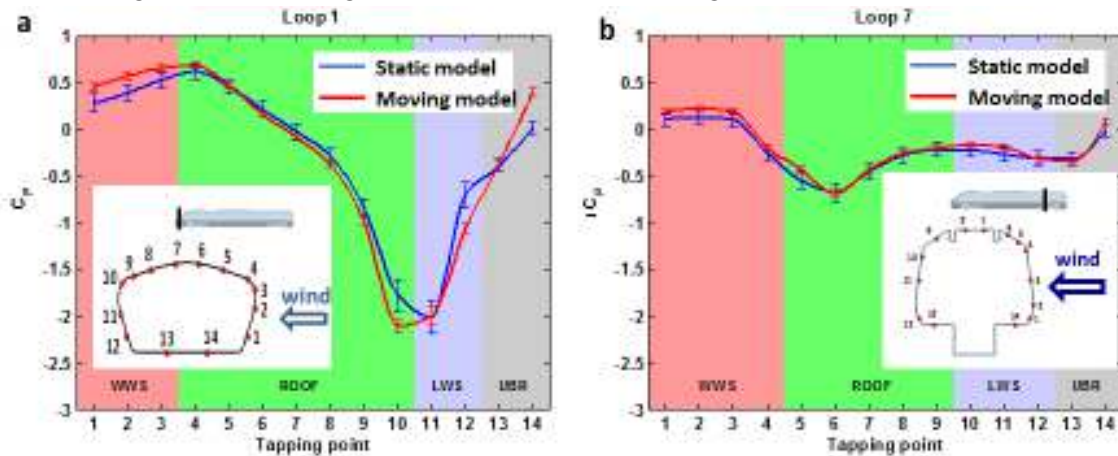
Figure 1. Non-dimensional pressure coefficient (C_p) on loop 1 on the train nose (a) and on loop 7 on the rear bogie of the leading car (b). Comparison between static and moving model tests
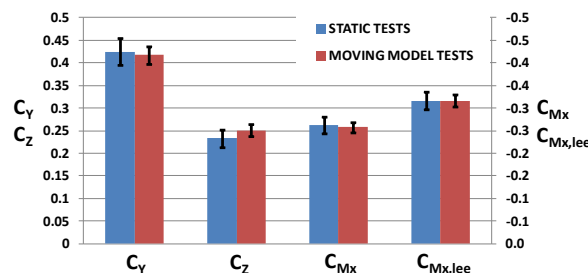
Figure 2. Overall mean aerodynamic load coefficients. Comparison between static and moving model tests.

Figure 1 illustrates the C_p distribution for two (of the totally 8) loops of pressure taps that were investigated: loop 1 on the train nose, and loop 7 on the rear bogie. A comparison is outlined between static and moving model tests taking into account the experimental uncertainty (specified by error bars). On the train nose positive values of C_p indicate stagnation on the windward side and windward portion of the roof, while negative values indicate suction on the leeward side of the roof and on the leeward face, with a suction peak arising on the leeward upper corner. In the underbody region, C_p changes from positive to negative moving from windward to leeward side. On the rear bogie C_p is smaller in magnitude and has a partially different trend than on the nose. Similar to loop 1, there is stagnation on the windward face and in the underbody, on windward side, while there is suction on the leeward face and on the leeward side of the underbody. Different from the nose, this suction now extends to the entire roof and the suction peak has moved from the leeward to the windward upper corner. The comparison between static and moving model tests reveals that a moving train has slightly larger C_p (both positive and negative) on the nose. Conversely, a general agreement between static and moving test results appears on loop 7, as well as on the other loops not shown here (Dorigatti, 2013).

The differences in pressure occurring on the nose are consistent with the skewed wind profile seen by a moving (but not by a static) vehicle, which is characterized by a higher relative wind velocity between the ground and the reference height (Dorigatti, 2013). However, the agreement found on the rest of the leading car indicates that such an effect of the vehicle movement is limited to the front of the train. Consistent with the characteristics of the flow surrounding a streamlined vehicle at a 30° yaw angle (Baker et al., 2009), it can be expected that the pressure on the train nose is sensitive to the onset

wind, while the pressure in the centre and rear is mainly determined by the vehicle-induced turbulence, i.e. by the vortices forming and rolling up along the train. Accordingly, what outlined above suggests that although a moving train sees a different relative wind profile with respect to a static train, the characteristics of the turbulent flow that develops around the vehicle are the same in the two cases.

Figure 2 compares static and moving model tests in terms of overall mean load coefficients. For the side force, as well as for both the rolling moment coefficients there is a remarkable agreement between the best-estimates associated with the two types of tests (i.e. differences < 2%). For the lift force coefficients slightly higher coefficients (~8%) characterise a moving train. However, it is important to note that any discrepancy found is smaller than the estimated experimental uncertainty. Therefore, to the level of accuracy of these measurements ($\leq$ 12%), the current comparison between static and moving model tests shows an overall agreement and, consequently, indicates no effect of the vehicle movement simulation on the mean aerodynamic coefficients.

4   Closing remarks

A comparison between a static and moving model-scale train in a crosswind has been carried out in this study. By developing a novel experimental methodology, for the first time, not only the overall aerodynamic load coefficients, but also the local surface pressure distribution was examined. The results outline only minor variations in the mean pressure between static and moving model tests localized on the nose. This suggests an overall similarity in the characteristics of the time-averaged flow field surrounding the rest of the train. Furthermore it leads to have no significant impact of the vehicle movement on the mean load aerodynamic coefficients. Accordingly, this work provides evidence that supports the use of wind tunnel static tests for estimating the train mean aerodynamic load coefficients. Nevertheless, a comparison of the correlation of the pressure fluctuations occurring along a static and a moving train (not shown here) reveals relevant differences. Hence, it warns on the accuracy of static tests for investigating unsteady aerodynamic parameters (such as peak coefficients and admittance functions). Finally, the present experimental results are viable for CFD benchmarking.

5   Acknowledgements

6   References

Baker, C.J. (1986). Train aerodynamic forces and moments from moving model experiments. *Journal of Wind Engineering and Industrial Aerodynamics* **24**, 227-251.

Baker, C.J., Cheli, F., Orellano, A., Paradot, N., Proppe, C., Rocchi, D. (2009). Cross-wind effects on road and rail vehicles. *Vehicle System Dynamics: International Journal of Vehicle Mechanics and Mobility* **47**, 983 - 1022.

CEN (2010). *Railway Applications - Aerodynamics - Part 6: Requirements and test procedure for cross wind assessment, EN 14067-6*. Brussels.

Cheli, F., Rocchi, D., Schito, P., Tomasini, G. (2011). Steady and moving high-speed train crosswind simulations. Comparison with wind-tunnel tests. *9th World Congress on Railway Research, Lille*.

Dorigatti, F. (2013). *Rail vehicles in crosswinds: analysis of steady and unsteady aerodynamic effects through static and moving model tests*. PhD Thesis. University of Birmingham.

Humphreys, N.D. (1995). *High Cross Wind Gust Loads on Ground Vehicles from Moving Model Experiments*. PhD Thesis. University of Nottingham.

Wind Loading on Multi-Layer Open Frame Structures:
A Comparison of International Code Provisions

Joelle K. Nelson, P.E.[1]

[1]Senior Project Director, Thornton Tomasetti, New York, NY, USA
jnelson@thorntontomasetti.com

Abstract

The effect of shielding in open frame structures from the upwind frames on the downwind frames causes significant reduction of the wind loading on the downwind frames. However, many international codes including Eurocode and ASCE 7 fail to provide guidance on the effects of shielding for these structures limiting their provisions to trussed towers and single plane lattice structures. This study examines the shielding provisions from both the British Standard and the Australian/New Zealand Standard comparing them to international code provisions for trussed towers and earlier wind tunnel studies. The shielding factors in both standards perform better for flat sided members and smaller arrays and conservatively in other cases with few exceptions. Even when these shielding factors produce highly conservative results compared to test data, they provide substantial reductions in wind loads from when shielding is neglected.

1   Introduction

Many building codes, such as Eurocode (2005) and ASCE7 (2010), provide wind force coefficients for a single plane open frame and for trussed towers, where a trussed tower consists of vertical trusses in a square or triangular plan configuration. Often, no other guidance is provided for the many other configurations of multiple layers of open frames such as can be found in scaffolding, petrochemical facilities, unclad buildings during construction, or any open structure with a non-square or non-triangular layout or more than two layers of frames. With no other provisions in place, the designer is left with the options of conservatively applying the single plane open frame coefficients to each frame with no consideration of the effects of shielding or performing a wind tunnel study, a process which can be cost prohibitive for many projects.

   Both the Australian/New Zealand Standard (2011) and the British Code, National Annex to Eurocode1 (BSI, 2010) and the superseded British Standard (BSI, 1997), by referencing Cook (1999) and (1990) respectively, address shielding for multiple layers of open frames. The two approaches vary substantially. This is a study comparing how the two sets of shielding coefficients perform when applied to lattice frame coefficients from multiple international codes.

2   Calculation of Shielding Factors

Both AS/NZS (2011) and Cook (1990) allow for the use of shielding factors to reduce calculated wind loads on multiple layers of open frames. However, the two standards take markedly different approaches to calculating these shielding factors.

   AS/NZS (2011) uses a simple approach where shielding factors for both the orthogonal and 45 degree wind direction can be looked up from a table using the parameters of the effective solidity ratio and the frame spacing ratio. No shielding factor is applied to the first frame in the upwind direction. The same shielding factor that is applied to the second frame is also applied to any subsequent frame. The increased shielding effect due to the increasing number of shielding frames is neglected. The provision specifies that the frames must be similar, so these provisions cannot be applied for a series

of open frames with widely different solidity ratios. Therefore, this study focuses only on arrays of frames that meet this requirement.

Cook (1990) recommends a simplified equation using only the parameters of the solidity ratio and the force coefficient of the shielding frame to calculate the shielding factor on the downwind frame. With this equation, the spacing ratio has no effect on the shielding coefficient. Cook also provides more complicated equations including the spacing ratio for shielding effects on the downwind frame from the upwind frame as well as for shielding effects on the upwind frame from the downwind frame. These provisions allow for the calculation of shielding coefficients for a series of open frames with varying solidity ratios. In this study, the more complicated equation including the spacing ratio is used to calculate the shielding factors for shielding from the upwind frame on the downwind frame. Shielding from the downwind frame on the upwind frame has been neglected except as noted.

Unlike the AS/NZS (2011) approach, the method in Cook (1990) calls for the calculation of a separate shielding factor for each frame in an array of open frames. This involves a summation of the solidity ratios, shielding coefficients, and force coefficients for all the shielding frames. While a more time consuming process, the method produces sharply reduced shielding coefficients for large arrays.

With the Cook (1990) method, the effects of a non-orthogonal wind direction are taken into account by applying a factor calculated through a nonlinear equation to the same shielding coefficients as for orthogonal winds. The method provides for the calculation of wind loads in any direction whereas the AS/NZS (2011) method only provides for an orthogonal and 45 degree wind loading. The Cook equation gives the component of the wind load acting in each of the orthogonal directions, and calculating the direction which produces the maximum total force on the structure is not straightforward.

3   Single Plane Frame Force Coefficients

In both the AS/NZS (2011) method and the British adopted method by NJ Cook (1990), wind loads on multiple planes of open frames are calculated by applying shielding coefficients to the force coefficients for single plane open frames. Therefore, in order to understand the shielding coefficients, the differences among the various code provisions in the force coefficients for single plane open frames must be recognized.

However, the various international code provisions take different approaches as to what portion of the calculated wind force is represented by the force coefficient and what portion is represented by other factors applied in combination with the force coefficient. The clearest discrepancy between the international codes occurs with what ASCE 7 (2010) calls the gust-effect factor and what AS/NZS (2011) calls the dynamic response factor. Both factors are designed to capture the effective increase in statically applied wind loads resulting from the dynamic response of the structure. Both have the same frequency lower limit of 1 Hz for rigid structures. However, in ASCE 7 (2010), the gust effect factor for rigid structures is 0.85 and in AS/NZS (2011), the dynamic response factor is 1.0. As a result, all AS/NZS (2011) force coefficients have been factored by 1/0.85 in order to compare them with ASCE7 (2010) provisions.

Once this adjustment has been made to AS/NZS (2011) force coefficients, Eurocode (2005), AS/NZS (2011), ASCE7 (2010), Cook (1990) have similar force coefficients for single plane open frames with flat sided members for solidity ratios greater than 30%. These range between 1.5 and 1.6. However, for frames with round members in the subcritical range, the various codes produce a wide range of force coefficients, and the difference in coefficients is even greater in the supercritical range (Fig 1).
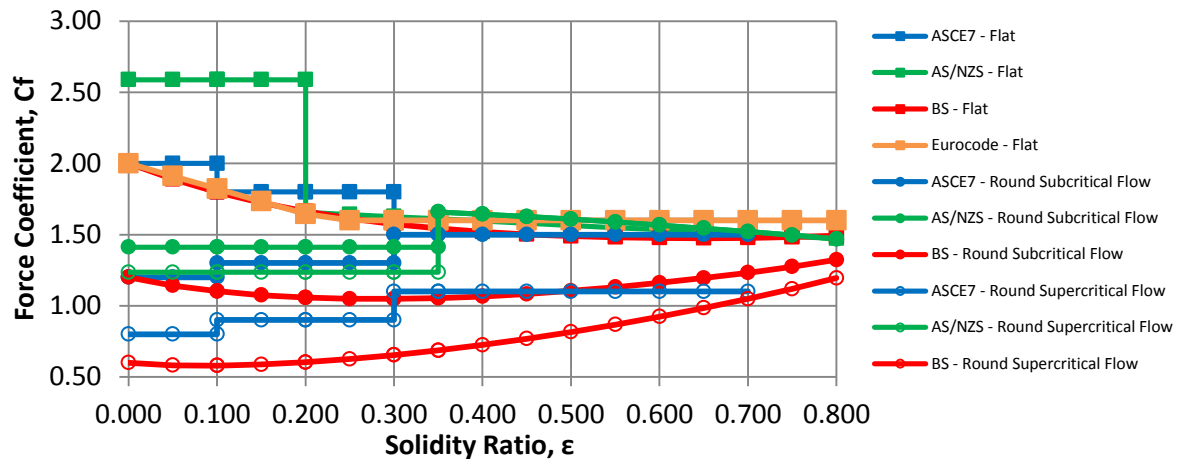
Figure 1. Force coefficients for lattice frames.

4   Comparison Tower Coefficients with Two Layers of Open Frames with Shielding

ASCE7 (2010), Cook (1990), and Eurocode (2005) provide force coefficients for towers consisting of two layers of open frames in a square configuration. Therefore, comparing the results of two lattice frames in a square configuration with a shielding factor applied with the tower coefficients from these codes is a simple way of gauging the effectiveness of the shielding factors in replicating the codes intent. In order to develop a better understanding of how much the variation in shielding factors effects the total force coefficient versus how much the variation in lattice frame force coefficient does, the shielding factors from both AS/NZS (2011) and Cook (1990) have been applied to the lattice frame force coefficients from ASCE 7 (2010), AS/NZS (2011), and Cook (1990).

ASCE7 (2010) does not provide force coefficients for towers with round members under supercritical flow. The tower force coefficients provided in ASCE7 correspond well with the force coefficients for trussed towers from the American standard for the telecommunications industry (ANSI/TIA, 2009), which does provide force coefficients for towers under supercritical flow. Therefore the ANSI/TIA (2009) tower force coefficients have been substituted for ASCE7 tower coefficients for supercritical flow comparisons.

For towers with flat members and a wind direction perpendicular to the frame, the various codes both for towers and for lattice frames with shielding factors applied produce similar results (Fig. 2a). The total coefficients vary by a maximum of 15% for solidity ratios between 30% and 95%.

For frames with round members and a perpendicular wind direction, the various codes produce similar force coefficients for towers. However these results are not replicated with lattice frame coefficients with shielding factors applied (Fig. 2b). These generally produce overly conservative values compared with tower coefficients. The large disparity in the results is mostly attributable to the differences in the lattice frame coefficients.   With either set of shielding factors applied, the lattice frame coefficients by Cook (1990) produce the results most similar to the tower coefficients for subcritical and supercritical flows but can provide lower values than the tower coefficients for supercritical flows (Fig. 2c).

For 45 degree wind directions on towers with flat members, the various codes both for towers and for lattice frames with shielding factors applied produce similar results within the range of 20% to 60% solidity. Within that range, the total coefficients vary by a maximum of 15%. For towers with flat members and solidity ratios greater than 60%, the tower force coefficients alone are within a much wider range than with the perpendicular wind direction. The lattice frames coefficients with shielding factors applied generally fall within or close to this range. The British lattice force coefficients for flat-sided members with British shielding factors applied produce total force coefficients that correspond well with the British tower coefficients. Thus while there is non-negligible difference
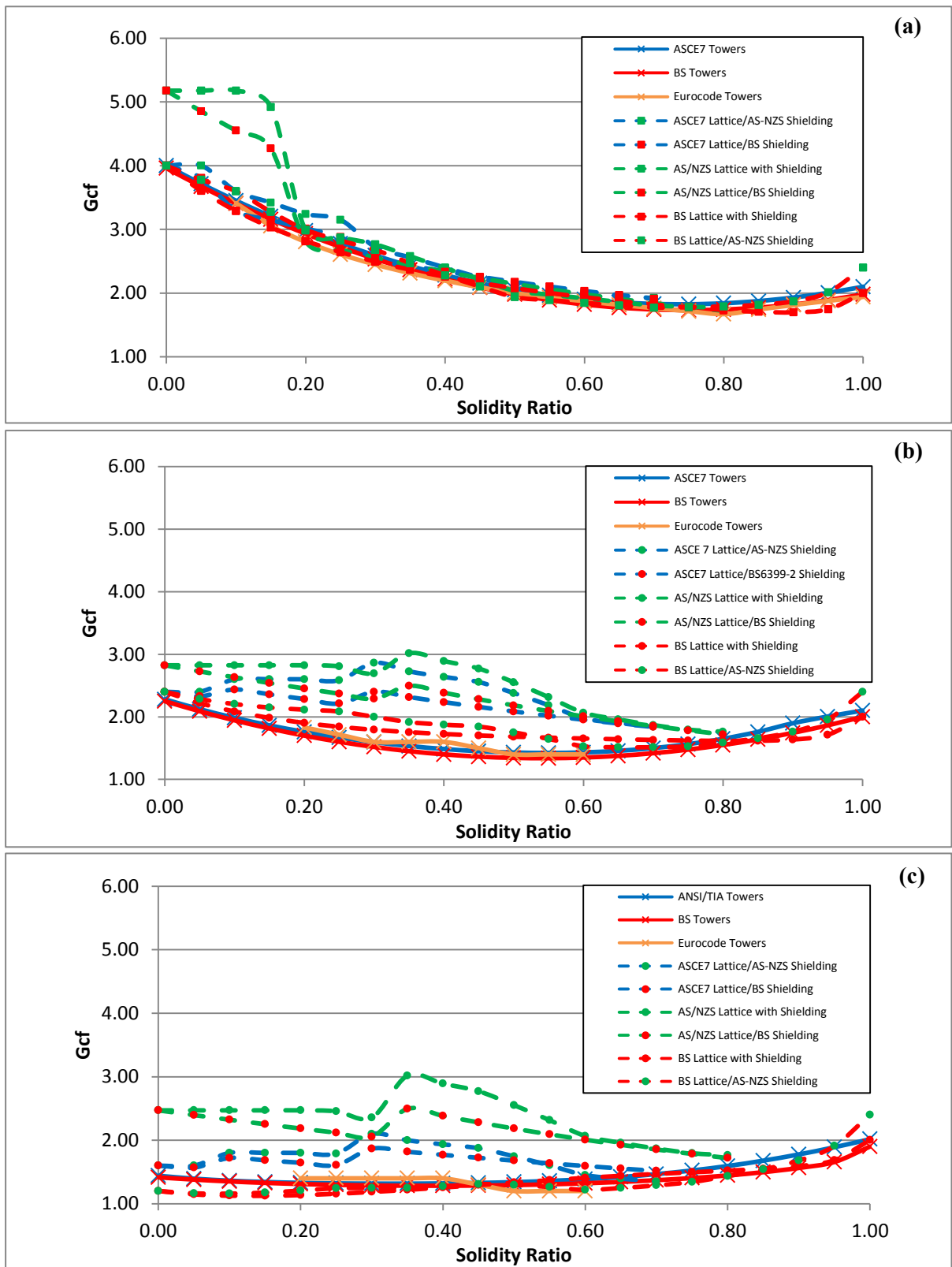
Figure 2. Force coefficients for orthogonal wind loads on square towers with (a) flat members (b) round subcritical members (c) round supercritical members.
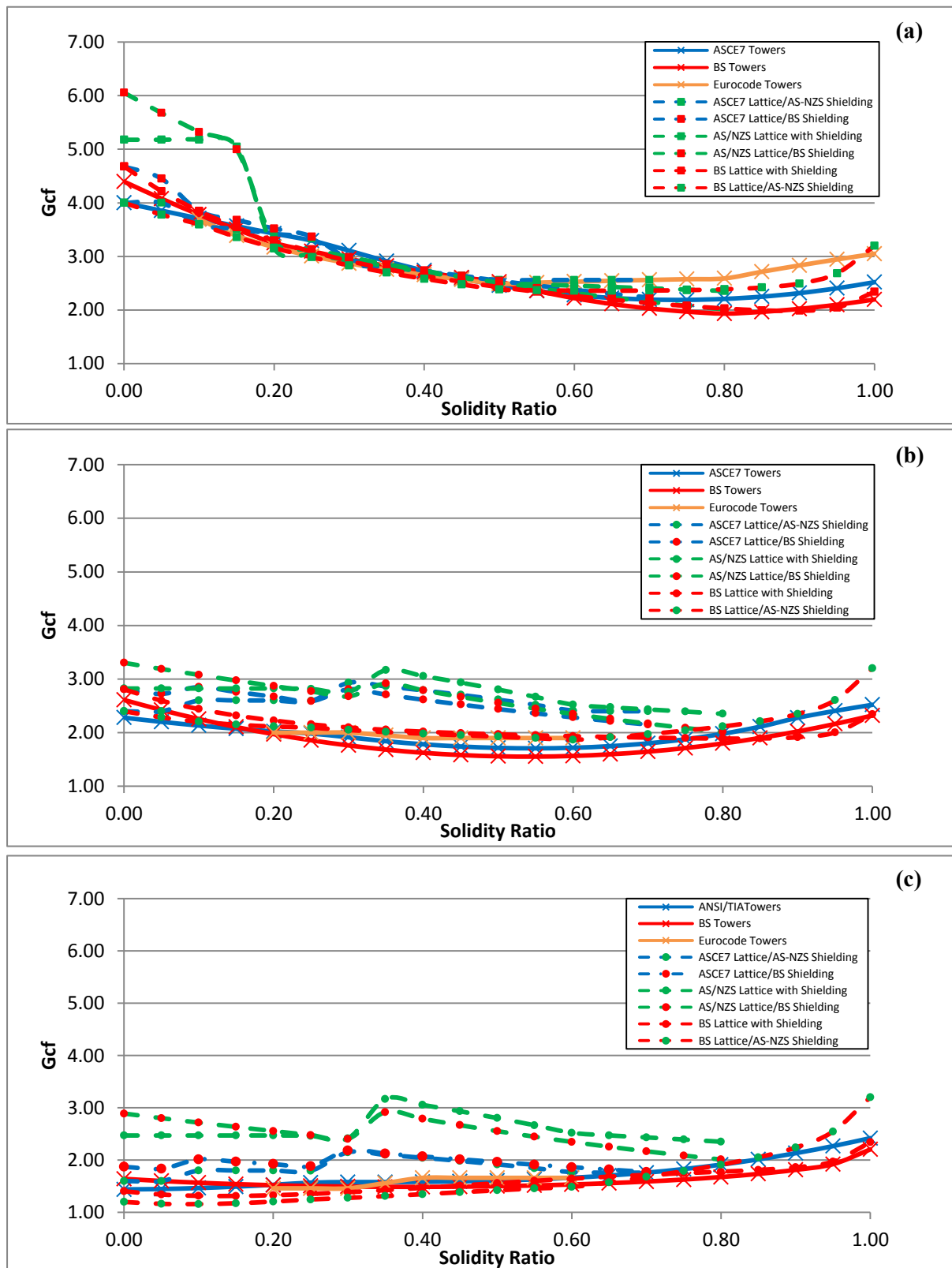
Figure 3. Force coefficients for 45 degree wind loads on square towers with (a) flat members (b) round subcritical members (c) round supercritical members.

between the coefficients in the higher solidity range, it should not be attributed to the failure of the shielding factors but to a general lack of consensus among the codes for angled wind directions.

As with the perpendicular wind direction, for round members in both the subcritical and supercritical ranges, the lattice frame coefficients with shielding factors applied fail to replicate the tower results. Here too, the British lattice frame coefficients with shielding factors applied produce the most similar but sometimes lower total force coefficient values when compared to the tower force coefficients (Fig. 3).

5   Two Planes of Frames with Varying Spacing Ratios

Cook (1990) cites tests performed by BRE for two open frames with three different solidity ratios and varying spacing ratios. This study focuses on two frames of equal solidity ratios for the purpose of comparison with code provisions. When comparing the BRE test results for the shielded frame with both the shielding factors proposed by Cook (1990) and AS/NZS (2011), the Cook shielding factors tend to match the test results more closely and conservatively than the AS/NZS factors. However, when considering the combined effect of both the shielding of the second frame from the first frame as well as the shielding of the first frame from the second frame, both the AS/NZS and the Cook factors produce a reasonably close fit to the test results (Fig. 4).

6   Multiple Planes of Frames

This study compares the total force coefficients using shielding factors in Cook (1990) and AS/NZS (2011) with test results from Whitbread (1979) for arrays of up to five lattice frames with spacing ratios of 0.5 and 1.0 and with solidity ratios varying between .163 and .543 (Fig. 5). Compared with the test results for frames with flat members, AS/NZS coefficients are overly conservative for solidity ratios under 20%. This can be attributed to the jump in the single plane frame coefficients for these solidity ratios as opposed to a failing in their shielding factors. With that exception, both provisions produce similar results to the test data for one and two frames with flat members and become increasingly conservative for increasing numbers of arrays. In general, the provisions developed by Cook produce slightly less conservative results. For frames with round members, the British force coefficients fit the single frame test data well and provide conservative but reasonable results for multiple frames when compared with the limited test data. The AS/NZS coefficients are overly conservative (Fig. 6).

Although both the AS/NZS (2011) and the Cook (1990) provisions for shielding for multi-layer open frames with flat sided members produce conservative values for large arrays, even these conservative values compared with test data represent a substantial savings as opposed to neglecting the effects of shielding altogether. Cook's methodology for an array of five frames with a solidity ratio of .543 and spacing ratio of 1.0 produces a total force coefficient that is 40% of that which would be used if shielding were neglected. AS/NZS provisions with a spacing ratio of 0.5 produces a total force coefficient that is 36% of that which would be used if shielding were neglected.

7   Conclusions

The AS/NZS Standard (2011) provides a simple approach to shielding which many engineers may prefer due to the ease of its use. The trade-off of the AS/NZS (2011) approach compared to Cook (1990) is increased conservatism, especially for large arrays of frames, and decreased flexibility, such as the inability to use AS/NZS provisions with frames of varying solidity ratios. Both methods allow for substantial reduction in wind loads on arrays of open frames. The adoption of either one would provide engineers with essential guidance.
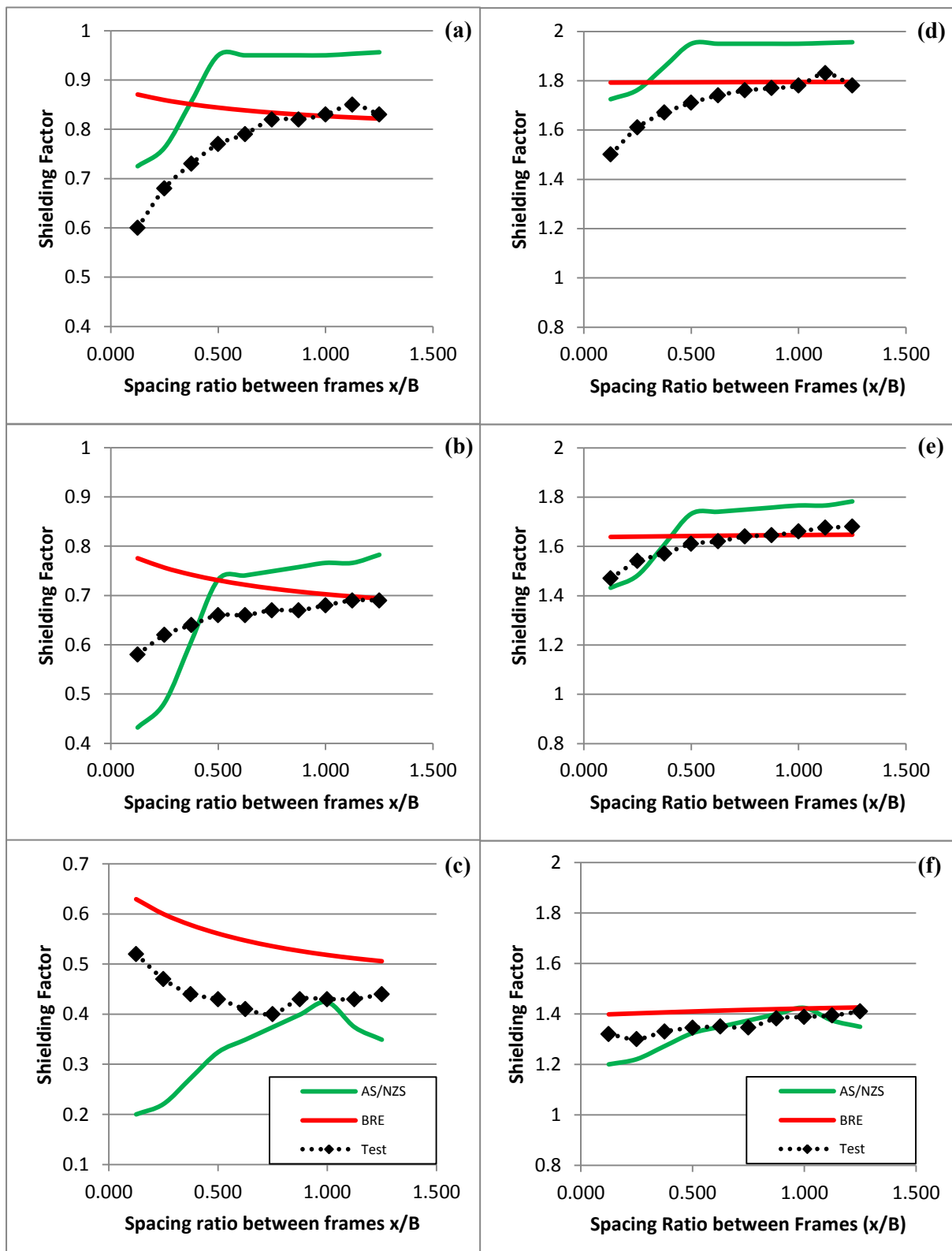
Figure 4. Shielding factor for shielded frame with solidity ratio of (a) 0.121 (b) 0.234 (c) 0.438 and combined shielding factor on both the shielding and shielded frame with solidity ratio of (d) 0.121 (e) 0.234 (f) 0.438
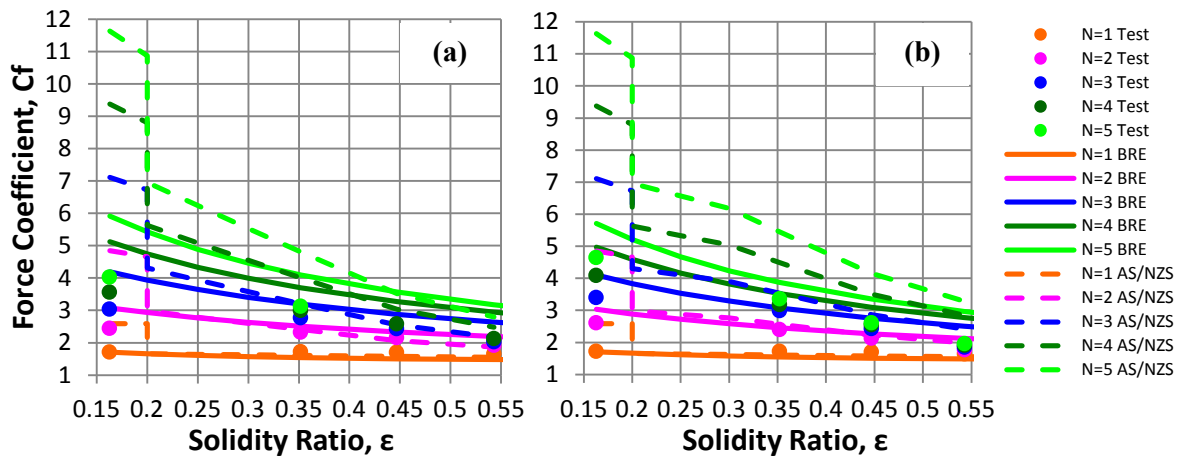
Figure 5. Arrays of flat membered lattice frames with (a) 0.5 spacing ratio (b) 1.0 spacing ratio.
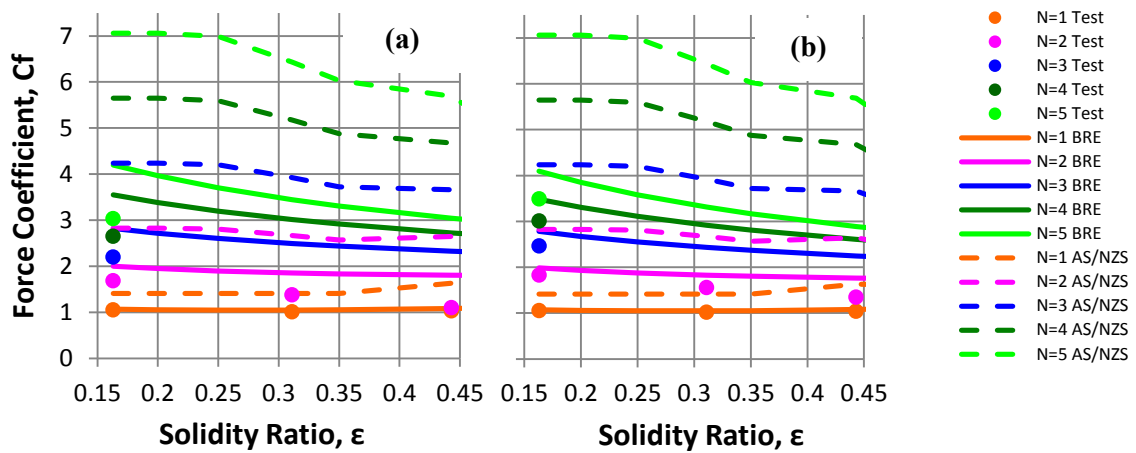
Figure 6. Arrays of round membered lattice frames with (a) 0.5 spacing ratio (b) 1.0 spacing ratio.

References

ANSI/TIA (2009), *ANSI/TIA-222-G-2005 Structural Standard for Antenna Supporting Structures and Antennas*. Arlington, VA: Telecommunications Industry Association.

ASCE (2010), *ASCE 7-10 Minimum Design Loads for Buildings and Other Structures*. Reston, VA: American Society of Civil Engineers.

BSI (1997), *British Standard BS6399-2:1997: Loading for Buildings – Part 2: Code of Practice for Wind Loads*. London: British Standards Institute.

BSI (2010), *UK National Annex to Eurocode 1 – Actions on Structures*. London: British Standards Institute.

Cook, N. J. (1990), *Building Research Establishment Report: The Designer's Guide to Wind Loading of Building Structures – Part 2: Static Structures*. London: Building Research Establishment.

Cook, N. J. (1999), *Wind Loading: A Practical Guide to BS 6399-2 Wind Loads on Buildings*. London: Thomas Teleford.

Eurocode (2005), *Eurocode 1: Actions on Structure - Part 1-4: General Actions - Wind Actions*. London: British Standards Institute.

Standards Australia & Standards New Zealand (2011), *Australian/New Zealand Standard AS/NZS 1170.2:2011: Structural Design Actions – Part 2: Wind Actions*. Sydney: SAI Global Limited & Wellington: Standards New Zealand.

Whitbread, R. E. (1979). The influence of shielding on the wind forces experienced by arrays of lattice frames. *Proceedings of the 5th International Conference on Wind Engineering*. Oxford: Pergamon Press.

Flutter of suspension bridges under nonuniform wind profiles

A. Arena[1], W. Lacarbonara[1] and P. Marzocca[2]

[1]Department of Structural and Geotechnical Engineering, Sapienza University of Rome, Rome, Italy

[2]Mechanical and Aeronautical Engineering Department, Clarkson University, Potsdam, NY, USA

Corresponding author: W. Lacarbonara, walter.lacarbonara@uniroma1.it

Abstract

A parametric one-dimensional model of suspension bridge is employed to investigate the effects of arbitrary wind distributions in the onset of flutter. A total Lagrangian formulation is adopted to obtain the equations of motion expressed in terms of kinematic variables and linearized about the prestressed aeroelastic equilibrium. The kinematics for the deck feature the vertical and the horizontal displacements of its elastic axis and the torsional rotations of the cross sections, the latter, are assumed rigid in their own plane. The elasto-geometric stiffness of the cables is obtained by condensing the bridge equilibrium under the self-weight in the longitudinal direction. The equations of motion are coupled with incompressible unsteady aerodynamics for which the aeroelastic loads are defined through a set of indicial functions specifically developed, by means of computational fluid dynamics simulations, for the cross section of the Runyang suspension bridge. The treatment of the aeroelastic system is performed by using the finite element approach and numerical investigations supply insights into the nonlinear flutter characteristics of such bridges.

1 Introduction

In highly flexible structures such as suspension bridges, typically exhibiting a very low bending-torsional stiffness, the flutter instability, that may arise from the wind-induced oscillations, can represent the major concern for the bridge designers. Moreover, when the bridge span becomes very long, the wind spatial profile can influence both the stability and the aeroelastic response of suspension bridges and need to be carefully investigated. For a bridge deck cross-section, the aeroelastic motion can be obtained by the combination of a torsional displacement in pitch and two bending displacements in plunge and lag (Salvatori and Borri, 2007). In the time domain, the aeroelastic response of a suspension bridge can be studied within a given range of wind speeds bracketing the flutter speed and the flutter condition can be evaluated when the bridge exhibits a limit cycle. Along with a proper representation for the structure to perform aeroelastic simulations, an accurate description of the aerodynamic forces is needed. To this aim, the indicial method represents a well-established approach adopted for the representation in the time domain of the unsteady aerodynamic loads in various flow speed regimes. These loads can be obtained as the convolution of the indicial responses, that is, the response in terms of lift, drag, and aerodynamic moment to a step-change of the aerodynamic input. This approach is proved to be suitable also for the investigation of the aeroelastic phenomena such as flutter (Salvatori and Borri, 2007) which, typically, for suspension bridges are studied in the frequency domain by means of aeroelastic derivatives. Herein the linear indicial unsteady aerodynamic functions are used for incompressible flow speed regimes, and the main assumption is that the viscous effects are blended into the indicial functions produced from the aerodynamic admittances evaluated for a bridge deck cross section. The unsteady aerodynamic loads for this incompressible flow regime do not refer to the Wagner's function, strictly only valid for thin airfoils, but in terms of new indicial functions derived from the aerodynamic admittance, or flutter derivatives, produced for a bridge deck cross section. In particular, the unsteady lift and aerodynamic moment considered in this study are pertinent to the Runyang Suspension Bridge in China (Zhang et al., 2002) and are described through indicial functions whose coefficients are numerically determined via computational fluid dynamic (CFD) investigations (Arena, 2012; Farsani et al., 2014). The inherent complexities presented in this formulation are bypassed, that is the Duhamel integrals, used to describe the unsteady

characteristics of the flow, are non directly solved, instead the aerodynamic loads are described using a state-space representation. In particular, the unsteady loads can be defined as a combination of aerodynamic states whose time evolution is described by a set of first-order differential equations coupled with the motion of the section. A linearized one-dimensional (1D) parametric model of suspension bridge is used (Lacarbonara, 2013; Arena and Lacarbonara, 2012) with the purpose of studying its dynamic aeroelastic stability under the action of a Gaussian-distributed wind speed and to evaluate the flutter boundary for different wind distributions. The aerodynamic loads, evaluated for a two-dimensional (2D) section model of the Runyang bridge deck, are introduced in the continuous 1D structural model, according to the strip theory, as loads per unit reference length. The aeroelastic equations of motions, together with the equations governing the time evolution of the aerodynamic added states are implemented and solved in a finite element (FE) solver, Comsol Multiphysics. The critical flutter speed evaluated under the assumption of uniform wind speed profiles is shown being not always the more conservative estimate.

2   1D parametric model of suspension bridge

The linear theory of elastic cables and unshearable elastic beams is here adopted to model the mechanics of the suspension bridge. The parametric modeling is based on a 1D continuous formulation where the space support is represented by the archlength x giving the position of the elastic center of the bridge deck cross sections (here assumed to be coincident with their center of mass) along the span l. The suspension elements are supposed to be unstretchable and uniformly distributed along the bridge span as an equivalent rigid membrane, therefore, the kinematics of the bridge can be defined through the component of the deck baseline displacement and of its cross sections torsional rotation. In particular, in the fixed reference frame (e_1, e_2, e_3) with origin in the center of mass of the left deck terminal section, the kinematic variables are thus defined through the horizontal and the vertical displacement $u_1(x, t)$ and $u_2(x, t)$, respectively, and the torsional rotation $\phi_3(x, t)$ of the generic bridge cross-section. Here, the direction e_3 is collinear with the bridge span whereas the deck cross-sections lay in the plane (e_1, e_2), being e_2 the vertical direction. The initial equilibrium of each suspension cable is described by the catenary nondimensional expression $y_c(\bar{x})$ which can be evaluated for a fixed sag-to-span ratio d_c/l. Under the action of dead loads and the static and aerodynamic wind loads per unit length, given in their nondimensional form by λ_2, D_S, L_S, M_S and D_AE, L_AE, M_AE, respectively, the first-order formulation of the aeroelastic equations of motion for the suspension bridge can be written in terms of nondimensional parameters and kinematic variables as

$$\dot{u}_1 = v_1 \ , \ \dot{u}_2 = v_2 \ , \ \dot{\phi}_3 = \omega_3 \ , \tag{1}$$
$$\dot{v}_1 = \left(-\chi\, u_1'''' - c_1 v_1 + D_\mathrm{S} + D_\mathrm{AE} \right) \ ,$$
$$\dot{v}_2 = \frac{1}{1 + 2\bar{m}_c}\left(-u_2'''' - c_2 v_2 + 2\alpha_c u_2'' + 2\kappa_c y_c'' \frac{1}{\eta_c} \int_0^1 y_c' u_2' \, dx + \lambda_2 + L_\mathrm{S} + L_\mathrm{AE} \right) \ ,$$
$$\dot{\omega}_3 = \frac{1}{\bar{J}_d^m + \frac{\delta_c^2}{2}\bar{m}_c}\left(\beta\, \phi_3'' - c_3 \omega_3 + \frac{\delta_c^2}{2}\alpha_c \phi_3'' + \frac{\delta_c^2}{2}\kappa_c y_c'' \frac{1}{\eta_c} \int_0^1 y_c' \phi_3' \, dx + M_\mathrm{S} + M_\mathrm{AE} \right)$$

where the overdot and the prime indicate differentiation with respect to the nondimensional time t and archlength x, respectively, and $\kappa_c = EA_c l^2/EJ_1$, $\alpha_c = H_c l^2/EJ_1$, $\eta_c = L_c/l$, $\beta = GJ_3/EJ_1$, $\chi = EJ_2/EJ_1$ and $\delta_c = B_c/l$ represent the nondimensional elasto-geometric parameters governing the mechanics of the bridge. Moreover, $\bar{m}_c = m_c/m_d$, $\bar{J}_d^m = J_d^m/\left(m_d l^2\right)$, are the nondimensional mass and mass moment, where EJ_1, EJ_2 and GJ_3 are the deck bending stiffness about e_1 and e_2, and the torsional stiffness about e_3 axis, respectively; L_c is the length of the cables under the effect of the dead loads, B_c is the distance among the two cables while A_c is the cables area section and H_c the horizontal component of the force in the cables due to the dead loads. Finally, the terms $c_1 v_1$, $c_2 v_2$ and $c_3 \omega_3$ represent the classical linear damping terms. The reference parameters adopted to perform the nondimensionalization of the mechanical system are the span length l and the characteristic frequency $\bar{\omega} = \sqrt{EJ_1/m_d l^4}$, where m_d is the deck mass per unit length. By defining the state vector $\xi(x, t) = \{u_1, u_2, \phi_3, v_1, v_2, \omega_3\}$, the expressions of the unsteady aerodynamic drag D_AE, lift L_AE and moment M_AE,

shown in the right side of Eq. (1), can be defined in the time domain through the indicial formulation as follows

$$F_{\text{AE}}^j(x,t) = P^j(x) \sum_{\xi} C_{\xi}^j \left(\Phi_{\xi}^j(0)\xi(x,t) + \int_0^t \dot{\Phi}_{\xi}^j(t-\tau)\xi(x,\tau)d\tau \right) \tag{2}$$

where F_{AE}^j represents the generic aerodynamic force and moment, assuming $j = 1, 2, 3$ for referring to D_{AE}, L_{AE} and M_{AE}, respectively. The function $\Upsilon(x) = \exp\left(-\frac{(x-\mu)^2}{2\sigma^2}\right)$ is adopted to represent the spatial distribution of the wind speed $U(x)$ along the bridge span, such that $U(x) = U\Upsilon(x)$, and $P^j(x) = \frac{1}{2}\frac{\rho_a Bl}{m_d}\bar{U}(x)^2$ for drag and lift and $P^j(x) = \frac{1}{2}\frac{\rho_a Bl}{m_d}\bar{U}(x)^2\delta$ for the aerodynamic moment, $\bar{U}(x) = \frac{U(x)}{\bar{\omega}l}$ is the dimensionless free stream wind speed, and $\delta = B/l$, where B the deck width, and $\rho_a = 1.225 \text{ kg/m}^3$ is the air density. The indicial function associated with the jth aerodynamic load and the dynamic state $\xi(x,t)$ is defined as a linear combination of exponential functions as: $\Phi_{\xi}^j(t) = 1 - \sum_{k=1}^2 a_{\xi,k}^j e^{-\tilde{b}_{\xi,k}^j t}$ where $\tilde{b}_{\xi,k}^j = 2(\bar{U}(x)/\delta)b_{\xi,k}^j$. The coefficients $a_{\xi,k}^j$, $b_{\xi,k}^j$ and C_{ξ}^j are taken from results obtained in (Arena, 2012) from CFD simulations performed with a two-dimensional discrete vortex method solver based on a fast-multipole method specialized for bluff-bodies accounting for flow separation and wake effects (DVMFLOW by COWI Inc.). Eq. (1), that accounts for the integral terms given by Eq. (2), can be solved via direct time integration by adopting an *ad hoc* numerical scheme in order to treat the convolution integrals. An alternative expression of Eq. (2) is produced by introducing a set of aerodynamic added states $W_{\xi}^{j,k}(x,t)$ and by defining the unsteady aerodynamic loads as their linear combination where the evolution in time of such states is governed by a set of ODEs coupled with the bridge equations of motion (1). The convolution term (2) can be then written as

$$F_{\text{AE}}^j(x,t) = P^j(x) \sum_{\xi} C_{\xi}^j \left(\Phi_{\xi}^j(0)\xi(x,t) + \sum_{k=1}^2 a_{\xi,k}^j \tilde{b}_{\xi,k}^j W_{\xi}^{j,k}(x,t) \right) \tag{3}$$

and the characteristic equation of the the ODEs system governing the evolution in time of the added aerodynamic states has the following expression

$$\dot{W}_{\xi}^{j,k}(x,t) = \xi(x,t) - \tilde{b}_{\xi,k}^j W_{\xi}^{j,k}(x,t) \tag{4}$$
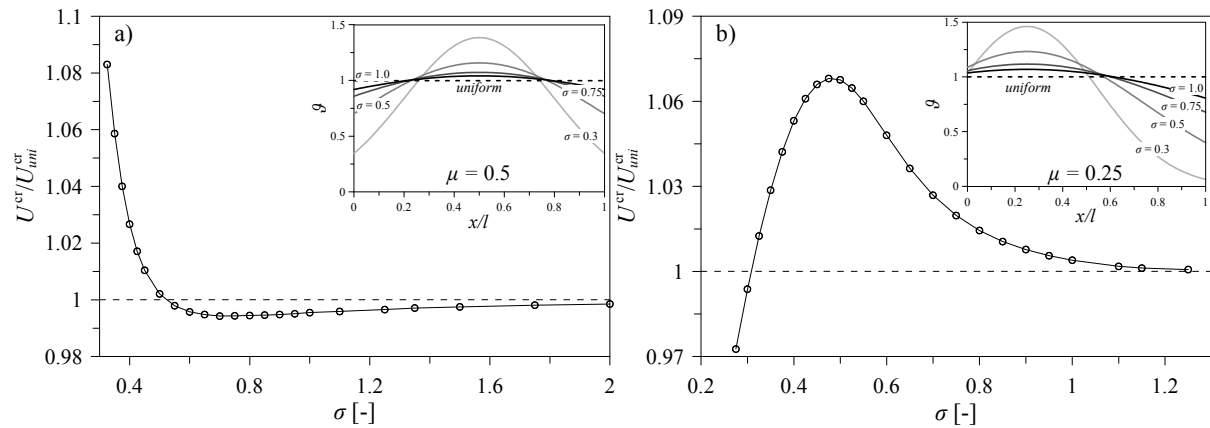
Figure 1. The parameter σ of the Gaussian function versus the flutter speed ratio: (a) for a symmetric ($\mu = 0.5$) and (b) for a non-symmetric ($\mu = 0.25$) wind speed profile.

3 Numerical results

Parametric analyses are carried out to study the onset of flutter for two Gaussian wind profiles. The elastogeometric properties of the deck-girder of the Runyang Bridge reported in (Zhang et al., 2002). When considering the Gaussian distribution of the wind speed the wind profiles are defined to have the same energy content as the uniform distribution. Therefore, to perform parametric analyses by varying μ and σ in the Gaussian function, its peak amplitude is determined coherently. The critical flutter speed is first evaluated under a uniform wind distribution. Numerical simulations were subsequently performed for the case of nonuniform Gaussian wind speed profile. Two main profiles were investigated, a symmetric shape ($\mu = 0.5$) and a non-symmetric shape with maximum speed at the quarter-span ($\mu = 0.25$). The parameter σ, regulating the width of the Gaussian function, was varied and the critical flutter speed U^{cr} was calculated through time marching simulations. In Fig. 1, the flutter speed ratio $U^{\mathrm{cr}}/U^{\mathrm{cr}}_{uni}$ between the nonuniform and uniform wind is given for several values of σ. For the considered bridge the flutter mode shape appear to be a skew-symmetric coupled flexural-torsional mode (Arena and Lacarbonara, 2012), hence the nonuniform wind distribution has the effect of leading to about 10% increase of critical wind speed with respect to a uniform wind distribution. While for a restricted range of wind distributions, conservative estimates are obtained by using a uniform flow spatial profile, the results obtained for the non-symmetric wind profile show that there is a large range of σ for which underestimated predictions are expected. On the other hand, symmetric wind distributions lead to a slight reduction of the flutter speed for a wide range of σ confirming the results shown in previous works (Sepe et al., 2000).

4 Conclusions

The aim of this work was to emphasize specific aspects of the aeroelastic behavior of long-span suspension bridges when subject to nonuniform wind speeds. A parametric model coupled with an unsteady aerodynamic model was used to explore the onset of flutter. Symmetric wind distributions showed that there is a not negligible range of nonuniform profiles leading to lower flutter speeds, while non-symmetric profiles may lead to nonconservative predictions. Thus, the proposed model intends to be a valid tool for bridge practitioners for the investigation of the flutter boundary when the bridge is exposed to nonuniform winds. This work was partially supported by the US-NSF (Grant n. CMMI-1031036).

References

Arena, A. (2012). Aeroelasticity of suspension bridges using nonlinear aerodynamics and geometrically exact structural models. PhD thesis. Sapienza University of Rome. URL: *http://hdl.handle.net/10805/1731*.

Arena, A. and Lacarbonara, W. (2012). Nonlinear Parametric Modeling of Suspension Bridges under Aeroelastic Forces: Torsional Divergence and Flutter. *Nonlinear Dynamics* **70**.4, pp. 2487–2510.

Farsani, H., Valentine, D. T., Arena, A., Lacarbonara, W., and Marzocca, P. (2014). Indicial Functions in the Aeroelasticity of Bridge Decks. *Journal of Fluids and Structures*. In press.

Lacarbonara, W. (2013). *Nonlinear Structural Mechanics. Theory, Dynamical Phenomena and Modeling.* ISBN 978-1-4419-1275-6. Springer, New York.

Salvatori, L. and Borri, C. (2007). Frequency- and time-domain methods for the numerical modeling of full-bridge aeroelasticity. *Computers and Structures* **85**.11-14, pp. 675–687.

Sepe, V., Caracoglia, L., and D'Asdia, P. (2000). Aeroelastic Instability of Long-span Bridges: Contributions to the Analysis in Frequency and Time Domains. *Wind and Structures* **3**.1, pp. 41–58.

Zhang, X., Xiang, H., and Sun, B. (2002). Nonlinear aerostatic and aerodynamic analysis of long-span suspension bridges considering wind-structure interactions. *Journal of Wind Engineering and Industrial Aerodynamics* **90**, pp. 1065–1080.

Targeted-Energy-Transfer devices for stay-cable vibration mitigation

Matteo Izzi[1], Luca Caracoglia[2] and Salvatore Noè[1]

[1]University of Trieste, 34127 Trieste, ITALY
[2]Northeastern University, Boston, MA 02115, U.S.A.
Corresponding author: Salvatore Noè, noe@units.it

Abstract

Free vibration of a taut-cable with an attached passive Targeted-Energy-Transfer (TET) device are investigated using an analytical formulation of the complex generalized eigenvalue problem. This problem is of considerable practical interest in the context of stay-cable vibration suppression in bridges, induced by wind, wind-rain and parametric excitation. The TET device was modelled as a dashpot with a viscous damper in parallel with a power-law elastic spring element; a linear elastic spring was also added between the dashpot and the deck. Two types of TET devices were analysed: a Linear TET and a Nonlinear TET. For both the devices a family of "universal design curves" was developed, by accounting the effect of the elastic stiffness and the flexibility of the support. To verify the adequacy of the universal curves and to evaluate the effectiveness of TET devices, numerical simulations were performed on a reference cable and subsequently extended to an existing stay, taken from the Fred Hartman Bridge (Houston, Texas, USA).

1 Introduction

The mitigation of large-amplitude oscillation on inclined stays associated with the effects of wind or wind-rain (FHWA, 2007; Xu, 2013) and parametric excitation (Gattulli and Lepidi, 2003; Liu et al., 2005; Gattulli and Lepidi, 2007) has been the focus of several investigations in recent years due to the potential high costs of maintenance or repair that can be caused by, for example, fatigue in the cables. To suppress the problematic vibrations, cable-damper system performance has been widely studied. In most investigations the damper unit was modeled as a linear viscous device, perfectly fixed and anchored to the deck (Main and Jones, 2002) or as a linear viscous damper with internal stiffness (Sun et al., 2004); other authors evaluated the effectiveness of the damping system by introducing the effects of the flexibility in the damper support (Huang and Jones, 2011). This paper is motivated by the necessity of extending the above-mentioned configurations to a generalized case, by first introducing a linear elastic stiffness element in parallel with the viscous damper and by simulating an imperfect anchorage to the deck with an elastic support. Also, the study investigates the use of Targeted-Energy-Transfer devices (Vakakis, 2001) by proposing a new device, which incorporates nonlinear stiffness in the model by means of a power-law elastic spring element (Fig. 1b).
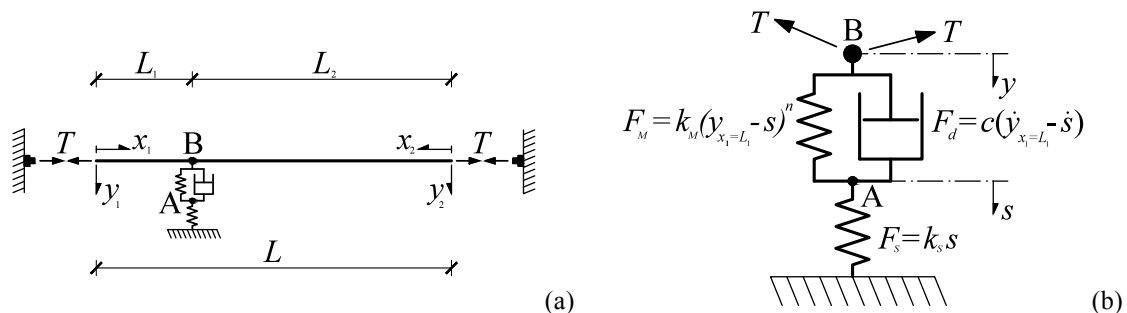
Figure 1. Taut-cable system model with a generic TET device (a), and NL-TET device schematization (b).

The performance of these systems was evaluated by analyzing the free-vibration response through a linearization of the equations of motion and a generalization of the wave equation (taut-cable theory) in the presence of two cable segments. "Universal design curves" (Krenk, 2000; Main and Jones, 2002) of the device were also analytically derived. For both cases, theoretical and numerical results were obtained and compared.

2   Linear Targeted-Energy-Transfer device (L-TET)

The cable and the Linear Targeted Energy Transfer device (L-TET) are shown in Fig. 1a. The length of the cable is L and the L-TET is located at a distance $x_1 = L_1$ from the left end; the cable force is T and the mass per unit length is μ. The attached L-TET device is modelled as a dashpot with a viscous damping coefficient c in parallel with an elastic spring with stiffness k_M and exponent $n = 1$ (Fig. 1b); a linear elastic spring with stiffness k_S is added between the dashpot and the ground (Huang and Jones, 2011). In the following it is convenient to introduce the complementary length $L_2 = L - L_1$ and the complementary coordinate $x_2 = L - x_1$.

Assuming that the tension T is large compared to the weight of the stay and under the hypothesis of small vibration, negligible bending stiffness and small mechanical damping in the stay, a taut-string model is used to simulate the dynamics of the system. Linear oscillations of the cable under the assumption of virtually unchanged cable force are described by the linear wave equation (Main and Jones, 2002):

$$\mu \frac{\partial^2 y_k(x_k,t)}{\partial t^2} = T \frac{\partial^2 y_k(x_k,t)}{\partial x_k^2} \tag{1}$$

being $y_k(x_k,t)$ the transverse vibration (deflection) and x_k the coordinate along the cable chord axis in the kth segment (with $k=1,2$). Equation (1) is valid everywhere except at the damper attachment point; at this location continuity of displacement and equilibrium of internal forces must be satisfied.

To solve Eq. (1) subjected to boundary, continuity and equilibrium conditions a non-dimensional time $\tau = \omega_{0,1} t$ is introduced (Pacheco et al., 1993), with $\omega_{0,1} = (\pi/L)(T/\mu)^{0.5}$, and two distinct shape functions over the two cable segments are assumed in the following form:

$$y_k(x_k,t) = Y_k(x_k) \cdot \exp(j\lambda\tau) \tag{2}$$

with λ non-dimensional eigenvalue, $Y_k(x_k)$ complex mode shape on kth cable segment and $j^2 = -1$.

The substitution of Eq. (2) into Eq. (1) yields to an ordinary differential equation where the solutions are the complex mode shapes of the system; enforcing the continuity of displacement at the damper linkage and the boundary conditions of zero displacement at the cable end leads to:

$$Y_k(x_k) = \gamma \frac{\sin(\pi\lambda x_k / L)}{\sin(\pi\lambda L_k / L)} \tag{3}$$

in which γ is the vibration amplitude at the damper location and L_k is the length of the kth cable segment. The equilibrium equation at node B for the damper in parallel with the elastic spring and support system (Fig. 1b) is:

$$T\left(-\frac{\partial y_2}{\partial x_2}\bigg|_{x_2=L_2} - \frac{\partial y_1}{\partial x_1}\bigg|_{x_1=L_1} \right) = c\left(\dot{y}_{x_1=L_1} - \dot{s} \right) + k_M\left(y_{x_1=L_1} - s \right) \tag{4}$$

where $y_{x_1=L_1} = y_1(x_1 = L_1, t)$; the "dot" marker denotes a differentiation with respect to time t, and the variable $s(t) = s_0 \cdot \exp(j\lambda\tau)$ is used to represent the displacement at node A. The equilibrium equation at node A is given by:

$$k_S s - c\left(\dot{y}_{x_1=L_1} - \dot{s} \right) - k_M\left(y_{x_1=L_1} - s \right) = 0 \tag{5}$$

By solving these equations the system equilibrium equation yields to:

$$\cot\left(\pi\lambda L_1 / L\right) + \cot\left(\pi\lambda L_2 / L\right) + \frac{\chi_S}{\pi\lambda}\left[\frac{\eta\pi\lambda - j\chi_M}{\eta\pi\lambda - j\left(\chi_S + \chi_M\right)}\right] = 0 \tag{6}$$

in which $\eta = c / (T / \mu)^{0.5}$ is the non-dimensional damper coefficient while the non-dimensional spring stiffness coefficients are $\chi_S = k_S L / T$ and $\chi_M = k_M L / T$. Equation (6) is also called frequency equation (Main and Jones, 2002; Krenk, 2000); its complex roots represent the "eigenvalues" (null space) of the system, each of which corresponds to a distinct mode of vibration. For specific values of η, χ_S, χ_M and L_1 / L Eq. (6) can be solved numerically to obtain frequencies and damping ratios of as many modes as desired, to an arbitrary degree of accuracy (Main and Jones, 2002). Each eigenvalue can be written in terms of real and imaginary part as $\lambda_i = (\omega_i / \omega_{0,1})[i\zeta_i + (1 - \zeta_i^2)^{0.5}]$ (Pacheco et al., 1993) where ζ_i is the damping ratio and ω_i is the modulus of the dimensional eigenvalue, which has been referred to as the pseudo-undamped natural frequency, in a given mode i.

When $L_1 / L \ll 1$ the damper-induced frequency shifts are small and Eq. (6) can be used to develop an asymptotic approximation of the modal damping ratios; introducing Krenk's approximations for the sinusoidal terms (Krenk, 2000), the damping ratio can be calculated as:

$$\frac{\zeta_i}{L_1 / L} = \frac{\pi^2\kappa}{\left(\pi^2\kappa\right)^2 \psi^2 + \left[1 + \psi\left(L_1 / L\right)\chi_M\right]^2} \tag{7}$$

where $\zeta_i / (L_1 / L)$ is the normalized modal damping ratio, $\psi = 1 + (\chi_S L_1 / L)^{-1}$ is the effective flexibility coefficient, defined by Huang and Jones (2011), and $\kappa = i\eta / \pi(L_1 / L)$ is a non-dimensional parameter group (Main and Jones 2002). The range of the non-dimensional parameter group κ, in the following referred as the normalized damper coefficient, is between zero and one; if $\kappa = 0$ the system is undamped and the stay is connected to an elastic device made by two elastic stiffness, respectively χ_S and χ_M, arranged in series. If $\kappa = 1$ the damper is perfectly clamped to the stay, the elongation between node A and B tends to zero and the amplitude of the vibration in the section of the TET is due to the flexibility of the support. Equation (7) is also named the "universal design curve" of modal damping ratio versus normalized damper coefficient.

3   Nonlinear Targeted-Energy-Transfer device (NL-TET)

The "universal design curve" of modal damping ratio obtained for the L-TET can be generalized for a Nonlinear Targeted-Energy-Target device (NL-TET), modelled as a dashpot, in which the damper is in parallel with a power-law elastic spring with stiffness k_M and exponent n (Fig. 1b); as previously, a linear elastic spring with stiffness k_S is added between the dashpot and the ground.

If n is defined positive and odd ($n=1, 3, \dots$), the equilibrium equations at node A and B for the NL-TET are easily obtainable from Eqs. (4) and (5). To solve these equations, an energy based approach was adopted, in which the nonlinear force-displacement relationship of the elastic spring with stiffness k_M is reduced to a linear equivalent law. After this approximation, the frequency equation of Eq. (6) leads to:

$$\cot\left(\pi\lambda L_1 / L\right) + \cot\left(\pi\lambda L_2 / L\right) + \frac{\chi_S}{\pi\lambda}\left\{\frac{\eta\pi\lambda - j\chi_{M\text{-NL}}\left(\Delta_{\tau,\text{sec}} / L\right)^{n-1}}{\eta\pi\lambda - j\left[\chi_S + \chi_{M\text{-NL}}\left(\Delta_{\tau,\text{sec}} / L\right)^{n-1}\right]}\right\} = 0 \tag{8}$$

with $\chi_{M\text{-NL}} = k_M L^n / T$, $\Delta_{\tau,\text{sec}}$ peak amplitude displacement between nodes A and B for the system characterized by linear equivalent spring and the other symbols as previously defined. As reported in Eq. (9) below, the value of $\Delta_{\tau,\text{sec}}$ is derived from the peak amplitude displacement Δ_τ of the nonlinear system (Fig. 2) through an energy-based approach by equating the elastic energy of the two systems:

$$\int_0^{\Delta_\tau} k_M x^n \, dx = \int_0^{\Delta_{\tau,\text{sec}}} k_M \Delta_{\tau,\text{sec}}^{n-1} x \, dx \tag{9}$$

where the variable x represents the relative displacement between node A and B (Fig. 1b).

The integration of Eq. (9) leads to the following expression:

$$\Delta_{\tau,\mathrm{sec}} = \sqrt[n+1]{\frac{2}{n+1}}\Delta_\tau \tag{10}$$
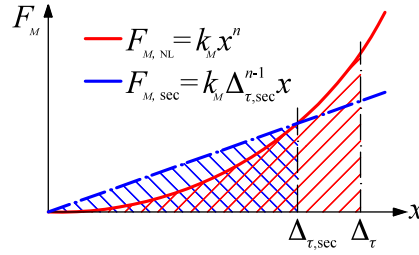
Figure 2. Schematization of the energy-based approach, used to describe the linear equivalent spring.

If the damper-induced frequency shifts are small, Eq. (8) can be used to derive an asymptotic approximation even for non-linear damping system, in which the modal damping ratio in a given mode i can be calculated as:

$$\frac{\zeta_i}{L_1/L} = \frac{\pi^2\kappa}{\left(\pi^2\kappa\right)^2\psi^2 + \left[1 + \psi\left(L_1/L\right)\chi_{M\text{-NL}}\left(\Delta_{\tau,\mathrm{sec}}/L\right)^{n-1}\right]^2} \tag{11}$$

The optimal damping ratio can be derived by setting the derivative of Eq. (11) with respect to κ equal to zero; this gives:

$$\kappa_{opt} = \frac{1}{\pi^2\psi}\left[1 + \psi\left(L_1/L\right)\chi_{M\text{-NL}}\left(\Delta_{\tau,\mathrm{sec}}/L\right)^{n-1}\right] \tag{12}$$

and the corresponding "optimal damping ratio" (Main and Jones, 2002) can be written as

$$\frac{\zeta_{i,opt}}{L_1/L} = \frac{1}{2\psi\left[1 + \psi\left(L_1/L\right)\chi_{M\text{-NL}}\left(\Delta_{\tau,\mathrm{sec}}/L\right)^{n-1}\right]} \tag{13}$$

Equation (13) shows that the optimal damping ratio for the NL-TET is amplitude dependent. Analogous results may be obtained for the L-TET with $n=1$; in this particular situation there is no relationship between the peak amplitude displacement in the section of the cable, anchored to the damper, and the optimal damping ratio. Since κ is proportional to the mode number i, it is important to note that the optimal damping ratio can be achieved in only one mode at a time; in particular, if the TET device is designed optimally for a particular mode, it will be more "rigid" in the higher modes and less compliant in the lower modes, showing suboptimal damping ratios in those situations (Main and Jones, 2002).

4   Formulation of the equally-spaced lumped mass model for the NL-TET

Numerical simulations were performed to evaluate the effectiveness of the TET devices (linear and nonlinear) and to explore the applicability of the concept of universal design curve to the TET devices. To verify the asymptotic approximations of Eq. (7) and Eq. (11) a time-domain lumped-mass model of a stay, equipped with the TET-device, was derived and numerically solved by step-by-step integration. The numerical algorithm was solved in MATLAB. In the model $\widehat{nn}$ concentrated masses, equally spaced at a distance Δx, are used to simulate the distributed mass of the stay μ; these points are linked by massless cable elements, axially loaded by a constant force T (Fig. 3a). A transverse discrete degree of freedom (y_i) is associated to each concentrated mass $M_i = \mu\Delta x$ (Giaccu and Caracoglia, 2011); an additional degree of freedom ($j_{\mathrm{sup}} = \widehat{nn}+1$) and a fictitious mass $M_{\mathrm{sup}} \ll M_i$ are also introduced in the model to evaluate the displacement in the section of the TET due to the flexibility of the support (node A, Fig. 1b). In the following it is convenient to define as j_{dev} the

degree of freedom, at which the TET device is attached to the cable (node B, Fig. 1b). The hypotheses of non-shallow cable, no mechanical damping and no flexural stiffness in the link elements were utilized.
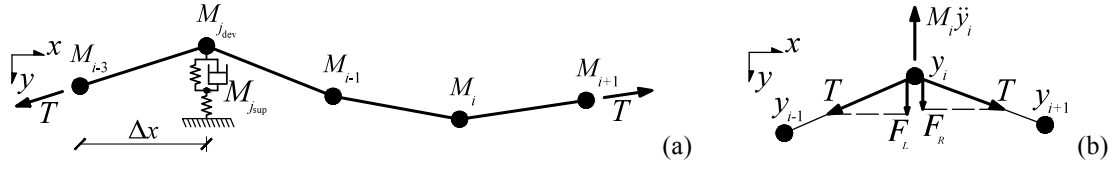
Figure 3. Lumped mass model of the stay (a) and free body equilibrium for the generic non-jointed node (b).

The free-body equilibrium equation for each non-restrained mass element of the taut-cable model incorporates the effects of the inertial force and those of the cable tension T (Fig. 3b), expressed through the transverce force components F_L and F_R (left, "L" and right, "R"), as follows:

$$M_i \ddot{y}_i - \frac{T}{\Delta x}\left(y_{i-1} - 2y_i + y_{i+1}\right) = 0 \tag{14}$$

being $\ddot{y}_i = \mathrm{d}^2 y_i / \mathrm{d} t^2$ and $i = 1 \ldots \widehat{nn}$, with $i \neq j_{\mathrm{dev}}$. Two additional force quantities are introduced in the dynamic equations at the degrees of freedom of j_{dev} and j_{sup} to characterize the effect of the TET damper device:

$$M_{j_{\mathrm{dev}}} \ddot{y}_{j_{\mathrm{dev}}} - \frac{T}{\Delta x}\left(y_{j_{\mathrm{dev}}-1} - 2y_{j_{\mathrm{dev}}} + y_{j_{\mathrm{dev}}+1}\right) = -c\left(\dot{y}_{j_{\mathrm{dev}}} - \dot{y}_{j_{\mathrm{sup}}}\right) - k_M\left(y_{j_{\mathrm{dev}}} - y_{j_{\mathrm{sup}}}\right)^n \quad \text{for } i = j_{\mathrm{dev}}$$

$$M_{j_{\mathrm{sup}}} \ddot{y}_{j_{\mathrm{sup}}} + k_{j_{\mathrm{sup}}} y_{j_{\mathrm{sup}}} = c\left(\dot{y}_{j_{\mathrm{dev}}} - \dot{y}_{j_{\mathrm{sup}}}\right) + k_M\left(y_{j_{\mathrm{dev}}} - y_{j_{\mathrm{sup}}}\right)^n \qquad \text{for } i = j_{\mathrm{sup}} \tag{15}$$

The dynamic system, obtained from Eqs. (14) and (15), was conveniently rewritten in matrix form as a function of a non-dimensional length $z_i = y_i / L$ and of a non-dimensional time $\tau = \omega_{0,1} t$, with derivative $\mathrm{d} y_i / \mathrm{d} t = \omega_{0,1}(\mathrm{d} y_i / \mathrm{d}\tau)$ and $\mathrm{d}^2 y_i / \mathrm{d} t^2 = \omega_{0,1}^2(\mathrm{d}^2 y_i / \mathrm{d}\tau^2)$:

$$\frac{\mathrm{d}^2 \mathbf{z}}{\mathrm{d}\tau^2} + \mathbf{K}_{\mathrm{nd}} \mathbf{z} = \mathbf{f} \tag{16}$$

in which $\mathbf{z}$ is the vectors of the transverse displacements and accelerations, $\mathbf{I}$ is the identity matrix of dimension $\widehat{nn}+1$ by $\widehat{nn}+1$, $\mathbf{K}_{\mathrm{nd}}$ is the stiffness matrix of the cable and elastic support, assembled as:

$$\mathbf{K}_{\mathrm{nd}} = \begin{bmatrix} -N_d^2 \pi^{-2} \mathbf{K}_1 & \mathbf{0}_{\left(\widehat{nn}\times 1\right)} \\ \mathbf{0}_{\left(1\times\widehat{nn}\right)} & N_d \pi^{-2} \chi_S \end{bmatrix} \tag{17}$$

where $N_d = L / \Delta x$; $\mathbf{K}_1$ is an $\widehat{nn} \times \widehat{nn}$ indicator-matrix of zeros, ones and minus twos defined as:

$$\mathbf{K}_1 = \begin{bmatrix} -2 & 1 & 0 & \cdots & 0 \\ 1 & \ddots & \ddots & \ddots & \vdots \\ 0 & \ddots & \ddots & \ddots & 0 \\ \vdots & \ddots & \ddots & \ddots & 1 \\ 0 & \cdots & 0 & 1 & -2 \end{bmatrix} \tag{18}$$

and $\mathbf{f}$ is a column vector employed to account for the presence of the TET, characterized by $\widehat{nn}-1$ zero elements and two non-zero elements, respectively:

$$\mathbf{f}_{j_{\mathrm{dev}}} = -\frac{N_d}{\pi}\eta\left[z_{j_{\mathrm{dev}}}^I - z_{j_{\mathrm{sup}}}^I\right] - \frac{N_d}{\pi^2}\chi_{M\text{-NL}}\left[z_{j_{\mathrm{dev}}} - z_{j_{\mathrm{sup}}}\right]$$

$$\mathbf{f}_{j_{\mathrm{sup}}} = -\frac{\mu \cdot \Delta x}{M_{j_{\mathrm{sup}}}} \cdot \mathbf{f}_{\mathrm{dev}, j_{\mathrm{dev}}} \tag{19}$$

To solve the nonlinear dynamic problem, the discrete vector $\mathbf{z}(\tau)$ was recast in state-space form as $\mathbf{w} = \{\mathbf{z}, d\,\mathbf{z}/d\,\tau\}^T$, with $\{\cdot\}^T$ denoting transpose operator and $d\,\mathbf{w}/d\,\tau = \{d\,\mathbf{z}/d\,\tau, d^2\,\mathbf{z}/d\,\tau^2\}^T$. A state-space system of $2\widehat{nn}+2$ first-order differential equations is consequently obtained, in the form:

$$\frac{d\,\mathbf{w}}{d\,\tau} = \mathbf{S}\mathbf{w} + \mathbf{f}^* \tag{20}$$

with $\mathbf{f}^* = \{\mathbf{0}_{(\widehat{nn}+1\times1)}, \mathbf{f}\}^T$ force-vector of the TET device and $\mathbf{S}$ state-space matrix, assembled as:

$$\mathbf{S} = \begin{bmatrix} \mathbf{0}_{(\widehat{nn}+1)\times(\widehat{nn}+1)} & \mathbf{I}_{(\widehat{nn}+1)\times(\widehat{nn}+1)} \\ \mathbf{K}_{nd} & \mathbf{0}_{(\widehat{nn}+1)\times(\widehat{nn}+1)} \end{bmatrix} \tag{21}$$

The vibration response of the discrete nonlinear dynamic system of Eq. (20) was numerically solved, with zero initial conditions $\mathbf{w}_0 = \mathbf{0}_{(2\widehat{nn}+2)\times1}$ at $\tau = 0$, by means of a fourth-order Runge-Kutta algorithm. After an initial phase in which the system is subjected to a transitory forced-vibration phase by applying a system of concentrated harmonic impulsive forces, suitably placed at selected degrees of freedom to excite the motion in one specific mode, the free-vibration response is analysed; the modal damping ratio, supplied through the TET device, is evaluated by applying the logarithmic decrement method (Chopra, 1995) to a reference degree of freedom, relevant to the entire system.

5   Numerical verification of the universal curves of the TET devices

Numerical analyses investigated the free-vibration response of the first five modes of a reference system, composed of a 20m-long stay-cable with $T = 1900kN$ and $\mu = 47.9kg/m$ and a TET damper device placed at $L_1/L = 0.02$. Five different flexibility coefficients ψ were analysed (Huang and Jones, 2011); Fig. 4a shows the normalized damping ratio $\zeta_i/(L_1/L)$ versus the non-dimensional parameter group κ for a L-TET device with $\chi_M = 10$ and exponent $n = 1$; a distinct curve is plotted for each mode.
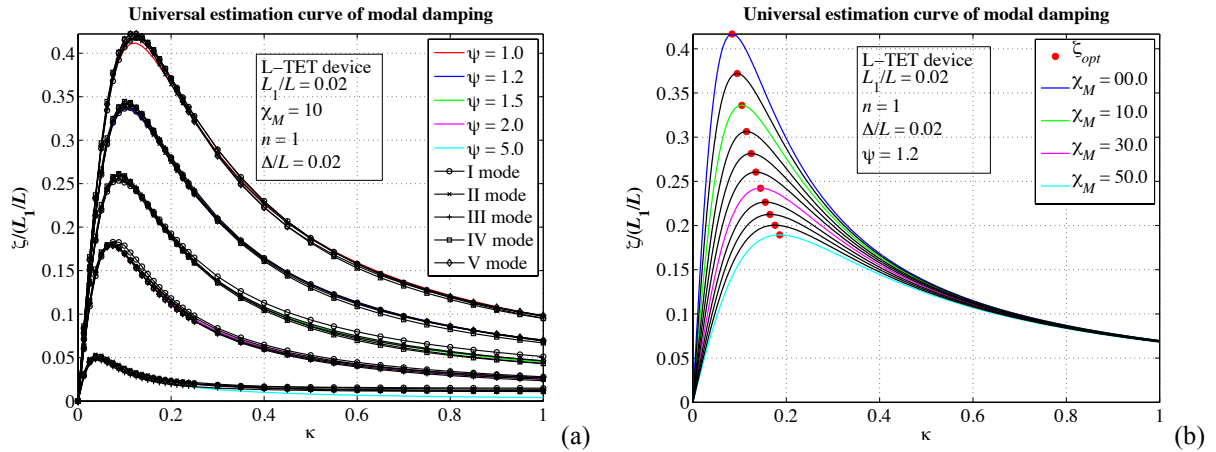
Figure 4. Numerical results for L-TET located at $L_1/L = 0.02$ (Fig. 1a) with $\chi_M = 10$ (a) and universal curves obtained when $\psi = 1.2$ and χ_M is varying between one and fifty (b).

The universal design curves (coloured lines without marker), obtained from Eq. (7), agree very well with the curves generated by numerical integration (black lines with marker) and corresponding to each of the five cable modes (Fig. 4a). The universal curves, found from Eq. (7) with $\psi = 1.2$ and with the elastic stiffness of the device χ_M varying between zero and fifty, are plotted in Fig. 4b; a red marker is used to label the local maxima, achieving optimal damping ratios. As shown in the same figure, an increase in the elastic stiffness χ_M yields to a reduction of both the optimal damping ratio and the slope of the curve in the proximity of the optimal-damping points, by "flattening" the bell-shaped curve in the interval of κ at which the highest damping ratios are achieved.

Figure 5 depicts the "plane of the optimal damping ratio", corresponding to an L-TET installed at the same stay location as in the previous cases, when the value of ψ varies between one (rigid support to ground) and five ("flexible" or imperfect support), and with χ_M varying between zero (linear dashpot with no spring in parallel) and five. For each value of the normalized damper coefficient κ_{opt} was defined as shown in Eq. (12). The results reveal that the optimal damping ratio is predominantly influenced by the flexibility of the support, compared to the elastic stiffness in parallel with the linear viscous damper.

Plane of the optimal damping ratio
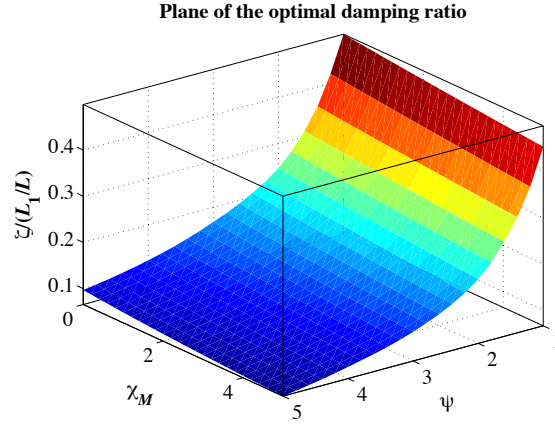
Figure 5. Plane of the optimal damping ratio of a L-TET when ψ and χ_M are varying.

As reported in Fig. 6a, analogous results were obtained for the NL-TET damper device with $\chi_{M\text{-NL}} = 2.000.000$ and exponent $n = 3$. As seen in Eq. (11), the performance of the nonlinear device, expressed through the damping ratio, is amplitude dependent; a numerical procedure was used to adjust the peak amplitude vibration of the cable in order to have, for each analysed mode, the same peak amplitude displacement $\Delta_{\tau,\sec}$.
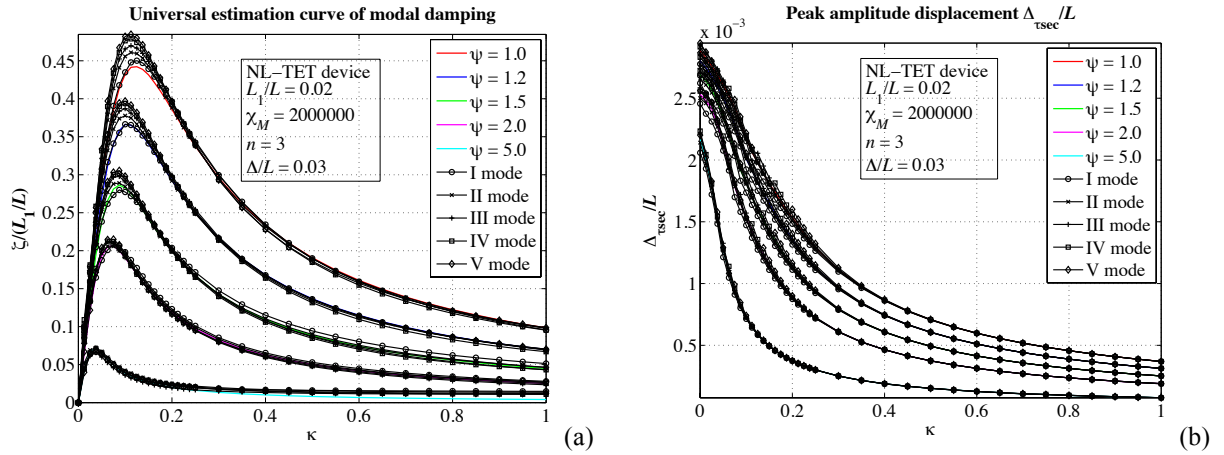
Figure 6. Numerical results for NL-TET located at $L_1 / L = 0.02$ (Fig. 1a) with $\chi_M = 2.000.000$ (a), and reference curves of the peak-amplitude displacement $\Delta_{\tau,\sec}$ in the cross-section of the damper (b)

Since vortex shedding and wind-rain induced phenomena usually happen in the first modes of the cable, causing peak oscillations of two or three times the diameter of the stay, or equivalently 0.02-0.03 times the length of the cable itself, the device used to perform the following analyses has been optimized for the second mode of the cable and for a peak amplitude displacement equal to $\Delta = 0.03L$ in the same mode. After this clarification, Fig. 6b shows the numerically-generated curves of the peak amplitude displacement $\Delta_{\tau,\sec}$ (black lines with marker), corresponding to each of the five modes of the cable, versus the non-dimensional parameter group κ. A set of reference curves (coloured lines

without marker) is obtained from the numerical simulations by means of the least-squares method; this set of values has been used to plot the universal curves in Fig. 6a.

The shape of the curves presented in Fig. 6b depends on several factors, as the peak amplitude displacement of the cable, the cross-section in which the TET device is applied, the non-dimensional elastic stiffness χ_M, the flexibility of the support ψ and the non-dimensional parameter group κ. To calculate the exact values of the universal design curves (Fig. 6a) it is important to identify the shape of the reference curve (Fig. 6b). Since this kind of investigation is time-consuming, a simplified approach has been preferred for practical purposes to define a "conservative" set of universal curves; for this reason, a constant value of the peak amplitude $\Delta_{\tau,sec}$ is used, obtained for the undamped system with $\kappa = 0$.
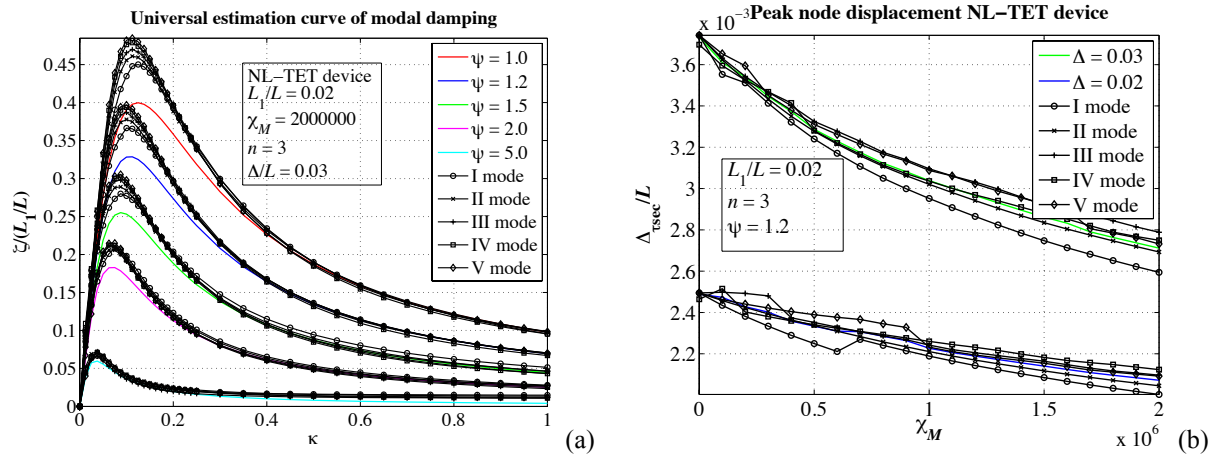
Figure 7. Conservative set of universal design curves, related to the numerical results of Fig. 5a (a), and simplified "abacus" for the prediction of the peak amplitude displacement $\Delta_{\tau,sec}$ of the undamped system (b) when the peak amplitude displacement of the cable is $\Delta = 0.03L$ (red line) and $\Delta = 0.02L$ (blue line)

The resulting curves are plotted in Fig. 7a; in comparison with the results of Fig. 6a, the damping ratios are lower near the point of optimal damping ratio but the values are very close to the "exact" solution everywhere else. A simplified "abacus" has also been proposed to predict the peak amplitude displacement in the section of the TET device; Figure 7b shows the results achieved a device placed at $L_1/L = 0.02$ when the optimal mode is the second and the peak amplitude displacement of the cable is, respectively, $\Delta = 0.03L$ (red line) and $\Delta = 0.02L$ (blue line). The curves have been obtained by combining the results of the first five modes by least squares (black lines with markers) and can be used to define the conservative universal design curves, previously mentioned.

6   An application on an existing stay: the Fred Hartman Bridge (Houston, Texas, USA)

The lumped-mass model, described in Chapter 4, was used to evaluate the effectiveness of NL-TET device applied on the AS16 stay of the Fred Hartman Bridge, Houston, Texas, USA (Main and Jones, 2001). The Fred Hartman Bridge (Fig. 8) is a twin-deck, cable-stayed bridge over the Houston Ship Channel with a central span of 380m and two side spans of 147m. Its deck is composed of precast concrete slabs on steel girders with four lanes of traffic, carried by a total of 192 cables, spaced at 15-m intervals in four inclined planes.

The system under evaluation is an 87m-long cable with $T = 2260 kN$, $\mu = 47.9 kg/m$ and diameter $D = 14.1 cm$ (FHWA, 2007), and by a NL-TET damper device placed at $L_1/L = 0.045$ with $\chi_{M-NL} = 200.000$ and exponent $n = 3$. The first five modes of the cable and four different flexibility coefficients ψ (1.00, 1.20, 1.50, 2.00) were analysed. The NL-TET device was designed for optimal performance in the fundamental mode of vibration and in the second one, which should provide adequate damping in the first several modes to suppress wind and wind-rain induced vibration. To define the peak amplitude displacement in the section of the damper, used to design the optimal

damper coefficient, a peak amplitude displacement of the cable of $\Delta = 0.02L$ in the fundamental mode (or in the mode designed for optimal damping) is was considered.

Figure 8. Fred Hartman Bridge, Houston, Texas, USA (image reproduced from: FHWA, 2007)

As mentioned in the introduction, 95% of stay cable vibrations is associated with wind-rain induced phenomena; to evaluate the susceptibility of the stays and to avoid this phenomena, it is common to refer to the Scruton number of the cable $S_{c,0} = (\mu\zeta)/(\rho D^2)$, where ρ is the density of the air and ζ is the structural damping ratio of the mode being investigated (Irwin, 1997). PTI Guide Specification (2000) and FHWA (2007), in particular, suggest increasing the Scruton number of the cable to values grater than 10; since cable mass and diameter are determined at the design stage and air density is constant, to satisfy this condition it is necessary to provide additional damping by means of an external mechanical device.
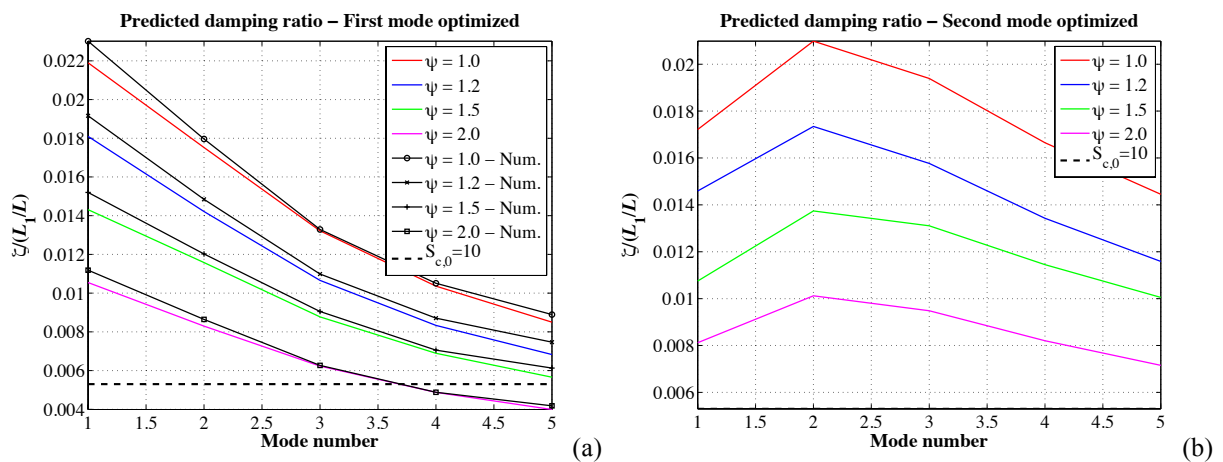
Figure 9. Predicted damping ratio for an NL-TET on AS16 stay of the Fred Hartman Bridge (Fig. 8) when the optimal damping ratio is achieved in the fundamental mode (a) and in the second mode (b).

Figure 9a depicts the modal damping ratios provided by the NL-TET when the optimal performance is achieved in the fundamental mode of vibration; mechanical damping of the stay or negative aerodynamic damping in the case of aeroelasic vibration were not included in the calculation (e.g., Main and Jones, 2001). The black-dotted line defines the minimum threshold given by the condition $S_{c,0} > 10$. As shown in the graph, the NL-TET device with $\psi = 2.00$ satisfies the Scruton number criterion in the first three modes only, while it appears inadequate for the higher modes and for larger flexibility in the support. It is important to note that this criterion is usually valid for the first few modes of vibration while its applicability to higher ones is less acceptable; for this reason, it might still be possible to mitigate the vibrations due to aeroelastic phenomena in this last case, by supplying smaller values of damping ratio. Analogous considerations are applicable to the analytical results shown in Fig. 9b, in which the optimal damping ratio is achieved in the second mode. In this second situation the TET damper device appears more "rigid" in the higher modes and less compliant in the lower modes, showing suboptimal damping ratios in both cases.

7   Conclusions

A new passive damper device, denoted as Nonlinear Targeted-Energy-Transfer-Device (NL-TET) was studied, both analytically and numerically. A new family of "universal design curves" was derived and verified through a time-domain lumped-mass model. Numerical analyses were performed on a reference stay and subsequently extended to an existing stay, currently installed on the Fred Hartman Bridge (Houston, Texas, USA), as a first example of application, to show the adequacy of the proposed device in suppressing the vibration. Future studies will possibly consider a systematic examination of the performance in comparison with other similar passive devices for stay-cable vibration mitigation.

Acknowledgments

References

Chopra, A. K. (1995). Dynamics of structures – Theory and Application to Earthquake Engineering. 3rd ed. (2007), Prentice-Hall, Upper Saddle River (N.J.).

FHWA - Federal Highway Administration – U.S. Department of Transportation (2007). Wind-Induced Vibrations of Stay Cables. Publication No. FHWA-HRT-05-083.

Gattulli, V., and Lepidi, M. (2003). Nonlinear interactions in the planar dynamics of cable-stayed beam. *International Journal of Solids and Structures*, 40 (18), 4729-4748.

Gattulli, V., and Lepidi, M. (2003). Localization and veering in the dynamics of cable-stayed bridges. *Computer and Structures*, 85 (21-22), 1661-1678.

Giaccu, G. F., and Caracoglia, L. (2012). Effects of modelling nonlinearity in cross-ties on the dynamics of simplified in-plane cable networks. *Struct. Control Health Monit.*, 18, 348-369.

Huang, Z. H., and Jones, N. P. (2011). Damping of taut-cable systems: Effects of linear elastic spring support. *J. Eng. Mech.*, 137, 512-518.

Krenk, S. (2000). Vibrations of a taut cable with external damper. *J. Appl. Mech.*, 67(4), 772-776.

Irwin, P. A. (1997). Wind vibrations of cables on cable-stayed bridges. *Proceedings of ASCE*.

Liu, M.-Y., Zuo, D., and Jones, N. P. (2005). Deck-induced stay cable vibrations: Field observations and analytical model. *Proceedings of the 6th International Symposium of Cable Dynamics*, 175-182.

Main, J. A., and Jones, N. P. (2002). Free vibrations of a taut cable with attached damper I: Linear viscous damper. *J. Eng. Mech.*, 128(10), 1072-1081.

Pacheco, B. M., Fujino, Y., and Sulekh, A. (1993). Estimation curve for modal damping in stay cables with viscous damper. *J. Struct. Eng.*, 119(6), 1961-1979.

PTI Guide Specification (2000). Recommendations for stay cable design, testing and installation. *PTI*.

Sun, L., Shi, C., Zhou, H. M., and Cheng, W. (2004). A full-scale experiment on vibration mitigation of stay cable. *IABSE Symposium, Shanghai 2004: Metropolitan Habitats and Infrastructure*, 31-36(6).

Xu, Y. L. (2013). Wind Effects on Cable-Supported Bridges. *John Wiley and Sons*.

Vakakis, A. F. (2001). Introducing passive nonlinear energy sinks in vibrating systems. *Trans. ASME, J. Vibr. Acoust.*, 123, 324-332.

Implementation of the non-flutter design principle

Michael Styrk Andersen[1], Emrah Sahin[2], Benjamin Laustsen[2], Michael Lenius[2] and Jesper Røssel Læsø[2]

[1]Research Assistant, University of Southern Denmark, Faculty of Engineering
[2]Student, M.Sc. Eng., University of Southern Denmark, Faculty of Engineering
Corresponding author: Michael Styrk Andersen, mian@iti.sdu.dk

Abstract

The non-flutter design principle is introduced. Aerodynamically stable section model tests performed by three different research groups indicate, that flutter might be avoided if the torsional-to-vertical frequency ratio is kept below 1. A case study of a suspension bridge spanning 3.7 km with a torsional-to-vertical frequency ratio $\gamma_\omega = 0.89$ is presented. Using a multimodal flutter approach and bridge deck flutter derivatives equal to those of a thin airfoil, classical flutter was shown not to occur.

1 Introduction

The aim of building super long span bridges in the future is challenging the civil engineering community. After the catastrophic collapse of the first Tacoma Narrows in 1940, modern bridge decks are designed with increased torsional stiffness to prevent flutter and torsional divergence. The introduction of the closed box girder amplified the torsional stiffness, but an increase in span width increase the cable contribution of the stiffness compared to the bridge deck it self which tends to decrease the torsional-to-vertical frequency ratio.

The torsional-to-vertical frequency ratio, $\gamma_\omega = \frac{\omega_\alpha}{\omega_\xi}$ where ω_α and ω_ξ is the torsional and vertical natural frequencies respectively, are decisive for the critical flutter wind velocity. In traditional bridge design, this means that the required torsional stiffness of the bridge deck is increased when the span goes up, which means that the mass of the bridge deck per unit length is increased as well as the total costs, because that is roughly proportional to the mass of the bridge deck. Aerodynamic countermeasures against flutter increases the unit cost of the bridge deck as well.

Richardson (1981) demonstrated that the cost of required torsional stiffness of the bridge deck to prevent flutter, is exponential to the span of the bridge. Therefore he introduced the idea of a twin suspension bridge having a torsional-to-vertical frequency ratio below unity. Lateral cross beams were placed between the twin girders and the cable planes were located at the internal side of the girders.

The principle of decreasing the torsional frequency to the level of the vertical frequency or below has been labeled the non-flutter design principle (Dyrbye and Hansen, 1997; Johansson et al., 2013). Dyrbye and Hansen (1997) explained that for very long span suspension bridges, the torsional rigidity of a closed box girder is too small to resist flutter. In order to obtain large critical flutter wind velocities, they proposed a design in which the torsional and vertical frequencies deliberately were made identical. This concept was validated experimentally by Bartoli et al. (2009).

1.1 Experimental validation

Bartoli et al. (2009) made wind tunnel experiments with a modified Messina twin bridge section model where $\gamma_\omega = 1.00$ and proved that it was stable against flutter, which confirms the thesis of (Richardson, 1981) and (Dyrbye and Hansen, 1997).

Wind tunnel tests performed recently (Johansson et al., 2013) and (Nowicki and Flaga, 2011) reports that flutter does not occur for flat plate section models with torsional-to-vertical frequency ratios below

1. Nowicki and Flaga (2011) reported, however, that this was not the case for bluff body bridge deck sections. Torsional divergence was not reported.

The aerodynamic derivatives and structural damping may be decisive for the limits of γ_ω, where the non-flutter frequency bandwidth is distinguished.

From the wind tunnel tests on section models, with frequency ratios close to or below unity, reported in the literature, there are no general value of the torsional-to-vertical frequency ratio γ_ω applicable to all bridge decks, which guarantees stability against violent flutter, because this limit depends on the aerodynamic derivatives of the section model.

The section model tests, reported in the literature, that do not show any sign of aerodynamic instability is:

- A single flat plate section model with a height-to-width ratio $h : b = 1 : 10$ and $\gamma_\omega = [0.71, 0.88]$ (Johansson et al., 2013)

- A single flat plate section model with a height-to-width ratio $h : b = 1 : 22$ and $\gamma_\omega = [0.81, 0.92]$ (Nowicki and Flaga, 2011)

- A single flat plate section model with a height-to-width ratio $h : b = 1 : 22$ and $\gamma_\omega = 1.08$ with increased structural damping (Nowicki and Flaga, 2011)

- A modified Messina Bridge section model (Twin boxes with curved shapes) and $\gamma_\omega = 1.00$ (Bartoli et al., 2008)

In the above mentioned wind tunnel tests, decreasing torsional frequencies have been reported due to increasing mean wind velocity. The decrease in torsional frequency is believed to increase the frequency separation between torsional and vertical modes, and thus, at least for the above mentioned cross section shapes, prevents the onset of classical coupled flutter.

Adapting the Theodorsen thin airfoil flutter derivatives (Theodorsen, 1934), there are no critical flutter wind velocity below a certain threshold, at $\gamma_\omega \approx 1.1$ (Dyrbye and Hansen, 1997). But the aerodynamically stable results of (Bartoli et al., 2008; Nowicki and Flaga, 2011; Johansson et al., 2013) with section models having torsional-to-vertical frequency ratios in the range $0.71 \leq \gamma_\omega \leq 1.08$ indicates that further experiments are needed to clarify the influence of $\gamma_\omega \leq 1.1$ for real bridge deck flutter derivatives.
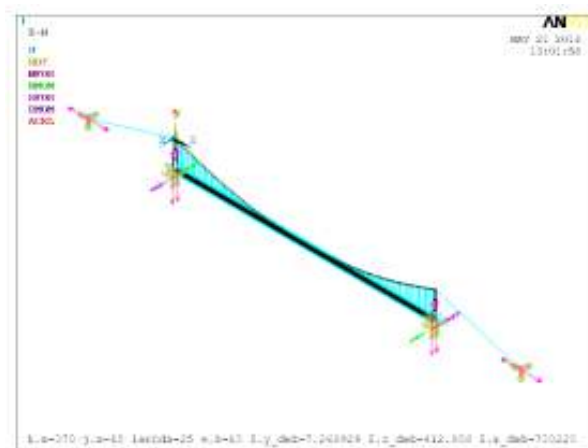
Figure 1. Finite element model used in a case study of a suspension bridge spanning 3.7 km. Various cross section properties are presented in Section 3, Table 2.

1.2   Present Study

In the present study, the aerodynamic coupling in classical bi-modal coupled flutter between pure vertical and torsional modes are investigated in section 2.1. The probability of classical bi-modal coupled flutter between all pure vertical and torsional modes are derived mathematically, eg. coupling between the second symmetric torsional mode with the first symmetric vertical mode. These results are verified in a case study of a suspension bridge design, illustrated in Figure 1, presented in Section 3.

It is, however, questionable whether flutter will occur between other modes than pure vertical and pure torsional modes. The presence of lateral torsional modes blurs the picture. In order to answer this question, a multimodal analysis with contributions of the first 20 bridge deck mode shapes is performed to reveal all possible flutter mechanisms in Section 3.3.

2   Probability of mode shape coupling

It is widely recognized that coupling of torsional and vertical mode shapes is considered to occur only between symmetric and antisymmetric pairs of mode shapes. But considering the structural mode shapes of the bridge deck as sine functions, it is seen that coupling is restricted only to occur between vertical and torsional mode shapes of the same order, due to the orthogonality of sine functions. An exception to this is coupling between the first and second symmetric mode shapes, which is described as the sum of two sines (Bleich et al., 1950). However, the product of the non dimensional mode shape coupling constants given in Equation (2) may become very close to zero.

The modes of a suspended bridge deck are strongly linked to the two main cable system modes. If the main cables oscillate in phase, pure vertical bending of the bridge deck will take place, while pure torsional oscillations of the bridge deck will take place when the main cables oscillate out of phase. (Bleich et al., 1950; Gimsing and Georgakis, 2012)

It is assumed that the mass and mass moment of inertia are uniformly distributed along the bridge deck axis. For super long span bridges the stiffness of the bridge deck itself is small compared to the stiffness provided by the cable suspension system. (Gimsing and Georgakis, 2012)

The vertical and torsional bridge deck mode shapes $\xi_n(y)$ and $\alpha_m(y)$ of the main span of a suspension bridge, has been described approximately by simple sine functions in the literature (Bleich et al., 1950), except the first and second symmetric modes, which can be described approximately as the sum of two sine functions. The former is considered below in Section 2.1 while the latter is treated in Section 2.2.

2.1   Mode coupling probability for antisymmetric and higher symmetric modes

The assumption of pure sine functions has been adapted in Equation (1) to show the tendency of mode coupling.

The bridge deck axis is denoted y. L is the main span width while n and m are the number of half-waves present in the respective mode shapes, where heave and pitch are denoted ξ and α respectively.

The natural frequencies ω_{ξ_n} and ω_{α_m} do not necessarily ascend according to the index n or m.

$$\xi_n(y) = \sin \frac{n\pi y}{L}, n \in N^+ \setminus \{1,3\} \tag{1a}$$

$$\alpha_m(y) = \sin \frac{m\pi y}{L}, m \in N^+ \setminus \{1,3\} \tag{1b}$$

The first 6 torsional and vertical mode shapes considered, are illustrated in Figure 2.

The similarity between mode shapes is described by the product of their mode shape coupling coefficients $c_{\xi,n}$ and $c_{\alpha,m}$ given in Equation (2). If the vertical bending mode shape $\xi_n(y)$ and the torsional mode shape $\alpha_m(y)$ has similar deflection curves along the bridge deck, the product $c_{\xi,n}c_{\alpha,m} = 1$. The bridge may be prone to classical flutter if $\frac{\omega_{\alpha_m}}{\omega_{\xi_n}} > 1$, but if $c_{\xi,n}c_{\alpha,m} = 0$ coupled flutter does not arise.

$$c_{\xi_n} = \frac{\int_0^L \xi_n(y)\alpha_m(y)\,dy}{\int_0^L \xi_n^2(y)\,dy} \tag{2a}$$
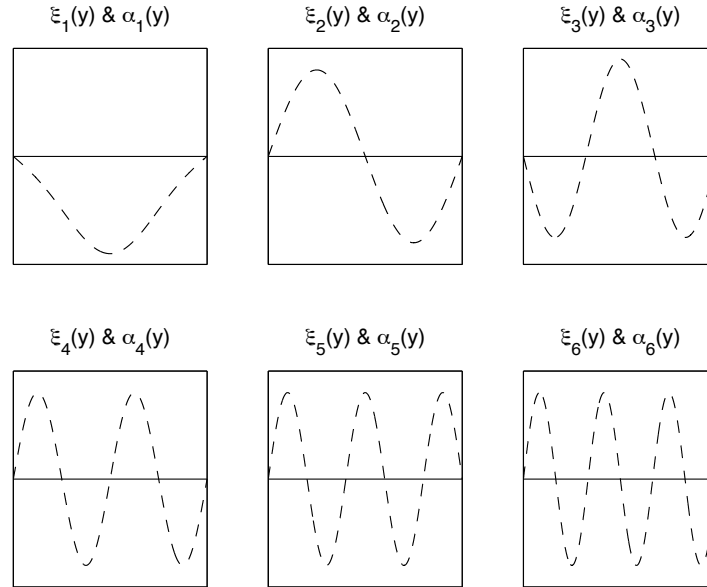
Figure 2. Vertical and torsional bridge deck mode shapes of the main span

$$c_{\alpha_m} = \frac{\int_0^L \xi_n(y)\alpha_m(y)\,dy}{\int_0^L \alpha_m^2(y)\,dy} \tag{2b}$$

The mode shape functions $\xi_n(y)$ and $\alpha_m(y)$ are mutually orthogonal on the interval $0 \leq y \leq L$. This means that the product of the mode shape coupling coefficients $c_{\xi,n}c_{\alpha,m} = 0$ if $n \neq m$, since

$$\int_0^L \sin\frac{n\pi y}{L}\sin\frac{m\pi y}{L}\,dy = \begin{cases} L/2 & \text{if } n = m \\ 0 & \text{otherwise} \end{cases} \tag{3}$$

2.2 Mode coupling probability for lower symmetric modes

For the first and second symmetric vertical and torsional mode shapes, where n and m equals 1 or 3, the curvature in Equation (4), along the bridge deck is defined as the sum of two sine terms.

$$\xi_n(y) = \sin\frac{\pi y}{L} + a_3\sin\frac{3\pi y}{L}, n = \{1, 3\} \tag{4a}$$

$$\alpha_m(y) = \sin\frac{\pi y}{L} + a_3\sin\frac{3\pi y}{L}, m = \{1, 3\} \tag{4b}$$

The coefficient a_3 depends on span width, side span width, girder stiffness, mass distribution and cable plane eccentricity.

The mode shape coupling coefficients between first ($n = 1$) symmetric vertical bending mode and second ($m = 3$) symmetric torsional mode must be analyzed in detail, because it is possible that $\gamma_\omega > 1$, even though the first symmetric vertical and torsional mode shape has $\gamma_\omega < 1$.

3   Case study: A concept for the Sognefjord Bridge

A twin suspension bridge with one central span of 3.7 km and a cable sag of 370 m has been modeled and analyzed with finite element software ANSYS Mechanical APDL, as illustrated in Figure 1.

The bridge deck is pinned to the pylons, but free at mid span. The cables are fixed at their ends and pinned to the top of the pylons. Three bracings connects the pylon legs 10, 130 and 250 meters from the

top level of the pylons. The pylon legs are fixed to the ground.

The cable cross sectional area has been estimated to withstand dead- and live load. The mechanical properties of the main cable and the hangers are given in (Gimsing and Georgakis, 2012). The total mass of the twin bridge cross section are $m = 14.57t/m$ while the mass moment of inertia depends heavily on the mass eccentricity between the cross section center of gravity and the local center of gravity of the twin boxes. Important cross section structural properties of the elements used in the model are given in Table 1, while different deck configurations are presented in Table 2. In the present case study, it was assumed that the cross beams between the twin boxes were infinitely stiff and their mass was neglected.

Table 1. Cross section structural properties in the finite element model

	Cross section structural properties					
	E	I_y	I_z	I_v	m	A
	$[GPa]$	$[m^4/m]$	$[m^4/m]$	$[m^4/m]$	$[t/m]$	m^2
Main cable	205	-	-	-	13.164	1.54
Hangers	180	-	-	-	0.05	0.005
Pylon legs	210	334	118	325	68.923	8.78
Pylon bracings	210	115	42	98	24.311	3.10

It is evident that the key to decrease γ_ω, is to decrease the cable eccentricity e_k compared to the mass eccentricity e_m. A twin bridge design, with the bridge deck placed external to the cable planes, as illustrated in Figure 3, allows this construction (Bartoli et al., 2008; Richardson, 1981).

Several models have been evaluated for their frequency ratios between vertical and torsional modes, of which three is presented in Table 2.

Table 2. Bridge deck cross section structural properties for three of bridge deck configurations

Deck	γ_ω	e_m	e_k	m	I	E	G	I_y	I_z	I_v
	-	$[m]$	$[m]$	$[t/m]$	$[t \cdot m^2/m]$	$[GPa]$	$[GPa]$	$[m^4/m]$	$[m^4/m]$	$[m^4/m]$
(a)	1.4	11.5	5	14.57	3101	210	81	7.27	147.74	2.08
(b)	0.89	20	10	14.57	7002	210	81	7.27	412.81	2.08
(c)	0.92	40	30	14.57	24488	210	81	7.27	1600.81	2.08

On the basis of these, it has been feasible to invert the natural frequencies with the following parameters: $e_k = 10$ m and $e_m = 20$ m, ie. bridge deck (b) in Table 2. The still air modal analysis of bridge deck (b) is presented in Section 3.1. Bi-modal coupling analysis of the vertical and torsional mode shapes and their respective frequency ratios of this model are presented in Section 3.2 while a multimodal analysis is presented in Section 3.3.
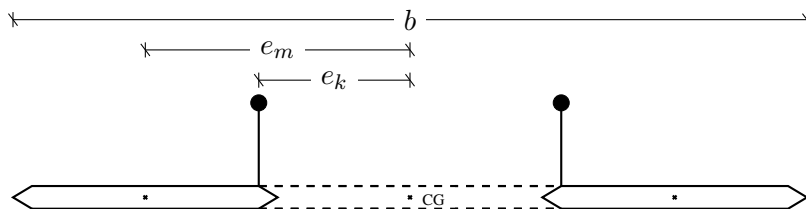
Figure 3. Cross section design principle

3.1 Global modal analysis

Prior to the modal analysis, the static force equilibrium equations were solved and the stiffness effects of deflection and internal forces due to dead load of the bridge was taken into account. The eigenvalue problem of the mass- and stiffness matrices were solved using block Lanczos algorithm.

The results of the global modal analysis for the first 20 modes are listed in Table 3, which fairly illustrate the incidence of the mode shape variations. Each mode shape is plotted along the bridge deck axis in the vertical and the horizontal plane.

Table 3. Modal analysis. The natural modes are listed according to their natural frequency ω in ascending order and their mode shapes are plotted and described where S: Symmetric. A:Anti-symmetric. L: Lateral. V: Vertical. T:Torsional.

			Modal analysis		
ID	ω $[Rad/s]$	f $[Hz]$	Description	Vertical plane	Horizontal plane
1	0.194	0.031	1SLT		
2	0.328	0.052	1AT		
3	0.369	0.059	1AV		
4	0.407	0.065	1ALT		
5	0.412	0.066	1ST		
6	0.463	0.074	Cables		
7	0.484	0.077	1SV		
8	0.519	0.083	Cables		
9	0.542	0.086	2ST		
10	0.591	0.094	2ALT		
11	0.603	0.096	LT + Pylons + Cables		
12	0.647	0.103	2SV		
13	0.651	0.104	2AT		
14	0.672	0.107	2SLT		
15	0.724	0.115	2AV		
16	0.797	0.127	Cables		
17	0.819	0.130	3ST		
18	0.86	0.137	LT + Pylons + Cables		
19	0.917	0.146	LT + Pylons + Cables		
20	0.919	0.146	3SV		

3.2 Bi-modal coupling coefficients

Selected results of the modal analysis are presented in Table 4 for the first five torsional and vertical mode shapes. The ID refers to Table 3, while α_m and ξ_n is the pitching and heaving mode where m and n is the number of half waves.

The natural frequency of the vertical mode shapes are higher than the corresponding torsional mode shapes, which is opposite traditional bridge design, ie. long span suspension bridges in service today.

Only mode shapes with dominating vertical displacements or torsional rotation has been selected. Lateral-torsional-bending mode shapes of the bridge deck, were observed in the modal analysis, but not included in the present bi-modal mode coupling analysis. The influence of these modes are considered in the multimodal analysis in Section 3.3.

Table 4. The five lowest pure torsional and vertical mode shapes of the bridge deck
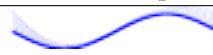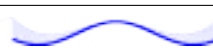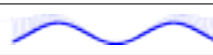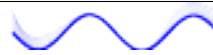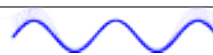
Torsional mode shapes (a)				Vertical mode shapes (b)			
ID	α_m	ω_{α_m}	Mode shape	ID	ξ_n	ω_{ξ_n}	Mode shape
2	α_2	0.328		3	ξ_2	0.369	
5	α_1	0.412		7	ξ_1	0.484	
9	α_3	0.542		12	ξ_3	0.647	
13	α_4	0.651		15	ξ_4	0.724	
17	α_5	0.819		20	ξ_5	0.919	

Table 5. Frequency ratios and mode shape coupling constants

Torsional-to-vertical frequency ratios (a) $\gamma_\omega = \dfrac{\omega_{\alpha_m}}{\omega_{\xi_n}}$					Mode shape coupling constants (b) $c_{\xi_n} c_{\alpha_m}$					
	ξ_2	ξ_1	ξ_3	ξ_4	ξ_5		ξ_2	ξ_1	ξ_3	ξ_4	ξ_5
α_2	**0.88**	0.68	0.51	0.45	0.36	α_2	**1**	0	0	0	0
α_1	1.11	**0.9**	0.64	0.57	0.45	α_1	0	**0.96**	0.05	0	0
α_3	1.47	1.12	**0.89**	0.75	0.59	α_3	0	0.04	**0.95**	0	0
α_4	1.76	1.34	1.01	**0.85**	0.71	α_4	0	0	0	**1**	0
α_5	2.22	1.69	1.27	1.13	**0.84**	α_5	0	0	0	0	**1**

From Table 4 and 5 it is seen that if the torsional-to-vertical frequency $\gamma_\omega > 1$, the mode shape coupling constants $c_{\xi_n} c_{\alpha_m} = 0$, except for the second torsional symmetric mode α_3 combined with the first vertical symmetric mode ξ_1, which has a mode shape coupling constant $c_{\xi_1} c_{\alpha_3} = 0.04$ and a torsional-to-vertical frequency ratio $\gamma_\omega = 1.12$. The root curves of the flutter determinant for this bi-modal combination is plotted in Figure 5 (b).

The numerical results of the case study verifies the theoretical analysis in Section 2.

3.3   Multimodal flutter analysis

The multimodal flutter approach developed by (Jain et al., 1996) has been implemented for the first 20 modes in order to estimate flutter instabilities of bridge model (b) presented in Section 3, Table 2.

The bridge deck flutter derivatives $A_1^*(K)$-$A_4^*(K)$ and $H_1^*(K)$-$H_4^*(K)$ where the non-dimensional frequency, $K = \frac{b\omega}{U}$ where ω is the circular frequency of the oscillation of the bridge deck at the wind velocity, U, are replaced with those of a thin airfoil and follows Dyrbye and Hansen (1997, page 151). The thin airfoil approximation of the bridge deck is an extreme assumption. The shape of the bridge deck in the case study is actually unknown, which complicate the choice of valid flutter derivatives. The lateral bridge deck flutter derivatives $P_1^*(K)$-$P_6^*(K)$, $A_5^*(K)$-$A_6^*(K)$ and $H_5^*(K)$-$H_6^*(K)$ are calculated according to quasi-steady theory, where the static drag, lift and moment coefficients are $c_d = 0.32$, $c_l = 0.0942$ and $c_m = 0.0104$ respectively. The slope of the lift curve at $\alpha = 0$ are considered flat, ie. $dc_d/d\alpha = 0$ (Chen et al., 2000).

The critical flutter wind velocity, U_{cr} is identified at the intersection point between a real and an imaginary root curve. Figure 4 plots real and imaginary root curves for the first 20 modes of bridge deck model (b), where the bridge deck width, $b = 60$ m. The areas highlighted in red on the plots corresponds to wind velocities $U \leq 100 m/s$. The root curves of mode 1, 2 and 3 becomes very close at low non-dimensional frequencies, but no intersection occurs for values of $0.02 \leq K$. The lowest frequency at $K = 0.02$ is $\omega = 0.02611 rad/s$ for the imaginary part of the root curve of mode 2, which corresponds to a full scale wind velocity $U = \frac{b\omega}{K} = 78.3 m/s$.

At a very high wind velocity, however, coupled flutter with participation of the second symmetric torsional mode and an antisymmetric lateral mode, appear. The still air mode shapes corresponds to mode 9 and 10, given in Table 3. The nature of this particular flutter instability mechanism is very rare. The intersection point between the root curves of mode 9 and 10 is found at $K = 0.025$ and $\omega = 0.46$ rad/s in Figure 4 (b), corresponding to a critical flutter wind velocity $U_{cr} = \frac{b\omega}{K} = 1104 m/s$, which is obviously beyond the scope of aerodynamic design of civil engineering structures.

3.4   Bi-modal flutter analysis

Considering the motion-induced wind load for the first antisymmetric modes α_2 and ξ_2 only, reveals that torsional flutter occur at a critical flutter wind velocity $U_{cr} = 56.7 m/s$, in bridge model (a), where the bridge deck width is $b = 26m$. For bridge model (b), no flutter instabilities were found between any bi-modal combinations of the first 20 modes. Figure 5 plots the root curves of α_2 and ξ_2 for bridge model (a) and (b) respectively.
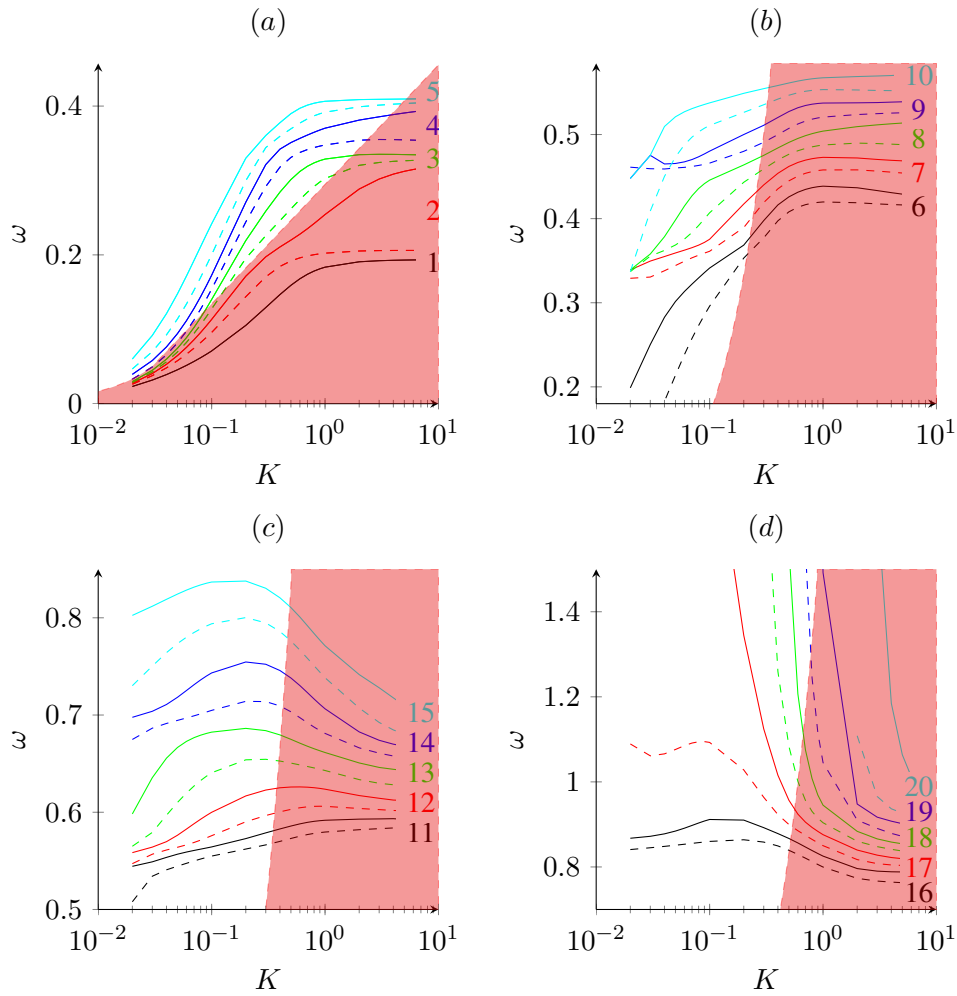
Figure 4. Multimodal flutter root curves of bridge model (b) presented in Section 3, Table 2. The cyclic frequency of oscillation ω in rad/s is plotted against the reduced frequency $K = \frac{b\omega}{U}$. Mode 1 to 5 is plotted in sub plot (a), mode 6 to 10 in sub plot (b), mode 11 to 15 in sub plot (c) and mode 16 to 20 is plotted in sub plot (d).
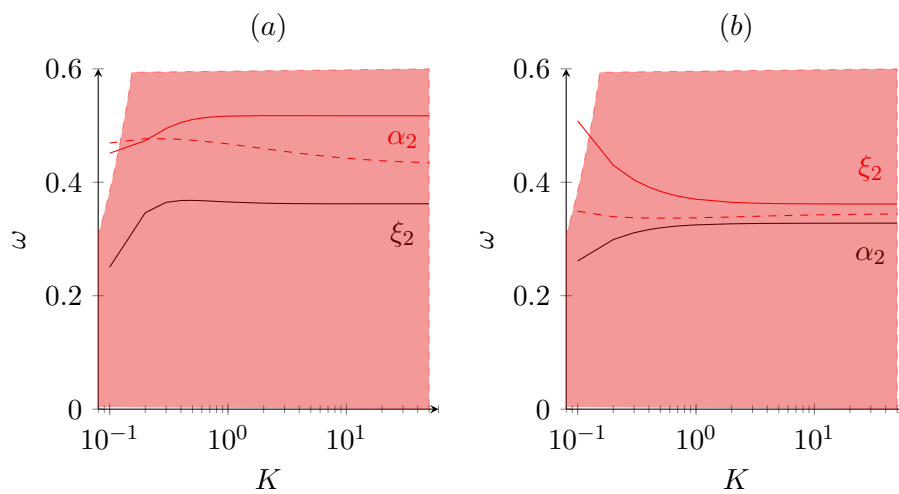
Figure 5. Bi-modal flutter root curves of the first antisymmetric vertical (α_2) and antisymmetric torsional (ξ_2) modes of bridge model (a) and (b) presented in section 3 Table 2, with bridge deck width $b = 26m$. Flutter occur in model (a) at $(K, \omega) = (0.22, 0.48)$ resulting in a critical flutter wind velocity $U_{cr} = 56.7m/s$.

4 Conclusion

It is possible to design a suspension bridge with a torsional-to-vertical frequency ratio below 1. Bimodal coupled flutter between higher torsional modes with lower vertical modes, where their respective torsional-to-vertical frequency ratio will be above 1, is avoided, because the mode shape coupling constants is zero or at least very close to zero.

A multimodal flutter analysis, considering the first 20 modes, revealed solely flutter mechanisms at very high wind velocities. The lowest flutter velocity was $U_{cr} = 1104$ m/s. for a lateral-torsional mode coupled with the second symmetric torsional mode.

Further studies are needed to clarify the influence of $\gamma_\omega \leq 1.1$ on twin bridges and the implementation of real bridge deck flutter derivatives in a multimodal flutter analysis of a suspension bridge.

5 Acknowledgments

6 References

References

Bartoli, G., D'Asdia, P., Febo, S., Mannini, C., Noe, S., and Procino, L. (2009). Innovative configurations for long-span suspension bridges. *Proceedings of the 5th European and African Conference on Wind Engineering*. Florence, Italy.

Bartoli, Gianni, D'Asdia, Piero, Febo, Sofia, Mannini, Claudio, Past, Stefano, and Procino, Lorenzo (2008). Innovative Solutions for long-span suspension bridges. *BBAA VI International Colloquium on: Bluff Bodies Aerodynamics Applications*.

Bleich, Freidrich, McCullough, C. B., Rosecrans, Richard, and Vincent, George S. (1950). *The mathematical theory of vibration in suspension bridges*. Department of commerce bureau of public roads.

Chen, Xinzhong, Matsumoto, Masaru, and Kareem, Ahsan (2000). Aerodynamic Coupling Effects on Flutter and Buffeting of Bridges. *Journal of Engineering Mechanics* **126**, pp. 17–26.

Dyrbye, Claus and Hansen, Svend Ole (1997). *Wind loads on Structures*. Wiley.

Gimsing, N. J. and Georgakis, C. T. (2012). *Cable Supported Bridges*. Third edition. Wiley.

Jain, A., Jones, N., and Scanlan, R. (1996). Coupled Flutter and Buffeting Analysis of Long-Span Bridges. *Journal of Structural Engineering* **122**, pp. 716–725.

Johansson, J., Andersen, M.S., and Øvre, M.S. (2013). Non-flutter design principle for long span bridges. *Proceedings of the Eighth Asia-Pacific Conference on Wind Engineering*.

Nowicki, T. and Flaga, A. (2011). Relation between shape and the phenomenon of flutter for bridge deck-like bluff bodies. *Archives of Mechanics* **63**.2, pp. 201 –220.

Richardson, J. R. (1981). The development of the concept of the twin suspension bridge. *NMI R125*.

Theodorsen, T. (1934). General theory of aerodynamic instability and the mechanism of flutter. *NACA Report* **496**, pp. 291–311.

Sectional load characteristics of a dry inclined helically filleted cable

Heidi Christiansen[1], Jasna B. Jakobsen[1], John H.G. Macdonald[2], Guy L. Larose[3] and Harold Bosch[4]

[1]Department of Mechanical and Structural Engineering and Material Science, University of Stavanger, Norway

[2]Department of Civil Engineering, University of Bristol, UK

[3]National Research Council Canada, 1200 Montreal Road, Ottawa, Ontario, Canada

[4]Aerodynamics Laboratory, Federal Highway Administration, McLean, Virginia, USA

Corresponding author: Heidi Christiansen, heidi.christiansen@uis.no

Abstract

An experimental study of an inclined stay cable with helical fillets in dry conditions carried out at the National Research Council Canada (NRC), revealed that a dry inclined helically filleted cable can experience wind-induced vibrations at a cable inclination angle of $60°$. The experiments, which were performed on a 1:1 scale cable model, furthermore showed that the occurrence of vibrations was highly dependent on the cable rotation about the cable's longitudinal axis, (Larose, 2013). The observation of vibrations of a helically filleted dry cable has spurred off the present investigation into the details of the loading characteristics of a cable with helical fillets in smooth flow at high Reynold numbers. The influence of the angular position of the helical fillet on the surface pressures and mean aerodynamic force coefficients, is presented along with time-dependent force coefficients showing that flow state jumps occur for an inclined helically filleted cable.

1 Introduction

The high-density polyethylene (HDPE) tubes on stay cables of any major cable-stayed bridge erected nowadays, are manufactured with a surface modification. This is either in the shape of a pattern-indented surface mostly used in Asia, or through the application of helical fillets. The first use of helical fillets was on the Normandy bridge in France as a mean to combat rain-wind induced vibrations. Initial wind-tunnel experiments in precipitation conditions were undertaken at CSTB, Nantes, by (Flamand, 1995), where an optimal fillet design was determined for the given cable diameter. Until recently, however, there has not been any records of dry inclined vibrations. In a study carried out at NRC for a helically filleted
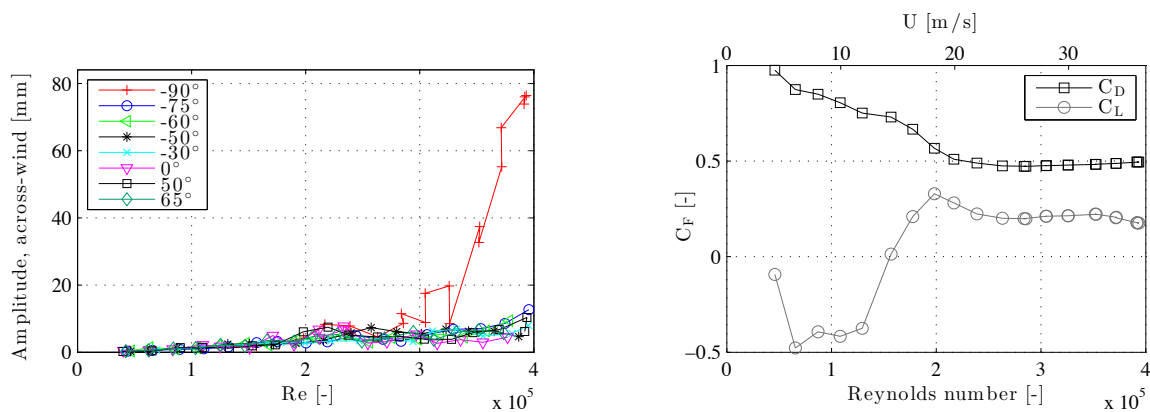
Figure 1. Amplitude in sway for different axial cable rotations (a) and force coefficients for the cable rotation of $-90°$ from mean of surface pressure measurements of the four pressure tap rings (b).

cable with a 60° inclination angle (Larose, 2013), vibrations of the cable model were observed, but only for a -90° rotation of the cable about its axis, yielding a dependency on surface irregularities, see Figure 1(a). The vibrations occurred in the supercritical Reynolds number region, i.e. where the drag and lift coefficients are nearly constant. Dry inclined vibrations of helically filleted cables have also been reported by (Kleissl, 2013), although at lower Reynolds numbers.

Throughout the years, many studies have been carried out considering the effects of adding a helical application to a circular cylinder, and a more "simple" single span-wise surface perturbation which may serve as a reference for the former. Studies have already shown a clear effect of the shape and size of the perturbation on the flow for both applications, and for the single perturbation in particular the angular position as well, (Igarashi, 1986) and (Ekmecki, 2010). Besides the size and shape, the number of protrusions and the pitch length for helical applications are governing parameters for the helical application, (Zdravkovich, 1981). No design specification exists for helical fillets and each cable manufacturer has therefore developed their own design resulting in different flow structures. With a helical fillet design representative of the current designs in use, this paper aims to highlight flow features important in the understanding of the flow around an inclined helically filleted cable.

2   Wind tunnel tests

The tests were conducted in the 3 m x 6 m x 12.2 m Propulsion and Icing Wind Tunnel at NRC which is an open-circuit tunnel. The experiments were performed on a 1:1 scale cable model with a mean diameter of 161.7 mm and a length of 6.7 m, only 6.1 m exposed to the flow. The section cable model was composed of a central steel core covered with a high density polyethylene (HDPE) tube obtained from a bridge construction site. The mass per unit exposed length of the cable model was equivalent to 66.7 kg/m. The fillet itself had a rectangular cross-section, 2.3 mm thick and 2.4 mm wide and was fixed to the surface of the model with double sided tape. It was installed as a double parallel helix with a pitch of 520 mm and a helix angle of 44.5°. Each end of the cable was supported on four springs allowing the cable to move in two orthogonal planes; along-wind motion and across-wind motion. The model aspect ratio was approximately 38 and the turbulence intensity $I_u \approx 0.5$ %. Both static and dynamic tests were undertaken for the cable with helical fillets, and as a reference, dynamic tests only were performed on the same cable without the fillet, i.e. a smooth cable surface.
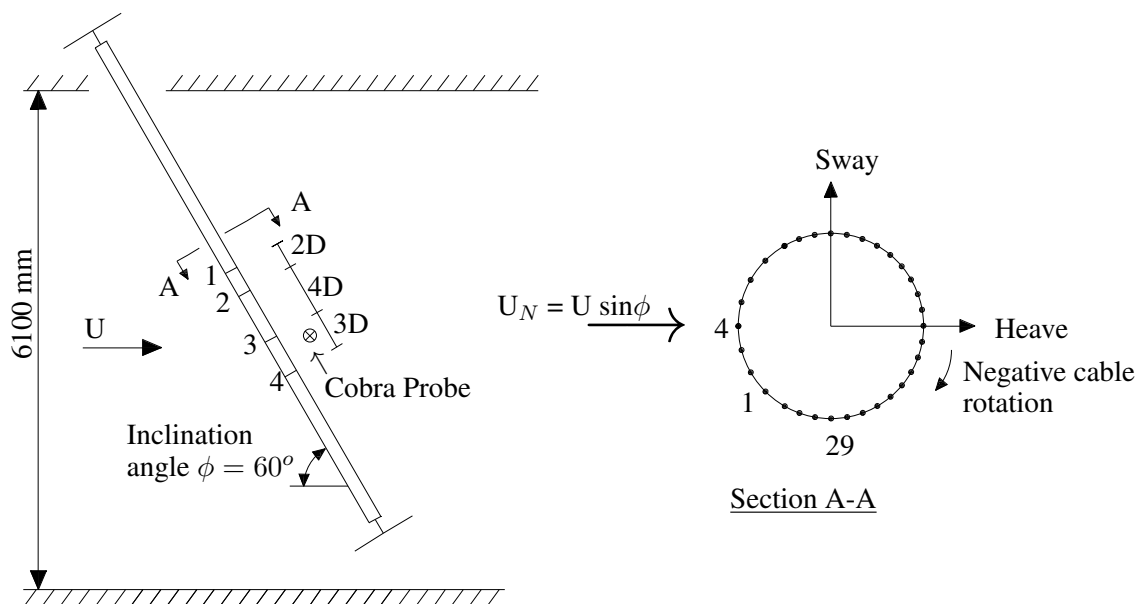
Figure 2. Cable geometry.

To measure the surface pressure distribution, four circumferential rings each consisting of 32 pressure taps were distributed on the model, see Figure 2. The taps were connected to four electronic pressure scanners sampling the signals at a frequency rate of 312.5 Hz for a time period of 90 s. No blockage correction is applied to the force coefficients because of a low blockage ratio of 5 %. Two laser displacement transducers were installed at each end of the cable to measure the sway and heave motion. Outdoor wind conditions and upwind flow conditions were recorded in terms of e.g. temperature and humidity. A Cobra Probe was installed in front of the cable and another in the cable wake to measure the flow characteristics. Measuring the outside diameter of the HDPE tube at every 10° of azimuth at the four rings, revealed that the tube was deviating from the mean circular shape by 1.3 mm at maximum (i.e. 1 % of the cable diameter) with the deviations being mostly consistent along the cable length. Assuming that the deformations were symmetric with respect to a circle, the local shapes are as shown in Figure 3, scaled up for visibility. Ring 2-4 are similar whereas ring 1 deviates.
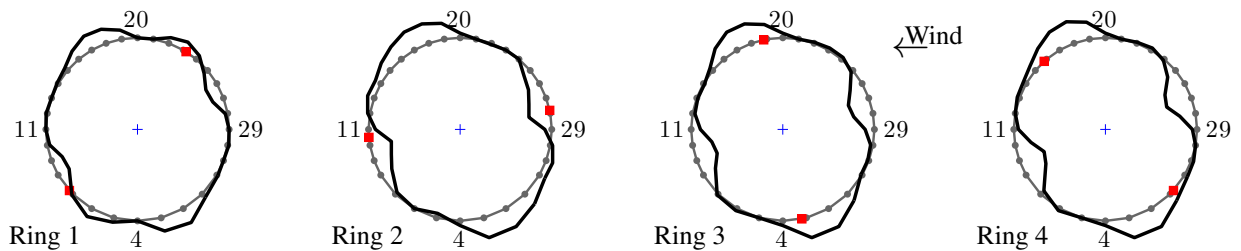
Figure 3. Enlarged cable surface deviations shown for a cable rotation of -90°. Based on diameter measurements of the HDPE-tube with the deformations assumed to be symmetric with respect to a circle. The markers indicate the fillet locations, the upper being nearly normal to the flow.

Reynolds number is in the following based on the oncoming wind speed U, and the drag C_D and lift coefficient C_L are defined as the components normal to the cable axis.

3   Load characteristics

The development of the mean force coefficient values with respect to Reynolds number of the four pressure tap rings are presented in Figure 4 for the cable rotation -90°. The drag coefficient depicts a slow transition from the subcritical to the supercritical flow state and settles at a mean value of 0.5. The lift coefficient is constantly non-zero, which is due to the asymmetry introduced by the helical fillets for an inclined cable, where one fillet is nearly aligned with the flow, the 'smooth' cable side, and the other is nearly normal to the flow, the 'rough' cable side. This yields different flow phenomena on the two sides and surface oil visualisations by (Kleissl, 2012) depicts this asymmetry where separation lines
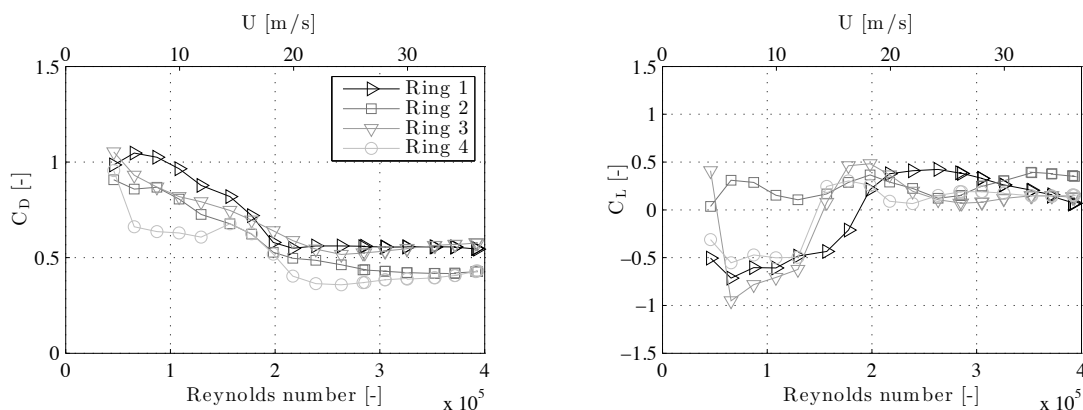
Figure 4. Drag coefficient (a) and lift coefficient (b) at the four rings for the cable rotation of $-90°$.

are different for the two opposing cable sides. The lift coefficient is negative in the subcritical Reynolds number region for ring 1, 3 and 4 and shifts sign between Re=$1.3 - 2 \cdot 10^5$, while it remains positive over the whole Reynolds number range for ring 2. This will all be looked further into.

3.1 Surface pressures and fluctuations

Surface pressure distributions and their fluctuations showing the influence of the angular position of the helical fillets, are depicted in Figure 5 and 6 for three different Reynold numbers; $1.3 \cdot 10^5$, where the lift coefficient is negative for ring 1, 3 and 4, $1.8 \cdot 10^5$ in the lift coefficient 'shift' region and $3.9 \cdot 10^5$ in the supercritical region. Surface pressure values C_p (black lines) are given on the left axis and surface pressure fluctuations (grey lines) on the right axis. The mean stagnation point is the starting point at $0°$. The rings are shown with respect to increasing value of the angular position of the fillet nearly normal to the flow, so that $0\text{-}180°$ shows the rough cable side and $180 - 360°$ the smooth cable side. The angular positions of the helical fillets are listed on Figure 6, where $\theta_\perp$ denotes the helical fillet nearly normal to the flow and $\theta_\parallel$ the helical fillet nearly aligned with the flow. It is noted that the helical fillet location at
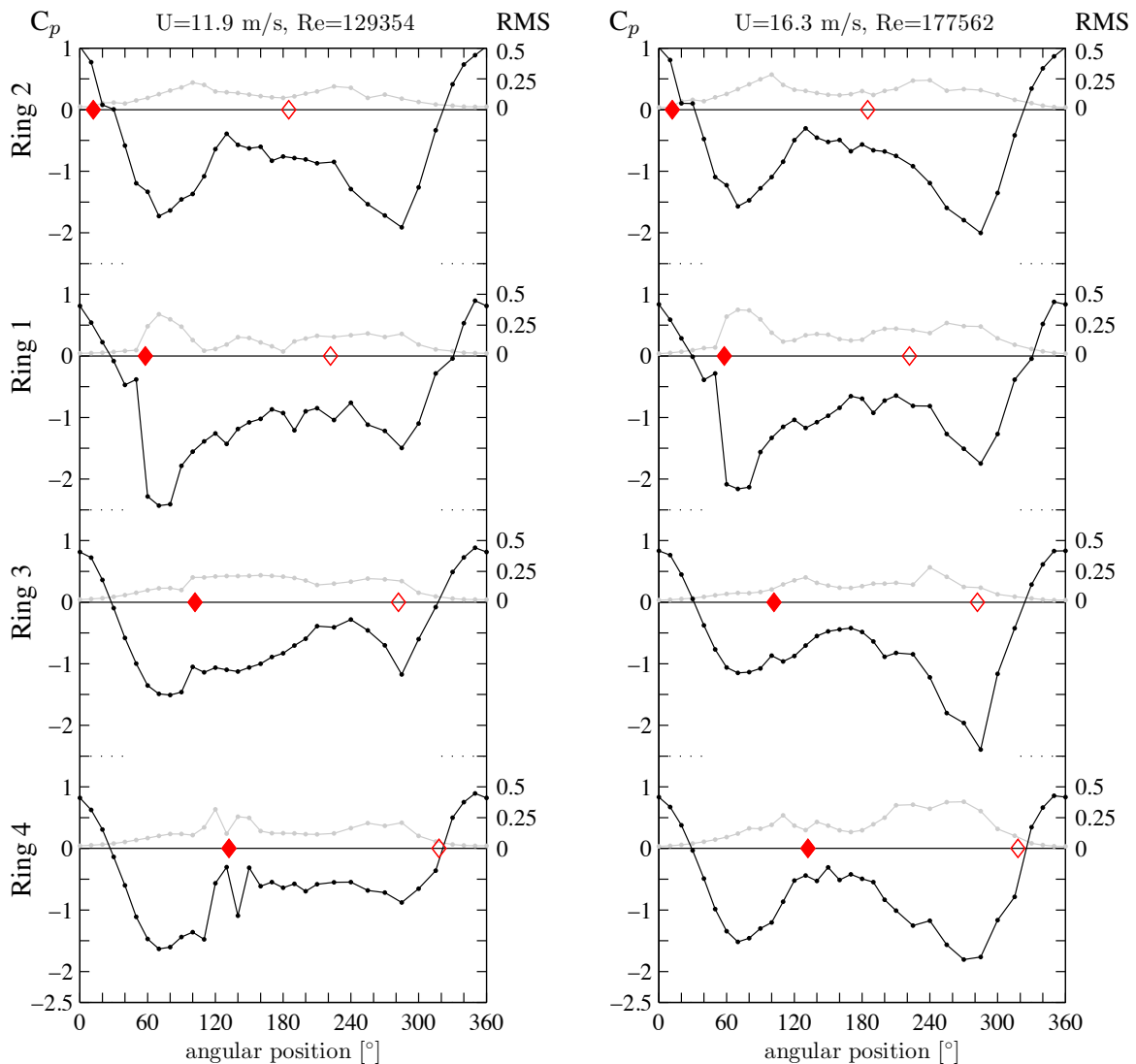
Figure 5. Mean pressure distributions and RMS of pressures for the helically filleted cable in dynamic tests at U=11.9 m/s (a) and U=16.3 m/s (b) for the four rings at the cable rotation of $-90°$. Angular position of $0°$ corresponds to the mean stagnation point. Black lines: C_p, grey lines: RMS, ◆: fillet normal to flow, ◇: fillet aligned with flow.

ring 1 is not symmetrical deviating with 16°, which proved necessary in order to avoid a pressure tap. Using the nomenclature from Zdravcovich, it is recalled that TrBL1 for a smooth cylinder normal to flow represents the single bubble regime, occurring in the critical Reynolds number region, and TrBL2 is the two-bubble regime, occurring in the supercritical Reynolds number region. The flow transition states for a smooth inclined cable is not revised here, but reference is made to (Jakobsen, 2012) where a thorough description is provided for a cable inclined 60° to the flow as in the current case.
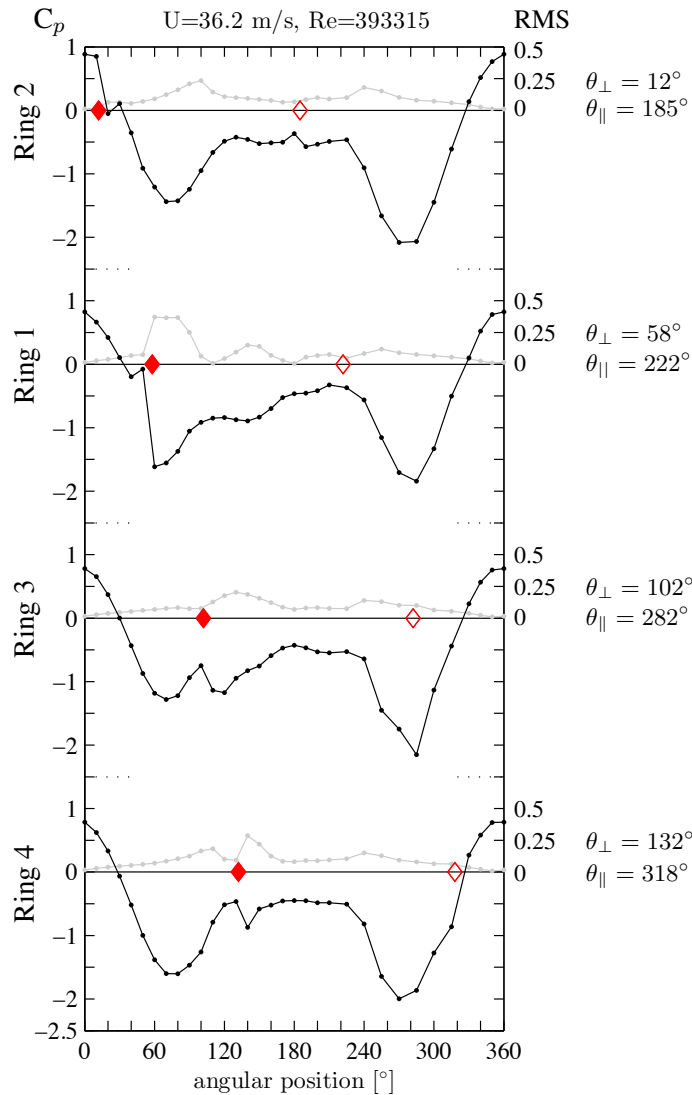
Figure 6. Mean pressure distributions and RMS of pressures for the helically filleted cable in dynamic tests at U=36.2 m/s for the four rings at the cable rotation of −90°. Angular position of 0° corresponds to the mean stagnation point. Black lines: C_p, grey lines: RMS, ◆: fillet normal to flow, ◇: fillet aligned with flow.

Observing first the smooth cable side, the flow seems nearly unaffected by the presence of the helical fillet nearly aligned with the flow at all Reynolds numbers. Only a minor effect appears for ring 3 at a helical fillet position of $\theta_\parallel = 282°$. At Re=1.3·10^5, a bubble has developed on the smooth cable side at ring 2, whereas the remaining rings are in a subcritical state. As the Reynolds number increases, the boundary layer transition at the rings resemble that of a smooth cylinder as bubbles are formed. Focusing now on the rough cable side, a change in the surface pressure as a function of the angular position of the helical fillet normal to flow is seen, but without any significant difference for varying Reynolds numbers. The flow on the rough cable side is thus controlled by the helical fillet nearly normal to the flow, whereas the smooth cable side experiences a Reynolds number dependency. It is though not said that the smooth

side is unaffected by the presence of the helical fillet. Studies by (Ekmecki, 2010) showed for example that a single wire along a cylinder normal to flow has global consequences on the flow.

The behaviour described above explains the shift seen for the lift coefficient in Figure 4 for ring 1, 3 and 4, so that the lift is directed towards the rough cable side at low Reynold numbers, where the flow is controlled by the helical fillets, but as the boundary layer on the smooth cable side undergoes transition, the lift on this cable side becomes dominating and the lift coefficient shifts direction. The lift coefficient development of ring 2, however, is only directed towards one side, since the helical fillets are located in the stagnation and base region, and therefore is seen to have reduced effect. It is though pointed out that the flow for an inclined cable is highly three dimensional and applying a surface modification adds to the complexity, so two-dimensional rings do not provide the full picture.

The surface pressure fluctuations indicate the influence of the helical fillet, and the high magnitudes occurring behind the helical fillets normal to flow at ring 1, 3 and to some extend ring 4, denote that the helical fillet trips the flow and thus increases the momentum as the flow passes the fillet. The pressure drops behind the helical fillet creating a sudden rise in suction which shows most clearly at ring 1 where $\theta_\perp = 58°$. These fluctuations prevail for all Reynolds numbers. For ring 2, the largest RMS-values are found near the separation points as for a smooth cylinder.

3.2   State jumps

Considering Figure 5- 6, a significant increase in RMS-values at Re=$1.8 \cdot 10^5$ compared to Re=$1.3 \cdot 10^5$ and $3.9 \cdot 10^5$ occur for ring 4 in particular, where some values have nearly doubled, and to a minor extend for ring 1 and 2. This is caused by state jumps during the boundary layer transition, i.e. at least three stable states occur within the same time series where a bubble may be formed on either side of the cable or not at all. This single bubble instability was first depicted in (Nikitas, 2012) for a smooth cable normal to flow, but the instability phenomenon was not recorded as such on inclined cables. Part of the 90 s time series at Re=$1.8 \cdot 10^5$ for the lift coefficient of ring 1 and 2 are shown in Figure 7 and the drag and lift coefficient of ring 4 in Figure 8, clearly depicting the alternating transition between symmetric and asymmetric states. Similar behaviour was found in the tests for a cable with a smooth surface, but since the main emphasis of this paper is on cables with helical fillets, this will not be shown.

Transitions at ring 2 follow those at ring 1 with what seems to be a small delay, see Figure 7, thus indicating a certain connection between the flow at the two rings separated by the distance 2D. The states at the two rings are, however, different due to the difference in helical fillet positions, and the jumps are randomly located supposedly because the shifts are connected to wind gusts. Ring 3 did not show any state jumps at this Reynolds number and is therefore not shown.
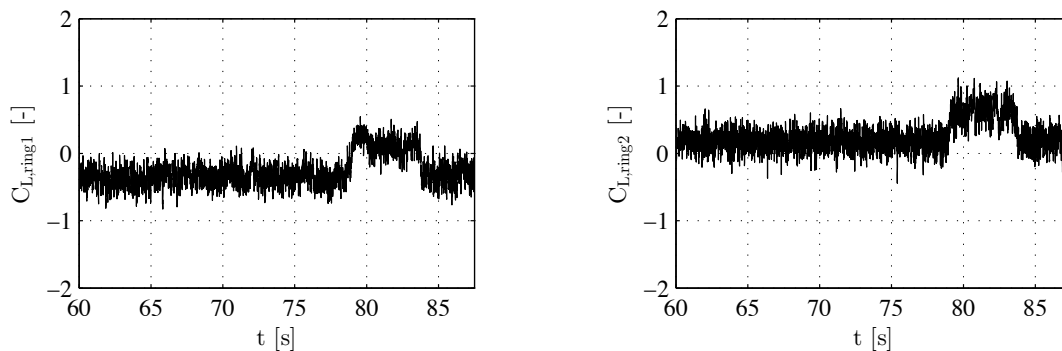
Figure 7. Time-history of C_L for ring 1 (a) and ring 2 (b), cable rotation $-90°$ dynamic case, at U=16.3 m/s, displaying the shift in states.

Pressure distributions at three time instants a, b and c for ring 4, the ring showing the largest pressure fluctuations, are depicted in Figure 9. The instantaneous pressure distributions show both signs of lift that can occur. The influence on the drag coefficient is, however, not as pronounced at ring 4, but this does vary from ring to ring. As the transition takes place there is though an instantaneous drop in drag,

time instant b, Figure 8 and 9. According to these findings, one must be careful considering only mean values of force coefficients for cables inclined to the flow as well as cables normal to the flow.
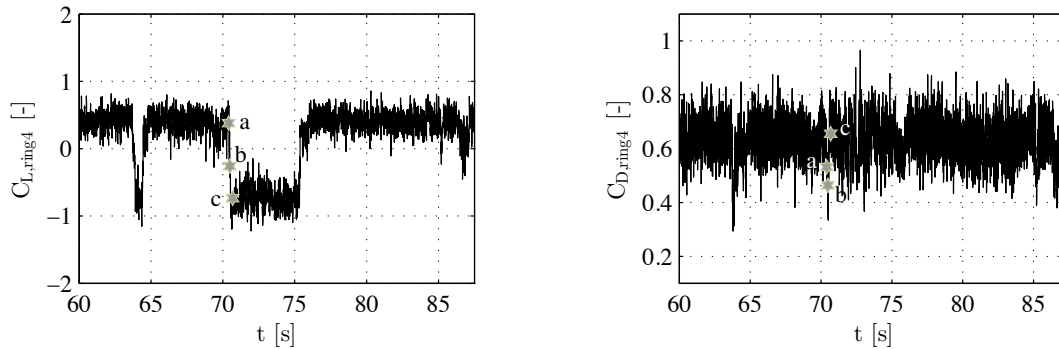
Figure 8. Time-history of the lift (a) and drag coefficient (b) for ring 4, cable rotation $-90°$ dynamic case, at U=16.3 m/s, displaying the shift in states. Pressure distributions at time instants a, b and c are given in Figure 9.
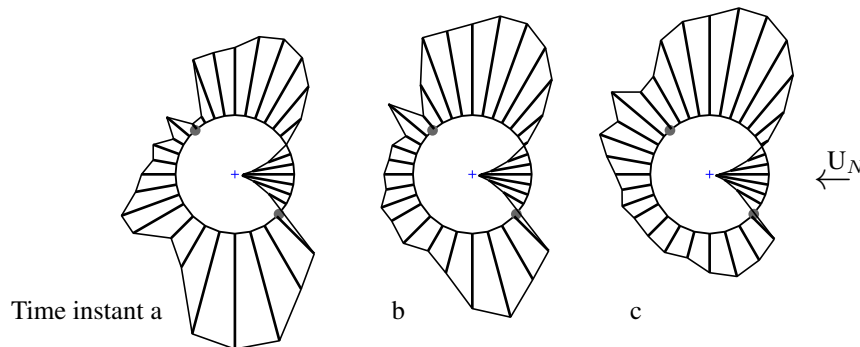
Figure 9. Pressure distributions for ring 4 at U=16.3 m/s at the time instants marked in Figure 8. The grey circles mark the fillets, the upper being nearly normal to the flow. Radius of the circle corresponds to $C_p = 1$.

The state jumps only take place in a narrow Reynolds number region, depicted in Figure 10 for ring 1 and Figure 11 for ring 4. For both the drag and the lift coefficient, the mean values of the 90 s time series are plotted together with the maximum and minimum mean values of the different states, if state jumps do occur in a given time series. For both rings the state jumps are found at the steepest drop of the drag coefficient. This is in interesting phenomenon, but in these tests, the single bubble instability is not the origin of the large amplitude cable vibrations observed in the supercritical Reynolds number region.

3.3   Influence of helical fillet position

It was previously shown that the flow around the cable is not significantly influenced by the fillet nearly aligned with the flow, but rather by the fillet nearly normal to the flow and its angular position. The dependence of the force coefficients on the angular position of the fillet normal to the flow is thus shown for a supercritical Reynolds number in Figure 12. The values are shown with four colors, each color indicating a certain ring. Hereby, it can for example be seen that the lift coefficients measured for ring 1 (red markers) deviates from the tendency seen for the lift of the other rings. This may have three origins, the first being the difference in surface shape of ring 1 (see Figure 3), the second the anti-symmetry of the helical fillets previously mentioned, and the last is possible end-effects. It is not certain which one of these that are governing.

In addition to the color differentiation, there are different types of markers representing a specific cable rotation. For each marker there are four points representing the angular position of the helical fillet nearly normal to the flow at each of the four rings for the given cable rotation. Thus, the angular positions
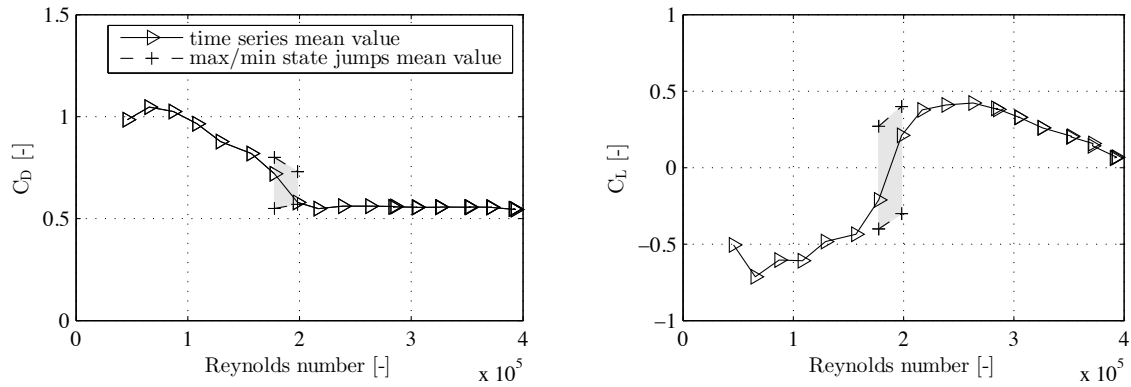
Figure 10. Drag C_D (a) and lift coefficient C_L (b) for ring 1 as a function of Reynolds number, cable rotation $-90°$ dynamic case. The mean values of the different states through a time series are shown.
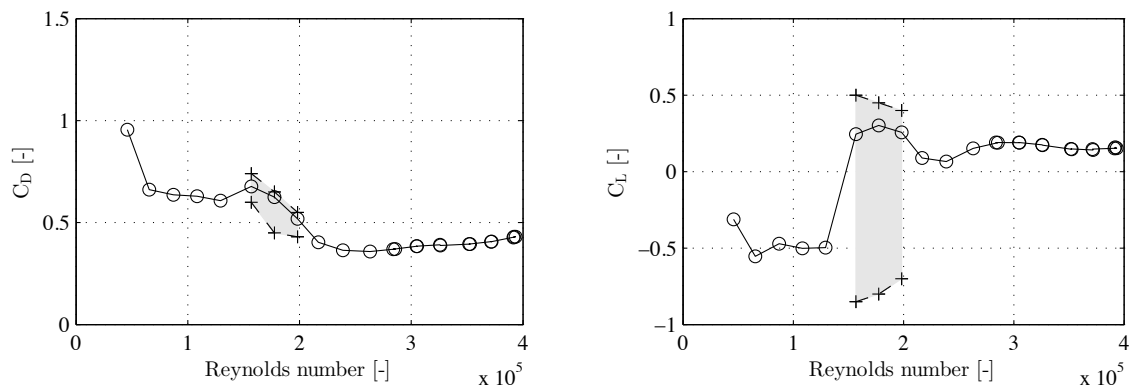
Figure 11. Drag C_D (a) and lift coefficient C_L (b) for ring 4 as a function of Reynolds number, cable rotation $-90°$ dynamic case. The mean values of the different states through a time series are shown.

for a cable rotation of -90° listed in Figure 6: 12°, 58°, 102° and 132°, can all be retrieved in Figure 12 with the marker ○, in four different colors. Results from both dynamic and static tests are shown and they are in good accordance.

The drag coefficient does not seem to be influenced significantly by the presence of the helical fillet in the stagnation and base region, as the values in these areas are located around that of a smooth inclined cable drawn as the dotted line. As the position of the helical fillet moves towards the shoulder of the cylinder, the drag starts increasing indicating a widening of the wake. At approximately 80° the drag decreases, hence a narrowing at the wake, until it 'settles' at the value for a smooth cylinder at approximately 130°. (Ekmecki, 2010) studied the flow around a circular cylinder with a fixed protrusion along the cylinder length, and showed that a wire with d/D=0.029 positioned before 40° or after 120° had relatively little influence on the near-wake structure at Re=$1 \cdot 10^4$. This corresponds well with the drag coefficient development for this setup, where the helical fillet thickness to outer cable diameter ratio is 0.014.

Contrary to the drag coefficient, the lift coefficient reveals that the flow is affected by the presence of the helical fillet in the stagnation and base region shown by the non-zero values, region 1 on Figure 12. Observing for example ring 2 in Figure 6 where $\theta_\perp = 12°$, the suction is reduced on the rough cable side compared to the smooth cable side due to the presence of the helical fillet. As for the drag coefficients, the lift coefficients in these areas are scattered, denoting an influence of surface irregularities. The dependency of aerodynamic force coefficients on cross sectional distortion and local changes in surface roughness of a smooth cable normal and inclined to flow, has previously been demonstrated by (Matteoni, 2012). Ignoring ring 1 in the interval of approximately 40-130°, region 2 on Figure 12, the fillet seems

to control the flow to a larger extent. The lift coefficient lies between 0.3-0.4 until approximately $100°$ where a sudden drop in lift occurs, corresponding to ring 3 in Figure 6 where $\theta_\perp = 102°$. The value then starts increasing. The exact flow mechanism present when the drop in lift occurs is not evident and it is pointed out that the rings, being perpendicular to the cable, are made up of several streamlines when the cable is inclined, each streamline being affected by the periodic pattern of the helical fillet.
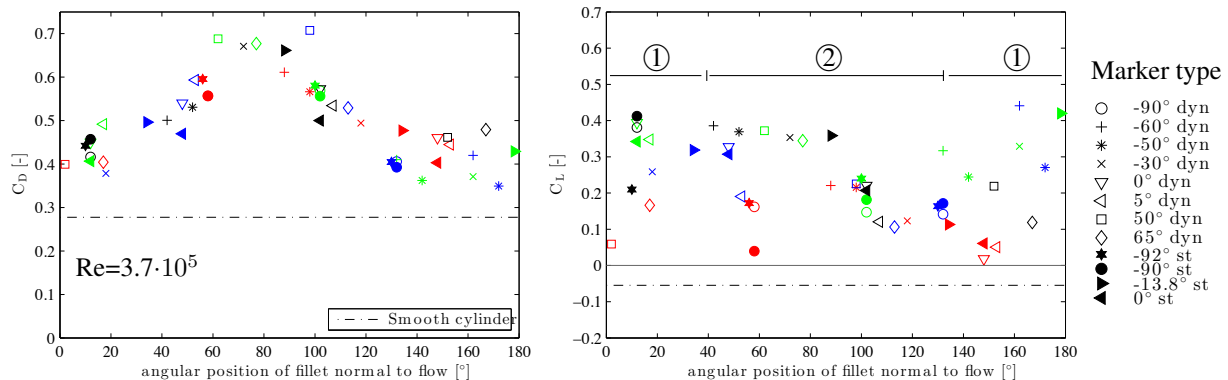
Figure 12. Local force coefficients with respect to the angular position of the helical fillet nearly normal to flow. The stagnation point equals $0°$. Both values from dynamic and static tests are shown. Red: ring 1, black: ring 2, green: ring 3, blue: ring 4. Dotted line marks value for a smooth cable. Region 1: controlled by surface irregularities, region 2: controlled by helical fillets.

4   Conclusion

This paper has presented different loading mechanisms for a helically filleted cable in dry conditions inclined to the flow. The helical fillet nearly aligned with the flow does not have a significant influence on the flow, and the boundary layer on this smooth cable side therefore undergoes what resembles a classical boundary layer transition. On the rough cable side, the flow is controlled by the helical fillet nearly normal to the flow and the local surface pressure distribution is governed by the angular location of the helical fillet. In the range of approximately $40\text{-}130°$, the helical fillet normal to the flow seem decisive regarding the magnitude of the aerodynamic force coefficients, whereas in the stagnation and base regions, approximately $0\text{-}40°$ and $130\text{-}180°$, the surface irregularities appear dominating. The helical fillet thickness (width) to outer cable diameter ratio was 0.014 (0.015) and the surface deviation from the mean circular shape 0.01 in this test round. For smaller or larger sizes of these parameters, the results presented here might be different. It was also proven that state jumps occur for a helically filleted cable inclined $60°$ to the flow.

References

Ekmecki A., Rockwell D. (2010). Effects of a geometrical surface disturbance on flow past a circular cylinder: a large-scale spanwise wire. *Journal of Fluid Mechanics* **665**, pp. 120–157.

Flamand, O. (1995). Rain-wind induced vibration of cables. *Journal of Wind Engineering and Industrial Aerodynamics* **57, 2-3**, pp. 353–362.

Igarashi, T. (1986). Effect of tripping wires on the flow around a circular cylinder normal to an airstream. *Bulletin of the Japan Society of Mechanical Engineers* **28**, pp. 2917–2924.

Jakobsen J.B., Andersen T.L. Macdonald J.H.G. Nikitas N. Larose G.L. Savage M.G. McAuliffe B.R. (2012). Wind-induced response and excitation characteristics of an inclined cable model in the critical

Reynolds number range. *Journal of Wind Engineering and Industrial Aerodynamics* **110**, pp. 100–112.

Kleissl K., Georgakis C.T. (2012). Comparison of the aerodynamics of bridge cables with helical fillets and a pattern-indented surface. *Journal of Wind Engineering and Industrial Aerodynamics* **104-106**, pp. 166–176.

Kleissl, K. (2013). *Cable Aerodynamic Control - Wind tunnel studies*. Ph.D. Thesis, Department of Civil Engineering, Technical University of Denmark.

Larose G.L., D'Auteuil A. Bosch H.R. Jakobsen J.B. Macdonald J.H.G. (2013). Wind-tunnel investigations of an inclined stay cable with a helical fillet. *6th European and African Conference on Wind Engineering, Cambridge, England, July 7-11*.

Matteoni G., Georgakis C.T. (2012). Effects of bridge cable surface roughness and cross-sectional distortion on aerodynamic force coefficients. *Journal of Wind Engineering and Industrial Aerodynamics* **104-106**, pp. 176–187.

Nikitas N., Macdonald J.H.G. Jakobsen J.B. Andersen T.L. (2012). Critical Reynolds number and galloping instabilities: experiments on circular cylinders. *Exp Fluids* **52**, pp. 1295–1306.

Zdravkovich, M.M (1981). Review and classification of various aerodynamic and hydrodynamic means for suppressing vortex shedding. *Journal of Wind Engineering and Industrial Aerodynamics* **7**, pp. 145–189.

Experimental Techniques for Super and Mega Yacht Aerodynamics Assessment

F. Fossati[1], S. Muggiasca[1] and F. Robustelli[1]

[1]Department of Mechanical Engineering, Politecnico di Milano, Italy
Corresponding author: F.Fossati, fabio.fossati@polimi.it

Abstract

The aerodynamics performances of hull and superstructure have became much more important in the years from the point of view of mega yacht designers because of the larger dimensions and the always superior comfort requests. Windage evaluation of very high superstructure, aerodynamic load assessment, and accurate air flow simulation are considered very important in the design procedure to get optimal layout and opening position. Moreover they are used to precisely evaluate thrusters and Dynamic Positioning Systems horsepower. The lack of data concerning the peculiar mega-yacht forms and the result requested accuracy lead to set up scale model wind tunnel tests. They are asked more and more frequently by designer and surveyors and considered a fundamental reference for any further CFD simulation. In this paper experimental methodologies developed at Politecnico di Milano Wind Tunnel in order to assess mega-yacht aerodynamics in terms of aerodynamic loads, comfort analysis, pollutants dilution and re-ingestion analysis using wind tunnel tests are described.

1   Introduction

Windage evaluation of high superstructure, aerodynamic load assessment, and accurate air flow simulation are considered very important in the mega-yacht design procedures to get optimal layout and opening position, as well as to Dynamic Positioning Systems (DPS) design purposes.

DPS is used to get and maintain a fixed point or to maintain a defined course at very low speed, for example ship position and orientation in sheltered waters without anchoring or course keeping in narrow passages. In these cases aerodynamic forces are very important. The experimental assessment of the ship aerodynamic behaviour through wind tunnel tests on a scale model can be very significant for the performances of the installed DPS system.

Reference data relative to aerodynamic forces on marine structures and ship superstructures are available but relative to shapes very different from mega yacht superstructure.

The lack of data concerning the peculiar mega-yacht forms and the result requested accuracy lead to set up scale model wind tunnel tests, that can also be used for any further CFD simulation.

Comfort on board a luxury yacht is obviously a key feature in all its aspects, like ship motions, noise and vibrations, windage and exhausts gases issues.

Since the speed-up comfort results are heavily dependent on the yacht exterior profile, these measurements are to be carried out at an early stage: excessive speed-up values in external areas like sunbathing or dining may be overcome by modifying the exterior shape, or by inserting glass or plexiglass windscreens, which can be fixed or removable. These elements usually have an impact on the aesthetics of the yacht, so they must be carefully designed together with the exterior stylist.

The positioning of HVAC external grids and generators exhausts can also be dependent on the aerodynamics of the flow around the yacht. Grids are usually placed according to the exterior profile design, so that they have the smallest possible aesthetic impact, and by using common practices in order to avoid pollution between exhaust and intake air (for example, usually the intake air grids are put on the opposite side than the exhausts). However, exhausts gas flow around the yacht superstructure may not be intuitive, therefore an experimental evaluation is very useful in order to detect possible re-ingestion problems and to ensure that gas is diluted or is flowing far enough from the external guest living areas.

The present paper describes experimental methodologies developed at Politecnico di Milano Wind Tunnel in order to assess mega-yacht aerodynamics in terms of aerodynamic loads, comfort analysis, pollutants dilution and re-ingestion analysis using wind tunnel tests on a scale model.

More in details with reference to aerodynamic loads assessment global aerodynamic forces are investigated at different wind exposures using a six component dynamometer, while comfort evaluation on the various yacht decks and relax areas are performed by means of speed up measurements in different positions on each yacht terrace and roof.

Finally in order to detect potential discomfort due to exhausts produced by diesel fuel combustion as well as potential plume re-ingestion problems, pollutants dilution lab-scale experiments are carried out using tracer gas dilution measurements.

Some results obtained with reference to aerodynamic investigations carried out, using a scale model of a 270' LOA mega-yacht in smooth and turbulent flow at different wind exposures, are presented and discussed. Obtained data represent a reference for a better consideration of aerodynamic aspects in maxi and mega-yacht design.

2   Experimental set-up

2.1   Politecnico of Milan Wind Tunnel

The Politecnico di Milano Wind Tunnel is a closed circuit facility having two test sections, a 4x4m high speed low turbulence and a 14x4m low speed boundary layer test section. As regard mega-yacht application tests are generally performed in the low speed Boundary Layer test section taking into account atmospheric turbulent flow characteristics. The model to be tested, together with the related environment, is usually set up on a 13m diameter turntable, included in the wind tunnel floor to allow computer pre-selected wind incidence angle changes.

2.2   Wind Characteristic

The atmospheric wind properties are a function of the environmental characteristics at full-scale: in the wind tunnel they can be achieved by using passive turbulence generators placed into the test section With reference to maxi and mega-yacht application the mean wind velocity and the wind turbulence intensity vertical profiles are generated according to the reference profiles of Eurocode specs relevant to marine areas. Wind tunnel tests are generally carried out firstly in smooth flow and then repeated in turbulent flow considering scaled simulation of the natural wind characteristic of the site according with turbulence and boundary layer similitude law.

2.3   Yacht scale model set up

Given the considerable dimensions of the wind tunnel, the optimal scale for yacht models is in the order of 1:20 – 1:30. These dimensions derive from a series of considerations, including reducing blockage as far as possible (normally less than 5%) while at the same time it is possible to reproduce with a good level of detail many of the elements of the boat that are useful for determining superstructure drag or windage effects. This geometric scale is also compatible with the scaled simulation of the boundary layer. The model is manufactured as a "rigid aerodynamic model", that is a static model that reproduces the geometry of the full-scale structure (aerodynamic surfaces and details).

2.4   Force Measurement

The measurement of the overall wind loads on the hull and yacht superstructures is achieved using a six components force balance, which is placed inside the hull. The model is manufactured using an internal structural frame which is rigidly connected to the dynamometer.

2.5   Speed Up Measurement

Comfort evaluation on the various yacht decks and relax areas are performed by means of wind speed measurements carried out in different positions according to yard and designer specifications (typically on yacht terraces and yacht decks) at different wind exposures.

Local wind speed measurements are performed by means of Irwin probes that allow to measure the magnitude of the wind speed at a given position at the desired height from the floor level.

Aerodynamic forces and speed-up measurements are generally performed at two different wind speeds in order to check any potential Reynolds effect.

3   Pollutant Dilution Measurement

3.1   Wind Tunnel Experiment on scaled models

The main requirement for pollutants dilution lab-scale experiments is related to release from the stacks of a gas having well defined properties in terms of density (to reproduce the buoyancy effect) and content of a suitable tracer gas, which is used to gain information about its dilution and dispersion in the ship wake. In the wind tunnel environment, having to reproduce the emission of exhausts produced by diesel fuel combustion, a mixture consisting of air and carbon dioxide, at room temperature, is fed to the yacht model stacks. The tracer flow-rate is controlled by means of a mass flow meter. In order to obtain a quantitative measure of the pollutant dilution conditions and the potential presence of the tracer gas into the ship wake or its possible accumulation in some parts of the vessel, a certain number of sampling ports are realized on the yacht model, placing them on decks or in areas that can be potentially critical for the dispersion of the tracer gas.

3.2   Scaling rules

As previously said the wind tunnel boundary layer reproduce at model scale the atmospheric boundary layer characteristics; therefore, the conditions necessary to ensure the flow similarity are obtained from the dimensional analysis of exhausts flow motion equations.

4   Some Results

4.1   Forces: Aerodynamic coefficients

The yacht aerodynamic forces are generally measured at different angles of attack from 0° to 180° with a step of 15 degrees: results are presented as function of the exposure angle (α – on the x-axis) in the wind coordinates system, in terms of drag coefficient, side force (lift) coefficient and aerodynamic moment coefficients.
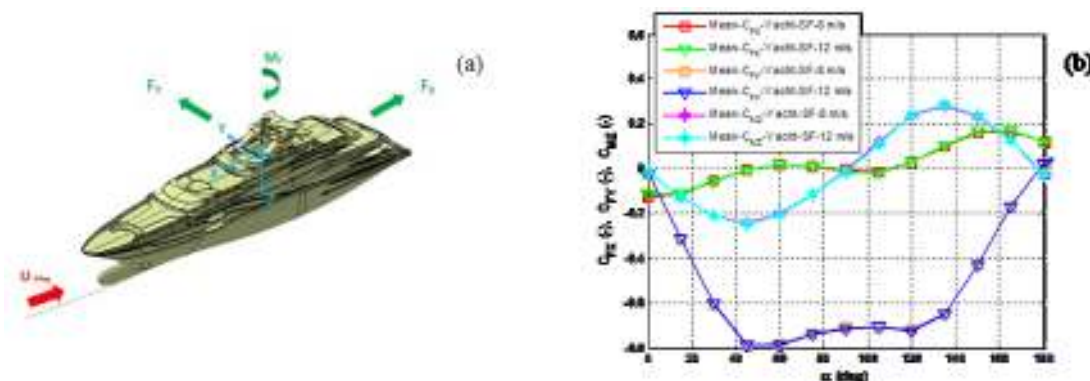
Figure 1: Yacht reference system (a) and (b) mean coefficient as function of the angle of exposure for two wind speeds: 8m/s and 12 m/s

4.2   Speed up

Figure 2a shows an example of the obtained results in smooth flow at 0 deg wind exposure with reference to the yacht sun deck level. The results are presented in a non-dimensional form by means of the speed-up factor that is defined as the ratio between the local mean wind speed in the measurement position and a reference wind velocity. The position of the local wind speed measurements points and their labels are sketched in the high part of Figure 2a. The histogram graph in the lower part of the figure shows the speed up values on the vertical-axis while on the x-axis the probes labels are reported.
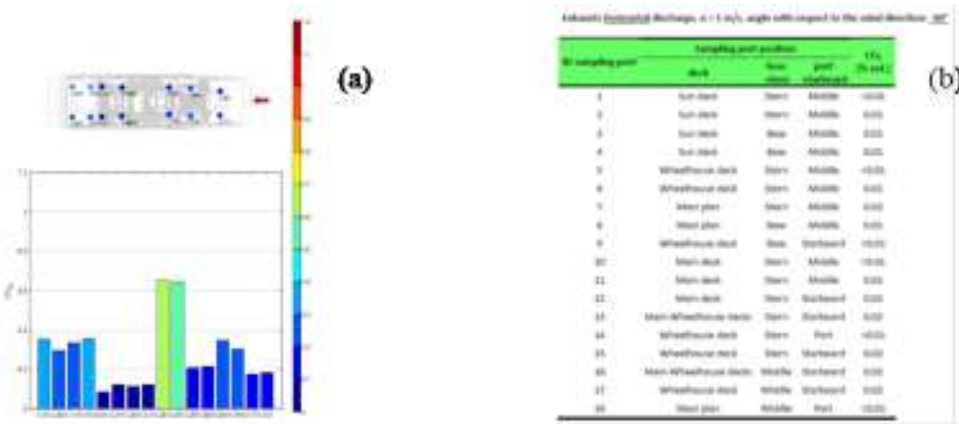
Figure 2: Speed Up - Sun Deck - angle 0 deg (a) and Exhausts horizontal discharge, u = 1 m/s, angle with respect to the wind direction: -90°

4.3   Exhaust dilution

Several tests with the aim to evaluate the effect of wind on the exhaust plume dispersion have been performed; different discharge layouts have been investigated at different wind speed in both smooth and turbulent flow. An example of the obtained results is summarized in Figure 2b: each sampling port is identified by an ID number and a short description which indicates the placement on the ship model; in the last right column the measured CO_2 concentration values are reported.

4.4   Flow visualization

Flow visualization techniques, for instance smoke visualizations, allows to collect qualitative information about the wind velocity field in correspondence of the open areas occupied by passengers.

References

Det Norske Veritas, (2011). *'Dynamic Positioning Systems'*. Rules for Classification of Ships. Special Equipment and Newbuildings System Additional Class, Part 6 Chapter 7.

Haddara, M.R., Guedes, C., (1999). Wind Loads on Marine Structures. *Marine Structures* 12:199-209.

Koop, A., Rossin, B., Vaz, G., (2012). Predicting Wind Loads on Typical Offshore Vessels Using CFD. *Proceedings of ASME 31th International Conference on Ocean, Offshore and Artic Engineering OMAE*.

Fujiwara T., Ueno M., Nimura T. (2001). An estimation method of wind forces and moments acting on ships. *Proceedings of the Mini-Symposium on Prediction of Ship Manoeuvring Performance, pp.83-92*.

Isherwood, R.M., (1972). Wind resistance of merchant Ships. *Trans RINA*.

Numerical and experimental optimization of a time-trial cycling helmet

M. Belloli[1], S. Giappino[1], P. Schito[1] and M. Tenni[2]

[1]Department of Mechanical Engineering, Politecnico di Milano, Italy
[2]MET Helmets, Italy

Corresponding author: Paolo Schito, paolo.schito@polimi.it

Abstract

Time-trial cycling is a very competitive and technological field. Research is not only related to the mechanical and aerodynamics of the bicycle, but is looking to the aerodynamics of the athlete itself, his position during the race and to the accessories. The helmet is a very important component for the aerodynamics of the body of the cyclist, therefore its aerodynamic optimization is a key point for the reduction of the total drag and the optimization of the performance of the athlete. The drag reduction analysis is studied using Computational Fluid-Dynamics for a preliminary analysis of the flow around the upper-body of the athlete; the chosen geometry is realized in prototypes and some wind tunnel tests are conducted to validate the CFD analysis. The final tests is represented by track tests where the power consumption of the athletes is compared between the different geometries.

1 Introduction

Time trial cycling is evolving towards more challenging technological aspects: the training of the athlete is not sufficient for a competitive result since also the whole cyclist gearand the bike have an influence on the performance (see Figure 1). The reduction of total drag is the target for every cyclist and for time trial athletes this aspect can be studied with much more accuracy than for other disciplines. Time trial cycling involves relatively high speeds, which increases the influence of the aerodynamic drag on the overall resistance to motion.

Current design of cycling suits and cycling helmets is carried out on empirical and using common sense. The evaluation of the performance in terms of energy consumption on the athlete is done in different ways: the more common approach during trial track testing: a torque-meter is applied at the hub of the pedal, and the power consumption of the athlete is evaluated for different runs. This approach is time consuming and requires several prototypes for the realization of a single efficient product.Most advanced helmet designs are supported by experimental wind tunnel testing. Track and wind tunnel testing are expensive ways for the assessment of the performance of a cycling helmet: in both approaches it is required to have a cyclist, a prototype of the helmet and the availability of the experimental facility.

The cyclist is important for the assessment of the aerodynamic performance of the helmet, since the resistance reduction is a function of the interaction between the helmet and the athlete. In this context it is fundamental that the cyclist finds the correct position on the bike as a function of the aerodynamic property of the helmet.

Track test results (especially for indoor tests) will represent the correct condition to assess the helmet performance, since the operating condition of the cyclist is the real one, but the results have often a large scatter: often on the athletes feeling the emotional reaction is dominant with respect to the real aerodynamic features of the helmet. It is very important to note that the track tests require the production of a prototype, with suitable protecting properties: it is not uncommon that the athletes fall during a specific test and it is necessary that the helmet playas his role and protects the rider from eventual injuries.

Figure 1. Cyclist during a time-trial race. (courtesy of www.cyclingfans.com / MET)

Wind tunnel testing allows for a better assessment of the aerodynamic performance of the helmet, since it is possible to perform the tests tracking and monitoring the position of the athlete. In this case it is possible to perform the measurement with the athlete pedalling or standing still. Wind tunnel tests require as the track tests the construction of a prototype, but in this case it is sufficient to reproduce the shape, that is fundamental for the evaluation of the aerodynamic resistance, while there is no need for the prototype to have also structural or protective features, since the rider stands still in the wind tunnel test section. It is therefore possible to produce through rapid prototyping helmets for the wind tunnel tests.

Computational fluid-dynamics (CFD) is rapidly developing in the last years, allowing for a more effective analysis on the aerodynamic features of a cycling helmet. Track tests and wind tunnel tests allow checking the aerodynamic performance of the single helmet, but the improvement in the shape and the design of the helmet can be only dependent from an intuition of the designer. CFD allows visualizing the actual flow features around the helmet and the rider, and the analysis of the flow can provide an enhancement in the helmet design to improve the resistance to motion performance with a successive revision of the design.

Current paper investigates the optimization of the time-trial cycling helmet reported in Figure 1. The optimization is conducted with CFD analysis improving the current design and optimizing the new design; the proposed designs are realized using rapid prototyping and tested in wind tunnel, in order to validate the outcome of the numerical investigation. The final version of the helmet selected from the wind tunnel tests will be tested in an indoor test track facility for the real life final performance assessment.

2   Methodology

The numerical analysis is conducted using the geometry of a biker and the CAD model of the helmet and of the visor.

The rider geometry is obtained by means of a three-dimensional scan. As can be seen in Figure 2 the geometry reproduces the upper-body of a real athlete, while some minor details, as the hairs (that will be shaded by the helmet), the hands, the legs and the bicycle are neglected.

Figure 2. Geometry of the rider: side view (left), front view (right).

The helmet and the visor are placed correctly on the rider head and this geometry is used as a reference for the CFD analysis as can be seen in Figure 3. The numerical analysis is conducted resolving steady state RANS with a kω-SST turbulence closure model.

Figure 3. Geometry of the rider and the helmet: side view (left), front view (right).

The rider is placed in the virtual wind tunnel as it can be seen in Figure 4. The wind velocity is defined on the right side of the domain, and the wind speed is coherent with the speed of a professional athlete: in particular the wind speed is 14m/s.
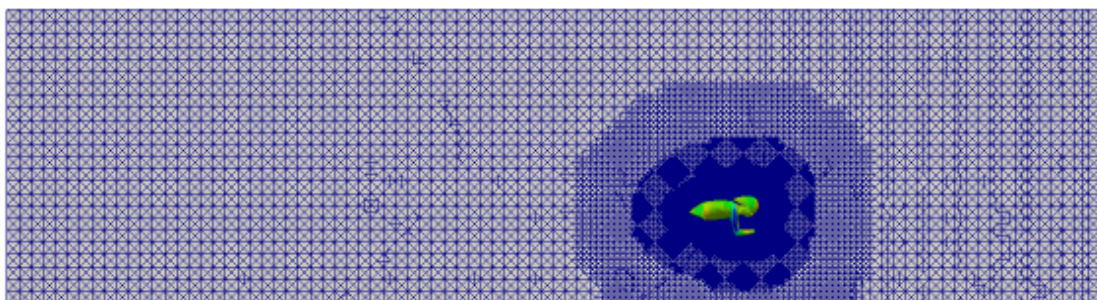
Figure 4. Domain of the numerical simulation.

The CFD framework that is used for the numerical analysis is OpenFOAM, where the pre-processor is snappyHexMesh, where the total number of cells is around 11 millions, with a special refinement close to the cyclist body and the helmet, as can be observed in Figure 5. In the same figure it is possible to observe the pressure distribution on the biker surface, in order to evaluate the overall performance of the helmet.
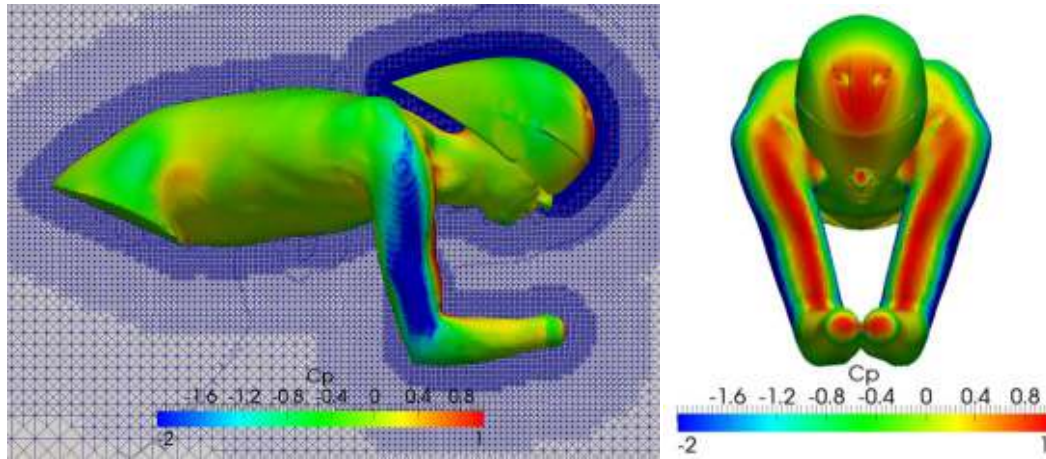
Figure 5. Mesh detail around the rider and the helmet and pressure distribution on the rider and helmet surfaces side view (left); pressure distribution on the surface of the rider and the helmet front view (right).

The pressure distribution on the surface together with the visualization of the path-lines and the oil flow pattern shown in Figure 6, allows defining possible directions for the improvement of the aerodynamic design of the helmet for achieving the drag reduction.
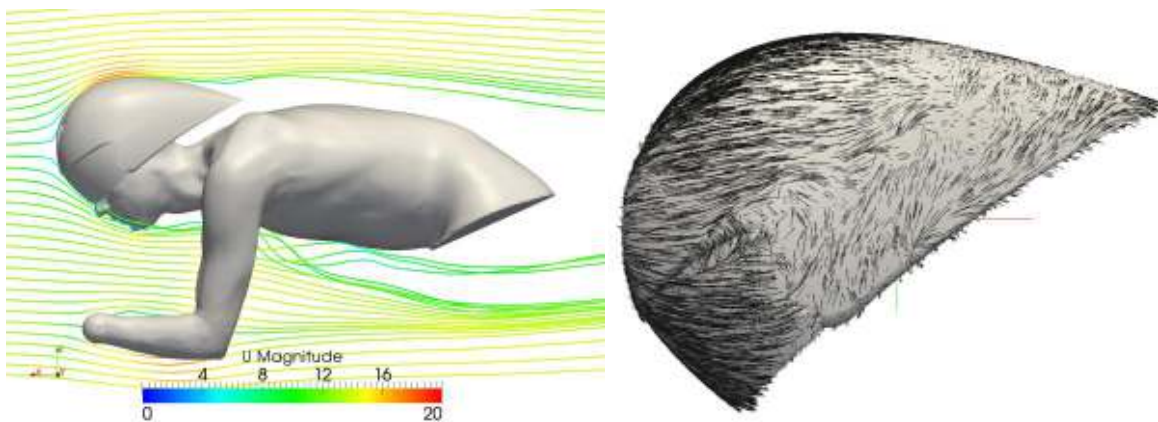
Figure 6. Path-lines coloured by velocity magnitude around the cyclist symmetry plane (right); oil flow on the helmet and visor to display the local velocity direction.

In the full paper will be presented the improvement steps and the final version of the helmet design, the comparison with the wind tunnel tests and the experimental track tests that at the moment are a confidential project.

References

Blocken B., Defraeye T., Koninckx E., Carmeliet J., Hespel P. (2013). CFD simulations of the aerodynamic drag of two drafting cyclists. *Computers & Fliods* **71**, 435–445.

Blocken B., Defraeye T., Koninckx E., Hespel P., Carmeliet J. (2010). Computational fluid dynamics analysis of cyclist aerodynamics: performance of different turbulence-modelling and boundary-layer modelling approaches. *CJournal of Biomechanics* **43(12)**, 2281–7.

Investigation of vortex-induced vibrations of the Ewijk Bridge during different stages of refurbishment

T. Argentini[1], D. Rocchi[1], A. Zasso[1]

[1]Department of Mechanical Engineering, Politecnico di Milano, Italy

Corresponding author: T. Argentini, tommaso.argentini@polimi.it

Abstract

This paper presents the results of sectional wind tunnel studies of the existing Ewijk Bridge, a 270m span cable-stayed bridge crossing over the river Waal in Netherlands, which is being refurbished. A recently constructed bridge, immediately to the west of the existing Ewijk Bridge, could affect the aerodynamic behaviour of the existing bridge and specific wind tunnel tests has been conducted. Sectional wind tunnel studies in a 1:50 scale are required to identify the aeroelastic stability of the bridge during various stages of refurbishment (as the deck profile, flexibility and mass changes). The aim of the wind tunnel studies is to assess the aeroelastic performance (vortex shedding, flutter and galloping risks) of the Ewijk Bridge deck during different stages of refurbishment, as the deck profile, stiffness, and mass change and might lead to potentially dangerous coupled vortex-induced vibrations.

1   Introduction

The Ewijk Bridge crosses the river Waal, which is the main branch of the Rhine in the Netherlands, and is a vital transportation route between the Port of Rotterdam and mainland Europe. The bridge opened to traffic in 1976, and the 1,055m-long structure has ten spans, with a 480m-long cable-stayed section over the river. This part of the bridge has a main span of 270m and back spans of 105m on each side.

The deck is a steel trapezoidal box girder with orthotropic plates to the top and bottom flanges. The box girder is continuous over the ten spans and supported by cable stays over the river crossing and the adjacent back spans. This bridge was selected for renovation due to problems with fatigue cracking in the deck. To this end, a second bridge was built, next to the existing structure, in order to divert all the traffic off the existing crossing to enable the repairs without loss of traffic capacity for the motorway (see Figure 1).

Figure 1. The Ewijk Bridge. On the left: original stand-alone configuration. On the right: the new configuration with the existing deck (in refurbishment) and the new deck.

The new construction is a cable-stayed bridge, with an asymmetric concrete deck made of two external trapezoidal hollow girders connected by transversal precast beams, evenly spaced along the bridge. Figure 2 shows a sketch of the two decks with their main dimensions.

During the refurbishment, the existing deck profile, its stiffness and mass are subjected to changes that affect its aerodynamics, structural frequencies, and relative height between new and existing (up to 1.2 m). The change of deck shape is due to the presence or not of parapets, traffic, and noise barriers. Table 1 summarizes some relevant configurations tested and the corresponding bridge properties.

Sectional wind tunnel studies are required to identify the aeroelastic stability of the bridge during the various stages of the refurbishment and to assess if vortex-induced vibrations arise for the existing deck, due to the presence of the new one, considering the closeness of the two bridges and their similar frequencies (especially at in-service configuration).
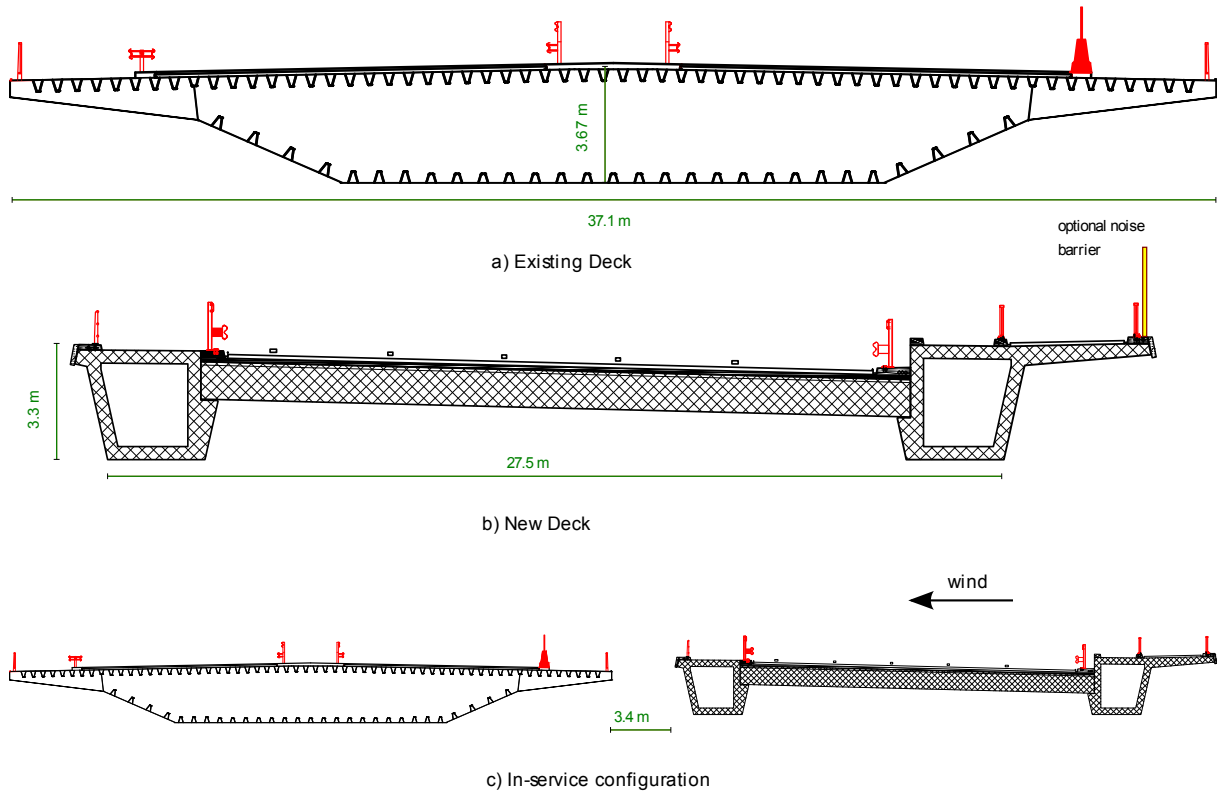
Figure 2. Existing and New deck sections.

Table 1. Configurations during the refurbishment stages.

Configuration	Relative height	Barriers on existing bridge	Frequencies (v: vertical; t: torsional)	
			existing	new
2 – Inner Cables Removed	+ 1.2 m	Removed	f_v=0.49 Hz; f_t=1.19 Hz	f_v=0.38 Hz; f_t=0.67 Hz
3 – Outer Cables Removed	0 m	Removed	f_v=0.49 Hz; f_t=1.19 Hz	f_v=0.38 Hz; f_t=0.67 Hz
4 – In-service	0 m	Reinstalled	f_v=0.36 Hz; f_t=0.71 Hz	f_v=0.38 Hz; f_t=0.67 Hz
5 – In-service + noise barriers on new bridge	0 m	Reinstalled + noise barriers on the new bridge	f_v=0.36 Hz; f_t=0.71 Hz	f_v=0.38 Hz; f_t=0.67 Hz

2   Experimental Setup

Two sectional 1:50 scale models were built and elastically suspended to identify possible vortex-induced excitation. The model were designed in order to reproduce the correct frequency ratios between the two decks while varying the Scruton number (either acting on mass or damping). Figure 3 shows some pictures of the experimental test rig.

a)

b)   c)
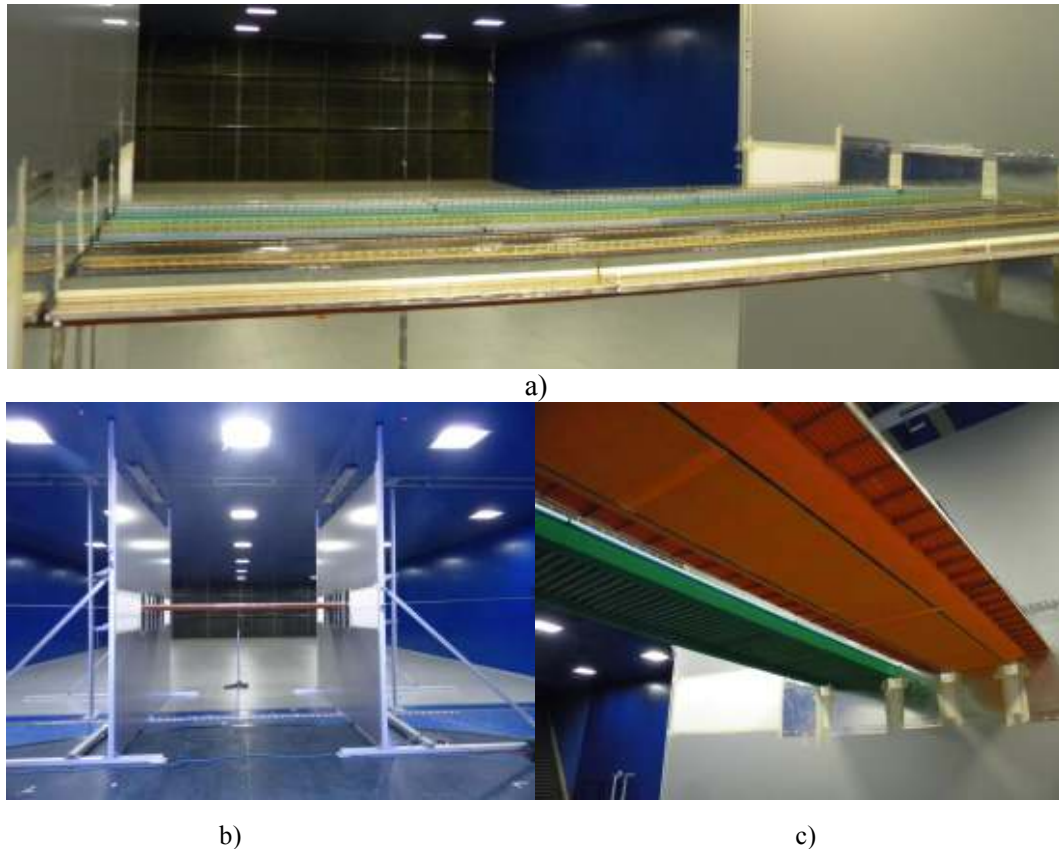
Figure 3. Experimental test rig: a) the two sectional models; b) overall view of the rig; bottom view of the two sectional models

3   Results

The New Bridge suffers from vortex-induced vibrations, when the Scruton number is sufficiently low, irrespective of the presence of the Existing Bridge (see Fig.4, conf. 1 and 4, where the non-dimensional vertical response of the bridge as a function of the reduced velocity is reported). The presence of an additional external noise barrier (conf. 5) enhances the phenomenon.

We can notice that, when the oscillations of the upwind bridge are sufficiently high, the vortexes shed force the existing bridge, and since the natural frequencies of both bridges are close, its response is not negligible. Moreover, for the New Bridge, a very small lock-in region at around half of the reduced frequency is present.

Figure 5 shows the dependence of the vortex-induced vibrations of the New Bridge upon the Scruton number ($Sc = m(2\pi\zeta)/(\rho B^2)$), and the corresponding resonant response of the existing one (whose Sc is kept constant). It can be seen that the downwind bridge response depends nonlinearly on the amplitude of oscillation of the upwind bridge, and that below a minimum level of forcing the response is negligible.
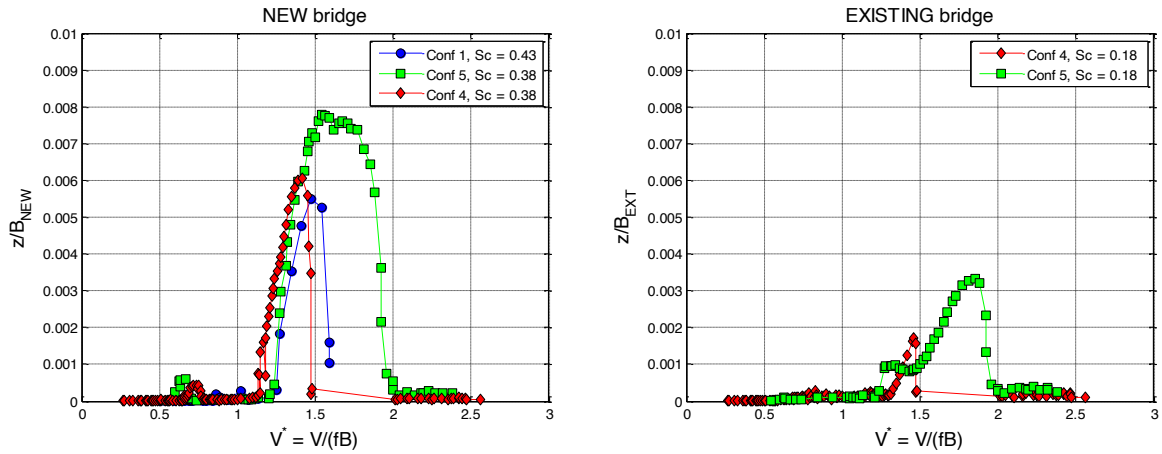
Figure 4. Lock-in region for different configurations: new deck (left) , existing deck (right)
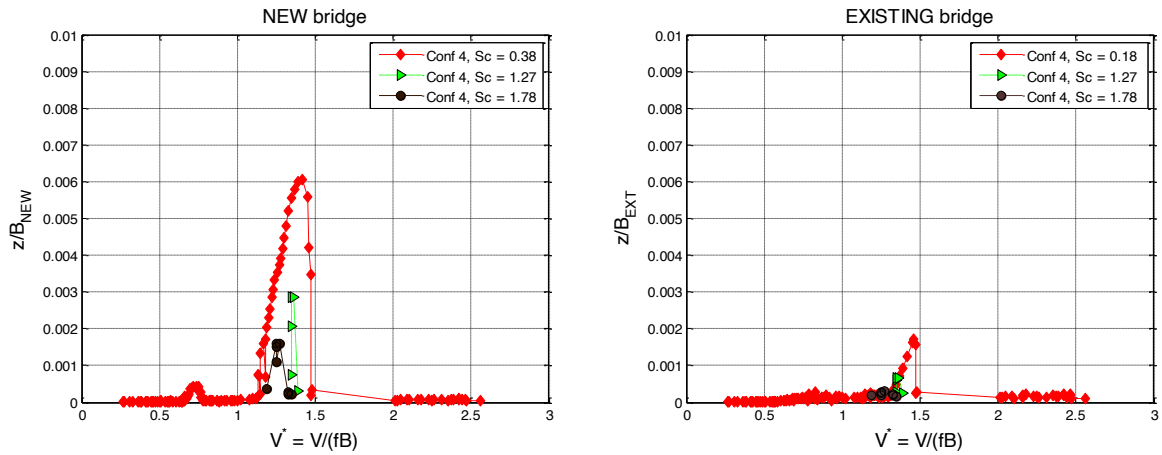
Figure 5. Lock-in region for different configurations: new deck (left) , existing deck (right)

4   Conclusions

The aerodynamic interaction of two different adjacent bridges was studied by means of wind tunnel tests on sectional scale models. The large-scale of the models allows to reproduce geometric details with accuracy and it is very suited for the study of vortex shedding and induced vibrations.

The two bridges are very close to each other and have similar frequencies. One of the bridges suffers from vortex shedding excitation and may influence the response of the other one, if Scruton numbers are sufficiently low. Wind tunnel testing is therefore necessary to assess the safety of the structure, and eventually to identify the minimum level of Scruton necessary to suppress vibrations.

5   Acknowledgements

Wind tunnel tests on "Arco estetico Expo 2015"

Marco Belloli[1], Fabio Robustelli[1] and Lorenzo Rosa[2]

[1]Department of Mechanical Engineering, Politecnico di Milano, Italy
[2]Galleria del Vento, Politecnico di Milano, Italy
Corresponding author: Marco Belloli, marco.belloli@polimi.it

Abstract

This paper presents the experimental activity carried out on the Arco Estetico Expo at Politecnico di Milano Wind Tunnel. The goal of the project is to define the structure response to the turbulent wind and the loads at foundations due to the wind effects. The particular shape of the real prototype suggests that it could experience a wind induced instability, driven by vortex shedding. It has been decided to build a full aeroelastic model in a quite large scale, to investigate all the over mentioned aspects. The study of the wind induced dynamics confirms the results previously highlighted in a different wind tunnel on a sectional model, putting in evidence a very important wind induced instability at quite low wind speed. Taking advantage of the availability of a full aeroelastic model, a damping system has been designed to avoid instability and tested on the model.

1 Introduction

The particular shape and the very low mass per unit length of the structure indicate that the Arco can be subjected to very large wind induced motions, both due to buffeting and to some wind induced instability. A key point to be studied is a galloping instability that occurs at quite high wind velocity, the section of the project is rectangular with 2/3 aspect ratio, which is known to be subject to galloping instability. Moreover at CRIACIV in Florence a sectional model suspended on springs has been tested and it highlights the occurrence of this instability, (Mannini et al. 2013, Mannini et al. 2013).

To well understand the dynamic response of the structure under wind loads it has been decided to build an aeroelastic model in a quite large scale (1/40) and to test it in smooth flow and in turbulent flow with different angles of exposure. The response has been characterized both in terms of accelerations of the Arco and in terms of wind loads at the bases.

2 Full aeroelastic model

A full aeroelastic model of the Arco has been built, adopting a 1/40 scale factor, in order to well represent the geometrical details and to have the larger possible Reynolds Number. The model has been designed and realized using as reference the modal parameters of the real structure, as designed. Natural frequencies, modal deflected shapes and mass distribution has been scaled adopting the Froude scaling rules, to have a unitary scale factor for the accelerations.

The model is realized using a spine structural scheme, the internal beam is an aluminium bar machined using CNC to control the flexural and torsional stiffness along the spine itself. Once built the spine has been calendered to obtain the correct arch shape. To grant the correct external shape and mass distribution an external cover in resin has been connected to the spine. Figure 1 shows the model during the construction stages, it is clearly visible how the external shells are connected to the spine to avoid any collaboration under the stiffness point of view. All the junction and connection between the different parts of the model are realized by glueing to grant the lowest possible damping of the whole structure, i.e. to have very evident wind induced vibrations.

Figure 1. Full aeroelastic model of the Arco while building it. The connection between the external shells and the spine are clearly visible.

Before testing the realized model has been characterized, in terms of modal parameters. The modal identification procedure is based on forced motion tests and free motion tests, to define the natural frequencies, the modal shapes and the damping to critical ration for the first modes.
Table 1 reports the main parameters as designed and as experimentally measured.

Table 1. Modal identification results.

Mode shape	Full scale frequency [Hz]	Model scale target frequency [Hz]	Measured frequency [Hz]	Structural damping [%]
1st flexural out of plane	0.55	3.53	3.43	0.08
1st flexural in plane	1.17	7.41	7.08	0.061
2nd flexural out of plane	1.49	9.42	9.68	0.056
2nd flexural in plane	1.94	12.3	12.92	0.05
3rd flexural out of plane	2.74	17.3	19.01	0.07
3rd flexural in plane	3.53	22.33	23.21	0.054

3 Wind tunnel testing

3.1 Smooth flow

Smooth flow testing highlighted very high acceleration values at high wind speed, in particular for wind speed higher than 23 m/s at full scale a strong dynamic instability – galloping – arises.

Figure 2 reports the antinode vibration amplitudes of the first flexural mode as function of the wind velocity, in particular the standard deviation of acceleration versus the wind velocity at full scale is reported. The different curves on the graph are for different damping to critical ratios. One can observe that the instability disappears for damping to critical ratios of around 2%. Figure 2 is referring to 90 deg incidence angle, or wind perpendicular to the plane of the arch. To have a safe structure at full scale a damping system has been dimensioned and tested on the full aeroelastic model, reaching the 2.7% of damping to critical ratios and supressing the instability. The damping system is a tuned mass damping, scaled according to Froude rules and applied to the model of the structure. In the following a brief description of the TMD is given.
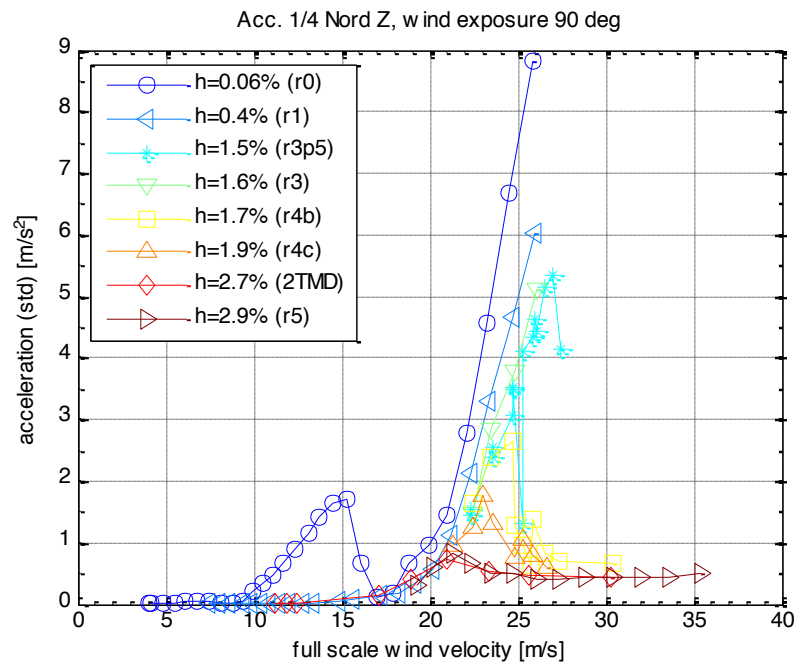
Figure 2. Standard deviation of acceleration at ¼ of the arch, first mode antinode; vertical direction; smooth flow wind perpendicular to arch plane.

The smooth flow conditions have been tested also with the vicinity model, i.e. the surrounding, to check if there is any wake effect on the structure. It has been noticed that the presence of the surrounding excludes the incoming of the instability at high wind speed. The occurrence of galloping instability is also strongly dependent on the angle formed by the wind direction and the plane of the arch, in particular with angle of exposure out of the range ± 15 deg from the perpendicular direction the instability does not appears also for very low damping values, less than 0.5% to critical.

3.2   Turbulent flow

To test the structure response to natural wind, or the so-called buffeting response, the aeroelastic model has been tested in turbulent flow conditions, reproducing the natural boundary layer in the appropriate scale factor, giving to the surrounding model the duty to reproduce the local flow field.

   The dynamic induced to the structure by the turbulent wind is very low if compared to the smooth flow accelerations due to instability, hence the TMD system applied to control the instability will assure very low response also to turbulent wind. Figure 3 reports the arch response to turbulent wind in terms of RMS of accelerations as function of full scale wind speed.
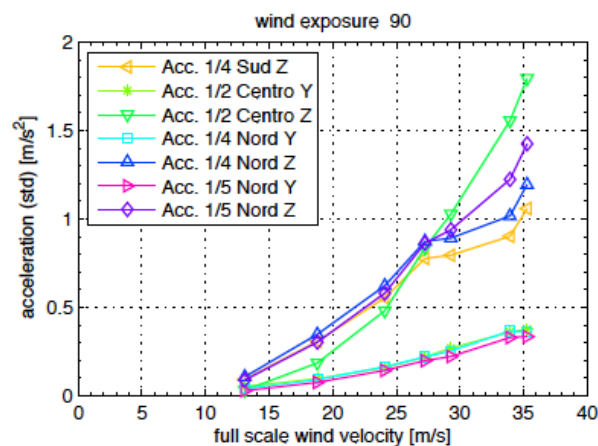
Figure 3. Standard deviation of acceleration at ¼ of the arch, first mode antinode; vertical direction;

4   Tuned Mass Damper

Two different possible solution have been identified to control the instability:
1. Introduce a change in the arch section shape;
2. Increase the damping of the whole system

The first solution is no feasible for aesthetic issues; the design of the arch is strictly connected to the design of the bridges that will be built in the neighbourhood so that under an architectural point of view it is not acceptable to change the shape of only one element. Moreover the structural design of the whole structure at the time we tested the arch in wind tunnel was at a very advanced stage, so changing the shape means to redo all the calculations.

It has been decided to follow the second possible solution to avoid the instability. Both the tests on the sectional model and on the full aeroelastic model highlight that a 3% of damping to critical ratio is enough to completely supress the galloping phenomenon. The only possible solution to increase so much the damping without visible elements is to add tuned mass dampers to the structure and this solution has been adopted also on the full aeroelastic model.

Two TMDs has been realized with mass equal to 22g and 24g, or 1408 kg and 1530 kg at full scale, and the damping of the secondary system is circa equal to 8%. The damping is given using eddy current dampers, using permanent magnets with an adjustable air gap in-between. Figure 4 shows a picture of the realized TMD and installed on the full aeroelastic model.
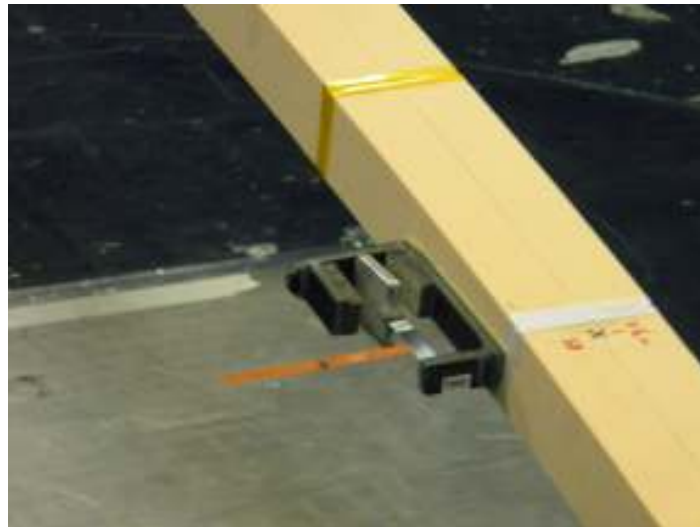
Figure 4. TMD installed on the full aeroelastic model of the Arco.

Using these devices it was possible to increase the damping, controlling the influence of the installation position and also the more effective installation position and damping to critical ratio of the secondary device.

References

Mannini C., Marra A. M., Bartoli G. (2013), Experimental investigation on the VIV-galloping instability of a 3:2 rectangular cylinder, *AIMETA Torino, Italy.*

Mannini C., Marra A. M., Massai T., Bartoli G (2013)., VIV and galloping interaction for a 3:2 rectangular cylinder, *6th European and African Wind Engineering Conference, Cambridge, UK.*

Sand transverse dune aerodynamics: a computational study

Luca Bruno[1], Davide Fransos[2], Alessio Merlo[3] and Luigi Preziosi[3]

[1]Department of Architecture and Design, Politecnico di Torino, Italy
[2]Optiflow Company, Marseille, France
[3]Department of Mathematical Sciences, Politecnico di Torino, Italy
Corresponding author: Luca Bruno, luca.bruno@polito.it

Abstract

The engineering interest about dune fields is dictated by the their interaction with a number of human infrastructures in arid environments. The aerodynamic behaviour of sand dunes in atmospheric boundary layer belongs to the class of bluff bodies. Because of their simple geometry and their frequent occurrence in desert area, transverse sand dunes are usually adopted in literature as a benchmark to investigate dune aerodynamics by means of both computational or experimental approach, usually in nominally 2D setups. The writers suspect the flow in the wake is characterised by 3D features and affected by wind tunnel setup - e.g. blockage effect, duct side wall boundary layer, incoming velocity profile - when experimental studies are carried out. The present study aims at evaluating the 3D flow features of an idealised transverse dune under different setup conditions by means of computational simulations and to compare the obtained results with experimental measurements.

1   Introduction

The engineering interest about dune fields is dictated by their interaction with a number of human infrastructures in arid environments, such as roads and railways, pipelines, industrial facilities, farms, buildings (e.g. Alghamdi and Al-Kahtani 2005). The development, shape and migration of dunes depend fundamentally on wind directionality and availability of mobile sediment. In areas of constant wind direction and under high sand availability, the transverse dune - which has nearly fixed profile in the direction perpendicular to the wind - is the prevailing dune type.

The aerodynamic behaviour of sand dunes in atmospheric boundary layer belongs to the general class of bluff bodies. For sake of clarity, a general 2D scheme of the transverse dune geometry and of the flow around it is given in Figure 1.
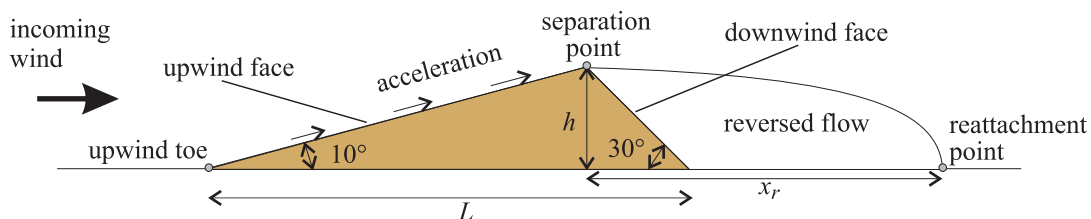
Figure 1 – Transverse dune aerodynamics scheme

The incoming wind flow is first fairly decelerated at the upwind toe, then strongly accelerated along the dune upwind face straight up to crest. The separation of the boundary layer then occurs at the crest itself. The naturally inclined downwind face is surrounded by a reversed flow region, whose extent is one of the key parameters describing the flow. Reattachment of the boundary layer occurs far downstream the dune crest, being x_r sensitive to a number of setup parameters. While nominally 2D flow structures have been extensively scrutinized (Livingstone et al 2007), current literature mainly disregards 3D flow features, if any.

The computational simulation of the flow field over the transverse dune is usually simplified to 2D condition (Livingstone et al 2007), as conducted by many researchers (e.g. Parsons et al. 2004, Schatz and Herrmann 2006, Araújo et al 2013). Analogously, Wind Tunnel (WT) tests adopt dune models spanning across the whole test section width, and with rather low values of the dune span/chord ratio (e.g. *S/L*= 1.28 in Walker and Nickling 2003, *S/L*= 5.4 in Liu et al 2011).

The present study aims at evaluating the 3D flow features around an idealised transverse dune and their sensitivity to setup conditions (incoming flow, side boundary conditions) by means of computational simulations and to compare the obtained results with experimental measurements.

2   Wind flow modelling

The incompressible, turbulent, separated, unsteady flow around the 3D dune is modelled by the classical Time-dependent Reynolds Averaged Navier-Stokes (T-RANS) equations. The *k-ω SST* turbulence model proposed by Menter (1994) is used to close the T-RANS equations. The complete set of governing equations, in Cartesian coordinates, reads

$$
\begin{cases}
\nabla \cdot \overline{u}_f = 0 & x \in \Omega \\[2mm]
\dfrac{\partial \overline{u}_f}{\partial t} + \overline{u}_f \cdot \nabla \overline{u}_f = -\dfrac{1}{\rho_a}\nabla \overline{p} + \nabla \cdot \left[\left(\nu_a + \nu_t\right)\nabla \overline{u}_f\right] & x \in \Omega \\[2mm]
\dfrac{\partial k}{\partial t} + \nabla \cdot \left(\overline{u}_f k\right) = \nabla \cdot \left[\left(\nu_a + \nu_t\right)\nabla k\right] + P_k - \gamma \omega k & x \in \Omega \\[2mm]
\dfrac{\partial \omega}{\partial t} + \nabla \cdot \left(\overline{u}_f \omega\right) = \nabla \cdot \left[\left(\nu_a + \nu_t\right)\nabla \omega\right] + P_\omega - C_\omega \omega^2 + 2\left(1 - F_1\right)\sigma_{\omega 2}\dfrac{1}{\omega}\nabla k \nabla \omega & x \in \Omega
\end{cases}
\tag{3}
$$

where the overbar denotes an average in the Reynolds sense, u_f is the flow velocity, p is the pressure, k is the turbulent kinetic energy, ω is the specific dissipation rate, t is the time, ν_a and ν_t are the air and the turbulent viscosity, respectively. P_k and P_ω are the production terms and are modelled upon the classic Boussinesq hypothesis.

A roughness wall function, or k_s-type wall function is adopted in the viscosity-affected near-wall region, following the best practice guidelines in Blocken et al (2007). A condition is imposed on the value of ν_t such that the velocity at the first grid point off the wall would match the expected logarithmic profile, i.e.

$$
\frac{\left|\overline{u}_f\right|_P}{u_*} = \frac{1}{\kappa}\log\left(\frac{u_* y_P}{\nu C_S k_S^+}\right) + 5.43
\tag{2}
$$

where subscript P indicates the value of the variable at the first off wall grid point, $u_* = C_\mu^{1/4}k_P^{1/2}$ is the friction velocity, $k_S^+ = u_* k_S/\nu$ is the dimensionless roughness height and C_S is a roughness constant usually set to 0.5. According to Blocken et al. (2007), the correct use of this type of boundary condition imposes the choice of the near wall grid discretization such that the first off wall point satisfies $y_P \geq k_S = 9.793 z_0/C_S$.

A quadrilateral grid is adopted to discretise the spatial computational domain. The total number of cells is about $1.e + 06$ and $y_p \approx 0.1h$.

The OpenFoam© Finite Volume open source code is used to numerically evaluate the flow field. The cell-center values of the variables are interpolated at face locations using the second order Central Difference Scheme. The convection terms are discretized by means of the Limited Linear Scheme. The advancement in time is accomplished by the implicit two-step second order Backward Differentiation Formulae (BDF) method. The pressure-velocity coupling is achieved by means of semi-implicit method for pressure-linked equations (SIMPLE) algorithm.

3   Application setup

Three setups are adopted and the corresponding flow compared. All of them generally refer to the 1:100 scaled experimental setup described by Liu et al 2011, but they differ in both the geometry of the analytical domain in space and in the boundary conditions applied. They are summarized in Figure 2 and briefly commented in the following:

s1   only 1/4 of the wind tunnel working section volume is retained. Symmetry conditions on the vertical plane because of the conjectured symmetry of the flow. Free stream conditions on the upper horizontal plane to disregard the influence of the WT upper wall. Incoming mean wind velocity and turbulence intensity profiles fitted on measurements in WT, turbulence length scale not available from measurements, conjectured L_t = 5 mm. This setup is often retained in CFD practice to reduce computational costs when the WT conditions are to be emulated (e.g. in Liu et al 2011). The setup in intended to discuss the accuracy of such an approach;

s2   reproduces exactly the size of the wind tunnel working section in Liu et al 2011. Wall conditions at the four alongwind boundary planes. A complementary simulation (s2-a, Figure 2) is preliminary performed along an empty channel with periodic conditions at inlet and outlet to obtain a fully self-developed incoming flow. The setup aims at removing the ansatz introduced in s1 in order to suggest best practice guidelines in CFD simulations of WT tests;

s3   The side walls of the working section are replaced by spanwise periodic conditions. The domain spanwise length w3 is 4 times the original wind tunnel width w2. The setup aims at evaluating 3D flow features under 2D conditions, if any, and at comparing to the S2 setup.
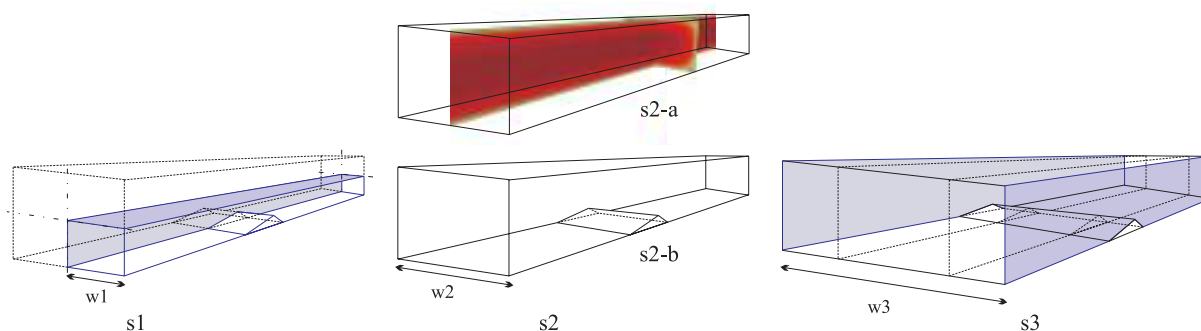
Figure 2 – Adopted setup conditions (wind from left to right)

In all setups, Neumann conditions involving the velocity field and the pressure (null normal component of the stress tensor) as well as k and ω are imposed at the outlet boundary. No-slip conditions are imposed at the wall surfaces. The roughness is set $z_0 = 1e - 4\ [m]$ according to Liu et al 2011. Uniform initial conditions are introduced.

4   Results

Time-averaged wind velocity vertical profiles are measured by PIV in WT tests at different positions in the central x-z vertical plan of the working section (Liu et al. 2011). These profiles are compared in Figure 3 to the obtained ones for the setup s2. The scatter with the WT data around the upwind face (Figure 3, a-b) are probably due, according to Liu et al 2011, to the limitation of the PIV system, which cannot fully resolve the high-speed gradient in the near-surface zone and leads to nonzero wind speed at the surface. The agreement in the reversed flow region (Figure 3, e-f) is excellent for setup s2, while results from setup s1, not included in this abstract for lack of space, strongly overestimate the speed deficit in the wake.

The final study will include the comparison of the wind speed profiles for every setup, and a detailed discussion about 3D flow features in the wake, with special attention to the reattachment line, pressure and shear stresses on the dune and ground surfaces.
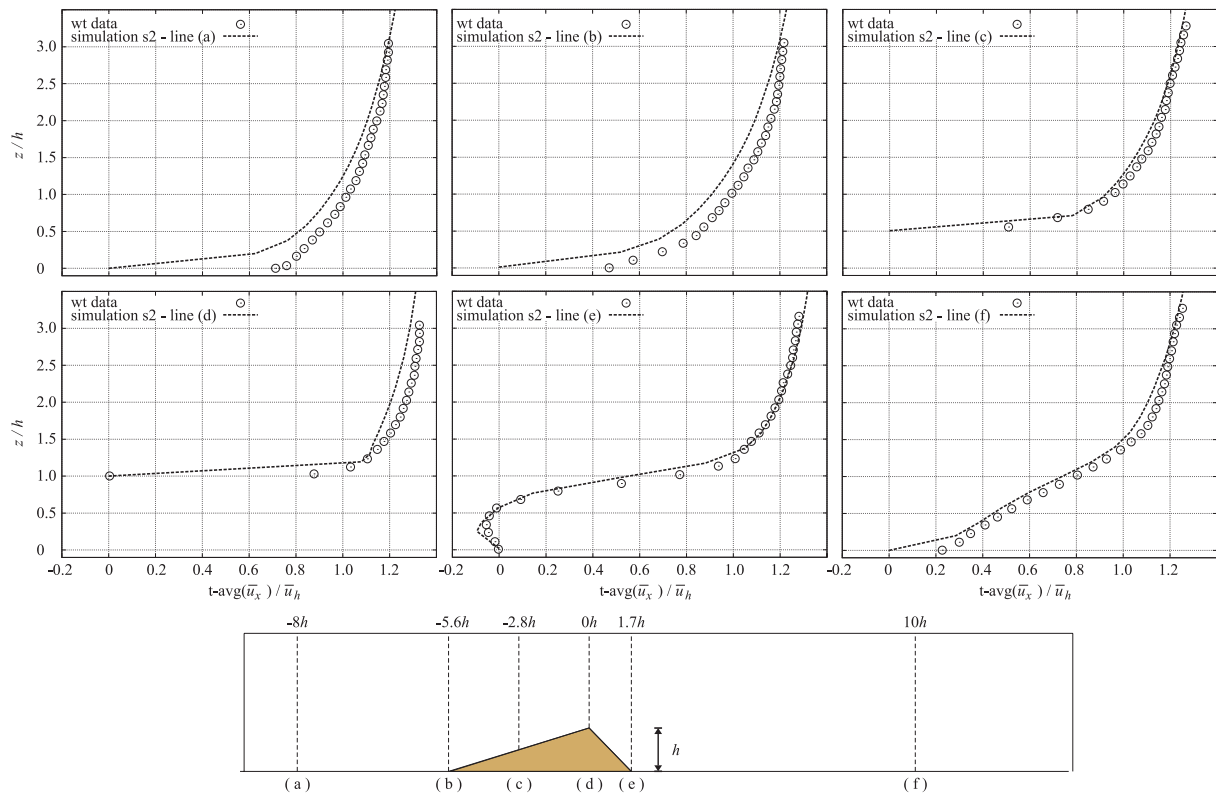
Figure 3 – Wind velocity profiles: wind tunnel measurements and CFD results from simulation s2

References

Alghamdi, A.A.A., Al-Kahtani, N.S. (2005). Sand Control Measures and Sand Drift Fences, *ASCE Journal of Performance of Constructed Facilities* **19:4**, 295-299.

Araújo, A.D. , Parteli, E. J. R., Pöschel, T., Andrade, J.S., Herrmann, H.J. (2013) Numerical modeling of the wind flow over a transverse dune, *Nature Scientific Reports* **3**, 1-9.

Blocken, B., Stathopoulos, T., Carmeliet, J. (2007). CFD simulation of the atmospheric boundary layer: wall function problems. *Atmospheric Environment* **41(2)**, 238–252.

Liu, B., Qu J., Zhang, W., Qian, G. (2011). Numerical simulation of wind flow over transverse and pyramid dunes. *Journal of Wind Engineering and Industrial Aerodynamics* **99(8)**, 879–888.

Livingstone, I., Wiggs, G.F.S., Weaver, C.M. (2007). Geomorphology of desert sand dunes: A review of recent progress *Earth-Science Reviews* **80**, 239–257.

Menter, F.R. (1994). Two-Equation Eddy-Viscosity Turbulence Models for Engineering Applications. *AIAA Journal* **32 (8)**, 1598-1605.

Parsons, D.R., Wiggs, G.F.S., Walker, I.J., Ferguson, R.I., Garvey, B.G. (2004). Numerical modelling of airflow over an idealised transverse dune. *Environmental Modelling and Software* **19**, 153–162.

Schatz, V., Herrmann, H.J. (2006). Flow separation in the lee side of transverse dunes: a numerical investigation. *Geomorphology* **81**, 207–216.

Walker, I.J., Nickling W.G. (2003). Simulation and measurement of surface shear stress over isolated and closely spaced transverse dunes in a wind tunnel. *Earth Surface Processes and Landforms* **28**, 1111–1124.

A generalised model of the lodging of cereal crops

[1]Chris Baker, [1]Mark Sterling, [2]Peter Berry

[1]Department of Civil Engineering, University of Birmingham, United Kingdom
[2]ADAS, Malton, North Yorkshire, United Kingdom
Corresponding author Chris Baker c.j.baker@bham.ac.uk

Abstract

This paper considers an application of wind engineering to a serious agricultural issue – the lodging (blowing over) of cereal crops in rainy and windy conditions. The paper begins by outlining the problem, and previous work on modelling the process for winter wheat is described. A new, generalised, model is then described that can calculate lodging risk for a much wider range of plant form, including crops where significant interlocking between individual plants occurs, such as oilseed rape. Sample results from the model are presented and a sensitivity analysis of lodging risk to various plant, soil and meteorological parameters is set out.

1 Introduction

Lodging, defined as the permanent displacement of plant stems from their vertical position, is a persistent problem for many crop species throughout the world, especially in regions where crops are irrigated or where high winds are common. As a result lodging resistance is considered one of the highest priorities for plant breeders worldwide (Reynolds et al., 2008). In the UK lodging is a particular problem in wheat, barley, oats and oilseed rape (figure 1). It has been shown that severe lodging years occur, on average, every 3 to 4 years when 16% of the wheat area and 35% of the oilseed rape areas are lodged (Berry et al., 1998; 2013). Yield losses from lodging in cereal crops and oilseed rape typically can be up to 25%, but can be up to 75% if lodging occurs early in the season (Berry and Spink, 2012; Berry et al., 2013). The cost of lodging from yield losses in a severe lodging year has been estimated at £105 million for wheat and £64 million for oilseed rape (Berry 2013). These estimates do not include the additional costs of greater grain drying, loss of bread making quality and longer harvesting time. Lodging in the other major UK cereals, barley and oats, is generally considered to be more prevalent than in wheat. If similar lodging costs per hectare are assumed for these cereal species as for wheat, then the total cost of lodging in a severe lodging year is conservatively estimated at £200 million, or approximately £60 million per year on average. Farmers attempt to reduce the risk of lodging by using lodging resistant cultivars and by using chemical plant growth regulators (PGRs). Little progress has been made in breeding varieties with greater lodging resistance and there is evidence in wheat that the lodging resistance of new varieties may in fact be increasing (Kendall et al., 2013). PGRs are used on the majority of UK cereal and oilseed rape crops. However, in future the number of products available may become restricted as a result of changing legislation in Europe (revision of 91/414/EEC). There is thus a need for research in this area to identify which characteristics of the plant / soil system make plants particularly susceptible to lodging.

Figure 1 Stem and root lodging of oats

2   Earlier investigations

The lodging of winter wheat was considered in a series of papers by the authors in the late 1990s and early 2000s, through the development of a model of the wheat lodging process, (Baker et al. 1998, Berry *et al*. 2003), which has since underpinned much of the current understanding of wheat lodging control. It was used to show that two types of lodging (stem and root) are both important. The former involves the bending failure of the stem and the latter involves the failure of the root / soil system. The model also underpins the most comprehensive guide that growers and agronomists use to minimise lodging risk (HGCA Guide: Avoiding lodging in winter wheat: Practical Guidelines) as well as being used by the agricultural industry to quantify the effect of PGRs on lodging risk. The work that led to the development of this model involved a series of field tests to observe and measure the lodging phenomenon, using a novel mobile wind tunnel that was placed over field grown crops. The results from these tests were used to develop a simple mathematical model of the lodging process that allowed the lodging wind speeds to be determined for crops of different types. This model assumes that the wheat plant can be represented by a two mass model connected by a weightless stem. The upper mass corresponds to the ear, whilst the lower mass corresponds to the root ball. A wind force due to a step change in wind speed is applied to the upper mass to cause displacement of the stem, which is resisted by the anchorage characteristics of the root mass. This allows the bending moment at the base of the stem to be determined, which is then compared with the strength at the base of the stem, or the root failure moment to determine whether or not lodging occurs.

Winter wheat is however not the only cereal crop to undergo lodging in adverse conditions and significant lodging has been observed in barley, oats, rice, oilseed rape and sunflowers. Now whilst one might expect the wheat lodging model to be generally applicable to other crops, and indeed it has been used with limited success for barley and sunflowers (Berry et al., 2006; Sporoso et al., 2010), the nature of the other above crops implies that significant modifications need to be made to the model to ensure its applicability. Specifically modifications are required in a number of areas.

- Different crops have different stem structures and plant morphologies between flowering and seed filling that need to be allowed for i.e. not all can be properly represented by the top mass model described above.
- Some crops, such as oats, rice and oilseed rape, have interlocking plant canopies, and, at least in part of the growth period, need to be considered as a complete canopy rather than as individual plants.
- For some crops, oilseed rape in particular, it is clear that stem bending/buckling at any point along the stem can occur, rather than just at the base of the stem.
- Some crops, again, such as oilseed rape, have a tap root anchorage system very different from that assumed in the current model;
- There is an overall need to fully understand the transmission of wind induced forces within crops, from the canopy to the root system, for the whole range of non-interlocking and inter-locking canopies, to enable a more robust model of the lodging of these crops to be developed.

3   The generalised lodging model

To address these issues a more complex generalised model of the lodging process has been developed and will be presented in this paper. This model builds on the earlier work but is different in a number ways. The major developments that have been made are as follows.

- The model now considers the dynamics of both isolated plants and a plant canopy and thus allows for the variation of plant and canopy morphology during the growing season to be taken into account, through a simple consideration of the effective intercrop stiffness and damping.
- The model allows the bending moment along the height of the stem to be calculated and thus enables the possibility of stem lodging at any point up the stem to be investigated.
- Different root forms are now considered – both the root ball type of winter wheat and the tap root type found in oilseed rape, with different root resistant models for each type.
- The new model has a more realistic model of the wind gust process than the old model, based on classical spectral and peak value analysis possible the inclusion of a realistic model for honami gusts
- The model takes as input the probability distributions of wind speed, rainfall, crop and soil characteristics, and through the modelling process arrives at probability distributions for stem and root lodging for a range of wind and rainfall conditions, and thus, through a convolution with the actual wind and rain probabilities, arrives at the overall lodging risk.

In what follows we present the basic outline of the model. A fuller description is given in Baker et al (2014). The modelling process begins by considering the dynamics of a plant canopy, that is either composed of individual plants or plants that are interlocking. A standard two degree of freedom dynamic model of the canopy is set up and results in the following expressions for the mean bending moment $\bar{M}$ and the fluctuating bending moment M' along the stem of an individual shoot of a plant.

$$\bar{M} = \frac{\left(\left(1+\omega_n^2\left(\frac{X}{g}\right)\right)\right)}{\omega_n^2\left(\frac{X}{g}\right)}(0.5\rho A_{CF}X)\left(\cos\left(\alpha\frac{x}{l}\right) - \cot\alpha\sin(\alpha\frac{x}{l})\right)\bar{U}^2 \tag{1}$$

$$M' = \frac{\left(\left(1+\omega_n^2\left(\frac{X}{g}\right)\right)\right)}{\left(\left(\omega_n^2\left(\frac{X}{g}\right)-\omega^2\left(\frac{X}{g}\right)\right)^2+\left(\frac{X}{g}\right)(\theta\omega)^2\right)^{0.5}}(\rho A_{CF}X)\left(\cos\left(\alpha\frac{x}{l}\right) - \cot\alpha\sin(\alpha\frac{x}{l})\right)\bar{U}U' \tag{2}$$

Here ω_n is the radial natural frequency and θ is the damping ratio. X is the height of the centre of gravity of the canopy above the ground, ρ is the density of air, x is the height above the ground, l is the length of the stem, $\bar{U}$ is the mean velocity at canopy top and U' is the fluctuating velocity magnitude at the canopy top at a frequency ω. A_{CF} is the drag area of the plant (effective area x drag coefficient). For crops with an interlocking canopy this is to be interpreted as the shear force area of the canopy top. The   natural frequency and damping ratio vary significantly between canopies with isolated plant and canopies with interlocking crops. The parameter α, which determines how the bending moment varies along the length of the stem, is related to the natural frequency through the following equation.

$$\omega_n = \left(\frac{g}{X}\right)^{0.5}\left(\frac{1}{\alpha^2\tan(\alpha)-1}\right)^{0.5} \tag{3}$$

To assess whether or not lodging occurs we need to define peak moments both at the base of the stem (for root lodging) and along the stem (for stem lodging). We proceed in a conventional way and define firstly a broad banded standard deviation of moment that does not take any resonant effects into account. This is given by

$$\sigma_{MB}{}^2 = \frac{\left(1+\omega_n^2\left(\frac{X}{g}\right)\right)}{\omega_n^2\left(\frac{X}{g}\right)}(\rho A_{CF}X\overline{U})^2(\cos(\alpha\bar{x}) - \cot\alpha\sin(\alpha\bar{x}))^2\sigma_U{}^2 = 4\overline{M}^2I^2 \tag{4}$$

I is the turbulence intensity. In addition we define a resonant component of the standard deviation of the bending moment using an approximation often used in structural design

$$\sigma_{MR}{}^2 = \overline{M}^2I^2\left(\frac{\pi}{\theta}\right)\left(\frac{n_nS(n_n)}{\sigma_U{}^2}\right) \tag{5}$$

Here the term in the final brackets is the normalised wind spectral density at the natural frequency of oscillation. For buildings this is in the tail of the spectra. However for cereal crops this peak coincides with a rather flat maximum in the normalised spectra with a magnitude of about 0.25 (Finnigan 2000). Thus the resonant component takes on the very simple form.

$$\sigma_{MR}{}^2 = \overline{M}^2I^2\left(\frac{\pi}{4\theta}\right) \tag{6}$$

To calculate the peak moment, we then follow the gust factor approach

$$\hat{M} = \overline{M} + ((g_{MB}\sigma_{MB})^2 + (g_{MR}\sigma_{MR})^2)^{0.5} \tag{7}$$

Root lodging takes place over a period of around a minute, and thus the resonant component of the fluctuation is not relevant. For such an averging time the appropriate value of the gust factor and is $g_{MB} = 1.7$ and thus, for root lodging

$$\hat{M} = \overline{M}(1 + 3.44I) \tag{8}$$

Now stem lodging takes place over a much shorter period of time – over one oscillation of the stem, and both broadband and resonant components need to be considered. For the broad banded gust factor with an averaging time of one second, $g_{MB} = 3.43$. From the usual "zero crossings" approach, the resonant gust factor can be calculated as $g_{MR} = 4.15$ for the range of natural frequencies for cereal crops. This gives, for stem lodging

$$\hat{M} = \overline{M}\left(1 + 6.86I\left(1 + 0.0.087\left(\frac{\pi}{4\theta}\right)\right)^{0.5}\right) \tag{9}$$

For stem lodging, the failure criterion is that the peak bending moment at some point along the stem should exceed the breaking strength of the stem. This occurs when the mean velocity at the canopy top exceeds the "stem lodging velocity" which can be shown to be given by the following formula.

$$\overline{U}_{LS} = \left(\frac{\omega_n^2\left(\frac{X}{g}\right)n(\sigma\pi a^3/4)\left(1-((a-t)/a)^4\right)}{\left(1+\omega_n^2\left(\frac{X}{g}\right)\right)(0.5\rho A_{CF}X)(\cos(\alpha x/l)-\cot\alpha\sin(\alpha x/l))\left(1+6.86I\left(1+0.366\left(\frac{\pi k}{2\theta}\right)\right)^{0.5}\right)}\right)^{0.5} \tag{10}$$

where n is the number of shoots per plant, σ is the yield strength of the stem, a is the stem radius and t is the stem thickness. Clearly these latter parameters vary along the stem, and in principle lodging can occur at any point. For root lodging the situation is somewhat more complex. The lodging criterion is that the peak stem base bending moment should be greater than the strength of the root / soil system, which gives

$$\overline{M}(1 + 3.44I) > \gamma s d^3 \tag{11}$$

where γ is a constant, σ is the soil shear strength and d is the effective root ball diameter. For plants with a root ball this can be simply estimated form the size of the ball. For tap root systems it is given by (root plate diameter^2 x tap root length)$^{1/3}$. The soil shear strength is however a function of the degree of saturation of the ground. This can be calculated following the procedure of Berry et al (1998) which effectively gives the degree of saturation as a function of daily rainfall. This enables us to define a reference daily rainfall and a "root lodging velocity" as follows

$$i_o = \frac{\left(\frac{\rho_s}{\rho_w}\right)(f-w)l}{\left(1-1.32e^{-5\left(\frac{f-w}{c}\right)}\right)} \tag{12}$$

$$\overline{U}_{LR} = \left(\frac{\omega_n^2\left(\frac{X}{g}\right)\gamma s_D d^3}{\left(\left(1+\omega_n^2\left(\frac{X}{g}\right)\right)(0.5\rho A_{CF}X)(1+3.44I)\right)}\right)^{0.5} \tag{13}$$

Here ρ_s is the soil density and ρ_w is the density of water, f is the water content of the soil at field capacity (saturated) and w is the water content of the soil at the wilting point (dry). c is the clay content of the soil. Lodging occurs when the daily rainfall exceeds a specific value.

$$i > \left(1-\frac{U^2}{\overline{U}_{LR}^2}\right)i_0 \tag{14}$$

This methodology allows a simple representation of the lodging phenomenon in a straightforward graphical way, as illustrated in figure 2 below.
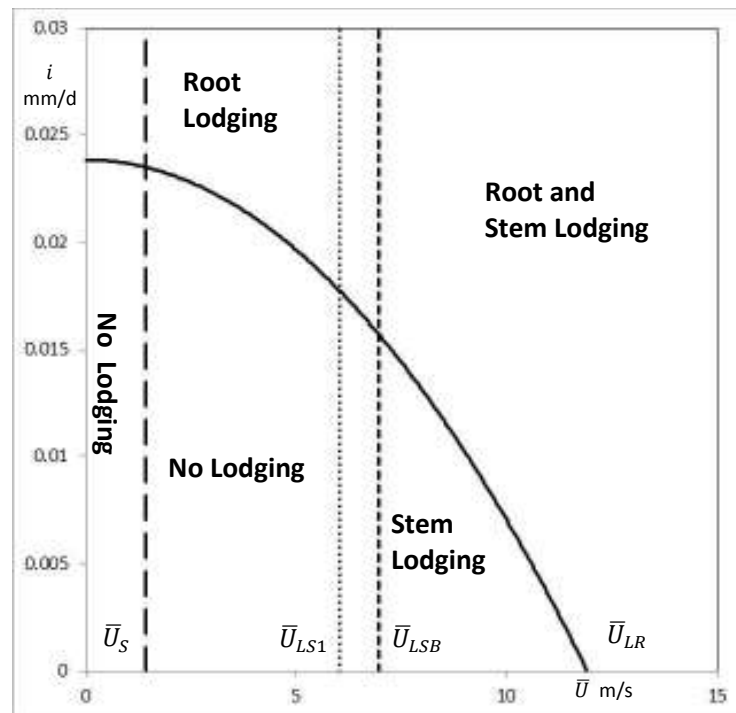
Figure 2 Lodging areas in the mean wind speed / daily rainfall plane

This figure shows regions of the daily rainfall / mean wind speed plane where lodging does and does not occur. It has been calculated for the parameters of a typical oat crop. The root lodging limit is a parabolic curve given by equation (14). Two stem lodging limits are given – one for lodging at the

stem base and one for lodging at the first internode, some way up the stem. There is a region at the left of the graph where the wind speed is never strong enough for lodging to occur, even when the soil is fully saturated. The wind velocity at which this occurs, $\overline{U}_S$, is given by

$$\frac{\overline{U}_S}{\overline{U}_{LR}} = \left(1 - \frac{i_s}{i_o}\right)^{0.5} \tag{15}$$

where i_s is

$$i_s = \left(\frac{\rho_s}{\rho_w}\right)(f-w)L = \left(1 - 1.32e^{-5\left(\frac{f-w}{c}\right)}\right)i_0 \tag{16}$$

4. The calculation of lodging risk

The risk of lodging can be calculated by specifying a joint probability distribution of wind speed and rainfall, and integrating this over the region of the lodging plane of figure 2 where lodging occurs. We assume that the wind speed and rainfall probability distributions are independent of each other. An analysis of UK data suggest that there is an interaction between the distributions but only in the high wind / rainfall region of the lodging plane, where one may assume lodging to always occur. In essence any probability distributions can be assumed, but for the sake of analytical simplicity we assume a Rayleigh distribution for wind speed and an exponential distribution for rainfall. Both of these are quite plausible representations of reality, and yet allows an analytical expression for risk to be calculated. These distributions are given by

$$p(\overline{U}) = \left(\frac{2}{\lambda}\right)\left(\frac{\overline{U}}{\lambda}\right)e^{-\frac{\overline{U}^2}{\lambda}} \tag{17}$$

$$p(i) = \left(\frac{1}{m}\right)e^{-\left(\frac{i}{m}\right)} \tag{18}$$

Here λ is a parameter that specifies the mean wind speed, and m is the daily rainfall. This distribution is shown in figure 3, using the same scales as in figure 2. It is clear that the high regions of the p.d.f are in the lower part of the windspeed / rainfall plane of figure 2. We now define the following dimensionless parameters

$$\widetilde{m} = \frac{m}{i_0} \tag{19}$$

$$\widetilde{U}_S = \frac{\overline{U}_S}{\lambda} \tag{20}$$

$$\widetilde{U}_{LS} = \frac{\overline{U}_{LS}}{\lambda} \tag{21}$$

$$\widetilde{U}_{LR} = \frac{\overline{U}_{LR}}{\lambda} \tag{22}$$

The parameters defined in equations (20) to (23) are effectively the governing parameters of the problem. The overall risk is then given by the following formula for when both root and stem lodging occur.

$$R = e^{-\widetilde{U}_{LS}^2} + e^{-\left(\frac{1}{\widetilde{m}}\right)}\left(\frac{\widetilde{U}_{LR}^2\widetilde{m}}{\widetilde{U}_{LR}^2\widetilde{m}-1}\right)\left(e^{-(\widetilde{U}_S)^2\left(\frac{\widetilde{U}_{LR}^2\widetilde{m}-1}{\widetilde{U}_{LR}^2\widetilde{m}}\right)} - e^{-\widetilde{U}_{LS}^2\left(\frac{\widetilde{U}_{LR}^2\widetilde{m}-1}{\widetilde{U}_{LR}^2\widetilde{m}}\right)}\right) \tag{23}$$

If only root lodging occurs this becomes

$$R = e^{-\tilde{U}_{LR}^2} + e^{-\left(\frac{1}{\tilde{m}}\right)}\left(\frac{\tilde{U}_{LR}^2\tilde{m}}{\tilde{U}_{LR}^2\tilde{m}-1}\right)\left(e^{-(\tilde{U}_S)^2\left(\frac{\tilde{U}_{LR}^2\tilde{m}-1}{\tilde{U}_{LR}^2\tilde{m}}\right)} - e^{-\tilde{U}_{LR}^2\left(\frac{\tilde{U}_{LR}^2\tilde{m}-1}{\tilde{U}_{LR}^2\tilde{m}}\right)}\right) \tag{24}$$

The variation of risk as given by this equation is shown in figures 4 and 5 below for root and stem lodging. Figure 4 shows that, for the root lodging only case, the lodging risk is primarily a function of the dimensionless root lodging velocity with the dimensionless rainfall having a smaller effect. When both stem and root lodging occurs the problem is more complex with both the dimensionless stem and root lodging velocities being of importance. Again variations in the dimensionless rainfall seem to be of little significance.
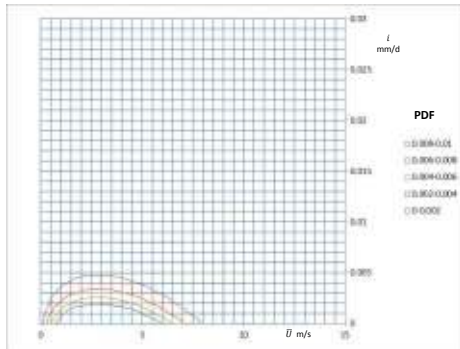
Figure 3 Wind speed / rainfall probability distributions
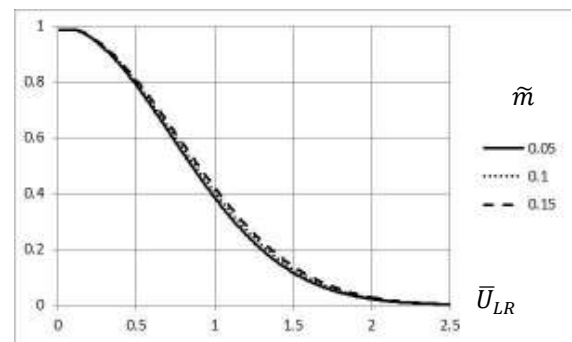
Figure 4 Variation of risk for root lodging
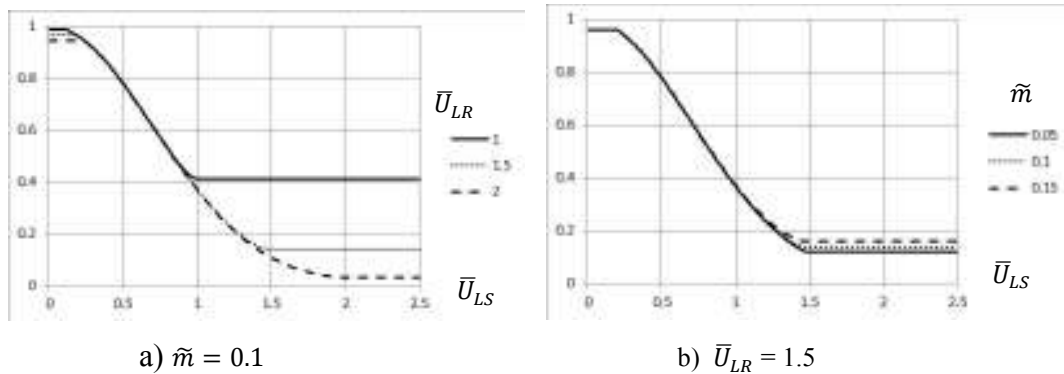
a) $\tilde{m} = 0.1$

b) $\overline{U}_{LR} = 1.5$

Figure 5 Variation of risk for stem and root lodging

5. Risk calculations for different crops

Risk calculations have been carried out for three distinct crop types – winter wheat, oats and oilseed rape. The assumed parameters, and the assumed uncertainties in these parameters, are given in table 1. Essentially the wheat characteristics are taken from those used by Berry et al (2003), the oat characteristics from the recent QUOATS project and the rape characteristics form a series of projects described in Berry et al (2013). At a number of points there are "author estimates" of certain parameters. The point made above concerning the arbitrariness of some of the modelling assumptions must be stressed, and the absolute of the risk not relied on. The most significant assumption is that for the root strength parameter γ for the tap root model for rape is taken as having a value of 4.0, ten times the experimentally measured values for wheat and oats . In each case a 100 realisations of the risk have been made, with the input parameters assumed to have rectangular probability distributions with

the mean ± limit range. It can be seen that for the wheat crop both root and stem lodging is predicted, with $\tilde{U}_{LS} < \tilde{U}_{LR}$. The same is true for the oats crop, but this time two values of $\tilde{U}_{LS}$ are given, with the values for the first node being less than that at the base and thus more critical. For the oilseed rape crop only root lodging is predicted with $\tilde{U}_{LR} < \tilde{U}_{LS}$. The uncertainties in the risk calculations can be seen to be relatively large (of the order of ±0.1).

One might expect the lodging risk to change through the season, and in particular over the period of crop interlocking. Whilst there is as yet no experimental data available to be able to study this in detail, a preliminary calculation can be made. For the oats crop the average value of risk was 0.22. Going from non-interlocking to interlocking crops one might expect the natural frequency to decrease, and the damping to increase. It was thus assumed that the natural frequency would fall from 1.4Hz to 0.7Hz, and the damping would increase from 0.05 to 0.5. A decrease in the natural frequency alone increases the risk to 0.27, whilst the increase in the damping decreases the risk to 0.19. When considered together the risk increases slightly to 0.24 i.e. the changes are well within the levels of uncertainty outlined above.

6. Conclusions and suggestions for further work

From the material presented in earlier sections the following conclusions can be drawn.

- The lodging phenomenon for both isolated plants and interlocking canopies can be simply modelled using a second order harmonic equation, provided that the natural frequencies, damping ratios and wind forces are suitably specified in each case. This results in simple expressions for both the mean and the fluctuating moments along the length of the plant stem.
- By applying suitable root and stem lodging criteria, it is possible to define mean wind velocities for the occurrence both root and stem lodging that are simple functions of a wide range of plant, soil and weather parameters.
- The definition of these velocities enables a graphical representation of the lodging process to be developed that clearly indicates regions of lodging and non-lodging in the rainfall / wind velocity plane.
- The assumption of a Rayleigh distribution for wind speed probabilities and an exponential distribution for rainfall probabilities allows simple formulae for lodging risk to be derived that are simple functions of dimensionless saturation, stem lodging and root lodging wind velocities, and dimensionless mean rainfall intensity.
- For most practical situations the stem and root lodging risks can be calculated from exponential functions of dimensionless stem and root lodging velocities.

Whilst the model presented in this paper thus represents a simple and effective way of studying lodging for a variety of crops, it still requires development in a number of ways.

- The firmer specification of the gust periods of relevance to root and stem lodging.
- The incorporation of honami dynamics into the model.
- The development and testing of a robust tap root model.
- The specification of crop parameters for interlocking canopies of different types.

These developments of course imply the need for field tests on different crops throughout the growing season.

Table 1. Crop parameters used in calculation

	Wheat		Oats		Rape	
	Assumed	Limits[9]	Assumed	Limits[9]	Assumed	Limits[9]
Growth stage	65[1]	-	71-83[1]	-	4,5[2]	-
Canopy height X (m)	0.43[3]	0.05	0.95[4]	0.15	1.52[7]	0.2
Canopy type	Isolated	-	Isolated	-	Isolated	-
Root type	Ball	-	Ball	-	Tap	-
Root constant γ	0.4[3]	0.1	0.4[5]	0.1	4.0[8]	1.0
Plant / canopy natural freq. f_n (Hz)	0.95[3]	0.2	1.4[5]	0.2	0.50[8]	0.1
Plant / canopy damping ratio θ	0.10[3]	0.02	0.10[5]	0.02	0.10[8]	0.02
Plant drag / shear coeff. area (m^2)	0.025[3]	0.003	0.01[5]	0.003	0.037[8]	0.003
Stem diameter a – internode 1 (mm)	3.25[3]	0.5	6[4]	1	11.1[8]	2
Stem diameter a – internode 2 (mm)	-	-	7[4]	1	-	-
Wall thickness t – internode 1 (mm)	0.64[3]	0.15	1[4]	0.2	2.2[8]	0.5
Wall thickness t – internode 1 (mm)	-	-	1[4]	0.2	-	-
Stem strength σ – internode 1 (MPa)	30[3]	5	30[4]	5	25[8]	5
Stem strength σ – internode 2 (MPa)	-	-	25[4]	5	-	-
Root plate diameter d (mm)	38[3]	10	50[4]	10	16.5[8]	3.0
Root plate depth l (mm)	40[3]	10	70[4]	10	123[8]	15
Number of stems/plant n	3.2[3]	0.5	2.5[4]	0.5	8.2[8]	1
Visual score v	5[3]	1	5[3]	1	5[3]	1
Clay content c	0.25[3]	0.03	0.25[3]	0.03	0.25[3]	0.03
Water content at wilting point w	0.27[3]	0.03	0.27[3]	0.03	0.27[3]	0.03
Water content at field capacity f	0.15[3]	0.03	0.15[3]	0.03	0.15[3]	0.03
λ_{10} (m/s)	4.0[6]	0.5	4.0[6]	0.5	4.0[6]	0.5
Mean daily rainfall m (mm)	2.0[6]	0.5	2.0[6]	0.5	2.0[6]	0.5
Turbulence intensity I	0.5[7]	0.1	0.5[7]	0.1	0.5[67]	0.1
$\bar{U}_S$ m/s	0.73		1.42		0.29	
$\bar{U}_{LS}$ m/s base	2.20		6.02		8.83	
$\bar{U}_{LS}$ m/s node 1	-		6.95		-	
$\bar{U}_{LR}$ m/s	6.12		11.91		2.43	
Risk	0.58		0.22		0.55	
Risk – 2 standard deviations	0.52		0.16		0.44	
Risk + 2 standard deviations	0.63		0.28		0.67	

[1] Tottman (1987), [2] Sylvester-Bradley and Makepeace (1984), [3] from Berry et al (2003) [4] Values from QUOATS trial for Balado –only info for internodes 1 and 2 – for other internodes, very similar to internode, [5] From UOB wind tunnel tests, [6] From MO data for Watnall *http://www.metoffice.gov.uk/climate/uk/mi/* [7] from Finnigan (2000), [8] from Berry et al (2013), [9] Author estimate

References

Baker C J, Berry P M, Spink J H , Sylvester-Bradley R, Griffin J M, Scott R K, Clare R W 1998. "A method for the assessment of the risk of wheat lodging", *Journal of Theoretical Biology* 194, 587-603

Baker C J, Stering M, Berry P M (2014) "A generalised model of crop lodging". Submitted for publication in the *Journal of Theoretical Biology*

Berry, P.M., Spink, J.H, Griffin, J.M., Sylvester-Bradley, R., Baker, C.J., Scott, R.K. and Clare, R.W (1998). "Research to understand, predict and control factors affecting lodging in wheat". Home-Grown Cereals Authority Research Project No. 169.HGCA, London, 131pp.

Berry, P.M., Sterling, M., Baker, C.J., Spink, J.H. & Sparkes, D.L. (2003). "A calibrated model of wheat lodging compared with field measurement"'s. *Agricultural and Forest Meteorology* 119, 167-180.

Berry, P.M., Sterling, M.S. and Mooney, S.J. (2006). "Development of a model of lodging for barley". *Journal Agronomy and Crop Science* 192, 151-158

Berry, P.M. and Spink, J. (2012). "Predicting yield losses caused by lodging in winter wheat". *Field Crops Research* 137, 19-26.

Berry, P.M., White, C., Sterling, M., Baker, C. (2013). "Develop a model of lodging risk in oilseed rape to enable integrated lodging control to reduce PGR use". Chemical Regulatory Directorate Report PS2146.

Berry, P.M. (2013). "New advances in PGRs". British Crop Protection Conference, Rothamsted, UK. 20 November 2013.

Finnigan J (2000) Turbulence in plant canopies, Annual Review of Fluid Mechanics 32:519–571

Kendall, S., Berry, P.M. and Griffiths, S. (2013). "Historical analysis of the effects of breeding on the height of winter wheat". AAB Conference 'Crop Breeding over 10,000 years; lessons for current and future challenges'. 7th October 2013, NIAB, Cambridgeshire, UK.

Reynolds MP, Dixon J, Ammar K, Kosina P, Braun HJ, 2008. "Stakeholder priorities for internationally-coordinated wheat research". In: Reynolds MP, Pietragalla J, Braun H. (Eds). International Symposium on Wheat Yield Potential: Challenges to International Wheat Breeding. CIMMYT.

Sporoso, M.M, Berry, P.M., Sterling, M., Hall, A.J., Chimenti, C.A. (2010). "Modelling root and stem lodging in sunflowers". *Field Crops Research* 119, 125-134

Totmann D R (1987) "The decimal code for the growth stages of cereals, with illustrations", *Annals of Applied Biology* 110, 2, 441–454, DOI: 10.1111/j.1744-7348.1987.tb03275.x

Sylvester-Bradley R, Makepeace R J (1984) "A code for stages of development in oilseed rape (Brassic napus L.)". *Aspects of Applied Biology* 6, 399-419.

Cross wind and rollover risk on lightweight railway vehicles

F. Cheli[1], S. Giappino[1], D. Rocchi[1], G. Tomasini[1]

[1]Politecnico di Milano, Department of Mechanical Engineering, Italy
Corresponding author: G. Tomasini, gisella.tomasini@polimi.it

Abstract

The paper investigates the effects of lateral wind on different type of railway vehicles, comparing the cross wind behaviour on a high speed train and on a modern train used for urban transportation. The second is characterized by a low operating speed, but also by a low mass that increases the risk of rolling over. In order to compare the two trains in terms of response to cross wind, two subsequent analyses have been performed: measurement of the force aerodynamic coefficients by means of wind tunnel tests on scale models and evaluation of the rollover risk by means of the definition of the Characteristic Wind Curve through a simplified numerical procedure, based on the static equilibrium, proposed by the TSI standard (three mass model).

1   Introduction

High cross-winds on rail vehicles may result in a risk of blowing over that can occur in practice, and in the design of any new train these risks have to be considered very seriously (Baker et al., 2009). This has led to the development of specific standards to lay out rigorous risk-assessment procedures for vehicles to operate (CEN, 2010; TSI, 2008) on exposed lines. All risk analysis methods require the knowledge of cross-wind aerodynamic force and moment coefficients that are generally obtained through wind tunnel testing on scaled models (Cheli et al., 2006; Bocciolone et al., 2008). Even if cross-wind effects are of critical importance in high-speed trains also lightweight railway vehicles can suffer of these problems.

In this research activity we compare the effects of lateral wind on a low speed, light-weight, train and a high speed train, in the following named *LS* and train *HS*. In order to compare the two trains in terms of response to cross wind, two subsequent analyses have been performed: win tunnel tests to measure the force aerodynamic coefficients and evaluation of the rollover risk by means of a numerical procedure (CWC).

2   Wind tunnels tests

2.1   Tests set-up

Wind tunnel tests on the two trains were carried out in the Politecnico di Milano Wind Tunnel employing a 1:20 scale model for the low speed train (Figure 1a) and a 1:15 scale model for the high speed train (Figure 1b). Tests were performed in the high-speed test section in low turbulence flow conditions. The convoy of the low speed train is composed by three vehicles while the convoy of the high speed train is composed by the power car and one half of the coach.

Table 1 summarizes the main dimensions (length, width and height) and the mass properties of the full scale vehicles for both the considered trains. Tests have been carried out on a flat ground scenario (without ballast and rails), which is one of the reference scenarios described in the TSI 232/2008 standard. To realize the flat ground scenario a splitter plate, 350mm high, has been adopted in order to have an equivalent block profile of the mean wind speed.

A force balance (RUAG 192) is used to measure the overall forces and moments on the vehicles. The non-dimensional aerodynamic coefficients are defined according to the CEN standard. The reference frame system is fixed to the carbody and its origin is coincident with the carbody centre, at ground level. The wind angle β_w with respect to the vehicle is zero when the wind is parallel to the vehicle, opposite to the running direction.

| (a) | (b) |

Figure 1. Wind tunnel models: low speed train (a) and high-speed train (b)

Table 1 Dimensions and mass properties of the two trains investigated

Train	Length [mm]	Width [mm]	Height [mm]	Total mass [kg]	Centre of gravity height [mm]
Low Speed	17455	2650	3600	29240	1680
High Speed	20250	3020	4000	66964	1329

2.2 Experimental results

Figure 3 shows the force coefficients most significant for the cross wind problem measured on the first vehicles of both the trains. It is possible to observe in the comparison that the lateral force coefficient (Figure 2a) on the low speed train is significantly lower.

| (a) | (b) |

Figure 2: Comparison between force aerodynamic coefficients of low speed and high speed train, first vehicle. C_{Fy} (a) and C_{Mxlee} (b)

Due to the coefficient definition, which uses a fixed value for parameters A (equal to 10 m^2) and h (equal to 3 m), the coefficients represent normalized forces based on the same reference dimensions that is a comparison in terms of actual forces on the full scale train. The C_{Mxlee} coefficient (Figure 2b)

shows the combined effect of the lateral and vertical forces in terms of overturning risk and it is used in the CWC calculation. The aerodynamic force is higher on the high speed train: this is mostly due to the train dimensions, in fact the lateral area of the high speed train is about 30% higher than the low speed one. On the other hand, the overturning risk is influenced not only by the aerodynamic forces but also by the inertial-dynamic properties of the rail vehicle: to evaluate the actual overturning risk it is necessary to calculate the Characteristic Wind Curves, as in the next section.

3   Characteristic Wind Curves

The two trains have been compared also in terms of CWC (Cheli et al., 2006; Baker et al., 2009; Cheli et al., 2012). As described in EN 14067-6, the most simple approach to calculate the CWC is the three mass model, based on the static equilibrium of all the acting forces and moments. The mass properties used to calculate the restoring moment due to the vehicle masses are reported in Table 1.

3.1   CWC results

Figure 3 shows the CWC evaluated for the two trains as a function of the absolute wind angle with respect to the track, for two vehicle speeds: V_{train}=80 km/h that corresponds to the commercial top speed for the low speed train (Figure 3a) and V_{train}=300 km/h that corresponds to the commercial top speed for the high speed train (Figure 3b). Figure 3a shows that the low speed train has lower CWC values with respect to the high speed train travelling at the same velocity: even if the high speed train has higher aerodynamic coefficients and so it experiences an higher aerodynamic moment, its high mass generates a corresponding high restoring moment increasing the CWC limit.

Figure 3. CWC for the two trains as a function of the wind angle (first vehicle only) for the maximum train speed: low speed train (a) and high-speed train (b)

In the same graph it is possible to observe that the lowest value of CWC in both the trains is reached not for perpendicular wind (β_w =90°), but at β_w =70°. This is due to the typical trend of the first vehicles aerodynamic coefficients that show the maximum value for a wind angle lower than 90° (see Figure 2). As expected a train speed increase reduces the CWC limit in the high speed train when it travels at the top speed (Figure 3b). It is interesting to compare the behavior of the two trains at their top speed; in fact, even if the low speed train has a maximum velocity equal only to 80 km/h, its CWC limit is even lower than the CWC limit of the high speed train travelling at 300 km/h. This behavior is also visible in the graph of Figure 4 that shows the CWC as a function of the train speed for the two wind angles β_w=70° and β_w =90°. The critical velocity decreases as the train speed increases and the limit value at the top speed is slightly lower for the low speed train.

Figure 4: CWC for the two trains as a function of the wind speed (first vehicle only). The CWC is limited to the maximum train speed

4 Conclusions

The paper investigated the cross wind effects comparing the behaviour of a high speed train and a low speed train. Modern low speed trains are often very light making them more sensitive to the overturning risk due to the lateral wind. The characteristic wind curves has shown that, limiting the analysis up to the commercial train top speed, a low speed train can have lower values of the critical wind velocity with respect to an high speed train.

Acknowledgements

References

Baker, C., Cheli, F., Orellano, A., Paradot, N., Proppe, C. & Rocchi, D. (2009). Cross-wind effects on road and rail vehicles. *Vehicle System Dynamics*, **47-8**, 983-1022.

Bocciolone M., Cheli F., Corradi R., Muggiasca S., Tomasini G. (2008). Crosswind action on rail vehicles: wind tunnel experimental analyses. *Journal of Wind Engineering and Indus-trial Aerodynamics*, **96**, 584-610.

CEN (2010), EN14067-6. Railway applications – Aerodynamics. - Part 6: Cross wind. CEN, Brussels.

Cheli, P. Belforte, S. Melzi, E. Sabbioni, G. Tomasini, (2006). A numerical-experimental approach for evaluating cross wind aerodynamic effects on heavy vehicles. *Journal of Vehicle System Dynamics Supplement*, **44**, 791-804.

Cheli, F., Corradi, R., Tomasini, G., (2012). Crosswind action on rail vehicles: A methodology for the estimation of the characteristic wind curves, *J. Wind Eng. Ind. Aerodyn.* **104–106**, 248–255.

TSI (2008), European Rail Agency. Technical Specification for Interoperability (TSI 232/2008) – Rolling Stock subsystem, 96/48/EC

Wind characteristics on a suspension bridge at the inlet of a fjord

Etienne Cheynet[1], Jasna Bogunović Jakobsen[2] and Jónas Þór Snæbjörnsson[3]

[1,2]Department of Mechanical and Structural Engineering and Materials Science, University of Stavanger, Norway

[3]School of Science and Engineering, Reykjavik University, Iceland

Corresponding author: Etienne Cheynet, etienne.cheynet@uis.no

Abstract

This paper discusses the wind field characteristics monitored on a suspension bridge located at the mouth of a fjord in Norway. The main focus is on the influence of the topography on the homogeneity of the flow as well as turbulence characteristics. The alignment of the fjord, its steep sides with local valleys and the islands transform the global airflow into the local wind, acting on the bridge. The influence of the terrain is examined by relating the mean wind speed and wind direction on the bridge to the data from the weather station at Sola airport, some 30 km west of the bridge. The fjord is found to have a channelling effect on the airflow resulting in a wind-rose that shows two dominating wind directions. The observed wind velocities have a different characteristics depending on the wind directions. For instance, higher turbulence intensities are observed for winds from North over the mountains, than from South over an extended fetch over sea. Variations in the flow along the bridge are also observed, most likely strongly influenced by the topography on each side of the bridge.

1 Introduction

The Coastal highway E39 project in Norway aims to join Kristiansand to Trondheim without using ferries to cross the fjords. Therefore, a number of cable-supported bridges, floating bridges, submerged bridges or combination are being considered for future construction. The high depth and width of the fjords makes the task particularly challenging. Detailed evaluation of wind induced vibrations for such structures, including the assessment of appropriate turbulence models for the complex topography of the fjords is required. Few studies of full-scale bridge in complex terrains such as fjords are available, among them one can cite the study of the Clifton bridge by Macdonald (Macdonald, 2004). The complex topography of fjords can perturb the wind field, in such a way that classical turbulence models become insufficient in describing the flow conditions, as they generally assume flat and homogeneous surface conditions. .

The Lysefjord Bridge located at the inlet of Lysefjord is used as study case. The bridge has a main span of 446 m, and is oriented from North-West to South-East. Both of the bridge extremities are close to the steep hills (see Figure 1). The first one is Sokkaknuten with a maximum altitude of 341 m approximately 0.6 km North-West of the bridge Northern tower. To the South-West, Bergefjellet has maximum altitude of 625 m, in 1.5 km distance from the bridge. The topography defines two main wind directions, which are indicated in Figure 1: North-East for wind coming from the inside of the fjord, and South-West for wind coming from the outside of the fjord.

The area to the South-West of the bridge is an open area, with 1.5 to 2 km of water before a transition to a hill. To the North-East, the fjord with its steep sides protrudes 35 km into the land. A small island called Bergsholmen is located at 1 km North-East of the bridge, with an altitude of 54 m, which coincides with the elevation of the central part of the bridge.
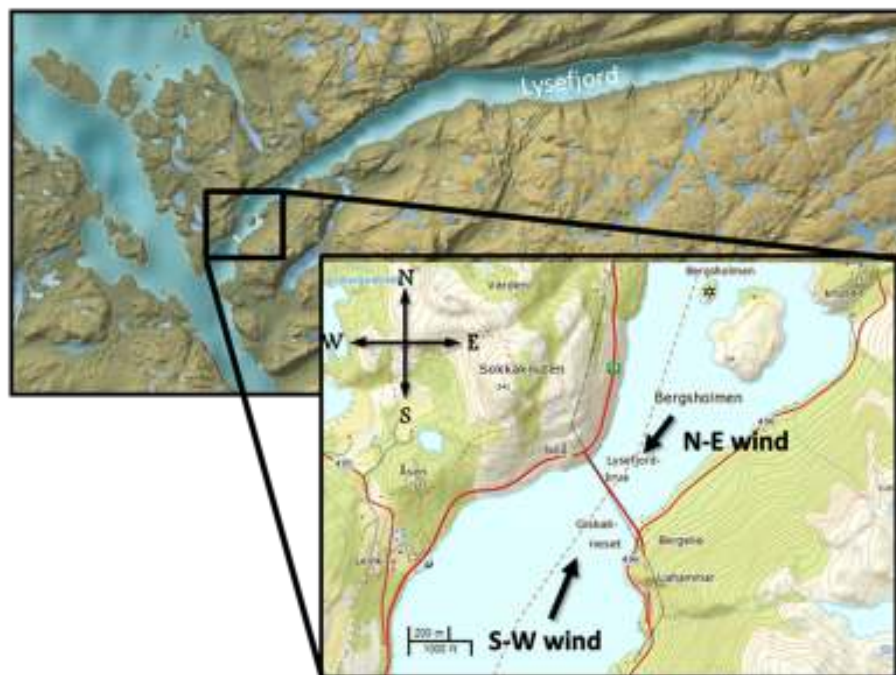
Figure 1. orientation and two main wind directions observed by the measurement system

Four 3D Gill WindMaster Pro sonic anemometers and one Vaisala weather transmitter WXT520 were installed at different locations on the bridge, in November 2013. The distance between anemometers varies from 24 m to 168 m. The sensors have been synchronized to provide a multiple-point measurement of the wind field. The Vaisala sensor and one of the Gill WindMaster are mounted on the hangers of the bridge, while the other anemometers are installed on the main cables. The sensors are mounted at the South-West side of the bridge, approximately 6 m above the bridge deck. Finally, two pairs of accelerometers are installed inside the bridge deck, one on the middle of the deck and the other 72 m toward south. The sensors are linked to CUSP[1] data acquisition units. GPS timing is used to synchronize the data, and a 3G router enables a wireless data access and transfer via a mobile net. The sampling rate for the WindMaster is 32 Hz and 4 Hz for the Vaisala weather station. The acceleration data is sampled at 200 Hz. The recorded data are registered on an online server, extracted with the software Matlab, and organised into daily events. The anemometers layout along the bridge is shown in Figure 2. Data from hanger 18, in the middle of the bridge, is used as reference data for the comparison of statistical flow properties of the recorded wind along the bridge. Hangers 10, 16, 18, 20 and 24 are noted H-10, H-16, H-18, H-20 and H-24 respectively.
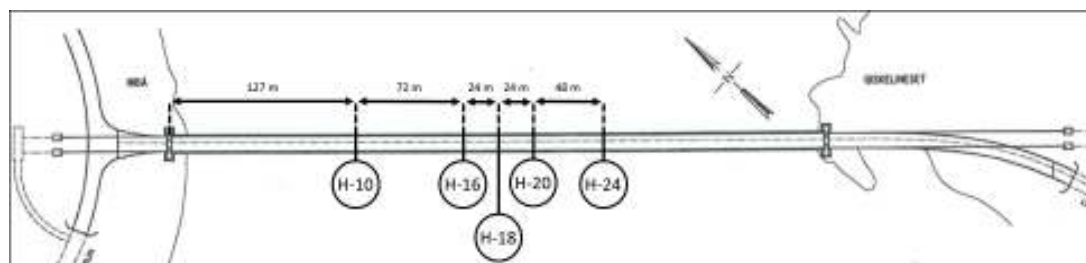
Figure 2. Position of the anemometers on the bridge deck: The Vaisala weather station is placed on H-10, and the Gill WindMaster Pro are on H-16, H-18, H-20 and H-24

---

[1]CANTERBURY SEISMIC INSTRUMENTS

2   Main wind conditions

Wind data for two days in December 2013 are selected for further studies and compared to the data from the Sola airport weather station, located at the coast 30 km West of the bridge. The influence of the topography is discussed in terms of mean wind speed, mean wind direction, and turbulence intensity.

Only the mean wind speed and the wind direction are available from Sola Airport. The information is provided as hourly reports freely accessible on Internet (MET, 2014). On December 6, 2013, at Sola, the mean wind speed for the whole day was 13.5 m/s with a N-NW direction, and on December 28, a wind from S-SW was monitored with a mean value of 10.9 m/s. At Lysefjord bridge, the horizontal mean wind speed measured on December 6 was lower than at Sola: 9.5 m /s with a direction N-NE. On December 28, the horizontal mean wind speed reached 13.0 m/s from S-SW, and was higher than at Sola (see Figure 2).
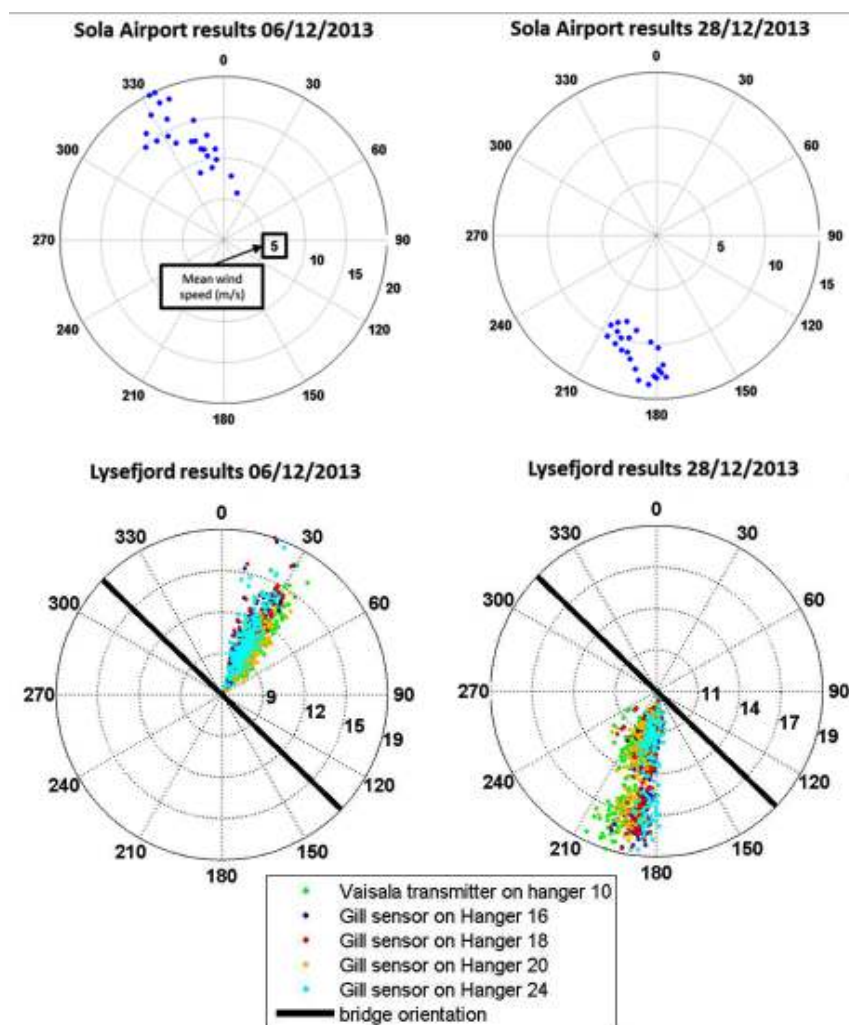
Figure 3. Wind roses obtained for the mean wind speed on Lysefjord Bridge, and Sola Airport, for all monitored data, for two different days.

On December 6, 295 samples, i.e. some 15 hours of data, were recorded at Lysefjord Bridge, and on 28th December, 325 time series were saved. Data recorded at H-10, H-16, and H-18 are synchronized, but not the data recorded at H-20 and H-24. Table 1 displays the mean value of the wind speed normal to the bridge, the turbulence intensity for the normal wind component, and the wind direction measured recorded at H-18:

Table 1. Mean wind speed normal to the bridge, turbulence intensity and mean wind direction, for each anemometer, for the two days studied

days	Hanger position	H-10	H-16	H-18	H-20	H-24
06/12/2013	U (m/s)	9.4	9.1	9.3	9.0	9.2
	Iu (%)	22.7	22.5	22.1	22.0	21.8
	Dir (^{o})	34.9	26.9	27.2	33.0	25.3
28/12/2013	U (m/s)	12.0	10.8	10.7	11.2	10.0
	Iu (%)	15.3	14.7	14.9	15.1	15.5
	Dir (^{o})	198.0	189.3	188.9	194.4	184.7

A high turbulence intensity was monitored on 06/12, i.e. 22 % for the component normal to the bridge and 10 % for the vertical component. The mean vertical speed measured is nearly nil (0.05 m/s). For the N-NE wind, the sensors are on the downstream side of the bridge deck which may partly perturb the recorded flow. At H-18, the mean wind direction is $27°$ relative to the North, with a standard deviations of $12°$. Therefore, the wind direction is not exactly normal to the bridge.

The turbulence intensity for the wind coming from SSE was 15% for the along wind component and 9% for the vertical component. The vertical mean speed is 1.0 m/s, corresponding to an angle of attack of 4 to 5 $°$, which cannot be neglected. At H-18, the wind direction has a mean value of $189°$ relative to the North, with a standard deviation of $9°$.

On Figure 4, three synchronized time-series and the corresponding power spectral density on Fig.5 of the along-wind turbulence are presented.
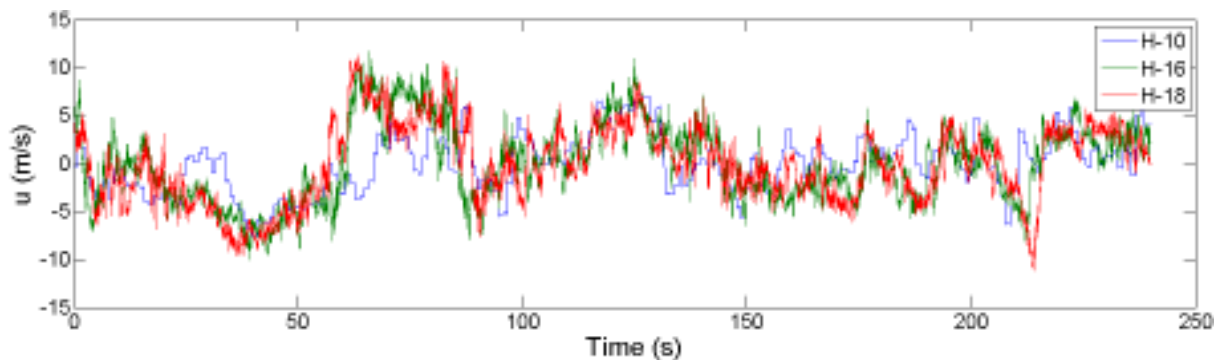
Figure 4. Example of the time-series of the wind velocity normal to the bridge deck, for three of the anemometers, for 06/12/2013.

The Power spectral density of a single sample on 06/12 and on 28/12 is compared with the classical Von Karman spectrum for the normal wind component, presented on equation 1, and it appears to be in a good overall agreement for both of these days.

$$S_u(f) = \frac{4L_u^x \sigma_u^2}{\overline{U}} \frac{1}{\left(1 + 70.7\left(\frac{fL_u^x}{\overline{U}}\right)^2\right)^{5/6}} \tag{1}$$
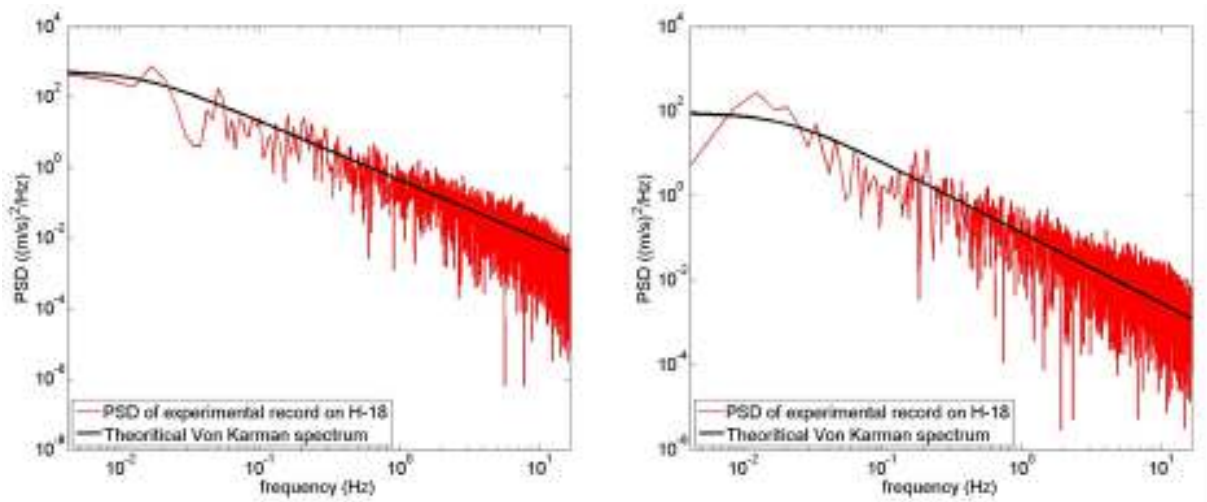
Figure 5. Experimental wind spectrum from Hanger 18, for 06/12/2013 (left), and for 28/12/2013 (right), compared to the theoretical Von Karman spectrum.

The differences observed between the wind conditions at Sola and Lysefjord are due to topography effects on the wind field. The wind from the North-West (as seen at Sola) descends and propagates from the inner part of the fjord towards the bridge. An airflow passage along the valley by Botnevatnet, North-East to the bridge, down towards the bridge is also anticipated. Bergsholmen island, situated on the North-East of the bridge, also perturbs the wind field, and may be responsible for an increased turbulence intensity, as it is shown on Fig. 6.
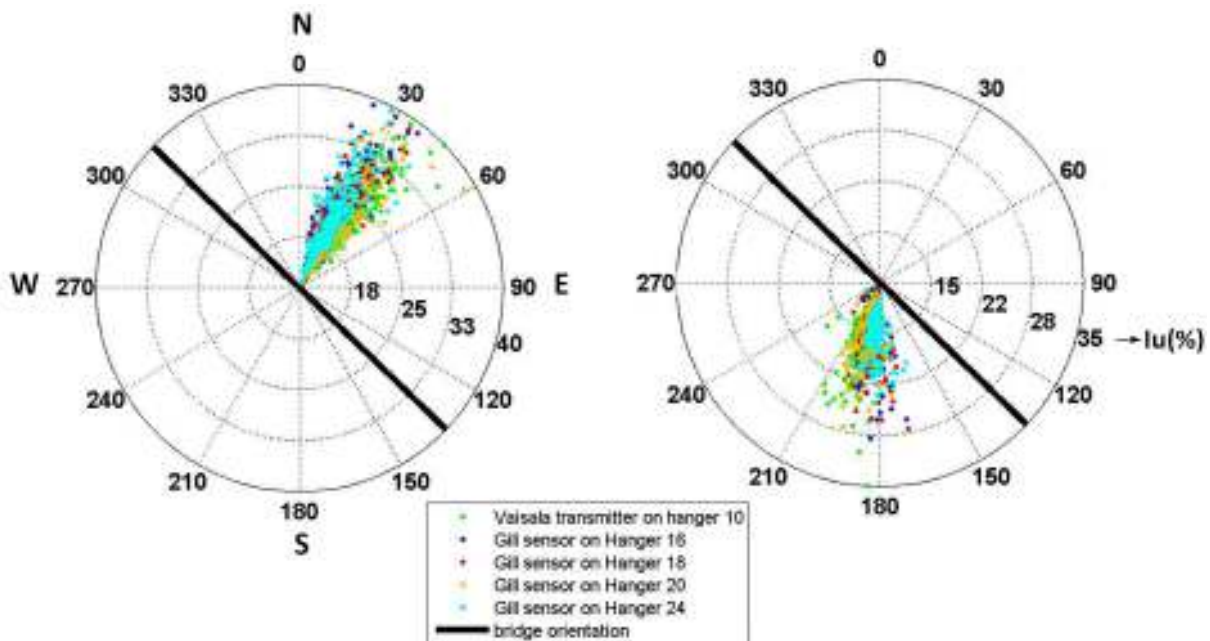
Figure 6. along-wind turbulence intensity measured by the five anemometers on 06/12 (left) and on 28/12 (right), and plotted as a function of the mean wind direction.

The directions monitored show that the wind follows the path of the fjord as the cliffs on either side are high enough to prevent the wind from coming from the North and North-West. The channelling influence of the fjord on the wind flow likely affects the turbulence length scales measured The wind monitored on the 28th of December is locally less perturbed by the landscape, as the turbulence intensity is lower than for the wind coming from the North-East. On the other hand, the mean wind speed is

higher than at Sola airport. A reason could be a Venturi effect. The measure of the atmospheric pressure at Lysefjord and Sola airport may give more information about this hypothesis.

In the case of a complex topography like the inlet of a fjord, some properties of the wind field must be studied more in details. Among them, the homogeneity of the wind field, the different turbulence length scales, and the coherence of the wind field along the bridge span.

3   Turbulence length scale

The axis convention adopted to calculate the turbulence length scales is presented in Fig.7, where U is the mean wind speed normal to the bridge deck, u, v, and w are the turbulent velocity components, normal to the bridge, along the bridge, and in the vertical direction respectively. In the frame of reference of the bridge, y is the axis along the bridge, x is the axis across the bridge, and z is the vertical axis.
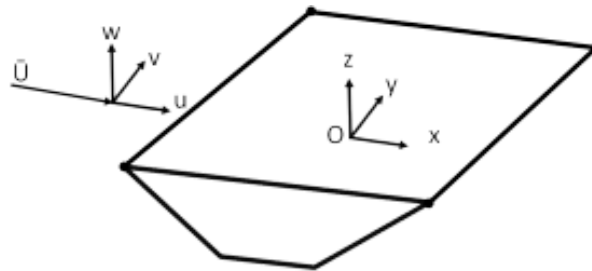
Figure 7. Axis convention defined for the bridge and the wind components.

The turbulence length scale in the wind direction L_u^x is calculated for every sample registered the 06/12 and the 28/12. L_u^x is obtained as the product between the mean wind speed and the integral of the normalized autocorrelation function of the turbulent component normal to the bridge:

$$L_u^x = U(z) \cdot \int_0^\infty R(z, \tau) \mathrm{d}\tau \tag{2}$$

The integral length scale of the turbulence component u in the lateral direction y, written L_u^y, is obtained from the correlation coefficient between the velocities measured by the anemometers installed on hangers 10, 16 and 18.

$$L_u^y = \int_0^\infty R(z, y) \mathrm{d}y \tag{3}$$

A distribution of length scales is obtained for 06/12/2013 and 28/12/2013. L_u^y has a mean value of approximatively 100 m for both of these days. However the distributions of length scales are different, and a gamma distribution is used to fit the set of data (Fig. 8).
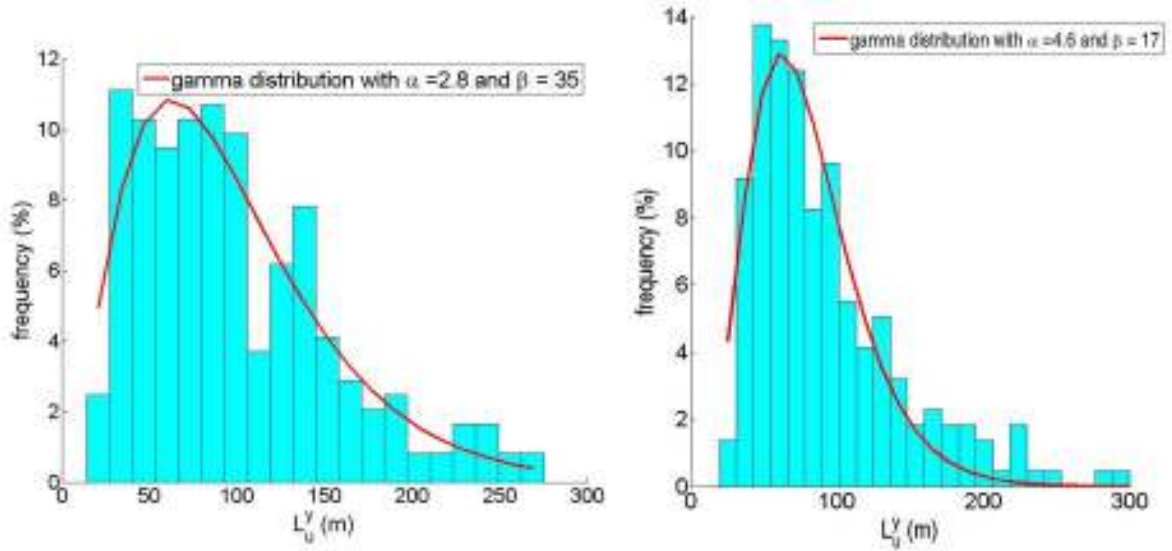
Figure 8. Distribution of integral length scales L_u^y for 06/12/2013 (left) and for 28/12/2013 (right)

The 28/12, most of the population of L_u^y ranges from 40 m to 100 m while on the 06/12 the distribution of length scale is wider, from 35 m to 140 m. More generally, the turbulence length scale along the bridge span tends to be higher when the wind comes from N-NE than when it comes from S-SW. The mean value of L_u^x is 147 m for 28/12 and 105 m for 06/12. The large spread of the length scales suggests that a statistical approach is relevant to estimate the turbulence length scale. The gamma distribution has been chosen quite arbitrary, but other distributions like a beta or a Weibull distribution might fit as well. The fitting of the length scale distribution may be useful for application of the Monte Carlo method to create several wind histories.

The mean value of the ratio L_v^x/L_u^x and L_v^y/L_u^y are quite different from the ratio predicted in the literature (ESDU, 2001), which might be due to the complex topography or an inhomogeneity of the wind flow. The vertical turbulence length scales L_w^x and L_w^y have respectively an average value of 45 m and 32 m for 06/12, and of 67 m and 34 m for 28/12. These values are higher than those generally seen in the literature (Cremona, 2012), but are still much lower than the vertical and along-wind turbulence length scales.

4   Coherence

The real part of the root mean square coherence, also called co-coherence is calculated from data registered on H-10, H-16 and H-18. The co-coherence is approximated by a exponential function, whose formulation is taken from (E. Strømmen et al., 1994), but with a coefficient $c = 1.0$ instead of $c = 1.5$. This function is expressed as a function of the lateral separation Δ_y along the bridge deck and the frequency f expressed in Herz:

$$\sqrt{Coh_u(\Delta_y, f)} = exp\left[-(\Delta_y\beta_u)^c\right] \tag{4}$$

with:

$$\beta_u = \left[b^2 + a^2(f/U)^2\right]^{0.5} \tag{5}$$

b is a coefficient that allow the coherence to be lower than 1 when the frequency is nearly zero. a is a decay coefficient that need ot be determined in addition to b.

On 28/12/2013, the co-coherence function for a 10 minutes sample measured at H-18 with a mean wind speed normal to the bridge equal to 16.2 m/s, a turbulence length scale along the bridge L_u^y equal to 131 m, a turbulence length scale in the direction of the wind L_u^x equal to 214 m and a turbulence intensity I_U equal to 16.6 % has been fitted. The averaged parameters a and b from equation 5 have been found to be:

$$a = 2.3 \text{ and } b = 0.005 \ m^{-1} \tag{6}$$

The experimental coherence is displayed on Fig. 9
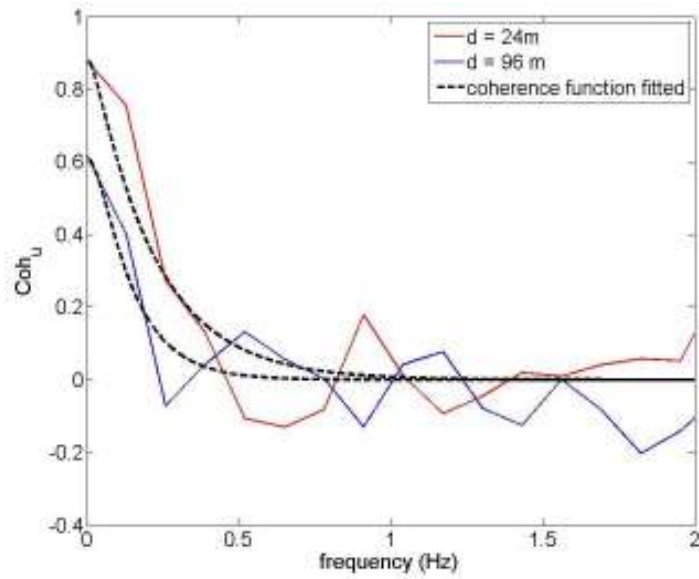
Figure 9. Experimental and fitted coherence functions for one selected time series from 28/12/2013.

The coherence function becomes nearly nil for frequencies higher than 1 Hz. However, the coherence decrease slowly when the distance Δ_y increase because the selected sample displays a high turbulence length scale L_u^y which implies a high coherence. The coefficient b is necessary here, since the coherence at low frequency is around 0.8 for a spatial distance of 24 m, and around 0.6 for a distance of 96 m. The latter value is rather high; whether it possibly reflects a genuine terrain influence or not will be addressed in a further analysis utilizing a larger set of data.

5   Homogeneity of the wind field along the bridge

The homogeneity can be evaluated by the evolution of the wind direction, the mean wind speed, and the turbulence intensity along the bridge. Assuming h_{Dir} is the heterogeneity of the wind field measured for the five anemometers, h_{Dir} is expressed in degrees and is defined as:

$$h_{Dir} = \langle Dir_{H_{18}} \rangle - \langle Dir_{H_k} \rangle \tag{7}$$

where $\langle Dir_{H_k} \rangle$ is the mean wind direction measured at hanger k, and $\langle Dir_{H_{18}} \rangle$ is the total mean wind direction measured at H-18.

It is also possible to study the variation of the mean wind speed along the bridge span. The reference point is on H-18, and this time the heterogeneity h_{vel}, expressed in % is defined as:

$$h_{vel} = 100 \cdot \frac{\langle U_{H_{18}} \rangle - \langle U_{H_k} \rangle}{\langle U_{H_{18}} \rangle} \qquad (8)$$

where $\langle U_{H_k} \rangle$ is the mean wind speed measured at hanger k, and $\langle U_{H_{18}} \rangle$ is the total mean wind speed measured at H-18.

Finally, the heterogeneity of the turbulence intensity along the bridge h_{turb}, expressed in % is defined as:

$$h_{turb} = 100 \cdot \frac{\langle Iu_{H_{18}} \rangle - \langle Iu_{H_k} \rangle}{\langle Iu_{H_{18}} \rangle} \qquad (9)$$

where $\langle Iu_{H_{18}} \rangle$ is the turbulence intensity measured at H-18, and $\langle Iu_{H_k} \rangle$ is the turbulence intensity measured at hanger k.

In tables 2 and 3, h_{Dir}, h_{vel}, and h_{turb} have been averaged for 20 samples of 10 min the 28/05/2014, for a wind from N-NE, and for 22 samples of 10 min the 22/05/2014, for a wind from S-SW:

Table 2. Heterogeneity of the wind field along the bridge (28/05/2014), for a wind direction measured on H-18 which is 29°,or N-NE.

Hanger position	H-10	H-16	H-18	H-20	H-24
$h_{Dir}(°)$	-7.4	0.4	0	-6.0	1.6
$h_{vel}(\%)$	-11.1	-0.4	0	1.3	11.0
$h_{turb}(\%)$	7.0	1.0	0	-1	-12
U (m/s)	7.3	6.6	6.6	6.5	5.9
Iu (%)	13.4	14.2	14.4	14.5	16.1

Table 3. Heterogeneity of the wind field along the bridge (22/05/2014), for a wind direction measured on H-18 which is 182°, or almost directly from South.

Hanger position	H-10	H-16	H-18	H-20	H-24
$h_{Dir}(°)$	-5.9	0.7	0	-6.6	0.6
$h_{vel}(\%)$	-9.3	1.4	0	-10.4	3.5
$h_{turb}(\%)$	-2.2	0.17	0	-0.9	1.5
U (m/s)	7	6.3	6.4	7.1	6.2
Iu (%)	21.6	21.1	21.2	21.4	20.9

A high difference for the mean wind direction is observed between H-18 and H-20 which is maybe influenced by a slight misalignment of the anemometer on H-20. Moreover, the low value of h_{Dir} for H-24 and H-16 tends to show that the wind direction is homogeneous near the middle of the bridge. h_{Dir} is also quite high at H-10, which may either be due to the heterogeneity of the wind field or the

misalignment of the anemometer on H-10. Information provided by the distribution of the mean wind speed normal to the bridge deck show different situations according to the wind direction: For the wind from N-NE, the mean wind speed normal to the deck increases from the South of the bridge toward the north of the bridge, while for a wind from S-SW, it appears more homogeneous. The turbulence intensity seems quite homogeneous along the bridge in the case of a wind from S-SW, while it decreases from the South to the North of the deck in the case of a N-NE wind.

Near the middle of the bridge, the wind field can be considered as homogeneous, but based on the data provided on H-10, the variations of the mean wind direction along the NW part of the bridge may not be negligible. Moreover, the variations of the mean wind speed U and of the turbulence intensity I_U along the span may give additional arguments to contradict the hypotheses of wind field homogeneity. To sum it up, the hypotheses of homogeneity appears to be respected in the case of a wind from S-SW, but it may not be the case for a wind from N-NE.

Ongoing studies involving wind Lidars will provide measurements of the wind filed along the bridge span. The installation of two additional anemometers on hanger 8, planned for June 2014, will provide more detailed information on the flow characteristic at the NW end of the bridge.

6   Conclusion

The comparison of the wind direction at Sola airport, and at Lysefjord bridge shows that the fjord "reroutes" the wind coming from North and North-West so that the wind follows the orientation of the fjord itself. The wind from South-West is less affected by the topography, and different turbulence characteristics are observed for each of these directions.

A large turbulent length scale along the bridge span is measured for winds coming from both N-NE and S-SW, but the statistical distribution fitted to the data is different for each wind direction. High coherence is observed along the bridge span, although more data should be included to verify the consistency of the exponential function model used.

Finally, the complex topography justifies the reassessment of the hypothesis of the homogeneity of the wind flow. Negligible variations of the wind speed, the wind direction and the turbulence intensity along the bridge are observed for a wind from the S-SW. However, higher variations are observed in the case of a wind from N-NE, which requires additional studies and instrumentation, that are already underway.

References

Cremona, C. (2012). *Structural Performance: Probability-Based Assessment*. ISTE. Wiley, pp. 306–308. ISBN: 9781118601150.

E. Strømmen, Jasna Bogunović Jakobsen, E. Hjorth-Hansen, S.O. Hansen, J.H. Kaspersen, and K. Handa (1994). *The Øresund link cable-stayed bridge*. SINTEF Structure and Concrete.

ESDU (2001). ESDU 86010: Characteristics of atmospheric turbulence near the ground Part III: variations in space and time for strong winds (neutral atmosphere).

Macdonald, John HG (2004). *Dynamic behaviour of the Clifton suspension bridge: response to wind loading*. Tech. rep. Bristol Earthquake and Engineering Laboratory Ltd.

MET, Norwegian Meteorological Institute (2014). *eKlima*. URL: *http://sharki.oslo.dnmi.no/portal/page?_pageid=73,39035,73_39049&_dad=portal&_schema=PORTAL*.

Structural dynamics modelling of floating wind turbines: a preliminary study on the role of large rotation

Alessandro Giusti[1], Enzo Marino[1] and Claudio Borri[1]

[1]DICeA, Department of Civil and Environmental Engineering, University of Florence, Italy
Corresponding author: Alessandro Giusti, alessandro.giusti@dicea.unifi.it

Abstract

This paper presents a preliminary study to asses the importance of modeling finite rotations in the structural dynamic analysis of offshore wind turbines. The dynamic problem is formulated with a dependent coordinate approach and the equations of motion are solved by using a suitable Lie-group time-integrator. This approach is aimed at handling with higher accuracy systems undergoing large displacements (rotations) as for the floating wind turbine. In the reality the problem is characterized by a rather complex hydro-aero-elastic interaction, but in this study it is strongly simplified with the intent to preliminary evaluate the benefits that a finite-rotations-based dynamic model can provide in comparison with more traditional time-integrator schemes. The examples presented show that when the system observes large displacements a finite rotation approach is much more accurate and it is strongly recommended.

1 Introduction

Due to the increasing importance that the exploitation of wind energy in deep-water sites is gaining, together with the fast growth of tower and rotor sizes, numerical simulation tools are required to face more and more complex dynamic problems. This work is focused on the use Lie-group time integrators (i.e. finite rotation approach) for the dynamic analysis of floating wind turbines and on the importance that these geometrically exact kinematics model have in the evaluation of the structural response. To this aim, the offshore wind turbine is sketched as a rigid body system with the same mass and inertia properties of a realistic floating offshore wind turbine developed by NREL (Jonkman et al., 2009; Jonkman, 2007): the support is the so called ITI Energy barge. This kind of floating platform is the most susceptible of large pitch displacements (Jonkman and Matha, 2010; Philippe et al., 2013) and can observe maximum pitch angles on the order of 0.2 rad, in the resonance peak at about 0.1 Hz, that is quite closed to the frequency of a typical wave load.

2 Dynamics of rigid bodies

The equations of motion, formulated by using the Lagrange Multipliers method, are a set of differential algebraic equations (Brüls and Cardona, 2010):

$$\mathbf{M}\dot{\mathbf{v}} + \mathbf{g}(\mathbf{q}, \mathbf{v}, t) + \mathbf{\Phi}_{\mathbf{q}}^T \boldsymbol{\lambda} = \mathbf{0} \qquad ; \qquad \mathbf{\Phi}(\mathbf{q}) = \mathbf{0} \tag{1}$$

where constraint equations $\mathbf{\Phi}$ are formulated at the position level and Lagrange multipliers $\boldsymbol{\lambda}$ are introduced in order to take into account of constraint reactions that make the coordinates dependent to each other; $\mathbf{M}$ is the mass matrix; $\mathbf{g}$ represents the external forces, velocity-dependent inertia forces and position-dependent forces (those obtained from a potential); $\mathbf{q}$ is the state vector whose elements are the translational and rotational parameters that describe the configuration of the system; $\mathbf{v}$ is the generalized velocity of the system. Equations (1) set up a system of differential algebraic equations (DAE) of index three.

2.1 Model of finite rotations

Finite rotations are described by means of the linear operator of rotations. Formally speaking, a rotation operator belongs to the special orthogonal group $SO(3)$. The main difficulty in the time integration of the equations of motion on $SO(3)$ arises from the fact that the rotation manifold is not an affine space, therefore the standard time integration models, routinely used for differential-algebraic equations, are no longer valid. Working with finite rotations means that composition rule is different and sums between incremental rotations are allowed only in the same tangent space to $SO(3)$. Let us focus on a material frame description and consider an incremental rotation applied to the actual configuration. The updated configuration is given by a composition of the actual rotation operator with the incremental one, i.e.:

$$\mathbf{R}_{upd} = \mathbf{R}_{act} \circ \mathbf{R}_{inc} = \mathbf{R}_{act}\mathbf{R}_{inc} = \exp(\tilde{\boldsymbol{\Theta}}_{act})\exp(\tilde{\boldsymbol{\Theta}}_{inc}) \tag{2}$$

where the rotation operator $\mathbf{R}$ is related to the rotational vector $\boldsymbol{\Theta}$ and to the associated skew-symmetric matrix $\tilde{\boldsymbol{\Theta}}$. The updated configuration can be also reached step by step by a vectorial composition of some incremental rotation vectors and a final projection on $SO(3)$ with the exponential map. This is possible if and only if the various incremental rotation vectors belong to the same tangent space to $SO(3)$ at the reference position. A tangent operator is used to project the incremental vectors belonging to different tangent spaces to the same tangent space (Cardona and Geradin, 1988; Simo and Vu-Quoc, 1988).

2.2 Time-integration scheme

It is used a Lie-group time integrator scheme that solves the differential dynamic problem by using the constraint equations formulated at the position level (Brüls and Cardona, 2010); this feature avoid using constraint violation stabilization procedures on the outputs (Terze et al., 2012). If the kinematics of motion is described in dependent coordinates, a numerical damping might be necessary in order to avoid computational instability (Géradin and Cardona, 2001).

Figure 1 compares the analytical (Romano, 2008) and numerical solutions, in terms of mean absolute error evaluated on the displacements, of a simple test case: rotating rigid body with spherical ellipsoid of inertia and follower torque, the same reported in (Brüls and Cardona, 2010). The convergence (quadratic) of the error proves the efficiency of the algorithm in the treatment of finite rotations. The case-dependent part of the code, that concerns the dynamic equilibrium formulation, has to be verified for every particular system.
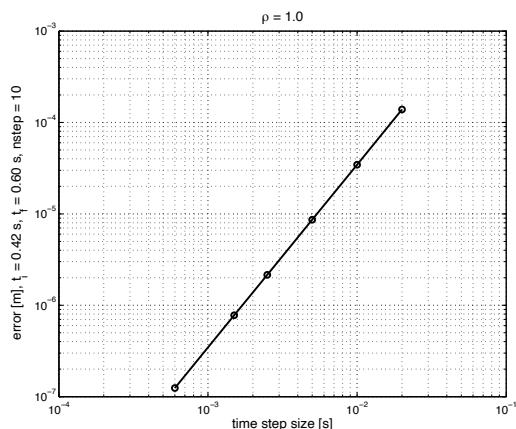
Figure 1. Rotating rigid body with spherical ellipsoid of inertia and follower torque: comparison between the anlytical solution and the numerical one for various time step sizes in the case of no numerical damping.
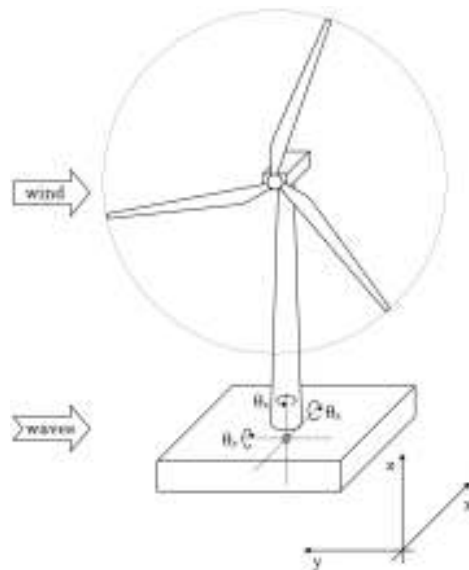
Figure 2. Single-rigid-body offshore wind turbine with three DOF.

3   Applications and preliminary results

In this section a very simple example of an offshore wind turbine is modeled. It is an idealized scheme that does not claim to reproduce the actual behaviour of a real system. It is only used to draw some preliminary considerations about the relevance of more sophisticated dynamical models.

   The system consists of a single rigid body (Figure 2) with the same mass and inertia properties of a realistic wind turbine (Jonkman et al., 2009; Jonkman, 2007). The system can rotate in the Euclidean space around a fixed point located at the platform centre of mass. The natural pitch and roll frequencies are respectively to 0.06 Hz and 0.12 Hz. External loads consist of a force $\mathbf{F}_{wind}$ applied at the hub height and a torque $\mathbf{M}_{wave}$ applied at the hinge. The forcing frequencies are set as shown in Figures 3.

   The equations of motion are solved with two different algorithms: the finite rotation approach and the classic Newmark scheme, that is different from the previous one only in the composition rule. The analyses are carried out for various amplitudes of the forcing components. Outputs are compared in terms of mean absolute error given by $err = \frac{1}{n_e}\sum_{i=1}^{n_e}\|\mathbf{x}(t_i) - \mathbf{x}^{ref}(t_i)\|$, evaluated on the top (hub height) displacements, between the solution obtained by the finite rotation algorithm and the other one.

   In Figure 3(a), by increasing the component $M_{wave,x}$, that leads the system to move out of the xz plane, it is shown that if the system rotates around a variable axis, the classic Newmark scheme becomes inaccurate; on the other hand, if the rotation axis is fixed, the two algorithms are equivalent. In Figure 3(b) pitch and roll angles are forced to grow by varying the amplitudes of external loads (parameter A in the figure). The plot shows that at maximum pitch angles of about 0.2 rad the error is non-negligible: about 10^{-1} m. Furthermore, the path in a bi-logarithmic plot is close to a straight line, it means that errors increase following a power low.

(a) effect of a variable rotation axis   (b) effect of the displacement amplitude
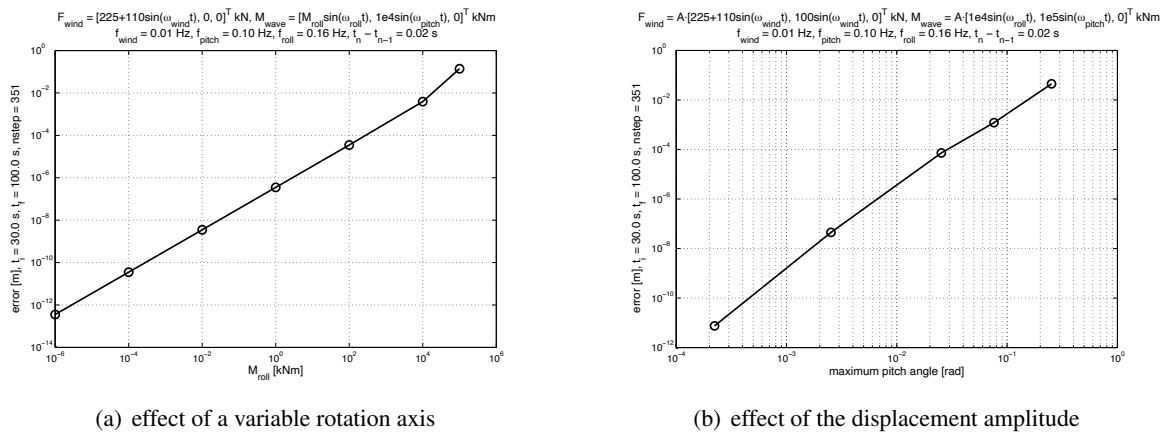
Figure 3. Simplified offshore wind turbine model: comparison between the numerical solution corresponding to a finite rotation approach with that obtained with a classic vectorial composition rule.

4   Conclusions and outlook

The previous simple example shows that different numerical approaches can leads to significant errors, especially when large pitch displacements are observed. Because of system loads depend significantly on platform pitch displacements (Jonkman and Matha, 2010), a reliable handling of finite rotations is strongly recommended. It has been observed that when rotations increase, the standard Newmark method is significantly inaccurate. The next step of the present work is to test a multi-rigid-body system reproducing more realistically the floating offshore wind turbine. The system consists of four main rigid parts linked together: rotor, nacelle, tower and substructure. The system has the same mass and inertia properties of the 5 MW wind turbine with barge floating platform concept, developed by NREL (Jonkman et al., 2009; Jonkman, 2007), unknown data are assigned in a plausible manner. Aerodynamic loads are modelled with the blade element momentum (BEM) theory starting from a time series of the incoming

turbulent wind. Hydrodynamic loads are treated with the same approach used by Jonkman (2009), i.e. as the sum of wave excitation loads, hydrostatic forces and an additional wave radiation load (not taken into account by the added mass matrix). The platform is modelled considering all six possible degrees of freedom, its dynamics is modelled by assembling in the global equation of motion the added mass, restoring and damping matrices obtained within the potential flow assumption for the fluid.

References

Brüls, O. and Cardona, A. (2010). On the Use of Lie Group Time Integrators in Multibody Dynamics. *Journal of Computational and Nonlinear Dynamics* **5**.

Cardona, A. and Geradin, M. (1988). A Beam Finite Element Non-linear Theory with Finite Rotation. *International Journal for Numerical Methods in Engineering* **26**. John Wiley & Sons, Ltd, pp. 2403–2438.

Géradin, M. and Cardona, A. (2001). *Flexible Multibody Dynamics - A Finite Element Approach*. John Wiley & Sons Ltd.

Jonkman, J. and Matha, D. (2010). *A Quantitative Comparison of the Responses of Three Floating Platforms*. Conference Paper NREL/CP-500-46726. Golden, Colorado: National Renewable Energy Laboratory.

Jonkman, J., Butterfield, S., Musial, W., and Scott, G. (2009). *Definition of a 5-MW Reference Wind Turbine for Offshore System Development*. Technical Report NREL/TP-500-38060. Golden, Colorado: National Renewable Energy Laboratory.

Jonkman, J. M. (2007). *Dynamics Modeling and Loads Analysis of an Offshore Floating Wind Turbine*. Technical Report NREL/TP-500-41958. Golden, Colorado: National Renewable Energy Laboratory.

— (2009). Dynamics of Offshore Floating Wind Turbines - Model Development and Verification. *Wind Energy* **12**. DOI: 10.1002/we.347. Wiley Interscience - www.interscience.wiley.com, pp. 459–492.

Philippe, M., Babarit, A., and Ferrant, P. (2013). Modes of response of an offshore wind turbine with directional wind and waves. *Renewable Energy* **49**. Elsevier, pp. 151–155.

Romano, M. (2008). Exact Analytic Solution for the Rotation of a Rigid Body Having Spherical Ellipsoid of Inertia and Subjected to a Constant Torque. *Celestial Mechanics and Dynamical Astronomy* **100**. Online version with Errata Corrige, pp. 181–189.

Simo, J. C. and Vu-Quoc, L. (1988). On The Dynamics in Space of Rods Undergoing Large Motions - A Geometrically Exact Approach. *Computer Methods in Applied Mechanics and Engineering* **66**, pp. 125–161.

Terze, Z., Zlatar, D., and Müller, A. (2012). Numerical Integration Algorithm in Lie-Group Setting for Dynamics of Mechanical Systems. *Proceedings of 7th International Congress of Croatian Society of Mechanics (7ICCSM 2012)*. Zadar, Croatia.

Coupled dynamic simulations of offshore wind turbines: influence of wave modeling on the fatigue load assessment

Enzo Marino[1,2], Claudio Lugni[2], Giovanni Stabile[1], Claudio Borri[1] and Lance Manuel[3]

[1]Dept. of Civil and Environmental Engineering, University of Florence, Italy

[2]CNR-INSEAN Maritime Research Institute Rome, Italy

[3]Dept. of Civil, Architectural, and Environmental Engineering University of Texas, Austin TX USA

Corresponding author: Enzo Marino, enzo.marino@dicea.unifi.it

Abstract

Nonlinear waves influence to a large extent the coupled hydro-aero-elastic response of offshore wind turbines. Higher-order contributions in the hydrodynamic forcing are responsible for resonant springing-like vibrations of the tower causing an increase of stress cycles and amplitudes. The present study investigates the effects of these amplifications in terms of fatigue load. Equivalent fatigue loads are estimated by means of both time and frequency domain methods. A comparison between linear, second-order and fully nonlinear wave models is proposed and it is shown that the weakly nonlinear model, widely used in the state-of-the-art simulations, may significantly underestimate the actual fatigue load. Hydrodynamic loads associated with the different wave models are coupled with aerodynamic loads acting on the rotor of a 5-MW wind turbine (fixed-bottom).

1 Introduction

The high demand for renewable energy requires the design of large offshore wind turbines. The associated increasing sensitivity of more and more slender components, such as tower and blades, to the coupled wind-waves dynamic excitation makes fundamental the development of more accurate simulation tools. Marino et al., 2013b has shown that the nonlinear hydrodynamic forcing has a large influence on the coupled hydro-aero-elastic response of fixed-bottom wind turbines. The response is generally underestimated when the linear wave theory is used – springing-like resonant phenomena, triggered by the passage of both steep non-breaking and breaking waves, are often missed. The importance of fully nonlinear wave models even in moderate sea states has been pointed out in Marino et al., 2013c. Moreover, the resonant vibrations of the tower are frequently associated with wave components higher than the second-order, proving the limitations of weakly nonlinear models in reproducing the actual structural response (Marino et al., 2013a). The amount of damage the tower accumulates directly depends on the number and amplitude of stress cycles it is subjected to during its lifetime. Therefore, amplifications in the structural response due to nonlinear hydrodynamics are expected to play a crucial role in the assessment of the structural safety. The present study aims at quantifying the effects in terms of fatigue load when a fully nonlinear (FNL) wave model is used in coupled hydro-aero-elastic simulations instead of more conventional linear (L) or weakly nonlinear (WNL) wave theories.

2 Fully and Weakly Nonlinear Irregular Wave Models

The nonlinear propagation of gravity waves is formulated, under the assumptions of inviscid and incompressible fluid in irrotational flow, within the potential-flow model. Laplace's equation for the velocity potential, together with the nonlinear kinematic and dynamic free-surface boundary conditions, is solved with a two-step Mixed Eulerian-Lagrangian (MEL) approach. At a given time instant, the solution of the Boundary Value Problem (BVP) for the Laplace equation with mixed Dirichlet and Neumann boundary conditions is reformulated in an integral representation of the velocity potential (using Green's second

identity) and numerically solved with a high-order boundary element method (HOBEM) (Marino et al., 2011). The integration in time is done using a 4th order RK method.

For WNL model Laplace's equation with nonlinear boundary conditions is solved by using a perturbation approach 2nd-order consistent (Sharma and Dean, 1981). The double summation involved in the second-order contributions is conveniently rewritten using only one summation and the use of the IFFT ensures efficiency and accuracy (Agarwal and Manuel, 2011).

3   Fatigue Loads Estimation

The standard definition of damage fraction D for constant-amplitude stress range S derived from Wöhler's equation is easily extended to the case of variable stress cycle amplitudes leading to the well know Miner's sum $D = \sum_i^N S_i^m / K$, where N is the number of stress cycles causing the damage D, K is proportional to the number of cycles a material can withstand before failure and m is another material parameter assumed equal to 3 (welded steel). As a measure of fatigue damage we use the equivalent fatigue load (EFL). The EFL is defined as the constant-amplitude stress range level which, over the same number of cycles, would cause an equivalent amount of damage as the original variable-amplitude stress time series. Estimates of EFL are carried out by using both the Rainflow Cycle-Counting (RCC) (time-domain approach) and a the Dirlik's spectral method (frequency domain) (Ragan and Manuel, 2007).

Fatigue damage cumulative theories can be generally linear or nonlinear. With Miner's rule, the total amount of damage due to an irregular loading is calculated by simply adding up the increments in damage due to each stress cycle; this is then used in a total life calculation. No memory or sequence effects are considered (i.e., the increment in damage manifested, say, in crack growth depends only on the current applied stress range and crack dimensions, and not on past loading). This is an approximation but Miner's rule is customarily used for wind turbine fatigue loads evaluation when simulation is involved. The application of more sophisticated nonlinear damage cumulative theories capable to account for the continuously deterioration of the material properties under cyclic loading is postponed to future studies.

4   Results and Discussion

Aero-hydro-elastic computations are performed with FAST (Jonkman and Marshall, 2005), a modal-multibody time domain solver. Within the global hydro-aero-elastic solver, the hydrodynamic forces associated with the three wave models (L, WNL, FNL) are modeled with the Morison equation. The turbine model used in this study is the 5-MW Reference Wind Turbine (Jonkman et al., 2009). The turbine is assumed in parked condition with blades pitched to feather (at a pitch angle of $90°$). The water depth is $20\,\mathrm{m}$. A sea state with by $H_s = 6\,\mathrm{m}$, $T_p = 9.8\,\mathrm{s}$ and a mean hub-height wind speed $U = 24\,\mathrm{m/s}$ reproduced. A normal turbulence model with Kaimal spectrum is used to generate e hub-height turbulent wind file according to the standard IEC 61400-1.

Figures 1(a) and 1(b) show, respectively, the time series and the PSDs of the dynamic response. The tower-base shear force (TwrBsFxt) mainly reflects the effect of the hydrodynamic forces. Due to the parked condition, the aerodynamic forces have minor effects. At the fundamental frequency of the sea, the wave elevation (WaveElev) PSD is overestimated by the linear and 2nd-order wave models. The response at the tower (fore-aft) natural frequency $0.28\,\mathrm{Hz}$ (see bending moment TwrBsMyt and tower-top fore-aft deflection TTDspFA) is amplified when the FNL model is used. This confirms that springing-like vibrations, clearly visible in the time series of Figure 1(a) bottom panel, are not properly captured by the weakly nonlinear model.

From the TrwBsMyt time series (Figure 1(a), second panel from bottom) and PSD (Figure 1(b) bottom-left panel) we observe that the FNL wave model is expected to have important effects on the stress cycles amplitudes. The EFL estimated with both RCC and Dirlik's methods associated with the three wave models are reported in Table 1. There is a quite large discrepancy between the two predictions. This indeed confirms what observed in Ragan and Manuel, 2007, that is the bad performances of the spectral method in comparison with the conventional RCC approach for signals characterized by a strong periodic component. A further verification has been done by repeating the simulation with the

Table 1. Comparison of EFL estimates using the RCC algorithm and the Dirlik spectral methods for linear (L), 2nd-order (WNL) and FNL wave kinematics models. Estimates refers to the 30-min time series.

Methods	RCC					Dirlik				
Wave model	L	WNL	$\Delta_{WNL/L}$	FNL	$\Delta_{FNL/L}$	L	WNL	$\Delta_{WNL/L}$	FNL	$\Delta_{FNL/L}$
EFL ($\times$ E4) [kNm]	2.194	2.217	1.02 %	2.42	10.34 %	1.441	1.454	0.88 %	1.586	10.09 %

turbine in power production under the same sea state and a full-field turbulent wind. The difference on the EFL between the two methods drastically reduces due to the attenuation of the structural response at 0.28 Hz induced by the aeroelastic damping (Marino et al., 2013d). However, from Table 1, we observe that two methods are in a good agreement in terms of EFL increments: an increase of about 1 % is observed using 2nd-order vs. linear, whereas an increase of about 10 % when using the FNL vs. linear.

5   Concluding remarks

A comparison of the effects of linear, weakly and fully nonlinear wave models on the fatigue loads on a fixed-bottom offshore wind turbine is presented. The structural response shows high sensitivity to resonant vibrations triggered by nonlinear wave contributions. These resonant springing-like phenomena are remarkably underestimated by both the linear and 2nd-order wave models. Direct consequences of such amplifications associated with the fully nonlinear wave modeling are observed in the estimates of the equivalent fatigue load. The weakly nonlinear model predicts an increase of equivalent fatigue load of only 1 % against the 10 % predicated by the FNL model. A more comprehensive work will follow in order to consider a wider range of sea states and operational conditions of the turbine and will investigate deeper the differences between the two methods used for the estimation of the equivalent fatigue load.

References

Agarwal, P and Manuel, L (2011). Incorporating irregular nonlinear waves in coupled simulation and reliability studies of offshore wind turbines. *Appl. Ocean Res.* **33**.3, pp. 215–227.

Jonkman, J, Butterfield, S, Musial, W, and Scott, G (2009). *Definition of a 5-MW Reference Wind Turbine for Offshore System Development*. Tech. rep. NREL/TP-500-38060.

Jonkman, J M and Marshall, L B Jr. (2005). *FAST User's Guide*. Tech. rep. NREL/EL-500-38230.

Marino, E, Borri, C, and Peil, U (2011). A fully nonlinear wave model to account for breaking wave impact loads on offshore wind turbines. *J. Wind Eng. Ind. Aerodyn.* **99**.4, pp. 483–490.

Marino, E, Stabile, G, Borri, C, and Lugni, C (2013a). A comparative study about the effects of linear, weakly and fully nonlinear wave models on the dynamic response of offshore wind turbines. *Res. Appl. Struct. Eng. Mech. Comput. SEMC 2013*. CRC Press.

Marino, E, Lugni, C, and Borri, C (2013b). A novel numerical strategy for the simulation of irregular nonlinear waves and their effects on the dynamic response of offshore wind turbines. *Comput. Methods Appl. Mech. Eng.* **255**, pp. 275–288.

Marino, E, Nguyen, H, Lugni, C, Manuel, L, and Borri, C (2013c). IRREGULAR NONLINEARWAVE SIMULATION AND ASSOCIATED LOADS ON OFFSHORE WIND TURBINES. *32nd Int. Conf. Ocean. Offshore Arct. Eng.* ASME Dig. Lib. ISBN: 978-0-7918-5542-3.

Marino, E, Lugni, C, and Borri, C (2013d). The role of the nonlinear wave kinematics on the global responses of an OWT in parked and oper. cond.sha. *J. Wind Eng. Ind. Aerodyn.* **123**, pp. 363–376.

Ragan, P and Manuel, L (2007). Comparing Estimates of Wind Turbine Fatigue Loads using Time-Domain and Spectral Methods by using Time-Domain and Spectral Methods. *Wind Eng.* **31**.2.

Sharma, N and Dean, R G (1981). Second-Order Directional Seas and Associated Wave Forces. *Soc. Pet. Eng. J.* **21**.01, pp. 129–140.
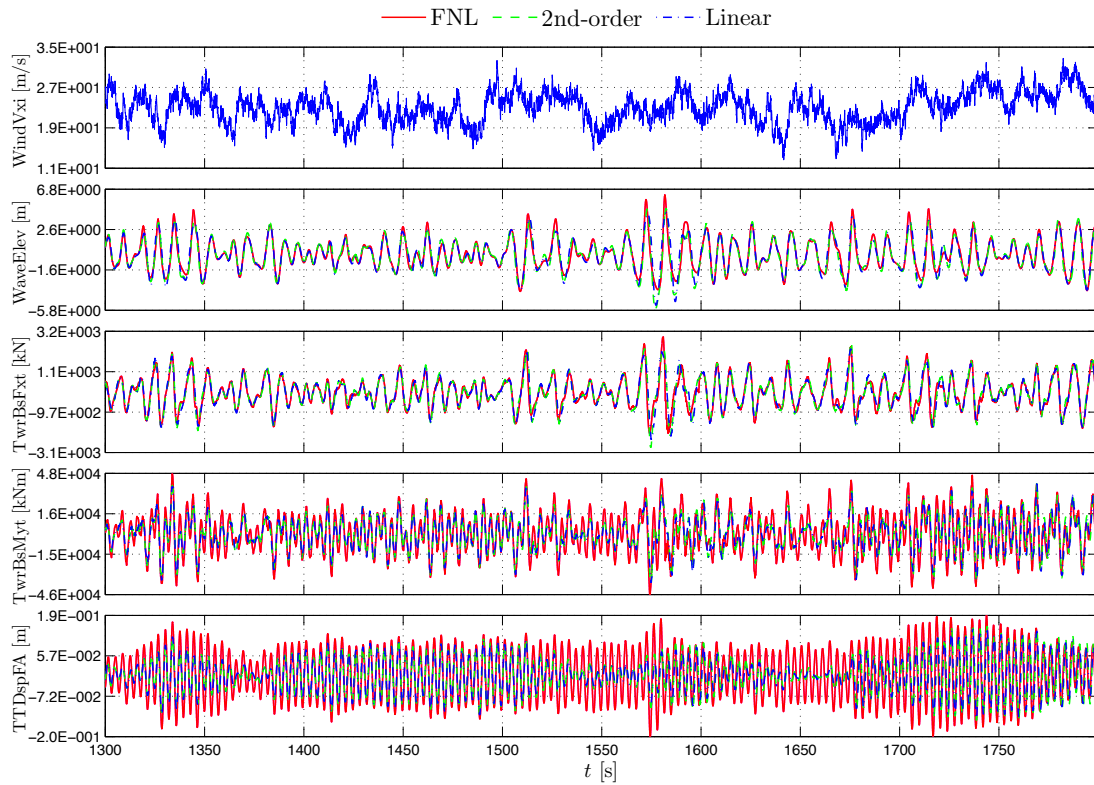
(a) Time series of the hub-height longitudinal wind velocity (WindVxi), wave elevation (WaveElev), tower base fore-aft shear force (TwrBsFxt), tower base fore-aft bending moment (TwrBsMyt) and tower-top fore-aft deflection (TTDspFA), corresponding to the linear (blue dash dot), 2nd-order (green dash), FNL (red solid) wave kinematic models.
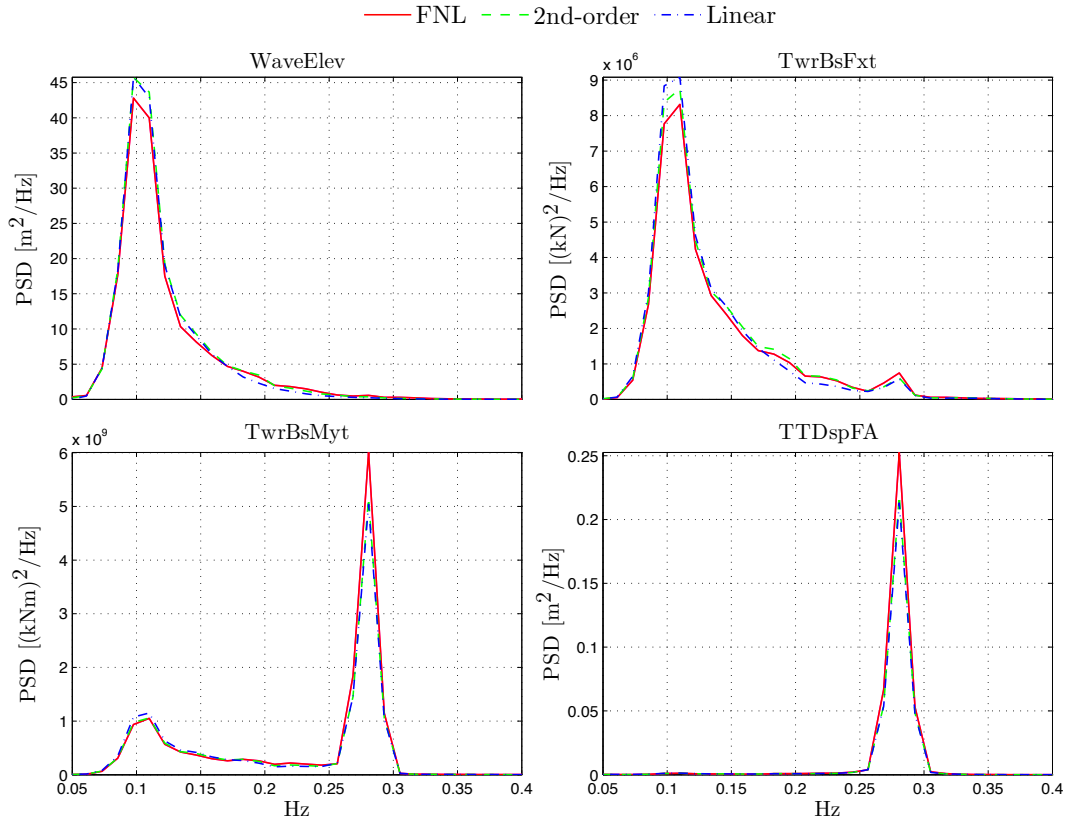
(b) PSDs of the wave elevation (WaveElev), tower base fore-aft shear force (TwrBsFxt), tower base fore-aft bending moment (TwrBsMyt) and tower-top fore-aft deflection (TTDspFA), corresponding to the linear (blue dash dot), 2nd-order (green dash), FNL (red solid) wave kinematic models.

Figure 1. Time series and PSDs of the system response comparing the three (L, WNL, FNL) hydrodynamic models.

Risk-consistent cladding pressures on the Isozaki tower in Milan

C. Pozzuoli[1], F. Mola[2] and C. Segato[1]

[1]ECSD Srl, Milan, Italy
[2]Politecnico di Milano, Milan, Italy
Corresponding author: C. Pozzuoli, chiara.pozzuoli@libero.it

Abstract

Risk-consistent wind loads on the cladding elements of the 202.2 m high Isozaki tower, located in new business and shopping district of CityLife in Milan, Italy, have been evaluated using the Database-Assisted Design (DAD) method (Rigato et al., 2001), considering directionality effects. The aerodynamic database, containing time series of pressures measured in a boundary layer wind tunnel, was combined with the climatological database, consisting of local information on directional extreme wind speeds. Comparing these pressures with those predicted neglecting the directionality effect, significant reductions in the peak wind loads and a meaningful redistribution of the 'hot spots' with the most critical pressures were observed when the directionality factor was included, resulting in a more economic, reliable and risk-consistent design of the cladding elements under wind loads.

1   Introduction

Differently from the conventional approach, the risk-consistent method for estimating design wind loads on cladding elements takes into account the dependence of the design wind speed with a given return period on the incoming wind direction, thus leading to a uniform safety level of the cladding elements under wind loads (Simiu and Hendrickson, 1987; Simiu and Scanlan, 1996).

In the definition of cladding loads from pressure coefficients measured in the wind tunnel for a building with a certain orientation, the design wind speed at reference height with a certain return period depends on incoming wind direction, because of two phenomena. Firstly, roughness upwind of the site changes with direction leading to different speed-up effects in different directions. Secondly, because of the local wind statistics, the design wind speed at a given height with a certain return period varies with approaching direction. This second effect is that called directionality effect.

The Database-Assisted Design (DAD) method (Rigato et al., 2001), which combines the aerodynamic database, containing time series of pressure coefficients measured in the wind tunnel at a large number of points, with the climatological database of the directional wind speeds at a meteorological station relevant to the building site, allows for the complete consideration of direction-related issues in the estimation of design wind loads. In particular, the DAD method takes into account the directional aerodynamic properties of the specific type of building being designed and the directional wind climate at the location of interest.

In this work the DAD method has been applied for defining the design wind loads on the cladding elements of the Isozaki tower, considering the wind directionality effect. The building, located in the new business and shopping district of CityLife in Milan (Fig. 1a), is 202.2 m tall and has an approximately rectangular footprint of dimensions 24 m x 60 m. The Isozaki tower, at the moment under construction (Fig. 1b), has six office floors in each of the eight modules clad with a double-glazed glass skin. The side façades are partly glazed and display the panoramic elevators. The cladding elements of the building comprise also parapets and fins that are exposed to the wind loads on their two sides (Fig.2).

In order to evaluate the directionality effect on the cladding loads, design wind pressures were compared with pressures calculated neglecting the dependence of wind speed on wind direction and

using the value of the design wind speed of 25 m/s recommended by the Eurocode (EN 1991-1-4:2005) and by CNR-DT 207 (2008).

Figure 1. Perspective view of the masterplan of the new business and shopping district of CityLife in Milan, Italy with Isozaki tower on the right (a); the Isozaki tower under construction (b).
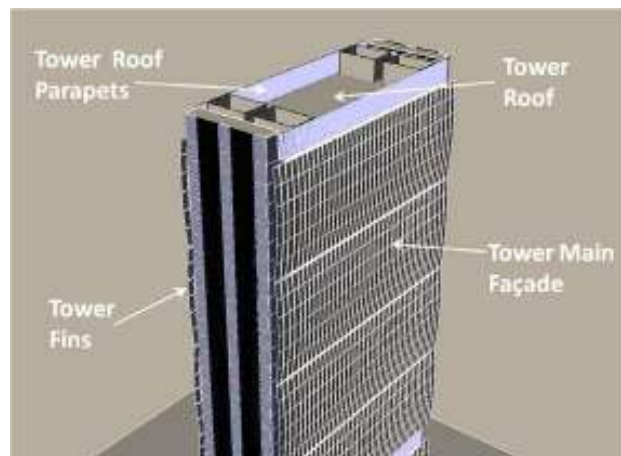
Figure 2. Labelling of Isozaki tower elements exposed to the wind action.

2   DAD approach for the definition of risk-consistent cladding pressures

Wind tunnel tests were carried out by CPP, Inc., Fort Collins, Colorado, in a boundary layer wind tunnel on a rigid model of the tower for two different configurations of surroundings. Configuration A consisted of the surrounding buildings including proposed buildings comprising the other two towers of the Citylife district. Configuration B consisted of the surrounding buildings excluding the other two towers of the Citylife development (Fig.1a). Cladding pressures characterizing the aerodynamic database were measured at 506 tap locations for 36 wind directions and were given in terms of positive and negative peak pressure coefficients as a function of incoming wind direction.

Full scale positive peak pressures were obtained according to Eq.1 (for negative pressures a similar equation was used) where A,B are the two topographic configurations, θ is the wind direction, $\hat{C}_{P,T}^{+}(\theta)$ is the peak positive pressure coefficient at tap T, function of θ and ρ is the air density.

(a)   (b)
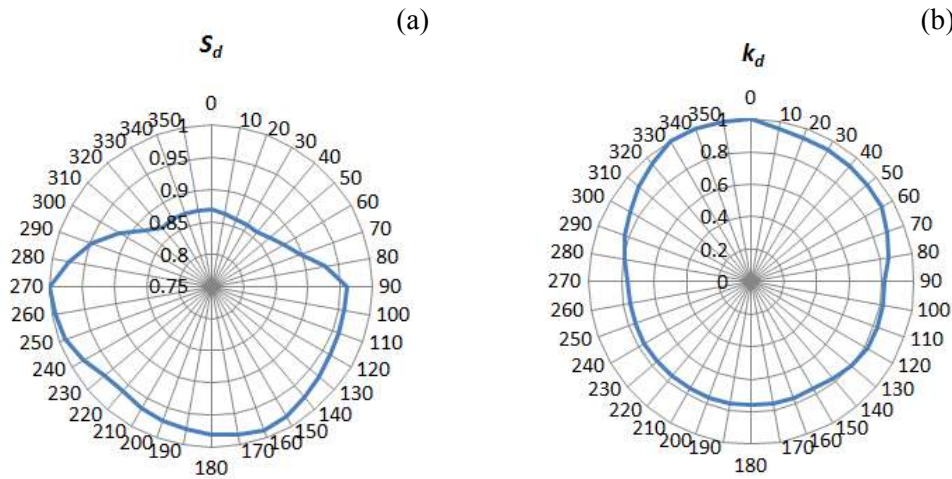
Figure 3. Smoothed load ratio S_d (a) and directionality factor k_d (b) as a function of wind direction.

$$\widehat{p}_T^+ = \max_{A,B} \left\{ \max_{\theta=1\div360} \left[\widehat{C}_{P,T}^+(\theta) \frac{1}{2} \rho U_{ref,50}^2(\theta) \right] \right\} \qquad (1)$$

The mean wind speed at reference height with 50-year return period, $U_{ref,50}$, is direction-dependent because of the two effects mentioned in the introduction. Firstly, roughness characteristics upwind of the site vary with direction, leading to different speed-up effects with height; secondly, the design wind speed at a given height and for a given return period, varies with direction according to the local climate. Changes in roughness upwind of the site were included in the calculation of the mean wind speed at reference height by means of a 'smoothed load ratio', S_d (Fig. 3a), using the ESDU Internal boundary layer analysis (ESDU 1993). For the second effect, i.e. the directionality effect, a directionality factor, k_d (Fig. 3b), was defined from the statistical analysis of wind speed data obtained from three nearby airports, namely Linate, Malpensa and Cameri airports. Consideration of these two effects was mathematically framed transforming Eq. (1) in Eq. (2), where the constant equal to 721 Pa is a value of the dynamic pressure taken as reference.

$$\widehat{p}_T^+ = \max_{A,B} \left\{ \max_{\theta=1\div360} \left[\widehat{C}_{P,T}^+(\theta) k_d^2(\theta) S_d(\theta) \cdot 721\ Pa \right] \right\} \qquad (2)$$

For façade cladding elements separating the internal building space from the external environment design wind loads were evaluated in terms of net pressures of the external pressure and the internal pressure taken equal to +0.3/-0.4 kPa, based on the Eurocode, whichever gave the most onerous net pressure. Cladding elements exposed on their two sides (parapets, fins…) were designed for the peak simultaneous differential pressures acting across the surfaces. The most severe net negative pressure value on the main facades is -2.2 kPa and was reached in small areas on the northwest elevation. An even more severe negative pressure equal to approximately -2.6 kPa was measured on tower fins at the top of the building. The highest values of positive pressures are in the range 1.6-1.8 kPa.

3   Wind directionality effect on cladding pressures

For evaluating the wind directionality effect on design cladding loads, pressures calculated according to Eq. 2 were compared with those calculated taking into account changes in roughness upwind of the site, but neglecting the directionality factor, considering, regardless for direction, the value of the design wind speed recommended by the Eurocode. The most severe negative pressure obtained in this way is -3.8 kPa and was reached in small regions on the southwest elevation. Positive pressure zones of approximately 2.0 kPa are quite common.

Comparing pressures calculated according to Eq. 2 with those predicted neglecting the directionality effect, significant reductions in the peak wind loads (up to 40% reductions) and a significant redistribution of the 'hot spots' with the most critical positive and negative pressures were observed when the directionality factor was taken into account, resulting in a more economic, reliable and risk-consistent design of the cladding elements of the Isozaki tower under wind loads.

4 Acknowledgements

References

CNR-DT 207 (2008) – *Istruzioni per la valutazione delle azioni e degli effetti del vento sulle costruzioni.* Consiglio Nazionale delle Ricerche. Commissione di studio per la predisposizione e l'analisi di norme tecniche relative alle costruzioni.

EN 1991-1-4:2005, *Eurocode1: Actions on Structures – General Actions – Part 1-4: Wind actions*, CEN TC250.

ESDU (1993). *Strong winds in the atmospheric boundary layer, Part 1: mean hourly wind speeds*, ESDU Report 82026, ESDU International.

Rigato, A., Chang, P., and Simiu, E. (2001). Database-assisted design, standardization and wind direction effects. *Journal of Structural Engineering*, **127** (8), 855-860.

Simiu, E., and Hendrickson, E.M. (1987). Design criteria for glass cladding subjected to wind loads. *Journal of Structural Engineering*, **113**, 501-518.

Simiu, E. and Scanlan, R. (1996). *Wind Effects on Structures*. John Wiley & Sons, Inc.

Predictions of VIV-mathematical models for a rectangular 4:1 cylinder

Antonino M. Marra[1], Claudio Mannini[1] and Gianni Bartoli[1]

[1]CRIACIV/Department of Civil and Environmental Engineering, University of Florence, Italy
Corresponding author: Antonino M. Marra, antonino.marra@dicea.unifi.it

Abstract

Results of aeroelastic tests on a rectangular 4:1 cylinder are compared with semi-empirical model predictions to show the inadequacy of existing models in estimating vortex-induced vibrations of bluff bodies. After estimating the input model parameters at a certain Scruton number, their predictions of the peak values of the limit-cycle oscillation amplitude at higher Scruton numbers are compared with the experimental responses. The variation of the aeroelastic parameters with the Scruton number of a van der Pol-type model clearly shows its inadequacy in predicting lock-in oscillations. Other models' predictions will be analyzed in the full-length paper.

1 Introduction

Significant flow-induced oscillations of the Volgograd bridge deck (800 mm peak-to-peak amplitude) were recently observed (Weber et al., 2013). The nature of the oscillations seems to be reconducible to vortex-induced vibrations, a phenomenon that has been imposing expensive interventions to mitigate the oscillations of several bridges to prevent fatigue problems and/or discomfort on users.

Vortex-induced vibration represents a non linear resonance between the Karman-vortex shedding action and the motion of the structure. Despite the work of many researchers in the last five decades, the phenomenon has not been properly modeled yet (Luo and Bearman, 1990; Marra et al., 2011). As confirmed by the number of works developed into the last years (Marra et al., 2011; Wu and Chang, 2011; Wu and Kareem, 2012; Wu and Kareem, 2013; Zhu et al., 2013), the topic still represents a priority in bridge aerodynamics.

In this work, wind tunnel tests on a rectangular 4:1 cylinder were carried out at different Scruton numbers to evaluate the VIV predictions of some semi-empirical models. In particular, Section 2 describes the experimental results. In Section 3, for the sake of brevity, only a van der Pol-type model is considered while other models are treated in the full-length paper. Finally, some preliminary remarks are reported.

2 Experiments

2.1 Experimental set-up

Experiments were conducted in the open-circuit boundary layer wind tunnel of CRIACIV, located in Prato, Italy. The test section is 2.42 m wide and 1.60 m high.

A wooden sectional model, 986 mm long, 300 mm wide (B) and 75 mm deep (D), was used to perform the tests (Figure 1). To enforce bidimensional flow conditions, rectangular plates in plywood were provided at the model ends (562 mm $\times$ 225 mm $\times$ 4 mm). The mass of the model with end-plates was about 3.3 kg. The blockage ratio given by the model alone, calculated as D/H_{wt}, being H_{wt} the height of the wind-tunnel test section, was 4.7%.

The model was connected through its longitudinal axis-tube to two shear-type frames. Only a vertical displacement was allowed by the two frames due to the very large flexural stiffness of the two vertical elements at which the model was connected. The aerodynamic damping due to the exposition to the flow of the plate-springs was verified to be very small. All the tests were carried out in a nominal smooth flow with a turbulence intensity slightly lower than 1%. The Reynolds number ($Re_r = U_r D / \nu$ where

Figure 1. Experimental set-up: sectional model (left), suspension system (right).

Table 1. Characteristics of the oscillating system for each configuration.

Configuration	l	m	m_a	n_0	$\zeta \times 10^{-3}$	m_r	Sc
	[mm]	[kg/m]	[kg]	[Hz]	[-]	[-]	[-]
I	674	6.5	0	8.4	0.7	0.0011	2.1
II	674	6.5	0	8.4	0.8	0.0011	2.3
III	490	6.3	0	13.9	1.6	0.0011	4.6
IV	550	6.2	6	8.2	1.1	0.0006	6.1
V	490	6.3	12	8.1	1.2	0.0004	9.9

$\nu = 0.154$ cm^2/s is the air kinematic viscosity) at the resonance wind speed ($U_r = n_0 D/St$) ranged from 23,450 to 38,600.

2.2   Free vibrations

Five dynamic configurations were considered to study the lock-in response of the system at different Scruton numbers. Since the damping ratio of the suspension system increases as the length of the plate-springs is reduced, the Scruton number was changed by combining different lengths of the plates with various masses added to the suspension system.

The vertical frequency and damping ratio for the oscillating system in still air were estimated for the five configurations reported in Table 1, where l is the length of the oscillating plate-springs; m represents the mass per unit length of the oscillating system; m_a is the added mass; n_0 denotes the vertical natural frequency; ζ is the vertical damping coefficient; $m_r = \rho D^2/m$ represents the mass ratio and $Sc = 4\pi m\zeta/(\rho BD)$ is the Scruton number. It can be seen that the Scruton number ranges from 2.1 to 9.9 (from 8.4 to 39.6 if the classical definition $Sc = 4\pi m\zeta/(\rho D^2)$ is adopted).

2.3   Lock-in response

Figure 2 reports the standard deviation of the dimensionless transverse displacement against reduced velocity for five Scruton numbers. For each configuration the lock-in oscillations start at a reduced velocity of about $1/St$ ($St = 0.136$ as obtained in Marra et al. (2011)). The increase of the Scruton number corresponds to a reduction of the peak vertical response as well as to a reduction of the lock-in range from the right side. A secondary resonance is also present around $1/(2St)$. The right-hand side of Figure 2 reports a table with the peak of the standard deviation values of the oscillation amplitudes for each Scruton number.

Configuration	Sc	$\tilde{y}_{peak}/D$
	[-]	[-]
I	2.1	0.0479
II	2.3	0.0414
III	4.6	0.0378
IV	6.1	0.0328
V	9.9	0.0260
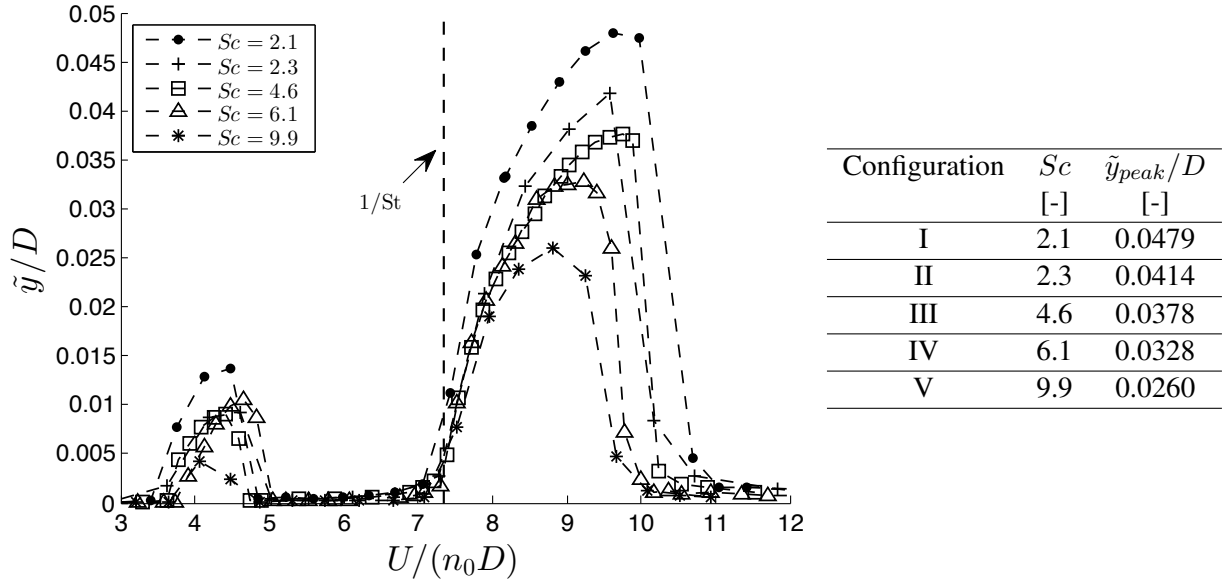
Figure 2. Standard deviation of dimensionless transverse displacement $\tilde{y}/D$ against reduced velocity $U/(n_0 D)$ for different values of the Scructon number.

3   Predictions of semi-empirical models

Ehsan and Scanlan (1990) proposed a semi-empirical nonlinear model for the across-flow response that considers the following van der Pol-type equation:

$$m(\ddot{y} + 4\pi n_0 \zeta \dot{y} + 4\pi^2 n_0^2 y) = \frac{1}{2}\rho U^2 (2D)\left[Y_1(K)\left(1 - \epsilon(K)\frac{y^2}{D^2}\right)\frac{\dot{y}}{U}\right] \tag{1}$$

where U is the mean wind speed and $Y_1(K)$ and $\epsilon(K)$ are parameters which have to be determined through wind tunnel tests being $K = 2\pi n_0 D/U$. The parameters Y_1 and ϵ are related, respectively, to the linear and nonlinear component of the aerodynamic damping. In particular, ϵ takes into account that the oscillations are self-limiting.

To obtain the aeroelastic parameters (ϵ and Y_1) one can conduct a decay-to-resonance test by fitting the decaying response with an approximate harmonic solution given by the method of slowly varying parameters (Ehsan and Scanlan, 1990). Figure 3 reports the aeroelastic parameters estimated for different Scruton numbers by decaying-to-resonance tests performed at the wind speeds of the peak responses. It can be seen the significant variation of the parameters with the Scruton number.

4   Preliminary remarks

The performance of a van der Pol-type model in estimating vortex-induced vibrations are assessed by identifying its aeroelastic parameters at different values of the Scruton number. The significant variation of the parameters with the Scruton number highlighted the inadequacy of the model in predicting such a complicated phenomenon. In fact, such a variation of the coefficients causes non-negligible changes in the response preditions at Scruton numbers different from that at which the parameters were estimated (Marra et al., 2011). The full-length paper will report more details on the present model as well as the analysis of other existing model.
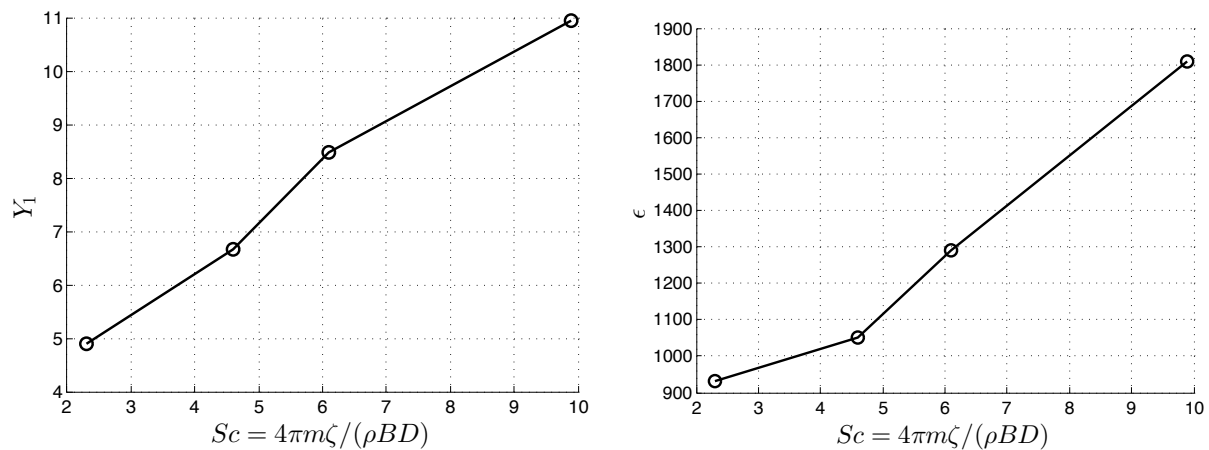
Figure 3. Variation of the aeroelastic parameters of the Ehsan-Scanlan model with the Scruton number.

Aknowledgements

References

Ehsan, F. and Scanlan, R. H. (1990). Vortex-Induced Vibrations of Flexible Bridges. *Journal of Engineering Mechanics* **116**.6, pp. 1392–1411.

Luo, S. C. and Bearman, P. W. (1990). Predictions of fluctuating lift on a transversely oscillating square-section cylinder. *Journal of Fluids and Structures* **4**.2, pp. 219–228.

Marra, A. M., Mannini, C., and Bartoli, G. (2011). Van der Pol-type equation for modeling vortex-induced oscillations of bridge decks. *Journal of Wind Engineering and Industrial Aerodynamics* **99**.6-7, pp. 776–785.

Weber, F., Distl, J., and Maslanka, M. (2013). Semi-active TMD Concept for Volgograd Bridge. *Conference Proceedings of the Society for Experimental Mechanics Series,* pp. 79–88.

Wu, J.C. and Chang, F.J. (2011). Aerodynamic parameters of across-wind self-limiting vibration for square sections after lock-in in smooth flow. *Journal of Sound and Vibration* **330**.17, pp. 4328 –4339.

Wu, T. and Kareem, A. (2012). An overview of vortex-induced vibration (VIV) of bridge decks. *Frontiers of Structural and Civil Engineering* **6**.4, pp. 335–347.

Wu, Teng and Kareem, Ahsan (2013). Vortex-Induced Vibration of Bridge Decks: Volterra Series-Based Model. *Journal of Engineering Mechanics* **139**.12, pp. 1831–1843.

Zhu, L.T., Meng, X.L., and Guo, Z.S. (2013). Nonlinear mathematical model of vortex-induced vertical force on a flat closed-box bridge deck. *Journal of Wind Engineering and Industrial Aerodynamics* **122**.1, pp. 69 –82.

Design of Industrial Chimneys for Gust and Vortex Resonance: Practice and Perspectives

Francesca Lupi[1], Claudio Borri[1] & Hans-Juergen Niemann[2], Ruediger Hoeffer[2]

[1]Department of Civil and Environmental Engineering, University of Florence, Italy
[2]Department of Civil and Environmental Engineering, Ruhr-University Bochum, Germany
Corresponding author: First Author, francesca.lupi@dicea.unifi.it

Abstract

Vibrations of chimneys under the wind action occur in the along-wind and in the across-wind direction. All the design load models to account for along-wind vibrations are based on the gust response concept, originally developed by Davenport. Two different models - developed by Ruscheweyh and Vickery&Basu, respectively - are available regarding the design for vortex resonance. They include the modelling of aeroelastic forces but they differ in the manner they incorporate aeroelastic effects. Ruscheweyh's approach deals with vortex resonance as a forced vibration and incorporates the aero-elastic effects into model parameters derived from experimental data. The Vickery&Basu model follows Scruton's approach and treats the aeroelastic lift force as a component in out-of-phase with the motion, acting as a negative aerodynamic damping. Experimental observations indicate the relative importance of parameters such as the Scruton number, the intensity of turbulence and the mode of vibration. Furthermore, regarding the in-line wind load, the mechanical model of the chimney (either beam or shell) also enters into the discussion. The paper applies different approaches and model codes to real samples of industrial chimneys and discusses the principal results, open problems and further improvements in the design of chimneys for the wind action.

1   Along wind action

1.1   Design models for gust wind load

All gust wind models presently utilized in modern wind loading codes go back to the classical Davenport approach (Davenport, 1962). It amplifies the mean wind force - which is a real physical quantity - applying the gust response factor G. The aim is to obtain an equivalent static load that reproduces the effects of the stochastic wind loading process on the most important structural stressing.

$$w(z) = G \cdot w_m(z) \tag{1}$$

In the Eurocode formulation, an important difference is that the wind force is based on the peak (or gust) velocity pressure. This is one of the merits of this model, because the profile of the wind force results in a more realistic image of the local gust loads at each level. As a result, the first term in equation (2), which is close to 1, quantifies the Eurocode modification to the Davenport approach.

$$w(z) = \frac{1+7I_v(z)}{1+7I_v(z_s)} \cdot G \cdot \frac{\rho_a V^2(z)}{2} \cdot C_D \cdot A_{ref} \tag{2}$$

Other formulations are for example proposed in the CICIND model Code for industrial chimneys (CICIND, 2010, 2011). It is unique in that it gives individual expressions for the mean wind load and the gust wind load (eqn. (3)). By separating both components, the gust load may be given any profile appropriate to reproduce the distribution of the real bending response due to gustiness. The CICIND adopts a linear profile with $w_g = 0$ at $z = 0$, able to reproduce the peak bending moment at the base.

$$w(z) = w_m(z) + w_g(z) \tag{3}$$

Further differences in the code stipulations concern the aerodynamic factor C_D. It is sensitive to Re, surface roughness and aspect ratio. Moreover, the three-dimensionality of the chimney and of the flow past it is responsible for the spanwise variation of C_D and its local increase in the tip region.

Figure 1a shows the differences in the in-line wind loading profile due to different gust wind load models. The Eurocode approach (2) is also applied to the non-uniform distribution of C_D resulting from wind tunnel tests (Lupi, 2013). Figure 1b shows the resulting bending moments. The differences in the response are predominantly due to the different values and distributions of C_D, whereas the accordance between the different models is good. On the basis of these and other results (see Niemann et al., 2013), the CICIND model code results in a simplified but conservative design. Even though the tip-effect is not included in the CICIND model, this is compensated by the relatively high and constant force coefficient. However, about 10% of reduction of stresses might be achieved through a more realistic distribution of C_D, e.g. resulting from wind tunnel tests.
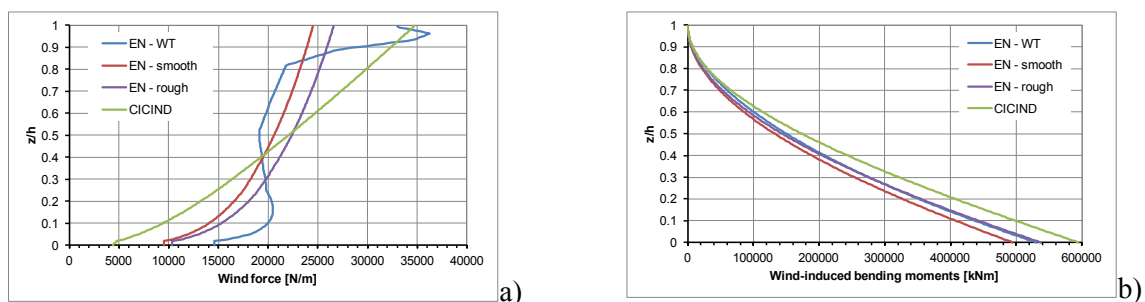
Figure 1. a) In-line wind loading on a real chimney sample according to different loading models and C_D distributions: [1] Eurocode model applied to C_D measured in the wind tunnel (EN-WT) and to those provided by the Code itself for [2] smooth or [3] rough surfaces and [4] CICIND Model Code. b) Resulting bending moments.

1.2 Structural behaviour: beam versus shell

Figure 2 a) shows that in case of low aspect ratio and/or low the thickness-to-radius, the deviation in the maximum membrane stress, compared to the beam distribution, may even exceed 30%. The departure is especially high at the bottom, but it extends over a relatively high portion of the cylinder height (Figure 2 b). As a result, the beam-like model might be neither realistic nor on the safe side and tensile stresses at the windward side become the leading stresses. When a shell model of the chimney has to be used, wind pressures and not forces have to be provided.
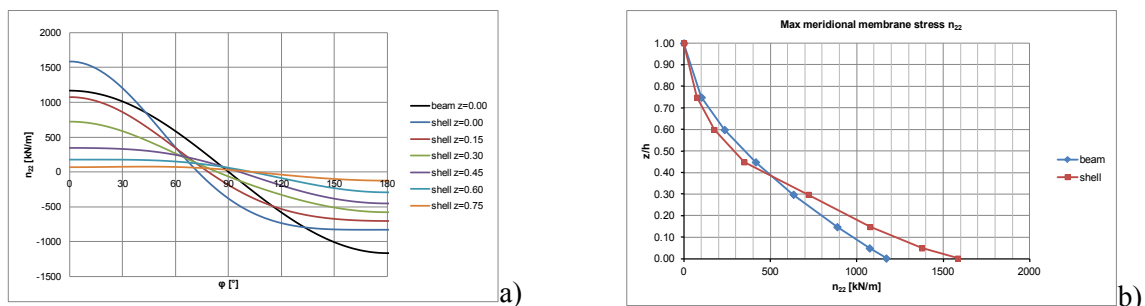
Figure 2. a) Meridional membrane stress n_{22} at different z/h levels on a real chimney sample, beam distribution at z = 0. b) Meridional membrane stress n_{22} at stagnation compared to beam distribution.

2 Design for vortex resonance

2.1 Design models for vortex resonance

Two different models - developed by Ruscheweyh and Vickery&Basu, respectively - are available regarding the design for vortex resonance. Ruscheweyh's approach is based on the concept of the

effective correlation length and accounts for aeroelastic forces by an iterative procedure. The model parameters are derived from experimental data, therefore the model is suitable for typical ranges of turbulence intensity. Ruscheweyh's approach is included in the Eurocode as Method 1. The typical feature of the Vickery&Basu model (which is included in its full and even extended formulation in the CICIND and in its simplified version in the Eurocode as Method 2) is to include the aeroelastic effects into the modelling of a negative aerodynamic damping. The approach goes back to Scruton (1963). Furthermore, as vortex excitation is characterized by the existence of a self-limiting cycle, the model is non-linear. A possible modelling of the non-linear and self-limited behaviour of the aeroelastic lift force is proposed by Marris (1964). However, Vickery revisits Marris's approach and removes the non-linearity by expressing the aerodynamic damping as function of the variance of the response and two independent model parameters, namely the negative aerodynamic damping for small amplitudes of oscillations K_{a0} and the self-limiting amplitude on the rms of the response a_L (Vickery&Basu, 1983):

$$\xi = \frac{\rho_a d^2}{m_e}\left[\frac{Sc}{4\pi} - K_{a0}\left(1 - \left(\frac{\sigma_y}{a_L d}\right)^2\right)\right] \tag{4}$$

Little information is available on the aerodynamic damping and it at least depends on the Reynolds number, the turbulence intensity, the mean wind velocity and the aspect ratio. In fact, the Scruton number ($Sc = 4\pi m\xi_s/(\rho D^2)$) - and in particular the ratio of Sc and the aerodynamic damping $4\pi Ka$ - governs the amplitude of the response. The response lies in the lock-in range when $Sc \ll 4\pi Ka$. Small amplitudes of vibrations are instead predicted when $Sc \gg 4\pi Ka$.

2.2   Application to a real chimney sample and identification of open problems

Figure 3a shows the response curves as function of the Scruton number at different levels of turbulence intensity. The calculation applies the Vickery&Basu model in its full (an extended) formulation, as described in the CICIND Commentaries. According to this formulation, the effect of turbulence intensity on the response is to reduce the critical Scruton number at which the jump between high and low levels of oscillation occurs. The reason is that the higher is the turbulence intensity, the lower is the negative aerodynamic damping, the higher is the ratio $Sc/4\pi Ka$. Mathematically, large amplitudes of vibrations occur when $Sc/4\pi Ka < 1$. This threshold is achieved at smaller Sc in case of higher Iv. Similarly, Figure 3b shows that, at a given level of mechanical damping (thus Scruton number), the effect of Iv may considerably reduce the response.
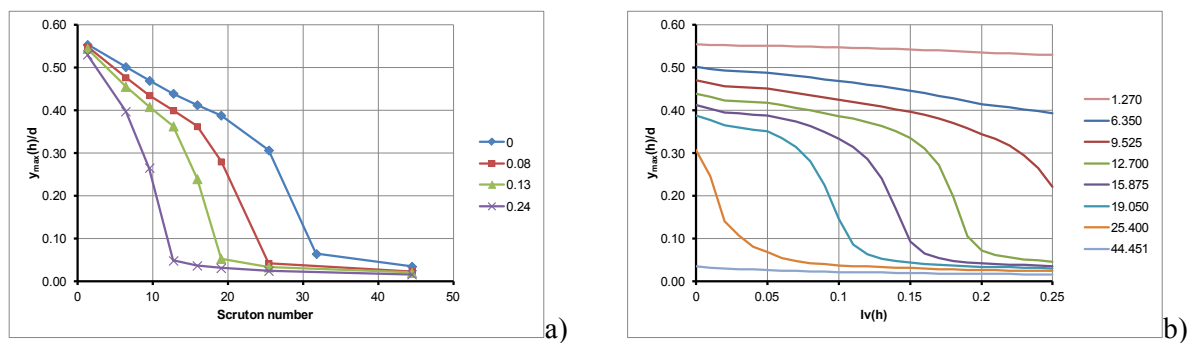
Figure 3. a) Cross-wind deflections as a function of the Scruton number Sc at different turbulence intensities; b) Cross-wind deflections as a function of turbulence intensity Iv at different Scruton numbers Sc.

Figure 4a shows the extension of the lock-in range at a given Sc and its dependency on the turbulence intensity. The figure is obtained by applying the CICIND model to a real chimney sample. This model is unique in the sense it includes the effect of turbulence and the dependency of the response on V/Vcr. The Eurocode design methods (Method 1 and Method 2), applied to the same chimney sample, provide very different results (Figure 4b). However, the figure proves that both methods turn to be correct if properly interpreted by including the effect of turbulence intensity. In fact, as the Eurocode Method 1 (after Ruscheweyh) is empirical and calibrated on the basis of experimental data, it should be reliable at higher values of turbulence intensity. The opposite holds for the Eurocode

Method 2 (a simplified version of the Vickery&Basu model), which only provides results for zero turbulence intensity and for this reason the response is often overestimated. The figure proves that the design load models for vortex resonance are in principle consistent and physically correct. However, at low values of Sc, as well as in the range Sc ≈ 4πKa, the model parameters as well as the influence of turbulence intensity should be carefully investigated, as the two methods differ considerably even at relatively high values of turbulence intensity. Figure 3b shows the impressively high amplitudes of vibrations at small values of Sc by applying the Vickery&Basu model.
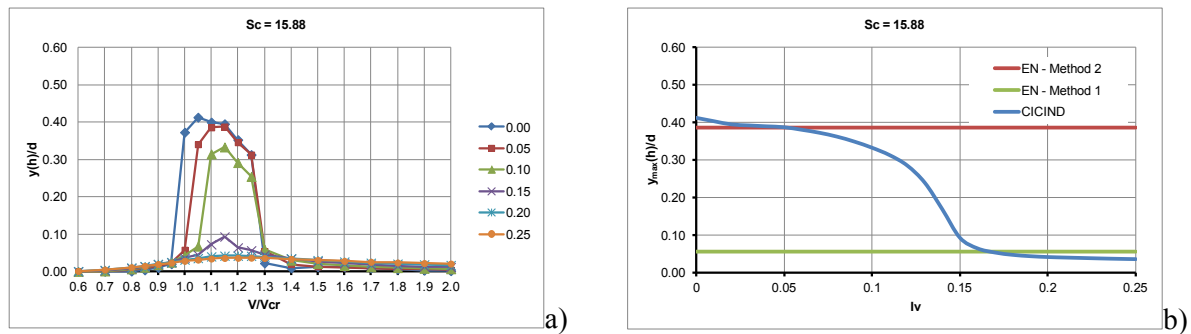
Figure 4. a) Extension of the lock-in range as a function of I_v; b) Comparison of model codes for vortex resonance.

3   Future outlooks

The investigation suggested that further improvement regarding the design of industrial chimneys for vortex resonance may be gained by further research, through wind tunnel tests in the values of the model independent variables (self-limiting amplitude of vibration and aerodynamic damping) and in the parameters they depend on (mode shape, intensity and scale of turbulence, the latter related to the cylinder diameter). A new research project has been just opened by the authors for this purpose and will be introduced at the conference.

References

Davenport, A.G., The response of slender line-like structures to a gusty wind. Proc. Soc. Civ. Engineers, vol. 23, pp. 389, 1962.

Scruton C., On the wind-excited oscillations of stacks, towers and masts. Proc. of Symposium no.6. Wind effects on Building and Structures, Teddington, UK, 26-28 June 1963.

CICIND Model Code and Commentaries for Steel and Concrete Chimneys, 2010-2011.

Lupi F., Eds., A new aerodynamic phenomenon and its effects on the design of ultra-high cylindrical towers. Phd Dissertation, Univ. of Florence / Technical Univ. Braunschweig, Shaker Verlag.

Niemann, H.-J., Lupi, F., Höffer R., International Standardizazion of Wind Actions on Chimeys, CICIND Report, 2013.

Marris, A.W., A review of vortex streets, periodic wakes and induced vibration phenomena. Journal Basic Eng., Trans. Am. Soc. Mech. Eng., 86, 185-193, 1964.

Vickery, B.J., Basu, R.I., Across-wind vibrations of structures of circular cross-section. Part I-II: Journal of Wind Engineering and Industrial Aerodynamics, Vol. 12, 49–97, 1983.

Wind tunnel study on urban wind flows

Maria P. Repetto[1], Andrea Freda[1], Marco Fia[1], Elisabetta Rebuffo[1], Massimiliano Burlando[1], Alessio Ricci[1]

[1]Department of Civil, Chemical and Environmental Engineering, University of Genoa, Italy
Corresponding author: Maria P. Repetto, repetto@dicca.unige.it

Abstract

This paper presents the results of an experimental study aimed at investigating the urban flow in a canopy layer. A quarter of Livorno city, placed in Tuscany, has been selected as test case and reproduced in scale 1:300 in the wind tunnel of the Department of Civil, Chemical, and Environmental Engineering (DICCA) of the University of Genova. Two sets of measurements have been carried out, aimed at measuring the wind velocity profiles in a curved street canyon and at characterizing the urban wind comfort in a square, respectively. The results are discussed with reference to similar experiences and analytical models reported in literature.

1 Introduction

The wind velocity models are generally well established in flat open terrain, where the wind profile can be described based on the roughness of the surface and on the thermal atmospheric conditions. On the contrary, the wind flow in urban environment is dominated by a variety of complex issues, such as the heterogeneous geometry of the areas and the thermal urban effects. The region above the buildings in the urban boundary layer (UBL) is characterized by continuously changing surface roughness, so the flow never reaches the equilibrium condition. The situation is even more complex within the canopy layer, where the streets give rise to complex canyoning effects, strongly dependent on their orientation with respect to the incoming wind.

Many research works have been done covering different aspects of urban flow (Fernando et al., 2010), however, at present, it is not yet completely understood. Several authors (e.g. Fernando, 2010, Barlow, 2013), stress that the complexity of the UBL requires studies with multiple approaches, having mutual strength and weaknesses. High-resolution numerical models and wind tunnel laboratory tests can help to identify basic processes, however results must be validated carefully, as they are strongly dependent on the model conditions (Blocken, 2013). Fields studies in real urban atmosphere can provide benchmark data for modelling, but they also can be affected by uncertainties due to the lack of spatial and time representativeness of single point measurements (Schatzmann and Leitl, 2011).

The present paper presents the first step of a wide research project aimed at investigating the urban flow in the canopy layer. A city district of Livorno, placed in Tuscany, has been selected as test case. The fluxes in the quarter will be measured and simulated extensively by means of wind tunnel tests and CFD numerical models, with the aim of providing a carefully validated benchmark.

The paper presents, in particular, the wind tunnel measurements, discussing the results on the basis of similar experiences and analytical models reported in literature.

2 Urban area and monitoring network

Livorno is an average size coastal Italian city (around 150.000 inhabitants) placed in Tuscany, in flat terrain. A district on the sea side has been selected, of about 36000 m^2, named "Quartiere La Venezia" for the presence of narrow canals, similar to the Venice ones. The district comprehends a linear narrow street and canal (Viale Caprera), a curved street and canal (Canale Rosciano and Fosso della Venezia)

and a square (Piazza del Luogo Pio). The urban fabric is very complex, with blocks of different shaped buildings and internal courts; the average height of constructions is 20 m. The selected area will be monitored by means of a series of instruments, reported in Figure 1. In particular, five sonic anemometers have already been placed in the framework of the 'Wind and Ports' European project (Solari et al., 2012), and have been measuring data since 2011. Figure 1 shows the position of two of them ($A_{vp}3$ and $A_{vp}4$) and reports, on the left, the wind rose obtained from the measurements, showing a prevalence of wind directions from East and West sectors, the latter corresponding also to the extreme wind velocity directions. Moreover, a Lidar is presently being installed in the framework of the "Wind, Ports, and Sea" European Project (Burlando et al., 2014), and five new sonic anemometers will be installed in the canopy layer (Fig. 1 right box). In the first phase of the research, four anemometers will be placed in different positions along the curved street, and one will be placed at the top of the highest roof of the area. In the second phase, the anemometers will be moved to the linear street and to the square.

Figure 1. Test area of Livorno city.

3   Wind tunnel tests

3.1   Model building and test set-up

The selected area has been reproduced in a 1:300 scale model and tested in the wind tunnel of DICCA. The realization of a detailed physical model required different stages of work, represented in Figure 2. In the first stage, a 2-D CAD model of the area has been elaborated, identifying the blocks (Fig. 2 a); in the second stage, a 3-D CAD model of each block has been produced, identifying each building of the block (Fig. 2 b); in the third stage, each building has been exploded into his main parts, identified by means of a numerical code (Fig. 2 c). The buildings parts have been then realised, using medium-density fibreboard (MDF) of different thickness for the plates and buildings walls, and 2 mm PVC panels for the roofs and bridges. Finally, each block has been composed (Fig. 2 d) and the physical model has been assembled completely.

The layout of the model and the position of the instruments are reported in Figure 3. Two sets of measurements have been carried out. The first set is aimed at measuring the wind velocity profiles in the curved street canyon Canale Rosciano; the positions corresponding to the anemometric stations (A1- A5) have been identified, and the profiles of the mean wind velocity and turbulence intensities in the centre and in a lateral point of the Canal have been measured at 7 height levels between 5 and 50 m (real scale) over the sea level by means of a multihole probe. The second set of tests is aimed at characterizing the urban wind comfort in the square Piazza del Luogo Pio, considering or neglecting the presence of the green area with high trees in its nearby (Fig. 1 right box). In this case, 8 positions

(P1- P8) have been selected and the mean wind velocity has been registered by means of thermistors, at 2 m and 5 m over the terrain level, in two different configurations, with and without the presence of trees.

The two sets of measurement have been repeated for three western sectors ($\alpha=240°$, $\alpha=270°$, $\alpha=300°$ from the North), corresponding to the extreme winds prevalent directions in the area, and for different wind tunnel velocities.
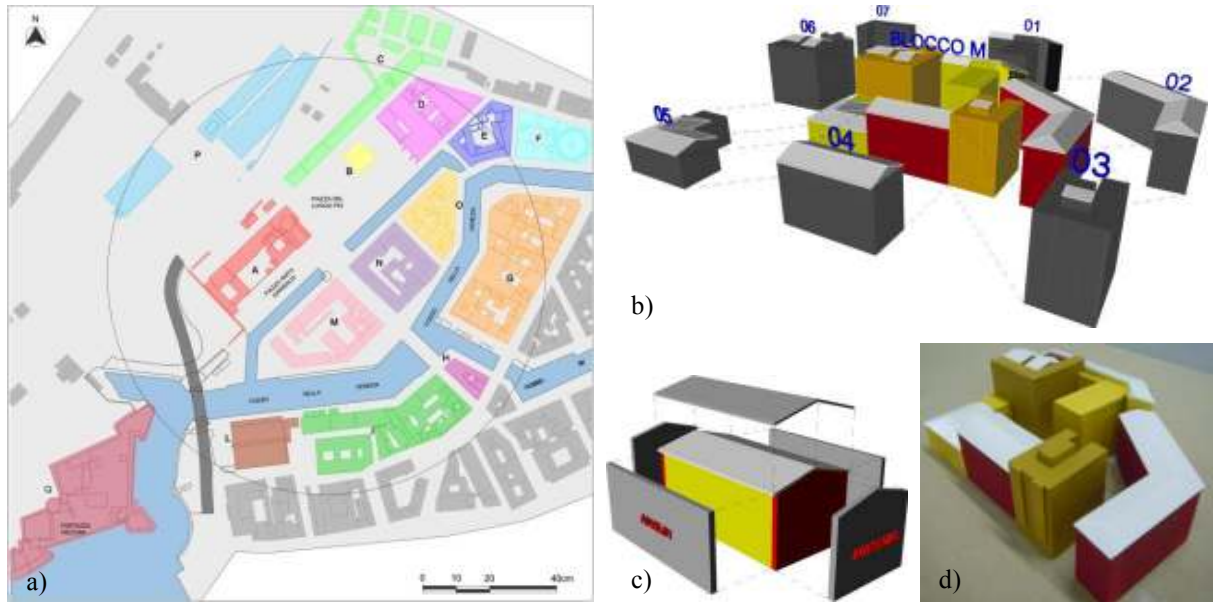
Figure 2 Different stages in the model construction: a) plan of the area with blocks identification; b) 3-d CAD model of one block, with identification of the buildings; c) 3-d CAD model of one building, with identification of elements; d) physical model of the block.
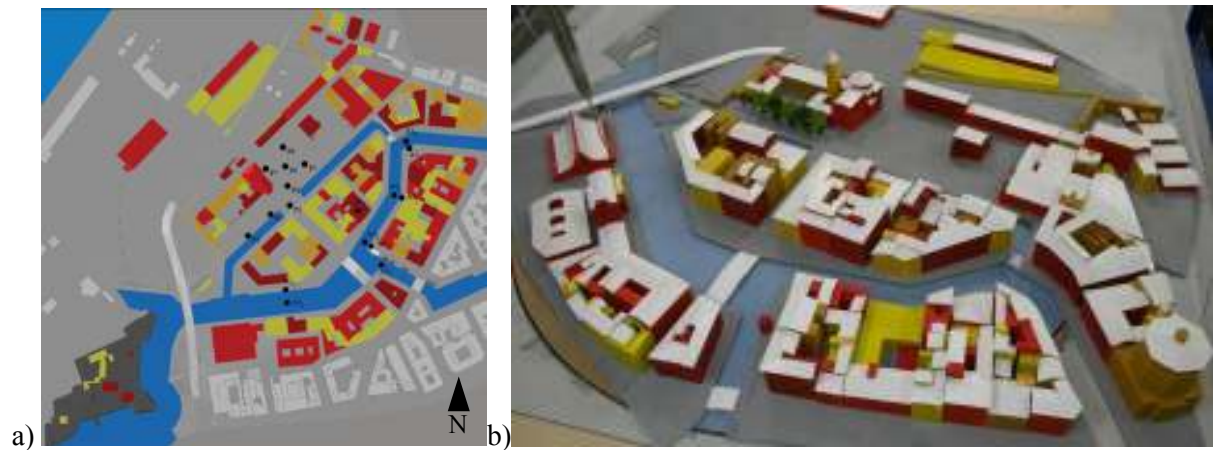
Figure 3. Scheme of the wind tunnel model and test positions (a) and picture of the model in the wind tunnel (b).

3.2   Urban canyons results

Figure 4 reports the mean wind velocity profiles measured at four positions (A2-A5) in the central line of Canale Rosciano, with incoming wind directions $\alpha=240°$ (Fig. 4 a), $\alpha=270°$ (Fig. 4 b) and $\alpha=300°$ (Fig. 4 c), respectively; the abscissa reports the ratio between the measured velocity at height z and the reference undisturbed incoming velocity (V_{ref}), corresponding to geostrophic conditions. For each measured z level, the yaw angle ϕ and the pitch angle θ are reported, showing the horizontal and vertical deviation from the incoming along wind direction, respectively. Each diagram also reports the

incoming wind profile (orange line). On the left, a schematic section of the canal is reported, showing the mean height of the buildings, h_b=20 m. On the right, a wind map at z=10 m is reported.
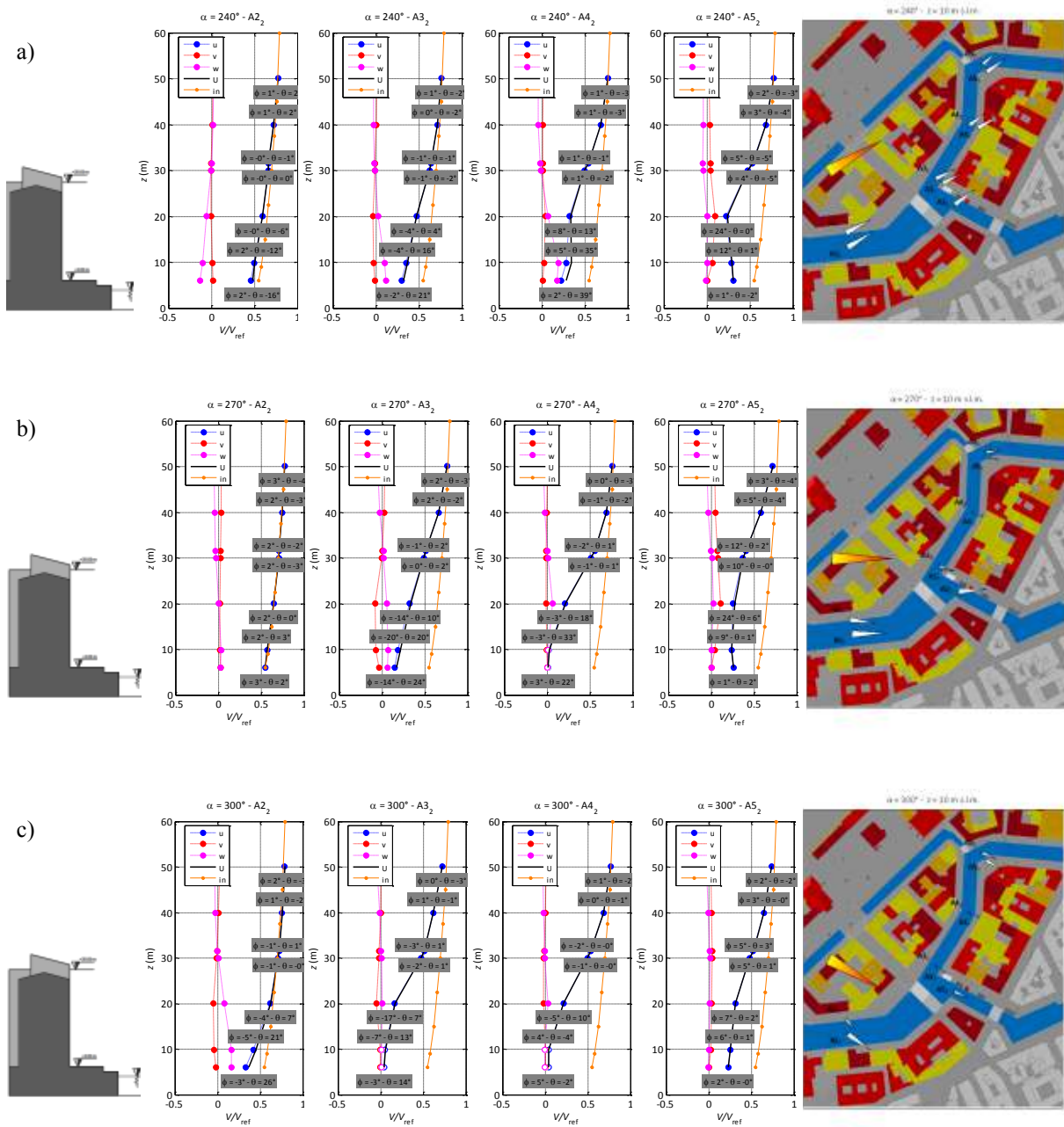
Figure 4. Mean wind velocity profiles measured in the four positions in the central line of Canale Rosciano, with wind direction α=240° (a), α=270° (b) and α=300° (c).

At z=50 m, corresponding to 2.5 h_b, the mean wind speed is almost constant in the four points, with yaw and pitch tending to zero, independently from the wind direction. At levels between 30 and 50 the wind speed in the horizontal plane is almost aligned with the incoming direction (yaw tending to zero), whereas some noticeable vertical deviation can be observed. The wind velocity is also progressively less intense from A2 to A5, showing the effect of the change in roughness. At levels lower that 30 m, the canyoning effect is emphasized.

Considering the inflow direction α=240° (Fig. 4 a), as the first section of the Canal is almost aligned with the incoming wind, at point A2 the canyoning effect produces an acceleration of the flow,

with negligible yaw and pitch. At points A3 and A4 the wind speed is progressively reduced, while the yaw and pitch grow up, highlighting the presence of large vortices typical of canyon streets not aligned with the incoming wind. This tendency is inverted at point A5, in which the flow tends to become more regular. Considering the wind directions α=270° and α=300° (Fig. 4 b and c), the canopy layer effect is much more evident, especially in the points A3 and A4, in which the Canal results almost orthogonal with respect to the inflow. In these points, wind velocity at low levels reduces almost to zero, as the flow tends to move over the building roofs. The wind velocity tends to increase in points A3₃ and A5, where the flow tends again to accelerate for canyoning effect.

It can also be noted that the wind velocity show some differences, considering the central and the side points of the Canal. Figure 5 show the mean wind profiles corresponding to the side and central points in correspondence of A2 position, with incoming wind direction α=300°; it can be seen that both the wind velocity and the flow deviation angles are completely different at levels lower that 30 m.
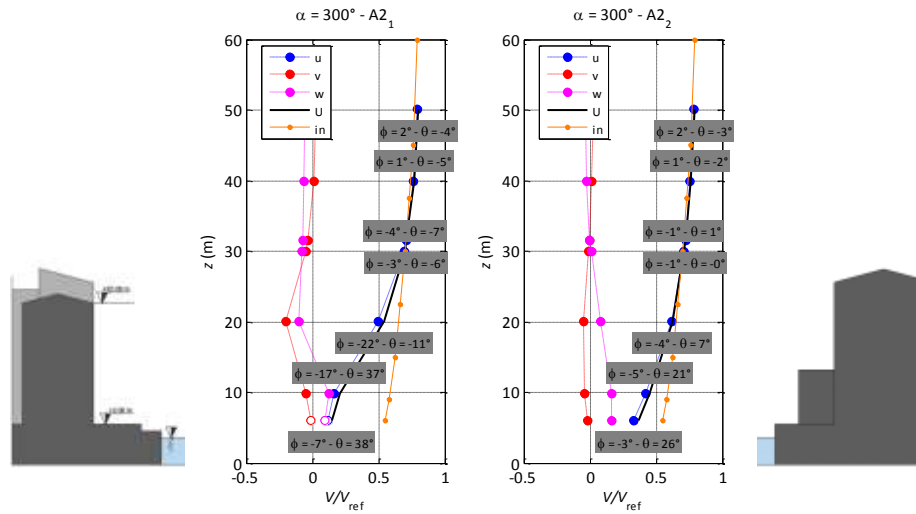
Figure 5. Mean wind velocity profiles measured in the side and central points of Canale Rosciano, at position A2, with wind direction α=300°.

Previous results confirm that the wind velocity in the canopy layer is very complex and difficult to be modelled. The wind tunnel measurements will be compared, in further step of the research, to a numerical CFD simulation and with full scale measurements, in order to deeper understand the physical mechanisms arising and to give some guidance on the best modelling strategy.

At this stage, the test results have been compared with analytical solution outside the canopy layer (Figure 6). In this layer, if the height of the buildings is quite regular, the wind velocity can be modelled adopting a logarithmic profile defined as (Garratt, 1992):

$$V(z) = \frac{1}{k} u * \ln\left(\frac{z-d}{z_0}\right)$$ (1)

where z is the height above the terrain level, d is the zero-plane displacement, z_0 is the roughness length, $u*$ is the shear velocity, k is the Von Karman constant. The zero-plane displacement is usually defined as a function of the mean height of the buildings.
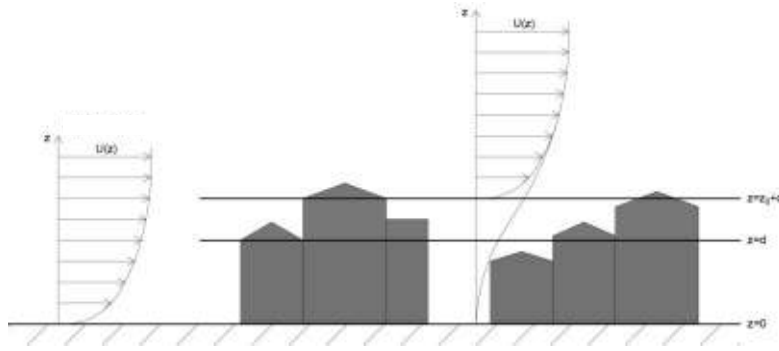
Figure 6. Analytical logarithmic profile over the building height.

The mean wind profiles measured in wind tunnel tests are represented in Figure 7, for incoming wind directions α=240° (Fig. 7 a), α=270° (Fig. 7 b) and α=300° (Fig. 7 c), respectively; the abscissa reports the ratio V/V_{ref} between the measured wind velocity and the undisturbed reference undisturbed incoming velocity, in logarithmic scale. If Eq. (1) was satisfied, the diagram should be linear in this scale. It is worth notice that the wind profile al level lower that z=30 m are strongly nonlinear, thus, as expected, in the canopy layer the logarithmic law is not adequate to model the wind profile.
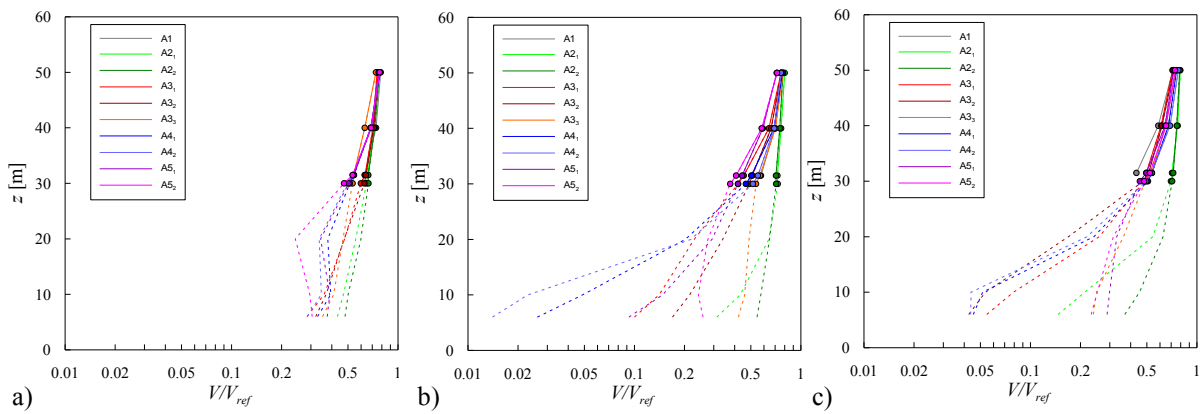
Figure 7. Mean wind velocity profiles measured in all the positions, with wind direction α=240° (a), α=270° (b) and α=300° (c), in logarithmic scale.

Considering only the measurements at level greater than z=30 m, the three parameters in Eq.(1), u^*, d, and z_0, are estimated, adopting the Marquardt-Levenberg nonlinear mean square algorithm (Marquardt, 1963). Table 1 summarizes the obtained values for the considered points and for the three incoming flow directions. Considering the inflow direction α=240° (Table 1 and Fig. 7 a), the obtained values are quite coherent for all the measured points, except in point $A3_3$. In these cases, the flow distortion are limited to the level lower that z=30 m and the analytical profile in Eq.(1) could be adopted to model the wind velocity above the buildings, paying particular attention to the estimate of the zero plane displacement and the corrected roughness length. Considering the inflow directions α=270° and α=300° (Table 1 and Fig. 7 b, c), the obtained values are reasonable only for few points. In these cases, in facts, the perturbation due to the canyon street lasts for higher levels and Eq.(1) cannot be used for describing the wind velocity profiles. Measurements at levels higher than z=50 m should be made in future works, in order to define a more reliable boundary of the canopy layer.

Table 1. Parameters estimates of the analytical logarithmic wind profile low (Eq. 1).

	α=240°			α=270°			α=300°		
	$u*$	d [m]	z_0 [m]	$u*$	d [m]	z_0 [m]	$u*$	d [m]	z_0 [m]
A1	0.634	28.3	0.0072	0.453	29.3	0.0002	2.988	10.8	7.8212
A2$_1$	0.880	15.7	0.1064	3.779	-100.4	36.4	0.343	27.4	0.0001
A2$_2$	0.993	15.2	0.1883	0.847	7.0	0.0892	0.699	11.2	0.0196
A3$_1$	0.550	25.5	0.0026	1.519	25.1	0.8660	2.814	5.1	8.1325
A3$_2$	0.677	22.9	0.0144	1.423	23.4	0.7314	5.749	-34.9	36.4783
A3$_3$	385.8	-5467.7	5447.6	1.095	24.7	0.2086	2.201	12.0	3.8586
A4$_1$	1.371	22.9	0.5986	0.903	28.6	0.0682	1.022	25.6	0.1700
A4$_2$	0.922	27.2	0.0856	0.765	27.9	0.0282	1.020	26.6	0.1445
A5$_1$	0.855	27.7	0.0551	3.185	7.6	9.4030	1.045	25.9	0.2281
A5$_2$	1.043	26.6	0.1604	2.615	16.4	5.2955	1.311	22.3	-0.6295

3.3   Wind velocity at pedestrian level

A preliminary analysis of the wind regimes at pedestrian level has been realized, measuring the wind velocity at eight positions (P1- P8) in Piazza del Luogo Pio, at level z= 2 m from the terrain, with the three incoming wind directions α=240°, α=270° and α=300°. In particular, two different set of measurements have been made, considering or neglecting the presence of the green area with high trees. Figure 8 shows in detail the model of the Piazza del Luogo Pio with (a) and without (b) trees.
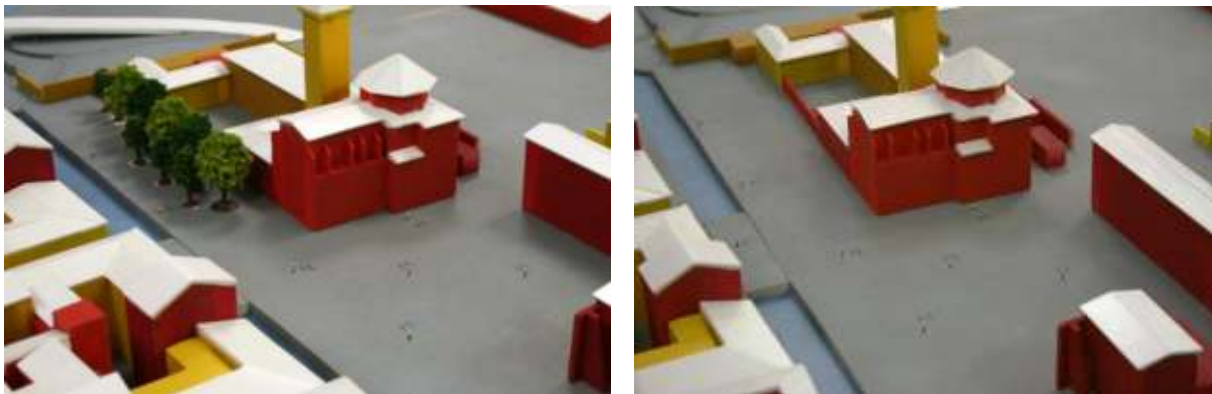
Figure 8. Pictures of the wind tunnel model of the Piazza del Luogo Pio, with (a) and without (b) trees.

Figure 9 shows the mean wind velocity maps corresponding to the configurations with and without trees (left and right panels, respectively), with wind direction α=240° (a), α=270° (b) and α=300° (c). It can be noted that also in this case a canyoning effect arises, in correspondence of Viale Caprera, which produces the worst situation at points P2, P3, P4 in the configuration without trees. As expected, such effect is usually mitigated by the presence of the trees; however, the presence of trees can sometimes increase the wind velocity.

In order to quantify such effect, Table 2 show the variation of wind velocity due to the presence of the trees, as a percentage of the value measured in the configurations without trees. Negative sign represents a decreasing velocity, positive sign represents an increasing velocity, due to the presence of the trees. The mitigating effect of the trees is quite evident in many points, reaching the maximum decreasing value in the order of 60% in point P4 and α=270°. The increasing effect of the trees is particularly evident in point P8, where the vegetation always increase the wind velocity of 10%; the maximum increasing value is 22% at point P1 and α=300°. Since this effect might also be imputed to the physical modelling of trees for wind tunnel tests, a comparison with vegetation having different porosity is going to be carried out in the prosecution of the current research.

Also, the overall effect of the trees cannot be evaluated in the present analysis, because it should be set in the framework of a pedestrian wind comfort evaluation, repeating the analysis for all the wind directions and considering the directional probability of incoming wind velocity. However, these preliminary results alert on possible unfavourable effects induced by trees in complex urban environment.

Table 2. Percentage of variation of wind velocity due to the presence of the trees

point	α=240°	α=270°	α=300°
P1	-6,3	-3,4	+22,2
P2	-10,8	-5,0	-19,6
P3	+8,8	-2,5	-34,0
P4	-38,1	-59,5	-27,3
P5	-43,8	-41,4	+18,2
P6	-32,0	-33,3	-4,2
P7	0,0	-5,0	-9,1
P8	+2,6	+7,7	+10,0

a)

b)

c)
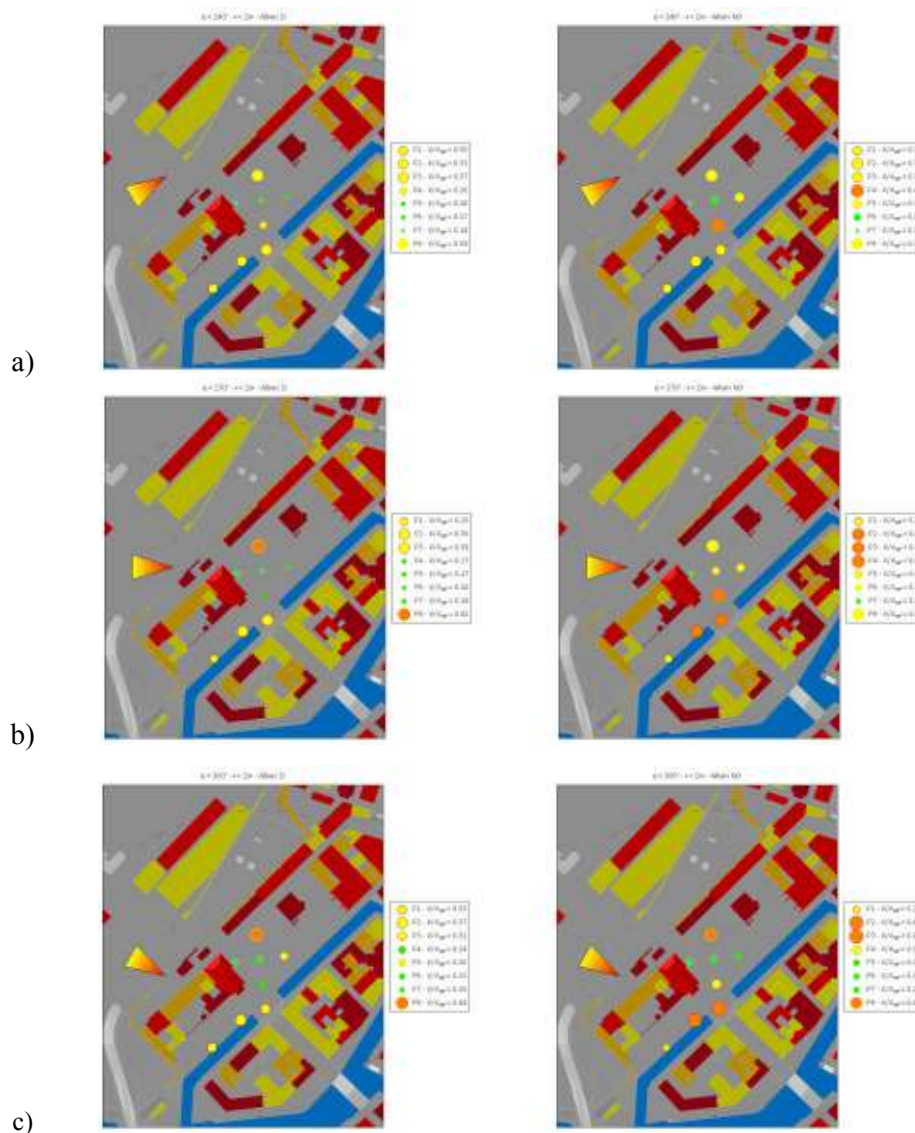
Figure 9. Mean wind velocity maps measured in the Piazza del Luogo Pio, at pedestrian level, with and without trees (left and right panels, respectively), with wind direction α=240° (a), α=270° (b) and α=300° (c).

4   Conclusions and perspectives

The paper reports the first step of a wide research project aimed at investigating the urban flow in the canopy layer, presenting, in particular, the wind tunnel measurements related to a quarter of Livorno city, reproduced in a detailed physical model in scale 1:300.

   The first set of test measures the mean wind profile in different points of the narrow and curved Canale Rosciano, for three inflow western sectors. The obtained values show a strong reduction of the wind velocity in the canopy layer, in particular for levels lower than 1.5 h_b. The measured wind profiles have been also compared with the analytical logarithmic power low, considering measured at levels between 1.5 h_b and 2.5 h_b, showing that, for internal points and wind directions orthogonal to the Canal, the perturbation due to the canyon street lasts until the highest levels.

   The second set of tests measures the wind velocity at pedestrian level in the open Piazza del Luogo Pio, discussing the effect of trees in mitigating wind effects. It has been shown, in particular, that the vegetation have usually a great mitigating effect, reducing wind velocity up to 60% in some points, but it can also increase the wind velocity in some other conditions.

   The research still in course is aimed at expand and strengthen the obtained results. More wind tunnel tests are going to be carry out, measuring wind profiles at higher levels over the terrain and in more points and completing the two set of measurements for all the incoming wind sectors. The effect of trees mitigation will be re-evaluated in a framework of a complete comfort analysis, and considering different vegetation porosities. In parallel, a CFD numerical model of the same area is under construction and a series of anemometric stations are going to be installed in the selected points. The numerical simulation and the full scale measurements will be adopted to complete the comparison, in order to obtain a benchmark solution, giving useful information on the best strategies for modelling wind in complex urban areas.

References

Barlow, J.F. (2013). The wind that shakes the buildings: wind engineering from a boundary layer meteorology perspective. In: *Fifty Years of Wind Engineering: Prestige Lectures from the Sixth European and African Conference on Wind Engineering*, Owen J.S. et al. (Eds.), University of Birmingham.

Blocken, B. (2013). Years of Computational Wind Engineering: Past, Present and Future. In: *Fifty Years of Wind Engineering: Prestige Lectures from the Sixth European and African Conference on Wind Engineering*, Owen J.S. et al. (Eds.), University of Birmingham.

Burlando M., Repetto M.P., Solari G., De Gaetano P., Pizzo M., Tizzi M. (2014). Wind and waves numerical forecasting for safety access to port areas: the "Wind, Ports, and Sea" project. *CWE 2014, June 8 - 12, 2014, Hamburg, Germany*.

Fernando, H.J.S. (2010). Fluid dynamics of urban atmospheres in complex terrain. Annual review of fluid mechanics, **42**, 365–389.

Fernando, H.J.S., Zajiic, D., Di Sabatino, S., Dimitrova, R., Hedquist, B., Dallman, A. (2010). Flow, turbulence and pollutant dispersion in urban atmospheres . *Physics of fluids*, **22**, 051301-1–20.

Garratt, J.R. (1992). The atmospheric boundary layer. Cambridge University Press, Cambridge, U. K.

Marquardt, D.W. (1963). An algorithm for least-squares estimation of nonlinear parameters, *Journal of the Society for Industrial and Applied Mathematics*, **11**(2), 431-441.

Schatzmann, M., Leitl, B. (2011). Issue with validation of urban flow and dispersion CFD models. *Journal of Wind Engineering and Industrial Aerodynamics*, **99**, 169–186.

Solari G., Repetto M.P., Burlando M., De Gaetano P., Parodi M., Pizzo M., Tizzi M. (2012). The wind forecast for safety management of port areas. *Journal of Wind Engineering and Industrial Aerodynamics*, **104–106**, 266–277.

Wake characteristics of an offshore wind turbine
in the vicinity of a coastal mountain

Hrvoje Kozmar[1], Davide Allori[2], Enzo Marino[2], Gianni Bartoli[2], Claudio Borri[2]

[1]Faculty of Mechanical Engineering and Naval Architecture, University of Zagreb,
Ivana Lučića 5, 10000 Zagreb, Croatia
[2]Department of Civil and Environmental Engineering, University of Florence,
Via di Santa Marta 3, 50139 Florence, Italy
Corresponding author: Hrvoje Kozmar, hrvoje.kozmar@fsb.hr

Abstract

An extensive set of experiments was carried out in the CRIACIV boundary layer wind tunnel in order to characterize flow and turbulence around an offshore wind turbine in complex coastal terrain. The wind-tunnel simulation of the atmospheric boundary layer (ABL) flow and turbulence developing upwind from the coastal mountain was achieved by using the castellated barrier wall, vortex generators and surface roughness elements. Once a well developed ABL simulation has been created, wake characteristics of an alone-standing offshore wind turbine were studied for three different mountain models (small and large mountain with laterally uniform height, mountain with a bay). A configuration without the mountain was tested as well in order to investigate flow and turbulence around an offshore wind turbine placed downstream of a plane coast. The wind turbine was in the parking position (no rotation of the rotor blades) in order to study wind characteristics for a strong wind situation with wind velocity larger than 25 m/s. The experimental results indicate a velocity decrease and stronger turbulence in the wind-turbine wake in presence of a coastal mountain.

1   Introduction

When offshore wind turbines are deployed off the orographically complex, mountainous coast, their ability to extract kinetic energy from the flow decreases due to wind characteristics significantly different than the 'classical' atmospheric boundary layer (ABL) flow that wind turbines are originally designed for. In addition, unsteady wind loading of wind energy structures in those areas is expected to reveal additional, unknown features. While there is a lot of information on onshore wind turbine aerodynamics, as exposed to 'classical' atmospheric boundary layer flow, little is known about their wake characteristics off the mountainous coast that is essential to extend their lifetime and to maximize energy production. Hence, carefully designed small-scale wind-tunnel experiments are expected to provide valuable information on those problems.

This project builds upon the findings of previous studies on onshore wind turbine aerodynamics, as exposed to 'classical' ABL flow. In particular, Zhang et al. (2012) identified localized regions of strong vorticity and swirling strength in the wind turbine near wake. Hu et al. (2012) characterized the dynamic wind loads and evolution of the unsteady vortex and turbulent flow structures. Chamorro and Porté-Agel (2010) found the velocity deficit has an axisymmetric shape; the turbulence intensity distribution is non-axisymmetric, velocity power spectra show a signature of the turbine blade tip vortices. In this study, the wake characteristics of an alone-standing wind turbine immediately downstream of the mountainous coast are investigated at different distances downstream from the wind turbine.

2   Experimental setup

Experiments are carried out in the CRIACIV boundary layer wind tunnel described in detail in Augusti et al. (1995) following standard wind-tunnel procedures (Simiu and Scanlan, 1996). This wind tunnel is designed as an open-return (Eiffel) suction-type wind tunnel with a closed test section. Wind velocity through the test section can be regulated between 0 m/s and 30 m/s by both adjusting the pitch blade angle and regulating the speed of the fan powered by a 160 kW engine, where the fan is placed at the outlet of the test section. The total length of the wind-tunnel test section is approximately 22 m. The test section is 1.6 m high and 2.2 m wide at the outlet of the nozzle, i.e. at the inlet to the test section. Due to diverging side walls in the longitudinal direction to avoid pressure gradients, the test section width at the centre of the turntable is 2.4 m. In this wind-tunnel it is possible to reproduce the ABL flow and turbulence along the first 11 m of the test section (8 m long fetch and 3 m at the turntable, where horizontal incidence angle of the flow can be varied). The ABL simulation upwind from the mountain is created by applying the Counihan (1969) technique. The simulation hardware consists of three Counihan 1.53 m high quarter-elliptic constant-wedge-angle spires, a castellated barrier wall and a fetch of roughness elements. Surface roughness consisted of 0.05 m high, 0.05 wide, 0.05 m long wooden cubes placed in a staggered pattern with lateral distance between the cubes 0.145 m in lateral and 0.110 m in longitudinal direction. Three different mountain models are used, as well as the smooth surface representing the sea. Each mountain model is 60 cm long in the main wind direction (along the wind-tunnel test section) and 100 cm wide (lateral to the main wind direction). Small mountain model is 10 cm high, large mountain model is 20 cm high, while the mountain with a bay is 20 cm high with a slope to 10 cm height in the lateral centre of the mountain. Leading edge of all terrain types is placed 5.3 m downwind from the trailing edge of the vortex generators. Downwind from the trailing edge of the mountain the test-section surface is smooth representing the sea. In all tests, the offshore wind turbine model is placed 5 cm downwind from the trailing edge of the mountain. The cylindrical wind turbine tower with diameter of 1.2 cm is 24 cm high. Three 16 cm long turbine blades designed similar to DOWEC-NREL 5MW and EU 56.1400-2 blades are fixed in a parking position (no rotation). An arrangement of the castellated barrier wall, vortex generators, surface roughness elements, as well as the coastal mountain and wind turbine model is presented in Figure 1.

a)   b)

Figure 1. Experimental setup in the wind tunnel test section: a) castellated barrier wall, vortex generators, surface roughness and the mountain with a bay model, b) the offshore wind-turbine model placed 5 cm downstream from the trailing edge of the large mountain model.

Measurement technique includes Cobra probe and Prandtl-Pitot tube for velocity measurements, as well as pressure and temperature sensors. The flow and turbulence are analyzed with respect to the mean velocity, turbulence intensity, Reynolds stress, integral length scales of turbulence, power spectral density of velocity fluctuations. The velocity profiles downstream of a mountain are evaluated using the freestream mean velocity $\bar{u}_\infty = 15$ m/s measured in the undisturbed flow at 93 cm height, 100 cm upwind from the leading edge of the mountain. The ABL velocity profiles without the mountain model are normalized using the reference velocity $\bar{u}_{ref} = 10.2$ m/s at the reference height

$z_{ref} = 0.216$ m. Initial velocity measurements carried out to investigate characteristics of the ABL simulations differed insignificantly for time records longer than 60 s. Hence, the time record length in the ABL simulations is 120 s, when analyzing the wind-turbine wake characteristics it is 60 s, while the sampling rate is 500 Hz in all tests.

3   Results

In a wind-tunnel test section without a mountain model in place, the power-law exponent for the mean velocity u profile in the main (x) wind direction is $\alpha = 0.26$ indicating an urban ABL simulation with the Prandtl constant-flux layer clearly exhibited in the lower part of the ABL simulation, as presented in Figure 2.
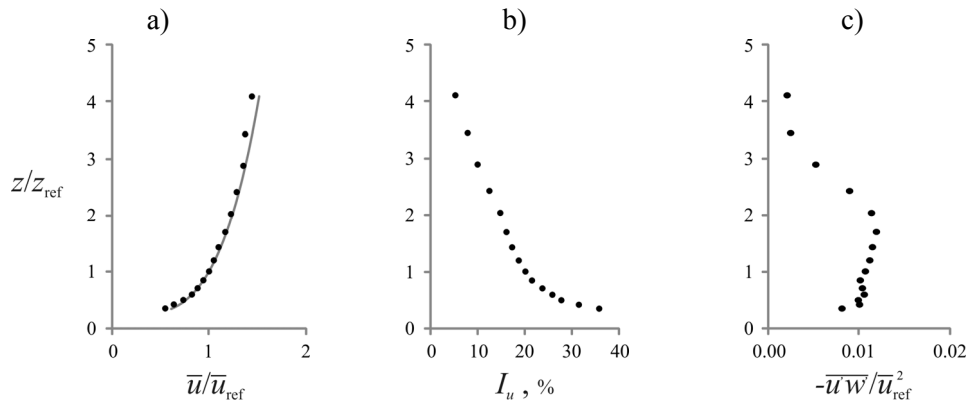
Figure 2. Characteristic profiles of the created ABL simulation: a) mean wind velocity profile (solid dots are experimental results, solid line is the power-law approximation with an exponent $\alpha = 0.26$), b) longitudinal turbulence intensity I_u profile (normalized locally with a mean wind velocity at the measurement point height), c) Reynolds shear stress profile; $\bar{u}_{ref} = 10.2$ m/s is mean wind velocity in the main wind direction x recorded at the reference height $z_{ref} = 0.216$ m.

Vertical profiles of the mean wind velocity and longitudinal turbulence intensity at the position of the wind turbine (without wind turbine in place), as well as at different streamwise positions downstream from the wind turbine (wind turbine in place) are presented in Figures 3 and 4, respectively, for three different shapes of the mountain and without the mountain (flat coastal terrain). Each profile is created based on measurements in ten different heights.
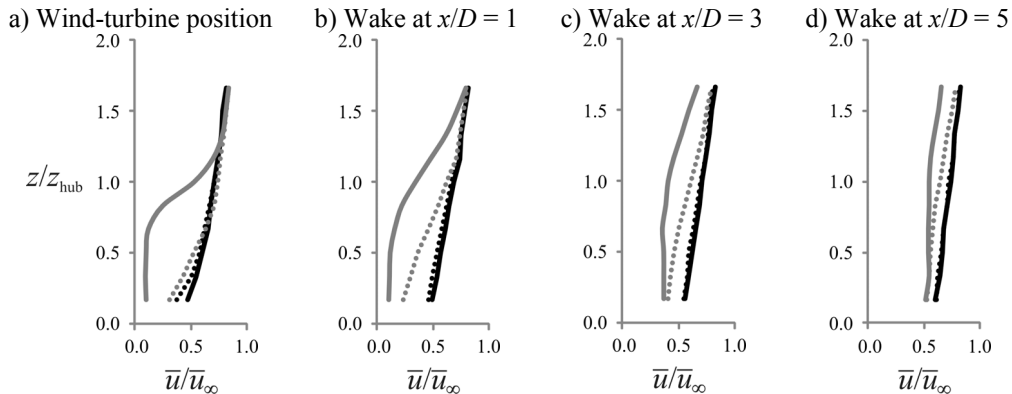
Figure 3. Mean wind velocity profiles at the position of the wind turbine (without wind turbine in place), as well as at different streamwise positions downstream from the wind turbine (wind turbine in place) for different coastal terrain types: black solid line is sea (without coastal mountain), black dotted line is small mountain, solid grey line is large mountain, dotted grey line is mountain with a bay; x/D is nondimensionalized downstream distance from the wind turbine, D is the wind-turbine rotor diameter, $\bar{u}_\infty$ and z_{hub} are mean wind velocity in the undisturbed freestream flow and the wind-turbine hub height, respectively.

a) Wind-turbine position   b) Wake at $x/D = 1$ c) Wake at $x/D = 3$ d) Wake at $x/D = 5$
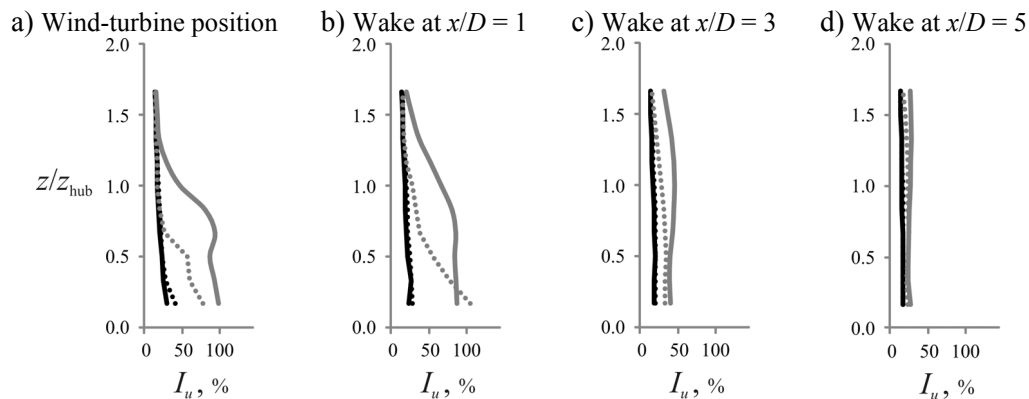
Figure 4. Turbulence intensity profiles at the position of the wind turbine (without wind turbine in place), as well as at different streamwise positions downstream from the wind turbine (wind turbine in place) for different coastal terrain types: black solid line is sea (without coastal mountain), black dotted line is small mountain, solid grey line is large mountain, dotted grey line is mountain with a bay.

The experimental results indicate a strong velocity deficit and an increase in turbulence intensity downstream from a large mountain in comparison to other configurations. Those trends are particularly exhibited from the sea surface up to the wind-turbine hub height and closer to the mountain. Further downstream the effects of a coastal topography on the wake characteristics of an offshore wind turbine considerably decrease.

Acknowledgements

References

Augusti, G., Spinelli, P., Borri, C., Bartoli, G., Giachi, M., and Giordano, S. (1995). The C.R.I.A.C.I.V. atmospheric boundary layer wind tunnel. *Proceedings of the 9th International Conference on Wind Engineering (ICWE), New Delhi, India*.

Chamorro, L.P., and Porté-Agel, F. (2010). Effects of Thermal Stability and Incoming Boundary-Layer Flow Characteristics on Wind-Turbine Wakes: A Wind-Tunnel Study. *Boundary-Layer Meteorology* **136(3)**, 515–533.

Counihan, J. (1969). An improved method of simulating an atmospheric boundary layer in a wind tunnel. *Atmospheric Environment* **3**, 197–214.

Hu, H., Yang, Z., and Sarkar, P. (2012). Dynamic wind loads and wake characteristics of a wind turbine model in an atmospheric boundary layer wind. *Experiments in Fluids* **52(5)**, 1277–1294.

Simiu, E., and Scanlan, R.H. (1996). *Wind Effects on Structures*, John Wiley & Sons.

Zhang, W., Markfort, C.D., and Porté-Agel, F. (2012). Near-wake flow structure downwind of a wind turbine in a turbulent boundary layer. *Experiments in Fluids* **52(5)**, 1219–1235.

Aeroelastic instabilities of rectangular cylinders with various side ratios

Claudio Mannini[1], Antonino M. Marra[1], Tommaso Massai[1] and Gianni Bartoli[1]

[1]CRIACIV/Department of Civil and Environmental Engineering, University of Florence, Italy

Corresponding author: Claudio Mannini, claudio.mannini@dicea.unifi.it

Abstract

A few two-dimensional prisms with rectangular cross section were tested in the wind tunnel. The models were free to vibrate in the plunging mode only and the smooth flow was perpendicular to a face of the cylinders. These clean and simple geometries are of great importance in bluff-body aerodynamics and in the wind engineering practice, showing a pronounced proclivity to several aeroelastic instabilities ranging from vortex-induced vibration to galloping, that in some cases can strongly interact. This paper presents also the results of analytical models which were applied to some particular test cases. The comparison with the experimental data underscored the complexity of the aeroelastic response of these structures.

1 Introduction

Slender prismatic structural elements with rectangular cross section are very important in bluff-body aeroelasticity, not only because they represent, sometimes in a clean schematic fashion, various kinds of existing structures or structural elements, but also because, depending on the side ratio, they are prone to different types of aeroelastic instabilities in the plunging and pitching degrees of freedoms, that in some cases can also coexist (see e.g. Matsumoto, 1996).

In particular, rectangular cylinders free to vibrate in the plunging mode, with a width-to-depth ratio in the range $0.75 \leq B/D \leq 3 \div 4$ according to Parkinson (1965), being B the width, i.e. the streamwise dimension, and D the depth, i.e. the cross-flow dimension of the section, are known to be unstable with respect to galloping. These sections can gallop spontaneously from rest and are therefore called "soft oscillators". By contrast, rectangular cylinders with shorter afterbody (at least for $0.375 \leq B/D \leq 0.683$ according to Parkinson (1965)) are "hard oscillators" in smooth flow, i.e., they cannot gallop from rest but they need an external initial energy input to reach the basin of attraction of the limit cycle (Parkinson, 1965). Nevertheless, the same bodies are expected to become soft oscillators in turbulent flow (Novak and Davenport, 1970). Mathematically speaking galloping is a supercritical Hopf bifurcation and then, once the critical wind speed has been exceeded, it manifests itself as a limit-cycle nearly-harmonic oscillation whose amplitude steadily grows by increasing the flow velocity. The critical wind speed is usually obtained by the linearized quasi-steady theory; it is proportional to a mass-damping parameter called Scruton number and inversely proportional to a galloping stability parameter obtained by measurements on the stationary body. Clearly, the quasi-steady theory is supposed to be suitable to predict galloping only at high reduced wind speed (therefrom the term "high-speed galloping"). Nakamura and co-workers opposed to this dynamic instability what they called "low-speed galloping" for rectangular cylinders with side ratio B/D significantly lower than unity (Nakamura and Hirata, 1991). This is a soft-type instability building-up in a very regular form for a restricted range of wind speeds, much lower than the vortex-resonance velocity. No model is available so far for this phenomenon.

Another common aeroelastic instability for rectangular cylinders is vortex-induced vibration (VIV), which is caused by the nonlinear resonance of the force due to the alternate shedding of vortices with one mode of vibration of the structure and self-excitation is a key issue in case of large-amplitude oscillations. The excitation starts at a critical wind speed which depends on the Strouhal number and disappears beyond a certain flow velocity. The amplitude of vibration and the extension of the so-called "lock-in" range depend on the mass ratio and structural damping, combined as Scruton number for conventional structures in airflow.

In slender prisms with bluff rectangular cross section and sufficient afterbody VIV and galloping can interact and give rise to an instability characterized by oscillations starting at the Kármán-vortex resonance wind speed but unrestrictedly growing with the wind speed, as typical for galloping. Also, in cases of weaker interaction the onset of the oscillations can be at a wind speed higher than the critical velocity of VIV but significantly lower than the quasi-steady theory prediction. Therefore VIV-galloping interaction is a potentially dangerous condition from the engineering point of view as excitation can occur in a wind speed range where it is not expected. In this phenomenon the parameter playing a crucial role is the ratio of quasi-steady galloping to VIV critical wind speed but Mannini et al. (2014) showed that the recommendations of Eurocode 1 (EN 1991-1-4: 2010), which excludes the possibility of interaction when the ratio of critical velocities for the two individual phenomena is either lower than 0.7 or higher than 1.5, are definitely non-conservative.

This paper presents a series of experimental results recently obtained in the CRIACIV wind tunnel laboratory on two-dimensional rectangular cylinders with various side ratios and a face perpendicular to the smooth airflow with the aim to better characterize the different phenomena and underscore their interaction. Finally, since it is evident that the estimation of the aeroelastic response of a rectangular cylinder is still today a very complicated task, this work attempts to apply some analytical models available in the literature to predict the different types of excitation.

2   Experimental set-up

A static rig was employed to measure the force coefficients and the Strouhal number of the cylinders, necessary for the modeling of their aeroelastic response. It was composed by two vertical beams fixed to both the floor and the ceiling of the wind tunnel; two rigid frames, overhanging on the upstream side of the tunnel, were fixed to these beams. These frames supported two six-component extensometric force balances (one for each side of the model) that allowed the measurement of lift, drag and torque.

In the aeroelastic set-up the model was connected to two shear-type steel frames allowing only a vertical displacement due to the very large in-plane flexural stiffness of the vertical elements. The stiffness of the suspension system was modified in the different tests by varying the length of the plate-springs. The displacements of the model were recorded respectively with two non-contact laser transducers. Finally, measurements with a hot-wire anemometer of the velocity fluctuations in the wake of both stationary and oscillating models were performed.

3   Wind-tunnel results and analytical models

3.1   VIV-galloping interaction: B/D = 1

The aeroelastic behaviour of the two-dimensional square cylinder was studied in great detail in the past. Nevertheless, in the literature there is no agreement on an important parameter such as the galloping stability parameter (i.e., the slope of the transverse force coefficient for a zero angle of attack), which is known to be very sensitive to the flow and boundary conditions during the tests (see Mannini et al. (2014) for a review), and an international document such as the Eurocode 1 provide a value which does not appear conservative at all. The square cylinder is known to be prone to a VIV-galloping instability and Bearman et al. (1987) claims that a ratio of the quasi-steady galloping critical wind speed to the Kármán-vortex resonance velocity equal to 4 or 5 is needed to fully separate the two phenomena and the quasi-steady theory to be applicable, especially in turbulent flow.

A few attempts to model the complex interaction between the two phenomena was done for this geometry. Bouclin (1977) proposed a model which coupled the quasi-steady load with the VIV model by Hartlen and Currie (1970) for a square cylinder in a waterflow. This model was later slightly modified by Corless and Parkinson (1988) who applied it to a square cylinder in an airflow. Comparison with the experimental data by Bearman et al. (1987) showed promising results. A similar model coupling the quasi-steady forces with the VIV model by Tamura and Matsui (1979) was presented by Tamura and Shimada (1987) and applied to the experimental test cases by Wawzonek (1979). This model was
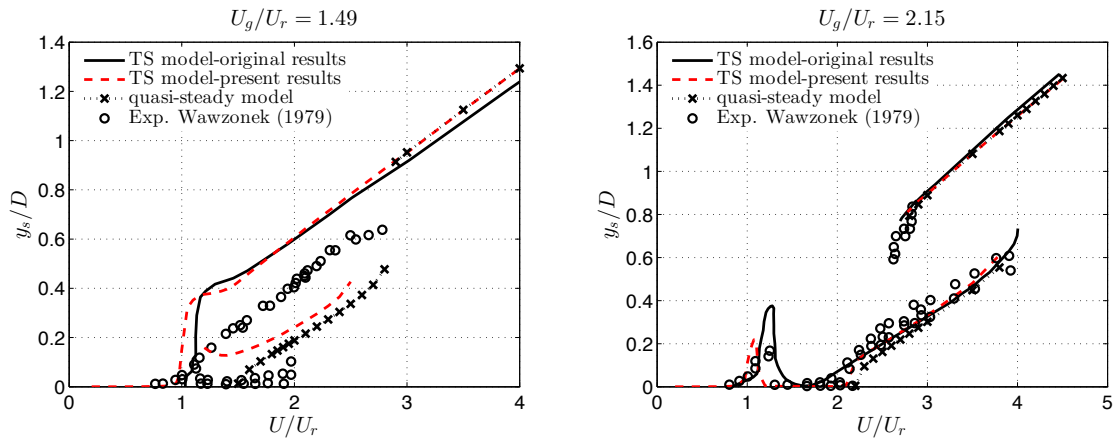
Figure 1. Comparison between experimental and numerical results for the square cylinder. "TS model" stands for the model by Tamura and Shimada (1987), y_s is the limit-cycle amplitude of oscillation, U the flow speed, U_r and U_g respectively the vortex-resonance and the quasi-steady galloping critical wind speed.

implemented also by the Writers and it was observed that, by extending the simulations for a larger number of cycles, the agreement with the experiments was even better than that obtained in Tamura and Shimada (1987), especially in the "lock-in" range (Fig. 1).

3.2   *VIV-galloping interaction: B/D = 1.5*

A vast experimental campaign was conducted at CRIACIV on a 3:2 rectangular cylinder, since this geometry was found extremely susceptible to a VIV-galloping combined instability, even more than the square cylinder. Two sectional models at different scales were employed to investigate two Reynolds number ranges and to span a large interval of Scruton numbers. The first model was made of wood (D = 77 mm, B = 116 mm, L = 986 mm, blockage ratio = 4.8%) and had a mass of 1.730 kg (including the end plates in plywood), whereas the second model was in aluminum (D = 30 mm, B = 45 mm, L = 1000 mm, blockage ratio = 1.9%) and had a mass of 2.672 kg (with steel end plates).

   Up to very high values of the Scruton number the models showed oscillations starting at the Kármán-vortex resonance velocity and unrestrictedly increasing in amplitude with the flow speed. Moreover, at low Scruton number a significant excitation in a low reduced velocity range was clearly observed due to the resonance with the third superharmonic of the Strouhal frequency component of the transverse force. Other nonlinear features of the fluid-structure coupled system were observed, such as hysteresis and frequency demultiplication. The previously mentioned analytical models by Tamura and Shimada (1987) and Corless and Parkinson (1988) were adapted to this test case and the results were compared with the experiments.

3.3   *"Hard-type" galloping: B/D = 0.66*

The aluminum section model described in the previous section was also turned by 90 degrees in order to test a rectangular 2:3 cylinder (D = 45 mm, B = 30 mm, L = 1000 mm, blockage ratio = 2.8%). Appropriate end plates were provided for this new case study. Both static and aeroelastic tests were performed to shed some light on the mechanism of instability of this supposed hard-galloping oscillator. Comparison is proposed with the results of the quasi-steady theory (Parkinson, 1965).

3.4   *Vortex-induced vibration: B/D = 4*

A wooden section model of a rectangular 4:1 cylinder (D = 75 mm, B = 300 mm, L = 986 mm, blockage ratio = 4.7%) was tested for different values of the Scruton number. The body resulted to be clearly susceptible to VIV excitation with moderate amplitudes. In addition, for low values of the mass-damping parameter a secondary resonance was clearly observed with oscillations starting at about one-half of the

VIV critical wind speed. Details of the experimental data and comparison with the results of a few analytical models can be found in Marra et al. (2014).

4   Concluding remarks

Several aeroelastic instabilities ranging from vortex-induced vibration to galloping were observed for two-dimensional rectangular prisms in smooth flow by changing the side ratio of the cross section and the value of the mass-damping parameter. A few nonlinear features of the fluid-structure coupled systems were also highlighted. The complexity of the phenomena for such simple geometries is apparent and the use of analytical models to predict experimental data is still a challenging task although some promising results were obtained.

References

Bearman, P. W., Gartshore, I. S., Maull, D. J., and Parkinson, G. V. (1987). Experiments on fluid-induced vibration of a square-section cylinder. *Journal of Fluids and Structures* **1**.1, pp. 19–34.

Bouclin, D. N. (1977). Hydroelastic oscillations of square cylinders. MA thesis. Vancouver, Canada: University of British Columbia.

Corless, R. M. and Parkinson, G. V. (1988). A model of the combined effects of vortex-induced oscillation and galloping. *Journal of Fluids and Structures* **2**.3, pp. 203–220.

Hartlen, R. T. and Currie, I. G. (1970). Lift-oscillator model of vortex-induced vibration. *Journal of Engineering Mechanics Division* **96**.5, pp. 577–591.

Mannini, C., Marra, A. M., and Bartoli, G. (2014). Aeroelastic instability of a rectangular 3:2 cylinder: review and new experiments. *Journal of Wind Engineering and Industrial Aerodynamics*. (submitted).

Marra, A. M., Mannini, C., and Bartoli, G. (2014). Predictions of VIV-mathematical models for a rectangular 4:1 cylinder. *These proceedings*.

Matsumoto, M. (1996). Aerodynamic damping of prisms. *Journal of Wind Engineering and Industrial Aerodynamics* **59**.2-3, pp. 159–175.

Nakamura, Y. and Hirata, K. (1991). Pressure fluctuations on oscillating rectangular cylinders with the long side normal to the flow. *Journal of Fluids and Structures* **5**.2, pp. 165–183.

Novak, M. and Davenport, A. G. (1970). Aeroelastic instability of prisms in turbulent flow. *Journal of Engineering Mechanics Division* **96**.1, pp. 17–39.

Parkinson, G. V. (1965). Aeroelastic galloping in one degree of freedom. *Wind Effects on Buildings and Structures: proceedings of the conference held at the National Physical Laboratory, Teddington, UK, Jun. 26-28, 1963*. HMSO, London, pp. 581–609.

Tamura, Y. and Matsui, G. (1979). Wake-oscillator model of vortex-induced oscillation of circular cylinder. *Proceedings of the 5th International Conference on Wind Engineering, Jul. 8-14, 1979, Forth Collins, US*. Elsevier, pp. 1085–1094.

Tamura, Y. and Shimada, K. (1987). A mathematical model for the transverse oscillations of square cylinders. *Proceedings of the 1st International Conference on Flow Induced Vibrations, May 12-14, 1987, Bowness-on-Windermere, UK*. Springer-Verlag, pp. 267–276.

Wawzonek, M. A. (1979). Aeroelastoc behavior of square section prisms in uniform flow. MA thesis. Vancouver, Canada: University of British Columbia.

Calculation of third order joint acceptance function for line-like structures

N. Blaise[1], T. Canor[2] and V. Denoël[1]

[1]Structural Engineering Division, Faculty of Applied Sciences, University of Liège, Liège, Belgium.
[2]F.R.S.-FNRS, National Fund for Scientific Research, University of Liège, Liège, Belgium
Corresponding author: N. Blaise, n.blaise@ulg.ac.be

1 Introduction

A horizontal line-like structure is exposed to a random stationary 1-direction wind flow with mean velocity $U(\xi)$ and a fluctuating gaussian turbulence component $u(\xi, t)$ with standard deviation $\sigma(\xi)$, see Fig. 1. The wind velocities are assumed to be perfectly correlated in the vertical direction $d(\xi)$ of the line-like structure. Turbulence intensity is defined as $I_u(\xi) = \sigma(\xi)/U(\xi)$.
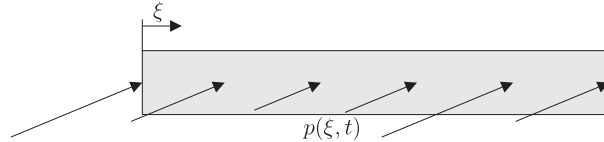
Figure 1. A line-like structure immersed in a wind velocity field. The dimensionless curvilinear abscissa is ξ.

The covariance between two wind velocities at two positions is defined by

$$\kappa_{2u}(\xi_i, \xi_j) \quad = \quad \sigma(\xi_i)\sigma(\xi_j)\rho\left(s_{ij}\right) \tag{1}$$

where the correlation function $\rho\left(s_{ij}\right)$ is assumed to be a function of only the absolute value of the spatial distance $s_{ij} = |\xi_i - \xi_j|$ between the two positions. Vertical line-like structures, such as buildings, do not meet this assumption because the correlation function is also function of the two distinct positions, i.e. $\rho\left(\xi_i, \xi_j, s_{ij}\right)$.

Assuming quasi-steady aerodynamics, neglecting aerodynamic damping and assuming that the velocity of the structural displacement aligned with the wind is low compared to the wind velocity, the total non-gaussian aerodynamic pressure $p(\xi, t)$ on the structure is expressed by

$$p = a + bu + cu^2 \tag{2}$$

where $a(\xi) = \gamma(\xi)U(\xi)^2$; $b(\xi) = 2\gamma(\xi)U(\xi)$; $c(\xi) = \gamma(\xi)$ with $\gamma(\xi) = \frac{1}{2}\rho(\xi)d(\xi)C(\xi)$ where $\rho(\xi)$ is the air density and $C(\xi)$ is the aerodynamic coefficient. The cross cumulants of order 2 $\kappa_{2p}(\xi_i, \xi_j)$ and order 3 $\kappa_{3p}(\xi_i, \xi_j, \xi_k)$ between aerodynamic pressures are respectively given by

$$\kappa_{2p_{ij}} = b_i b_j \rho_{ij} \sigma_i \sigma_j + 2c_i c_j \rho_{ij}^2 \sigma_i^2 \sigma_j^2 \tag{3}$$

and

$$\kappa_{3p_{ijk}} = 2\sigma_i \sigma_j \sigma_k \left(c_i b_j b_k \rho_{ij} \rho_{ik} \sigma_i + b_i c_j b_k \rho_{ij} \rho_{jk} \sigma_j + b_i b_j c_k \rho_{ik} \rho_{jk} \sigma_k\right) + 8c_i c_j c_k \rho_{ij} \rho_{ik} \rho_{jk} \sigma_i^2 \sigma_j^2 \sigma_k^2. \tag{4}$$

2   Background turbulent response

In its continuous form, the background structural response, $R(t)$, is derived from integration of the aerodynamic pressures field $p(\xi, t)$ multiplied by its response-influence function $I(\xi)$ over the line-like structure

$$R(t) = \int_0^1 I(\xi)p(\xi, t)\mathrm{d}\xi \tag{5}$$

and its second cumulant is obtained as

$$\kappa_{2R} = \iint_0^1 I(\xi_i)I(\xi_j)\kappa_{2p}(|\xi_i - \xi_j|)\mathrm{d}\xi_i\mathrm{d}\xi_j \simeq \iint_0^1 g_1(\xi_i)g_1(\xi_j)\rho(|\xi_i - \xi_j|)\,\mathrm{d}\xi_i\mathrm{d}\xi_j \tag{6}$$

where $g_1(\xi) = b(\xi)\sigma_u(\xi)I(\xi)$ and neglecting the second term in Eq. (3), which is marginal. Closed-form expressions of the double integrals in Eq. (6) are attractive in order to avoid numerical integrations and the consideration of numerical admittance (Denoël and Maquoi, 2012). This has been achieved by (Dyrbye and Hansen, 1988) who simplified this double integral thanks to the change of variable $s_{ij} = |\xi_i - \xi_j|$ and interchange of the order of integration, which finally yields

$$\kappa_{2R} = \int_0^1 k(s)\rho(s)\,\mathrm{d}s \tag{7}$$

with an influence function defined as

$$k(s) = 2\int_0^{1-s} g_1(\xi)g_1(\xi + s)\mathrm{d}\xi. \tag{8}$$

In the case of integrable expressions for $g_1(\xi)$, analytical formulations for the influence function $k(s)$ are derived and even if Eq. (6) has no analytical solution, Eq. (7) has the advantage to reduce the double integration to a single one which is also easier to treat numerically if it had to. Nonetheless, for specific $\rho(s)$ such as a decaying exponential function

$$\rho(s) = e^{-\phi s} \tag{9}$$

with parameter ϕ, analytical solutions of Eq. (7) can be derived. We must also emphasize that analytical expressions for $g_1(\xi)$ and $\rho(s)$ may not be available and even with analytical expressions, the double integrals may be awkward (or even impossible) to compute analytically. For simple cases, one may consider fitting those functions with simple polynomial functions which ensures integrability.

The third cumulant of the structural response is obtained as

$$\begin{aligned}
\kappa_{3R} &= \iiint_0^1 I(\xi_i)I(\xi_j)I(\xi_k)\kappa_{3p}(s_{ij}, s_{ik})\,\mathrm{d}\xi_i\mathrm{d}\xi_j\mathrm{d}\xi_k \\
&\simeq 6\iiint_0^1 g_2(\xi_i)g_1(\xi_j)g_1(\xi_k)\rho(s_{ij})\,\rho(s_{ik})\,\mathrm{d}\xi_i\mathrm{d}\xi_j\mathrm{d}\xi_k
\end{aligned} \tag{10}$$

where $g_2(\xi) = c(\xi)\sigma_u^2(\xi)I(\xi)$ and neglecting the fourth term in Eq. (4), which is marginal. Following the same strategy as discussed hereinbefore, this paper aims at extending the work of (Dyrbye and Hansen, 1988) to a third order analysis, i.e. simplifying triple integrals of Eq. (10) to double integrals as

$$\begin{aligned}
\kappa_{3R} &= 2\int_0^1\int_0^{s_1} [(k_1(s_1, s_2) + k_2(s_1, s_2))\rho(s_1)\rho(s_2)]\,\mathrm{d}s_2\mathrm{d}s_1 \\
&+ 2\int_0^1\int_0^{1-s_1} k_3(s_1, s_2)\rho(s_1)\rho(s_2)\mathrm{d}s_2\mathrm{d}s_1
\end{aligned} \tag{11}$$

where we define the third order influence functions as

$$k_1(s_1, s_2) = \int_{s_1}^{1} g_2(\xi) g_1(\xi - s_1) g_1(\xi - s_2) d\xi \tag{12}$$

$$k_2(s_1, s_2) = \int_{0}^{1-s_1} g_2(\xi) g_1(\xi + s_1) g_1(\xi + s_2) d\xi \tag{13}$$

$$k_3(s_1, s_2) = \int_{s_2}^{1-s_1} g_2(\xi) g_1(\xi + s_1) g_1(\xi - s_2) d\xi. \tag{14}$$

One could want to apply the same procedure for the fourth cumulant of the structural response, obtained as

$$\kappa_{4R} = \iiiint_{0}^{1} I(\xi_i) I(\xi_j) I(\xi_k) I(\xi_l) \kappa_{4p_{ijkl}} d\xi_i d\xi_j d\xi_k d\xi_l \tag{15}$$

where $\kappa_{4p_{ijkl}}$ is the cross cumulants of order 4 between the aerodynamic pressures. However it comes out that this is quite challenging as interchange of the order of integration is tricky for a four-dimensional domain.

Notice that if analytical expressions are derived for the cumulants of order 2, thanks to Eq. (7), order 3, thanks to Eq. (11), and order 4, thanks to Eq. (15), one could obtain analytical expressions for the skewness coefficient defined as $\gamma_{3R} = \kappa_{3R}/\kappa_{2R}^{3/2}$ and for the excess coefficient defined as $\gamma_{eR} = \kappa_{4R}/\kappa_{2R}^{2}$. These two coefficients are of paramount importance to assess the non-gaussianity of the structural response and the impact on its extreme values through non-gaussian peak factors (Gurley et al., 1997).

3   Illustration

A beam with constant section and length l is considered. The mean velocity U, standard deviation σ_u and coefficient γ are assumed to be constant along the beam. Table 1 collects the influence functions for uniform and linear response influence functions.

	Uniform	Linear
$k(s)/\left(b^2\sigma^2\right)$	$2(1-s)$	$\frac{1}{3}\left(s^3 - 3s + 2\right)$
$k_1(s_1, s_2)/\left(b^2 c\sigma^4\right)$	$(1-s_1)$	$\frac{1}{12}(s_1 - 1)^2\left(s_1^2 + 2s_1 - 2(s_1 + 2)s_2 + 3\right)$
$k_2(s_1, s_2)/\left(b^2 c\sigma^4\right)$	$(1-s_1)$	$\frac{1}{12}(s_1 - 1)^2\left(4s_2 - s_1(s_1 - 2s_2 + 2) + 3\right)$
$k_3(s_1, s_2)/\left(b^2 c\sigma^4\right)$	$(1-s_1-s_2)$	$-\frac{1}{12}(s_1 + s_2 - 1)^2\left(s_1(s_1 + 2) - s_2(s_2 + 2) - 3\right)$

Table 1. Second order and third order influence functions for uniform and linear response influence functions.

In the calculation of the cumulants, the correlation function is considered as a decaying exponential function (Holmes, 2007), see Eq. (9). The parameter $\phi = l/L_u^x$ is the ratio between the length of the structure and L_u^x, the integral length scale for the longitudinal turbulence u in direction $x(= \xi l)$. The integral length scale L_u^x is a measurement of the averaged size of the vortices in the wind. In this case, the cross cumulants of order 4 between aerodynamic pressures is given by

$$\kappa_{4p_{ijkl}} = 4b^2 c^2 \sigma^6 \left(12\rho_{ij}\rho_{ik}\rho_{jl}\right) + 16c^4\sigma^8 \left(3\rho_{ij}\rho_{ik}\rho_{jl}\rho_{kl}\right) \tag{16}$$

and neglecting the second term in Eq. (16), which is marginal, leading to

$$\kappa_{4p_{ijkl}} \simeq 48b^2c^2\sigma^6 \iiiint_0^1 I(\xi_i)I(\xi_j)I(\xi_k)I(\xi_l)\rho\left(s_{ij}\right)\rho\left(s_{ik}\right)\rho\left(s_{jl}\right)\,\mathrm{d}\xi_i\mathrm{d}\xi_j\mathrm{d}\xi_k. \tag{17}$$

Table 2 collects the analytical results for γ_{3R} and γ_{eR} for uniform and linear response influence functions.

	Uniform	Linear
$\dfrac{\gamma_{3R}}{3I_u}$	$\dfrac{e^{-2\phi}\left(2e^{\phi}(\phi+4)+e^{2\phi}(4\phi-7)-1\right)}{2\sqrt{2}\phi^3\left(\frac{\phi+e^{-\phi}-1}{\phi^2}\right)^{3/2}}$	$\dfrac{3\sqrt{3}e^{-2\phi}\left(-4e^{\phi}(\phi+5)+e^{2\phi}(2\phi(2\phi-7)+19)+1\right)}{4\phi^4\left(\frac{(2\phi-3)\phi^2+6(\phi+1)\sinh(\phi)-6(\phi+1)\cosh(\phi)+6}{\phi^4}\right)^{3/2}}$
$\dfrac{\gamma_{eR}}{12I_u^2}$	$\dfrac{e^{-3\phi}\left(e^{\phi}\left(e^{\phi}\left(2\phi(\phi+9)+2e^{\phi}(8\phi-19)+47\right)-2(2\phi+5)\right)+1\right)}{8\left(\phi+e^{-\phi}-1\right)^2}$	too long formula.

Table 2. Skewness and excess coefficients for uniform and linear response influence functions.

Figure 1 depicts the cumulants, γ_{3R} and γ_{eR} for ϕ ranging $[10^{-3};10^2]$. Notice for the limit case of quasi-full correlation, *i.e.* $\phi \ll 1; \rho(s) \simeq 1$, skewness and excess coefficients approach the values associated to an aerodynamic pressure (resp. $3I_u$ and $12I_u^2$) while in the limit case of no correlation, *i.e.* $\phi \gg 1; \rho(s) \simeq 0$, their values approach asymptotically the gaussian ones (*i.e.* zeros) explained by the central limit theorem (Papoulis, 1965) and the well-known scale effect.
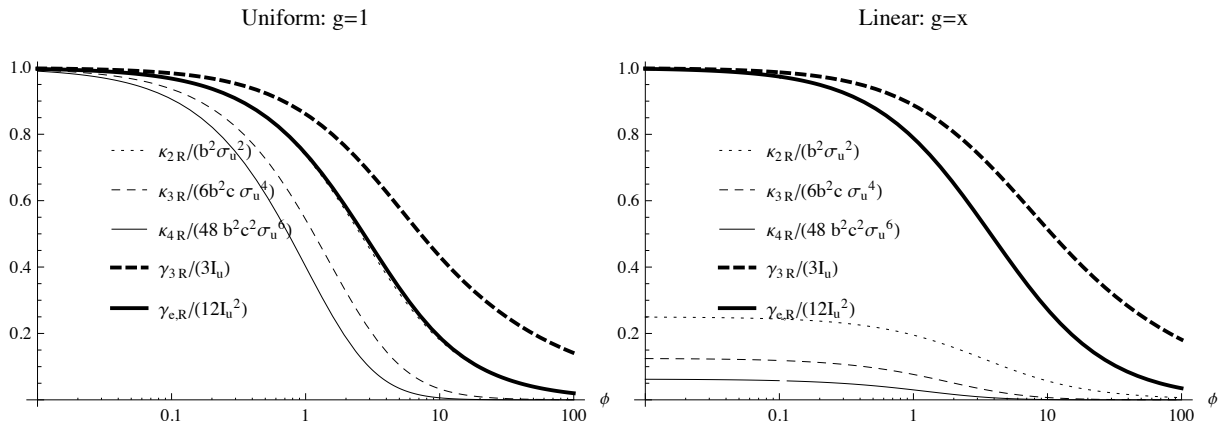
Figure 2. Cumulants and coefficients as function of ϕ for uniform and linear response influence functions.

References

Denoël, V. and Maquoi, R. (2012). The concept of numerical admittance. *Archive of Applied Mechanics* **82**.10-11, pp. 1337–1354.

Dyrbye, C. and Hansen, S. O. (1988). Calculation of joint acceptance function for line-like structures. *Journal of Wind Engineering and Industrial Aerodynamics* **31**.23, pp. 351–353.

Gurley, K. R., Tognarelli, M. A., and Kareem, A. (1997). Analysis and simulation tools for wind engineering. *Probabilistic Engineering Mechanics* **12**.1, pp. 9–31.

Holmes, J. D. (2007). *Wind Loading on Structures*. 2nd Edition. London: SponPress.

Papoulis, A. (1965). *Probability, Random Variables, and Stochastic Processes*. New York: McGraw Hill.

Aerodynamics of 5 MW Wind Turbine Using Boundary Element Method

Israa Al-Esbe, Moustafa Abdel-Maksoud

Institute for Fluid Dynamics and Ship theory,
Hamburg University of Technology, Germany.

Corresponding author: Israa Al-Esbe, israa.al@tuhh.de

Abstract

Numerical simulation of the aerodynamics of rotor and blade-tower interaction for the 5MW horizontal axis wind turbine (HAWT) is conducted using in-house boundary element solver *pan*MARE, which is based on potential flow theory. The numerical solution tool introduced here is a three-dimensional first-order panel method which can be used for various flow problems. In-house CAD code is used to build the geometry and create panels on geometry surfaces. This study has been performed for two configurations, HAWT rotor-only and complete wind turbine. The operation conditions include uniform wind speed 9 m/sec, rotational speed 1.08 rad/sec and zero yaw angles. This paper presents results, time histories of rotor torque coefficients for the two configurations, surface pressure distributions on blade on selected radial locations of different blades at different angular positions from the tower (0 deg.,120 deg.), and the pressure distribution on the tower leading edge.

The results show that the pressure on the blade suffers a drop 10-15% from its normal value, with a pressure drop on the tower when the blade passes in front of the tower. The results obtained by applying panel method have an acceptable agreement with those predicted by the CFD model and show the ability of the code to simulate a complex 3D wind turbine aerodynamic.

Keywords: HAWT, BEM, Panel method

1 Introduction

Wind turbines convert wind energy to electricity via mechanical energy, the production of which depends on the interaction between the rotor and the wind. Due to wind effects, aerodynamic forces act on the aerofoils blade. The aerodynamics of flow around wind turbine blades plays an important role in wind turbine efficiency. In order to better understand the complex flow around wind turbines, it is important to analyse unstable and unexpected aerodynamic performances on the rotor and the tower, and to take blade -tower interaction in to consideration.

The accurate prediction of wind turbine aerodynamics is necessary to reduce the risks involved in developing a new machine, and to reduce the cost of manufacturing and maintaining the turbine, as well as to increase power production, as the amount of available energy, which the wind transfers to the rotor, depends on mass density of the air, wind speed, sweep area of the rotor and blade design .

A number of different methods, varying in degree of complexity and accuracy, are used to model the aerodynamics of a wind turbine, such as the blade element momentum method, vortex methods, actuator disc method and Navier-Stokes solvers. Bazilevs et al., (2010) carried out CFD simulations on the flow over NREL 5MW offshore wind turbine rotor using a Navier−Stokes equation which involves incompressible flow with a rigidly rotating body based on rotationally periodic boundary conditions. Namiranian A. (2011) also used Navier−Stokes equations to simulate the three-blade 5MW wind turbine, with the presence of the tower. In order to incorporate the effect of the wind

turbine tower in the simulations, the rotationally-periodic boundary conditions were included, and as a result, the blade–tower interaction was successfully investigated.

Vortex method based on potential flow has been applied by Abedi et al. (2013) for wind turbine aerodynamic performance ,they used three different approaches of vortex theory, lifting line, lifting surface and panel method models, and the results show the ability of panel method to provide detailed load, pressure and velocity distributions over the blade surface compared to other approaches. Another method, such as general non-linear unsteady vortex-lattice method, has been used by Gebhardt et al. (2010) to simulate the unsteady aerodynamic behaviour of large horizontal-axis wind turbines in time domain. The aerodynamic blade-tower interaction has been satisfactorily captured as well as the effects of land surface and boundary layer. Hogeon et al. (2010) have used unsteady vortex lattice method (UVLM) for simulating the blade-tower interaction over the NREL Phase VI. Further, he used the nonlinear vortex correction method (NVCM) to investigate rotor turbine considering wind shear, yaw error, distance from blade to tower, and the size of the tower.

Three-dimensional panel method was used by Bermudez et al. (2000) for simulating the aerodynamics behaviour of horizontal-axis wind turbines, the comparison between experimental data and the computed results by panel method shows a good agreement.

The objectives of this paper are to analyse aerodynamic   performance and study   the blade-tower interaction for 5MW wind turbine at full scale.

2   Methodology

For the numerical simulation of this study the in-house boundary element solver *pan*MARE (panel Code for Maritime Applications and REsearch) is used, which is implemented to simulate arbitrary potential flows for different applications. The code is based on a three-dimensional first-order panel method, where the body's surfaces are discretized by means of quadrilateral panels, where each panel has a constant-strength singularity distribution of sources and dipole. For each N body's surface panel, the solver governing equation and the boundary conditions are satisfied at a control point (in the centre of panel).Potential theory drives the governing equation, where the flow is considered to be irrotational, incompressible and inviscid. The evolution of the total velocity potential (Φ) is governed by the continuity equation for incompressible flows, requiring the Laplace equation:

$$\nabla^2 \cdot \Phi = 0. \tag{1}$$

The solution of the Laplace equation is a linear combination of several sources and dipoles superimposed with the inflow velocity (Φ_∞). The strength of those sources and dipoles needs to be determined, so a boundary element method is used.

The general solution of Eq. (1) in an outer point of the body boundary is defined in Katz and Ploklin, (2001):

$$\Phi^*(x,y,z) = \Phi(x,y,z) + \Phi_\infty(x,y,z) = \frac{1}{4\pi}\int_{SB} \mu \frac{\partial}{\partial n}\left(\frac{1}{r}\right) dS - \frac{1}{4\pi}\int_{SB} \sigma\left(\frac{1}{r}\right) dS + \Phi_\infty(x,y,z), \tag{2}$$

where (μ) is dipole strength and (σ) source strength, which is defined as:

$$-\mu = \Phi \quad , \quad -\sigma = \frac{\partial \Phi}{\partial n}$$

The velocity potential can be calculated by applying the boundary condition directly when we consider Eq. (2) in an inner point of the body. We have an overall potential of the form:

$$\Phi^* = \Phi_{inner} - \Phi_\infty \tag{3}$$

In an inner point of the boundary, the inner potential is arbitrary. Thus, we choose $\Phi^* = \Phi_\infty$ and obtain the following equation for the velocity potential:

$$\frac{1}{4\pi} \int_{SB} \mu \frac{\partial}{\partial n} \left(\frac{1}{r} \right) dS - \frac{1}{4\pi} \int_{SB} \sigma \left(\frac{1}{r} \right) dS = 0. \tag{4}$$

For the unique solution of Eq. (4), the kinematic boundary condition (Neumann boundary condition) is applied on the surface: the total velocity normal to the surface is required to be zero:

$$\nabla \Phi^* \cdot \vec{n} = 0 \tag{5}$$

By applying the kinematic boundary condition, the value of source strength in case of lifting panel can be determined by:

$$-\sigma = \partial \Phi^* / \partial n \quad \text{and} \quad -\sigma = -\vec{n} \cdot \overrightarrow{V_\infty},$$

where n is the normal vector directed upwards to the surface and $\overrightarrow{V_\infty}$ is the inflow velocity vector, so in this case (lifting body) only the strength of each dipoles is unknown, and in case of a non-lifting body, there is no dipoles and the strength of each source are unknown quantities. Only dipoles with strength μ are applied on the free vortex surface (wake). The strength is constant over one panel but can vary among each other in case of unsteady flow.

The boundary conditions can be transformed into a set of linear equations. The solution gives the strength of each dipole (μ) and source (σ), and can be used to compute the induced velocities on the body surface. The induced velocities can be calculated as follows:

$$v_{ind}(\vec{x}) = \underbrace{(v_l(\vec{x}) + v_m(\vec{x}))}_{\text{tangential components}} + \underbrace{v_n(\vec{x})}_{\text{normal components}}$$

The tangential components are determined from the dipole distribution:

$$v_l(x_i) = -\frac{\partial \mu_i}{\partial \xi} \quad , \quad v_m(x_i) = -\frac{\partial \mu_i}{\partial \eta}$$

Where ξ and η are the local tangential coordinates of the panel after the calculation of all velocity components.

The pressure distribution on each panel of the body can be completed by applying the Bernoulli equation which is defined as:

$$p + \rho g z + 0.5 \rho v^2 + \rho \, \partial \Phi^* / \partial t = \text{const.} \tag{6}$$

The wake surface is a sheet of dipoles, generated from the blades' trailing edges according to the force-free condition, so a new boundary condition is needed. The Kutta boundary condition is applied, which is suitable for lifting bodies with sharp trailing edge in order to obtain a unique solution. The Kutta condition requires the total flow leaving the trailing edge of the airfoil to be smooth, which means the derivative of velocity potential at the airfoil trailing edge, is finite:

$$\nabla \Phi_w(t) < \infty \qquad \text{at the trailing edge}$$

The Kutta condition requires the jump of potentials at the trailing edge to convect the wake; hence it is necessary to impose a pressure Kutta condition to ensure a zero pressure difference at the trailing edge of the airfoil:

$$\Delta C_P = C_P^+ - C_P^- = 0. \tag{7}$$

The dipole strength in the wake surfaces behind the trailing edge can be calculated by using

$$\mu_{t.e} = \mu_{upper} - \mu_{lower} \tag{8}$$

Where μ_{upper} and μ_{lower} are the potentials at the upper and lower side of the airfoil trailing edge.

The dipole strength of each wake panel at the trailing edge is calculated at each time step. The flow field is history-dependent according to the force-free condition on the wake surface (Lei H.,

2010), where the strength on the shed wake is determined from the previous time step, meaning the current distributions of dipoles on the wake surface depend on some previous distributions of dipoles. Therefore, the history of the motion is stored in the wake.

3   Wind Turbine Geometry

First, the rotor blade consists of a several airfoils that are lofted in the blade axis direction. The geometry of the rotor blade considered in this study is based on the 5MW wind turbine described in Jonkman J., (2009) and the blade geometry data taken from this reference. A 61m-length blade is attached to a hub with a radius of 2m, which gives a total rotor radius of 63m. The blade is composed of several airfoil types and these profiles are given in different blade sections, see Table 1 in reference Bazilevs et al., (2010). The first portion of the blade is a perfect cylinder; further away from the root, the cylinder is smoothly blended into a series of DU (Delft University) airfoils. At the location away from the root 44.55 m, the NACA64 profile is used to define the blade all the way to the tip.

The tower diameter in this study is 6m at tower base and 3.87m at tower top. A panel method is applied to determine the most efficient wind turbine grid. The panels are generated   using in-house CAD as shown in Figure 1.
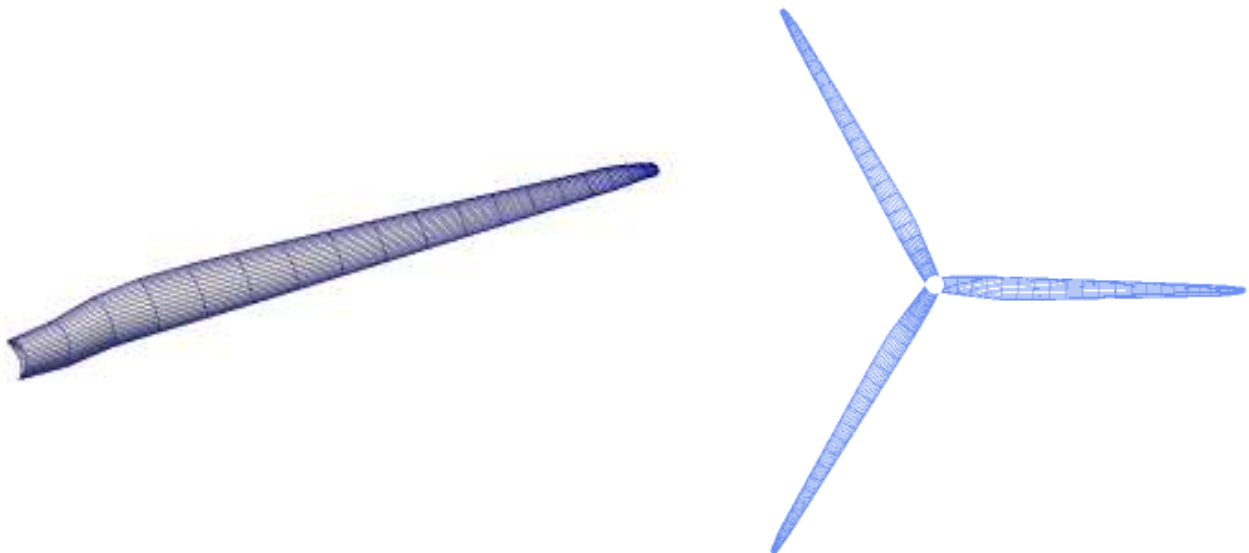
Figure 1. 5MW wind turbine blade and rotor geometry.

4   Blade-Tower Interaction

Blade-tower interaction of the wind turbines has become important for aerodynamic loading as the systems have become larger. However, there are not enough studies describing these phenomena. To investigate this case, the described methodology is used to solve the flow around the rotor and tower in an iterative manner by solving a two-equation system; the first one for the rotor and the second one for the tower, in addition to considering the time-dependent effect of one component on the other. The interactive effects of the components are taken into account by calculating the induced velocities of each component on the other component at every time step. Figure 2 shows the flowchart of solving the blade-tower interaction case by using an iterative procedure. In the first iteration process, the tower problem is solved without the presence of the rotor. Next, we solve the unsteady rotor problem by incorporating the unsteady tower-induced on rotor surface at the corresponding time. The last two steps are repeated until the solution converges.

4
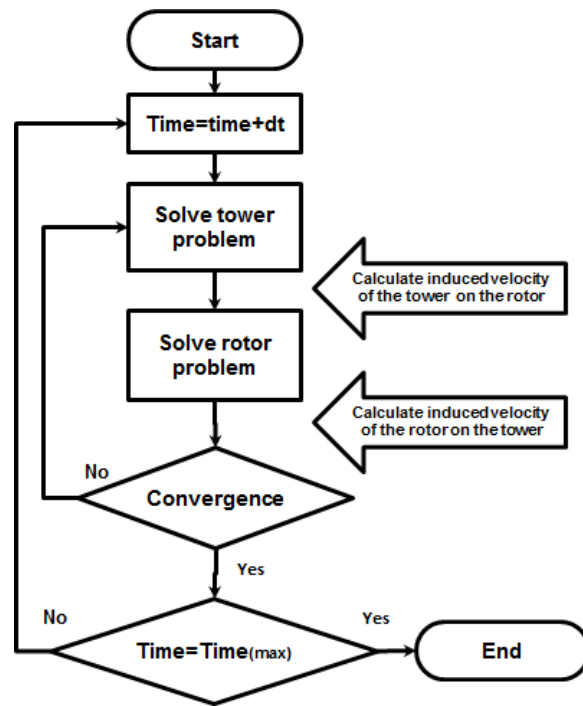
Figure 2. Flow chart of iterative procedure for solving blade-tower interaction.

5 Validation Cases

For the validation case, the calculated torque values for two cases are compared with the torque value in references Bazilevs et al., (2010), and Bazilevs et al., (2012). As shown in Figure 3, these two references simulate the same geometry of the 5MW wind turbine. Case 1 is compared with reference Bazilevs et al., (2012), where the simulation is carried out for complete wind turbine and the operation condition (inflow air velocity is 11.4 m/s and rotational speed is 1.267 rad/sec). Case 2 is compared with reference Bazilevs et al., (2010), where the simulation is done without the presence of the tower under the operation condition (inflow air velocity is 9 m/s and rotational rotor speed is 1.08 rad/sec). The comparison shows acceptable agreement with the published results.
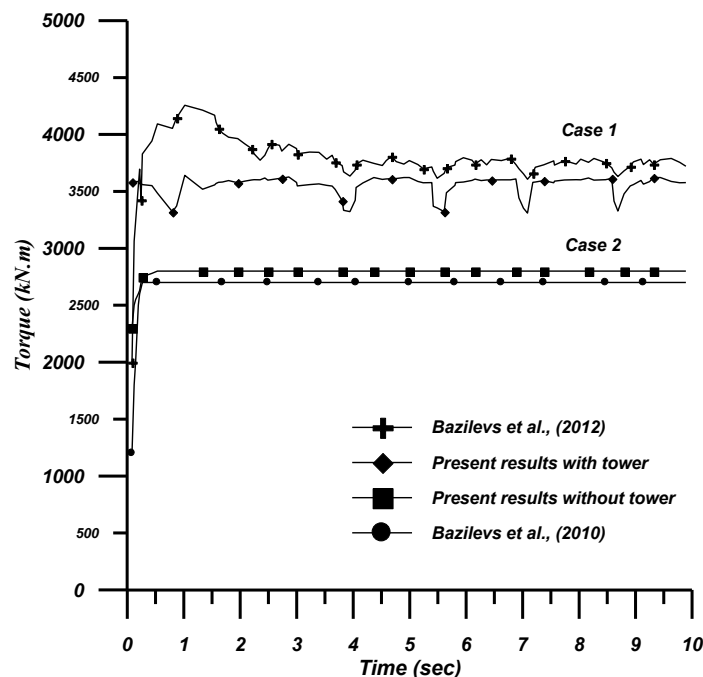
Figure 3. Time history of aerodynamic torque for validation cases.

6   Results

The results obtained using the computational tool   at the same operation condition in Case 2 give a tip speed ratio of 7.55; and the time of increment is chosen such that the rotor blades advance 6.118 degrees at each time step: therefore, one revolution is completed in 58 seconds. Figures 4 and 5 show the wake structure behind the wind turbine, both excluding and including the presence of the wind turbine tower. The wake is shed from the trailing edge of the rotor blades, and it gets convected downstream with the local fluid velocity.

At each time step, the free wake moves with the induced velocity that is calculated at each panel. Figure 6 shows a technique that is used when the wake collides with a tower. The wake element, which is recognized to be in collision with the tower, is excluded from the induced velocity calculation of the wake element so it will not have any effect on the tower panels.
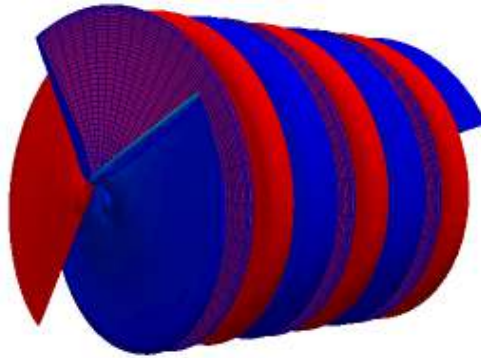
Figure 4. Wind turbine rotor panels and trailing wake surface without tower.
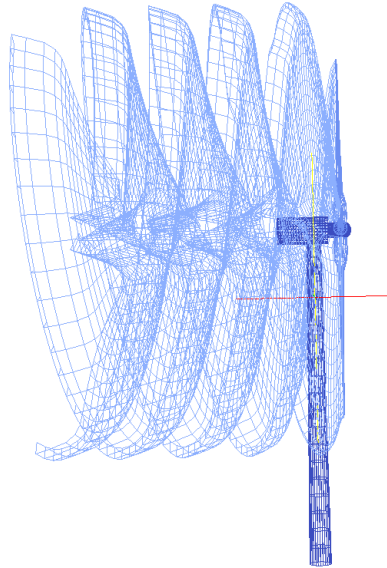
Figure 5. Wind turbine panels and trailing wake surface with tower.
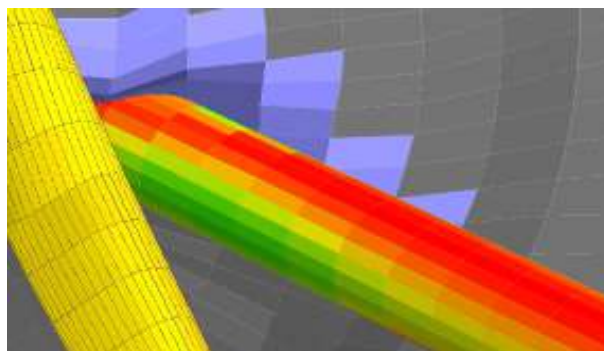
Figure 6. View of wake collided with a tower.

Figures 7 and 8 show of the pressure distribution on the face and back blade surface after 60 time steps; note the high pressure region on the pressure side (face side), especially near the leading edge, and the low pressure zone on the suction side (back side). The different pressures between the two sides will create forces (lift and drag) on the blade surface.
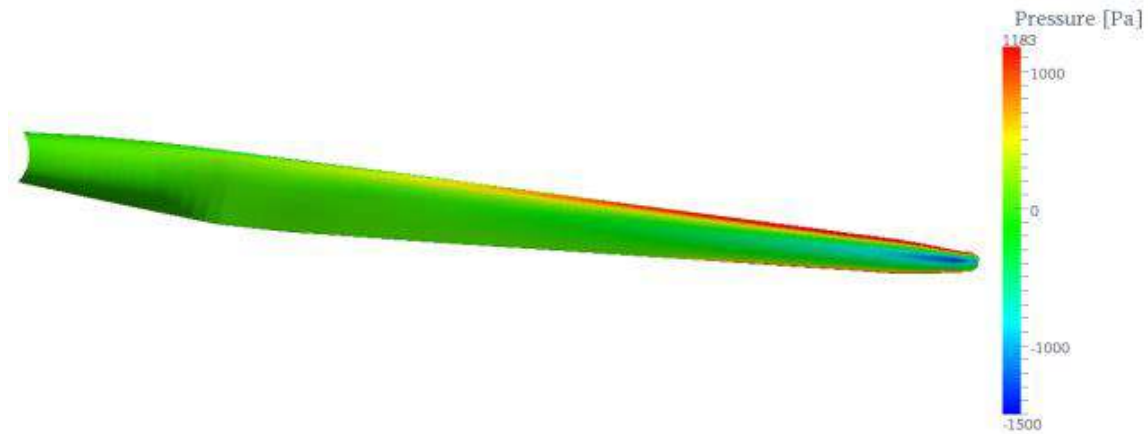
Figure 7. Pressure distribution on the pressure side of the blade surface.
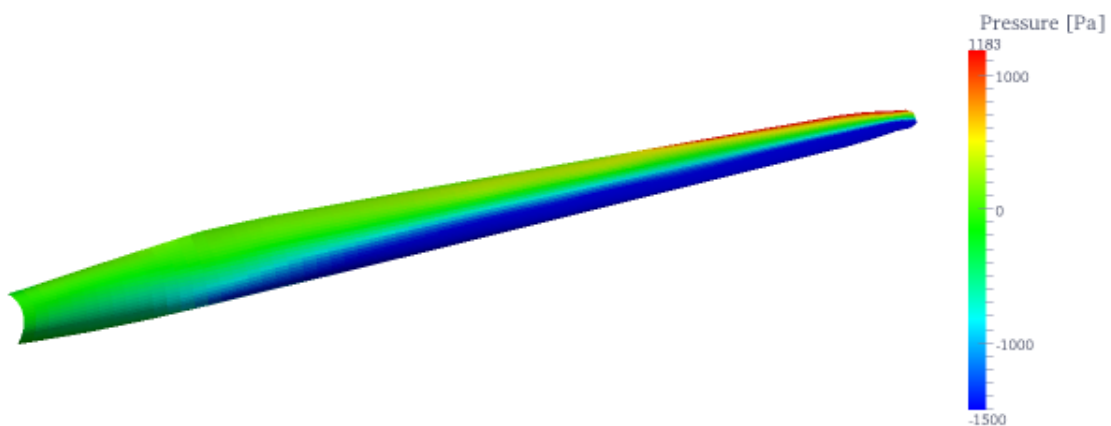
Figure 8. Pressure distribution on the suction side of the blade surface.

The aerodynamic effects of blade-tower interaction have two influences: the effect from tower on the blade and the impact of blade on tower. To discuss the first interaction part, Figures 9A through 9D show the pressure coefficient distribution at many sections (r/R= 0.25, and 0.75) on different blades rotor, which have different angular positions from the tower. The first blade has 120 degrees from the tower and the second blade is in front of the tower. The effect of the blade-tower interaction on the pressure coefficient is discussed below; where the maximum value of the pressure coefficient suffers a drop of 10-15% on the second blade.

Evaluating the rotor torque coefficient provides more information on tower influence on the aerodynamic rotor performance. Figure 10 presents the time history of the coefficient torque values with and without tower. The comparison shows several drops on the torque history, with each drop corresponding to one blade passing in front of the tower, this phenomenon was also analysed by reference Bazilevs et al., (2012).
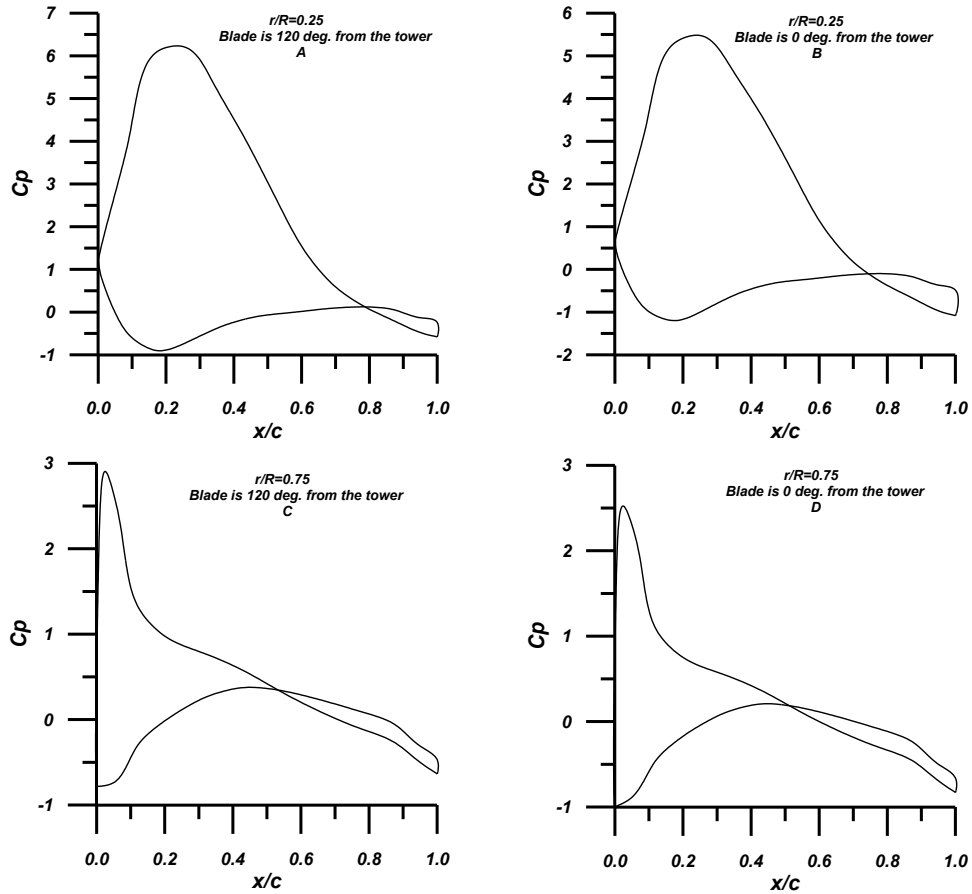
Figures 9 A – D. Effect the pressure coefficient distribution at (r/R= 0.25, and 0.75) for different blades position from the tower.
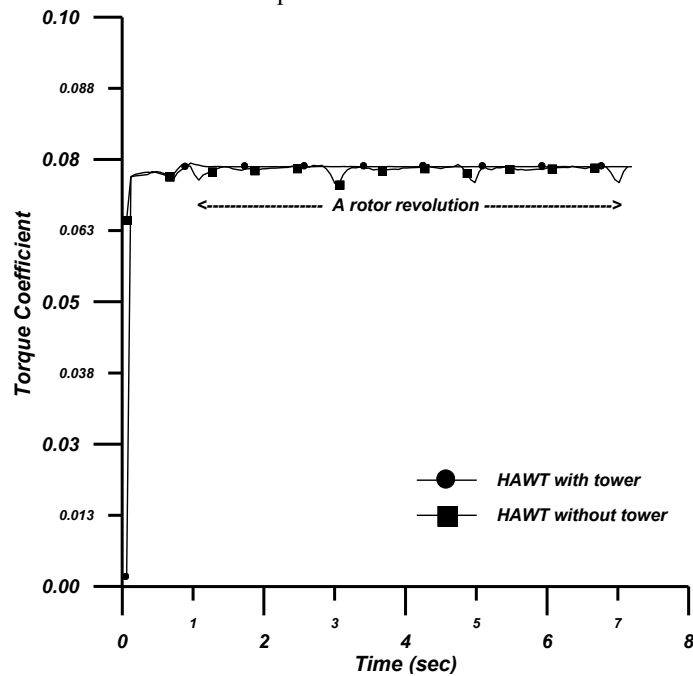
Figure 10. Time history of the torque value with and without tower.

In regards to the influence of the rotor on the tower surface, Figures 11 and 12 show the pressure distribution on the tower leading edge when the blade has 0 degrees (Fig. 11), and when the blade has 30 degrees (Fig. 12). As can be seen, the coefficient pressure decreases on the tower leading edge

when the blade passes the tower, where this sudden drop will create fluctuation forces on the tower. The maximum value of these forces is essential in tower design and for the calculation of fatigue. Also, the huge drop in pressure will effect deformation of the blade toward the tower, and this oscillation phenomenon is very dangerous in wind turbine working life. The results of behaviour on the tower leading edge have been satisfactorily captured and are in agreement with the results in reference Wang et al., (2012).
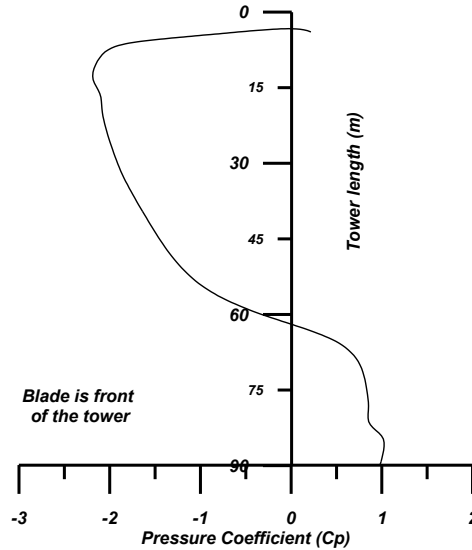
Figure 11. Pressure coefficient distribution on the tower leading edge.
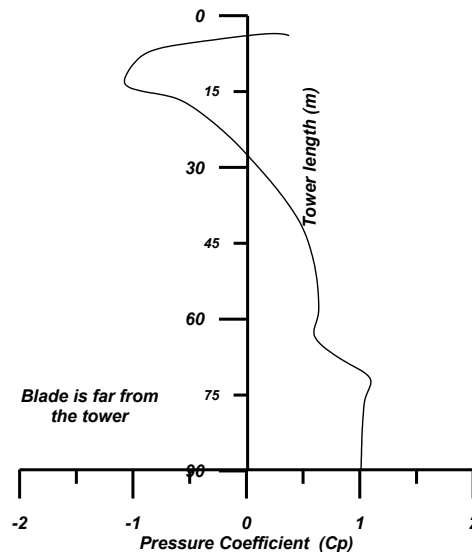
Figure 12. Pressure coefficient distribution on the tower leading edge (30° between tower and blade).

7 Discussion

We examined the interaction between a tower and a rotor blade in an upwind-type horizontal axis wind turbine system using the boundary element solver *pan*MARE. On both sides blades and tower, the maximum value component of the pressure coefficient suffers a drop of 10-15 % on the blade that pass from tower .and   drop on pressure coefficient tower leading edge at the same time. Some important conclusions can be drawn from the results presented here on both rotor and tower: they help to understand the aerodynamic behaviour associated with HAWT, the complexity of which is well-known and accepted.

9

In order to validate the boundary element solver, the simulation results were compared with results obtained from the literature under two operation conditions and they show a good agreement.

8   References

Abedi H., Lars D., and Spyros V. (2013). Vortex method application for aerodynamic loads on rotor blades. *EWEA 2013: Europe's Premier Wind Energy Event*, Vienna, 4-7 February 2013.

Bazilevs Y., Hsu M.-C. , Akkerman I., Wright S., Takizawa K., Henicke B., Spielman T., and Tezduyar T. (2010). 3D simulation of wind turbine rotors at full scale. Part I: Geometry modelling and aerodynamics. *International Journal for Numerical Methods in Fluids* **65**, 207–235.

Bazilevs Y., and Hsu M.-C. (2012). Fluid–structure interaction modelling of wind turbines: simulating the full machine, Springer-Verlag, *Comput Mech* **50**,821–833.

Boorsma K., Grasso F., and Holierhoek J.G. (2011). Enhanced approach for simulation of rotor aerodynamic loads. *EWEA Offshore*, Amsterdam. (ECN-M--12-003).

Bermudez L., Velazquez A., and Matesanz A. (2000). Numerical simulation of unsteady aerodynamics effects in horizontal-axis wind turbines. *Solar Energy* **68**, 1, 9-21.

Dnyanesh A. (2012). Simulation of flow over wind turbines. *M.Sc. Thesis*, University of Massachusetts, Amherst.

Gebhardt C.G., Preidikman S., Massa J.C. (2010). Numerical simulations of the aerodynamic behaviour of large horizontal-axis wind turbines. *International Journal of Hydrogen Energy* **35**, 6005–6011.

Hogeon K., Seungmin L., and Soogab L. (2010). Influence of blade-tower interaction in upwind-type horizontal axis wind turbines on aerodynamics. *Journal of Mechanical Science and Technology* **25**, 5, 1351-1360

Jonkman J., Butterfield S., Musial W., and Scott G. (2009). Definition of a 5-MW reference wind turbine for offshore system development, *Technical Report NREL/TP-500-38060*, National Renewable Energy Laboratory, Golden, CO.

Katz J., and Ploklin A. (2001). Low-Speed Aerodynamics. Cambridge University Press.

Lei H. (2010). Numerical Simulation of Unsteady Rotor/Stator Interaction and Application to Propeller/Rudder Combination. *Ph.D. Thesis*, University of Texas, Austin.

Namiranian A. (2011). 3D Simulation of a 5MW Wind Turbine. MSC Thesis, Department of Mechanical Engineering, Blekinge Institute of Technology, Karlskrona, Sweden.

Takizawa K., Henicke B., Tezduyar E., Ming-Chen Hsu, and Bazilevs Y. (2011). Stabilized space–time computation of wind-turbine rotor aerodynamics. Springer-Verlag, *Computational Mechanics* **48**, 3, 333-344.

Wang Q., Zhou H., and Wan D. (2012). Numerical simulation of wind turbine blade-tower interaction, *Journal of Marine Science and Application*, **11**, 321-327.

Yuwei Li A., Kwang-Jun P., Tao X., and Pablo M. Carrica (2012). Dynamic overset CFD simulations of wind turbine aerodynamics. *Renewable Energy* **37**, 285-298.

Pressure field around a rectangular 5:1 cylinder in smooth flow

Claudio Mannini[1], Davide Allori[1], Luca Pigolotti[1], Antonino M. Marra[1] and Gianni Bartoli[1]

[1]CRIACIV/Department of Civil and Environmental Engineering, University of Florence, Italy
Corresponding author: Claudio Mannini, claudio.mannini@dicea.unifi.it

Abstract

This paper reports the ongoing progresses on the experimental campaign on a rectangular 5:1 cylinder in the framework of the BARC benchmark. Measurements of surface pressures and velocity fluctuations in the wake of a section model in smooth flow are presented. The effects of a variation of the Reynolds number and of the angle of attack are studied and comparison with other experimental and numerical results is provided. The data analysis is particularly aimed at underscoring the details of the vortex-shedding mechanism for this bluff body.

1 Introduction

The simple shapes of many civil and industrial structures, such as tall buildings, towers, chimneys, antennas and bridges, characterized by circular or rectangular cross section, play a key role in bluff body aerodynamics, as they highlight complex fluid dynamic phenomena and allow a detailed study of the aerodynamic features of the flow field they generate. For these reasons in the literature there are several studies on rectangular cylinders in which the effects of various geometrical and flow parameters are experimentally and numerically investigated, such as the width-to-depth ratio, Reynolds number, Mach number, angle of attack, oncoming turbulence characteristics and blockage ratio.

The BARC benchmark, launched during the 6th International Symposium on Bluff Body Aerodynamics and Applications (Bartoli et al., 2008) has focused the attention on the rectangular cylinder with a 5:1 cross section, which is characterized by being close to the limit between fully separated and reattached flow. A synopsis of the experimental and numerical results obtained so far was recently published (Bruno et al., 2014).

This work reports the results of pressure measurements on the surface of the cylinder in different cross sections and of velocity fluctuations in the wake of the section model. Experiments were performed in smooth flow and the effects of a variation of the Reynolds number and of the angle of attack were studied. The data analysis was particularly aimed at underscoring the details of the vortex-shedding mechanism for this bluff body.

2 Experimental set-up

The tests were carried out in the open-circuit boundary-layer wind tunnel of CRIACIV in Prato. The free-stream turbulence intensity was about 1%.

The aluminum model (Fig. 1) was 300 mm wide (B), 60 mm deep (D) and 2380 mm long and was mounted horizontally in the wind tunnel, so that the blockage ratio at zero degree angle of attack was 3.75%. The length-to-width ratio was 7.93 and its mass was 42 kg. The model locking system was activated from its ends, so to avoid screws, keeping the lateral surfaces of the cylinder very smooth and minimizing the disturbances to the flow. The model was provided with 564 pressure taps and pressure data were recorded with two 32-channels miniaturized piezoelectric scanners and the system PSI DTC Initium at a sampling rate of 500 Hz. In a first configuration (called "A") three sections were instrumented (the central one and other two sections 595 mm and 690 mm apart from the former, respectively on the right and left side of the wind tunnel centerline). In this case several pressure taps on the downward

(a)   (b)

Figure 1. a) View of the model; b) model in the wind tunnel.
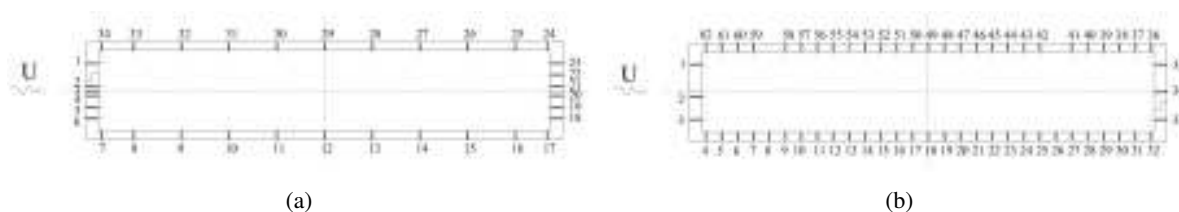
(a)   (b)

Figure 2. Instrumented pressure taps in the central section for a) configuration A and b) configuration B.

and leeward faces of the prism were connected with the pressure scanners in order to estimate also the drag coefficient of the cylinder. By contrast, in the second configuration (called "B") only the taps on the central section were connected to the pressure scanners and mainly those on the sides of the rectangle parallel to the flow. Tests at angles of attack different from zero were performed only with configuration B. Figure 2 shows the two arrangements of instrumented pressure taps.

Measurements of free-stream flow properties at the position of the model and of velocity fluctuations in the wake of the cylinder (in a point located 110 mm downstream and 32 mm below the lower trailing edge of the central section) were realized with a single-component hot-wire anemometer Dantec 55P11 connected to a Dantec CTA Bridge 56C01.

3 Results

Examples of pressure coefficients measured in the central section of the model are reported in Figure 3. The pressures are uncorrected with respect to blockage effects and this justifies the value slightly larger than unity at the stagnation position for a zero-angle of attack. The time histories were high-pass filtered at 8 Hz to eliminate the effects of wind-tunnel pressure low-frequency fluctuations. It is worth noting the symmetry of pressures on the upper and lower half of the section obtained by rotating nose-down the model of about $0.4°$, which demonstrates the good quality of the model.

The mean pressure distribution for $\alpha = 0°$ is in good agreement with the experimental data by Matsumoto (see Mannini et al. (2011)) and the 3-D DES numerical results by Mannini et al. (2011). Also the location of the maximum of the standard deviation of the pressures (about $s/D = 4.33$), which is known to be close to the shear-layer mean reattachment position, agrees well with those results. By contrast, the standard deviation of the pressure coefficients is significantly higher than that reported in the previously mentioned experimental and numerical works. The estimated drag coefficient is 1.127 to be compared with about 1.0 obtained in a few works in the literature (see Mannini et al. (2011)). The
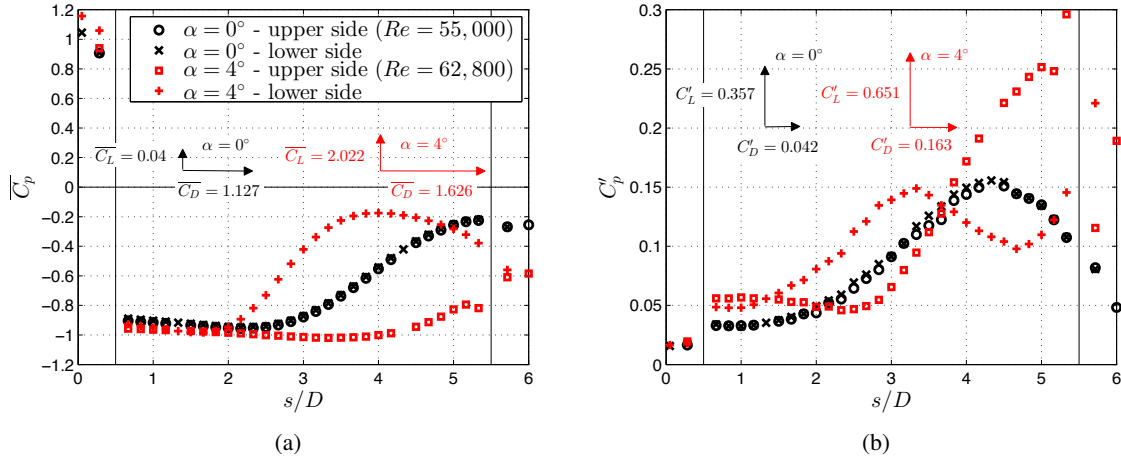
Figure 3. a) Mean and b) standard deviation of pressure coefficients (configuration B) for two angles of attack α. The mean and standard deviation values of lift and drag coefficients (C_L and C_D, normalized with respect to the cross-wind depth D of the section) are also reported. s denotes the coordinate describing the contour of the section: $s/D = 0$ and 6 indicate respectively the center of the downward and leeward sides of the rectangle.
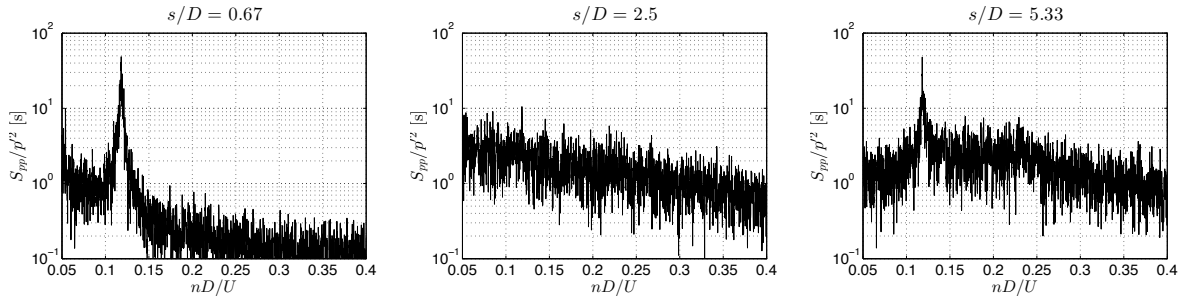
Figure 4. Power spectral density of the pressure coefficients at three different locations of the central cross section ($\alpha = 0°$ and $Re = 55,000$).

slight overestimation may partly be ascribable to blockage effects but it is mainly due to integration of pressures with not enough taps near the edges (Fig. 2). As expected the resultant mean lift coefficient is negligible. The standard deviations of the drag and lift coefficient are respectively 0.042 and 0.357, in good agreement with the numerical results by Mannini et al. (2011) and the measurements by Schewe (2013) ($C'_L \cong 0.4$). Figure 4 reports the spectra of pressures at three different positions on one side of the cylinder parallel to the flow. In the first part of the separation bubble and near the mean reattachment position a peak corresponding to a Strouhal number of 0.118 is apparent. This value is coherent with the literature results collected in Mannini et al. (2011) and is also confirmed by the hot-wire measurements of velocity fluctuations in the wake of the model (Fig. 5). It can be noted in Figure 4 that there is a portion of the separation bubble around $s/D = 2.5$, that is immediately before the pressure recovery zone (Fig. 3(a)), where the Strouhal peak is not visible. Moreover, near the end of the streamwise side of the cylinder and in the base region, a small peak in the spectra corresponding to a frequency double than the Strouhal one can also be detected.

Concerning the configuration with an angle of attack of $+4°$ (blockage ratio of 5.05%), the mean pressure distribution in Figure 3(a) confirms that the flow is fully separated on the upper side of the cylinder, while unsteady reattachment on the lower side is supposed to occur around $s/D = 3.33$ (peak value of C'_p in Figure 3(b)), which is in line with the 2-D URANS numerical results by Mannini et al. (2010). The mean values of drag and lift coefficients are respectively 1.626 and 2.022, while the standard deviations, as expected, are significantly larger than for the case $\alpha = 0°$. $\overline{C_D}$ is significantly larger than what measured by Schewe (2013) for the same value of the Reynolds number (slightly less
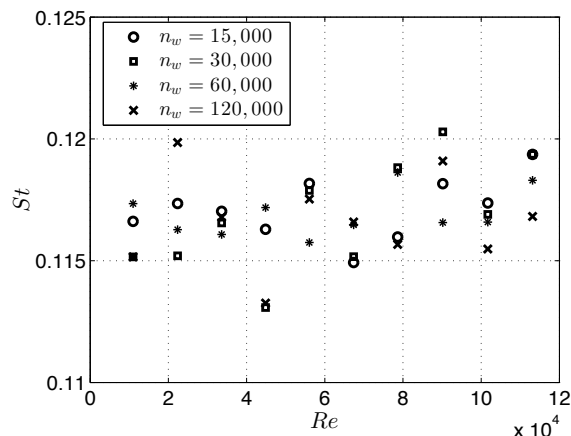
Figure 5. Strouhal number as a function of the Reynolds number obtained through measurements of velocity fluctuations in the wake of the model with a hot-wire anemometer (n_w denotes the number of points per window over which the spectra are calculated before averaging).

than 1.4) but this is probably due to the little number of pressure taps on the front face of the prism (configuration B, see Figure 2(b)). By contrast, the mean lift results to be slightly lower than the value obtained by Schewe for a similar Reynolds number (about 2.5). It is also worth noting the significant increase of standard deviation of pressure and small reduction of mean pressure for the last tap of the upper side of the cylinder ($s/D = 5.33$), which is a clue as to the counter-rotating secondary bubble shown by the numerical simulations in Mannini et al. (2010). Finally, the Strouhal number deduced from pressure spectra results to be slightly higher for $\alpha = +4°$, that is 0.126.

4   Concluding remarks

The wind tunnel measurements in smooth flow of surface pressures and velocity fluctuations in the wake of a two-dimensional model with a benchmark rectangular 5:1 cross section were compared with previous experimental and numerical results showing a general good agreement. Several Reynolds numbers and a few angles of attack were taken into account. Detailed data analysis will be also discussed to shed some light on the vortex-shedding mechanism for this particular bluff-body geometry.

References

Bartoli, G., Bruno, L., Buresti, G., Ricciardelli, F., Salvetti, M. V., and Zasso, A. (2008). *BARC overview document*. http://www.aniv-iawe.org/barc.

Bruno, L., Salvetti, M. V., and Ricciardelli, F. (2014). Benchmark on the Aerodynamics of a Rectangular 5:1 Cylinder: An overview after the first four years of activity. *Journal of Wind Engineering and Industrial Aerodynamics* **126**, pp. 87–106.

Mannini, C., Soda, A., and Schewe, G. (2010). Unsteady RANS modelling of flow past a rectangular cylinder: investigation of Reynolds number effects. *Computers and Fluids* **39**.9, pp. 1609–1624.

— (2011). Numerical investigation on the three-dimensional unsteady flow past a 5:1 rectangular cylinder. *Journal of Wind Engineering and Industrial Aerodynamics* **99**.4, pp. 469–482.

Schewe, G. (2013). Reynolds-number-effects in flow around a rectangular cylinder with aspect ratio 1:5. *Journal of Fluids and Structures* **39**, pp. 15–26.

Experimental investigation on small size wind turbines renovated

M. Burlando[1], L.C. Pagnini[1] , M.P. Repetto[1] and M. Rosasco[2]

[1]Department of Civil, Chemical and Environmental Engineering, University of Genoa, Italy
[2] S.V. Port Service Srl, Savona, Italy
Corresponding author: L.C. Pagnini, luisa.pagnini@unige.it

Abstract

A monitoring campaign has been undertaken since Jan 2012 over two commercial small size wind turbines located in the Savona Harbour (Northern Italy) characterized by comparable nominal power and having respectively vertical and horizontal axis. The investigation between 2012 and 2013 has shown that power production turned out to be well out underneath the expectations, especially due to gusts and wind fluctuations. For this reason, in late 2013 the control system of the turbines has been modified. The present paper presents new results after the improvements. Preliminary analyses reveal that the power production is now satisfactory and quite competitive when the medium speed wind is over 5 m/s.

1 Introduction

Wind power exploitation by large wind turbines is gaining more and more importance in the power production strategies (GWEC 2012). The great interest in this field has brought into being a large scientific and technical literature and has opened the way to advanced technologies and to an increasing number of realizations. Horizontal axis wind turbines constitute the most common type in use today for large realizations.

In most cases small size wind turbines don't provide the return on investment, due to the fact that construction and operating costs are often too high with respect to the power production. Notwithstanding this, small size turbines can be attractive from many points of view: the environmental impact is low; they do not cause instabilities in the power network distribution; they do not need large power storage capability and are therefore particularly suitable in isolated contexts, like small islands. The technical interest is thus increasing, with reference to the strategic aim of a diffuse micro-generation of renewable energy.

The present paper describes the results of a monitoring activity started in Jan 2012 at the Savona Harbour (Northern Italy) that is carried out to study the efficiency of two small size wind power generators, respectively with horizontal and vertical axis. During the experience carried out in 2012 and 2013 the power production turned out to be well out underneath the expectations. The energy production of the HAWT was higher than the VAWT, in the range of the registered wind velocities. However, the HAWT turned out to be very exposed to gusts and to large wind fluctuations in direction and intensity. Mainly for this reason, it had to be slowed down at moderate wind velocities, thus reducing the power production; moreover it needed much maintenance and suffered severe damages to the machine. For these reasons the control and inverter systems of both turbines were completely redesigned and renewed in Jan 2014, giving rise to a new setting which is now much more efficient and competitive.

2 The wind turbines and monitoring equipment

The investigated wind turbines are located on the quay of the Savona Harbour. Figure 1 shows the area and the location (red stars) of the HAWT and VAWT on the dam and their cup anemometers (circles).

Figure 1: Location of the two wind turbines (red stars) and of the anemometers (red circles).

The HAWT, shown on the right side in Figure 2, is provided by It-Energy (Vicenza, Italy). It has a three bladed turbine with an up-wind rotor with 10 m diameter, a synchronous generator and an active yaw system The turbine is made by three fiberglass blades and is supported by a 18m high steel pole. The slowing system is given by a hydraulic brake, yaw control and electrical brake. The VAWT, shown on the left side in Figure 2, is a H-rotor manufactured by Ropatec (Bolzano, Italy). The rotor diameter is 8 m and its height is 5.8 m; it is provided with 5 aluminium, steel and fiberglass blades. The machine's security is guaranteed slowing the turbine through its inverter apparatus, which requires, at high wind speed, larger power demand with respect to the available one. It is supported by a 10.5m high steel pole, which is much shorter than the HAWT's one. Besides, it is worth noting that the swept area of the HAWT is almost twice the area swept by the VAWT. Both turbines are placed upon the dam, at 4.5 m above the ground. They have been installed late in 2011, together with a monitoring system to register and collect the power production with a sampling rate of 10 seconds.

Figure 2: The wind turbines: HAWT (right) and VAWT (left).

Each wind turbine is equipped with its own cup anemometer; the wind monitoring system is integrated with the three-axial sonic anemometer installed in the Harbour nearby the turbines registering continuously three wind velocity components. This is part of a large monitoring network realized in the framework of the European Project "Wind and Ports" (Solari et al., 2012).

The nominal power given by the manufacturers is 20 kW, even if the VAWT may at least in principle go further. Both turbines are equipped by a suitable power control system and are slowed down and stopped by a hydraulic brake under strong winds. Notwithstanding the control system, after

the start-up of the machines, the HAWT suffered heavy damages because of strong wind gusts. It was therefore secured by reducing the slowing-down wind velocity threshold and the cut-off wind speed. Nevertheless, the HAWT turbine experienced severe damages in the last months of 2012 and went out of use. The VAWT proved to be less exposed to gust effects; unfortunately, it suffered severe damages due to a lightning and it went out of use too.

On the basis of the previous experience, both turbines were put back into operation at the beginning of 2014 with a control system completely renovated so as to exploit better the potential of the two machines, to ensure greater reliability and continuity of operation

3   Monitoring activity and data investigation

The dataset of the sonic anemometer provides the more reliable description of the wind and turbulence field nearby the turbines. These data are preliminary checked and corrected, and missing periods are reconstructed through an MCP (Measure Correlate Predict) procedure based on the correlation with the two cup anemometers available at the turbines' position; then, transfer coefficients are applied in order to transfer the wind speed and turbulence time series from the position of the sonic anemometer to the turbine hub heights. The transfer coefficients have been calculated by the procedures introduced by the Engineering Sciences Data Unit (ESDU, 1993), as described in Burlando et al. (2013).

Figure 3 and Figure 4 show some results obtained during 2012, *i.e.* before the turbines' refurbishment. Figure 3 represents a records of the mean power and mean wind speed recorded during a couple of day of moderate windiness. It is interesting to note that the blue line, which describes the HAWT power production, lies almost always above the red line, which refers to the VAWT production; nevertheless, the VAWT production turns out to be slightly larger during the stronger winds. It has been found that the slight decrease of the mean wind was due to a sudden change of the incoming wind direction (from sea at first, from land later), followed by the increase of the wind turbulence and gust which has caused the fall of the power production. Figure 4a,b report the power curves (blue solid line) obtained from the measures as 10-minute mean values (IEC 61400) and the dispersion of measures (symbols), for HAWT (a) and the VAWT (b), respectively. In the same figures, the data frequencies of the wind speed occurrence at the hub height and the theoretical power curves provided by the manufacturer (dashed line) are also shown. It is apparent that both the measured curves lay underneath the target power for wind velocities higher that 6-7 m/s. The HAWT seems to produce more in the range of the low wind velocities, which are more frequent, and has a lower cut in speed. It reaches the maximum power production at about 10 m/s. The VAWT, which almost follows the same trend in the range 0-12m/s, has an upturn after about 15m/s and reaches a higher power production, still much lower than the target one.
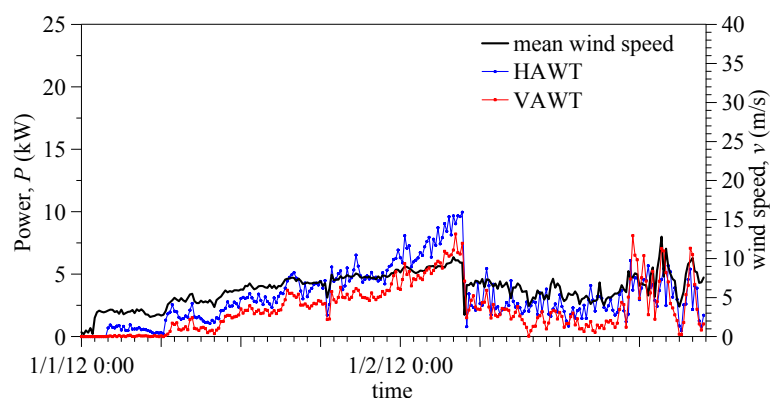
Figure 3. 10-min averaged values of power and wind speed collected the 1st-2nd January 2012.

Figure 5 shows the records of the mean power and mean wind speed during a couple of days in 2014, *i.e.* after that the turbine were renovated. This time, the power prediction of both turbines seems

to be much more efficient even at moderate windiness and is especially fitting with the target power curve.

The full paper will show the detailed study of the experimental investigation, focusing, in particular, on the influence of the ambient turbulence over the power production of such small size wind turbines. The change of the turbine behaviour before and after the system renovation will be fully detailed and the renovated power production will be investigated, also quantifying the sustainability of such small size power plants in urban areas.
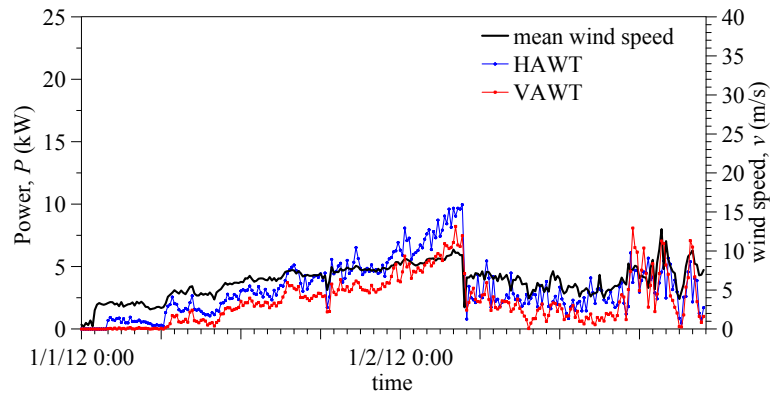
Figure 4: Power curve and wind speed frequencies of the (a) HAWT and (b) VAWT.
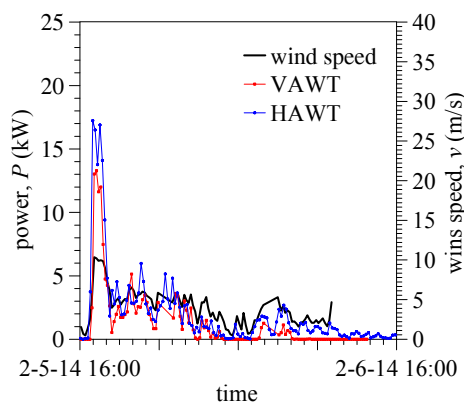
Figure 5. 10-min averaged values of power and wind speed collected the 5th-6th February 2014.

References

Burlando, M., Pagnini, L.C., Repetto, M.P. and Rosasco, M. (2013). Experimental investigation on small size wind turbines. *VI EACWE,* UK.

Global Wind Energy Council. Global Wind Report 2012.

Engineering Sciences Data Unit, 1993. Computer program for wind speeds and turbulence properties: flat or hill sites in terrain with roughness changes. *ESDU Item 92032*, London, UK.

IEC 61400-12-1, Power performance measurements of electricity producing wind turbines, 2005

Solari, G., Repetto, M.P., Burlando, M., De Gaetano, P., Pizzo, M., Tizzi, M. and Parodi, M. (2012). The wind forecast for safety management of port areas, *J. Wind Eng. Ind. Aerodyn.*, **104-106**, 266–277.

Galloping of slender tower buildings based on a shear-shear torsional equivalent beam model

Giuseppe Piccardo[1], Federica Tubino[1] and Angelo Luongo[2]

[1]Department of Civil, Chemical and Environmental Engineering, University of Genoa, Italy
[2] M&MoCS, University of L'Aquila, Italy
Corresponding author: Federica Tubino, federica.tubino@unige.it

Abstract

In this paper the aeroelastic behaviour of tall buildings or towers is studied based on an equivalent one-dimensional beam model immersed in a three-dimensional space. The beam is internally constrained, so that it is capable to experience shear strains and torsion only. The model accounts for the torsional effect induced by the rotation of the floors around the tower axis; the macroscopic shear strain is produced by bending of the columns, accompanied by negligible rotation of the floors. Aerodynamic forces are evaluated through the quasi-steady theory, referring to a section model under stationary wind. The effect of mechanical and aerodynamic coupling on the critical galloping conditions is analyzed.

1   Introduction

Tower buildings are usually slender structures very sensitive to wind-induced vibrations. Wind excitation may induce high vibrations and stresses; furthermore, if these structures are lightweight and with low damping capacity, they can be potentially subjected to aeroelastic instability phenomena called galloping.

In recent years there is a growing interest in the technical literature about simple models which can be useful for preliminary structural analysis. Semi-analytical approaches have been proposed to estimate lateral load effects on tall shear wall structures, aiming at the analysis of the distribution of the external forces on high rise buildings (e.g., Carpinteri et al. 2010), the evaluation of their dynamic characteristics (e.g., Dym 2013) and their dynamic response to wind loadings (e.g., Cluni et al. 2013).

The authors of the present paper have recently introduced a continuous model of beam immersed in a three dimensional space and capable to experience shear strains and torsion only, with the aim of studying the critical and postcritical aeroelastic behavior of slender tower-buildings (Piccardo et al. 2014). In this model, the macroscopic shear strain is produced by bending of the columns, accompanied by negligible rotation of the rigid floors, prevented by the high axial stiffness of the columns. The torsional effect induced by the rotation of the floors around the tower axis is included. Furthermore, the nonlinearities generated by the stretch of the columns are accounted for: a nonlinear constitutive law is thus introduced, which relates the internal forces to the three strain components. Aerodynamic forces are evaluated through the classic quasi-steady theory, referring to a section model, taking into account nonlinear terms up to the third order. The full nonlinear fundamental problem for the aeroelastic behaviour of tower-buildings is derived, including kinematics relationships, balance equations, elastic law and external forces (Piccardo et al. 2014).

In the present paper, the linearized form of the beam model proposed by Piccardo et al. (2014) is adopted in order to analyze the effects of the mechanical and aerodynamic coupling among torsional and translational vibrations on the critical galloping conditions of slender tower buildings. A preliminary numerical example considering a square building excited along a generic direction (generally not aligned with a symmetry axis) is shown.

2   Mechanical and aerodynamic model

A shear-beam is characterized by shear strains much larger than flexural ones: it is a coarse model for three-dimensional shear-type frames under planar excitation transverse to the axis. The shear-beam is considered as a one-dimensional polar continuum whose points, in the reference configuration, lie on the segment $s \in [0, \ell]$ (assumed to be coincident with the *centroidal axis* of the underlying three-dimensional model). It is assumed internally constrained, namely unflexurable and clamped at one end. The current configuration of the beam is described by three scalar configuration variables, the transverse displacement of the centroidal axis $\mathbf{u} := u_2(s,t)\,\overline{\mathbf{a}}_2 + u_3(s,t)\,\overline{\mathbf{a}}_3$ and the twist $\theta(s,t)$.

Starting from the structural model introduced by Piccardo et al. (2014), the linearized equations of motion may be expressed as follows:

$$
\begin{aligned}
& hK_2^f u_2'' - hx_{3F}K_2^f \theta'' + p_{a2} - m\ddot{u}_2 - c_2\dot{u}_2 = 0 \\
& hK_3^f u_3'' + hx_{2F}K_3^f \theta'' + p_{a3} - m\ddot{u}_3 - c_3\dot{u}_3 = 0 \\
& h\left(K^t + K^{tf}\right)\theta'' - hx_{3F}K_2^f u_2'' + hx_{2F}K_3^f u_3'' + c_a - I_1\ddot{\theta} - c_\theta\dot{\theta} = 0
\end{aligned}
\tag{1}
$$

where the prime symbol denotes differentiation with respect to s, the dot denotes differentiation with respect to time, h is the interfloor height, m is the mass per unit length, I_1 is the inertia mass moment of the cross section with respect to $\overline{\mathbf{a}}_1$, c_i ($i=2,3,\theta$) are the viscous damping constants, K_2^f and K_3^f are the total flexural stiffnesses, K^t is the total torsional stiffness and K^{tf} is the contribution to the torsional stiffness given by the flexural stiffness of the columns; x_{2F} and x_{3F} are the coordinates of the center F of the flexural stiffness.

Furthermore, p_{a2}, p_{a3}, c_a in Eq. (1) are the aerodynamic forces. Based on the linearized quasi-steady theory, neglecting the torsional damping contribution, they are given by (Piccardo et al. 2014):

$$
p_{ai} = \frac{1}{2}\rho_a bU\left(C_{ai2}\dot{u}_2 + C_{ai3}\dot{u}_3 + UC_{ait}\theta\right)\ (i=2,3) \qquad c_a = \frac{1}{2}\rho_a b^2 U\left(C_{at2}\dot{u}_2 + C_{at3}\dot{u}_3 + UC_{att}\theta\right)
\tag{2}
$$

where ρ_a is the air density, b is a characteristic dimension of the cross-section, U is the mean wind velocity; furthermore:

$$
C_{a2i} = C_{di}\cos\beta - C_{li}\sin\beta \qquad\qquad C_{a3i} = C_{di}\sin\beta + C_{li}\cos\beta \qquad\qquad C_{ati} = C_{ti} \qquad (i=2,3,t)
\tag{3}
$$

In Eq. (3), β is the wind angle of attack (i.e. the angle between the mean wind velocity U and $\overline{\mathbf{a}}_2$ axis) and the coefficients $C_{\varepsilon i}$ ($\varepsilon = d, l, t$; $i=2,3,t$) are given by:

$$
C_{\varepsilon 2} = c_{\varepsilon 2}\sin\beta - 2c_{\varepsilon 1}\cos\beta \qquad\qquad C_{\varepsilon 3} = -c_{\varepsilon 2}\cos\beta - 2c_{\varepsilon 1}\sin\beta \qquad\qquad C_{\varepsilon t} = -c_{\varepsilon 1}'
\tag{4}
$$

$c_{\varepsilon i}$ ($\varepsilon = d,l,m$, $i=1,2$) being functions of the following aerodynamic coefficients:

$$
c_{d1} = c_d \qquad c_{l1} = c_l \qquad c_{m1} = c_m \qquad c_{d2} = -c_l + c_d' \qquad c_{l2} = c_d + c_l' \qquad c_{m2} = c_m'
\tag{5}
$$

By direct inspection, the exact solution of Eq. (1) is expressed as follows:

$$
u_2(s,t) = \sin\!\left(\frac{\pi s}{2\,l}\right)q_2(t) \qquad u_3(s,t) = \sin\!\left(\frac{\pi s}{2\,l}\right)q_3(t) \qquad \theta(s,t) = \sin\!\left(\frac{\pi s}{2\,l}\right)q_t(t)
\tag{6}
$$

Introducing the non-dimensional parameters:

$$\tilde{t}=\omega_3 t, \quad \tilde{q}_2=\frac{q_2}{b}, \quad \tilde{q}_3=\frac{q_3}{b}, \quad \tilde{q}_t=q_t, \quad \xi_2=\frac{c_2}{2m\omega_2}, \quad \xi_3=\frac{c_3}{2m\omega_3}, \quad \xi_\theta=\frac{c_\theta}{2I_1\omega_\theta}, \quad \tilde{x}_{2F}=\frac{x_{2F}}{b}, \quad \tilde{x}_{3F}=\frac{x_{3F}}{b},$$

$$\alpha_{23}=\frac{\omega_2}{\omega_3}, \quad \alpha_{\theta 3}=\frac{\omega_\theta}{\omega_3}, \quad \eta=\frac{I_1}{mb^2}, \quad \mu=\frac{U}{\omega_3 b}, \quad \nu=\frac{1}{2}\frac{\rho_a b^2}{m} \qquad (7)$$

ω_2, ω_3 and ω_θ being the circular frequencies of the building in the uncoupled case (i.e., symmetrical cross-section with respect to the reference axes; Luongo and Zulli 2011):

$$\omega_2^2=\frac{hK_2^f}{m}\left(\frac{\pi}{2\ell}\right)^2, \quad \omega_3^2=\frac{hK_3^f}{m}\left(\frac{\pi}{2\ell}\right)^2, \quad \omega_\theta^2=\frac{h\left(K^t+K^{tf}\right)}{I_1}\left(\frac{\pi}{2\ell}\right)^2 \qquad (8)$$

the equations of motion can be written in the following matrix form:

$$\mathbf{M}\ddot{\tilde{\mathbf{q}}}+\mathbf{C}_s\dot{\tilde{\mathbf{q}}}+\mathbf{K}_s\tilde{\mathbf{q}}=-\mu\mathbf{C}_a\dot{\tilde{\mathbf{q}}}-\mu^2\mathbf{K}_a\tilde{\mathbf{q}} \qquad (9)$$

where $\tilde{\mathbf{q}}$ is the vector of the non-dimensional principal coordinates, $\mathbf{M}$, $\mathbf{C}_s$, $\mathbf{K}_s$ are the structural mass, damping and stiffness matrixes:

$$\tilde{\mathbf{q}}=\begin{Bmatrix}\tilde{q}_2\\\tilde{q}_3\\\tilde{q}_t\end{Bmatrix} \quad \mathbf{M}=\begin{bmatrix}1&0&0\\0&1&0\\0&0&\eta\end{bmatrix} \quad \mathbf{C}_s=\begin{bmatrix}2\xi_2\alpha_{23}&0&0\\0&2\xi_3&0\\0&0&2\xi_\theta\alpha_{\theta 3}\eta\end{bmatrix} \quad \mathbf{K}_s=\begin{bmatrix}\alpha_{23}^2&0&-\tilde{x}_{3F}\alpha_{23}^2\\0&1&\tilde{x}_{2F}\\-\tilde{x}_{3F}\alpha_{23}^2&\tilde{x}_{2F}&\alpha_{\theta 3}^2\eta\end{bmatrix} \quad (10)$$

Furthermore, $\mathbf{C}_a$ and $\mathbf{K}_a$ are the aerodynamic damping and stiffness matrixes:

$$\mathbf{C}_a=\nu\begin{bmatrix}-C_{a22}&-C_{a23}&0\\-C_{a32}&-C_{a33}&0\\-C_{at2}&-C_{at3}&0\end{bmatrix} \quad \mathbf{K}_a=\nu\begin{bmatrix}0&0&-C_{a2t}\\0&0&-C_{a3t}\\0&0&-C_{att}\end{bmatrix} \qquad (11)$$

3   Linear bifurcation analysis

The reduced equations of motion, Eq. (9), can be rewritten in the following state-space form:

$$\dot{\mathbf{x}}=\mathbf{A}\mathbf{x} \qquad (12)$$

being $\mathbf{x}=\left\{\tilde{q}_2 \quad \tilde{q}_3 \quad \tilde{q}_t \quad \dot{\tilde{q}}_2 \quad \dot{\tilde{q}}_3 \quad \dot{\tilde{q}}_t\right\}^{\mathrm{T}}$ the state-space vector and $\mathbf{A}$ the state-space matrix given by:

$$\mathbf{A}=\begin{bmatrix}\mathbf{0}&\mathbf{I}\\-\mathbf{M}^{-1}\mathbf{K}&-\mathbf{M}^{-1}\mathbf{C}\end{bmatrix} \qquad \mathbf{C}=\mathbf{C}_s+\mu\mathbf{C}_a \qquad \mathbf{K}=\mathbf{K}_s+\mu^2\mathbf{K}_a \qquad (13)$$

From Eq.(13) it should be noted that the total damping of the structure is proportional to the nondimensional wind velocity μ, which acts as a bifurcation parameter. Linear bifurcation analysis is carried out by evaluating the complex eigenvalues and eigenvectors of the state-space matrix $\mathbf{A}$ as functions of μ. The classic Den Hartog criterion corresponds to the critical velocity μ_{DH} of the sole crosswind degree of freedom, $\tilde{q}_3$, and it is achieved when $\beta=0$ and $\mathbf{C}(2,2)=0$: $\mu_{DH}=-2\xi_3/\left[\nu\left(c_d+c_l'\right)\right]$.

A first numerical application is proposed, considering a building with an external square shape, mechanically symmetric with respect to $\overline{\mathbf{a}}_2$ ($\tilde{x}_{3F}=0$), with coincident natural frequencies in the orthogonal directions $\overline{\mathbf{a}}_2$ and $\overline{\mathbf{a}}_3$ ($\alpha_{23}=1$), $\xi_2=\xi_3=\xi_\theta=0.01$, $\nu=0.004$, $\eta=1/6$. The effects on critical conditions of the eccentricity between flexural and inertia center $\tilde{x}_{2F}$ and of the torsional-to-shear

frequency ratio $\alpha_{\theta 3}$ are analyzed. Figure 1 shows the ratio between the critical non-dimensional mean wind velocity and the Den Hartog limit value as a function of $\alpha_{\theta 3}$ and $\tilde{x}_{2F}$ assuming the mean wind velocity aligned with $\overline{\mathbf{a}}_2$, so that $\beta=0$ ($c_d = 2.09$, $c_l = 0$, $c_m = 0$, $c_d' = 0$, $c_l' = -5.69$, $c_m' = 0.196$). It is evident that the coupling between shear and torsion has always a stabilizing effect, which in many cases causes a significant increase of the critical wind velocity with respect to the classic Den Hartog criterion.
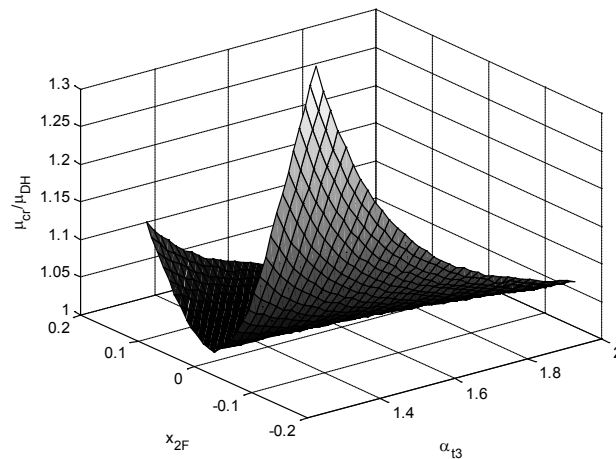
Figure 1. Ratio between the critical galloping velocity and the Den Hartog criterion as a function of $\alpha_{\theta 3}$ and $\tilde{x}_{2F}$.

It is currently under investigation the analysis of buildings excited along a generic direction (generally not aligned with a symmetry axis, $\beta \neq 0$).

Acknowledgments

References

Carpinteri, A., Lacidogna, G., and Puzzi, S. (2010). A global approach for three dimensional analysis of tall buildings, *The structural design of tall and special buildings* **19**, 518-536.

Cluni, F., Gioffrè, M. and Gusella, V. (2013). Dynamic response of tall buildings to wind loads by reduced order equivalent shear-beam models, *Journal of Wind Engineering and Industrial Aerodynamics* **123**, 339-348.

Dym, C.L. (2013). Approximating frequencies of tall buildings, *Journal of Structural Engineering ASCE* **139(2)**, 288-293.

Luongo, A. and Zulli, D. (2011). Parametric, external and self-excitation of a tower under turbulent wind flow, *Journal of Sound and Vibration* **330**, 3057-3069.

Piccardo, G., Tubino, F. and Luongo, A. (2014). An equivalent nonlinear beam model for the aeroelastic analysis of shear-type buildings, *Proc. VIIII European Conference on Structural Dynamics, EURODYN 2014,* July 2014, Oporto, Portugal, accepted.

The European project "Wind, Ports, and Sea"

M. Burlando[1], M.P.Repetto[1], G. Solari[1], P. De Gaetano[1], M. Pizzo[1], M. Tizzi[1], L. Iafolla[2,3], C. Carmisciano[2], V. Iafolla[3]

[1]Department of Civil, Chemical, and Environmental Engineering, University of Genoa, Italy
[2]Istituto Nazionale di Geofisica e Vulcanologia, (INGV), Sezione Roma2, sede Portovenere, Italy
[3]Assist in Gravitation and Instrumentation (AGI srl), Roma, Italy
Corresponding author: G. Solari, solari@dicat.unige.it

Abstract

This paper describes the European project "Wind, Ports, and Sea", which focuses on the safety management of the sea areas outside the main commercial ports in the Northern Tyrrhenian Sea. This project follows a previous European project, named "Wind and Ports", that focused on the safety management of the same port areas with reference to the problem of the wind effects on the land side, managed through the realisation of an integrated system including in situ wind monitoring, wind climatology evaluations, and the implementation of algorithms for medium- and short-term wind forecast. "Wind, Ports, and Sea" integrates "Wind and Ports", focusing on the sea side of the port areas, through the acquisition of new in situ wind and wave monitoring devices and the implementation of a wave forecast system coupled to the already existing wind forecast system.

1 Introduction

The European project "Wind, Ports, and Sea", financed by the European Cross-border Programme "Italy–France Maritime 2007-2013", aims at extending the results of the previous project "Wind and Ports" (Solari et al., 2012) to the sea outside the main ports of the Northern Tyrrhenian and Ligurian Seas, i.e. the Ports of Savona, Genoa, La Spezia, Livorno, Bastia, and Ile Rousse. The partnership, common to both the projects, consists of the University of Genoa, who is also the only scientific partner, the Port Authorities of Savona, Genoa, La Spezia, and Livorno, and the Chambre de Commerce et d'Industrie Territoriale de Bastia et de la Haute-Corse, who manages the Port of Bastia and Ile Rousse.

The "Wind and Ports" project, which lasted 3 years from July 2009 to June 2012, produced four main outcomes, common to all the above mentioned ports, apart from Ile Rousse that was not involved in the project at that time: a wind-monitoring network consisting of 23 sonic anemometers; the analysis and high-resolution mapping of the wind climatology in the port areas; a medium-term (up to +72 h) wind forecast system; a short-term (up to +1.5 h) wind forecast system. The project was intended to provide the Port Authorities with a set of tools to define operating strategies during real wind-induced risk conditions, in order to plan the work in safety conditions within their own port areas. Seaport areas are often exposed to high wind velocities, indeed, which can give rise to great risks for structures and infrastructures, ships and ferries approaching or docking in port, empty piled containers and, most of all, health hazard for workers, who need to work in safety conditions also on windy days, or stop working on extreme windy days. Moreover, too frequent and not regulated stops of the working activities inside the port areas can produce large economic losses. Therefore, the tools made available through the project were expected to be of great interest to all the stakeholders operating within the land-side of the port areas, e.g. terminal operators, ferries and cruise companies, etc.

The new project "Wind, Ports, and Sea", which started in June 2013 and will end in 2 years, is expected to produce two main outcomes: the strengthening of the existing monitoring network through the installation of new sensors to measure wind, waves, and the main meteorological parameters

(Section 2); and the implementation of a medium-term (up to +72 h) wave forecast system coupled to the existing medium-term wind forecast system (Section 3). The project, therefore, aims at integrating some of the outcomes realised in the framework of the "Wind and Ports" project by means of new tools that will provide the Port Authorities and their stakeholders with further information on the sea state conditions. The outcomes of the project are expected to be of great interest, in particular, for the pilots, the coast guard, and all the shipping companies, who are the main operators in the sea-side of the ports.

2   Installation of new monitoring devices

New monitoring devices will be installed in the framework of the project "Wind, Ports, and Sea" to integrate and strengthen the anemometric monitoring network realised during the "Wind and Ports" project. The new devices are intended to improve the already-implemented anemometric monitoring network, to provide new meteorological parameters, and to measure the sea state in terms of wave conditions. Figure 1 shows an overview of all the new devices that are being installed.

23 🟡 anemometers installed in the framework of "Wind and Ports"
5 🔵 weather stations (anemometer, barometer, thermometer, hygrometer)
3 🔴 LiDARs
3 🟤 seismometers + 1 🔵 buoy (pilot project in La spezia)
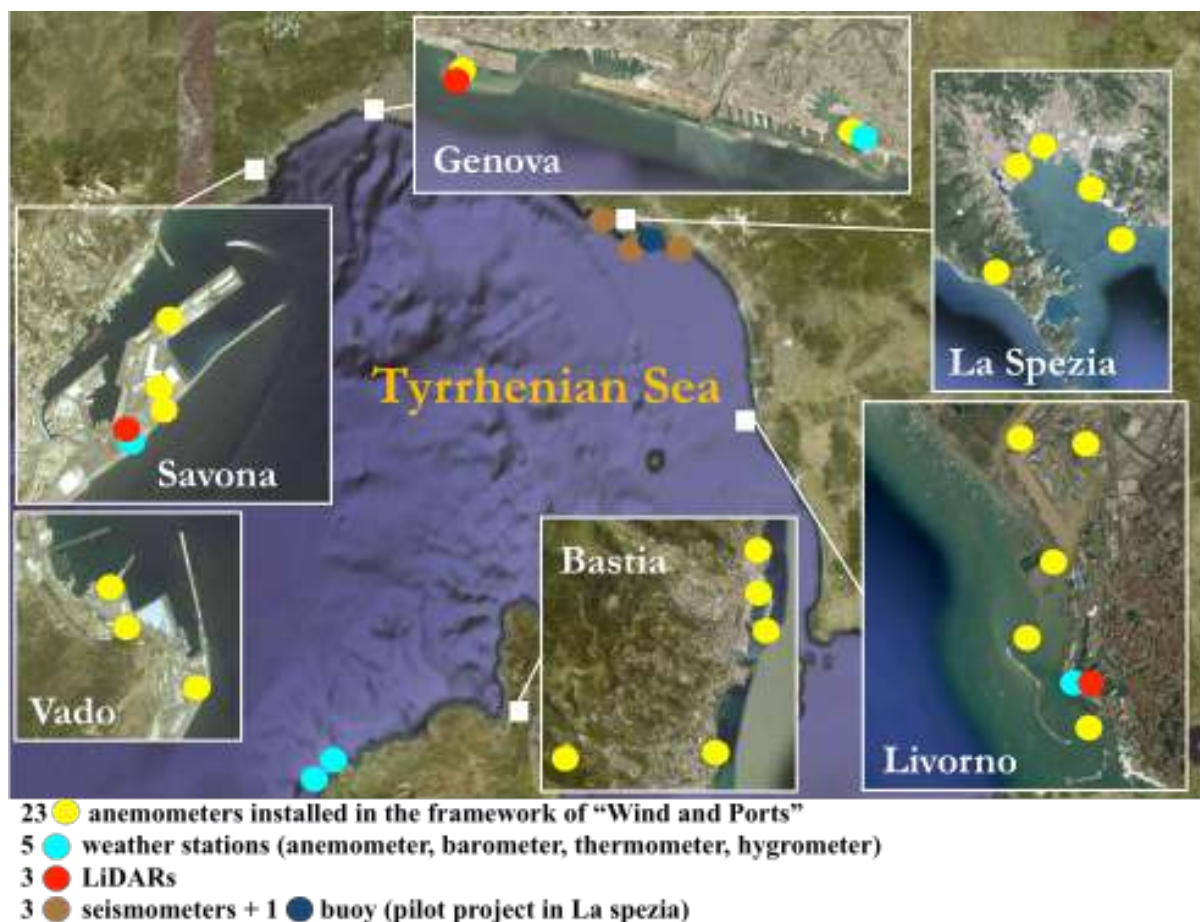
Figure 1. New monitoring devices that are being installed in the framework of the project "Wind, Ports, and Sea" with respect to the previously existing anemometric monitoring network.

The already-implemented anemometric monitoring network will be integrated with 3 weather stations mounted in the Port of Savona, Genoa, and Livorno, each one equipped with an ultra-sonic anemometer and the standard meteorological instruments to measure pressure, temperature, and humidity. Yet, 3 LiDARs (Light Detection And Ranging) will be installed in the Ports of Savona, Genoa, and Livorno, for the measurements of the vertical wind profiles up to a minimum height of about 150 m. Besides, 2 anemometric stations, equipped with ultra-sonic anemometers only, will be installed in the Port of Ile Rousse, where no anemometers had been placed during the "Wind and Ports"

project. Note that the two stations in the Port of Ile Rousse will allow obtaining a more evenly spaced coverage of the anemometric measurements in the Ligurian and Northern Tyrrhenian Sea, especially for the wind blowing from southwest (i.e. Libeccio), which is a very common wind condition in winter and it is usually quite strong. All the meteorological and anemometric measurements will be made available to the meteorological model (see Section 3) in order to provide it with very local data to assimilate through nudging techniques.

In the framework of a pilot project, three micro-seismic stations able to perform the sea-waves monitoring have been installed nearby the port of La Spezia. This technique is based on many experimental works done since the last century (Ardhuin, F. et al., 2012, Longuet-Higgins, 1950): it evaluates the significant height and the period of the sea-weaves by using the micro-seismic noise that they produce. More precisely, the sea-waves cause a variation of the pressure on the seafloor that produces a micro-seismic noise whose dominant frequency is the double of the sea-wave frequency. This micro-seismic signal can be detected inland even many kilometres far away from the coast, making possible indirect measurements of the sea state.

Each station is equipped with a high-sensitivity seismometer beside others sensors (weather station and GPS receiver) and a data-logger in order to provide multi-parameter measurements; a central server will collect and process the data from the three stations. Being inland, this system is much more reliable, maintainable and cost effective than other kinds of solutions (e.g. the buoys).

The main drawback is the difficulty of evaluating the waves height and period, which requires a good knowledge of the site and a preliminary calibration by comparison with a reference buoy. This calibration will be done during a first period of some months in which a temporary buoy anchored in La Spezia gulf will be used; after this characterization the buoy can be removed. Further developments of this method will be devoted to the evaluation of the direction of the sea-waves using the measurements from the three seismic stations.

3   Implementation of a coupled wind-wave forecast system

During the "Wind and Ports" project, a wind forecast system have been implemented based on two different numerical models: the meteorological model Weather Research and Forecasting (WRF), whose initial and boundary conditions are provided by the Global Forecast System (GFS), and the mass-consistent model WINDS (Burlando et al., 2007). This system calculates the wind forecast, every day, from 00 UTC to +72 h with a time-step of 1 h, through 3 runs of WRF and 2 runs of WINDS. Each run provides the wind forecast over a smaller and smaller domain with increasing resolution, as follows: the largest WRF domain covers all the Mediterranean Sea with a horizontal resolution of about 20 km and the forecast is performed with the initial and boundary conditions of the GFS; the second and third runs are performed by means of WRF through a 2-way nesting over two additional computational domains, centred over Italy and the Northern Tyrrhenian Sea, with an increasing horizontal resolution of 6.7 km and 2.2 km, respectively; the forth and fifth runs are performed by means of WINDS through a 1-way nesting within WRF, over two computational domains centred over the Province and the Port considered, with resolutions of about 230 m and 80 m, respectively.

In the framework of the "Wind, Ports, and Sea" project a new wave forecast system is being implemented that will be coupled to the already existing wind forecast system. The wave model adopted for this application (Sørensen et al., 2004) is a third generation spectral wind-wave model that simulates the growth, decay and transformation of wind-generated waves and swells in offshore and coastal areas. The model includes wave growth by action of wind, non-linear wave-wave interaction, dissipation by white-capping, wave breaking, and bottom friction, refraction due to depth variations, and wave-current interaction. This model will be connected to the meteorological model WRF through a pseudo-dynamic coupling, exchanging information each other every 1 h: on the one hand, the wind fields at 10 m height above the sea level produced by WRF will be the main input to the wave model to trigger the wind-generated wave conditions; on the other hand, the sea state will provide the meteorological model with updated, dynamic, and realistic boundary conditions as far as the sea surface roughness is concerned.

Figure 2 shows the extension of the computational domain of the currently-implemented wave model, which covers the whole Western Mediterranean Sea with a variable resolution ranging from about 16 km offshore in the Balearic Basin to 1 km along the coastline of Liguria, Tuscany, and Corsica regions. The unstructured triangular mesh and the bathymetry (shaded contours) are also represented.
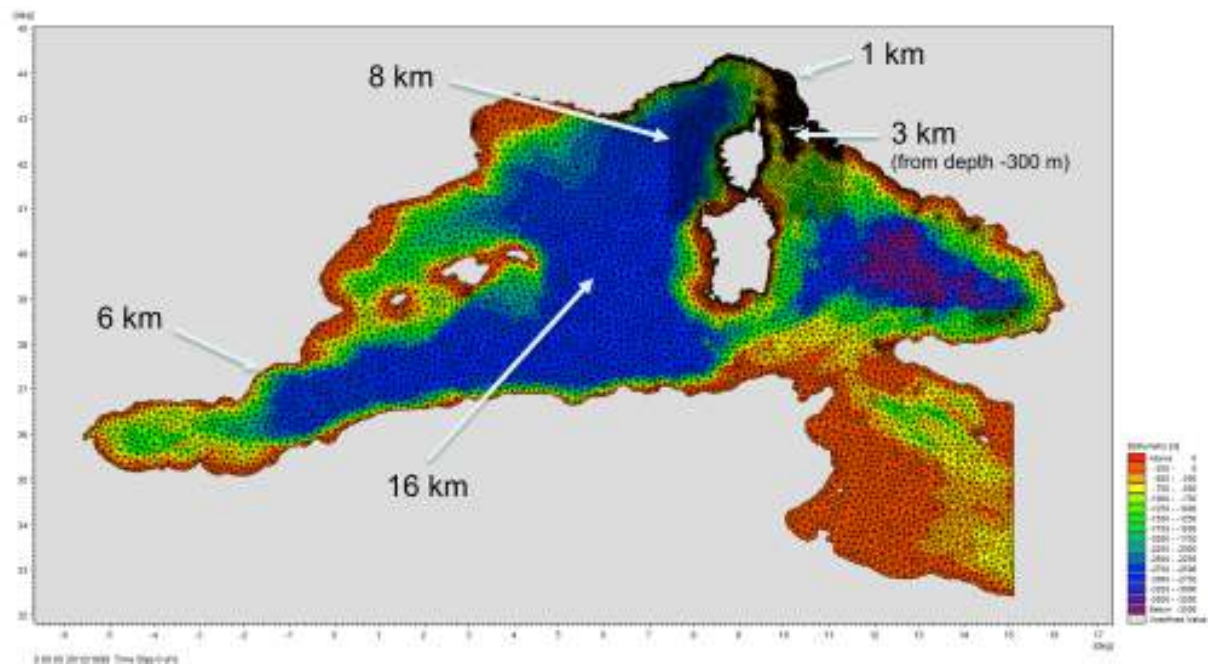
Figure 2. The extension of the wave model computational domain: bathymetry (shaded contours) and triangular mesh with the indication of the resolution for some different areas.

4   Conclusions

This paper provides an overview of the research activities related to a highly innovative project focusing on the wind and wave forecast in port areas. The system is realised through an integrated structure including numerical simulation models and in-situ monitoring, which are expected to provide new tools for the management and the safety of the port areas, especially for pilots, coast guard, and shipping companies.

References

Burlando, M., Georgieva, E., Ratto, C.F. (2007). Parameterisation of the planetary boundary layer for diagnostic wind models.*Boundary-LayerMeteorology,* **125**, 389-397

Solari, G., Repetto, M. P., Burlando, M., De Gaetano, P., Pizzo, M., Tizzi, M., and Parodi, M. (2012). The wind forecast for safety management of port areas. *Journal of Wind Eng. Ind. Aerodyn.***104-106**, 266–277.

Sørensen, O.R., Kofoed-Hansen, H., Rugbjerg, M., Sørensen, L.S. (2004). A third generation spectral wave model using an unstructured volume technique. *29th International Conference of Coastal Engineering, 19-24 September, Lisbon, Portugal.*

Ardhuin, F., Balanche, A., Stutzmann, E. Obrebski M. (2012). From seismic noise to ocean wave parameters: General methods and validation. *Journal of Geophysical research,* **117**, C05002, 1-19

Longuet-Higgins, M. S. (1950). A theory of the origin of microseisms. *Phylos. Trans. R. Soc. A,* **243**, 1-35

Efficient estimation of the high-order response statistics of a wind-excited oscillator with nonlinear velocity feedback

Vincent Denoël[1], Luigi Carassale[2]

[1]Structural Engineering Division, University of Liège, Belgium
[2]Dept. of Civil Chemical and Environmental Engineering, University of Genova, Italy
Corresponding author: Vincent Denoël, Vincent Denoël, v.denoel@ulg.ac.be

Abstract

The point-like quasi-steady aerodynamic loading in a turbulent flow is formally expressed as a function of the squared relative velocity between the fluid and the investigated structure. The three major terms governing the low-order statistics of the response are known to be related to the average loading, the linear turbulent loading and the aerodynamic damping. The three other terms in the loading, namely the quadratic turbulence term, the parametric velocity feedback term and the squared velocity term, may significantly affect the higher order statistical cumulants of the response. These latter two sources of fluid-structure interaction are usually disregarded, by lack of efficient simulation tools, except a Monte Carlo simulation of the nonlinear equation. In this paper, we provide a formal analysis of the complete nonlinear model, including thus all six terms, but mainly focusing on the importance of the two nonlinear coupling terms of the loading. Closed form solutions of the response are derived for a second-order Volterra model of this problem, under the assumption of different timescales in the loading and in the structural behaviour. Two major outcomes of the analysis are, on the one hand, that the squared structural velocity term has no influence on the cumulants of the response up to order 4 and, on the other hand, that the parametric velocity feedback acts as a reduction of the non Gaussianity of the response.

1 Introduction

The response of civil engineering structures to the wind turbulence is a multiple timescale process. Indeed, in a linear context, the structural response to very low frequency turbulence excitation may be approached by a sum of two components, a background component associated with the slow dynamics of the excitation and a fast resonant component associated with the structural timescale (Davenport, 1961).

The stochastic structural analysis of a linear structure subject to a stationary excitation, such as the wind turbulence, is usually performed with a spectral approach. While offering a clear understanding of the structural behaviour and the dispatching of energy in the different timescales, this approach also sidesteps the heavy generation of the wind velocity or pressure time histories. The stochastic approach is a useful tool to determine the Gaussian, but also non-Gaussian, response of a linear system. One drawback perhaps is that the evaluation of high-order statistics requires a multi-dimensional integration of spectral densities in spaces whose dimension increases with the order of the cumulants of the response under investigation. The application of the method in the context of non-Gaussian responses thus turns out to be challenging, from a computational viewpoint. This drawback is partly circumvented by considering the existence of the different timescales in the response. Doing so, the multiplicity of the integrals to be computed is decreased by one, which substantially speeds up the computation (Denoël, 2014).

In this paper, the concept described above is extended to the study of a linear oscillator whose excitation is defined as a quadratic function of the wind-structure relative velocity. The analysis still relies on a spectral approach and the structural system is modelled as a Volterra system (e.g. Schetzen, 1980). Developments are limited to the second-order Volterra operator which is shown to be accurate enough for the statistics up to order 4. The efficiency of the method is discussed with the determination

of the first four cumulants of the response. The quality of the result is assessed in terms of accuracy with respect to a reference solution obtained through Monte Carlo simulation. Under the quasi-steady assumption, the response of a point-like single degree-of-freedom structure subject to a 1-dimensional wind turbulence is governed by the nonlinear second order differential equation

$$m\ddot{x} + c\dot{x} + kx = \frac{1}{2}\rho C_d A\left(U + u - \dot{x}\right)^2 \tag{1}$$

where $x(t)$ is the structural displacement, m, c and k are mass, viscosity and stiffness, respectively, U is the mean wind velocity and $u(t)$ a Gaussian zero-mean random process representing the wind velocity fluctuation; ρ, A and C_d are, respectively, the air density, the area of the structure exposed to the wind and the aerodynamic drag coefficient. The overhead dot denotes differentiation with respect to time t. The nonlinearity of this equation results from the squared structural velocity $\dot{x}^2(t)$ and the parametric excitation $-2\dot{x}(t)u(t)$ terms obtained in the right-hand side after expansion.

The zero-mean Gaussian turbulence process $u(t)$ is fully described by its power spectral density $S_u(\omega)$. Following Kolmogorov's energy cascade, typical models for the turbulence decrease as $\omega^{-5/3}$ in the high-frequency range. This non Markovian behaviour makes any stochastic method based on the FPK equation and moment equation rather intricate since a proper approximation with a Markovian process has to be formulated. This argument drove the solution procedure of the considered problem toward spectral methods. It is thus possible to handle realistic power spectral densities of the wind turbulence such as

$$S_u\left(\omega;\frac{L}{U}\right) = \sigma_u^2 \frac{0.546\dfrac{L}{U}}{\left(1 + 1.64\dfrac{L}{U}|\omega|\right)^{5/3}} \tag{2}$$

in which L represents the integral length scale and σ_u the standard deviation of the turbulence velocity.

This problem might be formulated in a dimensionless manner leading to the governing equation

$$\tilde{x}'' + 2\left(\xi_s + \xi_a\right)\tilde{x}' + \tilde{x} = \frac{1}{2I_u} + \tilde{u} + \frac{1}{2}I_u\tilde{u}^2 - 2I_u\xi_a\tilde{u}\tilde{x}' + 2I_u\xi_a^2\tilde{x}'^2 \tag{3}$$

where the following dimensionless quantities are used

$$\begin{aligned}
\tilde{x} &= \frac{k}{\rho A C_d I_u U^2}x, & \tilde{u} &= \frac{u}{\sigma_u}, & \tilde{t} &= \sqrt{\frac{k}{m}}t = \omega_0 t, \\
\xi_s &= \frac{c}{2m\omega_0}, & \xi_a &= \frac{\rho A C_d U}{2m\omega_0}, & \alpha &= \frac{U}{L\omega_o}
\end{aligned} \tag{4}$$

and where a prime $'$ denotes differentiation with respect to the nondimensional time $\tilde{t}$. The power spectral density $S_{\tilde{u}}(\tilde{\omega};\alpha)$ of the dimensionless turbulence velocity $\tilde{u}$ is a function of the dimensionless frequency $\tilde{\omega}$ and of the small parameter α, which is the ratio of the characteristic turbulence frequency U/L and the structural natural frequency ω_0. The two coefficients ξ_s and ξ_a represent the structural and aerodynamic damping coefficients.

This formulation indicates that the solution of the problem at hand may evolve in different regimes, depending on the relative smallness of ξ_s, ξ_a and α. These three numbers are typically in the range $[10^{-3};$ $10^{-1}]$. A fourth small parameter of the problem is the turbulence intensity I_u, usually in the range $[10\%;$ $30\%]$, which scales the quadratic turbulence term and the nonlinear feedback terms on the right hand side of Eq. (3). The dimensionless version of the governing equation readily shows that the quadratic velocity term x'^2 is one order of magnitude smaller than its left neighbour ux', the parametric excitation

term, which presumably indicates that the former one would yield negligible contribution to the response. This is to be proved with a more formal derivation. Although the dimensionless version of the governing equation is definitely more convenient to identify the leading physics and its limiting cases, the paper is mainly developed with physical quantities, so as to provide a simpler understanding.

2   Second order Volterra model

2.1   The Volterra Frequency Response Functions

Inspired by former works (Carassale & Kareem, 2010), it is chosen to model the response of this nonlinear problem with a second order Volterra model. This choice is validated in Section 5, with the typical orders of magnitude of the parameters encountered in wind engineering applications.

In this framework, the response $x(t)$ is approximated as

$$x(t) \simeq x_o + x_1(t) + x_2(t) \tag{5}$$

where $x_1(t)$, respectively $x_2(t)$, is defined as the first (resp. second) order convolution of the zero-mean Gaussian input $u(t)$ with the Volterra kernel $h_1(t)$, respectively $h_2(t)$. In a stationary setting, this definition is advantageously translated into the frequency domain with the symmetrical Volterra frequency response functions (VFRF) $H_1(\omega)$ and $H_2(\omega_1,\omega_2)$.

These functions need to be established for the specific nonlinearity of the problem under consideration. This may be achieved with the harmonic probing technique (Bedrosian & Rice, 1971) or with the systematic procedure presented in Carassale & Kareem (2010). The same procedure as that developed in the later one has been used to derive the VFRFs as:

$$H_1(\omega) = \frac{\rho C_d A U}{D(\omega) + j\omega\rho C_d A U},$$

$$H_2(\omega_1,\omega_2) = \frac{\rho C_d A}{2} \frac{\left(1 - j\omega_1 H_1(\omega_1)\right)\left(1 - j\omega_2 H_1(\omega_2)\right)}{D(\omega_1 + \omega_2) + j(\omega_1 + \omega_2)\rho C_d A U} \tag{6}$$

where $D(\omega) = -m\omega^2 + j\omega c + k$ is the inverse of the FRF defining the mechanical part of the system.

These frequency response functions are sketched in Figure 1. The first one corresponds to the classical frequency response function of a linear oscillator, with additional aerodynamic damping. The second represents the interaction between the different harmonics in the response, especially the filtering of pairs of harmonics (ω_1, ω_2) that fall out of the band $|\omega_1 + \omega_2| \simeq \omega_o$.

2.2   Cumulants of the stationary response

In a second-order Volterra model, the total response is expressed as the sum in Eq. (5) involving the 0th-order constant term x_0, together with the fluctuating terms $x_1(t)$ and $x_2(t)$. When the input $u(t)$ is a stationary random process, the statistical properties of the total response $x(t)$ may be expressed in terms of its cumulants, which in turn can be written as functions of the cumulants of $x_1(t)$ and $x_2(t)$. Using some classical developments in the theory of probability (e.g. Papoulis, 1965) under the hypothesis that $u(t)$ is Gaussian distributed, we obtain

$$\kappa_2[x] = \kappa_2[x_1] + \kappa_2[x_2]$$

$$\kappa_3[x] = 3\kappa_3[x_1, x_1, x_2] + \kappa_3[x_2] \tag{7}$$

$$\kappa_4[x] = 6\kappa_4[x_1, x_1, x_2, x_2] + \kappa_4[x_2]$$

where $\kappa_k[\bullet]$ (when used with a single argument) represents the kth-order cumulant of its argument and $\kappa_k[\bullet,...,\bullet]$ represents the kth-order cross-cumulant associated with the product of the arguments.
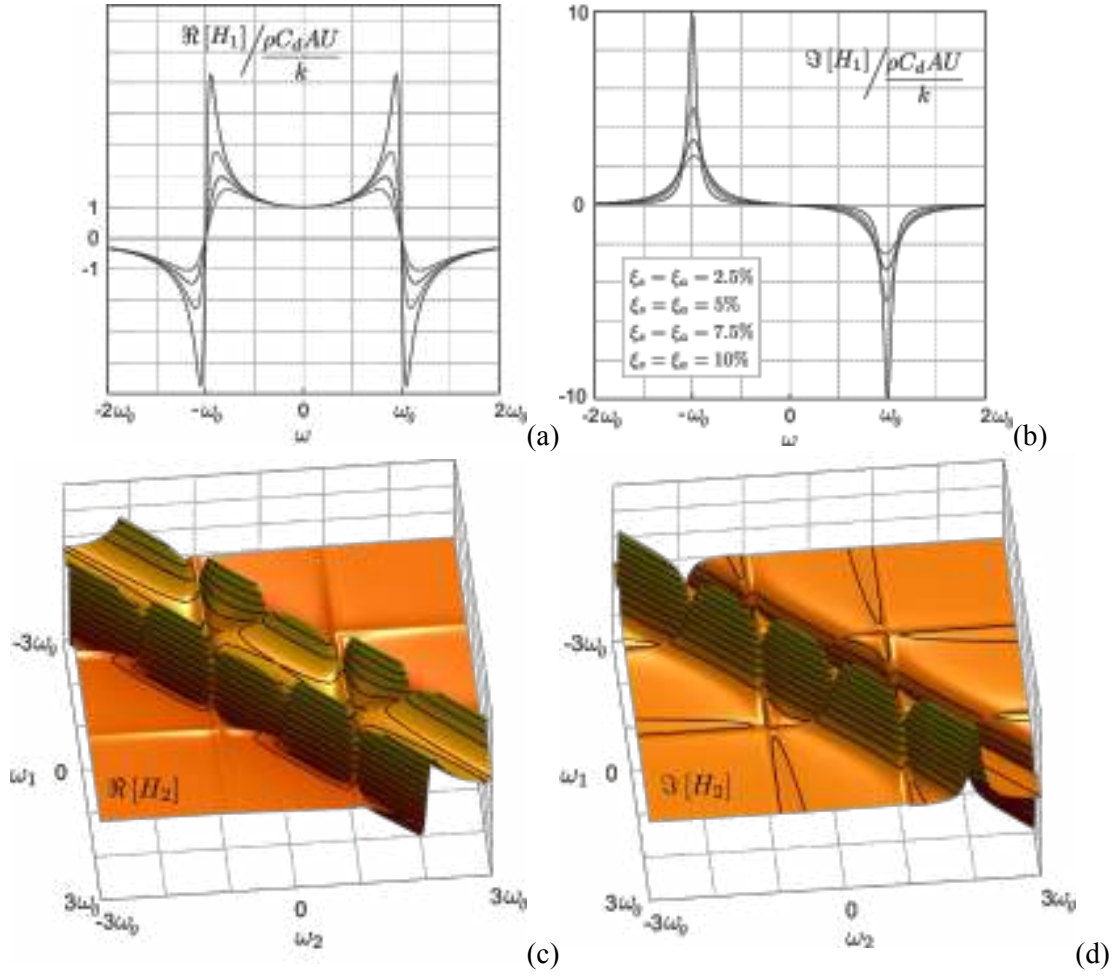
Figure 2. Second-order frequency response function ($\xi_s = \xi_a = 5\%$).

An analysis of the orders of magnitude of the two terms that compose each cumulant of the response reveals that the second terms in the expressions given in (7) are negligible in front of the first terms, at least for the small realistic values of the aerodynamic damping ξ_a encountered in typical wind engineering applications. The formal demonstration of this statement goes beyond the scope of this paper, but is available in Denoël and Carassale (2014) together with a deeper investigation of this problem.

Intuitively however, the second order response $x_2(t)$ is one or several orders of magnitude smaller than the first order response $x_1(t)$. The ratio of these two actually scales with the aerodynamic damping ξ_a. As a consequence, in Eq. (7), the cross-cumulant, involving more factors in $x_1(t)$ than the unilateral cumulants of $x_2(t)$ are expected to be leading.

2.3   *Power spectral density and higher order spectra of the response*

The power spectral density of the total response $x(t)$ of a second-order Volterra model reads

$$S_x(\omega) = |H_1(\omega)|^2 S_u(\omega) + 2 \int_{-\infty}^{+\infty} |H_2(\omega_1, \omega - \omega_1)|^2 S_u(\omega_1) S_u(\omega - \omega_1) \mathrm{d}\omega_1 \tag{8}$$

where $S_u(\omega)$ is the power spectral density of the turbulence, while H_1 and H_2 represent the Volterra frequency response functions, as given in (6).

The integration of the power spectral density $S_x(\omega)$ provides the second cumulant of the total response

$$\kappa_2[x] = \int\limits_{-\infty}^{+\infty} S_x(\omega)\,d\omega \tag{9}$$

Substitution of (8) into (9) indicates that the cumulant of the response is composed of two terms, as hinted by (7) anyway. The first one, involving $|H_1(\omega)|$, is responsible for the linear counterpart of the response $\kappa_2[x_1]$, while the second term, involving the second-order frequency response function $|H_2(\omega_1,\omega_2)|$ provides the second contribution $\kappa_2[x_2]$ to the total cumulant, after integration along the real axis. Following the former observation that the second terms in (7) are negligible, the second term in the power spectral density of the total response is dropped.

It finally turns out that the second order response is that of a linear system whose total damping is represented by the sum of the structural and aerodynamic damping. In this context, there exists a classical way to bypass the numerical integration of $S_x(\omega)$ in (9). It is based on the background/resonant decomposition of the response, a two-timescale approximation of the response usually attributed to the pioneering works of Davenport (1961). In this method, the variance of the response is simply expressed as the sum of a background and a resonant component as

$$\kappa_2[x] \simeq \kappa_2[x_1] \simeq (1+r)\kappa_{2,B} \tag{10}$$

where

$$\kappa_{2,B} = \left(\frac{\rho C_d A U \sigma_u}{k}\right)^2 ; \quad r = \frac{S_u(\omega_o)}{\sigma_u^2}\frac{\pi\omega_o}{2(\xi_s+\xi_a)} \tag{11}$$

are readily interpreted as the background response and the resonant-to-background ratio.

One major advantage of this two-timescale method is that it sidesteps any integration and offers an approximate solution of the problem at no computational costs. Extension of this method to higher-order statistics was the key motivation for the consideration of this problem as a Volterra model.

Similarly to the power spectral density, the bispectrum of the total response $x(t)$ is composed of two terms, among which only the first one is retained in the analysis, as it is responsible for the contribution $3\kappa_3[x_1, x_1, x_2]$ to the third cumulant. The bispectrum of the response is thus approximated as

$$
\begin{aligned}
B_x(\omega_1,\omega_2) = {} & 2H_1(-\omega_1-\omega_2)H_1(\omega_1)H_2(\omega_1+\omega_2,-\omega_1)S_u(\omega_1+\omega_2)S_u(\omega_1)+ \\
& +2H_1(-\omega_1-\omega_2)H_1(\omega_2)H_2(\omega_1+\omega_2,-\omega_2)S_u(\omega_1+\omega_2)S_u(\omega_2)+ \\
& +2H_1(\omega_1)H_1(\omega_1)H_2(-\omega_1,-\omega_2)S_u(\omega_1)S_u(\omega_2)
\end{aligned}
\tag{12}
$$

and the third cumulant of the response is approximated by

$$\kappa_3[x] \simeq 3\kappa_3[x_1,x_1,x_2] = \int\limits_{-\infty}^{+\infty}\int\limits_{-\infty}^{+\infty} B_x(\omega_1,\omega_2)\,d\omega_1\omega_2 \tag{13}$$

Similarly again, the trispectrum of the total response $x(t)$ is composed of two terms, among which only the first one is considered. In this simplified version, it reads

$$
\begin{aligned}
T_x(\omega_1,\omega_2,\omega_3) = 4\sum_{\substack{\alpha,\beta,\gamma=1,2,3\\ \alpha\neq\beta\neq\gamma}} & H_1(\omega_\alpha)S_u(\omega_\alpha)\Big[H_1(\omega_\beta)H_2(-\omega_\alpha,-\omega_\beta-\omega_\gamma)H_2(\omega_\beta+\omega_{\alpha_3},-\omega_\beta)S_u(\omega_\beta)S_u(\omega_\beta+\omega_\gamma)+ \\
& +H_1(-\omega_\alpha-\omega_\beta-\omega_\gamma)H_2(-\omega_\alpha,\omega_\alpha+\omega_\gamma)H_2(\omega_\alpha+\omega_\beta+\omega_\gamma,-\omega_\alpha-\omega_\gamma)S_u(\omega_\alpha+\omega_\beta+\omega_\gamma)S_u(\omega_\alpha+\omega_\gamma)\Big]
\end{aligned}
\tag{14}
$$

where the summation is performed on all six possible permutations of the indexes α, β, $\gamma = 1, 2, 3$. The fourth cumulant of the response is thus approximated by

$$\kappa_4[x] \simeq 6\kappa_4[x_1, x_1, x_2, x_2] = \int\limits_{-\infty}^{+\infty}\int\limits_{-\infty}^{+\infty}\int\limits_{-\infty}^{+\infty} T_x(\omega_1, \omega_2, \omega_3)\, d\omega_1\, d\omega_2\, d\omega_3 \qquad (15)$$

The purpose of the rest of the paper is to provide simple expressions for the integrals in (13) and (15).

3   Multiple Scale Spectral Analysis & Analysis of the Model

3.1   *Cumulants of the response*

The multiple timescale spectral analysis is a recent technique that allows decreasing by one (at least) the order of integration in the determination of the cumulants of the response. It hinges on the timescales separation between the loading and the structure and is able to deal with linear/nonlinear structures, stationary/evolutionary problems, SDOF/MDOF problems, and is fundamentally not limited regarding the statistical order (Denoël, 2014). The method is elaborated in the frequency domain and is not contingent upon the markovianity of the loading process; it thus deals with any complex analytical expression of the power spectral density of the loading –such as those that characterize the wind turbulence– without any artefact. The technique actually generalizes the background/resonant decomposition of the variance (Davenport, 1961) and the background/biresonant decomposition of the third cumulant (Denoël, 2011) of the response of a single degree-of-freedom linear system subject to slow stochastic loading.

Application of the general method requires the identification, in the response spectra, of the different components to the response. Among them the background component is easily identified. Its trivial subtraction from the initial response spectra leaves us with resonant and mixed background/resonant terms. Examples of applications in (Denoël, 2014) give some hints on how to determine and approximate these components.
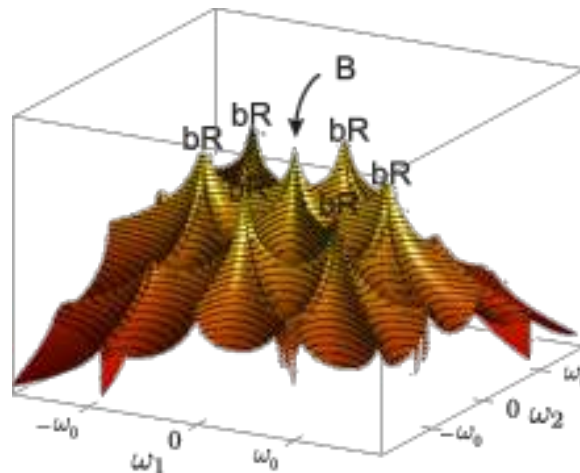
Figure 2. Sketch of the bispectrum of the response, (12).

At third order, the bispectrum of the response is expressed by (12) at leading order. This function is represented in Figure 2 which illustrates the background component as a central peak of the frequency space as well as six peaks, coined as *biresonance peaks* as they correspond to resonance in two factors out of three in the each term of $B_x(\omega_1, \omega_2)$. These peaks are located at $(\omega_1, \omega_2) = (\pm\omega_o, 0)$, $(0, \pm\omega_o)$ and $(\pm\omega_o, -\omega_o)$.

The background contribution to the integral in (13) is obtained by replacing the frequency response functions H_1 and H_2 by their local behaviour in Eq. (12), i.e. $H_1(\omega) = \rho C_d A U/k$ and $H_2(\omega_1, \omega_2) = \rho C_d A/2k$, which yields

$$\kappa_{3,B} = 3I_u \left(\frac{\rho C_d A U \sigma_u}{k} \right)^3 \tag{20}$$

Applying the procedure recommended in the multiple timescale spectral analysis, the additional contribution of the biresonance peaks is obtained as

$$\kappa_{3,R} = r \kappa_{3,B} \frac{2\xi_s + \xi_a}{\xi_s + \xi_a} \Psi_1 \tag{16}$$

with r the second-order resonant-to-background ratio introduced in (11) and

$$\Psi_1\left(S_u(\omega);\omega_o;\xi\right) = \int\limits_{-\infty}^{+\infty} \frac{S_u(\omega)}{\sigma_u^2} \frac{4\xi^2\omega_o^2}{\omega^2 + 4\xi^2\omega_o^2} d\omega \tag{17}$$

and where the shorter notation $\xi = \xi_s + \xi_a$ is used. The total cumulant of the response is finally written as the sum of the background and biresonant components, $\kappa_{3,B} + \kappa_{3,R}$.

The appreciable outcome of the method is that the order of integration to determine the third cumulant of the response has dropped from 2, in Eq. (13), to 1 in Eq. (17), as a result of the timescale separation.

A graphical representation of the trispectrum of the response (14) is a bit more involved as it concerns a function of three parameters. However the generic procedure developed at the third order may be replicated. It reveals the existence of four types of peaks, namely (i) a background peak located at the origin, as usual, (ii) four A-type mixed background-resonant peaks located in $(\omega_1,\omega_2,\omega_3)=\pm(\omega_o,0,-\omega_o)$ and $(\omega_1,\omega_2,\omega_3)=(\omega_o,\pm\omega_o,0)$, (iii) two B-type mixed background-resonant peaks located at $(\omega_1,\omega_2,\omega_3)=\pm(0,\omega_o,-\omega_o)$ and (iv) four (purely) resonant peaks located at $(\omega_1,\omega_2,\omega_3)=\pm(\omega_o,\omega_o,-\omega_o)$ and $(\omega_1,\omega_2,\omega_3)=\pm(\omega_o,-\omega_o,-\omega_o)$.

The natures of these peaks are different because they each maximize different factors in the expression of the trispectrum. To keep it simple, the background peak corresponds to the only possible value of $(\omega_1, \omega_2, \omega_3)$ that maximizes the factors in S_u, while the four resonant peaks correspond to the four possible combinations of $(\omega_1, \omega_2, \omega_3)$ that maximize three out of the four factors in H_1 or H_2. Mixed A- and B-type peaks maximize one (or two) factors in H_1 or H_2 and two (resp. one) factors in S_u.

Resorting again to the basic principles of the multiple timescale spectral analysis (Denoël, 2014), the integral in Eq. (15) can be approximated by the sum of the four terms:

$$\kappa_{4,B} = 12I_u^2 \left(\frac{\rho C_d A U \sigma_u}{k} \right)^4 ; \qquad\qquad \kappa_{4,BR_I} = r \kappa_{4,B} \frac{2\xi_s + \xi_a}{\xi_s + \xi_a} \Psi_1 ;$$

$$\kappa_{4,BR_{II}} = r \kappa_{4,B} \left(\Psi_2 - \frac{\xi_a}{\xi_s + \xi_a} \Psi_3 \right); \qquad \kappa_{4,R} = r^2 \kappa_{4,B} \frac{\xi_s + \dfrac{\xi_a}{2}}{\xi_s + \xi_a} \Psi_1 \tag{18}$$

with $\Psi_2(S_u(\omega);\omega_o;\xi)$ and $\Psi_3(S_u(\omega);\omega_o;\xi)$ are defined as

$$\Psi_2 = \int\limits_{-\infty}^{+\infty}\int\limits_{-\infty}^{+\infty} \frac{S_u(\omega_1)}{\sigma_u^2} \frac{S_u(\omega_2)}{\sigma_u^2} \frac{4\xi^2\omega_o^2}{(\omega_1 - \omega_2)^2 + 4\xi^2\omega_o^2} d\omega_1 d\omega_2 \tag{19}$$

$$\Psi_3 = \int\limits_{-\infty}^{+\infty}\int\limits_{-\infty}^{+\infty} \frac{S_u(\omega_1)}{\sigma_u^2} \frac{S_u(\omega_2)}{\sigma_u^2} \frac{2\xi^2\left[32\xi^4\omega_o^4 + \omega_1\omega_2\left(8\xi^2\omega_o^2 + (\omega_1 - \omega_2)^2\right)\right]}{\left(\omega_1^2 + 4\xi^2\omega_o^2\right)\left(\omega_2^2 + 4\xi^2\omega_o^2\right)\left((\omega_1 - \omega_2)^2 + 4\xi^2\omega_o^2\right)} d\omega_1 d\omega_2 \tag{20}$$

In our formulation, integrals are hidden in the coefficients Ψ_1, Ψ_2 and Ψ_3, but the dimensionality of the integrals is limited to 2, or even to 1 when mixed background-resonant components are dropped (which unfortunately degrades the quality of the result, see Denoël, 2012).

3.2 Skewness and Excess Coefficients

The skewness and excess coefficients of the response are readily obtained from the corresponding cumulant. With the multiple timescale approximation, they read

$$\gamma_3 = 3I_u \frac{1 + r \frac{2\xi_s + \xi_a}{\xi_s + \xi_a} \Psi_1}{(1+r)^{3/2}}; \quad \gamma_e = 12I_u^2 \frac{1 + r \left(\frac{2\xi_s + \xi_a}{\xi_s + \xi_a} \Psi_1 + \Psi_2 - \frac{\xi_a}{\xi_s + \xi_a} \Psi_3 \right) + r^2 \frac{\xi_s + \frac{\xi_a}{2}}{\xi_s + \xi_a} \Psi_1}{(1+r)^2} \tag{21}$$

What this model offers is a simple and attractive procedure for the computation of the skewness and excess coefficients of the nonlinear response of the considered problem. These coefficients are simply expressed as a function of the resonant-to-background ratio denoted by r, the damping coefficients, structural and aerodynamic, as well as the coefficients Ψ_1, Ψ_2 and Ψ_3 which holds the remaining computational issues.

Interestingly enough, these latter coefficients have closed-form asymptotic expressions, for large and small values of the total damping coefficient. The relative smallness has to be assessed by comparison with the ratio of the characteristic frequency of the wind velocity turbulence and that natural frequency of the structure, α introduced in (2). For instance, one may observe that all three factors tend to 1 when $\xi \gg \alpha$. This makes the estimation of the skewness and excess coefficients of the response promptly accessible.

The amplitude of the nonlinearity scales with the magnitude of the aerodynamic damping, see (2). For small values of that parameter, the response is still non-Gaussian as a result of the square transformation of the wind velocity turbulence u^2. In the limit case, the structural behavior is linear and the current formulation degenerates into existing approximation based on the multiple timescale spectral analysis too (Denoël, 2011). What mainly matters here is that the non-Gaussianity of the response (measured by the magnitude of the skewness and excess coefficients) decreases as some nonlinear feedback is injected into the structure. This is readily observed by substituting ξ_a by 0 in Eqs. (21); the coefficients of Ψ_1, Ψ_2 and Ψ_3 are systematically decreased. This validates the following statement. The differentiation in the feedback loop acts as a high-pass filter of the structural response. It is well known that the non-Gaussianity of the response mainly results from the low-frequency content while the resonant component of the response is simply Gaussian. Consequently the correction to the open-loop system is more or less Gaussian and this tends to diminish the non-Gaussianity of the loading. The model described in this paper is a simple tool to quantify this return to the Gaussian distribution.

The few details that were communicated in this paper are not really sufficient to understand that the local approximations of the kernel, that allowed the derivation of the low-dimensional integral solutions, are actually not affected by the presence of the square velocity feedback. In other words, the squared structural velocity $\dot{x}^2(t)$ term is definitely negligible in front of the parametric excitation $-2\dot{x}(t)u(t)$ term, no matter the values and relative smallness of the parameters of this problem. The only limitation on this observation is that the timescales remain well separated.

At last but not least, another interesting case is that of a small dynamic amplification, in the second-order sense, i.e. $r \ll 1$. In that case, both the mixed and resonant contributions vanish and the skewness and excess coefficients of the response match those of the quadratic transformation of the Gaussian wind velocity turbulence, i.e. $\gamma_3 = 3I_u$ and $\gamma_e = 12I_u^2$.

4   Numerical application

A Monte Carlo simulation of the original nonlinear system (1) and of its 2nd-order Volterra series approximation (5) provides realizations of the total response $x(t)$, as well as of the terms $x_1(t)$ and $x_2(t)$

of the Volterra series approximation. With the help of an online averaging method, the raw moments of $x(t)$, $x_1(t)$, $x_2(t)$ are readily obtained. They are finally translated into cumulants, as they offer a more convenient understanding. Figure 3 shows the comparison of the skewness (a) and coefficient of excess (b) of the full nonlinear response $x(t)$ (blue surface) and its Volterra series approximation $x_1(t)+x_2(t)$ (red surface). It can observed that, within the considered parameter space, the 2nd-order Volterra system provides a perfect representation of the skeness and a slight overestimation of the coefficient of excess. Figure 4 shows the comparison, again in terms of skewness (a) and coeffient of excess (b), of the solution provided by the numerical integration of the 2nd-order Volterra series (blue surface) and by the proposed analytical solution (red surface). The analytical solution provides a good estimation of skewness, while tends to overestimate a bit the numerical results. A good agreement is observed in the region of high aerodynamic damping and low structural damping, which is the most relevant from a technical point of view.

As far as the computational efficiency is concerned, it should be emphasized that the analytical solution is extremely convenient when the two timescales involved in the problem are very different from each other, i.e. α is small. In this case, indeed, the Monte Carlo simulation requires the integration of very long time series using a small time step. For example, the computation of the results shown in Figures 3 and 4 (400 points of the parameters space) required about five minutes for the analytical solution and about 2500 hours CPU time for the Monte Carlo simulation (mostly used for the solution of the full nonlinear system).

(a)   (b)
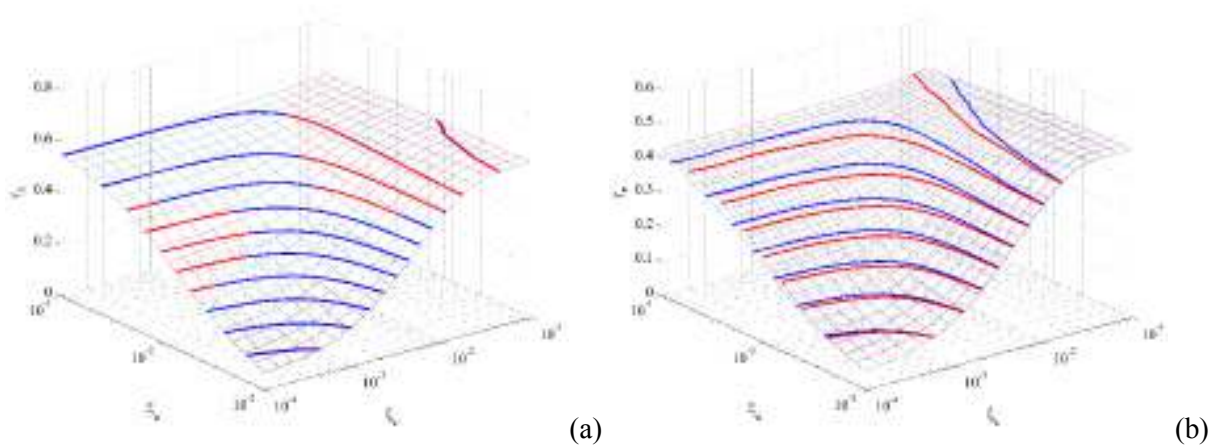
Figure 3. Skewness (a) and coefficient of excess (b) of full nonlinear response (blue) and 2nd-order Volterra series approximation (red).

(a)   (b)
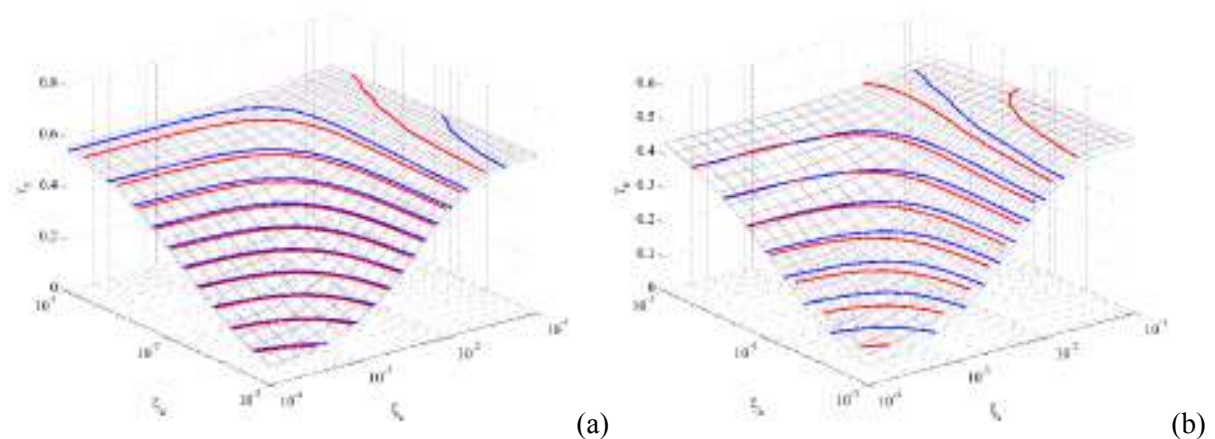
Figure 4 Skewness (a) and coefficient of excess (b) of 2nd-order Volterra series approximation (blue) and analytical solution (red).

5   Conclusions

There are two main contributions in this paper. The first one concerns the derivation of the very general solution, expressed as accurate approximations though, of the stochastic response of a second-order Volterra model. Equations presented in this paper are rather general and might be applied in other fields or problems, as long as the timescales separation hypothesis holds.

The second contribution concerns the application to a classical problem of wind engineering, namely the influence of the nonlinear quadratic velocity and parametric loading terms arising in a quasi-steady aerodynamic loading. Although not given with full details, the derivation demonstrates that the parametric loading term is mainly responsible for the non-Gaussianity of the response, while the squared structural velocity term has very few influence. As an interesting outcome too, it is demonstrated that the nonlinear quadratic velocity feedback systematically reduces the skewness and excess coefficients of the loading.

References

Davenport , A. G. (1961). The application of statistical concepts to the wind loading of structures. *Proceedings of the Institute of Civil Engineers* **19**, 449-472.

Denoël, V. (2014), Multiple Timescale Spectral Analysis. *Probabilistic Engineering Mechanics*. *Submitted*.

Schetzen, M. (1980). *The Volterra and Weiner theories of nonlinear systems*. John Wiley & Sons, Inc., New York.

Carassale, L. and Kareem A. (2010). Modeling nonlinear systems by Volterra Series. *Journal of Engineering Mechanics* ASCE **136**, 801-818.

Bedrosian, E. and Rice S. O. (1971). Output properties of Volterra systems (nonlinear systems with memory) driven by harmonic and Gaussian inputs. *Proceedings of the IEEE* **59**(12), 1688-1707.

Papoulis, A. (1965). *Probability, Random Variables, and Stochastic Processes*. New York, McGraw Hill.

Denoël, V. and Carassale L. (2014). Response of an oscillator to a random quadratic velocity-feedback loading. *Under preparation*.

Feijoo, J. A. V., Worden, K. and Stanway, R. (2005). Associated linear equations for Volterra operators. *Mechanical Systems and Signal Processing* **19**(1): 57-69.

Denoël, V. (2011). On the background and biresonant components of the random response of single degree-of-freedom systems under non-Gaussian random loading. *Engineering Structures* **33**(8): 2271-2283.

Denoël, V. (2012). Extension of the Background/biResonant decomposition to the estimation of the kurtosis coefficient of the response. *Uncertainty in Structural Dynamics 2012. Leuven, Belgium*.

Qualitative analysis of the motion-excited forces acting on a square prism

Luigi Carassale, Andrea Freda and Lorenzo Banfi

Department of Civil Engineering, University of Genoa, Italy
Corresponding author: Luigi Carassale, luigi.carassale@unige.it

Abstract

Unsteady aerodynamic forces on moving bodies are often classified as Vortex Induced Excitation and Motion Induced Excitation. These two classes of forces coexist and interact with each other in rather complicated manner. In order to shed some light on this phenomenon an experimental campaign involving pressure measurements of a square prism with controlled motion has been carried out. A preliminary analysis of the results includes the study of the mean force coefficients as a function of the motion frequency and amplitude, the harmonic analysis of the force fluctuation and the quantification of the motion excited forces in terms of amplitude and phase.

1 Introduction

Unsteady aerodynamic forces acting on a body exposed to a smooth flow are often classified into two categories. The Vortex Induced Excitation (VIE) is due to flow instabilities appearing in the neighbourhood of the body generating unbalanced time-variant pressure distributions. The Motion Induced Excitation (MIE) is produced by the body motion and disappears when the body is fixed. The mentioned classification is somehow arbitrary and has mostly a conventional value. VIE and MIE are, indeed, deeply coupled and are subject complicated interactions. It is well known, for example, that VIE can be affected by the body motion when its frequency is close to the Karman Vortex Shedding (KVS) frequency, giving rise to the lock-in phenomenon. On the other hand, when the body motion is very slow (i.e. its time scale is much slower that KVS time scale) VIE and MIE tend to be independent of each other and the quasi-steady formulation is employed to model MIE, while a stochastic model may be used to represent VIE. Between these two extreme conditions, a number of interactions phenomena exist making the development of phenomenological models challenging.

In order to shed some light on interaction between VIE and MIE, a series of tests has been carried out in the wind tunnel at the University of Genova. To this purpose, an experimental rig designed to test prisms moving in cross-flow direction with harmonic motion has been realized.

This paper described some results obtained using the mentioned facility to test a prism with square cross section. The results are mostly described from a qualitative point of view, however useful quantities such as mean force coefficients, power spectra density function of the fluctuation, as well as amplitude and phase of motion-excited forces are reported. Differently from previous published contributions (e.g. Bearman & Obasaju 1892; Bearman 1984; Sarpkaya 2004) the emphasis is not focussed on the lock-in region, but on the VIE-MIE interaction phenomena.

2 Experimental setup

The experimental setup is constituted by a square prism moving in cross-flow direction according to a controlled harmonic motion. The size of the prism cross-section is b = 50mm and its length in l = 500 mm. The angles of incidence investigated are α = 0°, 6° and 12°. The aerodynamic forces are estimated from the measurement of the pressure along an instrumented ring with 20 pressure taps located at the mid span of the model and connected to a pressure scanner mounted on-board. The

harmonic motion is generated by a crankshaft driven by an electric motor regulated in velocity by a closed-loop controller. The model is connected to the shaft by a long rod pinned on a flywheel. The investigated motion frequency is in the interval $f_m = 0.7 - 17.5$ Hz. Three amplitudes of motion are considered, namely $Y = 5, 10, 15$ mm corresponding to the ration $b/Y = 10\%$, 20% and 30%. The wind velocity is in the range $U = 5 - 20$ m/s, which corresponds to the range of Reynolds number $Re = 1.6 \cdot 10^4 - 6.6 \cdot 10^4$ and Reduced Frequency (RF) $f_m b/U = 2 \cdot 10^{-2} - 0.17$ or reduced velocity $U/f_m b = 5.9 - 200$.

Figure 1. Experimental setup.

3   Mean aerodynamic forces

Mean drag and lift coefficients are defined as:

$$C_D(f_m) = \frac{\mathrm{E}[D(t)]}{\frac{1}{2}\rho b U^2}; \qquad C_L(f_m) = \frac{\mathrm{E}[L(t)]}{\frac{1}{2}\rho b U^2} \qquad (1)$$

where D and L are, respectively, the drag and lift forces and ρ is the air density; $\mathrm{E}[\bullet]$ is the expectation operator that is implemented as a time average over time intervals in which the motion frequency is constant and equal to f_m.

Figure 2 shows C_D and C_L plotted as functions of the RF. For $\alpha = 0°$, C_D slowly decreases from its static value as the RF increases until a value about 0.10-0.12 where the coefficient drops. This change of behaviour corresponds to the lock-in region, which is expected in the neighbourhood of the Strouhal number, S_t, which for the static square prism is about 0.12. After this value of RF the static value of C_D is recovered, but another drop follows immediately. As the amplitude of motion increases, the behaviour remains qualitatively unchanged, but the region in which the drag drops becomes larger in terms of RF. The lift coefficient remains close to zero in the whole RF range.

For α = 6°, the behaviour of C_D is qualitatively similar to what has been observed for α = 0° with the relevant exception of the presence of a narrow peak for $f_m b/U = 0.07$. C_L is relatively independent of the RF for $Y/b = 10\%$, while its fluctuation increases for higher motion amplitudes. In particular, a discontinuity at $f_m b/U = 0.7$ appears and a significant reduction (in terms of absolute value) at high RF is well visible.

For α = 12°, the behaviour appears significantly different from the two cases above. C_D tends to increase as the RF increases and has two evident positive peaks that appear for $f_m b/U = 0.07$ and 0.12. C_L decreases (in terms of absolute value) as the RF increases reaching a value about 1/3 of the static one for $f_m b/U = 0.12$ and $Y/b = 30\%$. A further difference with respect to the previous cases is in the low RF range. For α = 0° and 6° the mean aerodynamic forces are practically independent of the motion amplitude for low RF (for α = 6° there is no amplitude effects until $f_m b/U = 0.06$). On the contrary, for α = 12°, both C_D and C_L departs from their static values with significantly different trends.
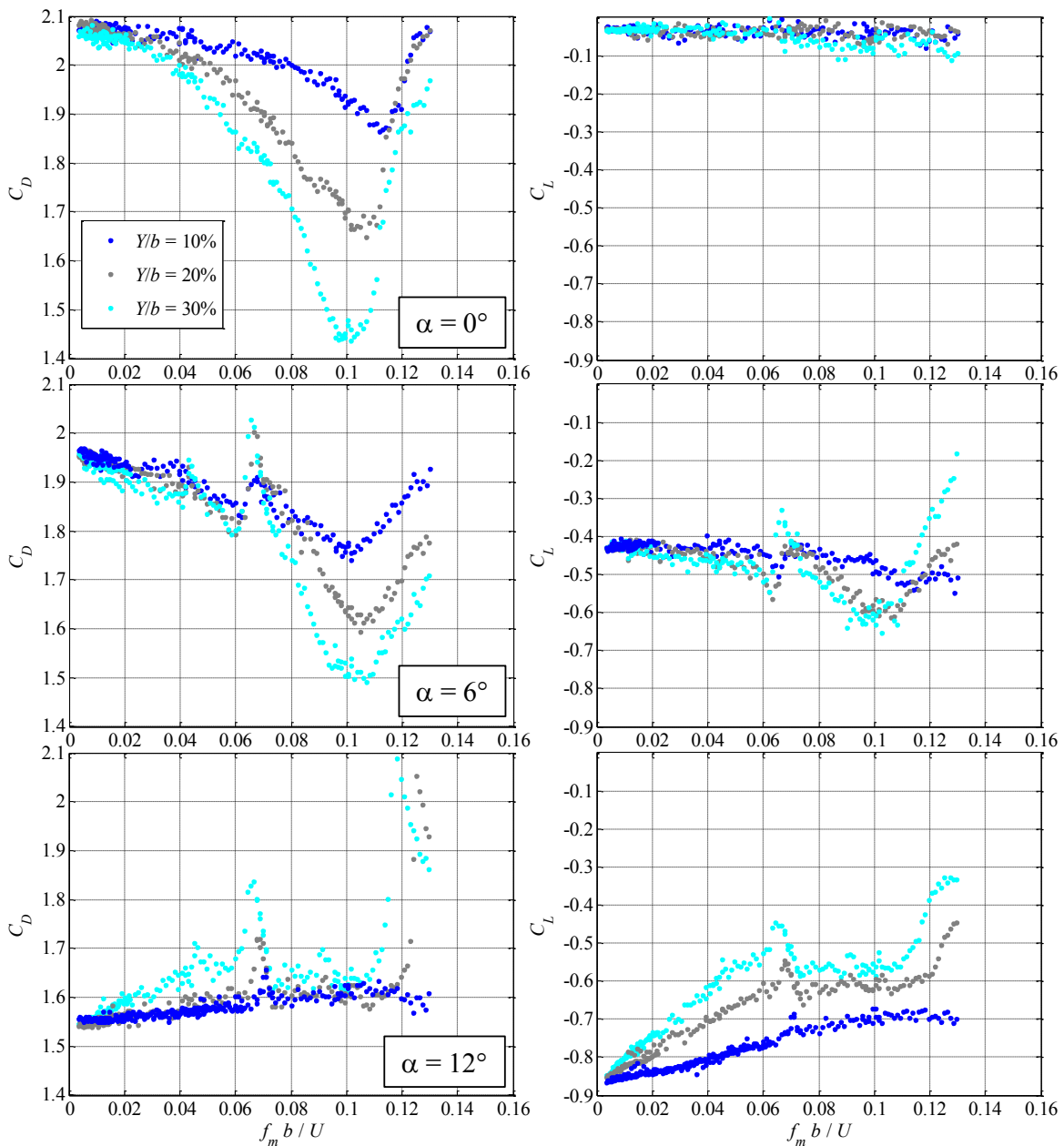
Figure 2. Mean drag and lift coefficients as functions of the RF.

4   Harmonic analysis of the fluctuating forces

This section describes the results of the harmonic analysis of the aerodynamic forces. For this purpose, the Power Spectral Density (PSD) function of the drag and lift forces is defined as:

$$S_X(f, f_m) = \frac{1}{T} \mathrm{E}\left[\left| \tilde{X}_T(f) \right|^2 \right] \qquad (X = L, D) \tag{2}$$

where $\tilde{X}_T(f)$ is the Fourier transform of $X(t)$ within a time window of length T and the expectation $\mathrm{E}[\bullet]$ is implemented as the statistic average including all the time windows in which the motion frequency is equal to f_m.
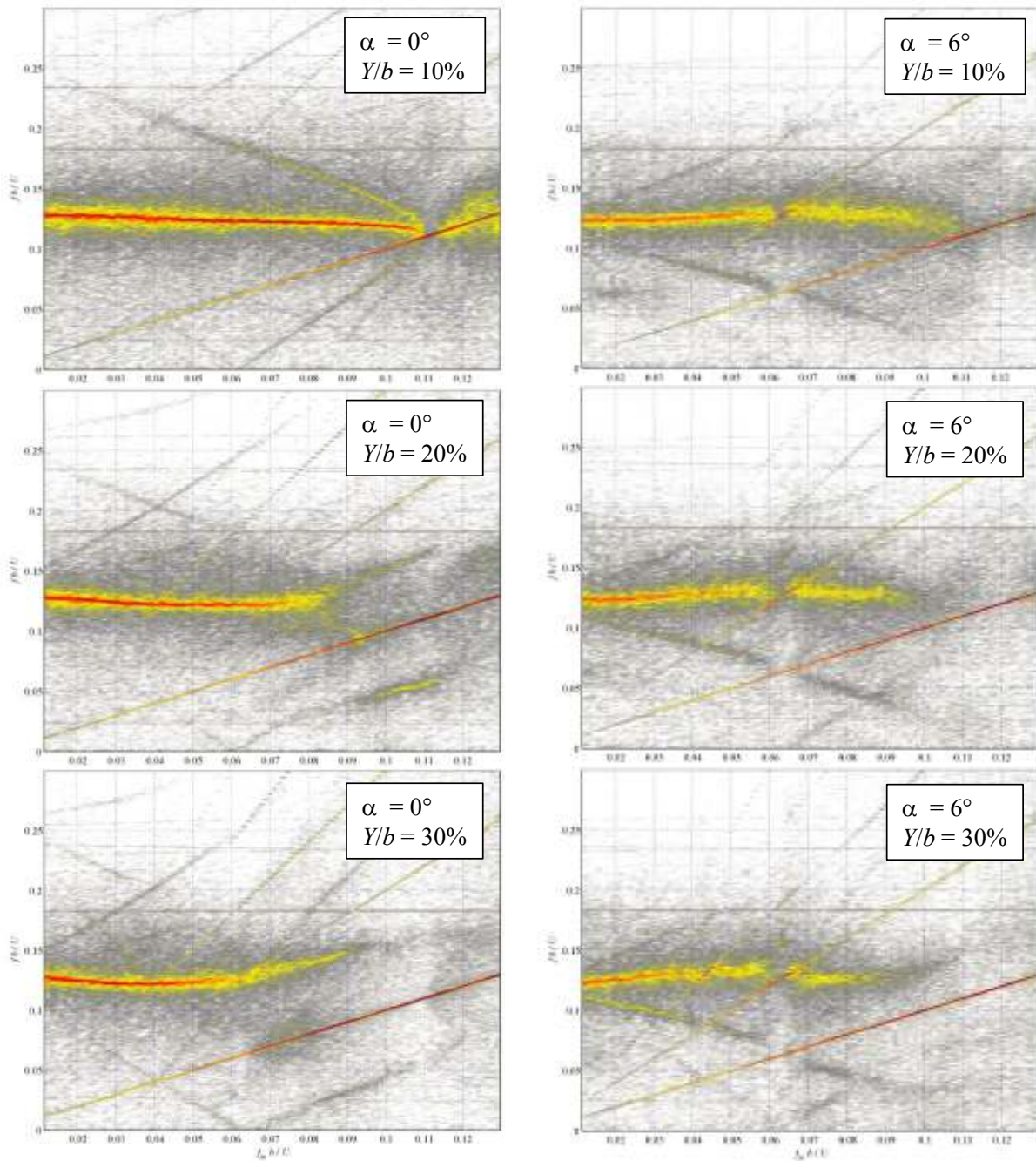
Figure 3. PSD maps of the lift force for $\alpha = 0°$ and $6°$; $Y/b = 10\%$, 20% and 30%.

Figure 3 shows colour maps representing S_L as a function of f_m and f, for $\alpha = 0°$ and $6°$ and for different motion amplitudes. In all the figures the motion frequency is well visible, as well as the KVS. Besides, traces of interaction between motion and KVS, which reflects into harmonics with sum and difference frequencies are well evident. For all the considered cases, the frequency of KVS is significantly affected by the RF. For $\alpha = 0°$, it tends to decreases as the RF increases, until KVS disappears due to lock-in. It must be emphasised that before disappearing, the frequency of KVS is attracted by motion frequency for $Y/b = 10\%$, while it is repelled for higher motion amplitudes. It can be observed that the width of the lock-in region increases as the motion amplitude increases. For the case of $\alpha = 6°$, the second harmonics of the motion is visible due to the lack of symmetry of the configuration. This harmonics produces a lock-in at $f_m U/b$ about 0.07, which justify the discontinuity in the mead aerodynamic coefficients observed in Figure 2.

5   Synchronous MIF

This section investigates the behaviours of the lift harmonic component that is synchronous with the motion. The amplitude and of such harmonics are represented through the complex-valued quantity:

$$H(f_m) = \frac{1}{\frac{1}{2}\rho Y U^2 T} \mathrm{E}\left[\int_0^T L(t) e^{2\pi \mathrm{i} f_m t}\,\mathrm{d}t\right] \qquad (3)$$

where the expectation represents the statistic average of the quantities evaluated for all the time intervals of length T in which the motion frequency is equal to f_m.

Figure 4 shows the function H in terms of amplitude and phase. The prediction given by the quasi-steady formulation is represented through a black dashed line. For $\alpha = 0°$ the lock-in region is well identified by the amplitude increment and by the sharp phase shift. The amplitude of H is almost independent of the motion amplitude (which means that the force amplitude increases linearly with the motion amplitude) in the low RF range. In the lock-in region $|H|$ decreases as the motion amplitude increases. The phase angle between motion and force is $\pi/2$ for very low RF and goes quickly to a value about $\pi/4$. For $\alpha = 6°$ a discontinuous trend for $f_m b/U$ about 0.06 - 0.07 is well visible and is related to the lock-in of KVS with the second harmonics of motion. The phase angle shifts progressively from π to $-\pi/2$ as the RF increases. For $\alpha = 12°$ the behaviour appears to be more complicated. In particular, two concurrent configurations have been observed in the low RF range for $Y/b = 10\%$. From a preliminary analysis it appears that the existence of the two configurations is governed by the Reynolds number. It can be observed that, in contrast with the quasi-steady prediction, both these configurations are stable (phase angle in the green area in Figure 4).

6   Closing remarks

Some experimental results including drag and lift forces on an oscillating square-section prism have been presented. Intense and complicated interactions between VIE and MIE have been observed, event well far from the lock-in region. In particular, for non-symmetric configurations lock-in on the second harmonics of the motion (i.e. about a RF half of S_t) has been clearly observed.

The comparison of amplitude and phase of the lift force component synchronous with the motion with the prediction of the quasi-steady formulation suggests several considerations. For $\alpha = 0°$ the quasi-steady formulation provides accurate results in terms of amplitude in the low RF range; the prediction of the phase angle, on the contrary, is accurate only for $f_m b/U$ tending to zero, i.e. extremely high reduced velocities. For $\alpha = 6°$ the amplitude prediction is still accurate (for low RF), but the phase observed experimentally does not tend to the quasi-steady value for $f_m b/U$ tending to zero. For $\alpha = 12°$ it appears that the quasi-steady formulation is totally unable to predict motion-excited forces.
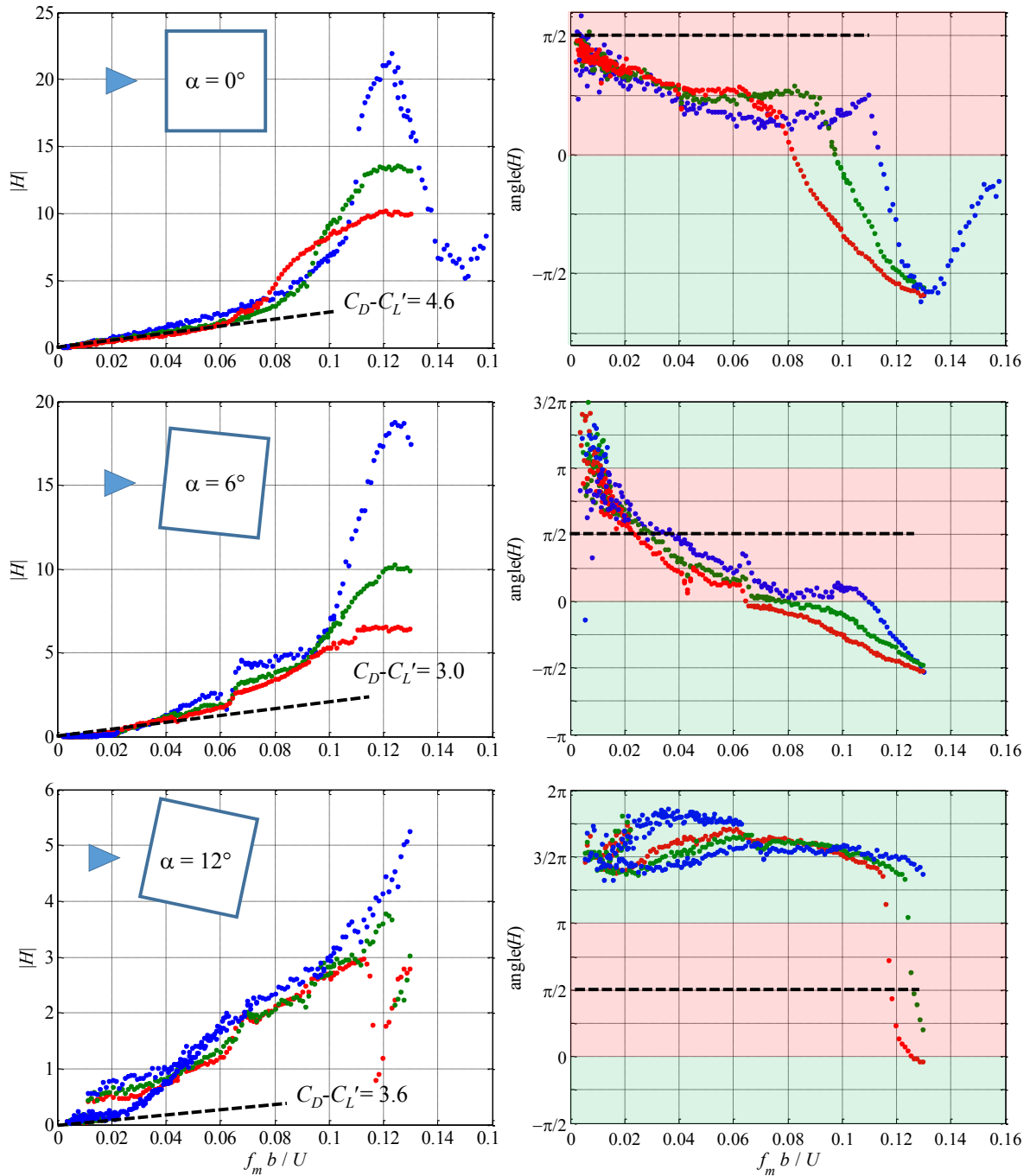
Figure 4. Amplitude and phase of the synchronous lift force. Motion amplitude Y/b = 10% (blue), 20% (green), 30% red. Stable region (green), unstable region (red). Quasi-steady prediction (black dashed line).

References

Bearman, P W. and Obasaju, E. D. (1892). An experimental study of pressure fluctuation on fixed and osciallting square-section cylinders. *Journal of Fluid Mechanics* **119**, 297–321.

Bearman, P. W. (1984). Vortex shedding from oscillating bluff bodies. *Ann. Rev. Fluid Mech*. **16**, 195-222.

Sarpkaya, T. (2004). A critical review of the intrinsic nature of vortex-induced vibrations. *Journal Fluids and Structures* **19**, 389-447.

The debate on the strengthening of San Gaudenzio dome in Novara (1931-1945): a contribution to the history of wind engineering

Chiara Calderini and Luisa C. Pagnini[1]

[1] Department of Civil, Environmental & Chemical Engineering
University of Genoa, Italy
C`rresp`nding auth`r: Chiara Calderini, chiara.calderini@unige.it

Abstract

The consolidation of the San Gaudenzio Basilica carried out between 1931 and 1945 raised a heated debate dealing with the dynamic response of the structure under wind actions and the reliability of the monitoring system. The dispute was held by Arnaldo Daverio (1909-1990) and Arturo Danusso (1880-1968), distinguished engineer and professor of Structural Mechanics that was charged with consolidating the Basilica after it suffered serious damages. The history of the debate that followed the consolidation intervention appears particularly interesting for the modernity of the topic discussed. It was carried out raising hypotheses and arguments that show the arduous path undertaken during the twentieth century on this aspect of structural engineering.

1 Introduction

There are many reasons for interest in the history of the S. Gaudenzio basilica, and in particular in the succession of failures and consolidation that it suffered between 1931 and 1945. Concerning wind engineering, two points should be considered. Firstly, at the time (and even today) the basilica was one of the highest (121 m) masonry buildings in Europe. As well as the Mole Antonelliana in Turin (163 m), it was designed by Alessandro Antonelli in the second half of XIX century. It was recognized as one of the best expressions of masonry art in Europe, but it appeared undoubtedly audacious for its epoch (and even for us). Secondly, the failures and consolidation interventions that it suffered raised a heated debate concerning the dynamic response of the structure to wind actions. This debate may appear rather naïve if seen with contemporary eyes; however, it is an interesting historical statement of how wind engineering and structural dynamics had developed in Italy. The interest in the debate is strengthened by the consideration that the role of protagonist was played by one of the most influential Italian engineers of his time, pioneer of structural dynamic and seismic engineering in Italy: Arturo Danusso.

2 The history of consolidation interventions

Figure 1 shows the main parts of the structure and the terms used for their description. The building is 121 m high and its base diameter is approximately 20 m. The structure is made of brick masonry (except for the small dome which is made of granite), with numerous metallic bindings. The Fabbrica Lapidea, which will be mentioned many times in the text, is the organization that has administered thebasilica since the sixteenth century, overseeing the building, maintenance and functional modifications. Antonelli's cupola was built above the pre-existing body of the S. Gaudenzio basilica designed by Pellegrino Tibaldi during the sixteenth century. The first alarm for the structural safety of the building was felt between 1882 and 1883, when some cracks were found in the structures at the base of the cupola, in particular in the large pre-existing base pillars (Daverio, 1940). Antonelli

himself took care of monitoring and consolidating the structure, partly rebuilding the pillars and/or underpinning them. The cracks, however, raised many doubts about the safety of the structure, and, more in general, about Antonelli's work. While he was consolidating the structure, numerous opinions were requested; a commission of experts was appointed in 1882 and an anonymous letter requesting the sending of a technical commission to Novara ''*t` witness the imminent and very seri`us danger*'' was sent to the Minister of the Interior in 1883 (Daverio, 1940, p. 130). It is worth noting that, in this period, Antonelli continuously demanded freedom of action, because he had ''*the resp`nsibility f`r the w`rk that was being carried `ut in the basilica*'' (Daverio, 1940, p.138), while the administration claimed the very same responsibility ''*in as much as `ne is dealing with public safety*'' (Daverio, 1940, p. 138).
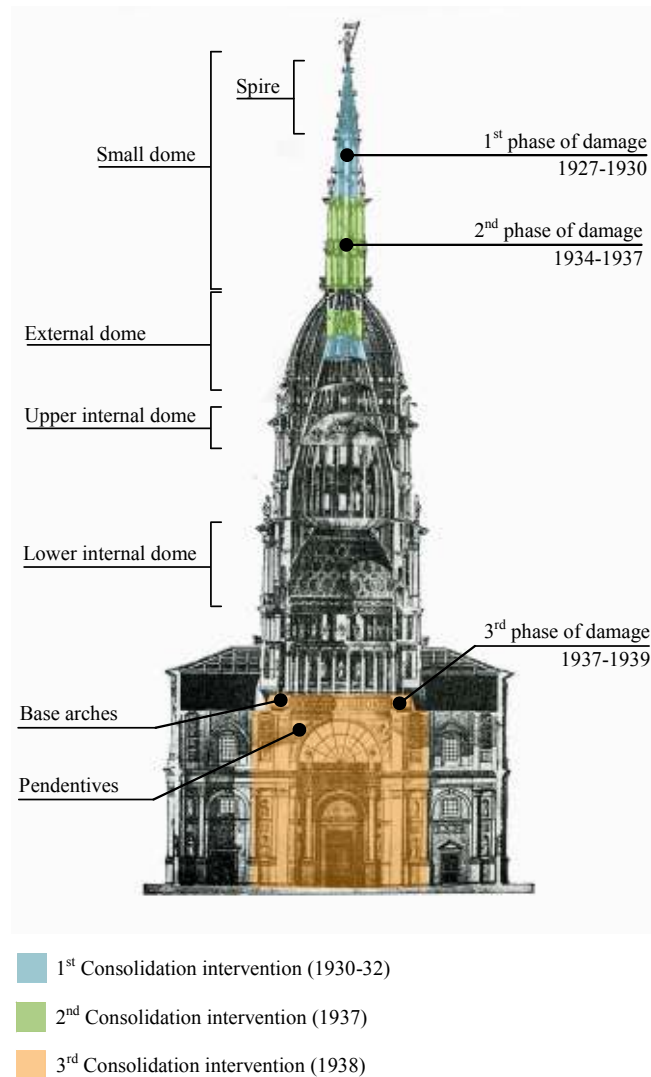
Figure 1. Section of the S. Gaudenzio basilica (from Caselli, 1877), containing the names attributed to the main parts of the building and information on the phases of damage and the consolidation interventions.

The consolidation works ended, despite everything, in 1885. Then, there followed a period of calm in which doubts about the safety of the building were no longer raised. A new phase of alarms began as a consequence of the sudden collapse of the Sanctuary of Boca, on August 29, 1907. Public opinion was struck by the news and the local press fomented a sentiment of mistrust among the population towards the building. There were similar reactions two years later, following the great earthquake of Messina and Reggio Calabria (Daverio, 1940). The memory of the uncertainties that emerged in the previous century about the structural safety of Antonelli's cupola was still alive. The technical reports written in those years were all aimed at testifying how the ancient cracks had not worsened and how, in general, the static conditions of the structure had not changed (Daverio, 1940). Actually, a totally new problem

was emerging: the failures on the small dome (Figure 1 —first phase of damage). The first failures on the small dome, consisting in slight cracking in the joints of the granite masonry structure, were found at the end of the nineteenth century. They worsened progressively until 1922, when cracks in the highest columns first appeared (SG1). The causes of the failures were traced back to the oscillations produced at the top of the cupola by the wind and the effect of freeze–thawing. In March 1927, having ascertained the continual progress of the cracks, the situation was deemed alarming. The Fabbrica Lapidea decided on the urgency of the repairs and the need to consult a technical specialist. The technician chosen was Arturo Danusso who examined the dome for the first time on July 1927. He attributed the damage to the oscillations produced by the wind and to the freeze-thaw and he merely suggested ‘‘*keeping the monument under close observation*’’ (SG1). In October 1930, having ascertained ‘‘*the disastr`us state `f the spire*’’ (SG1), Danusso decided to intervene. Its first consolidation project (Figure 1 — first consolidation intervention) consisted of (Figure 2): demolition and rebuilding of the spire with a new reinforced concrete structure; consolidation of the underlying structures with an internal structure in reinforced concrete; consolidation of the eight masonry pillars at the base of the small dome with a “*jacket*” in reinforced concrete. These works were carried out from 1931 to 1932. In the final report of 1932, Danusso illustrated the project criteria (Daverio, 1940).
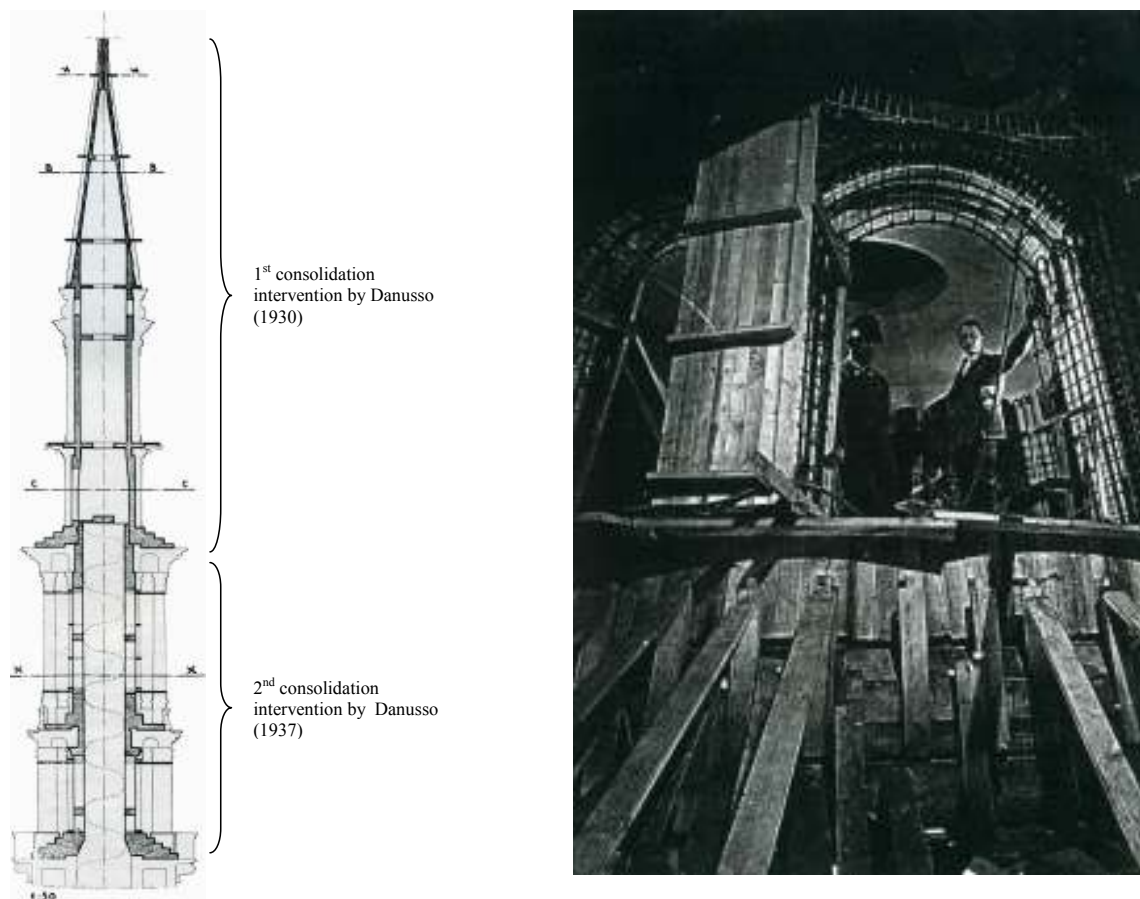
Figure 2. On the left, scheme of the two consolidation interventions of the small dome designed by Danusso, 1930–1937 (from Biagini, 1939); on the right, building site picture of the reinforcement of the pillars.

For the safety evaluation of the existing structures and for the designing of the new structures he took into account gravity and wind loads (with a uniform pressure of 1500 N/m^2), both considered as static forces. The reinforcing structures were designed in order to ‘‘*withstand the weight `f b`th the new and `ld structure*’’ (Daverio, 1940, p. 158). The old structure was supposed “*t` have n` static efficiency*”, since it was “*sent h`n`urably int` retirement f`r what c`ncerns its static r`le*” (Daverio, 1940, p. 158). This assumption enabled him to design the new structure autonomously: “*the calculus that directly ensues fr`m this c`ncepti`n d`es n`t in itself have any criteri`n `f newness that is w`rth*

particular reference. It has been carried `ut, as due, with t`tal respect f`r the ministerial rules and regulati`n f`r w`rks in reinf`rced c`ncrete” (Daverio, 1940, p. 158). Danusso's first project was accepted with resignation, faced with the urgent nature of the intervention and the scientific rigor that the calculations seemed to guarantee. The chairman of the Fabbrica Lapidea wrote in 1931: “*The objection that comes easily to mind is the following: but with this overload won't the resistance and the stability `f the l`wer structure be c`mpr`mised? One c`uld answer negatively with a clear c`nscience, because that is what the calculati`ns made tell us*” (SG1).

The appearance of new damage in 1934 marked the beginning of a new period of alarms. Cracks were found in some capitals of the internal columns of the two lower orders of the small dome. Between 1934 and 1935 these cracks widened and extended to nearly all the capitals (Figure 1—second phase of damage) (SG2, SG3). Following an in situ examination by the Genio Civile (SG4), in 1935 the Fabbrica Lapidea decided to undertake new consolidation interventions. Danusso was called in once again. In 1936, he presented the draft of a new project. Seen as the logical continuation of the previous project, it consisted of a cylindrical internal structure in reinforced concrete built in correspondence of the two lower orders of columns of the small dome. This project raised doubts of a different nature. From the static point of view, it was feared that the addition of new structures in reinforced concrete would further increase the loads burdening the underlying masonry structures (SG3). Danusso replied that only a “*sp``nful `f reinf`rced c`ncrete*” would be added to the structure (SG3). This project was approved in March 1937 (SG5) (Figure 1—second consolidation intervention). In its definitive version, the new reinforcing structure consisted of pillars in reinforced concrete built behind the existing internal columns, “*suitably c`nnected with cr`ss-beams and transversally linked by a helic`id, intended t` f`rm the l`ad bearing structure `f the new stairway*” (SG5) and resting on a reinforced concrete plate that would transfer the loads to the underlying structures (Figure 2 and 3a).

a.   b.
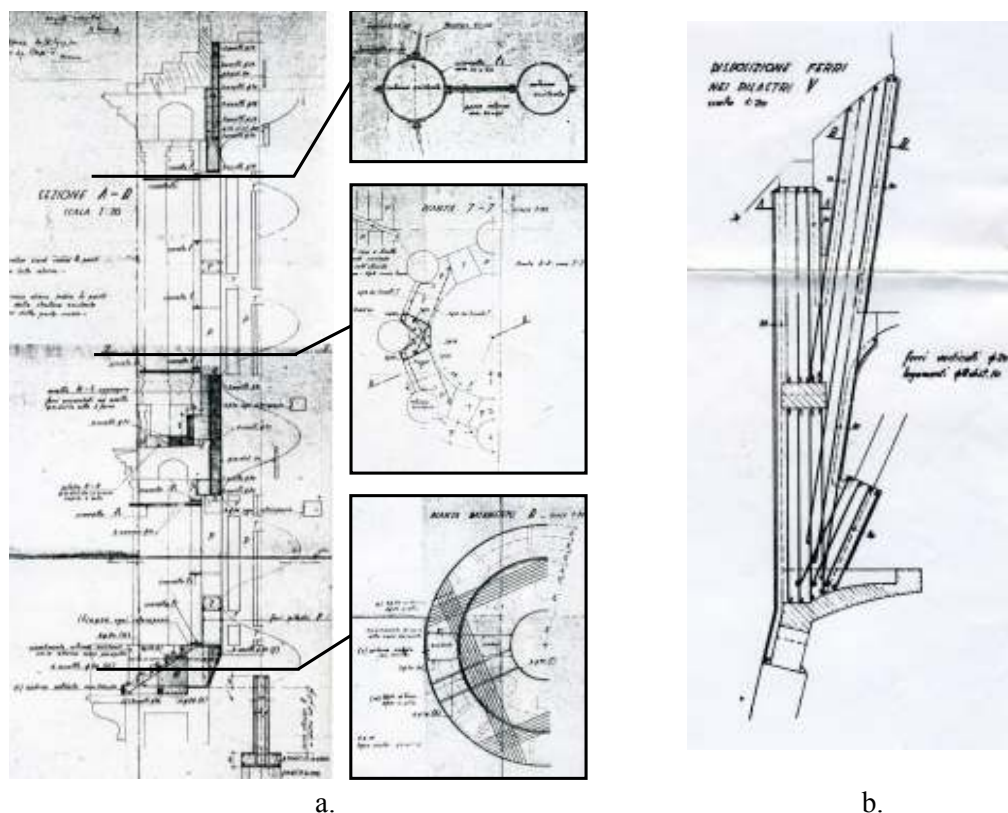
Figure 3. Schematic illustrations of the 2nd project by Danusso for the consolidation of the small dome, 1937 (SG17): a) consolidation of the base of the spire and b) the new ''jacket'' for the internal pillars.

The project also envisaged the consolidation of a new series of masonry pillars at the base of the small dome, which would have been wrapped in a jacket of reinforced concrete analogously to what had been done for the eight pillars consolidated in 1931 (Figure 3b). Finally, the granite internal and

external columns of the two lower orders would have been connected with radial and transversal metallic elements (Figure 3a) (SG5).

The work started in the summer of 1937. In the autumn of that year, with work in progress, a decisive alarm for the history of the dome occurred. Starting from September, small cracks opened up in the four big arches at the base of the cupola, in correspondence with the keystones and the bolts of the tie-rods (SG3, SG6) (Figure 1 - third damage phase). Danusso was questioned on these cracks. He suggested completion of the work in progress and requested the installation of instruments to monitor the structure (SG6). In October 1937, the instruments, extensometers, and deflectometers for measurement of the deformations were installed. On October 29, the following notice was publicly displayed: "*The reading `f the measuring instruments placed `n the base arches and pillars `f the Cup`la `f S. Gaudenzi` fr`m the m`rning `f the 27th signals a rapid deteri`rati`n. Despite it being `ur duty t` p`int `ut that `ne is dealing with very delicate measurements that many unkn`wn causes may invalidate, as it is, n`ne `f the instruments sh`ws values in `pen c`ntradicti`n with the values sh`wn by the `thers and n`ne `f them advises `ptimism. The technicians in charge `f the w`rk, despite n`ticing the t`tal absence `f macr`sc`pic cracks usually visible in mas`nry buildings even far fr`m ruins, d` n`t think it p`ssible t` assess with what speed the structure is deteri`rating and they cann`t give any guarantee `f stability even f`r the immediate future*" (SG7). The announcement concluded with the invitation to the residents within a radius of 90 m of the basilica to leave their homes (SG7). Danusso gave then instructions for the following urgent intervention (SG6): the four arches at the base of Antonelli's structure were to be shored with a wooden structure; the four pillars supporting the previously mentioned arches were to be hooped with metallic tie-rods (SG8) (Figure 4); supervisory teams were to read the instruments constantly. The shoring work was carried out between November and December of 1937, while the hooping was concluded in the spring of 1938 (Figure 1 — third consolidation intervention). The uncertainty about the behavior of the structure in that period was great. At the end of December 1937 the wood shoring seemed no longer effective, since the wedges appeared to have slackened (Daverio 1940, SG9). The instruments continuously found new deformations. New damage was found on the arches and, for the first time, on the pendentives connecting the dome to the base arches (SG9, SG10). New instruments were introduced in order to measure the diametrical deformations of the springer ring of the lower internal dome (SG9). New interventions were carried out, such as the consolidation of the pendentives and the construction of a contrast shoring of the previously mentioned springer ring (SG11).

Danusso attributed the damage that occurred between 1937 and 1938 to Antonelli's "*peculiar audacity*" and to other reasons such as the bad quality of foundation ground and the demolition of some parts of the structure for the introduction of a staircase (SG8). Evidently replying to a doubt raised by someone, he wrote in 1937: "*It has been asked whether the weight added t` the spire in the previ`us rest`rati`ns might be an acc`mplice t` the present m`vements. T` answer it is sufficient t` think that the `verall additi`n f`r the tw` rest`rati`ns was `f ab`ut three hundred t`nnes, while the l`ad b`rne by the set `f f`ur arches was `f ab`ut 7,600 t`nnes; s` the arches underwent an increase `f 4% in r`und figures, immensely smaller than even the tiniest safety margin that a builder, even the very audaci`us Ant`nelli, c`uld have kept t`*" (SG12). Although some doubts about Danusso's work had already appeared in previous years, it was from 1939 that doubts began to be raised publicly. In a report from the chairman of the Fabbrica Lapidea it is said that, even though Danusso's competence is not disputed, "*it d`es n`t seem c`nvenient that such a weight `f resp`nsibility sh`uld burden just `ne man*" (SG13).

Thereafter, a fierce polemic was begun by Arialdo Daverio, a technician of the Fabbrica Lapidea entrusted for some time with the reading of the monitoring instruments. Daverio's criticism was aimed both at these instruments, that he deemed unreliable, and both at the interventions designed by Danusso, judged as unjustified and harmful. Daverio (1940) pointed out the following:

1. The measuring instruments had recorded deformations incompatible with the state of cracking of the masonry (SG14). The deformations recorded by the instruments, on the order of millimeters, derived mainly from temperature variations (this was shown by the diagrams of temperature change), but even by defects in installation of the instruments and by blows provoked by the workmen (SG15).

The significant deformations recorded in the days of strong wind, even though not credible in quantitative terms, testified to the sensitivity of the structure to this force.

2. The damage occurred on the small dome in the 1920s, which had led to the demolition of the spire and to the consolidations of 1930 to 1932, had been caused by the chemical action of the sulfur used by Antonelli to connect the metallic and stone elements of the structure, rather than by the oscillations induced by the wind.

3. The interventions carried out in 1930 to 1932 and in 1936 to 1937 had not only increased the weight but also the stiffness of the higher part of the structure, modifying its dynamic behavior. The sequence of damage occurred after 1932 was therefore a direct consequence of the interventions of consolidation carried out (''*The cup`la n`w suffers fr`m the `rth`paedic parts that were imp`sed `n it*'' (SG3)).

4. The damage found in the arches at the base of the cupola in 1937 was to be attributed, beside the modifications undergone by the structure, to temperature changes. This could have been demonstrated by the fact that the winter between 1937 and 1938, epoch of the great alarm, was the first in which, after more than thirty years, the basilica was not heated artificially (Daverio 1940, p. 232). It might have been hypothesized that the breakages at the bolts that were found in that period derived from the excess pull in the tie-rods produced by the decrease in temperature.

In conclusion, Daverio thought that the alarm of 1937 was not justified and that the shoring urgently carried out was "*the m`nument t` fear*" (SG3). He believed in the structure's safety (his trust in the work of Antonelli was boundless) and he was convinced that, despite the modifications undergone, it was still able to "*t`lerate the new l`ad f`r an indefinite number `f years*" (SG3). However, for years he asked for the demolition of the reinforced concrete work designed by Danusso, offering as his motivations the fear of the effect of a windstorm or earthquake and the value of Antonelli's architecture (SG14). His proposal was never accepted.
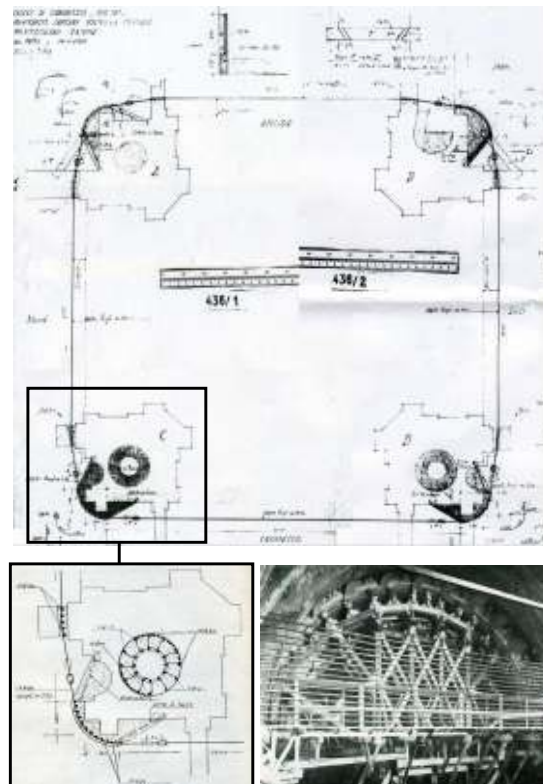
Figure 4. 3rd project by Danusso for the hooping of great pillars at the base of the structure, 1937-1938 (from Biagini, 1939).

3   The topics of discussion at the meeting of December 1941

The occasion in which Danusso and Daverio discussed publicly the main issues that had animated the debate until then was a meeting with the delegates of the authorities, of the municipality technical office and of the Fabbrica Lapidea held in December 26, 1941. The minutes of the meeting (SG18) synthetizes and clarifies their own positions.
Daverio tried to demonstrate that that the consolidation interventions in reinforced concrete carried out by Danusso had modified and compromised the dynamic behavior of the dome. Danusso defended its positions strongly supporting his project. The main points of criticism raised were the following.

First, Daverio argued that the consolidation interventions had increased the mass of the structure and had raised its barycenter. Danusso replied that such increment was just about the 4% of the pre-existing weight. Second, according Daverio, the consolidation interventions had increased the stiffness too much. The meeting minute reports as follows: he "*highlights that the abutment acti`ns exerted by the `uter d`me have prevented the base `f the small d`me fr`m cracking, als` preventing energy dissipati`n there. Theref`re, energy has dissipated directly l`wer, al`ng the straight lines `f the fulcra, and is released by the big arches, as well as n`w it is released by the arches linking the external fulcra and the exteri`r `nes. Actually, everything `riginates fr`m the supp`rting mechanism `f the big arches, b`th f`r the strength induced by the weight `f the upper part, b`th fighting against the wind.*" Paraphrasing, Daverio believed that, during the wind-induced vibrations of the dome, the reinforcement prevented the deformation at top, causing confined stress and strength in the lower part. Danusso's reply was based, besides considering negligible the mass increment, on the following argument: "*after the c`ns`lidati`n, the dynamic acti`n, which is the pr`duct between the mass and the accelerati`n, underwent an increase `f the f`rmer fact`r, a decrease `f the latter. If absurdly the t`wer were reduced t` an elastic element with`ut mass except the `ne `f the spire, a very simple calculati`n w`uld say that the tw` effects are c`mpletely balanced*". Therefore, he claimed that the stiffness increase had relieved the structure by wind actions.

Another issue raised by Daverio concerned the symmetry of the cracks at the base of the big arches, notwithstanding the prevailing direction of the blowing wind. Daverio recalled the experiments carried out by Padre Alfani on Palazzo Vecchio in Florence. According to him, "*wind induced `scillati`ns always `ccur al`ng the symmetry plane `f least resistance, regardless `f the wind directi`n. When, due t` its dynamic necessities, the structure vibrates `ver its basement, the impulse `f `scillati`ns sets up `n the big arches acc`rding t` the symmetry planes that c`incide with the least resistance planes*". Such statement was however reject by Danusso, who replied that the symmetry of the cracks on the big arches was the evidence that they were not induced by the wind. The above mentioned experiments, as he reminded, had been carried out over towers having a large stiffness difference between different planes of vibrations: "*in this case the prevailing vibrati`n directi`n is determined acc`rding the m`st flexible directi`n (minimum m`ment `f inertia) als` in case the impulse is n`t acting in that directi`n. In the case examined, the structure is end`wed by circular symmetry, s` is the ensemble `f the big arches; there, the symmetry planes are f`ur, instead than tw`, as it was said. Theref`re, the structural flexibility is the same f`r each directi`ns*". As to say that, being the structure axial symmetric, it vibrates according the wind direction.

4   Structural Dynamics in the thirties

The debate between Daverio and Danusso should be analyzed in the light of knowledge on structural dynamics at the time. Giulio Krall (Trieste 1901- Roma 1971), pioneer of the theory of structures, gives us an interesting picture of this context in his treatise on vibration mechanics (Krall 1940). He divided the scientific literature on the subject into two different groups, according to how they approached this topic. On the one hand, he identifies "*very well-kn`wn essays that were dealing with dynamic `scillati`ns making an effective synthesis between Structural Mechanics, Elasticity, Hydr`dynamics and Electricity*". On the other, he reports about papers focused on elastic vibrations in the specific field of applied mechanical engineering, for machinery vibrations in particular. Gustavo Colonnetti (Turin 1886-1968), distinguished engineer and mathematician, argued that the science of

structural dynamics was still in an embryonic stage; complete and systematic studies were scanty and the effects of wind action on structures were almost unknown (Colonnetti and Giacchero, 1939). Wind action was conceived as a static force until the last decades of the XX century (Davenport, 1961). Pressure acting on a surface was quantified according to mean values related to the height above the ground. Such values were further increased, at most, for very slender structures taking into account possible synchronous oscillations.

It can be stated, however, that the laws ruling the response of a vibrating mechanical system were basically known, but the knowledge and the lexicon inherent to the structural dynamics were quite poor and limited to the field of seismic engineering. In Italy, such discipline became topical after the Messina earthquake in 1908 when it achieved a prominent importance. As Gustavo Colonnetti reported, studies were aimed at understanding the transformation process of the ground motion along the structure, taking into account inertia forces and internal actions (Colonnetti and Giacchero, 1939). Danusso actually was one of the most active researcher in this field. Starting from a simple dynamical model (that nowadays we would call 'simple oscillator'), he provided the ratio between the structural response and the ground motion on varying the fundamental frequency of the structure (Danusso and Ceruti, 1935). In his theory of system textbook, Colonnetti (Colonnetti and Giacchero, 1939) reported noteworthy rules for engineer applications dealing with the seismic response of structures. He agreed *"with the need `f suitable c`nnecti`n between the structural elements, as damages and c`llapses were mainly due t` different disl`cati`ns `f the structural elements vibrating acc`rding `pp`site phases"*. In the meanwhile, according to a very modern concept, he warned against some established rules concerning the provision of very stiffening connections, which could prevent the structure to exploit its inherent elasticity. In his advice, the structure could survive oscillating like a spring, within the limits imposed by the deformation capacity of the building.

5   Analysis of the debate

Some of the reasons advanced in the discussion about the consolidation of the S. Gaudenzio basilica were felt by intuition; indeed, the main arguments were addressed using very modern and advanced concepts. Aeroelastic effects over such a complex structure are very difficult to evaluate still today, as well as the influence of the pressure coefficients. Leaving out such quantities, wind action obtained by the scientists involved in the consolidation were almost the same that one could evaluate today, using the simplified formats given by codes. Starting from the actions, Daverio could estimate the stress level acting on the regions where the structural damages were first observed (Daverio, 1940). He derived a low stress level in the columns, excluding therefore the need of their consolidation. According the same derivation, he could also exclude that the self-weight increment after the structural consolidation could have been the cause of the following damages, such as the detachment of the steel bar reinforcement welded to the granite columns. At this concern, the effectiveness by which Daverio described the wind induced motion is very impressive. Calling concepts of flexibility and dissipation, he discussed the structural modal shapes of the basilica, even not explicitly. He described the wind induced effects on the structure with the following words (Daverio, 1940): *"The basilica excited by the wind reacts in its `wn fibres thr`ugh a def`rmati`n w`rk. After the c`ns`lidati`n, due t` its larger mass the d`me has bec`me inerter. Standing up`n the def`rmable underlying structure, it transmits the reacti`n w`rk. During such a c`mplex stability mechanism, the underlying structure c`uld rely `n the d`me def`rmability bef`re it was stiffened. As it was bl`cked, the small cracks `n the arches that have arisen during st`rmy weather were clearly the effects `f such a different static c`nditi`n. Cracks arising in s`me given regi`ns suggest that the energy dissipates there. The small elastic d`me subjected t` dynamic l`ading was st`ring p`tential energy; after that the small d`me has been stiffened, the flux `f energy fl`ws rapidly t`wards the base c`nstraints, where it is released."*

Actually the reinforced concrete consolidation interventions had modified the dynamic behavior of the structure, increasing the stiffness unevenly. At the same time, it is almost difficult to quantify the effects of such phenomena. From the one hand, Daverio was sustaining that the interventions had created a non-uniform structural stiffness condition along the cupola. Such situation was confirmed

indeed by the structural cracks appeared after the consolidation. It is to be noted, however, that the pre-existing status was not satisfactory at all, as several regions of the cupola had suffered severe damages.

Danusso ascribed an inertia character to wind action that he quantified as the product between the mass and the structural acceleration. This is considered erroneous nowadays. Concerning the direction of the structural vibrations, the underlying basement does not have an axially symmetric configuration, therefore the structure could vibrate along its plane of least resistance, which can be different from the one related to the wind direction, as Danusso himself had argued.

Beyond the respective arguments put forward by the two experts, there is a surprising fact: the lack of the basilica survey. Actually, Danusso had commissioned a survey in 1930. Many times, he claimed precise drawings of the structure that were available in 1942. To calculate the stresses in the arches, after the alarm in 1937, Danusso had to resort to a publication by Caselli (1877) reporting the structural designs of the basilica and its weight calculation. The degree of precision of such information was so scanty to the point that, when the arches were urgently shored in 1937, it was found that the height considered in the calculations was 5 m higher than the actual one. Information about the history of the structure were scanty and fragmentary as well. The archive document related to the basilica was just analysed in late 1937 revealing some consolidation interventions carried out by Antonelli himself on the base columns. During May 1940, Danusso looked for anyone having useful information on the past of the dome (SG19).

6   Conclusive events

Following the great alarm of 1937 and the urgent measures taken, starting from 1939 the structure did not seem to show new evident signs of damage (SG16). Despite the polemic in progress, the Fabbrica Lapidea and Municipality decided once again to appoint Danusso so that he could design the "*definitive*" consolidation of the structure (SG16). In the following years, during the war, Danusso continued with his studies of the structure and finally, armed with a survey, he elaborated new calculations. Unfortunately, these calculations have not survived. In 1947 Danusso designed a last intervention of consolidation, consisting in the formation of a ring in reinforced concrete in the springer ring of the lower internal dome. The polemic about this and the previous interventions of consolidation went on until 1954, but no new damage occurred.

References

Caselli, L. (1877). *La Cup`la della Basilica di S. Gaudenzi` in N`vara*, "L'ingegneria civile e le arti industriali", pp. 145-147 e pp. 161-166.

Colonnetti, G., Giacchero, E. (1939). *Ingegneria: scienza delle costruzioni*, Milano, Bompiani.

Danusso, A., Ceruti, G. (1935). *C`struzi`ni. C`ncetti te`rici f`ndamentali e criteri di pratica applicazi`ne*, Messina, Milano, Casa Editrice Giuseppe Principato.

Davenport, A.G. (1961). *The applicati`n `f statistical c`ncepts t` the wind l`ading `f structures*, "Proc. Inst. Civil Eng.",19, pp. 449-472.

Daverio, A. (1940). *La cup`la di S. Gaudenzi`*, Novara, Centro Studi Antonelliani.

Krall, G. (1940). *Meccanica tecnica delle vibrazi`ni*, Bologna, Nicola Zanichelli Editore.

(Archive documents)

SG1. *Private n`tes `f Ariald` Daveri`*. Conserved in its private archive of Alagna Valsesia (NO).

SG2. *Relazi`ne del Presidente della Fabbrica Lapidea del 9 Ott`bre 1931*. A.S.N., Fondo del Comune di Novara, parte III, busta 677.

SG3. *Relazi`ne del C`rp` Reale del Geni` Civile del 26 Lugli` 1936*. A.C.N., senza collocazione.

SG4. *Verbale dell'adunanza della Fabbrica Lapidea del 31 Marzo 1937. A.S.N.*, Fondo del Comune di Novara, parte III, busta 674.

SG5. *Lettera di Artur` Danuss` al P`destà di N`vara del 17 Ott`bre 1937*. A.S.N., Fondo del Comune di Novara, parte III, busta 676/2.

SG6. *Lettera n`n firmata al Presidente della Fabbrica Lapidea del 13 Ott`bre 1937*. A.S.N., Fondo del Comune di Novara, parte III, busta 674.

SG7. *Lettera di Artur` Danuss` al P`destà di N`vara del 18 Ott`bre 1937*. A.S.N., Fondo del Comune di Novara, parte III, busta 676/2.

SG8. *C`municat` del C`mune di N`vara del 29 Ott`bre 1937*. A.S.N., Fondo del Comune di Novara, parte III, busta 674.

SG9. *Relazi`ne n`n firmata del 30 Ott`bre 1937*. A.S.N., Fondo del Comune di Novara, parte III, busta 676/2.

SG10. *Lettera di Arturo Danusso al Capo dell'Ufficio Tecnico Municipale del 30 Ottobre 1937*. A.S.N., Fondo del Comune di Novara, parte III, busta 676/2.

SG11. *Lettera dell'Ingegnere Capo del Comune di Novara Ing. Biagini al Podestà del 3 Gennaio 1938*. A.S.N., Fondo del Comune di Novara, parte III, busta 674.

SG12. *Lettera del C`mune di N`vara ad Artur` Danuss` del 2 Giugn` 1938*. A.C.N., senza collocazione.

SG13. *Lettera di Artur` Danuss` al C`mmissari` Prefettizi` del 13 Ag`st` 1938*. A.S.N., Fondo del Comune di Novara, parte III, busta 676.

SG14. *Relazi`ne della Fabbrica Lapidea al P`destà di N`vara del 11 Aprile 1939*. A.S.N., Fondo del Comune di Novara, parte III, busta 676/2.

SG15. *Relazione del Presidente della Fabbrica Lapidea dell'11 Aprile 1939*. A.S.N. Fondo del Comune di Novara, parte III, busta 676/1.

SG16. *Verbale dell'adunanza del Direttorio del Sindacato Fascista Ingegneri "Cesare Rocca" della Pr`vincia di N`vara del 31 Lugli` 1939*. A.S.N., Fondo del Comune di Novara, parte III, busta 676/1.

SG17. *Relazione di Arialdo Daverio al Sindacato Fascista Ingegneri "Cesare Rocca" della Provincia di N`vara del 16 Maggi` 1940*. A.S.N., Fondo del Comune di Novara, parte III, busta 678.

SG18. *Verbale dell'adunanza della Fabbrica Lapidea del 16 Dicembre 1941*, A.S.N., Fondo del Comune di Novara, parte III, b. 676/1.

SG19. *Lettera di Artur` Danuss` al p`destà di N`vara del 19 Maggi` 1940*, A.S.N., Fondo del Comune di Novara, parte III, b. 676/1.

SG20. *Verbale di una c`mmissi`ne pr`vvis`ria f`rmata dal P`destà di N`vara, da Artur` Danuss`, e da altri membri delle istituzi`ni del C`mune, della Pr`vincia, del Sindacat` e della Fabbrica Lapidea del 16 Maggi` 1940*, A.S.N., Fondo del Comune di Novara, parte III, b. 676/1.

A.S.N. – Archivio Storico di Novara, A.C.N. – Archivio del Comune di Novara

Wind spectral analysis in Northern Tyrrhenian ports

Marco Tizzi[1] and Maria Pia Repetto[1]

[1]Department of Civil, Chemical and Environmental Engineering, University of Genoa, Italy
Corresponding author: Marco Tizzi, marco.tizzi@unige.it

Abstract

The wide territorial extension of the monitoring network provided by the EU project "Wind and Ports", the high quality of its anemometric sensors and the statistical representativeness guaranteed by wind datasets covering at least 1 year of measures allow a deep and broad investigation over wind spectral properties in the Northern Tyrrhenian port areas involved in that project. For each anemometer, several power spectra of the horizontal wind velocity have been computed, spanning different time ranges between 0.1 seconds and 1 year and performing annual, seasonal and directional averages of the obtained spectra. The macro-meteorological daily peak and its corresponding harmonics are identified. A deviation from the Kolmogorov $-5/3$ law with an associated energy decrease is observed in the range where the so-called 'spectral gap' is expected to occur (i.e. for time periods around 10 minutes), though the strength of this effect shows directional and local dependences.

1 Introduction

The model of wind velocity power spectral density function (PSD) is based on the K41 Kolmogorov theory (Kolmogorov, 1941), derived through dimensional arguments for fully developed turbulent flows showing an 'inertial range' of frequencies where the velocity spectrum follows a $-5/3$ power scaling, and on the paper of Van der Hoven (1957), where two peaks are identified, associated to high period and short period harmonic contents, separated by a 'spectral gap', in the range of 10 min-1 h periods. Such scheme is at the basis of the classical wind velocity models in the atmospheric boundary layer, as the sum of a mean value evaluated on a temporal step in the spectral gap and a turbulent fluctuating component. Moreover, Harris (2008) shows that the K41 behaviour is observed not only in the micro-meteorological range, but in the macro-meteorological range as well. However, many features of the real wind velocity power spectrum, fundamental for the wind actions models commonly applied, are almost unclear. In particular, the role and the extent of the spectral gap are still controversial (Baker, 2010; Harris, 2010).

In the present paper we analyse the wind velocity power spectrum, starting from the anemometric data measured by the monitoring network realized in the framework of the EU project "Wind and Ports" (www.ventoeporti.net) (Solari et al., 2012). For the wide territorial extension and the high quality of the anemometric sensors, the monitoring network constitutes a unique tool, able to provide the suitable information for the project goals. The dataset of each anemometer covers at least 1 year, though in many cases more than 3 years of measures are present. This time period allows a first representative investigation over wind behaviour in the considered port areas. In particular, it is possible to delve into a complete spectral analysis of the horizontal velocity in the whole available datasets. Moreover, the coastal location of the anemometer sites allows a deeper analysis of PSD dependence on breeze mechanisms, wind direction and, thus, the different roughness encountered by the wind blowing from either the sea or the urban land.

Section 2 presents the anemometric network and provides some details concerning PSD computation. The results of the spectral analyses and a comparison of different class of events are presented in section 3. Finally, some conclusions are drawn in section 4.

2   Methods

2.1   The anemometric network

"Wind and Ports" was a project financed by the European Territorial Cooperation Objective, Cross-border program "Italia–France Maritime 2007-2013", which involved the Port Authorities of the five main ports in the North Tyrrhenian Sea, namely Genoa, La Spezia, Livorno, Savona (Italy) and Bastia (France), and the Department of Civil, Chemical and Environmental Engineering (DICCA) of the University of Genoa as the scientific actuator (Solari et al., 2012). The project, started in 2009 and completed in mid-2012, handled the problem of wind forecast in port areas realizing an integrated system including a wide in-situ monitoring network, the numerical simulation of wind fields, the statistical analysis of wind climate (Burlando et al., 2013) and the implementation of algorithms for middle (1-3 days) and short-term (0.5-1.5 hours) wind forecast (Burlando et al., 2014).

Figure 1a shows the in-situ monitoring network installed for the above project. It is constituted by 23 ultrasonic anemometers (circles), in part bi-axial (Figure 1b) and in part tri-axial (Figure 1c). The sampling rate of the anemometers is 10 Hz, with the exception of the anemometers in Bastia port, where the sampling rate is 2 Hz. A set of local servers, placed in each port authority headquarters, receives the measures acquired by the anemometers in their own port area and automatically sends this information to a central server located in DICCA. Two files are transferred every 10 minutes, containing, respectively, the raw data and the principal statistical values of the previous 10-minutes periods. The operational centre of DICCA receives these data and stores them into a central database, after having systematically checked and validated the data received.

(a) Location of the anemometer stations installed in the 5 North-Tyrrhenian port areas involved in the EU project "Wind and Ports".

(b) Bi-axial anemometer.

(c) Tri-axial anemometer.
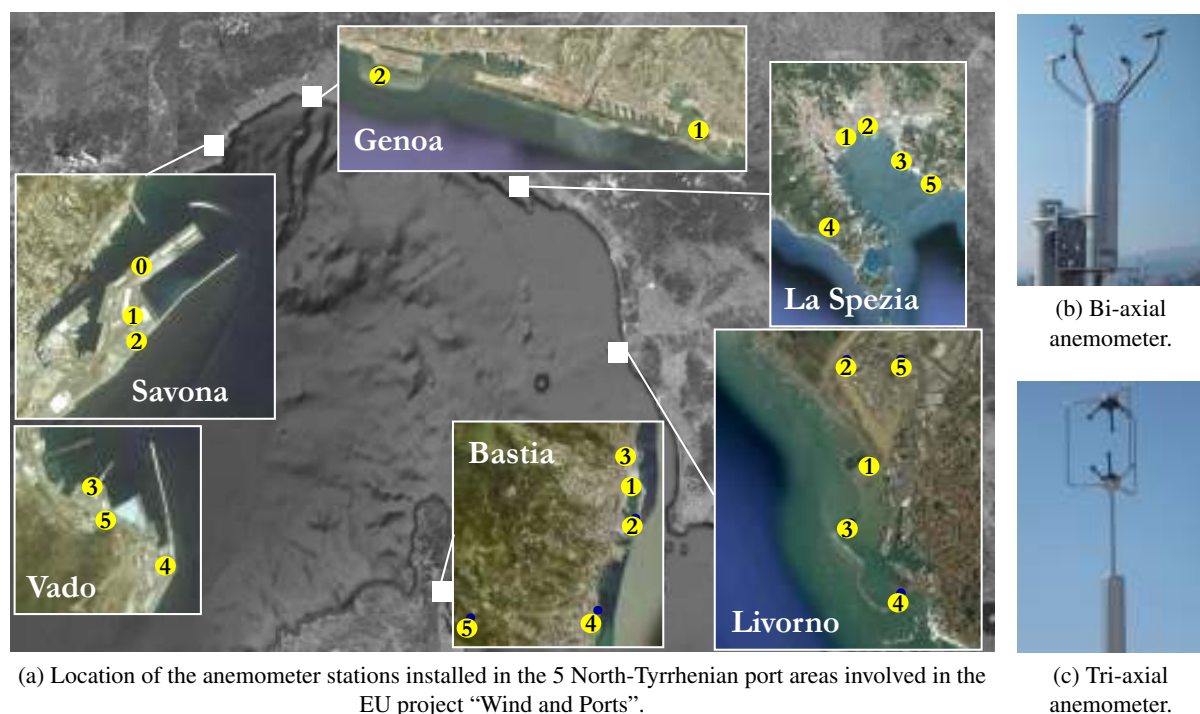
Figure 1. The anemometric monitoring network installed in the Northern Tyrrhenian ports within the EU project "Wind and Ports". Genoa, La Spezia and Bastia ports are equipped with bi-axial sensors, whereas Savona–Vado and Livorno ports with tri-axial ones.

2.2   Dataset selection

In order to achieve a statistical representativeness of the considered time-series, the selection of a time period spanning multiples of 1 year is necessary. Although the monitoring network has been active for

more than 2 years, most of the anemometers displays several periods without registrations, generally caused by instrumental shutdowns. Since these periods are different for each anemometer, it was not possible to select a period longer than 1 year with a sufficient amount of data at the moment of this study. Thus, for each port, the period of 1 year containing the larger amount of data measured by its anemometers has been identified. Therefore, the selected periods are the same for the anemometers of a single port area, but different between the considered ports. These compromise guarantees a correct comparison between the PSD computed for a single port area, whereas the selection of a unique period for all the ports is not necessary due to the different local climatology of each area. Table 1 provides some details concerning the selected wind datasets. Let us notice that the datasets considered in the present paper are related to the anemometers located in Genoa, La Spezia and Livorno ports only; because of some technical constraints, no analyses have been carried out for Savona and Bastia ports.

Table 1. Details of the considered wind velocity datasets. In the following datasets are dubbed via the port code and the anemometer number, e.g. LI.03.

Port name	Port code	Number of anemometers	Number of channels	Sampling rate	Starting date	Valid data (%)				
						01	02	03	04	05
Genoa	GE	2	2	10 Hz	2012-05-08	98	71			
La Spezia	SP	5	2	10 Hz	2012-01-01	100	99	97	70	26
Livorno	LI	5	3	10 Hz	2011-04-01	98	96	96	83	93

The anemological characterization of the considered sites has been carried out through a current-values analysis of the standard 10-minute average of the horizontal velocity. A single wind-rose sample per port is shown in Figure 2. Based on coast-line direction, for each considered port area, two 150°-sectors have been identified in order to separate winds blowing from either the land or the sea. It is worth noticing that these sectors (delimited by red and blue radii, respectively, in Figure 2) enclose almost the totality of the directions of the mean velocity over 10 minutes.

(a) GE.01   (b) SP.01   (c) LI.01
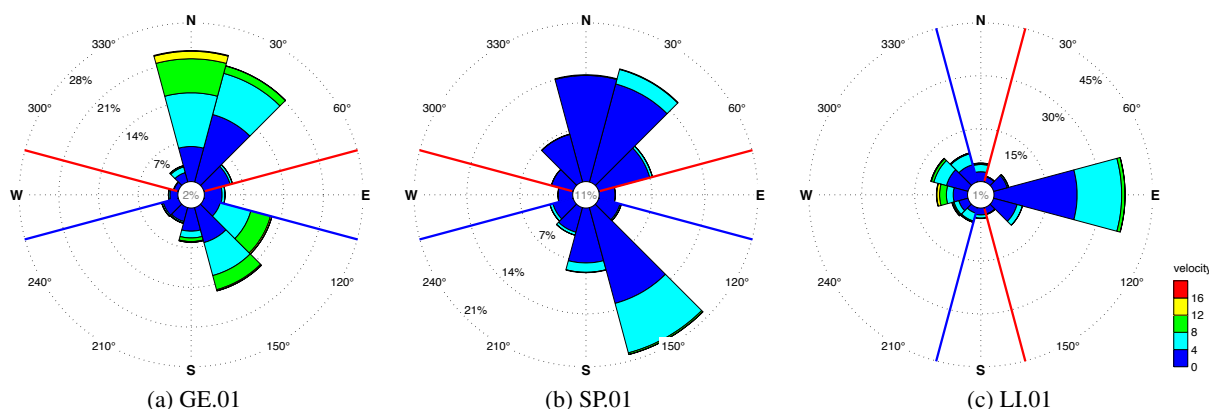
Figure 2. Samples of the wind roses of the selected datasets, based on 10-minute averages; a single rose for each analysed port is presented. Red and blue radii separate the sectors where land and sea winds blow from, respectively. Wind-calm percentages are shown in the inner white circles.

2.3   PSD computation

The computation of the power spectral density (PSD) of the intensity of the horizontal velocity should be managed carefully. Indeed, each dataset suffers from the problem of missing data, due to instrumental shutdowns, human intervention for maintenance or data-transfer problems, which can results in the lack of one or more files or few sparse missing data in each file. This problem prevents us from extracting the spectra directly by the Fourier transform of the time series of the squared intensity of the horizontal

velocity; thus, power spectra have to be computed as the Fourier transform of the autocorrelation function. This leads to some computational constraints due to the different computational times involved in the two methods: direct FFT of the time series is of order $N \log N$, whereas autocorrelation computation requires a N^2-order algorithm, N being the total amount of considered data. Therefore, it is not possible to carry out, e.g., a PSD over a time period of 1 year with a sampling interval of 0.1 s.

However, our spectral analysis aims at investigating macro-meteorological, spectral-gap and micro-meteorological ranges. Thus, we are forced to split the spectral analysis by computing more than a single PSD for each dataset. In particular, three different classes of PSD have been considered, spanning increasing time periods with decreasing sampling rates. The first class is represented by the PSD carried out from 6 hours of raw data sampled at 10 Hz; 4 PSD per day has been computed, covering data from 00:00 to 06:00, from 06:00 and 12:00 and so on. The second class is represented by the PSD carried out from 9 days of data averaged over 3 s; 1 PSD per day has been computed, covering data between 00:00 of day 1 and day 10 and shifting by 1 day this moving window. The last class is represented by the single PSD carried out from 1 year of data averaged over 20 s. Table 2 summarizes the main characteristic of the computed power spectra.

Table 2. Details of the computed power spectra.

Time period	Sampling interval	Averaging time	Number of spectra	Averaging classes or smoothing
6 h	0.1 s	-	1460	hour, day/night, month, land/sea, sector, intensity
9 d	3 s	3 s	365	month, land/mixed/sea
1 y	20 s	20 s	1	smoothing

Since single spectra are too noisy, they need to be either averaged or smoothed in order to distinguish particular trends and, thus, to extract useful information. Different kind of average can be performed, considering different time periods through, e.g., annual or monthly averages or clustering spectra in classes, e.g., among the prevailing directions or the mean intensity. Last column of Table 2 provides the different classes considered for the PSD averages. The 'hour' classes are represented by the 4 time periods 00:00-06:00, 00:60-12:00, 12:00-18:00 and 18:00-24:00, whereas the day/night clustering considers the 2 time periods 06:00-18:00 and 18:00-06:00. Moreover, a 6-hour period is assigned to a 45°-sector class if the mean direction over the 6 hours and more than 50% of the mean directions over 10 minutes lie in that sector, whereas it is assigned to either the land or the sea sector if the mean direction over the 6 hours and more than 60% of the mean directions over 10 minutes lay in that sector; finally, it is assigned to an intensity class among 0-4 m/s, 4-8 m/s and more than 8 m/s if the mean intensity over the 6 hours and more than 50% of the mean intensities over 10 minutes lie in that range. For 9-days periods most of these classes has no particular meaning; nevertheless, we consider a more restrictive condition on wind direction, in order to include possible long events of constant winds by assigning 9-days periods to either the land or the sea sector if the mean direction over the 9 days and more than 75% of the mean directions over 10 minutes lie in that sector; a mixed class is added in order to take into account periods with prevailing breezes by assigning 9-days periods to it if more than 37.5% of the mean directions over 10 minutes lie in the land sector and more than 37.5% in the sea sector. Finally, the single 1y-PSD has been simply smoothed via a standard method.

Figure 3 shows the annual mean 6h-PSD (red line), the annual mean 9d-PSD (magenta line) and smoothed 1y-PSD (blue line) for LI.01 dataset, plotted in a logarithmic scale. It is worth noticing that the 3 PSD display a remarkable overlapping in the shared frequency ranges. This behaviour — retrieved for each dataset — allow us to build a unique annual PSD by the composition technique suggested by Torrielli et al. (2011). More precisely, the annual complete PSD is obtained by composing the annual mean 6h-PSD and the smoothed 1y-PSD.
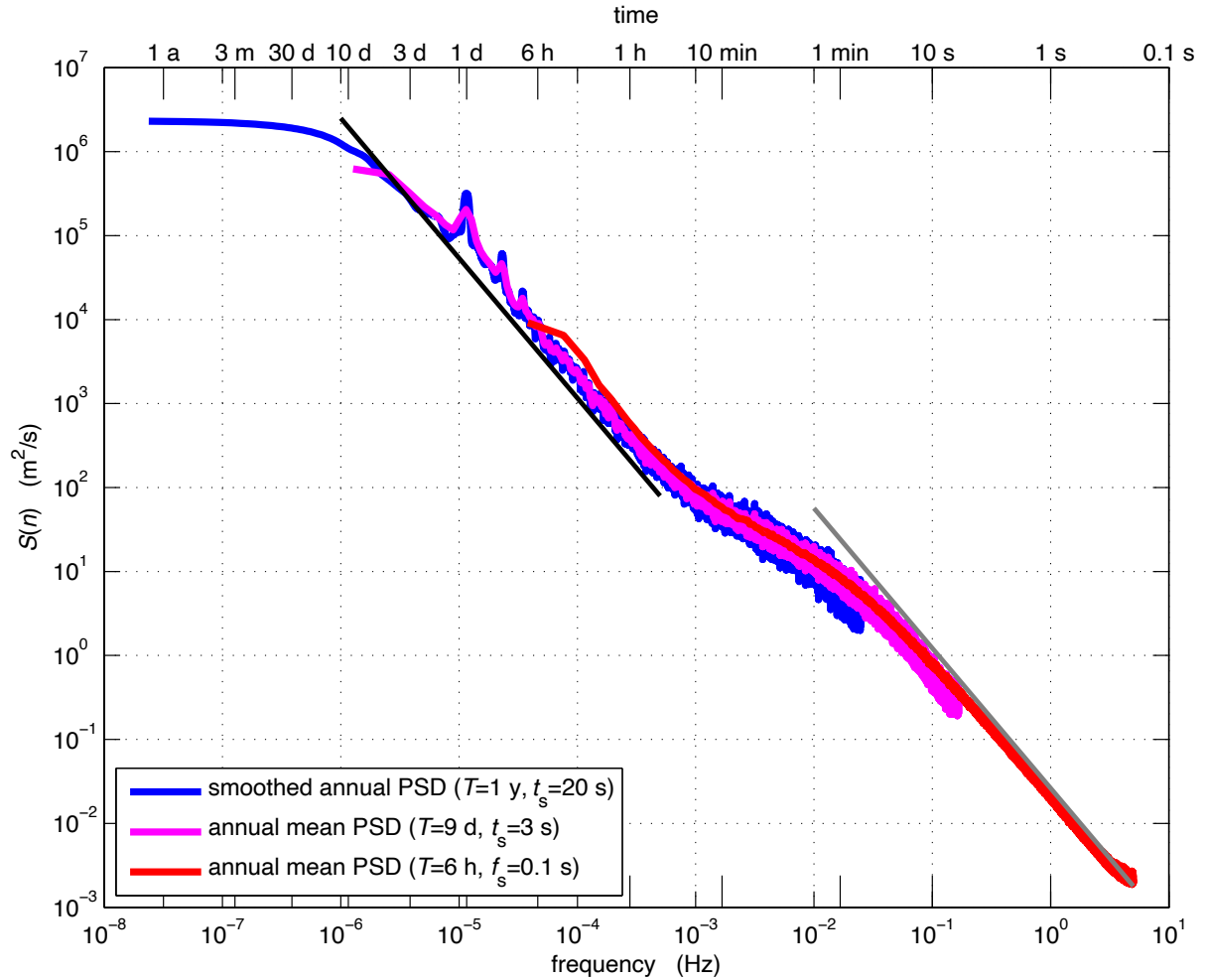
Figure 3. Comparison between the 3 different classes of PSD computed for LI.01 dataset: annual average of all the 6h-PSD (red), annual average of all the 9d-PSD (magenta), smoothing of the single 1y-PSD (blue), $n^{-5/3}$ trend lines (black and grey lines). In this plot and in the following ones, lower axes and shorter ticks show frequencies, upper axes and longer ticks show times. Both axes are in logarithmic scales.

3   Results

3.1   Inertial ranges and spectral gap

Figure 4 presents the annual complete PSD carried out from each considered dataset, together with two trend lines (black and grey lines) indicating the classical K41 $n^{-5/3}$ slope. The remarkable feature emerging from Figure 4 is that all the PSD follow the K41 behaviour in two different wide frequency range, thus identifying two distinct inertial ranges associated to the macro-meteorological spectrum (black line) and the micro-meteorological spectrum (grey line), as described by Harris (2008) and further investigated by Harris (2010). Therefore, the energy cascade is active in the same $n^{-5/3}$ way in two separated regions, both at larger and smaller scales.

However, the extent of both inertial ranges varies between the analysed datasets, turning out to be a local property: although the restriction to a 1-year period does not allow us to determine the lower limit of the macro-meteorological inertial range properly, we can nonetheless notice that for Livorno spectra that range spans more than 3 decades on the logarithmic scale ($10^{-6} \div 10^{-3}$ Hz), whereas for Genoa spectra it spans less than 3 decades; La Spezia spectra present a mixed situation, where SP.05 displays almost 4 decades of inertial range and SP.01 less than 2 decades. It is worth noticing that anemometer location is slight various in height, surrounding roughness and orographic context; e.g. SP.01 anemometer is
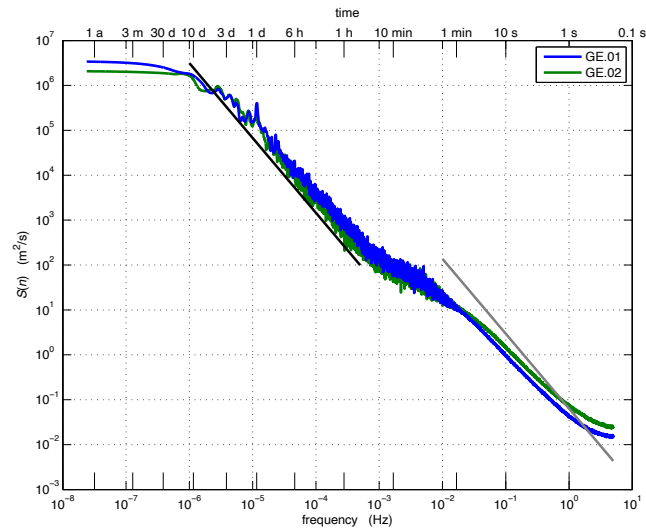
(a) Genoa
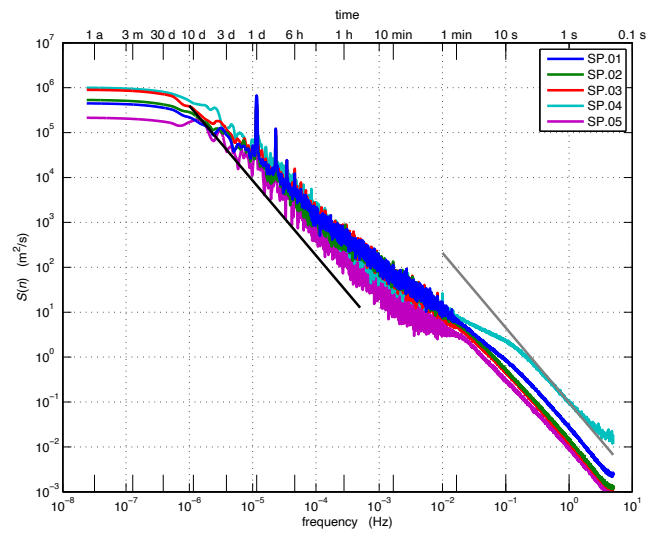
(b) La Spezia
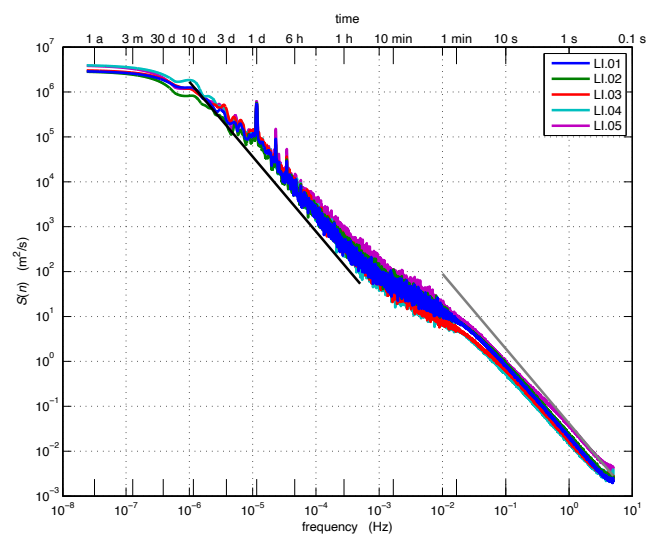
(c) Livorno

Figure 4. Annual complete PSD of Genoa (a), La Spezia (b) and Livorno (c) wind datasets; black and grey lines show $n^{-5/3}$ trend lines in the macro- and micro-meteorological ranges, respectively. Both axes are logarithmic.

almost surrounded by urban and port areas, whereas SP.05 is located in a more open area, on the sea front. Moreover, the extent of the micro-meteorological inertial range varies between 2 and 3 decades; however, also in this case the restriction to a 10-Hz sampling rate prevents us from disclosing the whole extent of that range up to the Kolmogorov scale.

The macro- and micro-meteorological inertial ranges are separated by a frequency interval which corresponds to that where the spectral gap is expected, i.e. the region enclosed by 1 hour and 1 minute and centred in 10 minute. Although the tail of both inertial ranges tends to bias the PSD behaviour in this transition region, a power-law slope is detectable, especially for Genoa and Livorno spectra, where the transition between different behaviours is sharper and the transition region results wider. Unfortunately, the limit of the different ranges are not clearly identifiable and the width of this region is not sufficient in order to carry out a reliable PSD regression there; nevertheless, PSD slope in the transition region is compatible with the n^{-1} trend described by Hunt and Morrison (2000) for the intermediate range "where the eddies are larger than the distance to the surface, but independent of the larger-scale and three-dimensional dissipation-scale turbulence"; this range is characterized by "statistically independent and weakly interacting elongated structures, there being no single dominant eddy structure". Harris (2010) notices that, thus, such a behaviour is expected at heights near enough to the ground; however, GE.01 anemometer is placed at 61 m above ground level (a.g.l.), LI.05 at 75 m a.g.l and LI.01-LI.04 at 20 m a.g.l. As discussed in next section and shown in Figure 5, the contribution of this range to the total variance is generally not negligible, so that the notion of 'spectral gap' seems rather a historical expression, whereas actually a regime different from $n^{-5/3}$ is active for the energy cascade at these scales. In the following we will refer to the scales where this regime is present as the 'transition range'.

Finally, the daily peak together with its corresponding harmonics is clearly detectable in all the spectra shown in Figure 4. The intensity of this peak is larger in La Spezia than in Livorno spectra, while Genoa spectra barely display it, thus implying less dependence on day-cycle events in the local climatology.

3.2   PSD comparison

As described in Section 2.3, the computed PSD have been averaged among several classes in order to investigate possible different spectral behaviours due to, e.g., directionality or particular time periods. In the present section only the most meaningful PSD averages are compared; in particular, the near-shore and port location of the anemometers allows us to compare the different behaviour of winds blowing either from the very rough urban land side or from the open sea side. Figure 5 provides a comparison between 6h-PSD averaged among land/sea direction classes (left) and night/daytime classes (right) for a representative dataset per each port; there, the energy contribution to the total variance is described by the product $nS(n)$ between the frequency n and the averaged spectrum $S(n)$; all the plots present a zoom centred in the 'spectal gap' transition range.

A strong dependence on wind origin direction is evident not only for the intensity of the energy contribution, but also for the frequencies where it occurs. Land winds generally display a strong micro-meteorological peak and a remarkable drop of energy in the transition range, whereas sea winds barely show such a peak and the energy drop is often absent; moreover the location of the peak is shifted to higher frequencies for land winds. This behaviour is clearly due to the more turbulent conditions experienced by land winds over the urban area. However, SP.02 PSD shows an inverted behaviour; indeed, land and sea winds are determined on a large scale, looking at the approximate coastline in the port areas, but SP.02 anemometer is in fact located over a building at the head of a dock. This indicates that the roughness in the immediate vicinity of the site is the determining factor. Moreover, let us notice that the location of both the micro-meteorological peak and the minimum varies between the port areas, turning out to be a local property, related again to the local roughness surrounding the anemometer site.

Although Genoa spectra do not show any dependence on night/daytime winds, La Spezia and Livorno daytime spectra result more energetic than the night ones in the transition range.

Finally, Figure 5 shows that the transition range does not identify a real spectral gap, since the energy drop does not occur in particular conditions and, anyway, the energy contribution of this range is not negligible with respect to that of the micro-meteorological range. However, the spectral gap can be still regarded as a separation region between two different inertial ranges, a region where a regime change occurs, the turbulent structures are less interactive and energetic and the classical $n^{-5/3}$ energy cascade
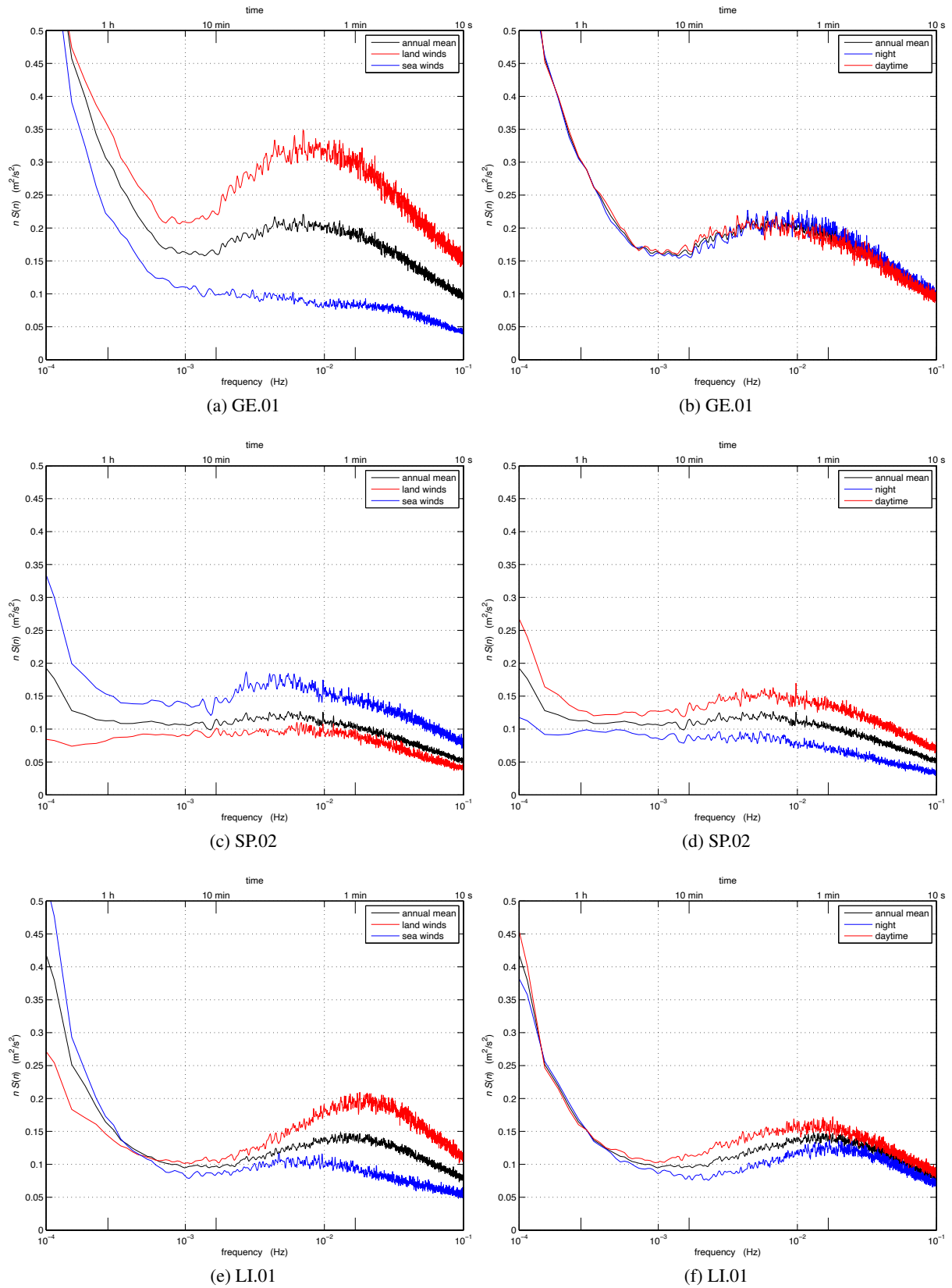
Figure 5. Comparison between 6h-PSD averaged among land/sea direction classes (left) and night/daytime classes (right) for GE.01 (top), SP.02 (centre) and LI.01 (bottom) datasets. In order to show the spectral contribution to the total variance, the frequency-PSD product $nS(n)$ is plotted; frequency axis is logarithmic.

slows down.

4   Conclusions

In this paper a wide investigation over wind spectral properties in the Northern Tyrrhenian port areas involved in the EU project "Wind and Ports" has been carried out by computing the power spectral densities of the intensity of horizontal wind velocity for 12 1-year datasets over different time ranges (between 0.1 seconds and 1 year), by composing the resulting spectra in a unique complete PSD for each dataset and by averaging them among different wind classes.

The macro-meteorological daily peak and its corresponding harmonics are clearly identified in all the spectra. A deviation from the Kolmogorov $n^{-5/3}$ law is observed in a 'transition range' between the macro and the micro-meteorological inertial ranges. In this transition range, spectra follow a power-law trend, compatible with a n^{-1} slope. This frequency range is the same where the 'spectral gap' is expected to occur, but that notion seems to be unsuitable to describe the regime change occurring in this region, where the active physical mechanisms generally result less energetic than in both inertial ranges. The extent of the three identified ranges and their energetic contribution shows directional and local dependences. In particular, the more the roughness experienced by the wind velocity is, the more energetic the micro-meteorological peak results; in this case the transition range come closer to the original notion of spectral gap, although its energetic contribution is not negligible.

References

Baker, C.J. (2010). Discussion of "The macro-meteorological spectrum — A preliminary study" by R.I. Harris, {JWEIA} 96 (2008) 22942307. *Journal of Wind Engineering and Industrial Aerodynamics* **98**.12, pp. 945–947. ISSN: 0167-6105.

Burlando, M., De Gaetano, P., Pizzo, M., Repetto, M.P., Solari, G., and Tizzi, M. (2013). Wind climate analysis in complex terrains. *Journal of Wind Engineering and Industrial Aerodynamics* **123, Part B**.0. The Twelfth Italian National Conference on Wind Engineering, IN-VENTO-2012, Venezia, Italy, October 7th10th 2012, pp. 349–362. ISSN: 0167-6105.

Burlando, M., De Gaetano, P., Pizzo, M., Repetto, M.P., Solari, G., and Tizzi, M. (2014). Short-term wind forecast for the safety management of complex areas during hazardous wind events. Submitted to *Journal of Wind Engineering and Industrial Aerodynamics*.

Harris, R.I. (2008). The macrometeorological spectrum — a preliminary study. *Journal of Wind Engineering and Industrial Aerodynamics* **96**.12, pp. 2294–2307. ISSN: 0167-6105.

Harris, R.I. (2010). Author's reply to discussion by C.J. Baker of "The macro-meteorological spectrum — A preliminary study" by R.I. Harris, {JWEIA} 96 (2008) 22942307. *Journal of Wind Engineering and Industrial Aerodynamics* **98**.12, pp. 948–950. ISSN: 0167-6105.

Hunt, J.C.R. and Morrison, J.F. (2000). Eddy structure in turbulent boundary layers. *European Journal of Mechanics, B/Fluids* **19**.5, pp. 673–694.

Kolmogorov, A. N. (1941). Local structure of turbulence in an incompressible fluid for very large Reynolds numbers. *Doklady Akademii Nauk SSSR* **30**, pp. 299–303.

Solari, G., Repetto, M.P., Burlando, M., De Gaetano, P., Pizzo, M., Tizzi, M., and Parodi, M. (2012). The wind forecast for safety management of port areas. *Journal of Wind Engineering and Industrial Aerodynamics* **104-106**. 13th International Conference on Wind Engineering, pp. 266–277. ISSN: 0167-6105.

Torrielli, A., Repetto, M.P., and Solari, G. (2011). Long-term simulation of the mean wind speed. *Journal of Wind Engineering and Industrial Aerodynamics* **99**.11, pp. 1139–1150. ISSN: 0167-6105.

Van der Hoven, I. (1957). Power spectrum of horizontal wind speed in the frequency range from 0.0007 to 900 cycles/h. *Journal of Meteorology* **14**, pp. 160–164. ISSN: 0095-9634.

An assertion for the annoyance of wind engineers

Chris Baker

School of Civil Engineering, University of Birmingham

The way that wind engineers have been carrying out statistical analysis of winds for the last 60 years is wrong.

Why?

➢ The analysis of winds has been carried out using data from single point near surface measurements at geographically fixed locations.

➢ These measurements are confounded by

  ➢ Changes to site surroundings over the decades

  ➢ The inability to distinguish between different storm types and physical causes (extra-tropical cyclones, thunderstorms, frontal winds, sting jets…)

UNIVERSITY OF BIRMINGHAM

Buildings around
measurement sites
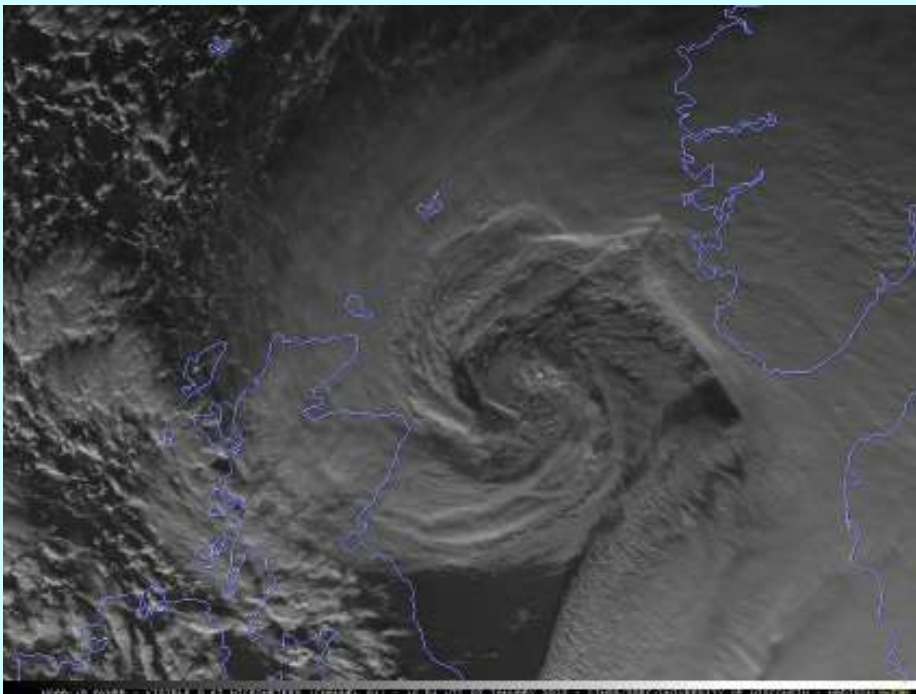
Sting jets and other
weather systems

Why?

➢ Current wind statistics contain no information on geographical scale (important for large network resilience studies)

➢ Current wind statistics do not allow for any consideration of climate change (mismatch between meteorological predictions and surface measurements)
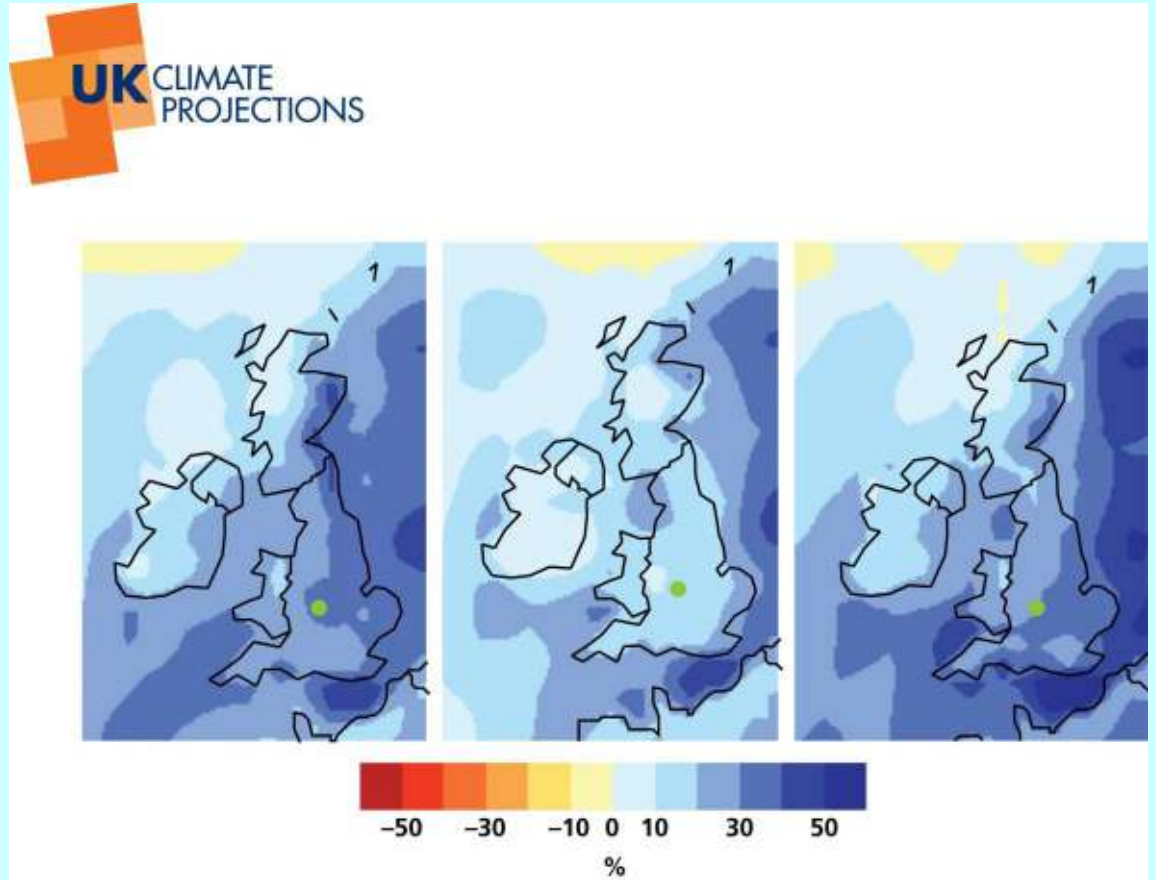
Is there anything better?

➢ Apply statistical modelling to physical parameters that are fundamental
  ➢ Storm track
  ➢ Strom strength
  ➢ Storm size
➢ Downscale to surface conditions from such data
➢ Debatable if current statistical methods (Extreme value analysis, Weibull) would be appropriate

UNIVERSITY OF BIRMINGHAM

Met Office

Most likely track

Monday 28 October 2013

MOST LIKELY
TRACK OF LOW

Be aware of very
strong winds and
heavy rain

Be prepared for
gusts of over 80mph

UNIVERSITY OF
BIRMINGHAM

SOME SLIGHTLY PROVOCATIVE STATEMENTS

- **Accurate boundary conditions** are **essential** for accurate and reliable wind-tunnel tests and CFD simulations.

- After many decades of wind engineering, we are **still not able** to specify/generate accurate boundary conditions. This particularly applies to approach flow conditions in combination with ground roughness.

- Problem of inaccurate boundary conditions is **insufficiently known**, and the related errors and uncertainties are **insufficiently assessed**.
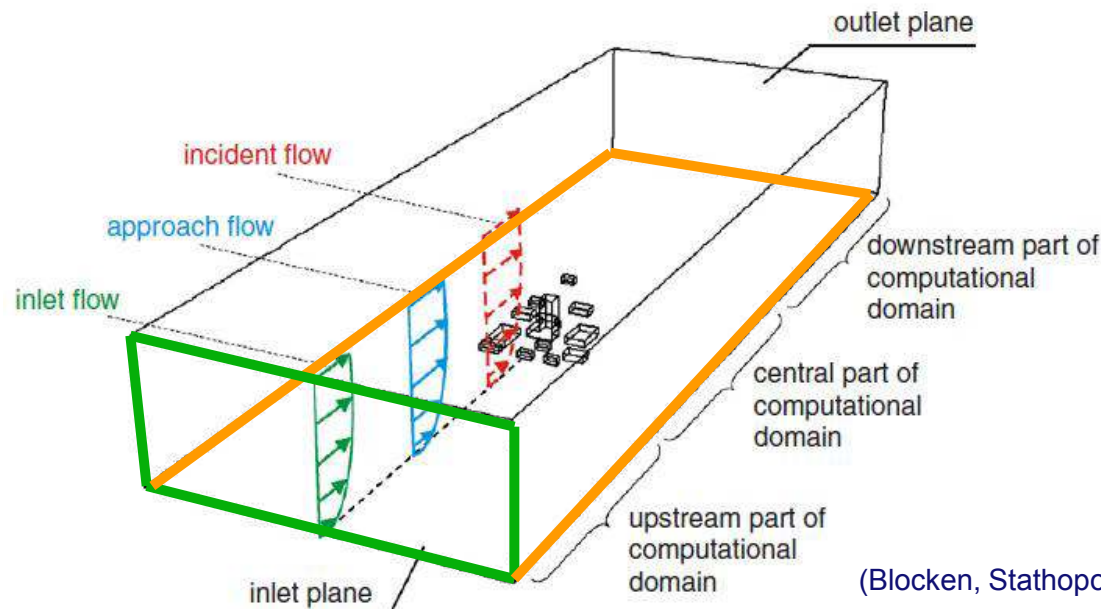
(Blocken, Stathopoulos, Carmeliet, Atmos. Env. 2007)

TWO QUOTES, TWO DECADES APART

- *"In 1958 Jensen showed that in wind-tunnel testing it is just as important to correctly model the wind as it is to correctly model the building. This lesson must surely carry over into the relatively new field of computational wind engineering." (Richards & Hoxey, 1993)*

Appropriate boundary conditions for computational wind engineering models using the k-ε turbulence model

P.J. RICHARDS
Senior Lecturer, Department of Mechanical Engineering, University of Auckland, Private Bag 92019, Auckland, New Zealand
R.P. HOXEY
Research Engineer, Silsoe Research Institute, Wrest Park, Silsoe, Bedford, MK45 4HS, England

- *" 'Appropriate boundary conditions for computational wind engineering' was an issue addressed by Richards and Hoxey at the first Computational Wind Engineering Conference and is still a relevant issue today."*
(Richards & Norris, 2011)

J. Wind Eng. Ind. Aerodyn. 99 (2011) 257–266

Contents lists available at ScienceDirect

Journal of Wind Engineering and Industrial Aerodynamics

journal homepage: www.elsevier.com/locate/jweia

ELSEVIER

Appropriate boundary conditions for computational wind engineering models revisited

P.J. Richards*, S.E. Norris

Mechanical Engineering, University of Auckland, New Zealand

HOT TOPIC

Non-exhaustive list of related papers:

2007: **Hargreaves, D.M., Wright, N.G.** On the use of the k–ε model in commercial CFD software to model the neutral atmospheric boundary layer. *J. Wind Eng. Ind. Aerodyn.*

2007: **Blocken, B., Stathopoulos, T., Carmeliet, J.** CFD simulation of the atmospheric boundary layer: wall function problems. *Atmos. Environ.*

2007: **Blocken, B., Carmeliet, J., Stathopoulos, T.** CFD evaluation of wind speed conditions in passages between parallel buildings—effect of wall-function roughness modifications for the atmospheric boundary layer flow. *J. Wind Eng. Ind. Aerodyn.*

2008: **Yang, W., Quan, Y., Jin, X., Tamura, Y., Gu, M.** Influences of equilibrium atmosphere boundary layer and turbulence parameter on wind loads of low-rise buildings. *J. Wind Eng. Ind. Aerodyn.*

2009: **Gorlé, C., van Beeck, J., Rambaud, P., Van Tendeloo, G.** CFD modelling of small particle dispersion: the influence of the turbulence kinetic energy in the atmospheric boundary layer. *Atmos. Environ.*

2009: **Yang, Y., Gu, M., Chen, S., Jin, X.** New inflow boundary conditions for modelling the neutral equilibrium atmospheric boundary layer in computational wind engineering. *J. Wind Eng. Ind. Aerodyn.*

2011: **Parente, A., Gorlé, C., van Beeck, J., Benocci, C.** Improved k-ε model and wall function formulation for the RANS simulation of ABL flows. *J. Wind Eng. Ind. Aerodyn.*

2011: **Richards, P.J., Norris, S.E.** Appropriate boundary conditions for computational wind engineering models revisited. *J. Wind Eng. Ind. Aerodyn.*

A MULTITUDE OF PROBLEMS

- Selection of aerodynamic roughness length of upstream terrain (used for "inlet profiles") in the Davenport-Wieringa roughness classification can easily be **one class off**.

	y_0 (m)	Landscape description
1	0.0002 Sea	Open sea or lake (irrespective of the wave size), tidal flat, snow-covered flat plain, featureless desert, tarmac, concrete, with a free fetch of several kilometres.
2	0.005 Smooth	Featureless land surface without any noticeable obstacles and with negligible vegetation; e.g. beaches, pack ice without large ridges, morass, and snow-covered or fallow open country.
3	0.03 Open	Level country with low vegetation (e.g. grass) and isolated obstacles with separations of at least 50 obstacle heights; e.g. grazing land without windbreaks, heather, moor and tundra, runway area of airports.
4	0.10 Roughly open	Cultivated area with regular cover of low crops, or moderately open country with occasional obstacles (e.g. low hedges, single rows of trees, isolated farms) at relative horizontal distances of at least 20 obstacle heights.
5	0.25 Rough	Recently-developed "young" landscape with high crops or crops of varying height, and scattered obstacles (e.g. dense shelterbelts, vineyards) at relative distances of about 15 obstacle heights.
6	0.50 Very rough	"Old" cultivated landscape with many rather large obstacle groups (large farms, clumps of forest) separated by open spaces of about 10 obstacle heights. Also low large vegetation with small interspaces such as bush land, orchards, young densely-planted forest.
7	1.0 Closed	Landscape totally and quite regularly covered with similar-size large obstacles, with open spaces comparable to the obstacle heights; e.g. mature regular forests, homogeneous cities or villages.
8	≥ 2.0 Chaotic	Centres of large towns with mixture of low-rise and high-rise buildings. Also irregular large forests with many clearings.

- Wind tunnels are usually only operated/equipped for **a few** of these eight roughness classes
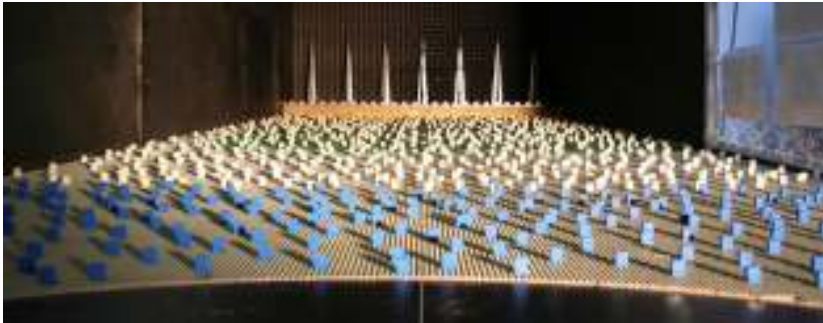
Courtesy of Christof Gromke
http://www.ifh.uni-karlsruhe.de/science/aerodyn/CODASC.htm

	y_0 (m)	Landscape description
1	0.0002 Sea	Open sea or lake (irrespective of the wave size), tidal flat, snow-covered flat plain, featureless desert, tarmac, concrete, with a free fetch of several kilometres.
2	0.005 Smooth	Featureless land surface without any noticeable obstacles and with negligible vegetation; e.g. beaches, pack ice without large ridges, morass, and snow-covered or fallow open country.
3	0.03 Open	Level country with low vegetation (e.g. grass) and isolated obstacles with separations of at least 50 obstacle heights; e.g. grazing land without windbreaks, heather, moor and tundra, runway area of airports.
4	0.10 Roughly open	Cultivated area with regular cover of low crops, or moderately open country with occasional obstacles (e.g. low hedges, single rows of trees, isolated farms) at relative horizontal distances of at least 20 obstacle heights.
5	0.25 Rough	Recently-developed "young" landscape with high crops or crops of varying height, and scattered obstacles (e.g. dense shelterbelts, vineyards) at relative distances of about 15 obstacle heights.
6	0.50 Very rough	"Old" cultivated landscape with many rather large obstacle groups (large farms, clumps of forest) separated by open spaces of about 10 obstacle heights. Also low large vegetation with small interspaces such as bush land, orchards, young densely-planted forest.
7	1.0 Closed	Landscape totally and quite regularly covered with similar-size large obstacles, with open spaces comparable to the obstacle heights; e.g. mature regular forests, homogeneous cities or villages.
8	≥ 2.0 Chaotic	Centres of large towns with mixture of low-rise and high-rise buildings. Also irregular large forests with many clearings.

A MULTITUDE OF PROBLEMS

- CFD simulations suffer from **incompatibility** between inlet profiles and wall functions, which gets even worse for stably and unstably stratified flows.
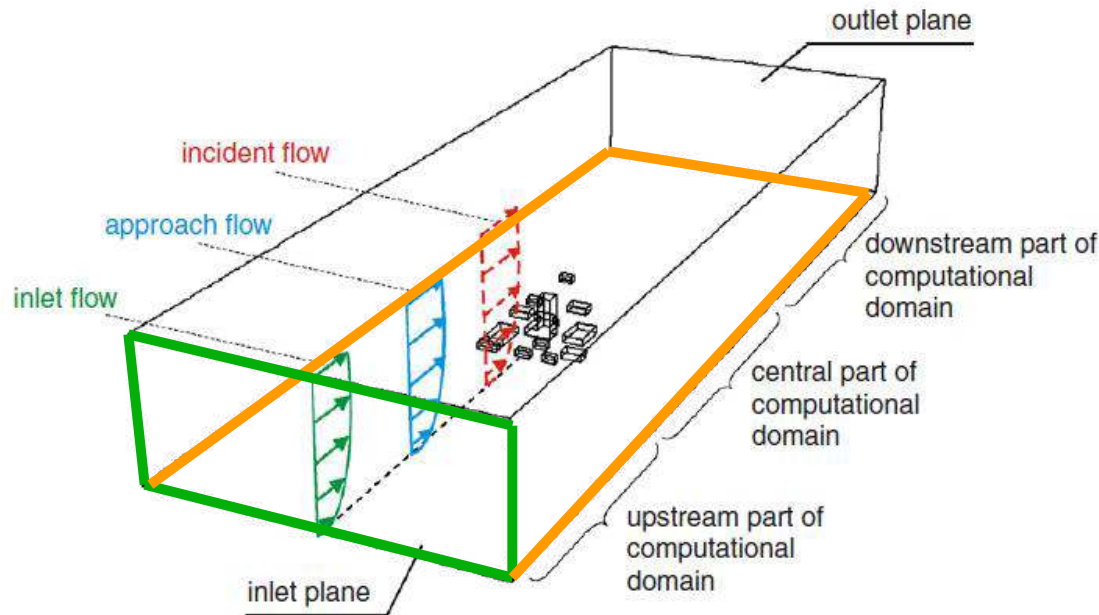
A MULTITUDE OF PROBLEMS

- Problem of inaccurate boundary conditions is **insufficiently realized**, and the related errors and uncertainties are **insufficiently assessed**.

Simulating and forecasting wind with meteorological models

Andrea Buzzi

Institute for Atmospheric Sciences and Climate
of the National Research Council
ISAC-CNR
and University of Bologna
Bologna, Italy

• The main job of our group of *Dynamic Meteorology* at ISAC in the last 25 yrs has been developing meteorological models for research and forecasting.

• A global hydrostatic model (**GLOBO** ~ 25 km), an intermediate scale hydrostatic limited-area model (**BOLAM** ~ 8 km) and a high-res. non-hydrostatic model (**MOLOCH** ~ 1.5 km) have been developed and are implemented for an experimental daily forecasting (used by the National Civil Protection).

GLOBO, 24 km
144 h

BOLAM, 8.3 km
72 h

MOLOCH, 1.5 km
48 h

Globo monthly forecasts

Globo archive

Blended precipitation

Moloch high res. wind

Bolam cross-sections

Moloch cross-sections

Bolam meteograms

Moloch meteograms

www.isac.cnr.it/dinamica/projects/forecasts/
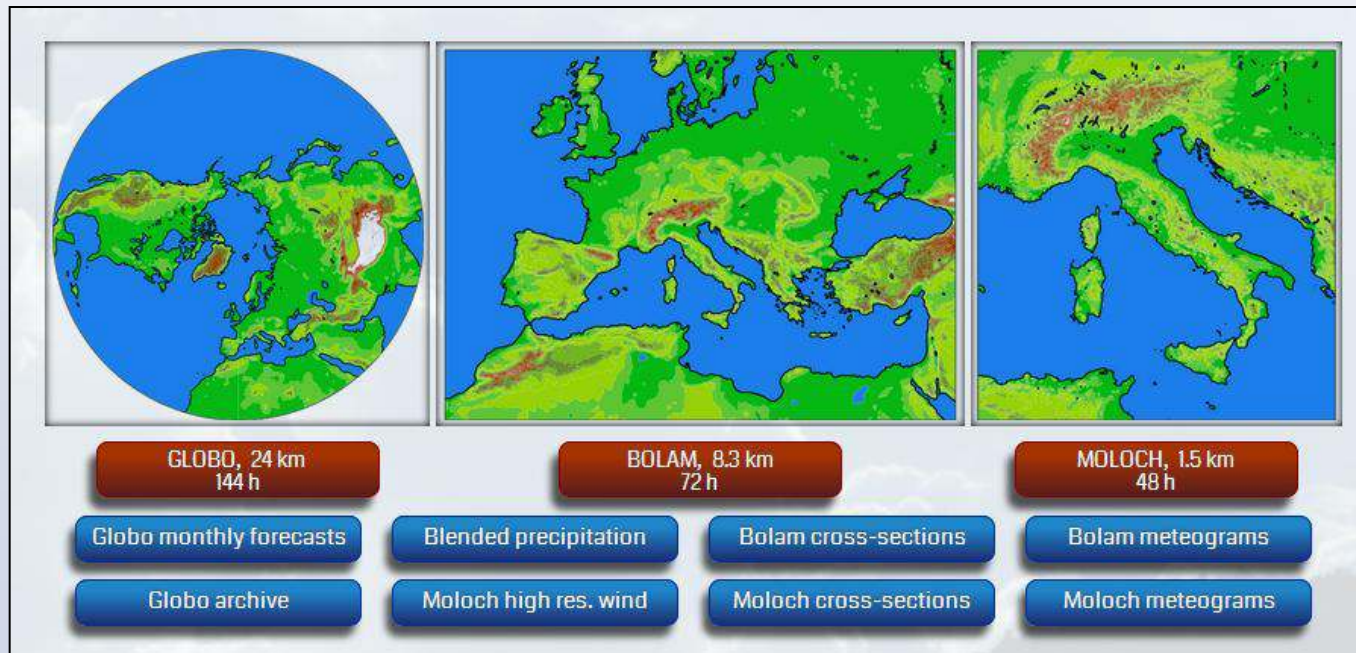
GENERAL CONSIDERATIONS:

• Energy (kinetic and potential) mainly comes from the large scales (astronomical forcing, baroclinic instability...) but partly propagates upscale (generated at smallest scales by turbulence, dry and moist convective instability, orography, land-sea contrast, latent heat exchanges...).

• The above physical processes impose severe limits of predictability (from 2 weeks down to less than one hour, depending on scales) and severe constraints on numerical methods.

• Weather forecasting requires a global model for more than 2-3 day forecast length, a continental scale model (~6000x6000 km) for 2 day forecasts, a ~1000x1000 km domain for 1 day forecasts - models are used in cascade (grid "nesting").

• Large errors derive from errors in initial conditions (errors of observations and errors of assimilation methods), model errors due to resolution but also parameterizations (necessary for subgrid phenomena), microphysical processes, turbulent fluxes inside and outside the atmospheric boundary layer, radiative transfer, soil and ocean surface fluxes, etc.

• We have mainly concentrated our efforts in improving forecasting of heavy precipitation and severe weather in general, that includes strong winds (disclaimer: we have no specific experience in wind forecasting for wind engineering applications!).

• Our "general purpose" forecasts seem popular among sailors... there is a surprising variability in our area around Italy, due mainly to complex orography - but verification over the sea is difficult.

• A part from errors due to the meteorological variability, we have for instance problems in representing well the diurnal cycle over land.

• Meteorological models, based on the definition of initial state and on the atmospheric equations, should not have particular limitations (except those buried in statistics related to data assimilation and parameterizations) in representing extreme events. However, they are not a suitable tool to generate statistics.
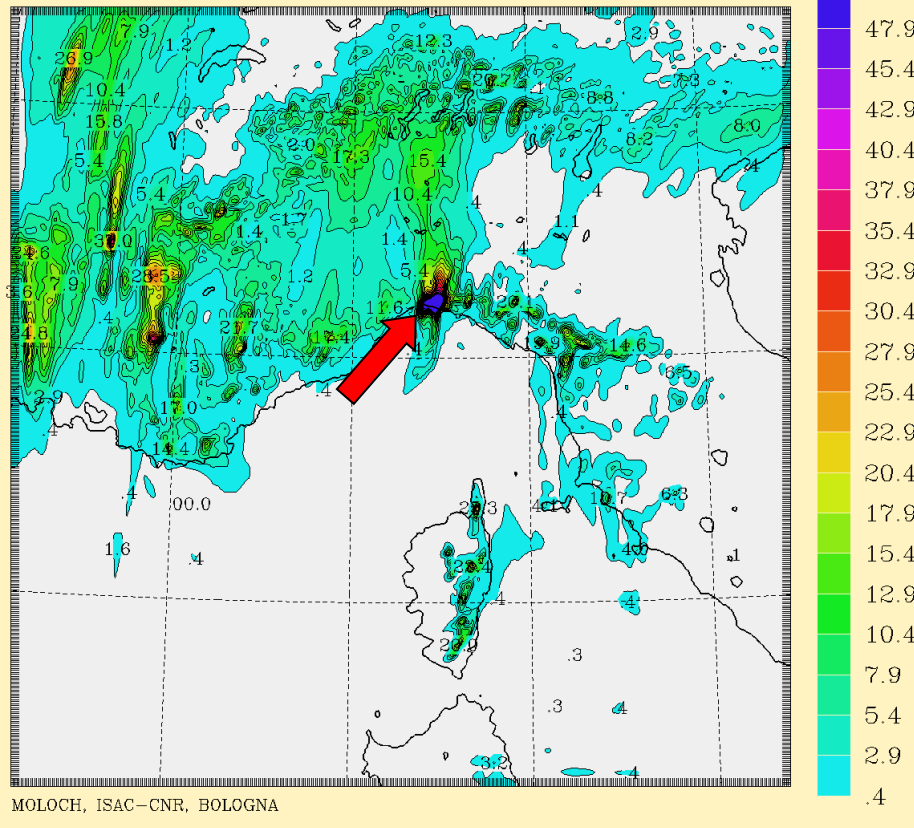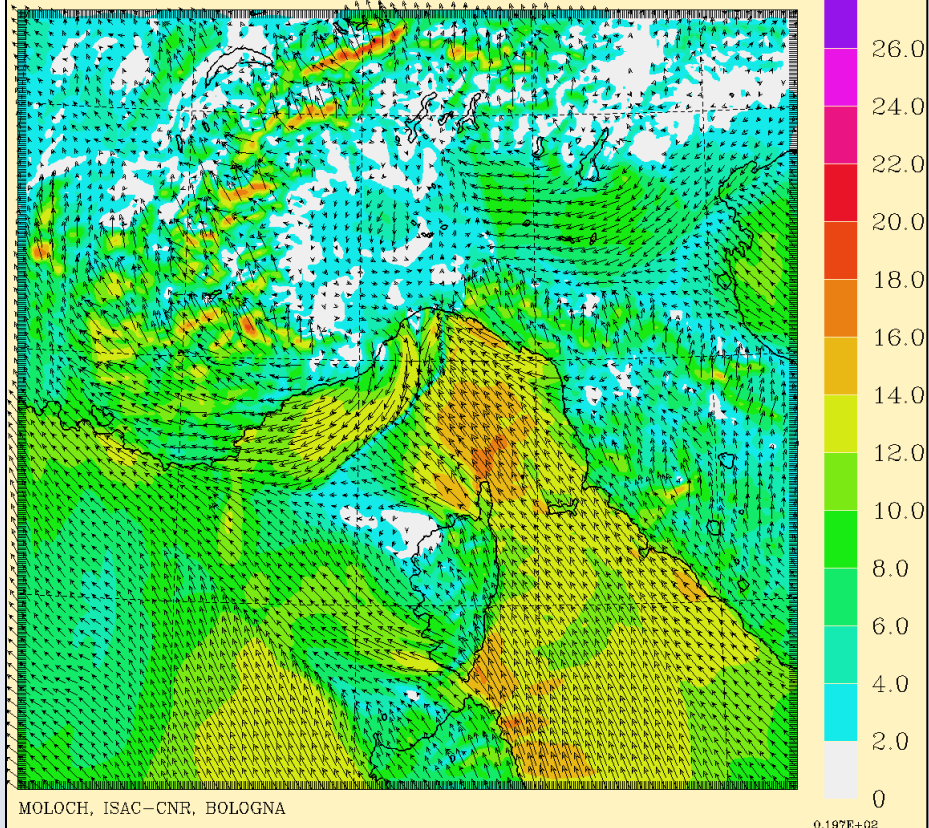
Example of precipitation (left) and wind forecast (right) at 1.5 km grid spacing, for the case of severe convection and flooding in Genoa, 4 Nov. 2011.

The complex surface wind is part of the mesoscale circulation maintaining the thunderstorm (arrow), but locally depends on the system dynamics.

(This organized convection exhibited a better predictability than normally expected)

Still, high resolution models seem to have difficulties in "beating" the ECMWF global model accuracy (except for precipitation), especially beyond 2 days.
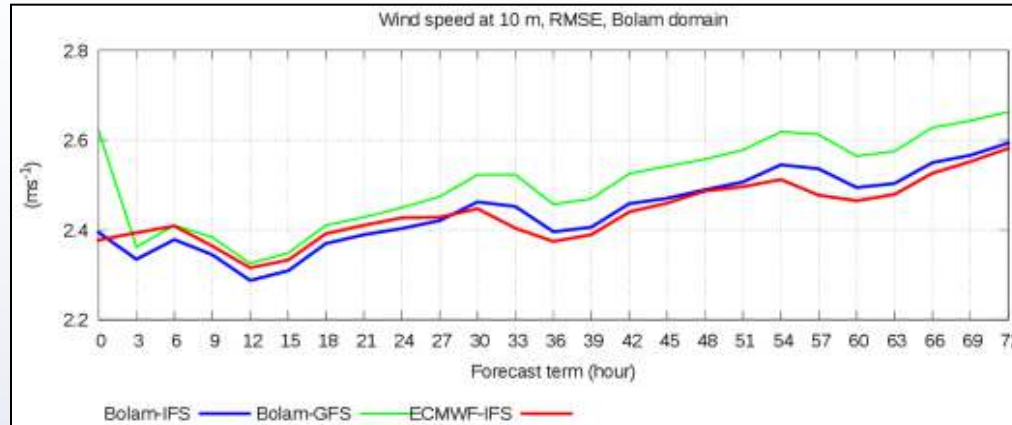
However, multimodel ensemble techniques (basically use of several meteorological models combined with statistical postprocessing) is an efficient (but expensive) tool to reduce not only systematic but also random errors of output variables, including wind.
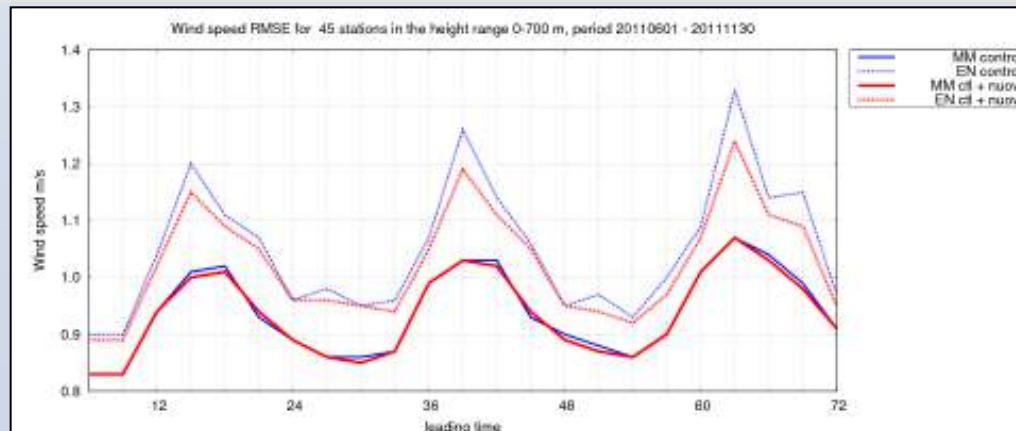
• Full meteorological models have practical (initial conditions, computational constraints) as well as theoretical (turbulence and microphysics representation) limitations for grid spacing less than ~1 km problem (probably one should jump to less than 100 m, using LES or DNS models.

• Use of simplified nested models (e.g. "mass consistent" wind models) in cascade, taking into account very small features in topography, are useful to improve wind representation (as it was done in a cooperation between us and the Wind Engineering group here in Genoa, for the assistance to the Italian sailing team during the London Olympic Games of 2012 in Weymouth).

The *past* (?)

- The twin towers of the *World Trade Center* in NYC were amongst some of the very first structures to be tested in a turbulent boundary layer wind tunnel..
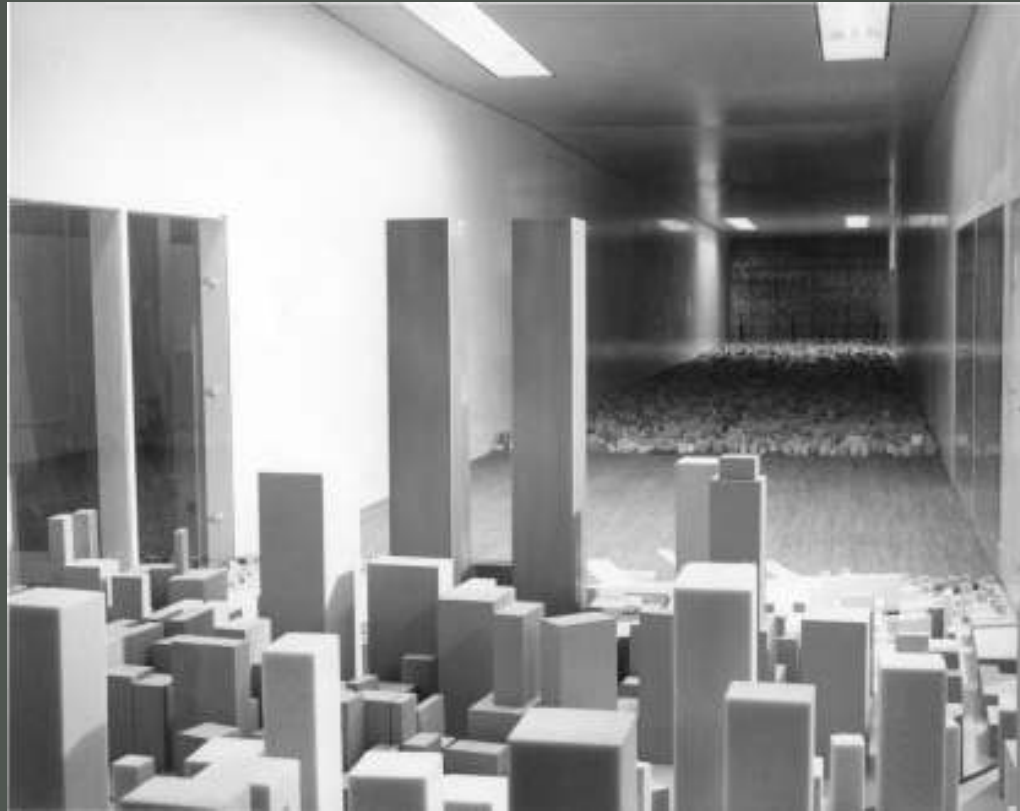
..has much changed since then?

BMT Fluid Mechanics

The *status quo*

- Synoptic scale low-pressure weather systems (e.g. extra-tropical depressions)

- Typhoons / Tropical cyclones / Hurricanes

- Topographical effects
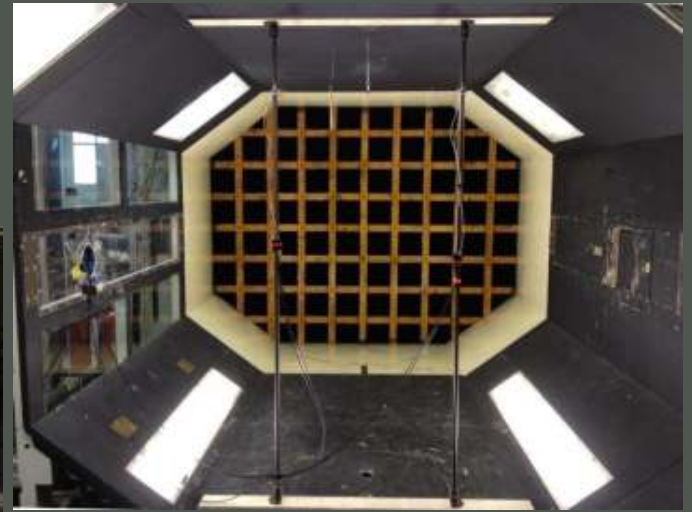
The *challenges*

- Improve simulation techniques for *transient flows* (e.g. microburst, tornados, thunderstorm)

- Have we got robust analytical models?

- Do we need more research / investments in **moving jet wind tunnel facilities**?

The *challenges*

- *Ekman spiral* and its potential effect on the design of super- & mega-tall buildings

- How much do we really know about 'winds' at high altitude?

- Is there anything we could perhaps learn from other industries (e.g. the yacht industry)?

- Could the *University of Auckland*'s Twisted Flow Wind Tunnel (TFWT) facility be a good starting point?

- If so, do we need more research / investments in **twisted flow wind tunnel facilities**?

The *challenges*

- *Scale effects* and their potential impact on the design of modern 'organic' architectural forms

- In the wind tunnel, have we got any realistic chance to get closer to the full-scale *Reynolds* number ($10^7 - 10^8$) flow regime?

- Do we need a new generation of wind tunnels for tomorrow's mega-tall & ultra-long structures?

- If so, is there anything we could perhaps learn from other industries (e.g. the aerospace industry)?

- Could we for instance get inspired by the *European Transonic Wind Tunnel* (ETW) in Cologne (Germany), a **cryogenic wind tunnel facility**..?

BMT Fluid Mechanics

Thank you

BMT Fluid Mechanics

Cross wind and rollover risk on lightweight railway vehicles

F. Cheli[1], S. Giappino[1], D. Rocchi[1], G. Tomasini[1]

[1]Politecnico di Milano, Department of Mechanical Engineering, Italy
Corresponding author: G. Tomasini, gisella.tomasini@polimi.it

Abstract

The paper investigates the effects of lateral wind on different type of railway vehicles, comparing the cross wind behaviour on a high speed train and on a modern train used for urban transportation. The second is characterized by a low operating speed, but also by a low mass that increases the risk of rolling over. In order to compare the two trains in terms of response to cross wind, two subsequent analyses have been performed: measurement of the force aerodynamic coefficients by means of wind tunnel tests on scale models and evaluation of the rollover risk by means of the definition of the Characteristic Wind Curve through a simplified numerical procedure, based on the static equilibrium, proposed by the TSI standard (three mass model).

1 Introduction

High cross-winds on rail vehicles may result in a risk of blowing over that can occur in practice, and in the design of any new train these risks have to be considered very seriously (Baker et al., 2009). This has led to the development of specific standards to lay out rigorous risk-assessment procedures for vehicles to operate (CEN, 2010; TSI, 2008) on exposed lines. All risk analysis methods require the knowledge of cross-wind aerodynamic force and moment coefficients that are generally obtained through wind tunnel testing on scaled models (Cheli et al., 2006; Bocciolone et al., 2008). Even if cross-wind effects are of critical importance in high-speed trains also lightweight railway vehicles can suffer of these problems.

In this research activity we compare the effects of lateral wind on a low speed, light-weight, train and a high speed train, in the following named *LS* and train *HS*. In order to compare the two trains in terms of response to cross wind, two subsequent analyses have been performed: win tunnel tests to measure the force aerodynamic coefficients and evaluation of the rollover risk by means of a numerical procedure (CWC).

2 Wind tunnels tests

2.1 Tests set-up

Wind tunnel tests on the two trains were carried out in the Politecnico di Milano Wind Tunnel employing a 1:20 scale model for the low speed train (Figure 1a) and a 1:15 scale model for the high speed train (Figure 1b). Tests were performed in the high-speed test section in low turbulence flow conditions. The convoy of the low speed train is composed by three vehicles while the convoy of the high speed train is composed by the power car and one half of the coach.

Table 1 summarizes the main dimensions (length, width and height) and the mass properties of the full scale vehicles for both the considered trains. Tests have been carried out on a flat ground scenario (without ballast and rails), which is one of the reference scenarios described in the TSI 232/2008 standard. To realize the flat ground scenario a splitter plate, 350mm high, has been adopted in order to have an equivalent block profile of the mean wind speed.

A force balance (RUAG 192) is used to measure the overall forces and moments on the vehicles. The non-dimensional aerodynamic coefficients are defined according to the CEN standard. The reference frame system is fixed to the carbody and its origin is coincident with the carbody centre, at ground level. The wind angle β_w with respect to the vehicle is zero when the wind is parallel to the vehicle, opposite to the running direction.

(a)   (b)

Figure 1. Wind tunnel models: low speed train (a) and high-speed train (b)

Table 1 Dimensions and mass properties of the two trains investigated

Train	Length [mm]	Width [mm]	Height [mm]	Total mass [kg]	Centre of gravity height [mm]
Low Speed	17455	2650	3600	29240	1680
High Speed	20250	3020	4000	66964	1329

2.2 Experimental results

Figure 3 shows the force coefficients most significant for the cross wind problem measured on the first vehicles of both the trains. It is possible to observe in the comparison that the lateral force coefficient (Figure 2a) on the low speed train is significantly lower.

(a)   (b)

Figure 2: Comparison between force aerodynamic coefficients of low speed and high speed train, first vehicle. C_{Fy} (a) and C_{Mxlee} (b)

Due to the coefficient definition, which uses a fixed value for parameters A (equal to 10 m^2) and h (equal to 3 m), the coefficients represent normalized forces based on the same reference dimensions that is a comparison in terms of actual forces on the full scale train. The C_{Mxlee} coefficient (Figure 2b)

shows the combined effect of the lateral and vertical forces in terms of overturning risk and it is used in the CWC calculation. The aerodynamic force is higher on the high speed train: this is mostly due to the train dimensions, in fact the lateral area of the high speed train is about 30% higher than the low speed one. On the other hand, the overturning risk is influenced not only by the aerodynamic forces but also by the inertial-dynamic properties of the rail vehicle: to evaluate the actual overturning risk it is necessary to calculate the Characteristic Wind Curves, as in the next section.

3   Characteristic Wind Curves

The two trains have been compared also in terms of CWC (Cheli et al., 2006; Baker et al., 2009; Cheli et al., 2012). As described in EN 14067-6, the most simple approach to calculate the CWC is the three mass model, based on the static equilibrium of all the acting forces and moments. The mass properties used to calculate the restoring moment due to the vehicle masses are reported in Table 1.

3.1   CWC results

Figure 3 shows the CWC evaluated for the two trains as a function of the absolute wind angle with respect to the track, for two vehicle speeds: V_{train}=80 km/h that corresponds to the commercial top speed for the low speed train (Figure 3a) and V_{train}=300 km/h that corresponds to the commercial top speed for the high speed train (Figure 3b). Figure 3a shows that the low speed train has lower CWC values with respect to the high speed train travelling at the same velocity: even if the high speed train has higher aerodynamic coefficients and so it experiences an higher aerodynamic moment, its high mass generates a corresponding high restoring moment increasing the CWC limit.

Figure 3. CWC for the two trains as a function of the wind angle (first vehicle only) for the maximum train speed: low speed train (a) and high-speed train (b)

In the same graph it is possible to observe that the lowest value of CWC in both the trains is reached not for perpendicular wind (β_w =90°), but at β_w =70°. This is due to the typical trend of the first vehicles aerodynamic coefficients that show the maximum value for a wind angle lower than 90° (see Figure 2). As expected a train speed increase reduces the CWC limit in the high speed train when it travels at the top speed (Figure 3b). It is interesting to compare the behavior of the two trains at their top speed; in fact, even if the low speed train has a maximum velocity equal only to 80 km/h, its CWC limit is even lower than the CWC limit of the high speed train travelling at 300 km/h. This behavior is also visible in the graph of Figure 4 that shows the CWC as a function of the train speed for the two wind angles β_w=70° and β_w =90°. The critical velocity decreases as the train speed increases and the limit value at the top speed is slightly lower for the low speed train.

Figure 4: CWC for the two trains as a function of the wind speed (first vehicle only). The CWC is limited to the maximum train speed

4 Conclusions

The paper investigated the cross wind effects comparing the behaviour of a high speed train and a low speed train. Modern low speed trains are often very light making them more sensitive to the overturning risk due to the lateral wind. The characteristic wind curves has shown that, limiting the analysis up to the commercial train top speed, a low speed train can have lower values of the critical wind velocity with respect to an high speed train.

Acknowledgements

References

Baker, C., Cheli, F., Orellano, A., Paradot, N., Proppe, C. & Rocchi, D. (2009). Cross-wind effects on road and rail vehicles. *Vehicle System Dynamics*, **47-8**, 983-1022.

Bocciolone M., Cheli F., Corradi R., Muggiasca S., Tomasini G. (2008). Crosswind action on rail vehicles: wind tunnel experimental analyses. *Journal of Wind Engineering and Indus-trial Aerodynamics*, **96**, 584-610.

CEN (2010), EN14067-6. Railway applications – Aerodynamics. - Part 6: Cross wind. CEN, Brussels.

Cheli, P. Belforte, S. Melzi, E. Sabbioni, G. Tomasini, (2006). A numerical-experimental approach for evaluating cross wind aerodynamic effects on heavy vehicles. *Journal of Vehicle System Dynamics Supplement*, **44**, 791-804.

Cheli, F., Corradi, R., Tomasini, G., (2012). Crosswind action on rail vehicles: A methodology for the estimation of the characteristic wind curves, *J. Wind Eng. Ind. Aerodyn.* **104–106**, 248–255.

TSI (2008), European Rail Agency. Technical Specification for Interoperability (TSI 232/2008) – Rolling Stock subsystem, 96/48/EC

The Case for Full-Scale Monitoring of Wind-Sensitive Structures: How to Capitalize on the Mutual Benefits for Structural Designers and Wind Engineers

Tracy L. Kijewski-Correa[1]

[1]Department of Civil & Environmental Engineering and Earth Sciences, University of Notre Dame, USA

Corresponding author: Tracy L. Kijewski-Correa, tkijewsk@nd.edu

Abstract

In recent decades, full-scale monitoring has proven to be a powerful tool for closing the gap between design predictions and actual as-built performance, particularly in seismic zones and for a growing portfolio of bridges. Why then has the wind engineering community not achieved similar large-scale monitoring campaigns and dense arrays on signature structures? How can we reverse this trend to take full advantage of this "living laboratory" to enhance our understanding of wind effects on structures? This paper will focus on these questions by overviewing the current state-of-the-art in full-scale monitoring of tall buildings, demonstrating the benefits that can be gained both for structural designers and wind engineers using examples from the author's personal experiences. Then the author will present a "roadmap to adoption" to capitalize on these mutual benefits using appropriate incentives and strategies to encourage widespread implementation of embedded sensing so that both communities can grow their knowledge base and enhance the safety, efficiency and economy of future structures.

1 Introduction

Ever since ancient times, Civil Engineers have been responsible for producing projects of impressive scale, cost and complexity, with significant life safety implications. The features that make these projects impressive, specifically their scale and cost, also prohibit the use of full-scale prototyping common in other engineering disciplines. Instead, numerous assumptions must be made each day by designers to simplify highly complex and uncertain structures into manageable finite element models, without ever truly knowing the implications of these choices. They are then forced to make even less guided choices when specifying the anticipated level of damping, having no reliable predictive tool to consult in the design stage. This information is then relayed to wind tunnel consultants, who rely on scaled models and simulated boundary layers to estimate equivalent static wind loads and acceleration responses. One can argue that these approaches, when coupled with modern codes and standards and sound heuristic principles, have historically enabled experienced engineers to efficiently develop safe designs; however, our inability to accurately simulate the actual performance of constructed systems has necessitated considerable conservatism in that design process…conservatism that will become even more challenging to assure due to the increasing complexity of our urban environments: according to the Rockafeller Foundation, 50% of the world's population now inhabits urban zones; by 2050, this is projected to grow to 75%. This implies that the demand for tall buildings will continue to grow worldwide, with mean heights rapidly ascending and often accompanied by the complexities of modern free-form architecture.

Such complexities in engineered systems warrant as-built performance validation using state-of-the-art sensing and diagnostics, which has been invaluable for a number of allied industries such as aerospace and automotive engineering. The manufactured systems developed in these fields are heavily instrumented to provide essential feedback both for quality assurance and design improvements, but also for maintenance and operations in-service. While these fields have embraced technology as an essential partner in their design and manufacturing process, the same sadly cannot be said in structural engineering, despite the fact that such systems arguably have even more to gain from

in-situ validation given their uniqueness, scale, complexity and cost. For example, modern tall buildings now attract price tags in the hundreds of millions of dollars and are responsible for providing safe and comfortable home and work environments for their occupants.

Perhaps the stark difference in attitudes toward the use of monitoring stems from history itself: the earliest uses of monitoring for assessment of tall building performance in the US were associated with "suspect" buildings, e.g., the John Hancock Tower in Boston (Durgin, 1990). These unsavory origins made the concept of proactive monitoring quite foreign, as owners were naturally reluctant to install instrumentation systems for fear that this may tarnish the reputation of their buildings. As a result, years later, designers continue to push the envelope with increasingly tall and complex structural forms whose designs remain underpinned by the same collection of un-validated tools and approaches. This lack of in-situ validation has not gone unnoticed by the tall buildings community. The recent CTBUH *Roadmap on the Future Research Needs of Tall Buildings* identified the top two priorities in the category of structural performance to be (1) "research on the development and implementation of **real-time structural monitoring** of completed tall buildings" and (2) research on the **validation of modelling assumptions for wind** and seismic **loading** (Oldfield et al., 2014).

CTBUH has rightfully recognized how large-scale strong motion monitoring campaigns in seismically active regions have done much to bring instrumentation into the mainstream of practice, not only to better understand the behavior of a diverse array of structures under earthquakes, but to aid in post-event evaluation and reoccupation. Similar strides have been achieved for other constructed systems like bridges, with numerous case studies of "Structural-Identification" recently chronicled (Catbas et al., 2013). So why then has the tall buildings community, which has been historically aligned with the wind engineering community, not achieved similar successes? Why are large-scale monitoring campaigns and even dense arrays on signature structures lacking? How can we reverse this trend to take full advantage of this living laboratory to enhance our understanding of wind effects on structures? This paper will focus on these questions by overviewing the current state-of-the-art in full-scale monitoring of wind-sensitive structures, demonstrating the benefits that can be gained both for structural designers and wind engineers using examples from the author's own experience to identify incentives and strategies that can further promote the use of full-scale monitoring in the tall building and wind engineering communities.

2   State-of-the-Art in Tall Building Monitoring

As tall building designs are generally governed by serviceability and habitability limit states under wind, they exhibit strong sensitivity to their dynamic properties. Thus the design process governing these buildings faces considerable need for validation in four critical stages:

(1) Accuracy of predicted natural frequencies and mode shapes from finite element models
(2) Appropriateness of assumed damping values
(3) Effectiveness of wind tunnel testing in predicting acceleration responses
(4) Acceptability of acceleration levels among occupants

Unfortunately, each of these four areas has scarcely benefited from full-scale validation. For instance, historical full-scale damping values are generally tied to comparatively shorter structures, whose underlying structural systems differ fundamentally from modern tall buildings, e.g., a large portion of the buildings in the well-known Japanese database (Satake et al., 2003) and the buildings involved in the full-scale measurement projects in the UK (Jeary and Ellis, 1979; Littler and Ellis, 1992). Meanwhile, in the case of habitability assessment, the determination of acceptable performance requires understanding the complex interaction between the human occupant and the structure, which in and of itself has stirred considerable debate. Unfortunately, only limited studies have attempted to resolve these debates through full-scale investigations (e.g., Ohkuma, 1991; Ohkuma, 1996; Denoon et al., 1999) and even fewer have been tied to actual validation of wind-induced response predictions (e.g., Littler, 1991). It was only recently that a handful of monitoring programs surfaced to validate the these four critical stages for modern tall buildings, including the author's own work in Boston, Chicago (Kijewski-Correa et al., 2006), Seoul (Abdelrazaq et al., 2005) and Dubai (Kijewski-Correa et al., 2013) and a collection of buildings in Hong Kong, mainland China and Taiwan, including Central
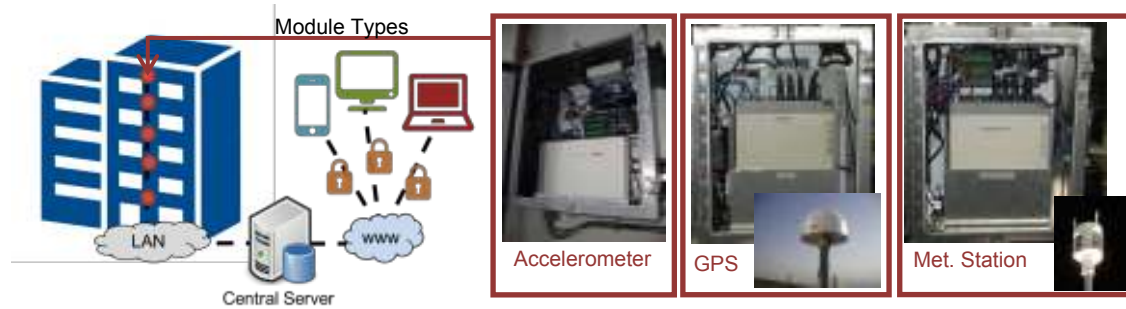
Figure 1. Schematic representation of Smart Sync concept with insets of hardware modules.

Plaza, Jin Mao, Bank of China and Taipei 101 (Li et al., 2002; Li et al., 2003; Li et al., 2004; Li et al., 2004; Li and Wu, 2004; Li et al., 2005; Li et al., 2006; Li et al., 2007; Li and Wu, 2007; Li et al., 2011; Campbell et al., 2005; Campbell, 2007; Xu and Zhan, 2001).

Traditionally, these monitoring programs have employed wired systems, often termed "hub and spoke" due to the fact that the sensors are located throughout the structure and then wired to a central data acquisition unit (datalogger). While reliable, the use of instrumentation cables presents significant cost and feasibility issues for distributed infrastructure monitoring. Thanks to a number of technology advancements taking advantage of wireless communications, multi-hop radio or cellular relays have replaced cables in some recent applications to ease installation, relocation and maintenance burdens. The SmartSync system was then introduced in the author's monitoring program for Burj Khalfia to utilize the building's existing Internet backbone as a system of "virtual" instrumentation cables (so called data acquisition over local area networks or DAQ over LAN) that connects a series of self-contained instrumentation modules, shown in Figure 1, that can be moved to any location with access to power and an Internet connection (Kijewski-Correa et al., 2013).

Regardless of the architecture of the data acquisition network, these systems rely on high precision, low-frequency accelerometers as the primary sensing element, generally supplemented by on-site wind velocity measurements. However, recognizing that wind-induced responses of tall buildings can only be truly characterized by displacement measurements capable of capturing the mean and background response, a number of tall building monitoring efforts have also employed Global Positioning Systems (GPS) (Kijewski-Correa and Kochly, 2007; Brownjohn et al., 2006; Tamura et al., 2002). Unfortunately, the use of pressure taps and other distributed displacement sensing is the exception, not the rule for tall building monitoring.

Even with only a handful of accelerometers, these isolated monitoring programs have made important contributions to our collective understanding of tall buildings under wind. Summarizing herein all that has been learned in a decade of such efforts by the author and her contemporaries would prove impossible; however, the following summarizes the author's personal inventory of some of the value that has been added by the full-scale monitoring she has been involved with:

- Comparisons of wind tunnel predicted and observed acceleration levels for a range of wind speeds and directions over periods of years (Bashor et al., 2012; Kijewski-Correa et al., 2013)
- Comparisons of wind tunnel predicted and observed displacements, isolating proportion of background response in full-scale using GPS (Kijewski-Correa and Kochly, 2007)
- Identification of in-situ damping levels over a range of amplitudes and correlation with structural system typologies for more reliable predictive damping models (Kijewski-Correa et al., 2013; Williams et al., 2013)
- Identification of in-situ natural frequencies over a range of amplitudes and correlation with finite element models to reveal implications of modelling assumptions related to cracked section properties, panel zones, boundary elements and participation of gravity elements in the lateral resistance (Kijewski-Correa et al., 2013; Bentz et al., 2010)
- In-situ quantification of occupant comfort through voluntary online surveys mapped to measured building responses and projected rates of disruption through pseudo-full scale

evaluation tools (Bentz and Kijewski-Correa, 2009; Kijewski-Correa and Pirnia, 2009; Weigand and Kijewski-Correa, 2013)

- Determination of root causes of unusual or unexpected behaviors, including large amplitude responses in transient wind events (Bentz and Kijewski-Correa, 2011)

3   Unique Barriers to Applications in Wind Engineering

Despite the fact that the only opportunity for our profession to advance its knowledge about the actual behavior of our "products" and the appropriateness of the assumptions, models and approaches used in their design is to observe them in-situ following construction, there remain comparatively limited applications of full-scale monitoring. While there has been general speculation about the reasons for this lack of uptake (Catbas and Kijewski-Correa, 2013), in the case of monitoring wind effects on structures there are some compounding difficulties, largely a function of scale.

3.1   A Problem of Temporal Scale

Contrary to allied professions whose design limit states recur more frequently or can even be artificially simulated at full-scale, monitoring of civil infrastructure under natural loading conditions requires a long-term commitment on the order of years that still in no way guarantees that any design-level events will be observed. Securing a commitment to not only maintain the hardware and communications backbone, but also the personnel processing the data for such a long duration can be especially challenging. While the long-term nature of required monitoring is true regardless of the hazard, in wind the support for data analysis is especially important as the annual recurrence of events implies that data will need to be processed and analyzed more frequently, whereas a seismic monitoring system may experience only a few noteworthy events in the entire lifetime of the structure. Unfortunately, the monitoring systems that are currently installed in tall buildings are generally viewed as an academic exercise rather than an integral component of the building operations worthy of a dedicated annual operating and maintenance budget.

3.2   A Problem of Spatial Scale

Monitoring wind effects on structures also suffers from barriers at a spatial scales. At the scale of the structure itself, the aforementioned issue of instrumentation cables, which is a non-issue for instrumentation in automobiles and even aircraft, presents major challenges in buildings. And while seismic monitoring applications focus on comparatively low-rise buildings for which a wired instrumentation system may still be feasible, wind-sensitive structures can have exceptional height, making the use of instrumentation cables especially daunting. This issue of scale also contributes to our inability to quantify wind loads in full-scale. The nature of earthquakes places few additional hardware requirements to capture the input to the system (ideally just nearby free-field accelerometers). In the case of wind, the load effects cannot be quantified without an additional significant investment in pressure taps whose density, particularly given the scale of tall buildings, can never be practically adequate to truly capture the load effect. Thus both the wind load effect and even the response, referring back to the previous section's discussion of the role of GPS in capturing mean and quasi-static responses, requires greater densities of sensors over greater spatial scales and supplementation of accelerometers with other sensing modalities that are not as affordable and/or simple to install. As such many programs will rely only on acceleration data, which then can only be analyzed by select system identification approaches due to the lack of measured system inputs and requires particular care in processing due to the signal's comparatively low frequencies and low amplitudes.

Then there is the issue of the hazard's geographic scale – while seismic monitoring programs are confined to select regions of high seismicity, wind affects structures essentially worldwide and thus instituting monitoring programs to capture the many unique wind climates and exposures means monitoring campaigns truly need to coordinate globally. As such, these problems of spatial scale have

significant implications for coordinating and financing the density and diversity of instrumentation programs truly needed.

4   Roadmap to Adoption

The aforementioned barriers are not trivial to overcome and ultimately reduce to a question of cost. While federal agencies engaged in seismic monitoring, e.g., USGS, have extended their mandates to buildings, those focused on meteorological phenomenon have not. Thus, the private sector will need to lead take charge in demanding the implementation of embedded sensing so that the both structural and wind engineers can grow their knowledge base and enhance the safety, efficiency and economy of future structures. To do so, appropriate incentives and strategies will be needed, since this will represent a major cultural shift a private sector who had not formally engaged in research & development (R&D). While a handful of leading structural engineering firms and wind tunnel consultants do engage in research and present and publish their findings, the majority of the private sector relies on academic, professional or governmental organizations to lead research initiatives that eventually translate into standards of practice. This culture is in sharp contrast to other engineering disciplines where the private sector not only leads R&D but even funds research activities at universities, but is understandable considering the slim profit margins and lack of a consumer-driven market to incentivize in-house R&D. However, there will be no progress in achieving this culture shift as long as the private sector remains unconvinced of the value of full-scale monitoring due to a lack of compelling evidence that these systems can deliver as promised and improve their ability to design and maintain their buildings. As such, we next consider potential incentivizes to help champion greater use full-scale monitoring, followed by the strategies necessary to maintain their cost effectiveness.

4.1   Incentive 1: Providing Value to Building Ownership

Direct financing by building ownership will occur only when true "value added" can be demonstrated. In seismic applications, the potential for rapid assessment and reoccupation following a major earthquake, through the use of pre- and post-event data analysis, can reduce downtime and enhance safety by revealing defects that may not be visually apparent. This has been taken to extreme cases through the requirement of monitoring for certain classes of buildings, which of course serves as the strongest incentive of all. Thus there have been genuine incentives for and even an openness toward sharing the insights gained through full-scale monitoring under earthquakes[1]. The same compelling life-safety arguments cannot be presented for wind, and thus other return on investment must be demonstrated. For most owners, evaluation of performance is not a sufficient motivator, though in the case of tall buildings, this may have some value if data can be translated to knowledge that drives decision making, e.g., in-situ assessments of occupant comfort (Kijewski-Correa and Pirnia, 2009; Weigand and Kijewski-Correa, 2013; Weigand and Kijewski-Correa, 2013). With the exception of signature structures like Burj Khalifa, many owners have yet to realize or, more appropriately, yet to be presented with a worthwhile value proposition by the engineering community.

4.2   Incentive 2: Providing Value to Engineers and Consultants

While the value proposition to building owners is more challenging, structural engineers and wind tunnel consultants have a clearer direct benefit from full-scale monitoring for their projects as a critical validation step for the assumptions made in the design process. In essence, firms that employ systematic monitoring as part of the project quality assurance processes would have a legitimate

---

[1] Interestingly, wind hazard monitoring of tall buildings in the US often requires strict anonymity, whereas in seismic applications, building identities have been revealed. Such lack of transparency in building names, details and other information truly needed for the community to benefit from published findings has been a further hindrance that the author again attributes to the differing attitudes towards "life safety" monitoring and serviceability/habitability monitoring.

competitive advantage in being able to deliver the optimized and efficient designs or reliable test results essential to maintain competitiveness in the global marketplace. Thus it is much more likely to incentivize firms to build monitoring programs into the project requirements and thus have the building owner indirectly finance the operation. Further, in reflecting back upon the author's experiences in full-scale monitoring, having the original engineers of record and the original wind tunnel consultants involved in the full-scale validation process is invaluable; however, when this process transitions from academic research to private-sector quality assurance, which is likely the only means to realize monitoring on a large scale, it is less likely to be disseminated and fully disclosed to grow the knowledge base of the community as a whole (if it were, the competitive advantage would be completely lost). Thus without a collection of major structural engineering firms and wind tunnel facilities forming a consortium to collude in both mandating the instrumentation of their projects as well as the open exchange of the findings, its potential impacts will never be realized.

4.3   Strategy 1: Rapidly Deployable Monitoring Modules

With the exception of buildings for which a local failure is concerning, e.g., fatigue of a specific element, global response monitoring is more than sufficient for validation of the design process. While accelerometers and dataloggers are fairly cost-competitive, the greater challenge lies in the installation of lengthy cables particularly vertically over the structure to allow quantification of mode shapes. Movement toward DAQ over LAN solutions, such as those described earlier in this paper, provides an attractive alternative. While this monitoring architecture is especially feasible for tall buildings, moving toward self-contained modules that are readily deployed with plug-and-play ease also makes the technologies more accessible to a wider segment of the engineering community who may wish to use them. Even in instances where the data is locally stored due to the lack of a reliable communication means (and given the low cost of memory, this enables operation over very long periods of time), moving toward such a modular approach to hardware design means that these units can be pre-fabricated and then deployed on structures on-demand. Thus while not every building may warrant a permanent monitoring system, in advance of a landfalling hurricane/typhoon or other major storm, these modules can be temporarily deployed on a large portfolio of buildings to capture responses that at least approach critical limit states of design. Regardless of whether permanently or temporarily deployed, wide-spread monitoring is a necessary strategy in order to systematically validate design practice. Considering the uniqueness of each building and the diversity of structural systems, geometries and materials to be canvased, the removal of instrument cables creates the most cost-effective approach to do so.

4.4   Strategy 2: Automated Data Processing and Mining

In order to achieve true systematic validation under a range of wind events with mean recurrence intervals on the order of 10 years or more and for various angles of attack, long-term monitoring is essential. Over the course of such extended monitoring, substantial quantities of data are generated and, while valuable, their effective mining can prove challenging. Maintaining the cost-competitiveness of large-scale monitoring programs precludes the contractual support for personnel to manually process and analyze the acquired data, though, as mentioned previously, some support for annual system (hardware, software) maintenance, upgrading or on-demand servicing should be expected. Unfortunately, enabling automated processing of data is challenging given that many established techniques do not lend themselves well to unattended operation, often requiring considerable skill and experience to obtain reliable estimates of quantities such as damping. However, without investing in the creation of automated frameworks to do so, long-term monitoring will never scale. Such automated processing must go beyond simply web-interfaces that enable users to process, archive, query and visualize acquired data (Kijewski-Correa et al., 2013). As such, we presently are developing automated frameworks to mine over a decade of data collected from over 70 tall buildings in our data warehouse. The framework, shown in Figure 2, passes data through a signal processing module that conducts a variety of statistical analyses, in parallel with a system identification module to extract the dynamic properties. The latter module is tightly coupled with a variety of quality assurance indicators appropriate for the system identification methodology employed, which specifies the reliability of the
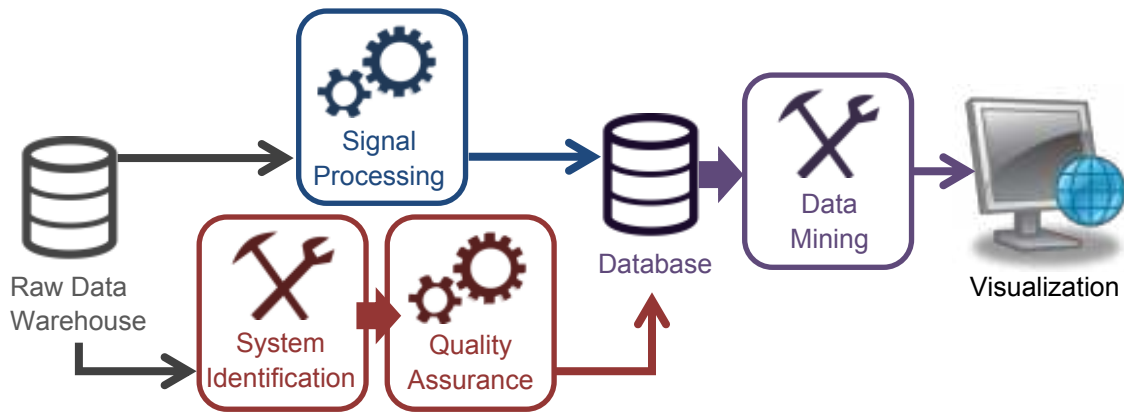
Figure 2. Schematic of automated processing framework long-term monitoring data.

estimated properties and flags records with anomalous features. The parameters extracted from these modules are then curated in a database that is then mined and visualized to reveal trends and relationships within the data that may have been obscured due to the inability to efficiently process such volumes of data manually. Ultimately, such approaches streamline the data management and, while they cannot replace the human analyst, provide a means to maximize the knowledge generated by years of archived data and can even identify evolving trends within the data that may suggest deterioration of the system. Of course, the types of data analyses and visualizations must be customized for the needs of the client, as the type of information desired by engineers varies significantly from that of building owners (Weigand and Kijewski-Correa, 2013).

4.5   *Strategy 3: Hybrid Sensing of Wind Loads on Structures*

The spatially distributed and random nature of wind loads on structures constitutes a major barrier to scalably quantifying them in full-scale. Even if one structure is pressure tapped with sufficient density to characterize its wind loading, it will do little to support the validation of current predictive tools for wind loading and ensuing response for a wide range of building geometries and exposures. Interestingly, a different issue of scale has recently been addressed in the earthquake engineering community through the use of real-time *hybrid simulation*: the use of a computational model that is dynamically integrated with experimental data collected from a component whose behaviors are not well understood. It may indeed be warranted that the wind engineering community similarly advocate for *hybrid sensing* as a compromise to the challenge of quantifying wind loads on structures. By integrating computational fluid dynamics (CFD) models with strategically placed point measurements, the computational model can be dynamically calibrated to offer a more reliable description of the pressures acting on the building envelope than a limited number of pressure taps alone could provide. Such hybrid approaches have been shown to be effective in enhancing the reliability of CFD models in predicting the evolution of contaminant plumes in urban zones (in real-time) and even in hindcasting the point origin of the contaminant (Kijewski-Correa et al., 2009). Of course the extension of this concept to the quantification of full-scale wind load effects requires greater fidelity in the underlying CFD model and as such may limit the ability to execute such operations in pseudo real time, though off-line analysis and dataset augmentation is completely feasible.

5   Closing Remarks

The uniqueness and uncertainties associated with constructed systems render their actual properties and response, particularly under wind, to be extremely difficult to predict accurately. Our work to date has affirmed how little is truly known about the performance of constructed systems and further has motivated the need for a sustained commitment to full-scale monitoring. While the value of full-scale monitoring cannot be denied, our current approach as a community to developing, promoting and implementing these systems simply cannot scale to the level needed to provide true, systematic

validation we require. This paper focused in particular on the state-of-the-art in full-scale monitoring of tall buildings as an example application where the wind and structural engineering communities can unite to achieve mutual benefits. In the processes, the unique barriers that these and any other monitoring programs focused on wind hazards inevitably face were presented. Noting these challenges presented by this application's spatial and temporal scales, the author then offered incentives to attract private sector investment for full-scale monitoring as well as strategies that can reduce the cost and maximize the coverage of monitoring programs for wind by focusing on re-deployable modular sensor networks, hybrid sensing of wind loads on structures, and automation of the data processing and management in long-term monitoring. There is no doubt that it will require considerable innovation and a truly cooperative effort across our community if we are truly take advantage of the living laboratory that full-scale provides; however, the benefits we will gain are too great to squander.

6   Acknowledgements

References

Abdelrazaq, A., Kijewski-Correa, T., Young-Hoon, S., Case, P., Isyumov, N., and Kareem, A. (2005). Design and Full-Scale Monitoring of the Tallest Building in Korea: Tower Palace III. *September, Seoul, Korea.*

Bashor, B., Bobby, S., Kijewski-Correa, T., and Kareem, A. (2012). Full-Scale Performance Evaluation of Tall Buildings Under Wind. *Journal of Wind Engineering & Industrial Aerodynamics* **104-106,** 88-97.

Bentz, A., and Kijewski-Correa, T. (2011). Wind-Induced Vibrations of Buildings: Role of Transient Events . *Proceedings of the ICE, Structures and Buildings* **164,** 273-284.

Bentz, A., Young, B., Kijewski-Correa, T., and Abdelrazaq, A. (2010). Finite Element Modeling of Concrete Lateral Systems in Tall Buildings: Insights from Full-Scale Monitoring. *10Th Annual Structures Congress, May 12-15, Orlando, FL.*

Bentz, A., and Kijewski-Correa, T. (2009). Wind-Induced Vibrations of Tall Buildings: The Role of Full-Scale Observations in Better Quantifying Habitability. *IMAC-XXVII: A Conference and Exposition on Structural Dynamics, Orlando, FL.*

Brownjohn, J. M. W., Stringer, M., Tan, G. H., Poh, Y. K., Ge, L., and Pan, T. C. (2006). "Experience with RTK-GPS System for Monitoring Wind and Seismic Effects on a Tall Building. *Structural*

Health Monitoring and Intelligent Infrastructure, Ou, Li, and Duan, eds., Taylor & Francis Group, 265-275.

Campbell, S., Kwok, K. C. S., and Hitchcock, P. A. (2005). Dynamic Characteristics and Wind-Induced Response of Two High-Rise Residential Buildings during Typhoons. *Journal of Wind Engineering and Industrial Aerodynamics* **93,** 461.

Catbas, F. N., and Kijewski-Correa, T. (2013). Structural Identification of Constructed Systems: A Collective Effort Toward an Integrated Approach that Reduces Barriers to Adoption. *Journal of Structural Engineering* **139,** 1648-1652.

Catbas, F. N., Kijewski-Correa, T. L., and Aktan, A. E. (2013). *Structural Identification (St-Id) of Constructed Systems: Approaches, Methods and Technologies for Effective Practice of St-Id* American Society of Civil Engineers (ASCE), Structural Engineering Institute (SEI), Reston, VA.

Denoon, R. O., Letchford, C. W., Kwok, K. C. S., and Morrison, D. L. (1999). Field Measurements of Human Reaction to Wind-Induced Motion. *Wind Engineering into the 21st Century, Proceedings of 10th International Conference on Wind Engineering, 21-24 June, Copenhagen, Netherlands.*

Durgin, F. H. (1990). Available Full-Scale on-Site Wind-Induced Data from a Major Tall Building. *J.Wind Eng.Ind.Aerodyn.* **36,** 1201-1215.

Jeary, A. P., and Ellis, B. R. (1979). A Study of the Measured and Predicted Behaviour of a 46 Storey Building. *International Conference on Environmental Forces on Engineering Structures.*

Kijewski-Correa, T., Henderson, A., Montestruque, L., and Rager, J. (2009). Real-Time Sensor Fusion to Enhance Plume Detection in Urban Zones. *11th Americas Conference on Wind Engineering, June 22-26, San Juan, Puerto Rico.*

Kijewski-Correa, T., Kareem, A., Guo, Y. L., Bashor, R., and Weigand, T. (2013). Performance of Tall Buildings in Urban Zones: Lessons Learned from a Decade of Full-Scale Monitoring. *International Journal of High Rise Buildings* **2,** 179-192.

Kijewski-Correa, T., Kilpatrick, J., Kareem, A., Kwon, D. K., Bashor, R., Kochly, M., Young, B. S., Abdelrazaq, A., Galsworthy, J., Isyumov, N., Morrish, D., Sinn, R. C., and Baker, W. F. (2006). Validating the Wind-Induced Response of Tall Buildings: A Synopsis of the Chicago Full-Scale Monitoring Program. *Journal of Structural Engineering* **132,** 1509-1523.

Kijewski-Correa, T., and Kochly, M. (2007). Monitoring the Wind-Induced Response of Tall Buildings: GPS Performance and the Issue of Multipath Effects. *Journal of Wind Engineering and Industrial Aerodynamics* **95,** 1176-1198.

Kijewski-Correa, T., Kwon, D. K., Kareem, A., Bentz, A., Guo, Y., and Bobby, S. (2013). SmartSync: An Integrated Real-Time Structural Health Monitoring and Structural Identification System for Tall Buildings. *Journal of Structural Engineering* **139**, 1675-1687.

Kijewski-Correa, T., and Pirnia, D. (2009). Pseudo-Full-Scale Evaluation of Occupant Comfort in Tall Buildings. *11th Americas Conference on Wind Engineering, June 22-26, San Juan, Puerto Rico.*

Li, Q. S., Fu, J. Y., Xiao, Y. Q., Li, Z. N., and Ni, Z. H. (2006). Wind Tunnel and Full-Scale Study of Wind Effects on China's Tallest Building. Engineering *Structures* **28,** 1745-1758.

Li, Q. S., and Wu, J. R. (2007). Time-Frequency Analysis of Typhoon Effects of a 79-Storey Tall Building. *Journal of Wind Engineering and Industrial Aerodynamics* **95,** 1648-1666.

Li, Q. S., and Wu, J. R. (2004). Correlation of Dynamic Characteristics of a Super-Tall Building from Full-Scale Measurements and Numerical Analysis with various Finite Element Models. *Earthq. Engin. and Struct. Dyn.* 1311-1336.

Li, Q. S., Xiao, Y. Q., Fu, J. Y., and Li, Z. N. (2007). Full-Scale Measurements of Wind Effects on the Jin Mao Building. *Journal of Wind Engineering and Industrial Aerodynamics* **95,** 445-466.

Li, Q. S., Xiao, Y. Q., Wong, C. K., and Jeary, A. P. (2004). Field Measurements of Typhoon Effects on a Super Tall Building. *Engineering Structures* **26,** 233-244.

Li, Q. S., Xiao, Y. Q., Wong, C. K., and Jeary, A. P. (2003). Field Measurements of Wind Effects on the Tallest Building in Hong Kong. *The Structural Design of Tall and Special Buildings* **12,** 67-82.

Li, Q. S., Zhi, L. H., Tuan, A. Y., Kao, C. S., Su, S. C., and Wu, C. F. (2011). Dynamic Behavior of Taipei 101 Tower: Field Measurement and Numerical Analysis. *Journal of Structural Engineering* **137,** 143-155.

Li, Q. S., Wu, J. R., Liang, S. G., Xiao, Y. Q., and Wong, C. K. (2004). Full-Scale Measurements and Numerical Evaluation of Wind-Induced Vibration of a 63-Story Reinforced Concrete Tall Building. *Eng.Struct.* **26,** 1779-1794.

Li, Q. S., Xiao, Y. Q., and Wong, C. K. (2005). Full-Scale Monitoring of Typhoon Effects on Super Tall Buildings. *J.Fluids Struct.* **20,** 697-717.

Li, Q. S., Yang, K., Zhang, N., Wong, and Jeary, A. P. (2002). Field Measurements of Amplitude-Dependent Damping in a 79-Storey Tall Building and its Effects on the Structural Dynamic Responses. *Struct.Des.Tall Build.* **11,** 129-153.

Littler, J. D. (1991). *The Response of a Tall Building to Wind Loading.* PhD thesis. University of London, London, UK.

Littler, J. D., and Ellis, B. R. (1992). Full Scale Measurements to Determine the Response of Hume Point to Wind Loading. *Journal of Wind Engineering and Industrial Aerodynamics* **42,** 1085-1096.

Ohkuma, T. (1996). *Japanese Experience with Motions of Tall Buildings.* Council on Tall Buildings in Urban Habitat (CTBUH) Committee 36: Motion Perception and Tolerance.

Ohkuma, T. (1991). Full-Scale Measurement of Wind Pressures and Response Accelerations of a High-Rise Building. *J.Wind Eng.Ind.Aerodyn.* **38,** 185-196.

Oldfield, P., Trabucco, D., and Wood, A. (2014). Roadmap on the Future Research Needs of Tall Buildings. CTBUH.

Satake, N., Suda, K., Arakawa, T., Sasaki, A., and Tamura, Y. (2003). Damping Evaluation using Full-Scale Data of Buildings in Japan. *Journal of Structural Engineering* **129,** 470-477.

Tamura, Y., Matsui, M., Pagnini, L. C., Ishibashi, R., and Yoshida, A. (2002). Measurement of Wind-Induced Response of Buildings using RTK-GPS. *J.Wind Eng.Ind.Aerodyn.* **90,** 1783-1793.

Weigand, T., and Kijewski-Correa, T. (2013). Automated Assessment of Tall Building Wind-Induced Response Data to Support Long-Term Monitoring Programs. *Proceedings of 12th Americas Conference on Wind Engineering, June 16-20, Seattle.*

Williams, S., Bentz, A., and Kijewski-Correa, T. (2013). A Typology-Driven Damping Model (TD2M) to Enhance the Prediction of Tall Building Dynamic Properties using Full-Scale Wind-Induced Response Data. *Proceedings of 12th Americas Conference on Wind Engineering, June 16-20, Seattle.*

Xu, Y. L., and Zhan, S. (2001). Field Measurements of Di Wang Tower during Typhoon York. *Journal of Wind Engineering and Industrial Aerodynamics* **89,** 73-93.

A new aerodynamic phenomenon
and its effects on the design
of ultra-high cylindrical towers

by
Francesca Lupi
born 21 April 1984
from Prato, Italy

Dissertation submitted to and approved by the Department of Architecture, Civil Engineering and Environmental Sciences of the University of Braunschweig - Institute of Technology and the Department of Civil and Environmental Engineering of the University of Florence in candidacy for the degree of a Doktor-Ingenieurin (Dr.-Ing.) / Dottore di Ricerca in Mitigation of Risk due to Natural Hazards on Structures and Infrastructures[*)]

*) Either the German or the Italian form of the title may be used.

Berichte aus dem Bauwesen

Francesca Lupi

**A new aerodynamic phenomenon and its effects on
the design of ultra-high cylindrical towers**

Shaker Verlag
Aachen 2013

Acknowledgments

Abstract

The dissertation addresses the design of ultra-high towers in the atmospheric boundary layer under the wind action and has a special application for Solar Updraft Power Plants (SUPPs). They represent a highly sustainable natural resource for electric power generation, based on a combined sun-wind energy solution.

The object of the investigation is a 1-km tall solar updraft tower, made of reinforced concrete and stiffened along the height by stiffening rings. Stiffening rings are usually introduced in the design of solar updraft towers in order to reduce their structural vulnerability to the wind action by enhancing a beam-like behaviour. However, wind tunnel experiments – which were performed for the first time on such a structure within this research – showed that the presence of ring beams along the height of the tower modifies the aerodynamics of the flow around the circular cylinder and creates a bi-stable and asymmetric load condition, which does not disappear even at moderately high Reynolds numbers. This phenomenon is new and unknown. Similar effects were observed around circular cylinders (without rings) in the critical range of the Reynolds number and around two side-by-side cylinders, but the conditions of occurrence and the physical reasons were profoundly different.

The discovery of the existence of such a bi-stable and asymmetric load condition induced by ring beams along the height of a finite length circular cylinder, its interpretation, as well as the cross-checked experimental evidence in different wind-tunnel laboratories confirmed also by numerical simulations, are the original contributions of this work. Then, the effect is quantified on the structural response. The bi-stable asymmetric load on the structure did not result to be a prohibitive load condition for solar updraft towers and the magnitude of the effect depends on the number and/or on the size of the rings. Mitigation strategies are then proposed in the work. Furthermore, the dissertation evaluates the shell response to the stochastic wind loading process, especially in the vicinity of the ring beams, and provides to the designer a general unified simple tool to define design wind loads for quasi-static calculations of ultra-high towers in any atmospheric boundary layer flow.

Sommario

La tesi riguarda il progetto di torri di altezza straordinaria nello strato limite atmosferico, soggette all'azione del vento. Un particolare campo di applicazione è quello degli impianti di torri solari ad aspirazione, "Solar Updraft Power Plants" (SUPPs). Questi rappresentano una nuova e sostenibile risorsa di energia rinnovabile, basata sullo sfruttamento combinato di energia solare ed eolica.

L'oggetto dello studio è una torre solare ad aspirazione in calcestruzzo armato alta 1 km e irrigidita lungo l'altezza da travi ad anello. Queste sono normalmente utilizzate nel progetto di torri solari per ridurre la vulnerabilità all'azione del vento, in quanto la loro presenza garantisce un comportamento strutturale predominante a trave. Tuttavia, gli esperimenti in galleria del vento – effettuati per la prima volta su una struttura di questo tipo nell'ambito del presente lavoro – hanno mostrato che gli anelli lungo l'altezza della torre modificano l'aerodinamica del flusso e creano attorno al cilindro una condizione di carico bistabile e non simmetrico. L'effetto non scompare a numeri di Reynolds moderatamente elevati ed il fenomeno è nuovo e sconosciuto. Effetti simili sono stati osservati attorno a cilindri circolari (senza anelli) nell'intervallo critico del numero di Reynolds e attorno a due cilindri affiancati. Tuttavia, le condizioni in cui si verificano e il principio fisico sono profondamente diversi.

La scoperta dell'esistenza di una tale condizione di carico bistabile e non simmetrica indotta da anelli disposti lungo l'altezza di un cilindro circolare di altezza finita, la sua interpretazione, così come l'evidenza sperimentale in gallerie del vento diverse e la sua conferma numerica, sono i contributi originali di questo lavoro. L'effetto è poi quantificato in termini di risposta strutturale. La condizione di carico bistabile e non simmetrica non risulta proibitiva per il progetto di torri solari e la sua incidenza dipende dal numero e/o dalla dimensione degli anelli. Strategie di mitigazione dell'effetto sono proposte nel lavoro. Inoltre, la tesi studia la risposta della torre al carico del vento, specialmente vicino agli anelli di irrigidimento. Infine, la tesi fornisce al progettista uno strumento semplice e di validità generale per definire i carichi di progetto dell'azione del vento, utilizzabili nel calcolo quasi-statico della risposta di torri di altezza elevata nello strato limite atmosferico.

Zusammenfassung

Die hiermit vorgelegte Doktorarbeit befasst sich mit der Einwirkung des natürlichen Windes auf ultra-hohe Turmbauwerke, die weit in die atmosphärische Grenzschichtströmung hineinreichen. Die Türme von Aufwindkraftwerken stehen hierbei im Vordergrund. Derartige Kraftwerke ermöglichen eine schadstofffreie Erzeugung elektrischer Energie. Sie stellen eine sehr nachhaltige Technologie dar, die thermische Energie der Sonne in Strömungsenergie umwandelt, die ihrerseits mit Hilfe von Turbinen als elektrische Energie nutzbar gemacht wird.

Als Untersuchungsgegenstand der Arbeit dient beispielhaft ein 1 km hoher Aufwindturm. Das Tragwerk ist als Stahlbetonschale, die durch Aussteifungsringe verstärkt ist, konzipiert. Die Versteifung vermindert die durch die Einwirkung von Winddrücken erzeugten Beanspruchungen, indem sie ein stabartiges Tragverhalten bewirkt. Erstmalig wurden im Rahmen dieser Forschungen Windkanalversuche an Aufwindtürmen durchgeführt. Sie zeigten, dass die außenliegenden Versteifungsringe die aerodynamischen Eigenschaften des Turmes im Vergleich zu einem endlichen Kreiszylinder ohne Ringe erheblich verändern: Zwischen den Ringen entsteht abschnittsweise ein unsymmetrischer, bi-stabiler Strömungs- und Belastungszustand, der bis zu den höchsten untersuchten Reynoldszahlen zu beobachten ist. Ähnliche Effekte sind zwar auch bei einem Zylinder ohne Ringe bekannt, sie sind dort jedoch auf einen schmalen Bereich kritischer Reynoldszahlen beschränkt. Ebenfalls zeigen sich derartige Strömungszustände bei 2 nebeneinanderliegenden Zylindern bei bestimmten Abstandsverhältnissen. Die physikalischen Ursachen des hier bei Zylindern mit Ringen erstmalig beobachteten Phänomens sind jedoch grundsätzlich unterschiedlich.

Originäre Beiträge der Arbeit sind die Entdeckung der abschnittsweise unsymmetrischen, bi-stabilen Windbelastung, die Bestätigung des experimentellen Befundes durch Versuche in einem zweiten Windkanallaboratorium und durch numerische Simulationen, sowie schließlich die Deutung des Phänomens. Weiterhin wird die Auswirkung der zusätzlichen Windbelastung auf die Strukturbeanspruchungen untersucht. Es wird gezeigt, dass Anzahl und Breite der Ringbalken die Größe des Lasteffekts bestimmen; Maßnahmen zu seiner Minderung werden entwickelt. Insgesamt bleiben die Zusatzbeanspruchungen beherrschbar. Abschließend befasst sich die Arbeit mit den Tragwerksbeanspruchungen infolge des stochastischen Windlastprozesses, insbesondere mit den Störungen des Membranzustands in der Umgebung der Ringsteifen. Für die Tragwerksplanung werden verallgemeinerte Wind-Ersatzlasten entwickelt, die geeignet sind, als Grundlage zur Berechnung der statischen und quasi-statischen Beanspruchungen ultra-hoher Türme in beliebiger atmosphärischer Grenzschichtströmung zu dienen.

Table of Contents

List of Figures

List of Tables

List of Symbols

A_c = area of the chimney

A_{coll} = area of the collector

C_D = drag coefficient

$C_{D,m}$ = mean drag coefficient

$C_{D, peak}$ = peak drag coefficient

$C_{D, \sigma}$ = standard deviation of the drag coefficient

C_L = lift coefficient

$C_{L,m}$ = mean lift coefficient

$C_{L, \sigma}$ = standard deviation lift coefficient

Co = co-spectrum

C_p = pressure coefficient (external)

$C_{p,air}$ = specific heat capacity of air

$C_{p,b}$ = base pressure coefficient

$C_{p,h}$ = pressure coefficient at φ_h

$C_{p,i}$ = internal pressure coefficient

$C_{p,m}$ = mean pressure coefficient

$C_{p,max}$ = maximum pressure coefficient

$C_{p,min}$ = minimum pressure coefficient

C_{pp} = decay coefficient of ρ_p

C_{uu} = decay coefficient of ρ_u

$C_{p,\sigma}$ = standard deviation of pressure coefficient

$C_{p,\sigma,BI}$ = standard deviation of pressure coefficient, body-induced part

$C_{p,\sigma,TI}$ = standard deviation of pressure coefficient, turbulence-induced part

D = diameter

D = damping matrix

D_{coll} = diameter of the collector

E = voltage measured by hot-wire anemometers (either E_a or E_{corr})

E_a = voltage measured by hot-wire anemometers, without temperature correction

E_{corr} = voltage measured by hot-wire anemometers, with temperature correction

EaR = element at risk

F_m = mean (drag) force

$\mathbf{F_r}$	= friction force (vector)
F_x	= friction force along x-axis
F_y	= friction force along y-axis
F_z	= friction force along z-axis
F_σ	= rms (drag) force
G	= [1] solar radiation (Chapter 1); [2] gradient wind speed (Chapter 2)
H	= height of the tower = 1000 m
H/D	= aspect ratio
H&D	= Harris and Deaves model
I_F	= intensity of force (standard deviation / mean value)
I_p	= intensity of pressure (standard deviation / mean value)
$I_{p,TI}$	= intensity of pressure (standard deviation / mean value), turbulence-induced part
I_u	= turbulence intensity (along wind component)
$\mathbf{K}$	= stiffness matrix
K_0	= Kolmogorov parameter
L	= [1] mixing length; [2] length scale of mid-latitude synoptic systems
L_f	= eddy formation region in the wake of a cylinder
L_{LIFT}	= correlation length of C_L
L_{pz}	= pressure correlation length (z direction)
L_{ux}, L_{uy}, L_{uz}	= integral length scales of the along-wind velocity component
L_{VS}	= correlation length of vortex shedding lift
L_{vx}, L_{vy}, L_{vz}	= integral length scales of the across-wind velocity component
L_{wx}, L_{wy}, L_{wz}	= integral length scales of the vertical component of wind velocity
$\mathbf{M}$	= mass matrix
M_D	= bending moment in the along-wind direction
$M_{D,m}$	= mean bending moment in the along-wind direction
$M_{D,peak}$	= peak bending moment in the along-wind direction
$M_{D,\sigma}$	= rms bending moment in the along-wind direction
$M_D, \sigma_B^{\ 2}$	= variance of M_D, quasi-static part (resonance not included)
$M_D, \sigma_B^{\ 2} + \sigma_R^{\ 2}$	= variance of M_D, including resonance
M_L	= bending moment in the across-wind direction
$M_{L,m}$	= mean bending moment in the across-wind direction
$M_{L,peak}$	= peak bending moment in the across-wind direction
$M_{L,\sigma}$	= rms bending moment in the across-wind direction
$M_L, \sigma_B^{\ 2}$	= variance of M_L, quasi-static part (resonance not included)

$M_L, \sigma_B{}^2 + \sigma_R{}^2$ = variance of M_L, including resonance

$M_{res,m}$ = mean resultant bending moment

$M_{res,peak}$ = peak resultant bending moment

$M_{res,\sigma}$ = rms resultant bending moment

$M_{res}, \sigma_B{}^2$ = variance of M_{res}, quasi-static part (resonance not included)

$M_{res}, \sigma_B{}^2 + \sigma_R{}^2$ = variance of M_{res}, including resonance

N = number of time steps

P_{el} = electric output

P_{tot} = power of the power plant

Qu = quad-spectrum

$\dot{Q}$ = heat increase in the collector

R = radius

Re = Reynolds number

Re_{cr} = critical Reynolds number

Re_e = effective Reynolds number

Ro = Rossby number

R_u = autocovariance function of u

S = [1] power spectral density function; [2] generic effect in the tower response (either n_{11}, n_{22}, …)

S_{cr} = Scrouton number

S_t = Strouhal number

SUPP = Solar Updraft Power Plant

T_0 = ambient temperature

T_a = ambient temperature during acquisition of hot-wire signals

T_{ux} = integral time scale

T_w = hot-wire operational temperature = 250°

T/D = centre-to-centre transverse pitch ratio in side-by-side cylinders

U = wind velocity in the along wind direction

U_{cr} = critical velocity

U_{FS} = full-scale velocity

U_g = gradient wind, component along x-axis (reference system as specified in the context)

U_m = mean along wind component

$U_{m,\infty}$ = mean along wind component in the undisturbed flow

U_{pra} = Prandtl velocity, i.e. wind tunnel velocity at the Prandtl tube

U_{ref} = reference wind velocity

U_{WT}	= wind tunnel velocity
V	= velocity vector
V_b	= basic wind velocity at 10 m height (code denomination)
V_c	= flow speed in the chimney
$V_{c,max}$	= maximum flow speed in the chimney
V_g	= gradient wind, component along y-axis (reference system as specified in the context)

c	= ratio between L_{uz} and L_{pz}
cov_D	= covariance matrix of drag force
f_c	= Coriolis parameter
f_{sz}	= correction factor on C_D for boundary layer flow (ESDU)
g	= gravitational acceleration
h	= gradient height
k	= von Karman constant (k = 0.4)
k_F	= peak factor of the force ($k_F = 3.5$)
ks	= thickness of ribs on the wind tunnel model
k_P	= peak factor of the velocity ($k_P = 3.5$)
k_{pw}	= pressure withdrawal factor for the turbines
$\dot{m}$	= mass flow rate
$m_{i,e}$	= equivalent mass of the structure per unit length, i^{th} vibration mode
m_{11}	= bending moment in the circumferential direction per unit length ($m_{11,m}$, $m_{11,\sigma}$, $m_{11,peak}$, see $n_{11,...}$)
m_{22}	= bending moment in the meridional direction per unit length ($m_{22,m}$, $m_{22,\sigma}$, $m_{22,peak}$, see $n_{11,...}$)
n	= frequency
n_s	= vortex shedding frequency
n_1	= first eigenfrequency
n_{11}	= internal force in the circumferential direction per unit length
$n_{11,m}$	= mean value of n_{11}
$n_{11,\sigma}$	= mean value of n_{11}
$n_{11,peak}$	= peak value of n_{11}
n_{22}	= internal force in the meridional direction per unit length ($n_{22,m}$, $n_{22,\sigma}$, $n_{22,peak}$, see $n_{11,...}$)
p	= pressure
p_m	= mean pressure

xxx

p_σ	= standard deviation of the pressure p
$p_{\sigma,BI}$	= standard deviation of the pressure p, body-induced part
$p_{\sigma,TI}$	= standard deviation of the pressure p, turbulence-induced part
q_m	= mean velocity pressure
q_{peak}	= peak velocity pressure
t	= time
u	= along-wind component
u_*	= friction velocity
v	= across-wind component
w	= [1] vertical wind component; [2] width of the ring beams
x	= along-wind direction in the wind tunnel
y	= across-wind direction in the wind tunnel
z_0	= roughness length
z	= vertical coordinate
z'	= downwards vertical coordinate with origin at z = H (tower top)
z_{ref}	= reference height
ΔC_p	= pressure recovery
Δp_d	= pressure difference, dynamic component
Δp_s	= pressure difference, static component
Δp_{tot}	= pressure difference, static + dynamic
ΔT	= temperature increase/decrease
Ω	= angular velocity of Earth rotation, magnitude
$\boldsymbol{\Omega}$	= angular velocity of Earth rotation, vector
α	= exponent of mean wind profile by using power law
δ	= [1] thickness of the boundary layer; [2] logarithmic decrement
ε	= dissipation
ξ	= modal damping ratio
η	= [1] efficiency of the power plant (Chapter 1); [2] influence coefficient (Chapter 7)
η_c	= efficiency of the chimney
η_{coll}	= efficiency of the collector
η_{turb}	= efficiency of the turbines
θ	= phase angle
ϑ_0	= maximum angle of turn due to Ekman spiral

λ_F	= frequency scale factor (wind tunnel and full scale)
λ_L	= length scale factor (wind tunnel and full scale)
λ_R	= roughness factor in the definition of Re_e
λ_T	= [1] time scale factor (wind tunnel and full scale); [2] turbulence factor in the definition of Re_e
λ_V	= velocity scale factor (wind tunnel and full scale)
μ	= dynamic viscosity
ν	= kinematic viscosity
ρ	= [1] mass density of air; [2] cross-correlation coefficient
ρ_0	= mass density of air at 20°
ρ_a	= mass density of air outisde the chimney
ρ_c	= mass density of air inside the chimney
ρ_{coll}	= mass density of air inside the collector
ρ_D	= correlation matrix of drag force
ρ_P	= cross-correlations of p
ρ_u	= cross-correlations of u
σ	= standard deviation
σ^2	= variance
σ_B	= standard deviation of background response
σ_u	= standard deviation of u
$\sigma_{u,\infty}$	= standard deviation of along wind component in the undisturbed flow
σ_v	= standard deviation of v
σ_w	= standard deviation of w
τ	= shear stresses
ϕ	= latitude
φ	= circumferential angle
φ_h	= angle of separation
φ_{min}	= angle of $C_{p,min}$
ω	= circular frequency
EXP	= experimental result
LM	= loading model
'	= fluctuating component

Chapter 1. **Introduction**

The design of ultra-high structures in the atmospheric boundary layer is a pioneering field of study, where research and application complement each other. The recent construction of super-tall skyscrapers – more than 800 m in height – represents today the highest synthesis of these efforts. This thesis proposes and investigates a new context of application – the Solar Updraft Power Plant Technology – a highly sustainable natural resource for electric power generation. This chapter introduces the technology, the working principle and the aim of the research.

1.1 **The Solar Updraft Power Plants technology**

The Solar Updraft Power Plants technology (SUPPs) produces renewable energy by sun-wind energy harvesting. Solar radiation is an inexhaustible input, which is converted into electric power through the natural updraft of heated air in a very high chimney.

Peculiar characteristics of this technology are its long lifetime (more than 100 years), its very low costs of operation, the no-need of water for power generation and the absence of pollutant emissions (if one incorporates the CO_2 emissions during construction, one ends up with a few grams of CO_2 per kWh of produced electricity (Backström et al., 2008)).

A SUPP consists of three elements (Figure 1.2): the collector, the turbine(s) with coupled generators as power conversion unit and the solar tower. The collector is a large glass-covered area where the visible and the ultraviolet wavelengths of the solar radiation heat the ground and consequently warm up the air under the roof, through the mechanism of natural convection. Meanwhile, the infrared wavelengths warm up the energy storage layer made of the soil itself, stones or, in case, water. Such an energy storage allows night operation. Then, the heated, less dense air rises up into the chimney of the plant, thereby drawing in more air at the collector perimeter and thus initiating forced convection. The driving force or potential that causes air to flow through the solar tower is the pressure difference between a column of cold air outside and a column of hot air inside the chimney. The stream of warm air turns the turbines at the chimney foot and in the power conversion unit the kinetic energy of the flow is transformed into electric power.
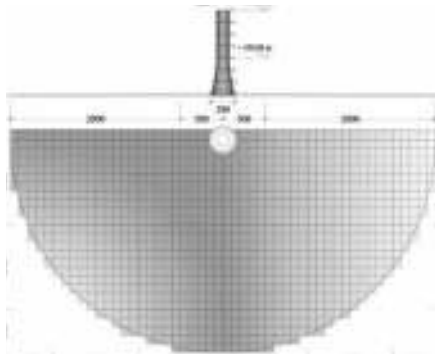
Figure 1.1 View of a Solar Updraft Power Plant
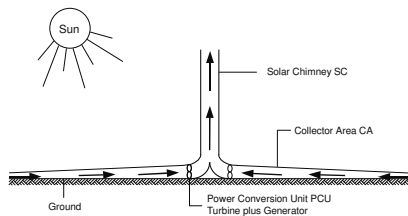
Figure 1.2 Working principle

The production of energy is proportional to the volume of the cylinder with the height of the tower and the diameter of the collector (Schlaich et al., 2005). For this reason, provided sufficiently high solar radiation input (e.g. 2000 kWh/m^2 or even more), very good efficiency of the power plant can be reached with extra-large dimensions of the tower and/or the collector.

A map of the yearly solar radiation distribution is shown in Figure 1.3. It suggests the most suitable locations for SUPPs around the world (Pretorius, 2007). In those areas, a plant with a collector diameter of 7 km and with solar tower height of 1500 m is estimated to deliver a maximum (peak) electricity power of 400 MW (Pretorius&Kröger, 2006). This assumption has been also assessed, both experimentally and theoretically for a wide range of plant geometries, as a reasonable global assumption (Fluri, 2008).
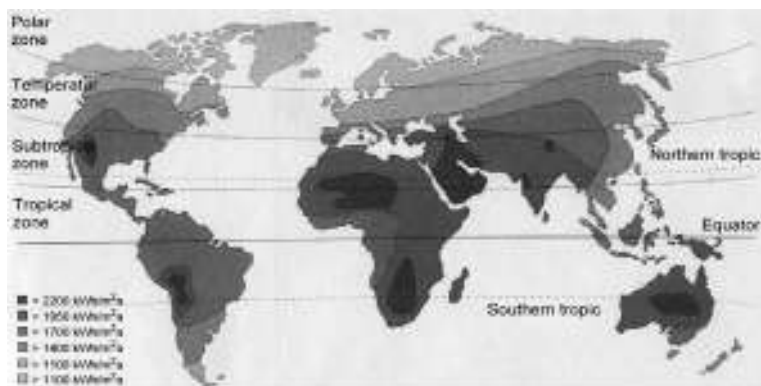
Figure 1.3 Solar radiation input (Pretorius, 2007)

1.2   **Historical review**

The paternity of the SUPPs idea is commonly attributed to the Spanish army colonel I. Cabanyes (Cabanyes, 1903), although a patent for "an improved temperature differential air motor" was invented even earlier – in 1896 – by A. R. Bennett (Bennett, 1896), a prototype of which is shown at the Science Museum in London.

The apparatus proposed by Cabanyes consisted of an air-heater attached to a house with a chimney. Inside the house, there was a wind propeller for electricity production (Figure 1.4).

Another early description of the SUPP principle can be found in the work of the German author Hanns Günther (Günther, 1931). The idea of the author was a solar chimney on the slope of a mountain (Figure 1.5). The very high air speed could deliver an enormous amount of energy, which could be extracted by means of wind turbines.

Figure 1.4 Article of Isidoro Cabanyes, published on "La Energia Electrica" (Cabanyes, 1903).
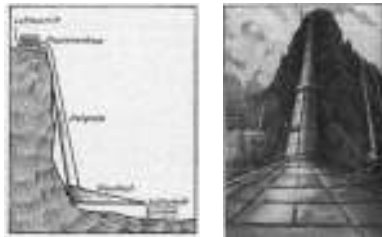
Figure 1.5 A solar chimney on the slope of a high mountain. (Günther, 1931)

Around 1975, a series of patents were granted to the US engineer R.E. Lucier in countries with deserts suitable for SUPPs, like Australia, Canada, Israel and the US. These patents concerned: "Apparatus for converting Solar to Electrical Energy", "Utilization of Solar Energy", "System and Apparatus for Converting Solar Heat to Electrical Energy", "System for converting solar heat to electrical energy".

Jörg Schlaich, Rudolf Bergermann and their team have been very active in developing and spreading the Solar Updraft Power Technology. Their first idea – as reported in (Schlaich, 2010) – goes back to 1972, when they were invited by the power industry to develop a large scale cooling tower for dry cooling. A new question arose among them, whether the natural updraft which is produced in such chimney tubes could not be utilized to produce electricity, provided an additional "fire" at the base of the chimney tube. And why not to use solar radiation and collect solar warm air by means

of a large greenhouse roof? All of that resulted, in 1979, in what they called the "Solar Chimney" (Schlaich, 2010). As they said, Schlaich and his team developed the whole idea on their own, and only some years later they got hold of the paper written in 1931 by Günther, describing the similar basic principle of the solar updraft tower. In 1980, thanks to a grant by the German Ministry for Research and Technology, J. Schlaich built a solar tower prototype with a maximum power output of 50 kW in Manzanares (Spain), in order to test the new technology and confirm analytical results through experimental data (Figure 1.6). "The aim of this research project was to verify, through field measurements, the performance projected from calculations based on theory, and to examine the influence of individual components on the plant' output and efficiency under realistic engineering and meteorological conditions" (Schlaich, 1995). The chimney was a cylindrical tube of 195 m in height and 10 m in diameter. It was surrounded by a collector of 240 m in diameter. The design was only made for experimental purposes, i.e. to collect measurements for a period of three years. The plant was intended to be removed without trace after that. Being a temporary structure, the chimney was made of a corrugated metal sheeting, whose thickness was only 1.25 mm and which could be used again after the experiment. In fact, the original plan was to take measurements in 1981 and 1982 and dismantle the structure in 1983, after three years from the construction, since the grant did not permit regular corrosion protection especially for the stay-cables. Anyway, years passed away permitting them to take more measurements. The chimney lasted for eight years, until spring 1989, when the cables broke in a storm and the chimney fell down. When it happened, the necessary measurements had largely been completed. Experimental results were very promising, a detailed analysis can be found in (Schlaich, 1995).
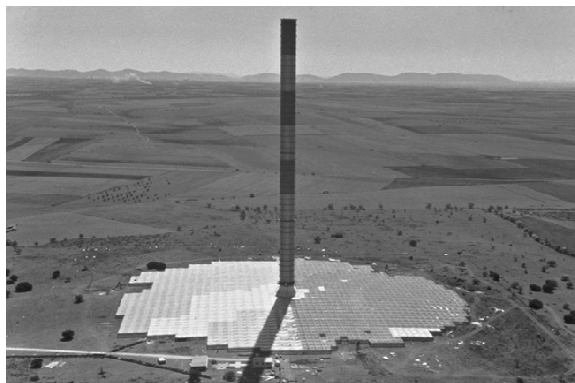
Figure 1.6 J. Schlaich's prototype in Manzanares/Spain (Schlaich, 1995)

In 1987, Pasumarthi and Sherif erected a small prototype installation in California and published the first thermo-mechanical plant model (Pasumarthi&Sherif, 1997).

A recent experimental investigation of the solar collector temperature field on a 9 m tall prototype with sloped collector is currently being performed by Kalash and others, 2012. A complete up-to-date bibliography of the latest worldwide studies can be found in the Proceedings of both the 2nd and the 3rd International Conferences on SUPPs (STPT2010, SUTPT 2012).

Up to now, several projects of large SUPPs have been developed in arid zones all over the world, but none of them has come to realization. In 2008, the Namibian government approved a proposal for the construction of a 400 MW solar chimney called the 'Greentower'. The tower was planned to be 1.5 kilometres tall and 280 m in diameter, and the base consisted of a 37 square kilometres greenhouse. In recent years EnviroMission (Australia) proposed a 200 MW power plant in the US deserts. Such a power plant could provide enough electricity to power around 100000 households (www.enviromission.com).

In October 2010 a so-called Solar Heated Wind Updraft Tower Power System became operational in the Wuhai desert, Inner Mongolia (China). It is a medium size power plant with a 53 m tall tower and a collector area of 6300 m^2. There are 5 turbines, each one having a capacity of 40 kW (Wei&Wu, 2012). In October 2010 the generating electricity system was combined to the grid and since then monitoring devices have been controlling the thermodynamic behaviour. Some pictures of the power plant, taken during a visit in October 2012, are reported in the following (Figure 1.7, Figure 1.8).

Figure 1.7 Solar Heated Wind Updraft Tower Power in Wuhai desert, Inner Mongolia (China). Visit to the prototype in October 2012, during the 3rd Int. Conf. on Solar Updraft Tower Power Technology.
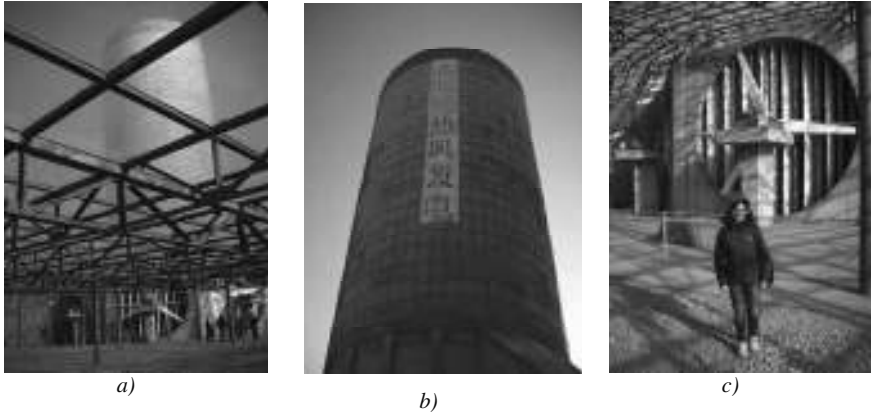
Figure 1.8 Solar Heated Wind Updraft Tower Power in Wuhai desert, Inner Mongolia (China). a) View of the tower under the glass collector, b) Tower, c) Turbine

1.3 **Production of energy**

The thermo- and fluid-dynamic behaviour of the power plant and the efficiency of energy production are crucial aspects for the development of the technology. However, they are not addressed in this work and only a simplified approach – resulting from documentation in literature – is presented now. For further details, the first wide studies of the multi-physics of solar updraft power plants can be found in Weinrebe (2000) and Bernades (2004). Then, Pretorius (2007) presents another milestone work. Recent studies are presented in Krätzig (2012a,b).

A simple theory to understand the mechanism of SUPPs is outlined in Schlaich (1995) and briefly addressed here. According to that, the efficiency of the power plant is the product of the individual component efficiencies, i.e. the collector roof, the solar tower and the turbines:

$$\eta = \eta_{coll} * \eta_c * \eta_{turb} \tag{1.1}$$

The efficiency of the collector (η_{coll}) describes the effectiveness with which solar radiation is converted into heat. The efficiency of the chimney (η_c) describes the effectiveness with which the quantity of heat delivered by the collector is converted into flow energy. η_{turb} is the efficiency of the wind turbines.

The collector

The collector converts solar radiation G (W/m^2) on the collector surface A$_{coll}$ (m^2) into heat increase in the collector airflow $\dot{Q}$ (W). Thus, the efficiency of the collector is defined by the ratio:

$$\eta_{coll} = \frac{\dot{Q}}{A_{coll} * G} \tag{1.2}$$

In recent publications, Krätzig (2012a,b) applies one-dimensional flow-tube theory and prosecutes a mass of air on its way through the collector, the turbines and the chimney. The efficiency of the collector is estimated successively and iteratively for each one-dimensional collector element with a characteristic finite volume of air. The thermo-fluidmechanics in the collector is described by fluid equations (conservation of mass, conservation of momentum and Bernoulli's energy equation to connect the ambient atmosphere around the plant at the collector rim with its interior) and thermodynamic conditions (conservation of energy). Fluid equations and thermodynamic conditions are coupled by the equation of state of air, as an ideal gas.

The heat output $\dot{Q}$ under steady conditions is expressed as the product of the mass flow rate $\dot{m}$ (kg/s), the specific heat capacity of the air C$_{p,air}$ (J/kgK) and the temperature difference between the collector inflow and outflow (a typical value is ΔT ≈ 30°K):

$$\dot{Q} = \dot{m} C_{p,air} \Delta T \tag{1.3}$$

According to Pretorius (2007) the efficiency of the collector η_{coll} can be approximated by the following interpolation relation, in which the diameter of the collector D_{coll} is measured in km:

$$\eta_{coll} = 0.680 * \left(1 - 0.229 \sqrt{D_{coll} - 2}\right) \tag{1.4}$$

In order to model the physical processes of transformation of solar radiation G into heat increase ΔT of the air flux, the specific design of the collector comes into play. In

fact, the manifold exchanges of convective and radiation heat power that exist in the different components of the collector – single or double glass panels, air flow, water heat storage or soil absorber – must be considered in the heat power balance conditions (Krätzig, 2012a,b).

The chimney

The chimney converts the heat flow $\dot{Q}$ produced by the collector into kinetic energy. The pressure difference Δp_{tot} between a column of cold air outside and a column of hot air inside the chimney is the driving force that causes air to flow through the Solar Updraft Power Plant.

$$\Delta p_{tot} = g \int_0^H \{\rho_a(z) - \rho_c(z)\} dz \tag{1.5}$$

$\rho_a(z)$ and $\rho_c(z)$ stand for the height-depending mass density (kg/m^3) of the air outside and inside the chimney, while g is the gravitational acceleration (m/s^2).

With the barometric pressure dependence from height, air as an ideal gas and ΔT constant over h, the pressure difference can be evaluated by solving analytically equation (1.5) over the tower height:

$$\Delta p_{tot} = g \rho_{coll} H \frac{\Delta T}{T_0} \tag{1.6}$$

being ρ_{coll} the density of air at temperature $T_0 + \Delta T$ at collector outflow and T_0 the ambient temperature at ground level.

The pressure difference can be divided into a static and a dynamic component (neglecting friction losses):

$$\Delta p_{tot} = \Delta p_s + \Delta p_d \tag{1.7}$$

Such a division is due to the energy taken by the turbines: the static pressure difference drops at the turbines, while the dynamic component describes the kinetic energy of the airflow. If the turbines are left out ($\Delta p_s = 0$), the maximum flow speed $V_{c,max}$ is achieved and the whole pressure difference is used to accelerate the air.

From Bernoulli's equation we calculate the maximum air velocity at the chimney's entrance:

$$V_{c,\max} = \sqrt{2gH\frac{\Delta T}{T_0}} \tag{1.8}$$

The whole pressure difference is then converted into kinetic energy. Therefore, the total power contained in the flow is:

$$P_{tot} = \Delta p_{tot}\frac{\overset{\bullet}{m}}{\rho} = \Delta p_{tot}V_{c,\max}A_c = \frac{1}{2}\overset{\bullet}{m}V_{c,\max}^2 \tag{1.9}$$

$V_{c,\max}$ and A_c are the maximum flow speed and the cross-section of the chimney, respectively.

The efficiency of the chimney can be calculated by combining equations (1.3), (1.8), (1.9):

$$\eta_c = \frac{P_{tot}}{\overset{\bullet}{Q}} = \frac{gH}{C_{p,air}T_0} \tag{1.10}$$

All of that is a simplified representation, but it highlights that the efficiency of the chimney is fundamentally dependent on its height. Pretorius (2007) also proposes an approximated expression to consider the influence of the mean chimney diameter D.

The turbines

The turbines at the base of the chimney convert free convection flow into rotational energy. The pressure drop at the turbines can be expressed, in a first approximation, by the Bernoulli equation:

$$\Delta p_s = \Delta p_{tot} - \frac{1}{2}\rho_c V_c^2 \tag{1.11}$$

being ρ_c and V_c the air density and the flow speed in the chimney, respectively.

Thus, the theoretically useful power at the turbines becomes, in analogy to equation (1.9):

$$P_{tot} = \Delta p_s \frac{\overset{\bullet}{m}}{\rho} = \Delta p_s V_c A_c = \frac{1}{2} \overset{\bullet}{m} V_c^2 \qquad (1.12)$$

By introducing η_{turb} for the turbine efficiency and the pressure withdrawal factor k_{pw} (so that $\Delta p_s = k_{pw}\Delta p_{tot}$)), the effective electrical power generated by the power plant can be finally expressed as:

$$P_{el} = k_{pw}\eta_{turb}\eta_{coll}\eta_c A_{coll}G \qquad (1.13)$$

The power is maximized if the pressure drop $\Delta p_s = k_{pw}\Delta p_{tot}$ is about two thirds of the total pressure difference available, i.e $k_{pw} = 2/3$ (Schlaich, 1995). By substitution, it results:

$$P_{el} = \frac{2}{3}\eta_{turb}\eta_{coll}\frac{gH}{C_{p,air}T_0}A_{coll}G \qquad (1.14)$$

The electrical output of the Solar Updraft Power Plant is then proportional to the product HA_{coll}, i.e. to the volume included within the chimney height and the collector area, as it was stated in section 1.1. Further detailed and updated studies can be found in Proc. SUTPT 2012.

Electric power and electricity costs

Despite the high initial cost of the SUPPs, the estimated leveled electricity costs LECs (due to IEA-guidelines) of the harvested energy are very low.

Krätzig (2012b) estimates a maximum electric power of 75 MW for a power plant with a 750 m tall chimney and 3500 m collector diameter, by assuming solar radiation G = 2.2 MWh/m^2. If the capacity factor (i.e. full load hours/24*365 hours in one year) is considered about 34%, - it means that the full load hours in one year are around 3000 - then the total annual energy harvest is around 75/0.34 = 220 GWh/a. The same paper provides an estimation of investment costs (around 340 M€, 60% of which due to the collector, 20% due to the chimney and 15% due to the turbines, plus extra costs). By considering a depreciation period of 33 years, it results in LECs equal to 9.9 €cent/kWh.

A similar value of LECs also resulted in other previous studies (Bergermann&Weinrebe, 2010). They estimated for a 200MW Solar Updraft Tower a total investment of 750 M€ and an average yearly production for a North African location of 650 GWh. It resulted, by assuming a depreciation period of 30 years, in LECs equal to 10.3 €cent/kWh.

Further studies about economic aspects can be found in (Breuer&Hüwe, 2010).

1.4 Main components of the power plant

1.4.1 The tower

Solar Updraft Towers (SUTs) are slender and extremely thin shells, usually made of reinforced concrete. In Europe, two main German schools are leading the structural design of Solar Updraft Towers, headed by J. Schlaich and W.B. Krätzig, respectively. J. Schlaich proposes tubes of cylindrical shape, usually stiffened along the height by spoke wheels. Various alternatives and non-linear structural analyses are reported in (Goldack, 2004, 2011). A double-wall tower is also presented in (Goldack, 2004). Two examples are shown in Figure 1.9 and Figure 1.10.
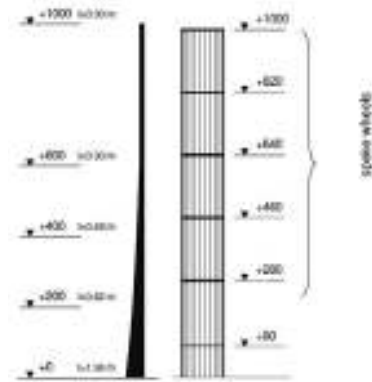
Figure 1.9 1-km tower (Goldack, 2004, 2011)   *Figure 1.10 Double-wall tower (Goldack, 2004)*
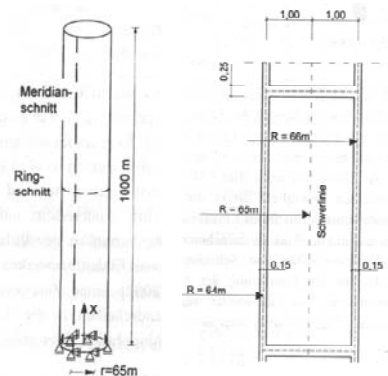
W.B. Krätzig transfers insights from designs of natural draft cooling towers' projects to solar chimneys. Figure 1.11 gives an overview over these attempts, demonstrating the way from cooling towers to chimneys of SUPPs up to an elevation of 1500 m (Krätzig et al., 2008-2009a,b).
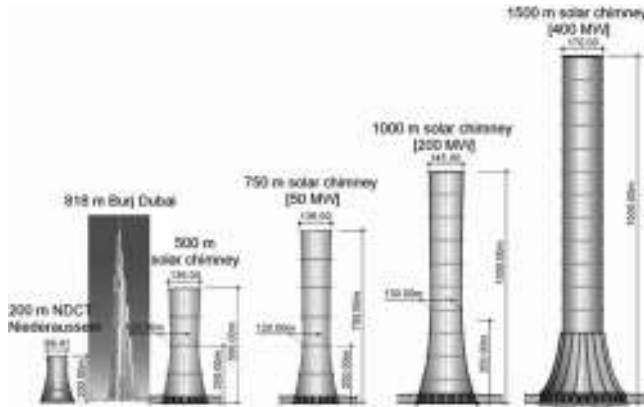
Figure 1.11 From cooling towers to chimneys of Solar Updraft Power Plants (Krätzig et al., 2008-2009a,b)

The distinctive feature is that the lower part of the tower turns into a hyperboloid. Thanks to the use of a double curvature surface, the structure applies the benefits of shape strengthening. Two recent pre-designs of a 1000 m high reinforced concrete solar tower are shown in Figure 1.12 and Figure 1.13 (Krätzig et al., 2008-2009a,b; Harte et al., 2010). With a collector size of 6000 m of diameter they shall produce a peak power of 200 MW_p (annual work of 600 GWh). In Figure 1.12, shortly above the throat at 400 m of height, the shell diameter is 130 m wide, while at the upper ring it is 145 m. Below 400 m the tower shell widens in strength-optimized hyperbolic shape up to a foot-diameter of 260 m. The wall thickness of high-performance reinforced concrete (C70/85) varies from 0.25 m to 0.65 m. In addition to the upper edge member, nine intermediate reinforced concrete ring-stiffeners are applied, fixed on the outer shell face. 16 turbo-generators deliver the mentioned plant capacity, see (Backström et al, 2008). In Figure 1.13 the upper part of the tower has a constant diameter of 150 m and the maximum shell thickness at the base is 0.60 m. This one drawn in Figure 1.13 is the reference structure which is always considered in this work.

From the structural viewpoint it is important to construct the solar tower as thin as possible. This can be achieved by using high-strength concrete and/or by installing stiffening rings along the chimney height and on top. Stiffening rings can be realized in several ways, e.g. classical reinforced concrete beams (Figure 1.14), composite steel-concrete, spoken wheels with carbon fiber strings (Figure 1.15). In order not to reduce the efficiency of production, the interference between stiffening rings and

internal efflux in the chimney has to be minimized. For this reason, it is preferable that stiffening rings are fixed on the outer surface.

Firstly, the intermediate stiffeners enhance a beam-like distribution of the meridional forces under wind loading. The second important contribution of the rings is the increase in the stability safety by localization of the buckling modes. For tower designs without ring-stiffeners one would recognize that instability modes dominate the entire shell, so that the concrete quality for this alternative had to be increased to a high performance reinforced concrete (e.g. C90/105), (Krätzig et al., 2008-2009a,b). Moreover, the vulnerability to vortex shedding would be strongly increased if the shell-like behaviour predominated at the first eigenmode.

Provided a very good soil, the foundation of 1 km tower may only consist of a reinforced concrete circular ring beam (Krätzig et al., 2008-2009a,b).
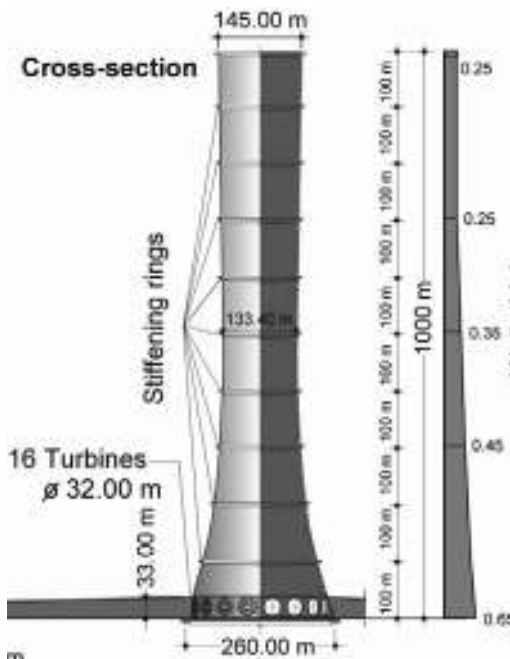
Figure 1.12 Example n.1 of 1-km tall solar tower (Krätzig et al., 2008-2009a,b; Harte et al. 2010)
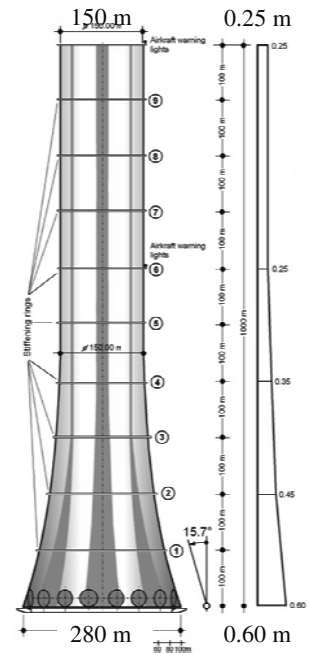
Figure 1.13 Example n.2 of 1-km tall solar tower (Krätzig et al., 2008-2009a,b; Harte et al. 2010)
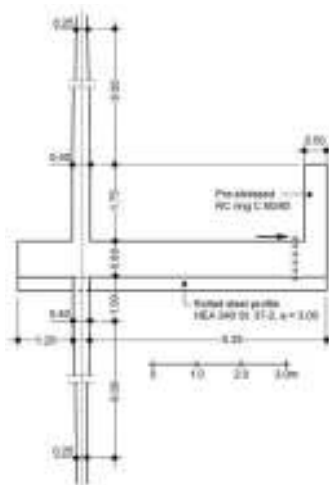
Figure 1.14 Reinforced concrete stiffening ring (Krätzig et al., 2008-2009a,b)
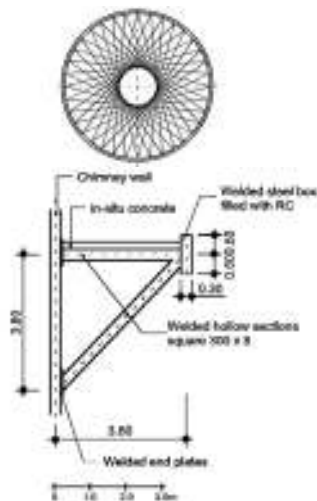
Figure 1.15 Spoke wheels with carbon fiber strings (Krätzig et al., 2008-2009a,b)

1.4.2   **The collector**

The collector area is not investigated within this work. However, the collector is one of the main components of the power plant. In fact, as previously mentioned, the power output of Solar Updraft Towers is proportional to the collector area (1.14). The diameter of the collector ranges from 1 up to 7 km, depending on the required energy output, it is usually made of glass and it could also take the secondary function of being a greenhouse for agricultural purposes. Its cost is a high percentage (between 40% and 60%) of the entire power plant, as reported in several publications (e.g. Krätzig , 2012b; Bergermann&Weinrebe, 2010). Thus, the collector plays a key role and the performances of the SUPP, in terms of energy production, can be significantly increased by improving the collector glass quality. In particular, the optical glass quality is of the greatest importance. The transmittance and absorptivity of glass depend on the solar radiation incident angle, the refractive index of the glass, the thickness of the glass and its extinction coefficient. The latter determines the amount of radiation absorbed and consequently transmitted by the medium (Pretorius, 2007). Moreover, a better quality of the glass implies a better transparency, allowing more solar radiation to penetrate it.

Several studies and on-going researches about the collector can be found in literature. For example, numerical simulations are performed in (Pretorius, 2007), referring to a SUPP located in South Africa, with a 5000 m collector diameter and a 1000 m high, 210 m diameter chimney. These simulations show that through the modification of the collector roof reflectance, collector roof emissivity, ground surface absorptivity and ground surface emissivity, major improvements on plant performance are possible. An improved plant performance can also be reached by introducing thermal insulation and double glazing of the collector roof. The better is the insulation of the warm collector air from the environment, the smaller are the heat losses through the roof. It is also predicted a notable sensitivity to the ground surface absorptivity value.

Techniques to control the power output of a SUPP according to specific demand patterns are investigated in (Pretorius, 2007). Without any control, SUPPs deliver electricity simultaneously to sun radiation and are designed neither for base load power generation nor for peak load. The introduction of a secondary collector roof beneath the main one is a strategy proposed by Pretorius to regulate the air-flow, and thus the energy production, according to specific demand patterns. Another strategy to control the power production of SUPPs is the incorporation of water tanks under the collector roof, so that the energy (heat) storage capability increases significantly thanks to the high specific heat capacity of water. In this way, the production during the day-time is lower, but the night-time production is much higher.

Recent studies about heat storage and heat transfer have been presented at the International conference SUTPT 2012 (e.g. Bernardes (2012) and Fasel (2012)).

1.4.3   The turbines

Milestones studies regarding the layout of the turbines of solar updraft towers belong to the University of Stellenbosch (Backström&Fluri, 2006; Fluri, 2008; Fluri&Backström, 2008; Backström&Fluri, 2010).

The two typical solar tower configurations are one with vertical axis (used in a single turbine layout) and one with horizontal axis (used in multiple turbine layout). Backström&Fluri (2010) explain that the vertical axis layout with horizontal entrance is favoured for layouts where there is one turbine per chimney, while the horizontal layout for many turbines per chimney. In Fluri (2008) it is stated that many smaller generators replacing a large one weigh and cost less than a huge one. Fluri investigated the optimum number of turbines for solar chimney power plants of various output. He found that for large plans with nominal power of 200 MW the optimal number of

turbines is about 30, and the turbine diameter is about 30 m. Each turbine will then have a rating of about 6.7 MW.

The turbine layout is not considered in this work. However, the reference structure of this Thesis, depicted in Figure 1.13 presents 16 turbines of 32 m in diameter.

1.5   **Aim of the research**

The dissertation investigates the Aeolian risk scenario on ultra-high structures, like solar updraft towers. For such structures, the wind action represents the main natural hazard.

At first, the dissertation aims to revise the knowledge about the nature of strong winds in the atmospheric boundary layer. The usual wind engineering applications are limited to the lowest 200-300 m of the atmosphere, where codified wind profiles can be applied. The coupling between wind engineering and meteorology allows to investigate higher levels. The problem is addressed in the thesis on theoretical bases, because experimental data at large heights in strong winds are, so far, inexistent. Several issues still remain unsolved and their uncertainty increases the structural risk of ultra-high towers. However, this should not prevent the design, provided that the vulnerability of the structure to the wind action is low.

The structural vulnerability of solar towers to the wind action is especially addressed in the dissertation. In fact, so far it was known that stiffening rings applied along the height of the tower reduce the vulnerability of the structure, because they enhance a beam-like behaviour. However, their effect on the load had never been investigated before. Moreover, no load model is so far available to the designer to calculate the structural response of a solar updraft tower to a stochastic wind loading process. Without that, the actual damage of such a structure due to the wind action could not be really estimated.

Thus, the main purpose of this research is to investigate – by means of wind tunnel experiments – the aerodynamics of the flow around circular cylinders, like solar towers. Beside the traditional case of study, i.e. a circular cylinder with a free-end (which is addressed in literature but not in all its aspects) the dissertation also investigates the effect of rings along the height of the tower. This case is not treated in literature. The dissertation aims at investigating the new phenomenon created by spanwise rings, both from the fluid dynamic point of view – by means of wind tunnel experiments and numerical simulations – and from the structural point of view.

The experimental investigation is performed in two wind tunnels, at WiSt Ruhr-University Bochum and at CRIACIV University of Florence. The comparative study aims to cross-check results. In view of that, numerical simulations represent a further support. However, the wind pressures depend on atmospheric boundary layer characteristics. Since the boundary layers in two different wind tunnels are necessarily different, the experiments also aim to investigate such a dependency. So, as a further result of this work, the designer will benefit of a quasi-static stochastic load model which is not referred to a pre-defined boundary layer, but it can be generalized to any atmospheric boundary layer flow. This tool allows to evaluate the structural damage even in the vicinity of the stiffening rings, where the shell-like behaviour predominates and no load model was available before.

The tower structure which is used as reference in the dissertation is the one in Figure 1.13. The height is 1-km, the diameter at the base is 280 m and at the top it is 150 m. However, the wind tunnel model has a simpler and more general shape. It is a circular cylinder with aspect ratio H/D = 1000/150 = 6.7.

Chapter 2. **Risk scenario for SUPPs technology**

This chapter describes the risk scenario of the apparently most economic and sustainable technology for renewable energy harvesting, with focus on the Aeolian risk. The theory of the atmospheric boundary layer at large heights – resulting from coupling wind engineering with boundary layer meteorology – is presented as the basis for a deeper knowledge of the natural hazard. Moreover, so far it is known that the structural vulnerability of the tower to the wind action can be reduced by introducing stiffening rings along the height.

2.1 **Aeolian risk**

Many studies around the world (SCPT, 2010; SUTPT, 2012) proved that Solar Updraft Power Plants would be the most economic technology for renewable energy harvesting in the world, as reported in section 1.3. The leveled electricity costs of the energy (according to the definition in the IEA-guidelines) would be of a few €cent/kWh, considerably lower than those for other competitive renewable energy concepts. So, why have big power plants not come to realization, yet? It is not only a matter of the high initial cost, because it would be retrieved after the amortization period, including depreciation. In fact, SUPPs are considered a highly risky technology. The high risk concerns especially two main aspects: the production of energy and the structural feasibility. Some projects stopped before being completed because it was realized that the production of energy of the power plant would have resulted lower than expectations, for which investors were gained. The structural aspect is another challenge, since 1 km tower would be the highest structure in the world.

The present work focuses on the structural aspect; the wind action on the tower is selected among all natural hazards. Thus, the focus is on the Aeolian risk scenario, which is first introduced in the next section within a general framework. In particular, the following issues are discussed in the dissertation:

NATURAL HAZARD

The state of knowledge of the nature of wind at high altitudes results from coupling boundary layer meteorology with wind engineering. Theoretical models like the Harris and Deaves (H&D) one (Harris&Deaves, 1980) describe the mean wind profile, the turbulence intensity and the integral length scale of turbulence in strong wind

conditions up to the boundary layer height, on the basis of order of magnitude analyses of the equations of motion. The Coriolis force is included. However, a further question is whether such mid-latitudes models could be applied at small latitudes, where the Coriolis force becomes smaller and smaller in the geostrophic balance. Moreover, to which extent can full-scale measurements at large heights (e.g. 1 km height) be used to study the turbulent properties of wind, for engineering purposes? These issues are addressed in section 2.3. Tropical cyclones and tornadoes are only mentioned but not included in this work.

Wind tunnel experiments performed in different boundary layers (and different wind tunnels) allowed to study the effect of certain boundary layer properties on wind forces and pressures. A simplified model of wind pressures on the tower shell, with regard to the turbulent properties of the incoming flow, is proposed in Chapter 7. It can be applied by the designer in any boundary layer flow to calculate the quasi-static response of the tower (resonance not included).

EXPOSURE

The tower is considered exposed to strong wind conditions (exposure factor $E = 1$).

VULNERABILITY

The main part of the dissertation studies the effect of stiffening rings applied along the height of the tower, like those reported in Figure 1.14 and Figure 1.15. They were originally introduced in the design in order to reduce the vulnerability of the structure, as explained in section 2.4, but their effect on the flow had never been investigated before. The thesis discovers and proves that this strategy for the reduction of structural vulnerability might induce an even more severe load condition, if improperly used.

2.2   **Risk management framework**

The risk scenario of the Solar Updraft Power Plants Technology can be described within the general approach of the risk management framework. The latter is outlined as a unified methodology throughout different disciplines in Pliefke (2010).

The risk management framework is organized in three main steps (see Figure 2.1), that are risk identification, risk assessment and risk treatment. They are performed sequentially and accompanied by a risk review step and a continuous risk monitoring.
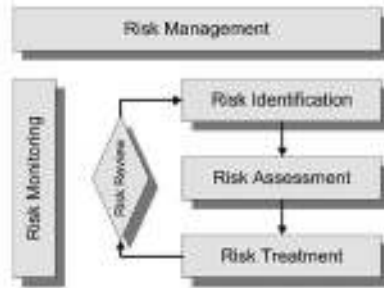
Figure 2.1 The general risk management framework (Pliefke, 2010)

As outlined in Pliefke (2010), the risk identification phase consists in the definition of the system under analysis and of the hazards that could endanger it. In the present work, the system is the solar tower and the natural hazard under investigation is the wind action.

The risk assessment phase is divided in two sub-steps (Figure 2.2): the risk analysis and the risk evaluation. The risk analysis (Figure 2.3) consists in a quantification of the risk. To do that, the hazard must be defined, for a certain return period, in term of its intensity and frequency parameters. Then, for each element at risk (EaR) of the system, i.e. for each element with a non-zero exposure to the hazard, the impact of the hazard is converted into hazard load. Depending on the structural response of the element at risk to the hazard load, the damage can be identified. The relation between the hazard load and the resulting damage is the structural vulnerability. It indicates "the degree of physical susceptibility towards the impact of the hazard". The expected damage per year can be interpreted as the structural risk. By definition, the structural risk is "the product of the annual probability of occurrence of damage multiplied by the potential damage that goes in line with it". Then, direct and indirect consequences, both tangible and intangible, are estimated in order to calculate the total risk, i.e. the expected loss per year, which is "the product of the annual probability of occurrence of the loss and the loss that goes in line with it". Tangible consequences are measured in monetary value. Intangible consequences must be converted in monetary values, otherwise no comparison of risks is possible. After that, the risk evaluation sub-step aims to find adequate risk measures, so that the risk under investigation can be compared to other risks for the system.

The last phase in Figure 2.1, that is the risk treatment, creates a rational basis to handle the risk and, if necessary, reduce it by risk mitigation initiatives. Then, for those risks that have already run through the whole process at least once, a risk review process can be performed.

Figure 2.2 The risk assessment phase (Pliefke, 2010)
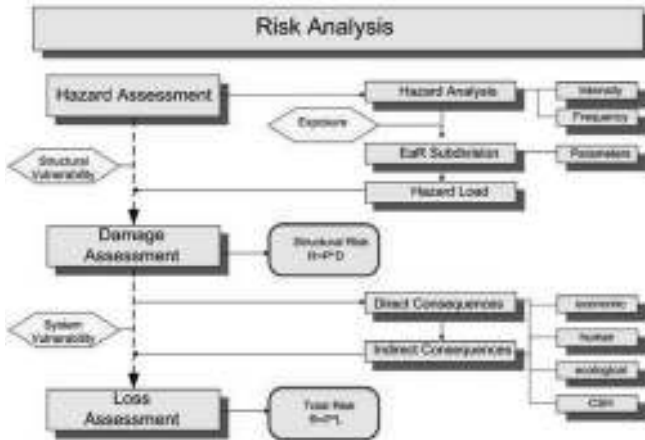
Figure 2.3 The risk analysis (Pliefke, 2010)

The risk management framework proposed by Pliefke is consistent with other definitions of risk in literature. In particular, Augusti et al., (2001) define the damage risk as "the risk associated with physical damage to constructed facilities". The probability of a negative consequence caused by a potentially dangerous event is "the product of three factors, namely: [1] hazard, i.e. the probability of occurrence of a dangerous event (the action); [2] exposition, i.e. the probability that the action finds something that can be damaged; [3] vulnerability, i.e. the (conditional) probability that the facility is damaged when hit by the dangerous action." The damage is associated to its consequences ("losses"). The latter can be considered as a measure of the damage itself, so that the three-factor formulation yields directly the risk as "expected cost of damage". Alternatively, the "expected cost of damage" can be split up into the product of the "probability of damage" times the "cost of damage". In this case, the cost of damage is the fourth factor to be included in the probabilistic definition of risk.

2.3   **Natural hazard – the wind action**

Solar Towers are subjected to loads and other actions that are typical for high reinforced concrete towers:

- dead load of the shell wall, the ring beams, the turbine houses, and the foundation ring;
- wind loading acting both on the external and the internal surfaces of the shell
- temperature effects, operational ones from the action of the heated air, axisymmetrical ones due to ambient air temperature, non-axisymmetrical ones due to solar irradiation on the tower shell;
- seismic action if the location of the Solar Updraft Power Plant exhibits sufficiently important seismicity;
- shrinkage effects;
- pre-stressing if applicable;
- construction loads, e.g. anchor forces from pre-stressed guys of the central crane;
- differential soil settlements of external origin.

Wind and seismic activity are the main natural hazards to be considered in the tower design. However, the very high first natural period of the tower (beam-like bending mode, like a soft cantilever), makes it isolated against strong earthquake excitations. Therefore, even in case of seismic hazard, the vulnerability of the structure to earthquake loading is not high. The seismic risk is thus neglected in this work. Instead, the main risk in the solar tower design is due to the wind action.

The wind hazard for strong winds in "well-behaved" wind climates (i.e. excluding tropical cyclones and tornadoes) is related to the design wind velocity. This is the 10-min-average velocity that has a 2% yearly probability of exceedance, which roughly corresponds to a 50-year-return period (Eurocode1). Tropical cyclones and tornadoes are not covered in this dissertation (they are only mentioned in section 2.3.4), as well as occurrence of low-level jets in the deserts.

The height of solar updraft towers (up to 1500m) exceeds by far the main definition domain of up to 300 m for established and codified wind profiles and wind load models. In this domain, the concept of the turbulent Prandtl layer with constant shear is a useful approximation. Above the Prandtl layer, in the Ekman layer, the shear turbulence decreases while the Coriolis force increases and tends to align the flow in the direction of the isobars according to the Ekman spiral.

The knowledge of the nature of the wind is a pre-requisite for investigating the wind load on solar towers. However, experimental data are scarce at large heights, and accurate measurements of wind turbulence are currently not available above 300 m. This section addresses the state of knowledge of the structure of strong winds at high altitudes and to which extent it can be enhanced by means of field measurements. The modelling of the wind action with regard to turbulent properties of the flow (Chapter 7) by means of wind tunnel experiments in different boundary layer flows is the way which is proposed in this work to approach the open problem concerning the nature of wind at large heights.

2.3.1 **The structure of strong winds in the atmospheric boundary layer**

Five equations form the foundation of boundary layer meteorology (Stull, 1988): [1] equation of state (ideal gas law), [2] conservation of mass (continuity equation), [3] conservation of momentum (Newton's second law), [4] conservation of moisture, [5] conservation of heat (first law of thermodynamics). In addition, there are equations for conservation of scalar quantities, e.g. a tracer in the atmosphere.

In strong winds, it can be assumed that the ambient temperature gradient is adiabatic (neutrally stable atmosphere), so that only the mechanical stirring and not the convective action of buoyancy forces will generate turbulence. Essentially, the conservation of momentum and the continuity equation govern the motion of strong atmospheric winds. The latter leads to the incompressibility approximation if typical velocity and length scales of the boundary layer are used. In a rotating Cartesian frame of reference the former equation is (Stull, 1988):

$$\frac{\partial U_i}{\partial t} + U_j \frac{\partial U_i}{\partial x_j} = -\delta_{i3} g + f_c \varepsilon_{ij3} U_j - \frac{1}{\rho} \frac{\partial p}{\partial x_i} + \frac{1}{\rho} \frac{\partial \tau_{ij}}{\partial x_j} \tag{2.1}$$

$$\text{I} \qquad \text{II} \qquad \text{III} \qquad \text{IV} \qquad \text{V} \qquad \text{VI}$$

where $i,j = 1,2,3$ and $\varepsilon_{ij3} = +1$ if $ij3 = 123$ and $= -1$ if $ij3 = 213$; $\varepsilon_{ij3} = 0$ if $i = j$ (alternating unit tensor) and $\delta_{i3} = +1$ if $i = 3$, otherwise it is 0 (Kronecker delta). The terms on the left-hand side represent the time rate of change of the wind velocity (i.e. acceleration) following a moving fluid element: the first contribution (term I) is the time rate of change at a fixed point (local derivative), while the second term (term II, advection) is the time rate of change due to the movement of the fluid element from one location to another in a flow field where the flow properties are spatially different. The terms on the right-hand side represent the sum of forces (per unit mass) acting on

24

a fluid particle. They are body forces (term III, due to gravity and acting only vertically), Coriolis force (term IV, an apparent force due to the earth rotation, f_c is the Coriolis parameter), pressure-gradient forces (term V) and viscous forces (terms VI).

To a close approximation, air in the atmosphere behaves like a Newtonian fluid (viscous stresses are proportional to the velocity gradients), so that, by assuming incompressibility, the term VI reduces to:

$$\text{Term VI} = \frac{1}{\rho}\frac{\partial \tau_{ij}}{\partial x_j} \rightarrow v\frac{\partial^2 U_i}{\partial x_j^2} \qquad (2.2)$$

$$\text{being: } v = \frac{\mu}{\rho} \text{ the kinematic viscosity and } \tau_{ij} = \mu\left(\frac{\partial U_i}{\partial x_j} + \frac{\partial U_j}{\partial x_i}\right) \qquad (2.3)$$

The horizontal pressure gradient term (V) can be expressed by using the definition of geostrophic wind:

$$f_c U_g = -\frac{1}{\rho}\frac{\partial p}{\partial y} \qquad \text{and} \qquad f_c V_g = +\frac{1}{\rho}\frac{\partial p}{\partial x} \qquad (2.4)$$

So that the horizontal equations of motion can be written as:

$$\frac{dU}{dt} = -f_c\left(V_g - V\right) + v\frac{\partial^2 U}{\partial x_j^2} \qquad (2.5)$$

$$\text{I+II} \qquad \text{IV+V} \qquad \text{VI}$$

$$\frac{dV}{dt} = +f_c\left(U_g - U\right) + v\frac{\partial^2 V}{\partial x_j^2} \qquad (2.6)$$

$$\text{I+II} \qquad \text{IV+V} \qquad \text{VI}$$

where the terms IV+V are sometimes called the geostrophic departure terms because they are zero when the actual winds are geostrophic.

Then, the wind velocity can be expanded into mean and fluctuating components. It is remarkable that, due to the non-linearity of the equations, unknown terms arise even in the equations of the mean fluid motion (equations (2.7)). They are the Reynolds stresses. Physically, this implication means that turbulence must be considered in making forecasts in the turbulent boundary layer, even if only mean quantities are of interest. The following forecast equation for mean wind is formally very similar to the basic conservation equation (2.1) except for the addition of the turbulence term at the end (VII):

$$\frac{\partial \overline{U_i}}{\partial t} + \overline{U_j}\frac{\partial \overline{U_i}}{\partial x_j} = -\delta_{i3}g + f_c\varepsilon_{ij3}\overline{U_j} - \frac{1}{\rho}\frac{\partial \overline{p}}{\partial x_i} + v\frac{\partial^2 \overline{U_i}}{\partial x_j^2} - \frac{\partial\left(\overline{u_i'u_j'}\right)}{\partial x_j}$$

$$\quad\text{I}\qquad\quad\text{II}\qquad\qquad\text{III}\qquad\text{IV}\qquad\text{V}\qquad\text{VI}\qquad\text{VII}$$

(2.7)

In order to solve the problem, the unknown Reynolds stresses must be somehow specified (closure problem).

Mean wind profile

Some simplifying assumptions are introduced in meteorology, in order to develop analytical expressions of the mean wind profile throughout the whole depth of the boundary layer, including the Coriolis force (Stull, 1988):

- steady state ($\rightarrow \partial\overline{(\ )}/\partial t = 0$, i.e. no time-dependence);
- horizontal homogeneous flow, as it happens in large-scale storms, on a horizontal site of uniform roughness over a sufficiently large fetch ($\rightarrow \partial\overline{(\ )}/\partial x = 0, \partial\overline{(\ )}/\partial y = 0$, i.e. no advection);
- barotropic flow, i.e. negligible horizontal density gradient ($\rightarrow$ constant geostrophic wind);
- geostrophic approximation ($\rightarrow$ the curvature of the isobars is negligible);
- no subsidence ($\rightarrow$ the mean vertical wind component is zero).

In these conditions, the equations of mean motion reduce to (Stull, 1988):

$$0 = f_c\overline{V} - \frac{1}{\rho}\frac{\partial p}{\partial x} + \frac{1}{\rho}\frac{\partial \tau_x}{\partial z} \qquad \rightarrow \qquad 0 = -f_c\left(\overline{V_g} - \overline{V}\right) + \frac{1}{\rho}\frac{\partial \tau_x}{\partial z}$$

(2.8)

$$0 = -f_c \overline{U} - \frac{1}{\rho} \frac{\partial p}{\partial y} + \frac{1}{\rho} \frac{\partial \tau_y}{\partial z} \qquad \rightarrow \qquad 0 = +f_c \left(\overline{U_g} - \overline{U} \right) + \frac{1}{\rho} \frac{\partial \tau_y}{\partial z} \qquad (2.9)$$

where τ_x and τ_y are the horizontal shear stresses, including both contributions from viscous forces and Reynolds stresses. $\overline{U}$ and $\overline{V}$ are the components of the mean wind. For convenience, it is chosen a reference system with the x-axis aligned with the direction of gradient wind G:

$$-\overline{V} f_c = +\frac{1}{\rho} \frac{\partial \tau_x}{\partial z} \qquad (2.10)$$

$$f_c \left(\overline{U} - G \right) = \frac{1}{\rho} \frac{\partial \tau_y}{\partial z} \qquad (2.11)$$

where:

$$G = \sqrt{U_g^2 + V_g^2} \qquad (2.12)$$

The boundary conditions are:

$$z = 0 \quad \rightarrow \quad \overline{U} = \overline{V} = 0 \qquad (2.13)$$

$$z \rightarrow \infty \quad \rightarrow \quad \overline{U} \rightarrow G, \, \overline{V} \rightarrow 0 \;\; \text{and} \;\; \tau_x, \; \tau_y, \; \frac{\partial \tau_x}{\partial z}, \; \frac{\partial \tau_y}{\partial z} \rightarrow 0 \qquad (2.14)$$

Meteorologists have attempted to solve equations (2.8) and (2.9) by introducing phenomenological relations to describe the shear stresses τ_x and τ_y.
A well-known assumption (Schlichting, 1960) is that an eddy viscosity K and a mixing length L may be defined, so that (first-order local closure K-theory):

$$\frac{\tau_x}{\rho} = -K \frac{\partial \overline{U}}{\partial z} \;\; \text{and} \;\; \frac{\tau_y}{\rho} = -K \frac{\partial \overline{V}}{\partial z} \qquad (2.15)$$

where:

$$K(x, y, z) = L^2(x, y, z) \left[\left(\frac{\partial U}{\partial z} \right)^2 + \left(\frac{\partial V}{\partial z} \right)^2 \right]^{1/2} \tag{2.16}$$

Either the eddy viscosity K or the mixing length L must be specified. An analytical solution of the equations (2.8) and (2.9) can be obtained under the assumption of a constant eddy viscosity (Ekman, 1905). That is the Ekman spiral model:

$$\overline{U}(z) = G \left[1 - e^{-\gamma_E z} \cos\left(\gamma_E z \right) \right] \tag{2.17}$$

$$\overline{V}(z) = G \left[e^{-\gamma_E z} \sin\left(\gamma_E z \right) \right] \tag{2.18}$$

where $\gamma_E = (f_c/2K)^{1/2}$, and $f_c = 2\Omega\sin\phi$ is the Coriolis parameter (ϕ = latitude, Ω = angular velocity of Earth rotation). The wind speed is geostrophic at height $z = \pi/\gamma_E$. This height is used as an estimate of the depth of the neutral boundary layer. Hence, the Ekman layer depth can be defined as $h = \pi/\gamma_E$.

A different type of approach, based on the asymptotic similarity theory, is developed in Csanady (1967). The boundary layer is divided in two regions: a surface layer and an outer layer. The theory is based on the attempt to express the profile of wind velocity as a function of height in non-dimensional form. This poses the problem of finding appropriate velocity and length scale parameters. It turns out that for the velocity, anywhere in the height range considered, the velocity scale parameter is the friction velocity u_*. In the case of the height scale, in the lower layer, close to the ground, the appropriate parameter is the roughness length z_0, while in the upper layer it is the gradient height h. The law of the wall describes the flow in the surface layer, while a velocity defect law applies in the outer layer.

The key to solve the problem lies in the assumption that a region of overlap exists, in which both laws are valid. It results in a logarithmic solution. Out of it, the gradient wind velocity can be calculated (Gill, 1968; Monin&Yaglom, 1971). It depends on two universal constants A and B:

$$G = \left[B^2 + \left(\ln \frac{u_*}{f_c z_0} - A \right)^2 \right]^{1/2} \frac{u_*}{k}$$

(2.19)

Several authors proposed values for A and B, as listed in Simiu&Scanlan (1996). It can be considered $0 < A < 2.8$ and $4.3 < B < 5.3$.

A similar approach, based on a modified version of the asymptotic similarity theory, was developed by Harris&Deaves (1980). The peculiar feature of the so-called H&D model is the closure assumption to solve the equations of motion (2.8) and (2.9): the shear stresses are assumed to decrease parabolically with height (equation (2.20)). Some justification for this assumption was found by the authors in full-scale data, but it is also justifiable on theoretical grounds, on the basis of an order of magnitude analysis between production, diffusion and dissipation of turbulent energy (Deaves, 1981).

$$\tau(z) = \rho u_*^2 \left(1 - \frac{z}{h} \right)^2$$

(2.20)

This expression is adopted by the ESDU Data Items (ESDU 85020).
Accordingly, the velocity defect law is parabolic for a substantial part of the boundary layer, so that:

$$\overline{U}(z) = \frac{1}{k} u_* \left\{ \ln \frac{z}{z_0} + a_1 \frac{z}{h} + a_2 \left(\frac{z}{h} \right)^2 + a_3 \left(\frac{z}{h} \right)^3 + a_4 \left(\frac{z}{h} \right)^4 \right\}$$

(2.21)

where z_0 is the roughness length, h is the atmospheric boundary layer thickness, u_* is the friction velocity and k the Von Karman constant ($k = 0.4$). The coefficients a_i, $i = 1$, ..., 4 are universal constants whose values are determined theoretically, in terms of two experimental parameters: β and A. From fitting a number of good quality wind profiles, it resulted $\beta = 6$ and $A = -1$ (Harris&Deaves, 1980). So that:

$$a_1 = 2(\ln \beta - A) + \frac{1}{6} \approx 5.750 \quad a_2 = 1 - \frac{a_1}{2} = -1.875 \quad a_3 = -\frac{4}{3} \quad a_4 = \frac{1}{4}$$

(2.22)

The H&D model thus extends the log-law (which fits good near the surface) through the Ekman layer, in order to blend into the gradient wind velocity at the gradient height. Indeed, if compared to both the well-known logarithmic and power laws, the Harris and Deaves model is the only one which recognizes the top of the atmospheric boundary layer.

It is known that the boundary layer height (h) in neutral atmosphere is proportional to the ratio between the friction velocity and the Coriolis coefficient (Csanady, 1967). In the H&D model such proportionality is expressed by the coefficient $1/\beta$:

$$h = \frac{1}{\beta} \frac{u_*}{f_c} \qquad (2.23)$$

In order to give an idea of the boundary layer height, at a latitude $\phi = 30°$ it results $h \approx 4300$ m, being $z_0 = 0.05$ m, $V_b = 25$ m/s (at 10 m). Thus, the Deaves and Harris model has three scaling parameters: z0 and u* – inherited from the log-law model – and the additional length parameter, h, which is the atmospheric boundary layer height. It is a function of the wind speed, the surface roughness and also the latitude.

Then, by evaluating the H&D wind profile at $z = h$, the gradient wind speed is given by:

$$G = \frac{1}{k} u_* \left\{ \ln \frac{u_*}{f_c z_0} - A \right\} \qquad (2.24)$$

This expression is comparable with equation (2.19), but the universal constants have different values. The same letter A is used in expressions (2.19) and (2.24), because this is the traditional nomenclature reported in the literature on this topic. This should not create confusion. Finally, by using the closure assumption (2.20) and by applying the boundary conditions to the equations of motion, the H&D model derives the following relationship involving ϑ_0, the total (maximum) angle of turn of the wind throughout the boundary layer:

$$\frac{G \sin \vartheta_0}{u_*} = 2\beta = 12 \qquad (2.25)$$

The model also suggests to use above the Prandtl layer a linear variation with height of the wind rotation angle. In fact, the variation of the wind angle would result from the solution of partial differential equations, but a linear approximation can be accepted.

In conclusion, relying on the closure assumption (2.20) – derived by an order-of-magnitude analysis – on the boundary conditions, on theoretical considerations and two constants (A and β) determined empirically, the H&D model gives a complete description of the mean flow in the atmospheric boundary layer (equation (2.21))[1]. However, this is valid at mid-latitudes, where a state of dynamic equilibrium establishes in strong wind conditions, so that the energy subtracted by the mean flow exactly balances that absorbed by the work done against surface friction and dissipated by the viscosity of air (Harris&Deaves, 1980). At tropical latitudes, strong winds are associated with large scale storms, but these may contain intense components of thermal origin. Moreover, the geostrophic assumption is more approximated as the Coriolis force becomes small. To which extent the H&D model is valid at small latitudes is addressed in section 2.3.3.

Standard deviation of the along-wind component σ_u

The H&D model also provides an analytical expression of the standard deviation σ_u of the along-wind component of turbulence at any height in the atmospheric boundary layer, that is valid over uniform flat terrain. On theoretical grounds, it has been seen that for a flow – which is fully in equilibrium with the surface – σ_u / u_* starts from a constant value near the surface and approximately constant within the inner layer, then it achieves a maximum before decreasing linearly with height. At large heights, it is (Harris&Deaves, 1980):

$$\frac{\sigma_u(z)}{u_*} \propto 1 - \frac{z}{h} \tag{2.26}$$

An empirical expression proposed in the H&D model, which matched the data set available to the authors, is:

---

[1] In the following, the horizontal superscript which distinguishes the mean velocity component $\overline{U}$ from the total velocity in the along wind direction $U = \overline{U} + u'$ is neglected, in order not to burden the treatment. Therefore, in the following it is normally referred to U_m as the mean wind velocity.

$$\frac{\sigma_u(z)}{u_*} = \frac{7.5\left[1-\frac{z}{h}\right]\left\{0.538+0.09\ln\left(\frac{z}{z_0}\right)\right\}^{\left[1-\frac{z}{h}\right]^{16}}}{1+0.156\ln\left(6\frac{h}{z_0}\right)} \tag{2.27}$$

This expression is adopted by the ESDU Data Items (ESDU 85020).

Integral length scales of turbulence

Harris and Deaves also propose an expression for the integral length scale of the longitudinal component of turbulence L_{ux}, which is adopted by the ESDU Data Items (ESDU 85020 and 86010). The length scale increases with increasing height above the ground up to a maximum value. Also, for a given height, it increases with increasing wind speed and surface roughness. As the wind strength increases, the boundary layer height increases and the eddies within the boundary layer are stretched accordingly. Moreover, apart from low levels close to the ground, the longitudinal length scale in the boundary layer is generally twice the value of the lateral scale.

The starting point to develop the H&D model of L_{ux} is to match the well-established Kolmogorov and Von Karman spectrum formulas (Harris and Deaves, 1980). For turbulent flows in which an equilibrium range exists (i.e. at high Re), the Kolmogorov formula for the high frequency range of the spectrum is:

$$nS(z,n) = K_0(\varepsilon U)^{2/3} n^{-2/3} \tag{2.28}$$

being K_o the Kolmogorv parameter.

The Von Karman form of the spectrum for the longitudinal component of turbulence is:

$$\frac{nS(z,n)}{\sigma_u^2} = \frac{4\frac{L_{ux}n}{U}}{\left(1+70.8\left(\frac{L_{ux}n}{U}\right)^2\right)^{5/6}} \tag{2.29}$$

At high frequencies, it reduces to:

$$\frac{nS(z,n)}{\sigma_u^2} = A\left(\frac{L_{ux}\,n}{U}\right)^{-2/3} \tag{2.30}$$

being $A = 0.115$.

By combining the Von Karman spectrum at high frequencies and the Kolmogorov formula, it is obtained:

$$L_{ux} = \left(\frac{A}{K_o}\right)^{3/2} \frac{\sigma_u^3}{\varepsilon} \tag{2.31}$$

This result is completely independent of the H&D model, which only becomes involved when the variation with height of the standard deviation σ_u (according to equation (2.27)) and the dissipation ε (using equation (2.32)) are introduced. The dissipation can be approximated by:

$$\varepsilon \cong \frac{\tau}{\rho}\frac{dU}{dz} \tag{2.32}$$

Moreover, two further questions are discussed in the H&D model, through the investigation of experimental data:

1. If autocorrelations and spectra are both derived from field measurements, the length scales derived by the integration of the autocorrelation functions are generally greater than the length scales required in the Von Karman formula to fit the measured spectral density data. It is due to the inadequacy of the Von Karman spectrum to represent the characteristic of turbulence closely at all frequencies. The disparity between length scales is a factor of around 1.4, but it decreases with height. A modification to the coefficient $A = 0.115$ in the formula of the spectrum is then suggested and adopted in (ESDU, 85020):

$$A = 0.115\left[1 + 0.315\left(1 - z/h\right)^6\right]^{2/3} \tag{2.33}$$

2. Due to anisotropy of turbulence near the ground, the Kolmogorov parameter should vary with height up to a constant value at sufficiently high altitude. An empirical relationship, based on a re-analysis of data by (Thompson, 1990), is defined by equation (2.34) (ESDU, 85020):

$$K_0(z) = 0.19 - \left(0.19 - \frac{0.39}{Ro^{0.11}}\right) \exp\left[-24Ro^{0.155}\left(\frac{z}{h}\right)^{1.24Ro^{0.008}}\right] \qquad (2.34)$$

where Ro is the Rossby number ($Ro = u_*/f_c z_0$). By combining equations from (2.31) to (2.34), the expression of the integral length scale of turbulence L_{ux} is thus obtained. Even though the H&D model of L_{ux} is adopted by the ESDU Data Items, it leads to values of the integral length scale which are larger than those recommended in other Codes of practice (e.g. Eurocodes). As a consequence, if the H&D model of L_{ux} is used in the calculations in place of the expressions recommended by other Codes (in case extrapolated at high altitudes), it results that the quasi-static loading is slightly increased, while dynamic loading is decreased.

Cross-correlation functions and cross-spectral densities of wind turbulence

The cross-correlations functions characterize the relationship between fluctuating velocity components at two points in space and in the general case at different times (time lag τ). The zero-lag cross correlations are especially important since they describe how the instantaneous fluctuating component of wind velocity varies in space. Because changes in the gust velocity at one point are not necessarily reflected immediately by similar changes in the gust velocity at another point, the cross-correlation functions are, in general, not symmetrical functions of τ. They can be considered to be composed of two components, the larger one being a symmetrical function of τ and the other being an anti-symmetrical function of τ. Once they are split up in the frequency domain, they are the Fourier transforms of the real (in-phase) and the imaginary (out-of-phase) components of the cross-spectral density. These are the co-spectral density and the quad-spectral density functions, respectively, and are related by the phase-lag angle. The latter is sometimes expressed in terms of an "eddy slope" (ESDU 86010). For most cases, the quad-spectra are small and often neglected, so that the coherence equals the co-coherence. Moreover, the out-of-phase component integrates to zero.

For points having a spatial separation Δx in the along-wind direction, if the assumption of frozen turbulence applies (Taylor's hypothesis), Δx can be converted into an equivalent time lag $\Delta x/U$, being U the mean velocity of the flow. In this case, the coherence function would be 1 and the phase angle $\theta = 2\pi n \Delta x / U$. In practice, Taylor's hypothesis is not always strictly applicable (particularly near the ground, when U/n is greater than 300 m, according to an ESDU 86010 recommendation).

The phase angle for separations normal to the wind direction can be taken as zero in the horizontal plane (lateral direction). Instead, for separations in the vertical directions the eddies are inclined with the mean wind shear, so that changes in the gust component higher up are followed by similar changes lower down at some time later. Thus, in general, the phase angles θ_{uu} and θ_{vv} (for the u- and v- wind components) are not zero. They are zero, no matter the value of z and Δz, only in case of isotropic turbulence. This applies to the high frequency range when, even near the ground, turbulent exhibits isotropic properties. However, θ_{uu} and θ_{vv} tend to zero as z increases and dU/dz tends to zero. Because of that, the ESDU 86010 provides the following formulas for the phase angles θ_{uu} and θ_{vv}:

$$\theta_{uu}\{\Delta z\} = \left(1.3\Delta z / z_m\right)\left(c-1\right)^{0.7}\left(2\pi n \Delta z / U_m\right) \tag{2.35}$$

$$\theta_{vv}\{\Delta z\} = \left(3\Delta z / z_m\right)\left(c-1\right)^{0.7}\left(2\pi n \Delta z / U_m\right) \tag{2.36}$$

where c is a frequency-dependent coefficient defined in the code, that varies between 2 (low frequencies) and 1 (high frequencies). The factors $1.3\Delta z/z_m$ and $3\Delta z/z_m$ are estimations – on the basis of different sources of data up to about 80 m – of the eddy slope for the u and v components.

The H&D model (ESDU Data Items) and other codes: comparison of wind profiles

For purpose of comparison, the H&D model – adopted by the ESDU Data Items and applicable throughout the whole height of the boundary layer – is compared to the extrapolations of the log- and power- law models, adopted by Eurocode and DIN. Rigorously, these would be limited to 200 m and 300 m, respectively. The dependence on latitude is included in the H&D model.

The following case studies are selected:
- terrain category II ($z_0 = 0.05$ m)

- $V_b(10m) = 25$ m/s
- Latitude $\phi = 30°, 23°$.

In these conditions, according to the Eurocode (up to 200 m), it is:

$$U_m(z) = V_b\, 0.19 \ln\left(\frac{z}{z_0}\right)$$

(2.37)

$$I_u(z) = \frac{1}{\ln\left(\dfrac{z}{z_0}\right)}$$

(2.38)

$$L_{ux}(z) = 300\left(\frac{z}{200}\right)^{0.67 + 0.05\ln(z_0)}$$

(2.39)

According to the DIN-EN (up to 300 m), it is:

$$U_m(z) = V_b\left(\frac{z}{10}\right)^{0.16} \qquad I_u(z) = \left(\frac{z}{10}\right)^{-0.16} \qquad L_{ux}(z) = 300\left(\frac{z}{300}\right)^{0.26}$$

(2.40)

All the previous models neglect the variation of air density with height. In Backström et al. (2008) the following expression is proposed:

$$\rho(z) = \rho_0\,\frac{22000 - z}{22000 + z}$$

(2.41)

where $\rho_0 = 1.25$ kg/m^3.

As shown in Figure 2.4, the profiles of mean wind and turbulence intensity recommended by the Codes do not differ significantly at low heights. The H&D model predicts much larger integral scales. This issue is further commented by Harris (1986), because the large values imply, from the structural point of view, an increase in the quasi-static response and a decrease in the dynamic response. The question about the representativeness of such large values is still open today.
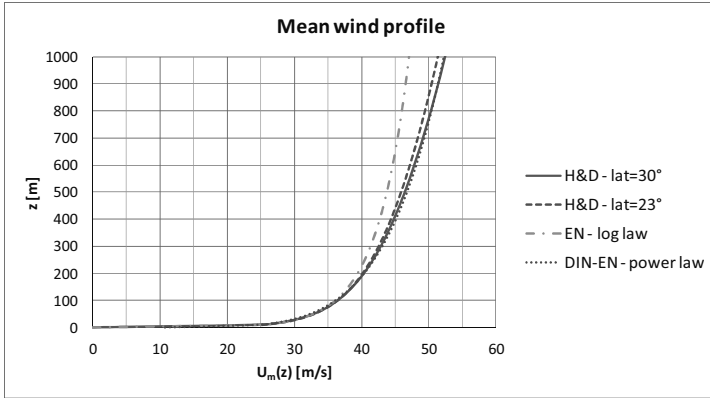
Figure 2.4 Mean wind profile: ESDU, EN, DIN-EN
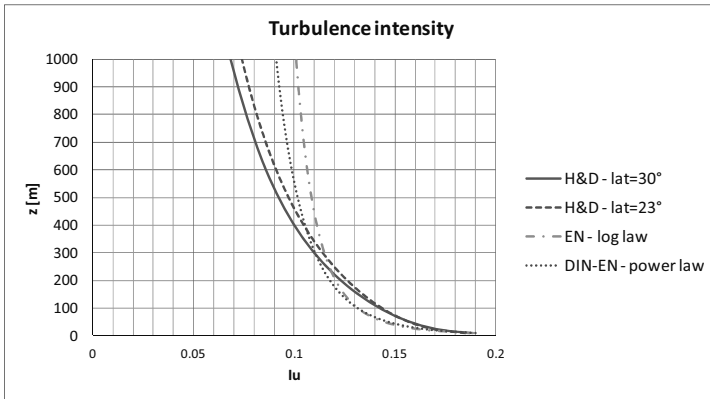
Figure 2.5 Turbulence intensity: ESDU, EN, DIN-EN
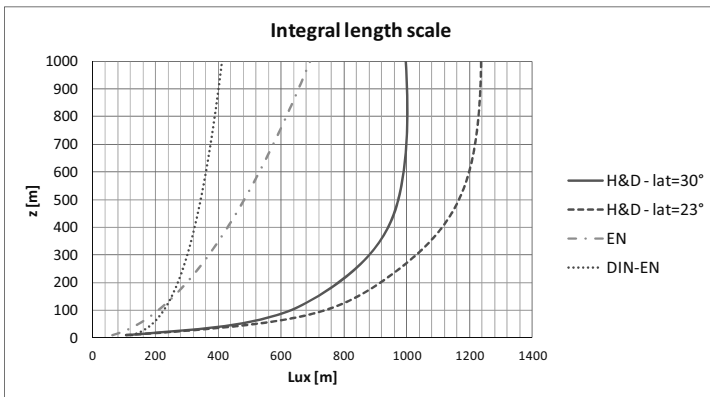
Figure 2.6 Integral length scale: ESDU, EN, DIN-EN

2.3.2   Experimental and numerical investigation of the ABL

Up to around 300 m, wind velocities can be accurately measured at sufficiently high frequency resolution (for example by means of anemometers on high towers, Figure 2.7). Therefore, the structure of wind turbulence up to that level is deeply investigated in literature (Peil et al., 1990, 1992, 1996; Clobes et al., 2009; Clobes&Willecke, 2009).
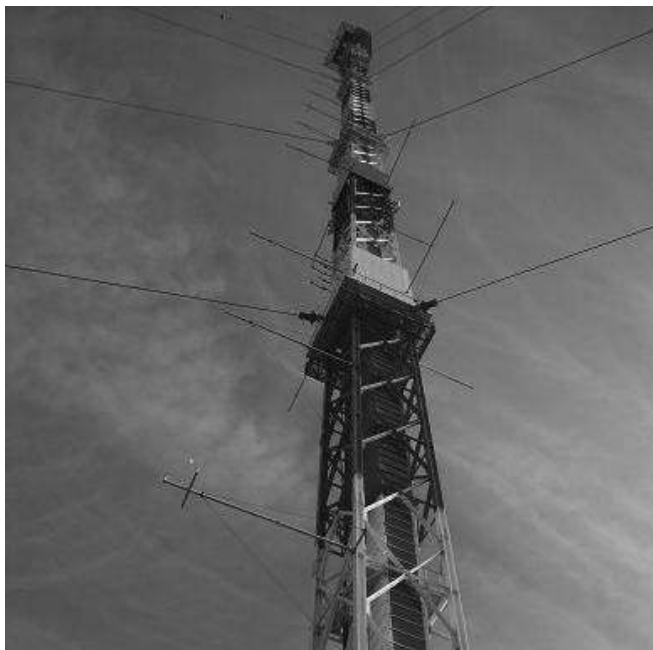
Figure 2.7 Gartow tower (344 m) equipped with anemometers
(picture from http://www.is.tu-braunschweig.de/)

As briefly mentioned in the previous section concerning strong wind conditions, there are still many open problems in the nature of wind at large heights. Recommendations of the Codes of practice are usually limited to 200-300 m. The ESDU Data Items provide profiles which are valid up to the boundary layer height, but there is considerable uncertainty in many parameters, for example the integral length scales of turbulence. Moreover, in light wind conditions the mean wind profile can assume different shapes and no information is currently codified for the designer of super-tall structures. Further investigation in the Ekman layer is thus needed. This section aims at providing an overview of the technologies which are available nowadays to investigate the atmospheric boundary layer at large heights.

Field experiments at large heights

Above 300 m, no experimental evidence is currently available for the purpose of structural wind engineering. It does not mean that no experimental evidence is available at all. In fact, measurements are usually performed at large heights (1000-1500 m) by meteorologists. However, for structural design, specific requirements should be fulfilled:

- sufficiently high frequency resolution, in order to measure turbulence fluctuations;
- spatial averages over big volumes should be avoided;
- relatively small distance between simultaneous measuring points, to calculate cross-correlations.

With regard to the design in the ultimate limit state, only the shear production of turbulence (due to surface friction) and not the buoyancy forces arising from convective motions and thermal stratification of the atmosphere should be considered. It corresponds to neutral stratification of the atmosphere. In these conditions, the scatter of data due to the thermal effects is much reduced, so that a more defined pattern can be evaluated (e.g. power- or log- law for the mean wind profile). Moreover, in the ideal condition of neutral atmosphere, wind is a stationary random process, in the sense that statistics are invariant with time. Instead, thermal effects, convective motions of the atmosphere and buoyancy production of turbulence play a role in light wind conditions. This is a wide field of research in meteorology. For this reason, the instruments that have been used since long time ago to measure wind at large heights are normally required to work only in light wind conditions.

For example, measurements with balloons and aircrafts are possible even at high altitudes. Examples of airborne measurements are reported in Figure 2.8 and Figure 2.9. Such aircrafts do not fly if the wind speed is higher than 10 m/s. In fact, accuracy of these measurements depends on the relative velocity of the aircraft and the wind speed, and it is much affected if they are of the same order.

Balloons represent a less expensive technique than aircrafts for atmospheric investigation. They can be tethered or free balloons. Measurements can be performed either along the vertical while the balloons are flying up, at a fixed point if they are tethered or in the mean wind direction, as they are transported by the flow. Kites are another choice. Again, the use of these instruments by meteorologists is only limited to light wind speeds.

Figure 2.8 Aircraft measurement during the field campaign in Emden, Germany, 2008 (Kroonenberg v.d., 2009)

Figure 2.9 Turbulence probe Helipod, field campaign in the Baltic sea (Bange, 2007)

The type of measurements described above fall in the broad category of in-situ sensors, because the sensing instrument (mounted either on towers, aircraft or balloons) lies in the probe volume. Another category is that one of remote sensing instruments. They can be mounted at ground level, on aircrafts or even on satellites. Their peculiarity is that they do not have a sensing element within or around the volume of interest. They infer atmospheric properties through their effects on acoustic, microwave and optical signals propagation through the air. They can be classified into three main groups:

- acoustic waves are used by SODARs (Sonic Detecting And Ranging)
- light waves are used by LIDARs (Light Detecting and Ranging)
- radio waves are used by RADARs (RAdio Detecting And Ranging)

The wind speed is measured through the doppler effects (in fact, the proper names of the instruments would be doppler-SODAR, doppler-LIDAR, doppler-RADAR). The doppler effect consists in the change of frequency between the emitted signal (known and fixed) and the returned signal. The latter depends on the velocity of the air particles which scatter the signal back. This shift in phase is the necessary information to calculate the velocity of air particles, that is the wind velocity.

Figure 2.10. Movable mono-static Doppler SODAR with three antennas for the measurements of mean wind and turbulence profiles (Emeis, 2010)

Some SODAR campaigns have been recently performed (e.g. Tamura et al., 2007), but results are only available for the mean wind up to 500 m. In fact, the main limit of SODARs is that they measure over an averaging time of several minutes (e.g. 30) and the resolution of measurements decreases with height. Thus, it is not possible to have good results above 400-600 m. This height decreases as the wind speed increases, because the backscattered signal tends to be displaced away from the receiver by the wind itself.

RADARs are not addressed in this context since their resolution of wind measurements is low for the scopes of structural engineers. The reason is that the radio wave is not so well aligned. Instead, conceptually similar but much more focused and precise is the light wave used by LIDARs. High frequency measurements are possible with these instruments, thanks to the high speed of light. Moreover, atmosphere can be investigated up to some kilometers, even if with a decreasing resolution as height increases.

Turbulence measurements using lidars are still a subject of research and the method of analysis of data is not fully established, yet. An attempt to answer the question "Can the available wind lidars measure turbulence?" has been recently presented in Sathe et al. (2011).

Conical scanning is the usual mode of operation of a wind LIDAR (see Figure 2.11), in order to measure vertical profiles of the three-dimensional wind vector. In fact, as the signal sweeps around the conical surface, at each altitude several measurements around the circumference are available. They are all needed to provide information about the wind speed at the circumference centre. However, as the height increases, the radius of the circumference increases, so that big horizontal distances are swept at high altitudes, providing information for wind speed only at the circumference centre.
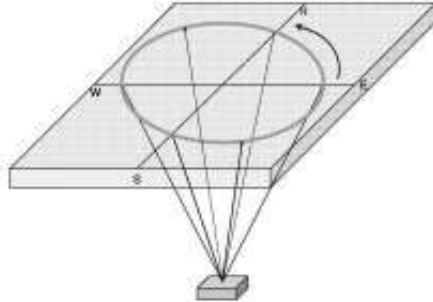
Figure 2.11 Conical scanning pattern of a wind LIDAR in order to measure profiles of the three-dimensional wind vector (Emeis, 2010)

Usually, the signal is transmitted in pulses (Range-resolved remote sensing systems), which are then scattered by atmospheric inhomogeneities or suspensions (e.g., aerosol, droplets), sending a small fraction of the transmitted energy back to the receiver. Distance to the measurement volume is determined by the time of flight of the signal pulse. The state of the art of LIDAR techniques for wind and turbulence measurements by using signal delay for range determination is given by Hardesty & Darby (2005) and Davies et al. (2003). An important point is the spatial resolution, i.e. the volume on which the measured wind speed is averaged. If the signal is sent in pulses in a certain direction, the spatial resolution is related to the distance swept by the pulse in the time interval. Due to the high speed of light, it is in the order of tens of meters (see Figure 2.12). Such a spatial average over big volumes is sometimes useful, for example for applications in the field of wind turbines (Emeis et al., 2007; Mikkelsen et al., 2008). In fact, the average volume is in the order of the volume swept by a blade of a wind turbine, thus it is some good information to design the rotor.
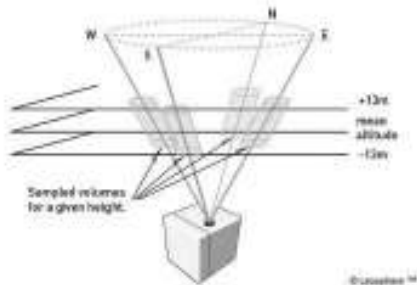
Figure 2.12 Sketch of the operation principle of the Leosphere Windcube
(Waechter et al., 2009)

A transportable continuous-wave wind LIDAR (Figure 2.14) has been recently designed and built (Emeis, 2010). The system emits a continuous-wave beam, so that detection of the wind speed at a given range is achieved by focusing, rather than by the time-of-flight method of pulsed systems (range determination by beam focusing). The system cannot distinguish between air motion towards and away from the LIDAR, and this leads to an ambiguity of 180° in the derived value of wind direction. This is easily resolved, however, by making reference to a simple wind direction measurement at a height of a few meters. The profile of the three-dimensional wind vector is yielded by scanning a cone with a 30° half angle once per second (Banakh et al. 1995, Emeis et al. 2007a, Kindler et al. 2007). Hence the diameter of the measured volume is 173 m at a height of 150 m. The probe length increases roughly as the square of the height. As an example, the vertical resolution is ~ ± 10 m at a height of 100 m. Strong reflections from particles and other moving objects outside the focal range (e.g. due to smoke, fog or birds) can lead to spurious Doppler returns (Harris et al. 2001), but these effects can be recognized and mitigated by signal processing techniques.

Figure 2.13 Small pulsed Doppler wind LIDAR for measurement of wind profiles in a height range between 40 and 200 m. Distance determination by pulse travel time (Emeis, 2010)

Figure 2.14 Small continuous-wave Doppler wind LIDAR for measurement of wind profiles in a height range between 10 and 200 m. Distance determination by beam focusing (Emeis, 2010)

Within the context of this dissertation, field measurements have not been available. Moreover, the concern in the Thesis is mainly on strong wind conditions, which so far have never been investigated in any experiment. However, the field of research on full-scale wind measurements at large heights is currently very active and in rapid development. For example, sophisticated mathematical models are being developed to

manage the major and unavoidable problem of spatial average as the height increases (see Emeis, 2010).

Numerical simulations of the atmospheric boundary layer

Numerical simulations of the atmospheric boundary layer are an alternative and a support to field measurements. For example, Canadillas (2010) presents the investigation of the marine boundary layer by means of a PArallelized Large eddy simulation Model (PALM Code), developed at the Institute of Meteorology and Climatology of the Leibniz University of Hannover (Raasch&Etling 1991, 1998 and Raasch&Schröter, 2001). Examples of results achievable with LES are reported in Figure 2.15 and compared to field data (Canadillas, 2010). In this case, the simulation is performed in neutrally stratified conditions of atmosphere. Such conditions are often achieved in the marine boundary layer even at low wind speeds (the ocean surface and the air flowing above it nearly have the same temperature), so that a comparison with field data can be made. However, these well-defined meteorological conditions (no large-scale advection, homogeneous surface, stationary conditions), like over the sea, should not be easily expected over land on heterogeneous terrain, so that such a comparison with observations is generally extremely difficult.
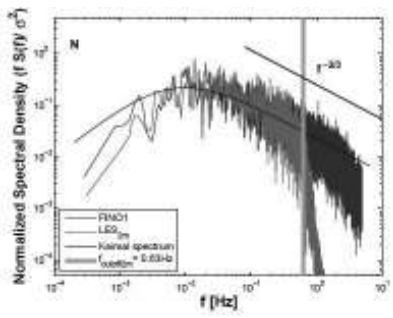
Figure 2.15 Normalized one-dimensional spectra of the horizontal wind velocity fluctuations: comparison between LES simulation of the marine boundary layer (red) and field data (blue) (Canadillas, 2010)
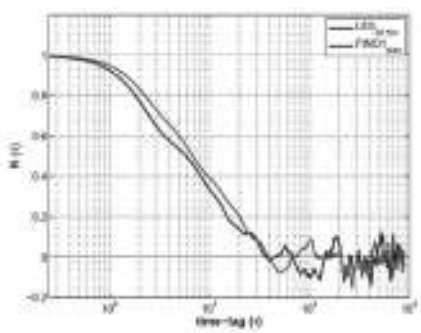
Figure 2.16 Autocorrelation function for the horizontal wind velocity fluctuations: comparison between LES simulation of the marine boundary layer (red) and field data (blue) (Canadillas, 2010)

2.3.3 The Coriolis force

An analytical expression of the Ekman spiral was previously described (equation (2.17)) and a useful approximation to define angle of turn of the mean wind profile is

44

included in the H&D model (equation (2.25)). However, two further questions need some attention:

1) which is the effect of the Coriolis force on turbulence;

2) which model should be used in tropical regions, where the Coriolis force is small (and becomes zero at the equator). In fact, the H&D model is a mid-latitude model.

These questions are addressed in the following.

The Coriolis force in the equations for turbulent departures

Equations for mean variables in turbulent flow have been previously introduced. In particular, equation (2.7) expresses the conservation of momentum. Turbulent departures of the variables are the deviations from their respective means. The equations for the variance of the wind speed are obtained by expansion of the momentum conservation equation and subtraction of the mean part. Such equations contain the local storage of variance, the advection of variance by the mean wind, the buoyancy production, the shear production, the turbulent transport term describing how variance is moved around by the turbulent eddies, the pressure redistribution term describing how variance is redistributed by pressure perturbations and the viscous dissipation term. The Coriolis term, instead, is identically zero for velocity variances (Stull, 1988).

Phisically, this means that Coriolis force cannot generate turbulence kinetic energy. The Coriolis term merely redistributes energy from one horizontal direction to another. Furthermore, the magnitude of the redistribution term is about three orders of magnitude smaller than other terms. For this reason, the Coriolis terms can be neglected in the turbulence equations, even for the cases where they are not identically zero (Stull, 1988).

The Coriolis force in tropical regions

The equations of motion, which describe all types and scales of atmospheric motions, are derived by the second Newton's law: "the rate of change of momentum of an object referred to coordinates fixed in space equals the sum of all the forces acting". Such forces are: the pressure gradient force, the gravitational force and friction. Moreover, since the motion in the atmosphere is usually referred to a coordinate system rotating with the Earth, the Newton's second law can still be applied provided certain apparent forces: the centrifugal force and the Coriolis force.

The centrifugal force is the force that an object at rest experiences in a rotating system. Usually, its effects are combined with those of the gravitational force, by defining a

gravity force which is everywhere directed normal to the local level. The Coriolis force is the force that a moving object (e.g. an air particle) experiences in a rotating system. Therefore, the Newton's second law for motions relative to a rotating coordinate frame – written in the notation used by Holton (1979) – is:

$$\frac{d\mathbf{V}}{dt} = -2\mathbf{\Omega} \times \mathbf{V} - \frac{1}{\rho}\nabla p + \mathbf{F}_r \tag{2.42}$$

The left-hand side represents the substantial derivative of wind flow (local + advective acceleration), while the terms on the right-hand side represent the Coriolis force, the pressure gradient force and the friction force. This is consistent with what has been described before. However, a deeper analysis is required to better understand the flow movements even at low latitudes.

If such an equation is written in spherical coordinates, being x the westward direction, y the northward direction and z the upward direction, it is (Holton, 1979):

$$\frac{du}{dt} - \frac{uv\tan\phi}{a} + \frac{uw}{a} = -\frac{1}{\rho}\frac{\partial p}{\partial x} + 2\Omega v \sin\phi - 2\Omega w \cos\phi + F_x \tag{2.43}$$

$$\frac{dv}{dt} + \frac{u^2 \tan\phi}{a} + \frac{vw}{a} = -\frac{1}{\rho}\frac{\partial p}{\partial y} - 2\Omega u \sin\phi + F_y \tag{2.44}$$

$$\frac{dw}{dt} - \frac{u^2 + v^2}{a} = -\frac{1}{\rho}\frac{\partial p}{\partial z} - g + 2\Omega u \cos\phi + F_z \tag{2.45}$$

where ϕ is the latitude and a the radius of Earth.

They are the complete equations for all motions in the atmosphere. Now, let us consider the synoptic scale motions, i.e. those systems of typically several hundred kilometers in horizontal direction. Characteristic scales of the field variables based on observed values for mid-latitude synoptic systems are (Holton, 1979):

- $U \sim 10$ m/s = horizontal velocity scale
- $W \sim 10^{-2}$ m/s = vertical velocity scale
- $L \sim 10^6$ m = length scale
- $D \sim 10^4$ m = depth scale

- $\Delta p / \rho \sim 10^3$ m^2/s^2 = horizontal pressure fluctuation scale
- $L/U \sim 10^5$ s = time scale

In the free atmosphere, i.e. by neglecting friction, an order-of-magnitude analysis of the equations shows that at mid-latitude the pressure gradient force and the Coriolis force are of the same order of magnitude (10^{-3} m/s^2) and approximately in balance, while all the other terms are one or more orders of magnitude smaller. Thus, the geostrophic approximation – which describes the familiar situation in which the wind blows parallel to the isobars and the Coriolis force balances the pressure gradient force – turns to be confirmed. In other words, being U_g and V_g the horizontal components of the gradient wind, it is:

$$- f_c V_g \cong - \frac{1}{\rho} \frac{\partial p}{\partial x} \tag{2.46}$$

$$+ f_c U_g \cong - \frac{1}{\rho} \frac{\partial p}{\partial y} \tag{2.47}$$

At lower altitudes, i.e. within the atmospheric boundary layer (ABL), the equations of motion are approximately a tree-way balance between the pressure gradient force, the Coriolis force and friction (see Figure 2.17 and Figure 2.18).
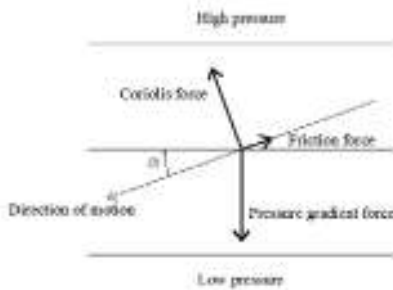
Figure 2.17 Balance of forces within the ABL at mid-latitudes
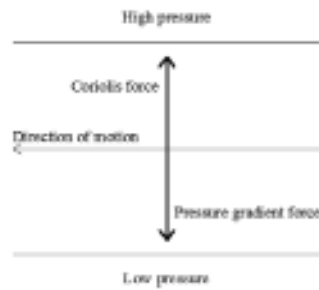
Figure 2.18 Balance of forces in the free atmosphere at mid-latitudes

If the same scale analysis of momentum equations is repeated in tropical regions, it turns out that it is not appropriate to assume that the Coriolis force term balances the pressure gradient. As the Coriolis force becomes smaller, the pressure gradient must be

balanced by the inertial acceleration term. As a consequence, in order to satisfy such a balance, for synoptic scale systems in tropical regions characterized by the same horizontal length and velocity scales as in mid-latitudes, the pressure gradient force is an order of magnitude smaller than at mid-latitudes (Holton, 1979).

Although it is only a rough calculation, it is apparent that large scale motions on the so-called equatorial beta-plane, i.e. in the tropical region including the effect of variation of the Coriolis force with latitude, are much more complicated and result in wave motions involving the balance between pressure gradient forces, inertial forces and a varying Coriolis force (latitude-dependent). Unfortunately, there is not as yet a single unifying theory for tropical motions comparable to the quasi-geostrophic theory for mid-latitude motions. This matter, which was firstly posed by Matsuno in 1966 ("is there quasi-geostrophic motion even at the equator?"), is still of relevance even today in Physics of the Atmosphere (e.g. Verkley&Velde, 2010).

Therefore, for wind engineering purposes, there is no other theory available which includes the effect of the Coriolis force on the mean wind by solving the equations of motion, apart from those proposed for mid-latitude models (e.g. Ekman, 1905 or Harris and Deaves, 1980) and addressed in section 2.3.1. They assume the geostrophic approximation in the free atmosphere, i.e. the balance between the Coriolis and the pressure gradient force. Therefore, the question is: to which extent, in terms of latitude, can we assume that these theories are approximately valid? The answer to this question is as follows: the horizontal frictionless flow can be approximated like geostrophic flow if the inertial acceleration term is sufficiently smaller than the Coriolis force. A convenient measure of the acceleration magnitude compared to the Coriolis force may be obtained by forming the ratio of the characteristic scales for the acceleration and the Coriolis force terms:

$$\frac{U^2/L}{f_c U} = \frac{U}{f_c L} = Ro \tag{2.48}$$

This ratio is a non-dimensional number called the Rossby number (Ro). Thus, the smallness of the Rossby number is a measure of the validity of the geostrophic approximation. At mid-latitudes (being $U \approx 10$ m/s, $f = 2\Omega\sin\varphi \approx 10^{-4}$ m/s, $L = 10^6$ m), it results $Ro \approx 0.1$. At lower latitude, e.g. $10°$, $Ro \approx 0.4$, but only at $4°$ Ro changes its order of magnitude (≈ 1.0). For this reason, it can be assumed that the geostrophic approximation can be accepted up to a latitude of about $4°$. Being on the safe side, the lower limit for latitude can be set at $10°$ (Houghton, 1977). In view of the solar updraft

tower design, such a limit encloses most of the possible locations for solar towers (see Figure 1.3). It means that the models based on the (frictionless) geostrophic balance can be applied, within an acceptable range of approximation.

However, even if the H&D model approximation is still acceptable at relatively low latitudes, the failure of the model is physically motivated by the different type of storms creating strong winds near the equator, which should be reflected in the design. This issue is addressed by Irwin (2009). The types of storms near the equator tend to be local, e.g. thunderstorms, and in these storms the boundary layer depth is limited by the small scale of the storm and not by Coriolis effects.

2.3.4 **Tropical cyclones and tornadoes**

Tropical cyclones and tornadoes are not included in this work. In these motions the Coriolis force is always of secondary importance with respect to the acceleration term in the equations of motion.

Tropical cyclones (called hurricanes in the Atlantic and typhoons in the Pacific) are intense vertical storms which develop over tropical oceans in regions of very warm surface water. They are characterized by a horizontal scale of the region where convection is strong of about 100 km in radius. Maximum tangential wind speeds in these storms range typically from 50 to 100 m/s. For such high velocities and relatively small scales, the centrifugal force term cannot be neglected compared to the Coriolis force. It means that, to a first approximation, the radial force balance in a steady-state hurricane satisfies the gradient wind relationship (equation (2.49)), but not the geostrophic balance.

$$\frac{U^2}{R} + f_c U = -\frac{1}{\rho}\frac{\partial p}{\partial n} \tag{2.49}$$

Anyway, tropical cyclones rapidly degenerate when they move on land and, as can be seen in Figure 2.19, they do not affect possible locations for solar towers.

Besides tropical cyclones, tornadoes are not considered in this Thesis as well. In fact, a methodology to design structures against tornadoes does not exist. Haan et al. (2008) designed a large tornado simulator for wind engineering applications, but physical model testing in wind tunnels is still in need of further development (Irwin, 2009). Usually, tornadoes are only treated in terms of their probability of occurrence (Goliger&Milford, 1998) and the great majority of structures (with exclusion of nuclear reactors and other critical facilities) is not designed to withstand them.
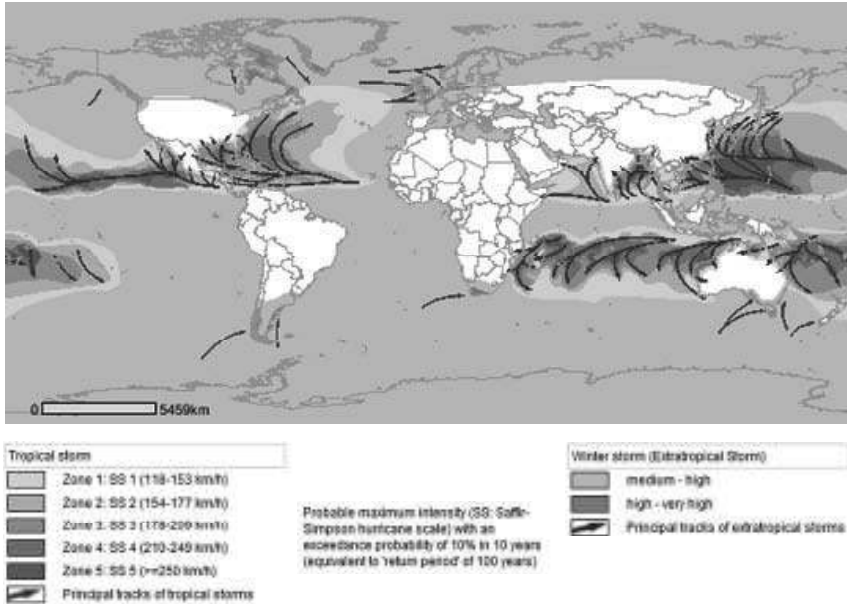
Figure 2.19 Principle tracks and intensities of tropical cyclonic storms

2.4   **Structural vulnerability of the tower to the wind action**

So far, it is known that the structural vulnerability of the solar tower to the wind action can be significantly reduced by applying stiffening rings along the height (Figure 1.9, Figure 1.12, Figure 1.13). As explained in several publications about solar towers (Goldack, 2004; Backström et al., 2008; Krätzig et al., 2008-2009a,b; Lupi, 2009, 2011; Niemann et al., 2009; Harte et al. 2010; Borri et al., 2010), the stiffening rings guarantee a beam like behaviour at the first eigenmode, reduce ovalling deformations of the shell, increase buckling safety and improve the distribution of internal forces. This is the same concept as for steel chimneys, which was first investigated by Peil&Nölle (1988) and constitutes the basis of the rule in the German Standard DIN 4133.

Figure 2.20 shows the natural vibration modes of the tower depicted in Figure 1.13, that is the reference structure in the Dissertation. The calculation on the left-hand side is done in absence of stiffening rings. The shell-like behaviour (modes with three and two waves, respectively) definitely predominates. Instead, in case of ten stiffening

50

rings (like those in Figure 1.14), the first vibration mode is a bending mode, with an eigenfrequency of about 0.17 Hz, and the second mode shape is a shell-like one, with two waves and no inversion along the meridian. A wider study about the influence of stiffening rings on the vibration modes can be found in Lupi (2009). It was seen that at least five rings would be necessary along the height, in order to promote a beam-like mode.

$f_1=f_2 = 0.073$ Hz $\qquad$ $f_3=f_4 = 0.086$ Hz $\qquad$ $f_1=f_2 = 0.172$ Hz $\qquad$ $f_3=f_4 = 0.311$ Hz

Figure 2.20 Natural vibration modes of 1000 m tower (Borri et al., 2010)
without stiffening rings $\qquad\qquad$ *with 10 stiffening rings*

The reduction of shell-like deformations significantly improves the distribution of internal forces. This diminishes the structural vulnerability, especially to the wind action, because the peaks of tension at the windward side are reduced. Ideally, the internal distribution of forces tends to a beam-like distribution, which is linear in the cross-section and crosses zero at 90°. In presence of ten stiffening rings like those in Figure 1.14, this ideal response distribution is achieved at about middle height of the tower, as shown in Chapter 7 (Figure 7.57). As the peaks of tension due to the wind action are reduced at the windward side, tensile stresses can even be completely balanced by the compressive stresses due to self-weight. Consequently, the amount of steel reinforcement is significantly reduced and if needed it can be restricted to the minimum percentage that is required by the Codes. It was calculated in Niemann et al. (2009) that even at the base of the tower and even at the ultimate limit states, the tensile stresses due to the wind action can be completely balanced by self-weight. This also means that the risk of an overturning of the tower is prevented and pales against overturning are not necessary in the foundations. It explains the relatively small foundation ring, which is depicted below the tower in Figure 1.12 and Figure 1.13.

However, even if the predominant behaviour of the solar tower is a beam-like bending mode, relevant shell stresses still arise, especially in the vicinity of the stiffening rings and in the tip region. The local effects in the vicinity of the stiffening rings are evaluated in Chapter 7. In the tip region, the ovalization of the shell is evident in Figure 7.57, where at high levels compressive forces arise at stagnation and lateral tension is present at the flanges. Therefore, even if the beam-like calculation of the structure provides a good estimation of global effects, it would not be sufficiently representative in view of the design. This is confirmed by Peil&Nölle (1988), who investigated the stress distribution in steel chimneys and proposed a simple formula (introduced in the Eurocodes) to identify the admissible shell geometries, i.e. those geometries that can be calculated by the beam theory. It depends on geometric parameters like H/R and R/t, being H, R and t the height of the tower, the radius and the wall thickness, respectively. The equation for allowable shell geometries is given by Peil&Nölle (1988):

$$\frac{H}{R} \geq 0.14 * \frac{R}{t} + 10 \qquad (2.50)$$

In the case of the solar tower, it results (measures are in m):

$$\frac{1000}{75} \geq 0.14 * \frac{75}{0.25} + 10 \quad \rightarrow \quad 13.3 \geq 52 \quad \rightarrow \quad FALSE \qquad (2.51)$$

It is then clear that the enhancement of the beam-like behaviour by introducing stiffening rings is a strategy of risk mitigation, because it reduces the structural vulnerability (especially to the wind action), but the design cannot neglect the shell-like behaviour.

In addition, the presence of rings is crucial in order to reduce the structural vulnerability to vortex shedding. The frequency of shedding (n_s) is conveniently represented in non-dimensional form by the Strouhal number:

$$S_t = \frac{n_s D}{U} \qquad (2.52)$$

where D is the diameter of the cylinder and U is the wind speed. For circular cylinders, S_t is of the order of 0.18-0.2 (but it varies with the Reynolds number). As wind speed increases, the dominant frequency of vortex shedding n_s increases, until the critical flow velocity U_{cr} is reached. It happens when n_s is close to a natural frequency of vibration of the body. At the critical flow speed, a significant amplification of the across-flow forces occurs and large amplitude of across-flow oscillations can result. The amplitude of the induced oscillations depends on the Scruton number:

$$S_{cr} = \frac{4\pi m_{i,e}\xi_i}{\rho D^2} \tag{2.53}$$

where $m_{i,e}$ is the equivalent mass of the structure per unit length corresponding to the ith mode of vibration and ξ_i is the damping ratio corresponding to the ith mode of vibration. If the Scruton number is large, the motion induced by the vortex shedding will not exceed a few per cent of the diameter, although fluctuating forces induced by vortex shedding will still be present. Instead, if the Scruton number is small, the motion of the body has a significant influence on the strength of the vortices shed and the forces induced by them, which in turn affect the oscillation amplitude. It is an aeroelastic effect.

When the amplitudes of oscillation are small, the fluctuating forces are generally random in nature, with significant energy distributed over a relatively broad band of frequencies centered on n_s. In this case, the distribution of the vortex-induced fluctuating forces along the length of the cylinder is also disorganized, which means that the maximum value of the fluctuating force does not occur simultaneously at all positions along the cylinder. The resulting response is a broad-band response of random amplitude nature at approximately the body frequency. For larger amplitudes of oscillation, the local forces due to vortex shedding are amplified. In such cases, the motion of the structure tends to cause the shedding frequency n_s to "lock-in" to the body frequency n_j over a range of local flow velocities. The fluctuating forces at various sections along the structure in the lock-in region are in phase with the body motion and thus completely correlated with each other, further enhancing the response. These forces are nearly periodic in nature, with significant energy confined to a relatively narrow band of frequencies centered on the body frequency n_j. The resulting response is a narrow-band response of an almost constant amplitude of sinusoidal nature at approximately the frequency n_j.

Solar towers are characterized by small Scruton numbers, therefore the lock-in phenomenon may be dangerous. However, the critical wind speed at which it would occur is so high that, in practice, it cannot be reached. It is primarily due to the aspect ratio of solar towers, which is generally not too high. It reduces the sensitivity to vortex-induced oscillations. In addition, the presence of the ring beams along the height is very important, because the beam-like behaviour at the first eigenmode increases the critical velocity, as calculated in the following.

The critical wind speed for 1-kilometer tall tower with ten stiffening rings ($n_1 = 0.17$ Hz), corresponding to a beam-like bending mode, is calculated as (by assuming $D = 150$ m, like in Figure 1.13 at the tower top):

$$U_{cr} = \frac{n_1 D}{S_t} = \frac{0.17*150}{0.20} = 127.5 \text{ m/s} \qquad (2.54)$$

As regards the ovalling modes of vibration, the critical wind speed corresponding to the second mode, characterized by two waves around the cross-section ($n_1 = 0.31$ Hz), can be calculated as:

$$U_{cr} = \frac{n_2 D}{2S_t} = \frac{0.31*150}{2*0.20} = 116.25 \text{ m/s} \qquad (2.55)$$

The Codes require that the critical wind speed is at least 25% higher than the design wind speed, assumed for a period of 50 years. Such requests are largely satisfied. However, in absence of rings (or with a few rings, like one or two, see Lupi (2009)), the critical velocity would be much lower. For example, if $n_1 = 0.073$ Hz and there are three waves, like in Figure 2.20, the critical velocity would have been only 18 m/s. In this case, the amount of steel reinforcement and width of cracks are secondary aspects, because the collapse of the structure would likely be produced by aeroelastic effects due to the lock-in.

Chapter 3. **Flow around circular cylinders: state of the art**

This chapter describes the current state of knowledge of the flow around smooth and rough circular cylinders. The Reynolds number is the single governing parameter in disturbance-free flow around a two dimensional circular cylinder. Real flows are affected by a wide variety of disturbances, classified as influencing parameters. In particular, three dimensional effects have to be considered in view of the design of structures. They can be enhanced in atmospheric flow and depend on the aspect ratio.

3.1   **The boundary layer and its separation**

A body is classified as aerodynamically bluff – in opposite to streamlined – "when the flow streamlines do not follow the surface of the body, but detach from it leaving regions of separated flow and a wide trailing wake" (Cook, 1985). Circular cylinders belong to the class of bluff bodies with rounded shape, characterized by a separation point which can move and adjust itself in response to the flow structure in the separated region. In particular, separation will generally be delayed when transition from laminar to turbulent boundary layer occurs (Buresti, 2012). According to Zdravkovich (1997), the disturbed flow field around a circular cylinder can be divided into four regions: [1] one narrow region of retarded flow close to stagnation; [2] two boundary layers attached to the surface of the cylinder; [3] two sidewise regions of displaced and accelerated flow; [4] a wide downstream region of separated flow, called the wake. The near wake is initially bordered by the separated boundary layers which continue to develop downstream as free-shear layers. The concept of a thin boundary layer which develops around a body as a result of viscous friction was first presented by Prandtl in 1904. He evaluated the boundary layer thickness (δ) around circular cylinders at high Re as:

$$\delta \propto \frac{D}{\sqrt{\text{Re}}} \tag{3.1}$$

The boundary layer has only a small thickness near the stagnation point and generally increases with distance along the surface. Zdravkovich (1997) uses a factor of proportionality equal to 5 at $\varphi = 60°$.

55

In the boundary layer, the velocity varies from the free stream value to zero at the wall, where fluid adheres to the boundary (no-slip condition). Therefore, a large velocity gradient exists normal to the surface and the shearing forces (which arise from the tangential shearing flow of the fluid along the surface of the body) are transmitted through the fluid shear layers adjacent to the surface. In the forward facing part of a circular cylinder, the flow accelerates and the boundary layers around the cylinder are subjected to a favorable (negative) pressure gradient. The region of accelerated flow is then followed by a small region of adverse (positive) pressure gradient before separation. In this decelerating flow region – over the rearward facing part of the body – the velocity at the edge of the boundary layer decreases. Due to the no-slip condition at the surface, at each value of z within the boundary layer the reduction of velocity in passing downstream varies from zero at the wall to a certain value at the edge of the boundary. There often comes a point at which the velocity gradient normal to the surface, at the surface, becomes zero. At this point, the viscous shear force must also be zero, which means that the boundary layer can no longer progress along the surface and thus separates. For this reason, the positive pressure gradient in the decelerating flow region is regarded as an adverse pressure gradient (ESDU 71012).

Downstream of the separation of the boundary layer, there is a region of reversed flow close to the surface. In fact, the region between the separated boundary layer and the surface is filled with an eddying flow in which the velocity and direction vary with time in an almost random manner and it has little or no relation to that of the free stream.

3.2   The state of the flow as a function of the Reynolds number

The state of the flow around a circular cylinder can be either fully laminar (at very low Re), fully turbulent (at very high Re, theoretically Re → ∞, in practice it is limited by occurrence of compressibility effects in air) or there can be a transition from laminar to turbulent state either in the wake, in the free shear layers or in the boundary layers. In laminar flow, the adjacent fluid layers in the flow slide over each other and only friction forces act between them, without macroscopic mixing. Transition from laminar to turbulent flow was first discovered by Reynolds (1883) in a smooth pipe and then the concept was applied by Rayleigh (1896, 1915) to the flow around spheres and cylinders. In this case, the external diameter of the sphere or the circular cylinder was taken as the characteristic length. The Reynolds number is thus the governing parameter of the state of the flow. However, as stressed by Zdravkovich (1997), it is the single governing parameter only in disturbance-free flow. Real flows around

circular cylinders in most practical applications are affected by a wide variety of disturbances, which are classified as influencing parameters. Turbulence of the incoming flow, surface roughness, aspect ratio, end-effects (ground-wall effects and free-end effects), oscillations and wall-blockage are the most common influencing parameters. Transition is very sensitive to small disturbances, which may initiate transition at lower Re and in case become themselves governing parameters.

In this section, it is referred to an idealized disturbance-free flow, so that it is allowed to classify the flow regimes on the only basis of the Reynolds number (the aspect ratio is an ever-present influencing parameter, but – as clarified by Zdravkovich – it becomes a governing one only for a short cylinder with a free end).

The adverse pressure gradient reduces the skin friction to zero and at that instant the separation of the flow from the surface takes place. The capability of the boundary layer to sustain higher adverse pressure gradients before separation depends on the state of the flow and thus on the Reynolds number. The effect of mixing of fluid elements in a turbulent boundary layer promotes a greater interchange of momentum between layers which in turn increases the thickness δ of the boundary layer. Furthermore, the mixing process produces an effective shear stress which is additive to the shear stress produced by the viscosity of the fluid. As a consequence, the retarded fluid layers adjacent to the surface can be pulled further along the surface into regions of higher pressure. Because of that, the thick turbulent boundary layer is able to progress further against an unfavorable pressure gradient and it separates at a point further along a surface. Instead, in free-disturbance conditions, fully laminar boundary layers can only exist when the external pressure gradient is favorable. This is the reason for the early occurrence of laminar separation. As it will be showed in the following, a useful parameter which quantifies the capability of the flow to sustain the adverse pressure gradients prior to separation around a circular cylinder is the adverse pressure recovery. Its magnitude can be expressed by $C_{p,b} - C_{p,min}$, being $C_{p,b}$ and $C_{p,min}$ the base pressure coefficient (at $\varphi = 180°$) and the minimum pressure coefficient.

A first classification of the states of the flow around a smooth cylinder is proposed by Roshko (1961). Four regimes are defined: subcritical, critical, supercritical and transcritical. Later, Achenbach (1971) also referred to this classification for rough cylinders (section 3.3). In the subcritical state, there is an early laminar separation (angle of separation $\approx 70°-80°$) and the drag is independent on Re. The critical regime is a range of transition between laminar and turbulent separation. It begins with the initial fall of the drag coefficient and ends with the formation of two laminar

separation bubbles at Re = Re$_{cr}$, which corresponds to the minimum drag. The supercritical range on smooth cylinders is still characterized by the two bubbles (rather constant low drag coefficient and narrow wake, with separation around 140°). After this first stable stage, the supercritical regime becomes unstable, with disruption of bubbles and suppression of vortex shedding. Roshko suggests that the disappearance of the bubbles marks the transition from supercritical to transcritical range, where the separation is purely turbulent and it occurs at lower angles ($\approx$ 110°). Vortex shedding reappears in the transcritical range, it was discovered by Roshko and published for the first time in 1961.

According to Zdravkovich (1997), the position of the separation point (with regard to the position of transition from laminar to turbulent boundary layer) is the key feature to classify a particular state of the flow around a circular cylinder. He proposes a detailed classification based on occurrence of transition in different regions around the circular cylinder. It is reported in Table 3.1 and briefly explained in the following.

Table 3.1 Epitome of disturbance-free flow regimes (Zdravkovich, 1997)

STATE			REGIME	Re RANGES
L	LAMINAR	1	No-separation	0 to 4-5
		2	Closed wake	4-5 to 30-38
		3	Periodic wake	30-48 to 180-200
TrW	TRANSITION IN WAKE	1	Lower transition regime	180-200 to 220-250
		2	Upper transition regime	220-250 to 350-400
TrSL	TRANSITION IN SHEAR LAYERS	1	Lower subcritical	350-400 to $1*10^3$-$2*10^3$
		2	Intermediate subcritical	$1*10^3$-$2*10^3$ to $2*10^4$-$4*10^4$
		3	Upper subcritical	$2*10^4$-$4*10^4$ to $1*10^5$-$2*10^5$
TrBL	TRANSITION IN BOUNDARY LAYERS	0	Pre-critical	$1*10^5$-$2*10^5$ to $3*10^5$-$3.4*10^5$
		1	Single bubble	$3*10^5$-$3.4*10^5$ to $3.8*10^5$-$4*10^5$
		2	Two-bubble	$3.8*10^5$-$4*10^5$ to $5*10^5$-10^6
		3	Supercritical	$5*10^5$-10^6 to $3.5*10^6$-$6*10^6$
		4	Post-critical	$3.5*10^6$-$6*10^6$ to (?)
T	FULLY TURBULENT	1	Invariable	(?) to ∞
		2	Ultimate	

3.2.1 Fully laminar state

The fully laminar state (L, Re < 200) is characterized by three basic flow regimes. In the first one, the creeping flow regime (L1), separation does not occur because the

cylinder at extremely low Re (Re < 5) is dominated by viscous forces. Then, the magnitude of viscous forces decreases at higher Re and a steady separation initiates; the free shear layers meet at the end of the near-wake at the so-called confluence point. Thus, a laminar, closed, steady near-wake is formed behind the cylinder (L2). The well-known Von Karman eddy street starts with the instability of such an elongated closed near-wake which commences a sinusoidal oscillation for Re > 30-48. As Reynolds increases, the amplitude of the trail oscillations increases and the shear layers start to roll up at crests and troughs. That is, according to the nomenclature chosen by Zdravkovich, the flow regime L3. In such a shedding mode, initiated by the instability of the laminar wake, the laminar eddies are not shed starting from the cylinder, but they are formed gradually as they are carried downstream. Kovasznay (1949) writes: "it is remarkable that the fluctuations close to the cylinder are very small and that they develop the maximum intensity only in the vicinity of X/D = 7. Thus, the eddies are not shed starting from the cylinder at this low Re, but develop several diameters downstream". This mode is also identified as the low-speed mode, as opposite to the high-speed shedding mode of turbulent eddies which are shed starting from the cylinder itself at higher Re. Karman (1912) derived the first theoretical model by considering the stability of staggered vortices in two parallel rows. However, it was Bénard in 1908 the first who sketched the alternate procession of eddies observed in water.

3.2.2   **Transitional states**

All laminar flows undergo transition to turbulence above a certain Re. Around circular cylinders, it is interesting to describe the succession of transitions in various regions of the disturbed flow as Re increases. Zdravkovich (1997) identifies three different transitional stages of flow, based on the fact that transition may occur in the wake (TrW), in the shear layers (TrSL) and in the boundary layers (TrBL). Gerrard (1978) noted that all transition states are characterized by the appearance, development and disappearance of an entirely new flow structure. As it will be explained later, such flow structures are called fingers in TrW, transition waves in TrSL and separation bubbles in TrBL.

Transition in the wake

As Reynolds number increases, the laminar wake undergoes transition to turbulence (TrW, Re from 180-200 until 350-400), due to random initiation and growth of irregularities. The progressive distortion of laminar eddy filaments is described by Gerrard (1978) as the onset of "fingers" at randomly disposed spanwise positions. The

name "fingers" describes the fact that such a distortion of filaments always points toward the cylinder.

In the so-called lower transition regime (TrW1), the eddies are formed laminar and become turbulent further downstream. Then, transition spreads gradually upstream with increasing Re, until the eddies become turbulent during its formation (TrW2). According to Gerrard (1978), it is the mixing with the free stream around the eddies that promotes the formation of turbulent eddies.

The key feature of this transitional state is the change of the shedding mode from low-speed mode (which characterizes L3 and TrW1) to high-speed mode, which appears in TrW2. This change – that represents the boundary between TrW1 and TrW2 – is marked by a jump in the Strouhal number. It has been measured at Re $\approx$ 250 by Roshko, (1954) and it distinguishes two different S_t-versus-Re curves, for the two shedding modes, respectively: while in L3 and TrW1 (low-speed mode) S_t increases with Re, later on S_t is almost constant with rising Re. Anyway, the transition from low- to high-speed mode of eddy shedding is not smooth and an overlapping of the two modes of shedding (two peaks in the frequency spectra) has also been argued (Zdravkovich, 1992).

The characteristic feature of the high-speed mode (Gerrard, 1966) is that the growth of an eddy on one side of the cylinder (in an almost stationary position) induces transverse flow across the wake, which is responsible for the cut-off of the subsequent eddy from a further supply of circulation. It is at this stage, and because of the shear layer crossing the wake, that the eddy is shed from the cylinder.

Transition in the shear layer

After transition in the wake, at higher Re, transition occurs in the shear-layer, TrSL (Re from 350-400 until $1-2*10^5$). Basically, it is the usually called subcritical flow state, meaning that the boundary layer remains laminar up to and beyond separation. In this state, the free shear layers which surround the near-wake are initially laminar but they become turbulent before rolling up into turbulent eddies.

More precisely, the TrSL is divided by Zdravkovich (1997) in three stages: the lower-, intermediate- and upper-subcritical regime. The typical flow structures of the TrSL state are the so-called transition eddies.

At first, undulations of both free shear layers develop from the separation lines in TrSL1. They are called Gerrard-Bloor transition waves and were first described by Gerrard (1978). Such waves are symmetric on the two sides of the cylinder and in-phase, therefore they are not related to the alternating eddy shedding. Zdravkovich (1997) describes an analogy between the onset of instability and oscillation of the

laminar Karman-Bénard street (L3) and the onset of these undulations in the free-shear layers (TrSL1).

In TrSL2, the transition eddies appear before transition to turbulence. They were firstly sketched by Couregelongue (1929) during outdoor experiments in a river and appeared as "chains" of small eddies along the free shear layers. As Re increseas, there is a progressive movement of transition towards separation and it is accompanied by a shortening of the eddy formation region (L_f), so that the eddies are brought closer to the base of the cylinder. A reduction in L_f is always reflected in a decrease in $C_{p,b}$ (higher suction in the wake, thus higher drag) and an increase in C'_L (higher lift fluctuations), because the eddies form closer to the body. However, the S_t number does not change significantly from TrSL1 (elongation of the formation region) to TrSL2 (shortening of the formation region). Because of that, Gerrard (1966) suggested that the shedding frequency is primarily related to the distance between the two free shear layers, which varies through TrSL but not so largely as the variation of L_f. In particular, according to Gerrard (1966) and Bloor and Gerrard (1966), two opposite tendencies seem to cancel each other in order to keep the same strength of the turbulent eddies in TrSL2, thus an almost constant S_t: the shortening of the formation region and the widening of the turbulent shear layers. In addition, in the TrSL2 regime the shortening of L_f counteracts the increase in the shear layer thickness, since thick turbulent shear layers need more time for a roll up to be carried across the wake.

As the shortening of the eddy formation region is completed, at the end of TrSL2, the transition eddies disappear and TrSL3 begins. It is characterized by a wide near-wake (small angle of separation), high suction in the wake, high drag and high lift fluctuations due to the very short length of the formation region L_f. Zdravkovich (1997) describes the transition to turbulence as a sudden burst in the free shear layers close to the cylinder. Three-dimensional flow structures develop in the near-wake, responsible for a significant reduction of the correlation length along the span. The interesting feature of TrSL3 is the stabilizing effect produced on the transition in the free shear layers in this range of Re, so that the upper subcritical regime is defined as a quasi-invariable flow. The reason is that the wide near-wake (produced by short L_f) displaces the free shear layers into the free stream and causes the acceleration of the stream adjacent to the near-wake. This has a stabilizing effect, so that the transition region does not progress upstream with increasing Re. As a consequence, TrSL3 is characterized by almost constant $C_{p,b}$, C_D (the horizontal stretch before the critical fall in the drag), C'_D and C'_L (see Figure 3.3) and S_t number as well.

Transition in the boundary layer

The stabilizing effect, which characterizes the quasi-invariable nature of the flow in the subcritical range - due to the accelerated free stream that squeezes the separated shear layers that surround the wide wake - gradually weakens with rising Re, as the free-shear layers become more aligned with the adjacent free stream. Transition to turbulence advances in the free shear layers towards separation until it reaches the separation line. It starts then a complex interaction between transition and separation, which was first observed by Taylor (1916) and better investigated by Fage in 1928. Zdravkovich (1997) names this regime transition in the boundary layer TrBL (Re from 10^5-$2*10^5$ – according to Zdravkovich, but generally somewhat arbitrary in literature – to an undefined upper limit, in the order of 10^6, which marks the entering in fully turbulent conditions).

The beginning of TrBL is marked, according to Zdravkovich, by the initial fall of the drag coefficient (Re = 10^5-$2*10^5$), due to a reward movement of the separation point. Instead, according to Schewe, 1983 the key feature which denotes such a boundary between subcritical and critical regimes is the onset of randomization of lift fluctuations, at a slightly higher Re (in Schewe's results, Re = $2.8*10^5$ marked the onset of random lift fluctuation, while Re = $1.4*10^5$ was at the initial fall of the drag).

This initial stage (TrBL0), which Zdravkovich includes in the critical regime, is named pre-critical. The decrease in the drag coefficient is the result of the narrowing of the wake and a gradual displacement of separation downstream with rising Re (Achenbach&Heinecke, 1981). The length of the eddy formation region L_f, which was short in TrSL3, elongates and the roll up of the free shear layers is displaced downstream. This reduces the negative base pressure and weakens the alternate pressure fluctuations on the two sides of the cylinder. The small suction in the wake is associated to high maximum lateral suction and this is the reason for the fall in the drag coefficient and the rise of the pressure recovery. Bearman (1969) noticed that the S_t number remains constant in TrBL0. Again, the constancy of S_t is related to two opposite tendencies: on one hand the free shear layers tends to get closer, but the elongation of L_f leads to a slight widening.

The state TrBL1 is named by Zdravkovich single bubble regime, followed by TrBL2 that is the two-bubble regime.

Eisner (1925) was the first who measured stable asymmetric mean pressure distributions around a circular cylinder in a certain range of Re. He concluded, correctly, that transition occurred on one side only of the cylinder. Only at slightly higher Re, transition could complete on the two sides. When this happens, C_D reaches

the minimum value (at Re = Re$_{cr}$). However, the state of flow in this particular range of Re was deeply investigated only several years later (Achenbach, 1968; Bearman, 1969; Farell and Blessmann, 1983; Schewe, 1983). The key feature is the formation of laminar separation bubbles, either on one side only or on two sides of the cylinder.

The formation of laminar separation bubbles on two sides of a cylinder (at Re ≈ Re$_{cr}$) was identified by Achenbach (1968) through measurements of skin friction. He found that at Re = 10^5, at $\phi = 105°$ ($\phi = 255°$) there was not a final separation. In fact, there was a region between laminar separation and turbulent reattachment in which the wall shear stresses theoretically vanished. Downstream, there was an intensive rise of the skin friction, showing that the boundary layer was turbulent. Turbulent separation occurred finally at $\phi = 147°$ ($\phi = 220°$).

In 1969, Bearman identified a bistability of the flow in a sub-range of Re before symmetric twin bubbles appeared by experimental evidence of discontinuous changes in C$_{p,b}$ and S$_t$ at Re = $3.4*10^5$ and $3.8*10^5$. He found the cause in the formation of a laminar separation bubble on one side only of the cylinder. The C$_{p,b}$ distribution along the height showed that the bubble took place along the complete length of the cylinder. He also noted that the asymmetric pressure distribution was accompanied by the displacement of the stagnation point away from the bubble.

Further studies on the formation of only one bubble are reported by Farell and Blessmann (1983). Contrary to the results of Bearman (1969), who found the single-bubble regime to occur always with the bubble consistently on the same side of the cylinder, in Farell and Blessmann's experiments no preference was detected for the bubble to form on either side of the cylinder.

Schewe (1983) described in detail the physical phenomenon of a laminar separation bubble on one side only of the cylinder. A discontinuity in the drag coefficient and a sudden jump of S$_t$ (up to 0.33) mark the onset of a bistable flow condition (Figure 3.1, letter c). The name explains that there are two stable states, corresponding to the two possible signs of the lift force. The asymmetric stable state persists for a very small range of Re. Then, a second discontinuity in the drag, as well as another sudden jump in S$_t$ (up to 0.48 that is the highest value, letter f in Figure 3.1) marks the abrupt disappearance of the steady lift and the attainment of the minimum drag, corresponding to the critical Re. The bistable flow condition is preceded and followed by two unstable ranges (corresponding to S$_t$ = 0.2 and 0.31 respectively, according to Figure 3.4). Such unstable ranges correspond to the letters a, b and d, e in Figure 3.1.

"The explanation for the phenomena", Schewe writes, "lies in the behaviour of the boundary layer. The asymmetric flow and thus the steady lift in the critical range is

caused by the fact that the boundary layer transition from laminar to turbulent has occurred on one side only of the cylinder. Thus a laminar separation bubble is formed as follows: the transition from laminar to turbulent flow occurs in the detached boundary layer just downstream from the separation point. After reattachment of the boundary layer on the back of the cylinder, the separation is turbulent." Figure 3.2 shows the asymmetry of laminar and turbulent separations on the two sides of the cylinder. Figure 3.6 reports a clear representation made by Basu (1985) of the flow field near the point of separation in transitional range of Re, with formation of a laminar separation bubble.
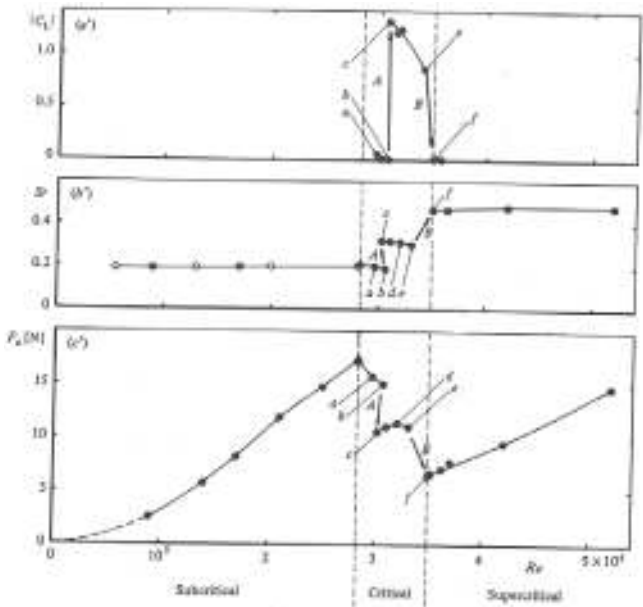
Figure 3.1 Steady lift, Strouhal number and drag force. Asymmetric bistable flow indicated by letter c (Schewe, 1983)

The reason for which transition in the detached boundary layer is initiated on one side only of the cylinder and not simultaneously on both sides is the occurrence on that side of perturbations or fluctuations, which are inherent in the boundary layer and in the free stream. Then, once transition and then reattachment have occurred on one side, there is an acceleration of the fluid on that side and deceleration on the other side. Since deceleration delays transition in the free shear layer (it reduces Re), the formation of the bubble also on the other side is delayed. According to Schewe (1983) this is the reason which stabilizes and fixes the asymmetric flow state. Of course, such

64

a bistable flow condition is extremely sensitive to Re and is possible only if there is a very low probability for simultaneous occurrence of perturbation on both sides. In fact, the bistable flow disappears on rough cylinders as well as in turbulent flow.
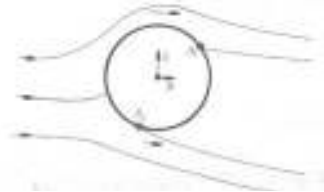
Figure 3.2 Asymmetric flow state in the critical regime of Re (Schewe, 1983)

As soon as the flow also reattaches on the other side of the cylinder, symmetric conditions are again achieved with two bubbles on the two sides of the cylinder: the drag is then minimum and that is the critical Re. Zdravkovich defines this symmetric state of the flow as two-bubble regime (TrBL2) and it precedes the supercritical (TrBL3) regime. The latter begins with the fragmentation and disruption of bubbles and it is characterized by large scatter of results and suppression of vortex shedding, due to high three-dimensionality of the flow. Slightly different in the nomenclature and in the subdivision of the flow regime, is the classification proposed by Roshko (1961) and Achenbach (1971): the supercritical regime starts immediately after the critical drop and for the smooth cylinder it is at first stable, with two separation bubbles and narrow band lift fluctuations, i.e. regular vortex shedding. According to this classification, vortex shedding is rather evident in the first stage of supercritical flow, with the highest Strouhal value ($S_t = 0.48$ according to Schewe, 1983). Then, the upper transition range is an unstable state, characterized by suppression of vortex shedding, which marks the transition to the transcritical regime.

Until the surprising discovery made by Roshko in 1961, it was believed that once the boundary layer becomes turbulent upstream of the separation the periodic eddy shedding should cease due to the irregular and chaotic state of the free shear layers. Instead, Roshko discovered that the periodic eddy shedding reappears in what he called transcritical regime. That is, referring to Zdravkovich's nomenclature, TrBL4 or post-critical regime. In this regime, all the C_D curves by different authors show the same trend: they rise up to a certain Re in the TrBL3 and level out in the TrBL4 regime. It means that the separation point is essentially fixed. According to Achenbach's classification, the more or less constant position of the separation point is

the boundary between what he defined supercritical and transcritical regimes, at about $Re = 5*10^6$.

3.2.3 Fully turbulent state

Above TrBL4, Zdravkovich concludes the classification with the fully turbulent state (T). Theoretically, it is reached when all the three disturbed regions (wake, free shear and boundary layers) are fully turbulent, i.e. transition is very close to stagnation. In practice, it is not defined, in terms of Re, neither the beginning of T (i.e. the end of TrBL4) nor the end. Transition should reach the stagnation point when Re → ∞, so that the final regime is called ultimate. However, compressibility effects in air appear at high Re and they become the governing parameters. Anyway, what is accepted for sure, is that (Roshko, 1961) "it seems unlikely that there will be any further transitions once all disturbed regions around the cylinder are turbulent". The invariance of the flow pattern implies that all coefficients remain constant as Re increases.

3.2.4 Summary

Figure 3.3 (Zdravkovich, 1990) summarizes the behaviour of the mean drag and rms value of the lift coefficients for the whole range of Re.

FIG. 2   Force Coefficients versus Reynolds Number; c_D – mean drag, c_{Df} – friction drag, c_{Dp} – pressure drag, c_L' – fluctuating drag, c_L – mean lift c_L' – fluctuating lift.
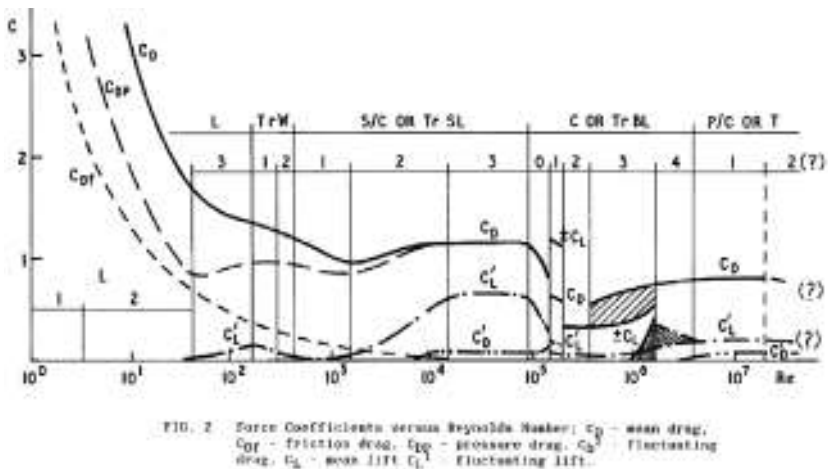
Figure 3.3 Force coefficients versus Reynolds number (Zdravkovich, 1990)

Relying on Schewe (1983)'s results and in accordance with Roshko and Achenbach's classification of the regimes of flow, Niemann&Hölscher (1990) suggest, for the smooth cylinder, the following review (Figure 3.8):

			discontinuity A, hysteretic		discontinuity B, hysteretic		upper transition	
	(1)	(2)	(3)	(4)	(5)	(6)	(7)	(8)
state of boundary layer	stable		unstable	bistable	unstable	stable	unstable	stable
10^5 Re	1,4	3,8	5,0	3,3	3,5	10	30	
mean drag c_D	1,2	1,2 - 1,0	1,0 - 0,7	0,5	0,5 - 0,4	0,32	0,32 - 0,52	0,52
mean lift c_L	0			± 1,3	1,3 - 0,4	0	0,1 ... 0,2	0
fluctuating lift: 1DOF	single narrow peak		random with two peaks	narrow peak	random + peak	narrow peak	random, two broad peaks	rather narrow peak
Sr	0,2		0,2	0,33	0,31	0,48	(0,1/0,45)	0,28
$c_{L,rms}$	0,4 - 0,25	0,25 - 0,09	0,09 - 0,06	0,06	0,06 - 0,01	0,02	0,04	0,05
boundary layer and separation								
	laminar separation S_l	laminar separation	random changes	one-sided separation bubble	random changes	two-sided separation bubble	random changes	turbulent separation S_t

Figure 3.4 Smooth circular cylinder – review (Niemann&Hölscher, 1990)

The flow field near the point of separation in different Re regimes is well depicted by Basu (1985). It is reported in Figure 3.5 (at subcritical Re), in Figure 3.6 (in the transitional range, with formation of a laminar separation bubble) and in Figure 3.7 (at transcritical Re).
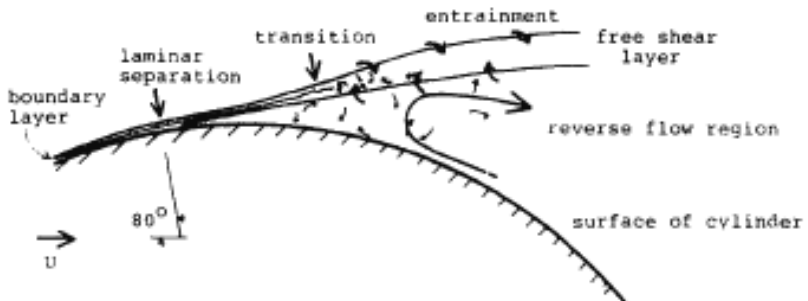
Figure 3.5 The flow field near the point of separation: subcritical Re (Basu, 1985)
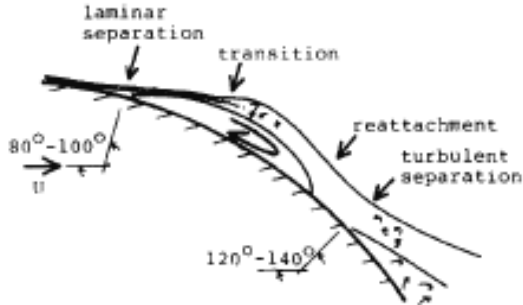
Figure 3.6 The flow field near the point of separation: transitional Re (Basu, 1985)
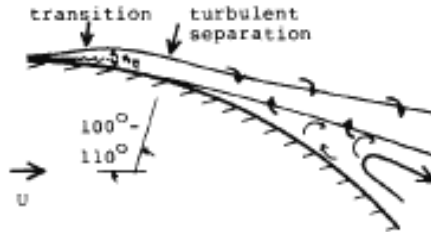
Figure 3.7 The flow field near the point of separation: transcritical Re (Basu, 1985)

3.3   **Effect of surface roughness**

The flow pattern around a circular cylinder is primarily determined by the position of the separation point. Such a location is governed by the Reynolds number and strongly influenced by the roughness of the cylinder surface and to some extent also by the turbulence characteristics of the approaching flow. Surface roughness is often used in wind tunnel tests as a simulation technique of high Reynolds numbers.

A practical approach to quantify this effect is proposed in the ESDU 74030 and results in the calculation of the so-called effective Reynolds number (Re_e). This is a modified Re, which incorporates a factor λ_R depending on surface roughness, and a factor λ_T depending on incoming turbulence. Re_e reproduces, at lower Reynolds numbers, the same effects in the flow that would occur at higher Reynolds numbers. It is then a useful tool in wind tunnel tests on scale models.

$$Re_e = Re\,\lambda_R\lambda_T \tag{3.2}$$

Increasing surface roughness and/or turbulence of the incoming flow has the effect of increasing the boundary layer thickness and enhancing transition from laminar to turbulent flow, so that transition occurs at progressively lower Re. This explains the decrease in the critical Re. In addition, increasing surface roughness increases the value of C_D at Re_{cr}, while increasing incoming turbulence does not change the value of C_D at Re_{cr} significantly. The effect of incoming turbulence will be addressed in the next section, while this section addresses the effect of surface roughness. Surface roughness is especially effective in triggering transition in TrBL and the effectiveness depends on the height of roughness elements with respect to the thickness of the boundary layer. Pioneering experiments on the effect of surface roughness were carried out by Fage and Warsap (1929). They showed that the steep drop in the steady drag occurs at progressively smaller Reynolds numbers with increasing surface roughness.

Milestone studies on the influence of surface roughness on circular cylinders at high Re (up to $3*10^6$), obtained in atmospheric and high-pressure wind tunnel, have been published by Achenbach (1971) and Achenbach&Heinecke (1981). Similarly to what Roshko (1961) proposes for a smooth cylinder, the curve representing the drag coefficient as a function of Reynolds number for a rough cylinder (Achenbach, 1971) is divided into four parts (Figure 3.8). Each range – subcritical, critical, supercritical, transcritical, respectively – is characterized by a special boundary layer behaviour. According to Achenbach, "the subcritical flow regime is not yet influenced by the surface roughness. In a large range of Reynolds number the drag coefficient is nearly constant. Increasing the Reynolds number the drag coefficient suddenly drops. This range, the lower limit of which is dependent upon the roughness conditions, is denoted the critical flow regime. Exceeding the Reynolds number of minimum C_D the drag coefficient grows up again (supercritical range) and reaches a nearly constant value in the transcritical range. This transcritical drag coefficient increases with rising roughness parameter".

Achenbach studied the behaviour of the boundary layer by measuring local pressures and skin friction. In subcritical flow regime the boundary layer separates laminarly. At immediately higher Re, the disturbances produced by surface roughness "support the boundary layer with energy from outside". Thus, the boundary layer can remain adjacent to the wall over a larger distance. The separation point shifts to the back of the cylinder and this reduces the drag coefficient, although the separation is still laminar (critical range). At minimum C_D, laminar separation and turbulent reattachment occur. This is the phenomenon of the separation bubbles, as previously

described on smooth cylinders. However, it is remarkable that this phenomenon – clearly visible in the horizontal plateau at $C_{D,min}$ for smooth cylinders (Figure 3.9) – is restricted to a very narrow flow range if the surface of the cylinder is rough. In fact, as proved by Buresti (1981) and stated in the review by Niemann&Hoelscher (1990), the extension of the critical and supercritical range is diminished on a rough cylinder. The critical range basically consists in a shift downstream of separation (without the unstable and bistable flow ranges observed on smooth cylinders) and then the drag increases to its transcritical value due to an upstream shift of the transition point. Moreover, as previously said, with increasing roughness the minimum of C_D at the critical Reynolds number increases.
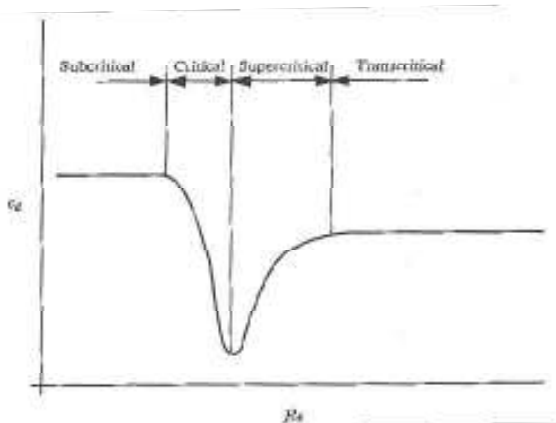
Figure 3.8 Definition of four ranges for the flow past a rough circular cylinder (Achenbach, 1971)

Figure 3.9 reports the different behaviour of the Strouhal-versus-Re curve on a rough cylinder. In particular, on a rough cylinder the Strouhal number exhibits an increase in the critical flow regime, but with growing roughness parameter the step in the curve becomes smaller (Achenbach&Heinecke, 1981). In any case, this is much smaller than the constant value of the Strouhal number due to the formation of laminar separation bubbles on a smooth cylinder (range 6 in Figure 3.9). The smaller S_t and the higher $C_{D,min}$ at critical Re on a rough cylinder, with respect to a smooth cylinder, are due to the upstream shift of the location of boundary layer separation. In other words, higher roughness produces earlier separation. This is confirmed by Achenbach (1971): "with increasing roughness parameter, the angle of separation becomes smaller ($\approx 110°$) compared with that of the smooth cylinder ($\approx 140°$) at critical flow conditions".
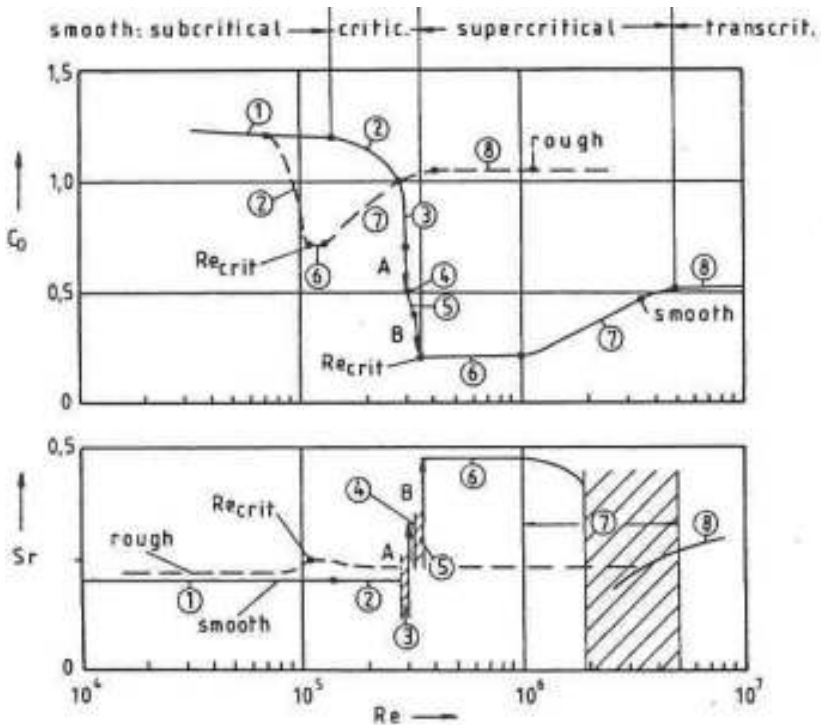
Figure 3.9 Flow regimes for smooth and rough cylinders. The corresponding flow regime description is counted in Figure 3.4 – review (Niemann&Hölscher, 1990)

Various surface roughness types are investigated by Achenbach&Heinecke (1981). Despite the differences in the curves (in terms, for example, of C_D and S_t), the fundamental boundary layer phenomena are the same for all roughness types. However, "the boundaries between the various regimes, as well the supercritical and post-critical drag coefficients and Strouhal numbers are a function of both the size and the type of surface roughness" (Buresti, 1981). In the same years, Güven et al. (1980) measures the effects on the mean flow past circular cylinders due to five different sizes of distributed sandpaper roughness. In particular, the pressure rise to separation results to be closely related to the characteristics of the boundary layer; smaller pressure rise is associated to thicker boundary layers. Larger roughness gives rise to a thicker and more retarded boundary layer which separates earlier and with a smaller pressure recovery. The influence of meridional ribs on the development of the boundary layer around a circular cylinder is calculated by an analytical method in Güven et al. (1983). Ribeiro (1991) investigates "which types of surface roughness are more efficient in

triggering a transition of the flow so as to simulate the mean and fluctuating pressures occurring at ultra-critical Reynolds numbers". Among sand paper, wire mesh screen and ribs, he finds that "all the roughness types were efficient in triggering regime transitions and in allowing the establishment of the ultra-critical regime with relatively low Reynolds numbers". However, "an increase in relative roughness progressively distorts the mean pressure distribution results (distorts in the sense of deviating from what is observed with smooth circular cylinders)". Therefore, he suggests that "the smallest relative roughness to establish ultracritical conditions should be chosen for simulation problems of cylindrical structures with circular cross-section and smooth surface". Moreover, Ribeiro also observed that "the mean values of the force and pressure coefficients obtained with the ribs model were closer than any of the others to the values observed on smooth circular cylinders. The behaviour was such that, with regard to mean values, the rib roughness type seems the most appropriate to be employed in simulation problems of cylindrical structures of circular cross-section and smooth surface, because of its efficiency in establishing the ultra-critical condition and because it does not interfere excessively with the mean force and pressure coefficients". According to Ribeiro, the same conclusion regarding the use of ribs also holds regarding the fluctuating loads, although the fluctuating values measured on the rough circular cylinders (at relatively low Re values) were larger than those observed on the smooth cylinder at high Re values.

Other important contributors on the topic are for example Batham (1973), who measured pressure distributions on smooth and rough cylinders at critical Reynolds numbers in uniform and turbulent flows; Szechenyi (1974, 1975), who performed supercritical Reynolds number simulations for two-dimensional flow over circular cylinders; Nakamura&Tomonari (1982), who studied the effect of different types of surface roughness at high Reynolds numbers; Basu (1985), who gathered data from a large number of experiments in order to describe the behaviour of the mean drag coefficient, the Strouhal number and the rms lift coefficient as functions of Re and relative roughness. In recent years, the effect of surface roughness on lift forces has been investigated by Eaddy (2004).

Last but not least, the effect of surface roughness is not only a simulation technique of high Reynolds numbers, but it is utilized for example on cooling towers to reduce wind-induced stresses in shell structures, by reduction of high lateral peaks of suction (VGB, 2010). However, this is not the case of solar towers, which should be smooth in full-scale in order to be subjected to lower drag forces (Figure 3.10b).

a)   *b)*
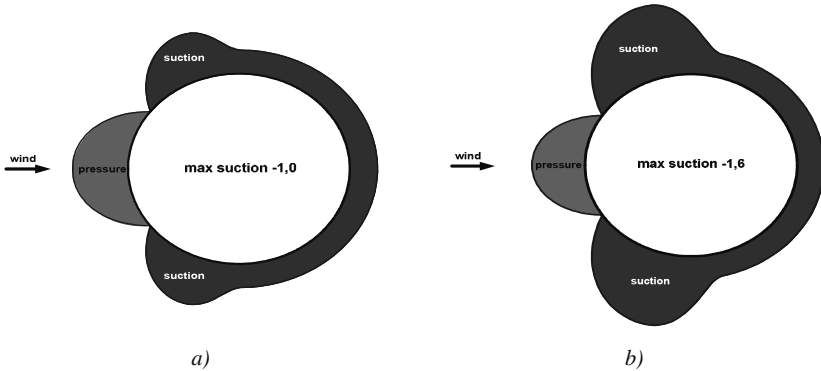
Figure 3.10 Mean pressure distribution at transcritical Re
a) rough surface, $C_{D,m} = 0.66$; b) smooth surface, $C_{D,m} = 0.46$ (Niemann, 2009).

3.4 **Effect of free-stream turbulence**

Free stream turbulence is basically characterized by two parameters: the turbulence intensity σ_U/U_m and the integral length scale of the longitudinal component L_{ux}. For very large ratios L_{ux}/D, longitudinal velocity fluctuations are perceived as slow changes in the mean wind speed and lateral fluctuations as slow changes in wind speed direction. Under these conditions, the quasi-steady approximation can be used to evaluate pressure fluctuations, by applying equation (3.3) (Basu, 1986). Instead, when L_{ux}/D ratios are small, further complication arises because turbulence is distorted by the presence of the body.

$$Cp_\sigma(\varphi) = \left\{ \left[\left(\frac{2\sigma_u}{U_m} \right) Cp_m(\varphi) \right]^2 + \left(\frac{dCp_m(\varphi)}{d\varphi} \right) \left(\frac{\sigma_v}{U_m} \right)^2 \right\}^{1/2} \tag{3.3}$$

Incoming turbulence modifies mean pressures and forces on a circular cylinder because it induces earlier transition to turbulence in the cylinder boundary layers or in the separated shear layers than would occur in smooth flow. Since small-scale turbulence is better able to interact with the cylinder boundary layers and shear layers than large-scale turbulence, at large turbulence scale-to-diameter ratios the interaction between free-stream turbulence and the cylinder boundary layers and wake is reduced, so that premature transitions are less likely to occur (Basu, 1986). Moreover,

depending on the intensity of turbulence, two mechanisms play a major role: at low levels of turbulence the main effect is to disrupt the coherence of vortex shedding; at higher levels of turbulence the enhanced entrainment from the near wake into the shear layers dominates. Because of this last mechanism, while the influence of incoming turbulence on the fluctuating pressures in the stagnation region is direct, in the wake region it is more subtle. In fact, the wake region is separated from the external flow by the presence of the free-shear layers and only at sufficiently high intensity the small-scale turbulence is able to penetrate. Since the principal influence of free-stream turbulence is in the stagnation region, while the influence on the wake is quite weak, it is often assumed that the pressure fluctuations at the rear of the cylinder are independent on the incident turbulence.

As previously mentioned, further complication arises from the distortion that the turbulence experiences as the flow approaches and passes the cylinder. Hunt (1972) developed a theory, namely rapid distortion theory, to predict the modification of turbulence near a structure, and how these changes depend on the shape of the structure and on the scale of the turbulence relative to the structure. Once the disturbed flow field near the structure is mathematically described, the pressure fluctuations on the body surface can be predicted. This is the core of the theory, which aims to identify the effects of the incident turbulent on the unsteady velocities near a bluff body invested by wind and on the fluctuating pressures on its surface.

The effects of the incident turbulence should be distinguished from the effects of the self-induced unsteady velocities and surface pressures, which are induced near a structure when a completely steady wind blows around it. They are due to separated flows at the sides and rear of the obstacle and to instability of the flow at the ground or at the tip. The theory assumes that the intensity of the upwind turbulence is weak and it does not interact with the velocity fluctuations induced by the wake. In this way, the velocity fluctuations outside the wake caused by eddies shed at the wake boundaries are statistically independent on the velocity fluctuations caused by the upwind turbulence. Therefore, the two types of velocity fluctuations can be analyzed separately (Hunt, 1975). This assumption is only approximately true. In fact, fluctuations of the incident wind can strongly effect the fluctuations caused by eddy shedding. For example, if there is a significant amount of energy in the velocity fluctuations of the incident wind at frequencies close to the eddy shedding in the wake, the eddy shedding may be amplified. Experiments by Britter et al. (1979) showed that the vortex shedding peak is altered by the incident turbulence, because it may occur at a slightly lower frequency and be more broad. In general, problems to the applicability

of the theory arise if there is an appreciable correlation between wake induced fluctuations and velocity fluctuations in the incident turbulence. The correlation results from the modification of the self-induced fluctuation due to incoming turbulence. However, this should not be significant if $\sigma_{u,\infty} << U_{m,\infty}$, i.e. the turbulence of the incoming (undisturbed) flow is weak. Moreover, it is interesting to note that the addition of a splitter plate, which is able to suppress vortex shedding, improves the agreement between the theory and the experiments.

The core of the theory – which allows to consider the self-induced velocity fluctuations in the external region (resulting by the unsteady wake) as statistically independent on the velocity fluctuations produced by upwind turbulence – is the rapid distortion of turbulence by changes in the mean velocity produced by the body. In other words, turbulence is disturbed so rapidly by changes in the mean velocities close to the body, that each wave number (or eddy) is distorted separately before it can exchange energy non-linearly with other wave numbers. Therefore, a limitation of the theory is that it is linear. In fact, non-linear effects can be important, especially at high frequencies, where non-linear terms do not decay as rapidly as the linear terms. In any case, a good applicability of the theory is guaranteed if the time scale for the non-linear interaction between energy-containing eddies (L_{ux}/σ_u) is large compared with the time required for the fluid to flow round the obstacle (a/U_m where "a" is used in Figure 3.11 to indicate the cylinder radius). In other words, if $(\sigma_u/U_m)(a/L_{ux}) << 1$, then the turbulence is primarily distorted by the mean velocity field before it can be modified significantly by non-linear interactions: the distortion is rapid. This criterion for linearization – suggested by Hunt (1973) – is considered even too restrictive in Durbin&Hunt (1980) and re-formulated in that paper.

The changes in the turbulent velocity field in the disturbed region near the structure have a simple physical explanation. Two phenomena explain qualitatively the amplification or reduction of the turbulent components: [1] distortion by the mean flow of the turbulent vorticity; [2] blocking or source effect caused by turbulence impinging on the cylinder surface. Near the stagnation point the vortex lines in the x-direction are decreased while those in the y-direction are stretched and those in the z-direction are unaffected (two dimensional case, far from end conditions). So, at stagnation, the eddies which are small compared to the structure are piled up and stretched out. Instead, if the turbulence scale is much larger than the radius of the cylinder there is no effect of vortex stretching, only a blocking effect of the cylinder (Hunt, 1975).
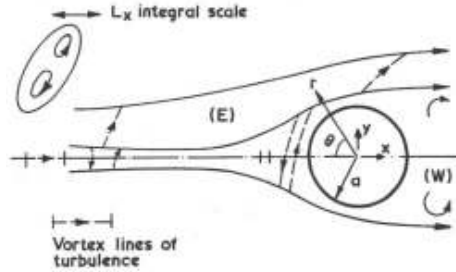
Figure 3.11 Mean streamlines around a circular cylinder showing compression and stretching of vortex lines (E stands for external region, W stands for wake region) (Hunt, 1975)

By assuming a rapid distortion, the movement of vortex elements can be described by the movement of line elements (Figure 3.11) and the movement of line elements is known if the mean velocity field near the body is known. The field of mean velocity will stretch and rotate vortex lines, altering the distribution of turbulent vorticity and thus changing the turbulent velocities. This stretching and rotating of vortex lines will take place over a distance in which the mean velocity field is significantly altered by the bluff body, i.e. over a distance a few times the radius of the cylinder (Britter et al., 1979). Instead, the blocking effect produces a change in the turbulence over a distance comparable to the scale of turbulence L_{ux} or the cylinder radius a, whichever is smaller. The relative importance of the distortion effect over the blocking one increases as a/L_{ux} increases or the distance from the cylinder increases. The effect of turbulence scale with respect to the diameter of the cylinder is demonstrated in (Hunt, 1973) by measuring the ratio between the rms values of the u-components in the undisturbed flow and in the disturbed flow near the structure ($\sigma_{u,\infty}/\sigma_u$) as a function of the ratio between cylinder radius and L_{ux} (a/L_{ux}). The issue is further addressed in Britter et al. (1979). Figure 3.12 (Britter et al., 1979) summarizes these results. If turbulent eddies are small with respect to the cylinder diameter (small scales, $a/L_{ux} \gg$ 1), on the stagnation line σ_u increases and σ_v decreases. However, close to the surface where both vorticity distortion and the source effect are significant, the amplification of σ_u decreases and σ_v increases. For large scales ($a/L_{ux} \ll$ 1) the source effect dominates, turbulence is blocked by the cylinder and consequently σ_u decreases and σ_v increases. At the flanges of the cylinder (90°) the opposite occurs. The vortex lines of small scale eddies are stretched in the x-direction, but reduced in the y-direction, so that σ_u is reduced (x-direction) and σ_v is increased (y-direction), while the blocking effect acts in the cross-wind direction.

Hunt's theory predicts results for the two asymptotic limits $L_{ux}/a \gg 1$ and $L_{ux}/a \ll 1$. The large scale limit is described by the well-known quasi-steady theory (equation (3.3)), while the small-scale limit is introduced by Hunt as a quasi-homogeneous or slowly varying approximation, where the turbulence vorticity around the body is given in terms of the upwind fluctuating vorticity and the mean velocity field. The latter is given by the standard potential-flow solution for a circular cylinder, as if separation does not take place. The quasi-steady theory for large scales is simpler than the small scale theory, because the incident vorticity is not distorted by the obstacle, which only blocks the flow. For intermediate scales, it is not practical to apply the rapid distortion theory, but reasonable extrapolation formulas (e.g. for the stagnation point) are proposed in Durbin&Hunt, 1980. In any case, whatever the value of L_{ux}/a, if the frequency is sufficiently high the results for spectra tend to the limiting situation where $L_{ux}/a \ll 1$.
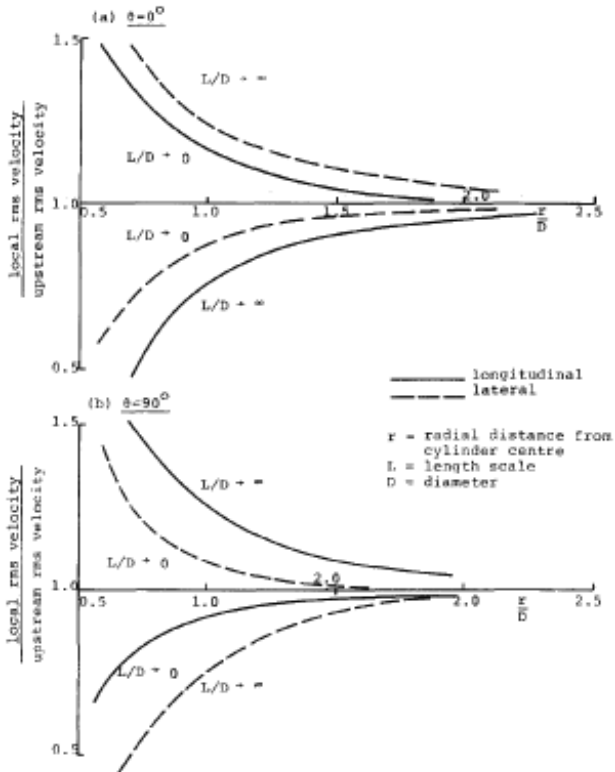
Figure 3.12 Modification of fluctuating velocities near the cylinder in small- and large-scale turbulence (Britter et al., 1979)

This Dissertation does not go further into the mathematical model behind Hunt's theory (Hunt, 1972, 1973). However, the physical principles represented the basis to develop the wind load model in Chapter 7. Such physical principles have been applied to experimental data measured in two wind tunnels (WiSt and CRIACIV) in order to separate turbulence-induced and body-induced pressure fluctuations (section 7.1.3).

3.5   **Three dimensional effects**

This section addresses the aerodynamic of the flow around finite-length circular cylinders of high aspect ratio, characterized by Karman vortex shedding, where end-effects still dominate for large part of the height. Solar updraft towers are represented at best by this category. Three dimensional effects arise at the top due to the free end and at the bottom due to the ground surface. They depend on the aspect ratio, on the boundary layer conditions (uniform or shear layer) and on Re. Literature at high Re is scarce, therefore most of the experiments and simulations mentioned in the following are performed in sub-critical conditions.

In the ground-wall region, a three dimensional separation of the boundary layer occurs upstream of an obstacle and a so-called horseshoe (or necklace) vortex system develops at the base of the body. In fact, the cylinder end is submerged in a retarded wall boundary layer and an adverse pressure gradient is created. This causes the three dimensional boundary layer separation at some distance upstream of the body, followed by a roll-up of the separated boundary layers into a system of swirls. The swirl system is swept around the base of the cylinder and assumes a characteristic shape, which is responsible for the name "horseshoe vortex".
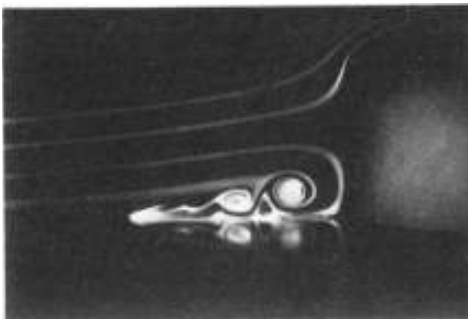
Figure 3.13 Horseshoe vortex system: experiment by Sutton (1960) in laminar boundary layer, reported in Baker (1991)
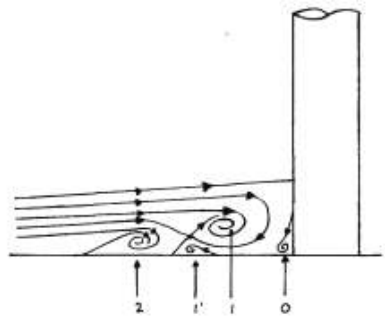
Figure 3.14 Turbulent horseshoe vortex system: sketch by Baker (1980)

As explained by Zdravkovich (2003), the physical parameters governing the horseshoe vortex system and the number of swirls are the thickness of the wall boundary layer and the cylinder diameter. The wall boundary layer may be laminar or turbulent, depending on the Re of the boundary layer, which includes the flow velocity and viscosity and – as characteristic length – the thickness of the boundary layer. If the upstream boundary layer on the wall is laminar, then the flow pattern results in steady laminar horseshoe vortices, as those shown in Figure 3.13. This is an early photograph taken by Sutton (1960) and reported in Baker (1991). There are three clockwise and three anticlockwise rotating vortices on the plane of symmetry upstream of the cylinder.

A literature review about laminar and turbulent vortex systems is presented in Baker, (1978, 1980). In particular, Figure 3.14 (Baker, 1980) shows the flow pattern of a turbulent horseshoe vortex upstream of a cylinder at low Re ($4*10^3 < Re < 9*10^4$). Four vortices (0, 1, 1' and 2) are detected in the figure. Vortex 1 is the main or primary vortex, vortex 1' is caused by separation of the boundary layer beneath vortex 1. Vortex 0 is caused by separation of the boundary layer on the upstream face of the cylinder. Baker (1990) studies the oscillatory behavior of horseshoe vortices in the transitional regime, between the steady laminar horseshoe vortices which occur at low Reynolds number and the fully turbulent horseshoe vortices that occur at higher Reynolds numbers.

The distance from the boundary layer separation to the cylinder depends on the height and diameter of the cylinder. When the height is greater than the wall boundary layer thickness, the separation is independent on the height of the cylinder. According to Belik (1973), such a distance lies between 0.45D and 0.65D. Baker (1991) also measured that for H/D > 1 the separation length tends to 1.1D, independent on H/D.

The size of the horseshoe vortices, relative to the height of the cylinder, decreases as the height of the cylinder increases (Okamoto&Sunabashiri, 1992). Zdravkovich (2003) estimates that the mean pressure distribution along the cylinder, at the cylinder foot, is modified by the horseshoe vortex system for a spanwise distance of about only one third of the diameter.

Hölscher (1993) measured the pressure distribution on the ground plane around a finite circular cylinder of low aspect ratio (H/D = 2). Roughly, the circumferential pressure on the cylinder surface is reflected on the ground plate. Positive pressures on the windward surface of the cylinder also act on the ground plate in the region upwind of the body. This study indicates that the extension is about one diameter upwind of the

junction for a body totally immersed in a turbulent boundary layer. It is directly correlated to the size of the horseshoe vortex system. As the surface pressures on the cylinder decrease with the circumference, negative pressures arise on the ground plate. However, maximum suction appears in the near wake in the plane of symmetry and not at the side of the cylinder. The unsteadiness of the wake flow generates significant pressure fluctuations. They even exceed the pressure fluctuations on the windward side, which are on the other hand directly determined by the turbulence intensity of the approaching flow. Due to the free-end effect, the base pressure in the wake of a short cylinder is higher than in the case of a tall cylinder. Taniguchi (1981) and Okamoto&Sunabashiri (1992) provide comparisons of surface pressure distribution on the ground plane for cylinders of different aspect ratios.
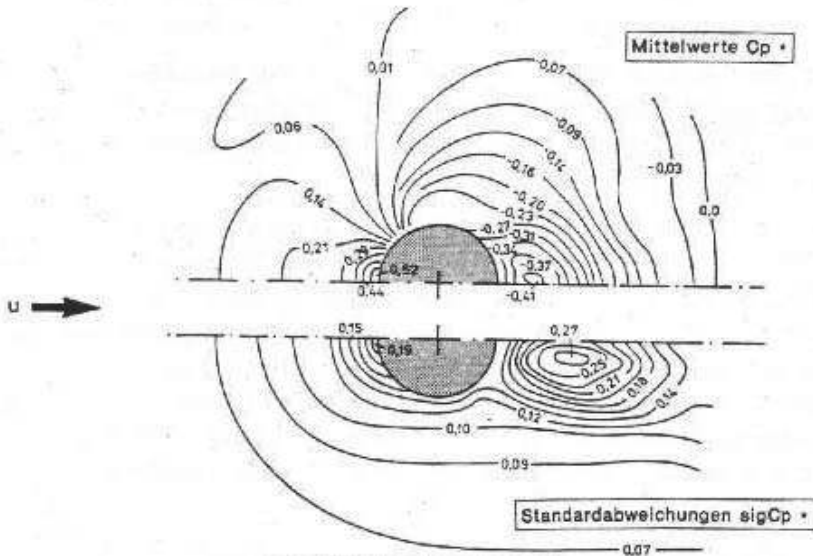
Figure 3.15 Pressure distribution on the ground plane around a finite circular cylinder. Top: mean pressure coefficient, bottom: rms-value of pressure fluctuations. H/D = 2, Re = 3.1*10^5 (Hölscher, 1993)

In the wake, the surface pressures on the ground plane are the result of a time-averaged recirculation region behind the cylinder and depend on the aspect ratio. For small aspect ratios, the streamlines over the top of the cylinder reattach to the ground plane downstream. Okamoto&Sunabashiri (1992) identified the size of such a recirculation region for cylinders of different aspect ratio. Tests were performed in uniform flow at

Re = 2.5-4.7*10^4. According to those results, the recirculation region enlarges with an increase in H/D, as long as H/D ≤ 4. But the recirculation region decreases in the case H/D ≥ 7, because the end effect is limited to the portion near the free-end. The steady recirculation region observed in the experiments by Palau-Salvador et al. (2010) on a H/D = 5 circular cylinder at Re = 2.2*10^4 is instead somewhat smaller (Figure 3.17).
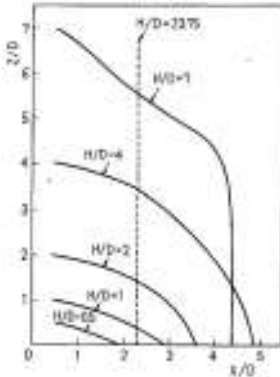
*Figure 3.16 Wake recirculation, Re= 2.5-4.7*10^4 (Okamoto&Sunabashiri, 1992)*
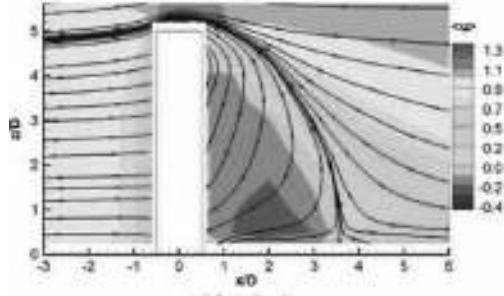
*Figure 3.17 Recirculation region in the wake, H/D = 5, Re = 2.2*10^4 (Palau-Salvador et al., 2010)*

A recent investigation on the influence of the aspect ratio on the wake structure is presented in Rostamy et al. (2012) and summarized in Figure 3.18. The study, based on a PIV visualization, is performed in flat-plate turbulent boundary layer on cylinders of aspect ratio H/D = 9, 7, 5, 3 and at Re = 4.2*10^4. The cylinders have a close end. The study highlights the strong downwash in the near-wake region, which originates near the free-end and descends in the central portion of the wake. The large recirculation zone is marked by the "dividing streamline"; the flow above it moves away from the cylinder. Within the recirculation zone, a small vortex forms immediately below the free-end. The size of this vortex varies with the aspect ratio; the largest vortex occurs for the smallest aspect ratio (H/D = 3). Depending on the size of this vortex, the flow in the tip region can move upwards along the cylinder wall toward the free-end, as it happens in Figure 3.18 c and d (H/D = 5 and 3, respectively). Near the ground, a weak upwash flow can be seen for H/D > 3, which moves towards the central region of the wake. This creates a vortex, namely base vortex, near the cylinder wall-junction. For H/D = 3 the base vortex and the upwash are absent. This is not surprising, because the wake structure of a low aspect ratio circular cylinder is completely different (for example symmetric arch-type vortices develop), as it will be

explained in the following. For all the aspect ratios, a saddle point (black point in the figure) is identified between the two vortices near the free-end and near the cylinder-wall junction. This point marks the streamwise extension of the recirculation zone, as previously identified by Okamoto&Sunabashiri (1992). Accordingly, the saddle point moves downstream as H/D increases, below H/D = 7 up to x/D = 3.8. Results are not too far from Palau-Salvador et al. (2010). For H/D = 9 the saddle point moves closer to the cylinder at x/D = 3.
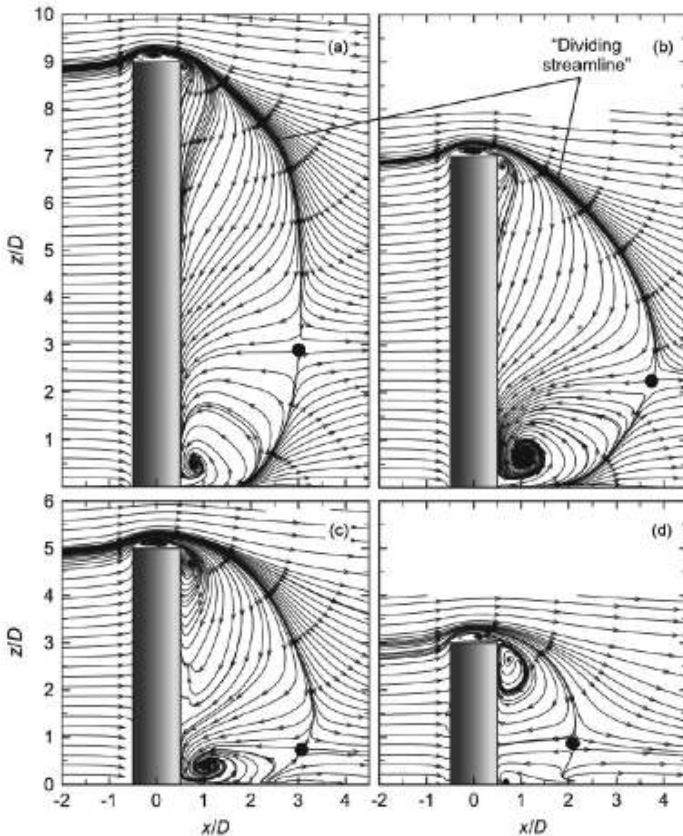
Figure 3.18 Mean streamline field in a vertical plane on the wake centreline for: a) H/D = 9; b) H/D = 7; c) H/D = 5; d) H/D = 3; Re = 4.2*10^4, flat-plate turbulent boundary layer (Rostamy et al., 2012)

A clear visualization of the near-wake flow behind a H/D = 6 circular cylinder at Re = 2*10^4 is described by using LES in Krajnovic (2011). Particular attention is paid to the upwash flow and the base vortices in uniform flow, namely N_w in the paper (with left

and right legs N_{wl} and N_{wr}). "As seen in Figure 3.19, the flow in the symmetry plane moves towards the cylinder near the ground and bends down after the stagnation point, forming the N_w vortex. While the lower part of the near wake is dominated by the downwash very close to the cylinder, the upwash dominates further downstream. This is a result of the two legs, N_{wl} and N_{wr}, rotating in counter-clockwise and clockwise directions, respectively (Figure 3.19 high right-hand side corner)". In the symmetry plane downstream of vortex N_w (Figure 3.19 low right-hand side corner), a focus F_{nw} and a saddle point S_{nw} are visible. They indicate the closure of the separation region in the near wake".
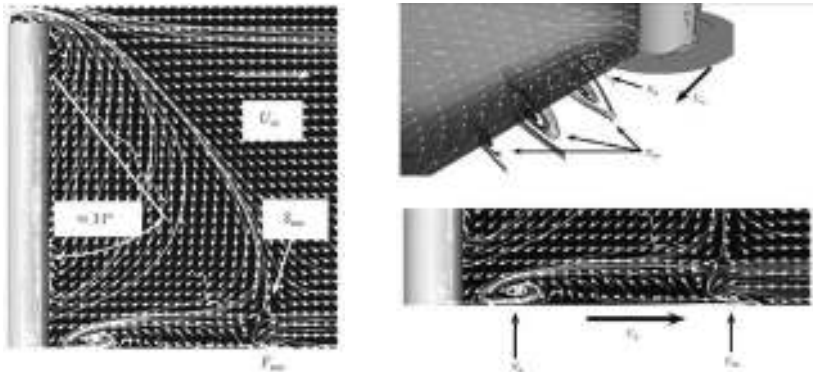
Figure 3.19 Near wake visualized with vortex cores, streamlines and velocity vectors H/D = 6, Re = 2*10^4, uniform flow (Krajnovic, 2011)

An analogous simulation, but in boundary layer flow (Sumner&Heseltine, 2008, H/D = 3 to 9, Re = 6*10^4) showed a similar base vortex pair (distinct from the horseshoe vortex) close to the ground. However, probably due to the boundary layer, the vortices are of different size and at higher position if compared to those in Figure 3.19. Figure 3.20 shows the strong downwash behind the cylinder and the weak upwash near the ground plane, which is associated to the base vortices. It is confirmed in this paper, that for low aspect ratios (e.g. H/D = 3) the downwash extends almost to the wall, while the base vortices and so the upwash are absent: the wake structure is then completely different. A further proof is observed by using PIV in Rostamy et al. (2012).

A flow visualization of the surface flow pattern at the base of a circular cylinder at high Re is also published by Gould et al. (1968) and shown in Figure 3.21. It refers to uniform flow conditions, but a certain boundary layer is naturally developed at the tunnel floor. The figure clearly shows the downstream movement of the separation line

at the ground. The importance of these experiments, is that they are performed on a smooth cylinder in a pressurized wind tunnel up to Re = 5.4*10⁶. Therefore, they represent one of the few tests available in literature in transcritical conditions. Because of that, they will be often used as reference in the following.
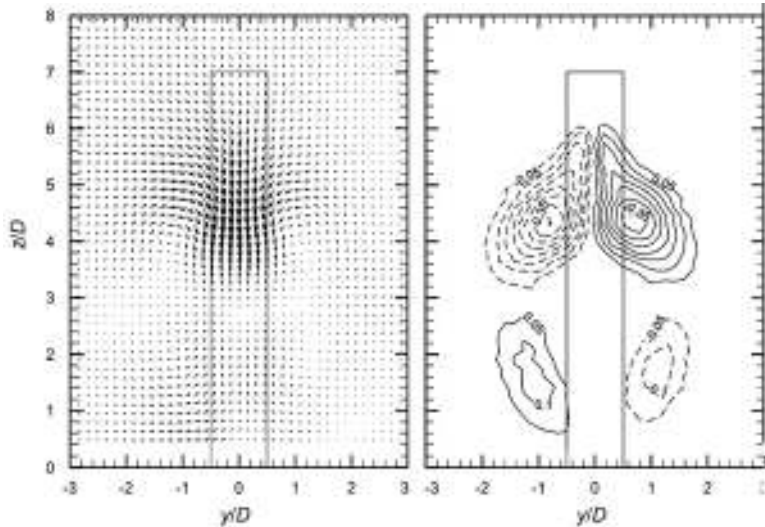
*Figure 3.20 Time-averaged wake structure: in-plane velocity field and streamwise vorticity field behind the cylinder (dimensionless vorticity contour increment 0.05, minimum vorticity contour ±0.05, solid line represent counter clockwise vorticity, dashed lines represent clockwise vorticity). H/D = 7, Re = 6*10⁴, boundary layer flow (Sumner&Heseltine, 2008)*

In the tip region (Figure 3.22), because the pressure induced by the flow on the forward facing surface is significantly higher than that on the rearward facing surface, a flow is induced over the tip of the cylinder from front to rear. The separated flow over the tip creates a region of very low pressure, which induces a spanwise flow towards the tip of the cylinder. This flow sweeps up the separated shear layers from intermediate heights. At short distance below the free-end (about D/2), vortex sheets roll up into a pair of trailing (tip) vortices, which form because of the interaction between the upward-directed separated flow at the sides of the cylinder and the downward-directed flow over the tip. The tip vortices are counter-rotating open vortex loops with their axis perpendicular to both the free-stream direction and the longitudinal axis of the cylinder. The tip effect is governed by the difference of pressure between the front and the rear surfaces of the cylinder and it extends for the upper two or three diameters. In sub-critical flow conditions the wake suction is high

(thus high drag), therefore it is expected that the tip effect in sub-critical conditions is more vigorous than in transcritical conditions, being the latter accompanied by a smaller wake with a lower base suction (ESDU 96030).
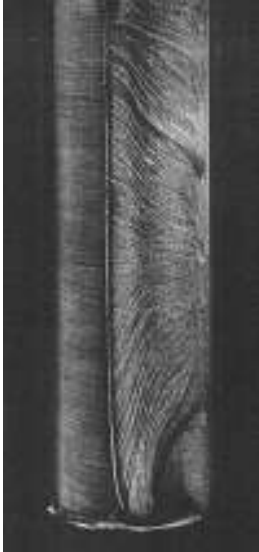
Figure 3.21 Flow pattern in the bottom region at high Re (Gould et al., 1968)
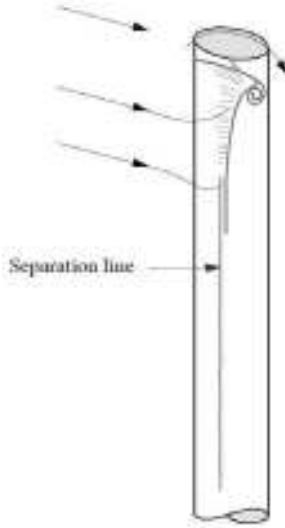
Figure 3.22 Flow pattern in the tip region:
a) Sketch of tip trailing vortices (ESDU 96030);
b) Flow visualization at high Re (Gould et al., 1968);

In presence of an efflux from a chimney, wind tunnel tests show that, at sub-critical Reynolds numbers ($Re < 10^5$), the effect of the efflux is to increase the response. However, at higher Reynolds number (as it is for solar towers) the effect is likely to be reversed (ESDU 96030).

Gould et el. (1968) also investigated the effect of efflux. In their experiments without efflux, it is confirmed the presence of tip vortices originating from the top of tower, within the plane where the local drag coefficient is maximum (i.e. at D/3 from the top, where D stands for diameter), as shown in Figure 3.22. In presence of efflux, it is noticed that there is a distortion of such a pattern. As a result, the vortices can be seen at one diameter from the top (instead of D/3). Gould et al. suggested that the effluent plume generates another pair of vortices just above the top of the chimney. These are opposite in sign to the original pair present in the absence of efflux. As the velocity of the efflux increases, the upper pair of vortices increases in strength and causes a displacement and weakening of the original pair. The apparent effect of an efflux is

thus to raise the height at which the peak loading is experienced to a level closer to the top of the chimney. In such a way, there is an extension of the quasi-two dimensional region (out of the influence of the tip effect), where the drag and lift coefficients are smaller. Moreover, it is also observed in practice that if a chimney is seen to oscillate, then increasing the efflux by opening the flues will generally reduce the oscillation amplitude. Thus, at high Reynolds numbers, it is likely to be conservative to assume that the no-efflux condition presents the more critical design case (for both the along and the across wind response). The ESDU Data Items (ESDU 81017) give the same recommendation. In particular, when H/D is greater than 4 the drag coefficient is larger when the free-end is not closed, but if there is an efflux from the open end the drag coefficient is reduced approximately to the value it would have with a closed end. It is then common practice (at least for what concerns the mean load) to design a stack with the top open and no-efflux.

In summary, the three-dimensional flow pattern around a slender finite length circular cylinder, is characterized by the horseshoe vortices forming upstream at the cylinder-wall junction, a recirculation region in the near-wake, with a small vortex below the free-end and base vortices near the ground plate. The latter develop strongly in boundary layer flows as a result of an upwash near the ground. In the tip region, there are counter rotating open vortex loops, named tip vortices. As regards the fluctuating field, there is the familiar Karman vortex shedding from the sides of the cylinder. This may present, along the height, a variation of the Strouhal number, as it will be explained afterwards. Now, the mean and rms loading pattern on the cylinder surface is analyzed.

In literature, one of the first studies of the spanwise distribution of mean force and pressure coefficients in uniform and shear flow for different aspect ratios has been carried out by Okamoto and Yagita (1973, 1984) at Re $= 1.3*10^4$. The mean iso-pressures lines for a slender circular cylinder (H/D = 9) in uniform flow and shear flow (uniform shear flow) are reported inFigure 3.23 and Figure 3.24, respectively. The velocity profile for the uniform shear flow of those experiments has a non-dimensional velocity gradient of 0.4 and it is expressed by the relation: U(z)/U(H/2) = 1 + 0.4*(z/H – 1/2).

Figure 3.23 and Figure 3.24 show that the free-end effect is limited to the upper three diameters and it is not affected by the boundary layer conditions. Only for smaller

aspect ratios (H/D ≤ 5 according to Okamoto&Yagita, 1984) the end effect would reach the root of the cylinder.

A typical feature of the mean surface pressure distribution in the tip region is the minimum pressure around $\phi \approx 70°$ at z' $\approx$ 2/3D from the free-end. It is due to the displacement of the separation to higher angles. Then, a second islet of minimum pressure appears at $\phi \approx 135°$ and z'/D $\approx$ 1/3 from the free-end. This second $C_{p,min}$ arises considerably the local drag near the free-end. In fact, the $C_{D,max}$ is more pronounced on slender cylinders (H/D ≥ 7) and it is followed by a decrease at lower levels. $C_{D,max}$ exceeds the value of the nominal drag for two-dimensional circular cylinders (Figure 3.27 and Figure 3.28)
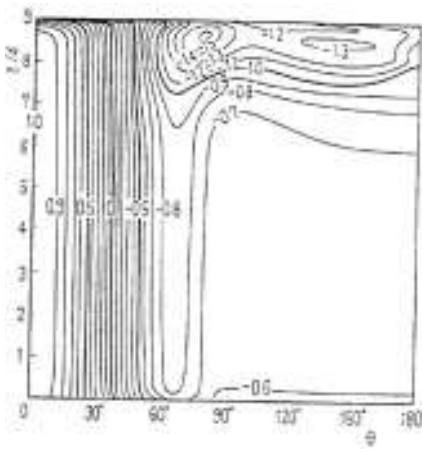
| Figure 3.23 $C_{p,m}$ in uniform flow. H/D = 9, Re = 1.3*10⁴ (Okamoto&Yagita, 1984) | Figure 3.24 $C_{p,m}$ in uniform shear flow. H/D = 9, Re = 1.3*10⁴ (Okamoto&Yagita, 1984) |
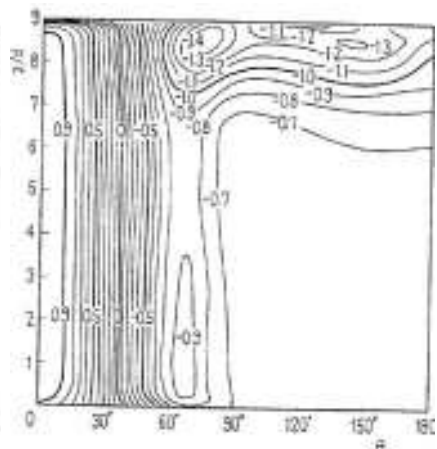
The bottom region of the cylinder in figure Figure 3.24 is influenced by the shear flow condition, but the effect is not so strong. In the low region, at the stagnation line, the C_p distribution tends to deviate from the unitary value due to the downflow produced by the horseshoe vortices. This effect is enhanced by the velocity gradient in shear flow. In shear flow there is also an increase in lateral suction at the base of the cylinder. It has, however, little effect on the drag, which results to be uniform along the height below the tip region for H/D = 9, both in uniform and in shear flow (Figure 3.27 and Figure 3.28).

At higher aspect ratios, e.g. H/D = 12, and in shear flow, the region of low pressures at the rear side gradually extends towards the root of the cylinder (Figure 3.25). The increase in wake suction at the bottom (see Figure 3.26 at high aspect ratios) implies

higher drag in the low region of the cylinder. It is remarkable that this occurs for sufficiently high aspect ratios and only in shear flow, as confirmed by Figure 3.28.
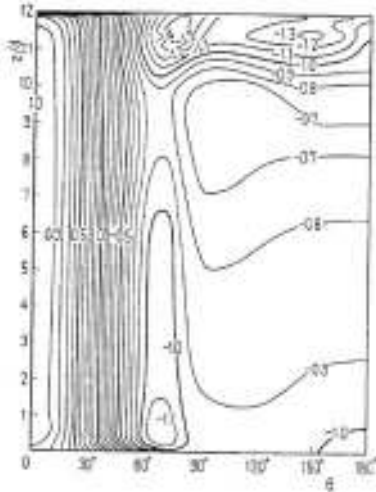
Figure 3.25 $C_{p,m}$ in uniform shear flow.
H/D = 12, Re = 1.3*10⁴
(Okamoto&Yagita, 1984)
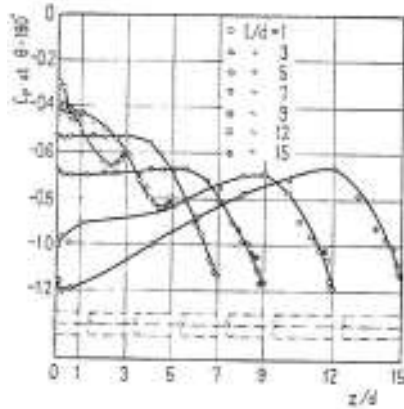
Figure 3.26 $C_{p,m}(180°)$ in uniform shear flow.
H/D from 1 to 15, Re=1.3*10⁴
(Okamoto&Yagita, 1984)

It is remarkable to further comment the comparison of local drag coefficients in uniform and shear flows in Figure 3.27 and Figure 3.28: the mean drag at low levels is constant in uniform flow, while it rises in shear flow when the aspect ratio is sufficiently high. The authors mention the existence of a secondary flow in the rear of the cylinder, which does not appear in the uniform stream. They conclude that "the pressure at the rear side of the cylinder of H/D ≥ 12 gradually decreases and the local drag coefficient increases as the root of the cylinder in a uniform shear stream is approached, while the pressure at the rear side of the cylinder of H/D ≥ 7 is nearly constant in the lower portion free from the end effect in a uniform stream".

With this regard, Farivar (1981) confirmed that in uniform flow (Re = 7*10⁴) the base pressure coefficient is independent on height in the range 0.39 ≤ z/H ≤ 0.81. At z/H ≤ 0.39 the variation of the base pressure was attributed to the boundary layer at the tunnel floor. Luo et al., 1996 showed that in uniform flow (at Re = 3.33*10⁴) the pressure in the stagnation region is relatively insensitive to variation of both H/D and spanwise location, with exception near the free-end. Instead, the pressure in the wake shows strong aspect ratio and spanwise position dependence. This is mainly due to tip

effects, while the spanwise dependence is greatly reduced at z/H ≤ 0.5. This is in agreement with other results in uniform flow.

In boundary layer flows, Garg&Niemann (1995) observed that on a smooth cylinder of H/D = 8.5 at Re = 6.7*10[4], the spanwise mean drag distribution is comparable to the ones in Figure 3.28, characterized by increasing values at the top (due to the tip effect) and also the bottom. The results in this Dissertation (Chapter 4) confirm this trend on a rough cylinder in atmospheric boundary layer, although this peculiar distribution is ignored in many Codes (e.g. Eurocodes).
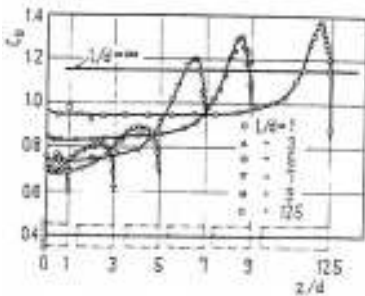
Figure 3.27 Local drag coeff. $C_{D,m}$ in uniform flow, Re=1.3*10[4] (Okamoto&Yagita, 1984)
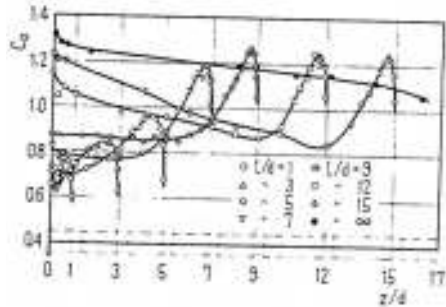
Figure 3.28 Local drag coeff. $C_{D,m}$ in uniform shear flow, Re=1.3*10[4]. (Okamoto&Yagita, 1984)

The non-uniformity of the drag coefficient along the height of the cylinder below the tip region (i.e. apart from tip effects) in boundary layer flow – which primarily depends on higher suction in the near wake at low levels – can also find an explanation by looking at Figure 3.19 compared to Figure 3.20 (Krajnovic, 2011 and Sumner&Heseltine, 2008, respectively): the position of the base vortex pair in the time-averaged wake structure rises significantly in boundary layer flow. On low aspect ratio cylinder (H/D < 3), instead, base vortices are absent.

Consistently with what has been said about the non-uniformity of the mean drag in the low region in boundary layer flows, the ESDU Data Items (ESDU 81017) suggest to apply – in boundary layer flows – a correction factor, which allows to calculate the value of the local mean drag coefficient in the specific boundary layer flow condition by amplifying the C_D value in uniform flow. The extent and the magnitude of the correction depend on the local shear flow gradient.

The reason provided by the ESDU for such a correction factor, namely f_{sz}, is that in boundary layer flows stronger spanwise velocity gradients enhance the flow movement

from regions of relatively high pressure to regions of relatively low pressure. This produces higher local drag coefficients at the base of the structure. In particular – as explained by the ESDU – on the front face of the cylinder in boundary layers flow the pressure decreases as z becomes smaller, because the free-stream velocity decreases. This pressure gradient induces a spanwise flow directed away from the tip. Thus, there is a flow down the front face which interacts with the free-stream flow and produces a net deflection towards the ground plane. This interaction reinforces the bound vortex system which is swept around the cylinder and downstream. The result of this three dimensional effect is to increase considerably the local drag coefficient over that occurring in uniform flow as z/H → 0. Moreover, compared to uniform flow, the bound vortex system tends to delay separation and assist the flow to attain a lower minimum pressure coefficient before separating. The larger lateral suction is accompanied by an increase in the wake suction, which is responsible for higher local drag coefficients at the base. As said, the extent of this modification depends on the local shear flow gradient. For shear flow profiles of the boundary layer type, the ESDU provides – on the basis of H/D and the profile exponent α – a correction factor to the value of the drag coefficient in uniform flow. As z/H → 0, the correction factor increases significantly the local drag coefficient, especially for high slenderness ratios. The expression for such a correction factor, namely f_{sz} in the ESDU, is as follows:

$$f_{sz} = a + b\left(\frac{z}{H} - 0.7\right)^2 \tag{3.4}$$

where:

$$a = 0.8 + 0.2 * \exp\left(-1000\alpha^3\right) \tag{3.5}$$

$$\frac{b}{b_1} = 1.5(1 - \exp(-5.5\alpha)) \quad and \quad b_1 = 2.222\left(1 - \exp\left(-0.00303\left(\frac{H}{D}\right)^4\right)\right) \tag{3.6}$$

If H/D ≥ 6 and α = 0.16, $f_{sz}(z=0) = 2.4$, meaning that the drag coefficient at the base in shear flow is more than twice the corresponding value in uniform flow, due to a bound vortex system enhanced by vertical pressure gradients. The ESDU recommends to use such a correction factor even at transcritical Re, although most of the experiments have been carried out at lower Re.

Kawamura et al. (1984) carried out experiments on circular cylinders of different aspect ratios (H/D = 1, 2, 4, 6, 8) in turbulent boundary layer flows at Re = $3.2*10^4$. The mean surface pressure distribution for the most slender case (H/D = 8) is reported in Figure 3.29. Close to the ground, the down-wash flow at stagnation decreases $C_p(0°)$ and the horseshoe vortices increase lateral suction and move downstream the separation line. All of that is in agreement with the ESDU recommendation. The tip effect, accompanied by high suction and downstream movement of the separation line, is evident at high levels.

According to Kawamura, the second islet of minimum pressure coefficient in the tip region, which is responsible for the high drag at about 1/3D (1/2D) from the top, is due to the attachment of trailing swirls, depicted in Figure 3.30 while they move downstream. As previously explained, longitudinal trailing vortices result from a coupling of the blow-down flow from the free-end and the separated up-wash flow along the side wall. The upward-directed flow sweeps the separated shear layers from intermediate heights towards the tip and rolls up in intense tip vortices with horizontal axis – counter rotating vortices – before passing downstream in a trailing vortex street (ESDU 96030).
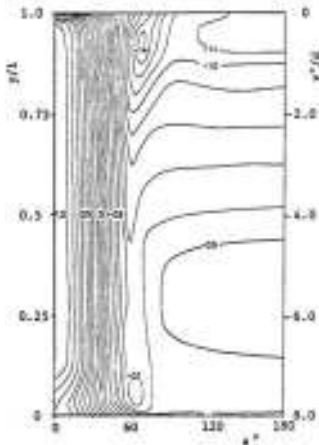
Figure 3.29 Surface pressure coefficients on a finite length circular cylinder H/D = 8 in turbulent boundary layer flow, Re = $3.2*10^4$. (Kawamura et al., 1984)
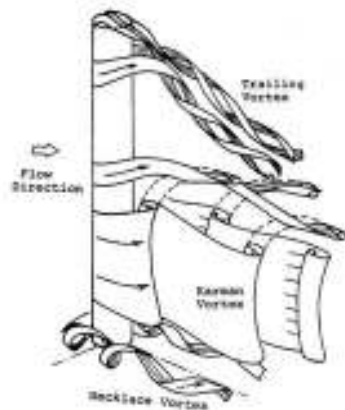
Figure 3.30 Model of the flow around a finite length circular cylinder H/D ≥ 2.5. (Kawamura et el., 1984)

Kawamura did not observe Karman vortex shedding near the free-end, because the free-end was dominated by the downwash. This issue, which will be addressed in the following, is questionable and it is contradicted by other authors.

The trailing vortices were observed by Kawamura even at low aspect ratios, while the formation of Karman vortex streets is suppressed below a critical H/D, which increases as the boundary layer grows thicker.

In contrast with Kawamura, Fox&West (1993) found that for low aspect ratios (H/D ≤ 4) longitudinal trailing vortices do not form. Consistently, there is no evidence of trailing vortices in the results by Uematsu et al. (1994) on cantilevers with aspect ratio in the range 1 to 4.

Sakamoto&Arie (1983) found a completely different flow structure, characterized by symmetric arch-type vortices at aspect ratios below 2.5. This is considered by the authors as the "critical" H/D value where the type of vortex shedding behind a circular cylinder changes from the Karman-type vortex to the arch-type vortex. However, the overall effect of changing the boundary layer height as well as the cylinder height or diameter is still not well understood and among different authors the critical aspect ratio varies in the range 1 to 7.

Below the tip region – which usually extends for two or three diameters and is characterized by high drag due to the high vorticity – the downwash flow leads to an increase in the wake pressure and then a reduced drag coefficient with respect to the two-dimensional situation (infinite cylinder). Therefore, the introduction of additional fluid from over the top relieves some of the negative base pressure. Consequently, the mean and fluctuating pressures below the tip region are lower than those obtained on a circular cylinder between two end plates and the mean drag coefficient decreases as H/D decreases (Okamoto&Sunabashiri, 1992).

As the distance from the tip increases, the strength of the downwash is reduced. This is consistent with what has been previously said about the size of the recirculation region in the wake. Because of that, Fox&West (1993) justified that, if the cantilever is sufficiently long (the value H/D ≥ 13 is chosen as reference to define a long cantilever), the C_D at low levels rises towards the infinite cylinder value. In their experiments they observed that such an infinite cylinder value (relatively high) is fully achieved at spanwise distance higher than 20 diameters from the top. Therefore, for longer circular cylinders, it is sufficient to consider that beyond 20 diameters from the top the conditions associated with the infinitely long circular cylinder are established. Only 3.5 diameters from the ground (Fox&West, 1990), the interference effect with the end-plate becomes significant and it is expressed by an increase in C_D.

Experiments by Fox&West are performed at subcritical Re (Re = $4.4*10^4$). The ESDU Data Items (ESDU 96030) observe that, at higher Re (Re > 10^6) the tip flow is weaker

and two-dimensional conditions are reached at smaller distance from the top than 20 diameters. Moreover, in presence of vertical velocity gradients and turbulence intensity due to a boundary layer, it can be supposed that the downwash is further weakened, so that the spanwise drag distribution at low levels tends to the high value of the two-dimensional drag coefficient, even at lower aspect ratios. This is a further explanation to the rise of C_D in Figure 3.28.

The weaker downwash in the wake in boundary layer flows compared to uniform flows is evident in Park&Lee' flow visualizations (2002). As a consequence of the weaker downwash, the recirculation bubble which normally develops on the rear side of the cylinder is smaller in boundary layer flows than in uniform flow. Therefore, at about middle height, the vortex formation region can move upstream, so that in boundary layer flows the vortices are formed closer to the cylinder, as shown by Figure 3.36.
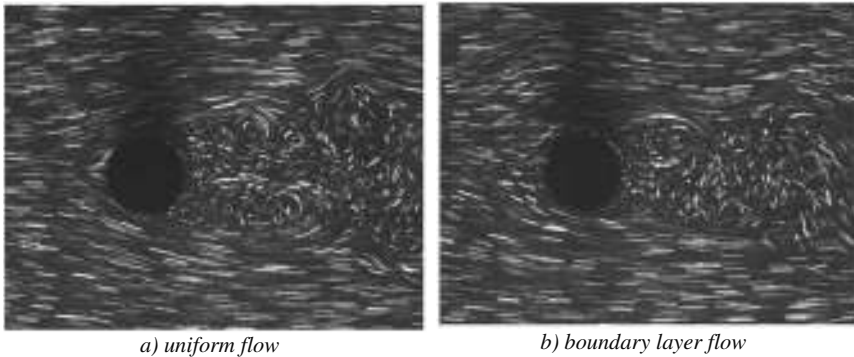
a) uniform flow   b) boundary layer flow
Figure 3.31 Top view of wake at middle height of the finite cylinder H/D = 6, Re = 2*10^4
(Park&Lee, 2002)

The free-end condition, allowed by the absence of a physical boundary between the free stream pressure and the base pressure in the wake, has also an effect on eddy shedding. In particular, as explained by Zdravkovich (2003), the secondary flow over the tip is responsible for: 1) elongation of the eddy formation region, widening of the near-wake, decrease in Strouhal number; 2) displacement downstream of eddy shedding; 3) suppression of eddy shedding for small aspect ratios, so that the secondary flow becomes the primary flow.

A spanwise variation of the Strouhal number has been observed at first by Farivar (1981) at Re = 7*10^4 in uniform flow (Figure 3.32a). He found a cellular shedding

with three distinctive regions: a small top region (z/H $\geq$ 0.9) characterized by low frequency of vortex shedding ($S_t \approx 0.08$), a middle region (0.6 < z/H < 0.9) characterized by higher frequency, but still lower than that for a classical wake flow ($S_t \approx 0.165$), and a lower region (z/H $\leq$ 0.6) characterized by a Strouhal number equal to that for the classical wake flow ($S_t \approx 0.19$). On the basis of Roshko's experiments with a splitter plate placed in the wake of a cylinder parallel to the stream – which proved a decreases of the Strouhal number depending on the position of the splitter plate in the wake (Roshko, 1959) – and on the basis of Gerrard's theory on the length of the eddy formation region related to the frequency of vortex shedding (Gerrard, 1966), Farivar gathered the following explanation: the decrease in the Strouhal number in the tip region is due to a lengthening of the formation region, as it can be produced by a splitter plate; in the case of a cylinder with a free-end, the flow over the top enters the wake region and this entrainment causes a blockage in the wake preventing the interaction between vortices. Because of that, the formation region elongates and the frequency of vortex shedding is reduced. However, this does not explain the cellular shedding along the height.
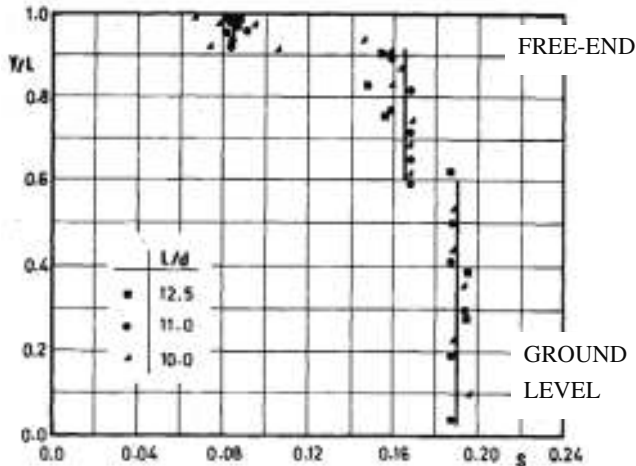
Figure 3.32 Variation of the Strouhal number with height along a finite circular cylinder. Uniform flow, Re = Re = 7*104, H/D = 10, 11, 12.5 (Farivar, 1981)

A decrease in the Strouhal number in the tip region of a finite length circular cylinder is also confirmed by Fox et al. (1993) and reported in Figure 3.32b. Cell-like structures were also detected in the wake by Ayoub&Karamcheti (1982), with vortex shedding occurring up to a short distance from the free-end.
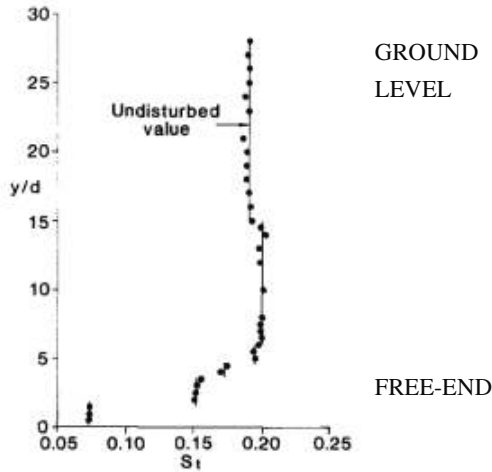
Figure 3.33 Variation of the Strouhal number with height along a finite circular cylinder. Uniform flow, Re = Re = 4.4*10⁴, H/D = 30 (Fox et al., 1993)

Park and Lee (2000) deeply investigated the shedding frequency at the free-end, in comparison with Karman vortex frequency along the height. They tested three finite circular cylinders with aspect ratios 6, 10 and 13 respectively, in uniform flow at Re = $2*10^4$. Near the free-end a peculiar spectral peak occurred at 24 Hz, which in the conditions of those tests corresponds to a reduced frequency nD/U = 24Hz*0.03m/10m/s = 0.072. At middle height the vortex shedding frequency depended on the aspect ratios and the following values were achieved: nD/U = 60*0.03/10 = 0.18 for H/D = 13; 0.16 for H/D = 10 and 0.14 for H/D = 6[2]. In the 2D conditions it resulted nD/U = 0.20, almost three times the reduced frequency in the tip region. The difference in the vortex shedding at middle height is attributed to the downwash flow along the central region of the wake. The strength of the downwash flow depends on the aspect ratio. It is interesting to note, instead, that the 24 Hz component is not modified by the different aspect ratio. However, several spanwise cells as those reported in Figure 3.32 are not observed by these authors. In agreement with Park&Lee's results, Luo et al. (1996) observed Strouhal numbers equal to 0.08 and 0.191 on their H/D = 8 cylinder at z/H = 0.95 and z/H ≤ 0.5 respectively, in uniform flow at Re = $3.33*10^4$.

---

[2] In Park&Lee (2002) the same tests are repeated in atmospheric boundary layers and the vortex shedding frequencies and the vortex formation regions are lower.

Another wide study in uniform flow regarding the existence of big vortices generated around the free-end of a finite circular cylinder, whose frequency is much lower than the Karman vortex shedding frequency, is documented by Kitagawa et al. (1999, 2001, 2002) at Re = $2.5*10^4$ (Figure 3.34, Figure 3.35). Such vortices are called tip-associated vortices (TAV) and tend to vanish if the end conditions are modified, for example by a sufficiently large end disk. Kitagawa et al. (1999) found that with a circular disk over the free-end, with a diameter which is 20% more than the cylinder diameter, the tip-associated vortices are weakened; with an increase in the disk diameter up to 60% more than the cylinder diameter , the tip-associated vortices are almost vanished.

The tip-associated vortices are something different from the previously mentioned counter rotating vortices with horizontal axis – usually called tip vortices – which are produced by the interaction between the upward flow at the side of the cylinder and the downward flow over the tip and the rear and pass downstream in a steady street of longitudinal trailing vortices (Figure 3.30). The shedding frequency of tip-associated-vortices measured by Kitagawa is about 1/3 of the Karman vortex shedding frequency. The tip-associated-vortices possibly correspond to one of the cells detected by Farivar (1981) and others close to the tip of the circular cylinder. Detection of vortex shedding near the top is in contrast with the results, previously mentioned, by Okamoto&Yagita (1973, 1984) and Kawamura et al. (1984). They did not observe vortex shedding near the top, but only stationary longitudinal trailing vortices (Figure 3.30).

a)   b)
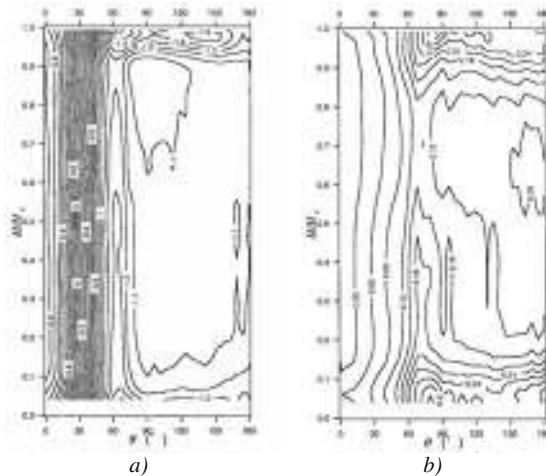
Figure 3.34 Pressures on a finite cylinder, uniform flow, H/D = 25, Re = $2.5*10^4$
a) $C_{p,m}$; b) $C_{p,\sigma}$; (Kitagawa et al., 2001)
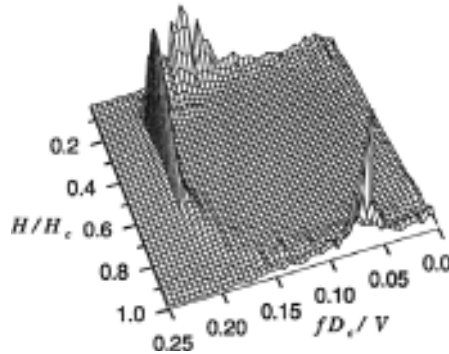
Figure 3.35 Power spectra of fluctuating pressures at 90°: existence of tip-associated-vortices, uniform flow, H/D = 25, Re = 2.5*10^4 (Kitagawa et al., 2001).

Aeroelastic tests by Kitagawa et al. (1999) studied the so-called end-cell-induced-vibrations (ECIV), which are similar to the vortex-induced-vibration (VIV), but they occur at a wind speed a few times higher than the threshold wind speed of VIV. Tip-associated-vortices are found to be the cause of ECIV. In fact, according to Kitagawa, ECIV could not be generated by sub-harmonic oscillations of the Karman vortex shedding, although they also occur at a flow velocity a few times higher than that for VIV. The difference is that ECIV tend to vanish with modification of the flow around the free-end, for example by using a disk plate. This would not happen if ECIV were generated by sub-harmonic oscillations and not by the tip-associated vortices.

Three dimensional effects on the flow around circular cylinders have been studied in recent years by numerical simulations. A few of them have been mentioned before. Some important ones are cited in the following. However, many of them are only for short aspect ratio cylinders. In particular, a large eddy simulation of a finite cylinder H/D = 2.5 at Re = 4.3*10^4 was performed by Fröhlich&Rodi (2004), who demonstrated the existence of tip vortices and an arch vortex in the average flow downstream of the free end. Similar results were obtained by Lee et al. (2007). Afgan et al. (2006) presented LES of the flows studied by Park&Lee (2000), i.e. circular cylinder with H/D = 6 in uniform flow at Re = 2.0*10^4. Palau-Salvador et al. (2010) made LES of their own experimental cases with H/D = 2.5 at Re = 4.3*10^4 and H/D = 5 at Re = 2.2*10^4. Krajnovic (2011), previously mentioned in the description of the near-wake flow, used LES to explore both the instantaneous and the time-averaged flows around a relatively tall cylinder (H/D = 6) in uniform flow at Re = 2*10^4.

3.6   **Bi-stable flows in literature**

Bistable flow conditions around isolated circular cylinders in the critical range of Re (section 3.2) represent a well-known and interesting fluid-dynamic phenomenon, but without any relevant application in the design of structures. As previously explained, the physical reason lies in the transition from laminar to turbulent boundary layer, which occurs on one side only of the cylinder. The transition to turbulent conditions is governed by the Reynolds number. The bistable regime occurs in a very small range of Re, just before Re_{cr}. Most of the structures are far beyond this regime. Moreover, the bistable phenomenon is extremely sensitive not only to Re, but also to any flow disturbance such as turbulence of the incoming flow and cylinder surface roughness.

Bistable flow conditions around circular cylinders are much more common in side-by-side configurations of cylinders in pair. In this case, the bi-stability is regarded as a phenomenon of interaction between cylinders and it can be of importance in the structural design. The fluid behaviour is primarily a function of the centre-to-centre transverse pitch ratio (T/D). Reynolds effects for the side-by-side configuration exist, but they are less prominent than, for example, the tandem configuration. Depending on T/D, three different flow patterns are possible for the side-by-side configuration (Zdravkovich, 2003):

- single-bluff-body behaviour at small pitch ratios (approximately 1.0 < T/D < 1.1-1.2, Figure 3.36a): the single eddy street is formed behind both cylinders, which appear as a single bluff body with a weak flow through the gap;
- a biased flow pattern at intermediate pitch ratios (approximately 1.1-1.2 < T/D < 2.0-2.2, Figure 3.36b): narrow and wide wakes are formed behind two identical cylinders. The gap flow forms a jet biased towards the narrow wake. The biased gap flow is bistable, and may intermittently switch to either side;
- coupled, parallel vortex streets at high pitch ratios (approximately T/D > 2.0-2.5, Figure 3.36c): both wakes are equal in size and eddy shedding is synchronized in frequency and phase. The predominant out-of-phase coupling produces two eddy streets, which mirror each other relative to the gap axis.

A recent review paper by Sumner (2010) further describes the asymmetrical or biased flow pattern at intermediate values of T/D for two side-by-side circular cylinders: the asymmetrical flow pattern is characterized by a gap flow biased towards one of the two cylinders. The cylinder towards which the flow is biased has a narrow near-wake, higher-frequency vortex shedding, and a higher drag coefficient, while the other

cylinder has a wider near-wake, lower-frequency vortex shedding, and a lower drag coefficient. Because of that, the two modes "narrow wake" and "wide wake" can be identified. The deflection of the biased gap flow varies with T/D. The trend is toward a smaller degree of deflection with increasing T/D. In some cases, the biased flow pattern switches intermittently from being directed towards one cylinder to the other, and the flow pattern is termed bistable. This ''flip-flopping'' of the gap flow direction and wake sizes occurs spontaneously and irregularly, but between switchovers the flow remains stably biased to one of the cylinders for long durations (perhaps a few orders of magnitude larger than the vortex shedding period). The bistable characteristic is not caused by misalignment of the cylinders or other extraneous influences, but is an intrinsic property of the flow.
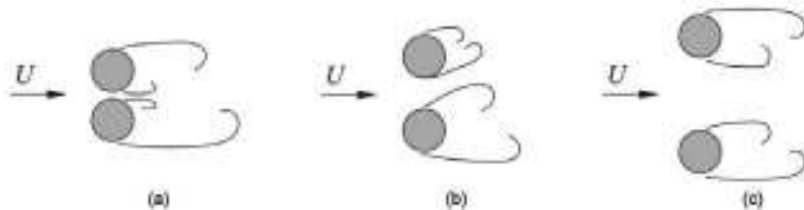
Figure 3.36 Flow patterns for two side-by-side circular cylinders: a) single-bluff-body behaviour; b) biased flow pattern; c) parallel vortex streets (Sumner, 2010);

Mahbub Alam et al. (2003) applied a wavelet analysis in order to detect the frequency of vortex shedding in the two modes (narrow wake, wide wake) and the switching phenomenon.

Three modes of flow, associated with wider wake, symmetric wake and narrow wake are described by Mahbub Alam&Meyer (2011) and sketched in Figure 3.37. The formation and burst of a separation bubble when the gap flow is biased towards one of the two cylinders can even produce a quadri-stable flip-flopping flow regime. A typical lift force signal is shown in Figure 3.38.

Zdravkovich (2003) stresses the paradox of Figure 3.36b, which shows the bistable biased gap flow. The paradox is due to two special features: the first is that an entirely symmetrical oncoming flow leads to the asymmetric narrow and wide wakes behind the two identical side-by-side cylinders. The second is that a uniform and stable flow induces a non-uniform and random bistable flow. The origin of bistable biased flow has been attributed to various causes, but still remains unresolved.

Ishigai et al. (1972) suggested that the Coanda effect is responsible for the biased gap flow. The Coanda effect is observed when a jet tangentially attached to a curved surface becomes deflected by following the surface. According to this definition, it is essential to have a rounded surface. Because of that, Bearman&Wadcock (1973) proved that the Coanda effect could not be the reason; the biased gap flow also appeared by using side-by-side flat plates.

Zdravkovich&Pridden (1977) and Zdravkovich (1987) also observed stable narrow and wide wakes on the upstream and downstream cylinders in staggered arrangement, respectively. As the side-by-side arrangement is approached, the distinction persists so that one cylinder remained upstream with a narrow wake, and the other downstream, with a wide wake. In a side-by-side configuration the asymmetric flow structure is preserved, but it becomes bistable because neither of the side-by-side cylinders is upstream nor downstream. Zdravkovich (2003) concludes that the flow structure consisting of two identical wakes appears to be intrinsically unstable and hence impossible.
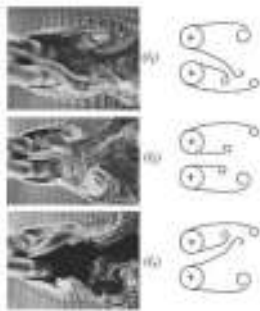
Figure 3.37 Tri-stable flow (T/D = 0.4) (Mahbub Alam&Meyer, 2011)
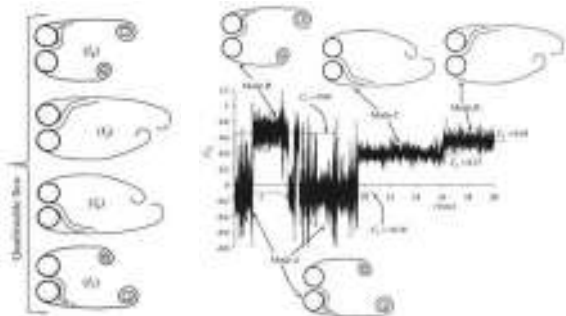
Figure 3.38 Quadri-stable flow due to formation and burst of a separation bubble (T/D = 0.13) (Mahbub Alam&Meyer, 2011)

This Dissertation addresses the case of only one isolated circular cylinder. However, a similar bistable phenomenon of interaction like the one previously described occurs in the wake between different compartments of the single cylinder, which are separated by stiffening rings. This effect is addressed in Chapter 5.

Chapter 4. **Experimental set-up for wind tunnel tests**

This chapter describes the boundary layer wind tunnel at the Ruhr-University Bochum, the model of the Solar Updraft Tower and an outline of the tests. Moreover, the preliminary results on the circular cylinder (without rings) are presented. Issues like the influence of the Reynolds number and the choice of surface roughness are also addressed in this chapter.

4.1 **WiSt wind tunnel (Ruhr-University Bochum)**

4.1.1 **Geometry of the boundary layer wind tunnel**

WiSt laboratory at Ruhr-University Bochum (Windingenieurwesen und Strömungsmechanik http://www.ruhr-uni-bochum.de/wist) is an open circuit wind tunnel with a total length of about 17 m. The tunnel itself has a length of 9.3 m. The test section is 1.8 m in width and 1.6 m in height. In case of need, the upper ceiling of the tunnel can be raised until 1.9 m. A turntable in the test section allows to test different wind directions, if necessary. A honeycomb grid is located at the inlet of the tunnel.

Figure 4.1 WiSt boundary layer wind tunnel at Ruhr-University Bochum

The turbulent boundary layer develops over a length of about 7.6 m. After a castellated barrier having a maximum height of 425 mm, there are three turbulent generators of 1.5 m in height. They are built according to Counihan's specifications (Counihan, 1969), as reported in the following sketch (Figure 4.2). The roughness field consists of six panels with 36*36*36 mm^3 cubes alternated to 36*36*18 mm^3 square prisms. It creates the lowest and most important part of the boundary layer, which undergoes a natural evolution along the wind tunnel and the largest eddy reaches approximately the

thickness of this surface layer, i.e. 30-40 cm. The turbulence in the upper layer is created by turbulence generators. At a distance of about 3.5 times the height of the turbulent generators, the two layers merge and continue to grow together. The castellated barrier acts as an adjustment element. All these facilities (castellated barrier, turbulence generators and roughness field) are removed in case of low-turbulence tests in empty tunnel and approximately uniform flow. The boundary layer at each wall affects a distance of about 30 cm.

$$x = \frac{H}{2}\sqrt{1 - \frac{y^2}{H^2}}$$

$$G = 2x\tan\frac{\varphi}{2}$$
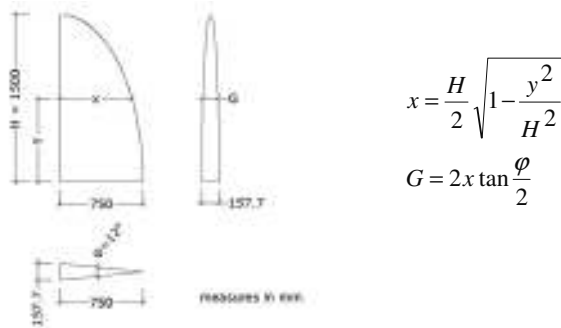
Figure 4.2 Turbulent generators of Counihan type

The diffusor and the centrifugal fan are placed at the end of the wind tunnel. The engine allows to attain a maximum wind speed of about 28-30 m/s with 1500 turns per minute of the fan. A Prandtl tube allows to measure the dynamic pressure of the incoming flow. Temperature sensors acquire temperature during the measurements. It allows to calculate the air density and therefore the mean wind speed by applying Bernoulli equation. The Prandtl tube is normally placed at 1.3 m in height – out of the influence of the wall of the wind tunnel – but its position may change depending on the tests.

Figure 4.3 View of the model in the wind tunnel with turbulent facilities

DRAWING n.1   WiSt Boundary layer wind tunnel Ruhr-University Bochum

0   1000   2000mm

VERTICAL CROSS-SECTION

HORIZONTAL CROSS-SECTION

Turbulence generators

Surface roughness panels

WIND

Z

Y

X

700
1400
1285
750
5580
1700
2100
1600
2000

425
225
1500
750

400
250
750   750

1600
2230
2800

1800
2230
2800

850
850
850

17115
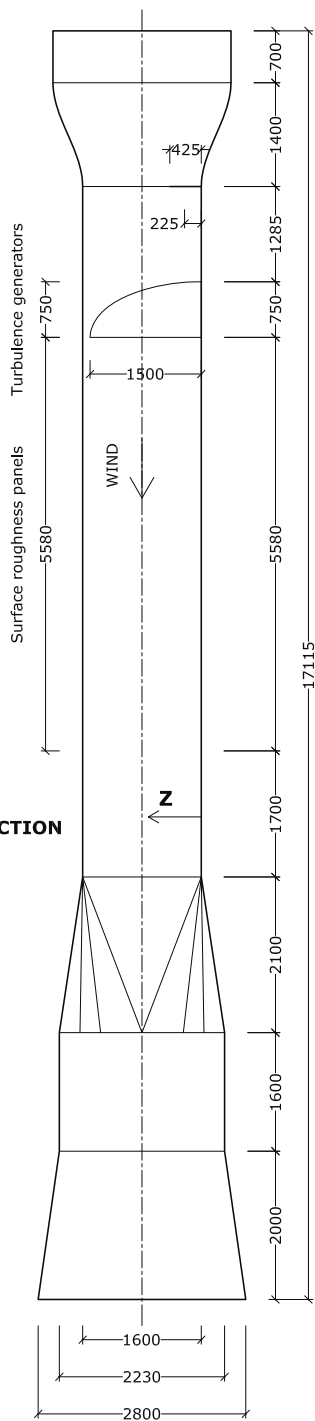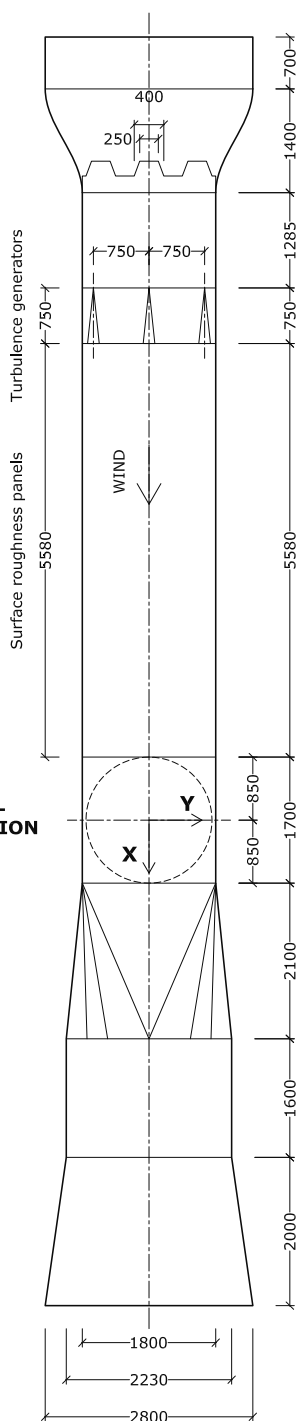
4.1.2 **Flow characteristics**

The castellated barrier, the turbulent generators and the roughness field, previously described, produce a certain boundary layer namely RAU8. For the wind tunnel tests on the solar tower, however, a slightly modified version of RAU8 is adopted, due to the presence of the collector. It is named RAU8+collector (Figure 4.1). The collector, i.e. a smooth panel of 4 m in length, centered at the tower position, was introduced with the aim of creating a two-phase profile, as it should be expected in full-scale. Due to the presence of the collector, the last roughness panel (the shortest one, 0.33 m in length) had to be removed. The final set-up of the wind tunnel resulted like that:
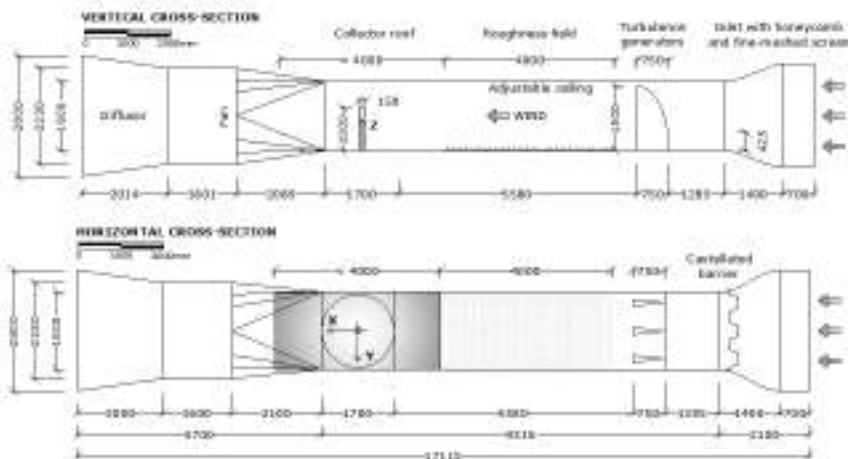
Figure 4.4 View of the Solar Tower in the wind tunnel at the Ruhr-University Bochum

The ESDU Data Items 82026 allow to estimate the height of the internal layer which develops after a roughness change, as that produced by the smooth collector roof. $z_{0,1}$ and $z_{0,2}$ are the roughness lengths corresponding to the upwind and downwind conditions, respectively. U_{z1} and U_{z2} are the resulting wind profiles. At a certain distance x from the step change in roughness, it can be assumed that the wind speed profile consists of a lower portion (internal layer), where the velocity is dependent on x and it is given by $K_x U_{z2}$, and an upper portion where the profile is the same as upwind. The height of the internal layer, at which the two portions intersect, can be estimated according to the ESDU procedure. If it is assumed that the smooth collector has a surface roughness $z_{0,2} = 0.005$ m, while the upwind conditions are those described in chapter 2 for the H&D model ($U_{z1}(10m) = 25$ m/s, $z_{0,1} = 0.05$ m, latitude $= 23°$), an internal layer of approximately 200 m can be calculated in the full-scale condition at a distance equal to the radius of the collector Rcoll (Table 4.1).

Table 4.1 Effect of a step change in roughness according to ESDU 82026
at the tower position

Upwind conditions (full-scale)			Downwind conditions (full-scale)		
z_{01}	0.05	m	z_{02}	0.005	m
u_{*1}	1.898	m/s	u_{*2}	1.638	m/s
Internal layer height in m (full-scale)			h_i	201	
K_x factor at $x = R_{coll} = 2000$ m after the roughness change				0.9070	

Instruments for velocity measurements

The velocity profile is measured with hot-wires anemometers. Cross wires allow to measure two wind components (either u and v, or u and w). More than one probe can record simultaneously in the wind tunnel; the Multichannel CTA 54N80 by Dantec is an amplifier which allows to measure up to 16 channels. In the experiments, however, only two cross-wire probes were used (four channels) plus temperature and Prandtl velocity (two other channels). The A/D converter is the same as for pressure measurements (see section 4.1.3) and it is set to a sampling frequency of 2 kHz.

a) *b)*
Figure 4.5 Miniature wires (X-array): a) during experiments; b) zoom

The multichannel CTA is designed for use with miniature wire probes (type 55P61-64) in combination with 4m probe cables. Each channel of the CTA can be set to a certain "decade resistance", defined as twenty times the operating resistance. The latter depends on the resistances of the sensor, of the probe support and of the probe cable. The wires are 5 μm in diameter and 1.2 mm long. They are suspended between two needle-shaped prongs. The frequency bandwidth is 10 kHz and filters can be applied.

The anemometers are calibrated in laminar flow in the calibration tunnel. The calibration establishes a relation between the CTA output (voltages) and the flow velocity. It is performed by exposing the probe to a set of known velocities, U, and the corresponding voltages E are recorded. A fitting curve through the points (E,U) represents the transfer function to be used when converting data records from voltages into velocities. The fitting curve which is adopted is a polynomial curve of 4th order (equation (4.1)). The coefficients are calculated by fitting the data in the least-squares sense. An example reported is in Figure 4.6.
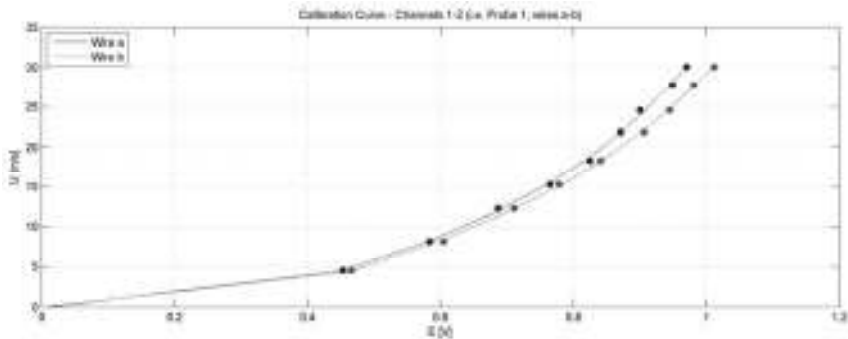
Figure 4.6 Calibration curve – wires a and b of one probe (experiment 24.10.2011)

$$U = C_0 + C_1 E + C_2 E^2 + C_3 E^3 + C_4 E^4 \qquad (4.1)$$

If the temperature varies during calibration and the experiment, the recorded voltages must be corrected (E_{corr}) with the formula:

$$E_{corr} = \left(\frac{T_w - T_0}{T_w - T_a} \right)^{0.5} E_a \qquad (4.2)$$

where: E_a = acquired voltage; T_w = sensor hot temperature = 250°; T_0 = ambient reference temperature (during calibration); T_a = ambient temperature during acquisition. The expression can be used for moderate temperature changes in air (± 5°C). The useful range may be expanded (Jørgensen Finn E., 2002) by reducing the exponent from 0.5 to 0.4 or 0.3.

This formula is suggested by the practical guide of Dantec, but it was checked by measurements at several different temperatures before being applied in the experiments.

Results of velocity measurements

Mean wind profile, turbulence intensity, integral length scales and spectra are evaluated by hot-wires anemometers measurements. The mean wind profile is defined by using a power law according to formula (4.3).

$$\frac{U_m(z)}{U_{ref}} = \left(\frac{z}{z_{ref}}\right)^{\alpha} \qquad (4.3)$$

The reference velocity is the velocity of the Prandtl tube U_{pra}. Unfortunately, during the tests, the mean level of the velocity measured by one of the two anemometers shifted to lower values. It is probably due to a sensible modification of the calibration curve. The mean values of that anemometer could not be used. Instead, the fluctuations did not result to be affected. The results of the available data for the mean wind profile are reported in Figure 4.7 and confirmed that the influence of the collector extends up to z = 200 mm. This fits very well the ESDU recommendation mentioned before (Table 4.1).

The turbulence intensity of the u-component is calculated according to the definition (4.4). The same applies to the components in the other directions, by using either σ_v or σ_w.

$$I_u(z) = \frac{\sigma_u(z)}{U_m(z)} \qquad (4.4)$$

The integral length scales of turbulence represent an average size of the vortices associated to longitudinal, transversal and vertical turbulence in the x, y and z directions, respectively. Nine integral scales of turbulence can be defined: L_{ux}, L_{uy}, L_{uz}, L_{vx}, L_{vy}, L_{vz}, L_{wx}, L_{wy}, L_{wz}. They are calculated by integration from zero to infinite of the zero-lag covariance functions divided by the variance, i.e. the cross-correlation coefficients. For example, for the u-component they are:

$$L_{ux} = \frac{1}{\sigma_u^2} \int_0^{+\infty} R_u(\Delta x, 0) d\Delta x = \int_0^{+\infty} \rho_u(\Delta x, 0) d\Delta x \qquad (4.5)$$

$$L_{uy} = \frac{1}{\sigma_u^2} \int_0^{+\infty} R_u(\Delta y, 0) d\Delta y = \int_0^{+\infty} \rho_u(\Delta y, 0) d\Delta y \qquad (4.6)$$

$$L_{uz} = \frac{1}{\sigma_u^2} \int_0^{+\infty} R_u(\Delta z, 0) d\Delta z = \int_0^{+\infty} \rho_u(\Delta z, 0) d\Delta z \qquad (4.7)$$

The integral length scale L_{ux} can be easily calculated by Taylor's hypothesis, which allows to use only one signal measured in one position, by assuming that the vortices move in the along-wind direction at the mean wind speed:

$$L_{ux} = U_m T_{ux} \qquad (4.8)$$

T_{ux} is the integral time scale, i.e. the integral of the auto-correlation function from zero until infinite (equation (4.9)). In practical terms, the integration can be extended until the first zero crossing, because all the following ondulations of the auto-correlation coefficient approximately average to zero. Also other methods exist, for example the exponential method, which assumes that the auto-correlation function has an exponential decay (Schrader, 1993). Alternately, T_{ux} can also be calculated by fitting the spectrum of the signal with an analytical expression of the velocity spectrum (e.g. von Karman spectrum in isotropic flow).

$$T_{ux} = \int_0^{\infty} \rho_{ux}(\tau) d\tau \qquad (4.9)$$

Besides L_{ux}, for the purpose of this work it is especially important to investigate the integral length scale of the u-component in the z direction, i.e. L_{uz}. Approximately, in the atmospheric boundary layer flow, it is one half of L_{ux}, apart from very close to the ground. In this work, L_{uz} is calculated at each height by integration of the cross-correlation coefficients from zero until infinite (equation (4.10)). This requires simultaneous measurements of wind velocity in at least two points (Figure 4.5).

$$L_{u_z}\left(z_{ref}, \Delta z\right) = \int_0^\infty \rho_u\left(z_{ref}, \Delta z\right) d\Delta z \tag{4.10}$$

Vertical cross-correlations of the u-component in the undisturbed flow are measured both upwards and downwards at the following reference heights: 100-300-500-700-900-1100 mm. They are fitted with a negative exponential function, from which L_{uz} is easily derived:

$$\rho_u\left(\Delta z\right) = e^{-\dfrac{\Delta z}{Luz}} \tag{4.11}$$

The spectra of the u and v components are reported in Figure 4.11 and Figure 4.12. In particular, the investigation of the cross-wind component (v) of the wind velocity is important for a deeper study of pressure fluctuations at the flanges of the cylinder and for transversal oscillations of the structure in a dynamic calculation. The spectrum of the v-component, compared to the spectrum of the u-component, appears to be shifted (Figure 4.13). It implies higher energy in the cross-wind direction at relatively high frequency, i.e. in the frequency range of most of structures sensitive to wind.
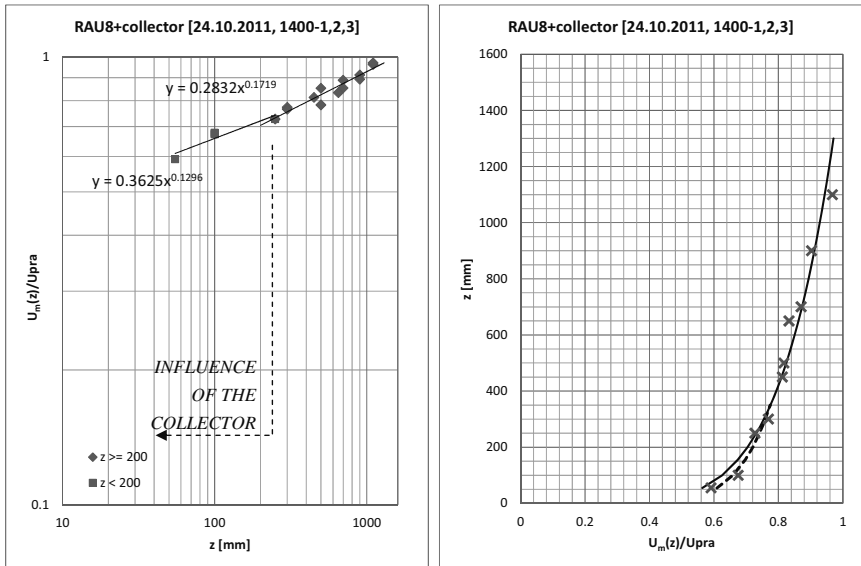
Figure 4.7 Mean wind profile (RAU8+collector)

109
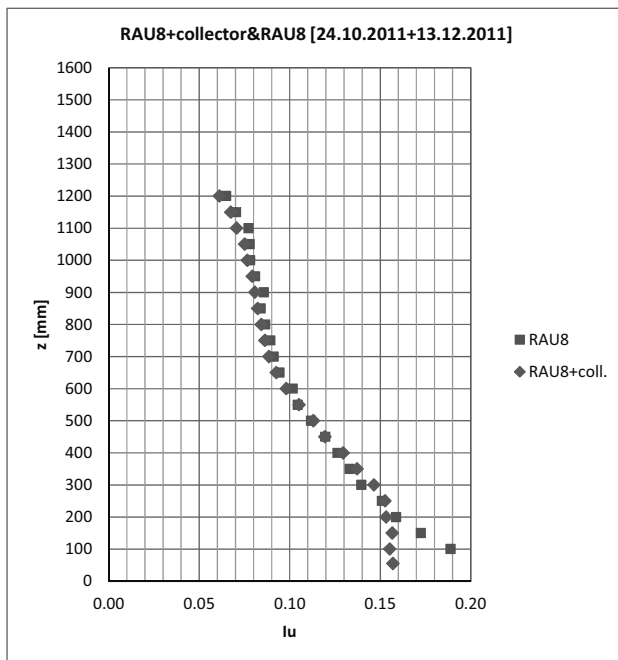
Figure 4.8 Turbulence intensity (RAU8+collector and RAU8)
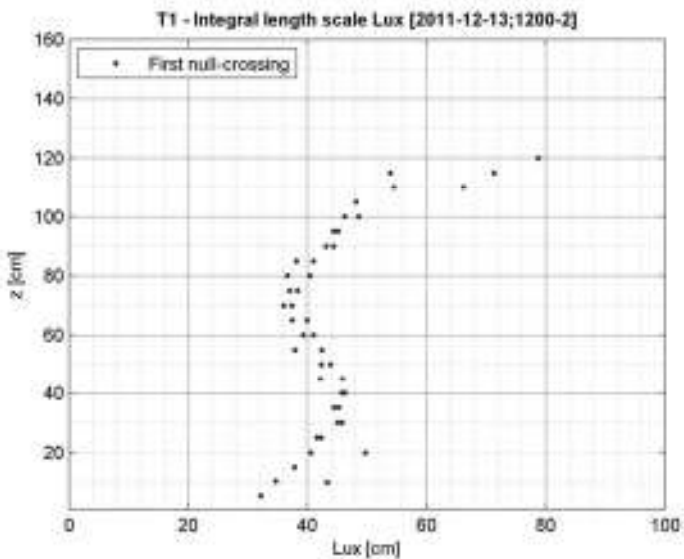
Figure 4.9 Integral length scale, L_{ux} (RAU8+collector) in the figure: first zero-crossing

Upwards   **Downwards**
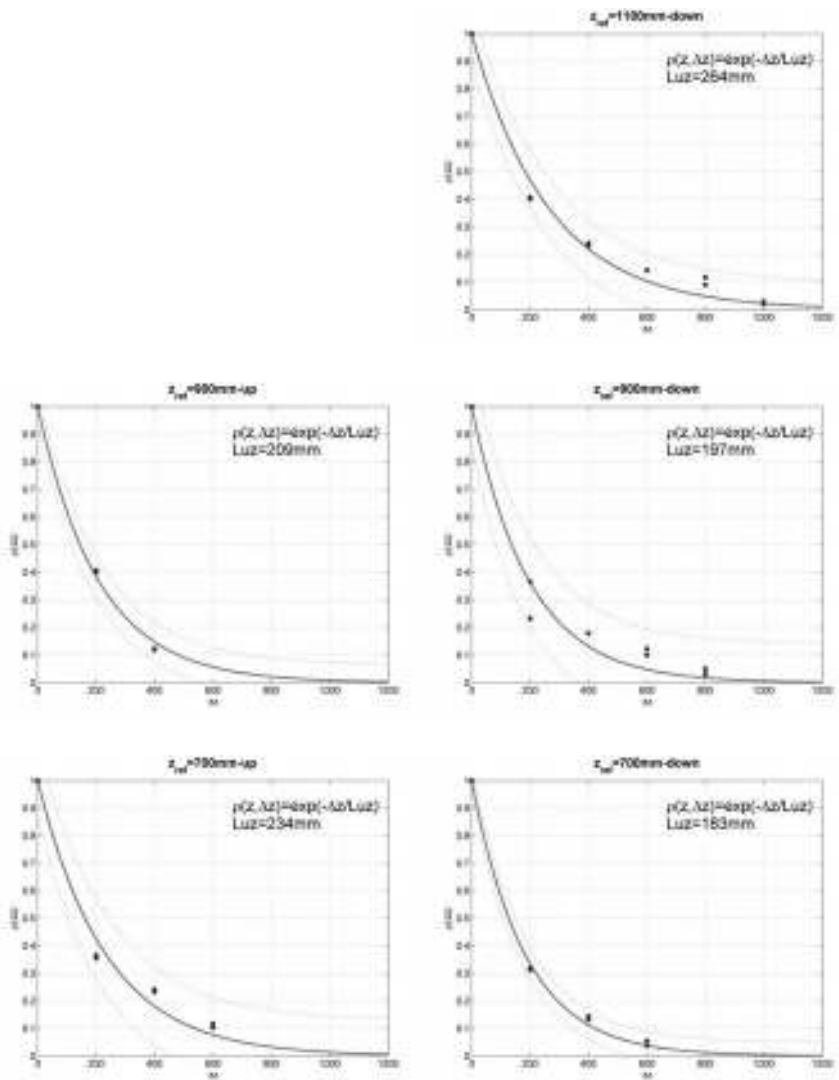
Figure 4.10 Cross-correlation coefficients $\rho_u(z,\Delta z)$ (RAU8+collector)
(continued in the next page)

Upwards   **Downwards**
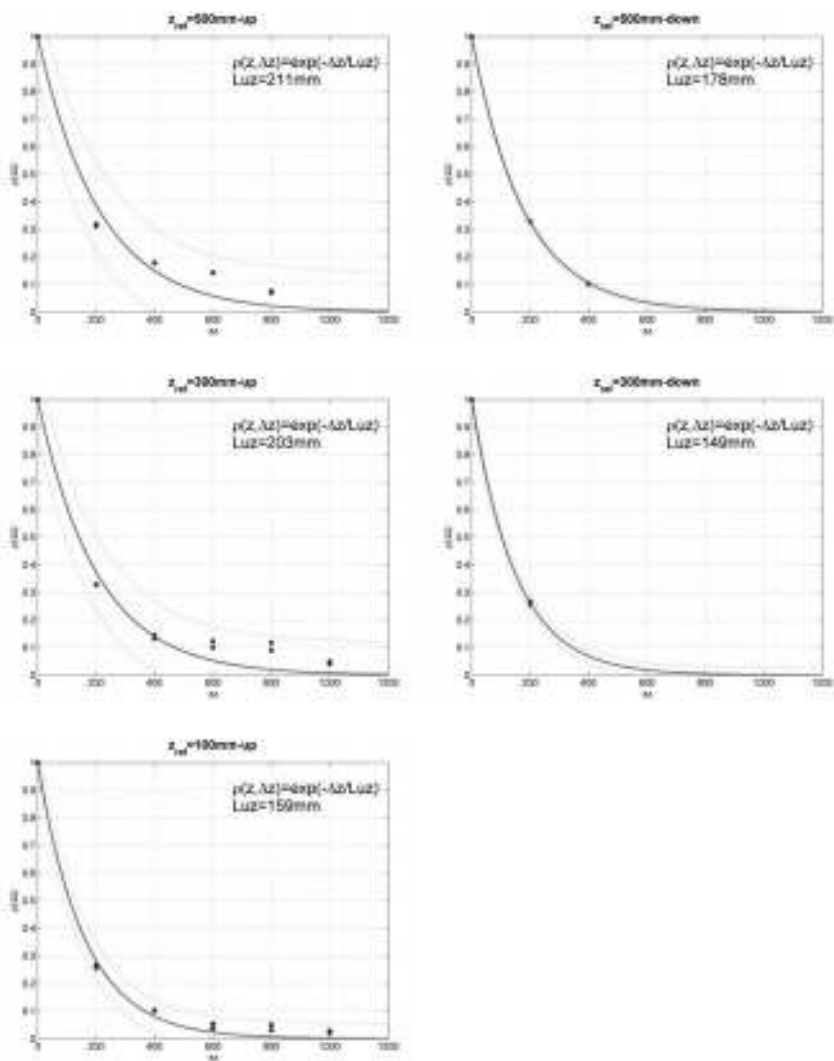
Figure 4.10 Cross-correlation coefficients $\rho_u(z,\Delta z)$ (RAU8+collector)
(continued)

The vertical scale of the u-component L_{uz} will be compared in Chapter 7 to the correlation length of pressures L_{pz}. In view of that, a representative value of L_{uz} is chosen at each level as the average of the values in the upward and downward directions. The final result is:

Table 4.2 L_{uz} (average between upward and downward directions), RAU8+collector

z [mm]	100	300	500	700	900	1100	mean
L_{uz} [mm]	159	176	194	209	203	264	200
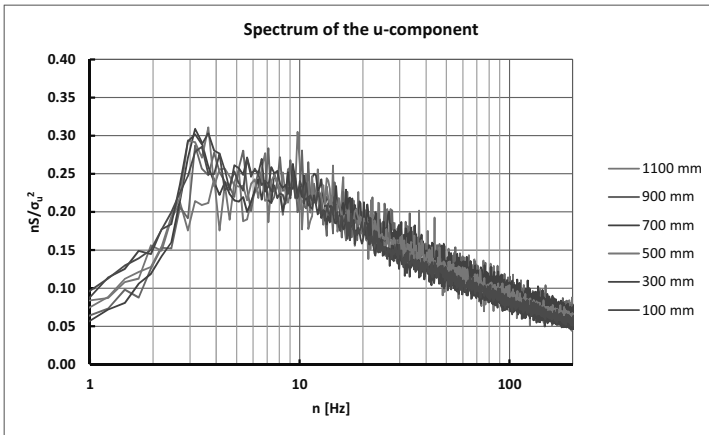
Figure 4.11 Spectra of wind fluctuations in the along-wind direction (u-component) at several levels (RAU8+collector)
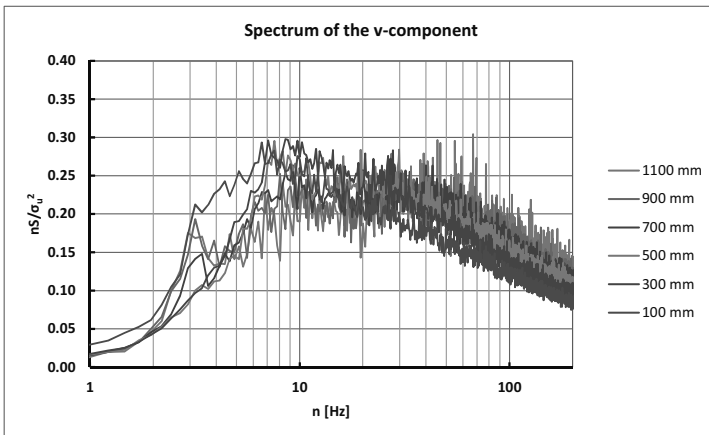
Figure 4.12 Spectra of wind fluctuations in the across-wind direction (v-component) at several levels (RAU8+collector)
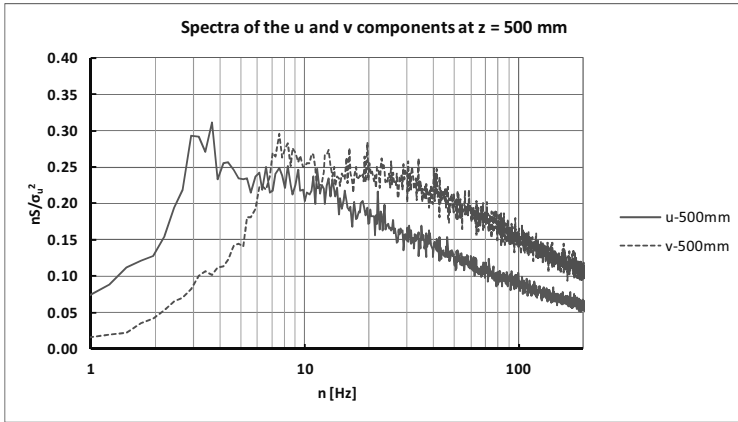
Figure 4.13 Spectra of wind fluctuations in the along-wind (u-component) and across-wind (v-component) directions at 500 mm (RAU8+collector)

The unusual peak at about 3-4 Hz in the u-spectrum in Figure 4.13 (detectable at higher frequencies also in the v-spectrum) is not produced by the slight modification of RAU8 by including the collector. It is difficult to find its precise cause. By the way, it is also recorded in pressure measurements. Once pressures are integrated along the circumference, for example to calculate the lift force, such a peak disappears in the lift spectrum because the two half lifts have negative correlation in that range of frequencies.

In any case, flow disturbances are not surprising in a wind tunnel. They can be produced by the rotor blades, the motor itself, the vibrations of the ground surface and of the wind tunnel walls or they can be electrical disturbances.

The similarity criteria between wind tunnel and full-scale require that the dimensionless parameters (e.g. S_t, Re, I_u,…) assume the same value in the wind tunnel and in full-scale. All the quantities which have the same dimension (for example, length, velocity or time) should be scaled according to the length scale λ_L, λ_V, λ_T, respectively. They represent the ratios between the values in the wind tunnel and the values in full-scale.

Due to the scale of the model, it is not possible in this work to reproduce in the wind tunnel the same Re as in full-scale. Its effects and the use of surface roughness in order to overcome the mismatch are discussed in section 4.4. The similarity of S_t requires that: $\lambda_L = \lambda_V * \lambda_T$.

$$S_t = \left(\frac{nD}{U}\right)_{WT} = \left(\frac{nD}{U}\right)_{FS} \quad \rightarrow \quad \lambda_L = \lambda_V * \lambda_T \tag{4.12}$$

If λ_L is equal to the scale of the model, i.e. 1:1000, the turbulence (in particular L_{ux}) and the boundary layer should be scaled accordingly. In fact, the full-scale value of L_{ux} is an uncertain parameter in itself. Chapter 2 proved that different codes and calculation methods provide more or less similar results in the surface layer, but very different ones in the Ekman layer. Similarly, T_{ux} can be directly calculated from wind tunnel data by equation (4.9); in full-scale it can be derived by Taylor hypothesis. The comparison between L_{ux} (T_{ux}) in the wind tunnel and in full-scale provides an estimation of the approximation, in case the data are used in a structural calculation on 1-km prototype. In any case, Figure 4.14 shows that the turbulence scale reproduced in the wind tunnel, multiplied by the scale factor 1000 (λ_L = 1:1000) is not too far from the Code predictions (even extrapolated at large heights). Instead, the H&D model would suggest much larger integral length scales, which cannot be reproduced in the wind tunnel. This partial simulation of turbulence implies, with regard to the H&D model, a smaller background response and higher dynamic amplification.

In conclusion, by assuming λ_L = 1:1000 and having λ_V = 1:2.05 (U_{FS}(z=H) = 51.31 m/s; U_{WT} (z=H) = 25.07 m/s), it results λ_F = 1/488; λ_T = 488. By looking at Figure 4.14 it can be inferred that it is not too far from the time scale that would be obtained by comparing T_{ux} in the wind tunnel and T_{ux} in full-scale.
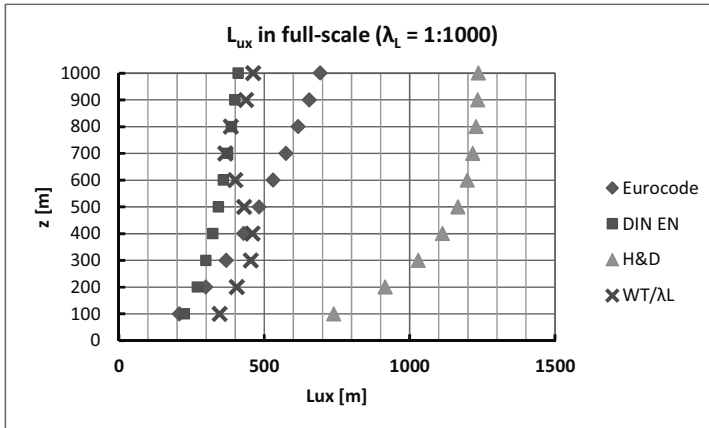
Figure 4.14 Integral length scale of turbulence L_{ux} in full-scale. The violet marks represent L_{ux} in the wind tunnel divided by the length scale factor 1:1000.

The following table summarizes the boundary layer characteristics (RAU8+collector). They are interpolated at levels of pressure measurements for further use.

z [mm]	$U_m(z)/U_{pra}$	$I_u(z)$	L_{ux} [mm]
990	0.927	0.077	459
950	0.920	0.079	448
910	0.914	0.081	440
890	0.910	0.081	429
850	0.903	0.082	396
750	0.884	0.086	377
650	0.862	0.093	387
550	0.838	0.105	402
520	0.830	0.110	425
505	0.826	0.112	429
495	0.823	0.114	432
480	0.818	0.116	437
450	0.809	0.119	440
350	0.775	0.137	448
250	0.741	0.153	419
150	0.694	0.157	379
50	0.602	0.157	322

Table 4.3 Summary: flow characteristics, RAU8+collector

Figure 4.15 RAU8+collector (WiSt wind tunnel)

Last but not least, some measurements are also done in empty tunnel. These are the characteristics of the flow:

- $U(z) \approx U_{pra}$ (uniform flow, apart from wall effects);
- $I_u \approx 5\%$
- $L_{ux} \approx 3\text{-}4$ cm (isotropic turbulence), by fitting Von Karman spectrum.

4.1.3   Pressure measurement technique

The wind tunnel facilities allow to measure 92 pressures simultaneously. The measurement chain consists of pressure sensors, amplifiers and analogic-digital (A/D) converters. The pressure sensors are four-active-element piezoresistive bridges. When a pressure is applied, a differential output voltage, proportional to that pressure, is

produced. Differential sensors provide a differential voltage proportional to the pressure differential between two ports. One port measures the wind pressure on the model, the other one is connected to the static pressure of the Prandtl tube. Two different pressure sensors are used:

- Type 1:   Honeywell 170 PC
                 Measurement range ± 35 mbar
- Type 2:   AMSYS 5812-0001-D-B
                 Measurement range ± 10.34 mbar

They are calibrated by using different factors, so that 5 mbar corresponds to 5 V for the type 1 (the most sensitive) and 5 mbar corresponds to 1 volt for type 2. A static calibration is performed to find pressure to voltage relations for each pressure sensor by using a Betz manometer, which allows to load the system with a known pressure.
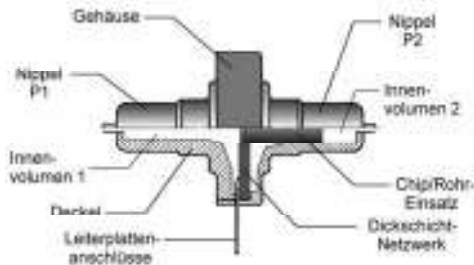
Figure 4.16 Pressure sensor Honeywell 170PC

Figure 4.17 Pressure cell AMSYS

The pressure cells AMSYS also incorporate the amplifiers. Instead, the amplifiers for the type 1 are external and independent from one another (Figure 4.18). Then, all the analogic signals are converted into a digital signal by the A/D converters. Eight cards with sixteen A/D each are available in the laboratory. The pressures are scanned in a sample-and-hold modus, which produces simultaneous sampling of the measurements. A sampling frequency of 2 kHz was selected for the measurements. The software used for recording is SBench 5.0.

Figure 4.18 External amplifiers for pressure sensors type 1

The pressure taps on the model surface are connected to the pressure sensor by a plastic tube. Special 1.5 m long tubes are used in this work, due to the dimension of the model (see section 4.2). The usual, optimized tubes of the laboratory are 60 cm in length, so they could not be used. The 1.5 m long tubes were used in previous work by Neuhaus (2009). The recorded pressures with the long tubes are corrected by a transfer function, in order to remove the dynamic effect produced by the tubes. Neuhaus (2010) explains how it is calculated. The response spectrum of the signal by using the long tube is compared to the response spectrum obtained by applying the sensor directly on the surface of a model. The latter is considered the right measurement. In fact, the transfer function is not evaluated in absolute terms, but relatively to the right measurement of the signal. The comparison shows that the tube tends to amplify the frequencies lower than 65 Hz (with maximum at about 30 Hz) and damps the frequencies higher than 65 Hz. At 200 Hz there is a damping of 50%. Therefore, the transfer function for the amplitude could be derived in the frequency domain. As regards the phase shift, it resulted to be a linear function of the frequency. Being k the slope of this linear function, the output of the pressure tubes has a constant time delay equal to $k/2\pi$. It is about 0.005 s and it is constant for each frequency, therefore no correction to the phase is applied.

The effective range in which the digital filter applied to the pressure corrects the signal is up to 200 Hz. Therefore, even if the sampling frequency is 2000 Hz, 200 Hz is the cut-off frequency. After that, the frequencies are damped. The reason for which such a high sampling frequency was chosen, despite the relatively lower cut-off frequency, is the higher accuracy in the time domain even for high-frequency (e.g. 200 Hz) fluctuations.

The time histories of pressures are acquired for a duration of $N/f_{sampl} = 2^{18}/2000 = 131.072$ s. 2^{18} is the number of time steps (N) in each recorded signal.

4.2   Model of the solar updraft tower

The model of the Solar Updraft Tower for wind tunnel tests is a circular cylinder of 1 m in height and 15 cm in diameter, made of plexiglass. The aspect ratio is about 1:7 (H/D = 6.7). The dimensions of the model are chosen in order not to have a too high blockage ratio. On the transversal plane the model occupies an area of $1*0.15m = 0.15$ m^2, while the wind tunnel cross-section is $1.8*1.6m = 2.88$ m^2. The ratio between the two values gives a blockage of 5%, which can be accepted without any correction of results. In scale 1:1000, the model represents a 1-km tall prototype.
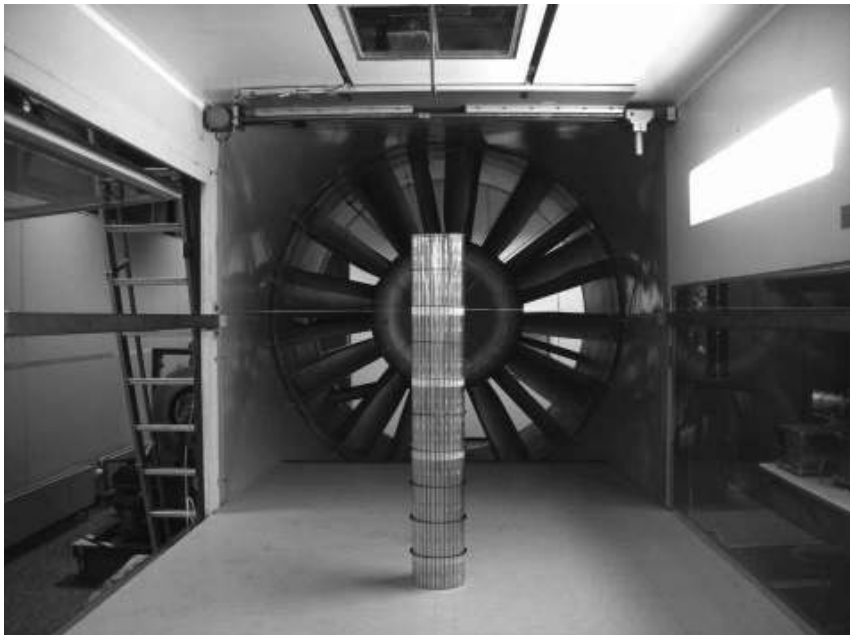
Figure 4.19 Wind tunnel model of the Solar Tower

Even though the real shape of the tower, according to the pre-designs mentioned in Chapter 1, may turn into a hyperboloid at lower levels, the wind tunnel model is a circular cylinder. This shape, which simplified the manufacturing, allows to evaluate the aerodynamic effects without any loss in generality. Moreover, the model is rigid and in order to avoid vibrations two wires[3] at 800 mm fix it at the wall of the wind tunnel.The tower model is equipped with 342 pressure taps, placed at several levels along the height and in the circumferential direction, in order to investigate vertical and horizontal cross-correlations. Both external and internal pressures are measured at each level. The external pressure taps are placed at 17 levels (990-950-910-890-850-750-650-550-520-505-495-480-450-350-250-150-50 mm) at an angular distance of 20° (≈ 26 mm) at each level. The internal pressure taps in the tip region are 9 per level (angular distance = 45°) at 990 and 950 mm. Along the height (at 850-750-650-550-520-450-350-250-150-50 mm) they are 2 per level, at 0° and 180°. This is better shown in the drawing of the model (Drawing 2 on page 125).

The wind tunnel scale of the model and of the boundary layer properties reduces by around three orders of magnitude the Reynolds number from full-scale to wind tunnel conditions (Re = UD/v; $Re_{,FS} \approx 50*150/1.5*10^{-5} = 5*10^8$; $Re_{,WT} \approx 30*0.15/1.5*10^{-5} = 3*10^5$). Because of that, surface roughness (ribs) is applied along the model, in order to reproduce the same state of the flow as in full-scale. The target condition is described in the VGB guideline for cooling towers (curves K1.5-1.6). The final choice for the surface roughness – as it will be proved in section 4.4 – is ks/D = 0.25mm/150mm, being k the thickness of the ribs. The ribs are at an angular distance of 20°, i.e. in between two pressure taps (Figure 4.20). In any case, ribs are only applied in the scaled wind tunnel model because of Re effects, while the surface of the tower in full-scale conditions must be smooth in order to reduce the drag (Figure 3.10, Niemann,2009) .

The collector roof (4 km in diameter in full-scale) is also modeled in the wind tunnel. It is a very smooth panel in HDF, ideally representing the smooth glass surface encountered by the incoming wind (Figure 4.4). Its function in the wind tunnel is only the creation of a two-phase wind profile. The efflux inside the tower is not reproduced by means of the collector, but artificially by using the pressure difference outside-inside the wind tunnel. In fact, one of the major difficulties in the design of the model was the creation of the efflux inside the tower, due to the presence of 342 tubes inside the cylinder, which connect each measuring point on the shell to the pressure

---

[3] The wires are too thin to modify the flow condition and disturb the measurements.

transducers. The presence of such a large number of tubes inside the tower would affect the internal flow. Moreover, the efflux had to be created somehow.

After having discussed several possibilities, it was decided to use a second circular cylinder, having a smaller diameter, to be placed inside the main cylinder representing the tower. This configuration of a pipe in a pipe allows placing all the tubes for measuring the pressures in the small cavity between the two cylinders. The two cylinders are glued together at the top through a union ring, as it can be seen in Figure 4.20.

Figure 4.20 Tube-in-a-tube solution.

The outer cylinder is shorter in length than the inner one, so that the pressure tubes can come out of the model (below the wind tunnel) when the outer cylinder ends. As said, the efflux inside the tower is created by the pressure difference inside-outside the wind tunnel. In addition, a ventilator is placed below the model - at the opening of the inner cylinder - in order to achieve higher efflux velocities, if needed. Below the ventilator there is a moving plate which allows to regulate the opening, so to achieve the desired air capacity for the efflux. In addition, tests are also made in no-efflux conditions (outage condition), by closing the opening below the ventilator. Even though in reality the value of the efflux velocity during operation of the power plant depends on several conditions (e.g. the temperature rise in the collector, the pressure drop at the turbines

etc.), a quite realistic condition for the design is achieved in the wind tunnel when the velocity of the efflux inside the tower is around one half of the wind tunnel velocity.

The peculiarity of the model is the presence of circular ring beams applied along the height (Figure 4.21). Tests are performed both without and with rings. The size and the number of the rings resulted to be influencing parameters of the flow around the tower. Ring beams of two sizes are tested, they are identified by the prefix SR and KR as follows:

- SR = big rings (usually called simply rings in the following): external diameter 164 mm, internal diameter 150 mm, width (w) = 7 mm → w/D = 7/150 = $4.67*10^{-2}$;
- KR = small rings: external diameter 157 mm, internal diameter 150 mm, width = 3.5 mm→ w/D = 3.5/150 = $2.33*10^{-2}$;

They represent the highest and one of the lowest limits in the design of a solar tower. They are placed along the height at the reference distance of 10 cm in the wind tunnel scale (10 rings). Due to their strong effect on the flow, tests have also been repeated with 5 rings at a distance of 20 cm and 7 rings at a distance of about 14 cm (see section 4.3).

Figure 4.21 Ring beams along the height of the cylinder.

Figure 4.22 The support system for installation
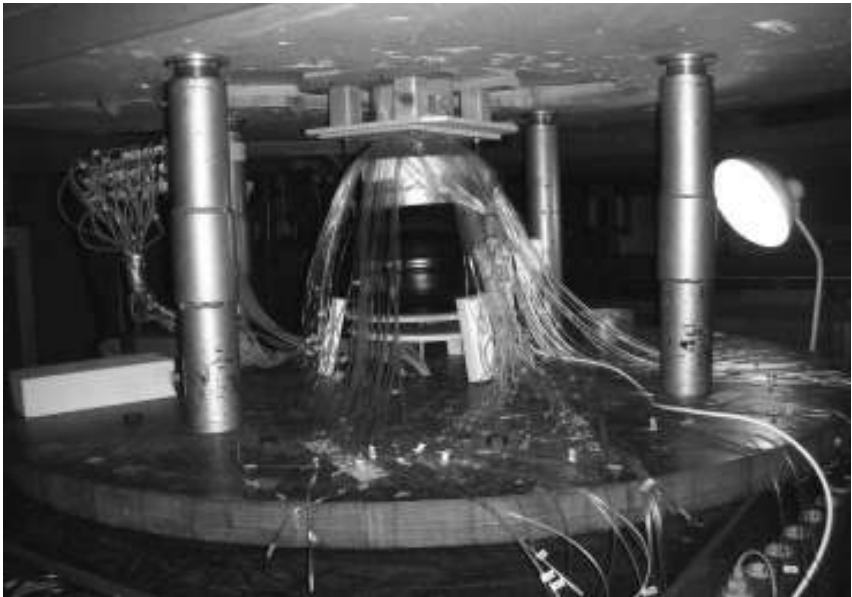
Figure 4.23 Complete installation

a)
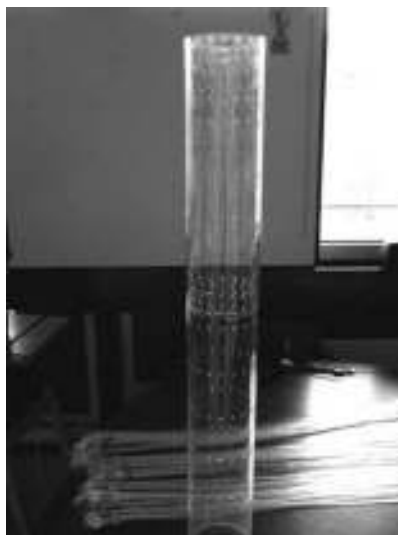
b)

c)

d)

e)

Figure 4.24 Model under construction: a) inner cylinder; b) outer cylinder; c) outer cylinder during application of pressure tubes; d) detail of the tip: the two cylinders are glued together; e) pressure taps and references on the outer cylinder

DRAWING n.2 Wind tunnel model of the solar updraft tower

TIP REGION
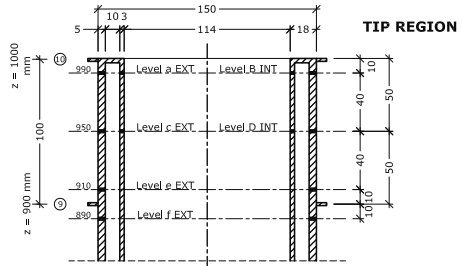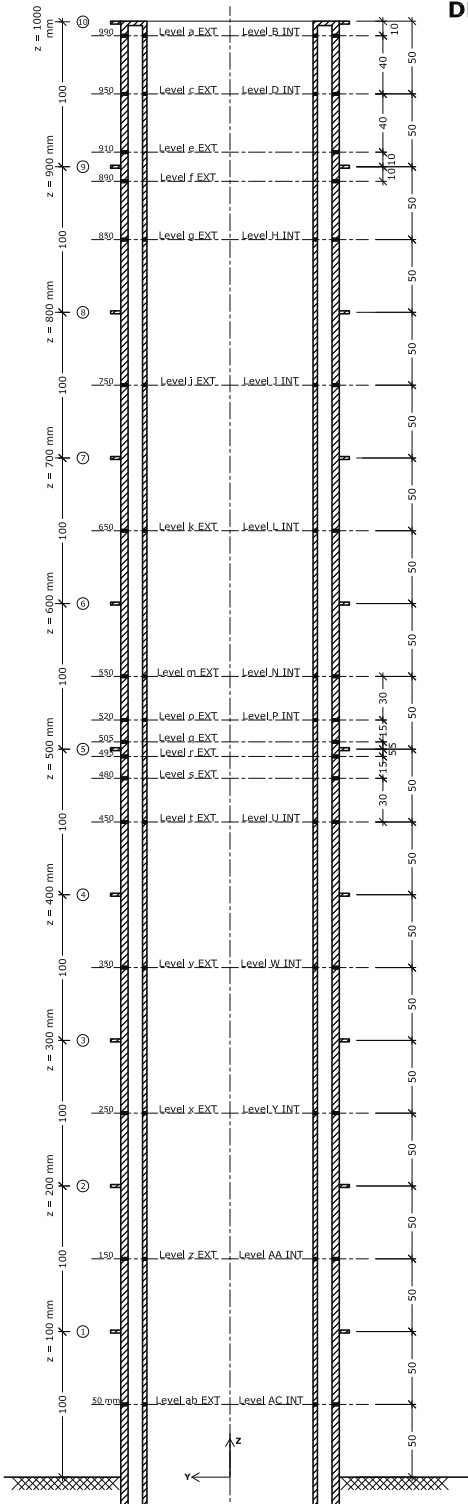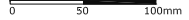
HORIZONTAL DISTRIBUTION OF PRESSURE TAPS

EXTERNAL PRESSURES:
Levels:
a-c-e-f-g-i-k-m-o-q-r-s-t-v
x-z-ab
18 pressure taps for each level
17 x 18 = 306
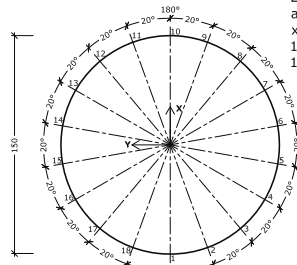
INTERNAL PRESSURES:
Levels: B-D
8 pressure taps for each level
2 x 8 = 16
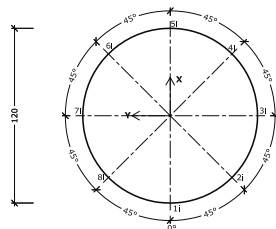
INTERNAL PRESSURES:
Levels: H-J-L-N-P-U-W-Y-AA-AC
2 pressure taps for each level
10 x 2 = 20
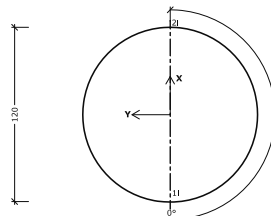
DETAIL OF THE STIFFENING RING

VERTICAL DISTRIBUTION OF PRESSURE TAPS

WiSt
Boundary layer wind tunnel
Ruhr-University Bochum
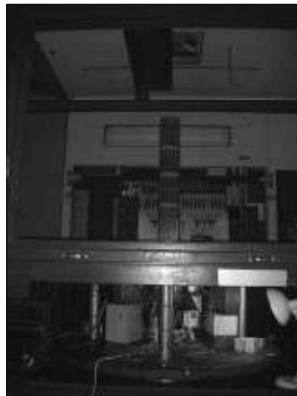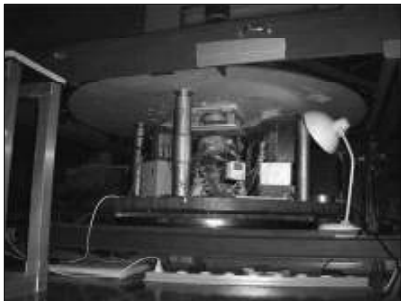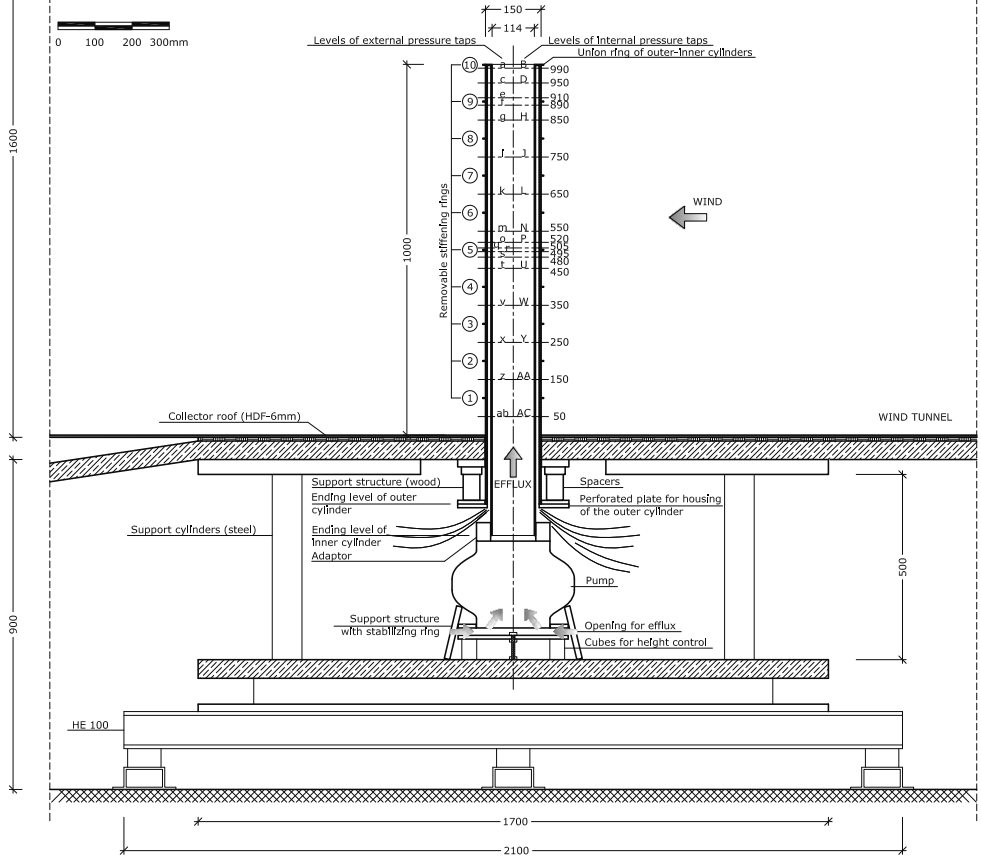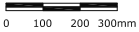
4.3   **Outline of the experiments**

The model of the tower without rings is the reference case to identify the flow condition and study the aerodynamic of the flow around a circular cylinder H/D = 7, immersed in boundary layer flow. Most of the studies in literature refer to sub-critical Re; in addition, the aspect ratio and the characteristics of the boundary layer influence the results (Chapter 3). Therefore, before investigating the effect of the ring beams, it is necessary to have a deep knowledge of the flow around the circular cylinder without ring beams. Because of that, each test is always made twice: once with the rings, once without them. In addition, several conditions, in terms of surface roughness, flow velocity, boundary layer, efflux, number of rings, size of rings are tested. The nomenclature used in the campaign is described in the following:

1. Boundary layer:
    - T1 = boundary layer flow RAU8 + collector;
    - T3 = uniform flow (empty tunnel);

2. Surface roughness conditions on the outer surface of the model:
    - R0 = smooth cylinder;
    - R1 = ribs at a spacing of 20°, ks = 0.250 mm (ks/D = $1.67*10^{-3}$);
    - R2 = ribs at a spacing of 10°, ks = 0.250 mm (ks/D = $1.67*10^{-3}$);
    - R3 = ribs at a spacing of 20°, ks = 0.375 mm (ks/D = $2.50*10^{-3}$);
    - R4 = ribs at a spacing of 10°, ks = 0.375 mm (ks/D = $2.50*10^{-3}$);
    - R5 = ribs at a spacing of 20°, ks = 0.500 mm (ks/D = $3.33*10^{-3}$);

    The surface roughness is always made of ribs. This choice is motivated by simplicity of manufacturing and consolidated experience on cooling towers (VGB, 2010).

3. Wind tunnel velocity: for practical reasons, the wind tunnel velocity to be used in each test is identified by the number of rounds per minute (rpm) of the fan. Depending on the static pressure and on the temperature during measurements, the density of air and consequently the velocity may change. A small difference in the measured velocity corresponding to the same rpm is also noted in presence or absence of boundary layer (RAU8 or empty tunnel) and in presence or absence of efflux in the chimney. Approximately, it results:
    - 100 rpm; $U_{pra} \approx 3$ m/s
    - 200 rpm; $U_{pra} \approx 5$ m/s

- 400 rpm; $U_{pra} \approx 8$ m/s
- 600 rpm; $U_{pra} \approx 12$ m/s
- 800 rpm; $U_{pra} \approx 16$ m/s
- 1000 rpm; $U_{pra} \approx 20$ m/s
- 1250 rpm; $U_{pra} \approx 25$ m/s
- 1400 rpm; $U_{pra} \approx 27$ m/s

1400 rpm is the highest velocity which was used, although the capacity of the wind tunnel was even higher, up to 1500 rpm. However, the resulting pressure at higher wind speed would have exceeded the sensitivity range of the pressure transducers type 2, which could not be regulated.

The low velocity range 100-200-400 rpm is tested only on the smooth cylinder, in the hope to reach subcritical conditions (laminar separation). However, at very low speed the wind tunnel velocity was not always stable.

4. Efflux condition:
    - EF0 = no efflux;
    - EF1 = efflux;

The velocity of the efflux is regulated at about one half of the wind tunnel velocity (section 4.4.1).

5. Effect of ring beams:
    - SR0 = no rings;
    - SR1 = ten big rings along the height, equally spaced at a distance of 10 cm;
    - SR7 = seven big rings along the height, equally spaced at a distance of 14 cm (15 cm in the two lowest compartment);
    - SR5 = five big rings along the height, equally spaced at a distance of 20 cm;
    - KR1 = ten small rings along the height, equally spaced at a distance of 10 cm;
    - KR7 = seven small rings along the height, equally spaced at a distance of 14 cm (15 cm in the two lowest compartment);
    - KR5 = five small rings along the height, equally spaced at a distance of 20 cm;

The wind tunnel equipment allows to measure maximum 92 pressures simultaneously. However, some sensors where out of use at the time of the tests, therefore no more than four levels (with 18 pressure taps each, on the external surface) could be measured at the same time, plus other positions at proper convenience. In the first plan of the experiments, it was decided to measure all the correlations of the 342 pressure taps in the basic conditions: T1(&T3)-SR0&SR1-EF0(&EF1)-R1, where the nomenclature out of brackets had the priority. In order to measure all the cross-correlation, the pressures had to be divided into groups and each group had to be measured with all the other ones. However, due to the appearance of the new phenomenon described in Chapter 5 – during the second set of measurements (May 2011) – the original plan of experiments was revised. Different experimental conditions had to be tested for a deeper understanding of the phenomenon: not only SR0 and SR1, but also SR5, SR7, KR1, KR5, KR7; not only R1, but also R0-R2-R3-R4-R5. Consequently, the complete correlation field could not be measured, but only the most important pressures were measured simultaneously.

In summary, the following series of measurements were defined (only pressures on external surface and complete circumference are mentioned):

- MS01: levels z = 990-950-910-890 mm;
- MS02: levels z = 910-890-850-750 mm;
- MS03: levels z = 750-650-550 mm;
- MS04: levels z = 550-520-505-495 mm;
- MS05: levels z = 505-495-480-450 mm;
- MS06: levels z = 450-350-250-150 mm;
- MS07: levels z = 250-150-50 mm + vertical at 0°;
- MS08: levels z = 990-950-750 mm;
- MS09: levels z = 550-450 mm;
- MS10: levels z = 450-50 mm + vertical at 80°;
- MS28: verticals at 20°, 120°, 180°, 300°;
- MS30/MS32: levels z = 950-850-750-650 mm;
- MS31: levels z = 950, 890, 750, 650 mm;
- MS33: levels z = 950-910-890-850 mm;
- MS34: levels z = 650-550-520-480 mm;

The experimental campaign was articulated in the following four sets, which became necessary as the investigation was proceeding:

Set n.1 (April 2011):

Turbulence setting:	T1
Rings:	SR0
Efflux:	EF0/EF1
Surface roughness:	R1
Wind tunnel velocity (rpm):	600/800/1000/1250/1400
Measurement series:	MS01/02/03/04/05/06/07/08/09/10/28;

Set n.2 (May 2011):

Turbulence setting:	T3
Rings:	SR0/SR1
Efflux:	EF0/EF1
Surface roughness:	R1
Wind tunnel velocity (rpm):	0600/0800/1000/1100/1250/1400
Measurement series:	MS01/02/04/05/08/09;

Set n.3 (October 2011):

Turbulence setting:	T1
Rings:	SR0/SR1/SR7/SR5/KR1/KR7/KR5
Efflux:	EF0/EF1
Surface roughness:	R0/R1/R2/R3/R4/R5
Wind tunnel velocity (rpm):	0600/0800/1000/1250/1400
Measurement series:	MS30/31;

Set n.4 (December 2011):

Turbulence setting:	T1
Rings:	SR0/SR1
Efflux:	EF0/EF1
Surface roughness:	R1/R3
Wind tunnel velocity (rpm):	0600/0800/1000/1250/1400
Measurement series:	MS32/33/34;

4.4   Preliminary results on the circular cylinder

In this section, preliminary results on the cylinder without rings are presented.

4.4.1   Velocity of efflux

The tests are performed in two conditions: open efflux (EF1) and closed efflux (EF0). The latter represents the condition of out of use of the power plant. For many aspects, EF0 is more dangerous than EF1. In particular, the tip effect in EF0 is stronger. In the condition of open efflux, the tests are performed with only one efflux velocity. The influence of different efflux velocities on the pressures is not investigated. The efflux velocity which acts in EF1 is around one half of the undisturbed flow velocity (U_{pra}). This is achieved in the experiments by defining a proper opening below the model, through the position of the wooden plate under the ventilator (Figure 4.23).

The efflux velocity was measured during a preliminary test by a second Prandtl tube placed inside the chimney close to the tip. Figure 4.25 shows the ratio between the Prandtl velocity U_{pra} and the efflux velocity at different U_{pra}, corresponding to a certain position of the wooden plate used in all the experiments.
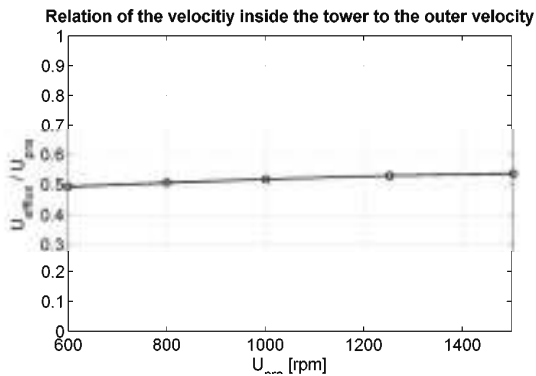
Figure 4.25 Efflux velocity

The effect of the efflux on the pressures is evident in the tip region, while it is not influent at lower levels. Figure 4.26 shows the modification of the external pressures at z/H = 0.95 due to the efflux. In EF1 the lateral suction is reduced and the separation point is shifted downstream. Moreover, the increase in suction in the wake of the cylinder, around $\varphi = 150°$ in EF0, due to tip vortices as explained in Chapter 3, is missing EF1. It is then confirmed (Gould et al., 1968) that the efflux displaces the tip vortices. The peak of pressure in the wake due to the entrainment of the flow is also leveled out in EF1, as expected.
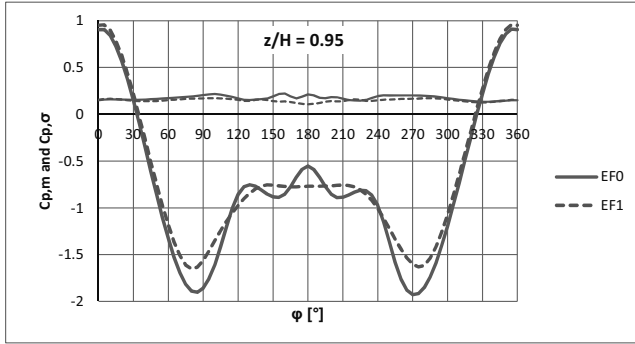
Figure 4.26 $C_{p,m}$ and $C_{p,\sigma}$ in the tip region ($z/H = 0.95$): influence of efflux.

4.4.2 Internal pressure

The internal pressure coefficient C_{pi} is calculated with reference to the velocity pressure at $z = H$. The pressure coefficient is higher is case of efflux, both in the mean as well as in the rms. Its value is approximately constant along the height and along the circumference. Only close to the tip it exhibits some variation. In any case, the value of C_{pi} is lower than the typical value for cooling towers ($C_{pi} = -0.5$ in VGB, 2010).
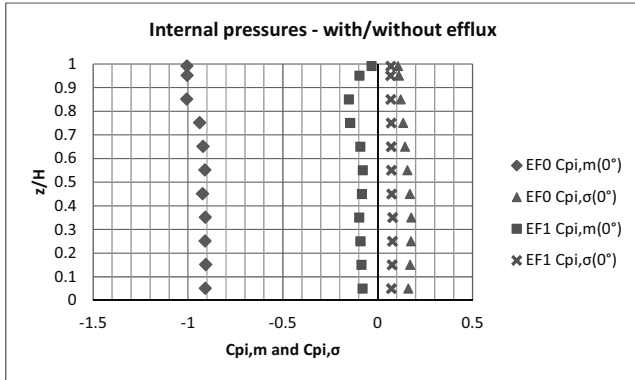
Figure 4.27 Internal pressures – spanwise varation

In absence of efflux, the internal pressure is somewhat higher at $z/H = 0.99$, $\varphi = 180°$, probably due to an entrainment of fluid inside the cylinder (Figure 4.28). However, the level $z/H = 0.95$ is already unaffected and the internal pressure does not show any circumferential variation.

132
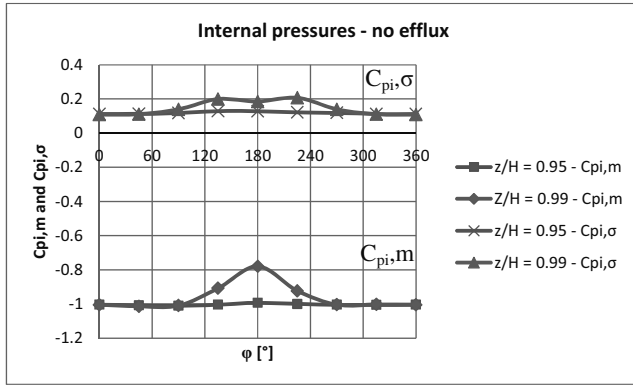
Figure 4.28 Internal pressures – circumferential varation

4.4.3 **Reynolds effects on the smooth and rough cylinder**

As mentioned before, due to the reduced scale of the model in the wind tunnel, the Reynolds number is around three orders of magnitude lower than in full-scale (Re = UD/ν; $Re_{,FS} \approx 50*150/1.5*10^{-5} = 5*10^{8}$; $Re_{,WT} \approx 30*0.15/1.5*10^{-5} = 3*10^{5}$). Because of that, surface roughness (consisting of ribs) is applied to the model. The effect of surface roughness on the circular cylinder in the wind tunnel is studied with regard to the following key parameters:

- $C_{D,m}$ = mean value of the drag coefficient;
- $C_{D,\sigma}$ and $C_{L,\sigma}$ = rms values of the drag and lift coefficients;
- $C_{p,min}$ = minimum pressure (lateral suction);
- $C_{p,b}$ = base pressure;
- $C_{p,b}$-$C_{p,min}$ = pressure rise to separation or pressure recovery;

Further comments concern the Strouhal number (S_t) and the angle of separation.

At first, the results are presented for the level z/H = 0.65, which is out of the tip region, approximately in the two-dimensional normal range and available in most of the tests. Then, the spanwise variation is considered. The tests are in turbulent boundary layer (T1), unless differently specified, and only results in EF0 are reported. The Reynolds number is uniquely defined with respect to the local velocity at the tower top (at z = H). The dependency of air viscosity on the temperature is neglected; the value $\nu = 1.5*10^{-5}$ at 20°C is used.

Figure 4.29 plots the drag coefficient distribution at z/H = 0.65 for different Reynolds numbers (i.e. different wind tunnel velocities) and for different surface roughness conditions. The blue curve (R0) refers to the smooth cylinder (according to the nomenclature in section 4.3). It can be seen that the flow around the smooth cylinder is at first in the critical state, characterized by the fall of C_D until the minimum at $Re_{cr} \approx$ $1.9*10^5$. After that, the horizontal plateau is typical of the supercritical range for smooth cylinders, according to Roshko's classification (Chapter 3). On the rough cylinder in turbulent boundary layer flow (T1), for any type of surface roughness (R1-R5) the state of the flow is already beyond the critical Re. This is not only due to the surface roughness, but it is also enhanced by the turbulence of the flow. In fact, it is interesting to compare these results to the black dashed line in the figure, which is the only one referring to uniform flow and lower I_u (empty tunnel). However, due to lack of data, it is at z/H = 0.55. In any case, it can be seen that at high (effective) Re the effect of turbulence on the drag coefficient is limited, while it is stronger at low Re: in empty tunnel the flow around the rough cylinder R1 undergoes the critical state at Re $\approx 1.5*10^5$. Moreover, the figure shows a certain similarity between the curves R2-R3 and R4-R5 for the whole range of Reynolds numbers. R2 and R4 have, with respect to R3 and R5, a double number of ribs with smaller height. Therefore, within a certain limit, the height of the rib and their distance act in the same manner.
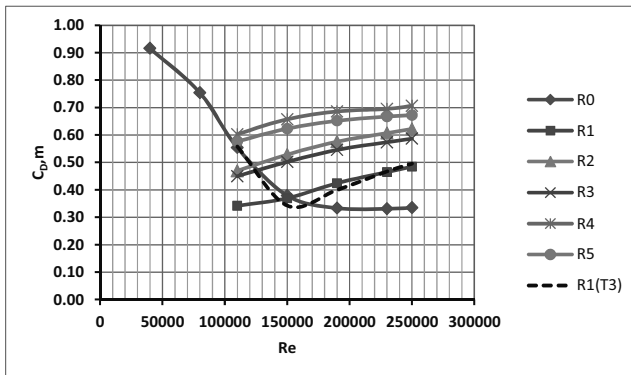
Figure 4.29 Drag coefficient vs Re (z/H = 0.65, R0-R5, T1 unless differently specified)

The rms values of both drag and lift coefficients on the rough cylinder do not show a large variability with Re (Figure 4.30 and Figure 4.31). The along wind fluctuations tend to increase with higher roughness. It is not surprising that in empty tunnel (black dashed line) the force fluctuations, especially in the along wind direction ($C_{D,\sigma}$), are lower, because turbulence is lower.
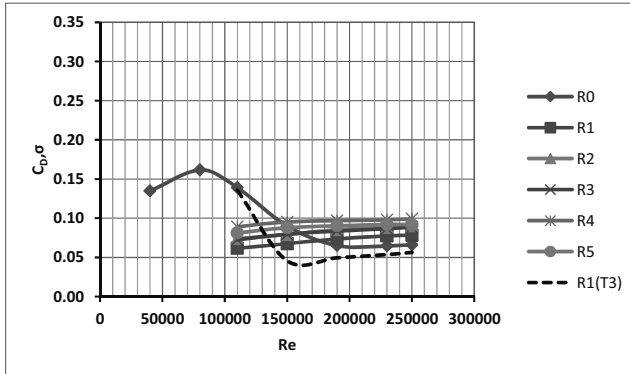
Figure 4.30 Rms drag coefficient vs Re (z/H = 0.65, R0-R5, T1 unless differently specified)
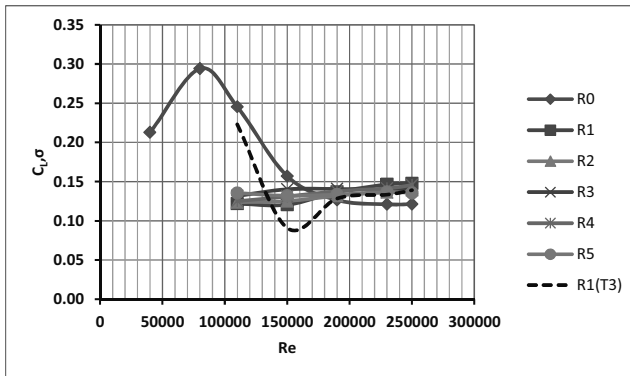
Figure 4.31 Rms lift coefficient vs Re (z/H = 0.65, R0-R5, T1 unless differently specified)

Figure 4.32, Figure 4.33 and Figure 4.34 complete the set of information by plotting the pressure recovery, the wake pressure and the minimum pressure, respectively.

On the smooth cylinder (R0) at $Re_{cr} \approx 1.9*10^5$, the blue curve reaches the maximum base pressure (the lowest wake suction) and the minimum pressure at the flanges. This corresponds to the largest value of pressure recovery, which is associated to the minimum drag. After that, the horizontal plateau in the supercritical range is confirmed. All of that is in accordance to literature (Chapter 3).

On the rough cylinder, the positive rise in terms of $C_{D,m}$ (Figure 4.29) corresponds to a decrease in the pressure recovery. It is due to the progressive increase in wake suction (which rises the drag) and decrease in lateral suction. In fact, according to Güven et al. (1980), the overall effect of surface roughness on the pressure distribution is best seen in the behaviour of the pressure rise to separation or pressure recovery $C_{p,b}$-$Cp_{,min}$. Such a parameter, which includes both variations of the base and minimum pressures

and shows opposite trend with respect to the drag, is especially important because it is almost insensitive to the effects of influencing parameters such as tunnel blockage, aspect ratio and even free-end effects. Furthermore, as explained by Güven et al. (1980), in the supercritical Reynolds number range, $C_{p,b}$-$Cp_{,min}$ decreases with increasing Re for a given relative roughness and decreases with increasing relative roughness for a given Re number. The incremental changes in $C_{p,b}$-$Cp_{,min}$ decrease with increasing roughness. Such a pressure difference is closely related to the characteristic of the boundary layer prior to separation and it is the reason for its strong dependence on surface roughness. All of that is confirmed by Figure 4.32.

The black curves of the rough cylinder in empty tunnel (R1-T3) confirm the critical Re at $\approx 1.5*10^5$. This represents a point of maximum of the pressure recovery. In fact, in the critical range before Re_{cr} the pressure recovery is a small value due to the early laminar separation. At high Re, the turbulence intensity has a negligible effect on the state of the flow, as it was shown by C_D.
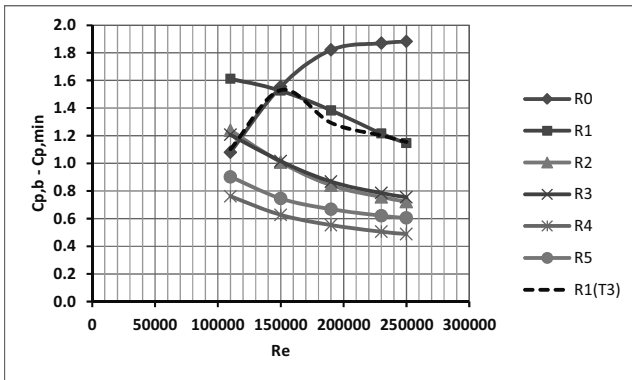
Figure 4.32 Pressure recovery (z/H = 0.65, R0-R5, T1 unless differently specified)
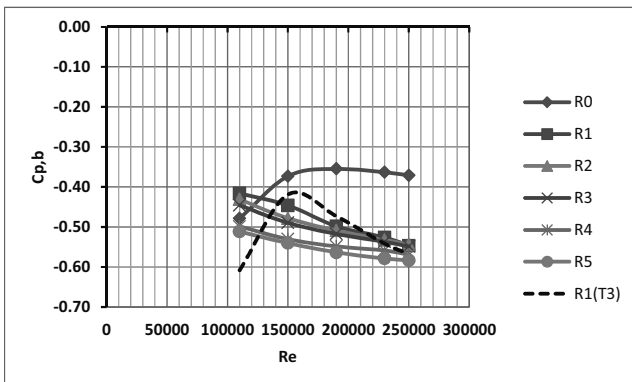
Figure 4.33 Base pressure (z/H = 0.65, R0-R5, T1 unless differently specified)
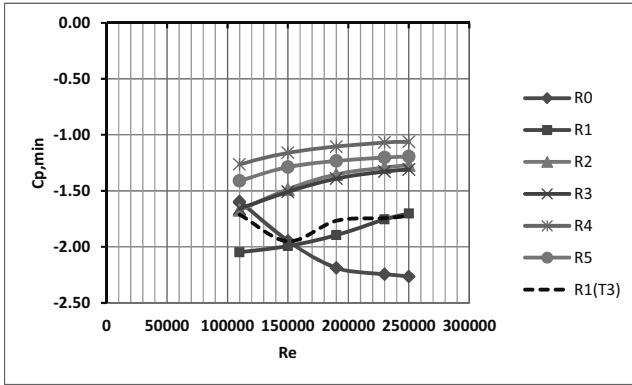
*Figure 4.34
Minimum pressure
at the flanges (z/H =
0.65, R0-R5, T1
unless differently
specified)*

The following figures show an overview of the variation of the mean pressure distribution with Re and surface roughness. On the smooth cylinder (R0) in Figure 4.35, it is clear that the increase in wind tunnel velocity progressively increases lateral suction and decreases wake suction. The blue and the red curves in the figure lie in the critical range (which is characterized by the fall in the drag). The critical condition is reached at first by the green curve (Re = $1.9*10^5$) and all the other curves collapse on that one, due to the horizontal plateau in the supercritical range. On the rough cylinder R1 (Figure 4.36), instead, the progressive increase in the Re is marked by decrease in lateral suction, accompanied by upstream movement of the separation point and increase in wake suction.
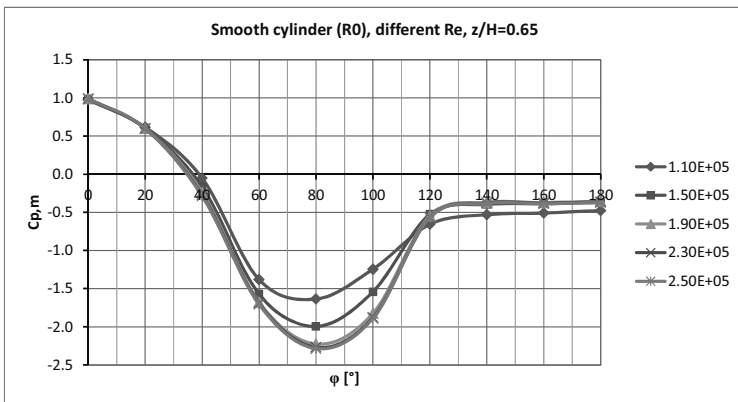
*Figure 4.35 Mean pressure distribution as a function of Re on the smooth cylinder
(z/H = 0.65)*
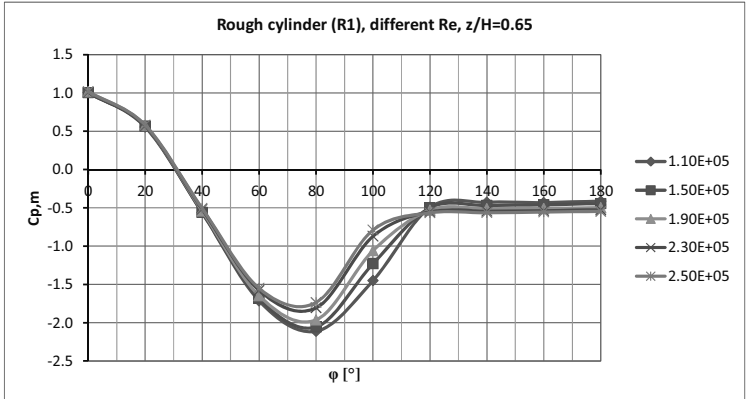
Figure 4.36 Mean pressure distribution as a function of Re on the rough cylinder (z/H = 0.65)

In time, the position of the separation point is not stationary, but it fluctuates around the average position, in full-scale as well as in the wind tunnel. The function of the ribs should not be to force the separation at precise locations, but to promote turbulent transition of the boundary layer. A turbulent boundary layer is able to overcome larger adverse pressure gradients and therefore separation is retarded. However, it can be argued whether such oscillations of separation are forced or prevented by the presence of the ribs on the wind tunnel model. Figure 4.37 clarifies that with small surface roughness (e.g. R1) the position of separation is not particularly fixed by the presence (and the specific distribution) of the ribs. The figure highlights the spatial oscillation of the separation point in a short time window. The roughness conditions R4 and R5 resulted, from this point of view, more invasive. In fact, it is not recommended to force the Reynolds regime by using high surface roughness. Ribeiro (1991) wrote: "the larger the relative roughness, the lower the Reynolds number with which the ultra-critical regime is established, but the greater the differences observed in this regime, between the parameters measured on the rough circular cylinder and those observed on smooth circular cylinders". For this reason, the surface roughnesses R4 and R5 are discarded for further studies on the tower.

The Strouhal number decreases on the rough cylinder (R1) from 0.22 to 0.20 as the transcritical conditions are approached (Figure 4.38) and the peak becomes narrower. Such a decrease in the Strouhal number is related to the upstream movement of the separation point. The lowest S_t on the rough cylinder (R1) at the highest Re ($2.5*10^5$) is associated to the a wider wake, as shown in Figure 4.36. This is consistent with Roshko's concept of universal Strouhal number, which is related not to the cylinder dimension but to the width of the wake (Roshko, 1955).
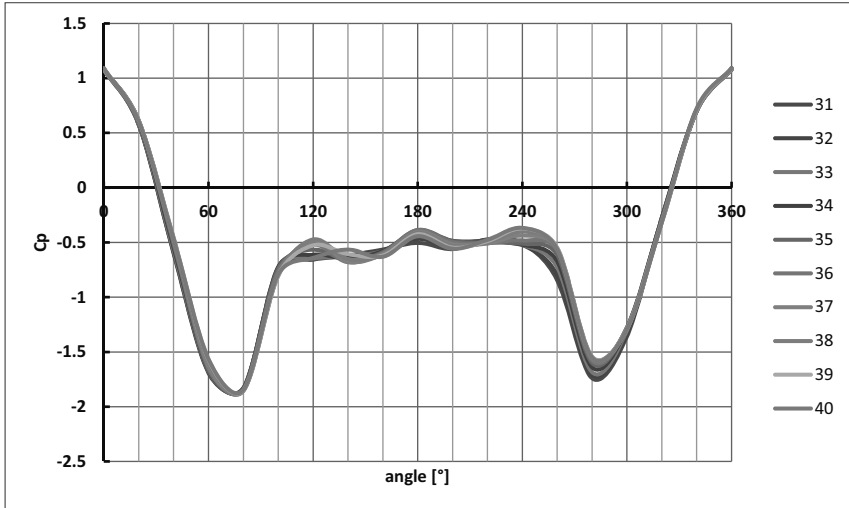
Figure 4.37 Momentary pressure distribution (z/H = 0.65, T1-R1, time steps 2897:2906)
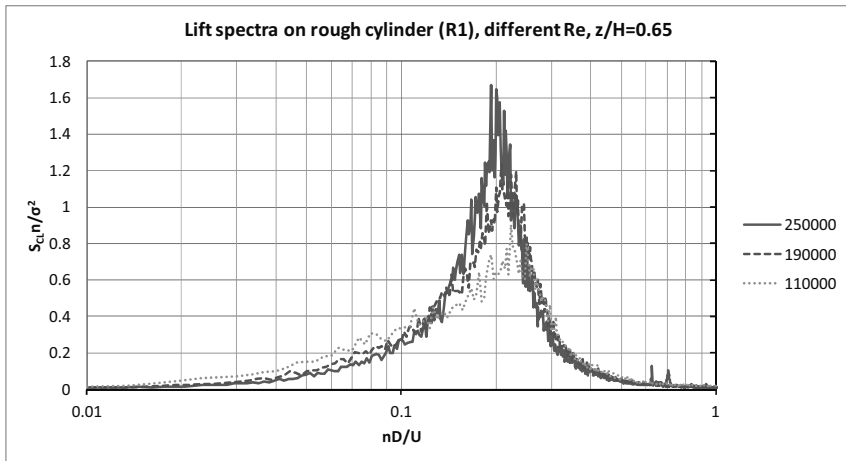
Figure 4.38 Spectra of the lift coefficient vs n [Hz] on the rough cylinder as a function of Re

The skewness of the spectra at z/H=0.65 in Figure 4.38, which is more evident at the lowest Re (green curve) but still present at the highest Re, is due to fluctuations produced at low frequencies by tip-associated-vortices. They are free-end effects, as mentioned in Chapter 3 and better investigated in Chapter 5.

So far, the discussion has been focused on the behaviour at middle height.

Figure 4.39 and Figure 4.40 describe the spanwise variation of the mean drag coefficient and of the pressure recovery at $Re = 2.5*10^5$. The tip effect is influenced by the surface roughness, because the rougher is the cylinder, the lower is the wake pressure (Figure 4.33). This enhances the flow over the tip of the body. For the same reason, the tip effect on the smooth cylinder is weaker: the smooth cylinder at $Re = 2.5*10^5$ is in supercritical conditions, characterized by minimum drag (horizontal plateau) due to small wake suction and very high pressure recovery due to large suction at the flanges. Moreover, in uniform flow (black curve) the tip effect is weaker than in boundary layer flow. It is in contradiction with Gould's conclusion (Gould et al., 1968) that the free-end effect is independent on the type of boundary layer. It is confirmed, instead, that the tip effect produces an increase in the lift fluctuations at about one diameter from the top, probably due to tip vortices, while the spanwise variation of drag fluctuations are less pronounced.

Another important feature in Figure 4.39 and Figure 4.40 is the ground effect, which extends up to $z/H = 0.5$. It is not only confined to the very low region. The higher drag at the base of the tower is probably enhanced by the presence of a boundary layer and thus vertical pressure gradients, as mentioned in Chapter 3. Unfortunately there are not so many measurements at low levels in uniform flow (T3). In this case, a significant variation of $C_{D,m}$ would not be expected. In the presence of atmospheric boundary layer, the ESDU Data Items (ESDU 81017) confirm the existence of higher wake suction and lower pressure at the flanges. The high wake suction is responsible for an increase in drag. The even larger lateral suction produces the increase in pressure recovery as $z \rightarrow 0$. In fact, the correction factor proposed by the ESDU Data Items to account for the atmospheric boundary layer profile (ESDU 81017, figure 5) shows the same trend as the red curve in Figure 4.39. A similar behaviour of the drag curve at low levels is confirmed in literature e.g. by Garg's results (1995) at sub-critical Re, but a systematic study does not exist. The blue curve in Figure 4.39 (smooth cylinder) would suggest an even higher three-dimensionality of the phenomenon. However, there are not measurements in the lower half to confirm it.

The choice of an appropriate surface roughness for the wind tunnel tests, in view of the evaluation of design wind loads, depends on the full-scale condition which one would like to achieve. For solar towers, the target full-scale condition is given by a smooth circular cylinder in transcritical Re. Codified data for smooth and rough surfaces at transcritical Re are available in the VGB guideline (2010). Further full-scale data on chimneys and TV towers are collected in (Niemann&Schräder, 1981).

Relying on the recommendation of the VGB guideline, the target value of the drag coefficient for a smooth surface is in the range 0.46-0.49. The value of the minimum lateral suction (1.5-1.6 for curves K1.5 and K1.6, respectively) should not be considered alone, rather, the difference $C_{p,b} - C_{p,min}$ is a much more significant parameter, since the base pressure depends on slenderness while the pressure recovery is not so influenced by the aspect ratio. Therefore, referring to cooling towers, for solar towers it should be expected $C_{p,b} - C_{p,min}$ in the range 1.0-1.1.

On the basis of these recommendations, three different alternatives in terms of rib height and rib distance seem to be equivalent. The highest surface roughness (R4-R5) is discarded, as previously said. By choosing an appropriate value for the wind tunnel velocity, R1, R2 and R3 may be used. Remarkable is also the similarity between R2 and R3 for the whole range of Re. In this work, in view of the design wind loads, the condition R1 at 1400 rpm (Re = $2.5*10^5$) is selected and it will be used in the next chapters.

The pressure results of the experiments, shown in terms of $C_{p,min}$, $C_{p,h} - C_{p,min}$ and $C_{p,h}$, are compared with literature (Figure 4.41). Wind tunnel tests in literature at transcritical Re on smooth circular cylinders, providing pressure distributions and not only force measurements, are rare. An investigation is contributed by Gould et al. (1968), who measured pressures on smooth cylinders having different aspect ratio in a pressurized wind tunnel (Re = $2.7-5.4*10^6$). This paper is used here as reference, also in order to prove the effectiveness of surface roughness in the experiments. However, Gould's experiments are in uniform flow and this should explain the departure of results at low levels, as previously mentioned.
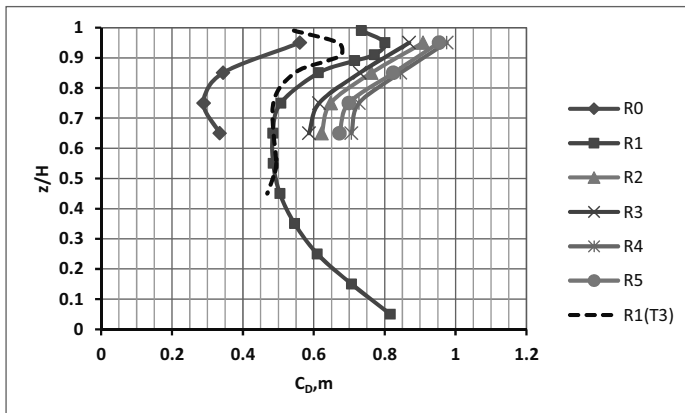
Figure 4.39 Mean drag coefficient along the height on the smooth cylinder and for different roughness conditions at $U_H \approx 25$ m/s, Re = $2.5*105$ (R0-R5, T1 unless differently specified)
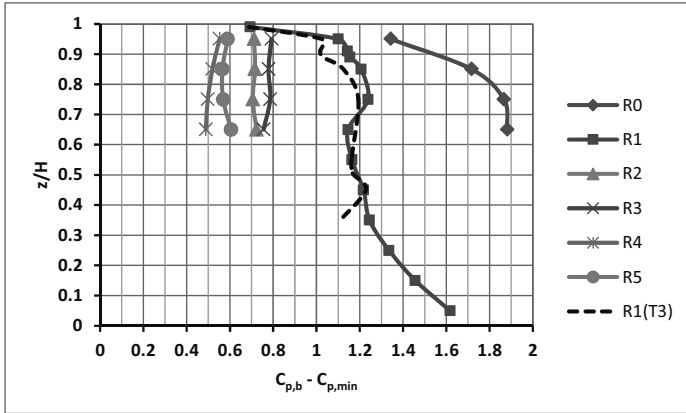
Figure 4.40 Pressure recovery along the height on the smooth cylinder and for different roughness conditions at $U_H \approx 25$ m/s, Re = $2.5*10^5$ (R0-R5, T1 unless differently specified)
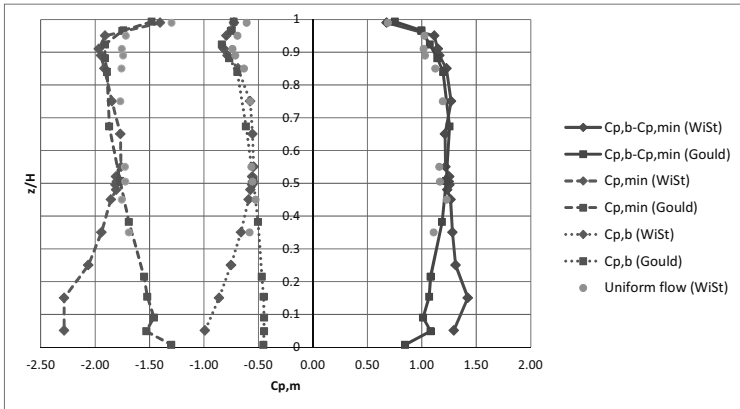
Figure 4.41 Mean pressure coefficients ($C_{p,min}$, $C_{p,b}$ - $C_{p,min}$, $C_{p,b}$): red = results by Gould et al., 1968 (H/D = 6, Re = $5.4*10^6$, uniform flow); blue = WiSt (R1-T1). Green = WiSt (R1-T3, i.e. uniform flow)

Chapter 5. **A new phenomenon around circular cylinders**

This chapter discusses the experimental evidence at WiSt wind tunnel of a new phenomenon around circular cylinders with a free-end. The peculiar feature is the presence of ring beams along the height of the cylinder. The physical interpretation proposed in this chapter is based on the investigation of pressure measurements through wind tunnel tests.

5.1 **Experimental observation**

The results of the first set of experiments (April 2011) on the rough circular cylinder without rings in turbulent boundary layer flow (T1-SR0-R1) at several wind tunnel velocities (and thus different Re) represented a good starting point for a deeper investigation (section 4.4). The tests were then repeated by adding 10 equally spaced ring beams along the height of the cylinder in both empty tunnel and turbulent atmospheric boundary layer flow.

Although a certain effect of the ring beams on the flow was expected, it was really surprising to see – immediately, during the first wind tunnel test on the tower with rings – a very interesting phenomenon, which was not just a local effect in the vicinity of the rings. During the experiments, the measurements at WiSt are usually checked and monitored by an oscilloscope, which plots the analogic signal coming out from the amplifiers, and by the computer, which plots on the screen the digitalized raw data. Unusual jumps in the time histories were immediately noted (Figure 5.1).
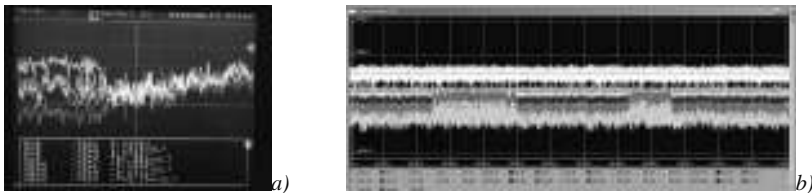
Figure 5.1 Wind tunnel experiments on the circular cylinder with rings: appearance of jumps in the analogic signals (fig. a. oscilloscope) and digital signals (fig. b. computer screen)

The post-processing of the time histories confirmed the presence of jumps at certain points around the circumference. An error during the measurements was at first hypothesized. An error could have occurred at every step in the measurement chain.

However, since the jumps occurred both in the analogic and in the digital signal, if there was an error it could not be in the A/D converter, but before it. Moreover, while the pressure cells AMSYS (type 2) also include the amplifiers, the amplifiers to the pressure sensors Honeywell (type 1) are completely independent from one another (Figure 4.18). Therefore, if there was an error in one of these amplifiers, the others would not be affected. Then, the first check was just to connect a pressure sensor showing the jump to another of these independent amplifiers. This check was repeated several times with different pressure sensors and different amplifiers, but the result did not change. Similarly, it did not seem to be a problem of the connections and of the plastic tubes, because the same test without rings did not show the jump. Therefore, it was decided to go ahead with the measurements because no experimental error could be detected. In addition, the jumps were more evident at angles around 100°-120°, i.e. around separation, so it could have been then reasonable that they were due to a physical cause.

A further proof of validity of the experiments resulted from a closer data inspection. In fact, the jumps were coordinated around the circumference and along the height; they occurred in opposite directions on the two sides of the cylinder and in neighbouring compartments. Furthermore, since the jumps in the time histories occurred mainly at the flanges of the cylinder, they produced jumps in the time histories of the lift, but not in the drag coefficient.

The phenomenon needed to be investigated more deeply and other sets of experiments were planned (section 4.3). This chapter comments on the experimental evidence and reports results of the complete wind tunnel investigation at WiSt laboratory.

The presence of efflux out of the chimney tends to destroy the phenomenon, therefore the undisturbed effect is described in section 5.2 with only reference to the no-efflux condition. The effect of efflux will be mentioned among "other conditions" in section 5.3.5. Moreover, the phenomenon seems to be more related to geometric characteristics of the body rather than to turbulent properties of the flow. In fact, the bistable flow occurs both in empty tunnel (uniform flow) and in atmospheric boundary layer flow. Section 5.2 refers to atmospheric boundary layer flow conditions, the most important ones for the design. A comparative study of uniform and shear flow is addressed in section 5.3.3. A further comparison between different atmospheric boundary layer flows results from the cross-checked investigation at WiSt and CRIACIV wind tunnels (Chapter 6). In fact, the dependency of the bistable flow on the type of atmospheric boundary layer is one of the important issues to be considered in view of the design. First, because the design situation can refer to a different type of

atmospheric boundary layer; secondly, because full-scale properties of strong winds like I_u, shear stresses, integral length scales might be not faithfully reproduced in the wind tunnel. Furthermore, the full-scale condition is associated to higher Re. This is likely the most important point, which is addressed in this chapter as well. The three-dimensionality of the cylinder with a the free-end, the spanwise distance from the tip and the distance between rings - related to the tower diameter - resulted to be key influencing parameters. The slenderness ratio, which was chosen as a fixed parameter in these experiments, should play a role as well (section 5.4), but the investigation of cylinders with different aspect ratios was not possible within this work (Chapter 8).

5.2   Description of a new cross-wind phenomenon

The phenomenon is described in this section with regard to the following condition of experiments: T1-SR1-R1-EF0. Re is $2.5*10^5$ (i.e. tests at 1400 rpm). Further conditions are introduced in the following sections.

5.2.1   Three main features

The occurrence of jumps in the time histories is only one aspect of the phenomenon – perhaps the most evident one – but the analysis of data suggested that three main features describe the flow condition around the circular cylinder with ten rings (Figure 5.3 and Figure 5.4):

1. Bi-stability of the flow: in time, the side pressures jump between two magnitudes;
2. Asymmetric flow around a symmetric structure: on opposite sides of the cylinder, the side pressures jump in opposite directions, so that a lower suction level on one side (e.g. $C_p(100°) \approx -1$) corresponds to a higher suction level on the other side (e.g. $C_p(260°) \approx -1.6$);
3. Spanwise inversion: in adjacent compartments the side pressures jump as well, in opposite directions. For example, if z_1 and z_2 belong to different compartments (e.g. $z_1 = 950$ mm and $z_2 = 850$ mm), then $C_p(z_1, 100°) \approx -1$ and $C_p(z_2, 100°) \approx -1.6$ and $C_p(z_1, 260°) \approx -1.6$ and $C_p(z_2, 260°) \approx -1$.
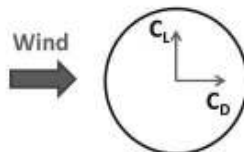
Figure 5.2 Definition of drag and lift coefficients

------------------------------------ *RING BEAM at 1000 mm* ------------------------------

------------------------------------ *RING BEAM at 900 mm* ------------------------------

------------------------------------ *RING BEAM at 800 mm* ------------------------------

------------------------------------ *RING BEAM at 700 mm* ------------------------------
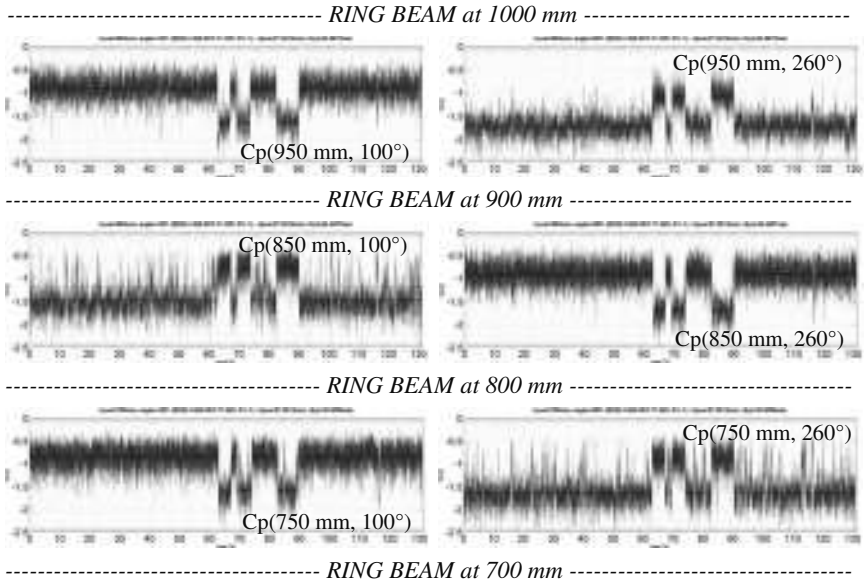
Figure 5.3 Bistable and asymmetric flow with spanwise inversion. Time histories of C_p at: 950-850-750 mm, 100° and 260° (WiSt, T1-SR1-EF0-R1, Re = 2.5*10^5)

------------------------------------ *RING BEAM at 1000 mm* ------------------------------

------------------------------------ *RING BEAM at 900 mm* ------------------------------

------------------------------------ *RING BEAM at 800 mm* ------------------------------

------------------------------------ *RING BEAM at 700 mm* ------------------------------
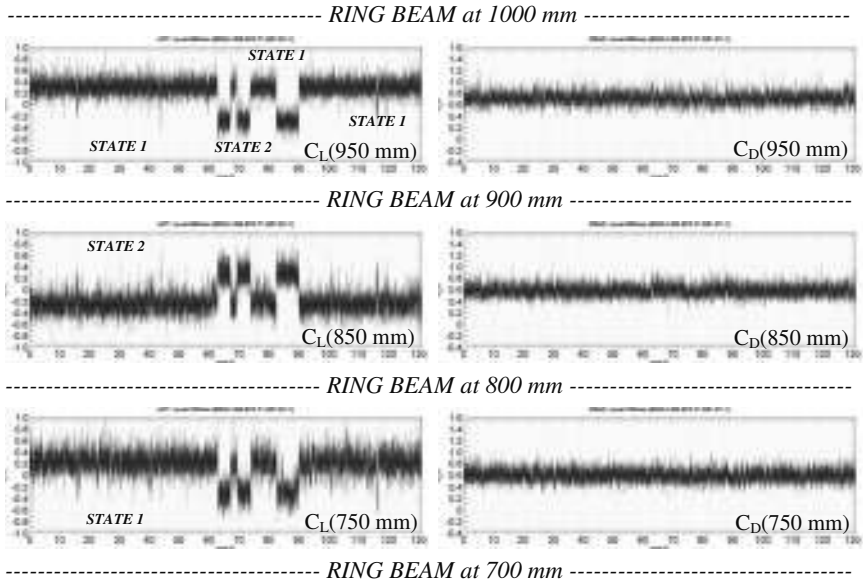
Figure 5.4 Time histories of C_L and C_D at 950-850-750 mm (WiSt, T1-SR1-EF0-R1, Re = 2.5*10^5)

The phenomenon continues along the height of the tower, but at low levels (z < 0.6H) the mixture between the two states is more pronounced. The progressive disruption of the bistable flow along the height, as the distance from the tip increases, is an issue addressed in Chapter 6.

The mean and the rms values of the time histories are calculated separately for each interval of time before and after a jump; their circumferential distribution proves that two states can be detected. They are asymmetric but identical, just mirrored (Figure 5.5 and Figure 5.6, z/H = 0.75). Because of that, the flow is called bi-stable. As a consequence of the asymmetry, that is created by higher suction on one side of the cylinder, the mean lift coefficient is not zero (Figure 5.4). Depending on the interval of time which is considered, the mean lift can be either positive or negative. For convention, the "state 1" identifies the intervals of time associated to positive mean lift and the "state 2" is associated to negative mean lift. In the reference system of the wind tunnel, being the x-axis along the wind tunnel and the y-axis in the across wind direction (see the Drawing 1 on page 103), the state 1 has the high-suction side between 180° and 360°.
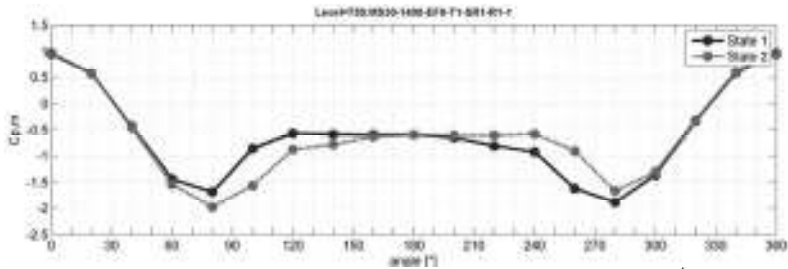
Figure 5.5 Cp,m at 750 mm (WiSt, T1-SR1-EF0-R1, Re = 2.5*10⁵)
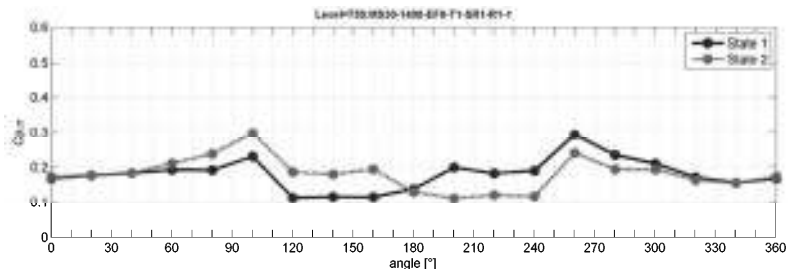
Figure 5.6 Cp,σ at 750 mm (WiSt, T1-SR1-EF0-R1, Re = 2.5*10⁵)

The state 1 at z/H = 0.75 is now analyzed in more detail in Figure 5.7 ($C_{p,m}$) and Figure 5.8 ($C_{p,\sigma}$). The asymmetric pressure distributions are fitted with spline curves. It can be seen that the higher suction on one side only of the cylinder is associated to a

rearward movement of the separation point ($\varphi_N \approx 240°$ in Figure 5.7) and a complicated flow structure in the wake. Usually, the recirculation region in the wake of a cylinder between the separated shear layers is characterized by random fluctuations; they are not relevant for the structural design, but the wake structure is of great interest from the fluid-dynamic point of view. In particular, in presence of 10 ring beams along the tower, a recirculation bubble can be detected in the mean and rms pressure distributions. In fact, between 240° and 200°, i.e. after separation on the high-suction side, the mean pressure distribution presents a horizontal step at the constant value ≈-0.8 and then it rises again until ≈-0.6, which remains constant in the rest of the wake, also on the other side of the cylinder (low-suction side). The presence of such a horizontal step after separation can be attributed to a reattachment of the separated shear layer and further separation (Zdravkovich, 1997, page 166), i.e. the formation of a separation bubble. In the range 240° and 200° the rms values undergo a horizontal step as well, at a rather high value (Figure 5.8): the value is, in fact, comparable to the fluctuations at stagnation, while fluctuations in the wake should normally have a standard deviation about one half of the ones at stagnation (as it is in the wake on the low-suction side of the cylinder). Because of that, in case of rings the two sides of the cylinder are named "normal side" and "bubble side", i.e. "low-suction side" and "high-suction side", respectively.
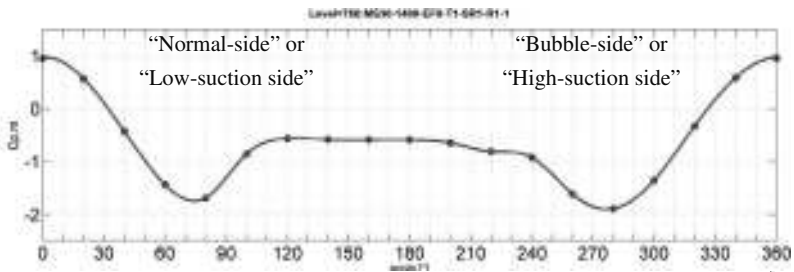
Figure 5.7 $C_{p,m}$ at 750 mm. State 1, spline fitting (WiSt, T1-SR1-EF0-R1, Re = 2.5*10⁵)
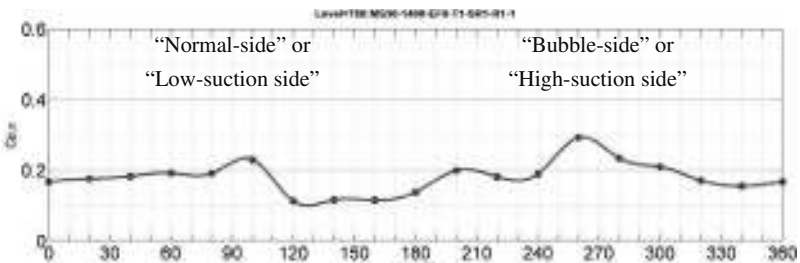
Figure 5.8 $C_{p,\sigma}$ at 750 mm. State 1, spline fitting (WiSt, T1-SR1-EF0-R1, Re = 2.5*10⁵)

Another peculiar feature is the spanwise inversion along the height of the cylinder, which means that the state of the flow is alternated in neighboring compartments. In fact, Figure 5.4 proves that during each stable interval of time the mean lift coefficient changes its sign in neighboring compartments, so that the steady cross-wind force changes its versus along the height of the cylinder. This is due to the vertical alternation of high- and low-suction sides of the cylinder, as shown in a transversal view in Figure 5.9.
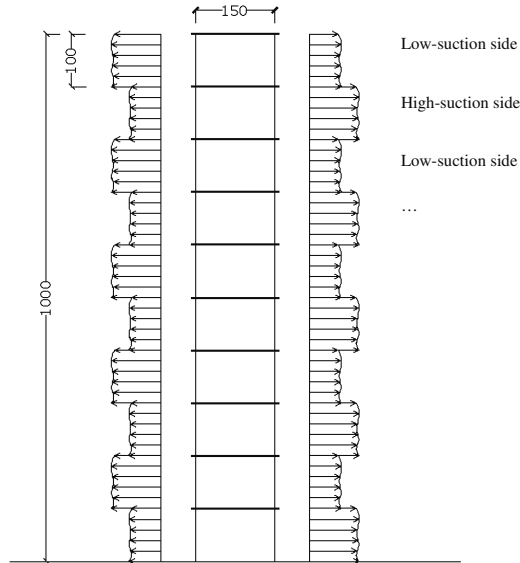
Figure 5.9 Spanwise inversion: high-suction and low-suction sides, transversal view.

5.2.2   **Step by step through a jump between two states**

The jump between the two states of the bistable flow is accompanied by a significant displacement of the stagnation point and the formation of a bigger separation bubble, which suddenly seems to move in the wake on the other side of the cylinder. This can be seen in a sequence of instantaneous pressure distributions within a jump. In particular, 8 significant time steps are highlighted in Figure 5.10, when the lift is either maximum or minimum in the vortex shedding cycle and crossing zero before changing state. The x-axis in the figure plots the number of time steps, it is remembered that the sampling frequency is 2000 Hz, therefore the figure plots a time window of 2 seconds.
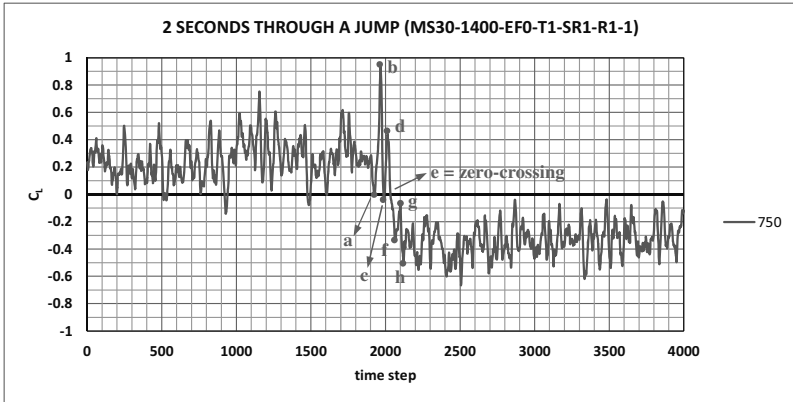
*Figure 5.10 2s-time history at 750 mm ($n_{sampling}$ = 2000 Hz) : transition from state 1 to state 2 (WiSt, T1-SR1, Re = 2.5*10^5)*

Figure 5.11 (a-d) plots instantaneous distributions in the state 1, i.e. the state of positive mean lift. Then, in figure e) the flow is changing state and after that the instantaneous distributions belong to the state 2 (figures f-g-h).

In the state 1, during a shedding cycle the lift oscillates between a minimum value which is close to zero and a maximum positive value which corresponds to a von Karman vortex shed on the bubble side. For example, in Figure 5.11a) the instantaneous pressure distribution results to be almost symmetric. In fact, the lift at those instants is around the minimum value because the vortex is shed on the normal side, where the mean lateral suction is lower than on the bubble side. Thus, the growth of the vortex on the normal side reduces the asymmetry. Instead, when the vortex is shed on the bubble side, the lift assumes an extreme value, which is either positive (state 1) or negative (state 2). In the compartment below the ring the situation is simultaneously reversed.

At some time, there might be the formation of a bigger bubble (Figure 5.11d), which is anticipated by a displacement of the stagnation point. Such a displacement occurs on the same side of the cylinder at diffetent levels (despite the spanwise inversion of lift) and it is sligthly anticipated at higher levels, so that the transition of state at 950 mm appears to be about 0.11 seconds (in the wind tunnel time scale) earlier than 20 cm below. This is a very short time in the wind tunnel, but it is remembered that the vortex shedding period is more than three times shorter ($S_t U/D$) ≈ 0.2*25/0.15 = 0.03s. After the zero crossing (Figure 5.11e) the state has changed and a separation bubble of smaller size (comparable with the one in the mean distribution, plotted in Figure 5.11) develops on the other side of the cylinder.

150
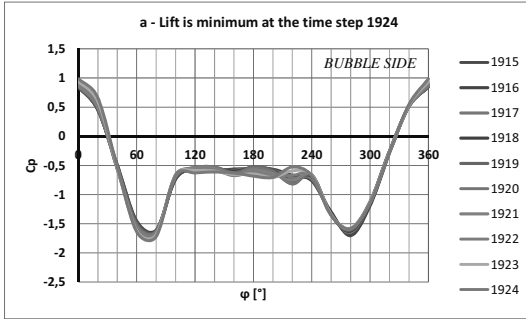
*Figure 5.11 a) State 1;
n. 1924 in the legend is the time
step "a" in Figure 5.10*
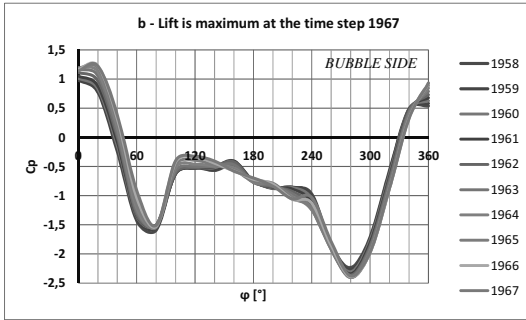
*Figure 5.11 b) State 1;
n. 1967 in the legend is the time
step "b" in Figure 5.10*
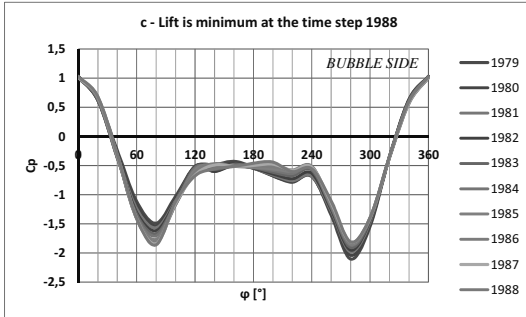
*Figure 5.11 c) State 1;
 n. 1988 in the legend is the time
step "c" in Figure 5.10*
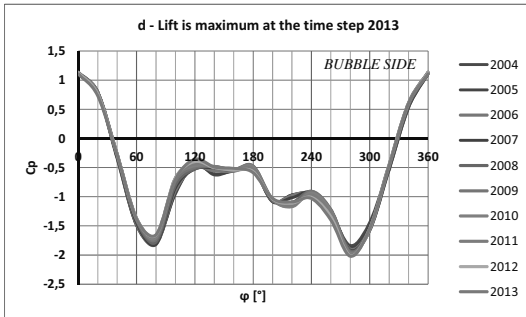
*Figure 5.11 d) State 1;
n. 2013 in the legend is the time
step "d" in Figure 5.10*
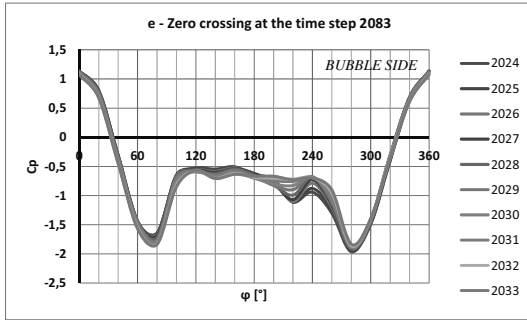
Figure 5.11 e) Change of state; n. 2033 in the legend is the time step "e" in Figure 5.10
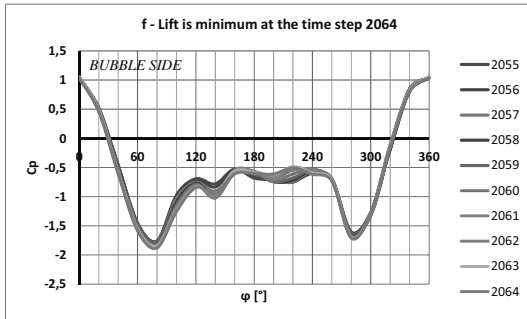
Figure 5.11 f) State 2; n. 2064 in the legend is the time step "f" in Figure 5.10
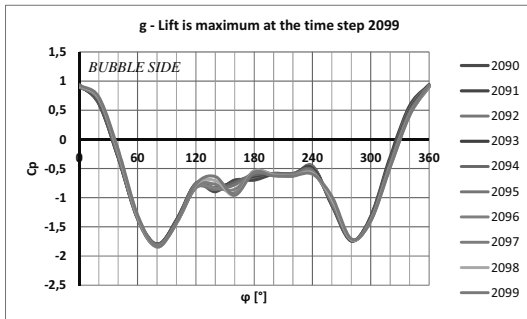
Figure 5.11 g) State 2; n. 2099 in the legend is the time step "g" in Figure 5.10
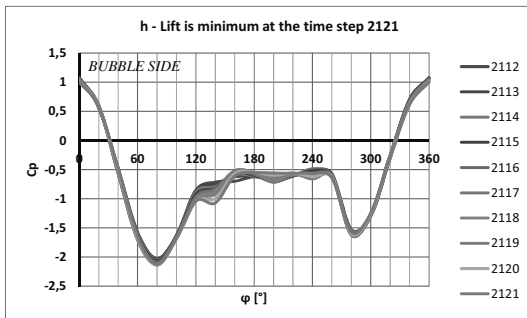
Figure 5.11 h) State 2; n. 2121 in the legend is the time step "h" in Figure 5.10

Figure 5.11 a-h) Momentary distributions during a jump (10 time steps = 10/2000 s), Re = 2.5*10⁵

5.2.3   **Literature and novelty**

The asymmetry of the pressure distribution created by the rings is associated to higher suction and formation of a separation bubble on one side only of the cylinder. This phenomenon might be - in itself - not new. A similar effect is well-known around circular cylinders (without rings) in the critical range of Re, as mentioned in Chapter 3. However, the conditions of occurrence (further discussed in section 5.3) of the bistable phenomenon evidenced in this Dissertation make it original and physically unique.

The similar case reported in literature (Figure 3.2) is very sensitive to Re and occurs in a small range of Re just before the critical value. Moreover, it is also sensitive to disturbances and perturbations in the flow (such as turbulence). The phenomenon is thus observed only in smooth flow on smooth cylinders. It is also very difficult to catch it. The physical reason which produces the separation bubble is strictly related to the Reynolds number, because it governs the transition from laminar to turbulent flow. In particular, the flow is asymmetric because such a transition has occurred in the shear layer after separation (laminar separation) on one side only of the cylinder. On that side where transition occurred the turbulent flow gets more energy and is able to reattach. The second separation is then turbulent. In between, there is the formation of a separation bubble, namely laminar separation bubble. Transition from laminar to turbulent flow, which occurs after the first laminar separation, is due to some random perturbations on that side of the cylinder. Therefore, in ideal conditions, the side on which it may occur is completely random. Moreover, it can occur on one side only of the cylinder only if there is a low probability that there are perturbations on the two sides able to initiate a transition to turbulent flow. Because of that, the asymmetric phenomenon disappears in turbulent flow and/or on a rough cylinder: perturbations and laminar separation bubbles likely develop on the two sides of the cylinder and that is the critical (symmetric) state.

In the present case of study, the incoming flow is turbulent and the cylinder is rough. In the pictures shown up to now the wind tunnel is at full-speed (Re $\approx$ 2.5*10^5, effective Re about one order of magnitude higher). In these conditions, laminar separation can be absolutely excluded. In fact, transition from laminar to turbulent boundary layer should occur very close to stagnation and certainly before separation. Consequently, even though the higher suction on one side of the cylinder may suggest the existence of a separation bubble, like in the well-known bistable flow in the critical range of Re, it cannot be a separation bubble in the classical sense, i.e. a laminar separation bubble. A laminar separation bubble is caused by a physical reason, that is transition to turbulent conditions in the free-shear layer after separation and

consequent reattachment. As the formation of the laminar separation bubble is excluded in the conditions of the experiments, the corresponding physical explanation fails. For the same reason, the high sensitivity of the laminar separation bubble to Re, to the surface roughness of the cylinder and to the turbulence of the incoming flow should not necessarily be confirmed in the present phenomenon. In fact, it is not. It should also be remembered that the result shown up to now in this chapter occurs in a state of the flow far beyond the critical drop (Re = $2.5*10^5$, surface roughness R1), as confirmed by Figure 4.29. Thus, although the dependency on Re is an issue which deserves particular attention, it is clear that it cannot be just an effect of Re_{cr}.

What is completely new is also the spanwise variation of the asymmetry. In the well-known case of literature, Bearman (1961) observed that "the distribution of base pressure along the span suggested that the establishment of a bubble on one side takes place along the complete length of the cylinder and this was later confirmed by surface oil flow patterns". In absence of ring beams along the height, in fact, there is no reason for a spanwise inversion. It is a peculiar effect of the compartments created by the rings. In particular, it must be a result of the interaction between compartments. The alternation along the height of higher and lower side pressures determines vertical pressure gradients and thus flow movements between different levels. It is believed that the key is in the recirculation bubbles in the near wake of the cylinder.

The occurrence of jumps between the two states does not present regularity. The random nature is, in any case, not surprising. It is typical, for example, of side-by-side cylinders. It reflects the random nature of the turbulent flow. Also the bistable flow in the critical range of Re presents the same characteristic: a random perturbation in the flow, on either side of the cylinder, may initiate the phenomenon.

What is interesting, moreover, is the stable nature within each state. After being initiated, a certain state establishes. This is completely different from the unsteadiness of vortex shedding, where cross-wind oscillations of the lift force average to zero. From the experiments, it was not straightforward to infer that symmetric conditions can be achieved by averaging on an infinitely long period. In any case, an infinitely long period cannot be justified in the design of a structure during a wind storm. But it must be remembered that the stable nature of the asymmetric condition is a peculiar feature of the well-known bistable flow of literature, too. The name itself, bi-stable flow, highlights that we are dealing with two conditions of stability, not with instability. In the case of literature, Schewe (1983) wrote "the immediate formation of a one-sided bubble leads to steady circulation around the cylinder. This effect results in acceleration of the fluid on the side where the boundary layer transition has

occurred and in deceleration at the other side of the cylinder. Deceleration of the fluid delays the transition in this detached boundary layer and hence the formation of the bubble. This coupled occurrence of the development of a bubble on one side with the deceleration of the fluid on the other side (i.e. decrease in the Reynolds number of this boundary layer) probably causes stabilizing and fixing of the asymmetric flow state". Acceleration of the flow on the bubble side is related, in a phenomenon which is highly sensitive to Reynolds effects, to the Reynolds number. Again, the reason here must be profoundly different, but the effect is the same.

The interesting debate between known and unknown, literature and novelty, motivated further investigation of the phenomenon and a proper revision of the wind tunnel experiments. It seemed worthwhile to go deeper in the study by testing different situations. The crucial question is not only the physical reason which produces the asymmetric and bistable effect, but also the systematic investigation of the conditions of occurrence and their dependency on the Re, i.e. on the wind tunnel scale. The two wind tunnels available for the experiments allowed to test only a limited range of Re, so that surface roughness was introduced to increase the effective range. Several different combinations of wind velocities and rib height and distributions were tested. Section 5.3 explains the details, but it is now anticipated the surprising result that the phenomenon seems to stabilize even more as Re increases. Further experiments at higher Re (like full-scale conditions) would require higher velocities and bigger wind tunnels (or pressurized flow); they would be much more expensive, but rather decisive. Fluid dynamic simulations (section 6.3) were performed in parallel to the last part of the experimental work (in CRIACIV) also with the aim to explore higher Re.

5.3   Conditions of occurrence

In order to accept and be convinced of the new experimental phenomenon, it has been tested with regard to the following conditions of occurrence: [1] different wind tunnel velocities (thus different Reynolds numbers); [2] different surface roughness on the model, in terms of height and distribution of ribs; [3] different boundary layers (uniform and shear flow); [4] removal of hypothesized experimental unintentional disturbances. The tests were also repeated in presence of [5] efflux. Then, a further question that was addressed regarded the sensitivity of the phenomenon to [6] different design choices, for example with a different number of ring beams (5 or 7) and with smaller rings (whose width is halved).

This sensitivity analysis has been performed in only one wind tunnel (WiSt laboratory) and mostly in turbulent boundary layer flow. Only the most representative tests were

repeated at CRIACIV for further validation in a different laboratory (Chapter 6). The results in WiSt tunnel are reported in the following. However, the sensitivity analysis with 10 rings did not suggest any reason for which the phenomenon should not be expected. The phenomenon is in any case mitigated by the presence of efflux and by using fewer and/or smaller rings.

Although the sensitivity analysis was carried out with the purpose of being as much general as possible, the tower model and the experimental set-up limited the experimental investigation to the 3D condition (cylinder of finite length with a free-end) and H/D = 6.7, as well as to a certain range of Re. Tests in two-dimensional flow and with different slenderness ratios would be recommended for future investigation, as well as tests with a different distribution of rings (Chapter 8). The load and response calculation (Chapter 7) should give an indication about the importance of additional experimental investigation in the structural design of Solar Updraft Towers. It basically depends on the level of structural optimization one wants to achieve.

5.3.1 Dependency on the Reynolds number

The dependency of the phenomenon on the Reynolds number is at first studied for a certain surface roughness by varying the wind tunnel velocity. The preliminary investigation described in section 4.4.3 showed that the best target condition, in terms of effective Reynolds number, is achieved by using the surface roughness condition R1. It is then the reference condition through the whole dissertation and also in this sub-section 5.3.1. In any case, the tests were also repeated with different surface roughness, in order to study its effect. The most representative results are reported in section 5.3.2.

As described in Chapter 4, five levels of wind velocity in the working range of the wind tunnel at WiSt were selected for most tests: 600-800-1000-1250-1400 rpm (corresponding to $U_{pra} \approx$ 12-16-20-25-27 m/s, respectively). Lower wind speeds (up to 3 m/s) were only tested on the smooth cylinder to reach the subcritical range (section 4.4.3).

Figure 5.12 plots the results versus Re at z = 950 mm in the two states, which can be considered reasonably equal. The dependency of the drag coefficient on Re is less pronounced than in SR0, at Re_{cr} there is only a small drop. The interesting and peculiar feature of the phenomenon is the presence of a mean steady lift throughout the whole tested range of Re. It does not show any tendency to disappear at higher Re. Because of that, so far (on the basis of these experiments) it is not expected any disappearance of the phenomenon at higher Re. The rms values in the two states do not show a significant dependence on Re.
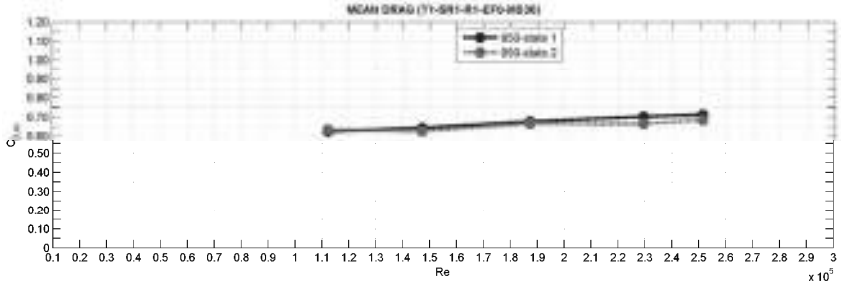
a)
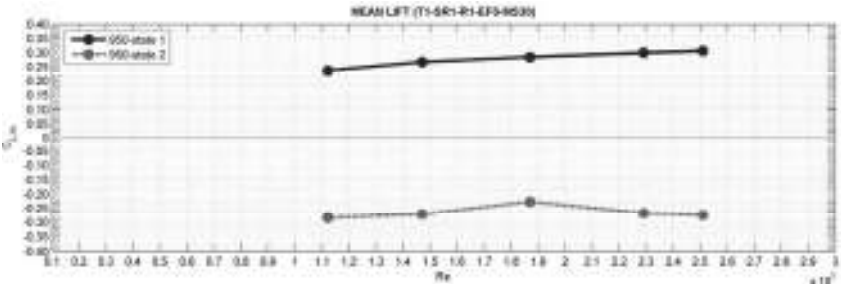
b)
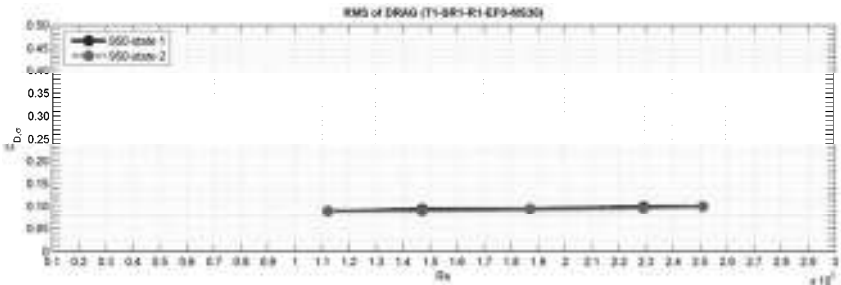
c)
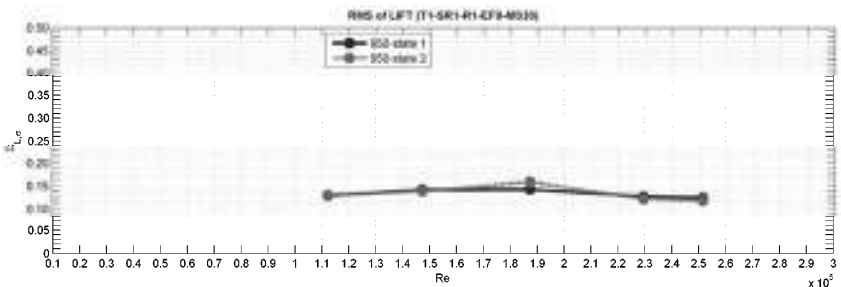
d)

Figure 5.12 a-d) Bistable and asymmetric flow within one state as a function of Re at 950 mm: a) $C_{D,m}$; b) $C_{L,m}$; c) $C_{D,\sigma}$; d) $C_{L,\sigma}$ (WiSt, T1-SR1-R1-EF0)

157

a)

Spanwise inversion between
neighbouring compartments

b)

c)

d)
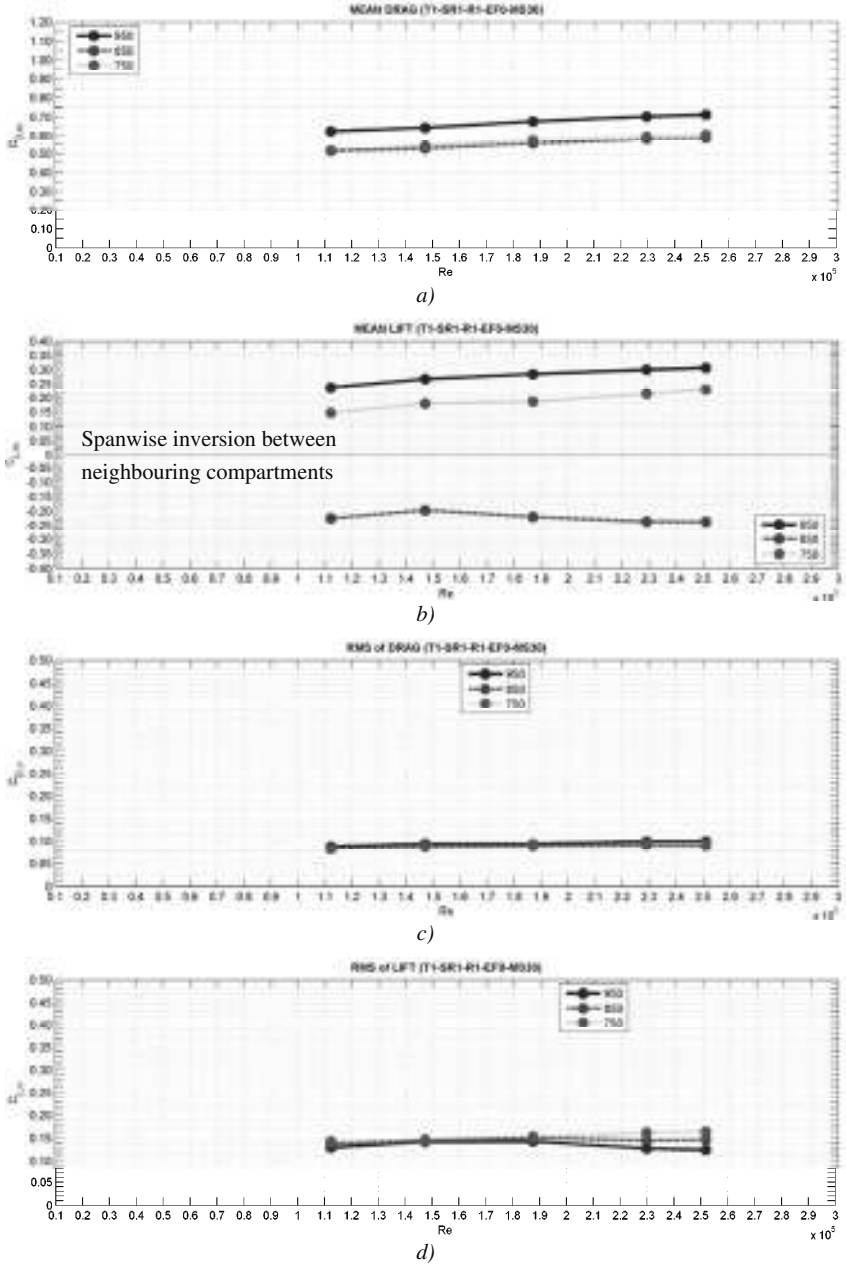
*Figure 5.13 a-d) Bistable and asymmetric flow within one state as a function of Re
at 950-850-750 mm: $C_{D,m}$, $C_{L,m}$, $C_{D,\sigma}$, $C_{L,\sigma}$ (WiSt, T1-SR1-R1-EF0)*

Figure 5.13 shows the dependency of the phenomenon on the height in the tip region (the situation at lower levels is explained in Chapter 6). Only one of the two states is considered. Due to the spanwise inversion, the mean steady lift alternates in sign between different compartments. This is a very peculiar feature of the phenomenon. It can also be observed that the tip effect is not so pronounced and, apart from the highest level (950 mm), the mean drag stabilizes on the same value. The rms values do not show significant dependency on height.

Figure 5.14 plots the mean pressure coefficients distributions at different Re and explains the weak dependency of the force coefficients on Re. On the normal side of the cylinder (0-180°), as the wind velocity increases, the lateral suction decreases and the separation point moves upstream (such a movement is maybe concealed by the linear interpolation in the figure). This is typical of the supercritical range on a rough cylinder (Figure 3.8). The suction in the wake tends to increase, but this is especially appreciable on the bubble side, where lateral suction remains high. Because of that, as Re increases, the asymmetric condition tends to stabilize.
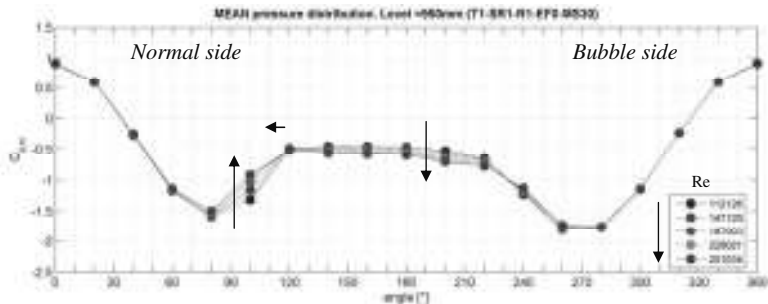
Figure 5.14 Bistable and asymmetric flow as a function of Re at 950 mm: $C_{p,m}$ in state 1 (WiSt, T1-SR1-R1-EF0)

5.3.2 **Effect of surface roughness**

Surface roughness, consisting of ribs, has a very strong effect on the flow because it changes the effective Reynolds number. As a consequence, it has an effect on the pressures, both with and without rings.

The most suitable flow condition for the design of the solar tower is achieved in the wind tunnel by using surface roughness R1, as already discussed in Chapter 4, whose result have been already presented (also in presence of rings, see section 5.2).

It is not in the purpose of this section to discuss the effect of a different state of the flow (produced by a different flow velocity and/or a different type of surface

roughness) on the bistable phenomenon, because it would not be relevant for the design of solar updraft towers. The aim of this section is to exclude that the occurrence of the bistable phenomenon may only be a matter of a certain choice – for experimental purposes – of surface roughness for the wind tunnel model. Thus, some tests were done by applying 10 rings in the following conditions: surface roughness R1, R2, R3, R4, R5 at 600, 800, 1000, 1250, 1400 rpm and on the smooth cylinder (R0) at 100, 200, 400, 600, 800, 1000, 1250, 1400.

Out of all the tests, the main result that can exclude that the ribs are responsible for creating the bistable flow is plotted in Figure 5.15. It has been measured on the smooth cylinder at low velocity (200 rpm, ≈ 5 m/s) in turbulent boundary layer flow. The state of the flow is at the very end of the subcritical state. The figure shows that the jumps in the time histories still occur and the histogram of the pressure coefficient highlights the bistability, even without ribs, even in a different state of the flow. The angle 100° at 950 mm is chosen as representative in the picture.
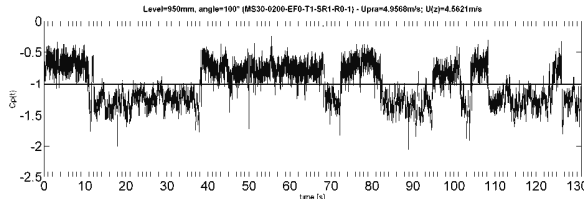
Figure 5.15 Bistable flow on the smooth cylinder (R0) with 10 rings ($U_{pra} ≈ 5$ m/s = 200 rpm): $C_p(950m,100°)$ (WiSt, T1-SR1-R0-EF0)
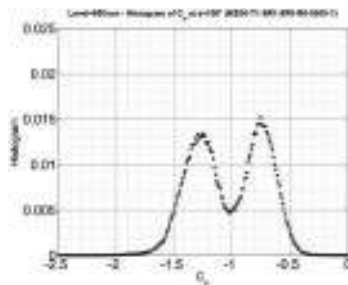
Figure 5.16 Histogram of C_p (time history in Figure 5.15)

Figure 5.17 is an example which shows that jumps in the time history also occur in a different surface roughness condition. In this example, higher roughness (R3) has been applied and the wind tunnel velocity is 800 rpm. This condition presents the same $C_{D,m}$ and pressure recovery as R1-1400rpm (section 4.4.3).
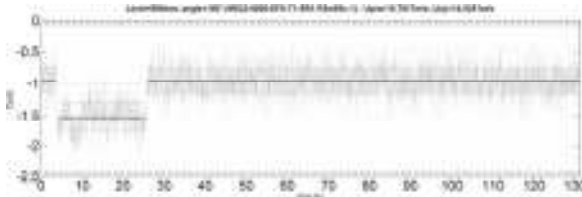
Figure 5.17 Bistable flow on a rougher (R3) cylinder with 10 rings ($U_{pra} \approx 16$ m/s = 800 rpm): C_p(950m,100°), (WiSt, T1-SR1-R3-EF0)
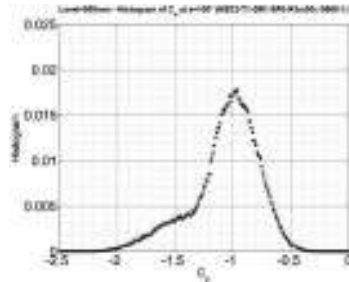
Figure 5.18 Histogram of C_p (time history in Figure 5.17)

5.3.3   Influence of boundary layer

The bistable flow occurs both in shear and in uniform flow. The values of the turbulence intensity and of the integral scales are not the governing parameter of the phenomenon, because the uniform and the shear boundary layer flow in WiSt (T1 and T3), as well as shear boundary layer in CRIACIV, are characterized by very different parameters (sections 4.1 and 6.1) and this does not prevent the occurrence of the phenomenon in the tip region. In fact, the phenomenon appears in the three cases. However, as it will be better explained in Chapter 6, the bistable flow tends to become a mixture of the two states at lower levels and there is a height at which the asymmetric flow starts to vanish. In particular, this disruption of the phenomenon starts at a certain level along the tower as a more rapid alternation of jumps on one side of the cylinder, that is the bubble side at that level.

Being the bistable flow a three-dimensional effect, it is basically governed by the free-end and the highest compartment, therefore it should not be surprising that the effect tends to disappear as the distance from the top increases. However, the experiments proved that the boundary layer influences the height at which the disruption starts. In fact, in the three boundary layers of the experiments it always starts at different levels. This will be better addressed in Chapter 6, once the CRIACIV results have been introduced. But it is now anticipated that: [a] in the shear flow in WiSt the disruption is

observed in the pressures at 650 mm (Figure 6.9); [b)] in the uniform flow in WiSt it is observed at 450 mm (Figure 6.13); [c)] in the shear flow in CRIACIV it is observed already at 750 mm (Figure 6.9 and Figure 6.12). However, a direct relationship between this height and a certain behaviour of a boundary layer property (such as I_u, L_{ux}, L_{uz} or σ_u) has not been detected.

5.3.4 Removal of experimental (unintentional) disturbances

The peculiarity of the observed phenomenon and the lack of a direct comparison with literature arose many questions and several doubts. Therefore, during the campaign some tests were repeated in order to verify that some experimental conditions should not have appreciably influenced the occurrence of the phenomenon.

For example, since separation bubbles develop in the wake of the cylinder, it was hypothesized that the ribs in the wake might have had a disturbing effect. Therefore, a few tests were repeated by removing the ribs in the separated region, which do not have any effect on the state of the flow. In the reference condition R1 the result did not change. In case of higher roughness (e.g. R3) the asymmetric condition could stabilize even better. Therefore, ribs in the wake were not responsible at all for creating the effect.

In order to allow the ribs to adhere to the model all along the cylinder without interruption, very small cuts were done in the ring beams for passage of the ribs. Although such cuts were very small, about 1 mm, they might have acted as holes in the rings. Therefore, the tests were repeated by accurately closing all these "holes" with tesa film. The result did not change significantly, but the removal of this disturbance allowed to the asymmetric flow to stabilize better. This enhanced the idea that the design of ring beams with some holes inside would have reduced the bistable effect on the structure. In fact, the asymmetry and the inversion in different compartments create pressure differences above and below the rings. The rings prevent the vertical flow along the tower surface and enhance the interaction between compartments due to gradients of pressure. Some holes inside the rings would reduce the pressure gradients. However, this mitigation proposal has not been extensively tested and validated. The experiments available before closing the cuts in the rings did not show a disappearance of the bistable flow, just a slight disturbance (i.e. more frequent jumps).

5.3.5 The effect of the efflux

The efflux suppresses the bistable phenomenon, even with 10 rings. It is easily seen in the histograms of the lift coefficients, which are approximately symmetric and centered in zero in presence of efflux (Figure 5.19, right column).

5.3.6   **The effect of number and size of rings**

The number and the size of the rings play a key role. So far, the reference condition with ten big rings at a distance of 10 cm in the wind tunnel scale (100 m in full-scale if λ_L = 1:1000) has been considered. This is just one design condition, and the bistable flow depends strongly on the distribution of rings and to some extent on the size of the rings. Therefore, once the bistable phenomena were ascertained in the previously described sensitivity analysis (influence of Re, influence of surface roughness, removal of disturbances), different design cases were studied. The main results (in the no-efflux condition) are presented here and a physical explanation will be proposed in section 5.4. Then, a conclusion and a proposed recommendation will be explained in section 5.6. Figure 5.20 plots the histograms of the lift coefficients in two situations:

1) 10 small rings (KR1) on the left column;
2) 5 big rings (SR5) on the right column.

On the left column, as well as in Figure 5.19, the distance between rings is 10 cm, i.e. 2/3 of the diameter; on the left column it is 4/3 of the diameter (20 cm). A first conclusion which can be drawn from the graphs is that the flow is bistable only in case of 10 big rings and no efflux (Figure 5.19, left column). In other words, the flow is able to undergo a jump, i.e. the bubble is able to pass on the other side of the cylinder, only if the rings are sufficiently big. As it was shown in Figure 5.11, a bigger bubble develops shortly before a jump, accompanied by a stronger deviation of the stagnation angle. This bubble is the result of 3D secondary vortices in the wake due to the flow over the tip which enters the wake. The spanwise inversion is a sort of cascade effect from the highest compartment. The trigger occurs randomly in time, according to the random nature of the flow. Apparently, smaller rings do not offer enough horizontal excrescence so that sufficiently big bubbles can develop. As long as the bubbles are small they produce asymmetric flow (because they are on one side only), but they do not pass on the other side. The size of the separation bubbles, related to the size of the rings should then explain the bistability of the flow.

However, in view of the design, the bi-stability (i.e. the jump) might not be the leading feature, because it is rapid in the wind tunnel but slower in full-scale (λ_T = 488, section 4.1.2). Instead, additional stresses in the shell may arise from the stable asymmetric condition. This is still present even with 10 small rings. Therefore, more than the size of rings, it is the distribution of rings which influences the design. In any case, if the rings are small, the asymmetry is limited to a smaller range (only two compartments in Figure 5.20a). When the distance between rings is large, e.g. 20 cm on the 1 m model

(whose diameter is 15 cm), both the bi-stability and the asymmetry vanish (Figure 5.20 right column). Increasing the distance between rings is then a safe mitigation strategy.

SR1-EF0: 10 big rings - without efflux (C_L)   *SR1-EF1: 10 big rings - with efflux (C_L)*
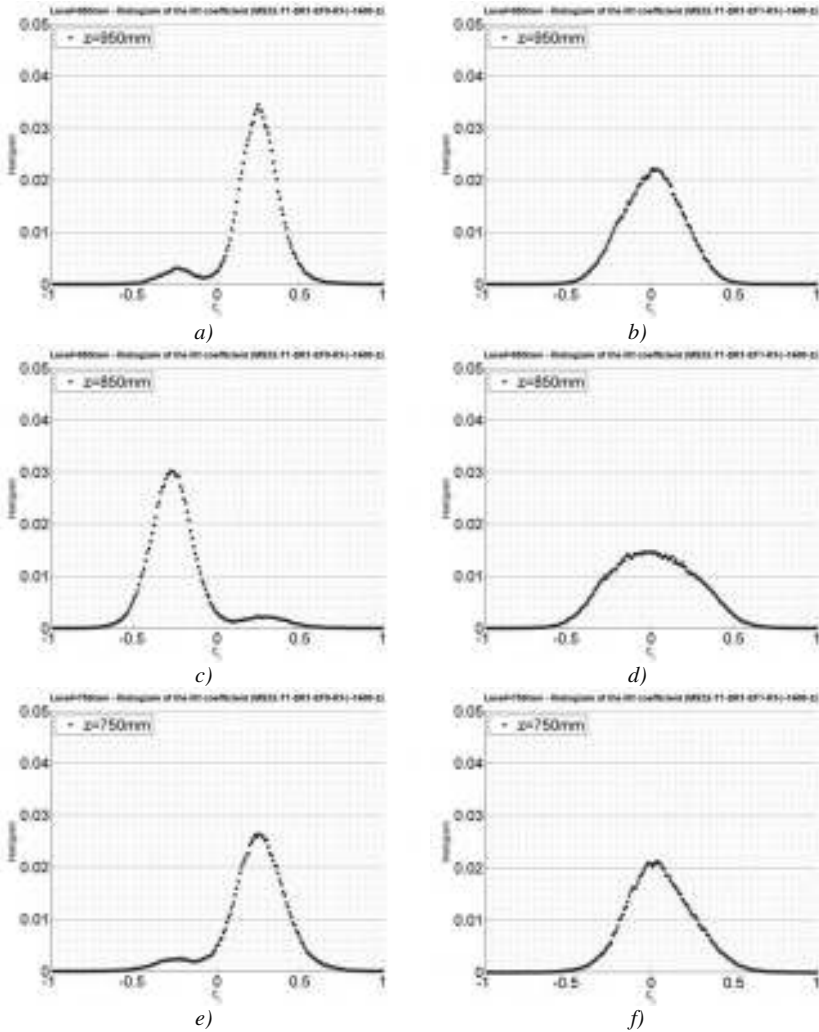
Figure 5.19 Effect of efflux on the bistable flow with 10 rings, histograms of C_L: a) level 950 mm (EF0); b) level 950 mm (EF1); c) level 850 mm (EF0); d) level 850 mm (EF1); e) level 750 mm (EF0); f) level 750 mm (EF1); (WiSt, T1-SR1-R1-EF0/EF1)

KR1-EF0: 10 small rings - without efflux (C_L)   *SR5-EF0: 5 big rings - without efflux (C_L)*
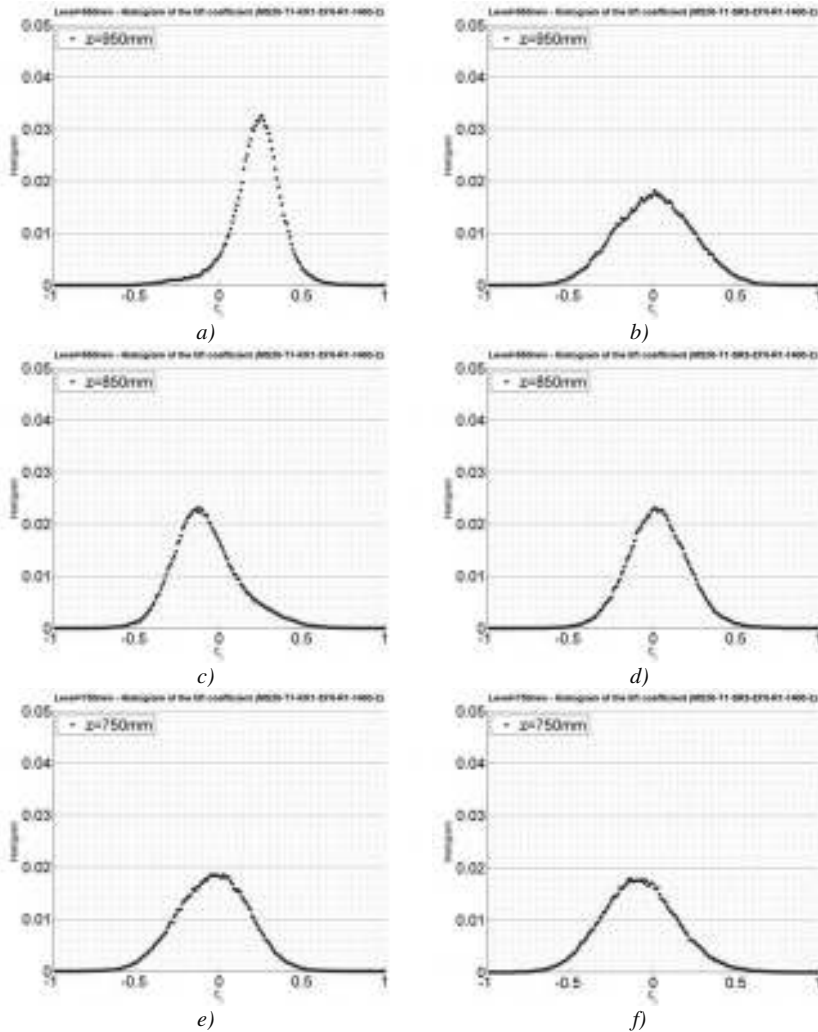
Figure 5.20 Effect of size and number of rings on the bistable asymmetric flow, histograms of C_L: a) level 950 mm (KR1); b) level 950 mm (SR5); c) level 850 mm (KR1); d) level 850 mm (SR5); e) level 750 mm (KR1); f) level 750 mm (SR5); (WiSt, T1-KR1/SR5-R1-EF0)

5.4   A physical interpretation

The key points of the cross-wind phenomenon described so far are first remembered in a brief summary.

Pressure measurements on 1 m circular cylinder with 10 rings of 7 mm in width at spacing of 100 mm (scale 1:1000 to the prototype) have shown:

1. two steady asymmetric states (namely "state 1" and "state 2");
2. a bi-stability of the flow, i.e. a change of state in time;
3. a spanwise inversion, i.e. a change of state in space.

It was not found, at increasing Re, any tendency for this phenomenon to disappear. Instead, the phenomenon is cancelled out by the efflux and the effect is mitigated by using fewer and/or smaller rings.

The phenomenon is more evident in the upper part of the tower, this would support the thesis that it is a 3D effect, related to the free-end. The occurrence of the phenomenon does not depend significantly on the atmospheric boundary layer. The characteristics of the atmospheric boundary layer are not governing parameters, they only influence the development – or the disruption – of the phenomenon along the height. The spanwise inversion may be interpreted as a cascade effect in the neighbouring compartments, starting from the highest one. The change of state in time, i.e. the jump, appears randomly: no periodicity has been found. This random nature of the bi-stability reflects the random nature of turbulent flow. Relying on the wind tunnel measurements, it is not straightforward to state that a symmetric state can be obtained if an infinitely long period is considered. In fact, the asymmetric conditions, once formed, tend to establish. Each state is intrinsically stable. The change of state must then receive some stronger input from the flow in order to initiate and take place. It is not astonishing, therefore, that sometimes this input is not found in the time window of a measurement. In any case, asymmetric states generally persist so long that the design of the structure should necessarily include the asymmetric interval, even though the structure is symmetric.

Secondary vortices like separation bubbles develop in the wake on one side only of the cylinder, that is called in this work "bubble side". A key role, from the fluid-dynamic point of view, is the near-wake structure. In fact, the structural design is not directly governed by wake fluctuations, but the development of a certain wake structure and a vortex street are responsible for cross-wind loads and body-induced fluctuations in the attached boundary layer before separation.

An in-depth examination of the cross-wind phenomenon introduced in section 5.2 has led to the physical interpretation proposed in the following. The focus is not in the jump between two states, rather on the asymmetric steady condition within each state.

Von Karman vortex separation produces an oscillation of the separation point. Instantaneously, the pressure distribution is not symmetric, but the lateral suction increases on the side of the cylinder where the vortex is growing, before being shed. However, the phenomenon described in section 5.2 is not dealing with an instantaneous asymmetry of pressures, which produces an oscillating cross-wind force. This would be the well-known phenomenon of vortex separation. Instead, section 5.2 describes a steady asymmetric state, which produces a mean lift. This is a first fundamental characteristic. Therefore, the asymmetry must be sought at first in the averaged position of the separation point in the mean pressure distribution. Separation angles are identified at $z/H = 0.95$ in Figure 5.21, referring to the state 1.
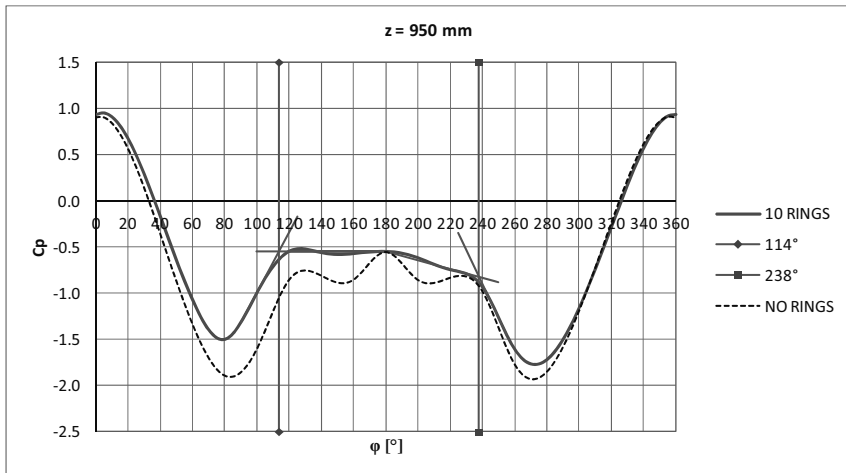
Figure 5.21 Mean pressure distribution and separation angles (WiSt, T1-SR1/SR0-R1-EF0)

Figure 5.21 describes the horizontal distribution and the strong asymmetry at a certain cross-section (z = 950 mm), but it cannot say anything about the three-dimensionality of the effect within the compartment and between different compartments. This issue is better addressed – in a first stage – by the cross-correlation coefficients; then they will be split up in the frequency domain. Since the phenomenon is a sort of cascade effect from the highest compartment (i.e. compartment number 10), the cross-correlations within this compartment and between it and the neighbouring one are investigated, both far from the rings and close to them. One state is considered alone.

Figure 5.22 shows the circumferential cross-correlations within compartment number 10, i.e. between levels $z_1 = 950$ mm and $z_2 = 910$ mm. The continuous line refers to the case with 10 rings (SR1), while the dashed line refers to the case without rings (SR0). At stagnation and for a certain region downstream the presence of rings does not modify the cross-correlations within the compartment: the ring beam is like not-existing. Then, at a certain angle, the cross-correlations SR1 drop down significantly. The asymmetry of the mean pressure distribution is also confirmed in the cross-correlations, because such a drop starts earlier on one side of the cylinder (0°-180° in this case). By looking at Figure 5.21, it can be seen that the drop starts earlier on the normal side. The earlier drop in the correlations likely reflects an anticipated separation of the boundary layer on the normal side of the cylinder, with respect to SR0, where separation is normally at large angles due to the tip effect. Since the cross-correlation is between two levels ($z_1 = 950$ mm, $z_2 = 850$ mm), the earlier separation may occur either at the level z_1, or at the level z_2, or on both levels.
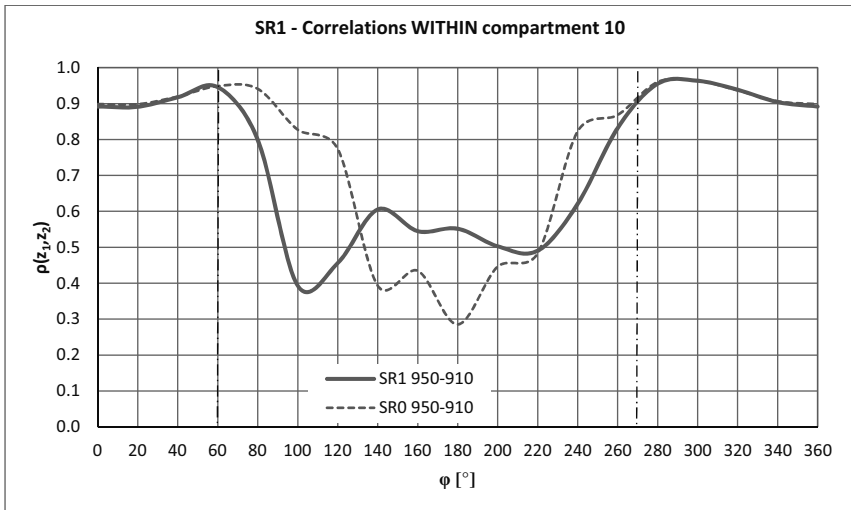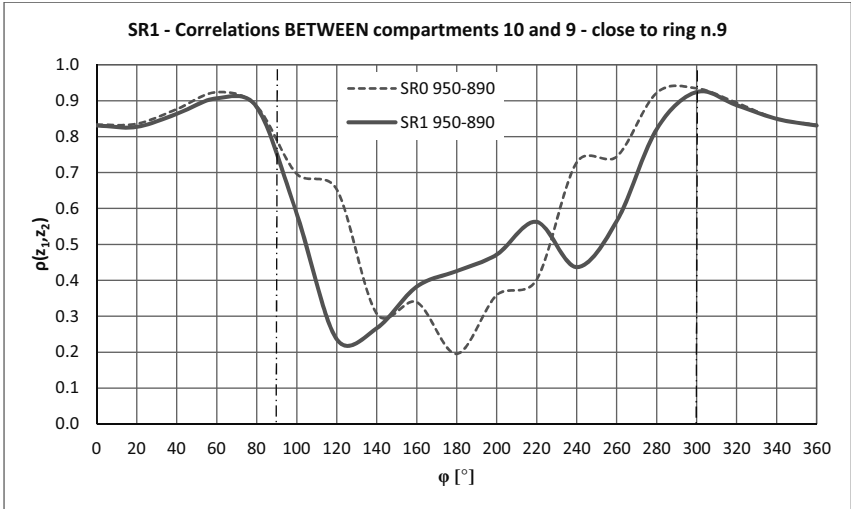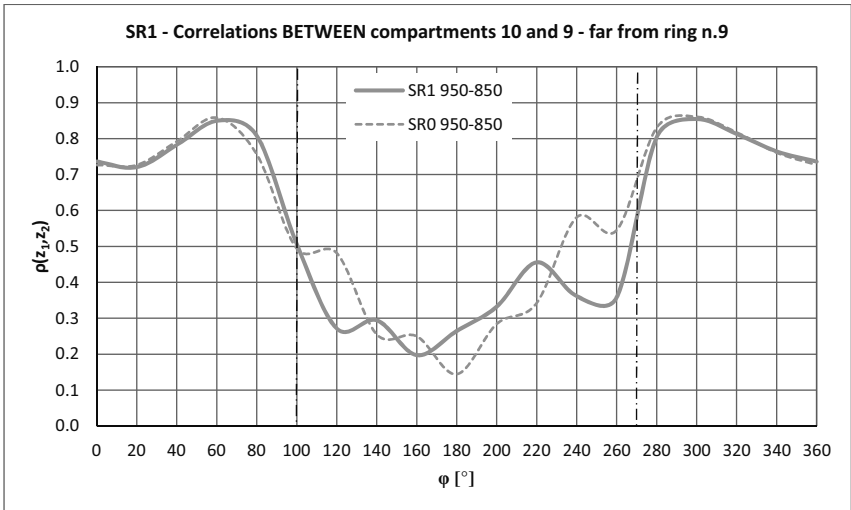

Figure 5.22 Cross-correlations of C_p between two levels
10 rings (continuous line SR1), without rings (dashed line SR0)
$z_1 = 950$ mm, $z_2 = 910$ mm (WiSt, T1-SR1/SR0-R1-EF0)

Let us consider the reference height $z_1 = 950$ mm, as before. Figure 5.22 described the cross-correlations of this level within the compartment. Now, the cross-correlations with the neighbouring compartment are added (Figure 5.23 and Figure 5.24). In particular, Figure 5.23 shows the cross-correlations of $z_1 = 950$ mm with a level close

to the ring n.9 (below it, $z_2 = 890$ mm) and Figure 5.24 shows the cross-correlations with a level in the middle of the compartment below ($z_2 = 850$ mm). It must be remembered, from Figure 5.22, that $\rho(950,910)$ drops early on one side at about 60° due to the effect of the ring. It is now remarkable to see that such an earlier drop on the same side of the cylinder, i.e. at 60°, does not appear neither in Figure 5.23 nor in Figure 5.24. In fact, $\rho(950,890)$ and $\rho(950,850)$ are not affected by the rings until about 90°-100°. Instead, perfectly consistent with the inversed mirrored condition previously described in terms of $C_{p,m}$ and $C_{p,\sigma}$, an earlier drop at 300° (i.e. -60°) occurs in $\rho(950,890)$. Even more remarkable, is that the correlation between middle levels in different compartments (950 and 850 mm) does not perceive the earlier drop (Figure 5.24). This suggests that the effect of the ring is an earlier separation that develops within the compartment on one side only of the cylinder, as we move closer to the ring. The cross-correlations between middle levels remain unaffected much longer downstream.

In Figure 5.22, the movement towards the ring is from above (because $z_1 > z_2$) and the earlier drop is at 60°. Figure 5.25 ($\rho(850,890)$) is like Figure 5.22 – i.e. it shows the cross-correlations within the compartment – but in the compartment below. The reference level is $z_1 = 850$ mm and the movement towards the ring is from below ($z_1 = 850$ mm $< z_2 = 890$ mm). The cross-correlations confirm not only the asymmetry of the pressures, but also the inversion between different compartments, because the earlier drop in the cross-correlations $\rho(850,890)$ occurs mirrored with respect to Figure 5.22, i.e. at 300°.

Therefore, the earlier drop of the correlation coefficient on one side only of the cylinder (normal side) and close to the ring (either above or below it) is explained by an earlier separation of the boundary layer at the ring (earlier than in absence of rings). On the other side of the cylinder, as well as in the neighbouring compartment on the same side, instead, the flow remains longer attached (separation is delayed). That is the bubble side. This movement of the mean separation line induced by the rings is confirmed by the mean pressure distributions calculated during only one state: the separation line is not at a symmetric position on the two sides of the cylinder (thus the steady asymmetry results, as shown in Figure 5.26 and Figure 5.27) and presents a discontinuity at the ring. In other words, the wake is not aligned in the rear of the cylinder.

Figure 5.23 Cross-correlations of C_p between two levels
10 rings (continuos line SR1), without rings (dashed line SR0)
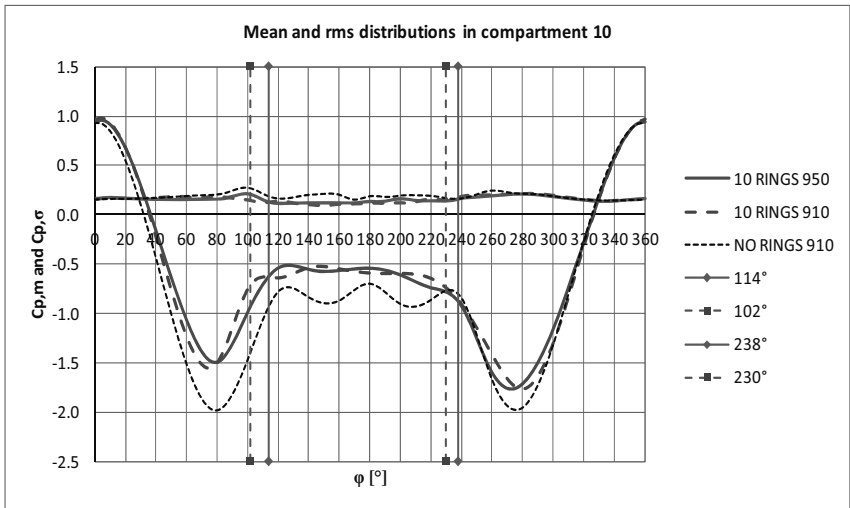*$z_1 = 950$ mm, $z_2 = 890$ mm (WiSt, T1-SR1/SR0-R1-EF0)*

Figure 5.24 Cross-correlations of C_p between two levels
10 rings (continuos line SR1), without rings (dashed line SR0):
$z_1 = 950$ mm, $z_2 = 850$ mm (WiSt, T1-SR1/SR0-R1-EF0)
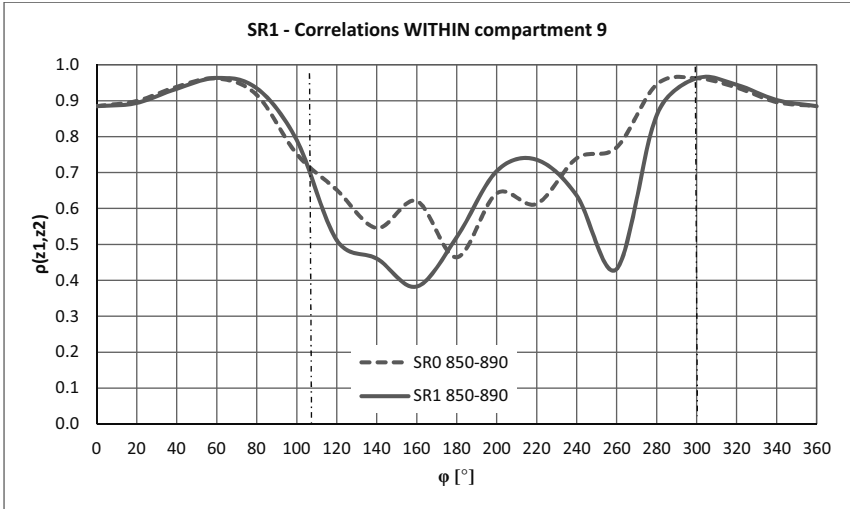
Figure 5.25 Cross-correlations of C_p between two levels
10 rings (continuos line), without rings (dashed line):
$z_1 = 850$ mm, $z_2 = 890$ mm (WiSt, T1-SR1/SR0-R1-EF0)

Figure 5.26 Angles of separation in the compartment n.10
(WiSt, T1-SR1/SR0-R1-EF0)
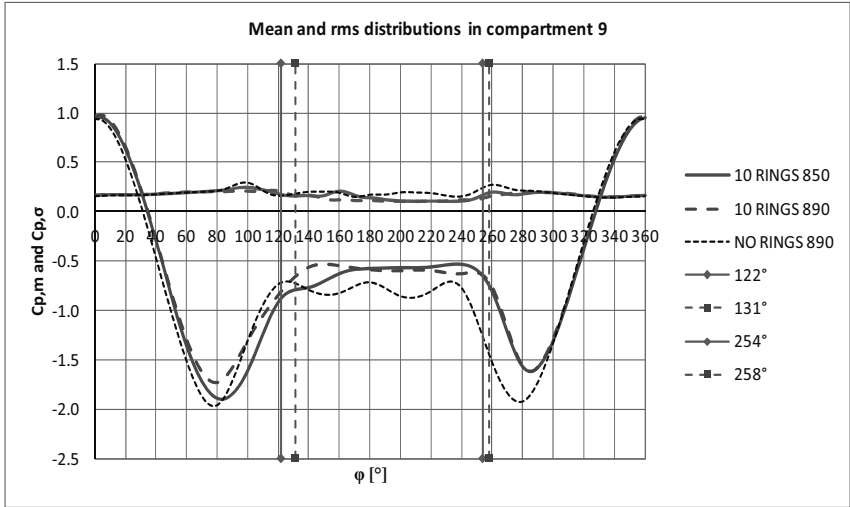
Figure 5.27 Angles of separation in the compartment n.9
(WiSt, T1-SR1/SR0-R1-EF0)
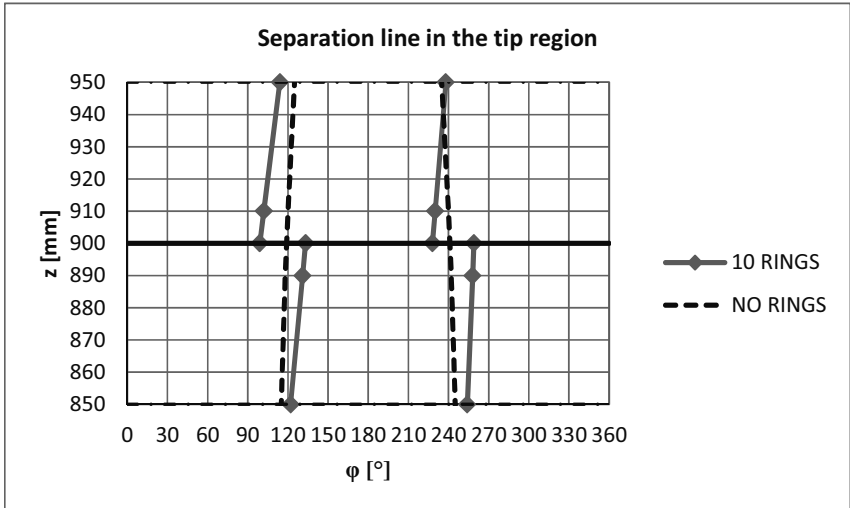
Figure 5.28 Discontinuity of the mean separation line within one state
(WiSt, T1-SR1/SR0-R1-EF0)

A jump between two states produces an inversion of the position of the separation line around the circumference. Then, around the circumference, there is an appreciable movement of the mean position of separation, which can be identified in the pressure measurements. For example at the level 890 mm, the separation point oscillates around two different mean positions, which alternate in time: one is before 120° and one is after that. Therefore, the time history recorded at $\varphi = 120°$ shows two different states of the flow (Figure 5.29): the pressure tap lies once in the attached boundary layer before separation (higher rms) and once in the wake (lower rms).
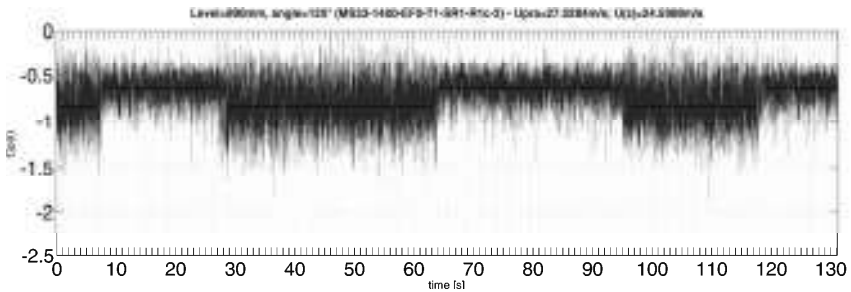
Figure 5.29 Bistability of the flow: movement of mean separation point
(WiSt, T1-SR1-R1-EF0)

Figure 5.22 (referring to compartment n. 10) showed an anticipated drop of the cross-correlation coefficients on the side 0°-180° in case of ten rings. The same happened in the compartment below on the side 180°-360° (Figure 5.25). It is now interesting to split up the cross-correlation coefficients between two levels at a certain angle in the frequency domain (Co-spectrum(z_1,φ_1; z_2,φ_1)/$\sigma_1\sigma_2$), in order to indentify the missing contributions with respect to the case without rings. The angle 100° and 260° are chosen as reference in both compartments 10 and 9. In particular, the angle 100° lies on the normal side in compartment 10 and on the bubble side in compartment 9. The opposite holds for the angle 260°. Figure 5.22 and Figure 5.25 show that ρ(950,910) at 260° and ρ(850,890) at 100° (bubble sides) are basically the same both in presence and in absence of rings (SR1 and SR0). It is then surprising that the difference in case of rings is on the so-called normal side. The missing contribution in SR1 can be identified in the frequency domain. It results to be a typical 3D effect of circular cylinders with a free-end. It is a proof that the rings interact, somehow, with the three dimensional flow. In fact, Figure 5.30 a), d) shows that the missing contribution in the co-spectra of C_p on the normal sides (0°-180° in compartment 10 and 180°-360° in

compartment 9) are not in the frequency range of Karman vortex shedding (nD/U ≈ 0.2), but at lower frequencies.

In order to understand the phenomenon created by the rings, it is now important to go one step back and investigate deeper the flow around the free-end, even in absence of rings. So far, the effect of the rings has been described as an asymmetric pressure distribution, associated to a fragmented separation line and a misaligned wake of the cylinder. The study of the cross-correlations within the same compartment and in different compartments has suggested that an earlier and a delayed separation develops at the rings. The phenomenon evolves within the compartment as one moves towards the ring; the cross-correlations at middle levels between rings are not affected much longer downstream. The frequency split-up of the cross-correlations at about 100° between different levels allowed to identify the range of frequencies where, in presence of rings, the phenomenon acts. It is not the range of Karman vortex shedding ($S_t ≈ 0.2$). Rather, it is a lower range, that results to be – by literature documentation – the frequency range of TAV, tip-associated-vortices (Kitagawa et al., 2001).

Tip-associated-vortices, described in Chapter 3, should not be confused with the longitudinal trailing vortices at the tip of the cylinder, which are created by the interaction between the upwards flow at the flanges and the downwards flow over the tip. The TAV are bigger Karman vortices, at a frequency around one third of the usual Karman frequency at intermediate levels. They are responsible for the variation of the Strouhal number in the tip region which is produced, according to Farivar (1981), by the entrainment in the wake and elongation of the eddy formation region. The tests performed by Kitagawa et al. (2001) constitute, so far, one of the deepest investigations of TAV. Those tests are performed in uniform flow on a H/D = 26 circular cylinder. Therefore, it is not surprising that the TAV are confined at high-levels and do not interact with the Karman vortex shedding at middle height (Figure 3.34c). A different situation and a stronger interaction should be expected on a H/D = 7 circular cylinder. In fact, in our experiments, double-peak spectra – low frequency peak due to TAV and Strouhal peak due to Karman vortex shedding – describe the cross-wind fluctuations at the high levels in SR0. As it will be shown in Chapter 6 by comparison with CRIACIV, the boundary layer influences the either stronger or weaker interaction between the two peaks at different levels. In any case, there is general agreement on the shedding frequency of TAV, about nD/U = 0.07, as confirmed by Kitagawa et al. (2001) and Park&Lee (2000). The results of the present work in SR0 are a further confirmation.
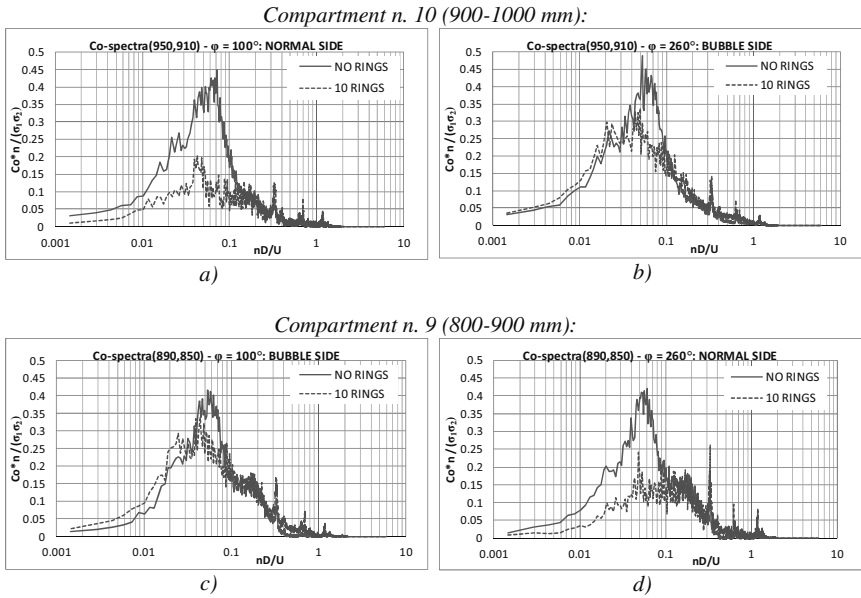
Compartment n. 10 (900-1000 mm):

a)

b)

Compartment n. 9 (800-900 mm):

c)

d)

Figure 5.30 Asymmetry of the of the flow in the frequency domain:
blue line: no rings; red line: 10 rings;
a) Co(950,910) at 100°; b) Co(950,910) at 260°;
c) Co(850,890) at 100°; d) Co(950,890) at 260°;
x-axis: nD/U_{1000}; y-axis = $Co_{Cp}(z_1,z_2)*n/(\sigma_1\sigma_2)$;
(WiSt, T1-SR0/SR1-R1-EF0)

Figure 5.31 shows the strong interaction in absence of spanwise rings between the low-frequency peak at $nD/U = 0.062$ and $S_t = 0.2$.

The TAV predominate at $z/H = 0.95$, where the Karman vortex shedding is weak (but not completely absent).

At $z/H = 0.85$ there is a strong interaction between the two peaks and then the low-frequency peak disappears at $z/H \leq 0.75$. Only a skewness of the spectra remains.

It is also observed (not shown) that in presence of efflux the low-frequency peak disappears. In Chapter 7 the effect of the low-frequency peak on the response will be investigated. It essentially gives a contribution in the quasi-static oscillation, on which Karman resonance is superimposed.

a) z = 950 m

b) z = 850 m

c) z = 750 m

d) z = 650 m
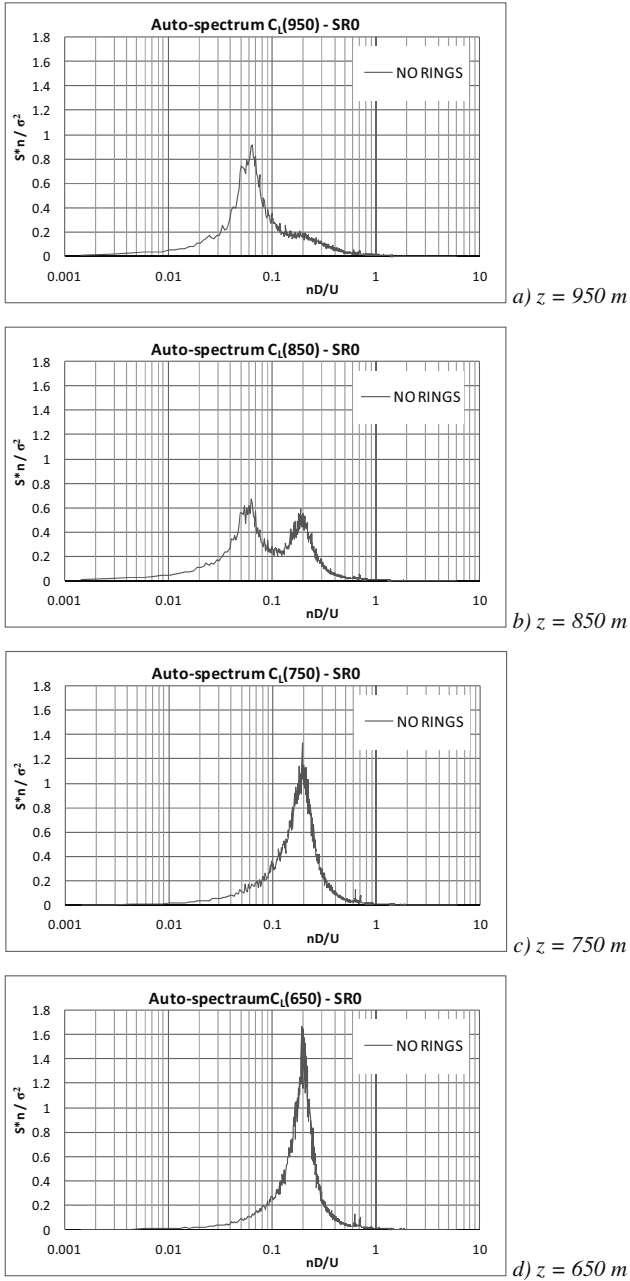
Figure 5.31 Lift spectra along the height without rings (WiSt, T1-SR0-R1-EF0)

In this section, it is interesting to analyze the effect of the rings on the TAV. It is interesting to see in Figure 5.32 that the spectra of lift coefficients in the tip region are not double-peak spectra (as they are in SR0), but they present only one peak at Strouhal number 0.2 (von Karman vortex shedding). Actually, it was for this reason, that the spectral analysis in case of ten rings alone could not say so much, before being compared with the corresponding case without rings. The single-peak lift spectra in SR1 appeared to be perfectly reasonable at first sight. Only the comparison with the results of the circular cylinder without rings highlighted the disappearance of tip-associated-vortices.

In terms of pressures, Figure 5.30 has suggested that the low frequency peak due to tip associated vortices is fragmented on the normal side of the cylinder at each level, while such bigger vortices still remain on the bubble side. These big vortices associated to low frequency contributions, which remain on one side only of the cylinder, are responsible for the delayed separation on the bubble side. This explains also the asymmetry. Moreover, since low frequency tip-associated vortices are fragmented on one side of the cylinder in case of ten rings, they do not produce lift fluctuations: the low-frequency peak in the lift disappears.

Compartment n. 10 (900-1000 mm):

a)   *b)*

Compartment n. 9 (800-900 mm):

c)   *d)*

Figure 5.32 a-d) Lift spectra at 950-910-890-850 mm. $S_{CL}(z_1)*n/\sigma$ vs nD/U_{1000}; (WiSt, T1-SR0/SR1-R1-EF0)

Kitagawa et al. (1999) placed a circular disk (not a ring) on the top of a circular cylinder of finite length and observed the disappearance of tip vortices. The disk had a diameter of 1.6 times the tower diameter. A smaller disk (with a diameter 20% larger than the tower diameter) was not able to suppress the tip vortices, it just reduced their strength. Kitagawa concluded correctly that the tip vortices were produced by the free-end and therefore some modification of the free-end conditions would have altered them. One may then think that the top ring on the solar tower could have, alone, the same effect as the disk placed by Kitagawa, although the diameter of the ring is only 10% larger than the tower diameter, comparatively smaller than what Kitagawa observed. Due to the small dimensions of the ring, such a strong effect would be surprising. In fact, by adding the results of the tests with the five ringed cylinder, a new explanation can be supposed.

Figure 5.33 shows the vertical cross-correlations of lift forces between different compartments. The reference level is 950 mm. A similar picture (Figure 6.15) will also be shown in Chapter 6 as further proof. Figure 5.33 shows that the lift cross-correlations in case of five rings follow the same bahaviour as in SR0 (no rings). The co-spectra divided by the product of the standard deviations, i.e. the split up over frequencies of the cross-correlation coefficients, prove that in case of five rings the tip vortices are not suppressed. It should also be remembered (Figure 5.20) that in case of five rings the flow is neither asymmetric nor bistable. Instead, in case of ten rings, $\rho, C_L(950,850)$ (i.e. $\rho, C_L (\Delta z=100)$) is much lower because the contribution of the tip-associated vortices is missing.

It follows that a certain distribution of rings, at a sufficiently small distance, interacts and kills the bigger vortices in the tip region. It should also be observed that in case of ten rings the distance between them is 10 cm in the scale of the wind tunnel model (i.e. 2/3 of the diameter) and in case of five rings the distance between them is 20 cm (i.e. 4/3 of the diameter). Between 10 and 20 cm, the value 15 cm lies. This is actually the tower diameter. Although so far there is not an experimental proof of it, it can be supposed that the tower diameter could be taken as reference to calibrate the distance between rings, in order not to interact with tip vortices. Even more, it could be supposed that, since the big tip vortices develop only in the tip region, the key feature is the distance between rings only in the tip region and not all along the tower. In this regard, Chapter 8 will mention, among future outlooks, the importance of doing tests where the ring beams are not equally distributed along the heihgt, but they are placed at larger distance (e.g. 4/3D) in the tip region only.
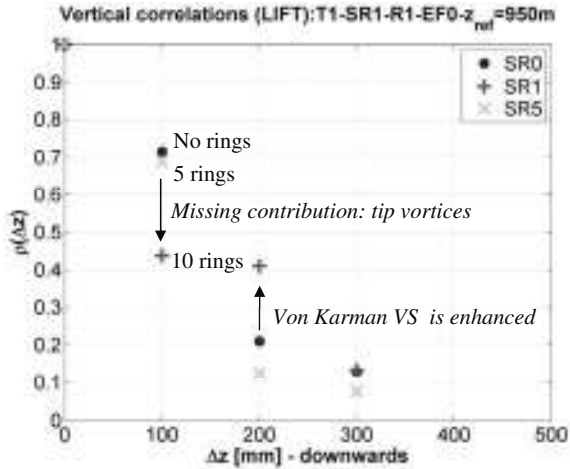
Figure 5.33 Cross-correlation coefficients of C_L
without rings (blue), 10 rings (red) and 5 rings (green). z_{ref} = 950 mm
(see also Figure 6.15)
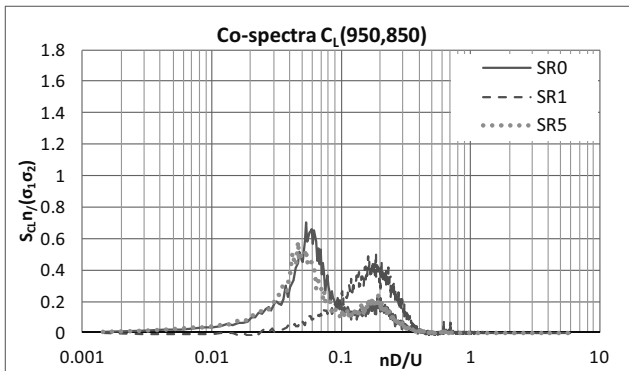
Figure 5.34 Co-spectra of C_L: $S_{CL}(z_1,z_2)*n/\sigma^2$ vs nD/U, z_1 = 950 mm, z_2 = 850 mm; (see also
Figure 6.16). (WiSt, T1-SR0/SR1/SR5-R1-EF0)

A further proof that the tip vortices are disturbed by rings placed at a too small distance is given by the experiments with 10 small rings (KR1). In that case, the flow is not able to undergo jumps, but it is asymmetric (Figure 5.20). Figure 5.35 shows that ten rings, at a smaller distance than the diamter (2/3 of it, in this case) are able to suppress tip associated vortices, even if the rings are small. Figure 5.36 proves that the Karman vortex shedding ($S_t \approx 0.2$) is not significantly affected by the rings. The low-frequency contributions in the spectra of SR1-SR5-KR1 represent the oscillations produced in the time histories by the changes of state (e.g. in Figure 6.9 at 650 mm).

The spectra are evaluated separately in each interval of time, the intervals are clearly detectable for example by looking at the time histories of either lift force or pressures in the tip region (see Figure 5.3 and Figure 5.4, the selection of intervals is evident). However, as it will be better explained in Chapter 6 (Figure 6.12), the stability within each state is progressively lost at low levels and even within the same interval of time the frequency of jumps between the two states increases. However, a predominant low frequency peak cannot be identified.
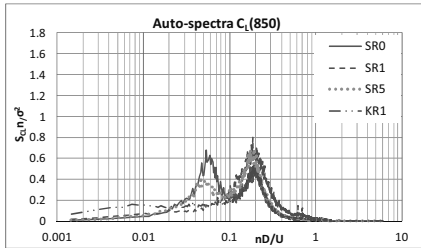
Figure 5.35 Lift spectra at 850 mm.
$S_{CL}(z_1)*n/\sigma^2$ vs nD/U_{1000}; (WiSt, T1-
SR0/SR1/SR5/KR1-R1-EF0)
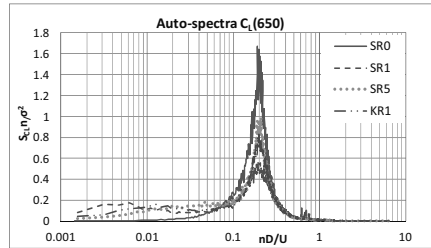
Figure 5.36 Lift spectra at 650 mm.
$S_{CL}(z_1)*n/\sigma^2$ vs nD/U_{1000}; (WiSt, T1-
SR0/SR1/SR5/KR1-R1-EF0)

The auto-spectra are normalized with respect to the variance, so that the area is one. The following table reports the variances, for the sake of completeness.

Table 5.1 Variances of C_L

	C_L, σ^2			
	SR0	**SR1**	**SR5**	**KR1**
950	0.020	0.014	0.053	0.027
850	0.033	0.017	0.034	0.042
750	0.020	0.022	0.053	0.044
650	0.022	0.039	0.030	0.035

The TAV are a typical three dimensional effect due to the free-end: the reason for the lower frequency contribution close to the top is the entrainment of flow in the wake from above the cylinder, as previously said. The numerical simulations in Chapter 6 will clarify that the entrainment of flow in the wake results to be significantly altered by the presence of rings. This motivates not only the disappearance of tip-associated-vortices, but also the asymmetry and the spanwise inversion.

It is straightforward to wonder what it may happen if the entrainment in the wake is prevented, for example by an end-plate. In other words, what would happen in 2D

flow? Within this work, it has not been possible to perform experiments in 2D flow, because a new wind tunnel model with two end-plates, as well as a different experimental set-up would have been necessary. However, on the basis of the results obtained, it is inferred that the bistable flow disappears in 2D conditions (Chapter Chapter 8).

5.5 Effect on wind load

In the tip region, where the asymmetric flow is particularly apparent in SR1 (Figure 5.37), the steady lift is enhanced by high suction on the bubble side (that is, in any case, comparable to SR0) and the relatively lower suction on the normal side. However, C_L remains in any case relatively low (about 0.2-0.3), and the resulting bending in the cross-wind direction is not significantly high (see section 7.2.2).

The typical second islet of $C_{p,min}$ in the wake of the cylinder (see e.g. Figure 3.23, Figure 3.24, Figure 3.25, Figure 3.29), produced – according to Kawamura et al. (1984) – by the attachment of trailing swirls, is clear in SR0, but it cannot be detected in SR1 (Figure 5.37a). Such a minimum pressure islet in the tip region is responsible, on free-end cylinders, for the increase in drag in the tip region. Therefore, the tip effect is less pronounced in presence of rings (Figure 5.39). Instead, along the height, the drag coefficient is higher in SR1 than in SR0, due to the separation bubble in the wake, as proved by the mean pressure distribution at 650 mm in Figure 5.38.

On the normal side of the cylinder at middle height the mean and rms distributions of C_p (averaged within only one state) resemble the corresponding distributions in absence of rings. On the bubble side, the negative mean pressures decrease after 90° and this increases the drag force. Also the rms values increase on the bubble side. The effect on the response is quantified in sections 7.2.2 and 7.3.4.

a) b)
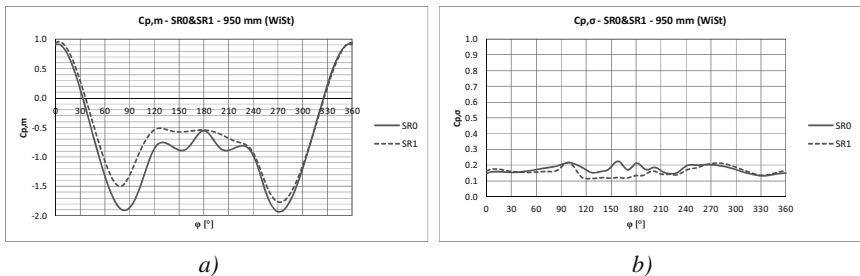
Figure 5.37 $C_{p,m}$ (a) and $C_{p,\sigma}$ (b) in the tip region with and without rings (WiSt, T1-SR0/SR1-R1-EF0)

a)   *b)*
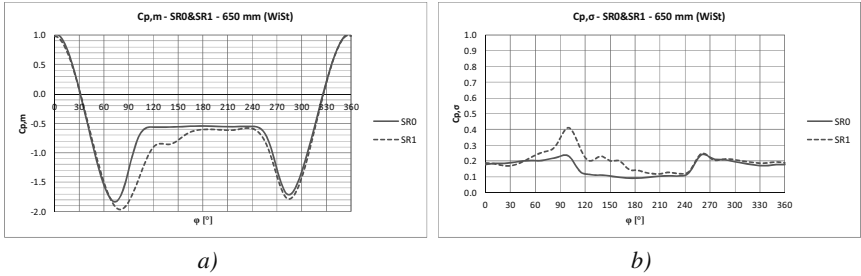
Figure 5.38 $C_{p,m}$ (a) and $C_{p,\sigma}$ (b) at middle height with and without rings
(WiSt, T1-SR0/SR1-R1-EF0)
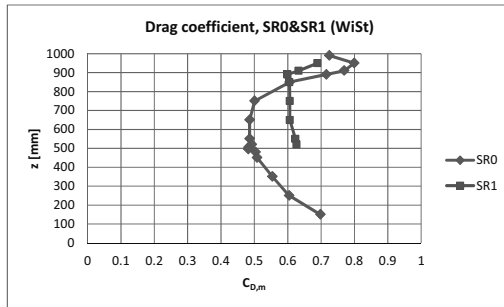
Figure 5.39 $C_{D,m}$ with and without rings (WiSt, T1-SR0/SR1-R1-EF0)

Measurements at low levels (z/H < 0.5) are not available in case of rings at WiSt. However, in order to figure out a three-dimensional distribution of the asymmetric load, the same behaviour as in Figure 5.38 is also hypothesized at lower levels so that, in practice, the presence of rings increases the load on the bubble side. Figure 5.40 and Figure 5.41 plot the resulting $C_{p,m}$ and $C_{p,\sigma}$ distributions, respectively. They are idealized distributions on the safe side, because the two states tend to be mixed as the height decreases (Figure 6.12).

a)   *b)*
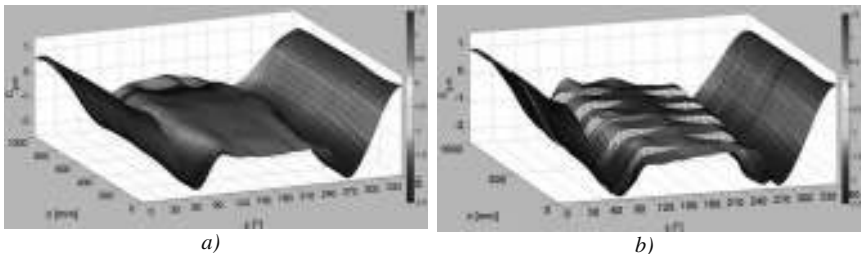
Figure 5.40 $C_{p,m}$ on the tower: a) without rings; b) with 10 rings (WiSt, T1-SR0/SR1 -R1-EF0)
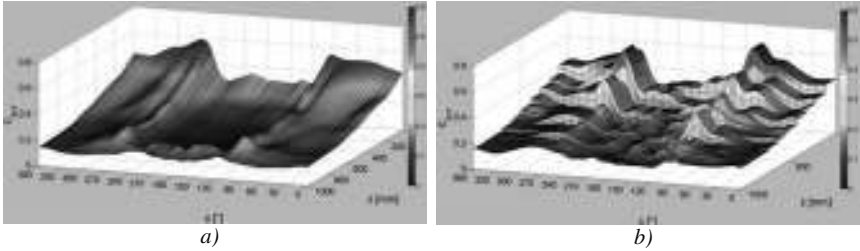
Figure 5.41 $C_{p,\sigma}$ on the tower: a) without rings; b) with 10 rings (WiSt, T1-SR0/SR1 -R1-EF0)

While in terms of $C_{p,m}$ and $C_{p,\sigma}$ the effect of the rings is a general increase in load, the correlation field is generally reduced.

In terms of horizontal correlations, in case of rings the matrices lose the symmetry with respect to the secondary diagonal, because of the asymmetric conditions between the two sides of the cylinder. Apart from that, the differences are not so relevant. The level z/H = 0.75 is chosen as representative in Figure 5.42, but the same concept applies at the other levels, too. In the case of rings, the correlation field is smoother on the bubble side (180°-360°), where the downstream movement of the separation point, together with the separation bubble, conceal the valley at the separation angle. In the wake, the correlation in case of rings is lower. It consequently decreases the drag force and partly counterbalances the higher Cp_{σ}. However, even though the analysis of the correlation field in SR1 resulted very important for the understanding of the fluid–dynamic phenomenon, structural calculations can safely use the correlation field in SR0 (see Chapter 7).

a)   b)
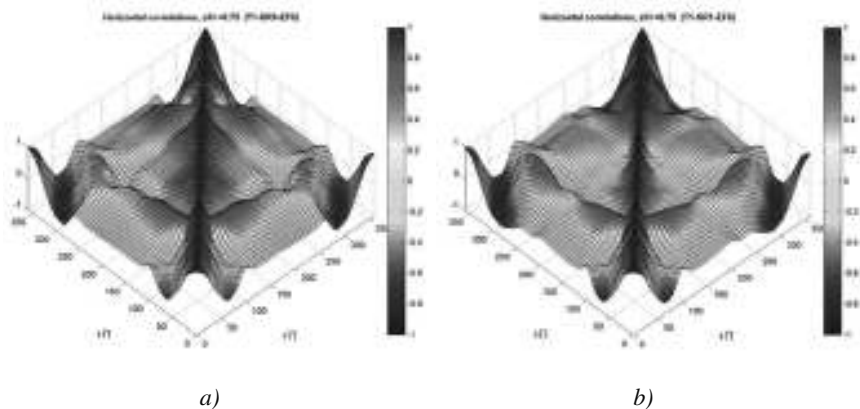
Figure 5.42 Horizontal correlation field at z/H = 0.75: a) without rings; b) with 10 rings
(WiSt, T1-SR0/SR1-R1-EF0)

The vertical cross-correlations are not modified at stagnation and in the frontal region, as motivated in section 5.4. Further downstream, the correlations between levels may show drops in the vicinity of the rings and even at middle levels, as in Figure 5.33. In the wake, there is a reduction of vertical correlations, which is, however, not particularly relevant because the fluctuations in the wake are small.

5.6   **Mitigation strategies**

After the full investigation, any reason could not be detected which suggested the disappearance of the phenomenon at higher Re. It is then believed – so far, on the basis of this work – that the same phenomenon should also occur in full-scale, whether the same number and size of rings of the experiments are used.

The case of ten big rings, i.e. SR1, represents the upper limit in a design condition. Such big rings may not be necessary. Nevertheless, the designer should be aware that an improper use of stiffening rings may produce a negative effect, i.e. the improvement in the structural response can be accompanied by an even more severe load condition.

In the case of rings, the wind load depends on the number, on the size and on the distribution of rings, because different flow structures, like tip-associated vortices and separation bubbles develop in a different way. Therefore, a unified wind load condition for the tower with rings does not exist. The experiments during this work tested several situations and even more are recommended for future research. In chapter 7, a simplified load modelling is provided to the designer. Being unique and being simplified, it cannot include all the load patterns produced by the many different distributions of rings along the height.

Therefore, the aim should be to mitigate, as much as possible, the effect of the rings on the load, in order to design the tower with reference to the design wind load in SR0, that is an established load condition.

Intuitively, small rings at large distance reduce the bistable asymmetric effect. Section 5.3.6 showed that with five rings, even big, the flow is neither bistable nor asymmetric. From the structural point of view, however, it might be preferred to use small rings but more than five. The use of small rings is of course a mitigation strategy, but the tests have shown that e.g. ten rings, even small, still produce an asymmetric flow. In this regard, it is also important to remember that with ten rings, either small or big, the tip-associated vortices are suppressed. Ten rings equally spaced are placed, in this case of study, at a smaller distance than the tower diameter (2/3D). This suggests that a too dense distribution of rings disturbs the tip-associated vortices.

The more pronounced fragmentation of the big vortices on one side of the cylinder produces the not-symmetry, once it is analyzed in the frequency domain. Therefore, rings at a larger distance than one diameter (or, more safely, at 4/3D as it is in SR5) mitigate the effect. If needed, the rings can be placed at larger distance only in the tip region, where the tip-associated vortices are confined.

In any case, it must be remembered that the bistable asymmetric effect is naturally mitigated by the presence of efflux inside the chimney. This is a great advantage, even though out-of-use conditions cannot be neglected.

Chapter 6.   **Experimental and numerical evidence**

This chapter confirms and further analyzes the experimental evidence of asymmetric bistable flow at WiSt laboratory, by a cross-checked investigation at CRIACIV wind tunnel and numerical simulations.

6.1   **CRIACIV wind tunnel (University of Florence)**

6.1.1   **Characteristics and instrumentation**

The CRIACIV laboratory (Centro di Ricerca Interuniversitario Aerodinamica delle Costruzioni e Ingegneria del Vento, www.criaciv.unifi.it) is an open-circuit wind tunnel located at Polo Universitario Città di Prato, which is a branch of the University of Florence. The total length is about 22 m. The tunnel itself has a length of 11 m, with a slightly divergent shape from the inlet (in order to guarantee a constant pressure along the x-axis) and a test section of 2.4 m in width and 1.6 m in height. A turntable in the test section allows to test different wind directions, if necessary. A honeycomb grid is located at the inlet of the tunnel. Details of the wind tunnel are reported in the Drawing 4 on page 194).

The motor – with a nominal power of 160 kW – and the fan are placed at the end of the wind tunnel, followed by a T-shaped symmetric diffuser. The engine allows to attain a maximum wind speed of about 30 m/s with 1500 rounds per minute of the fan. The variation of the rpm is controlled through an inverter up to 50 Hz. The air flow can also be regulated by adjusting the pitch angle of the ten blades of the fan between 7.7 and 15.4. The experiments in this work are performed by setting the frequency of the inverter at either 45 Hz or 50 Hz and the pitch angle at 15.4.

The atmospheric boundary layer profile which is used in these experiments is produced by three bigger "shark-fins" and four smaller spires, followed by roughness panels with wooden cubes (Figure 6.7).

The Prandtl tube allows to measure the static and the dynamic pressure of the incoming flow. During the experiments, only one Prandtl tube, placed above the tower, has been used during pressure measurements on the model. For specific purposes, for example the measurement of the efflux velocity or the mean wind profile at the tower position, a second Prandtl tube is introduced. For the acquisition of these signals, the instruments are connected to a pressure transducer (Setra System, model 239). The

signal is then converted by 32-bit NI card and acquired by a PC. A sampling frequency of 500 Hz is used in the experiments with the Setra System.

Figure 6.1 CRIACIV wind tunnel (University of Florence)

The mean wind profile at the tower position was measured during the experiments by using a mobile Prandtl tube. The mean wind velocity has been indirectly calculated from the dynamic pressure, by using Bernoulli equation. The variation of air density due to temperature variation during the experiments is considered. The result, with respect to the velocity at the main Prandtl tube, is plotted in Figure 6.2. In fact, in order to evaluate pressure coefficients from pressure measurements, the velocity pressure itself, and not the velocity, is used in the calculation.

The turbulence intensity and integral length scale of turbulence L_{ux} were previously measured and tabulated in an internal report of the laboratory. Those data, resulting from hot-wire measurements (Figure 6.3 and Figure 6.4) are referred to in this work.

The pressures on the tower are measured using two different types of pressure scanners:

- Type 1: PSI 8400, consisting of four acquisition units having 16 piezoelectric transducers each and two acquisition units having 32 transducers each. A total

amount of 128 pressures can be recorded simultaneously at a sampling frequency of 250 Hz[4] and a time duration of 30 s.

- Type 2: DTC-Initium, two acquisition units having 32 piezoelectric transducers each. A total amount of 64 pressures can be recorded simultaneously at a sampling frequency of 500 Hz.
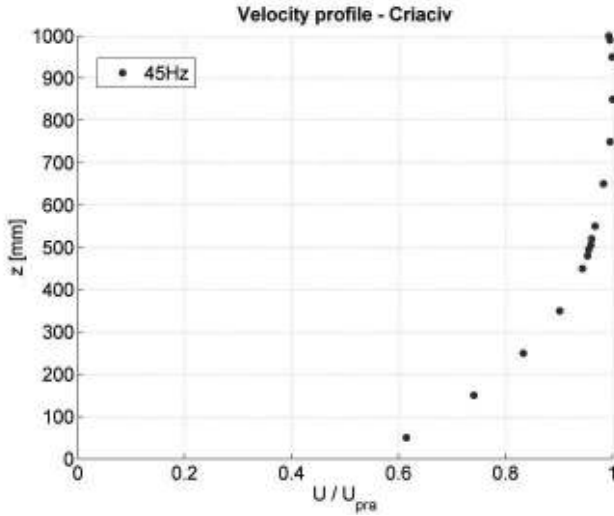
Figure 6.2 Mean wind profile
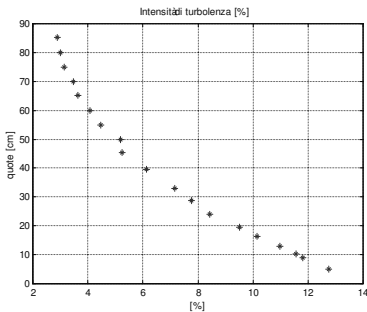
Figure 6.3 Turbulence Intensity Iu (%). (Procino, 2010)
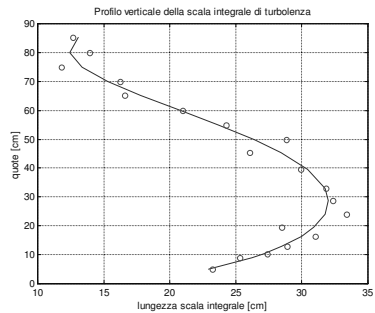
Figure 6.4 Integral length scale L_{ux} (cm). (Procino, 2010)

---

[4] Pressures can be measured with a sampling frequency up to 1 kHz, but the sampling frequency is inversely proportional to the number of channels which are used at the same time. if the maximum number of channels (128) is used simultaneously, the sampling frequency decreases to 250 Hz.

6.1.2 **Outline of the experiments**

The first purpose of CRIACIV experiments is to confirm the experimental evidence at WiSt laboratory, concerning the bistable and asymmetric flow. In every wind tunnel, it is absolutely common to have some disturbance in the flow. The comparison of results in the two wind tunnels proves that the occurrence of the bistable flow is not induced by some local distortion of a certain laboratory. Furthermore, the wind tunnel tests at CRIACIV allowed to better investigate the bistable flow, also at lower levels.

The two different types of pressure scanners cannot be combined together, therefore the tests are divided into two sets: one with 64 sensor type 2, distributed on three external levels in each measurements, able to measure for a relatively long time (131 s) at high sampling frequency, i.e. 500 Hz; one with 128 sensors type 1, distributed at several levels and able to measure at 250 Hz for a duration of 30 s. The set n.2 aims to attain a global correlation field, but with lower degree of detail.

The tests are repeated by using two wind tunnel velocities: $U_{pra} \approx 28$ m/s (frequency of the wind tunnel inverter = 45 Hz) and $U_{pra} \approx 30$ m/s (frequency of the wind tunnel inverter = 50 Hz). The Reynolds number are: $Re = 2.8*10^5$, $Re = 3.0*10^5$. The first one is more comparable with WiSt; the second one is a further test at a slightly higher Re, but it did not show any additional relevant feature. Therefore, the main study has been based on $Re = 2.8*10^5$.

The following series of measurements, associated to the measure of circumferential levels or vertical lines, are defined. Some of the 128 sensors type 1 were out of use at the time of the measurements. The internal pressures were measured, too, in some of the free channels.

- MS51: levels z = 990-950-910 mm;
- MS52: levels z = 910-890-850 mm;
- MS53: levels z = 850-750-650 mm;
- MS54: levels z = 650-550-520 mm;
- MS55: levels z = 520-505-495 mm;
- MS56: levels z = 495-480-450 mm;
- MS57: levels z = 450-350-250 mm;
- MS58: levels z = 250-150-50 mm;
- MS59: verticals at 0°, 20°, 40°;
- MS60: verticals at 60°, 80°, 100°;
- MS61: verticals at 120°, 140°, 160°;
- MS62: verticals at 180°, 200°, 220°;

- MS63: verticals at 240°, 260°, 280°;
- MS64: verticals at 300°, 320°, 340°;
- MS65: levels z = 950-850-750-650-550(only 9 taps)-450(only 9 taps)-50 mm;
- MS67: levels z = 950-850-750-650-550-450-350-250-150-50 mm (only 9 taps at each level);

The experimental campaign was articulated in the following two sets:

<u>Set n.1 (March 2012):</u>

Pressure scanners	type 2
Turbulence setting:	T5
Rings:	SR1
Efflux:	EF0/EF1
Surface roughness:	R1
Wind tunnel velocity (Hz):	45/50
Measurement series:	MS51/52/53/54/55/56/57/58/59/60/61/62/63/64;

<u>Set n.2 (April 2012):</u>

Pressure scanners	type 1
Turbulence setting:	T5
Rings:	SR0/SR1/SR5/SR7
Efflux:	EF0/EF1
Surface roughness:	R1
Wind tunnel velocity (Hz):	45/50
Measurement series:	MS65/67.

The efflux inside the tower is calibrated at a velocity about one half of U_{pra} (Figure 6.5). In order to adapt the model to the facilities of the laboratory, it was decided to simplify the installation (Drawing 3 on page 126, at WiSt) and remove the ventilator. In fact, a suitable opening below the model was enough to guarantee the proper efflux capacity and velocity (Figure 6.8).

However, as previously explained, the most interesting results referred to the condition without efflux.

Figure 6.5 Efflux velocity
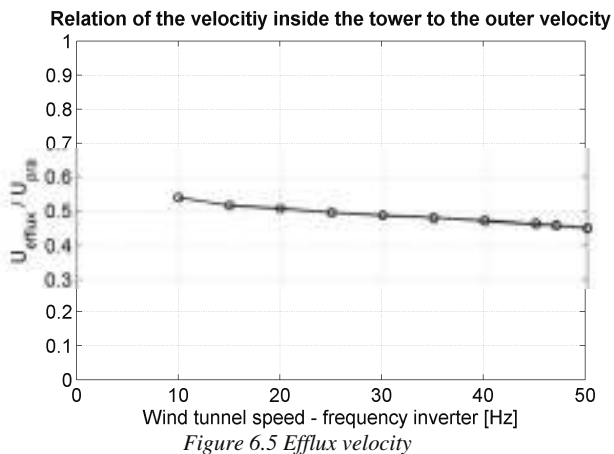
The model for the experiments is the same as in Bochum. A picture of it in CRIACIV wind tunnel is reported below (Figure 6.6). The smooth collector roof was not placed during these tests. In fact, it was seen that its presence did not affect significantly the substance of the results.
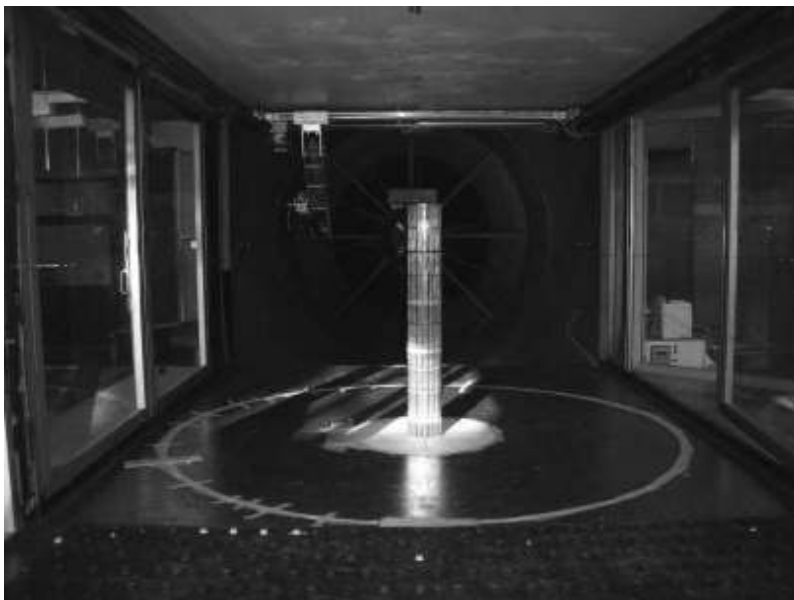
Figure 6.6 Solar tower at CRIACIV wind tunnel
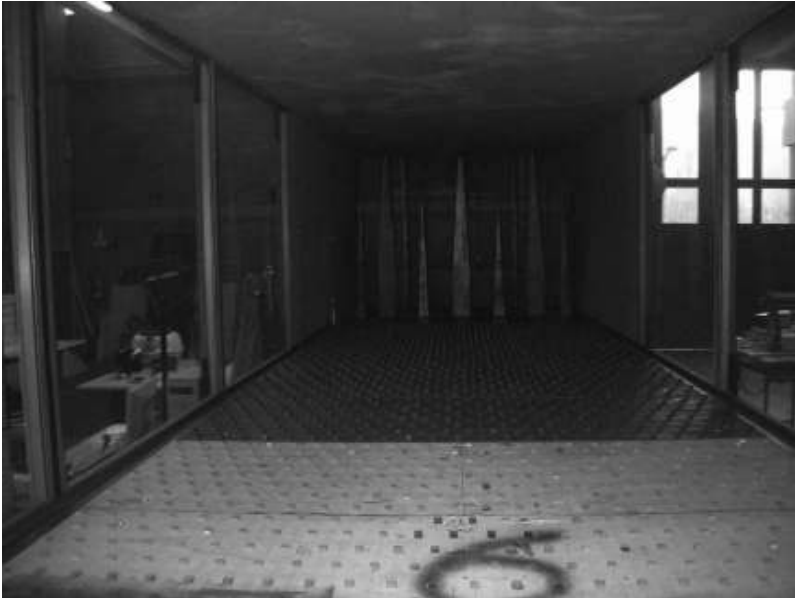
Figure 6.7 Atmospheric boundary layer facilities at CRIACIV
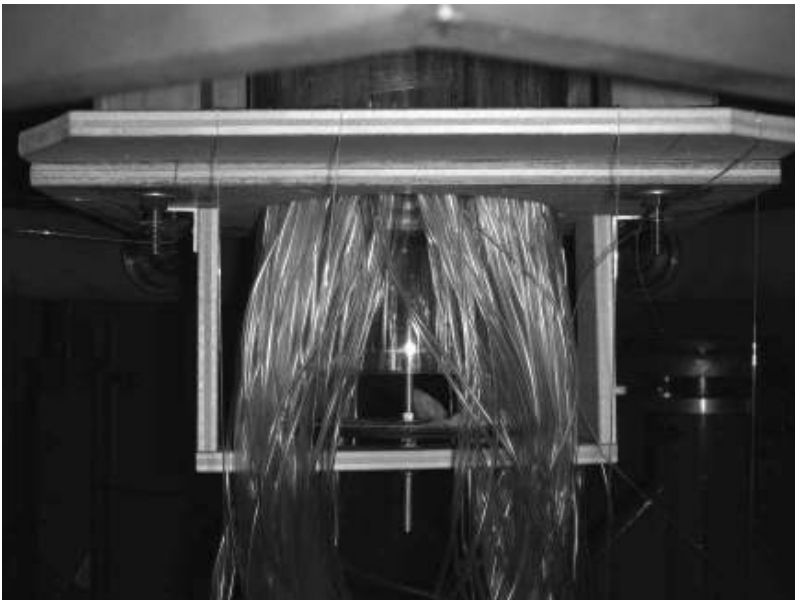
Figure 6.8 Opening below the model for creation of the efflux

0   1000   2000mm

14580
13400
2260   180   3440   2400   3440   200

600
200

310
1200
4590

END DIFFUSOR

1020
END DIFFUSOR

1500

2040

1700
200

2040X2040

DOUBLE BEND WITH VANES
ADAPTIVE SECTION

180
1363

Ø 1884
ELASTIC JOINT

1470

DRIVE AND FAH (157 KW)

180

Ø 2788
ELASTIC JOINT

2400

DIFFUSOR (1.6 X 2.4 - Ø 2788)

2400X1600

X

Y

22093

500

TURN TABLE

2400X1600

WORKING SECTION (2.4 X 1.6 m²)

24500

11000

TUNNEL AXIS

2200X1600

2000

CONTRACTION

3850X2800
3850X2800

600

INLET WITH HONEYCOMBS
STRATIFIER

3850

6700   6700
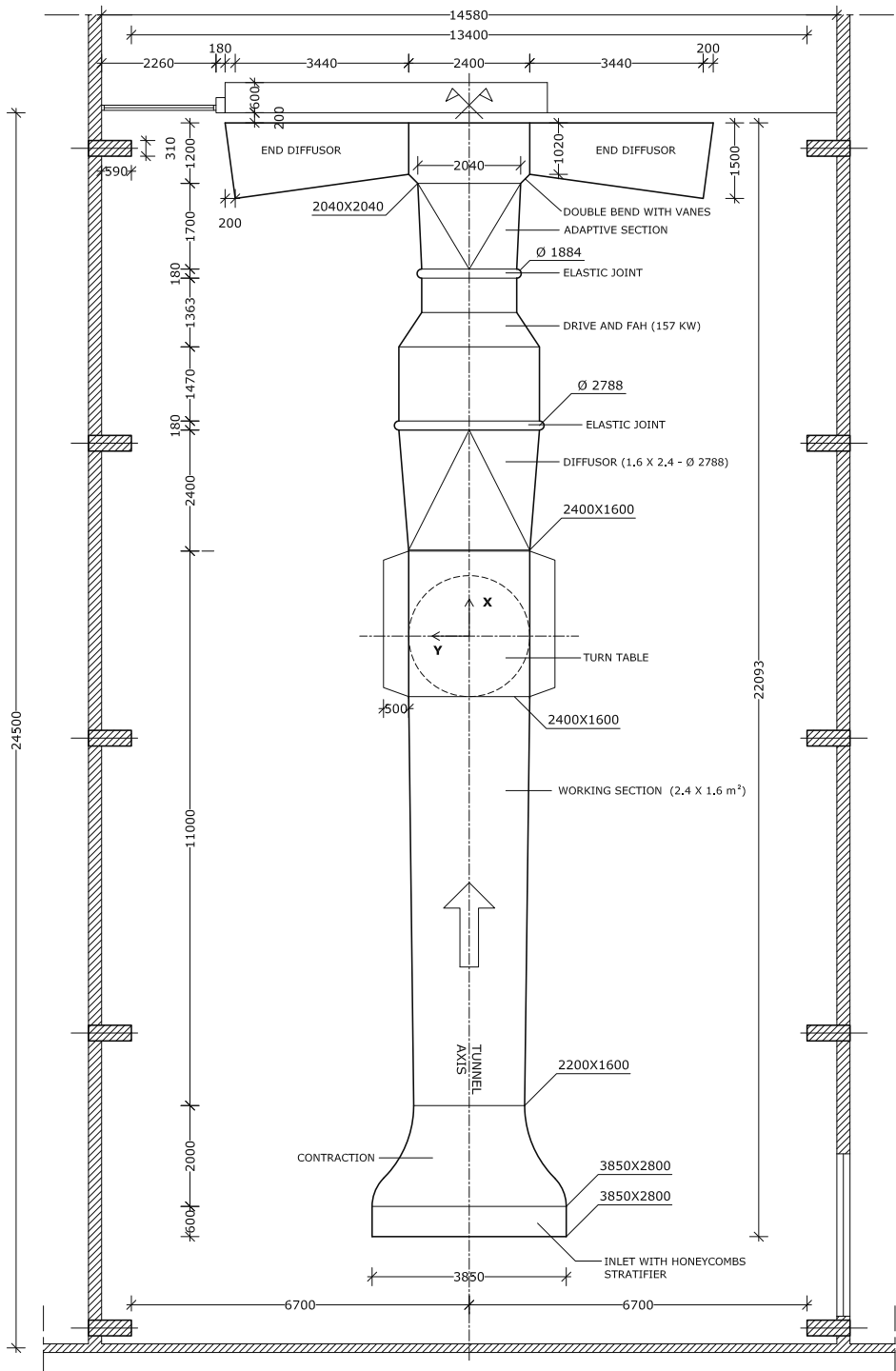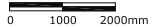
6.2 The bistable flow at CRIACIV

The wind tunnel tests at CRIACIV prove that the bistable flow is a fundamental physical phenomenon, which is not induced by some local distortion of the flow in a given laboratory. Figure 6.9 shows the comparison of pressure coefficients at 100° and at different levels along the height of the tower in the two wind tunnels, in case of ten rings along the height (SR1). The model is the same, therefore any difference between results is only attributable to the flow.

At first sight, it can be seen that the standard deviation of the time histories in each state is different at WiSt and CRIACIV, but this is not surprising, because of the different I_u. The corresponding values of I_u are reported in Table 6.1. Apart from that, the jumps occur in the same manner in the two wind tunnels.

By looking at the time histories, another evidence in the tip region is the existence, in the two wind tunnels, of a predominant state. This lasts longer in every time history. At WiSt, the predominant state in the highest compartment is state 1, i.e. the one which is characterized by positive mean lift in the reference system of the wind tunnel (Drawing 4, page 194). Being the x-axis in the along wind direction, the positive lift in the state 1 is created by a separation bubble on the 180°-360° side of the cylinder. At CRIACIV, the situation is reversed and the predominant state in the highest compartment is state 2, i.e. the one which is characterized by negative mean lift. It means that at CRIACIV the separation bubble in the highest compartment preferably develops on the 0°-180° side, instead of 180°-360° as in WiSt. Then, along the height, the inversion proceeds according to the top condition. In any case, the existence of a predominant state is not due to model imperfections, but to the flow. The question arises about what should be expected in ideal conditions. These cannot be perfectly reproduced in any experiment, but they can be reasonably assumed in a CFD simulation (this issue is addressed in section 6.4).

At a certain level along the height a sort of disruption of the bistable flow starts. The jumps between the two states become more rapid on one side of the cylinder, so that the actual state of the flow is a mixture between the two states. A further insight in this phenomenon will be discussed at the end of this section by using the histograms of pressures along the height until the very low levels. The disruption of the bistable flow starts on the high-suction side of the cylinder, i.e. on the bubble side. This is confirmed in the two wind tunnels by looking in Figure 6.9 at C_p(650mm,100°) in WiSt and C_p(750mm, 100°) in CRIACIV: those pressure taps lie, during the predominant state, on the bubble side. Figure 6.12 clarifies better what occurs at CRIACIV at the levels of disruption on the two sides of the cylinder. It can be seen that the normal side (NS)

remains unaffected until a lower level. This explains why the mixture in C_p(750mm, 260°) and C_p(650mm, 100°) in Figure 6.12 is not so evident. In fact, at those levels the separation bubble preferably develop on the other side of the cylinder, as confirmed by C_p(750mm, 100°) and C_p(650mm, 260°). There, instead, the disruption is clear because those pressure taps lie, during the predominant state, on the bubble side.
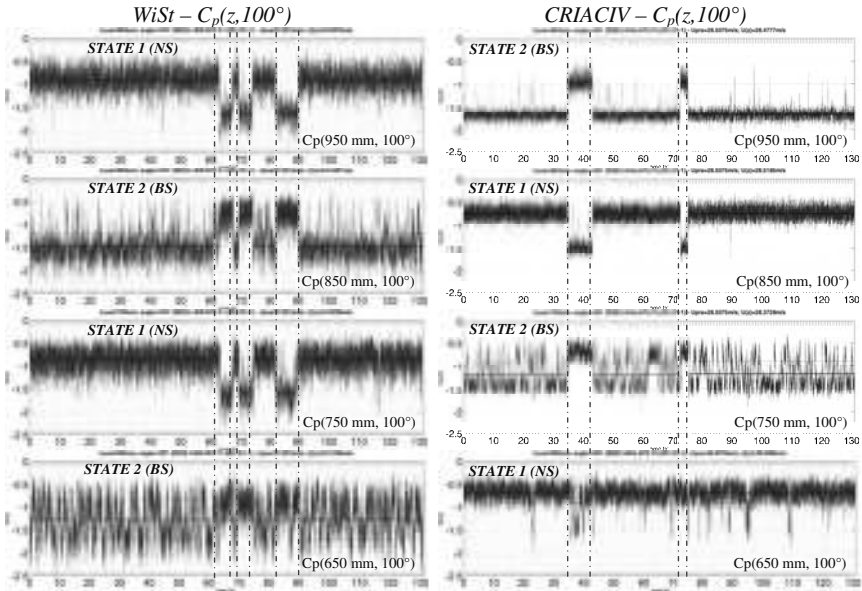

Figure 6.9 The validating result: Wist&CRIACIV (T1/T5-SR1-EF0-R1)
NS = normal side; BS = bubble side (Re = 2.5*10⁵ at WiSt, Re = 2.8*10⁵ at CRIACIV)

Table 6.1 Turbulence intensity at WiSt and CRIACIV

z [mm]	I_u at WiSt	I_u at CRIACIV
950	0.0794	0.0283
850	0.0823	0.0283
750	0.0863	0.0309
650	0.0925	0.0359

The level at which the bistable flow starts disrupting is different in WiSt and CRIACIV. In particular, at WiSt it starts at 650 mm, while at CRIACIV it starts one compartment above, i.e. at 750 mm. This is not related to I_u, because the value of I_u at

CRIACIV at 750 mm is much lower than the I_u at WiSt, even in the highest compartment (Table 6.1). However, this must be related to the type of atmospheric boundary layer, as it is further proved at WiSt, through the tests in uniform flow (namely T3), shown in Figure 6.13. The figure plots the time histories at levels 550 and 450 mm. The equivalency between the two states is not exactly fulfilled at those levels, but it can be seen that the disruption of the bistable flow, i.e. the more rapid alternation of the two states, starts at level 450 mm on the bubble side. In uniform flow (T3) this happens two compartments lower than in atmospheric boundary layer flow (T1), in the same wind tunnel. Therefore, the spanwise development of the bistable flow must be influenced by the type of atmospheric boundary layer. However, so far it has not been identified a certain property of the boundary layer which is univocally related to the disruption of the bistable flow at a certain level.

The equivalency of the two states, in terms of mean and rms values of the pressure coefficients, is shown in Figure 6.10 and Figure 6.11 (at z = 750 mm), which are comparable to Figure 5.5 and Figure 5.6 at WiSt, respectively.
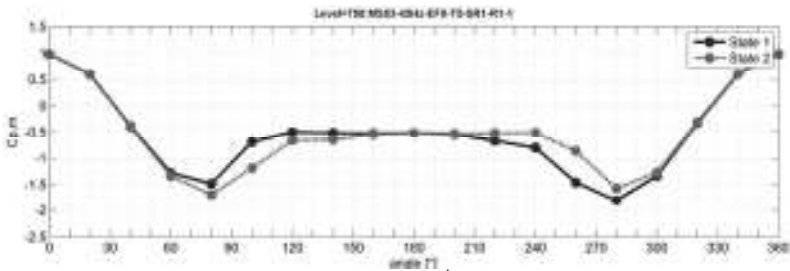
Figure 6.10 $C_{p,m}$ at 750 mm, Re = 2.8*10^5 (CRIACIV, T5-SR1-EF0-R1) to be compared with Figure 5.5
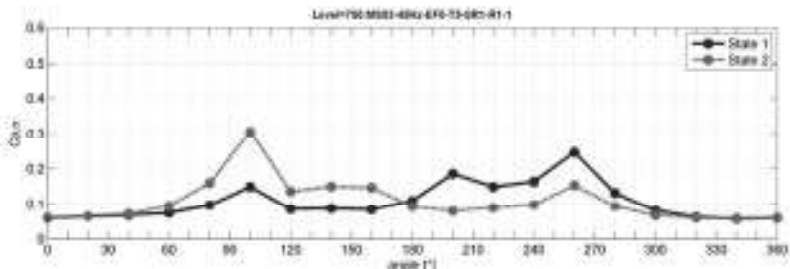
Figure 6.11 $C_{p,\sigma}$ at 750 mm, Re = 2.8*10^5 (CRIACIV, T5-SR1-EF0-R1) To be compared with Figure 5.6
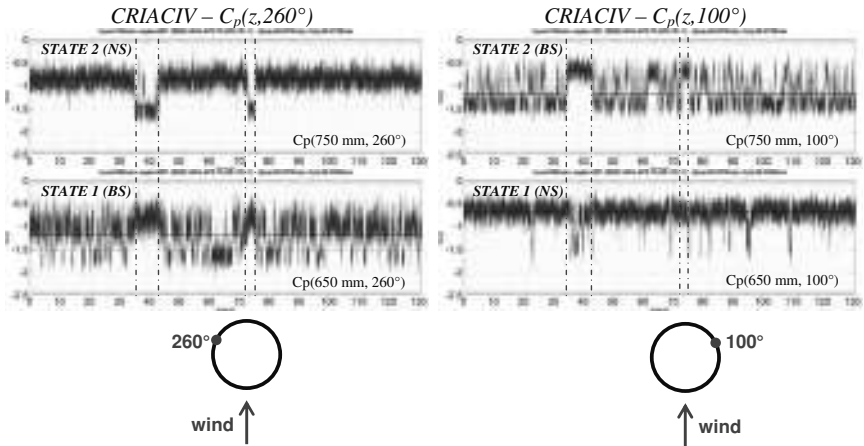
Figure 6.12 The levels of disruption (CRIACIV, T5-SR1-EF0-R1)
NS = normal side; BS = bubble side (Re = 2.8*10^5, z = 650, 750 mm)
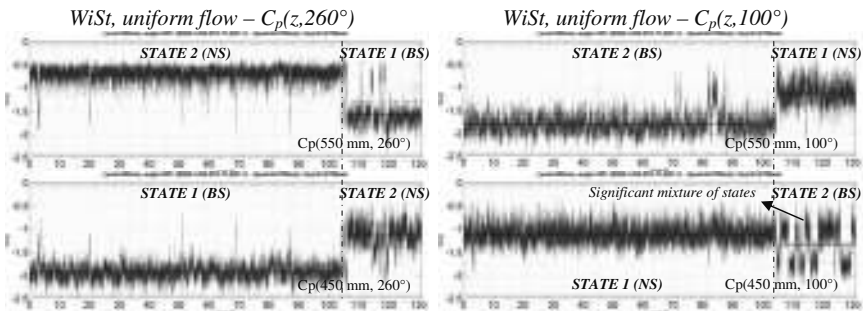
Figure 6.13 Lowering of disruption level in uniform flow (WiSt, T3-SR1-EF0-R1, Re =
2.5*10^5)

The inversion of the asymmetry along the height of the cylinder is confirmed at CRIACIV, as proved by the previous pictures. It is a sort of cascade effect, which is governed by the tip. Such a spanwise inversion is the result of an interaction between compartments. In order to motivate flow movements between compartments, the pressures and the pressure differences above and below one ring within only one state are plotted in Figure 6.14. The curves of $C_{p,m}$ at 910 and 890 mm are reported in the figure together with the green lines, namely Dp, which represent the difference $C_{p,m}(890) - C_{p,m}(910)$. At WiSt, on the side of the cylinder 0°-180°, the flow moves vertically towards the lower pressure, i.e. towards the compartment with the separation

198

bubble. This results, on the 0°-180° side of the cylinder, in a downwards movement. The opposite occurs on the other side of the cylinder, with an upwards movement, always towards the high-suction, i.e. the bubble-side. All of that is valid during each of the two stable states of the flow. In particular, in Figure 6.14 the results are averaged over the predominant interval. The results at CRIACIV are in wonderful agreement[5].
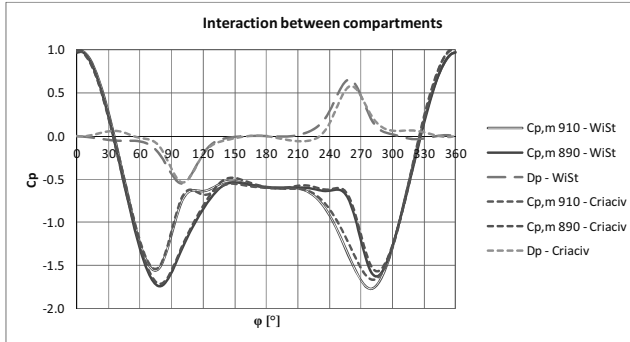
Figure 6.14 Pressures and pressure differences between compartments, above and below the ring n.9 (WiSt&CRIACIV, T1/T5-SR1-EF0-R1)

Figure 5.33 showed the cross-correlations of the lift coefficient at WiSt, with reference height z = 950 mm. In the case of ten rings, a drop of the cross-correlations at Δz = 100 mm due to the missing contribution of the tip-associated vortices was evident. Instead, such a contribution was not disturbed by the presence of only five rings. This is confirmed at CRIACIV in Figure 6.15, both in terms of cross-correlation coefficients and in terms of co-spectra.

In this regard, one comment deserves further attention. The results, so far, have shown:
-   the asymmetric flow with spanwise inversion along the height is a cascade effect from the tip (see also section 6.4);
-   although it seems to be a free-end effect, it is not merely governed by a modification of the top condition, i.e. by the top ring alone, because the bistable asymmetric flow disappears with five rings.. Rather, the phenomenon seems to be governed by the distribution of rings in the tip region. This conclusion would deserve to be further explored by experiments (Chapter 8).

---

[5] The predominant state at WiSt and Criaciv present separation bubbles on opposite sides. Therefore, in order to compare results in both wind tunnels within the predominant state, results at Criaciv are mirrored.
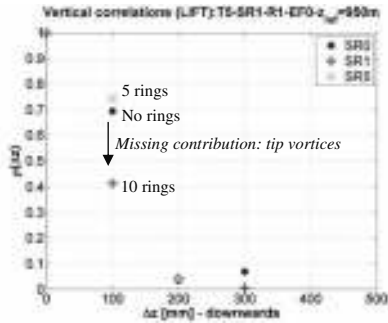
Figure 6.15 Cross-correlation coefficients of C_L without rings (blue), 10 rings (red) and 5 rings (green). z_{ref} = 950 mm. To be compared with Figure 5.33
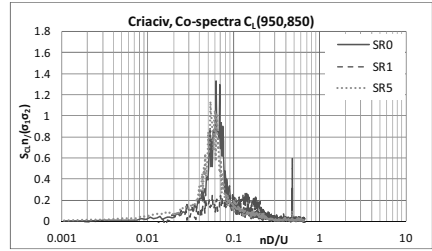
Figure 6.16 Co-spectra of C_L: $S_{CL}(z_1,z_2)*n/\sigma^2$ vs nD/U, z_1 = 950 mm, z_2 = 850 mm (CRIACIV, T5-SR0/SR1/SR5-EF0-R1). To be compared with Figure 5.34

6.3   Influence of the atmospheric boundary layer

The atmospheric boundary layer produces vertical velocity gradients which enhance the flow movement from regions of relatively high pressure to regions of relatively low pressure (Chapter 3). Because of that, differences between results in the two wind tunnels should be expected, even in the mean pressure and force coefficients. In addition, the fluctuating loads are related to the turbulence intensity of the flow and the different length scales influence the load correlation. Chapter 7 takes advantage of the tests in different conditions of the atmospheric boundary layer, in order to model the wind load with regard to the flow properties. In this section, the differences on the circular cylinder without rings are discussed at the beginning, the effect on the bistable flow is commented at the end.

As regards the mean pressure coefficients, the tests in the two wind tunnels on the circular cylinder without rings showed that the most significant differences occurred in the middle region of the tower. It should also be mentioned that below 600 mm in SR0 only 9 measurements per level (instead of 18) were available at CRIACIV. Fitting curves (splines) are used to interpolate data. The available measurements at CRIACIV are highlighted in the graphs in Figure 6.17. The graphs show that the tip effect is perfectly reproduced in the two wind tunnels, without significant influence of the different atmospheric boundary layer. In view of the investigation of the bistable asymmetric flow, this is a great advantage. Instead, lower suction in the wake, as well at the flanges, is apparent at CRIACIV e.g. at 450 mm (Figure 6.17c). The higher pressure at the flanges in CRIACIV may depend on the downstream movement of

200

spanwise flows, produced by the vertical pressure gradients. The mean suction in the wake is related to the steady recirculation region behind the tower and to the length of the eddy formation region. As shown in Chapter 3, the strength of the downwash in the near-wake may be weakened by the boundary layer. This issue is further addressed in the following with regard to the correlation coefficients.

In any case, the two wind tunnels agree in showing higher suction in the wake (and thus higher drag) close to the ground (see $C_{p,m}$ at 150 mm in Figure 6.17). The increase in the drag coefficient also in the lower half of the cylinder, and not only in the tip region was previously commented in Chapter 4, too, concerning preliminary results at WiSt.

Cp_σ is different in the two wind tunnels, due to different I_u. In particular, in Figure 6.17 at 950 mm Cp_σ at stagnation (directly related to I_u) is very small, much smaller than the fluctuations in the wake, which instead are almost the same in WiSt and CRIACIV. These latter are mainly body-induced. This issue, concerning body-induced and turbulence-induced pressure fluctuations, will be addressed in Chapter 7. The different values of Cp_σ (or, similarly, Cp_σ^2) in the two wind tunnels will be related to the corresponding turbulent intensities, in order to quantify the amount of body-induced fluctuations in laminar flow.
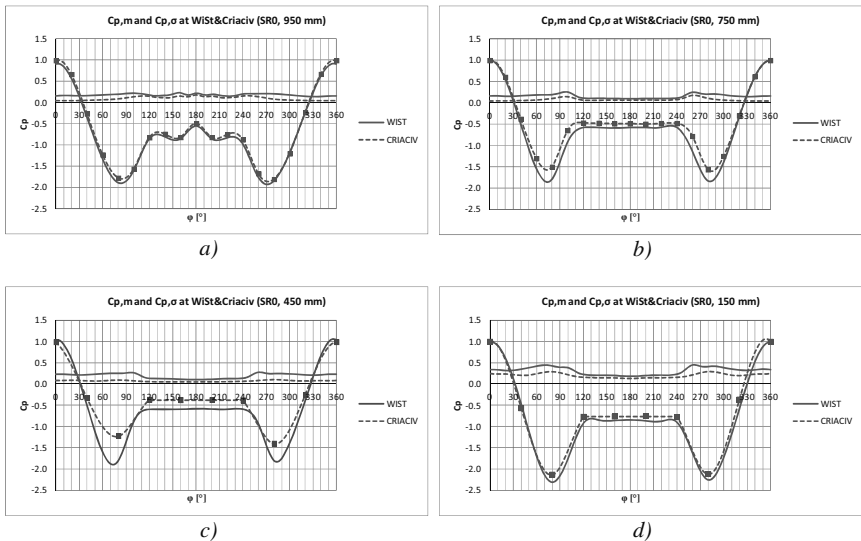
Figure 6.17 Mean and rms pressure coefficients at WiSt and CRIACIV (T1/T5-SR0-EF0-R1)

The cross-correlation coefficients and the correlation length L_{pz} depend on the correlation of the flow. In particular, L_{pz} can be related to L_{uz} (see Chapter 7). However, L_{uz} is not available at CRIACIV. In any case, the results at stagnation (where L_{pz} is directly related to L_{uz}) in the two wind tunnels do not show significant differences (Figure 6.18). L_{pz} at CRIACIV is generally lower, likely due to smaller L_{uz}.

The wake structure, instead, shows a certain dependency on the atmospheric boundary layer. As previously said, this is due to the strength of the downwash over the tip and to the formation of steady recirculation bubbles in the near-wake. The near-wake structure can be investigated by looking at the vertical cross-correlations. Representative graphs are shown in Figure 6.19, both in WiSt and in CRIACIV. Due to lack of data, the vertical cross-correlations at WiSt are measured at the angle 180°, while at CRIACIV the values at 160° are reported.

The cross-correlation $\rho(z_{ref}, \Delta z)$, with $z_{ref} = 950$ mm and Δz in the downward direction, shows that at WiSt there is a big steady vortex all along the height. Because of that, the cross-correlations are constant and different from zero even at large distance of separation. This cannot be modeled by a simple negative exponential function. The effect on the response will be quantified in Chapter 7, and it is now anticipated that it is not appreciably big (in the order of a few per cent of the response). In particular, the recirculation bubble at WiSt should arrive shortly above z = 50 mm (i.e. Δz = 900 mm). In CRIACIV, the same happens, but the recirculation bubble is smaller in size: it likely goes from the tip down to 450 mm. At larger distance of separation (Δz > 500 mm), the cross-correlation is zero. However, the steadiness of the recirculation bubble at CRIACIV is weaker, as shown by the rather low correlations even at small distance of separation, which weakly show a constant level.

In the lower half of the tower (z/H < 0.5), i.e. in the region of increase in the drag coefficient due to ground effects (see Chapter 4), a base vortex – maybe of the same type as that mentioned in Chapter 3 among the three-dimensional effects investigated by numerical simulations (Figure 3.18, Figure 3.19, Figure 3.20) – may be identified in the downwards cross-correlations with z_{ref} = 550 mm. The vortex can be identified by the still high correlation at Δz = 500 mm.
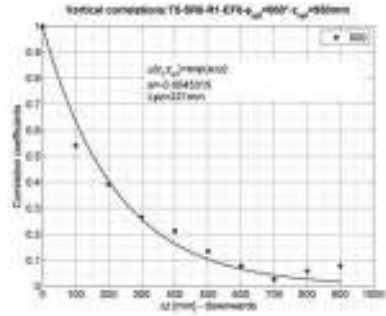
Last, but not least, it is interesting to observe that the upwards cross-correlations with z_{ref} = 50 mm show the same trend in the two wind tunnels. The base vortex is identified by the hump in the curve, at about Δz = 500 mm. At larger distances, the cross-correlations drop to zero.
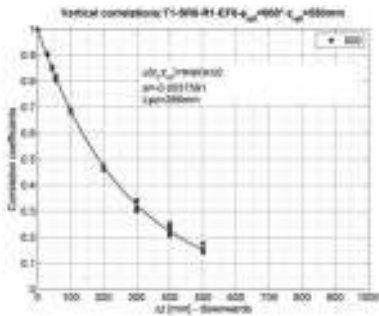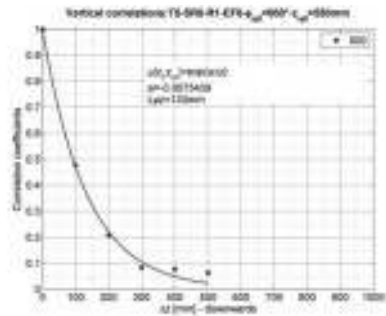
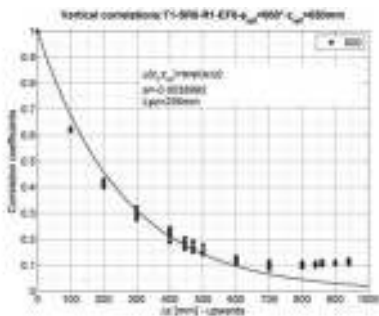*WiSt*   *CRIACIV*
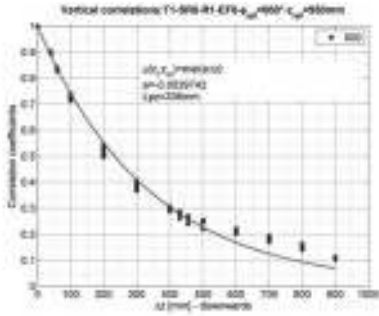
a)   *b)*
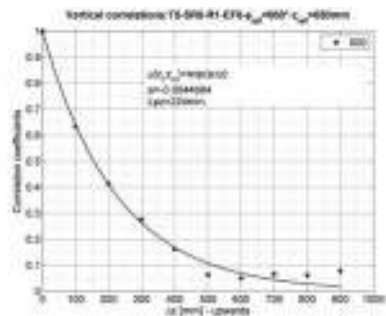

c)   *d)*

e)   *f)*

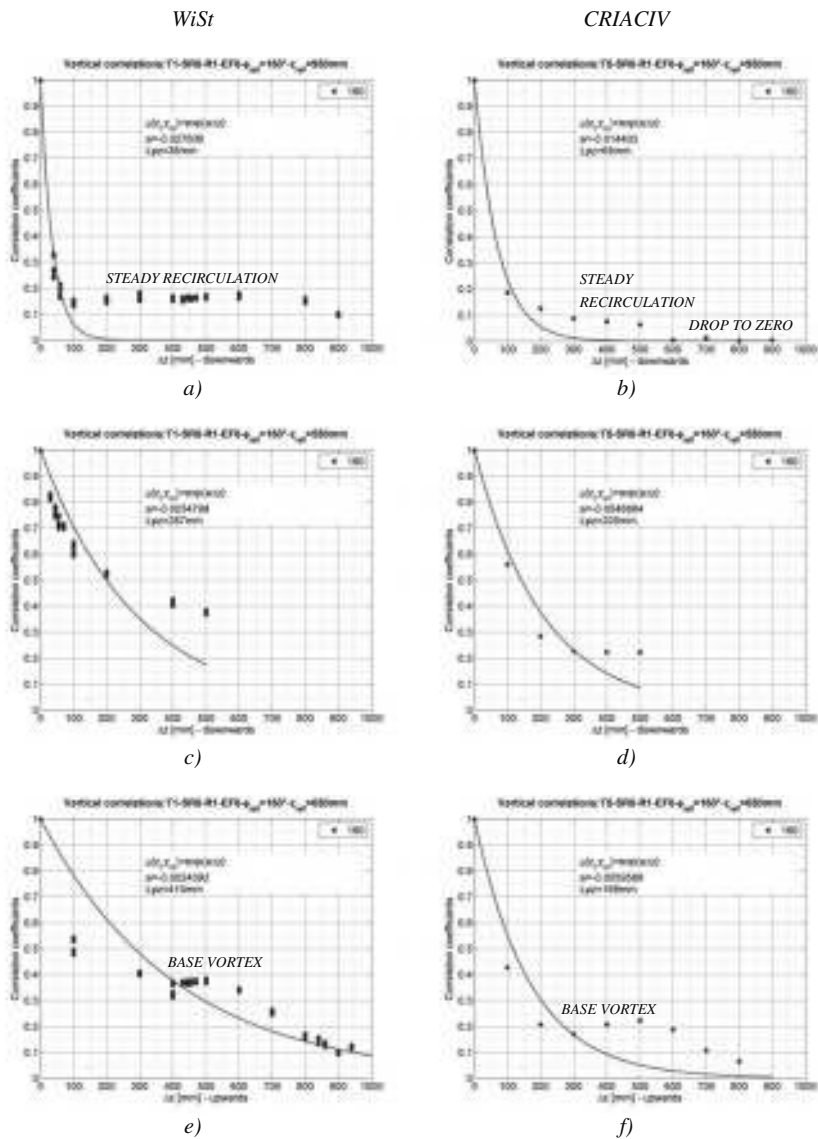*Figure 6.18 Cross-correlation coefficients at stagnation, WiSt and CRIACIV
(T1/T5-SR0-EF0-R1)*

WiSt *CRIACIV*

a) *b)*

c) *d)*

e) *f)*

Figure 6.19 Cross-correlation coefficients in the wake, WiSt and CRIACIV
(T1/T5-SR0-EF0-R1)

In the tip region of the cylinder, a low frequency peak – around one third of the Strouhal number – appears in the spectra due to the formation of tip-associated vortices.

As reported in literature (Kitagawa et al., 2001; Park&Lee, 2000), the shedding frequency of such big vortices is not deeply influenced by the boundary layer. The wind tunnel tests at CRIACIV, compared to those at WiSt, represent a further confirmation. However, the atmospheric boundary layer does influence the shedding along the height and the interaction between the low-frequency peak and the Karman vortex shedding. In particular, as proved by Figure 6.20, at WiSt the Karman vortex shedding ($S_t = 0.2$) strongly interacts with the tip-associated vortices already at $z/H = 0.85$ and definitely predominates at $z/H = 0.75$. All of that occurs at CRIACIV, too, but at a level which is lower of about 0.1H. In any case, it is confirmed in the spectra that in both wind tunnels the lower non-dimensional shedding frequency is about 0.065.

The explanation regarding the influence of the atmospheric boundary layer on the spanwise variation of the Strouhal number can be indirectly related to the different near-wake structure in the two wind tunnels (Figure 6.19). In fact, the decrease in the Strouhal number in the tip region is due to entrainment of flow over the tip (Farivar, 1981), as explained in the state of the art (Chapter 3). It is a sort of blockage effect, like a splitter plate, which elongates the eddy formation region. At CRIACIV, the atmospheric boundary layer is almost vanished in the tip region (i.e. the shear stress is almost null and the mean wind speed is constant). This can be a realistic situation, especially for the 1.5 km tower. In this condition, the effect is a stronger entrainment in the near-wake at high levels, as also confirmed by Park&Lee (2002) in uniform flow, with respect to boundary layer flow (Figure 3.31). So, at $z/H > 0.75$, the lower frequency peak predominates. Below such a level, the Karman vortex shedding peak arises. The almost constant noise at high frequencies in CRIACIV spectra, especially at $z/H = 0.65$, could be caused by the vibration of the turntable, which could not be completely avoided during the experiments.

It can be concluded that the near-wake structure is different in the two wind tunnels. Since the model is the same, such differences can only depend on the atmospheric boundary layer. In terms of mean wind load, this results in different wake suction (and thus different drag coefficient). In terms of fluctuating load, the spectra show a different interaction along the height between tip-associated vortices and Karman vortices.
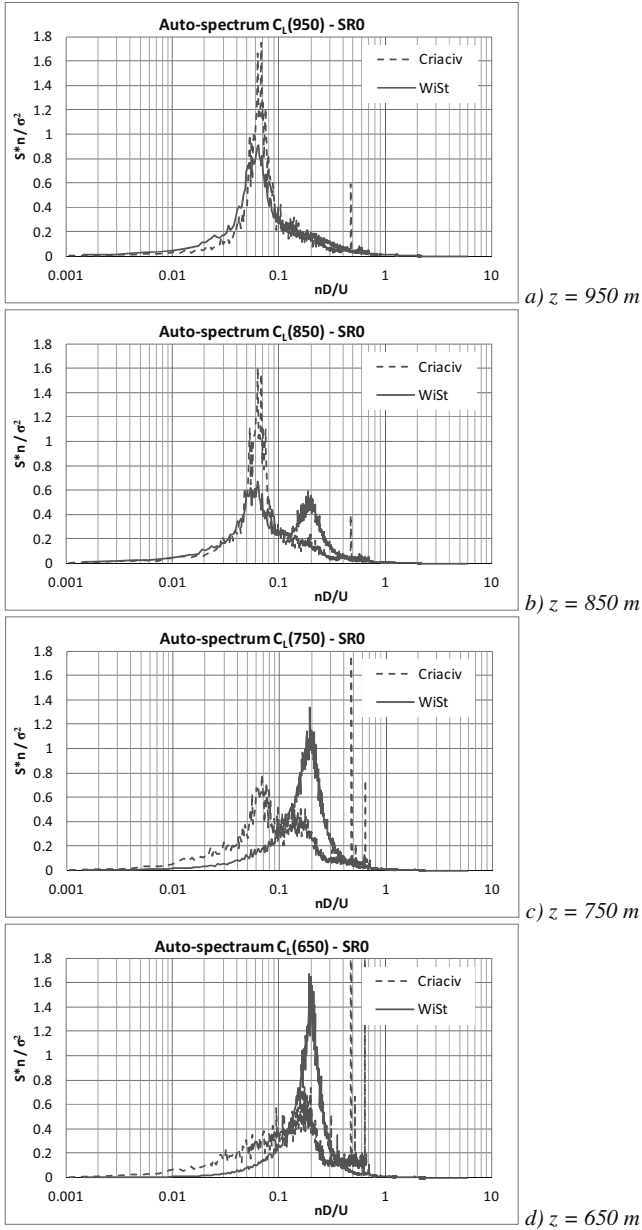
Figure 6.20 a-d) Lift spectra along the height without rings at WiSt and CRIACIV (T1/T5-SR0-R1-EF0)

Last but not least, the atmospheric boundary layer has an influence on the vertical development of the bistable flow. It has been already anticipated that the disruption of the boundary layer starts higher at CRIACIV, with respect to WiSt (Figure 6.9). Unfortunately, measurements at low levels in case of 10 rings were not available at WiSt. They are instead available at CRIACIV and allow to define a complete overview along the height.
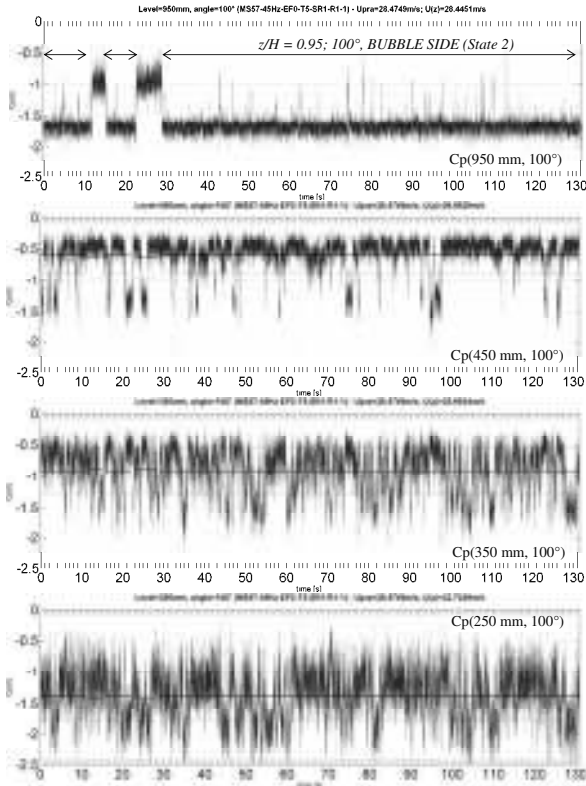
Figure 6.21 Bistability of the flow at low levels, $C_p(z/H,100°)$, simultaneous time histories (CRIACIV T5-SR1-R1-EF0, Re = $2.8*10^5$)
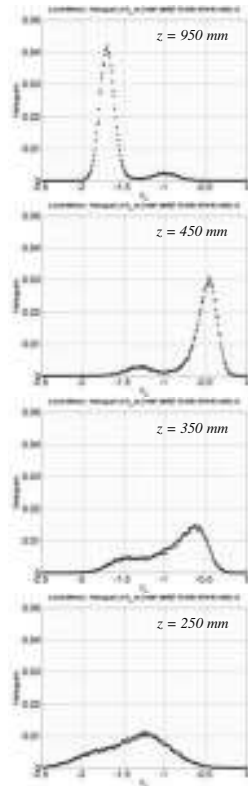
Figure 6.22 Bistability of the flow at low levels, histograms of $C_p(z/H,100°)$ (CRIACIV T5-SR1-R1-EF0)

The measurements along the height show that the flow is purely bistable and asymmetric only in the highest compartments (two at CRIACIV, three at WiSt). Here, bistable pressures produce bistable lift. Then, there is a region of transition (e.g. z =

650-750 mm in Figure 6.12, referring to CRIACIV data), where much more rapid jumps take place on the bubble side of the cylinder. The two states in the transition region are not well organized around the circumference, therefore they do not produce a purely bistable lift force. At lower levels (z < 500 mm, Figure 6.21) the time histories of pressures appear as an unstable sequence of states. In fact, the histograms of pressures on the right-hand side of the figure clarify that the pressures still oscillate between two states. Only closer to the ground (e.g. z = 250 mm in Figure 6.21), the bistability is substantially lost, not only in the lift but also in the pressures. The turbulence intensity certainly plays a role, although it is not the governing parameter of the bistable flow along the height.

6.4   Asymmetric bi-stable flow in CFD simulations

CFD simulations have been performed on the basis of CRIACIV experiments by the TEE group, Industrial Energy Dept. (formerly known as Energy Engineering Dept. "S. Stecco"), University of Florence (Salvadori&Mattana et al., 2013, unpublished personal communication).

The aim of the simulation is to provide numerical evidence of asymmetric bistable flow, as observed in the experiments. Therefore, the simulation refers to the most representative case: ten rings, no-efflux.

In the following, special attention is paid to those peculiar flow features which correspond to pressure characteristics observed in the experiments and commented up to now. However, the numerical study is only at the very first stage and it was not in the purpose of this work to proceed further. Further studies would be advisable in the future (Chapter 8).

The URANS simulation is performed by using the software Ansys Fluent 14. The incompressible fluid is solved by applying Navier-Stokes equations. The time step is 0.001 s, so about thirty time steps describe one period of vortex shedding. The turbulence model is the Shear Stress Transport (SST) k-ω. This is suitable to describe separated flows on smooth surfaces and adverse pressure gradients.

In order to reproduce the conditions of CRIACIV experiments, the tunnel and also the diffusor downstream of the test section were modelled. However, the presence of the diffusor is not relevant for the simulation and it can be ignored in further studies. Some pictures of the unstructured mesh are reported in Figure 6.23 and Figure 6.24.

The boundary conditions at the inlet are the velocity profile, the turbulence intensity and the turbulent length scale. The boundary conditions at the outlet are the pressure, the turbulence intensity and the turbulent length scale. No slip conditions are set to all

the other surfaces. The velocity profile at the inlet is like in Figure 6.2 (with maximum value equal to 28 m/s), while the turbulence intensity and the integral length scale L_{ux} are constant along the height, equal to 1% and 0.0075 m, respectively. These very low values will be increased in future studies, but may be representative in the tip region.
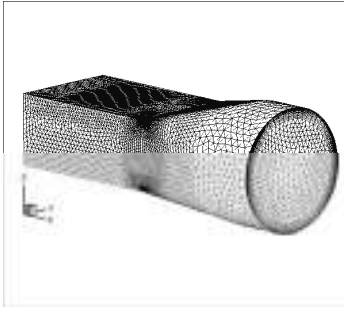

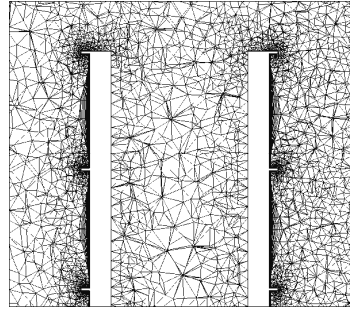*Figure 6.23 CRIACIV boundary layer wind tunnel – mesh*
(Salvadori&Mattana et al., 2013)

Figure 6.24 Detail of the mesh, transversal cross-section
(Salvadori&Mattana et al., 2013)

A peculiar feature of the simulations is the high Re number (Re = $2.8*10^7$), obtained by reducing the air viscosity of two order of magnitudes ($\nu = 1.5*10^{-7}$ m²/s). In these transcritical conditions of Re, surface roughness on the cylinder is not necessary. Moreover, differently from wind tunnel experiments, the simulation benefits of ideal test conditions.

The instantaneous flow picture in Figure 6.25 (horizontal cross-section at a representative level, 750 mm), clearly confirms the asymmetry due to a separation bubble on one side of the cylinder. This is consistent with the expectations on the flow, deduced on the only basis of pressure measurements in Figure 5.5 (WiSt) and Figure 6.10 (CRIACIV). The velocity magnitude shows the shift of the wake towards the bubble side. The streamline which separates on the normal side and reattaches on the bubble side motivates the high rms value on the bubble side in the wake. It is especially evident at about 200° in the state 1 (Figure 5.5/WiSt, Figure 6.10/CRIACIV).

Figure 6.26 plots the instantaneous vertical variation of the transversal velocity component, at the same time step as before. The cross-section cuts the cylinder in the across-wind direction Y at 120°-240° (X = 0.0375 m). The figure confirms the alternation between compartments (spanwise inversion), as observed in the experiments. The different colors in the figure on the two sides of the cylinder (i.e. blue on the right-hand side, standing for negative values and red on the left-hand side,

standing for positive values) are consistent with expectations: the transversal velocity vectors embrace the cylinder. In fact, what is interesting, and in agreement with the asymmetric phenomenon, is the different intensity of the transversal component on the two sides of the cylinder: in absolute value, the highest transversal velocity components are on the normal side. The differences in the transversal components on the two sides of the cylinder imply that the wake is not symmetrically aligned in each compartment, but it is shifted on one side. The same conclusion was also drawn from the experiments (Figure 5.40b).
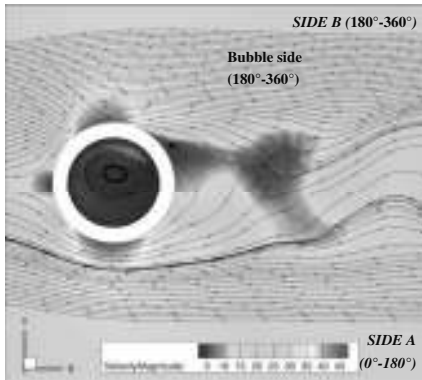
Figure 6.25 Horizontal cross-section, instantaneous flow velocity (magnitude, m/s) at z = 750 mm
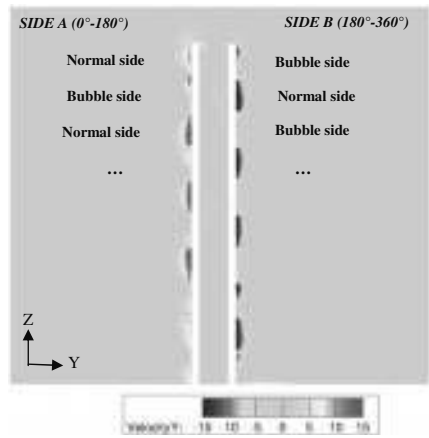
Figure 6.26 Transversal cross-sections, upstream view from the rear, instantaneous flow velocity (Y component, m/s) X = R/2 = 0.0375 m
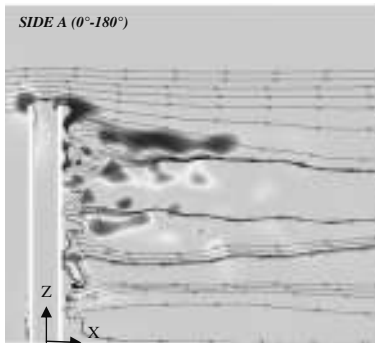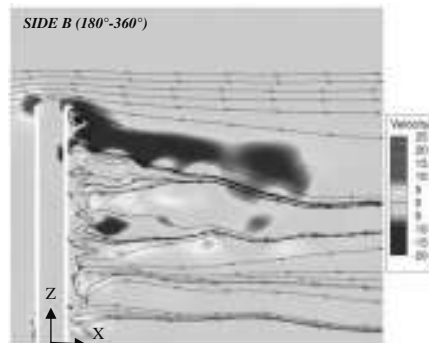
Figure 6.27 Longitudinal cross-sections, instantaneous flow velocity (Z component, m/s) Y = +/- 0.0257 m (Salvadori&Mattana et al., 2013)

So far, the numerical simulation has provided evidence of the asymmetry around a symmetric structure, due to the formation of a separation bubble on one side of the cylinder. The other fundamental issue which characterizes the phenomenon is the bistability. In order to detect, during the simulation, whether a jump takes place at a certain level, several monitoring probes were placed in the wake of the cylinder. As shown by Figure 6.28, there are two probes on each level for ten levels. The level number 1 is 49 mm above the cylinder, the level number 2 is at the tower top and so on, with a distance between levels of 50 mm. In this way, the probes are placed at each level of the ring and in between two rings, until $z/H = 0.6$. The probes allow to monitor the absolute pressure during the simulation. It is clear from Figure 6.29, in particular at level 5 ($z/H = 0.85$), that a jump has taken place at about $t = 0.2$ s.
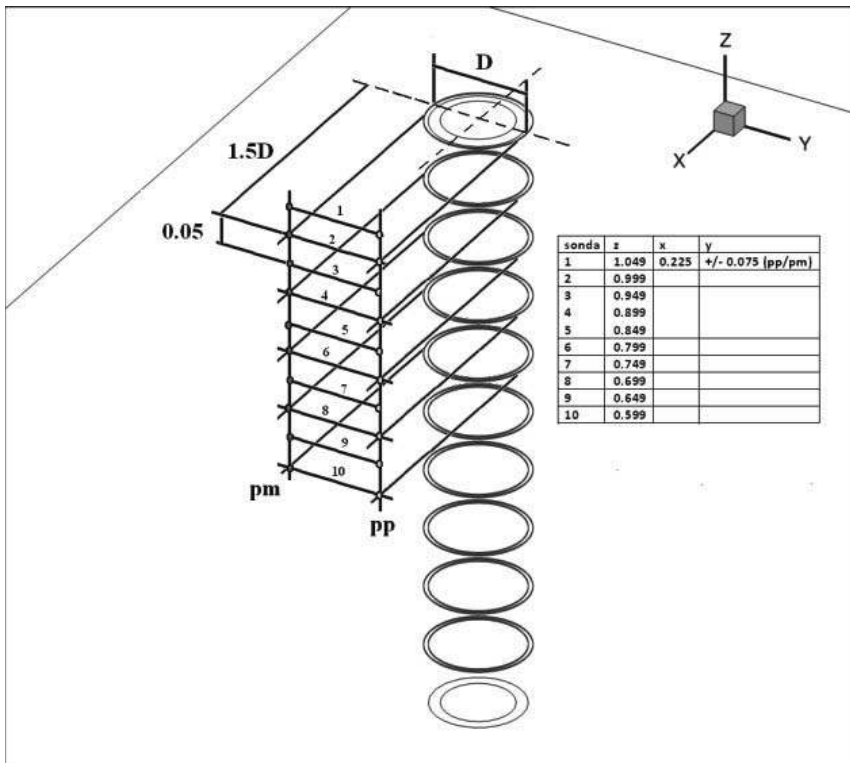

sonda	z	x	y
1	1.049	0.225	+/- 0.075 (pp/pm)
2	0.999		
3	0.949		
4	0.899		
5	0.849		
6	0.799		
7	0.749		
8	0.699		
9	0.649		
10	0.599		

Figure 6.28 Sketch of the probes to monitor flow pressures in the wake
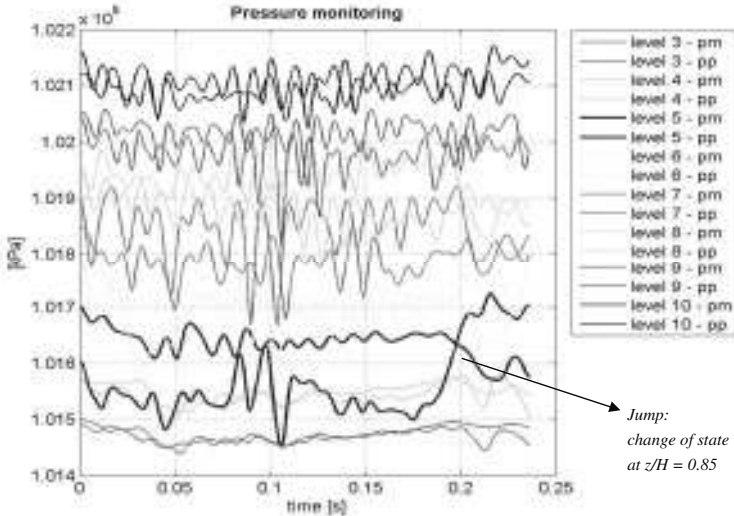*(Salvadori&Mattana et al., 2013)*

Figure 6.29 Time histories of flow pressures behind the tower
(Salvadori&Mattana et al., 2013)

The most representative flow picture which highlights the occurrence of a change of state is the transversal cross-sections at a downstream distance of one radius from the tower in the along-wind direction. Figure 6.30 reports an instantaneous flow picture before a jump, Figure 6.31 reports an instantaneous flow picture once the transition of state is initiated in the tip region.

The simulation shows that the downwash over the tip of the cylinder – the green tongue diverting towards side B in Figure 6.30 and side A in Figure 6.31 – guides the asymmetric flow, with spanwise inversion along the height. Due to the veer of the downwash flow, the sort of "snake" in the wake of the cylinder starts to invert its shape. At the time step in Figure 6.31 (that is the last monitored time step in Figure 6.29), the "snake" keeps the same shape from the ground until about two compartments from the top. There, the transition of state has occurred, as proved by the blue lines at level 5 in Figure 6.29. In fact, the time window of the simulation is relatively short. The experiments provided much longer measurements. Therefore, it cannot be stated whether Figure 6.31 testifies an actual jump, or just an attempt of jump, which is not able to develop along the height. The simulation should then proceed further, but this goes beyond the purpose of this Dissertation and it will be object of future research (Chapter 8).
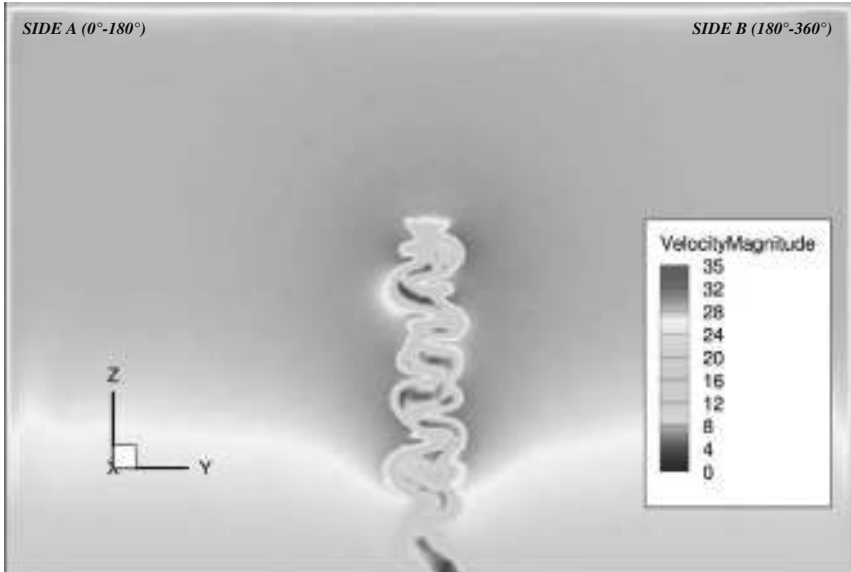
Figure 6.30 Transversal cross section in the wake at X = R from the tower (upstream view).
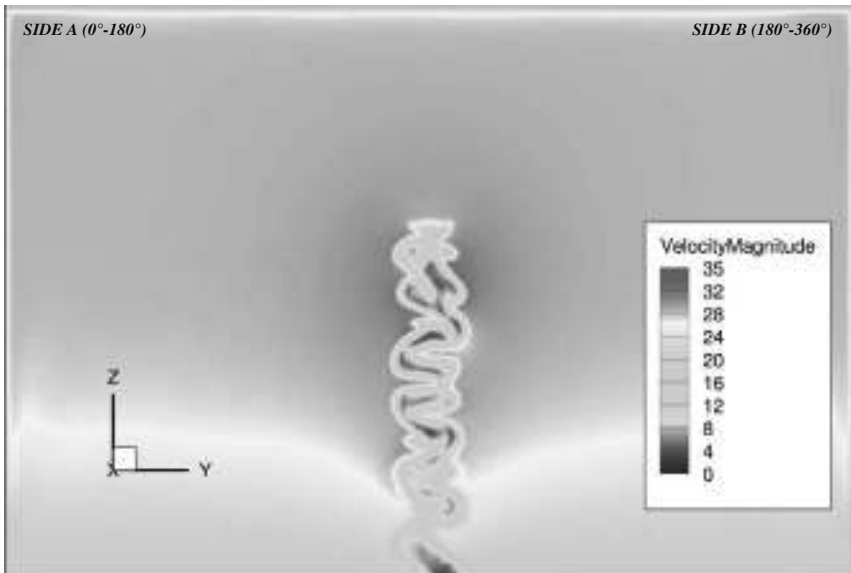*Before the jump (t = 0). (Salvadori&Mattana et al., 2013)*

Figure 6.31 Transversal cross section in the wake at X = R from the tower (upstream view).
After the jump (t = 0.024 s): transition of state is initiated in the tip region.
(Salvadori&Mattana et al., 2013)

213

6.5   **Concluding remarks**

The experiments at WiSt and at CRIACIV aimed to discover, prove and understand a new asymmetric and bistable flow condition around circular cylinders, even at moderately high Reynolds numbers. The URANS numerical simulation supports the experimental evidence. However, the numerical study has been just introduced in the Dissertation; it will be the object of future research.

The question of the Reynolds number could not be fully addressed in the wind tunnel, but it had to be limited to the range of Re of the experiments, accompanied by surface roughness on the model. Moreover, experimental conditions in any laboratory are never ideal ones. The existence of any kind of disturbance or local flow distortion can promote asymmetric results. It is, in any case, very unlikely that two different laboratories promote the same asymmetric results due to their own test conditions. However, the cross-check of experiments could not fully answer the question of what would happen in ideal test conditions. This question cannot be addressed experimentally anyhow. From this point of view, the CFD provides the most reliable answer. The proof of existence of an asymmetric effect on a symmetric structure in symmetric flow condition is one of the most important contributions of the CFD simulation. A further contribution is, of course, the occurrence of the jump. Further studies are now necessary to investigate the occurrence of jumps. What can be stated now, is that the occurrence of asymmetric and bistable condition is not a matter of the Re. Moreover, from the experiments it is clear that the stable condition in the highest compartments in the case of ten rings is the asymmetric one, on either side of the cylinder. The CFD is presently too short to confirm the same result. This is an issue which would deserve further attention in the future, especially with regard to the effect of the Reynolds number and ideal test conditions.

The CFD clarified a peculiar feature, also observed in the experiments: the formation of a separation bubble on one side of the cylinder and the misalignment of the wake between different compartments. This is due to the cross-wind component, which predominates on the normal side of the cylinder and diverts the wake towards the bubble side. In particular, the cross-wind component predominates on the side of the cylinder where the vertical downwash is weaker (i.e. on the normal side). This would confirm the key role of the flow over the tip of the cylinder, whose downwash is mainly reversed on the bubble side, where it creates a secondary vortex below the highest ring. For this reason, the presence of efflux inside the cylinder cancels the

asymmetric phenomenon. In fact, the downwash flow over the tip is disturbed by the upwards flow out of the tip. It can be then wondered whether it is possible to identify a critical ratio between the Reynolds number of the incoming flow and the Reynolds number of the efflux, which is able to suppress the phenomenon.

Along the height, strips of flow cross each other in neighboring compartments and are responsible for the spanwise inversion. It is reasonable that all these flow movements kill the shedding of tip-associated-vortices. In fact, the lower shedding frequency is due to entrainment in the wake. This is, in case of rings, displaced on either side of the cylinder.

It should also be remembered that the formation of asymmetric separation bubbles disappears if the rings are at a sufficiently large distance (experimental evidence only, CFD not performed). With regard to that, Figure 6.27 shows the effect of ring n.9 (z/H = 0.9) in constraining the recirculation vortex within the highest compartment. Therefore, the role of ring n.9 in the whole phenomenon should be further investigated.

The experimental and numerical evidence of the new phenomenon proposed in this Dissertation is now fully confirmed. It opens the doors to the last step of this work, that is the evaluation of load and response (Chapter 7). In this regard, it is important not to restrict the analysis to the interesting but unique design condition of ten rings along the height. Because of that, the study of the load and the response of the tower is addressed in a wider perspective. But of course, the response to the asymmetric and bistable flow needs to be quantified, too.

Chapter 7. **Load and response**

Wind tunnel experiments performed in different wind tunnels and thus different boundary layers allowed to study the effect of certain atmospheric boundary layer properties on wind forces and pressures. A simple design tool, generalizable to any atmospheric boundary layer flow is then derived by using the results in WiSt and CRIACIV (section 7.1). This model can be applied to calculate the quasi-static response of the tower to the stochastic wind loading process in any design conditions. Basic assumptions are linear structural analysis and quasi-static behaviour.
In sections 7.2 and 7.3 the beam and shell responses are analyzed. The effect of the asymmetric load due to the rings along the height is also quantified.

7.1   **Modelling of wind load**

The time-averaged mean load and the load covariances (i.e. rms values and correlation coefficients) are the input data to evaluate the quasi-static structural response to the stochastic wind loading process. The breaking-up of the covariances in the frequency domain is not necessary because the mechanical admittance is constant. More sophisticated methods to evaluate the structural response are the spectral method in the frequency domain, which is applicable to linear structures, and the time history method applicable to both linear and non-linear structures.

This section addresses the modelling of the stochastic quasi-static design wind load, with respect to the turbulent properties of the flow, by combining results of both WiSt and CRIACIV wind tunnels. The model refers to the basic configuration (without rings) and has a general application for cylindrical towers of any aspect ratio[6]. It also represents the reference case to evaluate the effect of the rings.

7.1.1   **Influence of boundary layer flows on force coefficients**

The comparison of experimental data recorded in different wind tunnels – and thus different atmospheric boundary layers – cannot be addressed without considering the properties of the flow in which such data are measured. This approach is pursued in this section with regard to the force coefficients.

---

6 For low-aspect ratio circular cylinders, i.e. for H/D less than a critical value (which ranges from 1 to 6, depending on the boundary layer thickness) a different flow structure develops in the wake (see section 3.5). The proposed wind load model is thus appropriate for sufficiently slender circular cylinders, e.g. H/D ≥ 6.

The local mean value of the drag coefficient that results from the experiments (^{EXP}) is calculated by definition as:

$$C_{D,m}^{EXP}(z) = \frac{F_m^{EXP}(z)}{q_m(z)D} \qquad (7.1)$$

where $q_m(z)$ is the local velocity pressure, i.e. at the level of the pressure measurement. Similarly, the coefficient can be defined with respect to the velocity pressure at the top of the tower:

$$C_{D,m}^{EXP,H}(z) = \frac{F_m^{EXP}(z)}{q_m(H)D} \qquad (7.2)$$

The comparison between results at WiSt and CRIACIV (Figure 7.1a) shows that the local mean force coefficients – calculated according to equation (7.1) – depend on the type of boundary layer. In fact, a certain boundary layer – characterized by its velocity and pressure gradients – may enhance certain flow movements. The time-averaged wake structure may also change, as addressed in section 6.3. While the tip effect is not so sensitive to the characteristics of the boundary layer, lateral and especially wake suction at middle height at CRIACIV are lower than at WiSt. This issue was commented with regard to Figure 6.17, which explains the differences between the two drag curves in Figure 7.1a.

The use of $q_m(H)$ instead of $q_m(z)$ allows to remove the differences due to the boundary layer and the results in the two wind tunnels are in wonderful agreement (Figure 7.1b). However, by using $q_m(H)$, an even more constraining dependency is gained: the one on the aspect ratio. The coefficients in Figure 7.1b are thus only valid for the aspect ratio of the experiments, that is $H/D = 6.7$.

The rms values of the forces (equation(7.3)) are necessarily different in the two wind tunnels (Figure 7.2), because the turbulence in the flow (σ_u) is different (Figure 7.3).

$$C_{D,\sigma}^{EXP,H}(z) = \frac{F_\sigma^{EXP}(z)}{q_m(z)D} \qquad (7.3)$$
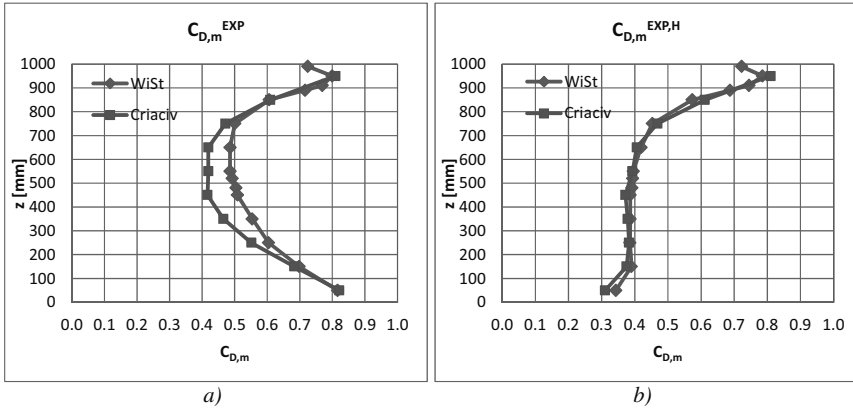
Figure 7.1 Mean drag coefficients $C_{D,m}$: comparison between WiSt and CRIACIV data (EXP)
a) $C_{D,m}$ by using local velocity pressure $q_m(z)$; b) $C_{D,m}$ by using velocity pressure on top
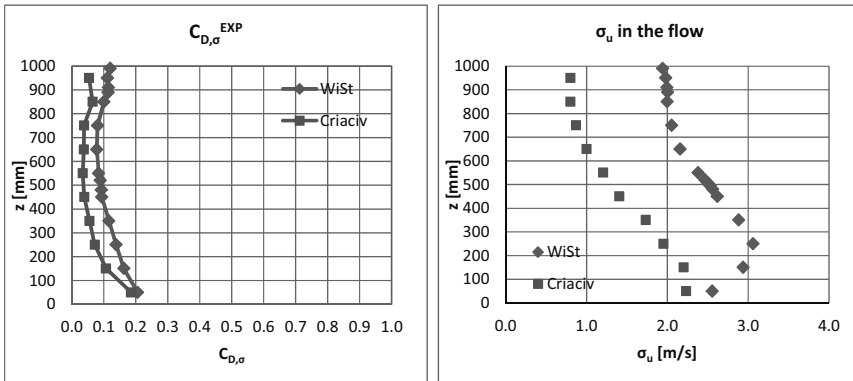*$q_m(H)$*

Figure 7.2 Rms drag coefficients $C_{D,\sigma}$: comparison between WiSt and CRIACIV experimental data (^{EXP})

Figure 7.3 Rms values of along wind velocity (σ_u) at WiSt and CRIACIV

It is then apparent that, in order to compare results obtained in different boundary layer flows and codify the force coefficients, a more general approach should be used, which includes the mean velocity pressure and the turbulence intensity.

The code approach is based on the peak force coefficient ($C_{D,peak}$), that is the ratio of peak (drag) force and peak velocity pressure (equation (7.4)). The latter is multiplied by D as usual, in order to obtain the dimension of force per unit length. In this way, the results in different boundary layer flows are more comparable even by using the local

velocity pressure and not the velocity pressure on top (Figure 7.4). The peak force coefficients are generalizable for load modelling.

$$C_{D,peak} = \frac{F_{peak}}{q_{peak} D} = \frac{F_m^{EXP} + k_F F_\sigma^{EXP}}{q_m\left(1 + 2k_p I_u\right)D} =$$

$$= \frac{C_{D,m}^{EXP} q_m D + k_F C_{D,\sigma}^{EXP} q_m D}{q_m\left(1 + 2k_p I_u\right)D} = \frac{C_{D,m}^{EXP} + k_F C_{D,\sigma}^{EXP}}{1 + 2k_p I_u}$$

(7.4)

The peak factors in equation (7.4) are assumed equal to 3.5 for both forces and velocities (k_F and k_p, respectively). The apex (^{EXP}) means resulting from experiments. It should be mentioned, however, that the code definition of the peak force includes the dynamic factor and the size factor. Relying on the experimental data, $C_{dyn} = 1$ because the model is rigid, C_s is assumed equal to 1, too, although it should take into account the decrease in correlation around the circumference. It could be partially responsible for the differences in the two curves in Figure 7.4.
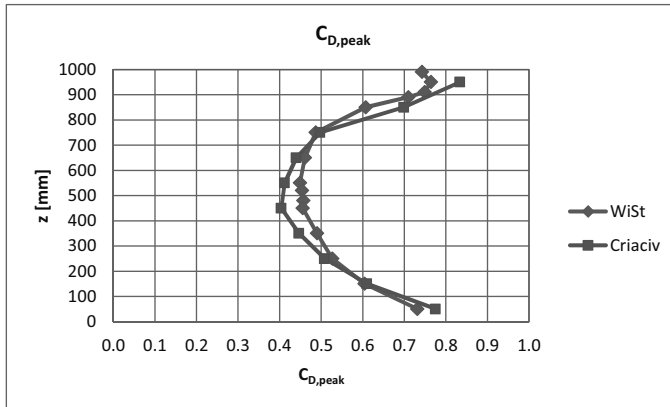

Figure 7.4 Peak drag coefficient $C_{D,peak}$ related to $q_{peak}(z)$

By assuming a quasi-stationary approach (the aerodynamic coefficient is invariant with respect to time) and linearized model ($I_u^2 \ll 1$), the intensity of force is twice the turbulence intensity and the peak force can be split up into its mean and fluctuating components as follows:

$$F_m = C_{D,\,peak}\, q_m D \tag{7.5}$$

$$F_\sigma = C_{D,\,peak}\, 2I_u q_m D \tag{7.6}$$

Therefore, the mean and the rms values of the force coefficients to be used in the proposed beam-load model (^{LM}) are:

$$C_{D,m}^{LM} = \frac{F_m}{q_m D} = C_{D,\,peak} \tag{7.7}$$

$$C_{D,\sigma}^{LM} = \frac{F_\sigma}{q_m D} = C_{D,\,peak}\, 2I_u \tag{7.8}$$

The behaviour of the peak drag coefficient along the height resembles the profile of the $C_{D,m}$, which increases both at tower top (tip effect) and at the bottom, as previously commented in sections 3.5 and 4.4.

The main results are reported in the following tables.

Table 7.1 Boundary layer flow at WiSt

	z [mm]	z/H	U [m/s]	σ_u	$q_m(z)/q_m(H)$	I_u
	990	0.99	25.16	1.9431	1.00	0.0772
	950	0.95	24.98	1.9826	0.98	0.0794
	910	0.91	24.79	1.9972	0.97	0.0806
	890	0.89	24.70	2.0041	0.96	0.0811
	850	0.85	24.30	2.0003	0.95	0.0823
	750	0.75	23.78	2.0536	0.91	0.0863
WiSt:	650	0.65	23.32	2.1580	0.86	0.0925
Boundary	550	0.55	22.66	2.3833	0.81	0.1052
layer	520	0.52	22.43	2.4656	0.80	0.1099
	480	0.48	22.16	2.5621	0.78	0.1156
	450	0.45	21.91	2.6181	0.76	0.1195
	350	0.35	21.01	2.8842	0.70	0.1373
	250	0.25	20.05	3.0614	0.64	0.1527
	150	0.15	18.77	2.9381	0.56	0.1566
	50	0.05	16.28	2.5565	0.42	0.1571

Table 7.2 Drag coefficients at WiSt

	z/H	$C_{D,m}^{EXP}$	$C_{D,m}^{EXP.H}$	$C_{D,\sigma}^{EXP}$	$I_F =$ $C_{D,\sigma}^{EXP}/$ $C_{D,m}^{EXP}$	I_F/I_u	$C_{D,peak}$
	0.99	0.7246	0.7221	0.1198	0.1654	2.1407	0.7425
	0.95	0.7992	0.7853	0.1112	0.1391	1.7528	0.7640
	0.91	0.7693	0.7447	0.1148	0.1492	1.8519	0.7487
	0.89	0.7158	0.6877	0.1134	0.1584	1.9523	0.7096
	0.85	0.6061	0.5732	0.1001	0.1652	2.0073	0.6069
	0.75	0.5007	0.4535	0.0801	0.1601	1.8539	0.4869
WiSt:	0.65	0.4858	0.4189	0.0781	0.1607	1.7366	0.4606
Drag	0.55	0.4859	0.3956	0.0838	0.1725	1.6401	0.4488
Coeff.	0.52	0.4924	0.3933	0.0888	0.1804	1.6411	0.4540
	0.48	0.5039	0.3915	0.0922	0.1830	1.5825	0.4568
	0.45	0.5083	0.3863	0.0937	0.1844	1.5430	0.4554
	0.35	0.5540	0.3862	0.1161	0.2095	1.5262	0.4897
	0.25	0.6044	0.3854	0.1386	0.2293	1.5015	0.5266
	0.15	0.6980	0.3899	0.1626	0.2330	1.4879	0.6046
	0.05	0.8160	0.3429	0.2055	0.2519	1.6034	0.7313

Table 7.3 Boundary layer flow at CRIACIV

	z [mm]	z/H	U [m/s]	σ_u	$q_m(z)/q_m(H)$	I_u
	950	0.95	28.36	0.8022	1.00	0.0283
	850	0.85	28.40	0.8033	1.00	0.0283
	750	0.75	28.26	0.8731	0.99	0.0309
	650	0.65	27.91	1.0020	0.97	0.0359
CRIACIV:	550	0.55	27.47	1.2085	0.94	0.0440
Boundary	450	0.45	26.79	1.4070	0.89	0.0525
layer	350	0.35	25.58	1.7340	0.81	0.0678
	250	0.25	23.65	1.9534	0.70	0.0826
	150	0.15	21.03	2.2015	0.55	0.1047
	50	0.05	17.44	2.2339	0.38	0.1281

Table 7.4 Drag coefficients at CRIACIV

	z/H	$C_{D,m}^{EXP}$	$C_{D,m}^{EXP.H}$	$C_{D,\sigma}^{EXP}$	$I_F = C_{D,\sigma}^{EXP}/C_{D,m}^{EXP}$	I_F/I_u	$C_{D,peak}$
CRIACIV: Drag Coeff.	0.95	0.8099	0.8099	0.0539	0.0666	2.3547	0.8337
	0.85	0.6096	0.6113	0.0650	0.1066	3.7681	0.6986
	0.75	0.4717	0.4682	0.0380	0.0806	2.6070	0.4972
	0.65	0.4193	0.4062	0.0375	0.0894	2.4899	0.4400
	0.55	0.4192	0.3932	0.0341	0.0814	1.8498	0.4118
	0.45	0.4164	0.3717	0.0388	0.0931	1.7725	0.4037
	0.35	0.4652	0.3784	0.0552	0.1186	1.7494	0.4465
	0.25	0.5510	0.3831	0.0716	0.1299	1.5729	0.5079
	0.15	0.6830	0.3755	0.1069	0.1564	1.4941	0.6100
	0.05	0.8213	0.3106	0.1852	0.2255	1.7602	0.7748

7.1.2 Mean pressure coefficient distribution

The circumferential distribution of the mean pressure coefficients C_p on the external surface of the tower is described by the following parameters:

- $C_{p,max}$ = maximum pressure coefficient (at stagnation);
- φ_{min} and $C_{p,min}$ = angle and pressure coefficient at maximum lateral suction;
- φ_h and Cp_h = angle of separation and pressure coefficient in the wake;

Depending on the circumferential angle φ, three ranges can be identified along the circumference, as shown in Figure 7.5. The distributions in the three ranges are described by expressions (7.9)-(7.11), derived by studies on cooling towers and codified in the VGB guideline (VGB, 2010).
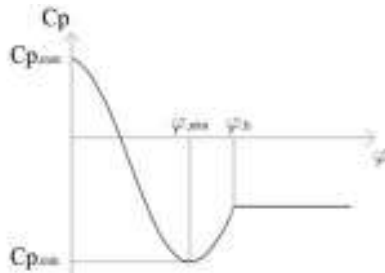
Figure 7.5 Pressure coefficients distribution in the three ranges
$(0<\varphi<\varphi_{min}; \varphi_{min}<\varphi<\varphi_h; \varphi_h<\varphi<180°)$

Range I: $\qquad 0° \leq \varphi \leq \varphi_{min}$

$$C_P(\varphi) = C_{P,max} - \left(C_{P,max} - C_{P,min}\right)\left(\sin\frac{90}{\varphi_{min}}\varphi\right)^{\varepsilon_{min}} \tag{7.9}$$

Range II: $\qquad \varphi_{min} \leq \varphi \leq \varphi_h$

$$C_P(\varphi) = C_{P,min} - \left(C_{P,min} - C_{P,h}\right)\left(\sin\frac{90}{\varphi_h - \varphi_{min}}\left(\varphi - \varphi_{min}\right)\right)^{\varepsilon_h} \tag{7.10}$$

Range III: $\qquad \varphi_h \leq \varphi \leq 180°$

$$C_P(\varphi) = C_{P,h} \tag{7.11}$$

This model is adapted to the experimental data of the solar tower along the height (WiSt results). The parameter ε_h has been chosen accordingly to the VGB guideline, while the parameter ε_{min} has been calibrated by fitting the measured C_p values and matching the value of the measured drag coefficient. The values are reported in Table 7.5 and plotted in the following graphs. In particular, three spanwise regions can be identified along the height of the cylinder:

- tip region (z' $\leq$ 2D, i.e. z > 0.7H, as z' starts at z = H in downwards direction);
- normal region (z > 0.5H and z' > 2D);
- low region (z $\leq$ 0.5H).

Table 7.5 Mean pressure coefficients

	z/H	Cp max	Cp min	φ,min [°]	Cp,h	φ,h [°]	ε,min	ε,h	ΔCp	C_D model	C_D meas.
	0.99	0.7	-1.40	85	-0.73	130	2.085	2.395	0.68	0.72	0.72
	0.95	0.9	-1.91	85	-0.79	125	2.189	2.395	1.11	0.80	0.80
TIP	0.91	0.9	-1.96	80	-0.82	120	2.390	2.395	1.15	0.77	0.77
REGION	0.89	0.9	-1.95	80	-0.78	118	2.277	2.395	1.16	0.72	0.72
	0.85	1.0	-1.91	75	-0.69	115	2.332	2.395	1.23	0.61	0.61
	0.75	1.0	-1.85	75	-0.58	110	2.395	2.395	1.27	0.50	0.50
NORMAL	0.65	1.0	-1.77	75	-0.55	110	2.248	2.395	1.21	0.49	0.49
REGION	0.55	1.0	-1.76	75	-0.54	110	2.238	2.395	1.22	0.49	0.49
LOW	0.45	1.0	-1.86	75	-0.59	110	2.261	2.395	1.26	0.51	0.51
REGION	0.35	1.0	-1.94	75	-0.66	110	2.359	2.395	1.28	0.55	0.55

0.25	1.0	-2.06	75	-0.75	115	2.474	2.395	1.31	0.60	0.60
0.15	1.0	-2.28	80	-0.86	120	2.256	2.395	1.42	0.70	0.70
0.05	1.1	-2.28	80	-0.99	110	2.052	2.395	1.29	0.80	0.80

The following figures (Figure 7.6, Figure 7.7, Figure 7.8) plot the circumferential distributions of mean pressure coefficients along the height. The three figures refer to the tip region, the normal region and the low region, respectively. Further variation of the distribution is also present within each region. Modelling according to equations (7.9), (7.10), (7.11) and experimental data are in good agreement.
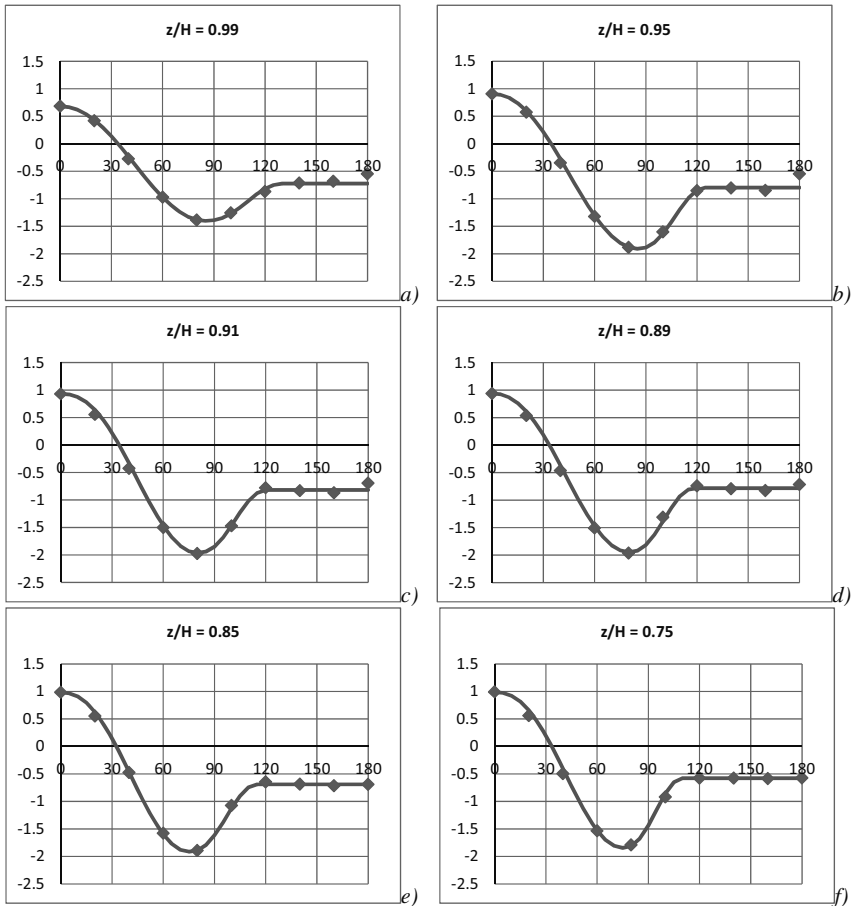
Figure 7.6 e-f) Mean pressure coefficients $C_{p,m}$: proposed model (red) and experimental data (blue) [x-axis = φ (°), y-axis = $C_{p,m}$]. Tip region (z' < 2D)
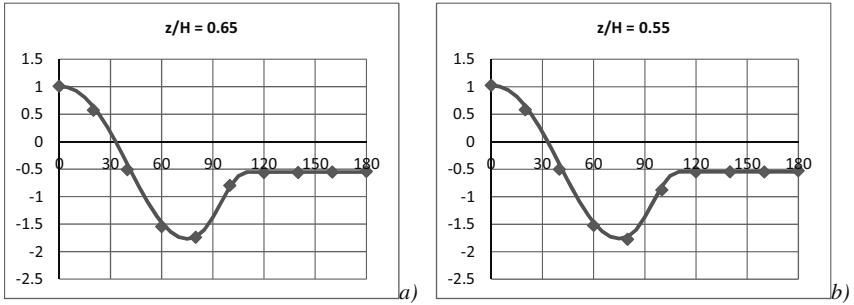
Figure 7.7 a-b) Mean pressure coefficients $C_{p,m}$: proposed model (red) and experimental data (blue) [x-axis = φ (°), y-axis = $C_{p,m}$]. Normal region (z' > 2D; z/H > 0.5)
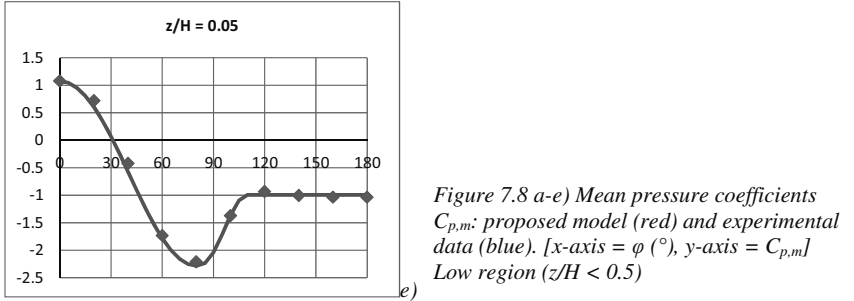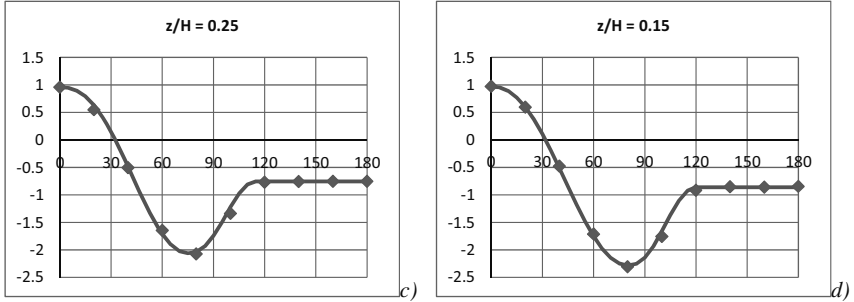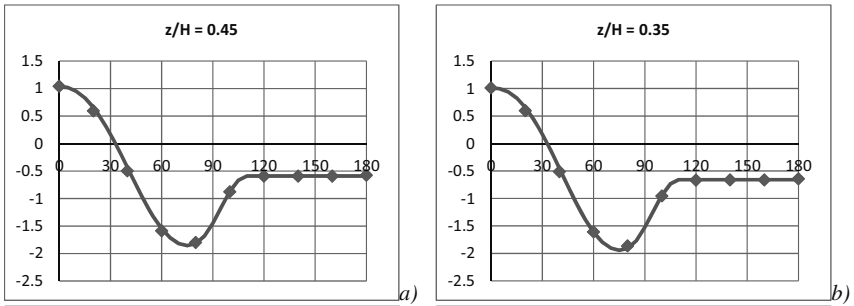
Figure 7.8 a-e) Mean pressure coefficients $C_{p,m}$: proposed model (red) and experimental data (blue). [x-axis = φ (°), y-axis = $C_{p,m}$] Low region (z/H < 0.5)

Finally, Figure 7.9 shows an overview of the distributions of the mean pressure coefficients along the height.

a) *Tip region (z' ≤ 2D)*

b) *Normal region (z > 0.5H and z' > 2D)*

c) *Low region (z ≤ 0.5H)*
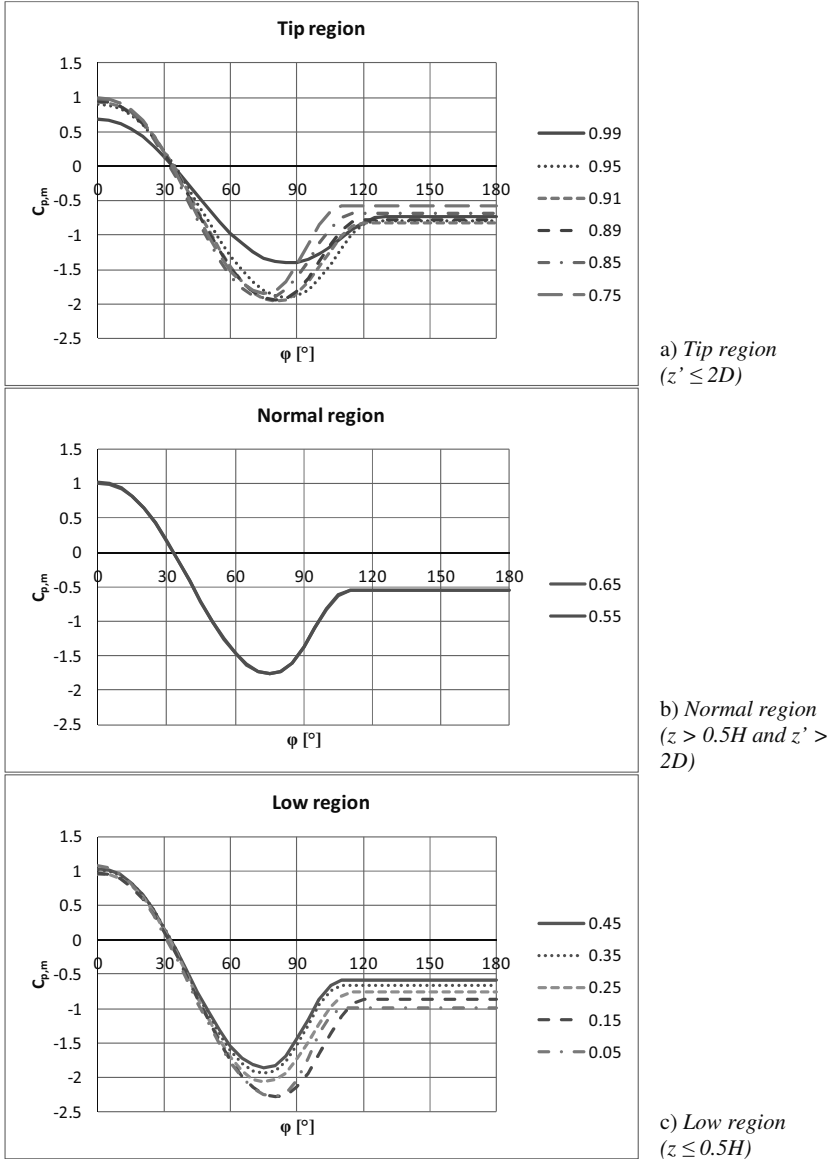
Figure 7.9 a-c) Mean pressure coefficients: variation along the height

227

7.1.3 Rms pressure coefficients: body-induced and turbulence-induced fluctuations

Pressure fluctuations on the shell surface are both body-induced and turbulence-induced. They are due to vortex shedding and to the turbulence of the incoming flow, respectively. In order to model the turbulence-induced fluctuations with regard to the turbulent properties of the boundary layer, the question arises whether it is possible to separate the two contributions. Then, the easiest approach would be to relate the turbulence-induced fluctuations around the circumference to the fluctuation at stagnation, which in turn depends on $I_u(z)$, and to measure the body-induced pressure fluctuations in smooth flow.

The problem cannot be addressed linearly in the rms values, but in the variances. Furthermore, the question is much more complicated because the turbulence of the incoming flow may be responsible for enhancing body-induced fluctuations. However, the simplifying assumption that body-induced pressure fluctuations ($p_\sigma^2{}_{,BI}$) and turbulence-induced pressure fluctuations $p_\sigma^2{}_{,TI}$ are statistically independent finds support in literature (see, for example, the rapid distortion theory by Hunt (1972/1975/1990), section 3.4) and can be accepted as long as I_u is not too high. This assumption is the basis for the model proposed in the following.

If the covariances between body-induced and turbulence-induced fluctuations are assumed to be zero (in view of the statistical independence), it follows that the pressure fluctuation which is measured during an experiment in turbulent flow is just the sum – in terms of variances – of the two contributions, the turbulence-induced one ($_{TI}$) and the body-induced one ($_{BI}$), as follows:

$$p_{\sigma^2} = p_{\sigma^2,TI} + p_{\sigma^2,BI} \tag{7.12}$$

Although it is apparent in the spectra that higher energy content is around the Strouhal peak, the separation of the two contributions is not immediate, especially in high turbulent flow. In terms of variances, the comparison of results in the two wind tunnels (WiSt and CRIACIV) resulted to be helpful. In fact, at CRIACIV the turbulence intensity is very low at high levels and this allows a first good estimation of the body-induced contribution at those levels. Then, extrapolation is made at $I_u = 0$, so that the actual body-induced fluctuations can be estimated all around the circumference. Since equation (7.12) holds in general, the theory can be further extended at low levels.

The validation of this simplified modelling is through comparison of full-scale results on cooling towers (Pröpper, 1977), as explained later on.

In the following, the level z/H = 0.85 is chosen as representative for explanation. At that level, $I_u = 0.028$ at CRIACIV and $I_u = 0.082$ at WiSt.

The circumferential distribution of the total variance of the pressure coefficients ($C_{p,\sigma}^2$) is shown in Figure 7.10. The two sides of the cylinder are not perfectly symmetric due to inhomogeneities of the flow in both wind tunnels. In fact, this is not surprising in experiments in turbulent boundary layer flows. Anyway, the differences between the two sides of the cylinder are small and they do not prevent the development of a model which is, of course, symmetric. Figure 7.10 shows that at stagnation the pressure fluctuations at CRIACIV are very small, resulting from low I_u. At 100° and 260° the fluctuations are instead high and they must be mostly body-induced. An insight in the spectra gives a more clear explanation over frequencies. As can be seen in Figure 7.11, at z/H = 0.85 it is not only the Karman vortex shedding that produces the majority of body-induced contribution, but there is a strong interaction with the tip-associated vortices.
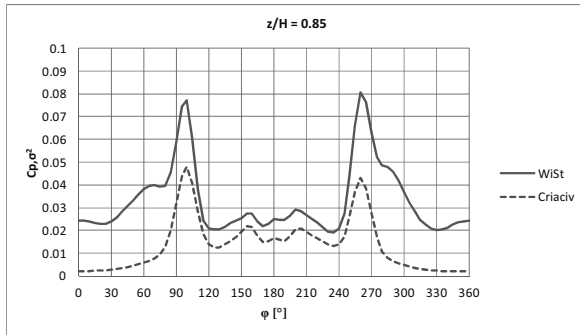
Figure 7.10 Circumferential distribution of the total variance $C_{p,\sigma}^2$ (body+turb.-induced)
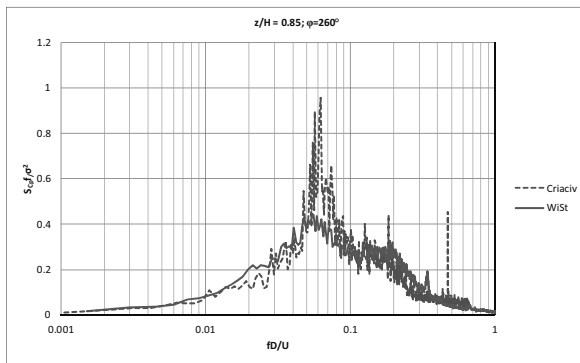
Figure 7.11 Power spectral densities of C_p at z/H = 0.85, 260°
$C_{p,\sigma}^2 = 0.0805$ (WiSt); $C_{p,\sigma}^2 = 0.0400$ (CRIACIV)

In order to separate body-induced and turbulence-induced contributions, the variances measured at CRIACIV (mostly body-induced) are compared to the variances measured at WiSt (mainly, but not only, turbulence-induced). A tentative extrapolation at $I_u = 0$ is proposed in Figure 7.12 and Figure 7.13. Since two experimental points are available at each angle, the extrapolation can only be linear in the plane σ^2, I_u^2. In any case, a linear extrapolation seems to be rather good for several reasons.

First of all, at 0° and up to 60° the body-induced contribution in smooth flow results to be zero and this confirms the expectations: at those angles the pressure fluctuations are mostly induced by the flow fluctuations. Then, moving downstream, the body-induced percentage increases and at 180° the slope of the line is almost flat (Figure 7.13). It means that the fluctuations in the wake are almost completely body-induced and they do not depend significantly on the upwind turbulence. It is also interesting to see that most of the lines in both figures are approximately parallel. It means that the rate of turbulence-induced fluctuations is almost the same at each circumferential angle. This is a further reason to relate the circumferential turbulence-induced distribution to only one reference angle, e.g. the stagnation angle, that can be related to the flow properties.
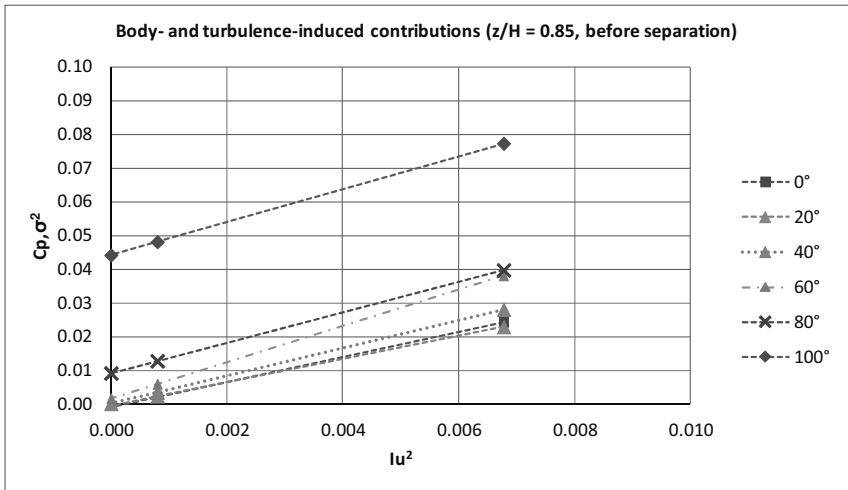
Figure 7.12 Extrapolations of body-induced contributions at angles before separation based on experiments at WiSt ($I_u = 0.082$ at $z/H = 0.85$) and at CRIACIV ($I_u = 0.028$ at $z/H = 0.85$)
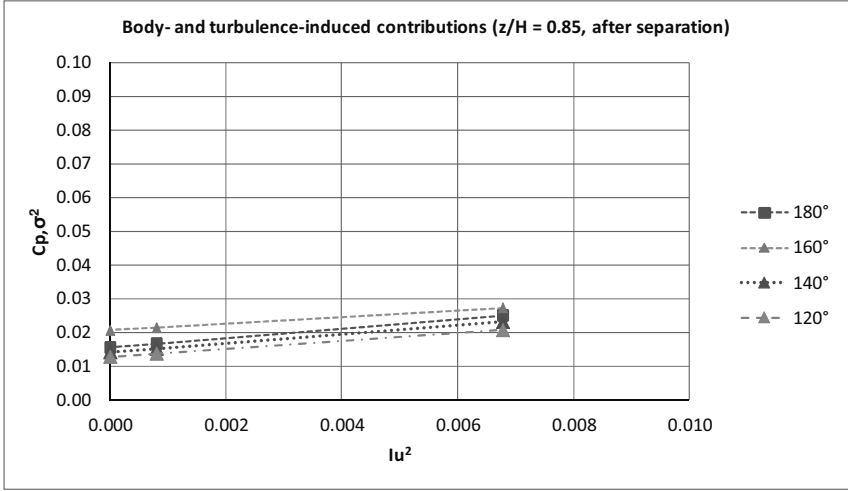
Figure 7.13 Extrapolations of body-induced contributions at angles after separation
based on experiments at WiSt ($I_u = 0.082$ at z/H = 0.85)
and at CRIACIV ($I_u = 0.028$ at z/H = 0.85)

The body-induced contribution extrapolated at $I_u = 0$ is then subtracted by the total variance measured at WiSt tunnel in high turbulent flow. The result represents the turbulence-induced part, which can be modeled around the circumference through the factor a(φ), defined as follows:

$$a^2(\varphi) = \frac{p_{\sigma^2, TI}(\varphi)}{p_{\sigma^2, TI}(0°)} \quad \rightarrow \quad a(\varphi) = \frac{p_{\sigma, TI}(\varphi)}{p_{\sigma, TI}(0°)} = \frac{C_{P, \sigma_{TI}}(\varphi)}{C_{P, \sigma_{TI}}(0°)} \tag{7.13}$$

$p_{\sigma,TI}(\varphi)$ is the standard deviation of the turbulence-induced contribution of the wind pressure; $C_{p,\sigma,TI}(\varphi)$ is the standard deviation of the corresponding pressure coefficient. In particular, at z/H = 0.85 it is:

Table 7.6 Body-induced and turbulence-induced pressure fluctuations (z/H = 0.85)

φ [°]	$C_{p,\sigma}^2$ (Wist)	$C_{p,\sigma}^2$ (CRIACIV)	$C_{p,\sigma,BI}^2$	$C_{p,\sigma,TI}^2$ (WiSt)	$a^2(\varphi)$	$a(\varphi)$
0	0.0242	0.0021	0.0000	0.0242	1.0000	1.0000
20	0.0229	0.0023	0.0000	0.0229	0.9428	0.9710
40	0.0280	0.0033	0.0000	0.0280	1.1529	1.0737
60	0.0381	0.0059	0.0016	0.0365	1.5044	1.2265

80	0.0397	0.0127	0.0091	0.0306	1.2602	1.1226
100	0.0772	0.0480	0.0441	0.0331	1.3660	1.1688
120	0.0207	0.0137	0.0128	0.0079	0.3271	0.5719
140	0.0231	0.0152	0.0141	0.0090	0.3720	0.6100
160	0.0273	0.0214	0.0206	0.0067	0.2769	0.5262
180	0.0251	0.0167	0.0155	0.0095	0.3929	0.6268
200	0.0290	0.0204	0.0192	0.0098	0.4043	0.6359
220	0.0237	0.0166	0.0156	0.0081	0.3341	0.5780
240	0.0207	0.0138	0.0129	0.0078	0.3226	0.5680
260	0.0806	0.0431	0.0381	0.0425	1.7527	1.3239
280	0.0486	0.0108	0.0058	0.0428	1.7673	1.3294
300	0.0369	0.0047	0.0004	0.0365	1.5056	1.2270
320	0.0225	0.0027	0.0001	0.0224	0.9254	0.9620
340	0.0212	0.0021	0.0000	0.0212	0.8755	0.9357
360	0.0242	0.0021	0.0000	0.0242	1.0000	1.0000

The same principle is attempted at other levels and the coefficient $a(\varphi)$ is calculated according to equation (7.13). The results along the height are plotted in Figure 7.14 and in the following ones . The stagnation value is well representative for the turbulence-induced fluctuations around the circumference in the attached region. In the wake the fluctuations drop at around one half. Relying on that, the following simple model $a^{LM}(\varphi)$ can be used to estimate turbulence-induced fluctuations, for any I_u:

$$a^{LM}(\varphi) = \begin{cases} 1 & \varphi \leq \varphi_h \\ 0.5 & \varphi > \varphi_h \end{cases} \qquad (7.14)$$

The apex (^{LM}) stands for load model. According to that, the intensity of pressure fluctuations varies along the circumference: it is constant before separation and drops to 50% in the wake.

The red dotted curve "0.85-tot" in Figure 7.14 represents the ratio $\sigma_p(\varphi) / \sigma_{p,0°}$, where the suffix "tot" means "without subtraction of body-induced fluctuations". It shows that a considerable contribution of body-induced fluctuations has been removed by the model, although the red curve (namely 0.85) still appears to be higher than 1 before separation. The reason is due to some body-induced contributions which are correlated to turbulent properties of the incoming flow and cannot be removed through tests in

smooth flow. These contributions are manly at the flanges of the cylinder. In any case, the departure from 1 is neglected in the proposed simplified model (equation (7.14)).
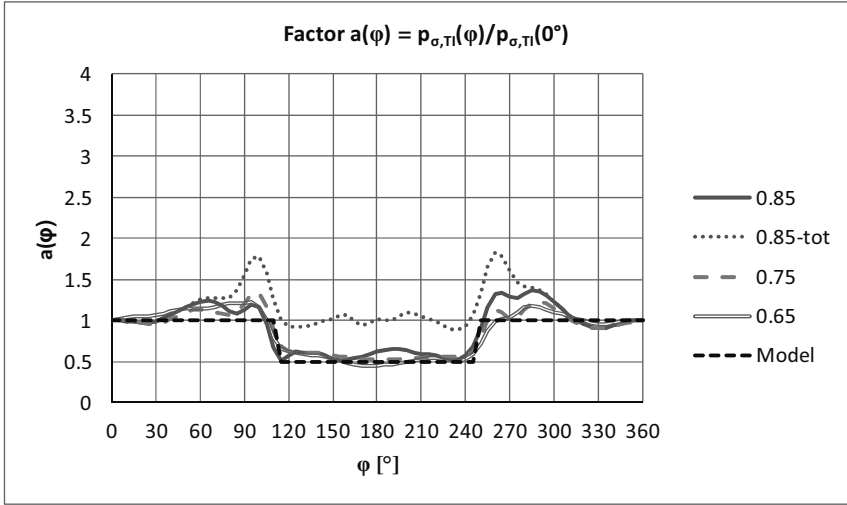

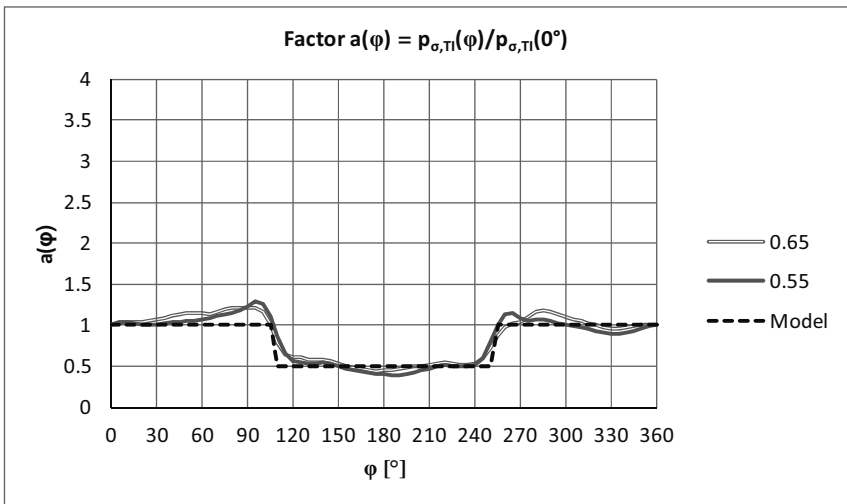*Figure 7.14 Factor a(φ) for modelling turbulence-induced pressure fluctuations (highest levels)*

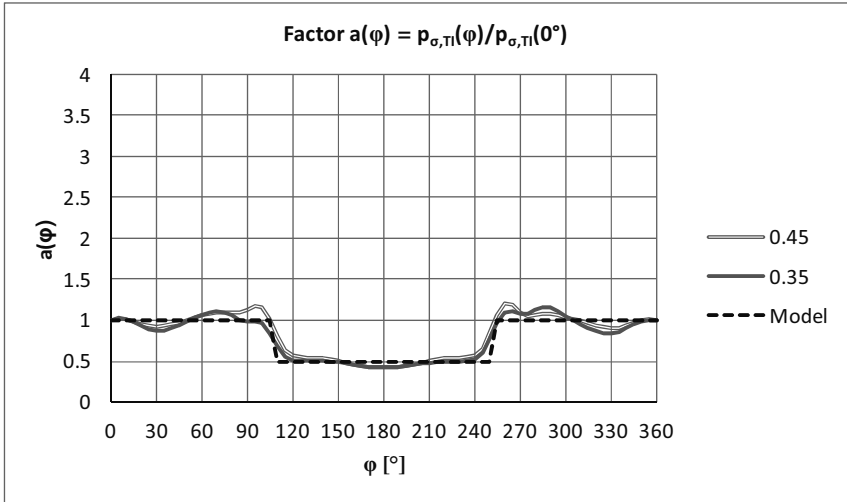*Figure 7.15 Factor a(φ) for modelling turbulence-induced pressure fluctuations (intermediate levels)*

233

Figure 7.16 Factor a(φ) for modelling turbulence-induced pressure fluctuations (low levels)

The comparison with results in literature is a proof of validity of the model, despite its approximations. In particular, similar results are obtained in full-scale data at transcritical Re by Pröpper (1977, fig. 8.8) on cooling towers. In that case, the contribution of vortex separation is low, so that the predominant contribution is turbulence-induced.

A further comment regards the linear extrapolation of the variances at $I_u^2 = 0$ in Figure 7.12 and Figure 7.13. It was an inevitable choice, since only two points per level at different I_u were available at each angle. However, the choice resulted to be rather reasonable. As a proof, the height-dependent variances at stagnation ($C_p,\sigma^2(z) \approx C_p,\sigma^2_{TI}(z)v$ c) are plotted as a function of I_u^2 in Figure 7.17. It shows that a linear relationship, whose extrapolation approximately crosses the origin of axes, is rather correct. The points at the highest turbulence intensity represent pressures on the tower at low levels ($z/H < 0.20$). The reason for which I_u is constant is the presence of the smooth collector roof (Figure 4.8). In any case, at $z/H < 0.20$ the model fails. The reason is that the horseshoe vortex system and the base vortices vary with the free-flow structures and the extrapolation at $I_u = 0$ is strongly non-linear.
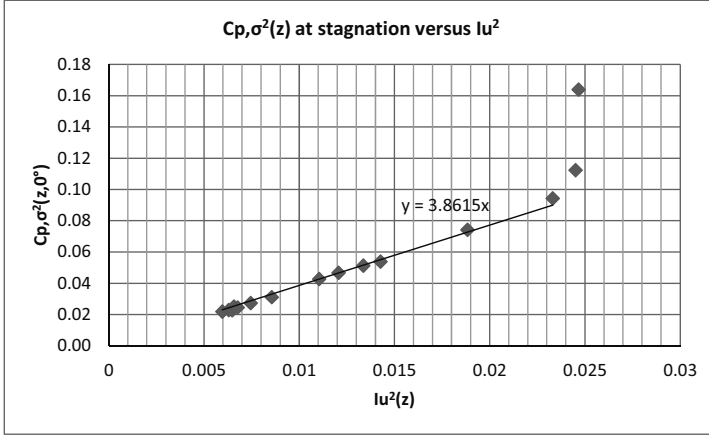
Figure 7.17 Variances C_p,σ^2 at stagnation versus I_u^2: a linear relationship (WiSt data)

So far, the factor $a(\varphi)$ has allowed to calculate the turbulence-induced fluctuations around the circumference provided their value at stagnation. Then, the latter can be calculated from the turbulence intensity of the incoming flow. This allows to generalize the model for any boundary layer condition. A first approach has already been proposed in Figure 7.17. A similar approach is based on the factor $A(z)$, which is the ratio between the intensity of pressures at stagnation (the turbulence-induced contribution, namely $I_{P,TI}(z)$) and the intensity of turbulence $I_u(z)$:

$$A(z) = \frac{I_{p,TI}(z)}{I_u(z)} \tag{7.15}$$

The intensity of pressures at stagnation $I_{P,TI}(z)$ is approximately equal to the standard deviation of the pressure coefficient at $0°$, being $p_m(z,0°)$ (mean pressure) approximately equal to the mean velocity pressure $q_m(z)$ (because $C_p(z,0°) \approx 1$) and $C_{p,\sigma TI}(z,0°) \approx C_{p,\sigma}(z,0°)$, as explained by equation (7.16).

$$
\begin{aligned}
I_{p,TI}(z) &= \frac{p_{\sigma,TI}(z,0°)}{p_m(z,0°)} = \frac{p_{\sigma,TI}(z,0°)}{C_p(z,0°)q_m(z)} \approx \\
&\approx \frac{p_{\sigma,TI}(z,0°)}{q_m(z)} = C_{P,\sigma,TI}(z,0°) \approx C_{P,\sigma}(z,0°)
\end{aligned}
\tag{7.16}
$$

Therefore:

$$A(z) \approx \frac{C_{P,\sigma}(z,0°)}{I_u(z)} \qquad (7.17)$$

The coefficient A(z) calculated on the basis of WiSt results is approximately constant along the height, as shown in Figure 7.18. Its mean value is around 1.93, which is approximately the square root of the slope coefficient of the equation y = 3.8615 in Figure 7.17. Only close to the ground (z/H ≤ 0.20) is the ratio A(z) higher than twice the turbulence intensity, due to the horseshoe vortex system, as previously mentioned with regard to Figure 7.17. Numerical values are reported in Table 7.7. The value $A^{LM}(z) = 2$, on the safe side, can be assumed by the designer without any significant overestimation (see section 7.3). It means that the intensity of pressure at stagnation is about twice the turbulence intensity of the flow.
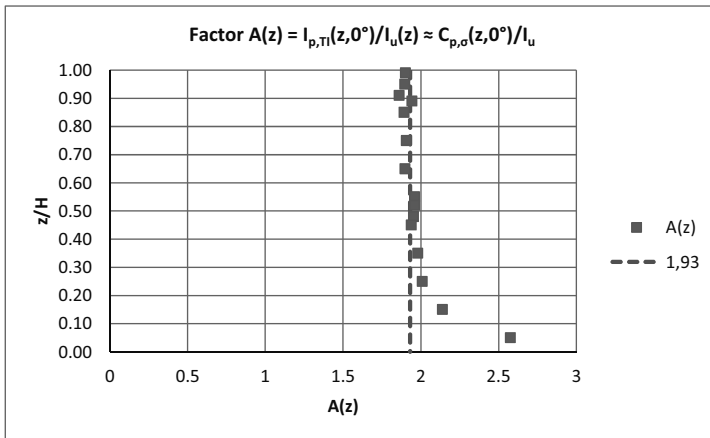
Figure 7.18 Factor A(z)

Table 7.7 Factor A(z) and simplified load modelling $A^{LM}(z)$

z/H	WiSt		
	I_u	$C_{p,\sigma}(z,0°)$	$A(z) \approx C_{p,\sigma}(z,0°)/I_u$
0.99	0.0772	0.1469	1.9016
0.95	0.0794	0.1506	1.8970
0.91	0.0806	0.1499	1.8609
0.89	0.0811	0.1578	1.9443

0.85	0.0823	0.1557	1.8917
0.75	0.0863	0.1646	1.9067
0.65	0.0925	0.1757	1.8985
0.55	0.1052	0.2061	1.9598
0.52	0.1099	0.2154	1.9599
0.48	0.1156	0.2259	1.9532
0.45	0.1195	0.2317	1.9394
0.35	0.1373	0.2719	1.9809
0.25	0.1527	0.3068	2.0095
0.15	0.1566	0.3349	2.1392
0.05	0.1571	0.4046	2.5761
Simplified load modelling: $A^{LM}(z) = 2$			

Under the basic assumption that body-induced fluctuations are statistically independent on turbulence-induced fluctuations (Hunt, 1975), the former can be evaluated by an experiment in smooth flow. The result of the extrapolation at $I_u = 0$ at all levels, based on WiSt and CRIACIV results, as previously described, is plotted in Figure 7.19. Numerical values can be found in the appendix (Table A.1). Differences between the two sides due to experimental asymmetries have been averaged out. The figure highlights three distinct regions: the tip region, with a strong effect of tip-associated vortices; the two-dimensional region, where the strength of Karman vortex shedding is practically absorbed by the stochastic fluctuation (the curves as z/H = 0.55, 0.45, 0.35 are close to zero); the low region with the ground effect.
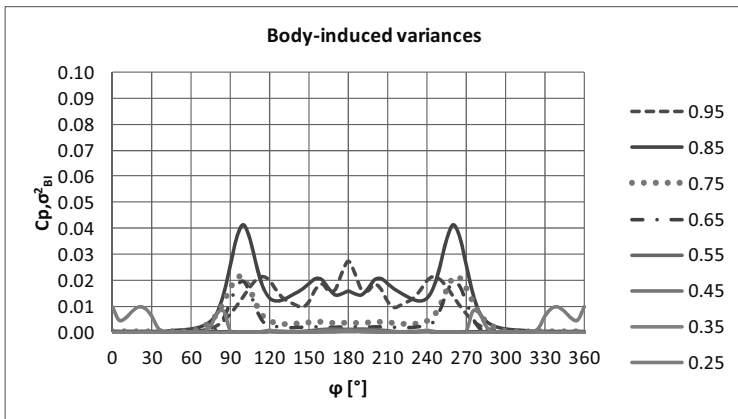
Figure 7.19 Body-induced fluctuations C_p, σ^2_{BI} all around the tower

237

7.1.4 **Cross-correlation coefficients**

The cross-correlation coefficients represent, beside the mean and the rms values, the third piece of information to calculate the quasi-static response of structures to the stochastic wind loading process. They give information about the lack of correlation (size effect). Simple models of cross-correlations of pressure coefficients are proposed in this section, they can be applied for calculation of shell stresses on the solar tower.

The analysis of cross-correlations of pressure coefficients is split up into the vertical and horizontal directions. Their cross product is used to approximate the cross-correlations between points having both horizontal and vertical separation, in case measured data are not available. The goodness of the approximation is discussed at the end of the section and later on in terms of the structural response. This simplification allowed to reduce significantly the total number of simultaneous measurements in the experiments, but a further refinement would be advisable for the future (Chapter 8).

Similarly, since force coefficients are calculated by integration of pressures at each level, the evaluation of their cross-correlations required simultaneous measurements of each level with all the other ones. Simultaneous data of forces at all levels are not available, therefore it is not possible to develop a complete model for cross-correlations of drag and lift coefficients to be used in beam-like calculations. Therefore, cross-correlations of forces are used whenever available for a deeper insight and clarification of pressure cross-correlations.

Vertical cross-correlation coefficients

The vertical correlation of pressures at stagnation depends on the turbulence structure of the incoming flow. As before, it would be important to generalize the results obtained for the specific turbulence condition tested in the wind tunnel to other turbulence conditions. For this purpose, it is mainly referred to results at WiSt, since measurements of both cross-correlations of pressures and velocities are available there. According to Teunissen (1970) the vertical correlation coefficients of wind velocities (along-wind component) in the atmospheric boundary layer have an exponential decay along the height:

$$\rho_u(\Delta z) = e^{-C_{uu}\Delta z} \tag{7.18}$$

By definition, the vertical integral length scale of turbulence (L_{uz}) is given by integration:

$$L_{uz} = \int_0^\infty \rho_u (\Delta z) d(\Delta z) \tag{7.19}$$

Therefore $C_{uu} = 1/L_{uz}$. If also the vertical correlations of pressures ($\rho_p(\Delta z)$) can be described by an exponential curve, then the vertical decay of pressure fluctuations can be related to the vertical decay of turbulence fluctuations. In general, it is:

$$\rho_p (\Delta z) = e^{-C_{pp}\Delta z} \tag{7.20}$$

L_{pz} is the pressure correlation length:

$$L_{pz} = \int_0^\infty \rho_p (\Delta z) d(\Delta z) \tag{7.21}$$

Similarly, $C_{pp} = 1/L_{pz}$ and a factor "c" is introduced to describe the relationship between L_{uz} and L_{pz}:

$$\rho_p (\Delta z) = e^{-\Delta z/L_{pz}} = e^{-c \cdot \Delta z/L_{uz}} \tag{7.22}$$

where:

$$c = \frac{L_{uz}}{L_{pz}} \tag{7.23}$$

However, provided the information regarding the vertical correlation of turbulence (L_{uz}), the relationship between L_{uz} and L_{pz} is in general unknown. It further depends, according to Hunt (1975), on the diameter of the structure. For example, for a circular cylinder ($L_{uz}/D = 0.2 \div 0.5$) Hunt finds $L_{pz}/L_{uz} = 1.5 \div 2.5$ (the factor c is the inverse value). According to him, the correlation length of pressure fluctuations (L_{pz}) is larger than the integral scale of turbulence L_{uz} because the vortices which are smaller than the diameter of the structure pile up at stagnation. This creates more similarity in the pressure fluctuations field.

In the case of the solar tower tested in the WiSt wind tunnel, the vertical integral length scale of the velocity fluctuation varies along the height around 200 mm (see Table 4.2). It is then of the same order of the tower diameter. Two representative levels at small and large heights (z_{ref} = 100 mm, upwards direction; z_{ref} = 700 mm, downwards direction) are reported in Figure 7.20, in view of a direct comparison with the pressure correlations. The vertical cross-correlations of pressures at stagnation are fitted with a negative exponential curve. Figure 7.21 reports L_{pz} at two levels, selected as the most suitable ones for the direct comparison with Figure 7.20.

a)   b)
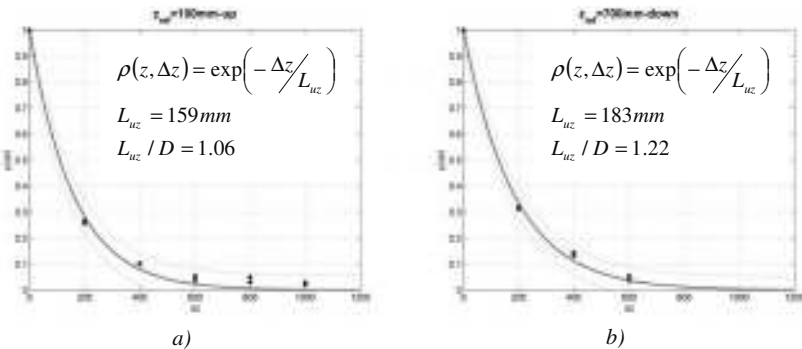
Figure 7.20 Vertical correlation coefficients of wind velocity (u-component)
a) z_{ref} = 100 mm (upwards); b) z_{ref} = 700 mm (downwards);

a)   b)
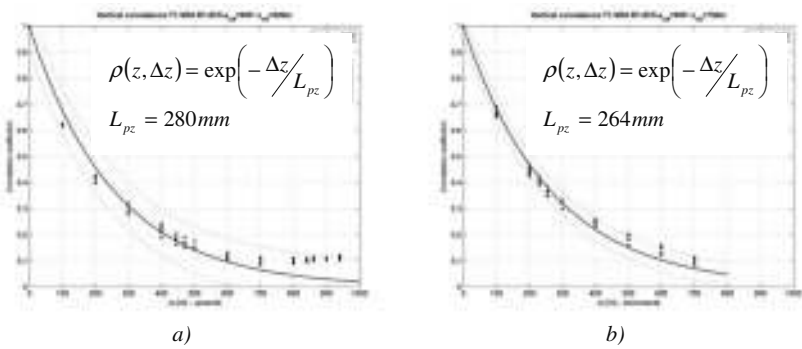
Figure 7.21 Vertical correlation coefficients of wind pressure at stagnation
a) z_{ref} = 50 mm (upwards); b) z_{ref} = 750 mm (downwards);

The comparison between Figure 7.20 and Figure 7.21 shows that $L_{pz} > L_{uz}$. It confirms Hunt's theory of the piling up of vortices at stagnation even for integral length scales of turbulence which are comparable to the tower diameter. Then, in order to develop a

general model, a more systematic study is needed at several reference heights and different meridians. It is reported in the following.

In principle, L_{pz} and L_{uz} depend on the direction of movement (Δz upwards, or Δz downwards). However, in view of a simplified model, the correlation coefficients are considered as a function of $|\Delta z|$. Figure 7.22 gives an overview of the pressure correlation lengths in the attached region of the cylinder (i.e. before separation). As said, they are calculated by integration of $\rho(|\Delta z|)$, i.e. assuming independence from the direction of movement. The largest correlation length is the angle $\varphi = 60°$. The figure also plots the integral length scales of the flow L_{uz}. Reference values, averaged along the height, are:

- $L_{uz} \approx 195$ mm $\qquad\qquad$ ($L_{ux}/D = 195/150 = 1.30$);
- $L_{pz} \approx 285$ mm at $\varphi = 0°$ $\quad$ ($c(0°) = L_{uz}/L_{pz} = 0.68$);
- $L_{pz} \approx 254$ mm at $\varphi = 20°$ $\quad$ ($c(20°) = L_{uz}/L_{pz} \quad = 0.77$);
- $L_{pz} \approx 341$ mm at $\varphi = 300°$ $\qquad$ ($c(300°) = L_{uz}/L_{pz} = 0.57$).

Figure 7.23 shows the experimental height-dependent ratio L_{uz}/L_{pz} (the so-called factor "c", equation (7.23)) at different circumferential angles before separation. The figures shows that the ratio L_{uz}/L_{pz} is different at each angle but it is approximately constant along most of the height.
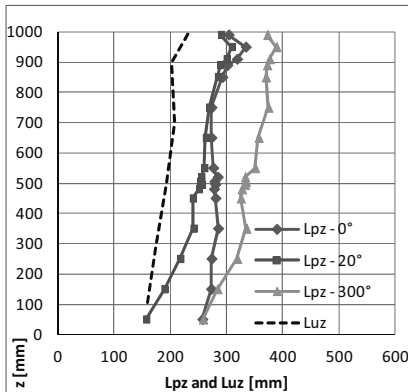
Figure 7.22 L_{pz} and L_{uz} in the attached region before separation, calculated by integration of $\rho(|\Delta z|)$, i.e. assuming independence of direction of movement (WiSt results)
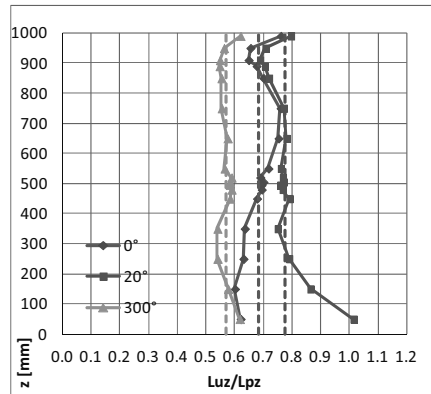
Figure 7.23 Factor $c = L_{uz}/L_{pz}$ (WiSt results)

The cross-correlation coefficients in the wake region drop faster with increasing distance. It would lead to small values of L_{pz}. In fact, at WiSt, the cross-correlation

remains almost constant to a non-zero value, around 0.18, at very large distances of separation (Figure 7.24). Such a constant correlation is not present in the undisturbed flow. The physical reason is probably a big steady vortex in the near-wake, due to the recirculating flow, as discussed in section 6.3 in the comparison with CRIACIV data. From a mathematical point of view, the negative exponential function would force the curve rapidly to zero and would not consider this quasi-asymptotic behaviour, leading to an underestimated value of L_{pz}. A double negative exponential function fits better in the wake (Figure 7.24, red curve). However, in this way the integration of the cross-correlation coefficients from zero to ∞ results in an impressively high value. Therefore, it is decided to calculate a so-called "equivalent correlation length" by integration of the double exponential fitting function along the tower height (from zero to $\Delta z = H$). It can then be used to model the correlations according to equation (7.22). The resulting values of the equivalent correlation lengths for the wake region are reported in Figure 7.25. Apart from the departure in the tip region, it can be approximately said that:

- $L_{pz} \approx 260$ mm at $\varphi = 120°$ $(c(120°) = L_{uz}/L_{pz} = 0.75)$;
- $L_{pz} \approx 340$ mm at $\varphi = 180°$ $(c(180°) = L_{uz}/L_{pz} = 0.57)$;
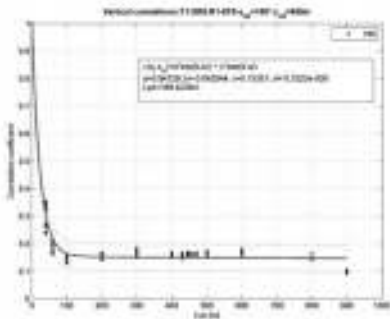
Figure 7.24 $\rho(0.95H,|\Delta z|)$ double negative exponential fitting curve, in order to fit the almost constant correlation at large distances (WiSt results)
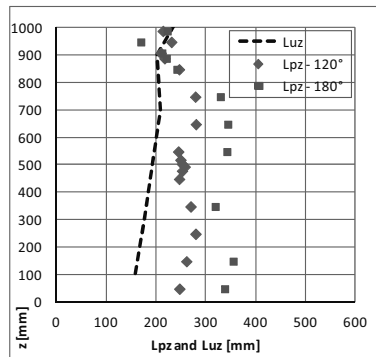

Figure 7.25 Equivalent L_{pz} in the wake region, calculated by integration along the tower height (WiSt results)

It results that around the circumference there is a certain variability of L_{pz}. In any case, provided the values of L_{pz} at different angles, the vertical cross-correlations are easily modelled by applying equation (7.22), i.e. by a negative exponential function.

In order to estimate the goodness of this modelling, Figure 7.26 plots the measured cross-correlations by using the dimensionless x-axis $|\Delta z|/L_{pz}$. The black line is the modeled curve by using a negative exponential function according to equation (7.22). In the dimensionless plane it is just $\rho(|\Delta z|/L_{pz}) = \exp(-1*|\Delta z|/L_{pz})$. It can be seen (Figure 7.26a), that the use of a negative exponential function provides a good estimation of the vertical cross-correlations in the attached region of the cylinder before separation. In the wake region (Figure 7.26b) the scatter is bigger, also because of the quasi-asymptotic behaviour at large distances. In any case, Figure 7.26b, compared to Figure 7.24, shows that this behaviour is partially removed by the use of the "equivalent" L_{pz}, as previously defined. However, at short distances it tends to overestimate the cross-correlations.

In any case, the goodness of the proposed stochastic model for vertical correlations does not depend on the scatter in the approximation of the load, rather on the effect on the response. A beam-like calculation (through the co-variance method) estimated that an even high non-zero drag correlation at large distance (e.g. 0.3) would produce an increase of around 3% of the base peak bending moment. This increase is further reduced by introducing the equivalent (larger) L_{pz}. Therefore, it can be concluded that a simple negative exponential function according to (7.22) can be used without any significant underestimation.
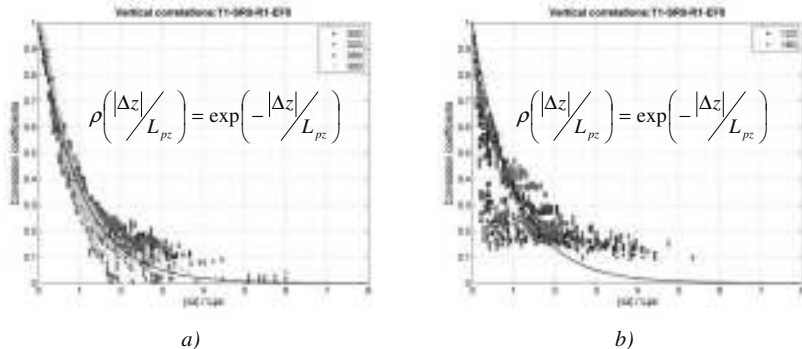

Figure 7.26 Modelling of vertical cross-correlations by negative exponential function
a) attached region before separation; b) wake region

In order to generalize the model to any turbulent boundary layer flow, which is characterized by a certain profile of $L_{uz}(z)$, L_{pz} should be evaluated from L_{uz} by using the factor "c" and equation (7.23). On the basis of WiSt results, such factors around the circumference are summarized in Table 7.8.

A further simplification can be introduced in the load model (^{LM}) by neglecting the circumferential variation of L_{pz}. This is reported in the last row of Table 7.8. Although the load input might be rather approximated, the calculation of the response did not show any significant change. Because of that, the approximation (^{LM}) is recommended.

Table 7.8 The factor "c" to relate L_{pz} and L_{uz}

Luz [mm] - WiSt	φ [°]	L_{pz} [mm] - WiSt	c = L_{uz}/L_{pz}
195	0	285	0.68
	20	254	0.77
	60	341	0.57
	80	296	0.66
	120	260	0.75
	180	340	0.57
(^{LM}) Load Model approx.	0-360		2/3

In conclusion, in the general case the vertical cross-correlations of pressures can be modelled as:

$$\rho_p\left(z,|\Delta z|\right) = e^{-\left(\frac{2}{3}\right)\frac{|\Delta z|}{L_{uz}(z)}}$$
(7.24)

Horizontal cross-correlation coefficients

The horizontal correlation coefficients around the circumference are governed by the mean flow pattern, while the structure of incoming turbulence is of secondary importance (Pröpper, 1977). Therefore, the first parameter to describe the cross-correlation matrix at a certain level is the separation angle φ_h (see Table 7.5).

By definition, $\rho(\varphi_1; \varphi_2) = \rho(\varphi_2; \varphi_1)$, therefore the correlation matrix is symmetric with respect to the main diagonal, whose values are equal to 1. Moreover, due to the symmetry between the two sides of the cylinder, the matrix is also symmetric with respect to the secondary diagonal. The description of one quarter of the matrix will then contain all the necessary information[7].

---

[7] In case of rings, instead, the presence of a bubble on only one side of the cylinder breaks the symmetry with respect to the secondary diagonal.

The correlation coefficients depend on the reference position and on the direction of movement. The reference position is classified in two groups: points before separation ($\varphi < \varphi_h$) and points after separation ($\varphi \geq \varphi_h$). The direction of movement is either downstream or upstream. The cross-correlations of stagnation and of rear stagnation (i.e. 0° and 180°) are the only ones which are symmetric around the circumference.

The circumferential correlations of the stagnation point with all the other points around the circumference resemble the mean pressure distribution (Figure 7.27). Stagnation and maximum suction have a strong negative correlation; stagnation and wake area have small negative correlations. It means that the fluctuations around the circumference appear to be organized by the mean flow and a considerable portion of them may be understood as a "breathing" of the mean flow.

The correlations of rear stagnation prove that the correlation between points in the wake and points before separation is not equal to zero. There is a relatively strong correlation between the maximum lateral suction and the wake ($\rho(180°,70°) \approx 0.6$) and even at 0° the correlation is not zero: $\rho(180°,0°) = -0.2$. These values are in agreement with Pröpper's results on cooling towers (Pröpper, 1977, figure 8.14). Therefore, Hunt's assumption of statistically independent pressure fluctuations due to incoming turbulence and vortex shedding is not completely confirmed.
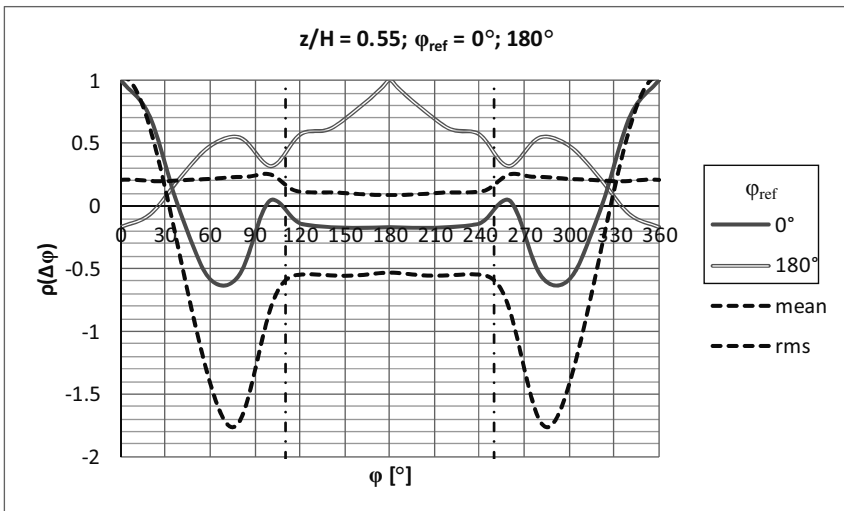
Figure 7.27 Cross-correlation coefficients ρ(0°,Δφ) and ρ(180°,Δφ) at z/H = 0.55

Figure 7.28 plots the circumferential cross-correlations at z/H = 0.55 when the reference position (listed in the legend, corresponding to $\rho=1$) is before separation. The downstream movement from the reference position has to be read in the graph from left to right, while the direction towards left refers to the upstream direction of movement. Similarly, Figure 7.29 plots the circumferential cross-correlations at z/H = 0.55 when the reference position is in the wake. All these pieces of information are then synthesized together in the correlation matrix in Figure 7.30.

Let us consider the cross-correlations to a reference angle φ_{ref} before separation (Figure 7.28). A significant difference between going downstream or upstream the cylinder from the reference position is the extension of the range of the negative correlations. In particular, in the downstream direction there is a weak negatively correlated range, which disappears in a positive plateau as the reference position approaches separation. Referring to $\rho(20°,\varphi)$, for example, the negative correlated range lies between $\rho(20°,60°)$ and $\rho(20°,100°)$, i.e. $\Delta\varphi = 40°$. The position $\varphi_{ref} = 60°$ is always positively correlated with the downstream positions. The upstream cross-correlations, instead, drop in a deep negatively correlated area when the two points belong to opposite sides of the cylinder. For example, at $\varphi_{ref} = 20°$ the negative range with circumferential positions on the other side lies between $\rho(20°,340°)$ and $\rho(20°,270°)$, i.e. $\Delta\varphi = 70°$ and the correlation drops till -0.7. The negative correlation between the two sides of the cylinder is marked by the dark blue on the upper right-hand-side corner in Figure 7.30 (or, similarly, the lower left-hand-side corner).

Along the height, the spanwise variation of the circumferential correlations follows the same organization of the mean flow. The following three main regions are detected along the height (Table 7.5):

- tip region (z' < 2D from the top, i.e. z' < 0.3H in the case study), Figure 7.31;
- normal region (z/H > 0.5 and z' > 0.3H), Figure 7.30
- low region (z/H < 0.5), Figure 7.32;

For simplicity, only one correlation matrix is proposed for the low region (Figure 7.32), that is an envelope of values on the safe side. Instead, the tip region can be further subdivided as follows:

- tip region (z' < 2D):   a) z' < 0.3D (Figure 7.31a)
                            b) $0.3D \leq z' \leq 0.5D$ (Figure 7.31b)

c) $0.5D \leq z' \leq D$ (Figure 7.31c)

d) $D \leq z' \leq 2D$ (Figure 7.31d)

Numerical values of correlation matrices for calculations are reported in the appendix (section 10.1).

Correlations between points with horizontal and vertical separation

The cross-correlations between points with horizontal and vertical separation ($\Delta\varphi$ and Δz) are approximated by the cross-products (equation (7.25)). The approximation in unavoidable, because the streamlines of the flow descend while flowing round the body. These movements are even enhanced by the velocity gradients in shear flow. Therefore, it is generally not possible to split the correlation into a height-dependent and a circumferential distribution. The topic is also addressed in Kasperski&Niemann (1988). However, the three dimensional correlation field has not been completely measured in the experiments on the tower. Because of that, the use of approximation (7.25) cannot be avoided. Further tests are advisable in the future for refinement of this model.

$$\rho(z_1, \varphi_1; z_2, \varphi_2) \cong \rho(z_1; z_2) \cdot \rho(\varphi_1; \varphi_2) \tag{7.25}$$

Equation (7.25) can be applied in two ways: the vertical correlation can be evaluated at $\varphi = \varphi_1$ and the horizontal correlation at $z=z_2$ or viceversa. Numerically, the results are different, but a general rule does not exist. Therefore, in this work the cross-product was calculated in both ways and the safest result was considered. Whenever measured, $\rho(\varphi_1, z_1; \varphi_2, z_2)$ is compared to its approximated modelling. The modelling results to be mostly on the safe side. Only the cross-correlations in the wake might be underestimated.
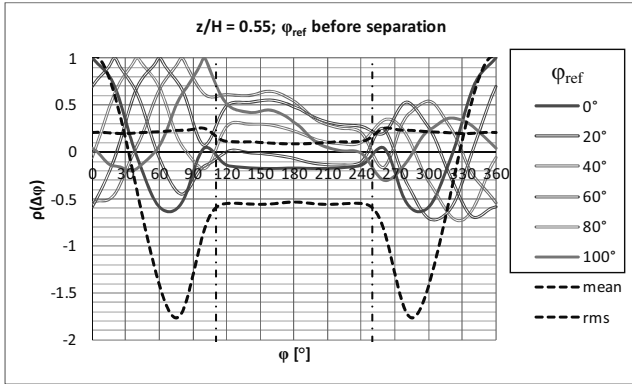
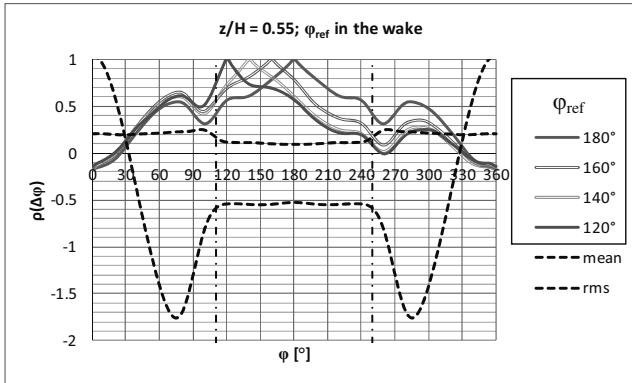*Figure 7.28 Horizontal cross-correlation coefficients at z/H = 0.55; φref before separation*

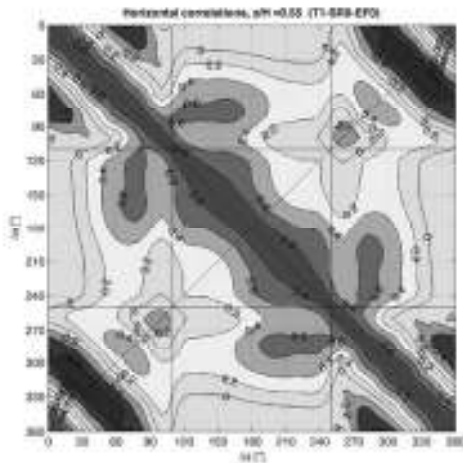*Figure 7.29 Horizontal cross-correlation coefficients at z/H = 0.55; φref in the wake*

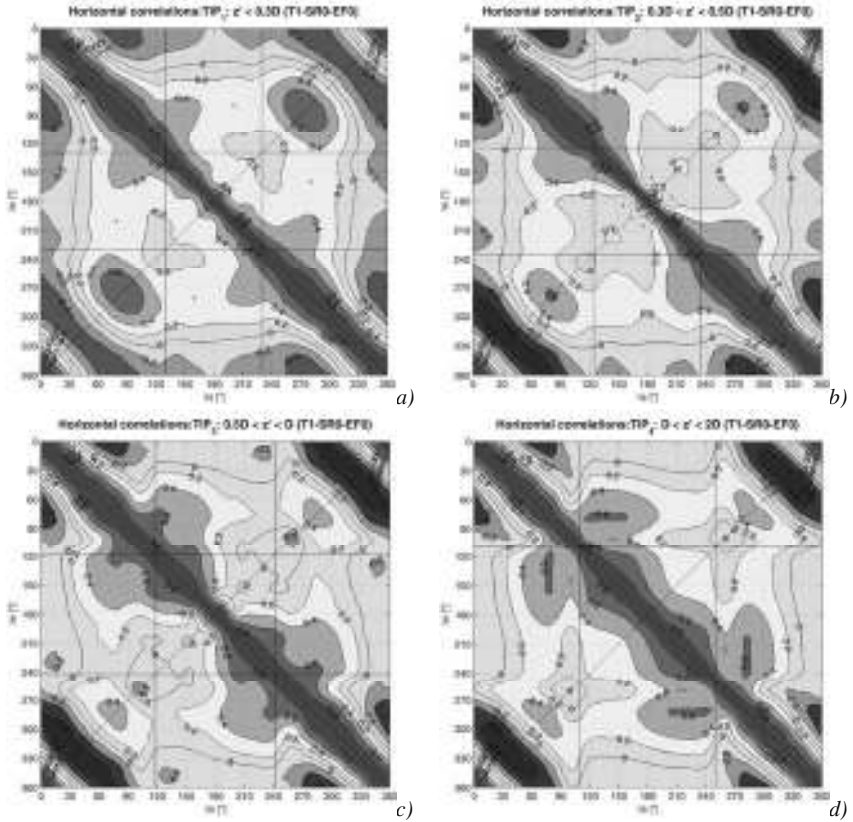*Figure 7.30 Horizontal cross-correlation coefficients at z/H = 0.55*

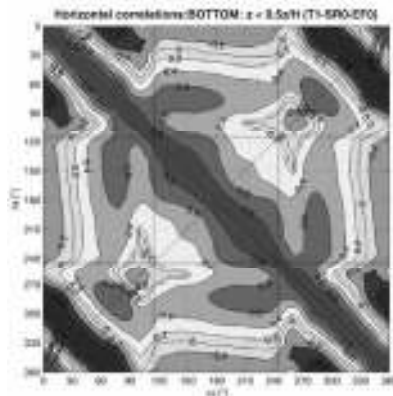Figure 7.31 a-d) Horizontal cross-correlation coefficients in the tip region (z' < 2D)

Figure 7.32 Horizontal cross-correlation coefficients in the low region (z/H < 0.5)

7.2 The beam response

The beam response of the solar tower is governed by the first natural vibration mode ($n_1 = 0.17$ Hz, Figure 2.20). Being $S_t \approx 0.2$ (Chapter 4), the critical velocity for vortex resonance is about $n_1 D / S_t = 0.17 \cdot 150/0.2 = 127$ m/s. This is much higher than the design velocity $U(1000) \approx 55$ m/s (Deaves&Harris model, Figure 2.4), so that resonance between the Strouhal frequency and the (transversal) vibration frequency is not expected. In these conditions, the design is led by the drag force, even though the cross-wind response remains an important contribution.

This section addresses both the along- and the across-wind beam response to the stochastic wind loading process. The background contribution is at first evaluated by the covariance method. Then, it is split up in the frequency domain by using time histories and influence coefficients. This calculation is then repeated by using the software Ansys, including inertial and damping forces. The first sub-section (7.2.1) considers the reference load condition, i.e. without any load modification produced by the rings. The effect of the rings is estimated in the second sub-section (7.2.2).

7.2.1 Quasi-static and dynamic beam response

The beam response of the tower is evaluated in this section by using the reference load condition, i.e. the effect of the rings on the load is not considered. This load configuration corresponds to the experimental results SR0.

At first, the background response to the drag force (σ_B^2), i.e. the response to the excitation that is transmitted without resonant amplification, is estimated without any split into frequencies through the covariance method (Niemann et al., 1996). This method uses statistical averages obtained from measured time series rather than the time series themselves.

$$\sigma_B^2 = \mathbf{\eta}^T \cdot \mathbf{cov}_D \cdot \mathbf{\eta} \qquad \text{and} \quad \mathbf{cov}_D = diag[F_\sigma] \cdot \mathbf{\rho}_D \cdot diag[F_\sigma] \qquad (7.26)$$

The matrix $\mathbf{cov}_D$ contains the covariances between drag forces at different levels and the vector $\mathbf{\eta}$ contains the influence coefficients for a certain effect at a certain cross-section. The covariances can be further split up into the product between rms values and correlation coefficients. The peak value of the bending moments ($M_{D,peak}$) is defined as:

$$M_{D,peak}(z) = M_{D,m}(z) + k_p M_{D,\sigma}(z) \qquad \text{where } k_p = 3.5. \qquad (7.27)$$

The load data ($C_{D,m}$, $C_{D,\sigma}$ and ρ_D) in the basic load configuration (without rings) and the results are listed in the appendix (Table A.8, Table A.9, Table A.10). A synthetic summary is reported here in Table 7.9 and plotted in Figure 7.33.

The base peak bending moment results in the order of $8.7*10^7$ kNm. The calculation does not include the quasi-asymptotic contribution due to the steady recirculation region in the near-wake (Figure 7.24 showed such a contribution in terms of pressure correlations at 180°). This would result in non-zero values of the cross-correlations of drag force at large distance. However, it has been estimated that even high asymptotic correlation in the drag to the constant value 0.3 instead of 0 would imply an increase in the base peak bending moment of only 3% (i.e. $M_{peak,base} = 9.01*10^7$ kNm). It is then negligible.

Table 7.9 Quasi-static beam response to drag force (effect of the rings on the load not included)

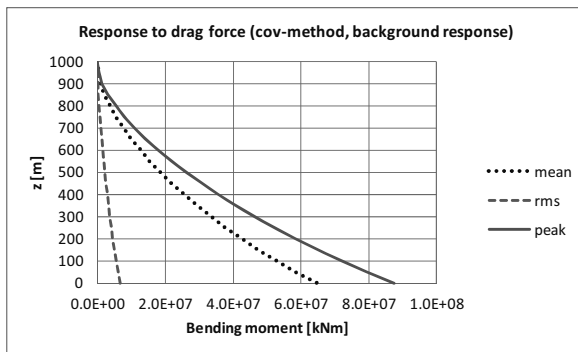| z [m]	$M_{D,m}$ [kNm]	$M_{D,\sigma}^2$ [kNm]^2	$M_{D,peak}$ [kNm]
0	6.45E+07	4.26E+13	8.74E+07
650	9.90E+06	1.45E+12	1.41E+07
750	5.42E+06	4.64E+11	7.80E+06
850	2.06E+06	7.17E+10	3.00E+06
950	2.14E+05	1.25E+09	3.38E+05

Figure 7.33 Quasi-static along-wind beam response (effect of rings on the load not included)

Then, the across and the along wind beam responses are calculated in the time domain. The background response to the stochastic process is evaluated by the use of measured time histories and influence coefficients, i.e. it is "manually" calculated by applying statically at each time step the influence coefficients of forces along the height. The

influence coefficients for the bending moment at the base are just the heights of the forces. The full dynamic response is calculated with the software Ansys by integration of the dynamic equations of motion (including damping and mass forces) and it shows the dynamic amplification at the first two vibration modes. Simultaneous time histories have to be used in the calculation. They have been measured at four levels (950-850-750-650 m) and - for the purpose of this analysis - all the other time histories are considered fully correlated with them.

The spanwise variation of the tower diameter (Figure 1.13) has been included in the calculation, in order not to underestimate the mass of the structure. The data in the wind tunnel ($_{WT}$) are transferred into full-scale ($_{FS}$) by scale factors applied on the length ($\lambda_L = L_{FS}/L_{WT}$), on the velocity ($\lambda_U = U_{FS}/U_{WT}$) and consequently on the frequency ($\lambda_F = \lambda_V/\lambda_L$) and on the time ($\lambda_T = 1/\lambda_F$), as explained in section 4.1.2. The reference length scale is the scale of the model (1:1000), because the tower diameter enters the Strouhal number. It is then assumed that the boundary layer in the wind tunnel is scaled similarly.

The main input data of the analyses are:

- $D_{FS}(H) = 150$ m; $D_{WT}(H) = 0.15$ m $\rightarrow \lambda_L = 1000$;
- U_{FS} (H) = 51.31 m/s (H&D model, $V_b = 25$ m/s, II terrain cat.); U_{WT} (H) = 25.07 m/s $\rightarrow \lambda_V = 2.05$;
- $\lambda_F = 1/488$; $\lambda_T = 488$; it is not too far from the time scale that would have been obtained by comparing T_{ux} in the wind tunnel and T_{ux} in full-scale, even though T_{ux} in full-scale is an uncertain parameter (see section 4.1.2).

In addition, the time domain analysis includes damping and inertial forces (full-transient analysis, Ansys):

- Integration time step = 0.244 s = $(1/n_{sampl})*\lambda_T = (1/2000)*488 < 1/20n_1 = 1/(20*0.17) = 0.29$;
- Rayleigh damping: $[D] = \alpha[M] + \beta[K]$. The coefficients are calculated assuming modal damping ratios ξ_i equal to 0.01 (corresponding to a logarithmic decrement $\delta = 2\pi\xi \approx 0.06$) at $n_1 = 0.17$ Hz (beam bending mode) and $n_3 = 0.65$ Hz (beam mode with two nodes), according to the formula $\xi_i = \alpha/2\omega_i + \beta\omega_i/2$, where $\omega_i = 2\pi n_i$.

Tapered elements "beam188" in Ansys library have been used in the finite element model of the tower.

Figure 7.34 shows the spectrum of the loading process in the across-wind direction (S_{CL}). Figure 7.35 and Figure 7.36 show the quasi-static and the dynamic responses, respectively, in the across-wind direction. Since the methods and the tools of

calculations are different, the good agreement of results is a further proof of validity. Instead, Figure 7.37, Figure 7.38, Figure 7.39 refer to the along-wind direction. In this regard, it is interesting to note the similarities to the undisturbed flow fluctuations (Figure 4.11).

Figure 7.34 shows the typical two-peaks lift spectra, due to tip-associated vortices. They are shed only in absence of ring beams (basic load configuration), that is the one considered in this section. The critical wind speed for the lower Strouhal number (around 0.07) is very high, so resonance between the structural mode the low-frequency peak will not occur[8]. On the other hand, there will be a quasi-static low frequency oscillation on which the Karman resonance is superimposed. It is then important to quantify the response contribution of the tip-associated vortices.

In the background response, the contribution of the low frequency peak in the bending moment at the base is around 7% (Figure 7.35). If resonance is included (Figure 7.36), the tip-associated vortices increase the variance of the total response of only 3%[9]. Therefore, the contribution of tip vortices in the total response is not so significant. Moreover, Figure 7.36 highlights the dynamic amplification at the base due to the structural vibration modes. The first mode ($n_1 = n_2 \approx 0.17$; $n_1D/U \approx 0,50$) is the beam bending mode, typical of the solar tower (see section 2.4). The filtering effect of the structure at higher frequencies (mechanical transmittance) is also evident in the graph: the black spectrum goes below the blue one after the resonant peak. The second vibration mode ($n_3 \approx 0.65$; $n_3D/U \approx 1,9$) is a beam mode with two nodes of inversion in the shape. It is typical for beams but its frequency is not the same as in the shell model of the solar tower. In the shell tower, the second beam mode has a much higher frequency. Many shell-like modes precede it. Therefore, the beam FE model does not reproduce faithfully the real structure, which is not, in fact, a beam. In any case, the vibration frequency of the second beam mode is high and it lies in a frequency range which is not reproduced accurately even in the load. In fact, as explained in section 4.1.3, the damping effect of 1.5m pressure tubes predominates at n > 200 Hz (wind tunnel scale), that is nD/U > 1.2. This is the cut-off frequency for the spectra.

---

8 In this work, non-linear geometrical effects arising from low frequencies of excitation are not considered, as well as the reduced stiffness due to concrete cracking. Further investigation in the non-linear behaviour is a future outlook.

9 In Figure 7.36 the spectra do not seem to decrease to zero as n→0. This is a matter of the log plot and Δn. For example, in the "0-qs" curve the first point has coordinate (nD/U = ΔnD/U = 0,00146074 ; Sn = 3,57E+11). The ordinate is more than two orders smaller than the highest magnitude. Moreover, the ordinate is a very small number close to zero once it is divided by the variance, as it is in the dimensionless plot (3,57E+11/1,61E+14 = 2.2*10^{-3}).
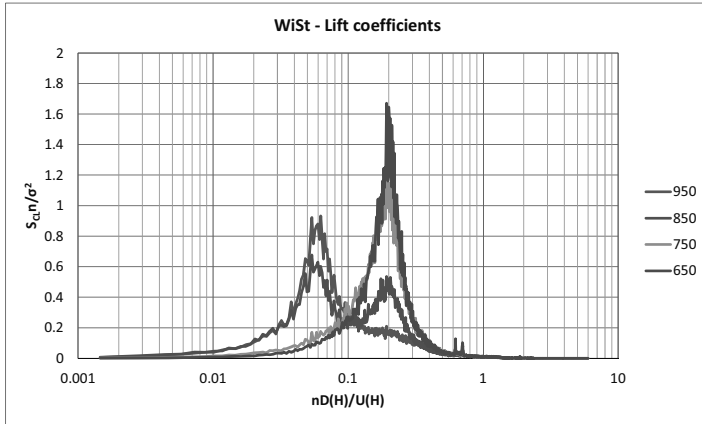
Figure 7.34 Spectra along the height of lift coefficient

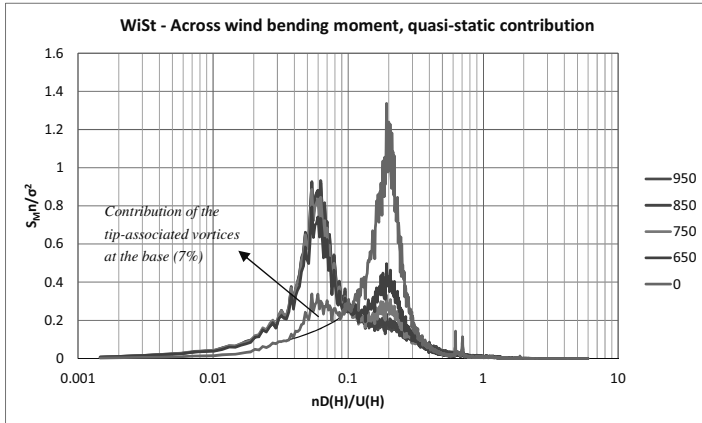*(SR0, effect of the rings on the load not included, WiSt data)*

Figure 7.35 Structural response in the across-wind direction. Resonance not included.

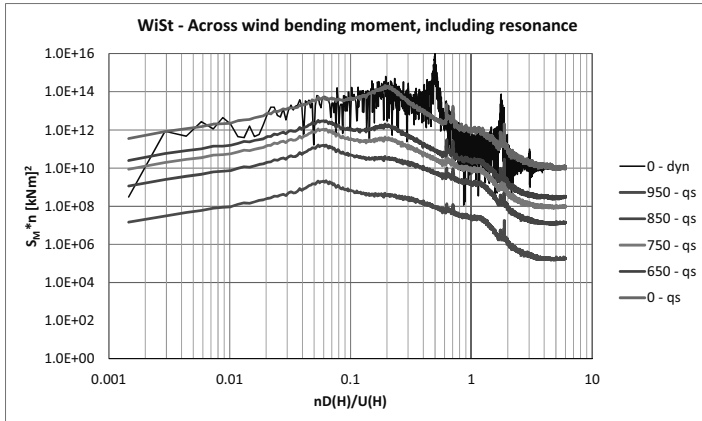*(SR0, effect of the rings on the load not included, WiSt data)*

Figure 7.36 Structural response in the across-wind direction. Resonance included.

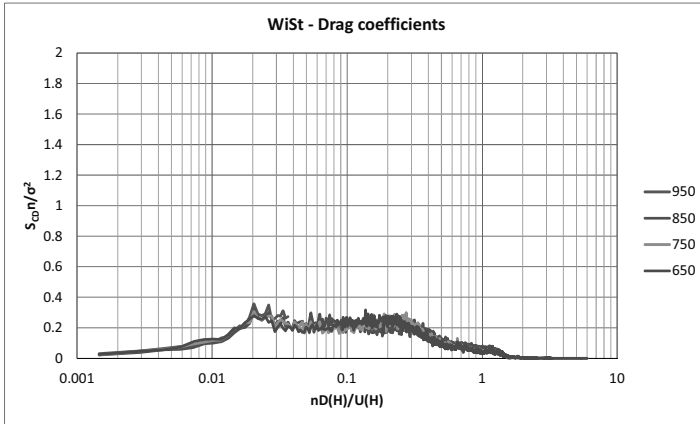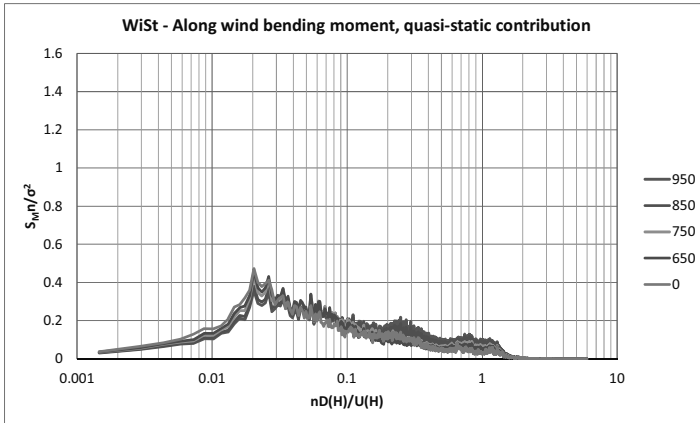*(SR0, effect of the rings on the load not included, WiSt data)*

Figure 7.37 Spectra along the height of drag coefficient

(SR0, effect of the rings on the load not included, WiSt data)

Figure 7.38 Structural response in the along-wind direction. Resonance not included.

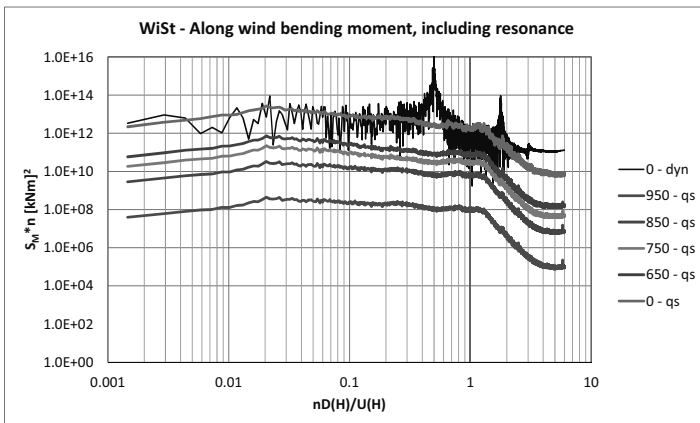*(SR0, effect of the rings on the load not included, WiSt data)*

Figure 7.39 Structural response in the along-wind direction. Resonance included.

(SR0, effect of the rings on the load not included, WiSt data)

Table 7.10 summarizes the results of the quasi-static and dynamic beam response. Results are separated in the along wind and across wind direction. The variance of the response in the across-wind direction is higher than in the along-wind direction. This can be explained by looking at Figure 4.13. At sufficiently high frequencies, the energy contribution of the v-component of wind speed is higher than the energy contribution of the u-fluctuations.

The effects in the two directions need to be combined in the resultant bending moment, which is a function of the along- and across-wind bending moments:

$$M_{res} = g\left(M_D, M_L\right) \rightarrow M_{res} = \sqrt{M_D^2 + M_L^2} \tag{7.28}$$

The resultant bending moment can be linearized with Taylor expansion around the middle value; in general it is:

$$
\begin{aligned}
M_{res} \cong {} & g\left(M_{D,m}, M_{L,m}\right) + \\
& + \frac{\partial g}{\partial M_D}\bigg|_{\left(M_{D,m}, M_{L,m}\right)}\left(M_D - M_{D,m}\right) + \\
& + \frac{\partial g}{\partial M_L}\bigg|_{\left(M_{D,m}, M_{L,m}\right)}\left(M_L - M_{L,m}\right)
\end{aligned}
\tag{7.29}
$$

Therefore, the mean and the variance of the resultant bending moment are:

$$M_{res,m} = g\left(M_{D,m}, M_{L,m}\right) = \sqrt{M_{D,m}^2 + M_{L,m}^2} \tag{7.30}$$

$$
\begin{aligned}
M_{res,\sigma^2} \cong {} & \left(\frac{\partial g}{\partial M_D}\right)^2 M_{D,\sigma^2} + \left(\frac{\partial g}{\partial M_L}\right)^2 M_{L,\sigma^2} + \\
& + \left(\frac{\partial g}{\partial M_D}\right)\left(\frac{\partial g}{\partial M_L}\right) M_{D,\sigma} M_{L,\sigma} \rho\left(M_D, M_L\right)
\end{aligned}
\tag{7.31}
$$

Where the derivatives are taken at the mean value of the independent variables. If $M_{L,m}$ = 0, by linearizing at the first order it results that $M_{res},\sigma^2 \approx M_{D},\sigma^2$.

By combining the effects at each time step in the time domain (equation (7.32)), the variance can be exactly evaluated by the resulting time history. It is reported in Table 7.10 and it allows to quantify the approximation by linearization. It can be seen that in the dynamic calculation $M_{res},\sigma_B^2+\sigma_R^2$ and $M_{D},\sigma_B^2+\sigma_R^2$ differ of only 6% at z/H = 0. The difference is higher in the quasi-static calculation (M_{res},σ_B^2 compared to M_{D},σ_B^2).

$$\mathrm{M}_{res}(t) = \sqrt{M_D^2(t) + M_L^2(t)} \qquad (7.32)$$

The dynamic amplification at the base (z/H = 0) is 22%, calculated according to equation (7.33):

$$dyn = \frac{M_{res,\,peak,\,B+R}}{M_{res,\,peak,\,B}} = \frac{M_{D,m} + k_p M_{res,\sigma,\,B+R}}{M_{D,m} + k_p M_{res,\sigma,\,B}} \qquad (7.33)$$

Table 7.10 [10] Beam response without and with resonance
(effect of the rings on the load not included, WiSt results)

z	950	850	750	650	0	m		
C_D,σ^2	0.013	0.010	0.007	0.006	0.006		drag coeff.	variance
C_L,σ^2	0.024	0.036	0.021	0.020	0.020		lift coeff.	variance
M_D,m	2.14E+05	2.06E+06	5.42E+06	9.90E+06	6.45E+07	kNm	along wind	mean
M_D,σ_B^2	1.25E+09	8.65E+10	5.20E+11	1.61E+12	5.75E+13	[kNm]^2	along wind	background
$M_D,\sigma_B^2+\sigma_R^2$	2.98E+10	5.93E+11	2.94E+12	8.53E+12	1.80E+14	[kNm]^2	along wind	with resonance
M_L,σ_B^2	2.31E+09	1.75E+11	1.28E+12	4.06E+12	1.58E+14	[kNm]^2	across wind	background
$M_L,\sigma_B^2+\sigma_R^2$	4.24E+10	9.10E+11	4.75E+12	1.40E+13	3.28E+14	[kNm]^2	across wind	with resonance
M_{res},σ_B^2	1.82E+09	1.02E+11	6.06E+11	1.85E+12	6.32E+13	[kNm]^2	tot. response	background

10 The mean response in Table 7.10 is evaluated by using the same load distribution as in Table 7.9. Instead, the background and the dynamic responses reported in Table 7.10 are evaluated by using simultaneous time histories measured in the wind tunnel. Since only four levels of simultaneous measurements were available (z/H = 0.95; 0.85; 0.75; 0.65, 18 pressure taps at each level), for the purpose of this analysis all the other time histories at other levels are considered fully correlated with them. Consequently, a higher value of the stochastic response is obtained. Even from the dynamic point of view, the fact that the time histories are fully correlated at lower levels is an overestimation on the safe side, because the first vibration mode does not have inversions of shape along the height.

$M_{res},\sigma_B{}^2+\sigma_R{}^2$	3.06E+10	6.17E+11	3.09E+12	9.02E+12	1.92E+14	[kNm]^2	tot. response	with resonance

In the dynamic calculation, time histories of around 80 minutes (full-scale time, based on the previously mentioned scale factor λ_T = 488) were applied as input in Ansys. This time window corresponds to 10 s in the acquisition of wind tunnel data. A zoom on a time window of 0.5 s (in the wind tunnel scale), which corresponds to 244 s in full scale, is plotted in Figure 7.40 and in the following ones. The aim of these figures is to study, in the time domain, the vortex separation and the structural vibration, both in the stochastic loading process and in the structural response.

The full-scale period of vortex separation is around 15 s ($S_tD/U \approx 0.2*51/150 = 0.068$ Hz). It corresponds to about 0.03 s in the wind tunnel. Therefore, about 16 vortex shedding periods occur in the time window of Figure 7.40. This oscillation is evident in the time history of the loading process (Figure 7.40), superimposed to the stochastic contribution due to turbulence fluctuations. In order to highlight vortex separation, the time histories have been filtered with a passband filter around the Strouhal peak (nD/U between 0.18 and 0.22). The blue lines represent the filtered time histories.

In particular, Figure 7.40 plots the lift coefficient at a representative level (z = 650 m). Figure 7.41 plots the corresponding effect, i.e. the across-wind bending moment, at the same level, both without and with filtering around Strouhal (magenta and blue lines, respectively). The magenta line highlights, in the response, the dominant oscillation at the frequency of the structural vibration: the structure is, itself, a filter. While the vortex shedding period is about 0.03 s in the wind tunnel scale, the structure vibrates with a shorter period, about 0.01 s ($1/n1/\lambda_T = 1/0.17/488$). It results that about 40 cycles occur in the time window of Figure 7.41 (that is 0.5 s).

It is interesting to analyze the response that there would be in conditions of resonance between vortex separation and structural vibration frequency (Figure 7.42). This is not a design condition, resonance has been imposed just for the purpose of this analysis by reducing the Young modulus of the material and increasing the wind speed. Resonant conditions are obtained at U_H = 74 m/s and reduced stiffness so that n_1 = 0.10116 Hz ($n_1D/U = 0.20 = S_t$). Figure 7.42 proves that in this condition stochastic properties of the load are completely filtered out in the response by the resonant vibration. The magnitude of amplitudes is also much higher (one order of magnitude, if compared to Figure 7.41). The cross-correlation functions in the resonant condition assume a value close to 1 along the whole height and decrease slowly in time.
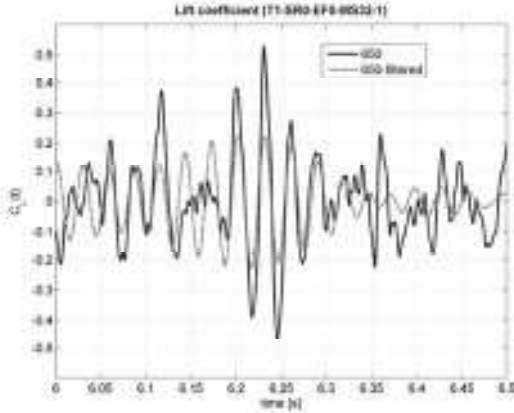
Figure 7.40 Stochastic loading process: time history of C_L , level 650 m. (SR0, effect of the rings on the load not included, WiSt data)
Blue line: bandpassfilter around S_t (0.18-0.22)
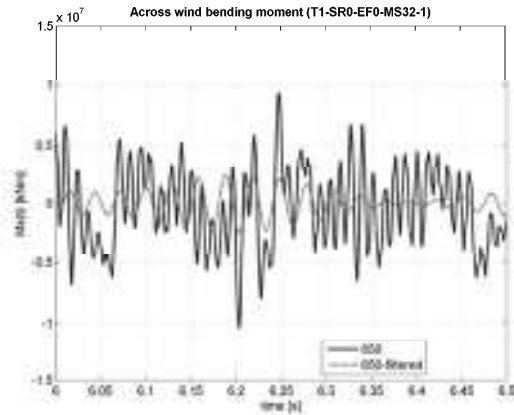*x-axis in wind tunnel scale*

Figure 7.41 Structural response to the stochastic process: across wind bending moment, level 650 m.
$S_t = 0.2$; $n_1 D/U = 0.5$
Blue line: bandpassfilter around S_t (0.18-0.22)
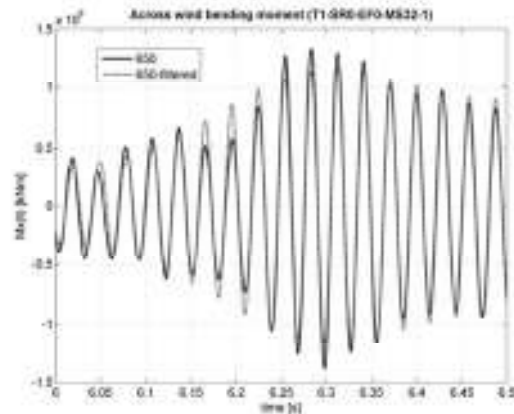*x-axis in wind tunnel scale*

Figure 7.42 Across wind bending moment, level 650 m. Resonant conditions:
$S_t = n_1 D/U = 0.2$
Blue line: bandpassfilter around S_t (0.18-0.22)
[The y-axis is one order of magnitude larger than in Figure 7.41]
x-axis in wind tunnel scale

259

Another important issue is the correlation along the height of the lift force and across-wind response.

The cross-correlations of the lift coefficients (z_{ref} = 650 m) are plotted in Figure 7.43. The correlation length of the "total" lift (i.e. unfiltered) is small, around one diameter (L_{LIFT} = 154 m), because of the stochastic effect of turbulence. The correlation length of the filtered time histories (so-called vortex shedding lift) is higher because the stochastic effect is largely removed. Nevertheless, it is still small (L_{VS} = 262 m), less than two diameters. However, the correlation of the response is much higher, being the structure itself, with its vibration frequency, a filter. In the time domain, this effect was clearly evident in Figure 7.41, where the structural oscillation governs the magenta line. In fact, the across-wind response is almost fully correlated along the whole height: Figure 7.44 shows $\rho(950,\Delta z)$ and proves that $\rho(950,1000)$ is more than 0.8.
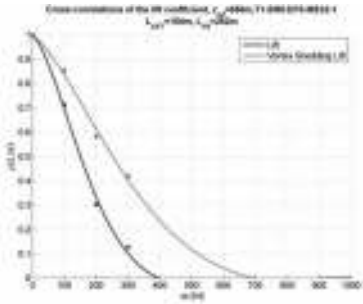

Figure 7.43 Cross-correlation coefficients of lift and vortex shedding lift (z_{ref} = 650 m)
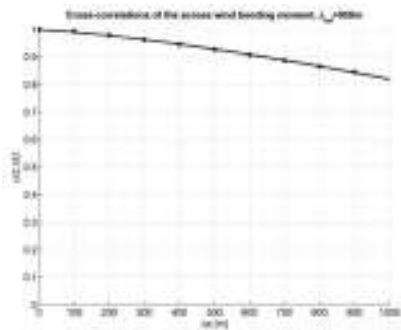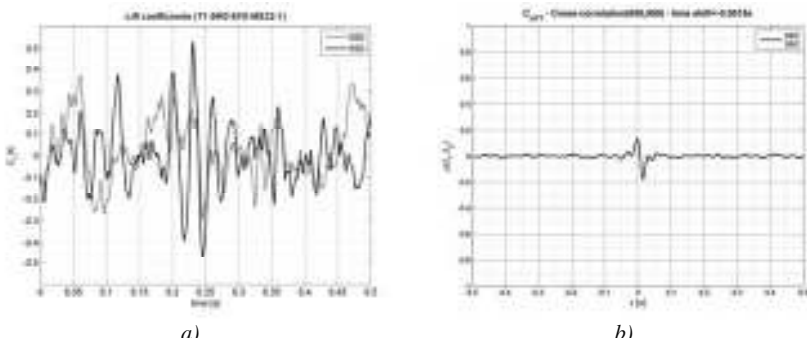
Figure 7.44 Cross-correlation coefficients of the response (across wind bending moment, z_{ref} = 950 m)

The spanwise correlation of the lift force and of the across-wind response is further analyzed in Figure 7.45, Figure 7.46, Figure 7.47. Two levels, 650 and 950 m, are chosen as representative. Load and response at these two levels are compared. Even if the fluctuations at 950 m are small, these levels are selected because simultaneous time histories were available at the largest separation distance (Δz = 300 m). Moreover, Figure 7.44 proves that, even if the fluctuations at 950 m are small, their correlation is high all along the tower, so that even this high level is representative.

Figure 7.45 shows that in the stochastic process the load correlation due to vortex separation is strongly diminished by turbulence (ρ = 0.1273). Once the time histories are filtered around the Strouhal peak (Figure 7.46), the cross-correlation is expectedly higher (ρ = 0.4197).

The modulation in amplitude of the filtered time histories is due to the beats phenomenon. It is produced by vortex shedding frequencies which are very close to each other, so that when the different waves are out of phase they tend to cancel each other and the resulting amplitude is small. Instead, when they are in phase they sum up and the resulting amplitude of oscillation is higher. This enhances the cross-correlation between different levels, too.

Figure 7.46 shows the correlation of the response at $z_1 = 950$ m and $z_2 = 650$ m. Consistently with Figure 7.44, the response has a much stronger correlation. The predominant oscillation is the bending vibration mode. The cross-correlation between the responses at the two levels is still close to 1 ($\rho = 0.9638$), although the two levels are at a distance of 300 m.

a)   *b)*

Figure 7.45 Lift coefficients at z = 650 and 950 m
a) time histories; b) cross-correlation function. ρ(650,950) = 0.1273
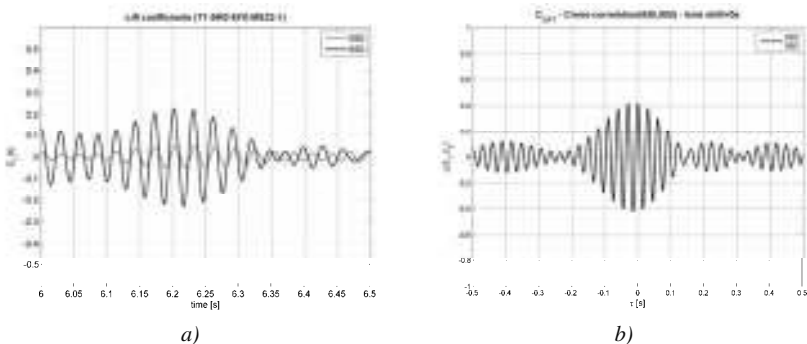
a)   *b)*

Figure 7.46 Lift coefficients at z = 650 and 950 m: filtered time histories, bandpass filter
around Strouhal (0.18-0.22).
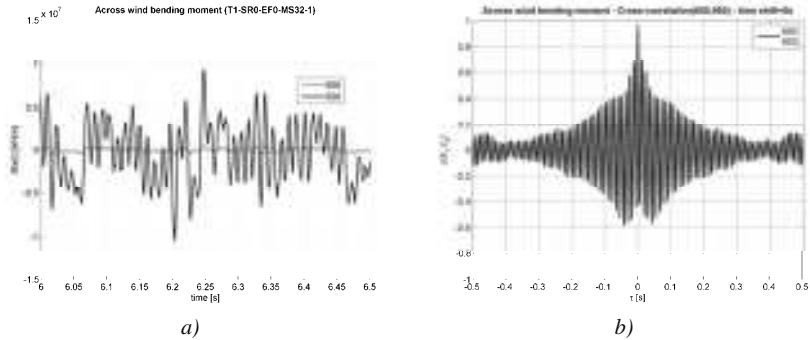*a) time histories; b) cross-correlation function. ρ(650,950) = 0.4197*

a)   *b)*

Figure 7.47 Cross-wind response at z = 650 and 950 m: a) time histories; b) cross-correlation function. ρ(650,950) = 0.9638

7.2.2   **The structural response to the asymmetric load**

The mean asymmetric load created by the rings is characterized by higher drag (Figure 5.39) and mean steady lift. $C_{L,m}$ is in any case considerable smaller than $C_{D,m}$. Moreover, the effect of the steady lift at the base is partially balanced by the inversion of the force along the height. In case of rings, the force coefficients (obtained by pressure integration) were not measured all along the height, therefore some approximation has been introduced in the calculation.

Relying on the measurements, a suitable resulting load model is plotted in Figure 7.48, together with its structural response in Figure 7.49. Numerical values are reported in the appendix (Table A.11, Table A.12).

At z = 0:

NO RINGS: $M_{D,m} = 6.45*10^7$ kNm (along wind, mean response)

$\qquad\qquad M_{res,m} = M_{D,m} = 6.45*10^7$ kNm

10 RINGS: $M_{D,m} = 7.01*10^7$ kNm (along wind, mean response)

$\qquad\qquad M_{L,m} = 3.14*10^6$ kNm (across wind, mean response)

$\qquad\qquad M_{res,m} = (M_{D,m}{}^2 + M_{L,m}{}^2)^{0.5} = 7.02*10^7$ kNm

Globally, in case of 10 rings, an increase in the mean bending moment at the base is estimated of about 9%:

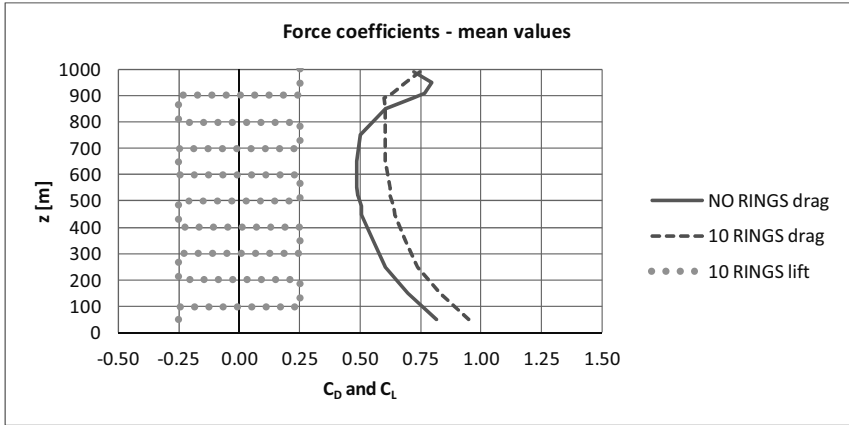$M_{res,m}$(10 rings) / $M_{res,m}$(no rings) $= 7.02*10^7/6.45*10^7 = 1.09$

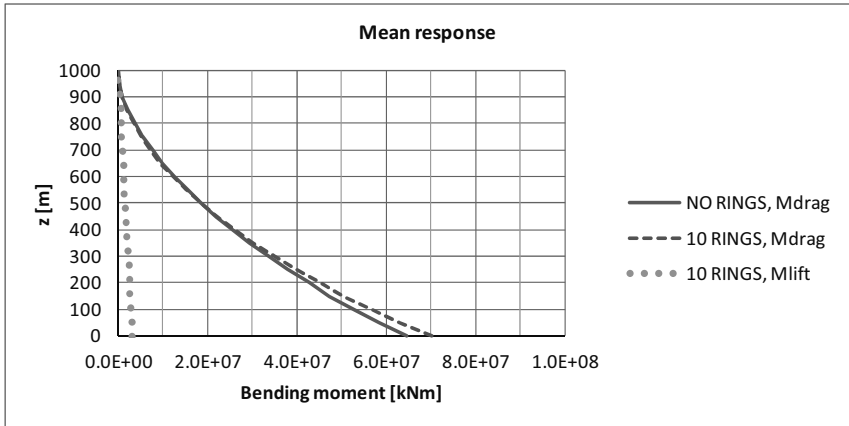*Figure 7.48 Effect of asymmetric flow due to ring beams: mean load*

Figure 7.49 Effect of asymmetric load due to ring beams: mean response

Then, the effect on the response is evaluated by applying simultaneous time histories in a quasi-static and a dynamic calculation. The calculation is performed like in section 7.2.1. Results are reported in Table 7.11.

Table 7.11 Beam response (along and across wind bending moment)
without and with resonance (load configuration with 10 rings, WiSt data)

z	950	850	750	650	0	m		
C_D, σ^2	0.101	0.095	0.095	0.104	0.104		drag coeff.	variance
C_L, σ^2	0.014	0.017	0.022	0.039	0.039		lift coeff.	variance
M_D, σ_B^2	9.24E+08	6.39E+10	3.92E+11	1.28E+12	6.59E+13	$[kNm]^2$	along wind	background

$M_D, \sigma_B^2 + \sigma_R^2$	4.08E+10	8.12E+11	4.08E+12	1.20E+13	2.60E+14	[kNm]^2	along wind	with resonance
M_L, σ_B^2	1.37E+09	9.56E+10	6.24E+11	2.20E+12	1.66E+14	[kNm]^2	across wind	background
$M_L, \sigma_B^2 + \sigma_R^2$	4.20E+10	8.50E+11	4.37E+12	1.32E+13	3.60E+14	[kNm]^2	across wind	with resonance
M_{res}, σ_B^2	1,30E+09	7,19E+10	1,36E+12	1,36E+12	7,19E+13	[kNm]^2	tot. response	background
$M_{res}, \sigma_B^2 + \sigma_R^2$	3,88E+10	7,82E+11	3,97E+12	1,18E+13	2,69E+14	[kNm]^2	tot. response	with resonance

Finally, through the comparison of Table 7.10 and Table 7.11, it can be quantified that the increase in the peak response at the base in case of ten rings is about 13% (Table 7.12, Table 7.13). It is basically an effect in the along-wind direction; in fact, the contribution given by the steady lift is one order of magnitude lower. Therefore, the effect of the rings on the beam response is not dramatic. Furthermore, the results presented here represent the highest limit, i.e. many rings (ten) and rather big.

Table 7.12 Across and along wind beam response (including resonance)
without and with rings:

	Along wind response (at z = 0)			Across wind response (at z = 0)		
	$M_{D,m}$ [kNm]	$M_{D,\sigma}$ [kNm]	$M_{D,peak}$ [kNm]	$M_{L,m}$ [kNm]	$M_{L,\sigma}$ [kNm]	$M_{L,peak}$ [kNm]
SR0	6.45E+07	1.34E+07	1.12E+08		1.81E+07	6.34E+07
SR1	7.01E+07	1.61E+07	1.27E+08	3.14E+06	1.90E+07	6.96E+07
SR1/SR0	1.09	1.20	1.13		1.05	1.10

SR0 = load modification due to the rings not included;
SR1 = load modification due to 10 rings included

Table 7.13 Resultant beam response (including resonance) without and with rings

	Resultant response (at z = 0)		
	$M_{res,m}$ [kNm]	$M_{res, \sigma}$ [kNm]	$M_{res,peak}$ [kNm]
SR0	6.45E+07	1.39E+07	1.13E+08
SR1	7.02E+07	1.64E+07	1.28E+08
SR1/SR0	1.09	1.18	1.13

SR0 = load modification due to the rings not included;
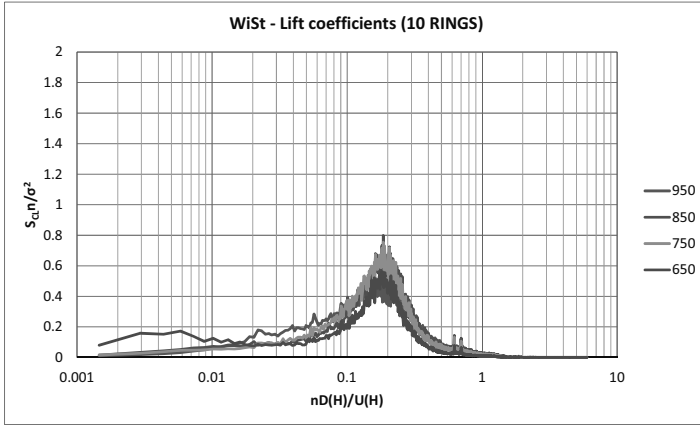*SR1 = load modification due to 10 rings included*

Figure 7.50 Spectra along the height of lift coefficient

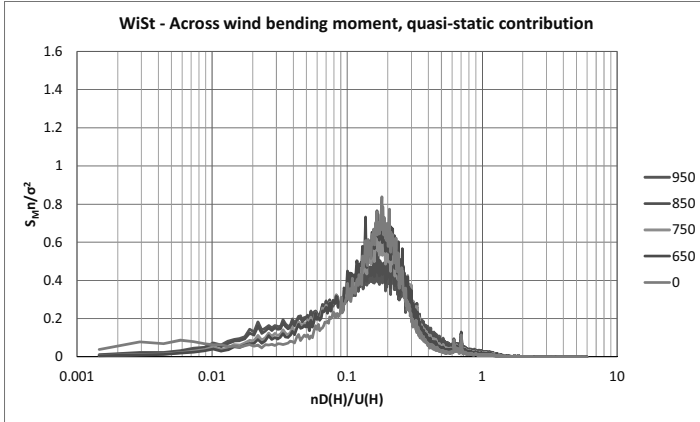*(SR1, effect of 10 rings on the load included, WiSt data)*

Figure 7.51 Structural response in the across-wind direction. Resonance not included.

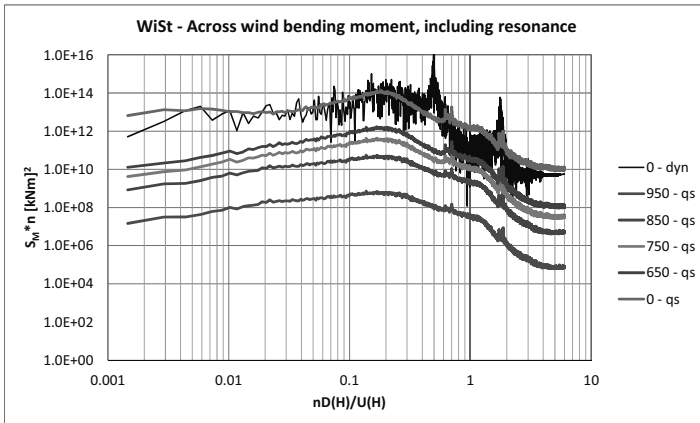*(SR1, effect of 10 rings on the load included, WiSt data)*

Figure 7.52 Structural response in the across-wind direction. Resonance included.

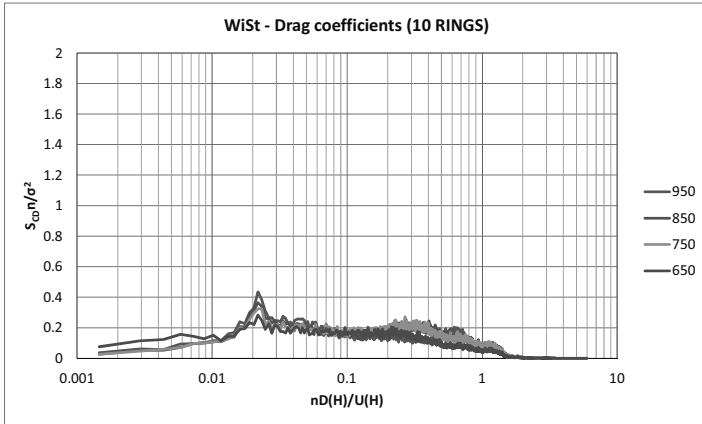*(SR1, effect of 10 rings on the load included, WiSt data)*

Figure 7.53
Spectra
along the
height of
drag
coefficient

(SR1,
effect of 10
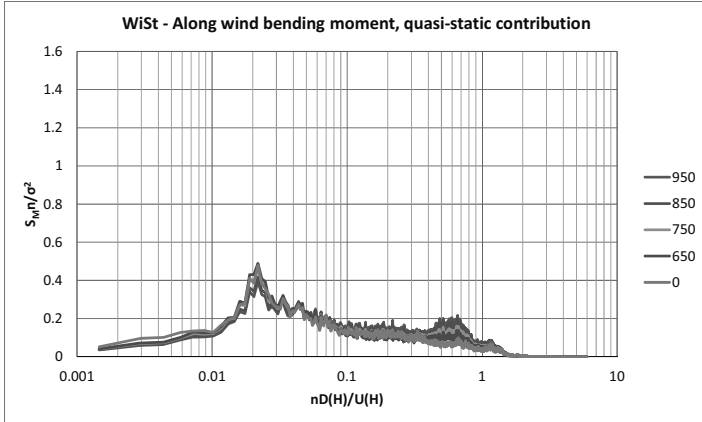rings on the
load
included,
WiSt data)

Figure 7.54
Structural
response in
the along-
wind
direction.
Resonance
not included.

(SR1,
effect of 10
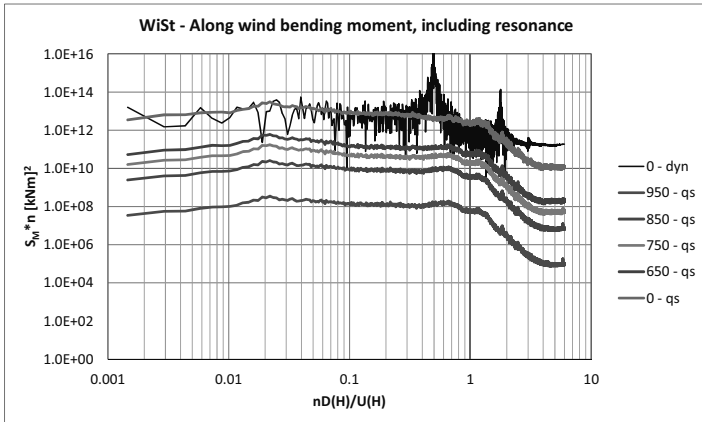rings on the
load
included,
WiSt data)

Figure 7.55
Structural
response in
the along-
wind
direction.
Resonance
included.

(SR1,
effect of 10
rings on the
load
included,
WiSt data)

7.3   The shell response

The shell response to the stochastic wind loading process is at first investigated through the covariance method. It is a quasi-static calculation (resonance not included) and it allows to consider the wind effect due to correlation of pressure. Input data are $C_{p,m}$, $C_{p,\sigma}$, $\rho(\Delta z, \Delta\varphi)$. They are all available by the experiments[11]. Then, dynamic calculations which include inertial and damping forces are performed on the tower by the software Ansys. The structural calculations always assume the presence of stiffening rings along the height (see Figure 1.13 and Figure 1.14 for the reference tower geometry), while the modification the rings create on the load is included only if specified.

In section 7.1 the big amount of experimental data has been simplified in a few parameters, which are of general application by the designer in any design condition. This simplified model is now validated through comparison of responses by applying either the experimental load data (directly measured) or the simplified load model. Results of the simplified model turn to be well representative of the experimental situation, so they can be extended in further applications to different boundary layer flows (and to structures of different aspect ratios). They allow to calculate the background response to the stochastic process in case of linear structural behaviour.

The wind load model derived from the wind tunnel investigation is then applied to a codified design wind profile for a certain location and terrain category. The local effects in the vicinity of the ring beams represent the substantial difference which is not included in the beam model presented before.

As the wind load is influenced by the actual number and size of rings, the quantification of the expected increase in stresses in the response due to the rings is another object of this section (see 7.3.4).

7.3.1   Validation of the simplified wind load model

The stochastic wind load model proposed in section 7.1 is suitable for being used in the quasi-static calculations through the covariance method (Niemann et al., 1996). The input data which are required are: $C_{p,m}$, $C_{p,\sigma}$, $\rho(\Delta\varphi)$ and $\rho(\Delta z)$. They have been modelled in section 7.1 with regard to the flow properties (especially I_u and L_{uz}) and summarized in the appendix (section 10.1).

---

[11] For locations where $\rho(\Delta z, \Delta\varphi)$ is not measured, it is substituted by the product between $\rho(\Delta z)$ and $\rho(\Delta\varphi)$.

In this section, the structural response of the tower is evaluated through the covariance method, both under the experimental data (directly measured at WiSt tunnel) and the simplified load model, applied to the same flow condition (the one at WiSt wind tunnel). The results are compared in order to identify to which extent the simplifying assumptions on the stochastic load in section 7.1 may affect the response. The aim is to validate the general use of the simplified stochastic load model for any atmospheric boundary layer flow. The wind load model (proposed in section 7.1) introduced the following approximations:

- the cross-correlations between points with horizontal and vertical separation are modeled as a product of $\rho(\Delta\varphi)$ and $\rho(\Delta z)$;
- $A(z) = 2$ constant along the height is a value on the safe side only at $z/H > 0.2$ (section 7.1.3) because it does not include horseshoe and base vortices;
- the body-induced fluctuations (Figure 7.19) are extrapolated at $I_u = 0$, through the assumption that they are not correlated to turbulence-induced fluctuations, although the wake fluctuations show a certain correlation with points before separation (Figure 7.27);
- the vertical correlations refer to the unified value around the circumference $L_{pz} = (3/2)L_{uz}$ (Table 7.8) and the constant almost asymptotic correlation at large distances, due to a large recirculation bubble in the near-wake, is neglected.

These approximations are accepted in view of the following results. Only the first simplifying assumption cannot be completely assessed because of the lack of the complete three dimensional correlation field; further experiments would be necessary (Chapter 8). The lack of a three dimensional correlation field might be one of the main reasons for the differences in the standard deviation of the stresses. In the following figures, the blue lines represent the effect that result from the experimental data, the red dots/lines from the simplified stochastic model applied to the same flow condition. The stochastic model underestimates of about 10% the rms values of internal forces. As regards the bending moments, the differences are less than 1 kNm/m. Moreover, the approximation is strongly reduced once the peak values are considered, so that the model can be accepted (Figure 7.56). The peak values of the structural response ($S =$ either n_{11}, n_{22}, m_{11} or m_{22}, i.e. circumferential or meridional forces and bending moments (direction 1 is circumferential, 2 is meridional)) are calculated as follows:

$$S_p = S_m + 3.5\sigma_s \qquad if \quad S_m \geq 0$$

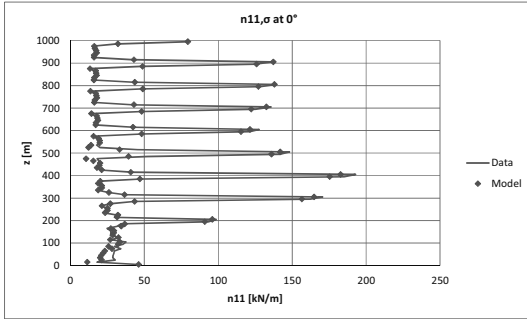$$S_p = S_m - 3.5\sigma_s \qquad if \quad S_m < 0$$

(7.34)

Figure 7.56 a)
Circumferential force,
rms values.
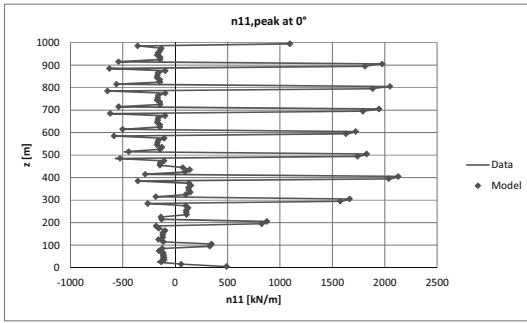*(continued)*

Figure 7.56 b)
Circumferential force,
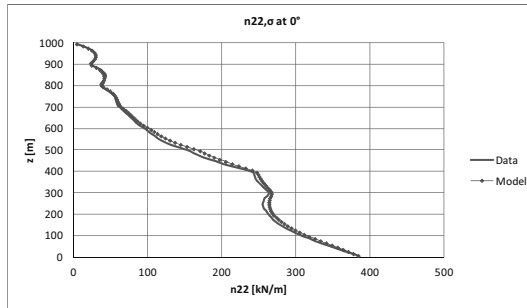*peak values.*
(continued)

Figure 7.56 c)
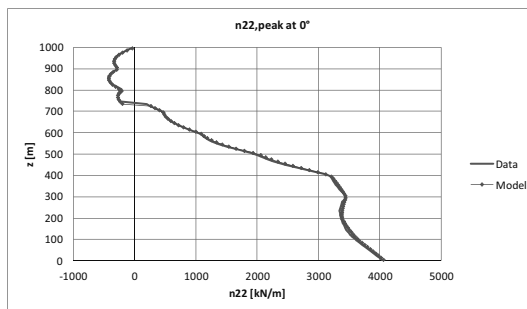*Meridional force,*
rms values
(continued)

Figure 7.56 d)
Meridional force,
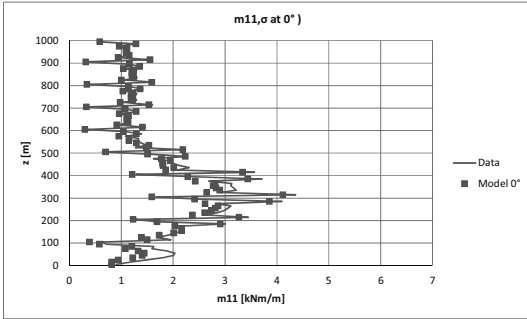*peak values*
(continued)

Figure 7.56 e)
Circumferential bending
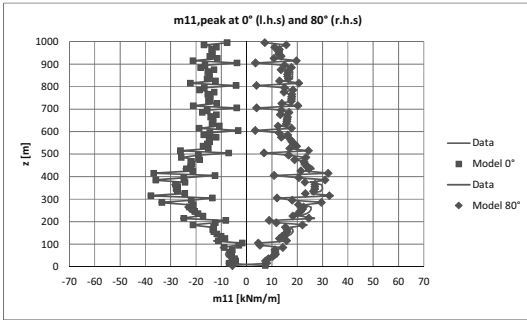moment, rms values
(continued)

Figure 7.56 f)
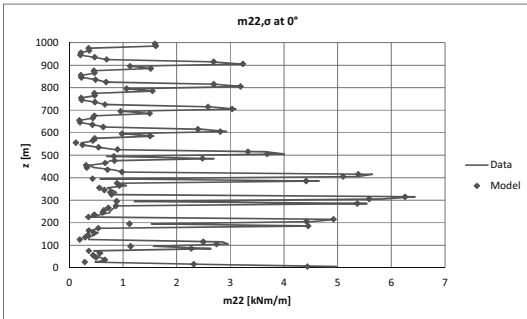Circumferential bending
moment, peak values
(continued)

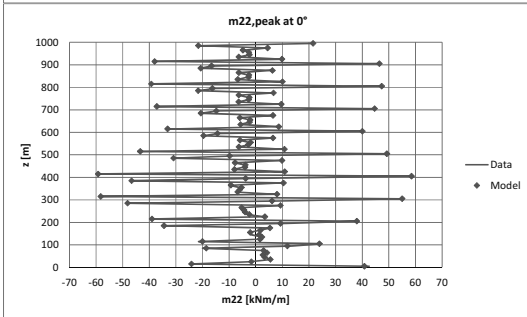Figure 7.56 g)
Meridional bending moment,
rms values
(continued)

Figure 7.56 h)
Meridional bending moment,
peak values
(continued)

Figure 7.56 Structural response along the height at significant angles, comparison by using experimental load data (blue lines) and proposed stochastic load model (red dots). Validation of the model. Resonance not included; effect of the rings on the load not included.

7.3.2   **Local effects in the vicinity of the stiffening rings**

The stiffening rings were originally introduced in the design (Goldack, 2004; Backström et al., 2008) in order to reduce ovalizations of the shell. A certain number of rings, properly stiffened, can guarantee a beam-like behaviour at the first eigenmode. As a result, the distribution of internal forces under the wind action is improved and the peaks of tension at the windward side are reduced. By increasing the stiffness and/or the number of rings, the circumferential distribution of meridional forces changes from a cosines-like distribution (typical for shells) to a linear distribution crossing zero at 90°, that is typical for beams (Lupi, 2009). With ten rings, such a beam-like distribution is achieved in the cylindrical shell at middle height (Figure 7.57, black curve). Ovalizations of the shell at the windward side in the upper part of the tower are responsible for the negative values of n_{22} at stagnation and lateral tension at the flanges, as it occurs for example at 850 m in the figure.
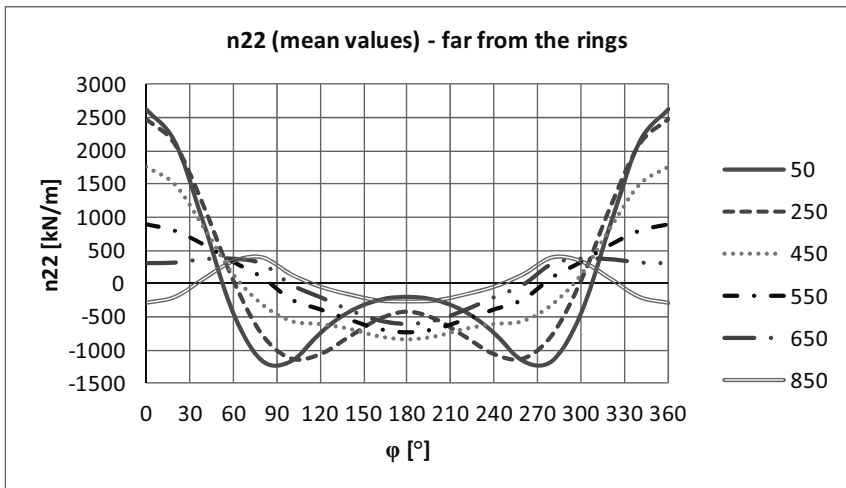

Figure 7.57 Circumferential distribution of meridional stresses – mean response

Even though the stiffening rings guarantee a global beam-like behaviour, evaluation of local effects in the vicinity of the ring beams requires the application of a shell-like model. The magnitude of such local effects – due to ovalization of the cross-section,

especially because of the constraining effect of the rings – confirms what was stated in section 2.4 by equation (2.50): a Solar Tower cannot be fully designed by using the beam theory.

The design of the tower is governed by the stresses in the half of the shell which is exposed to the wind. The meridians at stagnation and at 80° (maximum suction) have the highest tension stresses. The stresses at stagnation are reported in the following figures. The calculation is done by the covariance method (resonance not included). The stochastic wind load model results from wind tunnel investigation; this is now applied to the following design properties of the atmospheric boundary layer:

- terrain category II ($z_0 = 0.05$ m), $V_b(10m) = 25$ m/s, latitude = 23°;
- mean wind profile: according to H&D model;
- turbulence intensity: according to the H&D model;
- integral length scale: according to Eurocode;

All these profiles are plotted in Figure 2.4, Figure 2.5, Figure 2.6.
The H&D model would suggest a much larger integral length scale. The approach of the Eurocode is preferred in this calculation, but the designer should bear in mind that a larger integral length scale would imply higher background response.

The following figures show that the structural effect of the rings on the response has an extension in the shell of around 20 m both above and below each ring. In that region both positive and negative peaks of n_{11}, m_{11} and m_{22} arise, due to the constraining effect to the ovalization of the shell exerted by the rings.

Another issue, which is not addressed in this work, but it should be investigated in view of the design, is the correlation of peak effects. In particular, the design of the shell reinforcement should result from combination of axial force and bending moment. The highest limit, if their peaks are fully correlated, is their sum, while the lowest limit in case of zero correlation is the square root of the sum of single square values.

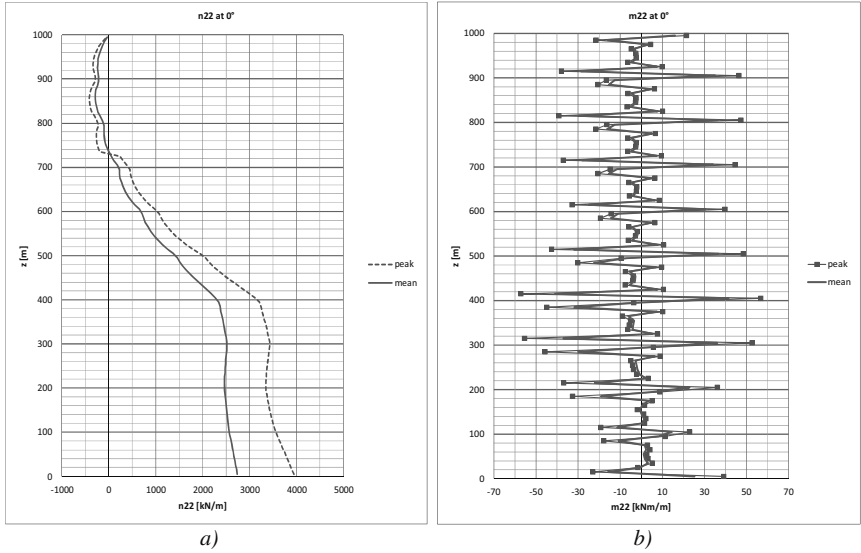*Figure 7.58 Shell response in a design condition: meridional force n_{22} (fig. a) and bending moment m_{22} (fig. b) at 0° (resonance not inlcuded, effect of the rings on the load not included)*
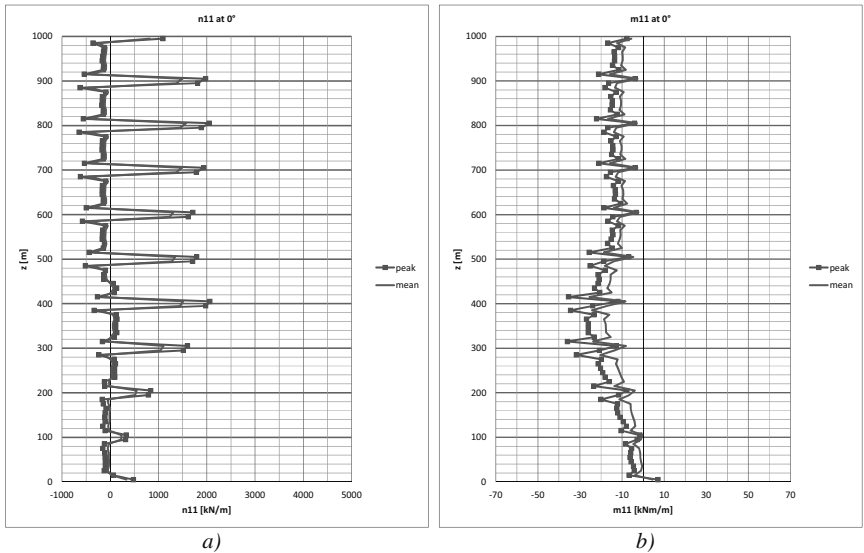

Figure 7.59 Shell response in a design condition: circumferential force n_{11} (fig. a) and bending moment m_{11} (fig. b) at 0° (resonance not included, effect of the rings on the load not included)

273

7.3.3 **Dynamic amplification**

The dynamic amplification is calculated by using the software Ansys. Simultaneous time histories measured in the wind tunnel along the circumference at $z/H = 0.95$; 0.85; 0.75; 0.65 are used for the purpose of this investigation. All the other loads are then fully correlated with them. The result is on the safe side because the predominant contribution is the bending mode, which does not present inversions of shape along the height. However, the result can be only considered as a global effect on the structure. A more sophisticated load condition should be considered in order to investigate dynamic effects in the vicinity of the ring beams. This is, however, beyond the purpose of this work.

The calculation includes mass and damping forces. The Rayleigh damping ($\mathbf{D} = \alpha\mathbf{M} + \beta\mathbf{K}$) is calculated assuming modal damping ratios ξ_i equal to 0.01 (corresponding to a logarithmic decrement $\delta = 2\pi\xi \approx 0.06$) at $n_1 = 0.17$ Hz (beam bending mode) and $n_3 = 0.33$ Hz (shell-like mode with two waves), according to the formula $\xi_i = \alpha/2\omega_i + \beta\omega_i/2$, where $\omega_i = 2\pi n_i$. As in the beam calculation (section 7.2.1), the time factor for transferring data from wind tunnel to full-scale is $\lambda_T = 488$. The integration time step is 0.244 s, as in the beam calculation.

In order to evaluate the dynamic amplification, the results of the dynamic analysis (including mass and damping forces) are compared with the results of a quasi-steady calculation, i.e. a static calculation (not including mass and damping forces) at each time step. The dynamic amplification is the ratio of peak responses, the one at the nominator results from dynamic calculation, the one at the denominator results from the quasi-steady calculation. The mean response is included in the definition of the dynamic amplification. Moreover, only representative results are considered. In fact, the interest of the designer is in the dynamic amplification of those parts of the tower which are especially exposed to the wind action and thus govern the design. In practice, the stagnation line plays the most important role. Since the tower thickness varies along the height, it is important to be aware of the dynamic amplification all along the height, although internal forces are smaller in the tip region. As shown by Figure 7.60, the dynamic amplification is around 10% only at the base of the tower. Along the height, it is much higher than what was expected according to Eurocode calculations (Cd = 1.04 in Lupi, 2009). Further studies are then necessary. The result does not depend significantly on the class of concrete which is selected for the calculation.

These calculations are performed with C50/60 concrete (so that $n_1 = 0.17$ Hz). In fact, the class could be even higher (C70/85) and in this case it would be $n_1 = 0.18$ Hz.

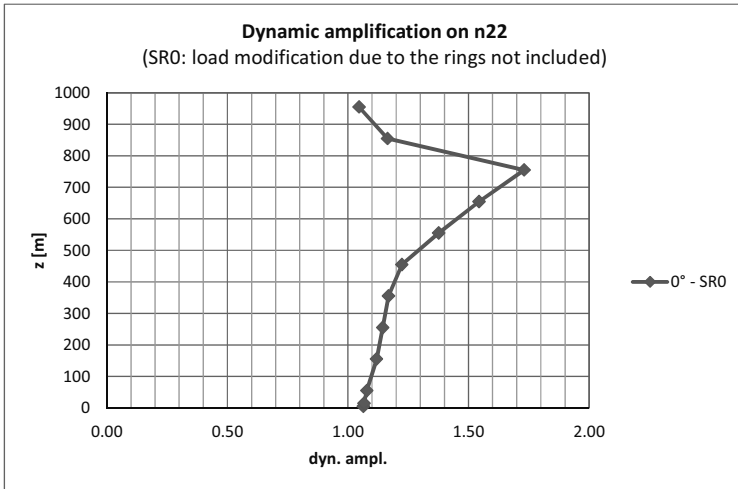However, as seen in a comparative calculation, this does not change significantly the dynamic response.

Figure 7.60 Dynamic amplification at stagnation – WiSt results
(load modification due to the rings not inclueded)

7.3.4 **The shell response under asymmetric wind load (10 ring beams)**

The asymmetric response of the tower, due to the load modification induced by the rings (SR1) is analyzed in this section, both in quasi-static and dynamic calculations.

The covariance method is applied to input data that describe the asymmetric load condition, with inversion along the height, created by 10 ring beams (section 5.5). This load condition corresponds to SR1. The response to the SR1 load condition (red lines in the following graphs) is compared to the response in SR0 (load modification due to rings not included, blue lines in the graphs). In any case, the calculation is made on a structure with ten rings (like in Figure 1.13). The flow condition (mean profile, turbulence intensity, integral length scale) is the one in the WiSt tunnel, properly scaled according to the prototype.

The most appreciable effect on the response, due to the load modification induced by the ring beams, is on the meridional forces n_{22} (Table 7.15, Figure 7.63). In particular, the increase in the peak meridional force (n_{22}) at the base is around 10%, comparable to the increase in bending moment in the beam-like model (section 7.2.2).

As regards the circumferential stresses (n_{11}), they are high only close to the rings and the highest ones are at the throat of the hyperboloid. The increase in stresses due to the

275

load modification induced by the rings is less than 10% in the peak response and somewhat higher in the standard deviations (Table 7.14, Figure 7.62).

The bending moments in both meridional and circumferential directions do not present significant variations due to rings; they do not differ more than 5 kNm/m in the peak response.

Numerical values are reported in the appendix (Table A.14, Table A.15, Table A.16).

In any case, these results represent the highest limit in case of ten big rings. Intermediate situations are expected with smaller rings and/or at larger distance. Moreover, the asymmetric load condition all along the height is the worst condition in which the two asymmetric states are never mixed. In fact, the mixture of the two states at low levels tends to weaken the asymmetry towards a mostly symmetric condition at the base, as observed in Chapter 6.

Table 7.14 Effect of load modification due to 10 rings on the quasi-static response (n_{11})
WiSt data; SR0 = load modification due to the rings not included;
SR1 = load modification due to 10 rings included

z [m]	n_{11},peak at 0° [kN/m]			n_{11},m at 0° [kN/m]			n_{11},σ at 0° [kN/m]		
	SR0	SR1	SR1/SR0	SR0	SR1	SR1/SR0	SR0	SR1	SR1/SR0
5	479	533	1.11	326	347	1.07	45	54	1.20
105	362	370	1.02	232	245	1.05	38	36	0.97
205	890	830	0.93	548	553	1.01	99	80	0.81
305	1672	1681	1.00	1078	1090	1.01	171	169	0.99
405	2144	2269	1.06	1472	1509	1.03	193	218	1.13
505	1841	1966	1.07	1324	1361	1.03	148	174	1.17
605	1737	1824	1.05	1292	1306	1.01	128	148	1.17
705	1945	2007	1.03	1472	1468	1.00	136	154	1.14
805	2039	2084	1.02	1553	1541	0.99	139	155	1.12
905	1965	2012	1.02	1490	1484	1.00	136	152	1.11
995	1090	1096	1.00	817	798	0.98	79	86	1.09

Table 7.15 Effect of load modification due to 10 rings on the quasi-static response (n_{22})
WiSt data; SR0 = load modification due to the rings not included;
SR1 = load modification due to 10 rings included

z [m]	n_{22},peak at 0° [kN/m]			n_{22},m at 0° [kN/m]			n_{22},σ at 0° [kN/m]		
	SR0	SR1	SR1/SR0	SR0	SR1	SR1/SR0	SR0	SR1	SR1/SR0
5	4039	4442	1.10	2695	2863	1.06	385	451	1.17
105	3581	3973	1.11	2520	2709	1.08	304	362	1.19
205	3364	3683	1.09	2447	2637	1.08	262	299	1.14

305	3440	3608	1.05	2519	2649	1.05	264	275	1.04
405	3100	3117	1.01	2278	2308	1.01	236	232	0.98
505	1893	1814	0.96	1376	1334	0.97	149	137	0.93
605	992	874	0.88	667	580	0.87	93	85	0.90
705	414	337	0.81	204	128	0.62	60	60	1.00
805	-220	-260	1.18	-94	-113	1.20	36	42	1.17
905	-280	-277	0.99	-197	-186	0.95	25	27	1.08
995	-43	-44	1.02	-30	-30	1.03	5	5	1.00

From the dynamic point of view, the calculation is repeated in SR1 as in section 7.3.3. The main difference between SR1 and SR0 is at level 650 m, where the bistable asymmetric flow starts its disruption on the bubble side.
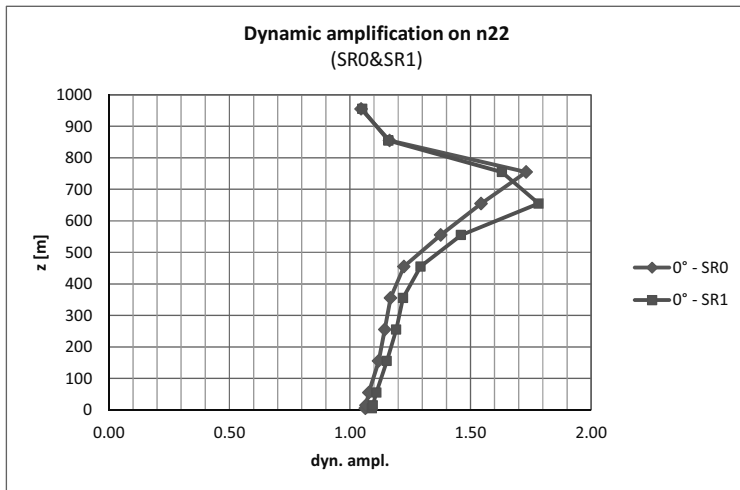

Figure 7.61 Dynamic amplification at stagnation: SR0&SR1– WiSt results

The presence of jumps in the time histories, which mark the transition from state 1 to state 2 or viceversa, should not create severe dynamic problems to the structure. The scale factor $\lambda_T = 488$ is applied to the jump reported in Figure 5.10, so that two seconds in the wind tunnel correspond to about 1000 s in full-scale. Figure 7.66 shows that the jump basically occurs between the time steps "d" and "f". It takes about 10 s, i.e. about twice the natural period of the structure. Nevertheless, the effect of the jump on the response should be further investigated in the future (see Chapter 8), because even in a time period comparable to the natural period of the tower, the load might undergo a steep change.

a) mean

b) rms

c) peak

Figure 7.62 Effect of the rings on the quasi-static response (n_{11})

a) mean

b) rms

c) peak

Figure 7.63 Effect of the rings on the quasi-static response (n_{22})
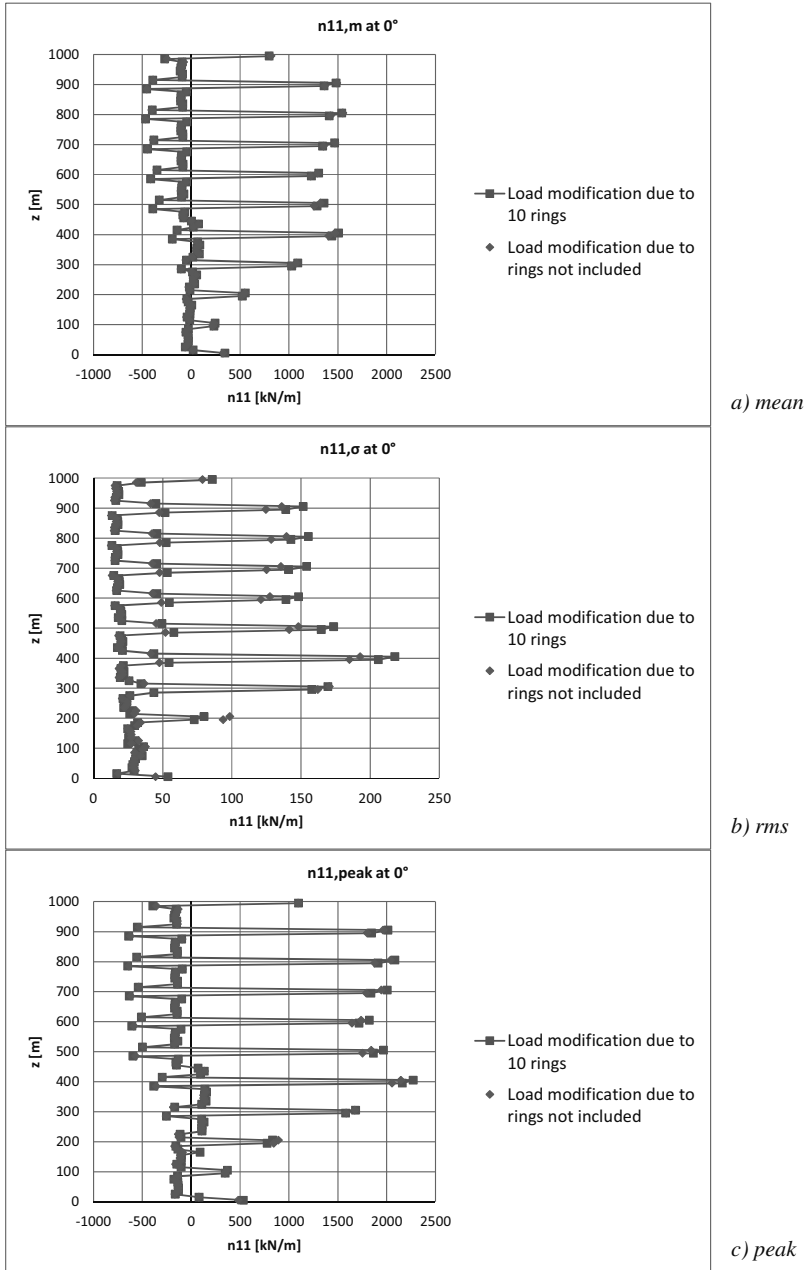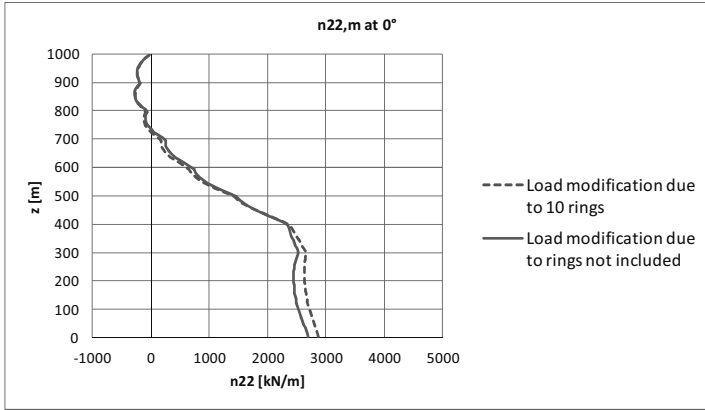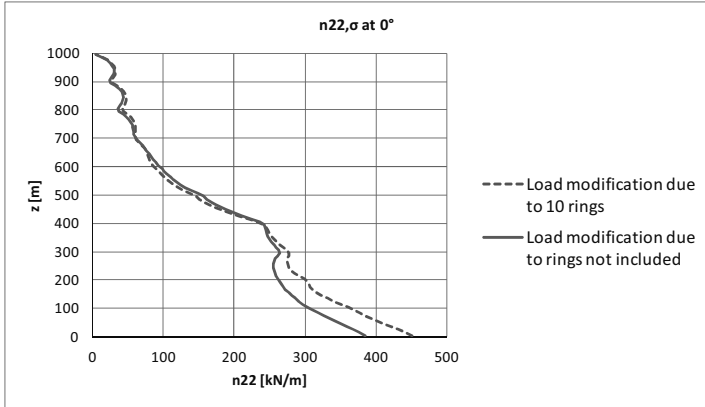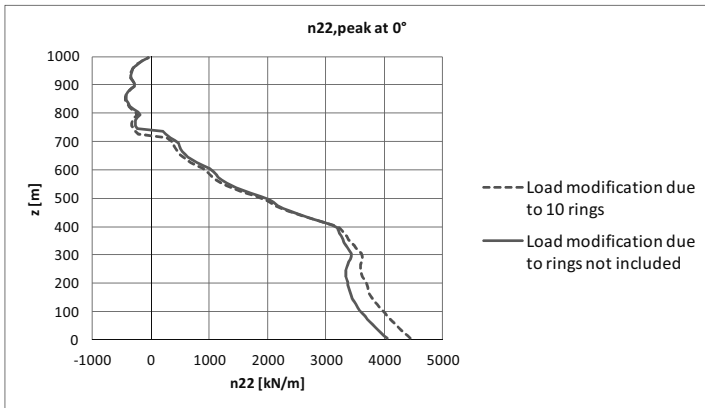
a) mean

b) rms

c) peak

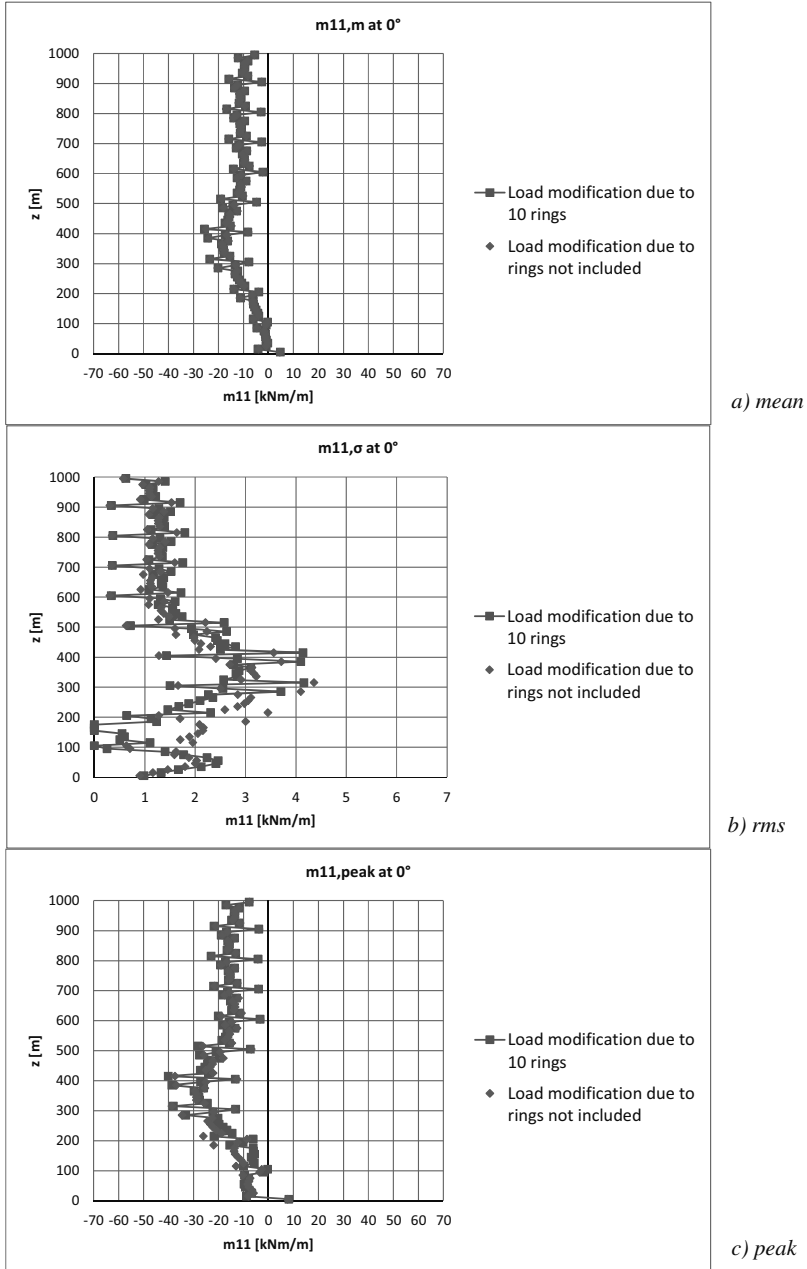*Figure 7.64 Effect of the rings on the quasi-static response (m_{11})*

a) mean

b) rms

c) peak
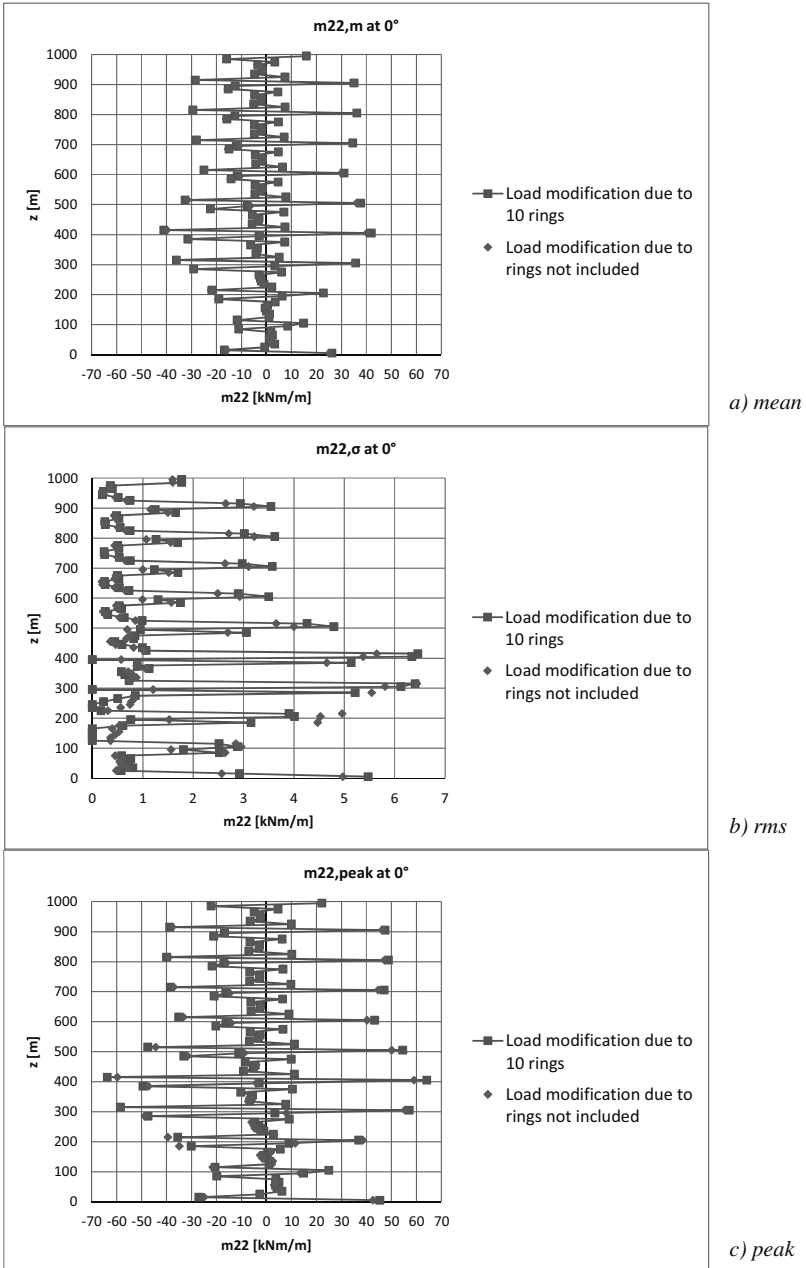
Figure 7.65 Effect of the rings on the quasi-static response (m₂₂)

Figure 7.66 Bistable load on the structure: change of state

Chapter 8.   **Conclusions and future outlooks**

The dissertation studies the Aeolian risk scenario in the design of ultra-high structures exposed to strong winds in the atmospheric boundary layer. Solar updraft towers represent the main application and constitute the thread of the dissertation.

A deeper knowledge of the natural hazard - the wind action - at large heights and also at small latitudes in the atmospheric boundary layer is addressed in Chapter 2. In the design of ultra-high structures, the coupling between wind engineering and boundary layer meteorology becomes stronger and it cannot benefit of experimental data, which are scarce at large heights and even inexistent in strong wind conditions. Therefore, Chapter 2 approaches the problem at first on theoretical bases, and then outlines the possible experimental and numerical investigations which could support future studies.

Then, the aerodynamic study of the flow around circular cylinders is required for the design of towers with circular cross-section. A large amount of literature has been written on the topic and it is reviewed in Chapter 3. However, the flow around circular cylinders is so sensitive to many either governing or influencing parameters (such as Re, aspect ratio, free-end, characteristics of the boundary layer…), that a unified and systematic investigation is currently not available to the designer.

In Chapter 4, the dissertation investigates the flow around a circular cylinder of finite length through wind tunnel tests at WiSt laboratory (Ruhr-University Bochum). The full understanding of such a reference case study is the basis to interpret the effect of spanwise rings along the height of the tower.

The discovery and the physical interpretation of a new phenomenon around circular cylinders, induced by stiffening rings along the height, is the original contribution of this research. The phenomenon is described in Chapter 5 on the basis of WiSt wind tunnel results. An asymmetric and bistable flow condition establishes around a symmetric structure like a circular cylinder and it does not disappear at moderately high Reynolds numbers, far beyond the Re_{cr}.

The debate between literature and novelty, between similar effects in completely different physical contexts, encouraged the deep investigation of this asymmetric and bistable flow condition. Similar cases of bistable flows are also described in literature.

283

They are well-known for example on isolated cylinders in the critical range of the Reynolds number, as well as on side-by-side cylinders. But despite the similarities, the physical reasons appeared to be profoundly different. This immediately resulted from the analysis of the conditions of occurrence. The Reynolds numbers at which this new bistable phenomenon occurs are not limited to a small range around Re_{cr}. The effect can also be considered as a sort of interaction phenomenon. However, the interaction is not between wide and narrow wakes, like in the case of side-by-side cylinders, but between the wake in different spanwise compartments along the height. In fact, the peculiar characteristic of the cylinder, which is responsible for the occurrence of the phenomenon, is the presence of spanwise rings at a certain distance along the height of the tower. The contribution of the flow over the tip seems to play a key role, so that the phenomenon is a cascade effect, alternated in different compartments, towards the base of the tower.

In order to confirm and provide experimental evidence of the same asymmetric bistable flow condition even in a different wind tunnel, the experiments are repeated on the same model at CRIACIV wind tunnel at University of Florence and documented in Chapter 6. It is confirmed that the phenomenon does not depend on some local conditions or disturbances of a certain laboratory, but it is induced by the ring beams. It is also confirmed that in the moderately high range of Re which was investigated on the rough cylinder (up to Re = $3*10^5$), the effect does not disappear. So far, no reason has been identified, which may suggest the disappearance of the phenomenon at higher Reynolds numbers, e.g. in full-scale conditions.

A further proof is provided by numerical simulations (Chapter 6). They have been performed on the basis of CRIACIV experiments by the TEE group, in the Industrial Energy Department at the University of Florence. The CFD simulation reproduces the experimental conditions but it benefits of two additional important aspects: ideal conditions and higher Reynolds numbers (in the order of 10^7, obtained by reduction of air viscosity). Even in this case, the asymmetric bistable phenomenon appears.

Therefore, the thesis can state that under peculiar conditions (the presence of spanwise rings along a circular cylinder of finite length), an asymmetric flow tends to stabilize around a symmetric structure. Random jumps occur in the time histories and reverse the situation. The wind tunnel experiments confirmed that the phenomenon belongs to one of those paradoxical cases where the symmetric flow structure appears to be intrinsically unstable and hence impossible. This was cited by Zdravkovich (2003)

concerning side-by-side cylinders, but the concept seems to be perfectly fitting also to the case of an isolated cylinder with spanwise rings.

Furthermore, this type of asymmetric flow is not only an interesting fluid dynamic phenomenon. In fact, the presence of rings along the height of the tower, which are responsible for creating the effect, has an important structural function. In many pre-designs of the solar tower, stiffening rings were introduced in order to reduce the structural vulnerability to the wind action. They enhance a beam-like behaviour and reduce the peaks of tension at the windward side. They also increase the buckling stiffness. The stiffening rings were then considered, for the solar tower, a strategy to mitigate the structural risk. However, the effect of the rings on the load had never been investigated before, so it was not expected that the improvement in the structural behaviour might also be responsible for an even more severe load condition. This increases the structural damage. For this reason, the effect of the fluid dynamic phenomenon had to be quantified in terms of structural response. Fortunately, the increase in internal forces did not result to be dramatic (in the order of 10-15%), but the designer should be aware that reduction of structural vulnerability, by adding stiffening rings, can become a double-edge sword. Because of that, further design conditions (with a different number and/or size of rings), as well as mitigation strategies are also investigated in this work. It resulted that the asymmetric bistable flow tends to disappear as the rings become smaller and/or at larger distance. Moreover, the presence of efflux inside the chimney is a natural rescue.

A further contribution of the research is the development of a stochastic load model to be used in quasi-static calculations of the tower in any atmospheric boundary layer flow. It could be developed thanks to the comparative studies between WiSt and CRIACIV results, which allowed to investigate the dependency of wind forces and pressures on the characteristics of the atmospheric boundary layer. This tool allows the designer to evaluate the structural damage even in the vicinity of the stiffening rings, where the shell-like behaviour predominates and no load model was available before.

The dissertation suggested many interesting aspects and new ideas, which would deserve further investigation in the future.
The asymmetric and bistable flow discovered in this work was completely unknown, so there are many issues which should be further addressed. The results suggested that the bistable asymmetric flow is a three-dimensional phenomenon, related to the flow

structures which develop around the free-end. This explains also the disruption along the height. In view of that, experiments in two dimensional conditions are recommended as a further proof. Moreover, it would also be important to test the influence of the aspect ratio of the cylinder. In any case, even if the phenomenon is related to the free-end condition, it is not the top ring alone which initiates the effect. In fact, in the case, for example, of five rings (instead of ten) the top ring is still there but the phenomenon disappears. This suggests to study the distribution of rings in the tip region more in detail. The thesis proved, by experiments, that equally distributed rings at sufficiently large distance mitigate the effect. However, the designer might need rings at smaller distance. Because of that, an important result would be to know whether it is sufficient, in order to mitigate the phenomenon, to outdistance the rings only in the tip region, as supposed in Chapters 5 and 6 on the basis of these results.

The CFD simulations presented in Chapter 6 are just at their first stage. The time window of the URANS is presently too short to be representative. More periods should be investigated. If it is the case, a large eddy simulation could allow to better investigate the bistability of the flow, being the bistability a stochastic effect.

Wind tunnel tests at higher Reynolds numbers on a smooth cylinder in three dimensional conditions would represent a decisive result to confirm what has been stated in this dissertation by using the concept of effective Reynolds number.

Moreover, the three dimensional correlation field should be investigated more extensively in the wind tunnel. This would allow to refine results in Chapter 7. A future aim of the research is to develop a simpler wind load model, e.g. an equivalent static wind load, which could be easily used to evaluate local effects. The approach could be the same as for cooling towers, by using the load response correlation method (Niemann, 1998).

The dynamic response of the solar tower should be further investigated, too. In the case of rings, a dynamic effect could rise within the jump. In this regard, it would be important to characterize the bistable pressure field and model bistable time histories. Moreover, the non-linear behaviour should be included in the analyses.

Chapter 9.   **Bibliography**

Achenbach E. (1968). Distribution of local pressure and skin friction around a circular cylinder in cross-flow up to Re=5×10^6. Journal of Fluid Mechanics, 34, 625-639.

Achenbach E. (1971). Influence of surface roughness on the cross-flow around a circular cylinder. Journal of Fluid Mechanics, 46, 321-335.

Achenbach E., Heinecke E. (1981). On vortex shedding from smooth and rough cylinders in the range of Reynolds numbers 6×10^3 to 5×10^6. Journal of Fluid Mechanics, 109, 239-251.

Afgan I., Moulinec C., Prosser R., Laurence D. (2006). Large eddy simulation of turbulent flow for wall mounted cantilever cylinders of aspect ratio 6 and 10. International Journal of heat and fluid flow, 28 (4), 561-574.

Augusti G., Borri C., Niemann H.-J. (2001). Is aeolian risk as significant as other environmental risks? Reliability Engineering and System Safety, 74 (3), 227-237.

Ayoub A., Karamcheti K. (1982). An experiment on the flow past a finite circular cylinder at high subcritical and supercritical Reynolds numbers. Journal of Fluid Mechanics, 118, 1-26.

Backström T.W. von, Fluri T.P. (2006). Maximum fluid power condition for solar chimney power plants – An analytical approach. Solar Energy, 80, 1417-1423.

Backström T.W. von, Harte R., Höffer R., Krätzig W.B., Kröger D.G., Niemann, H.-J., van Zijl, G.P.A.G. (2008). State and Recent Advances of Solar Chimney Power Plant Technology. VGB PowerTech, 88 Vol. 7, 64-71.

Backström T.W. von, Fluri T.P. (2010). Solar chimney turbine layout and design considerations. Proc. 2nd Int. Conf. Solar Chimney Power Technology, 239-246. Ruhr-Universität Bochum and Bergische Universität Wuppertal.

Baker, C.J. (1980). Vortex flow around the bases of obstacles. Dissertation, Cambridge.

Baker, C.J. (1980). The turbulent horseshoe vortex. Journal of Wind Engineering and Industrial Aerodynamics, 6 (1-2), 9-23.

Baker, C.J. (1991). Oscillation of horseshoe vortex systems. Journal of Fluids Engineering, Transactions of the ASME, 113 (3), 489-495.

Banakh V.A., Smalikho I.N., Köpp F., Werner C. (1995). Representativeness of wind measurements with a cw Doppler lidar in the atmospheric boundary layer. Applied Optics, 34 (12), 2055-2067.

Bange J. (2007). Airborne measurement of turbulent energy exchange between the earth surface and the atmosphere. Habilitationsschrift, Technical University Braunschweig, Germany.

Basu, R.I. (1985). Aerodynamic forces on structures of circular cross-section. Part 1. Model-scale data obtained under two-dimensional conditions in low-turbulence streams. Journal of Wind Engineering and Industrial Aerodynamics, 21 (3), 273-294

Basu, R.I. (1986). Aerodynamic forces on structures of circular cross-section. Part 2. The influence of turbulence and three-dimensional effects. Journal of Wind Engineering and Industrial Aerodynamics, 24 (1), 33-59.

Batham J.P. (1973). Pressure distributions on circular cylinders at critical Reynolds numbers. Journal of Fluid Mechanics, 57, 209-228.

Bearman P.W. (1969). On vortex shedding from a circular cylinder in the critical Reynolds number regime. Journal of Fluid Mechanics 37 (3), 577-585.

Bearman P.W., Wadcoc A.J. (1973). The interaction between a pair of circular cylinders normal to a stream. Journal of Fluid Mechanics, 61, 499-511.

Belik L. (1973). The secondary flow around circular cylinders mounted normal to a flat plate. Aero. Quart., 29, 47-54.

Bénard H. (1908). Formation of centres of circulation behind a mmoving obstacle (in French). Comptes Rendus Academie des Sciences, 147, 839-842.

Bendat J.S., Piersol A. (1993). Engineering Applications of Correlation and Spectral Analysis. John Wiley&Sons, Inc.

Bendat J.S., Piersol A. (2000). Random Data, analysis and measurement procedures. John Wiley&Sons, Inc.

Bennett A.R. (1896). An improved differential temperature air motor, adapted for scientific applications, for philosophical toys, for advertising and for other purposes. A.D. 1986, n. 8711. Printed by Darling and Son Ld, London.

Bergermann R., Weinrebe G. (2010). Realization and costs of solar updraft towers. Proceedings of the SCPT 2010 – International Conference on Solar Chimney Power Technology, 63-68. Ruhr-University Bochum and Bergische Universität Wuppertal, Bochum, Germany.

Bernardes M.A.d.S. (2004). Technische, ökonomische und ökologische Analyse von Aufwind-kraftwerken. Dr.-Ing. Thesis, University of Stuttgart.

Bernardes M.A.d.S. (2012). On the heat storage in solar updraft towers collectors. Proc. 3rd Int. Conf. on Solar Updraft Power Technology SUTPT 2012, 13-25. HUST, Wuhan, China.

Bloor M.S., Gerrard J.H. (1966). Measurements on turbulent vortices in a cylinder wake. Proceedings of the Royal Society of London, Series A (Mathematical and Physical Sciences), 294 (1438), 319-342.

Borri C., Pastò S. (2006). Lezioni di Ingegneria del Vento. Firenze University Press.

Borri C., Lupi F., Marino E. (2010). Optimum Shell Design of Solar Updraft Towers. Proc. 2nd Int. Conf. Solar Chimney Power Technology, Ruhr-Universität Bochum and Bergische Universität Wuppertal, 155-162.

Breuer W., Hüwe A (2010). Solar chimney power plants – An economist's point of view. International Conference on Solar Chimney Power Technology, 55-61. Ruhr-University Bochum and Bergische Universität Wuppertal, Bochum, Germany.

Britter R.E., Hunt J.C.R., Mumford J.C. (1979). The distortion of turbulence by a circular cylinder. Journal of Fluid Mechanics, 92 (2), 269-301.

Buresti G. (1981). The effect of surface roughness on the flow regime around circular cylinders. Journal of Wind Engineering and Industrial Aerodynamics, 8 (1-2), 105-114.

Buresti G. (2012). Elements of Fluid Dynamics. Ed. Imperial College Press.

Cabanyes I. (1903). Las chimeneas solares (Solar chimneys). La ernergia eléctrica. Cited due to Wikipedia.

Canadillas B. (2010). A study of the marine boundary layer by LES-modelling and experimental observations with a focus on offshore wind energy applications. Gottfried Wilhelm Leibniz Universitaet Hannover.

Clobes M., Willecke A., Peil U. (2009). A refined analysis of guyed masts in turbulent wind. Proc. 5th European and African Conference on Wind Engineering, EACWE 5, Florence, Italy.

Clobes M., Willecke A. (2009). On the numerical simulation of gust and vortex excitation of guyed masts. IASS 24th meeting, Helsinki.

Cook N.J. (1985). Designer's Guide to Wind Loading of Building Structures Part 1: Background, Damage Survey, Wind Data&Structural Classification. Department of the Environment Building research establishment.

Cook N.J. (1997). The Deaves and Harris ABL model applied to heterogeneous terrain. Journal of Wind Engineering and Industrial Aerodynamics, 66, 197-214.

Counihan J. (1969). An improved method of simulating an atmospheric boundary layer in a wind tunnel. Atmospheric Environment 3 (2), 197-214.

Couregelongue J. (1929). On the existence of two families of eddies behind immersed solids (in French). Comptes Rendus Academie Sciences, 189, 972-974.

Courtney M., Wagner R., Lindelöw P. (2008). Testing and comparison of lidars for profile and turbulence measurements in wind energy. IOP Conference Series: Earth and Environmental Science, 1.

Crandall S.H., Mark W.D. (1963). Random Vibration in Mechanical Systems. Academic Press, New Yoerk and London.

Csanady G.T. (1967). On the resistance law of a turbulent Ekman layer. Journal of the Atmospheric Sciences, 24 (5), 467-471.

Davies F., Collier C.G., Bozier K.E., Pearson G.N. (2003). On the accuracy of retrieved wind information from Doppler lidar observations. Quart. Journal. Royal. Meteorology. Society. 129, 321-334.

Deaves D.M. (1981). A note on the upper boundary conditions for turbulence models in the neutral atmosphere. Boundary Layer Meteorology, 21 (4), 489-493.

Deaves D.M., Harris R.I (1982). A note on the use of asymptotic similarity theory in neutral atmosphere boundary layers. Atmospheric Environment, 16 (8), 1889-1893.

DIN EN 4133 (2009). German industrial standards: Steel stack / Chimneys built of Steel.

Durbin P.A., Hunt J.C.R. (1980). On surface pressure fluctuations beneath turbulent flow round bluff bodies. Journal of Fluid Mechanics, 100 (1), 161-184.

Dyrbye C., Hansen S.O. (1997). Wind Loads on Structures. John Wiley & Sons.

Eaddy M. (2004). Lift forces on smooth and rough circular cylinders in low and high turbulence flows. Dissertation. Monash University, Victoria.

Eisner F. (1925). Pressure measurements in flow cylinders. Zeitschrift für agewandte Mathematik und Mechanik, 5, 486-489.

Ekman (1905). Influence of the Earth's rotation on ocean currents. Arkiv for Matematik, Astronomioch Fysik, 2 (11), 1-52.

Emeis S., Harris M., Banta R.M. (2007). Boundary-layer anemometry by optical remote sensing for wind energy applications. Meteorologische Zeitschrift, 16 (4), 337-347.

Emeis S. (2010). Surface-Based Remote Sensing of the Atmospheric Boundary Layer. Atmospheric and Oceanographic Sciences Library. Springer.

EN 1990:2001-11, Eurocode - Basis of structural design, CEN 2001.

ESDU 71012, Fluid forces on non-streamline bodies - background notes and description of the flow phenomena, Engineering Sciences Data Unit, London.

ESDU 74030, Characteristics of atmospheric turbulence near the ground. Part I: definitions and general information, Engineering Sciences Data Unit, London.

ESDU 80025, Mean forces, pressures and flow field velocities for circular cylindrical structures: single cylinder with two-dimensional flow, Engineering Sciences Data Unit, London.

ESDU 81017, Mean forces, pressures, and moments for circular cylindrical structures: finite-length cylinders in uniform and shear flow, Engineering Sciences Data Unit, London.

ESDU 82026, Strong Winds in the Atmospheric Boundary Layer. Part 1: Mean hourly wind speeds, Engineering Sciences Data Unit, London.

ESDU 83045, Strong Winds in the Atmospheric Boundary Layer. Part 2: Discrete Gust Speeds, Engineering Sciences Data Unit, London.

ESDU 85020, Characteristics of atmospheric turbulence near the ground. Part II: single point data for strong winds (neutral atmosphere), Engineering Sciences Data Unit, London.

ESDU 86010, Characteristics of atmospheric turbulence near the ground. Part III: variations in space and time for strong winds (neutral atmosphere), Engineering Sciences Data Unit, London.

ESDU 96030, Response of structures to vortex shedding, Engineering Sciences Data Unit, London.

Fage A. (1928). The air flow around circular cylinder in the region where boundary layer separates from the surface. Aeronautical Research Council, Rep&Memo 1179.

Fage A, and Warsap J.H. (1929). The effects of turbulence and surface roughness on the drag of a circular cylinder. Aeronautical Research Council, Rep.&Memo 1253.

Farell C., Blessmann J. (1983). On critical flow around smooth circular cylinders. Journal of Fluid Mechanics, 136, 375-391.

Farivar Dj. (1981). Turbulent uniform flow around cylinders of finite length. AIAA Journal, 19 (3), 275-281.

Fasel H. F. (2012). Fluid dynamics and heat transfer analysis of geometrically scaled models of solar updraft tower plants using CFD. Proc. 3rd Int. Conf. on Solar Updraft Power Technology SUTPT 2012, 126-127. HUST, Wuhan, China.

Ferziger J.H., Peric M. (2002). Computational Methods for Fluid Dynamics. Springer.

Fluri T.P. (2008). Turbine layout for and optimization of solar chimney power conversion units. Ph.D. thesis, University of Stellenbosch.

Fluri T.P., Backström T.W. von (2008). Performance analysis of the power conversion unit of a solar chimney power plant. Solar Energy, 82 (11), 999-1008.

Fox T. A., West G.S. (1990). On the use of end plates with circular cylinders in wind tunnel studies. Research Report Series - University of Queensland, Department of Civil Engineering, CE118, 1-17

Fox T.A., West G.S. (1993). Fluid-Induced Loading of Cantilevered Circular Cylinders in a Low-Turbulence Uniform Flow. Part 1: Mean Loading with Aspect Ratios in the Range 4 to 30. Journal of Fluids and Structures, 7 (1), 1-14.

Fox T.A., West G.S. (1993). Fluid-Induced Loading of Cantilevered Circular Cylinders in a Low-Turbulence Uniform Flow. Part 2: Fluctuationg Loads on a Cantilever of Aspect Ratio 30. Journal of Fluids and Structures, 7, (1), 15-28.

Fox T.A., Apelt C.J. (1993). Fluid-Induced Loading of Cantilevered Circular Cylinders in a Low-Turbulence Uniform Flow. Part 3: Fluctuating Loads with Aspect Ratios 4 to 25. Journal of Fluids and Structures, 7 (4), 375-386.

Fox T.A., Apelt C.J., West G.S. (1993). The aerodynamic disturbance caused by the free-ends of a circular cylinder immersed in a uniform flow. Journal of Wind Engineering and Industrial Aerodynamics, 49 (1-3), 389-399.

Fröhlich J., Rodi W. (2004). LES of the flow around a circular cylinder of finite height. International Journal of Heat and Fluid Flow, 25 (3), 537-548.

Garg R.K., Niemann H.-J. (1995). On three dimensionality of fluctuating aerodynamic forces on circular cylindrical structures. Proc. of the 9th International Conference on Wind Engineering, New Delhi, India.

Gerrard, J.H. (1966). Three-dimensional structure of wake of circular cylinder. Journal of Fluid Mechanics, 25, 143-164.

Gerrard J.H. (1978). The wakes of cylindrical bluff bodies at low Reynolds number. Philosophical Transactions of the Royal Society of London A (Mathematical and Physical Sciences), 288 (1354), 351-382.

Gill A.E. (1968). Similarity theory and geostrophic adjustment. Journal Royal Meteorology Society, 94, 586-588.

Goldack A. (2004). Tragverhalten und Aussteifung hoher Stahlbetonrohren fuer Aufwindkraftwerke (Load-bearing behaviour and stiffening of high-rise RC-tubes for updraft power plants). Dissertation, University of Stuttgart. (in German).

Goldack A. (2011). Natural frequencies and Mode Shapes of Towers for Solar Updraft Power Plants. Proc. 8th Int. Conf. Structural Dynamics, EURODYN 2011, Leuven, Belgium, 3575-3581.

Goliger A. M., Milford R. V. (1998). A review of worldwide occurrence of tornadoes. Journal of Wind Engineering and Industrial Aerodynamics, 74/76, 111-121.

Gould R.W.E., Raymer W.G., Ponsford P.J. (1968). Wind tunnel tests on chimneys of circular section at High Reynolds Number. Proceedings of the Symposium on wind effects on buildings and structures, Loughborough.

Günther H. (1931). In hundert Jahren - Die künftige Energieversorgung der Welt (In hundred years – World's future energy supply). Kosmos, Franckh'sche Verlagshandlung Stuttgart.

Güven O., Farell C., Patel V.C. (1980). Surface-roughness effects on the mean flow past circular cylinders. Journal of Fluid Mechanics, 98 (4), 673-701

Güven O., Farell C., Patel V.C. (1983). Boundary-layer development on a circular cylinder with ribs. Transactions of the ASME. Journal of Fluids Engineering, 105 (2), 179-184.

Haan F.L., Sarkar P.P., Gallus W.A. (2008). Design construction and performance of a large tornado simulator for wind engineering applications. Engineering Structures, 30, 1146-1159.

Hardesty R.M., Darby L.S. (2005). Ground-based and airborne lidar. Encyclopedia of Hydrologic Sciences. Malcolm G. Anderson (Ed.), Wiley, 697–712.

Harris R.I., Deaves D.M. (1980). The structure of strong winds. Proc. CIRIA Conference. London, Construction Industry Research and Information Association.

Harris R.I. (1986). Longer turbulence length scales. Journal of Wind Engineering and Industrial Aerodynamics, 24 (1), 61-68.

Harris M., Constant M., Ward C. (2001). Continuous wave bistatic laser Doppler wind sensor. Applied Optics, 40, 1501–1506.

Harte R., Graffmann M., Wörmann R. (2010). Progress in the Structural Design of Solar Chimneys. Proc. 2nd Int. Conf. Solar Chimney Power Technology, Ruhr-

Universität Bochum and Bergische Universität Wuppertal, 145-152, Bochum, Germany.

Holmes J.D. (2003). Wind Loading of Structures. Spon Press, Taylor&Francis Group.

Hölscher N., Niemann H.-J. (1993). On the flow around finite circular cylinders in turbulent shear flows. Physics of separated flows – Numerical, experimental and theoretical aspects. Ed.: Kl. Gersten, Notes on numerical fluid mechanics, Vol 40, pp. 216-244.

Hölscher N. (1993). Ein multivariater Ansatz fuer die aerodynamische Uebertragungsfunktion der Winddruecke in atmosphaerischer Grenzschichtstroemung. Dissertation 93-3, Ruhr University Bochum.

Holton J.R. (1979). An introduction to dynamic meteorology. Academic Press, New York.

Houghton J.T. (1977). The physics of the atmospheres. Cambridge University Press.

Hunt J.C.R. (1972). A theory for fluctuating pressures on bluff bodies in turbulent flows. Symposium on flow-induced structural vibrations. Karlsruhe, Germany.

Hunt J.C.R. (1973) A theory of turbulent flow round two-dimensional bluff bodies. Journal of Fluid Mechanics, 61, 625-705.

Hunt J.C.R. (1975) Turbulent velocities near and fluctuating surface pressures on structures in turbulent winds. Proc. International Conference on Wind Effects on Building and Structures.

Hunt J.C.R. (1990). A review of velocity and pressure fluctuations in turbulent flows around bluff bodies. Journal of Wind Engineering and Industrial Aerodynamics, 35, 49-85.

Irwin P. (2009). Wind engineering research needs, building codes and project scientific studies. Proc. 11th American Conference on Wind Engineering. San Juan, Puerto Rico.

Ishigai S., Nishikawa E., Nishimura K., Cho K. (1972). Experimental study on structure of gas flow in tube banks with tube axes normal to flow. Bulletin of the Japan Society of Mechanical Engineers, 15 (86), 949-956.

Isyumov N. (1999). Wind Tunnel Studies of Buildings and Structures. ASCE American Society of Civil Engineers.

Jørgensen Finn E. (2002). How to measure turbulence with hot-wire anemometers - a practical guide. Dantec Dynamics.

Kalash S., Naimeh W., Ajib S. (2012). A simplified analysis of the main parameters affecting the solar updraft power plants. Proc. 3rd Int. Conf. on Solar Updraft Power Technology SUTPT 2012, 101-106. HUST, Wuhan, China.

Karman Th. von, Rubach H. (1912). On the mechanism of resistance in fluids (in German). Physikalische Zeitschrift, 13.

Kasperski M, Niemann H.-J. (1988). On the correlation of dynamic wind loads and structural response of natural-draught cooling towers. Journal of Wind Engineering and Industrial Aerodynamic, 30, 67-75.

Kawamura T. Hiwada M, Hibino T., Mabuchi I., Kumada M. (1984). Flow around a finite circular cylinder on a flat plate. Cylinder height greater than turbulent boundary layer thickness. Bulletin of the Japan Society of Mechanical Engineers, 27 (232), 2142-2151.

Kindler D., Oldroyd A., Macaskill A., Finch D. (2007). An 8 month test campaign of the QinetiQ ZephIR system: preliminary results. Meteorologische Zeitschrift, 16, 463–473.

Kitagawa T., Fujino Y., Kimura K. (1999). Effects of free-end condition on end-cell-induced vibration. Journal of Fluids and Structures, 13 (4), 499-518.

Kitagawa T., Fujino Y., Kimura K., Mizuno Y. (2001). Wind pressures on end-cell-induced vibration of circular tower. Journal of Engineering Mechanics, 127 (11), 1135-1143.

Kitagawa T., Fujino Y., Kimura K., Mizuno Y. (2002). Wind pressures measurement on end-cell-induced vibration of a cantilevered circular cylinder. Journal of Wind Engineering and Industrial Aerodynamics, 90 (4-5), 395-405.

Kovásznay, L. S. G. (1949). Hot-Wire Investigation of the Wake behind Cylinders at Low Reynolds Numbers. Proceedings of the Royal Society of London. Series A, Mathematical and Physical Sciences, 198 (1053), 174-190.

Krajnovic, S. (2011). Flow around a tall finite cylinder explored by large eddy simulation. Journal of fluid mechanics, 676, 294-317.

Krätzig W.B., Harte R., Wörmann R. (2008). Large shell structures for power generation technologies. Proc. 6th Int. Conf. IASS-IACM 2008, Cornell University, Ithaca, NY, USA.

Krätzig W.B., Niemann H.-J., Harte R. and Höffer R. (2009a). Solar Updraft Power Plant with 750 m power towers and collector diameters of 3000 m to 4000 m. Internal manual, Bochum.

Krätzig W.B., Harte R., Montag U., Woermann R., (2009b). From large natural draft cooling tower shells to chimneys of solar upwind power plants. In: A. Domingo, C. Lazaro (eds.), IASS Symposium on Evolutions and Trends in Design, Analysis and Construction of Shells. CD-Rom, University of Valencia.

Krätzig W.B., Harte R., Montag U., Graffmann M. (2010). On Structural Engineering Problems of Solar Updraft Chimneys. Proc. 4th Int. Conf. Structural Engineering, Mechanics and Computation, SEMC 2010, Cape Town, South Africa.

Krätzig W.B., Gould Ph.L., Harte R. (2011). Shell structures for power technology. In: Mungan, I., Abel, J.F. (eds.) Fifty years of progress for shell and spatial structures. International Association for Shell and Spatial Structures (IASS), Madrid, 165-194.

Krätzig W.B. (2012a). Solar updraft power technology, State and advances of low-concentrated thermal solar power generation. VGB PowerTech 92, Vol. 11, 34-39.

Krätzig W.B. (2012b). Physics, Computer Simulation and Optimization of Thermo-fluidmechanical Processes of SUPPs. Proceedings 3rd Int. Conf. on Solar Updraft Power Tower Technology SUTPT 2012, 1-12. HUST Wuhan, China.

Krätzig W.B., Harte R., Graffmann M., Montag U. (2013). Load response and design of Giga-towres. CICIND Report 29 Vol. 1, 55-62.

Kroonenberg van den A. (2009). Airborne Measurement of Small-Scale Turbulence with special regard to the Polar Boundary Layer. Dissertation. Technical University Carolo-Wilhelmina, Braunschweig.

Lee T., Lin C.-L., Friehe C.A. (2007). Large-eddy simulation of air flow around a wall-mounted circular cylinder and a tripod tower. Journal of turbulence, 8 (29), 1-28.

Luo S.C., Gan T.L., Chew Y.T. (1996). Uniform flow past one (or two in tandem) finite length circular cylinder(s). Journal of Wind Engineering and Industrial Aerodynamics, 59 (1), pp. 69-93.

Lupi F. (2009) Structural behaviour, optimization and design of a solar chimney prototype under wind loading and other actions. Master Thesis, University of Florence in cooperation with Ruhr University Bochum.

Lupi F., Borri C., Krätzig W.B., Niemann H.-J., (2011). Solar Updraft Power Plant technology: basic concepts and structural design. In Encyclopedia Online of Life Support Systems (EOLSS) developed under the auspices of the UNESCO, Eolss Publishers, Oxford, UK.

Lupi F., Borri C., Niemann H.-J., Peil U. (2011) Non-conventional wind loading on ultra-high Towers in Solar Updraft Power Plants. International Journal of Shell and Space Structures, 52 (4), 257-264.

Mahbub Alam, Md., Sakamoto, H., Moriya, M. (2003). Reduction of fluid forces acting on a single circular cylinder and two circular cylinders by using tripping rods. Journal of Fluids and Structures 18 (3-4), 347-366.

Mahbub Alam Md., Meyer, J.P. (2011). Two interacting cylinders in cross flow. Physical Review Section E, Statistical Nonlinear and Soft Matter Physics 84 (5).

Mann J., Cariou J.P., Courtney M., Parmentier R., Mikkelsen T., Wagner R., Lindelöw P., Sjöholm M., Enevoldsen K. (2008). Comparison of 3D turbulence measurements using three staring wind lidars and a sonic anemometer. IOP Conference Series: Earth and Environmental Science, 1.

Matsuno T. (1966). Quasi-geostrophical motions in the equatorial area. Journal Meteorol. Jpn,. 44, 25-42.

Mikkelsen T., Mann J., Courtney M., Sjöholm (2008). Windscanner: 3-D wind and turbulence measurements from three steerable Doppler Lidars. Proc. 14th Int. Symposium for the Advancement of Boundary Layer Remote Sensing.

Monin A.S., Yaglom A.M. (1971). Statistical fluid mechanics: mechanics of turbulence, Vol. 1. Mit Press, Cambridge.

Nakamura Y., Tomonari Y. (1982). The effects of surface roughness on the flow past circular cylinders at high Reynolds numbers. Journal of Fluid Mechanics, 123, 363-378.

Neuhaus C. (2009). ZurIdentifikationselbsterregteraeroelastischerKräfte im Zeitbereich. Dissertation. BergischeUniversität Wuppertal, Germany.

Neuhaus C. (2010). Numerische frequenzabhängige Kalibrierung langer Druckmessschlauchsysteme. Internal report, Windingenieurwesen und Strömungsmechanik, Ruhr-Universität Bochum, Germany.

Newland D.E. (1993). An Introduction to Random Vibrations, Spectral & Wavelet Analysis. Dover Publications, Inc, Mineola, New York.

Niemann H.-J., Schräder P. (1981). Konstruktiver Ingenierbau Berichte, Heft 35/36, Gebäudeaerodynamik. DFG-Kolloquium, Ruhr-Universität Bochum, Germany.

Niemann H.-J., Hölscher N. (1990). A review of recent experiments on the flow past circular cylinders. Journal of Wind Engineering and Industrial Aerodynamics, 33 (1-2), 197-209.

Niemann H.-J., Flaga A., Höffer R., Hölscher N., Kasperski M. (1996). Structural response to wind. In: Dynamics of Civil Engineering Structures, Wilfried B. Krätzig & Hans-Jürgen Niemann (Eds.) A.A. Balkema, Rotterdam.

Niemann H.-J. (1998). Wind load modelling in the analysis of very high cooling towers. Proc. Wind effects on buildings and structures, A.A. Balkema.

Niemann H.-J-, Hölscher N., Meiswinkel R. (2007). A probabilistic approach for the determination of extreme actions with respect to the structural design. Proc. of ICAPP 2007, Nice, France.

Niemann H.-J., Höffer R. (2007). Wind loading for the design of the solar tower. Proc. 3rd Int. Conf. SEMC, Cape Town, South Africa.

Niemann H.-J (2008). Prototyp eines Aufwindkraftwerks. Windeigenschaften, winderregte Schwingungen und Windlasten zur Bemessung des Stahlbetonturms. Internal report, Bochum. (in German)

Niemann H.-J., (2009). A Refined Approach to Wind Loading for the Design of the Solar Tower. CICIND Report, 25 (2).

Niemann H.-J., Lupi F., Höffer R., Hubert W., Borri C., (2009). The solar updraft power plant: design and optimization of the tower for wind effects. Proceedings of the 5th European and African Conference on Wind Engineering EACWE5, Florence, Italy.

Niemann H.-J. (2010). Static, quasi-static and resonant wind effects on solar towers. 2nd International Conference on Solar Chimney Power Technology, Ruhr-University Bochum and Bergische Universität Wuppertal, Bochum.

Okamoto S., Yagita M. (1973). The experimental investigation on the flow past a circular cylinder of finite length placed normal to the plane surface in a uniform stream. Bulletin of the Japan Society of Mechanical Engineers, 16 (95), 805-814.

Okamoto S., Yagita M. (1984). Flow past circular cylinder of finite length placed normal to ground plane in uniform shear flow. Bulletin of the Japan Society of Mechanical Engineers. 27 (229), 1454-1459.

Okamoto S., Sunabashiri Y. (1992). Vortex shedding from a circular cylinder of finite length placed on a ground plane. Transactions of the ASME. Journal of Fluids Engineering, 114 (4), 512-521.

Palau-Salvador G., Stoesser T., Fröhlich J., Kappler M., Rodi W. (2010). Large Eddy Simulations and Experiments of Flow Around Finite-Height Cylinders. Flow, Turbulence and Combustion, 84 (2), 239-275.

Park C.-W., Lee S.J. (2000). Free end effects on the near wake flow structure behind a finite circular cylinder. Journal of Wind Engineering and Industrial Aerodynamics, 88, (2-3), 231-246.

Park C.-W., Lee S.J. (2002). Flow structure around a finite circular cylinder embedded in various atmospheric boundary layers. Fluid Dynamics Research, 30 (4), 197-215.

Parsumarthi N., Sherif S.A. (1997). Performance of a Demonstration Solar Chimney Model for Power Generation. Proc. 35th Heat Transfer and Mechanics Conference, 203-240. California State University, School of Engg. and Computer Science. Sacramento.

Peil U., Nölle H. (1990). Measurement of Wind Load and Response of a guyed Mast. Proc. European Conference on Structural Dynamics, Eurodyn '90, Bochum, Germany.

Peil U., Nölle H., (1992). Guyed masts under wind load. Journal of Wind Engineering and Industrial Aerodynamics, 43 (3), 2129-2140.

Peil U.,Nölle H., Wang Z.H. (1996). Dynamic behaviour of guys under turbulent wind load. Journal of Wind Engineering and Industrial Aerodynamics, 65 (1-3), 43-54.

Peil U., Nölle H., (1998). Stress distribution in steel chimneys. CICIND, Proc. 6th International Chimney Conference, 1. Brighton, England.

Plate E.L. (1982). Engineering meteorology. Elsevier Scientific Publishing Company.

Pliefke T. (2010). Public Investments in Disaster Risk Reduction – A Social Cost Benefit Analysis. Dissertation. Technical University of Braunschweig, University of Florence.

Pope S.B. (2000). Turbulent flows. Cambridge University Press.

Prandtl L. (1904). Fluid motion with very small friction (in German). Proc. of the 3rd International Mathemathical Congress, 484-491.

Pretorius J.P., Kröger D.G. (2006). Solar Chimney Power Plant Performance. ASME J. Solar Energy Engineering 128, 302-311.

Pretorius J.P. (2007). Optimization and Control of a Large-Scale Solar Chimney Power Plant, PhD-Thesis, University of Stellenbosch.

Pretorius J.P., Kröger D.G. (2010). Basic theory and numerical simulation of large scale solar updraft power plants. Proc. 2nd Int. Conf. Solar Chimney Power Technology, 45-54. Ruhr-Universität Bochum and Bergische Universität Wuppertal.

Procino L. (2010). Profilo mare. Internal report, CRIACIV.

Pröpper H. (1977) Zur aerodynamischen Belastung großer Kühltürme. Dissertation 77-3, Ruhr-Universitaet Bochum, Germany.

Raasch S., Etling D. (1991). Numerical simulation of rotating turbulent thermal convention. Beitr. Phys. Atmos. 64, 185-199.

Raasch S., Etling D. (1998). Modelling deep ocean convention: large eddy simulation in comparison with laboratori experiments. Journal of Physical Oceanography, 28, 1786-1802.

Raasch S., Schröter M. (2001). PALM – A large eddy simulation model performing on massively parallel computers. Meteorologische Zeitschrift, 10 (5), 363-372.

Rayleigh L. (1896). The theory of sound.

Rayleigh L. (1915). Aolian tones. Philosophical Magazine, 6th series, 42, 173-176.

Reynolds O. (1883). An experimental investigation of the circumstances which determine whether the motion of water shall be direct or sinuous, and the law of resistance in parallel channels. Philosophical Transactions, 174, 935-982.

Ribeiro D.J.L. (1991). Effects of surface roughness on the two-dimensional flow past circular cylinders I: mean forces and pressures. Journal of Wind Engineering and Industrial Aerodynamics. 37 (3), 299-309.

Ribeiro D.J.L. (1991). Effects of surface roughness on the two-dimensional flow past circular cylinders II: fluctuating forces and pressures. Journal of Wind Engineering and Industrial Aerodynamics. 37 (3), 311-326.

Roshko A. (1954). On development of turbulent wakes from vortex streets. National Advisory Committee for Aeronautics, Reports.

Roshko A. (1954). On the effect of air pressure on Strouhal number. Journal of the Aerospace Sciences, 26 (2), 121.

Roshko A. (1955). On the wake and drag of bluff bodies. Journal of the Aeronautical Sciences, 22 (2), 124-132.

Roshko A. (1961). Experiments on the flow past a circular cylinder at very high Reynolds number. Journal of Fluid Mechanics 10 (3), 345-356.

Rostamy N., Sumner D., Bergstrom D. J., Bugg J. D (2012). Local flow field of a surface-mounted finite circular cylinder. Journal of fluid and structures, 34, 105-122.

Sagaut P. (2006). Large eddy simulation for incompressible flows. Springer, Germany.

Sakamoto H., Arie M. (1983). Vortex shedding from a rectangular prism and a circular cylinder placed vertically in a turbulent boundary layer. Journal of Fluid Mechanics, 126, 147-165.

Salvadori S.&Mattana A., Barbanti G.&Vita G. (2013). CFD simulations on a Solar Updraft Tower on the basis of CRIACIV experiments, personal communication, unpublished.

Sathe A., Mann J., Gottschall J., Courtney M.S. (2011). Can wind lidars measure turbulence? Journal of Atmospheric and Oceanic Technology, 28 (7), 853-868.

Schewe G. (1983). On the forces acting on a circular cylinder in cross-flow from subcritical up to transcritical Reynolds numbers. Journal Fluid Mechanics 133, 265-285.

Schlaich J. (1995). The Solar Chimney, Electricity from the Sun. Edition A. Menges, Stuttgart.

Schlaich J., Bergermann R., Schiel W., Weinrebe G. (2005). Design of Commercial Solar Updraft Tower Systems. ASME J. Solar Energy Engineering, 127, 117-124.

Schlaich J. (2010). Concept and motivation of solar updraft power technology. Proc. 2nd Int. Conf. Solar Chimney Power Technology, 15-18. Ruhr-Universität Bochum and Bergische Universität Wuppertal, Bochum, Germany.

Schlichting, H. (1960). Boundary layer theory. McGraw-Hill.

Schrader P. (1993). Die statistische Stabiltät gemessener integraler Längenmaβe und anderer Windparameter. Dissertation, Ruhr-Universität Bochum, Germany.

Simiu E., Scanlan R.H. (1996). Wind effects on structures - Fundamentals and application to design. John Wiley&Sons, Inc. New York.

Simiu E. (2011). Design of Buildings for Wind. John Wiley&Sons, Inc.

Sjöholm M., Mikkelsen T., Mann J.,Enevoldsen K., Courtney M. (2008). Time series analysis of continuous-wave coherent Doppler Lidar wind measurements. IOP Conference Series: Earth and Environmental Science, 1 (1).

Stull R.B. (1988). An introduction to boundary layer meteorology. Kluwer Academic Publishers, Dordrecht, The Netherlands.

SCPT (2010). Proc. 2nd Int. Conf. on Solar Chimney Power Technology, Ruhr-Universität Bochum and Bergische Universität Wuppertal, Bochum, Germany.

Strømmen E.N. (2010). Theory of Bridge Aerodynamics. Springer.

Sumner D., Heseltine J.L. (2008). Tip vortex structure for a circular cylinder with a free end. Journal of Wind Engineering and Industrial Aerodynamics, 96, 1185-1196.

Sumner, D. (2010). Two circular cylinders in cross-flow: A review. Journal of Fluids and Structures 26 (6), 849-899.

SUTPT (2012). Proc. 3rd Int. Conf. on Solar Updraft Power Technology SUTPT 2012. HUST, Wuhan, China.

Szechenyi E. (1974). Simulation of high Reynolds numbers on a cylinder in wind tunnel tests. Recherche Aerospatiale, 3, 155-164.

Szechenyi E. (1975). Supercritical Reynolds number simulation for two-dimensional flow over circular cylinders. Journal of Fluid Mechanics, 70, 529-542.

Tamura Y., Iwatani Y., Hibi K., Suda K., Nakamura O., Maruyama T., Ishibashi R (2007). Profiles of mean wind speeds and vertical turbulence intensities measured at seashore and two inland sites using Doppler sodars. Journal of Wind Engineering & Industrial Aerodynamics, 95 (6), 411-427.

Taniguchi S., Sakamoto H., Arie M. (1981). Flow around a circular cylinder vertically mounted in a turbulent boundary layer. Bulletin of the Japan Society of Mechanical Engineers, 24 (193), 1130-1136.

Taylor G.I. (1916). Pressure distribution round the cylinder. Advisory Committee of Aeronautics, Rep&Memo.

Teunissen H.W. (1970). Characteristics of the mean wind and turbulence in the planetary boundary layer. UTIAS Review No 32. Institute for Aerospace Studies, University of Toronto.

Thompson N. (1990). Integral length scales of turbulence: a re-analysis including data from non-uniform terrain. ESDU Memorandum n.76.

Uematsu Y., Yamada M. (1994). Aerodynamic forces on circular cylinders of finite height. Journal of Wind Engineering and Industrial Aerodynamics, 51 (2), 249-265.

Verkley W.T.M., van der Velde I.R. (2010). Balanced dynamics in the Tropics. Quarterly Journal of the Royal Meteorological Society, 136 (646), 41-49.

Versteeg H.K., Malalasekera W. (1995). An Introduction to Computational Fluid Dynamics. The Finite Volume Method. Longman Scientific&Technical.

VGB (2005). Structural design of cooling towers. Guideline VGB R 610Ue, VGB PowerTech, Essen.

VGB (2010). Structural design of cooling towers. Guideline VGB R 610e, VGB PowerTech, Essen.

Waechter M., Rettenmeier A., Kuehn M., Peinke, J. (2009). Characterization of short time fluctuations in atmospheric wind speeds by LIDAR measurements. Meteorologischezeitschrift, 18 (3), 277-280.

Wie Y., Wu Z. (2012). Shed absorbability and tower structure characteristics of the Solar Heated Wind Updraft Tower Power. Proc. 3rd Int. Conf. on Solar Updraft Power Technology SUTPT 2012, 126-127. HUST, Wuhan, China.

Weinrebe G. (2000). Technische, ökologische und ökonomische Analyse von solarthermischen Turmkraftwerken. Dissertation, University of Stuttgart.

Zdravkovich M.M. (1987). The effects of interference between circular cylinders in cross flow. Journal of Fluids and Structures, 1 (2), 239-261.

Zdravkovich M. M. (1992). A reflection on two modes of eddy shedding at Re = 180-300. Iutam Symposium, Bluff body wakes, Dynamics and Instabilities, Göttingen, 631-639. Springer, Berlin.

Zdravkovich M. M., Pridden D.L., (1977). Interference between two circular cylinders; Series of unexpected discontinuities. Journal of Wind Engineering and Industrial Aerodynamics, 2 (3), 255-270

Zdravkovich, M. M (1997). Flow around circular cylinders, Vol. 1, Fundamentals. Oxford University Press.

Zdravkovich, M. M (2003). Flow around circular cylinders, Vol. 2, Applications. Oxford University Press.

Chapter 10. **Appendix**

10.1   **Modelling of wind load (Chapter 7)**

Table A.1 Load data: body-induced pressure fluctuations - variance (SR0, effect of the rings on the load not included)

					Cp,σ_B^2 = body-induced pressure fluctuations					
	0	**20**	**40**	**60**	**80**	**100**	**120**	**140**	**160**	**180**
0.95	0	0	0	1.04E-05	0.0023097	0.0136799	0.0198095	0.0102689	0.0184776	0.0273402
0.85	0	0	5.006E-05	0.00103	0.0074486	0.0411091	0.0128124	0.014862	0.0199033	0.0155416
0.75	0	0	0	0.000128	0.0070256	0.0211319	0.0041208	0.0030748	0.0037577	0.0034584
0.65	0	0	0	0	0.0014349	0.0192708	0.0023672	0.0017146	0.0019685	0.0020286
0.55	0	0	0	0	0	0	0.0005087	0.0002179	0.0009585	0.0010654
0.45	0	0	0	0	0	0	0.0001991	0	0.0004456	0.000387
0.35	0	0	0	0	0	0	0.0007821	0	5.383E-05	0.0002192
0.25	0.0099196	0.0097788	0	0	0.0072963	0	0	0	0	0.0006125
0.15	0.0373687	0.0325377	0.0093249	0.016141	0.0453442	0	0.0143486	0.0123303	0.012928	0.0100694
0.05	0	0	0	0	0.0669672	0	0.0596038	0.0943915	0.1293659	0.0646646

Table A.2 Load data: horizontal correlations tip region 1 (SR0, effect of the rings on the load not included)

									TIP REGION N.1										
	0	**20**	**40**	**60**	**80**	**100**	**120**	**140**	**160**	**180**	**200**	**220**	**240**	**260**	**280**	**300**	**320**	**340**	**360**
0	1.00	0.73	0.10	-0.40	-0.54	-0.43	-0.27	-0.28	-0.23	-0.19	-0.23	-0.28	-0.27	-0.43	-0.54	-0.40	0.10	0.73	1.00
20	0.73	1.00	0.64	0.02	-0.36	-0.40	-0.26	-0.22	-0.18	-0.14	-0.15	-0.21	-0.13	-0.24	-0.42	-0.53	-0.31	0.23	0.73
40	0.10	0.64	1.00	0.69	0.19	-0.05	-0.06	0.02	0.03	0.06	0.08	0.03	0.16	0.19	0.02	-0.31	-0.49	-0.31	0.10
60	-0.40	0.02	0.69	1.00	0.77	0.43	0.24	0.30	0.29	0.26	0.32	0.28	0.40	0.57	0.50	0.13	-0.31	-0.53	-0.40
80	-0.54	-0.36	0.19	0.77	1.00	0.79	0.46	0.45	0.43	0.33	0.40	0.37	0.42	0.68	0.75	0.50	0.02	-0.42	-0.54
100	-0.43	-0.40	-0.05	0.43	0.79	1.00	0.69	0.47	0.40	0.26	0.29	0.26	0.27	0.55	0.68	0.57	0.19	-0.24	-0.43
120	-0.27	-0.26	-0.06	0.24	0.46	0.69	1.00	0.62	0.35	0.26	0.15	0.12	0.07	0.27	0.42	0.40	0.16	-0.13	-0.27
140	-0.28	-0.22	0.02	0.30	0.45	0.47	0.62	1.00	0.52	0.36	0.23	0.21	0.12	0.26	0.37	0.28	0.03	-0.21	-0.28
160	-0.23	-0.18	0.03	0.29	0.43	0.40	0.35	0.52	1.00	0.39	0.31	0.23	0.15	0.29	0.40	0.32	0.08	-0.15	-0.23
180	-0.19	-0.14	0.06	0.26	0.33	0.26	0.26	0.36	0.39	1.00	0.39	0.36	0.26	0.26	0.33	0.26	0.06	-0.14	-0.19
200	-0.23	-0.15	0.08	0.32	0.40	0.29	0.15	0.23	0.31	0.39	1.00	0.52	0.35	0.40	0.43	0.29	0.03	-0.18	-0.23
220	-0.28	-0.21	0.03	0.28	0.37	0.26	0.12	0.21	0.23	0.36	0.52	1.00	0.62	0.47	0.45	0.30	0.02	-0.22	-0.28
240	-0.27	-0.13	0.16	0.40	0.42	0.27	0.07	0.12	0.15	0.26	0.35	0.62	1.00	0.69	0.46	0.24	-0.06	-0.26	-0.27
260	-0.43	-0.24	0.19	0.57	0.68	0.55	0.27	0.26	0.29	0.26	0.40	0.47	0.69	1.00	0.79	0.43	-0.05	-0.40	-0.43
280	-0.54	-0.42	0.02	0.50	0.75	0.68	0.42	0.37	0.40	0.33	0.43	0.45	0.46	0.79	1.00	0.77	0.19	-0.36	-0.54
300	-0.40	-0.53	-0.31	0.13	0.50	0.57	0.40	0.28	0.32	0.26	0.29	0.30	0.24	0.43	0.77	1.00	0.69	0.02	-0.40

320	0.10	-0.31	-0.49	-0.31	0.02	0.19	0.16	0.03	0.08	0.06	0.03	0.02	-0.06	-0.05	0.19	0.69	1.00	0.64	0.10
340	0.73	0.23	-0.31	-0.53	-0.42	-0.24	-0.13	-0.21	-0.15	-0.14	-0.18	-0.22	-0.26	-0.40	-0.36	0.02	0.64	1.00	0.73
360	1.00	0.73	0.10	-0.40	-0.54	-0.43	-0.27	-0.28	-0.23	-0.19	-0.23	-0.28	-0.27	-0.43	-0.54	-0.40	0.10	0.73	1.00

Table A.3 Load data: horizontal correlations tip region 2 (SR0, effect of the rings on the load not included)

TIP REGION N.2																		
	0	**20**	**40**	**60**	**80**	**100**	**120**	**140**	**160**	**180**	**200**	**220**	**240**	**260**	**280**	**300**	**320**	**340**	**360**
0	1.00	0.69	-0.05	-0.55	-0.65	-0.38	-0.18	-0.27	-0.21	-0.15	-0.21	-0.27	-0.18	-0.38	-0.65	-0.55	-0.05	0.69	1.00
20	0.69	1.00	0.61	-0.02	-0.39	-0.36	-0.14	-0.17	-0.15	-0.10	-0.12	-0.19	-0.08	-0.18	-0.52	-0.70	-0.55	0.07	0.69
40	-0.05	0.61	1.00	0.73	0.29	-0.02	0.06	0.14	0.07	0.06	0.11	0.08	0.13	0.21	-0.01	-0.37	-0.67	-0.55	-0.05
60	-0.55	-0.02	0.73	1.00	0.82	0.41	0.30	0.38	0.28	0.18	0.29	0.31	0.26	0.44	0.44	0.11	-0.37	-0.70	-0.55
80	-0.65	-0.39	0.29	0.82	1.00	0.78	0.54	0.50	0.40	0.21	0.34	0.39	0.24	0.45	0.63	0.44	-0.01	-0.52	-0.65
100	-0.38	-0.36	-0.02	0.41	0.78	1.00	0.79	0.46	0.41	0.13	0.21	0.23	0.04	0.18	0.45	0.44	0.21	-0.18	-0.38
120	-0.18	-0.14	0.06	0.30	0.54	0.79	1.00	0.56	0.37	0.11	0.11	0.12	-0.04	0.04	0.24	0.26	0.13	-0.08	-0.18
140	-0.27	-0.17	0.14	0.38	0.50	0.46	0.56	1.00	0.48	0.14	0.19	0.21	0.12	0.23	0.39	0.31	0.08	-0.19	-0.27
160	-0.21	-0.15	0.07	0.28	0.40	0.41	0.37	0.48	1.00	0.05	0.18	0.19	0.11	0.21	0.34	0.29	0.11	-0.12	-0.21
180	-0.15	-0.10	0.06	0.18	0.21	0.13	0.11	0.14	0.05	1.00	0.05	0.14	0.11	0.13	0.21	0.18	0.06	-0.10	-0.15
200	-0.21	-0.12	0.11	0.29	0.34	0.21	0.11	0.19	0.18	0.05	1.00	0.48	0.37	0.41	0.40	0.28	0.07	-0.15	-0.21
220	-0.27	-0.19	0.08	0.31	0.39	0.23	0.12	0.21	0.19	0.14	0.48	1.00	0.56	0.46	0.50	0.38	0.14	-0.17	-0.27
240	-0.18	-0.08	0.13	0.26	0.24	0.04	-0.04	0.12	0.11	0.11	0.37	0.56	1.00	0.79	0.54	0.30	0.06	-0.14	-0.18
260	-0.38	-0.18	0.21	0.44	0.45	0.18	0.04	0.23	0.21	0.13	0.41	0.46	0.79	1.00	0.78	0.41	-0.02	-0.36	-0.38
280	-0.65	-0.52	-0.01	0.44	0.63	0.45	0.24	0.39	0.34	0.21	0.40	0.50	0.54	0.78	1.00	0.82	0.29	-0.39	-0.65
300	-0.55	-0.70	-0.37	0.11	0.44	0.44	0.26	0.31	0.29	0.18	0.28	0.38	0.30	0.41	0.82	1.00	0.73	-0.02	-0.55
320	-0.05	-0.55	-0.67	-0.37	-0.01	0.21	0.13	0.08	0.11	0.06	0.07	0.14	0.06	-0.02	0.29	0.73	1.00	0.61	-0.05
340	0.69	0.07	-0.55	-0.70	-0.52	-0.18	-0.08	-0.19	-0.12	-0.10	-0.15	-0.17	-0.14	-0.36	-0.39	-0.02	0.61	1.00	0.69
360	1.00	0.69	-0.05	-0.55	-0.65	-0.38	-0.18	-0.27	-0.21	-0.15	-0.21	-0.27	-0.18	-0.38	-0.65	-0.55	-0.05	0.69	1.00

Table A.4 Load data: horizontal correlations tip region 3 (SR0, effect of the rings on the load not included)

TIP REGION N.3																		
	0	**20**	**40**	**60**	**80**	**100**	**120**	**140**	**160**	**180**	**200**	**220**	**240**	**260**	**280**	**300**	**320**	**340**	**360**
0	1.00	0.67	-0.09	-0.56	-0.61	-0.21	-0.19	-0.20	-0.19	-0.17	-0.19	-0.20	-0.19	-0.21	-0.61	-0.56	-0.09	0.67	1.00
20	0.67	1.00	0.65	0.06	-0.32	-0.22	-0.04	-0.04	-0.08	-0.10	-0.16	-0.19	-0.18	0.03	-0.47	-0.70	-0.63	-0.08	0.67
40	-0.09	0.65	1.00	0.76	0.32	-0.04	0.31	0.30	0.25	0.12	0.05	-0.02	0.00	0.25	0.04	-0.35	-0.69	-0.63	-0.09
60	-0.56	0.06	0.76	1.00	0.82	0.32	0.52	0.49	0.44	0.29	0.21	0.15	0.16	0.30	0.42	0.14	-0.35	-0.70	-0.56
80	-0.61	-0.32	0.32	0.82	1.00	0.71	0.65	0.57	0.54	0.35	0.23	0.19	0.15	0.20	0.52	0.42	0.04	-0.47	-0.61
100	-0.21	-0.22	-0.04	0.32	0.71	1.00	0.71	0.47	0.52	0.22	0.03	0.02	-0.10	-0.28	0.20	0.30	0.25	0.03	-0.21
120	-0.19	-0.04	0.31	0.52	0.65	0.71	1.00	0.75	0.67	0.36	0.01	0.01	-0.06	-0.10	0.15	0.16	0.00	-0.18	-0.19
140	-0.20	-0.04	0.30	0.49	0.57	0.47	0.75	1.00	0.74	0.39	0.08	0.08	0.01	0.02	0.19	0.15	-0.02	-0.19	-0.20
160	-0.19	-0.08	0.25	0.44	0.54	0.52	0.67	0.74	1.00	0.45	0.09	0.08	0.01	0.03	0.23	0.21	0.05	-0.16	-0.19

	0	20	40	60	80	100	120	140	160	180	200	220	240	260	280	300	320	340	360
180	-0.17	-0.10	0.12	0.29	0.35	0.22	0.36	0.39	0.45	1.00	0.45	0.39	0.36	0.22	0.35	0.29	0.12	-0.10	-0.17
200	-0.19	-0.16	0.05	0.21	0.23	0.03	0.01	0.08	0.09	0.45	1.00	0.74	0.67	0.52	0.54	0.44	0.25	-0.08	-0.19
220	-0.20	-0.19	-0.02	0.15	0.19	0.02	0.01	0.08	0.08	0.39	0.74	1.00	0.75	0.47	0.57	0.49	0.30	-0.04	-0.20
240	-0.19	-0.18	0.00	0.16	0.15	-0.10	-0.06	0.01	0.01	0.36	0.67	0.75	1.00	0.71	0.65	0.52	0.31	-0.04	-0.19
260	-0.21	0.03	0.25	0.30	0.20	-0.28	-0.10	0.02	0.03	0.22	0.52	0.47	0.71	1.00	0.71	0.32	-0.04	-0.22	-0.21
280	-0.61	-0.47	0.04	0.42	0.52	0.20	0.15	0.19	0.23	0.35	0.54	0.57	0.65	0.71	1.00	0.82	0.32	-0.32	-0.61
300	-0.56	-0.70	-0.35	0.14	0.42	0.30	0.16	0.15	0.21	0.29	0.44	0.49	0.52	0.32	0.82	1.00	0.76	0.06	-0.56
320	-0.09	-0.63	-0.69	-0.35	0.04	0.25	0.00	-0.02	0.05	0.12	0.25	0.30	0.31	-0.04	0.32	0.76	1.00	0.65	-0.09
340	0.67	-0.08	-0.63	-0.70	-0.47	0.03	-0.18	-0.19	-0.16	-0.10	-0.08	-0.04	-0.04	-0.22	-0.32	0.06	0.65	1.00	0.67
360	1.00	0.67	-0.09	-0.56	-0.61	-0.21	-0.19	-0.20	-0.19	-0.17	-0.19	-0.20	-0.19	-0.21	-0.61	-0.56	-0.09	0.67	1.00

Table A.5 Load data: horizontal correlations tip region 4 (SR0, effect of the rings on the load not included)

TIP REGION N.4																		
	0	**20**	**40**	**60**	**80**	**100**	**120**	**140**	**160**	**180**	**200**	**220**	**240**	**260**	**280**	**300**	**320**	**340**	**360**
0	1.00	0.66	-0.07	-0.55	-0.51	0.00	-0.14	-0.16	-0.15	-0.15	-0.15	-0.16	-0.14	0.00	-0.51	-0.55	-0.07	0.66	1.00
20	0.66	1.00	0.65	0.03	-0.35	-0.19	-0.01	0.00	-0.02	-0.05	-0.10	-0.12	-0.09	0.23	-0.29	-0.68	-0.62	-0.05	0.66
40	-0.07	0.65	1.00	0.73	0.17	-0.18	0.25	0.28	0.25	0.18	0.11	0.09	0.10	0.36	0.18	-0.31	-0.68	-0.62	-0.07
60	-0.55	0.03	0.73	1.00	0.70	0.07	0.47	0.51	0.48	0.40	0.30	0.28	0.26	0.29	0.51	0.20	-0.31	-0.68	-0.55
80	-0.51	-0.35	0.17	0.70	1.00	0.60	0.62	0.61	0.60	0.48	0.34	0.31	0.25	0.01	0.47	0.51	0.18	-0.29	-0.51
100	0.00	-0.19	-0.18	0.07	0.60	1.00	0.48	0.40	0.40	0.29	0.14	0.10	0.04	-0.22	0.01	0.29	0.36	0.23	0.00
120	-0.14	-0.01	0.25	0.47	0.62	0.48	1.00	0.71	0.63	0.49	0.32	0.27	0.23	0.04	0.25	0.26	0.10	-0.09	-0.14
140	-0.16	0.00	0.28	0.51	0.61	0.40	0.71	1.00	0.76	0.55	0.38	0.32	0.27	0.10	0.31	0.28	0.09	-0.12	-0.16
160	-0.15	-0.02	0.25	0.48	0.60	0.40	0.63	0.76	1.00	0.68	0.46	0.38	0.32	0.14	0.34	0.30	0.11	-0.10	-0.15
180	-0.15	-0.05	0.18	0.40	0.48	0.29	0.49	0.55	0.68	1.00	0.68	0.55	0.49	0.29	0.48	0.40	0.18	-0.05	-0.15
200	-0.15	-0.10	0.11	0.30	0.34	0.14	0.32	0.38	0.46	0.68	1.00	0.76	0.63	0.40	0.60	0.48	0.25	-0.02	-0.15
220	-0.16	-0.12	0.09	0.28	0.31	0.10	0.27	0.32	0.38	0.55	0.76	1.00	0.71	0.40	0.61	0.51	0.28	0.00	-0.16
240	-0.14	-0.09	0.10	0.26	0.25	0.04	0.23	0.27	0.32	0.49	0.63	0.71	1.00	0.48	0.62	0.47	0.25	-0.01	-0.14
260	0.00	0.23	0.36	0.29	0.01	-0.22	0.04	0.10	0.14	0.29	0.40	0.40	0.48	1.00	0.60	0.07	-0.18	-0.19	0.00
280	-0.51	-0.29	0.18	0.51	0.47	0.01	0.25	0.31	0.34	0.48	0.60	0.61	0.62	0.60	1.00	0.70	0.17	-0.35	-0.51
300	-0.55	-0.68	-0.31	0.20	0.51	0.29	0.26	0.28	0.30	0.40	0.48	0.51	0.47	0.07	0.70	1.00	0.73	0.03	-0.55
320	-0.07	-0.62	-0.68	-0.31	0.18	0.36	0.10	0.09	0.11	0.18	0.25	0.28	0.25	-0.18	0.17	0.73	1.00	0.65	-0.07
340	0.66	-0.05	-0.62	-0.68	-0.29	0.23	-0.09	-0.12	-0.10	-0.05	-0.02	0.00	-0.01	-0.19	-0.35	0.03	0.65	1.00	0.66
360	1.00	0.66	-0.07	-0.55	-0.51	0.00	-0.14	-0.16	-0.15	-0.15	-0.15	-0.16	-0.14	0.00	-0.51	-0.55	-0.07	0.66	1.00

Table A.6 Load data: horizontal correlations normal region (SR0, effect of the rings on the load not included)

NORMAL REGION																		
	0	**20**	**40**	**60**	**80**	**100**	**120**	**140**	**160**	**180**	**200**	**220**	**240**	**260**	**280**	**300**	**320**	**340**	**360**
0	1.00	0.70	-0.06	-0.59	-0.54	0.07	-0.14	-0.17	-0.18	-0.17	-0.18	-0.17	-0.14	0.07	-0.54	-0.59	-0.06	0.70	1.00
20	0.70	1.00	0.64	-0.03	-0.44	-0.16	-0.01	-0.02	-0.04	-0.07	-0.11	-0.13	-0.09	0.27	-0.29	-0.70	-0.60	-0.02	0.70

	0	20	40	60	80	100	120	140	160	180	200	220	240	260	280	300	320	340	360
40	-0.06	0.64	1.00	0.71	0.12	-0.19	0.27	0.29	0.29	0.23	0.15	0.11	0.12	0.37	0.24	-0.30	-0.68	-0.60	-0.06
60	-0.59	-0.03	0.71	1.00	0.69	0.06	0.50	0.54	0.56	0.48	0.36	0.30	0.28	0.24	0.54	0.26	-0.30	-0.70	-0.59
80	-0.54	-0.44	0.12	0.69	1.00	0.61	0.66	0.65	0.67	0.54	0.36	0.29	0.23	-0.14	0.38	0.54	0.24	-0.29	-0.54
100	0.07	-0.16	-0.19	0.06	0.61	1.00	0.54	0.44	0.45	0.32	0.14	0.07	0.03	-0.30	-0.14	0.24	0.37	0.27	0.07
120	-0.14	-0.01	0.27	0.50	0.66	0.54	1.00	0.75	0.70	0.58	0.38	0.28	0.25	0.03	0.23	0.28	0.12	-0.09	-0.14
140	-0.17	-0.02	0.29	0.54	0.65	0.44	0.75	1.00	0.83	0.64	0.44	0.33	0.28	0.07	0.29	0.30	0.11	-0.13	-0.17
160	-0.18	-0.04	0.29	0.56	0.67	0.45	0.70	0.83	1.00	0.79	0.56	0.44	0.38	0.14	0.36	0.36	0.15	-0.11	-0.18
180	-0.17	-0.07	0.23	0.48	0.54	0.32	0.58	0.64	0.79	1.00	0.79	0.64	0.58	0.32	0.54	0.48	0.23	-0.07	-0.17
200	-0.18	-0.11	0.15	0.36	0.36	0.14	0.38	0.44	0.56	0.79	1.00	0.83	0.70	0.45	0.67	0.56	0.29	-0.04	-0.18
220	-0.17	-0.13	0.11	0.30	0.29	0.07	0.28	0.33	0.44	0.64	0.83	1.00	0.75	0.44	0.65	0.54	0.29	-0.02	-0.17
240	-0.14	-0.09	0.12	0.28	0.23	0.03	0.25	0.28	0.38	0.58	0.70	0.75	1.00	0.54	0.66	0.50	0.27	-0.01	-0.14
260	0.07	0.27	0.37	0.24	-0.14	-0.30	0.03	0.07	0.14	0.32	0.45	0.44	0.54	1.00	0.61	0.06	-0.19	-0.16	0.07
280	-0.54	-0.29	0.24	0.54	0.38	-0.14	0.23	0.29	0.36	0.54	0.67	0.65	0.66	0.61	1.00	0.69	0.12	-0.44	-0.54
300	-0.59	-0.70	-0.30	0.26	0.54	0.24	0.28	0.30	0.36	0.48	0.56	0.54	0.50	0.06	0.69	1.00	0.71	-0.03	-0.59
320	-0.06	-0.60	-0.68	-0.30	0.24	0.37	0.12	0.11	0.15	0.23	0.29	0.29	0.27	-0.19	0.12	0.71	1.00	0.64	-0.06
340	0.70	-0.02	-0.60	-0.70	-0.29	0.27	-0.09	-0.13	-0.11	-0.07	-0.04	-0.02	-0.01	-0.16	-0.44	-0.03	0.64	1.00	0.70
360	1.00	0.70	-0.06	-0.59	-0.54	0.07	-0.14	-0.17	-0.18	-0.17	-0.18	-0.17	-0.14	0.07	-0.54	-0.59	-0.06	0.70	1.00

Table A.7 Load data: horizontal correlations bottom region (SR0, effect of the rings on the load not included)

		0	20	40	60	80	100	120	140	160	180	200	220	240	260	280	300	320	340	360
BOTTOM REGION																				
	0	1.00	0.71	-0.14	-0.66	-0.73	0.02	-0.25	-0.31	-0.32	-0.33	-0.32	-0.31	-0.25	0.02	-0.73	-0.66	-0.14	0.71	1.00
	20	0.71	1.00	0.66	-0.14	-0.51	-0.44	-0.16	-0.15	-0.16	-0.19	-0.21	-0.21	-0.15	0.24	-0.48	-0.75	-0.67	0.08	0.71
	40	-0.14	0.66	1.00	0.73	0.24	-0.29	0.27	0.31	0.29	0.26	0.20	0.18	0.24	0.51	0.33	-0.27	-0.68	-0.67	-0.14
	60	-0.66	-0.14	0.73	1.00	0.81	0.23	0.56	0.59	0.57	0.54	0.47	0.44	0.41	0.53	0.71	0.40	-0.27	-0.75	-0.66
	80	-0.73	-0.51	0.24	0.81	1.00	0.73	0.69	0.67	0.69	0.63	0.54	0.50	0.38	-0.13	0.79	0.71	0.33	-0.48	-0.73
	100	0.02	-0.44	-0.29	0.23	0.73	1.00	0.64	0.52	0.53	0.42	0.29	-0.03	-0.06	-0.35	-0.13	0.53	0.51	0.24	0.02
	120	-0.25	-0.16	0.27	0.56	0.69	0.64	1.00	0.78	0.72	0.58	0.36	0.32	0.25	-0.06	0.38	0.41	0.24	-0.15	-0.25
	140	-0.31	-0.15	0.31	0.59	0.67	0.52	0.78	1.00	0.84	0.65	0.44	0.39	0.32	-0.03	0.50	0.44	0.18	-0.21	-0.31
	160	-0.32	-0.16	0.29	0.57	0.69	0.53	0.72	0.84	1.00	0.78	0.52	0.44	0.36	0.29	0.54	0.47	0.20	-0.21	-0.32
	180	-0.33	-0.19	0.26	0.54	0.63	0.42	0.58	0.65	0.78	1.00	0.78	0.65	0.58	0.42	0.63	0.54	0.26	-0.19	-0.33
	200	-0.32	-0.21	0.20	0.47	0.54	0.29	0.36	0.44	0.52	0.78	1.00	0.84	0.72	0.53	0.69	0.57	0.29	-0.16	-0.32
	220	-0.31	-0.21	0.18	0.44	0.50	-0.03	0.32	0.39	0.44	0.65	0.84	1.00	0.78	0.52	0.67	0.59	0.31	-0.15	-0.31
	240	-0.25	-0.15	0.24	0.41	0.38	-0.06	0.25	0.32	0.36	0.58	0.72	0.78	1.00	0.64	0.69	0.56	0.27	-0.16	-0.25
	260	0.02	0.24	0.51	0.53	-0.13	-0.35	-0.06	-0.03	0.29	0.42	0.53	0.52	0.64	1.00	0.73	0.23	-0.29	-0.44	0.02
	280	-0.73	-0.48	0.33	0.71	0.79	-0.13	0.38	0.50	0.54	0.63	0.69	0.67	0.69	0.73	1.00	0.81	0.24	-0.51	-0.73
	300	-0.66	-0.75	-0.27	0.40	0.71	0.53	0.41	0.44	0.47	0.54	0.57	0.59	0.56	0.23	0.81	1.00	0.73	-0.14	-0.66
	320	-0.14	-0.67	-0.68	-0.27	0.33	0.51	0.24	0.18	0.20	0.26	0.29	0.31	0.27	-0.29	0.24	0.73	1.00	0.66	-0.14
	340	0.71	0.08	-0.67	-0.75	-0.48	0.24	-0.15	-0.21	-0.21	-0.19	-0.16	-0.15	-0.16	-0.44	-0.51	-0.14	0.66	1.00	0.71
	360	1.00	0.71	-0.14	-0.66	-0.73	0.02	-0.25	-0.31	-0.32	-0.33	-0.32	-0.31	-0.25	0.02	-0.73	-0.66	-0.14	0.71	1.00

10.2   **The beam response (Chapter 7)**

Table A.8 Load data: mean and rms drag forces (SR0, effect of the rings on the load not included)

z [m]	U [m/s]	q_m [kN/m²]	D [m]	Δz [m]	$C_{D,m}$	F_m [kN]	$C_{D,\sigma}$	F_σ [kN]
990	51.22	1.640	150	30	0.725	5346.37	0.120	884.04
950	50.86	1.616	150	40	0.799	7751.58	0.111	1078.48
910	50.48	1.593	150	30	0.769	5513.67	0.115	822.48
890	50.29	1.581	150	30	0.716	5091.11	0.113	806.49
850	49.89	1.556	150	70	0.606	9901.57	0.100	1635.98
750	48.83	1.490	150	100	0.501	11192.00	0.080	1791.60
650	47.64	1.419	150	100	0.486	10337.94	0.078	1661.10
550	46.30	1.340	150	65	0.486	6345.71	0.084	1094.48
520	45.85	1.314	150	22.5	0.492	2183.83	0.089	393.90
505	45.62	1.301	150	12.5	0.483	1177.26	0.090	219.80
495	45.46	1.292	150	12.5	0.482	1167.56	0.092	221.95
480	45.22	1.278	150	22.5	0.504	2173.84	0.092	397.82
450	44.73	1.250	150	65	0.508	6196.09	0.094	1142.33
350	42.83	1.147	158.94	100	0.554	10098.03	0.116	2115.57
250	40.43	1.021	183.15	100	0.604	11306.93	0.139	2592.24
150	38.34	0.919	217.59	100	0.698	13956.99	0.163	3251.36
50	33.26	0.691	258.20	100	0.816	14564.22	0.206	3668.03

$M_{D,m}(z=0)$	6.45E+07	kNm		
$M_{D,\sigma}(z=0)$	6.53E+06	kNm	including lack of correlation	
$M_{D,peak}(z=0)$	8.74E+07	kNm		

Table A.9 Load data: correlation matrix of drag forces (SR0, effect of the rings on the load not included)

Z [m]	990	950	910	890	850	750	650	550	520	505	495	480	450	350	250	150	50
990	1.000	0.683	0.445	0.387	0.357	0.316	0.214	0.129	0.031	0.028	0.026	0.023	0.019	0.009	0.004	0.002	0.001
950	0.683	1.000	0.705	0.614	0.519	0.425	0.341	0.155	0.112	0.104	0.099	0.091	0.078	0.047	0.028	0.017	0.010
910	0.445	0.705	1.000	0.863	0.610	0.393	0.308	0.187	0.117	0.108	0.102	0.094	0.079	0.046	0.026	0.015	0.009
890	0.387	0.614	0.863	1.000	0.710	0.398	0.337	0.205	0.130	0.120	0.114	0.105	0.089	0.051	0.029	0.017	0.010
850	0.357	0.519	0.610	0.710	1.000	0.477	0.365	0.247	0.160	0.148	0.140	0.129	0.109	0.063	0.036	0.021	0.012
750	0.316	0.425	0.393	0.398	0.477	1.000	0.583	0.407	0.329	0.306	0.291	0.271	0.234	0.144	0.089	0.055	0.034
650	0.214	0.341	0.308	0.337	0.365	0.583	1.000	0.610	0.497	0.458	0.433	0.399	0.343	0.202	0.119	0.070	0.041
550	0.129	0.155	0.187	0.205	0.247	0.407	0.610	1.000	0.845	0.775	0.735	0.685	0.613	0.347	0.204	0.120	0.071
520	0.031	0.112	0.117	0.130	0.160	0.329	0.497	0.845	1.000	0.916	0.856	0.806	0.687	0.410	0.240	0.188	0.084
505	0.028	0.104	0.108	0.120	0.148	0.306	0.458	0.775	0.916	1.000	0.945	0.847	0.722	0.444	0.260	0.201	0.091

495	0.026	0.099	0.102	0.114	0.140	0.291	0.433	0.735	0.856	0.945	1.000	0.905	0.763	0.468	0.274	0.210	0.096
480	0.023	0.091	0.094	0.105	0.129	0.271	0.399	0.685	0.806	0.847	0.905	1.000	0.839	0.506	0.297	0.225	0.103
450	0.019	0.078	0.079	0.089	0.109	0.234	0.343	0.613	0.687	0.722	0.763	0.839	1.000	0.606	0.348	0.326	0.121
350	0.009	0.047	0.046	0.051	0.063	0.144	0.202	0.347	0.410	0.444	0.468	0.506	0.606	1.000	0.590	0.431	0.205
250	0.004	0.028	0.026	0.029	0.036	0.089	0.119	0.204	0.240	0.260	0.274	0.297	0.348	0.590	1.000	0.637	0.348
150	0.002	0.017	0.015	0.017	0.021	0.055	0.070	0.120	0.188	0.201	0.210	0.225	0.326	0.431	0.637	1.000	0.590
50	0.001	0.010	0.009	0.010	0.012	0.034	0.041	0.071	0.084	0.091	0.096	0.103	0.121	0.205	0.348	0.590	1.000

Table A.10 Results – covariance method (SR0, effect of the rings on the load not included)

z [m]	$M_{D,m}$ [kNm]	$M_{D,\sigma}$ [kNm]	$M_{D,peak}$ [kNm]
0	6.45E+07	6.53E+06	8.74E+07
50	5.83E+07	5.98E+06	7.93E+07
100	5.28E+07	5.47E+06	7.20E+07
150	4.74E+07	4.98E+06	6.48E+07
200	4.26E+07	4.52E+06	5.84E+07
250	3.78E+07	4.08E+06	5.21E+07
300	3.36E+07	3.67E+06	4.64E+07
350	2.93E+07	3.26E+06	4.07E+07
400	2.56E+07	2.88E+06	3.57E+07
450	2.19E+07	2.51E+06	3.07E+07
500	1.85E+07	2.16E+06	2.61E+07
550	1.54E+07	1.82E+06	2.18E+07
600	1.27E+07	1.51E+06	1.79E+07
650	9.90E+06	1.20E+06	1.41E+07
700	7.66E+06	9.40E+05	1.09E+07
750	5.42E+06	6.81E+05	7.80E+06
800	3.74E+06	4.71E+05	5.39E+06
850	2.06E+06	2.68E+05	3.00E+06
900	9.24E+05	1.28E+05	1.37E+06
950	2.14E+05	3.54E+04	3.38E+05
1000	0.00E+00	0.00E+00	0.00E+00

Table A.11 Load data: mean drag forces (SR1, effect of ten rings on the load included)

z [m]	U [m/s]	q_m [kN/m2]	D [m]	Δz [m]	$C_{D,m}$	$F_{D,m}$ [kN]
990	51.22	1.640	150	30	0.746	5503.44
950	50.86	1.616	150	40	0.689	6684.68
910	50.48	1.593	150	30	0.633	4533.52
890	50.29	1.581	150	30	0.599	4261.88
850	49.89	1.556	150	70	0.605	9882.94

750	48.83	1.490	150	100	0.606	13548.72
650	47.64	1.419	150	100	0.606	12901.86
550	46.30	1.340	150	65	0.623	8140.94
520	45.85	1.314	150	22.5	0.626	2775.63
505	45.62	1.301	150	12.5	0.616	1502.75
495	45.46	1.292	150	12.5	0.615	1490.81
480	45.22	1.278	150	22.5	0.637	2749.58
450	44.73	1.250	150	65	0.642	7822.83
350	42.83	1.147	158.9367	100	0.687	12530.31
250	40.43	1.021	183.1461	100	0.738	13803.53
150	38.34	0.919	217.5889	100	0.831	16625.38
50	33.26	0.691	258.2017	100	0.949	16946.00

$M_{D,m}(z=0)$ 7.01E+07   kNm

Table A.12 Load data: mean lift forces (SR1, effect of ten rings on the load included)

z [m]	U [m/s]	q_m [kN/m2]	D [m]	Δz [m]	$C_{L,m}$	$F_{L,m}$ [kN]
950	50.86	1.616	150	100	0.250	6061.72
850	49.89	1.556	150	100	-0.250	-5834.30
750	48.83	1.490	150	100	0.250	5588.57
650	47.64	1.419	150	100	-0.250	-5320.27
550	46.30	1.340	150	100	0.250	5023.32
450	44.73	1.250	150	100	-0.250	-4688.45
350	42.83	1.147	158.9367	100	0.250	4556.57
250	40.43	1.021	183.1461	100	-0.250	-4677.06
150	38.34	0.919	217.5889	100	0.250	4998.87
50	33.26	0.691	258.2017	100	-0.250	-4461.95

$M_{L,m}(z=0)$ 3.14E+06   kNm

10.3   The shell response (Chapter 7)

Table A.13 Shell response (effect of the rings on the load not included)

Response at stagnation - wind tunnel model applied to codified wind profile												
	Mean				Rms				Peak			
z	n11	n22	m11	m22	n11	n22	m11	m22	n11	n22	m11	m22
[m]	kN/m	kN/m	kNm/m	kNm/m	kN/m	kN/m	kNm/m	kNm/m	kN/m	kN/m	kNm/m	kNm/m
5	335.32	2741.12	4.53	25.22	41.06	342.59	0.74	4.00	479.03	3940.17	7.11	39.21
55	-30.04	2651.49	-1.34	1.15	21.94	311.21	1.40	0.42	-106.83	3740.71	-6.22	2.61
85	-32.06	2597.99	-4.64	-10.72	24.94	291.88	1.06	2.02	-119.36	3619.56	-8.37	-17.80
95	222.23	2578.27	-1.06	8.03	26.92	285.34	0.51	0.96	316.45	3576.95	-2.85	11.40
105	233.55	2565.70	-0.39	14.53	28.21	280.28	0.33	2.41	332.27	3546.68	-1.53	22.97

115	-19.05	2552.11	-5.95	-11.41	25.31	275.53	1.29	2.22	-107.63	3516.45	-10.47	-19.19
155	-14.53	2507.25	-5.47	-0.44	26.56	261.37	1.89	0.40	-107.50	3422.06	-12.07	-1.83
185	-52.93	2477.19	-11.24	-19.16	31.85	255.38	2.50	3.83	-164.39	3371.02	-19.99	-32.58
195	515.17	2464.02	-6.58	5.46	78.50	253.57	1.44	0.97	789.91	3351.50	-11.64	8.86
205	547.41	2464.25	-3.98	22.90	83.14	253.12	1.05	3.79	838.40	3350.19	-7.66	36.16
215	-20.04	2466.68	-13.60	-22.08	26.55	252.82	2.80	4.22	-112.96	3351.54	-23.39	-36.86
255	17.78	2489.23	-11.93	-2.20	20.32	255.18	2.37	0.54	88.90	3382.37	-20.21	-4.08
285	-113.27	2510.73	-20.39	-29.92	34.99	260.08	3.24	4.51	-235.72	3421.00	-31.72	-45.71
295	1042.56	2512.81	-13.65	3.07	134.42	261.51	2.02	0.76	1513.03	3428.08	-20.73	5.75
305	1104.82	2511.19	-8.14	36.11	141.49	261.76	1.33	4.73	1600.02	3427.33	-12.78	52.68
315	-60.21	2497.76	-23.83	-36.98	29.41	260.20	3.46	5.27	-163.16	3408.47	-35.94	-55.41
355	50.31	2431.20	-17.84	-3.42	17.67	253.04	2.34	0.46	112.15	3316.84	-26.03	-5.05
385	-198.04	2369.43	-24.28	-31.75	38.45	248.09	2.92	3.76	-332.62	3237.75	-34.50	-44.89
395	1444.30	2342.28	-17.14	-2.28	152.59	245.97	1.94	0.37	1978.36	3203.19	-23.94	-3.56
405	1511.55	2273.12	-8.37	41.38	158.90	240.11	1.02	4.40	2067.69	3113.48	-11.95	56.80
415	-148.16	2173.71	-25.47	-41.04	33.57	231.74	2.85	4.61	-265.65	2984.78	-35.45	-57.16
455	-76.78	1758.99	-15.40	-2.81	17.09	197.91	1.57	0.27	-136.58	2451.67	-20.89	-3.77
485	-392.97	1516.14	-18.21	-22.41	35.29	177.32	1.98	2.22	-516.49	2136.75	-25.14	-30.18
495	1277.73	1455.16	-13.91	-6.96	122.81	171.26	1.35	0.75	1707.55	2054.56	-18.62	-9.57
505	1344.46	1359.20	-4.69	36.75	128.21	162.70	0.62	3.35	1793.18	1928.64	-6.85	48.47
515	-330.27	1248.70	-18.68	-32.04	29.86	153.43	1.97	3.01	-434.77	1785.70	-25.56	-42.56
555	-101.21	894.46	-10.62	-1.49	18.00	122.97	1.06	0.11	-164.20	1324.87	-14.33	-1.88
585	-418.55	742.47	-12.46	-14.42	45.33	107.04	1.21	1.42	-577.19	1117.09	-16.71	-19.38
595	1235.34	712.97	-10.92	-10.99	109.46	102.66	0.98	0.93	1618.46	1072.27	-14.37	-14.26
605	1306.75	643.71	-2.26	30.44	115.15	97.02	0.28	2.67	1709.76	983.29	-3.24	39.80
615	-354.78	557.16	-13.92	-24.87	40.06	91.46	1.33	2.27	-494.99	877.26	-18.59	-32.81
655	-103.39	305.08	-9.50	-1.47	17.60	75.48	1.06	0.18	-165.00	569.26	-13.22	-2.10
685	-453.16	230.75	-13.02	-15.39	47.03	65.96	1.25	1.46	-617.76	461.60	-17.40	-20.51
695	1368.64	226.78	-11.85	-11.48	119.31	62.18	1.05	0.94	1786.23	444.40	-15.52	-14.77
705	1487.98	178.65	-2.75	34.24	129.29	58.62	0.32	2.97	1940.51	383.82	-3.86	44.62
715	-390.52	111.66	-15.76	-28.18	41.92	56.65	1.50	2.52	-537.24	309.94	-21.00	-37.02
755	-105.66	-73.10	-10.28	-1.64	17.11	50.93	1.17	0.21	-165.53	-251.36	-14.37	-2.39
785	-475.22	-106.82	-13.86	-16.22	48.26	40.81	1.35	1.53	-644.14	-249.65	-18.57	-21.57
795	1444.15	-98.35	-12.73	-12.56	125.93	35.83	1.13	1.06	1884.89	-223.77	-16.67	-16.28
805	1571.51	-131.60	-2.95	36.27	136.62	34.26	0.33	3.17	2049.69	-251.52	-4.11	47.35
815	-408.62	-180.28	-16.64	-29.85	42.90	35.92	1.57	2.66	-558.77	-306.01	-22.14	-39.18
855	-107.58	-285.30	-10.46	-1.75	16.86	37.65	1.19	0.21	-166.61	-417.06	-14.62	-2.49
885	-456.89	-247.49	-13.43	-15.34	48.05	28.52	1.34	1.50	-625.07	-347.32	-18.12	-20.60
895	1371.62	-213.67	-12.38	-12.63	125.25	22.40	1.15	1.13	1810.01	-292.06	-16.40	-16.58
905	1496.61	-214.75	-2.71	35.16	136.46	21.47	0.31	3.22	1974.21	-289.91	-3.79	46.43
915	-390.32	-227.98	-15.79	-28.56	42.26	24.71	1.54	2.67	-538.21	-314.48	-21.18	-37.90
955	-99.88	-205.47	-9.70	-1.83	16.65	26.98	1.08	0.21	-158.17	-299.89	-13.47	-2.57
985	-245.32	-85.10	-12.36	-15.89	31.51	12.33	1.27	1.59	-355.60	-128.25	-16.80	-21.46
995	816.33	-28.47	-5.61	15.96	78.39	4.29	0.58	1.57	1090.70	-43.48	-7.63	21.47

Table A.14 Load modification induced by the rings: effect on the quasi-static response (peak values):
SR0 = load modification due to the rings not included;
SR1 = load modification due to 10 rings included

	n11,peak at 0°		n22,peak at 0°		m11,peak at 0°		m22,peak at 0°	
z	SR0	SR1	SR0	SR1	SR0	SR1	SR0	SR1
[m]	kN/m	kN/m	kN/m	kN/m	kNm/m	kNm/m	kNm/m	kNm/m
5	483	535	4042	4443	8	8	43	45
55	-137	-133	3802	4189	-8	-10	3	4
85	-138	-139	3666	4056	-10	-10	-20	-20
95	346	348	3619	4015	-4	-2	14	15
105	363	372	3584	3975	-3	0	25	25
115	-117	-101	3546	3924	-13	-10	-21	-21
155	-110	-101	3434	3766	-13	-6	-2	0
185	-171	-156	3385	3712	-22	-16	-35	-30
195	845	778	3370	3700	-12	-10	12	9
205	893	833	3365	3685	-9	-6	39	37
215	-124	-104	3352	3651	-26	-22	-39	-36
255	104	111	3357	3595	-23	-20	-5	-3
285	-257	-253	3419	3620	-35	-33	-49	-47
295	1587	1581	3442	3626	-22	-22	8	3
305	1675	1683	3442	3610	-14	-13	55	57
315	-183	-169	3408	3564	-39	-38	-58	-59
355	125	135	3287	3390	-29	-28	-6	-6
385	-356	-384	3221	3274	-37	-39	-47	-49
395	2056	2161	3196	3228	-25	-27	-4	-3
405	2147	2272	3103	3119	-13	-13	59	64
415	-286	-297	2958	2964	-37	-40	-60	-64
455	-147	-150	2393	2358	-22	-24	-4	-5
485	-570	-596	2091	2028	-26	-28	-32	-33
495	1754	1865	2020	1946	-19	-21	-9	-11
505	1842	1968	1896	1815	-7	-7	50	55
515	-484	-499	1747	1665	-26	-28	-44	-47
555	-169	-167	1295	1204	-15	-16	-2	-3
585	-586	-608	1113	1003	-17	-18	-20	-20
595	1646	1718	1078	961	-15	-16	-14	-16
605	1739	1825	993	876	-3	-3	40	43
615	-502	-510	885	776	-19	-20	-33	-35
655	-165	-166	581	496	-13	-14	-2	-2
685	-617	-634	483	401	-18	-18	-21	-21
695	1792	1839	475	390	-16	-16	-15	-16
705	1947	2007	415	338	-4	-4	45	47
715	-536	-542	331	268	-22	-22	-37	-38
755	-163	-164	-263	-321	-15	-15	-3	-3

785	-638	-650	-236	-284	-19	-19	-22	-22
795	1877	1912	-194	-239	-17	-17	-16	-17
805	2041	2085	-221	-261	-4	-4	47	49
815	-552	-558	-290	-322	-23	-23	-39	-40
855	-163	-166	-431	-436	-16	-16	-3	-3
885	-622	-639	-346	-344	-19	-19	-21	-21
895	1801	1846	-283	-280	-16	-17	-16	-17
905	1966	2014	-282	-279	-4	-4	46	48
915	-534	-550	-314	-313	-21	-22	-38	-39
955	-160	-170	-311	-316	-13	-13	-3	-3
985	-355	-393	-134	-137	-17	-17	-21	-22
995	1094	1099	-45	-47	-8	-8	21	22

Table A.15 Load modification induced by the rings: effect on the quasi-static response (mean values):
SR0 = load modification due to the rings not included;
SR1 = load modification due to 10 rings included

	n11,m at 0°		n22,m at 0°		m11,m at 0°		m22,m at 0°	
z	SR0	SR1	SR0	SR1	SR0	SR1	SR0	SR1
[m]	kN/m	kN/m	kN/m	kN/m	kNm/m	kNm/m	kNm/m	kNm/m
5	326	347	2695	2863	5	5	25	26
55	-34	-30	2603	2782	-1	-1	1	1
85	-34	-29	2551	2737	-5	-5	-11	-11
95	221	233	2533	2720	-1	-1	8	9
105	232	245	2520	2709	0	0	14	15
115	-21	-15	2506	2696	-6	-6	-11	-12
155	-15	-9	2465	2658	-6	-6	-1	0
185	-52	-45	2451	2644	-11	-11	-19	-19
195	517	523	2446	2637	-6	-6	6	6
205	548	553	2447	2637	-4	-4	23	23
215	-20	-12	2445	2631	-14	-14	-22	-22
255	19	26	2462	2630	-13	-12	-2	-2
285	-106	-100	2505	2652	-20	-20	-29	-29
295	1019	1029	2519	2657	-13	-13	4	3
305	1078	1090	2519	2649	-8	-8	35	36
315	-55	-48	2499	2621	-23	-23	-36	-36
355	52	57	2419	2504	-18	-18	-4	-4
385	-189	-193	2367	2419	-24	-24	-31	-31
395	1408	1440	2347	2387	-17	-17	-2	-3
405	1472	1509	2278	2308	-8	-8	40	42
415	-141	-144	2173	2196	-25	-26	-40	-41
455	-76	-76	1752	1747	-15	-16	-3	-3

485	-388	-392	1524	1497	-18	-18	-22	-22
495	1258	1289	1471	1435	-14	-14	-7	-8
505	1324	1361	1376	1334	-5	-5	36	38
515	-326	-326	1259	1215	-19	-19	-32	-33
555	-101	-97	897	837	-11	-11	-2	-2
585	-415	-415	758	680	-12	-13	-14	-14
595	1222	1231	735	651	-11	-11	-11	-12
605	1292	1306	667	580	-2	-2	30	31
615	-353	-349	574	489	-14	-14	-25	-25
655	-104	-101	312	232	-10	-10	-2	-2
685	-450	-447	250	169	-13	-13	-15	-15
695	1354	1346	254	173	-12	-12	-11	-12
705	1472	1468	204	128	-3	-3	34	35
715	-387	-382	127	58	-16	-16	-28	-28
755	-104	-103	-73	-114	-11	-11	-2	-2
785	-470	-466	-85	-112	-14	-14	-16	-16
795	1427	1413	-62	-87	-13	-13	-12	-13
805	1553	1541	-94	-113	-3	-3	36	36
815	-404	-397	-156	-166	-17	-17	-30	-29
855	-106	-104	-281	-272	-11	-11	-2	-2
885	-455	-457	-234	-222	-14	-14	-15	-15
895	1365	1360	-193	-182	-12	-12	-12	-12
905	1490	1484	-197	-186	-3	-3	35	35
915	-389	-393	-220	-211	-16	-16	-28	-28
955	-102	-107	-211	-210	-9	-9	-2	-2
985	-247	-272	-88	-89	-12	-12	-16	-16
995	817	798	-30	-30	-6	-6	16	16

Table A.16 Load modification induced by the rings: effect on the quasi-static response (rms values):
SR0 = load modification due to the rings not included;
SR1 = load modification due to 10 rings included

	n11,σ at 0°		n22,σ at 0°		m11,σ at 0°		m22,σ at 0°	
z	SR0	SR1	SR0	SR1	SR0	SR1	SR0	SR1
[m]	kN/m	kN/m	kN/m	kN/m	kNm/m	kNm/m	kNm/m	kNm/m
5	45	54	385	451	0.90	0.98	4.97	5.48
55	29	30	342	402	2.03	2.46	0.55	0.71
85	30	31	318	377	1.62	1.40	2.64	2.52
95	36	33	310	370	0.71	0.25	1.57	1.81
105	38	36	304	362	0.64	0.00	2.96	2.88
115	28	25	297	351	1.95	1.11	2.85	2.52
155	27	26	277	316	2.16	0.00	0.53	0.00

185	34	32	267	305	3.00	1.24	4.47	3.15
195	94	73	264	304	1.70	1.12	1.53	0.76
205	99	80	262	299	1.28	0.64	4.53	4.01
215	30	26	259	291	3.45	2.31	4.96	3.91
255	24	24	256	275	3.06	2.10	0.77	0.22
285	43	44	261	277	4.10	3.70	5.55	5.22
295	162	158	264	277	2.51	2.55	1.21	0.00
305	171	169	264	275	1.67	1.50	5.81	6.13
315	37	34	260	269	4.36	4.16	6.44	6.41
355	21	22	248	253	3.11	2.87	0.71	0.58
385	48	55	244	244	3.71	4.10	4.66	5.14
395	185	206	243	241	2.42	2.84	0.57	0.00
405	193	218	236	232	1.28	1.44	5.38	6.34
415	41	44	224	220	3.56	4.14	5.65	6.46
455	20	21	183	175	2.00	2.44	0.36	0.44
485	52	58	162	152	2.23	2.63	2.69	3.06
495	142	165	157	146	1.60	1.93	0.69	0.96
505	148	174	149	137	0.63	0.72	4.00	4.79
515	45	49	139	129	2.21	2.58	3.65	4.26
555	19	20	114	105	1.32	1.55	0.22	0.26
585	49	55	101	92	1.39	1.60	1.57	1.75
595	121	139	98	89	1.10	1.31	0.99	1.31
605	128	148	93	85	0.31	0.34	2.93	3.50
615	43	46	89	82	1.46	1.72	2.49	2.90
655	17	19	77	76	1.11	1.33	0.19	0.24
685	48	53	67	66	1.31	1.53	1.52	1.70
695	125	141	63	62	1.10	1.28	1.00	1.23
705	136	154	60	60	0.34	0.36	3.10	3.58
715	42	46	58	60	1.60	1.76	2.64	2.98
755	17	17	54	59	1.27	1.31	0.24	0.23
785	48	53	43	49	1.41	1.52	1.56	1.70
795	129	143	38	44	1.16	1.30	1.07	1.27
805	139	155	36	42	0.35	0.37	3.22	3.62
815	42	46	38	44	1.64	1.80	2.71	3.02
855	16	17	43	47	1.27	1.35	0.24	0.25
885	48	52	32	35	1.38	1.51	1.50	1.66
895	125	139	26	28	1.16	1.28	1.16	1.25
905	136	152	25	27	0.31	0.34	3.21	3.55
915	41	45	27	29	1.53	1.70	2.65	2.94
955	17	18	28	30	1.09	1.14	0.22	0.22
985	31	35	13	14	1.28	1.41	1.60	1.77
995	79	86	5	5	0.58	0.63	1.59	1.77

The number of decimals after the comma is just a matter of visualization. The values are calculated with higher precision in order to avoid significant truncation errors.

Curriculum Vitae

Personal information

First name / Surname	**Francesca Lupi**
Nationality	Italian
Date of birth	21/04/1984
Place of birth	Prato, Italy
Gender	Female
Mother tongue	Italian
Other languages	English, German

Occupational field **Civil Engineering**

Affiliation	DICEA - Department of Civil and Environmental Engineering University of Florence Via di S. Marta 3 50139, Florence Italy
E-mail	francesca.lupi@dicea.unifi.it

Education

Dates	2010 - April 2013
Title of qualification awarded	Dottore di Ricerca / Dr.-Ing. (grade: outstanding) International Research Doctorate on "Mitigation of risk due to natural hazards on structures and infrastructures"
Name of organisation	Università degli Studi di Firenze / Technical University Carolo-Wilhelmina Braunschweig
Dates	February 2010
Title of qualification awarded	Registered Professional Engineer (Civil and Environmental Engineering Sector, Section A)
Name of organisation	Ordine degli Ingegneri della Provincia di Prato, Italy
Dates	2007 - 2009
Title of qualification awarded	Master degree in Civil Engineering, major in Structural Engineering (110/110 cum laude) Thesis: "Structural behaviour, optimization and design of a solar chimney prototype under wind loading and other actions".
Name of organisation	Università degli Studi di Firenze, Florence, Italy

Dates	February - May 2009
	Erasmus placement
Name of organisation	Niemann&Partner Ingenieurgesellschaft, Bochum, Germany
Dates	2003 - 2007
Title of qualification awarded	Bachelor degree in Civil Engineering (110/110 cum laude)
	Thesis: "Progetto di parcheggio interrato in Piazza Mercatale a Prato" ("Desing of an underground parking in Piazza Mercatale, Prato")
Name of organisation	Università degli Studi di Firenze, Florence, Italy
Dates	1998 - 2003
Title of qualification awarded	Scientific High School Diploma (100/100)
Name and type of organisation	Liceo Scientifico "Conservatorio San Niccolò", Prato, Italy

Prizes and Awards

Date	September 2011
	"Outstanding young engineer contribution award" for the paper presented at IABSE-IASS 2011 symposium in London: "Non-conventional wind loading on ultra-high Towers in Solar Updraft Power Plants".

Università degli Studi di Genova

Scuola Politecnica

DICCA - Dipartimento di **I**ngegneria **C**ivile, Chimica e **A**mbientale

Dottorato di Ricerca in Ingegneria Strutturale e Geotecnica

XXV Ciclo

Tesi per il conseguimento del titolo di Dottore di Ricerca

Michela Marrè Brunenghi

Probabilistic Tools for the Qualitative Analysis of Wind Actions on Structures

Relatore:

Prof. Luigi Carassale – Università degli Studi di Genova

Revisori:

Prof. Guido Buresti – Università degli Studi di Pisa
Prof. Giovanni Solari – Università degli Studi di Genova

Università degli Studi di Genova

Scuola Politecnica

DICCA - Dipartimento di Ingegneria Civile, Chimica e Ambientale

Scuola di Dottorato in Scienze e Tecnologie per l'Ingegneria

Corso di Dottorato di Ricerca in Ingegneria Strutturale e Geotecnica

Ciclo XXV

Coordinatore del Dottorato:

Prof. Roberta Massabò – Università degli Studi di Genova

Prof. Sergio Lagomarsino (fino al 2012) – Università degli Studi di Genova

Commissione esaminatrice:

Prof. Mario Di Paola – Università degli Studi di Palermo

Prof. Luigi Gambarotta – Università degli Studi di Genova

Prof. Anna Saetta – Università degli Studi di Venezia

Esame finale:

09 Aprile 2014

To my family

PREFACE AND ACKNOWLEDGMENT

CONTENTS

INTRODUCTION

The large extent of civil and mechanical engineering structures are not usually designed to meet aerodynamic objectives and are classified as bluff bodies (e.g. high-rise buildings, bridges, heat-exchanger tubes). The flow pattern around a bluff-body is usually characterized by complex phenomena such as flow separation, vortex shedding and shear layer instability. When the Reynolds number is high enough, such phenomena can be revised as random processes and probabilistic tools are required for the analysis.

The prediction of the aerodynamic behaviour of bluff bodies on the basis of their shape is very difficult; experimentations – or numerical analyses – are practically unavoidable either when the intention is to gather a qualitative description of the phenomenon or to estimate quantitative indicators. Within experimental bluff-body aerodynamics, a common activity is the measurement of pressure fields acting on models by high-frequency multi-channel scanners. The intention of these experimentations is often twofold: 1) global and local wind actions are quantified for design purpose in terms of force and pressure coefficients; 2) the pressure field is analyzed to elaborate a qualitative interpretation of the phenomenon, enabling the engineer to predict the possible occurrence of behaviour that are not reproduced in the experimentation and to assess the plausibility of the experimental results. When the incoming flow is turbulent the problem becomes "so intractable", as defined in Holmes et al. (1997), therefore experimental tests and sophisticated statistical techniques have to be used jointly in order to identify simplified objects in a confused random datasets. In this sense, the belief in 1970 that some coherent structures (CS) exist, motivated scientist over the last 40 years to isolate (mathematically) these well-correlated portions of the pressure field with the hope of understanding some aspects of turbulence.

The activity research described in the present manuscript hinges on several wind tunnel tests carried out in the wind tunnel of the University of Genova. The experimental work enabled the application of different statistical techniques (traditional and innovative) to identify elementary pressure patterns (in this context defined as CS) whose characteristics reflect the aerodynamic behaviour of the tested models. The object of the experimentation are square section cylinders and prisms with sharp edge corners and rounded corners with different corner radii. These objects are geometrically very simple, but are relevant for civil and mechanical engineering. In fact structural elements similar to square cylinders may be present everywhere, for example high-rise buildings or single parts of long-span bridges and the wind action may be relevant for design purpose. To determinate the fluctuating

loads, local and global, that vary randomly in space and time, is fundamental to identify the flow pattern which develop around the bluff body for interpretation purpose.

The concept of coherent structure is rather artificial and does not necessarily reflect any feature of the physical world. However, the idea of extracting from a given turbulent flow (or associated pressure field) a family of deterministic shapes able to characterize qualitatively the phenomenon is not only conceptually appealing, but is also a natural choice. To be convinced about this latter sentence it is sufficient to observe a video animation of simulated flow or a measured pressure field. The observer will realize that her/his attention is naturally attracted by the shape of well-correlated regions of the field, which are distinctly detected by her/his eyes/brain. The time evolution of these shapes and patterns is a further ingredient that plays a role in the understanding of the visualization. As an example, **Figure 0.1** shows six snapshots of a typical (recurrent) pressure pattern in which the effect of the generation and advection of a vortex is well recognizable (upper side of the figure in gray). Due to the free-stream turbulence and the high Reynolds number, this pattern is all but deterministic, however, even a non-experienced eye can easily detect its occurrence within the pressure-field visualization.

As a matter of fact, it appears that eyes are much smarter than math in recognizing and tracking correlated features and that the development of mathematical tools for the extraction of coherent structures is a very complicated task. These tools have usually statistical nature and are based on modal expansions; their development and validation represents the core of the present work and will be fully described in the next sections.
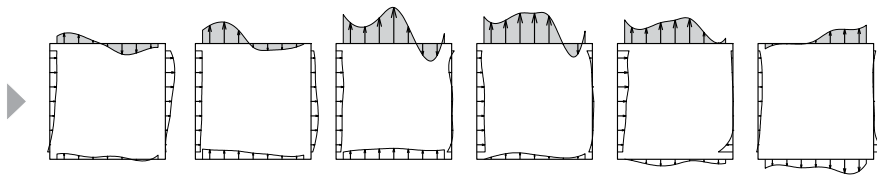
Figure 0.1   Time history of the pressure field (time step 10 ms), Carassale and Marrè Brunenghi (2011).

The concept of CS is intimately related to the technique traditionally employed for their estimation, the Proper Orthogonal Decomposition (POD, Lumley, 1970), which, in the discrete-space context, is often referred to as Principal Component Analysis (PCA). This modal expansion, probably the oldest and most used procedure in random multi-variate analysis, is a linear combination of deterministic vectors, the PCA modes, modulated by uncorrelated coefficients, depending on time, called Principal Components (PCs). A strong limitation involved in the use of PCA

as a pattern identification tool derives from the orthogonality of its modes that, from a physical point of view, is not justifiable (e.g. Holmes et al., 1997; Kareem and Cheng, 1999; Baker, 2000). Accordingly, Gilliam et al. (2004) observed that the ''orthogonal'' nature of POD modes is not supported by the mathematical theory of fluid flows. Besides, also the concept of linear combination may be questionable since the evolution of turbulent flows is driven by Navier–Stokes equations which are inherently nonlinear. On the other hand, from a probabilistic point of view, the PCs are statistically independent only if the original data are normally distributed. Since wind pressures often exhibit strong non-Gaussian properties, POD may be unsuited to separate the effects of physically-independent phenomena underlining the original data (He et al. 2007).

With the purpose of obtaining a representation formula analogous to PCA, but based on a non-orthogonal set of modes, the concept of Independent Component Analysis (ICA) has been introduced in the description of pressure fields acting on bluff bodies. This technique has a relatively recent formulation, but has been largely employed in several fields for the solution of the so-called blind source separation (BSS) or for feature extraction purpose. In the latter context, ICA has been implemented within image recognition tools (Bell and Sejnowski, 1997), biomedical signal processing (Jung et al., 1998), time-series forecast algorithms (Roth and Baram, 1996) and damage detection (Zang et al., 2004).

ICA is formulated assuming that the measured data derive from a generative model in which unknown sources, said Independent Components (ICs) are instantaneously mixed by an unknown mixing matrix. Both ICs and mixing matrix can be estimated from the data exploiting the condition that the ICs are mutually statistically independent. This kind of hypothesis is obviously correct for the BSS problem in which the existence of independent (though unknown) sources is postulated, while for the feature-recognition problem there is generally no physical reason to assume that independent sources exist.

Both the aforementioned techniques represent the measurements as a sum of deterministic modes, constant in time, which are therefore referred to as static. It is clear that the use of static modes is a strong limitation when the intent of the analysis is to identify coherent structures in a propagating phenomenon. In this thesis the convolutive versions of the PCA and ICA, dynamic-PCA (D-PCA) and dynamic-ICA (D-ICA) are applied to extract coherent structures evolving with time and containing information on both the spatial and temporal statistical structures of the pressure field.

MOTIVATIONS AND SCOPE

Based on the remarks in the previous section, the main aims of this thesis can be summarized as follows:

1. to present a general review of the state-of-art regarding bluff-bodies aerodynamics focusing on the square section cylinder and how multi-variate data analysis is used for interpreting experimental results;

2. to provide innovative statistical techniques oriented to the study of the wind effects on bluff bodies comparing their application with traditional statistical tools;

3. to provide mathematical models to describe the fluctuating loads on bluff-shaped structures in turbulent flow;

4. to classify systematically these data-processing techniques on the basis of their ability to describe the spatial and/or the temporal probabilistic structure of the pressure field;

5. to obtain low-dimensional models based on non-orthogonal modes able to represent typical or recurrent configurations of the pressure field providing qualitative interpretation of the phenomenon;

6. to define what a coherent structure is (or should be) - independently of the tools used for its identification – and apply the above mentioned techniques to several different case study;

7. to investigate non-stationary random processes using time-frequency analysis.

HOW TO READ THE MANUSCRIPT

The research work presented in this thesis is the result of a twofold activity:

1. wind-tunnel static tests on square cross-section cylinders and prisms;

2. post-processing analyses of the collected datasets through various statistical techniques reported in **Table 0.1**.

The backbone of the present manuscript follows the methodological perspective offered by such table. Each analyzed dataset is composed by simultaneous time histories coming from pressure taps located on the body surface. The spatial and temporal correlation structure of the samples is key ingredient of the discussion, together with their probability distribution.

In **Table 0.1**, the statistical techniques are classified on the basis of their ability to describe this spatial and/or temporal probabilistic structure of the dataset. In this sense four classes have been identified: statistical analysis of the pressure in single

points at single times (SPST), in single points at multiple times (SPMT), in multiple points at single time (MPST) and in multiple points at multiple times (MPMT). An orthogonal classification opposes techniques that rely on statistical information up to the second order to techniques that exploit the non-Gaussian nature of the measurements as a key element to describe the phenomenon. Each cell includes examples for each class of techniques and the chapter in which they are described. Multi-Spectra and Spectral Kurtosis (SK) are in the table but they have not been applied.

<table>
<tr><td rowspan="2"></td><td rowspan="2"></td><td colspan="2">Probabilistic order</td></tr>
<tr><td>2nd-order</td><td>High-order</td></tr>
<tr><td rowspan="8">Space/time correlation structure</td><td>SPST</td><td>Mean,
Standard Deviation (SD),
probability density function (pdf)
(Chapter 2)</td><td>Skewness,
Coefficient of excess (COE)
(Chapter 2)</td></tr>
<tr><td>SPMT</td><td>Power Spectral Density (PSD),
Wavelet Transform (WT)
(Chapter 2)</td><td>Multi-spectra,
Spectral Kurtosis (SK)</td></tr>
<tr><td>MPST</td><td>Principal Component Analysis (PCA)
(Chapter 3)</td><td>Independent Component Analysis (ICA)
(Chapter 4)</td></tr>
<tr><td>MPMT</td><td>Dynamic-PCA (D-PCA)
(Chapter 5)</td><td>Dynamic-ICA (D-ICA)
(Chapter 5)</td></tr>
</table>

Table 0.1 Systematic classification of the data-processing techniques employed to analyze datasets from pressure fields (adapted from Carassale and Marrè Brunenghi 2011). Each cell includes examples of the pertinent tools and the chapter in which they are presented.

The sections presenting the statistical techniques are from Chapter 2 to Chapter 5. Each of them contains few examples of application of the relative techniques to a selected case study. The selected dataset used to demonstrate the statistical quantities or methods comes from the experimental tests on a rigid prism with geometrical section shown in **Figure 0.2**. The pressure field has been measured along the mid-span cross section of the prism of length l=50 cm and side length b=7.5 cm. The corners are rounded with r/b=1/15. The Reynolds number was equal to 7.83×10^4 and the incoming flow was characterized by homogeneous turbulence with intensity equal to 5%. The angle of incidence of the flow was α=7°. In **Figure 0.3** the position of the pressure taps on the cross section are indicated and enumerated.

Figure 0.2   Experimental setup of the selected case study.

The main results obtained analyzing all the datasets, concerning different kind of cylinders and different flow condition are reported in Chapters 6 and Chapter 7.
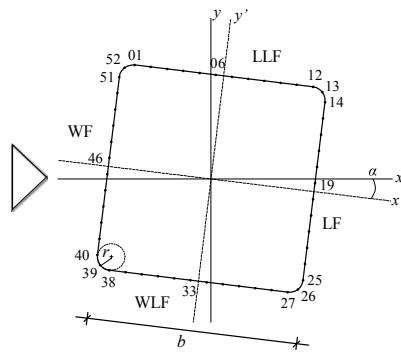
Figure 0.3   Cross section of the cylinders used as selected case study. Location and number of the pressure taps.

In this manuscript, vectors are denoted by bolded lowercase letters and matrices are bolded uppercase. Random variables and their realizations are not typographically different, but the index *t* always denotes realizations.

LAYOUT OF THE THESIS

Each paragraph of this section briefly describes the contents of each chapter.

Chapter 1 presents a general review on the state of knowledge concerning square cross-section cylinders from an aerodynamic point of view. The two main topics of the manuscript, (i.e. the aerodynamic behaviour of square cross-section cylinders and the concept of coherent structures) are presented. Some background on bluff-body aerodynamics is given, focusing on square cross-section prisms with sharp

edge and rounded corners. The actual knowledge on the flow behaviour around these models is presented; to this purpose, some results obtained through the research activity of the author are employed and are here anticipated. One section is dedicated to the review of the experimental activity on such models. For the sake of clarity some basics on aerodynamics are reported at the beginning.

In Chapter 2 statistical techniques defined SPST and SPMT are presented. The first class considers the measurements as a wide set of random variables deprived of their spatial and the temporal probabilistic structures. Cumulants and the probability density function are classical SPST tools. SPMT techniques such as Power Spectral Density (PSD) function and Wavelet Transform (WT) enable the exploration of the temporal structure of the data. Both these approaches are employed to provide a qualitative, and locally quantitative, description of the phenomena observed in the wind tunnel.

Chapter 3 presents the most popular modal expansion employed in bluff bodies aerodynamics: the Principal Component Analysis (PCA, Jolliffe, 2002) or covariance proper transformation (CPT, Carassale et al., 2001), also known as Proper Orthogonal Decomposition (POD, Lumley, 1970). PCA is a MPST tool, thus it takes into account of the spatial probabilistic structure of the pressure field ignoring its temporal characteristics. PCA is a 2nd-order tool because it is based on the properties of the covariance matrix of the data: given a set of multivariate measurements, the purpose is to find the best representation of the data finding a new orthogonal basis reducing the redundancy, which is quantified by correlations between data elements. This representation possesses the maximum possible velocity of convergence in the mean square sense and for this reason is often used to synthesize reduced order models from experimental or numerical datasets. In this chapter the analytical formulation of PCA is presented with the state-of-the-art on its use focusing on bluff body aerodynamics and fluid dynamic contexts. Furthermore it is discussed the effect of a possibly non-homogeneous spatial discretization of the domain.

Chapter 4 presents another MPST tool: the Independent Component Analysis (ICA). This technique has a relatively recent formulation but has been largely employed in several fields to solve blind source separation (BSS) problem (Antoni, 2005). This technique has been introduced to overcome some trouble involved in the PCA representation, due to the orthogonality of its modes. ICA expresses observed random data as a linear transform of components that are statistically independent from each other, instead of simply non-correlated as Principal Components. Such decomposition is well identifiable if the Independent Components are non-Gaussian (except for only one). Several methods have been formulated to estimate ICs (Hivärinen et al., 2001); this chapter employs a formulation based on the

maximization of the non-Gaussianity, which is measured by the information-theory quantity called neg-entropy.

Chapter 5 introduces the concept of Dynamic Coherent Structures presenting the Dynamic-PCA and Dynamic-ICA following the formulations proposed in Carassale (2012). Such techniques are classified as MPMT and are the natural evolution of PCA and ICA in order to catch the spatial and temporal probabilistic structure of the pressure field. The application presented in this chapter is borrowed from Carassale (2012) in order to show the potentiality of such techniques; other applications carried out by the author can be found in Chapter 6.

Chapter 6 presents the applications of the techniques, innovative (e.g. ICA and D-ICA) as well as conventional, to a simple but relevant case study involving a square-base prismatic body immersed in an artificial boundary layer. The model has aspect ratio 1:5 and different angles of incidence have been tested. All the experimental tests have been carried out at the University of Genova. The discussion of the results enables the definition of general criteria that can guide the selection of the most appropriate data-analysis technique for the study of a large class of aerodynamics-related problems.

Chapter 7 shows the application of the statistical techniques above described to a relevant case study involving a square-base cylinders immersed in homogeneous flow. The setup involves different models: beside the sharp-edge corner condition considered as benchmark, two different rounded-corner radii (r/b=1/15 and 2/15) are studied. Global forces and surface pressure are simultaneously measured in the Reynolds number range between 1.7×10^4 and 2.3×10^5. The measurements are extended to angles of incidence between 0 and 45°.

The conclusions summarize the most important results achieved and delineate the perspective for future research directions.

Appendix A collects the papers published by the Author; the present manuscript is partially based on these works.

"Finally, we must keep in mind the basic problem: to find suitable models for the forces on bluff bodies."

A. Roshko, 1993.

CHAPTER 1

SQUARE PRISMS AND COHERENT STRUCTURES

Ando Hiroshige, Rough Sea at Naruto in Awa Province.
Woodblock print,1858.

1.1 INTRODUCTION

Turbulence is the last great unsolved problem of classical physics[1] (Holmes et al.
1996). When the flow passes near a bluff body the problem becomes if possible
much more unpredictable. Very complex phenomena are usually induced in the
neighbourhood of the model surface, e.g. flow separation, vortex shedding, wake
instability. If the Reynolds number is high, the problem is necessarily approached as
a stochastic one, and a possible objective is the extraction/identification of well-
correlated portions of the flow field. These geometric features are commonly
referred to as coherent structures (CSs) and are employed as qualitative descriptors

---

[1] The sentence, or more generally the concept, have been variously attributed to
Sommerfeld, Einstein, Feyman and Lamb.

of the flow field. Various statistical techniques are applied in order to separate such coherent structures from a confused dataset. The classical choice is the modal expansion offered by the Principal Component Analysis (PCA). Its application may produce the extraction of highly energetic features, even if it has been demonstrated that, in general, PCA fails when the goal is a feature selection, i.e. finding modes that resemble the observed physical phenomena fading noise and redundancy. In this case the modes can be identified as coherent structures. Other techniques works better, e.g. Independent Component Analysis (ICA), which provides a reduced order model together with meaningful CSs.

In the present chapter, the two main topics of the manuscript are presented, i.e. the aerodynamic behaviour of square cross-section cylinders and the concept of coherent structures. Some background on bluff-body aerodynamics are given, focusing on square cross-section prisms with sharp edge and rounded corners. The actual knowledge on the flow behaviour around these models is presented; to do this some results reached through the research activity of the author are employed. One section is dedicated to the review of the experimental activity on such models. For the sake of clarity some basics on aerodynamics are reported at the beginning.

1.2 BASICS ON BLUFF-BODY AERODYNAMICS

In order to describe the flow behaviour around a bluff body, in particular a square cross-section cylinders, it is essential to define elementary basic aerodynamic quantities and parameters. The contents of this section are well known in the aerodynamic context and are reported here for completeness purpose. A wide dissertation on this topic can be found in Buresti (2012).

Any object immersed in a turbulent[2] air stream undergoes loads produced by normal and tangential stresses generated over its surface. The resultant fluid dynamic forces are strongly connected with the features of the flow produced by the relative motion between body and fluid and are in general represented as the sum of a steady part and a fluctuating components; this time-varying part is due to the complex random phenomena that may develop in the neighbourhood of the body, e.g. flow separation, vortex shedding and shear layer instability.

In particular, the aerodynamic force along the undisturbed flow direction is the result of two contributions: the friction drag and the pressure drag. The former is due to the friction between the body and the flow; this action is relevant for attached flow and is related to the surface area exposed to the flow. The pressure drag is

---

[2] In general turbulent flows occur when the inertial forces in the flow are dominant, i.e. with high values of Reynolds number, Eq. (1.6).

associated to the formation of the wake; this action is important for separated flow and is related to the cross-sectional area exposed to the flow. When the total drag is dominated by the friction drag the body is defined aerodynamic (or streamlined); otherwise if the drag is dominated by pressure drag the body is defined bluff. This thesis examines only bluff bodies, therefore the term drag will indicate the pressure drag.

The flow pattern around a bluff body is not definable a priori, neither quantitatively nor qualitatively. Experimentally it may be investigated by anemometric measurements in one or multiple discrete locations, as well as by optical measurements providing the velocity field in the neighbourhood of the body. More commonly, aerodynamic pressure acting on the body is directly measured through multi-channel pressure scanners able to acquire the pressure in several locations of the body surface with a practically simultaneous sampling and a relatively high speed. The results obtained from a pressure scanner may be collected in a vector $\mathbf{q}(t)=[q_1(t),...,q_N(t)]$ containing the values of pressure measured by the N pressure taps for each discretized time instant t. In the context of probability theory $\mathbf{q}(t)$ is identified as an N-variate, discrete-time random process[3].

The local pressure $q(t)$, measured in a single point on the body surface, is in general expressed by the non-dimensionalized pressure coefficient c_p defined as

$$c_p(t) = \frac{q(t)-q_0}{q_d} \tag{1.1}$$

where q_0 is the static wind tunnel pressure and $q_d=0.5\rho U^2$ is the dynamic, or kinetic, pressure of the flow being ρ the fluid density and U the free-stream mean velocity. The steady pressure coefficient is defined as $C_p=\mathrm{E}[c_p]$[4].

The spatial integration of the pressures in the alongwind direction provides the drag force f_D. Such action, or its mean value $D=\mathrm{E}[f_D]$, is the result of two pressure contributions: the pressure acting in the forebody, i.e. the portion of the body with attached boundary layer, and the pressure acting in the afterbody, or base region, i.e. the part of the body affected by the separated wake. The former contribution is characterized by overpressure while the latter is essentially dominated by suction. For this reason the drag coefficient is directly influenced by the wake width: if the

---

[3] Random or stochastic processes are defined as random functions of time; they are the generalization of the concept of random variables.

[4] $\mathrm{E}[\cdot]$ is the statistical expectation estimated by the temporal average on all the available samples. This operation is possible because experimental time histories are supposed to represent a stationary and ergodic random process, see Chapter 2 about single-point - single-time techniques.

wake narrows the resultant of the pressure in the afterbody decreases and, consequently, the total drag decreases.

In the aerodynamic context the non-dimensionalized drag is usually employed. It is called drag coefficient C_D and it is defined as

$$C_D = \frac{D}{q_d bl} \qquad (1.2)$$

where b is the cross-section size and l is the spanwise length of the model.

As aforementioned, bluff bodies leave behind themselves an highly-energetic wake characterized by the presence of a double row of alternate concentrated vortices known as Karman vortex street. Such phenomenon produces a continuous asymmetrical flow pattern around the body during the shed of each vortex. The resulting cross-flow fluctuating force is called lift force f_L and represents the spatial integration of the pressures in the crosswind direction. Its mean value $L=\mathrm{E}[f_L]$ is zero for symmetric configurations.

In analogy with the drag coefficient, the lift coefficient is defined as follows

$$C_L = \frac{L}{q_d bl} \qquad (1.3)$$

The harmonic contents[5] of the lift coefficient is concentrated on the frequency of vortex shedding n_s, which is expressed conventionally by the dimensionless Strouhal number defined as

$$St = \frac{n_s b}{U} \qquad (1.4)$$

The drag coefficient generally has a peak in the frequency spectrum near $2n_s$ because conveys the vortex shedding on both sides of the model.

The third effect caused on a bluff body by the flow, is the fluctuating moment f_M. Through its mean value $M=\mathrm{E}[f_M]$ it is possible to introduce the moment coefficient as

$$C_M = \frac{M}{q_d b^2 l} \qquad (1.5)$$

Summarizing, the aerodynamic loads depend on the flow pattern around the body and this is strictly related to the vortex shedding mechanism. Such mechanism depends on different parameters (i.e. the St is not a constant for each body) which

---

[5] For the spectral analysis see Chapter 2 about single-point - multiple-time techniques.

are: the body itself (in terms of surface roughness, cross section, afterbody shape and orientation with respect to the mean flow) and on the flow condition (i.e. the value of the Reynolds number, Re, intensity of turbulence, I_u, and integral length scale, L_u).

Re is a non-dimensional number representing the ratio of inertial to viscous forces and it is defined as

$$Re = \frac{\rho U b}{\mu} = \frac{U b}{\nu} \qquad (1.6)$$

where μ and ν are, respectively, the dynamic and the kinematic viscosity of the fluid. Aerodynamic forces induced on civil structures by the wind are characterized by Reynolds number of the order between 10^6 and 10^8; classical wind tunnel tests are executed in the range between 10^4 and 10^5.

The intensity of turbulence is defined as

$$I_u = \frac{\sigma_u}{U} \qquad (1.7)$$

where σ_u is the Standard Deviation (SD) of the along-wind velocity, identified by the subscript u.

The integral scale of turbulence L_u is a parameter to be estimated from the spectral analysis of the alongwind velocity and provides information about the mean dimension of the vortexes that produce the turbulence. Quantities analogous to I_u and L_u can be also defined for the lateral and vertical components of the wind velocity fluctuation v and w, respectively.

1.3 FLOW PATTERNS AROUND SQUARE CYLINDERS

The aerodynamic parameters described in the previous section may be more or less influential regarding the flow behaviour around bluff bodies. For instance, bluff bodies characterized by rounded corners, without fixed separation points, may be deeply affected by the Reynolds number. When the bodies have sharp-edge corners, the separation points are fixed and the angle of flow incidence α and the extent of the afterbody play the major role. The turbulence in the incident flow may affects the vortex shedding mechanism in different ways, depending on the body shape and

cross-section, because produces fluctuations in the stagnation[6] and separation regions modifying the evolution of the wake structures.

The flow pattern around a two-dimensional circular cylinder, in smooth flow condition, are usually distinguished into three regimes depending on *Re*: subcritical, supercritical and postcritical (Lienhard, 1966, Basu, 1985). Passing from subcritical to supercritical regime, increasing the Reynolds number, the separation point moves downstream and the flow reattaches on the body giving rise to a separation-reattachment bubble; the wake width narrows and the drag coefficient drops consequently reaching his minimum value. The Reynolds number for which the flow reattaches is called critical Reynolds, Re_{cr} and is about 3×10^5. Adding turbulence in the incoming flow the value of critical Reynolds is reduced; in particular low intensity of turbulence are sufficient to disorganise the coherence of the vortexes, while high level of turbulence increases the entrainment and the fluctuation near the model surface. In particular large scale of turbulence are less efficient in anticipating drag crisis than small scale (Surry, 1969).
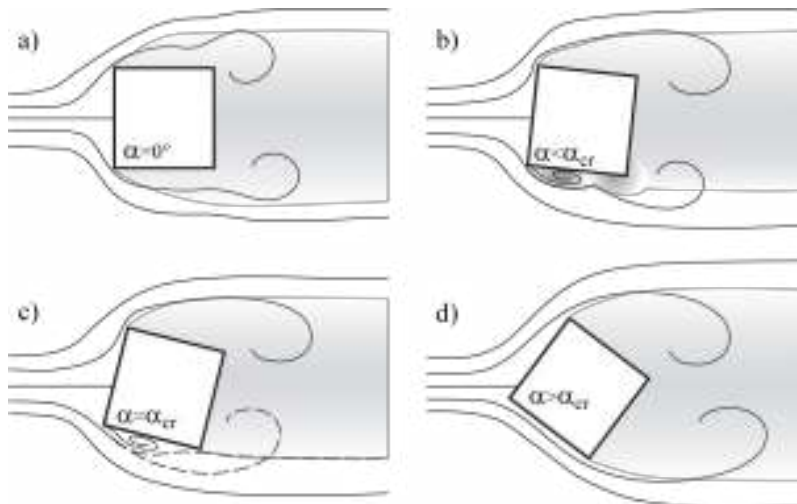
Figure 1.1 Flow pattern around square section cylinder according with the classification proposed in Huang et al. (2010): perfect separation type with symmetric flow (a), subcritical regime with a dual-ring bubble (b), reattachment-separation flow type, critical regime (c), wedge flow type, supercritical regime(c). $Re=2 \times 10^4$.

---

[6] In fluid dynamics, a stagnation point of a flow field is a point where the local velocity of the fluid is zero; consequently, due to Bernoulli equation, the static pressure in such point reaches its maximum value.

Similarly to circular cylinder, a critical condition takes place for square cylinder when the angle of attack α is equal to its critical value α_{cr}. **Figure 1.1** shows a typical flow behaviour changing with the angle of incidence and follow the instantaneous smoke flow patterns around a square cylinder reported in Huang et al. (2010). **Figure 1.1** (a) shows a symmetric configuration with $\alpha=0$ and the stagnation point is located at about the centre of the windward face (WF). The boundary layer is completely separated from both the lateral faces, the separated shear layer rolls up and reverse flow reattaches on the rear face. Increasing slightly the angle, **Figure 1.1** (b) the region of vortex formation moves closer the trailing edge and a little asymmetry appears; the stagnation point moves towards the lower part of the WF. In Huang et al. (2010) it is underlined the presence of two sub-regions near the windward lateral face (WLF) with accumulated smoke (dual-ring bubble). This is probably due to the reverse flow in the wake that interferes with the separated shear layer near the leading edge; the regime is defined subcritical. For $\alpha=\alpha_{cr}$, **Figure 1.1** (c), the reverse flow is obstructed by the trailing edge; as a consequence of the flow, that separates near the leading edge, reattaches on the windward lateral face giving rise to a single recirculation bubble. At the critical angle two concurrent flow regimes appear (subcritical and supercritical) with smooth and frequent transitions; this intermittent behaviour may be classified as irregular vortex shedding (Carassale et al. 2014) and in the figure is represented by the dashed line. Increasing the angle, **Figure 1.1** (d), the separation bubble slowly disappears shrinking towards the windward corner, the flow is completely attached on the lateral face and separates near the trailing edge. For $\alpha=45°$ the flow pattern is symmetric again.

The main effects on the aerodynamic coefficients due to transcritical regime, i.e. surrounding the critical angle, are: (1) a drastic reduction of the drag coefficient till its minimum, (2) the inversion of the lift coefficient slope, (3) the sharply increase of the Strouhal number. The patterns illustrated in **Figure 1.1** are Reynolds number independent, as already premised, but may be affected by high level of turbulence or by motion of the cylinder (Scruton, 1981); in such conditions the flow reattaches on the leeward lateral face (LLF) giving rise to a recirculation bubble until separates at the downstream corner.

The halfway point between the circular and the square cylinder is represented by the square prism with rounded corners. This cross-section shape is extremely interesting from an engineering (and architectural) point of view because it is the simplest strategy to reduce the drag force on square cross-section elements. Simultaneously, small corner modification entails a great sensibility to many parameters as the Reynolds number, the angle of attack, and the incident intensity of turbulence. In particular for these kind of sections both the critical angle α_{cr} and the critical Reynolds number Re_{cr} can be identified. Rounded corners promote the flow reattachment on the windward lateral face and the critical angle is smaller than for

sharp-edge corners; increasing *r/b* the drag decreases and the critical angle becomes smaller (Carassale et al., 2014). Rounded corners also produce the reattachment of the flow on both lateral face in supercritical regime $Re>Re_{cr}$ for $\alpha=0$ giving rise to two recirculation bubbles, exactly as it happen for the case elongated rectangles. The turbulence plays a fundamental role because anticipates the transition to supercritical regimes in terms of both angle of incidence and Reynolds number.
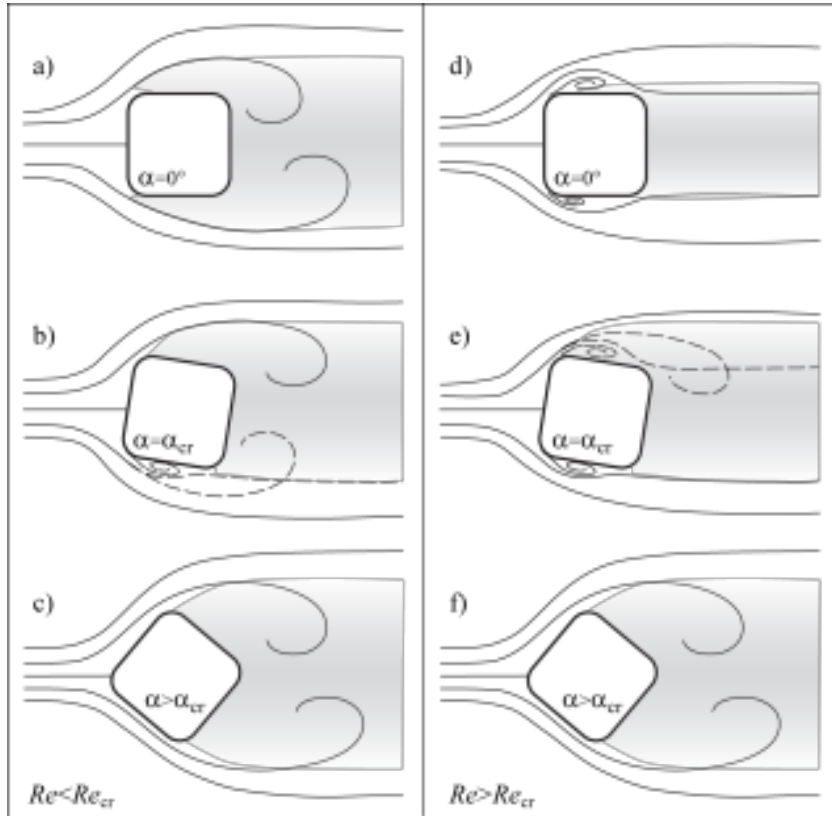
Figure 1.2 Typical flow behaviour around square section cylinder with rounded corners in subcritical condition (a, b and c) and supercritical condition (d, e and f) for different angles of incidence.

   Figure 1.2 clarifies such behaviour: the first column shows the flow patterns around a square cross-section cylinder with rounded corners for $Re<Re_{cr}$. The sketch is similar to **Figure 1.1** except for the value of α_{cr} which is smaller than for sharp-edge corners. In the neighbourhood of α_{cr} two concurrent flow regimes (subcritical and supercritical) appear but in this case they alternately remain stable for a relatively long time (Carassale et al., 2014). The right column shows an opposite behaviour: in supercritical conditions and for small angle of incidence the flow

separates near the leading edges and reattaches on the lateral sides of the cylinder, consequently the wake narrows. Rotating the prism up to the critical angle, the flow starts to be completely separated and a further rotation provides the same configuration in **Figure 1.1** (c). For square-section cylinders with rounded corners it is not clear if the dual-ring bubble appears near the critical angle, as found for the sharp-edge corner case; no observation about this behaviour have been found by the author.

1.4 EXPERIMENTAL ACTIVITIES ON SQUARE SECTION CYLINDERS AND PRISMS

"The best method for measuring air resistance is to put a model in an artificial stream of air, i.e. the method of the wind tunnel". This sentence appears in the first chapter of Theodor von Karman book "Aerodynamics" published in 1954. Till that time the focus of the aerodynamic research was essentially aeronautic, i.e. to find the most favourable wing shape with the highest lift-drag ratio. The discovery of vortex street phenomenon, jointly with its formulation and stability analysis, occurred many years before, in 1911, by von Karman observing a circular cylinder in a water channel. Such section continued to be the favourite one for many years, up to the increasing interest by engineers, when the bluff body aerodynamics became essential for structural design purpose. Square and rectangular cross-sections became more and more popular thanks to their frequent engineering applications, to the geometric simplicity and to their simplicity of fabrication for experimental tests (it is probably the simplest model to be mounted and instrumented by pressure taps in a wind tunnel).

   Two principal kind of experimentations about square prisms may be identify in literature: (1) two-dimensional tests involving cylinders mounted between end-plates (sectional models), usually immersed in homogeneous smooth or turbulent flow, (2) three-dimensional tests concerning prisms one side delimited (by just one end-plate or by wind tunnel floor) affected by homogeneous flow or an artificial boundary layer. Many papers focus on the influence of the angle of incidence, many others on the intensity and scale turbulence effects, a few are centred on the modification of the corner shape.

   Most of the literature is concern with the aerodynamic characteristics of square cylinders evaluating pressure distribution, drag and lift coefficients, vortex shedding frequency through high frequency pressure scanners and load cells. Recently flow visualization techniques are largely employed to analyze the global flow behaviour, e.g. laser doppler velocimetry (LDV) or particle image velocimetry (PIV). Relatively few investigations dealing with the flow structure very close to the

surface body can be found because of the difficulties of measurements in that region, e.g. smoke and surface-oil flow visualization.

One of the first and relevant paper concerning square-section cylinder was published by Vickery (1966). He studied the influence of turbulence on the aerodynamic coefficients and on the Strouhal number of a long square cylinder confined by end-plates. He used strain-gauge dynamometers and pressure taps. In the paper five different angles of attack are considered, between 0 and 40°, and have been observed that the effect of turbulence is mostly marked at low angles of incidence. In particular, the change in base pressure is attributed to the intermittent re-attachment of the separated flow. This intermittence is presented as an hypothesis and the whole graphs show an interpolation between experimental points; changing the angle of incidence, the behaviour of the aerodynamic parameters is presented as continuous.

Lee (1975) and Kareem and Cermak (1984) are two complementary and fundamental works on this argument. Both deal with turbulence effect; the former uses two-dimensional cylinder in homogeneous flow (also changing the angle of attack) while the latter uses three-dimensional prism in boundary layer for 0° angle of attack. They analyze the measurements coming from chordwise and spanwise direction and observe that increasing turbulence the spatial correlation decreases, the shear layer reattaches intermittently on the lateral face and the vortex formation region move downstraem. Furthermore, Lee's paper focus on the result for the angle of attack α_{cr}=12.5°: he notices that, in smooth flow, for such angle the drag coefficient has a minimum, the lift coefficient changes its slope and the Strouhal number has a maximum. This is due to the reattachment of the flow and the turbulent condition moves this behaviour to α=8°. Both papers decompose the nonperiodic pressure field in orthonormal eigenfunctions[7]. The first eigenvalue represents the most of the total energy associated to the vortex shedding; the incident turbulence involves a significant redistribution over a wider frequency range. Kareem and Cermak thanks to a spectral analysis locate the reattachment region where a redistribution of energy to a wider bandwidth than the vortex-shedding peak is visible and where the SD reaches its minimum.

Obasaju (1983) carried out an experimental similar to Lee (1975) founding the reattachment of the shear layer at the angle of attack α_{cr}=13.5°; for this value of incidence the Strouhal number reaches its maximum. He uses the sharpness factor, i.e. the peak frequency divided by the bandwidth of the half-power points, to indicate the degree of organisation of the vortex shedding process: he finds that for $\alpha=\alpha_{cr}$ very low value of such factor occurs suggesting that the flow switches

---

[7] For thorough details see Chapter 3 about Principal Component Analysis (PCA).

between different states because of the flow reattachment; together, the base pressure reaches its minimum value.

Igarashi (1984) formalizes these findings. He classifies the flow pattern around a square prism into three regimes: perfect separation type ($\alpha=[0°;13°]$), reattachment flow type ($\alpha=[14°;35°]$) and wedge flow type ($\alpha=[36°;45°]$). These results are obtained through wind tunnel visualization techniques by smoke (using incense stick embedded in the prism near the front stagnation point). He clearly photographs the separation bubble that appears passing the critical angle, when the flow starts to reattach on windward lateral face. Using pressure taps, the paper identifies the position of the flow reattachment and the flow separation respectively as the location of the maximum and the minimum pressure coefficient.

Nakamura and Ohya (1984, 1989) and Nakamura and Ozono (1987) explore the effect of turbulence on the mean pressure surface prisms with different rectangular cross-sections, both in two and three-dimensional conditions. They found that large-scale turbulence increases the base pressure of a two-dimensional flat plate, while it reduces that of a three-dimensional square plate vortex shedding from square prism.

Luo et al. (1994) analyze the afterbody shape effect viewing this as a changes in the angle of attack. They study a square, two trapezoids and one triangle; it is worth to notice that plotting, for each models, St (scaled by its maximum value) with respect to the angle of incidence (scaled by the angle when flow reattachment begins), the four curves coincide for $\alpha \geq \alpha_{cr}$. They also observe that, implementing a stability analysis, using Den Hartog's (1956) criterion, the definition of stability to galloping cannot be defined in terms of cross-sectional shape, but also including the angle of incidence.

Naudascher et al. (1981) and Kwok (1988) change the section shape of a square cylinder, in two-dimensional configuration, in order to mitigate galloping instability for all possible flow direction.

Tamura and Miyagi (1999) investigate the corner modification effect on the aerodynamic forces. They compare sharp-edge, chamfered and rounded corners, in smooth and turbulent flow, observing that wind loading can be reduced controlling the separated flow. Chamfered and rounded corner decrease drag force, in particular the square cylinder with rounded corners in turbulent flow promote the reattachment of the shear layer also for $\alpha=0$. They found that α_{cr} is equal to 12°.

Huang et al. (2010) investigates the velocity field around a square prism in two-dimensional condition providing a topological analysis. Different experimental techniques are employed: pressure scanners, smoke-wire flow visualization and surface-oil flow visualization. The incidence angle is changed between 0 and 45° and the three categories of flow pattern, i.e. subcritical, subcritical and wedge flow, according with Igarashi (1984) are fully described. After alpha critic $\alpha_{cr}=15°$ clearly

appears a recirculation bubble: the Strouhal number attains a maximum while the drag coefficient a minimum due to the minimum of the wake width.

1.5 COHERENT STRUCTURES AND LOW-DIMENSIONAL MODELS

The term coherent structure has been introduced for the first time in fluid-dynamics context for indicating a physical phenomena that emerge recurrently in flowing fluids (e.g. Holmes et al., 1996). A typical example of coherent structure is a vortex that sheds from a bluff-body surface; such mechanism is not just a transient phenomenon and is present in the flow for a relatively long time. In a turbulent flow, say two dimensional for simplicity, there are many structures that will look like vortices but only for a very short period of time. They will have a rotational velocity and will look about circular, but if they do not last more than a (few) dynamical time(s), then they are transient, non-coherent and are defined just as eddies. **Figure 1.3** shows an example of coherent structures generated by the Karman vortex shedding from an island and visualized by a fortunate combination of clouds and sun illumination.
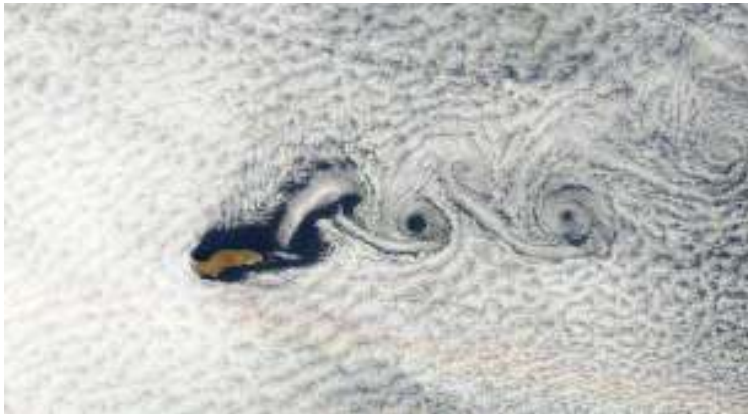
Figure 1.3   An example of coherent structures: Von Karman vortexes due to an island (NASA website).

When the incoming flow is turbulent the problem becomes "so intractable", as defined in Holmes et al. (1997), that experimental tests and sophisticated statistical techniques have to be used jointly in order to identify simplified objects in a confused random datasets. In this sense, the certainty that some coherent structures (CS) exists, motivated scientist over the last 40 years to isolate (mathematically) these well-correlated portions of the flow field with the hope of understanding some aspects of turbulence. Presently, the concept of coherent structures is employed as

qualitative descriptor of the flow velocity field characterized by highly-correlated regions, both in space and time. The relevance of these dominant flow phenomena is clarified by the sentence: "*...such persistent macroscopic structure amidst the small-scale activity and fluctuations provides a backbone for many turbulent flows, and hence that analysis of the dynamics of these structures may provide a basis for improved understanding of some aspects of turbulence*", (Holmes et al., 1997).

Analogously, in this context, the pressure signatures of the vortexes that develop in the neighbourhood of a body are defined as coherent structures (CSs). Such well-correlated portions of the pressure field emerge recurrently and possibly propagate due to advection effects. These mechanisms are usually well recognizable observing an animated video reconstruction of the measured pressure (e.g. **Figure 0.1**).

The concept of CS is intimately related to the technique traditionally employed for their estimation, the Proper Orthogonal Decomposition (POD, Lumley, 1970), which, in the discrete-space context, is often referred to as Principal Component Analysis (PCA). This modal expansion, probably the oldest and most used procedure in random multi-variate analysis, is a linear combination of deterministic vectors, the PCA modes, modulated by uncorrelated coefficients, depending on time, called Principal Components (PCs).

The intent of this kind of approach is to identify reduced order models (ROM). In machine learning and statistic, dimensionality reduction, or dimension reduction, is the process of reducing the number of random variables under consideration and can be classified into two strategies. Adopting the terminology usually employed in pattern recognition and in image processing, these strategies are:

1. feature extraction: to transform the data in the high-dimensional space to a space of fewer dimensions cancelling noise. A filter is an example of feature extraction;

2. feature selection: to compact wide dataset preserving the dominant or most significant mechanisms hidden in clouded or unclear data deleting redundancy.

PCA provides the best approximation – in the mean square sense, or in terms of energy - of the original dataset, but may fail as feature-selection operation and serious concerns on the meaningfulness of its modes have been risen (e.g. Holmes et al., 1997; Kareem and Cheng, 1999; Baker, 2000). A strong limitation involved in the use of PCA as a pattern identification tool derives from the orthogonality of its modes that, from a physical point of view, is not justifiable.

Figure 1.4 shows a six consecutive snapshots extracted from the pressure field on the lateral face of a square prism immersed in a boundary layer on the floor of the wind tunnel. The highly-correlated suction zone emerges at the windward corner close to the top of the model. Then, it evolves shifting downstream giving rise to a

pattern leaning in the flow direction. This sequence of snapshots is very recurrent in the data set and can be easily recognized observing a video animation of the measurements. The sequence, however, is not deterministic and shows itself different at every vortex-shedding cycle. This randomness, which is essentially due to the free-stream turbulence, as well as the high Reynolds number (about 10^5), also implies that the vortex-shedding period is not perfectly constant (i.e. the time between the generation of two subsequent vortices is random), therefore deterministic tools such as the phase averaging fail in extracting typical samples of the pressure patterns shown in the figure. As a matter of fact (Carassale 2012) also PCA demonstrated to be inadequate to identify these pressure patterns, in spite of the significant power associated to them, which is testified by high rate of recurrence, as well as the high levels of pressure locally measured at their occurrence.
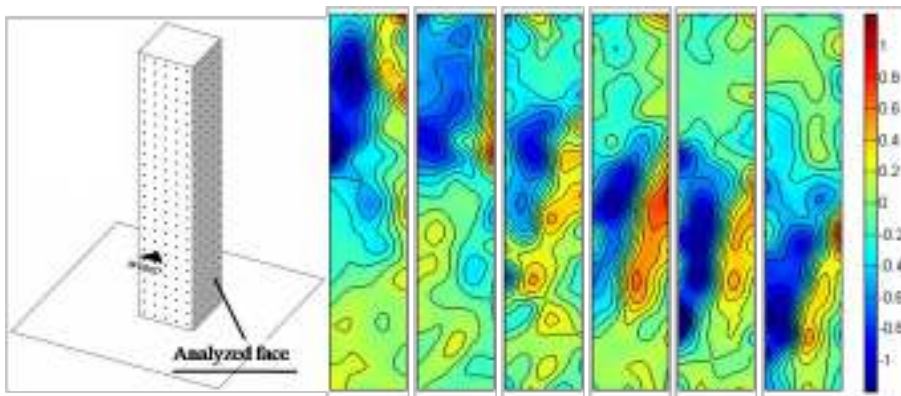
Figure 1.4   Recurrent sequence observed in the pressure field fluctuation interpreted as effects of Karman vortex shedding (down wash on the windward face), Carassale (2012).

With the purpose of obtaining a representation formula analogous to PCA but based on a non-orthogonal set of modes, the concept of Independent Component Analysis (ICA) has been introduced in the description of pressure fields acting on bluff bodies. This idea, borrowed from the so-called blind source separation (BSS) problem has been often adopted for feature extraction purpose, but its application in aerodynamics and wind engineering is at the very beginning.

Both PCA and ICA represent the measurements as a sum of deterministic modes, which are constant in time. It is clear that the use of static modes is a strong limitation when the intent of the analysis is to identify coherent structures in a propagating phenomenon like the example of **Figure 1.4** in which a vortex (and therefore its pressure signature on the body) is advected by the mean flow and shifts through the observation domain. In this thesis the convolutive version of the PCA

and ICA are proposed and are referred to as dynamic-PCA (D-PCA) and dynamic-ICA (D-ICA) to underline their (theoretical) ability to extract coherent structures evolving with time, containing information on both the spatial and temporal statistical structures of the pressure field.

Since CSs are determined on the basis of the mathematical principle used for their extraction, rather than on some mathematical property related to the flow governing equation, it is natural to ask whether or not the CSs posses any physical meaning or if there is any chance to related them to any physical process. To address this problem, the concept of meaningful CS has been proposed (Carassale and Marrè Brunenghi, 2012) introducing some necessary requirements. A meaningful CS must fulfil the following properties:

1. if two parts of the pressure field have distinct statistical characteristics (e.g. in terms of probability and power spectral distribution), then different CSs should represent the two parts of the pressure field separately;

2. the amplitude fluctuation of a CS should reproduce the local statistical properties of the pressure field in the zone where this CS has significant amplitude;

3. the CSs should represent typical or recurrent configurations of the pressure field;

4. CSs should be invariant with respect to the spatial discretization adopted to measure the pressure field.

In particular the present thesis investigates if the coherent structures, or modes, extracted by the statistical techniques above briefly described, are consistent with the picture we have about specific observed phenomena. It is the reason why all the application refers to very simple geometrical shapes such as square cylinders and prisms.

1.6 CONCLUDING REMARKS

Turbulent flow around bluff-bodies are characterized by very complex phenomena and experimental activities jointly with statistical tools are required. This chapter presents few basic knowledge about bluff-body aerodynamics and describes the phenomenological behaviour of the flow around square-section cylinder with rounded corners. These particular objects are very sensitive to Reynolds number and to the angle of flow incidence; for these two parameters may exist two different kind of critical regime, in general characterized by non-stationary behaviour and time-frequency analyses should be applied (see section 7 for some applications). For a qualitative interpretation of the observed mechanisms, probabilistic methods based

on modal representation may be useful in order to extract well-correlated portions of the flow field. These geometric features are commonly referred to as coherent structures (CSs) and may be used as feature-recognition tools. The concept of CS is intimately related to the technique traditionally employed for their estimation, the Proper Orthogonal Decomposition (POD, Lumley, 1970), which, in the discrete-space context, is often referred to as Principal Component Analysis (PCA). PCA has some limits because uses a second-order criteria neglecting extra-information contained in higher-order statistics. Based on this remark, other techniques will be presented and applied in the present manuscript.

CHAPTER 2

STATISTICAL ANALYSES AT SINGLE POINTS
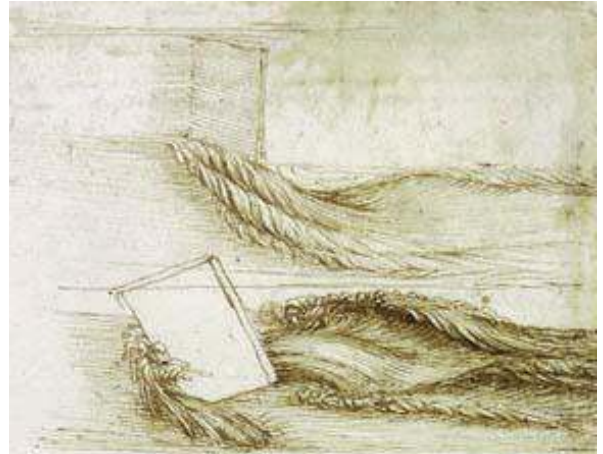
Leonardo Da Vinci, Study on water passing obstacle.
Pen and ink on paper, 1508.

2.1 INTRODUCTION

This chapter presents the statistical techniques defined as Single Point (SP). The spatial probabilistic structure of the process is neglected. Single Point - Single Time (SPST) techniques ignores also the temporal probabilistic structure. On the other hand, Single Point - Multiple Time (SPMT) methods exploit the information coming from the temporal dimension and the measurements are actually considered as time histories.

Thanks to their hierarchical character, cumulants are natural candidates as statistical quantities to be employed by SPST techniques. Cumulants of a probability distribution are a set of quantities that provide an alternative to the moments of the distribution. In practice, the 2nd-order cumulant is substituted by its square root (the

standard deviation, SD), and higher-order cumulants are non-dimensionalized by the SD obtaining, at the 3rd-order, the skewness and, at 4th-order, the flatness coefficient or coefficient of excess (COE). Together with the separation point, the reattachment point of the flow (when occurs) is the responsible of the aerodynamic response of a bluff body; unfortunately its position is totally unpredictable. These zones are characterized by high turbulent activity and analysis of the statistical moments may help in their location, e.g. Igarashi (1984).

Typical quantities considered in SPMT analyses are covariance functions and power spectral density (PSD) functions. The representation and interpretation of these functions for all the measurement points (possibly a few hundreds in wind tunnel tests or several thousands in numerical simulations) is usually unpractical; for this reason, they are usually studied in a very limited subset of locations or, whenever is relevant, synthetic quantities like peak amplitude or peak frequency of the PSD are mapped on the whole body surface (Kitagawa et al., 2002). High-order spectra may be used to represent the higher-order (non-Gaussian) characteristics of the temporal probabilistic structure of measured pressure fields; however, their complexity (they are multi-dimensional functions of frequency) may discourage their application as interpretative tools. More synthetic quantities as the spectral kurtosis (SK, Dwyer, 1984) have been successfully employed in several research fields to detect pure-tone components (Ottonello and Pagan, 1994) or identify intermittent behaviour (Antoni, 2006); however, to the authors' knowledge, no application has been proposed in bluff-body aerodynamics.

Pressure measurements characterized by intermittent behaviour, as well as frequency and/or amplitude modulations, are often analyzed by means of techniques able to detect and extract the transient components possibly present in the signals. Within this class of tools the wavelet transform (WT, e.g. Kijewski-Correa and Kareem, 2007) and the Hilbert–Huang transform (HHT, Huang et al., 1998) received numerous applications, also associated to ad-hoc filtering strategies (Buresti et al., 2004 and Olhede and Walden, 2004). Besides, the interpretative advantages deriving from the use of a data-driven (a-posteriori) basis to represent the measured signals have been investigated by several authors. Aysin et al. (2005) introduced the concept of orthonormal-basis partitioning consisting in projecting the measured signals onto local or global optimal functional bases obtained through the Karhunen–Loeve expansion. In bluff-body aerodynamics, a similar concept has been developed by Iungo and Lombardi (2011).

2.2 SINGLE POINT - SINGLE TIME ANALYSIS

The statistical analysis of a dataset in single point at single time (SPST) is the most basic statistical approach since the experimental measurements $q_j(t)$ ($j=1,...,N$, $t=1,...,N_t$) are interpreted as N_t outcomes of N random variables, which are analyzed independently from each other. In this context $q_j(t)$ includes N_t pressure measurements induced by the wind, recorded at each discrete time instant t by the jth pressure channel; N is the total number of the instrumented pressure taps. Both the spatial and the temporal probabilistic structure of the pressure field is neglected. Typical SPST tools are the cumulative distribution function (cdf), the probability density function (pdf) and the cumulants κ_k ($k=1,2,...$) or, in alternative, the statistical moments m_k and the statistical central moments μ_k. All these quantities are strictly connected and defined below; an exhaustive dissertation on the probability theory may be found in Papoulis (1991).

Initially, let q be a continuous-valued random variable, analogous to the above mentioned q_j neglecting the subscript for simplicity. The cumulative distribution function (cdf) F_q of q at the point $q=\xi$ is defined as the probability P that $q \leq \xi$, where ξ is a parameter in $\Re$:

$$F_q(\xi) = P(q \leq \xi) \tag{2.1}$$

The cumulative distribution function has the following properties:

1. it is a monotonically increasing function:

$$F_q(\xi_1) \leq F_q(\xi_2) \qquad \text{with} \quad \xi_1 \leq \xi_2 \tag{2.2}$$

2. it is a non-negative function:

$$F_q(\xi) \geq 0 \tag{2.3}$$

3. it is a bounded (above and below) function:

$$0 \leq F_q(\xi) \leq 1$$
$$F_q(-\infty) = 0 \tag{2.4}$$
$$F_q(+\infty) = 1$$

4. it is a continuous function (but not necessarily differentiable):

$$\lim_{\xi \to \bar{\xi}} F_q(\xi) = F_q(\bar{\xi}) \tag{2.5}$$

Formally, the probability density function (pdf) p_q is obtained as the derivative, wherever it exists, of the cdf:

$$p_q(\xi) = \frac{dF_q(\xi)}{d\xi} \qquad (2.6)$$

and represents the relative likelihood for the random variables to take values in the neighbourhood of the given value ξ. The probability density function has the following properties:

1. it is a non-negative function, as defined in Eq. (2.3);

2. it is a bounded (above and below) function and extinguishes for $\pm\infty$:

$$p_q(-\infty) = p_q(+\infty) = 0 \qquad (2.7)$$

3. its integral exists and has unitary value:

$$\int_{-\infty}^{+\infty} p_q(\xi) d\xi = 1 \qquad (2.8)$$

The expectation of q, denoted as E[q], is defined as

$$\mathrm{E}[q] = \int_{-\infty}^{\infty} \xi p_q(\xi) d\xi \qquad (2.9)$$

The kth statistical moment m_k of q is defined through the expectation, defined in Eq. (2.9), as follows

$$\mathrm{m}_k(q) = \mathrm{E}[q^k] = \int_{-\infty}^{\infty} \xi^k p_q(\xi) d\xi \qquad (k = 1, 2, ...) \qquad (2.10)$$

The first statistical moment of q, m_1, is the mean value of q and indicates the position of the pdf on the q-axis. The second moment m_2 is the average power of q usually denoted as φ^2. The kth statistical central moment of q, μ_k, is defined through the expectation as

$$\mu_k(q) = \mathrm{E}\left[(q - \mathrm{m}_1)^k\right] = \int_{-\infty}^{\infty} (\xi - \mathrm{m}_1)^k p_q(\xi) d\xi \qquad (k = 2, 3, ...) \qquad (2.11)$$

The first central moment is insignificant; the second central moment μ_2 is the variance of q, its root mean square, usually denoted as σ_q, is the standard deviation (SD) of q and indicates the variation, or dispersion, of the data from the mean value. Low SD indicates that the data points tend to be very close to m_1; high SD means that the data points are spread out over a wide range of values.

The normalized measure of dispersion is the coefficient of variation (CV) defined as

$$\mathrm{CV}(q) = \frac{\sigma_q}{\mathrm{m}_1} \qquad (2.12)$$

The absolute value of CV is the relative standard deviation RSD:

$$\text{RSD}(q) = |\text{CV}(q)| = \frac{\sigma_q}{|\text{m}_1|} \tag{2.13}$$

Higher-order moments, or their derived quantities, provide information about the shape of the pdf. The third and forth central moments, non-dimensionalized by the SD, are called, respectively, skewness and kurtosis:

$$\text{skewness}(q) = \frac{\text{E}\left[q^3\right]}{\sigma_q^3} \qquad \text{kurtosis}(q) = \frac{\text{E}\left[q^4\right]}{\sigma_q^4} \tag{2.14}$$

The former is a measure of the symmetry of the pdf (it is zero for probability density functions that are symmetric about their mean, as the Gaussian[8] pdf); the latter is a measure of "peakedness" and gives information about the tail weight.

In this thesis will be used an alternative version of the kurtosis, the coefficient of excess (COE), defined as

$$\text{COE}(q) = \frac{\text{E}\left[q^4\right]}{\sigma_q^4} - 3 \tag{2.15}$$

It is worth to notice that the COE is the simplest statistical quantity for indicating the non-Gaussianity rate of a random variable with symmetric distribution. The COE of any Gaussian random variable is zero. In statistical literature, distributions having a negative COE are called subgaussian, while if COE is positive they are called supergaussian. The coefficient of excess also may be defined as

$$\text{COE}(q) = \frac{\kappa_4}{\sigma_q^4} \tag{2.16}$$

where κ_4 corresponds to the fourth cumulant. The general definition of cumulants κ_k ($k=1,2,...$) needs the definition of the characteristic functions. The first characteristic function $\Phi_q(\theta)$ is defined as the continuous Fourier transform of the pdf $p_q(\xi)$:

$$\Phi_q(\theta) = \mathscr{F}\left\{p_q(\xi)\right\}(\theta) = \int_{-\infty}^{+\infty} p_q(\xi)e^{-i\theta\xi}d\xi = \text{E}\left[\exp(-i\theta\xi)\right] \tag{2.17}$$

---

[8] Gaussian probability density function for a generic random variable x has the form:

$$p_x(x) = \frac{1}{\sqrt{2\pi\sigma(x)^2}}\exp\left(-\frac{(x-\text{m}_1(x))^2}{2\,\sigma(x)^2}\right)$$

where $i=(-1)^{1/2}$ and θ is the transformed variable of ξ defined in $\mathfrak{R}$. The first characteristic function completely defines the probabilistic structure of q, which may be expanded into its McLaurin series:

$$\Phi_q(\theta) = \Phi_q(0) + \sum_{k=1}^{\infty} \frac{1}{k!} \frac{d^k \Phi_q}{d\theta^k}\bigg|_{\theta=0} \theta^k \tag{2.18}$$

From (2.17) it will be obtained

$$\Phi_q(0) = 1$$

$$\frac{d^k \Phi_q}{d\theta^k}\bigg|_{\theta=0} = i^k E\left[q^k\right] = i^k m_k\left[q\right] \tag{2.19}$$

and (2.18) becomes

$$\Phi_q(\theta) = 1 + \sum_{k=1}^{\infty} \frac{(i\theta)^k}{k!} \, m_k\left[q\right] \tag{2.20}$$

thus the first characteristic function, and consequently the pdf, may be expressed through the statistical moments; for this reason, $\Phi_q(\theta)$ is also called the moment generating function.

The second characteristic function $\Psi_q(\theta)$, or cumulants generating function, is given by the natural logarithm of the first characteristic function and may expressed, in analogy with Eq. (2.19), as follows:

$$\Psi_q(\theta) = \log\left(\Phi_q(\theta)\right) = \sum_{k=1}^{\infty} \frac{1}{k!} \frac{d^k \Psi_q}{d\theta^k}\bigg|_{\theta=0} \theta^k = \sum_{k=1}^{\infty} \frac{(i\theta)^k}{k!} \, \kappa_k\left[q\right] \tag{2.21}$$

Cumulats and statistical moments are connected through recursive functions based on Pascal's triangle with the form:

$$\kappa_k = m_k - \sum_{r=1}^{k-1} \binom{k-1}{r-1} \kappa_r m_{k-r} \tag{2.22}$$

The explicit expressions up to the forth order are listed below:

$$\begin{aligned}
\kappa_1 &= m_1 \\
\kappa_2 &= m_2 - m_1^2 = \mu_2 \\
\kappa_3 &= m_3 - 3m_2 m_1 + 2m_1^2 = \mu_3 \\
\kappa_4 &= m_4 - 3m_2^2 - 4m_3 m_1 + 12m_2 m_1^2 - 6m_1^4 = \mu_4 - 3\mu_2^2
\end{aligned} \tag{2.23}$$

Hence the first three cumulants are equal to the relative central moments and the fourth non-dimensionalized is the COE, as reported in Eq. (2.16). It is worth to underline that in order to obtain significant values of higher-order cumulants, it is necessary to have much more data available than for second-order statistics. For example, the former are very sensitive to outliers in the dataset and few samples with highest absolute value may significantly affect the COE estimation.

It could appear that dealing with statistical moments or cumulants is indifferent: both contain the same statistical information, because cumulants can be expressed in terms of sums of products of moments, as defined in Eq. (2.23). On the contrary, cumulants are able to present in a clearer way the additional information provided by higher-order[9] statistics, and have the following properties:

1. the first cumulant is shift-equivariant for any constant c:

$$\kappa_1(q+c) = \kappa_1(q) + c \tag{2.24}$$

2. all the cumulant higher than the first are are shift-invariant:

$$\kappa_k(q+c) = \kappa_k(q) \qquad (k = 2,3,...) \tag{2.25}$$

3. the kth cumulants is homogeneous of order k:

$$\kappa_k(cq) = c^k \kappa_k(q) \tag{2.26}$$

4. if q and v are two statistically independent random variables, the cumulant of their sum is equal to the sum of the single cumulants of q and v:

$$\kappa_k(q+v) = \kappa_k(q) + \kappa_k(v) \tag{2.27}$$

5. if the random variable q has Gaussian distribution, then all its cumulants of order higher than two are identically zero.

In wind engineering, especially in wind-loading codes and standards, the model representing the wind is assumed to have Gaussian pdf. The fluctuating loads (pressures and/or forces) on structures follows the variation of the longitudinal velocity stream, so the resulting wind actions are also Gaussian. This concept is only valid when the time scale of the velocity fluctuation in the incoming flow and in the wake are well separated enabling the adoption of a quasi-steady approach (e.g. Holmes, 2001) and for low levels turbulence intensity, which allows the linearization of the quadratic relationship between velocity and pressure. It is worth to notice that experimental research (concerning both wind tunnel tests and full-scale measurements) has shown the quasi-steady approach is, in general, unable to

---

[9] Higher than the second.

not predict the wind loads on structures (e.g. Holmes, 1981, Kawai, 1983) and that non-Gaussian features characterize the pressure field. In particular in the regions near the body surface characterized by high turbulent activity (i.e. base region, separation point, flow reattachment zone) the pressure field appears to be highly non-Gaussian. Kumar and Stathopoulos (1998) investigate the aerodynamic behaviour of a low-rise building roof by pressure scanners and suggest that a particular region can be considered non-Gaussian if the absolute values of skewness and kurtosis of the pressure fluctuations at various taps are greater than 0.5 and 3.5 respectively. Gioffrè et. al (2001) analyze a tall building model in wind tunnel boundary layer through statistical moments; the presented results show that non-Gaussianity appears rather evident in the separated flow regions where the flow is dominated by vortex shedding; in the wake regions non-Gaussian features appears with less emphasis.
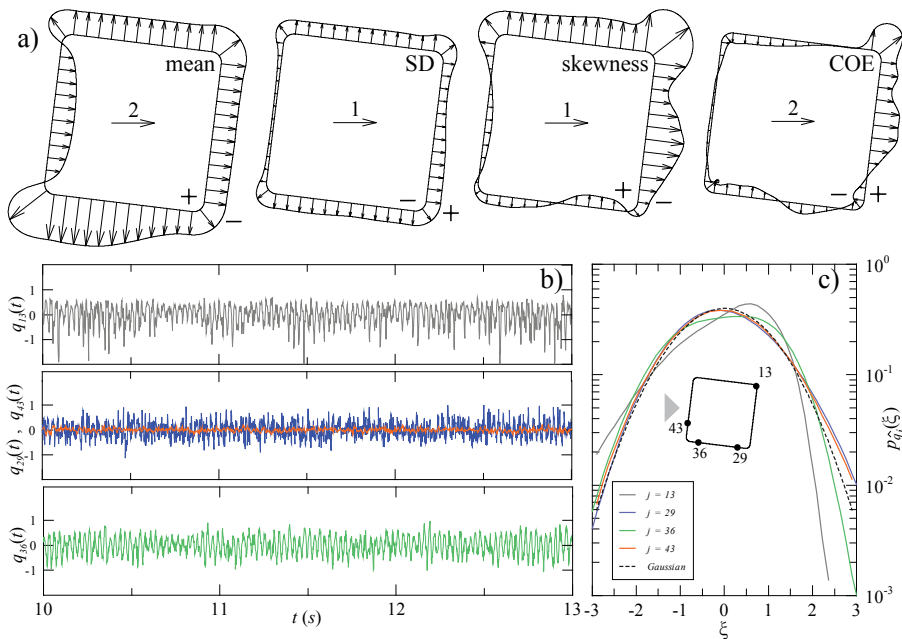
Figure 2.1 From left to right: mean, SD, skewness and COE (a) of the pressure field non-dimensionalized by kinetic pressure; zero mean time histories (b) and relative standardized probability density functions (c) of four pressure taps.

The higher-order statistical tools aforedescribed are simple but efficient tools to localize such non-Gaussian regions as they can be represented by means of contour plots or colour maps directly on the body surface. **Figure 2.1** shows an example of SPST application referred to a square prism immersed in a turbulent flow artificially

reproduced in the wind tunnel. For the details on the setup see the Introduction. **Figure 2.1** (a) shows, from left to right respectively, the mean, SD, skewness and COE of the recorded pressure signals; the overpressure is only on the windward face, lateral faces are dominated by similar values of suction. The windward face is characterized by high values of standard deviation but the statistics of the third and forth order are almost zero. In opposition to the case-study presented in Gioffrè et. al (2001), in the wake regions non-Gaussian features appears with more emphasis than in the separation flow regions.

Figure 2.1 (b) shows four time histories recorded during the wind tunnel test by two pressure taps; their location is visible in **Figure 2.1** (c). To allow the comparison, these quantities have been standardized. Sensor 43 is on the windward face near the stagnation point and reports an almost Gaussian distribution preserving the probabilistic structure of the incoming wind. According to the quadratic relationship between velocity and pressure that should hold at the stagnation point and assuming that the velocity fluctuation of the incoming flow is Gaussian distributed, the pressure should be distributed according to a non-centred Chi-square model. This corresponds to a positive value of the skewness that scales directly with the free-stream turbulence intensity. This scenario is substantially consistent with the results shown in **Figure 2.1** (a).

Sensor 13 is on the upper lateral face close to the trailing edge and is characterized by a very skewed and supergaussian behaviour due to the separation of the flow in such position. The skewness of sensor 13 is negative because the left tail is higher than the Gaussian curve, plotted as reference; this reflects the vortex shedding mechanism characterized by high level of suction that appear very quickly followed by a relatively slower pressure recovering. The COE is positive and indicates that positive and negative peaks of the pressure time histories tend to be more pronounced than the peaks of the Gaussian distribution; high-suction and high-overpressure events on the lateral faces appear and disappear quickly over a background of random fluctuations.

Sensor 29 and sensor 36 are both on the lower lateral face; the former is close to the trailing edge while the latter is close to leading edge. The behaviour of the flow near these two sensors is opposite. In the upstream region the skewness is negative and the COE is positive; in the downstream region the signs are inverted. In particular near sensor 29 the COE is almost zero and the probability density function (pdf) evaluated for such signal is very similar to the one evaluated for the sensor 43 (almost Gaussian) confirming the reattachment of the flow in that zone. Sensor 36 is located in the fully-separated region and its pdf is very far from the Gaussian bell.

The combined information obtained by the cumulants of order up to four enables the localization of some known phenomena discussed in Chapter 1. Namely:

1. the reattachment of the flow on the lower face of the prism is localized by the variation of the mean pressure and by the change of sign of both skewness and COE; on the contrary the SD is totally insensitive to the flow reattachment;

2. the fully-separated region on the upper face of the prism is characterized by highly-negative skewness, which, from a qualitative point of view, means that the pressure drops faster than it recovers;

3. the trailing-edge vortex at the end of the upper face is localized by high values of both skewness and COE.

It is worth to notice that the position of the reattachment or separated regions seems to be predictable, as first attempt, by the sign of the third cumulant. Further analyses by SPMT techniques, presented in the section that follows, clarify this sentence.

2.3 SINGLE POINT - MULTIPLE TIME ANALYSIS

The statistical analysis of a dataset in single point at multiple times (SPMT) focuses on the temporal probabilistic structure of the dataset neglecting the spatial correlation. To accomplish an exhaustive description of these tools, the concept of random process mono-variate is necessarily introduced.

A random, or stochastic, process may be reviewed - generalizing the classical definition of random variable – as a map leading any possible experimental result into a given functional space. In the present application, the members of such space are functions of time. For example is may be assumed that M sample functions $q_s(t)$ ($s=1,...,M$) of the process $q(t)$ are M registrations of the wind action through a single pressure tap. Let us assume that the recording time is the same for each experiment and the time instants t_1, t_2,..., on which the stochastic process is observed are discrete due to sampling; the total amount of samples is N_t for each recorded time history. For each time instant, for example $t=t_1$, is possible to define the random variable $q(t_1)$ and to obtain the relative pdf, $p_{q(t_1)}$ and the statistical moments as follows (in analogy with Eqs. (2.10) and (2.11)):

$$m_k(t_1) = E\left[q(t_1)^k\right] = \int_{-\infty}^{+\infty} \xi_1^k \, p_{q(t_1)}(\xi_1) d\xi_1 \qquad (k=1,2,...) \tag{2.28}$$

$$\mu_k(t_1) = E\left[\left(q(t_1) - m_1(t_1)\right)^k\right] = \int_{-\infty}^{+\infty} \left(\xi_1 - m_1(t_1)\right)^k p_q(\xi_1) d\xi_1 \quad (k=2,3,...) \tag{2.29}$$

m_k and μ_k are deterministic function in $\Re$ depending on time. These random variables are continuous values depending on the discretized time.

Let us consider now a pair of time instants, t_1 and t_2, giving rise to a pair of random variables, $q(t_1)$ and $q(t_2)$. The joint probability distribution function is defined as

$$F_{q(t_1)q(t_2)}(\xi,\eta) = P\big(q(t_1) \leq \xi \ \text{and} \ q(t_2) \leq \eta\big) \tag{2.30}$$

and the joint probability density function is defined as

$$p_{q(t_1)q(t_2)}(\xi,\eta) = \frac{\partial^2 F_{q(t_1)q(t_2)}(\xi,\eta)}{\partial\xi\partial\eta} \tag{2.31}$$

where ξ and η are parameters in $\Re$.

It is now possible to define second order statistics as the auto-correlation R_{qq} and the auto-covariance C_{qq} functions:

$$\begin{aligned} R_{qq}(t_1,t_2) &= \mathrm{E}\big[q(t_1)q(t_2)\big] = \\ &= \int_{-\infty}^{\infty}\int_{-\infty}^{+\infty} \xi_1\xi_2\, p_{q(t_1)q(t_2)}(\xi_1,\xi_2)d\xi_1 d\xi_2 \end{aligned} \tag{2.32}$$

$$\begin{aligned} C_{qq}(t_1,t_2) &= \mathrm{E}\Big[\big(q(t_1)-m_1(t_1)\big)\big(q(t_2)-m_1(t_2)\big)\Big] = \\ &= \int_{-\infty}^{\infty}\int_{-\infty}^{+\infty} \big(\xi_1-m_1(t_1)\big)\big(\xi_2-m_1(t_2)\big) p_{q(t_1)q(t_2)}(\xi_1,\xi_2)d\xi_1 d\xi_2 \end{aligned} \tag{2.33}$$

The auto-correlation R_{qq} and the auto-covariance C_{qq} are deterministic functions in $\Re^2$ and connected through the following relation

$$C_{qq}(t_1,t_2) = R_{qq}(t_1,t_2) - m_1(t_1)\,m_1(t_2) \tag{2.34}$$

If the process is zero-mean, the use of R_{qq} or C_{qq} is discretional; similarly for m_k and μ_k (except for $k=1$).

The normalized auto-covariance is defined by the ratio

$$\rho_{qq} = \frac{C_{qq}(t_1,t_2)}{\sigma_q(t_1)\sigma_q(t_2)} \tag{2.35}$$

In practice, these probability distributions must be estimation from data repeating a large number of experiments. It is clear that it results into a formidable job that cannot achieved unless some statistical assumption is made. The most popular assumption oriented to this purpose is the stationarity.

2.3.1 STATIONARY RANDOM PROCESSES

Formally a stochastic process is defined stationary (in the strict sense) if any of its statistical properties is invariant under any shift of the time origin; this means that the first-order pdf is time-invariant, while the second-order joint pdf depends only on the time lag $\tau = t_2 - t_1$ and not directly on the choice of the two instants.

A very important subclass of stationary random processes is called weak or wide-sense stationary (WSS) processes which are characterized by these properties: (1) the statistical means of the first order are time independent; (2) the statistical quantities of the second order are only time lag dependent ($\tau = t_2 - t_1$); (3) the variance of the process is finite. This leads to the definition of the statistical properties:

$$m_k = \mathrm{E}\left[q(t)^k\right] = \int_{-\infty}^{+\infty} \xi^k p_{q(t)}(\xi)d\xi \qquad (k = 1, 2, ...) \tag{2.36}$$

$$\mu_k = \mathrm{E}\left[\left(q(t) - m_1\right)^k\right] = \int_{-\infty}^{+\infty} \left(\xi - m_1\right)^k p_q(\xi)d\xi \quad (k = 2, 3, ...) \tag{2.37}$$

$$R_{qq}(\tau) = \mathrm{E}\left[q(t)q(t+\tau)\right] \tag{2.38}$$

$$C_{qq}(\tau) = \mathrm{E}\left[\left(q(t) - m_1\right)\left(q(t+\tau) - m_1\right)\right] \tag{2.39}$$

$$\rho_{qq}(\tau) = \frac{C_{qq}(\tau)}{\sigma_q^2} \tag{2.40}$$

From their definition it follows easily that R_{qq}, C_{qq} and ρ_{qq} are symmetric functions and assume positive values in the origin:

$$
\begin{aligned}
R_{qq}(0) &= \varphi_q^2 \\
C_{qq}(0) &= \sigma_q^2 \\
\rho_{qq}(0) &= 1
\end{aligned}
\tag{2.41}
$$

C_{qq} and ρ_{qq} are bounded (above and below) functions:

$$
\begin{aligned}
\left|C_{qq}(\tau)\right| &\leq \sigma_q^2 \\
\left|\rho_{qq}(\tau)\right| &\leq 1
\end{aligned}
\tag{2.42}
$$

Figure 2.2 shows, as an example, the normalized autocovariance function of the pressure field measured by taps 43 and 13. The peak in $\tau = 0$ is unitary due to

normalization. The other peaks identify time delays on which the pressure values are well correlated. These time delays correspond to integer multiples of the vortex shedding period. It can be observed that on the lateral face of the prism the normalized autocovariance retains values that are much higher that on the windward face. From a random-process view point this means that the pressure on the lateral face has longer memory than on the windward face, i.e. its present value is statistically conditioned by its past history. From a technical point of view it means that the pressure on the lateral face may be approximated to some extent by a deterministic model, which would reflect into a unitary value of the secondary peaks of the normalized autocovariance.
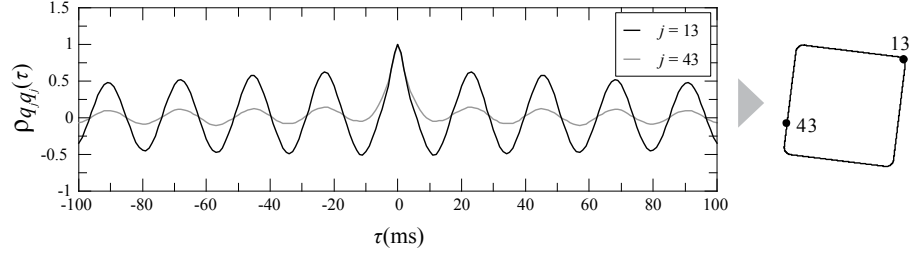
Figure 2.2   Normalized autocovariance functions of two pressure signals.

The WSS assumption is very useful for practical applications since it enables the definition of temporal statistics. For example the temporal mean and autocovariance can be defined as:

$$\overline{\mu_q} = \lim_{T_s \to \infty} \frac{1}{T_s} \int_{-T_s/2}^{+T_s/2} q(t)dt \tag{2.43}$$

$$c_{qq}(\tau) = \lim_{T_s \to \infty} \frac{1}{T_s} \int_{-T_s/2}^{+T_s/2} q(t)q(t+\tau)dt \tag{2.44}$$

where T_s is the temporal length of the time histories. In practise, when the time is discretized and the available samples are limited Eqs. (2.43) and (2.44) must be updated as:

$$\overline{\mu_q} = \sum_{j=1}^{N_t} q\left(t_j\right) \tag{2.44}$$

$$c_{qq}\left(\tau_k\right) = \sum_{j=1}^{N_t} q\left(t_j\right)q\left(t_j + \tau_k\right) \tag{2.44}$$

where $\tau_k = (k-1)\Delta t$, $(k = 1, N_\tau)$ is a discretized scale for the time delay. The temporal averages can be estimated for each sample function of the process generating sets of realizations of random variables. Since the process is stationary, it is possible to demonstrate that the expected values of such variables is equal to the corresponding statistical means.

A step forward may be done introducing the concept of ergodicity. In such case all the time averages estimated on each realization are coincident or, in other words, are deterministic. Hence, if the zero-mean process is stationary and ergodic, statistical and temporal means coincide as follows:

$$\mu_k = \overline{\mu_k} \tag{2.45}$$

$$C_{qq}(\tau) = c_{qq}(\tau) \tag{2.46}$$

The ergodic assumption is often invoked in the data processing of aerodynamic data, since usually only a few (or even only one) records are available. This assumption, however, should be introduced with care as, possible due bi-stable configurations, a single time history may not contain the complete statistical information about the random process.
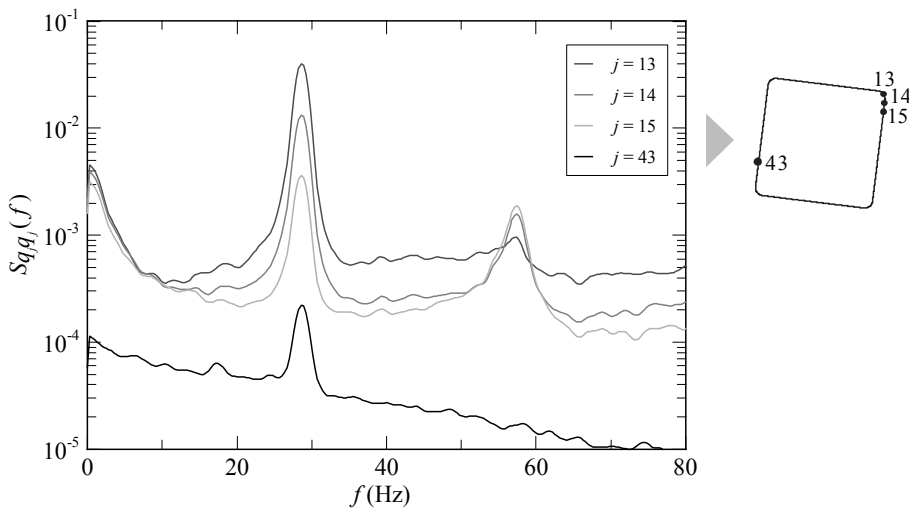
Figure 2.3 PSD functions of four pressure signals; the peak on the vortex shedding frequency is clearly visible. Sensors on downstream corner detect the vortexes on both sides of the cylinder.

A great amount of information of a stationary and ergodic random process may be extracted passing to frequency domain; such representation is offered by the Power Spectral Density (PSD) function. The PSD of a single realization $q(t)$, indicated as

$S_{qq}(\omega)$ where ω is the circular frequency, is defined as the Fourier transform of the autocorrelation function $C_{qq}(\tau)$ divided by 2π:

$$S_{qq}(\omega) = \frac{1}{2\pi} \mathscr{F}\{C_{qq}(\tau)\}(\omega) = \frac{1}{2\pi} \int_{-\infty}^{+\infty} C_{qq}(\tau) e^{-i\omega\tau} d\tau \qquad (2.47)$$

Figure 2.3 shows the PSD of four pressure signals recorded in the points on the windward face and near the trailing edge of the upper face. In all the signals a peak at about 29 Hz related to Karman vortex shedding is visible. On the leeward face the first superharmonics is visible as well, detecting a significant spectral component at twice the vortex shedding frequency.

Exploiting the concept of ergodicity and stationarity, an alternative definition of Eq. (2.47) and useful for practical application, is

$$S_{qq}(\omega) = \frac{1}{2\pi} \lim_{T \to \infty} \frac{1}{T} E\left[\left| \tilde{Q}_T(\omega) \right|^2 \right] \qquad (2.48)$$

where $\tilde{Q}_T(\omega)$ represents the random process (as a function of the frequency) collecting all the Fourier transforms $\tilde{q}_T(\omega)$ of each single realization of the process; T indicates the length of the window considered for the calculation of the Fourier transform, i.e.:

$$q_T(t) = \begin{cases} q(t) & \text{for } t \in (-T/2, T/2) \\ 0 & \text{otherwise} \end{cases} \qquad (2.49)$$

so the Fourier transform of the windowed realization is defined as

$$\tilde{q}_T(\omega) = \int_{-\infty}^{+\infty} q_T(t) e^{-i\omega t} dt = \int_{-T/2}^{+T/2} q(t) e^{-i\omega t} dt \qquad (2.50)$$

The introduction of the time window is functional to two purposes: 1) from a theoretical point of view it is necessary to assure the convergence of the integral in Eq. (2.50); 2) from a statistical point of view it is necessary to produce from one or a few available time series a suitable number of samples necessary to estimate the expectation present in Eq. (2.48).

In Eq. (2.49) a rectangular window function is used for the sake of clarity. In typical applications, the used window functions have various shapes, e.g. triangular, parabolic, bell-shaped curves. **Figure 2.4** shows few examples of cosine window functions which are typically smooth and necessarily non-negative. Dealing with such functions the term "tapering", instead of "windowing", is preferred. This operation is known as short-time Fourier transform (STFT) and is a Fourier-related transform enables to determine the frequency content and phase of a signal in a local

region of time domain. Formally, in the continuous-time case, the STFT of a sample function $q(t)$ is defined as

$$\text{STFT}\{q(t)\}(\omega,\tau) = \int_{-\infty}^{+\infty} q(t)w(t-\tau)e^{-i\omega t}dt \qquad (2.51)$$

In practice the STFT is the Fourier transform of the signal multiplying a window function $w(t)$ sliding along the time axis t, as in a convolution[10]. A more general definition of window functions does not require them to be identically zero outside an interval, as long as the product of the window multiplied by its argument is square integrable, which means that the function goes sufficiently rapidly to zero.

In the PSD estimation, the length of the window T is a fundamental parameter, but is not a free choice. In practical application the recorded signal is divided in parts of length T and their pertinent Fourier transforms are the realizations of the above mentioned random process $\tilde{Q}_T(\omega)$. Usually the STFT is performed on a computer using the Fast Fourier Transform (FFT) algorithm, so both the variables ω and τ are discrete and quantized. This approach is known as Welch method and is useful in reducing the variance of the spectral estimation. The windows may be more or less overlapped. The overlap tends to introduce redundant information but the non-rectangular shape reduces this effect low weighing the samples near the window limits. Narrowing the window the number of realizations increases but the frequency resolution decreases, while enlarging the window the contrary happens. Furthermore the windows may be more or less overlapped. So the windowing operation is a delicate question depending on the sample frequency and on the length of the time histories.

For the numerical applications of the present work a cosine window, in particular the Hamming function,, has been used. It can be generalized from the general formula

$$w(x) = \sum_{k=0}^{K} \alpha_k \cos\left(\frac{2\pi kx}{N-1}\right) \qquad x = 1,...,N-1 \qquad (2.52)$$

---

[10] The convolution integral between two generic functions, $f(t)$ and $g(t)$, is a mathematical operation defined as

$$(f * g)(t) := \int_{-\infty}^{+\infty} f(\tau)g(t-\tau)d\tau$$

where τ is a dummy variable generally equivalent to the time delay. The convolution formula can be described as a weighted average of the function $f(\tau)$ at the moment t where the weighting is given by $g(-\tau)$ simply shifted by amount t.

where α_k are weigh factors, K is the function order and N is the number of samples in T. The numerical coefficients of the window functions, plotted in **Figure 2.4**, are reported in **Table 2.1** for completeness purpose.
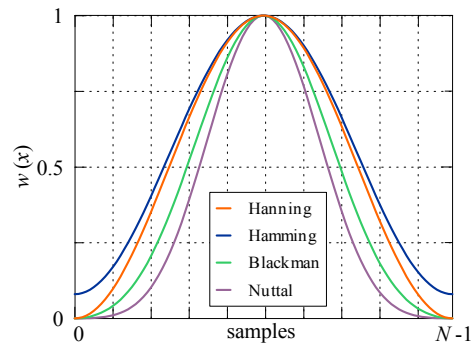
Figure 2.4   A few examples of cosine window functions commonly used in practice.

Window function	α_0	α_1	α_2	α_3
Hanning (Hann)	0.50	-0.50	-	-
Hamming	0.54	-0.46	-	-
Blackman	0.42	-0.50	0.08	-
Nuttal	0.3557	-0.4873	0.1442	-0.0126

Table 2.1   Weigh coefficients of some popular cosine window functions.

Quite often, the spectral information about a pressure or force measurement is condensed into the frequency of the spectral peak. It is especially true when dealing with regions characterized by regular vortex shedding in which the PSD is dominated by a narrow spectral band. The identification of the spectral peak can be done by simple inspection of the plots, but more accurately can obtained by fitting on the PSD a smooth curve like the Gaussian pdf (**Figure 2.5**).

Figure 2.6 a) shows the peak amplitude of the PSD evaluated for the each signals recorded during the wind tunnel test described in the introduction; the skewness is reported for comparison (**Figure 2.6** b). Through such representation it is possible to recognize three regions where the vortex shedding activities is particularly weak or absent:

1. the whole windward face under the incident flow direct action, except for the very close zones to the rounded corners;

2. part of the windward lateral face where the flow reattaches after separating near the lower upstream corner;

3. the upper part of the leeward face where the reverse flow appears in the wake.
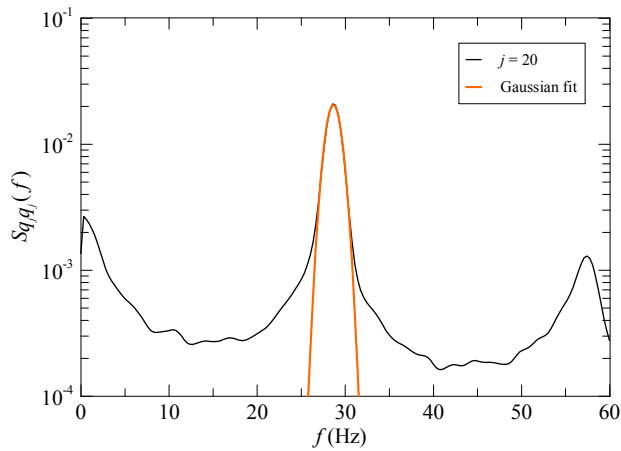
Figure 2.5   Line fitting of the PSD by a Gaussian curve to identify the spectral peak.
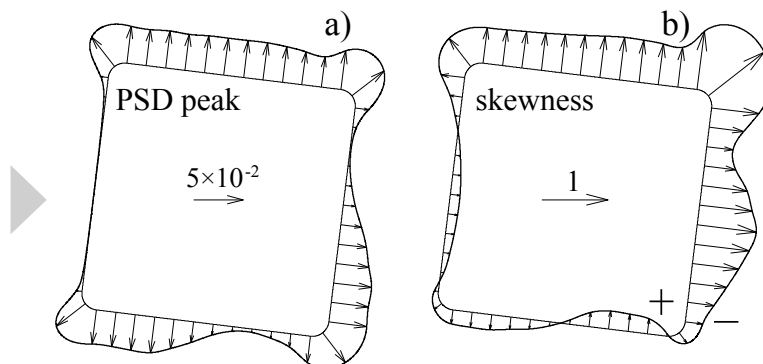
Figure 2.6   Peak amplitude of the PSD (a) and skewness (b) mapped on the body square section.

Near these three regions the skewness (**Figure 2.6** a) increases; in particular near the WF and in the WLF the skewness becomes positive (the right tail is higher than the Gaussian curve). This behaviour reflects the presence of attached flow.

2.3.2 NON-STATIONARY RANDOM PROCESSES

The wavelet analysis is a powerful tool frequently used in non-stationary signals processing; aperiodic, noisy, intermittent, transient signals are few examples. Its main ability is to explore a function, or signal, both in time and frequency simultaneously and in a more efficient, computationally, way with respect to the traditional short time Fourier transform (STFT), presented in the previous section, providing frequency resolution that is adaptive with respect to the frequency band investigated. The applications are various, for example the analysis of financial indices, the heart monitoring, the condition monitoring of rotating machinery, seismic signal analysis, denoising of astronomical images, video image compression and, as in the present case, the characterization of turbulent intermittency of a flow field.

The first application of wavelet concept to real problem was in the mid-1980s to seismic signals, but the most ideas which wavelet are based on have been existed for a long time. For almost ten years this kind of analysis remained within a small mathematical community; then its growth, in term of scientific papers concerning wavelet, was exponential. In Addison (2002) it is reported a curious graph about a web research[11] and the number of papers with the word "wavelet" or "wavelets" in the title, keywords, or abstract: from 1990 to 2001 such numbers was passing from 40 to 1400.
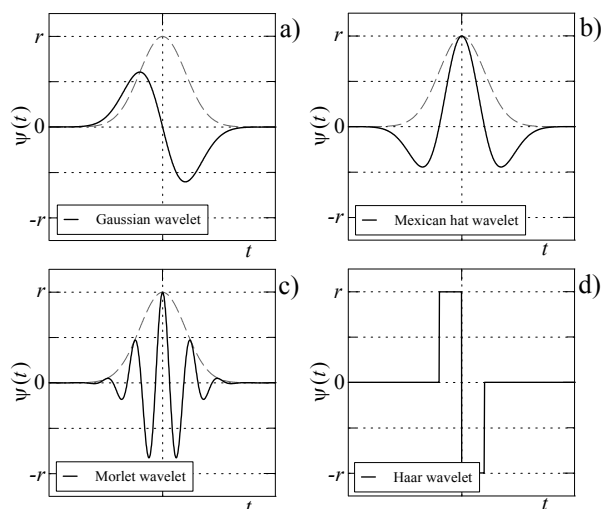
Figure 2.7   Few wavelets functions (continuous line); Gaussian bell (dashed line) for shape reference. Gaussian wavelet (first derivative of a Gaussian

---

[11] The source was: Web of Science, http//wos.mimas.ac.uk/.

bell, a), Maxican hat wavelet (second derivative of a Gaussian, b), Morlet wavelet, real part (the envelope is a Gaussian, c), Haar wavelet.

The term "wavelet" comes from the French word "ondelette" meaning small wave. In fact this kind of analysis is based on a little wavelike functions localized on the time axis and called mother wavelet; they, oscillating, begin at zero, increase, reach a maximum and go back to zero. **Figure 2.7** shows a few examples of wavelets commonly used in practice. Wavelets are employed to transform a signal into another form which happen to be more useful for extracting information hidden in the signal. This transformation is called wavelet transform (WT) and mathematically consists in a convolution of the wavelet function $\psi(t)$ with the original function. Note that the present manuscript refers to temporal signal just for being coherent with the applications proposed; the dependence could be also on space or other parameters.
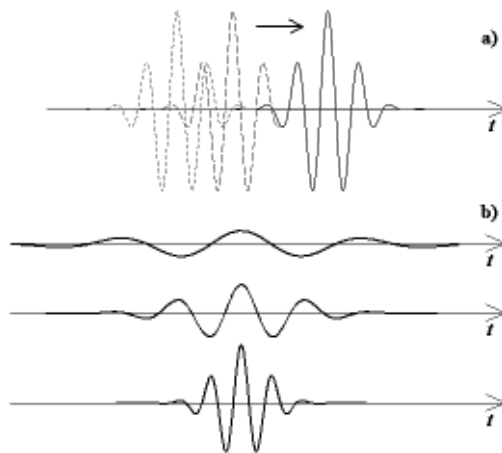
Figure 2.8   Morlet wavelet, location (a) and scale (b).

These wavelet functions are manipulated through two basic operation: translation along t axes (**Figure 2.8** a) and dilation (stretch and squeeze, **Figure 2.8** b); the wavelet analyses quantifies the local matching of the wavelet with the signal. The dilation, or contraction, of the mother wavelet is regulated by the scale factor a and the movement along t axes is governed by the location factor b. For a generic sample function $q(t)$ the wavelet transform is defined as

$$\text{WT}\{q(t)\}(a,b) = \frac{1}{a}\int_{-\infty}^{+\infty} q(t)\ \psi^*\left(\frac{t-b}{a}\right)\ dt \tag{2.53}$$

where $\psi*$ is the complex conjugate of the wavelet mother, if the wavelet mother is a complex function. A very large number of wavelets exist, real and complex; the Gaussian wave is a real wavelet with the form

$$\psi(t) = (-t)e^{-t^2/2} \tag{2.54}$$

which corresponds to the first derivative of the Gaussian bell; its second derivative provides another real-valued wavelet called Mexican hat (for an obvious reason, in Figure 2.7 b is plotted mirrored with respect t axis) defined as

$$\psi(t) = (t^2 - 1)e^{-t^2/2} \tag{2.55}$$

Making the Fourier transform of the Mexican hat, setting to zero the negative frequency component and making the inverse Fourier transform, it is possible to get a very famous complex wavelet, the Morlet wavelet, which has been used in the present work. Its shape has the form

$$\psi(t) = \left(1/\pi^{0.25}\right)e^{2\pi i f_0 t}e^{-t^2/2} \tag{2.56}$$

The time-frequency analysis is a very useful tool for investigating the flow behaviour around bluff bodies from a qualitative view point giving information about the features of the vortex shedding mechanism. A time-frequency representation may also be useful for the analysis of the dynamic response of a structure. In Carassale and Marrè Brunenghi (2013) the vibration of the foundation and the pressure generated by the train passage on a trackside structure is considered. The wavelet map allows to identify the passage of each single bogies distinguishing the driven cars from the towed ones.

In Buresti et al. (2004) an alternative procedure to the Empirical Mode Decomposition (EMD, Huang et. al., 1999) is proposed for investigating the vorticity structures of different size and dynamics in the wake of a bluff body. The proposed technique exploits first the Morlet wavelet as a sort of dynamical band-pass filter for the velocity measurements, i.e. a wavelet-ridge extraction procedure is applied for the selection of the main components of the signal modulated in frequency and amplitude. After that, the Hilbert transform technique is applied to each component, in order to obtain the required modulation laws.

Figure 2.9 shows the wavelet analysis of the time histories recorded by the pressure sensor number 32 during the experimental test presented in the introduction but for $Re=6.48\times10^4$. The colormap represents the amplitude of the wavelet transform of the pressure, plotted with respect to the time t and frequency f. The sensor is located on the midpoint of the windward lateral face. It can be observed that the dominant harmonic content of the pressure is in a band having central

frequency about 29 Hz and that it is visible a vibration component with amplitude at a very low frequency, within 5 Hz. The first harmonic content is related to the vortex shedding mechanism and the second is due to the incident flow turbulence. The intensity of the signature of the vortexes is characterized by amplitude modulation because the phenomenon is naturally intermittent. Furthermore, each vortex-shedding cycle is different with different period, thus the harmonic content is irregular. For about t=18.3 s there is a lack of vortex shedding, this means that the period doubles and the harmonic content halves.
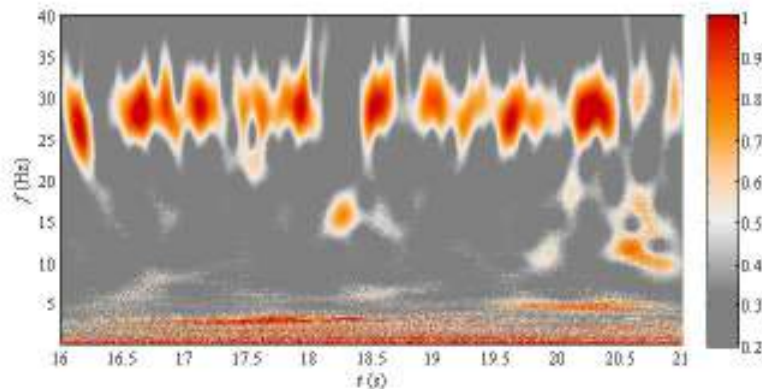
Figure 2.9 Wavelet map of the signal recorded by sensor 32 (windward lateral face); turbulent flow, Re=6.48×10^4.
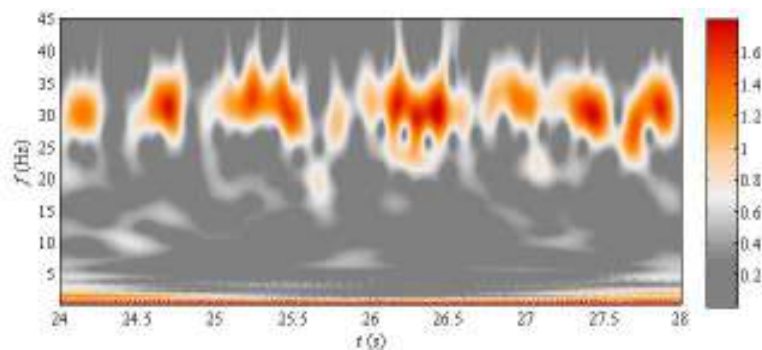
Figure 2.10 Wavelet map of the lift force at the critical angle (α=5°); Re=7.83×10^4.

Figure 2.10 shows a time-frequency analysis of the lift force measured at α=α_{cr}. The length of the considered time window is 4 seconds, which roughly includes 120 cycles of vortex shedding. From the wavelet map it can be observed that the vortex shedding peak frequency changes with time. This critical condition is due to the intermittent flow reattachment on the lateral face exposed to the wind. The technical

implications of this effect is relevant due to the variation of the aerodynamic coefficients as well as in relation to galloping instability. In Carassale et al. (2013) the effects of corner shaping and of the free-stream turbulence on the aerodynamic stability of square cylinders have been investigated with a quasi-steady approach. The corner radius seems to play a fundamental role in the galloping phenomenon and a series of aeroelastic tests is under design to clarify this issue.

2.4 CONCLUDING REMARKS

For the analysis of a dataset representing an *N*-variate random process, the classical (and the first) choice is to apply a SPST analysis. Mean value and SD have an obvious quantitative meaning, while higher-order quantities are often employed as qualitative descriptors to localize zones characterized by high activity of unstable phenomena. The temporal structure of the data can be investigated by SPMT analysis, in particular for stationary time histories, the covariance functions and PSD functions are used. This chapter presents an alternative technique to analyze the transient component possibly present in the signals: the wavelet transform (WT), a powerful method which correspond to a PSD localized on time.

CHAPTER 3

MULTIPLE POINT - SINGLE TIME ANALYSIS BY PCA

Vincent Van Gogh, Starry night.
Oil on canvas, 1889.

3.1 INTRODUCTION

Principal Component Analysis (PCA) represents a mainstay in modern exploratory data analysis from the beginning of 1900, when Karl Pearson, in the biological contest, presented its first version of PCA as geometrical procedure to find the "best-fitting" straight line or plane of a system of points in an N-dimensional space. In few decades the horizon of applications quickly expanded and the N-dimensional system of points became an N-variate random process: psychology, psychometrics, meteorological science, fluid dynamics, linear algebra, computer graphics, statistics, noise and vibration, data compression and structural dynamics are a few examples.

In the engineering field many relevant phenomena can be represented as quantities that vary randomly in space and time. The analyzed dataset derives from

measurements of a physical phenomenon taken in precise points in the space at different time instants. Such discretization is naturally involved due to the limits of experimental activities and is strictly necessary for computational purpose. The great amount of the data, usually confused and redundant, needs to be simplified and clarified by the help of statistical techniques. These two aspects are the fundamental features of PCA making it so attractive. PCA in fact is able to reduce the dataset to a lower dimension revealing some hidden (by noise) and possibly simplified structures that may underlie it. The PCA fascination also lies in its versatility and simplicity: through a non-parametric modal expansion, PCA is able to represent a random process as a linear combination of deterministic quantities, called modes, modulated by random coefficients called Principal Components (PCs). PCs are linear combinations of the original variables and are mutually orthogonal (i.e. non-correlated).

The modal representation offered by PCA is the best in the mean square (i.e. energetic) sense because has the fastest possible convergence among all the possible linear combinations. This means that only some (usually a few) terms of the series are usually needed to capture the relevant energetic part of the observed phenomenon. For this reason PCA is also identified as a method of dimensionality reduction involving the two aspects of this discipline: (1) the feature selection, because deletes part of noise discarding the lasts terms of the series with low variance (a classic strategy of feature selection is a filter); (2) the feature extraction, because transforms the data in the high-dimensional space to a space of fewer dimensions. Geometrically, the aim of PCA is to find a rotation of the reference system which minimizes the covariance (i.e. the redundancy) of the random variables maximizing the variance (i.e. the information) of the new variables in the new reference system. The change in basis can be seen as a change of the point of view that improves the "visible" information included in the dataset.

In the forties there was the first attempts to analyze turbulence trough dynamical system theory by Hopf (1942). He wrote about finite-dimensional attractor and in the seventies fluid dynamicists realized that low-dimensional models and strange attractors might have some practical interest for them. At the same time flow visualization techniques and simulation confirmed the existence of region of organized motion were large-scale ordered structures appear and disappear. This so called coherent structures (CS) are strongly dependent on flow condition and varied considerably in space and time. In this context, for its ability in feature extraction, PCA was naturally introduced in the field of turbulence by Lumley (1967). Later, Holmes et al. (1997) defined these persistent macroscopic structures the "backbone" for many turbulent flows; once get them, the problem of turbulence became less unattainable.

In the mid of fifties it was developed an experimental technique which is now a common activity in experimental aerodynamics: the measurement of pressure fields acting on models surface immersed in a flow by multi-channel scanners. These measurements are idealized as realization of multi-variate random processes and analyzed by means of statistical approaches usually involving some a-priori assumptions such as stationarity and ergodicity.

In the next section the interesting PCA properties are described with the state-of-the-art on the use of PCA, focusing on bluff-bodies aerodynamics and fluid dynamics context; in the same section it is defined what meaningful mode means and if can be defined as coherent structure. Next, the analytical formulation of the PCA is presented using one of the many ways usually employed to formulate this modal expansion. The effect of possibly non-homogeneous spatial discretization of the domain is considering and the use of a corrective term that is able to make PCA modes insensitive to non-homogeneous discretizations is proposed. The chapter follows with the application of PCA to two cases study. The results are discussed and the limitations of this statistical technique are outlined.

3.2 HISTORY OF PCA

Principal Component Analysis (PCA) is a mathematical procedure suitable to convert a set of observations of possibly correlated variables into a set of linearly uncorrelated variables called Principal Components (PCs). This method is largely employed as a tool in exploratory analysis; starting from a dataset, PCA entails the eigenvalue decomposition of the covariance matrix estimated from the mean-centered data.

The *N*-variate dataset may be identified as a set of *N* coordinates in an high-dimensional data space, one axis for each variables. PCA is able to find a new set of *N* coordinates in such a way that the first PC has the maximum variance and each succeeding component has the highest variance possible under the constrain that it is orthogonal to the preceding components. In this way the PCs are mutually uncorrelated. This operation is equal to find a linear orthogonal transformation (i.e. a rotation) in $\Re^N$ in which the new basis is represented by deterministic vectors of order *N* called PCA modes.

In mathematical terms, PCA representation can be written as:

$$\mathbf{q}(t) = \mathbf{m_1} + \mathbf{q'}(t) = \mathbf{m_1} + \sum_{k=1}^{\infty} \boldsymbol{\phi}_k(t) x_k(t) \tag{3.1}$$

where $\mathbf{q}(t)$ is the original dataset or, in this context, an N-variate random process, function of the discrete time t; $\mathbf{m}_1$ and $\mathbf{q'}(t)$ are respectively the expected value and the fluctuating part of $\mathbf{q}(t)$; $\boldsymbol{\phi}_k(t)$ are the PCA modes and $x_k(t)$ are the PCs, both depending on time. If the process $\mathbf{q}(t)$ is stationary, the zero-mean fluctuating component can be expressed as:

$$\mathbf{q'}(t) = \sum_{k=1}^{N} \boldsymbol{\phi}_k x_k(t) \tag{3.2}$$

where $\boldsymbol{\phi}_k$ are deterministic vector in $\Re^N$; Eq.(3.2) represents a t-invariant transformation, also known as Covariance Proper Transformation (CPT, Solari and Carassale, 2000). It is worth noting that the summation in the definition of PCA drops from infinite terms to N (the number of the pressure channels) as the stationarity assumption is invoked.

Observing the previous equation is possible to assert that PCA expands the original random process (omitting mean) in a linear combination of deterministic quantities, called modes, modulated by random coefficients (depending on time) called Principal Components. However, not all the PCs need to be kept; the sum in Eq.(3.2) may be truncated after a certain term $n < N$ because the modal representation offered by PCA possesses the maximum possible velocity of convergence, in the mean square sense (PCA has a hierarchical nature in terms of energy). PCA has the effect of concentrating the greatest part of the signal energy into the first few principal components and for this reason PCA is widely applied to identify Reduced Order Models (ROM). Simultaneously, dimensionality reduction may also be appropriate when the measured signals are noisy. The last PCs of the modal expansion offered by PCA are usually dominated by noise, so they can be usually dropped.

In the next chapter such dimensionality reduction will be a very useful step to analyse high-dimensional dataset prior to apply another kind of modal expansion, the Independent Component Analysis (ICA). ICA is based on a non-orthogonal set of modes and its advantage in respect to PCA will be discussed.

In aerodynamics and wind engineering literature PCA is best known as Proper Orthogonal Decomposition (POD) formally defined in the continuous space as

$$q(r,t) = \sum_{k=1}^{N} \phi_k(r) x_k(t) \tag{3.3}$$

where $q(r,t)$ is the random fluctuation (zero mean) of the process at the position r in the domain D; x_k are the PCs of $q(r,t)$ and $\phi_k(r)$ ($k = 1,\dots,N$) are the eigenfunctions referred to as POD modes.

Over the years many others names have been employed to indicate the same concept with similar formulations. In the original work by Pearson (1901) in the biology contest, the starting point was minimizing the squared reconstruction error to find the best-fitting straight line or plane of a system of point. Hotelling, (1933) in the same field, introduced the variance maximization criterion, deriving this method as a special case of Factor Analysis (FA) introduced by Spearman (1904) in psychology. FA is a method with an analogous formulation to PCA in which modes are substituted by specific loads and PCs are weighting coefficients referred to as common factors (Mulaik, 1972). Later PCA appeared in statistics thanks to Loeve (1945) and Karhunen (1946) being called Karhunen-Loeve Expansion (KLE) and used it for continuous second-order stochastic processes.

$$v(t) = \sum_{k=1}^{N} \phi_k(t) x_k \tag{3.4}$$

where $\phi_k(t)$ is the k-th eigenfunction of the covariance function $C_v(t,t')$ of the random process $v(t)$; x_k are uncorrelated random coefficients. The main difference with (3.2) is the presence of an infinite number of eigensolutions.

The use of PCA in fluid dynamics and in bluff bodies aerodynamics started almost at the same time (see Solari et al, 2007, Carassale et al, 2007 for a wide review). In the mid sixties, Lumley (1967) and Armitt (1968) firsts applied PCA respectively to a stochastic turbulent velocity field and to a pressure field. The former expanded the one-dimensional covariance tensor of the velocity field into a sum of eigenfunctions; the largest eddies were identified with the most energetic eigenfunctions. The latter expanded the full-scale pressure measurements on a cooling tower into a series of modes represented by the eigenvectors of the covariance matrix at the zero time lag.

The intents of the two works were, respectively, to extract organized structures hidden in the flow and to compact the pressure data preserving the dominant mechanisms of the wind loading on structures. Speaking about this subject, it is interesting to report a Theodore von Karman sentence, written in 1954, about aerodynamic science: *"...it is a rare example of co-operation between 'men of mathematics'[12] and creative engineers"*. As a matter of fact Lumley and Armitt never worked together (and probably never net each other), but from the point of view of my research their works mark the same fundamental starting point.

In 1970 Lumley provided an important contribute to PCA considering the process with finite and infinite total energy[13]. In the first case the eigenfunctions of the

---

[12] T. von Karman declares himself that the epithet comes from its friend Eric. T Bell. *T. von Karman, (1954), Aerodynamics, Cornell University Press, London.*

[13] A process has finite energy if the functions representing it are square-integrable.. This is the necessary condition to evaluate the Fourier transform of that functions.

covariance function are obtained by KLE and are orthogonal modes; the corresponding eigenvalue represents the energy content. In the second case the eigenfunctions are classical harmonic functions and KLE becomes a generalized Fourier transform. Next Lumley applied these concepts to *n*-dimensional processes and developed the first attempt to apply PCA to an *n*-variate random process.

When obtaining experimental measurements of velocity field became usual practice, PCA showed its utility. The experimental work carried out by Herzog (1986) who first measured three-dimensional velocity field in a pipe is considered the basic case study and the data-set will be used in the years after (e.g. Moin and Moser, 1989, Aubry et al., 1993).

Simultaneously, in bluff-body aerodynamics, PCA was applied to represent *N*-variate pressure fields measured on the surface of building models in homogeneous flow (smooth and turbulent) and boundary-layer flow to evaluate loading effects (Lee, 1975, Best and Holmes, 1983, Kareem and Cermak 1984). They observed that a very limited number of PCA modes was sufficient to represent wind-tunnel experimental results with a good accuracy and to reconstruct models of the wind action.

Bienkiewicz et al (1995) applied PCA to measurements derived from 494 pressure taps placed on building model surface; in this context, so many signals at the same time had never been recorded before. They observed that the first PCA mode was similar to the mean pressure distribution. Tamura et al. (1997) and Kikuchi et al. (1997) working with a high-rise building model observed that the first two modes were connected to the alongwind and crosswind forces separately.

Despite to these results, other authors asserted that PCA does not necessarily posses physical insight and that the identity between some PCA mode and known loading mechanisms may be purely accidental. For example Holmes et al. (1997), Tamura et al. (1999), Baker (2000), Carassale (2009 and 2012), Carassale and Marrè Brunenghi (2011 and 2012) observed that it may be difficult to associate just one flow mechanism to one PCA mode separating the effects of different physical phenomena.

3.3 PRELIMINARY ASPECTS AND KNOWLEDGE

According to Eq.(3.1), let $\mathbf{q}(t) \in \Re^N$ be an *N*-variate, stationary and ergodic random process, function of the discrete time $t=1,...,N_t$. Principal Component Analysis identifies $\mathbf{q}(t)$ as a random vector composed by N_t independent realizations. The ordering role of the time is disregarded and the index *t* could be dropped, i.e. $\mathbf{q}(t)$ can be redefined as

$$\mathbf{q}(t) = \begin{bmatrix} q_1(t) \\ q_2(t) \\ ... \\ q_N(t) \end{bmatrix} \rightarrow \mathbf{q} = \begin{bmatrix} q_1(t=1) & q_1(t=2) & ... & q_1(t=N_t) \\ q_2(t=1) & q_2(t=2) & ... & q_2(t=N_t) \\ ... & ... & ... & ... \\ q_N(t=1) & ... & ... & q_N(t=N_t) \end{bmatrix} \qquad (3.5)$$

where the column order of the matrix can be changed without any loss of information[14].

The spatial probabilistic structure of the random vector $\mathbf{q}$, exploited by PCA, can be represented at the second order by the correlation matrix $\mathbf{R_{qq}}$ defined as:

$$\mathbf{R_{qq}} = \mathrm{E}\begin{bmatrix} \mathbf{q}\mathbf{q}^\mathrm{T} \end{bmatrix} = \begin{bmatrix} \varphi^2(q_1) & R_{q_1 q_2} & ... & R_{q_1 q_N} \\ R_{q_2 q_1} & \varphi^2(q_2) & & \\ ... & & ... & \\ R_{q_N q_1} & & & \varphi^2(q_N) \end{bmatrix} \qquad (3.6)$$

where the diagonal contains the average power of the random variables; other elements are the correlations $R_{q_i q_j}$ of the all possible couples of random variables defined as

$$R_{q_i q_j} = \mathrm{E}\begin{bmatrix} q_i q_j \end{bmatrix} \qquad i = 1,...,N \qquad j = 1,...,N \qquad (3.7)$$

Alternatively, the covariance matrix $\mathbf{C_{qq}}$ of the random vector $\mathbf{q}$ is defined as

$$\mathbf{C_{qq}} = \mathrm{E}\begin{bmatrix} (\mathbf{q} - \mathbf{m_1})(\mathbf{q} - \mathbf{m_1})^\mathrm{T} \end{bmatrix} = \begin{bmatrix} \sigma^2(q_1) & C_{q_1 q_2} & ... & C_{q_1 q_N} \\ C_{q_2 q_1} & \sigma^2(q_2) & & \\ ... & & ... & \\ C_{q_N q_1} & & & \sigma^2(q_N) \end{bmatrix} \qquad (3.8)$$

where the vector $\mathbf{m_1}$ is the mean of the vector $\mathbf{q}(t)$ containing column-wise the mean of each component

$$\mathbf{m_1} = \mathrm{E}[\mathbf{q}] = \begin{bmatrix} \mathrm{m_1}(q^{(1)}) \\ \mathrm{m_1}(q^{(2)}) \\ ... \\ \mathrm{m_1}(q^{(N_t)}) \end{bmatrix} \qquad (3.9)$$

---

[14] In the literature about PCA, the index t is conventionally preserved.

The diagonal of $\mathbf{C_{qq}}$ collects the variances of the random variables; other elements are the covariances $C_{q_i q_j}$ of the all possible pairs of random variables defined as

$$C_{q_i q_j} = \mathrm{E}\left[\left(q_i - \mathrm{m}_1(q_i)\right)\left(q_j - \mathrm{m}_1(q_j)\right)\right] \tag{3.10}$$

The covariance is bounded by the following relationship

$$\left|C_{q_i q_j}\right| \leq \sigma_{q_i} \sigma_{q_j} \tag{3.11}$$

Using the properties of the expectation operator (2.9), it is easy to see that

$$\mathbf{C_{qq}} = \mathbf{R_{qq}} - \mathbf{m_1} \mathbf{m_1}^{\mathrm{T}} \tag{3.12}$$

If the mean vector $\mathbf{m_1} = \mathbf{0}$, the correlation and covariance matrices become the same.

The covariance matrix satisfies some important properties:

1. it is a symmetric matrix:

$$\mathbf{C_{qq}} = \mathbf{C_{qq}}^{\mathrm{T}} \tag{3.13}$$

2. it is a positive definite matrix:

$$\mathbf{a}^{\mathrm{T}} \mathbf{C_{qq}} \mathbf{a} > \mathbf{0} \tag{3.14}$$

for all *N*-vector $\mathbf{a} \neq \mathbf{0}$;

3. the eigenvalues of $\mathbf{C_{qq}}$ are real and positive; the relative eigenvectors are real and can always be chosen so that they are mutually orthonormal.

The covariance matrix $\mathbf{C_{qq}}$ generalizes the concept of variance, defined in Section 2.2, to multiple dimension. If $\mathbf{C_{qq}}$ is diagonal, all the elements of the random vector are mutually uncorrelated, i.e.

$$C_{q_i q_j} = \mathrm{E}\left[\left(q_i - \mathrm{m}_1(q_i)\right)\left(q_j - \mathrm{m}_1(q_j)\right)\right] = 0 \qquad (i \neq j) \tag{3.15}$$

This is the core of the PCA model, which allows to decorrelate the dataset finding the optimal basis for representing the data in a compact way. From a mathematical point of view this operation implies the diagonalization of the covariance matrix.

If the covariance matrix of $\mathbf{q}$, having zero mean, is equal to the identity matrix, i.e. the variances are equal to one and the covariances are equal to zero, the random vector is defined as a white random vector. Any original dataset can be whitened in infinitely many ways. Such operation is a very useful preprocessing step in independent component analysis (ICA) and will be discussed in more detail in Chapter 4.

A parameter alternative to the covariance, is the correlation coefficient, also known as the Pearson product-moment correlation coefficient, defined as

$$\rho_{q_i q_j} = \frac{C_{q_i q_j}}{\sigma_{q_i} \sigma_{q_j}}$$

(3.16)

It is bounded by the relationship

$$\left| \rho_{q_i q_j} \right| \leq 1$$

(3.17)

In analogy to (3.8) it is possible to define the matrix of correlation coefficients $\boldsymbol{\rho_{qq}}$ as

$$\boldsymbol{\rho_{qq}} = \begin{bmatrix} 1 & \rho_{q_1 q_2} & \cdots & \rho_{q_1 q_N} \\ \rho_{q_2 q_1} & 1 & & \\ \cdots & & \cdots & \\ \rho_{q_N q_1} & & & 1 \end{bmatrix}$$

(3.18)

The correlation coefficient is the best second order quantity for representing the rate of linear dependence between a pair of random variables. In general, two random variables with correlation coefficient equal to zero are uncorrelated but are not statistically independent. Uncorrelatedness means also statistical independence if and only if the random variables have Gaussian distribution. The independence condition for q_i and q_j is that the joint probability density function $p_{q_i q_j}$ is factorizable into the product of the two marginal densities $p_{q_i}(\xi)$ and $p_{q_j}(\eta)$, ξ and η are parameters in $\Re$, i.e.

$$p_{q_i q_j}(\xi, \eta) = p_{q_i}(\xi) p_{q_j}(\eta)$$

(3.19)

where

$$p_{q_i q_j}(\xi, \eta) = \frac{\partial^2 F_{q_i q_j}(\xi, \eta)}{\partial \xi \, \partial \eta}$$

$$p_{q_i}(\xi) = \int_{-\infty}^{+\infty} p_{q_i q_j}(\xi, \beta) d\beta$$

(3.20)

$$p_{q_j}(\eta) = \int_{-\infty}^{+\infty} p_{q_i q_j}(\alpha, \eta) d\alpha$$

On the other hand, if two random variables are independent, they are uncorrelated. The concept of uncorrelatedness and statistical independence are essential to understand the passage from PCA to ICA.

3.4 MODAL REPRESENTATION BY PCA

According to Eq. (3.1), let $\mathbf{q}(t) \in \mathfrak{R}^N$ be an N-variate, stationary and ergodic random process, function of the discrete time $t=1,...,N_t$. Considering just the fluctuating part, $\mathbf{q}(t)$ can be redefined as

$$\mathbf{q}(t) \rightarrow \mathbf{q}(t) - \mathbf{m_1} \qquad (3.21)$$

The application of PCA to $\mathbf{q}$ may be interpreted as:

1. to find an orthogonal linear transformation (i.e. a rotation) transforming $\mathbf{q}$ in a new vector $\mathbf{x}$ whose components are non-correlated or, in other words, making the correlation matrix $\mathbf{C_{qq}}$ of the data (**Figure 3.1**) diagonal;

2. to find a suitable orthogonal basis to define an optimal (in the mean square sense) reduced order model of $\mathbf{q}$;

3. to find a deterministic direction in $\mathfrak{R}^N$ representing a typical realization of $\mathbf{q}$.
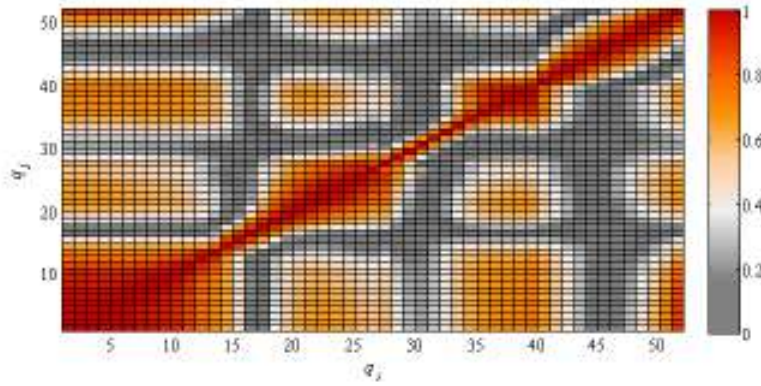
Figure 3.1 Absolute value of the normalized correlation matrix of the original dataset coming from the experimental test described in the Introduction.

Following the third formulation, the first PCA mode represents the "typical" direction $\boldsymbol{\phi}_1$ in $\mathfrak{R}^N$ as parallel as possible to the vector $\mathbf{q}(t)$, i.e. the direction that maximizes the parallelism measure:

$$J = E\left[x_1(t)^2\right] = E\left[\left(\boldsymbol{\phi}_1^T \mathbf{q}(t)\right)^2\right] \qquad (3.22)$$

with the constrain $\|\boldsymbol{\phi}_1\|=1$. The function $x_1(t)$ corresponding to the absolute maximum of J represents the first PC of $\mathbf{q}(t)$. In this sense, the first PC represent the projection of $\mathbf{q}$ (along a direction in $\mathfrak{R}^N$) having the maximum possible variance.

Eq.(3.22) can be translated into the unconstrained extreme value problem:

$$J_1 = E\left[\left(\boldsymbol{\phi}_1^T \mathbf{q}(t)\right)^2\right] - \lambda \|\boldsymbol{\phi}_1\|^2 \tag{3.23}$$

where λ is the Lagrange multiplier. The stationary points of J_1 can be obtained by equating to zero its gradiant with respect to $\boldsymbol{\phi}_1$

$$\frac{\partial J_1}{\partial \boldsymbol{\phi}_1} = 2E\left[\mathbf{q}(t)\mathbf{q}(t)^T\right]\boldsymbol{\phi}_1 - 2\lambda\boldsymbol{\phi}_1 = \mathbf{0} \tag{3.24}$$

The expectation in Eq. (3.24) produces the zero-time-lag covariance matrix $\mathbf{C_{qq}}$ of $\mathbf{q}$, which can be estimated from data as:

$$\mathbf{C_{qq}} = \frac{1}{N_t}\sum_{t=1}^{N_t} \mathbf{q}(t)\mathbf{q}(t)^T \tag{3.25}$$

Substituting in Eq.(3.24), the maximization problem becomes an eigenvalue problem as follow

$$\frac{\partial J_1}{\partial \boldsymbol{\phi}_1} = \left(\mathbf{C_{qq}} - \lambda\mathbf{I}\right)\boldsymbol{\phi}_1 = \mathbf{0} \tag{3.26}$$

where $\mathbf{I}$ is the unitary matrix. Thus the solution is represented by the eigenvalues λ_k and by the eigenvectors $\boldsymbol{\phi}_k$ ($k=1,...,N$) which satisfy the problem

$$\mathbf{C_{qq}}\boldsymbol{\phi}_k = \lambda_k\boldsymbol{\phi}_k \tag{3.27}$$

or alternatively

$$\mathbf{C_{qq}} = \boldsymbol{\Phi}\boldsymbol{\Lambda}\boldsymbol{\Phi}^T \tag{3.28}$$

The matrix $\boldsymbol{\Phi}$ is composed, column-wise, by eigenvectors which are normalized to have unite norm; $\boldsymbol{\Lambda}$ is the diagonal matrix of the eigenvalues of $\mathbf{C_{qq}}$.

The solution of Eq. (3.26) provides a set on N eigenvalues and eigenvectors, which represents the N stationary points of J_1. The eigenvector corresponding to the largest eigenvalues (the absolute maximum of J) represents the direction as parallel as possible to the data in the sense expressed by Eq. (3.22). The other eigenvectors represent other statiorary points (local maxima, minima o saddle points) of J.

Due to the properties of the symmetric eigenvalues problems, the second principal direction $\boldsymbol{\phi}_2$ (corresponding to the eigenvalues λ_2) maximizes the quantity

$$J_2 = E\left[x_2(t)^2\right] = E\left[\left(\boldsymbol{\phi}_2^T\mathbf{q}(t)\right)^2\right] \tag{3.28}$$

under the constraints:

$$\|\boldsymbol{\phi}_2\| = 1$$
$$\boldsymbol{\phi}_2{}^T \boldsymbol{\phi}_1 = \mathbf{0} \tag{3.29}$$

For this reason $\boldsymbol{\phi}_2$ can be interpreted as the direction in $\mathfrak{R}^N$ that is as parallel as possible to the data subspace orthogonal to $\boldsymbol{\phi}_1$. The subsequent principal directions can be interpreted in the same fashion as the direction that is as parallel as possible to the data subspace orthogonal to all the principal directions that have been already identified.

According to the above discussion, the principal directions of the process $\mathbf{q}$ can be obtained both by solving the eigenvalues problem stated by Eq. (3.26) or by solving a cascade of constrained optimization problems in the form of Eqs. (3.28) and (3.29) . The convenience of these two different approaches depends essentially on the size of the problem. In particular if N is small the analytic solution is preferable, while, for very large N, algorithms based on the optimization strategy are by far more efficient.

Once the N orthogonal directions $\boldsymbol{\phi}_i$ are obtained, it is possible to determinate the N Principal Components (PCs) from the data through a simple orthogonal projection as follows:

$$x_k(t) = \boldsymbol{\phi}_k{}^T \mathbf{q}(t) \tag{3.30}$$

so in general the PCA representation of $\mathbf{q}(t)$ is:

$$\mathbf{q}(t) = \sum_{k=1}^{N} \boldsymbol{\phi}_k x_k(t) = \boldsymbol{\Phi}\mathbf{x}(t) \tag{3.31}$$

where $\mathbf{x}(t)$ is the vector collecting the PCs and $\boldsymbol{\Phi}$ collects column-wise the eigenvectors. The eigenvectors and the PCs are enumerated in such a way that their corresponding eigenvalues are sorted in decreasing order λ_k.

Figure 3.2 shows values of the vector $\mathbf{q}=[q_1 \ \ q_2]^T$ representing the pressure fluctuation measured on two opposite lateral faces of a prism (the mean pressure has been removed). It can be observed that the data have negative correlation as a positive fluctuation of the pressure on one face tends to correspond to a negative fluctuation of the other face. The first principal direction is aligned with the largest axis of the cloud of the data points and has slope -1. The second principal direction is necessary orthogonal to the first one and, being in $\mathfrak{R}^2$, is univocally determined. **Figure 3.2** (b) shows the data points rotated according to the principal directions, so that the x and y axes of the figure represent, respectively, the PCs x_1 and x_2. The first PC represents a pressure component that acts on both the faces of the prism with the same random intensity and opposite sign. On the top of this, x_2 represents a random difference (actually it is an algebraic sum) between pressure measured in the two

considered points. The two PCs are uncorrelated due to their construction, but they are not statistical independent, as it can be clearly seen in **Figure 3.2** (b). Even from a simple observation of the data points it clearly emerges that, for example, the conditional pdf of x_2 given x_1=0 is different from the conditional pdf of x_2 given x_1=2.
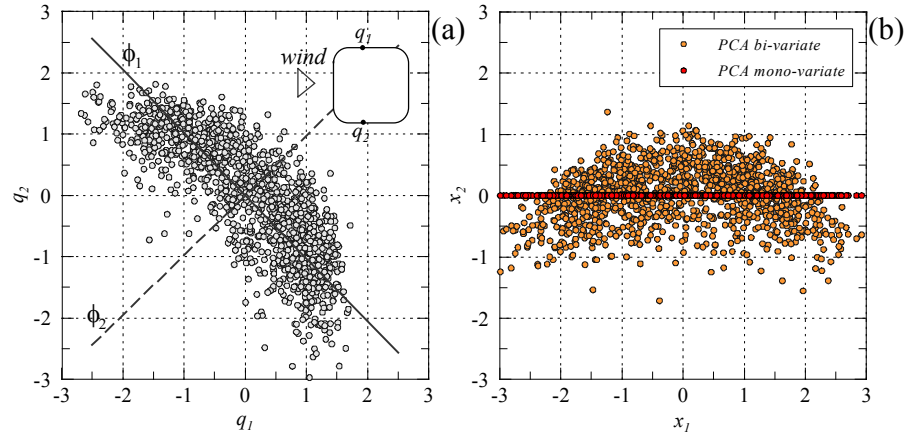
Figure 3.2   PCA application to pressure measurements on the lateral sides of a square-base prism with rounded corners in homogeneous turbulent flow.

The random process $\mathbf{q}(t)$ may be interpreted as experimental measurements derived from N pressure taps located on the body tested surface and, according with the modal representation offered by PCA, it may be represented as a sum of deterministic pressure distributions, the modes $\boldsymbol{\phi}_k$, modulated by random coefficients depending on time, the Principal Components x_k.

For practical purpose, the PCA representation is usually employed to synthesize the dataset in order to obtain a reduced order model deleting noise. For this it is reasonable to substitute Eq. (3.31) by the partial sum

$$\mathbf{q}^{(n)}(t) = \sum_{k=1}^{n} \boldsymbol{\phi}_k x_k(t) = \boldsymbol{\Phi}^{(n)} \mathbf{x}^{(n)}(t) \qquad (n \le N) \qquad (3.32)$$

where $\boldsymbol{\Phi}^{(n)}$ and $\mathbf{x}^{(n)}$ contains the first n PCA modes and PCs respectively. The number of modes n is estimated by counting the eigenvalues of $\mathbf{C_{qq}}$ that are above a suitable threshold[15]. The vector $\mathbf{q}^{(n)}$ represents the best (in the mean square sense) n-variare approximation of $\mathbf{q}$.

---

[15] Conventional threshold is fixed on the 80-90% of the total amount of variance of the process.

The relative importance of each mode may be quantified through the quantity:

$$\Sigma_n = \left(\frac{E\left[\left\| \mathbf{q}(t)^{(n)} \right\|^2 \right]}{E\left[\left\| \mathbf{q}(t) \right\|^2 \right]} \right)^{0.5} = \left(\frac{\sum\limits_{k=1}^{n} \lambda_k}{\sum\limits_{k=1}^{N} \lambda_k} \right)^{0.5} \leq 1 \tag{3.33}$$

which represents the percentage of the norm Standard Deviation (SD) contained in the reduced representation of order *n* with respect to the full-order dataset.

The principal direction are represented through the unit-vectors $\boldsymbol{\phi}_k$, while their importance (in the mean square sense) is represented by the corresponding eigenvalues λ_k. These two pieces of information can be combined together into the scaled PCA modes:

$$\overline{\boldsymbol{\phi}}_k = \lambda_k^{0.5} \boldsymbol{\phi}_k \tag{3.34}$$
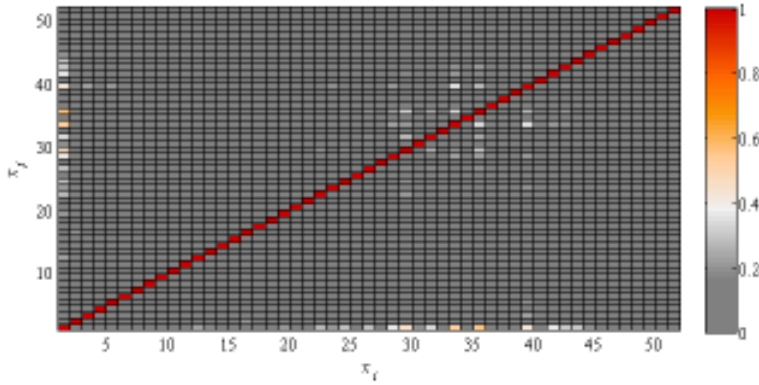
Figure 3.3 Absolute value of the correlation coefficients matrix of the principal components (PCs) obtained by PCA.

PCA properties may be summarized as follows:

1. PCA modes are orthonormal, thus Φ is an orthogonal matrix and represents a rotation in $\Re^N$:

$$\boldsymbol{\phi}_i^T \boldsymbol{\phi}_j = \delta_{ij} \tag{3.35}$$

2. the first PCA mode $\boldsymbol{\phi}_1$ is the best mono-variate representation, in the mean square sense, of the original dataset; its direction is as parallel as possible to the vector $\mathbf{q}(t)$.

3. PCs are zero-mean:

$$E[x_k] = \boldsymbol{\phi}_k^T \, E[\mathbf{q}] \; = \; 0 \tag{3.36}$$

4. PCs are mutually uncorrelated thus the relative covariance matrix (**Figure 3.3**) is diagonal:

$$E[x_j x_k] = \boldsymbol{\phi}_j^T E[\mathbf{q}\mathbf{q}^T] \boldsymbol{\phi}_k = \lambda_j \delta_{ij} \tag{3.37}$$

5. the eigenvalues represent the variance of the PCs:

$$E[x_k^2] = \boldsymbol{\phi}_k^T E[\mathbf{q}\mathbf{q}^T] \boldsymbol{\phi}_k = \lambda_k \tag{3.38}$$

6. the modal expansion has the maximum possible velocity of convergence; $\mathbf{q}^{(n)}$ in Eq. (3.32) is the best n-variate approximation of $\mathbf{q}$, in the mean square sense, because the approximation error

$$J_e^{(n)} = E\left[\left\|\mathbf{q} - \mathbf{q}^{(n)}\right\|^2\right] \tag{3.39}$$

is minimum and the energy of the reduced order model

$$J_E^{(n)} = \frac{E\left[\left\|\mathbf{q}^{(n)}\right\|^2\right]}{E\left[\left\|\mathbf{q}\right\|^2\right]} = \frac{\sum_{k=1}^{n}\lambda_k}{\sum_{k=1}^{N}\lambda_k} = (\Sigma_n)^2 \leq 1 \tag{3.40}$$

is maximum possible for an n-order model.

Figure 3.4 shows the cumulated SD obtained through Eq.(3.33) applied to a dataset deriving from the pressure measured along the mid-span cross section of a square prism in turbulent flow, see Introduction for the details on the setup. The 6th-order ROM retains about 95% of the SD of the full-order dataset and **Figure 3.5** shows the relative 6 PCA modes extracted. Mode 1 represents a pressure distribution on the leeward lateral face (LLF), on the leeward face (LF) and on the windward lateral face (WLF); the amplitude is almost constant except for the regions near sensors 14 and 30. Mode 2 represents pressure distribution acting on the same three faces but having two maximum values near the two downstream rounded corners. It is worth to notice that no mode presents a pressure distribution on the windward face (WF) because the vortex shedding mechanism prevails on the incident turbulence, characterized by intensity equal to 5%. The high activity region near the leeward rounded corner on the LLF, sensors 12 to 14, with high values of skewness and COE (**Figure 2.1** a) is represented by modes 1, 2 an 6. Modes 2 and 6 also provide a contribution to the pressure field acting on the downstream corner on the WLF, sensors 25 to 27. All the reported modes provide a contribution to the pressure field acting on the WLF, with higher modes representing details characterized by a

smaller spatial scale. This latter behaviour is encountered quite commonly in PCA applications and is essentially due to the constrain of orthogonality of the modes Carassale and Marrè Brunenghi (2011, 2012), Carassale (2012).
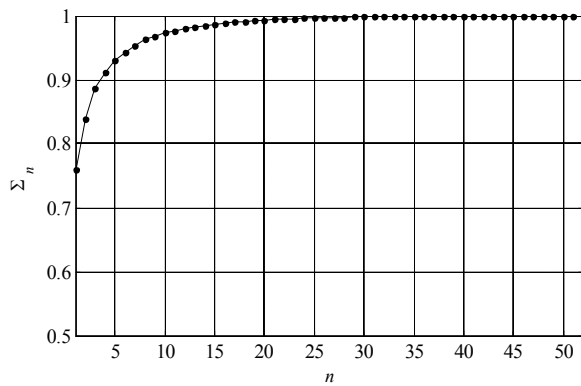
Figure 3.4   Cumulated SD of the PCs.
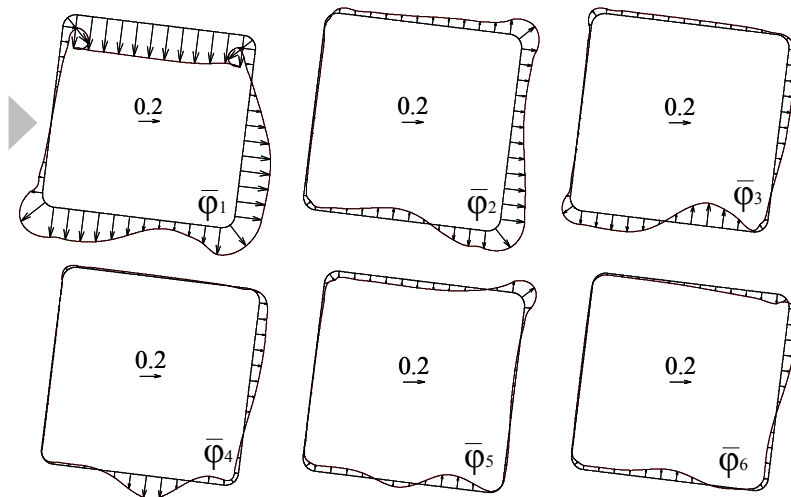
Figure 3.5   First 6 scaled PCA modes.

Figure 3.6 shows few seconds of the first two principal components x_1 and x_2 (left) and the relative probability density function (pdf, right). The Gaussian bell is reported for reference. The pdf of both components reflects an almost Gaussian feature. Modes 1 and 2 represent a pressure distribution acting on the lateral sides and in the base region but the relative PCs do not represent this behaviour from a probabilistic view point. For example, Sensor 13 is on the upper lateral face close to

the trailing edge and is characterized by a very skewed and supergaussian behaviour due to the separation of the flow in such position (see **Figure 2.1**).
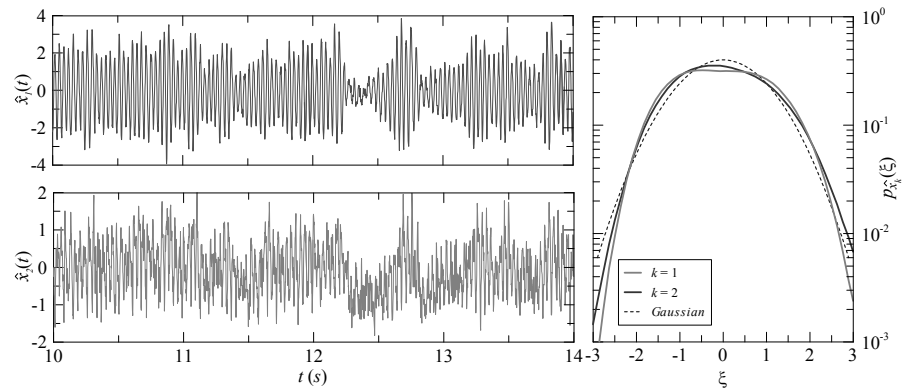
Figure 3.6   Time histories (left) and relative probability density functions (right) of the first two principal components x_1 and x_2.

This aspect reflects a limit adopting PCA representation as feature selection tool. As reported in Section 1.5, a meaningful CS must fulfil the following property: if two parts of the pressure field have distinct statistical characteristics (e.g. in terms of probability and power spectral distribution), then different CSs should represent the two parts of the pressure field separately. Furthermore, the amplitude fluctuation of a CS should reproduce the local statistical properties of the pressure field in the zone where this CS has significant amplitude.
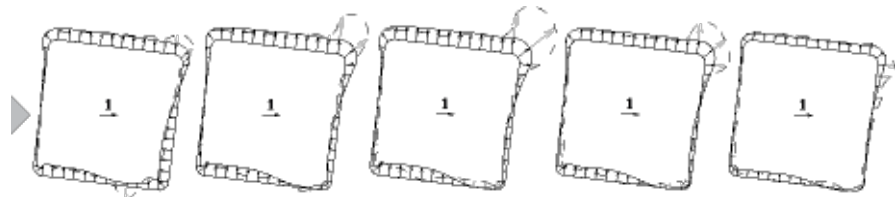
Figure 3.7   Time history of the pressure field (dashed line) and its reconstruction by first 2 PCA modes (continuous line); time step 1.5 ms.

Figure 3.7 shows five snapshot of the pressure time history compared with its approximation by the first two PCA modes. The amplitude of the pressure is almost the same except for the instability region in the neighbourhood of the sensor 13. Extreme values are not captured by PCs because PCA is a 2nd order tool. Anyway, higher order models don't reach the task. **Figure 3.8** represents the reconstruction of the pressure time history by 6 PCA modes; also in this case the high values of suction presented in the leeward rounded corner on the LLF are not reproduced by such method.
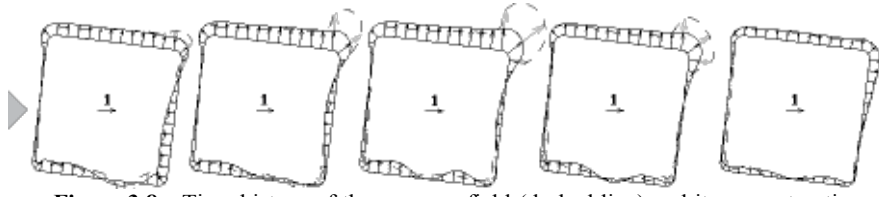
Figure 3.8   Time history of the pressure field (dashed line) and its reconstruction by first 6 PCA modes (continuous line); time step 1.5 ms.

3.5 SPATIAL DOMAIN DISCRETIZATION

The CSs are, at least in principle, an intrinsic property of the flow field and not should be affected by the subjective choice of the spatial discretization adopted for the pressure measurement. In other terms, two experimentalists that observe the same flow, but adopt two different pressure-tap layouts should be able to find the same CSs. Unfortunately it is not the case for PCA, which, due to its hierarchical mean-square nature, tends to capture in the lower order modes those parts of the pressure field that are more finely discretized. This issue has a technical relevance since in many situations a non-homogeneous layout of the pressure taps may be chosen to increase the spatial resolution in those parts of the model where the higher pressure gradients are expected.

In order to investigate this problem the CSs extracted by POD from an ideal continuous-space measurement of the pressure field are discretized and compared with PCA modes. On this basis, a correction procedure is proposed.

Let $q(r,t)$ be the random fluctuation (zero mean) of the pressure field at the position r in the domain D; r may be a scalar or a vector-valued variable, depending on the dimension of the domain D. Let $q_j(t) = q_j(r,t)$ ($j=1,...,N$) be the components of the vector $q(t)$ representing the discrete-space counterpart of $q(r,t)$.

According to POD, the continuous-space pressure is represented as

$$q(r,t) = \sum_{k=1}^{\infty} \phi_k(r) x_k(t) \tag{3.41}$$

where the x_k are the PCs of $q(r,t)$ and $\phi_k(r)$ ($k=1,2,...$) are the solutions of the continuous eigenvalue problem:

$$\int_D C_{qq}(r,r')\phi_k(r')dr' = \lambda_k \phi_k(r) \qquad (k=1,2,...) \tag{3.42}$$

where the $C_{qq}(r,r') = \mathrm{E}[q(r,t)q(r',t)]$ is the zero-time-lag auto-covariance function of $q(r,t)$. The integral in Eq.(3.42) can be discretized according to the experimental layout leading to the equation:

$$\sum_{j=1}^{N} C_{qq}\left(r_i, r_j\right)\phi_k\left(r_j\right)\Delta r_j = \lambda_k \phi_k\left(r_i\right) \qquad \left(k=1,2,\ldots; \quad i=1,\ldots,N\right) \qquad (3.43)$$

where Δr_j is tributary part of D for the node j. Adopting a matrix notation Eq.(3.43) becomes:

$$\mathbf{C_{qq}}\Delta\tilde{\boldsymbol{\phi}}_k = \lambda_k \tilde{\boldsymbol{\phi}}_k \qquad \left(k=1,2,\ldots\right) \qquad (3.44)$$

where $\mathbf{C_{qq}}$ is the covariance matrix of $\mathbf{q}$ defined by Eq.(3.8), $\tilde{\boldsymbol{\phi}}_k = [\phi_k(r_1),\ldots,\phi_k(r_N)]^{\mathrm{T}}$ and $\boldsymbol{\Delta}=\mathrm{diag}(\Delta r_1,\ldots,\Delta r_N)$. Eq.(3.42) provides an infinite number of eigenfunctions, however, as a consequence of the spatial discretization, the vectors $\tilde{\boldsymbol{\phi}}_k$ with k greater than a certain $\bar{N} \leq N$ are not significant due to aliasing.

Eq.(3.44) can be reduced to a symmetric eigenvalue problem by left-multiplying both sides of the equation by $\boldsymbol{\Delta}^{1/2}$. It yields to the new eigenvalue problem:

$$\mathbf{C_{\tilde{q}\tilde{q}}}\boldsymbol{\psi}_k = \lambda_k \boldsymbol{\psi}_k \qquad (3.45)$$

where $\mathbf{C_{\tilde{q}\tilde{q}}} = \boldsymbol{\Delta}^{1/2}\mathbf{C_{qq}}\boldsymbol{\Delta}^{1/2}$ is the covariance matrix of the modified pressure vector $\tilde{\mathbf{q}} = \boldsymbol{\Delta}^{1/2}\mathbf{q}$ and $\boldsymbol{\psi}_k = \boldsymbol{\Delta}^{1/2}\tilde{\boldsymbol{\phi}}_k$ are its eigenvectors.

On the basis of Eq.(3.45), the vector $\tilde{\mathbf{q}}$ can be represented by PCA as:

$$\tilde{\mathbf{q}} = \sum_{k=1}^{N} \boldsymbol{\psi}_k x_k \qquad (3.46)$$

and, left-multiplying by $\boldsymbol{\Delta}^{-1/2}$, $\mathbf{q}$ is obtained in the form:

$$\mathbf{q} = \sum_{k=1}^{N} \tilde{\boldsymbol{\phi}}_k x_k \qquad (3.47)$$

It is worth noting that the eigenvectors $\tilde{\boldsymbol{\phi}}_k$ represent the discretization of the continuous eigenfunctions $\phi_k(r)$ (at least for k not too large) and are in general different from the vectors $\boldsymbol{\phi}_k$ obtained by Eq. (3.27), which necessarily reflect the discretization layout. Since the eigenvectors are used to estimate the CSs which, in turns, are used as interpretative tools to study the pressure field, it is clear that the use of $\tilde{\boldsymbol{\phi}}_k$ instead of $\boldsymbol{\phi}_k$ is largely justified.

As an example, in Section 6.3.2 PCA modes extracted for a particular case-study are reported; these modes are evaluated for the dataset pruned removing the signals corresponding to three sensors. These modes are significantly different from the ones obtained from the complete dataset. Besides, it is worth noting that this

difference is not restricted to the zone where the sensors have been removed, but propagates to the whole domain. On the contrary the modes obtained from the pruned dataset using the correction procedure above described, are very close to the ones calculated from the complete dataset.

3.6 CONCLUDING REMARKS

PCA and the closely related Karhunen-Loève transform are classic techniques in statistical data analysis and they are the classic choice for the coherent structures (CS) extraction in fluid dynamics. PCA has hierarchical nature in terms of energy and it is a very good strategy in order to find a smaller set of variables with as less data redundancy as possible. PCA modes are mutually orthogonal and the relative principal components are non-correlated. Several applications (e.g. Carassale and Marrè Brunenghi, 2012, Baker, 2000) reveal that PCA is not the best choice to formulate qualitative interpretations of the observed physical phenomena. Moreover, the CSs are, at least in principle, an intrinsic property of the flow field and not should be affected by the subjective choice of the spatial discretization adopted for the pressure measurement. On this basis, a correction procedure has been proposed in this chapter.

CHAPTER 4

MULTIPLE POINT - SINGLE TIME ANALYSIS BY ICA

Gustave Klimt, The tree of life.
Oil on canvas, 1905.

4.1 INTRODUCTION

Independent Component Analysis (ICA) is a statistical and computational method for separating a multivariate signal into additive components by assuming that the subcomponents are as much as possible statistically independent from each other. ICA may be considered a special case of blind source separation (BSS). Its fundamental difference to classical multi-variate statistical methods as PCA, is that ICA exploits the non-Gaussian structure of the data, which is crucial for recovering hidden information that underlie sets of random variables. In particular this thesis deals with the instability regions in the neighbourhood of bluff bodies (square cylinders immersed in a wind flow) which are characterized by high values of skewness and coefficient of excess (COE). Furthermore ICA method enables to

estimate a linear transformation from the data itself. This important property allows to adapt the transformation to the data that is being processed.

The problem of dealing with noise in the ICA model is quite complicated. In this chapter it is proposed a method for pre-processing data through PCA; such method allows the dimensional reduction of the dataset deleting the least energetic component of the process. This operation is called whitening and is widely described in this chapter. The last section proposes some statistical quantities for reducing further the dimension of the dataset and for the selection of the best model order. This task may be challenging and requires a particular attention and discussion.

4.2 LINEAR NON-ORTHOGONAL REPRESENTATION BY ICA

Independent Component Analysis (ICA) is a multivariate statistical tool used to extract unknown independent components (ICs) or sources of information, given the observed data that are assumed to be a linear combination of such sources. When the dataset is Gaussian distributed, this task can be accomplished by PCA (described in Chapter 3), since the uncorrelated PCs are also statistically independent. In this case, however, the identification of the sources leads to an undetermined problem, as it will be explained in the following. When the dataset is characterized by a non-Gaussian probabilistic distribution, further information can be gather from high-order statistics. These information are exploited by ICA to remove the undetermination proper of PCA and obtain the identification of the unknown sources. What distinguishes this technique from other methods is that ICA extracts components that are both non-Gaussian and statistically independent. The most of real-world datasets follow a supergaussian distribution; in particular this thesis deals with the instability regions in the neighbourhood of bluff bodies (square cylinders immersed in a wind flow) which are characterized by high values of skewness and coefficient of excess (COE), see Chapter 2.

The ICA approach is a novel method in the field of wind engineering, however this technique is largely employed in different research fields that involve signal processing, in particular digital image and digital audio analysis. In these cases the main problems are: (1) to find a suitable representation of data to accomplish tasks like compression or denoising (feature extraction), (2) to transform data making its essential information more visible and comprehensible (feature selection). To these purposes, standard linear transformation are traditionally used, e.g. in image processing the Fourier, Haar and cosine transforms are in the common practise. Compared to these methods ICA has the advantage of using a representation that is

determined by data (i.e. adaptive) and is not postulated a priori like in most of the available techniques.

The independent Component Analysis has been originally applied to blind[16] source separation (BSS) problem. In Hyvärinen et al. (2001) a simple example of BSS is reported in order to introduce such method. The problem, known as cocktail-party problem, is the following: three people are speaking simultaneously in a room and three microphones are recording audio signals. Each of these registrations is a weighted sum of the three voices depending on the distances of the microphones from the speakers. ICA intends to separate the original speech signals (unknown) starting from their mixtures (known), together with the assumption of the statistical independence of the source signals. In this sense the modal expansion offered by ICA is a generative model, because the observed data come from a process of mixing independent components whose existence is postulated. The mixing system is unknown, but it is assumed as linear and memoryless.

Formally, using a vector-matrix notation, the mixing model (or the linear transformation) offered by ICA is defined as follows

$$\mathbf{q}(t) = \mathbf{m_1} + \mathbf{q'}(t) = \mathbf{m_1} + \mathbf{A}\mathbf{s}(t) \tag{4.1}$$

where $\mathbf{q}(t)$ is the original dataset or, in this context, an N-variate random process, function of the discrete time t; $\mathbf{m_1}$ and $\mathbf{q'}(t)$ are respectively the expected value and the fluctuating part of $\mathbf{q}$; $\mathbf{s}(t)$ is a vector of $n \leq N$ unknown and statistically independent sources s_k ($k=1,...,n$), the ICs, and $\mathbf{A}$ is an $N \times n$ full-rank matrix referred to as mixing matrix.

Note that in Eq. (4.1) (likewise for PCA) the time index t could be dropped because the basic ICA model belongs to the class of statistical methods defined as Multiple Point - Single Time (MPST). Accordingly, each source and each mixture are assumed to be a random variable, instead of a proper time signal or time series. Any time delays is also neglected in such method; for this reason is often called the instantaneous mixing method and is usually written as

$$\mathbf{q} = \mathbf{A}\mathbf{s} \tag{4.2}$$

neglecting the mean component of the mixtures as well as of the sources. This assumption simplifies the formulation and the algorithm of the ICA.

In case the IC mixture is contaminated by additive noise, the fluctuating part in Eq. (4.1) can be expressed as

$$\mathbf{q}(t) = \mathbf{A}\mathbf{s}(t) + \mathbf{r}(t) \tag{4.3}$$

---

[16] The word blind means that the original sources to be estimated are almost unknown from a probabilistic point of view.

where $\mathbf{r}(t)=[r_1(t),...,r_n(t)]$ is the noise vector and is assumed to be additive[17]. In the noisy ICA model, Eq. (4.3), the mixing matrix $\mathbf{A}$ can be estimated anyway under the same restrictions present in the basic ICA model, Eq. (4.1). The ICs, on the other hand, cannot be exactly estimated retrieved due to the effect of the noise (Hyvärinen et al. 2001). An alternative approach to deal with noise consist of applying PCA as a pre-processing stage to achieve a dimensionality reduction together with a noise cancellation, then applying ICA to the reduced-order dataset $\mathbf{q}^{(n)}$ in the form of Eq. (4.2)

$$\mathbf{q}^{(n)}(t) = \mathbf{A}\mathbf{s}(t) \tag{4.4}$$

where the model order n is estimated applying the PCA model, Eq. (3.32), and counting the eigenvalues of $\mathbf{C_{qq}}$ that are above a suitable threshold[18]. The vector $\mathbf{q}^{(n)}$ represents the best (in the mean square sense) n-variare approximation of $\mathbf{q}$ obtained by the combination of the first n PCA modes and PCs. In this way, the original dataset is compacted into a reduced order model deleting noise (at least to some extent).

The modal representation provided by ICA, Eq. (4.4), can be used to represent the pressure field acting on a body as a linear combination of deterministic pressure pattern identified by the columns $\mathbf{a}_k$ of the mixing matrix $\mathbf{A}$, modulated by statistically independent (as much as possible) amplitudes corresponding to the ICs.

$$\mathbf{q}^{(n)}(t) = \sum_{k=1}^{n} \mathbf{a}_k s_k(t) \tag{4.5}$$

This kind of representation is analogous to the modal expansion offered by PCA in Eq. (3.32) with the difference that the columns $\mathbf{a}_k$ are in general non-orthogonal and that the ICs are now statistically independent (instead of simply uncorrelated like PCs). Due to this analogy, ICA is used to estimate a set of $n<N$ coherent structures (CSs), from the experimental dataset, which evolve in time with amplitudes that are as much statistically independent as possible. It is worth to notice that in the observed physical system independent sources are not explicitly present and the concept of virtual sources (Zhou and Chelidze, 2007) must be invoked. Virtual sources, however, are not necessary statistically independent thus the ICA problem should be reformulated as: given the observed data $\mathbf{q}$, find a suitable number n of virtual sources that are as much statistically independent as possible and provide an nth-order approximation of $\mathbf{q}$ through Eq. (4.4). Also in this

---

[17] This assumption is standard in signal processing because allows for a simple formulation of the noisy model.

[18] Conventional threshold is fixed on the 80-90% of the total amount of variance of the process.

case the choice of the model order n may be based on the eigenvalues of $\mathbf{C_{qq}}$, but the brute application of this criterion cannot be exhaustive.

One of the major problem in synthesizing an ICA model from measured data is the selection of the model order. The reason of this difficulty will be clear from the following and will be discussed in Section 4.6.

4.3 HISTORY OF ICA

During the last thirty years, blind source separation by ICA has received growing interest because of its potential applications in signal processing such as in speech recognition systems, telecommunications and medical signal processing. ICA method is applied to identify independent sources given only sensor signals or measurements that are supposed to be instantaneously and linearly mixed. In contrast to correlation-based transformations such as PCA, ICA not only decorrelates the signals (2nd-order statistics), but also reduces higher-order statistical dependencies, attempting to make the signals as independent as possible. ICA was so named because of its analogies with PCA and because it is considered its higher-order generalization (Bell and Sejnowski, 1995).

From the early 1980s, two different research fields have considered the analysis of independent components (Kachenoura et al., 2008, Albera et al. 2004). On one hand, the study of separating mixed sources observed in an array of sensors has been a classical and difficult signal processing problem. The seminal work on blind source separation (BSS) is by Jutten et al (1987) in the neurophysiologic field. The problem was to define a simplified model for the movement of muscles during a contraction and they proposed an adaptive algorithm in a simple feedback architecture. This approach has been explained and further developed by Jutten and Herault (1991), Karhunen and Joutsensalo (1994), and others. Furthermore, Comon (1994) introduced the concept of independent component analysis proposing a maximization algorithm based on the forth cumulant. The contrast function was built from the mutual information of the standardized observations.

On the other hand and in parallel to BSS studies, unsupervised learning rules based on information-theory have been proposed. In Linsker (1992), Becker and Hinton (1992) and others, the idea was to maximize the mutual information between the inputs and outputs of a neural network. This approach is based on redundancy reduction, or feature extraction, which was suggested by Barlow (1961) as a coding strategy in neuron analysis. To achieve an optimal performance, each neuron of a network should posses information that are statistically independent from other neurons. Atick (1992) and Nadal and Parga (1994) applied these principles as visual processing strategy. Roth and Baram (1996) and Bell and Sejnowski (1995)

independently derived stochastic gradient learning rules for this maximization and applied them, respectively to forecasting and time series analysis, and the blind separation of sources. Bell and Sejnowski (1995) were the first explaining the blind source separation problem from an information-theoretic viewpoint and defined ICA as a self-organized learning method.

All through the 1990s several algorithms were proposed. Gaeta and Lacoume (1990) first proposed the maximum likelihood estimation approach. Cardoso and Souloumiac (1993) developed the JADE algorithm which used the forth-order cumulants. Karhunen and Joutsensalo (1994) and Oja (1997) proposed the nonlinear PCA algorithm. Girolami and Fyfe (1996) introduced the negentropy maximization approach; they used an extended exploratory projection pursuit network with inhibitory lateral connections that could separate sub- and super-Gaussian sources. Lee et al (1997) derive the same learning rule from the INFOMAX approach preserving the simple architecture and showing superior convergence speed. Hyvärinen and Oja (1997) presented the fixed-point or FastICA algorithm which has contributed to the applicaton of ICA to large-scale problems due to its computational efficiency (Hivärinen et al., 2001). FastICA iteratively maximizes a forth order contrast function. Chevalier (1999) proposed the efficient COM2 algorithm which uses higher-order cumulants. Kachenoura et al. (2008) applied and compared six of the widely used ICA algorithms; regarding performance JADE, FastICA and COM2 algorithms lead to the best results.

ICA is widely applied in biomedical data analysis. Makeig et al. (1996) applied the original INFOMAX algorithm to ElettroEnchefaloGrafic (EEG). Jung et al. (1998) show that the extended infomax algorithm is able to linearly decompose EEG artifacts such as line noise, eye blinks, and cardiac noise into independent components with sub- and super-Gaussian distributions. McKeown et. al. (1998) have used the extended ICA algorithm to investigate task-related human brain activity. By determining the brain regions that contained significant amounts of specific temporally independent components, they were able to specify the spatial distribution of transiently task-related brain activations. Other potential applications may result from exploring independent features in natural images. Bell and Sejnowski (1997) suggest that independent components of natural scenes are edge filters. The filters are localized, mostly oriented and similar to Gabor like filters. The outputs of the ICA filters are sparsely distributed. Bartlett and Sejnowski (1998) and Gray, Movellan and Sejnowski (1997) demonstrate the successful use of the ICA filters as features in face recognition tasks and lip-reading tasks respectively.

The basic ICA application is constrained by certain assumptions and restrictions, i.e. the sources have to be statistically independent with non-Gaussian distribution (Section 4.4). Hence some flexible nonlinearities have been included in the mixing model. Examples of nonlinear ICA may be found in Lin et al. (1997). Other

limitations due to the possibly not square mixing matrix, i.e. having less sensors than sources, led to the virtual array concept (Chevalier et al. 2005).

In the past ten years BSS and ICA methods have been applied also to structural dynamics. Gelle and Delaunay (2000) used BSS to a test bench where various machines operate simultaneously in order to diagnose each element. The problem was to remove the influence of the other machines, without having to stop them, which would be damaging for production. Zang et al. (2004) and Serviere and Fabry (2004) used ICA for reducing the dimension of the dataset composed by rotating machinery signals for further damage identification.

In wind engineering field, Gilliam et al. (2004) employed independent component to analyze a dataset coming from full-scale pressure measurements on a low-rise building. The aim was to give physical interpretation to intermittent conical vortexes that shed near the roof corner. He et al. (2007) implemented a non-parametric version of ICA to the same dataset attempting to decompose the measured wind pressures in independent flow modes. Carassale and Vernazzani (2009) Carassale and Marrè Brunenghi (2011, 2012), Carassale (2012) applied ICA to wind-tunnel measurements on a high-rise building model. They showed that ICA modes tend to identify some known features of the pressure field, also when PCA modes represent clearly unphysical pressure patterns.

4.4 PRELIMINARY ASPECTS AND KNOWLEDGE

Independent Component Analysis is a statistical and computational technique for revealing underling factors or sources hidden in a dataset of signals, measurements or random variables. ICA is a powerful tool applicable when classical methods, e.g. factor analysis or (PCA, Chapter 3), fail as feature-recognition methods.

However, the application of ICA requires the fulfilment of a few conditions and is affected by certain limitations. These aspects are listed below.

1. The mixing matrix $\mathbf{A}$ is assumed to have full column rank. If its inverse matrix $\mathbf{B}$ (or pseudo inverse if $n<N$, i.e. $\mathbf{A}$ is a non-square matrix) were evaluable (which is not since $\mathbf{A}$ is unknown), then the ICs could be obtained as:

    $$\mathbf{s} = \mathbf{Bq} \qquad\qquad (4.6)$$

    Set in this way, the identification of the ICA model focuses on the estimation of the matrix $\mathbf{B}$. This point entails an ambiguity: if both $\mathbf{A}$ (or $\mathbf{B}$) and $\mathbf{s}$ are unknown, any scalar multiplier c_k in one of the sources s_k could be nullified by dividing the relative $\mathbf{a}_k$ by those scalar, i.e.

$$\mathbf{q}^{(n)}(t) = \sum_{k=1}^{n} \left(\frac{1}{c_k} \mathbf{a}_k \right) \left(s_k(t) c_k \right) \tag{4.7}$$

In order to remedy to this ambiguity, the magnitude of the independent components is assumed to have unit variance:

$$\mathrm{E}\left[s_k^{\,2} \right] = 1 \tag{4.8}$$

This means that the ICA modes cannot be sorted in decreasing order exploiting the energy (variance) of the components (for PCA model this was possible, Eq. (3.38)), but it is necessary to invoke other strategies based on other statistical quantities (see Section 4.4.1).

2. The ICs, or sources s_k, are assumed to be statistically independent; the statistical independence entails uncorrelatedness. From a mathematical point of view this means that the zero-time-lag covariance matrix $\mathbf{C_{ss}}$ is diagonal. Furthermore in Eq. (4.8) the variance of each independent components is fixed to be one; consequently the covariance matrix $\mathbf{C_{ss}}$ is equal to the identity matrix

$$\mathbf{C_{ss}} = \mathrm{E}[\mathbf{ss}^{\mathrm{T}}] = \mathbf{I} \tag{4.9}$$

Due to this property the random vector $\mathbf{s}$ of the independent sources is a white vector (see Section 4.4.1).

3. The probabilistic structures of the ICs must follow a non-Gaussian distributions. The estimation of the mixing matrix is based on higher-order information (in term of cumulants or other statistical quantities) that is identically zero for Gaussian random variables, see Chapter 2. If all the sources are Gaussain the mixing matrix cannot be univocally estimated. If some ICs are Gaussian and some are not, ICA estimates the non-Gaussian components, but the mixing of the Gaussian components will remain unresolved. With just one Gaussian independent component, the method can be performed because it does not have any other Gaussian component to mix with.

4. The original data as well as the independent components are assumed to be zero-mean signals. As mentioned in the previous section, this assumptions leads to simplified formulations of the method.

The sections that follow present some mathematical preliminaries (just mentioned in this section) useful to the description of the estimation principles of ICA, i.e. whitening, statistical independence, mutual information, entropy of a random variable and central limit theorem.

4.4.1 PREPROCESSING BY WHITENING AND PCA

Dataset preprocessing is in general an important step in the data mining activities. For the ICA problem, the preprocessing is a fundamental tool because adds a constrain of orthogonality on the mixing matrix in the whitened space permitting its estimation. In this work, whitening operation is employed in order to preprocess the original data $\mathbf{q}$ obtaining a new vector $\mathbf{z}$ whose new components are mutually uncorrelated and have unit variance.

Uncorrelatedness is a weaker form of statistical independence. Two generic zero-mean random variables q_1 and q_2 are uncorrelated if

$$C_{q_1 q_2} = \mathrm{E}\left[q_1 q_2\right] = 0 \tag{4.10}$$

Consequently the covariance matrix $\mathbf{C_{qq}}$ of a generic zero-mean random vector $\mathbf{q}$ is diagonal if its components are mutually uncorrelated

$$\mathbf{C_{qq}} = \mathrm{E}\left[\mathbf{q}\mathbf{q}^{\mathrm{T}}\right] = \begin{bmatrix} \sigma^2(q_1) & 0 & \dots & 0 \\ 0 & \sigma^2(q_2) & & \\ \dots & & \dots & \\ 0 & & & \sigma^2(q_N) \end{bmatrix} \tag{4.11}$$

where $\sigma(q_i)$ ($i=1,\dots,N$) is the SD of the single components of the random vector.

Two generic zero-mean random variables q_1 and q_2 are statistically independent if their joint probability density function $p_{q_1 q_2}$ can be factorized into the product of their marginal densities (see Section 3.3)

$$p_{q_1 q_2}(\xi,\eta) = p_{q_1}(\xi) p_{q_2}(\eta) \tag{4.12}$$

and consequently, due to the definition of expectation, Eq. (2.9), for any two functions, h_1 and h_2,

$$\mathrm{E}\left[h_1(q_1) h_2(q_2)\right] = \mathrm{E}\left[h_1(q_1)\right]\mathrm{E}\left[h_2(q_2)\right] \tag{4.13}$$

It could be easy demonstrate that:

1. if two random variables are independent, they are also uncorrelated;
2. if two random variables are uncorrelated, they are also independent if and only if they have Gaussian distribution;

A generic zero-mean random vector $\mathbf{z}$ is white if $\mathbf{C_{zz}}$ is diagonal and is equal to the correlation coefficient matrix $\boldsymbol{\rho_{zz}}$, i.e. $\mathbf{C_{zz}}$ corresponds to the identity matrix

$$\mathbf{C_{zz}} = \mathrm{E}\left[\mathbf{z}\mathbf{z}^{\mathrm{T}}\right] = \boldsymbol{\rho_{zz}} = \mathbf{I} \tag{4.14}$$

Any random vector $\mathbf{q}$ can be transformed into a white random vector $\mathbf{z}$ through a linear transformation. This operation is called whitening or equalization. It is possible to assert that whiteness is a stronger property than uncorrelatedness because consists of a double transformation: the components of the random vector are mutually uncorrelated and are scaled in order to make their variances equal to one. This means that the original data $\mathbf{q}$ are transformed by a linear model as

$$\mathbf{z} = \mathbf{V}\mathbf{q} \tag{4.15}$$

where $\mathbf{V}$ is referred to as whitening matrix. The estimation of such matrix has a straightforward solution adopting the PCA expansion, Section 3.4. According to Eq. (3.28) the correlation matrix may be decomposed through its eigenvectors and eigenvalues as

$$\mathbf{C_{qq}} = \mathbf{\Phi}\mathbf{\Lambda}\mathbf{\Phi}^{\mathrm{T}} \tag{4.16}$$

where the matrix $\mathbf{\Phi}$ is composed column-wise by eigenvectors, which are normalized to have unite norm; $\mathbf{\Lambda}$ is the diagonal matrix of the eigenvalues. Considering the special form of $\mathbf{V}$ as follows

$$\mathbf{V} = \mathbf{\Lambda}^{-1/2}\mathbf{\Phi}^{\mathrm{T}} \tag{4.17}$$

and substituting Eq. (4.17) into Eq. (4.15), it is possible to demonstrate that the zero-time-lag covariance matrix of the white vector $\mathbf{z}$ is the identity matrix

$$\begin{aligned} \mathrm{E}\left[\mathbf{z}\mathbf{z}^{\mathrm{T}}\right] = \mathrm{E}\left[\mathbf{V}\mathbf{q}\mathbf{q}^{\mathrm{T}}\mathbf{V}^{\mathrm{T}}\right] = \mathbf{V}\mathrm{E}\left[\mathbf{q}\mathbf{q}^{\mathrm{T}}\right]\mathbf{V}^{\mathrm{T}} = \mathbf{V}\mathbf{C_{qq}}\mathbf{V}^{\mathrm{T}} = \\ = \mathbf{V}\mathbf{\Phi}\mathbf{\Lambda}\mathbf{\Phi}^{\mathrm{T}}\mathbf{V}^{\mathrm{T}} = \mathbf{\Lambda}^{-1/2}\mathbf{\Phi}^{\mathrm{T}}\mathbf{\Phi}\mathbf{\Lambda}\mathbf{\Phi}^{\mathrm{T}}\mathbf{\Phi}\mathbf{\Lambda}^{-1/2} = \mathbf{I} \end{aligned} \tag{4.18}$$

The elements of this vector $\mathbf{z}$ are defined Equalized Principal Components (EPC, Carassale and Marrè Brunenghi, 2012). Substituting the instantaneous mixing model offered by ICA (4.2) in (4.15), the mixing matrix $\mathbf{A}$ will be transformed in a new one $\mathbf{D}$ as follows

$$\mathbf{z} = \mathbf{V}\mathbf{A}\mathbf{s} = \mathbf{D}\mathbf{s} \tag{4.19}$$

where $\mathbf{s}$ is in $\mathfrak{R}^{N}$. From Eqs. (4.9) and (4.14) it is immediate to conclude that the matrix $\mathbf{D}$ must necessarily be an orthogonal matrix, i.e. $\mathbf{D}^{\mathrm{T}}=\mathbf{D}^{-1}$. Hence it is possible to invert Eq. (4.19) and to obtain the ICs

$$\mathbf{s} = \mathbf{W}\mathbf{z} \tag{4.20}$$

where $\mathbf{W}=\mathbf{D}^{\mathrm{T}}$ is an unknown orthogonal matrix to be estimated. In Section 4.4.2, an heuristic approach based on the central limit theorem is reported to estimate such matrix (Hyvärinen et al., 2001).

4.4.2 NON-GAUSSIANITY THROUGH NEGENTROPY

Following the classical ICA formulation, the original data vector $\mathbf{q}$ in $\Re^N$ is assumed to be the result of a mixing (by the $N \times n$ matrix $\mathbf{A}$) of independent sources s_k (ICs) contained in the vector $\mathbf{s}$ in $\Re^n$ ($n \leq N$)

$$\mathbf{q} = \mathbf{As} \tag{4.21}$$

Through a whitening process by PCA, the ICA model becomes

$$\mathbf{z} = \mathbf{Ds} \tag{4.22}$$

where the white vector $\mathbf{z}$ in $\Re^n$ represents the equalized, and possibly reduced-order, version of the original data $\mathbf{q}$. The $n \times n$ matrix $\mathbf{D}$ is an orthogonal matrix.

Inverting (4.22)

$$\mathbf{s} = \mathbf{D}^{-1}\mathbf{z} = \mathbf{Wz} \tag{4.23}$$

the estimation of the ICs becomes the estimation of an appropriate linear combination of the mixture data $\mathbf{z}$. Let $\hat{s}_k$ ($k=1,...,n$) be an estimator for a particular IC (the generic s_k). According to Eq. (4.23) it can be expressed through a linear combination of the EPC as:

$$\hat{s}_k = \mathbf{b}^\mathrm{T}\mathbf{z} \tag{4.24}$$

where $\mathbf{b}$ is a vector to be determined. Substituting Eq. (4.22) into Eq. (4.24), the estimator $\hat{s}_k$ of the IC s_k is expressed as a linear combination of the ICs themselves.

$$\hat{s}_k = \mathbf{b}^\mathrm{T}\mathbf{z} = \mathbf{b}^\mathrm{T}\mathbf{Ds} = \mathbf{x}^\mathrm{T}\mathbf{s} \tag{4.24}$$

Obviously, $\hat{s}_k$ correctly estimate s_k when $\mathbf{x}$ is a vector containing all zeros, but a one in the position k (e.i. x extracts s_k from $\mathbf{s}$). In practice, $\mathbf{x}$ cannot be evaluated since both $\mathbf{D}$ and $\mathbf{s}$ are unknown; however, it is possible to find a suitable estimator that provides a good approximation.

It may be argued that, if the ICs have non-Gaussian distribution, due to the central limit theorem[19], their linear combinations tend to be more Gaussian than the ICs themselves. Following this principle $\hat{s}_k$ estimates correctly s_k if it is more non-Gaussian than any other possible linear combinations of the ICs. Therefore, in order to estimate $\mathbf{x}$, it is necessary to maximize the non-Gaussianity of the linear combination $\mathbf{x}^\mathrm{T}\mathbf{s}$ with respect the vector $\mathbf{x}$ in $\Re^n$. This operation is not possible since $\mathbf{s}$ is unknown, but due to Eq. (4.24) the same result may be obtained maximizing the

---

[19] The central limit theorem asserts that the sum of independent random variables has a distribution that is more Gaussian than any of the original random variables.

non-Gaussianity of $\mathbf{b}^{\mathrm{T}}\mathbf{z}$ with respect to $\mathbf{b}$ in $\Re^n$ or, in analogy to Eq. (4.23), with respect to $\mathbf{w}_k$ (being $\mathbf{w}_k$ a column of the orthogonal matrix $\mathbf{W}$). As a consequence of the orthogonality of the mixing matrix (of the whitened data) $\mathbf{W}$, the optimization process can be repeated for each independent component under the constrain of mutual orthogonality of $\mathbf{w}_k$.

A typical measure for non-Gaussianity is the absolute value of COE due to its theoretical and computational simplicity (see Chapter 2 for definition and properties). However, COE is not a robust quantity because it is very sensible to outliers and needs a great amount of samples for its correct estimation.

In the present work, negentropy[20] has been used as alternative quantity to COE for measuring the non-Gaussianity of the independent components. Negentropy is an information-theory quantity based on the differential entropy H. For a continuous random variable q, H is defined as

$$H(q) = -\int p_q(\xi)\log\big(p_q(\xi)\big)d\xi \tag{4.25}$$

where $p_q(\xi)$ is the pdf of q. The entropy of a random variable reflects the rate of information carried by the variable itself. The more unstructured and unpredictable the variable is, the larger is entropy. A random variable with Gaussian distribution has the largest entropy (among variables with the same variance)[21]. To exploit this property the negentropy is defined as

$$J(q) = H(q_{\mathrm{G}}) - H(q) \tag{4.26}$$

where q_{G} is a Gaussian random variable with the same variance of q. The entropy of a Gaussian variable is known, hence negentropy can be written as

$$J(q) = 0.5 + \log\big(\sqrt{2\pi}\sigma(q)\big) + \int p_q(\xi)\log\big(p_q(\xi)\big)d\xi \tag{4.27}$$

where $\sigma(q)$ is the standard deviation (SD) of q. J is a non-negative quantity and is zero if and only q is Gaussian. This property makes negentropy a very good measure for non-Gaussianity.

Since a correct evaluation of the pdf is a complicated step for the estimation of J, approximated formula are usually employed. For example, the best cumulant-based approximation of negentropy is

---

[20] The concept of negative entropy was introduced by Irwin Schrödinger in his science book *What is life?* (1944). In 1962, the French physicist Lèon Brillouin coined the term negentropy.

[21] This is known as the maximum entropy principle.

$$J(q) \simeq \frac{1}{12}\kappa_3 (q)^2 + \frac{1}{48}\kappa_4 (q)^2 \tag{4.28}$$

where q is a standardized random variable (zero-mean and unit variance); κ_3 and κ_4 are respectively the third and forth cumulant of q. This representation is obtained representing the pdf through a type-A Gram-Charlier expansion and is affected by the nonrobustness encountered with kurtosis. For the applications presented in this thesis, the non-Gaussianity measure J_{NG} has been specified in the form

$$J_{NG}(q) = \left(E\big[g(q) \big] - E\big[g(q_G) \big] \right)^2 \tag{4.29}$$

where q_G is a Gaussian standardized random variable and g is a non-linear function with the form

$$g(q) = \frac{1}{a}\log(\cosh aq) \qquad a = 1.5 \tag{4.30}$$

where a is a constant.

The constrained maximization of J_{NG} has been carried out by the algorithm FastICA. The structure of this algorithm is reported in the next Section; full details and validation can be found in Hyvärinen et al. (2001).

4.5 MODAL REPRESENTATION BY ICA

Let $\mathbf{q}(t) \in \Re^N$ be a zero-mean, N-variate, stationary, zero-mean and ergodic random process, function of the discrete time $t=1,...,N_t$. In this context $\mathbf{q}(t)$ is a dataset obtained by an experimental test: a fixed cylinder, with regular cross section, immersed in an artificial wind flow. Its surface is instrumented by N pressure taps; $q_j(t)$ includes N_t pressure measurements recorded at each discrete time instant t by the jth pressure channel.

The first operation necessary to estimate ICs and mixing matrix is data reduction and whitening. Both these steps are made by PCA defining the EPC as

$$\mathbf{z} = \mathbf{V}^{(n)}\mathbf{q} \tag{4.30}$$

where the whitening matrix $\mathbf{V}^{(n)}$ has size $N \times n$ and is defined as

$$\mathbf{V}^{(n)} = \mathbf{\Lambda}^{(n)^{-1/2}} \mathbf{\Phi}^{(n)^{\mathrm{T}}} \qquad n \le N \tag{4.31}$$

where $\mathbf{\Phi}^{(n)}$ and $\mathbf{\Lambda}^{(n)}$ contain respectively the first n eigenvectors and eigenvalues of $\mathbf{C_{qq}}$.

Substituting the ICA model into Eq. (4.30) it yields

$$\mathbf{z} = \mathbf{V}^{(n)}\mathbf{As} = \mathbf{Ds} \tag{4.32}$$

and it is now possible to invert the equation since, after whitening, the new mixing matrix $\mathbf{D}$ is orthogonal, hence

$$\mathbf{s} = \mathbf{D}^{-1}\mathbf{z} = \mathbf{Wz} \tag{4.33}$$

1.	Center and whiten the data to obtain the EPC
2.	Select a suitable model order n on the basis the eigenvalues of $\mathbf{C_{qq}}$
3.	Choose random initial values for $\mathbf{w}_k$ ($k=1,...,n$)
4.	Orthogonalize the matrix $\mathbf{W}=[\mathbf{w}_1,..., \mathbf{w}_n]$ by updating its value as $$\mathbf{W} \leftarrow \left(\mathbf{WW}^{\mathrm{T}}\right)^{-1/2}\mathbf{W}$$
5.	Update $\mathbf{w}_k$ ($k=1,...,n$) as $$\mathbf{w}_k \leftarrow \mathrm{E}\left[\mathbf{z}g'\left(\mathbf{w}_k^{\mathrm{T}}\mathbf{z}\right)\right] - \mathrm{E}\left[\mathbf{z}g''\left(\mathbf{w}_k^{\mathrm{T}}\mathbf{z}\right)\right]\mathbf{w}_k$$ where g' and g'' are respectively the first and the second derivative of g (Eq. (4.30)) and the expectation is estimated by a statistical average on all the available samples.
6.	Orthogonalize the matrix $\mathbf{W}=[\mathbf{w}_1,..., \mathbf{w}_n]$ by updating its value as $$\mathbf{W} \leftarrow \left(\mathbf{WW}^{\mathrm{T}}\right)^{-1/2}\mathbf{W} \tag{4.36}$$
7.	Check the convergence of $\mathbf{W}$ in term of some norm; in the implementation adopted for this thesis the largest absolute row sum was used.
8.	If the prescribed tolerance is not reached go back to step 5. For the applications presented herein the tolerance value 10^{-12} was adopted.

Table 4.1   The FastICA algorithm for estimating several ICs, with symmetric orthogonalization.

Now the fastICA algorithm can be adopted for determining the n columns of $\mathbf{W}$, $\mathbf{w}_k$ ($k=1,...,n$), maximizing the non-Gaussianity of the product $\mathbf{w}_k^{\mathrm{T}}\mathbf{z}$ through the measure J_{NG} ,Eq. (4.29). In Hyvärinen et al. (2001) two versions of this algorithm are proposed: (1) the FastICA with deflationary orthogonalization, (2) the FastICA with symmetric orthogonalization. In the first method the vectors of $\mathbf{W}$ are estimated one by one constraining each vector to be orthogonal to the vectors that have been already estimated. It results that the errors in the estimation of the first vectors affect the estimation of the subsequent ones. The second method estimates all $\mathbf{w}_k$ in parallel imposing the orthogonality constraint on all the vectors simultaneously; in this way no vector is privileged over others and therefore the algorithm is defined as symmentic. For the applications presented herein, the second method, i.e. symmetric orthogonalization, has been adopted. The structure of this algorithm is reported in Table 4.1.

The $n \times n$ mixing matrix **A** is now easily evaluable as follows

$$\mathbf{A} = \mathbf{\Phi}^{(n)} \mathbf{\Lambda}^{(n)^{1/2}} \mathbf{W}^{-1} \tag{4.37}$$

and the vector **s** containing n independent components (statistically independent as much as possible) can be calculated as

$$\mathbf{s} = \mathbf{W} \mathbf{\Lambda}^{(n)^{-1/2}} \mathbf{\Phi}^{(n)\mathrm{T}} \mathbf{q} \tag{4.38}$$
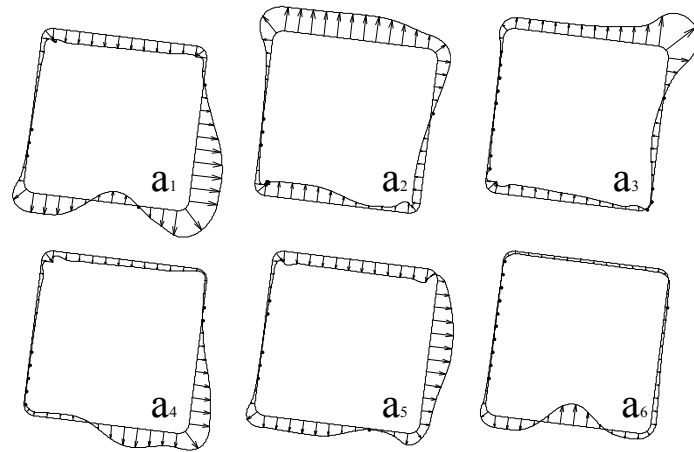
Figure 4.1   6 ICA modes evaluated for *n*=6.

Figure 4.1 shows the first 6 ICA modes estimated from the data. Mode 1 represents a pressure distribution mainly on the leeward lateral face (LLF) and on the leeward face (LF); the amplitude has two minima near the regions close to sensors 16 and 30. Mode 2 has an almost constant distribution on the leeward lateral face (LLF). It is worth to notice that no mode presents a pressure distribution on the windward face (WF) because the vortex shedding mechanism prevails on the incident turbulence, characterized by intensity equal to 5%. The high activity region near the leeward rounded corner on the LLF, sensors 12 to 14, with high values of skewness and COE (**Figure 2.1** a) is represented by mode 3. Mode 4 represents pressure distribution acting on the lower part of the LF and downstream part of the WLF with maximum values near the corner, sensor 26. Modes 2 and 6 also provide a contribution to the pressure field acting on the downstream corner on the WLF, sensors 25 to 27. All the reported modes provide a contribution to the pressure field acting on the WLF, with higher modes representing details characterized by a smaller spatial scale.

Figure 4.2 shows five snapshot of the pressure time history compared with its approximation offered by the superimposition of three ICA modes, in particular mode 1, 6 and 7 (see **Figure 4.1**). The instability region in the neighbourhood of the sensor 13 is characterized by negative skewness, i.e. high probability of having high values of suction. The ICA reconstruction, exploiting just three modes conveniently chosen, is able to reproduce the amplitude of the pressure in such regions, relevant from the design view point in term of fatigue damage.
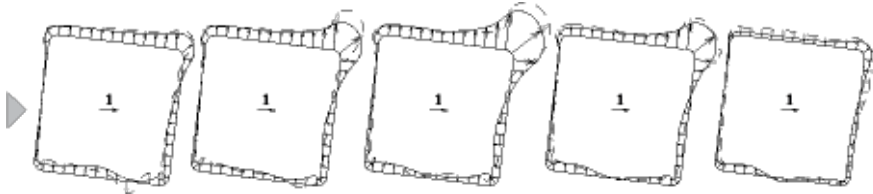
Figure 4.2   Time history of the pressure field (dashed line) and its reconstruction by 3 ICA modes (continuous line): a_1, a_2 and a_3; time step 1.5 ms.

From this latter consideration, two main questions deserve attention:

1. ICA is an higher-order technique and is able to catch the non-Gaussian feature of the dataset, comparing **Figure 3.8** and **Figure 4.2** the limits of PCA are evident;

2. working with ICA representations, the choice of the model order *n* can be more critical than for PCA; for the reconstruction presented in **Figure 4.2** the three modes have been chosen just looking at **Figure 4.3**. The selection could be made on mathematical bases and this issue is discussed in the next section.

4.6 ORDER SELECTION OF AN ICA MODEL

One of the major problem in synthesizing an ICA model from measured data is the selection of the model order. This difficulty is related to the different behaviour that PCA and ICA representations have as the model order is increased. In particular, when working with PCA, the passage from a model with order *n* to a model with order *n*+1 only involves the introduction of a new mode, without changing the modes from 1 to *n*. On the contrary, increasing the order of an ICA model produces, in general, the modification of all the modes involved in the representation. Indeed, even if the ICA model spans the same data subspace as the PCA model of the same order, ICA modes are determined by an optimization principle, whose results may change as fresh information is added increasing the model order. For this reason, it is clear that the model order should be selected as large enough to represent the

relevant part of the observation, but not larger since, due to the effect of equalization, high-order EPCs may bring amplified noise components into the model.

The tracking of the mode stability for different model orders, as well as the study of entropy and mutual information of the ICs are a valuable guides for the order selection. In Carassale and Marrè Brunenghi (2012), differential entropy and mutual information have been employed to accomplish such task. The entropy of a random variable is defined in Eq. (4.25) and quantifies the information carried by a random variable.

Another useful guide in order to identify a proper subspace dimension is the mutual information I between two random variables q_j and q_k. I is defined as

$$I(q_i, q_j) = \int_{\mathfrak{R}^2} p_{q_i q_j}(\xi, \eta) \log\left[\frac{p_{q_i q_j}(\xi, \eta)}{p_{q_i}(\xi) p_{q_j}(\eta)}\right] d\xi d\eta \tag{4.39}$$

and can be interpreted as a measure of the statistical dependency of two random variables, or from an information-theory view point, it measures the overlapping of the information carried by q_j and q_k.
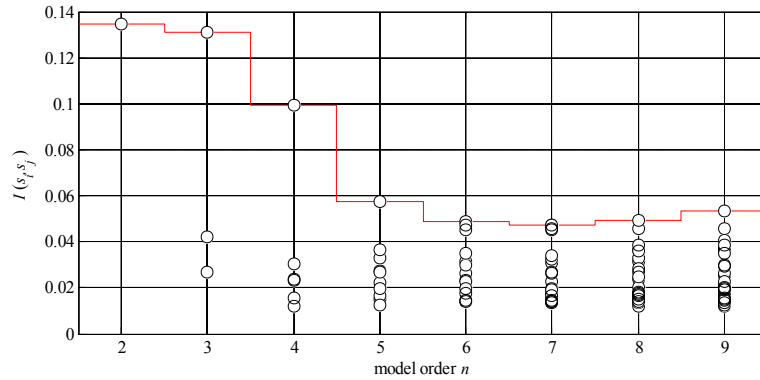
Figure 4.4   Mutual information between pairs of ICs as functions of model order *n*.

Figure 4.4 shows the mutual information between pairs of ICs evaluated for different model orders *n* from 2 to 9. The case study adopted for this application is described in the introduction. Observing the maximum value offered by each subspace dimension (red line) it is possible to exclude those orders that produce modes associated to ICs with large mutual information (like *n*=2,3 in the present application), and to privilege the orders for which this statistical quantity tends to be clustered about small values (like *n*=5,6,7 in the present application).

Figure 4.5 shows the ICA modes estimated for model orders n from 2 to 6. For each model, modes are plotted row-wise, labelled with a letter (from a to f) on the basis of their shape. The dotted red line tracks the evolution of each modal shape increasing the order. Mode a remains stable for n=2,3,4 representing the pressure field on the leeward lateral face (LLF), with an almost constant value; on the windward lateral face (WLF) and on the leeward face (LF), mode a presents a variable pressure distribution with two minimum values near sensors from 29 to 32 (where the flow reattaches on the lateral face, see section 2.3.1 and **Figure 2.6**) and near sensors from 14 to 16 (where the suction in the weak region is mitigated by the reverse flow). For n=5,6 mode a splits into two modes classified as a and f: mode a preserves the pressure distribution on the WLF and on the LF while mode f inherits the pressure distribution on the LLF representing the completely separated flow. The behaviour of mode b is almost equal to the behaviour of mode a: for n=2,3,4 mode b remains stable and for n=5,6 two modes, b and e, distil different local actions of the wake region; in particular mode b conserves the features of the high activity region near the leeward corner and mode e reproduces suction due to vortex shedding near the upper downstream corner. Modes c and d combine each other and separate alternatively from n=3 to 6 presenting, respectively, a pressure distribution essentially on the LF (mode c) and on the WLF (mode d). The tracking of the mode stability offered by **Figure 4.5** confirms the hypothesis made observing the mutual information in **Figure 4.4**, i.e. for the present application a good choice for obtaining a reduced order model is n=5,6. Higher order models are not suggested because of the amplified noise components introduced by the equalization procedure, essential for the ICA application.

Figure 4.6 reveals a complementary aspect of the modes evolution from n=2 to n=9, i.e. the differential entropy of the ICs associated to modes a to f. The reduction of entropy represents the increment of non-Gaussianity of the ICs (the maximum entropy corresponding to the Gaussian distribution is reported with dotted line). Furthermore the reduction of entropy reflects a reduction of the information content carried by each IC, which, in some sense, tends to separate a specific feature of the observed phenomenon. For the model order n=5, the entropy referred to modes b, c, e and f have local minima; for this reason jointly with the aforesaid results, n=5 represents the best choice for the present application. A further discussion of this issue is provided in Chapter 6 referring to another specific case study.

Figure 4.7 shows a comparison, in term of pdf, between the ICs relative to modes a, b, c, d and the pressure measurements in proximity of the pressure distributions presented by the modes for the model order n=5. It is possible to observe that the probabilistic properties of the ICs tend to assume a behaviour consistent with the local properties of the pressure field.
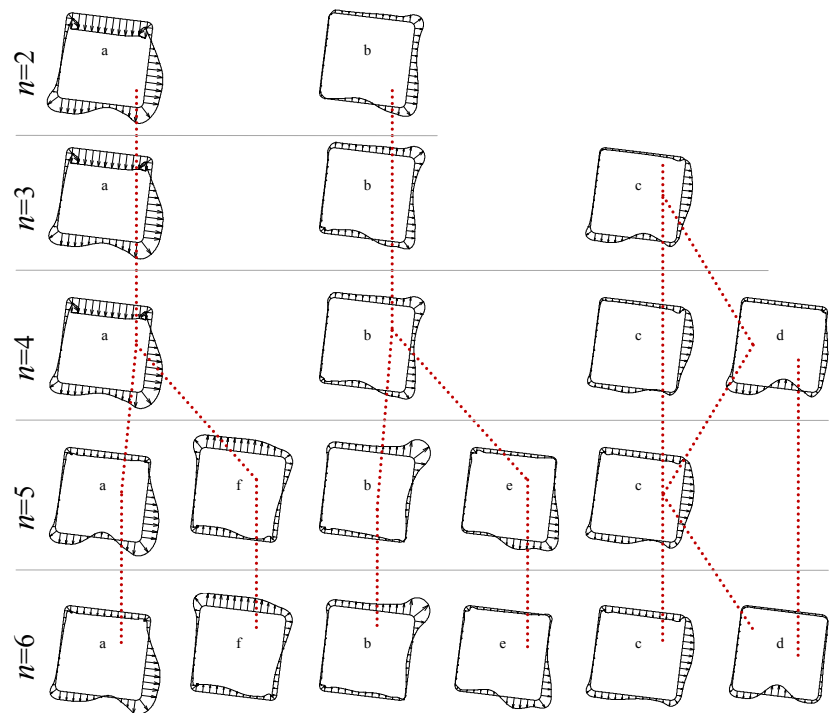
Figure 4.5   ICA modes for model orders *n*=2-6.
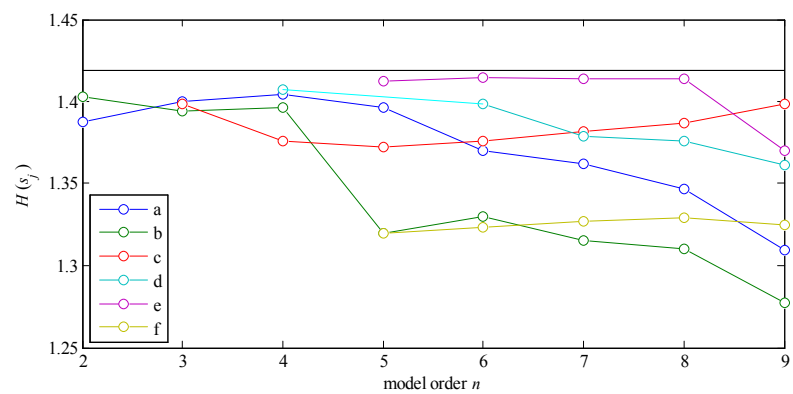
Figure 4.6   Entropy of the ICs as functions of model order *n*.
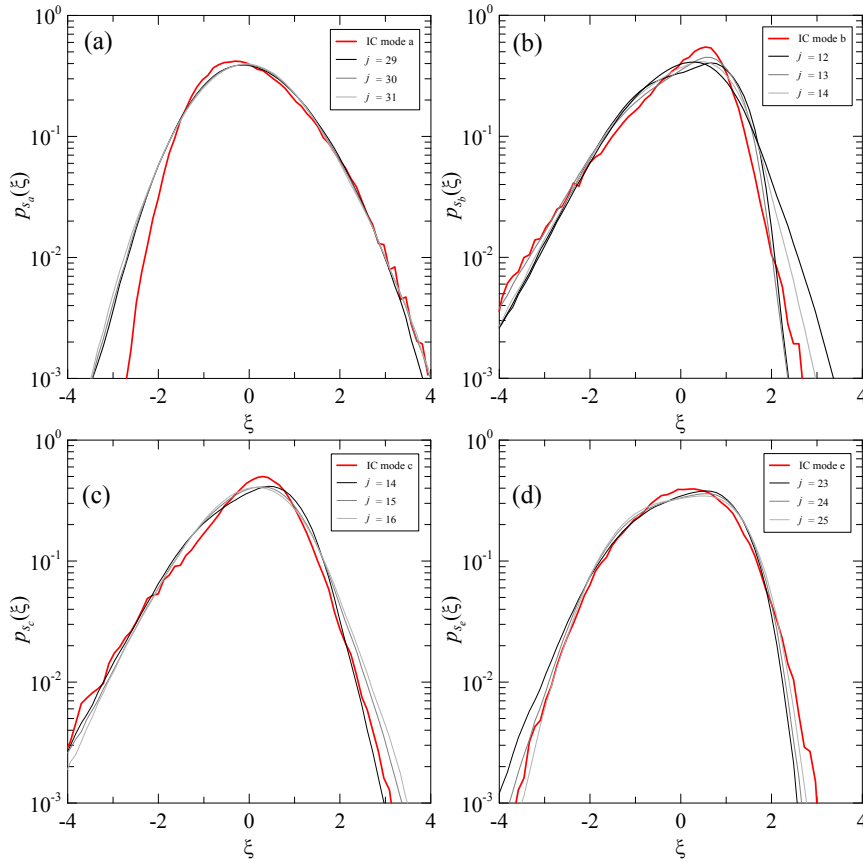
Figure 4.7   Pdf of the ICs for different model orders (red line) compared with the pdf of standardized pressure measurements of the sensors localized near the pressure distribution represented by the relative mode.

4.7 CONCLUDING REMARKS

ICA is a powerful statistical methods for representing the original observed data as a superimposition of components that are statistically independent, as much as possible, from each other. ICA is based on the maximization of nongaussianity. When the dataset is characterized by a non-Gaussian probabilistic distribution, further information can be gather from high-order statistics. These information are exploited by ICA to remove the undetermination proper of PCA and obtain the identification of the unknown sources. What distinguishes this technique from other methods is that ICA extracts components that are both non-Gaussian and statistically independent. Thanks to these properties, ICA is able to separate the pressure

fluctuation acting on different parts of a body surface, even if they have very different statistical characteristics. Different ICA modes reflect the local pressure in terms of pdf, thus ICA modes constitute meaningful local representations. The choice of the most appropriate model order for ICA may be critical; the tracking of the mode stability for different model orders, as well as the study of entropy and mutual information of the independent components (ICs), are valuable guides for the order selection.

CHAPTER 5

MULTIPLE POINT - MULTIPLE TIME ANALYSIS
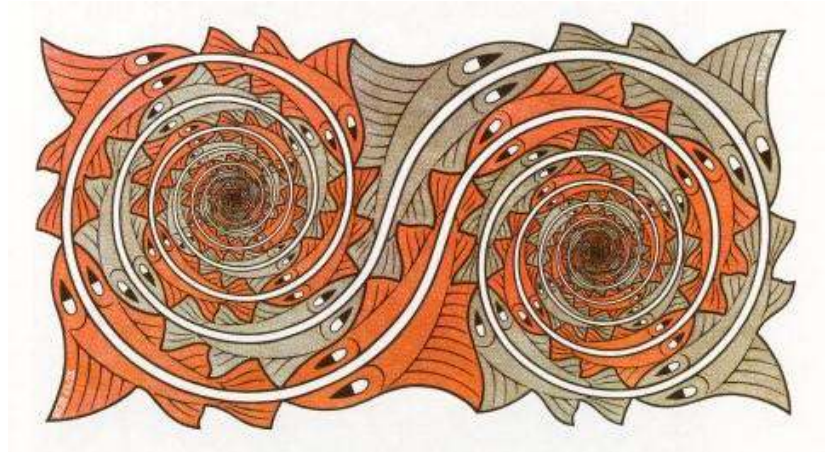
Maurits Cornelis Escher,Whirlpools.
Woodcut, 1957.

5.1 INTRODUCTION

This chapter deals with the Multiple Point - Multiple Time techniques (MPMT) presenting the convolutive version of PCA and ICA which are referred here as dynamic-PCA (D-PCA) and dynamic-ICA (D-ICA); the formulations of such techniques follow Carassale (2012). These modal representations rely on both spatial and temporal probabilistic information within the recorded dataset. In this context, these techniques have been adopted in order to represent (and interpret) propagating phenomena such as the pressure field generated by a vortex advected by the mean flow. The instantaneous mixing models offered by PCA and ICA are not adequate for fulfilling this task since they provide static modes; D-PCA and D-ICA enable the extraction of deterministic shapes evolving with time, which can be identified as dynamical coherent structures. The application presented in Carassale

(2012) are here reported as an example. Further applications of these techniques can be found in Chapter 6 regarding a square prism in atmospheric boundary layer.

5.2 N-Variate Random Processes

The statistical analysis of measurements carried out in several points at multiple times (MPMT) focuses both on the spatial and temporal probabilistic structure of the dataset. To accomplish an exhaustive description of these tools, the definition of N-variate random processes is necessarily introduced.

Let $\mathbf{q}(t) \in \mathfrak{R}^N$ be an N-variate, stationary and ergodic random process, function of the discrete time $t=1,...,N_t$. At the second order, considering a pair of time instants, t_1 and t_2, this random process can be described by the auto-correlation matrix $\mathbf{R_{qq}}(t_1,t_2)$ and by the auto-covariance matrix $\mathbf{C_{qq}}(t_1,t_2)$ defined as

$$\mathbf{R_{qq}}\left(t_1,t_2\right) = \mathrm{E}\left[\mathbf{q}\left(t_1\right)\mathbf{q}^\mathrm{T}\left(t_2\right)\right] \tag{5.1}$$

$$\mathbf{C_{qq}}\left(t_1,t_2\right) = \mathrm{E}\left[\left(\mathbf{q}\left(t_1\right) - \mathbf{m_1}\left(t_1\right)\right)\left(\mathbf{q}\left(t_2\right) - \mathbf{m_1}\left(t_2\right)\right)^\mathrm{T}\right] \tag{5.2}$$

where the mean vector $\mathbf{m_1}$ for the time instant t_1 is defined as

$$\mathbf{m_1}\left(t_1\right) = \mathrm{E}\left[\mathbf{q}\left(t_1\right)\right] = \begin{bmatrix} \mathrm{m_1}\left(q_1\left(t_1\right)\right) \\ \mathrm{m_1}\left(q_2\left(t_1\right)\right) \\ ... \\ \mathrm{m_1}\left(q_N\left(t_1\right)\right) \end{bmatrix} \tag{5.3}$$

The elements on the diagonal of $\mathbf{R_{qq}}(t_1,t_2)$ and $\mathbf{C_{qq}}(t_1,t_2)$ are, respectively, the auto-correlations and auto-covariances of the components of the process. The out-of-diagonal elements are, respectively, the cross-correlations and cross-covariances, defined for the time instants t_1 and t_2, as

$$R_{q_i q_j}\left(t_1,t_2\right) = \mathrm{E}\left[q_i\left(t_1\right)q_j\left(t_2\right)\right] \qquad i=1,...,N \qquad j=1,...,N \tag{5.4}$$

$$C_{q_i q_j}\left(t_1,t_2\right) = \mathrm{E}\left[\left(q_i\left(t_1\right) - m_1\left(q_i\left(t_1\right)\right)\right)\left(q_j\left(t_2\right) - m_1\left(q_j\left(t_2\right)\right)\right)\right] \tag{5.5}$$

The matrixes $\mathbf{R_{qq}}(t_1,t_2)$ and $\mathbf{C_{qq}}(t_1,t_2)$ satisfies the following properties:

$$\begin{aligned} \mathbf{R_{qq}}\left(t_1,t_2\right) &= \mathbf{R_{qq}}^\mathrm{T}\left(t_1,t_2\right) \\ \mathbf{C_{qq}}\left(t_1,t_2\right) &= \mathbf{C_{qq}}^\mathrm{T}\left(t_1,t_2\right) \end{aligned} \tag{5.6}$$

Formally a stochastic process is defined stationary (in the strict sense) if all its statistical properties is invariant under any shift of the time origin; this means that the first-order pdf is time-invariant, while the second-order joint pdf depends only on the time lag $\tau = t_2 - t_1$ and not directly on the choice of the two instants.

Wide-sense stationary (WSS) processes are a very important subclass of stationary random processes which are characterized by the properties: (1) the statistical means of the first order are time independent; (2) the statistical quantities of the second order are only time lag dependent ($\tau = t_2 - t_1$); (3) the variance of the process is finite. This leads to the definition of these statistical quantities:

$$\mathbf{R}_{\mathbf{qq}}(\tau) = \mathrm{E}\left[\mathbf{q}(t)\mathbf{q}(t+\tau)^{\mathrm{T}}\right] = \begin{bmatrix} R_{q_1 q_1}(\tau) & R_{q_1 q_2}(\tau) & \dots & R_{q_1 q_N}(\tau) \\ R_{q_2 q_1}(\tau) & R_{q_2 q_2}(\tau) & & \\ \dots & & \dots & \\ R_{q_N q_1}(\tau) & & & R_{q_N q_N}(\tau) \end{bmatrix} \tag{5.7}$$

$$\mathbf{C}_{\mathbf{qq}}(\tau) = \mathrm{E}\left[\left(\mathbf{q}(t) - \mathbf{m_1}(t)\right)\left(\mathbf{q}(t+\tau) - \mathbf{m_1}(t+\tau)\right)^{\mathrm{T}}\right] =$$

$$= \begin{bmatrix} C_{q_1 q_1}(\tau) & C_{q_1 q_2}(\tau) & \dots & C_{q_1 q_N}(\tau) \\ C_{q_2 q_1}(\tau) & C_{q_2 q_2}(\tau) & & \\ \dots & & \dots & \\ C_{q_N q_1}(\tau) & & & C_{q_N q_N}(\tau) \end{bmatrix} \tag{5.8}$$

where

$$R_{q_i q_j}(\tau) = \mathrm{E}\left[q_i(\tau)q_j(t+\tau)\right] \qquad i = 1,\dots,N \qquad j = 1,\dots,N \tag{5.9}$$

$$C_{q_i q_j}(\tau) = \mathrm{E}\left[\left(q_i(t) - m_1\left(q_i(t+\tau)\right)\right)\left(q_j(t) - m_1\left(q_j(t+\tau)\right)\right)\right] \tag{5.10}$$

Usually, a frequency-domain formulation can be conveniently adopted. Let $\mathbf{S}_{\mathbf{qq}}(\omega)$ be the Power Spectral Density matrix (PSDm) defined as

$$\mathbf{S}_{\mathbf{qq}}(\omega) = \frac{1}{2\pi}\int_{-\infty}^{+\infty}\mathbf{C}_{\mathbf{qq}}(\tau)e^{i\omega\tau}d\tau =$$

$$= \begin{bmatrix} S_{q_1 q_1}(\omega) & S_{q_1 q_2}(\omega) & \dots & S_{q_1 q_N}(\omega) \\ S_{q_2 q_1}(\omega) & S_{q_2 q_2}(\omega) & & \\ \dots & & \dots & \\ S_{q_N q_1}(\omega) & & & S_{q_N q_N}(\omega) \end{bmatrix} \tag{5.11}$$

where ω is the circular frequency. The elements on the diagonal of $\mathbf{S}_{qq}(\omega)$ are the PSD's of the components of the process. The out-of-diagonal elements are the cross-PSD functions defined as

$$S_{q_i q_j}(\omega) = \frac{1}{2\pi} \int_{-\infty}^{+\infty} C_{q_i q_j}(\tau) e^{i\omega\tau} d\tau \qquad i = 1, ..., N \qquad j = 1, ..., N \tag{5.12}$$

Exploiting the concept of ergodicity and stationarity, an alternative definition of Eq. (5.11) and useful for practical application, is

$$\mathbf{S}_{qq}(\omega) = \frac{1}{2\pi} \lim_{T\to\infty} \frac{1}{T} E\left[\tilde{\mathbf{q}}_T(\omega) \tilde{\mathbf{q}}_T^*(\omega)\right] \tag{5.13}$$

where $\tilde{\mathbf{q}}_T(\omega)$ represents the random process (as a function of the frequency) whose realizations are the Fourier transforms of the realizations of $\mathbf{q}(t)$ windowed within $t \in [-T/2, T/2]$; the symbol * represents the conjugate transpose.

$\mathbf{S}_{qq}(\omega)$ is a complex-valued Hermitian-symmetric matrix (the real part is symmetric and the imaginary part is anti-symmetric); the diagonal elements are necessary real because the PSD functions are real functions.

5.3 CONVOLUTIVE MIXTURE MODEL

In defining a convolutive mixture model, the classic cocktail-party problem[22] can be reformulated as follows: in a room, people are speaking simultaneously and a set of microphones are recording. Starting from the registrations, the task is to estimate the original source signals. These speech signals reach the microphones with different time delays due to their different relative positions. Furthermore, reverberation from obstacles in the room causes echoes of the voices. These two phenomena are modelled as a convolutive mixtures (Hivärinen et al., 2001).

A convolutive mixture can be seen as the superimposition of some kind of convolution simultaneously with a linear mixing. From the opposite point of view, blind source separation of convolutive mixtures is the result of two different problems:

1. an instantaneous linear blind source separation (BSS/ICA, see Chapter 4);
2. a blind deconvolution (Haykin, 1994).

---

[22] See Chapter 4 for the details.

In signal processing and communications, blind deconvolution[23] deals with only one observed signal (output) and only one source signal (input). The output signal is generated by the mixing of delayed versions of the source signal.
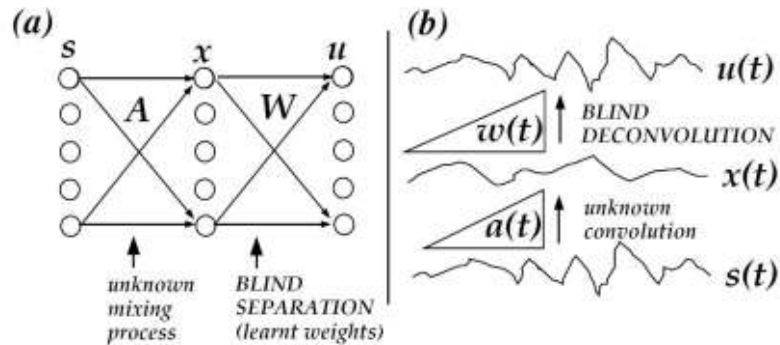
Figure 5.1   Network achitectures for blind separation of 5 mixed signals (a), blind deconvolution of a single signal. Figure from Bell and Sejnowski (1995).

Figure 5.1 shows the basic ideas of the blind separation and the blind deconvolution. In **Figure 5.1** a, a set of sources s_k (k=1,...,N) are mixed together by an unknown mixing matrix **A**; the result is a set of N known signals x_k. The separation problem offered by ICA concerns to recover the original sources by finding the matrix **W**, which is a permutation and rescaling of the inverse of the matrix **A**. **Figure 5.1** b shows the blind deconvolution problem: the observed discrete time signal $q(t)$ is originated by an unknown source signal as follows

$$q(t) = \sum_{\tau=0}^{t-1} a(\tau) s(t-\tau) \tag{5.14}$$

where $a(\tau)$ are called the convolution coefficients. The problem is to estimate the source signal $s(t)$ knowing $q(t)$, i.e. to find a deconvolution filter

$$y(t) = \sum_{\tau=0}^{t-1} h(\tau) q(t-\tau) \tag{5.15}$$

representing a good estimation of the source signal $s(t)$ at each time instant. Eq. (5.15) represents a deconvolution sum and the constant coefficients h_k define the Finite Impulse Response (FIR) part of the filter. For details on digital signal processing, see Oppenheim and Schafer (1989) or Haykin (1989).

---

[23] Blind deconvolution is also known as blind equalization.

At the second order, a modal representation belonging to the MPMT techniques, can be formulated by generalizing PCA. Let $\mathbf{q}(t)=[q_1(t),..., q_N(t)]$ be an N-variate random process containing the zero-mean fluctuation of the measurements deriving from N pressure taps located on the body surface. According to PCA model presented in Eq. (3.31), $\mathbf{q}(t)$ is represented by the modal expansion

$$\mathbf{q} = \sum_{k=1}^{N} \boldsymbol{\phi}_k x_k = \boldsymbol{\Phi}\mathbf{x} \tag{5.16}$$

where $\mathbf{x}$ is the vector collecting the principal components (PCs) uncorrelated for zero time lag and $\boldsymbol{\Phi}$ collects column-wise the PCA orthogonal modes. Note that in Eq. (5.16) the time index t is dropped because the temporal order is not relevant. The dynamic version of Eq. (5.16), defined as dynamic-PCA (D-PCA) and based on the blind deconvolution problem in Eq. (5.14), is given by

$$\mathbf{q}(t) = \sum_{\tau=0}^{t-1} \sum_{k=1}^{N} \boldsymbol{\phi}_k(\tau) x_k(t-\tau) = \sum_{\tau=0}^{t-1} \boldsymbol{\Phi}(\tau)\mathbf{x}(t-\tau) \tag{5.17}$$

where the column of the kernel $\boldsymbol{\Phi}(\tau)$ may be interpreted as time-variable coherent structures. The PCs result now uncorrelated for any time lag. The estimation of such a kernel can be carried out through the joint diagonalization of the data covariance matrix calculated for different time lags, however when $\mathbf{q}(t)$ is a stationary process, a frequency-domain formulation can be conveniently adopted. In section 5.5 , three alternative approaches to solve the D-PCA problem are discussed.

Analogously, the concept of dynamic-ICA (D-ICA) can be introduced, through the definition of blind deconvolution. The ICA model describing $\mathbf{q}(t)$ is

$$\mathbf{q} = \sum_{k=1}^{N} \mathbf{a}_k s_k = \mathbf{A}\mathbf{s} \tag{5.18}$$

where $\mathbf{s}$ is the vector collecting the independent components (ICs) as much as possible statistically independent and $\mathbf{A}$ collects column-wise the ICA modes and represents the instantaneous mixing matrix. Hence, a D-ICA model is offered by the following equation

$$\mathbf{q}(t) = \sum_{\tau=0}^{t-1} \sum_{k=1}^{N} \mathbf{a}_k(\tau) s_k(t-\tau) = \sum_{\tau=0}^{t-1} \mathbf{A}(\tau)\mathbf{s}(t-\tau) \tag{5.19}$$

where the column of the kernel $\mathbf{A}(\tau)$ may be interpreted as time-variable coherent structures or, alternatively, a filter. Also in this case, D-ICA can be formulated in the frequency domain and the dynamic coherent structures can be characterized in terms of amplitude and phase angle, see Section 0 for details.

Coherent structures provided by D-PCA and D-ICA are objects which evolve with time, containing information on both the spatial and temporal statistical structure of the pressure field.

5.4 STATE-OF-THE-ART ON DYNAMIC REPRESENTATION

The histories of D-PCA and D-ICA belong to different lines of research, likewise for PCA and ICA. The former, starting from the 50's, widely developed in sectors like fluid dynamics, turbulent flow, wind engineering and bluff-body aerodynamics. The latter developed later in signal processing and communications.

Obviously, Dynamic-PCA is intimately related to Proper Orthogonal Decomposition (POD); its formulation in frequency domain is equivalent to the Spectral Proper Transformation (SPT) which is considered a 'strong' form of POD (Solari and Carassale, 2000). The 'weak' form of POD is the Covariance Proper Transformation (CPT), analogous to PCA formulation. In SPT, the generalized Fourier transform of the process is given by a linear combination of frequency dependent modes, the eigenvectors of the power spectral density matrix (PSDm), modulated by random processes, as functions of frequency. The spectral principal components result uncorrelated for any time lag. In Carassale (2005) it is demonstrated that, for a certain class of random processes, CPT and SPT coincide.

SPT in bluff-body aerodynamics appeared first thanks to De Grenet and Ricciardelli (2004): the problem was to reproduce the wind loads on a vibrating bridge deck section. Carassale et al.(2004) developed a similar research analyzing pressure measurements on a tall building model. In these works it is shown that each spectral mode is able to capture more mechanisms changing the frequency ranges.

In structural dynamics SPT and CPT were employed for the expansion of the loading random process, formulating, jointly with the classic modal analysis of a structure, the Double Modal Transformation (Carassale et al. 1998, 1999, 2000). In Carassale and Kareem (2002) SPT is applied for decoupling the loading and a Volterra series is used to determine the nonlinear response of M-DOF systems. Carassale and Piccardo (2003, 2004) analyzed the wind-induced response of suspended cables by SPT and Volterra series. Di Paola et al. (2004) and Carassale and Piccardo (2010) analyzed a similar case by Monte Carlo simulation method and using DMT in a nonlinear environment.

SPT-based modal identification originated from Brincker et al. (2001) who proposed a method, the Frequency Domain Decomposition (FDD), closely related to classical peak picking technique. Two applications of FDD were reported by Yoshida and Tamura (2004) to identify the dynamic properties of a chimney and of a large span roof exposed to wind. Barroso and Rodriguez (2004) used FDD within

a benchmark study on structural health monitoring of a four-story building model. Carassale and Percivale (2006) investigated the relationship between SPT of stationary *N*-Variate processes and FDD as well as its range of applicability in the identification of linear systems.

Digital stochastic processes are frequently modelled in terms of autoregressive moving average (ARMA) processes or on the superimposition of harmonic waves with random phase angles. These methods involve the decomposition of covariance matrix or the psdm, closely related to SPT. These concept were applied by Dodds and Robson (1975) and Li and Kareem (1989, 1995). The spectral decomposition was applied by Yamazaki and Shinozuka (1990) to the covariance matrix at the zero time lag of a stationary process; this method focused on a quasi-static analysis.

Caddemi and Di Paola (1994) and Di Paola and Pisano (1996), independently of the previous papers, embedded the spectral decomposition of the PSDm of an *N*-Variate random process into a Monte Carlo procedure aimed at simulating wind velocity and sea wave fields, respectively. Di Paola (1998) acknowledged the contribution of Li and Kareem, emphasising the link between stochastic and spectral decompositions; in this context, he provided an interpretation of the eigenvectors of the PSDm of a turbulence field, referred to as "blowing modes of the wind", and discussed their limited variation on wide frequency ranges. Based on this remark, Benfratello and Muscolino (1999) applied the spectral decomposition of the PSDm of a turbulence field, calculating its eigenvectors in a suitable fixed frequency value; consequently, they modelled each eigenvalue of the PSDm as the power spectral density (PSD) function of a process dealt with as the output of digital filters driven by independent Gaussian white noises. Di Paola and Gullo (2001) further improved this method dividing the frequency domain into *p* sub-intervals where each eigenvector was approximated as a polynomial of order *q*; in this way, each incoherent fully coherent component process was given by the combination of *p* incoherent fully coherent (*q*+1)−Variate processes, whose generation was embedded into an Auto-Regressive (AR) procedure.

Carassale and Solari 2002 obtained an analytical expression of the eigenvalues and eigenfunctions of the cross spectral density function of the three wind turbulence components, assumed as uncorrelated.

The application of D-PCA in bluff-body aerodynamics is still very limited (Carassale et al. 2004, De Grenet and Ricciardelli, 2004, Carassale, 2012) and its potentiality are still unexplored.

Dynamic-ICA is intimately related to Independent Component Analysis (ICA) and Blind Source Separation (BSS) problems. The multichannel blind source separation problem has been addressed by Yellin and Weinstein (1994) and Ngyuen and Jutten (1995) and others based on 4th-order cumulants criteria. An extension to time-delays and convolved sources from the infomax viewpoint using a feedback architecture

has been developed by Torkkola (1996). Lee, Bell and Lambert (1997) have extended the blind source separation problem to a full feedback system and a full feed-forward system. The feed-forward architecture allows the inversion of non-minimum phase systems. In addition, the rules are extended using polynomial filter matrix algebra in the frequency domain (Lambert, 1996). The proposed method can successfully separate voices and music recorded in a real environment. Lee et al. (1997) show that the recognition rate of an automatic speech recognition system is increased after separating the speech signals.

Peled et. al (2005) convoluted mixing source for bearing diagnosis. Zhou and Chelidze (2007) used a novel BSS method in order to extract linear normal modes (LNMs). Modal coordinates are considered as a specific case of sources that have certain time structure.

Bell and Sejnowski (1995) showed that a variant on the network architecture is able to perform blind deconvolution cancellation of unknown echoes and reverberation in a speech signal.

5.5 DYNAMIC PRINCIPAL COMPONENT ANALYSIS (D-PCA)

Dynamic Principal Component Analysis (D-PCA) has been introduced in this context with the objective of extracting physically-meaningful coherent structures from phenomena characterized by a strong temporal (and spatial) correlation structure. As mentioned in the Section (5.17), the vector data $\mathbf{q}(t)$ can be represented as a convolutive mixture of the principal components (PCs)

$$\mathbf{q}(t) = \sum_{\tau=0}^{t-1} \mathbf{\Phi}(\tau)\mathbf{x}(t-\tau) \tag{5.20}$$

where $\mathbf{\Phi}(\tau)$ is the matrix of the D-PCA modes, which depend on the time delay τ. Such modes may be interpreted as time-variable coherent structures. The PCs defined by D-PCA (contained in the vector $\mathbf{x}(t)$) are fully uncorrelated, thus D-PCA represents the measurements as a sum of fully-correlated pressure distributions that are mutually uncorrelated.

In the sections that follow, $\mathbf{q}(t)$ is a stationary process and a frequency domain formulation can be conveniently adopted. Three different formulations are presented in Carassale (2012) and are reported here for completeness purpose.

5.5.1 D-PCA BY POWER SPECTRAL DENSITY MATRIX

Let $\mathbf{S_{qq}}(\omega)$ be the Power Spectral Density (PSD) matrix estimated from the data $\mathbf{q}(t)$ and let us consider the eigenvalue problem

$$\mathbf{S_{qq}}(\omega)\boldsymbol{\theta}_k(\omega) = \gamma_k(\omega)\boldsymbol{\theta}_k(\omega) \qquad k = 1,...,N \tag{5.21}$$

where $\boldsymbol{\theta}_k(\omega)$ are the eigenvectors, mutually orthogonal, and $\gamma_k(\omega)$ are the eigenvalues, real and non-negative ($\mathbf{S_{qq}}(\omega)$ is a complex-valued Hermitian-symmetric matrix). Assembling column-wise the eigenvectors, the obtained matrix $\boldsymbol{\Theta}(\omega)$ can be interpreted as the Frequency-Response Function (FRF) of the linear transformation defined by Eq. (5.20) and used to define a stationary D-PCA. This modal representation is referred to as Spectral Proper Transformation and fulfils the following properties

1. the PCs are uncorrelated for any time lag and their PSD is defined by the eigenvalues γ_k;

2. if the eigenvalues are enumerated in decreasing order, D-PCA possesses, for each harmonic component of $\mathbf{q}$, the same optimal properties discussed for PCA.

The eigenvectors $\boldsymbol{\theta}_k(\omega)$ are in this context interpreted as coherent structures evolving in time at the frequency ω, therefore called coherent structures; the corresponding eigenvalues $\gamma_k(\omega)$ represent their power. The use of such dynamic coherent structures is particularly useful to represent propagating phenomena for which highly correlated values appear in different locations with a time delay determined by the propagating velocity. The D-PCA modes are complex-valued and can be used to represent a phenomenon in a particular frequency range characterizing features concerning both amplitude and phase.

According to Eq.(5.21), a set of D-PCA modes can be defined for any values of ω, thus the dynamic coherent structures may be interpreted, in principle, as pressure configurations variable in frequency. This interpretation is not particularly useful because in practice it leads to a tremendous complexity of the modal representation; however in several applications, the spectral characteristics of the process suggest focusing the D-PCA analysis on a limited number of frequency bands that can be selected detecting the peaks of the eigenvalues $\gamma_k(\omega)$.

5.5.2 D-PCA BY SHORT-TIME FOURIER TRANSFORM OR WAVELET TRANSFORM

An alternative approach for the estimation of the matrix $\boldsymbol{\Theta}(\omega)$ can be defined converting Eq. (5.20) into the frequency domain as:

$$\tilde{\mathbf{q}}_T\left(\omega,\overline{t}\right) = \boldsymbol{\Theta}(\omega)\tilde{\mathbf{x}}_T\left(\omega,\overline{t}\right) \tag{5.22}$$

where $\tilde{\mathbf{q}}_T\left(\omega,\overline{t}\right)$ and $\tilde{\mathbf{x}}_T\left(\omega,\overline{t}\right)$ are the short-time Fourier transform of **q** and **x**, respectively, calculated on time windows with length T; $\overline{t}$ is a downsampled time, with a sample for each window. Starting from Eq.(5.22), D-PCA can be reformulated like the traditional PCA, on the basis of the zero-time-lag covariance matrix of $\tilde{\mathbf{q}}_T\left(\omega,\overline{t}\right)$

$$\mathbf{C_{qq}}\left(\omega\right) = \mathrm{E}\left[\tilde{\mathbf{q}}_T\left(\omega,\overline{t}\right)\tilde{\mathbf{q}}_T\left(\omega,\overline{t}\right)*\right] = \frac{1}{N_{\overline{t}}}\sum_{\overline{t}=1}^{N_{\overline{t}}}\tilde{\mathbf{q}}_T\left(\omega,\overline{t}\right)\tilde{\mathbf{q}}_T\left(\omega,\overline{t}\right)* \tag{5.23}$$

where $N_{\overline{t}}$ is the number of windows extracted from the measured signals. Accordingly, $\boldsymbol{\theta}_k(\omega)$ and $\gamma_k(\omega)$ are obtained as the eigenvectors and eigenvalues of the matrix $\mathbf{C_{qq}}(\omega)$.

It is clear that the width of the frequency bands in which $\boldsymbol{\Theta}(\omega)$ is defined is determined by the window length T; on the other hand, the statistical accuracy of the estimation is conditioned by the number of windows $N_{\overline{t}}$ extracted from the available signals. The choice of $N_{\overline{t}}$ is usually a compromise between the required statistical accuracy and the necessity of selecting precisely specific frequency bands.

The advantage of this approach with respect to the previous one is merely a computational one since it enables the use of the same algorithms developed to solve the traditional PCA problem with the only additional complication that here the covariance matrix is complex valued and the eigenvalue problem must be solved for each frequency band of interest. Besides, this approach can easily be generalized to ICA.

A more sophisticated version of this technique can be formulated by substituting the short-time Fourier transform with a wavelet transform. Although the two approaches are conceptually equivalent, this substitution enables a more accurate selection of the frequency bands to be employed for the analysis by a careful selection of an appropriate mother wavelet. In this case, $\boldsymbol{\theta}_k(\omega)$ and $\gamma_k(\omega)$ are obtained as the eigenvectors and eigenvalues of the matrix:

$$\mathbf{C_{ww}}\left(\omega\right) = \mathrm{E}\left[\mathrm{W_{q}}\left(t,s\right)\mathrm{W_{q}}\left(t,s\right)*\right] = \frac{1}{N_{\overline{t}}}\sum_{\overline{t}=1}^{N_{\overline{t}}}\mathrm{W_{q}}\left(t,s\right)\mathrm{W_{q}}\left(t,s\right)* \tag{5.24}$$

where $W_\mathbf{q}(t,s)$ is a complex analytic wavelet transform of $\mathbf{q}$ and s is the scale corresponding to the frequency ω.

5.5.3 D-PCA BY DIGITAL FILTERING AND HILBERT TRANSFORM

A further alternative approach based on the digital filtering of the measured data and on the Hilbert transform can be formulated as follows:

1. the signals $\mathbf{q}(t)$ are band-pass filtered with the central frequency ω and the bandwidth $\Delta\omega$, assumed small enough to treat the filtered signals $\mathbf{q}_\omega(t)$ as narrow-band processes;

2. an analytic signal $\tilde{\mathbf{q}}_\omega(t) = \mathbf{q}_\omega(t) + iH[\mathbf{q}_\omega(t)]$ is obtained through the Hilbert transform $H[\bullet]$;

3. the zero-time-lag covariance matrix of $\tilde{\mathbf{q}}_\omega(t)$ is computed as:

$$\mathbf{C}_{\tilde{\mathbf{q}}\tilde{\mathbf{q}}}(\omega) = \mathrm{E}\left[\tilde{\mathbf{q}}_\omega(t)\tilde{\mathbf{q}}_\omega(t)*\right] = \frac{1}{N_{\bar{t}}}\sum_{\bar{t}=1}^{N_{\bar{t}}}\tilde{\mathbf{q}}_\omega(t)\tilde{\mathbf{q}}_\omega(t)* \tag{5.25}$$

4. $\boldsymbol{\theta}_k(\omega)$ and $\gamma_k(\omega)$ are obtained as the eigenvectors and eigenvalues of the matrix $\mathbf{C}_{\tilde{\mathbf{q}}\tilde{\mathbf{q}}}(\omega)$;

5. steps 1–4 are repeated for any relevant frequency band.

From a computational point of view this approach is equivalent to the formulation based on the short-time Fourier transform; as an advantage, it enables a free adjustment of the frequency bandwidths for each of the relevant frequency contents considered in the analysis. This latter approach is adopted in the applications described in the next sections.

It should be mentioned that the eigenvalues $\gamma_k(\omega)$ obtained through the different procedures described above differ for a constant factor; however, this discrepancy does not produce any problem since the eigenvalues are used only to measure the relative energetic importance of different modes.

D-PCA modes are complex-valued vectors and should be represented in terms of amplitude and phase angle. This produces serious difficulties in the interpretation, thus an alternative form that enables a simple and intuitive representation is obtained defining the set of real-valued vectors as

$$\bar{\boldsymbol{\theta}}_k(\omega,\beta) = \mathrm{Re}\left[\boldsymbol{\theta}_k(\omega)e^{i\beta}\right] \tag{5.26}$$

where β is a real variable representing a common phase shift attributed to all the vector components. Since the vector $\boldsymbol{\theta}_k(\omega)$ are undetermined by a common phase

angle, the vectors $\overline{\boldsymbol{\theta}}_k$ can be represented for $\beta \in [0, \pi)$ without losing any information. Besides, the variable β may be related to the time lag $\tau = \beta/\omega$.
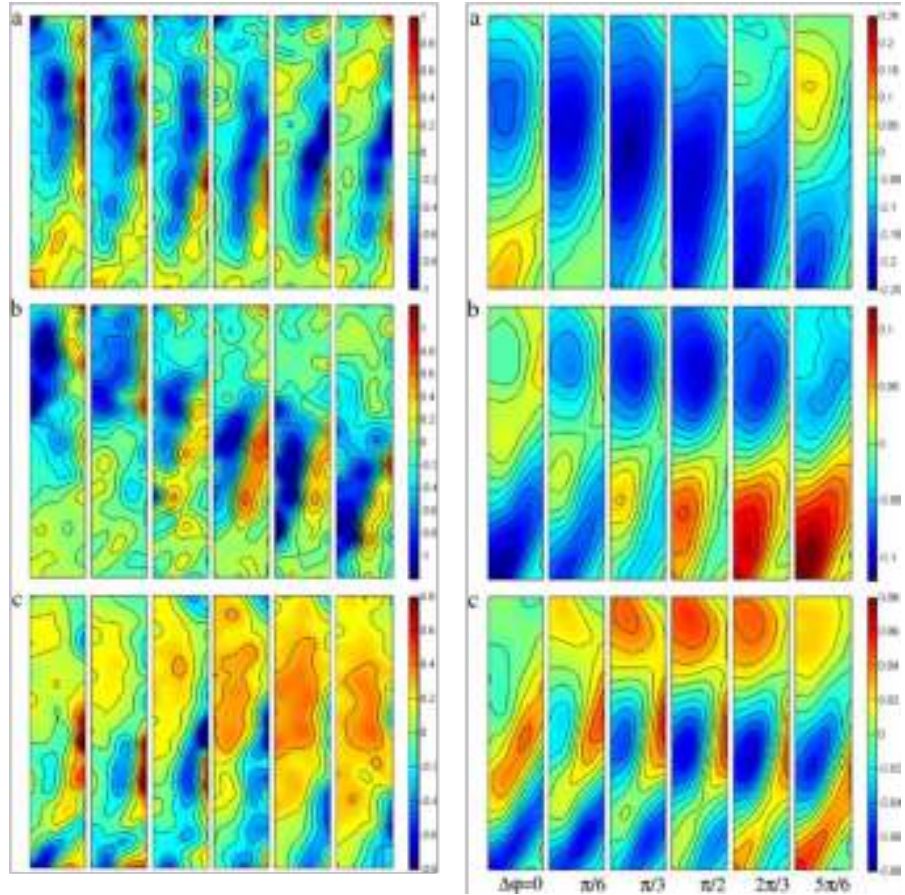
Figure 5.2   Figure from Carassale (2012). Left column: recurrent sequences observed in the pressure field fluctuation interpreted as effects of Kármán vortex shedding (a), down wash on the windward face (b) horseshoe vortex (c). Right column: scaled D-PCA modes at the vortex shedding frequency. Mode 1(a), mode 2(b), mode 3(c). Real value corresponding to six phase angle shifts uniformly spaced between 0 and π.

Figure 5.2 borrowed from Carassale 2012 presents an example of D-PCA application. **Figure 5.2** (left column) shows three selected sequences of the measured pressure field centered with respect to its mean value and non-dimensionalized with respect to the kinetic pressure; the time between frames is thrice the sampling period of the measured data (i.e. Δt=4 ms), and the total length

of sequences is about 25 ms that is about half vortex-shedding period, which is approximately 55 ms; negative values represent a suction superimposed to the mean pressure field. **Figure 5.2**a (left column) shows a very recurrent pressure pattern representing the signature of a vortex generated by the windward corner and advected along the lateral face of the model. It is worth noting that, as time passes, the vortex becomes inclined forwards due to the advection velocity, which is variable along the height because of the boundary layer developed on the floor. **Figure 5.2**b (left column) shows an intense suction region concentrated near the windward corner and shifting downwards; this effect may be related to the down-wash generated along the front face of the model. **Figure 5.2**c (left column) shows another quite recurrent pressure pattern, which can be associated to the well-known horse-shoe vortex appearing at the base of high-rise buildings.

The right column of **Figure 5.2** shows the first three scaled D-PCA modes in a frequency band centered at the frequency ω_s=18 Hz with a bandwidth $\Delta\omega$=6 Hz, containing the vortex shedding spectral peak. The six colour maps in each figure represent the real value of the mode corresponding to six phase-angle shifts between 0 and π; the phase delay between consecutive snapshots is $\Delta\varphi$=π/6, roughly corresponds to the time step Δt=4.6 ms. It seems that different phenomena are represented, at different times by the same mode: for example, frames 1–4 of mode 1 (**Figure 5.2**a (right column)) clearly represents Kármán vortex shedding, while frames 5 and 6 represent an intense pressure at the base of the model. This mixture of different phenomena is even more evident in modes 2 and 3 (**Figure 5.2** b and c (right column)), in which high-suction zones in different places of the model coexist at different times within the same mode.

5.6 DYNAMIC INDEPENDENT COMPONENT ANALYSIS (D-ICA)

The generalization of ICA to its dynamic version D-ICA can be carried out as discussed for PCA in Section 3.4. The procedure is discussed in detail considering the D-PCA formulation based on short-time Fourier transform (Section 5.5.2) since it is conceptually simpler, even if the D-PCA approach based on digital filtering and Hilbert transform (Section 5.5.3) can be successfully adopted as well.

As mentioned in the Section (5.17), the vector data $\mathbf{q}(t)$ can be represented as a convolutive mixture of the independent components (ICs)

$$\mathbf{q}(t) = \sum_{\tau=0}^{t-1} \mathbf{A}(\tau)\mathbf{s}(t-\tau) \tag{5.27}$$

D-ICA model can be formulated rewriting Eq. (5.27) in the frequency domain as:

$$\tilde{\mathbf{q}}_T\left(\omega,\overline{t}\right) = \mathbf{A}(\omega)\tilde{\mathbf{s}}_T\left(\omega,\overline{t}\right) \tag{5.28}$$

where $\tilde{\mathbf{s}}_T\left(\omega,\overline{t}\right)$ is the short-time Fourier transform of the ICs and $\mathbf{A}(\omega)$ is a frequency-variable, complex-valued $N \times n$ mixing matrix. Mixing matrix and ICs can be estimated, for each frequency band, maximizing the non-Gaussianity of the sources $\tilde{\mathbf{s}}_T\left(\omega,\overline{t}\right)$ as discussed for ICA.

Considering a particular frequency ω, the D-ICA problem can be solved following the procedure described below:

1. the number n of the ICs to be extracted is estimated according to a condition analogous to the one expressed by Eq.(3.40), but involving the eigenvalues $\gamma_k(\omega)$

$$J_E^{(n)} = \frac{E\left[\left\|\mathbf{q}^{(n)}\right\|^2\right]}{E\left[\left\|\mathbf{q}\right\|^2\right]} = \frac{\sum_{k=1}^{n}\lambda_k}{\sum_{k=1}^{N}\lambda_k} \geq 0.8 - 0.9 \tag{5.29}$$

2. the short-time Fourier transform of the data is projected onto the subspace defined by the first n eigenvectors $\boldsymbol{\theta}_k(\omega)$ ($k=1,...,n$) and whitened through the relationship

$$\tilde{\mathbf{z}}_T\left(\omega,\overline{t}\right) = \boldsymbol{\Gamma}^{(n)}(\omega)^{-0.5}\,\boldsymbol{\Theta}^{(n)}(\omega)^*\,\tilde{\mathbf{q}}_T\left(\omega,\overline{t}\right) \tag{5.30}$$

where $\boldsymbol{\Theta}^{(n)}(\omega)$ contains the first n columns of $\boldsymbol{\Theta}$ and $\boldsymbol{\Theta}^{(n)}(\omega)=\mathrm{diag}(\gamma_1(\omega),...,\gamma_N(\omega))$;

3. the non-Gaussianity measure $J_{NG}(y)$ of the real-valued random variable $y = \left|\mathbf{w}^*\mathbf{z}_T\left(\omega,\overline{t}\right)\right|$ is maximized with respect to $\mathbf{w} \in \mathbb{C}^n$ with the constraint $\|\mathbf{w}\| = 1$; the statistical expectation implicitly introduced by J_{NG} is computed by a time average on $\overline{t}$.

4. the *n* orthonormal vectors $\mathbf{w}_k$ (k=1,...,n) providing the local maxima of J_{NG} are collected row-wise in the matrix $\mathbf{W}$;

5. the mixing matrix $\mathbf{A}(\omega)$ and the sources $\tilde{\mathbf{s}}_T\left(\omega,\overline{t}\right)$ are calculated as:

$$\begin{aligned}
\mathbf{A}(\omega) &= \boldsymbol{\Theta}^{(n)}(\omega)\,\boldsymbol{\Gamma}^{(n)}(\omega)^{0.5}\,\mathbf{W}^* \\
\tilde{\mathbf{s}}_T\left(\omega,\overline{t}\right) &= \mathbf{W}\boldsymbol{\Gamma}^{(n)}(\omega)^{0.5}\,\boldsymbol{\Theta}^{(n)*}\tilde{\mathbf{q}}_T\left(\omega,\overline{t}\right)
\end{aligned} \tag{5.31}$$

Once $\mathbf{A}(\omega)$ has been estimated for all the pertinent frequency bands, its columns can be used to identify dynamic coherent structures, which evolve in time with the frequency ω and are mutually statistically independent as much as possible (for any time lag).

For interpretation purpose, D-ICA modes can be represented as sequences of real vectors defined as

$$\overline{\mathbf{a}}_k(\omega,\beta) = \mathrm{Re}\left[\mathbf{a}_k(\omega)e^{i\beta}\right] \tag{5.32}$$

for the parameter $\beta \in [0,\pi]$.

If the D-PCA approach based on digital filtering and Hilbert transform is adopted, Eq. (5.30) must be updated as:

$$\tilde{\mathbf{z}}_\omega(t) = \mathbf{\Gamma}^{(n)}(\omega)^{-0.5}\,\mathbf{\Theta}^{(n)*}\tilde{\mathbf{q}}_\omega(t) \tag{5.33}$$

The estimation of the vectors $\mathbf{w}$ is carried out by maximizing the non-Gaussianity measure $J_{NG}(y)$ with $y = \left|\mathbf{w}^*\tilde{\mathbf{z}}_\omega(t)\right|$.

In the application presented in the next sections this latter approach is employed. Besides, it is assumed that $J_{NG}(y)=\mathrm{E}[G(y)]^2$, with $G(y)=y^4-3$; the statistical expectation is estimated through a temporal average on t.

Figure 5.3, published in Carassale 2012, presents an example of D-ICA application. The left column of **Figure 5.3** (equals to the left column in **Figure 5.2**) shows three selected sequences of the measured pressure field centered with respect to its mean value and non-dimensionalized with respect to the kinetic pressure; the time between frames is thrice the sampling period of the measured data (i.e. Δt=4 ms), and the total length of sequences is about 25 ms that is about half vortex-shedding period, which is approximately 55 ms; negative values represent a suction superimposed to the mean pressure field. **Figure 5.3**a (left column) shows a very recurrent pressure pattern representing the signature of a vortex generated by the windward corner and advected along the lateral face of the model. **Figure 5.3**b (left column) shows an intense suction region concentrated near the windward corner and shifting downwards. **Figure 5.3**c (left column) shows another quite recurrent pressure pattern, which can be associated to the well-known horse-shoe vortex appearing at the base of high-rise buildings.

Figure 5.3 shows the first three D-ICA modes extracted from the reduced data space determined by the first four D-PCA modes. The colour maps represent the real value of the modes corresponding to six phase-angle shifts between 0 and π. Mode 1 (**Figure 5.3**a, right column) represents the time evolution of a vortex that, generated by the boundary layer separation at the windward corner, is advected along the lateral face of the model. As time passes (going from left to right in **Figure 5.3**a, right column), the high-suction zone moves forwards and the vortex starts leaning due to the velocity gradient in the floor boundary layer. It should be noted that the pressure distribution represented by the first D-ICA mode is extraordinarily similar to the measured pressure field reported in **Figure 5.3**a (left column) with roughly the same time delay between consecutive frames. D-ICA mode 2 (**Figure 5.3**b, right column) represents a pressure field shifting downwards on the lateral face just after the windward corner. This behaviour is compatible with the descendant flow often

recognized on the windward face of high-rise buildings as it is represented in **Figure 5.3**b (left column) D-ICA mode 3 **Figure 5.3**c (left column) represents the evolution of the pressure field at the base of the model. Also in this case, the shift of the high-suction zone is well visible and is substantially coherent with the measured sequence reported in **Figure 5.3**c (left column).
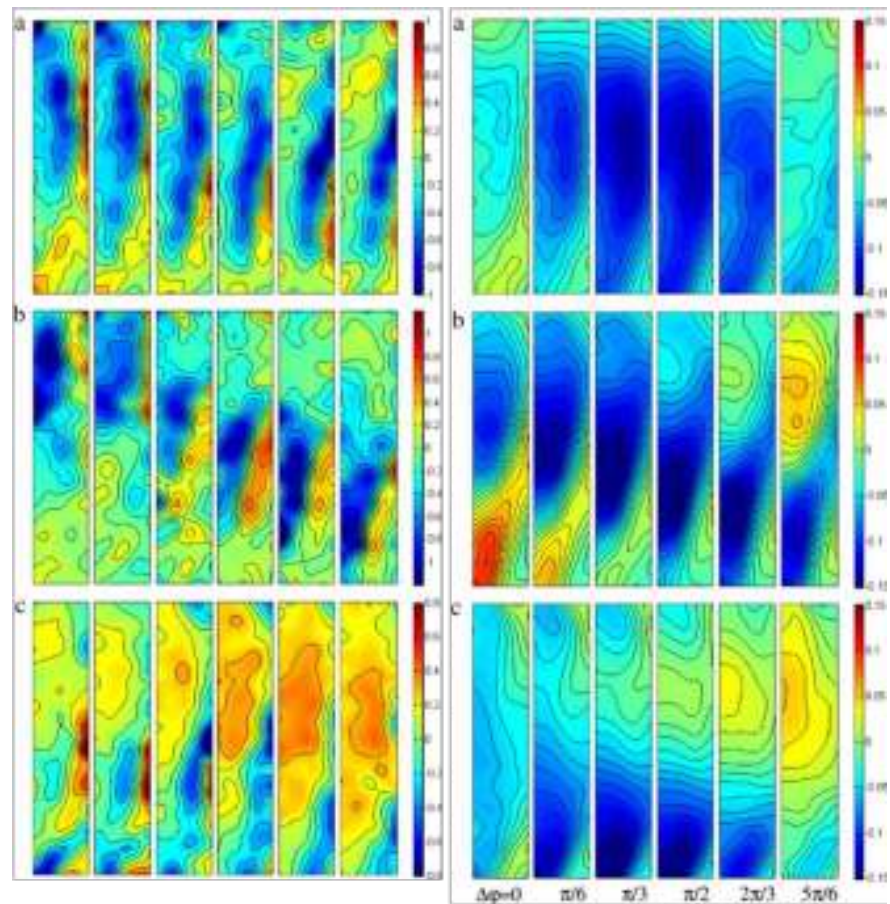
Figure 5.3   Figure from Carassale (2012). Left column: recurrent sequences observed in the pressure field fluctuation interpreted as effects of Kármán vortex shedding (a), down wash on the windward face (b) horseshoe vortex (c). Right column: D-ICA modes at the vortex shedding frequency. Mode 1(a), mode 2(b), mode 3(c). Real value corresponding to six phase angle shifts uniformly spaced between 0 and π.

5.7 CONCLUDING REMARKS

The use of modal representation techniques to provide qualitative interpretations of aerodynamic data is widely consolidated and PCA represents the standard tool to accomplish this task. In this paper this technical issue is reviewed in the wider context of the feature-extraction problem and alternative techniques are borrowed from different scientific fields. The theoretical formulation of ICA, D-PCA and D-ICA, are discussed. D-PCA is formulated according to three alternative formulations (Carassale, 2012). The formulation based on digital filtering and Hilbert transform is probably the most efficient and robust, while the other approaches are reported mostly because of their theoretical value. The solution based on the diagonalization of the PSD matrix derives straightly from the application of POD to stationary random processes and enables a simple demonstration of the optimal properties of the modal representation mentioned in this section. On the other hand, the solution based on the short-time Fourier Transform has the advantage of being formally analogous to PCA and, for this reason, it is employed to derive D-ICA from D-PCA through a simple analogy. Its main drawback, related to its poor statistical robustness, can be overcome by adopting a wavelet-based formulation.

CHAPTER 6

APPLICATION: SQUARE PRISM IN BOUNDARY LAYER

Vincent Van Gogh, Cornfield and wind vortex.
Oil on canvas, 1889.

6.1 INTRODUCTION

In the previous chapters several statistical techniques oriented to the study of the wind effects on bluff bodies have been extensively described. This section presents the applications of such techniques, innovative (e.g. ICA and D-ICA) as well as conventional ones, to a simple but relevant case study involving a square-base prismatic body immersed in an atmospheric boundary layer (ABL). The model has aspect ratio 5:1 and different angle of incidence have been tested. All the experimental tests have been carried out at the University of Genova. The discussion of the results enables the definition of general criteria that can guide the selection of the most appropriate data-analysis technique for the study of a large class of aerodynamics-related problems.

6.2 EXPERIMENTAL ARRANGEMENTS

The experimental tests have been carried out in the closed-circuit wind tunnel at the University of Genova, whose cross section is 1640×1350 mm^2 and the fetch for the generation of the boundary layer on the wind tunnel floor is 8.8 m long. The setup consists of a building model with aspect ratio 5:1 (high l=40 cm, square base with side b=8 cm). The incident boundary layer is produced by a set of triangular spires and a roughness fetch is realized by blocks with decreasing size (**Figure 6.1**). The mean wind velocity profile corresponds to a power law with exponent 0.22; at the top level of the model the mean wind velocity is U=12.2 m/s, the intensity of the longitudinal turbulence is I_u=13% and its integral length scale is L_u=40 cm. The high of the boundary layer at the model location is about 60 cm (1.5l).

Figure 6.1   Wind tunnel, experimental setup.

The measurements derive from an instrumented ring at the level of the stagnation point z=0.6l. The ring is composed by N=28 pressure taps connected through short tubes to a 32-channel PSI pressure scanner mounted inside the model (**Figure 6.2**). The recording time corresponds to about 2×10^4 vortex shedding cycles. The model is fixed to a turning table to explore different angles of wind incidence α. In particular, the results presented in the following section consider α=[0,15°,20°,25°,30°,35°,40°,45°] focusing on the symmetric configuration with α=0 and non-symmetric arrangement with α=15°.

In the discussion that follows, the analyzed dataset is composed by N time histories coming from the pressure taps located on the tested body surface. All the measurement channels are simultaneously sampled N_t times at a regular time rate; the vector $\boldsymbol{q}(t)$=[$q_1(t),...,q_N(t)$]^T contains the pressure measurements sampled at the discrete time t. The sampling frequency is n_s=325 Hz and N_t=6.5·10^4 samples per channel are available for the analysis. The observed phenomenon is assumed to be

statistically stationary and ergodic, thus time averaging is used as a surrogate of ensemble averaging to estimate any statistical quantity.
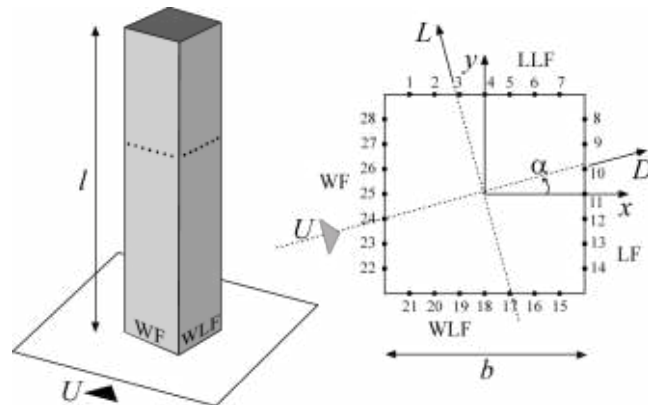
Figure 6.2   Experimental setup for square prism in atmospheric boundary layer; cross section with pressure taps and reference system.
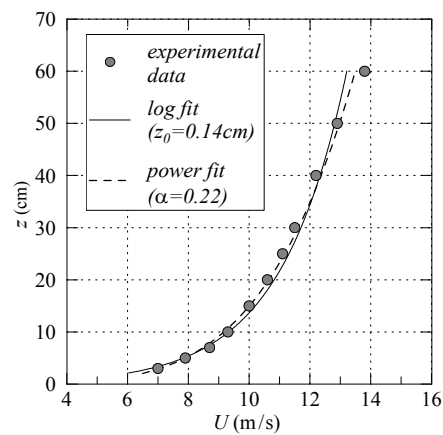
Figure 6.3   Incident flow features: boundary layer velocity profile with two different lines fitting.

6.3 DATASETS ANALYSES

This section presents the results obtained applying the statistical techniques, extensively described in the previous chapters, to the datasets collected during the wind tunnel tests described above, i.e. square prism in atmospheric boundary layer.
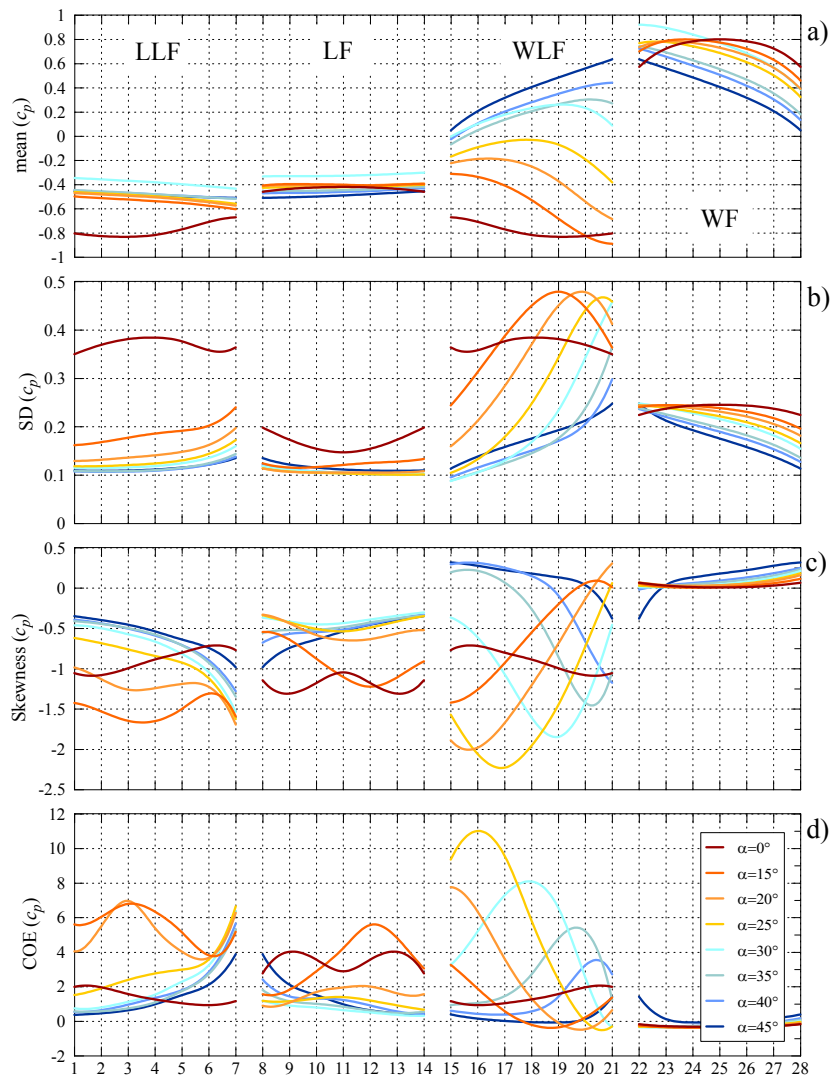
Figure 6.4   BL-setup, Single point-single time analysis for different angles of incidence.

Figure 6.4 shows the mean (a), Standard Deviation (SD; b), skewness (c) and Coefficient of Excess (COE; d) of the pressure coefficient c_p, i.e. the pressure field $q_j(t)$ (j=1,...,28) non-dimensionalized by the dynamic pressure q_d=$0.5\rho U^2$ evaluated at the top level of the model, for different angle of incidence, α=0,15,20,25,30,35,40,45°. The coloured lines interpolate the experimental results coming from the pressure taps. Passing from a symmetric configuration to other (i.e. from α=0, red line, to α=45°, blue line) the windward face (WF) is governed by

overpressure while the leeward lateral face (LLF) and the leeward face (LF) are affected by suction. In particular, the stagnation point approaches the leading edge increasing the angle and gives rise to a significant change in overpressure on the WF; the suction on the LF is practically constant with a value about $0.4q_d$, while on the LLF the suction is between $0.4q_d$ and $0.8q_d$. The mean pressure acting on the windward lateral face (WLF) is negative till $\alpha=25°$, beyond becomes positive; the minimum value is detected by sensor 19 with a value about $-0.8q_d$ for $\alpha=0$ and the maximum value is detected by sensor 21 and is about $0.6q_d$ for $\alpha=45°$. The SD on the LF and WF is between $0.1q_d$ and $0.25q_d$; higher values are reached on the WLF. The maximum values of SD, about $0.48\ q_d$ are localized on the WLF and moves towards the leading edge rotating the prism: for $\alpha=15°$ the maximum is recorded by channel 19, for $\alpha=20°$ by channel 20 and for $\alpha=25°$ by channel 21. At the same time the SD of the sensor 15 (near the trailing edge) decreases passing from 0.35 to 0.1. This may be interpreted as the complete reattachment of the fluid flow on the lateral side exposed to the wind.
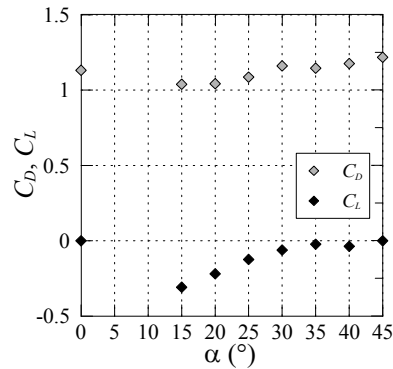
Figure 6.5   Steady drag and lift coefficients for different angles of incidence.

Figure 6.5 gives information about global aerodynamic forces changing the angle; unfortunately the data between $\alpha=0$ and $\alpha=15°$ are not available. The drag coefficient has its minimum value for $\alpha=15°$ and the lift slop is positive; such behaviour agrees with the pressure results concerning the reattachment of the flow on the windward corner.

The representation of the SPST analysis offered by **Figure 6.6** simplifies the qualitative interpretation of the results shown in **Figure 6.4** for $\alpha=15°$, 20° and 25°. Increasing the angle, on the WLF the mean and the SD decrease toward the trailing edge because the flow field reattaches on the lateral side. At the same time higher-order statistics increase due to the high instability of such region.
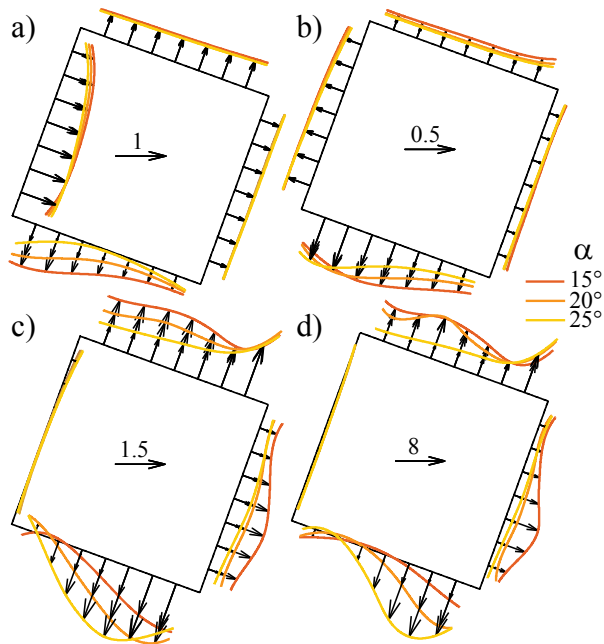
Figure 6.6   Mean (a), SD (b), skewness (c) and COE (d) of the pressure field non-dimensionalized by the kinetic pressure at the model top level; α=15° (red line), 20° (orange line), 25° (yellow line).

6.3.1 SYMMETRIC CONFIGURATION

This section focuses on the particular configuration with angle of attack α=0, further details can be found in Carassale and Marrè Brunenghi (2011).
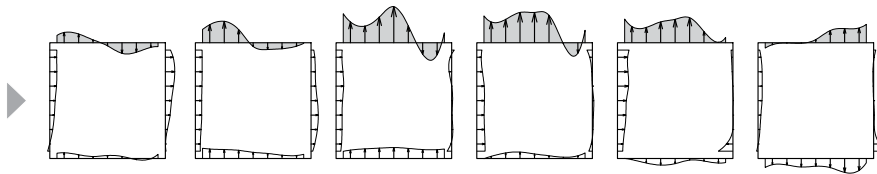
Figure 6.7   Time history of the pressure field (time step 10 ms), Carassale and Marrè Brunenghi (2011).

Figure 6.7 shows six snapshots of a typical (recurrent) pressure pattern in which the effect of the generation and advection of a vortex is well recognizable (upper

side of the figure in grey). The distance between subsequent snapshots is about 10 ms.

Figure 6.8 shows the SPST analysis (Section 2.2) of the dataset. In particular are reported mean (a), SD (b), skewness (c) and COE (d) of the pressure field non-dimensionalized by the dynamic pressure evaluated at the top level of the model. The maximum, mean, overpressure is in the stagnation point (sensor 25) and is about $0.7q_d$; the maximum value of suction, $0.8q_d$, is almost on the centre of the lateral sides (sensors 3 and 19). The maximum value of SD is about 0.4 q_d for the channel 18 suggesting that the lateral excitation mechanisms related to lateral turbulence and vortex shedding are the most relevant ones for this kind of model.
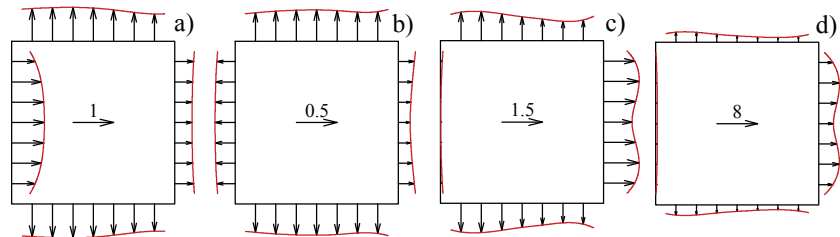
Figure 6.8   Mean (a), SD (b), skewness (c) and COE (d) of the pressure field non-dimensionalized by the kinetic pressure at the model top level; α=0.

While the 1st- and 2nd-order statistics mainly provide quantitative information, higher-order statistics furnish a qualitative description of the phenomenon. Skewness (**Figure 6.8** c) is negative and COE (**Figure 6.8** d) is positive everywhere with the exception of the wind ward face where they are practically zero. A negative skewness reflects a probability distribution having thicker tail on the suction side, while a positive COE indicates that positive and negative peaks of the pressure time histories tend to be more pronounced than the peaks of a Gaussian process with the same spectral characteristics. The 3rd- and 4th- order statistics testify two features of the pressure field that can be clearly noted observing an animated plot of the measurements: (1) suction in the separated region of the boundary layer appears very quickly (the physical reason is that it is related to the formation of vortices through a flow instability) leading to intense pressure peaks, while the subsequent over pressure phase tends to evolve more slowly, reaching lower pressure values; this behavior gives rise to a skewed probability density function (pdf) with negative skewness; (2) high-suction and high-overpressure events on the lateral faces appear and disappear quickly over a back ground random fluctuations, giving rise to a relatively high probability of having very high or very low pressure values.

The non-Gaussian nature of the pressure field is described with more detail in **Figure 6.9** a) where the pdf of the standardized (zero mean and unit variance) pressure is compared with the Gaussian pdf for the measurement Points 2, 13 and 25

(Fig. 1b). The pdf of the pressure near the sensor 2 (lateral face) and 13 (LF) are quite similar in spite of a great difference in the COE. At sensor 25 (WF) the pdf of the pressure is almost Gaussian; the right tail (suction) lower than the Gaussian pdf is compatible with the quadratic transformation between the incoming velocity (practically Gaussian) and pressure predicted by the quasi-steady assumption; on the contrary the behaviour of the left tail cannot be explained on this basis.
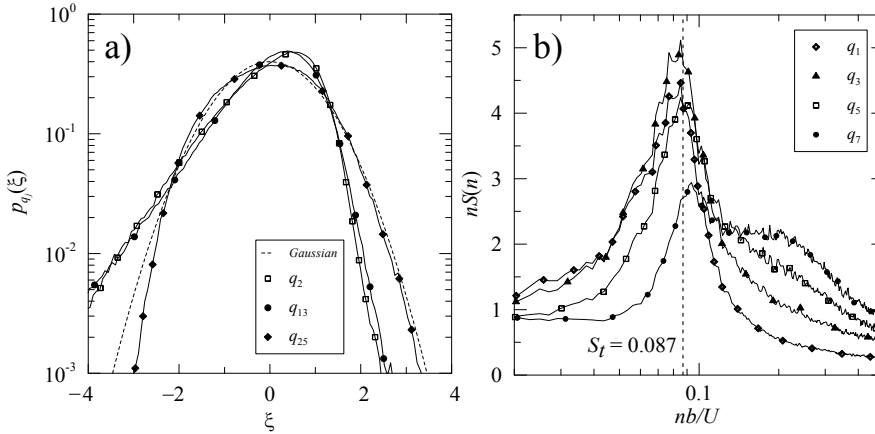
Figure 6.9   Left (a): pdf of standardized pressure channels q_2 (lateral face), q_{13} (LF) and q_{25} (WF). Right (b): PSD functions of the pressure along the lateral face.

As an example of SPMT analysis (Section 2.3), **Figure 6.9** b shows the PSD of the pressure measured on a lateral face of the model. The spectral peak due to vortex shedding is clearly visible in all the pressure taps and, even if the variance (the area below the curves) is almost constant along the face, some differences are clearly visible. In particular, the spectral peak shifts rightwards (towards higher frequencies) and decreases in amplitude moving from the windward to the leeward corner. The Strouhal number indicated in the figure refers to the global crosswind force and corresponds to an average of the peak frequencies estimated in the different points of the face.

The described behaviour may be explained with a mechanism in which the large vortices shed at the windward corners break into smaller vortices characterized by a faster time scale. This hypothesis cannot be proved on the basis of the results presented herein, but it is consistent with the analysis of the coherent structures extracted from the pressure field acting on the whole lateral face of the model (Carassale, 2012).
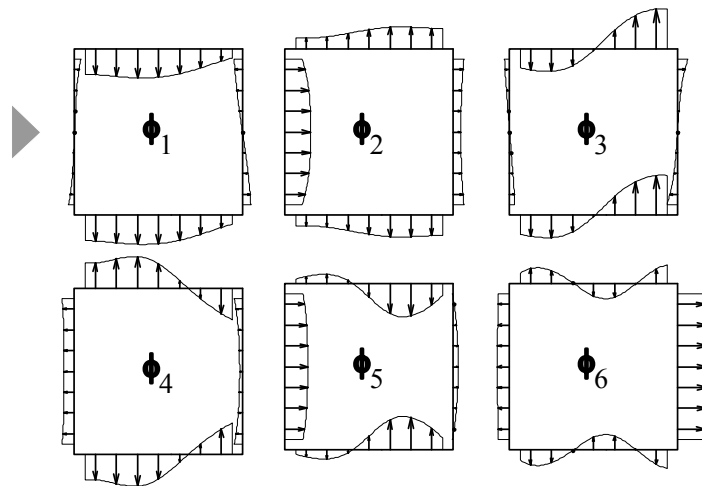
Figure 6.10 First six PCA modes extracted from the data.

An MPST analysis is carried out applying PCA (Chapter 3) and ICA (Chapter 4) to the measured data. **Figure 6.10** shows the first six PCA modes extracted from the pressure measurements $\mathbf{q}(t)$. PCA modes are necessarily symmetric or anti-symmetric (Carassale, 2009) and, as it has been observed by several authors (e.g. Kikuchi et al., 1997 for a very similar case study), the first few ones tend to be individually associated to different global actions. In this case, the first three PCA modes are associated, respectively, to cross-wind force, along-wind force and torsional moment, providing, respectively, 99%, 89% and 80% of their SD.

The use of PCA modes to identify, and possibly separate, physical mechanisms hidden in the random pressure field has often been justified by invoking two properties of PCA: (1) the PCs are uncorrelated, thus different modes may represent traces of different physical causes (unfortunately this condition is necessary, but is not sufficient); (2) PCA modes are separated by the maximum possible gap in terms of energy, thus physical phenomena located in well-separated energy bands are likely to be represented by different modes.

In spite of these observations, the PCA modes shown in **Figure 6.10** are clearly non-physical. In particular it can be noted that: (1) mode 1 represents pressure fields on the two lateral faces having the same intensity and opposite sign; on the contrary, it is known (and is confirmed by the negative skewness) that suction tends to be more violent than overpressure; (2) mode 4 suggests the presence of a symmetric vortex shedding that in reality does not occur.
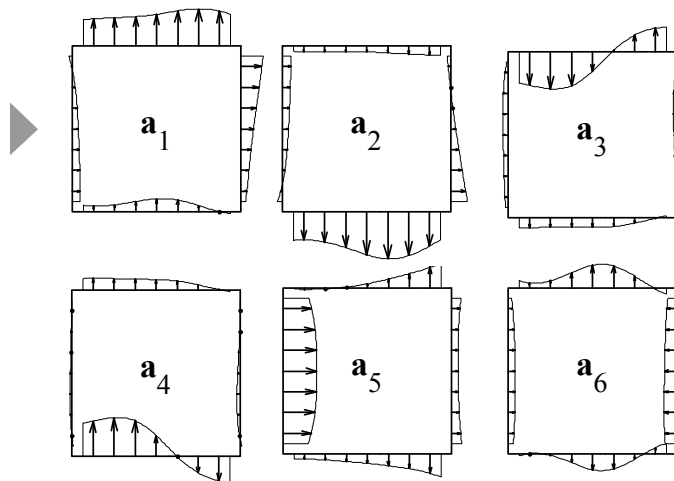
Figure 6.11 ICA modes extracted from the data space define by the first six PCA modes.

PCA modes are determined on the basis of the probabilistic structure of the pressure field without including any information on the physical nature of the observed phenomenon. For this reason, it should not be surprising if the shape of PCA modes does not reflect any specific physical mechanism. On the contrary, a reasonable expectation for a statistical technique like PCA would be to retrieve from the random measurements a set of pressure patterns that appear recurrently in the pressure field. Unfortunately, even this more limited task is not accomplished by PCA, as it can be observed comparing PCA modes and the measurements reported in **Figure 6.7**.

Figure 6.11 shows the six ICA modes estimated from the reduced data space defined by the first six PCA modes. With this condition, the six PCA modes shown in **Figure 6.10** and the six ICA modes shown in **Figure 6.11** contain exactly the same information; however, ICA modes are much more similar to the pressure patterns actually observed during the test (**Figure 6.7**). Modes 1 and 4 represent the pressure field on a lateral face (the upper one in the figure), while modes 2 and 5 represent, symmetrically, the field on the opposite face. The effect of the vortex shedding is, therefore, represented independently for the two lateral faces avoiding the non-physical results observed for PCA. Mode 3 mainly represents the pressure fluctuation on the windward face; Mode 6 contains a residual symmetric pressure distribution.

The better physical description offered by ICA has two main implications: (1) local features of the pressure field (like the pressure acting on a lateral face) are represented more efficiently (with less modes) by ICA than PCA; (2) the ICs tend to

inherit the probabilistic distribution of the local pressure field that they represent, while the PCs tend to produce wide distortions.

The latter property can be verified by comparing the pdf of the pressure measured at sensor 2 (**Figure 6.12** a), solid line) with the pdf of the PC x_1 (dashed line) and of the IC s_4 (dots). To allow the comparison, all the quantities have been standardized. Since ϕ_1 is anti-symmetric, then the pdf of x_1 is necessarily symmetric (Carassale, 2009), while the pdf of the actual pressure is strongly skewed as it is well reproduced by the pdf of s_4.

ICA modes 1 and 4 represent, satisfactorily, the pressure field on one of the lateral faces. Their respective amplitudes - the ICs s_1 and s_4 - are almost statistically independent, as it can be verified by observing **Figure 6.12** b) where their joint-pdf (solid line) almost coincides with the product of their marginal pdf (dots). In spite of this almost perfect statistical independence, it is clear that the description of the mechanism represented in **Figure 6.7** (generation and advection of a vortex) requires the use of both modes 1 and 4, which in this way are necessarily attributed to the same physical phenomenon. The reason of this apparent contradiction (two independent modes concurring to the representation of the same physical phenomenon) can be easily explained representing the cross-covariance of s_4 and s_1 defined as:

$$C_{s_4 s_1}(\tau) = \mathrm{E}\left[s_4(t) s_1(t + \tau) \right] \tag{6.1}$$

where $\mathrm{E}[\cdot]$ is the statistic expectation and τ is a delay time.
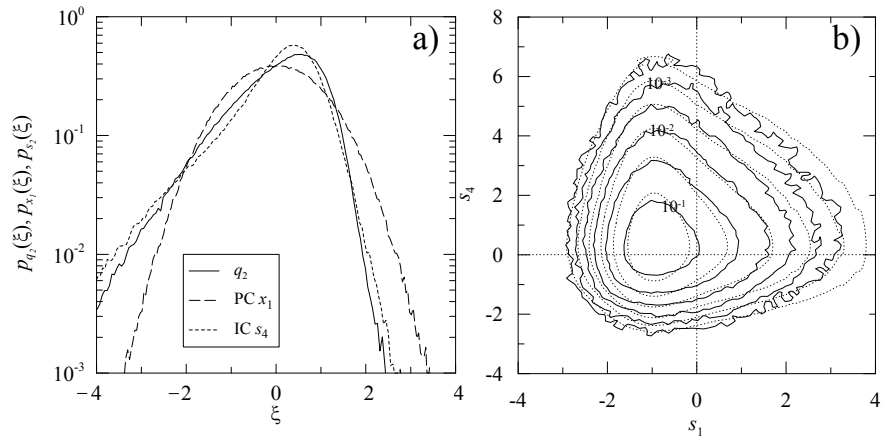
Figure 6.12 Left (a): pdf of standardized (zero mean, unit variance) pressure channels q_2 (solid line), the standardized PC x_1 (dashed line) and the IC s_4 (dots). Right (b): joint-pdf of the ICs s_1 and s_4 (solid line) and product of their marginal pdfs (dots).

It appears (**Figure 6.13**) that the cross-covariance of s_4 and s_1 has a peak with value about 0.45 (the ICs are unit variance for definition) for a delay time about 20 ms. It results that ICA modes 1 and 4 are definitely correlated if their amplitude is evaluated with a time delay roughly compatible with the advection time of a vortex (corresponding to the time between three consecutive snapshots in **Figure 6.7**).
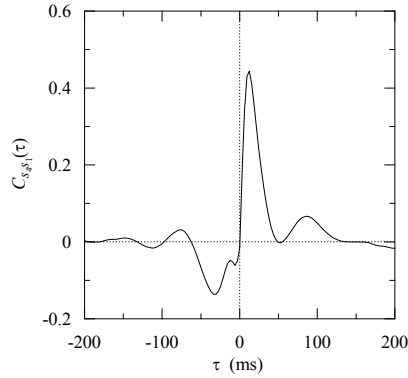
Figure 6.13 Cross-correlation of ICs s_4 and s_1.

Figure 6.14 shows the vectors $\overline{\theta}_k$ for $k=1,\dots,4$, $\omega=\omega_s$ (vortex shedding frequency) and $\alpha=0$, $\pi/6$, …, $5/6\pi$. Mode 1 is similar to PCA mode ϕ_1 and represents an anti-symmetric pressure distribution, fluctuating with frequency ω_s; the modification of the mode shape with the phase angle (i.e. with the time) is limited, but suggests the presence of a propagating pressure field, which can be associated to the advection of the vortexes. Modes 2 and 3 represent symmetric pressure distributions acting mainly on the lateral faces with a shape similar to PCA modes 2 and 4; propagation effects are present, but are substantially limited to the lateral faces. Mode 4 is anti-symmetric and is related to the pressure field acting on the lateral faces with a shape similar to PCA mode 3; the propagation in the wind direction appears evident.
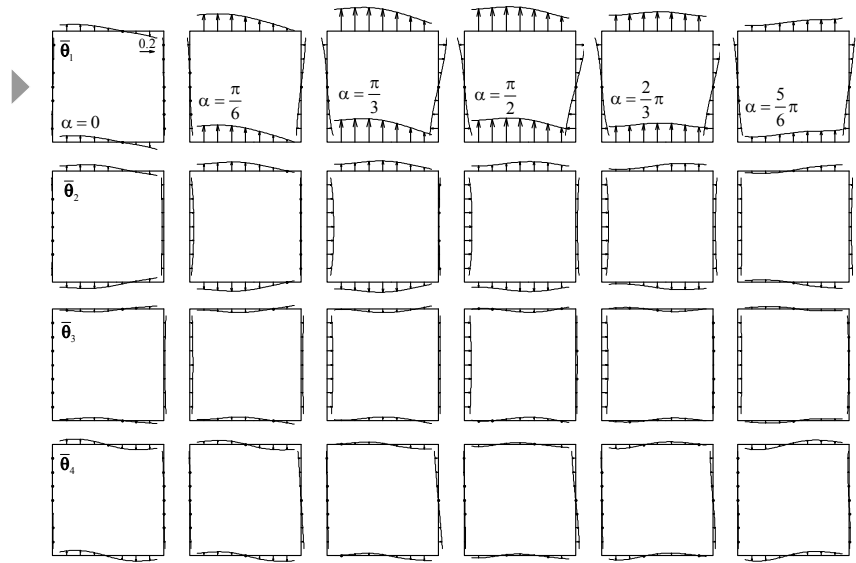
Figure 6.14 D-PCA modes $\boldsymbol{\theta}_1$ to $\boldsymbol{\theta}_4$ at the vortex-shedding frequency: real part for 6 phase shifts α=0, $\pi/6$,…,5/6π.

The dynamic coherent structures estimated by D-PCA are substantially similar to the coherent structures estimated by PCA, but provide information on the propagating direction and velocity of the pressure field. In spite of this more complete information, however, none of the D-PCA modes really resembles a realistic pressure time history of the pressure field like the one shown in **Figure 6.7**.

Figure 6.15 shows the vectors $\overline{\mathbf{a}}_k$ for k=1,…,4, $\omega = \omega_s$ and α=0, $\pi/6$, …, 5/6π estimated from the reduced data space determined by the first 4 D-PCA modes (**Figure 6.14**). Modes 1 and 3 are associated to the pressure field acting on a lateral face; Modes 2 and 4 are their symmetric counterparts and are referred to the opposite face. Modes 1 and 2 represent pressure distributions that are almost anti-symmetric with suction on a lateral face and overpressure with similar amplitude on the opposite face. On the contrary, Modes 3 and 4 represent pressure fields mainly acting on a single lateral face and characterized by an evident propagation in the wind direction.
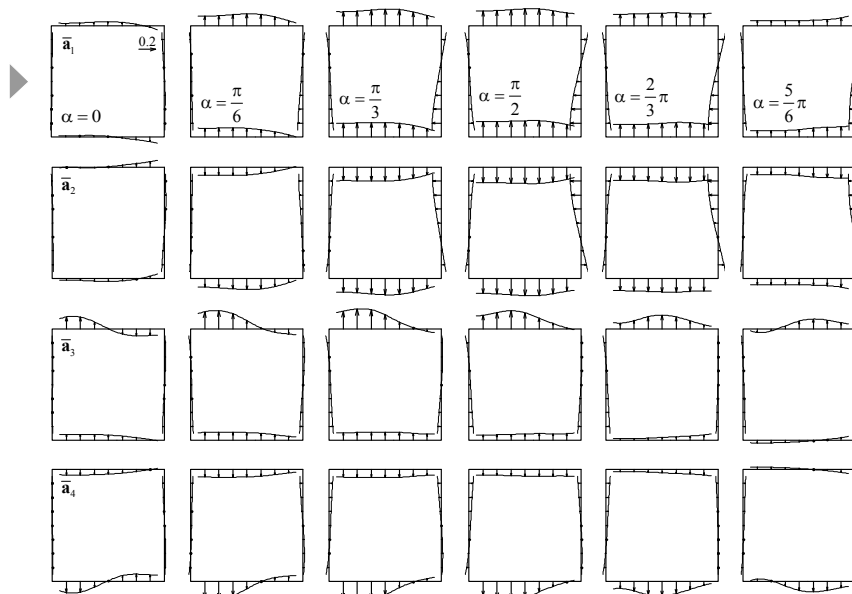
Figure 6.15 D-ICA modes $\mathbf{a}_1$ to $\mathbf{a}_4$ at the vortex-shedding frequency: real part for 6 phase shifts α=0, $\pi/6$,…,5/6π.

6.3.2 NON-SYMMETRIC CONFIGURATION

This section focuses on the particular configuration with angle of attack α=15°, further details can be found in Carassale and Marrè Brunenghi (2012).
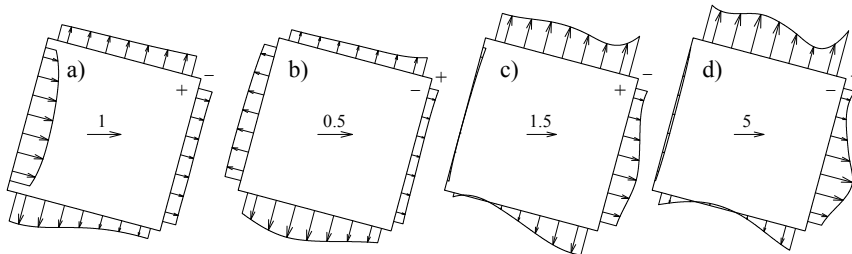
Figure 6.16 Mean (a), SD (b), skewness (c) and COE (d) of the pressure field non-dimensionalized by the kinetic pressure at the model top level.

Figure 6.16 shows the mean (a) SD (b), skewness (c) and COE (d) of the pressure field non-dimensionalized by the kinetic pressure evaluated at the top level of the model. The mean pressure field has maximum value ($0.8q_d$) on the windward face and minimum value ($-0.9q_d$) on the WLF, close to the windward corner. The mean

pressure acting on the LLF is negative and practically uniform about ($-0.4q_d$). The pressure fluctuation has maximum standard deviation on the WLF; it is substantially Gaussian on the windward face, while it is significantly non-Gaussian with negative skewness and positive COE on all the other faces with the exception of a limited portion of the WLF near the windward corner.
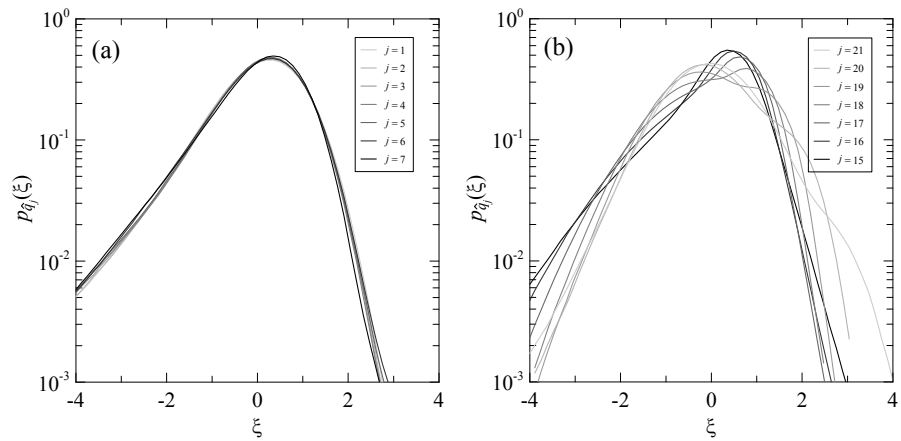
Figure 6.17 Pdf of standardized pressure measurements along LLF (a) and WLF (b).

Figure 6.17 shows the pdf of the standardized (zero mean, unit variance) pressure field $\hat{\mathbf{q}}(t)$ measured on the LLF (a) and WLF (b). All the sensors $\hat{q}_j(t)$ ($j=1, \ldots, 7$) on the LLF have similar super-Gaussian pdf with thicker tail on the suction side, likewise it has been observed on both the lateral faces for the case $\alpha=0$ (previous section, Carassale and Marrè-Brunenghi, 2011). On the WLF the pdf of $\hat{q}_j(t)$ ($j=15, \ldots, 21$) evolves moving downstream from the windward corner, gradually passing from a quasi-Gaussian distribution (like on the windward face) to a very skewed one. During this modification a secondary modal point appears (for positive pressure fluctuations) and increases its importance becoming the sole modal value. This behaviour seems to reveal a transition between two phenomena characterized by different pdf and may be related to the reattachment of the boundary layer producing a recirculation bubble (Huang et al., 2010).

Figure 6.18 shows the PSD function of the pressure field measured on the LLF (a) and WLF (b). On the LLF (a) the spectral content of the pressure fluctuation is similar to the one observed for the case $\alpha=0$: a clear peak at the vortex-shedding frequency (about 13 Hz) is accompanied by a low-frequency content similar to the spectra of the turbulence in the incoming flow. On the WLF, a low-frequency spectral peak at 2-2.5 Hz is clearly visible in all the pressure taps with the exception of the ones near the corners.
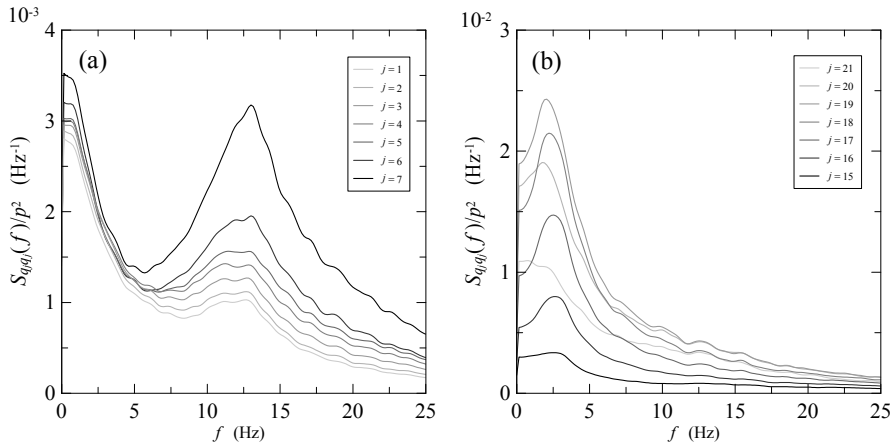
Figure 6.18 PSD of pressure measurements along LLF (a) and WLF (b).
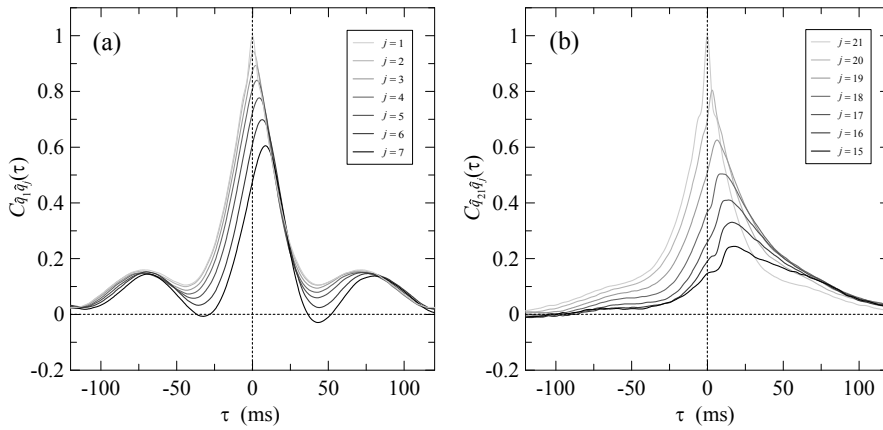
Figure 6.19 Correlation coefficients between the first pressure tap near the windward corners and the subsequent pressure taps along LLF (a) and WLF (b).

Figure 6.19 shows the correlation coefficients between the pressure measured by the first sensors near the windward corners and the other pressure taps along the LLF (a) and WLF (b). On the LLF the pressure field is well correlated, with a correlation coefficient between the first and the last pressure tap about 0.6 at the time lag $\tau \simeq 8.5$ ms. The time lags corresponding to correlation peaks are consistent with a propagation velocity about 9 m/s (about 75% of the top-model undisturbed velocity). Beside the main peak close to $\tau=0$, two peaks for $\tau \simeq \pm 75$ ms are clearly visible and represent the inter-cycle correlation of the pressure fluctuation due to

vortex shedding. On the WLF the loss of correlation moving downstream from the windward corner is larger than for the LLF (the correlation coefficient between the first and the last pressure tap is about 0.2), and the apparent propagation velocity estimated from the correlation peak time lags is lower (about 3 m/s).
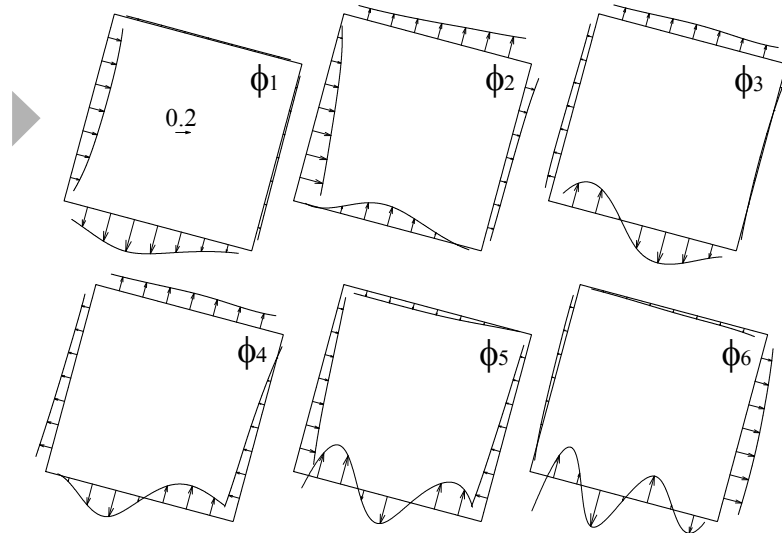
Figure 6.20 PCA modes

Figure 6.20 shows the first 6 PCA modes extracted from the data. The relative importance of each mode in the representation of the pressure field is quantified through the quantity defined by Eq (3.33); the 6th-order ROM defined through these modes retains about 93% of the norm SD of the full-order dataset. Mode 1 represents a pressure distribution acting on the windward face and the WLF with amplitude roughly proportional to the SD (**Figure 6.16** b) and provides about 67% of the SD of $\|\mathbf{q}\|$. The pressure on the LLF is represented, with a similar spatial distribution, by modes 2, 3 and 4. All the reported modes provide a contribution to the pressure field acting on the WLF, with higher-order modes representing details characterized by a smaller spatial scale. This latter behaviour is encountered quite commonly in PCA applications and is essentially due to the orthogonality constraint that is implicitly involved in the definition of the modes. Besides, it is worth noting that, even if the pressure fields acting on the two lateral faces have very different statistical properties (i.e. different probability distribution, spectral properties, propagation velocity), several modes provide contributions on both the lateral faces (modes 2, 3, 4).
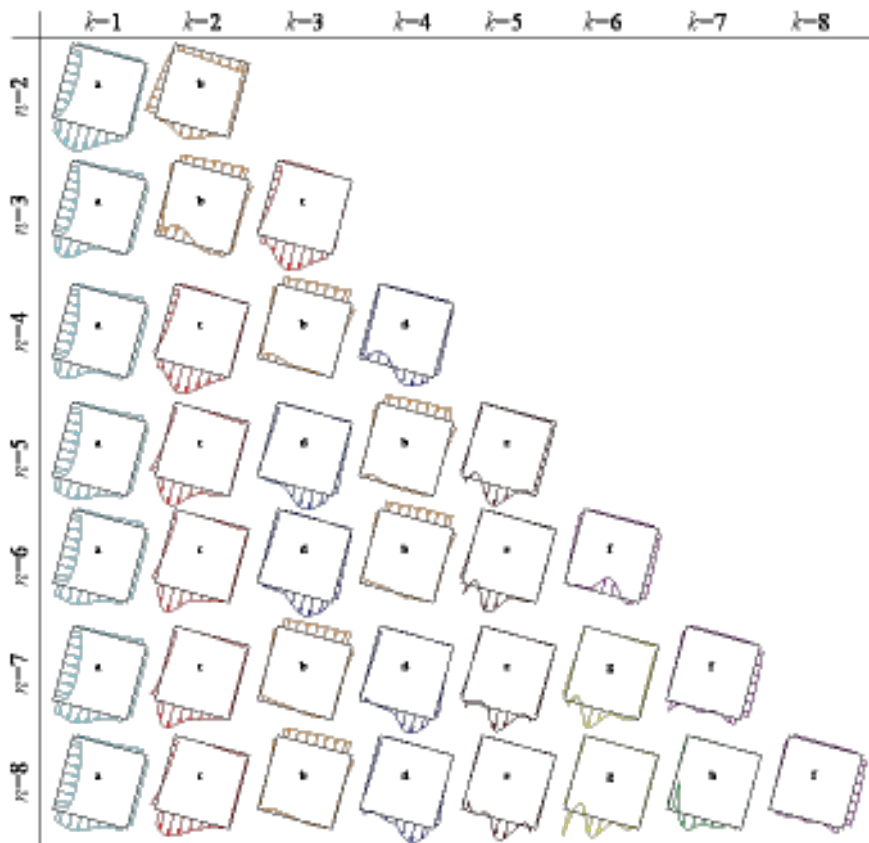
Figure 6.21 ICA modes for model orders $n = 2$ to 8.

It has been observed that, working with ICA representations, the choice of the model order n can be more critical than for PCA. To investigate this issue, **Figure 6.21** shows the ICA modes estimated for model orders n from 2 to 8. For each model, modes are plotted row-wise, sorted with respect to their norm and labeled with a letter (from a to h) on the basis of their shape. As the model order increases some modes (modes a, b and f) stabilize on a particular shape, while other modes split into different modes (modes c, d, e, g, h). The former behaviour belongs to the modes representing the pressure field on the windward face (mode a), on the LLF (mode b) and on the leeward face (mode f); the latter behaviour is shown by the modes involved in the representation of the pressure on the WLF (modes c, d, e, g, h).
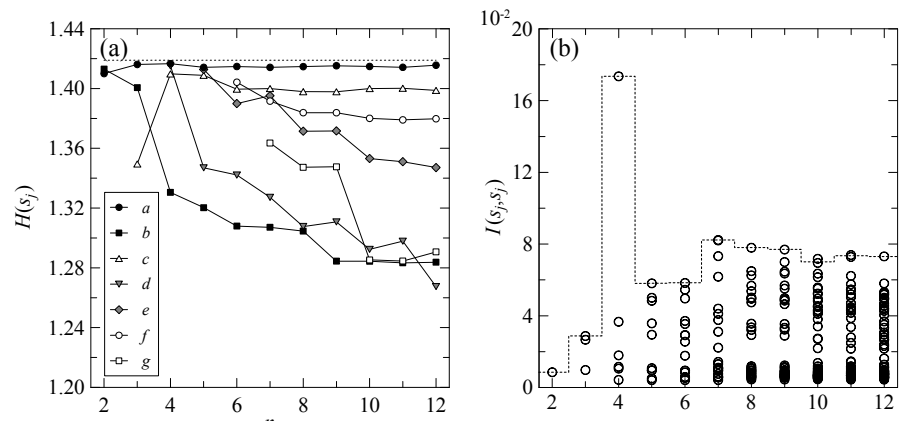
Figure 6.22 Entropy of the ICs (a) and mutual information between pairs of ICs (b) as functions of the model order.
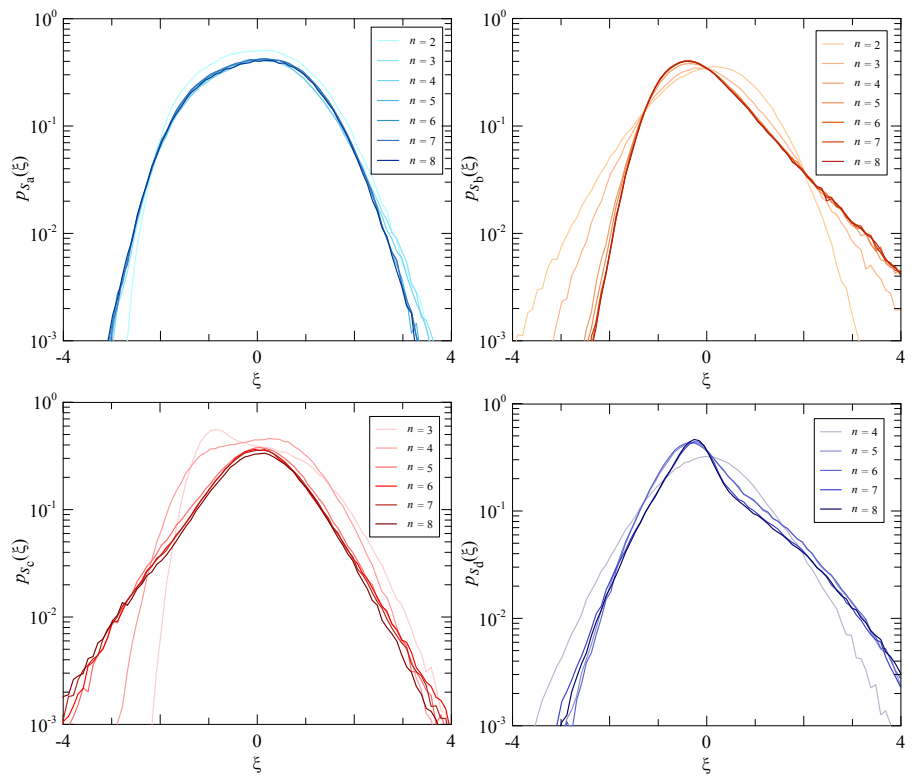
Figure 6.23 Pdf of the ICs for different model orders: s_a (a), s_b (b), s_c (c) and s_d (d).

Figure 6.22 reveals a complementary aspect of this evolution. **Figure 6.22** a) shows the differential entropy of the ICs corresponding to ICA modes *a* to *g*, defined by Eq (4.25) evaluated for s_k and being p_{S_k} the pdf of the kth IC. As the model order increases, the entropy of the ICs tends to decrease, indicating an increment of their non-Gaussianity (the maximum entropy corresponding to the Gaussian distribution is reported with dotted line). On the other hand, the reduction of entropy reflects a reduction of the information content carried by each IC, which, in some sense, tends to distill a specific feature of the observed phenomenon.

Figure 6.22 b) shows, for different model orders, the mutual information between pairs of ICs defined by Eq (4.39) and evaluated for s_j and s_k, being $p_{S_j S_k}$ the joint pdf of the jth and k^{th} ICs. The mutual information can be interpreted as a measure of the statistical dependency of two random variables, or from an information theory view point, it measures the overlapping of the information carried by s_j and s_k. The mutual information can be used as a guide to select the model order, for example excluding those orders that produce IC pairs with large mutual information (like $n = 4$ in the present application), and privileging the orders for which the mutual information of IC pairs are clustered about small values (like $n = 7, 8$ in the present application).
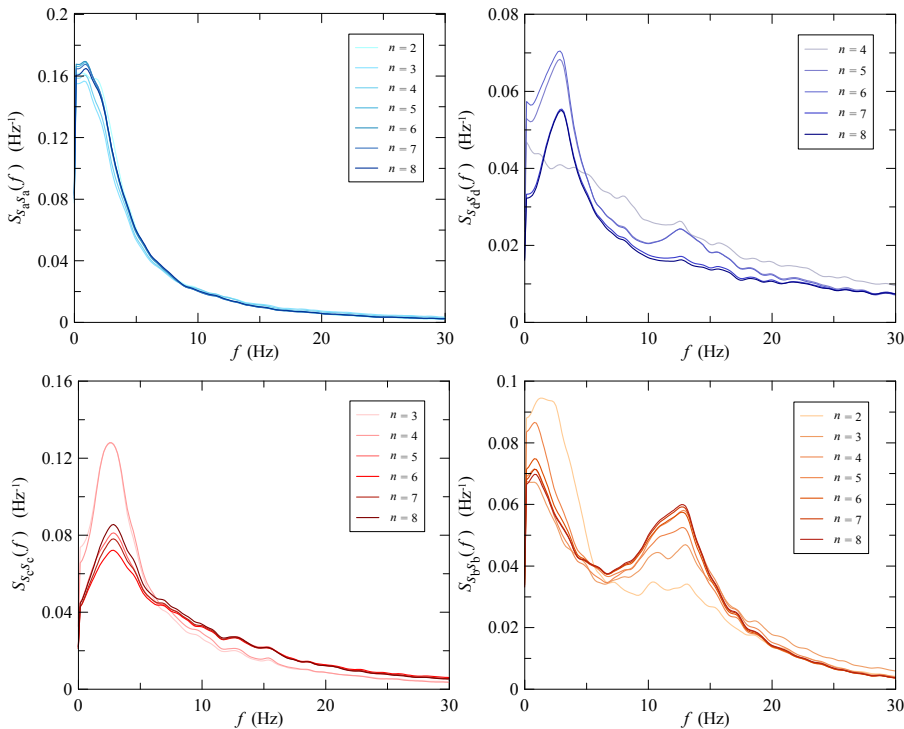
Figure 6.24 PSD of the ICs for different model orders: s_a (a), s_b (b), s_c (c) and s_d (d).

Figure 6.23 shows the pdf of the ICs corresponding to ICA modes *a* to *d*. As the model order increases the plots tend to converge to particular distributions, which recall the local feature of the pressure field (Fig. 3). In particular, the pdf of mode *a* is practically Gaussian like the pressure acting on the windward face; mode *b* has a pdf similar to the pressure on the LLF; modes *c* and *d* extract the two distinct features observed in the pressure on the WLF (Fig. 3b).

Figure 6.24 shows the PSD of the ICs corresponding to ICA modes *a* to *d*. As the model order increases, the spectral properties of the ICs tend to assume a behaviour consistent with the local properties of the pressure field, as the comparison with **Figure 6.18** can testify.
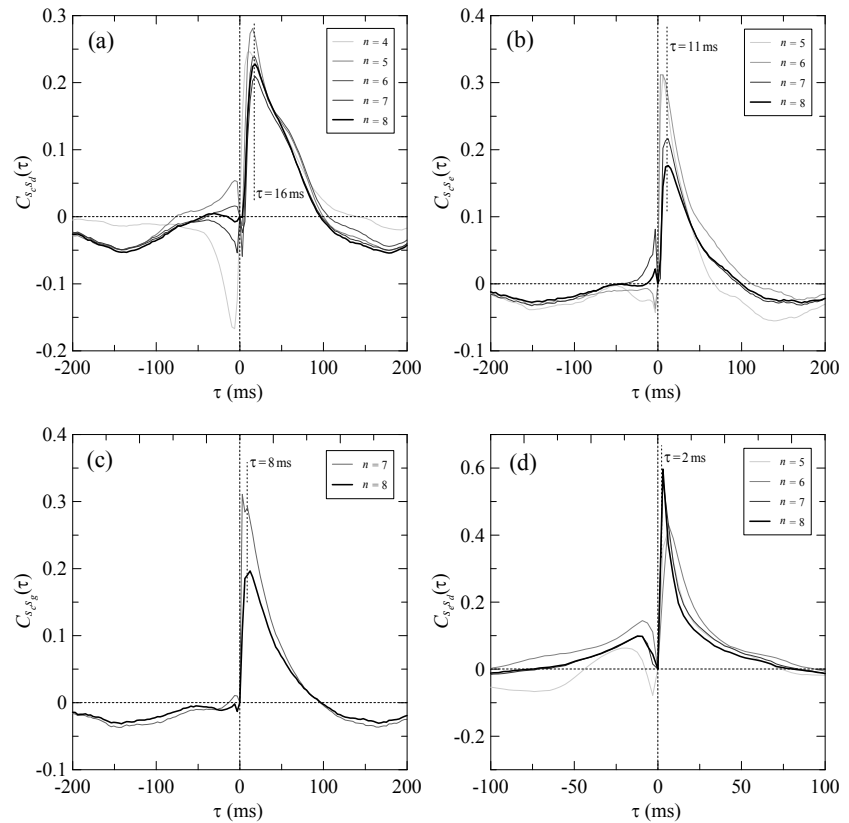
Figure 6.25 Correlation coefficients of the IC pairs s_c, s_d (a); s_c, s_e (b); s_c, s_g (c); s_e, s_d (d) for different model orders. The time lag corresponding to the peak for *n*=8 is indicated.

Figure 6.25 shows the cross-correlation of the ICs corresponding to ICA mode pairs *c-d* (a), *c-e* (b), *c-g* (c), *e-d* (d) representing the pressure on the WLF. Even if all the IC pairs are perfectly uncorrelated for zero time lag, a significant correlation

exists for $\tau \neq 0$; the time lags corresponding to the correlation peaks reported in the figure refer to the case $n=8$ and have been estimated by adopting a spline interpolation of the curves in the neighbourhood of the peaks. Analyzing these time lags, it can be concluded that the considered ICA modes tend to appear according to the sequence *c-g-e-d*, reproducing the propagation of the pressure fluctuation along the WLF.
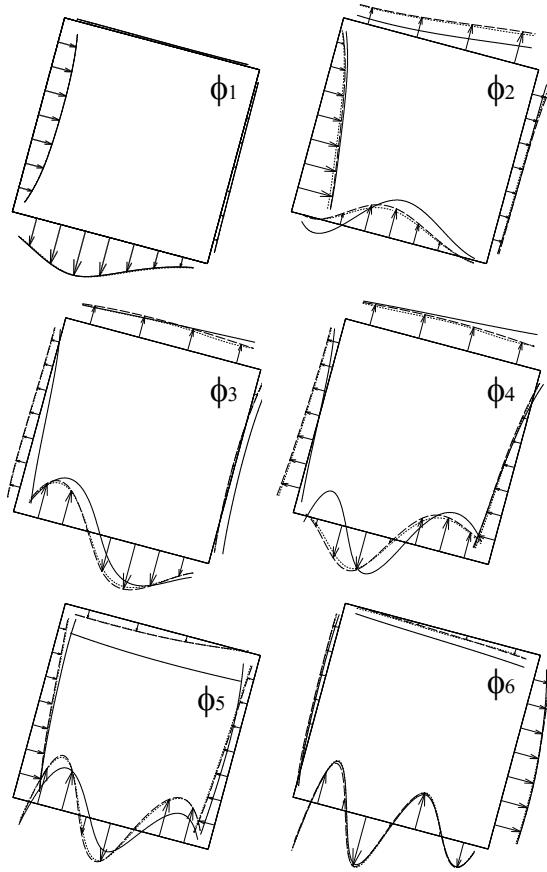
Figure 6.26 PCA modes φ_1 to φ_6 from the pruned dataset (solid line) from the full dataset (dots); corrected PCA modes $\tilde{\varphi}_1$ to $\tilde{\varphi}_6$ from the pruned dataset (dashed line).

In Section 3.5 it has been noted that PCA modes can be influenced by a non-homogeneous layout of the measurement points along the spatial domain. To investigate the impact of such effect on the CSs estimated for the present case study, **Figure 6.26** shows the first 6 PCA modes obtained from the same dataset used for Figure 6, but pruned removing the signals corresponding to sensors 2, 4 and 6 (solid

line). These modes are significantly different from the ones obtained from the complete dataset (reported for reference with dotted line), in particular as far as modes 2 to 5 are concerned. Besides, it is worth noting that this difference is not restricted to the zone where the sensors have been removed, but propagates to the whole domain. On the contrary the modes obtained from the pruned dataset using the correction procedure described in Section 3 (dashed line) are very close to the ones calculated from the complete dataset.

The same experiment has been repeated considering ICA modes estimated from the full and the pruned datasets. No significant differences have been observed, demonstrating that ICA is very robust with respect to non-homogeneous spatial discretizations.

6.4 CONCLUDING REMARKS

Aerodynamic data are analyzed by a wide set of statistical techniques that, at different levels of complexity, provide an insight of the physical nature of the observed phenomenon. From the perspective of the scientist, these techniques should possess some desirable features: (1) to provide quantitative representations of the measurements; (2) to emphasize aspects of the phenomenon that may be hidden within the random measurements; (3) to synthesize and represent qualitative features, like the existence of recurrent configurations or sequences, that cannot be directly isolated from the overall phenomenon, but a careful observed would recognize watching a flow visualization or an animated plot of the data. For the case study discussed herein it has been observed that the ability of the analysis techniques to accomplish the above tasks typically increases as their complexity increases.

Beside the issues that are specifically related to the present case study and have been discussed in this chapter, some general comments on the considered techniques and, more in general, on the statistical analysis of wind-generated pressure fields can be stated:

1. From a mathematical point of view, the four classes of techniques are well defined and separated, but the technical answers that they produce are somehow partially overlapped; in the present case it has been observed that high-order single-time statistics provide some information on the temporal structure of the pressure field acting on the lateral faces, while some aspects related to SPMT statistics suggest conclusions on its spatial probabilistic structure.

2. The coherent structures extracted by PCA can be non-physical and may lead to erroneous interpretations; on the other hand, PCA can be successfully adopted to extract ROMs to be employed for subsequent statistical analyses.

3. The coherent structures extracted by ICA tend to reproduce quite well recurrent configurations of the pressure field and may be used to represent efficiently local features of the field, preserving their probability distribution.

4. When a pressure field is generated by vortices advected by the mean flow, the coherent structures are necessarily represented using more than one ICA mode; in these cases the application of D-PCA and D-ICA enables a temporal tracing of the coherent structures moving through the spatial domain.

5. PCA is unable to separate the pressure fluctuation acting on different parts of the prism cross section, even if they have very different statistical characteristics; on the contrary, ICA separates in different modes the pressure field acting on the four faces of the prism.

6. The ICs reflect the local pressure field characteristics in terms of pdf and PSD, thus the ICA modes constitute meaningful local representations.

7. Different ICA modes on the WLF are almost statistically independent for zero time lag, but are well correlated for time lags compatible with the propagation velocity of pressure fluctuations advected by the mean flow. This suggests that ICA modes on the WLF represent subsequent snapshots of a dynamical phenomenon, like in the cases discussed in Carassale and Marrè-Brunenghi (2011) and Carassale (2012).

8. The non-homogeneous spatial distribution of the pressure taps affects the CSs estimated by PCA, while it is uninfluential for ICA. When PCA modes have to be estimated from a non-homogeneous dataset the use of the correcting procedure described in Section 3.5 is recommended.

9. The choice of the most appropriate model order for ICA may be critical; the tracking of the mode stability for different model orders, as well as the study of entropy and mutual information of the ICs are valuable guides for the order selection.

CHAPTER 7

APPLICATION: SQUARE CYLINDERS IN HOMOGENEOUS FLOW

Vladimir Kush, Departure of the winged ship.
Oil on canvas, 2000.

7.1 INTRODUCTION

In the first chapters of the present manuscript several statistical techniques oriented to the study of the wind effects on bluff bodies have been fully described. This section presents the applications of such techniques to a relevant case study involving a square-base cylinders immersed in homogeneous flow. It differs from the application shown in the previous Chapter 6 since the flow is 2-dimensional (at least in the mean) and the free-stream turbulence has lower intensity and smaller length scale. The setup involves different models: beside the sharp-edge corner condition considered as benchmark, two different rounded-corner radii (r/b=1/15 and 2/15) are studied. Global forces and surface pressure are simultaneously measured in the Reynolds number range between 1.7×10^4 and 2.3×10^5. The measurements are extended to angles of incidence between 0 and 45°.

All the experimental tests have been carried out at the University of Genova. The discussion of the results enables the definition of general criteria that can guide the selection of the most appropriate data-analysis technique for the study of a large class of aerodynamics-related problems.

7.2 EXPERIMENTAL ARRANGEMENTS

A wide set of cylinders with sharp-edge and rounded corners, with the same length but different cross-section size have been considered. They have been mounted between end plates in homogeneous flow condition (**Figure 7.1** left). The setup involves models with span length l=50 cm fabricated through the assemblage of aluminium plates and machined to reduce geometrical imperfections below 0.1% of the cross-section b. The influence of the Reynolds number is investigated varying both the wind-tunnel velocity U in the range 5–25 m/s, and the body size b in the range 50–150 mm; hence the Reynolds number range is between $1.7\times10^{4}$and 2.3×10^{5}. End plates are installed at the extremities of the models to confine the flow.

Figure 7.1   Wind tunnel, experimental setup: tested models (left) and turbulent flow condition by wood grid (right).

Global forces are measured by six resistive load cells and locale pressures are measured by pressure scanners mounted inside the models. Pressure taps are arranged in a ring in the mid-span cross-section; the number of instrumented points N ranges from 20 to 44 for different cylinders (**Figure 7.2**). Beside the section with sharp-edge corners, used as benchmark test, two rounded-corner configurations with r/b=1/15 and 2/15 (r being the corner radius) are considered. Two conditions of the incoming flow have been considered: 1) smooth flow (SF) characterized by a longitudinal turbulence intensity I_{u} about 0.2% and 2) turbulent flow (TF), produced through a grid realized by square bars (**Figure 7.1** rigth), characterized by I_{u} about

5% and integral length scale about 20 mm (**Figure 7.3**). The measurements are extended to angles of incidence α between 0 and 45°.
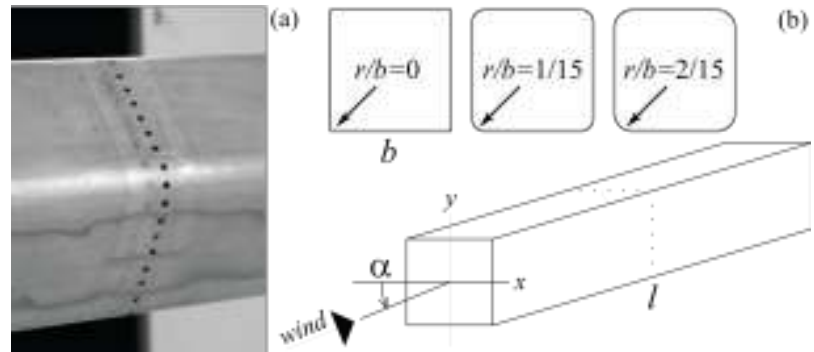
Figure 7.2   Experimental setup.
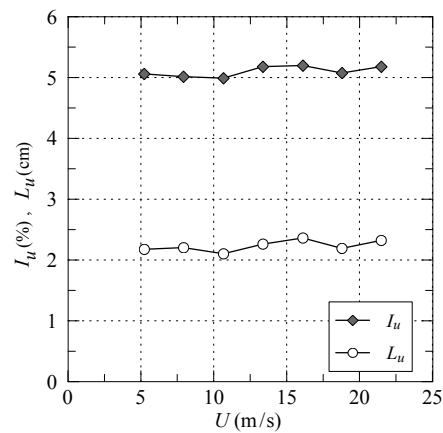
Figure 7.3   Turbulent flow features for TF tests: intensity of turbulence and integral length scale.

No blockage correction is adopted since the primary purpose of the study is the comparative analysis of the aerodynamic behaviour of bodies with similar shape and the qualitative description of some observed fluid-dynamic phenomena. Besides, since these phenomena are related to strong modifications of the flow topology, the use of blockage-correction rules should be necessarily restricted to flow configurations that are far enough from transition points. This would introduce artificial discontinuities in the experimental data that would complicate interpretation. On the other hand, it is important to mention that several models with different size (corresponding to the ratios b/B from 2.5% to 11%, B being the size of the wind tunnel cross-section in direction orthogonal to the prism axis) have been

tested and it emerged that the quality of the observed phenomena remains very consistent.

In the discussion that follows, the analyzed dataset is composed by N time histories coming from as many pressure taps located on the tested body surface. All the measurement channels are simultaneously sampled N_t times at a regular time rate; the vector $\boldsymbol{q}(t)=[q_1(t),...,q_N(t)]^{\mathrm{T}}$ contains the pressure measurements sampled at the discrete time t. The observed phenomenon is assumed to be statistically stationary and ergodic, thus time averaging is used as a surrogate of ensemble averaging to estimate any statistical quantity.

7.3 DATASETS ANALYSES

This section presents the results obtained applying the statistical techniques, fully described in the previous chapters, to the datasets collected during wind tunnel tests above described, i.e. square cylinders in homogeneous (smooth and turbulent) flow.

Figure 7.4 shows the variation of C_D (a), C_L (b), St (c) and $\tilde{C}_L$ (d) with respect to the angle of incidence for the three considered models in smooth flow. No significant influence of Re is found in the whole range explored during the experiments. It can be observed that these three models have a similar qualitative behaviour characterized by the inversion of the lift slope at the critical angle of incidence α_{cr}. For $\alpha=\alpha_{\mathrm{cr}}$ the steady drag and the fluctuating lift coefficients have a minimum value, while St increases sharply. The smooth fitting of the experimental data is interrupted at $\alpha=\alpha_{\mathrm{cr}}$ where a discontinuity exists (see Section 7.3.1 for a discussion about this issue). The value of α_{cr} decreases as r/b increases; for the sharp-corner model α_{cr} has been found about 12°, which is in substantial accord to previous experimentations (see Huang and Lin, 2011, for a review of previous results). In the case of rounded-corner models α_{cr} is about 7° and 5° for $r/b=1/15$ and 2/15, respectively. Tamura and Miyagi (1999), working in similar flow conditions, found $\alpha_{\mathrm{cr}} = 4°$ for $r/b = 2.5/15$.

Figure 7.5 shows the variation of C_D (a), C_L (b), St (c) and $\tilde{C}_L$ with respect to the angle of incidence, in turbulent flow at $Re=3.6\times10^4$ for $r=0$, $Re=7.9\times10^4$ for $r/b=1/15$ and $Re=2.5\times10^4$ for $r/b=2/15$. For the sharp-corner model α_{cr} has been found about 10°. In the case of rounded-corner models α_{cr} is about 5° and 3° for $r/b=1/15$ and 2/15, respectively. The qualitative comparison with the results presented in **Figure 7.4** shows that the increment of the free stream turbulence promotes a smooth transition from subcritical to supercritical angle regimes and produces a slight reduction of the critical angle for all the models. **Figure 7.6** shows the pressure patterns (mean) for the three kind of sections in smooth flow (solid line) and turbulent flow (dashed line); the rotation angles correspond to the critical angles

found for smooth flow condition. It is possible to observe that for such angles and for turbulent condition, the flow is widely reattached on the WLF. For smooth flow condition, the reattachment behaviour is slightly visible. The model with r/b=2/15 shows a significant difference between the two flow regimes in term of pressure distribution: in particular, the increment of turbulence produces a relevant increment of suction near the windward corners.

As far as the sharp-corner model and the rounded-corner model with r/b=1/15 are concerned, the quantities shown in **Figure 7.5** are practically invariant through the whole observed range of Re (Re=1.7×10^4 - 1.6×10^5 for sharp-corner model and Re=2.5×10^4 - 2.3×10^5 for r/b=1/15). On the contrary, the model with r/b=2/15 showed a strong dependency on Re, in particular for small angles of incidence.
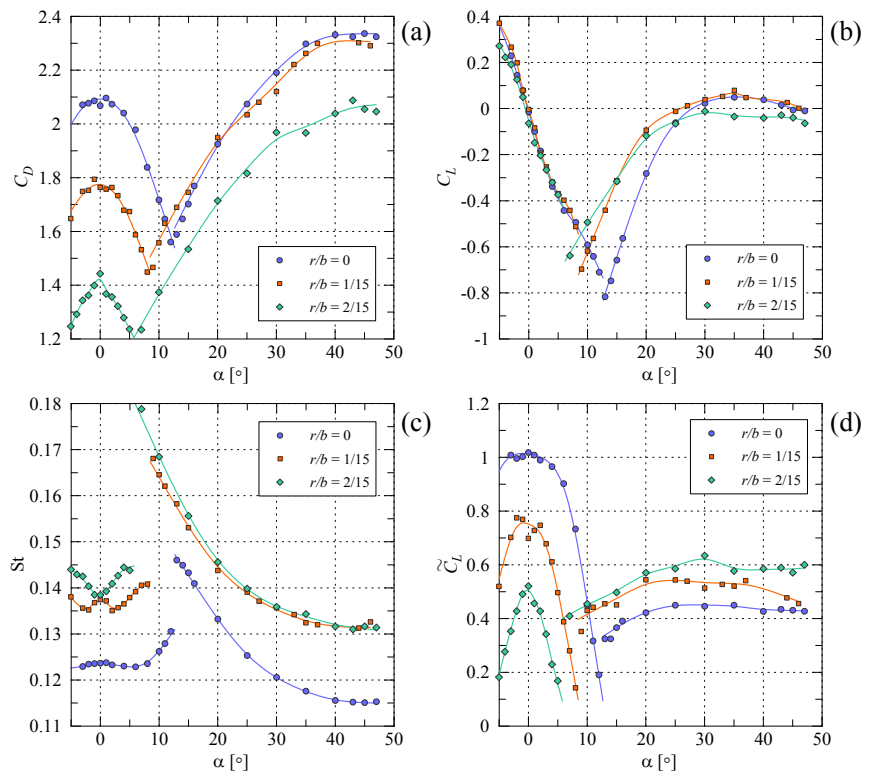
Figure 7.4   Aerodynamic coefficients in smooth flow: drag (a), lift (b), Strouhal number (c), fluctuating lift (d).

Figure 7.7 shows C_D (a), $dC_L/d\alpha$ (b), St (c) and $\tilde{C}_L$ (d) measured in turbulent flow for α=0 on the rounded-corner model with r/b=2/15. It can be observed that a drag crisis appears for Re between 5×10^4 and 1.2×10^5. Across this critical regime the drag coefficient drops from about 1.25 to 0.80; the lift slope passes from about -10 to +5

reaching values about -15 during the transition; *St* practically doubles jumping from 0.13 to 0.25; the fluctuating lift decreases significantly during the transition. Between Re=6.6×10^4 and 8.6×10^4 no regular vortex shedding was observed. Delany and Sorensen (1953) carried out experiments on rounded-corner square cylinders in smooth flow finding a drag crisis at Re≃6×10^5 for r/b=2.5/15 and Re≃2.5×10^5 for r/b=5/15 (in the mentioned reference Re is defined consistently with the definition adopted herein).
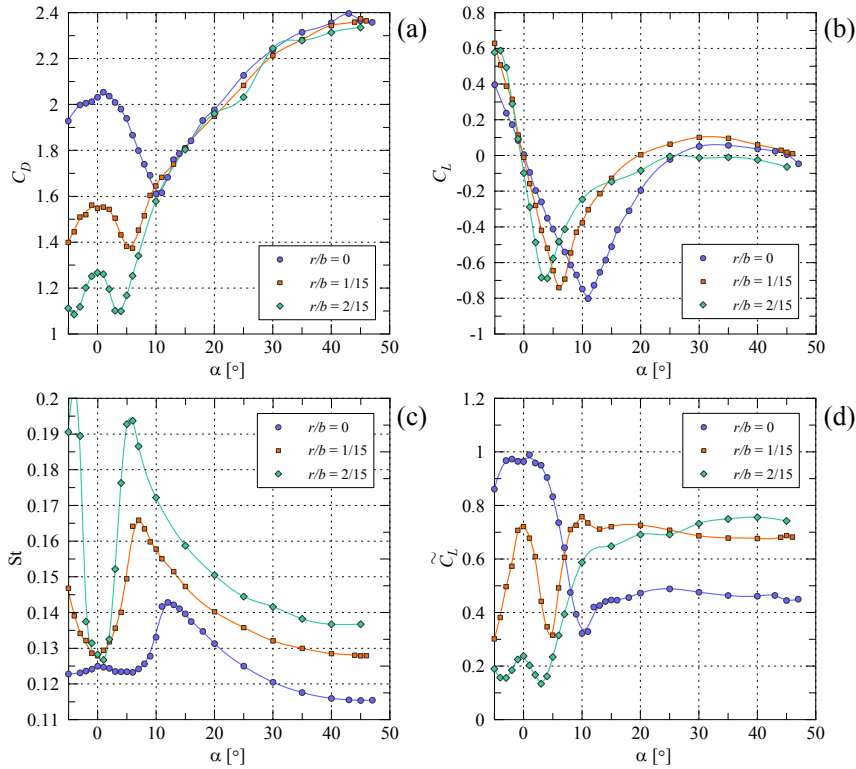
Figure 7.5   Aerodynamic coefficients in HF-T setup: drag (a), lift (b), Strouhal number (c), fluctuating lift (d).

Figure 7.8 shows the variation of C_D (a), C_L (b), *St* (c) and $\tilde{C}_L$ (d) with respect to the angle of incidence, for r/b=2/15, in turbulent flow at different Re between 4.90×10^4 and 1.81×10^5. The transition observed in Figure 4 reflects into the existence of two distinct behaviour referred to as subcritical (Re<Re_{cr}≃7.5×10^4) and supercritical regime (Re>Re_{cr}).
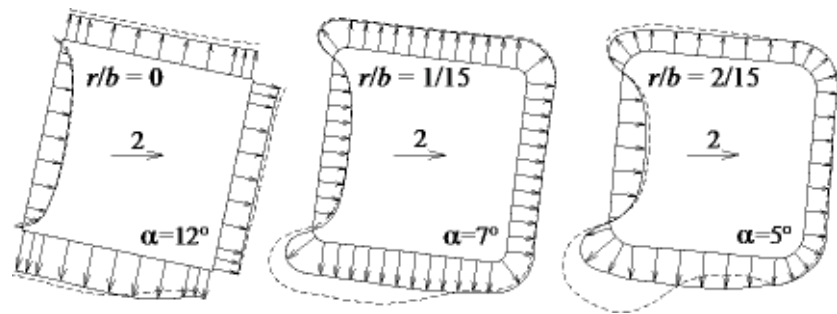
Figure 7.6   Mean pressure coefficients: smooth flow (solid line) and turbulent flow (dashed line). Re=2.9×10^4.

In the subcritical regime the drag coefficient for α=0 is about 1.3, (slightly lower than in smooth flow). The minimum value of the steady lift coefficient is about -0.7, and is obtained for α=3-4° (slightly before than α_{cr} in smooth flow). The Strouhal number is about 0.13 for α=0 and rapidly increases up to 0.18 for α=4° (again not far from the values observed in smooth flow). As Re increases, the steady lift slope for α=0 switches from negative to positive. Further increments of Re have the result of extending the range of α where the slope is positive. The maximum value of the steady lift coefficient increases as Re increases and is obtained for larger and larger angles of incidence. The maximum observed C_L is about 0.45 and appears for α=4° at Re=1.81×10^5. In the region where the steady lift slope is positive St is about 0.27 (approximately twice the value obtained in smooth flow) and is practically insensitive to Re. As the slope of C_L becomes negative, the regular vortex shedding disappears, until both C_L and St recover the trend observed in subcritical regime; in the observed range of Re it happens before α=10°. The minimum value of the drag coefficient is reached for the angle of incidence corresponding to the maximum vales for C_L.

The results shown in **Figure 7.7** and **Figure 7.8** are obtained using a model with b=150 mm. The tests carried out using models with different sizes (b=60, 75, 90 mm) provided very similar results as far as subcritical and supercritical regimes are concerned. The transition phase was qualitatively similar, but appeared at a slightly different Re.

Two main issues clearly emerged during the experimentation described in this Section and deserve to be discussed. The former concerns the sharp discontinuity of the aerodynamic behaviour observed for α=α_{cr} in smooth-flow condition. The latter issue is related to the two distinct flow behaviour observed for different Re in turbulent flow for r/b=2/15.
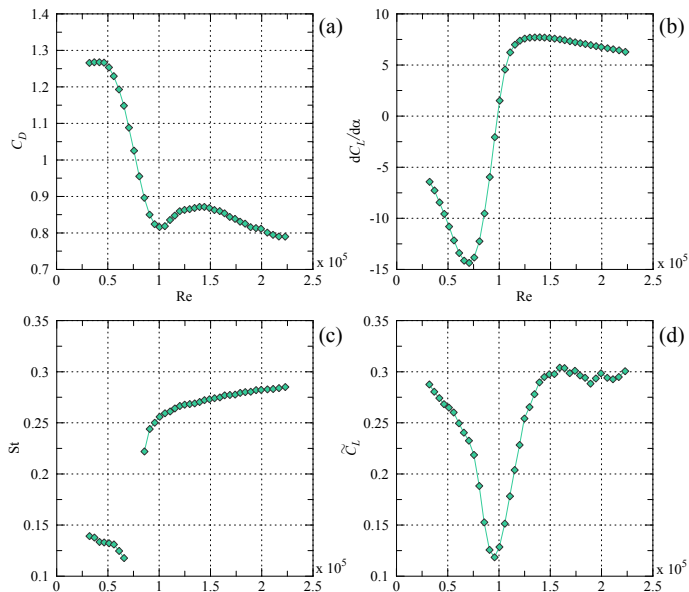
Figure 7.7   Steady drag (a) and lift (b) coefficients, Strouhal number (c) and fluctuating lift coefficient (d) for r/b=2/15 in turbulent flow at α=0 as functions of Re.
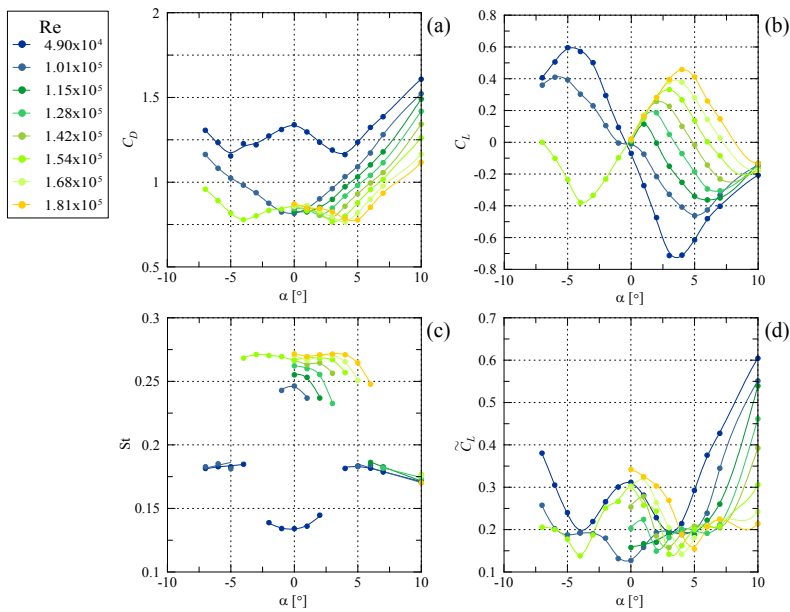
Figure 7.8   Steady drag (a) and lift (b) coefficients, Strouhal number (c) and fluctuating lift coefficient (d) for r/b = 2/15 in turbulent flow as functions of α; effect of Re in the range 4.9×10^4 - 1.8×10^5.

7.3.1 INTERMITTENT BEHAVIOUR NEAR THE CRITICAL ANGLE

For the case of sharp-corner square cylinders, the existence of two flow regimes separated by the critical angle of incidence has been clearly documented through accurate flow visualization techniques (Igarashi, 1984; Huang et al., 2010; Yen and Yang, 2011). The qualitative similarity of the behaviour observed for the three tested models suggests that a modification of the corner geometry (within the considered limits) does not produce qualitative variations of the flow pattern, but rather modifies the limit of existence of the flow regimes known for the sharp corner case. In particular, the increment of r/b produces a reduction of α_{cr}.
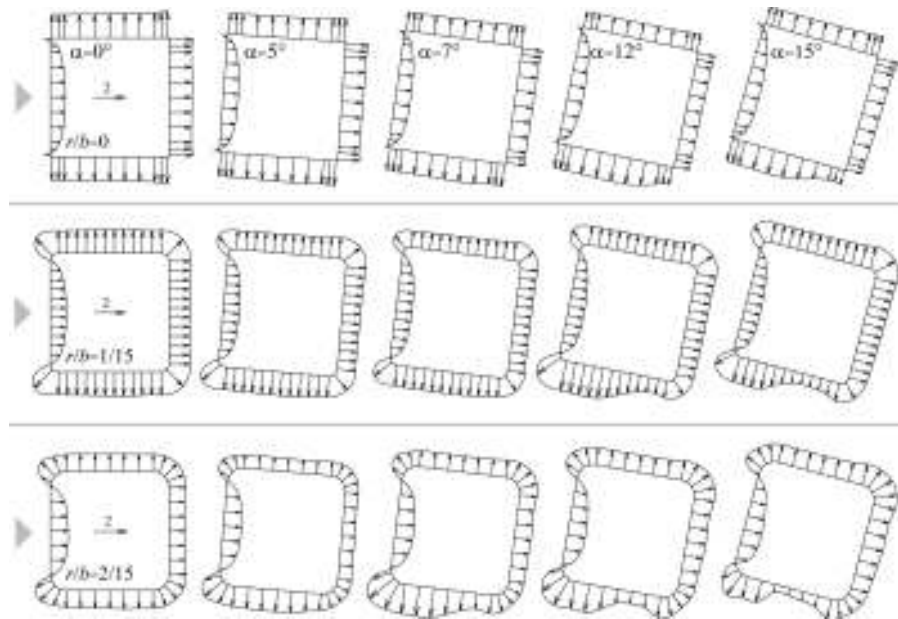
Figure 7.9   pressure coefficients in smooth flow. Re=2.9×10^4.

The transition between these two regimes is due to the reattachment of the mean flow on the lateral face exposed to the wind, and the consequent generation of a separation bubble. This behaviour is confirmed by the analysis of the pressure field measured on the mid-span cross section of the model. **Figure 7.9** shows the mean pressure distribution acting on the surface of the three models in smooth flow for the angles of incidence 0, 5, 7, 12 and 15°. Rotating the prism from α=0 to α=5° the mean pressure remains substantially unchanged and only a slight loss of symmetry is visible for the case r/b=2/15 for which α is approaching α_{cr}. Rotating the prism further to α=7° the pressure field on the lateral face exposed to the wind of the model with r/b=2/15 changes significantly. The suction increases near the leading

edge and decreases in a small portion of the face close to the trailing edge, testifying the reattachment of the flow and the generation of a separation bubble. A similar modification is visible on the model with r/b=1/15 for α passing from 7° to 12° and on the sharp-edge model for α increasing from 12° to 15°. Once the flow reattaches on the lateral face exposed to the wind, further increments of the angle of incidence produce a shrinking of the separation bubble towards the windward corner. This effect is well recognizable in particular for the case r/b=2/15.
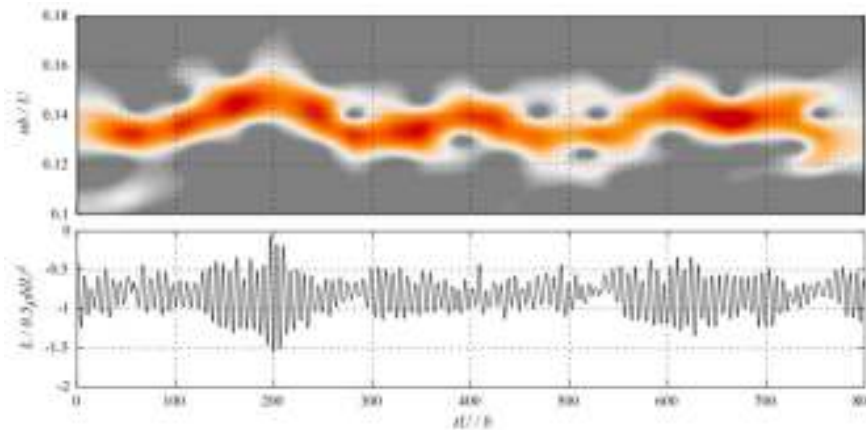
Figure 7.10 Wavelet map and time history of the lift force at $\alpha = \alpha_{cr}$ in smooth flow for square with sharp-edge corners. Re=4.7×10^4.

Figure 7.10, **Figure 7.11** and **Figure 7.12** show a time-frequency analysis of the lift force measured in smooth flow at $\alpha = \alpha_{cr}$ for the sharp-corner and rounded-corner models with r/b=1/15 and 2/15. The colormaps represent the amplitude of the wavelet transform of L, plotted with respect to the time t and the frequency n non-dimensionalized through b and U. The mother wavelet used for the analysis is an analytic Morlet type; the time histories of the lift coefficient are reported below the maps. The length of the considered time windows is 800 non-dimensional time units, which roughly correspond to 120 cycles of vortex shedding. From the wavelet maps it can be observed that the vortex-shedding peak frequency changes with time fluctuating between the values reported in **Figure 7.7** for angles just before and after α_{cr}. This result suggests that the wavelet maps can be employed to study, from a qualitative point of view, the stability of the two concurrent flow regimes (subcritical and supercritical) that appear in the neighbourhood of α_{cr}, as well as the transition from one regime to the other. The comparison of the three wavelet maps reveals that the flow past the sharp-corner cylinder tends to have smooth and frequent transitions between the two regimes giving rise to a behaviour that may be classified as irregular vortex shedding (**Figure 7.10**). On the contrary, in the case of

rounded-corner cylinders a proper intermittent behaviour appears as documented in **Figure 7.11** and **Figure 7.12**, where the transition is clearly visible and the flow remains stable in a regime for a relatively long time (for example in **Figure 7.12** the length of the subcritical phase corresponds to about 50 cycles of vortex shedding).
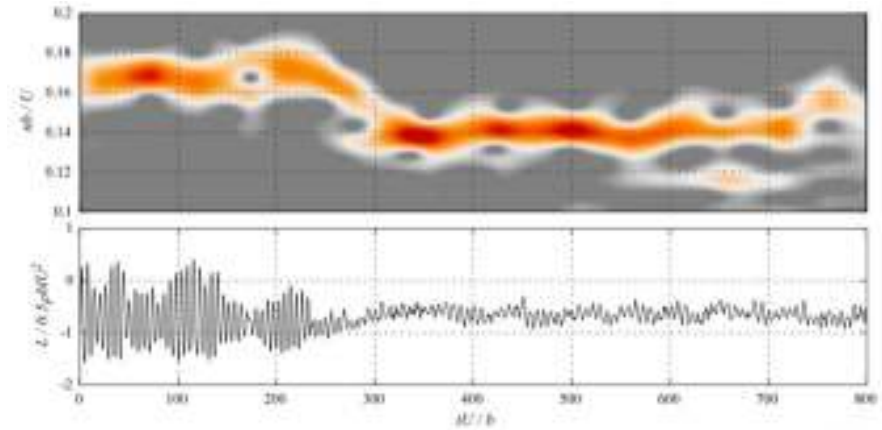
Figure 7.11 Wavelet map and time history of the lift force at $\alpha=\alpha_{cr}$ in smooth flow for square with rounded corners r/b=1/15. Re=4.7×10^4.
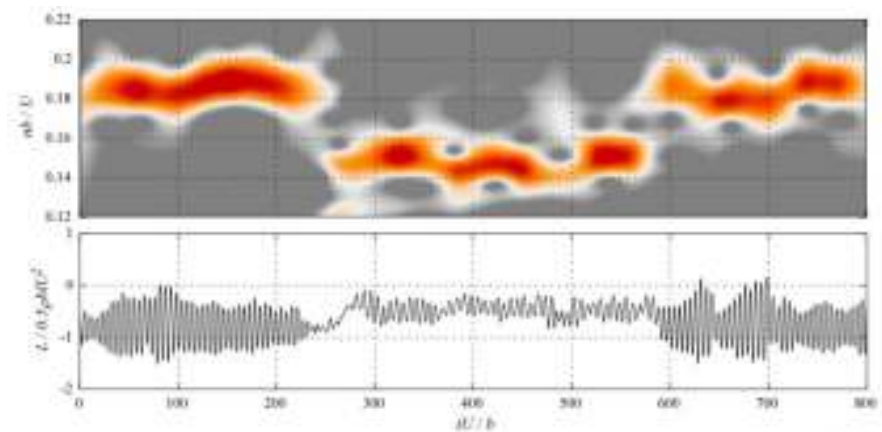
Figure 7.12 Wavelet map and time history of the lift force at $\alpha=\alpha_{cr}$ in smooth flow for square with rounded corners r/b=2/15. Re=4.7×10^4.

The comparison between **Figure 7.11** and **Figure 7.12** suggests that as r/b increases, the transition between the two regimes becomes sharper. A similar analysis has been carried out on the measurements obtained in turbulent flow, but no intermittence has been found. On the contrary, the transition through the critical

angle appears quite smooth and characterized only by a reduction of the intensity of vortex shedding.

7.3.2 REYNOLDS DEPENDENCY FOR TURBULENT FLOW

The analysis of the results obtained in turbulent flow for the rounded-corner cylinder with r/b=2/15 suggests the existence of two flow regimes for small angle of incidence, whose transition is governed by Re. The most evident characteristics of the transition between the two regimes is the inversion of the slope of steady lift coefficient for α=0 that passes from negative to positive with obvious implications for the stability of cross-wind oscillations in the quasi-steady limit. This phenomenon is accompanied by the reduction of C_D and the increment of St. A similar behaviour has been experimentally observed on elongated rectangular cylinders with aspect ratio 3:1 and has been related to the reattachment of the flow on both the lateral faces of the body (Norberg, 1993). The occurrence of the steady flow reattachment is regulated by Re and by the characteristics of the free-stream turbulence (Nakamura and Ozono, 1987; Li and Melbourne, 1995). For the 3:1 rectangle the transition between separated flow and reattachment-like behaviour has been identified between Re=5×10^3 and 10^4 (Re defined with respect to the cross-flow dimension) in smooth flow condition (Norberg, 1993), but several evidences suggest that it can be anticipated by the addition of small-scale free-steam turbulence or by the transverse vibration of the body (Nakamura and Ohya, 1984; Nakamura and Hirata, 1989). It should be noted that the mentioned transition phenomenon is probably very sensitive to several flow characteristics including the scale of the free-stream turbulence, the blockage ratio and possibly other parameters. Indeed, Larose and D'Auteuil (2008) observed a separated-like behaviour on a 3:1 rectangle at Re=2.0×10^6 (Re defined with respect to the cross-flow dimension) in smooth flow, which turned into a reattachment-like behaviour by adding 5% free-stream turbulence. Besides, they detected some unexplained effects of the Mach number.
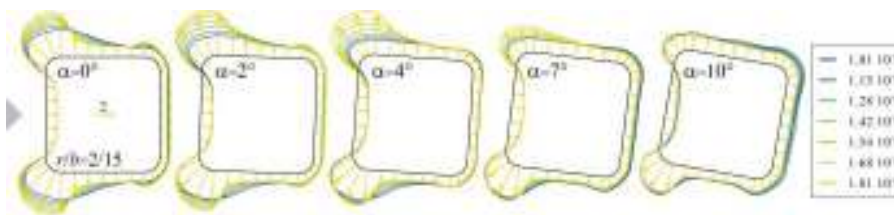
Figure 7.13 Steady pressure coefficient in supercritical Re regime for r/b=2/15 in turbulent flow.

Figure 7.13 shows the mean pressure coefficient measured on the rounded-corner model with r/b=2/15 in turbulent flow at supercritical Re (between 10^5 and 2×10^5) for different angle of incidence. For α=0, as Re increases the separation bubbles shrink towards the leading edges anticipating the recovery of the base pressure, while the suction near the leading edges increases. The rotation of the cylinder tends to prevent the flow reattachment on the upper lateral face reaching, eventually, a flow configuration with fully-separated flow on the upper lateral face and reattachment-like flow on the lower lateral face (exposed to the wind). This flow condition is similar to the one observed for subcritical Re and $\alpha>\alpha_{cr}$; this behaviour has already been observed on elongated rectangular cylinders (Schewe, 2013) and is confirmed by the coincidence of C_L and St for the two mentioned conditions (**Figure 7.8**), even if some difference in the strength of vortex shedding exists, which is reflected into a difference of C_D and $\tilde{C}_L$.
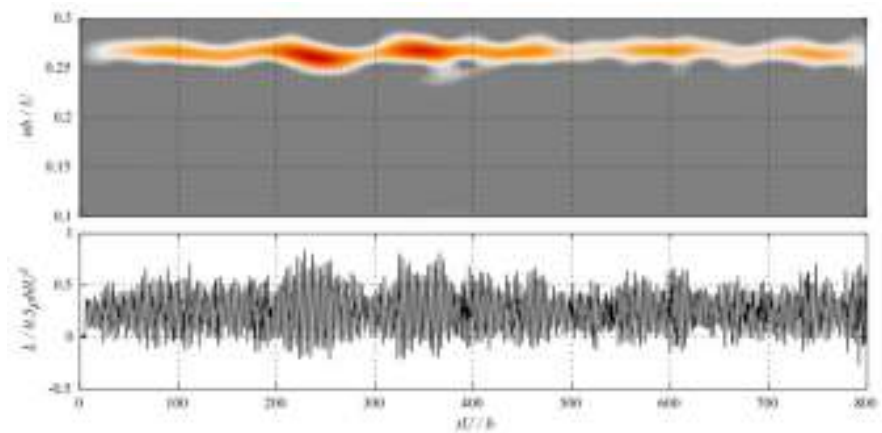
Figure 7.14 Wavelet map and time history of the lift force for r/b=2/15, at Re=1.42$\times10^5$ in turbulent flow; α=2°.

As Re increases, the maximum value of C_L increases because the separation bubble on the upper lateral face can be sustained for larger angles of incidence. Once the separation bubble becomes unstable, C_L decreases gradually to values typical of subcritical regime. During this transition, in which C_L has a negative slope, no regular vortex shedding appears, probably due to the recurrent formation of an unstable separation bubble on the upper face. This behaviour is documented in **Figure 7.14**, **Figure 7.15** and **Figure 7.16** where wavelet maps and the time histories of the lift coefficient are shown for different angles of incidence at Re=1.42$\times10^5$ in turbulent flow. For α=2°, **Figure 7.14**, the lift slope is positive and a regular vortex shedding appears with St about 0.26 (for α=0 the situation is similar); for α=5°, **Figure 7.15**, the lift slope is negative and no regular vortex shedding is

present; for $\alpha=10°$, **Figure 7.16**, regular vortex shedding reappears with *St* about 0.18.
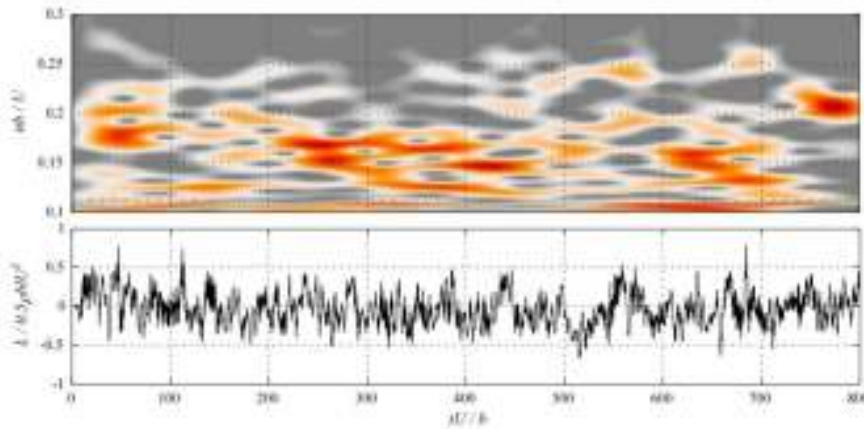
Figure 7.15 Wavelet map and time history of the lift force for *r*/*b*=2/15, at $Re=1.42\times10^5$ in turbulent flow; $\alpha=5°$.
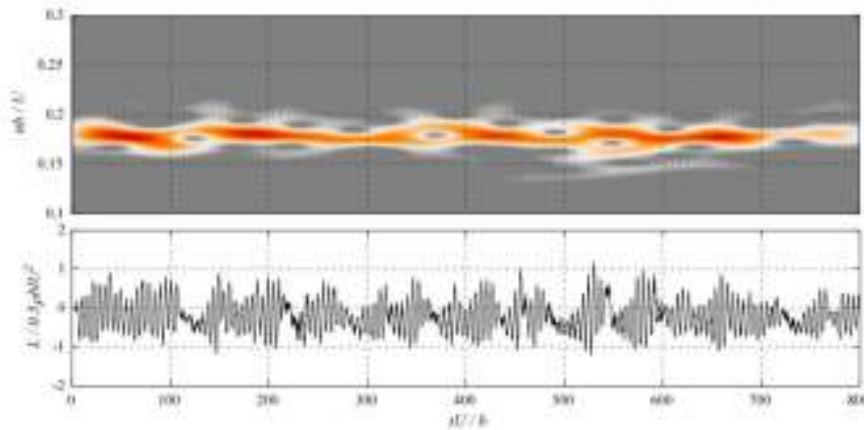
Figure 7.16 Wavelet map and time history of the lift force for *r*/*b*=2/15, at $Re=1.42\times10^5$ in turbulent flow; $\alpha=10°$.

7.4 CONCLUDING REMARKS

The effects of corner shaping on the aerodynamic behaviour of square cylinders have been investigated through the analysis and discussion of wind-tunnel experiments. It has been found that rounded corners promote the reattachment of the

flow on the lateral faces producing some significant effects that can be summarized as follows:

1. Rounded corners produces a reduction of the critical angle of incidence α_{cr} for which the flow reattaches on the lateral face exposed to the wind.

2. The transition between subcritical and supercritical angle regime is sharp in smooth flow and gradual in turbulent flow; the sharp transition is accompanied by an intermittent behaviour that in the sharp-corner case is not visible.

3. Rounded corners can produce the reattachment of the flow on the lateral faces for $\alpha=0$, exactly as it happen for the case elongated rectangles. The effects of this flow-field variation are confined in a range of relatively small angles of incidence and are characterized by the inversion of the lift slope and the strong increment of *St*.

4. The transition between subcritical and supercritical *Re* regime appeared very sensitive to the test conditions. Surely the scale of the free-stream turbulence plays a role, but probably other test parameters such as the blockage rate are important. These issues are currently under investigation.

5. The supercritical *Re* regime has been observed only for $r/b=2/15$ in turbulent flow, however it cannot be excluded that it may appear also for smaller r/b ratios and smooth flow at sufficiently high Reynolds numbers.

The technical implications of the mentioned effects are important due to the large variation of the aerodynamic coefficients as functions of r/b and possibly *Re*, as well as in relation to galloping instability. From the results obtained in smooth flow it can be concluded that the classical galloping model (based upon a quasi-steady assumption) cannot be adopted in the neighbourhood of $\alpha=\alpha_{cr}$ due to the observed intermittent behaviour. On the other hand, the results obtained in turbulent flow reveal that the lift coefficient of rounded corner cylinders can be negative or positive for different *Re* and that, in supercritical *Re* regime, the necessary condition for galloping (negative lift slope) does not appear at $\alpha=0$, but in a range of α between 5° and 10°.

CHAPTER 8

CONCLUSIONS AND FURTHER PERSPECTIVES

8.1 PREMISE

For the sake of clarity a conclusion section ends each chapter of the manuscript. In particular for the chapters containing the applications (Chapters 6 and 7), wide and detailed conclusions are proposed (see Sections 6.4 and 7.4). In the sections that follow general considerations about the complete thesis are presented jointly with suggestions for further researches.

8.2 CONCLUSIONS

Most of the mechanical and civil structures are not designed to meet aerodynamic objectives, hence the understand of their aerodynamic behaviour is a very important task for a wind engineer. Because of the complexity of the dynamic phenomena taking place in the flow past a bluff body, experimental tests and probabilistic tools for processing the data are required.

The research activity presented in the present manuscript aims at providing innovative statistical techniques for the quantitative evaluation and qualitative interpretation of the wind-induced pressure field on bluff bodies.

Square-section cylinders and prisms (with sharp-edge and rounded corners) have been tested in the wind tunnel of the University of Genova for several flow conditions, and an extensive dataset have been collected by means of load cells and multi-channel pressure scanners.

The statistical techniques applied to the pressure time histories have been classified on the basis of their ability to describe the spatial and/or the temporal probabilistic information that constitute the backbone of the dataset. From Chapter 2 to Chapter 5 such techniques are presented and critically analyzed. For the case studies discussed herein it has been observed that the ability of the analysis techniques to accomplish the aforementioned tasks typically increases as their complexity increases.

For the whole dataset, the aerodynamic coefficients have been estimated providing results that may be considered an interesting contribution to the base research on

bluff body aerodynamics. In particular, from the results obtained in Chapter 7 in smooth flow it can be concluded that the classical galloping model (based upon a quasi-steady assumption) cannot be adopted in the neighbourhood of $\alpha=\alpha_{cr}$ due to the observed intermittent behaviour. On the other hand, the results obtained in turbulent flow reveal that the lift coefficient of rounded corner cylinders can be negative or positive for different *Re* and that, in supercritical *Re* regime, the necessary condition for galloping (negative lift slope) does not appear at $\alpha=0$, but in a range of α between 5° and 10°.

Selected case studies enabled the application of different probabilistic tools in order to identify elementary pressure patterns (in this context defined as coherent structures, CSs) whose characteristics reflect the aerodynamic behaviour of the bluff bodies tested (Chapter 6). In particular Single point - single time (SPST) analyses, through the higher-order cumulants estimation, have been useful to localize zones characterized by high activity of unstable phenomena such as vortex shedding. In these areas the pressure field appears to be highly non-Gaussian.

Single point - multiple time (SPMT) analyses have been carried out through the PSD functions, for wide-sense stationary (WSS) processes, and through the wavelet transform (WT) for non-stationary processes. Synthetic quantity like the peak amplitude of PSD led to the localization of regions where the flow, for the present applications, tends to approach the body surface, due to physical mechanisms like the flow reattachment on the lateral side of the cylinder and the reverse flow near the leeward face. WT has been essential in order to investigate the critical condition generated by the irregular reattachment of the flow for critical angle of incidence.

Multiple point - single time (MPST) analyses have been conducted by means of modal expansions based on Principal Component Analysis (PCA) and Independent Component Analysis (ICA) in order to mathematically extract CSs. The modal representation determined by PCA is energetically optimal; on the other hand, the CSs extracted by PCA can be non-physical and may lead to erroneous interpretations. The CSs extracted by ICA tend to reproduce quite well recurrent configurations of the pressure field, preserving their probability distribution. Besides, while PCA modes tend to be affected by uneven spatial discretizations of the pressure field, ICA modes appeared practically insensitive to this issue.

ICA has become a classic tool in signal processing and machine learning to solve the Blind Source Separation (BSS) problem as well as to extract features from the data. At the beginning, serious concerns on the assumptions of non-Gaussianity and independence of the sources have been risen. Nowadays, it has been realized that in real scientific problems, non-Gaussian features are always present to an extent that is sufficient to make ICA algorithms working; the wind pressure measurements presented in the manuscript are a clear example. On the other hand, independence is now being considered as a useful approximation of reality and most ICA methods,

e.g. FastICA algorithm employed herein, are relatively robust regarding some dependence of the components.

Multiple point - single time (MPMT) analyses have been implemented through the convolutive version of PCA and ICA defined as dynamic-PCA (D-PCA) and dynamic-ICA (D-ICA) to underline their theoretical ability to extract coherent structures evolving with time. While D-PCA (like PCA) extracts clearly unphysical features, D-ICA modes are compatible with some known aerodynamic phenomena and are consistent with some recurrent pressure patterns extracted from the measured dataset (e.g. the vortex advection by the mean flow). The application of these dynamic techniques provided encouraging results regarding the prism in the atmospheric boundary layer (Chapter 6). For the case studies described in Chapter 7 the magnitude of the incident vortexes is smaller than the vortexes caused by the presence of the bluff body; through the filtering operation, the large extent of random components are suppressed and the process become almost deterministic. For this reason an higher level of the intensity of turbulence, characterized by a larger integral scale, is necessary in order to apply successfully such probabilistic techniques.

8.3 FURTHER PERSPECTIVES

Based both on the critical review of available papers related to bluff-body aerodynamics and to pressure field analysis through stochastic decomposition, jointly with the present investigations, the following suggestions for further researches can be summarized as follows:

1. the collected dataset has not been completely explored through advanced probabilistic tools due to its extent and allows further development of the presented statistical techniques;

2. the non-Gaussianity measure adopted to estimate the ICA and D-ICA modes is statistically symmetric, i.e. is insensitive to the odd-order statistical moments of the data. Since the wind-induced pressure has often very skewed probability distribution, this choice can be questionable and may be revised;

3. dynamic modes, in particular D-ICA modes, can be useful tools for investigating the transition regimes in terms of angle of incidence and Reynolds number; the evolution of coherent structures in such condition may be an useful guide for a better understanding the physical mechanism of the flow.

REFERENCES

Addison P.S., 2002, The illustrated wavelet transform handbook, Physics Publishing, London.

Ahn H., Choi E., Han I., 2007. Extracting underlying features and cancelling noise using independent component analysis for direct market. Expert Systems with Applications 33, 181-191, 2007.

Ahn H., Choi E., Ingoo H., 2007, Extracting underlying meaningful features and canceling noise using independent component analysis for direct marketing, Expert Systems with Applications, 33, 181–191.

Albera L., Ferreol A., Chevalier P., Comon P., 2004, ICAR: Independent Component Analysis using Redundancies, in ISCAS 04IEEE International Symposium on Circuits and Systems, Vancouver, Canada, May 23-26 2004, vol. 5, pp. 672-675.

Antoni J., 2005, Special Issue: Blind Source Separation, Mechanical Systems and Signal Processing, 19, 6, 1163-1380.

Antoni J., 2006, The spectral kurtosis: a useful tool for characterising non-stationary signals, Mechanical Systems and Signal Processing, 20, 282–307.

Armitt J., 1968, Eigenvector analysis of pressure fluctuations on the West Burton instrumented cooling tower, Internal Report RD/L/M 114/68, Central Electricity Research Laboratories, UK.

Atick J.J., 1992, Entropy minimization: A design principle for sensory perception?, Journal of Neural Systems, 3 81–90.

Aubry N., Lian W.Y., Titi E.S., 1993, Preserving symmetries in the proper orthogonal decomposition, SIAM Journal on Scientific Computing, 14, 483-505.

Aysin B., Chaparro L.F., Gravè I., Shusterman V., 2005, Orthonormal-basis partitioning and time–frequency representation of cardiac rhythm dynamics, IEEE Transactions on Biomedical Engineering, 52 (5), 878–889.

Baker C.J., 2000, Aspects of the use of proper orthogonal decomposition of surface pressure fields, Wind & Structures 3, 97-115.

Barlow H. B., 1961, Possible principles underlying the transformations of sensory messages, Sensory Communication, 217–234. MIT Press.

Barroso L.R., Rodriguez R., 2004, Damage detection utilizing the damage index method to a benchmark structure, Journal of Engineering Mechanics, ASCE, 130, 142-151.

Bartlett M.S., Sejnowsk T.J., 1998, Learning viewpoint invariant face representations from visual experience in an attractor network, Network: Computation in Neural Systems 9 (3), 399-417.

Basu R.I., 1985, Aerodynamic forces on structures of circular cross-section. Part 1. Model-scale data obtained under two-dimensional conditions in low-turbulence streams, Journal of Wind Engineering and Industrial Aerodynamics, 21, 273-294.

Bell A.J., Sejnowski T.J., 1995, An information-maximization approach to blind separation and blind deconvolution, Neural Computation, 7, 1129–1159.

Bell A.J., Sejnowski T.J., 1997, The independent components of natural scenes are edge filters, Vision Research, 37, 3327–3338.

Belouchrani A., Abel-Meraim K., Cardoso J.F., Moulines E., 1997, A blind source separation technique using second-order statistics, IEEE Trans. Signal Proc. 45(2), 434-444.

Benfratello S., Muscolino G., 1999, Filter approach to the stochastic analysis of MDOF wind-excited structures, Probabilistic Engineering Mechanics, 14, 311-321.

Best R.J., Holmes J.D., 1983, Use of eigenvalues in the covariance integration method for determination of wind load effects, Journal of Wind Engineering and Industrial Aerodynamics, 13, 359-370.

Bienkiewicz B., Tamura Y., Ham H.J., Ueda H., Hibi K., 1995, Proper orthogonal decomposition and reconstruction of multi-channel roof pressure, Journal of Wind Engineering and Industrial Aerodynamics, 54-55, 369-381.

Brincker R., Zhang L., Andersen P., 2001, Modal identification of output-only systems using frequency domain decomposition, Smart Material and Structures, 10, 441-445.

Buresti G., 2012, Elements of fluid dynamics, Imperial College Press, London.

Buresti G., Lombardi G., Bellazzini J., 2004, On the analysis of fluctuating velocity signals through methods based on the wavelet and Hilbert transforms, Chaos, Solitons and Fractals, 20, 149–158.

Caddemi S., Di Paola M., 1994, Second order statistics of the wind-excited response of structures, Proceedings on 4th Italian National Conference on Wind Engineering, Rome, 151-165.

Cao L.J., Chua K.S., Chong W.K., Lee H.P., Gu Q.M., 2003, A comparison of PCA, KPCA and ICA for dimensionality reduction in support vector machine, Neurocomputing, 55, 321-336.

Carassale L., 2009, Flow-induced forces on cylinders in statistically-symmetric cross flow. Probabilistic Engineering Mechanics, 24(3), 323-339.

Carassale L., 2010, Analysis of aerodynamics pressure measurements by dynamic coherent structures, in: G. Deodatis and P.D. Spanos (Eds.), Proc. of the 6th International Conference (CSM-6), Rhodos, Greece, June 13-16, 2010.

Carassale L., 2012, Analysis of the aerodynamic pressure measurements by dynamic coherent structures, Probabilistic Engineering Mechanics, 28, 66-74.

Carassale L., Freda A., Marrè Brunenghi M., 2013, Effects of free-stream turbulence and corner shape on the galloping instability of square cylinders, Journal of Wind Engineering and Industrial Aerodynamics, 123, 274-280.

Carassale L., Freda A., Marrè Brunenghi M., 2014, Experimental investigation on the aerodynamic behaviour of square cylinders with rounded corners, Journal of Fluids and structures, 44, 195-204.

Carassale L., Hibi K., Pagnini L.C., Solari G., Tamura Y., 2004, POD analysis of the dynamic wind pressure on a tall building, in: Proc., 5th Int. Coll. on Bluff Body Aerodynamics & Applications, Ottawa, Canada, 2004.

Carassale L., Marrè Brunenghi M., 2011, Statistical analysis of wind-induced pressure fields: a methodological perspective, Journal of Wind Engineering and Industrial Aerodynamics, 99, 700-710.

Carassale L., Marrè Brunenghi M., 2012, Identification of meaningful coherent structures in the wind-induced pressure on a prismatic body, Journal of Wind Engineering and Industrial Aerodynamics, 104-106, 216-226.

Carassale L., Marrè Brunenghi M., 2013, Dynamic response of trackside structures due to the aerodynamic effects produced by passing trains, Journal of Wind Engineering and Industrial Aerodynamics, 123, 317-324.

Carassale L., Percivale F., 2006, Frequency-domain output-only identification of linear structures subject to stationary excitation, Proceedings on 5th International Conference on Computational Stochastic Mechanics, CSM5, Rhodes, Greece, in press.

Carassale L., Piccardo G., 2003, Wind-induced nonlinear oscillations of cables by Volterra approach, Proceedings 5th International Symposium on Cable Dynamics, Santa Margherita, Italy, 149-156.

Carassale L., Piccardo G., 2004, A reduced model for nonlinear response of cables in turbulent wind, C.D. Proceedings, 3rd International Conference on Advances in Structural Engineering and Mechanics, Seoul, Korea.

Carassale L., Piccardo G., 2010, Nonlinear discrete models for the stochastic analysis of cables in turbulent wind, International Journal of Nonlinear Mechanics, 45, 219-231.

Carassale L., Piccardo G., Solari G., 2001, Double Modal Transformation and Wind Engineering Applications, Journal of Engineering Mechanics, ASCE 127(5), 432-439.

Carassale L., Solari G., 2002, Wind modes for structural dynamics: a continuous approach, Probabilistic Engineering Mechanics, 17, 157-166.

Carassale L., Solari G., Tubino F., 2007, Proper Orthogonal Decomposition in wind engineering: Part 2: Theoretical Aspects and Some Applications, Wind & Structures, 10 (2), 177-208.

Carassale L., Vernazzani A., 2009, Interpretation of aerodynamic pressure measurements by Independent Component Analysis, in: Proc. 5th European and African Conf. on Wind Engineering, EACWE 5, Florence, Italy, July 19-23, 2009.

Cardoso J.F., Souloumiac A., 1993, Blind beamforming for non Gaussian signals, IEE Proceedings, 140 (6) 362–370.

Chevalier P., Albera L., Ferreol A. Comon P., 2005, On the virtual array concept for higher order array processing, IEEE Trans. Signal Process., 53, 4, 1254-1271.

Comon P, Jutten C., 2010, Handbook of blind source separation, NY: Academic Press, New York,

Comon P., 1994, Independent Component Analysis, A new concept?, Signal Processing, 36, 287-314.

Comon P., Jutten C., Hérault J., 1991, Blind separation of sources, Part II: Problems statement, Signal Processsing 24, 11–20.

De Grenet E.T., Ricciardelli F., 2004, Spectral proper transformation of wind pressure fluctuations: application to a square cylinder and a bridge deck. J. of Wind Engrg. & Ind. Aerodyn. 92, 1281-1297.

Delany N.K., Sorensen N.E., 1953, Low-speed drag of cylinders of various shapes. National Advisory Committee for Aeronautics, Technical note 3038.

Den Hartog J. P., Mechanical Vibrations, 1956, McGraw-Hill Book Company, New York.

Di Paola M., 1998, Digital simulation of wind field velocity, Journal of Wind Engineering and Industrial Aerodynamics, 74-76, 91-109.

Di Paola M., Gullo I., 2001, Digital generation of multivariate wind field processes, Probabilistic Engineering Mechanics, 16, 1-10.

Di Paola M., Muscolino G., Sofi A., 2004, Monte Carlo simulation for the response analysis of long-span suspended cables under wind loads, Wind and Structures, 7, 107-130.

Di Paola M., Pisano A.A., 1996, Multivariate stochastic wave generation, Application Ocean Res, 18, 361-365.

Dodds C.J., Robson J.D., 1975, Partial coherence in multivariate random processes, Journal of Sound and Vibration, 42, 243-249.

Draper B. A., Baek K., Bartlett M. S., Beveridge J. R., 2003, Recognizing faces with PCA and ICA, Comp. Vision and Image Understanding 91, 115-137.

Dwyer R.F., 1984, Use of the kurtosis statistic in the frequency domain as an aid in detecting random signals, IEEE Journal of Oceanic Engineering 9(2), 85–92.

Gaeta M, Lacoume J.L., 1990, Source separation without prior knowledge: the maximum likelihood solution, Proceedings in EUSIPCO'90, 621–624.

Gelle M.C., Delaunay G., 2000, Blind source separation applied to rotating machines monitoring by acoustical and vibrations analysis, Mechanical Systems and Signal Processing, 14 (3), 427, 442.

Gilliam X., Dunyak J.P., Smith D.A., Wu F., 2004, Using projection pursuit and proper orthogonal decomposition to identify independent flow mechanisms, Journal of Wind Engineering and Industrial Aerodynamics 92, 53–69.

Gioffrè M., Gusella V., Grigoriu M., 2001, Non-Gaussian pressure on prismatic buildings. I: stochastic field, Journal of Structural Engineering, ASCE 127(9), 981-989.

Girolami M., Fyfe C., 1997, An extended exploratory projection pursuit network with linear and nonlinear anti-hebbian connections applied to the cocktail party problem, Neural Networks, 10, 1607–1618.

Gray M.S., Movellan J. R., Sejnowski T.J., 1997, A Comparison of Local Versus Global Image Decompositions for Visual Speechreading, Proceedings of the 4th Joint Symposium on Neural Computation, University of California, San Diego and University of Southern California 6, Institute for Neural Computation, La Jolla, CA, 92-98.

Haykin S., 1989, Modern Filters, Macmillan, London.

Haykin S., 1994, Blind Deconvolution, Prentice Hall, New Jersey.

He H., Ruan D., Metha K.C., Gilliam X., Wu F., 2007, Nonparametric independent component analysis for detecting pressure fluctuation induced by roof corner vortex, Journal of Wind Engineering and Industrial Aerodynamics, 95, 429–443.

Herzog S., 1986, The large scale structure in the near wall region of a turbulent pipe flow, Ph.D. Thesis, Cornell University.

Holmes J.D., 1981, Non-Gaussian characteristics of wind pressure fluctuations, Journal of Wind Engineering and Industrial Aerodynamics, 7, 103-108.

Holmes J.D., 1990, Analysis and synthesis of pressure fluctuations on bluff bodies using eigenvectors, Journal of Wind Engineering and Industrial Aerodynamics, 33, 219-230.

Holmes J.D., 2001, Wind loading of structures, 2001, Spon Press, London.

Holmes J.D., Sankaran R., Kwok K.C.S., Sume M.J., 1997, Eigenvector modes of fluctuating pressures on low-rise building models, Journal of Wind Engineering and Industrial Aerodynamics, 69-71, 697-707.

Holmes P.J., Lumley J.L., Berkooz G., 1996, Turbulence, coherent structures, dynamical system and symmetry, Cambridge University Press, Great Britain.

Holmes P.J., Lumley J.L., Berkooz G., J.C. Mattingly, R.W. Wittenberg, 1997, Low-Dimensional models of coherent structures in turbulence, Physics Reports, 287, 337-384.

Hotelling H., 1933, Analysis of a complex of statistical variables into principal components, Journal of Educational Psycological, 24, 417-441, 498-520.

Huang E.H., Shen Z., Long, S.R., 1999, Anew view of nonlinear water waves: the Hilbert Spectrum, Annual Rev Fluid Mechanics, 31, 417-457.

Huang N.E., Shen Z., Long S.R., Wu M.C., Shih H.H., Zheng Q., Yen N., Tung C.C., Liu H.H., 1998, The empirical mode decomposition and the Hilbert spectrum for nonlinear and non-stationary time series analysis, Proceedings

of the Royal society of London, Series A: Mathematical, Physical and Engineering Sciences, 454, 903–995.

Huang R. F., Lin B. H., Yen S. C., 2010, Time-averaged topological flow patterns and their influence on vortex shedding of a square cylinder in crossflow at incidence, Journal of Fluids and Structures, 26, 406-429.

Huang R.F., Lin B.H., 2011, Effect of flow patterns on aerodynamic forces of a square cylinder at incidence, Journal of Mechanics 27, 347-355.

Hyvärinen A., Karhunen J., Oja E., 2001, Independent Component Analysis. John Wiley and Sons, New York.

Hyvärinen A., Oja E., 1997, A fast fixed-point algorithm for independent component analysis, Neural Computation, 9 (7), 1483–1492.

Igarashi T., 1984, Characteristics of the flow around a square prism, Bulletin of JSME 27, 1858-1865.

Iungo G.V., Lombardi E., 2011, A procedure based on proper orthogonal decomposition for time–frequency analysis of time-series, Experiments in Fluids, 51 (4), 969-985.

Jolliffe I.T., 2002. Principal component analysis, Springer Verlag, New York.

Jung T.P., Humphries C., Lee T.W., Makeig S., McKeown M.J.,. Iragui V., Sejnowski T., 1998, Extended ICA removes artifacts from electroencephalographic recordings, Advances in Neural Information Processing Systems, 10, MIT Press.

Jutten C, Hérault J., 1991, Blind separation of sources, part I: an adaptive algorithm based on neuromimetic architecture, Signal Process. 24, 1–10.

Jutten C., 1987, Calcul neuromimètique et traitement du signal, analyse en composantes indèpendantes, PhD thesis, INPG, University of Grenoble, France.

Kachenoura A., Albera L., Senhadji L., Comon P., 2008, ICA: a potential tool for BCI systems, in IEEE Signal Processing Magazine, vol. 25, n°1, pp. 57-68.

Kareem A., Cermak J.E., 1984, Pressure fluctuations on a square building model in boundary-layer flows, Journal of Wind Engineering and Industrial Aerodynamics, 16, 17–41.

Kareem A., Cheng C.M., 1999, Pressure and force fluctuations on isolated roughened circular cylinders of finite height in boundary layer flows, Journal of Fluids and Structures 13, 907–933.

Karhunen J., Joutsensalo J., 1994, Representation and separation of signals using nonlinear PCA type learning, Neural Networks, 7(1), 113–127.

Karhunen K., 1946, Zur spektraltheorie stochastischer prozess, Annales Acaddemiae Scientiarum Fennicae Mathematica, 1, 34.

Katsamura N., Matsuyama Y., 2005, Database retrieval for similar images using ICA and PCA bases, Engrg. Appl. Artificial Intelligence 18, 705-717.

Kawai H., 1983, Pressure fluctuations on square prisms - Applicability of strip and quasy-steady theories, Journal of Wind Engineering and Industrial Aerodynamics, 13, 197-208.

Kermit M., Tomic O., 2003, *Independent component analysis applied on gas sensor array measurement data*, IEEE Sensors Journal, 3(2), 218-228.

Kijewski-Correa T., Kareem A., 2007, Nonlinear signal analysis: time–frequency perspectives, Journal of Engineering Mechanics, ASCE 133 (2), 238–245.

Kikuchi H., Tamura Y., Ueda H., Hibi K., 1997, Dynamic wind pressure acting on a tall building model - proper orthogonal decomposition, Journal of Wind Engineering and Industrial Aerodynamics 69-71, 631–646.

Kitagawa T., Fujinob Y., Kimurac K., Mizuno Y., 2002, Wind pressures measurement on end-cell-induced vibration of a cantilevered circular cylinder. J. of Wind Engrg. & Ind. Aerodyn., 90, 395–405.

Kumar K.S., Stathopoulos T., 1998, Power spectra of wind pressures on low buildings roofs, Journal of Wind Engineering and Industrial Aerodynamics, 74-76, 665-674.

Kumar K.S., Stathopoulos T., 1999, Synthesis of non-Gaussian wind pressure time series on low building roofs, Journal of Wind Engineering and Industrial Aerodynamics, 21, 1086-1100.

Kwok K.C.S., Wilhelm P.A., Wilkie B.G., 1988, Effect of edge configuration on wind-induced response of tall buildings, Engineering Structures 10, 135-140.

Lambert R. H., Multichannel Blind Deconvolution: FIR Matrix Algebra and Separation of Multipath Mixtures, PhD thesis, University of Southern California, 1996.

Larose G.L., D'Auteuil A., 2008, Experiments on 2D rectangular prisms at high Reynolds numbers in a pressurised wind tunnel, Journal of Wind Engineering and Industrial Aerodynamics, 96, 923-933.

Lee B.E., 1975, The effect of turbulence on the surface pressure field of a square prism, Journal of Fluid Mechanics 69, 321–352.

Lee T. W., Bell A. J., Lambert R., 1997, Blind separation of delayed and convolved sources. In Advances in Neural Information Processing Systems, volume 9, pages 758–764. MIT Press.

Lee T.W., Bell A.J, Lambert R., 1997, Blind separation of delayed and convolved sources, Advances in Neural Information Processing Systems, 9, 758–764.

Lee T.W., Koehler B.U., Orglmeister R., 1997, Blind source separation of nonlinear mixing models, In Neural Networks for Signal Processing VII, pages 406–415.

Leinhard J.H., 1966, Synopsis of lift, drag and vortex frequency data for rigid circular cylinders, Bulletin 300, college of engineering, Washington state University.

Li Q.S., Melbourne W.H., 1995, An experimental investigation of the effects of free-stream turbulence on stream wise surface pressures in separated and reattaching flows, Journal of Wind Engineering and Industrial Aerodynamics 54-55, 313–323.

Li Y., Kareem A., 1989, On stochastic decomposition and its applications in probabilistic dynamics, Proceedings on 5th International Conference On Structural Safety and Reliability, San Francisco, 1311-1318.

Li Y., Kareem A., 1995, Stochastic decomposition and application to probabilistic dynamics, Journal of Engineering Mechanics, ASCE, 121, 162-174.

Lin J.K., Grier D.G., Cowan J.D., 1997, Faithful representation of separable distributions, Neural Computation, 9(6), 1305–1320.

Linsker R., 1992, Local synaptic learning rules suffice to maximize mutual information in a linear network, Neural Computation, 4, 691-702.

Loeve M., 1945, Fonctions aléatoire de second ordre, Comptes Rendus de l'Acadèmie des sciences, Paris, 220.

Lucia D.J., Beran P.S., Silva W.A., 2004, Reduced-order modeling: new approaches for computational physics. Progress in Aerospace Sciences, 40, 51–117.

Lumley J.L., 1967, The structure of inhomogeneous turbulent flows, Proc. Int. Coll. on the fine scale structure of the atmosphere and its influence on radio wave propagation, Doklay Akademia Nauk SSSR, Moscow, 166-176.

Lumley J.L., 1970, Stochastic tools in turbulence, Academic Press, New York.

Luo S.C., Yazdani M.G., Chew Y.T., Lee T.S., 1994, Effects of incidence and afterbody shape on flow past bluff cylinders, Journal of Wind Engineering and Industrial Aerodynamics, 53, 375-399.

Makeig S., Jung T.P., Bell A.J., Ghahramani D., Sejnowski T., 1997, Blind separation of auditory event-related brain responses into independent components, Proceedings of National Academy of Sciences (USA), 94, 10979–10984.

McKeown M., Makeig S., Brown S., Jung T.P., Kindermann S., Bell A.J., Iragui V., Sejnowski T., 1998, Blind separation of functional magnetic resonance imaging (fMRI) data, Human Brain Mapping, 6(5-6), 368–372.

Moin P., Moser R.D., 1989, Characteristic-eddy decomposition of turbulence in a channel, Journal of Fluid Mechanics, 200, 471-509.

Mulaik S. A., 1972, The Foundations of Factor Analysis, McGraw-Hill, New York.

Nadal J.P., Parga N., 1994, Non-linear neurons in the low noise limit: a factorial code maximizes information transfer. Network, 5 565–581.

Nakamura Y., Hirata K., 1989, Critical geometry of oscillating bluff bodies, Journal of Fluid Mechanics 208, 375-393.

Nakamura Y., Ohya Y., 1984, The effects of turbulence on the mean flow past two-dimensional rectangular cylinders, Journal of Fluid Mechanics 149, 255-273.

Nakamura Y., Ozono S., 1987, The effects of turbulence on a separated and reattaching flow, Journal of Fluid Mechanics 178, 477-490.

Naudascher E., Weske J.R., Fey B., 1981, Exploratory study on dumping of galloping vibrations, Journal of Wind Engineering and Industrial Aerodynamics, 8, 211-222.

Nguyen Thi H.L., Jutten C., 1995, Blind source separation for convolutive mixtures, Signal Processing 45(2), 209-229.

Norberg C., 1993, Flow around rectangular cylinders: Pressure force and wake frequencies, Journal of Wind Engineering and Industrial Aerodynamics, 49, 187–196.

Obasaju E.D., 1983, An investigation of the effects of incidence on the flow around a square section cylinder, Aeronautical Quarterly, 34, 243-258.

Oja E., 1997, The nonlinear PCA learning rule in independent component analysis, Neurocomputing, 17 (1,) 25–46.

Okajima A., 1982, Strouhal numbers of rectangular cylinders. Journal of Fluid Mechanics 123, 379–398.

Olhede S., Walden A.T., 2004, The Hilbert spectrum via wavelet projections, Proceedings of the Royal Society of London A, 460, 955–975.

Oppenheim A., Shafer R., 1989, Discrete-Time signal processing, Prentice Hall, New Jersey.

Ottonello C., Pagan, S., 1994, Modified frequency-domain kurtosis for signal processing, Electronics Letters 30, 1117–1118.

Papoulis A., 1991, Probability, random variables and stochastic processes, McGraw-Hill, New York

Pearson K., 1901, On lines and planes of closet fit to systems of points in space, Philosophical Magazine, 2, 559-572.

Peled R., Braun S., Zacksenhouse M., 2005, A blind deconvolution separation of multiple sources with application to bearing diagnostics, Mechanical Systems and Signal Processing, 19 (6), 1181–1195.

Roshko A., Perspectives on bluff body aerodynamics, Journal of Wind Engineering and Industrial Aerodynamics, 49, 1-3, 79-100.

Roth Z., Baram Y., 1996, Multidimensional density shaping by sigmoids, IEEE Trans Neural Networks, 7, 1291-1298.

Rowley C. W. et al., 2009, Spectral analysis of nonlinear flows, Journal of Fluid Mechanics, 641, 115-127.

Schewe G., 2013, Reynolds-number-effects in flow around a rectangular cylinder with aspect ratio 1:5, Journal of Fluids and Structures 39, 15-26.

Serviere C., Fabry P., 2004, Blind source separation of noisy harmonic signals for rotating machine diagnosis, Journal of Sound and Vibration, 272, 317-339.

Shwartz S., Schechner Y., Zibulevsky M., 2006, Efficient separation of convolutive mixtures, in: Proc. ICA 2006, 246-253, Springer-Verlag, Berlin.

Solari G., Carassale L., 2000, Modal transformation tools in structural dynamics and wind engineering, Wind and Structures, 3, 221-241.

Solari G., Carassale L., Tubino F., 2007, Proper Orthogonal Decomposition in wind engineering: Part 1: A state-of-the-art and some prospects, Wind & Structures 10 (2), 153–176.

Spearman C., 1904, General intelligence, objectively determined and measured, The American Journal of Psychology, 15, 201-293.

Surry D., 1969, The effect of high intensity turbulence on the aerodynamics of a rigid circular cylinder at subcritical Reynolds numbers, UTIAS rep. 142.

Tamura T., Miyagi T., 1999, The effect of turbulence on aerodynamic forces on a square cylinder with various corner shapes, Journal of Wind Engineering and Industrial Aerodynamics, 83, 135-145.

Tamura T., Miyagi T., Kitagishi T., 1998, Numerical prediction of unsteady pressures on a square cylinder with various corner shapes, Journal of Wind Engineering and Industrial Aerodynamics, 74-76, 531-542.

Tamura Y., Suganuma S., Kikuchi H., Hibi K., 1999, Proper orthogonal decomposition of random wind pressure field, Journal of Fluids and Structures 13, 1069–1095.

Tamura Y., Ueda H., Kikuchi H., Hibi K., Suganuma S., Bienkiewicz B., 1997, Proper orthogonal decomposition study of approach wind-building pressure correlation, Journal of Wind Engineering and Industrial Aerodynamics 72, 421–432.

Torkkola K., 1996, Blind separation of convolved sources based on information maximization, Workshop on Neural Networks and Signal Processing (NNSP'96), 423–432, Kyoto, Japan.

Vickery B.J., 1966, Fluctuating lift and drag on a long cylinder of square cross-section in a smooth and in a turbulent stream, Journal of Fluid Mechanics 25, 481–494.

Von Karman T., 1954, Aerodynamics, Cornell University Press, Oxford.

Yamazaki F., Shinozuka M., 1990, Simulation of stochastic fields by statistical preconditioning, Journal of Engineering Mechanics, ASCE, 116, 268-287.

Yellin D., Weinstein E., Multichannel signal separation: Methods and analysis. IEEE, Trans. on Signal Processing, 44, 106–118, 1996.

Yen S.C., Yang C.W., 2011, Flow patterns and vortex shedding behaviour behind a square cylinder, Journal of Wind Engineering and Industrial Aerodynamics 99, 868–878.

Yoshida A., Tamura Y., 2004, System identification of structure for wind-induced response, Proceedings, 5th International Colloquium on Bluff Body Aerodynamics & Applications, Ottawa, Canada, 335-338.

Zang C., Friswel M.I., Imregun M., 2004, Structural damage detection using independent component analysis, structural health monitoring, 3, 1, 69-83.

Zdravkovich M.M., 1997, Flow around circular cylinder, Oxford University Press, Great Britain.

Zhou W., Chelidze D., 2007, Blind source separation based vibration mode identification, Mechanical Systems and Signal Processing, 21, 3072-87.

Zuo M.J., Lin J., Fan X., 2005. Feature separation using ICA foe one-dimensional time series and its application in fault detection. J. Sound & Vibration, 287, 614-624.

APPENDIX A

LIST OF PUBLICATIONS (PDF FILES - CD-ROM)

1. Carassale L., Freda A., Marrè Brunenghi M., 2014, Experimental investigation on the aerodynamic behaviour of square cylinders with rounded corners, Journal of Fluids and Structures, 44, 195-204.

2. Carassale L., Freda A., Marrè Brunenghi M., 2013, Effects of free-stream turbulence and corner shape on the galloping instability of square cylinders, Journal of Wind Engineering and Industrial Aerodynamics, 123, 274-280.

3. Carassale L., Marrè Brunenghi M., 2013, Dynamic response of trackside structures due to the aerodynamic effects produced by passing trains, Journal of Wind Engineering and Industrial Aerodynamics, 123, 317-324.

4. Carassale L., Marrè Brunenghi M., 2012, Identification of meaningful coherent structures in the wind-induced pressure on a prismatic body, Journal of Wind Engineering and Industrial Aerodynamics, 104-106, 216-226.

5. Carassale L., Marrè Brunenghi M., 2011, Statistical analysis of wind-induced pressure fields: a methodological perspective, Journal of Wind Engineering and Industrial Aerodynamics, 99, 700-710.

Aeroelastic Effects on Tall Buildings: Performance-Based Comfort Analysis

Dissertation

submitted to and approved by the

Department of Architecture, Civil Engineering and Environmental Sciences
University of Braunschweig – Institute of Technology

and the

Faculty of Engineering
University of Florence

in candidacy for the degree of a
Doktor-Ingenieur (Dr.-Ing.) /
Dottore di Ricerca in "Riduzione del Rischio da Catastrofi Naturali
su Strutture ed Infrastrutture" [*)]

by
Chiara Pozzuoli
Born 09.07.1983
from Perugia (PG), Italy

Submitted on	14 September 2012
Oral examination on	08 November 2012
Professorial advisors	Prof. G. Bartoli
	Prof. U. Peil

2012

*) Either the German or the Italian form of the title may be used.

To my family
for their love and support
every step of the way

Acknowledgements

Contents

List of Figures

xvi

xvii

List of Tables

List of Symbols

α exponent of the power law profile

$\chi^2()$ aerodynamic admittance function

δ boundary layer thickness

δ logarithmic decrement

κ von Kármán's constant

λ_a acceleration scale

λ_f frequency scale

λ_l length scale

λ_t time scale

λ_U velocity scale

$[C]$ damping matrix

$[K]$ stiffness matrix

$[M]$ mass matrix

μ dynamic viscosity

ν kinematic viscosity

ω circular frequency

ϕ mode shape

ρ density, air density

ρ_b bulk density

σ standard deviation

τ_0 shear stress at the ground surface

ξ damping ratio

ξ_s structural damping ratio

ξ_a aerodynamic damping ratio

ξ_{tot}	total damping ratio
a	linear acceleration
a_α	angular acceleration
b	breadth
C_D	drag coefficient
C_F	force coefficient
C_L	lift coefficient
C_M	moment coefficient
C_p	pressure coefficient
D	drag
d	depth
E	Young's modulus
F	force
f	frequency
$F()$	cumulative distribution function
$F()$	wind load
F_a	aeroelastic force
f_n	natural frequency
f_r	reduced frequency
F_s	aerodynamic force
f_s	shedding frequency
G	torsional modulus
$H()$	frequency response function
h, H	height
I	moment of inertia
I_u	turbulence intensity of the along-wind turbulent component
L	integral length scale
L	lift
l	length
M	moment

m	mass
M_D	mass-damping coefficient
$m_{i,e}$	equivalent mass per unit length for mode i
P	probability
p	pressure
$P()$	generalized wind load
$p()$	probability density function
p_0	static pressure
p_{dyn}	dynamic pressure
q	generalized displacement
R	return period
Re	Reynolds number
S	Power Spectral Density (PSD)
Sc	Scruton number
St	Strouhal number
U	mean velocity
u	longitudinal turbulent component
u_*	friction velocity
U_0	velocity of the undisturbed flow
U_∞	free-stream velocity
U_h	wind speed at model height
U_r	reduced velocity
U_{crit}	critical wind speed
$U_{r,crit}$	critical reduced velocity
v	lateral turbulent component
w	vertical turbulent component
z_0	roughness length
z_h	zero-plane displacement
z_{ref}	reference height

Abstract

Recent trends towards increasingly taller and slender buildings have led to a new generation of wind-sensitive structures, that can experience large wind-induced vibrations. Excessive dynamic oscillations can then cause discomfort to occupants, sometimes raising concerns about serviceability design problems. Vibration perception is subjective and depends on the vibration frequency and on physiological and psychological factors.

It is now widely accepted that the perception of wind-induced vibrations is closely related to the acceleration response of structures. It has, therefore, to be checked that the latter is limited under tolerable thresholds.

Wind risk assessment of tall buildings, related to occupant comfort under serviceability conditions, requires, therefore, the proper estimation of the acceleration responses. For tall, slender buildings, their across-wind dynamic responses usually exceed along-wind ones. The across-wind response, compared with that in the along-wind direction, is less related to fluctuations of the incoming wind, since it results mainly from the aerodynamic pressure fluctuations in the separated shear layers and wake flow fields.

Moreover, aeroelastic or motion-induced effects, such as lock-in and galloping, may take place and cause vibrations significantly different from those predicted with the assumption of rigid structures. For these reasons, wind tunnel tests represent the most reliable means for determining across-wind responses of slender structures susceptible of not negligible aeroelastic effects.

A wide experimental activity was carried out in the CRIACIV[1] (Centro di Ricerca Interuniversitario di Aerodinamica delle Costruzioni e Ingegneria del Vento) boundary layer wind tunnel, using a continuous equivalent aeroelastic model of a square-section building, previously investigated through rigid model tests.

The model, which is a "skin-skeleton" type one, is equipped with simultaneously measuring pressure taps and is mounted on a 5-components high-frequency force balance which enables the measurement of the overall forces at the base of the model. The dynamic characteristics (frequency, mode shape and damping) of the model-support system for the first three modes of vibration were identified by means of free vibration tests.

Wind tunnel tests were carried out orienting the model so that the incoming wind direction is perpendicular to the direction of the first identified bending mode. Three displacement laser transducers and three mono-axial accelerometers were used to measure across-wind displacement and along- and across-wind acceleration responses, respectively. Measurements were carried out for a wide range of wind speeds, including the critical velocity for vortex-induced vibrations. The main goal

---

[1]Interuniversity Research Center of Building Aerodynamics and Wind Engineering

of this experimental activity was the simultaneous measurement of pressures, overall forces, displacements and accelerations on an aeroelastic model, even in lock-in conditions.

From the analysis of the measured pressure field and responses, several results were obtained, including the possible variation of the Strouhal number with height over the tunnel floor, the correlation structure of pressures, the lock-in wind speed range, the RMS acceleration and displacement responses as functions of wind speed. Moderate motion-induced effects involving the pressure field were observed, while aeroelasticity was found to play an important role in the measured components of across-wind responses, in terms of displacements and accelerations.

A Finite Element Method model was also developed in order to compare the measured aeroelastic response with that predicted numerically from pressures measured on a rigid model. The benchmarking of the two responses allowed the identification of aeroelastic effects in terms of aerodynamic damping. The latter, in the case of high structural damping, gives a positive contribution, which means that, for the structure under investigation, aeroelastic effects decrease the across-wind response. Neglecting them is, therefore, a conservative choice. The identified aerodynamic damping as a function of reduced velocity was also compared with results from other literature works. The across-wind response of the model can be estimated from pressures on a rigid model, taking into account aeroelastic effects by means of an additional damping term.

A general procedure for the assessment of wind-induced discomfort risk of tall buildings is proposed. It is in line with the Performance-Based Wind Engineering approach and with the general risk management framework developed within the IGC 802. The procedure consists in two phases, namely the hazard analysis and the structural vulnerability analysis. According to any comfort criteria adopted, wind-induced risk is expressed in terms of the probability of exceeding the comfort threshold and can be translated into the average number of days per year in which the building experiences unacceptable vibrations. In order to illustrate how this risk assessment procedure works, it is applied to a square-section tall building whose response to the wind action is estimated from wind tunnel tests.

Sommario

L'attuale tendenza verso la costruzione di strutture sempre più alte e più snelle ha portato allo sviluppo di una nuova generazione di edifici alti particolarmente sensibili all'azione del vento. Quest'ultima può, infatti, dar luogo a vibrazioni importanti che causano problemi di discomfort degli occupanti, la cui entità varia da soggetto a soggetto e dipende dalla frequenza di oscillazione e da fattori fisiologici e psicologici.

La percezione delle vibrazioni indotte dal vento è strettamente correlata alla risposta in accelerazione, la quale dovrà essere contenuta entro definiti limiti di tollerabilità. La valutazione della performance degli edifici alti nei confronti del comfort richiede, quindi, la determinazione della risposta in accelerazione dovuta all'azione del vento. È nella direzione trasversale al vento (across-wind) che, in genere, si verificano le maggiori accelerazioni. La risposta across-wind è meno correlabile alle fluttuazioni turbolente del vento incidente rispetto alla risposta along-wind (nella direzione del vento), poiché è determinata prevalentemente dalle fluttuazioni della pressione aerodinamica nella zona di separazione e di scia vorticosa.

Fenomeni moto-indotti, detti aeroelastici, quali il lock-in ed il galloping, possono inoltre verificarsi e determinare risposte sensibilmente diverse da quelle ottenute nell'ipotesi di struttura indeformabile. Le prove sperimentali in galleria del vento su modelli aeroelastici costituiscono oggi lo strumento più diffuso per la stima della risposta trasversale al vento di edifici flessibili per i quali i fenomeni moto-indotti non sono trascurabili.

Un'ampia campagna sperimentale in condizioni di flusso turbolento è stata condotta nella galleria del vento del CRIACIV (Centro di Ricerca Interuniversitario di Aerodinamica delle Costruzioni e Ingegneria del Vento) su un modello aeroelastico equivalente continuo di un edificio regolare a base quadrata, oggetto di prove precedenti su modello rigido. Al fine di misurare la distribuzione delle pressioni durante il flusso in galleria, il modello è stato equipaggiato di prese di pressione acquisite simultaneamente. Il modello è stato inoltre montato su una bilancia aerodinamica per la misura delle forzanti alla base. Le caratteristiche dinamiche (frequenza, forma modale e smorzamento) del sistema modello-supporto così ottenuto sono state identificate, per i primi 3 gradi di libertà, mediante test in oscillazioni libere. Le prove sperimentali sono state quindi eseguite adottando una direzione del vento incidente ortogonale alla direzione di vibrazione del primo modo identificato.

Attraverso tre trasduttori laser e tre accelerometri istallati sul modello è stato possibile misurare, rispettivamente, lo spostamento across-wind e la risposta in accelerazione in sommità, sia in direzione along-wind che across-wind. Le misure sono state effettuate per un ampio range di velocità contenente la velocità critica di lock-in. La campagna sperimentale è stata realizzata con lo scopo fondamentale di

ottenere una misura simultanea di pressioni, forze, spostamenti ed accelerazioni su un modello aeroelastico in galleria del vento anche in condizioni di sincronizzazione.

Dall'analisi dei coefficienti di pressione e delle risposte sono stati ricavati la variazione del numero di Strouhal con la quota, la struttura di correlazione delle pressioni, l'intervallo di lock-in, la variazione delle accelerazioni e degli spostamenti con la velocità. Gli effetti aeroelastici osservati coinvolgono in modo lieve il campo di pressione e più significativamente la risposta across-wind in termini di spostamento e di accelerazione.

È stato inoltre sviluppato un modello agli elementi finiti al fine di confrontare la risposta aeroelastica misurata con quella ottenuta numericamente a partire dalle pressioni misurate su modello rigido. Il confronto tra le due risposte ha permesso di identificare gli effetti aeroelastici nella risposta across-wind in termini di smorzamento aerodinamico. Quest'ultimo, in caso di elevato smorzamento strutturale, rappresenta un contributo positivo per cui, nel caso in esame, gli effetti aeroelastici contribuiscono a ridurre la risposta trasversale. Trascurarli sarebbe quindi una scelta conservativa. La variazione dello smorzamento aerodinamico identificato con la velocità ridotta è stata confrontata con quella di altri lavori di letteratura.

Un ulteriore contributo di questo lavoro consiste nella definizione di una procedura di valutazione del rischio di discomfort indotto dall'azione del vento sugli edifici alti. Tale procedura è stata formulata in accordo all'approccio noto come Perfomance-Based Wind Engineering e può essere collocata all'interno del risk framework proposto dall'IGC 802. La tecnica di valutazione del rischio proposta si articola in due fasi corrispondenti all'analisi dell'hazard (pericolosità) ed alla valutazione della vulnerabilità. Il rischio di discomfort indotto dal vento è stimato in termini di probabilità di superamento di una qualsiasi soglia di comfort adottata e può essere tradotto facilmente in numero medio di giorni all'anno in cui l'edificio è soggetto a vibrazioni non accettabili. Al fine di fornire un esempio pratico di utilizzo della procedura di risk assessment proposta, quest'ultima è stata applicata ad un edificio alto di sezione quadrata, la cui risposta è stata valutata a partire dai dati sperimentali misurati in galleria del vento.

Zusammenfassung

Die derzeitige Tendenz zum Bau immer höherer und schlankerer Gebäude hat zur Entwicklung einer neuen Generation von Hochhäusern geführt, die besonders windempfindlich sind. Starke Gebäudeschwingungen können bei Personen, die sich im Hochhaus aufhalten, ein Gefühl des Unbehagens hervorrufen, dessen Stärke von der Intensität der Schwingungen und individuellen physiologischen und psychologischen Faktoren abhängt.

Die Wahrnehmung windbedingter Vibrationen steht in engem Zusammenhang mit dem Beschleunigungsverhalten, das gewisse Toleranzwerte nicht überschreiten darf. Die Bewertung von Hochhäusern in Bezug auf ihren Komfort erfordert daher die Bestimmung des windbedingten Beschleunigungsverhaltens.

Im Falle hoher und schlanker Gebäude entstehen gewöhnlich höhere Beschleunigungen quer zur Windrichtung (across-wind) als in der Windrichtung (along-wind). Im Unterschied zur Beschleunigung in Windrichtung steht diejenige quer zur Windrichtung nicht in einem direkten Zusammenhang zu turbulenten Schwankungen des betreffenden Winds, sondern hängt hauptsächlich von den aerodynamischen Druckschwankungen in den Scherschichten und den Nachlaufströmungsfeldern ab.

Außerdem können bewegungsbedingte und aeroelastische Phänomene wie Lock-in- und Formanregungs-Effekte (Galloping) auftreten und zu Schwingungen führen, die sich von denen starrer Gebäude stark unterscheiden. Experimentelle Versuche mit Hilfe aeroelastischer Modelle im Windkanal stellen heute die am weitesten verbreiteten Mittel zur Bestimmung des Beschleuningungsverhalten schlanker Gebäude quer zur Windrichtung dar, bei denen aeroelastische Effekte nicht vernachlässigt werden dürfen.

Eine umfangreiche Versuchsreihe unter turbulenten Windbedingungen ist im Windkanal des CRIACIV (Centro di Ricerca Interuniversitario di Aerodinamica delle Costruzioni e Ingegneria del Vento) mit Hilfe des aeroelastischen Modells eines regelmäSSigen Bauwerks mit quadratischem Grundriss durchgeführt worden, das Gegenstand vorheriger Versuche eines starren Modells gewesen war.

Zur Messung der Druckverteilung im Windkanal ist das Modell mit gleichzeitig messenden Druckkappen ausgerüstet worden. Ferner ist das Modell auf eine aerodynamische Waage zur Messung der Kräfte am Sockel montiert worden. Die dynamischen Charakteristiken (Frequenz, Schwingform und Dämpfung) des Modells sind mit freien Schwingungstests für die ersten drei Schwingungsformen bestimmt worden. Die Experimente sind so erfolgt, dass die Windrichtung senkrecht zur ersten festgestellten Schwingungsrichtung war.

Mit Hilfe von drei Laser-Abstandssensoren und drei einachsigen Beschleunigungsmessern konnten die Verschiebung quer zur Windrichtung (across-wind) und das Beschleunigungsverhalten an der Gebäudespitze sowohl quer als auch längs zur

Windrichtung (across-/along-wind) gemessen werden. Die Messungen sind für eine beträchtliche Spanne von Windgeschwindigkeiten einschlieSSlich der kritischen Lock-in-Geschwindigkeit durchgeführt worden.

Das wesentliche Ziel der Versuchsreihe war die gleichzeitige Messung von Drücken, Kräften, Verschiebungen und Beschleunigungen anhand eines aeroelastischen Modells im Windkanal, auch unter Lock-in-Bedingungen.

Durch die Auswertung der Druckkoeffizienten und der Beschleunigungswerte konnten die höhenbedingte Veränderung der Strouhal-Zahl, die Korrelationsstruktur der Drücke, der Lock-in-Windgeschwindigkeitsbereich sowie die Veränderung der Beschleunigungen und der Verschiebungen in Abhängigkeit von der Windgeschwindigkeit ermittelt werden. Die beobachteten aeroelastischen Effekte betreffen weniger stark das Druckfeld, spielen aber eine bedeutende Rolle bei den Beschleunigungen und den Verschiebungen.

Außerdem ist ein Modell nach der Finite-Elemente-Methode (FEM) entwickelt worden, um das gemessene aeroelastische Verhalten mit dem zu vergleichen, das von den an einem starren Modell gemessenen Drücken numerisch ermittelt worden ist. Der Vergleich der beiden Verhalten hat ermöglicht, die aeroelastischen Effekte quer zur Windrichtung (across-wind) im Sinne der aerodynamischen Dämpfung zu bestimmen. Im Falle einer hohen strukturellen Dämpfung hat letztere eine positive Auswirkung, weshalb im vorliegenden Fall die aeroelastischen Effekte dazu beitragen, das Beschleunigungsverhalten quer zur Windrichtung zu reduzieren. Es wäre daher eine konservative Wahl, sie zu ignorieren. Die Veränderung der aerodynamischen Dämpfung in Abhängigkeit von der Windgeschwindigkeit ist mit den Angaben in anderen wissenschaftlichen Arbeiten verglichen worden.

Das Verhalten quer zur Windrichtung (across-wind) des aeroelastischen Modells kann vom numerischen Modell auf der Grundlage der an einem starren Modell gemessenen Drücke abgeleitet werden, indem die aeroelastischen Effekte unter Hinzunahme eines zusätzlichen Dämpfungsterms berücksichtigt werden.

Ein weiterer Beitrag dieser Arbeit besteht in der Definition eines Verfahrens zur Bewertung der Gefahr des Empfindens windbedingten Unbehagens in Hochhäusern. Dieses Verfahren wurde in Übereinstimmung mit dem Perfomance-Based Wind Engineering Ansatz bestimmt und kann im Rahmen des Risikomanagements der IGC 802 betrachtet werden. Die Risikobewertung erfolgt in zwei Phasen: der Gefahrenanalyse und der Bewertung struktureller Schwachstellen. Die Gefahr des Empfindens windbedingten Unbehagens wird in Form der Wahrscheinlichkeit des Überschreitens von angenommenen Komfortgrenzwerten bestimmt und mit Hilfe der mittleren Anzahl von Tagen pro Jahr angegeben, an denen das Gebäude nicht akzeptable Schwingungen erfährt. Um ein praktisches Beispiel der Anwendung des vorgeschlagenen Risikomanagement-Verfahrens zu geben, ist das Verfahren auf ein Hochhaus mit quadratischem Grundriss angewandt worden, dessen Verhalten aufgrund der im Windkanal gemessenen Versuchsdaten bewertet wurde.

Chapter 1

Introduction

1.1 Background

Tall buildings, now approaching the frontier of 1000 m height, have enormously spread worldwide in recent years. This modern phenomenon has led to the introduction of new problems that the international engineering community is now facing.

One issue that has started to dominate the serviceability design of tall buildings is wind-induced discomfort. In the case of slender structures with low natural frequencies, the wind action can cause annoying vibrations which can interfere with building occupants' daily activities and general well-being.

Many literature works have been dedicated to the perception of vibrations. However, no single internationally accepted design standard for satisfactory levels of wind-induced vibrations in tall buildings has been set, yet.

If a modern building is prone to experience wind-induced vibrations, it is very important to estimate the risk of exceeding acceptable vibration limits and of causing discomfort. For this reason, management and treatment of wind risk related to motion perception in tall buildings is of major relevance today.

It is widely accepted that the perception of vibration is closely related to the acceleration response of buildings. Moreover, it is usually in the across-wind direction, that means perpendicular to the incoming wind direction, that buildings usually suffer greater vibrations. In order to satisfy comfort criteria, the wind-induced response has to be accurately estimated.

Many experimental and numerical studies have underlined the complexity of the wind flow and of the wind action around prismatic objects modeling possible tall buildings geometries. In the case of vibrating structures, aeroelastic or motion-induced effects can occur and lead to significantly different responses.

Recent improvements in Computation Fluid Dynamics techniques are very promising, however, wind tunnels have served as the most reliable means for estimating wind-induced responses of tall buildings experiencing aeroelastic phenomena.

One of the possible approaches used to identify aeroelastic effects of tall buildings is that of aerodynamic damping. While in the direction of wind aerodynamic damping is usually positive and small, in the across-wind direction it can be negative and relevant.

From this context it is clear that the accurate design of tall buildings in serviceability conditions is a challenging task involving several topics, including bluff body aerodynamics, aeroelasticity, human perception of vibrations, wind tunnel measure-

ments and also risk management and treatment.

1.2   Scope and Objectives

This research work aims to contribute to the understanding of the wind action and of the aeroelastic effects in tall buildings responses. One of this work purposes is to enlarge the database of wind tunnel measurements carried out on aeroelastic models. One important scope of the thesis is also to provide a general approach to evaluate discomfort risk of tall buildings.

1.3   Major challenges of the research

Serviceability design of tall buildings requires an in-depth study into the wind flow around structures, wind effects on buildings, including aeroelastic phenomena, dynamic properties of tall buildings and the risks of wind hazard. In this context, the primary research challenges of the thesis can be listed as follows:

- experimental wind tunnel tests on an equivalent aeroelastic model of a square-section tall building, aimed at the simultaneous measurement of pressures, overall forces and acceleration and displacement responses;

- experimental identification of the vortex resonance condition and analysis of its effects on the wind loads and responses;

- identification of aeroelastic effects in the across-wind response in terms of aerodynamic damping through an experimental-numerical procedure;

- development of a general procedure for wind risk assessment of tall buildings related to comfort thresholds and application of this procedure to a case study building.

1.4   Thesis organization

The content of the thesis is organized into nine chapters, including this introductory chapter (chapter 1). Chapter 2 formulates the problem of the wind-induced discomfort risk of tall buildings. A general probabilistic risk management framework, proposed for dealing with risk of structures, is illustrated. The Performance-Based Design approach for the assessment of risk is discussed. Some literature studies dedicated to motion perception of tall buildings occupants are reviewed and the comfort criteria currently used for the serviceability design of tall buildings are shown.

Chapter 3 is dedicated to the aerodynamics of the square-section bluff body. The knowledge of the flow behind prismatic bodies is judged of fundamental importance for the design of wind-sensitive tall buildings. The vortex-shedding phenomenon from fixed two-dimensional bluff-bodies is introduced. The aerodynamics of 2-D square-section cylinders is reviewed and then the three-dimensional flow behind square-section prisms of finite length is discussed.

Chapter 4 deals with aeroelastic effects in the wind-induced responses of tall buildings and discusses the aerodynamic damping approach for estimating the motion-induced effects. Literature studies focused on the across-wind aeroelastic response

of tall buildings are reviewed and later used for comparison with results obtained from the experimental activity carried out in this research.

In chapter 5 the experimental techniques of common use in wind tunnels are reviewed, with particular reference to aeroelastic simulations which provide the most complete characterization of the structural responses, including the effects of the motion-induced forces. Similarity requirements for the aeroelastic studies of buildings are also discussed.

Chapter 6 illustrates the wind tunnel tests carried out in the CRIACIV boundary layer wind tunnel on an aeroelastic model of a regular square-section tall building. Experimental results for a wide range of wind speeds, including the lock-in velocity condition, are investigated in detail and compared with data from other literature studies. The effects of vortex resonance on wind loads and model responses are discussed. The acceleration response of the model is found to be dominated by that in the across-wind direction, which is affected by the motion-induced lock-in phenomenon.

In chapter 7 the aeroelastic effects involving the across-wind response of the model tested in the wind tunnel are identified in terms of aerodynamic damping. For this identification procedure, a Finite Element Method model which replicates the physical wind tunnel model is developed. Across-wind aerodynamic damping is evaluated from the comparison between the aeroelastic response directly measured from the model in the tunnel and the response numerically predicted from wind loads measured on a rigid model.

In chapter 8 a general procedure for the serviceability wind risk assessment of tall buildings is presented. This procedure is applied to a case study building with the purpose of showing how the procedure can be used to assess the discomfort risk of tall buildings. Real wind data, registered from an anemometric station located in Italy, are used.

The last chapter (chapter 9) summarizes the major contributions and findings of this research study. Possible future developments of the work are suggested.

Chapter 2

Wind risk of tall buildings related to comfort thresholds

2.1   Introduction

Tall buildings emerged in the late nineteenth century in the United States of America. They constituted a so-called *American Building Type*, meaning that most important tall buildings were built in the USA. Today, however, they are a worldwide architectural phenomenon and the total number of tall buildings have grown up enormously. Ali and Moon (2007) refer to a number of 3482 tall buildings in 1982 and 108924 in 2006.

There is not an absolute definition of what constitutes a "tall building". According to the criteria proposed by the Council on Tall Buildings and Urban Habitat (CTBUH, `www.ctbuh.org`), a building can be defined as "tall" when it shows some element of "tallness" in one or more of the following three categories:

- *Height relative to context.* Differently from absolute height, it relates the building height to the context where it exists. Thus the same building, let's say 14-story building, may not be considered a tall building in a high-rise city, such as Chicago or Hong Kong, while it can be taller than the urban norm in a provincial European city or a suburb.

- *Proportion.* There are many buildings which are not particularly high, but are slender enough to have the appearance of tall buildings. Other buildings, on the other hand, are quite tall, but their size to floor ratio is so low that they can not be classed as tall buildings.

- *Technologies.* A building can be categorized as tall when it contains technologies that can be considered as a product of "tallness", such as, for example, vertical transport technologies and structural wind bracing as a product of height.

A multi-story structure between 35 and 100 meters tall, or a building of unknown height from 12 to 39 floors is classified as a high-rise building by the ESN 18727 Emporis Standards (`www.emporis.com`). The CTBUH defines a building as "supertall" when its height exceeds 300 meters.

In recent years tall buildings have encountered a deep change in geographical location, function and material used. Whereas as recently as 1990, 80% of the 100

world's tallest buildings were located in North America, by the end of 2012, the
number of the world's 100 tallest buildings in North America is expected to be only
20%, with 42% in Asia and 32% in the Middle East [Fig. 2.1(a)]. There has also
been a major moving away from the predominantly office buildings which have dom-
inated the tallest lists for many decades [Fig. 2.1(b)]. Residential and mixed-use
functions are currently heavily influencing the list, up to 38% from 12% in just the
last decade. The rapid urbanization of developing countries partially explains why,
in order to accommodate the growing populace in the city, many of these buildings
are now residential in nature rather than commercial. The changes in structural
material have also been very significant over the past few decades [Fig. 2.1(c)]. Steel
buildings have dropped in favor of concrete or composite structures.

    The major feature characterizing the evolution of tall buildings is, however,
the trend towards developing increasingly higher and more flexible structures. The
world's tallest buildings are now approaching the frontier of 1000 m height (Fig. 2.2).
As a consequence, a new generation of tall and slender structures, that are highly sen-
sitive to wind-induced deflections and vibrations, has developed. Therefore, concerns
of perceptible building motions and occupant discomfort have become prominent in
the design of tall buildings under the wind action.

    Management and treatment of risk related to wind-induced discomfort has be-
come today of major importance in the engineering community.

    In section 2.2 a risk management framework defining a general procedure for deal-
ing with risk of structures is briefly described. Section 2.3 refers to the Performance-
Based Design (PBD) approach, applied to wind engineering (Performance-Based
Wind Engineering, PBWE), as a methodology to be used for the quantitative esti-
mation of wind risk. In section 2.4 human comfort levels and perception criteria are
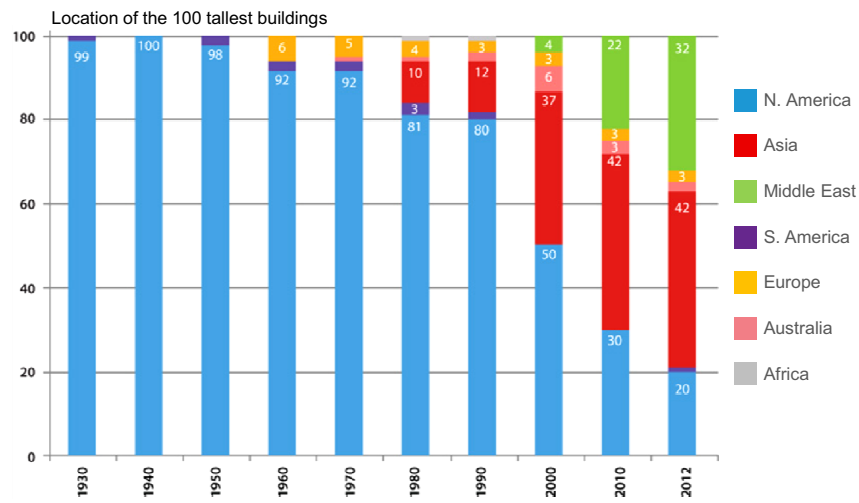illustrated.

2.2   Risk management

    The term *risk*, and therefore also *aeolian risk*, may take several meanings. Risk
is commonly identified with the presence of a certain danger, being its counter-
part, namely *safety*, identified with the absence of danger. This *yes-or-no* definition
doesn't apply to engineering facilities (Augusti *et al.*, 2001). The numerous uncer-
tainties involving natural disasters entail the necessity to assess risk in probabilistic
terms. A general *probabilistic risk management framework* (Fig. 2.3) was proposed
by Pliefke *et al.* (2006), in compliance with AS/NZS-Standard (1999) and consists
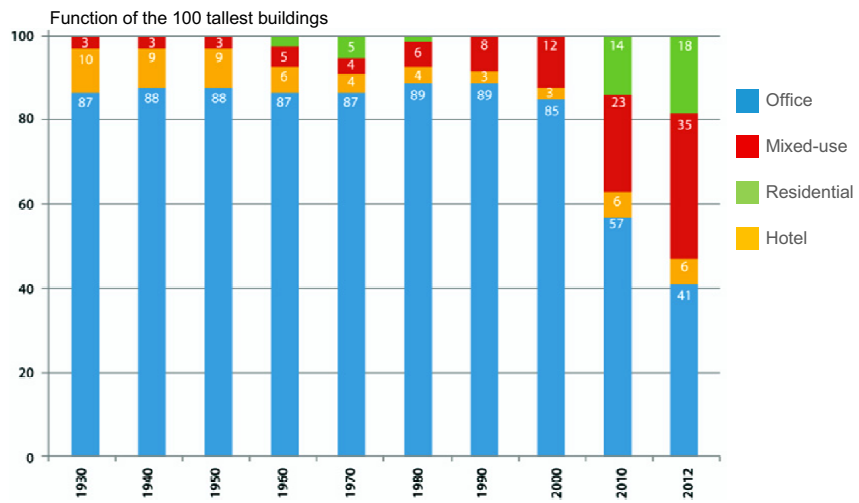of three major steps that are performed chronologically, corresponding to:

1. *risk identification*

2. *risk assessment*

3. *risk treatment*

2.2.1   Risk identification

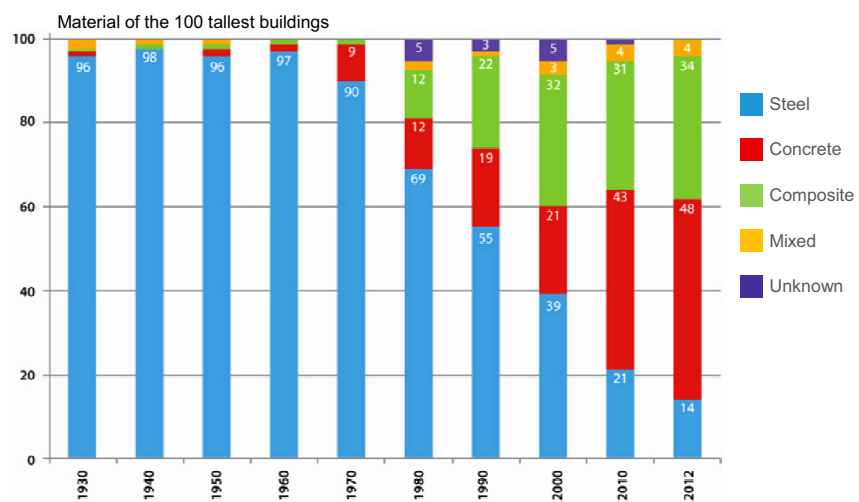   Risk identification is aimed at answering the question "what can happen and
where?" and requires first the definition of the system subjected to risk (e.g. a

Location of the 100 tallest buildings

(a)

Function of the 100 tallest buildings

(b)

Material of the 100 tallest buildings

(c)

Fig. 2.1 Recent trends of the 100 tallest buildings, from 1930 to 2012 (www.ctbuh.org): a) location; b) function; c) material.
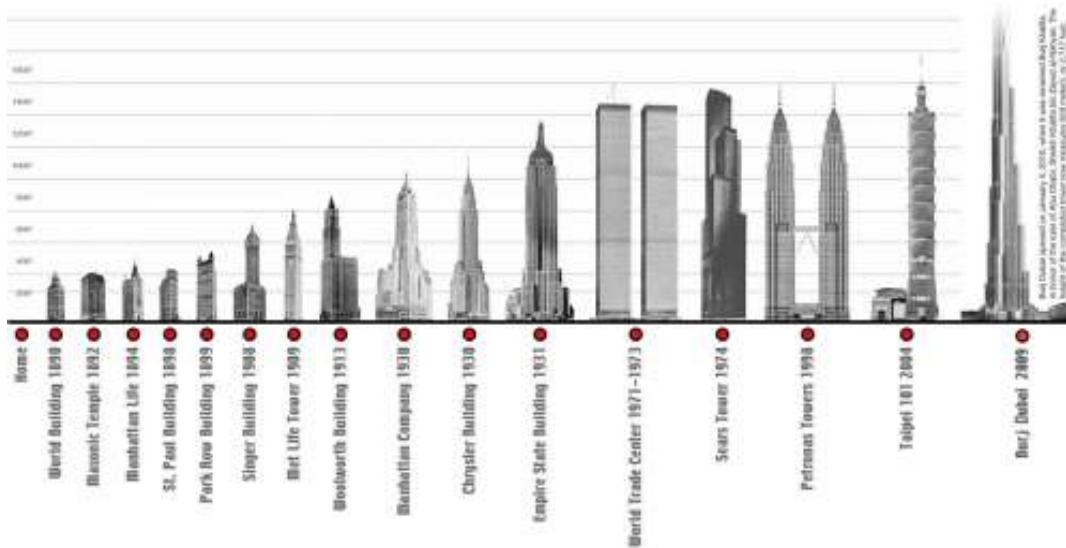
Fig. 2.2 World's tallest towers: timeline of all skyscrapers holding the title of tallest building in the world from 1890 to the present.

structure, a city, ...) and then all the sources of events that can compromise the system functionality (*hazard identification*).

2.2.2 Risk assessment

Risk assessment consists of two sub-procedures: *risk analysis* and *risk evaluation*.

The first phase of risk analysis is *hazard analysis*, aimed at the definition of the probability of occurrence of the previously identified hazards. Knowing the *structural vulnerability*, that is the relation between the hazard intensity and response of the system, damage is quantified (*damage assessment*). Finally, the consequences of damage in terms of losses are determined (*loss assessment*).

Direct losses occur when the disaster takes place, while *indirect losses* arise after a certain time delay. Losses can either be categorized in consequence classes, so that it is distinguished between economic loss, loss of life etc., or accumulated in one single number in order to define a common scale of evaluation for both *tangible* and *intangible* consequences. Tangible or economic consequences are those directly measurable in monetary terms. Intangible ones, are, on the other hand, not quantitatively appraisable losses, e.g. injuries and fatalities, pollution of the environment, loss of cultural, social and historical values, etc.

The final result of risk analysis is the quantification of risk in terms of both *structural risk* and *total risk*. Structural risk is the annual probability of occurrence of the hazard multiplied by the expected damage and can be expressed in [damage measure/year]. Total risk is defined as the product of the annual probability of occurrence or exceedance of the hazard or loss and the expected loss and is expressed in [loss unit/year].

The last stage of the risk assessment procedure is *risk evaluation*, whose purpose is to make the considered risk comparable to other competing risks to the system by the use of adequate risk measures.

2.2.3 Risk treatment

In the final phase pertaining *risk treatment*, a decision is made whether to accept, to transfer, to reject or to reduce a given risk. When *risk mitigation* is performed different risk reduction strategies can be followed, with the common purpose of reducing the vulnerability of the system. Among them, two types of strategies can be used, including pre-disaster interventions (*prevention*, *preparedness*), and post-disasters interventions (*response*, *recovery*).

Prevention includes technical measures that are to be performed with an accurate time horizon before the disaster takes place. Typical examples of prevention measures in the field of tall buildings design are auxiliary damping devices installed for the mitigation of wind-induced responses. A comprehensive description of the entire spectrum of techniques geared specifically toward reducing the effects of wind on structures, particularly those which involve occupant comfort can be found in Kareem *et al.* (1999).

Preparedness regards social activities limiting harm shortly before the disaster occurrence, such as evacuation plans and emergency training.

Response includes the variety of activities that are performed immediately after the occurrence of the disaster, such as the disposing of rescue and shelter for injured and harmed people as well as the coordination of emergency forces.

Finally, recovery embraces all activities that need to be held until the pre-disaster status of the system is restored again.
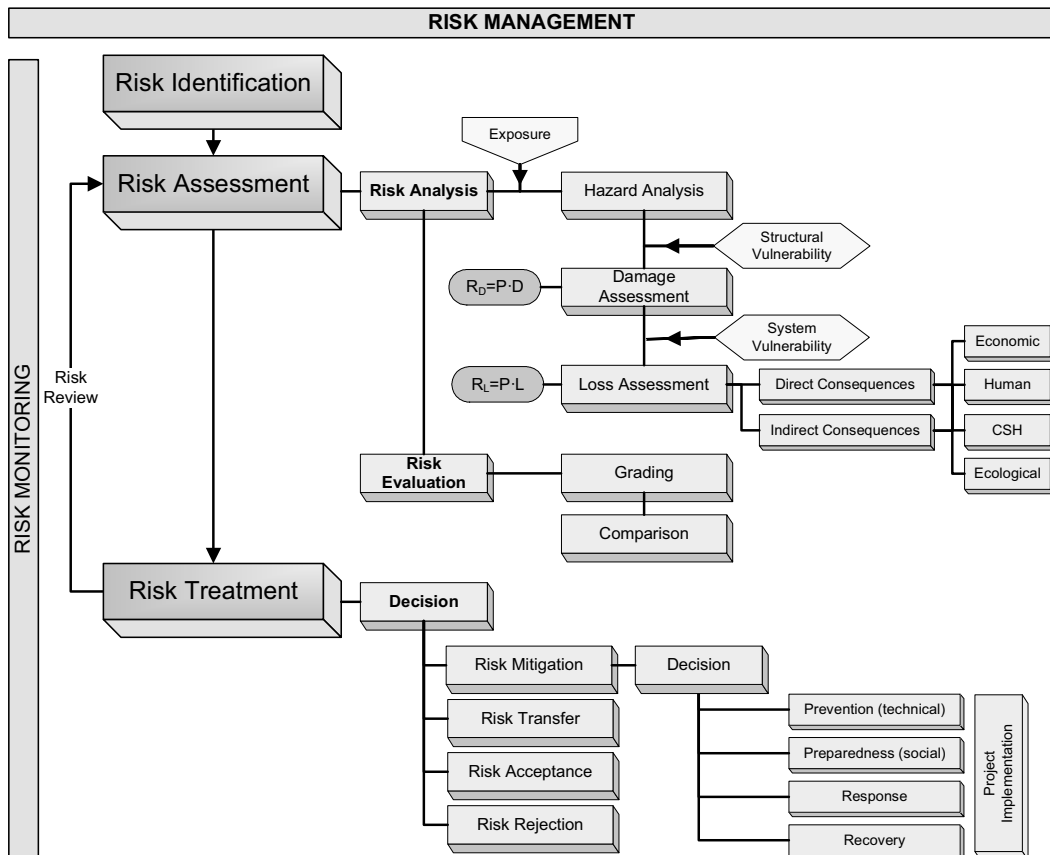

Fig. 2.3 Overview of the whole Risk Management process (Pliefke *et al.*, 2006, 2007).

2.3   PEER's approach for Performance-Based Design

2.3.1   PEER's methodology for Performance-Based Design

It has been recognized that Performance-Based Design (PBD) represents a rational approach to the assessment of risk, also in the wind engineering field. PBD is aimed directly at the achievement of well specified performance objectives with a sufficiently high probability and/or their optimization. PBD has developed mainly in the USA with reference to seismic risk and design. The Pacific Earthquake Engineering Research (PEER) Center, based at the University of California, Berkeley, has focused on the development of a PBD methodology. A central feature of the PEER's approach is that its principal outputs are system-level performance measures: probabilistic estimates of repair costs, casualties, and loss-of-use duration ("dollars, deaths and downtime"). Fig. 2.4 illustrates the PEER methodology (Porter, 2003), that, as shown, involves four stages: hazard analysis, structural analysis, damage analysis and loss analysis. In the scheme, the expression $p[X|Y]$ refers to the probability density of X conditioned on knowledge of Y, and $g[X|Y]$ is the occurrence frequency of X given Y.

The following equation, based on Porter (2003), can be used to frame the PEER methodology mathematically:

$$g[DV] = \iiint p[DV|DM]\, p[DM|EDP]\, p[EDP|IM]$$
$$g[IM]\, dIM\, dEDP\, dDM \tag{2.1}$$

where

- *IM* is the Intensity Measure and is a measure of the magnitude of the action;

- *EDP* is the Engineering Demand Parameter and describes the structural response;

- *DM* is the Damage Measure and expresses a certain level of damage;

- *DV* is the Decision Variable, the parameter indicating the probabilistic estimation of performance, that governs the design decision.

The term $g[IM]$, results from the *hazard analysis*, and evaluates the hazard at the facility, considering its location and structural, architectural and other features. The term $p[EDP|IM]$ is obtained from *structural analysis*, aimed at the estimation of the uncertain structural response, measured in terms of EDP, conditioned on the intensity measure. In the following damage analysis, EDP is input to a set of *fragility functions* that model the probability of various levels of damage, *DM*, conditioned on structural response, $p[DM|EDP]$. *Structural vulnerability* refers to the relation between the hazard measure and the resulting damage. The last stage is the probabilistic estimation of performance, parametrized by various decision variables, *DV*, conditioned on damage, $p[DV|DM]$. This is the stage of loss analysis that produces estimates of the frequency with which various levels of decision variables are exceeded. Loss analysis leads to the *decision-making* phase, in which, for example, one can determine whether the facility is safe enough or has satisfactorily low future
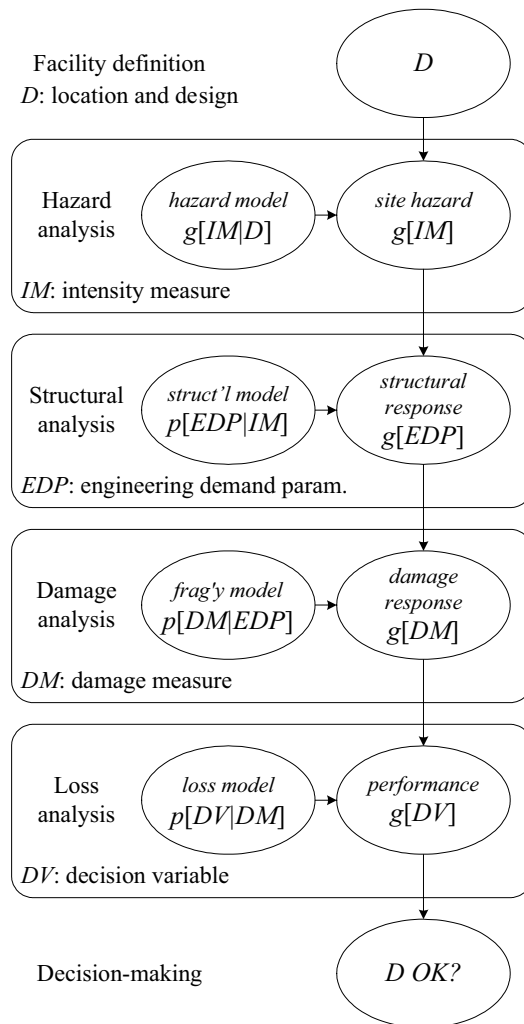
Fig. 2.4 PEER's analysis methodology (conditioning on D in the hazard term, indicates that the hazard at the facility has to be evaluated considering its location and structural, architectural and other features, jointly denoted by design, *D*) from Porter (2003).

repair costs.

It is easy to see that the logical scheme of the PEER's approach is comparable to that of the risk assessment procedure illustrated in Fig. **??**. As a result, PEER's equation will be used as the mathematical tool for the risk assessment procedure illustrated in this work.

2.3.2   Performance-Based Wind Engineering

As previously mentioned, the first applications of PBD were devoted to seismic engineering and design and often PBD is associated to Performance-Based Earthquake Engineering, PBEE, (Porter, 2003). Recently PBD approach is being applied to different problems, in particular to wind engineering.

The definition Performance-Based Wind Engineering, PBWE, appeared for the first time in 2004 (Paulotto *et al.*, 2004). Augusti and Ciampoli (2008) discussed the general approach of PBD and illustrated two examples of application to aeolian and seismic risk assessment, respectively. Dealing with PBD, as reported in Augusti and Ciampoli (2006) *low* and *high performances* can be considered: the former imply possible consequences on personal and structural safety (e.g. partial or total collapse and permanent damages), the latter are related to serviceability and comfort (displacements, vibrations). In Ciampoli *et al.* (2011) the general framework of the PBWE design approach is illustrated and applied to an example case: the assessment of the collapse and out-of-service risks of a long span suspension bridge. In Ciampoli and Petrini (2012) a probabilistic procedure for the Performance-Based Design of structures subject to the wind action is applied to a 74-story steel building. The performances considered are the occupant comfort, expressed in terms of perception of the wind-induced vibrations, and the structural reliability, evaluated in terms of deformation capacity. Marra (2011) recently used a PEER-type equation based on the PBWE approach in order to develop a procedure for the assessment of vortex-shedding risk of bridge decks.

2.4   Motion perception and human comfort levels in tall buildings

Recent trends towards structures with increasing height, often accompanied by increased flexibility (section 2.1) have led to a new generation of buildings with low natural frequencies of vibration, which position them within an operating range susceptible to wind excitations, particularly for buildings in regions of high wind speeds.

Wind-induced motions of tall buildings include sway motion of the first 2 bending modes, referred to as *along-wind* (in the direction of wind) and *across-wind* (normal to the wind direction) motions, a higher mode torsional motion about the vertical axis, or for buildings with stiffness and mass asymmetries, complex bending and torsion in the lower modes (Melbourne and Palmer, 1992). Prolonged exposure to these wind-induced motions can cause unnerving effects to the structure's occupants, giving rise to serviceability problems related to comfort. Symptoms of discomfort may range from concern, anxiety, fear and vertigo up to more severe effects of dizziness, headaches and nausea. As a result, numerous studies have been devoted to understanding human perception of vibration and determining tolerance thresholds of wind-induced vibrations of tall buildings. These studies generally fall into three

different categories:

- field experiments of building occupants conducted in wind-excited tall buildings;

- motion simulator and shake table experiments testing human test subjects;

- field experiments conducted in artificially excited structures.

In the following section a brief review of these studies is presented. A more detailed one is illustrated by Kilpatrick (1996) and Kwok *et al.* (2009).

2.4.1 Literature studies on comfort and motion perception in tall buildings

First studies concerning human comfort in tall buildings can be traced in very old times. As reported in Davenport (2002), the sky-scraper boom of the 1930s and later in the 1960s resulted in a growing curiosity in, and awareness of, vibrations through both experimental registrations and human perception of motion discomfort.

During the 1930s Rathburn (Rathburn, 1940) made extensive observations on the Empire State Building and stated that in wind it vibrated "*like the tines of a tuning fork*". In Spurr's treatise on wind bracing (Spurr, 1930) he stated: "*the whole question of the vibration in buildings from the effects of variable wind pressures is complicated by the indeterminate nature of the pressures themselves, as well as by the great variation in size, shape, weight, height and location of buildings*". In this work it was already stated that the perception of wind-induced motion is closely related to the acceleration response of buildings as it is nowadays widely accepted (Kwok *et al.*, 2009).

Fig. 2.5 illustrates the results of the study performed by Reiher and Meister (1931), concerning the human perception of steady-state vertical vibrations. The effects of amplitude and frequency of motion are related to different levels of perception.

As early as 1931, the Structural Division of the American Society of Civil Engineers (ASCE), Subcommittee No. 31, recommended that "*structural frames be so designed as to ensure that deflections will be kept within such limits as to render buildings comfortably habitable*"(ASCE, 1931).

One of the first in the literature to suggest limiting wind-induced displacements based on human comfort level was Chang (Chang, 1967). He noted that the strength of a structure is not the only consideration in the design of tall buildings and stated that "*rentals may depend on keeping movement in the upper levels of the building to acceptable human tolerance*". He suggested that, for the evaluation of human comfort levels, the return period of extreme winds is reduced from 50 years, a typical interval for strength consideration, to 10 or perhaps 2 years, depending on the nature of the structure. Considering that acceleration, the rate of change acceleration (commonly referred to as jerk) and frequency of vibration are often looked to as the main causes of discomfort, Chang developed tentative comfort criteria for building occupants. Fig. 2.6 describes the dynamic amplitude of vibration with period, for various acceleration levels. In Fig. 2.6, as a practical example, data points are reported from the earlier study on the Empire State Building by Rathburn (1940). Comfort limits for
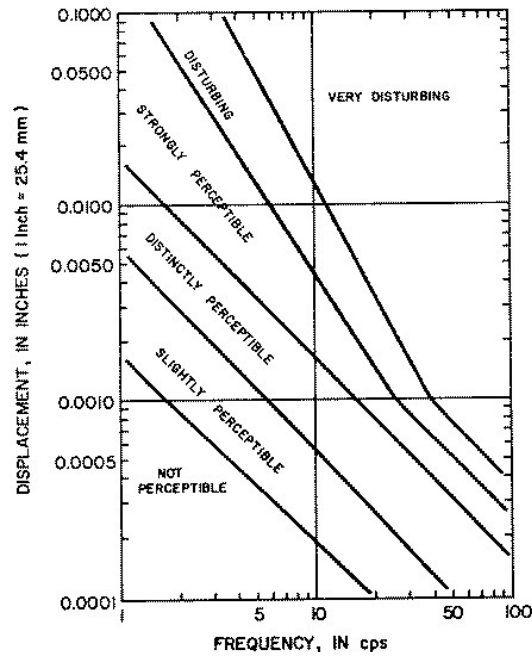
Fig. 2.5 Human perception levels related to steady-state vibration amplitude and frequency (Reiher and Meister, 1931).
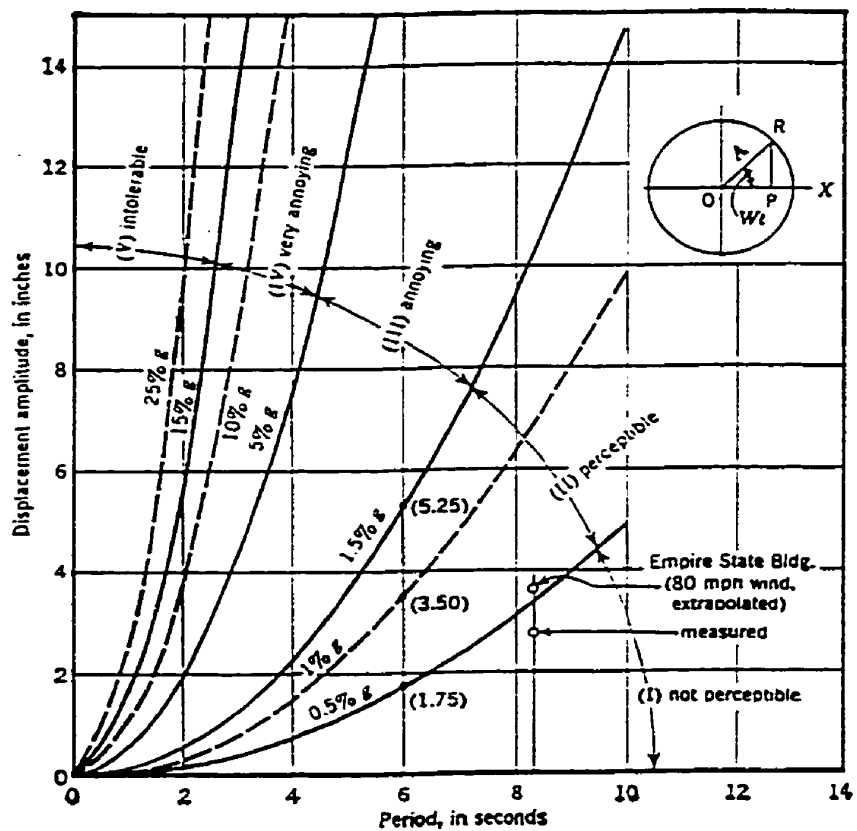

Fig. 2.6 Displacement amplitude versus period with comfort criteria (Chang, 1967).

building occupants with the corresponding acceleration level are listed in Table 2.1.
In a subsequent paper (Chang, 1973) Chang related to his suggested tenta-

Table 2.1 Comfort criteria for building occupants (Chang, 1967).

Acceleration in percent of g	Comfort limits
under 0.5	Not perceptible
0.5 to 1.5	Threshold of perceptibility
1.5 to 5	Annoying
5 to 15	Very annoying
over 15	Unbearable

tive comfort criteria curves (Fig. 2.7) the experimental data from four tall buildings
(the Empire State Building, the John Hancock Center, the 1000 Lakeshore Plaza in
Chicago and the World Trade Center in New York). The estimated performance and
the occupants experience of the four investigated tall buildings supported Chang's
comfort criteria.

The first attempt in the literature to examine human perception thresholds of

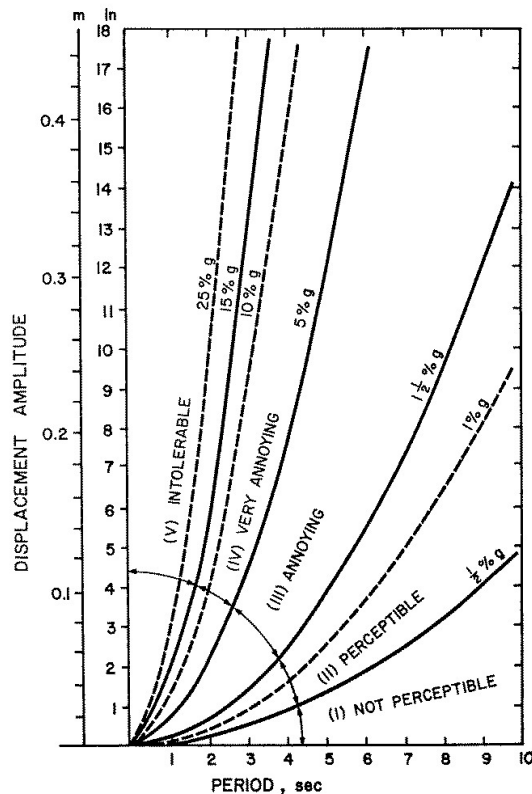**Fig. 2.7** Period dependent comfort criteria curves suggested by Chang (1973).

low frequency vibrations in the horizontal plane is represented by the work of Chen
and Robertson (1972). Two separate experiments during the design stage of the
World Trade Center in New York were carried out by the authors with the aim of
assessing acceptable thresholds of horizontal accelerations. The first one, designated

HATS-I, was addressed to the definition of proper thresholds of horizontal motions. The second one, HATS-II, was used to validate the results of the previous one. The effect of four factors corresponding to (1) period of oscillation, (2) body orientation, (3) body movement, (4) expectancy of building motion, was analyzed using HATS-I. It was assumed that the distribution of the perception threshold of horizontal acceleration was lognormal. Fig. 2.8 illustrates the geometric means of the thresholds under the four factors tested. In Fig. 2.9 an example of the cumulative frequency distribution of the perception threshold for HATS-I is shown.
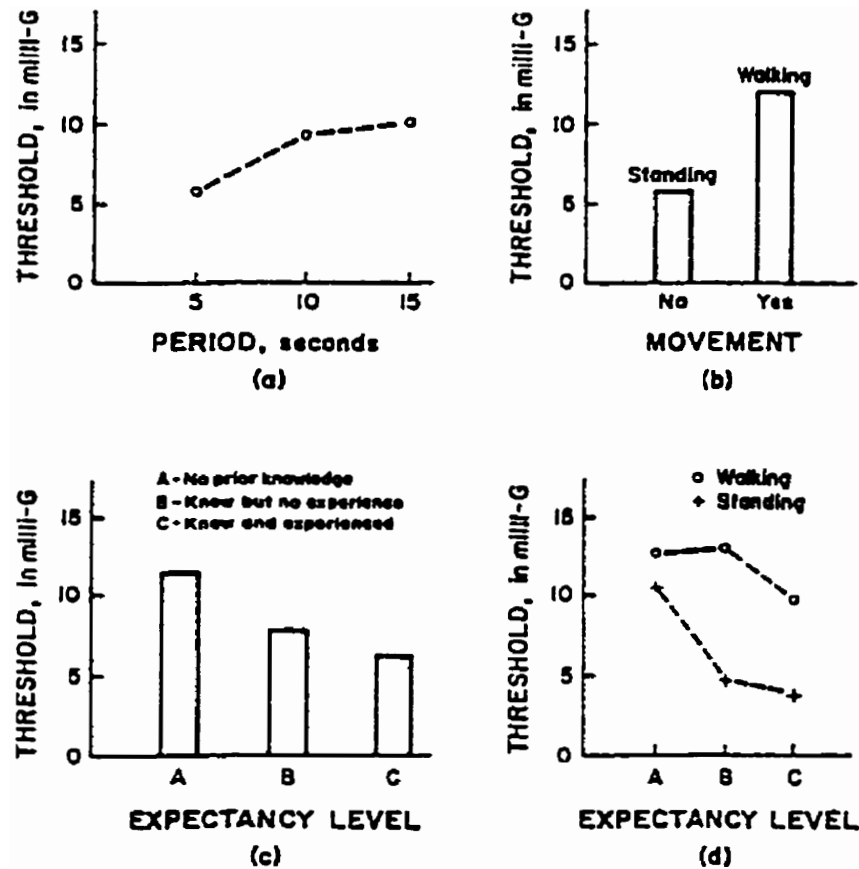

Fig. 2.8 Geometric means of perception thresholds: HATS-I (Chen and Robertson, 1972).

The second experiment, HATS-II, confirmed the results of HATS-I and verified the assumption that the perception threshold was lognormally distributed. In HATS-II only the effect on motion perception of body posture and that of expectancy level were investigated. The work of Chen and Robertson (1972) led to several important findings with implication in the design of tall buildings:

1. period of oscillation, body movement, expectancy of movement and body posture significantly affect the perception thresholds of low frequency horizontal periodic motion;

2. mean perception thresholds increase as the the period of oscillation increases from 5 to 15 seconds (hence, vibration perception is frequency dependent);

3. perception thresholds of standing subjects are significantly lower than those
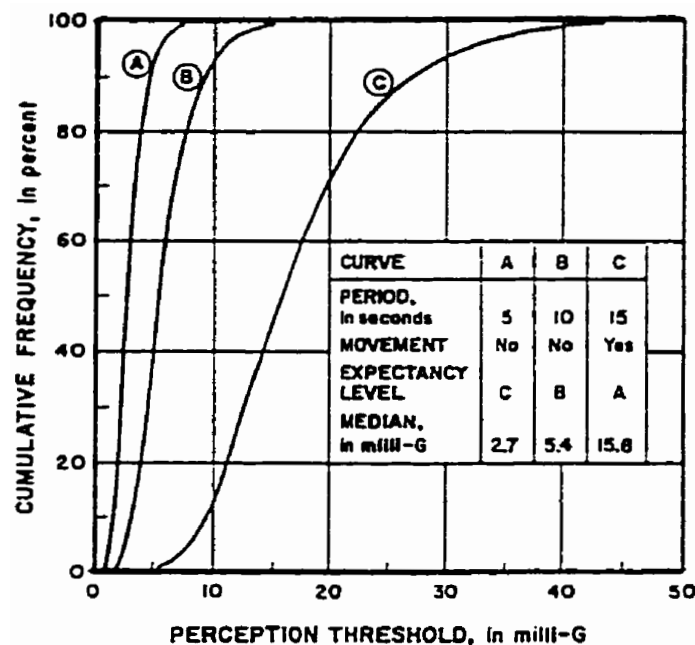
Fig. 2.9 Distribution of perception thresholds: HATS-I (Chen and Robertson, 1972).

of walking subjects (most probably because of the additional movement due to self-motion masking the sensation of vibration caused by the simulated vibration);

4. perception thresholds are smaller when subjects are anticipating motion;

5. perception thresholds are higher in the case of sitting position rather than those in the standing position.

Fig. 2.10 shows probability curves of the acceleration response. It is noteworthy that the research reported by Chen and Robertson (1972) 40 years ago is a landmark study and remains one of the most referenced studies to date.

Hansen *et al.* (1973) performed a study to correlate occupant discomfort with the wind-induced vibrations of two 167 m tall office buildings through occupant surveys after two major wind events that produced building vibrations, which disturbed a significant proportion of occupants of the upper floors. A tentative building vibration criterion was proposed by imposing a limit on RMS (Root Mean Square) acceleration of 5 milli-g occurring no more than once every six years on average, based on an average 2% occupant objection rate (Fig. 2.11).

In Fig. 2.12 the results of the study of Goldman and Von Gierke (Goldman and von Gierke, 1976) on the effects of steady-state vibration on human perception are shown.

Based on the review of the work of Chen and Robertson (1972) and Hansen *et al.* (1973), Irwin (1978) showed frequency dependence of uniaxial sinusoidal motion and recommended frequency dependent acceleration criteria for evaluating low-frequency motion within the range of 0.063 Hz to 1.0 Hz, which later led to the development of the ISO-6897 guidelines (ISO 6897, 1984).

In a more recent study, Von Gierke and Brammer (Von Gierke and Brammer, 1996) defined tolerance criteria for shock and for vibration exposure. Studies on
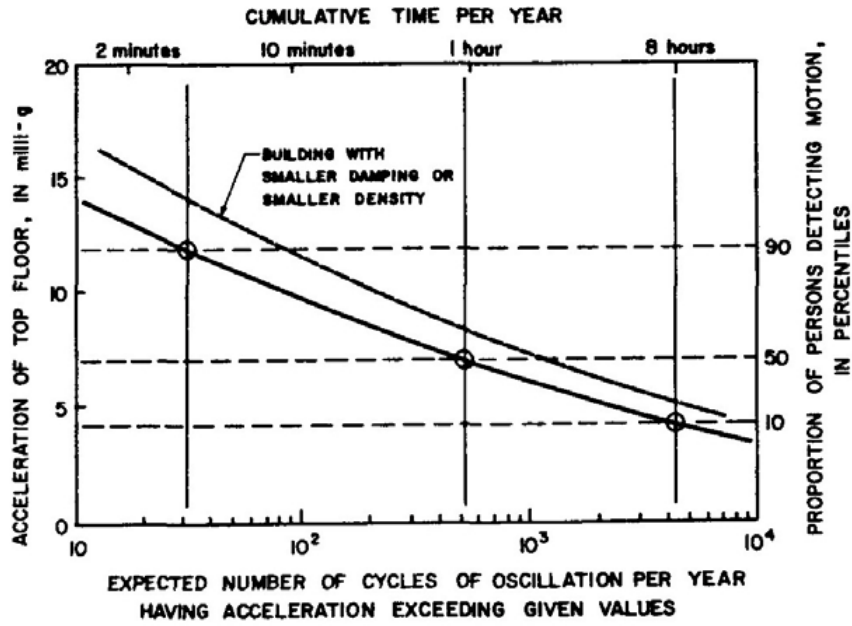
Fig. 2.10 Probability curves of horizontal accelerations (Chen and Robertson, 1972).
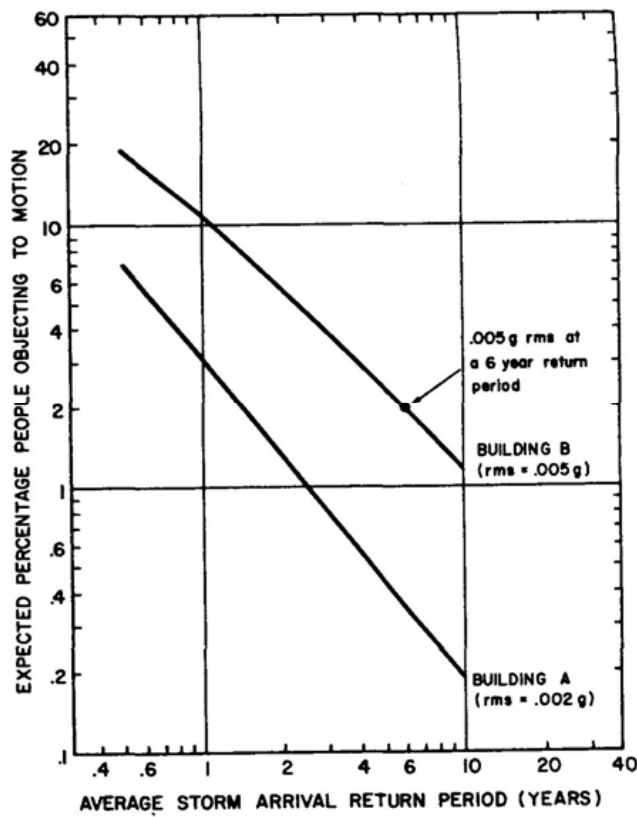

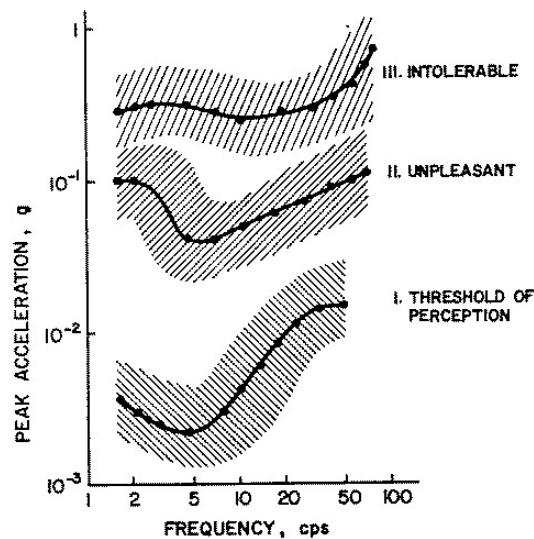**Fig. 2.11** Comfort criteria (Hansen *et al.*, 1973).

Fig. 2.12 Human perception levels related to steady-state vibration amplitude and frequency (Goldman and von Gierke, 1976).

perception thresholds based on motion simulator tests are illustrated in the work by Goto (1983), while Isyumov (1993) referred to tests on actual structures. Laboratory experiments using uni-axial motions are illustrated in Nakata *et al.* (1993) and in Shioya and Kanda (1993), while other tests were developed for random motions (Kanda *et al.*, 1988, 1990; Shioya *et al.*, 1992) and for bi-lateral elliptic motions (Shioya *et al.*, 1992), although the randomness did not seem to affect the perception threshold (Kanda *et al.*, 1990). Early laboratory tests showed discrepancies with actual building performance. Subjects isolated in the small rooms used in motion simulators were found to lack the visual and audio clues contributing to motion perception in actual buildings (McNamara *et al.*, 2002).

2.4.2 Occupant comfort assessment for wind-excited tall buildings. Considerations on recent developments

As seen in the previous section, great research effort has been devoted to investigate human perception thresholds of wind-induced building motion. Although some recommendations on acceleration limitations have been given in a number of current design codes, there is still no internationally accepted standard for limiting wind-induced motions of tall buildings.

Vibration perception and comfort related motion thresholds are still an active research topic in wind engineering (Kwok *et al.*, 2009). The results of several experiments and studies concerning wind-induced motion perception have been mainly collected by Kareem *et al.* (1999) and Tamura (2003) as shown in Fig. 2.14 and Fig. 2.13.

From literature studies on perception thresholds, comfort criteria are defined as limits which may be exceeded in a certain return period. Typically, in North America, a ten year interval is used; on the other hand, in region with frequent typhoon and hurricane events, a shorter return period may be more proper. Fig. 2.13 illustrates some of the perception criteria which are currently in use. North American practice is to use 10-15 milli-g peak horizontal accelerations at top floor for resi-
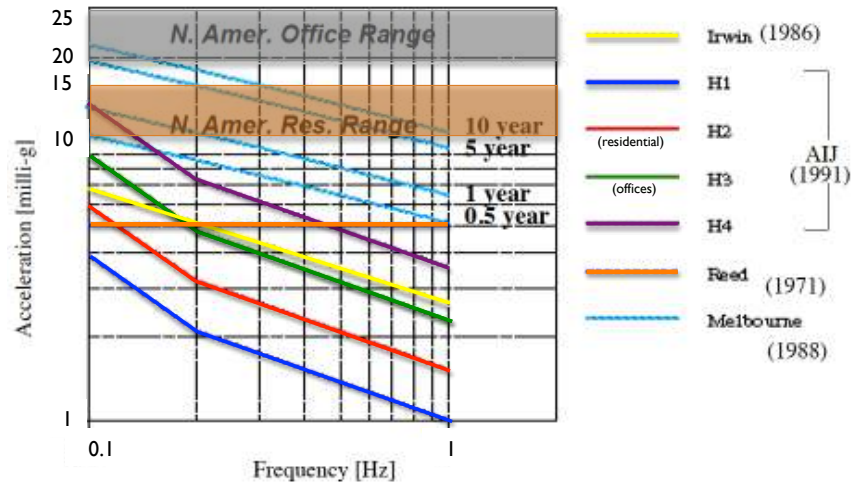
Fig. 2.13 Various perception criteria for occupant comfort (Irwin, 1986; AIJ, 1991; Reed, 1971; Melbourne and Cheung, 1988), from Kareem *et al.* (1999).
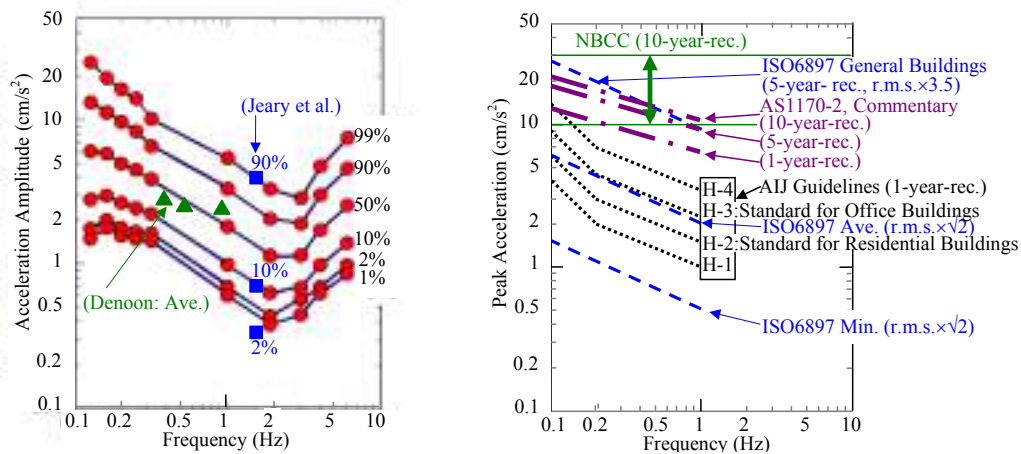
(a) *Probabilistic human perception threshold. (Jeary et al., 1988; Nakata et al., 1993; Denoon, 2000; Shioya et al., 1992)*

(b) *Guidelines / criterion for habitability to horizontal vibrations. (ISO 6897, 1984; Holmes et al., 1990; AIJ, 1991; NBCC, 1990)*

Fig. 2.14 Perception thresholds and guidelines for habitability to horizontal vibrations of buildings (Tamura, 2003).

dential buildings and 20-25 milli-g for office buildings, based upon a 10 year return period (Isyumov, 1993). Kareem (1988) proposed an RMS acceleration threshold of 8 to 10 milli-g for a 10 year recurrence interval. The lines H1-H4, taken from the Japanese AIJ standards (AIJ, 1991) represent various levels of peak acceleration perception, with H2 typically used for residential applications and H3 for office dwellings. It is also shown Reed's (Reed, 1971) constant perception limit of 5 milli-g for a 6-year return period and Irwin's curve (Irwin, 1986) for RMS accelerations, also given in ISO 6897 (1984), illustrating the difference between the use of RMS versus peak accelerations. The peak acceleration criteria of 15 milli-g for residential buildings and 25 milli-g for commercial buildings under 10-year return period are recommended in the National Building Code of Canada (NBCC, 1990), the Chinese code (JGJ 3-2002, 2002), and the Hong Kong Codes of Practice (HKCOP 2004, 2004; HKCOP 2005, 2005). The Japanese guidelines AIJ (2004) offer frequency dependent peak acceleration criteria (Fig. 2.15) and represent the reference basis of the acceleration thresholds given by the current Italian standard for wind action on buildings (CNR-DT 207, 2008). A comparison of perception criteria for 1-year return period
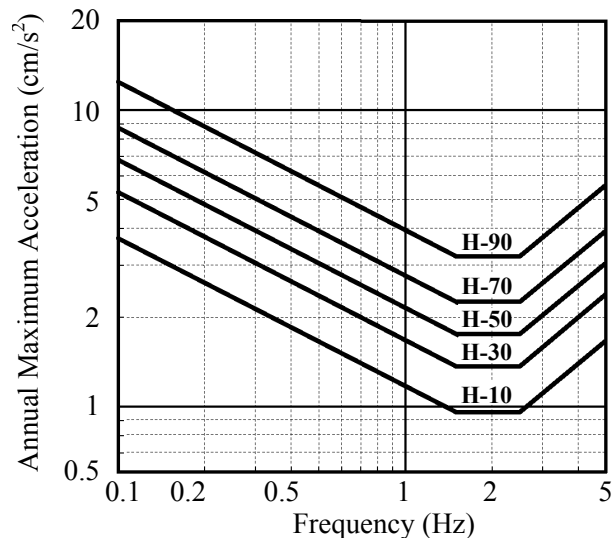
Fig. 2.15 Curves given in the AIJ-Guidelines-2004 (AIJ, 2004).

is reported in Bashor and Kareem (2007) and illustrated in Fig. 2.16.

Both peak and standard deviation acceleration thresholds are currently used. As reported in McNamara *et al.* (2002), the international community has not agreed on a universal descriptor of acceleration for a number of reasons. On one hand, negative reactions to motion may be the consequence of a sustained or ongoing phenomenon, best described by an averaged effect over some time period, leading to the common RMS descriptor. On the other hand, it has been also asserted that people are most dramatically injured by large events, impacting them far more than the typical phenomenon their bodies had become accustomed to. Many studies favor the RMS index due to the ease with which it is measured experimentally or predicted analytically, citing the variability in peak acceleration measurements in wind tunnel tests as one demonstration.

Boggs (1995) investigated the differences between the RMS and peak acceleration methods and the importance of making a rational selection of the appropriate

Fig. 2.16 Comparison of occupant comfort perception criteria for 1-year return period (Bashor and Kareem, 2007).
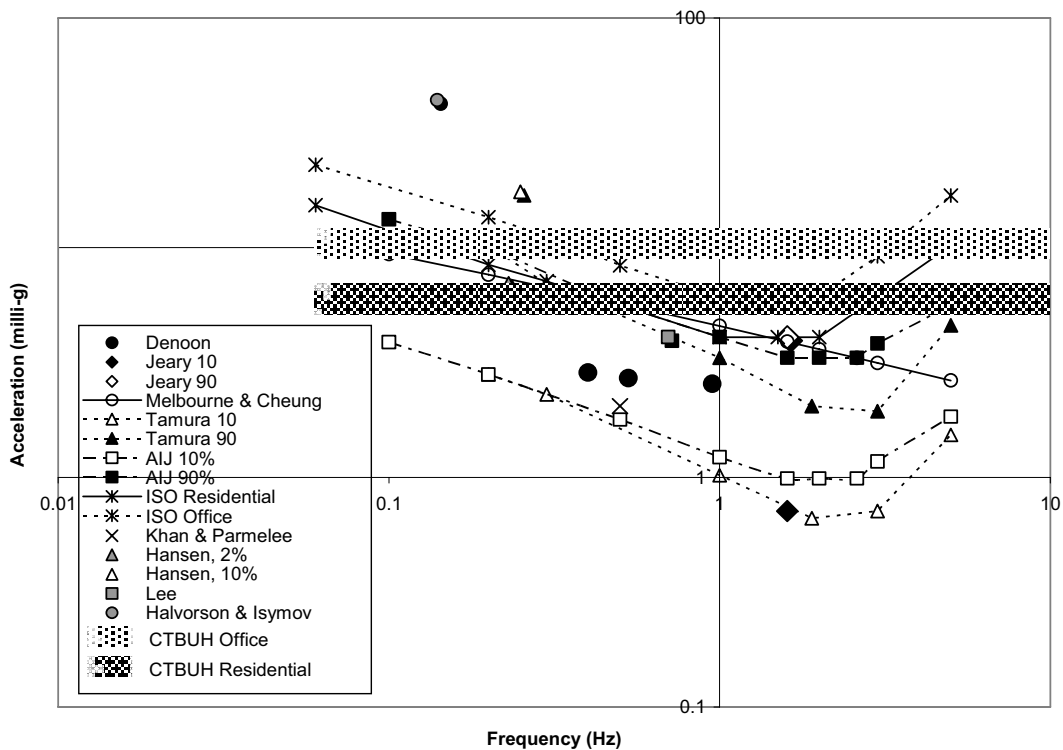
motion index for future standards. It was proposed to adopt the RMS value as the best available index. According to Kareem (1992), criteria based on RMS acceleration thresholds offer a more accurate means of combining response in different directions based on their respective correlations. In the peak acceleration criterion, the first peaks in each direction are determined and subsequently combined by an empirical correlation rule; however, since different response components may have a different probability structure, requiring different peak factors, care must be exercised (Kareem *et al.*, 1999). However, advocates of peak acceleration criteria contend that peak resultant accelerations are difficult to estimate when RMS accelerations are used (Isyumov, 1993). As reported in Huang (2008), since motion perception may be more dominated by the overall averaged effect for long duration events of a stationary vibration, the use of the RMS acceleration may be a reasonable choice to check the occupants comfort of buildings under more frequently occurring wind events, while for short duration infrequently occurring wind events, such as thunderstorms and typhoons, averaging the acceleration over the worst 10 minutes of the non-stationary motion of buildings may be statistically meaningless, and may also underestimate the effects of the largest individual peaks. It seems that peak and RMS acceleration response may characterize different motion effects on human response (Burton *et al.*, 2007). Hence, the choice of a particular acceleration criterion may depend on the type of dominating wind events in the geographical location of the building. Further investigations have shown that the *jerkiness* of the structural response may primarily be responsible for motion perception. While humans are capable of adjusting to acceleration, any change in the acceleration will require additional adjustments for equilibrium. As a result, perception criteria based on a

measure of *jerk* or the *rate of change of acceleration*, may better define perception thresholds under random motion. The adoption of such criteria may override the need of peak acceleration (McNamara *et al.*, 2002).

Finally, the debate about whether human response to wind-induced motion is dependent on the motion frequency is still open. As presented in subsection 2.4.1, Chang (Chang, 1967, 1973) was one of the first to suggest frequency independent occupant comfort criteria. The first code recommending frequency independent peak acceleration criteria was the NBCC (1977). On the other hand, Chen and Robertson (1972), Irwin (1978) and later the ISO 6897 (1984) guidelines suggested the frequency dependency of motion perception.

Burton *et al.* (2006) characterized the biodynamic human body vibration response, occurring during exposures to low-frequency, constant amplitude acceleration sinusoidal motion, and showed a physiological frequency dependence of this motion. The results from a series of motion simulator experiments showed that, as the frequency of oscillation increases from 0.15 to 1.00 Hz, acceleration measured at the head of a human test subject is increasingly magnified. This motion magnification demonstrates that biodynamic human body vibration is frequency dependent in this frequency range. Furthermore, there may also be further implications for visual perception of motion through parallax shift. Evidently, these effects have to be accounted for in developing more refined occupant comfort acceptable criteria for tall buildings motion.

According to the various considerations illustrated before, the comfort criterion which will be used in this research for the discomfort risk assessment and comfort checking under serviceability conditions of a case study tall building (chapter 8), is the ISO 6897's motion perception threshold, expressed in terms of standard deviation acceleration for a 10-minute duration in 5-year-recurrence wind and given as a function of frequency as:

$$\overline{\sigma_a} = exp(-3.65 - 0.41 \ln n) \tag{2.2}$$

where $\overline{\sigma_a}$ denotes the standard deviation modal acceleration response of the building and n is the natural frequency.

2.5 Summary and main remarks

This chapter deals with the problem of discomfort risk of tall buildings, induced by the wind action. A general probabilistic risk management framework is illustrated and the Performance-Based Design approach, based on the PEER's equation, for the assessment of risk is discussed and framed mathematically. The perception of vibration is becoming a more and more significant issue in the serviceability design of modern tall buildings, because the recent trends towards increasing height and slenderness is contributing to the generation of structures which are particularly sensitive to the wind excitation. Numerous studies have been dedicated to the definition of tolerance thresholds of wind-induced vibrations of structures. This chapter presents a brief review of them. It is now widely accepted that the perception of motion is closely related to the acceleration response of structures. However, the international community has not agreed on a universal comfort criterion. The debate about whether human response to wind-induced motion is dependent or not on the

frequency of vibration, together with that about the use of RMS or peak acceleration criteria, is still open. In this research, the comfort criterion proposed by the ISO 6897 standard is chosen and will be applied later for the discomfort risk assessment and comfort checking of a case study structure.

Chapter 3

Square section bluff-body aerodynamics

3.1 Introduction

Recent trends towards increasingly taller and slender structures have developed a new generation of buildings, particularly sensitive to the wind action. The knowledge of the flow field around prismatic objects of square and rectangular cross section is, therefore, receiving considerable attention for its relevance to tall buildings design. The understanding of the flow field around *bluff bodies*[1], such as buildings, and, consequently, the wind loads and effects on them, is a challenging task due to the complexity of the physical phenomena involved, including detachment of large eddies, massive flow separation and re-attachment. Furthermore, air flows around buildings are, usually, strongly three-dimensional (3-D), even for very slender and almost two-dimensional (2-D) geometries. All these aspects pose great difficulty for the accurate prediction of the flow field using computational methods. Current state-of-the-art Computational Fluid Dynamics (CFD) techniques are not able to fully substitute wind tunnel testing for bluff bodies aerodynamics, yet. Nevertheless, recent improvements in both software and hardware make the use of CFD methods ever more valuable to civil engineering applications.

This chapter is dedicated to the aerodynamics of prismatic objects, with particular focus on the square section prism. Section 3.2 is aimed at defining basic concepts and quantities of common use in bluff-body aerodynamics. Section 3.3 reviews the wake and the shedding of vortices from fixed bluff bodies in two-dimensional flows. Section 3.4 is devoted to the aerodynamics of two-dimensional square cylinders. Different flow patterns at various angles of incidence are illustrated. Strouhal number, fluctuating pressure coefficients and aerodynamic lift and drag forces are also discussed. Lastly, in section 3.5 the three-dimensional flow behind a finite-length square cylinder is presented.

---

[1] *"Bluff bodies"*, in contrast to *"streamlined bodies"*, such as aircraft wings, are characterized by the fact that, when immersed in a flow, the streamlines do not follow the surface of the body but detach from it creating regions of separated flow and a wide trailing wake (Cook, 1986).

3.2 Wind-induced pressures and forces in 2-D and 3-D flows

This section is aimed at the synthetic definition of basic concepts and quantities of bluff bodies aerodynamics that will be used in the following sections.

The flow around a bluff body of generic cross section develops local pressures, p, in accordance to the Bernoulli's equation. The surface pressure on the body could be expressed in the form of a non-dimensional *pressure coefficient*, C_p, defined as:

$$C_p = \frac{p - p_0}{\frac{1}{2}\rho U_0{}^2} \tag{3.1}$$

where p is the pressure, ρ is the air density and p_0 and U_0 are the pressure and velocity in the region outside the influence of the body, respectively. The quantity p_0 is also known as the *static pressure* of the undisturbed flow, while $\frac{1}{2}\rho U_0{}^2$ is called *dynamic pressure* of the undisturbed flow and is referred to as p_{dyn}.

The integration of the pressures over the body surface results in a net force, F, and a moment, M. Aerodynamic forces are conventionally resolved into two orthogonal directions, that may be parallel (along-wind) and perpendicular (across-wind) to the wind direction (or mean wind direction in the case of turbulent flow), in which case the axes are referred to as *wind axes*, or parallel and perpendicular to a direction related to the geometry of the body and referred to as *body axes* (Fig. 3.1). The components of the force in the along-wind and across-wind directions are commonly referred to as *drag* and *lift* respectively. The macroscopic effects of the flow around a bluff body can be, therefore, described in terms of a *drag force*, D, a *lift force*, L, an a *moment*, M.

Fig. 3.1 Wind force components along wind axes and body axes.
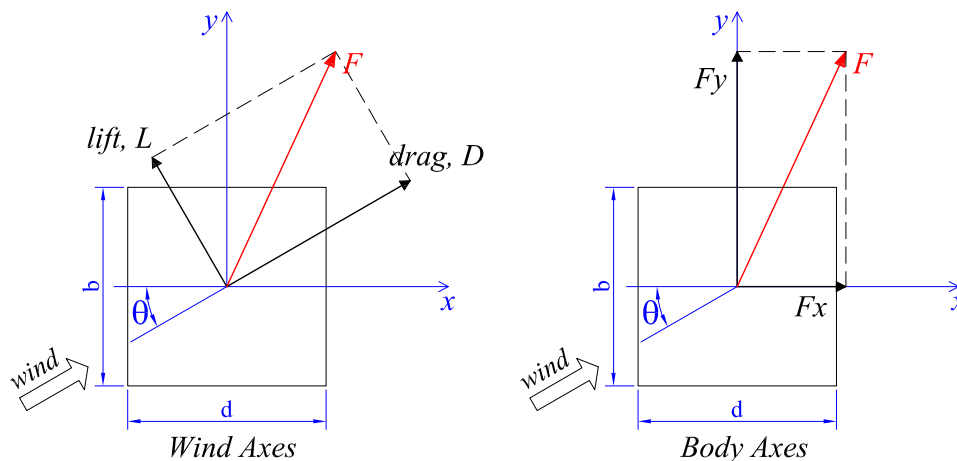
3.2.1 Aerodynamic forces in 2-D flows

In two-dimensional flows, that means independent of the coordinate normal to the plane of the body cross section, the aerodynamic forces, D, L and M, with reference to the wind axes in Fig. 3.1, represent values per unit of dimension normal to the plane of observation. They can be rendered dimensionless and expressed in

terms of *drag, lift* and *moment coefficients*, C_D, C_L, C_M, respectively, as follows:

$$C_D = \frac{D}{\frac{1}{2}\rho U_0{}^2 b} \tag{3.2}$$

$$C_L = \frac{L}{\frac{1}{2}\rho U_0{}^2 b} \tag{3.3}$$

$$C_M = \frac{M}{\frac{1}{2}\rho U_0{}^2 b^2} \text{ or } C_M = \frac{M}{\frac{1}{2}\rho U_0{}^2 bd} \tag{3.4}$$

where b and d are reference dimensions. Usually b is the *width* or *breadth* of the structure normal to the wind and d is the *depth* of the structure in the direction of wind.

3.2.2 Aerodynamic forces in 3-D flows

Fig. 3.2(a) shows the aerodynamic loads acting on a three-dimensional body, representing, for example, a tall building. The approaching wind direction is oriented of an angle θ with respect to the x and y body axes. The corresponding *drag* and *lift coefficients*, C_D and C_L, are defined as:

$$C_D = \frac{D}{\frac{1}{2}\rho U_0{}^2 A} \tag{3.5}$$

$$C_L = \frac{L}{\frac{1}{2}\rho U_0{}^2 A} \tag{3.6}$$

where D and L are the drag and lift forces, in the directions parallel and perpendicular to wind, respectively, and acting on the whole surface, and A is a reference area, often the projected frontal area, e.g. equal to width times height (bh). Analogously, the non-dimensional force components, C_{F_x} and C_{F_y} along x and y body axis, respectively, are defined as:

$$C_{F_x} = \frac{F_x}{\frac{1}{2}\rho U_0{}^2 A} \tag{3.7}$$

$$C_{F_y} = \frac{F_y}{\frac{1}{2}\rho U_0{}^2 A} \tag{3.8}$$

Wind-induced moments, M_x, M_y, M_z, result from the normal pressure and the shear stress actions multiplied by their moment arms and integrated over the building surface [Fig. 3.2(b)]. The corresponding non-dimensional moment coefficients, C_{M_x}, C_{M_y}, C_{M_z} may be defined as:

$$C_{M_x} = \frac{M_x}{\frac{1}{2}\rho U_0{}^2 A l} \tag{3.9}$$

$$C_{M_y} = \frac{M_y}{\frac{1}{2}\rho U_0{}^2 Al} \tag{3.10}$$

$$C_{M_z} = \frac{M_z}{\frac{1}{2}\rho U_0{}^2 Al} \tag{3.11}$$

where l indicates a reference dimension. The product Al is often assumed equal to bh^2.
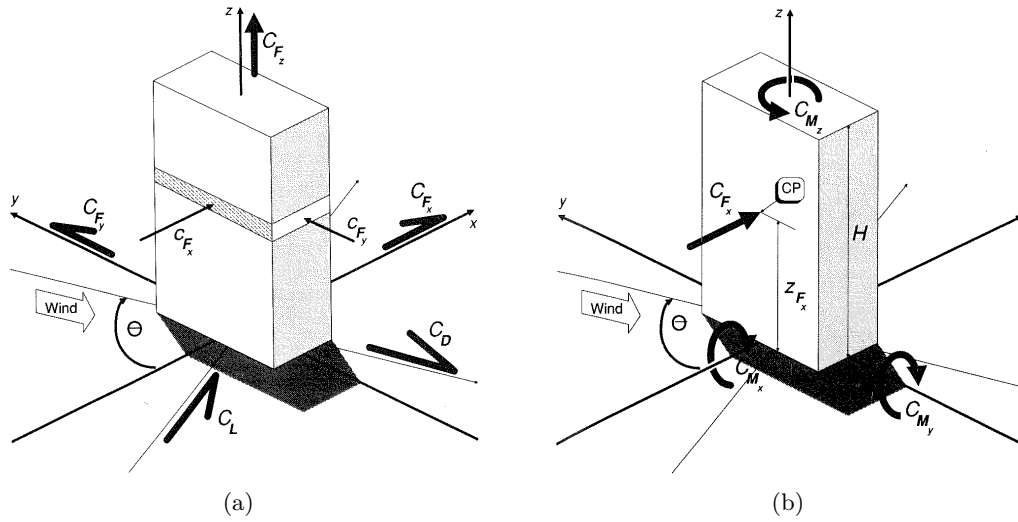

Fig. 3.2 Representation of wind directional loads: a) force coefficients; b) moment coefficients (Cook, 1990).

3.3   Wake and vortex shedding from fixed bluff bodies in two-dimensional flows

Unsteady flow over a 2-D fixed cylinder represents a classical flow paradigm in bluff-body aerodynamics. Even if the flow around buildings is usually three dimensional, in the case of slender structures exposed to cross air flows, the flow field can be studied as predominantly two-dimensional. For this reason, the study of the flow pattern around two-dimensional cylinders having building-type cross sections, such as the simplest case of the square section referred to in this study, is of primary importance in the design of slender structures.

A lot of work has been done so far on the 2-D flow about a circular cylinder rather than a square cylinder. In the renowned case of the circular cylinder, a number of flow patterns can be created by increasing the incoming flow velocity, each situation being identified by a specific range of the Reynolds number Re (Simiu and Scanlan, 1996). The latter expresses the ratio between inertial forces and viscous forces and is defined as:

$$Re = \frac{\rho U l}{\mu} = \frac{U l}{\nu} \tag{3.12}$$

where μ and ν are, respectively, the *dynamic* and *kinematic viscosities* of the fluid, U is the mean velocity of the approaching flow and l indicates here a typical length, that is usually the diameter in the case of a circular cylinder and the side dimension for a square section prism.

The flow regimes past a circular cylinder at varying Reynolds number values were reviewed in detail by Willamson (1996). For a wide range of Re, alternating vortices are shed from the cylinder surface and form the classical *vortex trail* or *vortex street* configuration downstream. This phenomenon was first reported by Bérnard (1908) and Von Kármán (1911) at the beginning of the XX century. Fig. 3.3 depicts the streamlines of the wake flow behind a circular cylinder for various Re values.

The principle of the vortex shedding phenomena is shown in Fig. 3.4, where an infinitely long, rigid circular cylinder is considered. The flow separation on the right side (in the direction of the incoming flow) produces a circulation, $+\Gamma$, in the cylinder wake. After Thomson's vortex law, a counter circulation, $-\Gamma$, occurs around the cylinder surface, producing a circulation current, ΔV, flowing clockwise around the cylinder. This velocity ΔV reduces the flow velocity, V_2, on the right side, while increases it on the left side. As a consequence, on the basis of the Bernoulli equation, the static pressure increases on the right side and decreases on the left side, leading to a cross wind force, indicated with F_y in Fig. 3.4, acting on the cylinder (Ruscheweyh, 2010). Since the vortices are shed alternately from opposite sides of the cylinder, the perpendicular force, F_y, alternates too, and its frequency is the same as the frequency at which the vortex shedding is formed.

Bluff bodies with other cross section shapes give rise to analogous vortex shedding phenomena. For a non-vibrating structure, the distance between vortices rotating in the same direction is proportional to the structure breadth, b, perpendicular to the direction of the wind (that coincides with the diameter in the case of a circular cylinder). The time between vortices is equal to this distance divided by the velocity of vortices, that is proportional to incoming wind speed, U. Therefore, the frequency of the lateral load caused by vortex shedding, f_s, is proportional to U/b. This linear relation, showed at the end of the nineteen century by a study of Strouhal (Strouhal, 1878), allows the definition of a nondimensional quantity, known as *Strouhal number*, St:

$$St = \frac{f_s b}{U} \tag{3.13}$$

Eq. (3.13) defines the Strouhal law, that is valid for stationary, two-dimensional bluff bodies. The frequency normalized by a value of the velocity and a reference dimension, as in the case of Eq. (3.13), is referred to as *reduced frequency*, and indicated hereinafter with f_r. The reciprocal of this parameter is called *reduced velocity* and is indicated with U_r.

Vortex shedding also generates a harmonically varying longitudinal load with a frequency of $2f_s$.

3.4 Aerodynamics of a 2-D square cylinder

The study of flow around prismatic objects of square section has received considerable attention motivated by fundamental aerodynamic interest, and its relevance
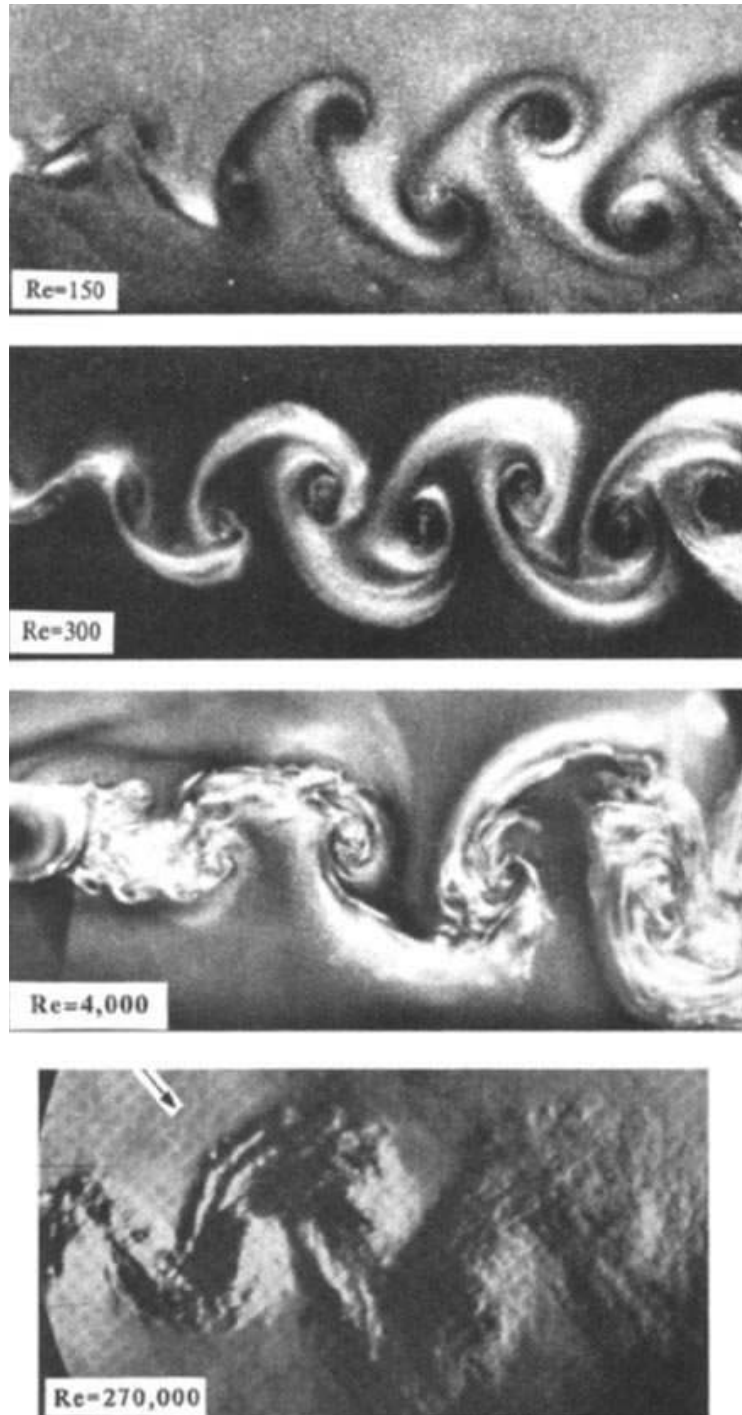
Fig. 3.3 Visualization of the vortex streets behind a circular cylinder over a wide range of Re (Willamson, 1996).
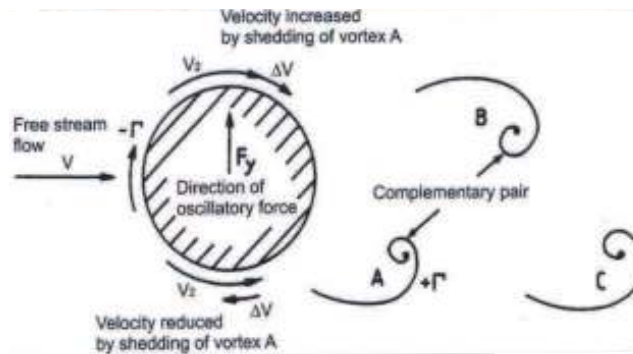
Fig. 3.4 The principle of the vortex shedding phenomena (Ruscheweyh, 2010).

to wind engineering and structural engineering applications, such as flow around buildings. Relevant experimental investigations on flow behind a square cylinder are, for example, those of Saha *et al.* (2000), Dutta *et al.* (2003), Ozgoren (2006), Dutta *et al.* (2008), Van Oudheusden *et al.* (2008). Moreover, many numerical studies (applications of Computational Fluid Dynamics - CFD) have been dedicated to the comprehension of the aerodynamics of square section cylinders [e.g. Bergstrom and Wang (1997); Taylor and Vezza (1999); Oka and Ishihara (2009); Šoda *et al.* (2011)], using different approaches. These include, for example, URANS (Unsteady Reynolds Averaged Navier Stokes), DNS (Direct Numerical Simulation), LES (Large Eddy Simulation) and DVM (Discrete Vortex Method).

3.4.1   Flow patterns

The flow structure behind a cylinder with square cross section resembles that behind a circular cylinder. However, the reasons for flow separation on the cylinder surfaces are totally different. Flow separation on the surfaces of the circular cylinder occurs due to an adverse pressure gradient in the downstream direction and the separation points move back and forth depending on the Reynolds number. On the other hand, in the case of the square section cylinder, as for other geometries with sharp corners, the separation points are fixed either at the leading edges (upstream corners), due to the abrupt geometrical changes at its sharp edges, or at the trailing edge, depending on the Reynolds number. The region of vortex formation is significantly broader and longer for a square section cylinder than for a circular cylinder (Dutta *et al.*, 2008).

Differently from behind circular cylinder, the flow pattern behind a fixed rectangular and, therefore, also square section cylinder is, even intuitively, sensitive to its orientation to the approaching flow, usually refereed to as *angle of incidence*, or *angle of attack*, indicated with θ in Fig. 3.5. While at moderate incidence, the separation points are fixed at the upstream corners, the orientation has a pronounced effect on the shear layer development, wake formation and resulting mean and fluctuating aerodynamic forces.

Dutta *et al.* (2003) examined the sensitivity of the wake properties to the cylinder orientation. Fig. 3.6 shows some images of the flow pattern behind the square cylinder recorded by the same authors in a smoke tunnel facility at a Reynolds number of 3920. At zero angle of incidence the flow separates from the corners of the
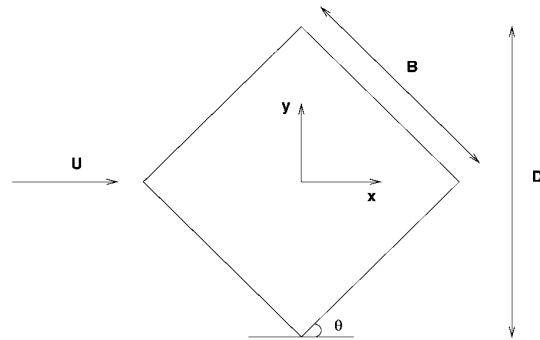
Fig. 3.5 Schematic drawing of a square section cylinder of side B, placed at an angle of incidence, θ to the incoming flow (Dutta *et al.*, 2003).
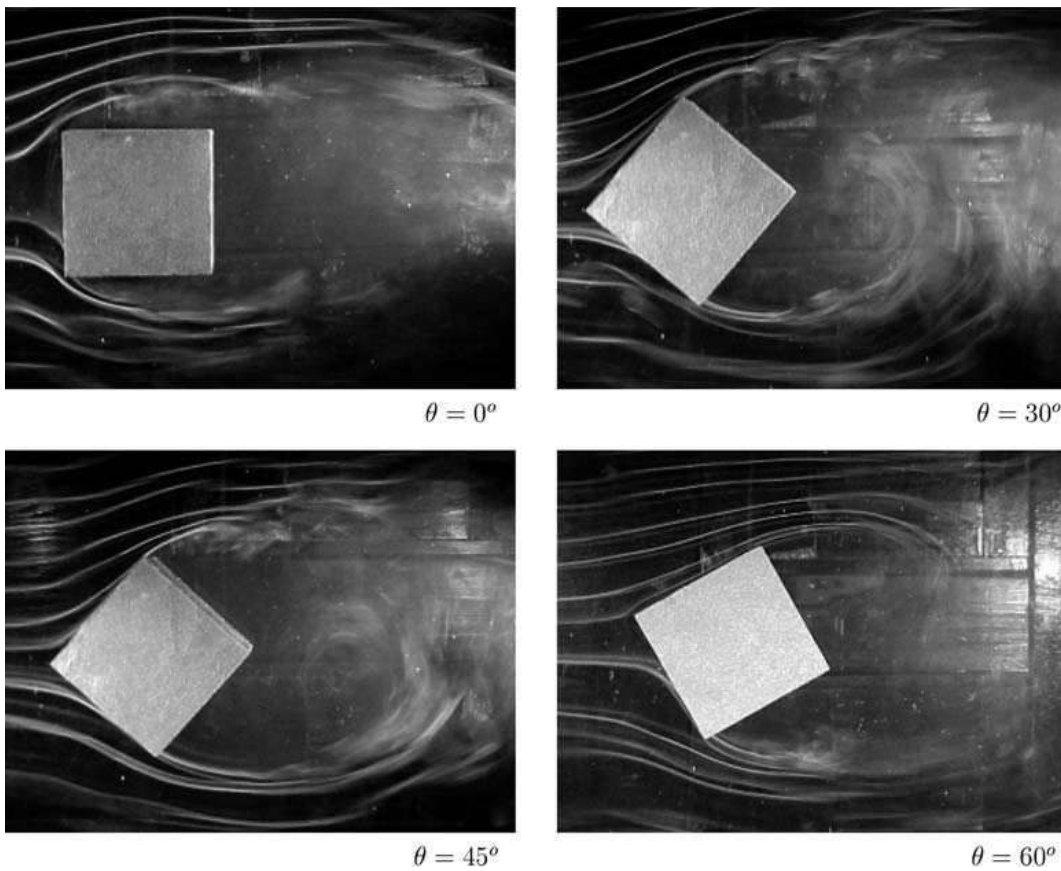

Fig. 3.6 Smoke visualization of flow around a square section cylinder at various angles of incidence with $Re = 3920$ from Dutta *et al.* (2003).

windward face. For inclinations greater than zero, the separation points is delayed up to the cylinder corners on the downstream side and the wake size increases, but the separated shear layer rolls up over a shorter distance. Flow patterns behind a square section cylinder have been classified into the following types depending on the cylinder orientation:

- perfect separation type

- reattachment type

The transition from the first to the second pattern occurs at a low value of the angle of incidence, often identified in the range $10° - 15°$. Van Oudheusden *et al.* (2008) investigated the flow field around a square section cylinder by means of Particle Image Velocimetry (PIV). According to their observations (Fig. 3.7 [2]), at zero incidence, the flow pattern is predominantly symmetric. Flow separation occurs at both upstream corners, small recirculation regions are observed above and below the model and two large recirculation regions appear in the wake behind the cylinder. At higher values of the angle of incidence, the separated region expands. At the leeward side, upper surface in Fig. 3.7, the side and rear recirculation regions gradually merge, while at the windward side, lower surface, the side recirculation is increasingly confined, with reattachment of the shear layer at an incidence between $10°$ and $15°$. It has been noted that the exact angle where reattachment begins to occur depends on the turbulence level and the Reynolds number as well (Vickery, 1966; Lee, 1975). Similar characteristics of the vortex trail behind a square section cylinder were obtained numerically by Taylor and Vezza (1999).

The distance between the end of the time-averaged separated wake, corresponding to the saddle point in the streamlines, and the center of the square is defined as *bubble* or *reattachment length*. The latter is found to be almost insensitive to Reynolds number for $0°$ and $15°$, while a pronounced effect is present for intermediate angles. This phenomenon is possibly due to a Reynolds number effect on the intermittent reattachment of the separated shear layer.

3.4.2 Strouhal number, pressures and aerodynamic forces on a 2-D fixed square cylinder

Fluctuating pressure coefficients and aerodynamic lift and drag forces on a 2-D square section cylinder have been measured by many authors [e.g. Vickery (1966); Chen and Liu (1999); Saha *et al.* (2000); Van Oudheusden *et al.* (2008); Liang *et al.* (2011)]. Fig. 3.8 shows the spectra of the lift force measured at $0°$ angle of incidence and $Re = 1.0 \times 10^5$ in both smooth and turbulent flow conditions. In both cases the bulk of the energy is in a very narrow band centered on the Strouhal frequency.

Liang *et al.* (2011) investigated Reynolds number effects on wind pressures over a square cylinder. The variation of the Strouhal number with increasing Reynolds number, ranging from 2.7×10^4 and 6.8×10^5, under a $0°$ angle of attack in smooth, 5% and 15% homogeneous turbulent flow fields was observed by analysing the position of the spectral peak of the across-wind force. As illustrated in Fig. 3.9, St is

---

[2]Unrealistic streamlines crossing the model surface are motivated by insufficient spacial resolution due to the finite window size of the PIV-image analysis. Higher resolution (zoom in) will resolve the flow details in these areas (Van Oudheusden *et al.*, 2008).
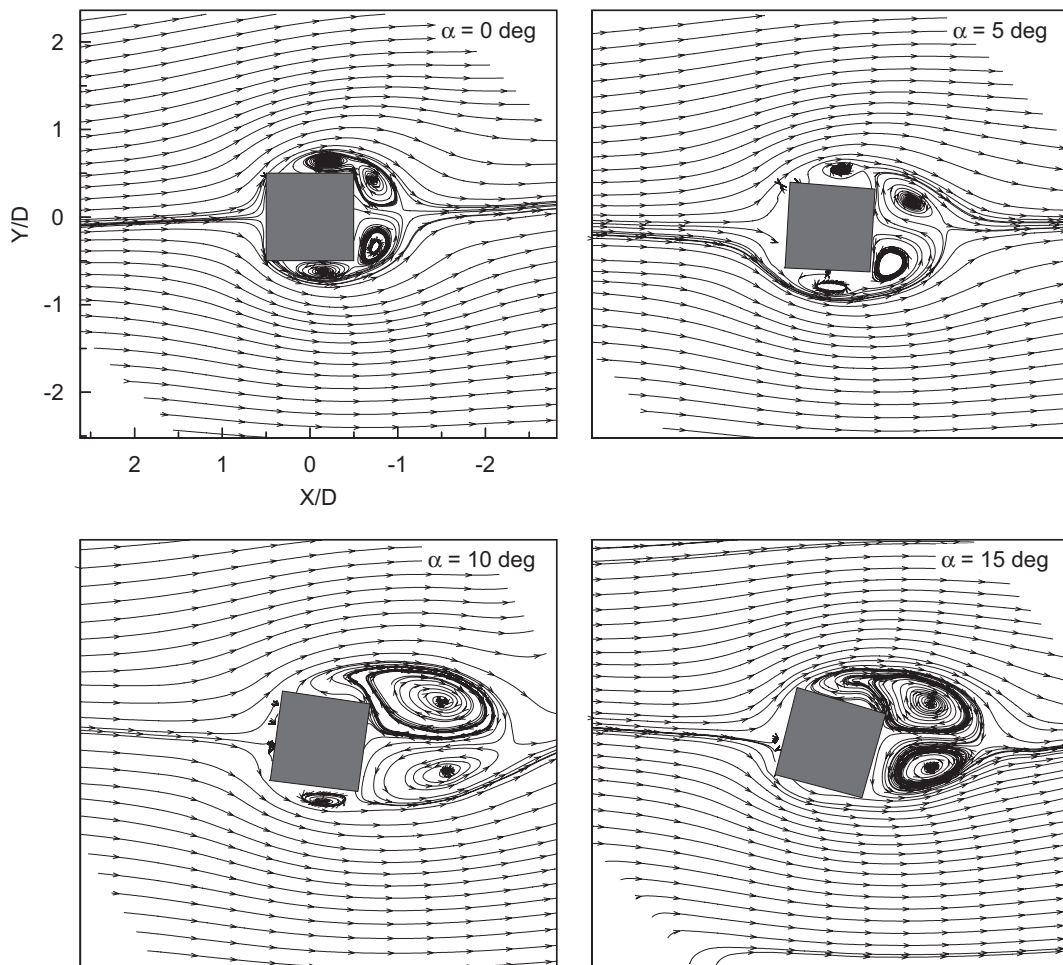
Fig. 3.7 Mean flow streamline pattern around a square section cylinder as a function of angle of incidence, at $Re = 20000$ from Van Oudheusden *et al.* (2008).
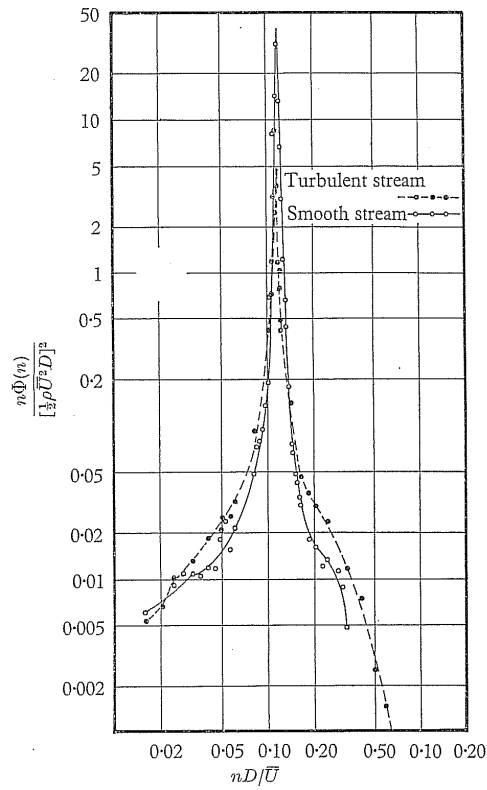
Fig. 3.8 Spectra of lift fluctuations on a square cylinder at 0° angle of incidence and $Re = 1.0 \times 10^5$ in both smooth and turbulent flow conditions (Vickery, 1966).

Fig. 3.9 Strouhal number variation with Reynolds number for a square section cylinder at 0° angle of attack (Liang *et al.*, 2011).

approximately equal to 0.1 in uniform and 5% homogeneous turbulent flow conditions, while values lower than 0.09 were observed for the 15% homogeneous turbulent flow field, showing an effect of turbulence on the Strouhal number in the Re range considered.

As seen in subsection 3.4.1, the formation of vortices behind a square cylinder

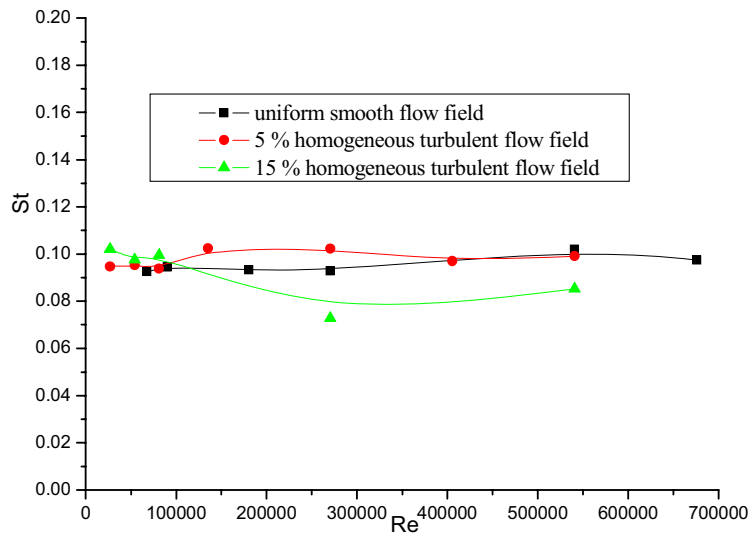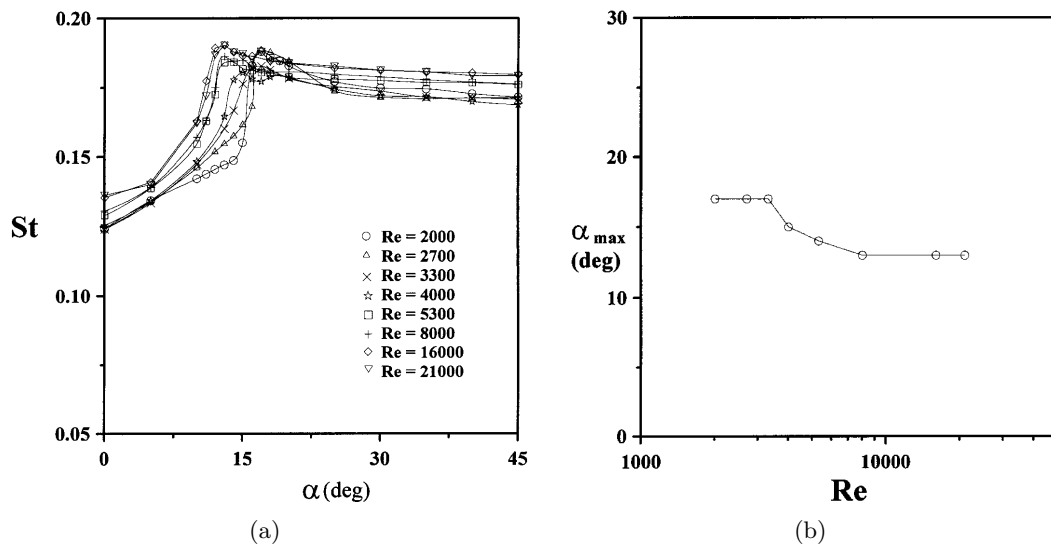**Fig. 3.10** Reynolds number and incidence effects on Strouhal number (Chen and Liu, 1999): a) St as a function of the angle of attack ($Re = 2000 - 21000$); b) angle at which St takes its maximum value as a function of Re.

depends on the orientation to the incoming flow. Fig. 3.10 shows the Strouhal number as a function of the angle of attack for Reynolds number ranging between 2000 and 21000 (Chen and Liu, 1999). At small incidence, St rises rapidly with increasing angle of attack, α, till a maximum at an angle α_{max}, and then it levels off between 0.17 and 0.18 at higher values of incidence [Fig. 3.10(a)]. Fig. 3.10(b) illustrates how α_{max} varies with Re. After a first Re number range where α_{max} takes its highest value, equal to 17°, and after a gradual descent for $Re = 3300 - 8000$, at higher Re values, α_{max} reaches a constant value of 13°.

A number of authors obtained similar relations between St and the angle of incidence, observing a sudden jump of St at comparable incidence, depending of Re [e.g. Vickery (1966); Dutta et al. (2008)]. The sudden jump of St at incidence between 13° and 17° is attributed to the onset of flow reattachment to the side face of the cylinder occurring, in fact, at the same incidence values, as seen in subsection 3.4.1, Fig. 3.7. From Fig. 3.10(b), at $Re = 20000$ the angle α_{max} is equal to 13°. This value of the angle of attack is in the range of incidence at which Van Oudheusden et al. (2008) observed flow reattachment for the same value of Re.

The achievement of a peak value of the Strouhal number at the onset of flow reattachment may be motivated by the fact that a decrease in the width of the wake can be linked to an increase in St. The angle at which reattachment of the shear layer to the windward side face of a square cylinder manifests corresponds to the narrowest wake and leads to the maximum Strouhal number.

Fig. 3.11(a) depicts the circumferential distribution of the mean pressure coefficients around a square section cylinder at zero incidence for a range of $Re = $

$2000 - 16000$ (Chen and Liu, 1999). The impingement pressure at the upstream face AB is not discernibly affected by Re. However, the pressure distribution on the side and rear faces, BC, CD and DA, appears to be influenced by Re in the range 2000-5300, while it levels off on the same curve for $Re > 5300$. Fig. 3.11(b) shows the pressure distribution measured at different angles of incidence for $Re = 5300$. The side face (BC) pressure distribution consists of a plateau of low pressure, followed by a recovery to a higher pressure nearing the trailing edge (C). The least pressure plateau as well as the strongest pressure recovery, indicating the onset of reattachment of the shear layer to the side face, occurs at the angle (14°) where the Strouhal number reaches its maximum value, as seen in Fig. 3.10.

Similarly to Chen and Liu (1999), Liang *et al.* (2011) investigated Reynolds
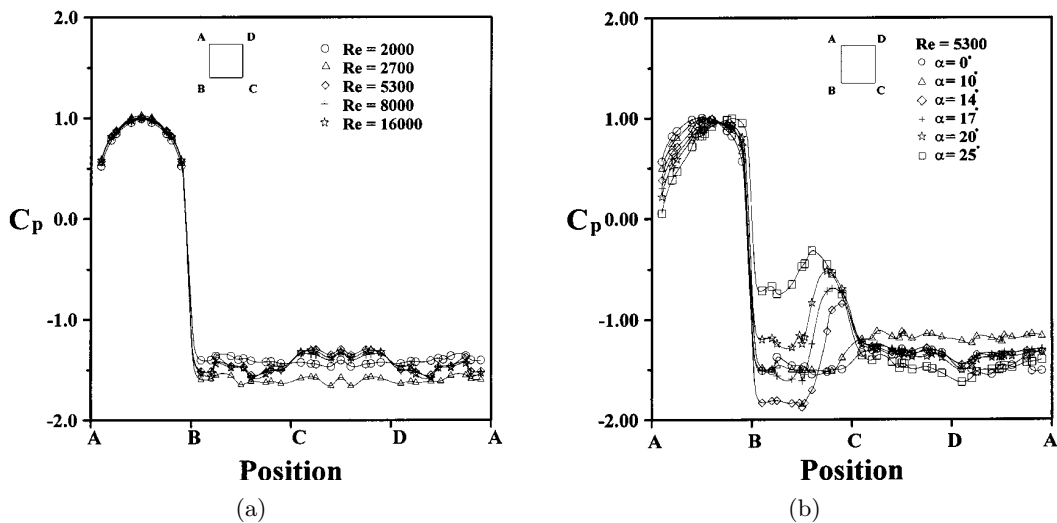

Fig. 3.11 Mean pressure coefficients distribution in uniform air stream at a turbulence level below 0.5%: a) zero incidence for various Reynolds numbers; b) variuos angles of incidence at $Re = 5300$ [Chen and Liu (1999)].

number effects on the pressure distribution around a square section cylinder. Their results concerning zero incidence and 15% homogeneous turbulent flow conditions are reported in Fig. 3.12. Reynolds number effects on the mean pressure coefficient [Fig. 3.12(a)] on the windward side are negligible, while the mean pressure distribution in the negative pressure regions on the sideward and leeward faces shows a sensitivity to Re. Two families of curves can be distinguished, the first for Re ranging from 27040 to 81120, and the second for Re from 270400 to 540800. The maximum difference of mean pressure coefficients in absolute values between the two families is 0.336. A bifurcation between these two Re families is also evident in Fig. 3.12(b). The RMS wind pressure coefficients all around the cylinder surface are much higher (maximum diffence equal to 0.2) for $Re = 27040 - 81120$ than for $Re = 270400 - 540800$.

The mean aerodynamic drag and lift coefficients, $\overline{C_D}$ and $\overline{C_L}$, at angles of incidence ranging from 0° to 45° were reported by several authors. Fig. 3.13 and Fig. 3.14 illustrate a summary of the results of two experimental works (Lee, 1975; Van Oudheusden *et al.*, 2008) and two numerical works (Taylor and Vezza, 1999; Oka and Ishihara, 2009).

At small incidence (perfect separation flow type, subsection 3.4.1), as the angle
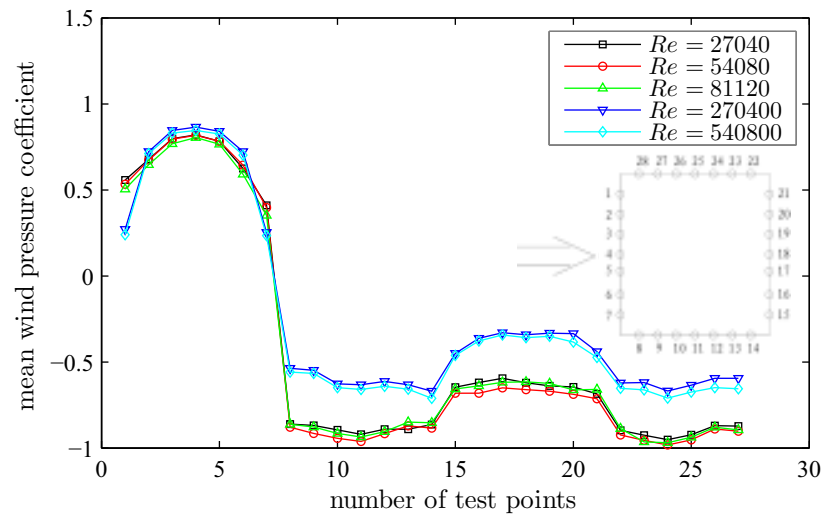
(a)
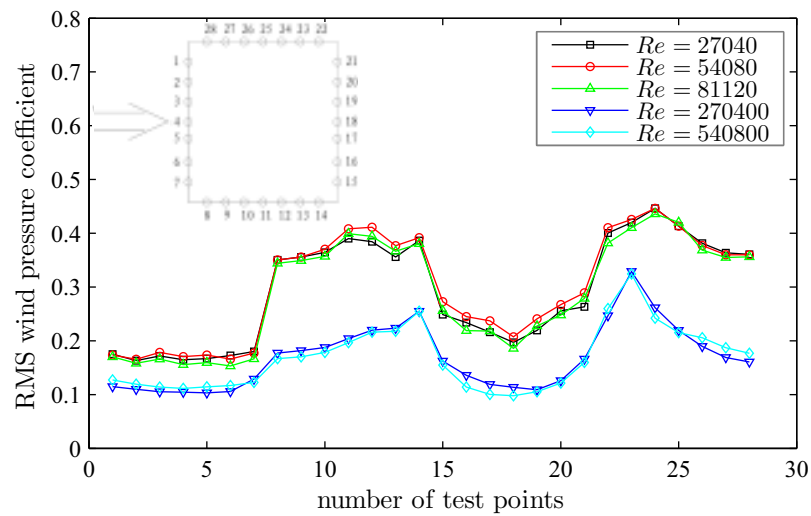
(b)

Fig. 3.12 Wind pressure coefficients in 15% homogeneous turbulent flow field at zero incidence: a) mean values; b) RMS values [Liang *et al.* (2011)].

of attack increases, the mean drag coefficients, $\overline{C_D}$, decreases (Fig. 3.13) primarily because of the shear layer that is shed from the upstream corner (on the lower surface with reference to Fig. 3.7), intermittently contacting the subsequent leeward corner. At the angle where reattachment occurs, between 10° and 15° according to different authors, the shear layer does not separate from the upstream corner on the lower side anymore, giving rise to a narrower wake and a lower value of the mean drag coefficient. Further increases in the angle of incidence simply lead to an enlargement of the wake and a gradual increase in $\overline{C_D}$, from approximately 15° to 45° (reattachment type flow pattern).

Transition from perfect separation to reattachment flow pattern explains also the variation of the mean lift coefficient, $\overline{C_L}$, with angle of incidence, illustrated in Fig. 3.14. Before reattachment, when the angle of incidence increases, side and rear recirculation (Fig. 3.7) gradually merge, giving rise to a separation bubble on the upper side. The separation bubble causes higher local suction pressures than those on the opposite side (lower surface), determining a negative lift coefficient with a maximum absolute value at the angle of full reattachment. As the angle further increases, the separation bubble decreases, so reducing the local suction pressures, which gradually balance with the ones at the opposite side, determining a decrease in the absolute value of $\overline{C_L}$.

Fig. 3.13 Variation of mean drag coefficient, $\overline{C_D}$, with angle of attack from different authors [Lee (1975); Taylor and Vezza (1999); Van Oudheusden *et al.* (2008); Oka and Ishihara (2009)].

The Root Mean Square (RMS) value of the fluctuating normal force coefficient on a square section is illustrated in Fig. 3.15, as a function of the angle of attack for both smooth and turbulent (turbulence intensity equal to 10%) incoming flow conditions (Vickery, 1966). Turbulence is seen to reduce the RMS value of the normal force below the corresponding laminar flow values at small angles, while increasing them at higher incidences.

The dependence of the drag coefficient, C_D, upon the turbulence intensity is il-
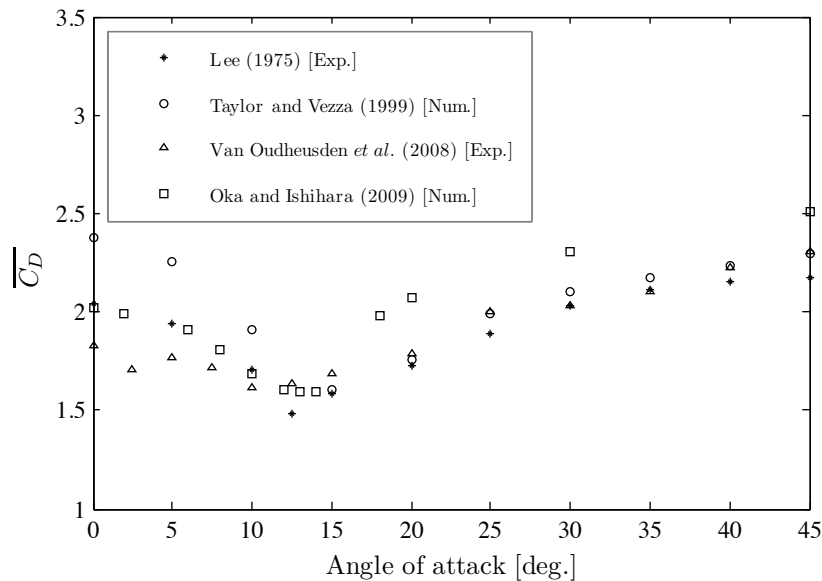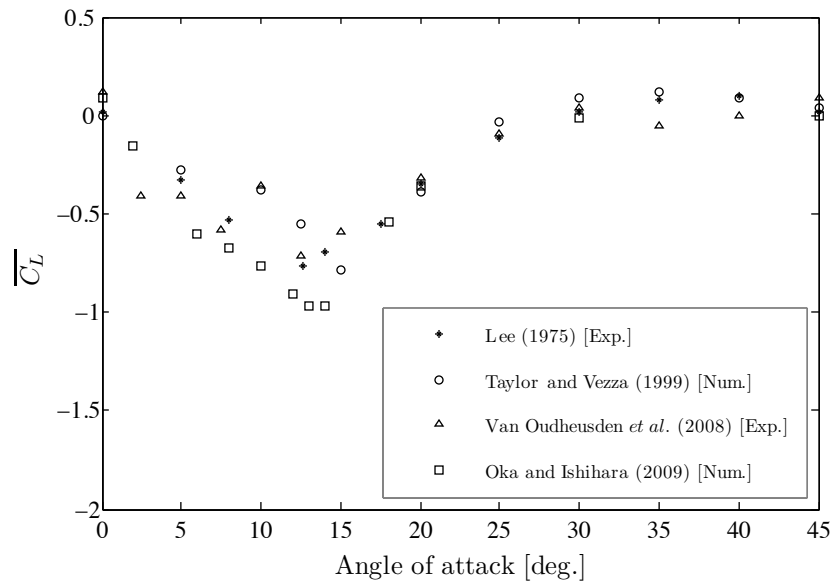
Fig. 3.14 Variation of mean lift coefficient, $\overline{C_L}$, with angle of attack from different authors [Lee (1975); Taylor and Vezza (1999); Van Oudheusden *et al.* (2008); Oka and Ishihara (2009)].
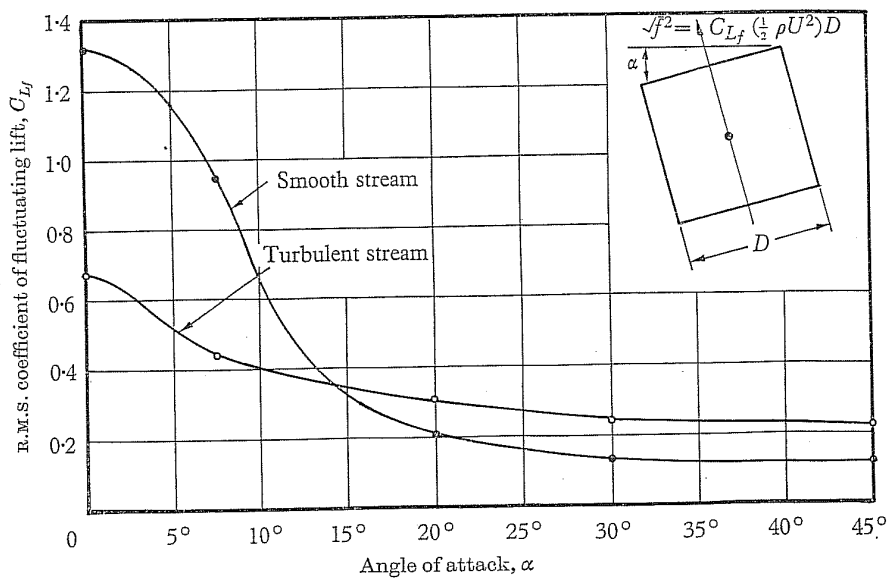

Fig. 3.15 Variation of the RMS normal force coefficient, indicated with C_{L_f} with angle of attack in smooth and turbulent flows (Vickery, 1966).

lustrated in Fig. 3.16, where the curve $b/h = 1$ refers to the square section cylinder. This picture shows that an increase in turbulence leads to a descrease of the drag coefficient.

For bluff bodies with rounded surfaces, the positions of the points of detach-
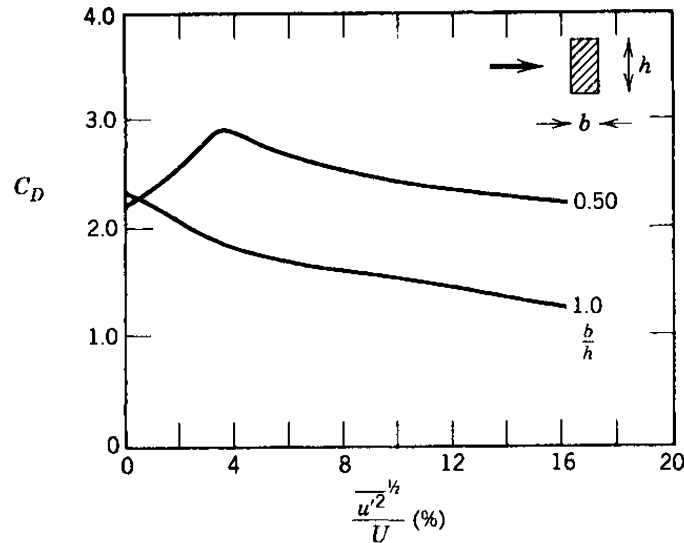

Fig. 3.16 Dependence of drag coefficient on turbulence intensity for rectangular section cylinders (Laneville *et al.*, 1977), from Simiu and Scanlan (1996).

ment of flow from the surfaces are much more dependent on viscous forces that in the case of sharp-edged bodies. This results in a variation of the drag coefficient with Reynolds number, which, as previously mentioned, is the ratio of inertial forces to viscous forces in the flow. Fig. 3.17 shows that a quite moderate rounding of the corners of a long square section prism results in a decrease of the drag coefficient, which also becomes Reynolds dependent. The critical Reynolds number at which the sudden decrease of the drag coefficient occurs is influenced both by surface roughness (see smooth surface and sanded surface lines in Fig. 3.17) and by turbulence in the approaching flow (Scruton, 1981). Both surface roughness and turbulence promote the transition to turbulent boundary layers at lower Reynolds number values. These layers detach from the surface at more rearward positions than do the laminar boundary layers found at sub-critical values. As a consequence, the wake width and the drag coefficient decrease.

In Table 3.1 some results of different numerical and experimental studies on the flow around a square cylinder at 0° angle of incidence are reported.

3.5 Three-dimensional air flows around finite-length square cylinders

In civil engineering applications cylinder-like structures have a finite length (or height), often with one free end and the other end fixed on the ground. These structures, including the case of high-rise buildings, cannot be treated as two-dimensional cylinders. It is now well established that, due to the end effects, the flow structure behind a finite-length cylinder differs drastically from that behind a two-dimensional cylinder, as unveiled in a number of previous studies, mostly focusing on circular
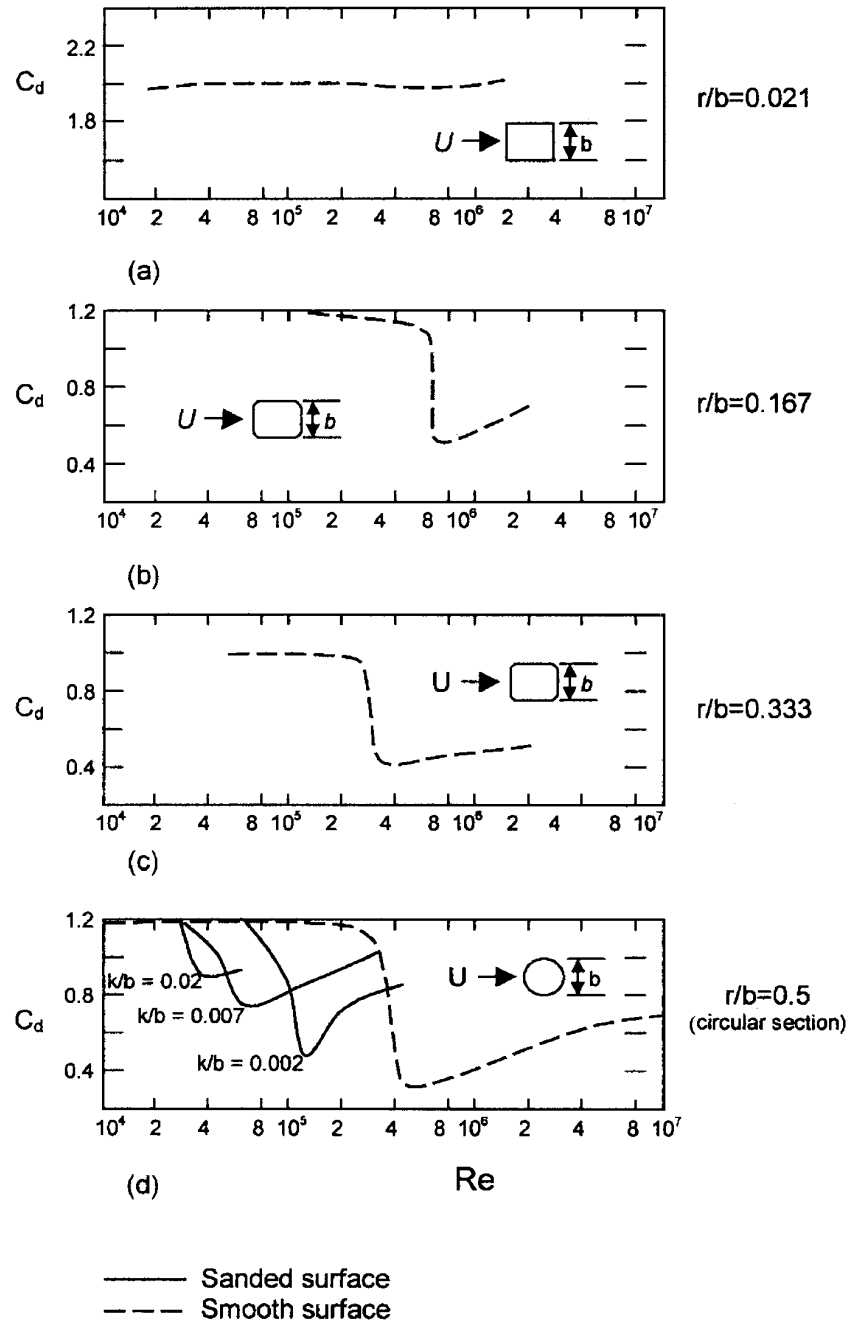
Fig. 3.17 Influence of Reynolds number Re, corner radius r/b and surface roughness k/b (where k is the size of grain) on drag coefficients C_D per unit span for 2-D (aspect ratio considered infinite) prisms of square section and circular cylinders, from Scruton (1981) [see also Holmes (2001)].

Table 3.1 Strouhal number and aerodynamic force coefficients for a square cylinder at 0°
angle of incidence, reported from different authors for different Re ($\overline{C_D}$ = mean
drag coefficient, $C_D{'}$ = standard deviation of drag coefficient, $\overline{C_L}$ = mean lift
coefficient, $C_L{'}$ = standard deviation of lift coefficient)

Author	St	$\overline{C_D}$	$C_D{'}$	$\overline{C_L}$	$C_L{'}$	Re
Experimental works						
Vickery (1966)	0.118	2.05	0.17		1.32	1.6e+5
Lee (1975)	0.1214	2.04	0.23	0.021		1.76e+5
Chen and Liu (1999)	0.124-0.138					0.2-2.1 e+4
Saha *et al.* (2000)	0.144-0.142	2.13-2.2				8700-17625
Liang *et al.* (2011)	0.085-0.1	1.05-1.35	0.035-0.28	0-0.05	0.043-0.6	0.27-6.8 e+5
Numerical works						
Taylor and Vezza (1999)	0.1278	2.38		0.019		2.0e+4
Oka and Ishihara (2009)	0.122-0.125	2.02-2.08	0.14-0.25	0-0.1	1.25-1.32	1e+4
Soda *et al.* (2011)	0.113-0.126	1.96-2.04	0.11-0.17		1.41-1.46	2.64e+4

cylinders.

The near wake of a wall-mounted finite-length circular cylinder, as reviewed by
Wang *et al.* (2004) and Wang and Zhou (2009), was found to be strongly three-
dimensional, due to the interaction of tip vortices sprung from the free end and
horseshoe vortices shed at the base. Furthermore, the ratio between the cylinder
height, h, and the diameter, d, i.e. the aspect ratio, has a great influence on the
wake structure. When h/d is below a critical value $(h/d)_{crit}$, vortex shedding changes
from the antisymmetrical Kármán type (the *vortex trail* illustrated in section 3.3), to
the symmetric arch-type, and the free-end downwash flow dominates the wake. For
$h/d > (h/d)_{crit}$, alternate Kármán vortex shedding occurs along the cylinder, except
near the free end, where the downwash interacts with the Kármán vortices, and near
the base. The critical aspect ratio value, $(h/d)_{crit}$, ranges from 2 to 6, depending on
different factors, such as the boundary layer thickness and turbulence intensity of
the incoming flow. The wake behind a finite-length cylinder is, therefore, character-
ized by the presence of the longitudinal tip and base vortices, in addition to possible
spanwise Kármán vortex shedding. The interactions between these three types of
vortices complicate significantly the flow and make it highly three-dimensional.

Motivated by its primary importance and practical significance in many branches
of engineering, such as aerodynamics of cooling towers and tall buildings, the flow
around a finite-length square prism has also attracted considerable attention in lit-
erature.

On the basis of hotwire and PIV measurements of the turbulent flow struc-
ture around a square cylinder of 3 to 7 aspect ratio, Wang *et al.* (2004) proposed the
schematic flow structure model illustrated in Fig. 3.18. At $h/b = 3$ [Fig. 3.18(a)], the
alternate spanwise Kármán vortex shedding is largely suppressed and the near wake
is dominated by tip and base vortices. At higher aspect ratios, $h/b \geq 5$ [Fig. 3.18(b)],
periodic spanwise vortex shedding occurs over almost the whole span except very
close to the wall. Power spectra of velocities in the flow direction revealed a broad
peak occurring at a reduced frequency, f_r, (that is the frequency normalized by ve-
locity and reference dimension, see Eqs. 3.13 and 5.6) equal to 0.09 for $h/b = 3$ and

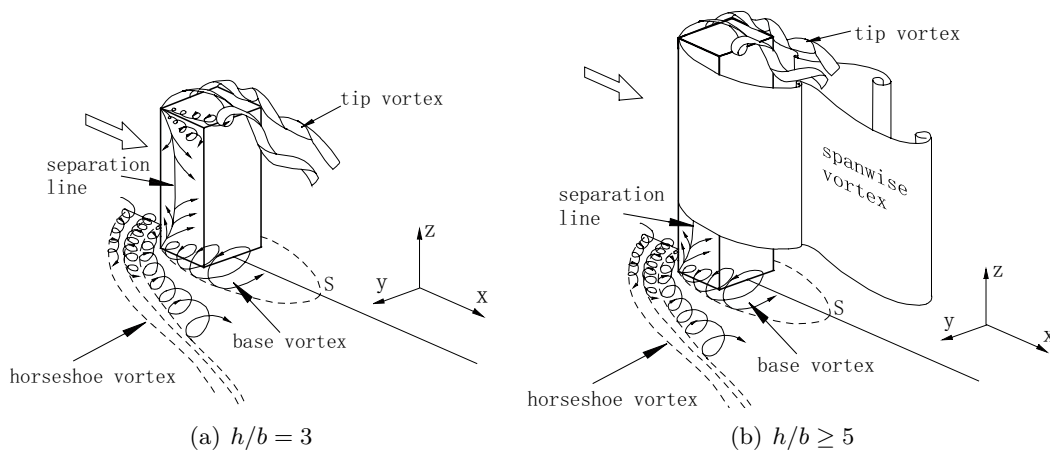(a) $h/b = 3$ (b) $h/b \geq 5$

Fig. 3.18 Flow structure behind a finite-length square prism (Wang *et al.*, 2004).

a pronounced sharp peak at approximately 0.12 and 0.13 for h/b equal to 5 and 7, respectively. The last mentioned values of the reduced frequency are close to those of dominant Kármán vortices in a two-dimensional square cylinder wake (see Table 3.1). It has to be specified that measurements were carried out by the authors at a free-stream velocity, U_∞, of 7 m/s, corresponding to $Re = 9300$, based on the side dimension of the square cylinder, b. The free-stream turbulence intensity, I_u [Eq. (6.16)], was about 0.7% and the boundary layer effect on the wake was judged negligible, because of the small thickness (2 mm) of the boundary layer at the cylinder position.

Flow around a finite-length wall-mounted square cylinder was systematically investigated by Wang and Zhou (2009). The cylinder was partially immersed in a boundary layer, characterized by a boundary layer thickness, δ, equal to $1.35b$, where $b = d$ indicates the side dimension of the square prism. The aspect ratio, h/b, examined ranged from 3 to 11. Planar PIV measurements were performed in the three orthogonal planes of the three-dimensional cylinder wake, along with flow visualization conducted simultaneously in two orthogonal planes. Laser Doppler Anemometry (LDA) and hotwire measurements were also performed. A huge amount of experimental evidences were discussed and compared by the authors with other literature works. In this section only a brief description of the main results is discussed.

Two distinct types of instantaneous sectional streamlines [Fig. 3.19(a,b)] were observed. One [Fig. 3.19(a)] is characterized by free-end downwash flow meeting with upwash flow from the wall. The saddle point results from interaction between downwash and upwash flows. The other one [Fig. 3.19(b)] is more complicated and characterized by more critical points, including two saddle points, three foci and a node. Time-averaged streamlines [Fig. 3.19(c)] are topologically similar to the instantaneous ones in Fig. 3.19(a) and to those behind a wall-mounted finite-length circular cylinder of the same aspect ratio.

Both symmetrically and antisymmetrically arranged spanwise vortices were distinguished on horizontal planes at different heights, reconfirming the observations of Wang *et al.* (2004). The investigated flow structure is highly three-dimensional, consisting of three types of vortical patterns:

- tip vortices emanating from the free end and constituting a downwash flow;

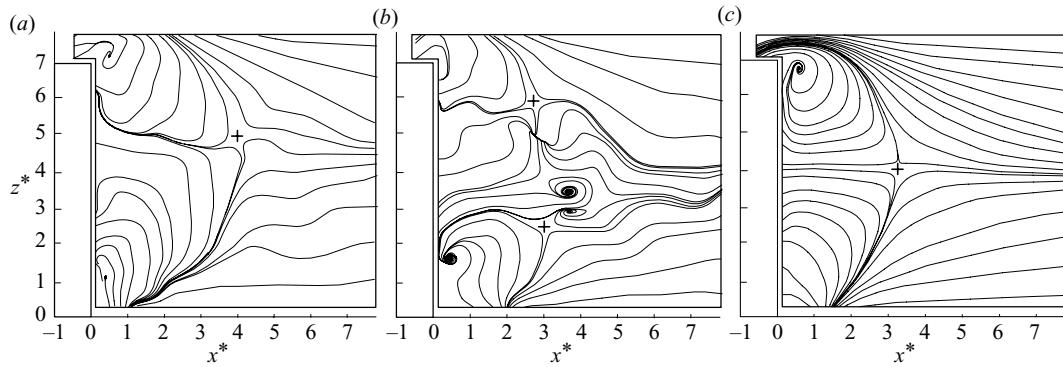**Fig. 3.19** Instantaneous (a,b) and time-averaged (c) sectional streamlines in the vertical plane, viewed on a fixed reference frame. Aspect ratio $h/b = 7$. Saddles denoted by '+' [Wang and Zhou (2009)].
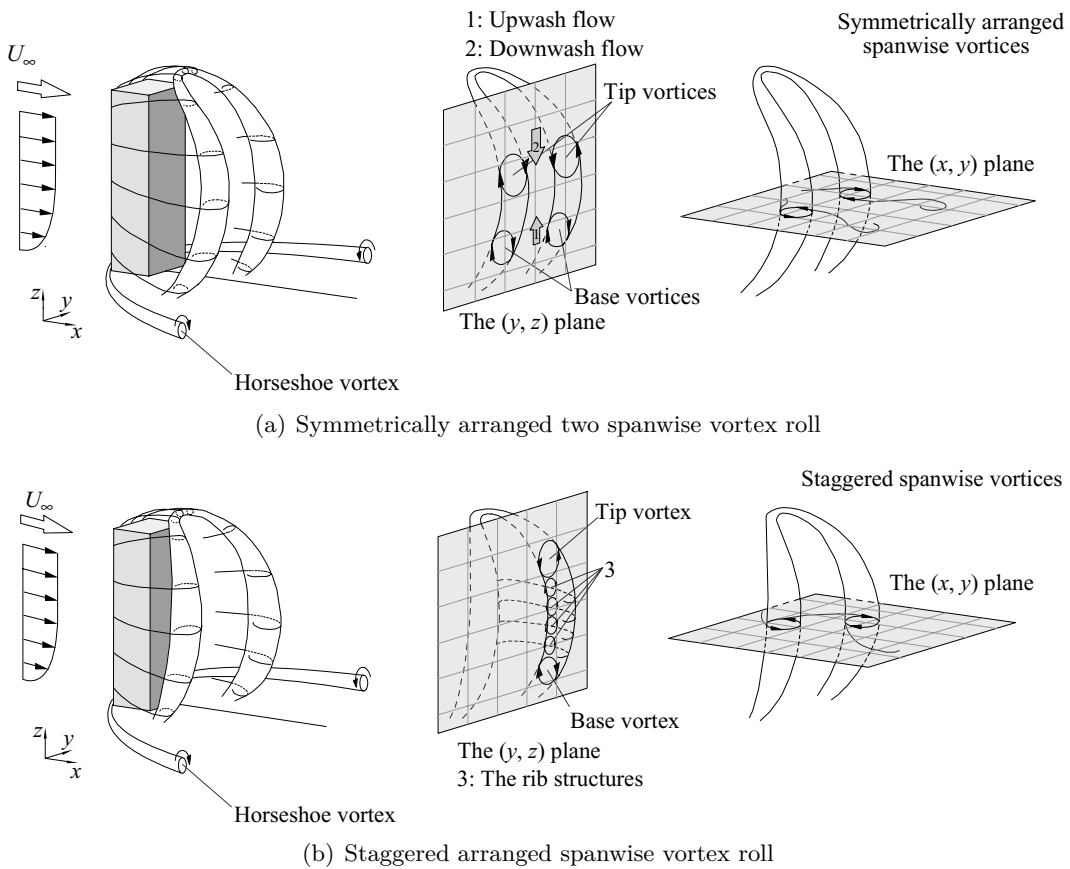

(a) Symmetrically arranged two spanwise vortex roll

(b) Staggered arranged spanwise vortex roll

Fig. 3.20 Model of the flow structure around a wall-mounted finite-length square cylinder proposed by Wang and Zhou (2009).

- Kármán vortices characterizing a spanwise shear flow;
- base vortices featuring an upwash flow from the wall.

The near wake is characterized by complex interactions between these components.

On the basis of experimental evidences and discussions, Wang and Zhou (2009) proposed the physical model for the flow structure behind a finite-length square cylinder, sketched in Fig. 3.20. In this model, spanwise vortices from both sides of the cylinder are connected with each other near the free end, forming an arch-type vortex. The latter consists of two 'legs' that immerse in the wall boundary layer and merge near the free end. Because of the influence of both the free-end downwash flow and the boundary layer over the wall, the upper and the lower regions of the arch-type structure are inclined upstream. Furthermore, a horseshoe vortex originates at the cylinder base.

Two instantaneous configurations of the arch-type vortex, corresponding to the two types of spanwise vortices observed, are illustrated in Fig. 3.20. Fig. 3.20(a) presents one configuration of the flow structure with spanwise vortices symmetrically arranged. The downwash and upwash flow is predominant. Symmetrically arranged spanwise vortex rolls do not occur frequently. In Fig. 3.20(b) another typical configuration is illustrated. This is characterized by staggered spanwise vortex rolls. The longitudinal rib structures occur on one side of the cylinder, so do the tip and base vortices. The two types of vortices follow rather distinct trajectories, which are, except near the free end, farther from the centerline than those in a two-dimensional wake, suggesting an increased wake width. This observation is ascribed to downwash and upwash flows, which entrain free-stream fluid into the wake and drive the spanwise vortices away from the centerline.

Many spacial configurations of instantaneous spanwise vortices are neither perfectly symmetric, nor perfectly antisymmetric, but, in fact, something in between. The probability of antisymmetrically arranged vortices is largest at midspan and reduces significantly when approaching the cylinder free end or the wall.

The occurrence of symmetrically arranged vortices around the finite-length
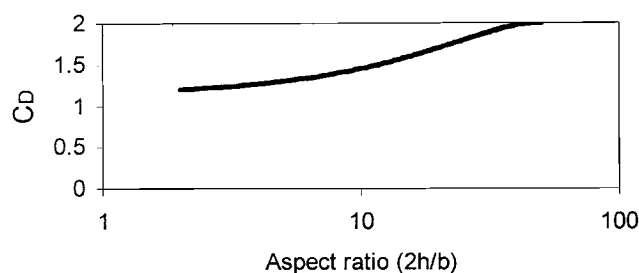
Fig. 3.21 Aspect ratio effect on drag coefficient for finite-length square section bodies (Scruton and Rogers, 1972), taken from Holmes (2001).

cylinder leads to lower drag (C_D) and fluctuating lift (C_L') coefficients, compared with those on a two-dimensional cylinder. Moreover, the maximum longitudinal extent of the reverse flow zone (at the saddle point) occurs near the midspan and is larger than in the 2-D case. Because of downwash and upwash flows, the reverse flow zone contracts when approaching the free end and the wall. The high three-dimensionality of the flow leads to a decrease in the Strouhal number compared to the two-dimensional wake.

Fig. 3.21 shows the drag coefficient for a square section prism with finite length with one free end in smooth flow conditions as a function of aspects ratio (Scruton and Rogers, 1972). The latter is defined, in this case, as $2h/b$, where h is the height and b is the breadth (side dimension), since it is assumed that the flow is equivalent to that around a body with a 'mirror image' added to give an overall height of $2h$ with two free ends. At high values of aspect ratio it is clear that the drag coefficient reaches the values corresponding to the 2-D flow conditions (see Table 3.1).

Even if the overall flow structure behind a finite-length square cylinder is independent on the aspect ratio, and increase in the latter is associated to enhanced upwash and downwash flows, such as tip and base vortices, similarly to what was observed in a finite-length circular cylinder.

The evidence that the unsteady spanwise vortices behind a 3-D square prism are connected to form an arch-type structure was also confirmed by Kawai *et al.* (2009, 2011).

3.6 Summary and main remarks

Modern tall and slender buildings are sensitive to the wind action. For this reason, the knowledge of the flow field around building-type prismatic shapes has been receiving increasing importance in the field of wind engineering and aerodynamics.

In this chapter the classical flow paradigm of the unsteady flow behind a fixed 2-D cylinder is presented at first, together with the principle of the vortex shedding phenomenon. The flow pattern behind a square-section cylinder, which this thesis is focused on, is reviewed. The flow behind a cylinder with square cross section is highly sensitive to the angle of attack, and the possible flow patterns can be categorized in two categories depending on the cylinder orientation, namely, perfect separation type and reattachment type. At zero incidence, the Strouhal number is affected by the Reynolds number and turbulence. A number of authors have investigated the influence of the angle of incidence on the Strouhal number. It shows, in general, a sudden jump till its maximum value at incidence between $10° - 15°$, that corresponds to the onset of flow reattachment to the side faces and to a decrease in the width of the wake. The distribution of the mean pressure coefficients around a square-section cylinder is discussed. Reynolds number effects on the windward side are negligible, while a certain sensitivity to Re is shown on the sideward and leeward faces. The strongest pressure recovery on the side face, indicating the onset of reattachment of the shear layer to the side face, occurs at the angle of incidence corresponding to the maximum Strouhal number. This value of the angle of attack corresponds also to a minimum of the mean drag and lift coefficients, reported by different authors. Turbulence is seen to affect the RMS value of the fluctuating normal force coefficient. Some literature results on the dependence of the drag coefficient on turbulence, Reynolds number, corner radius and roughness of the cylinder surfaces are also discussed. Data from different numerical experimental studies on square-section cylinders at zero incidence are collected in order to frame the variability range of some principle quantities, such as Strouhal number, mean and fluctuating drag and lift coefficients.

The last section of this chapter is devoted to the three-dimensional flow behind square section prisms of finite length. Due to the end effects, the wake behind a finite-length cylinder is drastically different from that behind a 2-D cylinder. It is

characterized by the presence of tip and base vortices, in addition to possible span-wise Kármán vortex shedding. The near wake is characterized by complex inter-actions between these components and both symmetrically and antisymmetrically arranged spanwise vortices may be distinguished on horizontal planes at different heights. The wake structure is influenced by the aspect ratio. The occurrence of symmetrically arranged vortices leads to lower drag and fluctuating lift coefficients than those on a 2-D cylinder.

Chapter 4

Aeroelastic effects in wind-induced responses of tall buildings

4.1 Introduction

This chapter addresses aeroelastic or motion-induced effects involving the wind-induced response of tall buildings. In section 4.2 the different components of the response of buildings to the wind action are discussed and aeroelasticity is introduced in the path from wind loads to wind-induced responses. Section 4.3 is devoted to the lock-in phenomenon which can play a significant role in the across-wind response, dominating the serviceability design of tall buildings.

Section 4.4, constituting the core of this chapter, illustrates, at first, the approach commonly used for estimating the response of tall buildings to aerodynamic loads which neglect motion-induced effects. Some experimental studies dealing with the across-wind aeroelastic response of tall buildings are reviewed in order to draw an overview for comparison for the results of the experimental campaign carried out in this research (chapter 6).

A brief description of the literature approaches for modeling the aeroelastic response is also given. Lastly, the approach of aerodynamic damping for dealing with the aeroelastic effects on tall buildings is illustrated and results from literature works on aerodynamic damping of tall buildings are reviewed. A particular attention is paid on those works which investigate the response of tall buildings with geometric and dynamic features similar to the model tested in the wind tunnel and under similar wind flow conditions.

4.2 Components of the wind-induced response and introduction to aeroelastic phenomena

Because of the fluctuating nature of wind velocity and, therefore, of wind loads, wind-induced response of structures is characterized by a *mean response*, due to the mean component of the wind load, and a *fluctuating response*, which can be further split into the *background* or *quasi-static response*, caused by the fluctuating components of the wind load, whose frequencies differ significantly from the natural

frequencies of the structures, and the *resonant response*, due to the fluctuating wind force components whose frequencies are equal or close to the structural natural frequencies. The natural frequencies of the structure determine whether the fluctuating dynamic response to the wind action is mainly driven by the background response or by the resonant response. Fig. 4.1[1] shows the response spectral density of a structure under wind loading. Subscripts B and R indicate background and resonant components, respectively. The area under the entire curve represents the total *mean-square* fluctuating response, whose square root is known as *Root Mean Square* and indicated with *RMS*. The background response, made up mainly of low-frequency contributions below the natural frequency of vibration, is the largest contributor in Fig. 4.1 and is usually dominant in the along-wind direction (Holmes, 2001). Due to their size and slenderness, tall buildings have, in general, several natural frequencies of vibration of less then 1 Hz, which, together with low damping values, make them susceptible to significant resonance when excited by extreme wind events.

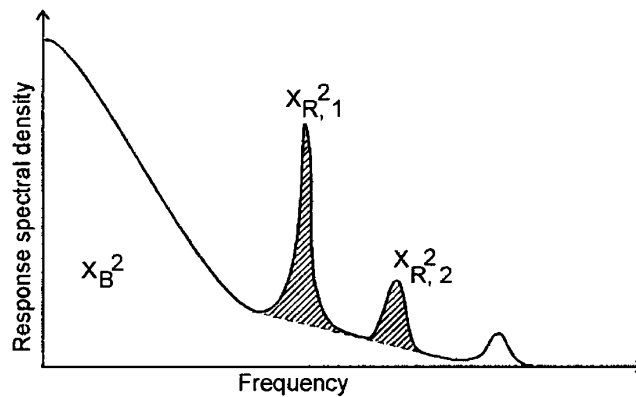If the structure moves or deforms appreciably under the wind-induced forces,

Fig. 4.1 Response spectral density for a structure with significant resonance contributions (Holmes, 2001).

these deflections may affect the fluid forces, which, in turn, will influence the deflections. *Aeroelasticity* describes phenomena involving the interaction between aerodynamic forces and structural deformations. These phenomena are known as *aeroelastic* or *motion-induced* effects. In case of lightweight, low damped, slender structures, these effects are not negligible and a proper assessment of the structural responses R, due to the wind action, can be performed considering that the structure is subject to overall forces $F = F_s + F_a$, where F_s are the *aerodynamic forces*, acting on the "fixed" structure (negligible displacements), and F_a are the motion-induced *aeroelastic forces* (Fig. 4.2).

The flutter of the Brighton Chain Pier Bridge in 1836 and, later, that of the Tacoma Narrows Bridge are notorious examples of aeroelastic behavior. Tall chimneys and high-rise buildings can also respond aeroelastically. The John Hancock building in Boston, which has a relatively flat shape in plan (Fig. 4.3), has experienced across-wind and torsional motions of sufficient severity to warrant the installation of a large tuned-mass damper system at its top. These motions may

---

[1]The mean response is not included in this plot
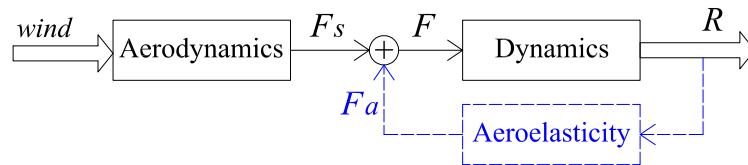
Fig. 4.2 Conceptual scheme illustrating the path from wind loads to structural responses including aeroelastic effects.

have been due to aeroelastic effects[2].

Different types of aeroelastic effects are known, such as torsional divergence,

Fig. 4.3 John Hancock Building, Boston (taken from Clark *et al.* (2004)).

flutter, lock-in and galloping. The most relevant phenomena for the across-wind response, which usually dominates the serviceability design of high-rise buildings are lock-in and galloping. However, the present research focuses only on lock-in, since galloping usually occurs at reduced velocities significantly different from those of synchronization for structures and wind conditions similar to that tested in the wind tunnel in this study [see, for example, Cheng *et al.* (2002)]. The main phenomenological aspects of the lock-in phenomenon are illustrated in the following section.

---

[2]For legal or other reasons, detailed technical reports on the wind-induced behavior of the John Hancock building are not available in the public domain (Clark *et al.*, 2004).

4.3   Lock-in phenomenon and Vortex-Induced Vibrations

It was seen in section 3.3 that alternating vortices are shed from a fixed (or stationary) bluff body, according to the Strouhal relation [Eq. (3.13)]. If the body is let free to vibrate, under the vortex shedding action, it will deflect, wholly or locally, and influence the local flow.

When the dominating shedding frequency f_s is equal or close to the natural frequency f_n of the structure, vibrating in a mode in the across-wind direction, a coupling between this motion and the wake dynamics exists. This results in a complex evolution of the shedding frequency, which deviates from the Strouhal law as the natural frequency of the solid is approached. The shedding frequency remains constant and locks on to the frequency of vibration for a certain range of flow speeds (Fig. 4.4). This aeroelastic or motion-induced phenomenon is referred to as *lock-in*.

Vortex-Induced Vibrations, referred to as VIV, corresponding to this locking-in of the wake to the body's oscillation frequency, occur over a larger velocity range than would be predicted using the Strouhal law. This speed range increases as the structural damping decreases.

The most commonly accepted interpretation of the mechanism underlying frequency lock-in is that of resonance: as the frequency of the unstable system (the wake) approaches that of the oscillator (the bluff body), the oscillating lift force causes an increasing amplitude of motion, by a standard resonance effect. Then, provided this amplitude is large enough, the wake is somehow affected and forced to move at the natural resonating frequency of the solid. This feedback mechanism is implicitly assumed to be nonlinear, as the existence of lock-in and its extent depend on the amplitude of motion.

The condition of "vortex resonance" occurs at a particular value of the wind speed, called "critical wind speed" U_{crit} and defined as:

$$U_{crit} = \frac{bf_n}{St} \tag{4.1}$$

For many structures, the critical wind speed for the first mode is of the order of 10 m/s, i.e. frequently recurring wind speeds that give rise to risk of fatigue.

In addition, the oscillation frequency, in this condition, does not always coincide with the natural frequency of the structure, because of the effect of the airflow added mass, and the drag is different from its steady-state value, e.g. Pastò (2008).

Dividing both terms in Eq. (4.1) by the quantity bf_n, one may conclude that the vortex resonance condition is achieved at a critical non-dimensional reduced velocity $U_{r,crit}$ equal to the reciprocal of the Strouhal number, as follows:

$$U_{r,crit} = \frac{U_{crit}}{bf_n} = \frac{1}{St} \tag{4.2}$$

The magnitude of vortex-induced vibrations is governed both by the structure's inherent damping characteristics and by the mass ratio between the structure and the fluid it displaces. These two effects are often combined in the Scruton number Sc, defined as (UNI-EN 1991-1-4, 2005):
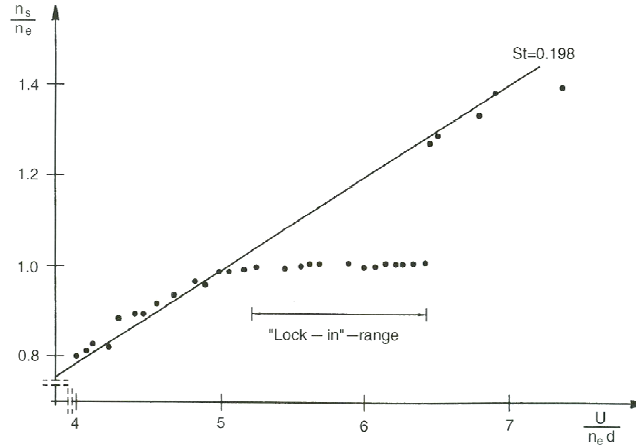
$$Sc = \frac{2\delta_s m_{i,e}}{\rho b^2} \tag{4.3}$$

Fig. 4.4 Experimental investigation of lock-in after Feng (1968), from Dyrbye and Hansen (1997).

where ρ is the air density, b is a reference dimension, δ_s is the logarithmic decrement that quantifies the structural damping and can be taken approximately equal to $2\pi\xi_s$, where ξ_s is the structural damping ratio. The equivalent mass per unit length for mode i, $m_{i,e}$, is equal to:

$$m_{i,e} = \frac{\int_0^h m(z)\phi_i^2(z)\,dz}{\int_0^h \phi_i^2(z)\,dz} \tag{4.4}$$

where $m(z)$ is the vibrating mass per unit length, h is height or length of the structure, ϕ_i is the mode shape for mode i.

An extensive review of vortex-induced vibrations of bluff bodies can be found in Willamson and Govardhan (2004, 2008).

As previously explained, the motion of the body leads to synchronization of vortex shedding. This phenomenon occurs along the longitudinal length of the body itself, providing an increase in the correlation of pressures when vortex-induced vibrations occur. Fig. 4.5 shows the spanwise correlation of fluctuating pressures along the center line of a side face of a square cylinder, forced to vibrate at an amplitude A of 1/10 times its cross dimension D ($A/D = 0.10$) for different values of the reduced velocity. Results are compared also with the case of a stationary cylinder ($\bigtriangledown$, $A/D = 0$). In the figure, $R(\rho, z)$ indicates correlation coefficient, plotted as a function of spanwise separation z/D. Results from the oscillating cylinder show much higher correlation than those from the rigid cylinder, particularly around the resonant velocity, U/fD within [7.3;8.5], where a correlation coefficient of 0.9 was recorded at the maximum spanwise separation of $z/D = 13.25$ (Bearman and Obasaju, 1982).

4.4   Aeroelastic effects in tall buildings response estimation

Comprehension of wind-induced loads and effects on tall buildings is a challenging task, motivated by both complexity of 3-D flow patterns (chapter 3) and occurrence
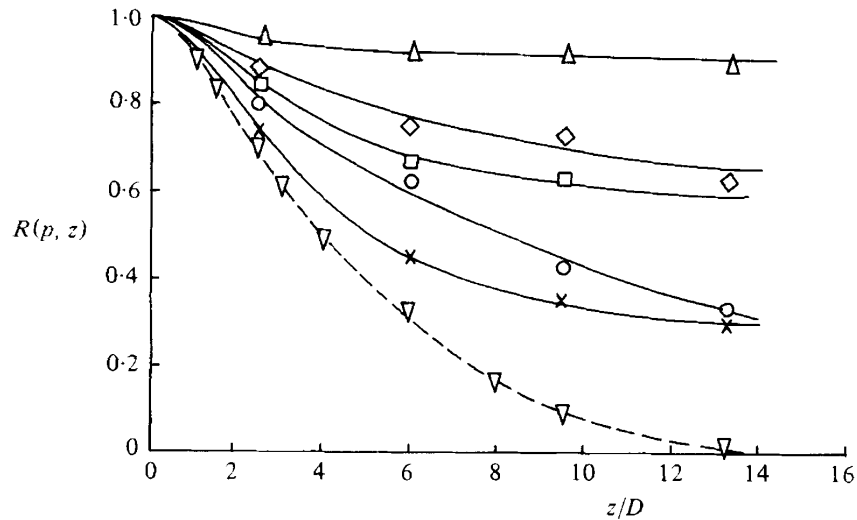
Fig. 4.5 Correlation of surface pressures on an oscillating square section cylinder vs. spanwise separation. $\triangledown$, stationary body ($A/D = 0$). Body oscillating with $A/D = 0.10$: $\times$, $U/fD = 6.2$; $\bigcirc$, 7.0; $\square$, 12.0; $\diamond$, 8.8; $\triangle$, U/fD within the lock-in range 7.3-8.5 (Bearman and Obasaju, 1982).

of the motion-induced effects, as previously illustrated. In broad terms, the wind forces resulting in dynamic excitation can be divided into three groups:

1. forces induced by the turbulent fluctuations in the incident flow;

2. forces induced by the unsteady nature of the wake and particularly by vortex shedding (section 3.3);

3. forces induced by motion of the structure (aeroelastic effects).

Furthermore, the three-dimensional simultaneous loading of a structure subject to the wind action results in the three structural components, sketched in Fig. 4.6. With reference to the wind axes, the along-wind component primarily results from pressure fluctuations in the approaching flow and leads to a swaying of the structure in the direction of wind. The across-wind component, due to side-face pressure fluctuations, primarily induced by the fluctuations in the separated shear layers, vortex shedding and wake flow fields, leads to a swaying motion perpendicular to the wind direction. Lastly, the torsional component results from imbalances in the instantaneous pressure distribution on the surfaces of the structure.

4.4.1   Response to aerodynamic loads

The along-wind component of the wind loading primarily results from turbulent velocity fluctuations in the approaching flow. It has been, therefore, successfully estimated using *strip* and *quasi-steady* theories, which imply that the wind pressure on a structure is determined by only the velocity at the height where the pressure acts and that the instantaneous pressure is proportional to the square of the instantaneous velocity pressure of the oncoming flow, respectively (Kawai, 1983). Velocity fluctuations in the oncoming flow may arise from the general nature of the earth's
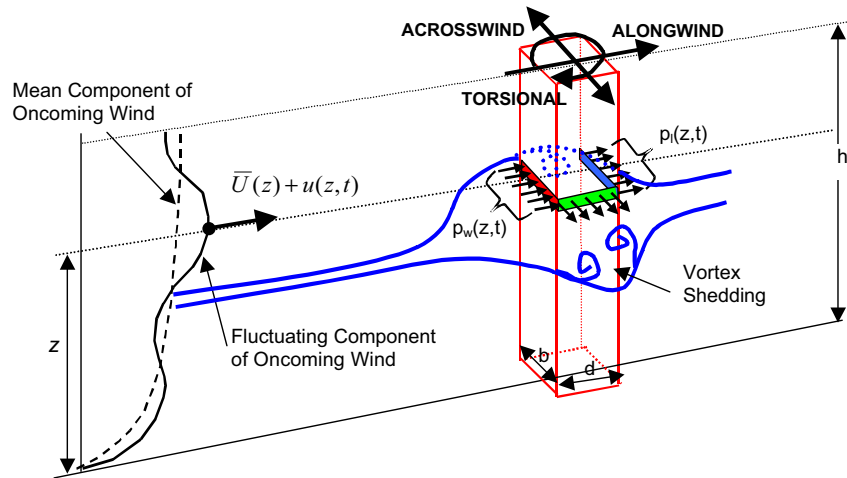
Fig. 4.6 Schematic description of oncoming wind field and resulting wind-induced response components [taken from Kijewski *et al.* (2000)].

turbulent boundary layer or from the unsteady wakes of one or more nearby structures. In the latter case the excitation is referred to as *buffeting*.

Although the along-wind response may include buffeting effects, it is the gust response due to the incoming wind that is of primary importance. Thus, the aerodynamic along-wind load may be expressed in terms of velocity fluctuations as:

$$F_D(t) = \frac{1}{2}\rho b^2 C_D[\overline{U} + u(t)]^2 \tag{4.5}$$

where b indicates the breadth of the structure. The quantity b^2 is often replaced with bh where h indicates the height. Eq. (4.5) implicitly assumes that velocity fluctuations are fully correlated over the entire structure. This assumption may hold for very small structures, but fails for structures with larger dimensions, such as the case of tall buildings, and leads to overestimation of loads. In this case imperfect correlation of wind fluctuations is introduced through an aerodynamic admittance function, $\chi^2(f)$. Describing the loading scenario in frequency domain, Eq. (4.5) is transformed accordingly as (Kijewski *et al.*, 2000):

$$S_{F_D}(f) = (\rho C_D)^2 \chi^2(f) S_u(f) b^4 \tag{4.6}$$

where $S_{F_D}(f)$ and $S_u(f)$ are the power spectral density (PSD) of along-wind load and wind fluctuations, respectively.

It has been recognized that the across-wind and torsional response for many high-rise buildings may exceed the along-wind response in terms of both serviceability and survivability designs [e.g. Kareem (1985); Liang *et al.* (2002)]. Nevertheless, most existing codes and standards provide only procedures for the along-wind response and little guidance for the critical across-wind and torsional responses. This is partially due to the fact that, differently from the along-wind loads, the across-wind and torsional loads and responses result mainly from the aerodynamic pressure fluctuations in the separated shear layers and wake flow fields. This fact has prevented to date any acceptable direct analytical relation between across-wind and torsional responses to the oncoming wind velocity fluctuations. Furthermore, higher order rela-

tionships may exist (Gurley *et al.*, 2001). As a result, experimentally derived loading functions have been introduced. Across-wind and torsional load spectra obtained by synthesizing the surface pressure field on scale models of typical tall building shapes are available in literature. Liang *et al.* (2002) proposed a complete analytical model of across-wind dynamic loads on rectangular tall buildings. This model was found to be in good agreement with some experimental results obtained by wind tunnel tests. Zhou *et al.* (2003) introduced an interactive database of aerodynamic loads obtained from High Frequency Base Balance (HFBB or High Frequency Force Balance - HFFB) measurements on a host of isolated tall building models, accessible to the worldwide Internet community at the URL address `http://aerodata.ce.nd.edu/`. The influence of key parameters, such as side ratio, aspect ratio and turbulence characteristics for rectangular sections was also discussed.

In order to derive the structural response from aerodynamic loads, basic random vibration theory is utilized, as briefly illustrated in subsection 4.4.2.

4.4.2   Random excitation model for aerodynamic response estimation

The equations of motion of a high-rise building represented by a discretized lumped-mass system are given by:

$$[M]\{\ddot{x}(t)\} + [C]\{\dot{x}(t)\} + [K]\{x(t)\} = \{F(t)\} \tag{4.7}$$

where $[M]$, $[C]$ and $[K]$ are the real symmetric mass, damping and stiffness matrices of the discretized system, respectively. $\{x\}$ is the displacement and $\{\dot{x}(t)\}$ and $\{\ddot{x}(t)\}$ are its first two time derivatives, representing velocity and acceleration, respectively. $\{F(t)\}$ indicates the stochastic wind loads applied. In general, Eq. (4.7) provides two translations and one rotation per story level, assumed rigid. For the sake of illustration, it is assumed here that the structure is uncoupled in each direction. By employing the standard transformation of coordinates, the wind response of a tall building vibrating in a natural translational mode, j, is described by:

$$\ddot{q}_j + 2\xi_j\omega_{n,j}\dot{q}_j + \omega_{n,j}^2 q_j = P_j(t) \tag{4.8}$$

where $P_j(t) = \{\phi_j\}^T \{F(t)\}$ are the generalized wind forces, ϕ_j, ξ_j and $\omega_{n,j}$ are the jth mode shape, modal critical damping ratio and circular frequency, respectively. The quantity q and its time derivatives represent generalized modal response quantities, related to x and its derivatives by:

$$\{x(t)\} = [\phi_j]\{q_j(t)\} \tag{4.9}$$

In the time domain, the generalized response, $q_j(t)$, can be calculated through integration of Eq. (4.8) and then any response parameter of interest can be obtained from the generalized displacements.

Using the frequency domain approach, the power spectral density (PSD) of the generalized displacement for mode j, is determined as:

$$S_{q_j}(\omega) = H_j(\omega)S_{P_j}(\omega)H_j^*(\omega) = |H_j(\omega)|^2 S_{P_j}(\omega) \tag{4.10}$$

where $H_j(\omega)$ is the jth-mode *frequency response function* (FRF). $H_j^*(\omega)$ indicates the complex conjugate of $H_j(\omega)$. The circular frequency ω is equal to $2\pi f$.

The square modulus of the FRF, $|H_j(\omega)|^2$, is called *mechanical admittance function* and is equal to:

$$|H_j(\omega)|^2 = \frac{1}{m_j^2 \omega_{n,j}^4} \frac{1}{\left[1 - \left(\frac{\omega}{\omega_{n,j}}\right)^2\right]^2 + 4\xi_j^2 \left(\frac{\omega}{\omega_{n,j}}\right)^2} \tag{4.11}$$

where m_j is the jth modal mass, equal to $\{\phi_j\}^T [M]$.

The mean square value of the modal response for the jth mode can be determined by integrating its PSD as follows:

$$\sigma_{q_j}^2 = \int_0^\infty S_{q_j}(\omega)\, d\omega \tag{4.12}$$

The mean square value of response in physical coordinates, $\sigma_{x^{(r)}}^2$, can be approximated by the weighted superposition of all N modal contributions:

$$\sigma_{x^{(r)}}^2 \approx \sum_{j=1}^N \frac{\phi_j^2 \pi f_{n,j} S_{P_j}(f_{n,j})(2\pi f_{n,j})^{2r}}{4(2\pi f_{n,j})^4 \xi_j m_j^2} + \sum_{j=1}^N \frac{\phi_j^2 \int_0^{f_{n,j}} S_{P_j}(f)\, df\, (2\pi f_{n,j})^{2r}}{(2\pi f_{n,j})^4 m_j^2} \tag{4.13}$$

where r indicates the derivative of response, i.e. $r = 0, 1, 2, 3$ denotes displacement, velocity, acceleration and jerk, respectively. The first term on the right side of Eq. (4.13) represents the resonant component and the second term the background component. Eq. (4.13) is an approximation of the area under the PSD of the response which is very close to exact for most lightly damped structures (Kijewski *et al.*, 2000).

Determination of wind-induced response based on random vibration theory, also known as spectral approach, is graphically illustrated in Fig. 4.7, which shows that the total mean square fluctuating response is computed from the spectral density of response. The latter is calculated from the spectrum of aerodynamic forces, which are in turn, calculated from the gust spectrum or wind turbulence. The frequency-dependent *aerodynamic admittance* and *mechanical admittance* functions constitute links between these spectra. For slender structures with low frequencies and damping, the dynamic amplification at the resonant frequency results in higher mean square (and, therefore RMS) and peak responses than structures with high frequencies, not excited by the wind action.

If response contributions from mode shapes higher than the fundamental mode of vibration of frequency f_1 can be neglected, the variance of the across-wind displacement ($r = 0$) response at the top of the building, σ_y^2, at which $\phi_1(h) = 1$, is calculated from Eq. (4.13) as:

$$\sigma_y^2 \approx \frac{\pi f_1 S_{P_1}(f_1)}{4(2\pi f_1)^4 \xi_1 m_1^2} + \frac{\int_0^{f_1} S_{P_1}(f)\, df}{(2\pi f_1)^4 m_1^2} \tag{4.14}$$

Although the wind force spectrum is usually broad band, modern tall buildings, being usually flexible and lightly damped (less than 10%), behave like narrow band filters, thus leading to the results of narrow band response output. Therefore, the
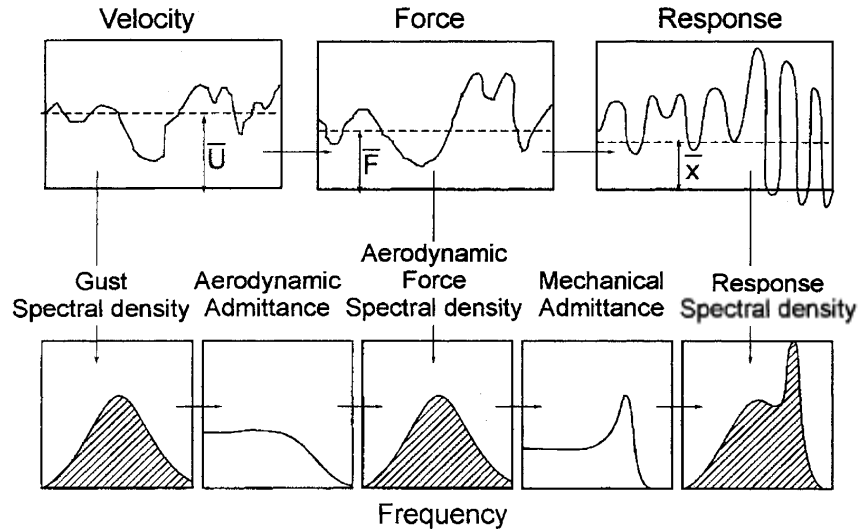
Fig. 4.7 The random vibration or spectral (frequency domain) approach for assessment of dynamic response, after Davenport (1963).

background component of the response can often be neglected (Kwok, 1982). Hence:

$$\sigma_y^2 \approx \frac{\pi f_1 S_{P_1}(f_1)}{4(2\pi f_1)^4 \xi_1 m_1^2} \tag{4.15}$$

so that the standard deviation cross wind response is proportional to $\xi^{-1/2}$. Analogously, the across-wind acceleration ($r = 2$) response may be written as:

$$\sigma_{\ddot{y}}^2 \approx \frac{\pi f_1 S_{P_1}(f_1)}{4 \xi_1 m_1^2} \tag{4.16}$$

4.4.3   Experimental studies on aeroelastic response of tall buildings

Aeroelasticity of tall buildings is mainly related to their across-wind response and to vortex-induced vibration and galloping phenomena. Vortex-induced vibrations and galloping of tall buildings have been investigated through several wind tunnel experiments.

In order to investigate across-wind response of tall buildings in lock-in conditions, wind tunnel model tests were carried out by Kwok and Melbourne (1981) on a circular and a square tower with an aspect ratio of 9 and on a square tower with an aspect ratio of 18. Base-pivoted, elastically mounted, rigid models were used, thus maintaining a straight-line deflection mode. Two boundary layer conditions were tested, corresponding to flow over a suburban area and a city center. The power law exponents of the mean longitudinal wind velocity profile were 0.23 and 0.44, and the longitudinal turbulence intensities at the building top were 0.07 and 0.14 for suburban and the city center conditions, respectively. When tested in city center wind conditions, the h:d:b=9:1:1 square tower did not exhibit any significant lock-in response for values of damping higher than 0.25% of critical. This result was thought to be due to the velocity profile and the high turbulence associated with the city center flow condition. Results for the 18:1:1 square tower in suburban wind model were found to be very similar to those for the 9:1:1 square tower. Fig. 4.8(a)

illustrates the normalized standard deviation across-wind displacement response as a function of reduced velocity, indicated with $\overline{U}(h)/(n_0 b)$, where $\overline{U}(h)$ is the mean wind speed at the top and n_0 is the natural frequency, and of structural damping ξ_s. As the structural damping is reduced, large increases of the lateral response are evident particularly at reduced velocity close to 10. This critical reduced velocity represents the wind condition at which the shedding frequency is close to the transverse natural frequency of vibration (vortex resonance condition).

Normalized across-wind tip response displacement versus structural damping ratio was also investigated [Fig. 4.8(b)]. At reduced velocities far from the critical value and at high values of the structural damping, the response is proportional to functions which lie between $\xi_s^{-1/3}$ and $\xi_s^{-1/2}$. Such dependence agrees with the fact that outside the lock-in conditions, the response is dominated by wake excitation of random nature, and, therefore, it can be adequately described by random vibration theory and is proportional to $\xi_s^{-1/2}$ (see subsection 4.4.2). However, the response increases much more rapidly with decrease in damping when the model operates close to the critical velocity, especially at low damping values. Such departure from the random excitation theory suggests that the enhance in across-wind response associated with a decrease in damping might have caused interdependence between excitation and response which resulted in well correlated forces along the structure. From these results, the authors concluded that it is possible to approximately determine a critical value of the normalized across-wind displacement amplitude above which the lateral response cannot be adequately estimated by using the random excitation theory.

The large across-wind response in Fig. 4.8(b) at a reduced velocity of 24 is believed to be caused by galloping excitation. At a reduced velocity of 15 wake excitation effects and displacement-dependent lock-in were increased by aerodynamic damping (see section 4.4.5) associated with galloping excitation which resulted in a significant response enhance, in particular at low structural damping values.

Kawai (1992) carried out wind tunnel tests on aeroelastic models of rectangular prisms with aspect ratio equal to 10, under smooth flow and turbulent (open terrain and urban) flow conditions and at zero incidence of the oncoming flow. Various side ratios (depth/breadth) were considered: 3/1, 2/1, 1/1, 1/2. In the case of the square prism in smooth flow conditions, it was found that, as the structural damping increases, the onset velocity of the VIV increases slightly, the peak of the vibration amplitude decreases and the velocity range of VIV is narrowed. No evidence of VIV was found for critical damping ratio equal to 0.113. The effect of turbulence on the response was also investigated and systematically discussed. Rather surprisingly, it was observed that for the 1/2 side ratio prism, as turbulence increases, the vortex-induced vibrations strengthen. This result was motivated by the fact that turbulence promotes the entrainment of flow through the separated shear layer to produce the stronger vortex shedding when the shear layer does not reattach on the side face. For deeper sections, on the other hand, as the turbulent level increases, the response reduces. It was, therefore, concluded that the response in turbulent flow corresponds to that for a deeper body in smooth flow.

Experiments from Kawai (1992) were limited to the case where the flow is normal to the windward face. In order to investigate the effect of the angle of attack on the occurrence of VIV and galloping, another series of wind tunnel tests was later carried out on the same building models and flow conditions (Kawai, 1995). Selected
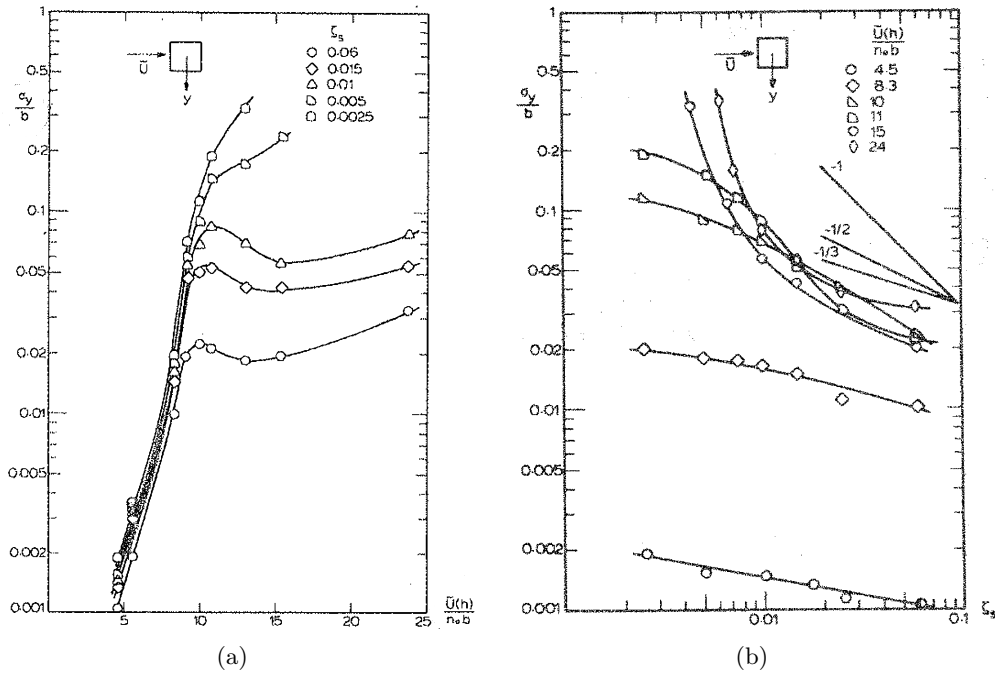
(a)   (b)

Fig. 4.8 Across-wind displacement response of a 9:1:1 square tower model in suburban wind
condition from Kwok and Melbourne (1981): a) normalized response as a function
of reduced velocity for various structural damping ratios; b) response dependence
on structural damping for different reduced velocities.

results, referred to the square section prism, of primary interest in this research, are
shown in Fig. 4.9. It is clear that VIV and galloping vibration are most violent
at zero incidence in both smooth and turbulent flow conditions. As the angle of
attack increases, the vibration amplitude rapidly decreases and the VIV ceases at
the ordinary damping level. It has to be clarified that the y direction in Fig. 4.9
means across-wind direction when the wind is normal to the windward face.

Boggs (1992) performed wind tunnel tests on an 8:1:1 building model. The wind
profile corresponded to suburban environment and was characterized by a power law
exponent of 0.22 and turbulence intensity at model height of approximately 0.09.
One rigid model and two pivoting-type aeroelastic models were used in order to
make comparisons between aerodynamic and aeroelastic results. Several values of
the mass ratio, corresponding to ratio of the generalized mass to the moment of
inertia of displaced air, were considered. The mass ratio can be written as:

$$\text{mass ratio} = \frac{3J}{\rho D^2 H L^2} \tag{4.17}$$

where J is the generalized mass (equal to the moment of inertia about the center
of rotation), ρ is the air density, D is the side dimension, H is the model height,
L is the length from tip to center of rotation, according to the notation used in
Boggs (1992). Comparisons between aerodynamic and aeroelastic results for two
values of the damping ratio and four mass ratios are displayed in Fig. 4.10. They
are given in terms of RMS moment coefficient $\tilde{C}_M$, normalized tip deflection $\frac{\tilde{\delta}}{D}$
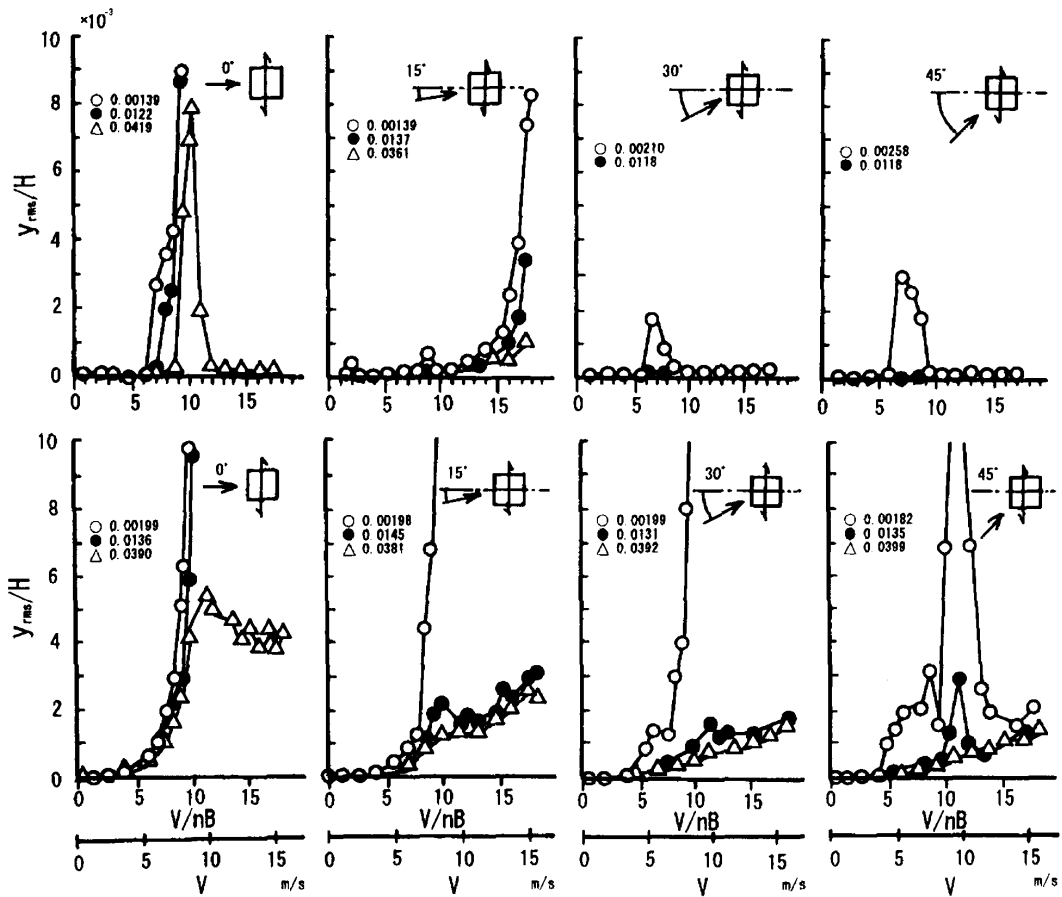and aeroelastic magnification factor AMF. The predicted RMS moment coefficient

Fig. 4.9 RMS response in y direction of a 10:1:1 prism for various angles of incidence: (top) smooth flow; (bottom) turbulent flow (urban, power law exponent, $\alpha = 0.3$). Numerical values beside the symbols show the critical damping ratio Kawai (1995).

was computed from hypothetical natural frequencies and damping ratios using the random vibration approach (subsection 4.4.2), according to the following equation:

$$\tilde{M}^2 = \int_0^\infty |H_M(f)|^2 \, S_M(f) \, df \qquad\qquad (4.18)$$

while, in the aeroelastic models the RMS moment coefficient was directly measured by the balance. Displacements were not measured directly, but were computed from the RMS moment coefficient for both the aerodynamic and aeroelastic models. Finally the aeroelastic magnification factor was defined as the ratio between the aeroelastic RMS normalized displacement and the aerodynamic one, allowing immediate comparison between the two results. It can be readily observed that the distance between the observed response and the predicted one may become quite large as the reduced velocity $U/f_0 D$ exceeds the critical value for vortex shedding, in particular for the lower mass ratios and damping. Furthermore, the AMF was plotted for two reduced velocity values (8 and 12) as a function of both aerodynamic and aeroelastic RMS normalized displacement and the product of density and damping (Fig. 4.11). This last parameter, similar to the Scruton number was selected as that describing best the observed-predicted response distance, producing the least scatter and defining a functional relationship with the AMF.

Marukawa et al. (1996) conducted wind tunnel tests of tall buildings, using a 1/500 scale aeroelastic stick model. The side ratio was varied in the range 0.33-3 and the aspect ratio was varied from 4 to 6. The simulated wind conditions corresponded to a mean velocity profile with a power index of 1/6 and the turbulence intensity at model height was 10.7%. The oncoming wind velocity range was 1-40 m/s.

The relation between the normalized standard deviation of the response displacement (measured by means of two laser displacement transducers) and the reduced velocity was investigated in both along and across-wind directions. According to the authors' observations, the standard deviation of the response increases in proportion to the power of 2.5 of wind velocity in the along-wind direction within the entire range of the wind velocities tested. On the other hand, in the across-wind direction, the standard deviation of the response displacement increases in proportion to the power of 2.5 to 3 of wind velocities, only for values of the reduced velocities not exceeding 8. Moreover, for the square section cylinder (side ratio equal to 1), an increase in the structural damping ratio was seen to lead to a decrease in the gradient of the displacements to wind velocities in both along and across-wind directions.

Aspect ratio was found to affect the response gradient, too. In particular, a higher aspect ratio of the model resulted in greater power index increase in the across-wind direction, while in the along-wind direction, there was scarcely any change. Motivated by their strict correspondence with tests conducted in this research, in Fig. 4.12 some selected results from Marukawa et al. (1996) are reported. They illustrate the above mentioned normalized response displacement for different values of the structural damping ratio and refer to a 6:1:1 square model at zero incidence.

Cheng et al. (2002) conducted aeroelastic tests in a boundary layer wind tunnel, aimed at studying the across-wind response and aerodynamic damping (see subsection 4.4.5) of isolated square-section high-rise buildings. Two boundary layer flows, BL1 and BL2, were generated in order to represent open terrain and urban terrain conditions, respectively. The exponent of the power law of the mean velocity profile
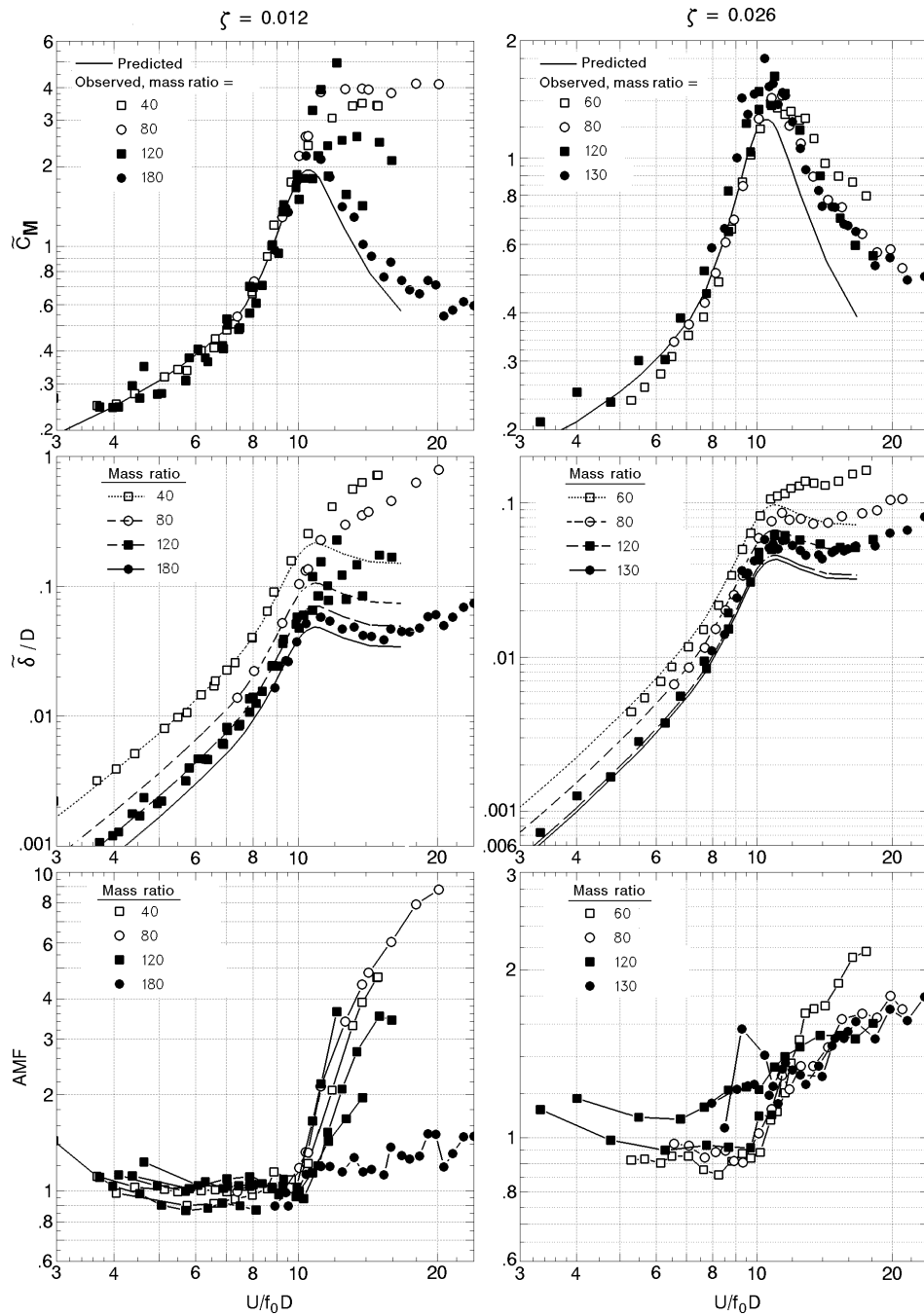
Fig. 4.10 Predicted (aerodynamic) and observed (aeroelastic) response of a 8:1:1 building as a function of reduced velocity for two damping values and four mass ratios (Boggs, 1992).
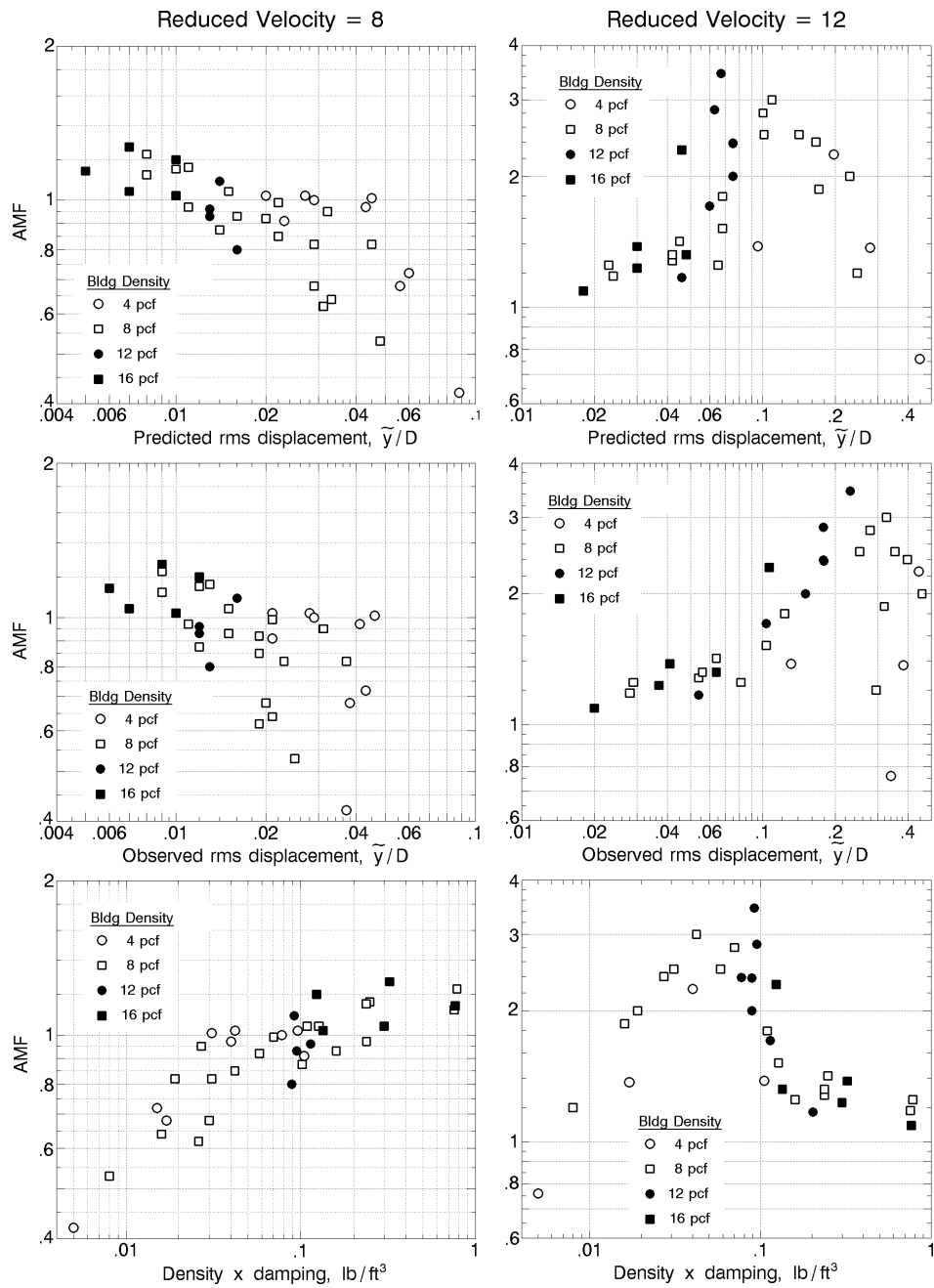
Fig. 4.11 Aeroelastic magnification factor as a function of various parameters for a 8:1:1 building at reduced velocities 8 and 12 (Boggs, 1992).
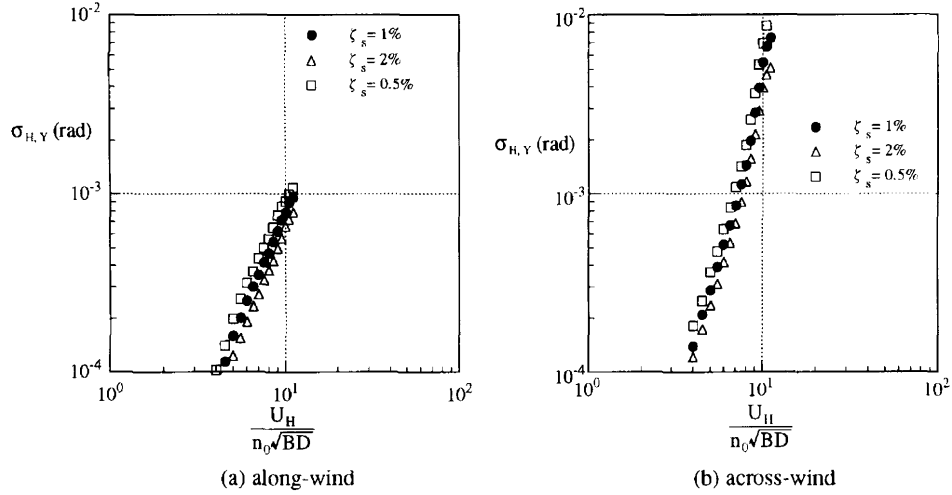
Fig. 4.12 Normalized standard deviation response displacement of a square section cylinder (H/B=6, B/D=1) with reduced velocity for different damping ratios in along and across-wind directions (Marukawa *et al.*, 1996).

α was equal to 0.15 for BL1 and 0.32 for BL2. The turbulence intensity varied from 20% near the ground to 3% at gradient height in BL1 and from 35% to 6% in BL2. A 7:1:1 rigid body base-pivoted aeroelastic model was considered, having two sway modes of vibration. Three structure densities equal to 151, 198 and 231 kg/m^3 were used and the structural damping ratio ξ_s varying from 0.4% to 6% was provided by an oil damper device at the model base. The following mass-damping coefficient M_D was chosen as the experimental controlling parameter:

$$M_D = \frac{\int_0^h m(z)\phi_i^2(z)\,dz}{\int_0^h \phi_i^2(z)\,dz} \frac{\xi_s}{\rho D^2} \qquad (4.19)$$

By using the definition of the Scruton number given in Eq. (4.3) and from the definition of the equivalent mass per unit length in Eq. (4.4), it can be easily observed that M_D is equal to $Sc/(4\pi)$ (D in Eq. (4.19) indicates the side dimension). Figs. 4.13 and 4.14 illustrate the RMS normalized across-wind responses in BL1 and BL2, respectively. The measured aeroelastic responses (circles) are compared with the aerodynamic ones (dashed lines), calculated from force spectra, and with the ones predicted from force spectra but having added the aerodynamic damping contribution (solid lines) [see subsection 4.4.5].

In BL1 three regions were defined for the across-wind response based on the M_D values. For $M_D \geq 6.28$, called *aerodynamic stable* region [Fig. 4.13(a)], the RMS tip across-wind response displays maximum value at a critical velocity approximately equal to 11. This maximum slightly increases when the mass-damping parameter decreases. The predicted response based on force spectra is in good agreement with the measured aeroelastic one for velocity values lower than the critical wind speed, while, for higher values of wind velocities the predicted response exceeds the measured one, showing that aeroelasticity plays a reducing effect on the across-wind response (positive aerodynamic damping). For $2.76 \leq M_D \leq 5.82$, *aerodynamic unstable* region [Fig. 4.13(b)], the predicted response merges with the measured one up to a reduced velocity of 8, while for higher values, the measured response exceeds the predicted

one. This aeroelastic magnification effects (negative aerodynamic damping) becomes stronger as M_D decreases. For even higher velocity values, above the critical wind speed, aeroelastic effects gradually weaken and the measured response meets the predicted one. Lastly, for $M_D \leq 2.18$, region of *aerodynamic divergence* [Fig. 4.13(c)] the across-wind response becomes even an order of magnitude greater than in the previous two regions. For reduced velocity less than 10, measurements form aeroelastic tests are approximately equal to predictions based on the across-wind force spectrum, while for reduced velocity greater than 10, a significant aeroelastic phenomenon occurs. For models with $M_D = 2.18$ and 1.54 the across-wind response increases monotonically with wind speed well beyond the critical vortex shedding value. At even higher reduced velocities the measured response is seen to decrease rapidly towards the predicted values. For low values of the mass-damping coefficient the across-wind galloping occurs and response diverges. As a matter of fact, the high values of aeroelastic responses observed well after lock-in conditions, where the shedding frequency identifiable from spectral analysis was well greater than the natural frequency of vibration, were attributed to galloping excitation. Examining different values of the mass-damping parameter, the authors identified the model's lock-in velocity U_{crit} and the critical velocity for galloping U_g and concluded that for a square-section building galloping does not trigger spontaneously at the critical galloping velocity. Instead, it is initiated by vortex resonance, i.e. when $U_{crit} \geq U_g$, galloping is delayed until vortex shedding resonance happens. On the other hand, if $U_{crit} < U_g$, vortex shedding resonance will trigger and accelerate the galloping excitation.

The across-wind responses measured in BL2 (Fig. 4.14) indicate that there is no peak value or resonance-then-galloping phenomenon, regardless of the mass-damping parameter value. The presence of high turbulence damps the aeroelastic effect and the predicted response is never lower than the aeroelastic one (positive aerodynamic damping).

4.4.4 Literature approaches for modeling aeroelastic across-wind response of structures

This section is intended to provide a brief description of some different approaches used in literature to deal with the aeroelastic response of structures. In the case of high-rise buildings this response, especially in the across-wind direction, can significantly differ from that estimated solely from lift force data from rigid model tests.

Even if the across-wind excitation mechanisms, namely the wake, incident turbulence and motion-induced forces, are separately identifiable, they often superimpose in causing the response. This is, probably, the main reason why a generalized analytical method for predicting across-wind vibrations of structures is still not available.

Holmes (1998) critically reviewed the commonly used methods for estimating across-wind responses of structures due to vortex shedding. They can be divided into two main classes:

- sinusoidal or harmonic excitation models,

- random excitation models.

Sinusoidal excitation models are based on the assumption that the vortex-shedding phenomenon generates near-sinusoidal cross wind forces. With reference to circular
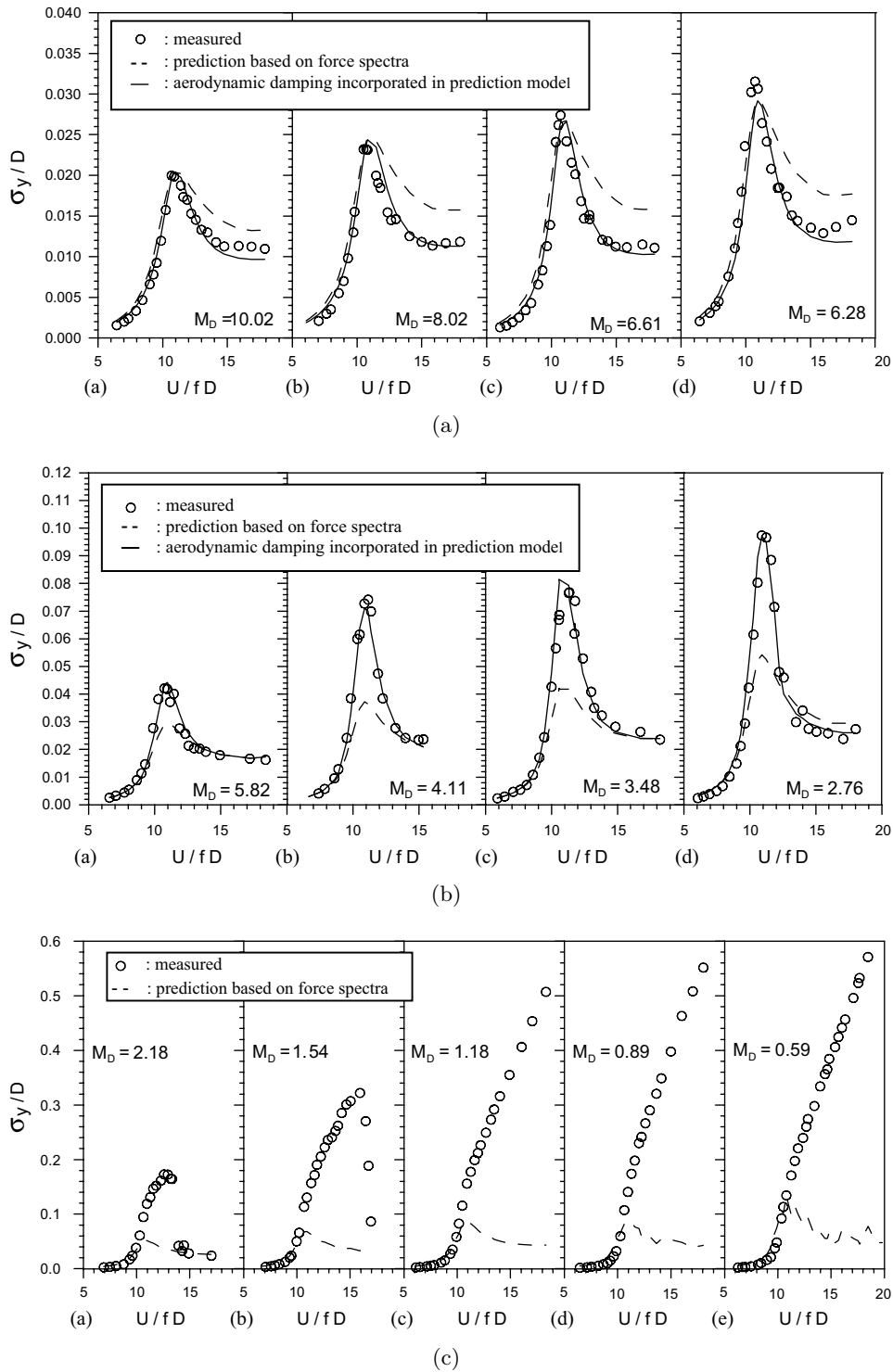
Fig. 4.13 Measured and predicted across-wind response of versus reduced velocity in BL1 from Cheng *et al.* (2002): a) $M_D \geq 6.28$; b) $2.76 \leq M_D \leq 5.82$; c) $M_D \leq 2.18$.
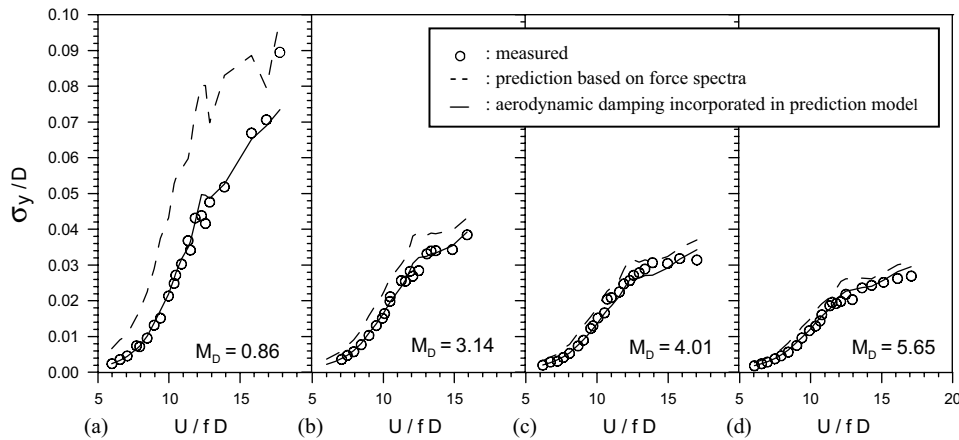
Fig. 4.14 Measured and predicted across-wind response of versus reduced velocity in BL2 from Cheng *et al.* (2002).

cylinders, this assumption is mostly related to the work of Scruton and co-workers in the 1950s and 1960s (Scruton, 1981). Sinusoidal models provide good estimates when large vibrations occur and the shedding has effectively locked-on to the across-wind motion of the structure. Ruscheweyh modified the basic sinusoidal model by the use of a correlation length, which takes into account that the vortex shedding mechanism is not uniformly distributed along the cylinder axis (Ruscheweyh, 2010). Because of lock-in, the exciting force has its maximum at the point of antinode of the mode shape. For a cantilever, for example, it is near the top[3] and for a simple supported beam it is in the mid span. The correlation length, which increases with vibration amplitude, serves the fact that vortex shedding forces are applied over a height range less than the total height of the structure.

Random excitation or spectral model was originally suggested by Vickery and Clark (Vickery and Clark, 1972) and further refined by Vickery and Basu (Vickery and Basu, 1983). In the case of random vibration, as seen in subsection 4.4.2, the response is inversely proportional to the square root of the damping, whereas in the case of sinusoidal excitation model, the peak response is inversely proportional to damping.

Eurocode 1 (UNI-EN 1991-1-4, 2005) proposes two approaches for predicting vortex-induced vibrations of structures. The first one is based on the vortex-resonance or sinusoidal model and the second one on the spectral model. The spectral model is also used in the Canadian and the Danish wind code and in the CICIND model code for chimneys.

Davenport and Novak (1976) proposed a two-stage vibration model for vortex-induced vibration, namely, random excitation and harmonic excitation stages. When the building tip vibration amplitude, in random excitation, exceeds 2% of the building width, harmonic excitation takes over.

On the basis of their experimental results, previously discussed, Kwok and Melbourne (1981) proposed a prediction procedure which consists of a random excitation model and a sinusoidal lock-in excitation model. When lock-in becomes significant, in fact, the response can be considered proportional to ξ_s^{-1}, rather than $\xi_s^{-1/2}$, as in

---

[3]At the free end of a cantilever, three dimensional flow around the top, tip effect, contrasts the vortex shedding and moves below the top the maximum of the exciting force.

the case of wake excitation. The selection of the excitation model to be used in the prediction process is determined by a critical across-wind displacement amplitude above which lock-in dominates the response. In suburban turbulent boundary layer flow, this was found to be approximately 0.025 of the side for a 9:1:1 square tower. Across-wind response predicted by these models was found to agree well with the measured response.

A number of researchers (Reinhold and Sparks, 1979; Kwok and Melbourne, 1981; Tschanz, 1982b; Kareem, 1982) have demonstrated conditions for both valid and invalid aerodynamic results for specific cases by comparing the results of aeroelastic and aerodynamic models of the same building. These researchers have not provided quantitative or general limits on conditions for validity and even the parameters of most significance have not been agreed upon. It may be stated, for example, that sufficient, but not necessary conditions, for the validity of the aerodynamic method for the response estimation, are that the reduced velocity be less than a critical value for vortex shedding, while others may demonstrate valid results provided the rms tip displacement (affected by varying the damping) is below a certain critical value. The effect of other parameters, including building density, building shape and boundary layer characteristics, have not been studied systematically, jet. Boggs (1992), as illustrated in subsection 4.4.3, compared aerodynamic (predicted) and aeroelastic (observed) response of an 8:1:1 square cylinder in a simulated suburban environment and showed that the reduced velocity, in conjunction with a mass-damping parameter, provides a good characterization of the *aeroelastic magnification factor (AMF)*, computing the distance between aeroelastic and aerodynamic responses.

4.4.5 Aerodynamic damping

The study of the aeroelastic behavior of structures can be addressed following different approaches, like that of flutter derivatives. In this study, however, the model of aerodynamic damping is used to deal with aeroelastic effects in tall buildings response. The generalized load, $P_j(t)$ in Eq. (4.8), may be dependent on the structure's response, so it should be written as:

$$P_j\left(t, q, \dot{q}, \ddot{q}\right) \tag{4.20}$$

The presence of q and its derivatives on the right side of Eq. (4.8) represents *aeroelastic feedback*, rendering the equation nonlinear. Depending on the phase of the force with respect to the motion, aeroelastic or motion-induced forces can be associated with the displacement, the velocity or the acceleration of the structure. Because of these associations, aeroelastic forces can be regarded as "aerodynamic contributions" to stiffness, damping and mass, respectively. They are therefore referred to as aerodynamic stiffness (in phase with displacement), aerodynamic damping (in phase with velocity), aerodynamic mass (in phase with acceleration).

In addition to inducing phase-related forces, the motion of a structure may influence the nature of those forces which already exist on the stationary body. The increase in correlation of the across-wind load with increasing amplitudes of vibration, discussed in section 4.3, is an example of this. Furthermore, aeroelastic effects can couple modes that are not coupled structurally.

Aeroelastic contributions to the overall aerodynamic loading are distinguished

from other unsteady loads by recognizing that aeroelastic loads vanish in absence of structural motion.

Aerodynamic mass and stiffness are not, normally, of great significance, except for very large light structures, such as large span roof systems and, to a lesser extent, bridges (Vickery, 1990).

Several methods have been used in order to estimate aerodynamic damping, using wind tunnel tests on aeroelastic models. They include, for example, the auto correlation function technique, the half power band width technique, the random decrement (RD) technique (Marukawa *et al.*, 1996). Other authors, e.g. Cheng *et al.* (2002), have estimated aerodynamic damping through an inverse approach by adjusting the damping value so that the aerodynamic response calculated from rigid model tests would have equaled the one measured from aeroelastic tests.

It is well known that along-wind aerodynamic damping is often small and positive and almost linearly increasing with the reduced velocity. Neglecting its effect in the response estimation is, therefore, conservative. Across-wind aerodynamic damping, however, may be negative and large for high wind speeds or large building displacements. This gives rise to a certain aeroelastic magnification, invalidating the response calculated using the aerodynamic method (Boggs, 1992).

Various studies have been dedicated to the identification of the aerodynamic damping of prisms. Here some results concerning aerodynamic damping of 3-D prisms are illustrated, with particular reference to the across-wind response of square-section prisms.

Marukawa *et al.* (1996) employed the RD technique to evaluate the aerodynamic damping ratio from the time series of the response displacement, using the stick aeroelastic models previously cited. The effect of side ratio, D/B, aspect ratio, H/B, and structural damping on aerodynamic damping, varying with reduced velocity, was investigated for both along-wind and across-wind directions.

The aerodynamic damping ratio observed in the along-wind direction was almost always positive. For side ratios lower than 1, the smaller the side ratio, the higher the aerodynamic damping ratio, while, for higher side ratios, no clear effect was found of the latter on aerodynamic damping. It increased, in most cases, monotonically with reduced wind velocities. For the square section model the observed values are smaller than those estimated by quasi-steady theory. No clear effect of aspect ratio on aerodynamic damping was found in along-wind direction. Fig. 4.15 illustrates the effect of structural damping on aerodynamic damping for the square section 6:1:1 model. For reduced wind velocities lower than 10, the smallest aerodynamic damping ratio was identified for 1% structural damping ratio. For reduced velocities beyond 10 and a structural damping of 0.5%, the aerodynamic damping ratio increased rapidly with reduced velocity.

Concerning the across-wind direction, models with side ratio lower than 1 showed positive aerodynamic damping at low wind velocities and negative values for higher speeds. The least reduced velocity value at which the negative aerodynamic damping ratio was observed was about 10 for the square section, 7 for side ratios of 0.5 and 0.33. The wind velocities from which positive aerodynamic damping changed to negative was much lower than the onset wind speed for galloping excitation. For side ratios greater than 1, positive aerodynamic damping ratios were observed for the entire range of tested wind speeds.

In across-wind direction, the wind velocity at which the aerodynamic damping
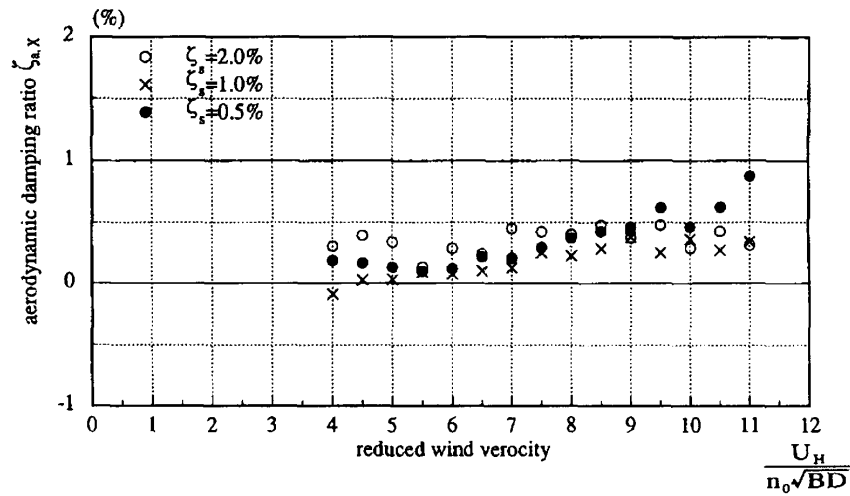
Fig. 4.15 Effect of structural damping ratio on aerodynamic damping ratio in along-wind direction for a 6:1:1 (D/B=1, H/B=6) square cylinder (Marukawa *et al.*, 1996).
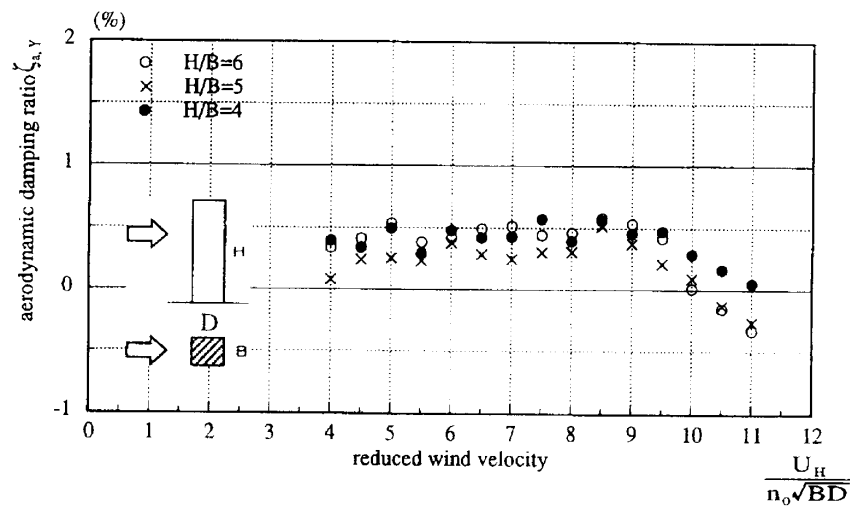

Fig. 4.16 Effect of aspect ratio on aerodynamic damping ratio in across-wind direction for a square cylinder with 1% structural damping (Marukawa *et al.*, 1996).

ratio changes from positive to negative is influenced by aspect ratio (Fig. 4.16). The wind speed where aerodynamic damping becomes negative increases as the aspect ratio decreases. This trend is believed to be related to the weaker Strouhal component of the power spectral density observed for smaller aspect ratios.

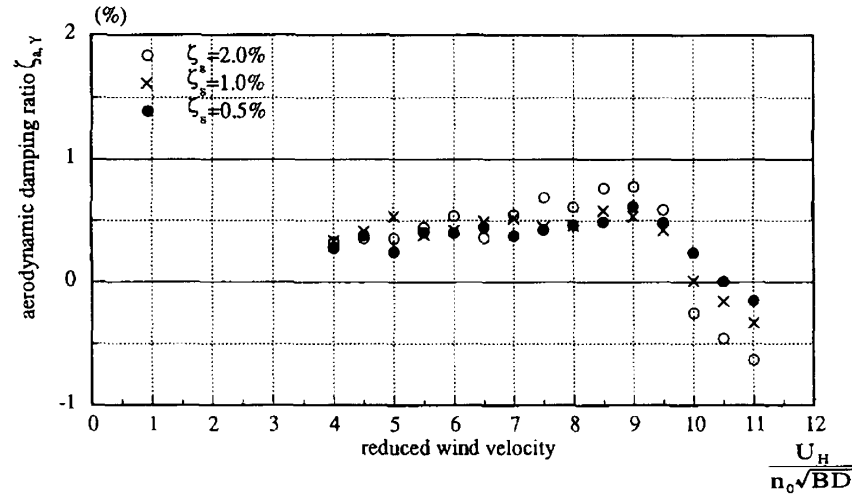In the across-wind direction, moreover, as depicted in Fig. 4.17, referred to the

Fig. 4.17 Effect of structural damping ratio on aerodynamic damping ratio in across-wind direction for a 6:1:1 (D/B=1, H/B=6) square cylinder (Marukawa *et al.*, 1996).

6:1:1 square section model, for reduced velocities lower than 9, positive aerodynamic damping ratio increases with structural damping ratio, while for higher reduced velocities, decreases more rapidly. The wind velocity at which aerodynamic damping becomes negative decreases with increasing structural damping.

With reference to the experimental results illustrated in subsection 4.4.3, Cheng *et al.* (2002) identified across-wind aerodynamic damping of a 7:1:1 building in open terrain (BL1) and urban terrain (BL2) conditions. Considering that the total damping of an aeroelastic system ξ_{tot} consists in the sum of the structural damping ξ_s and the aerodynamic damping ξ_a, the latter was identified through an 'inverse response approach'. First, the structural damping ratio of the aeroelastic model was determined, then the total damping was estimated adjusting it numerically so that the calculated response, based on the across-wind force spectra, was equal to the measurements. The aerodynamic damping was then calculated as the difference between total damping and structural damping. The inverse response approach based on the stochastic across-wind load was considered no longer valid in the aerodynamic divergence region, when the occurrence of galloping led from narrow bandwidth random to sinusoidal oscillations.

Fig. 4.18 shows the identified aerodynamic damping values as a function of the reduced velocity and the fitted curves proposed by the authors in order to derive an empirical aerodynamic damping model. In BL1 for $M_D \geq 6.28$ [Fig. 4.18(a)] aerodynamic damping is almost zero at the critical velocity and positive elsewhere. It is slightly influenced by the mass-damping parameter. The empirical model proposed by the authors is a function of the reduced velocity only. In the aerodynamic unstable region [Fig. 4.18(b)] aerodynamic damping becomes negative when the reduced velocity is greater than 8. Afterwards it reaches a minimum value around the critical velocity causing a maximum across-wind response. Aerodynamic damping in this
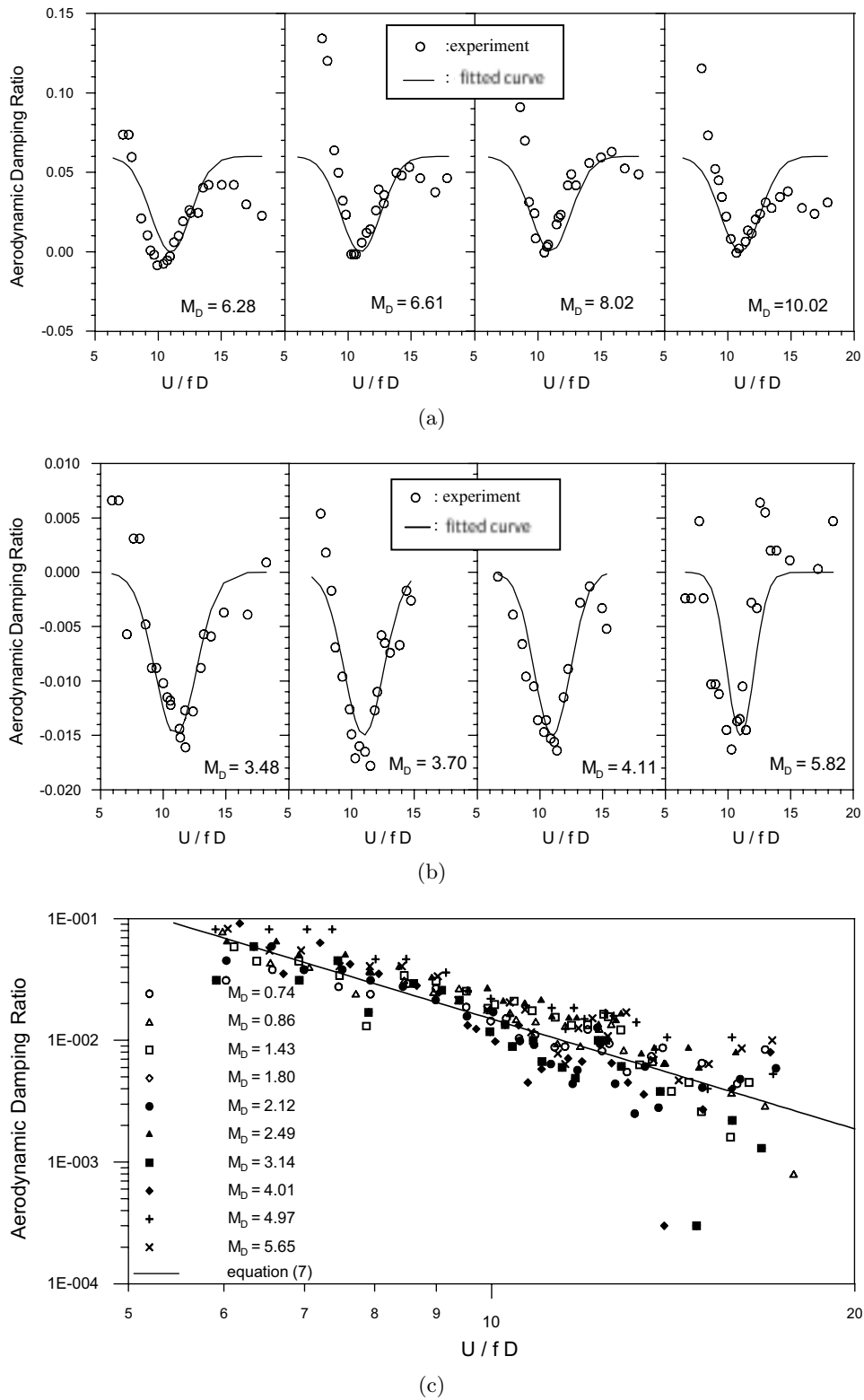
(a)

(b)

(c)

Fig. 4.18 Across-wind aerodynamic damping identified by Cheng *et al.* (2002): a) open terrain (BL1), $M_D \geq 6.28$; b) BL1, $2.76 \leq M_D \leq 5.82$; c) urban terrain (BL2).

region is influenced by both reduced velocity and mass-damping parameter. The empirical model proposed accounts for both these quantities. In BL2 [Fig. 4.18(c)] aerodynamic damping is always positive and proportional to -3 power of reduced velocity. The effect of the mass-damping parameter is negligible. The across-wind response of a high-rise building in this region can be conservatively estimated from the lift force spectrum. The authors, finally, showed that incorporating the identified aerodynamic damping values the response calculated from across-wind force spectra was in good agreement with the measured values.

Gu and Quan (2004) performed wind tunnel tests on a 6:1:1 base-pivoted aeroelastic model. Four kinds of wind conditions, corresponding to categories A, B, C, D, were simulated in the wind tunnel at a length scale of 1/500, according to the Chinese code (GB50009-2001, 2001). The exponents of the mean speed profiles for these categories orderly were 0.12, 0.16, 0.22, 0.30. The longitudinal turbulence intensities at the model top (0.60 m) were about 6.8%, 7.3%, 10% and 14% for the four categories of terrain, respectively. Four different values of the structural damping ratio, $\xi_s = 0.6\%$, 1.2%, 1.88%, 2.17%, were achieved in the wind tunnel, by selecting damping plates with different sizes [see also Quan *et al.* (2005)]. Fig. 4.19 shows the aerodynamic damping ratio ξ_a, identified with the time-averaging random decrement technique, as a function of the reduced velocity $U/(f_1 B)$ in the across-wind direction. Fig. 4.19(a) shows the variation of the aerodynamic damping with the terrain category. Under the conditions of terrain categories A, B and C, for reduced velocity lower than 9, ξ_a is positive and increases with reduced velocity. With a further increase in reduced velocity the aerodynamic damping suddenly decreases and changes from positive to negative values at a reduced velocity between 10 and 11. For terrain category D, however, ξ_a is always positive and its maximum value is much smaller than those under the first three terrain conditions. Fig. 4.19(b) depicts the variation of the aerodynamic damping ratio ξ_a with the structural damping ratio ξ_s under the terrain C conditions. The absolute values of ξ_a, in general, decrease with increasing structural damping. It may be observed that results from Gu and Quan (2004) are in evident agreement with those from Marukawa *et al.* (1996), illustrated before.

4.5   Summary and main remarks

In this chapter the wind-induced response of tall buildings is discussed, illustrating how aeroelastic effects can play an important role especially in the across-wind response of buildings. Aeroelastic phenomena, arising from the interaction between aerodynamic loads and structural deformations, are not negligible for lightweight, low damped, slender structures. In this case, motion-induced effects have to be carefully taken into account for a proper assessment of the responses induced by the wind action, in order to perform, for example, the serviceability design of the structures or to evaluate the comfort level of their occupants.

A vibrating structure, under the vortex shedding action, experiences the aeroelastic phenomenon known as lock-in when the dominating shedding frequency synchronizes with the natural frequency in the transverse direction. This phenomenon gives rise to the so-called Vortex-Induced Vibrations (VIV).

The movement of a structure immersed in an air flow can also affect the correlation structure of pressures.

The common used method for estimating the response of structures to aerody-
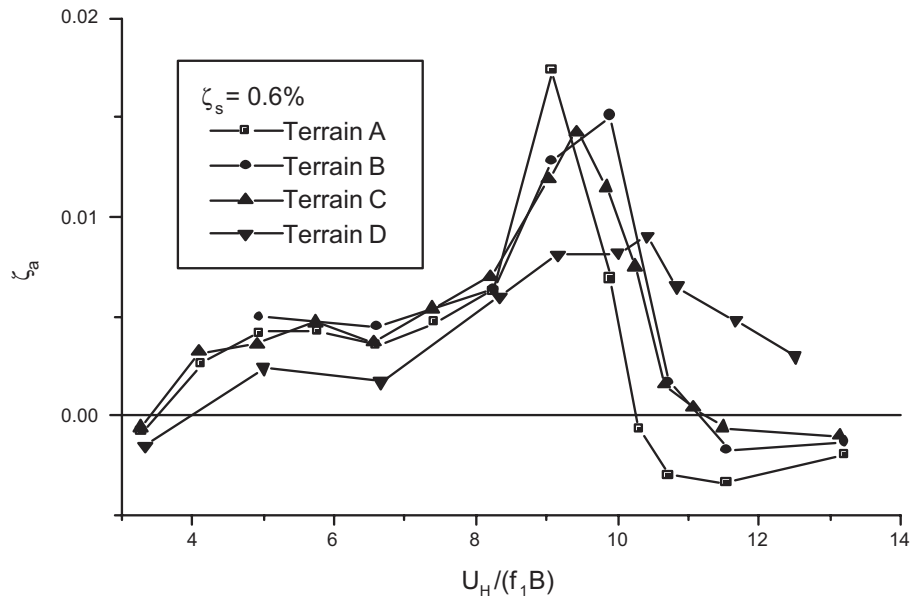
(a)
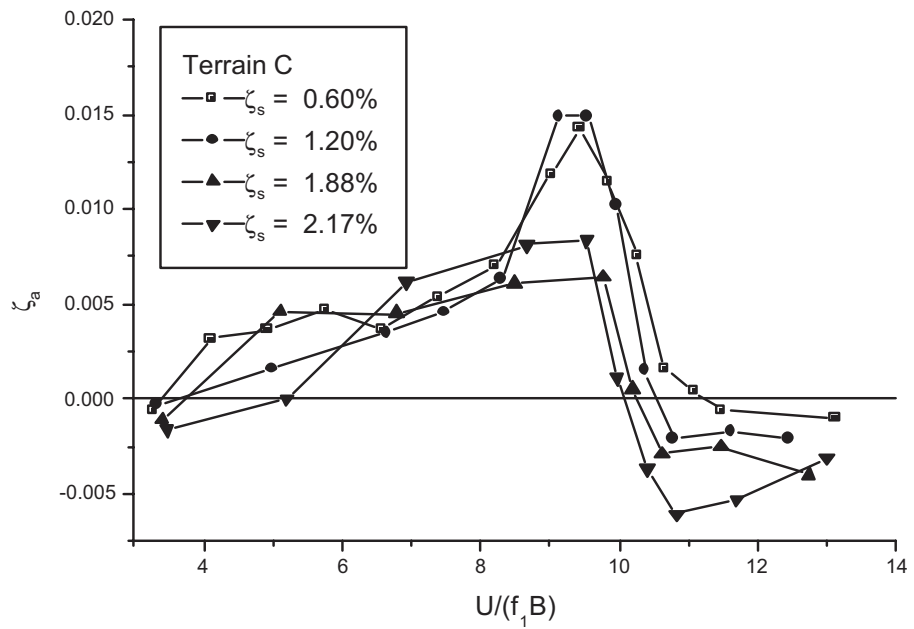
(b)

Fig. 4.19 Across-wind aerodynamic damping versus reduced velocity: a) variation of aerodynamic damping ratio with different terrain categories; b) variation of aerodynamic damping ratio with different structural damping ratios.

namic loads, neglecting aeroelastic effects is discussed. It leads to an approximate estimation of the standard deviation response which is proportional to $\xi^{-1/2}$, where ξ is the damping ratio.

Many literature studies have been devoted to the experimental evaluation of the across-wind response of buildings by means of aeroelastic models, often stick-type models. The across-wind response is usually evaluated in terms of the normalized standard deviation of the tip displacement, which shows a rapid increase at the critical reduced velocity. The latter, being the inverse of the Strouhal number, is approximately equal to 10 for a square section prism. The literature studies illustrated mostly refer to buildings with geometric and dynamic features similar to those of the structure tested in this work. Only in a few literature works the lateral response of square-section prisms, in turbulent flow conditions, was experimentally measured for various angles of incidence and a wide range of wind speeds including the synchronization range. Results from Kawai (1995) are reported in this chapter and will be used in chapter 8 as an illustrative example for the vulnerability analysis of tall buildings.

Different approaches exist in literature for modeling the aeroelastic across-wind response of structures.

The approach based on the aerodynamic damping is used in this work for the identification of aeroelastic effects on the across-wind response of tall buildings. Across-wind aerodynamic damping values identified in some literature works are discussed in this chapter. Differently from the along-wind aerodynamic damping which is often small, positive and linearly increasing with reduced velocity, across-wind aerodynamic damping may be negative and large for high wind speeds or large displacements.

Some experimental evidences are that across-wind aerodynamic damping is affected by the aspect ratio and structural damping of vibrating square-section prisms; at reduced velocities close to the critical value, aerodynamic damping is often observed to pass from positive to negative values; mass-damping characteristics (Scruton number) can define different aerodynamic damping conditions; turbulence of the approaching flow affects identified aerodynamic damping values; positive aerodynamic damping has been observed in high turbulence conditions at all tested reduced velocities, including the critical value.

Chapter 5

The role of wind tunnels in the prediction of tall buildings response

5.1 Introduction

The complete theoretical prediction of the wind-induced structural response is not feasible. The analytical modeling of wind-structure interactions is mathematically impracticable. Although recent advances in computational fluid dynamics are very promising, these are not at a stage of being a designer's tool, yet. Therefore, wind tunnels have served as the most reliable means of investigating the wind action effects on structures. Experimental techniques in common use can be categorized in the two following broad classes:

- rigid models;

- aeroelastic models.

In the case of rigid models (section 5.2), which are only geometrically scaled, the motion of the prototype is predicted by theoretical methods with the motion-induced forces either being ignored or estimated from existing data. Aeroelastic models (section 5.3) are geometrically and dynamically scaled and responses may be directly measured and transposed to prototype scale.

An exhaustive description of the practicable wind tunnel simulations can be found in ASCE (1999) and in Alan G. Davenport Wind Engineering Group (2007). In the following sections only a brief portraiture of them is given with particular reference to aeroelastic simulations of tall buildings. Scaling requirements for aeroelastic models of tall buildings are also illustrated.

5.2 Rigid model techniques

On structures or elements where aeroelastic effects, such as aerodynamic damping, are judged to be not significant, the overall external wind loads can be studied using rigid models, also referred to as *static* or, sometimes, even as *stationary* models, with geometrically scaled external features. The mean and dynamic wind-induced aerodynamic loads may be obtained by using different methods, basically including

High-Frequency-Force-Balance (HFFB) technique (subsection 5.2.1) and integration of surface pressures (subsection 5.2.2). Structural responses, e.g. deflections and accelerations, my be evaluated in *time domain*, using stored time-histories of the aerodynamic loads or, more commonly, in *frequency domain*, using power spectral densities of the applied modal wind loads and assuming steady-state conditions (ASCE, 1999).

5.2.1   High-Frequency Force Balance Tests

The High-Frequency Force Balance (HFFB) technique, first reported by Tschanz (1982a), is founded on an earlier approach proposed by Whitbread (1975). The technique, also known as High-Frequency Base Balance (HFBB), is based on the use of a very stiff high-frequency balance-model system that models only the exterior geometry of the structure. For this reason the HFFB technique can be employed at a stage in the design when only the exterior geometry of the structure has been decided. While with aeroelastic simulations (section 5.3) the measured quantity is the final response, the base balance technique allows direct measurements of good approximations to the steady and unsteady modal forces acting in the fundamental sway and torsional modes of vibration of the building.

The dynamic responses, including resonant amplification at the natural frequencies of the building, are derived analytically for each mode using random vibration analysis methods (subsection 4.4.2) and are subsequently used to estimate the full scale responses. Changes in the structural properties can be easily accommodated by iteration of the analytical procedures. Parametric studies, in which the responses are predicted as functions of the structural parameters, are often feasible. Furthermore, it is unnecessary to retest a new wind tunnel model unless significant changes in the exterior geometry are made. These reasons make the HFFB tests a widely accepted technique for wind tunnel model studies and a relatively economical and expeditious alternative to the aeroelastic model simulations.

The idea of measuring the modal force spectrum and then calculating the responses had been considered prior to the current base balance technique. Saunders and Melbourne (1975) attempted to record the modal spectrum by measuring it as seen through the mechanical admittance of an aeroelastic model. By knowing the model properties, reverse calculation yielded the modal spectrum which could then be combined with the desired structural properties. Major difficulties with this procedure are the errors introduced through aeroelastic model properties, in particular the damping estimation.

The fundamental assumption of the base balance technique is that the generalized or modal forces from the wind can be estimated from the measured base forces and moments experienced by a stationary model. The generalized or modal force is defined as the integral of the applied force weighted by the mode shape at the point of application. The three base moments, measured, for example, by a three component HFFB, including two overturning moments and the base torque, represent direct and exact measurements of the modal forces only when all the following conditions are met (ASCE, 1999):

1. The first three natural modes of the structure are decoupled and geometrically orthogonal in two sway directions and one twist direction.

2. The fundamental bending mode shapes are linear functions of height and piv-

oted at a point where the moments are measured.

3. The fundamental torsional mode shape is a constant (independent on height) over the height of the structure.

4. There are not significant motion-induced forces involved, so that the nature of the forces remains the same on a vibrating structure as it is on a rigid structure.

5. The balance-model system is substantially rigid, with a high natural frequency, so that the measured moments are not significantly amplified by the mechanical admittance of the system in the frequency range of interest.

6. The contribution to the response of the structure from higher modes is negligible.

In practice these requirements are never fully met and adjustments of the technique are needed for its proper application.

If the balance-model system responds dynamically to the wind-loading, then the measured base moments will include the *inertial loading effects* of the system itself. If the motions are large, then the aerodynamic interaction of the model with the wind could also contaminate the measurements. Therefore an attempt is made to take the balance-model system as rigid as possible, while being sensitive enough. In this way, it is ensured that the frequency range of interest falls at the low end of the mechanical admittance function where the dynamic amplifications are small. In cases where the natural frequency cannot be raised sufficiently high and the balance measurements are amplified, adjusting the spectral density is possible, in principle, providing the mechanical admittance of the system is well identified and may be treated as linear and uncoupled.

It must be checked in fact that the balance-model frequency is high enough to neglect the model motion (ASCE, 1999). In practice, however, it is difficult to avoid oscillatory movements of the model, which, together with intrinsic data acquisition system noise, might have a negative impact in the validity and/or accuracy of the measurements. A rough estimation of the magnitude of the inertia loads may be done calculating the acceleration from the amplitude of vibration and the oscillatory frequency and then multiplying it with the mass of the model (González *et al.*, 2011).

For buildings with uncoupled linear mode shapes, the generalized wind forces are equal to the measured base overturning moments and building dynamic responses can be exactly estimated directly solving a set of generalized equations of motion (see subsection 4.4.2). The evolution of tall buildings design and modern architectural forms towards irregular and elongated building shapes, illustrated in section 2.1, results in buildings having significantly nonlinear and/or three-dimensional coupled mode shapes and prone to significant wind-induced torsional loads. Many research works have been dedicated to address the effects of non-ideal mode shapes in the HFFB analysis technique and the use of mode shape corrections, such as Boggs and Peterka (1989); Zhou *et al.* (1999, 2002); Holmes *et al.* (2003). More recently, Tse *et al.* (2009) have proposed a HFBB analysis method, referred to as linear-mode-shapes (LMS) method, which allows the values of the sway components of the generalized wind force to be determined by establishing a new set of centers at which the translational mode shapes are linearized by axis transformation.

In a study by Tschanz and Davenport (1983) the use and advantages of the five component base balance are discussed. In particular, the additional measurement of the base shear forces in two orthogonal directions is shown to permit the magnitude and line of action of the mean forces to be defined and represented by a trapezoidal or parabolic distribution. Furthermore a correction procedure for developing a generalized torsional force from the measured torque component is described. The correction is quite appropriately determined by the ratio of the moments and shears in the translational modes.

5.2.2   Overall loads from local pressure measurements

The development of solid state pressure scanners has allowed the simultaneous measurement of pressures at several points distributed on the wind tunnel model of the building or structure in general. This experimental approach is known as *Synchronous Multi-Pressure Sensing System* (SMPSS) technique. Area loads may be assessed by measuring local pressures acting on tributary areas and used to determine overall loads through bending and torque arms. Key factor to be considered using pressure measurements for the determination of wind loads are the frequency response of the pressure measuring system and the distribution of the measuring points. The technique allows the direct computation of the steady and unsteady modal forces acting in any number of modes of vibration of the structure (Vickery, 1990; Alan G. Davenport Wind Engineering Group, 2007). Similarly to the HFFB approach, the resonant amplification due to the building structural dynamics is derived analytically for each mode using random vibration theory and results are used to estimate the response of the structure at full scale. Major vantages of the pressure measurements technique are that:

- a single model in a single testing session can produce both overall structural loads and cladding loads;

- the generalized forces can be properly determined also for three-dimensional non-linear mode shapes.

On the other hand, a disadvantage of this technique is that it typically includes more instrumentation and takes longer model construction time than the HFFB method. Furthermore, as in the case of the base balance, the method does not include any effects of the motion-induced forces.

5.3   Aeroelastic simulations

Aeroelastic modeling is the principle experimental technique in studies of structures which are sensitive to wind-induced dynamic effects. Aeroelastic wind tunnel models are designed to replicate the deformation and motion of prototype buildings and structures in a simulated flow field. If properly carried out, aeroelastic tests provide the most complete characterization of the wind-induced structural responses, inherently including additional effects of the motion-induced forces. Body motion-excited or aeroelastic forces, which can be significant for some lightweight, flexible and lightly damped structures, cannot be measured with stationary models, such as are used in pressure and force balance model studies.

Two approaches are common in aeroelastic wind tunnel studies. First, such tests

are carried out to provide particular empirical data for analytical formulations of wind-induced effects. Second, aeroelastic studies are carried out to simulate the "entire" process, including the salient characteristics of the structure and its specific setting. The latter approach provides "direct" estimates of the full scale wind-induced response and does not rely on analytical methods. To be representative, such studies must model the properties of the natural wind and the aerodynamically significant features of the exterior geometry, but have also to correctly simulate the stiffness, mass and damping properties of the prototype structure.

In general, aeroelastic simulations are performed at several speeds, selected to simulate a representative range of full-scale wind speeds and for a full range of wind directions, unless there are symmetries of shape, structural properties and surroundings, or unless the important directions of wind can be ascertained at the outset, as in the case of most bridges, or be determined from other studies.

Aeroelastic studies of tall buildings, described in detail by Isyumov (1982), generally fall into the category of direct modeling techniques. The action of wind on buildings is confined primarily to the lower modes of vibration and, as a result, the dominant aspects of wind actions can be studied with relatively simple dynamic models, which provide information that can be scaled up to full scale, without major corrections. The emergence of "direct" modeling approaches in aeroelastic studies of tall buildings is due to different reasons (Isyumov, 1982). Some of them are listed as follows.

1. The aerodynamics of buildings which, excluding super-tall structures, generally have aspect ratio (height/breadth) less than 6 and seldom above 10, tend to be more 3 than 2-dimensional (as explained in chapter 3) and many of the simplifying assumptions, possible in the formulation of wind loads on line-like structures, are not valid. This reduces also the feasibility of analytical methods.

2. Some analytical methods, such as the gust factor approach, are valid to describe the drag response of buildings due to the buffeting action of turbulence. In contrast, lift and torsional excitation are less analytically predictable (see chapter 4).

3. It is common that the influence of the surroundings plays an important role in modifying or determining the action of wind of building. Hence the validity of modeling the presence of surrounding structures directly in the tunnel.

4. The dynamic response of tall buildings can be complex with coupled degrees of freedom or three dimensional mode shapes. This compounds the difficulty of the analytical estimates and favors physical direct modeling.

5. Most tall buildings are sharp-edged and the information obtained in small scale wind tunnel studies is representative of full scale data. As a result, *direct translations* of the model findings to full scale are possible without major corrections.

Finally, a main reason for performing aeroelastic studies of tall buildings is that the detailed direct description of the responses they provide can be used as a basis for estimating the structural performances and developing safe and cost effective optimal designs.

5.3.1   Types of aeroelastic tests

Aeroelastic model techniques include *replica*, *equivalent* and *section models*. A detailed description of the different models can be found in ASCE (1999).

Replica models

Replica models reproduce the prototype in virtually all aspects. These are aeroelastic models in which the geometric scaling of all dimensions results in a scaled reproduction of elastic properties. The use of replica models is practical for structures in which the elastic properties are concentrated on the exterior geometry, such as slender chimneys, cooling towers, tubular structures and so on. Replica models result in *full dynamic similitude* and provide direct measures of the wind-induced response. Despite their advantages, there are also some drawbacks. These models tend to be expensive and are not suited for parametric studies in which structural parameters, such as stiffness, mass and/or damping, are varied. An example of a major concrete structure modeled as an approximate replica aeroelastic model is the 553 m CN Communications Tower in Toronto (Isyumov *et al.*, 1984), shown in Fig. 5.1. The concrete tower is modeled using a metalized epoxy, sold under the trade name Devcon. Devcon and concrete have essentially the same density but the lower modulus of Devcon results in a reduced velocity scale i.e.:

$$\frac{U_m}{U_p} = \frac{\sqrt{(E/\rho)_m}}{\sqrt{(E/\rho)_p}} \tag{5.1}$$

where ρ is the density and E is the elastic modulus.

Replica models are only used for comparatively simple structural systems and only if the model construction materials are available to produce a velocity scale that can be attained in the tunnel.

Equivalent aeroelastic models

Equivalent models are *mechanical analogues* designed to simulate only some aspects of the dynamic characteristics of the prototype structure. Both *continuous* and *discrete* equivalent aeroelastic models are used. The earliest type of equivalent aeroelastic model used in the wind tunnel is the *two-degree-of-freedom* or *"stick"* aeroelastic model, also referred to as *"aeroelastic balance"* (Zhou and Kareem, 2003). It is a rigid model, pivoted near the base, with the elasticity provided by appropriately selected springs, simulating, usually, two orthogonal fundamental sway modes of vibration. Implicit in this technique is the assumption that the sway modes do not include any coupling and can be approximated as linear, and that torsion is considered of secondary importance.

A typical set up of the "stick" type aeroelastic model is schematically shown in Fig. 5.2(a). The model in Fig. 5.2(b) also includes a provision for modeling the torsional degree of freedom, but it only represents a uniform mode shape.

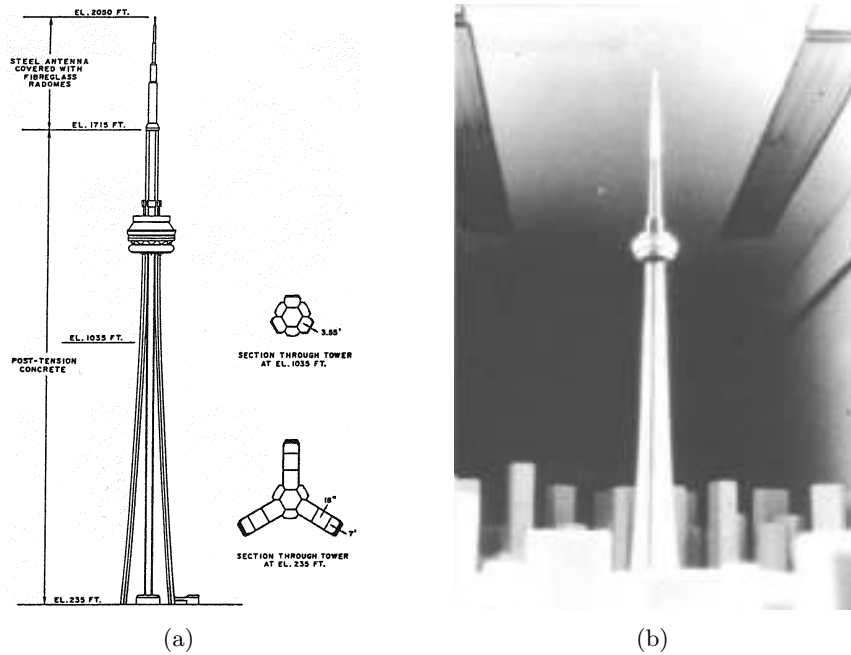(a)   (b)

Fig. 5.1 CN Communications Tower, Toronto: a) elevation of the tower and typical sections (ASCE, 1999); b) picture of the replica model of the tower in the wind tunnel, from Vickery (1990).
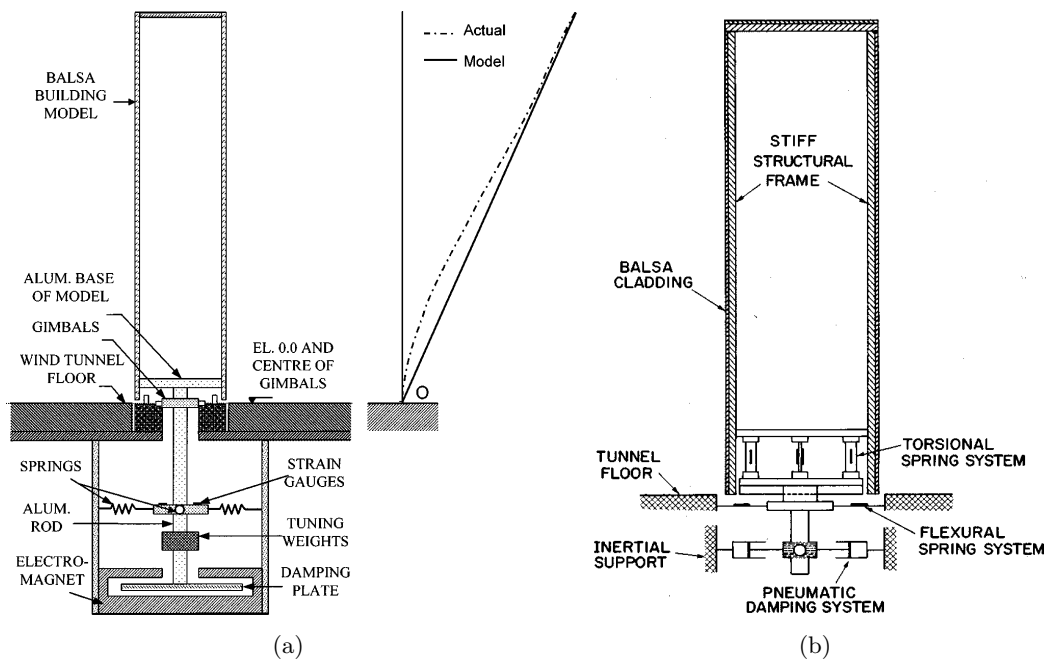

(a)   (b)

Fig. 5.2 "Stick" aeroelastic model from Zhou and Kareem (2003): a) schematic representation of a "stick" aeroelastic model, with mode shape modeling; b) "stick" aeroelastic model with a torsional spring system.

The paper by Zhou and Kareem (2003) focuses on the relevant features concerning the role of a "stick" type aeroelastic model in structural design. The direct

similarity between the model and the prototype structure, which is a prerequisite for accurate "direct" assessment of wind effects through the "stick" model, cannot be easily achieved in practice. The first issue concerns the mode shape modeling, because the "stick" model works best for structures with linear sway modes [Fig. 5.2(a)]. The second issue concerns the mass modeling, since tall buildings usually have a complex mass distribution that poses a difficulty in replicating it in a small scale aeroelastic model.

The inconsistency resulting from the mismatch in mode shape modeling has been generally treated in two ways. One approach makes use of a straight-line mode shape to fit a large portion of the actual mode shape, adjusting the pivot point at an "appropriate" height above the building base (Isyumov, 1982). Alternatively, analytical procedures, which follow the techniques routinely used in the HFFB method, may be invoked to adjust observations to nonlinear mode shapes, e.g. Kijewski and Kareem (1998), Zhou *et al.* (1999), Zhou *et al.* (2002).

The effect of imperfect modeling of mass distribution has received relatively less attention. In some of the literature (Cermak, 1977; Isyumov, 1982; ASCE, 1999), the similarities in the total and the first mode generalized masses and the mass moment of inertia are required, while in others the exact modeling of mass has been relaxed.

The category of discrete equivalent aeroelastic models includes also *multi-degree-of-freedom* models, which are discrete mechanical analogues of buildings comprising several interconnected lumped masses each having two translational and one rotational (rotation about a vertical axis) degrees of freedom. This type of model is suited for aeroelastic studies of more complex buildings, where torsional effects are judged to be important and/or in situations where the modes of vibration are highly three-dimensional because of inertial and/or elastic coupling. A schematic representation of a typical multi-degree-of-freedom aeroelastic model is presented in Fig. 5.3. In this case the building is divided into four zones, each represented by a lamped mass. Masses are concentrated at the floor diaphragms, that are connected by flexible columns and the entire mechanical system is enclosed in a non-structural skin which reproduces the exterior geometry. A full discussion on this technique is contained in Isyumov (1982) and Alan G. Davenport Wind Engineering Group (2007).

A common approach for the aeroelastic modeling of tall buildings have historically been the use of the "skin-skeleton" type continuous equivalent aeroelastic model. This model is made of an internal equivalent structural system, referred to as "skeleton" or "spine", which is used to model the mass and stiffness properties, and a non-structural skin to maintain the overall geometry. An example of such a model is shown in Fig. 5.4. Real tall buildings generally comprise of walls and frames. Under lateral load, the walls deflect in a flexural mode, while the frames in a shear mode. Since frames and walls are tied together by rigid floors, the building deflects in a shear-flexural mode. A "skin-skeleton" model with distributed mass and stiffness can simulate this shear-flexural mode of the prototype, as illustrated in Cheong *et al.* (1992).

Section models

Section models provide a rigid representation of a portion of the structure mounted dynamically and are valuable tools to study the action of wind on slender, high aspect ratio structures, which can be referred to as line-like structures, such as long-span
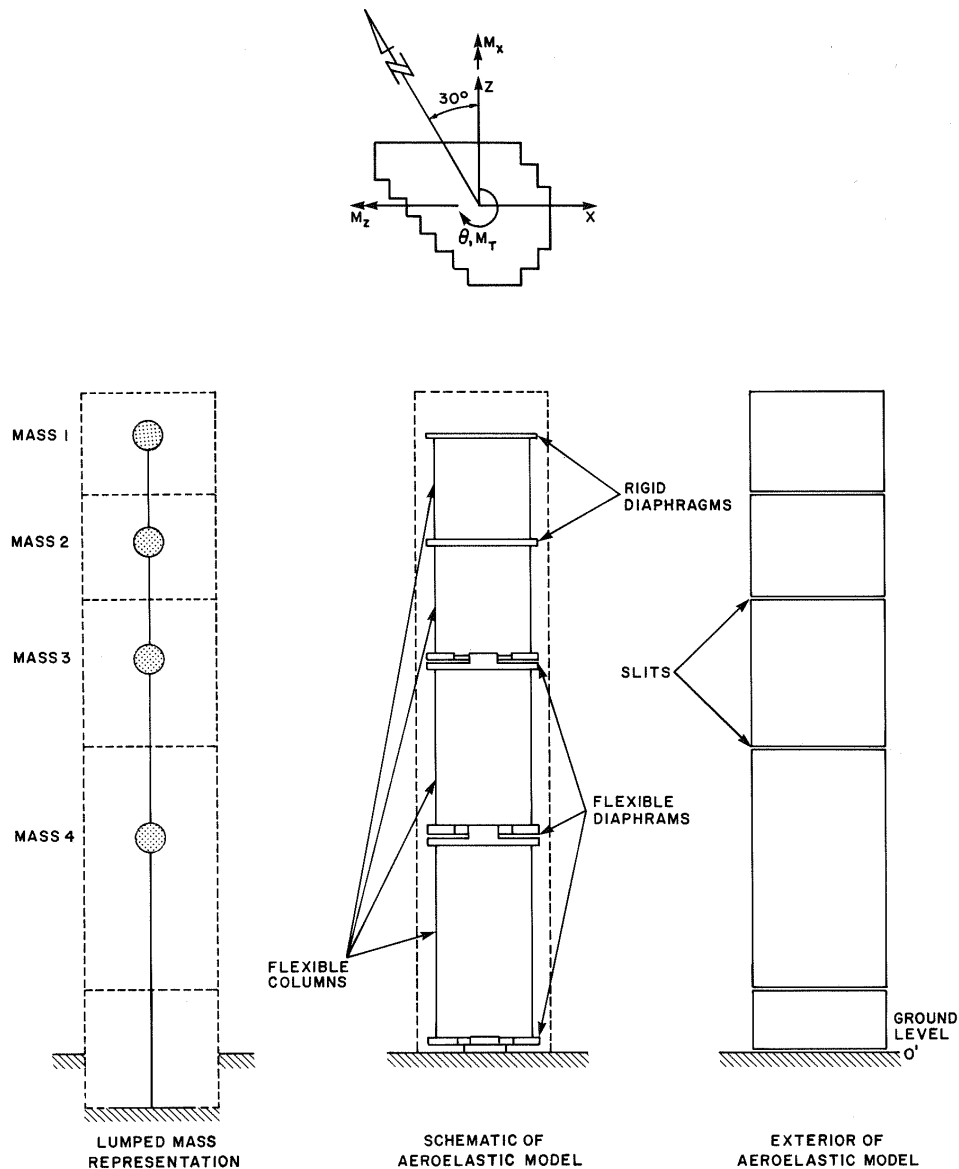
Fig. 5.3 Multi-degree-of-freedom aeroelastic model of a tall building (Isyumov, 1982).

bridges, cables and slender chimneys and towers and other structures in which the flow can be treated as two-dimensional. Typical geometric scales range from 1:10 to 1:100. A particularly important application of these models is the study of the aerodynamic stability of bridge sections. Section models are used to evaluate various aerodynamic derivatives, used in conjunction with theoretical models of the process. These models can be "driven" with controlled amplitudes and frequencies to study the effects of body motion on the aerodynamic forces. Section models are traditionally tested in smooth flow conditions. However, tests in turbulent flows generated with coarse girds or active turbulence generators can be carried out, too. A description of this technique is available in ASCE (1999).
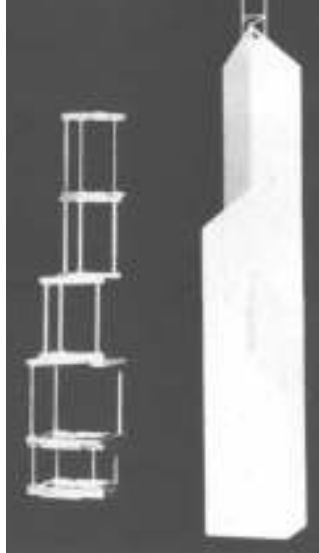
Fig. 5.4 "Skeleton" and completed aeroelastic model of Bank of China, Hong Kong (Steckley *et al.*, 1985), from Vickery (1990).

5.3.2   Scaling requirements for aeroelastic simulations of tall buildings

Unlike rigid model techniques, aeroelastic simulations provide a direct estimation of the wind-induced responses. Therefore, a direct similarity between the model and the prototype structure is a prerequisite for accurate assessment of wind effects.

Similarity requirements for aeroelastic studies are extensively treated in literature, e.g. Isyumov (1982), and based on established similarity theory (Cook, 1986). The principal requirements are:

1. similarity of the mean and turbulent characteristics of the flow;

2. geometric similarity to a scale consistent with the length scaling of the natural wind, including the depth of the boundary layer and the integral scale of turbulence;

3. similarity of aerodynamic forces (achieved by allowing for Reynolds number related differences for rounded shapes);

4. similarity of inertia forces;

5. similarity of stiffness characteristics;

6. similarity of damping.

Generally, the geometric or *length scale* of the model to the prototype, λ_l, defined as[1]:

$$\lambda_l = \frac{l_m}{l_p} \tag{5.2}$$

---

[1]m subscript refers to the model, p subscript to the prototype

is limited by the wind tunnel facilities and should be chosen with due regard to wind tunnel blockage. Corrections are generally required if the blockage exceeds 5%. Geometric scales of the order of 1:300 to 1:500, commonly used in aeroelastic tests, provide a representative simulation of the aerodynamic forces for sharp-edged structures.

Having selected the length scale, consistent with the length scale of the modeled wind, the similarity of the aeroelastic behavior of a sharp-edged building is achieved by maintaining equality of the following non-dimensional quantities in model and full scale:

$$\text{density ratio} = \frac{\rho_b}{\rho} \tag{5.3}$$

$$\text{elastic forces} = \frac{E}{\rho U^2}, \frac{G}{\rho U^2} \tag{5.4}$$

$$\text{damping ratio} = \xi_s \tag{5.5}$$

where ρ_b, ρ, E, G, U and ξ_s are, respectively, the bulk density, the air density, Young's modulus, the torsional modulus, the wind speed and the structural damping, expressed as a proportion of the critical damping.

Froude number scaling is of negligible consideration for tall buildings and free standing structures, in general, where the stiffness depends predominantly on elastic forces (Isyumov, 1982).

The similarity requirement for elastic forces in Eq. (5.4) can be replaced by the *reduced frequency*, f_r, defined as:

$$f_r = \frac{fb}{U} \tag{5.6}$$

where f is the modal frequency and b indicates a dimension, that has to be the same in model and full scale for the particular modes of vibration included in the simulation.

From Eq. (5.6), the *velocity scale*, λ_U, becomes:

$$\lambda_U = \frac{U_m}{U_p} = \lambda_L \lambda_f = \lambda_L / \lambda_t \tag{5.7}$$

where λ_f and λ_t are respectively the *frequency scale* and the *time scale*, defined as:

$$\lambda_f = \frac{f_m}{f_p} \tag{5.8}$$

and

$$\lambda_t = \frac{1}{\lambda_f}, \tag{5.9}$$

respectively. Consistent with the previous definitions, the *acceleration scale* becomes:

$$\lambda_a = \lambda_L \lambda_f^2. \tag{5.10}$$

For exact scaling it would also be necessary to maintain equality of the *Reynolds number*, *Re*, defined in Eq. (3.12). Reynolds similarity is not practical to be met as full scale Reynolds numbers are typically two or three orders of magnitude greater than those achieved in low speed wind tunnels. Although Reynolds number similarity is of primal importance for rounded shapes, where the location of flow separation from the curved surface is dependent on Reynolds number, it is less significant for sharp edged bodies, where flow separation tends to occur at the building corners (see chapter 3). Therefore, the influence of Reynolds number on the overall flow around buildings is, in general, considered not significant, especially in turbulent boundary layer flows.

Eqs. (5.3)-(5.5) define, in the most general form, the scaling requirements for the proper modeling of the oscillatory behavior of a structure. However, difficulties in the realization of aeroelastic models arise from the following causes (Scruton, 1981):

- the model does not replicate the correct structural damping and the structural damping characteristics on full-scale structures are generally unpredictable;

- it is usually not possible to build replica models using materials with the physical properties required by the similarity requirements.

Therefore, scaling rules are never exactly met. When dealing with aeroelastic simulations, elastic forces can be scaled according to the similarity requirement on reduced frequencies previously mentioned, while similarities on mass and damping characteristics can be expressed by means of the *Scruton number*, *Sc*, also known as "mass-damping parameter" (Holmes, 2001), defined as [see also Eq. (4.3)]:

$$Sc = \frac{2\delta_s m_{i,e}}{\rho b^2} \tag{5.11}$$

Reduced frequency and Scruton number have to be equal in model and full scale for those modes of vibration included in the simulation.

5.4   Summary and main remarks

This chapter reviews the main aspects of the wind tunnel experimental techniques in common use. With rigid model techniques, the responses are derived theoretically from aerodynamic loads, neglecting motion-induced forces. The use of aeroelastic models allows, on the other hand, the direct measurement of responses, inherently including additional effects of the motion-induced forces, which can be significant for some lightweight and lightly damped structures.

Aerodynamic loads may be obtained from rigid models by using different methods, basically corresponding to High Frequency Force Balance (HFFB) technique and integration of pressures, known as Synchronous Multi-Pressure Sensing System (SMPSS) technique. The main advantages and drawbacks of these two methods are discussed. The three base moments measured by a HFFB coincide with the first three generalized forces in the particular case of a system exhibiting uncoupled and linear mode shapes. Using the pressure measurements technique, a single model can be used for both overall structural loads and cladding loads, and the generalized forces can be properly evaluated also for three-dimensional non-linear mode shapes. However, the SMPSS technique typically includes more instrumentation and longer

model construction times.

Aeroelastic models, falling in the category of direct modeling techniques, replicate the deformation and motion of prototype structures in a simulated flow field. Listed in decreasing order of design and construction complexity, aeroelastic simulations include replica, equivalent and section model techniques. Equivalent models range form the "stick" type model, to the more complex multi-degree-of-freedom and continuous "skin-skeleton" type models. Several similarity requirements for aeroelastic studies have to be satisfied for the accurate assessment of wind effects. Such studies must model the properties of the natural wind flow and the aerodynamic features of the exterior geometry, but have also to simulate the stiffness, mass and damping properties of the prototype structure.

Chapter 6

Wind tunnel tests

6.1 Introduction

As explained in the previous chapter, if properly carried out, aeroelastic simulations provide the most complete characterization of the structural responses due to the wind action. An accurate knowledge of these responses, including the effects of possible motion-induced forces, is of primary importance for the serviceability design of tall buildings.

In this research a continuous equivalent aeroelastic model of a regular square-section tall building is built and tested in the wind tunnel in turbulent flow conditions.

A quite complex wind tunnel setup is adopted in order to carry out the simultaneous measurement of pressures, overall forces, across-wind displacements and along-wind and across-wind accelerations for a wide range of wind speeds including the lock-in critical wind speed condition.

The first two sections (6.2 and 6.3) of this chapter are dedicated to the description of the boundary later wind tunnel where the experimental activity is carried out and of the instrumentation used.

Section 6.4 describes the aeroelastic model tested in this research and includes a discussion about how the model geometry is designed on the basis of the experimental purposes. The principal stages of the assembly of the model are illustrated and the identification of its dynamic properties through free vibration tests is described.

Section 6.5 is devoted to the analysis of the simulated flow conditions. The experimental setup adopted and the instrumentation equipment of the model are shown in section 6.6.

The main results of this experimental activity include: the identification of the Strouhal number (section 6.7), the spectral analysis of the response (section 6.8), from which the identification of the lock-in range (section 6.9) and the analysis of modal frequencies (section 6.10) are carried out, the correlation analysis of the pressure-coefficients on the side-faces (section 6.11) and the analysis of the displacement (section 6.12) and acceleration (section 6.13) responses.

The overall forces from HFFB and SMPSS measurements are also analyzed and compared (section 6.14).

6.2 Wind tunnel description

The experimental activity is entirely carried out in the CRIACIV[1]-DICEA[2] Boundary Layer Wind Tunnel (BLWT), located in Prato, Italy (Fig. 6.1). Its technical characteristics are shown in Fig. 6.2.

It is an open-circuit suction-type wind tunnel with a convergent nozzle for the flow acceleration and a T-shaped symmetric diffuser. The total length is about 22 m. The cross-section slightly diverges from a width of 2.20 m and a height of 1.60 m at the inlet to a width of 2.42 m and a height of 1.60 m at the test section, allowing constant pressure along the axis.

The wind flow is generated by an axial fan, placed downstream of the test section, ensuring that the turbulence generated by the fan does not contaminate the flow.

The total length of the developing fetch is 8 m, while the length of the test section is 2.4 m. At the inlet the flow is regularized by a 5 cm thick honeycomb panel, followed by a squared mesh screen.

The growth of the boundary layer in the wind tunnel can be artificially developed through the use of *spires* and *Counihan devices*, which produce an immediate velocity gradient downstream, and which develop into a mean velocity profile representative of that in the atmosphere within a short downstream distance, and *roughness elements* on the floor of the wind tunnel aimed to increase the turbulence intensities on the basis of the full-scale values.

The wind speed, ranging from 0 to approximately 30 m/s, is regulated by both adjusting the pitch of the 10 blades of the fan and regulating the number of engine turns through an inverter. The fan has a power of 158 kW and is equipped with a servomotor for controlling the continuity of the flow. An elastic joint is placed between the test section and the axial fan, to isolate the former from the vibration produced by the propeller system. The exit of the flow is regularized by a T-shaped symmetric diffuser which minimizes the loss of pressure.

The tunnel is equipped with a turning table at the test section, which enables the incident wind direction to be changed with respect to the orientation of the model mounted on it.

6.3 Measurement instrumentation

6.3.1 Pitot tubes

The Pitot tube, consisting in a tube pointing directly into the fluid flow, allows the measurement of both the *stagnation pressure*, also known as the *total pressure* or (particularly in aviation) the *pitot pressure* and the *static pressure*. From the mean dynamic pressure, which is measured form the difference between the stagnation pressure and the static pressure, the mean wind speed can be derived.

During the experimental activity in the CRIACIV Wind Tunnel, 2 Pitot tubes are used. For the signals acquisition, the instruments are connected to a pressure

---

[1]Centro di Ricerca Interuniversitario di Aerodinamica delle Costruzioni e Ingegneria del Vento (Interuniversity Research Center of Building Aerodynamics and Wind Engineering). Web site: `www.criaciv.unifi.it`

[2]Dipartimento di Ingegneria Civile e Ambientale (Department of Civil and Environmental Engineering)

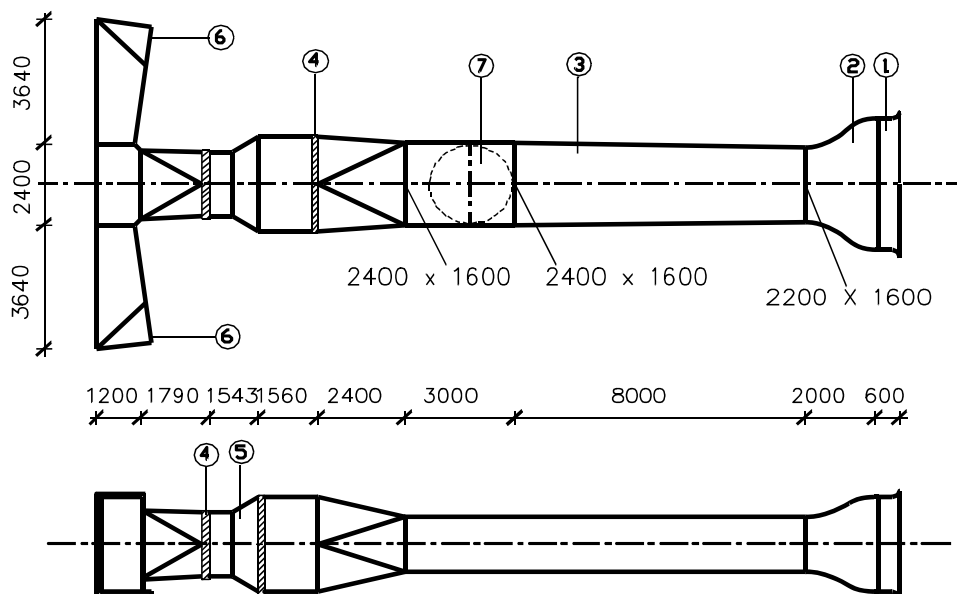**Fig. 6.1** View of the CRIACIV-DICEA Boundary Layer Wind Tunnel in Prato.

Fig. 6.2 Sketch of the CRIACIV-DICEA Boundary Layer Wind Tunnel: 1. Inlet with honeycomb grid; 2. Contraction; 3. Boundary Layer development zone; 4. Elastic joint; 5. Propelling System (160 kW); 6. Diffuser; 7. Test section with turning table.

Fig. 6.3 Pressure acquisition system PSI 8400.

transducer (Setra System, model 239), then the signal is converted by 32-bit NI card and finally is acquired by a PC.

6.3.2   Two-components hot-wire anemometer

A two components hot-wire anemometer is used to measure the characteristics of the incoming flow in the wind tunnel.

The hot-wire anemometer allows the measurement of the component of the instantaneous wind speed in the plane perpendicular to the wire. It is a thermic transducer with a platinum plated tungsten wire sensor. Electricity warms the sensor up by Joule effect, whereas air flowing past the wire has a cooling effect on the wire by convection. Since the electrical resistance is dependent upon the temperature of the metal, a relationship can be obtained between the resistance of the wire and the flow speed.

6.3.3   Pressure Transducers

Pressure measurements (SMPSS technique, see subsection 5.2.2) are performed by means of a PSI 8400 system by Pressure System (Fig. 6.3). The CRIACIV BLWT is equipped with four acquisition units having 16 piezoelectric transducers each (Fig. 6.4) and two acquisition units having 32 transducers each, so that a total amount of 128 pressures can be recorded simultaneously.

Dynamic pressures can be measured with a sampling frequency up to 1 kHz. The number of acquisition channels used is inversely proportional to the sampling frequency. For example, for the maximum number of pressure signals that can be contemporary measured (128 channels), the sampling frequency decreases to 250 Hz per channel.

Owing to their small dimensions ($13 \times 21.5 \times 69$ mm^3 for the 16-channel type and $26 \times 21.5 \times 69$ mm^3 for the 32-channel type), the PSI scanners can also be located inside the models.

Prior to the pressure data acquisition, the transducers calibration has to be performed, since piezoelectric transducers display drift effects and could be significantly affected by temperature variations. Once defined the expected pressure range,
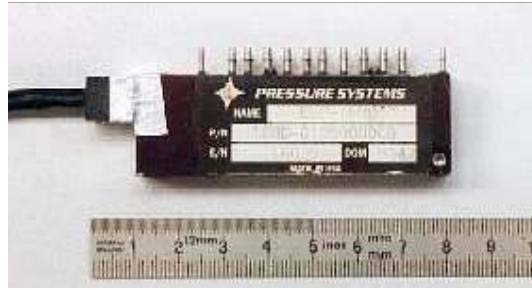
the calibration [...] ds five reference
pressures, withi[...] quires the corre-
sponding voltage [...] j, [...] a fourth degree
polynomial. This system allows pressure measurements in the range of [-254;+254]
mm H$_2$O. The accuracy of the calibration procedure is 0.05 % of the maximum al-
lowed pressure. The maximum error affecting the measured dynamic pressure values
0.2% of the the maximum allowed pressure (full scale) and is equal to:

$$err_{max} = 0.2\% \cdot 254 \approx 0.5 \text{ mm H}_2\text{O} \tag{6.1}$$

When, owing to the small dimensions of the model tested, it is not possible to
accommodate the sensors within the model, the pressures acting on the model surface
must be transmitted to the sensor without distortions. The transmission is carried
out through small highly flexible plastic tubes, manufactured in silicone or teflon.
To allow the pressures to be transmitted without distortions, each transmission tube
is equipped with a damper, which is obtained by a contraction of the tube diameter
(Fig. 6.5). The system constituted by tube and damper is properly calibrated so that
its frequency response does not influence the pressure measurements. The resulting
calibrated tube-damper system, used for this research, is that illustrated in Fig. 6.5,
where the total length, L1 + L2 + L3, is 500 mm, L3 is equal to 115 mm and the
damper is 20 mm long. The inner diameter of the pneumatic tube is 0.8 mm while
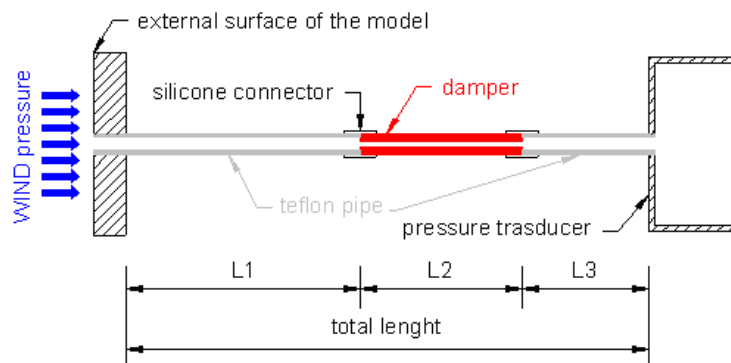that of the damper is 0.3 mm.

Fig. 6.5 Sketch of the tube-damper system for the transmission of pressures from the model
surface to the pressure transducer.

6.3.4   High Frequency Force Balance

A 5-component strain gauged balance (HFFB - High Frequency Force Balance), model FDC 010, manufactured by Metior S.r.l., Como, Italy (`www.metior.it`), is used (Fig. 6.6). It allows the measurement of 2 shear forces, F_x, F_y, 2 bending moments, M_x, M_y, along two orthogonal directions, and of the torque component, M_z (see Fig. 6.7). The capacity and accuracy of the balance corresponding to the different components are reported in Table 6.1.

Fig. 6.6 High Frequency Force Balance.

Table 6.1 HFFB capacity and sensitivity.

	Capacity	Sensitivity
F_x	10 kg	0.185 mV/V
F_y	10 kg	0.185 mV/V
M_x	5 kgm	0.270 mV/V
M_y	5 kgm	0.270 mV/V
M_z	5 kgm	0.270 mV/V

6.3.5   Displacement Transducers

Three non-contact optical laser transducers (Micro-epsilon Model OptoNCDT 1605) are available to determine the displacements of the model [Fig. 6.8(a)]. These lasers use a semiconductor with 675 nm wavelength and a maximum output power of 1 mW and their functioning principle is based on triangulation. The output voltage range is ±10 V which corresponds to a displacement of roughly ±100 mm. The lasers are connected to a PC acquisition card. The characteristics of the lasers are reported in Table 6.2. The actual linearity of these transducers and their conversion factor
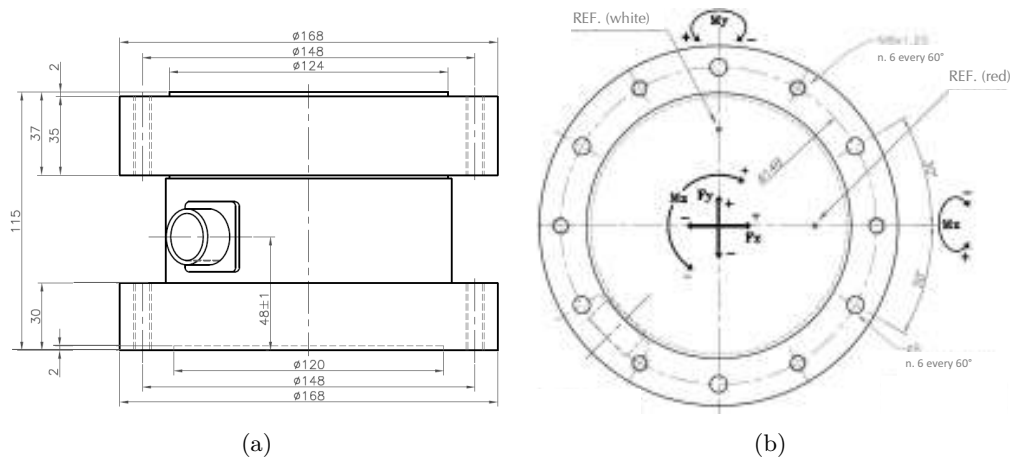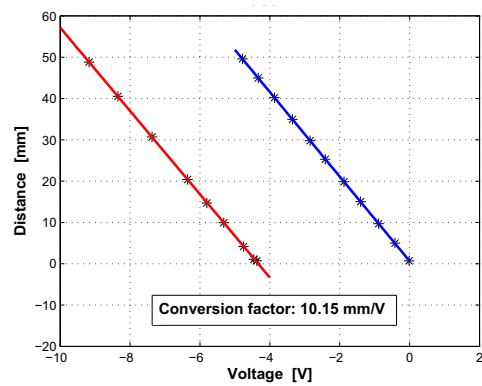
(a) (b)

Fig. 6.7 High Frequency Force Balance technical drawing: a) side view; b) plan view.

(a) (b)

Fig. 6.8 Micro-epsilon Model OptoNCDT 1605 laser tranducer: a) View of a laser triangulator device for displacement measurement; b) Relationship between laser output voltage and actual object distance (laser 1).

is checked for each laser by means of a high precision mechanical distantiometry [Fig. 6.8(b)].

Table 6.2 Micro-epsilon Model OptoNCDT 1605 laser characteristics.

Sensor type	Laser-Sensor
Model	LD 1605
Type	200
Measuring range	± 100 mm
Stand-off midrange	340 mm
Non-linearity $\leq \pm 0.3\%$ d.M.	600 μm
Resolution (noise) static	60 μm
Measuring spot dia. midrange	2 mm
Light source	Laser 1 mW, wavelength:red 675 nm
Sampling frequency	40 kHz
Laser class	2
Analogical output	
Displacement	± 10 V
Output impedance	appr. 0 Ohm (10 mA max.)
Angle dependence	appr. 0.5% when turning ± 30 about long.axis
Rise time	0.1/0.2/2 or 20 msec selectable
Frequency response	10 kHz, 3 kHz, 250 Hz or 25 Hz
Temperature stability	0.03%/K
Intensity of reflecting light	1 V bis 10 V/max; 0 V bis +13 V
Permissible ambient light	20000 Lux
Life time	50000 h for laser-diode
Insulation	200 VDC, 0 V against housing
Max. vibration	10 g to 1 kHz
Operation temperature	0 to 50 ℃

6.3.6   Accelerometers

A set of 4 mono-axial ICP® accelerometers (Fig. 6.9) produced by PCB Piezotronics, model 352C42, is used. Their technical characteristics are illustrated in Table 6.3.

6.4   The model

6.4.1   Design of the model

The equivalent continuous aeroelastic model (Fig. 6.10) used in this research is designed and built in order to simulate the dynamic response of a regular square-section tall building (the *side ratio*, defined as depth, d, over breadth, b, is equal to 1), which was previously tested in the wind tunnel using a rigid model (Spence, 2009). Its *aspect ratio*, defined as height, h, over breadth, b, is equal to 6. The choice of this dimensional proportion is also motivated by the richness in literature works on models with the same aspect ratio value [see, for example, Marukawa *et al.*

Table 6.3 Model 352C42 Accelerometer characteristics.

Performance	
Sensitivity ($\pm$10%)	10.2 mV/(m/s^2)
Measuring range	$\pm$491 m/s^2
Frequency range ($\pm$5%)	1.0 to 9000 Hz
Frequency range ($\pm$10%)	0.5 to 10000 Hz
Frequency range ($\pm$3 dB)	0.3 to 15000 Hz
Resonant frequency	$\geq$ 30 kHz
Broadband resolution (1 to 10000 Hz)	0.005 m/s^2 rms[a]
Non-linearity	$\leq$ 1%[b]
Transverse sensitivity	$\leq$ 5%[c]
Environmental	
Overload limit	$\pm$49050 m/s^2 pk
Temperature range	-54 to +121 ℃
Temperature response	see Fig. 6.9(b)[a]
Electrical	
Excitation voltage	22 to 30 VDC
Constant current excitation	2 to 20 mA
Output impedance	$\leq$ 200 Ohm
Output bias voltage	8 to 15 VDC
Discharge time constant	0.5 to 2.0 sec
Settling time (within 10% of bias)	$\leq$ 10 sec
Spectral noise (1 Hz)	1177 (μm/sec^2)/$\sqrt{Hz}$[a]
Spectral noise (10 Hz)	294 (μm/sec^2)/$\sqrt{Hz}$[a]
Spectral noise (100 Hz)	196 (μm/sec^2)/$\sqrt{Hz}$[a]
Spectral noise (1 kHz)	59 (μm/sec^2)/$\sqrt{Hz}$[a]
Physical	
Sensing element	Ceramic
Sensing geometry	Shear
Housing material	Titanium
Sealing	Welded hermetic
Size (Hex x Height)	9.7 mm x 9.7 mm
Weight	2.8 gm[a]
Electrical connector	10-32 Coaxial jack
Electrical connection position	Top
Mounting	Adhesive

[a] Typical
[b] Zero-based, least-squares, straight line method
[c] Transverse sensitivity is typically $\leq$ 3%

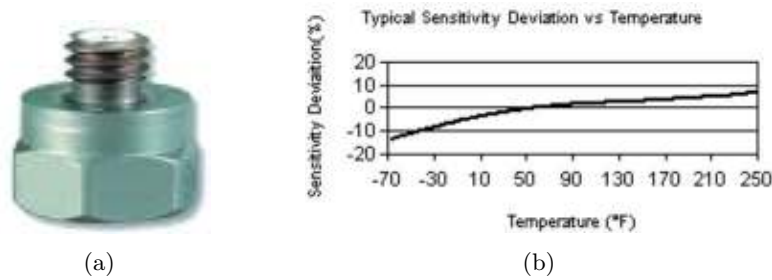(a)   (b)

Fig. 6.9 PCB Piezotronics Mod. 352C42 accelerometer: a) photo; b) temperature response.

(1996); Kijewski and Kareem (1998)]. The overall dimensions of the model, which replicate those of the rigid one, are 10.5 cm × 10.5 cm × 60.8 cm.

The model is a continuous "skin-skeleton" type aeroelastic model (see subsection 5.3.1). The external non-structural "skin", used to maintain the overall geometry and the aerodynamic forces is made of plexiglas. The internal structure, the "skeleton", is made of 4 continuous aluminum bars [Fig. 6.11(a)]. For the aluminum bars to move freely without any constraint from the outer shell, the latter is divided into three separate boxes [Fig. 6.11(b)]. Each box is made of 4 sides and one horizontal floor on the top, glued together. The internal structure and the external boxes are connected together at the three rigid horizontal floors, placed at $1/3\,h$, $2/3\,h$ and at the top [Fig. 6.11(c)], thus replicating the typical outrigger-braced system used in many buildings (McNabb and Muvdi, 1975; Stafford Smith and Coull, 1991).

The geometry of the different components of the model and the position of aluminum bars within the outer shell is decided on the basis of the testing purposes as explained in the following paragraphs.

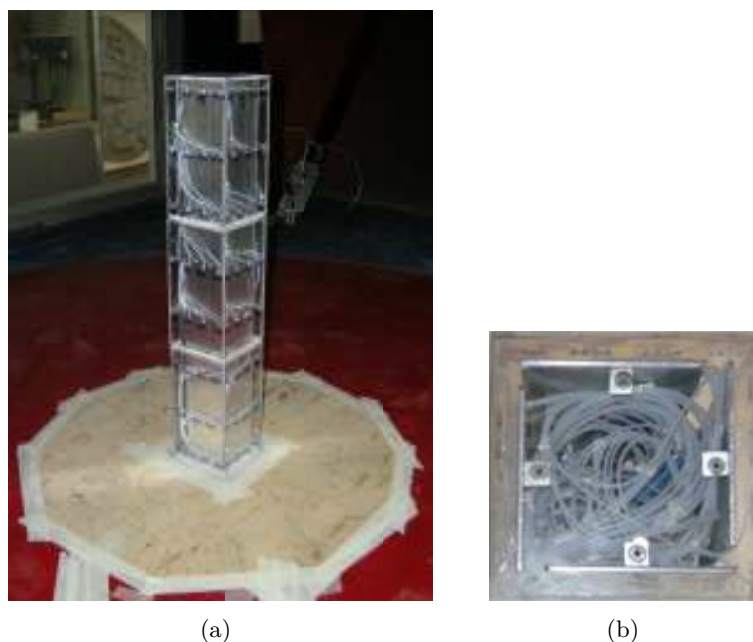The design and building of the model have resulted in a quite complicated stage

(a)   (b)

Fig. 6.10 The aeroelastic model: a) global view; b) plan view.

of the work. The reason for this lies in the quality and number of measurements that have been intended to be performed simultaneously. As a matter of fact, the major effort of the experimental activity has set to be the simultaneous measuring of:

1. pressures on the model surface,

2. overall forces and moments,

3. across-wind displacement response,

4. along-wind and across-wind acceleration responses,

in order to have an experimental characterization of the loads and responses of the model as complete as possible, even in lock-in conditions.

The measurement of pressures, using the maximum number of simultaneously measuring pressure taps allowed by the instrumentation capabilities, equal to 128 (see subsection 6.3.3), has led to the need to have a proper distribution of holes on the building surface, a proper path of the pneumatic tubes from the building sides to the pressure transducers and an adequate internal space to allow the casing of the pressure transducers. The last requirement is motivated by the need to avoid the employment of long tubes to limit as much as possible errors in the measurement of fluctuating pressures. As described in subsection 6.3.3, 50 cm long tubes are used in this work.

For the measurement of overall forces and moments a High Frequency Force Balance (subsection 5.2.1) is used. Hence the need to install the model over a supporting system which allows the connection with the balance.

One major purpose of the experimental activity is to measure the model response in lock-in conditions. The achievement of the critical wind speed in the wind tunnel is possible only designing the frequency of the model so that the critical velocity (see section 4.3):

$$U_{crit} = \frac{b f_n}{St} \tag{6.2}$$

where b is the side dimension of the model, f_n is the natural frequency and St is the Strouhal number, falls within the wind tunnel wind speed range, defined by the wind tunnel capabilities illustrated in section 6.2.

On the basis of these considerations, the geometry of the external and internal components of the model is set, even with the help of a simplified finite element model which enables a first control of the frequencies of the model. However, because of the complexity of the model and of the connections between the different components and with the real supporting system, the actual frequencies can be determined only through dynamic identification of the real model mounted in the wind tunnel (see subsection 6.4.3).

Fig. 6.12 illustrates the dimensional drawing of the model with the geometrical characteristics of the internal structure and of the outer shell.
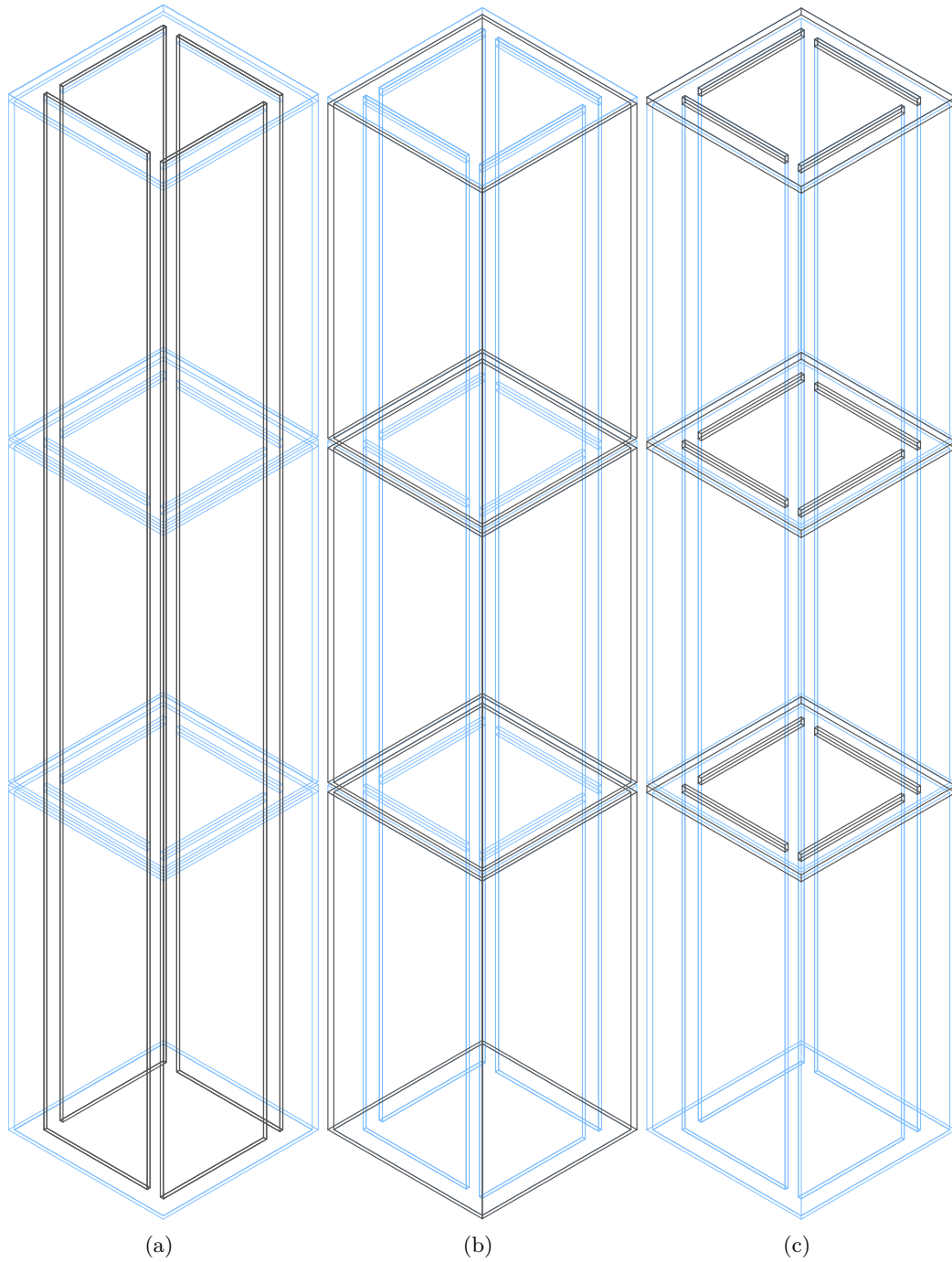
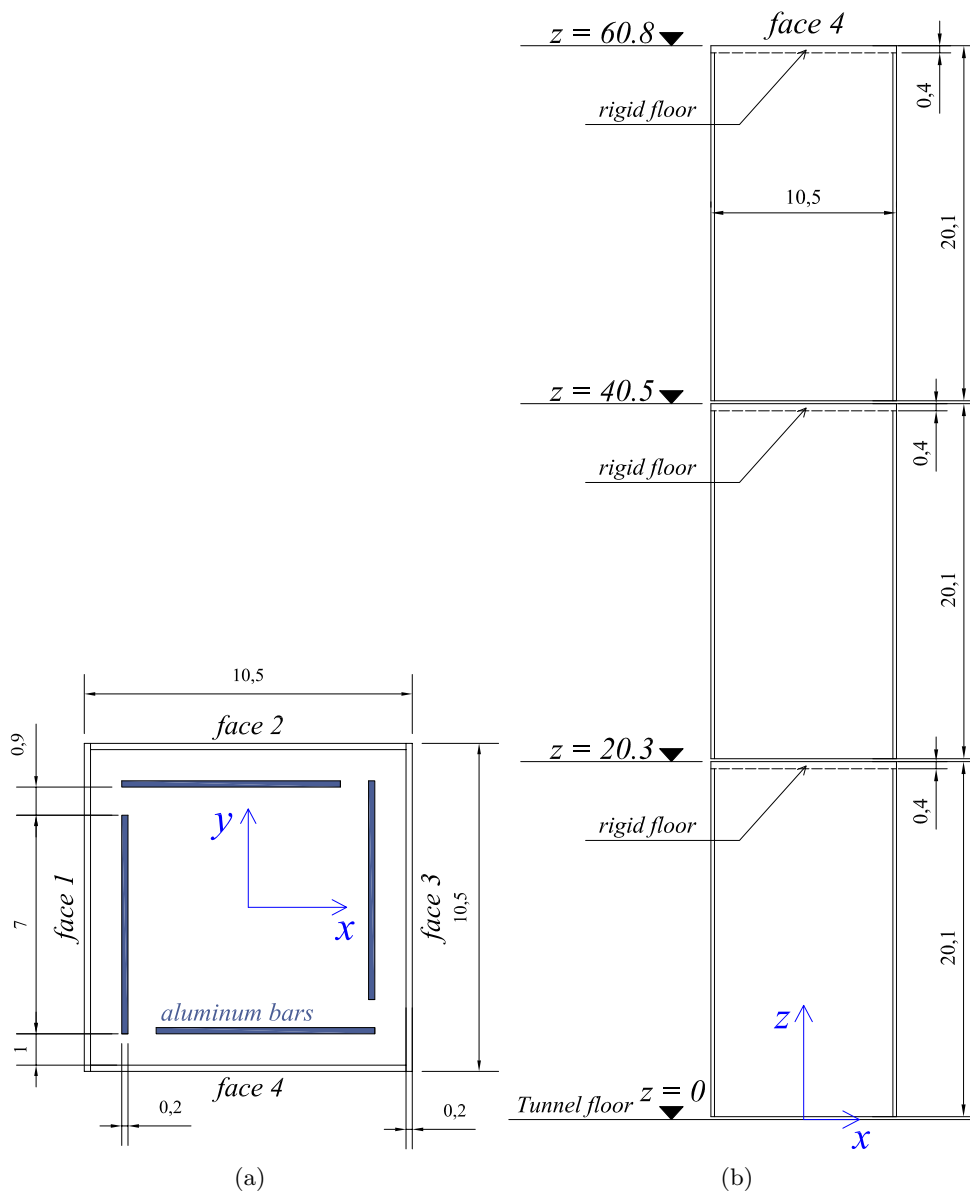**Fig. 6.11** 3D sketch of the model: a) the "skeleton"; b) the "skin"; c) rigid floors.

Fig. 6.12 Dimensional drawing of the model: a) plan view; b) side view (face 4).

6.4.2 The assembly of the model

Each side of the three external boxes, of 2 mm thickness, is equipped with the pneumatic tubes [Fig. 6.14(a)], according to the pressure tap distribution reported in Fig. 6.13. As explained later (see subsection 6.7.1), the total number of pneumatic tubes connected to the model outer surfaces is 126. Pressure taps are distributed on 8, approximately equally spaced, different levels whose height over the tunnel floor is reported in Fig. 6.13. As described in subsection 6.3.3, the pneumatic tubes
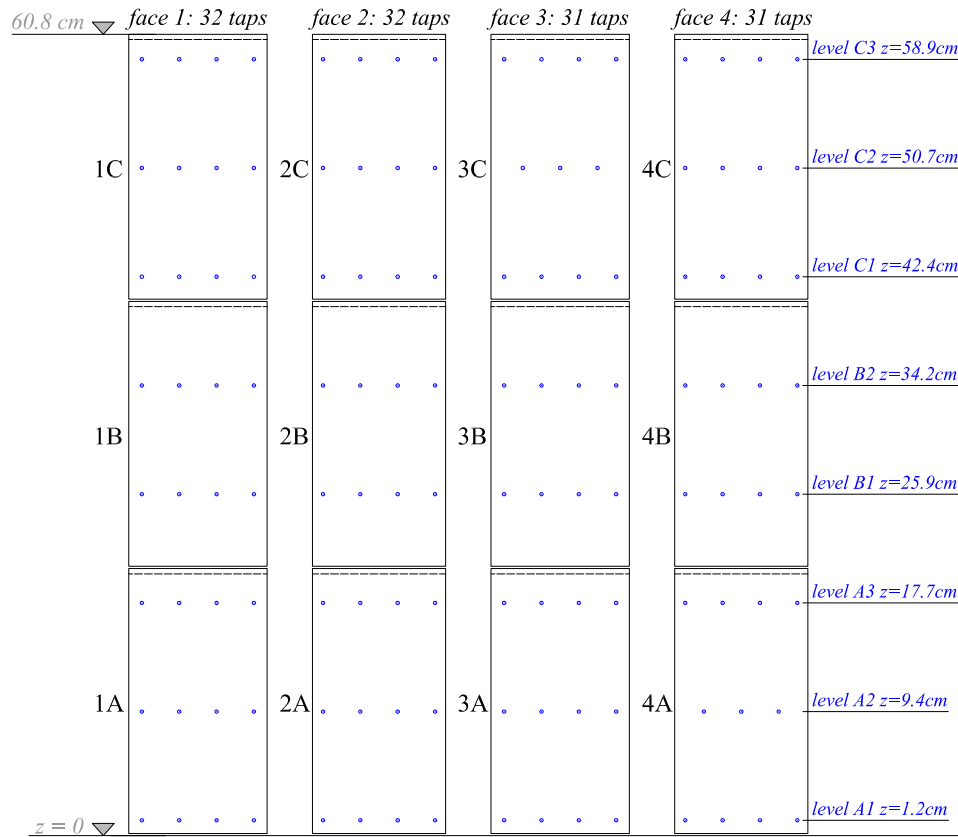
Fig. 6.13 Pressure taps distribution on the model surface.

have a total length of 50 cm, but their are divided in two parts, connected by a 2 cm long damper. As a consequence, the first part of each tube is glued to the model, the other part is installed to the PSI unit. The plexiglas, 4 mm thick, square plates constituting the horizontal floors are shaped with laser cuts in order to have 4 rectangular holes through which the continuous aluminum plates can be threaded. The four sides of each box are glued together and with one floor at the top. At this stage, the principal elements constituting the model, corresponding to the 4 plates and the three boxes are weighted [Fig. 6.14(b), Fig. 6.14(c), Fig. 6.14(d), Fig. 6.14(e)].

As shown in Fig. 6.13, the three boxes are referred to with the letters A, B and C, from the bottom to the top and each side with a number from 1 to 4, indicating the face of the model.

A preliminary mounting of the model outside the wind tunnel is performed. For the connection between the internal structure and the outer shell, a system of aluminum L-shape elements and screws is designed and realized (Fig. 6.15).
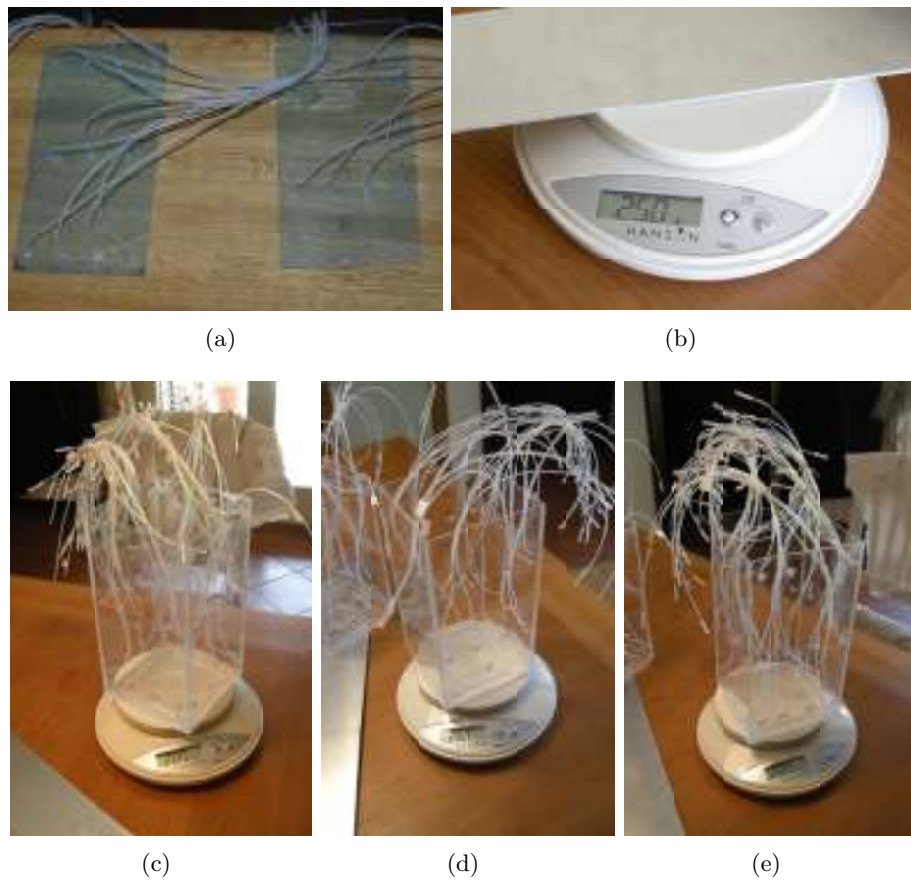
(a)

(b)

(c)

(d)

(e)

Fig. 6.14 Assembly of the model. First stage. a) pneumatic tubes glued on plexiglas surfaces; b) one aluminum plate weight; c), d), e) assembled plexiglas boxes and their total weight.

A wooden supporting system, visible in Figs. 6.15(e), 6.15(f), 6.16(b) and 6.16(c), is built in order to accommodate the aluminum bars in it and to provide a proper connection with the base balance. The wooden support is made of a prismatic core with a central circular hole with vertical axis and two horizontal lateral holes allowing the exit of the pneumatic tubes from the internal gap to below the tunnel floor. The presence of the two horizontal holes under two parallel faces (2 and 4) is responsible for a geometric asymmetry which translates into different stiffnesses in the two orthogonal directions.

The central prismatic core is connected to a circular disk at the bottom, which will be directly fixed to the balance and a second circular disk at the top, whose function will be only to close the hole on the tunnel floor between the lateral surfaces of the model and the circular plug of the floor which will be mounted in the test section (see Fig. 6.32). The overall thickness of the wooden support is approximately equal to 5 cm.

Since the outer shell is made of separate boxes, there are small slits between them. In order to prevent air from entering the model during wind tunnel tests, self adhesive felt strips [Fig. 6.15(e)] are glued at the top of box A and box B and on the support surface [Fig. 6.15(f)].

In order to perform wind tunnel tests, the model is mounted in the test section of the wind tunnel (Fig. 6.16). Fig. 6.16(a) shows the pneumatic tubes connections from the boxes sides to the pressure transducers. The 4 aluminum plates are first installed on the wooden support. The first box (box A) is positioned sliding from the top of the plates. The plates are inserted through the floor of the first box paying attention to the passage of the pressure tubes from the external faces, where they are fixed, to the interior area through the free spaces between the plates at the corners. The 47 pneumatic tubes of the first box are pulled outside from the model support and connected to three 16-channel type pressure transducers below it. The position of the first box with respect to the internal structure is fixed trough L-shaped aluminum elements and screws. The second box (box B) is then placed in its position [Fig. 6.16(b)], repeating the procedure illustrated for the first one. However, in this case, the 32 tubes on the box B surfaces are connected with one 32-channel type PSI unit, which is left inside the model. Finally, box C is inserted from the top [Fig. 6.16(c)]. Its 47 tubes are connected with one 32-channel type and one 16-channel type PSI units, both placed inside the model.

Finally, the model with its wooden support is installed on the balance which is mounted over the tunnel steel tripod, whose height is properly regulated in order to align the model basis to the tunnel floor.

Each pressure tap is identified with a 4-character code, "FBLN", where:

1. F=1,2,3,4 indicates the *Face* number;

2. B=A,B,C denotes the *Box*, from the bottom to the top;

3. L=1,2,3 is the *Level* (each box has up to three levels of taps);

4. N=1,2,3,4 is the *Number* which indicates the horizontal position of the tap from the left to the right side (each level has up to 4 taps per each side).

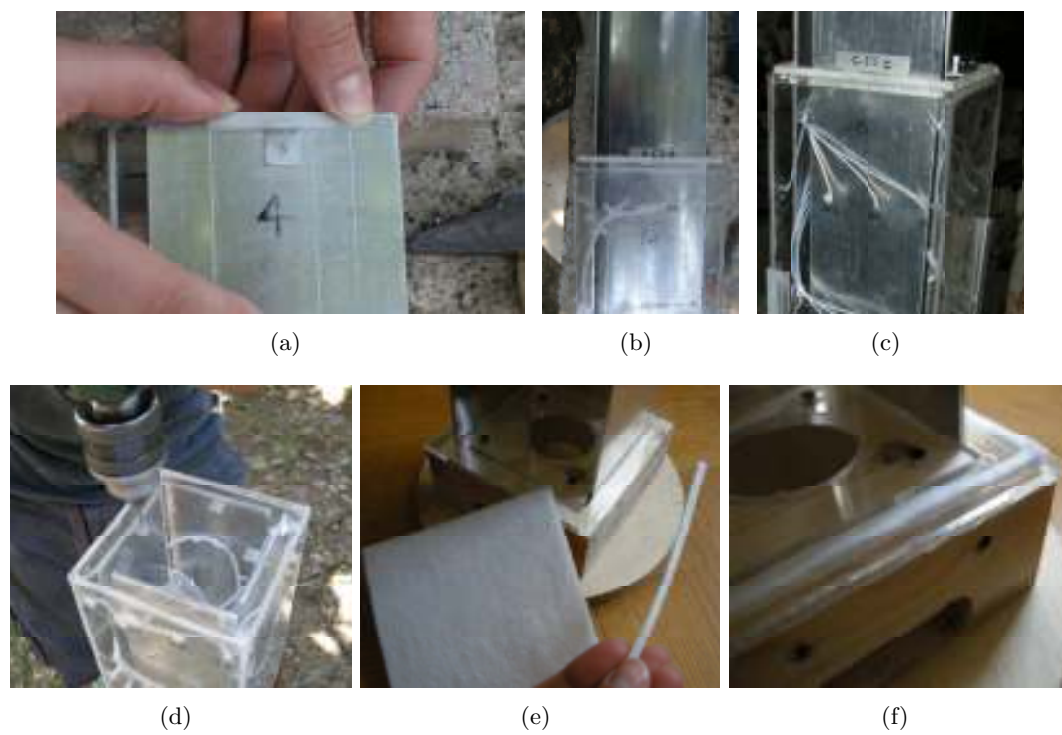Tap 4A31 is, for example, the first tap to the left side of the third level of box A on face 4.

Fig. 6.15 Model construction details: a) L-shaped aluminum element for the connection between the aluminum plates and the top floor; b) connection between the plates and the first box from the bottom (box A); c) connection between the plates and the second box (box B); d) connection between the plates and the box at the top (box C); e) self adhesive felt sheet; f) self adhesive felt strips mounted on the support surface at the level of the tunnel floor.
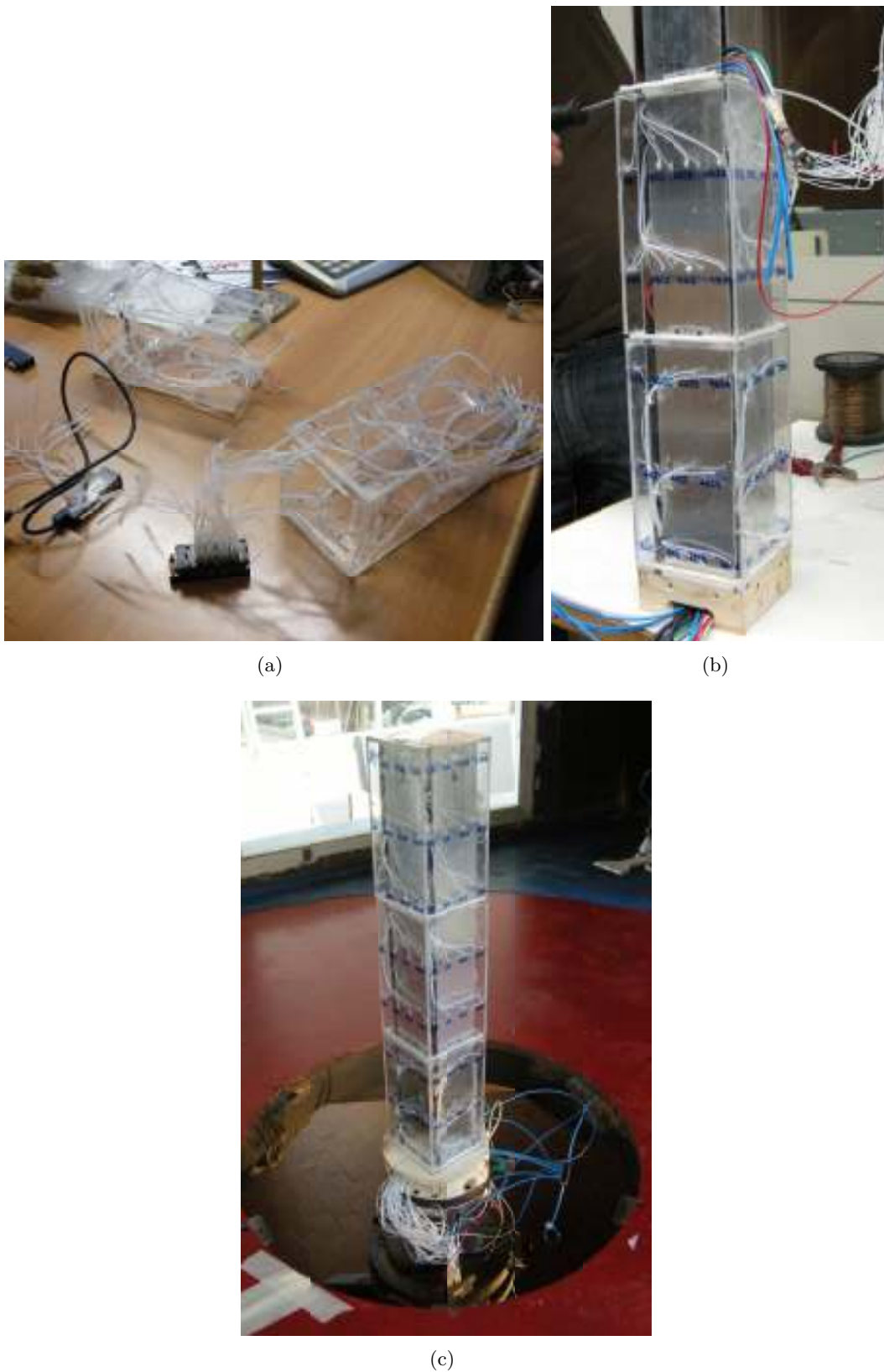
(a)

(b)

(c)

Fig. 6.16 Assembly of the model in the wind tunnel: a) pneumatic tubes connections from the boxes sides to the pressure transducers; b) box A and box B mounted; c) view of the model completely assembled and mounted in the test section of the wind tunnel.

6.4.3 Identification of dynamic properties

The natural frequencies and mode shapes of the model-support system are measured by means of four mono-axial accelerometers (their technical characteristics are illustrated in subsection 6.3.6). Two configurations are used in order to measure the free vibration response of the model along two orthogonal directions. Once they are mounted on face 4 (Fig. 6.17) and once on face 3 (Fig. 6.18). In both cases, three of them are placed along the mid axis of the model face, while one is eccentric. The model is then excited with both symmetric and eccentric impulsive excitations.

From the peaks of the power spectral density, S, of the measured acceleration
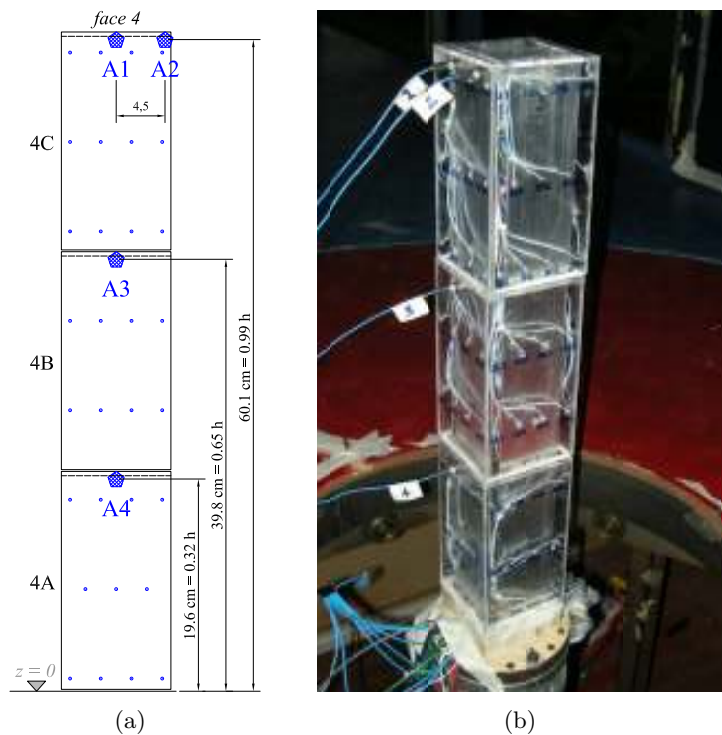
Fig. 6.17 Distribution of the accelerometers on the face 4 of the model: a) dimensional drawing; b) view from the wind tunnel.

signals (Fig. 6.19 and Fig. 6.20), the first three natural frequencies of the model are derived, corresponding to the first bending mode along the weak axis (face 2 - face 4 direction), the first bending mode along the strong axis (face 1 - face 3 direction) and the torsional mode. The presence of a weak and a strong axis related to different natural frequencies of vibration in the two orthogonal bending modes, is thought to be due to the asymmetric geometry of the model support, described in subsection 6.4.2. Moreover the complexity of the accommodation of pneumatic tubes and PSI units inside the model can also contribute to not symmetric characteristics of the model.

The free decay acceleration signals (Fig. 6.21, Fig. 6.22, Fig. 6.23) are compared with those simulated by means of the eigenvalues and eigenvectors estimated through the MULS method (Bartoli *et al.*, 2009). The latter is based on the improvement of the Unifying Least-Square (ULS) algorithm (Gu *et al.*, 2000) and is, therefore, called Modified Unifying Least-Square (MULS). This identification method is used
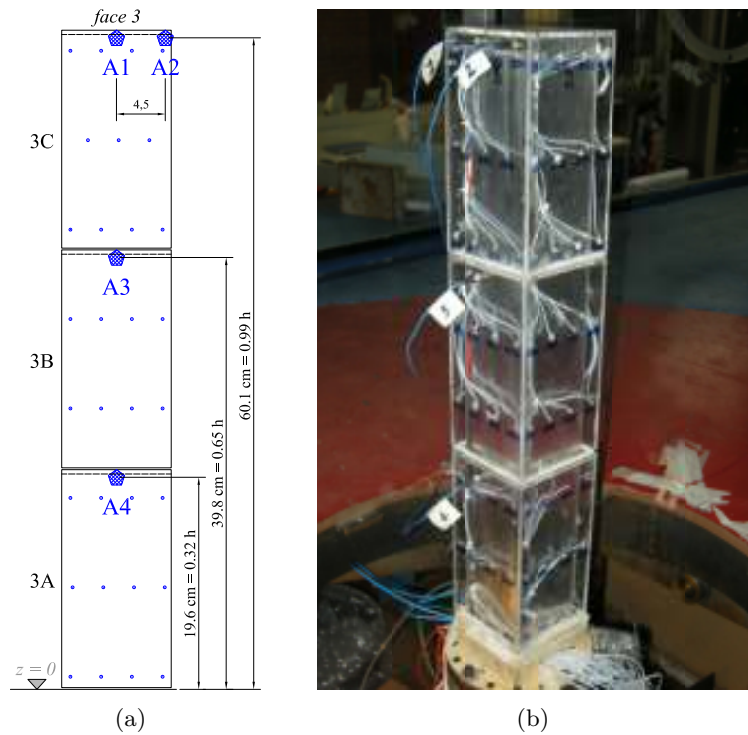
Fig. 6.18 Distribution of the accelerometers on the face 3 of the model: a) dimensional drawing; b) view from the wind tunnel.
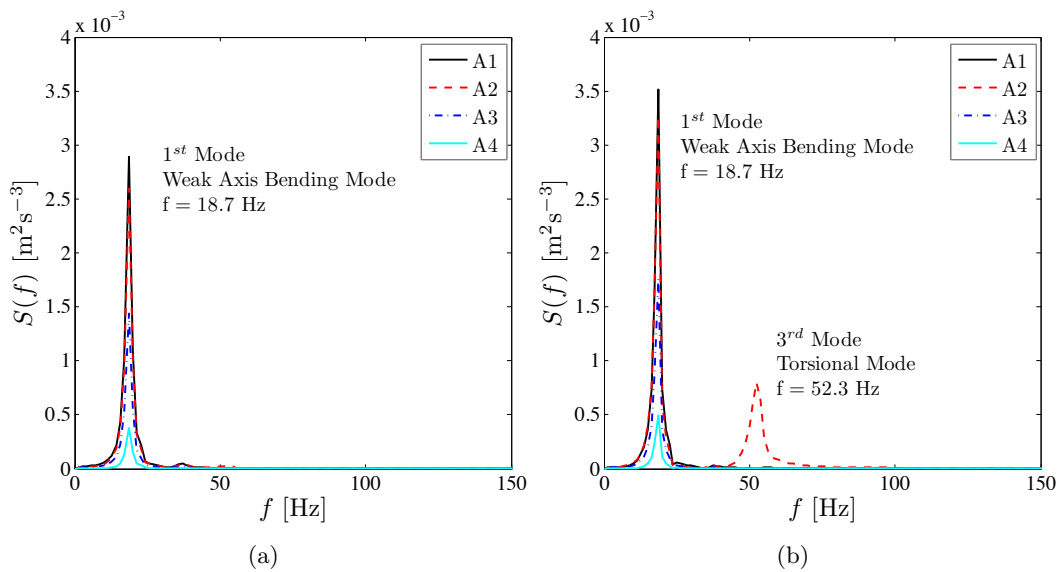

Fig. 6.19 Spectra of the measured accelerations. Free vibration response along the weak axis: a) symmetric excitation; b) eccentric excitation.
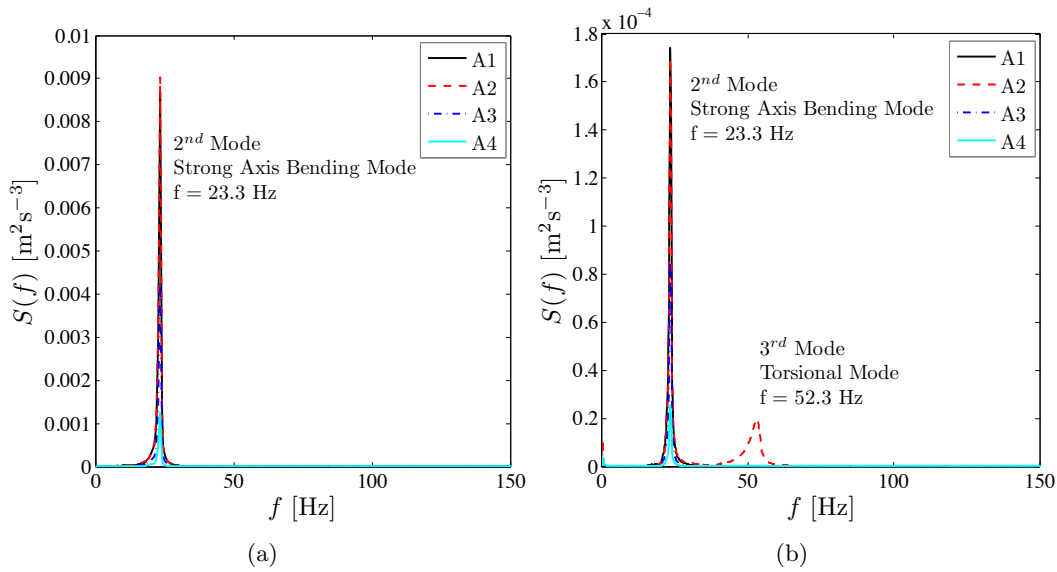
Fig. 6.20 Spectra of the measured accelerations. Free vibration response along the strong axis: a) symmetric excitation; b) eccentric excitation.

to confirm the natural frequencies of the model estimated by the spectral analysis, and to assess the mode shapes (Fig. 6.24) of the first two bending modes and the damping ratios. The results of the identification of the first three modal frequencies and damping ratios are illustrated in Table 6.4. The angular acceleration, a_α, (Fig. 6.23) that is the rate of change of angular velocity over time, measured in radians per second squared (rad/s^2), is obtained by the following relation:

$$a_\alpha = \frac{(a_{A2} - a_{A1})}{l} \qquad (6.3)$$

where a_{A1} and a_{A2} are the linear accelerations (in m/s^2), measured by the accelerometer A2 at the corner and by the accelerometer A1 at the center, respectively, and l is the horizontal distance between them, equal to 0.045 m.

Fig. 6.24 shows that the measured components of the identified mode shapes

Table 6.4 First three modes frequencies and damping ratios.

Mode	Description	Frequency Hz	Damping ratio %
1	bending - weak axis	18.7	5.0
2	bending - strong axis	23.3	1.6
3	torsional	52.3	4.6

are approximately linear.

Before wind tunnel tests, from the free vibration response of the model it has also been checked whether structural damping is stable, i.e. invariable with vibration amplitude of the building model. Fig. 6.25 shows the identified damping ratios from different sections of the free decay response with different vibration amplitude.
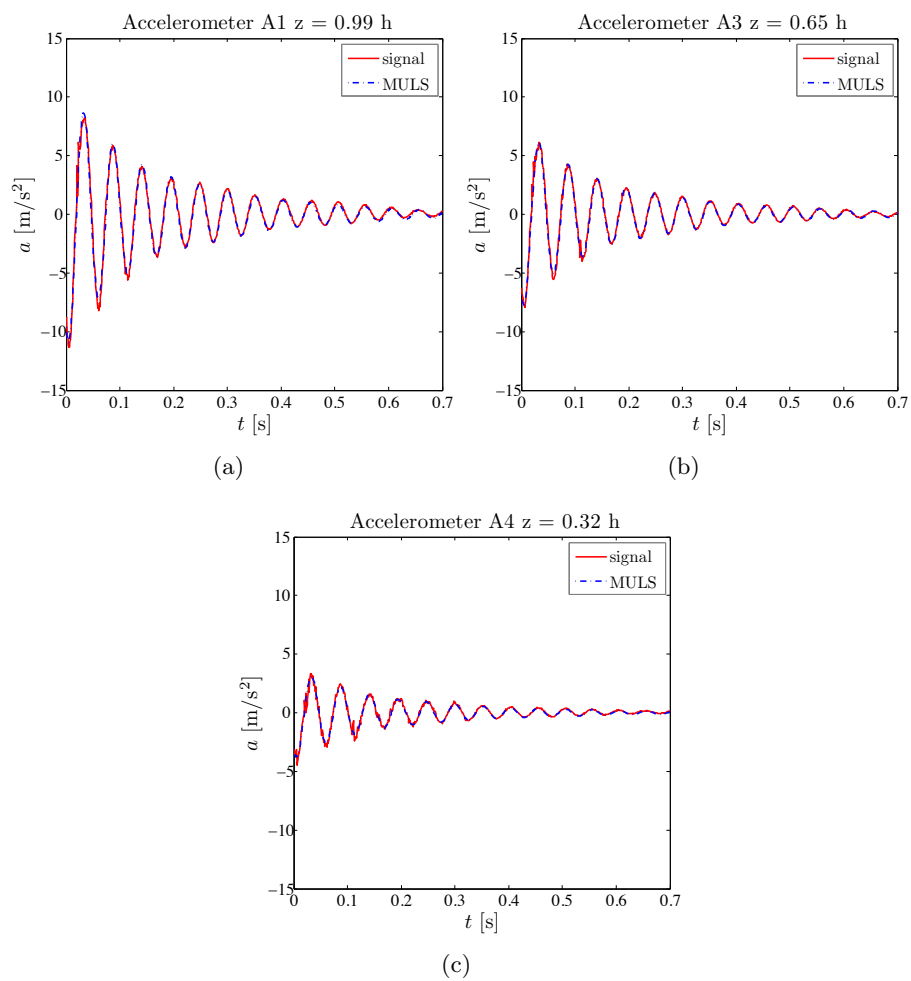
Fig. 6.21 Free vibration response. Decay acceleration signals along the weak axis direction: a) acceleration at $z = 0.99h$ (A1) ; b) acceleration at $z = 0.65h$ (A2); c) acceleration at $z = 0.32h$ (A3).
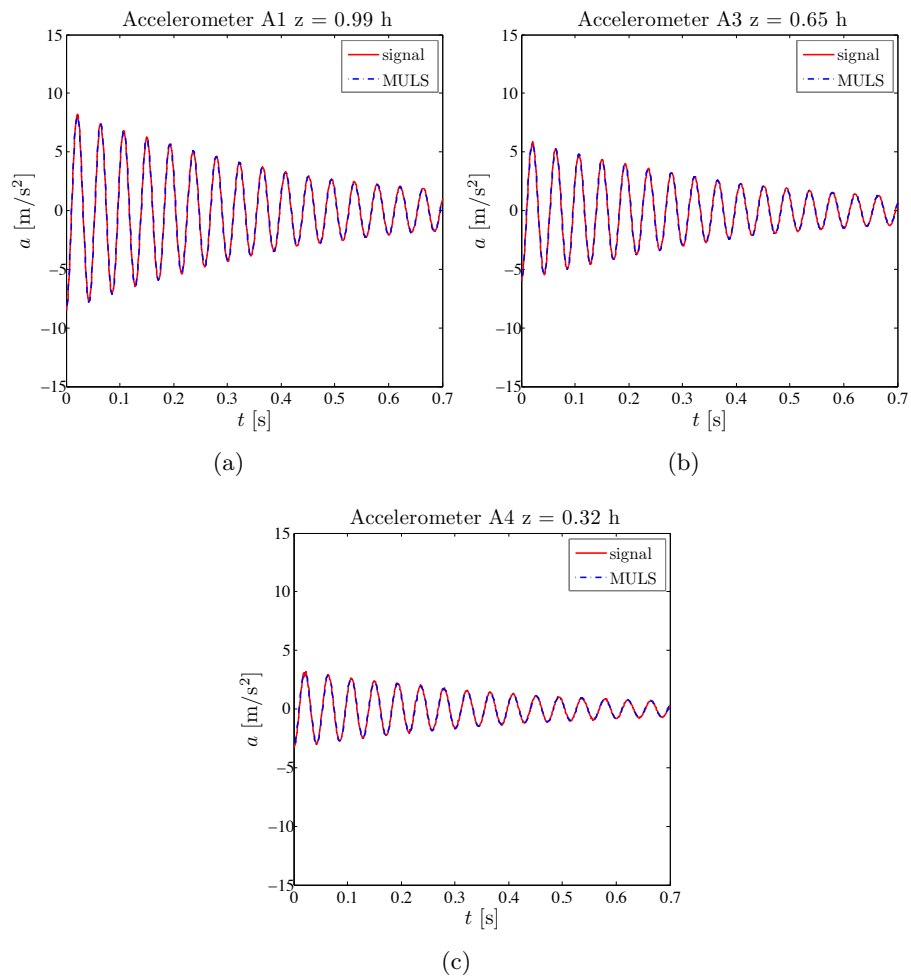
Fig. 6.22 Free vibration response. Decay acceleration signals along the strong axis direction: a) acceleration at $z = 0.99h$ (A1); b) acceleration at $z = 0.65h$ (A2); c) acceleration at $z = 0.32h$ (A3).
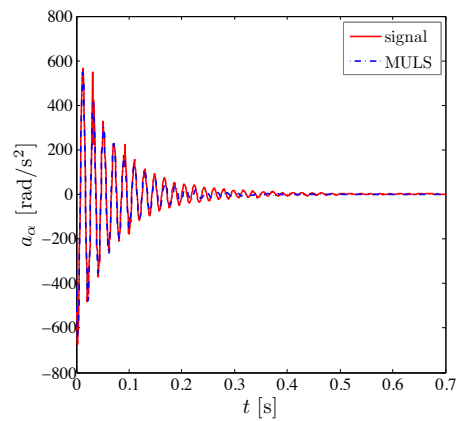

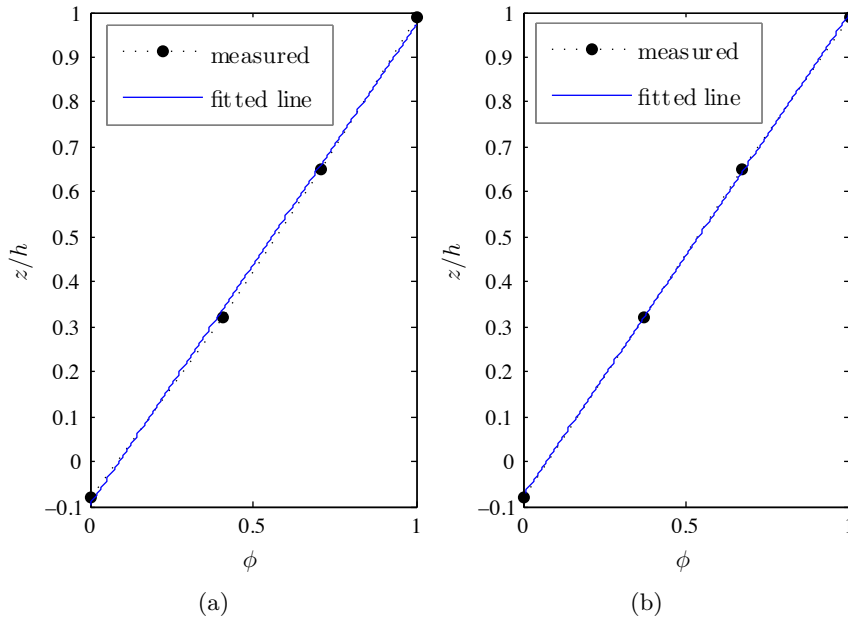Fig. 6.23 Torsional response from free vibration test.

Fig. 6.24 Identified mode shapes: a) first mode (measured component along the weak axis); b) second mode (measured component along the strong axis).

For the first and the second bending modes the signal registered by accelerometer A1 is used [Fig. 6.21(a) and Fig. 6.22(a)], while for the torsional response the signal shown in Fig. 6.23 is used.

From Fig. 6.25(b) and Fig. 6.25(c), the identified structural damping ratios for the second and the third identified natural modes of vibration are almost the same for different vibration amplitudes, while for the first bending mode the damping ratio largely varies with the vibration amplitude. This behavior is thought to be related to the presence and direction of the pneumatic tubes. As a matter of fact, the first mode is translational along the weak axis of the model which also corresponds to the direction along which the pneumatic tubes are aligned towards the exit from the model.

Assuming that the total mass of the model, approximately equal to 2.2 kg, is uniformly distributed along the model height and using the modal damping ratios reported in Table 6.4, from Eq. (4.3) and Eq. (4.4) the Scruton number is easily derived and it is equal to 165.0 and 52.8 for the first and the second bending modes, respectively. The air density ρ is taken equal to 1.25 kg/m^3. When a torsional mode is considered, the mass per unit span length in Eq. (4.3) is replaced by the moment of inertia per unit span, Iz, and the Scruton number, Sc_α, is, therefore, defined as:

$$Sc_\alpha = \frac{2\delta_\alpha I_z}{\rho b^4} \tag{6.4}$$

where δ_α indicates the logarithmic decrement for the torsional mode. For a rectangular building of height h, breadth b and depth d, the moment of inertia per unit
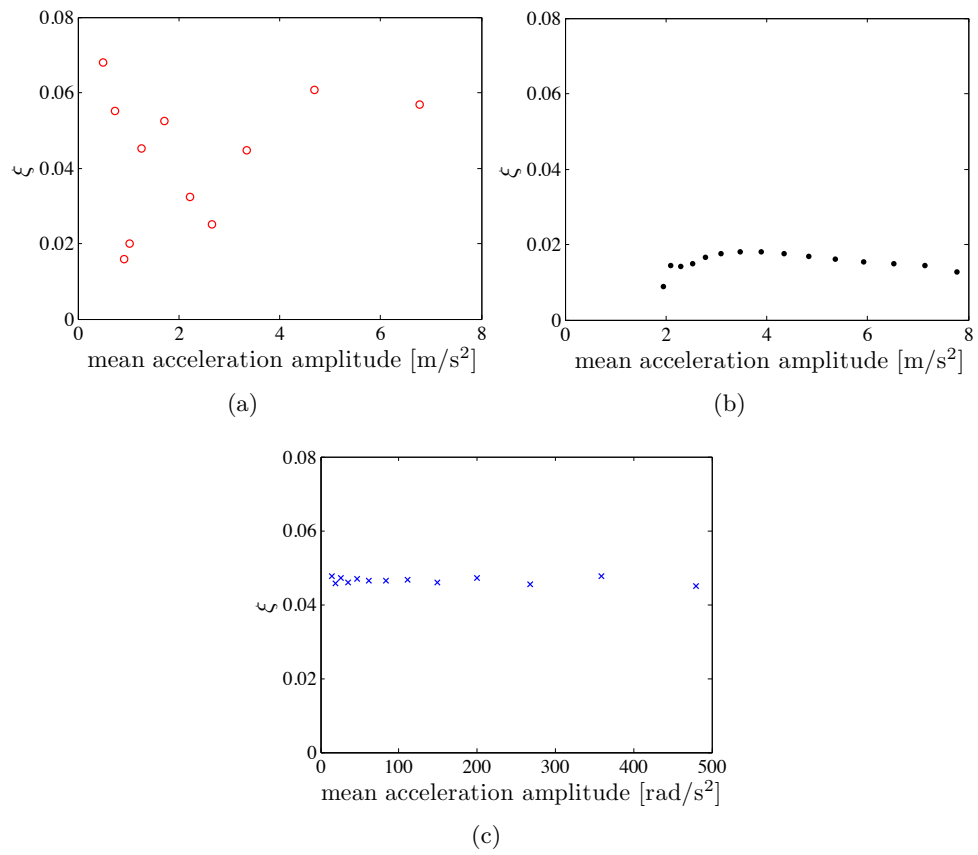
Fig. 6.25 Dependence of structural damping ratio on vibration amplitude: a) first bending mode; b) second bending mode; c) torsional mode.